

## EVALUATION OF COMPOSITE HARDNESS AND WEAR MECHANISM OF COPPER THIN FILM COATING

Sumaiya Islam, Raafat N. Ibrahim

Department of Mechanical & Aerospace Engineering, Monash University, Australia

### ABSTRACT

To measure the mechanical characteristics and the wear mechanism of the coating material, nano indentation and the nano scratching method were employed respectively with diamond Berkovich tip having tip radius of 100 nm. The results showed that the hardness decreased with the increase of the indentation depth. Therefore experimental data was interpreted with the Korsunsky model. Moreover the pile up along the indentation mark reveals that the ploughing mechanism is responsible for the material deformation in this range of indentation depth. After single scratching operation, the percentage of elastic recovery for this film/substrate combination decreased and the pile up volume increased with the increase of the depth of cut. The propagation of the pile up volume along the scratch length was clearly observed and there was no sign of crack propagation. Therefore for this film/substrate system ploughing wear mechanism is the dominant mechanism for the nano level deformation.

**Key Words:** Nano indentation, Nano scratch, Composite hardness

### 1. INTRODUCTION

Thin film coating is a promising technology and it has lot of applications in the field of semiconductor and biomedical industries. In order to increase the lifetime and reliability of thin film coatings, it is necessary to measure their mechanical properties and to characterize their wear mechanisms. In this paper nano indentation and nano scratching were chosen to investigate the composite hardness and the wear mechanism of the thin film coating.

Composite hardness describes the phenomenon where the measured hardness changes as depth of indentation increases, due to the combined responses of both the substrate and the film. The most commonly used model for composite hardness, the Bückle rule, which states that if the indentation depth is less than 10% of the film thickness, the hardness measured will be that of the film alone[1]. However, it is believed that the rule cannot accurately represent both hard film/soft substrate systems and soft film/hard substrate systems. Therefore there are different models available [2-7] to accurately represent the hardness data. However, for a specific thin coated system no specific model can be recommended. Generally a simple law of mixtures was used to describe the proportional contributions of both the film and substrate hardness, in relation to the ratio of film thickness to indentation depth. Beegan et. al [8] measured the hardness of copper films on oxidized silicon substrates (soft film / hard substrate), for different film thickness and indentation depths. Three distinct regions was identified with the increment of the indentation depth and shown in Fig 1. For a shallow penetration depths (region I), the measurement was that

of the film only ( $H_f$ ). As the depth increases (region II) the composite hardness was measured ( $H_c$ ). Then, at a large depth in region III the response was purely that of the substrate surface ( $H_s$ ).

To enhance the tribological properties of the surface, such as reducing the wear hard coating on a soft substrate

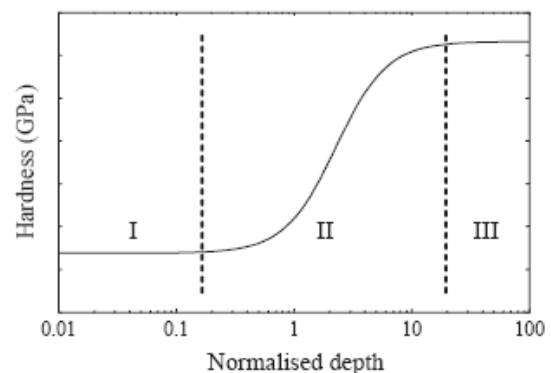


Fig 1. Composite Hardness for a soft film/hard substrate system [8]

was used [9]. The wear due to the contacting of the two metal surfaces was classified as abrasive wear. Recently it is speculated that ploughing mechanism is one of the dominant mode of abrasive wear [10]. However, the physics of such wear mechanism in the nanometer range still remains unclear because of the lack of experimental data. Therefore to establish the wear mechanism elastoplastic deformation behaviour can be considered as an indicator. Moreover elasto-plastic behaviour of the material have been reported by the variation of the

normal force using Atomic Force Microscope (AFM) [11-14]. AFM is a well recognised tool to measure the mechanical characteristics by the micro/nano scratching method[15, 16] The conventions of the AFM based lithographic technique is that the machined surface scale of the structure is solely determined by the geometry of the AFM probe[17-19]. Therefore the nano indenter produced by Hysitron utilises the same mechanism to create a scratch; however, a diamond probe is placed with the tool holder instead of the cantilever attachment used in AFM. The advantage of using nano indenter is to avoid the effect of the cantilever's geometry, stiffness and their respective calibration reliability on the measured nano machining parameters[20-22]. Moreover, AFM cannot directly measure the lateral force during scratching.

Therefore the objective of this study was to investigate the composite hardness and the wear mechanism studying elastoplastic deformation behaviour in hard film/soft substrate system utilizing indentation and scratching method for a nano meter range of dimensions. The effects of both the normal and the lateral cutting forces due to nano range variations in the depth of cut are reported in this study. The post scratch profiles were used to calculate the elastic deformation and pile up volume to identify the wear mechanism of the coated system.

## 2. EXPERIMENTAL CONDITION

Nickel was used as the substrate material in this study. The substrate materials were cut by the electro discharge machine (EDM) for making a completely flat surface. Before the deposition of the coating material, the substrate surfaces were polished with 1  $\mu\text{m}$  polishing pad to obtain a scratch free parallel surface[23]. The substrate specimens then underwent ultrasonic cleaning progressively in acetone and ethanol, and were subsequently dried in a vacuum dryer. After cleaning the substrate, Ni was electroplated at a current density of 3.5 Amps/dm<sup>2</sup> and at a deposition rate of 1.8  $\mu\text{m}$ /minute to form the Cu coatings. In the electroplating process, an electronic grade Cu metal sheet was used as the anode, while the substrate (Ni) acted as the cathode. After coating, the samples were not subjected to any further treatment to avoid additional effects resulting from surface preparation techniques (such as mechanical hardening due to polishing). For the measurement of composite hardness and elastoplastic behaviour to identify the wear mechanism nano indenter was used and the experimental conditions are presented in Table 1.

The topographic scanning method was employed to analyse the elastoplastic deformation behaviour. The area of the topographic measurement was 10x10  $\mu\text{m}^2$ . In scanning mode, 20  $\mu\text{m}$ /s tip velocity and 1 Hz scan rate were used. Before the scratching operation, the roughness of the surface was measured with the scanning mode. The average surface roughness for the investigated samples was found to be approximately 2 nm.

## 3. RESULT & DISCUSSION

### 3.1 Composite Hardness Evolution

In fig 2 the results for copper samples clearly showed that the hardness value decreased with the increase of indentation depth. The hardness was determined from the load displacement curve, using Oliver and Pharr method[24]. The variation of the hardness indicated that the composite hardness was being measured and therefore the response of the material to indentation changed with the increasing depth. As the indentation depth was equal to the film thickness, therefore the measured hardness could be the hardness of the substrate. The horizontal line at the bottom end represented the hardness of the substrate. It was observed in sample1 (thickness 300nm), the substrate hardness at 300 nm displacement of the indenter whereas sample2 (thickness 400nm), the substrate hardness at 400 nm. The individual substrate and the film hardness were 2.85 GPa and 15.95 GPa respectively

Table 1: Experimental Condition

Machine used	Triboindenter (Hysitron)
Cutting tip	Berkovich tip (100nm)
Room	20-24° C
Relative Humidity	50%
Nano indentation	
Sample 1	Coating Thickness 300 nm
Sample 2	Coating Thickness 400 nm
Displacement	50,75,100,150,200,300,400 nm
Nano scratching	
Material	Copper Coating
Feed rate	0.33 $\mu\text{m}$ /sec
Depth of cut	50,100,200,300 nm
Scratch length	10 $\mu\text{m}$

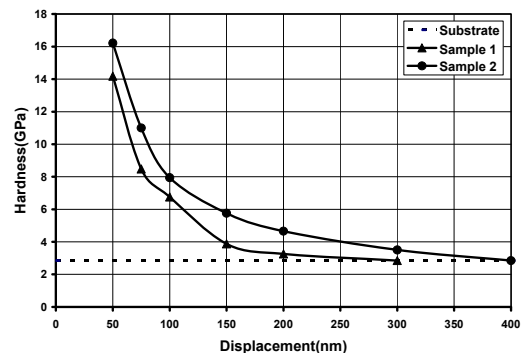


Fig 2. Variation of the Hardness with the Displacement



Different hardness models were compared to the collected data. The model which correlated best with the experimental data were found to be a Korsunsky model [6]. The equation used for the Korsunsky model is given below.

$$H_c = H_s + \frac{H_f - H_s}{1 + \kappa\beta^2}$$

(1)

$$\beta = \frac{\delta}{t}$$

where  $\beta$ ,  $\delta$  and  $k$  represent the normalised depth, indentation depth and constant related to the film thickness.

Fig 3 showed that the Korsunsky model [6] fits the experimental data well. The constant  $k$  was found to be 17.93 using equation 1. The trend of the data correlates with the trends of the models shown in [8] and [25]. There is variation in the fitted model at the smaller depths. This could be attributed to the uncertainty in hardness measurements at small depths, due to the very thin film used and large surface roughness. However, it can be seen that the Korsunsky model provides a sensible model for composite hardness of this thin film coatings.

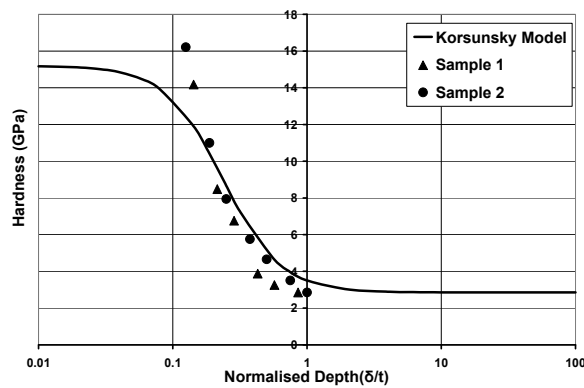


Fig 3. Fit of Korsunsky model to data

Fig 4 shows the surface topography and the indentation marks produced on a sample at different depths. The residual impression resembles the shape of the three sided pyramidal diamond tip. The slightly raised material at the indentation edges, in conjunction with the absence of cracks, was characteristics of the plastic flow behaviour of the ductile material. The smooth side walls of the residual impression and the absence of any surface or subsurface crack indicate that plastic flow was the principle deformation process in the nano indentation process.

### 3.2 Wear Mechanism Evaluation

To investigate the wear mechanism of the thin coated system nano scratching method was employed. The nano level elastoplastic deformation characteristics in the scratching operation was utilized for this purpose. The elastoplastic deformation of the material was determined by the percentage of elastic recovery and the pile up

volume. The elastic recovery (%) was calculated using the equation (2).

$$\text{Elastic Recovery (\%)} = \frac{h_1 - h_2}{h_1} \times 100 \quad (2)$$

where  $h_1$  is the depth of cut and  $h_2$  is the plastic depth that was measured from the post scratching profile.

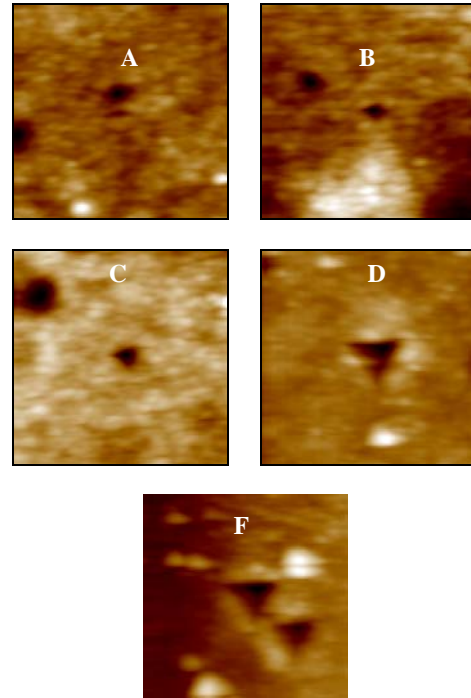


Fig 4. Indentation at different depth in sample 1 (A) 50 nm (B) 100 nm (C) 150nm (D) 200nm and (E) 300nm.

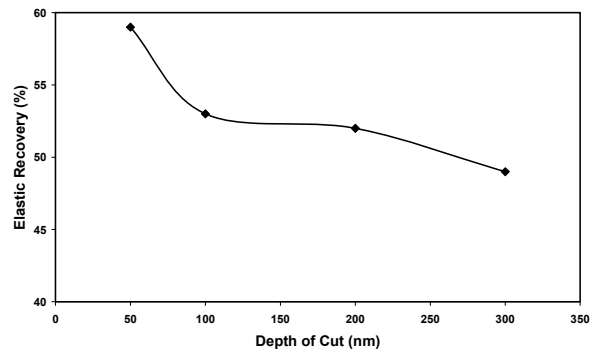


Fig 5. Variation of the elastic recovery (%) with the depth of cut.

Fig 5 presents the effect of the elastic recovery (%) with the variation of depth of cut. It was shown that percentage of elastic recovery decreased with the increase in the depth of cut. When the depth of cut increased the generated normal and lateral forces also increased as presented in fig 6. As a result, due to the increment of both forces elastic recovery was decreased and the plastic deformation of the material was

increased. The upward dislocation of the material due to plastic deformation is termed as pile up [26-28]. This pile up is the indicator to identify the ploughing abrasive wear mechanism.

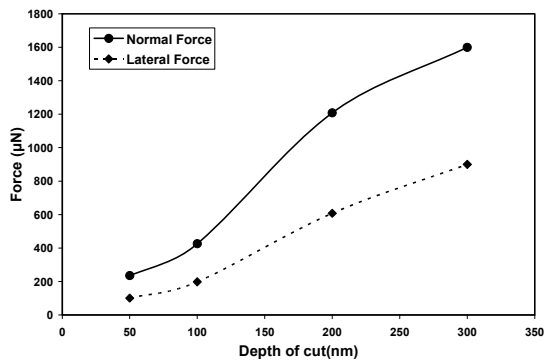


Fig 6. Variation of the normal and Lateral force with the depth of cut.

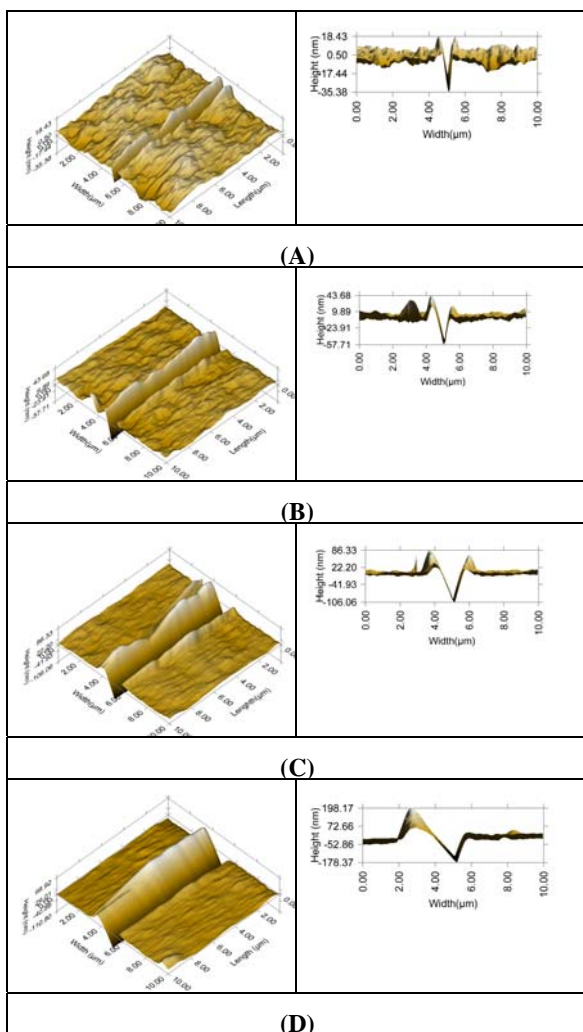


Fig 7. Scratches were done by using different depths of cut. (A) 50nm (B) 100 nm (C) 200nm and (D) 300 nm.

Fig 7 presented post scratch surface topography at different depths of cut. The pile up volume was generated

at one side of the scratch length during this nano scratching operation. Generally the pile up volume was generated at the edge of the cutting tool. Cutting tool (Berkovich tip) used in this experiment has an asymmetric shape [29]. The cutting edge faces at one side of the scratch length producing hydrostatic pressure that enables the plastic deformation.

Fig 8 shows the changes in the pile up volume with the depth of cut. The pile up volume increased with the increase of the depth of cut. This establishes that a higher plastic deformation leads to an increase in the pile up volume, which also implies a greater amount of plastic energy dissipation from the machining operation. Therefore, pile up volume was indicated that ploughing wear mechanism was the dominant factor for making this groove. Moreover, no crack was observed in this range of machining condition. Therefore it reveals that the wear has occurred due to the ploughing mechanism rather than the crack in this soft film hard substrate system.

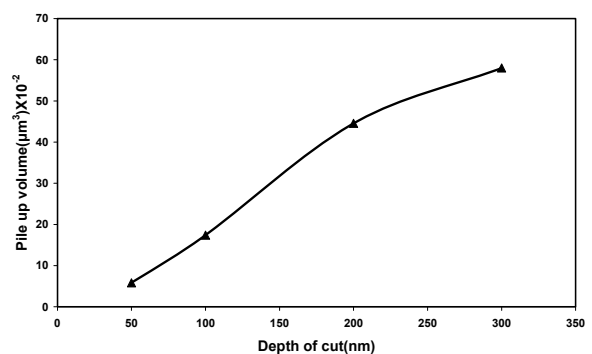


Fig 8. Variation of the pile up volume with the depth of cut.

#### 4. CONCLUSION

The hardness and wear characteristics of copper film/nickel substrate systems were experimentally investigated utilizing nano indentation and nano scratching technique. In view of the presented results and discussions, the following conclusion can be drawn.

- A composite hardness trend was observed for each of the samples. The hardness decreased with the increasing of the indentation depth. These hardness values provided the composite value for the hard film soft substrate system. The Korsunsky model was recommended to be a good fit for the data. Pile up volume was observed along the indentation mark rather than the crack.
- However, the hardness value changed with the increment of the indentation depth, therefore the wear mechanism remained unchanged. Hence the ploughing is the dominant mode for the wear mechanism during this range of indentation depth.
- The percentage of the elastic recovery of the coated system decreased with the increase of the depth of cut due to the increase of the generated normal and cutting forces during scratching. Therefore the pile up volume increased with the increase of the depth

of cut. Pile up along the scratch length reveals the ploughing mechanism. Therefore wear occurred due to the ploughing mechanism of the coated system in this range of depth of cut. Further more no crack or subsurface crack was observed along the scratch length.

## 5. REFERENCES

- Bückle, H., 1973, *Science of Hardness Testing and its Research Applications*, H. C. J.H. Westbrook. Metals Park, Ohio, USA.
- JijNSSON, B. and HOGMARK, S., 1984, "Hardness measurement of Thin Films", *Thin Solid Films*, 114: 257-269.
- Burnett, P. J. and Rickerby, D. S., 1987, "The Mechanical Properties of Wear-Resistant Coatings II: Experimentatl Studies and Interpretation of Hardness", *Thin Solid Films*, 148: 51-65.
- Bull, S. J. and Rickerbyt, D. S., 1990, "New developments in the modelling of the hardness and scratch adhesion of thin films", *Surface and Coatings Technology*, 42: 149-164.
- Chicot, D. and Lesage, J., 1995, "Absolute hardness of films and coatings", *Thin Solid Films*, 254 :123-130.
- Korsunsky, A. M., Mcgurk, M. R., Bull, S. J. and Page.T.F., 1998, "On the hardness of coated systems", *Surface and Coatings Technology*, 99: 171-183.
- Puchi-Cabrera, E. S., 2002, "A new model for the computation of the composite hardness of coatedsystems", *Surface and Coating Technology*, 160:177-186.
- Beegan, D. and Laugier, M. T., 2005, " Application of composite hardness models to copper thin film hardness measurement", *Surface and Coatings Technology*, 199: 32-37.
- Shen, W., Bin Jiang, Steven M. Gasworth and Mukamal, H., 2001, "Study of tribological properties of coating/substrate system in micrometer and nanometer scales with a scanning probe microscope", *Tribology International*, 34: 135-142.
- Zhang, L. and Tanaka, H., 1997, "Towards a deeper understanding of wear and friction on the atomic scale molecular dynamics analysis", *Wear*, 211: 44-53.
- Youn, S. W. and Kang, C. G., 2004, "A Study of Nanoscratch Experiments of the Silicon and Borosilicate in Air", *Material Science Engineering. A*, 384:275–283.
- Youn, S. W. and Kang, C. G., 2005, " FEA Study on Nano deformation Behaviors of Amorphous Silicon and Borosilicate Considering Tip Geometry for Pit Array Fabrication",. *Material Science & Engineering A*, 390: 233-239.
- Youn, S. W. and Kang, C. G., 2006, "Effect of nanoscratch conditions on both deformation behavior and wet-etching characteristics of silicon (1 0 0) surface", *Wear*, 261: 328-337.
- Komvopoulos, K., 1989, "Elastic-Plastic Finite Element Analysis of Indented Layered Media",. *ASME Journal of Tribology*, 111: 430-439.
- Bhushan, B., Israelachvili, J. N. and Landman, U., 1995d, "Nanotribology: Friction, Wear and Lubrication at the Atomic Scale", *Nature*, 374: 607-616.
- Fang, T. H., Chang, W. J. and Tsai, S. L., 2005, "Nanomechanical Characterization of Polymer using Atomic Force Microscopy and Nanoindentation", *Microelectronics .Journal*, 36: 55-59.
- Fang, T.-H., Chang, W., J. and Weng, C., I., 2006, Nanoindentation and Nanomachining Characteristics of Gold and Platinum Thin Films", *Material .Science & Engineering A*, 430: 332-340.
- Fang, T. H. and Chang, W. J., 2003, "Effects of AFM-based Nanomachining Process on Aluminum Surface", *Journal of Physics and chemistry of Solids*, 64: 913-918.
- Kawasegi, N., Takano, N., Oka, D., Morita, N., Yamada, S., Kanda, K., Takano, S., Obata, T. and Ashida, K., 2006, "Nanomachining of Silicon Surface Using Atomic Force Microscope with Diamond Tip", *Journal of Manufacturing science . E-T.ASME*, 128:723-729.
- Kawasegi, N., Morita, N., Yamada, S., Takano, N., Oyama, T. and Ashida, K., 2005, "Etch Stop of Silicon Surface Induced by Tribo-Nanolithography", *Nanotechnology*, 16 (8):1411-1414.
- K.Ashida., N. Morita. and Y.Yoshida., 2001, " Study on Nano-Machining Process Using Mechanism of a Friction Force Microscope", *JSME International Journal*, 44(1): 244–253.
- Park, J. W., Kawasegi, N., Morita, N. and Lee, D. W., 2004, "Tribo nanolithography of Silicon in Aqueous Solution Based on Atomic Force Microscopy", *Applied Physics Letter*, 85(10): 1766-1768.
- Takaduan, J. and Houmid Bennai, H., 1997, "Influence of substrate roughness and coating thickness on adhesion, friction and wear of TiN films", *Surface and Coating Technology*, 96:272-282.
- Oliver, W.C. and Pharr, G. M., 1992, "An improved technique for determining hardness and elastic modulus using load and displacement sensing indentation experiments", *Journal of Materials Research*, 7:1564-1583.
- Korsunsky, A. M. and Constantinescu, A., 2006 "Work of indentation approach to the analysis of hardness and modulus of thin coatings", *Materials Science and Engineering: A*, 423:28-35.
- Cheng, Y. T. and Cheng, C. M., 2004, "Scaling, Dimensional Analysis, and Indentation Measurements", *Material Science & Engineering R*, 44: 91-149.
- Mott, B. W., 1956, *Micro-indentation Hardness Testing*, Butterworths, London, UK.
- Tabor, D., 1951, *The Hardness of Metals*, Clarendon Press, Oxford, UK.
- Tribolab, U. M., 2008, *Hysitron Incorporated*, Minneapolis, MN 55344, USA.

## 6. NOMENCLATURE

<i>Symbol</i>	<i>Meaning</i>	<i>Unit</i>
$\delta$	Indentation depth	nm
T	Film thickness	nm
$H_f$	Film hardness	GPa
$H_s$	Substrate hardness	GPa
$H_c$	Composite hardness	GPa
$h_1$	Depth of cut	nm
$h_2$	Plastic Depth	nm
K	Constant	
$\beta$	Normalised depth	

## 7. MAILING ADDRESS

Raafat N. Ibrahim  
Department of Mechanical & Aerospace Engineering,  
Monash University  
Clayton, Victoria 3800, Australia.  
Corresponding author. Tel.: +61-3-99051982;  
Email: raafat.ibrahim@eng.monash.edu.au

## ANALYSIS ON SOUND ABSORPTION OF NATURAL COIR FIBER USING DELANY-BAZLEY MODEL

Md. Ayub<sup>1</sup>, M. J. Mohd Nor<sup>1</sup>, Nowshad Amin<sup>2</sup>, Rozli Zulkifli<sup>1</sup>,  
M. Hosseini Fouladi<sup>1</sup> and A. Rasdan Ismail<sup>1</sup>

<sup>1</sup>Department of Mechanical and Materials Engineering,

<sup>2</sup>Department of Electrical, Electronic and System Engineering,

Faculty of Engineering & Built Environment,

National University of Malaysia, 43600, Bangi, Selangor, Malaysia.

### ABSTRACT

This paper explores the sound absorption capacity of natural coir fiber. Absorption coefficient of coir fiber is calculated using Delany-Bazley model. Experiments are conducted in impedance tube to validate the analytical outcomes for three samples having different thickness. Increasing the thickness of coir fiber enhances sound absorption and shifts noise absorption peak towards low frequency. Moreover, effect of air gap on sound absorption performance of coir fiber has also been investigated. Increasing air gap thickness usually shifts the peak of absorption coefficient towards lower frequency. Then, the noise absorption of coir fibers with and without air gap is compared and shows that earlier one has greater absorption at low frequency than the later one. However, resonances can not be predicted using this technique. Results also indicate that Delany-Bazley equations can justify the overall trend of absorption coefficient of coir fiber perfectly as demonstrated in this study.

**Keywords:** Noise absorption, Natural coir fiber, Delany-Bazley equation.

### 1. INTRODUCTION

At present, green technology is widely used to replace the agricultural waste with synthetic fiber for noise absorption purposes. Natural fibers such as coir fiber can be used as a potential acoustic porous material since they are easily obtained from the nature. Coir fiber is a natural organic resource which is the seed-hair fiber obtained from the outer shell (endocarp) or husk of coconut.

It is well known that the absorption characteristics of porous material vary with type of porous materials. Numerous models were proposed to study the sound propagation in porous materials. Delany and Bazley [1] studied the impedance and wave propagation properties of fibrous materials. They proposed a normalized model based on dimensionless groups and developed an empirical formula to estimate the characteristics impedance and propagation constant of fibrous absorbent material. Their method was very simple and considered as the fast approximation to the solution as this method used only flow resistivity parameter which is an intrinsic property of the material. Dunn and Davern [2] studied on acoustic impedance of multilayer absorbers using Delany-Bazley method. Qunli [3] made an empirical relation for acoustical impedance of foam materials using a large amount of experimental data with a wider range of flow resistivity. It was observed that the Delany-Bazley model can sometimes predict non-physical results for low frequencies and layered

media. Hence, Miki [4] suggested an improved relationship based on the same model for wider range frequency with respect to porosity, tortuosity and the pore shape factor ratio.

Equivalent electrical circuit approach (EECA) [5, 6] is an usual method to analyze the multilayer panel, in which surface acoustic impedance of back air gap is assumed as the acoustic impedance of rigid wall even when the air space were actually backed with perforated plates. Jinkyu *et al.* [5] studied the assembly with two layers of perforated plates backed with air spaces by EECA. Lee and Chen [7] further studied the transmission analysis for multilayer absorbers consisting of several layer of porous material, air gap and perforated plate using a new technique named ATA (Acoustic-Transmission Approach). The effects of the back air gap and porous material was considered in ATA method. Results showed that ATA method can give the better result than the conventional EECA method for multilayer absorber.

However, the microscopic model of sound propagation is more complicated. More sophisticated models like Biot Model [8], Zwicker and Koston Model [9], Allard Model [10], Johnson-Allard Model [10] will not be considered in this analysis because they feature a large number of parameters which are rarely available. They require uncommon procedures for their determination and can't be deduced from simple acoustic



measurements. Delany-Bazley model is used in this work to predict the absorption coefficient of coir fiber as a preliminary study and as a simple method. However, this model is not suitable for very low and high frequency.

The sound absorption of coir fiber was investigated previously in Automotive Research Group Laboratories, Universiti Kebangsaan Malaysia [11, 12]. Those studies were based on simulation program WinFLAG™ and compared with experimental data obtained in reverberation room using diffuse sound field of noise source. This present study is analytical and compared with experimental data obtained by impedance tube with normal incidence sound field of noise source. The purpose of this current study is to explore the absorption capacity of coir fiber and to establish an analytical technique which can be able to describe the acoustic characteristics of coir fiber. A panel composed of coir fiber layer and air gap backed by rigid wall was used to analyze the acoustic absorption performance of coir fiber. This paper is just the preliminary study based on Delany-Bazley model to make an analytical technique for coir fiber. For further improvement, sound propagation of coir fiber can be analyzed more accurately based on Biot model [8], Jhonson-Allard model [10].

## 2. ANALYTICAL MODEL OF THE PANEL

According to Delaney-Bazley empirical model, for a homogenous and isotropic fibrous material, complex wave propagation constant  $\gamma_f$  and characteristic impedance  $Z_f$  of porous material can be expressed by flow resistivity  $\sigma$  as [2, 7],

$$\gamma_f = 2\pi f / c_a [0.189 b^{-0.595} + i(1 + 0.0978 b^{-0.7})] \quad (1)$$

$$Z_f = \rho_a c_a [1 + 0.057 b^{-0.754} - i(0.087 b^{-0.732})] \quad (2)$$

$$b = \rho_a f / \sigma \quad (3)$$

If the porous material is backed with a rigid wall, the surface acoustic impedance of the porous material can be expressed as [2, 7],

$$\Gamma_f = Z_f \coth(\gamma_f L_f) \quad (4)$$

If the air gap is backed with a rigid wall, the surface acoustic impedance of the air space can be expressed as [7],

$$\Gamma_a = Z_a \coth(\gamma_a L_a) \quad (5)$$

Where,  $Z_a (= \rho_a c_a)$  and  $\gamma_a (= i(2\pi f / c_a))$  are wave propagation constant and characteristic impedance of air.

Considering the geometry of Fig. 1, that illustrates a cross section of the panel consisting porous layer and air gap backed by rigid wall, the resultant surface acoustic impedance of the panel can be expressed as [2, 7],

$$\Gamma_p = Z_f [\cosh(\gamma_f L_f) + (Z_f / \Gamma_a) \sinh(\gamma_f L_f)] / [\sinh(\gamma_f L_f) + (Z_f / \Gamma_a) \cosh(\gamma_f L_f)] \quad (6)$$

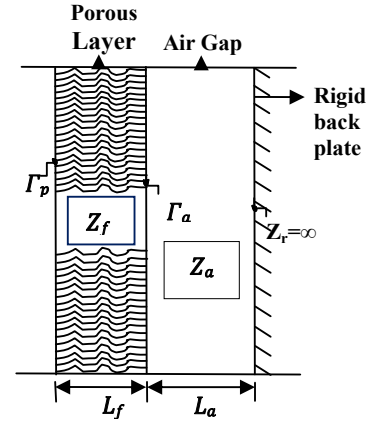


Fig 1. Schematic of the cross-section of absorber panel.

Where,  $\gamma_f$ ,  $Z_f$  and  $\Gamma_a$  are calculated according to equation (1), (2) and (5) respectively.

The surface acoustic impedance of panel without air gap  $\Gamma_f$  and that of with air gap  $\Gamma_p$ , is calculated from equations (4) and (6) respectively. This result can be expressed as,

$$\Gamma_f \text{ or } \Gamma_p = R + iX \quad (7)$$

For a normal incident plane sound wave, the absorption co-efficient of the absorption panel is expressed as,

$$\alpha = [4 \rho_a c_a R] / [(\rho_a c_a + R)^2 + X^2] \quad (8)$$

## 3. MATERIALS

In this study two types of coir fiber (CF) sample were used for experimental validation. These two samples are named as fresh CF and industrial CF. Fresh CF was collected from fresh coconut husk available in local wet market and then compressed it to make the sample using molds and punches with an average pressure of 20 kg/cm<sup>2</sup>. Industrial CF was prepared industrially using binder as a mixer with the fiber to keep it in shape.

Raw fiber thickness of the material was measured by dial thickness gauge meter in the scale of one hundredth of millimeter. Fifteen randomly selected fibers were used to measure the average thickness and weight of the fiber. Average diameter of the fiber was taken as 273  $\mu$ m and 248.22  $\mu$ m for fresh and industrial coir fiber respectively as found from the experimental measurements. The shape of the fiber was considered as cylindrical shape. Bulk density of the material was measured from mass and volume of the sample. Flow resistivity of the material was estimated using the empirical equation (9) based on mass, thickness and fiber diameter of each sample [13],

$$\sigma = 490 \rho_{bulk}^{1.61} / d_{fiber} \quad (9)$$

#### 4. EXPERIMENTS FOR ANALYTICAL VALIDATION

Experimental measurements were conducted in impedance tube according to ISO 10534-2 [14] standard to validate the analytical analysis. The components of the measurement system mainly include two impedance tubes with diameters 28 mm and 100 mm each contains ½” microphones type GRAS-40BP, plane wave source, two channel data acquisition system and 01dB software package. Small tube of diameter 28 mm was used to measure the absorption coefficient in high frequency range 1600 Hz - 6300 Hz and large tube of diameter 100 mm was used in low frequency range 31.5 Hz - 1600 Hz. One calibrator type GRAS-42AB was used for microphone sensitivity calibration at 114 dB and 1 KHz frequency.

Before starting the measurement, two microphones used in the impedance tube were calibrated relatively to each other using the standard switching technique by mounting a sample in the sample holder to make sure that the sound field inside the tube is well defined. The measurements were done with 3 Hz frequency resolution and sample records of finite duration about 10 s.

#### 5. RESULTS AND OBSERVATIONS

Fig. 2 and 3 represent the analytical analysis of sound absorption of coir fiber (CF) for different layer thickness with and without air gap. Additionally, Fig. 4 represents the analysis of absorption with bulk density of the material. This analysis will give an overall knowledge of sound absorption capacity of coir fiber which can be designed further to form an optimal sound band absorber.

##### 5.1 Coir Fiber Thickness

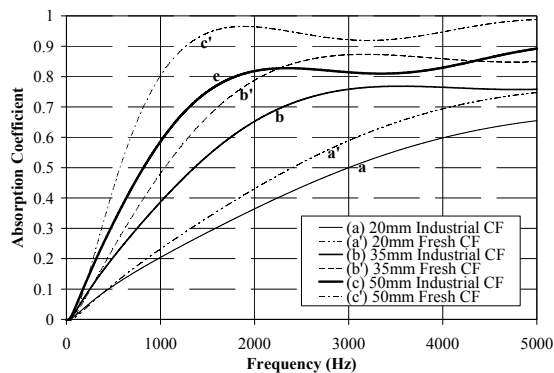


Fig 2. Numerical simulations of absorption coefficient of industrial and fresh coir fiber layer having thickness 20mm, 35mm and 50mm.

In this section, the effect of material layer thickness on sound absorption of coir fiber is investigated as shown in Fig. 2. It shows that increasing coir fiber layer thickness increases the absorption and moves absorption peak towards low frequency. In case of 20 mm layer (Industrial CF) thickness, maximum absorption occurs above 5000 Hz frequency at 6704 Hz with coefficient 0.68. When the layer thickness becomes 35 mm, the absorption peak moves towards lower frequency 3554 Hz

Hz with the increased coefficient of 0.76 from 0.68 and so on for 50mm. It indicates that the absorption increases as impinging wave has to go long way through the material and losses its energy. According to absorption phenomena inside a porous material, long dissipative process of viscosity and thermal conductions in the fluid inside the material due to increased thickness, improves the absorption.

If it is closely observed in Fig. 2, it seems that fresh coir fiber has better absorption for the same thickness of the material. This is because of the increased flow resistivity of fresh coir fiber comparatively that of industrial fiber for the same thickness of material. The main factors influencing the flow resistivity of fibrous material are the fiber size and the bulk density [1]. During the preparation of fresh coir fiber it was found that coir fiber contains some matrix material with the fiber which increased the bulk density of the material, as a result flow resistivity also increased. However, fresh coir fiber without any treatment (or binder) can not be used regularly as an absorber for long time period because of the moisture and stiffness effect [15] of the fiber which may decrease the thickness of the porous material later on and change the absorption characteristics.

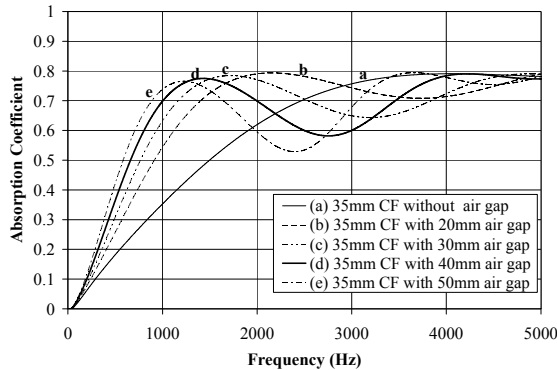
##### 5.2 Air Gap Thickness

Fig. 3(i), represents the effect of addition of air gap with coir fiber layer on sound absorption. Addition of 20mm air gap with coir fiber layer increases absorption towards low frequency compare to coir fiber without air gap. As shown in Fig 3(i), 20 mm coir fiber layer with 20 mm air gap moves the absorption peak towards 2740 Hz frequency with almost same coefficient 0.66 from 6704 Hz frequency that of fiber layer without air gap. In case of 35 mm thickness, it moves to 2019 Hz frequency from 3554 Hz with coefficient 0.77 and for 50 mm thickness, it moves to 1556 Hz frequency from 2344 Hz with coefficient 0.84. These results indicate that absorption can be increased in low frequency region with the addition of air gap between the layer of coir fiber and rigid wall.

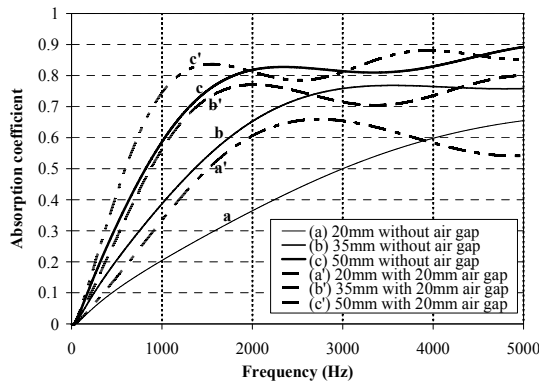
Fig. 3(ii), illustrates the effect of increasing air gap thickness on sound absorption for particular CF layer thickness of 35mm. It shows that increasing air gap shifts the absorption peak further towards low frequency. This is due the fact that air gap between porous layer and back plate creates resonance, which moves the absorption peaks towards low frequency and increasing air gap thickness moves further towards low frequency.

It can also be observed from Fig. 3(i), that the noise absorption at a particular region of the low frequency end can be achieved with coir fiber by either increasing the coir fiber layer thickness without air gap or increasing the air gap keeping the coir fiber layer thickness in a minimum value. As shown in Fig. 3(i), it can be seen that almost same trend of absorption line up to 2000 Hz frequency can be achieved using 20 mm coir fiber layer with 20 mm air gap instead of 35 mm coir fiber without air gap. Further, same trend of absorption line up to 1700 Hz frequency can be achieved using 35 mm coir fiber layer with 20 mm air gap instead of 50 mm coir fiber

without air gap. It indicates that absorption can be enhanced almost the same amount at a particular region by the addition of air gap instead of increasing fiber layer thickness.



(i)



(ii)

Fig 3. Numerical simulations of absorption coefficient of industrial coir fiber (i) with 20 mm air gap and without air gap having CF thickness 20 mm, 35 mm and 50 mm. (ii) 35 mm CF with 20 mm, 30 mm, 40 mm, 50 mm air gap and without air gap.

### 5.3 Effect of Bulk Density

Absorption coefficient of 35mm coir fiber layer with different bulk density is presented in Fig. 4. Four sample mass of 20, 25, 30 and 35 gm were considered for coir fiber sample of 100 mm diameter to change the bulk density of the material. Fig.4 shows that increasing bulk density of the porous material enhances the absorption property of coir fiber from 0.7 to 0.87. Enhancement of absorption occurs due to increased flow resistivity with increased bulk density.

It can also be observed from Fig. 4 that the profile of the graphs is same, though the additional bulk density increases the absorption. It means that increasing bulk density does not change the position of absorption peak. As long as there is no additional layer (porous or air) with the existing layer, absorption peak does not change its position.

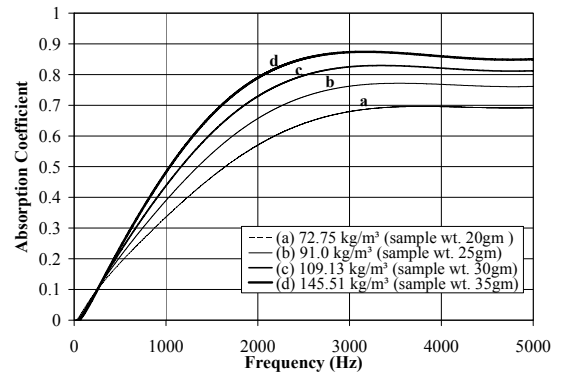
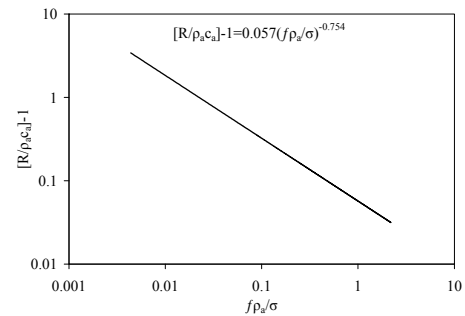


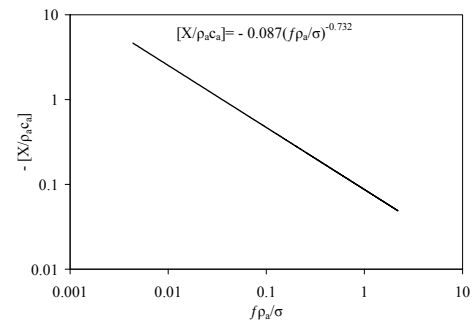
Fig 4. Numerical simulations of absorption coefficient of 35 mm industrial coir fiber with different bulk density.

These results denote that porous absorber prepared with larger bulk density will increase the absorption of the material. However, increased bulk density should be within a limit which will allow the sound wave to go through the material. Otherwise, there will be a probability of sound wave to be reflected by congested material surface rather than absorption.

## 6. LIMITATIONS OF DELANY-BAZLEY MODEL



(i)



(ii)

Fig 5. Normalization of real and imaginary component of characteristics impedance  $Z_f$ . (i) Real component and (ii) Imaginary component.

Delany-Bazley is considered to give good agreement between the theoretical and experimental results for the following limitations as explained in Ref. [1],

$$0.01 < \rho_{af}/\sigma < 1.0 \quad (10)$$

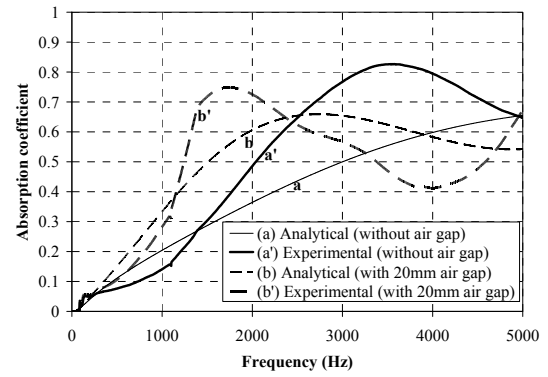
To verify the validity of this model for coir fiber, real and imaginary component of characteristics impedance ( $Z_f$ ) is normalized into two dimensionless group with free field wave impedance  $\rho_a c_a$  and plotted against normalized dimensionless frequency group  $\rho_{af}/\sigma$  as shown in Fig. 5. It can be seen that the frequency range ( $\rho_{af}/\sigma$ ) is within the given dimensionless limit 0.01 to 1.0 for the majority of the normalized real and imaginary components of  $Z_f$ . However, beyond this range this model can not be able to predict the material property as good as it can within the approximate frequency range of equation (5). Sometimes in the case of multilayer, real part of the surface impedance (when computed using this model) becomes negative at low frequencies as Miki [4] mentioned it as a non-physical result.

## 7. VERIFICATION OF THE ANALYTICAL MODEL

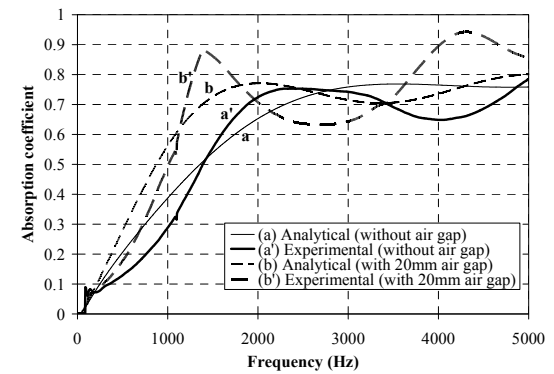
Verification of Delany-Bazley Model was done for three samples of industrial coir fiber with and without air gap, as shown in Fig. 6 (here shown for two samples 20 mm and 35 mm). Experimental results for 20 mm and 35 mm fresh coir fiber layer with and without air gap is also plotted in Fig. 7. The measured plots agree fairly well with analytical prediction. The profiles of the graphs are the same. However, the results also show that analytical model can not be able to predict the resonance peak. This resonance may be for frame resonance and Delany-Bazley model did not consider bulk modulus of elasticity which has been considered in Biot-Allard elastic model [10].

The graph in Fig. 6, also shows that analytical plot gives better agreement with experimental measurements at larger thickness of the sample increases from 20 mm to 50 mm. It may be due to one reason was addressed by Delany-Bazley [1] to show this type of behavior, at lower value of  $\rho_{af}/\sigma$  many materials exhibit significant structural non-rigidity and under these circumstances simple normalization is not possible as shown in Fig. 5.

In case of these three samples, it is found that increasing coir fiber layer (sample) thickness, decreases flow resistivity from  $3206 \text{ Nsm}^{-4}$  to  $2613 \text{ Nsm}^{-4}$  and those samples maintain almost equal thickness to mass ratio (TMR) between 1.3~1.45. Although, flow resistivity should be increased with increased thickness, but in this case flow resistivity is decreased because of bulk density. Bulk density is a factor of both mass and thickness, which is also decreased with increased layer thickness due to constant TMR. As a result, for larger thickness with the same TMR, gives a higher value of  $\rho_{af}/\sigma$  ratio compare to smaller thickness of the same material, which produces a better agreement of analytical model with experimental results.



(i)



(ii)

Fig 6. Experimental data compared to numerical simulations of the absorption coefficient of industrial CF with and without air gap having CF thickness (i) 20 mm (ii) 35 mm.

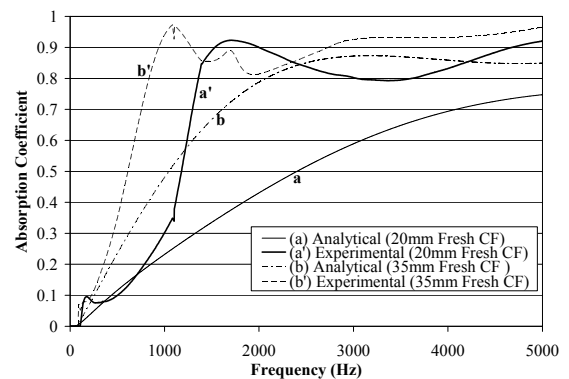


Fig 7. Experimental data compared to numerical simulations of the absorption coefficient of fresh CF having thickness 20 mm and 35 mm without air gap.

## 8. CONCLUSION

In this study, it is shown that, coir fiber has the potential to be replaced with the common synthetic fibrous material such as glass, mineral wool, felts or polyester fibers.

Analyses from this study give an overall idea about the factors that are able to enhance the absorption of coir fiber. Increasing coir fiber layer thickness will increase absorption and move the absorption peak towards low frequency. Increasing air gap thickness will increase the absorption at low frequencies, though it will increase absorption only at resonance frequencies. Absorption characteristics of coir fiber can also be increased by increasing bulk density of the material. Fresh coir fiber seems to give better absorption characteristics because of increased bulk density due to extra matrix material and moisture content with fiber. These results demonstrate that more strategically designed layers and configurations of coir fiber could increase the noise reduction.

An analytical model for theoretical prediction has been obtained. It can justify the overall trend of the absorption spectrum. For accurate prediction of overall absorption including the frame resonance, more sophisticated model like Johnson-Allard [10] or Biot-Allard model [10] can be used. Application of perforated plate and making multilayer structure are necessary to improve the absorption in low frequency. They may help to reduce the thickness of the panel which is a very important factor for limited space structure.

## 9. REFERENCES

1. Delany, M.E., Bazley, E. N., 1970, "Acoustical properties of fibrous absorbent material", Applied acoustics, 3: 105-116.
2. Dunn, I.P., Davern, W. A., 1986, "Calculation of Acoustic impedance of Multi-layer absorbers", Applied acoustics, 19: 321-334.
3. Qunli, W., 1988, "Empirical relations between acoustical properties and flow resistivity of porous plastic open-cell foam", Applied Acoustics, 25: 141-148.
4. Miki, Y., 1990, "Acoustical properties of porous materials, Modifications of Delany-Bazley models", Journal of Acoustical Society of Japan, 11: 19-24.
5. Jinkyo, L., George, W. and Swenson, J., 1992, "Compact sound absorbers for low frequencies", Noise Control Engineering Journal 38: 109-117.
6. Congyun, Z., Qibai, H., 2005, "A method for calculating the absorption coefficient of a multi-layer absorbent using the electro-acoustic analogy", Applied Acoustics, 66: 879-887.
7. Lee, F.-c., Chen, W.-h., 2001, "Acoustic transmission analysis of multi-layer absorbers", Journal of Sound and vibration 248(4): 621-634.
8. Biot, M.A., 1962, "Generalized Theory of Acoustic Propagation in Porous Media", J. Acoust. Soc. Am., 34(9): 1254-1264.
9. Zwikker, C., Kosten, C. W., 1949, "Sound Absorbing Materials", Elsevier, Amsterdam.
10. Allard, J.F., 1993, "Propagation of Sound in Porous Media-Modelling Sound Absorbing Materials", Elsevier Applied Science, London.
11. Nor, M.J.M., Jamaludin, N. and Tamiri, F. M., 2004, "A preliminary study of sound absorption using multi-layer coconut coir fibers", Electronic Journal: Technical Acoustics, <http://ejta.org/en/tamiri.1> [27th March 2004].
12. Zulkifli, R., Nor, M. J. M., Tahir, M. F. M., Ismail, A. R. and Nuawi, M. Z., 2008, "Acoustic properties of multilayer coir fibres sound absorption panel", Journal of Applied Sciences, 8(20): 3709-3714.
13. Ballagh, K.O., 1996, "Acoustical properties of wool", Applied Acoustics, 48(2): 101-120.
14. ISO10534, 1998, "Determination of sound absorption coefficient and impedance in impedance tubes", International Organisation for Standardization, Case postale 56, Gene`ve, 20.
15. Wassilieff, C., 1996, "Sound Absorption of Wood-Based Materials", Applied Acoustics, 48(4): 339-356.

## 10. NOMENCLATURE

Symbol	Meaning	Unit
$f$	Frequency	(Hz)
$c_a$	Sound speed	(ms <sup>-1</sup> )
$\rho_a$	Air density	(Kgm <sup>-3</sup> )
$\sigma$	Flow resistivity	(Nsm <sup>-4</sup> )
$L_f$	Thickness of Coir fiber layer	(m)
$L_a$	Thickness of air gap	(m)
$\alpha$	Absorption coefficient	(%)
$d_{fiber}$	Diameter of fiber	$\mu$ m
$\rho_{bulk}$	Bulk density of material	(Kgm <sup>-3</sup> )
$\gamma_f$	Propagation constant of CF	
$Z_f$	Characteristic impedance of CF	
$\Gamma_f$	Surface acoustic impedance of CF backed by rigid wall	
$\gamma_a$	Propagation constant of air gap	
$Z_a$	Characteristic impedance of air gap	
$\Gamma_a$	Surface acoustic impedance of air gap backed by rigid wall	
$\Gamma_p$	Resultant surface acoustic impedance of panel composed of CF, air gap and rigid wall.	
R	Real part of surface impedance $\Gamma_f$ or $\Gamma_p$ .	
X	Imaginary part of surface impedance $\Gamma_f$ or $\Gamma_p$ .	

## 11. MAILING ADDRESS

Md. Ayub  
 Department of Mechanical and Materials Engineering,  
 Faculty of Engineering & Built Environment,  
 National University of Malaysia, 43600, Bangi,  
 Selangor, Malaysia.



## EFFECT OF VARIOUS AMOUNT OF Cu ON THE THERMAL AND MECHANICAL BEHAVIOR OF Sn-9Zn EUTECTIC Pb-FREE SOLDER ALLOY

M. Rahman, A. Sharif, and Mansur Ahmed

Department of Materials and Metallurgical Engineering, Bangladesh University of Engineering and Technology, Dhaka-1000, Bangladesh.

### ABSTRACT

In this work, Cu content in the range between 0-1.0 wt.% with Sn-Zn eutectic system were examined in order to understand the effect of Cu addition on the microstructural and mechanical properties as well as the thermal behaviour of the solders. The melting temperature of Sn-9Zn eutectic solder alloy did not alter significantly with small amount of Cu addition. Only a 3°C increase in melting temperature was observed with the 1.0 wt. % Cu addition. The flower shaped  $\text{Cu}_6\text{Sn}_5$  and rod shaped  $\text{Cu}_5\text{Zn}_8$  IMCs were found to be uniformly distributed in the  $\beta$ -Sn phase for Sn-9Zn-0.4Cu, which resulted in an increase in the tensile strength. It was also found that the microhardness of the solder alloy was increased with the addition of Cu up to a certain limit. Finally, it can be concluded that the addition of a little amount of Cu can improve the mechanical properties of Sn-9Zn eutectic solder alloy.

**Keywords:** Sn-Zn Eutectic Solder, Microstructure, Mechanical Property, Thermal Behavior, Intermetallic Compounds, Strengthening Mechanism.

### 1. INTRODUCTION

The ban of lead in electronic products will occur in most industrialized countries before the end of this decade. Extensive investigations have been on-going over the last few years to find an acceptable Pb-free solder for various electronic attachment applications [1-3]. All alternatives to the standard eutectic tin-lead solder investigated so far are based on tin alloys with a tin content significantly over 90 wt. % in combination with copper, silver, antimony, bismuth, or zinc. Among the binary alloys, recently, Sn-Zn solder has become highly recommended as a substitute for Sn-Pb eutectic solder due to its lower melting point [4]. Sn-Zn solder can also be used without replacing the existing manufacturing lines or electronic components. Again, Sn-Zn is advantageous from an economic point-of-view because Zn is a low cost metal. However, Sn-Zn eutectic solder is difficult to handle practically due to its highly active characteristics [5]. As reported by S. Vaynman et al. [6] Sn-9Zn eutectic solders have limited commercial viability due to its serious oxidation and wetting problems.

The addition of Cu may increase the melting point of solder alloy, as Cu has far higher melting point (1084°C) than that of Sn-9Zn solder alloy (198°C), thus increasing the alloy melting process. The Sn-Zn-Cu (SZC) solder had a near eutectic reaction in 214.93°C [7]. By using mildly active rosin (RMA) flux, the wetting angle of Sn-9Zn was found to be 89°, and with addition of 4% Cu

with 0.05% of rare earth, the alloy wetting angle was found to be minimum 49° [8]. It had been proven that by alloying Cu with Sn-Zn-Al the melting temperature increases about 210°C. Cu has the ability to stabilize Zn in the solder and controls the growth of the reaction layer [9]. With the addition of Cu in the Sn-Zn alloy, the Cu-Zn compound formed in the solder matrix prevent the Zn atoms to diffuse in the Cu foil, which causes the planar rod-shape  $\text{Cu}_5\text{Zn}_8$  IMC at the interface change into scallop  $\text{Cu}_6\text{Sn}_5$  IMC. It was observed that the IMC of Sn-Zn-xCu/Cu joint is mainly  $\text{Cu}_5\text{Zn}_8$  when the content of Cu is 0-1%; when the content of Cu is 2%-6%, the IMC is  $\text{Cu}_6\text{Sn}_5$  and  $\text{Cu}_5\text{Zn}_8$  together; when the content of Cu is 8%, the IMC is  $\text{Cu}_6\text{Sn}_5$ . With the increasing of Cu in the Sn-Zn-xCu solder, the shear strength of the Sn-Zn-xCu/Cu solder joint is enhanced with the transformation of IMC type from planar  $\text{Cu}_5\text{Zn}_8$  to scallop  $\text{Cu}_6\text{Sn}_5$  at the interface [10].

Addition of a third element significantly changes Sn-9Zn eutectic binary alloys microstructure, and mechanical properties have a large extent of dependency on mechanical properties. It has already proven that addition of a third element in the Sn-9Zn eutectic solder greatly improves its mechanical properties [11-13]. Thus, the objective of this study is to find out the relation between the microstructure and mechanical properties that alters with the formation of IMCs for various amount of Cu addition. This study concerns with the melting temperature, microstructure, microhardness and tensile

properties on Sn–9Zn eutectic solder alloy that may alter after addition of various amount of Cu in it.

## 2. EXPERIMENTAL PROCEDURE

The Sn–9Zn, Sn-9Zn-0.4Cu, Sn-9Zn-0.7Cu and Sn-9Zn-1.0Cu lead-free solders were prepared with commercially available pure tin, zinc, and copper (purity of 99 %). The constituent elements were melted in a furnace. The molten alloys (in the alumina crucible) were homogenized at 500°C and then poured in a steel mold to prepare the chill cast ingot. Consequently, chemical analyses were done by volumetric method to determine the exact composition of the casting ingots. The chemical compositions of the alloys were listed in Table 1. The melting temperatures of the solder alloys were determined with differential scanning calorimeter (DSC Q 10).

Table 1: Chemical composition of starting materials (wt. %)

Alloys	Sn	Zn	Cu	Pb	Bi	Sb
Sn-9Zn	Bal.	8.692	-	0.346	0.253	0.009
Sn-9Zn-0.4Cu	Bal.	8.683	0.413	0.343	0.251	0.012
Sn-9Zn-0.7Cu	Bal.	8.601	0.682	0.346	0.252	0.010
Sn-9Zn-1.0Cu	Bal.	8.626	1.057	0.340	0.260	0.008

The as-cast solders were sectioned and polished according to non-ferrous metallography with 0.5µm Al<sub>2</sub>O<sub>3</sub> particles in order to obtain the microstructure. After cleaning with acetone and alcohol, the samples were investigated by an optical microscope with digital camera (LEICA-MZFLIII) which was followed by SEM. A Philips XL40 FEG scanning electron microscope (SEM) equipped with an energy dispersive X-ray (EDX) analysis system was used to inspect and analyze the microstructure of the three different solders and to perform the semi quantitative analysis on those structures in order to determine the phases. The accuracy of the compositional measurement was about ±5%. To determine the formula composition of the intermetallic compounds (IMCs), the chemical analyses of the EDX spectra were corrected by standard ZAF software. The backscattered electron imaging mode of the SEM was used for the microstructural study. EDX analysis has been done to support the phase identification of the structure. Grinding and polishing were necessary to obtain polished, smooth and flat parallel surface before indentation testing. Thus, the polished samples were placed in a Vickers Shimadzu microhardness tester to measure the microhardness. The applied load was 50g for 10s and at least ten readings of different indentation were taken for each sample at room temperature to obtain the mean value.

The rectangular solder ingots were then mechanically machined into tensile specimens with a gauge length marked 32.00 mm for each samples, the width and thickness of the samples were 6.00 mm and 5.00 mm respectively. Tensile tests were carried out with a tensile

testing machine (Instron 3369 Universal Testing Machine) at a strain rate of 1.00 mm/min at 25°C to obtain data on the stress-strain curves which contain information of elongation at fracture and the UTS. The fracture surfaces of these lead-free alloys were also investigated under SEM to find the fracture mode.

## 3. RESULTS AND DISCUSSIONS

### 3.1 Melting Temperature

DSC analysis was carried out in order to investigate the fundamental thermal reactions on heating of these alloys. Figure 1 shows the typical DSC curves obtained for Sn-9Zn, Sn-9Zn-0.4Cu, Sn-9Zn-0.7Cu, and Sn-9Zn-1.0Cu alloys on heating. With the addition of small amount of Cu, the melting temperatures changed slightly. The melting temperatures were found 199.33°C, 200.13°C and 200.28°C for the Sn-9Zn-0.4Cu, Sn-9Zn-0.7Cu, and Sn-9Zn-1.0Cu, respectively, as compared with 197.59°C for Sn–9Zn eutectic alloy. Lee et al. [14] reported that the addition of Cu even up to 4% did not significantly alter the melting point of the Sn-9Zn alloy. For Cu addition here the melting temperature increases only 3°C than that of Sn-9Zn binary eutectic alloy.

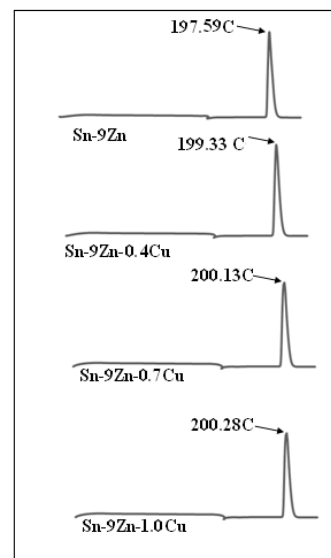


Fig 1. DSC curves of Sn-9Zn, Sn-9Zn-0.4Cu, Sn-9Zn-0.7Cu, and Sn-9Zn-1.0Cu alloys.

### 3.2 Microstructure and Elemental Analysis

The optical and SEM micrograph of the Sn-9Zn in Figure 2 (a and b) shows the typical lamella of eutectic microstructure. It has been mentioned that the eutectic Sn-9Zn alloy consists of β-Sn and Zn-rich phases. In the micrograph, the bright regions are the β-Sn phase and the primarily solidified phases; the dark phases are fine needlelike Zn-rich phase in β-Sn matrix. Also some Zinc spheroids are observed in the microstructure.

With the addition of 0.4% Cu, the eutectic Sn-9Zn alloy shows some precipitates distributed in the eutectic phase shown in Figure 2 (c and d). When 0.7% Cu is added with the eutectic Sn-9Zn alloy, the microstructure changes with some planar and flower shaped intermetallic compound distributed in the typical eutectic lamella as shown in Figure 3 (a and b). After the Cu

addition increases to 1% the number of intermetallic also increase while eutectic phase decreases and at the same time IMC size become larger, as shown in Figure 3 (c and d). The micrograph of the ternary alloys can be distinguished into three phases, i.e. the matrix  $\beta$ -Sn, the needle-like eutectic  $\alpha$ -Zn, and the flower or rod like dark grey phases. EDX analyses were carried out to clarify the composition of the dark grey phases. And interestingly it was found that Cu forms IMC of two different shapes reacting with both Zn and Sn. As can be seen in Figure 4 (a and b), the rod shaped dark gray phases revealed that the phases are composed of Cu and Zn and the Cu percentage of these phases are about 32 at. %. This observation implies that these rod shaped dark gray phases are actually  $\gamma$ -Cu<sub>5</sub>Zn<sub>8</sub> IMC. From the EDX analysis of flower shaped dark gray phases as shown in Figure 4 (c and d) were found to be made of Cu and Sn. And from the stoichiometrical ratio it was found that these flower shaped IMCs were Cu<sub>6</sub>Sn<sub>5</sub>.

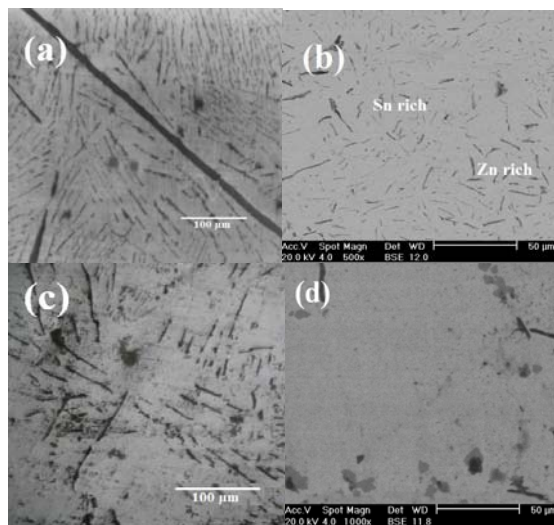


Fig 2. Optical and SEM micrograph respectively (a), (b) of Sn-9Zn and (c), (d) of Sn-9Zn-0.4Cu.

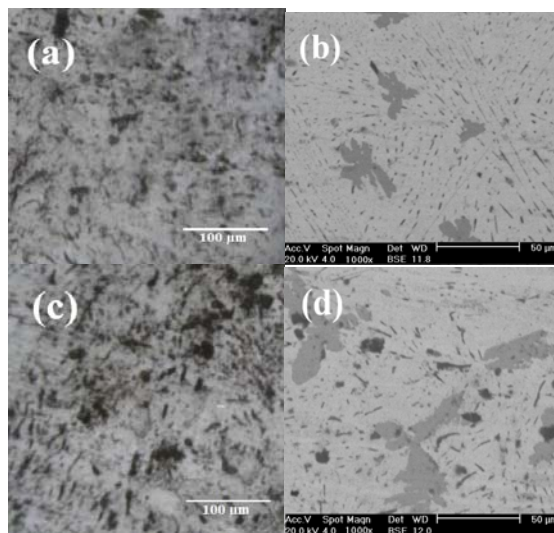


Fig 3. Optical and SEM micrograph respectively (a), (b) of Sn-9Zn-0.7Cu and (c), (d) of Sn-9Zn-1.0Cu.

Thus, we can see when a third element Cu is added with the Sn-9Zn eutectic alloy, the  $\alpha$ -Zn phases decreased and changes to finer structure. As Zn is a very reactive material (electro negativity: -1.65), it forms compound with the Cu. Cu also reacts with Sn as well to form intermetallic compound. And due to the high reactivity of Cu (electro negativity: -1.90), the microstructure of Sn-9Zn-0.7Cu and Sn-9Zn-1.0Cu deprived of thick Zn-rich eutectic lamella and consists of fine eutectic colonies dispersed with large Cu<sub>5</sub>Zn<sub>8</sub> and Cu<sub>6</sub>Sn<sub>5</sub>.

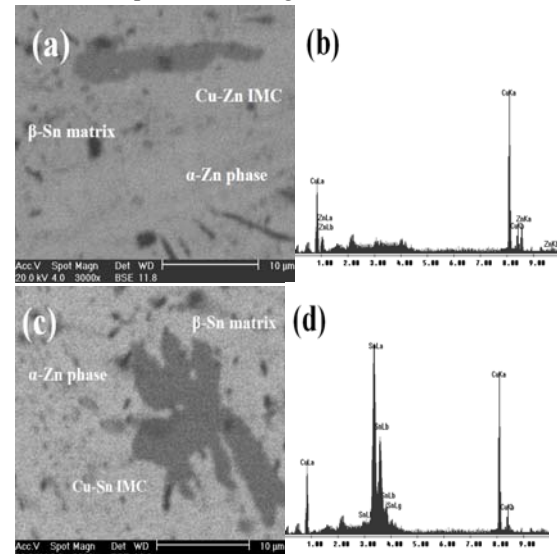


Fig 4. The dark gray phases and their quantitative analyses with EDX for Sn-9Zn-0.4Cu alloy (a), (b); (c), and (d).

### 3.3 Microhardness

The microhardness of a solder alloy depends on the motion of dislocation, growth and configuration of grains. The processes are more sensitive to the microstructure of the solder alloy than its chemical composition. So the mechanical property such as the microhardness depends especially on the microstructure, processing temperature, the composition, etc. [15]. In the present study the microhardness test was performed to observe the change of mechanical properties associated with the microstructural changes. Figure 5 shows the microhardness results with standard deviation as a function of alloy composition. In general, the hardness of Sn-based solders strongly depends on the alloying elements; the more the alloying elements, the higher the hardness. This is attributed to the fact that the volume fraction of the other phases increases as there are more alloying elements in solder. The same trend was confirmed for Sn-9Zn and Sn-9Zn-0.4Cu alloys; the average hardness value increases when small amount of Cu is added to the Sn-9Zn eutectic alloy as a third alloying element, as shown in Figure 5.

In Figure 5, it can be seen that the VHN of eutectic Sn-9Zn was 16.8, while those of Sn-9Zn-0.4Cu, Sn-9Zn-0.7Cu, and Sn-9Zn-1.0Cu were 21, 16.6 and 15.5 respectively. The hardness increases for Sn-9Zn eutectic alloy after addition of a third element can be understood by dissolution of Cu atoms for Sn-9Zn-xCu ternary alloys and formation of IMC particles in the

solder matrix to promote precipitation hardening. This may also be explained by the microstructural observations for the corresponding ternary alloy. Figure 3 represents that all the Sn-9Zn-xCu alloys are composed of three different phases; the matrix  $\beta$ -Sn, small amount of needle-like eutectic  $\alpha$ -Zn, and the dark gray phases of IMCs, while the Sn-9Zn eutectic alloy consists of only first two phases with some Zn spheroids in it. And also the amount of eutectic  $\alpha$ -Zn phase quantity is high and thick compared to that of the Zn-rich phases of the ternary alloys, which in turns results in a lower hardness value. Unfortunately for higher amount of Cu addition the hardness value starts to decrease gradually. This happens due to the formation of large IMC in the  $\beta$ -Sn matrix, which consumes more Zn and Sn from original bulk solder and eventually develops some sort of weak interface with the parent matrix.

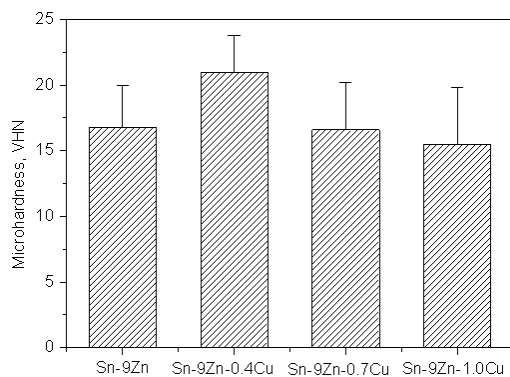


Fig 5. Graphical representation of Vickers Hardness Number (VHN) with Standard-deviation for Sn-9Zn, Sn-9Zn-0.4Cu, Sn-9Zn-0.7Cu, and Sn-9Zn-1.0Cu alloys.

### 3.4 Tensile Properties

The ultimate tensile strength (UTS) is the maximum engineering stress, which a material can withstand in tension, on the engineering stress-strain curve [16]. For solder alloys, the yield stress is commonly defined by the stress on the stress-strain curve at 0.2% strain offset. The effect of third alloying additives on mechanical properties of Sn-9Zn eutectic solder alloy can be seen from the strain-stress curves shown in Figure 6. The tensile strength of the Sn-9Zn, Sn-9Zn-0.4Cu, Sn-9Zn-0.7Cu, and Sn-9Zn-1.0Cu were 52, 53, 48 and 43 MPa, respectively. The elongation at failure of the Sn-9Zn, Sn-9Zn-0.4Cu, Sn-9Zn-0.7Cu, and Sn-9Zn-1.0Cu were 62, 47, 38 and 38%, respectively. The Sn-9Zn-0.4Cu alloy had the higher UTS and Sn-9Zn alloy exhibit higher elongation, while Sn-9Zn-1.0Cu had the lowest UTS and elongation. In the tensile stress-strain curves shown in Figure 6, after the peak tensile stresses are reached at  $\approx 0.05$  strain, the binary Sn-9Zn alloy has a less steep slope than the Sn-9Zn-xCu alloys. This steeper slope indicates that the eutectic structure becomes a hypoeutectic structure. The formation of Cu-Sn and Cu-Zn compound occurs at the expense of the Zn-rich phase. The variation in Sn content renders the eutectic structure into a hypoeutectic structure.

Figure 7 shows the tensile properties for Sn-9Zn, Sn-9Zn, Sn-9Zn-0.4Cu, Sn-9Zn-0.7Cu, and Sn-9Zn-1.0Cu alloys. An increase in 2% proof strength is observed for 0.4% Cu addition in Sn-9Zn alloy, while a 24% drop in elongation is observed for it. For 0.7 and 1.0% Cu addition both proof strength and elongation decreases in larger extent. As per dispersion strengthening theory [17], the strength must increase with the addition of a second phase particle in the matrix. And for the case of small amount of Cu addition in Sn-9Zn the theory proved right, while for the amount of Cu increases the theory contradicts with the results. These contradictory results can be explained from the microstructure and tensile fracture surface of the alloys very clearly.

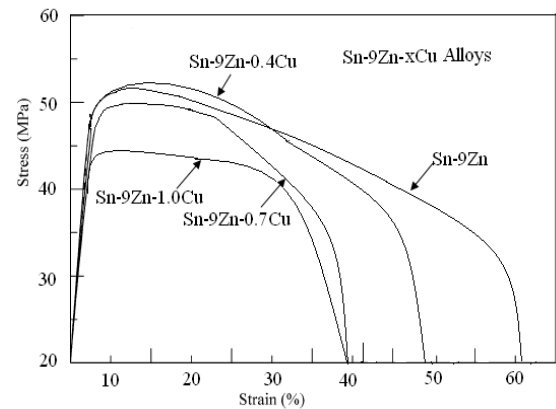


Fig 6. Tensile stress-strain curves of Sn-9Zn, Sn-9Zn-0.4Cu, Sn-9Zn-0.7Cu, and Sn-9Zn-1.0Cu alloys.

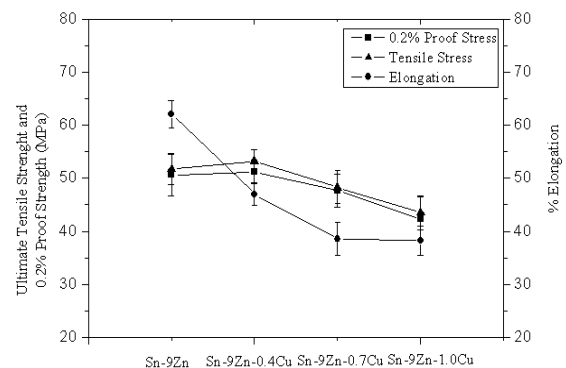


Fig 7. Tensile properties of Sn-9Zn, Sn-9Zn-0.4Cu, Sn-9Zn-0.7Cu, and Sn-9Zn-1.0Cu alloys.

### 3.5 Fracture Mode

Figure 8 shows the fractography of the alloys after tensile tests. All alloys displayed a typical ductile fracture mode. The dimpled pattern is represented in all fracture surfaces. The dimple size of the alloys varies for different element content. The dimples size for Sn-9Zn-0.4Cu is much finer compared to others. For Sn-9Zn-0.4Cu, Sn-9Zn-0.7Cu and Sn-9Zn-1.0Cu alloys, some Cu-Sn and Cu-Zn compounds were observed in the fracture surfaces. The fracture surface of the Sn-9Zn-0.4Cu alloy shows many fine dimple structures (Figure 8b). On the other hand, the fracture surfaces of

the Sn-9Zn-0.7Cu and Sn-9Zn-1.0Cu alloys exhibit some cleavage patterns, as shown in Figure 8 (c and d). Thus, Sn-9Zn-0.7Cu and Sn-9Zn-1.0Cu alloy undergoes a complex fracture pattern. From the results of tensile tests on Sn-9Zn-0.4Cu alloy, the formation of small size of Cu-Sn and Cu-Zn compounds promote tensile strength and deteriorate elongation slightly, while the tensile tests for Sn-9Zn-0.7Cu and Sn-9Zn-1.0Cu alloys reveal that the large intermetallic compounds deteriorates both tensile strength and elongation.

The both phenomenon of tensile strength and elongation can be clearly explain by the dispersion strengthening theory; i.e. the second phase formed by Al generates obstacle for the dislocation at the grain boundary (the maximum region of mismatch), dislocation piles up results in a increase in tensile strength, the term also called precipitation strengthening. On the other hand due to movement restriction of dislocation densities the slip planes cannot find their suitable direction to move freely results lack in ductility; i.e. elongation decreases. For higher amount of Cu in Sn-9Zn eutectic solder alloy tensile properties deteriorates. The fall of tensile strength is believed for the weak interface formed between the IMC and the matrix, which in turn decrease the tensile strength. According to Dieter [17], the second phase element increases the tensile strength up to a certain extent and beyond that the precipitate starts to grow non-coherently which results in the decrease of the overall strength. And for the case of Sn-9Zn-0.7Cu and Sn-9Zn-1.0Cu alloys the IMCs growth is beyond that limit which results in a decrease in the tensile strength. Also from figure 3 (a), (c) and 4 (a), (c), it can be observed that the flower and rod shaped IMCs have several edges, which may acts as crack initiators during tensile loading. Thus, rather than ductile cup-cone, complex cleavage type fracture surface is exposed after tensile test. The reduction of elongation for Cu addition may also be related to the weak interface between the large IMCs with the  $\beta$ -Sn matrix.

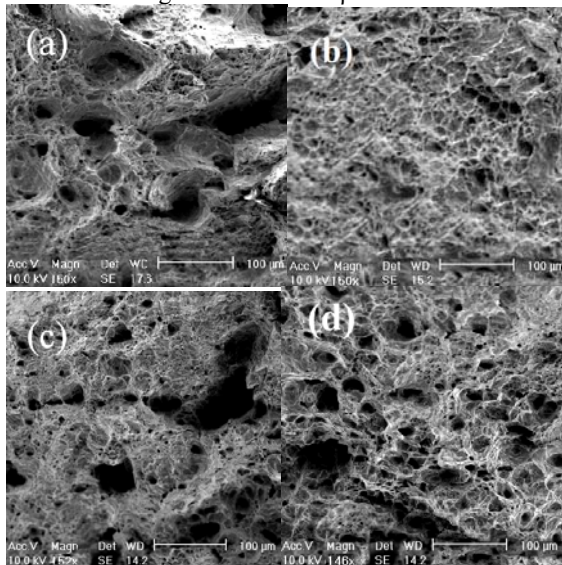


Fig 8. SEM fractograph in SE mode for (a) Sn-9Zn, (b) Sn-9Zn-0.4Cu, (c) Sn-9Zn-0.7Cu, and (d) Sn-9Zn-1.0Cu alloys.

#### 4. CONCLUSIONS

The melting temperature of Sn-9Zn eutectic solder alloy doesn't alter significantly after small amount of Cu in it, only a 3°C increase is observed up-to 1.0 wt. % Cu addition. The volume fraction of IMCs in Sn-9Zn-xCu ternary alloys increased in contrast to that of the eutectic  $\alpha$ -Zn phase, which decreased with Cu addition. At the same time the eutectic  $\alpha$ -Zn phase converts into fine needle-like structures rather than thick rod-like lamella. The flower and rod shaped precipitate of  $\text{Cu}_6\text{Sn}_5$  and  $\text{Cu}_5\text{Zn}_8$ , respectively were observed in the Sn-Zn-Cu ternary alloys. The mechanical properties of Sn-9Zn-0.4Cu are found to be higher compared to the Sn-9Zn eutectic solder alloy. As the amount of Cu further increases, both tensile strength and elongation drops. Sn-9Zn and Sn-9Zn-0.4Cu alloys showed a ductile fracture pattern, while Sn-9Zn-0.7Cu and Sn-9Zn-1.0Cu alloys showed a complex cleavage failure pattern.

Finally, it can be concluded that the addition of a little amount of Cu can improve the mechanical properties of Sn-9Zn eutectic solder alloy. As the Cu content in Sn-9Zn increases, the mechanical properties start to deteriorate.

#### 5. REFERENCES

1. Suganuma, K., 2004 "Preface-Special Issue on Lead-Free Soldering in Electronics," Mater. Trans. 45:605-605.
2. Zeng, K. and Tu, K.N., 2002 "Six cases of reliability study of Pb-free solder joints in electronic packaging technology," Mater Sci Eng R. 38:55-105.
3. Abtew, M. and Selvaduray, G., 2000, "lead-free solders in microelectronics," Mater Sci Eng R 27:95-141.
4. Song, J. M. and Wu, Z.M., 2006 "Variable eutectic temperature caused by inhomogeneous solute distribution in Sn-Zn system," Scripta Metall. 54:1479-1483.
5. Kim, K.S., Yang, J.M., Yu, C.H., Jung, I.O. and Kim, H.H., 2004 "Analysis on interfacial reactions between Sn-Zn solders and the Au/Ni electrolytic-plated Cu pad," J. Alloys and Compounds 379:314-318.
6. Vaynman, S. and Fine, M. E., 1999, "Development of fluxes for lead-free solders containing zinc" Scr. Mater. 41:1269-1271.
7. Xie, H. P., Yu D. Q. and Wang, L., 2005 "Effects of Bi, Ni additives on the microstructures and wetting properties of Sn-Zn-Cu lead-free alloy", Proc. the International Conference on Asian Green Electronics.
8. Xiaoyan, Z., Qun, Z., Wang, X. C. and Zhang, W. T., 2007 "Influence of Cu, Ce on Physics and Chemistry Properties of Sn-Zn System Solder Alloys", New technologies and process, 1.
9. Ichitsubo, T., Matsubara, E., Fujiwara, K., Yamaguchi, M., Irie, H., Kumamoto, S. and Anada, T., 2005 "Control of compound forming reaction at the interface between SnZn solder and Cu substrate", J. Alloy. Comp. 392:200-205.
10. Wang, L., Ma H. T., and Xie, H. P., 2005 "Interfacial Reaction and Shear Strength of Sn-Zn-Cu/Cu Joints",



- J. Dalian Uni. Tech. 45:663-667.
11. Soares, D., Vilarinho, C., Barbosa, J., Silva, R., Pinho, M. and Castro, F., 2004 "Effect of the Bi content on the mechanical properties of a Sn-Zn-Al-Bi solder alloy", *Mater. Sci. Forum* 455-456:307-311.
  12. Chuang, C. M., Lui, T. S., Chen, L. H., 2002, "Effect of aluminum addition on tensile properties of naturally aged Sn-9Zn eutectic solder", *J. Mater. Sci.* 37:191-195.
  13. Wu, C. M. L. and Wong, Y. W., 2007 "Rare-earth additions to lead-free electronic solders", *J. Mater. Sci.: Mater. Electron.* 18:77-91.
  14. Lee, J. E., Kim, K. S., Inoue, M., Jiang, J. and Sukanuma, K., 2008 "Effects of Ag and Cu addition on microstructural properties and oxidation resistance of Sn-Zn eutectic alloy", *J. Alloys and Compounds* 454:310-320.
  15. Frear, D., Morgan, H., Burchett, S., Lau, J., 1994 "The Mechanics of Solder Alloy Interconnects", Van Nostrand Reinhold, New York.
  16. Callister, W. D., 1996 "Materials Science and Engineering an Introduction", 4th Edition, John Wiley & Sons Inc., Canada.
  17. Dieter, G. E., 1986 "Mechanical Metallurgy", McGraw-Hill Book Co., New York.

## 6. MAILING ADDRESS

M. Rahman  
Department of Materials and Metallurgical Engineering,  
Bangladesh University of Engineering and Technology,  
Dhaka-100, Bangladesh.

## A FINITE ELEMENT STUDY OF ELASTIC-PLASTIC HEMISPHERICAL CONTACT BEHAVIOR AGAINST A RIGID FLAT UNDER VARYING MODULUS OF ELASTICITY AND SPHERE RADIUS

Biplab Chatterjee and Prasanta Sahoo

Department of Mechanical Engineering, Jadavpur University, Kolkata, India

### ABSTRACT

The present study considers a finite element analysis of elastic-plastic axi-symmetric hemispherical contact for a frictionless deformable sphere pressed by a rigid flat. The material of the sphere is modeled as elastic perfectly plastic. Analysis is carried out to study the effect of varying modulus of elasticity and sphere radius in wide range of dimensionless interference until the inception of plasticity as well as in plastic range. Results are compared with previous elastic-plastic models. It is found that materials with Young's modulus to yield strength ( $E/Y$ ) ratio less than and greater than 300 show strikingly different contact phenomena. The dependency of  $E$  on dimensionless interference at which the plastic region fully covers the surface is observed. However with different radius, finite element study exhibits similar elastic-plastic phenomena.

**Keywords:** Elastic-plastic contact, Sphere against flat, ANSYS, Modulus of elasticity, Sphere radius.

### 1. INTRODUCTION

Contact is necessary in any engineering application to transfer force and power hence it is almost an indispensable field of study. The elastic-plastic contact of a hemisphere with a rigid surface is a fundamental problem to study the major characteristics like localized deformation, the variation in the contact area, the contact force, displacement and the stress distribution in the deformable body. Much interest is devoted in the literature to the reverse case of indentation loading where a rigid sphere penetrates an elasto-plastic half space. It is worthy to emphasize that indentation and hemispherical deformation (this work) are significantly different in the elasto-plastic and fully plastic regimes. One of the earliest models of elastic asperity contact is that of Greenwood and Williamson [1]. This model uses the solution of the frictionless contact of an elastic hemisphere and a rigid flat plane, otherwise known as the hertz contact solution [2]. Some works are restricted to pure plastic deformation of the contacting sphere, based on Abbot and firestone [3]. The works on either pure elastic or pure plastic deformation of the contacting sphere overlook a wide intermediate range of interest where elastic-plastic contact prevails. An attempt to bridge this gap was made by Chang et al [4]. Zhao et al [5] used mathematical manipulation to smooth the transition of the contact load and contact area expressions between the elastic and elastic-plastic deformation regimes. Mathematical models are replaced using finite element model (FEM) concepts recently. Kogut and Etsion (KE) [6] used FEM concept and analyzed the evolution of the elastic-plastic contact with

increasing interference revealing three distinct stages that ranges from fully elastic, elastic-plastic up to fully plastic ( $0 < \omega^* \leq 110$ ). The model provides dimensionless expression for contact area, contact load and mean contact pressure covering a large range of interference values. They inferred that their analysis is normalized in such a way that allowed a general solution, which is independent of specific material and radius of the sphere. A change in the behavior of the mean contact pressure was observed in their analysis at  $\omega^* = 6$ , which marks the elastic limit of the contact area. To generalize their solution, the numerical solutions were normalized with respect to their corresponding critical values at yielding inception,  $\omega_c$ , the validity of this normalization was tested by solving the problem for several different material properties ( $100 < E/Y < 1000$ ,  $\nu = 0.3$ ) and sphere radii ( $0.1 \text{ mm} < R < 10 \text{ mm}$ ). Their results show that the entire contact zone is plastic when the dimensionless interference ratio ( $\omega/\omega_c = \omega^*$ ) is 68 and the rate of its radial expansion increases substantially. Moreover when  $\omega/\omega_c = 110$ , the dimensionless mean contact pressure ( $p/Y$ ) approaches the value of 2.8. This is identical to the ratio between the hardness and yield strength found experimentally for many materials as indicated by Tabor [7].

Kogut and Etsion [8] studied the maximum tangential load that can be supported by a normally preloaded elastic perfectly plastic spherical contact at the inception of sliding using an approximate semi analytical solution. Sliding inception was interpreted as a failure of the contact. They found that when the normal load is less

than the Hertzian critical load the failure occurs on the contact area. If the normal load exceeds that critical one, the failure occurs below the contact area. Brizmer et al. [9] analyzed and compared the ductile material yielding inception and the brittle material failure inception for two different contact conditions between a smooth elastic sphere and rigid flat and the effect of contact condition and material properties on the termination of elasticity. Jackson and Green (JG) [10] extended the KE model to account the geometry and the material effects in the analysis. They used finer mesh than the KE model and solved for five different yield strengths. They showed markedly different behaviors for the materials with different strengths in the transition from elastic-plastic to fully plastic deformations. For calculating the critical interference, they used material yield strength (Y) directly in their expressions. Their results show that the dimensionless mean contact pressure does not reach 2.8 for most of the yield strength values. The JG solution used E/Y ratio of 952.4, 356.6, 219, 158.1 and 137.74 by varying the values of 'Y' with constant E = 200 GPa. They also analyzed the interference when plastic deformation first reaches the contacting surface at the far right end and the contact surface first becomes entirely plastic for yield strength of 1.619, 1.2653, 0.9115 GPa. Quicksall et al. [11] have taken five hypothetical material properties and studied the error of formulation for KE and JG model. The first test generated contact area and contact force data for five hypothetical metals with Poisson's ratio, yield strength and elastic modulus typical of aluminum, bronze, copper, titanium and malleable cast iron. Non-dimensional interference between  $\omega^*=5$  and  $\omega^*=250$  were used to generate data in both the elastic-plastic and the plastic regimes except for aluminum at  $\omega^*=250$  and malleable cast iron above  $\omega^*=10$ . Second set of tests generated non-dimensional contact area and contact force data for a generic material in which the elastic modulus and Poisson's ratio were independently varied with yield strength held constant at 200 MPa. Firstly Poisson's ratio was varied between 0.28 and 0.36 with the elastic modulus held constant at 200 GPa. Then the elastic modulus was varied between 160 and 240 GPa with Poisson's ratio held constant at 0.32. The dimensionless interference was set at  $\omega^*=20, 80$  and 250 for each test iteration. Jackson et al. [12] used mesh size same as that of JG model and presented results for a range of normalized interference  $\omega^*$ , from 0.571 to 171. Then the contact force, stress tensor, von mises stresses and the displacement in both the radial and axial directions were recorded. After loading conditions had been simulated; the solution was then restarted and unloaded completely to simulate the residual stresses and the displacements. In order to measure the effect of the material properties on the hemispherical deformation, both aluminum and steel sphere unloaded from  $\omega^*=135$ ; they inferred that the deformation of the hemisphere is dependent on the properties of the material and the interference.

Shankar and Mayuram (SM) [13] studied the evolution of elastic core and the plastic region within the asperity for different Y/E ratios. They varied the yield strength from 250 N/mm<sup>2</sup> to 2250 N/mm<sup>2</sup>. E equals to

2.07 x 10<sup>5</sup> N/mm<sup>2</sup>. The range of E/Y is from 83.333 to 500. It was revealed from their analysis that higher dimensionless interference;  $\omega^*$  is required for the plastic region to just touch the contact surface when E/Y > 166.66 and this  $\omega^*$  is varied with E/Y ratio. For E/Y < 166.667, this  $\omega^*$  is constant and equals to 6. Same trend was observed for the entire contact surface to be in plastic. For E/Y > 166.66, the value of  $\omega/\omega_c$  decreases with decrease of E/Y ratio. When E/Y ratio is less than 166.66, the fully plastic contact condition exists at a constant interference ratio of 54. They studied the variation of mean contact pressure (p/Y) as a function of dimensionless interference ratio and observed that materials having low yield strength (i.e. when E/Y > 300) produces results similar to the KE model but p/Y ratio never reaches 2.8. Malayalamurti and Marappan (MM) [14] analyzed the elastic-plastic behavior of a sphere loaded against a rigid flat in two region. One is when E/Y > 300, another when E/Y < 300. They observed that when E/Y < 300, the fully plastic average contact pressure or hardness is not constant. However, the hardness and interference at the inception of fully plastic condition are constant for materials with E/Y > 300. The present work aims to study the qualitative and quantitative contact characteristics of single asperity contact using commercial FEM software ANSYS. Analysis is carried out to study the effect of varying modulus of elasticity and sphere radius in wide range of dimensionless interference until the inception of plasticity as well as in plastic range.

## 2. FINITE ELEMENT MODEL AND PROCEDURE

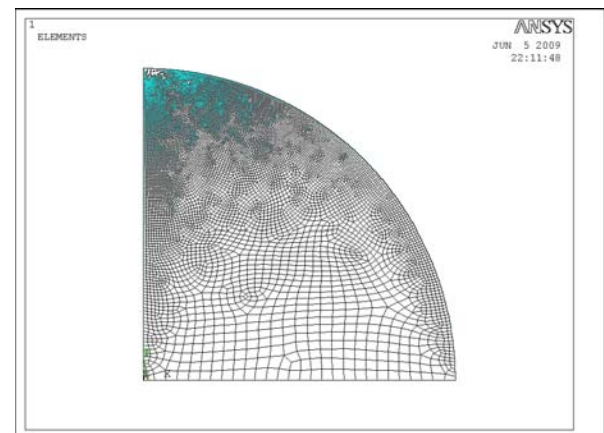


Fig 1. Finite element mesh of a sphere generated by ANSYS

To improve upon the efficiency of computation, an axi-symmetric 2-D model is used. The present study utilizes the commercial program ANSYS. The hemisphere is modeled by a quarter of a circle, due to its axisymmetry. A line models the rigid flat. The model refines the element mesh near the region of contact to allow the hemisphere's curvature to be captured and accurately simulated during deformation. The model uses quadrilateral, four node elements to mesh the

hemisphere. The resulting ANSYS mesh is presented in Fig.1. The nodes on the axis of symmetry are fixed in radial direction. Likewise the nodes on the bottom of the hemisphere are fixed in both axial and radial direction. The bilinear isotropic hardening (BISO) option in the ANSYS program is chosen to account the elastic-plastic material response for the single asperity model. The rate independent plasticity algorithm incorporates the von Mises criterion. Tangent modulus is assumed as zero for validating the results with other elastic perfectly plastic models. The KE model uses a maximum of 2944 nodes and JG model uses a constant of 11,101 elements for their analysis. However the present work uses a maximum of 11069 elements for the radius of 1 mm. The mesh density is iteratively increased until the contact force and contact area differed by less than 1% between iterations. In addition to mesh convergence, the model also compares well with the Hertz elastic solution at interferences below the critical interference. This work uses Lagrangian multiplier method. The tolerance of current work is set to 1% of the element width.

There are two ways to simulate the contact problem. The first applies a force to the rigid body and then computes the resulting displacement. The second applies a displacement and then computes the resulting contact force. In both methods, the displacement, stress, and strain can be determined as well as the contact pressure. In this work the latter approach is used. This method is used because the resulting solution converges more rapidly than the former. In this work contact parameters are normalized using the JG model's expression for critical interference ( $\omega_c$ ), critical load ( $P_c$ ) and critical contact area ( $A_c$ ) to form dimensionless parameters. Thus,

$$\omega_c = (\pi CY/2E')^2 R \quad (1)$$

$$P_c = (4/3)(R/E')^2 (C\pi Y/2)^3 \quad (2)$$

$$A_c = \pi^3 (CYR/2E')^2 \quad (3)$$

Where  $C=1.295 \exp(0.736\nu)$

$E'$  is defined as

$$1/E' = (1-\nu_1^2)/E_1 + (1-\nu_2^2)/E_2 \quad (4)$$

where  $E_1$ ,  $E_2$ , and  $\nu_1$ ,  $\nu_2$ , are Young's moduli and Poisson's ratios of the two materials, respectively. In case of the rigid flat,  $E_2 \rightarrow \infty$ . The dimensionless parameters are as follows:  $\omega^* = \omega/\omega_c$ ,  $P^* = P/P_c$ ,  $A^* = A/A_c$ .

### 3. NUMERICAL RESULTS AND DISCUSSION

The results of the finite element model are presented for a variety of interferences. The materials selected cover steel, grey cast iron and aluminum used in engineering applications. While yield strength and Poisson's ratio are held constant, four different elastic modulus ( $E$ ) are chosen. They are 70, 80, 103, 200 Gpa.

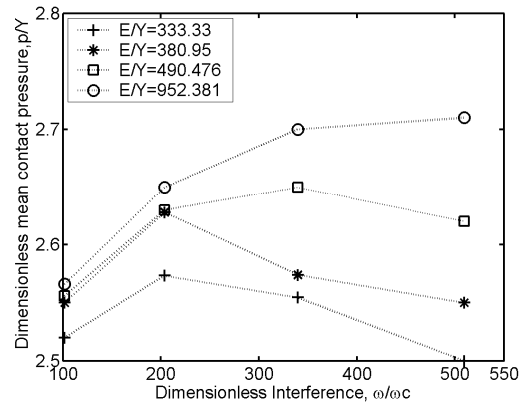


Fig 2. Dimensionless mean contact pressure versus dimensionless interference for  $E/Y > 300$ .

Fig 2 represents the results of the mean contact pressure to yield strength ratio ( $p/Y$ ) as a function of dimensionless interference ratio ( $\omega/\omega_c$ ) obtained from the finite element analysis. Here the study is made with constant yield strength ( $Y$ ) and Poisson's ratio ( $\nu$ ). The values of which are taken as 0.21 GPa and 0.32 respectively. With the variation of elastic modulus different  $E/Y$  ratios are obtained. Thus the  $E/Y$  ratios are 333.31, 380.95, 490.476 and 952.4 for the elastic modulus of 70, 80, 103, 200 GPa respectively. The range of  $\omega/\omega_c$  is from 100 to above 500. It is revealed from Fig 2 that when  $E/Y > 300$ ; the trend obtained is similar to the JG [10] model with small changes in magnitude. JG inferred that a material with higher  $Y$  has less mean contact pressure in plastic range. Here material with higher  $E$  has higher mean contact pressure as the dimensionless interference increases in the plastic range. MM [14] concluded the material independent behavior for  $E/Y > 300$ . They had taken the average results of four materials. Moreover they modeled the material of the sphere as an elastic linear hardening material A 1% linear hardening was selected for their work. The present work modeled the material of the sphere as an elastic perfectly plastic material and the results entirely deviate from their result as mean contact pressure to yield strength ratio ( $p/Y$ ) never reaches 2.8. Fig 3 shows the variation of dimensionless contact load as a function of dimensionless interference, when  $E/Y$  is greater than 300. The result indicates the similarity with Quicksall et al. [11] findings. With the increased modulus of elasticity ( $E$ ) the value of dimensionless load increases in the plastic range.

Dimensionless contact area as a function of  $\omega^*$  (dimensionless interference) is plotted in Fig 4. The values for dimensionless contact area continue to increase with interference even past fully plastic condition. For the contact area all the models follow the same general trend, but they differ only in magnitude. The result shows that the dimensionless contact area is independent of  $E$  when  $E/Y > 300$ .

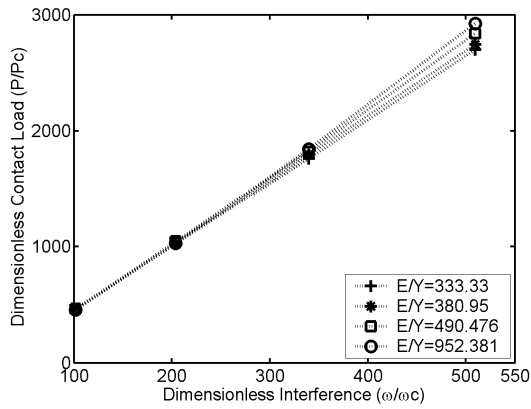


Fig 3. Dimensionless contact load as a function of dimensionless interference for  $E/Y > 300$ .

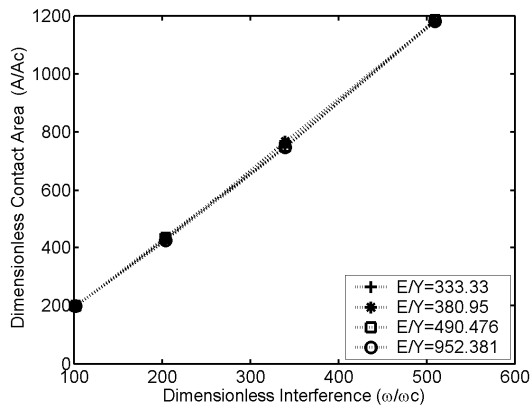


Fig 4. Dimensionless contact area as a function of dimensionless interference for  $E/Y > 300$ .

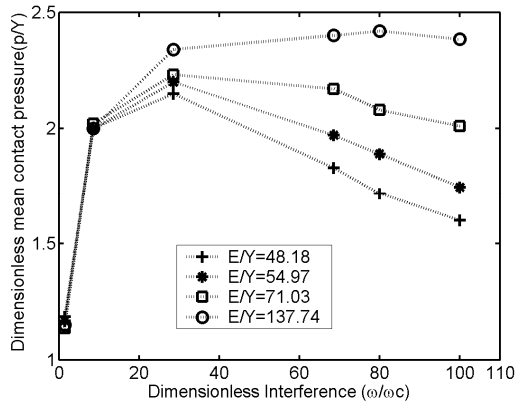


Fig 5. Dimensionless mean contact pressure as a function of dimensionless interference for  $E/Y < 300$ .

Study is also made for the materials of  $E/Y < 300$ . For this case  $Y$  is taken as 1.619 GPa, with constant Poisson's ratio of 0.32. With four  $E$  values of 70, 80, 103 and 200 GPa the corresponding  $E/Y$  ratios are 48.178, 54.972, 71.0315 and 137.739 respectively. These values

are well below 300. The behaviors of these materials in elastic as well as in elastic-plastic ranges are also analyzed. The average contact pressure to yield strength ratio is plotted in Fig 5 as a function of dimensionless interference ( $\omega^*$ ). It is clearly evident from the plot that dimensionless mean contact pressure does not reach the value of 2.8 even if for steel with  $E = 200$ Gpa. There is a decrease in mean contact pressure after reaching its peak value, though the peak value is dependent on  $E$ . As the value of  $E$  is increasing peak mean contact pressure also is high. There is a similarity of the trend with the findings of MM [14]. But MM inferred that peak value would reach after the dimensionless interference of 90 only. Present work observed that the peak value of mean contact pressure in all the cases occurred well below the dimensionless interference of 90. It can be seen from the figure 5, the location at which the mean pressure attain its peak value and the magnitude is entirely dependent on modulus of elasticity ( $E$ ) of the material.

Fig. 6 represents the plot of dimensionless load ( $P^*$ ) versus  $\omega^*$ . It is clear from the figure that for different value of  $E$  up to the inception of fully plastic contact the trend is linear with marginal change in magnitude. This is similar to the prediction of KE [6]. This trend is not observed in higher interference ratio. Fig. 7 represents the plot of dimensionless contact area with  $\omega^*$  when  $E/Y < 300$ . The FEM results from this study indicate that dimensionless contact area decreases slightly with increased elastic modulus of elasticity. Same trend was observed by Quicksall et al. [11].

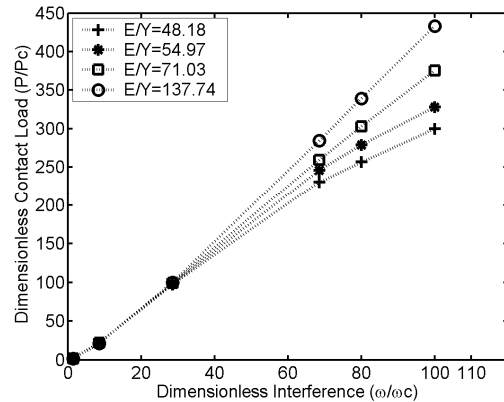


Fig 6. Dimensionless contact load versus dimensionless interference for  $E/Y < 300$ .

When interference increases, the elastic core completely disappears and the fully plastic region reaches the contact surface as shown in fig 8; thus the transition to the fully plastic state occurs. KE model predicted this transition limited to specific dimensionless ratio of 68. JG [10] and SM [13] predicted that this ratio at which this transition occurs is not constant. In the present work it is observed that this ratio is dependent on  $E$ . As the value of  $E$  increases the dimensionless ratio at which the transition occurs is also increasing. There is no indication of constant value for the present four  $E/Y$  ratio though SM also observed a constant value of 54 when  $E/Y < 166.66$ . Fig 9 is the plot of  $\omega^*$  versus  $E/Y$  where it is



clear that in the present domain of work SM overestimates the current work marginally. The present work also studied the values of dimensionless contact load, contact area and mean contact pressure with different sphere radii, the study is made with radii of 1, 2, and 3 mm. No significant deviation is observed. Thus it can be inferred that earlier mentioned dimensionless contact characteristics are independent of the sphere radius.

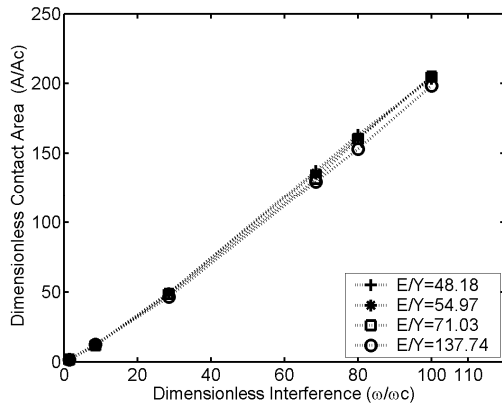


Fig 7. Dimensionless contact area versus dimensionless interference for  $E/Y < 300$ .

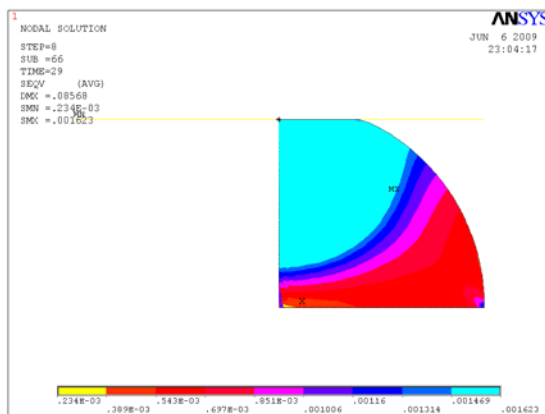


Fig 8. Inception of fully plastic contact

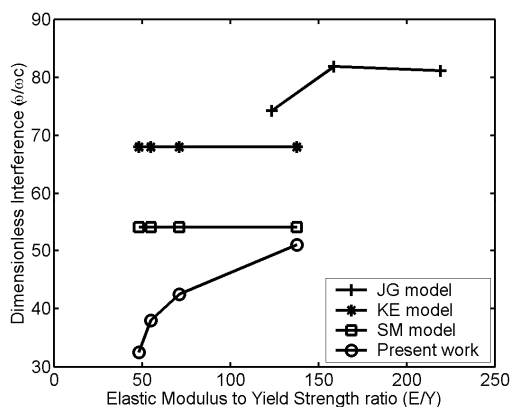


Fig 9. End of elastic-plastic region based on the disappearance of elastic core.

#### 4. CONCLUSIONS

The present work considers 2D axi-symmetric finite element model of an elastic perfectly plastic hemisphere in contact with a rigid flat surface. A comparison is also made with other existing models. The material is modeled as elastic perfectly plastic, and yielding occurs according to the Von Mises criterion. It has been clearly shown that the dimensionless mean contact pressure ratio is not constant at 2.8 in the plastic range but dependent on modulus of elasticity whether  $E/Y$  is greater or lesser than 300. But the peak value (i.e. maximum mean contact pressure ratio), the dimensionless interference at which this value occurs, the trend of changing is dependent on  $E/Y$  ratio. Dimensionless contact area, contact load also depends on modulus of elasticity. But dimensionless contact load, contact area and mean contact pressure is independent of changing radius of sphere. The development of the elastic core and the transition to the plastic region within the surface for the wide range of interference is studied using Von Mises stress. It is observed that the dimensionless interference ratio at the instance when the plastic region fully covers the surface is dependent on the values of modulus of elasticity when other properties are kept constant.

#### 5. NOMENCLATURE

Symbol	Meaning	Unit
P	Contact load	N
R	Radius of the sphere	mm
p	Pressure	GPa
$\omega$	Interference	$\mu\text{m}$
A	Contact area	$\mu\text{m}^2$
E	Modulus of Elasticity	GPa
Y	Yield strength of sphere	GPa
$\nu$	Poisson's ratio	

##### 5.1 Subscripts

c = critical values

##### 5.2 Superscripts

/ = equivalent

\* = dimensionless

#### 6. REFERENCES

- Greenwood, J. A. and Williamson, J. B. P., 1966, "Contact of nominally flat surfaces." Proc. R. Soc. London, Ser. A, 295: 300-319.
- Timoshenko, S. and Goodier, J. N., 1951, "Theory of Elasticity", McGraw-Hill, New York
- Abbott, E. J. and Firestone, F. A., 1933, "Specifying surface quality – A method based on accurate measurement and comparison", ASME J. Mech. Engg., 55:569-572.
- Chang, W. R., Etsion, I. and Bogy, D. B., 1987, "An elastic-Plastic model for the contact of rough surfaces," ASME J. Tribol., 109:257-263.
- Zhao, Y., Maietta, D. M. and Chang, L., 2000, "An asperity micro contact model incorporating the

- transition from elastic deformation to fully plastic flow”, ASME J. Tribol., 122(1):86-93.
6. Kogut, L. and Etsion, I., 2002, “Elastic-plastic contact analysis of a sphere and a rigid flat,” J. Appl. Mech., 69:657-662.
  7. Tabor. D., 1951, “The hardness of metals”, Clarendon Press Oxford.
  8. Kogut, L. and Etsion, I., 2003, “A semi-analytical solution for the sliding inception of a spherical contact”, ASME J. Tribol., 125:499-506.
  9. Brizmer, V., Kligerman, Y. and Etsion, I., 2005, “The effect of contact conditions and material properties on the elasticity terminus of a spherical contact,” Int. J. Solids and Structures, 43: 5736-5749.
  10. Jackson, R. L. and Green, I., 2005, “A finite element study of elasto-plastic hemispherical contact against a rigid flat”, ASME J. Tribol., 127: 343-354.
  11. Quicksall, J. J., Jackson, R. L. and Green, I., 2004, “Elasto-plastic hemispherical contact models for various mechanical properties”, J. Engg Tribol., 218: 313-322.
  12. Jackson, R., Chusoipin, I. and Green, I., 2005, “A finite element study of the residual stress and deformation in hemispherical contacts”, ASME J. Tribol., 127:484-493.
  13. Shankar, S. and Mayuram, M. M., 2008, “A finite element based study on the elastic –plastic transition behavior in a hemisphere in contact with a rigid flat”, ASME J. Tribol., 130:1-6.
  14. Malayalamurthi, R. and Marappan, R., 2008, “Elastic-plastic contact behavior of a sphere loaded against a rigid flat.” Mech. Adv. Mat. Struct., 15: 364-370

## 7. MAILING ADDRESS:

Biplab Chatterjee  
Department of Mechanical Engineering,  
Jadavpur University, Kolkata, India  
E-mail: psjume@gmail.com

## EFFECT OF STRAIN HARDENING ON ELASTIC-PLASTIC CONTACT BEHAVIOUR OF A SPHERE AGAINST A RIGID FLAT – A FINITE ELEMENT STUDY

Biplab Chatterjee, Dipankar Adhikary and Prasanta Sahoo

Department of Mechanical Engineering, Jadavpur University, Kolkata, India

### ABSTRACT

The present study considers an elastic-plastic contact analysis of a deformable sphere with a rigid flat using finite element method. The effect of strain hardening on the contact behaviour of a non-adhesive frictionless elastic-plastic contact is analyzed using commercial finite element software ANSYS. To study the strain hardening effect we have taken different values of tangent modulus. The result of strain hardening effect clearly shows that a generalized solution can not be applicable for all kind of materials as the effect of strain hardening differently influenced the contact parameters. With the increase in the value of hardening parameter this effect also increases. For higher value of hardening parameter the effect of strain hardening is severe on contact parameters. With the increase in strain hardening the resistance to deformation of a material is increased and the material becomes capable of carrying higher amount of load in a smaller contact area.

**Keywords:** Elastic-plastic contact, Strain hardening, Sphere against flat, ANSYS.

### 1. INTRODUCTION

Surface interactions are dependent on the contacting materials and the shape of the surface. The shape of the surface of an engineering material is a function of both its production process and the nature of the parent material. When studied carefully on a very fine scale, all solid surfaces are found to be rough. So when two such surfaces are pressed together under loading only the peaks or the asperities of the surface are in contact and the real area of contact is only a fraction of the apparent area of contact. In such conditions the pressure in those contact spots are extremely high. Accurate calculation of contact area and contact load are of immense importance in the field of tribology and leads to an improved understanding of friction, wear, and thermal and electrical conductance between surfaces. But it is a difficult task as rough surfaces consist of asperities having different radius and height. The problem is simplified when Hertz [1] provides the contact analysis of two elastic solids with geometries defined by quadratic surfaces. From then the assumption of surfaces having asperities of spherical shape is adopted to simplify the contact problems and the elastic plastic contact of a sphere and flat becomes a fundamental problem in contact mechanics. Greenwood and Williamson [2] used the Hertz theory and proposed an

asperity based elastic model where asperity heights follow a Gaussian distribution. The first plastic model was introduced by Abbot and Firestone [3] which neglects volume conservation of the plastically deformed sphere. The first model of elasto-plastic contact was proposed by Chang et al. [4]. In CEB model the sphere remains in elastic contact until a critical interference is reached, above which the volume conservation of the sphere tip is imposed. The CEB model suffers from a discontinuity in the contact load as well as in the first derivative of both the contact load and the contact area at the transition from elastic to elastic-plastic region. Later Evseev [5], Chang [6] and Zhao et al. [7] have made attempt to improve the elasto-plastic contact model.

Kogut and Etsion [8] (KE Model) first provide an accurate result of elasto-plastic contact of a hemisphere and a rigid flat. Kogut and Etsion used a finite element method to study the evaluation of the plastic zone in elastic-plastic contact between a sphere and rigid flat under frictionless contact condition. They study it for a wide range of material properties and sphere size and provide generalized empirical relations for contact area and contact force in terms of dimensionless contact interference for elastic, elastic-plastic and fully plastic region. They also studied their model for tangent modulus up to 0.1E and found negligible effect of it's in the contact parameters. Similar analysis has been done

by Jackson and Green [9] (JG Model). In JG model they incorporated variation of material property (e.g. Hardness) on deformed geometry and presented some empirical relations of contact area and contact load. Kogut and Etsion [10] developed a statistical contact model based on the results of KE model [8]. Jackson and Green [11] have also done similar reaserch. Quicksall et al. [12] used finite element technique to model the elasto-plastic deformation of a hemisphere in contact with a rigid flat for various materials such as aluminum, bronze, copper, titanium and malleable cast iron. They also studied the contact parameters for a generic material in which the elastic modulus and poisson's ratio were independently varied with the yield strength held constant and all the results are compared with the results of KE and JG Model. Brizmer et al. [13] have done elastic-plastic contact analysis between a sphere and rigid flat under perfect slip and full stick conditions for a wide range of material properties using FEM. According to the literature review contact analysis of a deformable sphere with a rigid flat using FEM has done by several researchers and some of these studies consider the effect of material properties. But the effect of strain hardening on contact of deformable sphere and rigid flat in a detailed way is still missing. The present work aims to study the effect of strain hardening for single asperity contact for different values of hardening parameter which is related to the tangent modulus.

## 2. FINITE ELEMENT FORMULATION

The contact of a deformable hemisphere and a rigid flat is shown in figure 1 where the solid and dashed lines represent the situation before and after contact respectively of the sphere of radius  $R$ . The figure also shows the interference ( $\omega$ ) and contact radius ( $a$ ) corresponding to a contact load ( $P$ ). The contact of deformable sphere with a rigid flat is modeled using finite element software ANSYS 10.0. Due to the advantage of simulation of axi-symmetric problems the model is reduced to a quarter circle with a straight line at its top.

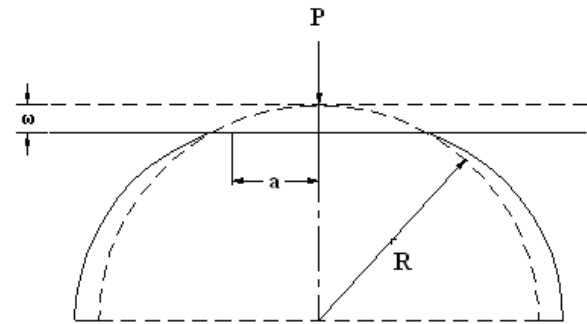


Fig 1. A deformable sphere pressed by a rigid flat.

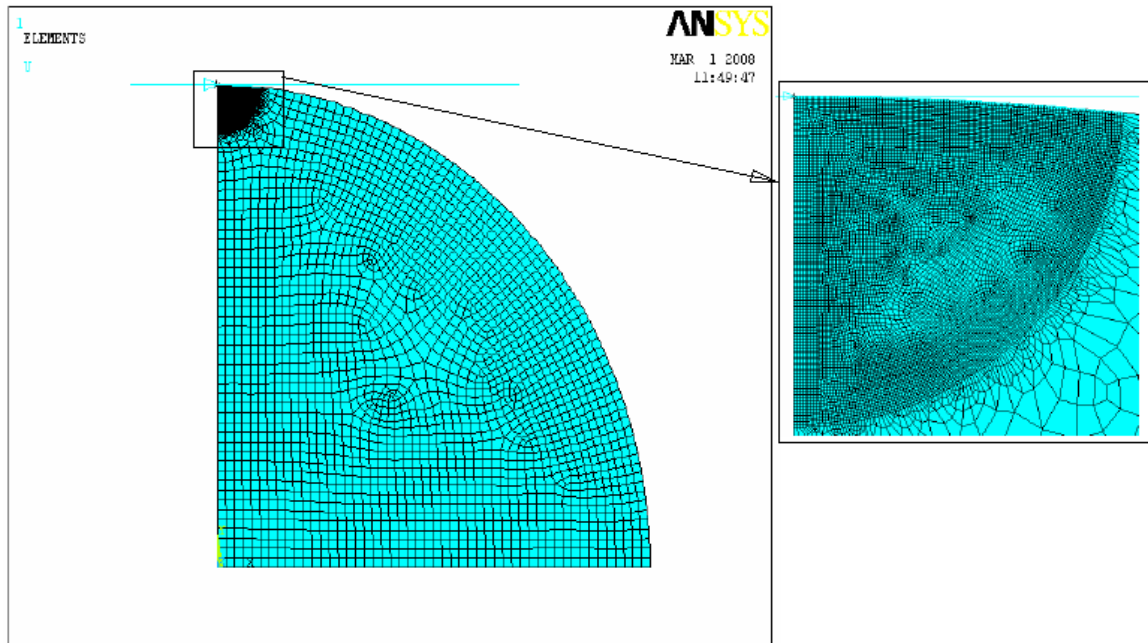


Fig 2. Meshed model of the hemispherical contact

The quarter circle is divided into two different zone, e.g., zone I and zone II. Here zone I is within  $0.1R$  distance from the sphere tip and zone II is the remaining region of the circle outside zone I. these two zones are significant according to their mesh density. The mesh

density of zone I is high enough for the accurate calculation of the contact area of the sphere under deformation. Zone II has a coarser mesh as this zone is far away from the contact zone. The meshed model is shown in figure 2. The resulting mesh consists of 12986

no of PLANE82 and 112 no of CONTA172 elements. Here the arc of the circle represents the deformable contact surface and the straight line is the rigid flat.

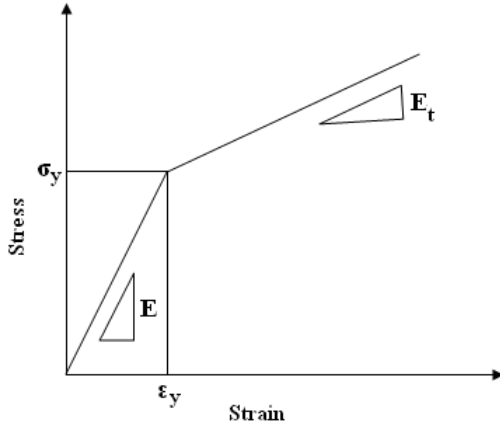


Fig 3. Stress-strain diagram for a material having bilinear isotropic properties

The nodes lying on the axis of symmetry of the hemisphere are restricted to move in the radial direction. Also the nodes in the bottom of the hemisphere are restricted in the in the axial direction due to symmetry. The sphere size is used for this analysis is  $R = 0.01$  mt. the material properties used here are Young's Modulus ( $E$ ) = 70 GPa, Poission's Ratio ( $\nu$ ) = 0.3 and Yeild stress ( $\sigma_y$ ) = 100 MPa. Here a frictionless rigid-deformable contact analysis is performed. In this analysis a bilinear material property, as shown in figure 3, is provided for the deformable hemisphere. To study the strain hardening effect we have taken different values of tangent modulus ( $E_t$ ). The Tangent Modulus ( $E_t$ ) is varied according to a parameter which is known as Hardening parameter and defined as,  $H = \frac{E_t}{E - E_t}$ . The

value of  $H$  is taken in the range  $0 \leq H \leq 0.5$  as most of the practical materials falls in this range. The value of  $H$  equals to zero indicates elastic perfectly plastic material ( $E_t$ ) behavior which is an idealized material behavior. The hardening parameters used for this analysis and their corresponding values are shown in Table 1. The wide range of values of tangent modulus is taken to make a fair idea of the effect of strain hardening effect in single asperity contact analysis. The solution type is chosen as large deformation static analysis. Here we have applied displacement on the target surface and the force on the hemisphere is found from the reaction solution. As this is an axi-symmetric analysis the force is calculated on a full scale basis. The radius of contact area is found from the last activated node for a particular analysis. In our analysis we have validated our mesh configuration by iteratively increasing the mesh density. The mesh density is increased by 1% until the contact force and contact area is differed by less than 1% between the iterations. In addition to the mesh

convergence the model also compared with the Hertz elastic solution. The results of contact load are differed by maximum 3% and contact radius by not more than 5% below the critical interference.

Table 1: Different H and  $E_t$  values used for the study of strain hardening effect

H	$E_t$ in %E	$E_t$ (GPa)
0	0.0	0.0
0.1	9.0	6.3
0.2	16.7	11.7
0.3	23.0	16.1
0.4	28.6	20.0
0.5	33.0	23.1

### 3. RESULTS AND DISCUSSION

As discussed earlier the strain hardening effect is studied by varying the hardening parameter which in turn changes the value of tangent modulus while other material properties are kept constant. The model is validated by comparing the results for elastic perfectly plastic material condition, i.e. for  $H = 0$ , with the results of KE model [8]. The results are normalized according to the following normalization scheme. Interference is normalized by the critical interference, provided by Chang et al. [4]. The critical interference is defined as,

$$\omega_c = \left( \frac{\pi K S}{2 E^*} \right)^2 R$$

where,  $K$  is the hardness coefficient [ $K = 0.454 + 0.41\nu$ ],  $S$  is the hardness of the material, according to Tabor [14]  $S$  is related to yield strength by  $S = 2.8\sigma_y$  and  $E^*$  is the equivalent young's Modulus,  $E^* = E/(1-\nu^2)$  in this case [ $E$  is the young modulus and  $\nu$  is the poisson's ratio of the deformable body]. The contact load is normalized according to critical contact load, i.e., load corresponding to critical interference and written as,

$$P_c = \frac{4}{3} E^* R^{1/2} \omega_c^{3/2}$$

The contact area is normalized according to critical contact area, i.e., area corresponding to critical interference and written as,

$$A_c = \pi R \omega_c$$

The results for elastic perfectly plastic material behavior are compared with the results of Kogut and Etsion. The calculated contact areas are exactly matched in the elastic and certain portion of the elastic plastic region and we found a maximum of 1% difference with the results KE model. In case of load vs. displacement we found there is a maximum of 3% difference with the results of KE model. Figure 4 and 5 shows the comparison of the

load-interference and contact area-interference for the present case and the KE model.

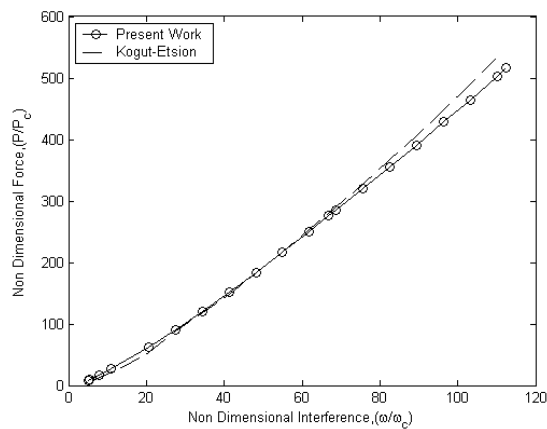


Fig 4. Plot of contact load vs. interference for elastic perfectly plastic material

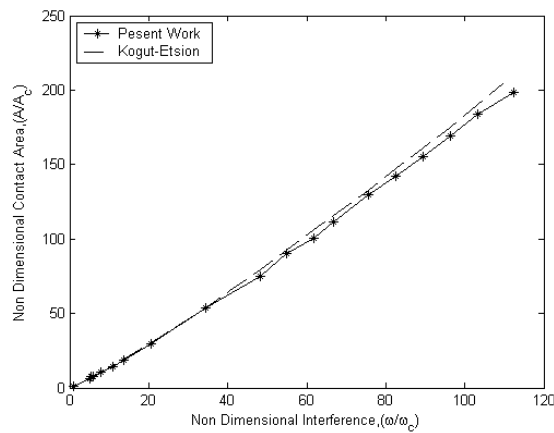
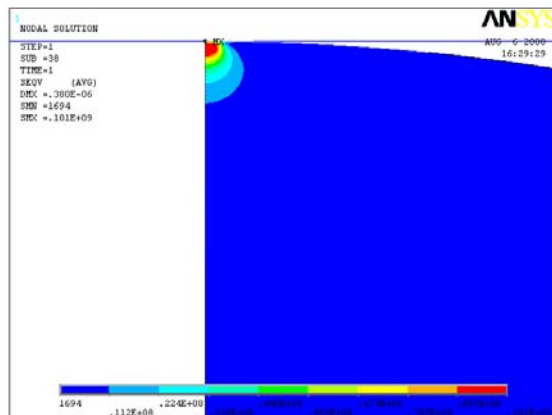
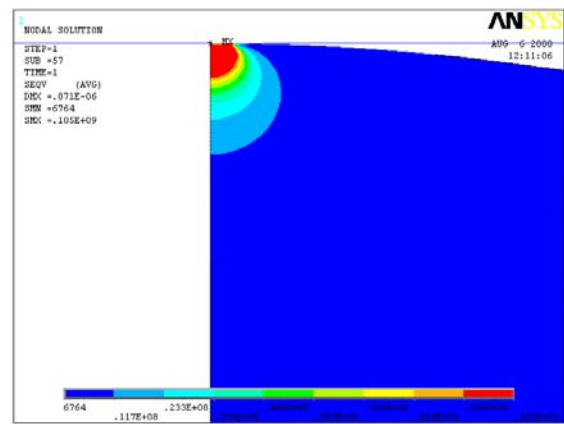


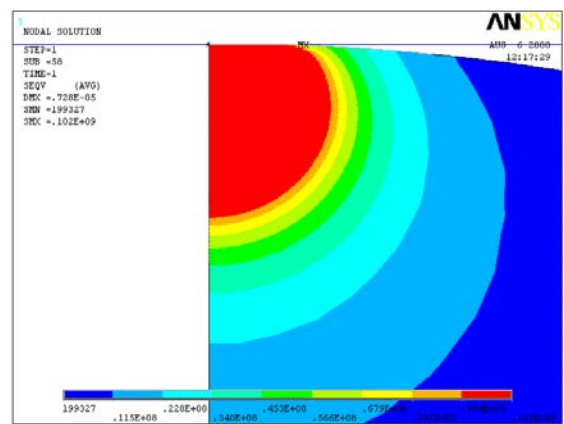
Fig 5. Plot of contact area vs. interference for elastic perfectly plastic material.



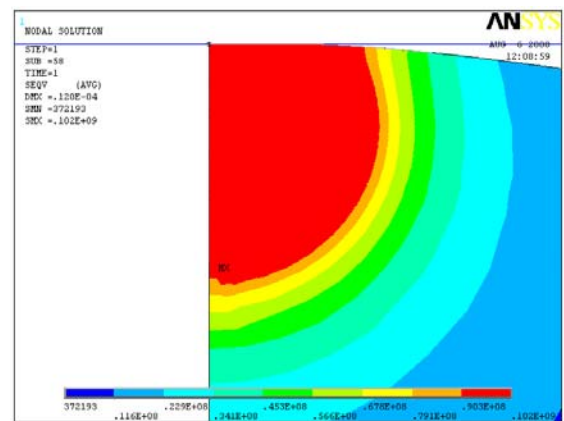
(a)



(b)



(c)



(d)

Fig 6. Plot of von-mises stress for (a)  $\omega = \omega_c$ , (b)  $\omega = 6\omega_c$ , (c)  $\omega = 68\omega_c$  and (d)  $\omega = 110\omega_c$

The possible reason of this differences in the results is may be due to the fact that Kogut and Etsion have done this analysis for a large no of sphere radius in the range of  $0.1 \leq R \leq 10$  (mm.) as well as for a large no of material

properties in the range  $100 \leq (E/\sigma_y) \leq 1000$  and they also found differences in their results up to 3%. Among all those results they provided the generalized one. Here we are representing the different contact conditions at different interference by means of stress contours of the deformed asperity. We found slightly higher values of interferences for the initiation of plastic and fully plastic deformation and as the differences are marginal, can be neglected. Von mises yield criterion is used to find the initiation of plastic deformation and fully plastic region is found when the mean pressure reaches the hardness value. The contour plots of von mises stress for different interference values are shown in figure 6.

The effect of strain hardening effect in single asperity contact is studied for materials having different values of tangent modulus with the other material properties are taken as constant. Here we have studied it for an applied interference range of  $10\omega_c \leq \omega \leq 200\omega_c$ . Figure 7 shows the variation of contact load at different interference for materials having different values of tangent modulus. The plot shows a non linear behavior in between the load and interference as the results are in the elasto-plastic and fully plastic region. Similar non linear behavior is found in between contact area and interference which is shown in figure 8. These plots show that up to a certain value of non-dimensional interference ( $\omega/\omega_c = 10$ ) the effect of strain hardening on contact parameters become negligible. Here we found below this value the variations of results are in the range of 2-5% from that of elastic perfectly plastic material behavior. But a significant effect of strain hardening on contact parameters for higher interference values is found. It is also found that a small amount of stain hardening (with in 2% of  $E$ ) helps in convergence of the solution and the results are quite close to the results of elastic perfectly plastic case. The variation of hardening parameters shows that for a small hardening parameter  $H = 0.1$  the results of load and contact area varies 3-15% and 5-17% respectively from the results of elastic perfectly plastic case with in the elasto-plastic region, i.e.  $10\omega_c \leq \omega \leq 110\omega_c$ . For fully plastic region, i.e.,  $\omega > \omega_c$  these variations are quite high and increase monotonically with the increase in interference. While for the large hardening parameter  $H = 0.5$  the variation in load and area are in the range of 11-52% and 5-33% respectively from that of elastic perfectly plastic case in the elasto-plastic region. In fully plastic region these variations are significantly high and increase monotonically with the increase in interference.

Figure 7 also shows that with the increase in tangent modulus value the contact load increases at a particular interference value. This clearly indicates that the resistance to deformation of a material increases with the increase in tangent modulus value. Figure 9 shows the variation of contact area at different applied load for materials having different values of tangent modulus. The figure shows a non linear behavior in between contact area and contact force. Here it is observed that the contact area decrease at a particular load for a material having higher tangent modulus value than that of a material having lower one. This indicates that with

the increase in the effect of strain hardening the material can support the same applied load in a smaller contact area.

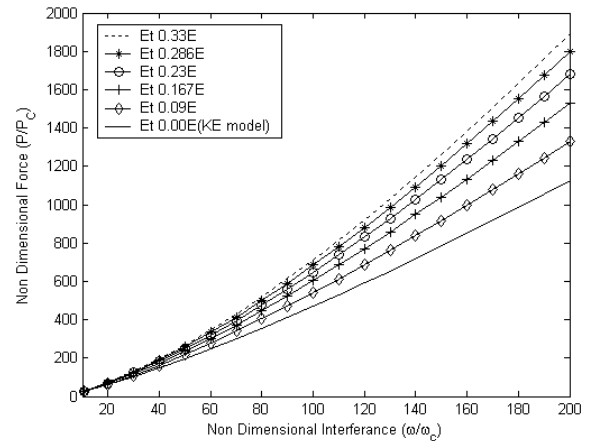


Fig 7. Plot of Contact Load vs. interference for materials having various  $E_t$  values.

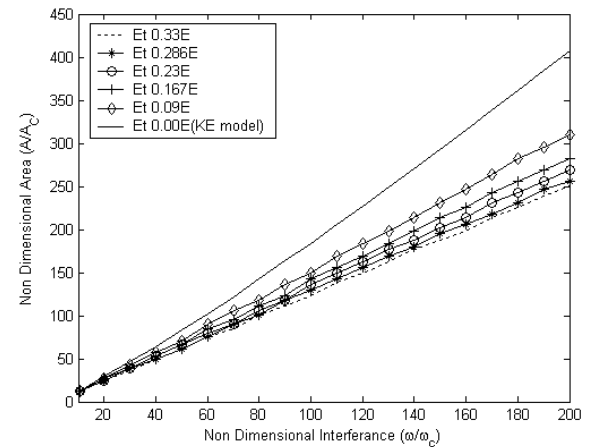


Fig 8. Plot of Contact Area vs. Interference for materials having different  $E_t$  values.

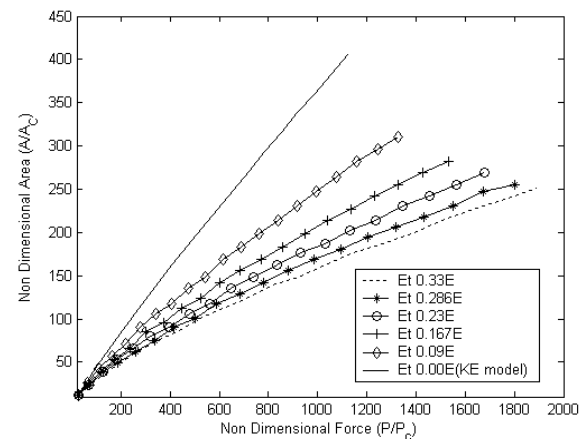


Fig 9. Plot of Contact Area vs. Force for materials having different  $E_t$  values.



#### 4. CONCLUSIONS

The result of strain hardening effect clearly shows that a generalized solution can not be applicable for all kind of materials as the effect of strain hardening greatly influenced the contact parameters. With the increase in the value of hardening parameter this effect also increases. Thus for a particular material this parameter should be taken care appropriately to get the accurate prediction of contact load and contact area. It is also observed that a small amount of strain hardening improves the solution convergence. It is noticed that in the elasto-plastic region up to a certain interference value ( $\omega = 10_c$ ) strain hardening have negligible effect on the contact parameters. If we assume that the material has very low hardening parameter, i.e.  $H \leq 0.1$ , the effect of its quite small and can be neglected with marginal error in the elasto-plastic region but a significant effect of its is found in fully plastic region that can not be neglected. For higher value of hardening parameter the effect of strain hardening is severe on contact parameters. With the increase in strain hardening the resistance to deformation of a material is increased and the material becomes capable of carrying higher amount of load in a smaller contact area.

#### 5. REFERENCES

1. Hertz, H., 1882, "Über die Berührung fester elastischer Körper", *J. Reine und Angewandte Mathematik*, 92:156-171.
2. Greenwood, J. A. and Williamson, J. B. P., 1966, "Contact of nominally flat surfaces", *Proc. Roy. Soc. London, A* 295:300-319.
3. Abbott, E. J. and Firestone, F. A., 1933, "Specifying surface quality - a method based on accurate measurement and comparison", *ASME J. Mech. Engg.*, 55:569-572.
4. Chang, W. R., Etsion, I. and Bogy, D. B., 1987, "An elastic-plastic model for the contact of rough surfaces", *ASME J. Tribol.*, 109:257-263.
5. Evseev, D. G., Medvedev, B. M. and Grigoriyan, G. G., 1991, "Modification of the elastic-plastic model for the contact of rough surfaces", *Wear*, 150:79-88.
6. Chang, W. R., 1997, "An elastic-plastic contact model for a rough surface with an ion-plated soft metallic coating", *Wear*, 212:229-237.
7. Zhao, Y., Maietta, D. M. and Chang, L., 2000, "An asperity micro-contact model incorporating the transition from elastic deformation to fully plastic flow", *ASME J. Tribol.*, 122:86-93.
8. Kogut, L. and Etsion, I., 2002, "Elastic-plastic contact analysis of a sphere and a rigid flat", *ASME J. Appl. Mech.*, 69:657-662.
9. Jackson, R. L. and Green, I., 2005, "A finite element study of elasto-plastic hemispherical contact against a rigid flat", *ASME J. Tribol.*, 127:343-354.
10. Kogut, L. and Etsion, I., 2003, "A finite element based elastic-plastic model for the contact of rough surfaces", *ASME J. Tribol.*, 46:383-390.
11. Jackson, R. L. and Green, I., 2006, "A statistical model of elasto-plastic asperity contact of rough surfaces", *Tribol. International*, 39:906-614.
12. Quicksall, J. J., Jackson, R. L. and Green, I., 2004, "Elasto-plastic hemispherical contact models for various mechanical properties", *Proc. Instn. Mech. Engrs., Part J: J. Engg. Tribol.*, 218:313-322.
13. Brizmer, V., Kligerman, Y. and Etsion, I., 2006, "The effect of contact conditions and material properties on the elasticity terminus of a spherical contact", *Int. J. Solids Struct.*, 43:5736-5749.
14. Tabor, D., 1951, *The Hardness of Metals*, Clarendon Press, Oxford.

#### 6. MAILING ADDRESS:

Biplab Chatterjee  
Department of Mechanical Engineering,  
Jadavpur University, Kolkata, India  
E-mail: psjume@gmail.com

## COMPARATIVE PERFORMANCE AND VERIFICATION STUDY OF SIMPLIFIED SPOT WELD MODELS

K. N. Ahsan Noman<sup>1</sup>, Monir Takla<sup>1</sup>, Thomas Ting<sup>2</sup>, Daniel Belton<sup>3</sup>

<sup>1</sup> School of Aerospace, Mechanical and Manufacturing Engineering,  
RMIT University, Melbourne, Australia

<sup>2</sup> Cooperative Research Centre for Advanced Automotive Technology (AUTOCRC), Australia

<sup>3</sup> Holden Innovation Ltd, Australia.

### ABSTRACT

A simple representation for spot weld joints is desirable for crashworthiness assessment of complicated and huge automotive body in white structures which generally contains thousands of spot weld joints. Hence, in this paper six different individual new spot weld joint finite element models simplified in terms of their geometric and constitutive representations were developed including the one that is currently used in automotive industries. The stiffness characteristics of these developed models were compared with the experimental results obtained following a simple strategy to design the welded joint based on the desired mode of nugget pull out failure. It was found that the current spot weld modeling practice in automotive industry under predict the maximum joint strength nearly by 50% for different loading conditions. The comparative study was related with the computational cost incurred by the developed effective models in different loading conditions. Hence, a suitable model for spot welded joints is established which is very simple to develop but relatively cheap in terms of computational costs.

**Keywords:** Spot weld, Non-linear finite element analysis, Experimental verification.

### 1. INTRODUCTION

Spot welding is the most common joining process for automotive body-in-white structures due to its production convenience and cost effectiveness. Generally most of the automotive components are designed and tested in a virtual design environment by using finite element analysis which requires the correct representation of the physical body. Spot welds used for joining purposes behave like an individual identity which affects the value of empirical relationships like structural effectiveness, which is proposed by Schneider and Jones [1]. Hence it necessitates accurate representation of the spot weld joints in finite element models.

The simplest and widely used model to represent the spot weld itself is the coincident nodes or two point rigid beam element [2]. Sheppard [3] had modified the idea of using a single rigid beam element, by utilizing a number of rigid beams to represent the spot weld joint. Similarly Xu and Deng [4] have used several numbers of rigid beams (increased with the level of mesh refinements around the nugget) and different arrangement patterns to represent the spot weld nugget. Recently S. Dincer et al. [5] had reported that the spot weld model with nine rigid elements around the nugget provided the best result for fatigue life testing. But proper design criterion for non linear analysis such as crashworthiness assessment of simplified spot welds models with direct experimental verification is not properly achieved yet. Besides the issue of computational efficiency in these analyses were

not addressed in any of the previous studies. Therefore, realistic spot weld models simplified in terms of their geometric representation for mechanical design engineering point of view and constitutive relationship are developed and experimentally verified in this study. Performance of these models will be studied for their load bearing capabilities and compared for computational efficiency. Generally the quality of spot welds is tested by destructive testing methods [6-8]. For these destructive tests single spot weld on test coupons are used. Hence to compare and judge the performances of different developed spot weld models a simple test coupon configuration is chosen for both the experimental and numerical analysis schemes presented in this paper.

### 2. EXPERIMENTAL ANALYSIS

#### 2.1 Materials

In this research a cold rolled ductile sheet metal with general purpose surface finish was used for making the spot welded test coupons. The chemical composition of the selected material is given in Table – 1. The mechanical material property characterization was carried out by uniaxial tensile tests in a preloaded ball screw driven Instron machine. These characteristic results have been used as input material parameters in the developed finite element models. Dog bone specimens were prepared according to the specifications provided by ISO 6892 [9]. The thickness of the tensile test specimens was same as spot welded coupon thickness

(1.2 mm). Three specimens were tested for each of the test speed configurations of 500 mm / min, 100 mm / min, 20 mm / min and 5 mm / min. Different loading rates were chosen to ensure correct repeatable quantification process by observing the gradual incremental changes in the stress strain relationship. The average true stress strain tensile properties were calculated from the force displacement relationship and are presented in Figure –1.

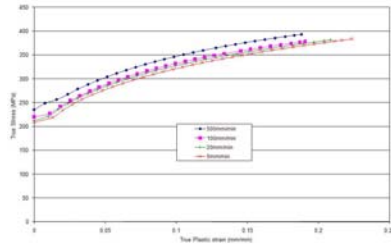


Fig 1. True stress strain curve of sheet metal

For the spot welding process a spot welding machine with rated configuration of 7.5 KVA, 18 amps with a supply voltage of 415V – 50Hz was used. The welding current was set to the maximum available level in this machine for a welding period of 50 cycles (1.0 second) and for a squeeze time of 70 cycles (1.4 seconds) for each of the fabricated test sample joints. The variations of the joint dimensions with the manufacturing process variables were not considered in this study. But failure mode based desirable spot weld nugget diameter was calculated. Thereafter it was cross checked whether the utilized manufacturing process parameters could obtain the previously calculated dimension. These are presented in the following sections.

## 2.2 Spot Weld Joint Tests

The spot welded coupons were tested in universal tensile testing machine. For each testing configurations 5 samples were tested. The shear loading condition was tested using a lap shear coupon. The bending and tensile loading conditions were tested by L shaped coach peel coupon and U shaped u tension coupons respectively. The lap shear and coach peel coupons were gripped directly by the testing machine jaws. The u tension test was performed utilizing special designed grip consisting of coupon holders and supporting side cushions plates. All experiments were conducted in displacement controlled mode. The displacement was recorded from the cross head displacement of the testing machine. As a force transducer a 50kN load cell was used to obtain the applied load data for these tests. AWS [10] recommended conducting such experimental tests below the speed of 20 mm/min test speed was chosen for experimental investigation. For each testing speed configurations five specimens were used to represent the repetitive nature of the test results.

Proper geometric dimensions of the test coupon may influence the testing of the spot welded joint. Zhou [11] reported that the width of the test coupon is the most influential dimension. Wung et al. [12] has determined the critical width dimension (to avoid distinctive variations) experimentally to be at least more than 35 mm. So for the present study the overall width of all the coupons was chosen as 50.8 mm. The spot weld nugget joint on the test coupon was designed based on the mode

of failure. In case of destructive testing procedures with the spot welded coupons, two distinctive desirable failure modes are observed [13]. They are “Nugget pull out failure” mode where the failure occurs around the spot weld nugget in the coupon sheet metal and it separates completely from the test coupon and “Interfacial failure” mode where the failure occurs inside the spot weld nugget only and breaking it apart without damaging the test coupon. Chao [13] studied both the failure modes and proposed an equation to predict the critical nugget diameter (d) for the transition of the spot weld failure mode from the “interfacial failure” to “nugget pull out failure” as a function of sheet metal thickness (t) as follows.

$$d_{cr} = 8.41t^{4/3} \quad (1)$$

The spot weld nugget diameter (recommended, minimum and nominal) can also be calculated using the following empirical equations found in different standards [13, 14].

$$d = 4\sqrt{t} \quad (2)$$

$$d = 0.89(1.05t - 0.007)^{1/2} \quad (3)$$

$$d = 0.88(1.05t - 0.007)^{1/2} \quad (4)$$

Apart from all of the above equations, VandenBossche [15] introduced material properties (yield strength,  $S_{YPM}$ ) and physical dimensions of the test coupon (width, w) other than the sheet thickness (t). This expression is given as follows.

$$\frac{d}{t} = \left( 0.34 \frac{S_{YPM}}{1.34S_{YPM} + 372 t} \frac{w}{t} \right)^{1/2} + 3.0 \quad (5)$$

The experiments in this study were designed with the target sheet metal thickness of 1.2 mm as it was either the exact or the median value of the reported previous researches [13-15]. The average thickness dimension (1.19 mm) of the prepared test coupons were used to calculate the preferred spot weld nugget diameter. According to the above mentioned equation numbers the results of these calculations are 4.3 mm, 4.36 mm, 4.57 mm, 5.79 and 6.05mm. The welding schedule was set to obtain the maximum possible spot weld nugget due to conservative engineering practice. The obtained spot weld nugget diameter of the prepared samples was checked by measuring hardness distribution along the spot welded surfaces. The hardness testing procedure is presented in the following section.

## 2.3 Hardness Measurement

After spot welded the test coupons diameter of the nugget was checked by utilizing hardness testing method. The Vickers hardness testing was performed with Future Tech Hardness Tester (Model FV – 700). The applied force level (5 kgf) for hardness measurement was determined by using a four point calibration procedure in both the hardest (spot weld nugget) and the softest (base metal) parts of the test samples. The HAZ was kept out of this calibration consideration due to variable hardness values in the region. A number of spot welded joints were tested starting from the nugget centre towards various radial directions. The averaged and linearized hardness distribution results (Figure-2) revealed the nugget dimensions to be near about 4.5 mm in diameter which is greater than both the critical and recommended nugget diameter dimensions as mentioned previously. This

nugget diameter dimension will be used for the numerical modeling which is presented in the next section.

### 3. NUMERICAL ANALYSIS

#### 3.1 Finite Element Models

Fig 3 presents the developed finite element models to characterize spot weld strength and to predict the nugget pull out type of failure for the joint as it is the desired mode of failure for the spot weld joint [14, 16].

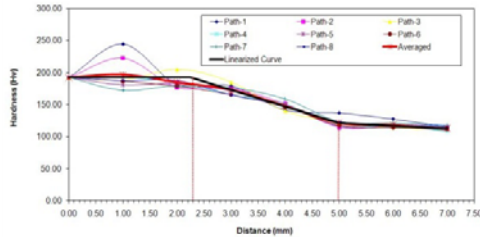


Fig 2: Hardness distribution along the radial directions of manufactured spot weld joints.

The geometric dimensions used for the developed full model were identical to the experimental test coupon and the spot weld nugget (4.5 mm conformed from hardness testing results) dimensions. The test coupons are modeled with homogeneous isotropic material properties determined experimentally from uniaxial tensile tests to implement Mises plasticity based constitutive model. This homogenous material model did not include the strength gradient of the heat affected zone around the spot weld nugget. It should be noted here that recently Wang *et al.* [17] has considered the HAZ properties in spot weld modeling with some assumptions which are scaled values of the base metal stress strain curve. Kong *et al.* [18] modeled the HAZ material properties using inverse finite element modeling and incorporated in the spot welded joint model. But this will be difficult to be incorporated in large scale CAE models. However analysis of heat affected zones in spot welds by Mignone [19] combining indentation technique and FE study reported that additional material zone representation in spot weld joint FE model follows the law of diminishing returns as its gain is small. Therefore homogenous material property was used to make the developed models as simple as possible so that they can be easily replicated in large automotive assembly system which may contain few thousands of spot welds [20]. Therefore one of the intentions of this study is to evaluate the achievable accuracy level with simplified spot weld models. Wung *et al.* [12, 21] reported that the spot weld nugget itself does not face any metallurgical changes after complete failure. Hence the nugget can be modeled with rigid elements. The only exception in this study was the solid nugget model in which case the nugget was modeled with the same material property as the coupon sheet metal.

There are six individual spot weld models developed for this comparative strength and performance study. The Individual Rigid Beam model (IRB) is the most widely used spot weld model for body in white structures [2] represented by a connection between two points through single rigid beam element. Parallel Multiple Rigid Beam (PMRB) spot weld model is a modification of the IRB model by physically representing the spot weld nugget

diameter utilizing several rigid beams (16 elements) along its circumference. In case of the Solid Element Model (SEM) the spot weld nugget is represented by three dimensional solid elements joined with shell elements representing the coupon sheet metal. For Spider Configuration (SC) models the spot welded joint is represented by spider patterns as presented in Figure – 3.

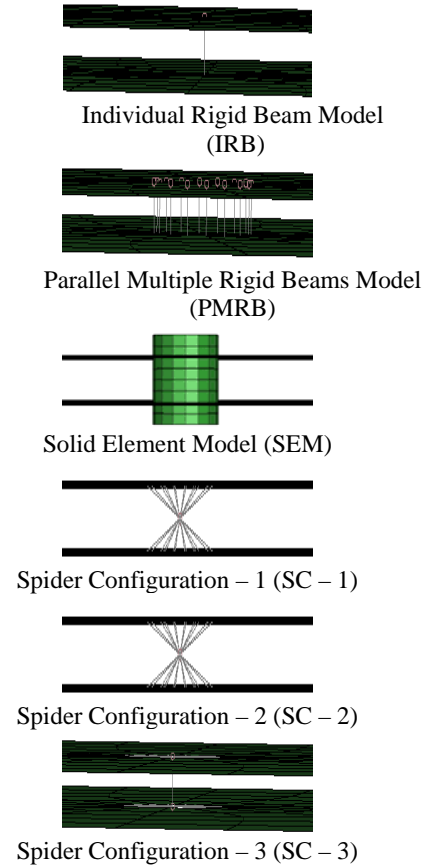


Fig 3: Simplified spot weld joint models.

In SC – 1 the nugget diameter region is represented by rigid shell elements. However in SC – 2 the diameter region is completely hollow and in SC – 3 this hollow region is filled up with rigid beam elements. The boundary conditions were imposed on the full spot welded coupon model to simulate the actual gripping situations of the tests. One end of the coupons was restricted for all the degrees of freedom. On the other end displacement boundary conditions were used to apply the load. The choice of the elements for these simulations is presented in the next section.

#### 3.1 Mesh Verification

In this study the coupons were modeled with quadrilateral linear 3D shell elements with reduced integration scheme because the thickness to length ratio for the chosen dimension was very low. These elements were arranged along the circumference of the nugget region to represent the exact diameter dimension measured in the experiments. Due to stress concentration in the overlap region near the nugget boundary, it was identified as the critical area of the coupons. Therefore five different mesh configurations around the spot weld nugget were studied to identify the most suitable mesh.

These meshes (in bracket the number of elements around the nugget) are Mesh – A (8 elements), Mesh – B (16 elements), Mesh – C (32 elements), Mesh – D (32 elements) and Mesh – E (32 elements). The number of elements in the length and the width directions of the test coupon did not vary for the first two mesh types. But for the rest of the three designs (Mesh C, D and E), a gradual finer mesh with more elements both in the width and length directions were used. To choose a particular mesh design, a relative error study was performed with one of the spot weld models for all the loading conditions. The Spider Configuration – 3 (SC – 3) model was chosen for this purpose because this was one of the spot weld models which represented a complete rigid spot weld nugget. For relative error study the maximum force values attained by the spot weld joints (as observed from the presented averaged experimental curves) for the different loading conditions were utilized using the following Equation 6

$$\% RE = [(EFV - SFV) / EFV] \times 100 \quad (5.1) \quad (6)$$

where RE = Relative Error, EFV = Experimental Force Value and SFV = Simulation Force Value. These results are presented in Table 2. The average error values presented in the table is the arithmetic average of all the relative errors in the considered loading situations. It was evident from these relative error studies that Mesh – A had a better performance in the tensile loading situation. Mesh – B had better performance for the bending loading situation and Mesh – C was better for the shear loading situation. But on the basis of the average error values Mesh – B had the best performance among the designed mesh configurations. Hence Mesh – B (16 elements around the nugget) configuration was chosen to conduct all the numerical analyses for this study and presented in next section.

## 4. Result and Discussion

### 4.1 Deformation Patterns

The failure patterns of the spot welded joints were critically observed. In spite of different loading conditions, all the test coupons spot welded according to the aforementioned simple design strategy failed in nugget pull out mode. Figure 4 presents the deformation patterns for the lap shear, coach peel and U tension coupons. The nugget came out of the joint system completely leaving a clear mark of degradation in the coupon material.

### 4.2 FE Model Verification and Strength Prediction

The force displacement diagrams are the major results obtained from the conducted experiments. They represent the load bearing capabilities of the spot welded joints. The resulting force displacement performances of the developed spot weld models were compared with the experimental results to validate and to evaluate the responses of the developed FE models. These force displacement curves were analysed from a global perspective as both the force and displacement data were obtained from one end of the coupon (the load application point) for both the experiments and simulations. An average force displacement curve from the five identical test coupons were obtained for the

specific loading rate at the averaged force value for a certain displacement position in equal intervals. The averaged experimental force displacement curves along with the simulated response (force displacement) curves for different developed spot weld models are presented in Figure 5.

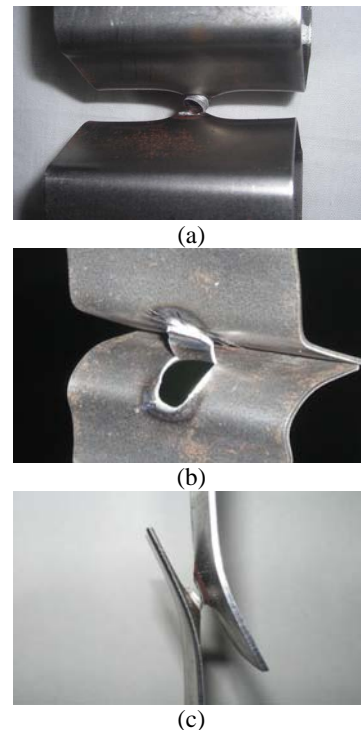


Fig 4. Failed spot weld joint connection. (a) U tension coupon. (b) Coach peel coupon (c) Lap shear coupon

Initially the force displacement response from five developed models (Parallel Multiple Rigid Beams, Spider Configuration - 1, Spider Configuration - 2, Spider Configuration - 3 and Solid Element Model) followed quite similar trend as the average experimental curves. The increment trend of the force level is also quite similar. It gradually increased to represent the maximum load bearing characteristics. It can be clearly seen that the developed five models are behaving closely according to the expected outcome of the experimental investigations even though the strength gradient for the heat affected zone are not included in these models. But the force displacement response obtained in case of the individual rigid beam (IRB) model which happens to be the current trend in automotive industry for modelling spot weld joint, showed an early collapse situation. The reason behind this kind of early collapse response (caused by the local buckling) is due to the way of making the connection between the top sheet and the bottom sheet of the test coupon configurations. For the IRB model the connection was made from one point to another point only. Hence this connection actually did not represent the diameter of the actual spot weld. So it did not represent the actual stiffness of a single spot weld as observed from the experimental force displacement response. Hence the force displacement response from the IRB model could not follow the average experimental force displacement curve in any of the above described



different stages (IDS and LWS) for all the loading conditions. Hence, IRB model predicts the maximum force level for spot weld joints with error level of 67.77%, 50.58% and 45.33% for shear, bending and tensile loading conditions respectively.

### 4.3 Comparative Computational Performance

The comparison of results through the characteristics responses (force displacement curve) verifies the model performances with respect to the accuracy from mechanics point of view. To clarify the complete performances of the developed spot weld models, the computational costs occurring for each model should also be considered. The computational cost is defined here as the CPU time which is the total approximate computation time required by the FE code for completing the analysis. Other than the CPU time two other parameters were considered for the comparison purposes. These parameters are the "Memory Used" for the FE code to solve the problem and the "Required Disk Space" for storing the scratch files during the analysis. All the computations were performed on WINDOWS (X-86, 32 bit) based platform. The comparison results are given in Table 3. It can be observed from the data of the following table that in general the IRB model is incurring more CPU time and disk space than any other models for the implicit analysis. This is due to the fact that this model needs more equilibrium iterations to complete the analysis. Based on the discussed computational performances SC – 2 model performed best.

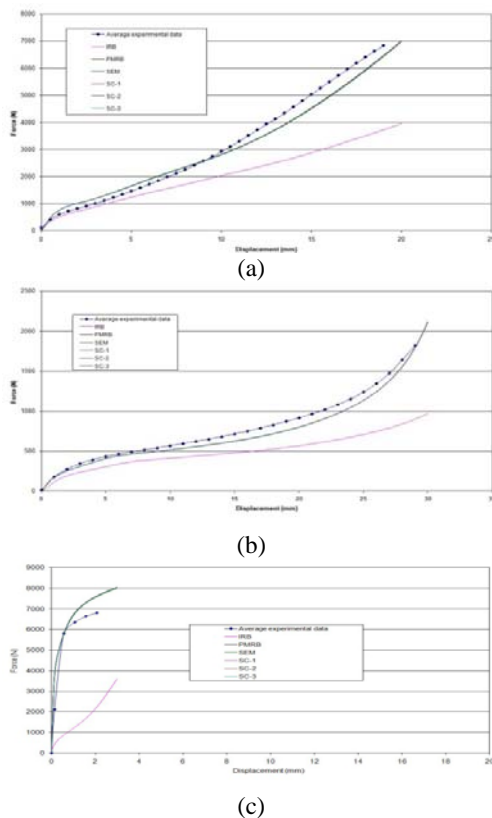


Fig 5. Force displacement response for spot welded coupons. (a) U tension coupon. (b) Coach peel coupon. (c) lap shear coupon

## 5. CONCLUSION

Six different simplified spot welded joint finite element models were developed and their performances were compared in this study. The stiffness characteristics of these models were verified through experimental analysis. A simple experimental strategy to design a spot welded joint based on its failure mode in over loaded situation is presented in this paper. The spot weld size guidance of  $d = \left( 0.34 \frac{\sigma_{max} \pi}{\sigma_{yield} \pi} \right)^{1/3} + 3.0$  by VandenBossche [11] over estimated the spot weld nugget diameter to ensure the nugget pull out failure mode. The conventional spot weld model used in crashworthiness assessment of large automotive body in white structures cannot represent the proper load bearing capability of a spot welded joint. Hence, five different simple but effective spot weld finite element models are developed and evaluated in this research. It is shown that these models can predict reasonably accurate response characteristics of the joint without considering the strength gradient of the heat affected zone in their constitutive relationship. Comparative performance evaluations of these developed simplified spot weld joint models reveal that the SC-2 model is relatively preferable.

## 6. ACKNOWLEDGEMENT

This study was supported by the Cooperative Research Centre for Advanced Automotive Technology (AUTOCRC), Australia.

## 7. REFERENCES

- Schneider, F., and Jones, N., 2003, "Influence of Spot Weld Failure on Crushing of Thin Walled Structural Sections," International Journal of Mechanical Science, 45: 2061-2081.
- Anonymus, 1994, "Optimizer Locates Welds to Stiffen Structure " Machine Design, News Trends, May: 18-19.
- Sheppard, S. D., 1993, "Estimation of Fatigue Propagation Life in Resistance Spot Welds," Advances in Fatigue Lifetime Predictive Techniques; 2nd Volume, ASTM STP, 1211: 169-185.
- Xu, S., and Deng., X., 2004, "An Evaluation of Simplified Finite Element Models for Spot-Welded Joints," Finite Elements in Analysis and Design, 40: 1175-1194.
- Dincer, S., Cinar, A., Kepenek, D. A., Asureciler, B., Duran, E. T., and Mugan, A., 2006, "A Comparative Study on the Finite Element Models for Spot Welds and Their Verification," SAE Technical Paper, 2006-01-0590.
- Zilincik, S. E., Frank, W. J. D., Monre, E., and Khan, S., 1998, "A New Approach to Evaluating Spot Welds for Automotive Durability," SAE Technical Paper, 982277.
- 1980, "Welding Handbook," American Welding Society.
- Pollard, B., 1974, "Spot Welding Characteristics of Hsla Steel for Automotive Applications," Welding Journal, Welding Research Supplement, 343s-350s.
- Iso, 1998, "Metallic Materials: Tensile Testing at Ambient Temperature".

10. A. W. S., and A. N. S. I., 2005, "Recommended Practices for Automotive Weld Quality - Resistance Spot Welding".
11. Zhou, M., H. A., and J. H. S., 1999, "Critical Specimen Sizes for Tensile Shear Tests", *Welding Journal, Welding Research Supplement*, 78: 305s-313s.
12. Wung, P., 2001, "A Force Based Failure Criterion for Spot Weld Design," *Experimental Mechanics*, 41: 107-113.
13. Chao, Y. J., 2003, "Failure Mode of Spot Welds: Interfacial Versus Pullout," *Science and Technology of Welding and Joining*, vol. 8:133-137.
14. Ewing, K. M. W., Cheresch, M., Thompson, R., and Kukuchek, P., 1982, "Static and Impact Strengths of Spot Welded Hsla and Low Carbon Steel Joints," SAE Technical Paper, 820281.
15. Vandenbossche, D. J., 1977, "Ultimate Strength and Failure Mode of Spot Welds in High Strength Steels," SAE Technical Paper, 770214.
16. Zuniga, S., and Sheppard, S. D., 1997, "Resistance Spot Weld Failure Loads and Modes in Overload Conditions".
17. Wang, J., Xia, Y., Zhou, Q., & Zhang, J. , 2006, "Simulation of Spot Weld Pullout by Modeling Failure around Nugget", SAE Technical Paper, 2006-01-0532.
18. Kong, X., Yang, Q., Li, B., Rothwell, G., English, R., and Ren, X. J., 2008 "Numerical Study of Strengths of Spot-Welded Joints of Steel," *Materials and Design*, 29: 1554-1561.
19. Mignone, P. J., 2006, "The Computational Analysis of Heat Affected Zones in Spot Welds", B. Eng. RMIT University, AUS.
20. Sawai, N. P., Ingle, R. B., Patakdar, S. K., and Mahajan, R. S., 2005, " Finite Element Modelling Strategy for Spot Welds in Thin Walled Sections and Its Verification," ASME, Orlando, Florida, USA.
21. Wung, P., 2001, "A Method for Spot Welded Structure Analysis," SAE Technical Paper, 2001-01-0427.

**8. NOMENCLATURE**

Symbol	Meaning	Unit
d	Diameter of the spot weld nugget	mm
t	Sheet thickness	mm
w	Coupon width	mm
S <sub>v</sub>	Yield strength	MPa

**9. APPENDIX**

Table 1: Chemical composition of sheet metal

Chemical properties	Carbon	Phosphorus	Manganese	Sulphur
wt %	0.04 - 0.06	0.005 - 0.02	0.2 - 0.26	0.008 - 0.02

Table 2: Relative error study for different mesh configurations

Mesh configuration	Loading situation	Maximum experimental force (N)	Simulation force value (N)	Relative error (%)	Averaged relative error
Mesh A	U tension	6827.86	6604.94	3.26	9.21
	Lap shear	6810.80	7684.74	12.8	
	Coach peel	1820.96	2031.77	11.58	
Mesh B	U tension	6827.86	6488.44	4.97	5.69
	Lap shear	6810.80	7596.06	11.50	
	Coach peel	1820.96	1831.70	0.59	
Mesh C	U tension	6827.86	5837.12	14.51	12.04
	Lap shear	6810.80	7257.70	6.55	
	Coach peel	1820.96	1546.90	15.05	
Mesh D	U tension	6827.86	5614.20	17.78	13.97
	Lap shear	6810.80	7019.50	3.05	
	Coach peel	1820.96	1437.25	21.07	
Mesh E	U tension	6827.86	5482.35	19.71	14.96
	Lap shear	6810.80	6830.05	0.28	
	Coach peel	1820.96	1367.94	24.88	

Table 3: Computational performances of different spot weld models.

Criterion / Spot weld model	U tension coupon			Lap shear coupon			Coach peel coupon		
	Required Disk Space (MB)	Total CPU time (sec)	Memory used (MB)	Required Disk Space (MB)	Total CPU time (sec)	Memory used (MB)	Required Disk Space (MB)	Total CPU time (sec)	Memory used (MB)
IRB	4.28	56.6	16.46	34.11	121.30	24.27	11.05	130.90	20.27
PMRB	4.44	63.5	16.51	33.72	108.60	24.31	10.95	126.30	20.27
SEM	6.27	88.30	16.73	25.38	117.1	21.54	12.79	149.4	18.99
SC – 1	3.92	62.90	16.47	31.45	99.2	24.36	10.10	109.60	20.30
SC – 2	3.66	53.50	16.29	20.46	88.2	20.26	9.99	93.10	18.65
SC – 3	3.70	55.0	16.32	20.59	89.8	20.594	10.02	93.60	20.12





## VARIATIONAL FORMULATION BASED POST-ELASTIC ANALYSIS OF ROTATING DISKS WITH VARYING THICKNESS

Shubhankar Bhowmick<sup>1</sup>, Dipten Misra<sup>2</sup> and Kashi Nath Saha<sup>3</sup>

<sup>1</sup>Research Scholar, Department of Mechanical Engineering, Jadavpur University, Kolkata

<sup>2,3</sup>Faculty member, Department of Mechanical Engineering, Jadavpur University, Kolkata

### ABSTRACT

Numerical solutions under plane stress conditions for elasto-plastic deformation and stress states of rotating solid disks with variable thickness have been reported. The problem is formulated through a Variational method. Assuming a series solution and using Galerkin's principle, the solution of the governing partial differential equation is obtained. The formulation is based on von Mises yield criterion and linear strain hardening material behavior. The approximate solution is obtained using an iterative method. Results are validated with benchmark solutions.

**Keywords:** Variational method, von Mises, Plastic front, Limit angular speed.

### 1. INTRODUCTION

Due to widespread applications, the analysis of rotating disk behavior has been of great interest to many researchers. Assuming linear strain hardening material behavior, Gamer [1-2] reported the elasto-plastic behavior of rotating disk of constant thickness using Tresca's yield criterion and its associated flow rule. Güven [3-4] carried out the analysis of rotating solid disk with variable thickness up to fully plastic state for linearly strain hardening material behavior. Based on both Tresca's and von-Mises yield criterion, Rees [5] investigated the elasto-plastic behavior of rotating disks of uniform thickness made of elastic-perfectly plastic material and reported the comparative results. You and Zhang [6] presented an approximate analytical solution for rotating solid disk of uniform thickness with plane stress assumption for non-linear strain hardening material behavior based on von-Mises yield criterion, deformation theory of plasticity and a polynomial stress-strain relationship. Based on similar assumptions, You et al. [7] developed a unified numerical method to report the elasto-plastic behavior of rotating disk of varying thickness made up of non-linearly strain hardening material. A unified yield criterion was proposed by Ma et al. [8] to report the plastic limit angular velocity and stress distribution in fully plastic state of rotating disks with variable thickness.

Eraslan and Orcan [9] obtained an analytical solution of elasto-plastic deformation field of rotating solid disks with exponentially varying thickness using Tresca's yield criterion and its associated flow rule for linear strain hardening material behavior. Eraslan and Orcan [10] extended the study for disks where, yielding initiates not at the centre but at an intermediate radial location.

Eraslan [11] studied the inelastic behavior of variable thickness rotating solid disks with linear strain hardening material behavior using both Tresca's and von Mises yield criterion.

Elasto-plastic behavior of rotating disks of variable thickness in power function form for both linear and non-linear strain hardening material behavior had been studied by Eraslan and Argeso [12] using von Mises yield criterion. In another research paper [13], Eraslan carried out the elasto-plastic analysis of rotating solid and annular disks with elliptical thickness variation and made of linearly hardening material using both Tresca and von-Mises criteria. The application of variational method, proposed by Bhowmick et al. [14] has yielded a generalized approach to study the behavior of rotating solid disks of variable thickness in the elastic regime. In another paper, the method has been further extended into elasto-plastic domain [15].

In the present study, a numerical method based on variational principle for elasto-plastic analysis of rotating variable thickness disks using von Mises yield criterion has been proposed. A solution algorithm has been developed to obtain an approximate solution of the unknown displacement field from the governing set of equations in an iterative manner.

### 2. MATHEMATICAL FORMULATION

The centrifugal loading on a rotating disk produces radial and tangential strain field, which in turn produces stresses. The present analysis is carried out based on the assumptions that material of the disk is isotropic and homogeneous and a state of plane stress exists in the loaded condition. Stress-strain relation of the disk is

linear elastic followed by linear strain hardening as shown in Fig. 1. In case of two-dimensional stress, the general condition of yielding based on von-Mises theory is given by,  $\sigma_1^2 - \sigma_1\sigma_2 + \sigma_2^2 = \sigma_y^2$ , where  $\sigma_y$  is the uniaxial yield stress value of the disk material and  $\sigma_{vm}$  is the von-Mises stress. At a certain speed, known as elastic limit angular speed ( $\Omega_1$ ), the stress field of the disk exceeds the yield limit value, thus giving rise to a plastic front. On further increase in rotational speed, a certain region of the disk attains post-elastic state and when this region encompasses the entire disk we get plastic limit speed or collapse speed ( $\Omega_2$ ). The present method captures the location of plastic front numerically by using an iterative method.

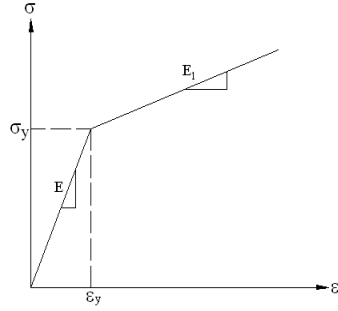


Fig 1. Linear elastic linear strain hardening material behavior.

For a uniform thickness disk the yielding initiates at the root. As a result the disks are made thicker near the hub and the thickness is reduced towards the periphery which results in variable thickness disks having higher elastic limit angular speeds. On varying the geometry it is observed that maximum stresses at elastic limit angular speed ( $\omega_l$ ) may occur at locations other than the root of the disk. Under such a situation, initiation of yielding occurs at location away from the root ( $r = r_y$ ). With increasing angular speed, the centrifugal load on the disk increases and the plastic front originated at  $r = r_y$  starts to spread in two directions; towards the root as well as the periphery. At such load increment ( $\omega = \omega_l + \Delta\omega$ ), the plastic region spans between  $r = r_i$  to  $r = r_o$ . Further load increment gives rise to two possibilities depending on the geometry parameters. Firstly the plastic region may collapse at the root before reaching the periphery or secondly the plastic region may reach the periphery before reaching the root. The angular speed at which the plastic front reaches either root or periphery is designated as  $\omega_1^i$  and  $\omega_1^o$  respectively. Additional load increments cause the disk to attain a fully plastic state and the corresponding plastic limit angular speed is designated as  $\omega_2$ .

Variational principle based on minimization of total potential energy functional states that

$$\delta(U + V) = 0 \quad (1)$$

where,  $U = U_e^i + U_p + U_e^o$ , i.e., total strain energy,  $U$  consists of two elastic  $\{(U_e^i) \text{ and } (U_e^o)\}$  and a plastic

$(U_p)$  part,  $V$  is the potential of the external forces and  $\delta$  is the variational operator. The interface between the inner elastic and the intermediate plastic region is demarcated by the radius  $r = r_i$  and that between the plastic region and the outer elastic region is demarcated by the radius  $r = r_o$ . The variation of elastic part of strain energy (for  $r = a$  to  $r = r_i$ ) is given as,

$$\delta(U_e^i) = \frac{2\pi E}{1-\mu^2} \int_a^{r_i} \left\{ \frac{u\delta u}{r} + v u \delta \left( \frac{du}{dr} \right) + v \frac{du}{dr} \delta u + r \frac{du}{dr} \delta \left( \frac{du}{dr} \right) \right\} h dr \quad (2)$$

Similarly the variation of elastic part of strain energy (for  $r = r_o$  to  $r = b$ ) is given as,

$$\delta(U_e^o) = \frac{2\pi E}{1-\mu^2} \int_{r_o}^b \left\{ \frac{u\delta u}{r} + v u \delta \left( \frac{du}{dr} \right) + v \frac{du}{dr} \delta u + r \frac{du}{dr} \delta \left( \frac{du}{dr} \right) \right\} h dr \quad (3)$$

Based on Hencky's deformation theory of plasticity the variation of post elastic part of strain energy (for  $r = r_i$  to  $r = r_o$ ) is given by,

$$\delta U_p = \delta \left\{ \int_{vol} (dU_r + dU_t) dv \right\} \quad (4)$$

where,  $dU_r$  and  $dU_t$  are the contributions coming from radial and tangential stresses and strains and are given as

$$dU_r = \frac{1}{2} \sigma_r^0 \varepsilon_r^0 + \frac{1}{2} \sigma_r^p \varepsilon_r^p + \sigma_r^0 \varepsilon_r^p \quad (5a)$$

$$dU_t = \frac{1}{2} \sigma_t^0 \varepsilon_t^0 + \frac{1}{2} \sigma_t^p \varepsilon_t^p + \sigma_t^0 \varepsilon_t^p \quad (5b)$$

From the stress-strain compatibility relations and strain-displacement relations it is known that

$$\sigma_r^0 = \frac{E}{(1-\nu^2)} [\varepsilon_r^0 + \nu \varepsilon_t^0], \sigma_t^0 = \frac{E}{(1-\nu^2)} [\varepsilon_t^0 + \nu \varepsilon_r^0]$$

$$\sigma_r^p = \frac{E_1}{(1-\nu^2)} [\varepsilon_r^p + \nu \varepsilon_t^p], \sigma_t^p = \frac{E_1}{(1-\nu^2)} [\varepsilon_t^p + \nu \varepsilon_r^p]$$

$\varepsilon_r^p = \frac{du}{dr} - \varepsilon_r^0$ ,  $\varepsilon_t^p = \frac{u}{r} - \varepsilon_t^0$ , where the super-script <sup>0</sup> refers to the state of initiation of yielding,

Substituting the abovementioned relations in the expressions of  $dU_r$  and  $dU_t$  the final expression for  $\delta U_p$  is obtained as

$$\delta U_p = \frac{E_1}{(1-\nu^2)} \int_{r_i}^{r_o} \left\{ \frac{u\delta u}{r} + r \left( \frac{du}{dr} \right) \delta \left( \frac{du}{dr} \right) + v \left( \frac{du}{dr} \delta u + u \delta \left( \frac{du}{dr} \right) \right) \right\} 2\pi h dr \quad (6)$$

$$+ \frac{E-E_1}{(1-\nu^2)} \int_{r_i}^{r_o} \left\{ \varepsilon_r^0 \left( v\delta u + r \delta \left( \frac{du}{dr} \right) \right) + \varepsilon_t^0 \left( \delta u + v \delta \left( \frac{du}{dr} \right) r \right) \right\} 2\pi h dr$$

The variation of the potential of the external forces is given by,

$$\delta(V) = -2\pi \rho \omega^2 \int_a^b r^2 h \delta(u) dr \quad (7)$$

The normalization of Eqs (2, 3, 6 and 7) is carried out with four parameters ( $\Delta, \Delta_1, \Delta_2$  and  $\Delta_3$ ) and four normalized coordinates ( $\xi, \xi_1, \xi_2$  and  $\xi_3$ ), where  $\Delta = b-a$  and  $\xi = (r-a)/\Delta$ ,  $\Delta_1 = r_i - a$  and  $\xi_1 = (r-a)/\Delta_1$ ,  $\Delta_2 = r_o - r_i$  and  $\xi_2 = (r-r_i)/\Delta_2$ ,  $\Delta_3 = b - r_o$  and  $\xi_3 = (r-r_o)/\Delta_3$ .

The global displacement field  $u(\xi)$  is approximated by co-ordinate functions  $u(\xi) \cong \sum c_i \phi_i$ ,  $i=1, 2, \dots, n$ , where  $\phi_i$  is the set of orthogonal functions developed through Gram-Schmidt orthogonalization scheme. The necessary starting function to generate the higher order orthogonal functions is selected by satisfying the relevant boundary conditions ( $u|_{r=0} = 0$  and  $\sigma_r|_{r=b} = 0$ ), of a rotating solid disk in elastic regime. For an annular disk boundary conditions become ( $\sigma_r|_{r=a} = 0$  and  $\sigma_r|_{r=b} = 0$ ). To facilitate computation, displacement functions in the elastic and post-elastic regions are expressed as  $u(\xi_1) \cong \sum c_i \phi_i^{e1}$ ,  $u(\xi_2) \cong \sum c_i \phi_i^p$  and  $u(\xi_3) \cong \sum c_i \phi_i^{e2}$  respectively.

On substituting the normalized expressions of  $\delta(U_e^i)$ ,  $\delta(U_p)$ ,  $\delta(U_e^o)$ ,  $\delta(V)$ , in Eq. (1), replacing the displacement field with assumed co-ordinate functions and replacing operator  $\delta$  by  $\partial/\partial c_j$ , the governing set of equations is obtained in matrix form as follows:

$$\frac{E}{1-\mu^2} \sum_{j=1}^n \sum_{i=1}^n c_i \int_0^1 \left\{ \frac{\phi_i^{e1} \phi_j^{e1}}{(\Delta_1 \xi_1 + a)} + \frac{(\Delta_1 \xi_1 + a)}{(\Delta_1)^2} \phi_i^{e1} \phi_j^{e1} + \frac{v}{\Delta_1} (\phi_i^{e1} \phi_j^{e1} + \phi_i^{e1} \phi_j^{e1}) \right\} h \Delta_1 d \xi_1$$

$$+ \frac{E_1}{(1-\nu^2)} \sum_{j=1}^n \sum_{i=1}^n c_i \int_0^1 \left\{ \frac{(\Delta_2 \xi_2 + r_i)}{(\Delta_2)^2} \phi_i^p \phi_j^p + \frac{\phi_i^p \phi_j^p}{(\Delta_2 \xi_2 + r_i)} + \frac{v}{\Delta_2} (\phi_i^p \phi_j^p + \phi_i^p \phi_j^p) \right\} h \Delta_2 d \xi_2$$

$$+ \frac{E}{1-\mu^2} \sum_{j=1}^n \sum_{i=1}^n c_i \int_0^1 \left\{ \frac{\phi_i^{e2} \phi_j^{e2}}{(\Delta_3 \xi_3 + r_o)} + \frac{(\Delta_3 \xi_3 + r_o)}{(\Delta_3)^2} \phi_i^{e2} \phi_j^{e2} + \frac{v}{\Delta_3} (\phi_i^{e2} \phi_j^{e2} + \phi_i^{e2} \phi_j^{e2}) \right\} h \Delta_3 d \xi_3$$

$$= \rho \omega^2 \sum_{j=1}^n \int_0^1 \left\{ (\Delta \xi + a)^2 \phi_j \right\} h \Delta d \xi$$

$$- \frac{E-E_1}{(1-\nu^2)} \int_0^1 \left\{ \varepsilon_r^0 \left( v \phi_j^p + \frac{(\Delta_2 \xi_2 + r_i)}{\Delta_2} \phi_j^p \right) + \varepsilon_t^0 \left( \phi_j^p + v \frac{(\Delta_2 \xi_2 + r_i)}{\Delta_2} \phi_j^p \right) \right\} h \Delta_2 d \xi_2 \quad (8)$$

In the above equation ()' indicates differentiation with respect to normalized coordinates. It should be noted further that the mathematical formulation is presented in generalized form, to be applicable both for solid and annular disks. However, in the present study the case of solid disks are only considered by setting  $a = 0$ .

## 2.1 Solution Algorithm

The governing Eq. (8) can be expressed in matrix form as,  $[K]\{c\} = \{f\}$ , where  $[K]$  is the stiffness matrix and  $\{f\}$  is the load vector and the required solution of unknown coefficients  $\{c\}$  is obtained numerically by using an iterative scheme. A brief description of the solution algorithm is provided below.

1. Solve for limit angular speed [14] and initiate three loops.
2. Start the outer (first) loop and increase the rotational speed through a suitable step size,  $(\Omega_j + \Delta \Omega_j)$ .
3. Start intermediate (second) loop and give  $r_o$  a small increment.
4. Start inner (third) loop and give  $r_i$  a small increment.
5. The ratio of  $\sigma_t^0$  and  $\sigma_r^0$  in the elastic region is constant for a particular radial location. This ratio ( $k$ ) is stored during elastic analysis. Whenever yield front expands at a particular radial location, the values of  $\sigma_t^0$  and  $\sigma_r^0$  at that point can be obtained as follows (considering that up to yield point the ratio  $k$  is maintained):
$$\sigma_{vm} = (\sigma_t^2 + \sigma_r^2 - \sigma_t \sigma_r)^{\frac{1}{2}}$$

$$= \sigma_r (1 + k - k^2)^{\frac{1}{2}}$$
6. Obtain the displacement field using the elastic-plastic formulation of Eq. (8) and post process to check whether von Mises stress attains the value of yield stress at the yield front location.
7. If the condition in step 6 is true within the set error limit then current position is the exact yield front location and go to step 2.

8. If the condition in step 6 is not satisfied, go to step 3, refine the increment on  $r_0$  and continue the iterative process.

### 3. RESULTS AND DISCUSSIONS

The results are presented in terms of the following dimensionless and normalized variables: radial coordinates  $\xi = r/b$ , angular velocity  $\Omega = \omega b \sqrt{\rho / \sigma_y}$ , stress  $\bar{\sigma} = \sigma / \sigma_y$ , displacement  $\bar{u} = uE / b\sigma_y$  and hardening parameter  $\bar{H} = E_1 / (E - E_1)$ . The results are generated using  $b=1.0\text{m}$ ,  $\rho = 7850 \text{ kg/m}^3$ ,  $E=210 \text{ GPa}$  and  $\sigma_y = 350 \text{ MPa}$ . The value of poisson's ratio  $\nu$  is taken as  $1/3$  unless otherwise stated. For the validation purpose, the value of  $\nu$  is taken as  $0.5$  in post-elastic region. Validation of the numerical scheme is presented for disks with uniform and elliptical thickness variation whereas results are presented for disks of exponential thickness variation. The mathematical expressions for thickness variations are defined below:

$$h(\xi) = h_0 \exp[-n\xi^k] \text{ for exponential disk,}$$

$$h(\xi) = h_0 \sqrt{1 - n\xi^2} \text{ for elliptical variation.}$$

Here,  $n, k$  are the parameters defining the geometry and  $h_0$  is the thickness at the root. From the above expressions, disk of uniform thickness is obtained for  $n = 0.0$ . The disk profiles treated in the present study are shown in Fig. 2 (a-b). In Fig. 2 (a), the profile of uniform disk and elliptical disk is illustrated. In Fig. 2 (b) profile of exponential disks for different geometry parameters is shown.

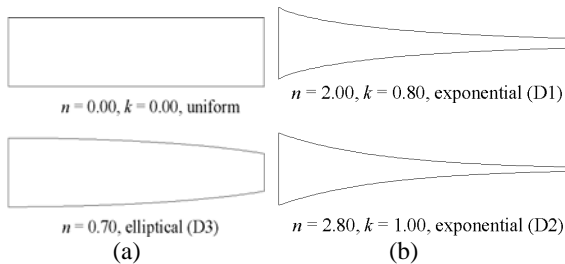


Fig 2. Disk profiles with geometry parameters

Table1: Validation of results on  $\Omega_2$

Geometry	Parameters	$\Omega_2$	
		Present method	Existing results
Uniform	$n=0.0$	2.13726	2.11747 [11]
Elliptical	$n=0.7$	2.28764	2.25761[13]

Results for linear strain hardening material behavior have been generated using  $\bar{H}=0.5$ . A validation on the plastic limit angular speed  $\Omega_2$  is carried out and the results are presented in Table 1. The plots for normalized displacement and normalized radial and tangential

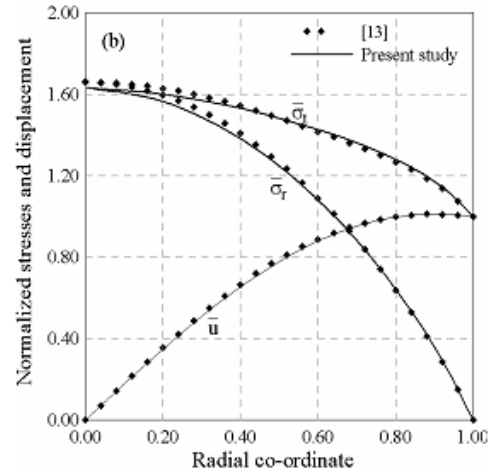
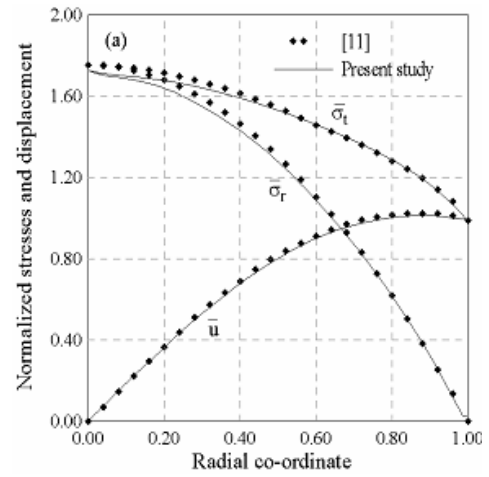


Fig 3. Validation of normalized displacement and normalized radial and tangential stresses at  $\Omega_2$  for (a) Uniform disk and (b) Elliptical disk.

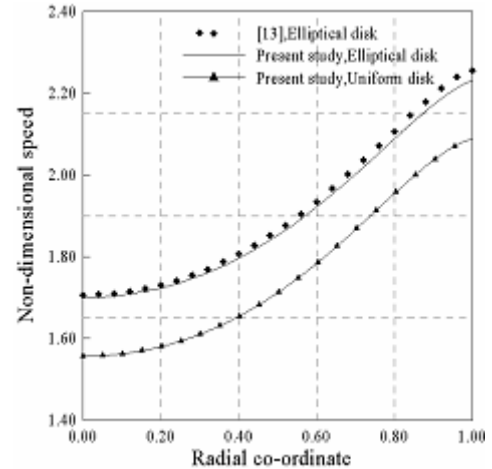


Fig 4. Propagation of elastic-plastic interface for Uniform and Elliptical disk.

stresses at the plastic limit speed  $\Omega_2$  obtained by the present study for uniform and elliptical disk is presented in Fig.3 (a, b). In Fig.4, the propagation of elastic-plastic interface radius with angular speed is plotted for an

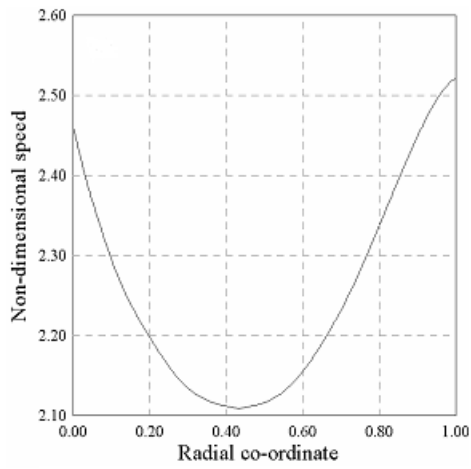


Fig 5. Propagation of elastic-plastic interface for Exponential disk (D1) at  $\Omega_2 = 2.5213$

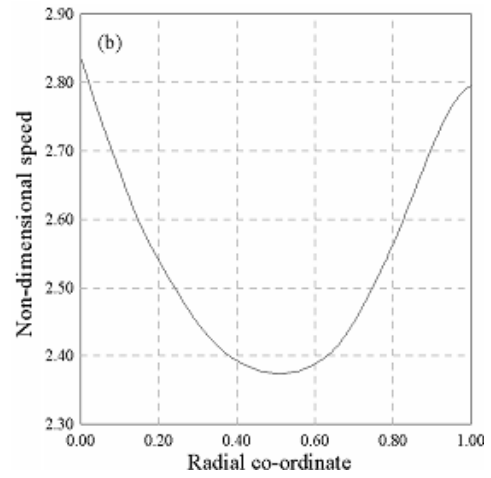


Fig 7. Propagation of elastic-plastic interface for Exponential disk (D2) at  $\Omega_2 = 2.8372$

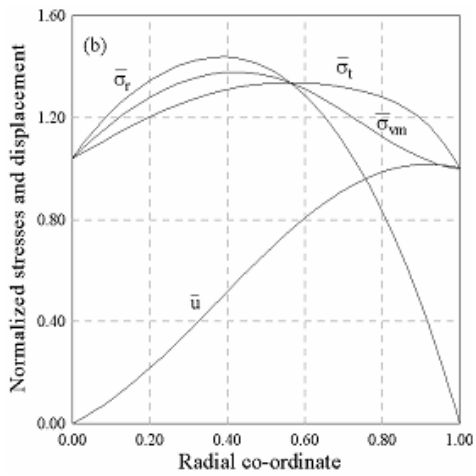
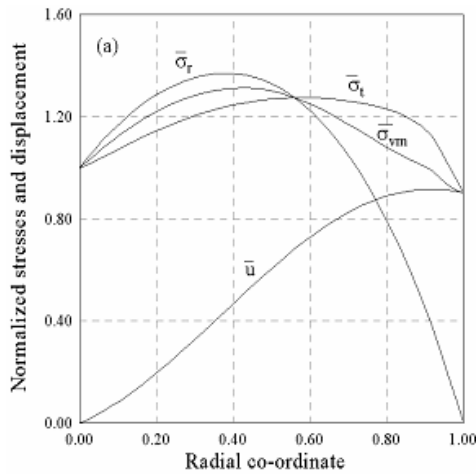


Fig 6. Normalized displacement, radial, tangential and von-Mises stresses for Exponential disk (D1) at (a)  $\Omega_1^i = 2.4621$  and (b)  $\Omega_2 = 2.5213$

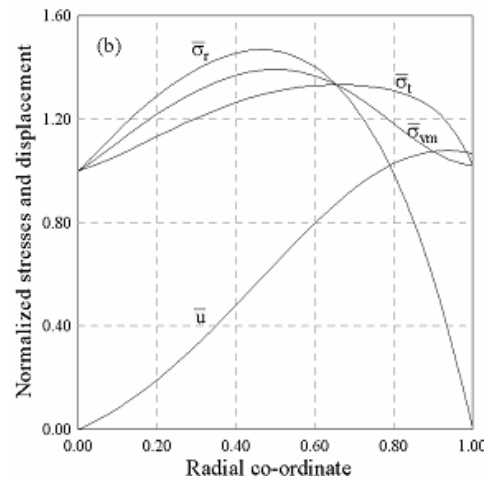
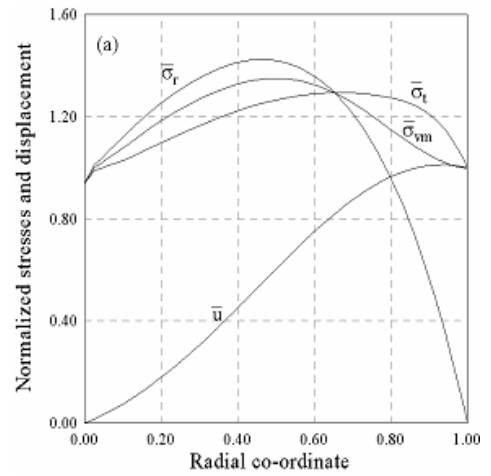


Fig 8. Normalized displacement, radial, tangential and von-Mises stresses for Exponential disk (D2) at (a)  $\Omega_1^o = 2.7948$  and (b)  $\Omega_2 = 2.8372$



elliptical disk and is validated with the results available in [13]. These plots exhibit very good agreement establishing validity of the present elasto-plastic analysis method.

The displacement and stress state of exponential disk is investigated next. The geometry parameters ( $n = 2.0, k = 0.8$  (D1) and  $n = 2.8, k = 1.0$  (D2)) are selected to ensure yielding at locations away from the root. Furthermore, for disk type D1, the yield front propagates in a manner to reach root first and then the periphery, whereas for disk type D2 the yield front reaches periphery first.

For disk type D1, the dimensionless angular speed ( $\Omega_1^i$ ) at which the yield front reaches the root is 2.4621.

The fully plastic state is attained at  $\Omega_2 = 2.5213$ . In Fig.5 the propagation of elastic-plastic interface is plotted against increasing speed. The corresponding normalized radial, tangential and von Mises stresses and normalized displacement at  $\Omega_1^i$  and  $\Omega_2$  for disk type D1 is plotted in Fig. 6(a, b).

For disk type D2, the dimensionless angular speed ( $\Omega_1^o$ ) is 2.7948 and the fully plastic state is attained at  $\Omega_2 = 2.8372$ . The propagation of elastic-plastic interface is plotted against increasing speed in Fig.7 for disk type D2. The corresponding normalized radial, tangential and von Mises stresses and normalized displacement at  $\Omega_1^o$  and  $\Omega_2$  is plotted in Fig. 8(a, b).

#### 4. CONCLUSION

The present work gives an approximate solution in the elasto-plastic region of a solid rotating disk of varying thickness assuming linear strain hardening material behavior following von Mises yield criterion. The results obtained by the present methodology have been validated and it showed a close conformity with the existing results of similar problem.

Some new results for displacement field and radial, tangential and von Mises stress field at plastic limit speed for exponential disks yielding at locations away from the root for linear strain hardening material behavior have been furnished and plots showing the bi-directional advancement of the plastic front with increase in rotational speed have been presented.

The method of formulation readily gives the kernel for dynamic analysis and many other complicating effects. The results are presented graphically so that they become designer friendly. The method developed has application potential in various other problems, e.g., shrink fitted rotating disk, pre-stressed rotating disk, compound disk made from different materials, etc.

#### 5. ACKNOWLEDGEMENT

The present study is financially supported by Council of Scientific and Industrial Research, India (Ref. File/letter No. 9/96[514]2K7-EMR-I) and the support is duly acknowledged by the first author.

#### 6. REFERENCES

1. Gamer U., 1985, "Elastic-plastic deformation of the rotating solid disk", *Ingenieur-Archiv*, 54:345-354.
2. Gamer U., 1984, "The rotating solid disk in the fully plastic state", *Forschung im Ingenieurwesen*, 50:137-140.
3. Güven U., 1994, "The fully plastic rotating solid disk of variable thickness", *Zeitschrift für Angewandte Mathematik und Mechanik*, 74(1):61-65.
4. Güven U. 1995, "On the applicability of Tresca's yield condition to the linear hardening rotating solid disk of variable thickness", *Zeitschrift für Angewandte Mathematik und Mechanik*, 75: 397-398.
5. Rees DWA. 1999, "Elastic-plastic stresses in rotating disks by von Mises and Tresca", *Zeitschrift für Angewandte Mathematik und Mechanik*, 79(4):281-288.
6. You LH, Zhang JJ. 1999, "Elastic-plastic stresses in a rotating solid disk", *International Journal Mechanical Sciences*, 41:269-282.
7. You LH, Tang YY, Zhang JJ, Zheng CY. 2000, "Numerical analysis of elastic-plastic rotating disks with arbitrary variable thickness and density", *International Journal of Solids and Structures* 37:7809-7820.
8. Ma G, Hao H, Miyamoto Y. 2001, "Limit angular velocity of rotating disk with unified yield criterion", *International Journal Mechanical Sciences*, 43:1137-1153.
9. Eraslan AN, Orcan Y. 2002, "Elastic-plastic deformation of a rotating solid disk of exponentially varying thickness", *Mechanics of Materials*, 34:423-432.
10. Eraslan AN, Orcan Y. 2002, "On the rotating elastic-plastic solid disks of variable thickness having concave profiles", *International Journal Mechanical Sciences*, 44:1445-1466.
11. Eraslan AN. 2002, "Inelastic deformations of rotating variable thickness solid disks by Tresca and Von Mises criteria", *International Journal of Computational Engineering science*, 3(1):89-101.
12. Eraslan AN, Argeso H. 2002, "Limit angular velocities of variable thickness rotating disks", *International Journal of Solids and Structures*, 39:3109-3130.
13. Eraslan AN. 2005, "Stress distributions in elastic-plastic rotating disks with elliptical thickness profiles using Tresca and von Mises criteria", *Zeitschrift für Angewandte Mathematik und Mechanik*, 85:252-266.
14. Bhowmick S, Misra D, Saha KN. 2008, "Approximate solution of limit angular speed for externally loaded solid rotating disk", *International Journal Mechanical Sciences*, 50: 163-174
15. Bhowmick S, Das D, Saha KN. 2006, "A study on the elasto-plastic behavior of a rotating solid disk having variable thickness", *Proc. International Congress on Computational Mechanics and Simulation, IIT Guwahati*, 825-832.

## LARGE AMPLITUDE PERIODIC VIBRATION OF COMPOSITE CYLINDRICAL PANELS

M. K. Singha and R. Daripa

Department of Applied Mechanics, Indian Institute of Technology, Delhi, India

### ABSTRACT

Large amplitude free flexural vibration characteristics of isotropic and multi-layered composite cylindrical shell panels are studied here using the finite element method. Formulation is based on first order shear deformation theory incorporating geometric nonlinearity. Periodic solution in time is assumed and the Galerkin's method is applied on the nonlinear governing equation to generate the matrix amplitude equation which is solved by direct iteration technique to obtain the disturbing energy *versus* vibration amplitude relationship. Dynamic response for the nonlinear free vibration of composite cylindrical panels is also obtained using Newmark's time integration technique. Specific numerical results are reported to show the effects of radius-to-span ratio, thickness-to-span ratio, and boundary condition on the large amplitude free vibration characteristics of laminated cylindrical shell panels.

**Keywords:** Nonlinear Vibration, Cylindrical Panels, Composite Material.

### 1. INTRODUCTION

Thin-walled structural components, made of isotropic or composite materials are increasingly used in high performance engineering applications and are subjected to hostile environment, resulting in a strong need to understand their nonlinear dynamic behaviour. Extensive literature review on the geometrically nonlinear flexural vibration characteristics of circular cylindrical shells and shell panels is given by Amabili and Paidoussis [1]. The flexural vibration characteristics of shell type of structures are complex due to the asymmetric oscillation with respect to the un-deformed middle surface. The mid-surface gets compressed while deflecting inward (towards the center of curvature), while the mid-surface is subjected to tensile in-plane stress when deflecting outwards. It is observed from the existing literature, that the assumed space-mode analytical methods are widely used by different investigators while studying the geometrically nonlinear flexural vibration characteristics of curved panels [2-5]. Extensive theoretical and experimental studies on the large amplitude flexural vibration characteristics of cylindrical and doubly-curved panels are reported by Amabili [6-8]. The nonlinear strain-displacement relationships from Donnell's shell theory and Novozhilo's shell theory were employed. A multi-mode expansion with assumed approximate time functions was employed to obtain the nonlinear governing equation with finite degrees of freedom, which was solved by arc-length continuation method to investigate the

flexural vibration characteristics of such panels.

Numerical techniques, such as finite element method, overcome the limitations of assumed space-mode. However, the selection of appropriate time function and determination of a steady-state periodic solution of the differential equations with quadratic and cubic nonlinearity is a challenge to the researchers working in the area of nonlinear dynamics of composite shells. Ribeiro [9-11] employed *p*-version finite element with hierarchic basis functions and harmonic balance method to get the equation of motion in frequency domain, which was solved by predictor-corrector method [9] or arc-length continuation method [10] for nonlinear free vibration or by shooting and Newton's method [11] for nonlinear forced vibration of shell panels. A strong modal interaction with even and odd harmonics was observed in the geometric nonlinear vibration, which was characterized by time plots, phase planes and Fourier spectra. Few nonlinear transient analyses of shell panels are available in the literature [12-14]. However, further study is required to understand the steady-state periodic and asymmetric vibration behavior of curved panels under transverse dynamic load.

In the present paper a sixteen noded shell finite element [15] is employed to study the nonlinear free flexural vibration behavior of shallow composite cylindrical panels. Time function is assumed for the nonlinear equation and Galerkin's method is employed to obtain the nonlinear frequencies of vibration. Dynamic response of curved panels is also obtained by Newmark's

direct time integration method. The effect of boundary condition and curvature on the large amplitude vibration characteristics of composite cylindrical panels is investigated in details.

## 2. FORMULATION

A sixteen noded degenerated isoparametric finite element is employed here to model a circular cylindrical shell panel of constant thickness  $h$ , radius  $R$ , axial length  $L$ , having plan-form width  $a$  and rise  $H$  as shown in Fig 1 (a). The sixteen-noded shell element is schematically shown in Fig 1(b). The normal to the mid-surface at node “ $k$ ” at any time “ $t$ ” is defined by the unit vector  ${}^tV_n^k$ .  ${}^tV_1^k$  and  ${}^tV_2^k$  are two unit vectors orthogonal to  ${}^tV_n^k$ .

Each node “ $k$ ” has five degrees of freedom namely;  $u_1$ ,  $u_2$ ,  $u_3$ ,  $\alpha$  and  $\beta$ . The mid-surface displacement components  $u_1$  and  $u_2$  are along the unit vectors  ${}^0V_1^k$  and  ${}^0V_2^k$  respectively; and  $u_3$  is the normal displacement along  ${}^0V_n^k$ . The changes in the direction cosines of the shell normal, given by  $V_n^k (= {}^tV_n^k - {}^0V_n^k)$  may be expressed in terms of nodal rotations ( $\alpha$  and  $\beta$ ) about the two vectors  ${}^0V_1^k$  and  ${}^0V_2^k$  as [15, 16]

$$V_n^k = -{}^0V_2^k \alpha + {}^0V_1^k \beta - \frac{1}{2}(\alpha^2 + \beta^2) {}^0V_n^k \quad (1)$$

The linear ( $e_{ij}$ ) and nonlinear ( $\eta_{ij}$ ) components of the Green-Lagrange strain tensors  $\varepsilon_{ij}^{DI} = (e_{ij} + \eta_{ij})$  may be written in terms of displacement components  $u_i$  ( $i = 1, 3$ ) as

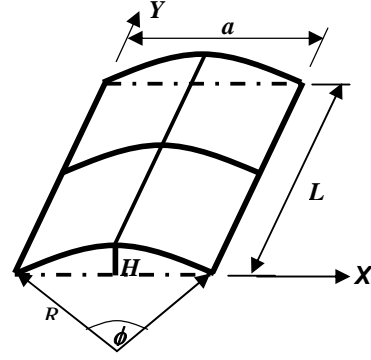
$$e_{ij} = \frac{1}{2}(u_{i,j} + u_{j,i}) \quad \text{and} \\ \eta_{ij} = \frac{1}{2}u_{k,i}u_{k,j}; \quad k = 1, 3 \quad (2)$$

Here, the strain components are obtained by direct interpolation using the finite element displacement assumptions. The coordinate system is defined element-wise by the element isoparametric coordinates. The normal strain component  $\varepsilon_{33}$  is zero. To avoid the shear and membrane locking phenomenon, mixed-interpolated elements are constructed by using the assumed strain-fields  $\varepsilon_{ij}^{AS}$  in place of  $\varepsilon_{ij}^{DI}$ . The covariant strain components  $\varepsilon_{ij}^{AS}$  are defined as

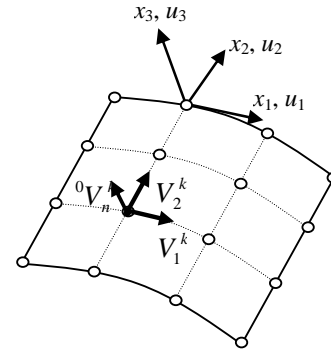
$$\varepsilon_{ij}^{AS}(r,s) = \sum_{k=1}^{n_{ij}} N_k^{ij}(r,s) \varepsilon_{ij}^{DI}(r,s) \quad (3)$$

where, the  $N_k^{ij}(\mathbf{r}, s)$  are interpolation functions (polynomials in  $r$  and  $s$ ) associated with the strain component  $\varepsilon_{ij}$  at tying point  $k$  and  $n_{ij}$  is the number of tying points as described in Bathe [16]. For a composite laminate of thickness  $h$ , comprising  $N$  layers with stacking angles  $\theta_i$  ( $i = 1, 2, \dots, N$ ) and layer thicknesses  $h_i$  ( $i = 1, 2, \dots, N$ ), the necessary expressions to compute

the stiffness coefficients are available in the literature [17].



(a) Geometry of cylindrical



(b) Geometry of 16 node shell

Fig 1. The geometry of a cylindrical panel and the shell element.

Following standard procedure (Lagrange's equation of motion), the nonlinear equation of equilibrium of the cylindrical shell panel under periodic transverse load may be written as

$$\begin{bmatrix} M_{mm} & 0 \\ 0 & M_{bb} \end{bmatrix} \begin{Bmatrix} \ddot{\delta}_m \\ \ddot{\delta}_b \end{Bmatrix} + \begin{bmatrix} K_{mm} & K_{mb} \\ K_{bm} & K_{bb} \end{bmatrix} \begin{Bmatrix} \delta_m \\ \delta_b \end{Bmatrix} + \begin{bmatrix} 0 & KN_1(w) \\ KN_2(w) & KN_3(w,w) \end{bmatrix} \begin{Bmatrix} \delta_m \\ \delta_b \end{Bmatrix} = \begin{Bmatrix} 0 \\ q(t) \end{Bmatrix} \quad (4)$$

Here,  $\mathbf{K}$  is the linear stiffness matrix;  $\mathbf{M}$  is the mass matrix;  $\mathbf{KN}_1$  and  $\mathbf{KN}_2$  are the nonlinear stiffness matrices, linearly depend on transverse displacement  $w$ ; and  $\mathbf{KN}_3$  is the nonlinear stiffness matrix, which is a quadratic function of transverse displacement  $w$ . The subscripts ‘ $m$ ’ and ‘ $b$ ’ correspond to membrane ( $u_1, u_2$ ) and bending ( $u_3, \alpha$  and  $\beta$ ) components of the degrees of freedom and corresponding mass and stiffness matrices respectively.

## 3. LARGE AMPLITUDE FREE VIBRATION

For the case of large amplitude vibration of shell panels, the vibration amplitude ( $w_{in}$ ) towards the center of curvature is more than the corresponding amplitude in the outward direction ( $w_{out}$ ), as schematically shown in

Fig 2. Hence, the displacement components in the inward (towards center of curvature) and outward direction may be individually expressed as

$$\delta_{in}(t) = \left\{ \begin{matrix} u_{in} \sin^2 \theta_1 t, v_{in} \sin^2 \theta_1 t, w_{in} \sin \theta_1 t, \\ (\gamma_{xz})_{in} \sin \theta_1 t, (\gamma_{yz})_{in} \sin \theta_1 t \end{matrix} \right\}^T \quad (5)$$

$$\delta_{out}(t) = \left\{ \begin{matrix} u_{out} \sin^2 \theta_2 t, v_{out} \sin^2 \theta_2 t, w_{out} \\ \sin \theta_2 t, (\gamma_{xz})_{in} \sin \theta_2 t, (\gamma_{yz})_{in} \sin \theta_2 t \end{matrix} \right\}^T \quad (6)$$

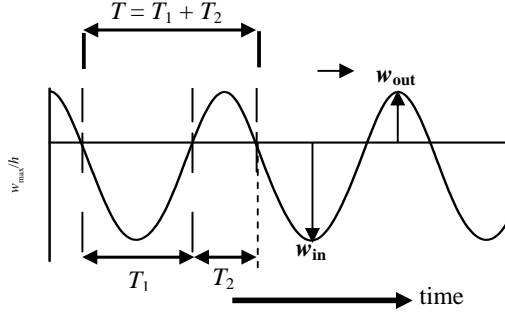


Fig 2. Schematic diagram for the large amplitude oscillation of a cylindrical shell panel.

Here, the total time period “ $T$ ” is divided between the time taken “ $T_1 = \pi/\theta_1$ ” for the inward motion and time taken “ $T_2 = \pi/\theta_2$ ” for the outward motion (as schematically shown in Fig 2). For the case of free vibration, the strain energies  $U(\delta_{in})$  and  $U(\delta_{out})$  for the inward and outward vibration amplitudes should match, i.e.,

$$U(\delta_{in}) = U(\delta_{out}) \quad (7)$$

Substituting the assumed solutions (5, 6) into the governing equation (4) and evaluating the weighted residual along the path

$$\int_0^{T_1/2} \{R_m\} \sin^2 \theta_1 t = \{0\} \text{ and } \int_0^{T_1/2} \{R_b\} \sin \theta_1 t = \{0\}$$

$$\text{or } \int_0^{T_2/2} \{R_m\} \sin^2 \theta_2 t = \{0\} \text{ and } \int_0^{T_2/2} \{R_b\} \sin \theta_2 t = \{0\}$$

the following matrix-amplitude equations are obtained

$$\begin{bmatrix} \frac{3}{4} K_{mm} & \frac{8}{3\pi} K_{mb} + \frac{3}{4} KN_1 \\ \frac{8}{3\pi} K_{bm} + \frac{3}{4} KN_2 & K_{bb} + \frac{3}{4} KN_3 \end{bmatrix} \begin{Bmatrix} \delta_m \\ \delta_b \end{Bmatrix}_{in} - \theta_1^2 \begin{Bmatrix} \delta_m \\ \delta_b \end{Bmatrix}_{in} = \begin{Bmatrix} 0 \\ 0 \end{Bmatrix} \quad (8a)$$

$$\begin{bmatrix} -M_{mm} & 0 \\ 0 & M_{bb} \end{bmatrix} \begin{Bmatrix} \delta_m \\ \delta_b \end{Bmatrix}_{in} = \begin{Bmatrix} 0 \\ 0 \end{Bmatrix}$$

$$\begin{bmatrix} \frac{3}{4} K_{mm} & \frac{8}{3\pi} K_{mb} + \frac{3}{4} KN_1 \\ \frac{8}{3\pi} K_{bm} + \frac{3}{4} KN_2 & K_{bb} + \frac{3}{4} KN_3 \end{bmatrix} \begin{Bmatrix} \delta_m \\ \delta_b \end{Bmatrix}_{out} - \theta_2^2 \begin{Bmatrix} \delta_m \\ \delta_b \end{Bmatrix}_{out} = \begin{Bmatrix} 0 \\ 0 \end{Bmatrix} \quad (8b)$$

$$\begin{bmatrix} -M_{mm} & 0 \\ 0 & M_{bb} \end{bmatrix} \begin{Bmatrix} \delta_m \\ \delta_b \end{Bmatrix}_{out} = \begin{Bmatrix} 0 \\ 0 \end{Bmatrix}$$

The matrix amplitude equations (8a, b) are solved separately to get the vibration mode shapes  $\{\delta_m, \delta_b\}_{in}^T$  or

$\{\delta_m, \delta_b\}_{out}^T$  corresponding to inward ( $w_{in}$ ) and outward ( $w_{out}$ ) vibration amplitudes. Thereafter, the vibration amplitudes ( $w_{in}$  and  $w_{out}$ ) are adjusted iteratively to satisfy equation (7). Further, a time history analysis is carried out starting from the initial condition  $\{\delta_m, \delta_b\}_{out}^T$ , obtained from the equation (8b) to get the time history of central displacement, strain energy and kinetic energy of the shell panel.

#### 4. RESULTS AND DISCUSSIONS

Large amplitude free flexural vibration characteristics of thin isotropic and laminated composite cylindrical panels of constant thickness  $h$ , radius  $R$ , axial length  $L$  and plan-form width  $a$  (as shown in Fig 1) is considered here. The non-dimensional material properties, unless specified otherwise, used in the present analysis are  $E_L/E_T = 40.0$ ,  $G_{LT}/E_T = 0.6$ ,  $G_{TT}/E_T = 0.5$ , and  $\nu_{LT} = 0.25$ , where,  $E$ ,  $G$ , and  $\nu$  are Young’s modulus, shear modulus and Poisson’s ratio respectively. Subscripts  $L$  and  $T$  represent the longitudinal and transverse directions with respect to fiber directions. The ply-angles are measured from the circumferential direction to the fiber direction. All the layers are of equal thickness.

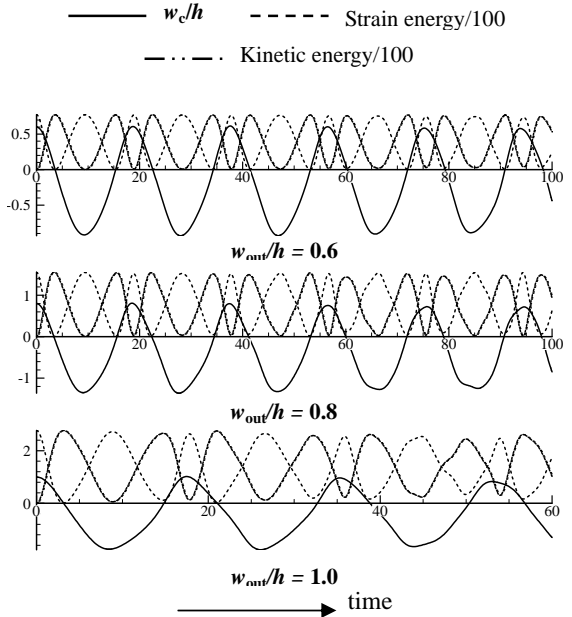


Fig 3. The time history of central displacement ( $w_c/h$ ), strain energy and kinetic energy of an isotropic simply supported (SS1) cylindrical panel at different amplitudes of vibration. ( $R/a = 10$ ,  $a/h = 100$ ,  $L/a = 1$ ).

The efficacy of the present element for linear free vibration analysis of composite cylindrical panels has been tested earlier [15] and the same is not presented here for the sake of brevity. 16 node MITC shell element has good convergence property for both thin and thick panels and a  $4 \times 4$  mesh is chosen to model the cylindrical panels. The different boundary conditions considered in the present analysis are:

**Simply supported cases:**

All edges simply support (SS1):  $u_1 = u_2 = u_3 = 0$  along the boundary nodes

Straight edges simply supported, curved edges free (SS2):  $u_1 = u_2 = u_3 = 0$  at  $x_1 = 0, a$

**Clamped case:** (CC1)

$u_1 = u_2 = u_3 = \alpha = \beta = 0$  along the boundary nodes

At the beginning, the large amplitude free flexural vibration characteristics of a simply supported (SS1) thin isotropic cylindrical shell panel ( $R/a = 10, a/h = 100, L = a$ ) are studied from a time history analysis. The nonlinear mode shapes  $\{\delta_m, \delta_b\}^T$  are obtained from the matrix-amplitude equation (8b) corresponding to different amplitudes of vibration ( $w_{out}/h$ ). Thereafter, a dynamic response analysis is performed starting from the initial condition  $\delta = \{\delta_m, \delta_b\}^T$  and the variation of non-dimensional central displacement ( $w_c/h$ ), strain energy and kinetic energy with time is presented in Fig 3. The strain energy and kinetic energy are evaluated using the non-dimensional material properties ( $E = 100000.0$  and  $\nu = 0.3$ ) and divided by 100, while plotting with the central displacement ( $w_c/h$ ) in Fig 3.

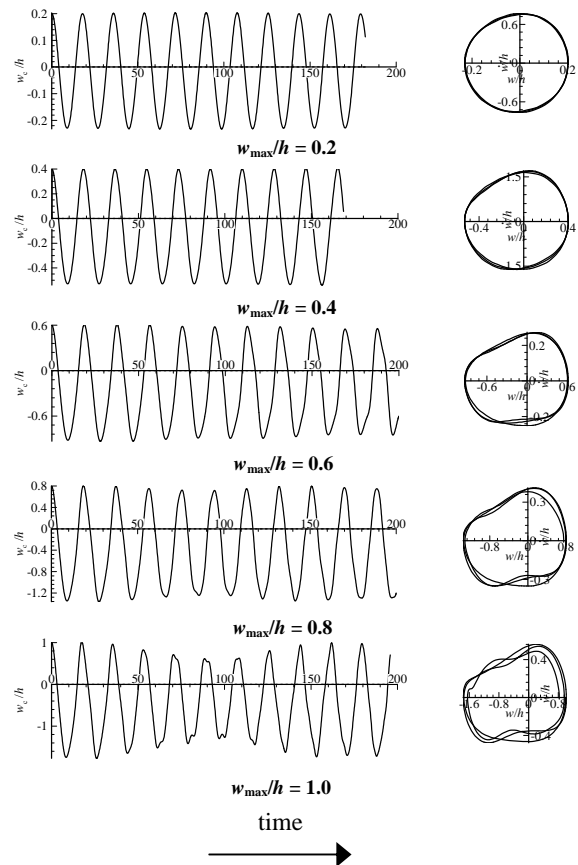


Fig 4. Nonlinear response curves and phase plots of a simply supported (SS1) isotropic cylindrical panel ( $R/a = 10, a/h = 100, L/a = 1$ ) at different amplitudes of vibration.

From the figure, it is observed that the response is approximately steady-state. In addition, a smooth

exchange of the strain energy and kinetic energy (strain energy + kinetic energy is constant) is noticed during the vibration cycle. Hence, it appears that, the vibration mode shapes obtained from equation (8b) is approximately correct, which is further investigated in detail.

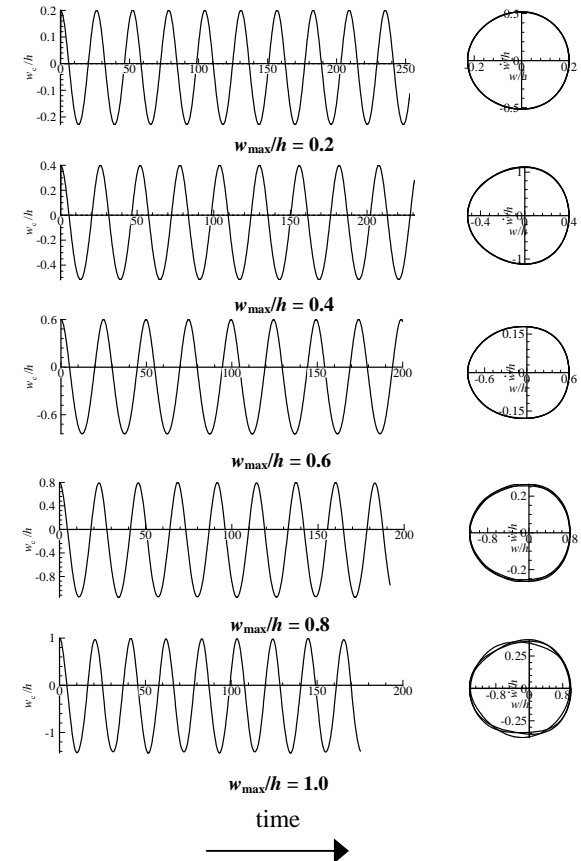


Fig 5. Nonlinear response curves and phase plots of a simply supported (SS1) isotropic cylindrical panel ( $R/a = 20, a/h = 100, L/a = 1$ ) at different amplitudes of vibration.

The nonlinear dynamic response curves and corresponding phase plots of simply supported (SS1) isotropic cylindrical panels are shown in Fig 4 and Fig 5 for radius-to-thickness ratio ( $R/a$ ) of 10 and 20 respectively. Time history analysis is also repeated for a cylindrical shell panel ( $R/a = 10$ ) with SS2 boundary condition, (*i.e.*, straight edges simply supported and curved edges are free) and the corresponding dynamic response along with phase plots are reported in Fig 6.

The vibration mode shapes in the outward and corresponding inward directions of an isotropic cylindrical panel ( $R/a = 10, a/h = 100$ ) are shown in the Fig 7 and Fig 8 for two different boundary conditions SS1 and SS2 respectively. From the time response curves and the mode shapes, the following major observations are made

- The maximum transverse deflection in the inward direction (towards center of curvature) is more compared to outward displacement ( $w_{out}/h$ ). The difference between the inward and outward

displacements ( $w_{in} - w_{out}$ ) increases with the increase of amplitude of vibration. For example, the inward vibration amplitudes are  $0.92h$ ,  $1.348h$  and  $1.747h$  corresponding to the outward displacement of  $0.6h$ ,  $0.8h$  and  $1.0h$  respectively for a simply supported (SS1) cylindrical shell panel with  $R/a = 10$ .

- For low amplitudes of vibration, the mode shape is symmetric and maximum displacement occurs at the center ( $w_{max} = w_c$ ). The vibration response is steady state. Hence, a harmonic time function assumption of the transverse displacement in equation (6) appears to be reasonable.
- With the increase of vibration amplitude, the mode shape becomes un-symmetric with the maximum displacement shifts away from the center ( $w_{max} > w_c$ ). The steady state nature of the vibration gets slowly disturbed. This disturbance is more for the panel with  $R = 10a$  compared to the panel with  $R = 20a$ . Further, the disturbance is more for SS2 boundary condition compared to SS1 boundary condition.

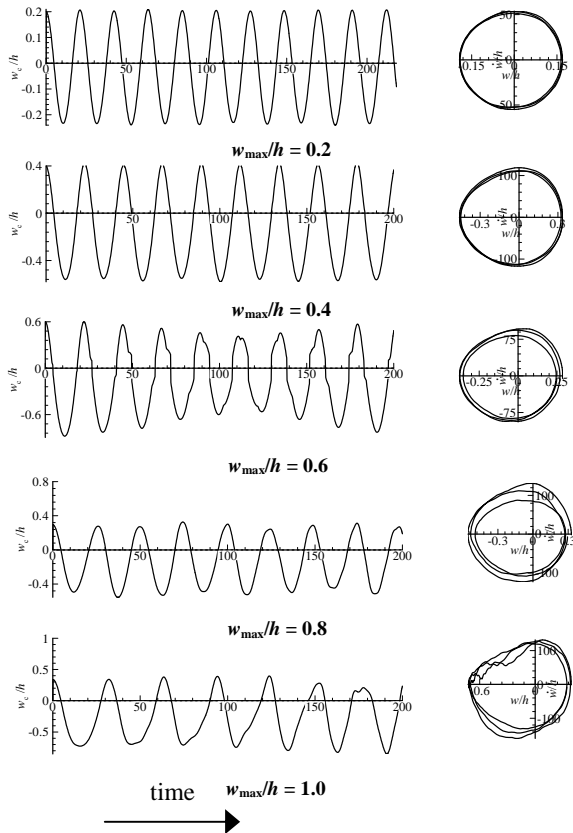


Fig 6. Nonlinear response curves and phase plots of simply supported (SS2) isotropic cylindrical panel ( $R/a = 10$ ,  $a/h = 100$ ,  $L/a = 1$ ) at different amplitudes of vibration.

Next, the variation of maximum transverse displacements in the inward ( $w_{in}$ ) and outward ( $w_{out}$ ) directions of thin simply supported (SS1) isotropic cylindrical panels with the total disturbing energy (strain energy + kinetic energy) is studied in Fig 9 for four different values of radius of curvature ( $R/a = 8, 10, 20$  and infinite, *i.e.*, plate). It is observed that, the vibration

amplitudes ( $w_{in}$  and  $w_{out}$ ) increase with the increase in disturbing energy, followed by a sudden jump in the outward displacements associated with a change in deflection shape

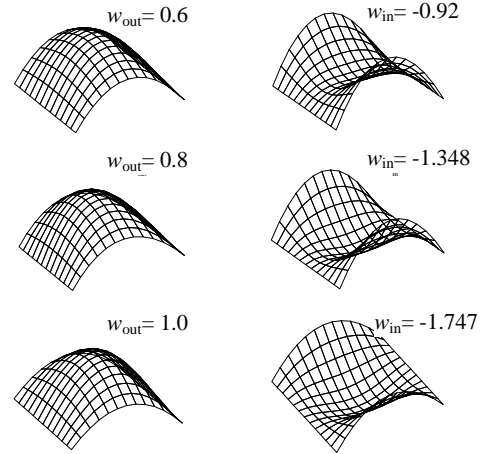


Fig 7. Vibration mode shapes for the outward and the corresponding inward directions of a thin simply supported (SS1) isotropic cylindrical panel ( $R/a = 10$ ,  $a/h = 100$ ,  $L/a = 1$ ).

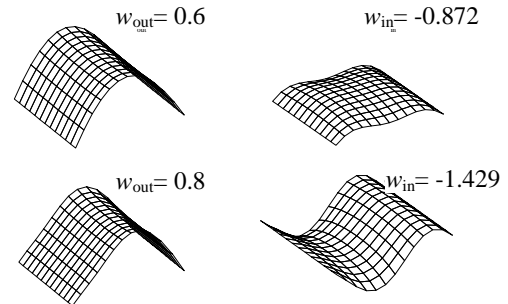


Fig 8. Vibration mode shapes for the outward and the corresponding inward directions of a thin simply supported (SS2) isotropic cylindrical panel ( $R/a = 10$ ,  $a/h = 100$ ,  $L/a = 1$ ).

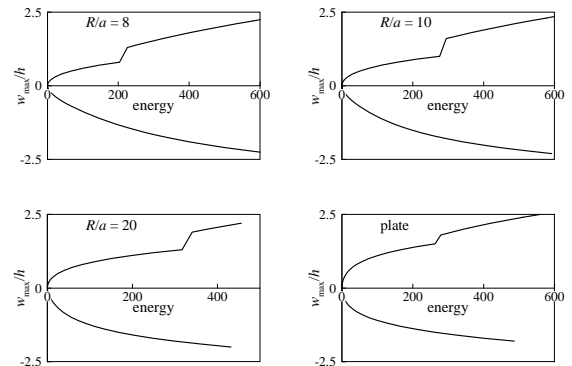


Fig 9. Effect of curvature on the non-linear free vibration characteristics of isotropic simply supported cylindrical panels.

Finally, the nonlinear free vibration behaviors of thin ( $a/h = 100$ ) angle-ply  $[45^0/-45^0/45^0/-45^0/45^0]$  simply



supported (SS1) and clamped (CC1) cylindrical shell panels of square plan-form ( $L/a = 1$ ) are studied in Fig. 10 for different values of radius of curvature ( $R/a$ ). The nonlinear frequency ratio ( $\omega_{NL}/\omega_L$ ) increases with the increase of vibration amplitude ( $w_{in}/h$ ) for the case of flat plate. This degree of hardening nonlinearity decreases with the increase of curvature (decrease of radius of curvature). For the case of cylindrical panels with *radius-to-span* ratio 10 and 20, the frequency-amplitude relation initially shows a softening behavior. But, at higher amplitudes of vibration, this softening behavior is transformed to hardening behavior. The frequency-amplitude relationship for the clamped cylindrical panel is qualitatively similar to those of simply supported panels.

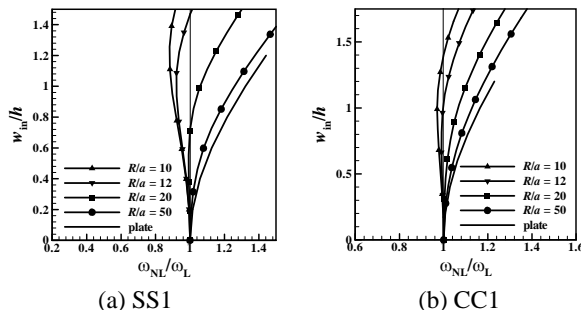


Fig 10. Effect of curvature on the non-linear vibration frequencies of simply supported and clamped (CC1) angle-ply  $[45^0/-45^0/45^0/-45^0/45^0]$  thin cylindrical panel ( $a/h = 100, L/a = 1$ ).

## 5. CONCLUSIONS

Large amplitude flexural vibration characteristics of isotropic and composite cylindrical panels are investigated here using a shear deformable finite element approach. The “vibration amplitude versus disturbing energy” and “vibration amplitude versus nonlinear frequency” relationships are studied using approximate matrix-amplitude equation obtained from single harmonic approximation to the asymmetric vibration. The present qualitative numerical results are examined thoroughly by a time history analysis. The time history and corresponding phase plots offer a good understanding of the nonlinear vibration characteristics of composite cylindrical panels.

## 6. REFERENCES

- Amabili, M. and Paidoussis, M. P., 2003, “Review of studies on geometrically nonlinear vibrations and dynamics of circular cylindrical shells and panels, with and without fluid–structure interaction”, *Applied Mechanics Reviews*, Transactions of the ASME, 56: 349–381.
- Hui, D., 1984, “Influence of geometric imperfections and in-plane constraints on nonlinear vibrations of simply supported cylindrical panels”, *Journal of Applied Mechanics*, Transactions of the ASME, 51: 383–390.
- Raouf, R. A. and Palazotto, A. N., 1992, “Nonlinear free vibrations of symmetrically laminated, slightly compressible cylindrical shell panels”, *Composite Structures*, 20: 249–257.
- Raouf, R. A. and Palazotto, A. N., 1994, “On the non-linear free vibrations of curved orthotropic panels”, *International Journal of Non-linear Mechanics*, 29: 507–514.
- Leissa, A. W. and Kadi, A. S., 1971, “Curvature effects on shallow shell vibrations”, *Journal of Sound and Vibration*, 16: 173–187.
- Amabili M. (2006). Theory and experiments for large-amplitude vibrations of circular cylindrical panels with geometric imperfections. *Journal of Sound and Vibration*, 298, 43–72.
- Amabili M. (2007). Effect of boundary conditions on the nonlinear vibrations of circular cylindrical panels. *Journal of Applied Mechanics*, 74, 645–657.
- Amabili M. (2008). *Nonlinear Vibrations and Stability of Shells and Plates*, Cambridge University Press, New York, USA.
- Ribeiro P. (2003). A hierarchical finite element for geometrically non-linear vibration of doubly curved, moderately thick isotropic shallow shells. *International Journal for Numerical Methods in Engineering*, 56 (5), 715–738.
- Ribeiro P. (2008), Non-linear free periodic vibrations of open cylindrical shallow shells. *Journal of Sound and Vibration*, 313 (1-2), 224–245.
- Ribeiro P. (2009). On the influence of membrane inertia and shear deformation on the geometrically non-linear vibrations of open, cylindrical, laminated clamped shells. *Composite Science and Technology*, 69 (2), 176–185.
- Kant T. and Kommineni J. R. (1994). Geometrically nonlinear transient analysis of laminated composite and sandwich shells with a refined theory and  $C^0$  finite elements. *Computers and Structures*, 52 (6), 1243–1259.
- Kommineni J. R. and Kant T. (1995). Pseudo transient large deflection analysis of composite and sandwich shells with a refined theory. *Computer Methods in Applied Mechanics and Engineering*, 123(1), 1–13.
- Nanda N. and Bandyopadhyay J.N. (2008). Nonlinear transient response of laminated composite shells. *Journal of Engineering Mechanics*, 134 (11), 983–990.
- Singha, M.K. and Mandal, M., 2008, “Supersonic flutter characteristics of composite cylindrical panels”, *Composite Structures*, 82: 295–301.
- Bathe, K.J., 1996, *Finite element procedures*, Englewood Cliffs, NJ: Prentice-Hall.
- Jones, R.M., 1975, *Mechanics of Composite Materials*, McGraw-Hill, New York.

## 7. MAILING ADDRESS

M. K. Singha  
 Department of Applied Mechanics,  
 Indian Institute of Technology Delhi 110106, INDIA  
 E-mail: maloy@am.iitd.ernet.in

## SYNTHESIS OF Mg-SiC COMPOSITES USING UNDERWATER SHOCK WAVE BY CHANGING MILLING PARAMETERS

A. Nayeem Faruqui<sup>1</sup>, Palavesamuthu Manikandan<sup>2</sup>, Takashi Sato<sup>3</sup>, Kazuyuki Hokamoto<sup>2</sup>

<sup>1</sup>Graduate School of Science and Technology, Kumamoto University,

<sup>2</sup>Shock Wave and Condensed Matter Research Center, Kumamoto University,

<sup>3</sup>Faculty of Engineering, Kumamoto University, Kurokami, Kumamoto, Japan

### ABSTRACT

The weight reduction demand, in particular for aerospace and automotive applications, has renewed interest in magnesium (Mg) based materials. Though magnesium has numerous desirable properties, its elastic modulus is low in comparison with other structural materials. Incorporation of ceramic reinforcement in the form of particulates is known to improve the properties of magnesium composites. Among the various reinforcements, SiC is the most commonly used reinforcement and also it has high wettability with magnesium. In this present investigation, 70 mass% Mg- 30 mass% SiC are used for the shock compaction of the powder. This composite has high specific strength, excellent machinability, castability and good recyclability. In the fabrication of magnesium-silicon carbide composite, conventionally used process expose the composite to a high temperature for a prolonged time resulting in undesirable reaction product. Thus a fabrication technique that involves less temperature and micro second time is necessary in the manufacturing of magnesium-silicon carbide composites. Underwater shock consolidation process is a one-stage densification process, which involves a very rapid and intense deposition of shock energy on powder particle surface using transmission of shock waves in water. Here the pressure during the shock consolidation is about 10-13.2 GPa. In the shock consolidation process, the important step is the powder milling using a ball mill for the uniform distribution of the matrix (Magnesium) and the reinforcement (Silicon carbide). However, for the best realization of mechanical properties various parameters of powder mixing must be optimized. In this work, parameters such as ball to powder ratio (10:1, 20:1 mass%), milling speed (100,150 and 250 rpm) milling time (3.6, 18, 36 and 54 ks), are varied and the structural changes in the powders are observed. Several experiments on shock consolidation are conducted. Microstructural characterization using scanning electron microscope and optical microscope of the mixed powders and the recovered composites are examined.

**Keywords:** Milling Parameters, Shock Wave, Microstructural Characterization.

### 1. INTRODUCTION

In the world of modernization, light-weight magnesium alloys have recently received much more attention due to their attractive properties. With its ~ 35% lower density when compared to aluminum, it carries tremendous potential for engineering applications requiring high specific mechanical properties. Magnesium based composites due to their inherently low density and ensuring potential to exhibit high specific mechanical properties are demandable for weight-critical structural application. Increasing demand for fuel consuming and low-level emissions in the automobile industry has favorably increased the use of these materials in recent years. A recent industrial review revealed that there are 60 different types of components, from instrument panel to engine component is developed for uses. The uses of magnesium in automobile parts are increased in the world at an average rate 15% per year [1].

The properties of metal-matrix composites (MMC) depend upon the properties of the reinforcement phase of the matrix and of the interface. A strong interfacial bonding without any degradation of the reinforcing phase is one of the prime objectives in the development of MMC. One of the major limitations of magnesium and its alloys is their low elastic modulus, which limits its use in conventional and critical engineering applications as structural materials. With the advent of the metal matrix composites, it is possible to increase the stiffness and hardness of the metallic matrices by addition of stiffer and harder ceramic reinforcement. In addition, judicious selection of the type, size and volume fraction of ceramic particulates for a given metallic matrix also enhance tribological characteristics, dimensional stability, damping capacity and elevated temperature creep properties [2,3]. SiC are very easily available in the economic point of view and have high wettability with magnesium matrix [2]. A uniform distribution is essential

for fabrication of good composites. High-energy ball mill is effective to mix the reinforcement and the matrix. Ball mill can reduce the particle size with the attention of the speed, time and grinding medium. After fixing the milling condition, underwater shock wave was applied. In a microsecond of time the desired composites are obtained. The unique potential of the shock consolidation of powders results from a combination of very high pressure, high velocity and the simplicity of equipment.

The present research focused on the changing milling parameters to fix the Mg-SiC powder mixing by ball mill. Uniform distributions of the metal-matrix are desirable. After shock wave loading on the powder Mg-SiC composites are formed and microstructure of the composite is studied.

## 2. EXPERIMENTAL PROCEDURE

### 2.1 Materials

In the present study, pure magnesium of 99% purity, with an average particle size 100 mesh was used as a base material and silicon carbide of 99% purity, with an average particle size 8000 mesh, were used as the ceramic reinforcement phase.

### 2.2 Processing

Mechanical alloying, which is usually achieved by high-energy ball milling has been utilized for producing metal or ceramic based composite powders. In this work, high-energy ball mill was used to reduce the particle size and uniformed distribution of the metal-matrix. At first 70 mass% Mg and 30 mass% SiC were taken for mixing as a weight ratio. The milling process was carried out in a planetary ball mill at room temperature using hardened still steel vial and under high purity argon atmosphere. The powder handling was done in the gloves box in the argon atmosphere. The milling medium was steel balls, 5 mm in diameter. The ball to powder weight ratio (BPR) and rotational speed were 10:1, 20:1 and 100, 150, 250 rpm, respectively [4]. The powder was milled for 3.6, 18, 36 and 54 ks respectively to achieve homogeneous distribution. XRD analysis was performed by means of X-ray diffractometer with Cu K $\alpha$  radiation. The amounts and distribution of morphology of the powder were studied in the polished sections by scanning electron microscopy (SEM) and optical microscopy.

Shock consolidation is one of the techniques to produce composites from powders. By shock wave crack free material can be obtained. Good consolidation results in the case of soft powder. The very short time scale of the shock pulse during compaction is through to strongly inhibit the usual quasi-static kinetic processes that tend to have much longer time. An advantage is the capability to densify powders into near-net-shaped compacts with essentially no thermal effects, such as grain growth and crystallization of amorphous structure.

The explosive assembly (Fig. 1) fabricated using mild steel, consisted of three parts: (i) the explosive region in which high explosive was packed; (ii) the water container in which the shock transmitting medium, water

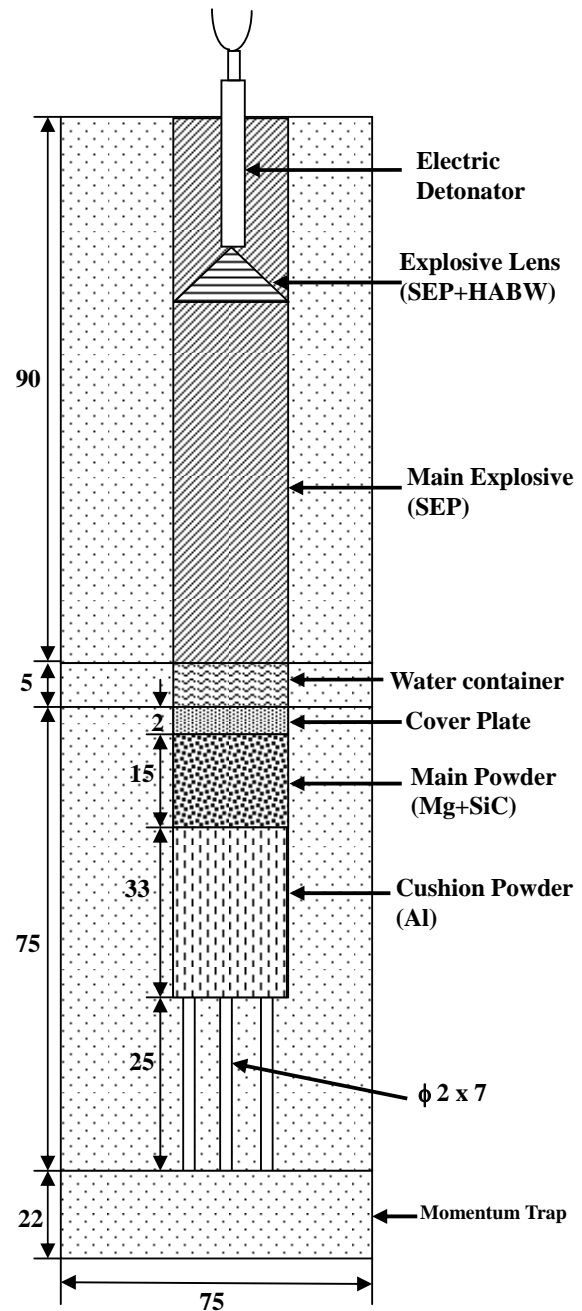


Fig 1. Schematic illustration of under water shock compaction

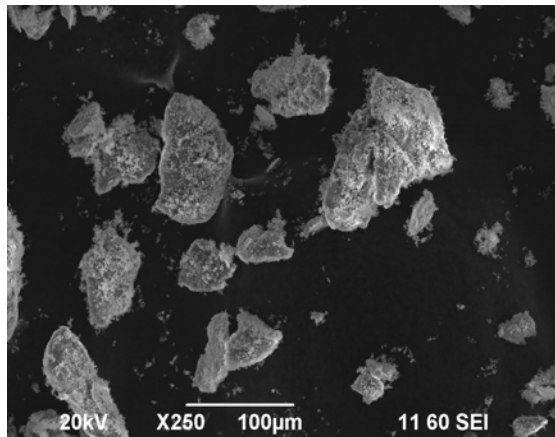
was stored; (iii) the powder mix region where the mixed powder were stacked. The detonation of an explosive by an electric detonator generates a detonation wave. The detonation wave propagates from the top to the bottom of the explosive chamber. When the detonation wave impinges on the water, an underwater shock wave is generated in the water chamber. As the underwater shock wave travels straight through the water chamber and at last it interacts with the main powder container. By adjusting the mass and the detonation velocity of the explosive shock pressure and shock duration can be controlled.

The containers are unusable following shock compaction. The shock waves generated using a planar

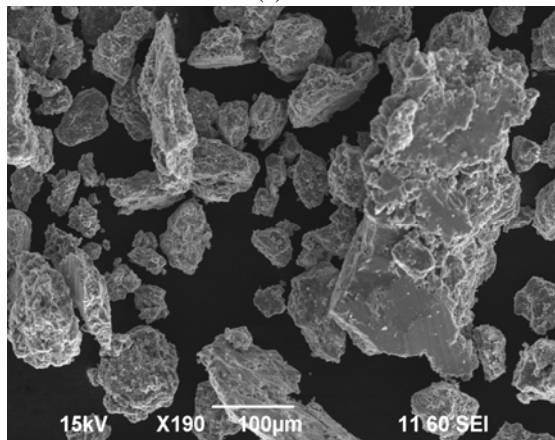
impact system by the use of an explosive lens [5], which was made, by the use of two explosive, SEP and HABW (both of Asahi-Kasei Corp., Japan; detonation velocity: 6.97 and 4.75 km/s, density: 1310 and 2200 kg/m<sup>3</sup>, respectively) were uniform applied on the blend. Changing the water column can change the shock pulse. Three-layered stacking arrangement [6] was adopted for the easy recovery of the sample. In order to take out the compacts from the powder containers machining was done. After obtaining the specimens, some of their properties were measured and the cross-sectional areas of the samples were analyzed by scanning electron microscope (SEM) and optical microscope.

### 3. RESULTS AND DISCUSSION

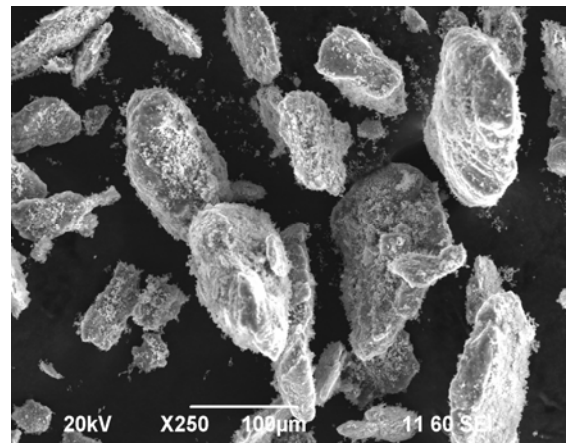
High-energy mechanical milling was used for the uniform distribution of the magnesium and SiC powder mixing. The effect of milling time and milling speed are taken into account in the case of this experiment. In the case, when the milling speed is 100 rpm the particle size are small and homogeneous with the increase of the milling time of 36 ks and 54 ks, respectively. We used two balls to powder ratio, which are 10:1 and 20:1, respectively.



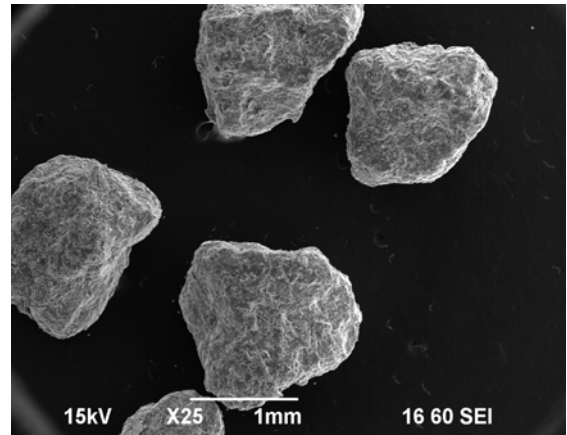
(a)



(b)



(c)

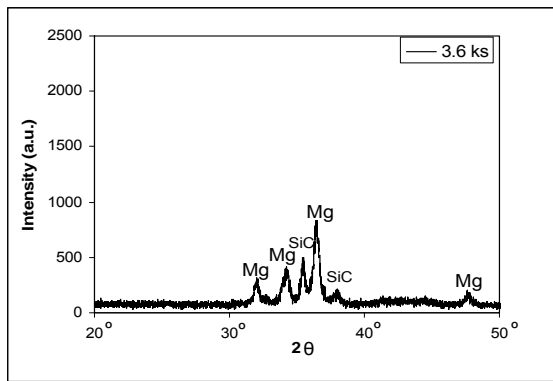


(d)

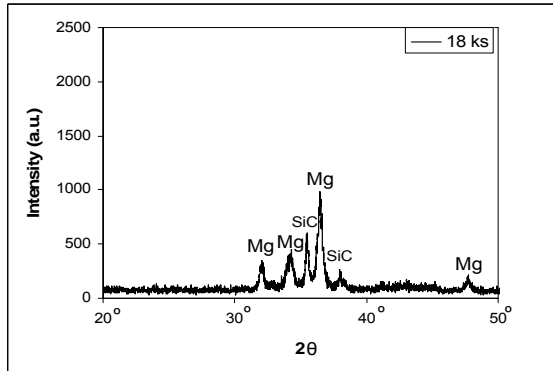
Fig 2. SEM micrographs of different particle morphologies of magnesium and silicon carbide powders in 54 ks mixing: a) 100 rpm b) 150 rpm (10:1 BPR) and c) 100 rpm d) 150 rpm (20:1 BPR).

The results of the SEM studies conducted on the Mg/SiC specimens revealed the existence of a completely recrystallised matrix. The presence of the porosity was minimal and the distribution of SiC particulate was fairly uniform. The interfacial integrity between SiC reinforcement and Mg matrix was found to be good in the case of 100 rpm specimens (Fig. 2(a), the other (Fig. 2 (c)) investigated in the present study. But in case of 150 rpm the particle size was not uniform and homogeneous. The particle become big and agglomeration were seen. The powder taken from the container of the ball mill was difficult because of powder sticking on the container. Where as, it was easy to take mixed powder in 100 rpm.

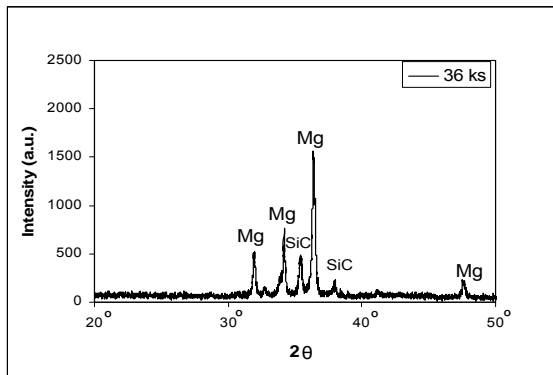
Fig. 3. shows there is no change of phase in the X-ray patterns of the mixed powder for the composite. It is known that mechanical milling reduces the particle size and creates a large surface area of the particle.



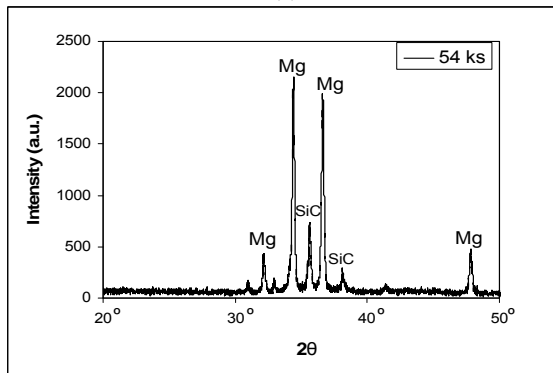
(a)



(b)



(c)



(d)

Fig 3. XRD spectra of mechanically milled 70 mass% Mg and 30 mass% SiC powders at different milling duration (a) 3.6 ks, (b) 18 ks, (c) 36 ks and (d) 54 ks (Cu-K $\alpha$ ).

In the case of 100 rpm in 20:1 BPR it has been observed that the particle size has been reducing and creates large surface area with the increase of milling duration. From the observation of the XRD the picks are increase with increase of the milling hours. That is a clear evidence of reduction of the particle size. There was no intermetallic compound formation.

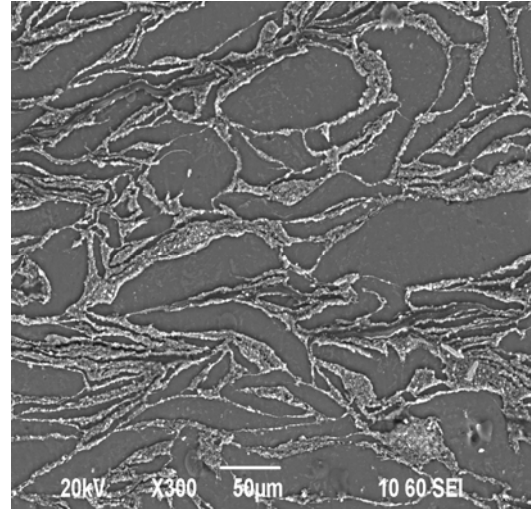


Fig 4. SEM micrographs of the magnesium and silicon carbide composites after compaction.

After shock wave deployed to the mixed powder with pressure the plastic flow of magnesium particles in the extrusion direction is disrupted by the interaction with SiC, which showed from the Fig. 4. As magnesium is softer than the ceramic, magnesium particle have to flow around the particles, changing the initial orientation. For highly elongated particles, it can be observed that the flow lines deviate from the original orientation near the particles.

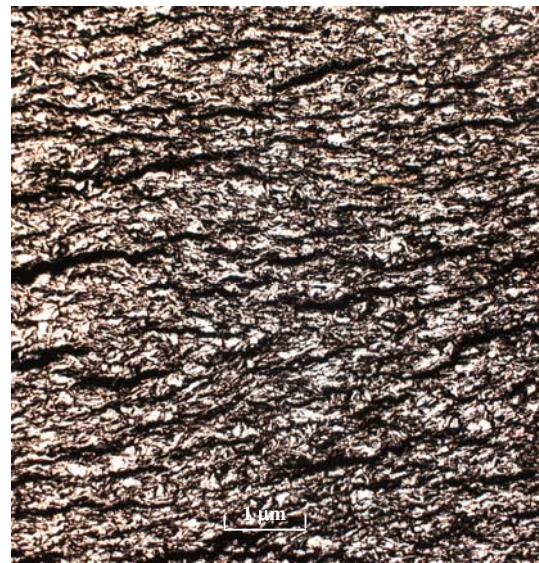


Fig 5. Optical micrograph of the recovered sample.

The experiment on 20:1, 100 rpm and 10:1, 100 rpm was recovered and the other experiment was not recovered. The microstructure of the recovered sample is shown in Fig. 5. In general, a homogeneous distribution of the particles was observed.

#### 4. CONCLUSION

By using high-energy ball milling of the mixture of powders, SiC particle reinforced 70 mass% Mg- 30 mass% SiC composite powder can be obtained. From the microstructure characterization, it has been observed that with the increase of the milling speed Mg powder become very reactive. In this respect, 100 rpm is the best milling speed than all other milling speed. The particle become very sticky to the container and recovery process were very difficult in the case of 150 and 250 rpm. Uniform distribution of the Mg and SiC reinforcement can be obtained with 100 rpm milling speed. From the XRD we found that there were no intermetallic compound formation and with the increase of milling hours in the case of 100 rpm particle size become reduced. So, we were chosen the best condition 100 rpm, 54 ks, 20:1 BPR and 70 mass% Mg- 30 mass% SiC for shock compaction. With this milled powder, composites were made in a microsecond with under water shock wave methods.

#### 5. REFERENCES

1. D. Magers, J. Brussels, in: B. L. Mordike, K.U. Kainer (Eds.), 1998, *Magnesium Alloys and Their Applications*, Werkstoff-Informationsgesellschaft, Wolfsburg, Germany.
2. D.J.Lloyd, 1994, "Particle Reinforced Aluminium-Magnesium Matrix Composites", *Int. Mat. Reviews*, 39(1): 1.
3. D.M. Lee, B. K. Suh, B. G. Kim, J. S.Lee and C. H. Lee, 1997, "Fabrication, Microstructures, and Tensile Properties of Magnesium alloy AZ91/SiCp Composites Produced by Powder Metallurgy", *Materials Science and Technology*, 13: 590.
4. F. Delogu, G. Cocco, 2006, "Microstructural Refinement of Ceramic Powders Under Mechanical Processing Conditions", *Journal of Alloys Compounds*, 420: 246-250.
5. K. Raghukandan, K. Hokamoto, J. S. Lee, A. Chiba and .C. Pai., 2003, " An Investigation on Underwater Shock consolidated Carbon Fiber Reinforced Al Composites", *Journal of Materials Processing Technology*, 134: 329-337.
6. S. Kimura, A. Chiba, Y. Morizono, 2001, "Fabrication of titanium/hydroxyapatite functionally graded bio-materials by underwater shock compaction", *Proc. 4<sup>th</sup> Int. Symp. on Impact Engineering, Kumamoto, Japan*, p.905.

#### 6. NOMENCLATURE

Symbol	Meaning	Unit
rpm	Revolution Per Minute	(r/min)
BPR	Ball to Powder Ratio	(mg/mg)

#### 7. MAILING ADDRESS

A. Nayeem Faruqi  
 c/o., Professor Kazuyuki Hokamoto  
 Shock Wave and Condensed Matter Research Center  
 Kumamoto University,  
 2-39-1 Kurokami, Kumamoto 860-8555,  
 JAPAN.  
 Phone: +81-9028547687(cell).  
 E-mail: nayeemfaruqi@yahoo.com



## VIBRATION CONTROL OF SMART COMPOSITE SHELL STRUCTURES USING GENETIC ALGORITHM

Debabrata Chakraborty<sup>1</sup> and Tarapada Roy<sup>2</sup>

<sup>1</sup>Mechanical Engineering, IIT Guwahati, India

<sup>2</sup>Mechanical Engineering, NIT Rourkela, Orissa, India

### ABSTRACT

The present article deals with the optimal vibration control of smart fiber reinforced polymer (FRP) composite structures using layered shell finite element and linear quadratic regulator (LQR) optimal control scheme. Coupled electromechanical finite element (FE) formulations have been developed for analysis of smart curved shell structures having piezoelectric sensors and actuators patches. A real coded GA based LQR control scheme has been used for designing an optimal controller to maximize closed loop damping ratio while keeping actuation voltage within the limit. The developed GA based LQR control has been applied to smart FRP ellipsoidal composite shells structures for simulation of active vibration control. It has been observed that the present GA based design of smart structures for determination of optimal control gain is far superior to the conventional design using LQR in terms of effective closed loop damping ratio.

**Keywords:** Smart Structures, Active Control, Genetic Algorithm.

### 1. INTRODUCTION

Most of the lightweight FRP structures are susceptible to large vibration with long decay time and thus require suitable integration of active control means to show better performance under operation. Piezoelectric materials integrated with such structures can act as sensors and actuators thus making the structure smart. This kind of smart structures could be used for active vibration control. At present, the linear quadratic regulator (LQR) control approach has been extensively used in vibration control with appropriate weighting matrices, which gives optimal control-gain by minimizing the performance index. Even though, trial and error method is used to select the weighting matrices, an optimal selection of weighting matrices is of significant importance from the control point of view. Some of the important works in this direction are presented in the following paragraph.

Bhattacharya et al [1] used linear quadratic regulator (LQR) strategy for vibration suppression of spherical shells made of laminated composites by trial and error selection of [Q] and [R] matrices. Ang et al [2] proposed the use of total weighted energy method to select the weighting matrices. Narayanan and Balamurugan [3] presented finite element modeling of laminated structures with distributed piezoelectric sensor and actuator layers and applied LQR control scheme to control the displacement by trial and error selection of [Q] and [R] matrices. In recent years, genetic algorithm (GA) has been extensively applied for optimization of engineering problems and some of the important works on application of GA are described here. Binary coded

GA has been applied by Han and Lee [4] to find locations of two piezoelectric sensors and actuators in a cantilever composite plate based on the open loop performance. Sadri et al [5] used Gray coded GA to find the eight coordinates of two piezoelectric actuators in a simply supported plate based on the open loop performance. Abdullah et al [6] used GA to simultaneously place collocated sensor/actuator pairs in multi-storey building while using output feedback as the control law in terms of minimizing the quadratic performance i.e. weighted energy of the system and concluded that the decision variables in this optimization problem were greatly dependent on the selection of weighting matrices [Q] and [R]. Robandi et al [7] presented the use of genetic algorithm for optimal feedback control in multi-machine power system. Deb and Gulati [8] presented simulated binary crossover (SBX) and parameter based mutation operator to be used for effective creation of children solutions from parent solutions. Yang and Soh [9] presented a simultaneous optimization method considering several design variables such as placement of collocated piezoelectric sensors/actuators and size of sensor/actuator and feedback control gain for vibration suppression of simply supported beam by minimizing the equivalent total mechanical energy of the system. However, they did not consider input energy in the used objective function i.e. equivalent total mechanical energy as such did not show the actuators voltages. Wang et al [10] addressed the topology optimization of collocated sensors/ actuators pairs for torsional vibration control of a laminated composite cantilever plate using output feedback control. Liu et al [11] used a spatial H2 norm of



the closed loop transfer matrix for finding the optimal nodal points for sensing displacement and applying actuation for the control of a fixed-fixed plate. Swann and Chattopadhyay [12] developed an optimization procedure to detect arbitrarily located discrete delamination in composite plates using distributed piezoelectric sensors.

From the literature review, it has been observed that a number of works have been reported on the vibration control of simple beam or plate structures.. Most of the published work in this direction used LQR control scheme where [Q] and [R] matrices have been chosen by trial and error, however choice of [Q] and [R] decides the optimal gain. Very few works discussed about actuation voltage while maximizing control performance. Keeping in mind the above points, the present work aims at developing a vibration control module of smart shell structures where the optimal controller will be designed based on a GA-LQR scheme, so that input /actuation voltage is kept within limit.

## 2. FE FORMULATION AND LQR CONTROL

Figure 1 shows a smart laminated structure having two thin patches of piezoelectric material bonded on the top and bottom surfaces of the base structure. The control laws determine the feedback signal to be given to the actuator depending upon the sensor signal. In Fig.1,  $F(t)$  is the excited force,  $\phi_s$  is the voltage generated by the sensor and  $\phi_a$  is the voltage input to the actuator in order to control the displacement by developing effective control force.

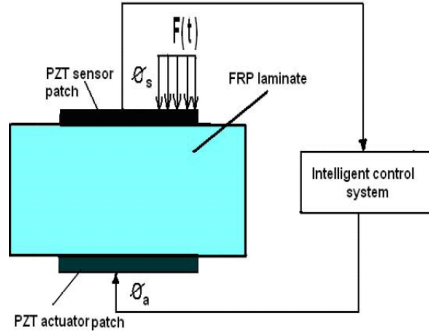


Fig 1. Schematic of a smart laminated plate

In the present formulation, the degenerate shell element [13] kinematics has been considered using a first-order shear deformation theory based on the Reissner–Mindlin assumptions. Figure 2 shows the general smart shell element with composite and piezoelectric layers. It has been assumed that the thin piezoelectric patches are perfectly bonded to the surface of the structure.

In the isoparametric formulation, the coordinates of a point within an element are obtained as

$$\begin{Bmatrix} x \\ y \\ z \end{Bmatrix} = \sum_{k=1}^8 N_k(\xi, \eta) \begin{Bmatrix} x_k \\ y_k \\ z_k \end{Bmatrix}_{mid} + \sum_{k=1}^8 N_k(\xi, \eta) \frac{h_k}{2} \zeta V_{3k} \quad (1)$$

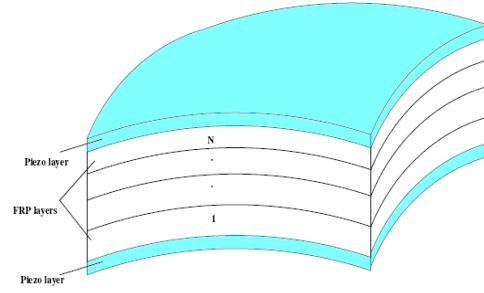


Fig 2. Smart layered shell element.

$$\text{where } \begin{Bmatrix} x_k \\ y_k \\ z_k \end{Bmatrix}_{mid} = \frac{1}{2} \left( \begin{Bmatrix} x_k \\ y_k \\ z_k \end{Bmatrix}_{top} + \begin{Bmatrix} x_k \\ y_k \\ z_k \end{Bmatrix}_{bottom} \right) \text{ and } h_k \text{ is the shell}$$

thickness at the node  $k$ .

The displacement field is described by the five degrees of freedom of a normal viz. the three displacements of its mid-point  $(u_k \ v_k \ w_k)^T_{mid}$  and two rotations  $(\beta_{1k}, \beta_{2k})$ . The displacements of a point on the normal resulting from the two rotations are calculated as

$$\begin{Bmatrix} u \\ v \\ w \end{Bmatrix} = \sum_{k=1}^8 N_k \begin{Bmatrix} u_k \\ v_k \\ w_k \end{Bmatrix}_{mid} + \sum_{k=1}^8 N_k \zeta \frac{h_k}{2} \begin{bmatrix} V_{1k}^x & -V_{2k}^x \\ V_{1k}^y & -V_{2k}^y \\ V_{1k}^z & -V_{2k}^z \end{bmatrix} \begin{Bmatrix} \beta_{1k} \\ \beta_{2k} \end{Bmatrix} \quad (2)$$

where  $u_k, v_k, w_k$  are the displacements of node  $k$  on the mid-surface along the global directions respectively, and  $N_k$  is the shape function at  $k^{th}$  node. Neglecting normal strain component in the thickness direction, the five strain components in the local coordinate system are given by

$$[\varepsilon] = \begin{Bmatrix} \varepsilon_x' \\ \varepsilon_y' \\ \varepsilon_z' \\ \gamma_{xy}' \\ \gamma_{xz}' \\ \gamma_{yz}' \end{Bmatrix} = \begin{Bmatrix} \frac{\partial u'}{\partial x'} \\ \frac{\partial v'}{\partial y'} \\ \frac{\partial w'}{\partial z'} \\ \frac{\partial u'}{\partial y'} + \frac{\partial v'}{\partial x'} \\ \frac{\partial u'}{\partial z'} + \frac{\partial w'}{\partial x'} \\ \frac{\partial v'}{\partial z'} + \frac{\partial w'}{\partial y'} \end{Bmatrix} \quad (3)$$

If  $\{d_k^e\} = \{u_k \ v_k \ w_k \ \beta_{1k} \ \beta_{2k}\}^T$  is the vector of nodal variables corresponding to  $k^{th}$  node of the element, the generalized nodal variables of an element  $\{d^e\}$  is expressed as  $\{d^e\} = [d_1^e]^T \ [d_2^e]^T \ [d_3^e]^T \ [d_4^e]^T \ [d_5^e]^T \ [d_6^e]^T \ [d_7^e]^T \ [d_8^e]^T$ . The

strain displacement equation relating the strain components  $\{\varepsilon\}$  in global coordinate system to the nodal variables  $\{d^e\}$  is expressed as

$$\{\varepsilon\} = \sum_{k=1}^8 [(B_u)_k]^e \{d_k^e\} = [B_u^e] \{d^e\} \quad (4)$$

and the stress-strain relation in the global coordinate system is

$$\{\sigma\} = [c] \{\varepsilon\} \quad (5)$$

where  $\{\sigma\} = [\sigma_x \ \sigma_y \ \tau_{xy} \ \tau_{xz} \ \tau_{yz}]^T$  are the stress components and  $[c]$  is the elastic constitutive matrix in global

coordinate system.

The linear piezoelectric constitutive equations coupling the elastic and electric fields can be respectively expressed as the direct and converse piezoelectric equations as

$$\{D\}=[e]\{\varepsilon\}+[e]\{E\} \quad (6)$$

$$\{\sigma\}=[C]\{\varepsilon\}-[e]^T\{E\} \quad (7)$$

where  $\{D\}$  denotes the electric displacement vector,  $\{\sigma\}$  denotes the stress vector,  $\{\varepsilon\}$  denotes the strain vector and  $\{E\}$  denotes the electric field vector. Further  $[e]=[d][C]$ , where  $[e]$  comprises the piezoelectric coupling constants,  $[d]$  denotes the piezoelectric constant matrix and  $[e]$  denotes the dielectric constant matrix. The element has been assumed with one electrical degree of freedom at the top of the piezoelectric actuator and sensor patches,  $\phi_a^e$  and  $\phi_s^e$  respectively. Electrical potential has been assumed to be constant over an element and vary linearly through the thickness of piezoelectric patch. For a thin piezoelectric patch, the component of the electric field in the thickness direction is dominant. Therefore, the electric field can be accurately approximated with a non-zero component only in the thickness direction. With this approximation, the electric field strengths of an element in terms of the electrical potential for the actuator and the sensor patches respectively are expressed as

$$\{-E_a^e\} = [B_a^e] \begin{Bmatrix} 0 \\ 0 \\ 1/h_a \end{Bmatrix} \begin{Bmatrix} \phi_a^e \\ \phi_s^e \end{Bmatrix} \quad (8)$$

$$\{-E_s^e\} = [B_s^e] \begin{Bmatrix} 0 \\ 0 \\ 1/h_s \end{Bmatrix} \begin{Bmatrix} \phi_a^e \\ \phi_s^e \end{Bmatrix} \quad (9)$$

where subscripts  $a$  and  $s$  refer to the actuator patch and the sensor patch, respectively. The superscript  $e$  denotes the parameter at the element level.  $[B_a^e]$  and  $[B_s^e]$  are the electric field gradient matrices of the actuator and the sensor elements respectively. It should be noted that the electric potential is introduced as an additional degree of freedom on an element level.

The coupled finite element matrix equation derived for a one-element model becomes

$$\begin{bmatrix} [M_{uu}^e] & [0] & [0] \\ [0] & [0] & [0] \\ [0] & [0] & [0] \end{bmatrix} \begin{Bmatrix} \ddot{d} \\ \ddot{\phi}_a \\ \ddot{\phi}_s \end{Bmatrix} + \begin{bmatrix} [K_{uu}^e] & [K_{ua}^e] & [K_{us}^e] \\ [K_{au}^e] & [K_{aa}^e] & [0] \\ [K_{su}^e] & [0] & [K_{ss}^e] \end{bmatrix} \begin{Bmatrix} d \\ \phi_a \\ \phi_s \end{Bmatrix} = \begin{Bmatrix} F^e \\ G^e \\ 0 \end{Bmatrix} \quad (10)$$

Considering a laminate made up of  $N$  layers with a total thickness of  $T$ , the elemental mass and transformed stiffness matrices can be written as

$$\text{Structural mass: } [M_{uu}^e] = \int_V \rho [N]^T [N] dV \quad (11)$$

Structural stiffness:

$$[K_{uu}^e] = \frac{2}{T} \int_{-1}^1 \int_{-1}^1 \sum_{k=1}^N \frac{t_k - t_{k-1}}{2} \int_{-1}^1 [B_u]^T [C] [B_u] |J| d\xi d\eta d\zeta \quad (12)$$

Dielectric conductivity:

$$[K_{\phi\phi}^e] = -\frac{2}{T} \int_{-1}^1 \int_{-1}^1 \sum_{k=1}^N \frac{t_k - t_{k-1}}{2} \int_{-1}^1 [B_\phi]^T [\varepsilon] [B_\phi] |J| d\xi d\eta d\zeta \quad (13)$$

Piezoelectric coupling matrix:

$$[K_{u\phi}^e] = \frac{2}{T} \int_{-1}^1 \int_{-1}^1 \sum_{k=1}^N \frac{t_k - t_{k-1}}{2} \int_{-1}^1 [B_u]^T [e]^T [B_\phi] |J| d\xi d\eta d\zeta \quad (14)$$

After assembling the elemental stiffness matrices, the global set of equations become

$$[M_{uu}] \ddot{d} + [K_{uu}] d + [K_{ua}] \phi_a = \{F\} \quad (15)$$

$$[K_{au}] d + [K_{aa}] \phi_a = \{G\} \quad (16)$$

$$[K_{su}] d + [K_{ss}] \phi_s = 0 \quad (17)$$

For open electrodes, charge can be expressed as

$$\{G\} = 0 \quad (18)$$

The overall dynamic finite element equation can be is

$$[M_{uu}] \ddot{d} + [K_{uu}] d + [K_{ua}] [K_{aa}]^{-1} [K_{au}] - [K_{us}] [K_{ss}]^{-1} [K_{su}] d = \{F\} - [K_{ua}] \phi_a \quad (19)$$

where  $[M_{uu}]$  is the global mass matrix,  $[K_{uu}]$  is the global elastic stiffness matrix,  $[K_{ua}]$  and  $[K_{us}]$  are the global piezoelectric coupling matrices of actuator and sensor patches respectively.  $[K_{aa}]$  and  $[K_{ss}]$  are the global dielectric stiffness matrices of actuator and sensor patches respectively. The displacement vector  $d(t)$  is approximated by the modal superposition of the first ' $r$ ' modes as

$$d(t) \approx [\psi] \{\eta(t)\} \quad (20)$$

where  $[\psi] = [\psi_1 \psi_2 \dots \psi_r]$  is the truncated modal matrix.

The decoupled dynamic equations considering modal damping can be written as

$$\{\ddot{\eta}_i(t)\} + 2\xi_{di} \omega_i \dot{\eta}_i(t) + \omega_i^2 \eta_i(t) = [\psi]^{-T} \{F\} - [\psi]^T [K_{ua}] \phi_a \quad (21)$$

where  $\xi_{di}$  is the damping ratio. In state-space form

$$\dot{X} = [A] X + [B] \phi_a + [\hat{B}] u_d \quad (22)$$

where,  $[A] = \begin{bmatrix} [0] & [I] \\ [-\omega_i^2] & [-2\xi_{di}\omega_i] \end{bmatrix}$  is the system matrix,

$[B] = \begin{bmatrix} [0] \\ -[\psi]^T [K_{ua}] \end{bmatrix}$  is the control matrix,  $[\hat{B}] = \begin{bmatrix} [0] \\ [\psi]^T \{F\} \end{bmatrix}$  is the

disturbance matrix,  $\{u_d\}$  is the disturbance input vector,

$\{\phi_a\}$  is the control input, and

$$\dot{X} = \begin{Bmatrix} \dot{\eta} \\ \eta \end{Bmatrix} \quad \text{and} \quad X = \begin{Bmatrix} \eta \\ \dot{\eta} \end{Bmatrix} \quad (23)$$

The sensor output equation can be written as

$$y = [C_0] X \quad (24)$$

where output matrix  $[C_0]$  depends on the modal matrix  $[\psi]$  and the sensor coupling matrix  $[K_{us}]$ .

LQR optimal control theory has been used to determine the control gains by minimizing a cost function or a performance index given by

$$J = \frac{1}{2} \int_0^t (y)^T [Q](y) + (\phi_a)^T [R](\phi_a) dt \quad (25)$$

where  $[Q]$  and  $[R]$  are the semi-positive-definite and positive-definite weighting matrices on the outputs and control inputs, respectively.

Minimization of  $J$  leads to the steady-state matrix Riccati equation whose solution leads to the gain as

$$[G_c] = [R]^{-1} [B]^T [K] \quad (26)$$

Considering output feedback, actuation voltage can be calculated as

$$\{\phi_a\} = -[G_c] \{y\} \quad (27)$$

Ang and Quek [2] proposed that  $[Q]$  and  $[R]$  matrices could be determined considering weighted energy of the system as follows

$$[Q] = \begin{bmatrix} \alpha_2 [\psi]^T [K] [\psi] & [0] \\ [0] & \alpha_1 [\psi]^T [M] [\psi] \end{bmatrix}, \text{ and } [R] = \gamma [\hat{R}] \quad (28)$$

The proposed weighted energy of the system in the quadratic form is

$$\bar{\Pi} = \frac{1}{2} \alpha_1 \{X\}^T [M] \{X\} + \frac{1}{2} \alpha_2 \{X\}^T [K] \{X\} + \frac{1}{2} \gamma \{\phi_a\}^T [\hat{R}] \{\phi_a\} \quad (29)$$

where,  $\alpha_1, \alpha_2$  and  $\gamma$  are the coefficients associated with total kinetic energy, strain energy and input energy respectively. These coefficients will take different values in the control algorithm apart from the value of unity to allow for the relative importance of these energy terms.

Therefore, a search algorithm is required for finding  $[Q]$  and  $[R]$  by taking  $\alpha_1, \alpha_2$  and  $\gamma$  as variables, which will

$$\text{Maximize } \xi_d = \frac{1}{\sqrt{\left(1 + \frac{4\pi^2}{p^2}\right)}} \quad (30)$$

Subjected to  $\phi_i < \phi_{max}, i = 1, \dots, n_a$  (31)

where  $p = \ln\left(\frac{x_i}{x_{i+1}}\right)$ ,  $n_a$  is the number of actuators and  $\phi_{max}$

refers to the maximum voltage that can be applied on the actuators depending on the piezoelectric materials and thickness of the piezolayers.

### 3. GA APPROACH TO LQR

In the present work, weighting matrices have been determined by the genetic search to obtain best control gain for the optimal LQR scheme. Parameters  $\alpha_1, \alpha_2$  and  $\gamma$  in Eq. (36) have been represented by real-valued genes for finding  $[Q]$  and  $[R]$  matrices. The fitness value has been calculated with respect to each chromosome using the following expression.

$$\xi_d = \begin{cases} \frac{1}{\sqrt{\left(1 + \frac{4\pi^2}{p^2}\right)}} & \text{if } \phi_i < \phi_{max} \\ 10^{-8} \times \frac{1}{\sqrt{\left(1 + \frac{4\pi^2}{p^2}\right)}} & \text{otherwise} \end{cases} \quad (32)$$

The ranges of  $\alpha_1, \alpha_2$  and  $\gamma$  are taken as  $0 < \alpha_1 \leq 200$ ,  $0 < \alpha_2 \leq 200$  and  $0 < \gamma \leq 2$  where controlled

response depends on  $\alpha_1, \alpha_2$  and  $\gamma$ . Parents have been selected through roulette wheel operator and offspring have been created using simulated binary crossover and polynomial mutation operator [8]. Genetic evolution has been continued for large number of generations till the fitness converges.

## 4. RESULTS AND DISCUSSIONS

Based on the formulations described in the previous section a code has been developed. The code is first validated with benchmark problems and then applied for simulation of vibration control.

### 4.1 Validation

A cantilever bimorph (as shown in Fig. 3) made of two PVDF layers laminated together is subjected to a unit external voltage. The transverse deflections calculated have been compared with the already published results of Hwang and Park [14] in the Table 1 and excellent agreements have been achieved.

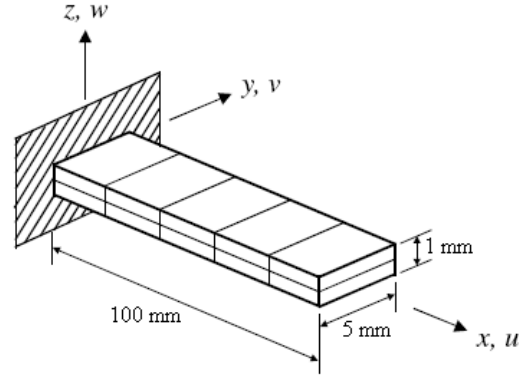


Fig 3. Schematic view of a cantilever bimorph beam.

Table 1: Deflections of piezoelectric bimorph actuator

Distance from fixed end (mm)	Deflection ( $\mu\text{m}$ )	
	Hwang and Park [14]	Present FEM
20	0.0131	0.0136
40	0.0545	0.0540
60	0.1200	0.1223
80	0.2180	0.2181
100	0.3400	0.3416

### 4.2 Control of an Ellipsoidal Shell Panel

In this study, a simply supported smart graphite/epoxy composite ellipsoidal shell panel on a square base ( $a = b = 0.04$  m) has been considered to study the vibration control. The major axis length is  $2 \times R$  and minor axis length is  $1.5 \times R$ . The radius is taken as  $R = 0.06$  m. The stacking sequence of each smart graphite/epoxy laminated structure considered is  $[p/[0/90]_s/p]$ . Here 'p' stands for piezo-patches one for sensing and the other for actuation. In all the cases, thickness of each piezoelectric patch has been considered as 0.5 mm, the allowable voltage of each PZT patch has been taken as 500V[15]

and thickness of each FRP composite ply has been considered as 0.75 mm. Table 2 shows the material properties considered in the present study.

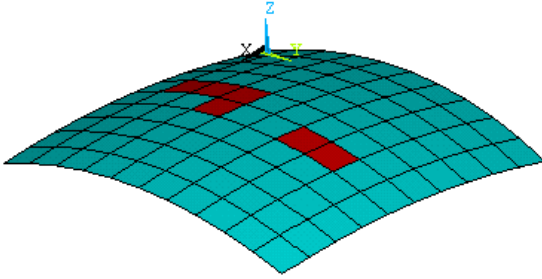


Fig 4. Collocated sensors and actuators location

Six numbers of collocated sensors and actuators have been considered and based on an optimal placement scheme those are placed as shown in figure 4. A modal damping ratio ( $\xi_d$ ) of 1% has been assumed to obtain open loop response and to calculate LQR gains. The smart panel has been subjected to an impulse load of 10 N at the center for a duration of  $\tau / 25$  seconds (where  $\tau$  is the time period corresponding to first natural frequency of the system) and impulse responses of this panel have been calculated with a time step of  $\tau / 100$  seconds.

Table 2: Material Properties

Material properties	Structural laminae	PZT
$E_1$	172.5 GPa	63.0 GPa
$E_2 = E_3$	6.9 GPa	63.0 GPa
$G_{12} = G_{13}$	3.45 GPa	24.6 GPa
$G_{23}$	1.38 GPa	24.6 GPa
$\nu_{12} = \nu_{13} = \nu_{23}$	0.25	0.28
$\rho$	1600 kg m <sup>-3</sup>	7600 kg m <sup>-3</sup>
$e_{31} = e_{32}$	0.0	10.62 C m <sup>-2</sup>
$\epsilon_{11} = \epsilon_{22} = \epsilon_{33}$	0.0	0.1555x10 <sup>-7</sup> F m <sup>-1</sup>

Uncontrolled displacement of the ellipsoidal shell panel is shown in Fig.5. The LQR and GA-LQR controlled displacement histories of smart ellipsoidal panel have been depicted in Fig. 6. It could be observed from figure 6 that both simple LQR and GA-LQR could control the vibration. However, in the GA-LQR controlled response of the panel, the closed loop-damping ratio achieved has been 17% compared to only 3.12% in the case of simple LQR control scheme. The maximum actuator voltage variations for simple LQR and GA-LQR control scheme have been shown in Fig. 7, which clearly shows that the GA-LQR control scheme could achieve, better control with minimum actuation voltage requirement. From this study it could be concluded that GA-LQR control scheme leads to the maximization of closed loop damping ratio with minimum input/actuator voltage within the limit.

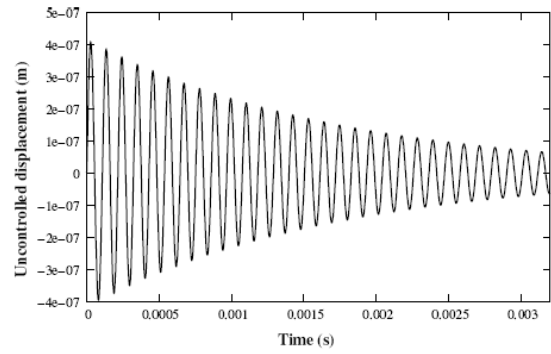


Fig 5. Uncontrolled displacement history

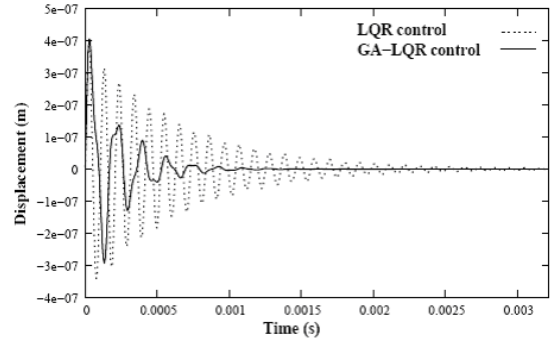


Fig 6. LQR and GA-LQR controlled displacements

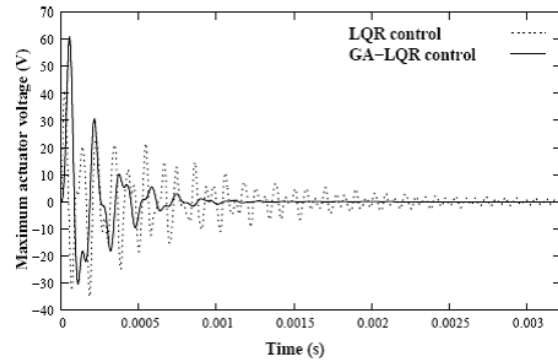


Fig 7. Maximum actuator voltage variation using LQR and GA-LQR control schemes

## 5. CONCLUSIONS

In the present work, a GA based LQR optimal control scheme have been developed for optimal vibration control of smart shell structures. This module along with layered shell finite element analysis has been used to simulate active vibration control of smart ellipsoidal shell FRP structures. It has been observed that the present GA based LQR scheme is far superior to conventional LQR scheme in terms of effective closed loop damping ratio and minimizing the actuator voltage requirement while keeping it within limit. Therefore this could be advantageously used in design of control gains in smart structures applications.

## 6. REFERENCES

1. Bhattacharya, P., Suhail, H. and Sinha, P. K., 2002, "Finite Element Analysis and Distributed Control of Laminated Composite Shells using LQR/IMSC Approach", *Aerospace Science and Technology*, 6:273–281.
2. Ang, K. K., Wang, S.Y. and Quek S. T., 2002, "Weighted Energy Linear Quadratic Regulator Vibration Control of Piezoelectric Composite Plates", *Journal of Smart Materials and Structures*, 11:98-106.
3. Narayanan, S. and Balamurugan, V., 2003, "Finite Element Modeling of Piezolaminated Smart Structures for Active Vibration Control with Distributed Sensors and Actuators", *Journal of Sound and Vibration*, 262:529–562.
4. Han, J.H. and Lee, L., 1999, "Optimal Placement of Piezoelectric Sensors and Actuators for Vibration Control of a Composite Plate using Genetic Algorithms", *Journal of Smart Materials and Structures*, 8:257-267.
5. Sadri, A.M., Wright, J.R., and Wynne, R., 1999, "Modeling and Optimal Placement of Piezoelectric Actuators in Isotropic Plates using Genetic Algorithm", *Journal of Smart Materials and Structures*, 8:490-498.
6. Abdullah, M. M., Richardson, A. and Hanif, J. 2001, "Placement of Sensors/Actuators on Civil Structures using Genetic Algorithms", *Earthquake Engineering & Structural Dynamics*, 30 (8):1167-1184.
7. Robandi, I., Nishimori, K., Nishimura, R. and Ishihara N., 2001, "Optimal Feedback Control Design using Genetic Algorithm in Multimachine Power system", *Electrical Power and Energy Systems*, 23:263-271.
8. Deb, K. and Gulati, S., 2001, "Design of Truss-Structures for Minimum Weight Using Genetic Algorithms", *Finite Elements in Analysis and Design*, 37:447-465.
9. Yang, Y., Jin, Z. and Soh, C.K., 2005, "Integrated Optimal Design of Vibration Control System for Smart Beams using Genetic Algorithm", *Journal of Sound and Vibration*, 282:1293-1307.
10. Wang, S.Y., Tai, K. and Quek, S.T., 2006, "Topology Optimization of Piezoelectric Sensors/Actuators for Torsional Vibration Control of Composite Plates", *Journal of Smart Materials and structures*, 15(2):253-269
11. Liu, W., Hou, Z.K. and Demetriou, M.A., 2006, "A Computational Scheme for the Optimal Sensor/Actuator Placement of Flexible Structures using Spatial H-2 Measures", *Mechanical Systems and Signal Processing*, 20 (4):881-895.
12. Swann, C. and Chattopadhyay, A., 2006, "Optimization of Piezoelectric Sensor Location for Delamination Detection in Composite Laminates", *Engineering Optimization*, 38 (5):511-528.
13. Ahamad, S., Irons, B.M. and Zienkiewicz, O. C., 1970, "Analysis of Thick and Thin Shell Structure by Curved Elements", *Int. J. Numer Meth Engg*, 2:419-451.
14. Hwang, W. S. and Park, H. C. 1993, "Finite Element Modeling of Piezoelectric Sensors and Actuators", *AIAA Journal*, 31 (5):930-937.
15. Bruch, J.C., Sloss, J.M. and Sadek, I. S., 2002, "Optimal Piezo-Actuator Locations/Lengths and Applied Voltage for Shape Control of Beams", *Journal of Smart Materials and Structures*, 9:205-211.

## 7. ACKNOWLEDGEMENT

The authors gratefully acknowledge the support of the SERC (Grant No. SR/S3/MERC/0017/2008) of the Department of Science and Technology, Government of India.

## 8. MAILING ADDRESS

Prof. Debabrata Chakraborty  
Mechanical Engineering,  
IIT Guwahati, Guwahati 781 039, India  
E-mail: chakra@iitg.ernet.in

## WATER DISSOCIATION AND ADSORPTION ON NI-CR (111) BINARY ALLOY SURFACE AT 325 °C

N. Kumar Das and Tetsuo Shoji

Fracture and Reliability Research Institute, Graduate School of Engineering  
Tohoku University, Japan

### ABSTRACT

Tight-binding quantum chemical molecular dynamics study has been considered to analyze the Ni-Cr (111) surface primary stage oxidation at pressurized water reactor (PWR) environments. The present study has identified the water molecules adsorbed on top site of the surfaces by oxygen with 2.85 Å metal-oxygen bond distance. The simulated results are in well consistent with the previous theoretical study. Chromium-oxygen preferential bonds assisted to trap oxygen atoms around chromium which initiates the early stage passivation. Applied strain and defect raised the oxygen diffusion in the surface. It seems that the employed parameters heighten water dissociation. However, small atomic hydrogen diffused faster in the lattice than oxygen and it stands ahead of oxygen. Deeply diffused hydrogen is changed into negatively charged by taking electron from metallic atoms. It introduces reaction very early stage in the surface. Consequently, metal atoms become positively charged. Thus, it can originate slight repulsion in between them and works as an oxygen carrier. Thus, the process can be able to accelerate oxidation or primary stage crack initiation in surface.

**Keywords:** Strain, Atomic Defect, Water Dissociation, Oxidation, SCC Initiation.

### 1. INTRODUCTION

Nickel base alloy are widely used as structural materials for high temperature environment, such as boundary components of light water reactors (LWR), turbine blades etc. It requires very severe in-service conditions both mechanical and oxidation resistance [1]. Environmentally assisted cracking or more generally stress corrosion cracking (SCC) of structural materials is one of the limiting factors for the safe and economic operation of plants that cause an unauthorized shutdown. Recently, SCC has been found in pressurized water reactor (PWR) components such as vessel head penetrations and bottom mounted instrument nozzles fabricated with Alloy 600 and its weld metals [2, 3]. SCC initiation involves with many variables and it is a synergistic failure that is the combined actions of materials, mechanics and environment. SCC initiation is related with the localization and acceleration of oxidation at the interfaces considering microstructure, surface condition, and local environments. The localized mass transfer at the crack tip region is necessary to consider for fundamentals of SCC. Computational chemistry is a tool that can be able to incorporate with the existing methods to investigate the mechanism from atomistic level.

It is a challenging task to simulate SCC initiation of nickel-base alloy by computational chemistry. It comprised of several elements among them nickel and chromium are the major ingredients. X-ray photoelectron

spectroscopy (XPS) study of Ni-Cr alloy demonstrated that Cr is oxidized preferentially to Cr<sub>2</sub>O<sub>3</sub> initially but that Ni in the alloy is oxidized more rapidly to NiO than Ni metal [4]. Another XPS study of Alloy 600 found the chromite-rich inner layer due to inward oxygen penetration and simultaneously with outward migration of nickel [5]. On the other hand, there are several studies have been performed of the Ni/H<sub>2</sub>O, Ni/O or O<sub>2</sub> or oxygen preadsorbed Ni/H<sub>2</sub>O by first principles, molecular dynamics and experimental methods to elucidate water dissociation and adsorption phenomena [6-11]. In one of the studies suggested that preadsorbed oxygen plays an important role in industrial reactions on transition metal catalysts. The adhesion of water to nickel surfaces is very weak. Most recently, we have successfully applied multiscale methods to examine the initial stage oxidation of Ni-Cr (111) surface with different stress intensity [12]. Stress intensity significantly increases oxygen diffusivity in the surface subsequently it can intensify crack initiation. In this paper, we adhere to a tight-binding quantum chemical molecular (QCMD) approach to the early stage oxidation of the Ni-Cr binary alloy with applied external strain and atomic defect on the surfaces. Mainly we focus on the water dissociation and diffusion process because the surface reaction dynamics has not been considered so far.

### 2. COMPUTATIONAL DETAILS

We have designed well set of parameters for analyz-

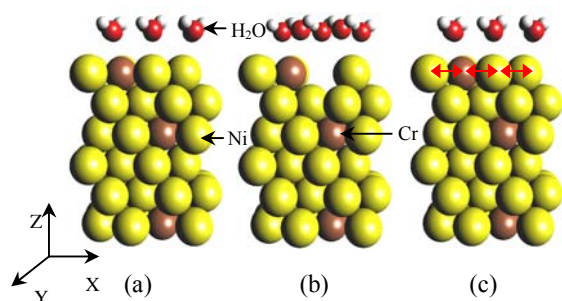


Fig 1. Slab surfaces for simulations (a) Ni-Cr (111) regular surface, (b) Ni-Cr (111) defect surface and (c) Ni-Cr (111) surface with applied strain.

-ing reaction dynamics of binary or ternary nickel base alloy or austenitic stainless steels. Diatomic calculation have been performed followed by the bulk systems by considering several parameters such as binding energy, equilibrium bond distance, cohesive energy, lattice constant and so on. The set of parameters are well consistent with the experimental and first principles calculated data, as for example, the calculated cohesive energy of nickel is 4.42 eV and the experimental value is 4.44 eV. More details about the parameterization can be seen elsewhere [13]. Tight-binding QCMD code ‘colors’ developed by Tohoku University has been employed for the water dissociation and adsorption on Ni-Cr (111) binary alloy surface at high temperature environment. This code is five thousand times faster than conventional density functional theory (DFT) and it can handle reaction dynamics of metal surfaces efficiently. Ni-Cr surface crystal structure has been created by using the software Material Studio. Figure 1 shows the slab models of Ni-Cr binary alloy. It consists of 48 atoms (42 of Ni and 6 of Cr atoms) with monolayer six water molecules embedded on the surfaces. Water molecules placed 3Å away from the surfaces. To analyze the strain and defect dependence of the chemical reaction with water, the metal structure deformed. The uniaxial tensile strain has been applied by extending one percent of lattice constant along the x-axis of metallic surfaces as well as one atomic defect introduced on top of surface. Total 5000 number of simulation steps have been carried out where each step was 0.2 femto second (fs) with the Verlet algorithm. The advantage of this algorithm is that it requires less computer memory, because only one set of positions, forces and velocities need to be carried at any one time. The ensemble for this simulation was constant volume and constant temperature (NVT) and the temperature is controlled by using scaling the atom velocities. Temperature was considered 325 °C represents the PWR condition and atmospheric pressure was assigned.

### 3. RESULTS

DFT is the most precise tools to analyze the surface phenomena at the atomic level but it requires huge computational power and it is expensive. On the contrary, tight-binding self consistent field is another worthy method to describe the dynamical features of surfaces.

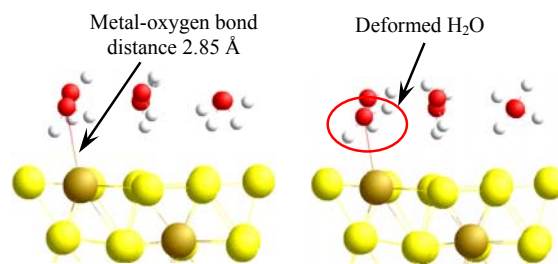


Fig 2. Birds eye view of water adsorbed surface.

### 3.1 Water Dissociation and Diffusion

Water molecules moved toward the metal surfaces with respect to time of simulation. It adsorbed on top site with the oxygen due to the most stable site. Theoretical and experimental studies have demonstrated that top site is the most stable for water absorption [13]. It stays on top site and starts deformation quickly. Figure 2 shows a close view of simulated surfaces where it is clearly observe the water adsorption and deformation on Ni-Cr surface. The thermal desorption spectroscopy study demonstrated that water molecules adsorbed molecularly on the Ni (111) surface from 165 K at low coverage to 170 K at saturation [10] and it can absorb up to 260 K when oxygen-predosed on surface. The results recommend that water molecules dissociate on the surface more than 260 K. The higher temperature initiates water dissociation quickly at the same time, metal atoms commence to dissolution from the surfaces. The bond distance in between the oxygen of adsorbed water molecule and metal atom is found 2.85 Å (see Fig. 2). A. Michaelides *et al.* have proposed that the metal-oxygen bond distance is 2.29 – 3.02 Å [14] and LEED results have demonstrated a bond distance 2.23 Å of Ni-O [15], in favor of the present calculation. H, O and OH generated from dissociation of water molecules. Hydrogen mobility is higher than other elements due to small atomic size. It can penetrate easily through interstitial sites. Several hydrogen atoms diffuse in the surface shortly and rest of them remain above the surface. It can be absorbed by the solution. Metal water interaction raises the dissociation rate of water molecules with respect to time. It is reasonable to diffuse these elements in the surfaces; subsequently surface can be modified. Figure 3 shows that oxygen concentration is significantly high around the chromium atom. It is well

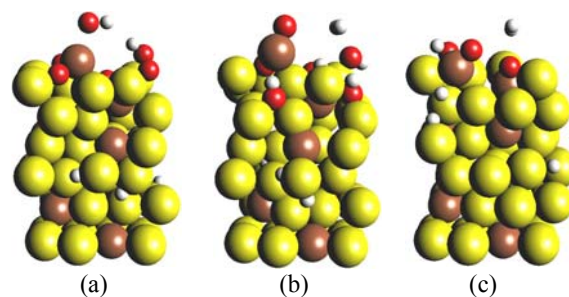


Fig 3. The calculated surface morphologies of (a) Ni-Cr regular surface, (b) Ni-Cr regular surface with applied strain and (c) Ni-Cr defect surface, after 1000 fs.



known mechanism both experimentally and theoretically that chromium forms a protective passive film by making preferential bonds with oxygen. It is difficult to quantify from the present study due to the limitation of time and length scale but qualitatively simulated results observe the initiation of passive film formation on the surface. The calculated surfaces show that the chromium moves upward to the surface because it dissolves faster than nickel atoms. Scanning electron microscopy (SEM) analysis of alloy 600 examined that chromium and iron are selectively dissolved and nickel remain at the surface of matrix [16]. The results obtained by the simulation are qualitatively well consistent with SEM study. Cr-O diatomic binding energy (4.78 eV/mole) is higher than Ni-O (3.79 eV/mole); therefore, it can assist oxygen to make preferential bond with chromium [17]. Moreover, the cohesive energy of nickel is higher than chromium that may lessen segregation of nickel atoms from the surface. Applied strain and atomic defect enhance oxygen diffusivity in the lattice along the z-axis. Figure 4 shows oxygen mean square displacement (MSD) of different surfaces. The value clearly replied that oxygen diffusivity in regular surface is lower than the other two surfaces. Thus, water dissociation on the surface is augmented by these two localized parameters. Applied strain or defects generated free more space in the lattice that helps to move metallic atoms frequently during the reaction occur. Oxygen adsorption weakens the metallic bond as a consequence metal-metal bond breakage and can easily dissolve from the surface.

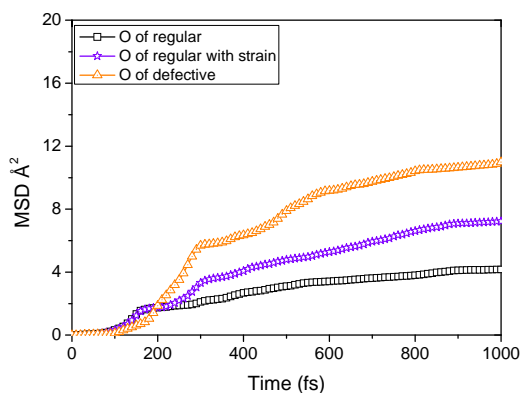


Fig 4. MSD of oxygen for different Ni-Cr surfaces.

From the fundamental aspects, essential element hydrogen is necessary to look at seriously. It diffuses faster than oxygen or any other species in addition to it can trap into interstitial sites owing to small atomic size. It has detrimental effect on materials properties such as hydrogen embrittlement, hydrogen oxidation etc. The simulated surfaces demonstrated that the dissociated hydrogen travel ahead of the oxygen or OH. These atoms can be able to lessen the strength of metallic bonds. Thus, it can empower oxygen diffusion in the metal.

### 3.2 Atomic Trajectories

Trajectory is a process to describe the dynamical features of atoms. Figure 5 shows the atomic advance-

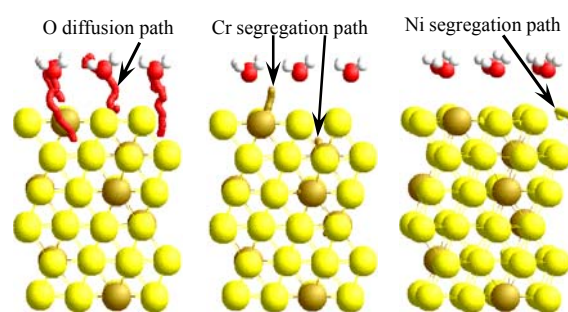


Fig 5. Simulated atomic trajectories.

ment during the simulation. Water molecules adsorb on top site but the dissociated oxygen diffuse through the hollow site. The experimental and theoretical studies examined that the hollow site is energetically most preferential for oxygen adsorption [8]. Oxygen adsorption and diffusion path in the present study are good agreement with the previous observation. The dissociated oxygen trajectory shows that atoms remain around the chromium and the bonding decelerates further diffusion. The chromium atoms move upward from the surface whereas nickel segregation rate is very slow.

### 3.3 Mulliken Population Analysis

Atomic charge with diffusion is calculated by using Mulliken population analysis, as shown in Fig. 6. The calculated results for other surfaces become harmonious with this figure, provided that it is not necessary to show them here. At the elementary stage, chromium and hydrogen are positive in charge and oxygen atoms are negative in charge besides, nickel atoms are not designated to any remarkable charges. The atomic charge modify with respect to time evolution. The negative oxygen atoms are strengthening value by taking electron from metals and metal atom are becoming positively charged. Especially, chromium atoms present noteworthy positive in charge. Figure 6 with the simulated surface of 700 fs suggests that the top three layers of metal atom content higher charges than the bottom layers. So, the top layer atoms are taking part actively in the reaction process at the beginning stage that raises electron transfer. Hydrogen atom on top of surfaces exhibit positively charged whereas the penetrated hydrogen notice negatively charged. Hydrogen negative charge in metal is interesting but not surprising and it is well consistent with our previous

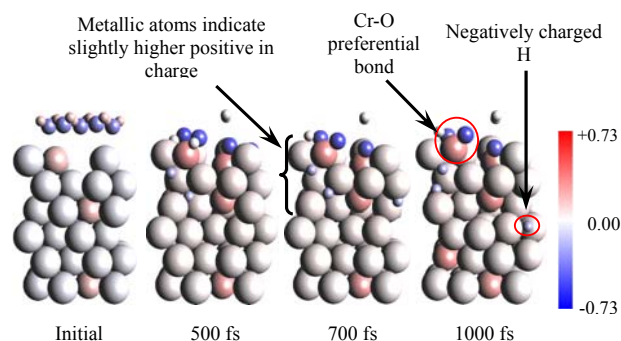


Fig 6. Atomic charge variation with time evolution.



results [18,19]. Although, the positively charged hydrogen is well known in the literature and it acts for decohesion. Hydrogen decohesion mechanism cause embrittlement. However, three highly simplified models have been proposed by Fiks in 1959 [20]. The models are: the protonic, the hydrogenic and the anionic. According to the anionic model, hydrogen receives electron from metal and change into negative in charge. Thus, the deeply diffused hydrogen interacts with metallic atom comparatively longer period of time and it takes electron from metal. The electron transfer process activates the surface chemically for further reaction. It makes easier for oxygen diffusion accordingly oxidation accelerates.

#### 4. IMPLICATIONS

The overall material degradation behavior involves many interrelated and often complex processes and reactions [21]. Fundamental aspects of the reaction mechanism comprise as follows: a) adsorption at the surface, b) diffusion or transport of reactants, c) film growth, development of voids or porosity, and d) stress produce in the scale and subsequent deformation or failure. The elucidation of cracking or material degradation requires atomistic fundamental knowledge of surfaces. The elements adsorb on the metal surface to lose metal-metal bond strength. The high metal-oxygen bond energy initiates the nucleation and new bond formation in between metal and oxygen. The process is essentially required to form protective passive film on the surface. Higher diffusivity of environmental species resulting in accelerates the surface oxidation. The protective film rupture may not necessary to crack advancement. Film degradation losing protective capability can cause a metal dissolution through the degraded film as well as film rupture [22]. Thus, the oxidation reaction, including anodic dissolution and formation of an oxide film, is a crucial process in crack initiation. The elements which can enhance oxidation and degrade the passive film stability, in the long run it is detrimental for material in the SCC standpoint

#### 5. CONCLUSIONS

The calculated results reveal that the water molecules adsorbed on top site of the surfaces by oxygen. The metal oxygen bond distance is 2.85 Å, showing good agreement with the previous theoretical study. Oxygen concentration is substantially high around the chromium. It reveals the early stage passivation initiation. We detect that the chromium dissolution rate is higher than nickel. Lower nickel segregation might help to form a nickel enrich inner oxide layer. Moreover, hydrogen atoms diffused faster in the lattice than oxygen and it stands ahead of oxygen. The applied strain and atomic defect heighten the permeation of hydrogen and oxygen atoms into lattice. Water dissociation on the surface is increased by these two localized parameters. It directly correlates with the surface oxidation. The initially penetrated hydrogen weakens the metallic bond by taking electron and the process make easier for oxygen further permeation in the surface. Negative in charge hydrogen commencing surface oxidation and consequently, it

works as an oxygen carrier. Therefore, it can accelerate oxidation and/or very beginning stage of SCC initiation.

#### 6. ACKNOWLEDGEMENTS

This work has been performed under the support of Grant-in-Aid for Scientific Research (S) 17106002, Japan Society for the Promotion of Science, and the support of the PEACE E program jointly supported EDF, EPRI, SKI, TEPCO, KEPCO, Tohoku EPCO, JAPCO, HITACHI Ltd., MHI, TOSHIBA Co., and IHI.

#### 7. REFERENCES

1. Douglas, D. L., 1995, "A Critique of Internal Oxidation in Alloys during the Post-Wagner Era", *Oxidation of Metals*, 44:81-111.
2. Scott, P. M. and Benhamou, C., 2001, "An Overview of Recent Observation and Interpretation of IGSCC in Nickel base Alloys in PWR Primary Water", *Proc.10<sup>th</sup> Int. Symp. On Environmental Degradation Materials Nuclear Power Systems – Water Reactors*, NACE, CDROM.
3. Scott, P. M. and Combrade, P., 2003, "On the Mechanism of Stress Corrosion Cracking Initiation and Growth in Alloy 600 Exposed to PWR Primary Water", *Proc.11<sup>th</sup> Int. Symp. On Environmental Degradation Materials Nuclear Power Systems – Water Reactors*, ANS, CDROM.
4. Jeng, S. P., Holloway, P. H. and Batich, C. D., 1990, "Surface Passivation of Ni/Cr Alloy at Room Temperature", *Surface Science*, 227:278-290.
5. Ziemniak, S. E. and Hanson, M., 2006, "Corrosion Behavior of NiCrFe Alloy 600 in High Temperature, Hydrogenated Water", *Corrosion Science*, 48:498-521.
6. Sebastiani, D. and Site, L. D., 2005, "Adsorption of Water Molecules on Flat and Stepped Nickel Surfaces from First Principles", *Journal of Chemical Theory and Computation*, 1:78-82.
7. Wang, G. C., Tao, S. X. and Bu, X. H., 2006, "A Systematic Theoretical Study of Water Dissociation on Clean and Oxygen-preadsorbed Transition Metals", *Journal of Catalysis*, 244:10-16.
8. Yamagishi, S., Jenkins, S. J. and King, D. A., 2003, "First Principles Studies of Chemisorbed O on Ni{111}", *Surface Science*, 543:12-18.
9. Mittendorfer, F., Eichler, A. and Hafner, J., 1999, "Molecular Precursors in the Dissociative Adsorption of O<sub>2</sub> on Ni (111)", *Surface Science*, 433-435:756-760.
10. Pache, T., Steinrück, H. -P., Huber, W. and Menzel, D., 1989, "The Adsorption of H<sub>2</sub>O on Clean and Oxygen precovered Ni(111) Studied by ARUPS and TPD", *Surface Science*, 224:195-214.
11. Netzer, F. P. and Madey, T. E., 1981, "Coadsorption-Induced Azimuthal Ordering in Molecular Adsorbate Layers: H<sub>2</sub>O and NH<sub>3</sub> on Oxygen-Precovered Ni(111)", *Physical Review Letters*, 47:928-931.
12. Das, N. K., Tirtom, I. and Shoji, T., 2009, "A Multiscale Modelling Study of Ni-Cr Crack Tip Initial Stage Oxidation at Different Stress Intensity",

- Materials Chemistry and Physics, under review.
13. Das, N. K., 2008, Fundamental Mechanistic Study of Stress Corrosion Cracking – Quantum Chemical Molecular Dynamics Approach”, Ph.D. thesis, Tohoku University, Sendai, Japan.
  14. Held, G. and Menzel, D., 1994, “The structure of the  $p(\sqrt{3} \times \sqrt{3})R30^\circ$  bilayer of  $D_2O$  on  $Ru(001)$ ”, Surface Science, 316: 92-102.
  15. Michaelides, A., Ranea, V. A., Andres, P. L. D. and King, D. A., 2003, “General model for water monomer adsorption on closed-packed transition and noble metal surfaces”, Physical Review Letters, 90:216102.
  16. Terachi, T., Totsuka, N., Yamada, T., Nakagawa, T., Deguchi, H., Horiuchi, M., and Oshitani, M., 2003, “Influence of Dissolved Hydrogen on Structure of Oxide Film on Alloy 600 Formed in Primary Water of Pressurized Water Reactors”, 40:509-516.
  17. Lide, D. R., Editor-in-Chief, 2007-2008, “CRC Hand Book of Chemistry and Physics”, 88<sup>th</sup> Edition, New York, USA.
  18. Das, N., K., Suzuki, K., Takeda, Y., Ogawa, K. and Shoji, T., 2008, “Quantum Chemical Molecular Dynamics Study of Stress Corrosion Cracking Behavior for fcc Fe and Fe-Cr surfaces”, Corrosion Science, 50:1701-1706.
  19. Das, N., K., Suzuki, K., Ogawa, K. and Shoji, T., 2009, “Early Stage SCC Initiation Analysis of FCC Fe-Cr-Ni Ternary Alloy at 288 °C: A Quantum Chemical Molecular Dynamics Approach”, Corrosion Science, 51: 908-913.
  20. Fiks, V. B., 1959, Soviet Physics Solid State, 14.
  21. Kofstad, P., 1988, “High Temperature Corrosion”, Elsevier, London.
  22. Takeda, Y., 2004, “Mechanistic Study of Intergranular Stress Corrosion Cracking in High Temperature Water Based on Electric Properties of Oxide Film”, PhD Thesis, Tohoku University, Sendai, Japan.

## 8. MAILING ADDRESS

Nishith Kumar Das  
 Fracture and Reliability Research Institute,  
 Graduate School of Engineering  
 Tohoku University,  
 Sendai 980-8579 Japan

## MECHANICAL AND THERMAL CHARACTERIZATION OF CNF-FILLED POLYESTER NANOPHASED COMPOSITE

Mohammad Kamal Hossain, Muhammad Enayet Hossain, Mahesh Hosur and Shaik Jeelani

Tuskegee University, Tuskegee, USA

### ABSTRACT

A high intensity ultrasonic liquid processor was used to infuse carbon nanofibers (CNFs) into polyester matrix which was then mixed with catalyst using a high speed mechanical agitator. Results showed the significant improvement in the dispersion of CNFs in sonication over the mechanical mixing method. Flexure tests performed on the neat polyester (NP), 0.1wt. %, 0.2 wt.%, 0.3 wt.% and 0.4 wt.% CNF-filled polyester (CNF-FP) showed 86% and 16% increase in flexural strength and modulus, respectively, compared to the unfilled polyester with increasing loading percentage of CNF up to 0.2%. Similar trend was found with CNF-filled glass reinforced polyester (CNF-FGRP) composites manufactured by vacuum assisted resin transfer molding (VARTM). Dynamic mechanical analysis (DMA) studies indicated an increasing trend of storage modulus and glass-transition-temperature ( $T_g$ ) values of all nanophased composites compared to neat polyester. Scanning electron microscopy (SEM) micrographs of fracture surfaces revealed relatively smooth surface of neat polyester compared to the nanophased polyester.

**Keywords:** Polyester, CNF, Mechanical and Thermal Properties.

### 1. INTRODUCTION

Fiber reinforced polymer matrix composites due to their high specific strength and specific stiffness to weight ratios have become attractive structural materials in aerospace industry, marine, armor, automobile, railways, civil engineering structures, sport goods etc. [1]. The incorporation of inorganic fillers has proved to be an effective way of improving the mechanical and thermal properties of these materials. However, the typical filler content needed for significant enhancement of these properties can be as high as 10-20% by volume. The processing of the materials often becomes difficult at such high particle volume fractions due to the higher density of the inorganic filler than the resin and the increased density of the filled resin [2]. In this rationale, nanoparticles such as CNFs, CNTs, clay, metallic nanoparticles filled fiber reinforced polymer matrix composites are attracting considerable attention since they can enhance properties that are sometimes even higher than the conventional filled polymers composites at volume fractions in the range of 1 to 5%.

Improvements in mechanical, electrical, and chemical properties have resulted in major interest in nanocomposite materials in numerous automotive, aerospace, electronics and biotechnology applications. These nanoscale materials provide the opportunity to explore new behavior and functionality beyond those found in conventional materials. It has been established that the addition of small amounts of nanoparticles (<5 wt. %) to a matrix system can increase thermal and mechanical properties without compromising the weight

or process-ability of the composite [3]. The higher surface area is one the most promising characteristics of the nanoparticles due to its ability of creating a great interface in a composite. An interphase of 1 nm thick represents roughly 0.3% of the total volume of polymer in the case of micro particle filled composites; whereas it can reach 30% of the total volume in the case of nanocomposites [4]. Contribution made by the interphase modified by the low nanofiller loading provides possibilities of enhanced performance by reinforced composites with a small percentage of strong fillers can significantly improve the mechanical, thermal, and barrier properties of the pure polymer matrix [6].

Choi et al. [7] have fabricated and studied the Epoxy/CNF composite with different proportions of CNFs by the in situ process modifying both low and high viscous epoxies. The SEM images showed a high level of dispersion for all materials, although occasional small aggregates were observed in high viscosity epoxy of 20 wt%. The storage modulus and  $T_g$  of the polymer were increased by incorporation of CNFs. The results showed the maximum tensile strength and Young's modulus at 5 wt% of CNF and reduction of the fracture strain with increasing filler content. Mechanical, electrical and thermal properties of low viscosity epoxy composites were resulted better than that of the high viscosity composites. Hussain et al. [8] have investigated the effect of nanoscale  $Al_2O_3$  particles in filament wound carbon fiber/epoxy composites and found an increase in modulus, flexural strength,

interlaminar shear strength, and fracture toughness when the matrix was filled with 10% by volume of alumina particles of 25 nm diameter. Seferis et al. [9] have shown the ability to incorporate nanosized alumina structures in the matrix and interlayer regions of prepreg based carbon/epoxy composites. Timmerman et al. [10] studied the influence of nanoclay on the carbon fiber/matrix composites under thermal cyclic loading and reported that the transverse cracking in symmetric carbon fiber/epoxy laminates was significantly reduced when nanoparticle fillers were used. Pervin et al. [11] evaluated the thermal and mechanical properties of carbon nanofiber reinforced SC-15 epoxy and documented the significant improvement in the thermal and mechanical properties of this material system. Mahfuz et al. [12] synthesized and characterized the carbon nanoparticles/whiskers reinforced polyethylene filament. SEM and TEM micrographs showed uniform dispersion and unidirectional alignment of carbon whiskers. They also documented the higher tensile strength and modulus by about 15–17% and increased thermal stability and crystallinity of the system as compared to the neat polyethylene control samples.

The primary focus of this paper was to characterize the effect of CNF on the mechanical and thermal behavior of the nanophased polyester and its laminate performing the flexure tests, TGA and DMA, respectively. Fracture morphology of the tested specimens was studied by SEM.

## 2. EXPERIMENTAL

### 2.1 Materials Selection

Commercially available B-440 premium polyester resin and styrene from US Composite, heat treated PR-24 CNF from Pyrograf Inc., and plain weave E-glass fiber from fiberglasssite.com were considered as matrix, nanoparticle, thinner and reinforcement, respectively, in this current study because of their good property values and low cost. Polyester resin contains two-part: part-A (polyester resin) and hardener part-B (MEKP- methyl ethyl ketone peroxide).

### 2.2 Resin Preparation

Ultrasonic cavitation technique is one of the most efficient means to disperse nanoparticles into a polymer [13]. In this study, sonication was performed using a high intensity ultrasonic irradiation (Ti-horn, 20 kHz Sonics Vibra Cell, Sonics Mandmaterials, Inc, USA) for 60, 90, and 120 minutes, respectively, adding 0.1, 0.2, 0.3, and 0.4 wt.% CNF with corresponding percent polyester resin with and without 10 wt% styrene in a glass beaker. The mixing process was carried out in a pulse mode of 30 sec. on/15 sec. off at amplitude of 50%. Continuous external cooling was employed by submerging the beaker in an ice-bath to avoid temperature rise during the sonication process. The intense mixing of polyester and CNF with or without styrene produced highly reactive volatile vapor bubbles at the initial stages of the reaction, which could detrimentally affect the properties of the final product

by creating voids. To reduce the void formation, high vacuum was applied using Brand Tech Vacuum system for about 90-120 minutes. Once the bubbles were completely removed from the mixer, 0.6 wt% catalyst was mixed with the mixer using a high-speed mechanical stirrer for about 2-3 minutes and vacuum was again applied for about 6-8 minutes to degasify the bubbles produced during the catalyst mixing. In parallel, neat polyester samples were fabricated by using the same method to compare with the nanophased system. The whole mixing system is shown in Figure 1.



1a. Sonication



1b. Degasification



1c. Mechanical Mixing

Fig 1. Mixing Method

### 2.3 Composite Fabrication

Both conventional and nanophased E-glass/CNF-polyester composites were manufactured by VARTM process. Arrangement of the fabrication process is detailed schematically in Figure 2. The VARTM process uses vacuum pressure to remove air from the fabric lay-up before and during the resin infusion to the fabric reinforcement. The pressure difference between the atmosphere and the vacuum is the driving force for infusion of the resin into the lay-up. Vacuum was maintained until the end of cure to remove any volatiles generated during the polymerization, in addition to maintaining the pressure of one atmosphere. The panel was cured for about 15-18 hours at room temperature. The room temperature cured material was taken out from the vacuum bagging and trimmed, and test samples were machined according to ASTM D 790-02. They were thermally post cured at 110 °C for 3 hour in a mechanical convection oven.

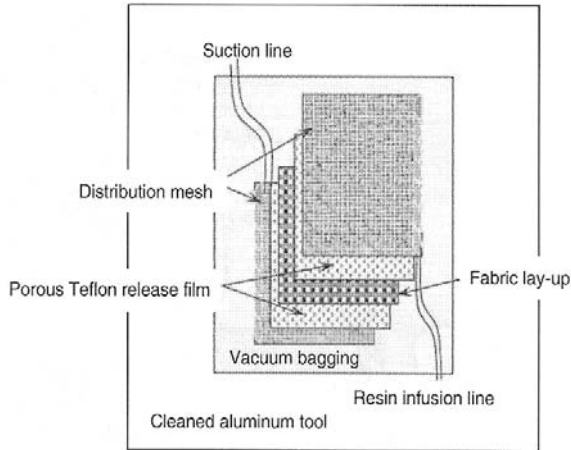


Fig 2. VARTM Layup Sequence

## 2.4 Test Procedure

### 2.4.1 Flexure Test

Flexural tests under three-point bend configuration were performed on the Zwick Roell testing unit shown in Figure 3 according to ASTM D790-02 to determine the ultimate strength and young modulus of the polymer nanocomposites and its laminates. The machines were run under displacement control mode at a crosshead speed of 2.0 mm/min [11] and tests were performed at room temperature.



Fig 3. Zwick Roell Setup

### 2.4.2 Thermogravimetric Analysis (TGA)

Thermo gravimetric analysis (TGA) was conducted with a TA Instruments Q 500, shown in Figure 4, which was fitted to a nitrogen purge gas. The temperature was from increased from ambient temperature to 500 °C at a ramp rate of 10 °C/min.

### 2.4.2 Dynamic Mechanical Analysis (DMA)

Storage modulus, glass transition temperature ( $T_g$ ), and loss factor,  $\tan\delta$ , of the fully cured samples were obtained from a TA instruments Q 800 operating in the three point bending mode at a heating rate of 3°C/min from 30°C to 160°C and an oscillation frequency of 1 Hz as shown in Figure 5. The sample specimens were cut by a diamond cutter in the form of rectangular bars of nominal dimensions 3mm×60mm×12mm. The test was carried out according to ASTM D4065-01 [14].



Fig 4. TGA Setup



Fig 5. DMA Setup

## 2.4.3 Morphological Characterization

Microstructure of neat and nanocomposite samples was examined under a Field Emission Scanning Electron Microscope (FE-SEM Hitachi S-900) JEOL JSM 5800), pictured in Figure 6. An accelerating voltage was applied to accomplish desired magnification. Micrographs were taken after the flexural tests were carried out.



Fig 6. SEM Setup

## 3. RESULTS AND DISCUSSIONS

### 3.1 Flexural Properties

Flexure tests were performed on the NP, 0.1, 0.2, 0.3, and 0.4 wt.% CNF-FP nanocomposites and its laminates to evaluate their bulk stiffness and strength and their typical stress-strain behaviors are shown in Figures 7 and 8, respectively. It is clear from these stress-strain curves that all the samples of CNF-FP composites failed immediately reaching to their maximum values showing significant improvement in the mechanical properties up to 0.2 wt% of CNF loading, beyond that there was decreasing trend. Similar trend was found for the CNF-filled nanophased E-glass/polyester composites showing considerable nonlinearity before reaching the maximum stress. However, more or less ductility was observed in each type of laminate sample but no obvious yield point was found.

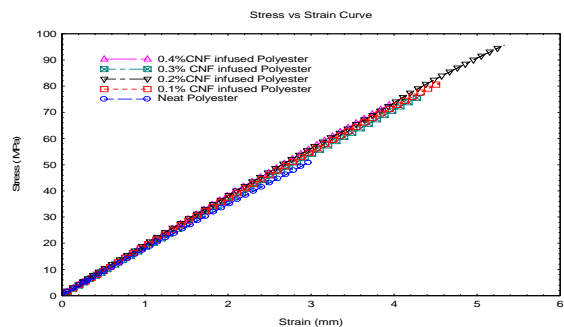


Fig 7. Flexural Stress-Strain Curves of Neat and

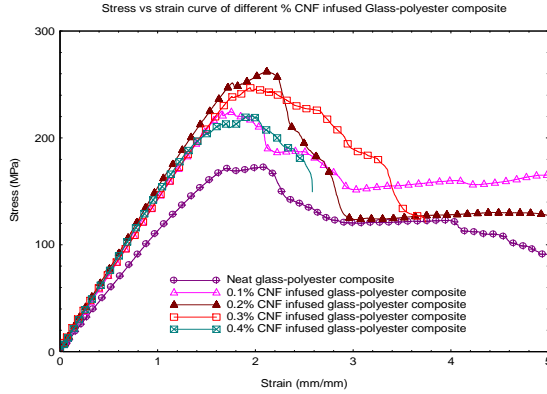


Fig 8. Flexural Stress-Strain Curves of NP and Nanophased CNF-FGRP Composites

Five samples were tested for each condition and the average properties obtained from these tests are listed in Tables 1 and 2. Table 1 shows the properties of the NP and CNF-FP samples loaded up to the 0.4 wt.% CNF with increment of 0.1 wt.%. It is evident that for 0.2 wt.% loading the flexural strength and modulus increased by about 76% and 16%, respectively, as compared to the NP samples. Similar trend was observed for the CNF-FGRP composites in Table 2.

Table 1: Results of CNF-FP with different % CNF

Sample	Flexural Strength (MPa)	% Gain in Strength	Flexural Modulus (GPa)	% Gain in Modulus
NP	51±2	-	3.44±0.21	-
0.1% CNF-FP	81±2	59	3.86±0.03	12.21
0.2% CNF-FP	95± 4	86	4.00±0.15	16.28
0.3% CNF-FP	77± 6	51	3.99±0.07	15.98
0.4% CNF-FP	73±4	43	3.83±0.14	11.34

Table 2: Results of CNF-FGRP composites

GRP	Flexural Strength (MPa)	% Gain in Strength	Flexural Modulus (GPa)	% Gain in Modulus
NP	174±5.8	-	16±0.8	-
0.1% CNF	228±9.4	31%	19±0.5	19%
0.2% CNF	260±4.3	49%	21±1.3	31%
0.3% CNF	248±8.3	43%	20±1.7	25%
0.4% CNF	220±5.2	26%	18±0.1	13%

From the resultant data it was found that the sonication mixing method is better than the mechanical one. 90 minutes sonication time and 0.2 wt.% CNF were explored the optimized conditions for this material system listed in Table 3.

Table 3: Sonication over mechanical mixing method

Sample Type	Flexural Strength (MPa)	Flexural Modulus (GPa)
NP	51±2	3.44±0.21
0.2%CNF-FP-90m-Sonication	95± 4	4.00±0.15

3.2 Thermal Response

TGA responses of NP and CNF-FP have been shown in Figure 9 as a function of temperature. It is clear from the plots that the decomposition temperature is slightly improved and overall weight loss was less for the 2 wt.% CNF-FP sample compared to all other samples.

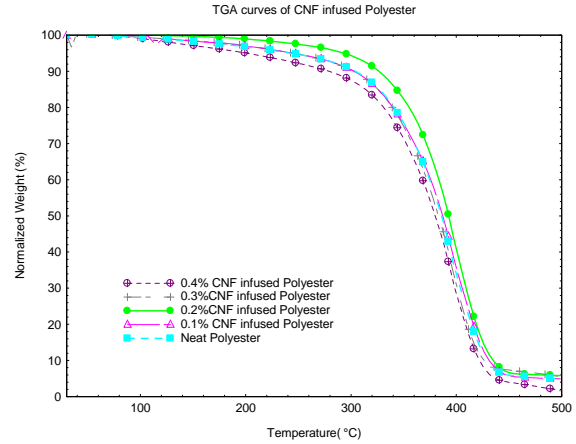


Fig 9. TGA Results of NP and CNF-FP Samples

The storage modulus and loss factor  $\tan \delta$  plotted as functions of temperature from DMA are shown in Figures 10 and 11. It is observed from the analysis that the storage modulus increases and peak height of the loss factor decreases with the addition of CNF. The addition of 0.2 wt.% of CNF infused polyester showed the maximum improvement of 20 % in the storage modulus at room temperature. The CNF infusion does not affect the  $T_g$  of this material. DMA results are given in Table 4.

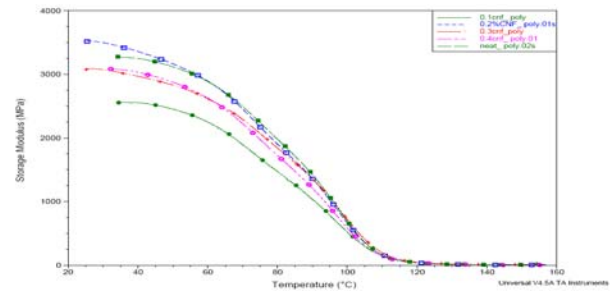


Fig 10. Storage Modulus-Temperature Curve

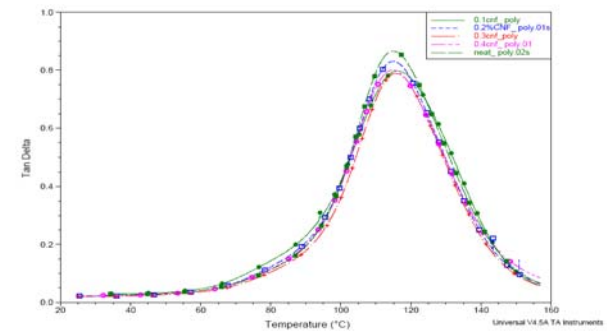


Fig 11. Loss Factor-Temperature Curve



Table 4: DMA results for NP and CNF-FP sample

Sample Type	Storage Modulus (MPa)	T <sub>g</sub> (°C)
NP	3272	114.82
0.1%CNF-FP	2557	116.22
0.2%CNF-FP	3936	115.01
0.3%CNF-FP	3078	115.65
0.4%CNF-FP	3082	114.89

### 3.3 Fracture Surface Analysis

Scanning electron microscopy was performed on the NP, 0.2% CNF-FP, GRP, and 0.2% CNF-FGRP tested samples to study the fracture morphology. The SEM micrographs of the fractured surfaces of NP, CNF-FP, GRP, and CNF-FGRP are illustrated in Figures 12, 13, 14, and 15, respectively.

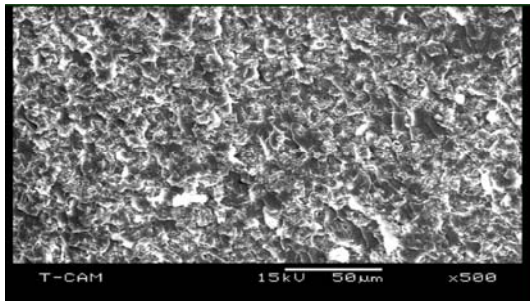


Fig 12. Fracture Surface of NP

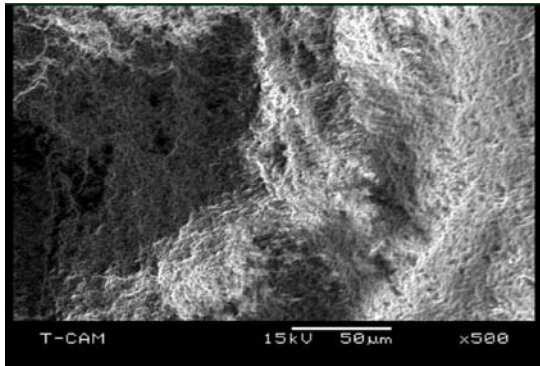


Fig 13. Fracture Surface of 0.2% CNF-FP

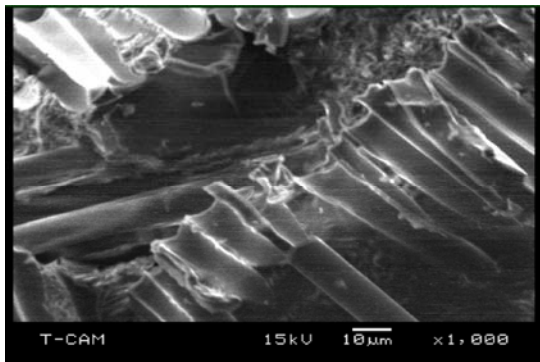


Fig 14. Fracture Surface of GRP Composite

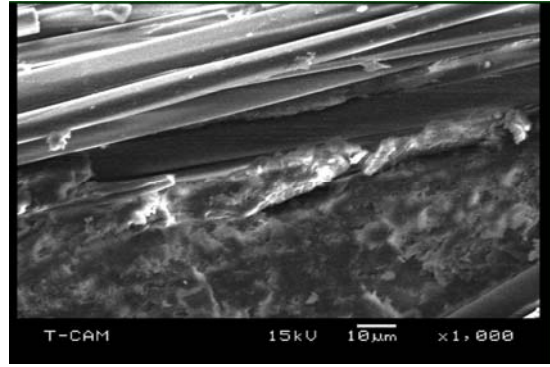


Fig 15. Fracture Surface of CNF-FGRP Composite

It is evident from the CNF-FP fractured surface is rougher compared to the NP fractured surface that gives rise to the mechanical and thermal properties. The rough surface attributes to the higher strength and modulus in the nanophased composites. Comparative analyses of the fractured surfaces of glass reinforced polyester composites and the CNF-filled glass reinforced polyester composites shows that the CNF-FGRP composites shows better adhesion between the fiber and matrix due to the addition of CNF than that of the GRP composites [15]. This better adhesion provides the less damage in the nanophased composites in terms of matrix cracking, fiber breakage, matrix fiber debonding, and delamination.

### 4. CONCLUSION

A high intensity ultrasonic liquid processor was used to infuse CNFs into polyester matrix which was then mixed with catalyst using a high speed mechanical agitator. The neat, CNF-filled polyester, conventional and nanophased composites samples were prepared and tested under the flexural and thermal loading condition. The fractured surfaces of the failed samples were examined under the SEM. The significant conclusions drawn from the investigation are given below.

1. Sonication mixing method is better than that of the mechanical mixing method to disperse the CNFs uniformly in the polyester.
2. 90 minutes sonication time and 0.2 wt.% CNF are the optimum condition to achieve the maximum mechanical and thermal properties.
3. 0.2% CNF-FP and 90 minutes sonication enhanced the 86% and 116% improvement of flexural strength and flexural modulus, respectively.
4. 0.2% CNF-FGRP exhibited the 49% and 31% improvement of flexural strength and flexural modulus, respectively.
5. TGA results showed the addition of CNF has insignificant improvement in the decomposition temperature.
6. DMA results illustrated 0.2 wt.% CNF-FP improved 20% of storage modulus and negligible effect on the T<sub>g</sub>.
7. SEM micrographs showed the rougher

fractured surfaces with addition of 0.2 wt.% CNF that attributed to the improved mechanical properties.

8. SEM studies revealed the better adhesion of fiber –matrix in the CNF-FGRP composites due to the uniform dispersion of the CNF.

## 5. ACKNOWLEDGEMENTS

The authors would like to gratefully acknowledge the financial support of Department of Energy (DOE) through Mississippi State University.

## 6. REFERENCES

1. Millerschin, E., 1999, “The Rise of Composites in the Automotive Market”, *Composites Fabrication*, 40-42.
2. Rajapakse, Y. D. S., Editor, 2002, *Composites for Marine Structures*. University of Maryland, USA.
3. Sandler, J., Werner, P., Shaffer, M. S. P., Denchuk, V., Altstadt, V. and Windle, A. H., 2002, “Carbon-Nanofiber-Reinforced Poly(ether ether ketone) Composites”, *Composites: Part A: Applied Science and Manufacturing*, 33:1033-1039.
4. Reynaud, E., Gauthier, C. and Perez, J., 1999, “Nanophases in Polymers”, *Review Metallurgie*, 96 (2):169-176.
5. Wu, C.L., Zhang, M. Q., Rong, M. Z. and Friedrich, K., 2002, “Tensile Performance Improvement of Low Nanoparticles Filled-Polypropylene Composites”, *Composites Science and Technology*, 62: 1327-1340.
6. Adams, W. W. and Kumar, S., 1992, *Conventional and Molecular Composites - Past, Present, and Future in Ultrastructure Processing of Advanced Materials*, editors D. R. Uhlmann and D. R. Ulrich, John Wiley, 343- 359.
7. Choi, Y. K., and Koh-ichi, 2005, “Mechanical and Physical Properties of Epoxy Composites Reinforced by Vapor Grown Carbon Nanofibers” *Carbon* 43:2199-2208.
8. Hussain, M., Nakahira, A. and Niihara, K., 1996, “Mechanical Property Improvement of Carbon Fiber Reinforced Epoxy Composites by Al<sub>2</sub>O<sub>3</sub> Filler Dispersion”, *Materials Letters*, 26: 185-191.
9. Hayes, B. S., Nobelen, M., Dharia, A. K. and Seferis J. C., 2001, “Development and Analysis of Nanoparticle Modified Prepreg Matrices”, *33<sup>rd</sup> International SAMPE Symposium and Exhibition*, Seattle, WA.
10. Timmerman, J. F., Hayes, B. and Seferis J. C., 2002, “Nanoclay Reinforcement Effects on the Cryogenic Micro Cracking of Carbon Fiber/Epoxy Composites”, *Composites Science and Technology*, 62: 1249-1258.

11. Pervin, F., Zhou, Y., Rangari, V. J., and Jeelani, S., 2005, “Testing and Evaluation on the Thermal and Mechanical Properties of Carbon Nanofiber Reinforced SC-15 Epoxy”, *Materials and Science Engineering A*, 405:246-253.
12. Mahfuz, H., Adnan, A., Rangari, V. K., 2004, “Carbon Nanoparticles/Whiskers Reinforced Composites and their Tensile Response”, *Composites 2004 Part A: Applied Science and Engineering*, 35 (5): 519-527.
13. Eskin, G.I., 2001, “Broad Prospects for Commercial Application of the Ultrasonic (cavitation) Melt Treatment of Light Alloys”, *Ultrasonic Sonochemistry*, 8 (3): 319-325.
14. Annual Book of ASTM Standards, D 4065-01, 2002, “*Standard Practice for Determining and Reporting Dynamic Mechanical Properties of Plastics*”.
15. Chowdhury, F. H., Hosur, M. V. and Jeelani, S., 2006, “Studies on the Flexure and Thermomechanical Properties of Woven Carbon/Nanoclay-Epoxy Laminates”, *Materials and Science Engineering A*, 421:298-306.

## 7. NOMENCLATURE

Symbol	Meaning
CNF	Carbon nanofiber
NP	Neat polyester
CNF-FP	CNF-filled polyester
GRP	Glass-reinforced polyester
CNF-FGRP	CNF-filled glass-reinforced polyester

## 8. MAILING ADDRESS

Assistant Prof. Mohammad Kamal Hossain  
E-mail: [hossainm@tuskegee.edu](mailto:hossainm@tuskegee.edu)

Muhammad Enayet Hossain  
E-mail: [mh0684160@tuskegee.edu](mailto:mh0684160@tuskegee.edu)

Associate Prof. Mahesh Hosur  
E-mail: [hosur@tuskegee.edu](mailto:hosur@tuskegee.edu)

Prof. Shaik Jeelani  
Director of T-CAM & Ph. D Program in Materials Science and Engineering, and Vice President for Research and Sponsored Program  
Center for Advanced Materials (T-CAM),  
Tuskegee University  
101 Chappie James Center  
Tuskegee, AL 36088, USA

E-mail: [jeelanis@tuskegee.edu](mailto:jeelanis@tuskegee.edu)

## EVALUATION OF THERMOELASTIC PROPERTIES OF CARBON NANOTUBE-BASED COMPOSITES USING FINITE ELEMENT METHOD

Sushen Kirtania<sup>1</sup> and Debabrata Chakraborty<sup>2</sup>

<sup>1</sup>Department of Mechanical Engineering, Tezpur University Assam, India.

<sup>2</sup>Department of Mechanical Engineering, Indian Institute of Technology Guwahati, Assam, India

### ABSTRACT

This article deals with the determination of the thermoelastic properties of single-walled carbon nanotube (SWNT)-reinforced composites using finite element (FE) analysis. A full three-dimensional (3-D) FE analysis has been performed using general purpose FE software ANSYS. SOLID45 elements embodied in ANSYS have been used for modeling a square representative volume element (RVE). Both carbon nanotubes (CNTs) and matrix materials are assumed to be isotropic. Effect of different important parameters on the properties of the CNT-based composites has been studied. Present work concludes that by adding ~3% of CNT in epoxy, the effective axial Young's modulus as well as axial coefficient of thermal expansion (CTE) of composites could be increased and decreased by 776.61% and 91% compared to the Young's modulus and CTE of the epoxy, respectively. It is observed that axial CTE of the SWNT/EPOXY composites could be reduced to zero corresponding to a volume fraction of ~13%.

**Keywords:** Cnt-Based Composites, Finite Element Analysis, Coefficient of Thermal Expansion.

### 1. INTRODUCTION

Among many potential applications of nanotechnology, nanocomposites have been one of the recent research areas. Carbon nanotubes due to their inherent advantages like high strength, stiffness, resilience along with superior thermo-electro-mechanical properties are believed to be ideal reinforcing materials for high performance structural composites. There have been good numbers of works reported in the broad area of nano-composites in recent times. One of the major difficulties in the study of CNT-based composites is experimental characterization of such materials due to their small size. On the other hand, modeling and simulation of nanocomposites can be easily analyzed by a computer. Determination of thermoelastic properties is one of the important tasks where simulation can be used advantageously. Therefore, computational approach played a significant role in the development of the CNT-based composites by providing simulation results to help in understanding, analyzing and designing of such nanocomposites

Carbon nanotubes first discovered by Sumio Iijima in 1991 [1] and subsequently there were many papers published to determine the Young's modulus [2-5], Poisson's ratio [6-7] and CTE [4, 8-9] of CNTs. From the above literatures, it was found that the Young's modulus, Poisson's ratio, and CTE of CNTs are in the order of 1

TPa, 0.28, and  $-1.5 \times 10^{-6} \text{K}^{-1}$ , respectively. Due to superior mechanical, thermal and electrical properties of CNTs, they provide the ultimate reinforcing materials for the development of a new class of nanocomposites [10-11]. The mechanical load carrying capacities of carbon nanotubes in nanocomposites have been investigated in some experimental works [12-13]. Qian and Dickey [12] conducted experiments and concluded that with only 1% (by weight) addition of CNTs in polystyrene (PS), elastic modulus and breaking stress have been observed to increase by 36%-42% and ~25%, respectively.

Jia et al. [14] explained the reasons and possibility of strong (C-C) bond between the CNTs and matrix, as well as the importance of interface in CNT-based composites. Lusti and Gusev [15] performed FE analysis of Young's modulus and CTE of CNT/epoxy composites for different orientation of CNTs in matrix, and concluded that CNTs could be more efficient as reinforcement compared to conventional glass or carbon fibers. Guo et al. [16] compared the CTE and Young's modulus of PAN/SWNT composites by performing experiments.

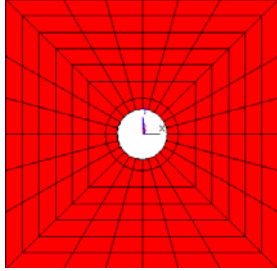
The effective mechanical properties of CNT-based composites are evaluated using a 3-D nanoscale representative volume element based on the 3-D elasticity theory and solved by the FEM [17-18] and observed that with the addition of 3.6% volume fraction of the CNTs in a matrix, axial Young's modulus of the

composites increased by 33% for the case of long CNT fibers. The tensile strength, modulus and electrical conductivity of a pitch composite fiber with 5 wt % of purified SWNTs are enhanced by ~90%, ~150%, and 340% respectively, as compared to the corresponding values in unmodified isotropic pitch fibers [19]. Han and Elliott [20] performed molecular dynamics simulation and determined axial and transverse elastic moduli using constant-strain energy minimization technique and reported that interfacial bonding effect is important.

Literature review reveals that even though number of work have been reported in the direction of characterization of CNT-based composites, especially using FE method, not many work in thermo-elastic characterization in CNT-based composites have been reported. Therefore the present work aims at FE based estimation of thermo-elastic properties of CNT-based composites and studying the effect of different important parameters on such properties which will be useful in design of such composites.

## 2. FORMULATION OF THERMOELASTIC PROPERTIES OF CARBON NANOTUBE-BASED COMPOSITES

In this present work, it has been assumed that the CNTs and matrix in a RVE are linear elastic, isotropic and homogeneous materials, with given Young's modulus and Poisson's ratios. It has also been assumed that the CNTs and matrix are perfectly bonded with no slip at the interface in the RVE to be studied. The RVE has been modeled by taking different materials like epoxy to steel and different volume fraction of SWNT in the matrix ranging from 0.5% to ~15%. The FE mesh of a cross section of the CNT-composites of the square RVE is shown in fig. 1.



Total number of nodes = 9,792, Total number of elements = 8,400, Total number of CNT layer = 1, Total number of matrix layers = 6, Thickness of CNT layer = 0.34 nm, Thickness of each matrix layer = 0.5 nm, Volume fraction of the CNT in the matrix i.e.  $V_{nt}$  = 3.056%

Fig 1. FE mesh of a cross section of the CNT-composites (square RVE)

The square RVE is used for calculation of the effective Young's modulus as well as CTE of the CNT-based composites. The diameter of CNTs has been chosen as 1.88 nm which is equal to the diameter of zigzag (24, 0) CNTs. The thickness of CNT layer  $t = 0.34$  nm but thickness of matrix layers are different for different volume fraction of CNT in composites. The

length of the CNTs has taken as 200 nm keeping the aspect ratio of the SWNT as 106. Even though it was reported in the literature [15] that the elastic modulus of CNTs does not change beyond an aspect ratio of 300, but it was observed in the present work that after an aspect ratio of 106, change in elastic modulus is insignificant.

### 2.1 Effective Young's Modulus of the Nanocomposites Based on Strength of Materials Approaches

Figure 2 shows a simple strength of materials model for calculating the effective axial Young's modulus of a long CNT reinforced inside the matrix of a square RVE. All the nodes at one end are fully restrained and the nodes at other ends are subjected to uniform tensile load ( $F$ ). The axial Young's modulus have been evaluated using

$$E_1 = \frac{F_1 / A_c}{\Delta L_a / L_a} \quad (1)$$

where,  $F_1$  (i.e.  $F$ ) stands for the total axial force acting at one end,  $A_c$  is the cross sectional area,  $L_a$  (i.e.  $L$ ) is the initial axial length and  $\Delta L_a$  is elongation of the nanocomposites in axial direction. In calculating the cross sectional area of the nanocomposites, the thickness  $t$  of the CNT is taken as 0.34 nm [21, 6] which is the interlayer spacing of graphite. The volume fraction of the CNT in matrix of the square RVE is defined by

$$V_{nt} = \frac{\pi(r_0^2 - r_i^2)}{4a^2 - \pi r_i^2} \quad (2)$$

where,  $r_0$  is the outer radius of the CNT,  $r_i$  is the inner radius of the CNT and  $2a$  is the thickness (or width) of the nanocomposites model.

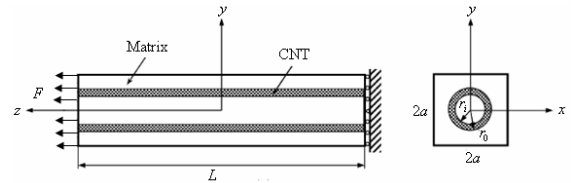


Fig 2. A simple strength of materials model for calculating effective axial Young's modulus of a long CNT reinforced inside the matrix of a square RVE

For a fiber composite under uniaxial loading, the dependence of the effective Young's modulus in terms of the modulus and the volume fraction of each constituent can be estimated by the rule of mixture (ROM) [22]. The same equations of the ROM are used to predict the effective Young's modulus of the CNT-based composites. The longitudinal elastic modulus or effective axial modulus  $E_1$ , of the nanocomposites with long CNT is

$$E_1 = E_{nt} V_{nt} + E_m V_m \quad (3)$$

where  $E_{nt}$  and  $E_m$  are the elastic modulus of the CNT and matrix, respectively, and  $V_{nt}$  and  $V_m$  are the volume fractions of the CNT and matrix, respectively.

Where

$$V_{nt} + V_m = 1 \quad (4)$$

These ROM formulae are applied to verify the computational results of the effective Young's modulus

of the CNT-based composite materials.

## 2.2 The Effective Coefficient of Thermal Expansion of the CNT-Reinforced Composites

The thermal expansion of a solid can be anisotropic if the coefficients of thermal expansion are direction dependent. This situation occurs in composite or nanocomposites materials with a directional reinforcement. In the present study, the axial and transverse linear CTE of the nanocomposites have been evaluated using finite element method (FEM). The uniform temperature is applied on each node by fixing the nodes at one end (zero displacement). The axial CTE of the composites in the axial direction is given by

$$\alpha_1 = \frac{1}{L_a} \frac{\Delta L_a}{\Delta T} \quad (5)$$

where,  $\Delta T$  is the change in temperature. Similarly, the coefficient of thermal expansion of the nanocomposites in the transverse direction is given by

$$\alpha_2 = \frac{1}{L_t} \frac{\Delta L_t}{\Delta T} \quad (6)$$

To verify the computed CTE of the CNT-based composite materials, following are the expressions developed for the two thermal expansion coefficients using the thermoelastic extremum principle [23].

$$\alpha_1 = \frac{\alpha_{nt} V_{nt} E_{nt} + \alpha_m V_m E_m}{E_{nt} V_{nt} + E_m V_m} \quad (7)$$

$$\alpha_2 = (1 + \nu_{nt}) \alpha_{nt} V_{nt} + (1 + \nu_m) \alpha_m V_m - \alpha_1 \nu_{12} \quad (8)$$

where,  $\alpha_1$  and  $\alpha_2$  are the linear CTE in axial and transverse direction,  $\alpha_{nt}$  and  $\alpha_m$  are the CTE for the CNT and matrix, and  $\nu_{nt}$  and  $\nu_m$  are the Poisson's ratio for the CNT and matrix, respectively. The effective axial Poisson's ratio,  $\nu_{12}$  is

$$\nu_{12} = \nu_{nt} V_{nt} + \nu_m V_m \quad (9)$$

which is approximated by the ROM expression [22], as in axial effective Young's modulus of the nanocomposites.

## 3. RESULTS AND DISCUSSION

The effective Young's modulus as well as the CTE of the CNT-reinforced composite has been evaluated considering a square RVE using FEM. The computed Young's modulus and CTE are compared to the Young's modulus and CTE of the matrix, respectively. To get a clear idea on the variation of the Young's modulus and CTE of the different types of nanocomposites, four types of matrix materials have been chosen. The matrix materials are epoxy, lead, titanium and steel i.e. from low strength to high strength materials. Effect of volume fraction on the variation of the Young's modulus as well as the CTE of the nanocomposites has also been studied. SOLID45 elements embodied in ANSYS10 have been used for modeling the RVE. Properties of epoxy have been chosen from literature [24] and densities of epoxy and SWNT are chosen from books [22, 25], respectively. Properties of the matrices materials and the SWNT [2-7] are as follows

SWNT:  $E_{nt} = 1000$  GPa,  $\nu_{nt} = 0.28$ ,  $\rho_{nt} = 1300$  kg/m<sup>3</sup>

Epoxy:  $E_m = 3.89$  GPa,  $\nu_m = 0.37$ ,  $\rho_m = 1380$  kg/m<sup>3</sup>

Lead:  $E_m = 16$  GPa,  $\nu_m = 0.44$ ,  $\rho_m = 11340$  kg/m<sup>3</sup>

Titanium:  $E_m = 116$  GPa,  $\nu_m = 0.32$ ,  $\rho_m = 4500$  kg/m<sup>3</sup>

Steel:  $E_m = 210$  GPa,  $\nu_m = 0.29$ ,  $\rho_m = 7800$  kg/m<sup>3</sup>

## 3.1 Effective Axial Young's Modulus of CNT-Reinforced Composites

Figure 3 shows the 3-D view along with the applied boundary conditions of a FE model for the square RVE with a long CNT. In the present model, the  $x$ - $y$  plane is the transverse plane and the  $z$ -axis is the axial direction of the CNT which is shown in Fig. 2. All the nodes at  $z = 0$  are fully restrained and the nodes at  $z = L_a$  are subjected to uniform tensile load. The average displacement along  $z$ -direction is calculated for all the nodes in the cross section at  $z = L_a/2$  and effective axial Young's modulus is calculated using Eq. (1).

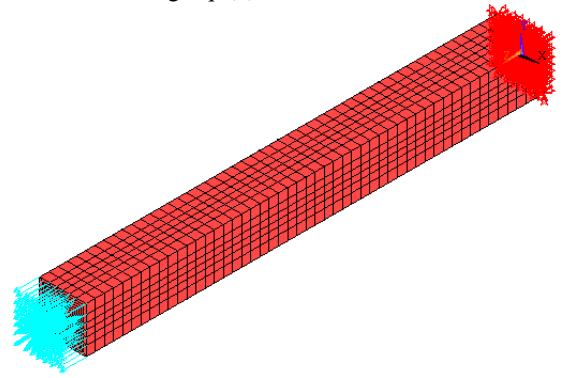


Fig 3. A 3-D model of FE meshes for the square RVE ( $V_{nt} \sim 8\%$ ) with a long CNT along with the applied boundary conditions

Table 1 : Computed axial effective Young's modulus of the CNT-based composites of RVE by using volume fraction = 3.056%

Types of nanocomposites	$E_{nt} / E_m$	% of increased $E_1$ w.r.t $E_m$ (Computed)	% of increased $E_1$ w.r.t $E_m$ (ROM)
SWNT/EPOXY	257	776.61	782.66
SWNT/LEAD	62.5	186.93	187.98
SWNT/TITANIUM	8.6	23.47	23.29
SWNT/STEEL	4.76	11.75	11.49

Based on the formulation described in section 2, effective axial Young's modulus of the CNT-based composites have been determined from the present FEA of the RVE. Table 1 shows the axial Young's modulus of the CNT-based composites compared with that of the matrix for a constant volume fraction 3.056%. For comparison the strength of materials solution based on ROM is calculated using Eq. (2) and also listed in Table 1.

Results in Table 1 show that by adding 3.056% CNT



in a matrix, the axial Young's modulus ( $E_1$ ) of CNT-based composites could be increased by 11.75% compared to the Young's modulus of the matrix, when the ratio of the Young's modulus of CNT and matrix i.e.  $E_{nt} / E_m = 4.76$ . In the case of  $E_{nt} / E_m = 257$ , the Young's modulus of the composites in the axial direction ( $E_1$ ) has been observed to have increased by about nine times compared to that of the matrix. Fig. 4 shows that percentage increase of effective axial Young's modulus of different nanocomposites at a constant volume fraction of 3.056%.

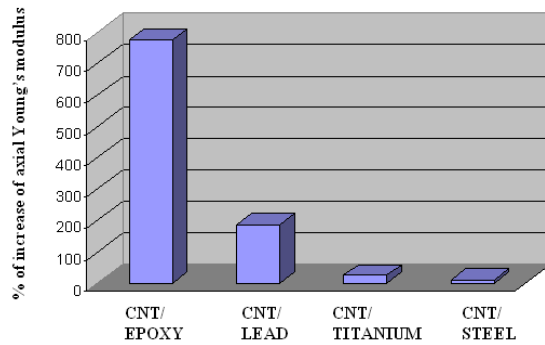


Fig 4. The variation of the percentage of increase of effective axial Young's modulus of different nanocomposites at a constant volume fraction (3.056%)

In practice the weight fraction of CNT in CNT-based composites is limited to 10% [25] and hence in the present analysis the range of the volume fraction is taken between 0.5%-10.3%. Table 2 shows the variation of  $E_1$  with increasing volume fraction in a CNT/Titanium composite. Results in table 2 show that there is a very high percentage increase of  $E_1$  as the volume fraction is increase from 0.5% to 10.3%. Same trend has also been observed for CNT/Epoxy composite.

Table 2: Computed effective axial Young's moduli of the CNT-Titanium nanocomposites taking volume fraction 0.5% to 10.3%

$V_{nt}$	% of increased $E_1$ w.r $E_m$ (computed)	% of increased $E_1$ w.r.t $E_m$ (ROM)
0.5%	4.1044	3.76
1%	7.91	7.64
3%	23.475	23.29
5.45%	41.6865	41.56
7.9%	60.34	60.29
10.3%	78.544	78.5548

From the results shown in Table 1 and Table 2 it could be observed that the effective axial Young's modulus of composites calculated from the present study appear very close to those obtained from ROM. Fig. 5. shows that by taking 0.5% to 10.3% volume fraction of CNT in Titanium matrix, the percentage of increase in effective axial Young's modulus of nanocomposites vary from 4.1% to 78.54% with respect to the Young's modulus of

Titanium.

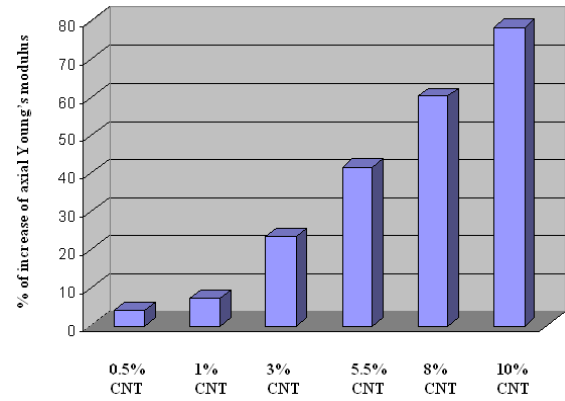


Fig 5. The variation of the percentage of increase of effective axial Young's modulus of CNT-Titanium composites in different volume fraction (0.5% to 10.3%)

### 3.2 Effective Coefficient of Thermal Expansion of CNT-Reinforced Composites

The effective CTE of CNT-based composites have been evaluated by using FEM. The effective axial CTE of the composites have been calculated by taking a constant volume fraction as well as by varying the volume fraction of the CNT in matrix. The same 3-D FE model for the square RVE with a long CNT is used which was used for the calculation of the effective Young's modulus of composites. The CTEs of SWNT, epoxy, lead, titanium, and steel are  $-1.5 \times 10^{-6} K^{-1}$ ,  $58 \times 10^{-6} K^{-1}$ ,  $29 \times 10^{-6} K^{-1}$ ,  $8.6 \times 10^{-6} K^{-1}$ , and  $12 \times 10^{-6} K^{-1}$ , respectively.

#### 3.2.1 Effective CTE of CNT-Reinforced Composites at a Constant Volume Fraction

The effective axial as well as transverse CTE of the composite are calculated by taking a constant volume fraction 3.056%. All the nodes at  $z = 0$  are fully restrained and a uniform temperature,  $\Delta T = 10^0 C$  is applied on all nodes. The effective axial CTE are calculated using equation (5). The calculated effective axial CTE of the CNT-based composites by using FEM are listed in Table 3 and compared with the theoretical values using equation (7).

Table 3: Computed axial CTE of the CNT-based composites of RVE by using a constant volume fraction = 3.056%

Types of nanocomposites	% reduction of $\alpha_1$ w.r.t $\alpha_m$ (Computational)	% reduction of $\alpha_1$ w.r.t $\alpha_m$ (Theoretical)
SWNT/EPOXY	-91.2	-91.32
SWNT/LEAD	-69.23	-69.7669
SWNT/TITANIUM	-25.33	-25.1
SWNT/STEEL	-15.0833	-14.6858

For all the four composite materials the axial CTE have

been observed to have decreased and the percentage of reduction of axial CTE of nanocomposites is maximum for SWNT/EPOXY (~91%) and minimum for SWNT/STEEL (~15%) is shown in Fig. 6.

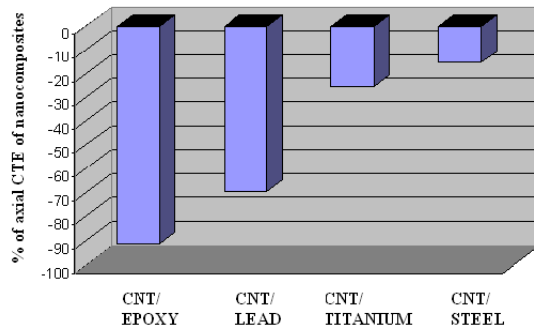


Fig 6. The variation of the percentage of axial CTE for different type's nanocomposites by taking a constant volume fraction ~3%

### 3.2.2 Effect on Volume Fraction on the Effective CTE of CNT-Reinforced Composites

Effective axial and transverse CTE are calculated using Eq. (5) and (6), respectively. For comparison of the calculated values with the theoretical values, equations (7) and (8) have been used. The calculated effective axial and transverse CTE of the CNT/EPOXY composites by using FEM for different volume fractions are listed in Table 4.

Table 4: Computed effective axial and transverse CTE of the CNT/EPOXY nanocomposites taking volume fraction from 0.5% to 15.77%

$V_{nr}$ (%)	$\alpha_1$ $\times 10^{-6} K^{-1}$ (Computed)	$\alpha_1$ $\times 10^{-6} K^{-1}$ (Theoretical)	$\alpha_2$ $\times 10^{-6} K^{-1}$ (Computed)	$\alpha_2$ $\times 10^{-6} K^{-1}$ (Theoretical)
0.5	25.203	24.462	69.754	70.01
1	15.302	15.043	72.867	73.1
3	5.0978	5.0349	74.7155	75.123
5.45	2.267	2.2593	73.5434	74.2
7.9	1.0643	1.0775	71.7165	72.631
10.3	0.4253	0.44798	69.7879	71.0713
15.77	-0.3201	-0.2894	65.1728	66.7249

In this study, the axial as well as transverse CTE of the SWNT/EPOXY composites are calculated by varying volume fraction from 0.5% to 15.77%. The variation of the axial CTE of SWNT/EPOXY with volume fraction of CNT is plotted in Fig. 7. It can be seen that the axial CTE of the nanocomposites are  $25.2 \times 10^{-6} K^{-1}$  and  $-0.32 \times 10^{-6} K^{-1}$  corresponding to its volume fractions of 0.5% and 15.77%, respectively. Another important observation from Fig. 7 is that the axial CTE of the composites is zero at a volume fraction ~13%. The same reduction trend of axial CTE with CNT volume fraction is also observed for CNT/Titanium composites. The computed effective CTE using FE results are very close to the computational [15] and experimental [16] results.

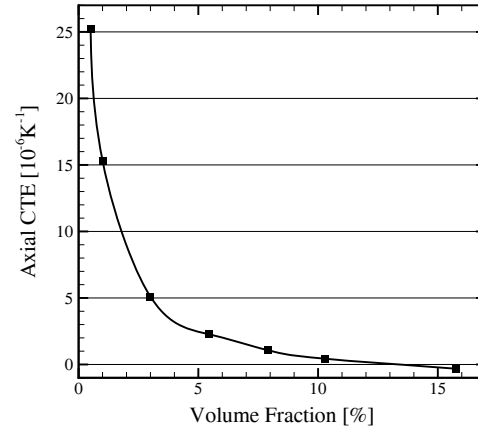


Fig 7. The variation of the axial CTE with respect to the volume fraction of the CNT in epoxy matrix

## 4. CONCLUSIONS

- In general, the load carrying capacity is enhanced and CTE is reduced due to addition of CNTs in matrices.
- By adding ~3% of CNT in a particular matrix, the axial Young's modulus of CNT-based composites could be increased between 1.11 times to 8.76 times that of the matrix, depending upon the ratio of the Young's moduli of CNT and matrix.
- The increase in effective CTE in transverse direction is very less compared to the increase in effective CTE in axial direction.
- By adding 3% of CNT in epoxy matrix, the axial CTE of CNT-based composites could be reduced by 91% compared to the CTE of the matrix.
- Increase in volume fractions of CNT in matrix lead to decrease in CTE and the axial CTE of the SWNT/EPOXY could be reduced to zero corresponding to a volume fraction of ~13%.

## 5. REFERENCES

1. Iijima S., "Helical microtubules of graphitic carbon" Nature (London), 354, pp. 56-58, (1991)
2. Li C., Chou T-W, "A structural mechanics approach for the analysis of carbon nanotubes" Int. J. Solid Struct., 40, pp. 2487-99, (2003)
3. K.I. Tserpes, P. Papanikos, "Finite element modeling of single-walled carbon nanotubes" Composites: Part B, 36, pp. 468-477, (2005)
4. S. Kirtania and D. Chakraborty, "Finite element based characterization of carbon nanotubes" J. Reinforced Plastics and Composites, 40(15), pp. 1557-70, (2007)
5. M. J. Treacy, T. W.Ebbesen and J. M. Gibson, "Exceptionally high Young's modulus observed for individual carbon nanotubes" Nature, 381, pp. 678-80, (1996)
6. Lu J. P., "Elastic properties of carbon nanotubes and nanoropes" Phys. Rev. Lett., 79(7), pp. 1297-300, (1997)
7. T. Belytschko, S. P. Xiao, G. C. Schatz, and R. S.



Ruoff, "Atomistic simulation of nanotube fracture" *Phy. Rev. B*, 65, pp. 235430-1-4, (2002)

8. Jiang H., Liu B., Huang Y., Hwang K. C., "Thermal expansion of single wall carbon nanotubes" *J. Engg. Mat. Technol.*, 126, pp. 265-270, (2004)
9. Kwon Y-K., Berber S., and Tomanek D., "Thermal contraction of carbon fullerenes and nanotubes" *Phys. Rev. Lett.*, 92(1), pp. 015901-1- 015901-4, (2004)
10. Thostenson E. T., Ren Z., Chou T-W., "Advance in the science and technology of carbon nanotubes and their composites: a review" *Compos. Sci. Technol.*, 61, pp. 1899-1912, (2001)
11. Lau K-T., Hui D., "The revolutionary creation of new advanced materials-carbon nanotube composites" *Composites: Part B Eng.*, 33, pp. 263-77, (2002)
12. D. Qian and E. C. Dickey, "Load transfer and deformation mechanisms in carbon nanotube-polystyrene composites" *Appl. Phys. Lett.*, 77(20), pp.2868-70, (2000)
13. L. S. Schadler, S. C. Giannaris, and P. M. Ajayan, "Load transfer in carbon nanotube epoxy composites" *Appl. Phys. Lett.*, 73(26), pp.3842-44, (1998)
14. Z. Jia, Z. Wang, C. Xu, Ji Liang, B. Wei, D. Wu and S. Zhu "Study on poly(methyl methacrylate)/carbon nanotube composites" *Mat. Sc. and Engg. A271*, pp. 395-400, (1999)
15. H. R. Lusti and A. A. Gusev, "Finite element predictions for the thermoelastic properties of nanotube reinforced polymers" *Modelling simul. Mater. Sc. Engg.*, 12, pp. S107-S119, (2004)
16. H. Guo, T. V. Sreekumar, T. Liu, M. Minus, S. Kumar, "Structure and properties of polyacrylonitrile/single wall carbon nanotube composites films" *Polymer*, 46, pp. 3001-5, (2005)
17. Y. J. Liu and X. L. Chen, "Evaluations of effective material properties of carbon nanotube-based composites using a nanoscale representative volume element" *Mechanics of materials*, 35, pp. 69-81, (2003)
18. Y. J. Liu and X. L. Chen, "Square representative volume elements for evaluating the effective material properties of carbon nanotube-based composites" *Computational materials Sc.*, 29, pp. 1-11, (2004)
19. R. Andrews, D. Jacques, A. M. Rao, T. Rantell, and F. Derbyshire, "Nanotube composite carbon fibers" *Appl. Phys. Lett.*, 75(9), pp.1329-31, (1999)
20. Yue Han and James Elliott, "Molecular dynamics simulations of the elastic properties of polymer/carbon nanotube composites" *Computational materials Sc.*, 39, pp. 315-23, (2007)
21. Dresselhaus M. S., Dresselhaus G., and Saito R., "Physics of carbon nanotubes" *Carbon*, 33(7), pp.

- 883-891, (1995)
22. Carl T. Herakovich, "Mechanics of Fibrous Composites" John Wiley & Sons, Inc., (1998)
23. R. A. Schepery, "Thermal expansion coefficient of composite materials based on energy principle" *J. of comp. materials*, 2(3), pp. 380-404, (1968)
24. M. R. Nedele and M. R. Wisnom, "Three-dimensional finite element analysis of the stress concentration at a single fiber breaks" *Comp. Sc. and Tech.*, 51, pp. 517-24, (1994)
25. M. Meyyappan, "Carbon Nanotubes Science and Applications" CRE Press LLC, (2005)

## 6. NOMENCLATURE

Symbol	Meaning	Unit
$A_c$	Cross sectional area	nm <sup>2</sup>
$E_1$	Young's modulus	GPa
$E_m$	Young's modulus of Matrix	
$E_{nt}$	Young's modulus of CNT	GPa
$L_a$	Initial axial length	nm
$L_t$	Initial transverse length	nm
$\Delta L_a$	Change in axial length	nm
$\Delta L_t$	Change in transverse length	nm
$r_i$	Inner radius of CNT	nm
$r_o$	Outer radius of CNT	nm
$T$	Temperature	K
$\Delta T$	Change in temperature	K
$V_m$	Volume fraction of Matrix	$V_m$
$V_{nt}$	Volume fraction of CNT	
$\alpha_1$	Axial CTE of Nanocomposites	K <sup>-1</sup>
$\alpha_2$	Transverse CTE of Nanocomposites	K <sup>-1</sup>
$\alpha_m$	CTE of Matrix	K <sup>-1</sup>
$\alpha_{nt}$	CTE of CNT	K <sup>-1</sup>
$\nu_{nt}$	Poisson's ratio of CNT	
$\nu_m$	Poisson's ratio of Matrix	

## 7. MAILING ADDRESS

Assistant Prof. Sushen Kirtania  
 Department of Mechanical Engineering,  
 Tezpur University  
 P.O.:- Napaam, Tezpur-784028, Assam, India  
 Phone : + 91-3712-267007/8/9 (Extn 5857)  
 Fax: 091-3712-267005/06  
 E-mail: sushen.kirtania@gmail.com

## A COMPARATIVE STUDY OF TRACK BUCKLING PARAMETERS OF CONTINUOUS WELDED RAIL

S. S. Nafis Ahmad, N. Kumar Mandal and Gopinath Chattopadhyay

Centre for Railway Engineering, Central Queensland University, CRC for Rail Innovation, Australia

### ABSTRACT

Track buckling has been considered as a major concern for Continuous Welded Rail (CWR) since the introduction of CWR on railway networks. Both static and dynamic loadings on track can cause track buckling. Track can be subjected to static loads such as tensile and compressive loads due to temperature differential, and misalignment due to maintenance operations and cumulative deflections. Dynamic parameters include vehicle loading on track under different speeds, Net Axle Lateral to Vertical (L/V) force ratio and bogie centre spacing. A number of research studies have been carried out to investigate the effect of different parameters of track buckling to establish a safety operating criteria. Railways around the world follow their own specific standards to safeguard against track buckling. However, all the studies differ in environment and operational characteristics. Hence unification of knowledge concerning different track buckling parameters is important. In the present study a comparative analysis of different parameters of track buckling is presented. An experimental design has been proposed to investigate variation of Rail Neutral Temperature (RNT) and dynamic effect on track buckling.

**Key word:** Continuous Welded Rail, Track Buckling Parameters, Safety Criteria

### 1. INTRODUCTION

Continuous welded rail (CWR) has replaced the jointed rail for the last four to five decades to reduce maintenance cost and improve ride comfort. High compressive forces, weakened track conditions and vehicle loads are major issue concerning buckling [1]. Compressive force is mainly caused by thermal force generated by the temperature differential between Rail Neutral Temperature (RNT) and actual rail temperature. The thermal force can be obtained from the following formula

$$F = \alpha EA_r(T_N - T_R) \quad (1)$$

Symbols are defined in nomenclature section.

The rail is constrained by sleepers, fasteners and ballast (Fig. 1). A well constrained track prevents the longitudinal and lateral movements of the rail caused by thermal force and train load. Track condition can be weakened by initial misalignment, lack of consolidation of ballast, inappropriate fastening, sleeper types etc. A weak track cannot provide the required resistance to the loads that cause buckling. Vehicle load and speed also play an important role in promoting buckling. Currently empirical formulae are mostly used to analyse safe operating criteria. Prud'homme developed a formula [2] for allowable axle load, which is followed by many of the railways of the world.

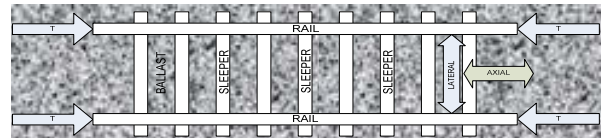


Fig 1. Compressive thermal force on a track [3]

The Prud'homme limit is however only applicable for vehicle approval and since it had been established in 1950s and 1960s, the value is somewhat conservative. The present track structure is stronger than that of that time.

### 2. TRACK BUCKLING PARAMETERS

Track buckling potential is characterized by upper ( $T_{B, MAX}$ ) and lower ( $T_{B, MIN}$ ) buckling temperatures. It can be noted from Fig 2 that, if the track is subjected to a temperature of  $T_{B, MAX}$ , the energy required to buckle the track will be zero, i.e. the track will buckle spontaneously. After buckling, the track reaches a stable state where buckling temperature is  $T_{B, MIN}$ . Fig 2 also shows that buckling energy requirement at  $T_{B, MIN}$  is much higher than that at  $T_{B, MAX}$ .

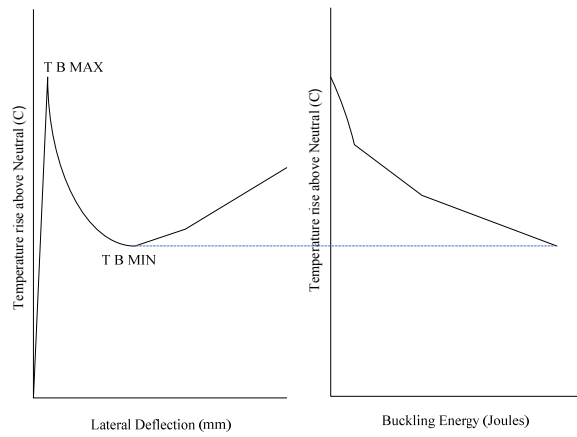


Fig 2. Buckling temperature and energy [4]

### 2.1 Initial Misalignments

Misalignments present in the track play an important role in triggering track buckling. It is considered that rail is manufactured to an initial straightness, which typically permits maximum defect amplitudes of 0.5 mm over 2 m of rail length [2].

F. Birman and F. Raab [5] show that straight tracks with smaller lateral imperfections buckled at much higher temperature increases than those tracks with noticeable lateral imperfections. Again, one train can create a small amplitude line defect which can increase the buckle proneness for the next train coming.

Samavedam et al. [6] show that negative deflection occurs under locomotive axles while the central bending wave under the hopper car increases the potential for lateral deflection. This is more severe for larger bogie centre spacings. The upper buckling temperature condition has been found to be more sensitive to misalignment than lower buckling temperature. It has been found that both upper and lower buckling temperatures increase with the increase of half wavelength and decrease with the increase of amplitude. Esveld's [7] investigation shows similar trends considering the fixed relationship between amplitude and half wavelength.

### 2.2 Lateral Resistance

The track must have the ability to resist lateral forces generated by train passing. Amans and Suavage [6] developed some empirical formulae for determining lateral resistance of a track, which do not include unloaded ballast resistance, sleeper-ballast friction coefficients, curvature and thermal load, effect of track misalignment, dynamic and multiple loads.

Samavedam et al. [6] sorted peak lateral resistance as the primary parameter in studying the effects of lateral resistance on buckling strength. It has also been observed that upper buckling temperature increases more rapidly than lower buckling temperature for higher peak lateral resistance. Track lateral resistance is highly variable as it is affected by many track conditions and maintenance parameters, including ballast section, consolidation, and maintenance.

Esveld [4] shows that a non-linear relationship exists

between lateral resistance and vertical loading. Elasto-plastic with softening behaviour is typical for well consolidated ballast, while the bi-linear model is usually used for describing ballast lateral behaviour. A 3D elastic beam element is used for the analyses and lateral resistance is investigated in relation to displacement.

Kish et al. [8] show the effect of lateral resistance on residual deflection considering multiple train passes. It has been found that residual deflection decreases non-linearly (softening) with the increase of peak lateral resistance. Esveld [7] states that vertical vibration caused by passing trains needs to be considered in determining lateral resistance.

### 2.3 Sleeper Ballast Friction

Sleeper ballast friction is the main contributor to lateral and longitudinal resistance. Friction coefficients between the ballast and sleeper end, sleeper bottom and sleeper side provide the resistance to track movement. Samavedam et al. [6] studied the effect of roughness of sleeper in relation to lateral resistance of the track. Lateral resistance of the track has been expressed by the following equations in [6].

$$F = F_b + F_s + F_e \quad (2)$$

$$F_b = \mu_r Q \quad (3)$$

$$F_{Pdynamic} = \begin{cases} [F_P - \mu_f Q] & \text{for uplift} \\ [F_P + \mu_f R_V(x)] & \text{otherwise} \end{cases} \quad (4)$$

Symbols are defined in nomenclature section.

Uplift of track occurs when the sum of vertical deflection forces caused by vehicle loads and the self-weight of the track is less than zero. It has been found that increasing the coefficient of roughness increases both upper and lower buckling temperature. For timber sleepers, track roughness factor increases with time as ballast tends to incise and lock itself into the timber. On the other hand, concrete sleepers become smooth over time and hence roughness factor is reduced. It has also been observed that base lateral resistance contributes most to the lateral resistance.

Kish et al. [9] show an analytical equation of friction coefficient considering vertical load influence over concrete and timber sleepers.

$$\mu = \mu_2 + (\mu_1 - \mu_2)e^{-\beta R} \quad (5)$$

$\mu_1$ ,  $\mu_2$  and  $\beta$  vary for concrete and timber sleepers. While the static value of lateral resistance increases with level of consolidation, value of friction coefficients were found to be decreasing with the number of train passes. Thus the consequence of vehicle passing is to affect the lateral resistance significantly. It has been observed that a reduction of 5% in friction coefficient happens in every 100 train passes.

Kish et al. [9] use Beam on Elastic Foundation (BOEF) to obtain vertical loads on sleepers. The BOEF assumes that the rail is supported by a single layer with uniform stiffness and it experiences a two-dimensional state of stress. Chrismer's [10] analysis shows that the actual distribution of vertical sleeper loads can be better

predicted by layer elastic modelling which considers multiple horizontal layers to represent the ballast, subballast and subgrade layers. Vertical force on the sleeper under the axle has been found to be approximately 10% greater using the layer elastic model than in BOEF method.

## 2.4 Rail Properties

Analysis by Tew et al. [11] shows the result of Miyai and concludes that lateral stability of any track section decreases with the increase of rail size. However they found one anomaly with the 53 kg/m rail which has higher horizontal moment of inertia compared to that of other larger rail sizes. This property helps to resist lateral bending. This effect was also verified by Railways of Australia (1988) by using Association of American Railroad's (AAR) track buckling model.

Samavedam et al. [6] show that track buckling temperature decreases with the increase of rail size more rapidly than the lower buckling temperature. This is because of the fact that increased area contributes to more thermal force and thereby reduces the effect of increasing bending stiffness. Again, though smaller rail section shows better buckling strength that does not allow for lower bending stiffness and hence maximum axle load of smaller rail. Hence an optimization between wheel load and fatigue is necessary to select an appropriate rail size.

## 2.5 Torsional Resistance

D L Bartlett of British Rail [5] shows that buckling load is proportional to torsional resistance of the rail to sleeper connection. New Zealand Railways carried out tests on torsional resistance of various types of fasteners [12]. However the tests were conducted with new timber sleepers and variation of fastener resistance with sleeper age was not conducted.

Samavedam et al. [6] examined concrete and timber sleepers with different fastener systems (McKay Safeelok and Pandrol fastener) showing that the timber sleeper fastening systems are much stiffer than concrete Pandrol and McKay systems. It has been shown that sleeper type or condition has no significant influence on torsional resistance, while fastener type is a significant parameter. Again, lower buckling temperature is more sensitive to torsional resistance increase compared to the negligible change of upper buckling temperature. Hence buckling strength of the track is not consistently affected by this phenomenon. European Rail Research Institute (ERRI) developed a simulation software 'CWERRI' by which Van [13] verifies the result of Samavedam et al. [6].

## 2.6 Curvature

Samavedam et al. [6] show that upper buckling temperature decreases more rapidly than lower buckling temperature with the increase of curvature. Strong, weak and medium track have been considered for the test. It has been found that progressive buckling can occur at 7 degree or higher curvature for weak track. However the model does not consider effects of non-uniformly distributed ballast resistance along the track, missing sleepers and fasteners, variation of track gauge and

differing neutral temperatures between two sites [14].

Esveld [7] study uses CWERRI model to observe curvature effect on track buckling and it has been found that, although the characteristics are similar to the study of [6], the temperature range is different. Different track conditions in USA and Europe are probably behind this difference.

## 2.7 Longitudinal resistance

Thermal gradient, dynamic braking and rail creep generate longitudinal forces in the rail. Track must provide adequate longitudinal resistance to restrict longitudinal movement. Ballast mass between the sleepers and rail to sleeper connection friction (from toe load grip on the rail foot and the use of rail anchor devices) provide longitudinal resistance. For initial longitudinal displacement up to 6.35 mm (0.25 inch), Samavedam et al. [6] assume the following relationship between longitudinal resistance ( $f$ ) and displacement ( $u$ ).

$$f = k_f u \quad (6)$$

Samavedam et al. [6] show that lower buckling temperature increases with the increase of longitudinal resistance, while upper buckling temperature remains almost constant. Esveld [7] investigation shows the same trend of longitudinal resistance characteristic using CWERRI software. If the track has no/little misalignment, longitudinal resistance will have little effect on buckling.

Grissom et al. [15] considered the effects of the torsional stiffness of the rail fasteners, the lateral bending stiffness of the cross-sleeper, and the track gauge to model the lateral response to temperature increases and approximated the axial resistance curve by the following formula

$$f(x) = f_0 \tanh [\mu u(x)] \quad (7)$$

## 2.8 Temperature

Currently empirical relations have been used to determine rail temperature from the ambient temperature. F. Birmann and F. Raab [5] concluded that there is an accumulation of permanent lateral track deformations due to reversal of temperature over a period of time, which increases buckle potential.

Kish et al. [8] show that residual deflection varies linearly with temperature difference, and 20- 40 % increase in the residual deflection can result by a  $\Delta T$  of 28° C. Van [13] states that buckling is not only based on maximum temperature at which buckling starts, but also on minimum temperature after buckling, which can be found with a post-buckling computation.

In all cases rail neutral temperature affects the result most significantly. However a potential difficulty is the variable nature of neutral temperature. RNT tends to shift downward over time due to the effects of traffic, rail movement and track maintenance. Longitudinal stiffness plays an important role in controlling neutral temperature variations. Pandit [5] describes the theoretical formula of neutral temperature using longitudinal strain in rail

$$T_N = T_L + \frac{1}{\alpha} \left\{ \frac{\partial u}{\partial x} + \frac{1}{2} \left( \frac{\partial v}{\partial x} \right)^2 + \frac{1}{2} \left( \frac{\partial w}{\partial x} \right)^2 \right\} \quad (8)$$

On a curve of radius R, if the track is shifted by an amount equal to C, the above formula can be changed to

$$T_N = T_L + \frac{1}{\alpha} \left\{ \frac{\partial u}{\partial x} + \frac{C}{R} + \frac{1}{2} \left( \frac{\partial v}{\partial x} \right)^2 + \frac{1}{2} \left( \frac{\partial w}{\partial x} \right)^2 \right\} \quad (9)$$

From equation (8) and (9) it is clear that if the displacements u, v and w cause compressive strains (-ve) neutral temperature ( $T_N$ ) will be lower than the laying temperature ( $T_L$ ). Rail longitudinal movement can be caused by train action (acceleration and braking) or wheel rolling action. Track lateral shift may occur due to hunting motion of bogie or curving. Non-uniform vertical settlement of ballast caused by vertical wheel load can generate longitudinal strain in the track, which further changes the rail neutral temperature.

### 2.8 Track Foundation Vertical Stiffness

Samavedam et al. [6] show the effect of track foundation vertical stiffness on track buckling potential, and it has been observed that upper buckling temperature increases with the increase of vertical stiffness. Lower buckling temperature also increases with the increase of stiffness, but this increase is less sensitive to that of upper buckling temperature. However an initial downward slope is visible in both the temperatures due to the complex relationship between the vehicle induced uplift wave and buckling lengths.

### 3. VEHICLE PARAMETERS

Axle load, Net Axle L/V ratio, bogie or truck centre spacing (TCS) and number of passes contribute to the static track buckling parameters. Samavedam et al. [6] show that upper buckling temperature decreases with the increase in axle load, while lower buckling temperature remains almost constant. It has been found [6] that longer TCS provide higher safety margins against possible explosive buckling.

Kish et al. [8] show that deflections over 5 mm are likely to be unstable after 20 passes. Samavedam et al. [2] observed that track tends to stabilize after several passes of a constant load. But after reaching a critical value of load, residual deflection tends to increase. Hence lateral load calculation is recommended.

Lateral load does not remain constant when a train passes over any misalignment in the track [8]. Spirals on curves, gauge narrowing, switch points, and other discontinuities can also produce large dynamic axle loads spread over relatively small wavelengths.

### 4. SAFETY CRITERIA

Rail longitudinal force needs to be less than the critical buckling load. From the theory of engineering mechanics, critical load for the buckling of rail acting as a column can be determined using the following formula

$$P_{cr} = \frac{\pi^2 EI}{l^2} \quad (10)$$

However the above formula does not consider lateral resistance of the track. Wen Pei et al. [16] show the following relation considering lateral resistance of the

track using the beam column principle..

$$P_{cr} = 2\sqrt{Elk_0 \left[ 1 - \left( 1 + \frac{8}{3\pi} \right) \frac{H}{d} + \left( \frac{7}{16} + \frac{4}{3\pi} \right) \frac{H^2}{d^2} \right]} \quad (11)$$

In order to maintain rail longitudinal force within safe limits, measurement of RNT is necessary. Most of the railways use a fixed value of RNT with one or two degree allowance. RNT varies due to rail longitudinal movement, radial breathing in curves, track vertical settlement and maintenance activities. RNT may even vary between two rails (up to 5<sup>0</sup> C) due to destressing operations.

Samavedam et al. [6] show buckling temperatures are functions of peak lateral resistance and the amplitude of misalignment for a given track curvature and rail size. From this analysis, the allowable temperature rise can be determined based on the criteria setup for different track strengths. Minimum required lateral resistance (MRL) for a given allowable rail temperature has been derived as a function of track curvature for rail size and amplitude of misalignment. This theory does not allow for the variable nature of ballast resistance with track deflection.

Table 1: Lateral limit load and L/V ratio with respect to axle load

Axle Load (KN)	Lateral Limit Load (KN)			Axle L/V Ratio			
	75	150	225	75	100	150	225
Prud'homme limit	35	60	85.0	0.47	0.43	0.40	0.38
85% Prud'homme limit	29.7	51	72.2	0.40	0.37	0.34	0.32
A & S Concrete Sleepered Track	38.5	66	93.5	0.51	0.48	0.44	0.42
A & S Wood Sleepered Track	29.7	51	72.2	0.40	0.37	0.34	0.32
A & S Recently maintained Track	35	60	85.0	0.47	0.43	0.40	0.38
Kish et al [12] 6 deg. Curve with Misalignment	38.6	59.6	80.6	0.52	0.46	0.40	0.36
Kish et al [12] 6 deg. Curve	40.8	61.8	83	0.54	0.48	0.41	0.37
Kish et al [12] Tangent track with Misalignment	41.9	62.2	82.4	0.56	0.49	0.41	0.37
Kish et al [12] Tangent track	44.6	64.8	85.1	0.59	0.51	0.43	0.38
US X 2000 Vehicle	37.5	75	113	0.50	0.50	0.50	0.50
FRA 96/ 03 [2]	68.4	91.1	114	0.91	0.76	0.61	0.51
SNCF for Tamped Track	54.8	85.5	116	0.73	0.65	0.57	0.52
SNCF for Consolidated Track	85.3	133	180	1.14	1.01	0.88	0.8

A & S – Amans and Suavage, FRA- Federal Railroad Administration, SNCF- French National Railways

Railway industries use wheel L/V, axle sum L/V, net axle L/V and truck side L/V for vehicle certification. Net axle L/V for high speed trains is used here for comparing different studies. Table 1 shows the comparison among different studies on determining lateral limit loads in relation to various axle loads. Prud'homme limit considers an indefinite number of axle passes with no allowance for misalignment. It seems impractical, as it requires rigorous maintenance activity. Again, Prud'homme considered the constant lateral force only but high lateral forces over short wavelengths can occur in field conditions [9]. 85% Prud'homme limit considers thermal and curvature effects. The Amans and Suavage investigation specifies different limits for different types of sleeper and track construction. Amans and Suavage developed a semi empirical formula which can take into



account misalignment amplitude for dynamic loads. Kish et al. [9] show different limit loads for a 6 degree curve and tangent track with and without misalignment. USDOT's [2] investigation reveals a higher L/V ratio than the current US practice. However, the USDOT [2] study deals with stationary loads only. SNCF developed lateral limit loads for dual block concrete sleepers which are much higher than that for the mono-block sleeper track.

Investigations through all studies except for the US X2000 vehicle presented in Table 1 show that allowable net axle L/V decreases with the increase of axle load. The Kish et al. [9] investigation on L/V ratio over several numbers of passes using the Track Residual Deflection Analysis (TREDA) model determined a safe ratio of 0.37. This analysis assumes constant lateral load and track with no initial line defects. However, TREDA can take into account variable lateral resistance and line defects.

A probabilistic approach has been proposed by Kish [17]. It determines probability of buckling at a given rail temperature and thus railroads can perform trade-offs between different maintenance practices for a given level of buckling probability using 'CWR Safe' software. However 'CWR Safe' does not consider parameters related to grade, train braking and acceleration, longitudinal movement etc.

Zarembski et al [18] propose a site specific track buckling risk analysis methodology which uses the available track database of the railway industry. However this model is site specific and requires experienced personnel for that site to develop an accurate model.

## 5. EXPERIMENTAL DESIGN

At present the track stability is managed in different railway industries by using some empirical formulas and experiences where dynamic effects are not quantified. However effect of different parameters and dynamic effect are needed to be incorporated in the track stability management tool. The present experimental design has been proposed (Fig 3 and Fig 4) to investigate the parametric effects (static and dynamic) on different track conditions.

A curved track with switches and cutting (Fig 3) has been considered appropriate for the test as it can handle radius, irregular track structure and non-uniform temperature effect on revenue track. Rail Stress Modules (RSM) will be used to monitor data in the revenue track. Details of RSM technology can be found in [19]. Through this investigation, it is aimed to develop a suitable RNT measuring and analysing tool for Australian track conditions in addition to observing the effect of track radius, braking zone, and irregular track structure and temperature distribution on the variation of RNT.

Fig 4 shows the setup to monitor change of axial stress along with lateral and vertical load due to dynamic effect. A trigger is proposed to record data during train passing. The setup in fig 4 will be placed in a braking zone to monitor change of strain due to braking, and thereby variation of RNT can be observed.

Currently Design Neutral Temperature (DNT) is used to keep track stable (neither buckle nor break) throughout

the year, based temperature of the region. However dynamic effect and different track constructions are not included in DNT selection. From the present experimental design it is aimed to find a better method of selecting DNT.

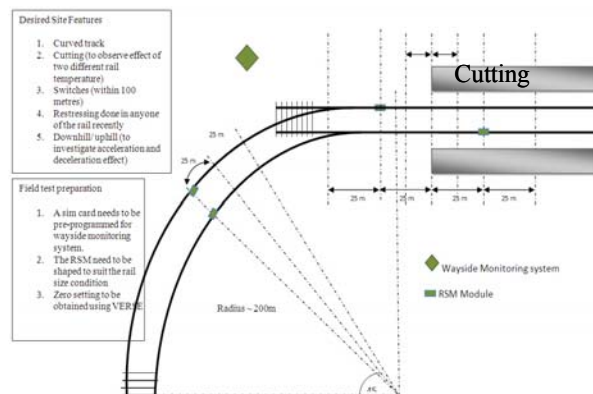


Fig 3. Monitoring of RNT for a long duration

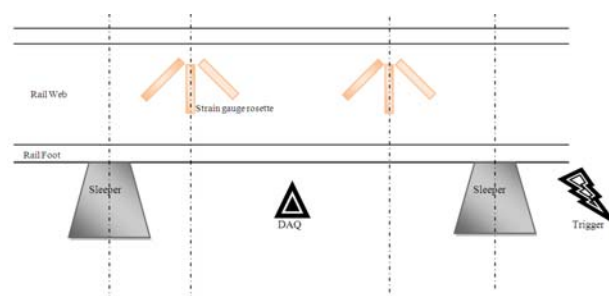


Fig 4. Monitoring dynamic effect on track buckling parameters

## 6. CONCLUSION

The track is managed by using some empirical relationships among different parameters, most of which were developed 30-40 years ago. It is necessary to incorporate the improved understanding of different parameters on the track stability management tool. A comparative study on track buckling parameters has been carried out. It is necessary to consider different track construction standards and vehicle parameters over a specific track to determine safe operating practice.

An experimental design has been proposed to investigate effect of dynamic parameters on different track conditions. The experimental setup will help to generate an improved track stability analysis with the inclusion of dynamic effect on track buckling potential in different track constructions.

Each track buckling parameter has its own individual effect on track shift. In revenue track, each parameter often depends on other parameters. Correlations among different parameters need to be established to provide better maintenance and inspection guidelines for the railway industry.

## 7. ACKNOWLEDGEMENT

The authors are grateful to the CRC for Rail Innovation (established and supported under the Australian Government's Cooperative Research Centres program) for the funding of this research. Project No.

## 8. REFERENCES

1. John A. Volpe National Transportation Systems Center, Track Buckling Research. Viewed 9 June 2009, <<http://www.volpe.dot.gov/sdd/docs/buckling.pdf>>.
2. Samavedam, G., Blader, F. & Thomson, D., 1996, "Safety of High Speed Ground Transportation Systems Track Lateral Shift: Fundamentals and State-Of-The-Art Review", US DOT Report No. DOT/FRA/ORD- 96/03
3. Van, M. A., 1996, "Buckling Analysis of CWR", Heron, 41.
4. Esveld, C., 2001, *Modern Railway Track*, MRT-Productions, the Netherlands.
5. Pandit, S. A., *Long Welded Rail*, Pune, Indian Railways Institute of Civil Engineering.
6. Samavedam, G., Kish, A., Purple, A. & Schoengart, J., 1993, "Parametric Analysis and Safety Concepts of CWR Track Buckling", US DOT Report No. DOT/FRA/ORD- 93/26.
7. Esveld, C., 1998, "Improved Knowledge of CWR Track", *D 202. Paris*.
8. Kish, A., Samavedam, G. & Wormley, D., 1998, "Fundamentals of Track Lateral Shift For High-Speed Rail Applications", *ERRI Interactive Conference on Cost Effectiveness and Safety Aspects of Railway Track, Paris*.
9. Kish, A., Samavedam, G. & Wormley, D., 2001, "New Track Shift Safety Limits for High-Speed Rail Applications", *Proc. of World Congress on Railway Research, Germany*.
10. Chrimer, S. M., 2005, "Analysis of Lateral Track Strength for High Speed Rail", *ASME International Mechanical Engineering Congress and Exposition, Orlando, Florida, USA*.
11. Tew, G. P., Marich, S. & Mutton, J. P., 1991, *A Review Of Track Design Procedures*, BHP Research- Melbourne Laboratories For Railways of Australia, Australia.
12. Doyle, N. F., 1980, *Railway Track Design: A Review of Current Practice*, Bhp Melbourne Research Laboratories, Canberra, Australia.
13. Van, M. A., 1997, "Stability of CWR Track", Phd Thesis, Civil Engineering. Delft University of Technology, The Netherlands.
14. Lim, N. H.-Y., Park, N.-H. & Kang, Y. J., 2003, "Stability of Continuous Welded Rail", *Computers and Structures*, 81: 2219- 2236.
15. Grissom, G. T. & Kerr, A. D., 2006, "Analysis Of Lateral Track Buckling Using New Frame-Type Equations", *International Journal Of Mechanical Sciences*, 48: 21- 32.
16. Wen-Pei, S., Ming-Hsiang, S., I, L. C.-. & Germ, G. C., 2005, "The Critical Loading For Lateral Buckling of CWR", *Journal Of Zhejiang University Science*, pp . 878- 885.
17. Kish A., 2009, 'Track Lateral Stability' in *International Heavy Haul Association (ed.), "Guidelines to Best Practices for Heavy Haul*

*Railway Operations Infrastructure Construction and Maintenance Issues*", USA.

18. Zaremski, A. M., Grissom, G. T. & Lees, H. M., 2004, "Development Of Track Buckling Risk Analysis Methodology", *AREMA 2004 Conference Proceedings*, pp. 1- 32.
19. Harrison H., McWilliams R. & Kish A., 2007 "Handling CWR Thermal Forces", *Railway Track and Structures*, New York, USA.

## 9. NOMENCLATURE

Symbol	Meaning	Unit
F	Longitudinal Force	N
$\alpha$	Coefficient of thermal expansion	$^{\circ}\text{C}/\text{m}$
E	Modulus of Elasticity	$\text{N}/\text{m}^2$
$A_r$	Area of rail	$\text{m}^2$
$T_N$	Neutral Rail Temperature	$^{\circ}\text{C}$
$T_R$	Rail Temperature	$^{\circ}\text{C}$
$T_L$	Rail Laying Temperature	$^{\circ}\text{C}$
$T_{B\text{MAX}}$	Upper buckling Temperature	$^{\circ}\text{C}$
$T_{B\text{MIN}}$	Lower buckling Temperature	$^{\circ}\text{C}$
$\mu_f$	Coefficient (index of bottom roughness)	Dimens ionless
$F_L$	Lateral Resistance	$\text{N}/\text{m}$
$F_b$	Base lateral resistance	$\text{N}/\text{m}$
$F_s$	Side lateral resistance	$\text{N}/\text{m}$
$F_e$	End shoulder lateral resistance	N
$F_p$	Peak Lateral Resistance	$\text{N}/\text{m}$
Q	Weight of sleeper	N
$R_v$	Distributed vertical forces between sleeper and ballast	N
$\mu_1$	Friction coefficient (index) at zero vertical load	Dimens ionless
$\mu_2$	Friction coefficient (index) at large vertical load (>89 KN)	Dimens ionless
$\beta$	In terms of 1/KN	1/KN
u	Rail displacement axial direction	m
v	rail displacement in lateral direction	m
w	rail displacement in vertical direction	m
C	Track shift due to curving	m
$\frac{\partial u}{\partial x}, \frac{\partial v}{\partial x}, \frac{\partial w}{\partial x}$	Tensile strains in x direction	Dimens ionless
R	Radius of the track	m
$k_f$	Longitudinal stiffness	MPa
f	Longitudinal resistance	N
$f_0$	Maximum axial resistance	N
$\mu$	Constant for fitting the expression to the non-linear test data	Dimens ionless
I	Moment of Inertia	$\text{mm}^4$
$k_0$	Unit Lateral resistance force before the rail is lifted	N
d	depth of rail clip covered into the sleeper and ballast	mm
H	lift height	mm
l	Column Length	m



## CONTACT STRESSES IN CONICAL ROLLERS UNDER NORMAL AND TANGENTIAL LOADINGS

M. Wasim Akram<sup>1</sup>, A. Rayhan Md. Ali<sup>2</sup> and S. C. Chowdhury<sup>2</sup>

<sup>1</sup>Department of Ocean Engineering, Florida Atlantic University, Florida, USA

<sup>2</sup>Department of Mechanical Engineering, Bangladesh University of Engineering and Technology, Dhaka, Bangladesh

### ABSTRACT

In this paper, the stresses distributions arising from the contact between two complex geometrical bodies have been analyzed using finite element simulation software by considering two conical rollers, where two rollers have been subjected under normal compressive and tangential loading. Due to these types of loading the contact patch has been found trapezoidal shape which is in contrast with cylindrical contact, where contact patch is rectangular. The trapezoid shape of the contact area arises because the radius of curvature of either cone varies along the axial direction and contact length. So, radius of curvature is a function of vertex angle and contact length. Maximum pressure distribution and half width distribution has been found along contact length. Stresses in different directions have been analyzed and shown with different contact geometries. Maximum stresses have been found at contact surface for three normal stress components under combined loadings, and maximum shear stress has been found at some distance into the solid from contact surface. The results have been verified with analytical solutions. The finite element simulation results have been found consistent with the analytical results in predicting pressure, its distribution and stresses in contact rollers.

**Keywords:** Conical Rollers, Radius of Curvature, Finite Element Simulation, Stress Distribution.

### 1. INTRODUCTION

Loading transfer between components in engineering assemblies often causes very high localized stresses, generally called contact stresses, which lead to component failure by different forms of surface contact fatigue. Consequently, the evaluation of contact area geometries, pressure distribution, stresses is imperative to prevent premature failure such as pitting, spalling, false brinelling.

The analysis of contact stresses between simple geometries like cylindrical elements or spherical elements have attracted the attentions of many researchers. There are lots of works on these simple geometries. Heinrich Hertz[1] for the first time analyzed the contact stresses by determining the loading distribution over the contact area and provided the mathematical models for the stress field using a potential function for the case of spherical contact. He deduced that an ellipsoidal distribution of pressure would satisfy the boundary conditions of the problem for the case of spherical contact. He verified his analytical results by running a series of experiments. Hertz only considered spherical contact for his analysis. And for a long time there was no remarkable research on contact problems. Every contact problems were solved on Hertz spherical contact theory. Lundberg [2] analyzed the problem when two bodies of different geometries come in contact. He calculated the stresses for the case of a cylinder and a

spherical ball pressed on a flat plate and verified his findings by photo elastic technique. Both (Hertz and Lundberg) considered only normal loading for their analysis. But for the case of contact between two rotating elements, there is always tangential traction except pure rolling. So in that case there exist some tangential loading. Mindlin [3] investigated the stress distribution due to tangential loading when one elastic body slides over the other across the contact area for the case of cylindrical contact. Mindlin found that the stresses on the bounding curve of the contact area due to bounding curve are infinite and consequently a state of impending slipping prevails. Smith and Liu [4] studied the contact between parallel rollers in combined rolling and sliding for spherical contact only. Though there are lots of works on gear contact, cam – follower contacts and so on, but all of these were based on simple contact geometries. With advent of time more complex geometries evolved and hence researches were needed on complex geometries. Al Zain [5] analyzed the contact problem between two conical rollers only under the normal loading. Shakoor[6] also agreed with Zain's proposal while he was doing research on special cam follower contact problems. Later Litvin [7] has used Zain's proposal for his research of bevel gear. But no one did research on conical rollers for complex loading and also finite element verification.

This work was based on more complex geometries

rather than simple geometries by considering conical rollers are in contact [8] under both normal and tangential loading. The stresses due to conical rollers in contact with application of both normal and tangential loading have been solved using finite element simulation software ANSYS [9]. The results obtained from ANSYS have been verified with analytical solution. The distribution of stresses has been observed for different contact geometrical parameters and loading conditions.

## 2. ANALYTICAL SOLUTION

When two geometrically and materially identical conical rollers come into contact with each other under the application of a uniform compressive normal loading in rolling, the contact patch appears in the form of trapezoid, in contrast with two cylinders where the contact area is a rectangle.

### 2.1 Radius of Curvature

The radius of curvature of a conical roller is equal to the radius of curvature of an ellipse formed by a cut plane normal to the external surface of the conical roller. This radius of curvature varies as the cut plane moves along the contact length. Figure -1 shows two ellipses in a side view formed by sectioning conical rollers by the cut plane at  $t$ .

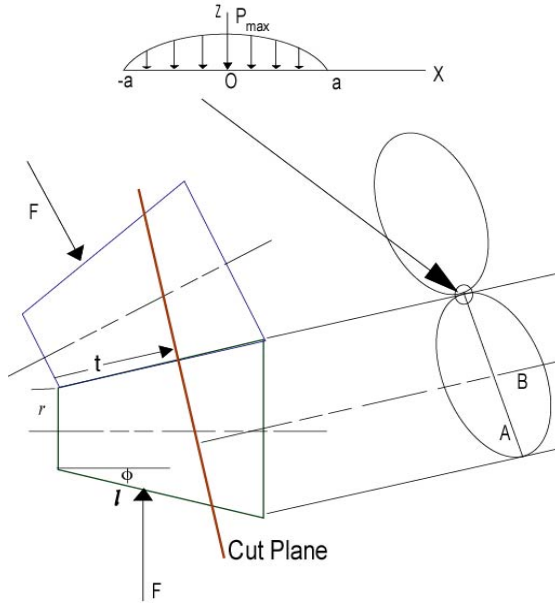


Fig 1. Two conical rollers in contact

The radius of curvature of the osculating rollers for the section at  $t$  is –

$$R_1 = R_2 = R = f(t) = \frac{B^2}{A} \quad 0 \leq t \leq l \quad (1)$$

Equation (1) is a parametric form of radius  $R$  of curvature, where all values of  $R$  along the contact length can be determined as  $t$  increases from 0 to  $l$ .  $A$  and  $B$  are the lengths of the major and minor axis respectively of the ellipses of osculating rollers 1 and 2 at  $t$ , when viewed perpendicular to the section, as shown in figure 1. The lengths of the major and minor axes, which are also

function of  $t$ , are determined by visualizing the cone in a three dimensional space. From figure 2 the length of the minor axis of each cone is –

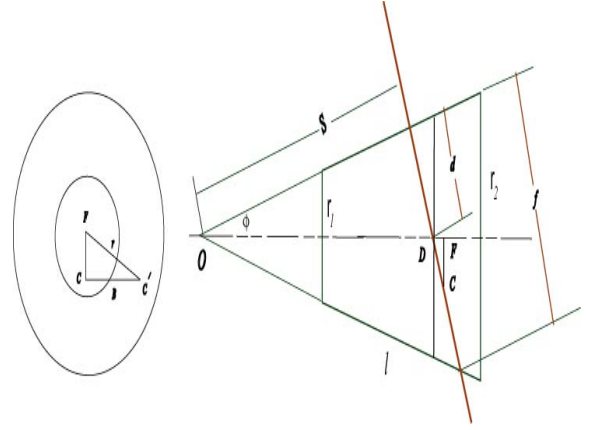


Fig 2. Front side view of conical cylinder

$$B = \sqrt{r^2 - FC^2} = \sqrt{(OD + DF)^2 \tan^2 \phi - DC^2 \cos^2 \phi}$$

$$\text{for } 0 < \phi < 45 \quad (2)$$

Where  $r$  is the radius of each cone at  $t$  and  $\phi$  is the vertex angle. The application of the above equation requires a vertex angle greater than  $0^\circ$  and less than  $45^\circ$ . At 0, the cone reduces to a line and at  $45^\circ$  the cutting plane  $t$  becomes parallel to the side  $l$ .

Putting the values of  $OD$ ,  $DF$  and  $DC$  in the above equation gives

$$B = \sqrt{\left[ \frac{S^2}{\cos^2 \phi} + \left( \frac{f-d}{2} \right)^2 \sin^2 \phi + 2 \left( \frac{S}{\cos \phi} \right) \left( \frac{f-d}{2} \right) \right] \tan^2 \phi - \left( \frac{f-d}{2} \right)^2 \cos^2 \phi}$$

$$\text{For } 0 < \phi < 45 \quad (3)$$

where  $S$  is the distance from the apex, and  $f$  is length of the section, perpendicular to the cone surface, at  $t$  projected on the  $Y-Z$  plane passing through the axis of the cone. The above equation can be written in terms of  $t$  as

$$B = K \left( \frac{r_1}{\sin \phi} + t \right) \quad 0 \leq t \leq l, \quad 0 < \phi < 45^\circ \quad (4)$$

where  $K$  is a constant which is given by

$$K = \sqrt{\left( \frac{1}{\cos^2 \phi} + H^2 \sin^2 \phi + \frac{2H}{\cos \phi} \right) \tan^2 \phi - H^2 \cos^2 \phi} \quad (5)$$

$$H = \frac{\tan(2\phi)}{2} - \tan \phi$$

The length of the major axis of each cone is –

$$A = \left( \frac{r_1}{\sin \phi} + t \right) \frac{\tan(2\phi)}{2} \quad 0 \leq t \leq l \quad 0 < \phi < 45^\circ \quad (6)$$

Putting the values of equations (4) and (6) in equation (1) gives –

$$R = \frac{2K^2}{\tan(2\phi)} \left( \frac{r_1}{\sin \phi} + t \right) \quad 0 \leq t \leq l \quad 0 < \phi < 45^\circ \quad (7)$$

The conical roller geometric constant  $b$  that depends only on the radii of curvature of two cones, at  $t$  is –

$$b = \frac{1}{2} \left( \frac{1}{R} + \frac{1}{R} \right) = \frac{1}{R} \quad 0 \leq t \leq l \quad (8)$$

It may be noted that like  $b$ , has a unique value for each value of  $t$  as long as long radius of curvature is not infinite or undefined.

## 2.2 Stress Distribution

Plane strain conditions have been assumed. The other two stresses ( $\sigma_x$  and  $\sigma_z$ ) have been determined first by considering point loading distribution for normal and tangential loading and hence integrating over the deformed area i.e. contact patch. Von misses shear stress ( $\tau_{xz}$ ) has been analyzed using normal stresses. Following equations were used for stress distribution-

$$\sigma_x = -\frac{2z}{\pi} \int_{-a}^a \frac{p(s)(x-s)^2 ds}{\{(x-s)^2 + z^2\}^{3/2}} - \frac{2z}{\pi} \int_{-a}^a \frac{q(s)(x-s)^3 ds}{\{(x-s)^2 + z^2\}^{3/2}} \quad (9)$$

$$\sigma_z = -\frac{2z^3}{\pi} \int_{-a}^a \frac{p(s)ds}{\{(x-s)^2 + z^2\}^{3/2}} - \frac{2z^2}{\pi} \int_{-a}^a \frac{q(s)(x-s) ds}{\{(x-s)^2 + z^2\}^{3/2}}$$

$$\sigma_y = \nu(\sigma_x + \sigma_z) \quad (10)$$

$$\tau_{xz} = \left| \frac{\sigma_x - \sigma_z}{2} \right| \quad (11)$$

## 2.3 Other Equations

For tangential loading –

$$q(x) = \pm \mu p(x) \quad (12)$$

Half width-

$$a = \sqrt{\frac{2(m_1 + m_2)F}{\pi bl}} \quad (13)$$

It is noted that half width does not vary with tangential loading if the material properties of two mating bodies are identical.

Pressure Distribution and Maximum Pressure

$$p(x) = P \max \sqrt{1 - \frac{x^2}{a^2}} \quad (14)$$

$$P_{\max} = 2*F / \pi a l \quad (15)$$

## 3. FINITE ELEMENT SIMULATION

In order to analyze conical rollers in finite element model, a geometrical model was created using Solid Works software. The length of the two rollers was 20 mm and vertex angle was 5 degree. The radiuses at the tip were 5 mm for both rollers. Then the geometrical model was transferred to ANSYS finite element software. After that, geometrical modeling was completed by creating surfaces using the loft method. In the meshing process, tetrahedral 10-Node element (SOLID 187) elements were employed to increase accuracy of the modeling. Materials have been used steel with  $E=209$  GPa and poisson's ratio 0.3 As in case of contact problems stress are concentrated close to contact region. So, fine mesh is required in the contact region. To do so, first all the geometrical models have been meshed freely. Then the contact surface has been mapped mesh to finer the meshing

Convergence criteria should be considered to evaluate

the results. Convergence analysis is performed on a metallic model of the conical rollers. By improving mesh density step-by-step a suitable number of elements is obtained. The stabilization of deformation and Von-Misses equivalent stress at a location far from the applied loadings are the criteria of convergence. The depiction of the FE model is shown in figure. 3. To give uniform compressive loading an almost zero thickness plate has been used.

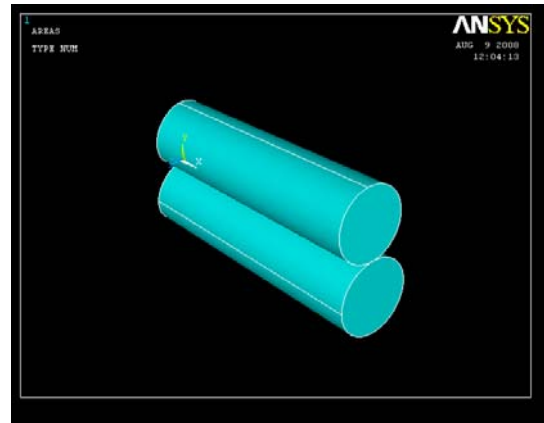


Fig 3. Finite element model

## 4. RESULTS AND DISCUSSION

In case of conical rollers in contact, the contact area is in form of trapezoid. So half width is not constant like cylindrical contacts. Though the half width is axis symmetric along line of contact but it varies along the length of the conical roller which has been shown in the figure 4. From the graph it has been observed that at the tip of conical rollers, half width has minimum dimension and it increases with the increase of length of the rollers.

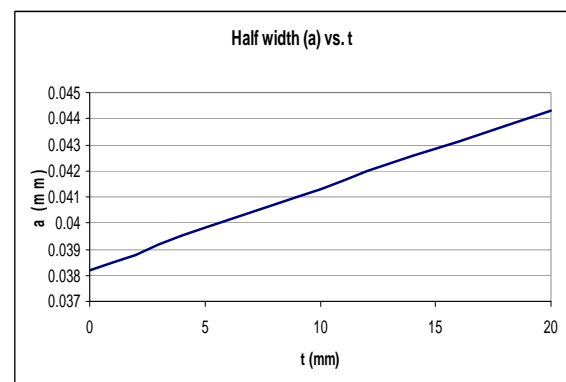


Fig 4. Half width distribution

As the maximum pressure under contact region depends on the deformed shape of the rollers, so maximum pressure has been found varying with the length of the conical rollers. At the tip of the conical rollers, the half-width is the minimum, so maximum pressure has been found largest at the tip as  $P_{\max}$  inversely proportional to half-width. The variation has been shown in the figure 5.

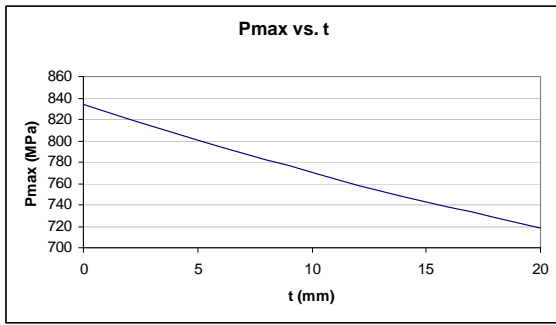


Fig 5. Maximum pressure distribution

Stress distribution for X axis ( $\sigma_x$ ) in case of normal loading has a maximum stress ratio i.e.  $\sigma_x / P_{max}$  is -1. It means that stress is compressive and maximum stress has a value same as maximum pressure. The maximum stress has been found at contact surface i.e.  $z/a=0$  and at  $x/a = 0$  i.e. at line of symmetry. For the case of tangential loading, the distribution is linear. In leading edge i.e. where rolling starts, the stress type is compressive and in trailing edge its type is tensile. The maximum stress ratio occurs at contact surface i.e.  $z/a = 0$  and a value of 0.6. In leading edge it has been found compressive at  $x/a=1$  i.e. where contact begins. In trailing edge it has been found tensile at  $x/a= -1$  i.e. where contact ends. For combined loading, the maximum stress has been found at contact surface i.e.  $z/a=0$  and it has been found at  $x/a=0.5$  distance towards the leading edge with a value of -1.167. So in case of combined loading stress component in X direction has a value 16.7% higher than that for normal loading and has been found 50% shifted towards the leading edge from symmetry. The stresses distributions for different loading have been shown from figure 6 to 8.

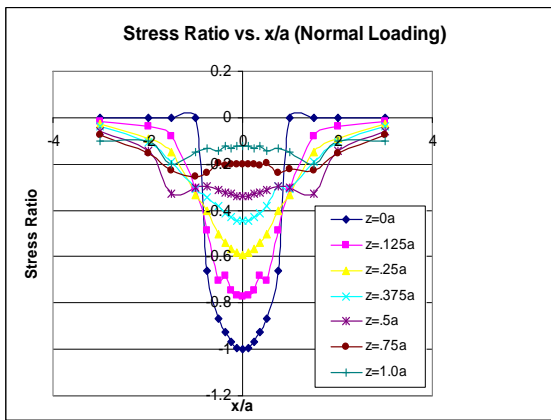


Fig 6. Distribution of  $\sigma_x$  under normal loading

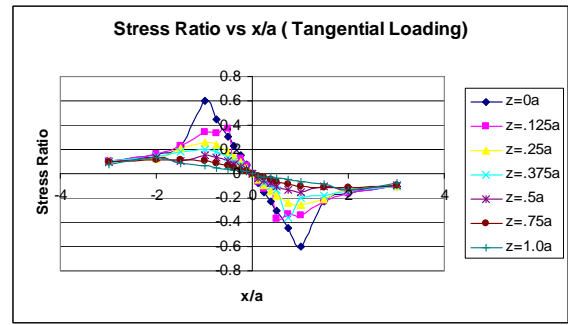


Fig 7. Distribution of  $\sigma_x$  under tangential loading

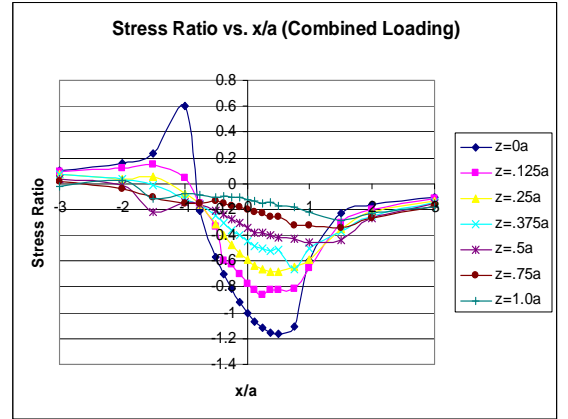


Fig 8. Distribution of  $\sigma_x$  under combined loading

As the maximum contact pressure is higher at the tip of the conical roller, so stress will be high at the tip. It decreases in value with the increases the length from the tip. In the figure 9 the stress distribution in X axis (at surface i.e.  $z/a=0$ ) for combined loading has been shown

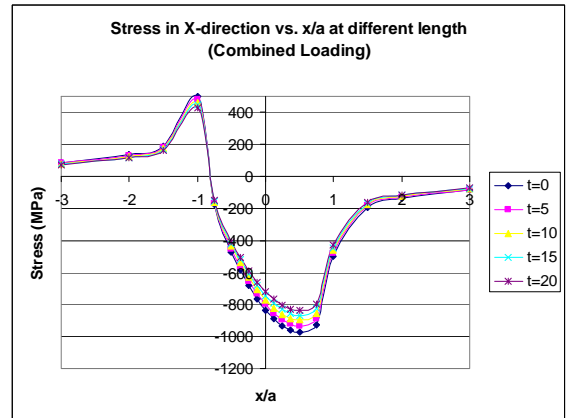


Fig 9. Distribution  $\sigma_x$  along contact length

Stress distribution in Z axis i.e. axis directed to solid vs.  $x/a$  shows that there is same distribution as pressure distribution for normal loading. The maximum stress ratio that is stress to maximum pressure has been found at  $x/a=0$  and at the surface. With increasing of the distance from the surface it decreases. The maximum value of

stress ratio is -1 that is exactly same what the value for maximum normal pressure.

The stress distribution (for tangential loading) vs.  $x/a$  shows linear relation. The stress ratio has very negligible value. It means by applying tangential loading in X direction, stress components in Z axis don't vary so much. So, for combined loading the stress distribution has shown same like for normal distribution. The stress distributions in Z axis for different loadings have been shown from figure 10 to 12.

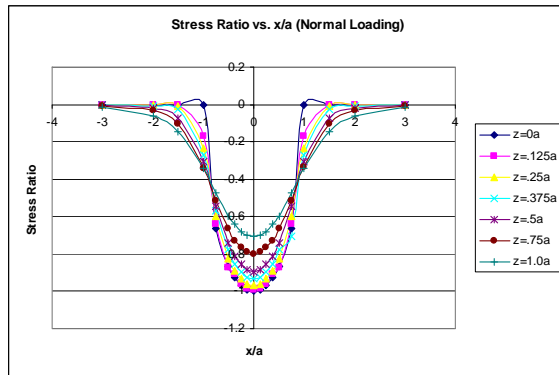


Fig 10. Distribution of  $\sigma_z$  for normal loading

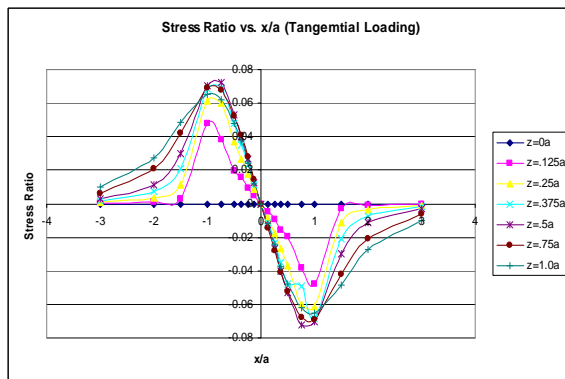


Fig 11. Distribution of  $\sigma_z$  for tangential loading

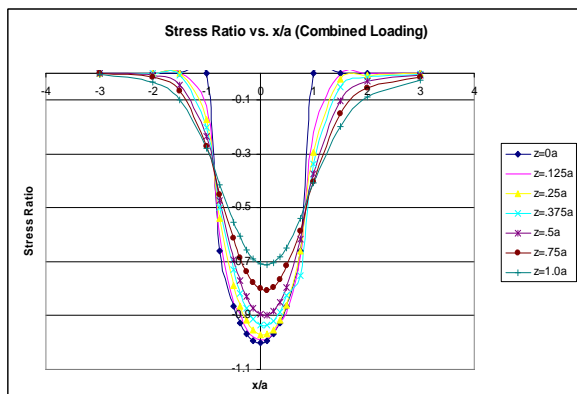


Fig 12. Distribution of  $\sigma_z$  for combined loading

Like the stress distribution in X axis, stress in Z axis also varies with varying distance from tip. At the tip i.e.

at  $t=0$ , the stress is maximum and its value decreases with increasing the distance from tip. The variation of stress along the contact length has been shown in figure 13.

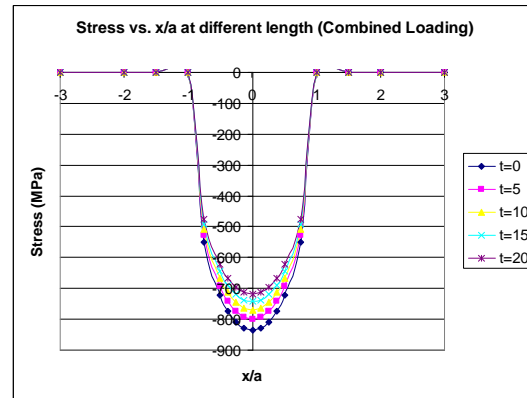


Fig 13. Distribution  $\sigma_z$  along contact length

From the distribution of stress in Y axis, we have seen that the distribution is as like as that for X axis, i.e. maximum value has been found some value tilted towards leading edge. But value of stress ratio is of 0.60 which is lower than other two components. So this stress component does not have significant role for contact stresses. The location where maximum stress has been found is at contact surface ( $z=0$ ) and at a distance ( $x/a=0.5$ ) from line of symmetry. The stress distribution has been shown in figure 14.

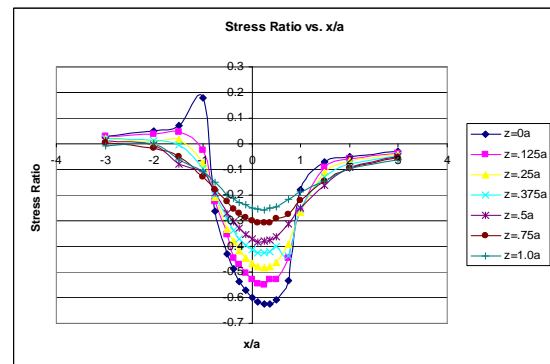


Fig 14. Distribution of  $\sigma_y$  for combined loading

From Von Mises stress distribution along  $x/a$  it has been found that maximum value for shear stress has been found that for  $z/a=0.34$  at it has been found at  $x/a=0$  with a stress ratio of 0.4. At surface  $z=0$  the value is not as high as that for  $z/a=0.30$ , though all other stress components are high at surface. The shear stress also varies with contact length. The distribution of shear stress with the variation of  $x/a$  and  $z/a$  as well contact length have been shown from figure 15 to 18.

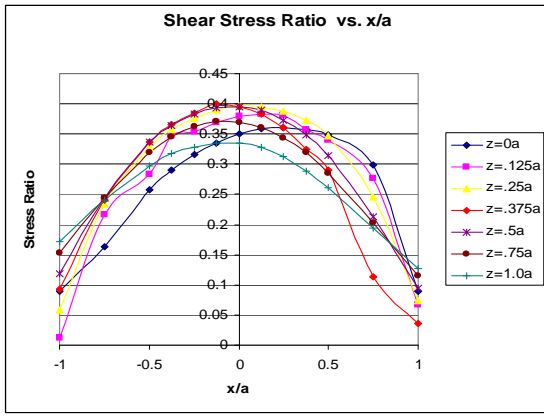


Fig 15. Distribution of shear stress along  $x/a$  (combined loading)

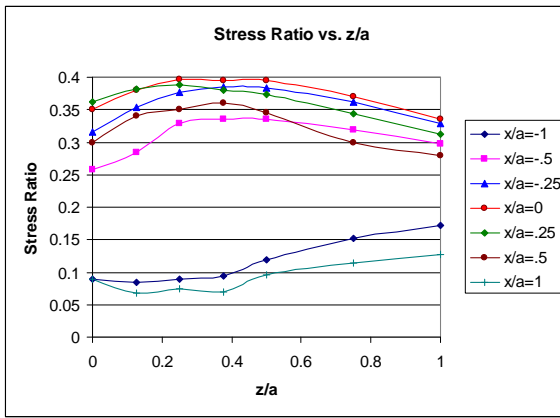


Fig 16. Distribution of shear stress along  $z/a$  (combined loading)

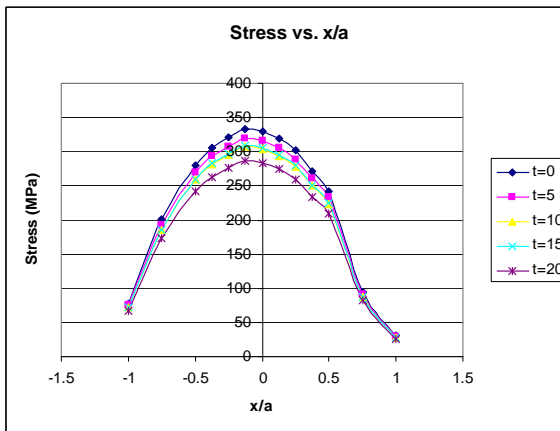


Fig 17. Distribution shear stress along contact length and  $x/a$

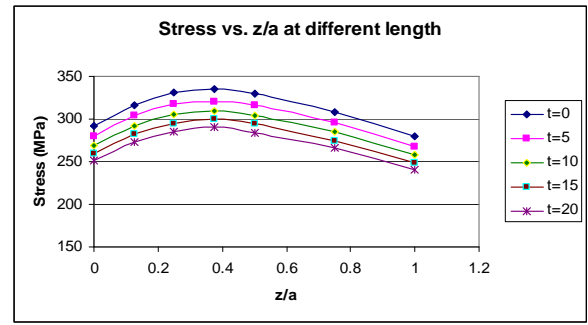


Fig 18. Distribution Shear Stress along contact length and  $z/a$

The results those have been obtained from ANSYS are very close to analytical solutions. Stress components in each direction are almost same with that of analytical results which have been solved by integration. To compare results only steel material has been considered with same loading conditions. The overall geometry and contact geometries were identical. The comparisons of the results have been shown from figure 19 to 21.

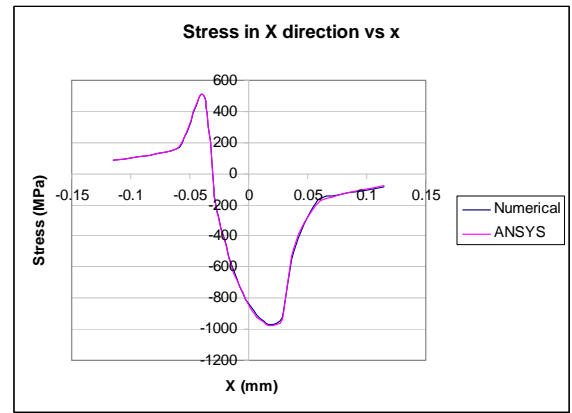


Fig 19. Comparison of  $\sigma_x$  with analytical solution

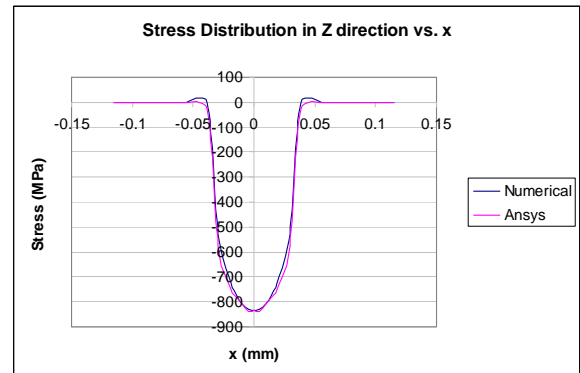


Fig 20. Comparison of  $\sigma_z$  with analytical solution



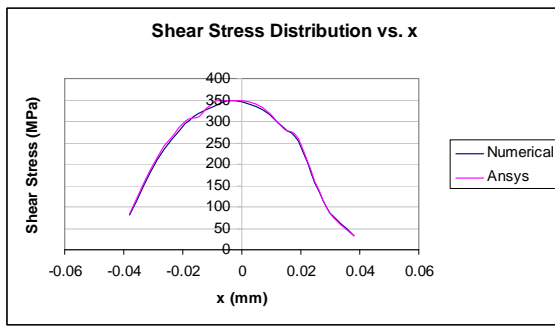


Fig 21. Comparison of shear stress with analytical solution

## 5. CONCLUSION

For simple geometries like sphere to sphere contact, cylinder to cylinder contact or cylinder to plane contact, the contact area or deformed area is either circular or rectangular based on type of contacts. But for conical rollers are in contact, the deformed area is trapezoid so half width varies with distance (from smaller end).

In case of combined loading stress component in X direction has a value 16.7% higher than for normal loading and has been found 50% shifted towards the leading edge from symmetry.  $\sigma_x$  varies along the contact length. With increasing of the distance from the apex of the roller  $\sigma_x$  decreases. The variation of stress between apex and larger end of the conical roller is 13.8% i.e. at the apex of the cone the stress is 13.8% higher than that at the large end.

The maximum value of stress ratio in Z direction for the case of tangential loading is .072 i.e. very negligible in compare with normal loading which is -1. So, for combined loading the distribution is almost like stress distribution for normal loading. In case of combined loading the stress ratio is -1 and it has been found as like as normal distribution i.e. at contact surface and in the line of symmetry of pressure distribution.

For the case of contact problems, the main cause of the initiation and propagation of crack or cracks is the maximum value of shear stress. In this present work to predict maximum shear stress Von Mises Maximum Shear Stress principle has been used. The maximum value as well as location of that peak value is important. From this work, for the case of combined loading we have found that the peak value of shear stress ratio i.e. ratio of maximum shear stress and maximum pressure is 0.39 which is 7.6% higher than that for only normal loading. The location of the maximum shear stress has been found at  $x/a=0$  i.e. the line of symmetry and at  $z/a=0.30$ . So from this two works it can be found that for combined loading the location of the maximum shear stress is 20% less deep from contact surface. The results obtained from ANSYS have been found consistent with those analytical results.

## 6. REFERENCES

1. Hertz, H. Gesammelte Werke, Band I, 1895 (Basth, Leipzig) (English transl. Hertz J,H Miscellaneous papers, 1896 (Macmillan, London)

2. Lunderberg, G. Elastiche Beruehrung Zweier Halbraeume Forsch. Geb Ingenieurwesens A, 1936, 10, 201-211
3. Mindlin, F. M. Hertz Contact Problem For Elastic Anisotropic Halfspace with Initial Stress, Plenum Publishing Corporation, 1990, 126-132
4. Smith, J.O. and Liu, C.K. , Stresses due to tangential and normal loadings on an elastic solid with application to some contact stress problems. Trans. ASME J. Appl. Mechanics, 1953, 75, 157-166
5. Al-Zain, H.O. Contact stresses in conical shaped rollers. Masters thesis, Department of Mechanical Engineering, Iowa State University, 2004.
6. Ali M, Shakoor M, Fluggrad D and Qamhiyah A. Cam optimization based on a fatigue life model. In proceedings of ASME 2006 International Design Engineering Technical Conferences and Computer and Information in Engineering Conference, Philadelphia, Pennsylvania, USA, 2006, pp 1- 8 (American Society of Mechanical Engineers, Newyork).
7. Litvin, L. E. Fuentes A. and Hayasaka, K. Design manufacture, stress analysis and experimental test of low noise high endurance bevel gears. Mechanism Mach Theory, 2006 41(1), 83 -118
8. Johnson, K. L. Contact Mechanics, 1985 (Cambridge University Press)
9. ANSYS user's manual, Version 10.0 , 2007

## 7. NOMENCLATURE

Symbol	Meaning	Unit
$\sigma_x$	Stress in X direction (Along Contact)	(MPa)
$\sigma_z$	Stress in Z direction ( Into the solid)	(MPa)
$\sigma_y$	Stress in Y direction (Along the length of the roller)	(MPa)
R	Radius of curvature	(mm)
t	Distance from tip of the rollers	(cm)
l	Length of the roller	(cm)
$\phi$	Vertex Angle	( $^\circ$ )
a	Half Width	(mm)
P(x)	Normal Pressure Distribution	(MPa)
$P_{max}$	Maximum Pressure	(MPa)
q(x)	Pressure Due to Tangential Loading	(MPa)
S	Cut plane distance	(mm)
s	Integrating variable	(-)
E	Young's Modulus	(GPa)
$\nu$	Poisson's Ratio	(-)
$\mu$	Kinetic Friction between two rotating rollers	(-)
F	Applied Compressive Loading	(N)
r	Radius at tip of the rollers	(mm)

## 8. MAILING ADDRESS

Mohammad Wasim Akram  
 Department of Ocean Engineering ,  
 Florida Atlantic University, Florida, USA



## DEVELOPMENT OF ARTIFICIAL SUB-SURFACE CRACKS IN WELDED PLATE AND THEIR NON-DESTRUCTIVE TESTING

Faizul Mohammad Kamal<sup>1</sup>, Jafar Sadique<sup>1</sup> and S. R. Ahmed<sup>2</sup>

<sup>1</sup>Atomic Energy Centre, Ramna, Dhaka, Bangladesh.

<sup>2</sup>Department of Mechanical Engineering,  
Bangladesh University of Engineering & Technology (BUET), Dhaka, Bangladesh

### ABSTRACT

This work has been carried out to study the optimum condition of generating cracks in welded structures. A sample welded test plate was designed for fabrication of artificial cracks in plate. The test plate was fabricated from mild steel by applying manual metal arc welding technique. Two test pieces of (304 × 152 × 13) mm have been fabricated. Sub-surface cracks were generated. During the welding non-destructive testing was applied to control the quality of weld as well as the size and location of the crack. After finishing the welding, magnetic particle and ultrasonic testing techniques were applied to evaluate the cracks generated. Finally, a comparative study was done to assess the appropriateness of the geometry and location of the crack generated with respect to the design intended. This method is verified to be a useful and effective method to generate artificial cracks in welded samples.

**Keywords:** Welded plate, sub-surface crack, non-destructive testing.

### 1. INTRODUCTION

There are inherent flaws in materials due to crystal lattice imperfections and dislocations however microscopic they may be. Manufacturing processes such as welding, casting, forging, surface treatment, etc. may cause further flaws or defects. Materials are used under various conditions of stress, fatigue and undesirable environment, which may create additional defects or aggravate present ones. It has been established that most material failures occur because these defects reach dangerous proportions such that remaining parts of the materials could not withstand the stress they are subjected to, thus become ductile or brittle.

Defects are found in several types and in different location and orientation in the steel materials and equipments that are used in different industries. Especially cracks in welding are very crucial variable for catastrophic failure of an industrial component. Therefore unwanted shutdown of an industrial plant can be occurred. Besides shutdown, human life and equipments of an industrial plant are to be in risk always. Periodic maintenance and checking of the boiler, pressure vessel, pipelines, welded joints of an industrial plant is necessary. In periodic maintenance and integrity assessment of industrial components and welding joints, non-destructive testing (NDT) can play an important role. Non-destructive testing has come into stable practice in assessing product quality and predicting of the cause and time of failures associated with the components of producing equipment [1, 2, 3]. Therefore, appropriate training and certification on NDT is essential for

checking integrity of materials.

NDT test specimens constitute a very important part of training and certification of NDT personnel and also important for carrying out actual inspection, and for achieving international recognition of NDT practices [4]. Therefore, there is a need to pay greater attention to this subject.

The present work has been carried out to study the optimum condition of generating artificial crack in welded plate of steel material. Two-test piece have been developed with artificial sub-surface defects. Defects have been evaluated in different stages of the development using non-destructive testing techniques. Later in this paper, a comparison has also been made between the theoretical knowledge and the experimental work of generating artificial defects in welded steel plate.

### 2. METHODOLOGY AND DEVELOPMENT PROCEDURE

#### 2.1 Mechanism of Crack Formation

Weld cracks are seldom encountered in mild steel welding when the sections are less than 10 mm thick. In thicker sections, cracks may appear in the welds due to one or more of the following factors: (a) rapid cooling of the deposit, (b) heavy restraint in the joint, (c) excessive dilution of the weld with the parent material, resulting in pick-up of carbon and other alloying elements and consequent hardening, (d) excessive hydrogen in the arc derived from moisture, grease, oil, etc. In butt welds, abnormal bead shape is often the cause of cracking.

In the present work, artificial cracks have been fabricated using rapid cooling of the deposit technique. By applying this technique, longitudinal cracks of designed length and location have been generated in the welded steel plate. The fabrication of artificial crack has been performed using manual metal arc welding.

## 2.2 Design of Welding Plate

Two test pieces having the dimension of 304 mm × 152 mm has been designed for generating artificial cracks of 10 mm length at different depth. The thickness of the welded plate is considered 13 mm. The cap width is considered 14 mm, bevel angle or weld preparation angle 60°, root face and root gap 2 to 5 mm. Longitudinal cracks are intended to generate in the welded plate in defined location.

## 2.3 Manual Metal Arc Welding

Manual metal arc welding (MMAW) is an electric arc welding process where the heat for welding is generated by an electric arc between a flux covered metal electrode and the work. The filler metal is deposited from the electrode and the electrode covering provides shielding. Other names for this process include the North American term “Shielded metal arc welding” (SMAW), “stick welding” or “stick electrode welding”.

This process is used predominantly to weld ferrous metals and it can weld thickness above about 2 mm in all positions. The arc is under the control of the welder and is visible. The welding process leaves a slag on the surface of the weld bead that must be removed. The most popular use for this process is for the welding of structural steel including low alloy and other higher strength steels [5]. The process is flexible, as the welder only needs to take the electrode holder and work lead to the point of welding. The equipment for the MMAW process consists of a power source, welding cable, electrode, electrode holder, and work clamp or attachment.

## 2.4 Procedure

Mild steel plates of 162 mm × 162 mm × 15 mm were taken and machined to 152 mm × 152 mm square by using shaper machine. The thickness then reduced from 15 mm to 13 mm by machining. The two plates of having size 152 mm × 152 mm × 13 mm were perfectly aligned with the help of T-scale maintaining 3 mm root gap. Then the two plates were tack welded at two ends.

For welding a backing strip was used to prevent burn-through caused by excessive penetration, which was difficult to avoid even with a 1.6 mm diameter electrode used at 30 amps. If the backing strip were mild steel, it would get welded to the joint by the penetrated weld bead. The strip was retained as an integral part of the joint or removed by machining. The backing strip can be of copper, which does not fuse with the penetrated weld metal and can easily be detached later. Thin sheets would better welded by the oxy-acetylene or argon-arc process, if use of backing strip is to be avoided, because with these processes the welder has better control on weld penetration. Two back strips were welded below the plates in order to avoid deformation.

The down hand or flat welding position is defined as a position in which the weld slope does not exceed 10° and the weld rotation does not exceed 10°. In this present work, the welding has been performed in flat or down hand position.

The sequence of weld passes with specified electrode sizes and currents for 13 mm thickness is described below. In this case, after the V has been filled up, the joint has been turned over and the root has been machined or gouged out by an oxy-acetylene gouging torch, or by a carbon electrode using the air-arc process, till sound metal has reached. The root has then been covered with a sealing pass deposited with a 4 mm electrode at 180 amps. The first weld pass has been performed with a 3.15 mm electrode at 110 amps. The welding metal has been covered with a sealing pass deposited in the second pass with a 4 mm electrode at 180 amps. Then third pass has been performed using a 5 mm electrode at 210 amps to get deeper penetration and a better guarantee that slag inclusions were completely dissolved out. Finally, a 6.3 mm electrode at 290 amps has been used for the fourth and fifth pass to complete the welding. These procedures have been carried out with selected electrodes at specified location.

## 3. NON DESTRUCTIVE TESTING OF WELDED PLATE

Different Non Destructive Testing (NDT) method has been applied during and after completion of the development of the artificial weld specimens to reveal cracks.

### 3.1 Ultrasonic Testing Method

Ultrasonic testing has been one of the most indispensable techniques in metal industries for detection and characterization of defects by analyzing variation in amplitude and frequency of the scattered ultrasonic waves [6,7,8]. In the present work, ultrasonic testing has been performed using pulse-echo technique to find cracks in the welded test plate. The pulse-echo technique is the simplest of all the ultrasonic testing methods and also most commonly used methods in industries. It consists basically of measuring the time taken for a short train of sound waves to move through a given distance. This distance can be determined if the speed of sound in the material is known or, if the distance were known; the speed of sound can be readily calculated. By measuring the relative amplitudes of pulses, which have traveled different distances, one can determine attenuation coefficients. Observing the patterns of the received pulses can provide valuable information about the nature of a defect at which the pulses have been reflected and, perhaps, of the structure of the material being tested. With the pulse-echo method, the time taken for sound pulses, generated at regular intervals, to pass through the object being tested and to return is measured. The returned pulses may be received either after a single reflection at a discontinuity of characteristic impedance (i.e. a boundary or a defect) or multiple reflections between the discontinuity and the front surface of the object [9].

After producing cracks to the desired location and

depth, the welded plate was machined and polished to remove the dust or spatter. Then the specimen was ready for ultrasonic testing. All the testing have been performed at room temperature. A pulse-echo transducer (Krautkramer ) of diameter,  $d = 10$  mm, transmitting a longitudinal wave of nominal frequency 5 MHz has been used for both generating and detecting the elastic waves for checking lamination. The space between the transducer and top surface of the specimen has been filled with motor oil used as a medium for ultrasonic wave propagation. After checking the lamination, an angle beam of  $70^\circ$  probe transmitting compression wave of frequency 4 MHz has been used for detecting cracks in the welding. All the signal from the oscilloscope has been recorded and then determined the location, length and depth of the crack.

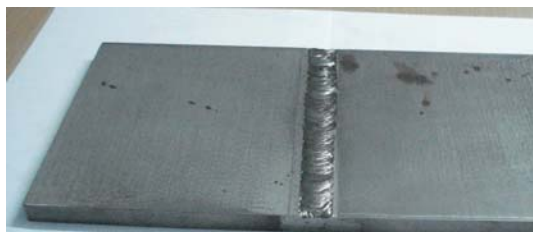
### 3.2 Magnetic Particle Testing Method

Magnetic particle testing method has been used to evaluate the welding quality during the welding process and finally after completion of the welding. Yoke magnetization method has been applied to evaluate the cracks of the welded test plate up to 5 mm from the top of the surface being tested [10]. When any form of electromagnetic or permanent magnet is used, a magnetic field is induced in the test component or work piece in a direction between the poles. The distribution of the field is such that the area of the surface, which is magnetized sufficiently for magnetic particle inspection to be carried out, is bounded by convex curves joining the poles of the magnet.

Before applying the yoke method, the iron particle settlement test has been performed for checking the concentration of particles. Pie gauge has been used for showing the existence and direction of magnetic fields above the surface of magnetized welded test plate. Yoke has been applied to the test plate and the cracks were revealed under ultraviolet light in the dark environment. Finally, after completion of the inspection, demagnetization has been done with an a.c. yoke magnet.

## 4. RESULTS AND DISCUSSION

In this present work, longitudinal cracks of designed size & location have been fabricated by applying rapid cooling of the deposit technique. The welded test specimens of mild steel have been developed using manual metal arc welding technique. The two test specimen A1 and A2 that were developed are shown in Figure 1.



(a) Specimen A1



(b) Specimen A2

Fig 1. Welded test plates (a) Specimen A1 (b) Specimen A2

### 4.1 Specimen A1

Test piece A1 was fabricated with a sub-surface longitudinal crack during the sixth pass of the welding process. The crack has been fabricated using rapid cooling technique. The developed crack after sixth pass is shown in Figure 2. The depth is approximately 4 mm from the top of the surface. After development of the crack final passes have been performed with special care so that no unwanted cracks or defects would be formed. After completion of the welding, magnetic particle testing technique has been applied to find the location and size of the crack. The crack has been found successfully using magnetic particle testing technique. The dimension measured is 7 mm. Photograph of the crack developed in Specimen A1 after applying magnetic particle testing technique and UV light is shown in Figure 3.



Fig 2. Photograph of the cracked welded plate (Specimen A1).

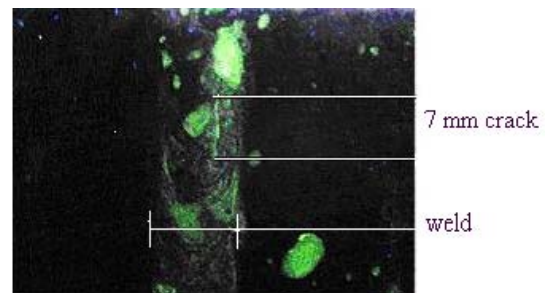


Fig 3. Photograph of the crack developed in Specimen A1 under magnetic particle testing and UV light.

## 4.2 Specimen A2

Test piece A2 has been fabricated with a sub-surface longitudinal crack during the third pass of the welding process. The developed crack, after third pass, is shown in Figure 4. After development of the crack, final passes have been performed with special care so that no unwanted cracks or defects would be formed. After completion of the welding, magnetic particle testing technique has applied to find the crack but failed. Then ultrasonic method has been applied to find the location, size and depth of the crack. The crack has been found using ultrasonic testing method perfectly. The fabricated test plate, A2 was inspected using ultrasonic flaw detector with compression wave and 8 mm length crack has been detected. In Figure 5, ultrasonic crack signal is shown in the welded plate, A2.

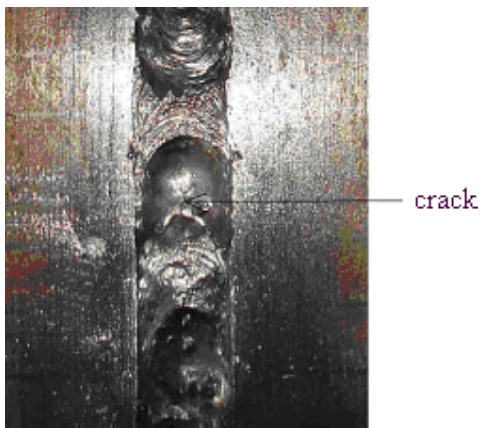


Fig 4. Photograph of the crack formed after third welding pass in Specimen A2.



Fig 5. Observation of crack signal in the welded plate, A2 under ultrasonic testing.

Some other defects were observed during the different welding passes. But finally, those defects were eliminated or fused during the next welding passes. Some unwanted cracks were formed at the edges or heat affected zones of the welding.

## 5. CONCLUSIONS

The following conclusions can be drawn from the present study:

- (i) Two welded test specimen have been

developed with artificial cracks as the design intended although there were some unavoids defects developed at the edges of welding.

- (ii) In welded test plate A1, a seven (7) mm length crack was developed where in its intended design length was 10 mm.
- (iii) In welded test plate A2, the fabricated crack length is 8 mm while the design length was 10 mm.
- (iv) The generated crack was verified and studied applying different non-destructive testing methods, i.e., ultrasonic and magnetic particle testing techniques.
- (v) The crack of Specimen A1 is revealed by magnetic particle testing method. In case of Specimen A2, magnetic particle testing method was applied, but no crack was found. Then ultrasonic testing method with shear wave was applied and a crack of 8 mm length was found.
- (vi) Thus it can be concluded from the present study that this rapid cooling technique is effective method for generating artificial sub-surface cracks in mild steel welded plates.

## 6. REFERENCES

1. Nadkarni, S. V., *Modern Arc Welding Technology*, Oxford & Ibh Publishing, India.
2. Gibbs, J. N., 1983, "A Third Party Look at NDT Inspection", *Proc. Of Qual Test-2 Conference*, Section 10-10, Dallas, USA.
3. Khan, F. and Howard, R., 2007, "Statistical Approach to Inspect Planning and Integrity Assessment", *Insight*, 49:1.
4. Khan, A. A., 2001, *Guide Book for the Fabrication of Non-Destructive Testing (NDT) Test Specimen*, IAEA, Austria.
5. Bongio, E. P. and Wiley, R. C., 1958, *Arc Welding Manual*, Fearon Publishers, USA.
6. Krautkramer, J and Krautkramer, H., 1983, *Ultrasonic Testing of Materials*, Springer, Berlin, Germany.
7. Sharp, R. S., 1982, *Research Techniques in Non-Destructive Testing*, Academic Press, London.
8. Komura, I, Hirasawa, T, Nagai, S., Takabayashi, J. and Naruse, K., 2001, "Crack Detection and Sizing Technique by Ultrasonic and Electromagnetic Methods", *Nucl Eng Des*, 206:351-62.
9. Blitz, J. and Simpson, G., 1996, *Ultrasonic Methods of Non-Destructive Testing*, Chapman & Hall, UK.
10. Lovejoy, D., 1993, *Magnetic Particle Inspection-A Practical Guide*, Chapman & Hall, UK.

## 7. MAILING ADDRESS

Faizul Mohammad Kamal  
Atomic Energy Centre,  
Ramna, Dhaka-1000, Bangladesh

## FREE AND FORCED VIBRATION EXPERIMENTS ON A CROSSBEAM SYSTEM

Anirban Mitra, Prasanta Sahoo and Kashinath Saha

Department of Mechanical Engineering, Jadavpur University, Kolkata, India

### ABSTRACT

In the present paper free and forced vibration experiments are carried out on a crossbeam system, made up of two slender beams in contact with their longitudinal axes perpendicular to each other. The experiments performed are the first of its kind in case of two beam systems. The free vibration experimentation is carried out by exciting the system with the blow of a soft rubber hammer, whereas study of forced vibration behaviour involves excitation by an external harmonic force having a specific magnitude, generated by a function generator and delivered to the system through an electrodynamic oscillator. The results of the free vibration experiments are presented in terms of the natural frequencies of the system and the response of the system to external excitation is presented in amplitude-frequency plane. Also the changes in system response due to change in position of the supporting beam has been observed.

**Keywords:** Crossbeam System, Free Vibration, Forced Vibration.

### 1. INTRODUCTION

A beam is one of the basic structural elements, which is extensively used in many branches of modern civil, mechanical, and aerospace engineering separately or in association with other beams or plates to satisfy different structural requirements like stiffness enhancement, light weight, low cost, material saving etc. Therefore, dynamic response analysis of single beam and beam systems has always been an area of immense interest to researchers.

One of the earlier works in this field was by Srinivasan [1, 2], who employed the Ritz-Galerkin technique to solve the governing nonlinear differential equation of dynamic equilibrium for free and forced vibration of a simply supported beam. Ray and Bert [3] carried out experimental studies to verify the analytical solutions for the nonlinear vibrations of simply supported beam. Yamamoto et al [4] conducted experimental analysis for a beam subjected to harmonic excitation, with a view to validate their analytical results for forced vibrations and subharmonic oscillations. They utilised ball bearings to simulate simply supported boundary conditions and used two magnets to provide the external excitations. The effects of large amplitude vibrations on dynamic strain and fundamental mode shape of a clamped-clamped beam were investigated analytically and experimentally by Bennouna and White [5, 6]. Leissa [7] described an exact method for determining the vibratory displacements of an Euler-Bernoulli beam subjected to distributed excitation forces Chen et al [8] performed experiments on a pre-stretched clamped beam in order to compare their results of finite element model for the nonlinear random

response under acoustic and thermal loads. In this set up also permanent magnets and excitor coils were used to apply external excitation. Experimental investigations on multimode responses in a cantilever beam were undertaken by Tabaddor and Nayfeh [9]. Ribeiro et al [10] experimentally investigated the phenomenon of internal resonance for the case of a clamped beam. Lee and Feng [11] carried out experiments using an electromagnetic shaker to determine the dynamic response of a beam with a frictional joint. Geometrically non-linear vibration of a hinged-hinged beam excited transversely with a harmonic excitation by an electromagnetic exciter was investigated experimentally by Ribeiro and Carneiro [12].

Forced vibration study of beam systems consisting of more than a single beam has also been a popular area of research. Ewing and Mirsafian [13] put forward an analytical model for forced vibration of a system of two Euler-Bernoulli beams joined with a nonlinear rotational torsional spring with linear and cubic stiffness. Oniszcuk [14] applied the classical modal expansion method for analysing undamped forced transverse vibrations of an elastically connected complex simply-supported double-beam system. It is evident from the review of existing literature that experimental investigations of a single beam under different loading and boundary conditions have been carried out extensively. But such experiments for a beam system are quite rare and the system response has not been studied.

In the present paper experiments are carried out on a two beam system, termed as crossbeam, which consists of two perpendicular slender beams in contact so as to form a 'cross', as shown in figure 1(a). The experiments



are devised to validate the sanctity of a theoretical model presented in a separate work. Such crossbeam systems are quite common in civil, mechanical and construction engineering applications. They also can effectively be used separately or with plate elements to construct marine and aerospace structures. At no loading condition there is no interaction between the beams of the system, though they are in surface contact. But when some transverse load is applied on the upper beam (Beam-1), it pushes down on the lower beam (Beam-2), which in turn provides a resistance to deformation of beam-1. It is assumed that external loading in the form of transverse harmonic excitation acts on beam-1 only and the purpose of beam-2 is to give the system a stiffening effect. The contact point between the two beams can be specified by two coordinates,  $x_r$  and  $y_r$ , as shown in figure 1(b). In the present paper, the contact point is assumed at the mid-span of beam-2, i.e.,  $y_r = 0.5L_2$ . However  $x_r$  can vary along the span of the beam and the effect of this change on the natural frequencies and forced vibration response of the system has been studied. The external harmonic excitation is always provided at the point of contact between the two beams.

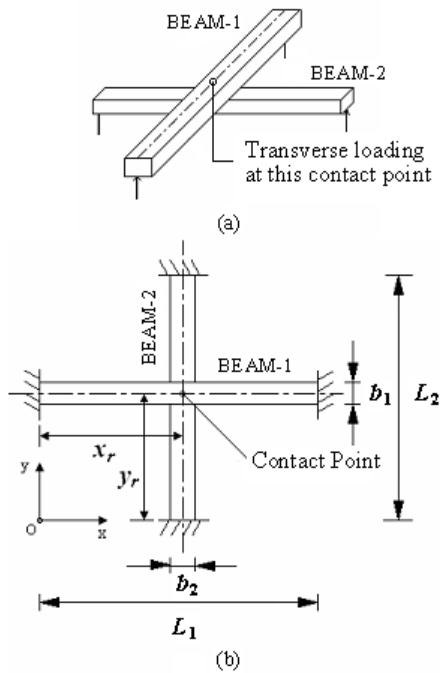
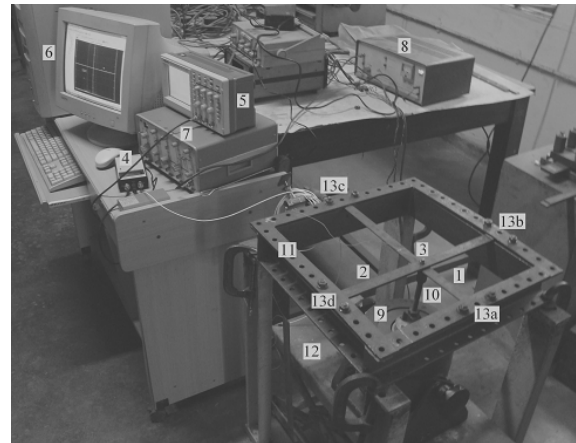


Fig. 1: Crossbeam system with significant dimensions

## 2. EXPERIMENTAL DETAILS

An experimental set up, as shown in figure 2, is prepared to carry out free and forced vibration experiments on the crossbeam system. Figure 3(a) shows the schematic diagram of the free vibration set up with indications of the major components and the schematic diagram of figure 3(b) refers to forced vibration set up. The free vibration experimentation is carried out by exciting the system with the blow of a soft rubber hammer, whereas experimental study of forced vibration behaviour involves excitation by a harmonic force

having a specific magnitude. To achieve this, the set up is slightly modified and a function generator, a power amplifier and an electrodynamic oscillator are introduced. The following section provides a brief description of the set up and test procedure.



1. Beam-1
2. Beam-2
3. Accelerometer on the contact point
4. Coupler
5. Digital storage oscilloscope
6. Desktop computer
7. Function generator
8. Power Amplifier
9. Electrodynamic oscillator
10. Rubber padded end of oscillator rod
11. Channel frame
12. Mechanical jack
- 13(a-d). Fixed ends ensured by bolting tightly to the frame

Fig 2. Photograph of the experimental set up

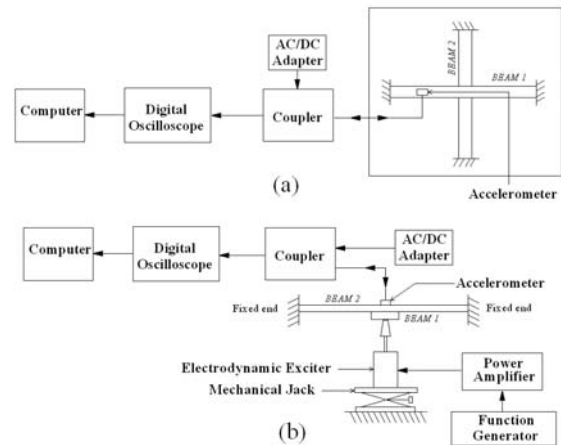


Fig. 3. Schematic diagram of experimental setup for (a) Free vibration and (b) Forced vibration experiments on crossbeam system

### 2.1 Experimental Set-up

Two slender beams are positioned perpendicularly and their ends are bolted firmly to the channel frame so as to simulate clamped boundary condition. The frame along with the crossbeam system is rigidly fixed to a heavy base with C-clamps. The accelerometer (Manufacturer: Kistler Instrument Corporation, Type: 8728A500, acceleration range:  $\pm 500g$  ( $g = 9.80665 \text{ m/s}^2$ ), frequency range: 1 Hz–10 kHz ( $\pm 5\%$ )) is a shear mode piezoelectric sensor and is mounted on the beam at a suitable position using Petro-Wax adhesive material.

The locations of the accelerometer are carefully selected to avoid any nodal points. The mass of the accelerometer (1.6 grams) is significantly less than the mass of the crossbeam system and hence it can be assumed that system response is not significantly affected by the effect of mass loading of the accelerometer. The accelerometer is connected to a coupler (Manufacturer: Kistler Instrument Corporation, Type: 5114, Frequency response: 0.07 Hz – 60 kHz ( $\pm 5\%$ )), which provides the constant current power supply to the impedance converter of the accelerometer and decouples the DC bias voltage from the output signal. The coupler provides the electrical interface between the accelerometer and the display device, which is a digital storage oscilloscope (Manufacturer: Tektronix Inc., Model: TDS 210) with the following specifications: peak detect bandwidth: 50MHz, sample rate range: 50 samples/s–1Gigasamples/s, record length: 2500 samples, and lower frequency limit: 10 Hz. It has the capability to transform a time domain signal into frequency domain through a Fast Fourier Transform (FFT) module. The oscilloscope is connected to a desktop computer through RS-232 communication ports. The data acquired through the oscilloscope are sent to the computer and saved to its hard disk using WSTRO Wavestar software for storage and off-line post-processing.

The external excitation for the forced vibration experimentation is provided through a function generator (Manufacturer: Aplab, Model: 2119, frequency output range: 0.0002 Hz – 20 MHz (in 10 ranges)). It can generate continuous sinusoidal signal of a specific frequency with a precision of  $\pm 3\%$  of the full range and ensures minimal distortion of the waveform. The generated harmonic signal is amplified using a 50W power amplifier (Manufacturer: VEB Metra Meß- und Frequenztechnik, Type: LV 102, frequency response: 3 Hz – 40 kHz) and sent to an electrodynamic oscillator (Manufacturer: VEB RFT Messelektronik, Model: ESE 221, Type: 11077), which provides the excitation to the crossbeam system. A rod with a soft rubber pad at one end is screwed to the top plate of the oscillator. The oscillator is placed on the platform of a mechanical jack and positioned appropriately below the crossbeam system. At the time of forced vibration experiment the oscillator is lifted with the help of the jack to touch the crossbeam system at the desired location. The contact between the lower beam and the padded rod should ensure that contact is maintained throughout the cycle of excitation and yet contribute minimum pre-stressing to the system. In case of free vibration experiment the jack is lowered so that there is no contact between the oscillator rod and the beam and excitation is provided by striking the system with a soft rubber hammer.

## 2.2 Test Procedure

Experiments are carried out to determine the free and forced vibration characteristics of the crossbeam system. The set up is readied by making the electrical connections for computer, oscilloscope, coupler and accelerometer and also for function generator, power amplifier and electrodynamic exciter. The accelerometer is mounted on the test specimen at a predefined location

using adhesive. A two-wire cable between the accelerometer and the coupler is used and the signal and power share the same line. Output from the coupler is connected to one of the channels of the oscilloscope. The oscilloscope is set to 'math' mode and 'auto' trigger mode is kept on. It is then kept ready by pressing the 'RUN' button as the system is hammered to provide disturbance and it captures the signal from the vibrating beams and plots the signal in frequency domain. The data is then transferred to the computer hard disk through the RS-232 ports and saved under an appropriate file name and format. The oscilloscope captures and plots the signal from the vibrating system in frequency-amplitude plane. Using horizontal and vertical cursors the amplitude (in dB) and frequency (in Hz) of the signal are read from the display and the data is tabulated in an excel sheet in the computer. The free vibration experiment is carried out first and for the subsequent forced vibration test the mechanical jack is lifted to put the oscillator in contact with the crossbeam system. A sinusoidal signal of a specified frequency, lower than the natural frequency of the system, is used as the initial external excitation. Now the excitation frequency is increased gradually by turning the dial of the function generator and the procedure of noting frequency and amplitude is repeated. The excitation frequency is increased beyond resonance till the amplitude of the signal falls to a sufficiently low level. The whole experimental procedure is repeated for different positions of the supporting beam (beam-2).

## 3. RESULTS AND DISCUSSION

The experiments carried out on the crossbeam system have the objective of determining the natural frequency of the system and to observe the system response due to an external harmonic excitation. Also the changes in system response due to change in position of the supporting beam (beam-2) has been observed.

The specimens used to construct the crossbeam system are two slender beams of rectangular cross-section. Figure 4 shows the schematic diagram of one such beam with representative dimensions. Different cross-sectional dimensions used for the present experiments are mentioned in Table 1. The material of the beams is mild steel.

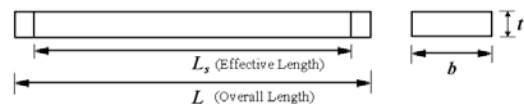


Fig 4. Schematic diagram of a slender beam

Table 1. Beam dimensions in mm

Specimen No.	$L$	$L_s$	$b$	$T$
A1	500	400	20.513	2.753
A2	500	400	18.367	5.373
B1	500	400	24.680	3.000
B2	500	400	24.720	5.000

The results of the free vibration experiments are presented in terms of the natural frequencies of the system, whereas the response of the system to external



excitation is presented in amplitude-frequency plane. The ordinate represents maximum amplitude of vibration and abscissa represents the frequency in Hertz. The amplitude data noted from the oscilloscope is in dB, which corresponds to the ratio of output and input voltages to the oscilloscope, as given by the following relation.

$$dB = 20 \log_{10} (V_o/V_i)$$

To validate the experimental procedure a free vibration experiment is carried out on a single beam and the results are compared with commercial finite element package ANSYS (version 11.0) and also with analytical results. The comparison of the natural frequencies from the three different methods is compared in Table 2. From the table it can be seen that the analytical and simulation results are in good agreement, but the experimental results differ from them. The difference can be attributed to insufficiency in replicating stretching boundary conditions of the system.

Table 2. Comparison of natural frequencies of a single beam obtained through experimental, analytical and simulation (ANSYS) methods.

Specimen No.	Free Vibration Frequency (Hz)			Mode
	Experimental	Analytical	ANSYS	
A1	75.0204	91.4552	91.482	1 <sup>st</sup>
	217.793	251.9252	252.160	2 <sup>nd</sup>
	435.196	493.3565	494.280	3 <sup>rd</sup>
A2	136.672	178.4944	178.52	1 <sup>st</sup>
	409.237	491.6796	491.98	2 <sup>nd</sup>
	876.492	962.8785	964.09	3 <sup>rd</sup>

Table 3 presents the natural frequencies of the crossbeam system with different combinations of the constituent beams. The effect of shift in position of the supporting beam (beam-2) is also studied and the results in terms of natural frequencies are shown in Table 4. It is evident from the results that as beam-2 shifts towards one of the ends the natural frequencies of the system increase. It can be concluded that the off-set position of beam-2 increases the overall stiffness of the system and hence an increase in the natural frequencies is observed.

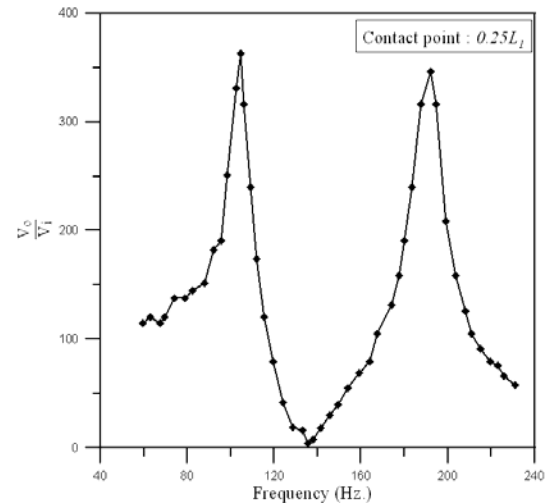
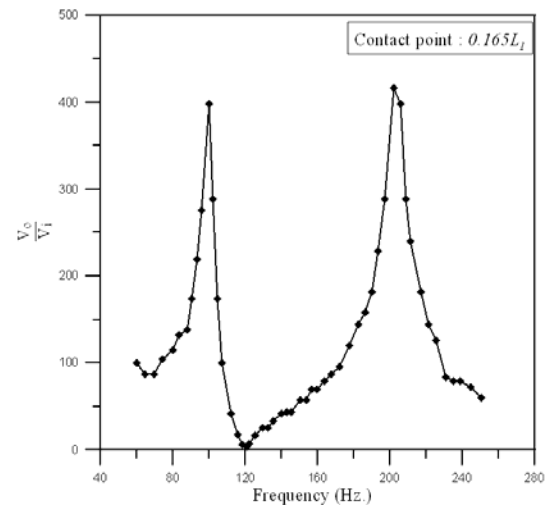
Table 3. Free vibration frequency (1<sup>st</sup> Mode) of a crossbeam system with different cross-sectional dimensions

Sl. No.	Specimen Arrangement	Free Vibration Frequency (Hz) (1 <sup>st</sup> Mode)
1	A1-A1	77.8998
2	A2-A2	139.917
3	A1-A2	123.693
4	A2-A1	126.938

Table 4. Free vibration frequency (1<sup>st</sup> Mode) of a crossbeam system for change in position of beam-2

Sl. No.	Specimen Arrangement	Beam-2 position	Free Vibration Frequency (Hz) (1 <sup>st</sup> mode)
1	A1-A1	0.5	77.8998
2		0.35	84.7548
3		0.125	87.9997

The system behavior under forced vibration is also studied for different positions of beam-2 along the span of beam-1. Results are presented in figures 5 and 6 as frequency-amplitude plots, where frequency is in Hertz and amplitude is proportional to the output voltage of the oscilloscope. Figure 5 presents the plots for crossbeam system with specimen arrangement B1-B1, whereas Figure 6 shows the same for arrangement B1-B2. Both the figures include frequency-amplitude plots of the system for five different positions of beam-2 as mentioned in the figure legends.



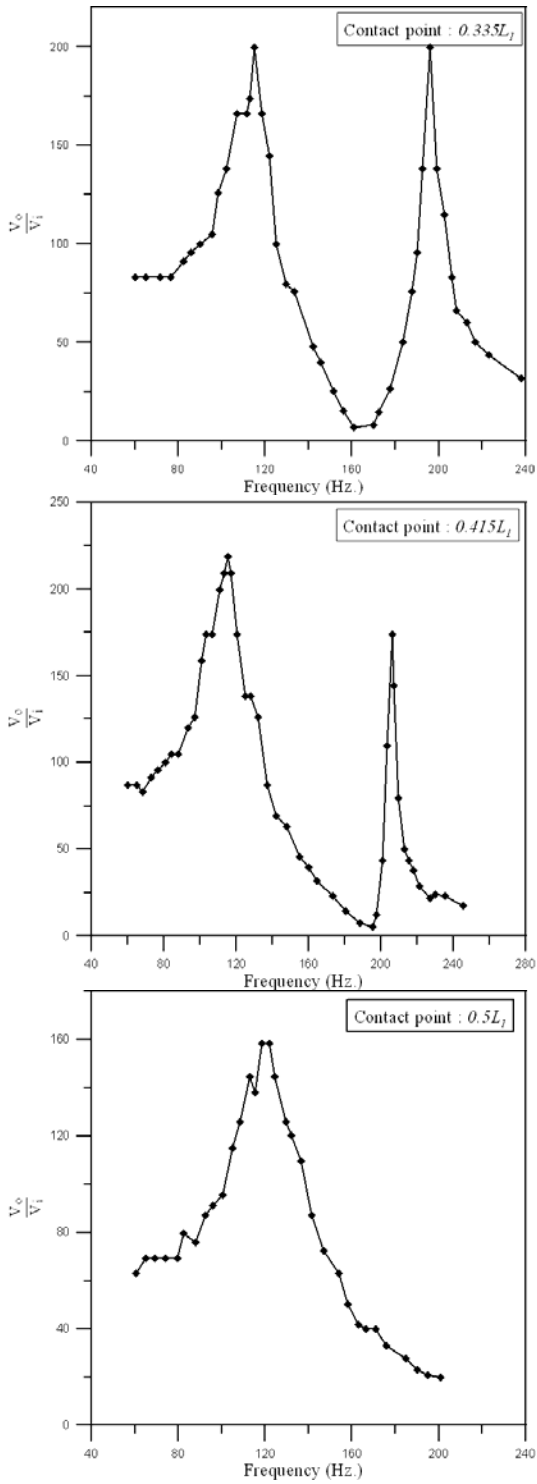
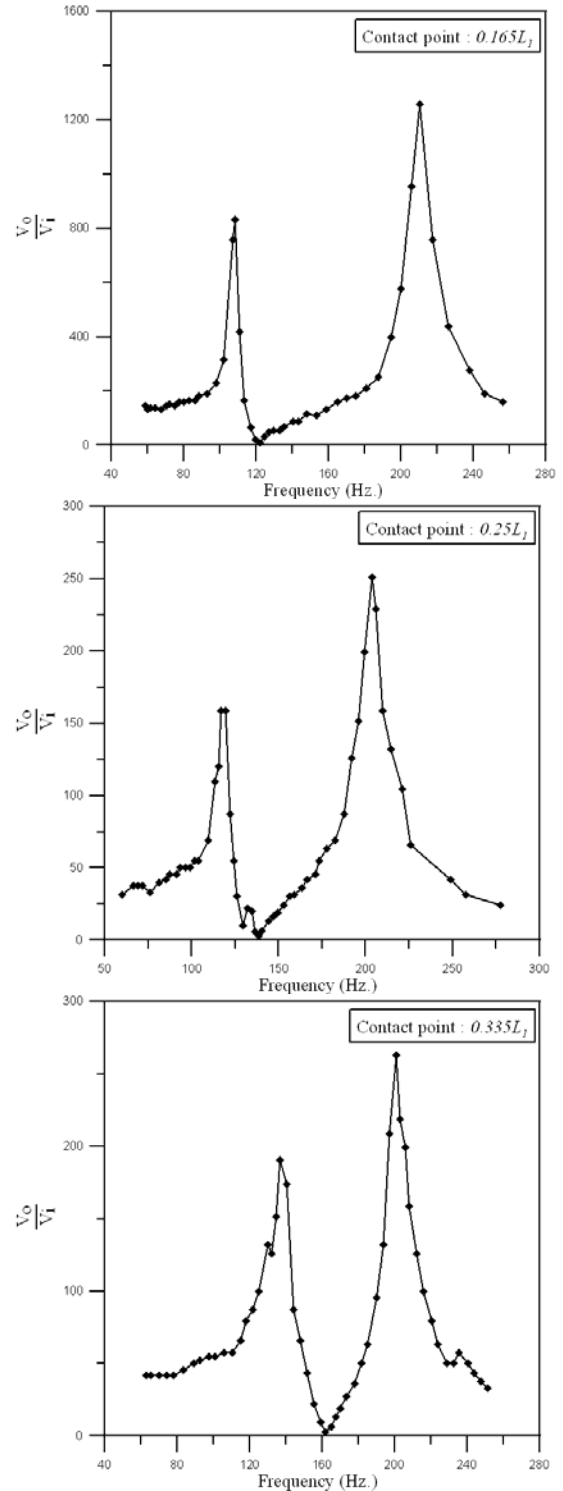


Fig 5. Frequency amplitude plots for forced vibration experiment for crossbeam system with specimen arrangement B1-B1

All the corresponding plots in figures 5 and 6 exhibit similar characteristics. However the particular case of contact point at the middle ( $x_r = 0.5L_j$ ) shows marked difference. The plots show that for a symmetric configuration of the system only one amplitude peak is obtained, whereas for an off-set position of the

supporting beam (beam-2) two peaks are present. It is seen from the plots that with increase in excitation frequency the amplitude response increases and attains a peak value. This corresponds to the resonant frequency. After this particular value, with further increase in excitation frequency the amplitude drops sharply. However, if frequency value is still increased another amplitude peak is obtained. It is also apparent from the plots that the distance between the two peaks increases as beam-2 shifts outward.



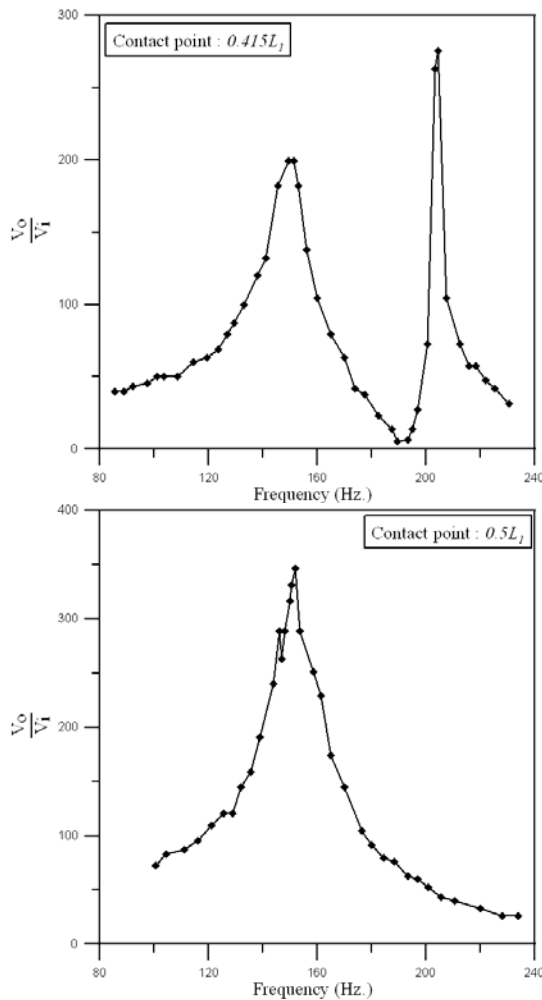


Fig 6. Frequency amplitude plots for forced vibration experiment for crossbeam system with specimen arrangement B1-B2

#### 4. CONCLUSION

The present paper undertakes an experimental free and forced vibration analysis of a two beam system under harmonic excitation. The experimental study undertaken is the first of its kind for a two beam system. A set up simulating clamped boundary conditions is developed and experimentations are carried out for different dimensions of the cross-section of the beams. The effect for shift in position of the lower beam is also observed. The results for free vibration case are presented in terms of natural frequencies of the system. Validation of the experimental process is carried out by comparing the results obtained from free vibration test on a single beam with analytical and simulation results. The results for forced vibration experiments are presented in terms of frequency-amplitude plots. The results indicate a shift in the resonant frequency which calls for further analytical study.

#### 5. ACKNOWLEDGEMENT

The first author acknowledges the research support received from AICTE, India, vide File No.: 1-10/RID/NDF/PG/(17)2008-09 Dated : 13.03.2009.

#### 6. REFERENCES

1. Srinivasan, A. V., 1965, "Large Amplitude Free Oscillations of Beams and Plates", American Institute of Aeronautics and Astronautics Journal, 3:1951-1953.
2. Srinivasan, A. V., 1966, "Nonlinear Vibrations of Beams and Plates", International Journal of Nonlinear Mechanics, 1:179-191.
3. Ray, J. D. and Bert, C. W., 1969, "Nonlinear Vibrations of a Beam with Pinned Ends", Journal of Engineering for Industry, Transactions of the ASME, 91: 977-1004.
4. Yamamoto, T., Yasuda, K. and Aoki, K., 1981, "Subharmonic oscillations of a slender beam", Bulletin of the Japan Society of Mechanical Engineers, 24(192): 1011-1020.
5. Bennouna, M. M. and White, R. G., 1984, "The Effects of Large Vibration Amplitudes on the Dynamic Strain Response of a Clamped-Clamped Beam with consideration on Fatigue Life", Journal of Sound and Vibration, 96: 281-308.
6. Bennouna, M. M. and White, R. G., 1984, "The Effects of Large Vibration Amplitudes on the Fundamental Mode Shape of a Uniform Clamped-Clamped Beam", Journal of Sound and Vibration, 96(3): 309-331.
7. Leissa, A. W., 1989, "Closed Form Exact Solutions for the Steady State Vibrations of Continuous Systems subjected to Distributed Exciting Forces", Journal of Sound and Vibration, 134: 435-453.
8. Chen, R. R., Mei, C. and Wolfe, H., 1996, "Comparison of Finite Element Non-linear Beam Random Response with Experimental Results", Journal of Sound and Vibration, 195(5): 719-737.
9. Tabaddor, M. and Nayfeh, A.H., 1997, "An Experimental Investigation of Multimode Responses in a Cantilever Beam", Journal of Vibration and Acoustics, Transactions of the American Society of Mechanical Engineers, 119: 532-538.
10. Ribeiro, P., Alves, L. and Marinho, J., 2001, "Experimental Investigation on the Occurrence of Internal Resonances in a Clamped-Clamped Beam", International Journal of Acoustics and Vibration, 6: 169-173.
11. Lee, Y. and Feng, Z. C., 2004, "Dynamic Responses to Sinusoidal Excitations of Beams with Frictional Joints", Nonlinear Science and Numerical Simulation, 9: 571-581.
12. Ribeiro, P. and Carneiro, R., 2004, "Experimental Detection of Modal Interaction in the Non-linear Vibration of a Hinged-Hinged Beam", Journal of Sound and Vibration, 277: 943-954.
13. Ewing, M. S. and Mirsafian, S., 1996, "Forced Vibration of Two Beams Joined with a Non-linear Rotational Joint: Clamped and Simply Supported End Conditions", Journal of Sound and Vibration, 193(2): 483-496.
14. Oniszczuk, Z., 2003, "Forced Transverse Vibrations of an Elastically Connected Complex Simply Supported Double-Beam System", Journal of Sound and Vibration, 264: 273-286.

## RECYCLING OF THERMOPLASTIC COMPOSITES: QUALITY AND DURABILITY

M. D. H. Beg<sup>1</sup>, K. L. Pickering<sup>2</sup>, I. Ahmed<sup>1</sup>, Z. Hassan<sup>1</sup>

<sup>1</sup>Faculty of Chemical and Natural Resources Engineering, Universiti Malaysia Pahang, Malaysia

<sup>2</sup>Department of Engineering, University of Waikato, Hamilton, New Zealand

### ABSTRACT

This paper describes the effects of reprocessing on the physical and mechanical properties of composites based on radiata pine (*Pinus Radiata*) fiber in a polypropylene (PP) matrix. Composites, containing 40 wt% fiber with 4 wt% maleated polypropylene (MAPP) as a coupling agent, were reprocessed up to eight times. Tensile strength (TS) and Young's modulus (YM) were found to decrease with increased reprocessing by up to 25% for TS and 17% for YM (after reprocessed 8 times). Hygrothermal ageing was also carried out by immersing specimens in distilled water at 50°C over a 9 month period. The diffusion coefficient of moisture absorption was obtained for composites by measuring water uptake of specimens at regular time intervals. It was found that the diffusion coefficient and the equilibrium moisture contents of composites decreased with increased number of times the materials were reprocessed. After hygrothermal ageing, tensile strength (TS) and Young's modulus (YM) of both virgin and reprocessed composites were found to decrease.

**Keywords:** Composites, Recycling, Weathering, Coupling Agent.

### 1. INTRODUCTION

It is estimated that globally, more than 6 million tonnes of polymer matrix composite products are manufactured each year, largely dominated by glass fibre reinforced polymers [1]. Furthermore, the amounts used are increasing annually. Concern for the environment, both in terms of limiting the use of finite resources and the need to manage waste disposal, has led to increasing pressure to recycle materials at the end of their useful life. In the metals industries, for instance, materials recycling operations are already well established and are driven by economics [2]. Polymers are generally more difficult to recycle and the economic incentives to recycle have been less favourable, particularly when waste disposal in landfills is relatively cheap. However, waste management is now a high priority within the European Union. As a consequence, it is already illegal to landfill composites waste in many EU countries. The "End-of-Life Vehicle Directive" (Directive 2000/53/EC) regulates the disposal of vehicles and the requirements include that from 2015, 85% of the weight of all "End-of-Life" vehicles must be re-used or recycled, a further 10% may be subject to energy recovery with a maximum of only 5% of the vehicle allowed to be disposed of in landfill. As vehicles have a life expectancy of more than 10 years, vehicles currently being manufactured must meet the 2015 requirements [2]. As a consequence of increasing legislation, there is a need for recycling routes to be established [2]. Although there are governmental regulations recycled materials are avoided, not only due to their physical properties, but mainly

because of their surface appearance. Indeed, many designers are reluctant to use them as they can be rejected by the market. However, this is an attitude that can change, as demonstrated in Brazil where around 15% of all rigid plastics and films consumed, are recycled and returned to industry [3]. Some states in the US are also concerned with recycling. For example, in Michigan, the recycling rate is close to 100 % and proves the potential for recycling plastic waste as well as changes in market attitude [4].

One major factor determining the route for recycling of composites is whether the matrix is thermoplastic or a thermoset plastic. Thermoplastics can be melted and therefore lend themselves more readily to recycling by reshaping. Indeed, there is much interest in the area of thermoplastic matrix composites, particularly in the automotive area, due the readiness with which they are expected to be recyclable. Thermoset matrix composites are less obviously recyclable due to the inability to remould them. However, increased adoption of these materials, along with increased cost of landfill and the use of more expensive fibres than are commonly used in thermoplastics, in particular carbon fibre, has driven interest in re-use of these materials. Potential techniques that could be in used for these materials include mechanical break-down, thermal recycling as well as chemical recycling. Although these techniques could also be used for thermoplastic matrix composites, energy considerations would suggest remoulding to be a much more desirable option. Due to the ability to melt thermoplastics, mechanical break-down into granules for

use in the original processing stream is the most obvious technique for recycling fiber reinforced thermoplastics. However, for fiber reinforced thermoplastics, fiber breakage induced by grinding and subsequent processing (e.g. injection moulding) leads to reduction of material properties. For these reasons, recycling by dissolution of the polymer matrix, often at elevated temperatures has also been considered. The simplicity of mechanical recycling and its relatively low cost give it the greatest potential, particularly for short fiber reinforced thermoplastics, for which fiber breakage during reprocessing has a lower impact on reinforcing properties than for long fiber reinforced plastics [5].

No post-consumer based recycling studies have been carried out on agro-based fiber composites [6] but there have been a number of studies on reprocessing. Agro-based fibers are less brittle and softer than glass fibers and are therefore more likely to retain properties during recycling. Bourmaud and Baley [7] compared reprocessing of hemp and sisal with glass fiber reinforced polypropylene (PP) composites. They observed reduction of both tensile strength (TS) and Young's modulus (YM) for all composites, with greater reduction found for glass fiber reinforced PP (about 52% for TS and 40% for YM) than PP reinforced with sisal (17% for TS and 10% for YM) or hemp (13% for TS and 1% for YM) after being reprocessed seven times. Walz et al. [8] studied reprocessing of 50 wt% kenaf fibre reinforced PP composites. Both tensile and flexural properties were found to decrease (by about 20%) with increased number of times the materials were reprocessed (up to nine times). A similar trend was shown by Joseph et al [9] for 20 wt% sisal fibre/LDPE matrix composites.

Cellulose fibres contain many hydroxyl groups (-OH) and readily interact with water molecules by hydrogen bonding. In contrast to glass fibres, where water adsorption only occurs at the surface, cellulose fibres can interact with water throughout their bulk. Moisture penetration into composite materials occurs by three different mechanisms. The main process consists of diffusion of water molecules inside the microgaps between polymer chains. The other mechanisms are capillary transport into the gaps and flaws at the interfaces between fibres and polymer because of incomplete wettability and impregnation, and transport by microcracks in the matrix, formed during the compounding process [10]. The capillary mechanism involves the flow of water molecules into the interface between the fibres and the matrix. It is particularly significant when the interfacial adhesion is weak and when the debonding of the fibres and the matrix has started. In addition, transport by microcracks includes the flow and storage of water in the cracks, pores or small channels in the composite structure. These imperfections can be originated during the processing of the material or due to environmental and service effects. The diffusion coefficient is the most important parameter for water absorption as this shows the ability of solvent molecules to penetrate inside the composite structure. Over short times, such that  $M_t/M_\infty \leq 0.5$ , the following equation can be used to determine the diffusion coefficient [11]:

$$\frac{M_t}{M_\infty} = \frac{4}{L} \left( \frac{D}{\pi} \right)^{0.5} t^{0.5} \quad (1)$$

where  $M_t$  is the moisture content at time  $t$ ,  $M_\infty$  is the moisture content at the equilibrium,  $L$  is the thickness of the sample and  $D$  is the diffusion coefficient.  $D$ , can be obtained from the slope of the linear part of the plot of  $M_t$  versus the square root of time  $t$ .

It is difficult to entirely eliminate the absorption of moisture in composites without using expensive surface barriers [12]. Good wetting of the fibre by the matrix and adequate fibre-matrix bonding can decrease the rate and amount of water absorption in the interface region of the composite [13]. Optimization of interfacial adhesion between cellulose-based fibres and thermoplastics has been the focus of a large amount of research conducted during the last two decades [14]. Coupling agents in wood fibre reinforced plastic composites play an important role in improving compatibility and adhesion between polar wood fibre and non-polar polymer matrices by forming bridges of chemical bonds between the fibre and the matrix. So far, more than forty coupling agents have been used in production and research. Among them, maleated polypropylene (MAPP) is the most popular one [15]. Several authors have investigated hygrothermal ageing of natural fibre composites. Panthapulakkal et al. [16] studied water absorption of agro-residue reinforced high-density polyethylene composites and found the tensile strength and Young's modulus to decrease despite the presence of compatibilizers. Espert et al. [17] found that the water absorption of natural fibre/PP composites followed the kinetics of a Fickian diffusion process, where the kinetic parameters are influenced by the fibre content, the type of matrix and mainly, the temperature by means of the Arrhenius law. Mechanical properties were found to be dramatically affected by water absorption. Prior to this current study, fibre content had already been optimised (from 30, 40 and 50wt%) to give the highest composites tensile strength [18] and Maximum tensile strength of composites was found for 40 wt% fibre content with 4 wt% MAPP. In this study, effects of reprocessing on the mechanical and hygrothermal behavior was studied.

## 2. MATERIALS AND METHODS

### 2.1 Materials

Radiata pine (*Pinus Radiata*) bleached wood fiber (Kraft) was supplied by Tasman Pulp & Paper Co Ltd, New Zealand. The average fiber length was 2.36 mm and the fiber diameter was 25  $\mu\text{m}$ . The lignin content of the fiber was zero. The matrix polymer was a standard polypropylene (PP) powder with a density of 0.9 g/cc supplied by the Aldrich Chemical Company, Inc and MAPP (AC 950P) with a saponification value of 35-40 mg KOH/g, a density of 0.93 g/cc and free maleic anhydride content of less than 0.5% was supplied by Honeywell international, Inc, USA.

### 2.2 Methods

Composite fabrication: Composites were fabricated with

40 wt% fiber with MAPP and PP using a TSE-16-TC twin-screw extruder with a 15.6 mm screw blade diameter at 180°C (maintaining 5 different temperature zones 100, 130, 160, 180 and 175°C from feed zone to exit die) and a screw speed setting of 100 rpm. Prior to extrusion, wood fiber, PP and coupling agent were dried in an oven at 80°C for a minimum of 48 hours. Following extrusion, the material was pelletised into lengths of less than 5 mm and injection moulded into specimens for tensile and 4-point bend testing using a BOY 15-S injection moulder. Specimens for tensile testing were randomly selected from approximately one hundred and fifty of each type to evaluate the mechanical properties. The remaining specimens were granulated and injection moulded. Again specimens were randomly selected from these recycled reprocessed materials for physical and mechanical property evaluation. The procedure of injection moulding and granulation was repeated for a total of eight times.

**Water absorption:** Water absorption studies were performed following the ASTM D 570-98: Standard Test Method for Water Absorption of Plastics. Six specimens of tensile and bending from every batch were submerged in distilled water at 50°C. The specimens were removed from the water after certain periods of time, weighed in a high precision balance to find the amount of water taken up and then resubmerged in water.

**Tensile testing:** Tensile testing was carried out according to the ASTM 638-03: Standard Test Method for Tensile Properties of Plastics using an Instron-4204 tensile testing machine fitted with a 5 kN load cell operated at a cross-head speed of 5 mm/min. An Instron 2630-112 extensometer was used to measure the strain. Six specimens were tested for each batch with a gauge length of 50 mm.

**Digital microscopy:** Following mounting, grinding and polishing, the fiber distribution and alignment of the fiber in the composites was observed using an Olympus B X 60 microscope.

**Scanning Electron Microscopy (SEM):** The fractured surfaces of the tensile test specimens were examined using a Hitachi S-4000 field emission scanning electron microscope, operated at 5 kV. Samples were mounted with carbon tape on aluminium stubs and then sputter coated with platinum and palladium to make them conductive prior to SEM observation.

**Extraction of fiber from composites:** Fiber was extracted by dissolving the matrix in hot xylene at 110°C followed by Soxhlet extraction in xylene for 72 hours.

**Fiber length measurement:** The length and fiber distribution of virgin and extracted fiber from the composites was measured using a Kajaani FS-200 electronic sequential fiber analyzer. Fiber count of about 15,000-20,000 was used to determine the fiber length distribution.

**Thermogravimetric analysis (TGA):** Thermogravimetric analysis was carried out using a TA Instruments n SDT 2960 Simultaneous DTA-TGA in air (flow rate 150 ml/min) with a heating rate of 10°C/min. The temperature range scanned was from 25°C to 600°C. The weights of all specimens were approximately 10 mg. Alumina open crucible was used for sample holding.

**Differential scanning calorimetry (DSC):** DSC was carried out using a TA Instruments DSC 2920 Differential scanning calorimeter in air (flow rate 50 ml/min) with a heating rate of 10°C/min. The temperature range scanned was from 25°C to 200°C. The weights of all specimens were approximately 10 mg. Aluminium open crucible was used for sample holding.

### 3. RESULTS AND DISCUSSION

#### 3.1 Effects on Reprocessing

Reprocessing was carried out for 40 wt% fibre (with 4 wt% MAPP) reinforced composites. Very little change on TS and YM was found for PP during reprocessing (Figs 1 and 2).

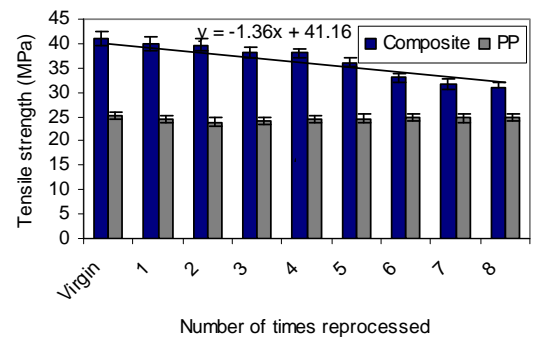


Fig 1. Tensile strength versus number of times reprocessed.

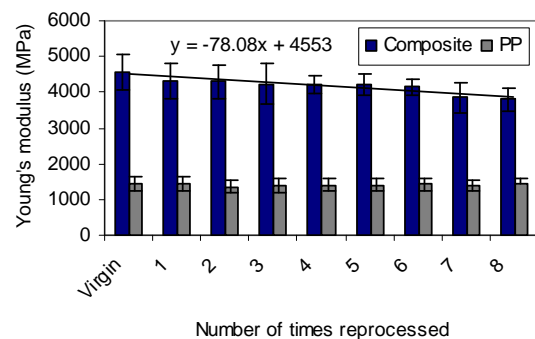


Fig 2. Young's modulus of composites versus number of times the materials were reprocessed.

The TS and YM of composites decreased with increased number of times the materials were reprocessed in a linear fashion. The virgin composites showed an average TS of 41 MPa and YM of 4553 MPa which reduced after being reprocessed 8 times to 31 MPa and 3800 MPa respectively.

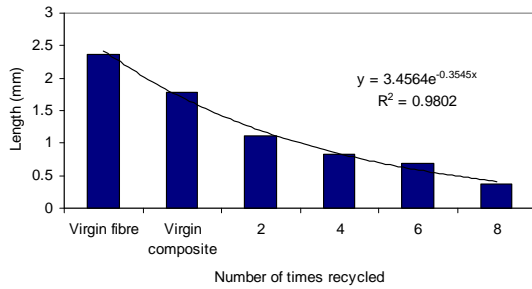


Fig 3. Weighted average fibre length of virgin fibre and the fibre extracted from composites.

One of the reasons for the changes in mechanical properties is likely to be due to the fact that reprocessing resulting some fibre damage. The average fibre length was found to decrease from 2.36 mm for virgin fibre to 0.37 mm for the fibre extracted from the 40 wt% fibre composites reprocessed 8 times (Fig. 3). The shorter fibre lengths and the increased fines percentage with reprocessing were also observable by light microscopy (Fig 4). The reductions of fibre length would be expected to reduce reinforcing efficiency, leading to the observed reduction in TS, YM.

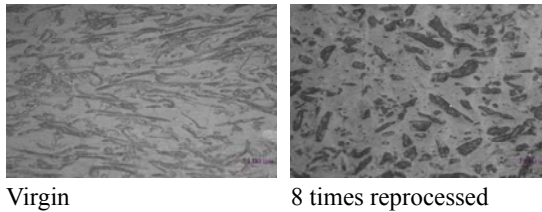


Fig 4. Fiber distribution in virgin and reprocessed composites.

### 3.2 Durability of Reprocessed Composites

Moisture absorption increased with increased soaking time for virgin and reprocessed composites until saturation at about 5 months (Fig. 5).

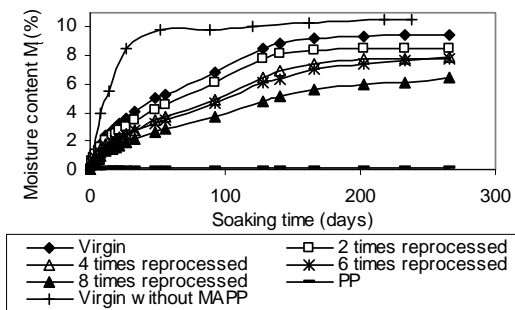


Fig 5. Moisture content of composites and PP versus hygrothermal ageing time.

As no significant weight gain was found for PP during this period, it seemed likely that moisture only penetrated into the composites through the fiber and fiber matrix interface. Both the equilibrium moisture content and diffusion coefficient decreased with increased number of

times the materials were reprocessed respectively from 9.42% and  $2.54 \times 10^{-13}$  m<sup>2</sup>/s for virgin composites to 6.41% and  $1.01 \times 10^{-13}$  m<sup>2</sup>/s for composites reprocessed 8 times (Table 1).

Table 1: Equilibrium moisture content and diffusion coefficient of virgin and reprocessed composites (with and without MAPP).

Composites	Equilibrium moisture content $M_{\infty}$ (%)	Diffusion coefficient $D$ (m <sup>2</sup> /s)
Virgin Without MAPP	10.51	$5.70 \times 10^{-13}$
Virgin (with 4 wt% MAPP)	9.42	$2.54 \times 10^{-13}$
2 times reprocessed	8.46	$1.53 \times 10^{-13}$
4 times reprocessed	7.93	$1.19 \times 10^{-13}$
6 times reprocessed	7.75	$1.10 \times 10^{-13}$
8 times reprocessed	6.41	$1.01 \times 10^{-13}$

The decrease in moisture content and diffusion coefficient with increased number of times the materials were reprocessed was explained by a number of effects. As the fiber length decreased with increased number of times the materials were reprocessed, it was considered that it would have been more difficult to form finite clusters which serve as passages for water molecules to travel through the lattice from one side to another. Also, reduction of micro-voids as evaluated by the increased density of composites with increased reprocessing would be expected to result in a decrease in moisture content and diffusion coefficient.

Table 2: Mechanical properties of 40 wt% fiber virgin (with and without MAPP) and reprocessed composites (made with 4 wt% coupling agent) before and after ageing.

Composites	TS (MPa)		YM (MPa)	
	Unaged	Aged	Unaged	Aged
Without MAPP	23	17.5	3619	1226
With 4 wt% MAPP	41	27.7	4553	2734
2 times reprocessed	40	26.3	4295	2776
4 times reprocessed	38	25.2	4215	2847
6 times reprocessed	33	23.5	4148	3002
8 times reprocessed	31	22.7	3800	2769



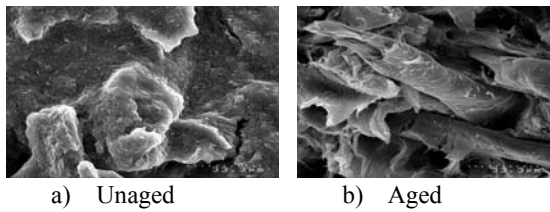


Fig 6. Effects of hygrothermal ageing showing SEMs of  
 a) fracture surface of an unaged virgin composite,  
 b) fracture surface of an aged virgin composite.

TS and YM after have been observed to decrease after hygrothermal ageing for virgin and reprocessed composites (Table 2) and it can be seen that the extent of reduction in properties decreased with increased number of times the materials were reprocessed. After ageing, reductions in TS of 33% and YM of 40% were found for virgin composites compared to reductions for both TS and YM of 27% for composites reprocessed eight times. This was considered to be due to the equilibrium moisture content decreasing with increased number of times the materials were reprocessed, and therefore having less effect on behaviour. Degradation of fibre and fibre matrix interface bonding was highlighted to explain the physical and mechanical properties of composites (Fig. 6).

### 3.3 Effects of Recycling on Thermal Stability

The melting temperature ( $T_m$ ) of PP in composites was found to be reduced slightly from 171°C for virgin composites to 167°C for composites reprocessed eight times which was considered to be due to reduced molecular weight as a consequence of thermo-mechanical degradation and chain.

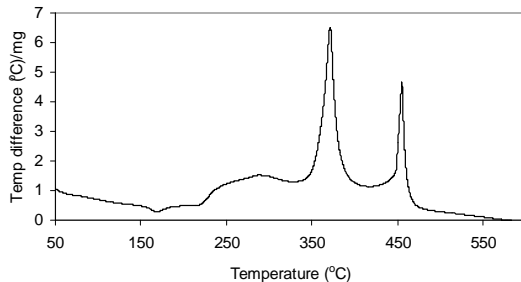


Fig 7. DTA trace of virgin composite.

Three stages of decomposition have been observed for virgin and reprocessed composites (Fig. 7), starting with dehydration and decomposition of volatile components at around 250°C, followed by rapid weight loss for oxidative decomposition and finally slow decomposition corresponding to formation of char as the temperature increased. Kinetic parameters for the various stages of thermal degradation were determined from the TGA graphs using the following equation, given by Broido [19].

$$\ln\left(\ln\frac{1}{y}\right) = -\frac{E_a}{RT} + \ln\left(\frac{RZ}{E_a\beta} T_m^2\right) \quad (3)$$

where  $y$  is the fraction of nonvolatilized material not yet decomposed,  $T_{max}$  is the temperature of maximum reaction rate,  $\beta$  is the heating rate,  $Z$  is the frequency factor and  $E_a$  is the activation energy. Initially, plots of  $\ln\ln(1/y)$  versus  $1/T$  for various stages of decomposition were drawn and found to be linear, suggesting good agreement with the Broido equation. The activation energies,  $E_a$  determined from the slopes of these plots are given in Table 3.

Table 3: Thermal properties of composites

Type	Stage	Wt. loss (%)	Temp. range (°C)	$T_{max}$ (°C)	$E_a$ (kJ/mol)
Virgin	1st	61	226-351	285	85
	2nd	31	351-436	371	68
	3rd	7	436-508	455	60
8 times re-processed	1st	30	230-340	289	87
	2nd	52	340-447	412	71
	3rd	15	470-512	470	81

$T_{max}$  and  $E_a$  for PP in composites have been found to increase with increased number of times the materials were reprocessed. The positions of weight loss on the TGA traces of composites (Fig. 8) increased number of times the materials were reprocessed suggesting increased thermal stability. The increase in thermal stability has been considered to be due to an increase in crystallinity of PP resulting from molecular weight reduction.

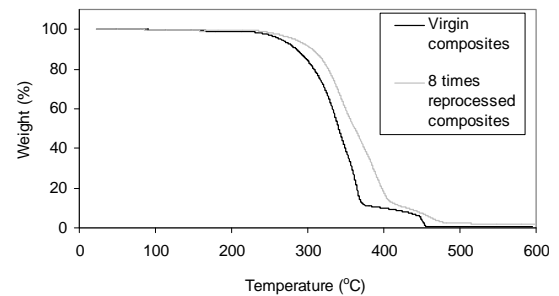


Fig 8. TGA trace of virgin and reprocessed composites.

## 4. CONCLUSION

Mechanical break-down is also the most progressed recycling method for thermoplastic matrix composites. Research based on reprocessing of thermoplastic matrix composites shows some reduction of tensile strength and Young's modulus, with poor surface appearance but increased failure strain and better moisture resistance. Reductions of fibre length and polymer degradation have been highlighted to explain the change in properties of reprocessed composites. Overall, issues of contamination and separation will also need to be addressed for increased mechanical recycling and therefore the development of infrastructure and systems. For 40 wt% fibre reinforced composites reprocessed 8 times, a 25% reduction in TS and 16% reduction in YM was found. The reduction of TS, YM was considered to be due to

fibre damage that occurred during reprocessing as evaluated by the associated reduction of the average fibre length from 2.36 mm for virgin fibre to 0.37 mm for the fibre extracted from the composites reprocessed 8 times. Moisture absorption increased with increased soaking time for all composites until saturation at about 5 months. Equilibrium moisture content and diffusion coefficient decreased with increased number of times the materials were reprocessed. For virgin and 8 times reprocessed composites, the equilibrium moisture contents were respectively 9.42% and 6.41% and the diffusion coefficients were  $2.54 \times 10^{-13}$  m<sup>2</sup>/s and  $1.01 \times 10^{-13}$  m<sup>2</sup>/s. TS and YM was found to decrease after hygrothermal ageing. A 33% reduction of TS and 40% reduction of YM was found for virgin composites and 27% reduction of both TS and YM was found for composites reprocessed 8 times. However, the extent of reduction was lower for reprocessed composites. Degradation of fibre and fibre matrix interface bonding was highlighted to explain the physical and mechanical properties of composites.

## 5. REFERENCES

- Lester, E. S., 2004, "Microwave heating as a means for carbon fibre recovery from polymer composites: a technical feasibility study.", *Materials Research Bulletin*, 39(10): 1549-1556.
- Pickering, S. J., 2006, "Recycling technologies for thermoset composite materials current status", *Composites: Part A*, 37 (8): 1206-1215.
- Martins, M. H. and Paoli, A., 2001, "Polypropylene compounding with recycled material I. Statistical response surface", *Polymer Degradation and Stability*, 71 (2): 93-98.
- Selke, S. E., 2002, "Plastics recycling. Handbook of plastics, elastomers and composites", McGraw- Hill, New York, 4th edition: 693-757.
- Bernasconi, A. D., 2007, "Analysis of the effect of mechanical recycling upon tensile strength of a short glass fibre reinforced polyamide 6,6.", *Engineering Fracture Mechanics*, 74(4): 627-641.
- Rowell, R. M., 1996 "Paper and composites from agro-based resources."
- Bourmaud, A., and Baley C., 2007, "Investigations on the recycling of hemp and sisal fibre reinforced polypropylene composites.", *Polymer Degradation and Stability*, 92(6): 1034-1045.
- Walz, K., Jacobson, R., et al., 1994 "Effect of reprocessing/recycling on the mechanical properties of kenaf-PP composites".
- Joseph, K., Thomas, S., et al., 1993, "Tensile properties of short sisal fibre-reinforced polyethylene composites.", *Journal of Applied Polymer Science*, 47: 1731-9.
- Lin, Q., Zhou, X., Dai, G., 2002, "Effect of hydrothermal environment on moisture absorption and mechanical properties of wood flour-filled polypropylene composites", *Journal of Applied Polymer Science*, 85(14): 2824-32.
- Crank, J., 1956, "The mathematics of diffusion", Clarendon Press, Oxford: 347.
- Rowell, R. M., Tillman, A. M., R. J. Simonson, 1986, *Wood Chem Tech*; 6: 427.
- Tajvidi, M., Ebrahimi, G., 2003, "Water Uptake and Mechanical Characteristics of Natural Filler-Polypropylene Composites", *Journal of Applied Polymer Science*, 88: 941-946.
- Weyenberg, I. Van. de., Ivens, J., Coster, A., Kino, De. B., Baetens, E. and Verpoest, I., 2003, "Influence of processing and chemical treatment of flax fibres on their composites", *Composites Science and Technology*, 63(9): 1241-1246.
- Lu JZ, Wu Q and Harold SM., 2000, "Chemical coupling in wood fibre and polymer composites", a review of coupling agents and treatments, *Wood and Fibre Science* 32 (1): 88 - 104.
- Panthapulakkal S and Sain M., 2007, "Agro-residue reinforced high-density Polyethylene composites", *Fiber characterization and analysis of composite properties*, 38 (6): 1445-154.
- Espert A, Vilaplana F and Karlsson S. 2004, "Comparison of water absorption in natural cellulosic fibres from wood and one-year crops in polypropylene composites and its influence on their mechanical properties", *Composites Part A* 35 (11): 1267-1276.
- Beg, MDH., 2007, "The improvement of interfacial bonding, weathering and recycling of wood fibre reinforced polypropylene composites", PhD Thesis, University of Waikato. New Zealand.
- Broido, A., 1969, "A simple, sensitive graphical method of treating thermogravimetric analysis data." *Journal of Polymer Science, Part A-2* 7: 1761.

## 6. MAILING ADDRESS

### M. D. H. Beg

Faculty of Chemical and Natural Resources Engineering,

Universiti Malaysia Pahang

**E mail:** [mdhbeg@ump.edu.my](mailto:mdhbeg@ump.edu.my)

**Phone:** +60 9549 2816

**Fax:** +60 9549 2889

## INFLUENCE OF ACETONE ON THE PERFORMANCE OF POLYETHERSULFONE MEMBRANES

Iqbal Ahmed<sup>1</sup>, Ani Idris<sup>2</sup>, M.D.H Beg<sup>1</sup>, Shaharuddin Kormin<sup>1</sup>

<sup>1</sup> Faculty of Chemical and Natural Resources Engineering, Universiti Malaysia Pahang, Malaysia

<sup>2</sup> Department of Bioprocess Engineering, Faculty of Chemical and Natural Resources Engineering,  
Universiti Teknologi Malaysia

### ABSTRACT

In this study polyethersulfone (PES) ultrafiltration (UF) membrane were prepared from mixtures of two solvents containing N,N-dimethylformamide (DMF) as core solvent, acetone (AC) as co-solvent and tape water were used as coagulant bath. Throughout the study, the concentration of PES is kept fixed at 20 wt % and the AC is varied in the range of 20-25wt. %. The dope solutions were prepared under closed heating system and PES asymmetric membrane was cast by dry/wet phase inversion process. The solution viscosity was measured using a standard Brookfield viscometer. Membrane performance was characterized in terms of pure water permeation (PWP), permeation rate (PR) and solute separation of polyethylene glycol (PEG) solution of various molecular weights ranging from 600-35000 Dalton. Results revealed that the 22 wt% AC exhibits the best performance with MWCO at 90% rejection in the range of 9.13 kDa and low flux range of 6.70 (L.m<sup>-2</sup>. hr<sup>-1</sup>).

**Keywords:** Asymmetric, Polyethersulfone, Mixtures, Solvents.

### 1. INTRODUCTION

The introduction of additive or non solvent into casting solutions plays a significant role in the formation process of macrovoids. The important effects of this non solvent are suppression of macrovoids, improved interconnectivity of the pores and higher porosities in the top-layer and sub-layer [1-4]. The presence of the non solvents in the dope not only changes the thermodynamic state of the dope but also influences the conformation and dynamics of the polymer, which affects the kinetics of phase separation in turn. Several authors [5-10] have studied the performance and microstructures of polysulfone membranes with polyvinyl pyrrolidone (PVP) as additive. Hwang et al [11] prepared PES asymmetric membranes with a co-solvent system of dichloromethane and NMP as volatile and nonvolatile solvent, respectively, and the effect of PVP additive was examined in terms of pure water flux and solute rejection of the membrane. Kim and Lee [12] investigated the effect of PEG additive as a pore-former on the structure formation of PES membranes and their performances of thermodynamic and kinetic properties in phase inversion process. The effects of the water/PVP or water/PEG mixed non solvent were also studied. Chaturvedi et al. [13] focused on the effects of nature of non solvent, solvent, ambient humidity on membrane performance behavior of PES UF membranes. Xu et al [14] studied the effect of ethanol concentration on characterization and performance of PES hollow fiber UF membranes fabricated using dry/wet spinning process. Besides

ethanol, the effect of methanol, n-propanol and water as non-solvent additives were also investigated. In another paper [15, 16] PVP and PEG were used as additives and NMP as solvent. Extensive research has been carried out to study the influence of additive such as PEG and PVP, on morphology and performance of polysulfone-NMP and PES-NMP membranes. However, very little is known regarding the usage of halogenated-based additives [17-21].

So far, study on acetone has been extensively performed. Ohya et al 1996. has reported that the addition of acetone in polymer solution has decreased the permeability but incredibly enhanced the solute rejection [22]. While Barth et al. investigated the physical properties of PSf-DMF-acetone polymer solution [23]. However, there are no reports yet on the effect of maximum concentration of acetone as co-solvent on the performance of polyether sulfone membranes. Thus, in this research, the effect of maximum concentration acetone as co-solvent on the performance of PES membranes is investigated.

### 2. EXPERIMENTAL DETAILS

#### 2.1 Materials

PES (Ultrasont E 6020P); weight-average molecular weight ( $M_w$ ) 58,000, weight-average molecular weight/number-average molecular weight ( $M_w/M_n$ ) 3.6 procured from BASF was the base polymer used in the membrane casting solution. Analytical grade N,

N-dimethylformamide DMF [ $\text{HCON}(\text{CH}_3)_2$ ,  $M=73.10$  g/mol] purchased from Merck (Germany) was used as the solvent. Commercial grade acetone was used as co-solvent in this study. Water was used as the coagulation bath. For the ultrafiltration experiments, PEG with various molecular weights (from PEG 600 to PEG 40000), were obtained from Fluka and used as the testing solution.

## 2.2. Preparation of Dope Solution

The dope solutions prepared consist of 20% PES and various compositions of DMF and acetone as tabulated in Table 1. The polymer dissolution process was carried out in a 1 liter 4 necked round bottomed flask with stainless steel stirrer and reflux condenser as described elsewhere [24]. Barnstead electro thermal heater with a rating of 230V~50/60 Hz, 300 Watts was used. The dope temperature was kept constant at 90-95 °C for single solvent and 55-58 57 °C for double solvent by stirring at the rate of 1200 rpm. Dissolution of the polymer and additive took 7 hrs.

Table 1: Dope composition

Membr. No.	PES% Wt. %	DMF Wt. %	Acetone Wt. %
1	20	80	0
2	20	60	20
3	20	59	21
4	20	58	22
5	20	57	23
6	20	56	24
7	20	55	25

## 2.3. Viscosity Measurement of Dope Solutions

The average apparent viscosities of polymer dope solutions were measured using Brookfield Digital Rheometer (model DV-III, USA) equipped with a suitable sample adaptor (SC4-31). At each dope solution concentration, spindle SC4-31 which is a high-viscosity adaptor was used at different shear rates (3.4-44.2 sec<sup>-1</sup>) as a function of time and at 25 °C.

## 2.4. Membrane Casting

The dope solution was poured onto a clean glass plate at room temperature and it was casted on a glass plate using a casting knife with a thickness of 200 μm. Immediately after casting, the glass plate with the casted film was dipped into ordinary tap water at room temperature. After few minutes, a thin polymeric film separated out from the glass plate due to the phase inversion process. The membrane was washed with distilled water and transferred to another container ready to be tested in the cross flow filtration cell. All flat sheet membranes were visually inspected for defects and good areas were chosen for membrane evaluation.

## 2.5. Membrane Evaluation

The performances of the various lithium halides flat sheet membranes were evaluated in terms of pure water permeation fluxes (PWP), solute permeation fluxes (PR)

and solute rejection rates (SR) in a stainless steel cross flow test cell at 3.5 bars [24]. All experiment was conduct at room temperature 25-26 °C. Membrane sample with an area of  $2.0 \times 10^{-3}$  m<sup>2</sup> was placed in the cross flow filtration test cell with the active skin layer facing the incoming feed. A minimum of three flat sheet samples were prepared for each condition so as to ensure the reproducibility and the average value was tabulated. Pure water permeation experiments were performed using double distilled deionized water. Pure water permeation fluxes (PWP) and solute permeation fluxes (PR) of membranes were obtained as follows:

$$J = \frac{Q}{\Delta t \times A} \quad (1)$$

where  $J$  is the permeation flux for PEG solution (Lm<sup>-2</sup>h<sup>-1</sup>) or pure water,  $Q$  is the volumetric flow rate of permeate solution and  $\Delta t$  is the permeation time (h).

Solute rejection of membranes were evaluated with various molecular weight PEG solutions ranging from 200 to 36,000 kDa at 3.5 bar. The concentration of PEG solution used was 1000-500 ppm. The concentration of the feed and permeate solution were determined by the method described by Sabde, [20]. The absorbance was measured using the spectrophotometer (Shidmadzu UV-160) at a wavelength of 535 nm against a reagent blank [20]. The membrane solute rejection (SR) is defined as

$$SR = \left( 1 - \frac{C_p}{C_f} \right) \times 100\% \quad (2)$$

where  $C_f$  and  $C_p$  are the polyethylene glycol concentration in the feed solution and permeate solution, respectively.

## 3. RESULTS AND DISCUSSION

### 3.1. Effect of AC on the Viscosity of Dope Solution

Viscosity is considered as one of the important parameters influencing the exchange rate between solvent and non-solvent during the phase inversion process [8]. Therefore, the viscosities of the various dope solutions at different shear rates are illustrated in Fig. 1. Results show that most of the dope solutions prepared by co-solvent have a lower viscosity compared to prepare by PES/DMF dope solution. Specifically, the dope solution prepared by 20-22 wt.% AC has a lower apparent viscosity (approximately 50% lower) than the one prepared using the PES/DMF (Fig. 1). Since DMF penetrates most engineered polymers and makes them swell, therefore higher viscosity might be attributed to the fact that dimethylformamide is as a solvent with low evaporation rate with leophilic and swilling tendency over AC due to formamide group when this group are heated at around 90-95 °C, it will attempt to swell rapidly to the ether group, respectively.

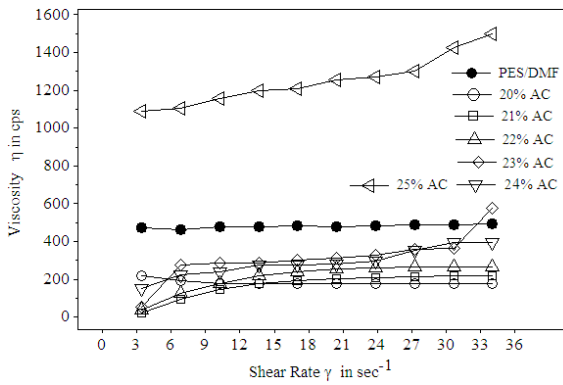


Fig 1. Viscosity versus shear rate of dope solution PES/DMF with various wt.% of AC.

Besides that the drop of dope solution viscosity revealed that with the increase of the AC ratio, the average viscosity was decreased while this behavior is proportional to shear rate, which can be attributed to the higher polarity and boiling point of DMF over that of AC [23]. It can also be concluded that the decreased of solution viscosity with mixture of DMF/AC over DMF due to the nature of two solvents, since DMF is electrophilic solvent and AC is hydrophobic nature for PES therefore, up to particular ratio of AC over DMF were stable for PES dope solution homogeneity and showed lower viscosity as compare to PES/DMF solution. However, beyond this ratio at 25 wt% of AC the viscosity dramatically increased due to the limited solubility of AC over DMF for PES and we can clearly observed in Fig. 1, this behavior attributed due to hydrophobic and hydrophilic moiety of both solvents for PES. Thus the concentration dependences of some properties exhibit extreme points in the  $X = 0.1 - 0.3$  range (from here on,  $X$  is the mole fraction of the PES in the mixture). According to the character of AC interaction with DMF, hydrophilic and hydrophobic groups are conventionally distinguished in molecules of PES. It is also attributed that the solvation of PES in DMF/AC type of solvents mainly occurs through charge-dipole type of interaction, in the situation of higher amount of AC, the increment methyl groups of acetone with DMF are responsible for the solvation of the PES. However it is observed that in these solvent mixtures, if increasing the amount of AC for PES shall break these interactions. Iqbal [24] and Wang [25] has also reported similar behavior for PES and PVDF polymer solution.

### 3.2. Performance of the Membranes

#### 3.2.1. Influence of Acetone on PWP and PR

The pure water permeation rates (PWP) and permeation rate of the membranes 1-7 produced from the various solutions are depicted in Figure 3 and 4. It is observed that the concentration of acetone is increased beyond 25 wt% the PWP rate begins to decrease. However when the concentration of acetone increases the PWP rates decreases up to ratio 20-21 wt.%. The highest PWP rate is obtained when acetone concentration is 23 wt. %. The reason for this behavior could be attributed

substantial mixture ratio of DMF/AC for PES due to significant hydrophilic and hydrophobic moiety balance. In general, the single solvent prepared membrane 1 have almost closed PWP rates over AC ratio 20 wt% and this is clearly observed in Table 2. It is believed that the higher viscosity of the single solvent solution compared to DMF/AC mixture solution contributed to different rates of exchange between solvent and non solvent during the precipitation process. The high viscosity solution has the tendency to promote delayed demixing and this feature decreased the membrane resistance and increased the PWP.

The permeate rates (PR) of the single and mixture of DMF/AC solvents prepared membranes are shown in Fig. 2. The results showed that the ratio of AC 23 wt.% over DMF exhibits highest permeation rates when separating various PEG solutions. In general the single solvent membrane has closer PR rate with membrane 2 and 3.

Table 2: Pure water permeation of UF membrane prepared by different wt% of AC.

Membr No.	PWP ( $L.m^{-2}.hr^{-1}$ )
1	8.50
2	8.00
3	9.40
4	10.00
5	25.65
6	14.20
7	8.80

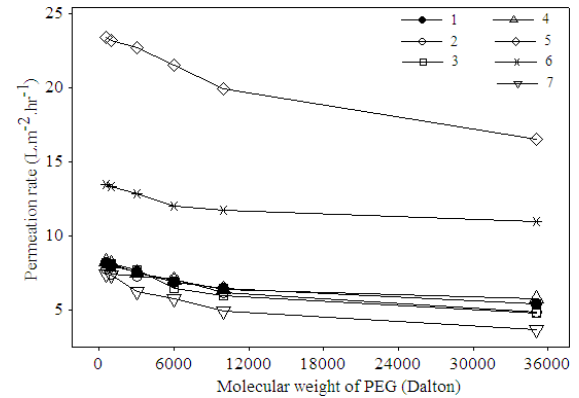


Fig 2. Permeation rate versus different molecular weight of PEG solution (Dalton)

However, when the AC ratio increases up to 23-25 % the PR rates of membrane 4-7 turns to increase but membrane 2-3 results clearly indicate that AC when used at that ratio as co-solvent has reduced the hydrophilic properties of the membrane and this is displayed by the lower PWP and PR rates. On the other hand, in the case of membrane 5 and 6, the PR increased almost 1.6-2.5 times higher as compare to membrane 1, 2, 3. There is the possibility that at this concentration between DMF/AC for PES shows significant balance of the hydrophilic and hydrophobic moieties has prevailed. Whereas the interaction can also be occurs due to hydrogen bonding in

water besides the usual ion-dipole interaction between two solvents for PES during phase inversion process.

The overall PWP and PR results indicate that the ratio of AC as a co-solvent has a strong effect on the structure of the casting solution which in turn affects the membrane performance. It appears that the AC nature of the hydrogen bond donating probably the process of attraction and association of two solvents polarities with molecules of PES. the PES polymer by hydrogen bonding with the carbonyl carbon as well as react with the amide solvent altering the solvent power [9]. This could lead to an optimum swelling of the polymer with desirable distribution of the size of the super molecular polymer aggregates and the degree of polymer network within the aggregates. It is significant to note that the casting solution viscosity is lower at control molar volume of AC which is attributed to the balance moieties for PES membrane.

Figure 3 show the rejection rates of the PES/DMF and PES/DMF/AC membranes for the various PEG solutions. Results revealed that the presence of control amount AC has not only improved the permeation rates but also the rejection rates as compared t. Increases in AC concentration to 22-23 wt.% has increased the membrane permeation and rejection rate. In membranes 1, 2 and 3 AC beyond 24-25wt% value does not result in increase rejection and permeation rates. The MWCO of the 4 & 5 membranes at 90% rejection rates is 9.7 kDa and 31.5 kDa with permeation rates of 7 and 17 L.m<sup>-2</sup>.hr<sup>-1</sup> for PEG 10,000 and 35000 Dalton solutions. It is observed that using 22-23 wt.% of AC as co-solvent in the casting solutions causes the development of a denser upper coating in the membrane. A further increase in AC beyond 24, 25 wt% of AC does not improve its rejection rates although its permeation rate also decreased. Maximum permeation rate can be obtained at 22 wt% AC with some reduction in rejection rates.

The PES/DMF membranes without AC exhibited MWCO of approximately 37 kDa. Meanwhile the PES/DMF/AC membranes have maximum MWCO around kDa and 39.5 kDa respectively, which is even lower than membrane 1. In general the AC prepared membranes has smaller pore sizes thus explaining for the higher rejection rates. It appears that the presence of control molar volume of AC as co-solvent with DMF has improved the hydrophilic and hydrophobic moieties properties of the membrane thus improving not only the permeation rate but also the rejection rates of the membranes. It seems that AC acts as a pore reducer observed by the reduction in the permeation rate. MWCO of the membranes and smaller pore sizes, the swelling property is balanced by the introduction of AC thus producing membranes with excellent rejection rates and reasonably high flux. In addition the production cost of the membranes is lower because AC is a cheaper solvent compared to DMF.

Another observation is the good and improved rejection rates observed for all the membranes 1, 2 and 3 compared with the membrane 1. In the AC membranes high rejection rates are contributed to the smaller pore sizes membranes produced as observed in Fig. 3.

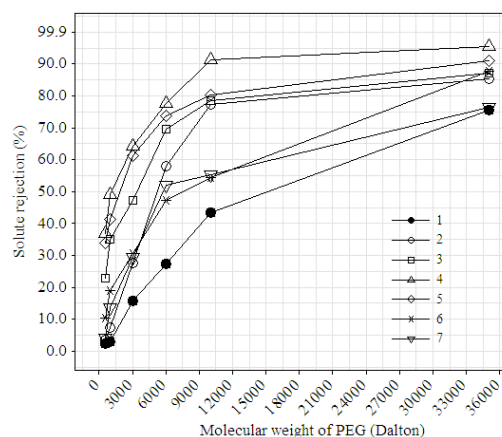


Fig 3. Rejection rate versus different molecular weight of PEG solution (Dalton).

The observation of lowered PR and higher rejection rates in the case of membranes prepared with the low volatile additive AC is confirmed by findings in the literature. Barth [12], who performed the phase inversion and membranes evaluation of PES and PSU with AC exhibiting similar properties, also obtained lower fluxes and higher retention after storing the membrane forming films in water for prolonged times.

#### 4. CONCLUSION

In summary membranes produced from dope solutions containing co-solvent acetone are superior in terms of permeation flux rates, rejection rates and quality of membranes compared to those membranes prepared without AC. The addition of AC to PES-DMF casting solutions has a significant effect on both solution properties as observed from its viscosities. The results indicates that AC interact very strongly with DMF and under closed heating system leading to the formation of DMF-acetone complexes and, hence, retain in the solvation power of DMF for PES. With addition of AC in the casting solution, membranes porosity decreases, asymmetric skin layer becomes very thin, producing membranes with slightly lower permeation rates but excellent the rejection rate.

#### 5. ACKNOWLEDGEMENT

Financial support from the University Malaysia Pahang through the funding, Vote No. RDU 090317 is gratefully acknowledged.

#### 6. REFERENCES

1. Jung, B. Yoona, J. K., Kima, B. and Rhee, H. W. 2004, "Effect of molecular weight of polymeric additives on formation, permeation properties and hypochlorite treatment of asymmetric polyacrylonitrile membranes", J.Membr. Sci. 243: 45-57.
2. Tasselli, F., Jansen, J.C. Sidari, F. and Drioli, E., 2005, "Morphology and transport property control of modified poly(ether ether ketone) (PEEKWC) hollow fiber membranes prepared from



- PEEKWC/PVP blends: influence of the relative humidity in the air gap”, *J. Membr. Sci.* 243:13-22.
3. Won, J., Kang, Y. S., Park, H. C and Kim, U. Y., 1998, “Light Scattering and Membrane Formation Studies on Polysulfone Solutions in NMP and in Mixed Solvents of NMP and Ethylacetate”, *J. Membr. Sci.* 243: 45-52.
  4. Lafreniere, L. Y. Talbot, F. D. F. Matsuura, T and Sourirajan, S., 1987, “Effect of poly(vinylpyrrolidone) additive on the Performance of poly(ether sulfone) Ultrafiltration Membranes”, *Ind, Eng. Chem. Res.* 26: 2385-2393.
  5. Xu, Z. L. Chung, T. S and Huang, Y., 1999, “Effect of polyvinylpyrrolidone molecular weights on morphology, oil/water separation, mechanical and thermal properties of polyetherimide/polyvinylpyrrolidone hollow fiber membranes”, *J. Appl. Polym. Sci.* 74:2220-2233.
  6. Han, M. J and Nam, S. T., 2002, “Thermodynamic and rheological variation in polysulfone solution by PVP and its effects in the preparation of phase inversion membrane”, *J. Membr. Sci.* 202: 55-67.
  7. Qin, J. J. Wong, F. S. Li, Y. and Liu, Y. T., 2003, A High Flux Ultrafiltration Membrane Spun from PSU/PVP (K90)/DMF/1,2-propanediol”, *J. Membr. Sci.* 211: 139-145.
  8. Sanchez, B. T. Ortiz-Basurto, R. I and Fuente, E. B., 1999, “Effect of Nonsolvents on Properties of Spinning Solutions and Polyethersulfone Hollow Fiber Ultrafiltration Membranes”, *J. Membr. Sci.* 152: 19-28.
  9. Zaidi, S. K and Kumar, A., 2004, “Effects of Ethanol Concentration on Flux and Gel Formation in Dead end Ultrafiltration of PEG and Dextran”, *J. Membr. Sci.* 237:189-197.
  10. Ochoa, N. A., Pradanos, P., Palacia, L., Paglearo, C., Marchese J. and Hernandas, A., 2004, “ Pore Size Distributions Bsed on AFM Imaging and Retention of Multidisperse Polymer Solutes: Characterisation of Polyethersulfone UF Membranes with Dopes Containing different PVP”, *J. Membr. Sci.* 187: 227–237.
  11. Hwang, J. R. Koo, S. H., Kim, J. H., Higuchi, A and Tak, T. M., 1996, Effects of Casting Solution Composition on Performance of Poly(ether sulfone) Membrane”, *J. Appl. Polym. Sci.* 60:1343-1348.
  12. Kim, J. H and Lee, K. H., 1998, “Effect of PEG additive on membrane formation by phase inversion”, *J. Membr. Sci.* 138: 153-163.
  13. Chaturvedi, B. K., Ghosh, A. K., Ramachandran, V. Trivedi, M. K., Hanra, M. S and Misra, B. M., 2001, Preparation, Characterization and Performance of Polyethersulfone Ultrafiltration Membranes *Desalination* 133: 3- 40
  14. Xu, Z. L and Qusay, F. A., 2004, “Effect of Polyethylene Gglycol Molecular Weights and Concentrations on Polyethersulfone Hollow Fiber Ultrafiltration Membranes”, *J. Appl. Polym. Sci.* 91: 3398-3407
  15. Idris, A., Zain, N, M and Noordin, M. Y., 2007, “Synthesis, Characterization and Performance of Asymmetric Polyethersulfone (PES) Ultrafiltration Membranes with Polyethylene glycol of Different Molecular Weights as Additives. *Desalination* 207: 324-339
  16. Munari, S., Bottino, A., Capannelli, G, Moretti, P. and Bon, P, 1988., “Preparation and Characterization of Polysulfone Polyvinylpyrrolidone Based membranes. *Desalination.* 70(1-3): 265-275.
  17. Zhang, Z., Wang, Y. Y., Wang, C. L and Xiang, H., 2008, “Synthesis and Characterization of a PVA/LiCl Blend Membrane for Air Dehumidification”, *J. Membr. Sci.* 308:198-206.
  18. Lee, H. J. Won, J. H and Kanga, Y. S., 2002, “Solution Properties of Poly(amic acid)-NMP Containing LiCl and their Effects on Membrane Morphologies” *J. Membr. Sci.* 196: 267-277.
  19. Ani, I and Iqbal, A., 2007, “Viscosity Behavior of Microwave-Heated and Conventionally Heated Poly(ether sulfone)/Dimethylformamide/Lithium bromide Polymer Solutions “, *J. Appl. Polym. Sci.* 108:302-307.
  20. Sabde, A. D., Trivedi, M. K., Ramachandran, V., Hanra, M. S and Misra, B. M., 1997, “Casting and characterization of cellulose acetate butyrate based UF membranes “, *Desalination.* 114: 223-232.
  21. Singh, S., Khulbe, K. C., Matsuura, T and Ramamurthy, P., 1998, “Membrane Characterization by Solute Transport and Atomic Force Microscopy”, *J. Membr. Sci.* 142: 111-127.
  22. Ohya, H., Vladislav, V., Kudryavtsev, Svetlana I. Semenova. (19996). *Polyimide membranes: applications, fabrications, and properties.* Gordon & Breach, Chapter 5, pp 201-206.
  23. Barth, C., Gonçaves, M. C., Pires, A. T. N., Roeder, J and Wolf, B. A., 2000, “Asymmetric Polysulfone And Polyethersulfone Membranes: Effects of Thermodynamic Conditions During Formation on their Performance”, *J. Membr. Sci.* 152: 19-28.
  24. Iqbal, A., Ani, I., Nasrul, F. C. P., 2009, “Novel Method of Synthesizing Poly(Ether Sulfone) Membranes Containing Two Solvents and A Lithium Chloride Additive and their Performance”, *J. Appl. Polym. Sci.*, Articles online in advance of print.
  25. Wang, D., Li, K and Teo, W. K., 1996, “Polyethersulfone hollow fiber gas separation membranes prepared from NMP/alcohol solvent systems”, *J. Membr. Sci.*, 115: 85-108.

## 7. MAILING ADDRESS

Iqbal Ahmed  
 Faculty of Chemical and Natural Resources Engineering,  
 Universiti Malaysia Pahang,  
 Lebuhraya Tun Razak, 26300  
 Gambang, Kuantan, Pahang, Malaysia  
 E mail: [mdhbeg@ump.edu.my](mailto:mdhbeg@ump.edu.my)  
 Phone: +60 9549 2816  
 Fax: +60 9549 2889

## A VIBRATION ISOLATION SYSTEM USING STIFFNESS VARIATION CAPABILITY OF ZERO-POWER CONTROL

M. Emdadul Hoque<sup>1,2</sup>, Takeshi Mizuno<sup>2</sup>, M. M. Zaglul Shahadat<sup>1,2</sup>, Yuji Ishino<sup>2</sup> and Masaya Takasaki<sup>2</sup>

<sup>1</sup>Department of Mechanical Engineering, Rajshahi University of Engineering & Technology  
Rajshahi, Bangladesh.

<sup>2</sup>Department of Mechanical Engineering, Saitama University, Japan.

### ABSTRACT

This paper presents a vibration isolation system combining a positive stiffness spring in series with a negative stiffness spring. The negative spring is realized by an active zero-power control. The conventional zero-power control system yields constant negative stiffness, and the stiffness depends on the capacity of the permanent magnets or the gap-force coefficient of the magnets. This is one of the bottlenecks in the fields of application of zero-power control where adjustment of stiffness is necessary, such as developing vibration isolation system. To overcome the above problem, the basic zero-power control system is modified such that it can adjust stiffness by adding a minor proportional feedback of displacement to the zero-power control current. Some experiments have been carried out to measure the efficacy of the control system, as well as the vibration isolation system.

**Keywords:** Active Control, Vibration Isolation, Zero-Power Control, Zero-Compliance System, Magnetic Bearing.

### 1. INTRODUCTION

Vibration isolation system is widely used in many researches and precise manufacturing systems, such as semiconductor industries, high precision measurement, etc. There are two kinds of vibrations that may hamper desired operations. They are direct disturbance on the table and ground vibration. Both vibration disturbances can be suppressed by using passive technique or using active control. Vibration absorbers extract kinetic energy from the vibrating host system and the active system introduces opposing forces in the structure to affect compensation.

Vibration isolation of mechanical systems is achieved with passive technique because of its low cost. However, passive techniques need the trade-off between the isolation elements where high stiffness suspension are used for suppressing direct disturbance, and suspension with soft stiffness are used for ground vibration isolation [1,2]. On the other hand, active techniques do not have such limitations, and performances are better as well [3-7]. Recently vibration isolation systems have been developed using active zero-power controlled magnetic suspension in the view of reducing system development costs as well as maintenance costs [8,9]. The above systems use a combined system with positive and negative springs in series. A middle table is introduced in

this system between base to isolation table. Positive stiffness spring is used between base to middle table, and a suspension with negative stiffness is used between middle table to isolation table.

In this research, an active zero-power control is used to realize negative stiffness by using a hybrid magnet consists of electromagnet and permanent magnets. This control achieves the steady state in which the attractive force produced by the permanent magnets balance the weight of the suspended object, and the control current converges to zero. Since there is no steady energy consumption for achieving stable levitation, it has been applied to space vehicles [10], and to the magnetically levitated carrier system in clean rooms [11].

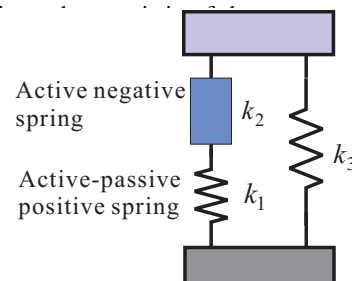


Fig 1. Principle of vibration isolation system using zero-power control

infinite stiffness by combing a mechanical positive spring with it is a very troublesome task, because a lot of mechanical springs are to be used to adjust both stiffnesses. This is one the obstacle to develop vibration isolation system using zero-power control.

Moreover, it can be noted that realizing negative stiffness can also be generalized by using linear actuator (voice coil motor) instead of hybrid magnet [13].

This paper demonstrates a control method of zero-power magnetic suspension system that has capability to adjust stiffness. This modified zero-power control introduces a proportional feedback of displacement to the original zero-power controller. The characteristics of the modified control system design are discussed analytically. Finally, a vibration isolation system is developed by connecting a mechanical spring in series with the modified zero-power control. Some experimental results are presented to show the efficacy of the control system, as well as the vibration isolation system.

## 2. PRINCIPLE OF VIBRATION ISOLATION

The vibration isolation system is developed to generate infinite (high) stiffness for direct disturbing forces and to maintain low stiffness for floor vibration. Infinite stiffness can be realized by connecting a mechanical spring in series with a magnetic spring that has negative stiffness [8, 9]. When two springs with spring constants of  $k_1$  and  $k_2$  are connected in series, the total stiffness  $k_c$  is given by

$$k_c = \frac{k_1 k_2}{k_1 + k_2}. \quad (1)$$

The above basic system has been modified by introducing a secondary suspension to avoid some limitations for system design and supporting heavy payloads [14]. The concept is demonstrated in Fig. 1. A spring  $k_3$  is added in parallel with the serial connection of positive and negative springs. The total stiffness  $\tilde{k}_c$  is given by

$$\tilde{k}_c = \frac{k_1 k_2}{k_1 + k_2} + k_3. \quad (2)$$

However, if one of the springs has negative stiffness that satisfies

$$k_1 = -k_2, \quad (3)$$

the resultant stiffness becomes infinite for any finite value of  $k_3$ , that is

$$|\tilde{k}_c| = \infty. \quad (4)$$

This research applies this principle of generating infinite stiffness against direct disturbance to the system. On the other hand, if low stiffness of mechanical springs for system ( $k_1, k_3$ ) are used, it can maintain good ground

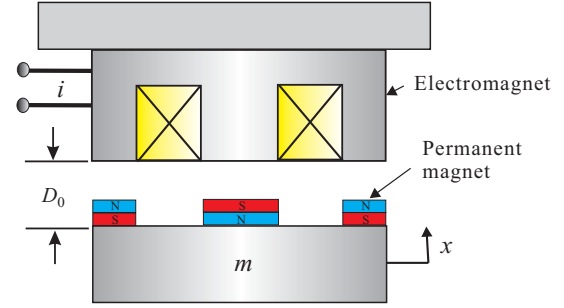


Fig 2. Basic model of zero-power control

vibration isolation performance as well.

## 3. ZERO-POWER CONTROL SYSTEM

Negative stiffness is generated by actively controlled zero-power magnetic suspension. The basic model, controller and the characteristic of the zero-power control system is described below.

### 3.1 Model

A basic zero-power controller is designed for simplification based on linearized equation of motions. It is assumed that the displacement of the suspended mass is very small and the nonlinear terms are neglected. The suspended object with mass of  $m$  is assumed to move only in the vertical translational direction as shown by Fig. 2. The equation of motion is given by

$$m\ddot{x} = k_s x + k_i i + w, \quad (5)$$

where  $x$ : displacement of the suspended object,  $k_s$ : gap-force coefficient of the permanent magnet,  $k_i$ : current-force coefficient of the electromagnet,  $i$ : control current,  $w$ : disturbance acting on the suspended object. The coefficients  $k_s$  and  $k_i$  are positive. When each Laplace-transform variable is denoted by its capital, and the initial values are assumed to be zero for

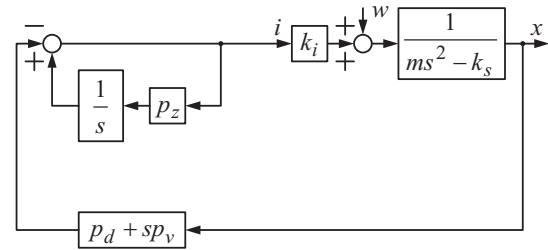


Fig 3. Block diagram of the zero-power controller

simplicity, the transfer function representation of the dynamics described by Eq. (5) becomes

$$\begin{aligned} X(s) &= \frac{1}{ms^2 - k_s} (k_i I(s) + W(s)) \\ &= \frac{1}{s^2 - a_0} (b_0 I(s) + d_0 W(s)), \end{aligned} \quad (6)$$

where  $a_0 = k_s / m$ ,  $b_0 = k_i / m$ , and  $d_0 = 1/m$ .

$$\lim_{t \rightarrow \infty} i(t) = \lim_{s \rightarrow 0} sI(s) = 0. \quad (12)$$

### 3.2 Zero-Power Controlled Negative Stiffness

Zero-power can be achieved either by feeding back the velocity of the suspended object or by introducing a minor feedback of the integral of current in the PD (proportional-derivative) control system [12]. Since PD control is a fundamental control law in magnetic suspension, zero-power control is realized from PD control in this research using the second approach. In the current controlled magnetic suspension system, PD control can be represented as

$$I(s) = -(p_d + p_v s)X(s), \quad (7)$$

where  $p_d$ : proportional feedback gain,  $p_v$ : derivative feedback gain. Figure 3 shows the block diagram of a current-controlled zero-power controller where a minor integral feedback of current is added to the PD control. The control current of zero-power controller is given by

$$I(s) = -(p_d + p_v s)X(s) + \frac{p_z}{s}I(s), \quad (8)$$

where  $p_z$ : integral feedback gain in the minor current loop. From Eqs. (6) to (8), it can be written as

$$\frac{X(s)}{W(s)} = \frac{(s - p_z)d_0}{s^3 + (b_0 p_v - p_z)s^2 + (b_0 p_d - a_0)s + a_0 p_z}, \quad (9)$$

$$\frac{I(s)}{W(s)} = \frac{-s(p_v + p_d)d_0}{s^3 + (b_0 p_v - p_z)s^2 + (b_0 p_d - a_0)s + a_0 p_z}. \quad (10)$$

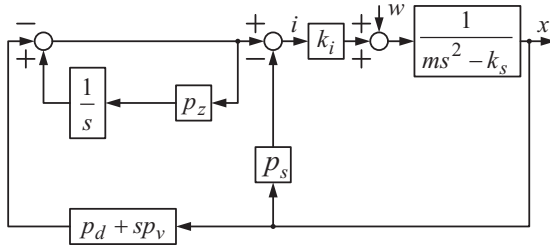


Fig 4. Block diagram of the modified zero-power controller that can adjust negative stiffness

To estimate the stiffness for direct disturbance, the direct disturbance,  $W(s)$  on the isolation table is considered to be stepwise, that is

$$W(s) = \frac{F_0}{s}, \quad (F_0 : \text{constant}). \quad (11)$$

From Eqs. (10) and (11)

It indicates that control current always converges to zero in the zero-power control for any load. The steady displacement of the suspension, from Eqs. (9) and (11), is given by

$$\lim_{t \rightarrow \infty} x(t) = \lim_{s \rightarrow 0} sX(s) = -\frac{d_0}{a_0} F_0 = -\frac{F_0}{k_s}. \quad (13)$$

The negative sign in the right-hand side illustrates that the new equilibrium position is in the direction opposite to the applied force. It means that the system realizes negative stiffness. Assume that stiffness of any suspension is denoted by  $k$ . The stiffness of the zero-power controlled magnetic suspension is, therefore, negative and given by

$$k = -k_s. \quad (14)$$

### 3.3 Stiffness Adjustment

The stiffness realized by zero-power control is constant, as shown in Eq. (14). However, it is necessary to adjust stiffness of the zero-power control system in many applications, such as vibration isolation systems. There are two approaches to adjust stiffness of the zero-power control system. The first one is by adding a minor displacement feedback gain to the zero-power control current, and the other one is by adding a proportional feedback in the minor current feedback loop [15]. In this work, stiffness variation capability of zero-power control is realized by the first approach. Figure 4 shows the block diagram of the modified zero-power controller that is capable to adjust stiffness. The control current of the modified zero-power controller is given by

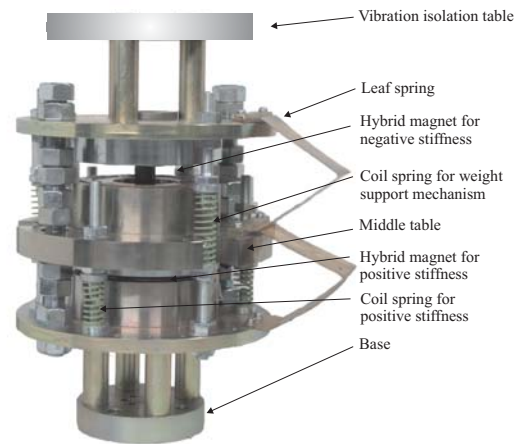


Fig 5. Photograph of the vibration isolation system

$$I'(s) = -\left(\frac{p_d s}{s - p_z} + p_v s + p_s\right)X(s), \quad (15)$$

where  $p_s$  : proportional displacement feedback gain across the zero-power controller.

The transfer-function representation of the dynamics shown in Fig. 4 is given by

$$\frac{X(s)}{W(s)} = \frac{(s - p_z)d_0}{s^3 + (b_0p_v - p_z)s^2 + (b_0p_d - a_0)s + a_0p_z + b_0p_s}. \quad (16)$$

From Eqs. (16) and (11), the steady displacement becomes

$$\begin{aligned} \lim_{t \rightarrow \infty} x(t) &= \lim_{s \rightarrow 0} sX(s) = -\frac{d_0p_z}{a_0p_z + b_0p_s} F_0 \\ &= -\frac{p_z}{k_s p_z + k_i p_s} F_0 \\ &= -\frac{F_0}{k_s + k_i p_s / p_z}. \end{aligned} \quad (17)$$

Therefore, the stiffness of the modified system becomes

$$k = -k_s - k_i \frac{p_s}{p_z}. \quad (18)$$

It indicates that the stiffness can be increased or decreased by changing the feedback gain  $p_s$ .

#### 4. EXPERIMENTAL SET UP

A single-axis vibration isolation system combining positive and negative stiffness suspension in series is shown in Fig. 5. It consisted of a circular base, a circular middle table and a circular isolation table. The height, diameter and weight of the system were 300mm, 200mm

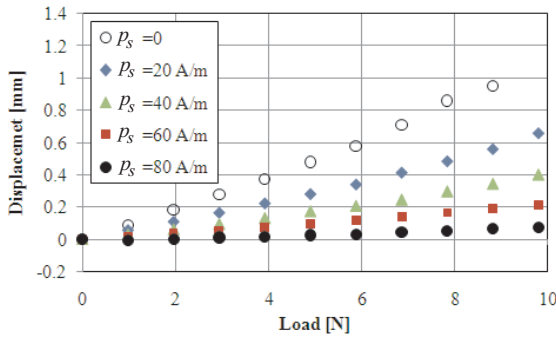


Fig 6. Load-displacement characteristics of the modified zero-power controller

and 20 kg, respectively. The relative displacement of the base to middle table was measured by an eddy-current displacement sensor, and positive stiffness was realized by a hybrid magnet consisted of an electromagnet (180-turns) that was fixed to the base, and four permanent magnets (15mm×2mm) attached to the

middle table. The permanent magnets are made of Neodymium-Iron-Boron (NdFeB). The middle table was also supported by three coil springs. The hybrid magnet and the coil springs were used in tandem to generate positive stiffness suspension. Another displacement sensor was used to measure the relative displacement between middle table to isolation table. A different hybrid magnet consisted of an electromagnet and six permanent magnets was used to realize negative stiffness. The isolation table was also supported by three coil springs as weight support mechanism.

The motion of the isolation table and that of the middle table were restricted to move only in the vertical direction. It was done by using a vertical shaft which was fixed to be base and passed through the center of the isolation table and middle table. The friction between the shaft and the isolation table and middle table were reduced to a minimum possible level by using suitable lubricant and ball bearings. Two additional threaded shaft and several hexagonal nuts were employed as stopper and limiter for the movement of the isolation table and the middle table. Two leaf springs were used to confine the rotational motions of the isolation table and middle table. These leaf springs were also behaved as damper for the both tables.

#### 5. EXPERIMENTAL RESULTS

The experiments have been carried out to measure the performances both for the modified zero-power controller, as well as for the vibration isolation system. Figure 6 shows the load-displacement characteristics of the system with the modified zero-power controller (Fig. 4). When the proportional feedback gain,  $P_s=0$ , it can be considered as a conventional zero-power controller (Fig. 3). The result shows that when the payloads were put on the suspended object, the table moved in the direction of load application, and gap was widened. It indicates that the zero-power control realized

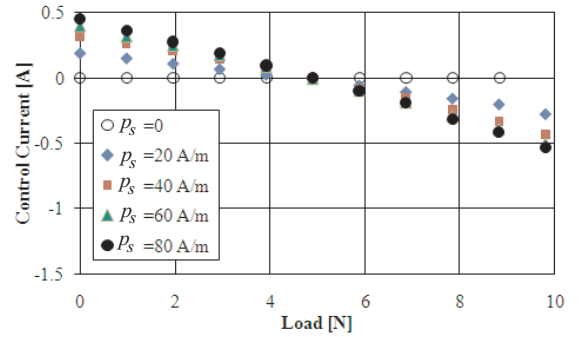


Fig 7. Load-current characteristics of the modified zero-power controller



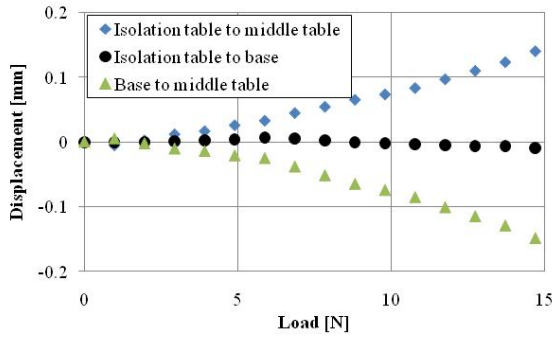


Fig 8. Zero-compliance characteristics of the isolation table to static direct disturbance using modified zero-power controller

negative displacement, and hence its stiffness is negative, as described by Eqs. (13) and (14). The conventional zero-power controller ( $P_s=0$ ) realized fixed negative stiffness of magnitude  $-9.2$  N/mm. When the proportional feedback gain,  $P_s$  was changed, the stiffness also gradually increased. When  $P_s=80$ A/m, negative stiffness was increased to  $-103.1$  N/mm. It confirms that proportional feedback gain,  $P_s$  can change the stiffness of the zero-power controller, as explained in Eq. (18).

Figure 7 shows the load-current characteristics of the zero-power controller. The control current necessary for the conventional zero-power controller ( $P_s=0$ ) was always zero. It proves the analysis described in Eq. (12). When the gain  $P_s$  was increased, a minor control current was necessary. The maximum control current for  $P_s=80$ A/m was  $\pm 0.5$ A up to 10 N load. However, the zero-power characteristic can be restored again by adjusting the weight support spring, once the system is stabilized.

Finally, experiments have been carried out with the developed vibration isolation system. Zero-compliance characteristics of the isolation table to static direct disturbance using modified zero-power controller is shown in Fig. 8. In this case, stepwise static direct disturbance in the vertical direction of the table was generated by putting payloads on the center of the table. The displacements of the isolation table to middle table and that of the middle table to base were measured by eddy-current displacement sensors. It is seen from the figure that positive stiffness was realized between base to

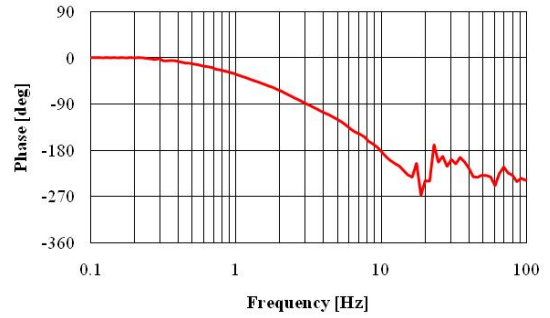
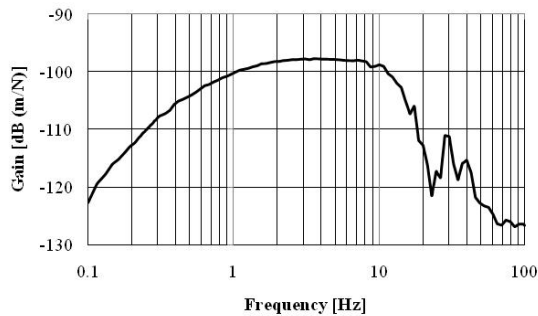


Fig 9. Frequency response of the isolation table to dynamic direct disturbance

middle table, and negative stiffness was realized between isolation table to middle table. Zero-compliance to direct disturbance of the isolation table to base was achieved when Eq. (3) was satisfied. In other words, an infinite stiffness of the isolation system was realized that confirms Eq. (4). At higher load, the zero-compliance characteristic may be lost due to the nonlinearity of the zero-power control system. A nonlinear compensation to zero-power controller can solve such problem [16].

Figure 9 shows the frequency response of the isolation table to dynamic direct disturbance. In this experiment, the isolation table was excited by an electromagnet which was fixed to the base above the isolation table. The displacement of the table was considered as output in this case. The frequency response was measured by a dynamic signal analyzer. The result shows that the table generated very low displacement at the low frequency region. The displacement of the table at 0.1 Hz was  $-122$  dB [m/N]. It confirms that isolation table generated very high stiffness at low frequency dynamic direct disturbance.

Finally, step response of the developed vibration isolation system was measured as shown in Fig. 10. An electromagnet was employed to generate stepwise disturbance [0 to  $-10$ N] at 0.25 Hz. The results demonstrate that the gap between isolation table to middle table was increased and the displacement of the middle table to base was decreased for downward disturbance on the table. However, the isolation table returned to the original position within 0.5s. The displacement and transient period to return to the original position can further be reduced by introducing feedforward control with the zero-power control system.

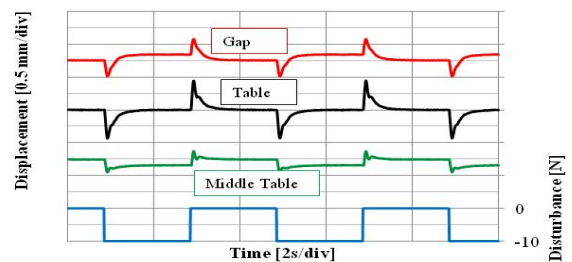


Fig 10. Step response of the isolation table



## 6. CONCLUSIONS

A vibration isolation system has been developed by combining an active zero-power control with mechanical springs. The zero-power control is modified by introducing a proportional displacement feedback to the zero-power control current. The modified zero-power controller yielded negative stiffness with the capability of adjusting negative stiffness. The concept was investigated by some experiments. The experimental results showed that the stiffness of the magnetic suspension system depends on the proportional gains of the displacement feedback. The modified zero-power control had wide stiffness range, and could be applied to develop vibration isolation system. The system can further be improved by providing minor current feedback to the integral of the zero-power control system.

A single-degree-of-freedom vibration isolation system has been developed using the fixed positive suspension and the modified zero-power controller. Infinite stiffness of the isolation system was realized when the negative stiffness was equal in magnitude with the positive stiffness. The static and dynamic response of the isolation table showed that the developed isolation system could effectively suppress the effect of direct disturbance.

## 7. ACKNOWLEDGMENT

The authors gratefully acknowledge the financial support made available from Japan Society for the Promotion of Science (JSPS) as a Grant-in-Aid, and from the Ministry of Education, Culture, Sports, Science Technology of Japan, as a Grant-in-Aid for Scientific Research (B).

## 8. REFERENCES

1. Rivin, E. I., 2003, "*Passive Vibration Isolation*," ASME Press, New York.
2. Harris, C. M., 1996, "*Shock and Vibration Handbook*," McGraw Hill, 4<sup>th</sup> Ed., New York.
3. Yoshioka, H., Takahashi, Y., Katayama, K., Imazawa, T., and Murai, N., 2001, "An Active Microvibration Isolation System for Hi-Tech Manufacturing Facilities," *ASME Journal of Vibration and Acoustics*, 123:269-275.
4. Benassi, L., Elliot, S. J., and Gardonio, P., 2004, "Active Vibration Isolation Using an Inertial Actuator with Local Force Feedback Control," *Journal of Sound and Vibration*, 276(3):157-179.
5. Daley, S., Hatonen, J., and Owens, D. H., 2006, "Active Vibration Isolation in a "Smart Spring" Mount Using a Repetitive Control Approach," *Control Engineering Practice*, 14:991-997.
6. Yasuda, M., and Ikeda, M., 1993, "Double-Active Control of Microvibration Isolation Systems to Improve Performances (Application of Two-Degree-of-Freedom Control)," *Transactions of the Japan Society of Mechanical Engineers, Series C (in Japanese)*, 59(562): 1694-1701.
7. Yasuda, M., Osaka, T., and Ikeda, M., 1996, "Feedforward Control of a Vibration Isolation System for Disturbance Suppression," *Proc. of the 35<sup>th</sup> Conf. on Decision and Control*, Japan, pp.1223-1228.
8. Mizuno, T., 2001, "Proposal of a Vibration Isolation System Using Zero-Power Magnetic Suspension," *Proc. of the Asia-Pacific Vibration Conference*, pp. 423-427.
9. Hoque, M. E., Takasaki, M., Ishino, Y., and Mizuno, T., 2006, "Development of a Three-Axis Active Vibration Isolator Using Zero-Power Control," *IEEE/ASME Transactions on Mechatronics*, 11(4):462-470.
10. Sabnis, A. V., Dendy, J. B., and Schmit, F. M., 1975, "A Magnetically Suspended Large Momentum Wheel," *Journal of Spacecraft*, 12: 420-427.
11. Morishita, M., Azukizawa, T., Kanda, S., Tamura, N., and Yokoyama, T., 1989, "A New Maglev System for Magnetically Levitated Carrier System," *IEEE Transactions on Vehicular Technology*, 38(4): 230-236.
12. Mizuno, T., and Takemori, Y., 2002, "A Transfer-Function Approach to the Analysis and Design of Zero-Power Controllers for Magnetic Suspension Systems," *Electrical Engineering in Japan*, 141(2):933-940.
13. Mizuno, T., Furushima, T., Ishino, Y., and Takasaki, M., 2007, "General Forms of Controller Realizing Negative Stiffness," *Proc. of the SICE Annual Conference 2007*, Kagawa University, Japan, Sept. 17-20, 2007, pp. 2995-3000.
14. Mizuno, T., Hoque, M. E., Takasaki, M., and Ishino, Y., 2006, "Development of A Six-Axis Hybrid Vibration Isolation System Using Zero-Power Control," *Proc. of the 45<sup>th</sup> IEEE Conference on Decision and Control*, San Diego, USA, paper no. 1400, pp. 6531-6536.
15. Ishino, Y., Mizuno, T., and Takasaki, M., 2009, "Stiffness Control of Magnetic Suspension by Local Feedback," *Proc. of the European Control Conference 2009*, Budapest, Hungary, 23-26 August, 2009, pp. 3881-3886.
16. Hoque, M. E., Mizuno, T., Takasaki, M., and Ishino, Y., 2006, "A Nonlinear Compensator of Zero-Power Magnetic Suspension for Zero-Compliance to Direct Disturbance," *Transaction of the Society of Instrument and Control Engineers*, 42(9):1008-1016.

## THEORETICAL AND NUMERICAL OPTIMIZATION OF AUTOFRETTAGE IN STRAIN HARDENED THICK-WALLED CYLINDERS.

Nidul C. Ghosh<sup>1</sup>, Tanvir-E-Alam<sup>2</sup>, A. R. M. Ali<sup>3</sup>.

Department of Mechanical engineering, BUET, Dhaka, Bangladesh.

### ABSTRACT

The optimum autofrettage pressure and the optimum radius of elastic-plastic junction of strain-hardened thick walled cylinders have been studied theoretically by finite element modeling. Equivalent von-mises stress is used as yield criterion. Influence of autofrettage on stress distribution and load-bearing capacity of a cylinder is studied and it has been observed that optimum autofrettage pressure is not a constant value rather depends on the working pressure. It has also been seen that to reduce the flow stress within the wall of the cylinder, the autofrettage pressure must be greater than the working pressure. For a particular working pressure, the effect of the ratio of outside to inside radius ( $b/a=k$ ) on the optimum autofrettage pressure is also observed. Maximum von-mises stress developed at different autofrettage pressure is compared for different material models. It has also been seen that the number of autofrettage stages has no effect on the maximum pressure carrying capacity of the cylinder.

**Keywords:** Autofrettage, thick wall cylinder, elastic plastic junction.

### 1. INTRODUCTION

The ever increasing industrial demand for axisymmetric pressure vessels which have applications in chemical, nuclear, fluid transmitting plant, power plant and military equipment, have concentrated the attention of designers on this particular area of engineering. Therefore, the prevention of pressure vessel failure to enhance safety and reliability has received considerable attention. On the other hand, the increasingly scarcity of materials and higher costs have led researchers not to confine themselves to the customary elastic regime but attracted their attention to the elastic-plastic along with optimization approach which offer more efficient use of materials. So the main concern is to increase the safety factor without increasing its weight. This purpose can be fulfilled successfully by means of autofrettage process. In this technique, the cylinder is subjected to an internal pressure so that its wall becomes partially plastic. The pressure is then released and the resulting residual stress lead to a decrease in the maximum von mises stress in the working loading stage. That means the increase in the pressure capacity of the cylinder in the next loading stage [1 & 2]. A key problem in the analysis of autofrettage process is to determine the optimum autofrettage pressure and corresponding radius of elasto-plastic boundary where the maximum equivalent von mises stress in the cylinder becomes

minimum. The analysis of residual stresses and deformation in an autofrettaged thick-walled cylinder has been given by Chen [3] and Franklin and Morrison [4]. Harvey's report [6] gave only a concept about autofrettage but detail result was missing. Brownell and Young [7], and Yu [8] proposed a repeated trial calculation method to determine the optimum radius of elastic plastic junction which was a bit too tedious and inaccurate; moreover this method is based on the first strength theory which is in agreement with brittle materials. But pressure vessels are generally made from ductile materials [9 & 10] which are in excellent agreement with the third or the fourth strength theory [11 & 13]. The graphical method presented by Kong [12] was also a bit too tedious and inaccurate. Based on the third and the fourth strength theory, Zhu and Yang [14] presented an analytic equation for optimum radius of elastic-plastic juncture,  $opt r$  in autofrettage technology. Ghomi & Majzoobi [15] proposed set of equations that used for determining optimum radius of elastic plastic junction. In the present work, Zhu & Yang's equations based on fourth strength theory are employed to predict the optimum autofrettage radius. Numerical simulation is done by using ANSYS for calculating optimum autofrettage pressure.

## 2. ANALYTICAL APPROACH

Bi-Linear elasto-plastic behavior has been considered in this work.

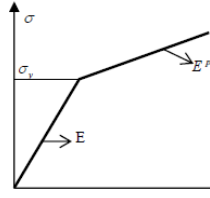


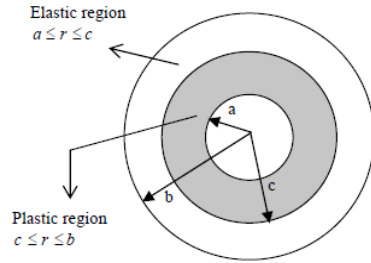
Fig 1. Bi-linear stress strain curve

The model, shown in figure 1 is described as follows:

$$\sigma = \sigma_y + E^p \hat{\epsilon} \quad (1)$$

In which  $\sigma$  is the effective stress,  $\sigma_y$  is the initial yield stress,  $E^p$  is the slope of the strain hardening segment of stress strain curve,  $\hat{\epsilon}$  is the effective strain.

Cylinder is subjected to autofrettage pressure and become partially plastic.



Ghomi & Majzoubi [16] proposed set of equations for determining radial and hoop stresses at different location along the cylinder wall in autofrettaged cylinder.

For the elastic-plastic material with linear strain hardening: In plastic region,  $a = r = c$ , for an internal pressure  $P$ :

$$\sigma_r = \frac{\sigma_y}{2} \left[ \left( 1 + \frac{c^2}{b^2} \right) + \ln \frac{c^2}{r^2} + (1-\nu^2) \frac{E^p}{E} \left( \frac{c^2}{r^2} - \frac{c^2}{b^2} \right) \right] \left[ 1 + (1-\nu^2) \frac{E^p}{E} \right] \quad (2)$$

$$\sigma_\theta = \frac{\sigma_y}{2} \left[ \left( 1 + \frac{c^2}{b^2} \right) - \ln \frac{c^2}{r^2} + (1-\nu^2) \frac{E^p}{E} \left( \frac{c^2}{r^2} - \frac{c^2}{b^2} \right) \right] \left[ 1 + (1-\nu^2) \frac{E^p}{E} \right] \quad (3)$$

When the cylinder is pressurized to the autofrettage pressure and the pressure is removed, the residual stress distribution across the wall of the cylinder can be expressed as follow [16]:

For elasto-plastic material:

Residual stresses in plastic region  $a = r = c$ :

$$\sigma_{rr} = \frac{\sigma_y \left( \frac{b^2}{r^2} - 1 \right) \left[ 1 - \frac{c^2}{b^2} + 2 \ln \frac{c}{a} + (1-\nu^2) \frac{E^p}{E} \left( \frac{c^2}{a^2} - \frac{c^2}{b^2} \right) \right]}{2(k^2 - 1) \left[ 1 + (1-\nu^2) \frac{E^p}{E} \right]} - \frac{\sigma_y \left[ 1 - \frac{c^2}{b^2} + 2 \ln \frac{c}{r} + (1-\nu^2) \frac{E^p}{E} \left( \frac{c^2}{r^2} - \frac{c^2}{b^2} \right) \right]}{2 \left[ 1 + (1-\nu^2) \frac{E^p}{E} \right]} \quad (4)$$

$$\sigma_{\theta\theta} = \frac{\sigma_y \left( \frac{b^2}{r^2} + 1 \right) \left[ 1 - \frac{c^2}{b^2} + 2 \ln \frac{c}{a} + (1-\nu^2) \frac{E^p}{E} \left( \frac{c^2}{a^2} - \frac{c^2}{b^2} \right) \right]}{2(k^2 - 1) \left[ 1 + (1-\nu^2) \frac{E^p}{E} \right]} + \frac{\sigma_y \left[ 1 + \frac{c^2}{b^2} - 2 \ln \frac{c}{r} + (1-\nu^2) \frac{E^p}{E} \left( \frac{c^2}{r^2} + \frac{c^2}{b^2} \right) \right]}{2 \left[ 1 + (1-\nu^2) \frac{E^p}{E} \right]} \quad (5)$$

Residual stresses in elastic region  $c = r = b$ :

$$\sigma_{rr} = \frac{\sigma_y \left( \frac{b^2}{r^2} - 1 \right) \left[ 1 - \frac{c^2}{b^2} + 2 \ln \frac{c}{a} + (1-\nu^2) \frac{E^p}{E} \left( \frac{c^2}{a^2} - \frac{c^2}{b^2} \right) \right] \sigma_y c^2 (b^2 - r^2)}{2(k^2 - 1) \left[ 1 + (1-\nu^2) \frac{E^p}{E} \right] 2b^2 r^2} \quad (7)$$

$$\sigma_{\theta\theta} = \frac{-\sigma_y \left( \frac{b^2}{r^2} + 1 \right) \left[ 1 - \frac{c^2}{b^2} + 2 \ln \frac{c}{a} + (1-\nu^2) \frac{E^p}{E} \left( \frac{c^2}{a^2} - \frac{c^2}{b^2} \right) \right] \sigma_y c^2 (b^2 - r^2)}{2(k^2 - 1) \left[ 1 + (1-\nu^2) \frac{E^p}{E} \right] 2b^2 r^2} \quad (8)$$

If the cylinder is loaded again by the internal working pressure, by superposing the residual stresses due to autofrettage and the working pressure, the final stress distribution in the wall of the cylinder will becomes:

For elastic-plastic material:

Overall stresses in plastic region  $a = r = c$ :

$$\sigma_{rr} = \frac{\sigma_y \left( \frac{b^2}{r^2} - 1 \right) \left[ 1 - \frac{c^2}{b^2} + 2 \ln \frac{c}{a} + (1-\nu^2) \frac{E^p}{E} \left( \frac{c^2}{a^2} - \frac{c^2}{b^2} \right) \right]}{2(k^2 - 1) \left[ 1 + (1-\nu^2) \frac{E^p}{E} \right]} - \frac{\sigma_y \left[ 1 - \frac{c^2}{b^2} + 2 \ln \frac{c}{r} + (1-\nu^2) \frac{E^p}{E} \left( \frac{c^2}{r^2} + \frac{c^2}{b^2} \right) \right]}{2(k^2 - 1) \left[ 1 + (1-\nu^2) \frac{E^p}{E} \right]} - \frac{P \left( \frac{b^2}{r^2} - 1 \right)}{k^2 - 1} \quad (9)$$

$$\sigma_{\text{ef}} = \frac{-\sigma_y \left( \frac{b^2}{r^2} + 1 \right) \left[ 1 - \frac{c^2}{b^2} + 2 \ln \frac{c}{a} + (1-\nu^2) \frac{E^p}{E} \left( \frac{c^2}{a^2} - \frac{c^2}{b^2} \right) \right]}{2(k^2 - 1) \left[ 1 + (1-\nu^2) \frac{E^p}{E} \right]} + \frac{\sigma_y \left[ 1 + \frac{c^2}{b^2} - 2 \ln \frac{c}{a} + (1-\nu^2) \frac{E^p}{E} \left( \frac{c^2}{r^2} - \frac{c^2}{b^2} \right) \right]}{2(k^2 - 1) \left[ 1 + (1-\nu^2) \frac{E^p}{E} \right]} + \frac{p \left( \frac{b^2}{r^2} + 1 \right)}{k^2 - 1}$$

(10)

Overall stresses in elastic region  $c = r = b$  :

$$\sigma_{\text{rf}} = \frac{\sigma_y \left( \frac{b^2}{r^2} - 1 \right) \left[ 1 - \frac{c^2}{b^2} + 2 \ln \frac{c}{a} + (1-\nu^2) \frac{E^p}{E} \left( \frac{c^2}{a^2} - \frac{c^2}{b^2} \right) \right]}{2(k^2 - 1) \left[ 1 + (1-\nu^2) \frac{E^p}{E} \right]} - \frac{\sigma_y c^2 (b^2 - r^2)}{2b^2 r^2} - \frac{p(b^2 - 1)}{k^2 - 1} \quad (11)$$

$$\sigma_{\text{ef}} = \frac{-\sigma_y \left( \frac{b^2}{r^2} + 1 \right) \left[ 1 - \frac{c^2}{b^2} + 2 \ln \frac{c}{a} + (1-\nu^2) \frac{E^p}{E} \left( \frac{c^2}{a^2} - \frac{c^2}{b^2} \right) \right]}{2(k^2 - 1) \left[ 1 + (1-\nu^2) \frac{E^p}{E} \right]} + \frac{\sigma_y c^2 (b^2 + r^2)}{2b^2 r^2} + \frac{p(b^2 - 1)}{k^2 - 1} \quad (12)$$

According to tresca yield criterion, the equivalent stress

$\sigma_{\text{eq}}$  can be defined as:  $\sigma_{\text{eq}} = \sigma = \sigma_{\text{e}} - \sigma_{\text{r}}$

$$\sigma_{\text{eq}} = \sigma = \sigma_{\text{e}} - \sigma_{\text{r}} \quad (13)$$

If the cylinder is intended to remain elastic throughout the loading process of the cylinder, then the equivalent stress should not exceed the yield stress of the material. i.e.:

$$\sigma_{\text{eq}} = \sigma_{\text{e}} - \sigma_{\text{r}} = \sigma_y \quad (14)$$

A simple case study:

Let's consider an Aluminum cylinder where internal radius,  $a = 0.01$  m and external radius,  $b = 0.02$  m. Material properties are summarized in table 1.

Table 1: Material properties

	$\sigma_y$ (MPa)	E (GPa)	$E^p$ (GPa)	$\nu$
Al	90	72	1.75	0.33

## 2.1 RESIDUAL STRESS PATTERN

This cylinder is subjected to an internal pressure so that its wall becomes partially plastic and the pressure is then released. Ghomi & Majzoubi [16] proposed set of equations for determining radial and hoop stresses at different location along the cylinder wall in autofretted cylinder. By using the equations the resulting residual stress pattern is shown in figure 2:

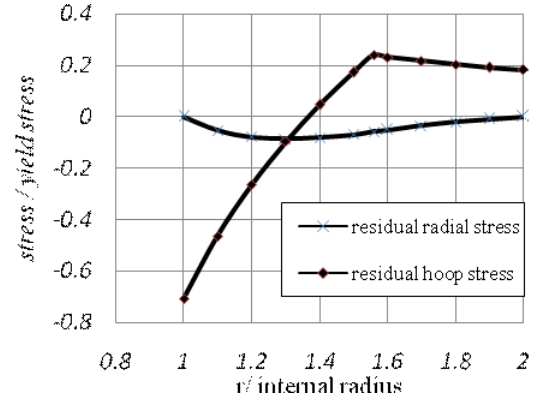


Fig 2. Residual Stress Distribution

From the figure, it is observed that residual compressive hoop stress occurs in near-bore region while residual tensile hoop stress occurs at outer portion. The resulting residual compressive hoop stress leads to a decrease in the maximum value of the von mises stress in the next loading stage.

## 2.2 Comparison Of Stresses With And Without Autofrettage

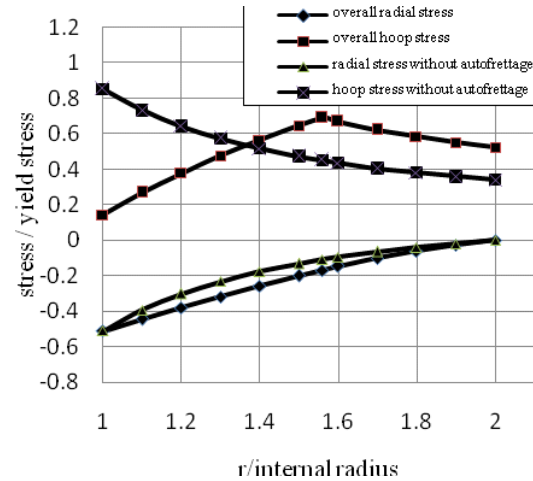


Fig 3. Comparison of Stresses with autofrettage and without Autofrettage.

By using Lamé's equation for thick wall cylinder the stress pattern is obtained. If the same cylinder undergoes autofrettage process then the overall stress pattern will change, which is shown on the graph. From figure 3, following points are observed:

Because of compressive hoop stress at inner bore, the resultant hoop stress becomes significantly lower in the

autofrettaged cylinder than the original hoop stress developed without autofrettage process at the same cylinder. Radial stress doesn't vary significantly after autofrettage process. The cylinder which undergoes autofrettage process has maximum stress occurring at the point of elasto-plastic junction.

### 2.3 OPTIMUM ELASTIC PLASTIC RADIUS

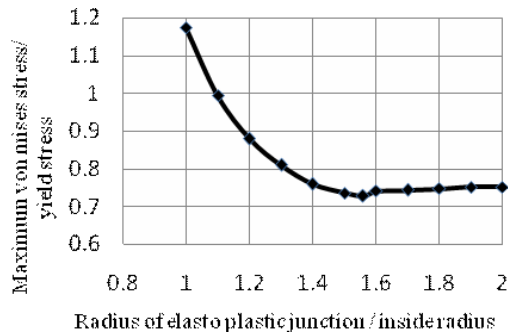


Fig 4. Maximum Von Mises Stress At Different Radius of Elasto Plastic Junction

When the ratio of radius of elasto plastic junction to inside radius equals to one (there is no autofrettage), then the maximum von mises stress exceeds yield stress, thus the material fails. Maximum von mises stress started to decrease as the radius of elastic plastic junction increases. After attaining a certain value of elastic plastic junction, maximum von mises stress started to increase. The point at which maximum von mises stress is minimum, is the optimum radius of elasto-platic junction.

### 2.4: Zhu & Yang Model For Optimum Elastic Plastic Radius

Zhu & Yang has developed an equation to determine  $opt r$  which we can calculate just using a pocket calculator.

(a) based on third strength theory,

$$r_{opt} = a \exp(p_w / \sigma_y) \quad (2)$$

(b) based on fourth strength theory,

$$r_{opt} = a \exp(\sqrt[3]{3p_w} / 2\sigma_y) \quad (3)$$

Ghomi & Majzoobi deduced  $r_{opt}$  by using MATLAB. For determining optimum radius of elastic plastic junction “Ghomi & Majzoobi’s model” and “Zhu & Yang’s model” are compared. It has been observed that these values vary between 5-7% only.

#### Sample calculation:

In this case study  $a=0.01m$ ,  $b= 0.02m$ , working pressure  $p_w = 46$  MPa.

From Zhu & Yang’s model,

Based on third strength theory  $r_{opt} = 0.01667$  m.

Based on fourth strength theory  $r_{opt} = 0.0156$  m.

From Ghomi & Majzoobi’s model (fig. 4), it is observed that  $r_{opt}$  is occurring in between 0.015 to 0.016 m. Indeed there is no significant variation between these two models.

Zhu Yang model based on fourth strength theory is considered for calculating  $opt r$  that simplifies the calculation.

### 3. NUMERICAL RESULTS

Single cylinder with the dimensions;  $a=0.1$  m,  $b=0.2$  m and an elastic plastic material’s model with  $\sigma_y = 800$  MPa; Modulus of elasticity  $E = 207$  GPa; Slope of the strain hardening segment  $E^p = 4.5$  GPa;  $i = 0.29$ ; were used for numerical modeling. The two pressure limits  $Py1$  and  $Py2$  can be computed as follows [1 & 17]:

$$Py1 = \sigma_y (1-1/k^2)/\sqrt{3}$$

$$=347 \text{ MPa}$$

$$Py2 = \sigma_y \ln(k)$$

$$=555 \text{ MPa}$$

If the autofrettage pressure is lower than 347MPa, then there will be no autofrettage effect. If the pressure is higher than 555MPa, then there will be converse effect. That means, instead of increasing, pressure capacity of the cylinder will decrease.

On this paper, effect of following factors is checked in autofrettage process. The considered factors are :

1. Working pressure; 2. Value of  $k$  ( $b/a$ ); 3. Material model (elastic perfectly plastic and elastic plastic with different slope of strain hardening segment); 4. Autofrettage Stages.

#### 3.1 Working Pressure

The cylinders were subjected to autofrettage pressures ranging from 350 MPa to 650 MPa. After removing the autofrettage pressure (AP), the cylinders were subjected to the working pressures(WP) of 100, 200, 300 and 400 MPa. From the numerical simulations, the curve of the von-Mises stress distribution was obtained for each autofrettage and working pressure (WP). From the curve, the value and the position of maximum von-Mises stress (MVS) were extracted. This stress and its position were then plotted versus autofrettage pressure for each working pressure. The results are shown in figure 5.

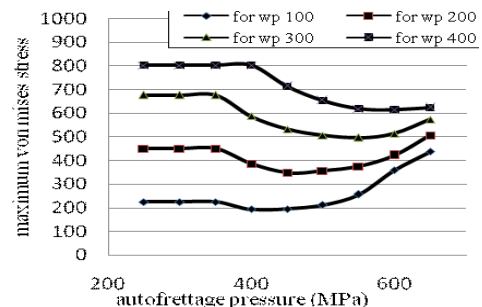


Fig 5. Variation of MVS versus autofrettage pressure at four working pressures.

It is observed that for each working pressure, the MVS remains constant up to an autofrettage pressure which is nearly equal to  $Py1$ . The curve then

begins to decline to a certain point thereafter, begins to rise or remains constant. It can be seen that for all working pressures, the rising portion of the curves end at a point which is nearly equal to  $P_{y2}$ .

From the numerical results, it can be concluded that: (i) The MVS depends on the working pressure and for any WP, the best AP lies between  $P_{y1}$  and  $P_{y2}$ ; (ii) For autofrettage pressures lower than  $P_{y1}$  and higher than  $P_{y2}$  the MVS remains unchanged; (iii) The position of MVS moves towards the outer radius as AP increases, (iv) For working pressure less than 300MPa, the autofrettage effect starts when the autofrettage pressure attain a value of 350 MPa. For working pressure 400MPa it is also observed that autofrettage pressure should be more than 400MPa to initiate the autofrettage effect. This means autofrettage pressure must be greater than the working pressure.

Table 2: Effect of working pressure at maximum von mises stress

WP (MPa)	MVS Without autofrettage (MPa)	MVS With autofrettage (MPa)	%Reduction Of MVS
100	225	193	14.22
200	450	348	22.67
300	676	496	26.62
400	840	615	26.78

For constant value of K, percent reduction of MVS is observed for different working pressures. From the table, it is observed that percent reduction of MVS is higher at higher working pressure. This means the autofrettage effect is more beneficial at higher working pressure.

### 3.2 Value Of K (B/A)

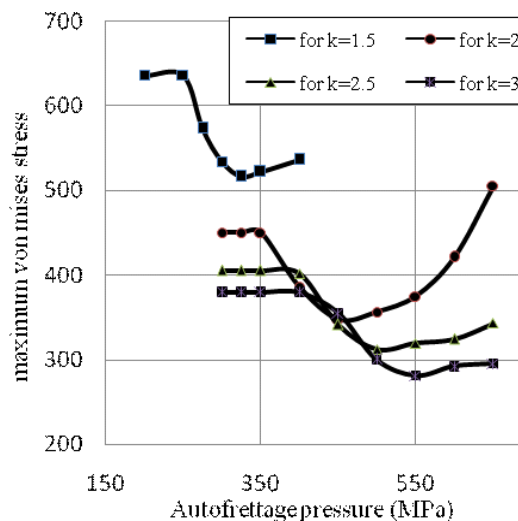


Fig 6. Effect of K (b/a) On Optimum Autofrettage Pressure

For constant working pressure (200 MPa) with different K values (inside radius constant), von mises stresses are observed for different autofrettage pressure. From graph, it is seen that optimum autofrettage pressure increases along with the k value.

Table 3: Effect of k (b/a) on MVS

K(b/a)	MVS Without autofrettage (MPa)	MVS With autofrettage (MPa)	%Reduction Of MVS
1.5	636	516	18.88
2.0	450	348	22.67
2.5	405	312	22.97
3.0	380	281	26.05

For constant working pressure, percent reduction of MVS is observed for different value of K. From the table 3, it is observed that the percent reduction of MVS is higher at higher values of K. This means the autofrettage effect is more beneficial with the increase of the thickness of the cylinder wall.

### 3.3. Material model

For working pressure of 200 MPa, the cylinder is subjected to autofrettage pressure ranging form 250 to 700 MPa. Here, the material of cylinder wall is varied form elastic perfectly plastic ( $E^p= 0$ ) to elastic plastic with different slope of strain hardening segment ( $E^p= 4.5, E^p= 30, E^p= 50$ ). From the numerical simulations, the curve of von-Mises stress distribution was obtained for each autofrettage pressure and different material models. From the curve, the value and the position of the maximum von-Mises stress (MVS) were extracted.

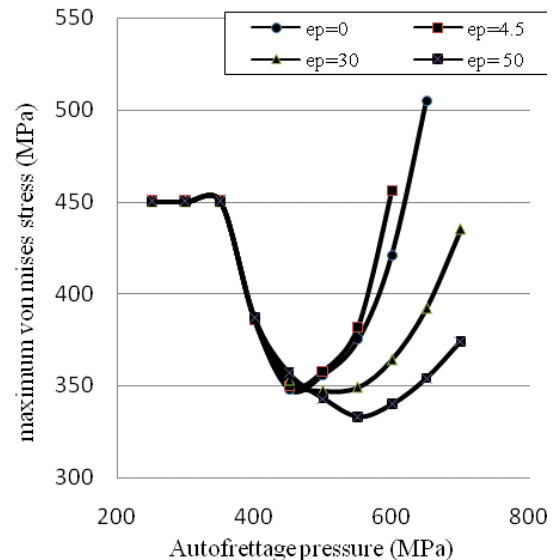


Fig 7. Effect of Material Model on Optimum Autofrettage Pressure

From the graph, it is observed that von mises stress varies in nominal manner in between  $P_{y1}$  (347MPa) and



Py2 (555 MPa). Variation becomes significant after exceeding Py2. The optimum autofrettage pressure is higher at higher value of the slope of strain hardening segment. The resultant von mises stress decreases as the slope of the strain hardening segment increases. So if the cylinder wall material has higher value of slope of strain hardening segment, then the autofrettage process can give us much more benedictions.

### 3.4. Autofrettage Stages

Consider a cylinder with working pressure of 300 MPa, where autofrettage pressure is 500 MPa. At first step, the autofrettage is done in three loading stages and at second step; autofrettage is done in nine loading stages. From the numerical simulation, it is observed that in both cases the MVS is 505 MPa and the stress pattern is almost similar. So there is no effect of loading stages on autofrettage process.

### 4. CONCLUSION

From the analytical and numerical results the following conclusions can be drawn:

1. In autofrettaged cylinder, maximum stress does not occur at inner bore instead, it occurs at the radius of elastic plastic junction. As the autofrettage pressure increases the point of maximum stress moves toward the outer bore.
2. Optimum autofrettage pressure is not a constant value rather it depends on the working pressure. The optimum autofrettage pressure increases along with the increase of working pressure.
3. For same working pressure, increasing the ratio of outer to inner radius K leads to an increase in the optimum autofrettage pressure.
4. It has also been observed that if the slope of strain hardening segment increases then the optimum autofrettage pressure also increases.
5. Because of autofrettage, percent reduction of maximum von mises stress increases for higher K value and for higher value of the slope of strain hardening segment.
6. Number of autofrettage stages has no effect on pressure capacity.

### 5. REFERENCES

1. T.Z Blazinski, Applied elasto-plasticity of solids, Hong-Kong: Macmillan, 1983.
2. GH Majzoobi, GH Farrahi, AH Mahmoudi, A finite element simulation and an experimental study of autofrettage for strain hardened thick-walled cylinders, J. Mater. Sci. Eng. A., vol. 359 pp. 326-31, 2003.
3. PCT. Chen, Stress and deformation analysis of autofrettaged high pressure vessels, ASME special publication, vol. 110, PVP. New York: ASME United Engineering Center; pp. 61-71, 1986.
4. G.J. Franklin, JLM. Morrison, Autofrettage of cylinders: prediction of pressure, external expansion curves and calculation of residual stresses Proceeding

of institute of Mechanical Engineers, vol. 174, pp. 947-74, 1960.

5. G.H. Majzoobi, G.H. Farrahi, M.K. Pipelzadeh and A. Akbari, Experimental and Finite Element Prediction of Bursting Pressure in Compound Cylinders, International Journal of Pressure Vessels and piping, vol 81, pp. 889-896, 2004.
6. J.F. Harvey, Theory and design of pressure vessels, New York: Van Nostrand Reinhold Company Ltd., 1985.
7. Brownell LE, Young EH. Process equipment design. New York: John Wiley & Sons, 1959.
8. G. Yu, Chemical pressure vessel and equipment (in Chinese). Beijing: Chemical Industrial Press, 1980.
9. E. David, An overview of advanced materials for hydrogen storage, Journal of Material Processing Technology, vol. 162-163, pp. 169-177, 2005.
10. H.H. Lee, J.H. Yoon, J.S. Park, Y.M. Yi, A study of failure characteristic of spherical pressure vessels, Journal of Material Processing Technology, vol. 164-165, pp. 882-888, 2005
11. AP Boresi, OM. Sidebottom, FB Seely, JO Smith, Advanced Mechanics of Materials, 3rd edition. New York: John Wiley & Sons, 1978.
12. F. Kong, Determining the optimum radius of the elastic-plastic juncture for thick-walled autofrettage cylinder by graphic method, (in Chinese), Petrochemical Equipment, 15:11, 1986.
13. S. Timshenko, Strength of Materials, New York: Van Nostrand Reinhold Company Ltd, 1978.
14. Ruilin Zhu, Jinlai Yang Autofrettage of thick cylinders, International Journal of Pressure Vessels and Piping, vol. 75 , pp. 443-446, 1998.
15. G.H. Majzoobi, A. Ghom Optimisation of autofrettage in thick walled cylinders of journal Achievements in Materials and Manufacturing Engineering volume 16 issue 1-2 may-june 2006.
16. A. Ghomi, Optimum Design of Thick-walled Pressure Cylinders (in Persian), MS.c final project, Bu-Ali Sina University, Hammadan, Iran, 2005.
17. GH. Majzoobi, A. Ghomi, Optimization of compound pressure cylinder, , Journal of Achievements in Materials and Manufacturing Engineering, In press, 2006.

### 6. NOMENCLATURE

Symbol	Meaning	Unit
a	Internal radius	(m)
b	External radius	(m)
$\sigma_{\text{er}}$	Residual hoop stress	(MPa)
$\sigma_{\text{rr}}$	Residual radial stress	(MPa)
$\sigma_{\text{rf}}$	Overall radial stress	(MPa)
$\sigma_{\text{ef}}$	Overall hoop stress	(MPa)
$P_w$	Working pressure	(MPa)

### 7. MAILING ADDRESS:

Nidul C. Ghosh  
 Department of Mechanical engineering,  
 BUET, Dhaka, Bangladesh.  
 Email: nidulme@yahoo.com  
 Phn:+08801717447151

## NUMERICAL ANALYSIS TO INVESTIGATE THE FIBER SIZE EFFECTS ON COMPOSITE STRENGTH

N.M. Awlad Hossain

Department of Engineering and Design, Eastern Washington University, Cheney, USA

### ABSTRACT

Currently many metallic structures are replaced with advanced composites to minimize the structural weight. The primary focus of this research was to examine the effects of fiber geometry to improve the strength of composites, and to pursue the possible advantages of using nanofibers instead of conventional fibers. Three different RVE models were analyzed where the fiber volume fraction kept constant through using reduced fiber diameter. Therefore, the surface area of fiber was increased gradually in each RVE model. The effects of fiber geometry were studied by comparing axial and shear stresses. As the cross sectional area of fiber remained the same in all RVE models, the axial stress of fiber was found relatively unchanged. The surface area of fiber was found important in shear stress distribution. The shear stress of fiber was found to be reduced significantly with increasing its surface area. An RVE model with the highest surface area of fiber was found to offer the lowest shear stress compared to the other RVE models. Therefore, if the composite strength depends on surface area of fiber, then a composite consisting of nanofibers will be stronger than a conventional composite prepared with same volume fraction, or conversely will be lighter at the same strength.

**Keywords:** Composite, Fiber Volume Fraction, Representative Volume Element.

### 1. INTRODUCTION

Structural weight reduction with improved strength is one of the targeted outcomes of composite materials. Currently, many metallic structures are replaced with advanced lightweight composites. The primary focus of this research was to examine the effects of fiber geometry to improve the strength of composite materials. The proposed research investigated the possible advantages of using nanofibers instead of conventional fibers. Mathematically, it can be shown that the nanofiber composite contains significantly more surface area over the conventional composite at no cost of volume fraction. The increased surface area can help to compensate for the imperfect bonding between the fiber-matrix interphase. Therefore, composite materials consisting of nanofibers are expected to offer higher strength than a conventional composite prepared with the same volume fraction.

Composite materials (or composites for short) are engineered materials made from two or more constituent materials with significantly different physical or chemical properties, and remain separate and distinct on a microscopic level within the finished structure. The two constituent materials are matrix and fiber (or reinforcement). The matrix material surrounds and supports the fiber materials by maintaining their relative positions. The fibers impart their special mechanical and physical properties to enhance the matrix properties. A synergism produces material properties unavailable from

the individual constituent materials, while the wide variety of matrix and fiber materials allows the designer of the product or structure to choose an optimum combination. Figure 1(a) represents a simplified concept of composite material with fiber and matrix constituents. Figure 1(b) depicts the Representative Volume Element (RVE) – the smallest cell, as shown by dotted line, to describe the individual composite constituents. The RVE is then divided into four subcells, as shown in Figure 1(c), all of rectangular geometry.

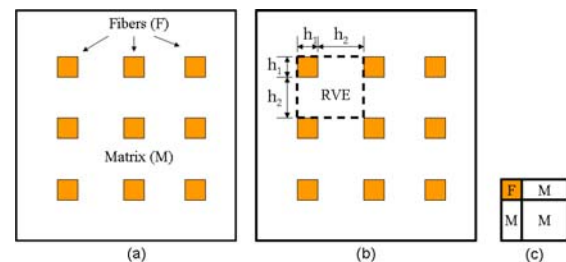


Fig 1. Simplified concept of composite materials and the Representative Volume Element (RVE).

In a series of papers documented by Dr. Jacob Aboudi [1, 2], the overall behavior of composite materials was explored through micromechanical analysis. The analysis was performed using an RVE approach to predict the elastic, thermoelastic,

viscoelastic and viscoplastic responses of composites. The composite material was assumed homogeneously anisotropic continuum without considering the interaction effects between fibers and matrix. Goh et al. [3] developed an analytical solution describing the average fiber stress ( $\sigma_f$ ), where the fiber was surrounded by an elastic matrix. The model proposed in [3] consists of a differential equation whose solution provided the distribution of fiber stress ( $\sigma_f$ ) and shear stress between fiber and matrix ( $\tau$ ) as a function of length. Expressions for ( $\sigma_f$ ) and ( $\tau$ ) were derived without considering the effect of fiber geometry and fiber-fiber interaction. According to the micromechanics theory, an increase in strength cannot be obtained from scaling fiber size while maintaining the same fiber volume fraction. Assuming a unit depth, volume fraction ( $V_f$ ) of fiber for the RVE model is defined as follows

$$V_f = \frac{h_1^2}{(h_1 + h_2)^2} \quad (1)$$

It can be seen that if the volume fraction is maintained while scaling  $h_1$  down, this will directly affect the value of  $h_2$ . Consequently, the ratio  $h_1/h_2$  in the micromechanics equation will remain the same, and therefore not affect the strength at all. In conclusion, higher strength to weight ratios cannot be obtained from scaling fiber size down at constant volume fraction.

One of the focal points of the proposed research was to determine the strength of composites by creating a more effective RVE model that incorporated the effects of fiber geometry. It has been suggested through other studies that the surface area ( $A_s$ ) of fibers plays an important role in strength of the composites. An advantage of using nanofibers is to increase the surface area, which can help to compensate for imperfect bonding. Figure 2 illustrates the concept of maintaining the same fiber cross-sectional area while increasing fiber surface area.

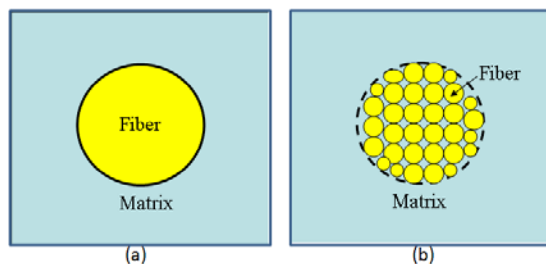


Fig 2. (a) Illustration of RVE of conventional composite with single unidirectional fiber. (b) Illustration of RVE of modified nanocomposite with many unidirectional fibers.

Mathematically it can be proved that the surface area of fiber in nanofiber composite will be higher than that of conventional composite by a factor of  $\sqrt{N}$ , where  $N$  represents the total number of nano fibers. Therefore, if the composite strength depends on fiber surface area, then a composite consisting of nanofibers will be stronger than a conventional composite prepared with

same volume fraction. However, this strength advantage is not apparent in Aboudi's micromechanics theory. The primary purpose of this research was to examine the effects of fiber geometry, and pursuing the possible advantages of utilizing nanofibers within composite materials.

## 2. ANALYSIS

### A. Numerical Models

Numerical models of conventional and nanofiber composites were developed using nonlinear finite element code ABAQUS and ANSYS. First, three different RVE models were developed as shown in Figure 3. For simplicity in the following sections, these numerical models are called RVE-1, RVE-2, and RVE-3. Note that all dimensions are in micrometer ( $\mu\text{m}$ ).

RVE-1, as shown in Figure 3(a), represents a conventional composite with one complete fiber connected with matrix. RVE-2, as shown in Figure 3(b) represents a nanofiber composite, with two nano fibers (one complete + four quarters) connected with matrix. Similarly, RVE-3, as shown in Figure 3(c), also represents a nanofiber composite with four nano fibers (one complete + 4 halves + 4 quarters). In RVE-2 and RVE-3, the fiber size was scaled down from radial dimension 5 micron to 3.5 micron and 2.5 micron, respectively. All RVE models have the same volume fraction of fiber (20%). The surface area of fiber in RVE-2 and RVE-3 was increased by 40% and 100%, respectively compared to the RVE-1. For analysis simplicity and to minimize the computational time, quarter symmetric models of the conventional and nanofiber composites, as shown in Figure 4, were used.

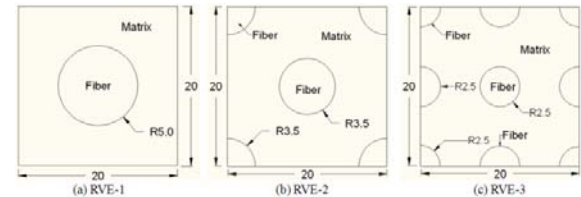


Fig 3. Illustration of different RVE model with increased fiber surface area while keeping the same fiber volume fraction.

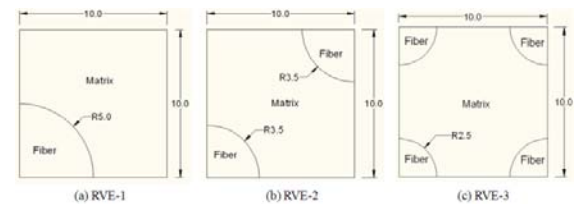


Fig 4. Quarter symmetric models of conventional and nanofiber composites used in the numerical analysis.

### B. Boundary Conditions and Loading

Numerical analyses were performed with the following boundary conditions and loading. For better understanding, a 3D view of the quarter symmetric conventional composite model is shown in Figure 5. The

entire back surface ( $z = 0$ ), which contains both fiber and matrix nodes, was constrained in its normal direction.

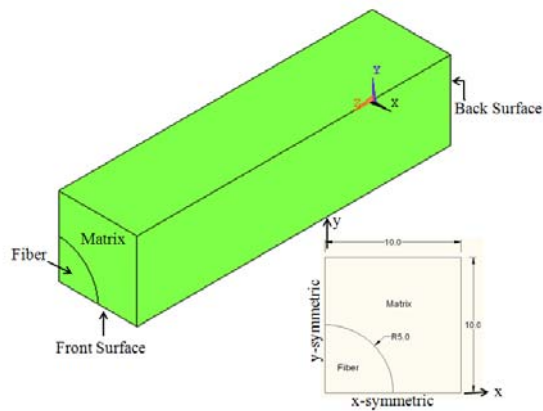


Fig 5. 3D view of the conventional composite model.

Symmetric boundary conditions were applied at the left and bottom edges. In addition, to constrain the rotational motion, two adjacent sides ( $x = 10$ , and  $y = 10$ ) were also constrained to their normal directions. Also, one node point on the back surface was pinned to prevent translation in the global  $x$ - and  $y$ - directions. Boundary displacement loading was assigned only to the matrix nodes of the front surface.

The fiber surface was connected by ties to all correlated matrix surface. The numerical model did not consider any interphase zone. The other quarter symmetric models, as shown in Figure 4, were also analyzed using the same boundary conditions and loading as discussed above.

### C. Material Properties

The materials properties are simply elastic and include Young's modulus and Poisson's ratio. Standard mechanical properties of E-glass and Epoxy were used to mimic the fiber and matrix, respectively.

## 3. RESULTS AND DISCUSSION

The following results were obtained when the entire back surface was constrained to its normal direction, and the boundary displacement was applied to matrix at the front surface. All three quarter symmetric models, as shown in Figure 4, were analyzed. For each case, axial and shear stress distribution of the fiber was studied. As the matrix region of nanofiber composite models has different geometry compared to the conventional composite, boundary displacement assigned to the nanofiber composites was tuned until they offered the same reaction force (at the back surface) found for the conventional composite model.

First, we compared the stress distribution of the RVE-1 and RVE-2. The axial stress distribution along a nodal path coincident with the fiber axis ( $x = 0$  and  $y = 0$ ) is shown in Figure 6. The cross sectional area of fiber remains the same between the conventional and nanofiber composite models. Therefore, the axial stress distribution was found to be fairly unchanged. The axial stress was found higher near the fixed end and gradually

decreased near the free end where load was applied. The numerical results match with expected outcomes.

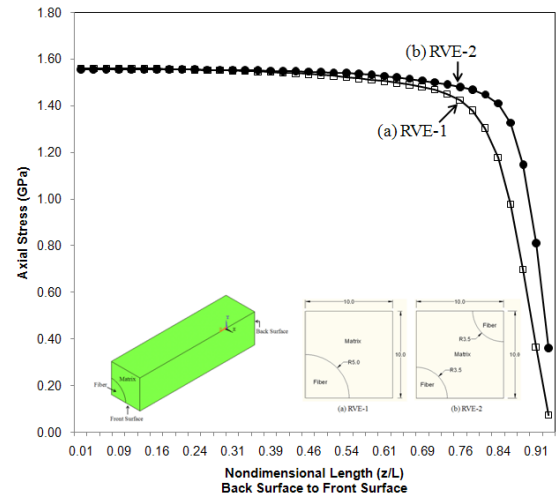


Fig 6. Axial stress ( $z$ -direction) distribution along the fiber axis between conventional and nanofiber composite models.

The shear stress distribution along a nodal path (at angular orientation  $\theta = 90$  degree – as named 12 o'clock section) on the topmost fiber layer is shown in Figure 7. The surface area of fiber was increased by 40% in the RVE-2 compared to the RVE-1. Therefore, the shear stress distribution in the RVE-2, representing a nanofiber composite, was found significantly reduced. A closer observation of the shear stress distribution, up to nondimensional length ( $z/L$ ) equal to 0.5, is shown in Figure 8. Shear stress in the RVE-2 was found to be reduced by approximately 50% compared to the RVE-1. Shear stress was also found to be smaller near the fixed end and increased exponentially towards the free end. The numerical results also match with expected outcomes.

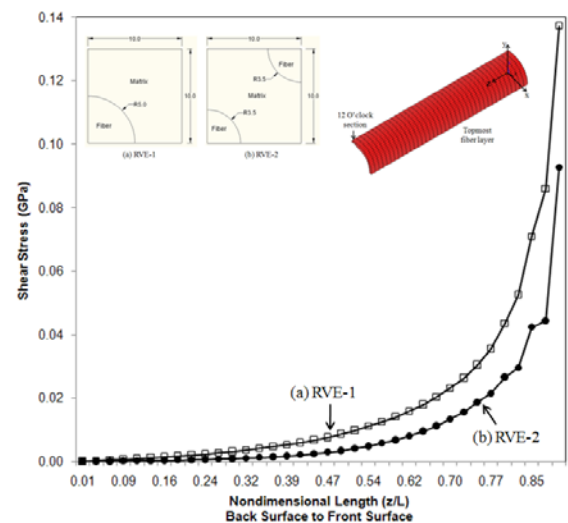


Fig 7. Shear stress distribution along a nodal path (at 12 o'clock section) on the topmost fiber layer between the conventional and nanofiber composite models.

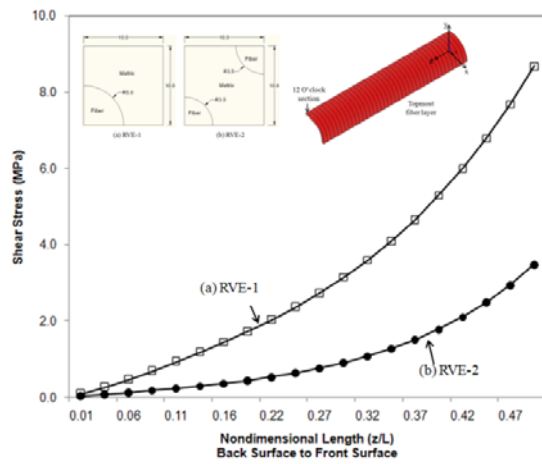


Fig 8. Shear stress ( $yz$ -direction) distribution along a nodal path (at 12 o'clock section) on the topmost fiber layer between the conventional and nanofiber composite. A closer view,  $z/L = 0$  to  $0.5$ , is shown.

The axial stress distribution along the fiber axis of all three different RVE models is shown in Figure 9. As the fiber cross sectional area is the same in each RVE model, the axial stress was found almost unchanged up to the nondimensional length ( $z/L$ ) equal to  $0.75$ . Some discrepancies were observed near the free end where boundary displacement was applied.

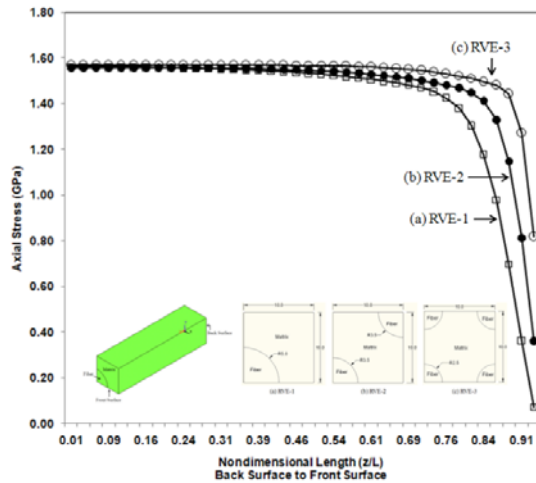


Fig 9. Axial stress ( $z$ -direction) distribution along a nodal path coincident to the fiber axis between the conventional and two other nanofiber composites.

On the other hand, the shear stress distribution of the topmost fiber layer of all three different RVE models is shown in Figure 10. The shear stress in the RVE-2 and RVE-3, representing nanofiber composites, was found to be reduced more with increasing the fiber surface area. The surface area of fiber in the RVE-3 is 60% more compared to the RVE-2. Subsequently, the shear stress in the RVE-3 was also found much smaller compared to the RVE-2.

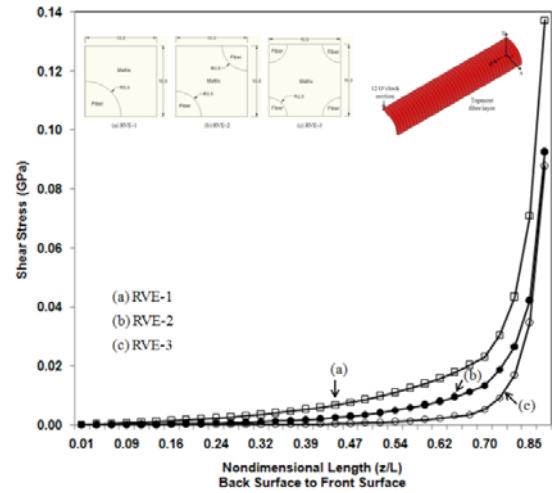


Fig 10. Shear stress distribution along a nodal path (at 12 o'clock section) on the topmost fiber layer between the conventional and two other nanofiber composite models.

For closer observation, the shear stress distribution of RVE-3, up to nondimensional length ( $z/L$ ) equal to  $0.50$ , is plotted separately with RVE-1 and RVE-2. These results are shown in Figures 11 and 12, respectively. The surface area of fiber in RVE-3 is increased by 100% compared to the RVE-1, and by 60% compared to RVE-2. Shear stress of the fiber, as shown in Figures 11 and 12, is expected to decrease more with further increment of its surface area.

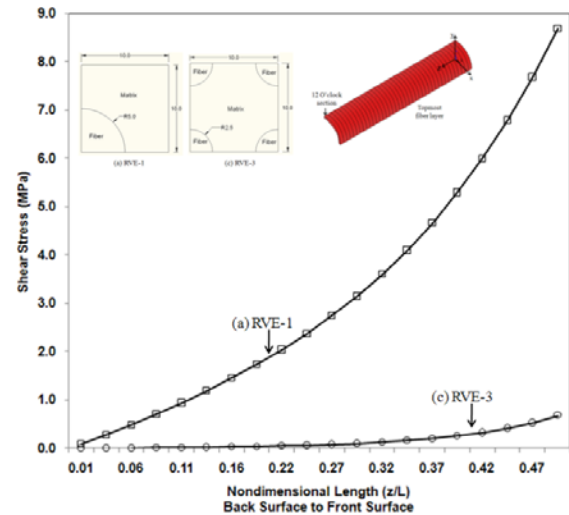


Fig 11. Shear stress ( $yz$ -direction) distribution along a nodal path (at 12 o'clock section) on the topmost fiber layer between the conventional and nanofiber composite, RVE-3.



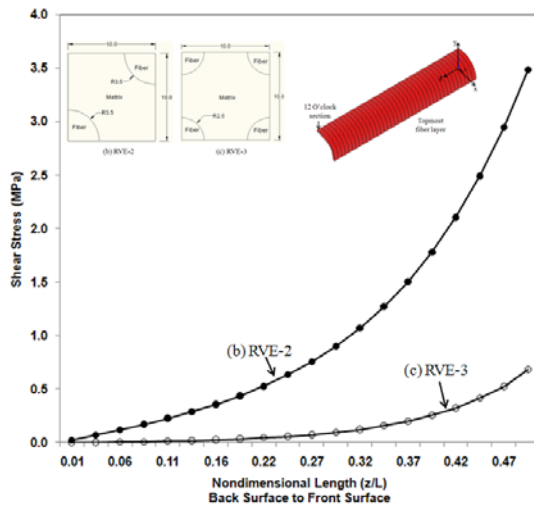


Fig 12. Shear stress (yz-direction) distribution along a nodal path (at 12 o'clock section) on the topmost fiber layer between two nanofiber composites RVE-2 and RVE-3.

Numerical simulation of the RVE models was then repeated with changing the boundary condition as follows. Instead of constraining the entire back surface, only the fiber nodes at the back surface were constrained to their normal z-direction. Therefore, matrix nodes at the back surface were released to translate along the global z-direction. Boundary displacement was assigned to the matrix nodes at the front surface, as used before.

The shear stress distribution of the three different RVE models is shown in Figure 13. Due to change in boundary condition, the shear stress distribution pattern observed in Figure 13 is significantly different from Figure 10. Shear stress was found to be smaller near the mid section and increased exponentially towards the fixed and free ends. However, as the surface area of fiber was increased in the RVE-2 & RVE-3, the shear stress in RVE-2 & RVE-3 was found significantly reduced compared to the RVE-1.

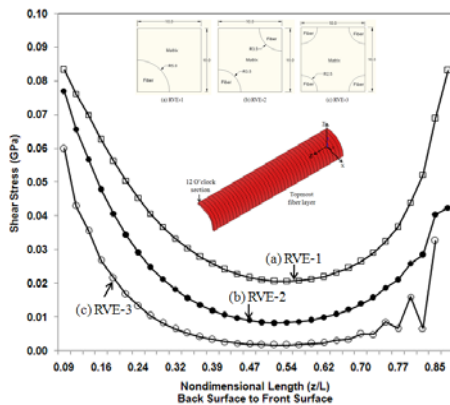


Fig 13. Shear stress (yz-direction) distribution along a nodal path (on 12 o'clock section) on the topmost fiber layer between conventional and two nanofiber composite models.

#### 4. CONCLUSION

In this paper, the effect of fiber geometry on composite strength was studied by numerical simulations. Three different RVE models were used where the surface area of fiber was increased gradually, keeping the fiber volume fraction constant. As the cross sectional area of fiber remained the same in all RVE models, the axial stress of fiber was found almost unchanged. The shear stress of fiber was found to be reduced significantly with increasing the surface area of fiber. An RVE model with the highest surface area of fiber was found to offer the lowest shear stress compared to the other RVE models. Numerical simulations were repeated with changing the boundary conditions. In all cases, an RVE model with increased surface area of fiber was found to offer reduced shear stress. Therefore, on the basis of shear stress developed in the fiber region, a composite consisting of nanofibers will be stronger than a conventional composite prepared with same fiber volume fraction, or conversely will be lighter at the same strength.

#### 5. REFERENCES

1. Aboudi, J., "Micromechanical Analysis of Composites by the Method of Cells," ASME, 1989.
2. Aboudi, J., "Micromechanics Prediction of Fatigue Failure of Composite Materials," Journal of Reinforced Plastic Composites, 1989.
3. Goh, K.L., Aspden, R.M., and Hukins, D.W.L., "Shear Lag Models for Stress Transfer from an Elastic Matrix to a Fiber in a Composite Materials," Int. J. Materials and Structural Integrity, Vol. 1, Nos. 1/2/3, 2007.

#### 6. NOMENCLATURE

Symbol	Meaning	Unit
RVE	Representative volume element	
$\sigma_f$	Fiber axial stress	(Pa)
$\tau$	Shear stress	(Pa)
$V_f$	Fiber volume fraction	
$h_1$	Dimension of fiber	( $\mu\text{m}$ )
$h_2$	Dimension of matrix	( $\mu\text{m}$ )
N	Number of nanofibers	

#### 7. MAILING ADDRESS

N.M. Awlad Hossain  
 Assistant Professor  
 Department of Engineering and Design  
 Eastern Washington University  
 Cheney, WA-99004, USA



## **\*Polyimide Nano-Hybrid : Enhance Mechanical-Thermal Performance**

**Shaikh Md. Mominul Alam, Ismat Ara, Mashud Ahmed**

College of Textile Technology, Tejgaon, Dhaka-1208, Bangladesh,

### **ABSTRACT**

Polyimide (PI) hybrids were synthesized from PI and inorganics like silica (1%) and polydimethylsiloxane (PDMS) (3%) through in-situ sol-gel process of inorganics. PI was prepared from 3, 3', 4, 4'-biphenyltetracarboxylic dianhydride (BPDA), p-phenylenediamine (PDA) (95%) and small amount of 4, 4'-Diamino-3, 3'dihydroxybiphenyl (HAB) (5%) to introduce poly(imide benzoxazole) unit in PI. These hybrids provided us higher performance in thermal properties like 5 and 10% degradation temperature, weight residue % at 800°C, glass transition temperature and mechanical properties like tensile modulus, strength, elongation at break (%) than pristine PI from BPDA, PDA. All the hybrids are also transparent.

**Key words:** Polyimide, Silica, Polydimethylsiloxane, sol-gel process.

***\*Full paper was not received before publication deadline***

## DETERMINATION OF CHIRALITY (n,m) OF SINGLE-WALLED CARBON NANOTUBES FROM ABSORPTION SPECTRA

M. Monzur Morshed, S. Arefin Siddiqui, Raju Sinha and S. Mohammad Mominuzzaman

Department of Electrical and Electronics Engineering,  
Bangladesh University of Engineering and Technology, Dhaka, Bangladesh

### ABSTRACT

Carbon nanotube sample-produced by alcoholic catalytic chemical vapor deposition (CVD) method on quartz substrate is analyzed using absorption spectroscopy. The sample on quartz substrate is in bundle state and the peak separation in the absorption spectrum is not much clear. However, the absorption spectrum of the sample is examined and a series of optical absorptions are identified. For this sample's spectrum, elemental Gaussian shape tends to dominate in the best curve fitting. On the basis of the electronic band theory, the spectral features are systematically assigned to the electronic transitions between pairs of van Hove singularities of semiconducting and/or metallic single wall nanotubes (SWNTs) and corresponding chiralities (n,m) and diameter distribution are determined.

**Keywords:** Single-walled Nanotubes (SWNTs), Alcohol Catalytic Chemical Vapor Deposition (ACCVD), Chirality (n,m).

### 1. INTRODUCTION

Carbon nanotube has become a promising material in various fields since its discovery due to its extraordinary electronic, mechanical, optical characteristics [1]. The most eye-catching features of these structures are their electronic, mechanical, thermal, optical and chemical characteristics, which has opened a way to future applications. For example, metallic nanotubes can carry an electrical current density of  $4 \times 10^9$  A/cm<sup>2</sup> which is more than 1,000 times greater than metals such as copper [2]. In terms of mechanical properties, nanotubes are among the stiffest (Young's modulus) and strongest (yield strength) materials yet measured. Their Young's modulus is 0.64 TPa [3–5], roughly five times greater than steel, which matches theoretical predictions [6]. Specially, its tunability in the wide range from soft to hard, semiconducting to metallic attracts the scientist in various fields of applications. However, electro-optical or mechanical properties are interrelated. Nanotubes can be single walled or multi walled, isolated or bundled. The properties of nanotubes strongly depend on chirality (n,m). Fundamental and practical nanotube researches have shown possible applications in the fields of energy storage, molecular electronics, nanomechanic devices, and composite materials. But before any research in any field, it is necessary to determine the type of carbon nanotubes, i.e. chirality. Carbon nanotubes are determined by the resonant Raman spectroscopy (RRS), photoluminescence spectroscopy (Spectrofluorometry), etc. RRS can give reliable results [7], but high resolution

of laser energy makes it difficult for use. And, photoluminescence can detect only semiconducting types and also cannot detect quenched, damaged or defective nanotubes. Absorption spectroscopy is a unique tool to characterize carbon nanotubes, to analyze its structure etc. Kataura et al. [8] first applied absorption spectroscopy to SWNTs and observed three absorption bands, originating from the overlapping van Hove transitions of varying size SWNTs. They also confirmed the inversely proportional relationship between the nanotube diameter and the energy of the absorption features, just as was predicted by theoretical calculation [9]. Here, we have determined the chirality (n,m) of carbon nanotubes in the sample produced by alcohol catalytic CVD method on quartz substrate using the optical absorption spectra of the sample. Estimated chirality of the nanotubes observed to be dependent on method of the synthesis and substrates. The investigation reveals interesting method of chirality estimation. Detailed analyses to obtain chirality of the nanotubes from absorption spectra will be reported in this paper.

### 2. EXPERIMENTAL DETAILS

This experimental section has been performed by the research group of Professor Shigeo Maruyama (Department of Mechanical Engineering, The University of Tokyo). A catalytic powder was prepared by impregnating iron acetate (CH<sub>3</sub>CO<sub>2</sub>)<sub>2</sub>Fe and cobalt acetate (CH<sub>3</sub>CO<sub>2</sub>)<sub>2</sub>Co-4H<sub>2</sub>O on to USY-zeolite powder (HSZ-390HUA, over 99% SiO<sub>2</sub>) [10-11]. The weight

concentration of Fe and Co was chosen to be 2.5 wt% each over the catalytic powder. Molybdenum acetate and cobalt acetate were employed for the catalytic loading on to the quartz substrate using a dip-coat technique. The adoption of Mo instead of Fe in the case of quartz is based on knowledge obtained by preliminary experiments. The schematic of the CVD apparatus and the procedure of the CVD are reported in elsewhere [12].

In brief, the specimen was placed on a quartz boat and the boat was set in the centre of a quartz tube (internal diameter = 26 mm, length = 1 m). One end of the quartz tube was connected to a rotary pump by two different paths, a 25 mm and a 6 mm diameter tube, to select the pumping power. The central 30 cm of the quartz tube was surrounded with an electric furnace. As the furnace was heated up from room temperature, a flow of about 300 sccm of Ar/H<sub>2</sub> (3% H<sub>2</sub>) was used, with only the smaller evacuation path open, to maintain the inside of the quartz tube at 300 ± 20 Torr. After the electric furnace reached the desired temperature, the Ar/H<sub>2</sub> flow was stopped and the larger evacuation path was opened to bring the inside of the quartz tube to vacuum. Subsequently, ethanol vapor was supplied from an ethanol reservoir at a constant pressure of 10 Torr into the quartz tube. After the CVD reaction, the electric furnace was turned off and brought back to room temperature with a 100 sccm flow of Ar/H<sub>2</sub>. CVD temperatures of 800°C was employed for the quartz substrate because this is the optimum temperature when ethanol vapor pressure is 10 Torr [12-14].

The VIS-NIR absorption spectra were measured with a HITACHI U-4000. Fig. 1 shows the absorption spectra of the sample in the visible and near-infrared ranges.

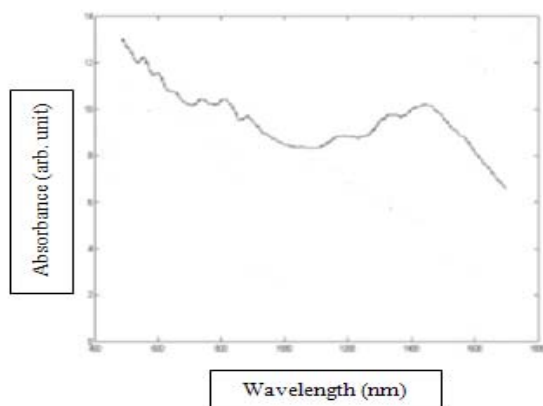


Fig 1. Optical absorption spectrum of alcohol catalytic chemical vapor deposition (ACCVD) single-walled nanotubes directly synthesized on a quartz substrate.

### 3. RESULTS AND DISCUSSIONS

In the optical spectra of SWNTs sample, three characteristic absorption bands are usually observed, superimposed on a broad background [15]. The first two bands are attributed to electronic transitions between the first and second pairs of VHSs in sem-SWNTs, and the last one to the first pair of singularity in *met*-SWNTs.

Demonstrated in Fig. 2 is the UV-VIS-NIR spectrum of ACCVD SWNTs directly synthesized on a quartz substrate in the range of 400-1700 nm after baseline

correction. The base line corrected absorption spectra are fitted with elemental Gaussian and Lorentzian shapes using our own matlab program. Sub peaks or shoulders are resolved here and these features could be correlated with a series of distinct electronic transitions between the pairs of VHSs of sem- and *met*-SWNTs.

According to the electronic band theory [16], the vertical interband transition energy between the *i*<sup>th</sup> pair of VHSs in both the valence and the conduction bands of a semiconducting (S) or metallic (M) nanotube (<sup>S,M</sup>*E*<sub>*ii*</sub>) are correlated with the diameter of the SWNT (*d*<sub>*t*</sub>) by

$${}^{S,M}E_{ii} = 2na_{C-C} \gamma_0 / d_t \quad (1)$$

Where *a*<sub>C-C</sub> is the nearest-neighbor carbon-carbon distance (~0.144 nm),  $\gamma_0$  is the nearest-neighbor carbon-carbon interaction energy (~2.9 eV), and *n* is an integer. <sup>S,M</sup>*E*<sub>*ii*</sub> corresponds to the first, second, third, fourth, and fifth interband transition of semiconducting SWNTs when *n* = 1, 2, 4, 5, and 7, and to the first and

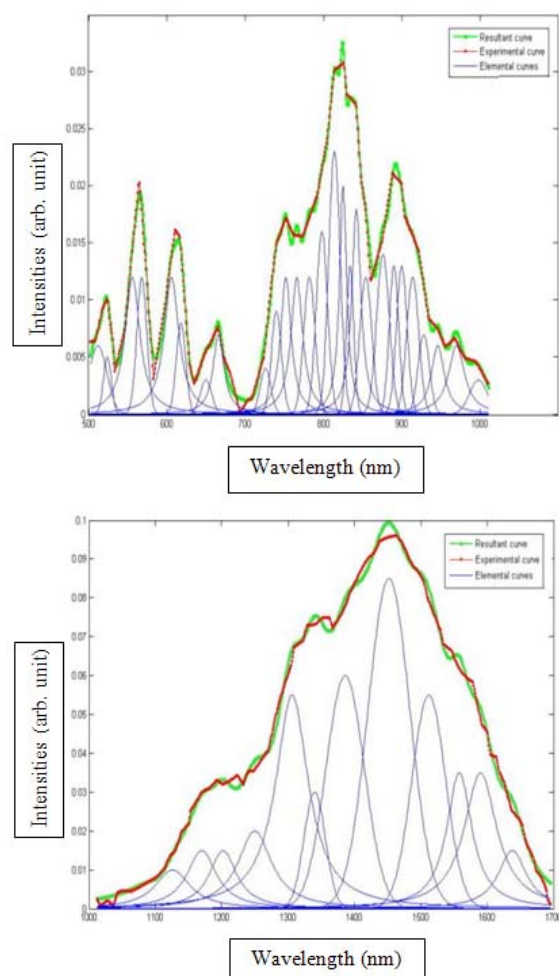


Fig 2. Optical absorption spectrum of alcohol catalytic chemical vapor deposition (ACCVD) single-walled nanotubes directly synthesized on a quartz substrate after background correction (the bold dot lines-experimental data) with Gauss-Lorentz fitting (the light solid and bold cross lines). Upper figure is for 500-1000nm and lower figure is for 1000-1700nm range.

second interband transition of metallic SWNTs when  $n = 3$  and  $6$ , respectively.

The diameter distribution and mean diameter can be obtained from the width and absorption maximum of this absorption band. After an energy calibration owing to Coulomb effects [17-18], mean diameter and diameter distributions are achieved (Table 1) for the SWNTs in the sample.

The sample grown on quartz substrate is in bundled state and the absorption peaks are not much clear. This has absorption peaks of slightly smaller energy. Observed in Fig 2 are fine structures, originating from the first inter band transitions of met-SWNTs and the first, second and third counterparts of sem-SWNTs. Analysis of them in details leads us to determine the diameter and chirality distributions and hence the chiral indices ( $n, m$ ) of SWNTs presented in the sample and the results are tabulated in Table 1.

Table 1: Spectral Data and Assignment of the Inter band Transitions and Chiral Indices of ACCVD SWNTs (grown on quartz substrate)

Abs. Wavelength (nm)	Inter band Transitions	Calculated Diameter (nm)	(n,m)
524	M <sub>11</sub>	1.057	(9,6)
556	M <sub>11</sub>	1.122	(8,8)
568	M <sub>11</sub>	1.146	(11,5)
604	M <sub>11</sub>	1.218	(10,7)
650	M <sub>11</sub>	1.311	(11,8)
724	S <sub>22</sub>	0.973	(9,5)
738	S <sub>22</sub>	0.99	(8,6)
774	S <sub>22</sub>	1.041	(8,7)
812	S <sub>22</sub>	1.092	(11,3)
892	S <sub>22</sub>	1.199	(11,6)
1176	S <sub>11</sub>	0.89	(7,6)
1216	S <sub>11</sub>	0.92	(11,1), (9,4)
1264	S <sub>11</sub>	0.956	(10,3), (8,6)
1310	S <sub>11</sub>	0.991	(9,5), (11,3)
1350	S <sub>11</sub>	1.021	(8,7), (12,1)
1398	S <sub>11</sub>	1.057	(10,5), (12,2)
1456	S <sub>11</sub>	1.102	(10,6), (13,2)
1508	S <sub>11</sub>	1.141	(12,4)
1548	S <sub>11</sub>	1.171	(13,3)
1580	S <sub>11</sub>	1.195	(12,5)

The average diameter for the sample grown on quartz substrate is found to be around 1.1nm with diameter distribution from 0.85nm to 1.35nm. For this sample's spectrum, elemental Gaussian shape tends to dominate in the best fitting. The ( $n, m$ ) assignment for both the sample have been calculated from the absorption spectra considering Coulomb effect for the first semi-conducting transition band (S<sub>11</sub>).

The relative abundance of the nanotubes with respect to diameters is shown in Fig 3. We have utilized the elemental curve areas in Fig 2 to find the relative distribution in Fig 3. We have also found that, semiconducting nanotubes are produced in much proportion than metallic nanotubes for the sample.

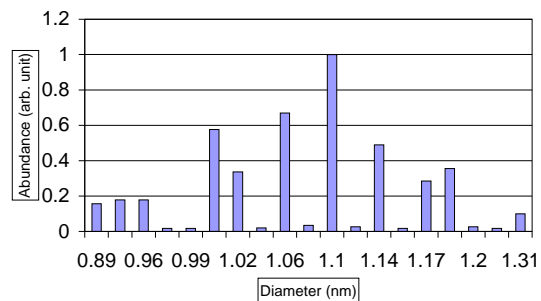


Fig 3. Abundance of nanotubes with respect to diameter in the sample grown on quartz substrate.

#### 4. CONCLUSIONS

There are different direct methods for characterization such as scanning electron microscopy (SEM), transmission electron microscopy (TEM), transmission electron diffraction, scanning tunneling microscope (STM) which are very delicate and can be destructive. On the other hand, there are quick and non-destructive methods using the optical properties of carbon nanotubes such as resonant Raman spectroscopy (RRS), photoluminescence and absorption spectroscopy. Here, we have worked with absorption spectroscopy and a detailed analysis of the optical properties of SWNT's of the sample produced on quartz substrate was presented.

The absorption properties of SWNTs is measured by using a technique of synthesizing a SWNT directly on to the surface of quartz substrates, by which any effects of post-treatments are excluded. From the absorption peaks in the spectra, the electronic state of the produced SWNTs is characterized since each peak corresponds to a band gap of the obtained SWNTs. Since the SWNTs on quartz are in the bundled state and not sonicated or dispersed in liquid at all, the peak separation is ambiguous.

Further study can be made using roughly estimates of the mixture ratio between semiconducting and metallic tubes from the intensities of absorption peaks in different samples as well as using abundance of produced nanotubes in different samples by analyzing the area of the elemental curves in the fitted resultant curve and all this estimation can be useful to establish a production technique with preferred and pre-selected chirality distribution.

#### 5. ACKNOWLEDGEMENT

The authors gratefully thank Professor Shigeo Maruyama (Department of Mechanical Engineering, The University of Tokyo) for sharing his experimental data and stimulating discussions.

#### 6. REFERENCES

1. Saito R, Dresselhaus G and Dresselhaus M S 1998 Physical Properties of Carbon Nanotubes (London: Imperial College Press).
2. Hong, Seunghun; Sung Myung (2007). "Nanotube Electronics: A flexible approach to mobility". Nature Nanotechnology 2: 207–208.
3. Treacy, M. M. J., Ebbesen, T. W., and Gibson, J. M.,

Exceptionally high Young's modulus observed for individual carbon nanotubes, *Nature* 381, 678–680, 1996.

4. Krishnan, A., Dujardin, E., Ebbesen, T. W., Yianilos, P. N., and Treacy, M. M.J., Young's modulus of single-walled nanotubes, *Physical Review B* 58, 14013–14019, 1998.
5. Yu, M.-F., Files, B. S., Arepalli, S., and Ruoff, R. S., Tensile loading of ropes of single-wall nanotubes and their mechanical properties, *Physical Review Letters* 84, 5552, 2000.
6. Gao, G., Agin, T., and III, Goddard, W. A., Energetics, structure, mechanical and vibrational properties of single-walled carbon nanotubes, *Nanotechnology* 3, 184, 1998.
7. Jorio, A.; Saito, R.; Hafner, J. H.; Lieber, C. M.; Hunter, M.; McClure, T.; Dresselhaus, G.; Dresselhaus, M. S. *Phys. Rev. Lett.* 2001, 86, 1118.
8. Kataura, H.; Kumazawa, Y.; Maniwa, Y.; Umezu, I.; Suzuki, S.; Ohtsuka, Y. Achiba, Y. *Synth. Met.* 1999, 103, 2555.
9. Hamada, N.; Sawada, S. I.; Oshiyama, A. *Phys. Rev. Lett.* 1992, 68, 1579.
10. Mukhopadhyay K, Koshio A, Tanaka N and Shinohara H 1998 *Japan. J. Appl. Phys.* 37 L1257
11. Mukhopadhyay K, Koshio A, Sugai T, Tanaka N, Shinohara H, Konya Z and Nagy J B 1999 *Chem. Phys. Lett.* 303 117
12. Murakami Y, Miyauchi Y, Chiashi S and Maruyama S 2003 *Chem. Phys. Lett.* 374 53.
13. Murakami Y, Yamakita S, Okubo T and Maruyama S 2003 *Chem. Phys. Lett.* 375 393.
14. Murakami Y, Miyauchi Y, Chiashi S and Maruyama S 2003 *Chem. Phys. Lett.* 377 49.
15. Kataura, H.; Kumazawa, Y.; Maniwa, Y.; Umezu, I.; Suzuki, S.; Ohtsuka, Y. Achiba, Y. *Synth. Met.* 1999, 103, 2555.
16. Charlier, J. C.; Lambin, Ph. *Phys. Rev. B* 1998, 57, R15 037.

17. Ichida, M.; Mizuno, S.; Saito, Y.; Kataura, H.; Achiba, Y.; Nakamura, A. *Phys. Rev. B* 2002, 65, 241407.
18. Pichler, T.; Knupfer, M.; Golden, M. S.; Fink, J.; Rinzler, A.; Smalley, R. E. *Phys. Rev. Lett.* 1998, 80, 4729.

## 7. NOMENCLATURE

Symbol	Meaning	Unit
${}^{SM}E_{ii}$	The vertical interband transition energy between the $i^{\text{th}}$ pair of VHSs in both the valence and the conduction bands of a semiconducting or metallic nanotube	(eV)
n	An integer	dimensionless
$a_{C-C}$	Nearest-neighbor carbon-carbon distance	(nm)
$\gamma_0$	Nearest-neighbor carbon-carbon interaction energy	(eV)
$d_t$	Diameter	(nm)

## 8. MAILING ADDRESS:

Muhammad Monzur Morshed,  
 Shamsul Arefin Siddiqui,  
 Raju Sinha  
 Sharif Mohammad Mominuzzaman.  
 Department of Electrical and Electronics Engineering,  
 Bangladesh University of Engineering and Technology,  
 BUET, Dhaka-1000, Bangladesh.  
 E-mail: momin@eee.buet.ac.bd,  
 Tel: (880 2) 8611594, Fax: (880 2) 8613046.

## DETERMINATION OF HARDENING MODULUS OF PLATINUM NANOWIRES

M. A. Salam Akanda, H. Tohmyoh and M. Saka

Department of Nanomechanics, Tohoku University, Japan

### ABSTRACT

In this study an experimental procedure together with finite element simulation procedure for determining the hardening modulus of Platinum nanowires is described. Platinum (Pt) wires with the nominal diameter of 625 nm are used for this study. The wire with suitable length is taken on a metallic substrate by nano welding just like a micro cantilever. A miniature setup for localized bending of the wire cantilever by using two opposite micro-probes under the continuous observation by a digital microscope is used. In the setup a force sensor, a piezo stage and two nano-manipulators have been accommodated on a single platform. The bending load is applied far from the root of the wire to ensure the failure in the wire across the loading point, and the load-displacement data are recorded. From the load-displacement data the elastic modulus and yield strength of the wire material are directly determined. For estimating the hardening modulus finite element (FE) analysis of the bending problem using the elastic modulus and yield strength with appropriate loading configuration has been performed. The hardening modulus of the Pt wires is successfully determined by fitting the load-displacement relationship obtained in FE analysis to the experimental one.

**Keywords:** Hardening Modulus, Finite element analysis, Pt nanowire.

### 1. INTRODUCTION

Knowing the mechanical properties of nanowires is of considerable interest for their uses as nanoscale interconnects and as the active components of electronic and electromechanical devices. An effective technique for quick evaluating the mechanical properties of the nanowires becomes necessary. Determination of elastic-plastic properties especially the hardening modulus is a difficult task. Among the conventional methods, tensile tests are superior in obtaining a stress-strain relation directly. For micro machined samples [1-3] the technique can effectively be used but handling of wire like samples on a nanometer scale is a difficult task, especially for holding with strong adhesive or grips or both, which makes it limited to micro- and millimeter-scale specimens [4-5]. In AFM based tensile tests the nanowire samples can be fixed with AFM tips by using deposition of metal or carbonaceous material [6]. But preparation of sample with such a technique having proper alignment is difficult and during testing most failures occur at the joint due to the combined effect of tension and bending. On the other hand, bending tests are comparatively easier test methods to handle a small size specimen than tensile tests, but there is a big hindrance to induce sufficient bending strain in nanowires. Elastic bending has been reported for various nanowires systems, and involve either positioning the wires across pores on substrates [7-9] or pinning one end of these wires to the substrate. In general, the bending configurations are not visible in these tests as the testing

is performed by applying force using AFM cantilever. In case of pinned wires, the flexure lengths are uncertain due to leakage of pinning materials in the shadow-mask process [10]. Atomic force microscope (AFM) and Nanoindentation techniques in evaluating the properties of nanomaterials are well reported. In AFM based tensile or bending tests, the samples are normally fixed on AFM tip or substrate. The roots of the samples on AFM tip or the substrate are very weak under mechanical loading. As a result it is often difficult to establish whether the measured failure is due to the wire itself or the contact between the wire and the AFM tip or the substrate. Moreover, in the AFM based technique, the deformation shape is difficult to be monitored during experiment. In nanoindentation techniques the results are sometimes qualitative and it can hardly predict the elastic-plastic behavior of materials. The methods available at present are not capable of providing reliable measures of nanowire strength or their behavior during plastic deformation and failure. Therefore, a reliable mechanical testing in evaluating their properties becomes indispensable.

In this study a smallscale bending test methodology with a new setup for the mechanical properties of nanowires is presented. The major limitations, i.e., failure at root, wire substrate friction, uncertainty in flexural length due to leakage of pinning material incase of pinned wire, etc., associated in the conventional techniques are removed and the elastic-plastic behavior of Pt nanowires is successfully determined.



## 2. EXPERIMENTAL DETAILS

### 2.1 Testing Methodology

Accurate estimation of nanowire mechanical properties by conventional tensile or bending tests is a difficult task. The bending technique is rearranged here in a way to overcome the major limitations. In this technique, a one end fixed beam is considered for small-scaled bending at its free end by closely positioned two opposite probes as shown in Fig. 1. The root A of the sample is considered rigidly fixed. The force  $P$  at B is considered very close to a fixed support at C. As the loading is considered close to the rigid support and far from the root of the sample, large bending can be obtained across the loading probe inducing a little bending at the root. Therefore, yielding of the wire can be induced across the loading probe without affecting the root by a large stress. The mechanical properties can be determined from the force-deformation relation obtained in this fashion.

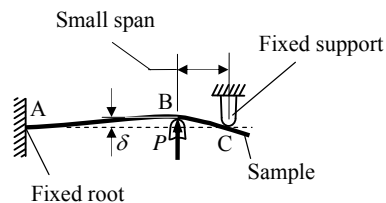


Fig 1. Bending configuration of Nanowire sample.

### 2.2 Sample Preparation

Nanomaterials prepared by chemical, electromigration or stressmigration processes are normally within the range of a few hundred microns in length. Manipulation of such a small sample in a testing base needs suitable carrier with proper gripping. In this study considering the above matter commercially available silver coated Pt nanowire as testing sample and Indium (In) wire as carrier for manipulating the sample are used for establishing a suitable testing methodology. The nominal diameter of Pt nanowire is 625 nm. The coated wire is cut into a small piece and glued on the tip of a small needle. The silver coating from the tip part of the wire is removed by inserting the free end into a nitric acid solution. The In wire with diameter of a few hundred microns is cut into small piece by scissors to have a sharp tip at the end. The In wire and the clean Pt wire are brought in tip to tip contact and joined by Joule-heat welding [11-12]. In the weld joining process properties of Pt are assumed to be unaltered as the melting point of In is very low compared to that of Pt. The Pt wire to form a micro cantilever on In carrier is cut to a desired length (about 200  $\mu\text{m}$ ) by Joule-heat cutting [11-12]. A number of samples prepared in this fashion are used for mechanical testing.

### 2.3 Test Setup

A setup is design and developed for bending the cantilever like micro/nanowire samples by using tiny loading probes in a testing base under a digital microscope. In the setup, a height adjustable rigid stand

for carrying support probe and two xyz-manipulators, one for carrying test sample and the other for carrying loading probe, are set on a single platform in similar height level. For measuring the force on the loading probe, it is placed on a force sensor. For computer controlled motion of the loading probe, the force sensor is attached to a piezo stage, which is placed on the xyz-manipulator. The initial setting of the loading probe to any desired xyz position can be done by using the manual manipulator and the precision control of the loading probe motion can be done by the piezo stage. The force sensor is devised as an integrated unit with the combination of a small capacitance sensor, an elastic cantilever and the loading probe as individual and interchangeable tools. The deflection of the cantilever due to forces at the loading tip causes change in gap distance between the cantilever head and the capacitive sensor. This change in gap distance or in other words the force on loading tip is calibrated with the capacitance sensor output.

### 2.4 Bending Test

The force sensor is set for measuring 0-25  $\mu\text{N}$  force with the rate  $1\mu\text{N}/\mu\text{m}$  by adjusting the pre-calibration length of the cantilever. The test base is taken on an anti-vibration table. The nanowire sample with the In substrate is taken on the carrier and fixed with a small piece of cellulose tape. By the nanomanipulators the sample is first set in contact with the fixed probe with desired length,  $L$  and then the loading probe is set in contact with the sample with the desired bending spans  $a$  and  $b$  as shown in Fig. 2. Note that the rigid stand contains an additional fixed probe, which is not used for bending test but for cleaning the dust (if any) from the sample or other probes. The manual manipulations of the

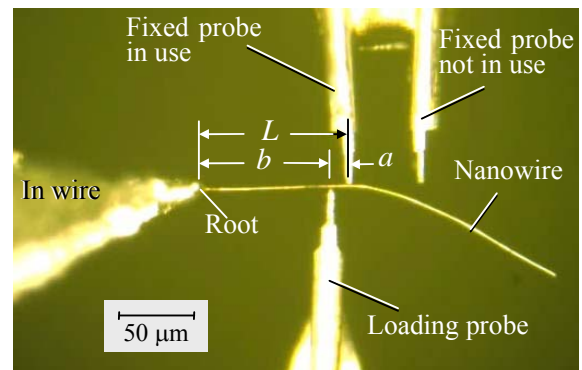


Fig 2. Bending parameters are shown on the microscopic image of the probe-sample assembly.

sample or the probes are performed precisely by the observation of the digital microscope. A computer controlled displacement (constant rate) is applied by the piezo stage and the corresponding capacitance change in potential is recorded. From these measurements the applied force and the corresponding deformation in the sample at loading point are determined. During the experiment the bending configuration of the sample is recorded as video clip by the digital microscope. Since  $a$  is very small compared to  $b$  during bending yielding

occurs only across the loading probe. After a test a large part of the length  $b$  remains unaffected and thus can be used for further bending test with shorter span. Three samples having different diameters have been tested. Several bending tests are performed on each sample with the variation of bending parameters ( $a$ ,  $b$  and  $L$ ). For any consecutive test the length,  $L$  is selected such that the material within it does not yielded in the former test. The option of the use of a single sample for multiple tests minimizes the number of individual samples need to be prepared and many tests can be performed in a short time in similar environmental condition.

### 3. RESULTS AND DISCUSSION

#### 3.1 Measured $P$ - $\delta$ relation and Bending Pattern

A typical force-displacement relationship obtained from experiment for a sample of diameter,  $d = 640$  nm with the flexural lengths,  $L = 100\mu\text{m}$  and  $a = 12\mu\text{m}$  is shown in Fig. 3. The little zigzags of the force-deformation curves are due to stick and slip for small friction between the probe and sample. As observed very good linearity in small deflection, the force-displacement data clearly depicts that very small forces (up to a few micronewtons) corresponding to the small deformation are precisely measured. Note that in Fig. 3 the horizontal axis indicates the displacement of loading-probe tip. The part AB of the curve shows no change in force but displacement of probe tip. This means for this part the loading probe was not in contact with the sample and contact starts at point B. Therefore, the true displacement of the sample can be determined by subtracting the displacement AB from the probe-tip displacement. The part BC shows linear force-deformation relationship for small deformation of few micrometers. This indicates the elastic bending of the wire. The force with deformation nonlinearly increases in part CD and then decreases in part DE. This confirms that plastic strain is induced in bending the wire.

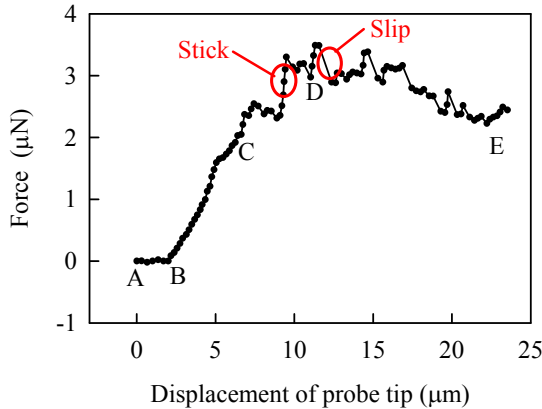


Fig 3. Measured force-displacement relation

#### 3.2 Evaluation of Properties

From the linear part of the force-deformation relation the elastic modulus of the wire material can be determined from the following equation [13].

$$E = \frac{Pb^4(2L+a)^2}{12L^3I\delta} - \frac{Pb^3}{3I\delta} \quad (1)$$

Here,  $I$  is the area moment of inertia of the wire cross section,  $P$  is the applied force,  $\delta$  is the corresponding deformation and the other parameters ( $a$ ,  $b$  and  $L$ ) are lengths as shown in Fig. 2. Using Eq. (1) the evaluated the average Young's modulus for the three samples under different loading spans is found to be  $134 \pm 22$  GPa. The estimated values for tensile modulus of the nanowires show reasonable agreement with their polycrystalline buck property.

The starting point of nonlinearity in force-deformation curve can be considered as yielding of material throughout the full cross section of the wire. As the hardening modulus of pure material is very small compared to Young's modulus, the stress distribution at this section can be considered as constant magnitude of yield stress  $\sigma_y$ . Therefore, for the loading configuration shown in Fig. 2 the yield stress,  $\sigma_y$  can be determined from the following formula [13].

$$\sigma_y = \frac{3P_y ab^2}{L^3 d^3} (2L+a) \quad (2)$$

where,  $P_y$  is the yield load corresponding to the starting point of nonlinearity in force-deformation curve and  $d$  is the diameter of the wire. Using Eq. (2) the evaluated average yield strength of the three samples for different loading spans is found as  $475 \pm 37$  MPa.

For FE analysis, the material is assumed linear-hardening elastic-plastic behavioral. The stress-strain relationship of such a material is given by

$$\varepsilon = \frac{\sigma}{E} \quad (\text{for } \sigma \leq \sigma_y), \quad (3)$$

and

$$\varepsilon = \frac{\sigma_y}{E} + \frac{\sigma - \sigma_y}{E'} \quad (\text{for } \sigma > \sigma_y), \quad (4)$$

where  $\varepsilon$ ,  $\sigma$ ,  $\sigma_y$ ,  $E$  and  $E'$  are strain, stress, yield strength, Young's modulus and hardening modulus respectively. The hardening modulus of wire material is determined from FE analysis by repeatedly doing the FE simulation till the load-displacement relationship obtained by FE analysis is coincident with the experimental one. The procedure is briefly described as follows. Let consider the particular experiment on a sample (diameter =  $770\text{nm}$ ) with loading parameters,  $L = 65\mu\text{m}$  and  $a = 12\mu\text{m}$  for FE model. The FE model is prepared with sufficient meshes and with proper boundary conditions that best suit the experimental conditions. At first the elastic FE analysis is performed on the model considering the Young's modulus obtained by Eq. (1) based on experimental data. The experimental data (round symbol) and the elastic FE analysis results (curve I) as force-displacement ( $P$ - $\delta$ ) relationships are plotted for comparison, see Fig. 4. The linear part (up to point B) of the experimental measurement show excellent matching with the elastic FE curve. This confirms that

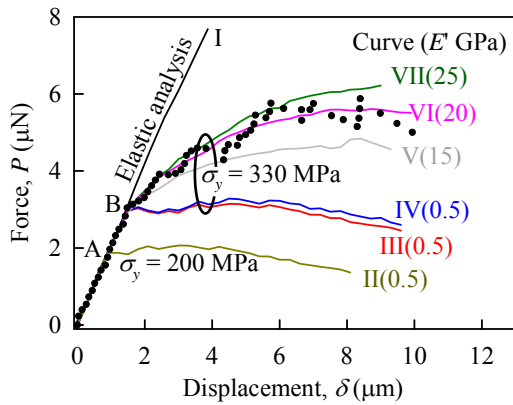


Fig 4. Finite element simulation

the measured force-displacement data are accurate. After that elastic-plastic FE analysis is performed based on the experimentally measured values for  $E$  and  $\sigma_y$ , and an assumed value for  $E'$ . In the elastic-plastic FE analysis the suitable values for  $\sigma_y$  and  $E'$  are looked into for which the best matching between FE and experimental  $P$ - $\delta$  relations is obtained. At first assuming a small value for  $E'$  the value of  $\sigma_y$  is adjusted in FE analysis. The curves II and III are for same  $E'$  (0.5 GPa) but for different values of  $\sigma_y$ , which are 200 and 330 MPa, respectively. These two curves clearly show their first-point of nonlinearities, i.e., points A and B. Note that with the increase in  $\sigma_y$  the point of nonlinearity moves from point A to point B; therefore it is easy to find the appropriate value of  $\sigma_y$  in FE simulation by a few trials. The curve III shows very good matching of the first point of nonlinearity with that of experimental measurements. Therefore, the value ( $\sigma_y = 330$ MPa) for curve III is considered appropriate and keeping this  $\sigma_y$  fixed the value of  $E'$  is adjusted in the FE simulation (see curves V-VII). Here it is observed that with the increase in  $E'$  the FE analysis curves become stiffened having the point of nonlinearity (point B) unchanged. Note that all the curves described above are obtained for a friction coefficient of 0.1 between the probe and sample. The curve IV is obtained for the same properties of curve III but the friction coefficient of 0.2. These two curves are very close therefore the friction coefficient has a little effect on the  $P$ - $\delta$  relation. In all analysis the friction coefficient is assumed in the range of 0.1 to 0.2 and the value of  $E'$  has been determined by matching the  $P$ - $\delta$  relation for large deformation in elastic-plastic range. The hardening modulus of the Pt wire is found as  $18 \pm 3$  GPa.

#### 4. CONCLUSIONS

The experimental and finite element simulation scheme can successfully produce the elastic as well as the elastic-plastic bending in the nanowire. The deformation pattern ensures that the difficulties associated with the root or holding points are removed completely. Very small force corresponding to the small deformation is effectively measured. Good matching of the FE analysis data with the experimental ones is obtained and eventually, the hardening modulus of 625

nm Pt sample is successfully determined.

#### 5. ACKNOWLEDGEMENTS

This work was supported by Grant-in-Aid for Scientific Research (S) 18106003 and Grant-in-Aid for JSPS Fellows 19-07379.

#### 6. REFERENCES

1. Sharpe Jr., W. N., Yuan, B. and Edwards, R. L., 1997, "A new technique for measuring the mechanical properties of thin films", *J. Microelectromech. Syst.*, 6-3, pp.193-199.
2. Greek, S., Ericson, F., Johanson, S., Furtch, M. and Rump, A., 1999, "Mechanical characterization of thick polysilicon films: Young's modulus and fracture strength evaluated with microstructures", *J. Micromech. Microeng.*, 9, pp.245-251.
3. Tsuchiya, T., Tabata, O., Sakata, J. and Taga, Y. 1998, "Specimen size effect on tensile strength of surface-micromachined polycrystalline silicon thin film", *J. Microelectromech. Syst.*, 7-1, pp.106-113.
4. Brenner, S. S., 1956, "Tensile strength of whiskers", *J. Applied Physics*, 27-12, pp.1484-1491.
5. Pan, Z. W., Xie, S. S., Lu, L., Chang, B. H., Sun, L. F., Zhou, W. Y., Wang, G., and Zhang, D. L., 1999, "Tensile tests of ropes of very long aligned multiwall carbon nanotubes", *Appl. Phys. Lett.*, 74-21, pp.3152-3154.
6. Yu, M. F., Lourie, O., Dyer, M. J., Moloni, K., Kelly, T. F. and Ruoff, R. S., 2000, "Strength and Breaking Mechanism of Multiwalled Carbon Nanotubes under Tensile Load", *Science* 287, pp.637-640.
7. Salvetat, J. P., Kulik, A.J., Bonard, J. M., Briggs, G. A. D., Stöckli, T., Méténier, K., Bonnamy, S., Béguin, F., Burnham, N. A., and Forró, L., 1999, "Elastic modulus of ordered and disordered multiwalled carbon nanotubes", *Adv. Mater.*, 11-2, pp.161-165.
8. Kis, B. A., Mihailovic, D., Remskar, M., Mrzel, A., Jesih, A., Piwonski, I., Kulik, A. J., Benoit, W., and Forró, L., 2003, "Shear and Young's modulus of MoS2 nanotube Ropes", *Adv. Mater.*, 15-9, pp.733-736.
9. Cuenot, S., Champagne, S. D., and Nysten, B., 2000, "Elastic modulus of polypyrrole nanotubes", *Phys. Rev. Lett.*, 85-8, pp.1690-1693.
10. Wong, E. W., Sheehan, P. E., and Lieber, C. M., 1997, "Nanobeam mechanics: elasticity, strength, and toughness of nanorods and nanotubes", 277, pp.1971-1975.
11. Tohmyoh, H., 2009, "A Governing Parameter for the Melting Phenomenon at Nanocontacts by Joule Heating and Its Application to Joining Together Two Thin Metallic", *J. Appl. Phys.*, 105, pp. 014907-1 - 014907-9
12. Tohmyoh, H. and Fukui, S., 2009, "Self-Completed Joule Heat Welding of Ultrathin Pt Wires", *Phys. Rev. B*, 80 (Issue 15) pp.155403-1 - 155403-7.
13. Timoshenko, S, 1930, *Strength of Materials, Part I: Elementary Theory and Problems*, D. Van Nostrand CompPany, Inc., New York, 203.

#### 7. MAILING ADDRESS

M. A. Salam Akanda,  
H. Tohmyoh  
M. Saka  
Department of Nanomechanics,  
Tohoku University, Aoba 6-6-01, Aramaki, Aobaku,  
Sendai 980-8579, Sendai, Japan.

## MECHANICAL PROPERTIES OF LYOCELL FIBER REINFORCED POLYPROPYLENE COMPOSITES

F. A. Mirza<sup>1</sup>, A. M. Afsar<sup>1</sup>, B. S. Kim<sup>2</sup>, and J. I. Song<sup>1</sup>

<sup>1</sup>Dept. of Mechanical Engineering, Changwon National University, Changwon, South Korea  
<sup>2</sup>Composite Materials Lab., Korea Institute of Materials Science (KIMS), Changwon, South Korea

### ABSTRACT

The major disadvantage of the hydrophilic natural fibers and hydrophobic polymer matrices is the poor compatibility between the fibers and matrices. In order to improve the affinity and adhesion between fibers (lyocell) and thermoplastic matrix (polypropylene) during manufacturing, maleic anhydride (MA) as a coupling agent has been employed. Physical properties such as void contents and water absorption rate were studied. Tensile and flexural tests were carried out to evaluate the composite mechanical properties. Tensile test results showed the higher strength and modulus of composite than pure polypropylene (PP). In addition, these properties were better for 2 wt% MA content than 1 wt% MA content. Thus, 2 wt% MA content ensured better interfacial adhesion between fibers and matrix. Like tensile properties, the flexural properties of the composites were not improved. However, between 1 and 2 wt% MA content, the composites containing 2 wt % MA showed better flexural properties than 1 wt % MA.

**Keywords:** Natural fibers, Polypropylene, Maleic anhydride, Interfacial bonding, Mechanical properties.

### 1. INTRODUCTION

In the recent years, considerable research and development have been done in natural fibers as reinforcements for thermoplastic resinous matrix. These reinforced plastics serve as an inexpensive, biodegradable, renewable, and nontoxic alternative to conventional fiber reinforced composites. The various advantages of natural fibers over man-made fibers like glass and carbon are low-cost, low density, competitive specific mechanical properties, reduced energy consumption, and biodegradability. The common thermoplastic materials that currently dominate as matrix materials for natural fibers are polypropylene and polyethylene while phenolics and polyesters are two widely used thermoset matrixes for the natural fibers. With a view to replacing the wooden fittings, fixtures, and furniture, organic matrix and resin reinforced with natural fibers, such as jute, kenaf, sisal, coir, straw, hemp, rice husk, bamboo, lyocell etc., have been explored in the past decades [1-21].

Recently, there is an increasing demand from automotive industries for materials with sound abatement capability as well as reduced weight for fuel efficiency. Natural fibers possess excellent sound absorbing efficiency and are more shatter resistant and have better energy management characteristics than conventional fiber reinforced composites. In automotive parts, such composites not only reduce the mass of the component but also lower the energy needed for production by 80%. Demands for natural fibers in plastic composites are forecast to grow at 15-20% annually in

automotive applications and 50% or more in selected building applications [1].

However, the primary disadvantages of natural fiber reinforced plastic composites are (a) poor interfacial adhesion and dispersion in olefinic thermoplastic matrix materials due to hydrophilic character of cellulose [12], (b) high moisture absorption leading to dimensional instability, and (c) low permissible temperatures of processing and use due to their limited thermal stability. The hydrophilic groups present in unmodified cellulose are detrimental to the performance of the cellulose based composites if the fibers are exposed to the outside atmosphere. Water, in liquid or vapor form, can diffuse into the composite, and the properties (including dimensional stability) are hampered due to hydration. Similar to the study on cellulose based composites by Rowell [13], modification of cellulose by esterification may solve this problem by reduction in hygroscopicity. Sanadi *et al.* [14] pointed out that the processing temperature for cellulose based reinforced composites is limited to 200°C although higher temperatures can be used for short periods of time.

The hydrophilic character of cellulose is usually incompatible with hydrophobic matrix material unless a compatibilizer or coupling agent is used [15]. This leads to poor interfacial adhesion between the fiber and matrix as well as poor fiber dispersion. Various coupling or compatibilizing agents are used for improving the interfacial adhesion, dispersion within the matrix, and compatibility of the system.

Surface modification of cellulose fibers with polypropylene-maleic anhydride copolymer resulted in improved mechanical properties of the cellulose-polypropylene composites as shown by Felix and Gatenholm [15]. Scanning electron microscopy (SEM) studies revealed improved dispersion and adhesion when the fibers were surface modified. Similar studies were reported by Karmaker and Youngquist [16] for jute fiber reinforced polypropylene composites, and by Chen *et al.* [17] for bamboo fiber reinforced polypropylene composites. Both of these studies used maleic anhydride-grafted polypropylene as coupling agent.

A study by Hendenberg and Gatenholm [18] showed improved stiffness in cellulose-thermoplastic composites containing polyethylene-polystyrene blend (70:30 proportion) as a matrix material when a functionalized copolymer (maleic acid anhydride grafted styrene-ethylene/butylene-styrene block copolymer) was used.

A study by Trejo-O'Reilly *et al.* [19] revealed the possible use of grafting agents bearing anhydride or isocyanate reactive groups for introducing non-polar characteristics to the surface of cellulose fiber in view of improving interfacial wetting with polymeric matrices. The interactions of various oligomeric (e.g. oligomeric isocyanate) and polymeric reagents, such as poly(styrene-co-maleic anhydride) and poly(styrene-co-3-isopopenyl- $\alpha,\alpha'$ -dimethylbenzyl isocyanate) (PSTMI), with the OH groups on the surface of different cellulose materials were studied using Fourier transform Infrared Spectroscopy (FTIR), scanning electron microscopy (SEM), X-ray photoelectron microscopy, and elemental analysis. It was found that the accessibility of the OH groups varied as a function of the coupling agent in terms of molecular size and chemical nature. In addition, fiber surface property studies revealed considerable changes in contact angle of water when the appended moieties were long-chain hydrophobic structures like PSTMI.

Improvement in mechanical properties and interfacial wetting was noted for steam-exploded fiber from Yellow poplar (*Liriodendron tulipifera*) when the fibers were acetylated [20]. The thermal stability of the fibers was also improved when the fibers were extracted with water and alkali and later acetylated. Cellulose fiber surface treatment by pre-impregnation of henequen cellulosic fibers in LDPE-xylene solution improved the interfacial adhesion between the fiber and matrix as well as the shear properties of the composites [21]. Also the silane coupling agent (A-172 Union Carbide) improved the properties of these henequen cellulosic fiber composites.

Lyocell is a new cellulosic fiber spun from wood or pulp in a closed amine oxide solvent system [12]. It is environmentally benign and has the shorter processing time than conventional viscose rayon in the production. Also, lyocell fibers are known to have good mechanical properties, good wettability, high tenacity, and good drapability as well as environmentally friendliness. Thus, these fibers have potential applications as reinforcements for polymer matrix materials to offer improved mechanical and physical properties. This urges to analyze various aspects of these composite systems to

understand, improve and quantify their properties. The objective of the present study is to manufacture lyocell fiber reinforced polypropylene matrix composites followed by the evaluation of their mechanical as well as physical properties. Special attention is paid to the interfacial adhesion, uniform distribution of fibers, and proper alignment of fibers with a view to improving the mechanical properties of the composites.

## 2. EXPERIMENTAL

### 2.1 Materials

In this study, lyocell fibers were used as reinforcement which supplied by KOLON Inds. (USA). The diameter of single strand was 10 micron. The ultimate tensile strength of mono filament was 0.5-0.8 GPa. The elongation at break and initial elastic modulus were 6-8% and 10-16GPa, respectively.

Polypropylene (PP) supplied by Honam Petrochemical Corp. (Korea) was used as the matrix. The specific weight, the melting point, and the molecular weight of PP were 0.95 g/cm<sup>3</sup>, 170°C, and 10,000 g/mol, respectively. Maleic anhydride (MA) (Eastman, USA) was used as a coupling agent.

### 2.2 Composite Fabrication

Composites were prepared by compounding with extrusion and processing with compression molding. The fabrication process of the composites is outlined below.

PP and MA were melt mixed by twin-screw extruder (PRIM TSC 16TC, Thermo Electron Corp.) to form continuous rod of diameter 1.0mm. MA contents were varied from 1 to 2 wt%. After extrusion, the rods were vacuum dried for 24hrs. A grooved mold was used (250x250 mm<sup>2</sup>) to distribute the fibers in matrix uniformly as shown in Fig. 1. Releasing agent was used for easy removal of composites. The lyocell fibers were laid along the grooves of the mold. The dried rods were then uniformly placed over the fibers. For compression molding, a hot press machine (Model: WES-A300, Wetech, Korea) was used. At first, mold was preheated at 150°C temperature for 10min. Then the mold was compressed at 3ton pressure and 180°C temperature for 20min to get a composite panel. This panel was formed with grooved in one side. Two grooved composite panels were then compressed to get the flat composite panel. The consolidation cycle was chosen as shown in Fig. 2. An adequate flow of matrix (reduction in viscosity) was allowed before any pressure was applied.

### 2.3 Voids Contents

The void contents of composite may significantly affect some of its mechanical properties (ASTM D-2734). Higher void contents usually mean lower fatigue

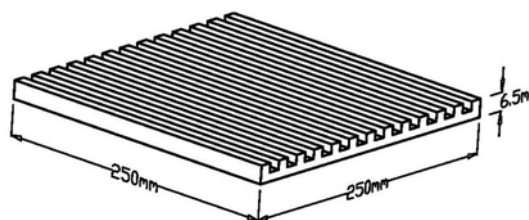


Fig 1. Grooved mold.

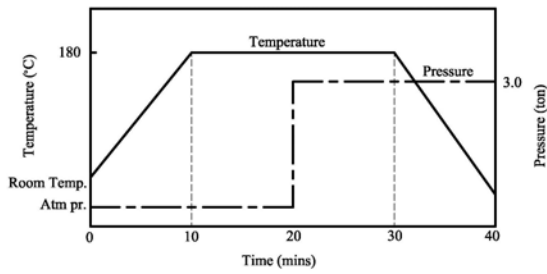


Fig 2. Time-temp-pressure cycle.

resistance, greater susceptibility to water penetration and weathering, and increased variation or scatter in strength properties. The void content is determined for the estimation of the quality of composites.

The densities of the composites were determined in accordance with ASTM-D792. The calculation was based the following equation:

$$M_d = a/(a + w - b) \quad (1)$$

where  $a$  represents apparent mass of specimen in air (g),  $b$  stands for apparent mass of specimen completely immersed and of the wire partially immersed in water (g) and  $w$  stands for apparent mass of totally immersed sinker and partially immersed wire (g).

The theoretical densities and voids contents of the composites were determined in accordance with ASTM D 2734-94. The theoretical density was determined using the following equation:

$$T_d = 100/(R/D + r/d) \quad (2)$$

where  $T_d$  = theoretical density ( $\text{g}/\text{cm}^3$ ),  $R$  = resin in composite (weight %),  $D$  = density of resin ( $\text{g}/\text{cm}^3$ ),  $r$  = reinforcement in composite (weight %), and  $d$  = density of reinforcement ( $\text{g}/\text{cm}^3$ ).

The void content was calculated from

$$V = 100(T_d - M_d)T_d \quad (3)$$

where  $V$  = voids contents (volume %).

## 2.4 Water Absorption of Composites

The mechanical properties of composites degrade if the composites absorb moisture. Thus, moisture absorbing capability of our lyocell fiber/PP composites is investigated in an attempt to know the degree of degradation of the mechanical properties of the composites. The tests were performed according to the ASTM D570-95 standard procedure for two and twenty four hour immersions (i.e. repeated immersion). Specimens of the composite panel were cut into dimensions of 76.2 mm in length by 25.4 mm in width by the thickness of the panel. The specimens were dried in an oven at 110°C, cooled in a desiccator and weighed. The conditioned specimens were fully immersed in

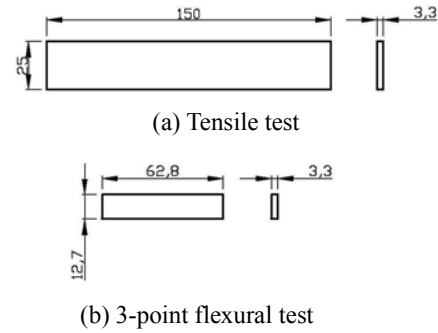


Fig 3. Dimensions of specimens (dimensions are in mm).

distilled water maintained at 23°C. The two-hour immersion method is used for materials having a relatively high rate of absorption and thin specimens, which can gain an equilibrium water content in 2 hours. For the composite panels under consideration, both the two hours and twenty-four hours methods were used to

compare the rate of absorption of water. Therefore, the specimens were removed from water after 2 hours, all surfaces were wiped off, and weighed. They were again placed in water, and weighed again after another 22 hours. Since there are no water soluble materials present in the composites, there was no need for any reconditioning. The percentage of water absorbed was calculated from

$$M(\%) = (M_t - M_o)/M_o \times 100 \quad (4)$$

where  $M_o$  is the mass of the dried specimen (g) and  $M_t$  is the mass of wet specimen (g).

## 2.5 Mechanical Properties

The tensile tests were carried out according to the ASTM D3039 standard (rectangular specimens) using a Universal Testing Machine (RB 301 Unitech M). The gage length was 25mm and the crosshead speed was 2.00mm/min. At the same time, strain was measured by an extensometer over a gage length of 25.0mm. The tensile modulus and strength were computed from the stress-strain curves.

According to the ASTM D790 standard, 3-point flexural test was performed by using the same Universal Testing Machine (RB 301 Unitech M) along with the flexural test fixture. The span length was 50mm and the test speed was 1.5mm/min. Figures 3(a) and 3(b) illustrate the specimens geometry for tensile and flexural test.

## 3. RESULTS AND DISCUSSION

### 3.1 Void contents

The experimental and theoretical densities are determined using Eq.s (1) and (2), respectively. Then, the void contents of composites are determined by using Eq. (3). Table 1 shows the densities and void contents of the lyocell/PP composites manufactured in the laboratory.



Table 1: Void contents of Lyocell/PP composites

Composite	Void (vol%)	$M_d$ (g/cm <sup>3</sup> )	$T_d$ (g/cm <sup>3</sup> )
1% MA	2.3	0.91	0.93
2% MA	6.4	0.87	0.93

Table 2: Water absorption of Lyocell/PP composites

Immersion time	Water absorption (wt %)	
	1% MA	2% MA
2 hr	0.508	0.625
24 hr	6.29	7.62

The average void contents of the composites were found to be 2.3 and 6.4 %, respectively, for 1 wt % and 2 wt % of MA contents. A good composite should have less than 1 % voids. The amount of voids in our case is large due to the lack of uniformity of surface coverage and insufficient (gap-filling) melt-flow of oversized matrix particles. In addition, the use of water as a suspension medium for extruded PP rods during prepregging can absorb water and cause these voids.

### 3.2 Water Absorptions

Water absorption of composites relates to composite properties such as dimensional stability. The results of the water absorption tests are summarized below in Table 2. It can be observed that the fiber-based composites showed significantly higher water absorption than pure PP due to the hydrophilic character of lyocell fibers. However, compared to water absorption of lyocell fibers, average of  $52.6 \pm 3.7\%$ , composites exhibit much lower water absorption values. These much lower values obtained for composites than for fibers themselves are because cellulose fibers are covered by PP layers that slow down the diffusion of water. Moreover, the hydrophilic -OH groups present in the lyocell fibers react with the acid anhydride group present in MA to form ester linkages. This reduces the water absorbing capacity in the lyocell/PP composites.

### 3.3 Mechanical Properties

The typical stress-strain curves for tensile test specimens of the composites are shown in Figure 4. It shows the effect of MA as a coupling agent on the tensile properties of the composites. It is observed that 2 wt % MA content shows better properties than 1 wt % MA content.

The improvement of tensile strengths of the composites can be observed from Fig. 5. The addition of 1 wt % MA increased the tensile strengths of the composites than the pure PP. The average tensile strength of the composites containing 1 wt % MA was 53.02 MPa. It was observed that with the increased of MA content from 1 to 2%, there was a relative rise in the tensile strengths. The average tensile strength of the composites

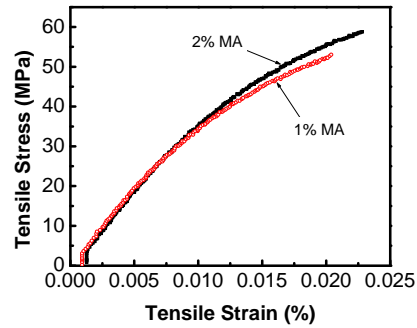


Fig. 4. Stress-strain curves for tensile test specimens.

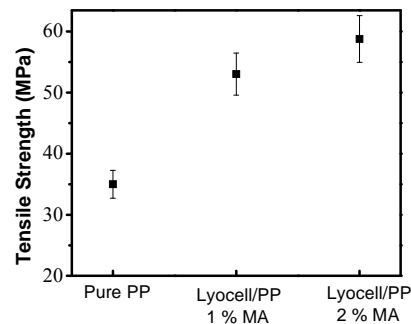


Fig. 5. Tensile strength of Lyocell/PP composites.

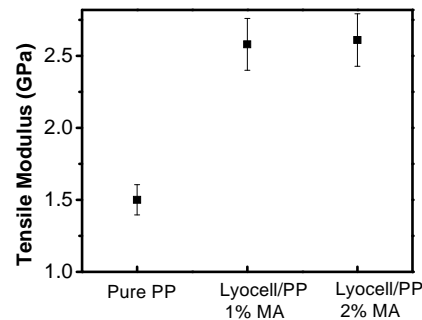


Fig. 6. Tensile modulus of Lyocell/PP composites.

containing 2 wt % MA was 58.76 MPa. It ensures good interfacial adhesion between lyocell fibers and PP matrix.

Figure 6 shows the tensile modulus of lyocell/PP composites. Similar improvements were achieved in tensile modulus of the composites. The average tensile modulus of the composites containing 1 wt % MA content was 2.58 GPa while it was 2.61 GPa for the composites containing 2 wt % MA. The average elongations at break of 1 wt % MA and 2 wt % MA content composites were 5.2% and 6.8%, respectively.

The flexural properties of lyocell/PP composites were also studied (Figures 7, 8, and 9). The Typical stress-strain curves for flexural test specimens are shown in Fig. 7.

Figure 8 shows the flexural strength of the composites. The average flexural strength of the composites containing 1 wt % MA and 2 wt % MA were 32.58 MPa

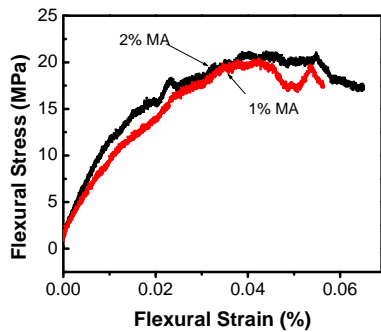


Fig 7. Stress-strain curves for flexural test specimens.

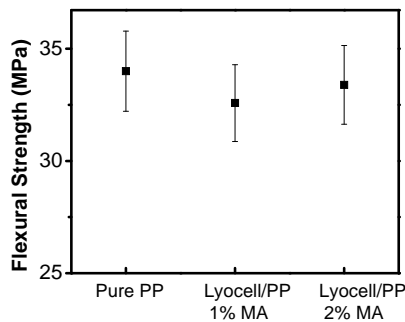


Fig 8. Flexural strength of Lyocell/PP composites.

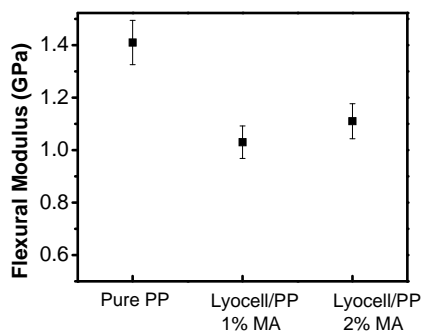


Fig 9. Flexural strength of Lyocell/PP composites.

and 33.39 MPa, respectively. It ensures that increasing MA contents can improve the flexural properties of the composites.

Figure 9 shows the flexural modulus of the composites. Similar trends can be observed as flexural strengths. The average flexural modulus of the composites containing 1 wt % MA and 2 wt % MA were 1.03 GPa and 1.11 GPa, respectively. It is observed that the flexural properties of the composites were not improved as tensile properties. Although, the properties are lower than the pure PP, it is observed that composites containing 2wt % MA shows better properties than 1 wt % MA. Overall observation of flexural properties shows that increasing the amount of the coupling agent can result in improved flexural properties.

#### 4. CONCLUSION

Lyocell fiber reinforced polypropylene matrix composites were successfully developed by compression molding technique and by using maleic anhydride as a coupling agent.

Results shows that average void contents of lyocell/PP composites are high. This is due to the lack of uniformity of surface coverage and insufficient (gap-filling) melt-flow of oversized matrix particles.

The improvement of tensile strengths and modulus of the composites can be observed. The tensile strengths of the composites were higher than the pure PP. It is observed that there is a relative rise in the tensile strengths and modulus upon increasing the content of the MA from 1 to 2%. It ensures that coupling agent can improve the interfacial adhesion between lyocell fibers and PP matrix.

The flexural properties for lyocell/PP composites do not show improvement. The results showed that increasing the amount of the coupling agent could improve the flexural properties.

It can be observed that the natural fiber-based composites show significantly higher water absorption than pure PP due to the hydrophilic character of lyocell fibers. However, compared to fibers, composites exhibit much lower absorption values.

#### 5. ACKNOWLEDGEMENT

This work was partially supported by Brain Korea 21 (BK-21) Projects Corps. of the second phase. We are thankful to Korean Institute of Composite Materials (KIMS) for providing the lyocell fibers and polypropylene.

#### 6. REFERENCES

1. Khondker, O. A., Ishiaku, U. S., Nakai, A., and Hamada, H., 2006, "A novel processing technique for thermoplastic manufacturing of unidirectional composites reinforced with jute yarns", *Composites: Part A*, 37:2274-2284.
2. Abdelmouleh, M., Boufi, S., Belgacem, M. N., and Dufresne, A., 2007, "Short natural-fibre reinforced polyethylene and natural rubber composites: Effect of silane coupling agents and fibres loading", *Composites Science and Technology*, 67:1627-1639.
3. Wulin, Q., Takashi, E., and Takahiro, H., 2006, "Structure and properties of composites of highly crystalline cellulose with polypropylene: Effects of polypropylene molecular weight", *European Polymer Journal*, 42:1059-1068.
4. Andrzej, K. B., and Faruk, O., 2006, "Injection moulded microcellular wood fibre-polypropylene composites", *Composites: Part A*, 37:1358-1367.
5. Mariano, P., Donatella, C., Irene, A., Zbigniew, K., and Poirkowska, E., 2006, "Functionalization compatibilization and properties of polypropylene composites with Hemp fibres", *Composites Science and Technology*, 66:2218-2230.
6. Johnson, R. K., Sharp, A. Z., Renneckar, S. H., and Wolfgang, G. G., 2008, "Mechanical properties of wetlaid lyocell and hybrid fiber-reinforced

- composites with polypropylene”, *Composites: Part A*, 39:470-477.
7. Pickering, K. L., Beckermann, G. W., Alam, S. N., and Foreman, N. J., 2007, “Optimising industrial hemp fibre for composites”, *Composites: Part A*, 38: 461-468.
  8. Doan, T. T. L., Shang, L. G., and Edith, M., 2006, “Jute/polypropylene composites I. Effect of matrix modification”, *Composites Science and Technology*, 66:952-963.
  9. Yang, H. S., Kim, H. J., Park, H. J., Lee, B. L., and Hwang, T. S., 2007, “Effect of compatibilizing agents on rice-husk flour reinforced polypropylene composites”, *Composite Structures*, 77:45-55.
  10. Girones, J., Mendez, J. A., Boufi, S., Vilaseca, F., and Mutje, P., 2007, “Effect of Silane Coupling agents on the properties of Pine fibers/polypropylene composites”, *Journal of Applied Polymer Science*, 103:3706-3717.
  11. Kim, H. S., Kim, S., Kim, H. J., and Yang, H. S., 2006, “Thermal properties of bio-flour-filled polyolefin composites with different compatibilizing agent type and content”, *Thermochimica Acta*, 451:181-188.
  12. Reddy, N., and Yang, Y., 2006, “Properties of high-quality long natural cellulose fibers from rice straw”, *Journal of Agricultural and Food Chemistry*, 54 (21):8077-8081.
  13. Rowell, R. M., 1991, “Recent advances in Lignocellulosic derived composites”, *Polymers from Bio-based Materials*, Noyes Data Corporation, pp. 35-57.
  14. Sanadi, A. R., Caulfield D. F., Jacobson R. E., and Rowell R. M., 1995, “Renewable Agricultural Fibers as Reinforcing Fillers in Plastics: Mechanical Properties of Kenaf Fiber–Polypropylene Composites,” *Industrial & Engineering Chemistry Research*, 34 (5):1889-1896.
  15. Felix, J. M., and Gatenholm, P., 1991, “The nature of adhesion in composites of modified cellulose fibers and polypropylene”, *J Journal of Applied Polymer Science*, 42:609-620.
  16. Karmaker, A. C., and Youngquist, J. A., 1996, “Injection Molding of Polypropylene Reinforced with Short Jute Fibers”, *Journal of Applied Polymer Science*, 62:1147-1151.
  17. Chen, X., Guo, Q., and Mi, Y., 1998, “Bamboo Fiber-Reinforced Polypropylene Composites: A Study of the Mechanical Properties,” *Journal of Applied Polymer Science*, 69:1891-1899.
  18. Hendenberg, P., and Gatenholm, P., 1995, “Conversion of Plastic/Cellulose Waste into Composites. I. Model of Interphase,” *Journal of Applied Polymer Science*, 56:641-651.
  19. Trejo-O’Reilly, J. A., Cavaille, J. Y., and Gandini, A., 1997, “The Surface Chemical Modification of Cellulosic Fibers in view of their use in Composite Materials,” *Cellulose*, 4:305- 320.
  20. Glasser, W. G., Taib, R., Jain, R. K., and Kander, R., 1999, “Fiber-Reinforced Cellulosic Thermoplastic Composites,” *Journal of Applied Polymer Science*, 73:1329-1340.
  21. Herrera-Franco, P. J., and Aguilar-Vega, M. J., 1997, “Effect of Fiber Treatment on Mechanical Properties of LDPE-Henequen Cellulosic Fiber Composites,” *Journal of Applied Polymer Science*, 65:197-207.

**7. MAILING ADDRESS:**

A. M. Afsar  
 Dept. of Mechanical Engineering,  
 Changwon National University, Changwon, South Korea.  
 Email:mdafsarali1967@yahoo.com

## MODELLING AND ANALYSIS OF A FEMORAL NECK PROSTHESIS

A.S.Blicblau and M.Lew

Faculty of Engineering and Industrial Sciences, Swinburne University of Technology,  
Hawthorn, Victoria, Australia

### ABSTRACT

This paper investigates the stresses around the femoral neck of hip replacements when compared with a repair procedure of hips, which include either a complete hip replacement, or the installation of a Dynamic Hip Screw to hold the hip together. Models were developed and analyzed to determine the high stress regions inside the bone which may cause pain or failure. For the Dynamic Hip Screw (DHS) the highest amount of stress on the bone was found to be near the top screw, and the screw supporting the head/neck of the femur. However, for a total hip replacement, the point of highest stress is located on the prosthetic-bone interface on the opposite side of the bone from the ball of the hip. Caution is required when selecting an appropriate hip repair or replacement for different people.

**Keywords:** Dynamic Hip Screw, Total Hip replacement, femoral, repair.

### 1. INTRODUCTION

Elderly people are at the greatest risk of hipbone fracture, which is partly due to Osteoporosis and Osteoarthritis[1]. The lifetime risk for a wrist, hip or vertebral fracture has been estimated to be in the order of 30% to 40% in developed countries – in other words, very close to that for coronary heart disease.

Osteoporosis is not only a major cause of fractures, it also ranks high among diseases that cause people to become bedridden with serious complications. Because of the morbid consequences of osteoporosis, the prevention of this disease and its associated fractures is considered essential to the maintenance of health, quality of life, and independence in the elderly population[1-3].

Osteoarthritis is a degenerative joint disease where the cartilage and lubricant between joints is decreased[2]. Severe cases of Osteoarthritis require joint replacement, as cartilage cannot be regenerated with current technology. According to Medicare Australia, over 16,000 hip repair procedures were conducted in 2007 in Australia[4]. This number includes both screw type repairs as well as total hip replacements. Of this number, roughly 1,300 (8%) were revision surgeries to repair or replace an existing implant. Current methods of repair involve either a complete hip replacement, or the installation of a Dynamic Hip Screw. In elderly patients however, several complications may arise such as osteoporosis and other bone weakening conditions associated with age.

This research expanded upon previous research to examine the bone surrounding hip replacements[5]. The aim of the current investigation was to study the stress in bone matter surrounding artificial implants so that future

patients can avoid repeat operations. It is important to study these stresses because they can be caused by of non uniform material in femur, weakened bone conditions from osteoporosis, and the resulting thinning of bone sections in some locations within the hip associated with possible high stress regions inside the bone, especially in the face of Dynamic Hip Screws.

The scope of this work resulted in a data analysis of failure of hip replacements with a view to targeting an at risk population, and so developing information suitable for simple hip repair utilizing finite element modelling (FEM) techniques[6-8]. A model of the load-bearing structure of the femoral head of the hip with associated reaction forces within the bone itself was analyzed[9, 10].

### 2. HIP FRACTURE AND JOINT REPAIR

In general, there are three types of fracture; at the femoral head; transcervical neck fracture which occurs in the region of the femoral neck; intertrochanteric fracture, which occurs at the base of the femoral neck; and ,subtrochanteric fracture which appears as a horizontal fracture below the femoral neck[2].

All three forms of failure require either total hip replacement (THR) or insertion of Dynamic Hip Screws (DHS) which is dependent on the severity of the fracture and the condition of the patient. Total hip replacement involves the removal of the femoral head and surrounding bone[11]. An artificial replacement is then installed in its place.

THR's are often used to treat joint failures due to Osteoarthritis. This type of surgery is generally known to be highly invasive as it involves not only the removal

of the femoral head, but also the removal of cancellous bone. A long section is inserted into the cancellous section of bone in order to stabilize it. The cup of the hip is replaced with a plastic or Teflon ball surface for low friction and bonded to the bone using bone cement. However, the DHS (also known as intramedullary hip screw) is a less invasive procedure which involves inserting a screw across the fracture and into the ball of the hip. This sort of repair is designed for intertrochanteric and subtrochanteric fractures[2].

The number of screws can vary according to the procedure from one to three. This method of repair requires less time and complexity compared to the THR and does not require the removal of significant amounts of bone. Its primary function is to allow the bone to heal the fracture instead of replacing the entire hip.

### 3. HIP POPULATION

In total, there were 13035 hip replacement procedures using a variety of techniques, performed in Australia in the period of January to December 2007, and 2041 Intramedullary screws installed, as shown in Figure 1. The number of total hip replacements is roughly equal for both genders. This number is expected to increase as the median age of the nation increases from 35.7 to 36.6.

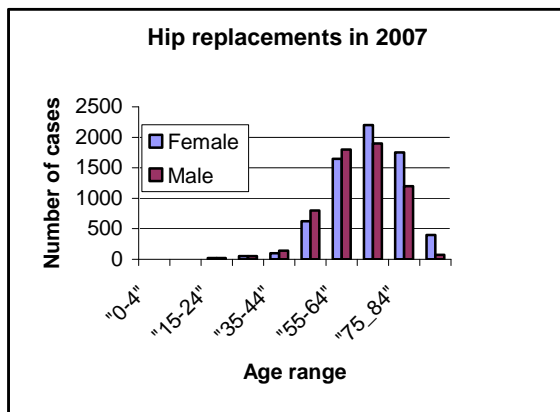


Fig 1. Number of cases versus age range in 2007

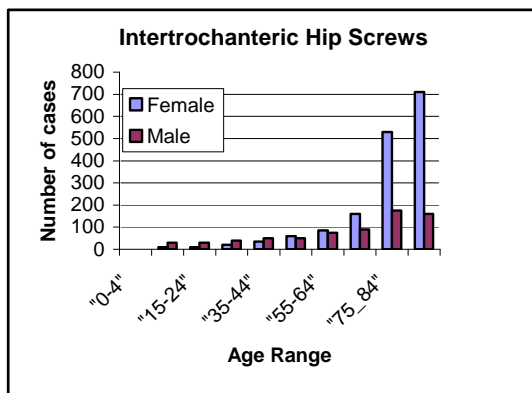


Fig 2. Number of cases versus age for intertrochanteric screws.

When analyzing specific data, as shown in Figure 2, a much larger proportion of females over the age of 65 undergo hip repair, compared to men and have an intertrochanteric hip screw inserted. The data indicates that a much larger proportion of females over the age of 65 undergo hip repair compared to men. This is in part due to the more profound effects of Osteoporosis This paper focused on female hip replacements for the over 75 year old persons.

### 4. PRELIMINARY MODEL

Anatomical and anthropological studies to-date have failed to establish a standard model for bone dimensions at the head of the femur. It is commonly accepted that bone dimensions are affected by diet, lifestyle, and heredity of a particular region of the world, were employed in this study, and are given in Table 1.

Table 1: Dimension of femoral head

Parameter of Femur	Dimension (mm)
Maximum length	422.5
Proximal breadth	90.2
Head vertical diameter	44.3
Head transverse diameter	44.5
Neck vertical diameter	30.6
Neck transverse diameter	25.9
Midshaft circumference	87.7
Midshaft antero-posterior diameter	26.9
Midshaft transverse diameter	26.6
Distal breadth	77.1
Collo-diaphyseal angle	119.6°

Although the data is mainly sourced from Anatolian individuals, the challenges of age, sex, and ethnicity should not affect the overall model. A further complication encountered while trying to model the femur is that the cross section of the femur itself also varies along its length. The cross-sectional geometry of the human femur is shown in Figure 3[10, 12]. The cortical wall thickness varied between 4.0mm to 7.6mm and was dependent on its position along the femur.

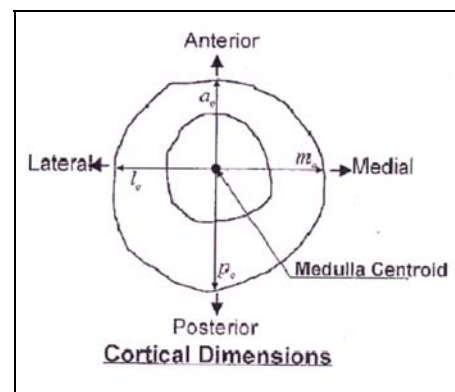


Fig 3. Geometry of the shaft of a real femur

The materials used in orthopaedic implants are typically stainless steels or Titanium alloys (used in the model). Two approaches were considered in modeling: a complete bone analysis without a screw and a model with a screw and the results were compared. Total hip replacements and Dynamic Hip Screws. The femoral head and part of the femur were modelled in Solidworks as two separate parts. These two parts were mated together with the Dynamic Hip Screw. This is the most realistic approach, as it simulates how a hip repair will be made during an actual surgery. The analysis will take the entire structure of the bone and implant into account. For the screw bone model because of complexities in the modeling and analysis process, only the proposed repair was modelled. Force restraints simulate the bone adhesion to the implant surface[7, 8, 13]. The resulting stresses on the implant can be safely assumed to have equal and opposite reaction forces from the bone. Again, in our case the analysis only considered the implant and not the surrounding bone.

The finite element(FE ) solid model was constructed in Solidworks®, and was made up of three components: the hard Cortical bone shell; the soft Trabecular bone core; and the. Prosthetic device[6, 9]. The FE model of the human femur is shown on Figures 4a and 4b.



Fig. 4a. FE side view model of human femur.

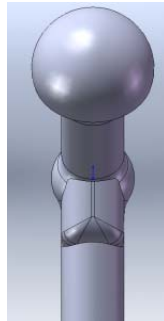


Fig. 4b. FE head on view of human femur.

The FE SOLID model of the dynamic hip screw and total hip replacement are shown on Figures 5a and 5b



Fig. 5a. FE side view model of commercial total hip replacement

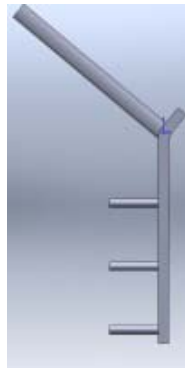


Fig. 5b. FE model of the Dynamic Hip Screw.

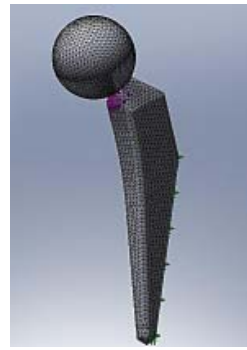


Fig. 6a. FE mesh of commercial hip replacement

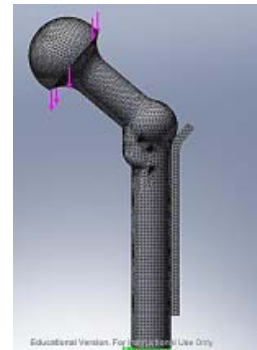


Fig. 6b. FE mesh of a complete bone and hip screw

## 5. RESULTS AND ANALYSIS

The highest stress for the complete bone study of the total hip replacement was found deep in the root of the bone. It was noted that there was a high fluctuation of stress in this region.

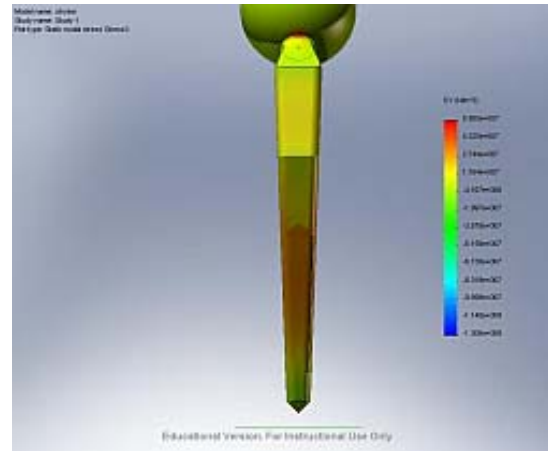


Fig 7. Location of highest stresses

This might be due to minor imperfections in the model where the prosthesis was in contact with the bone. The average stress on the face carrying most of the load was 8.5 MPa and the maximum stress was 33 MPa. However, the accuracy of this value is suspect due to the high amount of fluctuations. The highest stress for the reaction force study of the hip replacement was found at the sharp edge. This force is due to the boundary condition at that location and is pressing against the top surface of the bone. The average stress down the middle of the high stress area was 10 MPa. The highest stress was found to be 52 MPa

For the DHS, detail of stress on the top screw shows a high stress region at the root and at the tip of the screw, as shown in Figure 9. This area corresponds to the cortical bone part of the femur. The average stress recorded was 150 MPa while the maximum stress was 1 GPa (disregarding the outlying value of 3.5 Pa).



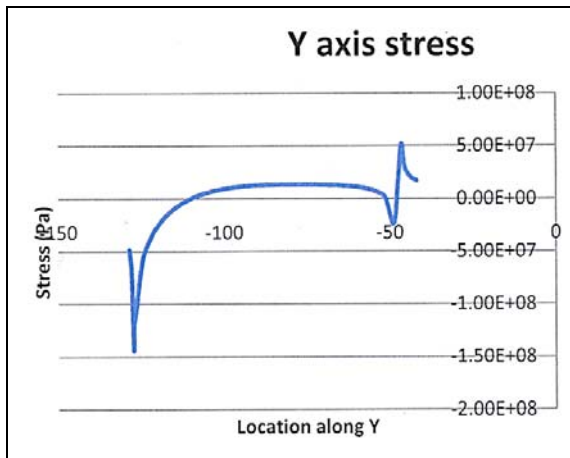


Fig. 8. Reaction force of the hip replacement

Detail of stress on the top screw shows a high stress region at the root and at the tip of the screw. This area corresponds to the cortical bone part of the femur. The average stress recorded was 150 MPa while the maximum stress was 1 GPa. When the stresses were plotted, it was found that each subsequent screw had progressively lower stress at the tips, as shown in Figure 9.

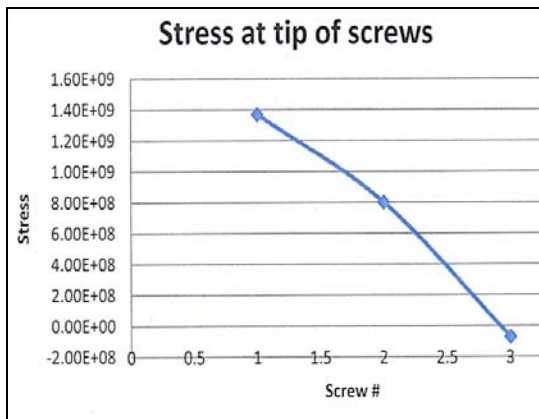


Fig 9. Stress at DHS Screw Tips

The stress for the reaction force case produced a more symmetrical stress distribution around the top screw. In this case, there was no sign of any stresses in the tip. The average stress was 63 MPa while the highest stress is 480 MPa. Unlike the complete bone model, there were some low stresses near the root of the subsequent screws.

For the case with no prosthesis, the highest stress is located on the outside of the femur away from the body. The average stress is 33 MPa as shown in Figure 10.

**6. DISCUSSION**

The average stress in the total hip replacement models showed a 1.5 MPa (15%) difference. This difference is largely due to sudden drops in stress on the surface of the Complete Bone study. Without these drops, the average stress would have been closer to that of the reaction force study.

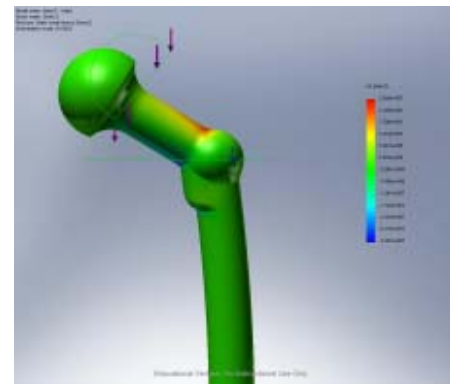


Fig 10. Stress distribution on the bone without a prosthetic.

In the case of the Dynamic Hip Screw, the difference in stress is much more dramatic with an error of 50%. This difference is probably due to the difference in mating conditions. The Complete Bone model had a mate through the cortical and Trabecular bone, which had different properties. For the Reaction Force case, all the screws were assumed to be fixed, treating the bone as a single, homogeneous material. The author feels that this also accounts for the lack of screw tip stress. A summary of the overall stress modeling results is given in Table 2.

Table 2 Modelling of Stress at various Locations

Model	Highest Stress Location	Average Stress (MPa)
Complete Bone -Total Hip replacement	Base of prosthetic embedded in the bone	8.5
Reaction Force -Total Hip replacement	Base of prosthetic embedded in the bone	10
Complete Bone -Dynamic Hip Screw	Root and tip of the first screw	150
Reaction Force -Dynamic Hip Screw	Root of the first screw	63
No Prosthetic	Outside of Femur	333

Hip Replacement surgery is a far more invasive approach compared to hip screws. In the case of the elderly, hip replacements has a longer recovery period and higher short term risk compared to hip screws. However, the long-term risk of failure is higher for a Dynamic Hip screw due to higher stress concentrations.

For hip replacement, the point of highest stress is located on the prosthetic-bone interface on the opposite side of the bone from the ball of the hip. This is consistent in both cases although the actual values are different. The implication of this is that the bone in this region has a higher concentration of stress, and thus a

higher chance of failure at this location. This needs to be taken into account when performing a bone repair to minimize stress in the bone, and patients should pay attention to pain in that region as it may be a sign of impending failure.

When analyzing the Dynamic Hip Screw the highest points of stress for the Dynamic Hip Screw on the bone are located around the top screw, and the screw supporting the head/neck of the femur. Subsequent screws bear a comparatively low load. This is consistent in both cases, though the values show a large amount of error, and implies that subsequent screws mainly help to stabilize the head. Therefore, a larger diameter first screw should be considered in order to reduce the amount of stress concentration.

## 7. CONCLUSIONS AND RECOMMENDATIONS

The complete bone study of the Dynamic Hip Screw indicates that the amount of stress taken up by subsequent screws decreases in a linear fashion. In particular, the highest points of stress for the Dynamic Hip Screw on the bone are located around the top screw, and the screw supporting the head/neck of the femur. The investigation established the maximum stress in bone matter surrounding artificial implants (DHS prosthesis.) so that future patients can avoid repeat operations.

From these conclusions, there are two possible avenues for further study;

(a) the influence of a larger screw in the first position, and (b) how it would affect the stress on subsequent screws; and the influence of the number of screws, and the extent that a larger number would help to even out the load.

## 8. REFERENCES

1. WHO, *Assessment of fracture risk and its application to screening for postmenopausal osteoporosis*, in *Report of a WHO Study Group World Health Organization*. 1994: Geneva.
2. Wheelless, C.R., *Wheelless' Textbook of Orthopaedics*, in *Femoral Shaft Fracture* J.A. Nunley and J.R. Urbaniak, Editors. 2009, Duke Orthopaedics <http://www.wheelsonline.com/>.
3. Kanis, J.A., 2002,"Diagnosis of osteoporosis and assessment of fracture risk ", *The Lancet*, 359(9321): 1929-1936
4. Medicare, *Medicare Statistics*. 2008, AGP <http://www.medicareaustralia.gov.au/about/stats/index.jsp>. Canberra.
5. Arundell, J., A. Blicblau, D. Richards, and M. Singh, 2008,"Dynamic Hip Fracture Modelling", *ANZIAM J (CTAC 2008)*: C220-C236.
6. Majumder, S., A. Roychowdhury, and A. Pal, 2007,"Simulation of hip fracture in sideways fall using a 3D finite element model of pelvis–femur–soft tissue complex with simplified representation of whole body", *Medical Engineering & Physics*, 20(10): 1167-1178.

7. Perilli, E., M. Baleani, C. Öhman, F. Baruffaldi, and M. Viceconti, 2007,"Structural parameters and mechanical strength of cancellous bone in the femoral head in osteoarthritis do not depend on age", *Bone*, 41(5): 760-768.
8. Helgason, B., E. Perilli, E. Schileo, F. Taddei, S. Brynjólfsson, and M. Viceconti, 2008,"Mathematical relationships between bone density and mechanical properties: A literature review", *Clinical Biomechanics*, 23(2): 135-136.
9. Stephenson, P. and B.B. Seedhom, 1998,"Cross-sectional geometry of the human femur in the mid-third region ", *Proceedings of the Institution of Mechanical Engineers, Part H: Journal of Engineering in Medicine*, 213 (2).
10. Ziylan, T. and K.A. Murshid, 2002,"An Analysis of Anatolian Human Femur Anthropometry", *Turkish Journal of Medical Science* 32(3): 231-235.
11. Bonshahi, A.Y., D. Knowles, and S.P. Hodgson, 2003,"Isolated lesser trochanter fractures in elderly-a case for prophylactic DHS fixation A case series", *Injury*, 35(2): 196-198.
12. Sun, S.S., H.-L. Ma, C.-L. Liu, and C.-H. Huang, 2008,"Difference in femoral head and neck material properties between osteoarthritis and osteoporosis", *Clinical Biomechanics*, 23(5): S39-S47.
13. Duchemin, L., V. Bousson, C. Raossanaly, C. Bergot, J.D. Laredo, W. Skalli, and D. Mitton, 2008,"Prediction of mechanical properties of cortical bone by quantitative computed tomography", *Medical Engineering & Physics* 30(3): 321-328.

## 9. NOMENCLATURE

Symbol	Meaning	Unit
DHS	Dynamic Hip Screw	N/A
FEM	Finite Element model	N/A
FE	Finite Element	N/A
THR	Total Hip Replacement	N/A
GPa	Stress	(Pa x 10 <sup>9</sup> )
MPa	Stress	(Pa x 10 <sup>6</sup> )

## 10. MAILING ADDRESS

A.S. Blicblau  
 Faculty of Engineering and Industrial Sciences  
 Swinburne University of Technology  
 PO Box 218 Hawthorn  
 Victoria AUSTRALIA.  
 Phone : 61392148531  
 FAX : 61392148264  
 E-mail : ablicblau@swin.edu.au

## NONLINEAR ANALYSIS OF SHOCK ABSORBERS

M. Ashiqur Rahman, A. Uddin Ahmed, M. Sayem Uddin

Department of Mechanical Engineering,  
Bangladesh University of Engineering & Technology, Dhaka

### ABSTRACT

Nonlinear dynamics of a two degrees-of-freedom (DOF) shock absorber or, untuned vibration damper system having nonlinear springs and dampers is treated as a boundary value problem. For the different cases, a comparative study is made varying the frequency ratio ( $r$ ). Another comparison is for response versus time for different spring and damper types at three important frequency ratios: one at  $r = 1$ , one at  $r > 1$  and one at  $r < 1$ . Response of the system is changed because of the spring and damper nonlinearities; the change is different for different cases. Accordingly, an initially stable absorber may become unstable with time and vice versa. Analysis also shows that higher nonlinearity terms make the system more unstable. Change in response is more evident near the frequency ratio of unity.

**Keywords:** shock absorber, nonlinear response, initial value problem (IVP), boundary value problem (BVP), multi segment method of integration.

### 1. INTRODUCTION

Shock absorbers are basically untuned viscous vibration dampers designed to smooth out or damp shock impulse, and dissipate kinetic energy. A tuned vibration absorber is only effective at one frequency, the tuned one, and its usefulness is narrowly limited in the region of the tuned frequency [1]. In contrast, when the forcing frequency varies over a wide range, an untuned viscous damper (also called a shock absorber) becomes very useful [2]. Vibration problems become nonlinear in nature as amplitude of oscillation becomes large in numerous engineering applications [3, 4]. The problem becomes more involved as springs and dampers do not actually behave linearly in vibration problems [4-6]. Zhu et al. [6] extensively studied nonlinear response of two degrees of freedom (2DOF) vibration system with nonlinear damping and nonlinear springs. Recently, Mikhlin and Reshetnikova [5] studied the nonlinear 2DOF system. In papers [7-8], theoretical investigation and some experimental verification on the use of nonlinear localization for reducing the transmitted vibrations in structures subjected to transient base motions have been presented. Nakhaie et al. [9] used the root mean square of absolute acceleration and relative displacement to find the optimal damping ratio and natural frequency of the isolator. Shekhar et al. [10, 11] have considered different alternatives to improve the performance of an isolator having a nonlinear cubic damping over and above the usual viscous damping. Alexander et al. [12] explored the performance of a nonlinear tuned mass damper (NTMD), which is modeled as a TDOFS with a cubic nonlinearity.

Most numerical studies regarding nonlinear vibration

of structures, particularly involving multi degrees of freedom system (MDOFS), have been carried out in the form of initial value problems: all the boundary conditions, termed as system's responses (displacement, velocity etc.), were specified at an initial time reference, followed by numerical integration of the governing differential equation. Such type of analysis involves simultaneous solution of a system of nonlinear equations where the number of equations to be solved is determined by order of the governing equations. This type of problem needs to simultaneously solve a large number of nonlinear equations that depends on the number of intermediate grid points in between the two time references. Though, Newton-Raphson method can be used to solve that large number of equations, there are chances of non-convergence of solutions.

Present work aims to solve both boundary and initial value problems for untuned vibration damper system. Generally, stability of the MDOFS system is studied by the method of perturbation. But a simple and direct method, like that of multisegment integration technique [13], that helps to directly visualize the system's response with time, would be very useful, in particular for the present study, when a boundary value problem is dealt with.

Thus results have been obtained for different shock absorbers (Cases 1 – 16 in Table 1) for chosen boundary conditions and different parameters of interest (Tables 2 – 3 and Fig. 1). Ideally, an untuned viscous damper is basically a 2DOFS with a very small mass ratio, having zero damping for the main mass ( $m_1$ ) and zero spring force for the absorber. Again both the main mass spring and absorber's damper are linear. Such an ideal case has

been symbolized as case 1 in this paper. However only to simulate practical situations, a small damping for the main mass ( $m_1$ ) and a small spring force for the absorber are assumed. It is also assumed that these two nonzero forces can be nonlinear as well (cases 2-16).

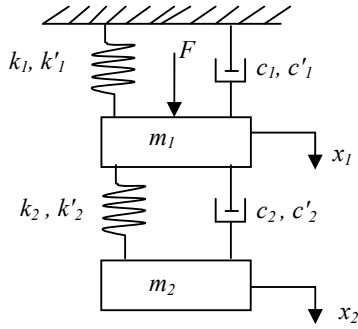


Fig 1. Arrangement of masses, springs and dampers for TDOF vibration system (nonlinear shock absorber).

Table 1: Different cases of shock absorbers

Case	Combinations of Springs	Combinations of Dampers
1	Linear spring with main mass only	Linear damper with second mass only
2	Both springs linear	Linear dampers
3	Both springs hard	
4	1 <sup>st</sup> spring: hard 2 <sup>nd</sup> spring: soft	
5	1 <sup>st</sup> spring: soft 2 <sup>nd</sup> spring: hard	
6	Both springs soft	
7	Both springs linear	Hard dampers
8	Both springs hard	
9	1 <sup>st</sup> spring: hard 2 <sup>nd</sup> spring: soft	
10	1 <sup>st</sup> spring: soft 2 <sup>nd</sup> spring: hard	
11	Both springs soft	
12	Both springs linear	Soft dampers
13	Both springs hard	
14	1 <sup>st</sup> spring: hard 2 <sup>nd</sup> spring: soft	
15	1 <sup>st</sup> spring: soft 2 <sup>nd</sup> spring: hard	
16	Both springs soft	

Table 2: Chosen Parameters of shock absorbers

Parameters	Initial Problem Value	Boundary Value Problem
$m_1$ (kg)	100.0	100.0
$m_2$ (kg)	100.0	1.0
$k_1$ (N/m)	1000.0	1000.0
$k'_1$ (N/m <sup>3</sup> )	0.0	±0.5
$k_2$ (N/m)	0.0	10.0
$k'_2$ (N/m <sup>3</sup> )	0.0	±0.005
$c_1$ (Ns/m)	0.0	0.03139
$c'_1$ (Ns/m <sup>3</sup> )	0.0	±0.003

$c_2$ (Ns/m)	63.246, 182.174, 316.23, 632.46	3.139
$c'_2$ (Ns/m <sup>3</sup> )	0.0	±0.03
$\sqrt{\frac{k_1}{m_1}}$	3.162	3.162
$\mu$	1.0	0.01
$\zeta$	0.1, $\zeta_0 = 0.288, 0.5,$ 1.0	$\zeta_0 = 0.00496$
$f$ (N)	20.0	20.0
$\omega_1$ (rad/s)	3.162	3.006
$\omega_2$ (rad/s)	-	3.326

Table 3: Prescribed boundary conditions

Parameters	BVP	IVP
$y_1(t=0.0s)$ (m)	0.05	0
$y_2(t=50.0s)$ (m/s)	0.06	0
$y_3(t=0.0s)$ (m)	-0.07	0
$y_4(t=50.0s)$ (m/s)	-0.06	0

For Table 2, damping constant equals to the optimum damping ratio ( $\zeta_0$ ). These data are so selected to demonstrate the fact that untuned viscous vibration dampers become highly unstable because of increased nonlinearity.

## 2. MATHEMATICAL MODELS

Fig. 1 shows the proposed model for the TDOFS while Table 1 shows the different cases of shock absorbers. Following Fig. 1, the equations of motion are as follows for the main mass and the damper mass, respectively,

$$m_1 \ddot{x}_1 + (k_1 x_1 + k'_1 x_1^3) + (c_1 \dot{x}_1 + c'_1 \dot{x}_1^2) + \{k_2 (x_1 - x_2) + k'_2 (x_1 - x_2)^3\} + \{c_2 (\dot{x}_1 - \dot{x}_2) + c'_2 (\dot{x}_1 - \dot{x}_2)(x_1 - x_2)^2\} = F \quad (1)$$

$$m_2 \ddot{x}_2 - \{k_2 (x_1 - x_2) + k'_2 (x_1 - x_2)^3\} - \{c_2 (\dot{x}_1 - \dot{x}_2) + c'_2 (\dot{x}_1 - \dot{x}_2)(x_1 - x_2)^2\} = 0 \quad (2)$$

For transformations, let

$$x_1 = y_1, x_2 = y_3, \frac{dx_1}{dt} = \dot{x}_1 = y_2$$

$$\text{and } \frac{dx_2}{dt} = \dot{x}_2 = y_4$$

With those transformations, Equations 1 and 2 become,

$$m_1 \frac{dy_2}{dt} + (k_1 y_1 + k'_1 y_1^3) + (c_1 y_2 + c'_1 y_2 y_1) + \{k_2 (y_1 - y_3) + k'_2 (y_1 - y_3)^3\} + \{c_2 (y_2 - y_4) + c'_2 (y_2 - y_4)(y_1 - y_3)^2\} = F \quad (3)$$

$$m_2 \frac{dy_4}{dt} - \{k_2(y_1 - y_3) + k'_2(y_1 - y_3)^3\} - \{c_2(y_2 - y_4) + c'_2(y_2 - y_4)(y_1 - y_3)^2\} = 0 \quad (4)$$

Rearrangement of Equation (3) & (4) gives,

$$\frac{dy_2}{dt} = \frac{1}{m_1} \left[ F - (k_1 y_1 + k'_1 y_1^3) - (c_1 y_2 + c'_1 y_2 y_1^2) - \{k_2(y_1 - y_3) + k'_2(y_1 - y_3)^3\} \right] \quad (5)$$

$$\frac{dy_4}{dt} = \frac{1}{m_2} \left[ \{k_2(y_1 - y_3) + k'_2(y_1 - y_3)^3\} + \{c_2(y_2 - y_4) + c'_2(y_2 - y_4)(y_1 - y_3)^2\} \right] \quad (6)$$

The governing Equations (5) and (6) can now be rewritten as a set of four nonlinear first order ordinary differential equations (ODE) as follows:

$$\frac{dy_1}{dt} = y_2 \quad (7)$$

$$\frac{dy_2}{dt} = \frac{1}{m_1} \left[ F - (k_1 y_1 + k'_1 y_1^3) - (c_1 y_2 + c'_1 y_2 y_1^2) - \{k_2(y_1 - y_3) + k'_2(y_1 - y_3)^3\} \right] \quad (8)$$

$$\frac{dy_3}{dt} = y_4 \quad (9)$$

$$\frac{dy_4}{dt} = \frac{1}{m_2} \left[ \{k_2(y_1 - y_3) + k'_2(y_1 - y_3)^3\} + \{c_2(y_2 - y_4) + c'_2(y_2 - y_4)(y_1 - y_3)^2\} \right] \quad (10)$$

The additional field equations, needed for multisegment method of integration are derived now from the above Equations. This is done by differentiating both sides of Governing Equations partially w.r.t.  $y(a)$ . More details can be found in [1,2].

## 2.1 Boundary Conditions

For different cases and chosen parameters (Tables 1, 2) prescribed boundary conditions are as given in Table 3. According to the multisegment method of integration, the boundary conditions for any boundary value problem are arranged in the following matrix form,

$$Ay(a) + By(b) = C \quad (11)$$

Solutions of the boundary value problem with any arbitrarily chosen boundary conditions are possible by the present method.

## 3. RESULTS AND DISCUSSION

Fig. 2 shows the absolute non-dimensional displacement ( $|d|$ ) versus frequency ratio ( $r$ ) for case 1. This problem is solved as initial value problem. No nonlinearity is taken into consideration. As seen from the figures, peak amplitude is lowest when  $\zeta_0 = 0.288$  which is known as optimum damping ratio of the system. This analysis was made intentionally to compare the exact results for untuned viscous damper in [4].

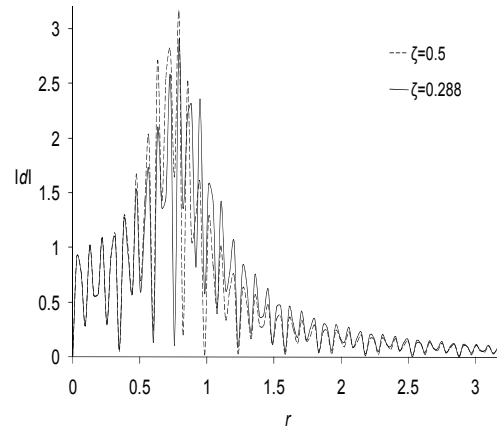


Fig 2.  $|d| - r$  for case 1 at  $t=20s$  having  $\mu=1.0$  and solved as initial value problem  $\zeta=0.288, 0.5$ .

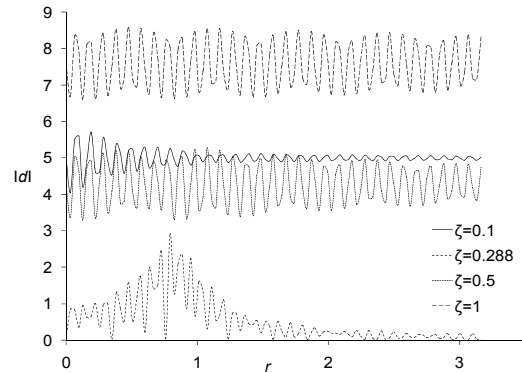


Fig 3.  $|d| - r$  for case at  $t=20s$  having  $\mu=1.0$  and solved as boundary value problem.

These results of Thompson [4] are, of course, for steady state vibrations but present study includes the transient terms. Fig. 2 for the main mass prove the reliability of the code again as these give very similar curves given in Thompson [4].

Next,  $d - r$  curves for case 1 having  $\mu=1.0$  solved as boundary value problem are shown in Fig. 3. The boundary conditions given in Table 3 were used for this observation. As the boundary conditions were fixing final velocity of the system and damping force is proportional to velocity, eventually the damping force became fixed at that particular boundary ( $t=b$ ). Damper in this case has little effect on the system's final displacement unless optimum  $\zeta = \zeta_0$  is used. As seen from the figure, for  $\zeta=1.0$ , amplitude ( $d$ ) range varies from 6.60 – 8.59, for  $\zeta=0.1$  range of  $d$  varies from 5.0 - 5.7 and for  $\zeta=0.5$   $d$  varies from 3.295 to 5.28. But, for optimum damping ratio ( $\zeta=0.288$ ) system shows similar deflection to that of initial value problem. This also indicates that the effect of optimum damping ratio ( $\zeta_0$ ) on the system's response is independent of boundary conditions. This figure also proves the fact that  $\zeta_0$  gives the minimum  $d$ .

$d_{\max} - \zeta$  relation for varying mass ratio is shown

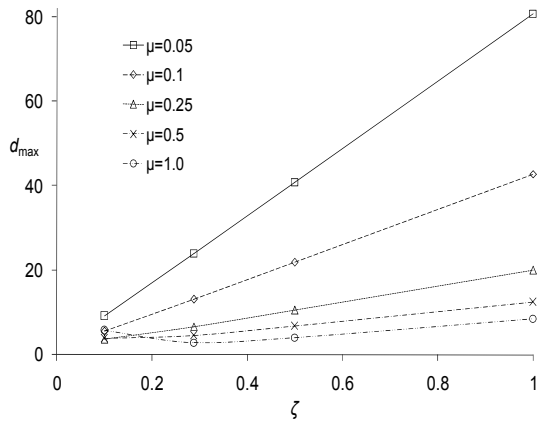


Fig 4.  $d_{\max} - \zeta$  with varying mass ratio ( $\mu$ ) for case 1 and solved as boundary value problem at  $t=20s$ .

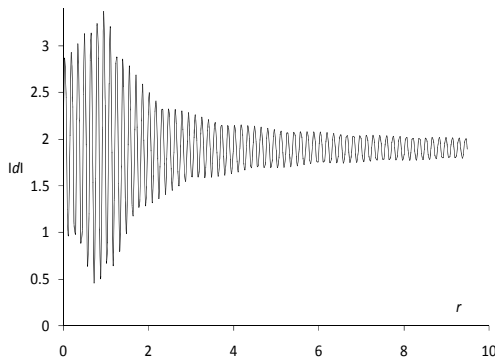


Fig 5.  $|d| - r$  for case 2 having  $\mu=0.01$  and  $\zeta=0.00496$  at  $t=50s$  and solved as boundary value problem.

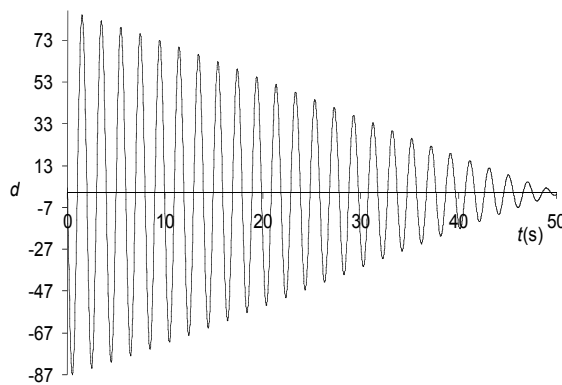


Fig 6.  $d - t$  for case 6 with  $\mu=0.01$ ,  $\zeta=0.00496$  and  $r=1.012$ .

in Fig. 4. Each curve in this figure was drawn by taking the peak amplitudes of a particular mass ratio while varying the damping ratio. From Fig. 4 the line of a particular  $\mu$  becomes steeper with the decrease of its value. So system with lower mass ratio but with fixed

damping ratio gives larger vibration. For cross-check it can be readily seen that for  $\mu=1.0$  and  $\zeta=0.288$ ,  $d_{\max}$  is minimum as discussed earlier.

System response for cases 2 – 16 can be seen in Figs. 5-7.

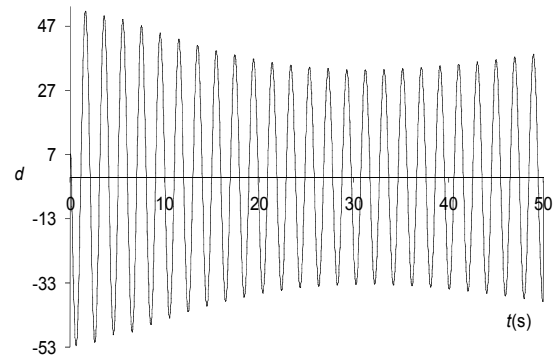


Fig 7.  $d - t$  for case 11 with  $\mu=0.01$ ,  $\zeta=0.00496$  and  $r=1.0$ .

Fig. 5 is for absolute non-dimensional displacement versus frequency ratio for case 2 at  $t=50s$ . At  $r \cong 1$  resonance occurs as the system behaves as SDOFS. Due to imposed velocity of the system at final condition the damper force also becomes fixed at the end. As seen from the figure, peak amplitude occurs at frequency ratio near unity and the peak value is 3.37. Cases 3 – 16 show similar type of deflection at  $t=50s$ .

Fig. 6 shows the  $d - t$  curves for case 6 at  $r = 1.012$ . Case 4 also shows similar type of response at  $r=1.012$ . Solution for this type of spring and damper combination, does not converge with time, resulting an unstable system at  $r=1.0$ . This happens due to soft springs in absorber side with linear damping (case 4, case 6). Spring force of 2<sup>nd</sup> mass becomes negative due to negative index and this force cannot be diminished by the linear or soft damper. This problem is eliminated when hard damper is used. Another way to solve this type of problem is to reduce the value of spring index of 2<sup>nd</sup> mass. As seen from figure, amplitude  $d$  ranges from 86.53 – 2.09. Here again system approaches to stability with time.

In Fig. 7,  $d - t$  curve for case 11 at  $r=1.0$  is shown. Amplitude ranges from 52.07 – 32.28. Cases 12 – 16 at  $r=1.0$  show similar response. Those cases, not discussed in detail here can be seen in Ahmed [2].

#### 4. CONCLUSIONS

As found in this study case 1 appears to be stable for any value of damping ratio but other cases 2-16 becomes unstable with increase of any nonlinearity index. A few causes of instability can be attributed to jump phenomenon and negative damping for the present study.



Jump phenomenon is for nonlinearity in the spring's response. The amplitude suddenly jumps discontinuously near the resonant frequency making the unstable. The instability region near the resonant frequency depends on amount of damping and rate of change of forcing frequency among others.

Soundness of the code has been demonstrated comparing a few results of present analysis with available exact results. Following conclusions can be drawn from the present study:

- Effect of optimum damping ratio ( $\zeta_0$ ) on the system's response is independent of boundary conditions. In case of optimum damping, untuned vibration damper vibrates with minimum amplitude. This happens for both initial value and boundary value problems. For example, case 1 with optimum damping ratio ( $\zeta_0=0.288$ ) shows similar deflections for initial value and boundary value problems.
- Mass ratio ( $\mu$ ) plays a significant role on the maximum deflection of untuned vibration damper. For the same damping ratio, system with larger mass ratio shows smaller peak amplitude. But all the systems with a particular mass ratio show minimum peak at optimum damping ratio.
- Increased nonlinearity in spring and damper makes the system more unstable.
- Untuned system with different cases (2 – 16) shows similar responses for both lower and higher forcing frequency ratios. For example, at forcing frequency ratio  $r=0.3162$  and  $4.744$  all the systems show similar responses.
- From this study, we can conclude that practical springs and dampers should contain smaller nonlinearity indices as systems with lower nonlinearity indexes approached to more stability.
- Practically no spring or damper remains linear with ever-increasing response. Therefore, this study is particularly useful for cars' shock absorber design and application. As stability of a shock absorber can easily change because of damper and spring nonlinearities.

## 5. REFERENCES

1. Rahman, M. A. and Ahmed, A. U. (2009), "Boundary value problem analysis of a tuned vibration absorber having nonlinear springs", Int. J. Structural Engineering (Inderscience Enterprises Ltd., Switzerland)- In press.
2. Ahmed, A. U., (2009), "Stability analysis of vibration absorbers", M. Sc. Engg. Thesis, Department of Mechanical Engineering, BUET, Bangladesh.
3. Kalnins A. and Dym C. L.,(1976), "Vibration Beams, Plates, and Shells", Dowden, Hutchinson & Ross, Inc.
4. Thomson, W. T., (1981). "Theory of Vibrations with Applications (2<sup>nd</sup> Edition)", George Allen & Unwin.
5. Mikhlin Y. V., Reshetnikova S. N., (2005). "Dynamical Interaction of an Elastic System and Essentially Nonlinear Absorber", Journal of Sound and Vibration 283 (1-2), pp. 91-120.
6. Zhu S.J., Zheng Y.F., Fu Y.M., (2004). "Analysis of Non-linear Dynamics of a Two Degree of Freedom Vibration System with Non-linear Damping and Nonlinear Spring", Journal of Sound and Vibration 271, pp. 15-24.
7. Manevitch L. I., Gendelman O., Musienko A. I., Vakakis A. F., and Bergman L., (2003), "Dynamic interaction of a semi-infinite linear chain of coupled oscillators with a strongly nonlinear end attachment", Physica D. Nonlinear Phenomena 178(1-2), pp. 1-18.
8. McFarland D. M., Bergman L. A., Vakakis A. F., Manevitch L. I., and Gendelman O., (2002), "Energy pumping into passive nonlinear energy sinks attached to forced linear substructures: analytical and experimental results", 9th Conference on Nonlinear Vibrations, Stability, and Dynamics of Structures, Virginia Polytechnic Institute and State University.
9. Nakhai G, Narimani A., Golnaraghi M. F., Swanson D.A, (2003), "Practical Frequency and Time Optimal Design of Passive Linear Vibration Isolation Mounts," 1. Vehicle System Dynamics 39, pp. 437-466.
10. Shekhar N. C., Hatwal H. , Mallik A. K., (1998), "Response of Non-linear Dissipative Shock Isolators," Journal of Sound and Vibration 214, pp. 589-603.
11. Shekhar N. C., Hatwal H., Mallik A. K., (1999), "Performance of Nonlinear Isolators and Absorbers to Shock Excitation," Journal of Sound and Vibration 227, pp. 293-307.
12. Alexander N. A., Schilder F., (2009), "Exploring the Performance of a Nonlinear Tuned Mass Damper" Journal of Sound and Vibration 319, pp. 445-462.
13. Kalnins, A., and Lestingi, J. E., (1967). "On Nonlinear Analysis of Elastic Shells of Revolution", J. Appl. Mech. 34, pp. 59-64.

## 6. NOMENCLATURE

$a$	Initial time reference
$b$	Final time reference
$c$	Damping coefficient (N-s/m)
$c_1, c_2$	Main mass and absorber mass damping coefficients (N-s/m)
$c'$	Damping nonlinearity index (N-s/m <sup>3</sup> )
$c'_1, c'_2$	Main mass and absorber mass damping nonlinearity indexes (N-s/m <sup>3</sup> )
$d$	$k_1 * x_1 / f$ : Nondimensional displacement for main mass
$e$	$k_1 * x_2 / f$ : Nondimensional displacement for absorber mass
$f$	Amplitude of the applied force (N)
$F$	$f \sin(\omega t)$ (N)
$k$	Spring constant (N/m)
$k_1, k_2$	Main mass and absorber mass spring constants (N/m)
$k'$	Spring nonlinearity index (N/m <sup>3</sup> )
$k'_1, k'_2$	Main mass and absorber mass spring nonlinearity indexes (N/m <sup>3</sup> )
$m_1, m_2$	Main mass and absorber mass (kg)
$r$	Frequency ratio: $\frac{\omega}{\sqrt{k_1/m_1}}$

$r_1$	Value of $r$ at first natural frequency of the system
$r_2$	Value of $r$ at second natural frequency of the system
$t$	Time (s)
$x_1$	$x$
$x_1, x_2$	Main mass and absorber mass deflections (m)
$y_1, y_3$	$x_1, x_2$ (m)
$\dot{x}_1, \dot{x}_2$	Main mass and absorber mass

	velocities (m/s)
$y_2, y_4$	$\dot{x}_1, \dot{x}_2$ (m/s)
$\zeta$	Damping ratio: $\frac{c_2}{2\sqrt{m_1 k_1}}$
$\zeta_0$	Optimum damping ratio : $\frac{\mu}{\sqrt{2(1+\mu)(2+\mu)}}$
$\mu$	Mass ratio: $m_2/m_1$
$\omega$	Forcing frequency (rad/s)
$\omega_1, \omega_2$	Natural frequencies of the main mass and absorber masses
DOF	Degrees of Freedom
DOFS	Degrees of Freedom System
MDOF	Multiple Degrees of Freedom
SDOF	Single Degree of Freedom
Tuned Absorber	2 DOFS without damping
Untuned Absorber	2 DOFS with damping
Spring force	$kx \pm k'x^3$
Damping force	$c\dot{x} \pm c'\dot{x}^2$
Hard spring	Nonlinearity index ( $k'$ ) is positive
Soft spring	Nonlinearity index ( $k'$ ) is negative
Hard damper	Nonlinearity index ( $c'$ ) is positive
Soft damper	Nonlinearity index ( $c'$ ) is negative
Linear spring	Nonlinearity index $k' = 0.0$
Linear damper	Nonlinearity index $c' = 0.0$

## 7. MAILING ADDRESS

Muhammad Ashiqur Rahman  
 Professor  
 Department of Mechanical Engineering,  
 Bangladesh University of Engineering & Technology  
 (BUET), Dhaka-1000  
 Telephone & Fax: 88-02-9665636  
 Email: ashig@me.buet.ac.bd

## HARNESSING RAINDROP ENERGY IN BANGLADESH

PV Biswas, MA Uddin, MA Islam, MAR Sarkar, VG Desa, MH Khan and AMA Huq

<sup>1</sup>Department of Mechanical Engineering, BUET  
Dhaka-1000, Bangladesh

### ABSTRACT

The kinetic energy of raindrops can be converted into electricity by using piezoelectric materials. This paper explains behavior of raindrops at impact and of piezoelectricity. The physics of monsoon and rain pattern are also described in detail. It has been found that Polyvinylidene Fluoride called PVDF is the most suitable type of material for power harvesting application. Raindrops of 1 to 5 mm diameter are suitable for harnessing energy in Bangladesh. According to the data in Bangladesh we have around four months (June-September) of massive rainfall. In Bangladesh this time is very potential for harnessing this kind of energy.

**Keywords:** Energy Harnessing, Piezoelectric material, Mechanical vibration

### 1. INTRODUCTION

Energy is the most important issue in the world and in Bangladesh also. It is true that it is not easy to override the conventional energy sources. But to meet the large energy demand we need some substitutes. And due to recent environment concern issue the energy should be greener. So it is true that we need to try to move towards harnessing the energy from the nature which can be very much potential in some respect. There are some energy which are low in energy density but can provide sufficient energy to our sensors and MEMS. One of the energy sources is raindrop energy. We are trying to explore the possibility and probability of raindrop energy potential in Bangladesh.

Several experiments and theory have been developed [1, 2]. The idea is rain falls from a significant height which has significant kinetic energy. It is possible to convert this kinetic energy into electric power by using piezoelectric materials which converts the stress into electrical energy. Basically it is vibration energy. Because of rain drop impact is being converted to electrical energy the amount of rain and the size of the rain drop is very important. In France raindrop size can vary from 1mm to 5 mm [1]. The terminal velocity of raindrop also has a major role play.

In Bangladesh June July August and September (JJAS) we have large amount of rain falls all over the country [3]. So there is a huge potential to collect the rainfall energy in the four months where other popular non conventional energy (e.g. solar energy) may not play a major role at that time.

### 2. REVIEW

#### 2.1 Behavior of raindrops at impact

It is essential to understand underlying mechanisms

governing the impact and spread of liquid droplets upon a solid surface for harnessing rain drop energy. Although this subject has been studied for more than a century, it is still not fully understood and therefore not perfectly modeled.

In general, three different types of behaviors are observed during drop impact on a solid surface: splashing, spreading and bouncing as illustrated in Fig 1 [4-5]. Drops impinging on solids can adhere to or bounce off the surface and can break up after impact or it can spread smoothly. An obvious difference is between processes that cause a disintegration of the drop and those that do not. Typically, the former case is called a splash. Often the conditions leading to splashing and spreading, respectively, are of particular interest. Hence, the desired behavior depends on the objectives of the particular process.

Many studies have been carried out to predict the behavior of a drop during its impact. Stow and Hadfield [6] established a splash parameter for the occurrence of splash, which depends on the surface roughness. The correlation for splashing/deposition limit expressed as  $Re^{31}We^{69} = \xi$ , where  $\xi$ , splash deposition value is dependent upon the surface roughness. Mundo *et al* [7] determined the limit between the splash and deposition modes for rigid impact surface based on experiments.

$$K = Oh*Re^{1.25} > 57.7 \quad (1)$$

If K is larger than a critical empirical value of 57.7, then it is in splashing regime. However, this empirical formula does not include other factors such as surface roughness, which is known to affect the contact angle between liquid drop and solid surface. Thoroddsen and Sakakibara's [8] experiments on a rigid impact surface showed that some of their test conditions in Mundo's splashing regime but

close to the splashing line did not splash. They suspected that surface roughness plays an important role and caused the ineffectiveness of Mundo's criteria, i.e.,

rougher solid surface will trigger splashing for drops in conditions near the splashing line.

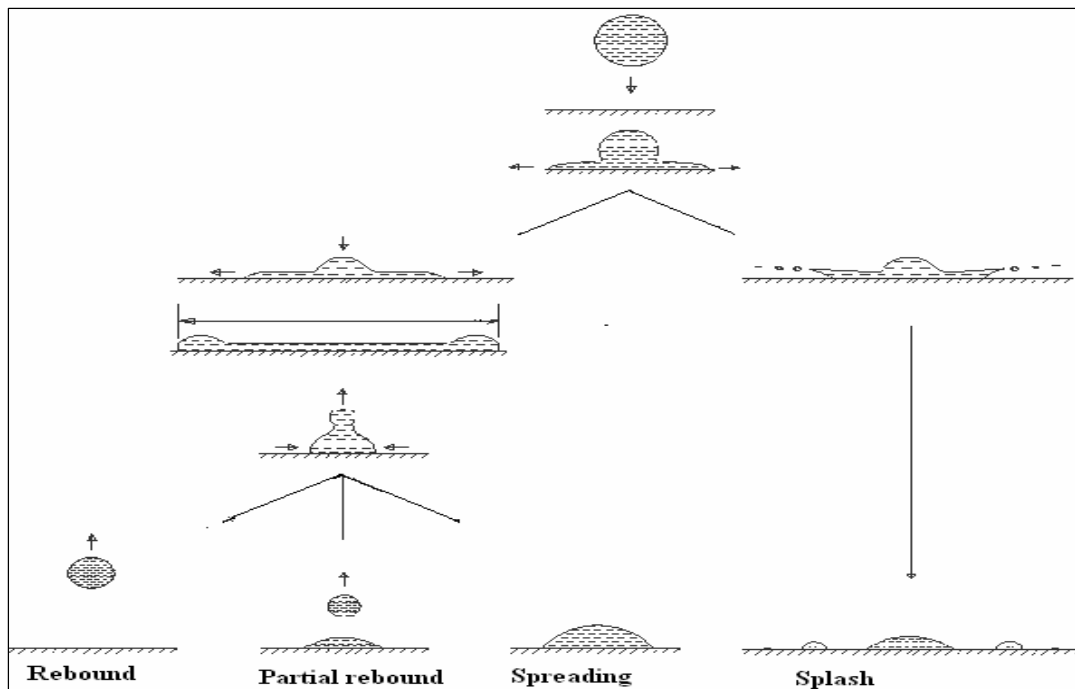


Fig 1. Scenarios of drop impact on a solid surface [5]

## 2.2 Piezoelectricity

Piezoelectricity describes the phenomenon of generating an electric charge in a material when subjecting it to a mechanical stress (direct effect); conversely, generating a mechanical strain in response to an applied electric field (converse effect).

The type of piezoelectric material selected for a power harvesting application can have a major influence on the harvester's functionality and performance. The most common type of piezoelectric used in power harvesting applications is lead zirconate titanate, a piezoceramic, known as PZT. Although PZT is widely used as a power harvesting material, the piezoceramic's extremely brittle nature causes limitations in the strain that it can safely absorb without being damaged. Lee et al [9] note that piezoceramics are susceptible to fatigue crack growth when subjected to high frequency cyclic loading. Another common piezoelectric material PVDF is a piezoelectric polymer that exhibits considerable flexibility when compared to PZT. Though the piezoelectric strain constant ( $d_{31}$ ) and coupling coefficient ( $k_{31}$ ) for PVDF is lower than that of PZT, PVDF is flexible, lightweight, tough, ecological properties (it does not contain lead) (Table 1).

A method of increasing the amount of energy harvested from a piezoelectric is to utilize a more efficient coupling mode. Two practical coupling modes exist; the  $-31$  mode and the  $-33$  mode. In the  $-31$  mode, a force is applied in the direction perpendicular to the poling direction, an example of which is a bending beam that is poled on its top and bottom surfaces. In the  $-33$  mode, a force is applied in the same direction as the

poling direction, such as the compression of a piezoelectric block that is poled on its top and bottom surfaces.

Conventionally, the  $-31$  mode has been the most commonly used coupling mode: however, the  $-31$  mode yields a lower coupling coefficient,  $k$ , than the  $-33$  mode [12, 13]. Table 3.4 shows a few of the most promising piezoelectric materials and their key properties. It was concluded that in a small force, low vibration level environment, the  $-31$  configuration cantilever proved most efficient [13].

Table 1: Comparison of Properties of Standard Piezoelectric Polymer and Ceramic Materials [10]

	$d_{31}$ , pm/V	$k_{31}$	Salient features
PVDF	28	0.12	Flexible, lightweight, low acoustic and mechanical impedance
PZT	175	0.34	Brittle, heavy, toxic

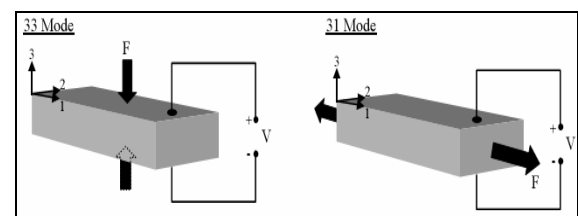


Fig 2. Illustration of 33 mode and 31 mode operation of piezoelectric material [11]

### 2.3 Energy harnessing from raindrop

Harnessing rain drop energy is a very recent research. Guigon *et al.* [1, 2] have recently developed a system that scavenges the vibration energy from a piezoelectric structure impacted by a water drop. In their papers they describe in detail the theoretical study undertaken to optimize the mechanical system and present an experimental device that validates the theoretical results.

Piezoelectric materials are widely used to convert mechanical energy into electrical energy. Majority of studies focus on the harvesting of vibration energy using piezoelectric beams subjected to pure bending [14,15]. For harvesting raindrop energy Guigon *et al.* [2] consider a piezoelectric membrane sensitive to surface impacts. The diagram in fig 3 shows the device used to recover the impact energy of raindrops. In the system the piezoelectric PVDF (Polyvinylidene fluoride) was used for power harvesting and it is used in -31 mode. In their study, they used mono-stretched PVDF polymers (thickness  $H = 25 \mu\text{m}$ , piezoelectric strain coefficient  $d_{31} = 15 \text{ pC N}^{-1}$ ) and bi-stretched PVDF polymers (thickness  $H = 9 \mu\text{m}$ , piezoelectric strain coefficient  $d_{31} = 5 \text{ pC N}^{-1}$ ), with a length  $L$  of 10 cm. Fig 4 shows the system with two transparent PVDF bands embedded in a Plexiglas structure, the electrodes on the surface of the piezoelectric membrane having been positioned by the manufacturer.

The impact of rain drop causes a deformation of the piezoelectric PVDF polymer membrane and a consequent strain. The resulting electrical energy in the PVDF material is formulated as [16]

$$W_{\text{elect}} = k \frac{Y_{\text{PVDF}}}{L} \Delta x \quad (2)$$

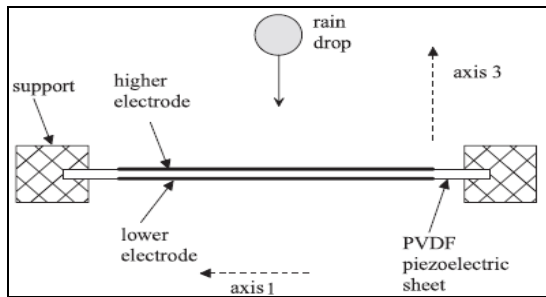


Fig 3. System of raindrop energy harvesting [2]

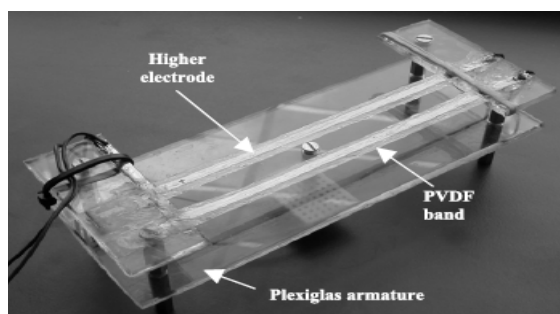


Fig 4. Mechanical system embedding the PVDF bands [2]

The electrical energy generated within the material is proportional to the deformation (Eq. 2), and thus to the amplitude of vibrations. It appears that 0.1 N pre-stressing of the cable decreases the amplitude by a factor of 10 after a water drop impact [1].

In the analysis Guigon *et al.* [1, 2] used the Mundo's [7] criteria to determine the mode of impact. They assumed that the energy balance of the splash mode drop is very close to the inelastic impact of a ball on a plate, where the energy lost during the collision is quantified by a restitution coefficient, namely the ratio of the relative speeds before and after the collision. They considered a standard rain drop of diameter 1mm and speed 3 m/s. Theoretical study shows that in order to maximize the deformation energy transferred to the material (and thus the recovered energy): the optimal width of which must be equal to approximately 2/3 of the maximum spread diameter of the drop (3.3 mm for a standard raindrop [17]).

It appears that, a  $25 \mu\text{m}$  thick, mono-stretched PVDF material with a piezoelectric strain coefficient  $d_{31} = 20 \text{ pC N}^{-1}$  is much more effective than a  $9 \mu\text{m}$  thick, bi-stretched PDVF material with a piezoelectric strain coefficient  $d_{31} = 5 \text{ pC N}^{-1}$ . Table 2 shows recoverable electrical quantities in various situations, with a single drop.

The results of these impacts are very close to those produced in the simulation, as shown in table 3. Note that the higher the speed of impact, the more the experimental results differ from the simulation results. Nevertheless, the theoretical and experimental results remain reasonably close.

Table 2: Recoverable electrical quantities in various situations [1]

Types of drop	Cable dimension	Recoverable voltage	Recoverable electrical energy	Recoverable instantaneous power
Rain; D:1mm; v:2.8m/s	L:10cm; W:3 mm; H: 25 $\mu\text{m}$	1.6 V	1.7 nJ	0.8 $\mu\text{W}$
Medium; D:2mm; v: 0.75 m/s	L:10cm; W:3 mm; H: 25 $\mu\text{m}$	3 V	5 nJ	2.5 $\mu\text{W}$
Downpour : 5mm; v: 5.7 m/s	L:10cm; W:1.3 cm; H: 25 $\mu\text{m}$	98 V	25 $\mu\text{J}$	12.5 mW

Table 3: Theoretical/experimental results for high-speed impact on 25  $\mu\text{m}$  thick PVDF [2]

Impact velocity and drop size	Simulation result	Experimental result	Ratio experimental/simulation results
4.5 m/s and 3 mm	24 V	17.2 V ( $\approx 147 \text{ nJ}$ ; $73 \mu\text{W}$ )	0.72
3.2 m/s and 1.6 mm	5.7 V	4.68 V ( $\approx 16 \text{ nJ}$ ; $8 \mu\text{W}$ )	0.82

### 3. RAIN SCENARIO IN BANGLADESH

#### 3.1 Physics of Monsoon in Bangladesh

The time of monsoon in South East Asia is from June to September. Prior to June, the months of May, April and March are summer months during which solar energy pours through the cloudless skies heating the South East Asia land mass which in turn heats air above the land. This hot air expands and rises. The solar energy also heats up the surface of the seas in Arabian Sea and the Bay of Bengal encouraging evaporation that generates considerable water vapor above the warm tropical water sea surface. At this time these months are autumnal months for the Indian Ocean south of the equator. The ocean is cool and the dense air settles over the surface of the ocean. This differential heating generates massive cool aerial current (Carnot Cycle) from the Indian Ocean south of the Equator heading northward to the hot land mass of South East Asia. As it passes over the Arabian Sea and Bay of Bengal, the cool dry air mass picks up tropical warm water vapor becoming moist air. The cool moist air consequently warms and rises, further picking up water vapor. As the moist unsaturated air parcel rises adiabatically, it cools and eventually reaches a relative humidity of 100%. This saturated moist air, under certain pressure and certain conditions, forms into cloud droplets when there are existing nuclei. Clouds now begin to appear. If the vapor will further condense on these cloud droplets increasing their size. This vapor condensation releases latent energy which in turns warms the air pushing it further upwards and allowing even more wet air to come in from the sea. All this heralds the growth of the dark monsoon clouds.

This massive aerial monsoon current conveying condensed cloud drops sweeps northward branching into a number of streams. It appears these streams are attached towards forested areas before making land. During their transverse over the forested areas, the monsoon cloud drops are transformed into raindrops and precipitation begins. One stream moves to Sumatra. Finally another stream moves north along the forested Arakan coast emerging into Assam (Cherapunji with nearly 300 inches annual rainfall) and Bangladesh before turning westwards over the Gangetic basin.)

The monsoon stream is made up of rain squalls. It is during the squalls that the monsoon rain comes down to earth and accounts for the intermittency in the monsoon rains. The squalls length is about 535km and speed 8m/s [18].

#### 3.2 Rain Pattern in Bangladesh

In Bangladesh in June, July, August and September we have the maximum down pour. The interesting part is in the peak season (Jun-Jul-Aug) average rainfall in the Western Ghat of India was only 224cm, contrasted to the peak season average rainfall from the Bay of Bengal branch ( Baisakkali ) of the monsoon stream (Bengal, Bangladesh and Assam) amounting to 762cms, nearly three and half fold.

Table 4 exhibits the available rainfall at Dhaka. For the purpose of comparison, the available rain power in France is almost 1 Wh per square meter per year. If 15 raindrops of 5mm size falls per second on a square meter

flat surface in Bangladesh (i.e.900 raindrops per minute), the impact energy equals to 0.18 watts.

PRECIS generated simulation data for the year of 2009 (Fig 6). Annual cycle of projected rainfall in Bangladesh projected (from year 2010-2020) (Fig 7) that the rainfall would be normally what it is in the major monsoon period.

It also shows that for the next ten years in Bangladesh the rain pattern is almost the same. Which is a good sign because we can go for long term plan and research for the technology development of harnessing rain energy in Bangladesh.

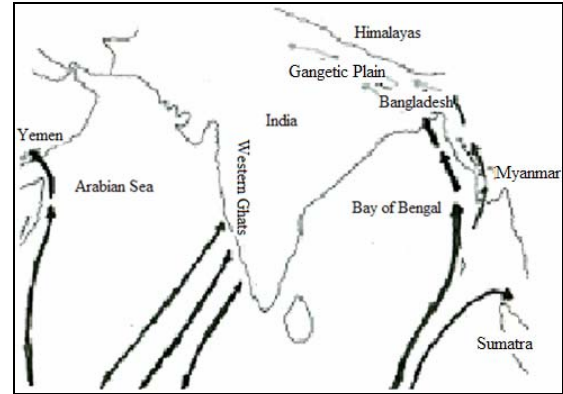


Fig 5. Map of North Asia

Table 4: Bangladesh cities monthly rainfall in mm [19]

	May	Jun	Jul	Aug	Sep	Oct	Total
Dhaka	428	348	553	282	361	368	2340
Sylhet	731	472	775	503	253	344	3078
Rajshahi	144	348	349	354	502	155	1852
Chittagong	463	879	491	848	203	201	3085

#### 3.3 Rain Drop Pattern

Raindrop is common occurrence that everyone has experienced. A raindrop occurs when the water vapor from a cloud wraps itself around tiny particles during condensation. Contrary to popular opinion, raindrops are not shaped like teardrops. In fact, they are actually oblate spheroids, or spheres with the nose smashed in [20]. Different sources approximate different ranges for the measure of a diameter of a raindrop. However, on the average, a raindrop is between 0.1 to 5 millimeters. There are some exceptions; rarely, raindrops of 8 millimeters were known to occur [20]. Rain drops size normally larger than the normal doesn't occur because when they come down they break down simply or by colliding with their neighbors. Presently, precipitation is believed to be triggered by a course of action called the collision-coalescence process [20]. The cloud droplets are small in size. So motion of the air keeps them suspended. Larger droplets are faster than the small ones so on the way down they sweep the small droplets and become large in size. Several important factors affect the diameter or size of a raindrop. First, the fall velocity of a raindrop particle is directly proportional to its diameter [20]. The larger the particle, the faster it falls. The same



follows for the maximum fall distance before evaporation or the process in which a liquid turns into a gas. The larger the diameter, the greater the distance it will fall due to gravity, the force that pulls a water droplet toward the earth's surface.

As a droplet falls, it also encounters air resistance or frictional force. The magnitude of this force depends on

the size of the drop's "bottom", or the surface area resisting the fall [20]. As the particle accelerates the frictional drag increases. Finally the frictional and gravitational forces balance and the droplet fall at a constant speed, which is called terminal velocity. This again depends on size; smaller droplets have a lower terminal velocity than larger droplets.

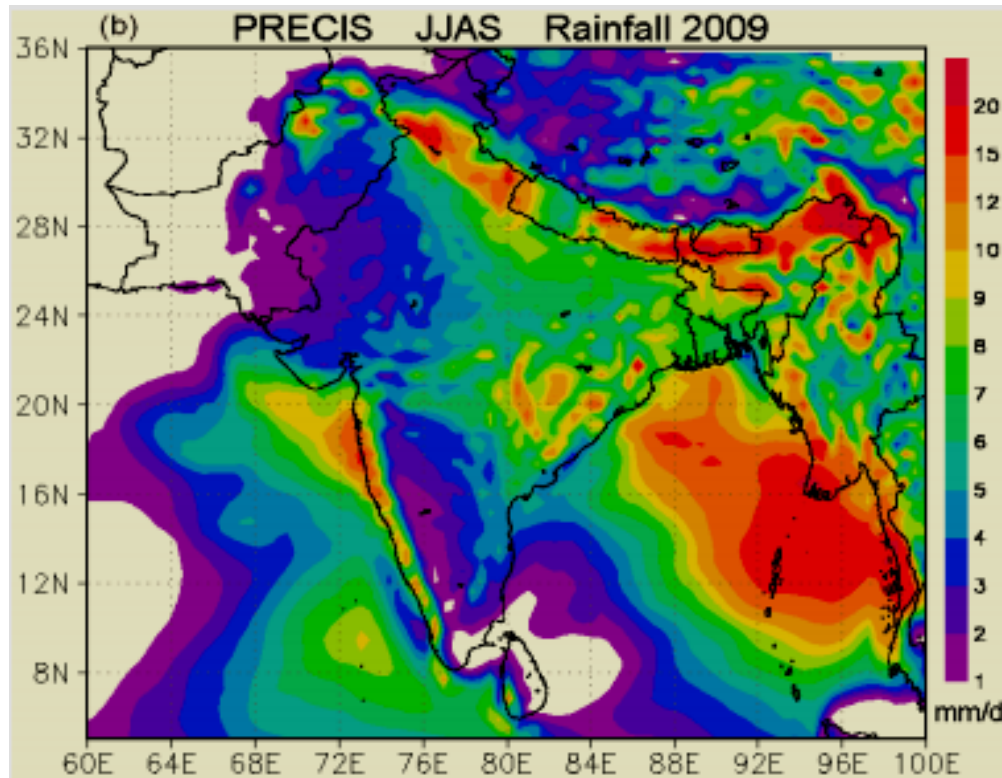


Fig 6. Projection of annual rainfall (mm/d) in the SAARC for the month of JJAS [3]

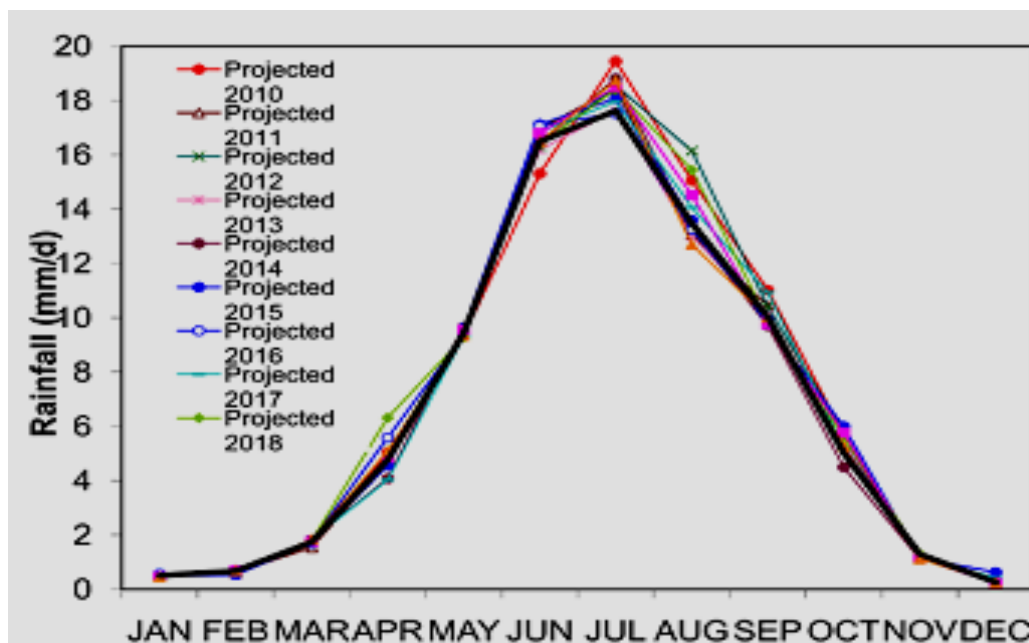


Fig 7. Annual cycle of projected rainfall (mm/d) in Bangladesh [3]

Table 5: Rain drop size assumption [20]

Bibliographic Entry	Result (w/surrounding text)	Standardized Result
"Precipitation." <i>Earth Science</i> . Illinois: Heath, 1999	"A raindrop may have a maximum diameter of 0.25 centimeter."	2.5 mm
"Rain." <i>Encyclopedia Encarta</i> . 1st ed. CD-ROM. New York: Microsoft, 2000.	"Raindrops generally have a diameter greater than 0.5 mm (0.02 in.). They range in size up to about 3 mm (about 0.13 in.) in diameter."	0.5–3 mm
Davis, Neil T. "Raindrop Size Article #236." <i>Alaska Science Forum</i> . 28 June 1978.	"The 4 mm maximum diameter of raindrops probably results because raindrops larger than this size tend to break up when colliding with other large raindrops."	< 4 mm
"Characteristics of Particles and Particle Dispersoids." <i>Handbook of Chemistry and Physics</i> . 62nd Edition. New York: CRC, 1981.	"Chart"	0.5–10 mm
Formation of Raindrops. Encyclopedia.com.	"Raindrops vary in size from about 0.02 in. (0.5 mm) to as much as 0.33 in. (8 mm) in thunderstorms."	0.5–8 mm

### 3.4 Measurement Techniques

Because of raindrop size, terminal velocity and quantity is very important here we need to go through some measurement technique.

To determine the terminal velocity of the falling monsoon raindrops ( $v$ ), we can use a stroboscopic flash lamp, adjusting the frequency to get a stationary image of the falling raindrops. The distance between successive falling drops can allow us to compute the frequency of the raindrops ( $f$ ). For determining the size of the raindrops, a camera with an electronic flash and close up lens can give a reasonable idea of the size of raindrops. Random distribution of drop sizes can also be gained by rapid collection of rain on a waxed surface or a shallow pan of oil. This size distribution of raindrop should be in conformity with raindrop size distribution law, found in books on meteorology.

### 4. JUSTIFICATION FOR THE STUDY

In Bangladesh only 47,084 (56%) villages out of the total 84,320 villages have been electrified as of April 2009 [21]. Furthermore, the year wise village electrification has been shown in Table 6.

Table 6: Number of villages electrified in Bangladesh under the project SHS [21]

Fiscal Year	98/99	99/00	00/01	06/07	07/08
No. of Villages electrified	3399	3463	2821	926	926

To provide electricity in areas not reached by electric grid, REB is supporting a renewable energy option by making

solar home system (SHS) available to households. A total of 13000 SHS has been installed.

Solar home systems are effective in the sunny months but inefficient during the monsoon months. It behooves to investigate other measures to ensure electricity availability during the monsoon months to these home systems. One such investigation is to explore the possibility to harness the energy of monsoon rains.

### 5. CONCLUSION

Energy is the major concern in the coming world. It must be remembered it is impossible to replace the mainstream energy by the use of non conventional energy. Rain drop energy is low grade energy. Due to that reason it would be used in sensors, MEMS those which consume very low amount of energy.

Because it is low grade energy the conversion mechanism should be highly efficient. Recent development in piezoelectric materials has made this energy harnessing more easy. Again the system should be sensitive to both raindrops (1mm diameter) and downpour drops (5mm diameter) because the average size of the drops are in that region.

This potential energy is under development. Some major works are being done in both raindrop energy and such kind of vibration energy. Georgia Institute of technology had made an umbrella with PVDF which is capable of harnessing energy from raindrop and powers its LED light. Researchers of the same university also have made a flexible fiber coated with zinc oxide nanowires that harvest any kind of vibration or motion for electric current.

According to the data in Bangladesh we have around four months of massive rainfall. In Bangladesh this time is very potential for harnessing this kind of energy.

## 6. REFERENCE

- [1] Guigon, R., Chaillout, J. J., Jager, Th. and Despesse, G., 2008a, "Harvesting raindrop energy: theory", *Smart Mater. Struct.* 17 015038.
- [2] Guigon, R., Chaillout, J. J., Jager, Th. and Despesse, G., 2008b, "Harvesting raindrop energy: experimental study", *Smart Mater. Struct.* 17 015039.
- [3] Islam, M. N., 2009, "Rainfall and Temperature Scenario for Bangladesh," the *Open Atmospheric science Journal*, 3, 93-103.
- [4] Rein, M., 1993, "Phenomena of liquid drop impact on solid and liquid surfaces", *Fluid Dynamics Research*, 12(2):61–93.
- [5] Rein, M., 2002, *Drop-surface interactions*, Springer, Wien; New York.
- [6] Stow, C. D. and Hadfield, M. G., 1981, "An experimental investigation of fluid flow resulting from the impact of a water drop with an unyielding dry surface", *Proc. R. Soc. of London, Ser. A* 373,419.
- [7] Mundo, CHR, Sommerfeld, M. and tropea, C., 1995, "Droplet-wall Collisions: Experimental studies of the deformation and break-up processes", *Int. J. Multiphase Flow*, Vol. 21, No. 2, 151-173.
- [8] Thoroddsen, S. T. and Sakakibara, J., 1998, "Evolution of the fingering pattern of an impacting drop," *Physics of Fluids*, Vol. 10, No. 6, 1359-1374.
- [9] Lee, C. S., Joo, J., Han, S., Lee, J. H. and Koh, S. K. 2005, "Poly(vinylidene fluoride) transducers with highly conducting poly (3, 4-ethylene dioxythiophene) electrodes", *Proc. Int. Conf. on Science and Technology of Synthetic Metals*, Vol 152 pp 49–52.
- [10] Harrison, J. S. and Unaies, Z., 2001, "Piezoelectric Polymers," NASA/CR-2001-211422 ICASE Report No. 2001-43.
- [11] Roundy, S. J., 2003, "Energy scavenging for wireless sensor nodes with a focus on vibration to energy conversion", Ph.D. thesis, University of California, USA.
- [12] Starner, T., 1996, "Human-powered wearable computing", *IBM Systems Journal*, 35(3) 618-629.
- [13] Baker, J., Roundy, S. and Wright, P., 2005, "Alternative geometries for increasing power density in vibration energy scavenging for wireless sensor networks", *Proc. 3rd Int. Energy Conversion Engineering Conf. (San Francisco, CA, Aug.)*, pp 959–70.
- [14] Roundy, S., 2005, "On the effectiveness of vibration-base energy harvesting", *J. Intelligent Material*

- Systems and Structures, Vol. 16.
- [15] Rabaey, J. M., Ammer, M. J., Silva, J. L., Patel, D. and Roundy S., 2000, "PicoRadio Supports Ad Hoc Ultra-Low Power Wireless Networking", *IEEE Computer*, Vol. 33, No. 7, pp. 42-48.
- [16] Courbon, J., 1980, "R'esistancedesmat' eriaux—Th' eoriesdes poutres Techniquesdel' Ing' enieur" C, 2, 010.
- [17] Clanet, C., Beguin, C., Richard, D. and Quere, D., 2004, "Maximal Deformation of an impacting drop" *J. Fluid Mech.*, 517 199–208.
- [18] Rafiuddin, M. and Islam, M. N., 2009, "Water and Flood Management", *Proc. 2<sup>nd</sup> Int. Conference*.
- [19] Ahmed, F., 1999, "Rainwater harvesting potential in Bangladesh", *Proc. 25<sup>th</sup> WEC Conference*.
- [20] Elert, G, 2001, *The Physics Factbook*, Available from URL: <http://hypertextbook.com/facts/2001/IgorVolynets.shtml>
- [21] Chowdhury, M. N. H., 2009. African Electrification Workshop.

## 7. NOMENCLATURE

Symbol	Meaning	Unit
H	Thickness	( $\mu\text{m}$ )
L	Length	(cm)
W	Width	(mm)
$d_{31}$	Strain coefficient	(pC/N)
$U_{\text{elec}}$	Electrical energy	J
k	Coupling coefficient	[-]
Y	Young's modulus	[-]
V	Volume	$\text{m}^3$
$S_{\text{aver}}$	Average voluminal deformation	[-]
D	Drop diameter	mm
v	Velocity	m/s
Re	Reynolds number	[-]
We	Weber number	[-]
Oh	Ohnesorge number	[-]
$\xi$	Splash deposition value	[-]

## 8. MAILING ADDRESS

M A Islam  
 Department of Mechanical Engineering,  
 BUET, Dhaka-1000, Bangladesh.  
 Email:aislam@me.buet.ac.bd

## STRESS ANALYSIS OF STEEL PLATE HAVING HOLES OF VARIOUS SHAPES, SIZES AND ORIENTATIONS USING FINITE ELEMENT METHOD

T. Hasan, A. Das, T. Rahman, S. C. Chowdhury, and M. T. Alam

Department of Mechanical Engineering, Bangladesh University of Engineering and Technology,  
Dhaka, Bangladesh

### ABSTRACT

Steel is widely used in machine parts, structural equipment and many other applications. In many steel structural elements, holes of different shapes and orientations are made with a view to satisfy the design requirements. The presence of holes in steel elements creates stress concentration, which eventually reduce the mechanical strength of the structure. Therefore, it is of great importance to investigate the state of stress around the holes for the safety and proper design of such elements. In this paper, the effects of hole size, shape and orientation on the stress-strain distribution are investigated. Finite element method, one of the popular numerical techniques, is used for the solution of two-dimensional elastic plates incorporating hole located at the centre of the plate. Results from finite element method have been compared with the analytical results for different shapes.

**Keywords:** Finite Element Method, Stress Concentration.

### 1. INTRODUCTION

Almost all structures consist of assembly of simple elements, which are connected to each other by joints. Joints or connections that are usually made in steel structures are mechanical fastening using bolts or rivets. In the mechanical fastening, holes are made to place the bolts or rivets; these make the structure weak and susceptible to failure. Therefore, it is necessary to investigate the state of stress around the holes for the safety and proper design of such structures.

From the point of view of the above facts, it is of great importance to understand the behavior of the steel structures with holes. For the solution of the problem several methodologies can be followed, however, all of these methods can be classified in the following three general categories: experimental, analytical and numerical method. Though experimental methods give the most reliable results, it is very costly, as it requires special equipments, testing facilities etc. Analytical solution of every problem is almost impossible because of complex boundary conditions and shapes. For this reason the numerical methods had become the ultimate choice by the researchers in the last few decades. Invention and rapid improvement of the computing machines, i.e. sophisticated high performance computers, also played an important role for the increasing popularity of the numerical methods.

Stress analysis of a steel structure with holes requires the solution of partial differential equations. There are various numerical methods available for the solution of

partial differential equations. Among them most popular methods are: Finite Element Method (FEM) and Finite Difference Method (FDM). The finite element method is a numerical technique for obtaining approximate solution to a wide variety of engineering problems. Although originally developed to study stresses in complex airframe structures, it has since been extended and applied to the broad field of continuum mechanics because of its diversity and flexibility as an analysis tool. The finite difference model of a problem gives a point wise approximation to the governing equations. This model is improved as more points are used. With finite difference techniques we can treat some fairly difficult problems; but for example, when we encounter irregular geometries or an unusual specification of boundary conditions, we find that finite difference techniques become hard to use.

Unlike the finite difference method, which envisions the solution region as an array of grid points, the finite element method envisions the solution region as built up many small, interconnected sub regions or elements. A finite element model of a problem gives a piece wise approximation to the governing equations. Since these elements can be put together in a variety of ways, they can be used to represent exceedingly complex shapes.

## 2. DESCRIPTION OF THE PROBLEM

The geometry of the problem is shown in Fig 1. The material of the plate is high strength alloy steel; Poisson's ratio  $\nu=0.33$ , Young's modulus  $E=200$  GPa. Uniform tensile load ( $\sigma_x$ ) is applied to the plate's lengthwise direction.

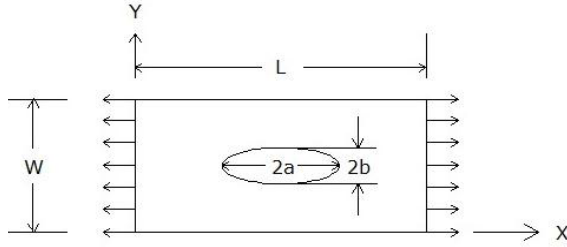


Fig 1. Rectangular plate with centrally located elliptical hole under uniform tensile loading

## 3. EQUATIONS USED

Stress analysis of an elastic body is usually three dimensional problem. But, most of the practical problems appear in the state of plane stress or plane strain. Stress analysis of three-dimensional bodies under plane stress or plane strain can be treated as two-dimensional problems. The solution of two-dimensional problems require the integration of the different equations of equilibrium together with the compatibility equations and boundary conditions. If body force is neglected, the equations to be satisfied are

$$\partial\sigma_x / \partial x + \partial\sigma_{xy} / \partial y = 0 \quad (1)$$

$$\partial\sigma_y / \partial y + \partial\sigma_{xy} / \partial x = 0 \quad (2)$$

$$(\partial^2 / \partial x^2 + \partial^2 / \partial y^2)(\sigma_x + \sigma_y) = 0 \quad (3)$$

Substitution of stress components by displacement components  $u$  and  $v$  into Eqs. (1) to (3) makes Eq. (3) redundant and Eqs. (1) and (2) transforms to

$$\partial^2 u / \partial x^2 + (1-\nu)/2(\partial^2 u / \partial y^2) + (1+\nu)/2(\partial^2 v / \partial x \partial y) = 0 \quad (4)$$

$$\partial^2 v / \partial y^2 + (1-\nu)/2(\partial^2 v / \partial x^2) + (1+\nu)/2(\partial^2 u / \partial x \partial y) = 0 \quad (5)$$

Now the problem is to find  $u$  and  $v$  from a two dimensional field satisfying the two elliptical partial differential Eqs. (4) and (5).

Instead of determining the two functions  $u$  and  $v$  the problem can be reduced to solving a single function  $\psi(x,y)$ , which can be determined by satisfying Eqs. (4) and (5). The displacement potential function  $\psi(x,y)$  can be defined as

$$u = \partial^2 \psi / \partial x \partial y \quad (6.a)$$

$$v = -[(1-\nu) \partial^2 \psi / \partial y^2 + 2\partial^2 \psi / \partial x^2] / (1-\nu) \quad (6.b)$$

By the above definitions the displacement components  $u$  and  $v$  satisfies Eq. (4) and the only condition reduced from Eq. (5) that the function  $\psi(x,y)$  has to satisfy is

$$\partial^4 \psi / \partial x^4 + 2 \partial^4 \psi / \partial x^2 \partial y^2 + \partial^4 \psi / \partial y^4 = 0 \quad (7)$$

So, now the problem is to evaluate a single function  $\psi(x,y)$  from the bi-harmonic Eq. (7), satisfying the boundary conditions specified at the boundary

## 4. RESULTS AND DISCUSSION

The solution of the displacement and stress components  $u_x$ ,  $u_y$ ,  $\sigma_x$ ,  $\sigma_y$  and  $\sigma_{xy}$  for elliptical hole and  $\sigma_x$  for square hole are obtained. Their distributions along some selected sections are described below. Also the changes of maximum stress for elliptical and square hole with angular orientations and with sizes are described.

### 4.1 Solution for Rectangular Plate with Elliptical Hole

#### a) Distribution of $\sigma_x$

Figure 2 shows a problem of rectangular plate with elliptical hole at the centre ( $a/b=2$ ) and two ends of plate are subjected to uniform tensile stress along X-direction and other two ends are kept free. At the extreme right end, the magnitude of normalized axial stress equals to unity, i.e. actual stress is equal to the applied stress.

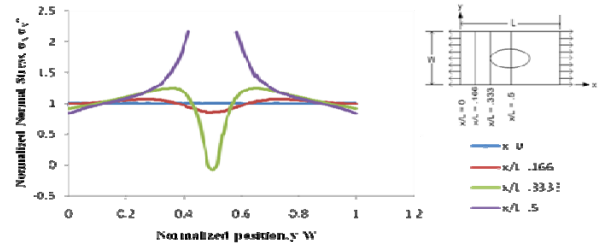


Fig 2. Distribution of normalized axial stress component at different sections of the plate.

Maximum compressive stress exists at two ends of elliptical hole on its major axis. Then it propagates towards the ends at a declining rate. From section  $y/W=0.42$  to section  $y/W=0.58$  compressive stress is generated. Most critical section is  $x/L=0.5$ . At  $x/L=0.5$  section the magnitude of axial stress is more than 2 times of the applied stress.

#### b) Distribution of $\sigma_y$

Figure 3 illustrates the normalized axial normal stress ( $\sigma_y / \sigma_x$ ) with respect to  $y$ -axis ( $y/W$ ). At  $x/L=0$  throughout the section the value is positive. The value of tensile stress then decreases and compressive stress dominates over the later sections. Compressive stress develops due to the effect of hole. The effect of hole starts at the section  $x/L=0.333$  where the major axis of hole exists in the corresponding section. At this section maximum compressive stress develops at the point where the major axis touches the section. The value of compressive stress develops is much more than the developed axial stress through applied load. The value of compressive stress decreases at the further outer sections from the hole. And it diminishes at the boundary of the plate. Again it is seen that after crossing the section

$x/L=0.333$  along X-direction, the value of tensile stress increases. This is due to the effect of minor axis of hole. At the section  $x/L=0.5$  the maximum tensile stress occurs because the ends of minor axis (vertical axis) of elliptical hole touches with this section.

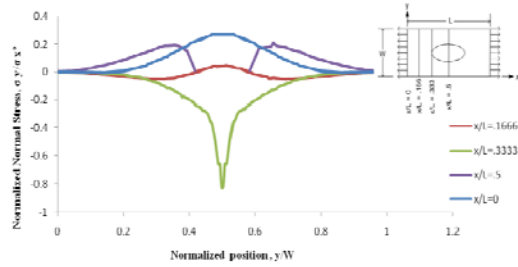


Fig 3. Distribution of normalized lateral stress component at different sections of the plate.

### c) Distribution of $\sigma_{xy}$

Figure 4 illustrates the normalized shear stress ( $\sigma_{xy} / \sigma_x^*$ ) with respect to y-axis ( $y/W$ ). The trends of these graphs except the end section and middle section of the plate are wave shaped. As the hole is located at the centre of the plate, so due to the effect of hole half of the sections goes positive value and others half goes negative value. With the development of normal stress, shear stress also developed in the plate but this value is much smaller compared to normal stress. As the load is applied over a ductile material a small amount of shear stress developed which is not dominant over normal stress but for brittle material the value of shear stress is dominant over normal stress. If we apply load over brittle material, then the value of shear stress will be considerable.

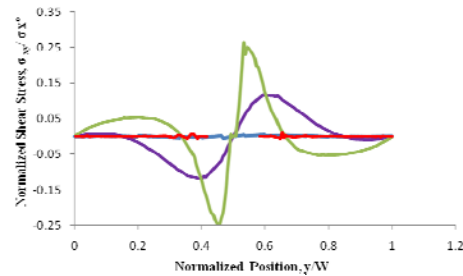


Fig 4. Distribution of normalized shear stress component at different sections of the plate.

### d) Distribution of $u_x$

Figure 5 represents the normalized displacement component ( $u_x/W$ ) with respect to y-axis ( $y/W$ ). From the graph it is seen that displacement at any section reaches maximum at  $y/W=0.5$ . As area is small here, less material is present here. So bonding force between molecules is weaker and as a result axial displacement will be higher. Again the value is higher in the outer layer. From the graph, it is also seen that after  $x/L=0.5$  the value of displacement is negative. This is due to the fact that, uniform tensile load is applied over the both ends of the plate.

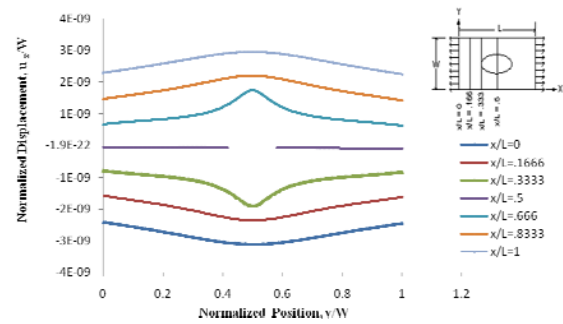


Fig 5. Distribution of normalized displacement component ( $u_x/W$ ) at different sections of the plate.

### e) Distribution of $u_y$

Figure 6 illustrates the normalized displacement component along y-axis ( $u_y/W$ ) with respect to y-axis ( $y/W$ ). With the development of  $\sigma_x$  a small amount of  $\sigma_y$  develops over the plate. Due to the effect of lateral normal stress, lateral normal strain develops. From the graph it is seen that for the half of each section the value is positive and for other sections value is negative. And value will be zero at  $y/W=0.5$ . Actually the deformation along y-direction starts from the position of  $y/W=0.5$ . Then it propagates through the both lateral ends of the plate. The two halves of each section from  $y/W=0.5$  tends to extend along the positive and negative direction of Y-axis. They oppose each other at the midpoint of each section. For this reason, the value of lateral strain is zero at midpoint of each section. Again it is seen that, as we go towards the inner sections of the plate the value of lateral displacement increases due to the hole effect.

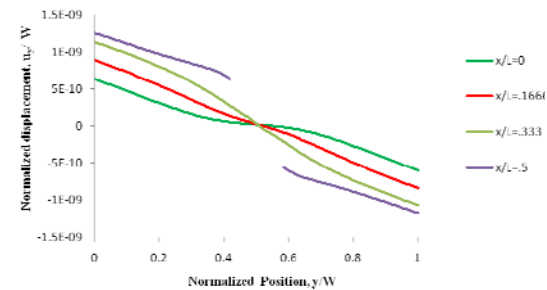


Fig 6. Distribution of normalized displacement component ( $u_y/W$ ) at different sections of the plate.

### f) Variation of Maximum Stress in the Plate Due to the Variation of Size of Hole

Figure 7 shows the variation of maximum longitudinal stress developed over a rectangular plate with the size variation of elliptical hole inserted into the plate. From the graph it is seen that with the increase of  $b/a$  ratio, maximum stress increases for 0 degree angle. For other angles maximum stress also decreases with decrease of  $b/a$  ratio, but after a certain  $b/a$  ratio instead of decrease of maximum stress, the value increases with decrease of  $b/a$  ratio. This is due to the fact that for large decrease of  $b/a$  means effect of one axis of hole, rejects the effect of other axis of hole. As a result, the desired value will not be found.



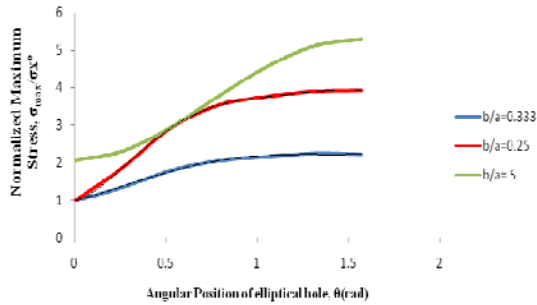


Fig 7. Variation of maximum stress in the plate due to the variation of size of hole.

**g) Variation of Maximum Stress Due to the Orientation of Elliptical Hole**

Figure 8 represents the variation of maximum axial stress due to variation of angular orientation of the elliptical hole inside the plate ( $a/b=2$  and  $L/W=1$ ). From the graph it is seen that the value of maximum stress not only depends on hole size but also depends on the angular position of hole which is located at the centre of the plate. With increase of angle, the value of maximum stress increases and it reaches maximum at 90 degree. At 0 degree the area under applied load is higher compared to other orientations. As a result, the value of maximum stress will be lower. This maximum stress exists at the ends of the vertical axis of the hole. At 90 degree, the position of major axis interchanges with the position of the minor axis. As a result, the area under the applied load decreases and maximum stress increases.

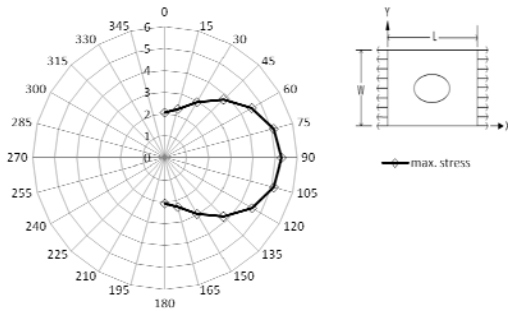


Fig 8. Variation of maximum stress due to the orientation of elliptical hole.

Many computational efforts are applied for the development of equation, for orientation of hole. All equations are developed based on the well known equation for elliptical hole at 0 degree angular orientation which is

$$\frac{\sigma_{\max}}{\sigma} = \left(1 + 2 \frac{b}{a}\right) \quad (8)$$

For  $a/b=2$ , the equation which gives less error than other equations is an exponential equation is represents as

$$\frac{\sigma_{\max}}{\sigma} = \left[1 + 2 \times \frac{b}{a} \times e^{(-.5366 \theta^6 + 2.2419 \theta^5 - 2.8179 \theta^4 + .0012 \theta^3 + 1.7398 \theta^2 + 0.6013 \theta)}\right] \quad (9)$$

For  $a/b=3$ , the equation found from the finite element method is

$$\frac{\sigma_{\max}}{\sigma} = \left[1 + 2 \frac{b}{a} (-4.842 \theta^3 + 10.93 \theta^2 + 0.251 \theta + 1.034)\right] \quad (10)$$

**4.2 Solution for Rectangular Plate with Square Hole**

**a) Variation of Stress at Different Cross Sections**

Figure 9 shows the normalized axial normal stress ( $\sigma_x/\sigma_0$ ) with respect to y-axis ( $y/a$ ) for a rectangular plate with square hole at the centre. Two ends of plate are subjected to uniform tensile stress along X-direction and other two ends are kept free. In order to present the graphs of stress in dimensionless form, actual values of stress are divided by the applied stress. At the extreme right end, the magnitude of normalized axial stress equals to unity, i.e. actual stress is equal to the applied stress. In all sections except ( $x/L=0$ ) the axial normal stress exceeds the applied stress and there is also compressive stress exists. In a material molecules are arranged in parallel layers. Due to the presence of hole all layers cannot move at a same rate. Maximum compressive load exists at two extremities of square hole along longitudinal axis. Then it propagates through the plate and its value declines towards the ends. The value of compressive stress goes to zero at ends of the plate and only applied load exists there. Stress concentration at sharp edge at the square hole, so we get the maximum value of tensile stress there. The value of stress increases up to the sharp edge, then it begins to decrease due to the flat region of square from which the compressive stress originates.

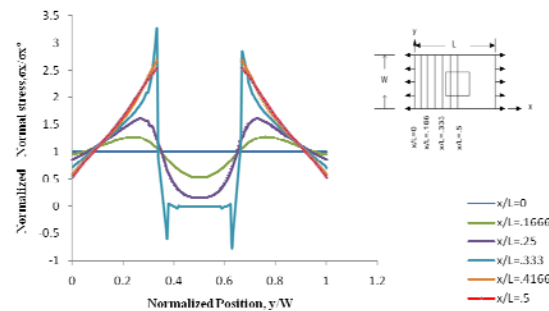


Fig 9. Distribution of normalized axial stress along the plate having square hole at the center.

**b) Variation of Maximum Stress due to Orientation of Square Hole**

Figure 10 represents variation of maximum stress due to variation of angular orientation of the square hole inside the plate ( $L/A=3$  and  $L/W=1$ ). It is seen that maximum stress increases with increasing angle of hole. It reaches maximum value at 30 degree and after that value decreases. As it is a square hole the value of maximum stress at 0 degree and 90 degree are same.

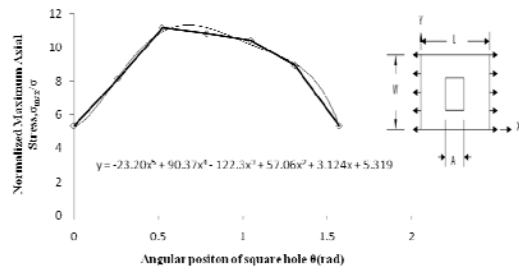


Fig 10. Variation of maximum stress due to orientation of square hole.

### 4.3 Variation of Maximum Stress due to Orientation of Rectangular Hole

Figure 11 represents Cartesian graph for maximum stresses developed in a plate with rectangular holes ( $A/B=2$  and  $L/W=1$ ) located at centre with various angular orientation. From the graph it is seen that it follows a fourth order polynomial

$$Y = -2.29x^4 + 7.066x^3 - 9.66x^2 + 7.279x + 2.393 \quad (11)$$

The value of maximum stress increases up to 30 degree then decreases up to 45 degree. After having a maximum value at 60 degree it again decreases.

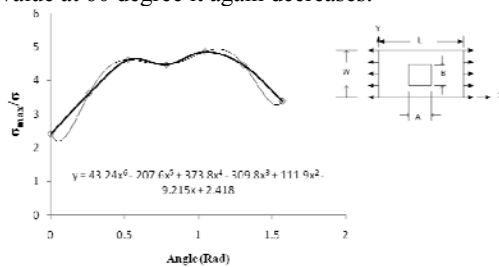


Fig 11. Variation of maximum stress due to orientation of rectangular hole.

## 5. CONCLUSION

In this study finite element method is used for the solution of two-dimensional problems of rectangular plate having centrally located holes of various shapes. Finite element results are carried out by using the commercial software COMSOL 3.3. Results are presented in the form of non-dimensional graphs. Effects of hole shape are critically analyzed from the results of the finite element method and analytical methods. The following conclusions are drawn in regard to the present study. Comparisons between the results by the present finite element method and the analytical solution technique yield good agreement. At  $0^\circ$  angular position of elliptical hole, maximum stress occurs at the two ends of hole on its minor axis. At  $90^\circ$  angular position of elliptical hole, maximum stress occurs at the two ends of hole on its major axis. For elliptical hole, with the increase of plate length to width ratio the maximum stress at all angular position increases. Moreover, with the increase of elliptical hole major diameter to minor diameter ratio, the maximum stress at all angular position increases. In case of rectangular plate under uniform tensile loading, square hole experiences more

longitudinal stress than elliptical hole. If the holes are made to rotate, the value of maximum stress increases with rotation. For square hole, the maximum value of maximum stress occurs at  $45^\circ$  angular position and it decreases with increase of plate length to hole length ratio. In case of rotation of square hole, for very small or very large plate length to hole length ratio, the highest value of maximum stress is found at  $30^\circ$  of rotation.

## 6. REFERENCES

1. Timoshenko, S. P. and Goodier, J. N., Theory of Elasticity, 3<sup>rd</sup> Ed., McGraw-Hill, Book Company, New York, N. Y., 1982
2. Airy, G. B., Brit. Assoc. Advan. Sci. Rept., 1862.
3. Rankine, Applied Mechanics, 14<sup>th</sup> Ed., pp. 344, 1895.
4. Mesnager, A., Compt. Rend., Vol. 132, pp. 1475, 1901.
5. Gatewood, B. E. and Dale, R., J. Appl. Mech., Vol. 29, pp. 747-749, 1962.
6. Hetenyi, M. (ed.), Handbook of Experimental Stress Analysis, John Wiley & Sons.
7. Frocht, M. M., Photoelasticity, Vol. 2, John Wiley & Sons, Inc., New York, 1940 and 1948.
8. Ribiere, M. C., Compt. Rend., Vol. 126, pp. 402-404 and 1190-1192, 1898.
9. Filon, L. N. G., Trans. Roy. Soc. (London), ser. A, Vol. 201, pp. 97, 1903.
10. Conway, H. D. and Ithaca, N. Y., "Some Problems of Orthotropic Plane Stress", Journal of Applied Mechanics Trans. ASME, pp. 72-76, 1953.
11. Kolossoff, G., Z. Math. Physik., Vol. 62, 1914.

## 7. NOMENCLATURE

Symbol	Meaning	Unit
x,y	Rectangular co-ordinate	
E	Modulus of Elasticity	(Pa)
v	Poisson's Ratio	
u, v	Displacement component in the x and y direction	(mm)
$\sigma_x, \sigma_y,$ $\sigma_{xy}$	Stress component in the x, y direction and xy plane	(Pa)
$\Psi$	Potential function	
W	Width of the plate	(mm)
L	Length of the plate	(mm)
a, b	Elliptical hole dimension	(mm)
A, B	Rectangular hole dimension	(mm)

## 8. MAILING ADDRESS

Dr. Sanjib Chandra Chowdhury  
 Assistant Professor  
 Department of Mechanical Engineering  
 BUET, Dhaka-1000, BANGLADESH.  
 Phone : 88029665636,  
 FAX : 880-2-8613046  
 E-mail : sanjib@me.buet.ac.bd

## MODELING OF THE LONGITUDINAL ELASTIC MODULUS OF CARBON NANOTUBE REINFORCED NANOCOMPOSITES

S. C. Chowdhury<sup>1</sup>, M. S. Islam<sup>2</sup> and A. R. M. Ali<sup>3</sup>

Department of Mechanical Engineering, BUET, Dhaka, Bangladesh.

<sup>2</sup>BSTI, Tejgaon, Dhaka, Bangladesh.

<sup>3</sup>Department of Mechanical Engineering, BUET, Dhaka, Bangladesh.

### ABSTRACT

Carbon nanotubes (CNTs) possessing extremely high stiffness, strength, and resilience may be the ultimate reinforcing materials for the development of nanocomposites. Unlike conventional fiber reinforced composites, there are wide variations in the diameter and length of the CNTs in the CNTs reinforced composites. In this work a numerical model has been developed to calculate the longitudinal elastic modulus of short CNTs reinforced composites considering the variation of diameter and length of the CNTs. According to this model, the whole composite is divided into several composite segments which contain CNTs of almost same diameter and same length. Longitudinal elastic modulus of the composite is then calculated by weighted summation of the longitudinal modulus of each composite segment. Existing micromechanical approach for modeling of short fiber composites is modified to account for the structure of the CNTs to calculate the elastic modulus of each segmented CNTs reinforced composites. Statistical variations of the diameter and length of the CNTs are modeled by the normal distribution. Results obtained from this numerical model are compared with the available experimental results and the comparison concludes that the developed model can be used to predict the elastic modulus of CNTs reinforced composites.

**Keywords:** Modeling, Elastic modulus, Nanocomposites.

### 1. INTRODUCTION

The discovery of carbon nanotubes (CNTs) in the early 1990's by Iijima [1] has sparked a revolution in research activities in science and engineering devoted to nanostructures and their application. A single-walled nanotubes (SWNTs) is a hollow structure formed by covalently bonded carbon atoms [2-3]. It can be visualized a graphene sheet rolled into a cylindrical tube. For multi-walled nanotubes (MWNTs), a number of graphene layers are co-axially rolled together to form a cylindrical tube. The spacing between graphene layers is about 0.34 nm. CNTs have exceptional mechanical, electrical and thermal properties [4-5]. For example, the stiffness and strength of CNTs are in the range of TPa and GPa, whereas the nearest competing materials exhibit these properties in the range of GPa and MPa respectively. CNTs are now being used in the fields of electronics, field emission devices, nano-electro-mechanical (NEMS) devices, sensors, medical appliances, nano robotics and of course in light weight structural composites [6-7]. The use of CNTs in polymer materials is now being increasingly studied to produce advanced nanocomposites for aerospace, automotive, and military applications [7-9].

However, super strong CNTs alone do not ensure super strong composites because the mechanical

properties of CNTs reinforced composites are strongly influenced by the amount of load transfer from the matrix to the CNTs within the composites. Load transfer within the CNTs reinforced composites is influenced by the physical structure (i.e. diameter and length) of the CNTs and the interfacial conditions (i.e., with or without cross-link) between the CNTs and matrix. It should be mentioned that although CNTs can now be readily produced, it is quite difficult to produce CNTs with completely perfect structure with specific diameter and length. Depending on the production process, CNTs are of different diameters and lengths with different imperfections (i.e., missing atoms in the wall of CNT, curved CNTs etc.) [3, 10].

In the literature on CNTs based composites (especially polymer composites), there is wide variation in the reported elastic properties [11-14]. Reported improvements in the elastic modulus are lower than the expected if the CNTs are assumed to act as reinforcing elements with an elastic modulus of 1 TPa. Discrepancies in the reported elastic moduli as well as reported lower elastic moduli in the literature may be due to the insufficient load transfer through the interface between CNT and polymer matrix of the composites. Since load transfer through the interface is affected by several factors like CNTs diameter, CNTs length and

interface condition, it is necessary to investigate their effects on the elastic properties of CNTs based polymer composites. Thostenson et al. [15] have developed a model to predict the elastic modulus of CNTs based composites considering the variation of nanotube diameter. However, numerical model to predict the elastic properties of CNTs based composites considering the variation of nanotube diameters and lengths simultaneously is necessary in designing CNTs based composites.

Here a numerical model has been developed to calculate the longitudinal elastic modulus of CNTs based composites considering the variation of diameter and length of the CNTs. According to this model, the whole composite is divided into several composite segments which contain CNTs of almost same diameter and same length. Elastic modulus of the composite is then calculated by weighted summation of the modulus of each composite segment. Existing micromechanical approach for modeling of short fiber composites [16] is modified to account for the structure of the CNTs to calculate the elastic properties of each segmented CNTs reinforced composites. In the conventional micromechanical approach, where the model deal with the geometric heterogeneity is at the microscopic level (i.e., microstructure), the reinforcing fibers have solid structure. However, CNTs have hollow structure. Therefore, here the hollow structured CNTs are converted into equivalent solid fibers and elastic properties of the equivalent solid fibers are determined as well. The variations of the diameter and length of the CNTs are modeled by the normal distribution. Results obtained from this numerical model are compared with the available experimental results of CNTs reinforced composites.

## 2. MODULUS OF EQUIVALENT SOLID FIBER

To model the properties of the nanotube based composite, it is important to consider the nanoscale structure of SWNTs and MWNTs and how the nanotube interacts with the polymer matrix. For fibre-like materials, load is transferred to the reinforcement through shear stresses at the fibre/matrix interface. As mentioned earlier, CNTs can be visualized as a graphene sheet, where carbon forms a planar hexagonal structure, rolled into a seamless cylinder. In SWNT there is only one graphene layer whereas MWNT is simply formed of concentric SWNTs with an interlayer spacing equal to about 0.34 nm. In each concentric layer the bonding is covalent, but there is no bonding between the walls of the MWNT. As a consequence of this weak layer-to-layer nonbonded interaction in the MWNT, the outer layer of the multi-walled tube will carry almost the entire load transferred at the nanotube/matrix interface [17].

To determine the elastic modulus of the equivalent solid fiber, the load carrying capability of the outer layer of the nanotube must be applied to the entire solid cross-section of the equivalent fiber. The elastic modulus of the nanotube is modelled by considering that the outer wall of the nanotube acts as an effective solid fiber with the same deformation behavior and same diameter and length as shown in Fig. 1. An applied external force on

the nanotube and the equivalent solid fiber will result in an iso-strain condition. Therefore,

$$\varepsilon_{NT} = \varepsilon_{eqv}, \quad (1)$$

where the subscripts NT and eqv refer to the nanotube and equivalent solid fiber, respectively. Using equation (1) we can relate the elastic properties of the nanotube to that of an equivalent solid fiber as

$$E_{eqv} = \frac{\sigma_{eqv}}{\sigma_{NT}} E_{NT}. \quad (2)$$

Because the applied external force is the same, the moduli of the equivalent solid fiber can be expressed in terms of the ratio of their cross-sectional areas given as

$$E_{eqv} = \frac{A_{NT}}{A_{eqv}} E_{NT}. \quad (3)$$

After substituting, the modulus of the equivalent solid fiber can be expressed in terms of the elastic modulus of the nanotube, the nanotube outer layer thickness ( $=0.34$  nm) and the nanotube diameter given as

$$E_{eqv} = \frac{4t}{d} E_{NT}. \quad (4)$$

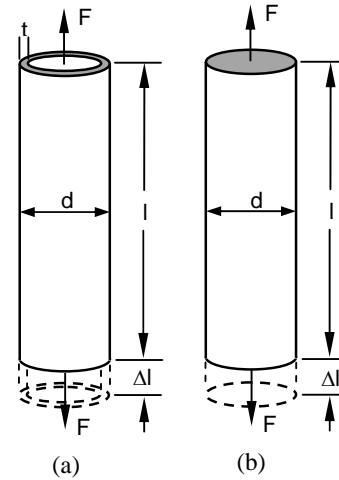


Fig 1. Schematic of (a) nanotube and (b) equivalent solid fiber.

## 3. NANOTUBE DENSITY

For the conversion of weight fraction, measured when processing the nanocomposite, to volume fraction, needed for predicting the elastic properties, we must know the density of the nanotubes and the matrix. For fibrous composites, the fiber volume fraction can be calculated based on the density of the constituents using the following equation [16].

$$V_f = \frac{W_f}{W_f + (\rho_f / \rho_m) - (\rho_f / \rho_m) W_f}. \quad (5)$$

Where subscripts f, m and c refer to the fiber, matrix and composite, respectively.

From the measurements of outside diameter and inside diameter the nanotube density can be calculated to be

$$\rho_{NT} = \frac{\rho_g (d^2 - d_i^2)}{d^2}. \quad (6)$$

Here  $d$  and  $d_i$  refer to nanotube outer and inner diameter respectively and subscript g refers to fully dense graphite. Obviously, the density of a MWNT will increase with the number of walls. The variation of density of equivalent solid nanotubes with outer diameters is shown in Fig. 2.

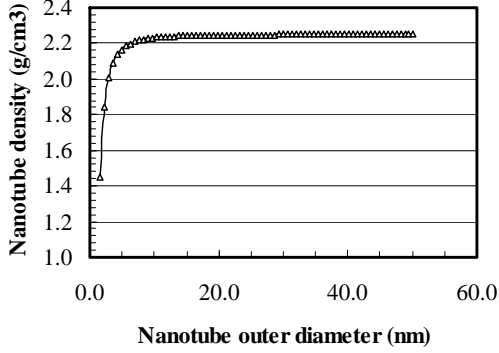


Fig 2. Variation of density with outer diameter for equivalent solid nanotubes.

#### 4. NANOTUBE DIAMETER AND LENGTH DISTRIBUTION

Although CNTs can now be readily produced, it is quite difficult to produce CNTs with completely perfect structure with specific diameter and length. Depending on the production process, CNTs are of different diameters and lengths. The distribution of nanotube diameter and length for a specific nanotube sample can be determined by measuring the outside diameter and length of a statistically large sample of nanotubes and then using the experimental data to determine the probability distribution of nanotubes for diameter and length  $\xi(d, l)$ . With a view to model the composite elastic properties, we study the volume fraction of carbon nanotubes within the composite. From the diameter and length distribution we can define the volume distribution of nanotubes  $\psi(d, l)$  as follows

$$\psi(d, l) = \frac{d^2 l \xi(d, l)}{\int_0^\infty \int_0^\infty d^2 l \xi(d, l) d(d) d(l)}. \quad (7)$$

The above volume distribution will need to be considered when calculating the overall nanocomposite properties.

#### 5. CALCULATION OF NANOCOMPOSITE ELASTIC MODULUS

A wide variety of models have been developed to predict the elastic properties of fiber composites in terms of the properties of the constituent materials [16]. Here we have used the most popular Halpin and Tsai [18] model according to which the longitudinal Young's modulus of composites can be determined from the following equations

$$E_{11} = E_m \left( \frac{1 + \zeta \eta_l V_f}{1 - \eta_l V_f} \right), \quad (8)$$

$$\eta_l = \frac{(E_f / E_m) - 1}{(E_f / E_m) - \zeta}. \quad (9)$$

Here the value of  $E_f (= E_{eqv})$  can be obtained from equation (4). In equations (8) and (9), the parameter  $\zeta$  is dependent on the geometry and boundary conditions of the reinforcement phase. For an aligned short fiber composite with low fiber volume fraction, this parameter can be expressed as [16]

$$\zeta = 2 \frac{l}{d}. \quad (10)$$

By substituting equations (4), (9) and (10) into (8) we can express the nanocomposite longitudinal Young's modulus in terms of the properties of the polymer matrix and the nanotube reinforcement given as

$$E_{11} = E_m \left( 1 + 2 \left( \frac{l}{d} \right) \left( \frac{(E_{NT} / E_m) - (d / 4t)}{(E_{NT} / E_m) + (l / 2t)} \right) V_{NT} \right) \times \left( 1 - \left( \frac{(E_{NT} / E_m) - (d / 4t)}{(E_{NT} / E_m) + (l / 2t)} \right) V_{NT} \right)^{-1} \quad (11)$$

Equation (11) expresses the diameter and length dependence of the carbon nanotube reinforcement on the nanocomposite elastic modulus. However, with distribution of nanotube diameters and lengths we can not use equation (11) directly to calculate the nanocomposite elastic modulus. To accurately model the elastic properties of the composite, we must take into account the contribution to the overall elastic modulus for each nanotube diameter and length and the volume fraction that tubes of a specific diameter and length occupy within the composite. If the nanotubes are uniformly dispersed and aligned throughout the matrix phase, the contribution of each diameter and length can be considered to act in parallel. Therefore, the elastic modulus of the composite can be calculated as a summation of parallel composites over the range of nanotube diameters and length.

The concept of parallel composites is illustrated in Fig. 3. Within the entire volume of the composite we can divide the volume into  $N$  individual composites containing nanotube with specific diameter and length. Each of the  $N$  individual composites will have a specific elastic modulus that depends on the local volume fraction of nanotubes at a given diameter and length. With the assumption of iso-strain, we can express the modulus of the whole composite as a summation of the moduli scaled by the partial volume of each  $n$ th composite given as

$$E_c = \sum_{n=1}^N v_n E_n(d_n, l_n). \quad (12)$$

Where  $E_n(d_n, l_n)$  is the elastic modulus of the  $n$ th composite segment calculated from equation (11) at the

specific nanotube diameter and length and  $v_n$  is the partial volume of the nth composite segment given as

$$v_n = \frac{VC_n}{VC} \quad (13)$$

$$\sum_{n=1}^{\infty} v_n = 1. \quad (14)$$

To calculate the modulus at a given nanotube diameter and length,  $E_n$  in equation (12), the local volume fraction at a given nanotube diameter and length can be calculated from the volume distribution of nanotubes (equation (7)) given as

$$V_{NT}(d_n, l_n) = \frac{\int_{d_n}^{d_n+\Delta d_n} \int_{l_n}^{l_n+\Delta l_n} (V_{NT} \psi(d, l)) d(d) d(l)}{v_n} \quad (15)$$

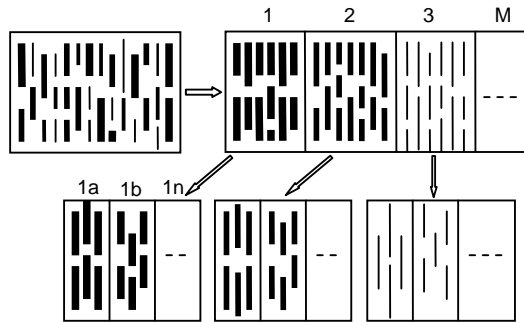


Fig 3. Composite segments. (Composite segment numbering with 1, 2, 3 etc. have CNTs of same diameter and different length whereas segments numbering with 1a, 1b etc. have CNTs of same diameter and same length.)

## 6. RESULTS AND DISCUSSION

To determine the longitudinal elastic modulus of the CNTs reinforced composites, the variation of the nanotube diameters and lengths are modeled with normal distribution. To calculate the composite elastic modulus, the whole composite is divided into 1000 composite segments with specific nanotube diameter and length. Young's modulus of the CNT and matrix are considered to be 1000 GPa and 1.2 GPa, respectively. To validate the present simulation model, we have compared our simulation result with that of Qian et al. [11] for the same type of nanotubes and polymer matrix. Figure 4 shows the comparison of present simulation results with that of Qian et al. Qian et al. have reported that adding 1% wt. of nanotubes (with average dia 34 nm and average length 15  $\mu\text{m}$ ) to polystyrene matrix increases the overall tensile modulus of composite by 35%. Using our model we have observed such increase in the composite modulus for 2.5 % wt. of nanotube, which is comparable. Figure 5 shows the effects of variation of nanotube diameter on the elastic modulus of composite. It is seen that with the increase of nanotube diameter elastic modulus of the composite decreases for a particular nanotube weight fraction. Figure 6 shows the effects of variation of nanotube length on the elastic modulus of composite. It is

seen that with the increase of nanotube length elastic modulus of the composite increases for a particular nanotube weight fraction.

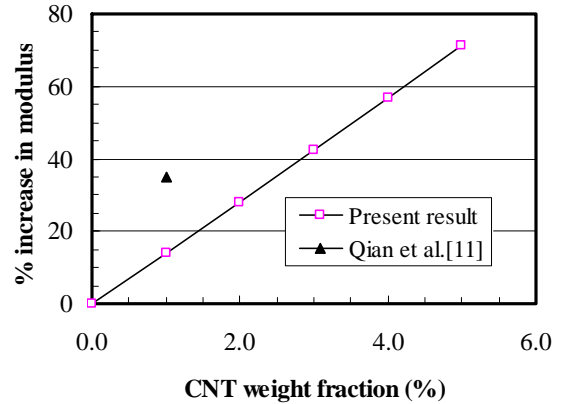


Fig 4. Variation of composite modulus with nanotube weight fraction.

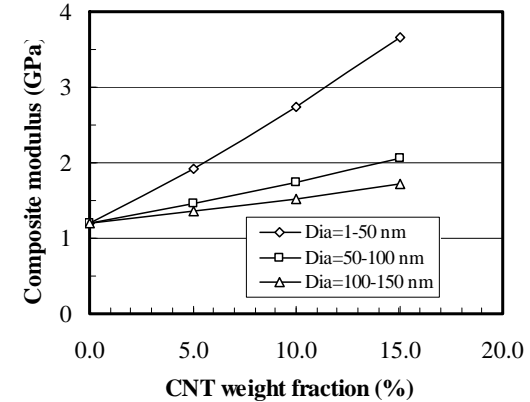


Fig 5. Variation of composite modulus with nanotube diameter (tube length = 800-1200 nm).

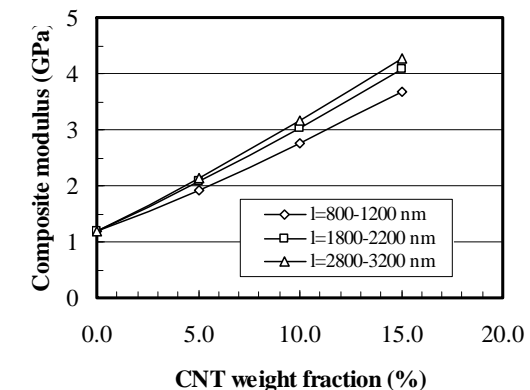


Fig 6. Variation of composite modulus with nanotube length (tube dia = 1-50 nm).

## 7. CONCLUSIONS

A numerical model has been developed to calculate the longitudinal elastic modulus of short CNTs

reinforced composites considering the variation of diameter and length of the CNTs. According to this model, the whole composite is divided into several composite segments which contain nanotubes of almost same diameter and same length. Longitudinal elastic modulus of the composite is then calculated by weighted summation of the longitudinal modulus of each composite segment. Existing micromechanical approach for modeling of short fiber composites is modified to account for the structure of the CNTs to calculate the elastic modulus of each segmented CNTs reinforced composites. Statistical variations of the diameter and length of the CNTs are modeled by the normal distribution. Results obtained from this numerical model are compared with the available experimental results and the comparison concludes that the developed model can be used to predict the elastic modulus of CNTs reinforced composites. It has also been observed that composite modulus increases with the increase of nanotube length and decrease of nanotube diameter.

## 8. REFERENCES

- Iijima S., 1991, "Helical Microtubules of Graphitic Carbon", *Nature*, 56:354.
- Dresselhaus M. S., Dresselhaus G. and Saito R., 1995, "Physics of Carbon Nanotubes", *Carbon*, 37: 883-891.
- Dresselhaus M. S., Dresselhaus G. and Avouris P., 2001, "Carbon Nanotubes: Synthesis, Structure, Properties and Application", Springer, Berlin, Germany.
- Miyagawa H., Misra M. and Mohanty A. K., 2005, "Mechanical Properties of Carbon Nanotubes and Their Polymer Composites", *Journal of Nanoscience and Nanotechnology*, 5:1593-1615
- Namilae S. and Chandra N., 2005, "Multiscale modeling to study the Effect of Interfaces in Carbon Nanotube-based Composites", *Transaction of the ASME*, 127:222-232
- Sinha N., Ma J. and Yeow J. T. W., 2006, "Carbon Nanotube based Sensors", *Journal of Nanoscience and Nanotechnology*, 6:573-590.
- Li C., Thostenson E. T. and Chou T. W., 2008, "Sensors and Actuators based on Carbon Nanotubes and Their Composites: A review", 68:1227-1249.
- Lau K. T. and Hui D. 2002, "The Revolutionary Creation of New Advanced Materials-Carbon Nanotube Composites", *Composites; Part B*, 33:263-277.
- Desai A. V. and Haque M. A., 2005, "Review-Mechanics of the Interface for Carbon Nanotube-Polymer Composites", *Thin-walled structures*, 43:1787-1803.
- Ebbesen T. W. and Takada T., 1995, "Topological and SP3 Defect Structures in Nanotubes", *Carbon*, 33 (7):973-978.
- Qian D., Dickey E. C., Andrews R. and Rantell T., 2000, "Load Transfer and Deformation Mechanism in Carbon Nanotube -Polystyrene Composites", *Applied Physics Letter*, 76:2868-2870.
- Gong X., Liu J., Baskaran S., Voise R. D. and Young J. S., 2000, "Surfactant-Assisted Processing of Carbon Nanotube /Polymer Composites", *Chemistry of Materials*, 12:1049-1052.
- Shaffer M. S. P. and Windle A. H., 1998, "Fabrication and Characterization of Carbon Nanotube /Polyvinylalcohol Composites", *Advanced Materials*, 11:937-941.
- Schadler L. S., Giannaris S. C. and Ajayan P M, 1998, "Load Transfer in Carbon Nanotube/Epoxy Composites", *Applied Physics Letter*, 73(26):3842-4.
- Thostenson E. T. and Chou T. W., 2003, "On the Elastic Properties of Carbon Nanotube -based Composites: Modeling and Characterization", *Journal of Physics D: Applied Phys.*, 36:573-582.
- Auter K. K., 1997, "Mechanics of Composite Materials", CRC Press, Newyork, USA.
- Li C. and Chou T. W., 2003, "Elastic Moduli of Multi-Walled Carbon Nanotubes and the Effect of van der Waals Forces", *Composites Science and Technology*, 63:1517-1524.
- Halpin J. C. and Tsai S. W., 1967, "Environmental Factors in Composite Materials Design US Air Force Technical Report AFML TR", 67-423.

## 9. NOMENCLATURE

Symbol	Meaning	Unit
d	CNT diameter	(nm)
l	CNT length	(nm)
$\epsilon$	Strain	(nm/nm)
$\sigma$	Stress	(Pa)
E	Young's Modulus	(Pa)
A	CNT cross section area	m <sup>2</sup>
t	CNT layer thickness	(nm)
F	Force	(N)
$\Delta l$	Length increment	(nm)
V	CNT volume fraction	--
W	CNT weight fraction	--
$\rho$	Density	(kg/m <sup>3</sup> )
v	Volume fraction of composite segment	--
$\Psi, \xi$	Distribution function	--
VC	Whole Composite volume	m <sup>3</sup>
VCn	Composite segment volume	m <sup>3</sup>

## 10. MAILING ADDRESS

Dr. Sanjib Chandra Chowdhury  
 Assistant Professor  
 Department of Mechanical Engineering  
 BUET, Dhaka-1000, BANGLADESH.  
 Phone : 88029665636,  
 88029665650-80 (Extn. 7994),  
 FAX : 880-2-8613046, 880-2-8613026.  
 E-mail : sanjib@me.buet.ac.bd



## ON THE DISPLACEMENT-POTENTIAL SOLUTION OF PLANE PROBLEMS OF STRUCTURAL MECHANICS WITH MIXED BOUNDARY CONDITIONS

S. K. Deb Nath<sup>1</sup> and S. R. Ahmed<sup>2</sup>

<sup>1</sup> Division of Mechanical and Automotive Engineering, Kongju National University, South Korea

<sup>2</sup> Department of Mechanical Engineering, Bangladesh University of Engineering and Technology, Bangladesh

### ABSTRACT

The present paper describes the advancement of displacement-potential approach in relation to solution of plane problems of structural mechanics with mixed mode of boundary conditions. Both the conditions of plane stress and plane strain are considered for analyzing the displacement and stress fields of the structural problem. Using the present approach an elastic plate is solved in which one of its ends is kept fixed and the opposite end is subjected to a combined loading of uniform compression and shear. Finite-difference technique is used to solve the problem numerically. Superiority of the present approach over the usual mathematical models as well as computational approaches is discussed.

**Keywords:** Elastic analysis, plane problems, displacement potential, finite-difference method.

### 1. INTRODUCTION

In order to reduce complexities as well as computational effort, a large number of three-dimensional problems are reduced to two-dimensional ones following the standard simplifying assumptions of either plane strain or plane stress condition. If one of the dimensions of a three-dimensional body is larger than other two dimensions, the problem can be considered as plane strain problem. A number of elastic problems have been solved using either plane strain or plane stress conditions based on existing elasticity formulations. Ogden and Isherwood [1] developed new formulations of the governing equations for finite plane-strain deformations of compressible isotropic elastic solids. Shuguang and Lim [2] used variational principles for the generalized plane strain problem of elasticity and they formulated total complementary potential energy functional has been applied to some classic problems in composite materials, viz. the analysis of transversely cracked laminates and the micromechanics of unidirectionally fiber-reinforced composites. Amadei and Goodman [3] developed a more general formulation of plane strain. They applied it to calculate the displacement and stress distributions around a circular hole drilled in a regularly jointed rock described as an equivalent anisotropic continuum. Tewary and Kriz [4] modified elastic plane strain Green's function to account for generalized plane strain and applied to calculating the stress and

displacement field in a biomaterial composite containing a free surface normal to the interface and subjected to an out-of-numerically as well as analytically. A generalized plane strain model was employed for the simulations of cold pilgering of fuel cladding for nuclear applications by Harada et al [5]. The difficulties involved in trying to solve the practical stress problems using the existing approaches, for example, the stress function approach or the displacement-functions approach [6], are clearly pointed in Ref. [7]. In the present paper, the displacement potential approach is extended for solving both the categories of plane problems of elasticity. Using this approach, a one-end fixed steel plate subjected to a combined loading of axial compression and shear, at its opposite end, is solved numerically.

### 2. DISPLACEMENT-POTENTIAL FORMULATION FOR PLANE PROBLEMS OF ELASTICITY

The stress at a point of a two-dimensional elastic body can be represented by three dependent variables, namely,  $\sigma_{xx}$ ,  $\sigma_{yy}$  and  $\sigma_{xy}$ . With reference to a rectangular coordinate system and in the absence of body forces, these three variables for the case of isotropic materials are governed by the two equilibrium equations [6].

$$\frac{\partial}{\partial x}(\sigma_{xx}) + \frac{\partial}{\partial y}(\sigma_{xy}) = 0 \quad (1)$$

$$\frac{\partial}{\partial y}(\sigma_{yy}) + \frac{\partial}{\partial x}(\sigma_{xy}) = 0 \quad (2)$$

To express the equilibrium equations in terms of displacement components, three stress-displacement relations are needed, which are obtained from Hooke's law as [6], are valid for plane stress and plane strain conditions.

$$\sigma_{xx} = \frac{\bar{E}}{1-\bar{\nu}^2} \left[ \frac{\partial u_x}{\partial x} + \bar{\nu} \frac{\partial u_y}{\partial y} \right] \quad (3)$$

$$\sigma_{yy} = \frac{\bar{E}}{1-\bar{\nu}^2} \left[ \frac{\partial u_y}{\partial y} + \bar{\nu} \frac{\partial u_x}{\partial x} \right] \quad (4)$$

$$\sigma_{xy} = \frac{\bar{E}}{2(1+\bar{\nu})} \left[ \frac{\partial u_x}{\partial y} + \frac{\partial u_y}{\partial x} \right] \quad (5)$$

where  $\bar{E} = E, \bar{\nu} = \nu$  ..... for plane stress condition

$\bar{E} = \frac{E}{1-\nu^2}, \bar{\nu} = \frac{\nu}{1-\nu}$  ..... for plane strain condition

Substituting the above stress-displacement relations into equations (1) and (2), two equilibrium equations for two-dimensional plane problems of isotropic materials in terms of the two displacement components are obtained as [7].

$$\frac{\partial^2 u_x}{\partial x^2} + \frac{1-\bar{\nu}}{2} \frac{\partial^2 u_x}{\partial y^2} + \frac{1+\bar{\nu}}{2} \frac{\partial^2 u_y}{\partial x \partial y} = 0 \quad (6)$$

$$\frac{\partial^2 u_y}{\partial y^2} + \frac{1-\bar{\nu}}{2} \frac{\partial^2 u_y}{\partial x^2} + \frac{1+\bar{\nu}}{2} \frac{\partial^2 u_x}{\partial x \partial y} = 0 \quad (7)$$

Although the above two differential equations are theoretically sufficient to solve the mixed-boundary value elastic problems of isotropic materials, in reality it is extremely difficult to solve for two functions simultaneously satisfying the two second-order elliptic partial differential equations. In order to overcome this difficulty, the existence of a new potential function of the space variables is investigated in an attempt to reduce the problem to the determination of a single variable from a single differential equation of equilibrium. In the present formulation, the potential function  $\psi(x, y)$  for plane strain conditions is thus defined in terms of the displacement components as [7]

$$u_x(x, y) = \frac{\partial^2 \psi}{\partial x \partial y} \quad (8)$$

$$u_y(x, y) = -\frac{1}{1+\bar{\nu}} \left[ 2 \frac{\partial^2 \psi}{\partial x^2} + (1-\bar{\nu}) \frac{\partial^2 \psi}{\partial y^2} \right] \quad (9)$$

Substitution of equations (8) and (9) into equations (6) shows that the equilibrium equation (6) for plane stress and plane strain conditions is automatically satisfied. Therefore,  $\psi$  has to satisfy the equilibrium equation (7) only. Expressing equation (7) in terms of the potential function,  $\psi$  the condition that  $\psi$  has to satisfy for the case of isotropic plane problems becomes [8]

$$\frac{\partial^4 \psi}{\partial x^4} + 2 \frac{\partial^4 \psi}{\partial x^2 \partial y^2} + \frac{\partial^4 \psi}{\partial y^4} = 0 \quad (10)$$

Substituting the expressions as given by equations (8) and (9) into equations (3) to (5), one obtains the explicit expressions of three major stress components in terms of the potential function,  $\psi$ , for both the cases of plane stress and plane strain conditions, as follows:

$$\sigma_{xx}(x, y) = \frac{\bar{E}}{(1+\bar{\nu})^2} \left[ \frac{\partial^3 \psi}{\partial x^2 \partial y} - \bar{\nu} \frac{\partial^3 \psi}{\partial y^3} \right] \quad (11)$$

$$\sigma_{yy}(x, y) = -\frac{\bar{E}}{(1+\bar{\nu})^2} \left[ (2+\bar{\nu}) \frac{\partial^3 \psi}{\partial x^2 \partial y} + \frac{\partial^3 \psi}{\partial y^3} \right] \quad (12)$$

$$\sigma_{xy}(x, y) = \frac{\bar{E}}{(1+\bar{\nu})^2} \left[ \bar{\nu} \frac{\partial^3 \psi}{\partial x \partial y^2} - \frac{\partial^3 \psi}{\partial x^3} \right] \quad (13)$$

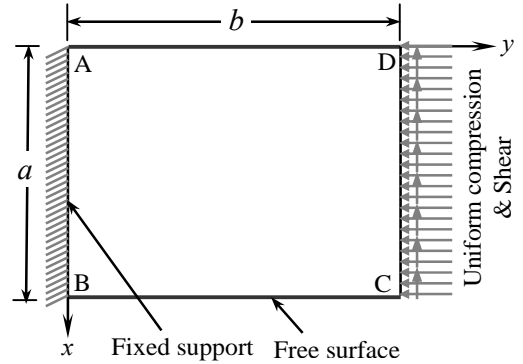


Fig.1 Model of a fixed-ended plate subjected to a combined loading

### 3. NUMERICAL SOLUTION

Finite-difference technique is used to discretize the governing differential equation (10) and also the differential equations associated with the boundary conditions (Eq. (8), (9), (11) to (13)). The discrete values of the displacement potential function,  $\psi(x, y)$ , at the mesh points of the domain concerned, is solved from the system of linear algebraic equations resulting from the discretisation of the governing equation of equilibrium and the associated boundary conditions. The complete finite-difference expression of the governing equation (10) as well boundary conditions are available in Ref. [8]. Details of the computational scheme as well as management and placement of boundary conditions in terms of finite difference expressions are described in Refs. [7-8].

A square steel plate, ABCD, subjected to a uniform compression and shear loading is shown in Fig. 1. Its supporting edge is AB and a combined loading is applied at its right lateral edge, DC. The intensity of both the components of applied stress is 30 MPa. The Young's modulus and Poisson's ratio of steel are taken as 200 GPa and 0.3, respectively, to solve the problem.

### 4. RESULTS AND DISCUSSIONS

In this section, the elastic field of the plate, whose one end is kept fixed and the opposite end is subjected to a combined loading, as shown in Fig. 1, is analyzed with the help of graphical representation. The variation of all

displacement and stress components is shown graphically as a function of  $x/a$  as well as  $y/b$ .

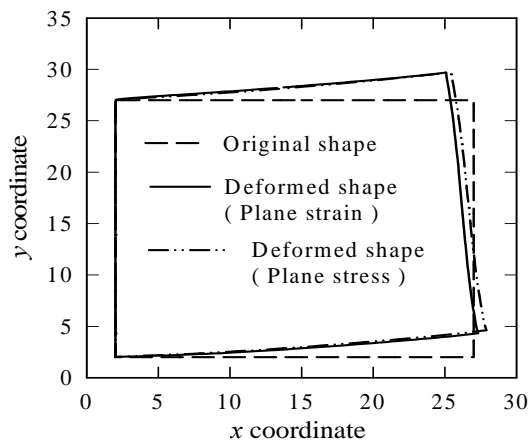


Fig. 2 Deformed shapes of the plate (magnification factor x100)

Figure 2 shows the deformed shapes of the plate for the case of plane stress and plane strain conditions in comparison with the original undeformed configuration. Effect of plane stress as well as plane strain conditions is clearly observed, particularly along the  $x$ -direction of the plate. At the supporting edge, both of the displacement components are zero, which is in good agreement with the physical characteristics of the problem. The plane strain solution gives a bit lower axial deformation of the plate than that of the plane stress condition. The lateral deformation is also found to be slightly lower for the case of plane strain solution.

The distributions of axial stress component at different sections of the plate are illustrated in a comparative fashion in Fig. 3. It is observed that the magnitude of axial/bending stress is found to be higher for the case of plane stress solution when compared it with the corresponding solutions of plane strain approximation, particularly around the fixed support of

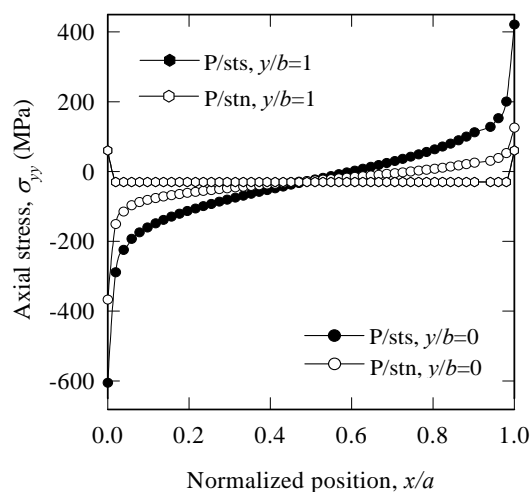


Fig. 3 Distribution of axial stresses at different sections of the plate under different conditions

the plate. The magnitude of the axial stress at the loaded lateral end is found to be identical to that of the applied one, which verifies the accuracy of reproducing the state of stresses at the loaded region. For the remaining longitudinal sections of the plate, the axial stress varies nearly anti-symmetrically with respect to the plate width, for both of the plane stress and plane strain conditions. For almost all sections except the loaded edge of the plate, the overall magnitude of axial stress is observed higher for plane stress condition than that of plane strain condition. Between the two corner regions of the supporting edge, top corner is identified to be more critical than the bottom corner, as far as the axial stress component is concerned.

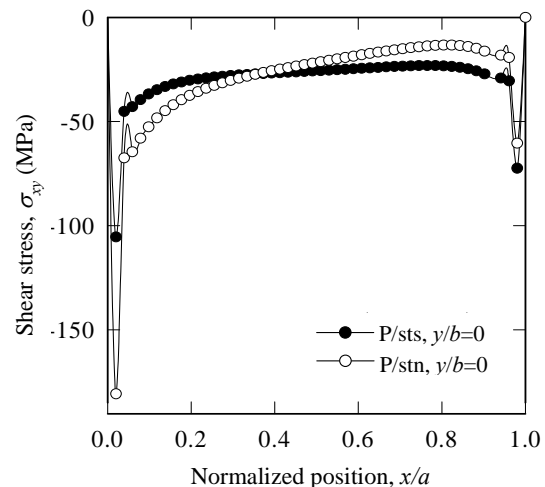


Fig. 4 Distribution of shear stresses at the fixed end of the plate under different conditions

Fig. 4 illustrates the comparison of distributions of shear stress component at different sections of the plate for both the plane stress and plane strain conditions. For both the cases, the shear stress at the right lateral edge of the plate is found identical to that of the applied shear stress, which is again in good agreement to the physical model of the problem. At the supporting end, the effect of the approximation used (*i.e.*, plane stress and plane strain conditions) is observed to be quite significant, which is, however, not that significant for the remaining sections of the plate. At the supporting end of the plate, the maximum shear stress under plane strain condition is found to be more than 1.5 times higher than that of the plane stress condition. Likewise the case of axial stress, the upper corner region of the supporting end is identified as the most critical section in terms of shearing stress.

As the lateral displacement in most of the sections of the plate under plane strain condition is lower than that of the plane stress approximation, the body under plane strain is stiffer in lateral direction than that of plane stress condition. If the stiffness characteristic of the plate in different direction is considered, the lateral stress at different sections of the plate under plane strain should be higher than that of plane stress condition, and this phenomenon is reflected in the solution as observed in

Fig. 5. From the comparative analysis of different displacement components at different sections of the plate under the two conditions it is observed that, away from the supporting end, the stiffness variation due to different simplifying approximations becomes more prominent as we move towards the loaded end. 5.

Finally, from the analysis of the normal stress component,  $\sigma_{zz}$ , at different sections of the plate it is observed that, at the loading and supporting ends, the distribution of this stress are found to be highly nonlinear and significant, however, for the remaining sections, the distribution of the normal stress is nearly linear and less significant in terms of magnitude.

## 5. CONCLUSIONS

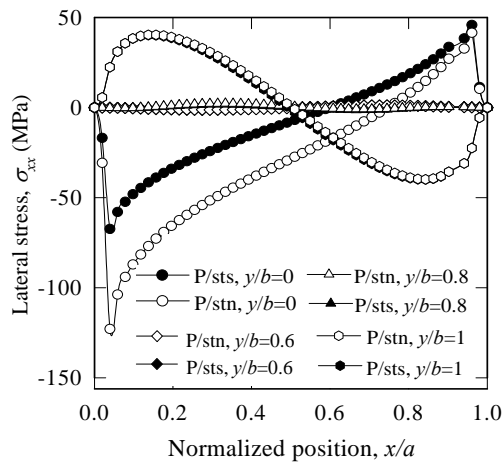


Fig. 5 Distribution of lateral stresses at different sections of the plate under different conditions

In the present article, the displacement-potential approach is extended for the solution of both plane stress and plane strain problems of solid mechanics. A one end fixed plate subjected to a combined loading of uniform compression and shear is solved using finite-difference technique, considering plane stress as well as plane strain conditions. The solutions of the elastic field are presented in a comparative fashion for plane stress and plane strain conditions. The present solution satisfies all the physical characteristics of the problem, which is clearly reflected by the deformed configuration of the plate. Loading and supporting edges of the plate are identified to be highly critical regions for both of the cases, which are realized by the detailed analysis of the results.

## 6. REFERENCES

1. Odgen, R.W. and Isherwood, D.A., (1979), "Solution of some finite plane-strain problems for compressible elastic solids". *J. Mechanics Appl Math*, 31(2): 219-249.
2. Shuguang, L. and Lim, S-H., (2005), "Variational principles for generalized plane strain problems and their applications". *Composites, Part A, Applied Science and Manufacturing*, 36(3):353-365.
3. Amadei, B. and Goodman, R.E., (1981), "Formulation of complete plane strain problems for regularly jointed rocks", *The 22<sup>nd</sup> U.S. Symposium on Rock Mechanics (USRMS)*, June 29 - July 2, Cambridge, MA.
4. Tewary, V.K. and Kriz, R.D., (1991), "Generalized plane strain analysis of a biomaterial composite containing a free surface normal to the interface". *J Mat. Res.*, 2609-2622.
5. Harada, M., Honda, A. and Toyshima, S., (2005), "Simulation of cold pilgering process by a generalized plane strain FEM". *Journal of ASTM International (JAI)*, 2 (3).
6. Timoshenko, S.P. and Maccullough, G.H., (1949), "Elements of strengths of materials.Princeton", NJ: Van Nostrand.
7. Ahmed, S. R., Khan, M. R., Islam, K. M. S. and Uddin, M.W., (1998), "Investigation of stresses at the fixed end of deep cantilever beams". *Computers and Structures*, 69: 329-338.
8. Ahmed, S. R., Nath, S.K.D., and Uddin, M.W., (2005), "Optimum shapes of tire treads for avoiding lateral slippage between tires and roads". *International Journal for Numerical Methods in Engineering*, 64: 729-750.

## 7. NOMENCLATURE

Symbol	Meaning	Unit
$u_x$	Lateral displacement	(mm)
$u_y$	Axial displacement	(mm)
$\sigma_{xx}$	Lateral stress component	(MPa)
$\sigma_{yy}$	Axial stress component	(MPa)
$\sigma_{zz}$	Normal stress component	(MPa)
$\sigma_{xy}$	Shear stress component	(MPa)
$G$	Shear modulus of material	(MPa)
$E$	Elastic modulus of material	(MPa)
$\nu$	Poisson's ratio	--
$\psi$	Displacement potential	
$a$	Plate width	(mm)
$b$	Plate length	(mm)

## 8. MAILING ADDRESS

S K Deb Nath  
 Division of Mechanical and Automotive Engineering,  
 Kongju National University, South Korea

## VIRTUAL IMPACTORS: A NOBLE DEVICE TO GENERATE HIGH CONCENTRATION MONODISPERSE AEROSOLS

M. Shamim Akhter<sup>1</sup>, M. Ariful Islam<sup>2</sup> and M.R. I. Sarker<sup>1</sup>

<sup>1</sup>Department of Mechanical Engineering, RUET, Rajshahi, Bangladesh

<sup>2</sup>Department of Industrial & Production Engineering, RUET, Rajshahi, Bangladesh

### ABSTRACT

A solid or liquid particle suspended in a gas which is usually air is called an aerosol. Dust, fume, smoke, mist, fog, smog, and cloud are all examples of aerosols found in nature. One of the important applications of aerosol technology is the production of monodisperse test aerosols used for aerosol research, calibration, testing and development of air-cleaning and air-sampling equipments and pollution abatement. The characteristics of an ideal aerosol generator are a constant and reproducible generation of monodisperse, stable, uncharged, spherical aerosol particles whose size and concentration can be easily controlled. Atomization produces aerosols with sufficient mass concentration but the generated aerosols are highly polydisperse. Therefore, polydisperse aerosols produced by atomization should be subsequently segregated to narrow size range so as to obtain aerosol appropriate for use as a test aerosol. A monodisperse aerosol is usually defined as one that has a geometric standard deviation of less than 1.2. An aerosol having geometric standard deviation from 1.2 to 1.5 is said to be narrowly distributed. Polydisperse aerosols have geometric standard deviation greater than 2.0. Virtual impactors are widely used in the sampling of particles because they generate high concentration aerosols. This technology is new in Bangladesh. This paper describes the technical aspects of virtual impactor so as to introduce the reader with this new technology. Results of experimental studies performed with an improved virtual impactor have also been described. It was possible to generate narrowly distributed aerosols with the improved virtual impactor employed.

**Keywords:** Aerosols, Virtual impactors, Monodisperse.

### 1. INTRODUCTION

A monodisperse virtual impactor type aerosol generator is used for various purposes, e.g., instrument calibration, aerosol research, development and testing of air-cleaning and air-sampling equipments, inhalation tests etc. Various devices have been employed to produce aerosol droplets (Hinds 1982; Berglund and Liu 1973), namely liquid atomizer, compressed air nebulizer, vibrating orifice aerosol generator, spinning disk generator (Simpkins 1997) and condensation generator. Liquid atomizers produce polydisperse aerosols of high mass concentration whereas the other aerosol generators produce monodisperse aerosols of very low mass concentration (Chein 1994). However, characteristic of an ideal monodisperse aerosol generator is a constant and reproducible output of single-sized, spherical aerosol droplets which are electrically neutral and whose size and concentration can be easily controlled. The virtual impactor is a device which is used for the inertial separation of airborne particles (Loo et al. 1976; Dzubay et al. 1975). In a conventional type of virtual impactor, particle laden air is accelerated through a nozzle and then impinges into a collection probe that is slightly larger in diameter than the nozzle. The particles larger than the cut off size have enough inertia to penetrate deep into the receiving tube and follow the minor flow (Marple et al.

1990) which is usually about 5-10% of the mainstream flow. The major flow, containing particles smaller than the cut off size, makes a sharp turn around the collection probe and exits. However, the minor flow would still contain a small amount of fine particles. An improved virtual impactor employs a central clean air flow to reduce or eliminate the fine particle contamination in the minor flow (Masuda et al. 1979; Chen et al. 1986). The clean air core prevents small particles from entering the center of the acceleration nozzle and, therefore, small particles can follow the major flow better. Recently, it was experimentally determined (Li and Lundgren 1997) that to reduce fine particle contamination in the minor flow, the clean air core diameter should be at least twice the converging nozzle diameter and that the clean air core should be positioned so that the ratio of the clean air flow velocity to the aerosol flow velocity ranges from 1.5 to 5.0 at the outlet of the clean air tube. A well-designed virtual impactor should have good separation characteristics like no fine particle contamination in the coarse particle flow (minor flow) and few or no internal losses (Asgharian and Godo 1997).

Controlling the size of the aerosols in the minor flow is very important to obtain the test aerosols. No work has yet been reported showing the effect of controlling parameters on which the size of the output aerosols. The

present study is an attempt to investigate the effect of solution concentration and minor flow rate on the size of aerosol particles in the minor flow and also to prescribe the relationship between them. The type of aerosol generator described in this study has the ability to produce a high concentration of monodisperse aerosols. It has two stages - a generation chamber stage and a virtual impactor stage as explained in experimental procedure. An atomizer is used to produce polydisperse aerosols at the bottom of the aerosol generation chamber. The larger droplets are removed by gravitational settling as the polydisperse aerosol travels vertically through the generation chamber. Droplets smaller than cut off size are subsequently eliminated in the virtual impactor stage.

## 2. THEORY

The size of monodisperse aerosols generated in the aerosol generator can be controlled by controlling minor flow rate and solution concentration used.

### 2.1 Particle size variation with the concentration of solution

The size of monodisperse aerosols can be controlled by changing the concentration of liquid solution according to the relation:

$$C_c = \frac{V_p}{V_d} = \frac{d_p^3}{d_d^3} \quad (1)$$

where,  $C_c$  = solution concentration,  $V_p$  = Volume of solute from which final particles are formed,  $V_d$  = Volume of solvent from which initial droplets are formed, since the volume of solute is negligible compared to the volume of solvent  $d_p$  = diameter of particle and  $d_d$  = diameter of droplet. The value of the cut off diameter of droplets in the generation chamber and can be determined from the analytical studies (Nevers 1995). Cut off diameter in the generation chamber is always fixed since the flow rate through the generation chamber is fixed. Hence, depending on the final particle diameters  $d_p$ , the solution concentration,  $C_c$  is varied to obtain it.

The particle diameter is related to aerodynamic diameter as follows:

$$d_p = D_{pa} \left( \frac{\rho_a}{\rho_p} \right)^{\frac{1}{2}} \quad (2)$$

where,  $D_{pa}$  = aerodynamic diameter of the particle,  $\rho_a$  = water density and  $\rho_p$  = particle density. Aerodynamic diameter may be defined as the diameter of unit density particle whose settling velocity is the same as original particle. Since the solute DOP (di-octyl phthalate) density is very close to water (unit) density, therefore, the relationship can be used here also. Subsequently, Eq. (1) yields:

$$C_c = \frac{D_{pa}^3}{d_d^3} \left( \frac{\rho_a}{\rho_p} \right)^{\frac{3}{2}} \quad (3)$$

Eq. (3) exhibits the relationship between aerodynamic diameter of the particle and solution concentration of solution strength.

In a real impactor, the nozzle flow divides equally into two flows due to impaction on the flat plate placed at right angles to the nozzle flow. Hence, the flow field is uniform in a real impactor provided the flow rate ( $Q_1$ ) through the nozzle is constant. But in a virtual impactor, this is not the case. Here, keeping the total flow rate ( $Q_1$ ) through nozzle constant, the minor flow rate ( $Q_m$ ) through collection probe can be changed by changing the major flow rate ( $Q_2$ ) operating the vacuum pump.

So, in a virtual impactor, the effective velocity responsible for pushing the particles into minor flow is the difference of velocities ( $V_1 - V_2$ ),  $V_1$  and  $V_2$  being the velocities in nozzle (total) flow and major flow respectively. Stokes number for a virtual impactor is given by:

$$S_{ik} = \frac{\tau(V_1 - V_2)}{D/2},$$

where,  $\tau$  is the relaxation time of the particle. Putting

$$\tau = \frac{\rho_p d_p^2}{18\mu}$$

in the above equation gives

$$9\mu D(S_{ik})_{50} = \rho_p d_{p50}^2 \left\{ \frac{Q_1}{A_1} - \frac{Q_1 - Q_m}{A_2} \right\} \quad (4)$$

Where  $S_{ik50}$  and  $d_{50}$  are stoke number and cut-off diameter respectively at 50% collection efficiency,  $A_1$  and  $A_2$  are areas of totals and major flows respectively and  $Q_2 = (Q_1 - Q_m)$ .

The collection efficiency may be defined as the ratio of the number of particles collected in the minor flow to the total number of particles delivered by the atomizer. Keeping  $Q_1$  to be constant and separating the constant terms, Eq. (4) yields:

$$d_{p50}^2 = \frac{C}{Q_m} \quad (5)$$

where  $C$  is a constant. Hence the cut off diameter of generated particles is inversely proportional to the square root of minor flow rate. Thus, by varying the minor flow rate, the desired particle size can be produced.

## 3. EXPERIMENTAL PROCEDURE

The experimental set up is shown in Fig. 1. A simplex, solid-cone atomizer (Delavan, Model DLN 29713-2) was installed at the bottom of a vertical perspex generation chamber 0.15 m in diameter and 1.5 m height. The atomizer generates clouds of aerosols from a liquid

solution of 10% DOP in ethyl alcohol at a constant atomizing air pressure of about 117 kPa. Polydisperse aerosols move upwards in the generation chamber of the aerosol generator and enter the mixing box placed at the

top of the chamber. From there, the aerosols move downwards and enter the improved virtual impactor of the generator. The improved virtual impactor separates larger diameter

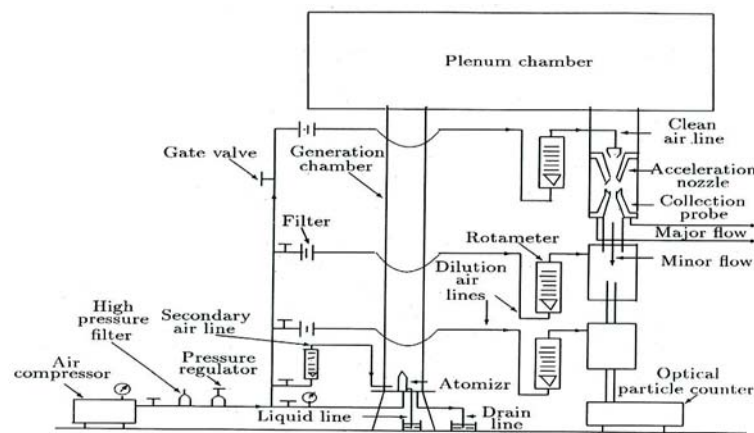


Fig 1. Experimental set up

particles from the aerosol stream by virtual inertial impaction into the collection probe. Improved virtual impactors have been discussed in the literature in terms of their design philosophy by Chen and Yeh (1987). Two sets of improved virtual impactor has been designed, fabricated and one set has been used for size control by varying the solution concentration and the other set has been employed for size control by controlling the minor flow rate. Secondary air flow is supplied at the bottom of the generation chamber so that the flow rate through the chamber is maintained constant at 50 lpm in case of size control by varying the solution concentration and 40 lpm in case of size control by controlling the minor flow rate. Clean air at a flow rates of 16 lpm and 17 lpm is also supplied through the clean air tube at the center of the acceleration nozzle in case of size control by varying solution concentration and minor flow rate respectively. A vacuum pump was employed to extract most of the aerosols through the major flow line and the rest of the coarse aerosols passed through the outlet pipe as minor flow. The minor flow was diluted with clean air and a small portion of it was ejected by a mechanism followed by further dilution to the allowable concentration before entering the Optical Particle Counter, LASAIR-2500 (Particle Measuring System Inc., USA). The sampling time was set to 30 minutes. To have statistically meaningful data, at least 28000 particles were measured by LASAIR-2500 during each sampling.

During this experiment, the liquid pressure was maintained at atmospheric pressure (liquid surface maintained at atomizer entrance height). The conditions in the laboratory were fairly stable during the tests with the ambient pressure and temperature being 760 mm of Hg and 33°C respectively. So, all pressures and flow rates mentioned in this work are relative to the above.

### 3.1 Effect of solution concentration

During the tests for investigating the effect of solution

concentration on the particle size in the minor flow, all flow rates were kept constant and only the solution strength (concentration of DOP in ethyl alcohol) was varied. The minor flow rate was kept at 10% of total flow rate. The solution concentration was varied from 5% to 100%.

### 3.2 Effect of minor flow rate

The variation in minor flow rate was made by changing the major flow rate (drawn by the vacuum pump) keeping all other flow rates constant and at a constant concentration of 10% of DOP. The major flow rate was varied in such a way so that the minor flow varied from 3 lpm (4.47% of total flow) to 11 lpm (16.41% of total flow).

## 4. RESULTS AND DISCUSSION

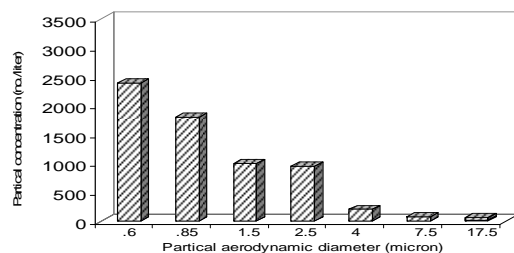


Fig 2. Particle size distribution for an atomizing air pressure of 17.1 kPa and chamber flow rate of 40 lpm

Fig. 2 shows the DOP particle size distribution histograms measured by LASAIR-2500 at an atomizing pressure of 117 kPa and chamber flow rate of 40 lpm. The size distribution has a number mean aerodynamic diameter (NMAD) of 1.23  $\mu\text{m}$ , geometric mean aerodynamic diameter (GMAD) of 1.02  $\mu\text{m}$  and geometric standard deviation (GSD) of 1.77. Thus the



particles generated by the atomizer at the atomizing pressure and chamber flow rate is fairly polydisperse in nature and ready for subsequent separation in the improved virtual impactor to monodisperse (GSD<1.5) test aerosols.

#### 4.1 Size control by varying the solution concentration

The DOP particle size distribution in the minor flow measured by LASAIR-2500 for solution concentrations of 5%, 10%, 25%, 50%, 75% and 100% DOP in ethyl alcohol have been shown in Fig. 3. They have NMADs of 1.41, 1.78, 2.57, 3.02, 3.54 and 4.07 respectively. This shows that as the solution strength increases, the particle size increases validating the theoretical predictions. All the size distributions mentioned above have GSD<1.5 indicating monodisperse aerosol.

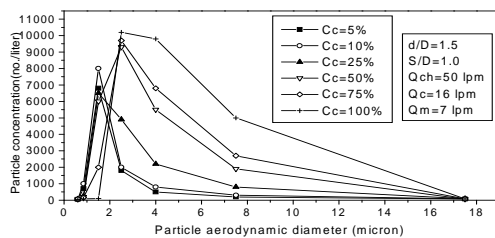


Fig 3. Variation of particle aerodynamic diameter with particle concentration for various solution concentrations.

#### 4.2 Size control by varying the minor flow rate

Graph showing the variation of DOP particles size distribution in minor flow as measured by the optical particle counter for different minor flow rates is given in Figure 4; the corresponding minor flow rates were 11 lpm, 9.5 lpm, 8 lpm, 7 lpm, 5.5 lpm and 3 lpm respectively. They have NMADs of 1.90, 1.98, 2.18, 2.63, 3.00 and 3.86, respectively with GSD less than 1.5 in all the cases ensuring acceptable monodispersity for the final output aerosols.

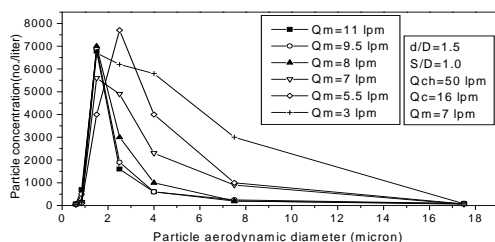


Fig 4. Variation of particle aerodynamic diameter with particle concentration for various minor flow rates.

## 5. CONCLUSIONS

Size control of generated monodisperse aerosols of DOP in minor flow of a virtual impactor type aerosol generator has been achieved by controlling the concentration of liquid solution (DOP in ethyl alcohol) atomized and the minor flow rate. By varying the solution strength from 5% to 100%, NMADs of DOP particles from 1.41 to 4.07  $\mu\text{m}$  have been achieved; while changing the minor flow rate from 11 lpm to 3 lpm produced a change in NMADs of DOP particles from 1.90 to 3.86.

## 6. ACKNOWLEDGEMENT

This work was funded by CSIR, New Delhi, India with IIT, Kharagpur, India under project no. 22(0283)/98/EMR-II. The research described in this paper has not been subjected to review by CSIR and therefore does not necessarily reflect the views of the Council.

## 7. REFERENCES

1. Asgharian, B. and Godo, M.N. (1997). *Aerosol Science and Technology*. 27:499-506.
2. Berglund, R.N. and Liu, B.Y.H. (1973). *Environmental Science and Technology*. 7(2):147-153.
3. Chen, B.T., Yeh, H. and Cheng, Y.S. (1986). *Aerosol Science and Technology*. 5:369-376.
4. Chen, B.T. and Yeh, H.C. (1987). *Journal of Aerosol Science*. 18(2):203-214
5. Dzuby, T.G., Stevens, R.K. *Environment Science and Technology*. (1975). 9: 633-638.
6. Hinds W.C. (1982). *Aerosol Technology*. John Wiley and Sons, Inc., New York, USA.
7. Li, S.N. and Lundgren, D.A. (1997). *Aerosol Science and Technology*. 27:625-635.
8. Loo, B.W., Jaklevic, J.M., Goulding, F.S. (1976). *Aerosol Generation Measurement, Sampling and Analysis in Fine Particles*.
9. Liu, B.Y.H., Ed.; Academic Press, New York.
10. Masuda, H., Hochrainer, D. and Stober, W. (1979). *Journal of Aerosol Science*. 10: 275-287.
11. Nevers, N.D. (1995). *Air Pollution Control Engineering*. McGraw-Hill, Inc., New York, USA.
12. Simpkins, P.G. (1997). *Aerosol Science and Technology*. 26:51-54.

## 8. MAILING ADDRESS:

**Md. Shamim Akhter**  
Department of Mechanical Engineering,  
RUET, Rajshahi 6204, Bangladesh

## PREDICTION OF STANDPIPE PRESSURE USING REAL TIME DATA

Dipankar Chowdhury<sup>1</sup>, Pål Skalle<sup>1</sup> and Mahbubur Rahman<sup>2</sup>

<sup>1</sup>Department of Petroleum Engineering and Applied Geophysics,  
Norwegian University of Science & Technology, NO- 7491, Trondheim, Norway

<sup>2</sup>Department of Petroleum and Mineral Resources Engineering,  
Bangladesh University of Engineering and Technology, Dhaka-1000, Bangladesh

### ABSTRACT

Standpipe pressure (SPP) represents the total frictional pressure drop in the hydraulic circuit used for rotary drilling operation. Conventional approach for SPP calculation is based on a number of simplifying assumptions that cannot be realized in real drilling operation. Hence the conventional approach does not produce SPP estimates with sufficient accuracy. The limitations of conventional approach led to the development of alternative methods for SPP estimation using real time data. In this paper, SPP was estimated by regression models and by instance-based reasoning (IBR) models using real time data collected while drilling a deviated well in the North Sea. These models were developed using mud flow rate and bit measured depth as independent parameters. For the real time data considered in this paper, the IBR models produced much better SPP estimates than the regression models.

**Keywords:** Standpipe pressure, Regression, Instance-based reasoning, Real time drilling data

### 1. INTRODUCTION

Rotary drilling is the most widely used drilling method. Drilling fluid is an essential component of a rotary drilling system. It is circulated through different parts of the hydraulic circuit by the mud pump principally for removing cuttings. During its circulation, pressure drop occurs at different segments of the hydraulic circuit due to friction between the drilling fluid and the surface in contact. The total frictional pressure drop in the hydraulic circuit, which equals the pump pressure, is termed as standpipe pressure (SPP). The hydraulic circuit typically consists of standpipe, rotary hose, swivel, kelly, drillstring, drill bit, and annular section between the drillstring and the casing or borehole wall.

SPP is an important drilling parameter that must be known with sufficient accuracy for selecting proper jet bit nozzle size, determining optimum flow rate to ensure efficient hole cleaning and for selecting proper mud pump liner. Continuous monitoring of SPP also helps in identifying downhole problems. For example, too low SPP can be caused by washed out pipe or bit nozzle, loose joint or broken drill

string, worn pump packing or liner, or lost returns due to formation fracture. On the other hand, too high SPP could indicate a plugged drill bit or increased mud density or viscosity. SPP anomalies can provide an early warning of circulation problems and thus can help the driller to make corrections before the situation is out of control.

SPP can be estimated using analytical frictional pressure drop relations. These relations are available for the three widely used rheological models namely Bingham plastic, Power law and Herschel-Bulkley. A detail description of this conventional approach is presented in [1]. However, the relations used in the conventional approach are based on a number of simplifying assumptions, such as concentric annular and circular sections, non-rotating drillstring, isothermal conditions in the bore hole and steady state axial flow. These simplifying assumptions are not completely valid in real life [2]. The effect of pipe eccentricity, pipe rotation, and temperature and pressure variations can have significant effect on frictional pressure drop in the annulus. Accurate determination of SPP is necessary for safe drilling because too high SPP can fracture the formation

resulting in lost circulation and too low SPP can cause kick which can lead to a blow out.

The limitation of the conventional approach led to the development of alternative method of SPP prediction using real time data. In this paper, the methodology used for estimating SPP using real time drilling data for a deviated well drilled in the North Sea is presented. Two approaches are considered for this purpose – i) regression analysis and ii) instance-based reasoning (IBR).

## 2. REAL TIME DATA COLLECTION

Real time data are collected by measurement while drilling (MWD) systems. Unlike wireline logging, MWD systems can be used for gathering and transmitting data from bottom-hole back to the surface without any interruption of the drilling operation. The data transmitted can be directional data, data related to the petrophysical properties of the formations and data related to drilling parameters such as SPP, weight on bit (WOB), mud flow rate, downhole temperature and torque. Relevant sensors and transmission equipment housed in a non-magnetic drill collar in the bottom hole assembly are used for data collection and transmission to the surface. A typical MWD system consists of a downhole system (power source, sensors, transmitter and control system), a telemetry channel (mud column used for sending pulses to surface) and a surface system (used for detecting pulses, decoding the signal and presenting numerical display, geological log etc.). A typical MWD system is shown in Fig 1.

The real time drilling operation data used in this paper were collected while drilling the 8.5" diameter deviated section of a well drilled in the Gullfaks field of the North Sea. The section was drilled using an oil based mud. Twelve measurements for each of the 37 drilling parameters (including SPP, WOB, bit measured depth, bit torque, travelling block position, mud flow rate, mud density, equivalent circulating density, hook load and gas content in the mud) were made simultaneously every minute. A total of 386,128 measurements were made for each drilling parameter from a measured depth of 5060 m to 6221 m. The collected data were analyzed using MATLAB.

### 2.1 Parameter Selection and Data Segregation

Among the different drilling parameters measured, mud flow rate and bit depth (DBTM) were considered for developing regression and IBR models. These are two of the four parameters that principally affect the pressure drop in a wellbore. The other two parameters are density of the fluid and flow

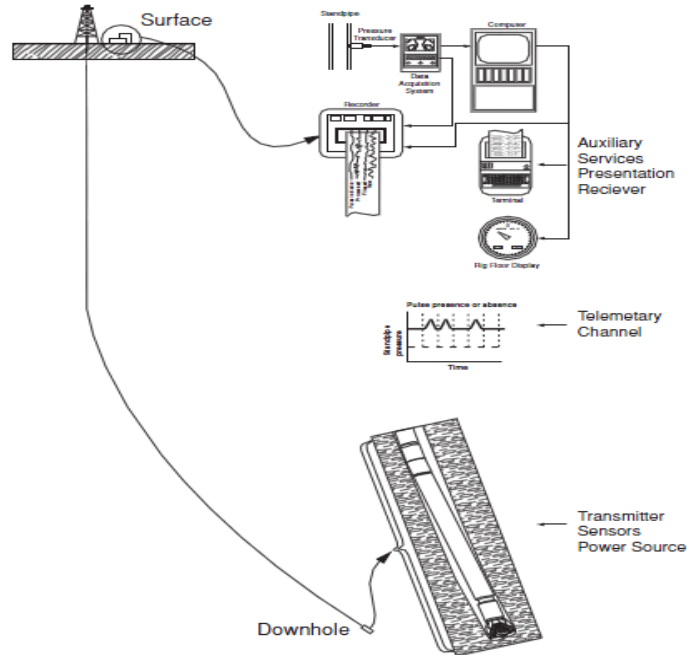


Fig 1. A typical MWD system<sup>3</sup>

area. Since an oil based mud was used throughout the operation, and the dimensions of the drillstring and the hole remained the same during data collection, the last two parameters were not considered for model development.

The collected data were divided into two groups: data collected during tripping-in and data collected during drilling. This was necessary because tripping-in (i.e. the process by which the drillstring is run into the hole) and drilling (i.e. the process by which the formation is penetrated by the drill bit) represent two different phenomena. During tripping-in, mud is circulated at times at constant flow rates with or without rotating the drillstring keeping the bit off bottom to clean up the hole. The flow can be either laminar or turbulent. On the other hand, dynamic condition prevails in the hole during drilling as the drillstring is rotating and vibrating. Hence the flow is usually turbulent during drilling.

Measured depth (i.e. the distance measured along the path of the wellbore) and bit measured depth (i.e. the distance travelled by the drill bit along the path of the wellbore) were used for data segregation. For tripping-in data, the two depths were considered different. But they were assumed to have an absolute difference of less than or equal to 0.1 m for the data collected during drilling. Furthermore, WOB (i.e. the load put on the bit by the drill collars to make penetration) was zero for tripping-in data and nonzero for drilling data. Also, the bit torque assumed nonzero values for drilling data while it was either zero or nonzero for tripping-in data.

## 2.2 Determination of Stationary SPP

To detect stationary SPP, determination of stationary flow rate and travelling block position is necessary. A flow rate was considered stationary if it had an absolute difference of less than or equal to 0.1 lpm (1 lpm = 0.000167 m<sup>3</sup>/s) with its previous or next measured flow rate. The block position was considered stationary if it had an absolute difference of less than or equal to 0.1 m with its previous and next measured block positions. The SPP was considered stationary if the absolute difference between the previous measured value and the present one, and that between the present measured value and the next one was less than or equal to 0.1 bar.

Using the criteria mentioned earlier, 10035 measured mud flow rate, DBTM and SPP during tripping-in, and 4320 measured mud flow rate, DBTM and SPP during drilling were found. However, several similar measured data sets were found at particular bit depths. This happened because the measurements were made after a short time interval of five seconds. To overcome this, the mean of all the flow rates at a particular bit depth interval of one meter was calculated and only one flow rate closest to the mean was determined. The SPP corresponding to this flow rate was considered for further work. This action reduced the number of tripping-in data set to 828. The same refinement when used for drilling data reduced the number of data set to 729. After removal of outliers (i.e. observations that are indicative of measurement error), the number of data set was further reduced to 764 for data collected during tripping-in and to 728 for data collected during drilling.

## 2.3 Selection of Training Examples and Query Instances

Training examples constituted of measured mud flow rate, DBTM and SPP were used for model development. Query instances consisting of the same parameters mentioned earlier were used for SPP prediction using the developed regression and IBR models. Among the 764 tripping-in data sets, every fifth data set is selected as a query instance including the first data set. This resulted in 611 training examples and 153 query instances. Same procedure produced 582 training examples and 146 query instances for the data collected during drilling.

## 3. MODEL DEVELOPMENT

To estimate SPP for the tripping-in query instances, four regression models and nine IBR models were used. Same approach was used for the data collected during drilling.

## 3.1 Regression Analysis

Regression analysis is a statistical technique for investigating functional relationship between the response variable, and one or more predictor variables. Regression models are most commonly developed using an error minimization criterion known as *Least Squares Regression*. In this method, the regression models are produced by minimizing the sum of the squares of the residuals. These models are based on three principal assumptions - independent predictor variables, equally reliable observations and normally distributed residuals. There are a number of least squares regression methods, such as linear least squares, weighted least squares, robust least squares and nonlinear least squares. Linear and nonlinear least squares methods produce regression models with acceptable goodness of fit parameters (such as SSE, RMSE and R-square) when none of the assumptions mentioned earlier is violated.

The parameters of a nonlinear model are adjusted using a fitting algorithm. Most widely used fitting algorithm is *Trust-Region*. This algorithm must be used if coefficient constraints are present. Another popular algorithm is *Levenberg-Marquardt*. It can be tried when the Trust-Region method does not produce a reasonable fit and there is no coefficient constraint [4].

There are several robust regression schemes. But the most widely used schemes are *Least Absolute Residuals (LAR)* and *Bisquare Weights*. In LAR scheme, a curve is found that minimizes the absolute value of the residuals instead of the squared differences. Bisquare weights scheme, on the other hand, minimizes a weighted sum of squares.

For a regression model that fits the observed data well, SSE is close to zero, R-square is close to one and RMSE is close to zero.

### 3.1.1 Regression Models for Tripping-in Data

Following four regression models were developed-

$$\text{Model1: } SPP = 0.0001521Q^{1.873} + 18.44$$

$$\text{Model2: } SPP = 0.002844Q^{1.497}$$

$$\text{Model3: } SPP = 20.2 + 2.46 \times 10^{-8} (DBTM)(Q^{1.75}) + 0.000241Q^{1.75}$$

$$\text{Model4: } SPP = 15.2 + 8.42 \times 10^{-10} (DBTM)(Q^{1.76}) + 0.000358Q^{1.76}$$

Both Model1 and Model2 were developed using robust least squares regression with LAR scheme and Trust-region algorithm. The curve fitting toolbox of MATLAB was used for this purpose. Model3 and Model4 were multiple regression models developed using linear least squares regression and robust least

squares regression respectively. All the models were developed using MATLAB

Among the four models, Model1 fitted the training data well with SSE=3488, R-square=0.9992 and RMSE=2.395. On the other hand, Model4 produced the worst fit of the training data with SSE=195000, R-square=0.955 and RMSE=17.9.

### 3.1.2 Regression Models for Drilling Data

Similar procedure as tripping-in data was followed for drilling data. Four regression models were developed as before. They are designated as 'Model1D', 'Model2D', 'Model3D' and 'Model4D'. The four models are as follows-

$$\text{Model1D: } SPP = 0.0002494Q^{1.811} + 10.31$$

$$\text{Model2D: } SPP = 0.0005629Q^{1.709}$$

$$\text{Model3D: } SPP = -162 - 1.57 \times 10^{-6} (DBTM)(Q) + 0.216Q$$

$$\text{Model4D: } SPP = -168 + 1.32 \times 10^{-6} (DBTM)(Q) + 0.202Q$$

Model1D and Model2D were found using nonlinear least squares regression. Model3D was found using linear least squares regression while Model4D was found using robust least squares regression. Among the four models, Model1D fitted the training data well with SSE=1213, R-square=0.9864 and RMSE=5.578. On the other hand, Model4D produced the worst fit of the training data with SSE=37500, R-square=0.924 and RMSE=8.05.

### 3.2 Instance-based Reasoning

Instance-based reasoning (IBR) is a machine learning method. Machine learning aims at developing computer programs which will learn from an existing database formed by real life experience and predict the value of the desired parameter (i.e. output) for a new unobserved situation using its learning experience.

The following methods were used to develop IBR models to estimate SPP for the deviated long well drilled in the North Sea:

- k-nearest neighbor learning algorithm
- Distance-weighted k-nearest neighbor learning algorithm
- Locally weighted linear regression

The k-nearest neighbor learning algorithm is the most basic IBR method [5]. It predicts the output parameter based on the k-nearest neighbors of the query instance. The value of k can be any positive integer starting from one to N. When k=N, the prediction becomes the global average of all the

training examples. The most frequently used value of k is three.

Distance-weighted k-nearest neighbor learning algorithm is a refinement to the previous learning algorithm. In this method, the contribution of each of the k-nearest neighbors is weighted with respect to its Euclidian distance from the query instance.

In locally weighted linear regression method, a different local approximation is calculated for each distinct query instance. In this method, weights are determined by minimizing the error in prediction using the training examples near the query instance. For error minimization, Quasi-Newton method and genetic algorithm were used in the current work. The Quasi-Newton method uses gradient to search for the minimum point of the objective function while genetic algorithm uses parallel search technique to find the optimal point.

A detail description of all these IBR methods can be found in [3] and [5].

Nine IBR models for tripping-in data and nine IBR models for drilling data were developed. The basic structure of these models is shown in Fig 2. Every model worked on the basis of an instance base. It was a database containing both training examples and the query instances. The instance base was formed with the help of MS Excel. The Euclidean distance between the query instance and a training example was determined using two attributes (DBTM and mud flow rate) for every query instance. The Euclidean distance was used to find the nearest neighbors and also to calculate the weights for every training example for distance-weighted models. For locally weighted models, the attributes were weighted.

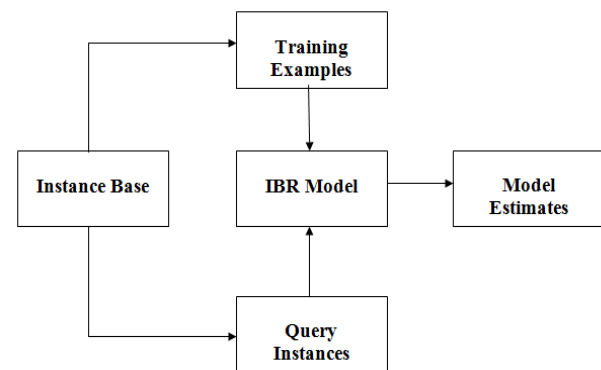


Fig 2. Basic structure of IBR models

Among the nine IBR models developed for each of the two groups of data, four models were based on the k-Nearest neighbor learning algorithm, three were

based on distance-weighted learning algorithm and two were based on locally weighted linear regression.

The locally weighted linear regression model was of the following form:

$$SPP = w_0 + w_1 DBTM + w_2 Q \quad (1)$$

The weights were found by minimizing the following distance weighted error function for the three nearest neighbors of the query instance in the Euclidean space:

$$Error = \sum_{i=1}^3 \frac{(SPP_{measuredi} - SPP_{estimatei})^2}{d(x_q, x_i)} \quad (2)$$

Here  $SPP_{measuredi}$  is the measured SPP and  $SPP_{estimatei}$  is the estimated SPP for the  $i$ th nearest neighbor. For error minimization, two MATLAB functions `fminunc()` and `ga()` were used. The function `fminunc()` uses Quasi-Newton algorithm while `ga()` uses genetic algorithm for minimizing the error function. The weights corresponding to minimum error were used in Eq. (1) for estimating SPP for the query instance.

A detail of the IBR models used can be found in [3].

#### 4. RESULTS AND DISCUSSION

The results obtained for tripping-in data and drilling data are presented in this section's two subsections.

##### 4.1 Tripping-in Data

The absolute error in predicted SPP for the 153 tripping-in query instances is presented in Fig 3.

Among the nine IBR models, Model1KT based on k-nearest neighbor learning algorithm outperformed the other three k-nearest neighbor models. Similarly, Model1WT among the distance-weighted models and Model2LGT among the linear regression models provided good estimates of SPP. For Model1KT, the data were not normalized (i.e. dividing all the values of an attribute by the largest value among them). The model also did not include updating the training example database (i.e. addition of the current query instance to the training example database). Model1WT estimated SPP for the query instance based on the weighted average of the three nearest neighbors of the query instance. Model2LGT predicted SPP using Eq. 1. The optimum weights were found by genetic algorithm using the three nearest neighbors of the query instance. Model1WT and Model2LGT used normalized data. They also updated the training example database after estimating the SPP for a query instance.

Fig 3 shows that the regression models predicted SPP with absolute errors in the range of zero to 20 bars while the IBR models predicted SPP with absolute errors in the range of zero to 10 bars for most of the query instances. A close observation of the error plots reveals that the regression models produced SPP estimates with errors greater than three bars for a large number of instances. It is 92 for Model1, 116 for Model2, 108 for Model3 and 91 for Model4. On the other hand, Model1KT produced SPP estimates with errors greater than three bars for 42 query instances, Model1WT did it for 41 instances and Model2LGT did the same for 45 instances. These numbers are approximately half of those observed for the four regression models.

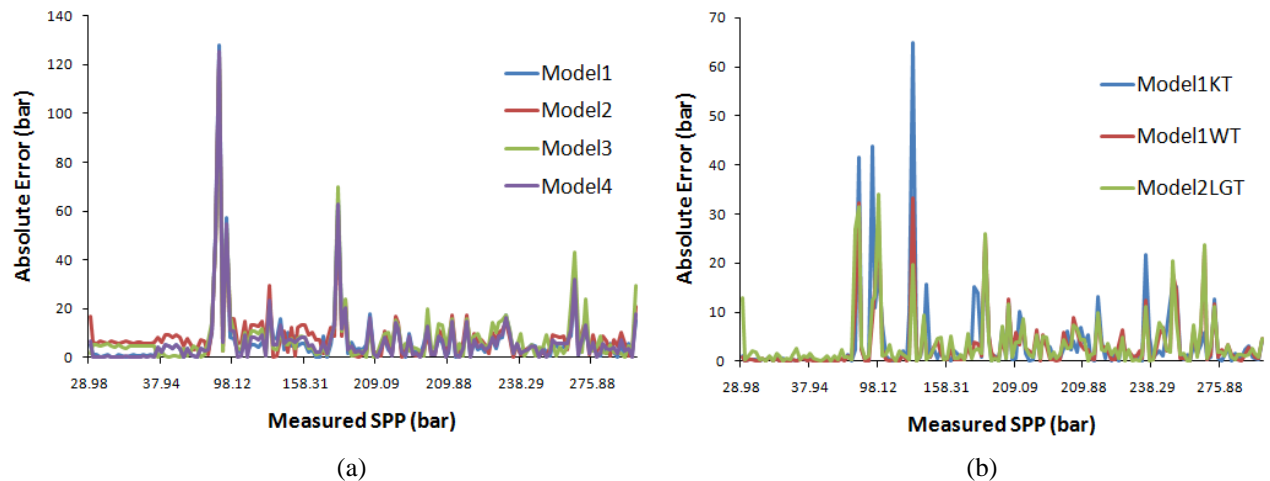


Fig 3. Comparison of absolute error for (a) tripping-in regression models and (b) tripping-in IBR models



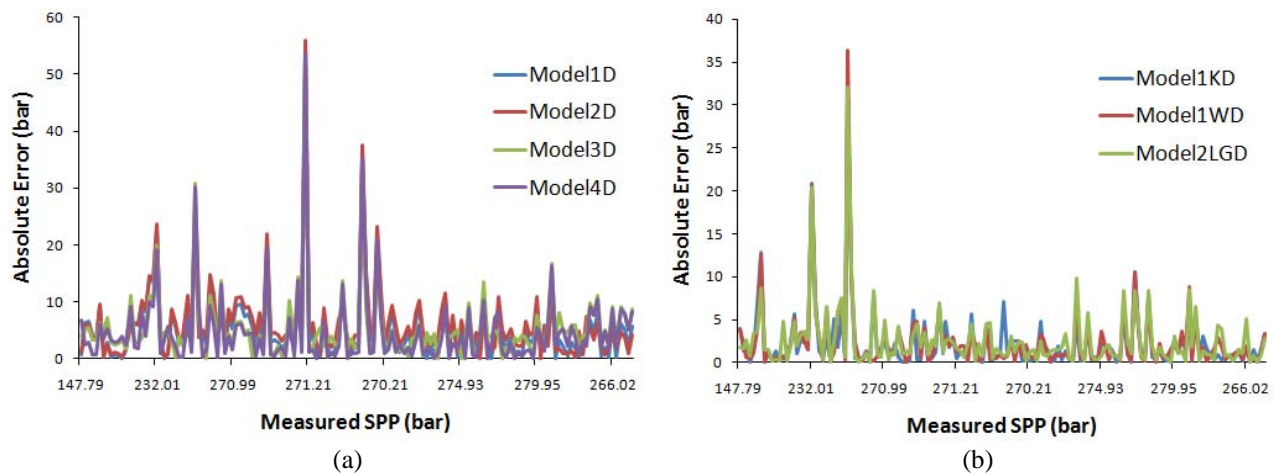


Fig 4. Comparison of absolute error for (a) drilling regression models and (b) drilling IBR models

#### 4.2 Drilling Data

Similar results were obtained for the drilling data. The results are shown in Fig 4. Fig 4 shows that the highest absolute error in predicted SPP was well over 50 bars for regression models while for IBR models it was around 35 bars. A close observation of the two error plots reveals that Model1D produced SPP estimates with absolute error greater than three bars for 80 query instances, Model2D did it for 101 instances, Model3D did the same for 92 instances and Model4D did it for 68 query instances. On the other hand, Model1KD produced SPP estimates with absolute error greater than three bars for 30 instances, for Model1WD it was 33 and for Model2LGD this number was 39. All these numbers are even less than half of those for the regression models. This indicates the credibility of IBR models as better estimators of SPP than the regression models for the present data.

#### 5. CONCLUSION AND FURTHER RECOMMENDATIONS

Due to the limitations of the conventional approach, alternative methods for SPP estimation using real time data were developed. IBR is one such method. In this paper, IBR models along with regression models are presented. For the real time data used in this paper, IBR models produced more accurate estimates of SPP compared to the regression models tried.

However, the results obtained are limited by the fact that the data used were collected while drilling the deviated segment of a well using an oil based mud. Therefore, it is recommended that the regression analysis and IBR approach should be tried with real time data collected while drilling wells in different geological locations using different drilling muds. Also, other machine learning methods such as case-based reasoning (CBR) and neural network can be tried. Furthermore, the results obtained by the IBR

approach can be compared with those obtained by the CBR and neural network approach.

#### 6. ACKNOWLEDGEMENT

A special thanks to Dr. Sigve Hovda of Verdande Technology AS for his support during the work.

#### 7. REFERENCES

1. Chowdhury, D., 2008, "Hydraulic Pressure Losses in Drilling Fluid", MSc Project Report, Norwegian University of Science and Technology, Trondheim, Norway.
2. Bourgoyne, Jr. A. T., Chenevert, M. E., Millheim, K. K. and Young, Jr. F.S., 2003, *Applied Drilling Engineering*, Society of Petroleum Engineers, Texas, USA, pp. 12-17,131-157.
3. Chowdhury, D., 2009, "Prediction of Standpipe Pressure Using Real Time Data", MSc Thesis Report, Norwegian University of Science and Technology, Trondheim, Norway.
4. *Curve Fitting Toolbox User's Guide* (Version 1), The MathWorks Inc., 2002, Massachusetts, USA, pp 1-40 (Chap. 3).
5. Mitchell M. T., 1997, *Machine Learning*, The McGraw-Hill Companies Inc., Singapore, pp. 1-18, 20-45, 230-245.

#### 8. NOMENCLATURE

Symbol	Meaning	Unit
Q	Mud flow rate	(m <sup>3</sup> /s)
DBTM	Bit measured depth	(m)
N	Number of training examples	dimensionless
w <sub>0</sub> , w <sub>1</sub> , w <sub>2</sub>	Weights	dimensionless
d(x <sub>q</sub> , x <sub>i</sub> )	Euclidean distance between normalized query instance and training example	dimensionless



## STUDY ON REAL GAS FLOWS THROUGH A CRITICAL NOZZLE

Mamun Mohammad<sup>1</sup>, Junji Nagao<sup>2</sup>, Shigeru Matsuo<sup>3</sup>, Tokitada Hashimoto<sup>3</sup> and Toshiaki Setoguchi<sup>4</sup>

<sup>1</sup> Dept. of Mechanical Engineering, BUET, Dhaka, Bangladesh.

<sup>2</sup> Graduate School of Science and Engineering, Saga University, Japan

<sup>3</sup> Dept. of Mechanical Engineering, Saga University, Japan.

<sup>4</sup> Institute of Ocean Energy, Saga University, Japan.

### ABSTRACT

A critical nozzle is used to measure the mass flow rate of gas. It is well known that the coefficient of discharge of the flow in a critical nozzle is a single function of the Reynolds number. The purpose of the present study is to investigate high-pressure gas flow of air through a critical nozzle. A computational analysis has been carried out to simulate a critical nozzle flow with real gas effects. A modified Berthelot's equation of state is incorporated into the axisymmetric, compressible Navier–Stokes equations. The computational results show that the discharge coefficient for ideal gas assumptions is significantly different from those of the real gas, as the Reynolds number exceeds a certain value. It is also known that the real gas effects appear largely in terms of the compressibility factor and the specific heat ratio, and these become more remarkable as the gas pressure increases. Furthermore, the effects of amplitudes and frequencies of the pressure disturbance on the gas flow through a critical nozzle were investigated numerically.

**Keywords:** Compressible flow, Critical nozzle, Real gas effects, Discharge coefficient, Simulation.

### 1. INTRODUCTION

The minimum pressure ratio for the flow to choke is called the critical pressure ratio. Once choked, the flow is no longer dependent on the pressure change in the downstream flow field. In this case, the mass flow is determined only by the stagnation conditions upstream of the flow passage. The critical nozzle is defined as a device to measure the mass flow with only the nozzle supply conditions, making use of the flow-choking phenomenon at the nozzle throat.

In the past, much attention has been paid to the prediction of mass flow through a flow passage, since it was of practical importance in a variety of industrial and engineering fields. The mass flowrate and critical pressure ratio are associated with the working gas consumption and the establishment of safe operation conditions of the critical nozzle. According to previous researches [1-3], the mass flowrate and critical pressure ratio are strong functions of the Reynolds number ( $Re$ ).

Of many kinds of working gases employed in industrial field, it is being recognized that hydrogen gas is one of the most promising gases as a future alternative energy source. In such an application, precise measurement of flowrate is of practical importance for mileage and power output of the vehicle. A large number of works [4–7] has been made to investigate the thermo-physical properties of hydrogen gas, which are specified by some different kinds of the equations of state, the critical pressure, the compressibility factor of hydrogen gas, etc. However, only a few researches have been made to date on the mass flowrate of the

high-pressure hydrogen gas through a critical nozzle, due to difficulties of treatment. Recently, Nakao [8] has conducted the flowrate measurement of hydrogen gas using a critical nozzle experimentally. It was shown in the range of high Reynolds number that the coefficient of discharge decreased with an increase of  $Re$ .

The objectives in the present study are to investigate the flow features of high-pressure air gas through a critical nozzle, with the help of a CFD method and to clarify the effects of amplitudes and frequencies of the pressure disturbance on the gas flow through a critical nozzle numerically. Modified Berthelot's equation of state [9] is employed to consider the force and volume effects of inter-molecules of air gas, and it is incorporated into the axisymmetric, compressible Navier–Stokes equations. Furthermore, the computational results (coefficient of discharge) are validated with some experimental data available.

### 2. CFD ANALYSIS

#### 2.1 Governing Equations

The governing equations, i.e., the unsteady compressible Navier-Stokes equations written in an axisymmetric coordinate system ( $x, y$ ) are as follows :

$$\frac{\partial U}{\partial t} + \frac{\partial E}{\partial x} + \frac{\partial F}{\partial y} = \frac{1}{Re} \left( \frac{\partial R}{\partial x} + \frac{\partial S}{\partial y} \right) + \frac{1}{y} H_1 + H_2 \quad (1)$$

where

$$\mathbf{U} = \begin{bmatrix} \rho \\ \rho u \\ \rho v \\ \rho k \\ \rho \varepsilon \end{bmatrix}, \mathbf{E} = \begin{bmatrix} \rho u \\ \rho u^2 + p \\ \rho uv \\ u(E_t + p) \\ \rho ku \\ \rho \varepsilon u \end{bmatrix}, \mathbf{F} = \begin{bmatrix} \rho v \\ \rho uv \\ \rho v^2 + p \\ v(E_t + p) \\ \rho kv \\ \rho \varepsilon v \end{bmatrix},$$

$$\mathbf{R} = \begin{bmatrix} 0 \\ \tau_{xx} \\ \tau_{xy} \\ \alpha \\ \left(\mu + \frac{\mu_t}{\sigma_k}\right) \frac{\partial k}{\partial x} \\ \left(\mu + \frac{\mu_t}{\sigma_\varepsilon}\right) \frac{\partial \varepsilon}{\partial x} \end{bmatrix}, \mathbf{S} = \begin{bmatrix} 0 \\ \tau_{xy} \\ \tau_{yy} \\ \beta \\ \left(\mu + \frac{\mu_t}{\sigma_k}\right) \frac{\partial k}{\partial y} \\ \left(\mu + \frac{\mu_t}{\sigma_\varepsilon}\right) \frac{\partial \varepsilon}{\partial y} \end{bmatrix},$$

$$\mathbf{H}_1 = \begin{bmatrix} -\rho v \\ \tau_{xy} - \rho uv \\ \alpha - \rho v^2 \\ \beta - (E_t + p)v \\ 0 \\ 0 \end{bmatrix}, \mathbf{H}_2 = \begin{bmatrix} 0 \\ 0 \\ 0 \\ 0 \\ P_k - \rho \varepsilon \\ C_{1\varepsilon} \frac{\varepsilon}{k} P_k - C_{2\varepsilon} \rho \frac{\varepsilon^2}{k} \end{bmatrix} \quad (2)$$

$$E_t = \rho C_p T + \frac{1}{2} \rho (u^2 + v^2) \quad (3)$$

$$p = (\gamma - 1) \left[ E_t - \frac{1}{2} \rho (u^2 + v^2) \right] \quad (4)$$

$$\alpha = u \tau_{xx} + v \tau_{yx} + \kappa \frac{\partial T}{\partial x}, \quad \beta = u \tau_{xy} + v \tau_{yy} + \kappa \frac{\partial T}{\partial y} \quad (5)$$

$$\mu_t = \rho C_\mu \frac{k^2}{\varepsilon} \quad (6)$$

$$P_k = 2\mu_t \left[ \left( \frac{\partial u}{\partial x} \right)^2 + \frac{1}{2} \left( \frac{\partial v}{\partial x} + \frac{\partial u}{\partial y} \right) + \left( \frac{\partial v}{\partial y} \right)^2 \right] \quad (7)$$

$$C_{1\varepsilon} = 1.44, C_{2\varepsilon} = 1.92, C_\mu = 0.09, \sigma_k = 1.0, \sigma_\varepsilon = 1.3 \quad (8)$$

For air, a modified Berthelot was used to obtain the compressibility factor as follows [9]:

$$p = \frac{RT}{v} \left\{ 1 + \frac{9pT_c}{128p_c T} \left( 1 - \frac{6T_c^2}{T^2} \right) \right\} \quad (9)$$

$p_c$  and  $T_c$  are critical pressure and critical temperature, respectively. In Eq.(2),  $\mathbf{U}$  is the conservative vector,  $\mathbf{E}$  and  $\mathbf{F}$  are inviscid flux vector and  $\mathbf{R}$  and  $\mathbf{S}$  are viscous

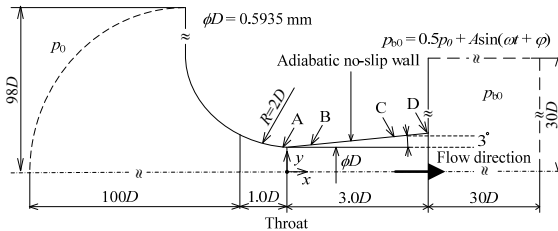


Fig 1. Details of critical nozzle

flux vectors.  $\mathbf{H}_1$  and  $\mathbf{H}_2$  are the source terms corresponding to axisymmetry and turbulence,

respectively.  $\tau_{xx}$ ,  $\tau_{xy}$ ,  $\tau_{yx}$  and  $\tau_{yy}$  are components of viscous

Table 1: Initial conditions

$Re$	$p_0$ (kPa)	$A$ (kPa)			$f$ (kHz)	
500	6.6	0.01 $p_{b0}$	0.05 $p_{b0}$	0.1 $p_{b0}$	30	60
700	9.3					
3,750	49.6					
7,548	99.8					
14,952	197.7					
76,631	1,013	-	-	-	-	-
153,263	2,026	-	-	-	-	-

shear stress.

The governing equation systems that are non-dimensionalized with reference values at the reservoir condition are mapped from the physical plane into a computational plane of a general transform. To close the governing equations, standard  $k$ - $\varepsilon$  model [10] is employed in computations. A third-order TVD (Total Variation Diminishing) finite difference scheme with MUSCL [11] is used to discretize the spatial derivatives, and a second order-central difference scheme for the viscous terms, and a second-order fractional step method is employed for time integration.

## 2.2 Computational Conditions

Figure 1 shows an ISO-type toroidal throat sonic Venturi nozzle [12] used in the present study. The radius of curvature at the throat of the nozzle is twice the throat diameter  $\phi D$  ( $= 0.5935$  mm). The straight divergent part has a half angle of  $\theta = 3^\circ$  and its axial length is  $3.0D$ . In order to simulate the pressure disturbance downstream, a sudden enlargement section that is  $30D$  long and  $30D$  high is connected to the nozzle exit. The nozzle inlet is located at  $100D$  upstream of the nozzle throat.

In the steady computations, the total pressure  $p_0$  (reservoir) and back pressure  $p_{b0}$  are given at the inlet and outlet of the critical nozzle, respectively. The back pressure  $p_{b0}$  is kept constant at  $0.5p_0$  and the inlet total pressure  $p_0$  is varied to change the Reynolds number. Ranges of Reynolds number are from 500 to 153,263 (Table 1). Total temperature is  $T_0 = 298K$ .

In order to simulate the effects of pressure disturbance on the critical flows, a sinusoidal wave with an amplitude  $A$ , an angular frequency  $\omega$  ( $= 2\pi f$ ) and a phase  $\varphi$  is assumed at the exit of the sudden enlargement section as illustrated in Fig.1. As shown in this figure, point A is located at  $-0.1D$  upstream of nozzle throat and points B, C and D are located at  $0.5D$ ,  $2.0D$  and  $3.0D$  downstream of the nozzle throat, respectively. Combinations of  $A$  and  $f$  used in the present simulation are shown in Table 1.

## 3. RESULTS AND DISCUSSIONS

### 3.1 Flow Characteristics in Case without Pressure Disturbance

Figures 2 show the effects of temperature and pressure on the compressibility factor  $Z$ . If the gas is assumed to be an ideal gas, the compressibility factor is 1.0, regardless of pressure. As seen from this figure, the

virial equation of state predicts a monotonous change in  $Z$  with pressure. Modified Berthelot's equation of state gives similar results with the virial equation of state for air gas. In the present study, modified Berthelot's equation of state is selected to simulate the air gas through the critical nozzle because it exhibits better agreement with the virial equation of state.

In Fig. 3, the present computations are validated with the experimental results [13] using air gas in which the Reynolds number is based on the diameter of the nozzle throat and the total properties at the inlet of the nozzle. It is known that the coefficient of discharge is a strong function of the Reynolds number, and the predicted coefficients of discharge are in good agreement with the experimental results below  $Re=14,952$ . It is believed that the present computational method effectively predicts the gas flow through the critical nozzle for low Reynolds number.

Furthermore, noticeable trend in the coefficient of the discharge can be found in the range of Reynolds numbers above 14,952 for air, where the coefficient of the discharge decreases with an increase in Reynolds number. This obviously differs from the trend that has reported by many researchers [16–18]. A similar trend is found in Johnson's data for hydrogen gas [19].

For an ideal gas assumption, the present computational results predict the coefficient of the discharge, which increases with the Reynolds number and then approaches a certain constant value [20]. However, the present computation taking into account the real gas effect is qualitatively similar to results

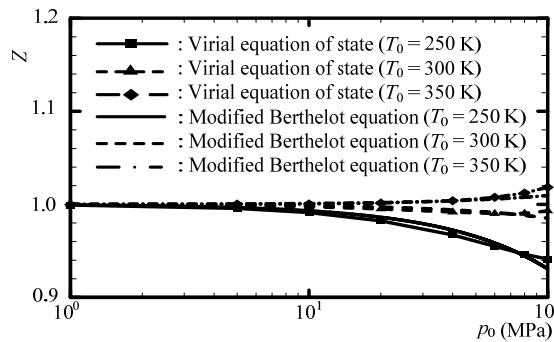


Fig 2. Comparison of the equation of state

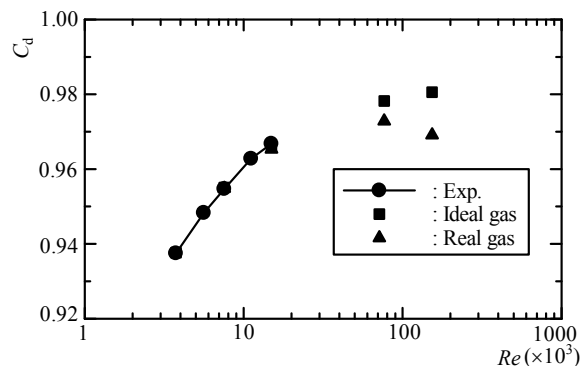


Fig 3. Effect of Reynolds number on discharge coefficient obtained by Johnson [19] and Nakao [2]. Unfortunately,

a clear and persuasive reasoning for this is, at present, not known. Such a trend in the discharge coefficient can give rise to a significant error in the mass flow at high-pressure conditions. More studies are needed to elucidate this ambiguous problem.

Figure 4 shows the effect of Reynolds number on the mass fluxes at the nozzle throat in the range from  $Re=7,548$  to  $153,263$ . In case of  $Re = 7,548$  and  $14952$ , the mass flux distributions for both the real and ideal gases are nearly the same. However, with an increase of Reynolds number, a little difference between ideal and real gases is mainly recognized in the region outside the boundary layer and the mass flux of real gas becomes slightly small. It is considered that a decrease of  $C_d$  with an increase of Reynolds number in case of real gas in Fig.3 may be due to the decrease of mass flux.

Figure 5 shows the axial distributions of the computed values of ratio of specific heats. Note that ratio of specific heats of ideal gas is constant at 1.4. Ratio of specific heats increases through the nozzle with an increase of Reynolds number. This variation in the ratio of specific heats with Reynolds number has a significant

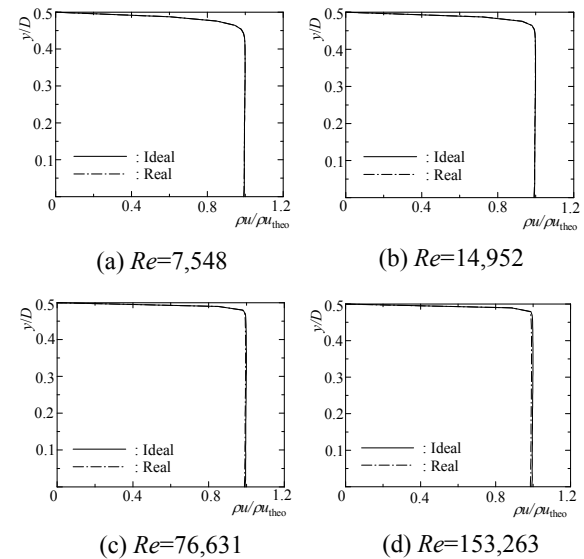


Fig 4. Comparison of average mass fluxes of ideal and real gas

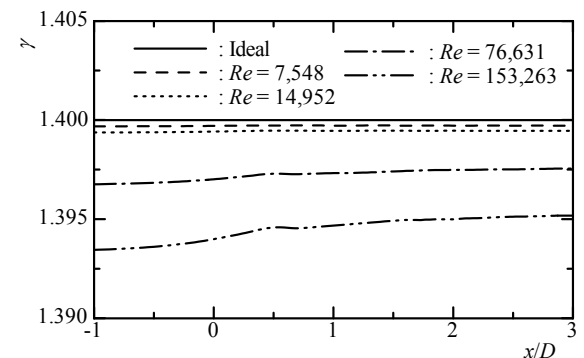


Fig 5. Effect of Reynolds number on ratio of specific heats influence on the mass flow.

In order to investigate the real gas effects, the computed compressibility factors along the nozzle axis are shown in Fig.6. The computed compressibility factors for the real gas seem to decrease during the process of the flow to be accelerated through the nozzle throat.

### 3.2 Effects of Pressure Disturbance on the Flows

For unsteady computations, the pressure signal imposed on the downstream boundary is given as a sinusoidal periodic wave in the range from  $Re = 500$  to  $14,952$ . For the pressure fluctuation of  $f = 60$  kHz ( $A = 0.01p_{b0}$ ,  $0.05p_{b0}$ ,  $0.1p_{b0}$ ), the computed pressure-time histories at the measuring point A on the nozzle wall are shown in Fig. 7. Figures 7(a) and 7(b) are pressure-time histories for  $Re = 700$  and  $3,750$ , respectively, and  $p_{av}$  means the time-mean local static pressure.

For  $Re = 700$ , the static pressures fluctuate with time and they are quite periodic. Furthermore, it is found that the unsteady effects of the pressure fluctuations can propagate upstream of the throat of the critical nozzle. Amplitude becomes large with an increase of  $A$ . For  $Re = 3,750$ , fluctuations in the static pressure are not observed for all cases. The fluctuations of static pressure for  $Re = 500$  was similar tendency to result of  $Re = 700$ . For  $Re = 7,548$  and  $14,952$ , they showed similar tendency to result of  $Re = 3,750$ .

Figures 8 shows pressure-time histories at point A for  $f = 30$  kHz. Figures 8(a) and 8(b) are pressure-time histories for  $Re = 700$  and  $3,750$ , respectively. As seen from these figures, in case of the pressure disturbance with large amplitude and small frequency, the pressure fluctuations could propagate upstream of the nozzle throat. Similar tendency is obtained in the range from  $Re = 500$  and  $14,952$ .

Figures 9 and 10 show time-dependent sonic lines of the flow through the critical nozzle for  $f = 60$  kHz in cases of  $Re = 700$  and  $3,750$ , respectively ( $A = 0.01p_{b0}$ ,  $0.05p_{b0}$ ,  $0.1p_{b0}$ ). In Fig.9, the sonic line fluctuations are slightly observed with an increase of amplitude. However, for  $Re = 3,750$  (Fig.10), it is found that the sonic line close to the throat do not fluctuate for three amplitude.

Figures 11 and 12 show time-dependent sonic lines for  $f = 30$  kHz in cases of  $Re = 700$  and  $3,750$ , respectively ( $A=0.01p_{b0}$ ,  $0.05p_{b0}$ ,  $0.1p_{b0}$ ). In Fig.11, a considerable amount of excursion of the sonic line is found near the nozzle throat for three amplitudes. The sonic lines appear highly distorted and they strongly depend on time.

However, for  $Re = 3,750$  (Fig.12), it is found that the sonic line downstream of the nozzle throat fluctuates largely for  $A = 0.01p_{b0}$  and  $0.05p_{b0}$ .

Figures 13(a) and 13(b) show the computed mass flow rate fluctuations for  $f = 60$  kHz in cases of  $Re = 700$  and  $3,750$ , respectively. Here  $\dot{m}_c$  means the time-mean mass flow rate that is obtained from the steady computations

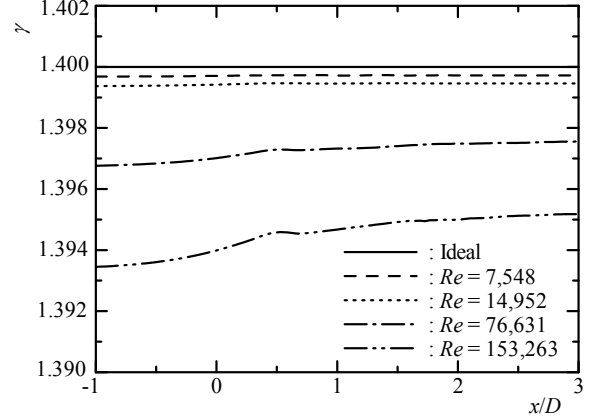


Fig 6. Effect of Reynolds number on compressibility factor

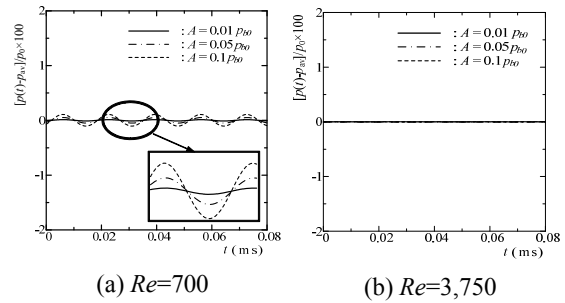


Fig 7. Pressure-time histories at point A ( $f = 60$  kHz)

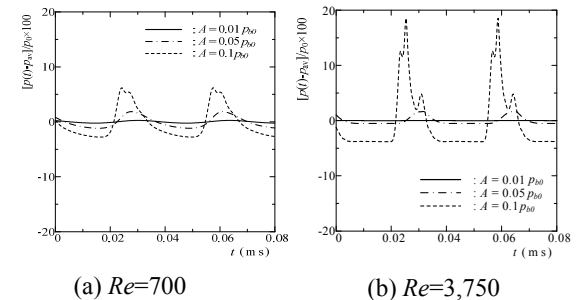


Fig 8. Pressure-time histories at point A ( $f = 30$  kHz)

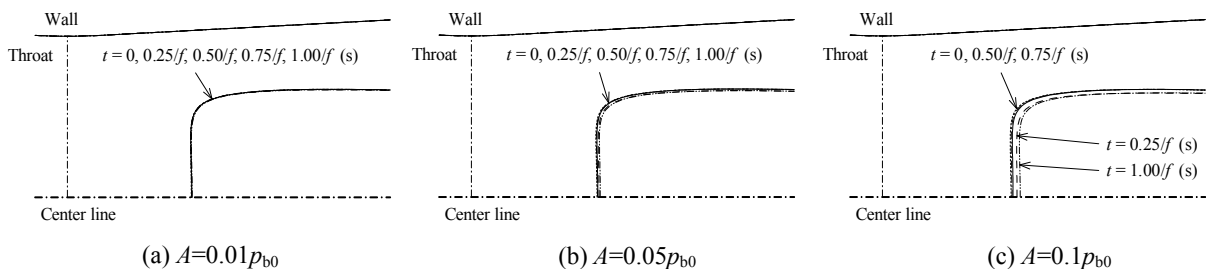


Fig 9. Time dependent sonic lines ( $Re = 700$ ,  $f = 60$  kHz)

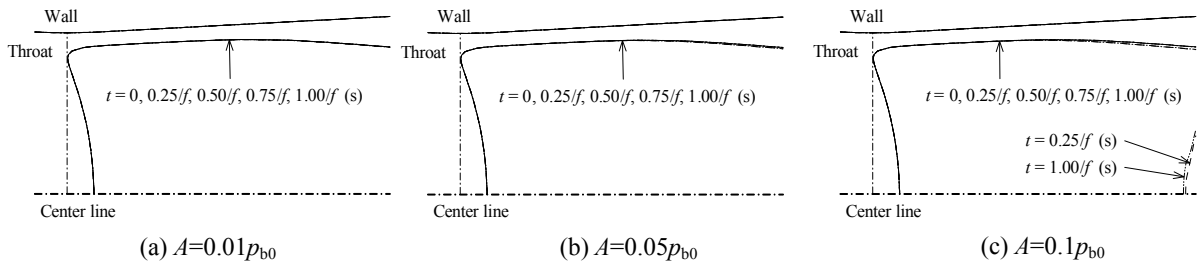


Fig.10 Time dependent sonic lines ( $Re = 3,750$ ,  $f = 60$  kHz)

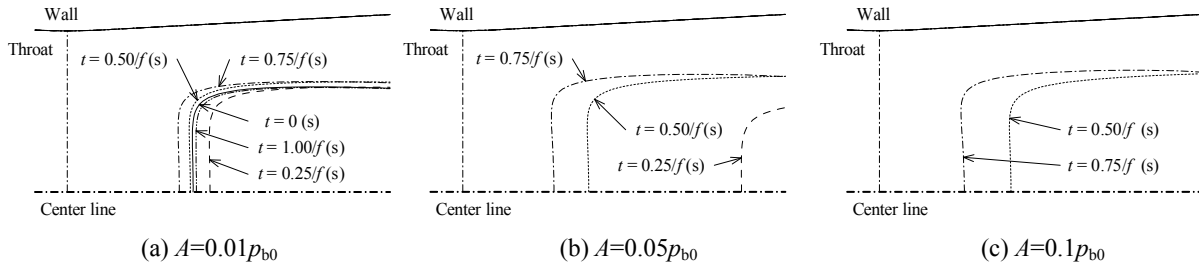


Fig.11 Time dependent sonic lines ( $Re = 700$ ,  $f = 30$  kHz)

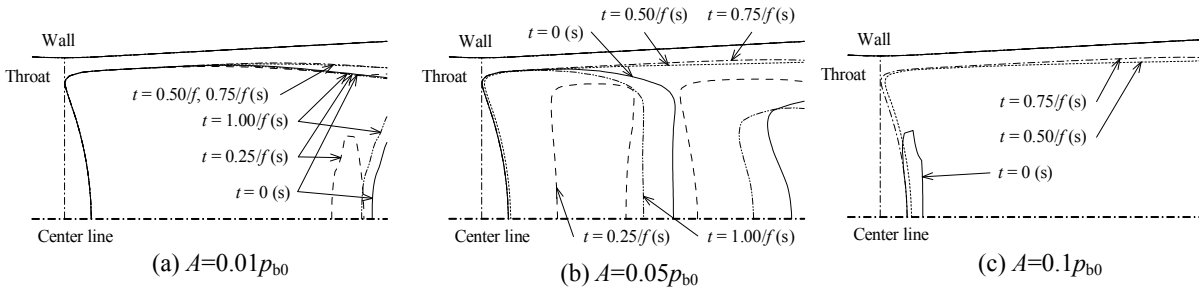


Fig.12 Time dependent sonic lines ( $Re = 3,750$ ,  $f = 30$  kHz)

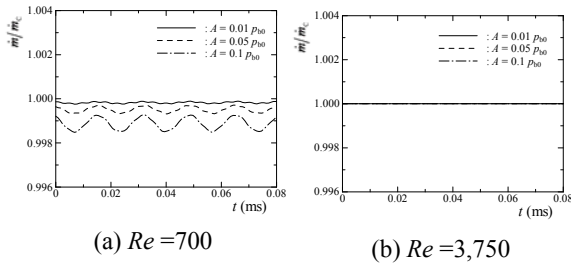


Fig.13 Mass flow rate fluctuation with time ( $f=60$ kHz)

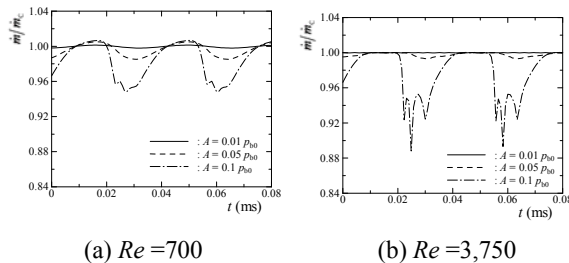


Fig.14 Mass flow rate fluctuation with time ( $f=30$ kHz)

for each Reynolds number. It is found for  $Re = 700$

(Fig.13(a)) that the mass flow rate for three amplitudes fluctuates even under the condition of flow choking. The mass flow rate becomes large with an increase of amplitude. However, the mass flow rate is constant for  $Re = 3,750$ .

Figures 14(a) and 14(b) show the computed mass flow rate fluctuations for  $f = 30$  kHz in cases of  $Re = 700$  and  $3,750$ , respectively. It is found that the fluctuation of the mass flow rate for  $A = 0.05 p_{b0}$ ,  $0.1 p_{b0}$  becomes large compared with cases of  $f = 60$  kHz.

#### 4. CONCLUSIONS

A computational study has been made to investigate the flow features of air through the critical nozzle. In order to simulate the real gas effects which appear at high-pressure conditions, modified Berthelot's equation of state has been employed for air and incorporated into the axisymmetric, compressible Navier-Stokes equations. The results obtained are as follows : Mass fluxes of real gas became small compared with ideal gas with an increase of Reynolds number. The coefficient of discharge of real gas through the critical nozzle decreased with an increase of Reynolds number. In high Reynolds number, the thermodynamics properties of real gas, such as the compressibility factor and the ratio of specific heats changed compared with ideal gas.

For low Reynolds number ( $Re = 500, 700$ ), the unsteady effects of the pressure fluctuations could propagate upstream of the nozzle throat and it had effect on thereby fluctuations in mass flow rate through the critical nozzle. In case of the pressure disturbance with large amplitude for high Reynolds number ( $Re = 3,750, 7,548, 14,952$ ), the pressure fluctuations could not propagate upstream of the nozzle throat. However, in case of the pressure disturbance with large amplitude and small frequency, the pressure fluctuations could propagate upstream of the nozzle throat.

## 5. REFERENCES

1. Tang, S. P. and Fenn, J. B., 1978, "Experimental determination of the discharge coefficients for critical flow through an axisymmetric nozzle", Am. Inst. Aeronaut. Astronaut. J., vol.16, no.1, pp.41-46.
2. Nakao, S., Yokoi, Y. and Takamoto, M., 1996, "Development of a calibration facility for small mass flow rates of gas and uncertainty of a sonic Venturi transfer standard", J. Flow Measmt Instrumentation, vol.7, pp.77-83.
3. Nakao, S., Irayama, T. and Takamoto, M., 2000, "Relations between the discharge coefficients of the sonic Venturi nozzle and kind of gases", J. Japan Soc. Mech. Engrs, Ser. B, vol.66, no.642, pp.438-444.
4. Johnson, R. C., 1965, "Real - gas effects in critical - flow - through nozzles and tabulated thermodynamic properties", NASA TN D-2565.
5. McCarty, R. D. and Weber, L. A., 1972, "Thermophysical properties of parahydrogen from the freezing liquid line to 5000R for pressures to 10,000 Psia", NBS TN 617.
6. McCarty, R. D., Hord, J., and Roder, H.M, 1981, "Selected properties of hydrogen (engineering design data)", NBS MN 168.
7. McCarty, R. D., 1975, "Hydrogen technological survey thermophysical properties", NASA SP 3089.
8. Nakao, S., 2005, "Development of critical nozzle flow meter for high pressure hydrogen gas flow measurements", In Proceedings of JSME, Fluid Dynamics Section, Kanazawa, Japan, G201.
9. Computational chemistry list, ltd. "Equations of State". CCL. NET, available from < http : // www.ccl.net / cca / documents / dyoung / topics-orig/eq\_state.html >, (accessed 2008-11).
10. Launder, B. E. and Spalding, D. B., 1974, "Computer Methods in Applied Mechanics and Engineering", vol.3, pp.269-289.
11. Yee, H.C., 1989, "A class of high-resolution explicit and implicit shock capturing methods", NASA TM-89464.
12. ISO 9300, (1990).
13. Nakao, S., 2001, "A Study on the Conversion Factor of Sonic Venturi Nozzles", Proc. of NCSL International Workshop & Symposium.
16. Bignell, N., 1996, "The use of small sonic nozzles at low Reynolds numbers", Flow Meas. Instrum., Vol.7, pp.77-83.
17. Choi, Y. M., Park, K. A., Park, J. T., Choi, H. M., and

Park, S. O., 1999, "Interference effects of three sonic nozzles of different throat diameters in the same meter tube", Flow Meas. Instrum., Vol.10, pp.175-181.

18. Kim, H. D., Kim, J. H., Park, K. A., Setoguchi, T., and Matsuo, S., 2004, "Study of the effects of unsteady downstream conditions on the gas flow through a critical nozzle", Proc. Instn Mech. Engrs, Part C: J. Mechanical Engineering Science, Vol.218, No.10, pp.1163-1173.
19. Johnson, R. C., 1965, "Real-gas effects in critical - flow - through nozzles and tabulated thermodynamic properties", NASA TN D-2565.
20. Kim, H.D., Kim, J. H., Park, K. A., Setoguchi, T. and Matsuo, S., 2003, "Computational study of the gas flow through a critical nozzle", Proc. Instn Mech. Engrs, Part C: J. Mechanical Engineering Science, Vol.217, No.10, pp.1179-1189.

## 6. NOMENCLATURE

Symbol	Meaning	Unit
$A$	Cross-section area	(m <sup>2</sup> )
$C_d$	Discharge coefficient	(-)
$C_p$	Specific heat at constant pressure	(J/kg·K)
$D$	Diameter of the critical nozzle throat	(m)
$E, F$	Inviscid flux vectors	(-)
$E_t$	Total energy per unit volume	(J/m <sup>3</sup> )
$H_1$	Source term for axisymmetry	(-)
$H_2$	Source term for Turbulence	(-)
$L$	Characteristic length	(m)
$J$	Jacobian	(-)
$\dot{m}$	Mass flow rate	(kg/s)
$p$	Pressure	(Pa)
$p_b$	Back pressure	(Pa)
$R$	Radius of the critical nozzle	(m)
$R, S$	Viscous flux vectors	(-)
$Re$	Reynolds number	(m)
$T$	Temperature	(K)
$t$	Time	(s)
$U$	Conservative vector	(-)
$u, v$	Velocity components	(m/s)
$v$	Specific volume	(m <sup>3</sup> /kg)
$x, y$	Cartesian coordinates	(m)
$Z$	Compressibility factor	(-)
Greeks		
$\gamma$	Ratio of specific heats	(-)
$\kappa$	Thermal conductivity	(W/mK)
$\rho$	Density	(kg/m <sup>3</sup> )
$\tau$	Shear stress	(Pa)
$\theta$	Angle of attack	( <sup>o</sup> )
Subscripts		
0	Stagnation point	
c	Critical point	
theo	theory	

## 7. MAILING ADDRESS

Mamun Mohammad  
 Dept. of Mechanical Engineering,  
 BUET, Dhaka-1000, Bangladesh.

## EXPERIMENTAL STUDY OF FRACTAL TURBULENCE

S.M. Muztaba Salim, F.C.G. Nicolleau , M. Borkowski

University of Sheffield, Dept of mechanical Engineering, UK

### ABSTRACT

Fractal turbulence is deemed much more efficient than grid turbulence in terms of the flow mixing properties. In this paper, we present our hotwire experimental results of fractal turbulence generated by fractal orifice. The self-similar edge characteristic of the fractal orifice is thought to play the vital role in the enhanced mixing properties. We used four fractal orifices, each paired with a smooth orifice of equivalent flow area. The objectives were two folds, the first was to study the fractal scaling influence on the flow and the second was to explore the potential of the fractal orifice flow meter to determine the flow rate in a pipe. The results provided an excellent insight of the fractal generated turbulence and the fractal flow physics. Across the fractal orifice, the pressure drop was lower but the turbulence intensity was higher than those across the paired smooth orifice.

**Keywords:** Fractal, Turbulence, Hotwire.

### 1. INTRODUCTION

Study of fractal property can be traced back to as far as 650 AD in the page design layout of the *Book of Durrow*, Ireland. Yet the term *fractal* was first coined by the famous Polish Mathematician, Benoît Mandelbrot, only in 1975. His difficulty in describing the shapes in details at various scales made him pick the word, *fractal*, where the Euclidean geometries such as triangle, rectangle or a circle did not fit to do the job. Take a tree for example. In a three dimensional world, the shape of a tree can be roughly visualized as a sphere on top of a cylinder or in a two dimensional world, the same tree can be viewed as a circle on the top of a long narrow rectangle. But how about when we try to describe the same tree in its micro scale, i.e., how its branches bifurcate or how is the distribution of the leaves? Here comes the fractal property as a savior. Another famous example is the cauliflower. Any smaller portion of it resembles the exact whole of it no matter how many times the same dissection is repeated.

Fractal geometry, as defined in [1], is a derivative of classical Euclidean geometry characterized by infinite detail where the edge smoothness is absent. Mandelbrot [2] defined the fractal property to be the self similar infinite repetition of the whole object from macro to micro scale.

The above definitions can easily be realized in the case of any turbulent flow. In a turbulent flow, the flow pulsations of lower order, mentioned by Kolmogrov [3], absorb energy of the motion and transfer it to the higher order pulsations until the finest pulsation is overcome by the flow viscosity. Stewart [4] mentioned this as energy cascade and showed that only under certain circumstance

the flow becomes turbulent. The turbulent flow takes energy from the large scales which themselves are unstable and break into smaller scales. However, during the breaking process the self similarity of the structures are preserved. This evidently represents the fractal characteristic of the turbulence.

Despite the inherent fractal property of turbulence, very few attempts have been made to generate turbulence by fractal grids as opposed to usual grid turbulence [5, 6, 7] where the grids are evenly distributed. The turbulence generated by fractal grids is referred to as fractal turbulence. Kearney [8] tried to exploit the fractal property of the turbulence in fluid scaling. He engineered a 3D fractal grid to create low energy fractal turbulence to control the geometry of fluid scaling process and implemented it in molasses chromatography process successfully. Queiros-Conde and Vassilicos [9] found that by using the fractal grids a well developed turbulence can be generated. When the fractal dimension is increased the velocity fluctuations tend to be more evenly distributed. More about the fractal dimension may be found in [10]. Staicu *et al.* [11] demonstrated that the flow is significantly affected by the orientation of the fractal grid. To illustrate the influence of the fractal grid on the flow, they compared their results with non-fractal grid turbulence. Keylock *et al.* [12] studied fractal fences, a variant of fractal grids and postulated that the use of fractal fences may suppress the high wind to protect flash flood or avalanche. Seoud and Vassilicos [13] concluded that using the fractal grids as higher as three times turbulence intensities may be produced than classical non fractal grids. They also concluded that their space filling fractal square grids generated a kind of



homogeneous isotropic turbulence whose decays locked into a single length scale. Hurst and Vassilicos [14] conducted an extensive work on 21 planar fractal grids to study scaling and decay of fractal turbulence. They found that the turbulence decay is strongly dependent on the fractal dimension, effective grid mesh size and the ratio between the largest to smallest bar thickness. However, the use of the fractal turbulence was never attempted in the pipe flow until very recently some attempts were made to associate the fractal turbulence with the orifice flow meter [15,16]. A flow meter is a device which is used to determine the flow rate in a pipe flow. With an orifice flow meter, the pressure drop across the orifice is measured. Then the flow rate can be calculated by the flow area of the orifice. The motivation behind this present work arose from the two practical points. One from the engineering point of view is to explore the potential of fractal orifice meter to determine the flow rate in a pipe and the other is from the point of understanding the fractal scaling effect.

## 2. EXPERIMENTAL SET UP

The following sections describe the experimental set up covering the details of the measurement.

### 2.1 Fractal vs. Smooth Orifices

As mentioned in the preceding section, a fractal orifice is a flow meter at its simplest form. The popular Koch curve by the famous Swedish mathematician Helge Von Koch (1870-1924) was adopted to design the fractal orifice shown in Fig. 1.

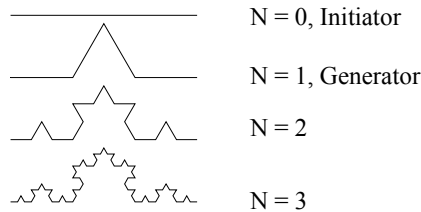


Fig 1. The Koch Curve was constructed by the Swedish Mathematician Von Koch in 1904

The inner edge of the orifice used in this experiment had the characteristics of the Koch curve. At each iteration, the edge lost the “smoothness” and the flow area increased. On the other hand, a smooth orifice is the one whose inner edge is smooth, a very distinguishable characteristic than that of the fractal orifice. Like the fractal orifice, the flow area of the smooth orifice is also increased at each iteration. The total area after each iteration was calculated by the following formula:

$$A_N = A_0 \left[ 1 + \frac{1}{3} \sum_{i=0}^{N-1} \left( \frac{4}{9} \right)^i \right] \quad (1)$$

Where  $A_N$  = total area after one iteration,  $A_0$  = area after previous iteration,  $N$  = number of iteration step. Fig. 2 shows the fractal orifices, each combined with a smooth

orifice of equivalent flow area. The outer diameter of the orifice was 140.8 mm which was kept constant for each orifice. The orifice was made of aluminum and had a thickness of 2 mm. For the naming purpose, we adopted the following convention that would be used throughout this paper; F0 was the fractal orifice at the zero-th iteration, while F1 was the fractal orifice after first iteration and so on. Similarly, S0 was the smooth orifice at the zero-th iteration and S1 was the smooth orifice after first iteration and so on. The pairs were F0-S0, F1-S1, F2-S2 and F3-S3, as shown in Fig. 2. Each pair had an equivalent flow area.

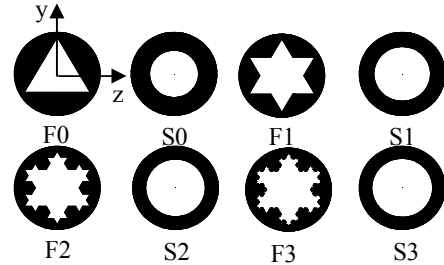


Fig 2. Four fractal orifices,  $N = 0 - 3$ , each paired with a smooth orifice of equivalent flow area

It is to bear in mind that the fractal orifice ( $N = 0$ ) at the zero-th iteration was not essentially a fractal orifice but involved only one scale and hence it was topologically the same as a circular smooth orifice except that some roughness was introduced through the triangle apex.

### 2.2 Wind Tunnel

The wind tunnel used in the experiment had a bell-mouth inlet for uniform flow and reduced inlet pressure losses [16]. The schematic of the wind tunnel is shown in Fig. 3. It had a working section of 3820 mm length and the inner diameter of 140.8 mm and was made of 5 mm thick polycarbonate. A motor driven fan was used to “suck down” the ambient air into the tunnel through the bell mouth and leave through a controlling valve. The controlling valve could be regulated to achieve the desired flow velocity in the tunnel. A maximum of 17 m/s flow velocity could be attained by the electric motor fitted at the other end of the tunnel. The motor had a rating of 372.85 J with a speed of 2850 rpm.

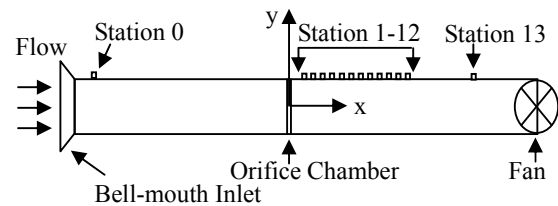


Fig 3. Bell-mouth wind tunnel

The orifice chamber was located  $14.50D$  away from the entrance. Of the fourteen Stations, one was  $14.15D$  upstream of the orifice chamber near the entrance, named Station 0, and one was  $13D$  downstream of the orifice chamber, named Station 13. The remaining twelve

Stations were immediately behind the settling chamber. The first Station of the twelve was  $1D$  behind the orifice chamber, named Station 1, followed by Station 2 to Station 12. The distance between the two successive remaining Stations was  $0.04D$  from Station 1 to 12. Each Station was further divided into 15 Substations (A to N) vertically from the wall to the center of the tunnel each with 5 mm apart. The Substation xA was located at the wall and the Substation xN was located at the center of the tunnel where x was any Station.

### 2.3 Experimental Devices

A constant temperature type hotwire system manufactured by Dantec Dynamics (Model 54T30 miniCTA) together with the hotwire probe (Model 55P16) from the same manufacturer was used to collect the velocity data. The output signal from the anemometer was continuously analogue. An analog-to-digital converter from the National Instrument (Model PCI-6023E) was used to obtain the digital signal. This anemometer allowed only one input from the hotwire and one output to a digital analogue converter. It was equipped with a Wheatstone bridge circuit connected to a servo-amplifier, signal conditioner, low-pass filter and dipperswitches. It was necessary to do this when the hotwire probe was changed and the new one had different resistance or when the ambient fluid temperature had changed a lot. Overheat ratio was the ratio between the wire resistivity when warmed up and the resistivity at room temperature,  $20^\circ\text{C}$ . This overheat ratio was defined by the temperature at which the wire was maintained during operation. During measurements overheat ratio was 1.8. Dipperswitches were adjusted according to the spreadsheet supplied by Dantec. TSI 1125 calibrator and Furness FC0510 micro manometer was used during the calibration. The manometer was capable of measuring 2000 to 0.001 Pa.

### 2.4 Experimental Procedures

Prior to the data collection during each measurement, hotwire calibration was done to ensure reliable data.

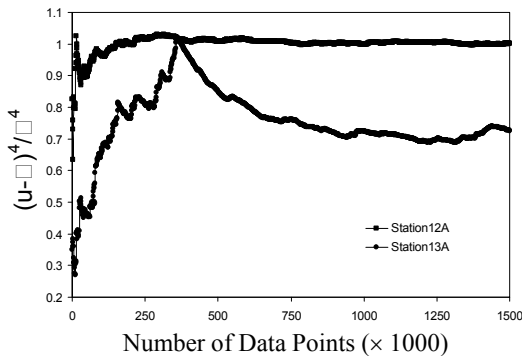


Fig 4. Convergence test to decide the sufficient number of data points for the velocity measurement

Each measurement was carried out at a maximum frequency of 10 kHz. To decide the number of hotwire sampling data for each point, a velocity convergence test was conducted at Station 12 and Station 13. We randomly

picked fractal orifice F2 for the convergence test. A total of  $3 \times 10^6$  velocity data was measured. The convergence test was done in the following way. We averaged the first 100,000 data points, then the first 200,000 data points, then the first 300,000 and so on until all  $3 \times 10^6$  data were covered. Finally we constructed the “number of data vs velocity curve”. Fig. 4 shows the fourth order velocity fluctuation normalized by the mean velocity as a function of the number of data point plot from the convergence test and we decided that  $1 \times 10^6$  data would be sufficient to get the velocity information without jeopardizing the accuracy. The velocity measurement was limited to the one half of the tunnel diameter assuming the flow had a radial symmetric profile as it was a circular wind tunnel. The flow rate at each measurement run was kept constant by regulating the control valve adjusting the mass flow rate. The inlet velocity was 9.75 m/s. Figure 5 shows the pdf of the inlet velocity. The Reynolds number was 95,000 based on the tunnel diameter.

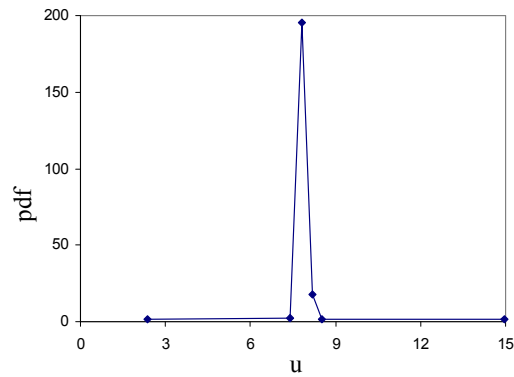


Fig 5. PDF of inlet velocity at Station 0

The pressure measurements were conducted at constant flow rate. The pipe connections between the Stations and the pressure measuring device were carefully checked to avoid any pressure leakage. Prior to each measurement, the flow was initiated and let it run for an appreciated time to ensure the tunnel was filled with the working fluid in motion. The pressure drops were measured between the Station 0 and the Station 13 across both the fractal and smooth orifices.

### 2.5 Normalization

In order to normalize both the pressure drop and velocity, we used the following two equations,

$$\Delta p_{norm} = \frac{2\Delta p}{\rho U_{inlet}^2 \left( \frac{A}{A_i} \right)} \quad (2)$$

and

$$U_{norm} = \frac{\bar{U}}{U_{inlet} \left( \frac{A}{A_i} \right)} \quad (3)$$

where,  $\Delta p_{norm}$  was the normalized pressure,  $\Delta p$  was

the pressure drop in Pa,  $\rho$  was the density of the working fluid which was air in our case,  $A$  was the area of the wind tunnel cross section,  $A_i$  was the flow area of the orifice, the index- $i$  represents the number of iteration,  $U_{norm}$  was the normalized velocity and  $U\text{-bar}$  was the average velocity.

### 3. ERROR ANALYSIS

Two types of measurements were conducted. One was the hotwire measurement and the other one was the pressure measurement. Below a brief description of the related errors are given.

#### 3.1 Hotwire Measurement Error

Errors associated with hotwire measurement could be further divided into two categories.

##### 3.1.1 Global Error

These inherent errors were always present regardless of any special care taken mostly due to the commonly known limitations associated with hotwire measurement technique such as the intrusive nature of the technique itself. The flow was always disrupted by the probe. We assumed that because of the high Reynolds number ( $Re_D = 9.55 \times 10^4$ ) this error was negligible.

Another error was the gradual decrease of the probe performance which was a function of time. We had fourteen Stations each with fifteen Substations. For eight orifices and the number of data points of 1000,000 made, it was impossible to run the experiments in one go to comply with the ideal measurement practice. To tackle this, we divided the experiments in several days. It is to be noted that hotwire measurements are highly sensitive to ambient temperature, humidity and air pressure. Keeping them in mind we took extra care and in some cases used two different probes.

##### 3.1.1 Local Error

These errors were due to the limitation of the experimental set up. The probe properties were also very sensitive to micro size dust when used for a longer period. To handle the dust problem, we tried to install air filter at the bell-mouth inlet. But this dramatically increased the pressure drop across the filter due to its low filter face velocity. The motor induced vibration also affected the velocity measurement. Although the vibration had negligible influence on the measurement but at the time of measurement, complete removal or isolating the vibration failed due to the set up limitation.

#### 3.2 Pressure Measurement Error

The pressure drop,  $\Delta p$ , calculated always had a fluctuation of about  $\pm 20$  Pa due to the negligible vibration induced by the motor fan. To minimize the error, an average was taken over the several measurements.

$$\sigma_r = \frac{\left\langle (\Delta p - \langle \Delta p \rangle)^2 \right\rangle^{\frac{1}{2}}}{\langle \Delta p \rangle} \quad (4)$$

Applying Equation 4 the relative pressure r.m.s.  $\sigma_r$  was

used to determine the relative error for each measurement. The maximum r.m.s. value did not exceed 4.3%. To further minimize the pressure error, the differential pressure,  $p$ , was averaged over twenty seconds. This significantly improved the pressure measurements.

## 4. RESULTS AND DISCUSSIONS

The objectives of this experimental work were two folds, the first: to understand the fractal scaling effects on the flow and the second: to distinguish the fractal orifice induced flow properties from the smooth orifice. We conducted both velocity and pressure measurements separately. In the following section, some key findings will be reported and discussed.

### 4.1 Pressure Measurements

Two sets of pressure measurements were done. The first set was to measure the pressure drops across the fractal and smooth orifices between Station 0 and Station 13 and the second set was to measure the atmospheric pressure drops for all the twelve stations, from Station 1 to Station 12. Both fractal and smooth orifices,  $N = 0 - 3$ , were used and this allowed a direct comparison between them and thus the study of the fractal scaling properties were possible. Fig. 6 shows the pressure drops across the fractal and the smooth orifices between Station 0 and Station 13. The pressure drop was higher for both the fractal and the smooth orifices at the zero-th iteration but significantly increased after first iteration. As the number of the fractal iteration increased the pressure drop recovery was observed or at least remained constant.

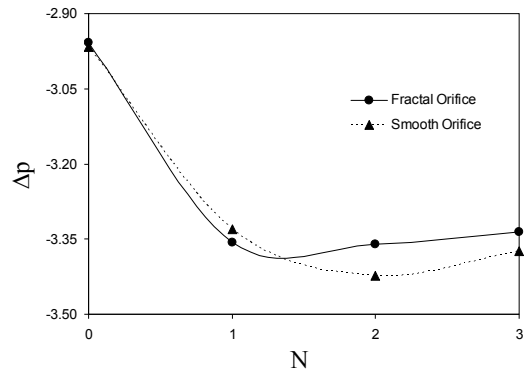


Fig 6. Pressure drops across the fractal and smooth orifices. The x-axis shows the number of iteration.

It could be intuitively said that with the increase of the number of the iterations, the pressure drop curve would show an asymptotic behavior. Also it was observed from Fig. 6 that the pressure drop was lower for the fractal orifice than for the smooth orifice. This was much more pronounced at the second iteration and was an indication that across the fractal orifice flow recovery occurred faster than across the smooth orifice. This could be further verified from Fig. 7, where x-axis was the position behind the orifice from Station 1 to Station 12. The fractal orifices induced lower pressure drops than their counterparts and as seen in Fig. 6, pressure drop dramatically reduced after the first iteration. The further

the downstream position was, the faster the flow recovered as expected. For the fractal orifices, this recovery was quicker than the smooth orifices. Also, the lower pressure drop behind the fractal

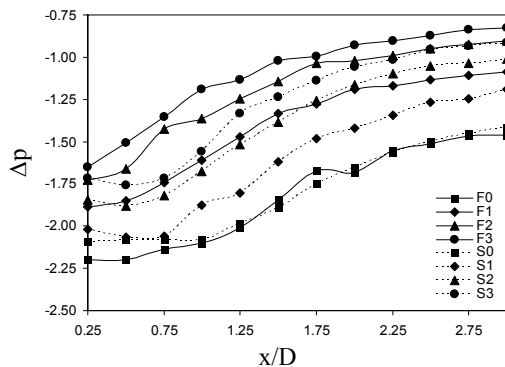


Fig 7. Normalized pressure drops behind the fractal and the smooth orifices at different stations

orifice was consistent at each iteration and downstream Station to a good extent. This was an obvious indication that the fractal scaling had significant effects on the flow properties which enhanced the mixing leading to a pressure reduction and a faster flow recovery. The results also showed that the differences in pressure drops between the fractal and the smooth orifices reduced as the iteration number reached to the higher one. From this it was deduced that as the number of iteration would increase the characteristics of the fractal orifices would asymptote the characteristics of the smooth orifice and the flow would continue independent of the orifice types.

#### 4.2 Hotwire Measurements

We measured velocity at each Station and its Substations.

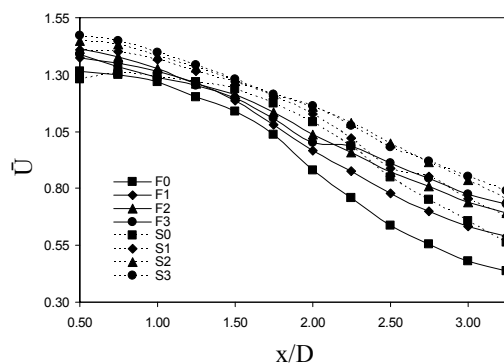


Fig 8. Mean velocity at centerline

Fig. 8 shows the mean velocity distribution along the centerline of the tunnel from Station 1 to Station 12. The solid lines correspond to the fractal orifices and the dashed lines correspond to the smooth orifices. It was clearly noticeable that the fractal orifices created smaller velocity scales than that of the smooth orifice. On the other hand from Fig. 9, we see that the fractal orifices

created larger range of the scales of the flow structures.

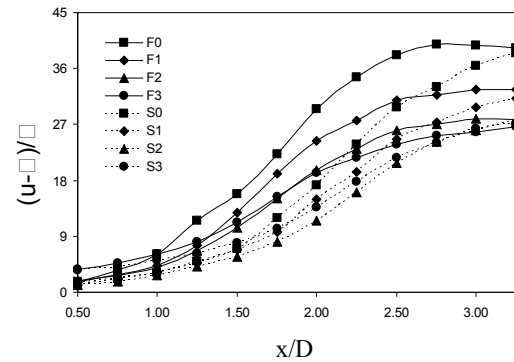


Fig 9. Turbulence Intensity at centerline

This was the process that initiated energy cascades leading to a better flow mixing properties. This also explained the lower pressure drop across the fractal orifices in contrast with the smooth orifice. Fig. 10 shows the velocity pdf at Station 12 downstream the orifice chamber. From the top left corner, clockwise, the pdfs clearly confirm that the larger range of velocity scales for fractal orifices were associated with the fractal scaling in comparison with the smooth orifices.

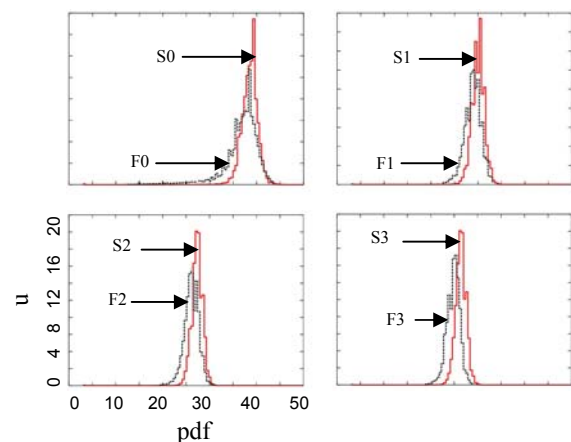


Fig 10. Velocity pdf at Station 12 across both the fractal and smooth orifices

#### 5. CONCLUSION

An experimental study of the fractal turbulence was conducted in an open circular wind tunnel. Hotwire measurement technique was implemented for the study. Both the fractal and the smooth orifices of equivalent flow area were used. The following conclusions were drawn from the results. Across the fractal orifice, as opposed to the smooth orifice,

1. flow mixing enhanced,
2. pressure drop lowered,
3. velocity scale decreased and
4. range of different velocity scales increased.

These were the clear indication of the influence of the fractal characteristics of the fractal orifice.

At the zero-th iteration, similar flow properties were

observed across both the fractal and smooth orifice. This was because at the zero-th iteration, the edge of the fractal orifice was not actually fractal. Topologically, it was just another smooth orifice except some friction was introduced by the sharp triangle apex as opposed to the smooth circular orifice of the equivalent flow area. As the number of iteration of fractal scaling increased, the flow properties were influenced by the fractal edge which was clearly distinguishable from the smooth orifice. It was assumed that at further higher iteration, the flow properties again would become identical to that of the smooth orifice.

## 6. REFERENCES

1. Nigel Lesmoire-Gordon, Will Rood and Ralph Edney, 2000, "Introducing Fractal Geometry", Icon Books, UK
2. Mandelbrot, J., 1974, "On the Geometry of Homogeneous Turbulence with Stress on the Fractal Dimension of the Iso-Surfaces of a Scalar, Journal of Fluid Mech., 72 (2), 401-416
3. Kolomogorov, A. N., 1941, "The Local Structure of Turbulence in Incompressible Viscous Fluid for Very Large Reynolds Numbers", C. R. Acad. Sci. U.R.S.S. 30, 301
4. Stewert, R.W., 1969, "Notes on Turbulence", NASA No. 21626
5. Salim, S.M.M., Saga, T. and Taniguchi, N., 2004, "Experimental Analysis of the Control of Turbulent Intensity in a Square Channel", The Japan Society of Mechanical Engineers 10, pp. 563-564
6. Zwart, P.J., Budwig and Tavoularis, S., 1997, "Grid Turbulence in Compressible Flow", Experiments in Fluids 23, 520-522
7. Antonia, R.A. and Burattini, P., 2006, Approach to the 4/5 Law in Homogeneous Isotropic Turbulence, J. Fluid Mech. 550, pp. 175-184.
8. Kearney, M., Kochergin, V. Petersen, K., Mumm, M., Jacob, W. and Velasquez, L., 1999, "Applications of Engineered Fractals in the Sugar Industry", Amalgamated Research Inc. ASSBT.
9. Queiros-Conde, D. and Vassilicos, J. C., 2000, "Intermittency in Turbulence and Other Dynamical Systems", Chapter: Turbulent wakes of 3-D fractal grids, Cambridge University Press.
10. <http://math.bu.edu/DYSYS/chaos-game/node6.html>
11. Staicu, A. et al., 2003, "Turbulent wakes of fractal objectes", Physical Review E 67, 066306.
12. Keylock C. and McElwaine J. 2005, "Understanding snow avalanches: Recent progress from a British perspective", Presented at the 2005SET for BRITAIN meeting for younger British scientists and engineers, House of Commons.
13. Seoud, R. and Vassilicos, J., 2007, Dissipation and Decay of Fractal-generated Turbulence, Physics of Fluids 19, 105108
14. Hurst, D. and Vassilicos, J., 2007, "Scaling and Decay of Fractal-generated Turbulence", Physics of Fluids, 19, 035103
15. Ahmadi, A. 2006, "The swirling orifice plate independent of inlet conditions", PhD Thesis, University of Sheffield, Department of Mechanical Engineering.
16. Abou-El-Azm, A. et al., 2009, "Experimental study of the pressure drop after fractal orifices in turbulence pipe flows", Exp. in Fluid & Thermal Science, (In Press).
17. Mehta, R.D. and Bradshaw, P., 1979, "Design Rules for Small Low Speed Wind Tunnels", The Aero. J. of the Royal Aero. Soc., Technical Notes.

## 5. MAILING ADDRESS

S.M. Muztaba Salim  
 University of Sheffield,  
 Dept of mechanical Engineering,  
 Mapping Street, Sheffield S13JD, UK

## CONVECTIVE HEAT TRANSFER FROM HEATED OBJECT IN A SQUARE ENCLOSURE

M. I. Haque,<sup>1</sup> and K. A. Hossain,<sup>2</sup>

Department of Mechanical Engineering, Khulna University of Engineering & Technology, Bangladesh.

### ABSTRACT

This paper presents, the computational analysis of natural convection heat transfer from a heated object in an square enclosure. The enclosure has two ventilators at the top of the vertical side walls. An isothermally heated object is placed at the middle of the bottom of the container and all walls are assumed to be adiabatic. The SUR method is used to solve discretized two dimensional continuity, Navier-Stokes and energy equation on the basis of stream function-vorticity formulation by the finite difference method. Uniform grids are used throughout the computational domain. The fluid flow characteristics and temperature behavior is investigated throughout the enclosure. The fluid from the surrounding entrains into the enclosure and fills up the empty space. Rayleigh numbers in the range from  $1.0 \times 10^2$  to  $1.0 \times 10^4$  is considered for the investigation. The heating efficiency of the enclosure is increases with the decrease of Rayleigh numbers.

**Keywords:** Free Convection, Heating efficiency, Enclosure, Recirculation, Separating Stream line.

### 1. INTRODUCTION

Natural convection heat transfer plays important role in the industrial application. Investigation about buoyancy dominated flow is carrying out for long time by the researchers. The investigation about heat transfer characteristics of a submerged heated object in fluid such as electrical winding in transformers, crops in green house, human body in atmosphere and electronic parts in enclosure etc. have attracted the researcher. The study of natural heat transfer characteristics is very important in engineering applications.

The cooling of mechanical or electronic devices is increasing in almost every branch of industry due to their continuous application. Introduction of microelectronics together with increasing demands on cryogenic engineering, especially in the field of refrigeration with micro fins is growing up. The ever increasing miniaturization, packaging density, quality demands and reduction in life costs will put ever-increasing pressure on the solutions of these problems.

The solution of such heat transfer depends on successful and accurate solution of the nonlinear Navier-Stokes equation along with the energy equation. Various attempts have been made in obtaining approximate solutions based on simplified Navier-Stokes equations. With the advent of high speed computers, numerical modeling of complex free convective heat transfer solutions has become simpler. The specific problem dealt with here is dependent on a number of parameters, an optimization of which is

necessary to yield reasonably accurate results.

The demand of high performance heat exchanger having spatial dimensions is increasing due to their need in applications such as transformer cooling, comfortableness of human body, electronic equipments and so on. Enhancement technique that improves over all heat transfer characteristics, are important to heat exchanger designers. However, it is important to have knowledge of the characteristics of laminar free convection heat transfer from isothermal surface of objects in order to exercise a proper control over the performance of the heat exchanger and to economize the process.

Natural air ventilation in partially open cavities is encountered in many practical applications such as energy conservation in buildings and the heating or cooling of environmental systems. In this work, natural convection heat transfer in a partially open cavity is investigated. A vertical isothermal object is placed inside the middle of the enclosure, acts as the thermal source which is responsible for the buoyant force of the inside fluid and the lighter fluid exits from the enclosure through the ventilators. At the same time, cold surrounding fluids enter into the container through the lower portion of the same openings and becomes hot and exit through the openings again.

Chu and Churchill [1] have studied the natural convection caused by a heat-generating conducting body located inside an enclosure. Numerical studies of natural convection heat transfer and flow in closed enclosures without a local heat source are reported in the literature;

it can be cited the work of Davis [2]. Numerous studies on natural convection caused only by external heating in partially open enclosures have been conducted by Chan and Tien [3]. Nara [4] was one of the first researchers to perform numerical simulations of air circulation within Greenhouse. He used the vortices and stream functions as field variables to solve the finite difference scheme of the Navier-stokes equation for a two dimensional cross-section on a mono span greenhouse with a fixed temperature difference between a warm soil and a colder roof to simulate soil surface heated by solar radiation. Aubinet and Deltour [5] who studied natural convection for heating pipes in greenhouse tomato canopy and characterized the plume generated by the heating pipes in the crop rows. However, few results have been reported for natural convection caused by an internal local heat source, although problems of this type are frequently important and their study is necessary for understanding the performance of complex natural convection flow and heat transfer.

## 2.MODEL DESCRIPTION

The geometry for the consideration is shown in Fig. 1. The model considered here is a rectangular enclosure with two side openings on two side walls with an object, isothermally heated is placed on the bottom surface at the middle of the enclosure. The enclosure dimensions is  $L=6$  and  $H=6$  and opening width  $W=1$ . All walls of the enclosure are assumed to be adiabatic. The out flow openings are located on the top of left and right vertical walls as shown in the Fig. 1.

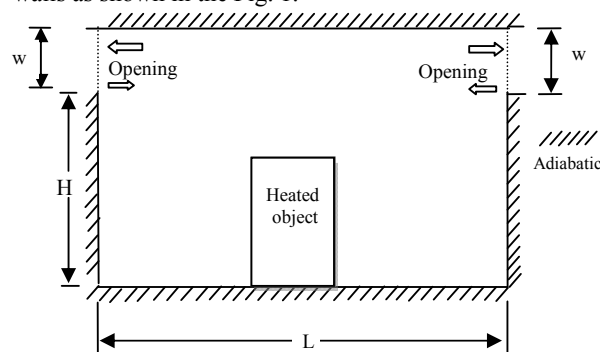


Fig 1. Schematic diagram of the problem considered and coordinate system.

## 3. MATHEMATICAL FORMULATION

Thermo physical properties of the fluid in the flow model are assumed to be constant except the density variations causing a body force term in the momentum equation. The Boussinesq approximation is invoked for the fluid properties to relative density changes to temperature changes and to couple in this way the temperature field to the flow field. The governing equations for laminar, steady, free convection flow using conservation of mass, momentum and energy equation can be used. The two dimensional, steady, incompressible, constant properties laminar flow from the heated object in a container with two side ventilators has been investigated.

## 4.GOVERNING EQUATIONS

Now for incompressible fluid and for two dimensional flow, steady flow the Navier-Stokes equation and continuity equation can be written as follows,

$$\frac{\partial u}{\partial x} + \frac{\partial v}{\partial y} = 0$$

$$u \frac{\partial u}{\partial x} + v \frac{\partial v}{\partial y} = -\frac{1}{\rho} \frac{\partial p}{\partial x} + \nu \left( \frac{\partial^2 u}{\partial x^2} + \frac{\partial^2 u}{\partial y^2} \right)$$

$$u \frac{\partial v}{\partial x} + v \frac{\partial v}{\partial y} = -\frac{1}{\rho} \frac{\partial p}{\partial y} + \nu \left( \frac{\partial^2 v}{\partial x^2} + \frac{\partial^2 v}{\partial y^2} \right) + g \beta (T_{obj} - T_{\infty})$$

The two dimensional energy equation is,

$$u \frac{\partial T}{\partial x} + v \frac{\partial T}{\partial y} = \alpha \left( \frac{\partial^2 T}{\partial x^2} + \frac{\partial^2 T}{\partial y^2} \right)$$

Now, to make this above equation in non dimensional form, the width of two equal opening sides  $W$  is considered as the characteristic length, maximum velocity,  $u_{\infty}$  as the characteristic velocity and initial pressure  $p_0$  as the characteristic pressure

$$x = \frac{x}{W}; \quad y = \frac{y}{W}; \quad U^* = \frac{u}{u_{\infty}}; \quad P^* = \frac{p - p_0}{\frac{1}{2} \rho u_{\infty}^2}$$

$$\theta = \frac{T(x, y) - T_{\infty}}{T_{obj} - T_{\infty}}$$

Now, putting these values in the above equations, the final non-dimensional form will appear,

$$\frac{\partial U}{\partial X} + \frac{\partial V}{\partial Y} = 0$$

$$U \frac{\partial U}{\partial X} + V \frac{\partial V}{\partial Y} = -\frac{1}{2} \frac{\partial P}{\partial X} + Pr \left( \frac{\partial^2 U}{\partial X^2} + \frac{\partial^2 U}{\partial Y^2} \right)$$

Similarly,

$$U \frac{\partial V}{\partial X} + V \frac{\partial V}{\partial Y} = -\frac{1}{2} \frac{\partial P}{\partial Y} + Pr \left( \frac{\partial^2 U}{\partial X^2} + \frac{\partial^2 U}{\partial Y^2} \right) + Ra \cdot Pr \cdot \theta$$

and

$$U \frac{\partial \theta}{\partial x} + V \frac{\partial \theta}{\partial y} = \left( \frac{\partial^2 \theta}{\partial x^2} + \frac{\partial^2 \theta}{\partial y^2} \right)$$

## 5. BOUNDARY CONDITIONS

**At all walls:** Since the Velocity Component,  $u$  and  $v$  both are zero at the walls and applying no-slip conditions,  $u=0$  and  $v=0$ , then stream function  $\psi=c$  and  $\omega=c$  the wall are considered as adiabatic.

**At the object:** Since the velocity component,  $u$  and  $v$  both are zero at the walls and applying no-slip conditions,  $u=0$  and  $v=0$  then, stream function  $\psi=c$  and  $\omega=c$ . The object is assumed to be heated. So, the dimensionless temperature  $T=1.0$

### Boundary Conditions at both openings:

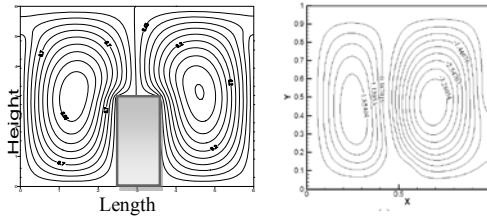
Velocity gradients are assumed to be zero for the flow variables as:



$$\frac{\partial u}{\partial x} = 0; \frac{\partial v}{\partial x} = 0; \frac{\partial \psi}{\partial x} = 0; \frac{\partial \omega}{\partial x} = 0; \frac{\partial T}{\partial x} = 0$$

## 6. RESULTS AND DISCUSSION

The grid independency test has been performed. It is observed that more than  $120 \times 120$  grid size does not give more accurate result, but increases the computational time only. The maximum error is obtained as  $10^{-11}$ . Fig.2 shows the comparison between present investigation and the published work of V.C. Mariani and L.S. Coelho[6]. It is observed that there is good agreement between two results.



Present investigation V.C. Mariani and L.S. Coelho[6]

Fig 2. Comparison between present work and V.C. Mariani and L.S. Coelho[6].

Figure 3, shows the stream function pattern at  $Ra = 1.0 \times 10^3$ . It is observed that there forms two recirculation on both sides of the heated object and it extended up to the exit openings.

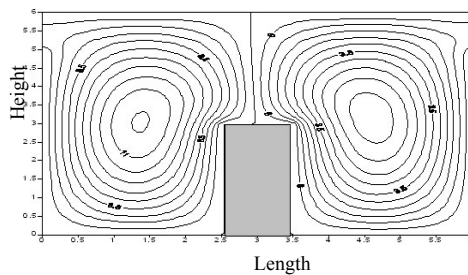


Fig 3. Stream function at  $Ra = 1.0 \times 10^3$ .

The fluid becomes heated as it comes to contact with the heated object and becomes lighter and goes up due to buoyancy force and exit from the openings. As a result a vacuum is created inside the enclosure and fluid comes from the surrounding through the opening to fill up that vacuum inside the enclosure.

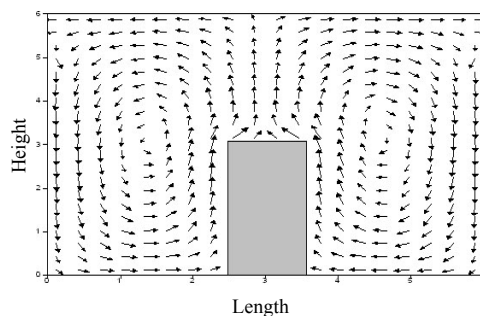


Fig 4. Velocity Vector for  $Ra = 1.0 \times 10^3$ .

Figure 4 shows the velocity vector for  $Ra = 1.0 \times 10^3$  as the heated object placed at the middle of the enclosure. The velocity vector shows the two recirculation region on two sides of the heated object and the separating stream line is shown at the middle plane of the object. The eye of the recirculation created at the same distance on either sides of the object. The direction of the recirculation is opposite in direction. On the left side of the object the fluid is rotating counter clockwise and on the right side of the object the fluid is rotating clockwise direction.

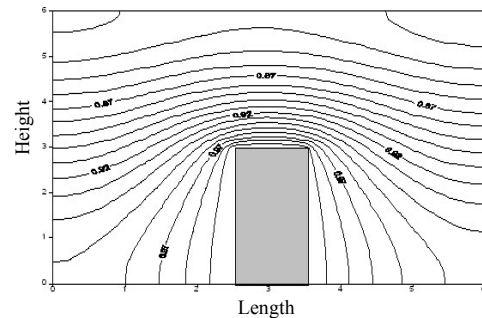


Fig 5. Isotherm at  $Ra = 1.0 \times 10^3$ .

Figure 5 shows the isothermal lines at  $Ra = 1.0 \times 10^3$ . The cold fluid comes into contact with the heated object and becomes heated and goes up to the top insulated surface.

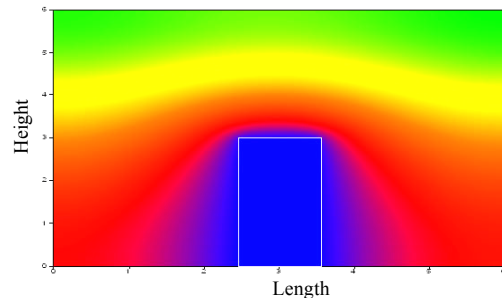


Fig 6. Temperature contour at  $Ra = 1.0 \times 10^3$ .

Figure 6 shows the color contour of the flow field at  $Ra = 1.0 \times 10^3$ . It is observed that the temperature of the fluid is varying in the whole domain. The blue color predicts the highest temperature, whereas the green color predicts the lower temperature in the domain.

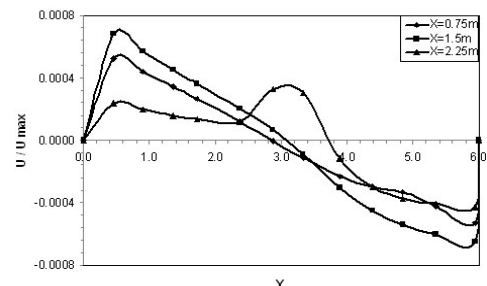


Fig 7. Velocity profile at the left side of the object at  $Ra = 1.0 \times 10^3$ .

different axial locations from the left vertical side wall for  $Ra = 100$ .

Figure 7 shows that the velocity varies positive to negative from bottom to top of the enclosure, which is due to the recirculation of the fluid in the enclosure. It is observed that the velocity at the left side of the object increases and then decreases with vertical height and goes to negative value because of recirculation near the object. Very close to the object the magnitude of the velocity is less than the velocity profile at the far distance from the object. Similar trend is observed at the right side of the object, but negative value starts near the bottom of the square enclosure.

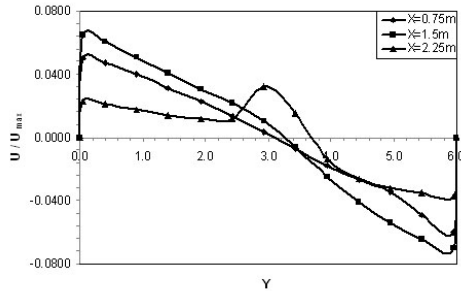


Fig 8. Velocity profile at the left side of the object at different axial locations from the left vertical side wall for  $Ra = 1.0 \times 10^4$ .

Comparing Fig. 7 and Fig. 8, it is observed the same trends follows for higher Rayleigh no. but the magnitude of the velocity is increased.

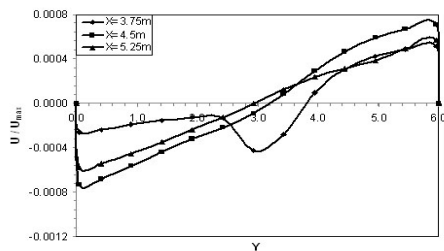


Fig 9. Velocity profile at the right side of the object at different axial locations from the left vertical side wall for  $Ra = 100$ .

Figure 9 shows the variation of velocity along vertical height at different axial locations from the left vertical side wall. The velocity varies negative to positive value from bottom to the top of the enclosure surface due to the clockwise recirculation.

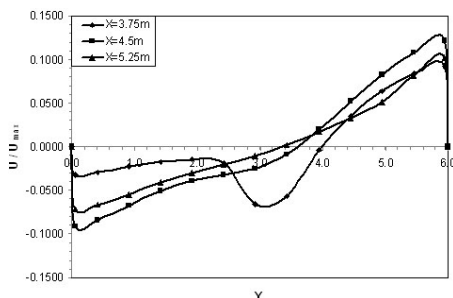


Fig 10. Velocity profile at the right side of the object at

different axial locations from the left vertical side wall for  $Ra = 1.0 \times 10^4$ .

Comparing Fig. 9 and Fig. 10, it is observed the same trends follows for higher Rayleigh no. but the magnitude of the velocity is increased.

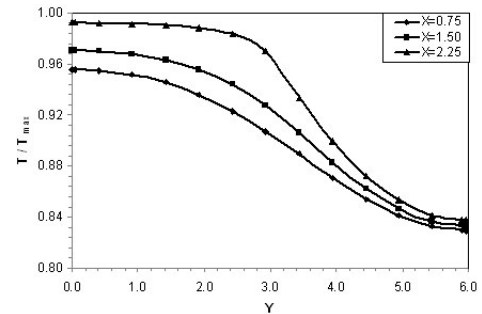


Fig 11. Temperature profile at the left side of the object at different axial locations from the left vertical side wall for  $Ra = 1.0 \times 10^3$ .

Figure 11 shows that the temperature of the fluid decreases with the increase of vertical height. The fluid very close to the object remains hot up to the height  $Y=2$  and then starts decayed. The fluid far from the heated object starts its decay from the beginning. The temperature profile predicts that the temperature decreases with vertical distance and also decreases with the axial distance far from the object.

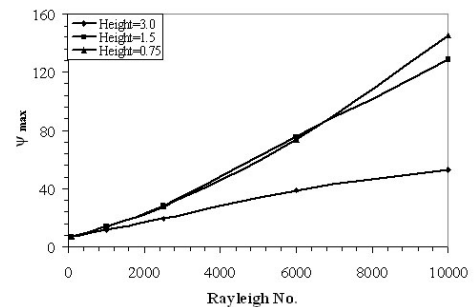


Fig 12. Maximum value of stream function with Rayleigh no. for different object heights.

Figure 12 shows that the maximum value of stream function increases with the increase of Rayleigh no. The maximum value of stream function increases with the increase of Rayleigh number. Also, the value of maximum stream function increases with the decrease of height of the object.

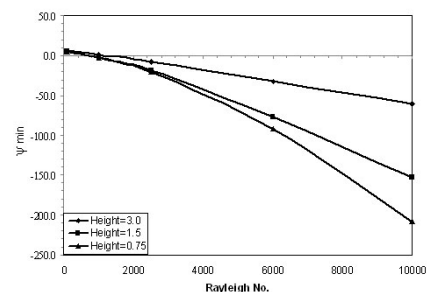


Fig 13. Minimum value of stream function with Rayleigh no. for different object heights

Figure 13 shows that the minimum value of stream function decreases with the increase of Rayleigh no. The minimum value of stream function decreases with the increase of the Rayleigh number. It is observed that the value of Rayleigh number more than 900 predicts the negative value of minimum stream function.

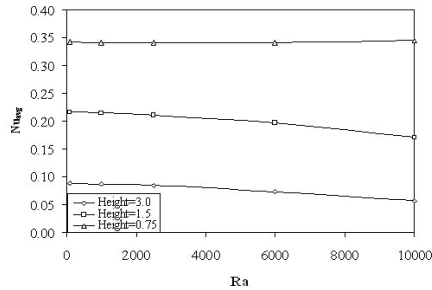


Fig 14. Variations of average Nusselt no. at different Ra & different heights.

Figure 14 shows the variation of average nusselt no. with Rayleigh no. for different object heights. It is observed that the average nusselt no. decreases with the increasing of Rayleigh no., but for object height=0.75 the average nusselt no. remains more or less constant for all values of Rayleigh no. The average value of Nusselt number decreases with the increase of Rayleigh number.

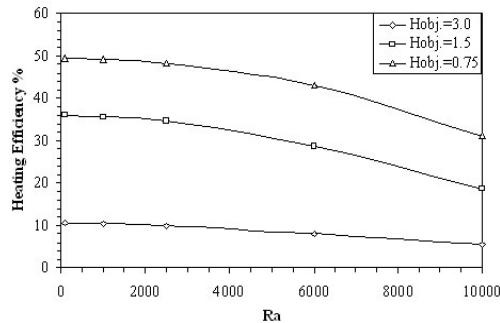


Fig 15. Variation of heating efficiency with Rayleigh no. for different object heights.

The heating efficiency is calculated according to the way described in Singh, S. and Sharif, M.A.R. [7]. The heating efficiency of the enclosure increases with the decrease of Rayleigh numbers. The heating efficiency is higher for the small object size.

## 7. CONCLUSION

Finite difference numerical method was used for laminar free convection flow in a square container with adiabatic side walls and heated object placed on bottom. The considered range of Rayleigh Number form  $1.0 \times 10^2$  to  $1.0 \times 10^4$ .

This investigation led the following conclusions.

Higher recirculation zones are formed at the two sides of object. The average value of Nusselt number decreases with the increase of Rayleigh number. The

heating efficiency decreases with the increase of Rayleigh number and heating efficiency is higher for the small object size.

## 8. NOMENCLATURE

Symbols	Descriptions
B	The length of space between object surface & container's wall
$C_p$	Specific heat of fluid at constant pressure
H	Height of the container
$H_{obj}$	Height of the object
I, J	Index along the X-axis and Y- axis respectively
K	Thermal conductivity
L	Length of the container
$L_{obj}$	Length of the object
P	Pressure of the flowing fluid
Pr	Prandtl Number
$p_0$	Initial pressure
$P^*$	Pressure in the dimension less form, $\frac{p}{\frac{1}{2} \rho u_\alpha^2}$
Re	Reynolds number = $\frac{u_\infty W}{\nu}$
Ra	Rayleigh Number, Gr.Pr
$T(x,y)$	Local fluid temperature
$T_{obj}$	Temperature of the object.
$T_\infty$	Fluid temperature
$u_\infty$	Free stream velocity
u, v	Velocity components
$U^*, V^*$	Dimensionless velocity component, $\frac{u}{u_\alpha}, \frac{v}{u_\alpha}$
W	Outlet opening of the container
x, y	Cartesian coordinates
X, Y	Dimensionless Cartesian coordinates, $\frac{x}{W}, \frac{y}{W}$
$\rho$	Density of fluid
$\omega$	Vorticity
$\omega^*$	Dimensionless Vortices $\omega^* = \frac{\omega}{\omega_0}$
$\nu$	Kinematics viscosity of fluid
$\theta(x,y)$	Dimensionless temperature, $\frac{T(x,y) - T_\infty}{T_{obj} - T_\infty}$
$\psi$	Stream function
$\psi_0$	Initial value of Stream function
$\psi^*$	Dimensionless Stream function , $\psi^* = \frac{\psi}{\psi_0}$

## 9. REFERENCES

1. Chu, H.H. and Churchill, S.W., "The effect of heater size, location, aspect-ratio and boundary conditions on two-dimensional laminar natural convection in rectangular channels, *Journal of Heat Transfer*, Vol. 98, No.2, pp 194-201, 1976.
2. Davis, G. de V., Natural convection of air in a square cavity: A benchmark solution, *International Journal of Numerical Methods in Fluid*, Vol.3, No.3, pp. 249-264, 1983.
3. Chan, Y.L. and Tien, C.L., A numerical study of two-dimensional laminar natural convection in shallow open cavities, *International Journal of Heat Mass Transfer*, Vol. 28, No. 3, pp. 603-612, 1985.
4. Nara M. Studies on air distribution in farm buildings two dimensional numerical and experiment. *Journal of the Society of Agricultural Structures*, 9(2), 18-25.
5. Aubinet M, Deltour J; Natural convection above line heat sources in greenhouse canopies. *International Journal of Heat and Mass Transfer*, 37(12), 1795-1806.
6. V.C. Mariani and L.S. Coelho, "Natural convection Heat Transfer in Partially open enclosures containing an internal heat Sources" *Brazilian Journal of Chemical Engineering*, Vol. 24 No. 03, 2007.
7. S. Singh and M.A.R. Sharif, "Mixed convective cooling of a rectangular cavity with inlet and exit openings on differentially heated side walls" Taylor and Francis, *Numerical Heat Transfer .Part-A*, 44:233-253, 2003.

## 10. MAILING ADDRESS

Haque, M. I.  
Under graduate student,  
Department of Mechanical Engineering,  
Khulna University of Engineering & Technology,  
Khulna 9203, Bangladesh.  
Email: ehasan\_04@yahoo.com

## THE EFFECT OF GAS FLOW RATE ON DEPOSITION RATE USING CVD

M A Chowdhury<sup>1</sup>, D M Nuruzzaman<sup>1</sup>, M L Rahaman<sup>1</sup> and M S Islam<sup>2</sup>

<sup>1</sup>Department of Mechanical Engineering

Dhaka University of Engineering and Technology, Gazipur, Bangladesh

<sup>2</sup>Mymensingh Polytechnic Institute, Mymensingh, Bangladesh

### ABSTRACT

Solid thin films have been deposited on stainless steel 314 substrates in a hot filament thermal chemical vapor deposition (CVD) reactor at different flow rates of natural gas. The variation of thin film deposition rate with the variation of gas flow rate has been investigated experimentally. During experiment, the effect of gap between activation heater and substrate on the deposition rate has also been observed. Results show that deposition rate on SS 314 increases with the increase of gas flow rate. It is also seen that deposition rate increases with the decrease of gap between activation heater and substrate within the observed range. In addition, friction coefficient and wear rate of SS 314 sliding against SS 304 under different normal loads are also investigated before and after deposition. The obtained results reveal that the values of friction coefficient and wear rate are lower after deposition than that of before deposition.

**Keywords:** Deposition rate, Gas flow rate, CVD.

### 1. INTRODUCTION

Chemical vapor deposition (CVD) is a process in which a solid material formed from a vapor phase by chemical reaction, is deposited on a heated substrate. The controlling parameters in CVD process are surface kinetics, mass transport in the vapor, thermodynamics of the system, chemistry of the reaction and processing parameters like temperature, pressure etc. The deposition rate which is the prime limiting factor in a CVD process is mainly controlled by the formation of required species to be deposited and its transportation in the vapor and surface kinetics [1-3]. Thin film synthesis via chemical vapor deposition (CVD) has been the subject of active research over the last two decades. Numerous studies have been carried out to examine the effects of the process parameters, such as temperature of the substrate and filament, gas flow rate, gas composition, chamber pressure etc on different types of materials [4-9]. The CVD process of thin film growth may be divided into two important sequential steps, the transport of the radicals through the gas toward the surface and their consumption on the surface leading to the crystal growth. Experimental results and numerical calculations of thermal conduction and diffusion have shown that the mass transport in the gas phase plays an important role during thin film growth, and growth of thin films are mainly controlled by the mass transport rate rather than by the surface reaction rate at substrate temperatures [10,

11]. Gas flow rate is an important parameter for CVD thin film growth because the gas flow rate is closely related to the gas transport in the CVD reactor [10]. To date, efforts have been made to investigate the effects of the gas flow rate on thin film growth and conflicting results have been reported by different groups. Celii et al. [12, 13] reported that varying the gas flow rate could change markedly the resultant microcrystalline diamond (MCD) crystal texture and surface morphology but has little effect on the growth rate. Yu et al. [14] have found that CVD thin film growth by hot filament CVD depends on a mass transfer controlled process and the growth rate was increased by increasing the gas flow rate, while other groups have reported that the gas flow rate does not appear to have a significant influence on thin film growth [15, 16].

From the previous experimental study discussed above it can be concluded that several experiments were conducted at different gas flow rate conditions and the effects on thin film growth differ significantly. Even now a day, the effects of gas flow rate on thin film deposition for different materials, especially, at varying gap between substrate and activation heater is less understood. This means that more work is needed for a better understanding of CVD film deposition under different gas flow rate, gap and other related parameters. Therefore, in this study an attempt is made to investigate the effect of gas flow rate and gap between activation

heater and substrate on the thin film deposition rate on SS 314. With its remarkable physical properties, thin film coatings on different substrates are expected to have many applications in industrial and engineering fields. A low friction coefficient combined with a very low wear rate is two of the numerous advantages which make it suitable for machining.

However, the tribological behavior of thin film deposition on SS 314 is yet to be clearly investigated. Therefore in this study, experiments are also conducted to observe the tribological properties of SS 314 under deposited and undeposited conditions.

It is expected that the application of these results will contribute to the different concerned mechanical processes.

## 2. EXPERIMENTAL DETAILS

### 2.1 Hot Filament CVD Unit

A thermo-chemical vapor deposition (hot filament) setup (Fig. 1) was designed and fabricated. The set-up is a CVD system comprised a reactor chamber supported by some sub assemblies and sub systems. The sub assemblies are (i) Heater (ii) Connector and (iii) Cooling line; and the subsystems are (i) Gas evacuation system (ii) Electric supply system (iii) Heating system (iv) Cooling system (v) Gas supplying system (vi) Measuring system and (vii) Structure and handling system. These arrangements of the experimental setup (Fig.1) are similar to the conventional thermo-chemical vapor deposition (hot filament) unit. The substrate as shown in Fig.1 is placed on the substrate holder in between substrate heater and activation heater.

To deposit carbon, thermal CVD requires high temperature, generally from 800 to 2000<sup>0</sup>C, which can be generated by resistance heating, high frequency induction, radiant heating, hot plate heating, or any combination of heating systems. Resistance heating is used here to obtain the required temperature. In substrate heating, there is a rectangular opening at the top of the substrate heater box. The substrate is placed through the opening, so that heat generated from Nichrome heater, inside the rectangular box is transferred through the opening to the substrate as required by adjusting the supply voltage to the heater by variac. Activation heater operates directly by supplying voltage from variac and the temperature can be adjusted by varying the variac voltage also. During CVD process, the temperature of the substrate and the temperature of the activation tungsten heater are measured by optical pyrometer (Brand: Foster, England, Model: AJ/ON/19.5). The process pressure during CVD process is continuously measured by a digital vacuum gauge meter (Brand: vacuubrand, German, Model: VAP 5). The weight of the deposited substrate was measured on a high-resolution weighing scale.

Gas flow inside the reactor chamber during CVD process is measured by a gas flow meter whose range is 0 to 2.0 liter per minute. This flow meter is connected to the supply line of the gas inside the reactor chamber. Natural gas is used as reactant gas for CVD process. The test sample used in this investigation is stainless steel

314. Experimental conditions are shown in table 1. During tests, each experiment was repeated several times and their average results are presented.

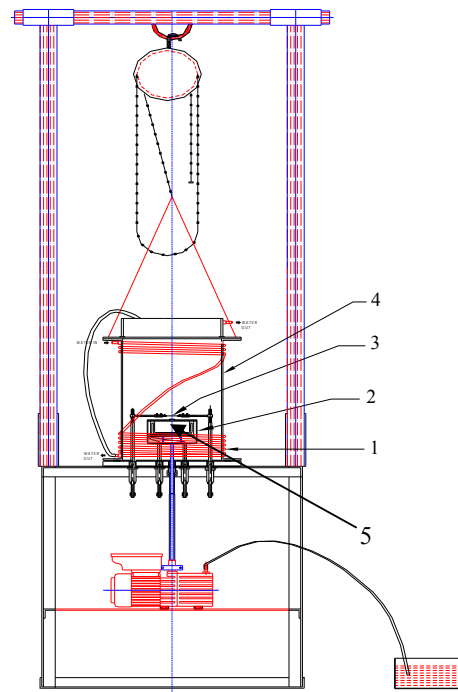


Fig 1. Schematic diagram of chemical vapor deposition (hot filament) setup [1. Cooling tube, 2. Substrate heater, 3. Activation heater, 4. Reactor chamber, 5. Substrate]

Table 1: Experimental Conditions (For CVD)

Sl. no.	Parameters	Range/conditions
1.	Substrate	SS 314
2.	Reactant gas	Natural gas mostly Methane (CH <sub>4</sub> )
3.	Substrate thickness	1.5-4mm
4.	Substrate size	20mmX20mm
5.	Distance between activation heater and substrate	4-6.5mm
6.	Flow rate	0.5-2.0 l/min
7.	Pressure	0.085 MPa
8.	Substrate heater temperature	800-1000 <sup>0</sup> C
9.	Activation heater temperature	1800-2000 <sup>0</sup> C
8.	Deposition duration	1 hr

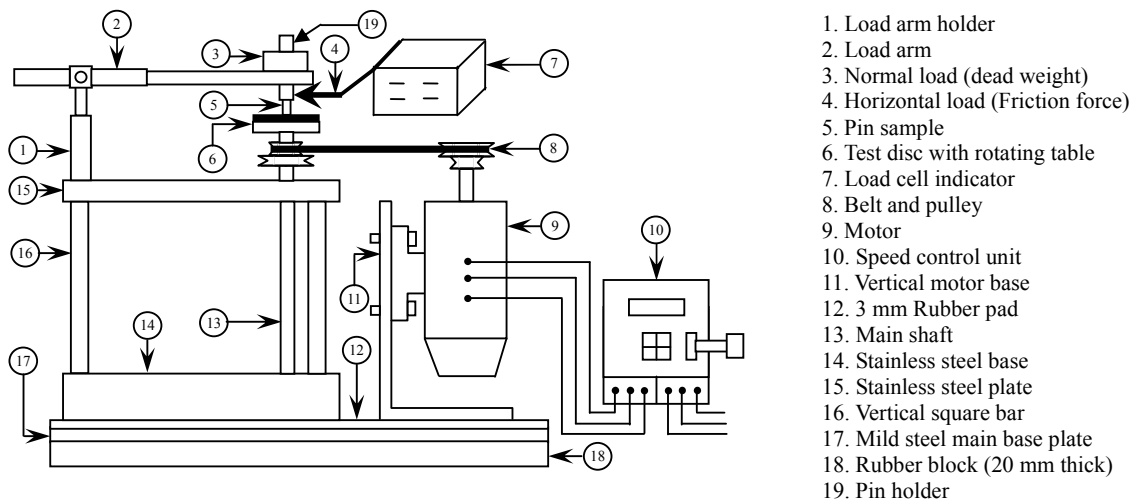


Fig 2. Block Diagram of the Experimental Set-up

## 2.2 Tribometer for Tribological Test

This is a pin-on-disc machine (Fig.2) i.e. a pin which can slide on a rotating horizontal surface (disc). In this set-up a test sample is to be fixed on a rotating plate (table) having a long vertical shaft clamped with a screw from the bottom surface of the rotating plate.

To rotate the shaft with the table a 1 hp motor is mounted vertically on a separate base having rubber damper. This separate base was arranged to reduce the effect of vibration of the motor, which may transmit to the main structure. An electronic speed control unit is used to vary the speed of the motor as required.

A cylindrical pin whose contacting foot is flat made of SS 304, fitted on a holder is subsequently fitted with an arm. The arm is pivoted with a separate base in such a way that the arm with the pin holder can rotate vertically and horizontally about the pivot point with very low friction. This pin can be put to slide at any point of the test sample (disc). Pin holder is designed with the facility of putting dead weight on it so that required normal force will act on the test sample through the pin. The shape of the pin was maintained cylindrical so that due to loss of surface material of the pin the contacting surface will remain almost constant. To measure the frictional force acting on the pin during sliding on the rotating plate, a load cell (TML, Tokyo Sokki Kenkyujo Co. Ltd, CLS-100NA, Serial no. MR2947) is fitted with a side support such that the load cell prevents the movement of the pin holder. During the rotation of the test sample, pin holder creates pressure on the load cell which gives the measure of the frictional force acting on the pin. Load measuring arrangement was constructed from a separate base to take care the probable fluctuation of friction force that may arise due to the vibration of the test disc. Another load cell of the same kind was also used to measure the vertical force acting on the pin. The coefficient of friction was measured as the ratio between horizontal and vertical forces. Each experiment was carried out for 20 minutes and average values of all these data were considered as friction coefficient. A load cell along with its digital indicator (TML, Tokyo Sokki

Kenkyujo Co. Ltd, Model no. TD-93A) was used for measuring loads. The total set-up was placed inside a chamber whose relative humidity can be adjusted by supplying requisite amount of moisture and dehumidifier. A hygrometer (Wet and Dry Bulb Hygrometer, ZEAL, England) was used to measure the relative humidity of the chamber. All experiments were conducted at about 75% relative humidity. A tachometer was used to measure the rpm of the rotating shaft. The surface roughnesses of the test sample were also measured by surface roughness tester (Taylor Hobson Precision Roughness Checker). Wear rates were calculated from the measured weight loss of the disc after rubbing for definite time. Initial and final weights of the disc before and after rubbing were measured on a high-resolution weighing scale. During tests each experiment was repeated several times with new sample of pin and disc.

## 3. RESULTS AND DISCUSSIONS

### 3.1. Experimental Results for Deposition Rate

In this study the effects of gas flow rate on deposition rate are investigated at different gaps between activation heater and substrate. The deposition rates are calculated in two ways: (i) the deposition rates of the coating in gram per unit time (mg/min) were calculated from the weight difference of substrate before and after deposition and (ii) the deposition rates of the coating in microns per unit time ( $\mu\text{m}/\text{min}$ ) were calculated from the thickness difference of substrate before and after deposition.

#### 3.1.1 Variation of Deposition Rate (g/min)

Fig. 3 shows the variation of deposition rate (mg/min) on SS 314 with the variation of gas flow rate. Curves 1, 2, 3 and 4 are drawn for gap between activation heater and substrate 6.5, 6, 5.5 and 4 mm respectively. From the curves of this figure it is found that deposition rate increases with the increase of gas flow rate. Results also show that the lower the gap between activation heater and substrate, the higher the values of deposition rate (mg/min) are obtained.



### 3.1.2 Variation of Deposition Rate ( $\mu\text{m}/\text{min}$ )

Several experiments are conducted to investigate the effects of gas flow rate on deposition rate ( $\mu\text{m}/\text{min}$ ) and these results are presented in Fig. 4. Curves 1, 2, 3, and 4 of this figure are drawn for gap between activation heater and substrate 6.5, 6, 5.5 and 4 mm respectively. Curve 1 shows that deposition rate increases with the increase of gas flow rate. Similar trends of results are observed for curves 2, 3 and 4. Results also indicate that the lower the gap between activation heater and substrate, the higher the values of deposition rate are obtained.

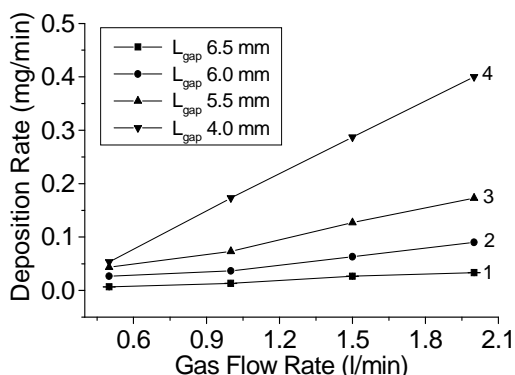


Fig 3. Variation of Deposition Rate (g/min) with the Variation of Gas Flow Rate at Different Gaps between Activation Heater and Substrate for SS 314.

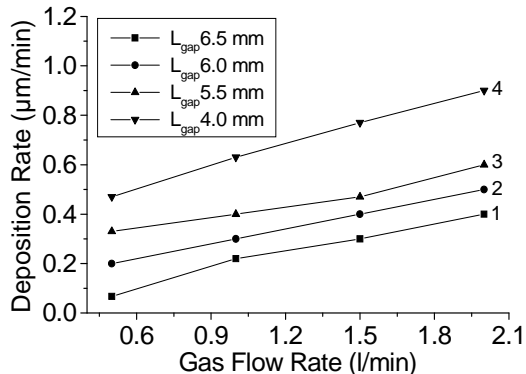


Fig 4. Variation of Deposition Rate ( $\mu\text{m}/\text{min}$ ) with the Variation of Gas Flow Rate at Different Gaps between Activation Heater and Substrate for SS 314.

### 3.2 Mechanism of Thin Film Growth and Possible Causes of Higher Deposition Rate

The mechanism of thin film growth and the possible causes of deposition with gas flow rate and the gap between activation heater and substrate can be explained as follows:

a) The process of CVD thin film growth can be divided into two steps: (i) the transport of active species and (ii) the incorporation of carbon atoms into the substrate lattice. Under fixed conditions of activating source gases, the production rate of active species is

fixed and the thin film growth depends on the rate of the above two steps, that is the transport rate of source gases to the substrate surface and the rate of thin film growth reactions on the growth surface. The surface growth process is controlled by a mass transport process rather than the reaction rate occurring in the growth surface [12, 13]. The direction of gas flow does not influence the thin film growth rate of substrate and growth is affected by the mass diffusion. If the gas flow rate near the growth region is sufficiently strong, convective mass transport will play an important role in thin film growth and gas flow rate markedly affect the growth rate of thin film [12, 13].

b) The complex chemical and physical processes, which occur during CVD, comprise several different but interrelated features. The process gases of the chamber before diffusing toward the substrate surface pass through an activation region (a hot filament), which provides energy to the gaseous species. This activation causes molecules to fragment into reactive radicals and atoms, creates ions and electrons, and heats the gas up to temperatures approaching a few thousand Kelvin. Beyond the activation region, these reactive fragments continue to mix and undergo a complex set of chemical reactions until they strike the substrate surface. At this point the species are adsorbed and entrapped within the surface, some portions are desorbed again back into the gas phase, or diffuse around close to the surface until an appropriate reaction site is found. If a surface reaction occurs, one possible outcome, if all the conditions are suitable, is thin film coating. During this process, the higher the gas flow rate the higher the density of carbon particles is obtained. That is more the density of carbon particle, more amount of deposition on the substrate may be occurred. The increase of deposition rate might be due to elimination or reduction of the local energy barrier during the chemical activity by increasing the gas flow rate.

c) In the case of increased flow rate, higher deposition rates are obtained. One of the conditions required for high deposition rate is that the diffusion of gas toward the substrate is the rate-determining stage. It was considered that the high flow rate made this mechanism possible [17].

d) At high flow rate, diffusion and convection are equally important. While the residence time of the rapid diffusion of atomic hydrogen is not significantly altered, the residence time of heavier carbon-containing species is sensitive to the change in gas flow pattern. The flux of carbon containing species on thin film growth surface is higher at higher flow rate. Celii et al. suggested that the changes of carbon containing species flux with gas flow rates were responsible for the changes in the morphology of the deposited thin films [12, 13].

e) The number of activated carbon species and atomic hydrogen are more near the activation heater [1]. The higher the substrate thickness, the lower the gap between activation heater and substrate are obtained. As the gap between activation heater and substrate reduces, more amounts of activated carbon species may be deposited on substrate and hence increase the deposition rate (coating thickness and weight of deposited materials).

### 3.3. Comparison of Tribological Behavior before and after Deposition

#### 3.3.1. Surface Roughness

The average roughness of SS 314 before deposition was 0.65  $\mu\text{m}$ . After deposition the average value of roughness becomes 0.50  $\mu\text{m}$ . This indicates smoother surface is obtained after deposition than that of before deposition.

#### 3.3.2. Frictional Behavior

Fig. 5 shows the variation of friction coefficient with the variation of duration of rubbing for SS 314. This figure is drawn for normal load 10-20 N, sliding velocity 1 m/s and relative humidity 75%. At normal load 10 N,

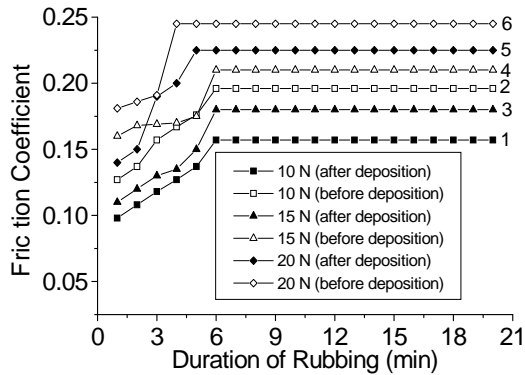


Fig 5. Variation of Friction Coefficient with the Variation of Duration of Rubbing at Different Normal load [Sliding velocity 1 m/s, Relative humidity=75%, Surface roughness before coating 0.65 microns, Surface roughness after coating 0.50 microns, Substrate: SS 314]

curve 1 is drawn for after deposition and curve 2 is drawn for before deposition. It is observed from curve 1 that at initial stage of rubbing, friction coefficient is low (0.098) and then increases almost linearly up to 0.157 and after that it remains constant for the rest of the experimental time. Similarly curve 2 drawn for before deposition shows that at the starting friction coefficient is 0.127 and then increases very steadily up to 0.196 and after that the values of friction coefficient remain almost constant. At starting of experiment the friction force is low due to contact between superficial layer of pin and disc. Then the friction coefficient increases due to ploughing effect and because of roughening of the disc surface. After a certain duration of rubbing, the increase of roughness and other parameters may reach to a certain steady value and for this reason the values of friction coefficient remain constant for the rest of the time. Similar results are obtained for normal load 15 and 20 N i.e. the coefficient of friction is lower for after deposition than that for before deposition. Moreover, the higher the normal load the higher the values of friction coefficient are obtained for before and after deposition. The steady values of friction coefficient at different normal load for after and before deposition are shown in Fig. 6.

#### 3.3.3 Wear Rate

Fig. 7 shows the variation of wear rate with the variation of normal load before and after deposition. Curve drawn for before deposition indicates that wear rate varies from 1.05 mg/min to 1.5 mg/min while for after deposition it varies from 0.5 mg/min to 0.8 mg/min

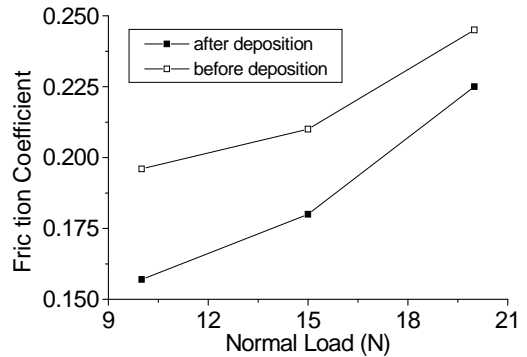


Fig 6. Variation of Friction Coefficient with the Variation of Normal load [Sliding velocity 1 m/s, Relative humidity 75%, Surface roughness before coating 0.65 microns, roughness after coating 0.50 microns, Substrate: SS 314]

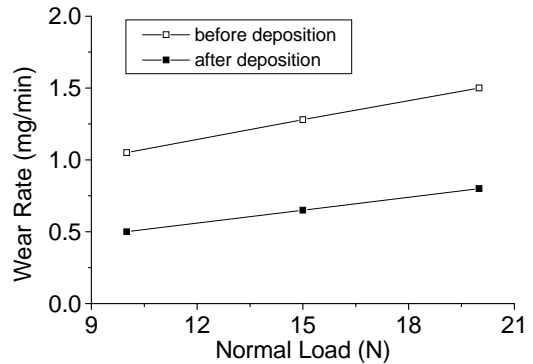


Fig 7. Variation of Wear Rate with the Variation of Normal load [Sliding velocity 1 m/s, Relative humidity 75%, Surface roughness before coating 0.65 microns, roughness after coating 0.50 microns, Substrate: SS 314]

with the variation of normal load from 10 to 20 N. That is the wear rate after deposition is less compared to that for before deposition.

### 4. CONCLUSIONS

The presence of gas flow rate and gap between activation heater and substrate significantly affect the deposition rate on SS 314. The deposition rate increases with the increase of gas flow rate and it decreases with the increase of gap between activation heater and substrate. The values of friction coefficient, wear rate and surface roughness are lower for deposited condition than that for without deposited condition. Therefore maintaining an appropriate level of gas flow rate and gap between activation heater and substrate, deposition rate may be kept to some optimum value.

## 5. REFERENCES

1. Huges, O. Pierson., 1999, Handbook of Chemical Vapor Deposition, second edition, Noyes publications, Norwich, New York, U.S.A.
2. Bunshah, R.F., 1994, Handbook of Deposition Technologies for films and Coatings, second edition, Noyes publications, New Jersey, U.S.A.
3. Regel, L.L., and Wilcox, W.R., 2001, "Diamond film Deposited by Chemical Vapor Transport," *Acta Astronautica*, 48:129-144.
4. Van der Werf, C.H.M., Goldbach, H.D., Löffler, J., Scarfó, A., Kylner, A.M.C., Stannowski, B., ArnoldBik, W.M., Weeber, A., Rieffe, H., Soppe, W.J., Rath, J.K., Schropp, R.E.I., 2006, "Silicon nitride at high deposition rate by Hot Wire Chemical Vapor Deposition as passivating and antireflection layer on multicrystalline silicon solar cells," *Thin Solid Films*, 501:51-54.
5. Stannowski, B., C, H.M., van der Werf., and R, E.I., Schropp., 2000, "Hot-Wire Chemical-Vapour Deposition For Low-Temperature Deposition Of Silicon-NitrideLayers," *Proc. of the 3rd Intern. Conf. on Coatings on Glass*, Oct 29 - Nov 2, Maastricht, pp. 387-394.
6. William, N., Shafarman., and Jie, Zhu., 1998, "Effect of Substrate Temperature and Deposition Profile on Evaporated Cu(InGa)Se<sub>2</sub> Films And Devices," paper reference: 0-624 Institute of Energy Conversion University of Delaware, Newark, DE 19716 USA.
7. Corata, E. J., and Goodwin, D. G., 1993, "Temperature dependence of species concentrations near the substrate during diamond chemical vapor deposition", *Journal of Applied Physics*, 74:2021-2029.
8. Mark, C., McMaster, I., Wen, L., Hsuap, Michael. E., Coltrin, B., David, S. Dandy., Ciaran Fox, D., 1995, "Dependence of the gas composition in a microwave plasma-assisted diamond chemical vapor deposition reactor on the inlet carbon source: CH<sub>4</sub> versus C<sub>2</sub>H<sub>2</sub>," *Diamond and Related Materials* 4:1000-1008.
9. Yongqing Fu., Chang Q., Sun, Hejun Du., Bibo Yan., 2002, "From diamond to crystalline silicon carbonitride: effect of introduction in CH<sub>4</sub>/H<sub>2</sub> gas mixture using MW-PECVD," *Surface & coating Technology*, 160:165-172.
10. H. Rau, F. Picht, 1992, "Rate limitation in low pressure diamond growth," *Journal of Materials Research*, 7:934-939.
11. D.W. Kweon, J.Y. Lee, D. Kim, 1991, "The growth kinetics of diamond films deposited by hot-filament chemical vapor deposition," *Journal of Applied Physics*, 69:8329-8335.
12. F.G. Celii, D. White Jr., A.J. Purdes, 1991, "Effect of residence time on microwave plasma chemical vapor deposition of diamond," *Journal of Applied Physics*, 70:5636-5646.
13. F.G. Celii, D. White Jr., A.J. Purdes, 1992, "Deposition of smooth, oriented diamond films using microwave plasma chemical vapor deposition," *Thin Solid Films*, 212:140-149.
14. J. Yu, R. Huang, L. Wen, C. Shi, 1999, "Nucleation kinetics of diamond in hot filament chemical vapor deposition," *Materials Research Bulletin*, 34:2319-2325.
15. Q.H. Fan, E. Pereira, J. Cracio, 1999, "Diamond deposition on copper: studies on nucleation, growth, and adhesion behaviours," *Journal of Materials Science*, 34:1353-1365.
16. H. Buchkremer-Hermanns, H. Ren, H. Weiß, 1996, "Optimization of diamond nucleation and growth using MW-PACVD method," *Diamond and Related Materials*, 5:312-316.
17. Kawai, C, 1994, "High-rate deposition of titanium silicides under high gas flow rate by chemical vapor deposition," *Journal of Materials Science Letters*, 13:860-862.

## 6. MAILING ADDRESS:

**M A Chowdhury**

Department of Mechanical Engineering,  
Dhaka University of Engineering and Technology,  
Gazipur-1700, Bangladesh.

**E-mail:** asadzmn2003@yahoo.com

## ANALYSIS OF WEIBULL PARAMETERS FOR THE THREE MOST PROSPECTIVE WIND SIDES OF BANGLADESH

M. M. Alam<sup>1</sup>, A. K. Azad<sup>2</sup>

Department of Mechanical Engineering, Bangladesh University of Engineering & Technology, BUET,  
Dhaka, Bangladesh

### ABSTRACT

The present demand of energy is increasing day by day due to various reasons such as increasing population the aspiration for improved living standards and general economic and industrial growth. In the wake of the increasing world energy crisis, which mostly affected the least developed countries, the interest in alternative energy resources has been increased considerably. In this regard, wind as a source of energy can hold good prospect for a underdeveloped country like Bangladesh. Besides, utilization of wind energy has been growing rapidly in the whole world due to environmental pollution, consumption of the limited fossil fuels and global warming. Bangladesh has fairly wind energy potential, exploitation of the wind energy is still in the crawling level. In the current study, wind characteristics and wind energy potential of (KKK) Kuakata, Kutubdia, and Khagrachari in the Coastal Areas are investigated. First of all the wind data of the coastal areas in Bangladesh from January to December, 2006 is to be collected and sorted in sequence in appropriate frequency. The data are further analyzed and converted into several useful parameters, like daily mean wind speed, monthly mean wind speed, and mean annual wind speed. After that, the velocity frequency bar graph, energy bar graph, velocity duration curve, etc. have been plotted and analyzed. The wind speed data of a location has been fitted to Weibull function to find different parameters for that site. The value of Weibull shape factor (k) and Weibull scale factor (c) have been calculated by different methods and compared and plotted them by employing different methods. Then a Wind Turbine has been designed for an effective location for electricity generation in Bangladesh.

**Keywords:** Wind Energy, Weibull Distribution, Wind Power, Energy Pattern Method, Standard Deviation Method.

### 1. INTRODUCTION

Wind energy is now being used in almost every country of the world as an important and pollution free renewable source of energy. In Bangladesh, research in the field of wind energy began only a few years ago, which has shown that some southern districts of Bangladesh have a very good potential of wind energy [1]. This wind energy can be used in many production areas [2]. In view of exhausting conventional energy sources and the green house effect due to their conversion, many scientist and engineers have been doing research extensively for pollution free renewable energy sources. As a result of technological advancement, the wind energy generation cost has come down from 25 cents (TK. 17.51) to 8 cents (TK. 5.60) per Kwh during the last 15 years in USA (according to 25<sup>th</sup> May,2009 money market). It is expected that by the year of 2015, the price will be reduced to 4cents (TK.2.80) [3]. Wind energy conversion system (WECS) are now extensively

used in Germany, Denmark, UK, Netherlands, Russia and Australia. Asian countries like China, India, Indonesia, Japan etc are also used these technology [4]. The wind resource assessment has completed in Srilanka and Malaysia. Now they are going to install wind farms in wind prospective areas in their respective countries [4]. Compared to other developing countries, Bangladesh is in its initial stage for utilizing WECS [5]. Some organizations like BCSIR, LGED and BUET already started measuring wind speeds at some typical location of Bangladesh [1,5&10]. Now, "RENEWABLE ENERGY POLICY OF BANGLADESH" is a new policy given by Power Division, Ministry of Power, Energy and Mineral Resources, government of the People's republican of Bangladesh [Published on 6<sup>th</sup> November,2008]. There are many objectives of this policy such as Scale up contributions of renewable energy to Electricity production, Harness the renewable energy resources and dissemination of renewable energy

technologies in rural, pre-urban and urban areas, Create enabling environmental [6,7]and legal support to encourage the use of renewable energy etc. The policy sets targets for developing renewable energy resources to meet 5% of the total power demand by 2015 and 10% by 2020. So, it is obvious that Bangladesh is encouraged to use renewable energy. Since we are in the initial stage of utility of wind energy, we should follow the steps as implemented by other country in this region. Some of the information may be available from [9,10]. These include mainly two types of uses. First one is pumping water [8,9,10] and second is electricity generation [7&10].

## 2. WIND DATA

In the present study, the objective is to statistically analyze of wind characteristics in some coastal region of Bangladesh and make a comparison between various methods to determine Weibull parameter. Wind data of some coastal areas in Bangladesh such as Kuakata, Munshigonj, Khagrachari, Kishorgonj, Naogaon, Pakshey, Panchagarh, Rauzan, Sitakundu, Kutubdia (Cox's Bazar) and Teknaf (Cox's Bazar) from January to December, 2006 have been considered [4]. The wind data measured in ten minutes interval and then further processed to hourly time series. All data are supplied by LGED, Renewable energy department. For Weibull parameters analysis the 3 most important wind sides are Kuakata, Kutubdia and Khagrachari with comparison to others.

## 3. OUTLINE OF METHODOLOGY

In the current study, wind characteristics and wind energy potential of (KKK) Kuakata, Kutubdia, and Khagrachari are the most important windy areas Coastal Areas are investigated. First of all the wind data of the coastal areas in Bangladesh from January to December, 2006 is to be collected and sorted in sequence in appropriate frequency. The data are further analyzed and converted into several useful parameters, like daily mean wind speed, monthly mean wind speed, and mean annual wind speed. After that, the velocity frequency bar graph, energy bar graph, velocity duration curve, etc. have been plotted and analyzed. The wind speed data of a location has been fitted to Weibull function to find different parameters for that site. The value of Weibull shape factor ( $k$ ) and Weibull scale factor ( $c$ ) have been calculated by different methods and compared and plotted them by employing different methods. There are several methods to calculate the Weibull parameter  $k$  and  $c$  such as, Weibull paper method, Standard deviation method, Energy pattern factor method etc. Then a Wind Turbine has been designed for an effective location for electricity generation in Bangladesh.

## 4. PREDICTING OF WIND DATA

The potential benefits of having wind speed predictability are obvious in wind power generation (knowing wind speed ahead of time is useful in automatic power dispatch, load scheduling and wind turbine control). A new approach for wind speed

forecasting is presented. This method makes use of memorized wind speed to predict the next step wind speed. It is shown that as long as the wind speed variation is not extremely brisk, the proposed predicting algorithm is able to predict wind speed with a fairly good precision. The proposed predicting scheme does not assume the precise knowledge of the wind model. The result is verified via computer stimulation. The proposed prediction algorithm as described previous chapter for seven orders. Based on daily wind speed variation, we simulate the algorithm for each time instance (the sampling period 10 min).

## 5. ESTIMATION OF THE WEIBULL PARAMETERS FROM THE PROCESSED DATA

The Weibull distribution shows its usefulness when the wind data of reference station are being used to predict the wind regime in the surrounding of that station. The idea is that only annual or monthly average wind speeds are sufficient to predict the complete frequency distribution of the year or the month. This section deals with methods to extract the Weibull parameter  $k$  and  $c$  from a given set of data. There are several methods by which  $k$  and  $c$  can be determined. Three different methods are described below.

1. Weibull paper/ Regression analysis
2. Standard - deviation analysis
3. Energy pattern factor analysis.

## 6. WEIBULL PAPER METHOD

In this method at first percentage of cumulative distribution have been calculated then these are plotted for corresponding wind speed as shown in Fig. 1.

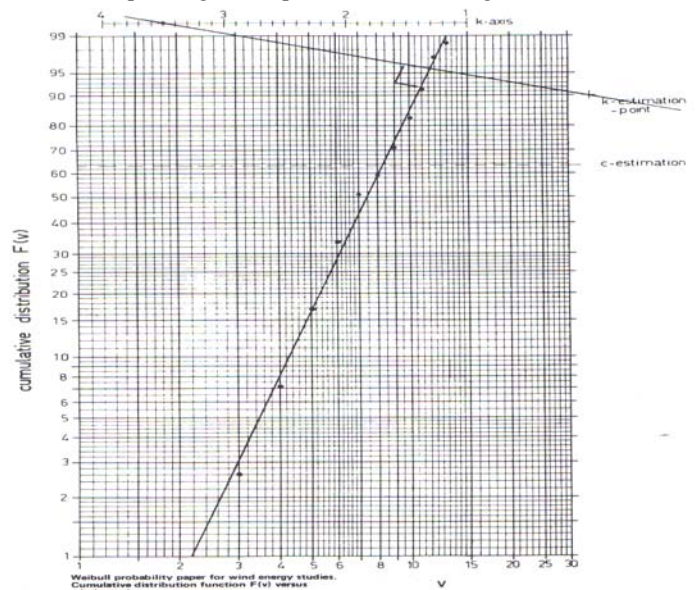


Fig 1. Cumulative distribution Vs wind speed graph

Then a straight line have been drawn in such a way that it can cover maximum point and from this line an intersection with  $c$  estimation line (dotted mark) gives the corresponding value of  $c$  for the location. A normal from “+” of the graph have been drawn upon the previous

straight line, the point of intersection with the “k” axis line (top) gives the value of k.

### 7. STANDARD-DEVIATION ANALYSIS METHOD

By determining the mean wind speed  $V_{mean}$  and standard deviation  $\sigma$  of wind data, k and c can be obtained from equation mentioned below,

$$\sigma = \sqrt{\int_0^{\infty} (v - \bar{v})^2 f(v) dv} \dots\dots\dots(1)$$

And the expression for f(v),

$$f(v) = \frac{dF(v)}{dv} = \left(\frac{k}{c}\right) \left(\frac{v}{c}\right)^{k-1} \times e^{-\left(\frac{v}{c}\right)^k} \dots\dots(2)$$

One can find next expression for  $\sigma$ ,

$$\sigma = c \sqrt{\left[ \Gamma\left(1 + \frac{2}{k}\right) - \Gamma^2\left(1 + \frac{1}{k}\right) \right]} \dots\dots(3)$$

Or with  $\bar{v} = c \times \Gamma\left(1 + \frac{1}{k}\right)$

$$\frac{\sigma}{\bar{v}} = \frac{\sqrt{\left[ \Gamma\left(1 + \frac{2}{k}\right) - \Gamma^2\left(1 + \frac{1}{k}\right) \right]}}{\Gamma\left(1 + \frac{1}{k}\right)} \dots\dots\dots(5)$$

The standard deviation of the distribution is calculated with

$$\sigma^2 = \frac{\sum (V_n)^2 - \frac{(\sum V_n)^2}{N}}{N - 1} \dots\dots\dots(6)$$

Then corresponding k value can be found from Fig 2

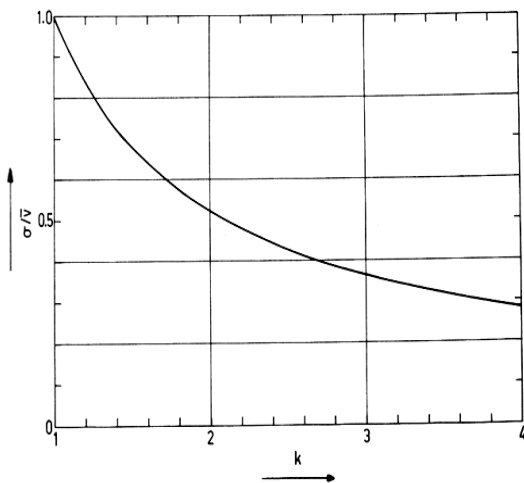


Fig 2. The relative standard deviation of a Weibull distribution as a function of Weibull shape factor (K).

Value of k and c from Standard Deviation method for each station for each month is given in result & discussion section.

### 8. ENERGY PATTERN FACTOR ANALYSIS

The energy pattern factor  $K_E$  is defined by Golding [5] as,

Total amount of power available in the wind

$$K_E = \frac{\text{Power calculated by cubing the mean wind speed}}{\dots\dots\dots}$$

Realizing that the power density of the wind is given by-

$$\frac{P(v)}{A} = \frac{1}{3} \rho V^3 \quad [W/m^2] \dots\dots\dots(7)$$

Then the total amount of energy available in the wind in a period T [26] is equal to

$$\frac{E}{A} = T \int_0^{\infty} \frac{1}{2} \rho v^3 f(v) dv \quad [J/m^2] \dots\dots\dots(8)$$

Whereas the energy [26] is calculated by cubing the mean wind speed is equal to  $\frac{E}{A} = \frac{1}{2} \rho V^3 T$

Using Weibull probability density function f(v) in (7) results,

$$K_E = \frac{\frac{1}{N} \sum_{n=1}^N (V_n)^3}{\left(\frac{1}{N} \sum_{n=1}^N V_n\right)^3} \dots\dots\dots(10)$$

Using the above expression the Weibull shape parameter k is easily found by the following figure.

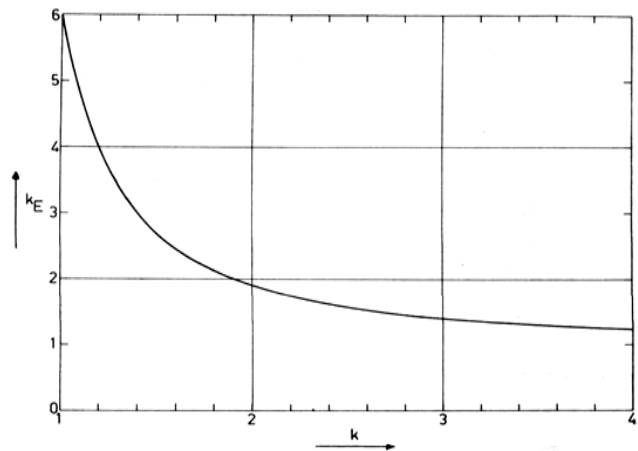


Fig 3. The energy pattern factor of a Weibull wind speed distribution as a function of the Weibull shape factor, k .

### 9. ESTIMATION OF WIND POWER DENSITY

The available power in the wind flowing at mean speed  $v_m$  through a wind rotor blade with sweep area A at any given site can be estimated as follows [3]:

$$P(v) = \frac{1}{2} \rho A v_m^3 \dots\dots\dots(11)$$

And the wind power density (wind power per unit area) based on the Weibull probability density function can be calculated as [3]:

$$p(v) = \frac{P(v)}{A} = \frac{1}{2} \rho c^3 \left( 1 + \frac{3}{k} \right) \dots\dots\dots(12)$$

Where is  $P(v)$  the wind power (W),  $p(v)$  is the wind power density ( $W/m^2$ ),  $\rho$  is the air density at the site =  $1.21(kg/m^3)$ ,  $A$  is the swept area of the rotor blades ( $m^2$ ),  $v_m$  is the wind speed at that location (m/s).

**10. PREDICTION PERFORMANCE OF THE WEIBULL DISTRIBUTION MODEL**

The prediction accuracy of the model in the estimation of the wind speeds with respect to the actual values were evaluated based on the correlation coefficient or determination coefficient,  $R^2$ , root mean square error (RMSE), and coefficient of efficiency (COE). In this paper, for wind speed data, the root mean square error (RMSE), determination coefficient ( $R^2$ ) are used in statistically evaluating the performance of the Weibull probability density functions. These parameters were calculated based on the following  $K_E$  equation in section 7 by programming language C, which is not shown in this paper.

**11. RESULT AND DISCUSSION**

**Value of k and c by Various Methods**  
(k is a dimensionless number and c in m/s)

**Weibull paper Method**

Location	Month	K	C
Kuakata	April	2.9	5.4
	May	2.6	5.2
	June	2.4	5.8
	July	2.2	6.2
	August	2.0	6.9
	September	2.6	5.6
Kutubdia	April	1.90	3.70
	May	2.30	4.60
	June	2.50	5.20
	July	2.80	6.00
	August	2.60	5.80
	September	1.50	3.40
Khagrachari	April	3.30	4.60
	May	2.40	3.80
	June	2.00	5.00
	July	2.70	3.80
	August	2.70	3.20
	September	3.00	4.00

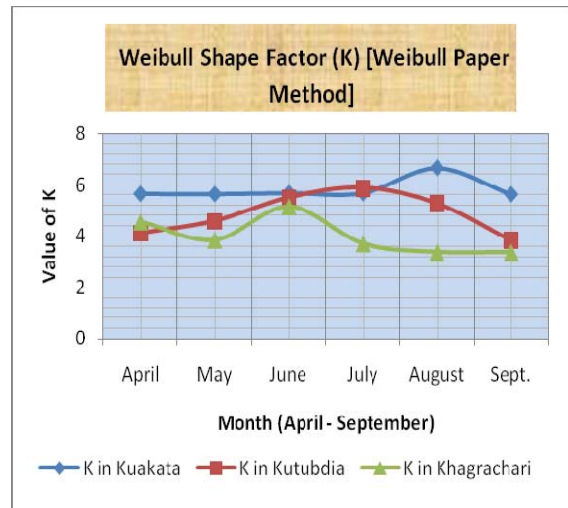
**Standard Deviation Method**

Location	Month	K	C
Kuakata	April	3.65	6.09
	May	3.16	5.49
	June	3.50	5.71
	July	3.92	6.46
	August	3.00	6.66
	September	2.41	5.64
Kutubdia	April	3.38	4.12

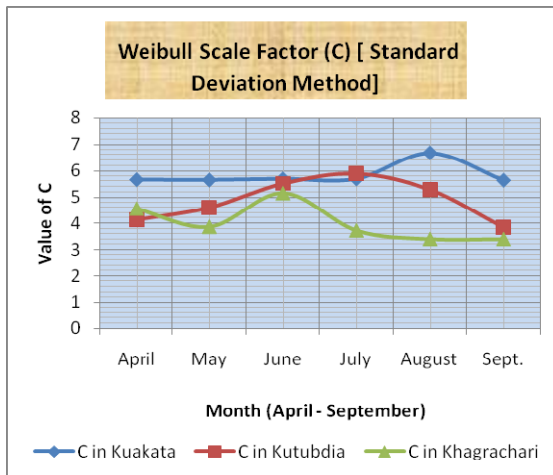
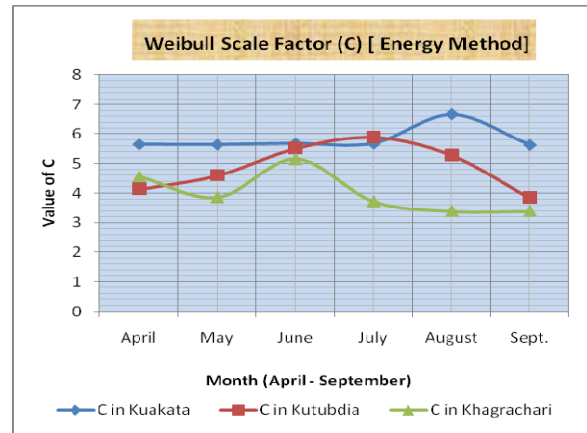
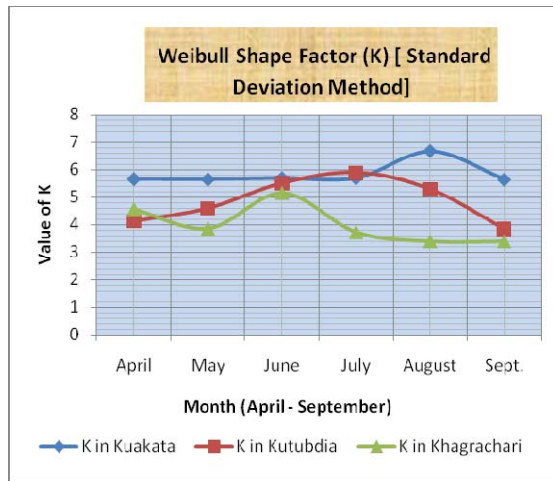
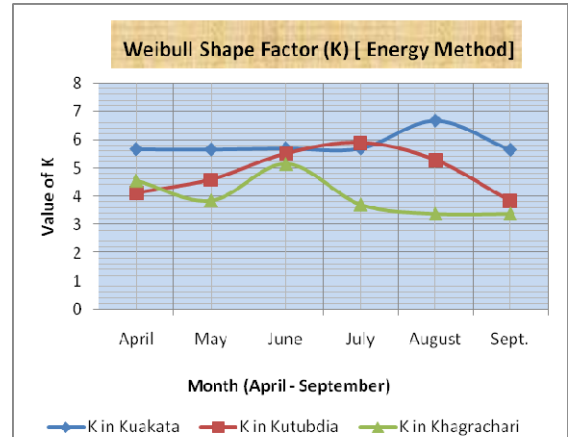
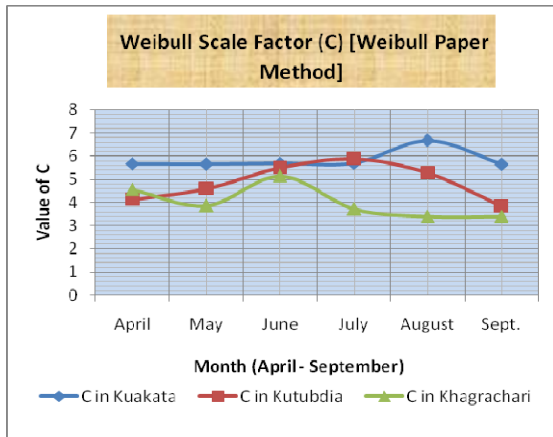
	May	3.2	4.60
	June	3.29	5.48
	July	4.00	5.89
	August	3.50	5.28
	September	2.1	3.96
Khagrachari	April	4.00	4.56
	May	2.61	3.86
	June	2.38	5.15
	July	4.00	3.72
	August	4.00	3.39
	September	4.00	3.38

**Energy Method**

Location	Month	K	C
Kuakata	April	3.19	5.66
	May	3.12	5.65
	June	3.65	5.69
	July	3.65	5.69
	August	2.85	6.67
	September	2.45	5.64
Kutubdia	April	3.21	4.13
	May	3.05	4.60
	June	3.00	5.51
	July	4.00	5.89
	August	3.65	5.28
	September	2.00	3.84
Khagrachari	April	4.00	4.56
	May	2.48	3.86
	June	2.30	5.15
	July	4.00	3.72
	August	4.00	3.39
	September	4.00	3.39







## 11.1. DISCUSSION

From the tables and graphs the Weibull distribution parameter such as Weibull shape factor ( $k$ ) and Weibull scale factor ( $c$ ) are calculated by different methods. It is found that the value of  $k$  remains between 1.5 to 4.0 and that of  $c$  remains between 3.20 to 6.9. In most cases of the Weibull functions follow very close to the shape factor ( $k=2$ ) for the selected sites. The mean wind speed ( $v_{\text{mean}}$ ) for each location remains 2.37 to 5.97 m/s and highest two mean wind speed are found in Kuakata (5.74m/s) and 5.97 m/s respectively. The maximum wind power is obtained from Kuakata which is 5895.6 Wh/m<sup>2</sup>. In Khagrachari, April 12<sup>th</sup> to 17<sup>th</sup> this five days data prediction was done by programming language C which is not shown in this paper.

## 12. CONCLUSION

In this study, assessments of wind characteristic for Coastal region of Bangladesh were made. The following conclusion can be drawn from the present analysis. The shape factor ( $k$ ) and scale factor ( $c$ ) are determined for each month. It is found that the value of  $k$  remains between 1.5 to 4.0 and that of  $c$  remains between 3.20 to 6.9. In most cases of the Weibull functions follow very close to the shape factor ( $k=2$ ) for the selected sites. Although some values are far beyond. The Weibull probability distribution scale parameters ( $c$ ) are consistently higher in values and variability than the shape parameters ( $k$ ) monthly distributions.

### 13. REFERENCES

1. "Wind Energy Resources Mapping (WERM), 2003", a project of Local Government Engineering Department (LGED) financed by United Nation Development Program (UNDP).
2. Lancashire, S and other, "Wind pumping Hand-book", IT Publication, London,UK,1987.
3. Cerrolaza, M., Berrios, R. and Bucarito, D., "Determination of the Venezuelan coastal-zone wind atlas by using Numerical method", Journal of wind Engineering, vol.19 No.4, Page. 213-233, 1995.
4. Hossain A, Mainuddin K. and Sayeed A., "Energy Needs and wind energy potential in the costal areas of Bangladesh", Presented at the 2<sup>nd</sup> seminar on wind energy study (WEST) project, LGED Auditorium, Agargaio, Dhaka, 23th November, 1997.
5. Alam, M. M. and Burton, J. D. (1998) "The Coupling of Wind Turbine to Centrifugal Pumps", Journal of Wind Engineering. Vol. 22, No. 5: pp223-234
6. Hussain, M., Alam, S. Reza, K.A. and Sarkar, M, "A Study of Wind Speed and Wind Energy Characteristics in Bangladesh", Journal of Conversion Management.. Vol. 26, No. 3/4: pp 321-327
7. Robert, G., Kortenkamp, R. and Twele, J. (1997), "A Simple Method for Near Optimum Design of Wind Turbines with Centrifugal Pumps", Journal of Wind Engineering. Vol.11, No. 5, pp: 293-312
8. Siddig, M.H. (1996), "Design Optimization of Wind Powered Piston Pumps", Journal of Wind Engineering. Vol. 20, No. 25: pp 63-71
9. Sarkar, M. and Hussain, M. (1991), "The Potential of Wind Electricity Generation In Bangladesh",

Journal of Renewable Energy. Vol. 1, No. 5/6: pp 855-857

10. Choi, E. C. C. and Hidayat, F. A. (2002): Gust factor for thunderstorm and non-thunderstorm winds, Journal of wind engineering and industrial aerodynamics, 90, 1683–1696.

### 14. NOMENCLATURE:

Symbol	Meaning	Unit
K	Shape factor	...
C	Scale factor	m/s
$K_E$	Energy pattern factor	...
$f(v)$	Provability density function	...
A	Area	$m^2$
E	Available energy	$wh/m^2$
$\rho$	Air density	$Kg/m^3$
$\sigma$	Standard Deviation	....
v	Velocity of Air	m/s
N	Total number of hours	hurs
T	Total time	hurs
$P(v)$	Wind Power	W
$p(v)$	Wind power density	$W/m^2$
P	Power	wat
$V_m$	Mean wind Speed	m/sec
R	Correction Co-efficient	...

### 15. MAILING ADDRESS

Dr. Mohammad Mahabubul Alam  
 Professor, Department of Mechanical Engineering,  
 Bangladesh University of Engineering & Technology,  
 BUET, Dhaka-1000, Bangladesh  
 E-mail: mmalam@me.buet.ac.bd

## EXPERIMENTAL INVESTIGATION ON FLUID FLOW SEPARATION CONTROL

Mohammad Mashud, A. Al Bari and T. P. Bhowmick

Department of Mechanical Engineering  
Khulna University of Engineering & Technology  
Khulna-9203, Bangladesh

### ABSTRACT

The aim of the research is to control the flow separation of an airfoil by providing a partial bumpy on the upper surface. The presence of friction in the flow causes a shear stress at the surface of the body, which in turn contributes to the aerodynamic drag of the body i.e. skin frictions drag. However, friction also causes another phenomenon called flow separation, which in turn creates another source of aerodynamic drag called pressure drag due to separation. From a fluid dynamist's point of view, the performance of an aircraft is essentially controlled by the development of the boundary layer on its surface and its interaction with the mean flow. This interaction decides the pressure distribution on the airfoil surface, and subsequently the aerodynamic loads on the wing. In order to obtain the highest levels of performance efficiencies for mission varying aircraft, it is necessary to either: (a) alter the boundary layer behavior over the airfoil surface—flow control methods of interest here, and/or (b) change the geometry of the airfoil real time for changing free stream conditions—adaptive wing technology. Geometry of the airfoil can be changed by providing bumpy on the upper surface. The value of the aerodynamic efficiency needs to be maximum i.e. the lift to the drag ratio needs to the maximization. For this case lift should be high and drag should be low, which increases aircraft efficiency. To investigate the effect of introducing large scale surface roughness through static curvature modifications on the low speed flow over an airfoil, two types model are prepared. One is regular surface model another is bumpy surface model. All the models are prepared by wood and the experiments are conducted using 36×36×100 cm subsonic wind tunnel. . From the experimental investigations it has been observed that the flow separation on the airfoil can be delayed by using the bumpy on the upper surface. Flow separation occurs at 8° angle of attack in the smooth surface. But in bumpy surface it occurs at 14° angle of attack. That indicates the bumpy surface successfully controls the flow separation and increases the lift force of an airfoil.

**Keywords:** Flow Separation Control, Partial Bumpy surface, Airfoil and Aerodynamics.

### 1. INTRODUCTION

When a real fluid flows past a solid boundary a layer of fluid which comes in contact with the boundary surface adheres to it on account of viscosity. Since this layer of fluid cannot slip away from the boundary surface it attains the same velocity as that of the boundary. In other wards at the boundary surface there is no relative motion between the fluid and the boundary. If the boundary is stationary, the fluid velocity at the boundary surface will be zero. Thus at the boundary surface the layer of fluid undergoes retardation. This retarded layer of fluid causes retardation for the adjacent layer of the fluid, thereby developing a small region in the immediate vicinity of the boundary surface in which the velocity of flowing fluid increases gradually from zero at the boundary surface to the velocity of the mainstream. This region is known as boundary layer. The boundary layer develops, up to a certain portion of the plate from the

leading edge, the flow in the boundary layer exhibits all the characteristics of laminar flow. This is so irrespective of whether the flow of the incoming stream is laminar or turbulent. This is known as laminar boundary layer. If the plate is sufficiently long, then beyond some distance from the leading edge the laminar boundary layer becomes unstable and then turbulent boundary layer is formed. This turbulent boundary layer may be formed by using external disturbance like passing outside a series of cylinder near the leading edge. The boundary layer thickness is considerable affected by the pressure gradient in the direction of flow. If the pressure gradient is zero, then the boundary layer continues to grow in thickness along a flat plate. With negative pressure gradient, the boundary layer tends to be reduced in thickness. With positive pressure gradient, the boundary layer thickens rapidly. The adverse pressure gradient plus the boundary shear decreases the momentum in the

boundary layer, and if they both act over a sufficient distance they cause the fluid in the boundary layer to come to rest. In this position the flow separation is started. Also when the velocity gradient reaches to zero then the flow becomes to separate. So when the momentum of the layers near the surface is reduced to zero by the combined action of pressure and viscous forces then separation occur. So boundary layer separates under adverse pressure gradient as well as zero velocity gradient. Fluid flow separation can be controlled by various ways such as motion of the solid wall, slit suction, tangential blowing and suction, continuous suction and blowing by external disturbances, providing bumpy the surface/surface roughness etc. Among them here the surface roughness method is used to control flow the flow separation.

#### **A. Roughness Application**

In certain cases when the pressure gradient imposed on the flow is not too adverse, transition and reattachment may occur after laminar separation, and the resultant turbulent boundary layer is found to be more resistant to flow separation. This provides a reasonable justification for separation control by means of promoting early transition in laminar flows, thereby reducing the otherwise imminent form drag. Experimental observations show that “rough” airfoils on upper surface perform better than the “smooth” surface airfoils at low  $Re$  values. The turbulence promoting devices (or turbulators) may range from passive methods such as mechanical roughness elements (strips, bumps), to active methods such as acoustic excitation, surface vibration. These methods introduce large disturbances in the flow so as to cause bypass transition, and are hard to analyze. One of the earliest studies of the effect of surface protuberances on airfoil and wing characteristics can be found in NACA reports. The chord based  $Re$  of the flow in these experiments was approximately 3.1 million; and the effects of variations in shape, span length, height and position of protuberances were considered. Four protuberances were placed on the upper surface at leading edge, front spar, maximum thickness and rear spar locations. It was observed that the loss of lift was directly proportional to the height of protuberances (order of 1/100-1/500 of chord length). At higher angles of attack, the protuberances had an adverse effect, especially when moved closer to the leading edge. Most of the work in roughness-related research has been aimed to understand the effects of icing on unsteady flow over an airfoil. Drag reduction by employing boundary layer trips was reported by Lyon and coworkers. They observed that thicker trips showed slightly better performance than thinner trips, and simple 2D trips provided the same advantage (if any) as complex 3D trips. The effects of large distributed surface roughness on airfoil boundary layer development and transition to turbulence has been investigated for  $Re$  values of

0.5, 1.25 and 2.25 million by Kerho et al. Hot wire measurements were conducted for a NACA 0012 airfoil with hemispherical disturbances of 0.35 mm height taped up to a maximum chordwise extent of 0.5 inches. They examined a variety of roughness ranging in heights lesser and greater than the boundary layer thickness. They observed that the roughness promoted the growth of a transitional boundary layer, which required substantial chordwise extent (downstream of the roughness) to become fully turbulent. The fluctuating streamwise velocity and turbulence intensity in the roughness-induced boundary layer was found to be lower than the smooth case. In general, longer the chordwise extent of the roughness and larger the roughness dimensions, length of the transitional region was found to decrease.

#### **B. Present Flow Control Approach**

The proposed method of flow control here is in introducing “large-scale” roughness to the upper surface of airfoil, such that the resultant shape would have a minor change in curvature. Due to this manufacturing constraint, the NACA 4315, a relatively thick airfoil, was selected. The radius of the bumps was of the order of 2.5% $c$ . While covering the airfoil with a membrane (to mimic the smooth profile) and adding a trailing edge extension were considered, it was decided to leave the airfoil unskinned to keep the flow tripped at all times along the surface. It is interesting to note that this bumpy profile has a blunt trailing edge. When using roughness elements to alter flowfield behavior, the effects of changing the following parameters should be considered: (a)  $Re_c$ , (b) imposed pressure gradient (angle of attack), (c) roughness placement, (d) number of roughness elements, (e) geometric roughness configurations, and (f) height of roughness with respect to the boundary layer. In the present case, factor (c) translates to chordal/spanwise bump location, while factor (e) translates to size and shape of bumps and “inter-bump” spacing. In this paper, the effects of variations in factors (a) to (d) will be considered. For flow control to be of any advantage, the following recommendations are available in the literature: (i) the roughness height ( $k$ ) should be small as compared with the boundary layer height, (ii) roughness location prior to the region of separation is “optimal”. It is important to note at this juncture that considering the flow over the bumps in the NACA 4315 profile as a roughness-induced effect would not be accurate. Specifically, one is faced with the question: what would be the length scale to safely consider “roughness” as a “curvature” related problem (and vice versa)? It is intuitive to expect that both these effects have some similarity in their mechanism of affecting the fluid, and that there should be a limiting length scale when both these effects become one and the same.

## 2. EXPERIMENTAL SETUP

### A. Test Airfoils

For this experiment NACA 4315 aerofoil profile has been selected as a model. There are two types of models are prepared.

- a) Regular surface model
- b) Partial bumpy surface model.

To investigate the effect of introducing large scale roughness through static curvature modifications on the low speed flow over an airfoil, two types model are prepared. All the models are prepared by wood. The chord of regular surface airfoils is 260 mm. For bumpy surface airfoils the bumpy height and the arc length both are constant. So the length is carefully taken so that the surface had enough bump or wave. The chords of these models are also 260 mm. Maximum height of the bumpy surface is 6.35 mm i.e. about 2.5% of total chord length. Total 4 bumpy models are constructed; here the bumpy is used for 10%, 20%, 40% and maximum wing thickness of chord length. For 10%, 20%, 40% and maximum wing thickness of chord length the no. of bumpies are 1, 2, 5 and 10 respectively. The experiments conducted on all the above models spanned a wide Re range from 50,000 to 150,000. In all the experiments, the model was mounted such that the flow over the airfoil was completely two-dimensional. The chord  $c$  was used as the length scale for Re calculation ( $Re$  and  $Re_c$  mean the same, and would be used interchangeably hereon).



(i) Regular Surface



(ii) Bumpy Surface

Fig 1. Models to be tested

### B. Wind Tunnel

The experiments were conducted using 36×36×100 cm subsonic wind tunnel. A small sized model is appropriate to examine the aerodynamic characteristics for the experiments. If we desire to examine the aerodynamic characteristics of a large model, a large scale wind tunnel facility is necessary for testing or the inflatable wing must be drastically scaled down to match the usual wind tunnel size violating the Reynolds number analogy requirements. Furthermore, it would be difficult to support the inflatable wing a desirable attitude in these wind tunnel experiments. Since the vertical part of the aerodynamic force produces the lifting force necessary to suspend the load. The main interest is to examine the aerodynamic characteristics of each model. The model was placed in the middle of the test section supported by a frame. The frame is constructed by four 5mm diameter threaded iron rod, bolts, a flat plate and two bars with

angle measuring system. The four threaded rods placed the plate tightly inside the wind tunnel. This plate holds the two bars, and these bars hold the model tightly inside the wind tunnel. One bar has an extended part which is used to measure the angle of attack of the model. The surface of the model is drilled through 2 mm diameter holes and small sizes pressure tubes are placed inside the drilled holes. One end of the vinyl tubes are attached to each pressure tube and the other end are connected to a digital manometer for measurement of the surface pressure of the model at different points.

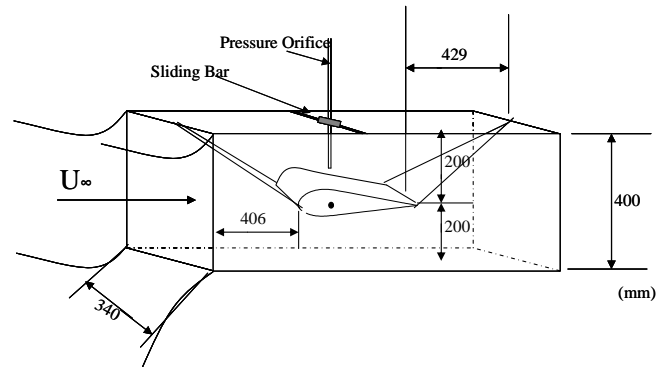


Fig 2. Schematic diagram of wind tunnel test section

### C. Pressure Measurement Technique

For this purpose a digital manometer was placed outside of the wind tunnel test section. There were drilled holes vertically in every 1.5 cm distance of the model and vinyl tubes were placed in these holes. The vinyl tubes connected between the pressure tubes and the manometer. The model surface pressure varies according to the scale of the chord length, which is much larger than the boundary layer thickness. For three constant motor speeds of the wind tunnel, difference of the inside surface pressure of wind tunnel and the surface pressure of the model were measured. So finally the static surface pressure at different points on the surface of the model was obtained.

## 3. RESULTS AND DISCUSSION

The results are prepared in the form of graph. The graphs are plotted Co-efficient of Pressure Vs  $x/c$ .

The Co-efficient of Pressure is

$$C_p = \frac{P - P_\infty}{q_\infty}$$

$$C_p = \frac{P - P_\infty}{\frac{1}{2} \rho_\infty u_\infty^2}$$

Where,

$p_\infty$  = free stream pressure

$u_\infty$  = free stream velocity

$q_\infty$  = dynamic pressure

and the  $x/c$  is the ratio of distance from leading edge to the chord length.

In this paper

Cp1 = Upper surface Co-efficient of Pressure at 4 m/s  
 Cp2 = Upper surface Co-efficient of Pressure at 5 m/s  
 Cp3 = Upper surface Co-efficient of Pressure at 6 m/s  
 Cpl = Lower surface Co-efficient of Pressure

In those graph here for the model of two surfaces regular at zero attack angle, there was no separated flow. As the attack angle increased from 0° to 12°, flow separation occur at 70% of the chord length from the leading edge and did not reattach to the rest of the upper surface. Due to flow separation, the value of the pressure coefficient was almost zero. As the attack angle increased from 12° to 16° clear flow separation appeared on the upper surface, the separation point was 40% of the chord length from the trailing edge of the upper surface. And when the angle of attack was increased to 20° the flow was separated from very early to the leading edge. We use 3 models where the bumpy surface was varied from 20% to maximum wing thickness of chord length. The 20%, 40% & maximum bumpy can control the flow separation upto 12° angle of attack.. The effect of bumpy surface is shown in fig. 4 ,6 and 8 where 20%, 40% and maximum bumpy is provided and it is seen that at 12° AOA the flow is attached but in fig 5 , 7 and 9 it is shown that the bumpy has no effect at 20° AOA.

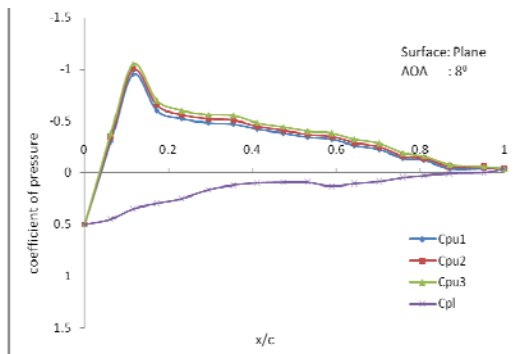


Fig 3. Coefficient of pressure vs. distance at 8° angle of attack

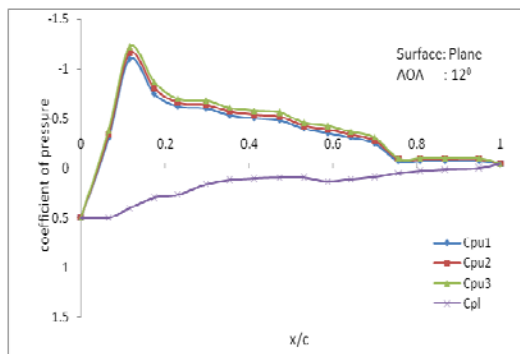


Fig 4. Coefficient of pressure vs. distance at 12° angle of attack

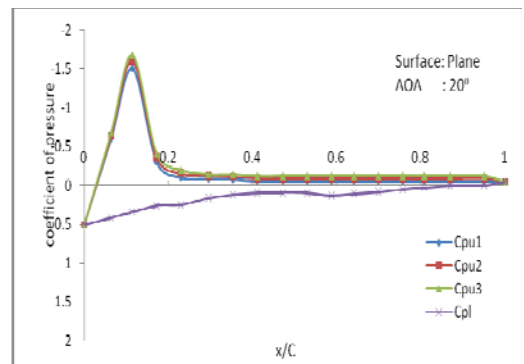


Fig 5. Coefficient of pressure vs. distance at 20° angle of attack

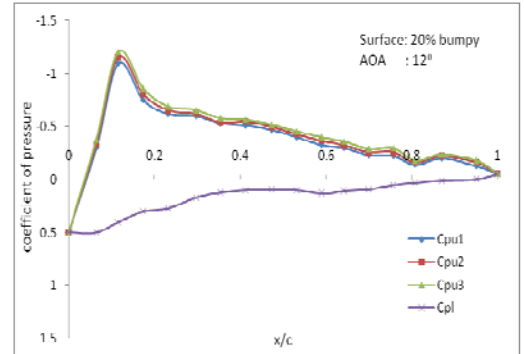


Fig 6. Coefficient of pressure vs. distance at 12° angle of attack

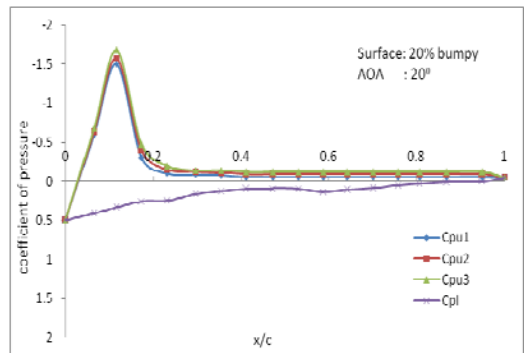


Fig 7. Coefficient of pressure vs. distance at 20° angle of attack

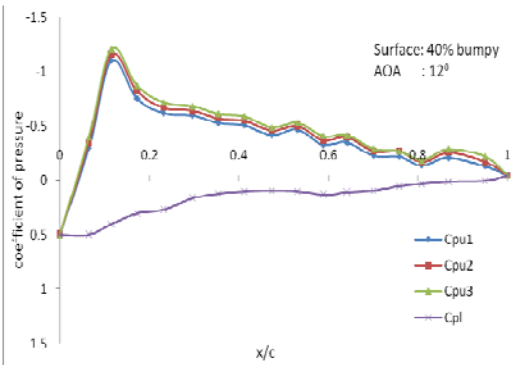


Fig 8. Coefficient of pressure vs. distance at 12° angle of attack

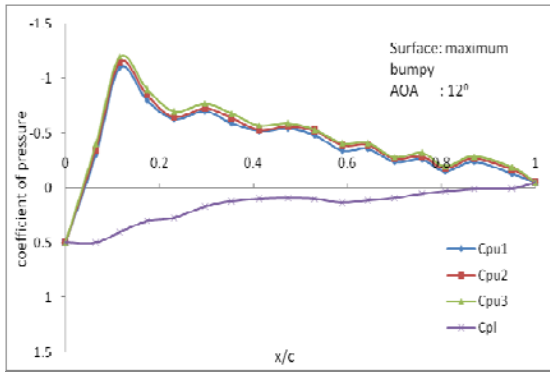


Fig 9. Coefficient of pressure vs. distance at 12° angle of attack

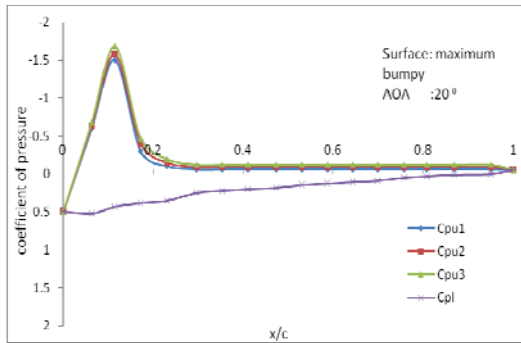


Fig 10. Coefficient of pressure vs. distance at 20° angle of attack

#### 4. CONCLUSION

From this experimental investigation it has been observed that the flow separation on the surface of the airfoil can be delayed by the modification with regular perturbations or “bumps”. The attached flow on the bumps surface is appeared at higher attack angle than the smooth surface. The lift of bumps surface airfoil will be

greater than the smooth surface.

#### 5. REFERENCES

1. Mueller, T. and DeLaurier, J., “Aerodynamics of Small Vehicles,” Annual Rev. of Fluid Mech., Vol. 35, 2003, pp. 89–111.
2. Stanewsky, E., “Adaptive Wing and Flow Control Technology,” Progress in Aerospace Sciences, Vol. 37, 2001, pp. 583–667.
3. Lissaman, P., “Low-Reynolds-Number Airfoils,” Annual Rev. of Fluid Mech., Vol.115, 1983, pp. 223–239.
4. Carmichael, B., “Low Reynolds Number Airfoil Survey,” NASA CR–165803, 1981.
5. Jacob, J., “On the Fluid Dynamics of Adaptive Airfoils,” Proc. ASME International Mechanical Engineering and Exposition, ASME, Anaheim, CA, 1998.
6. Gad-El-Hak, M., “Flow Control: The Future,” Journal of Aircraft, Vol. 38, 2001, pp. 402–418.
7. McMasters, J. and Henderson, M., “Low-Speed Single Element Airfoil Synthesis,” Technical Soaring, Vol. 6, 1980, pp. 1–21.
8. Gad-El-Hak, M., “Control of Low-Speed Airfoil Aerodynamics,” AIAA Journal, Vol. 28, 1990, pp. 1537–1552.
9. Jacobs, E., “Airfoil Section Characteristics as Affected by Protuberances,” NACA TR–446, 1932.
10. Jacobs, E., “Wing Characteristics as Affected by Protuberances of Short Span,” NACA TR–449, 1932.

#### 6. MAILING ADDRESS

Mohammad Mashud  
 Department of Mechanical Engineering  
 Khulna University of Engineering & Technology  
 Khulna-9203, Bangladesh  
 EMAIL: [mdmashud@yahoo.com](mailto:mdmashud@yahoo.com)



## A COMPUTATIONAL STUDY OF TRANSONIC MOIST AIR FLOW AROUND A SYMMETRIC DISK BUTTERFLY VALVE

A. B. M. Toufique Hasan<sup>1</sup>, Mohammad Mamun<sup>2</sup>, Shigeru Matsuo<sup>3</sup> and Toshiaki Setoguchi<sup>4</sup>

<sup>1</sup> Graduate School of Science and Engineering, Saga University, Saga, Japan

<sup>2</sup> Department of Mechanical Engineering, Bangladesh University of Engineering and Technology, Dhaka ,  
Bangladesh

<sup>3</sup> Department of Mechanical Engineering, Saga University, Saga, Japan

<sup>4</sup> Institute of Ocean Energy, Saga University, Saga, Japan

### ABSTRACT

Transonic flow around a symmetric disk butterfly valve is associated with the appearance of shock waves standing on valve surfaces. In this case, the interaction between shock wave and boundary layer becomes complex and thus generates the flow induced aerodynamic instability. In the transonic or supersonic flow where vapour is contained in the main flow, the rapid expansion of the flow may give rise to non-equilibrium condensation. In the present study, the effect of non-equilibrium condensation of moist air on the shock induced flow field oscillation around a butterfly valve was investigated numerically. The results showed that in case with non-equilibrium condensation, the flow field aerodynamic instabilities such as root mean square of pressure oscillation and shock induced oscillation frequency are reduced significantly compared with those without the non-equilibrium condensation. Moreover, the total pressure loss increases and the vortex shedding frequency is reduced with non-equilibrium condensation.

**Keywords:** Transonic Flow, Shock Induced Oscillation, Moist Air.

### 1. INTRODUCTION

Shock-boundary layer interaction (SBLI) is often observed in many transonic internal aeronautical applications such as turbine cascades, compressor blades, butterfly valves, fans, nozzles, diffusers and so on. Shock induced oscillations (SIO), aerodynamic instabilities (buffet), high cycle fatigue failure (HCF), nonsynchronous vibration (NSV), flutter, aeroacoustic noise and vibration and so on are the detrimental consequences of this unsteady interaction [1-2]. In transonic or supersonic flow where water vapour is contained in the main flow, rapid expansion may give rise to non-equilibrium condensation [3-5]. In this case, the degree of supersaturation  $S = p_v/p_{s,\infty}(T)$  (where  $p_v$  is the water vapour pressure and  $p_{s,\infty}(T)$  is the saturation pressure of water vapour at a given temperature  $T$ ) may reach much above one ( $S \gg 1$ ) without condensation because the liquid droplets do not reach the critical size for growth and collapse back to water vapour. At the critical state, known as supersaturation state, the liquid droplets reach the critical size. A significant nucleation of water droplets is suddenly initiated by spontaneous fluctuations in water vapour itself, known as homogenous nucleation [3]. Further, the condensation of the vapour takes place on these nuclei, known as droplet growth. This condensation process releases thermal

energy to the surrounding gaseous medium and considerably modifies their thermo-fluid behaviors.

Butterfly valve disks behave similarly to airfoils in that the angle of attack influences the flow field characteristics [6]. However, under certain combinations of valve disk opening angle and pressure difference across the valve, compressible flow effects can significantly alter the performance characteristics and flowfield of a butterfly valve. At these conditions, regions of transonic and supersonic flow can develop in the vicinity of the valve disk and downstream of it. Recently, butterfly valve performance coefficients in compressible flow field were predicted using computational fluid dynamics (CFD) [6-7]. However, in transonic or supersonic flow field, expansion of vapor/carrier gas mixture (moist air) or steam is often so rapid that the flow field gives rise to non-equilibrium condensation process. Till now, there is no investigation concerning the working medium as a moist air in the flow field around a butterfly valve.

In the present study, the effect of moist air with the occurrences of non-equilibrium condensation on transonic internal flow around a symmetric disk butterfly valve is investigated numerically. The computational results are also validated with experiments. Furthermore, various aerodynamic aspects for the case of moist air are

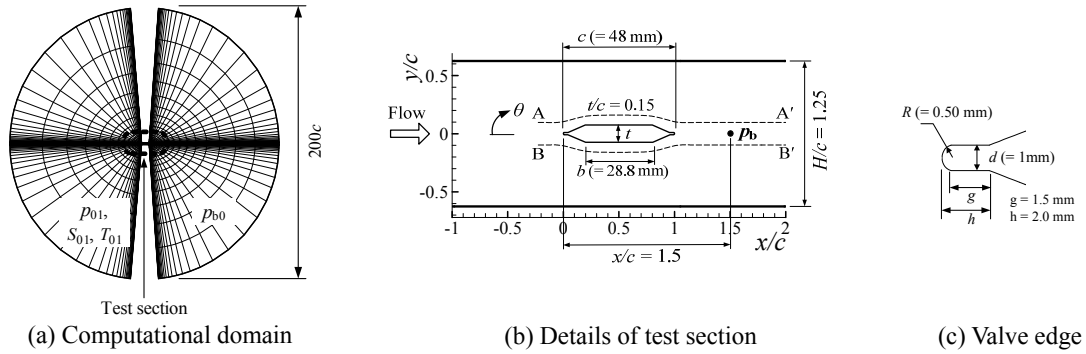


Fig 1. Computational domain, test section and valve edge geometry

discussed and compared with results of dry air.

## 2. NUMERICAL METHODS

Governing equations of the present flow field are unsteady compressible Navier-Stokes equations written in two-dimensional coordinate system. To link the heat supply by condensation process with flow, a rate equation of liquid-phase production [8] is coupled. As a turbulence model, a modified two-equation  $k$ - $R$  model [9-10] was used in the present computation where  $k$  is the turbulent kinetic energy and  $R$  being the undamped eddy viscosity.

These equations were discretized by the finite difference technique. A third order TVD (total variation diminishing) finite difference scheme with MUSCL [11] was employed to discretize the spatial derivative, and a second order central difference scheme for viscous terms, and a second order fractional step was used for time integration. For simplicity of the computation, assumptions are as follows; no velocity slip and no temperature difference between condensate particles and gas medium, and the effect of condensate particles on pressure is negligible.

Figure 1 shows the computational domain of the flow field, details of test section and valve edge geometry. Chord length  $c$  and the thickness of the butterfly valve  $t$  are 48 mm and 7.2 mm ( $t/c = 0.15$ ), respectively. Valve leading and trailing edges are rounded with radius of 0.5 mm. The height of the test section  $H$  is 60 mm ( $H/c = 1.25$ ). Computational domain is discretized by structured mesh. The mesh size is  $351 \times 101$ . The origin of  $(x, y)$  coordinate is located at leading edge of the valve. Aerodynamic and condensate properties are measured along lines A-A' and B-B' which are vertically  $0.075c$  apart from the valve upper surface and lower surface, respectively.

Working gas used in the present study is moist air which is assumed to be thermally and calorically perfect. Inlet Mach number upstream of the valve is 0.6 and Reynolds number based on valve chord length is  $5.4 \times 10^5$ . The pressure ratio  $p_{b0}/p_{01}$  ( $p_{b0}$ : total back pressure,  $p_{01}$ : reservoir total pressure) was kept at 0.739 [12]. Initial degrees of supersaturation  $S_{01}$  are 0 for dry air and 0.6 for moist air. Total temperature  $T_{01}$  and total pressure  $p_{01}$  in the reservoir are 298.15 K and 101.3 kPa, respectively.

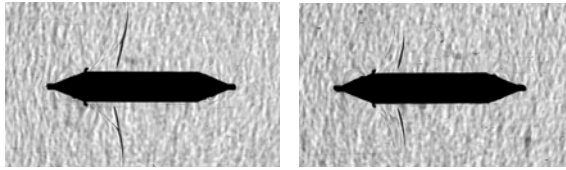
Inlet boundary was fixed, and exit boundary was constrained with free boundary condition. Non-slip and adiabatic wall conditions were applied at the solid

boundary. The pressure at the wall was obtained from zero normal pressure gradient on the body surface. Condensate mass fraction  $g$  was set to zero on the solid wall.

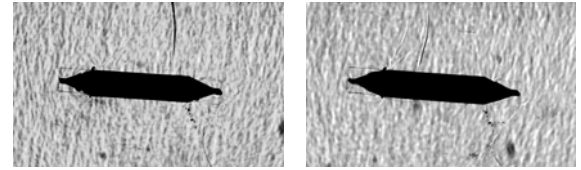
## 3. RESULTS AND DISCUSSION

Figures 2(a) and 2(b) show instantaneous schlieren photographs around a symmetric disk butterfly valve in cases without and with non-equilibrium condensation by experiments, respectively ( $\theta = 0^\circ$  and  $p_b/p_{01} = 0.650$ ). Figures 3 show instantaneous schlieren photographs around a symmetric disk butterfly valve obtained by experiments for  $\theta = 3.2^\circ$ . Results for  $S_{01} = 0.17$  (Figs. 2(a) and 3(a)) are shown in these figures. In this case, the degree of supersaturation is so small that the air can be considered to be almost dry [5]. In case with non-equilibrium condensation (Figs. 2(b) and 3(b)), it seems that the configuration of the shock wave changes largely and its strength becomes weaker compared to those in Figs. 2(a) and 3(a). However, in case of  $S_{01} = 0.6$ , the shock wave moves further upstream to that of dry air for  $\theta = 3.2^\circ$ . Figures 4 and 5 show computer generated schlieren pictures (density gradient) corresponding to each figure in Figs. 2 and 3, respectively. As seen from these figures, the flow structures obtained by simulation are similar to experimental results. However, small difference in shock structure in between experiment and simulation is due to presence of three-dimensional phenomena in the actual flow field.

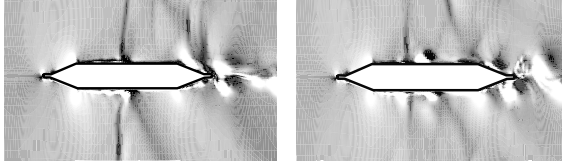
Figure 6 shows the distributions of static pressure  $p/p_{01}$ , nucleation rate  $I$  and condensate mass fraction  $g$  along the lines A-A' and B-B' during one cycle of shock oscillation  $T_s$  for  $\theta = 0^\circ$ .  $T_s$  is the time period of one cycle of shock induced oscillation measured at the peak position of RMS value of pressure oscillation (will be discussed latter). In case of  $S_{01} = 0$ , shock waves along line A-A' are observed to develop from  $x/c \approx 0.5$  and travel toward the leading edge during the cycle. Along line B-B', shock waves are moving from leading to trailing edge. Thus, shock waves are oscillating alternatively in between the upper and lower passages during the cycle. In case of  $S_{01} = 0.6$ , the maximum degree of expansion in the flow field is reduced and thus strength of shock wave becomes weak compared to the case of  $S_{01} = 0$ . Furthermore, the distribution of  $p/p_{01}$  indicates that the strength of shock wave gradually decreases when shock wave is moving towards the leading edge of the valve in both the cases. With the



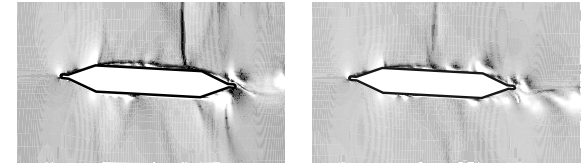
(a)  $S_{01} = 0.17$  (b)  $S_{01} = 0.6$   
Fig 2. Schlieren photographs ( $\theta = 0^\circ$ ,  $p_b/p_{01} = 0.650$ )



(a)  $S_{01} = 0.17$  (b)  $S_{01} = 0.6$   
Fig 3. Schlieren photographs ( $\theta = 3.2^\circ$ ,  $p_b/p_{01} = 0.650$ )



(a)  $S_{01} = 0.17$  (b)  $S_{01} = 0.6$   
Fig 4. Computer numerical Schlieren  
( $\theta = 0^\circ$ ,  $p_b/p_{01} = 0.650$ )



(a)  $S_{01} = 0.17$  (b)  $S_{01} = 0.6$   
Fig 5. Computer numerical Schlieren  
( $\theta = 3.2^\circ$ ,  $p_b/p_{01} = 0.650$ )

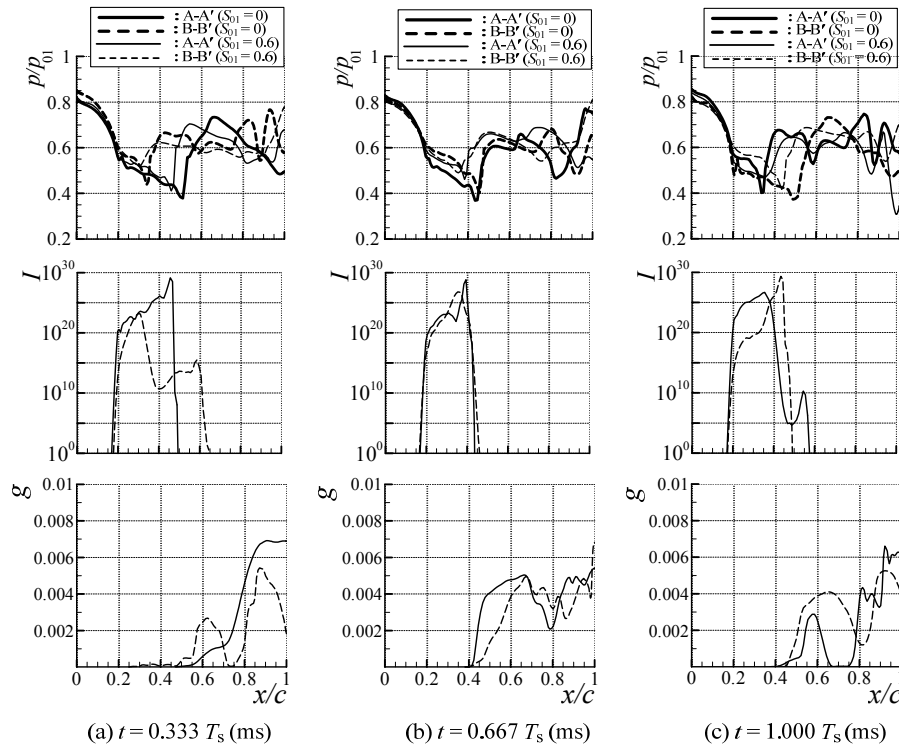


Fig 6. Distributions of static pressure ( $p/p_{01}$ ), nucleation rate ( $I$ ) and condensate mass fraction ( $g$ ) around a valve  
( $\theta = 0^\circ$ ,  $p_{b0}/p_{01} = 0.739$ )

occurrence of non-equilibrium condensation ( $S_{01} = 0.6$ ), a nucleation zone is observed to develop in the region close to rapid flow expansion at  $x/c \approx 0.2$ . Nucleation rate  $I$  reaches the peak value and then decreases with sharp gradient where static pressure falls to a minimum. Condensate mass fraction  $g$  begins to increase approximately from the position where nucleation rate decreases sharply. At upper region (along line A-A'),  $g$  starts to increase at  $x/c = 0.48, 0.40$  and  $0.35$  for  $t = 0.333T_s, 0.667T_s$  and  $1.000T_s$ , respectively. It is found from the above results that in upper region, positions where  $g$  begins to increase move towards the leading edge of the valve during the cycle. For lower region (along line B-B'), the positions where  $g$  begins to develop move towards the trailing edge of the valve during the

cycle. Thus, condensate properties  $I$  and  $g$  generate alternatively between the upper and lower regions around the valve. After the initial development,  $g$  varies unevenly further downstream. The maximum of  $g$  values are about 0.006 along the lines A-A' and B-B'. The reduction of shock strength is considered to be due to reduction of Mach number upstream of the shock by the generation of liquid droplets in case of moist air.

Figure 7 shows the distributions of static pressure  $p/p_{01}$ , nucleation rate  $I$  and condensate mass fraction  $g$  along the lines A-A' and B-B' during one cycle of shock oscillation  $T_s$  for  $\theta = 3.2^\circ$ . At  $\theta = 3.2^\circ$ , stronger shock wave is generated around the valve upper surface compared to  $\theta = 0^\circ$  (Fig. 6) in the range of  $x/c \approx 0.5 \sim 1.0$  for  $S_{01} = 0$ . In the lower surface, the shock wave is weaker

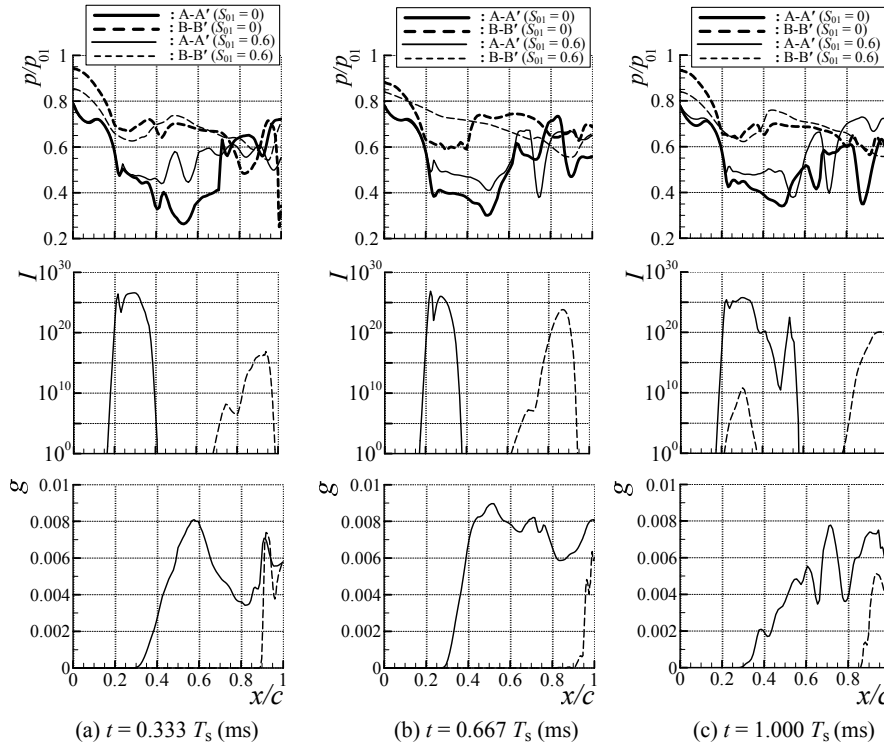


Fig 7. Distributions of static pressure ( $p/p_{01}$ ), nucleation rate ( $I$ ) and condensate mass fraction ( $g$ ) around a valve ( $\theta = 3.2^\circ$ ,  $p_{b0}/p_{01} = 0.739$ )

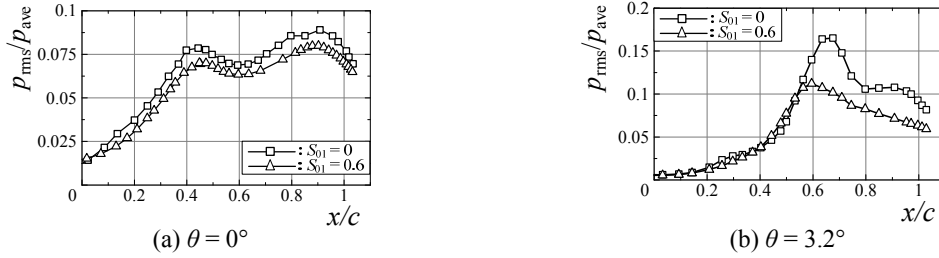


Fig 8. Distribution of RMS value of pressure oscillation around the valve ( $p_{b0}/p_{01} = 0.739$ )

than the upper one. In case of the occurrence of non-equilibrium condensation ( $S_{01} = 0.6$ ), along line A-A', a nucleation zone is developed around the valve leading edge. Then a sharp gradient in decrease of nucleation rate is observed at about  $x/c = 0.25$ . This initiates the development of condensate mass fraction from this position ( $x/c \approx 0.25$ ). In lower region along line B-B', the reduction of degree of flow expansion causes in decrease of peak nucleation rate compared to upper region.  $g$  begins to increase from  $x/c \approx 0.85$  along this line. The maximum of  $g$  values are about 0.008 and 0.006 along the lines A-A' and B-B', respectively. Furthermore, generation of liquid droplets also reduces the shock strength in both upper and lower regions at this angle of attack ( $\theta = 3.2^\circ$ ).

Flow field aerodynamic instability around the valve due to shock induced oscillation can conveniently be explained by the distribution of root mean square (RMS) value of pressure oscillation. Figure 8 shows the distribution of RMS value of pressure oscillation  $p_{rms}/p_{ave}$  ( $p_{rms}$ : RMS of pressure oscillation;  $p_{ave}$ : average of pressure oscillation) around upper passage of the test section for  $\theta = 0^\circ$  and  $3.2^\circ$  in cases without and with

non-equilibrium condensation. At  $\theta = 0^\circ$  (Fig. 8(a)), two peaks are observed in both the cases of  $S_{01} = 0$  and  $S_{01} = 0.6$ . However, the second one is more dominating than the first and located at about  $x/c = 0.9$ . In all axial locations, the RMS values are smaller in case of  $S_{01} = 0.6$  to those of  $S_{01} = 0$ . The peak  $p_{rms}/p_{ave}$  values are 0.09 and 0.08 for  $S_{01} = 0$  and  $S_{01} = 0.6$ , respectively. For  $\theta = 3.2^\circ$  (Fig. 8(b)), the RMS values are comparable up to  $x/c = 0.55$  in both the cases of  $S_{01} = 0$  and 0.6. After that, the RMS values are reduced in case of  $S_{01} = 0.6$ . The peak RMS values are 0.17 and 0.11 for  $S_{01} = 0$  and  $S_{01} = 0.6$ , respectively. However, in case of  $S_{01} = 0.6$ , peak RMS position is moved further upstream ( $x/c = 0.58$ ) to that of  $S_{01} = 0$  ( $x/c = 0.68$ ).

Dominant frequencies of shock induced oscillation measures at the peak position of RMS value of pressure oscillation (Fig. 8) are shown in Table 1. For all angles of attack, the frequencies are reduced significantly with the occurrences of non-equilibrium condensation compared with the case of no condensation. Reduction of dominant frequency is considered to be due to the decrease of turbulent fluctuation energy by the relaxation process of condensation and evaporation of vapour molecules on

Table 1: Dominant frequency (kHz) of shock induced oscillation at peak RMS position of pressure oscillation

$S_{01}$ \ $\theta$	$0^\circ$	$3.2^\circ$
0	1.26	1.20
0.6	0.51	0.50

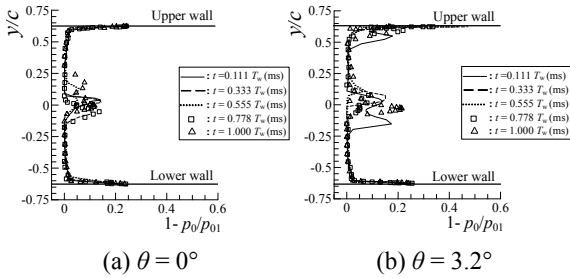


Fig 9. Total pressure losses during one cycle of flow oscillation ( $x/c = 1.5$ ,  $S_{01} = 0$ )

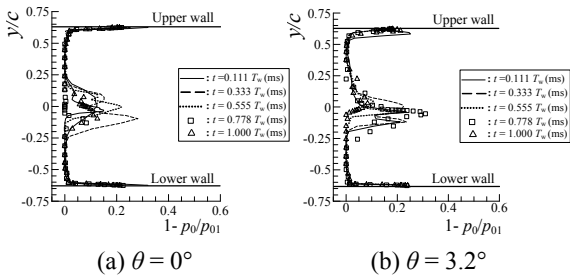


Fig 10. Total pressure losses during one cycle of flow oscillation ( $x/c = 1.5$ ,  $S_{01} = 0.6$ )

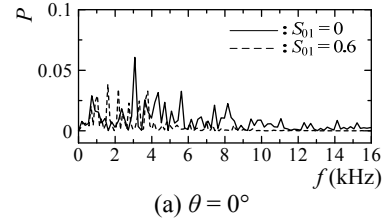
small droplet surfaces, and the interaction of boundary layer with shock wave becomes weak due to reduction of Mach number upstream of the shock wave.

Figure 9 shows distributions of total pressure loss ( $1-p_0/p_{01}$ ) ( $p_0$ : local total pressure) along  $y$ -direction at the position of  $x/c = 1.5$  in case without non-equilibrium condensation during one cycle of flow oscillation  $T_w$  ( $S_{01} = 0$ ).  $T_w$  is the time period of vortex shedding frequency measured at  $x/c = 1.5$ ,  $y/c = 0$  (will be discussed latter). For all angles of attack,  $\theta = 0^\circ$  and  $3.2^\circ$  (Figs. 9(a) and 9(b)), total pressure loss changes largely during one cycle. However, unsteadiness of total pressure losses increases with an increase of angle of attack. The maximums of total pressure loss values for  $\theta = 0^\circ$  and  $3.2^\circ$  are observed in the range of  $y/c = -0.2 \sim 0.2$  and  $-0.25 \sim 0.25$ , respectively. For  $\theta = 3.2^\circ$  (Fig. 9(b)), much variation of total pressure losses are observed in the region close to the upper wall compared with  $\theta = 0^\circ$ . This is due to the boundary layer separation induced by shock wave at the upper wall. Total pressure losses in case with non-equilibrium condensation along  $y$ -direction during one cycle of flow oscillation  $T_w$  are shown in Fig. 10 ( $x/c = 1.5$ ,  $S_{01} = 0.6$ ). It is found from this figure that values of total pressure loss become larger compared with case of dry air in Fig. 9. Moreover,  $y$ -range of occurrence of total pressure losses is increased for angles of attack of  $0^\circ$  and  $3.2^\circ$  compared to Figs. 9(a) and 9(b), respectively. This is considered to be due to the generation of condensate droplets induced by non-equilibrium condensation.

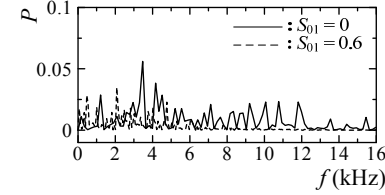
Total pressure losses were integrated from the lower wall to the upper wall at  $x/c = 1.5$  and the time averaged value  $\beta$  is shown for each angles of attack in Table 2.

Table 2: Time average integrated total pressure loss,  $\beta$  (-) ( $x/c = 1.5$ ,  $p_{b0}/p_{01} = 0.739$ )

$S_{01}$ \ $\theta$	$0^\circ$	$3.2^\circ$
0	0.035	0.041
0.6	0.044	0.048



(a)  $\theta = 0^\circ$



(b)  $\theta = 3.2^\circ$

Fig 11. Distributions of power spectrum densities in the wake region at  $x/c = 1.5$

With an increase of angle of attack,  $\beta$  increases in cases without and with non-equilibrium condensation. In case of the occurrence of non-equilibrium condensation, values of  $\beta$  for  $\theta = 0^\circ$  and  $3.2^\circ$  increase approximately by 25 % and 17 % compared to the case of no condensation, respectively.

Figure 11 shows the distributions of power spectrum densities (PSD) for wake static pressure measured at  $x/c = 1.5$ ,  $y/c = 0$ . For all angles of attack ( $\theta = 0^\circ$  and  $3.2^\circ$ ), it is observed that the vortex shedding frequency contains a frequency band width. However, in case of dry air, the dominant frequencies are 3.08 kHz and 3.48 kHz for  $\theta = 0^\circ$  and  $3.2^\circ$ , respectively. In case of moist air, the corresponding frequencies are 1.60 kHz and 2.08 kHz. In addition, the frequency band width and peaks of power spectrum densities are reduced in case of moist air to those of dry air.

#### 4. CONCLUSIONS

A computational study has been made to investigate the transonic flow around a symmetric disk butterfly valve at Mach number of 0.6 upstream of the valve for two different angles of attack. Aerodynamic features of the compressible flow field in case of moist air with non-equilibrium condensation were compared with those of dry air numerically and experimentally. The results obtained are summarized as follows: with the occurrence of non-equilibrium condensation, the strength of shock wave was reduced in case of valve with or without angle of attack. In case of valve without angle of attack ( $\theta = 0^\circ$ ), the condensate nuclei and droplets were observed around the valve upper and lower passages alternatively including downstream range. However for  $\theta = 3.2^\circ$ , condensate properties are observed mainly around the valve upper passage. The shock induced flow field aerodynamic instabilities such as root mean square (RMS) of pressure oscillations and flow oscillation

frequency were reduced significantly with non-equilibrium condensation compared to no condensation case. The peak of RMS value of pressure oscillation was shifted towards the upstream of the valve in case of moist air for valve with angle of attack ( $\theta = 3.2^\circ$ ). However, generation of condensate mass fraction and thus irreversible heat transfer in the flow field increased the total pressure loss in case of moist air. Furthermore, in the wake region, the vortex frequencies as well as peaks of power spectrum densities were reduced in case of moist air to those of dry air.

## 5. REFERENCES

1. McBean, I., Hourigan, K., Thompson, M. and Liu, F., 2005, "Prediction of Flutter of Turbine Blades in a Transonic Annular Cascade", ASME Journal of Fluids Engineering, 127: 1053-1058.
2. Caruana, D., Mignosi, A., Robitaille, C. and Corrège, M., 2003, "Separated Flow and Buffeting Control", Flow, Turbulence and Combustion, 71: 221-245.
3. Rusak, Z. and Lee, J.-C., 2000, "Transonic Flow of Moist Air around a Thin Airfoil with Non-Equilibrium and Homogeneous Condensation", Journal of Fluid Mechanics, 403:173-199.
4. Bakhtar, F., Young, J. B., White, A. J. and Simpson, D. A., 2005, "Classical Nucleation Theory and its Application to Condensing Steam Flow Calculations", Proceedings of the Institution of Mechanical Engineers, Part C: Journal of Mechanical Engineering Science, 219:1315-1333.
5. Huang, J. C., Gault, R. I., Benard, E. and Raghunathan, S., 2008, "Effect of Humidity on Transonic Flow", Journal of Aircraft, 45: 2092-2100.
6. Leutwyler, Z., and Dalton, C., 2006, "A Computational Study of Torque and Forces Due to Compressible Flow on a Butterfly Valve in Mid-Stroke Position", ASME Journal of Fluids Engineering, 128: 1074-1082.
7. Leutwyler, Z. and Dalton, C., 2008, "A CFD Study of The Flow Field, Resultant Force, and Aerodynamic Torque on a Symmetric Disk Butterfly Valve in a Compressible Fluid", ASME Journal of Pressure Vessel Technology, 130: 021302-1-021302-10.
8. Sislian, J. P., 1975, *Condensation of Water Vapour with or without a Carrier Gas in a Shock*

*Tube*. UTIAS Report No. 221.

9. Goldberg, U. C., 1994, "Toward a Pointwise Turbulence Model for Wall-Bounded and Free Shear Flows", ASME Journal of Fluids Engineering, 116: 72-76.
10. Heiler, M., 1999, "Instationäre Phänomene in Homogen/Heterogen Kondensierenden Düsen- und Turbinenströmungen", Ph.D. Thesis, Universität Karlsruhe (TH), Germany. (in German)
11. Yee, H. C., 1989, *A Class of High-Resolution Explicit and Implicit Shock Capturing Methods*. NASA TM-89464.
12. Hasan, A. B. M. T., Matsuo, S., Setoguchi, T., Kim, H. D. and Yu, S., 2009, "Control of Transonic Flow with Non-Equilibrium Condensation around a Circular Arc Blade using Bump", International Journal of Turbo and Jet Engines, 26: 33-49.

## 6. NOMENCLATURE

Symbol	Meaning	Unit
$c$	Chord length of butterfly valve	(mm)
$f$	Frequency	(kHz)
$g$	Condensate mass fraction	(-)
$H$	Height of test section	(mm)
$I$	Nucleation rate per unit volume and time	( $1/m^3 \cdot s$ )
$P$	Power spectrum density	(-)
$P_{01}$	Reservoir total pressure	(kPa)
$P_b$	Back pressure	(kPa)
$P_{b0}$	Total back pressure	(kPa)
$p_v$	Water vapour pressure	(Kpa)
$P_{s,\infty}$	Saturation pressure of water vapour	(Kpa)
$S$	Degree of supersaturation	(-)
$t$	Time /Thickness	(ms/mm)
$T_s$	Time period of shock induced oscillation	(ms)
$T_w$	Time period of wake frequency	(ms)
$T_{01}$	Reservoir total temperature	(K)
$x, y$	Cartesian coordinates	(mm)
$\beta$	Integrated total pressure loss	(-)
$\theta$	Angle of attack	( $^\circ$ )
0	Local stagnation state	(-)
01	Reservoir state	(-)

## 7. MAILING ADDRESS

A. B. M. Toufique Hasan  
 Graduate School of Science and Engineering  
 Saga University, 1 Honjo-machi,  
 Saga 840-8502, Japan  
 Phone: +81 (0)952 28 8606,  
 FAX: +81 (0)952 28 8587

## INDUCED DRAG REDUCTION FOR MODERN AIRCRAFT WITHOUT INCREASING THE SPAN OF THE WING BY USING WINGLET

Mohammad Mashud, Md. Hasan Ali, Abdullah-Al-Nahian and S. M. S. Selim

Department of Mechanical Engineering  
Khulna University of Engineering & Technology, Khulna

### ABSTRACT

This paper describes the potential of winglets for the reduction of induced drag without increasing the span of the aircraft. For this experiment a model aircraft has been constructed by aluminum-alloy whose wings profile is NACA 4315. There are three different types (rectangular, triangular and circular) of winglet are constructed for experiment. Aerodynamic characteristics for the model aircraft wing with rectangular, triangular and circular winglets and without winglet have been studied using a subsonic wind tunnel of 36cm×36cm rectangular test section. Drag measurements are carried out using an external balance. Tests are carried out on the aircraft model with and without winglet at the Reynolds numbers  $0.16 \times 10^6$ ,  $0.18 \times 10^6$ ,  $0.20 \times 10^6$ ,  $0.23 \times 10^6$  and  $0.25 \times 10^6$ . The experimental results show that the drag decreases by 26.4% - 30.9% as compared to the aircraft model with and without winglet for the maximum Reynolds number considered in the present study.

**Keywords:** Induced Drag, Wing, Winglet, Aircraft and Aerodynamics.

### 1. INTRODUCTION

The wings are the most important lift-producing part of the aircraft. Wings vary in design depending upon the aircraft type and its purpose. Most airplanes are designed so that the outer tips of the wings are higher than where the wings are attached to the fuselage. This upward angle is called the dihedral and helps to keep the airplane from rolling unexpectedly during flight. Wings also carry the fuel for the airplane.

Wingtip devices are usually intended to improve the efficiency of fixed-wing aircraft. There are several types of devices, and though they function in different manners, the intended aerodynamic effect is to modify the aircraft's wake in some beneficial manner. Wingtip devices can also improve aircraft handling characteristics. From a marketing standpoint, they are also valued for their aesthetic appeal.

Such devices increase the effective aspect ratio of a wing, with less added wingspan. An extension of span would lower lift-induced drag, but would increase parasitic drag, and would require boosting the strength and weight of the wing. At some point there is no net benefit from further increased span. There may also be operational considerations that limit the allowable wingspan.

The wingtip devices increase the lift generated at the wingtip, and reduce the lift-induced drag caused by wingtip vortices, improving lift-to-drag ratio. This increases fuel efficiency in powered aircraft, and

cross-country speed in gliders, in both cases increasing range. US Air Force studies indicate that a given improvement in fuel efficiency correlates directly with the causal increase in L/D ratio.

A winglet is a near vertical extension of the wing tips. The upward angle (or cant) of the winglet, its inward angle (or toe), as well as its size and shape are critical for correct performance, and unique in each application. The vortex which rotates around from below the wing strikes the cambered surface of the winglet, generating a force that angles inward and slightly forward, analogous to a sailboat sailing close hauled. The winglet converts some of the otherwise wasted energy in the wing tip vortex to an apparent thrust. This small contribution can be very worthwhile, provided the benefit offsets the cost of installing and maintaining the winglets during the aircraft's lifetime. Another potential benefit of winglets is that they reduce the strength of wingtip vortices, which trail behind the plane. When other aircraft pass through these vortices, the turbulent air can cause loss of control, possibly resulting in an accident.

Aerodynamic characteristics for the aircraft model with and without winglet having wing with NACA 4315 has been presented in this paper. The study on the enhanced performance of the aircraft models is also given by incorporating different shaped winglets.



## 2. MODEL CONSTRUCTION

The cambered airfoil sections of all NACA families considered herein are obtained by combining a mean line and a thickness distribution. The necessary geometric data and some theoretical aerodynamic data for the mean lines and thickness distributions obtained from the supplementary figures by the methods described for each family of airfoils. The process for combining a mean line and a thickness distribution to obtain the desired cambered airfoil section is shown in figure below.

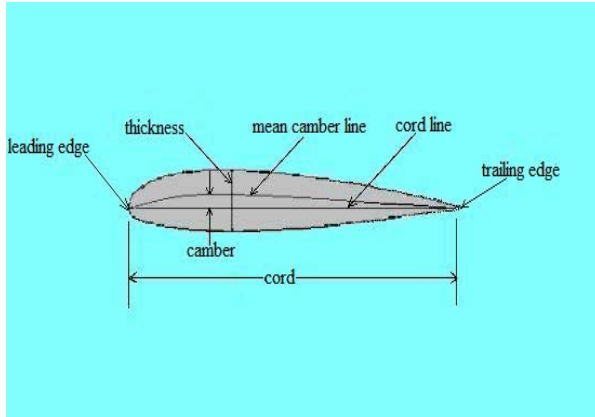


Fig 1. A typical airfoil

The cross sectional shape obtained by the intersection of the wing with the perpendicular plane is called an airfoil. The major design feature of an airfoil is the mean cambered line, which is the locus of points halfway between the upper and lower surfaces as measured perpendicular to the mean cambered line itself. The most forward and rearward points of the mean cambered line are the leading and trailing edges respectively. The straight line connecting the leading and trailing edges is the chord line of the airfoil and the precise distance from the leading to the trailing edge measured along the chord line is simply designated the chord of the airfoil, given by the symbol C. The camber is the maximum distance between the mean camber line and the chord line, measured perpendicular to the chord line. The camber, the shape of the mean camber line and to a lesser extent, the thickness distribution of the airfoil essentially controls the lift and moment characteristics of the airfoil. If  $X_u$  and  $Y_u$  represent respectively the abscissa and ordinate of a typical point of the upper surface of the airfoil and  $y_t$  is the ordinate of the symmetrical thickness distribution at chord wise position  $X_1$ , the upper surface coordinates are given by the following relations:

$$X_u = x - y_t \sin \theta$$

$$Y_u = Y_c + y_t \cos \theta$$

The corresponding expressions for the lower surface coordinates are

$$X_l = x + Y_c \cos \theta$$

$$Y_l = Y_c - Y_c \cos \theta$$

As is  $\theta$  very small,  $\sin \theta = 0$ ,  $\cos \theta = 1$

$$X_u = x \quad Y_u = y_c + y_t \sin \theta$$

$$X_l = x \quad Y_l = y_c - y_t \sin \theta$$

The center for the leading edge radius is found by drawing a line through the end of the chord at the leading edge with the slope equal to the slope of the mean line at that point and laying off a distance from the leading edge along this line equal to the leading edge radius. This method of construction causes the cambered airfoils to project slightly forward of the leading edge point. Because the slope at the leading edge is theoretically infinite for the mean lines having a theoretically finite load at the leading edge, the slope of the radius through the end of the chord

For such mean lines is usually taken as the slope of the mean line at  $x/c = 0.005$ . This procedure is justified by the manner in which the slope increases to the theoretically infinite value as  $x/c$  are reached. Large values of the slope are thus limited to values of  $x/c$  very close to 0 and may be neglected in practical airfoil design.

We have made software for the profile generation by using some basic equations of airfoil. They are as follows:

From leading edge to maximum wing thickness

$$Y_c/c = f/c (1/X_1^2) [2 X_1 (X/c) - (X/c)^2]$$

Valid for  $0 \leq X/c \leq X_1$

From maximum wing thickness to trailing edge

$$Y_c/c = f/c \{1/(1-X_1)^2\} [(1-2X_1) + 2X_1 (x/c) - (x/c)^2]$$

Valid for  $X_1 \leq x/c \leq 1$

Maximum wing thickness

$$Y_c = 5t (0.2969 \sqrt{x} - 0.126 x - 0.3516 x^2 + 0.2843 x^3 - 0.1015 x^4)$$

Where,  $f$  = maximum camber

$X_1$  = distance from leading edge to maximum wing thickness

C = chord of the airfoil

t = maximum wing thickness

$Y_c$  = vertical distance between mean camber line and chord line.

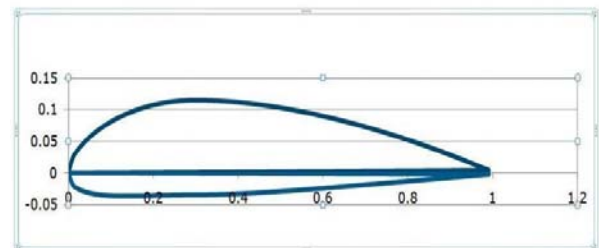


Fig 2. NACA 4315 Airfoil (Designed)

By applying Computer C++ Programming Language the regular surface profile of the NACA 4315 model was made. The thickness and chord length of the model is 15 cm and span is 10 cm respectively. Thus the chord length

based Reynolds number relevant at low flight speeds, which are a concern for the exploration of wing formation mechanism, is estimate to be about  $10^5$ . The chord length of the model was determined to have Reynolds number of the same order. The span length of the model, relative to the chord length is one of the important design parameters. Obviously, it should be made as large as possible so that the weight of the model can be reduced. To ensure the aerodynamic characteristics of an airfoil, it is important that the trailing edge of the model have a sharp edge form. After construction of the wing now it is time to construct the winglet. Three shapes of winglet are used for this experiment. The shapes are rectangular, triangular and half circular. The winglet is attached with the wing at the tip. Now the model is ready for testing.

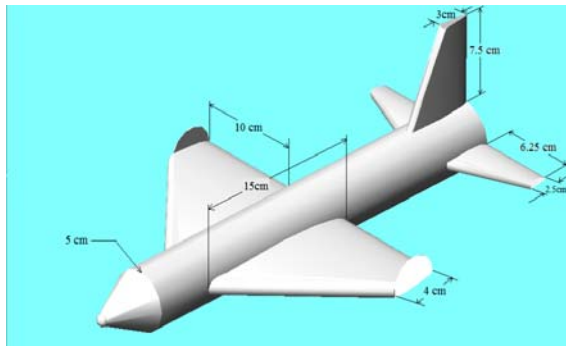


Fig 3. Designed Aircraft model

### 3. EXPERIMENTAL SET-UP AND PROCEDURE

The experiments were conducted using wind tunnel. Figure: 2 shows a schematic of the experimental set up. A small sized model is appropriate to examine the aerodynamic characteristics for the experiments. If we desire to examine the aerodynamic characteristics of a large model, a large scale wind tunnel facility is necessary for testing or the inflatable wing must be drastically scaled down to match the usual wind tunnel size violating the Reynolds number analogy requirements.



Fig 4. Experimental Setup (Actual investigation)

Furthermore, it would be difficult to support the inflatable wing a desirable attitude in these wind tunnel experiments. Since the vertical part of the aerodynamic force produces the lifting force necessary to suspend the load. We are mainly interested in the aerodynamic characteristics of each model. The model was placed in the testing section of the wind tunnel. Then the testing procedure is started of measuring the drag and lift of the constructed model from the wind tunnel scale.

For the complete testing the constructed model, subsonic wind tunnel and pressure measuring instrument were used as required apparatus. At the first step of the experimental procedure the constructed model aircraft with NACA 4315 along with winglets was placed inside the testing section of the wind tunnel. Three shaped winglets were used and those were half circular, triangular and rectangular. The half circular winglets were attached to the wing of the model aircraft at the wing tip. At the vertical position of the winglet which means  $0^\circ$  angle of the winglet the testing section was closed to start the measurement. For different velocities of the wind tunnel the lift and the drag forces were measured from the scale and pressure was also measured. After this the winglet angle was changed to  $5^\circ$  and then the lift and drag forces were measured along with pressure from the relative scales for different velocities. Next the winglets were changed. Then triangular and rectangular shaped winglets were attached one after another to measure the necessary data as the same way of half circular shaped winglets. The velocity of the wind tunnel was controlled by a regulator attached with the wind tunnel.

When the measurement of data had been complete then the calculation process was started. From the measured pressure the stream velocity was calculated by using the mathematical relation. Lift to Drag ratio was calculated by using the measured lift and drag forces.

$$\text{Reynolds number, } R_o = \frac{\rho v l}{\mu}$$

Here,

$\rho$  = Density of free stream or air

$v$  = Velocity of free stream or air

$l$  = Model length

$\mu$  = Dynamic viscosity

To calculate the Reynolds number at first we have to measure the velocity of the free stream of air. To measure the velocity the pressure is measured by a inclined manometer which pressure tube is connected into the wind tunnel.

Now,

$$\text{Velocity of free stream or air, } v = \sqrt{2gh}$$

Here,

$g$  = Acceleration due to gravity

$h$  = Pressure in the air stream

Again,

Pressure in the air stream,  $h = \frac{\Delta p}{\gamma}$

Here,

$\Delta p$  = Difference of pressure

$\gamma$  = Specific weight

#### 4. RESULTS AND DISCUSSION

Wind tunnel measurements using the constructed aircraft model without winglet and with winglet of different configurations were done. The coefficient of lift and the coefficient of drag have been calculated from the experimental results. Also various graphs have been drawn to examine the measured and calculated data nature.

The lift and drag depends on several factors, the most important of which are:

- 1) Airstream velocity
- 2) Plan form area S (ft<sup>2</sup>)
- 3) Profile shape of the airfoil
- 4) Viscosity of the air
- 5) Angle of attack (degrees)
- 6) Angle of winglet (considering the initial position perpendicular with wing)

The first two factors determine the dynamic pressure  $q$  of the airstream. Factors 4, 5, and 6 influence the amount of drag that an airfoil will develop at a certain angle of attack. It is convenient to express the lift and drag forces in terms of non-dimensional co-efficient that are functions of angle of attack. These are called the *co-efficient of lift* ( $C_L$ ) and the *coefficient of drag* ( $C_D$ ).

$$\text{Co-efficient of lift, } C_L = \frac{2F_L}{L^2 \rho v^2}$$

$$\text{Co-efficient of drag, } C_D = \frac{2F_D}{L^2 \rho v^2}$$

Coefficient of lift can be said to be “the ratio between the lift pressure and the dynamic pressure”. It is a measure of the effectiveness of airfoil to produce lift. Values of coefficient of lift have been obtained from experimental data. The importance of angle of attack in determining wings performance cannot be overemphasized. An airfoil has its maximum climb angle at a certain angle of attack, will achieve maximum rate of climb at another angle of attack, and will get maximum range at still another angle of attack. All airfoil i.e. aircraft performance depends on angle of attack. The lift characteristic is also depends upon or affected by thickness and location of maximum thickness, camber and other factors.

Increasing the thickness which results in lower static pressure and more lift. Our designed NACA 4315 models of airfoils have a maximum camber of 4% c, located at the 30%c position. Our designed NACA 4315 airfoils are 15%c thick. So this have much higher value of coefficient of lift and the stall is also higher. The drag

increases with increase in angle of attack to a certain value and then it increases rapidly with further increase in angle of attack. The rapid increase in drag coefficient, which occurs at higher values of angle of attack, is probably due to the increasing region of separated flow over the wing surface, which creates a large pressure drag. From the figure it is observed that the values of the minimum drag coefficients are 0.065, 0.052, 0.050, 0.049, and 0.047 respectively of different configurations for the maximum Reynolds number of  $0.23 \times 10^6$  which occur at zero angle of attack. In particular the measured drag against the angle of attack is minimum for the triangular winglet of configuration 1 and 2 over the values of the range of angle of attack considered under this study.

The measured drag values for the aircraft model with rectangular winglet of configuration 2 are also practically same as triangular winglet compared to the circular winglet. Other details of drag coefficients are given in Table 1. From this investigation it is observed that at the maximum Reynolds number of  $0.23 \times 10^6$  triangular winglet of configuration 1 and 2 (Figure 5) provides the significant decreases in drag ranging from 18% to 26.4%, giving an edge over other configurations. Decisively it can be said that the triangular winglet of configuration 2 (Winglets inclination at 5°) has the better performance giving about 26.4% - 30.9% decreases in drag as compared to other configurations.

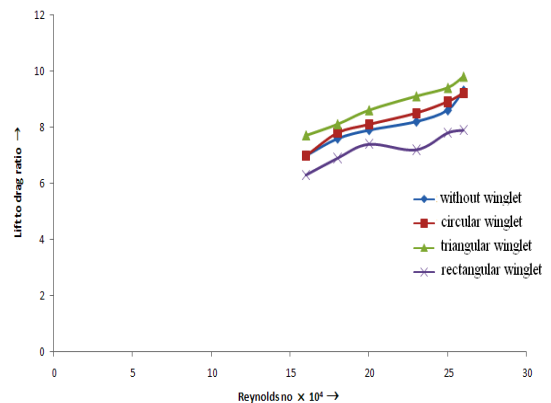


Fig 5. Lift to drag ratio Vs Reynolds no.

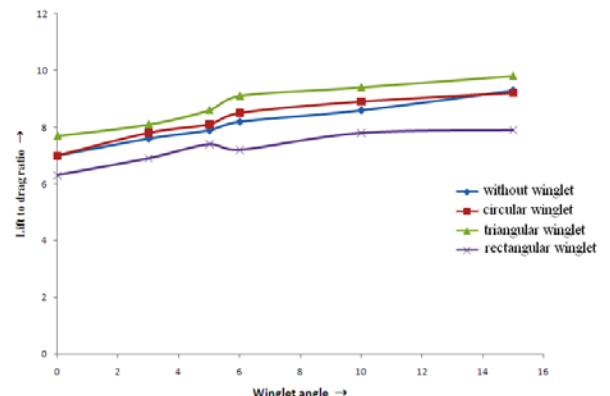


Fig 6. Lift to drag ratio Vs Winglet angle

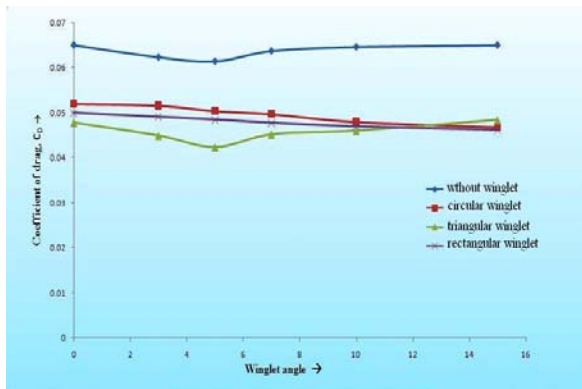


Fig 7. Coefficient of drag vs. winglet angle

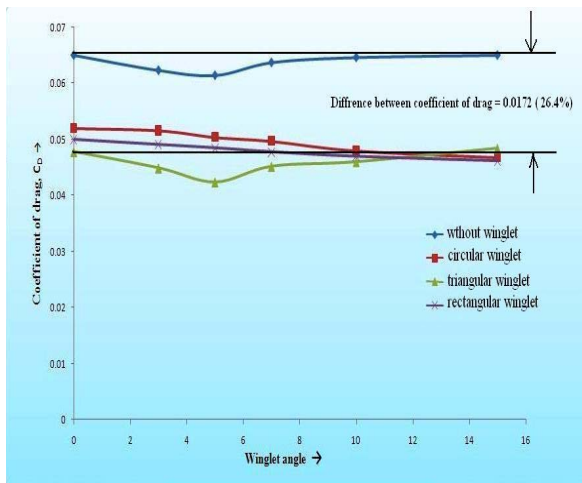


Fig 8. Variation of  $C_D$  with winglet angle

Winglets have the potential to give the following benefits:

- ❖ Reduced climb thrust. A winglet equipped aircraft can typically take a 3% derate over the non-winglet equivalent aircraft. This can extend engine life and reduce maintenance costs.
- ❖ Reduced cruise thrust. Cruise fuel flow is reduced by up to 6% giving savings in fuel costs and increasing range.
- ❖ Improved cruise performance. Winglets can allow aircraft to reach higher levels sooner.
- ❖ Good looks. Winglets bring a modern look and feel to aircraft, and improve customers' perceptions of the airline.

## 5. CONCLUSION

Following are the conclusions drawn from this investigation,

Aerodynamic characteristics for the aircraft model with and without winglet having NACA wing section no. 4315 have been presented.

Triangular winglet at  $5^\circ$  inclination has the better performance giving about 30.9% decreases in drag as compared to other configurations for the maximum Reynolds number considered in the present study.

So we have to suggest the triangular shape of winglet for the maximum lift and minimum drag among the other shapes

## 6. REFERENCES

1. John D. Anderson, J.R, "Introduction to Flight", Third Edition, Mc Graw--Hill International Editions, Aerospace Science Series
2. Dr. P. N. Modi & Dr. S. M Seth, "Hydraulics and Fluid Mechanics Including Machine" (In SI Unit), new edition 2005-2006, Standard Book House
3. Dr. K. R. Arora, Fluid Mechanics, "Hydraulics and Hydraulic Machine" (In SI Unit), Ninth revised and enlarged edition August 2005, Standard Publishers Distributors.
4. William H. Rae, Jr. & Alan pope, "Low Speed Wind Tunnel Testing", Second Edition, A Wiley – Inter science Publication
5. Charles E. Dole, "Flight Theory and Aerodynamics", A Wiley Interscience Publication.
6. Bernard Etkin, "Dynamics of Flight- Stability and Control", Third edition, John Wiley & Sons, INC.
7. Donald T. Ward, "Introduction to Flight Test Engineering", Elsevier Science Publishers.
8. Austyn Mair & David L. Birdstall, "Aircraft Performance", Cambridge University Press, Cambridge.
9. Francis J. Hale, "Introduction to Aircraft Performance, Selection and Desion", John Wiley & Sons Publishers.
10. Richard Eppler, "Airfoil Design and Data."
11. E. L. Houghton and P. W. Carpenter, "Aerodynamics for Engineering Students", Fourth Edition, Edward Arnold Publisher.

## 7. MAILING ADDRESS

Mohammad Mashud  
 Department of Mechanical Engineering  
 Khulna University of Engineering & Technology,  
 Khulna  
 E-mail: mdmashud@yahoo.com

## NUMERICAL SIMULATION OF A CONFINED LAMINAR DIFFUSION FLAME WITH VARIABLE PROPERTY FORMULATION

B. K. MANDAL<sup>1</sup>, A.K. CHOWDHURI<sup>1</sup> and A. J. BHOWAL<sup>2</sup>

<sup>1</sup>Bengal Engineering and Science University, Howrah, India

<sup>2</sup>Heritage Institute of Technology, Kolkata, India

### ABSTRACT

A numerical model is used for simulation of a confined axisymmetric laminar jet diffusion flame under normal gravity and pressure conditions to predict the velocity, temperature and species distributions. An explicit finite difference technique has been adopted for the numerical simulation of reacting flow with finite rate chemistry and variable thermodynamic and transport properties. The predictions match well with the experimental results available in the literature. A recirculation of ambient air is observed to extend from the exit plane into the domain adjacent to the wall. Radial velocity is never positive (away from the axis) in the solution domain. High temperature and high CO<sub>2</sub> concentration zone are confined to a small radial distance.

**Keywords:** Diffusion flame, Recirculation, Temperature distribution.

### 1. INTRODUCTION

The numerical simulation is a useful tool because it can easily employ various conditions by simply changing the parameters. Confined diffusion flames are commonly found in practical combustion systems, such as the power-plant combustor, gas turbine combustor, and jet engine afterburner. In these systems, fuel is injected into a duct with a co-flowing or cross-flowing air stream. The diffusion flame is found at the surface where the fuel jet and oxygen meet, react, and consume each other. The overall combustion in such situations is governed by a complex interaction of chemical reactions, transport and gas dynamic processes that are strongly dependent on physical boundary conditions and the type of the chemical system. The ability to predict the coupled effects of various complex transport processes and chemical kinetics in these systems is critical in obtaining velocity, temperature and different species concentration distributions. Computer simulation of the combustion process enables the prediction of optimal operating conditions for achieving high combustion efficiency and low emissions in the exhaust, and aids in the development of optimal burner designs.

Experimental and numerical investigations of steady confined laminar diffusion flame were carried out by Mitchell *et al.* [1] to study the temperature, velocity and concentration profiles of stable species. Smooke *et al.* [2] obtained the numerical solution of the two-dimensional axi-symmetric laminar co-flowing jet diffusion flame of methane and air both in the confined and the unconfined

environment. A numerical simulation of an axi-symmetric confined diffusion flame formed between a H<sub>2</sub>-N<sub>2</sub> jet and co-flowing air, each at a velocity of 30 cm/s, were presented by Ellzey *et al.* [3]. Li *et al.* [4] investigated a highly over-ventilated laminar co-flow diffusion flame in axi-symmetric geometry considering unity Lewis number and the effects of buoyancy. Katta *et al.* [5] developed a time dependent, axi-symmetric H<sub>2</sub>-air diffusion flame model to study the effects of Lewis number and finite rate chemistry on the steady state and dynamic flame structures.

The simulation described here is pertinent to laboratory scale studies of diffusion flames in burners commonly referred to as Wolkard burners, A numerical model was constructed for the purpose of understanding the interplay of diffusion, convection and chemical kinematics. In the present formulation, finite rate chemistry as well as the non-unity Lewis number and property variation have been considered.

The combustion system considered is the laminar diffusion flame in a confined physical environment with co-flowing fuel and air (oxidizer) streams. Two concentric vertical tubes comprise the burner. The fuel is admitted as a central jet through the inner tube and air as a co-flowing annular jet through the outer tube. The inner fuel tube diameter is 12.7 mm and the outer tube diameter is 50.4 mm. The thickness of the inner tube wall is neglected here. The dimensions are in conformity with the earlier experimental work of Mitchell *et al.* [1] and the numerical work of Smooke *et al.* [2]. The two



streams diffuse into each other at the outlet of the inner tube in order to produce a flammable mixture of fuel and air. A cylindrical shield of diameter 50.4 mm defines an impervious outer boundary (wall) of the axisymmetric system. The length of the computational domain in the axial direction is taken to be 30 cm.

## 2. NUMERICAL MODEL

The combustion process is simulated with a detailed numerical model, solving the governing equations for reacting flow with appropriate boundary conditions. The flow is assumed to be laminar and axi-symmetric produced by a jet of fuel emerging from a circular nozzle, which burns in a co-flowing stream of air in a confined environment. The reaction between the fuel and oxidizer proceeds through two-step irreversible chemical reactions. The flow is vertical through the reaction space and the gravity effect is included in the momentum equation. A variable property formulation has been made for the transport and thermodynamic properties. The radiation heat exchange within the gas phase is neglected because the soot loading with methane fuel is low. The Soret effect due to thermal diffusion is also neglected. Considering the axi-symmetric geometry, the numerical simulations have been performed on one side of the axis.

### 2.1 Governing Equations

The description of a problem in combustion can be given by the conservation equations of mass, momentum, species concentrations and energy. The gas phase conservation equations in cylindrical co-ordinate system have been used to model the reacting flow. The conservation equations with transient terms for mass, radial momentum, axial momentum, species concentrations and energy are presented in Eq.(1) to Eq.(5) respectively.

$$\frac{\partial \rho}{\partial t} + \frac{1}{r} \frac{\partial}{\partial r} (r \rho v_r) + \frac{\partial}{\partial z} (\rho v_z) = 0 \quad (1)$$

$$\begin{aligned} \frac{\partial}{\partial t} (\rho v_r) + \frac{1}{r} \frac{\partial}{\partial r} (r \rho v_r^2) + \frac{\partial}{\partial z} (\rho v_r v_z) = -\frac{\partial p}{\partial r} + \\ \frac{2}{r} \frac{\partial}{\partial r} \left( r \mu \frac{\partial v_r}{\partial r} \right) - \frac{2}{r} \mu \frac{v_r}{r^2} + \frac{\partial}{\partial z} \left\{ \mu \left( \frac{\partial v_z}{\partial r} + \frac{\partial v_r}{\partial z} \right) \right\} \\ - \frac{2}{3} \frac{\partial}{\partial r} \left( \mu \left( \frac{\partial v_r}{\partial r} + \frac{v_r}{r} + \frac{\partial v_z}{\partial z} \right) \right) \end{aligned} \quad (2)$$

$$\begin{aligned} \frac{\partial}{\partial t} (\rho v_z) + \frac{1}{r} \frac{\partial}{\partial r} (r \rho v_r v_z) + \frac{\partial}{\partial z} (\rho v_z^2) = -\frac{\partial p}{\partial z} + \\ \frac{1}{r} \frac{\partial}{\partial r} \left\{ r \mu \left( \frac{\partial v_z}{\partial r} + \frac{\partial v_r}{\partial z} \right) \right\} + 2 \frac{\partial}{\partial z} \left( \mu \frac{\partial v_z}{\partial z} \right) \\ - \frac{2}{3} \frac{\partial}{\partial z} \left\{ \mu \left( \frac{\partial v_r}{\partial r} + \frac{v_r}{r} + \frac{\partial v_z}{\partial z} \right) \right\} + \rho g \end{aligned} \quad (3)$$

$$\begin{aligned} \frac{\partial}{\partial t} (\rho C_j) + \frac{1}{r} \frac{\partial}{\partial r} (r \rho v_r C_j) + \frac{\partial}{\partial z} (\rho v_z C_j) \\ = \frac{1}{r} \frac{\partial}{\partial r} \left( r \rho D_{jm} \frac{\partial C_j}{\partial r} \right) + \frac{\partial}{\partial z} \left( \rho D_{jm} \frac{\partial C_j}{\partial z} \right) + \dot{S}_{cj} \quad (4) \\ \frac{\partial}{\partial t} (\rho h) + \frac{1}{r} \frac{\partial}{\partial r} (r \rho v_r h) + \frac{\partial}{\partial z} (\rho v_z h) = \frac{1}{r} \frac{\partial}{\partial r} \left( r \frac{\lambda}{c_p} \frac{\partial h}{\partial r} \right) \\ + \frac{\partial}{\partial z} \left( \frac{\lambda}{c_p} \frac{\partial h}{\partial z} \right) + \frac{1}{r} \frac{\partial}{\partial r} \left[ r \frac{\lambda}{c_p} \sum_{j=1}^n h_j (Le_j^{-1} - 1) \frac{\partial C_j}{\partial r} \right] \\ + \frac{\partial}{\partial z} \left[ \frac{\lambda}{c_p} \sum_{j=1}^n h_j (Le_j^{-1} - 1) \frac{\partial C_j}{\partial z} \right] \end{aligned} \quad (5)$$

where,  $C_j$  is the mass fraction of the respective species and  $D_{jm}$  is the diffusion coefficient of the species in a binary mixture of that species and nitrogen and  $Le_j$  is the local Lewis number defined as

$$Le_j = \frac{\lambda}{c_p} \frac{1}{\rho D_{jm}} \quad (6)$$

The source term,  $\dot{S}_{cj}$  appearing in Eq.(4) is the rate of production or destruction of the species  $j$  per unit volume due to chemical reaction. The temperature dependence of viscosity ( $\mu$ ), thermal conductivity ( $\lambda$ ), mass diffusivity ( $D_{jm}$ ) and specific heat ( $c_p$ ) has been taken into account using suitable correlations available in the literature. The axial and radial directions are denoted by  $z$  and  $r$  respectively. The conservation equation for chemical species is solved for five gaseous species, viz. CH<sub>4</sub>, O<sub>2</sub>, CO<sub>2</sub>, CO and H<sub>2</sub>O. The concentration for N<sub>2</sub> is obtained by difference.

### 2.2 Boundary Conditions

Boundary conditions at the inlet are given separately for the fuel stream at the central jet and the air stream at the annular co-flow. The streams are considered to enter the computational domain as plug flow, with velocities calculated from their respective mass flow rates. The temperatures of fuel and air are specified. In conformation with the conditions used by Mitchell *et al.* [1] and Smooke *et al.* [2], the fuel flow rate is taken as  $3.71 \times 10^{-6}$  kg/s and the air flow rate is taken as  $2.214 \times 10^{-4}$  kg/s. Considering the length of the computational domain to be 0.3 m, the fully developed boundary conditions for the variables are considered at the outlet. In case of reverse flow at the outlet plane, which occurs in the case of buoyant flame, the stream coming in from the outside is considered to be ambient air. Axi-symmetric condition is considered at the central axis, while at the wall a no-slip, adiabatic and impermeable boundary condition is adopted.

### 2.3 Solution Methodology

The conservation equations of mass, momentum, energy and species concentrations are solved simultaneously, with their appropriate boundary conditions, by an explicit finite difference computing technique. The solution yields velocity, temperature, and

species concentration. The numerical scheme adopted for solving the reacting flow problem is based on a straight-forward, yet powerful algorithm called SOLA (Solution Algorithm) developed by Hirt and Cook [6]. The algorithm is based on primitive variables and the variables are defined following a staggered grid arrangement. The solution is explicitly advanced in time till a steady state convergence is achieved. A variable size adaptive grid system is considered using hyperbolic distribution to capture the sharp gradients of the field variables. After extensive grid independence test, an optimal numerical mesh with  $85 \times 41$  grid nodes is finally adopted. The diffusion terms are discretized by a central differencing scheme, whereas the advection terms are discretized by a hybrid differencing schemes as described by Patankar [7]. The fluid properties like density, specific heat and viscosity are calculated at the cell faces by linear interpolation between the corresponding property values at the adjacent cell centres. The source terms are considered to be constant throughout the volume of each cell. The ignition of the fuel-air mixture in the combustion chamber is simulated by raising the temperature of the mixture within a few cells, to 1000 K, near the fuel-air interface (slightly above the burner tip) and maintaining till the local temperature of the mixture is raised beyond the ignition temperature due to reaction.

### 3. RESULTS AND DISCUSSION

The predictions from the present simulation are compared with the experimental results of Mitchell *et al.* [1] for the same operating conditions. Radial distributions of temperature and major product species ( $\text{CO}_2$  and  $\text{H}_2\text{O}$ ) concentrations at a height of 12 mm above the burner rim are shown in Fig. 1(a) and Fig. 1(b) respectively. Clearly the figures show a good agreement between the predicted values and experimental values of Mitchell *et al.* [1].

Combustion in diffusion mode is simulated with air of inlet temperature 300 K and also methane (fuel) of inlet temperature 300 K. The shape and size of the steady state flame in the computational zone is shown in Fig. 2 with the help of flame front. The investigation shows that the steady state flame has an over-ventilated shape.

#### 3.1 Velocity Distributions

The velocity field has been described by showing the axial velocity and radial velocity distributions at six different axial heights,  $z$ , above the burner. The axial heights, considered here are 2 cm, 6 cm, 10 cm, 15 cm, 20 cm and 30 cm. Figures 3 and 4 show variations of axial velocity and radial velocity with radial distance from the centreline at the above mentioned axial heights. Figure 3 clearly depicts that the axial velocity around the central region is high and also increases with height. The maximum centreline axial velocity at the exit plane is as high as 4.0 m/s. The axial velocity away from the centreline decreases at all heights and becomes very low beyond a radial distance of 0.015 m. It is also interesting to note that the axial velocity becomes negative above an axial position of 10 cm upto the exit plane (30 cm). This indicates that ambient air from the exit plane is entering

into the computational domain near the periphery. This penetrates upto a depth of 20 cm from the exit plane and a large recirculation from outside is noted.

Figure 4 shows that the radial velocity is always negative (i.e. towards the centre) except at the exit plane. This also confirms the presence of the recirculation from the exit plane near wall. There is also entrainment of air from the air side to the reaction zone. The maximum negative value of radial velocity at a radial position of around 0.0065 m indicates that the entrainment is more near the fuel-air interface. It is also clear that the entrainment is maximum at a lower axial position of 2 cm. The recirculation zone acts a barrier for the upward motion of the gas mixture towards the exit plane. Also the high temperatures in the reaction zone within the flame sets strong buoyant force near the axis. All these facts together explain the presence of high axial velocity near the axis. Also as the air is entering from the exit plane near the wall, the velocity in the central zone has to be high to satisfy the continuity equation.

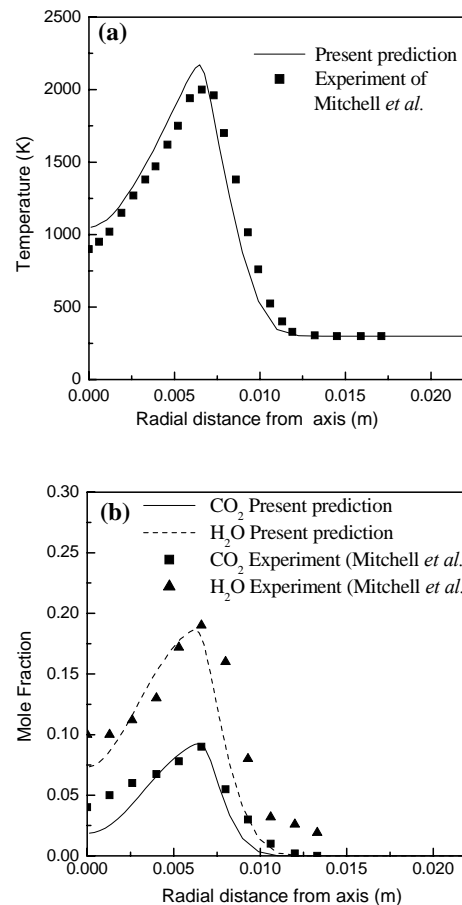


Fig 1. Comparison of the radial (a) temperature (b) species ( $\text{CO}_2$  and  $\text{H}_2\text{O}$ ) distributions at 12 mm axial height above the burner



### 3.2 Temperature Distributions

The temperature distributions for the diffusion flame have been described in Fig. 5 by plotting temperature as a function of radial distance from the centreline for different axial positions mentioned earlier. The temperature distributions as shown in figure 5 indicate that high temperature zone is limited only upto a certain

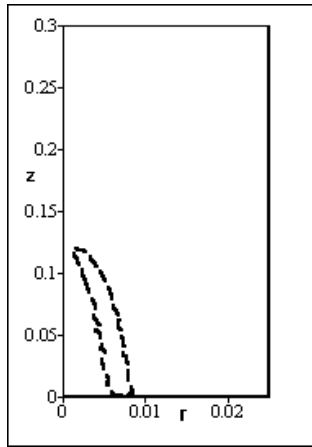


Fig.2. Shape and size of the flame

radial position (approx. 0.007 m) for all axial positions. Beyond that the temperature remains very low (almost 300 K). This is due to the recirculation of ambient air from the exit plane. The maximum temperature observed in this case is about 2250 K at an axial position of 10 cm. Above this the temperature becomes lower. This indicates that the flame height is in between 10 cm and 15 cm. Also, from  $z = 2$  to 10 cm, the radial position of the maximum temperature shifts towards the axis confirming the overventilated flame shape under the present operating condition. The temperature values in the high temperature regions are overpredicted by 50-100 K. This may be attributed to the fact that the present model has not considered the radiative exchange.

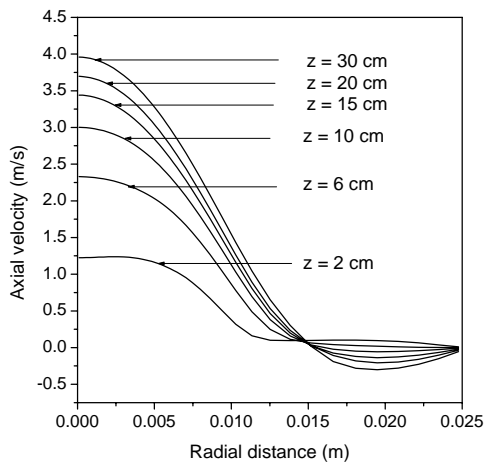


Fig. 3. Radial distributions of axial velocity at different axial heights,  $z$ .

### 3.3 Species Concentrations

The radial distributions of  $\text{CO}_2$  (one of the major product species) have been shown for different axial positions in Fig. 4. The peak values of  $\text{CO}_2$  concentration decrease after an axial position of 10 cm indicating the reaction zone to be limited to around 10 cm in the axial direction. The trend of  $\text{CO}_2$  distributions has a similarity with the temperature distributions.  $\text{CO}_2$  is present only in the high temperature zone, i.e., within the flame and above the flame. The concentration decreases above the flame due to the entrainment of ambient air entering through the exit plane near the wall.

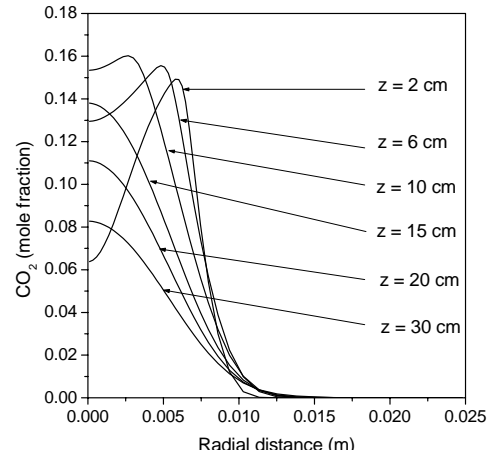


Fig 4. Radial distributions of  $\text{CO}_2$  concentrations at different axial heights,  $z$ .

### 4. CONCLUSION

Numerical computations of axisymmetric laminar diffusion flame for methane in air have been carried out to examine the nature of flame shape, distributions of velocity, temperature, and different species concentrations in a confined geometry. Initial conditions for diffusion flame for methane and air correspond to 300 K and 0.1 MPa. Different conservation equations for mass, momentum, energy and species concentration for reacting flows are solved in an axisymmetric cylindrical co-ordinate system. A two-steps chemical reaction of methane and air (oxidizer) has been considered to capture some of the features of chemical reaction mechanisms. The CFD model based on SOLA algorithm predicts velocity, temperature and species distributions throughout the computational zone of the cylindrical burner having the dimensions of 30 cm (axial length), 12.7 mm (inner diameter) and 50.4 mm (outer diameter). The predictions from the model match well with the experimental results available in the literature. The research results show that the highest calculated value of temperature near the flame tip is of the order of 2250 K, which is slightly overpredicted. The velocity distributions show that the fluid elements near the axis have been accelerated due to strong buoyant force. There is a recirculation of atmospheric air from the exit plane near the wall. As a result, the temperature near the wall is almost atmospheric temperature of 300 K. The higher temperature zone is confined only around the axis only.

The CO<sub>2</sub> concentration distribution characteristics are almost same as that of temperature distributions. It can be concluded that the present model of two-steps reaction mechanism is fairly useful for determining the combustion characteristics of laminar diffusion flame.

## 5. REFERENCES

1. Mitchell, R. E., Sarofim, A. F. and Clomburg, L. A., 1980, "Experimental and Numerical Investigation of Confined Laminar Diffusion Flames", *Combustion and Flame*, 37: 227 -244.
2. Smooke, M. D., Mitchell, R. E. and Keys, D. E., 1989, "Numerical Solution of Two-Dimensional Axisymmetric Laminar Diffusion Flames", *Combustion Science and Technology*, 67: 85 - 122.
3. Ellzey, J. L., Laskey, K. J. and Oran, E. S., 1991, "A Study of Confined Diffusion Flames", *Combustion and Flame*, 84: 249-264.
4. Li, S. C., Gordon, A. S. and Williams, F. A., 1995, "A Simplified Method for the Computation of Burke-Schumann Flames in Infinite Atmospheres", *Combustion Science and Technology*, 104: 75 – 91.
5. Katta, V. R., Goss, L. P. and Roquemore, W.M., 1994, "Effect of Nonunity Lewis Number and Finite Rate Chemistry on the Dynamics of Hydrogen- Air Jet Diffusion Flame", *Combustion and Flame*, 96: 60 - 74.
6. Hirt, C. W. and Cook, J. L. 1972, "Calculating Three-Dimensional Flows Around Structures and over Rough Terrain", *Journal of Computational Physics*, 10 : 324 – 338.
7. Patankar, S. V., 1980, "Convection and Diffusion", *Numerical Heat Transfer and Fluid Flow*. Hemispherical Publishing Corporation.

## 6. NOMENCLATURE

Symbol	Meaning	Unit
$C_j$	Concentration of jth species	--
$c_p$	Specific heat	J/kgK
$D$	Mass diffusivity	m <sup>2</sup> /s
$g$	Acceleration due to gravity	m/s <sup>2</sup>
$h$	Enthalpy	J/kg
$Le$	Lewis number	--
$p$	Pressure	Pa
$r$	Radial distance	m
$T$	Temperature	K
$t$	Time	s
$v$	Velocity	m/s
$z$	Axial distance	m
$\mu$	Viscosity	kg/ms
$\rho$	Density	kg/m <sup>3</sup>
$\lambda$	Thermal conductivity	W/mK

## 7. MAILING ADDRESS

Prof. Bijan Kumar Mandal  
 Department of Mechanical Engineering  
 Bengal Engineering and Science University, Shibpur  
 Howrah-711103, INDIA.  
 Phone : 91-033-26887619  
 91-033- 26684562-64 (Extn. 279)  
 FAX : 91-033-26684561  
 E-mail : bijan@mech.becs.ac.in  
 bkm375@yahoo.co.in

## NUMERICAL SIMULATIONS OF SUPERSONIC MICROJETS

A. M. M. Ashraful<sup>1</sup>, A. M. Mahabubul<sup>2</sup>, Matsuo Shigeru<sup>3</sup>, Setoguchi Toshiaki<sup>4</sup> and K. Heuy Dong<sup>5</sup>

<sup>1</sup>Graduate School of Science & Engineering, Saga University, Saga, Japan.

<sup>2</sup>Department of Mechanical Engineering, Chittagong University of Engineering & Technology, Chittagong, Bangladesh.

<sup>3</sup>Department of Mechanical Engineering, Saga University, Saga, Japan.

<sup>4</sup>Institute of Ocean Energy, Saga University, Saga, Japan.

<sup>5</sup>School of Mechanical Engineering, Andong National University, Andong, Korea

### ABSTRACT

Supersonic microjets acquire considerable research interest from a fundamental fluid dynamics perspective in part because the combination of highly compressible flow at low-to-moderate Reynolds number is not very common, and in part due to the complex nature of the flow itself. In addition, microjets have a great variety engineering applications such as micro-propulsion, MEMS (Micro-Electro Mechanical Systems) components, microjet actuators and fine particle deposition and removal. Numerical simulations have been carried out at moderate nozzle pressure ratios and for different nozzle exit diameters to investigate and to understand in-depth of aerodynamic characteristics of supersonic microjets.

**Keywords:** Compressible, Microjets, Supersonic, Jet structure, Numerical simulation

### 1. INTRODUCTION

Recently, miniaturization and micromation have been experienced in manufacturing and as well as in Aerospace industries. Developments in micro electrical mechanical systems (MEMS) have guided the construction of many small-sized devices. Aerospace industry has benefited from these devices particularly in development of new micro-size spacecraft and satellites. However, the studies involving fluid flows at microscales have brought new challenges especially micronozzles, microjets, etc.

Microjets acquire considerable research interest due to their potential use in various engineering applications such as micro-propulsion, MEMS components, and fine particle deposition and removal. Supersonic microjets provide several advantages over subsonic jets in a number of applications. Microjets are also used as actuators to control the ground effect created by large supersonic impinging jets, typically occur in STOVL (Short Take-off and Vertical Landing) aircraft [1] during hover. More recently, micro-jet actuators have also been used for controlling the flow separations [2], cavity flows, jet noise, and for suppressing turbulence [3] in jet flows. In addition, the flowfield of microjets is also of interest from a fundamental fluid dynamics perspective, in part because the combination of highly compressible flow at low-to-moderate Reynolds number is not very common, and in part due to the complex nature of the flow itself.

To-date most studies involving fluid flows at microscales have mainly focused on internal flows in

nozzles and micro-channels. Meinhart et al [4] describe a MicroPIV investigation of flow through an inkjet printer. A detailed computational and experimental study examining the flowfield inside silicon-etched converging-diverging (c-d) micronozzles with throat heights ranging from 10-50mm was carried out by Breuer and Bayt [5]. The study underlined the behavior and influence of the nozzle boundary layer on the thrust performance of these micronozzles. No measurements of the external flow were made in their work, the presence of supersonic flow was estimated via mass flow and thrust measurements. Bayt [6] has been conducted a comprehensive analysis of MEMS based Microthruster system. Scroggs and Settles [7] fabricated micronozzles by heating and stretching glass capillaries. Using this method, they fabricated converging-diverging nozzles and obtained schlieren images and pitot pressure surveys along the centerline for supersonic jets issuing from the c-d nozzles, ranging in size from 600  $\mu\text{m}$  to 1,200 $\mu\text{m}$ . Smedley et al. [8] discuss an application of supersonic microjets for surface entrainment of particles for shock induced cleaning. Phalnikar et al. [9] described a micro-schlieren system with a large magnification to visualize the flowfields qualitatively. More recently, Vela'squez-Aguilar et al. [10] applied the dual-hologram techniques to measure the same phase object by reference beam and shear techniques using only three Mach-Zehnder holograms: one comparison hologram and two identical signal ones. In most recent, Phalnikar et al. [11] conducted experiments on free and impinging

supersonic microjets using micro-schlieren system and through pitot pressure measurements. Since, the numerical simulation is an extremely important and most widely used tool to analyze and understand the in-depth of fluid flow behaviors. Moreover, till date, no considerable numerical work has been done to investigate the aerodynamic behavior of supersonic microjets. Therefore, it requires performing numerical investigation the aerodynamic characteristics of supersonic microjets.

The present study pertains with numerical simulations of supersonic microjets at moderate nozzle pressure ratios. Especially, we focused on the effect of nozzle exit diameter on the aerodynamic characteristics of microjets.

## 2. NUMERICAL APPROACHES

The two-dimensional viscous flow solver, developed at our laboratory, is used for these computations. It is based on the compressible Reynolds and Favre-averaged Navier-Stokes equations, and modified Goldberg's  $k$ - $R$  turbulence model [12]-[14] is used for closure. The governing equations are non-dimensionalized with reference values at the inlet conditions upstream of the nozzle written in an axisymmetric coordinate system. The 3rd order TVD (Total Variation Diminishing) finite difference scheme with MUSCL approach [15] is used to discretize the spatial derivatives, a second order-central difference scheme for the viscous terms, and a second-order fractional step is employed for time integration.

## 3. COMPUTATIONAL CONDITIONS

Axisymmetric supersonic microjets flow driven by the sonic nozzle [16] with exit diameters of  $\phi D_e = 400 \mu\text{m}$ ,  $200 \mu\text{m}$ , and  $100 \mu\text{m}$  (characteristic length) are considered in the present computation, as shown in Fig.1. The dry air as working gas is issued from that sonic nozzle. The structured clustered grids are used for these computations to obtain reasonable solutions in a flow with large pressure and velocity gradient. Several tests are conducted to select a suitable grid for obtaining grid-independent solutions. The resulting number of grids applied is  $50 \times 60$  in the nozzle region and  $200 \times 111$  in the jet plume region.

In the present study, three nozzle pressure ratios, the ratio of the reservoir pressure  $p_0$  (atmospheric pressure) to back pressure  $p_b$  ( $= p_0/p_b$ ), used are 4.57, 5.23 and 6.2, respectively. Total temperature  $T_0$  and total pressure  $p_0$  in the reservoir are 298.15 K and 101.3 kPa, respectively.

At the inflow boundary upstream of the nozzle, all variables are fixed at the initial values and all variables are extrapolated at the outflow boundary downstream of nozzle. The non-slip wall condition is used on the solid surface. The axisymmetric condition is used at the boundary of the nozzle centre line. Iso-pressure and no heat transfer are constrained on the solid wall.

## 4. RESULTS AND DISCUSSION

### 4.1 Comparison with Experimental Results

The comparisons of predicted iso-density contour with schlieren photograph obtained by experiment for

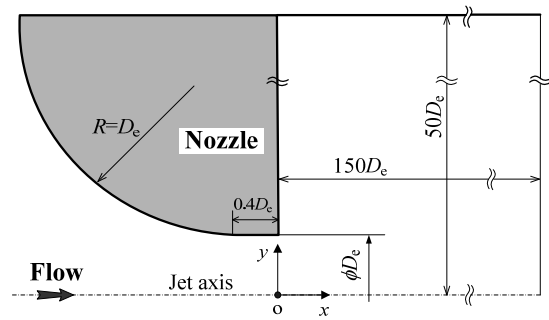


Fig 1. Computational domain

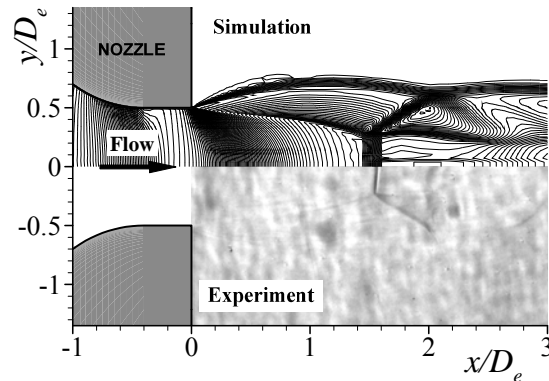


Fig 2. Comparison of the present computation with experiment ( $p_0/p_b=6.2$ )

$p_0/p_b=6.2$ , is shown in Fig. 2. The sonic nozzle [16] with exit diameters of  $\phi D_e = 12.7\text{mm}$  are used in the computation and experiment. The jet is underexpanded at the nozzle exit and barrel shocks are formed due to the differences in pressure between the underexpanded gas and the ambient gas. Therefore, these shocks reflect from the jet axis. Consequently the Mach disk is formed near the jet axis. At the intersection of the Mach disk with the barrel shock, a triple-point is formed. In the downstream of the triple-point the slip line is observed. The predicted iso-density contour is nearly same as the experimentally visualized result. Furthermore, the predicted Mach disk location and diameter are  $L_m/D_e=1.5613$  and  $D_m/D_e=0.5394$ , respectively, while the experimental values are 1.5646 and 0.5264, respectively. Here, location of Mach disk is measured from the nozzle exit, and both the location and diameter of the Mach disk are normalized by nozzle exit diameter. Thus, the present computational works predict well the flow structures of the highly underexpanded supersonic jets.

### 4.2 Structure of Supersonic Microjets

Computer schlieren images of the supersonic underexpanded jets from the nozzle with  $100 \mu\text{m}$  of exit diameter at pressure ratios of 4.57, 5.23 and 6.2 are shown in Fig. 3(a-c). Similarly, Figs. 4(a-c) and 5 (a-c) show the flowfields for the  $200\mu\text{m}$  and  $400 \mu\text{m}$ , respectively. In these figures, the jet flowfields evolve from weak underexpansion to strong underexpansion.

An increase in the nozzle pressure ratio makes the streamwise extent of the shock cells that roughly indicated increased length of the ‘supersonic core’. This trend has also been depicted for larger jets operating at higher Reynolds number [17] as well as for supersonic microjets [7], [11].

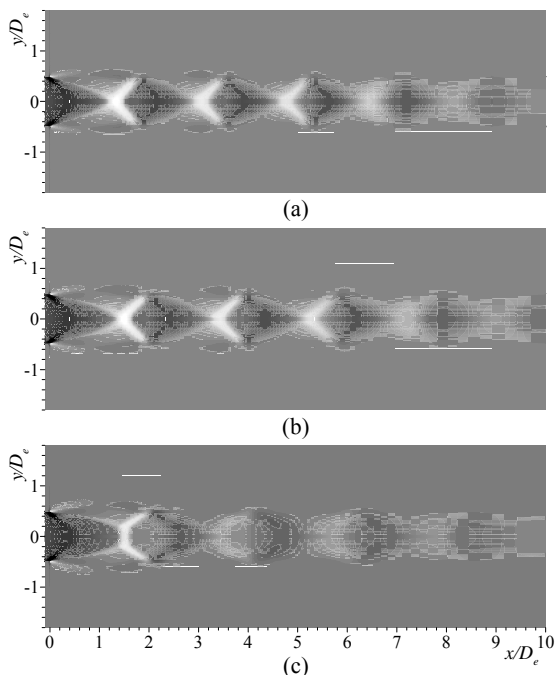


Fig 3. Numerical schlieren images of 100  $\mu\text{m}$  microjets. (a)  $p_0/p_b=4.57$ , (b)  $p_0/p_b=5.23$ , (c)  $p_0/p_b=6.2$

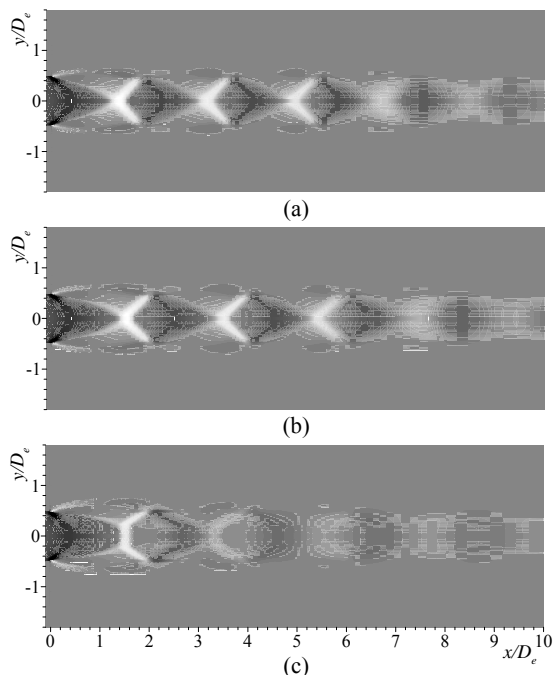


Fig 4. Numerical schlieren images of 200  $\mu\text{m}$  microjets. (a)  $p_0/p_b=4.57$ , (b)  $p_0/p_b=5.23$ , (c)  $p_0/p_b=6.2$

The jet is in moderately underexpanded condition, at lower nozzle pressure ratio  $p_0/p_b$ , the oblique shocks almost crosses on the jet axis. However, as the jet underexpansion ratio increases, central Mach disk appears near the jet axis. The presence of such Mach disks is clearly visible in Figs. 3(c), 4(c) and 5(b, c). At triple-point the oblique shock, the Mach disk, and the rear shock are confluences and leads to a characteristic lambda ( $\lambda$ ) shock structure. The velocity difference between the fluid streams that pass above and below this triple-point results in a shear layer or slip line. These slip lines emanating from the triple-point can be seen in Figs. 3(c), 4(c) and 5(b, c). Similar underexpanded flow features in supersonic microjets of 600  $\mu\text{m}$  and 1,200  $\mu\text{m}$  in diameter has been observed by Scroggs and Settles [7], [11]. These features are also similar to larger jets operating at much higher Reynolds numbers [17].

### 4.3 Properties of Underexpanded Microjets

#### 4.3.1 Surveys of Jet Centerline Pressure

The static pressure distributions downstream of the nozzle exit are strongly dependent on the nozzle exit diameter i.e. on jet diameter. This fact can be confirmed from the numerically predicted static pressure distributions along jet centerline at a nozzle pressure ratio of 5.23 in Fig. 6. The location of the sharp jump in the static pressure distribution is slightly varied with the jet diameter.

The centerline static pressure distributions for the 200  $\mu\text{m}$  and 400  $\mu\text{m}$  jets, are presented in Figs. 7(a) and (b), respectively. The pressures under each operating condition ( $p_0/p_b$ ) exhibit unique characteristics. From Fig. 7(a), the variation in pressure shows the characteristic quasi-periodic structure, due to the presence of shock

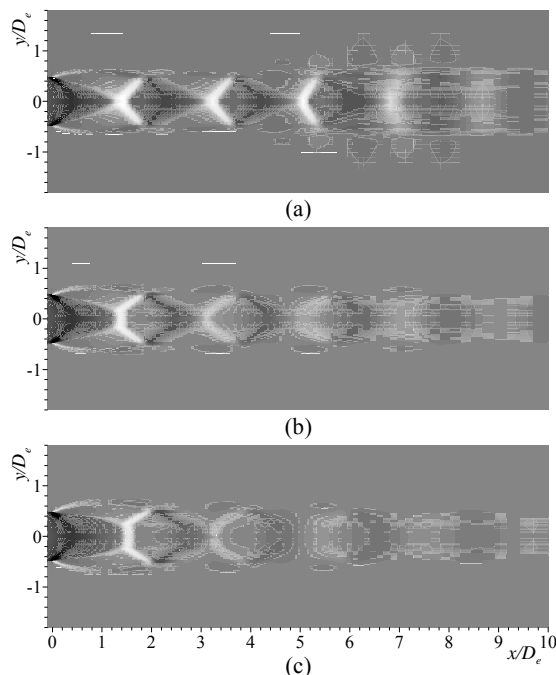


Fig 5. Numerical schlieren images of 400  $\mu\text{m}$  microjets. (a)  $p_0/p_b=4.57$ , (b)  $p_0/p_b=5.23$ , (c)  $p_0/p_b=6.2$

cells in the jet flow fields. Moreover, as the nozzle pressure ratio  $p_0/p_b$  is increased, the flow field is seen to stretch, where the shock cell spacing increases, leading to an increase in the length over which the shocks are present. At low  $p_0/p_b$ , the oblique shocks cross in a normal fashion, which changes to irregular crossing as the  $p_0/p_b$  is increased.

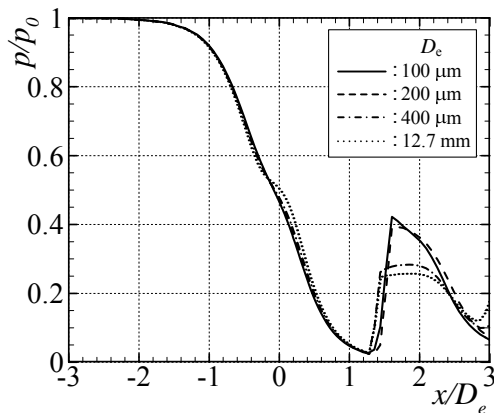
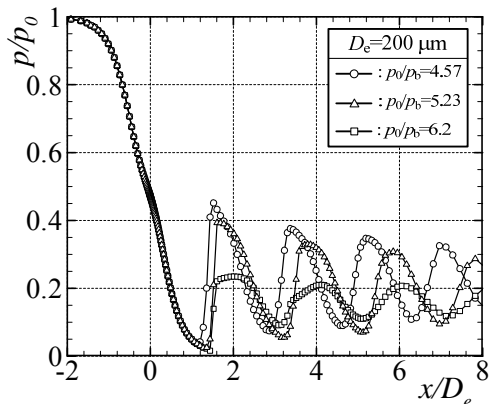
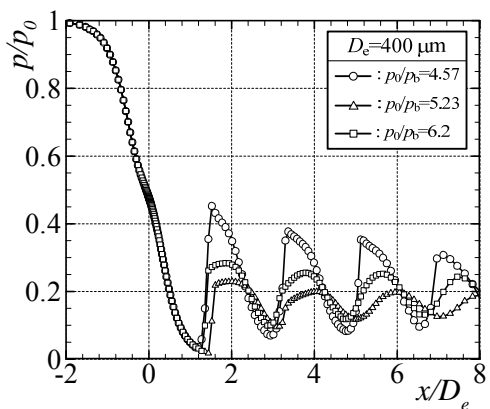


Fig 6. Static pressure distributions along jet axis ( $p_0/p_b=5.23$ )



(a) 200  $\mu\text{m}$  jets



(b) 400  $\mu\text{m}$  jets

Fig 7. Effect of nozzle pressure ratio on the static pressure distributions along jet axis

For 400  $\mu\text{m}$  jet, the centerline pressure distributions displays characteristics very similar to 200  $\mu\text{m}$  jet, as shown in Fig. 7(b). Furthermore, from Figs. 7(a) and (b), when the highly underexpanded condition is reached ( $p_0/p_b=6.2$ ), a Mach disk is first visually observed at the end of the first shock cell. At downstream of the first shock cell, the flow become subsonic, leading to a sudden drop in the pressure. The formation of Mach disk can also be clearly seen from the computer schlieren, in Figs. 3, 4 and 5.

### 4.3.2 Properties of Jet Structure

The configuration of jet boundary and barrel shock for different jet diameters at a nozzle pressure ratio of  $p_0/p_b=5.23$  is shown in Fig. 8. The locations of jet boundary and barrel shock were defined with the greatest value of density gradient ( $d\rho/dy$ ) on an arbitrary cross section normal to  $x$ -axis. For a given nozzle pressure ratio, the jet diameter exhibits no significance influence on the configuration of jet boundary. However, the present data shows a trend of outward expansion of barrel shock with the increase in jet diameter.

Figure 9 shows the configuration of jet boundary and barrel shock for 400  $\mu\text{m}$  jet at nozzle pressure ratio of  $p_0/p_b=4.57, 5.23$  and  $6.2$ . From this figure, it is found that

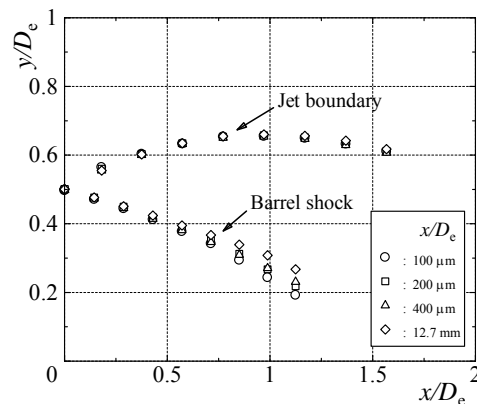


Fig 8. Effect of nozzle exit diameter on jet boundary and barrel shocks ( $p_0/p_b=5.23$ )

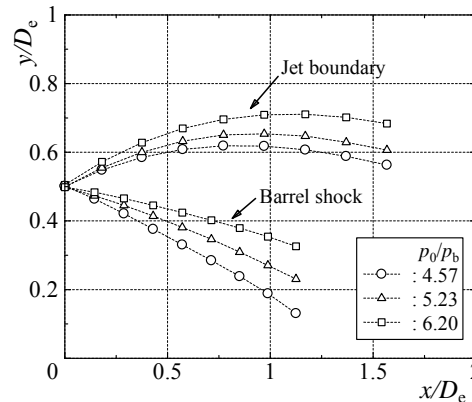


Fig 9. Effect of nozzle pressure ratio on jet boundary and barrel shocks ( $D_e=400 \mu\text{m}$ )

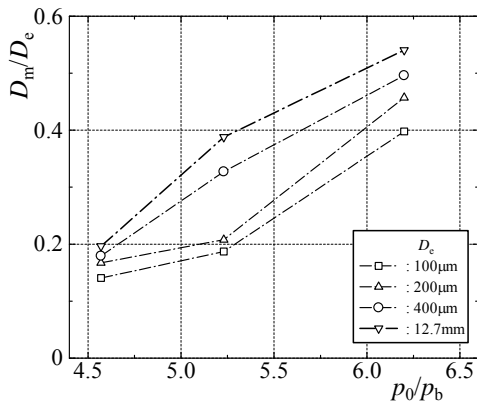


Fig 10. Variation of Mach disk diameter with nozzle pressure ratio,  $p_0/p_b$

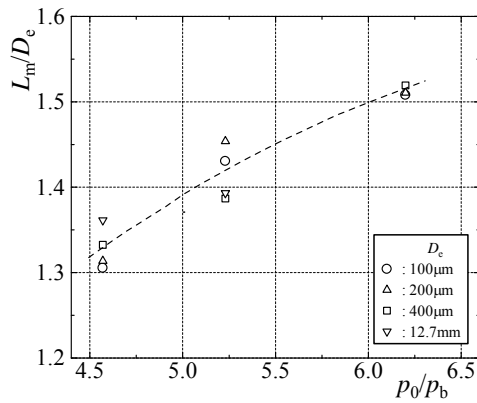


Fig 11. Variation of Mach disk location with nozzle pressure ratio,  $p_0/p_b$

both the configuration of jet boundary and barrel shock are significantly influenced by the nozzle pressure ratio  $p_0/p_b$  and the jet is expanded outward with the nozzle pressure ratio  $p_0/p_b$ .

#### 4.3.3 Properties of Shock Structure

The relation between the diameter  $D_m$  of Mach disk for the present microjets and the nozzle pressure ratio  $p_0/p_b$  is shown in Fig.10, where the present computational results of microjets are compared with large-scale jet. As seen from Fig.10, for different jet diameters, the diameter of Mach disk is an increasing function of the pressure ratio. It is also noted that for a given pressure ratio, the Mach disk diameter is significantly influenced by the jet diameter.

Figure 11 shows the relation between the location  $L_m$  of Mach disk from the nozzle exit and the nozzle pressure ratio  $p_0/p_b$ . It is found that the Mach disk location  $L_m$  is given by a function of the pressure ratio ( $p_0/p_b$ ) and it is not so sensitive to the jet diameter, unlike the Mach disk diameter.

#### 4.3.4 Surveys of Cross Stream Pressure

The cross-stream static pressure variations at different axial location of jet are examined under each operation

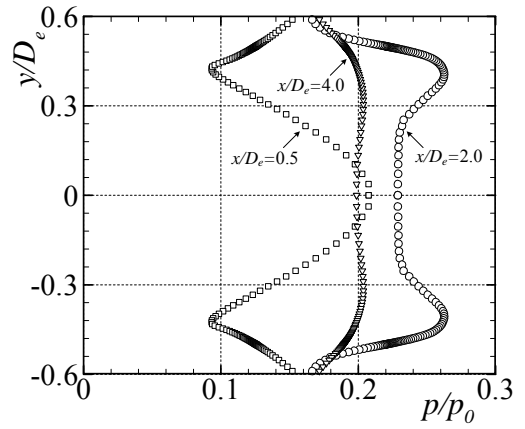


Fig 12. Cross-stream pressure profiles at different axial location of jet ( $p_0/p_b=6.2$ ,  $D_e=400 \mu\text{m}$ )

condition ( $p_0/p_b$ ). Cross-stream pressure profiles for 400  $\mu\text{m}$  jet with the nozzle pressure ratio of  $p_0/p_b=6.2$ , which are the representative of other conditions, at axial locations of  $x/D=0.5$ , 2.0 and 4.0 are shown in Fig. 12. Initially, at  $x/D=0.5$ , the pressure profile exhibits a central peak, which is mainly due to the expansion fan located just after the nozzle exit. At the axial location just after the Mach disk, at  $x/D=2.0$ , central depression is shown in the pressure profile due to the flow becoming subsonic. Further away from the nozzle exit, at  $x/D \geq 4.0$ , the shape of the pressure profile relaxes back to the central peak profile because of the weaker shock cells and shear layers merge.

## 5. CONCLUSIONS

In the present study, axisymmetric supersonic microjets flow was investigated numerically under different operating conditions ( $p_0/p_b$ ). Aerodynamic features of the jet flow field were compared with experimental results. Results obtained are summarized as follows: The presence of shock cells in the jet flow fields exhibit the characteristic quasi-periodic structure in the jet centerline pressure distributions. Moreover, at highly underexpanded condition, the Mach disks can be clearly visualized at the end of the first shock cell and the jet flow field is seen to stretch, where the shock cell spacing increases. For a given pressure ratio, the jet diameter has a significant influence on the configuration of barrel shock and the diameter of Mach disk. Other hand, the configuration of jet boundary and the location of Mach disk is not so sensitive to the jet diameter, for a given  $p_0/p_b$ . However, significant influence was observed on the configuration of jet boundary and barrel shock under different operating conditions ( $p_0/p_b$ ), and the microjet is expanded outward with  $p_0/p_b$ .

## 6. REFERENCES

1. Alvi, F. S., Elavarasan, R., Shih, C. and Garg, G., 2000, "Active Control of Supersonic Impinging Jets Using Microjets", AIAA Paper 2000-2236.
2. Alvi, F.S., 2007, "Active-Adaptive Control of Inlet Separation Using Supersonic Microjets", NASA Rept NAG-1-02059.



3. Araker, V.H., Krothapalli, A., Siddavaram, V., Alkislal, M.B., and Lourenco, L.M., 2003, "On the use of microjets to suppress turbulence in a Mach 0.9 axisymmetric jet", *Journal of Fluid Mechanics*, Vol. 490.
4. Meinhart, C. D. and Zhang, H., 2000, "The Flow Structure Inside a Microfabricated Inkjet Printhead", *Journal of Microelectromechanical Systems*, Vol. 9, No. 1.
5. Bayt, R. and Breuer, K., 1998, "Viscous Effects in Supersonic MEMS-Fabricated Micronozzles", *Proceedings of the 3rd ASME Microfluids Symposium*.
6. Bayt, R., 1999, "Analysis, Fabrication and Testing of a MEMS – Based Micropropulsion System", Ph. D. Dissertation, MIT.
7. Scroggs, S.D. and Settles, G.S., 1996, "An Experimental Study of Supersonic Microjets" *Experiments in Fluids*, Vol. 21.
8. Smedley, G.T., Phares, D.J. and Flagan, R.C., 1999, "Entrainment of fine particles from surfaces by impinging shock waves" *Experiments in Fluids*, Vol. 26.
9. Krothapalli, A., Alvi, F.S., and Shih, C., 2001, "Behavior of Free and Impinging Supersonic Microjets", *AIAA Paper 2001-3047*.
10. Vela'squez-Aguilar, J. G., Toker, G., Zamudio-Lara, A., and Arias-Estrada, M., 2007, "Visualization of a supersonic air micro jet by methods of dual-hologram interferometry", *Experiment in Fluids*, Vol. 42.
11. Phalnikar, K.A., Kumar, R. and Alvi, F.S., 2008, "Experiments on free and impinging supersonic microjets", *Experiment in Fluids*, Vol. 44.
12. Goldberg, U. C., 1994, "Toward a Pointwise Turbulence Model for Wall-Bounded and Free Shear Flows", *Transactions of the ASME*, Vol.116, pp.72-76.
13. Goldberg, U.C., 1996, "Exploring a Three-Equation R-k-ε Turbulence Model", *J. Fluids Engg.*, Vol.118, pp.795-799.
14. Heiler, M., 1999, "Instationäre Phänomene in Homogen/Heterogen Kondensierenden Düsen- und Turbinenströmungen", Dissertation, Fakultät für Maschinenbau, Universität Karlsruhe (TH), Germany.
15. Yee, H. C., 1989, "A class of high-resolution explicit and implicit shock capturing methods", NASA TM-89464.
16. Addy, A.L., 1981, "Effects of Axisymmetric Sonic Nozzle Geometry on Mach Disk Characteristics", *AIAA Journal*, Vol.19, No.1.
17. Wishart, D.P., 1995, "The structure of a heated supersonic jet operating at design and off-design conditions", Ph.D. Thesis, Florida State University, Tallahassee, FL.

## 7. NOMENCLATURE

Symbol	Meaning	Unit
$a$	speed of sound	(m/s)
$\rho$	density	(kg/m <sup>3</sup> )
$D_e$	nozzle exit diameter	(mm)
$D_m$	diameter of Mach disk	(mm)
$p$	static pressure	(Pa)
$L_m$	location of Mach disk	(mm)
<b>Subscripts</b>		
0	stagnation point	
b	ambient	

## 8. MAILING ADDRESS

Alam Miah Md. Ashraful  
 Graduate School of Science & Engineering,  
 Saga University,  
 1 Honjo-machi, Saga 840-8502, Japan.

## COMBINED EFFECTS OF CURVATURE AND TORSION ON FLUID FLOW IN A HELICAL RECTANGULAR DUCT

P. Kumar Bhattacharjee<sup>1</sup> and M. Mahmud Alam<sup>2</sup>

<sup>1</sup>Natural Science Group, National University, Gazipur, Bangladesh

<sup>2</sup>Mathematics Discipline, Khulna University, Khulna, Bangladesh

### ABSTRACT

This paper is concerned with the steady incompressible fully developed flow through a left-handed helical rectangular duct and presents the flow structure for various Dean number ( $D_n$ ), non-dimensional torsion ( $\tau'$ ) and non-dimensional curvature ( $\kappa'$ ) at aspect ratio  $\gamma = 1.5$ . Numerical study is performed to investigate the flow characteristics under various flow conditions. The flow structure in the helical rectangular duct is investigated numerically to examine the combined effects of non-dimensional curvature and torsion. Spectral method is used as a main tool for numerical calculations, where the Chebyshev polynomial, the collocation methods, the Arc-length method and the Newton-Raphson method are also used as secondary tools.

**Keywords:** Curvature, Torsion, Rectangular Duct.

### 1. INTRODUCTION

The flows through curved and helical ducts are encountered in various industrial processes. Flows in separation processes, heat exchangers, physiological systems, chemical processes, medical equipments and centrifugal compressors are examples of such processes. At first, Dean[1] formulated the curved pipe problem in mathematical terms under the fully developed flow conditions. He found the two-vortex counter rotating secondary flow patterns originated by the centrifugal force. Since then, there have been a lot of theoretical and experimental work concerning this flow and the review articles by Berger et al.[2] and Ito[3] may be referred. Cheng et al.[4] reported two-vortex secondary flow patterns in a curved duct with square cross-section by using finite difference method. One of the interesting phenomena of flow through the curved duct is the bifurcation of the flow. Yang and Wang[5] studied numerically the bifurcation structure and stability of the solutions of fully developed viscous flow in curved square duct. The governing equations were discretized by using the finite volume method.

The helical duct has been used extensively in various industrial applications to enhance the rate of heat, mass and momentum transfers. In order to improve the performance of these devices, an accurate and reliable analysis of the flow in the helical duct is necessary, which can also be used as the basis for studying the flow in other devices. The geometry of a helical pipe, as shown in Fig 1, is characterized by the curvature and

<sup>†</sup>O.S.D., Directorate of Secondary and Higher Education Dhaka, Bangladesh.

torsion. These non-dimensional curvature and torsion are defined respectively as,  $\kappa' = \frac{r'}{r'^2 + \alpha'^2}$ ,

$\tau' = \frac{\alpha'}{r'^2 + \alpha'^2}$  where  $r'$  is the radius of the helix

and  $\alpha' = \frac{\text{pitch}}{2\pi}$ . The secondary flow caused by the

centrifugal force due to curvature can be affected by torsion. If the pitch is equals to zero, then the torsion is equals to zero and the helical duct reduces to a toroidally curved duct. In a helical duct the centrifugal force plays an important role in creating a pair of vortices. However, above a critical value of the Dean number  $\left( D_n = \frac{\sqrt{2\kappa'} a^3}{\mu\nu} G \right)$ , the secondary flow is

changed from the appearance of several pair of vortices structure, due to the balance of the acting centrifugal and pressure gradient forces on the flow. The torsion causes the distortion in the symmetry of the flow, enlarging the upper vortex of the secondary flow at the expense of the lower vortex. Wang[6] was the pioneer author who formulated the helical pipe flow for circular cross-section using non-orthogonal co-ordinates and analyzed the flow for small curvature and torsion by taking series expansions of these parameters. He found that the secondary flow is a single vortex cell. There have been very few studies regarding the torsion effect on the flow in a helical square duct or rectangular duct. The effect of small torsion on the helical square ducts has been

investigated by Bolinder and sunden[7] and Sakalis et al.[8]. Recently, Bhattacharjee and Alam[9] investigated the torsion effect on fluid flow in a helical square duct. They found the bifurcation flow structure. They also found that multiple pair of vortices appeared on the bifurcation areas. Again, Wang and Andrews[10] investigated the flow in a helical rectangular duct. They studied the effect of the pitch ratio, pressure gradient and curvature ratio on the velocity distribution and fluid resistance in fully developed laminar flow of an incompressible fluid in a helical rectangular duct.

The main object of the present study is to investigate numerically the flow through a *left-handed helical rectangular duct* for a wide range of the Dean number, torsion and curvature. The non-dimensional governing equations have been solved numerically by employing spectral method as a main tool.

## 2. Governing Equations

A viscous incompressible fully developed steady flow through a *left-handed helical duct* with rectangular cross-section as shown in Figure 1 is considered. Let  $2a$  and  $2b$  be the width and the height of the cross-section respectively.

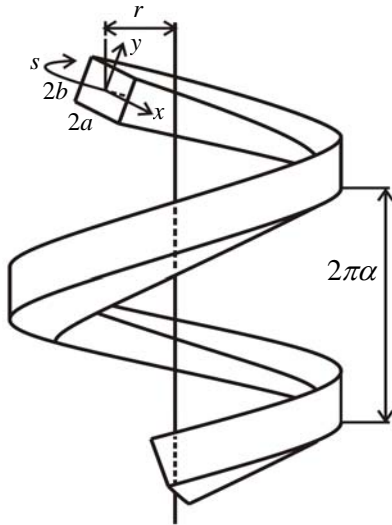


Fig 1. Helical duct with rectangular cross-section.

Thus, the Continuity and Navier-Stokes equations in terms of curvilinear co-ordinates are given by

$$\frac{\partial}{\partial \xi^i} (\sqrt{g} q_j \gamma_j^i) = 0 \quad (1)$$

$$\begin{aligned} \gamma_j^k \left( \frac{\partial q_i}{\partial \xi^k} - q_l E_{lik} \right) q_j &= -\frac{1}{\rho} \frac{\partial p}{\partial \xi^i} \gamma_i^j \\ -\nu \varepsilon_{ijk} \gamma_j^l \left( \frac{\partial (\nabla \wedge \mathbf{q})_k}{\partial \xi^l} - (\nabla \wedge \mathbf{q})_m E_{mkl} \right) & \quad (2) \end{aligned}$$

where the physical components of  $\nabla \wedge \mathbf{q}$  are defined by

$$(\nabla \wedge \mathbf{q})_i = \varepsilon_{ijk} \gamma_j^l \left( \frac{\partial q_k}{\partial \xi^l} - q_m E_{mkl} \right) \quad (3)$$

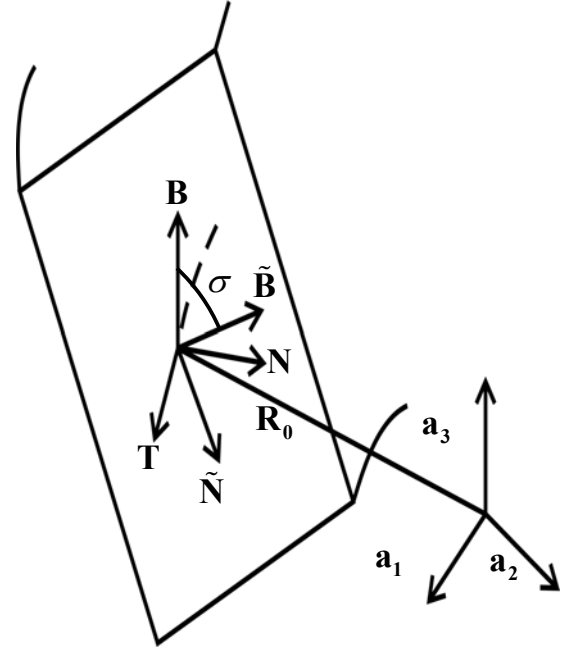


Fig 2. Various vectors related to the centre line of a duct.

Let the centre line of the duct be the smooth space curve  $\mathbf{R}_0(s)$ , where the parameter 's' is the arc-length. The unit tangent  $\mathbf{T}$ , normal  $\mathbf{N}$  and binormal  $\mathbf{B}$  vectors of the space curve  $\mathbf{R}_0(s)$  are given by the relations

$$\mathbf{T}(s) = \frac{d\mathbf{R}_0}{ds}, \quad \mathbf{N}(s) = \frac{1}{\kappa} \frac{d\mathbf{T}}{ds}, \quad \mathbf{B}(s) = \mathbf{T} \wedge \mathbf{N} \quad (4)$$

The curvature  $\kappa$  and torsion  $\tau$  are determined by the Serret-Frenet formulae

$$\frac{d\mathbf{T}}{ds} = \kappa \mathbf{N}, \quad \frac{d\mathbf{N}}{ds} = \tau \mathbf{B} - \kappa \mathbf{T}, \quad \frac{d\mathbf{B}}{ds} = -\tau \mathbf{N} \quad (5)$$

Let  $x$  be a coordinate along the direction of  $\tilde{\mathbf{N}}$  and  $y$  be a coordinate along the direction of  $\tilde{\mathbf{B}}$ . Here  $\tilde{\mathbf{N}}$  and  $\tilde{\mathbf{B}}$  are the orthogonal unit vectors obtained by a rotation of the physical basis vector  $\mathbf{N}$  and  $\mathbf{B}$  with the angle  $\sigma(s)$  in the  $\mathbf{N}-\mathbf{B}$  plane which is shown in Fig 2. Therefore, we have

$$\begin{cases} \tilde{\mathbf{N}} = \cos \sigma \mathbf{N} - \sin \sigma \mathbf{B} \\ \tilde{\mathbf{B}} = \sin \sigma \mathbf{N} + \cos \sigma \mathbf{B} \end{cases} \quad (6)$$

The position vector  $\mathbf{R}$  of any points in the duct is thus written in the following form:

$$\mathbf{R}(s, x, y) = \mathbf{R}_0(s) + x\tilde{\mathbf{N}}(s) + y\tilde{\mathbf{B}}(s) \quad (7)$$

The variables are non-dimensionalised by the characteristic length  $a$  (half width) and the kinematic viscosity  $\nu$  as follows:

$$\left. \begin{aligned} u &= \frac{\nu}{a} u', \quad v = \frac{\nu}{a} v', \quad w = \frac{\nu}{a} \frac{w'}{\sqrt{2\kappa'}} \\ \kappa &= \frac{\kappa'}{a}, \quad \tau = \frac{\tau'}{a}, \quad p = \rho \frac{\nu^2}{a^2} p' \\ s &= s'a, \quad x = x'a, \quad y = y'a \end{aligned} \right\} \quad (8)$$

Here  $w', u', v'$  are non-dimensional velocity components in the direction of  $s', x', y'$  respectively and  $p', \kappa', \tau'$  are the non-dimensional pressure, curvature and torsion respectively. The variables without prime are the dimensional quantities. For the incompressible fully developed flow, the velocity is independent of  $s'$ . We further introduce a new variable  $y' = \gamma \bar{y}$ , where  $\gamma \left( = \frac{b}{a} \right)$  is the aspect ratio of the cross-section. Since the flow field is uniform in the axial direction, we can introduce a stream function  $\psi = \psi(x', y')$  such that

$$\left. \begin{aligned} \frac{\partial \psi}{\partial y'} &= Ju' \sqrt{2\kappa'} + \tau' y' w' \\ -\frac{\partial \psi}{\partial x'} &= Jv' \sqrt{2\kappa'} - \tau' x' w' \end{aligned} \right\} \quad (9)$$

where  $J = 1 - \kappa' x'$ .

Therefore, the basic equations for  $w'$  and  $\psi$  are derived from the Navier-Stokes equations as follows:

$$\begin{aligned} D_x \left( \frac{\tau' x'}{J} \left( 1 + \frac{\tau'^2 \gamma^2 \bar{y}^2}{J^2} \right) \psi_{x'x'x'} - \frac{\tau' \bar{y}}{J} \left( 1 + \frac{\tau'^2 \gamma^2 \bar{y}^2}{J^2} - \frac{2\tau'^2 x'^2}{J^2} \right) \psi_{x'x'\bar{y}} \right. \\ - \frac{\tau' \bar{y}}{J \gamma^2} \left( \frac{\tau'^2 x'^2}{J^2} + 1 \right) \psi_{\bar{y}\bar{y}\bar{y}} + \frac{\tau' x'}{J \gamma^2} \left( \frac{2\tau'^2 \gamma^2 \bar{y}^2}{J^2} - 1 - \frac{\tau'^2 x'^2}{J^2} \right) \psi_{x'\bar{y}\bar{y}} \\ - \frac{3\kappa' \tau' \bar{y}}{J^2} \left( 1 + \frac{\tau'^2 \gamma^2 \bar{y}^2}{J^2} - \frac{2\tau'^2 x'}{\kappa' J} - \frac{\tau'^2 x'^2}{J^2} \right) \psi_{x'\bar{y}} \\ - \frac{\tau'}{J^2} \left( \frac{2\tau'^2 \gamma^2 \bar{y}^2}{J} + \kappa' x' + \frac{3\kappa' \tau'^2 x' \gamma^2 \bar{y}^2}{J^2} - \frac{\tau'^2 x'^2}{J} \right) \psi_{x'x'} \\ + \frac{\tau'}{J \gamma^2} \left( \frac{3\kappa' \tau'^2 x' \gamma^2 \bar{y}^2}{J^3} - \frac{2\tau'^2 x'^2}{J^2} + 2\kappa' x' + \frac{\tau'^2 \gamma^2 \bar{y}^2}{J^2} \right) \psi_{\bar{y}\bar{y}} \\ - \frac{\tau' \bar{y}}{J^3} \left( \frac{3\kappa'^2 \tau'^2 \gamma^2 \bar{y}^2}{J^2} - \frac{4\kappa' \tau'^2 x'}{J} - \tau'^2 + 3\kappa'^2 \right) \psi_{\bar{y}} \\ - \frac{\tau'}{J^2} \left( \frac{3\kappa' \tau'^2 \gamma^2 \bar{y}^2}{J^2} + \frac{\kappa'^2 x'}{J} + \frac{3\kappa'^2 \tau'^2 x' \gamma^2 \bar{y}^2}{J^3} - \frac{\kappa' \tau'^2 x'^2}{J^2} \right. \\ \left. - \frac{\tau'^2 x'}{J} + \kappa' \right) \psi_{x'} - \frac{2\tau'^2 x' \bar{y}}{J} \left( \frac{\tau'^2 \gamma^2 \bar{y}^2}{J^2} + \frac{\tau'^2 x'^2}{J^2} + 1 \right) w'_{x'\bar{y}} \\ + \left( \frac{2\tau'^2 \gamma^2 \bar{y}^2}{J} + \frac{\tau'^4 \gamma^4 \bar{y}^4}{J^3} + \frac{\tau'^2 x'^2}{J} + \frac{\tau'^4 x'^2 \gamma^2 \bar{y}^2}{J^3} + J \right) w'_{x'x'} \end{aligned}$$

$$\begin{aligned} + \left( \frac{\tau'^2 \bar{y}^2}{J} + \frac{\tau'^4 x'^2 \bar{y}^2}{J^3} + \frac{2\tau'^2 x'^2}{J \gamma^2} + \frac{J}{\gamma^2} + \frac{\tau'^4 x'^4}{J^2 \gamma^2} \right) w'_{\bar{y}\bar{y}} \\ + \left( \frac{3\kappa' \tau'^4 \gamma^4 \bar{y}^4}{J^4} + \frac{\tau'^2 x'}{J} - \frac{\tau'^4 x' \gamma^3 \bar{y}^2}{J^3} + \frac{2\kappa' \tau'^2 \gamma^2 \bar{y}^2}{J^2} + \frac{\kappa' \tau'^2 x'^2}{J^2} \right. \\ \left. + \frac{3\kappa' \tau'^4 x'^2 \gamma^2 \bar{y}^2}{J^4} - \kappa' - \frac{\tau'^4 x'^4}{J^3} \right) w'_{x'} + \frac{\tau'^2}{J} \left( -\frac{\kappa' x' \bar{y}}{J} - \frac{\tau'^2 x'^2 \bar{y}}{J^2} + \bar{y} \right. \\ \left. - \frac{\tau'^2 \gamma^2 \bar{y}^3}{J^2} - \frac{3\kappa' \tau'^2 x' \gamma^2 \bar{y}^3}{J^3} - \frac{3\kappa' \tau'^2 x'^3 \bar{y}}{J^3} \right) w'_{\bar{y}} + \frac{\kappa'}{J} \left( \frac{3\kappa' \tau'^4 \gamma^4 \bar{y}^4}{J^4} \right. \\ \left. - \frac{\tau'^4 x' \gamma^2 \bar{y}^2}{J^3} - \frac{\kappa' \tau'^2 \gamma^2 \bar{y}^2}{J^2} + \frac{\tau'^2 x'}{J} + \frac{\kappa' \tau'^2 x'^2}{J^2} - \kappa' \right. \\ \left. + \frac{3\kappa' \tau'^4 x'^2 \gamma^2 \bar{y}^2}{J^4} - \frac{\tau'^4 x'^3}{J^3} + \frac{3\kappa' \tau'^2 \gamma^2 \bar{y}^2}{J^2} \right) w' \\ - \frac{1}{\gamma \sqrt{2\kappa'}} \left[ \left( \frac{\tau'^2 x'^2}{J^2} + \frac{\tau'^2 \gamma^2 \bar{y}^2}{J^2} + 1 \right) w'_{x'\bar{y}\bar{y}} \right. \\ \left. - \frac{\kappa' \tau' x'}{J^3} \psi_{x'} \psi_{\bar{y}\bar{y}} \left( \frac{\kappa' \tau'^2 x'^2}{J^3} + \frac{\kappa' \tau'^2 \gamma^2 \bar{y}^2}{J^3} - \frac{\kappa'}{J} + \frac{2\tau'^2 x'}{J^2} \right) w'_{\bar{y}\bar{y}} \right. \\ \left. - \left( \frac{\tau'^2 x'^2}{J^2} + \frac{\tau'^2 \gamma^2 \bar{y}^2}{J^2} + 1 \right) w'_{\bar{y}\bar{y}} \psi_{x'} \right] - \frac{\tau'}{J^2 \sqrt{2\kappa'}} \left( \frac{\bar{y}}{\gamma} \psi_{x'} \psi_{\bar{y}\bar{y}} \right. \\ \left. + \frac{x'}{\gamma} \psi_{x'} \psi_{x'\bar{y}} - \frac{\bar{y}}{\gamma} \psi_{\bar{y}\bar{y}} \psi_{x'\bar{y}} - 2\tau' \gamma \bar{y} w' \psi_{x'} - \frac{x'}{\gamma} \psi_{\bar{y}\bar{y}} \psi_{x'x'} \right) \\ + \frac{\kappa' \tau' \bar{y}}{J^3 \gamma \sqrt{2\kappa'}} \psi_{\bar{y}}^2 = 0 \end{aligned} \quad (10)$$

$$\begin{aligned} \frac{1}{J \sqrt{2\kappa'}} \left[ \left( 1 + \frac{\tau'^2 \gamma^2 \bar{y}^2}{J^2} \right) \psi_{x'x'x'x'} + \left( 1 + \frac{\tau'^2 x'^2}{J^2} \right) \frac{1}{\gamma^4} \psi_{\bar{y}\bar{y}\bar{y}\bar{y}} \right] \\ - \frac{2\tau'^2 x' \bar{y}}{J^3 \sqrt{2\kappa'}} \psi_{x'x'x'\bar{y}} + \frac{1}{J \sqrt{2\kappa'}} \left( \frac{\tau'^2 x'^2}{J^2} + 2 + \frac{\tau'^2 \gamma^2 \bar{y}^2}{J^2} \right) \frac{1}{\gamma^2} \psi_{x'x'\bar{y}\bar{y}} \\ - \frac{2\tau'^2 x' \bar{y}}{J^3 \gamma^2 \sqrt{2\kappa'}} \psi_{x'\bar{y}\bar{y}\bar{y}} + \frac{1}{J^2 \sqrt{2\kappa'}} \left( 2\kappa' + \frac{6\kappa' \tau'^2 \gamma^2 \bar{y}^2}{J^2} \right. \\ \left. - \frac{\tau'^2 x'}{J} \right) \psi_{x'x'x'} + \frac{1}{J^2 \sqrt{2\kappa'}} \left( \frac{3\kappa' \tau'^2 x'^2}{J^2} + \frac{3\kappa' \tau'^2 \gamma^2 \bar{y}^2}{J^2} + 2\kappa' \right. \\ \left. - \frac{\tau'^2 x'}{J} \right) \frac{1}{\gamma^2} \psi_{x'\bar{y}\bar{y}} - \frac{\tau'^2 \bar{y}}{J^3 \sqrt{2\kappa'}} \left( \frac{9\kappa' x'}{J} + 1 \right) \psi_{x'x'\bar{y}} \\ - \frac{\tau'^2 \bar{y}}{J^3 \gamma^2 \sqrt{2\kappa'}} \left( \frac{3\kappa' x'}{J} + 1 \right) \psi_{\bar{y}\bar{y}\bar{y}} + \frac{\kappa'}{J^3 \sqrt{2\kappa'}} \left( 3\kappa' + \frac{15\kappa' \tau'^2 \gamma^2 \bar{y}^2}{J^2} \right. \\ \left. - \frac{4\tau'^2 x'}{J} \right) \psi_{x'x'} + \frac{\kappa' \tau'^2}{J^4 \gamma^2 \sqrt{2\kappa'}} \left( 2x' + \frac{3\kappa' \gamma^2 \bar{y}^2}{J} \right) \psi_{\bar{y}\bar{y}} \\ - \frac{6\kappa' \tau'^2 \bar{y}}{J^4 \sqrt{2\kappa'}} \left( \frac{2\kappa' x'}{J} + 1 \right) \psi_{x'\bar{y}} + \frac{\kappa'}{J^4 \sqrt{2\kappa'}} \left( -\frac{4\kappa' \tau'^2 x'}{J} + 3\kappa'^2 \right. \\ \left. + \frac{15\kappa'^2 \tau'^2 \gamma^2 \bar{y}^2}{J^2} - \tau'^2 \right) \psi_{x'} - \frac{\kappa' \tau'}{J^3 \sqrt{2\kappa'}} \left( 4\kappa' + \frac{3\kappa'^2 x'}{J} \right. \\ \left. + \frac{15\kappa'^2 \tau'^2 x' \gamma^2 \bar{y}^2}{J^3} - \frac{4\kappa' \tau'^2 x'^2}{J^2} + \frac{12\kappa' \tau'^2 \gamma^2 \bar{y}^2}{J^2} \right. \\ \left. - \frac{3\tau'^2 x'}{J} \right) w' - \frac{6\kappa'^2 \tau'^2 \bar{y}}{J^5 \sqrt{2\kappa'}} \psi_{\bar{y}} - \frac{\tau'}{J^2 \sqrt{2\kappa'}} \left( 4\kappa' + \frac{15\kappa'^2 \tau'^2 x' \gamma^2 \bar{y}^2}{J^3} \right. \end{aligned}$$

$$\begin{aligned}
& + \frac{3\kappa'^2 x'}{J} - \frac{4\kappa' \tau'^2 x'^2}{J^2} - \frac{3\tau'^2 x'}{J} + \frac{12\tau'^2 \kappa' \gamma^2 \bar{y}^2}{J^2} \Big) w'_{x'} \\
& + \frac{\tau' \bar{y}}{J^3 \sqrt{2\kappa'}} \left( \frac{12\kappa'^2 \tau'^2 x'^2}{J^2} + \frac{16\kappa' \tau'^2 x'}{J} + 3\tau'^2 \right. \\
& + \kappa'^2 - \frac{3\kappa'^2 \tau'^2 \gamma^2 \bar{y}^2}{J^2} \Big) w'_{\bar{y}} + \frac{\tau' \bar{y}}{J^2 \sqrt{2\kappa'}} \left( \frac{9\kappa' \tau'^2 x'^2}{J^2} + \frac{10\tau'^2 x'}{J} \right. \\
& - \left. \frac{3\kappa' \tau'^2 \gamma^2 \bar{y}^2}{J^2} + \kappa' \right) w'_{x'\bar{y}} - \frac{\tau'}{J^2 \sqrt{2\kappa'}} \left( \frac{6\kappa' \tau'^2 x' \gamma^2 \bar{y}^2}{J^2} + 2\kappa' x' \right. \\
& + 4J + \frac{4\tau'^2 \gamma^2 \bar{y}^2}{J} - \frac{\tau'^2 x'^2}{J} \Big) w'_{x'x'} - \frac{\tau'}{J \sqrt{2\kappa'}} \left( \frac{4}{\gamma^2} + \frac{3\kappa' x'}{J \gamma^2} + \frac{4\tau'^2 x'^2}{\gamma^2 J^2} \right. \\
& + \frac{3\kappa' \tau'^2 x'^2}{\gamma^2 J^3} - \frac{\tau'^2 \bar{y}^2}{J^2} - \frac{3\tau'^2 \kappa' x' \bar{y}^2}{J^3} \Big) w'_{\bar{y}\bar{y}} + \frac{\tau' x'}{J \sqrt{2\kappa'}} \left( \frac{2\tau'^2 \bar{y}^2}{J^2} \right. \\
& - \left. \frac{\tau'^2 x'^2}{\gamma^2 J^2} - \frac{1}{\gamma^2} \right) w'_{x'\bar{y}\bar{y}} - \frac{\tau' x'}{J \sqrt{2\kappa'}} \left( 1 + \frac{\tau'^2 \gamma^2 \bar{y}^2}{J^2} \right) w'_{x'x'x'} \\
& + \frac{\tau' \bar{y}}{J \sqrt{2\kappa'}} \left( \frac{2\tau'^2 x'^2}{J^2} - 1 - \frac{\tau'^2 \gamma^2 \bar{y}^2}{J^2} \right) w'_{x'x'\bar{y}} \\
& - \frac{\tau' \bar{y}}{J \gamma^2 \sqrt{2\kappa'}} \left( 1 + \frac{\tau'^2 x'^2}{J^2} \right) w' - \frac{1}{\gamma^3 J^3} \Psi_{\bar{y}} \Psi_{\bar{y}\bar{y}} - \frac{3}{2\gamma J^3} \Psi_{\bar{y}} \Psi_{x'x'\bar{y}\bar{y}} \\
& + \frac{\tau'}{\gamma J^2} \left( \frac{2}{\kappa'} + \frac{3x'}{2J} \right) w_x \Psi_{\bar{y}} - \frac{3\kappa'}{2\gamma J^3} \Psi_{x'} \Psi_{\bar{y}} - \frac{1}{2\kappa' \gamma^3 J^2} \Psi_{x'\bar{y}\bar{y}} \Psi_{\bar{y}} \\
& + \frac{1}{2\kappa' \gamma^3 J^2} \Psi_{x'} \Psi_{\bar{y}\bar{y}\bar{y}} - \frac{1}{2\kappa' \gamma J^2} \Psi_{\bar{y}} \Psi_{x'x'x'} + \frac{1}{2\gamma J^3} \Psi_{x'} \Psi_{x'\bar{y}} \\
& - \frac{\tau'}{\gamma J^2} \left( \frac{2}{\kappa'} + \frac{x'}{J} \right) w'_{\bar{y}} \Psi_{x'} + \frac{1}{2\kappa' \gamma J^2} \Psi_{x'} \Psi_{x'x'\bar{y}} + \frac{\tau' \bar{y}}{2\kappa' \gamma J^2} w'_{x'\bar{y}} \Psi_{\bar{y}} \\
& + \frac{\tau' x'}{2\gamma J^3} w' \Psi_{x'\bar{y}} + \frac{3\tau'}{\gamma J^3} \left( 1 + \frac{\kappa' x'}{2J} \right) w' \Psi_{\bar{y}} + \frac{\tau' x'}{2\kappa' \gamma J^2} w'_{x'} \Psi_{x'\bar{y}} \\
& - \frac{\tau' \bar{y}}{2\kappa' \gamma J^2} w'_{\bar{y}} \Psi_{x'\bar{y}} - \frac{1}{\gamma J} \left( 1 - \frac{\tau'^2 x'}{\kappa' J} \right) w' w'_{\bar{y}} - \frac{\tau'^2 \gamma \bar{y}}{J^3} w'^2 \\
& - \frac{\tau'^2 \gamma \bar{y}}{\kappa' J^2} w' w'_{x'} + \frac{\tau' \bar{y}}{2\gamma J^3} w' \Psi_{\bar{y}\bar{y}} + \frac{\tau' \bar{y}}{2\kappa' \gamma J^2} w'_{x'} \Psi_{\bar{y}\bar{y}} + \frac{\tau' \bar{y}}{2\gamma J^3} w'_{\bar{y}} \Psi_{\bar{y}} \\
& - \frac{\tau' \bar{y}}{2\kappa' \gamma J^2} w'_{\bar{y}\bar{y}} \Psi_{x'} + \frac{\tau' x'}{2\kappa' \gamma J^2} w'_{x'x'} \Psi_{\bar{y}} - \frac{\tau' x'}{2\kappa' \gamma J^2} w'_{x'\bar{y}} \Psi_{x'} = 0
\end{aligned} \tag{11}$$

### 3. METHOD OF NUMERICAL CALCULATIONS

The spectral method is applied in the present numerical calculation. The expansion by polynomial functions is utilized to obtain steady solution. Variables are expanded in series of functions consisting of Chebyshev polynomials. We expand  $w(x', \bar{y})$  and  $\Psi(x', \bar{y})$  as

$$\left. \begin{aligned}
w'(x', \bar{y}) &= \sum_{m=0}^M \sum_{n=0}^N w_{mn} \Phi_m(x') \Phi_n(\bar{y}) \\
\Psi(x', \bar{y}) &= \sum_{m=0}^M \sum_{n=0}^N \Psi_{mn} \Psi_m(x') \Psi_n(\bar{y})
\end{aligned} \right\} \tag{12}$$

where  $M$  and  $N$  are the truncation numbers along  $x'$  and  $\bar{y}$  direction respectively and  $w_{mn}$  and  $\Psi_{mn}$  are the coefficients of expansion.

The expansion functions  $\Phi_n(x')$  and  $\Psi_n(x')$  are

expressed as

$$\Phi_n(x') = (1 - x'^2) C_n(x'), \quad \Psi_n(x') = (1 - x'^2)^2 C_n(x') \tag{13}$$

where  $C_n(x') = \cos(n \cos^{-1}(x'))$  is the  $n$ -th order Chebyshev polynomial.

In order to obtain the solutions for  $w_{mn}$  and  $\Psi_{mn}$ , the expansion series (12) are then substituted into the basic equations (10) and (11) and apply the collocation method (Gottlieb and Orszag[11]), then we obtain the non-linear algebraic equations for  $w_{mn}$  and  $\Psi_{mn}$ . The collocation points are taken as:

$$\left. \begin{aligned}
x'_i &= \cos \frac{\pi i}{M+2}, \quad (i = 1, \dots, M+1) \\
\bar{y}_j &= \cos \frac{\pi j}{M+2}, \quad (j = 1, \dots, N+1)
\end{aligned} \right\}$$

The non-linear algebraic equations for  $w_{mn}$  and  $\Psi_{mn}$  are solved by the Newton-Raphson method starting with an initial guess of the solution.

The convergence is assured by taking  $\epsilon_{\bar{p}} < 10^{-8}$ , where subscript  $\bar{p}$  denotes the iteration number and  $\epsilon_{\bar{p}}$  is defined as

$$\epsilon_{\bar{p}} = \sum_{m=0}^M \sum_{n=0}^N \left[ \left( w_{mn}^{(\bar{p}+1)} - w_{mn}^{(\bar{p})} \right)^2 + \left( \Psi_{mn}^{(\bar{p}+1)} - \Psi_{mn}^{(\bar{p})} \right)^2 \right] \tag{14}$$

### 4. FLUX THROUGH THE HELICAL DUCT

The dimensional total flux,  $Q'$  through the duct is obtained as:

$$Q' = \int_{-a\gamma}^{a\gamma} \int_{-a}^a w' dx dy \tag{15}$$

where,  $w'$  is the component of the velocity normal to  $x' - y'$  plane and the dimensionless total flux is

$$Q = \gamma \int_{-1}^1 \int_{-1}^1 w'(x', \bar{y}) dx' d\bar{y} \tag{16}$$

The non-dimensional Resistance coefficient ( $R_c$ ) takes the following form

$$R_c = \frac{128\gamma \sqrt{2k}}{1 + \gamma} D_n \frac{1}{\left( \int_{-1}^1 \int_{-1}^1 w(x', \bar{y}) dx' d\bar{y} \right)^2} \tag{17}$$

### 5. RESULTS AND DISCUSSION

Left-handed helical duct with rectangular cross-section has been taken to investigate the flow characteristics for wide range of Dean number ( $D_n$ ), fixed curvature ( $\kappa' = 0.1$ ), different torsions ( $\tau' = 0.0, 0.1$ ) and aspect ratio ( $\gamma = 1.5$ ). In this article, the left side is the outer wall and the right side is the inner wall of the cross-section of the duct.

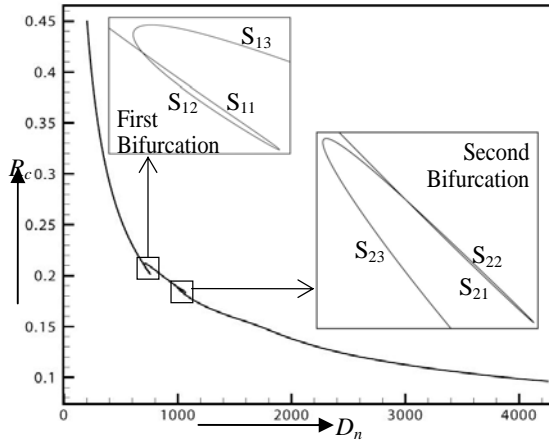


Fig 3. Solution Curve for steady fluid flow in Curved duct for  $\kappa' = 0.1, \gamma = 1.5, \tau' = 0.1$  and  $0 \leq D_n \leq 4258$ .

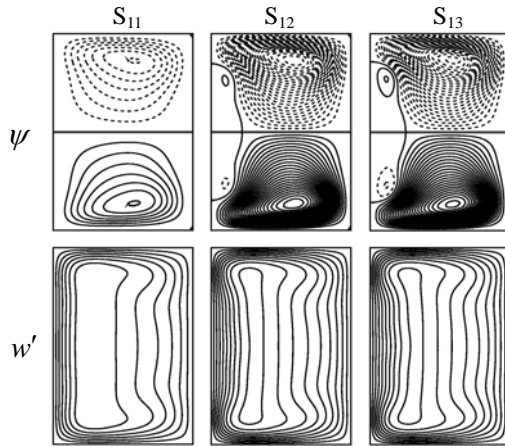


Fig 4. Stream lines of the secondary flow and contour plots of the axial flow on solution curves at  $D_n = 706$ .

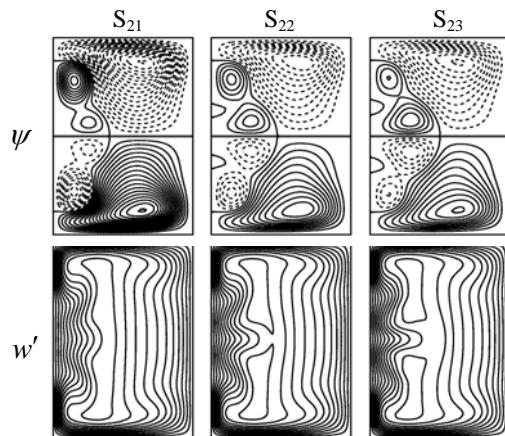


Fig 5. Stream lines of the secondary flow and contour plots of the axial flow on solution curves at  $D_n = 1005$ .

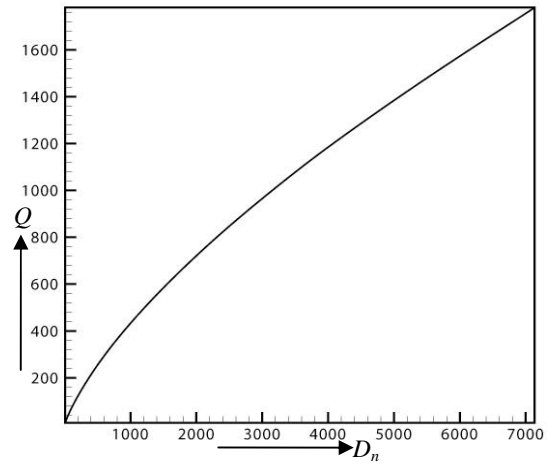


Fig 6. Solution Curve of steady flow through a helical rectangular duct for  $\kappa' = 0.1, \gamma = 1.50, \tau' = 0.1$  and  $0 \leq D_n \leq 7134$ .

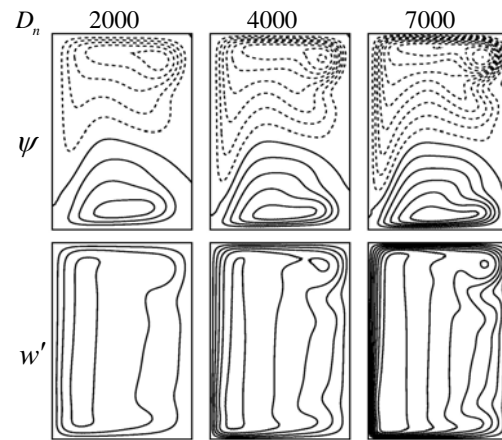


Fig 7. Stream lines of the secondary flow and contour plots of the axial flow on the solution curve for  $\gamma = 1.5, \kappa' = 0.1$  and  $\tau' = 0.1$  for various Dean number.

### 5.1 Case I ( $\kappa' = 0.1, \tau' = 0.0$ and $\gamma = 1.5$ )

Fig. 3 shows that the resistance coefficient ( $R_c$ ) through the duct versus Dean number ( $D_n$ ) and this is called solution curve. In this solution curve two bifurcation areas have been obtained which are the most important characteristic of the flow in the duct. After a comprehensive study over a parametric space, steady solution curve is obtained for  $\kappa' = 0.1, \tau' = 0.0, \gamma = 1.5$  and Dean number in the range of  $0 \leq D_n \leq 4258$ . In order to visualize the bifurcation areas more explicitly the enlargement of the solution curve areas are necessary. The above mentioned numerical solution curve areas are obtained by arc-length method as discussed in Keller et. al [12]. In fig. 3 it is seen that resistance coefficient decreases as Dean number increases along the curves  $S_{11}, S_{13}, S_{21}$  &  $S_{23}$  and resistance coefficient increases as

Dean number decreases along the curves  $S_{12}$ ,  $S_{22}$  in the bifurcation areas. From fig. 4 it is seen that the secondary flow patterns consists of two-vortex, four-vortex with two minor very weak vortices and four-vortex with two minor weak vortices for same Dean number  $D_n = 706$ . It is clear that weak vortices have been created near the outer wall of the cross-section and axial flow is gradually shifted towards the outer wall of the cross-section. In fig.5 It is seen that four-vortex secondary flow patterns are found along the curve  $S_{21}$  while six-vortex secondary flow patterns are observed along the curves  $S_{22}$  and  $S_{23}$  for same Dean number  $D_n = 1005$ . The axial flow is shifted more quickly to the outer wall of the cross-section. It is also seen that axial flow is stronger near the outer wall on the curves  $S_{22}$  and  $S_{23}$ .

### 5.2 Case II ( $\kappa' = 0.1$ , $\tau' = 0.1$ and $\gamma = 1.5$ )

The solution curve (Dean number versus flux) is depicted in the fig. 6. In this figure it is seen that steady solutions are found in the range of  $0 \leq D_n \leq 7134$ . It is also observed that the flux increases as Dean number increases. The secondary and axial flow patterns on the solution curve are shown in fig. 7. In these flow patterns  $\psi$  and  $w'$  are drawn with  $\Delta\psi = 1.75$  and  $\Delta w' = 90.0$ . Two-vortex non-symmetric secondary flow patterns are found on the solution curve for several Dean numbers and maximum axial flow is shifted to the lower part of the outer wall of the cross-section.

## 6. CONCLUSIONS

According to the present results, we can draw the following Concluding remarks:

- Several pair of vortices has been found in the bifurcation areas due to centrifugal and pressure gradient forces.
- Axial flow is shifted quickly to the outer wall of the cross-section for large Dean number.
- Torsion causes the distortion of the symmetry of the flow enlarging the upper vortex to the expenses of the lower vortex.
- The multiple solutions have not been found for torsion 0.1 and aspect ratio 1.5.

## 7. REFERENCES

1. Dean, W. R., 1927, "Note on the motion of fluid in a curved pipe", *Philosophical magazine and Journal of Science*, 4(20): 208-223.
2. Berger, S. A., Talbot, L. and Yao, L. S., 1983, "Flow in curved pipes", *Annual Reviews of fluid Mechanics*, 15: 461-512.
3. Ito, H., 1987, "Flow in curved pipes", *JSME International Journal*, 30(262): 543-552.
4. Cheng, K. C., Lin, R. and Ou, J. W., 1975, "Graetz

problem in curved square channels", *Trans. ASME Journal of heat transfer*, 97: 244-248.

5. Yang, T. and Wang, L., 2001, "Solution Structure and Stability of Viscous Flow in Curved Square Ducts", *ASME Journal of Fluids Engineering*, 123: 863-868.
6. Wang, C. Y., 1981, "On the low-Reynolds number flow in a helical pipe", *Journal of Fluid Mechanics*, 108:185-194.
7. Bolinder, C. J. and Sundén, B., 1995, "Flow visualization and LDV measurements of laminar flow in a helical square duct with finite pitch", *Experimental Thermal and Fluid Science*, 11: 348-363.
8. Sakalis, V. D., Hatzikonstantinou, P. M. and Papadopoulos, P. K., 2005, "Numerical Procedure for the Laminar Developed Flow in a Helical Square Duct", *Journal of Fluids Engineering*, 127: 136-148.
9. Bhattacharjee, P. K. and Alam, M. M., 2008, "Torsion Effect on Fluid Flow in a Helical Pipe with Square Cross-section", *Proc. 4<sup>th</sup> BSME-ASME Int. Conf. on Thermal Engineering*, pp. I: 198-203.
10. Wang, J. W. and Andrews, J. R. G., 1995, "Numerical Simulation of Flow in Helical Ducts", *AIChE Journal*, 41(5): 1071-1080.
11. Gottlieb, D. and Orszag, S. A., 1977, "Numerical Analysis of Spectral Methods", *Society for Industrial and Applied Mathematics*, Philadelphia.
12. Keller, H. B., 1987, "Lectures on Numerical Methods in Bifurcation problems", Springer, Berlin.

## 8. NOMENCLATURE

Symbol	Meaning
$D_n$	Dean number
$\gamma$	Aspect ratio
$\kappa'$	Dimensionless curvature
$\tau'$	Dimensionless torsion
$w', u', v'$	Dimensionless velocity along axial, radial, circumferential direction respectively
$s', x', y'$	Dimensionless length coordinates along axial, radial, circumferential direction respectively
$\psi$	Stream function
$R_c$	Resistance coefficient
$Q$	Dimensionless total flux

## 9. MAILING ADDRESS

M. Mahmud Alam  
 Mathematics Discipline,  
 Khulna University,  
 Khulna-9208, Bangladesh  
 E-mail: alam\_mahmud2000@yahoo.com



## ENTRANCE FLOW THROUGH ROTATING CURVED PIPE OF CIRCULAR CROSS-SECTION

M. A. Masud and M. Mahmud Alam

Mathematics Discipline, Khulna University, Khulna, Bangladesh

### ABSTRACT

A numerical study is performed regarding entrance flow of a viscous incompressible fluid through rotating curved pipe of circular cross-section. The flow depends on the pressure gradient force, centrifugal force due to curvature and coriolis force due to rotation. The effects of all these forces result in interesting flow behaviours in the entry region which are analyzed in the present study. The mathematical model is established considering three dimensional momentum equation. The problem is solved by finite difference method in a computational mesh extending from the inlet immediately adjacent to the reservoir to the fully developed region.

**Keywords:** Entry Flow, Rotation, Curved Pipe.

### 1. INTRODUCTION

Fluid flow in curved pipes is of considerable importance. It has large applications in chemical and mechanical engineering. Curved tube geometries are also found in bio-fluid-mechanics. It is extensively used in piping systems such as intakes in aircraft.

In case of curved pipe centrifugal force originates due to the curvature of the pipe. For flow through a straight pipe, the axial velocity in the core region is much larger than that near the wall which is due to no-slip condition at the wall. But when the fluid flows through a curved pipe, the particles experience centrifugal force which brings about the secondary flow. This was first noticed by Williams et al.[1]. They also found that the location of the maximum axial velocity is shifted towards the outer wall as an effect of the occurrence of secondary flow.

Dean [2,3] was the foremost author to formulate the problem theoretically. Here incompressible viscous fluid flow under constant pressure gradient force has been investigated and the flow is found to be dependent on a parameter termed as Dean number  $D_n$  given by

$$D_n = \frac{a^3}{\mu\nu} \sqrt{\frac{2a}{L}} G ; \text{ where, } \mu \text{ is the coefficient of}$$

viscosity,  $\nu$  is the kinematic viscosity,  $G$  is the constant pressure gradient force,  $L$  is the radius of the pipe and  $a$  is the radius of the cross-section.

After this, a lot of research works regarding fully developed flow have been carried out at different times. But in practice the flow is not always fully developed. So developing or entry flow is of utmost importance specially in case of physiological phenomena. Austin [4], Patankar et al. [5] and Humphrey [6] carried out study on developing flow through curved pipe beginning with

Poiseuille flow at the inlet using finite-difference technique. Singh [7] obtained a series solution for the entry-flow problem. He found a saddle-point-like stagnation point and a node-like sink near and at the centre of the pipe. Yao and Berger [8] obtained a solution for the flow from the entry to the fully developed region. Soh and Berger [9] solved elliptic Navier-Stokes equation for entrance flow into a curved pipe using the artificial compressibility technique. Secondary flow separation was observed near the inner wall in the developing region of the curved pipe.

But if the curved pipe rotates, in addition to centrifugal force the fluid experiences Coriolis force. The rotation is considered to be positive if it is in such a direction that the Coriolis force results a positive effect to that of the centrifugal force and this case is known as co-rotating case. Otherwise the rotation is considered to be negative and is known as counter rotating case. These types of rotating ducts are used in cooling systems for conductors of electric generators.

Since the pipelines have more or less a bent or a curved section, it is interesting to investigate the combined effects of curvature and rotation, which are relevant to the flow in rotating curved ducts. Miyazaki [10] examined the solutions for co-rotating case. Ito and Motai [11] investigated both co-rotating and counter rotating cases. At this time the concept of bifurcation was not so rich. Later Daskopoulos and Lenhoff [12] showed the bifurcation study of the flow combined with curvature and rotation.

In this paper, our aim is to study the entrance flow through a curved pipe of circular cross-section rotating at a constant angular velocity about an axis passing through the center of curvature of the pipe and perpendicular to the plane of the pipe.

## 2. GOVERNING EQUATIONS

A curved pipe of uniform circular cross-section has been considered. The pipe is rotating at a constant angular velocity about an axis passing through the centre of curvature of the pipe and perpendicular to the plane containing the axis of the pipe. The radius of the pipe is  $R$  and the radius of the cross-section is  $a$ . Toroidal coordinate system  $(r', \theta, s')$  has been considered to describe the motion of the fluid particles in the pipe which is illustrated in Fig 1.  $u', v', w'$  are the velocity components along  $r', \theta, s'$  directions respectively,  $p'$  is the pressure and  $\rho$  is the constant density of the fluid.

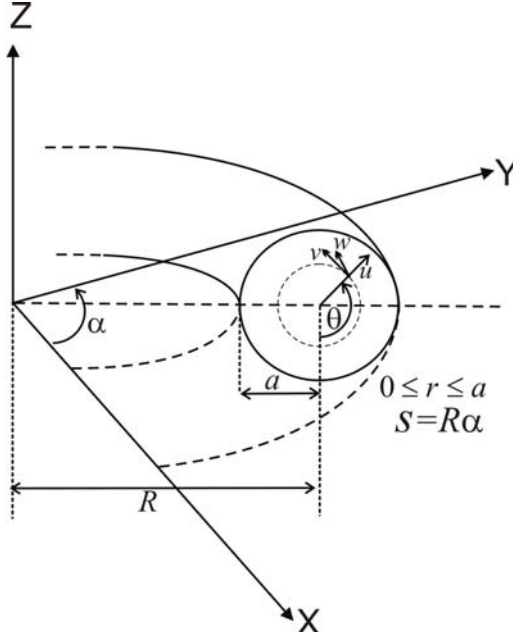


Fig 1. Toroidal coordinate system for a curved pipe with circular cross-section.

Introducing the non-dimensional variables,

$$u = \frac{u'}{W_o}, v = \frac{v'}{W_o}, w = \frac{w'}{W_o}, p = \frac{p'}{\rho W_o^2}, r = \frac{r'}{a}$$

we get the following momentum equations,

radial momentum equation,

$$\begin{aligned} & \frac{1}{r\omega} \left[ \frac{\partial}{\partial s} (ruw) + \frac{\partial}{\partial r} (r\omega u^2) + \frac{\partial}{\partial \theta} (\omega uv) - \omega v^2 - \delta r w^2 \sin \theta \right] - T_{r,v} \\ &= -\frac{\partial p_1}{\partial r} + \frac{1}{R_e} \left[ \frac{1}{r\omega} \left\{ \frac{\partial}{\partial r} \left( r\omega \frac{\partial u}{\partial r} \right) + \frac{\partial}{\partial \theta} \left( \frac{\omega}{r} \frac{\partial u}{\partial \theta} \right) + \frac{\partial}{\partial s} \left( \frac{r}{\omega} \frac{\partial u}{\partial s} \right) \right\} \right. \\ & \left. - \frac{1}{r^2} \left( 2 \frac{\partial v}{\partial \theta} + u \right) - \frac{v\delta}{\omega r} \cos \theta - \frac{\delta^2}{\omega^2} \left( \frac{2}{\delta} \frac{\partial w}{\partial s} + u \sin \theta + v \cos \theta \right) \sin \theta \right] \end{aligned} \quad (1)$$

circumferential momentum equation,

$$\begin{aligned} & \frac{1}{r\omega} \left[ \frac{\partial}{\partial s} (rvw) + \frac{\partial}{\partial r} (ruv\omega) + \frac{\partial}{\partial \theta} (\omega v^2) + \omega uv - \delta r w^2 \cos \theta \right] - T_{r,u} \\ &= -\frac{1}{r} \frac{\partial p_1}{\partial \theta} + \frac{1}{R_e} \left[ \frac{1}{r\omega} \left\{ \frac{\partial}{\partial r} \left( r\omega \frac{\partial v}{\partial r} \right) + \frac{\partial}{\partial \theta} \left( \frac{\omega}{r} \frac{\partial v}{\partial \theta} \right) + \frac{\partial}{\partial s} \left( \frac{r}{\omega} \frac{\partial v}{\partial s} \right) \right\} \right. \\ & \left. + \frac{1}{r^2} \left( 2 \frac{\partial u}{\partial \theta} - v \right) + \frac{u\delta}{\omega r} \cos \theta - \frac{\delta^2}{\omega^2} \left( \frac{2}{\delta} \frac{\partial w}{\partial s} + u \sin \theta + v \cos \theta \right) \cos \theta \right] \end{aligned} \quad (2)$$

Axial momentum equation,

$$\begin{aligned} & \frac{1}{r\omega} \left[ \frac{\partial}{\partial s} (rw^2) + \frac{\partial}{\partial r} (r\omega uw) + \frac{\partial}{\partial \theta} (\omega vw) + rw\delta (u \sin \theta + v \cos \theta) \right] \\ &= -\frac{1}{\omega} \frac{\partial p_1}{\partial s} + \frac{1}{R_e} \left[ \frac{1}{r\omega} \left\{ \frac{\partial}{\partial r} \left( r\omega \frac{\partial w}{\partial r} \right) + \frac{\partial}{\partial \theta} \left( \frac{\omega}{r} \frac{\partial w}{\partial \theta} \right) + \frac{\partial}{\partial s} \left( \frac{r}{\omega} \frac{\partial w}{\partial s} \right) \right\} \right. \\ & \left. + \frac{2\delta^2}{\omega^2} \left( \frac{\sin \theta}{\delta} \frac{\partial u}{\partial s} - \frac{\cos \theta}{\delta} \frac{\partial v}{\partial s} - \frac{w}{2} \right) \right] \end{aligned} \quad (3)$$

and the continuity equation takes the form,

$$\frac{\partial}{\partial r} (r\omega u) + \frac{\partial}{\partial \theta} (\omega v) + \frac{\partial}{\partial s} (rw) = 0 \quad (4)$$

where,  $R_e = \frac{aW_o}{\nu}$ ,  $T_r = \frac{2a\Omega}{W_o}$ ,  $\omega = 1 + r\delta \sin \theta$  and

$$\delta = \frac{a}{R}$$

## 3. BOUNDARY CONDITIONS

In the present study the fluid flow boundary is considered to be consists of three regions: the inlet cross-section where the fluid is entering, the rigid wall surrounding the fluid and the cross-section far downstream where the flow is assumed to be fully developed.

The initial conditions at the inlet is considered as,

$$w(r, \theta, 0) = \frac{1}{1 + \delta r \sin \theta}, \quad u(r, \theta, 0) = v(r, \theta, 0) = 0 \quad \text{and}$$

$$p = -\frac{1}{2(1 + \delta r \sin \theta)^2}$$

Due to the no-slip condition, all the velocity components vanish at the rigid boundary, i.e.,

$$u(1, \theta, s) = v(1, \theta, s) = w(1, \theta, s) = 0$$

At far down stream when the flow gets fully developed,  $\frac{\partial u}{\partial s} = \frac{\partial v}{\partial s} = \frac{\partial w}{\partial s} = 0$

## 4. FINITE DIFFERENCE FORMULATIONS

To rewrite the momentum equations (1-3) and 4 into a practical finite-difference scheme of computation, the grid arrangement shown in Fig 2 and Fig 3 has been chosen. The grid has been arranged in such a way that pressure is defined at the centre of a cell and  $u, v, w$  are defined at different positions on the pressure cell boundaries.

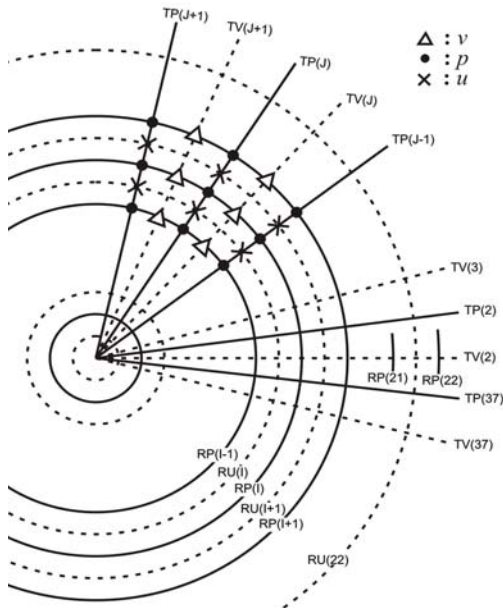


Fig 2. Grid system in the cross-section.

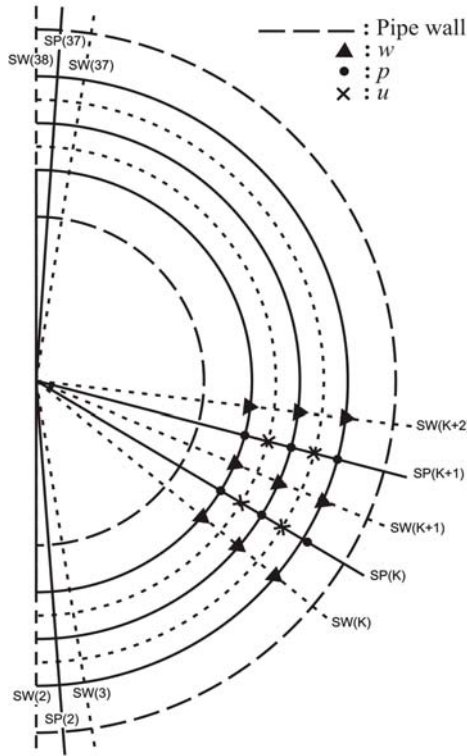


Fig 3. Grid system in the horizontal plane passing through the axis of the pipe.

Then the momentum equations in  $u, v, w$  -directions reduces to,

$$a_{ijk}^u u_{ijk} = a_{i+1,jk}^u u_{i+1,jk} + a_{i-1,jk}^u u_{i-1,jk} + a_{ij+1k}^u u_{ij+1k} + a_{ij-1k}^u u_{ij-1k} + a_{ijk+1}^u u_{ijk+1} + a_{ijk-1}^u u_{ijk-1} + b^u + A_{ijk}^u (p_{i-1,jk} - p_{ijk})$$

$$a_{ijk}^v v_{ijk} = a_{i+1,jk}^v v_{i+1,jk} + a_{i-1,jk}^v v_{i-1,jk} + a_{ij+1k}^v v_{ij+1k} + a_{ij-1k}^v v_{ij-1k} + a_{ijk+1}^v v_{ijk+1} + a_{ijk-1}^v v_{ijk-1} + b^v + A_{ijk}^v (p_{ij-1k} - p_{ijk})$$

$$a_{ijk}^w w_{ijk} = a_{i+1,jk}^w w_{i+1,jk} + a_{i-1,jk}^w w_{i-1,jk} + a_{ij+1k}^w w_{ij+1k} + a_{ij-1k}^w w_{ij-1k} + a_{ijk+1}^w w_{ijk+1} + a_{ijk-1}^w w_{ijk-1} + b^w + A_{ijk}^w (p_{ijk-1} - p_{ijk})$$

respectively. And the continuity equation reduces to,

$$a_p p'_p = a_E p'_E + a_W p'_W + a_N p'_N + a_S p'_S + a_T p'_T + a_B p'_B + b$$

The accuracy is assured by taking  $DIF < 10^{-6}$ , where

$$DIF = \sum \sum \sum \left\{ u_{n+1}(i, j, k) - u_n(i, j, k) \right\}^2 + \left\{ v_{n+1}(i, j, k) - v_n(i, j, k) \right\}^2 + \left\{ w_{n+1}(i, j, k) - w_n(i, j, k) \right\}^2$$

## 5. RESULTS AND DISCUSSION

Calculations were carried out for  $Re = 242$  &  $900$  and  $\delta = 0.1$  in a computational mesh extending from inlet ( $0^\circ$ ) to the outlet ( $180^\circ$ ).

### 5.1 Secondary Flow Development

Vector plots of the secondary flow have been shown in Fig 4(a) and 4(b) for  $Re = 242$  &  $900$  respectively at different positions. The secondary flow is set up just after entering the inlet due to the effect of centrifugal force. Most of the particles get radial velocity. Circumferential velocity is greater for the particles near the upper and lower boundary due to the friction with the wall. Also the velocity of the particles at the centre of cross-section is radially outward for the effect of centrifugal force. As the flow goes downstream the secondary velocity of the particles near the centre of the cross-section increase in the direction of the centrifugal force and the flow in the core region moves radially outward along the horizontal plane passing through the centre of the cross-section. At the same time, the particles near the upper and lower boundary experience high circumferential velocity in the direction opposite to the velocity of the particles at the core region. As a result, two vortex secondary flow is set up, which is symmetric about the horizontal plane passing through the centre of cross-section.

Increase in Reynold's number decrease the velocity of he particles near the core region remarkably. For  $Re = 900$  the secondary velocity of the particles in the inner half is higher than the velocity of the particles at the centre and outer half of the cross-section. As a result, two vortices are set up in the inner half. The strength of these vortices is lower than that of the vortices for  $Re = 242$ .

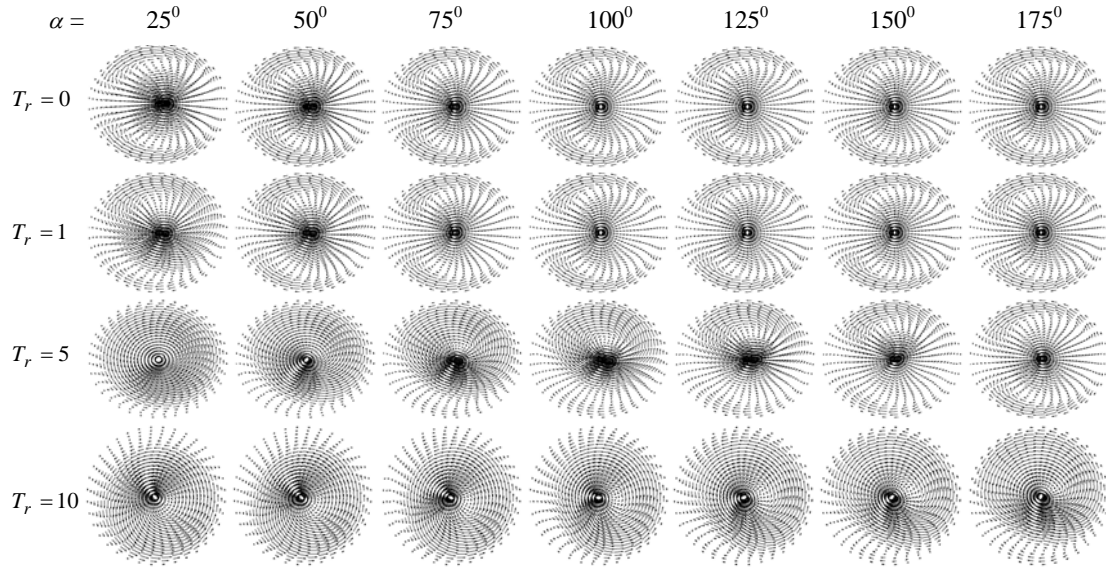


Fig 4a. Vector plots of the secondary flow for  $R_e = 242$  and  $\delta = 0.1$

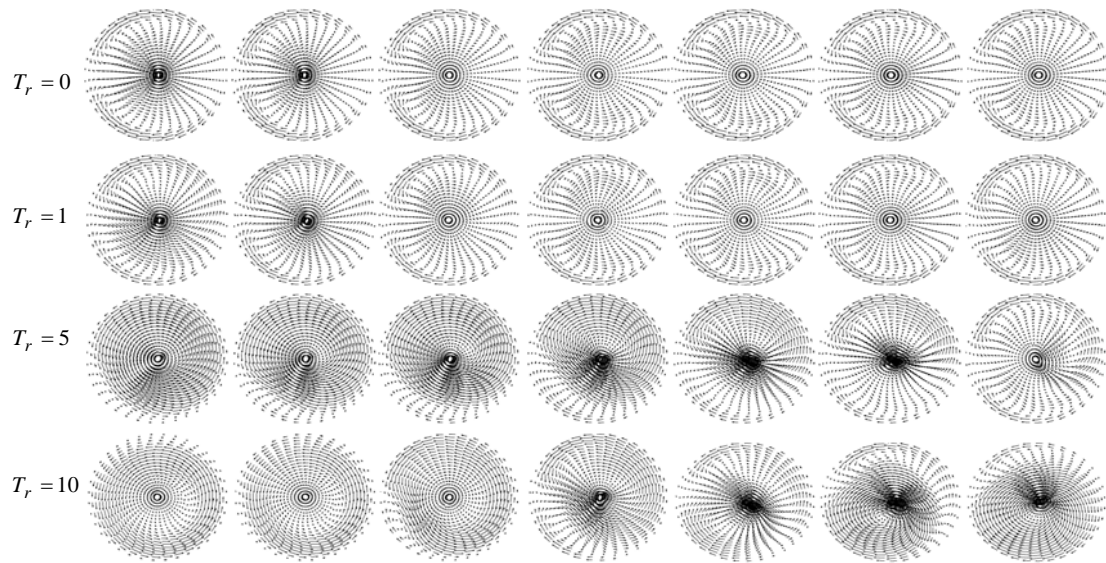


Fig 4b. Vector plots of the secondary flow for  $R_e = 900$  and  $\delta = 0.1$

When rotation comes to play, centrifugal force and Coriolis force work simultaneously in addition to pressure gradient force. The Coriolis force breaks down the symmetry. The particles get high circumferential velocity due to Coriolis force. As the flow proceed downstream a vortex originates from the lower portion and two vortex secondary flow is set up. Gradually the lower vortex gets stronger. At far downstream the centrifugal force prevails over Coriolis force and the secondary flow become symmetric. If rotation is increased the Coriolis force increases and consequently the flow needs to traverse more towards downstream to be symmetric. For high rotation ( $T_r = 10$ ) remain

asymmetric even at the outlet.

### 5.2 Axial Flow Development

The contour plots of the axial velocity has been shown in Fig 5(a) and 5(b) for  $Re = 242$  &  $900$  respectively. As the flow enters the pipe boundary layer begins to develop. Boundary layer near the inner wall develops faster than that at the outer wall. And with the development of the flow the strength of the axial flow is increased and is shifted towards the outer wall of the cross-section, which is effect of the centrifugal force due to curvature. The axial flow is symmetric about the plane passing through the centre of cross-section at the absence of rotation.

When the pipe rotates the symmetry breaks down. Due to Coriolis force the strength of the axial flow is shifted towards the lower portion of the cross-section. As the flow proceeds downstream the strength of the axial flow is shifted towards the middle of the outer half. Finally the centrifugal force dominates the Coriolis force and symmetry is attained. But for higher rotation the Coriolis force is too high to be dominated by the centrifugal force. As a result symmetry is not attained finally.

For high rotation initially two peaked axial velocity is found. With the development of the flow the outer

peak diminishes while the inner peak develops and gradually shifted outward. Finally, it took place diagonally between the upper part of the outer half and lower part of the inner half.

For  $Re = 900$  symmetric axial velocity profile has been found which is strong in the outer half when rotation is absent. When  $T_r = 10$  two peaked axial velocity is found, one peak in the inner half and another in the outer half. With the development of the flow the vortices took place in the upper and lower half of the cross-section respectively.

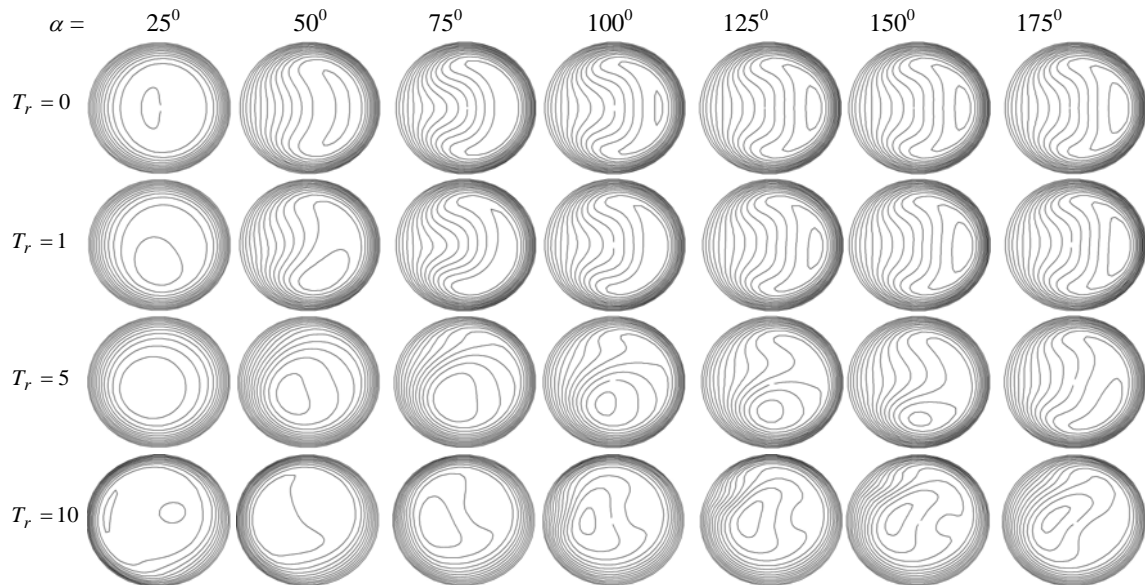


Fig 5a. Contour plots of the axial flow for  $R_e = 242$  and  $\delta = 0.1$

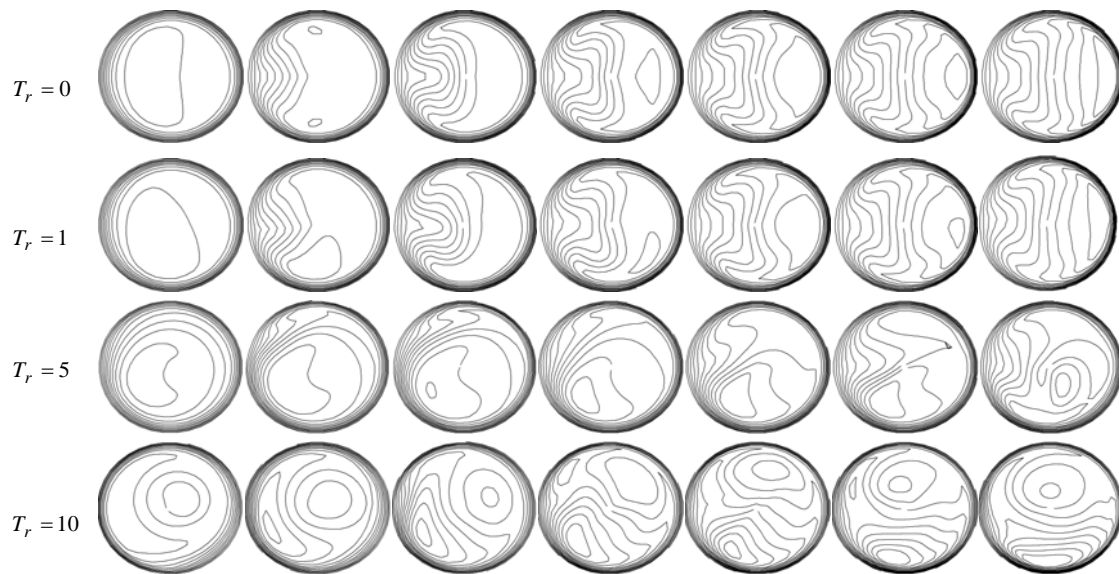


Fig 5b. Contour plots of the axial flow for  $R_e = 900$  and  $\delta = 0.1$

## 6. REFERENCES

1. Williams, G. S., Hubbell, C. W. and Finkell, G. H., 1902, "Experiments at Detroit, Michigan on the effect of curvature on the flow of water in pipes", Trans. ASCE, 47:1-196.
2. Dean, W. R., 1927, "Note on the Motion of Fluid in a Curved Pipe", Philosophical Magazine and Journal of Science, 4(20):208-223.
3. Dean, W. R., 1928, "The Stream-line Motion of Fluid in a Curved Pipe", Philosophical Magazine and Journal of Science, 5(30):673-695.
4. Austin, L., 1971, *The development of viscous flow within helical coils*, Ph. D. thesis, University of Utah, Salt Lake City.
5. Patankar, S. V., Pratap, V. S. and Spalding, D. B., 1974, "Prediction of laminar flow and heat transfer in helically coiled pipes", Journal of Fluid Mechanics, 62:539.
6. Humphery, J. A. C., 1977, *Flow in ducts with curvature and roughness*. Ph. D. thesis, Imperial College of Science and Technology.
7. Singh, M. P., 1974, "Entry flow in a curved pipe", Journal of Fluid Mechanics, 65:517.
8. Yao, L. S. and Berger, S. A., 1975, "Entry flow in a curved pipe", Journal of Fluid Mechanics, 88: 339.
9. Soh, W. Y. and Berger, S. A., 1984, "Laminar entrance flow in a curved pipe", Journal of Fluid Mechanics, 148:109-135.
10. Miyazaki, H., 1971, "Combined free- and

forced-convective heat transfer and fluid flow in rotating curved circular tube", International Journal of heat mass transfer, 14:1295-1309.

11. Ito, H. and Motai T., 1974, "Secondary flow in rotating curved pipe", The reports of the Institute of high speed Mechanics, Tohoku University, Sendai, Japan, 29(270):33-57.
12. Daskopoulos, P. and Lenhoff, A. M., 1990, "Flow in curved ducts: Part 2. Rotating ducts", Journal of Fluid Mechanics, 217:575-593.

## 7. NOMENCLATURE

Symbol	Meaning
$u, v, w$	Dimensionless velocity components along radial, circumferential and axial direction respectively
$Re$	Reynold's Number
$T_r$	Taylor Number
$\delta$	Dimensionless curvature

## 8. MAILING ADDRESS

Md. Mahmud Alam  
 Mathematics Discipline,  
 Khulna University, Khulna-9208, Bangladesh  
 E-mail: alam\_mahmud2000@yahoo.com

## FLOW THROUGH A CURVED RECTANGULAR DUCT

R. Nath Mondal, B. Roy and A. Kumar Datta

Mathematics Discipline; Science, Engineering and Technology School,  
Khulna University, Khulna, Bangladesh

### ABSTRACT

Flow through a curved rectangular duct of aspect ratios  $0.5 \leq l \leq 1.5$  is investigated numerically by using a spectral and covering a wide range of the Dean number. First, bifurcation structure of the steady solutions is investigated. As a result, a number of steady solution branches with asymmetric two-vortex and symmetric two- and multi-vortex solutions are obtained. The main concern of the present study is to investigate the transitional behavior of the unsteady solutions such as periodic, multi-periodic and chaotic solutions, as the aspect ratio changes. Time evolution calculations as well as their phase spaces show that the steady flow turns into chaotic flow through periodic and multi-periodic flows, if the Dean number is increased no matter what the aspect ratio is. It is found that the flow oscillates periodically or aperiodically between two-, four-, six-, eight- and ten-vortex solutions, as the aspect ratio is increased. It is also found that the axial flow shifted at the outer wall of the duct as the Dean number is increased.

**Keywords:** Curved Duct, Secondary Flow, Time Evolution, Periodic Solution, Chaos.

### 1. INTRODUCTION

The study of flows through curved ducts and channels has been and continuous to be an area of paramount interest of many researchers because of the diversity of their practical applications in fluids engineering, such as in fluid transportation, turbo machinery, refrigeration, air conditioning systems, heat exchangers, chemical reactors, ventilators, centrifugal pumps, internal combustion engines and blade- to-blade passage for cooling system in modern gas turbines. Blood flow in the human and other animals also represents an important application of this subject because of the curvatures of many blood vessels, particularly the aorta.

Considering the non-linear nature of the Navier-Stokes equation, the existence of multiple solutions does not come as a surprise. However, an early complete bifurcation study of fully developed flows in a curved duct was conducted by Winters (1987). Yanase *et al.*, (2005) performed numerical investigation of isothermal and non-isothermal flows through a curved duct of rectangular cross-section. Mondal *et al.* (2006) performed numerical prediction of non-isothermal flows through a curved square duct over a wide range of the curvature and the Dean number. Recently, Mondal *et al.* (2007) numerically investigated the bifurcation diagram for two-dimensional steady flow through a curved square duct. Very recently, Mondal *et al.* (2009) performed bifurcation structure of the steady solutions and investigated linear stability of the solutions for the flow through a curved rectangular duct.

Time dependent analysis of fully developed curved duct flows was initiated by Yanase and Nishiyama (1988) for a rectangular cross section. Mondal *et al.* (2007) performed numerical prediction of the solution structure, stability and transitions of isothermal flow through a curved square duct. They showed that there is a close relationship between unsteady solutions and the bifurcation diagram of steady solutions. To the best of the authors' knowledge, however, there has not yet been done any substantial work studying the effects of aspect ratio on unsteady solutions through a curved rectangular duct flows. This paper is, therefore, an attempt, to fill up this gap with a view to study the non-linear nature of the unsteady solutions for various aspect ratios, because this type of flow of often encountered in engineering applications.

In the present study, a numerical result is presented for the fully developed two-dimensional flow of viscous incompressible fluid through a curved rectangular duct. The main objective of the present study is to obtain solution structure of the steady solutions and to discuss the unsteady flow behavior through a curved rectangular channel.

### 2. MATHEMATICAL FORMULATION

Consider a viscous incompressible fluid streaming through a curved duct with rectangular cross-sections. The coordinate system with relevant notations is shown in Fig. 1. It assumed that the flow is uniform in the z-direction which is driven by a constant pressure gradient  $G$  along the centre of the duct.  $u$ ,  $v$  and  $w$  are the



velocity components in the  $x$ -,  $y$ - and  $z$ -directions, respectively. The variables are non-dimensionalized by using the representative length and the representative velocity.

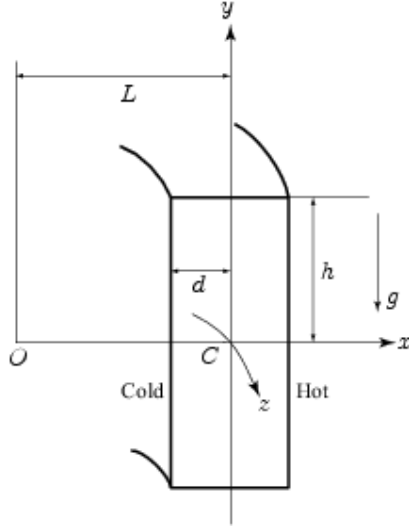


Fig 1. Coordinate system of the curved rectangular duct.

The sectional stream function  $\psi(x, y)$  is introduced in the  $x$ - and  $y$ - directions as

$$u = \frac{1}{1 + \delta x} \frac{\partial \psi}{\partial y}, \quad v = \frac{1}{1 + \delta x} \frac{\partial \psi}{\partial x} \quad (1)$$

Then the basic equations for  $w$  and  $\psi$  are derived from the Navier-Stokes equations as

$$(1 + \delta x) \frac{\partial w}{\partial t} + \frac{1}{l} \frac{\partial(w, \psi)}{\partial(x, y)} - Dn + \frac{\delta^2 w}{1 + \delta x} = \quad (2)$$

$$(1 + \delta x) \Delta_2 w - \frac{\delta}{l(1 + \delta x)} \frac{\partial \psi}{\partial y} w + \delta \frac{\partial w}{\partial x}$$

$$\begin{aligned} \left( \Delta_2 - \frac{\delta}{1 + \delta x} \frac{\partial}{\partial x} \right) \frac{\partial \psi}{\partial t} &= - \frac{1}{l(1 + \delta x)} \frac{\partial(\Delta_2 \psi, \psi)}{\partial(x, y)} \\ &+ \frac{\delta}{l(1 + \delta x)^2} \left[ \frac{\partial \psi}{\partial y} \left( 2\Delta_2 \psi - \frac{3\delta}{1 + \delta x} \frac{\partial \psi}{\partial x} + \frac{\partial^2 \psi}{\partial x^2} \right) \right. \\ &- \left. \frac{\partial \psi}{\partial x} \frac{\partial^2 \psi}{\partial x \partial y} \right] + \frac{\delta}{(1 + \delta x)^2} \left[ 3\delta \frac{\partial^2 \psi}{\partial x^2} - \frac{3\delta^2}{1 + \delta x} \frac{\partial \psi}{\partial x} \right] \\ &- \frac{2\delta}{1 + \delta x} \frac{\partial}{\partial x} \Delta_2 \psi + \frac{1}{l} w \frac{\partial \psi}{\partial y} + \Delta_2^2 \psi \end{aligned} \quad (3)$$

where

$$\Delta_2 \equiv \frac{\partial^2}{\partial x^2} + \frac{1}{l^2} \frac{\partial^2}{\partial y^2}, \quad \frac{\partial(f, g)}{\partial(x, y)} \equiv \frac{\partial f \partial g}{\partial x \partial y} - \frac{\partial f \partial g}{\partial y \partial x}$$

and  $Dn$  is Dean number defined as  $Dn = \frac{Gd^3}{\mu\nu} \sqrt{\frac{2d}{L}}$ ,

$l$  is the aspect ratio defined as  $l = \frac{h}{d}$ .

The no-slip boundary conditions for  $w$  and  $\psi$  are used as:

$$w(\pm 1, y) = w(x, \pm 1) = \psi(\pm 1, y) =$$

$$\psi(x, \pm 1) = \frac{\partial \psi}{\partial x}(\pm 1, y) = \frac{\partial \psi}{\partial y}(x, \pm 1) = 0 \quad (4)$$

### 3. NUMERICAL CALCULATION

In order to obtain the numerical solutions, spectral method is used. The main objective of the method is to use the expansion of the polynomial functions that is the variables are expanded in the series of functions consisting of Chebyshev polynomials. The expansion function  $\phi_n(x)$  and  $\psi_n(x)$  are expressed as

$$\phi_n(x) = (1 - x^2) C_n(x), \quad (5)$$

$$\psi_n(x) = (1 - x^2)^2 C_n(x)$$

where  $C_n(x) = \cos(n \cos^{-1}(x))$  is the  $n^{\text{th}}$  order Chebyshev polynomial.  $w(x, y, t)$  and  $\psi(x, y, t)$  are expanded in terms of the expansion functions  $\phi_n(x)$  and  $\psi_n(x)$  as:

$$\left. \begin{aligned} w(x, y, t) &= \sum_{m=0}^M \sum_{n=0}^N w_{mn}(t) \phi_m(x) \psi_n(y) \\ \psi(x, y, t) &= \sum_{m=0}^M \sum_{n=0}^N \psi_{mn}(t) \psi_m(x) \psi_n(y). \end{aligned} \right\} \quad (6)$$

where  $M$  and  $N$  are the truncation numbers in the  $x$  and  $y$  directions respectively. Steady solutions are obtained by the Newton-Raphson iteration method. Finally, for the unsteady solutions, Crank-Nicolson and Adams-Bashforth methods together with the function expansion and collocation methods are applied.

### 4. RESISTANT CO-EFFICIENT

The resistant coefficient  $\lambda$  is used as the representative quantity of the flow state and is generally used in fluids engineering, defined as

$$\frac{P_1^* - P_2^*}{\Delta_{z^*}} = \frac{\lambda}{d_h^*} \frac{1}{2} \rho \langle \omega^* \rangle^2 \quad (7)$$

where quantities with an  $P_1^*$  be asterisk denote dimensional ones,  $\langle \rangle$  stands for the mean over the cross section of the duct and  $d_h^* = 4(2d \times 2dl)/(4d + 4dl)$  is the hydraulic diameter. The main axial velocity  $\langle \omega^* \rangle$  is calculated by

$$\langle \omega^* \rangle = \frac{v}{4\sqrt{2\delta}l} \int_{-1}^1 dx \int_{-1}^1 \omega(x, y, t) dy \quad (8)$$

Since  $(P_1^* - P_2^*)/\Delta_{z^*} = G$ ,  $\lambda$  is related to the mean

non-dimensional axial velocity  $\langle \omega \rangle$  as

$$\lambda = \frac{8l\sqrt{2\delta}Dn}{(1+l)\langle \omega \rangle^2} \quad (9)$$

where  $\langle \omega \rangle = \sqrt{2\delta d} \langle \omega^* \rangle / \nu$ .

## 5. RESULTS AND DISCUSSION

### 5.1 Case I: Aspect Ratio $L = 0.5$

#### 5.1.1 Solution Structure of the Steady Solutions

We obtained a single branch of steady solution for the aspect ratio  $l = 0.5$ . The solution branch is shown in Fig. 2(a). It is found that the steady solution branch consists of symmetric two- and four-vortex solutions. It is also found that as  $Dn$  increases, the centrifugal force becomes strong and consequently the axial flow shifted to the outer bend of the wall.

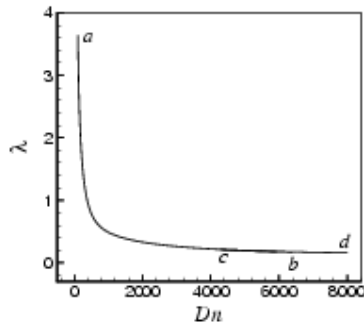


Fig 2. Steady solution branches for the aspect ratio

#### 5.1.2 Unsteady Solutions

To investigate non-linear behavior of the unsteady solutions, time-evolution calculation of the resistance co-efficient  $\lambda$  is performed. Since the steady solution is stable for  $Dn \leq 6404$  (Mondal *et al.*, 2009), we performed unsteady solutions for  $Dn > 6404$ . Time evolution of  $\lambda$  for  $Dn = 6500$  is shown in Fig. 3(a), where it is found that the flow is multi-periodic. Then we draw some contours of secondary flow and axial flow distribution in Fig. 3(b), where we observe that the unsteady flow oscillates between symmetric two- and four-vortex solutions.

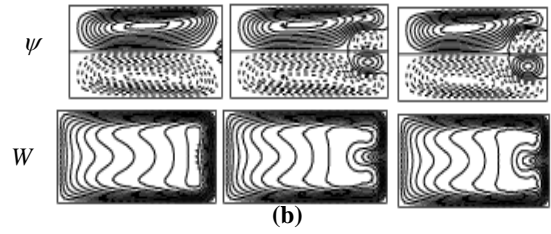
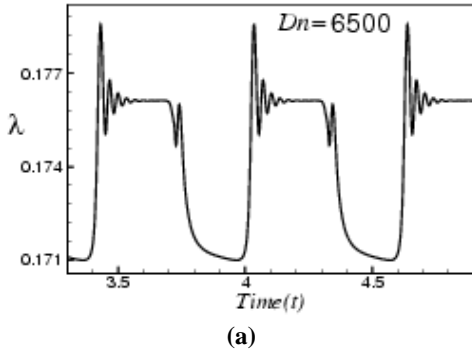


Fig 3.(a) Time evolution of  $\lambda$  for  $Dn = 6500$  and  $l = 0.5$ . (b) Secondary flow patterns (top) and axial flow distribution (bottom).

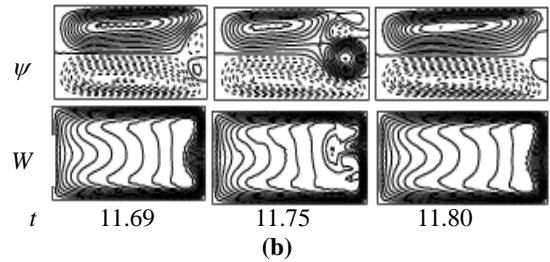
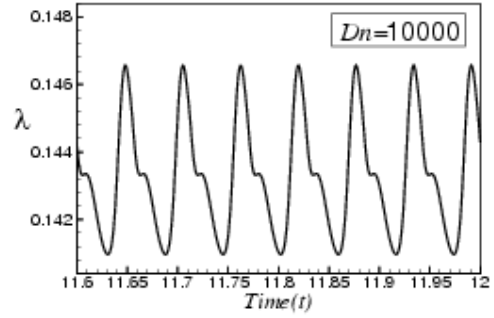


Fig. 4. (a) Time evolution of  $\lambda$  for  $Dn = 10000$  and  $l = 0.5$ . (b) Secondary flow patterns (top) and axial flow distribution (bottom).

Then we performed time evolution of  $\lambda$  for  $Dn = 10000$  as shown in Fig 4(a). It is found that the flow is multi-periodic for  $Dn = 10000$ . Contours of some secondary flow patterns and axial flow distributions are shown in Fig. 4(b), where it is seen that the multi-periodic oscillation at  $Dn = 10000$  oscillates between asymmetric two-, three- and four-vortex solutions.

### 5.2 Case II: Aspect Ratio $L = 1.5$

#### 5.2.1 Solution Structure of the Steady Solutions

We obtained four branches of steady solutions for the aspect ratio  $l = 1.5$ . The bifurcation diagram is shown in Fig. 5(a). It is found that there exists a bifurcating relationship between the first and second steady solution branches. The second branch bifurcates from the second branch by a sub-critical pitchfork bifurcation. We obtained two-, four-, six-, eight-, ten- and twelve-vortex solutions on various branches. Figure 5(b) shows contours of some secondary flow patterns and axial flow distribution at various  $Dn$ .

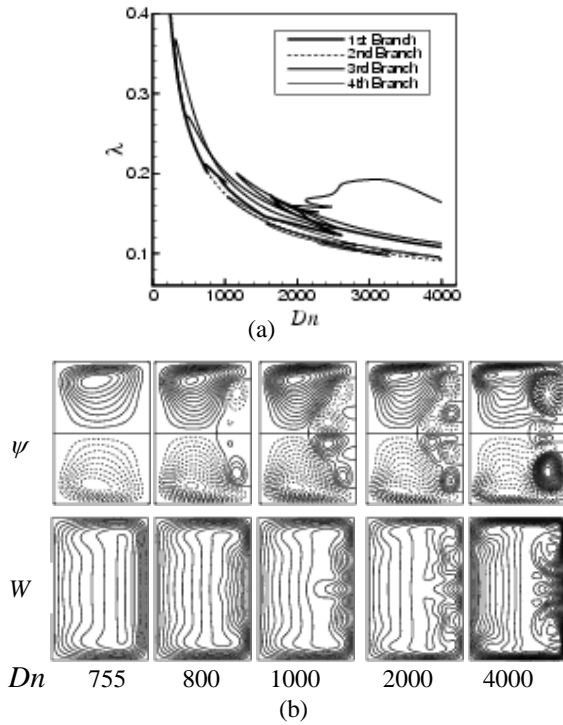


Fig 5. (a) Bifurcation structure of steady solutions for  $l = 1.5$ . (b) Secondary flow patterns (top) and axial flow distribution (bottom) for  $l = 1.5$ .

### 5.2.2 Unsteady Solutions

Unsteady solutions are obtained for  $Dn > 625$ , where the flow is stable for  $Dn \leq 625$ .

As the steady solution for  $Dn > 625$ , we performed time evolution of  $\lambda$  for  $Dn = 1225$  as shown in Fig. 6(a). It is found that the flow is time periodic. Contours of secondary flow and axial flow distribution are shown in Fig. 6(b), where it is seen that the periodic solution at  $Dn = 1225$  oscillates between symmetric four-vortex solutions.

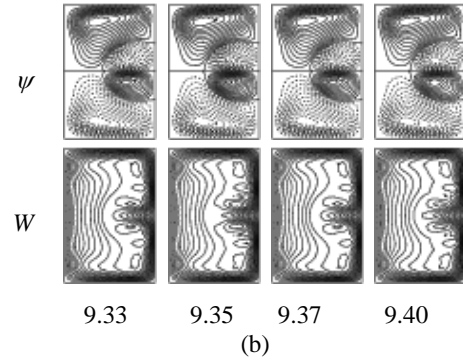
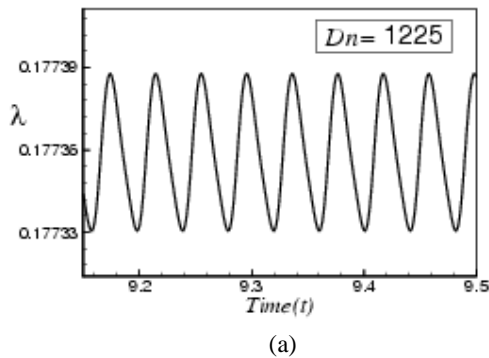


Fig 6. (a) Time evolution of  $\lambda$  for  $Dn = 1225$  and  $l = 1.5$ . (b) Secondary flow patterns (top) and axial flow distribution (bottom)

Then we performed unsteady solution for  $Dn = 1230$  as shown in Fig. 7(a). It is found that the flow oscillates irregularly, that is the flow is chaotic. Secondary flow patterns and axial flow distribution is shown in Fig. 7(b), where we find that the unsteady flow oscillates between two- and multi-vortex solutions. Since the nature of the flow characteristics changes between  $Dn = 1225$  and  $Dn = 1230$ , a transition from periodic to chaotic state occurs between  $Dn = 1225$  and  $Dn = 1230$  for the aspect ratio  $l = 1.5$ .

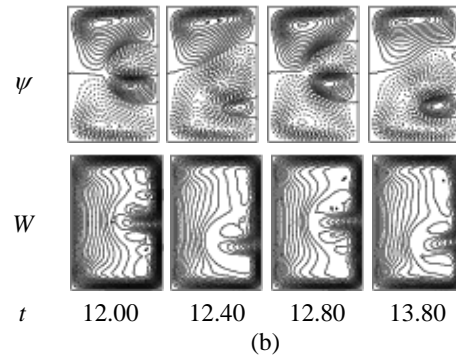
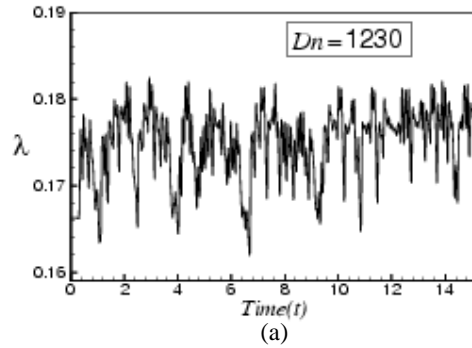


Fig 7. (a) Time evolution of  $\lambda$  for  $Dn = 1230$  and  $l = 1.5$ . (b) Secondary flow patterns (top) and axial flow distribution (bottom).

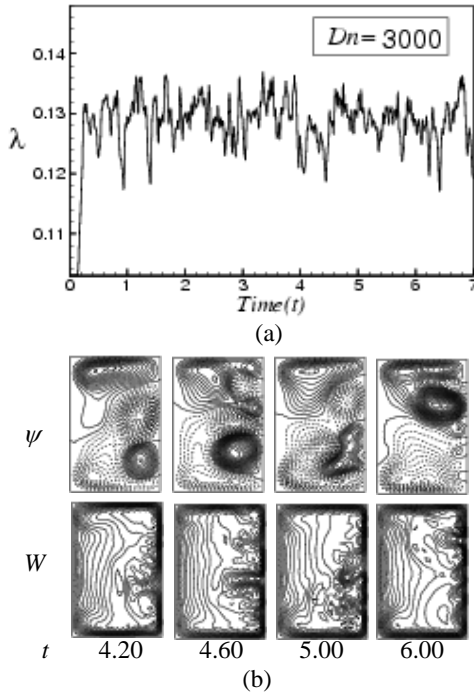


Fig 8. (a) Time evolution of  $\lambda$  for  $Dn = 3000$  and  $l = 1.5$ . (b) Secondary flow patterns (top) and axial flow distribution (bottom)

Finally, we performed time evolution calculations of  $\lambda$  for  $Dn = 3000$  as shown in Fig. 8(a). It is found that the flow is chaotic. Then contours of some secondary flow patterns and axial flow distributions are shown in Fig. 8(b). It is found that the chaotic solution at  $Dn = 3000$  oscillates between asymmetric two- and multi-vortex solutions. The chaotic solution at  $Dn = 1230$  is called *weak chaos* and that for  $Dn = 3000$  *strong chaos* (Mondal *et al.*, 2007).

## 6. CONCLUSIONS

In this study, we obtained solution structure of the steady solutions as well as unsteady solutions for the flow through a curved rectangular duct for the aspect ratios  $0.5 \leq l \leq 1.5$ . We obtained a number of steady solution branches with two- and multi-vortex solution on various branches. Time evolution calculation of the unsteady solutions for the aspect ratio 0.5 shows that the flow is periodic or multi-periodic for  $6404 < Dn < 10000$ , which oscillates between asymmetric two-, three- and four- vortex solutions. Then we studied time evolution of the unsteady solutions for  $Dn > 625$  for the aspect ratio  $l = 1.5$ , and it is found that the flow is periodic for

$Dn = 1225$  but chaotic for  $Dn = 1230$ . Thus the transition from periodic to chaotic state occurs between  $Dn = 1225$  and 1230. We also obtained chaotic solution at large values of the Dean number and it is found that chaotic solution becomes strong at large  $Dn$ . It is found that as the chaotic solution becomes strong, the number of secondary vortices also increases and the axial velocity shifted at the outer wall of the duct.

## 7. REFERENCES

1. Mondal, R. N., Kaga, Y., Hyakutake, T. and Yanase, S. (2006). Effects of Curvature and Convective Heat Transfer in Curved Square Duct Flows, *Journal of Fluids Engineering*, Vol. **128**, pp. 1013-1022.
2. Mondal, R. N., Kaga, Y., Hyakutake, T. and Yanase, S. (2007). Bifurcation diagram for two-dimensional steady flow and unsteady solutions in a curved square duct, *Fluid Dynamics Research*, Vol. **39**, pp. 413-446.
3. Mondal, R. N., Uddin, M. S., Ali, M. A. and Datta, A. K. (2009). Laminar flow through a curved duct with rectangular cross section, *Bulletin of pure and applied Mathematics*, Vol. **3**(1), pp. 55-71
4. Winters, K. H. (1987). A bifurcation study of laminar flow in a curved tube of rectangular cross section, *Journal of Fluid Mechanics*, Vol. **180**, pp. 343-369.
5. Yanase, S. and Nishiyama, K. (1988). On the bifurcation of laminar flows through a curved rectangular tube, *J. Phys. Soc. Japan*, Vol. **57**(11), pp. 3790-3795.
6. Yanase, S. Mondal, R. N., Kaga, Y. and Yamamoto, K. (2005). Transition from Steady to Chaotic States of Isothermal and Non-isothermal Flows through a curved Rectangular Duct, *Journal of the Physical Society of Japan*, Vol. **74**(1), pp. 345-358.

## 7. MAILING ADDRESS

Rabindra Nath Mondal  
 Mathematics Discipline;  
 Science, Engineering and Technology School,  
 Khulna University, Khulna-9208, Bangladesh  
 Phone: 0088-01710851580,  
 Fax: 0088-041-731244  
 E-mail: rmondal71@yahoo.com

## FLOW CHARACTERISTICS THROUGH A ROTATING CURVED DUCT WITH SQUARE CROSS SECTION

R. N. Mondal, A. K. Datta, M. A. Ali and M. S. Uddin

Mathematics Discipline; Science, Engineering and Technology School,  
Khulna University, Khulna, Bangladesh

### ABSTRACT

In this paper, a comprehensive numerical study is presented for the thermal flow through a rotating curved duct with square cross section. Numerical calculations are carried out over a wide range of the Taylor number  $0 \leq Tr \leq 3000$  for the Dean numbers  $Dn = 1000$  and  $Dn = 2000$  with the Grashof number  $Gr = 500$ , where the outer wall is heated and the inner one cooled. Spectral method is used as a basic tool to solve the system of non-linear differential equations. The rotation of the duct about the center of curvature is imposed, and the effects of rotation (*Coriolis force*) on the flow characteristics are investigated. As a result, multiple branches of asymmetric steady solutions with two- and four-vortex solutions are obtained. Linear stability of the steady solutions is then investigated. When there is no stable steady solution, time evolution calculations of the unsteady solutions are obtained, and it is found that there occur only periodic and multi-periodic solutions where the solution is unstable.

**Keywords:** Curved Square Duct, Secondary Flow, Steady Solutions, Dean Number, Taylor Number.

### 1. INTRODUCTION

The study of flows and heat transfer through a curved duct is of fundamental interest because of its importance in chemical, mechanical and biological engineering. Due to engineering applications and their intricacy, the flow in a rotating curved duct has become one of the most challenging research fields of fluid mechanics. Since rotating machines were introduced into engineering applications, such as rotating systems, gas turbines, electric generators, heat exchangers, cooling system and some separation processes, scientists have paid considerable attention to study rotating curved channel flows. The readers are referred to Berger *et al.* [1] and Nandakumar and Masliyah [2] for some outstanding reviews on curved duct flows.

One of the interesting phenomena of the flow through a curved duct is the bifurcation of the flow because generally there exist many steady solutions due to duct curvature. Many researches have performed experimental and numerical investigations on developing and fully developed curved duct flows. An early complete bifurcation study of two-dimensional (2D) flow through a curved channel was conducted by Winters [3]. However, an extensive treatment on the flow characteristics for both the isothermal and non-isothermal flows through curved duct with rectangular cross section was performed by Mondal [4].

The flow through a rotating curved duct is another

subject, which has attracted considerable attention because of its importance in engineering devices. The fluid flowing in a rotating curved duct is subjected to two forces: the Coriolis force due to rotation and the centrifugal force due to curvature. For isothermal flows of a constant property fluid, the Coriolis force tends to produce vortices while centrifugal force is purely hydrostatic. When a temperature induced variation of fluid density occurs for non-isothermal flows, both Coriolis and centrifugal type buoyancy forces can contribute to the generation of vortices (Wang and Cheng [5]). These two effects of rotation either enhance or counteract each other in a non-linear manner depending on the direction of wall heat flux and the flow domain. Therefore, the effect of system rotation is more subtle and complicated and yields new; richer features of flow and heat transfer in general, bifurcation and stability in particular, for non-isothermal flows. Recently, Mondal, Alam and Yanase [6] performed numerical prediction of non-isothermal flows through a rotating curved square channel with the Taylor number  $0 \leq Tr \leq 2000$  for the Grashof number  $Gr = 100$ .

In the present paper, a comprehensive numerical study is presented for the flows through a rotating curved duct with square cross section. Flow characteristics are studied over a wide of the Taylor number for the Grashof number  $Gr = 500$ . Studying the effects of rotation on the flow characteristics, caused by the buoyancy forces, is an important objective of the present study.

## 2. BASIC EQUATIONS

Consider a hydro-dynamically and thermally fully developed two-dimensional flow of viscous incompressible fluid through a rotating curved duct with square cross section, whose height and wide are  $2h$  and  $2l$ , respectively. In the present case, we consider  $h = l$ . The coordinate system with the relevant notation is shown in Fig. 1, where  $x'$  and  $y'$  axes are taken to be in the horizontal and vertical directions respectively, and  $z'$  is the axial direction. The system rotates at a constant angular velocity  $\Omega_r$  around the  $y'$  axis. It is assumed that the outer wall of the duct is heated while the inner wall cooled. The temperature of the outer wall is  $T_0 + \Delta T$  and that of the inner wall is  $T_0 - \Delta T$ , where  $\Delta T > 0$ .  $u, v$  and  $w$  be the velocity components in the  $x', y'$  and  $z'$  directions respectively. All the variables are non-dimensionalized.

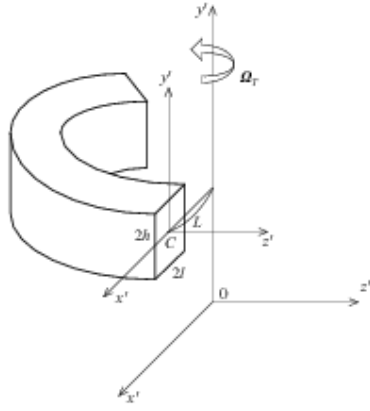


Fig 1. Coordinate system of the rotating curved square duct

The sectional stream function  $\psi$  is introduced as

$$u = \frac{1}{1 + \delta x} \frac{\partial \psi}{\partial y'}, \quad v = -\frac{1}{1 + \delta x} \frac{\partial \psi}{\partial x'} \quad (1)$$

Then, the basic equations for the axial velocity  $w$ , the stream function  $\psi$  and temperature  $T$  are expressed in terms of non-dimensional variables as:

$$\begin{aligned} (1 + \delta x) \frac{\partial w}{\partial t} + \frac{\partial(w, \psi)}{\partial(x, y)} - Dn + \frac{\delta^2 w}{1 + \delta x} = \\ (1 + \delta x) \Delta_2 w - \frac{\partial}{1 + \delta x} \frac{\partial \psi}{\partial y} w + \delta \frac{\partial w}{\partial x} \\ - \delta Tr \frac{\partial \psi}{\partial y} \end{aligned} \quad (2)$$

$$\begin{aligned} \left( \Delta_2 - \frac{\delta}{1 + \delta x} \frac{\partial}{\partial x} \right) \frac{\partial \psi}{\partial t} = -\frac{1}{(1 + \delta x)} \frac{\partial(\Delta_2 \psi, \psi)}{\partial(x, y)} \\ + \frac{\delta}{(1 + \delta x)^2} \left[ \frac{\partial \psi}{\partial y} \left( 2\Delta_2 \psi - \frac{3\delta}{1 + \delta x} \frac{\partial \psi}{\partial x} + \frac{\partial^2 \psi}{\partial x^2} \right) \right. \\ \left. - \frac{\partial \psi}{\partial x} \frac{\partial^2 \psi}{\partial x \partial y} \right] + \frac{\delta}{(1 + \delta x)^2} \left[ 3\delta \frac{\partial^2 \psi}{\partial x^2} - \frac{3\delta^2}{1 + \delta x} \frac{\partial \psi}{\partial x} \right] \\ - \frac{2\delta}{1 + \delta x} \frac{\partial}{\partial x} \Delta_2 \psi + w \frac{\partial w}{\partial y} + \Delta_2^2 \psi \\ - Gr_r (1 + \delta x) \frac{\partial T}{\partial x} + \frac{1}{2} Tr \frac{\partial w}{\partial y}, \end{aligned} \quad (3)$$

$$\frac{\partial T}{\partial t} + \frac{1}{(1 + \delta x)} \frac{\partial(T, \psi)}{\partial(x, y)} = \quad (4)$$

$$\frac{1}{Pr} \left( \Delta_2 T + \frac{\delta}{1 + \delta x} \frac{\partial T}{\partial x} \right)$$

where

$$\Delta_2 \equiv \frac{\partial^2}{\partial x^2} + \frac{\partial^2}{\partial y^2}, \quad (5)$$

$$\frac{\partial(T, \psi)}{\partial(x, y)} \equiv \frac{\partial f}{\partial x} \frac{\partial g}{\partial y} - \frac{\partial f}{\partial y} \frac{\partial g}{\partial x}$$

The non-dimensional parameters  $Dn$ , the Dean number,  $Gr$ , the Grashof number,  $Tr$ , the Taylor number and  $Pr$ , the Prandtl number, which appear in equation (2) to (4) are defined as:

$$\begin{aligned} Dn = \frac{Gl^3}{\mu\nu} \sqrt{\frac{2l}{L}}, \quad Gr = \frac{\beta g \Delta T l^3}{\nu^2}, \\ Tr = \frac{2\sqrt{2\delta} \Omega_r l^3}{\nu\delta}, \quad Pr = \frac{\nu}{\kappa} \end{aligned} \quad (6)$$

where the parameters denote their usual meaning.

The rigid boundary conditions for  $w$  and  $\psi$  are used as

$$\begin{aligned} w(\pm 1, y) = w(x, \pm 1) = \psi(\pm 1, y) = \psi(x, \pm 1) \\ = \frac{\partial \psi}{\partial x}(\pm 1, y) = \frac{\partial \psi}{\partial y}(x, \pm 1) = 0 \end{aligned} \quad (7)$$

and the temperature  $T$  is assumed to be constant on the walls as:

$$T(1, y) = 1, \quad T(-1, y) = -1, \quad T(x, \pm 1) = x \quad (8)$$

### 3. NUMERICAL METHODS

In order to solve the Equations (2) to (4) numerically, the spectral method is used. By this method the expansion functions  $\phi_n(x)$  and  $\psi_n(x)$  are expressed as

$$\left. \begin{aligned} \phi_n(x) &= (1-x^2) C_n(x), \\ \psi_n(x) &= (1-x^2)^2 C_n(x) \end{aligned} \right\} \quad (9)$$

Where  $C_n(x) = \cos(n \cos^{-1}(x))$  is the  $n^{\text{th}}$  order Chebyshev polynomial.  $w(x, y, t)$ ,  $\psi(x, y, t)$  and  $T(x, y, t)$  are expanded in terms of the expansion functions  $\phi_n(x)$  and  $\psi_n(x)$  as

$$\left. \begin{aligned} w(x, y, t) &= \sum_{m=0}^M \sum_{n=0}^N w_{mn}(t) \phi_m(x) \phi_n(y) \\ \psi(x, y, t) &= \sum_{m=0}^M \sum_{n=0}^N \psi_{mn}(t) \psi_m(x) \psi_n(y). \\ T(x, y, t) &= \sum_{m=0}^M \sum_{n=0}^N T_{mn} \phi_m(x) \phi_n(y) + x \end{aligned} \right\} \quad (10)$$

where  $M$  and  $N$  are the truncation numbers in the  $x$  and  $y$  directions respectively.

First, steady solutions are obtained by the Newton-Raphson iteration method and then linear stability of the steady solutions is investigated against only two-dimensional ( $z$  – independent perturbations. Finally in order to calculate the unsteady solutions, the Crank-Nicolson and Adams-Bashforth methods together with the function expansion (10) and the collocation methods are applied to Eqs. (2) to (4).

### 4. FLUX THROUGH THE DUCT

The dimensional total flux  $Q'$  through the duct in the rotating coordinate system is calculated by:

$$Q' = \int_{-d}^d \int_{-d}^d w' dx' dy' = v dQ \quad (11)$$

Where

$$Q = \int_{-1}^1 \int_{-1}^1 w dx dy \quad (12)$$

is the dimensionless total flux. The mean axial velocity  $\bar{w}'$  is expressed as

$$\bar{w}' = \frac{Qv}{4d}.$$

In the present study,  $Q$  is used to denote the steady solution branches and to pursue the time evolution of the unsteady solutions.

### 5. RESULTS AND DISCUSSION

We take a curved duct with square cross section and rotate it around the center of curvature with an angular velocity  $\Omega_T$ . In the present study, we investigate the flow characteristics and discuss the flow phenomena for two cases of the Dean numbers, *Case I*:  $Dn = 1000$  and *Case II*:  $Dn = 2000$ , over a wide range of the Taylor number  $0 \leq Tr \leq 3000$ , for the Grashof number  $Gr = 500$ . Thus an interesting and complicated flow behavior will be expected if the duct rotation is involved for these two cases.

#### 5.1 Case I: $Dn = 1000$

##### 5.1.1 Steady solutions and their linear stability analysis

With the present numerical calculation, we obtain two branches of steady solutions for  $Dn = 1000$  over the Taylor number  $0 \leq Tr \leq 3000$ . The two steady solution branches are named the *first steady solution branch* (first branch, thin solid line) and the *second steady solution branch* (second branch, dashed line), respectively. Figure 2 shows the flux  $Q$  through the duct versus the Taylor number  $Tr$  for the Dean number  $Dn = 1000$ . It is found that the steady solution branches are independent and there exists no bifurcating relationship between the two branches in the parameter range investigated in this study. It is found that the first branch is composed of two-vortex solutions only, while the second branch consists of two- and four-vortex solutions.

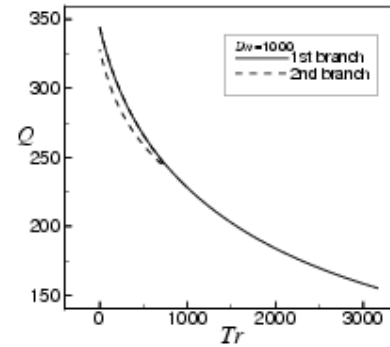


Fig 2. Steady solution branches for  $0 \leq Tr \leq 3000$  and  $Gr = 500$ .

Linear stability of the steady solutions shows that only the first steady solution branch is partly unstable for small  $Tr$  ( $Tr \leq 15.3$ ). However, as  $Tr$  increases, the steady solution becomes stable and remains stable onwards for larger  $Tr$ . Thus we find that the steady solution is linearly stable for  $15.4 \leq Tr \leq 3000$ . The second steady solution branch is linearly unstable everywhere.



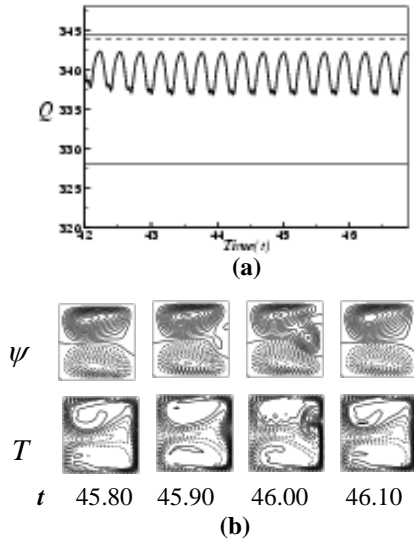


Fig 3. Unsteady solutions for  $Dn = 1000$  and  $Tr = 0$ . (a) Time evolution of  $Q$  and the values of  $Q$  for the steady solutions. (b) Contours of secondary flow (top) and temperature profile (bottom) for one period of oscillation at  $45.80 \leq t \leq 46.10$ .

### 5.1.2 Unsteady solutions

In order to study the non-linear behavior of the unsteady solutions, time-evolution calculations are performed for  $Dn = 1000$ . Time evolution of  $Q$  for  $Tr = 0$  is shown in Fig. 3(a). It is found that the flow is time periodic. In the same figure, the relationship between the periodic solution and the steady states, the values of  $Q$  for the steady solution branches at  $Tr = 0$ , are also shown by straight lines using the same kind of lines as were used in the bifurcation diagram in Fig. 2. The periodic solution at  $Tr = 0$  oscillates in the region between the upper and the lower parts of the second steady solution branch. Then, in order to see the change of the flow characteristics, as time proceeds, contours of typical secondary flow and temperature distribution are shown in Fig. 3(b), where it is seen that the periodic solution at  $Tr = 0$  oscillates between asymmetric two- and four-vortex solutions.

## 5.2 Case II: $Dn = 2000$

### 5.2.1 Steady solutions and their linear stability analysis

We obtain four branches of steady solutions for  $Dn = 2000$  over a wide range of  $Tr$  for  $0 \leq Tr \leq 3000$ . The bifurcation diagram of steady solutions is shown in Figure 4. The four steady solution branches are named the *first steady solution branch* (first branch, thick solid line), the *second steady solution branch* (second branch, dashed line), the *third steady solution branch* (third branch, thin solid line) and the *fourth steady solution branch* (fourth branch, dashed

dotted line), respectively.

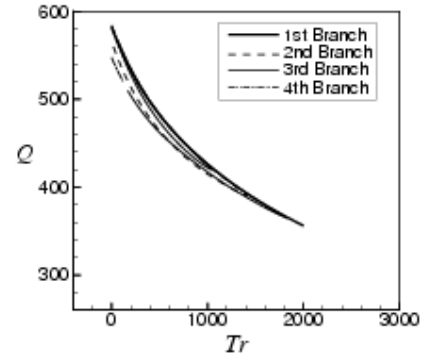


Fig 4. Steady solution branches for  $Dn = 2000$ .

The steady solution branches are obtained by the path continuation technique with various initial guesses as discussed by Mondal [4] and are distinguished by the nature and number of secondary flow vortices appearing in the cross section of the duct. The first branch is composed of only two-vortex solutions. The second branch consists of asymmetric two- and nearly symmetric four-vortex solutions. The third branch is comprised of two- and four- vortex solutions while the fourth branch is composed of four-vortex solutions. It is found that, at the same value of  $Tr$  we obtain both two- and four-vortex solutions. In the case of temperature transmission from inner wall to the fluid, it is found that the convection becomes more frequent with the increase of rotation.

Linear stability of the steady solutions shows that only the first branch is linearly stable in a couple of interval of  $Tr$ , while the other branches are linearly unstable at any value of  $Tr$ . The first branch is linearly stable for  $0 \leq Tr < 279.1$  and  $922.8 < Tr \leq 3000$  and unstable for  $279.1 \leq Tr \leq 922.80$ .

### 5.2.2 Unsteady solutions

We perform time-evolutions of the unsteady solutions for  $Dn = 2000$  and  $0 \leq Tr \leq 3000$ . The time evolutions of  $Q$ , together with the values of  $Q$  for the steady solution branches, are shown in Fig. 5(a) for  $Tr = 500$ . It is found that the flow oscillates multi-periodically. The associated secondary flow patterns and temperature profiles are shown in 5(b) for  $18.97 \leq Tr \leq 19.06$ . As seen in Figs. 5(a) and 5(b), the unsteady flow at  $Tr = 500$  oscillates between the asymmetric two-vortex solutions. Next, the time evolution of  $Q$  is shown in Fig. 6(a) for  $Tr = 900$ . It is found that the flow oscillates periodically. The associated secondary flow patterns and temperature profiles are shown, for one period of oscillation, in Fig. 6(b) at  $7.81 \leq Tr \leq 7.89$ . It is found that the unsteady flow at  $Tr = 900$  also oscillates between the asymmetric two-vortex solutions.

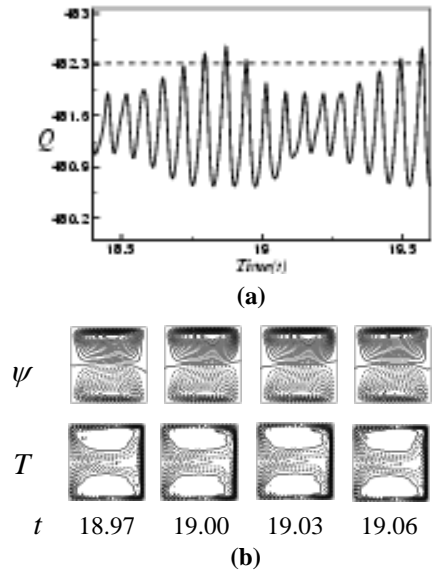


Fig 5. Unsteady solutions for  $Dn = 2000$  and  $Tr = 500$ . (a) Time evolution of  $Q$  and the values of  $Q$  for the steady solutions. (b) Contours of secondary flow (top) and temperature profile (bottom) for  $Dn = 2000$  and  $Tr = 500$  at  $Gr = 500$ .

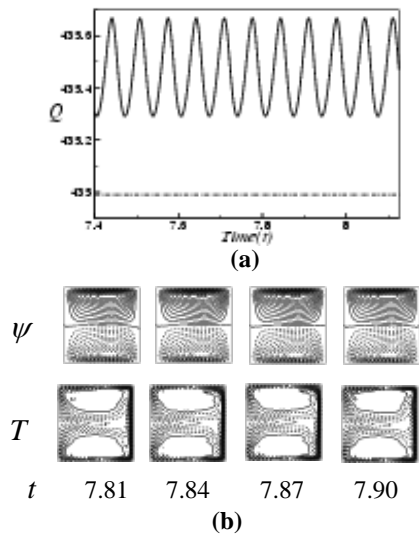


Fig 6. Unsteady solutions for  $Dn = 2000$  and  $Tr = 900$ . (a) Time evolution of  $Q$  and the values of  $Q$  for the steady solutions. (b) Contours of secondary flow (top) and temperature profile (bottom) for one period of oscillation at  $7.81 \leq t \leq 7.90$ .

## 6. CONCLUSIONS

In this study, a numerical result is presented for the fully developed two-dimensional flow of viscous incompressible fluid through a rotating curved square duct over a wide range of the Taylor number,

$0 \leq Tr \leq 2000$  and the Dean number,  $0 \leq Dn \leq 2000$  for the curvature  $\delta = 0.1$ . Spectral method is used as a basic tool to solve the non-linear system of equations. In this study, a detail discussion on  $Dn = 1000$  and  $Dn = 2000$  are presented with a temperature difference between the vertical sidewalls for the Grashof number  $Gr = 500$ , where the outer wall is heated and the inner wall cooled.

We obtain two and four branches of asymmetric steady solutions for  $Dn = 1000$  and  $Dn = 2000$  respectively. It is found that there exist two-and four-vortex solutions on various branches. These vortices are generated due to the combined action of the centrifugal force and Coriolis force. It is found that as  $Dn$  increases the number of steady solutions also increases. Linear stability of the steady solutions shows that only the first branch is linearly stable while the other branches are linearly unstable. In the unstable region, we perform time evolution calculations of the unsteady solutions and it is found that for  $Dn = 1000$  flow becomes periodic before turning to steady state. For  $Dn = 2000$ , however, the unsteady flow becomes steady-state first, then periodic or multi-periodic and finally steady state once again, if  $Tr$  is increased.

## 7. REFERENCES

- Berger, S.A., Talbot, L., Yao, L. S. (1983). Flow in Curved Pipes, *Annu. Rev. Fluid. Mech.*, Vol. 35, pp. 461-512.
- Nandakumar, K. and Masliyah, J. H. (1986). Swirling Flow and Heat Transfer in Coiled and Twisted Pipes, *Adv. Transport Process.*, Vol. 4, pp.49-112.
- Winters, K. H. (1987). Bifurcation Study of Laminar Flow in a Curved Tube of Rectangular Cross-section, *Journal of Fluid Mech.*, Vol. 180, pp.343-369.
- Mondal, R. N. (2006) Isothermal and Non-isothermal Flows through Curved ducts with Square and Rectangular Cross Sections, *Ph.D. Thesis*, Department of Mechanical Engineering, Okayama University, Japan.
- Wang, L. Q. and Cheng, K.C. (1996). Flow Transitions and Combined Free and Forced Convective Heat Transfer in Rotating Curved Channels: the Case of Positive Rotation, *Phys. of Fluids*, Vol. 8, pp.1553-1573.
- Mondal, R. N., Alam M. M. and Yanase, S. (2007). Numerical prediction of non-isothermal flows through a rotating curved duct with square cross section, *Thommasat Int. J. Sci and Tech.*, Vol. 12, No. 3, pp. 24-43.

## 7. MAILING ADDRESS

R. N. Mondal  
 Mathematics Discipline;  
 Khulna University, Khulna-9208, Bangladesh  
 Phone : 0088-01710851580,  
 FAX : 0088-041-731244  
 E-mail : rnmondal71@yahoo.com

## A STUDY OF BADMINTON SHUTTLECOCK AERODYNAMICS

Firoz Alam, Harun Chowdhury, C. Theppadungporn and Aleksandar Subic

School of Aerospace, Mechanical and Manufacturing Engineering, RMIT University,  
Melbourne, Australia

### ABSTRACT

Being a bluff body, the shuttlecock generates significant aerodynamic drag and complex flight trajectory. Despite the popularity of the game, scant knowledge is available in the public domain about the aerodynamics of shuttlecocks. The primary objectives of this study were to experimentally measure the aerodynamic properties of a series of natural feather and synthetic shuttlecocks under a range of wind speeds and pitch angles. The drag coefficients for shuttlecocks were determined and compared. The natural feather shuttlecock indicated lower drag coefficient at low speeds and significantly high value at high speeds. On the other hand, the synthetic shuttlecocks have shown opposite trends. The average drag coefficient for shuttlecocks found in this study was between 0.5 and 0.6.

**Keywords:** Aerodynamics, Shuttlecock, Wind Tunnel, Drag Coefficient.

### 1. INTRODUCTION

Badminton is one of the oldest and popular games in the world. It is believed to be originated from ancient Greece and China. However, the modern version of Badminton game was imported by the British from India to Great Britain in the middle of 19th century and spread to other parts of the world. Although the modern Badminton rules and regulations were introduced in 1887, the first Badminton World Championship was not taken place until 1977. The Badminton game was initially dominated by the Europeans and Americans; however, currently the game is besieged by the Asian nations especially, China, Indonesia, Malaysia, Japan and Singapore. Today the game is so popular that over 160 countries are now the official member of the Badminton World Federation (BWF) - a governing body of the game. Its initial name "International Badminton Federation" (established in 1934 with its headquarter in England) was renamed as BWF in 2006 and its headquarter has been moved to Kuala Lumpur in Malaysia in 2005 from England. According to BWF estimates, at present, the game is played by over 200 million people worldwide and over thousand players participate in various competitions and tournaments around the world. One of the exciting moments of the game is shown in Figure 1. The centre piece of the game is shuttlecock which is made of either natural feathers or synthetic rubber with an open conical shape (shown later). The cone comprises of 16 overlapping goose feathers embedded into a round cork base which is covered generally with a thin leather or synthetic material. Unlike most racquet sports, a badminton shuttlecock is an extremely high drag projectile and

possesses almost parabolic flight trajectory. Most amateur players use synthetic shuttlecock as it lasts longer and exhibits less aerodynamic drag compared to feather shuttlecock which is predominantly used by the professional players and have high initial velocity. Generally, three types of synthetic shuttlecocks (distinguished by colour code) are available in the market. They are: a) Green shuttlecock (for slow speed), b) Blue shuttlecock (for middle speed), and c) Red shuttlecock (for fast speed). Frequently, the red shuttlecock is used in colder climates and the green shuttlecock is used in warmer climates.



Fig 1. An exciting moment in Badminton game after Ref. [4]

Although the Badminton game is one of the most popular games in the world, the aerodynamic behaviour of the shuttlecock (be it feather or rubber made) is virtually unknown. Its flight trajectory is significantly different from the balls used in most racquet sports due to very high initial speeds (highest speed is 332 km/h by Chinese player Fu Haifeng in 2005) that decay rapidly due to high drag generated by feathers or rubber skirts. While many studies by Alam [2, 3], Mehta [6], Smits and Ogg [9] and Seo [8] were conducted on spherical and ellipsoidal balls, no study except Cooke [5] and more recently by Alam [1] was reported to the public domain on shuttlecock aerodynamics. The knowledge of aerodynamic properties of shuttlecocks can greatly assist both amateur and professional players to understand the flight trajectory as player requires considerable skills to hit the shuttlecock for the full length of the court. The parabolic flight trajectory is generally skewed heavily thus its fall is much steeper angle than the rise. The understanding of aerodynamic properties can significantly influence the outcome of the game. Therefore, the primary objective of this work is to experimentally measure the aerodynamic properties of a series of shuttlecocks (synthetic and feather made) under a range of wind speeds, and compare their aerodynamic properties.

## 2. EXPERIMENTAL PROCEDURE

Ten new shuttlecocks were selected for this study. These shuttlecocks are: Grays nylon, Grays plastic, Grays volante, Mavis – Yonex 500, RSL standard, Grays volant en plumes, Yonex mavis 350, RSL silver feather, Arrow 100, RSL classic tourney. The dimensions of all these shuttlecocks are given in Table 1. All shuttlecocks are shown in Figures 2-6. A sting mount was used to hold the shuttlecock, and the experimental set up in the RMIT Industrial Wind Tunnel test section is shown in Figures 7(a, b, c & d).

The aerodynamic effect of sting on the shuttlecock was measured and found to be negligible. The distance between the bottom edge of the shuttlecock and the tunnel floor was 420 mm, which is well above the tunnel boundary layer and considered to be out of significant ground effect.

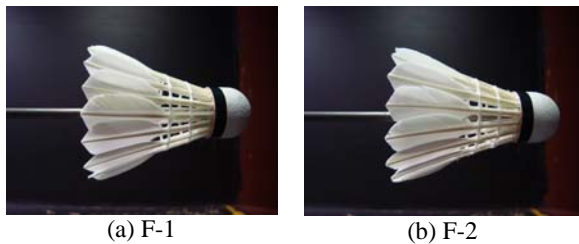


Fig 2. Natural feather shuttlecocks

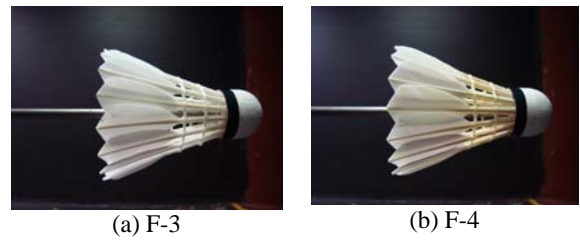


Fig 3. Natural feather shuttlecocks

Table 1. Physical parameters of shuttlecocks

ID	Type	Length of shuttle mm	Length of cock mm	Width at the end of skirt mm	Mass g
S-1	Synthetic	84	25	65	5.2
S-2	Synthetic	82	25	63	4.9
S-3	Synthetic	83	25	66	6.2
S-4	Synthetic	78	25	68	5.3
S-5	Synthetic	80	25	65	5.2
F-1	Feather	85	25	66	5.0
F-2	Feather	86	25	65	4.9
F-3	Feather	85	25	66	5.1
F-4	Feather	85	25	65	5.2
F-5	Feather	85	25	65	4.9

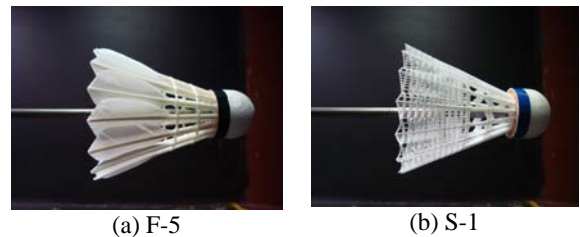


Fig 4. Natural feather shuttlecock (a) and synthetic shuttlecock (b)

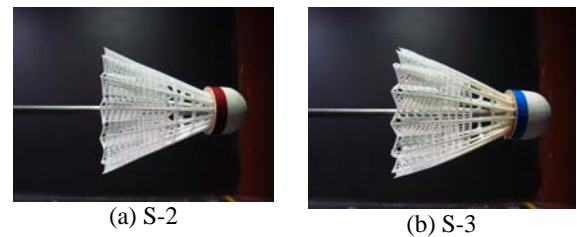


Fig 5. Synthetic shuttlecocks

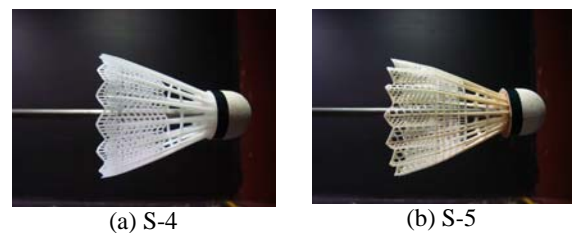


Fig 6. Synthetic shuttlecocks



In order to measure the aerodynamic properties of the shuttlecock experimentally, the RMIT Industrial Wind Tunnel was used. The tunnel is a closed return circuit wind tunnel with a maximum speed of approximately 150 km/h. The rectangular test section dimension is 3 m (wide) x 2 m (high) x 9 m (long), and is equipped with a turntable to yaw the model. The stud (sting) holding the shuttlecock was mounted on a six component force sensor (type JR-3), and purpose made computer software was used to digitise and record all 3 forces (drag, side and lift forces) and 3 moments (yaw, pitch and roll moments) simultaneously. More details about the tunnel can be found in Alam et al. [2].

The aerodynamic drag coefficient is defined as:

$$C_D = \frac{D}{\frac{1}{2}\rho V^2 A}$$

where  $D$ ,  $\rho$ ,  $V$  &  $A$  are the drag, air density, wind speed and undeformed projected frontal area of shuttlecock respectively. The Reynolds number

is defined as  $Re = \frac{VD}{\nu}$ , where  $V$ ,  $D$  &  $\nu$  are the

wind speed, skirt diameter and kinematic viscosity respectively. The lift and side forces and their coefficients were not determined and presented in this paper. Only drag and its coefficient are presented here.



Fig 7a. Experimental setup of sting



Fig 7b. With shuttlecock (side view)



Fig 7c. With shuttlecock (top view)



Fig 7d. Complete setup (sting & shuttlecock)

### 3. RESULTS

Shuttlecocks were tested at 60, 80, 100 and 120 km/h speeds. The shuttlecock was yawed relative to the force sensor (which was fixed with its resolving axis along the mean flow direction) thus the wind axis system was employed. The aerodynamic force was converted to non-dimensional parameter (drag coefficient,  $C_D$ ) and tare forces were removed by measuring the forces on the sting in isolation and removing them from the force of the shuttlecock and sting. The influence of the sting on the shuttlecock was checked and found to be negligible. The repeatability of the measured forces was within  $\pm 0.1$  N and the wind velocity was less than 0.5 km/h. The drag coefficient ( $C_D$ ) variation with Reynolds number (varied by velocity) for all shuttlecocks is shown in Figure 8. The  $C_D$  variation with Reynolds numbers for feather shuttlecock and synthetic shuttlecock is shown in Figures 9 and 10 respectively. The  $C_D$  was calculated using undeformed projected frontal area of the shuttlecock.

The average  $C_D$  value for all shuttlecocks is lower at low Reynolds number initially and increases with an increase of  $Re$ . However, the  $C_D$  value drops over 80 km/h (see Figure 8). Figure 10 shows a significant variation in drag coefficients among the synthetic shuttlecocks which is believed to be due to varied geometry of skirts and deformation at high speeds. On the other hand, less variation of drag coefficients was

noted for feather shuttlecocks (see Figure 9). As expected, the variation in  $C_D$  is minimal for the feather shuttlecock due to less deformation at high speeds and also less variation in skirt geometry. The average  $C_D$  value for

feather shuttlecock is higher at low speeds compared to synthetic shuttlecocks. In contrast, the average  $C_D$  value for the synthetic shuttlecock is higher at high speeds compared to the  $C_D$  value for feather shuttlecock.

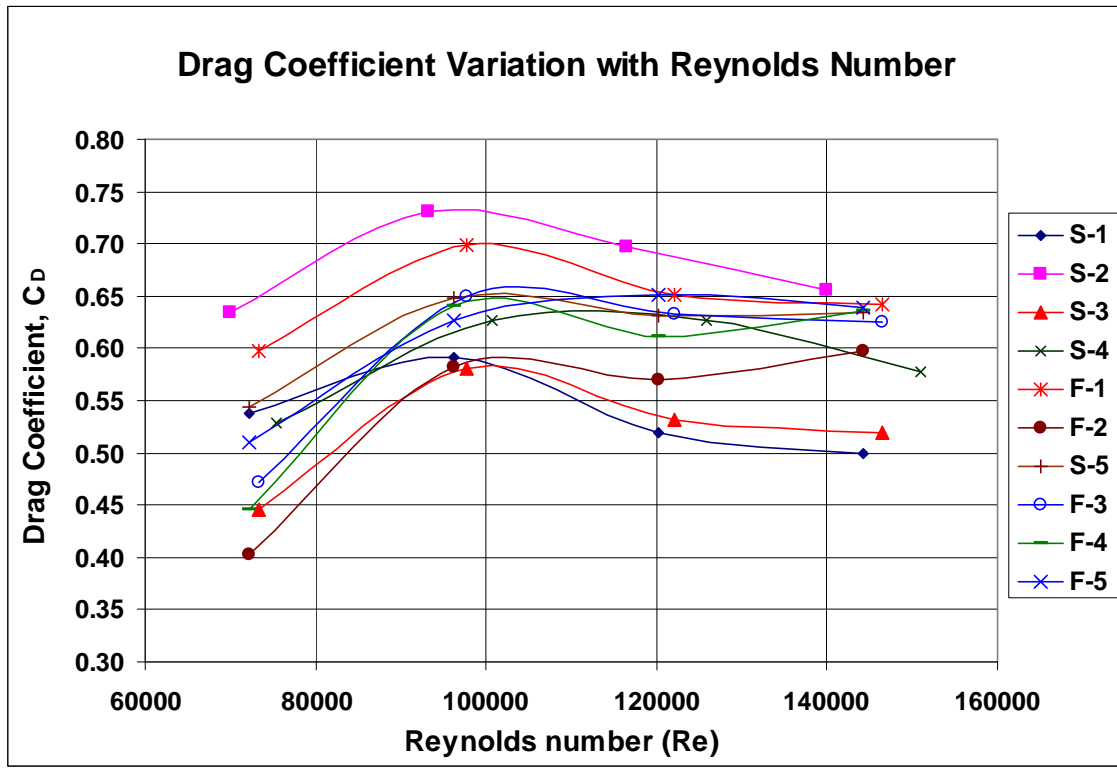


Fig 8. Drag coefficient variation with Reynolds number for all Shuttlecocks

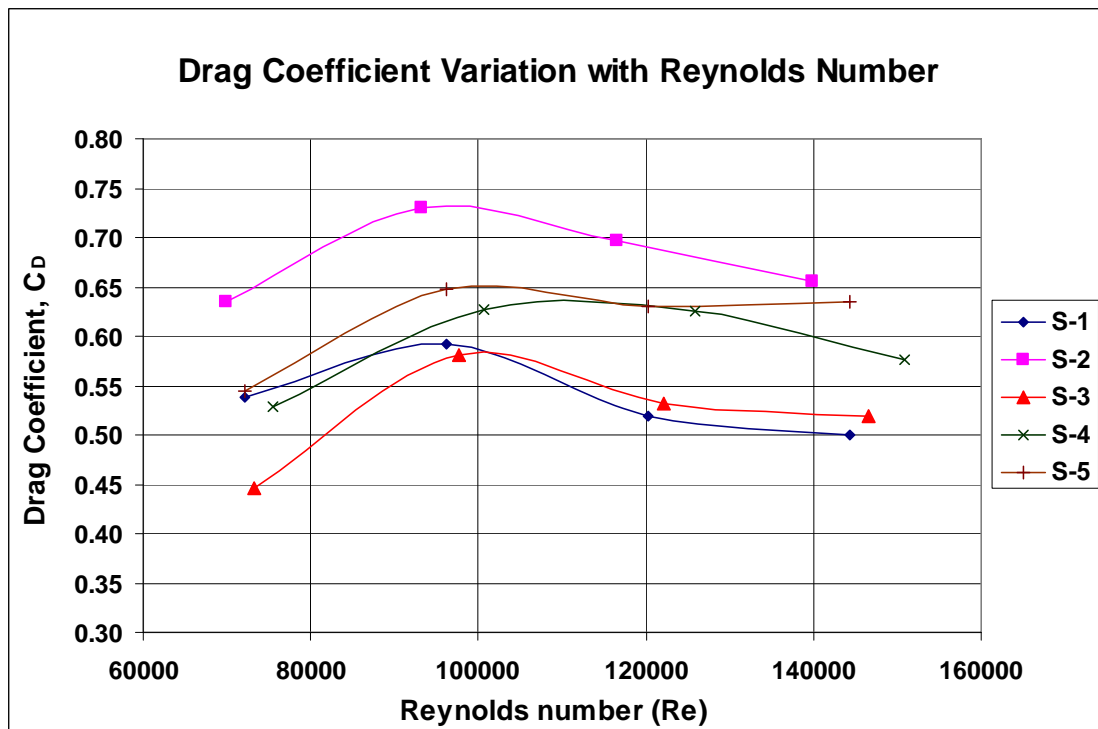


Fig 9. Drag coefficient variation with Reynolds number for feather made shuttlecocks

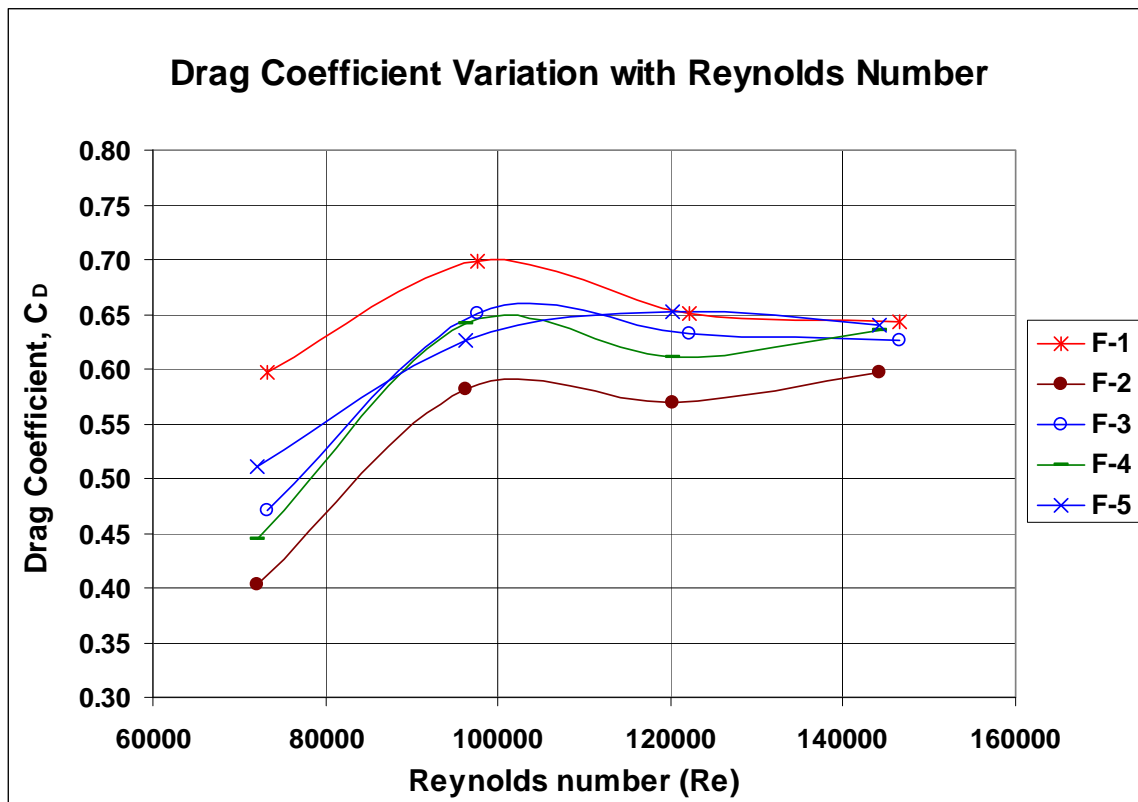


Fig 10. Drag coefficient variation with Reynolds number for synthetic shuttlecocks

#### 4. DISCUSSION

Two types of shuttlecock have been studied here. The experimental results indicate that there is notable variation in drag coefficients between the natural (feather) and synthetic shuttlecocks. These variations are believed to be due to structural deformation of the synthetic shuttlecocks at high speeds. Additionally, the skirt perforation and geometry of some synthetic shuttlecocks are significantly different from their counterpart, feather shuttlecocks. As a result, the airflow behaviour around the synthetic shuttlecocks differs notably compared to natural (feather) shuttlecocks. The degree of structural deformation of synthetic shuttlecocks was not determined in this study. However, work is underway to address this issue.

#### 5. CONCLUSION

The following conclusions are made from the work presented here:

- The average drag coefficient for all shuttlecocks tested is approximately 0.61 over 100 km/h and 0.51 at 60 km/h.
- The average drag coefficient for shuttlecocks made of feathers is approximately 0.62 over 100 km/h and 0.49 at 60 km/h.
- The average drag coefficient for shuttlecocks made of synthetic rubber is approximately 0.59 over 100 km/h and 0.54 at 60 km/h.
- The synthetic shuttlecock is subjected to higher deformation at high speeds compared to feather shuttlecock resulting in lower drag coefficients.

#### 6. FUTURE WORK

The effect of pitch angle is important and worthwhile to investigate.

The skirting design is believed to have effect on aerodynamic properties. Further study is required to quantify the effects.

Although Badminton is predominantly played in door, the effects of yaw on aerodynamic properties can be detrimental. Further investigation on this would be useful.

#### 7. ACKNOWLEDGMENT

The authors express their sincere thanks to Mr Patrick Wilkins and Mr Gilbert Atkin, School of Aerospace, Mechanical and Manufacturing Engineering, RMIT University, Melbourne, Australia for their technical assistance with the win tunnel testing.

#### 8. REFERENCES

1. Alam, F., Theppadungporn, C., Chowdhury, H. and Subic, A., 2009, "Aerodynamics of Badminton Shuttlecock", *The Impact of Technology on Sports III*, ISBN 13: 978-1-921426-39-1, pp. 239-243.
2. Alam, F., Subic, A., Watkins, S., Naser, J. and Rasul, M. G., 2008, "An Experimental and Computational Study of Aerodynamic Properties of Rugby Balls", *WSEAS Transactions on Fluid Mechanics*, 3:279-286.



3. Alam, F., Subic, A., Watkins, S. and Smits, A. J., 2009, "Aerodynamics of an Australian Rules Foot Ball and Rugby Ball", *Computational Science and Engineering (edited by M. Peters)*, Springer, Germany.
4. Badminton World Federation (BWF): <http://www.internationalbadminton.org/> accessed on 12 October, 2009.
5. Cooke, A. J., 1992, "The Aerodynamics and Mechanics of Shuttlecocks", PhD thesis, University of Cambridge, UK.
6. Mehta, R. D., Alam, F. and Subic, A., 2008, "Aerodynamics of Tennis Balls- a Review", *Sports Technology*, 1:1-10.
7. Seo, K., Kobayashi, O. and Murakami, M., 2004, "Regular and Irregular Motion of a Rugby Football During Flight", *The Engineering of Sport 5*, ISBN 0-9547861-0-6, pp. 567-573.
8. Smits, A. J. and Ogg, S., 2004, "Golf Ball Aerodynamics", *The Engineering of Sport 5*, ISBN 0-9547861-0-6, pp. 3-12.

## 9. NOMENCLATURE

Symbol	Meaning	Unit
D	Drag Force	(N)
L	Lift Force	(N)
$C_D$	Drag Coefficient	-
$C_L$	Lift Coefficient	-
Re	Reynolds Number	-
V	Velocity of Air	m/s
$\rho$	Density of Air	kg/m <sup>3</sup>
$\nu$	Kinematic Viscosity of Air	kg/m <sup>3</sup>
A	Projected Area	m <sup>2</sup>

## 10. MAILING ADDRESS

Dr Firoz Alam  
 School of Aerospace, Mechanical and Manufacturing  
 Engineering, RMIT University  
 Plenty Road, Bundoora, Melbourne, VIC 3083, Australia  
 Telephone: +61 3 99256103  
 Fax: +61 3 99256108  
 E-mail: [firoz.alam@rmit.edu.au](mailto:firoz.alam@rmit.edu.au)

## FUZZY LOGIC APPROACH FOR PREDICTION THE LIFT COEFFICIENT OF AN AIRCRAFT MODEL WITH AND WITHOUT WINGLET

A. Hossain<sup>1,2</sup>, A. Rahman<sup>2</sup>, A.K.M Mohiuddin<sup>2</sup>, A.K.M.P. Iqbal<sup>1</sup>, M. Arifin<sup>1</sup>, M. Mazian<sup>1</sup>

<sup>1</sup>Department of Mechanical Engineering, Faculty of Engineering, University Industry Selangor, Malaysia

<sup>2</sup>Department of Mechanical Engineering, Kulliyah of Engineering, International Islamic University  
Malaysia

### ABSTRACT

This paper describes the unique structure of an aircraft model with and without winglet tested at Aerodynamics Laboratory, Faculty of Engineering (University Putra Malaysia) using subsonic wind tunnel of 1000 mm × 1000 mm rectangular test section and 2500 mm long. Focusing on predicting the aerodynamic characteristics of the aircraft model, three main issues are studied in this paper. First, a six component wind tunnel external balance is used for measuring lift, drag and pitching moment. Secondly, Tests are conducted on the aircraft model with and without winglet. And thirdly, Artificial intelligence system such as fuzzy logic approach is used to predict the lift coefficient performance. Therefore, the primary purpose of this work was to investigate the relationship between lift coefficients, with free-stream velocities and angle of attacks, and to illustrate how fuzzy system might play an important role in prediction of lift coefficient with the addition of certain winglet configurations.

**Keywords:** Winglet, External Balance, Lift Coefficient, Fuzzy Logic.

### 1. INTRODUCTION

The aerodynamic efficiency of an aircraft can be improved through a wingtip device which diffuses the strong vortices produced at the tip and thereby optimize the span wise lift distribution, while maintaining the additional moments on the wing within certain limits. For a number of years many investigations have been carried out to prove the possible benefits of modifying wing tip flow. Modern interest in winglets spans the last 25 years. Small and nearly vertical fins were installed on a KC-135A and flight was tested in 1979 and 1980 [1-2]. Whitcomb showed that winglets could increase an aircraft's range by as much as 7% at cruise speeds. A NASA contract [3] in the 1980s assessed winglets and other drag reduction devices, and they found that wingtip devices could improve drag due to lift efficiency by 10 to 15% if they are designed as an integral part of the wing. The "spiroid" wingtip [4] produces a reduction in induced drag at the same time blended winglet reduces drag by eliminating the discontinuity between the wing tip and the winglet. Flight tests on the Boeing Business Jet 737-400 resulted in a 7% drag reduction. Theoretical predictions had indicated that the configuration would have only a 1-2% improvement, and wind tunnel tests had shown only 2% drag reduction [5]. The advantages of single winglets for small transports were investigated

by Robert Jones [6], on which they can provide 10% reduction in induced drag compared with elliptical wings.

The Pennsylvania State University (PSU) 94-097 airfoil has been designed for use on winglets of high-performance sailplanes [7]. To validate the design tools, as well as the design itself, the airfoil was tested in the Penn State Low-Speed, Low-Turbulence Wind Tunnel from Reynolds numbers of  $2.4 \times 10^5$  to  $1.0 \times 10^6$ . Another investigation was carried out on wing tip airfoils by J. J. Spillman at the Cranfield Institute of technology in England [8]. He investigated the use of one to four sails on the wingtip fuel tank of a Paris MS 760 Trainer Aircraft. Experiments on flight test confirmed the wind tunnel tests and demonstrated shorter takeoff rolls and reduced fuel consumption [9]. Spillman later investigated wingtip vortex reduction due to wing tip sails, and found lower vortex energy 400-700 m behind the aircraft, although the rate of decay beyond that was somewhat lower [10]. There has been limited investigation of multiple winglets for aircraft. The split-tip design [11] by Heinz Klug for an aircraft wing is considered a primitive multiple winglets which was created to exploit the non-planar wake geometry by reducing induced drag and wing stress. A biologist with an aerodynamic background has done extensive

investigation of the split wingtips of soaring birds and he demonstrated that the tip slots of soaring birds reduce induced drag and increase the span factor of the wings [12]. He found remarkable improvements of slotted wingtips compared with conventional wing with a Clark Y airfoil and he investigated that with the same increase in angle of attack, the Clark Y tip increased the base wing drag by 25%, while the feathered tip actually reduced the drag by 6%.

To improve the performance of a wing, the multi-winglet [13] design was evaluated to demonstrate its advanced performance potential over the baseline wing and an equivalent single winglet. The results of their wind tunnel testing show that certain multi-winglet configurations reduced the wing induced drag and improved L/D by 15-30% compared with the baseline 0012 wing. In Europe, an extension to the wing tip airfoils has been developed called Wing-Grid [14]. But this concept is limited, since it is not able to change configuration in flight to optimize drag reduction.

Aerodynamic characteristics for the aircraft model with and without winglet having NACA wing No. 65-3-218 has been explained [15]. An interaction matrix method has also been presented to revalidate the calibration matrix data provided by the manufacturer of the six-component external balance. The calibration of free stream velocity and flow quality in the test section has been established and documented [16].

At present, various techniques exist in soft computing method such as neural network, simulated annealing (SA), genetic algorithms, and fuzzy data analysis. Based on the studies on characteristics of the aircraft, an intelligent system using Fuzzy Logic was proposed to predict the aerodynamic characteristics of the aircraft model. Fuzzy Logic has been applied successfully to a large number of expert applications. Fuzzy [17-18]. This work presents the model of fuzzy system, comprising the control rules to express vague human concepts using fuzzy sets and also describe the corresponding inference systems based on fuzzy rules [19]. The aim of this study was the construction of fuzzy knowledge-based models for the prediction of aerodynamic characteristics of the aircraft model by controlling free stream velocities and angle of attack based on the Mamdani approach. A comparative performance analysis of this approach, by sampling data collected from the operation, was used to validate the fuzzy models.

## 2. METHODOLOGY

Experiments were conducted in the Aerodynamics Laboratory Faculty of Engineering (University Putra Malaysia) with subsonic wind tunnel of 1000 mm × 1000 mm rectangular test section and 2500 mm long. The wind tunnel can be operated at a maximum air speed of 50 m/s and the turntable has a capacity for setting an angle of attack of 14 degree. Fig. 1 shows a photograph of the aircraft model with elliptical shaped winglet, which is mounted horizontally in the test section of the wind tunnel.

## 2.1 Calibration of the Balance

Calibration of the six-component balance has been done to check the calibration matrix data provided by the manufacturer Fig. 2 shows a photograph of the calibration rig used for the validation of calibration matrix, which is mounted on the upper platform of the balance in place of model. The relationship between signal readings,  $L_i$  and the loads,  $F_i$  applied on the calibration rig are given by the following matrix equation, the detailed procedure of calibration using Matlab software is explained elsewhere [16].

$$\{L_i\} = [K_{ij}] \{F_i\} \quad (1)$$

Where,  $[K_{ij}]$  is the coefficient matrix,  $\{L_i\}$  is the signal matrix, and  $\{F_i\}$  is the load matrix. The calibration matrix is obtained and it compares well with the calibration matrix data supplied by the manufacturer with six component external balance.



Fig. 1. Aircraft Model with Elliptical shaped Winglet



Fig. 2. Calibration rig mounted on the floor of the wind tunnel test section

## 2.2 Lift coefficient model and Analyses

Coefficient of lift is defined as [20]

$$C_L = \frac{L}{\frac{1}{2} \rho_{\infty} V_{\infty}^2 S} \quad (2)$$

where  $L$  is the lift force in N,  $\rho_{\infty}$  is the air density in  $\text{kg/m}^3$ ,  $V_{\infty}$  is the free stream velocity in m/s,  $c$  is the

chord length in m, and  $S$  is reference area in  $m^2$ .

Using equations of state for perfect gas the air density,  $\rho_\infty$  in  $kg/m^3$  is defined as

$$\rho_\infty = \frac{p}{RT} \quad (3)$$

Where,  $p$  is the absolute pressure in  $N/m^2$ ,  $T$  is the temperature in K, and  $R$  is the gas constant of air in  $Nm/(kg)(K)$ .

Reynolds number based on the chord length is defined

$$Re = \frac{\rho_\infty v_\infty c}{\mu_\infty} \quad (4)$$

Where,  $v_\infty$  is the free stream velocity in m/s;  $\mu_\infty$  is the dynamic viscosity in  $kg/(m)(s)$  and  $c$  is the chord length in m.

The air viscosity,  $\mu_\infty$  is determined using the Sutherland's equation [21] described below

$$\mu_\infty = 1.458 \times 10^{-6} \frac{T^{1.5}}{T + 110.4} \quad (5)$$

Where,  $T$  is the temperature in K.

The tests were carried out with free-stream velocity of 21.36 m/s, 26.76 m/s, and 32.15 m/s respectively with and without winglet of different configurations. The coefficient of lift (Table 1) is obtained from the experimental results as per the procedure explained in [16]. The simulations on the parameters are conducted by using the MATLAB/Simulink.

Table 1: Lift coefficients from experimental data

S. No.	Winglet Configuration	Reynolds Number $10^6$	Lift coefficient, $C_L$		
			Initial Angle of Attack $0^\circ$	Stall Angle of Attack $8^\circ$	Final Angle of Attack $14^\circ$
1	WW	0.17	0.237	0.805	0.657
		0.21	0.259	0.817	0.584
		0.25	0.306	0.879	0.733
2	EWC1	0.17	0.299	0.829	0.641
		0.21	0.327	0.889	0.700
		0.25	0.359	0.934	0.713
3	EWC2	0.17	0.386	0.930	0.729
		0.21	0.394	0.934	0.815
		0.25	0.416	1.018	0.885

**Notifications:** WW-Without Winglet; EWC1-Elliptical Winglet, Configuration 1 ( $0^\circ$  angle); EWC2-Elliptical Winglet, Configuration 2 ( $60^\circ$  angle)

### 3. FUZZY LOGIC SYSTEM

There are a number of different techniques that would

work here. Some of the techniques require a relatively accurate model of the system in order to develop a satisfactory system. Fuzzy expert system, on the other hand, does not require a model of the system. Instead, they rely on the knowledge of an expert for the particular system. Therefore, a Fuzzy Logic expert system is introduced for the prediction of aerodynamic characteristics of the aircraft model. The general configuration of the fuzzy expert system, which is divided into four main parts, is shown in Fig. 3. For implementation of fuzzy values into the model by using Fuzzy expert system (FES), free stream velocity (FV) and angle of attack (AA) were used as input parameters and lift coefficient (CL) was used as output. The linguistic variables very low (VL), low (L), medium (M), high (H), and very high (VH) were used for the inputs and output. In this study, the center of gravity (Centroid) method for defuzzification was used.

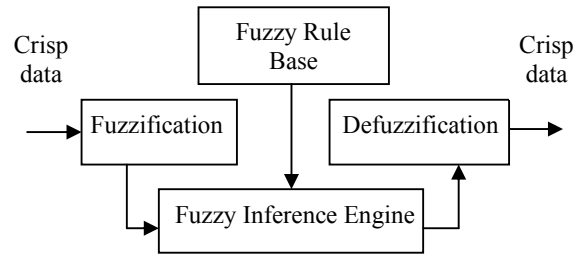


Fig 3. The diagram of the fuzzy system.

The units of the used factors were: FV (m/s), AA (degree), and CL is dimensionless. For the two inputs and one output, a fuzzy rule table is developed as shown in Table 2. Total of 25 rules were formed.

Table 2: Rule base of fuzzy expert system.

Rules	Input variables		Output variable
	FV	AA	CL
Rule1	VL	VL	VL
.....	....	....	....
Rule5	VL	VH	VH
Rule 9	L	H	H
.....	....	....	....
Rule 14	M	H	H
.....	....	....	....
Rule 19	H	H	H
.....	....	....	....
Rule 25	VH	VH	VH

#### 3.1 Fuzzification

The first block inside the fuzzy expert system (FES) is fuzzification, which converts each piece of input data to degrees of membership by a lookup in one or several membership functions. There is a degree of membership for each linguistic term that applies to that input variable. Using MATLAB FUZZY Toolbox, prototype triangular fuzzy sets for the fuzzy variables, namely, free stream velocity (FV), angle of attack (AA), and coefficient of lift

(CL) is set up. The term of parameters (membership functions) are presented in the Fig. 4 (a), (b), and (c)).

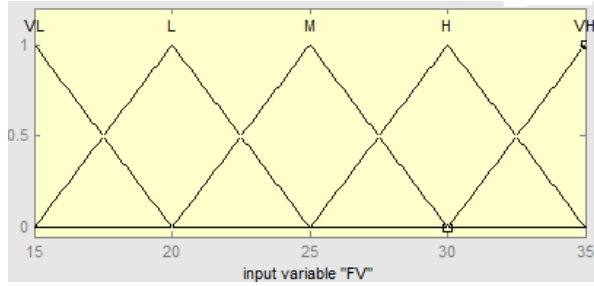


Fig 4 (a). Prototype membership functions for free stream velocity (FV).

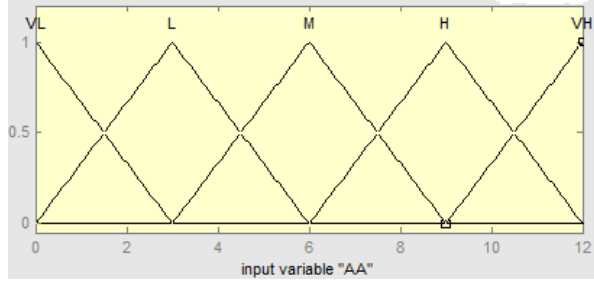


Fig 4(b). Prototype membership functions for angle of attack (AA).

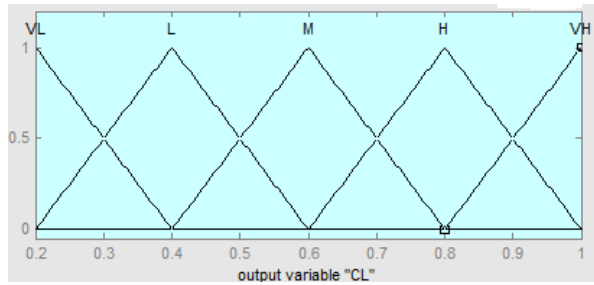


Fig 4 (c). Prototype membership functions for coefficient of lift (CL).

The membership values used for the FES were obtained from the formulas presented analytically in Eqns. (6-8). These membership functions helped in converting numeric variables into linguistic terms.

### 3.2 Inference step

The determination of conclusion is taken when the rules that are applied to deciding what the output to the plant (aircraft model) should be. In defuzzification stage, truth degrees ( $\mu$ ) of the rules were determined for the each rule by aid of the min and then by taking max between working rules. For example, for  $FV = 27$  m/s and  $AA = 8^\circ$ , the rules 13, 14, 18 and 19 will be fired.

The strength (truth values) of the four rules are obtained as

$$\alpha_{13} = \min\{\mu_M(FV), \mu_M(Aa)\} = \min(0.6, 0.33) = 0.33$$

$$\alpha_{14} = \min\{\mu_M(FV), \mu_H(AA)\} = \min(0.6, 0.67) = 0.6$$

$$\alpha_{18} = \min\{\mu_H(FV), \mu_M(AA)\} = \min(0.4, 0.33) = 0.33$$

$$\alpha_{19} = \min\{\mu_H(FV), \mu_H(AA)\} = \min(0.4, 0.67) = 0.4$$

For rule (13) the consequent is ‘‘coefficient of lift (CL) is medium’’. The membership function for the conclusion reached by rule (13), which is denoted as  $\mu_{13}$ , is given by

$$\alpha_{13}(CL) = \min\{0.33, \mu_M(CL)\}$$

Similarly, the membership functions for the conclusion reached by rule (14), (18) and (19), are

$$\alpha_{14}(CL) = \min\{0.6, \mu_H(CL)\},$$

$$\alpha_{18}(CL) = \min\{0.33, \mu_M(CL)\}$$

$$\alpha_{19}(CL) = \min\{0.4, \mu_H(CL)\}$$

$$\mu_{FV}(i_1) = \left\{ \begin{array}{l} \mu_{VL}(i_1) = \frac{20-i_1}{5}; 15 \leq i_1 \leq 20 \\ \mu_L(i_1) = \left\{ \begin{array}{l} \frac{i_1-15}{5}; 15 \leq i_1 \leq 20 \\ \frac{25-i_1}{5}; 20 \leq i_1 \leq 25 \end{array} \right. \\ \mu_M(i_1) = \left\{ \begin{array}{l} \frac{i_1-20}{5}; 20 \leq i_1 \leq 25 \\ \frac{30-i_1}{5}; 25 \leq i_1 \leq 30 \end{array} \right. \\ \mu_H(i_1) = \left\{ \begin{array}{l} \frac{i_1-25}{5}; 25 \leq i_1 \leq 30 \\ \frac{35-i_1}{5}; 30 \leq i_1 \leq 35 \end{array} \right. \\ \mu_{VH}(i_1) = \frac{i_1-30}{5}; 30 \leq i_1 \leq 35 \end{array} \right. \quad (6)$$

$$\mu_{AA}(i_2) = \left\{ \begin{array}{l} \mu_{VL}(i_2) = \frac{3-i_2}{3}; 0 \leq i_2 \leq 3 \\ \mu_L(i_2) = \left\{ \begin{array}{l} \frac{i_2}{3}; 0 \leq i_2 \leq 3 \\ \frac{6-i_2}{3}; 3 \leq i_2 \leq 6 \end{array} \right. \\ \mu_M(i_2) = \left\{ \begin{array}{l} \frac{i_2-3}{3}; 3 \leq i_2 \leq 6 \\ \frac{9-i_2}{3}; 6 \leq i_2 \leq 9 \end{array} \right. \\ \mu_H(i_2) = \left\{ \begin{array}{l} \frac{i_2-6}{3}; 6 \leq i_2 \leq 9 \\ \frac{12-i_2}{3}; 9 \leq i_2 \leq 12 \end{array} \right. \\ \mu_{VH}(i_2) = \frac{i_2-9}{3}; 9 \leq i_2 \leq 12 \end{array} \right. \quad (7)$$

$$\mu_{CL}(o_1) = \left\{ \begin{array}{l} \mu_{VL}(o_1) = \frac{0.4 - o_1}{0.2}; 0.2 \leq o_1 \leq 0.4 \\ \mu_L(o_1) = \left\{ \begin{array}{l} \frac{o_1 - 0.2}{0.2}; 0.2 \leq o_1 \leq 0.4 \\ \frac{0.6 - o_1}{0.2}; 0.4 \leq o_1 \leq 0.6 \end{array} \right. \\ \mu_M(o_1) = \left\{ \begin{array}{l} \frac{o_1 - 0.4}{0.2}; 0.4 \leq o_1 \leq 0.6 \\ \frac{0.8 - o_1}{0.2}; 0.6 \leq o_1 \leq 0.8 \end{array} \right. \\ \mu_H(o_1) = \left\{ \begin{array}{l} \frac{o_1 - 0.6}{0.2}; 0.6 \leq o_1 \leq 0.8 \\ \frac{1 - o_1}{0.2}; 0.8 \leq o_1 \leq 1.0 \end{array} \right. \\ \mu_{VH}(o_1) = \frac{o_1 - 0.8}{0.2}; 0.8 \leq o_1 \leq 1.0 \end{array} \right. \quad (8)$$

### 3.3 Defuzzification Module

In this stage defuzzification operation is considered that is the final component of the fuzzy controller. Defuzzification operates on the implied fuzzy sets produced by the inference mechanism and combines their effects to provide the “most certain” controller output (plant input). Due to its popularity, the “center of gravity” (COG) defuzzification method is used for combing the recommendations represented by the implied fuzzy sets from all the rules [19].

The output membership values are multiplied by their corresponding singleton values and then are divided by the sum of membership values.

$$CL^{crisp} = \frac{\sum b_i \mu_i}{\sum \mu_i} \quad (9)$$

Where  $b_i$  is the position of the singleton in  $i$  the universe, and  $\mu_{(i)}$  is equal to the firing strength of truth values of rule  $i$ . Using the above mentioned rules in Fig. 4(c), the following values are obtained as

$$b_{13} = 0.6, b_{14} = 0.8, b_{18} = 0.6, b_{19} = 0.8$$

Using equation (9) with membership values obtained from the rules, the coefficient of lift (CL) could be obtained as the crisp output of 0.72.

In addition, the predictive ability of developed system was investigated according to mathematical and statistical methods. In order to determine the relative error ( $\varepsilon$ ) of system, the following equation was used:

$$\varepsilon = \sum_{i=1}^n \left| \frac{y - \hat{y}}{y} \right| \frac{100\%}{n} \quad (10)$$

Where  $n$  is the number of observations,  $y$  is the actual value, and  $\hat{y}$  is the predicted value. The relative error gives the deviation between the predicted and

experimental values and it is required to reach zero. In addition, goodness of fit ( $\eta$ ) of predicted system was calculated by following equation:

$$\eta = \sqrt{1 - \frac{\sum_{i=1}^n (y - \hat{y})^2}{\sum_{i=1}^n (y - \bar{y})^2}} \quad (11)$$

Where  $\bar{y}$  is the mean of actual values. The goodness of fit also gives the ability of the developed system and its highest value is 1.

## 4. RESULTS AND DISCUSSIONS

### 4.1 Simulation Condition

The lift coefficient characteristics of the aircraft model without winglet under test are shown in Fig. 5 for all Reynolds numbers. The lift increases with increase in angle of attack to a maximum value and thereby decreases with further increase in angle of attack. At the maximum value of the angle of attack the lift coefficient characteristic has a mixed behavior e.g. the value of the lift coefficient first decreases with increase in Reynolds number and then increases with further increase in Reynolds number. At the maximum angle of attack of 14 degree the lift coefficients are 0.657, 0.584, and 0.733 respectively for the Reynolds numbers of  $1.7 \times 10^5$ ,  $2.1 \times 10^5$ , and  $2.5 \times 10^5$ .

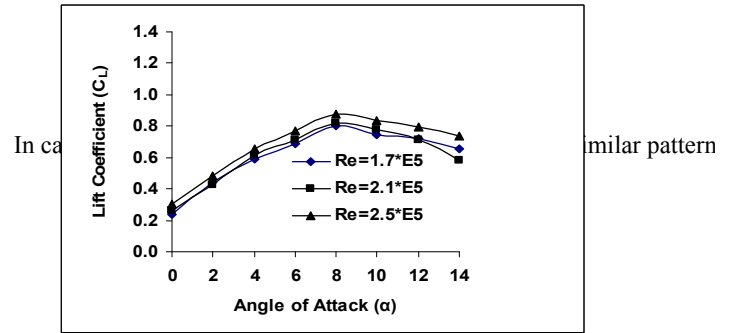


Fig 5. Lift Coefficients for the Aircraft Model without Winglet.

The reason for a drop in lift coefficient beyond a certain angle of attack e.g.  $8^\circ$  is probably due to the flow separation, which occurs over the wing surface instead of having a streamlined laminar flow there. This condition is called stalling condition and the corresponding angle of attack is called stalling angle. The stalling angle happens to be approximately  $8^\circ$  for all the Reynolds numbers under the present study. The lift coefficient data for elliptical winglet of two configurations i.e. configuration 1 (winglet inclination  $0^\circ$ ), and configuration 2 (winglet inclination  $60^\circ$ ) is given in Fig. 6 and 7 respectively.

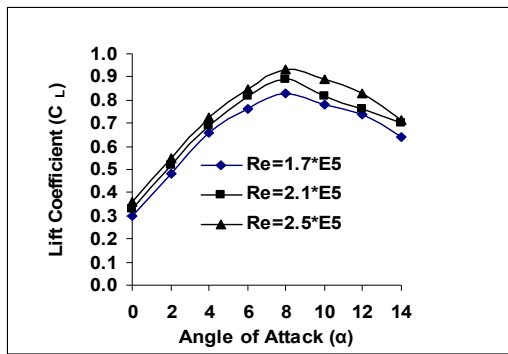


Fig 6. Lift Coefficients for the Aircraft Model with Elliptical Winglet at 0° (Configuration 1).

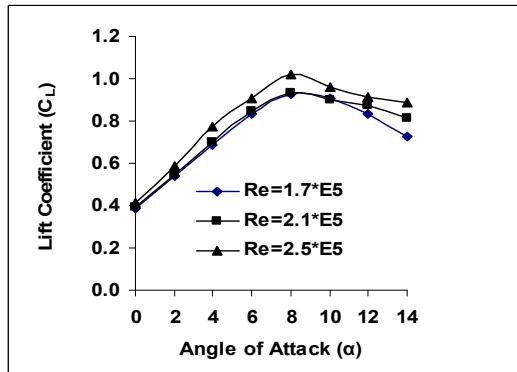


Fig 7. Lift Coefficients for the Aircraft Model with Elliptical Winglet at 60° (Configuration 2).

In case of the winglet for both configurations 1 and 2 a similar pattern is observed. For maximum Reynolds number of  $2.5 \times 10^5$  lift coefficients for config.- 1 (Fig. 6) and for config.-2 (Fig. 7) are 0.934 and 1.018 respectively corresponding to an angle of attack of 8°.

The results of the developed fuzzy expert system (FES) were compared with the experimental results. For lift coefficient analysis, the mean of actual and predicted values were 0.62 and 0.60 respectively. The correlation between actual and predicted values (from FES model) of lift coefficient in different angle of attack was given in Fig. 8. The relationship was significant for all parameters. The correlation coefficient of relationship was found as 0.99. The mean relative error of actual and predicted value (from FES model) was found as 5.18% for the velocity of 26.36 m/s which was found to be less than the acceptable limits (10%). The goodness of fit of prediction (from FES model) value was found as 0.95 which was found to be close to 1.0. The above indices indicate that the system is qualified to replace the work of an operator.

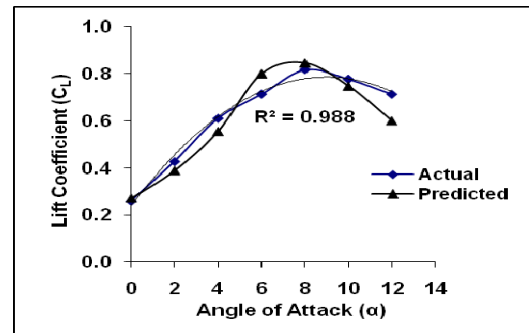


Fig 8. Correlation between actual and predicted values of lift coefficient.

## 5. CONCLUSION

Prediction of aerodynamic characteristics for an aircraft model is necessary for aerospace industry. In comparison to other predictive modeling techniques, fuzzy models have the advantage of being simple (rule base and membership functions) and robust. In this study, according to evaluation criteria of predicted performances of developed fuzzy knowledge-based model was found to be valid. However, the conclusions drawn from this investigation are as follows:

- The developed model can be used as a reference for the full scale aircraft.
- This system can be developed further by increasing the knowledge rules and by the addition of neural network to the system.

## 6. REFERENCES

- Whitcomb, R. T. 1976. A Design Approach and Selected Wind-Tunnel Results at High Subsonic Speeds for Wing-Tip Mounted Winglets. NASA TN D-8260.
- Whitcomb, R. T. 1981. Methods for Reducing Aerodynamic Drag. NASA Conference Publication 2211, Proceedings of Dryden Symposium, Edwards, California.
- Yates, J. E., and C. Donaldson. 1986. Fundamental Study of Drag and an Assessment of Conventional Drag-Due-To-Lift Reduction Devices. NASA Rep 4004.
- Louis, B. Gratzler. 1992. Spiroid-Tipped Wing. U. S. patent 5, 102,068.
- Reginald, V. French. 1978. Vortex Reducing Wing Tip. U. S. Patent 4, 108, 403.
- Jones, Robert T., 1984. Improving the Efficiency of Smaller Transport Aircraft. 14th Congress of the International Council of the Aeronautical Sciences, proceeding, Vol. 1, Toulouse, Fr.
- Maughmer, M. D., S. S. Timothy., and S. M. Willits. 2001. The Design and Testing of a Winglet Airfoil for Low-Speed Aircraft. AIAA Paper 2001-2478.
- Spillman, J. J., 1978. The use of wing tip sails to reduce vortex drag. Aeronautical Journal, pp. 387-395.
- Spillman, J. J., Ratcliffe, H. Y., and McVitie, A., 1979. Flight experiments to evaluate the effect of wing-tip sails on fuel consumption and handling



- characteristics. *Aeronautical Journal*, July, pp. 279-281.
10. Si Spillman, J. J., and Fell, M. J., 1983. The effects of wing tip devices on (a) the performance of the Bae Jetstream (b) the far-field wake of a Paris Aircraft. Paper 31A, AGARD CP No. 342, *Aerodynamics of Vortical Type Flows in Three Dimensions*, April, pp. 31A-1-11.
  11. Heinz G. Klug, 1988. Auxiliary Wing Tips for an Aircraft, U. S. Patent 4722499, February.
  12. Vance A.T., 1993. Gliding Birds: Reduction of Induced Drag by Wing Tip Slots between the Primary Feathers. *Journal of Experimental Biology*, Vol. 180 (1), pp. 285-310.
  13. Smith, M. J., N. Komerath., R. Ames., O. Wong., and J. Pearson., 2001. Performance Analysis of a Wing with Multiple Winglets. AIAA Paper-2001-2407.
  14. Roche La. U., and Palfy S., "WING-GRID, a Novel Device for Reduction of Induced Drag on Wings," Proceedings of ICAS 96, Sorrento, September, 1996.
  15. A. Hossain, P. R. Arora, A. Rahman, A. A. Jaafar, and A. K. M. P. Iqbal. 2008. Analysis of Aerodynamic Characteristics of an Aircraft Model with and Without Winglet. *Jordan Journal of Mechanical and Industrial Engineering*. Vol. 2, No. 3, pp. 143-150.
  16. Prithvi, R. A., A. Hossain, A. A. Jaafar, P. Edi, T. S. Younis, and M. Saleem. 2005. Drag Reduction in Aircraft Model using Elliptical Winglet. *Journal of IEM, Malaysia*, Vol. 66, No. 4, pp. 1-8.
  17. A. Al-Anbuky, S. Bataineh, and S. Al-Aqtash. Power demand prediction using fuzzy logic. *Control Engineering Practice*, Vol. 3, No. 9, pp. 1291-1298, 1995.
  18. K. Carman. Prediction of soil compaction under pneumatic tires a using fuzzy logic approach. *Journal of Terramechanics*, Vol.45, pp.103-108, 2008.
  19. Kevin M. Passino, and Stephen Yurkovich. *Fuzzy control*. Addison Wesley Longman, Inc. Menlo park, CA, USA, 1998.
  20. Bertin, John. J., 2002. *Aerodynamics for Engineers*. New Jersey, Prentice-Hall, Inc.

## 7. MAILING ADDRESS

Md. Altab Hossain  
 Lecturer, Department of Mechanical Engineering,  
 Faculty of Engineering, University Industry Selangor,  
 45600 Selangor, Malaysia  
 Phone: +6-03-3280 5122 (7187), Fax : +603-3280-6016  
 E-mail: altab75@unisel.edu.my

## PERFORMANCE OF A CIRCULAR ARC HORIZONTAL AXIS WIND TURBINE

Sayeda Nazma Yeasmin and M. Quamrul Islam

Atlas Bangladesh Limited, BSEC, Tongi, Gazipur  
Department of Mechanical Engineering, BUET, Dhaka-1000, Bangladesh

### ABSTRACT

An experimental investigation and design analysis of a Horizontal Axis Wind Turbine with arched steel plate section has been performed. Wind characteristics of different regions of Bangladesh have been analyzed and hence, a compatible design of Horizontal Axis Wind Turbine applicable to the pump has been carried out. Performance of the wind turbine models with circular arc blade section for different number of identical blades have been studied at constant wind velocity. The theoretical analysis has been done using momentum theory and Blade element theory. It is observed that the calculated results of the wind turbine with circular arc blade profile are comparable with those of the turbine with airfoil blade section. An extensive experimental investigation of the performance of the designed wind turbine model has been conducted in the wind tunnel. The wind turbines with 2, 3, 4, 5 and 6 blades for linearized chord and twist angle have been considered. The experimental investigation was performed for each turbine at various blade pitching and at different wind velocities. Finally, the calculated results of the wind turbine have been compared with the existing experimental results. It is observed that there are good agreements between the present experimental result and the existing other experimental results.

**Keywords:** Horizontal Axis Wind Turbine, Circular Arc Blade, Power Coefficient, Pitching Angle.

### 1. INTRODUCTION

For exploitation of energy in the field of wind, there have been reasonable developments. Still people are doing further research and development in this sector to find more efficient and cost effective machinery. Now-a-days both horizontal and vertical axis wind machines of different kinds have been developed in different parts of the world. For the present study attention has been focused on horizontal axis wind machines only. A horizontal axis wind machine with circular arc blade section has been chosen for the present theoretical and experimental investigation. This machine can be constructed with semi-skilled technicians and also the cost of production is not high. Most horizontal axis turbines built today are two or three-bladed, although some have fewer or more blades.

A prime objective in wind turbine design is for the blade to have a relatively high lift-to-drag ratio. This ratio can be varied along the length of the blade to optimize the turbine's energy output at various wind speeds [2,3,5]. Energy that comes from converting kinetic energy that is present in the wind into more useful forms of energy such as, mechanical energy or electricity.

### 2. EXPERIMENTAL SET-UP AND PROCEDURE

The schematic diagram of the experimental set-up of the present investigation is shown in Figure: 1. An open circuit subsonic type wind tunnel was used to develop the required flow and the rotor was positioned at the exit section of the wind tunnel. The tunnel was 6.55 m long with a test section of (490mm × 490mm) cross-section. The central longitudinal axis of the wind tunnel was maintained at a constant height from the floor. The converging mouth entry was incorporated into the system for easy entry of air into the tunnel and maintains uniform flow into the duct free from outside disturbances. The induced flow through the wind tunnel was produced by two-stage rotating axial flow fan of capacity 30,000 cfm at the head of 152.4 mm of water and 1475 rpm. A butterfly valve, actuated by a screw thread mechanism was placed behind the fan and was used to control the flow. A silencer was fitted at the end of the flow controlling section in order to reduce the noise of the system. The diverging and converging section of the wind tunnel was

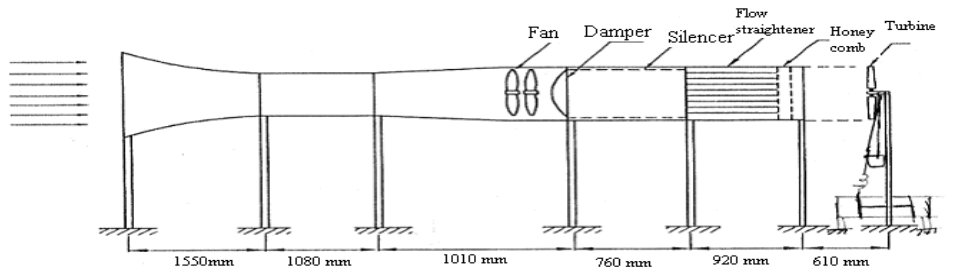


Fig 1. Schematic Diagram of Wind Tunnel

460 mm long and made of 16 SWG black sheets. The angle of divergence and convergence was  $7^\circ$ , which was done with a view to minimizing expansion and contraction loss and to reduce the possibility of flow separation. Other three outlet square (610 mm each) sections were used to make the flow straight and uniform. The flow velocity in the test section was adjusted within 15 m/s covering Reynolds no up to  $2 \times 10^5$ .

Al-blades were used with camberness ratio 0.07. For camberness ratio 0.07: rotor radius 250 mm, root chord length 37.50 mm, Tip Chord length 12.00 mm, Root twist angle  $13^\circ$ , Tip Twist angle  $2^\circ$ . For this type of blade 2, 3, 4, 5 and 6 number of blades was used.

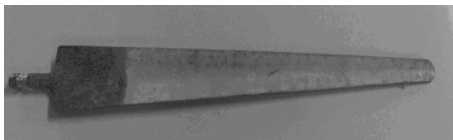


Fig 2. Blade Profile with  $f=0.07c$



Fig 3. Experimental Set-up with  $B = 4$

At first, the velocity was measured without the model turbine at the sections which was placed in front of the rotor at different locations and average velocity was measured directly. The experimental set-up is shown in Figure 3. The model turbine was placed at 0.5 - rotor diameter downstream from the wind tunnel exit end. This velocity distribution was along the vertical direction passing through the axis of the wind tunnel. It can be seen that the velocity is more or less uniform throughout. Similar velocity distribution had been observed in the

horizontal direction as well. Non-contact electrical tachometer was used to measure the speed of the model wind turbine at different loadings.

Wind speed behind the rotor was measured by a digital anemometer and the speed of the model wind turbine shaft having 2, 3, 4, 5 and 6 blades with different pitching were determined using a non-contact digital tachometer at different loading.

### 3. RESULT AND DISCUSSION

Effect of number of blades or solidity and pitching are taken into consideration in the study. The blade pitching angles are chosen as  $2^\circ$ ,  $4^\circ$ ,  $6^\circ$  and  $8^\circ$  for each set of rotor consisting of fixed number of blades. Blade pitch angle of  $0^\circ$  is seemed to be less convenient.

A wind rotor can only extract power from the wind, because it slows down the wind: The maximum power extraction is reached when the wind velocity in the wake of the rotor is  $1/3$  of the undisturbed wind velocity. If the wind speed increase, power increase. Multi-bladed rotors operate at low tip speed ratios and two or three-bladed rotors operate at high tip speed ratios.

#### 3.1 Comparison of the Results with Earlier Experimental Data

Comparison of the experimental results of power coefficients of wind turbines having circular arc blade section with camberness ratio  $f = 0.07c$  are made with those having the conventional NACA 4418 [1] blade section and CABS [4] blade section. It can be observed from these figures that as the number of blade increase, the maximum power shifted towards the lower tip speed ratio. The experimental results are good at tip speed ratio around 5. The experimental results turbine having NACA 4418 [1] blades section is good at tip speed ratio around 6 and CABS [4] at tip speed ratio around 5. It can also observe from these figures that the experimental results of the peak power coefficients of the turbine with NACA 4418 [1] blade section is higher. At low tip speed ratio, the power coefficient of the turbine CABS [4] are significantly higher than those with conventional NACA 4418 [1] and circular arc blade section with camberness ratio  $f = 0.07c$ . It is indicating that at relatively low tip speed ratio wind turbine with circular arc section is better.

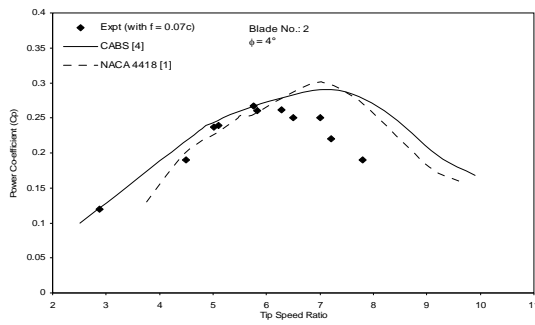


Fig 4. Power Coefficient vs Tip Speed Ratio for B = 2 and  $\phi = 4^\circ$  with  $f = 0.07$

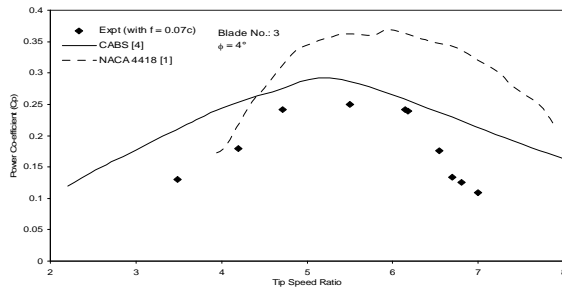


Fig 5. Power Coefficient vs Tip Speed Ratio for B = 3 and  $\phi = 4^\circ$  with  $f = 0.07$

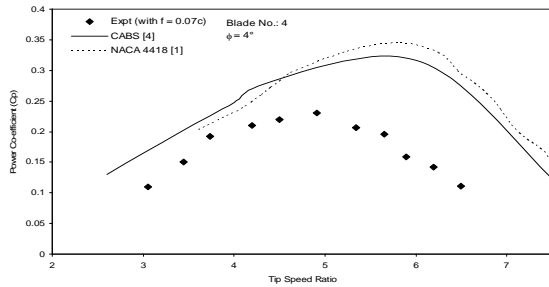


Fig 6. Power Coefficient vs Tip Speed Ratio for B = 4 and  $\phi = 4^\circ$  with  $f = 0.07c$

Experimental results showing the effect of blade pitching on the performance characteristics of HAWT having circular arc blade section are presented in Figure 7 with camberness ratio  $f = 0.07c$

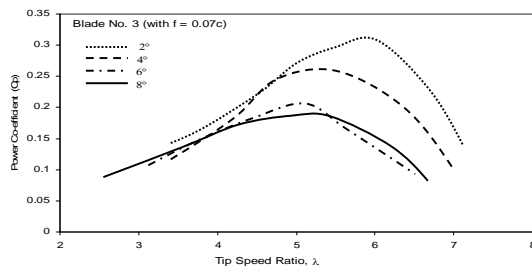


Fig 7. Power Coefficient vs Tip Speed Ratio for B = 3 ( $f = 0.07c$ ) with different pitching

As the blade pitching angle increases the power coefficient values drops and shifting of maximum power coefficient to the smaller values of tip speed ratio.

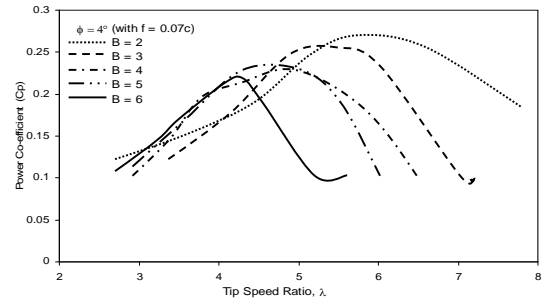


Fig 8. Power Coefficient vs Tip Speed Ratio for  $\phi = 4^\circ$  ( $f = 0.07c$ ) with different Number of Blades

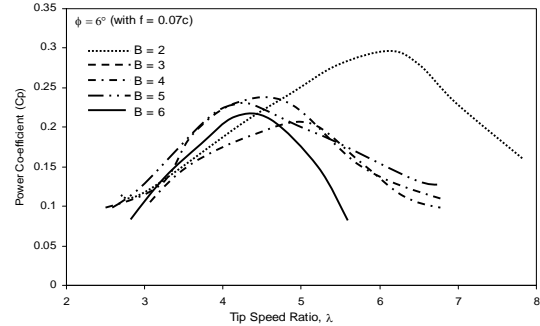


Fig 9. Power Coefficient vs Tip Speed Ratio for  $\phi = 6^\circ$  ( $f = 0.07c$ ) with different Number of Blades

The variations of result for changing number of blades in terms of  $C_p$  versus  $\lambda$  are shown in Figures 8 to 9 for camberness ratio 0.07. However, the maximum power coefficient is affected by changing the number of blades. It can be observed from these figures that increase of number of blades, higher power coefficients move to the region of smaller values of tip speed ratios.

#### 4. CONCLUSION

In regards to the present experimental investigation and design analysis of the horizontal axis wind turbines the following conclusions can be drawn:

1. For horizontal axis wind turbines, classical Strip theory have been found to give adequate results under normal operating conditions near the design tip speed ratio are comparable to those with conventional blade section.
2. The power coefficient values of the horizontal axis wind turbine with circular arc blade profile are comparable to those with conventional blade section. As the solidity (or number of blade) increases, the peak power co-efficient is shifted towards the lower tip speed ratio value.
3. With the increase of the pitch angle, the power co-efficient decrease in general expect of blade pitching angle of  $2^\circ$ , for which the power co-efficient value improves a little at high tip speed ratio range.
4. To produce the same power, it will be wise to choose small number of blades (say 2) in place of large number of blades.

## 5. REFERENCE

1. Ahmmed, S., "Investigation and Analysis of Wind Pumping System for Irrigation in Bangladesh", Ph.D. Thesis, Bangladesh University of Engineering and Dhaka, Bangladesh, 2002.
2. Chowdhury, S. C., Ramana Rao, B. V. and Sharma P., "Performance of Low cost Sail-Wind Windmill", Journal of Agricultural Mechanization in Asia, Africa and Latin
3. Hirsch, Ch., Derdelinckx, R. and Islam, M. Q., "A Theoretical Investigation of the Design of a Horizontal Axis Wind Turbine", Proceeding of the European Wind Energy Conference, Hamburg, 22 - 26, October, pp. 124 - 129, 1984.
4. Hosna, A. B., "An Experimental Investigation and the Design Analysis of a HAWT with Circular Arc Blade Section.", Ph.D. Thesis, Bangladesh University of Engineering and Dhaka, Bangladesh, 2002.
5. Islam, M. Q., "Theoretical Investigation of the Design of HAWT", Ph.D Thesis, Verije University Brussel, Belgium, 1986.

## 6. NOMENCLATURE

Symbol	Meaning	Unit
A	Turbine disc cross-sectional area	mm <sup>2</sup>
B	Number of blades in the rotor	No.
C	Chord of the Blade	mm
D	Diameter of the Rotor	mm
C <sub>D</sub>	Blade drag coefficient	
C <sub>L</sub>	Blade lift coefficient	
C <sub>P</sub>	Power coefficient	
$\lambda$	Tip speed ratio	
$\rho$	Air density	Kg/m <sup>3</sup>
$\varphi$	Angle of relative wind velocity	<sup>0</sup>

## 7. MAILING ADDRESS

Sayed Nazma Yeasmin  
Atlas Bangladesh Limited, BSEC, Tongi, Gazipur,  
Mobile: 01912-426486  
E-mail: ynazu@yahoo.com

## AERODYNAMICS OF TEXTILES FOR ELITE CYCLIST

Harun Chowdhury<sup>1</sup>, Firoz Alam<sup>1</sup>, David Mainwaring<sup>2</sup>, Jordi Beneyto-Ferre<sup>2</sup>, Margaret Tate<sup>2</sup>,  
Dorothy Forster<sup>2</sup> and Aleksandar Subic<sup>1</sup>

<sup>1</sup>School of Aerospace, Mechanical and Manufacturing Engineering, RMIT University, Australia

<sup>2</sup>School of Applied Sciences, RMIT University, Melbourne, Australia

### ABSTRACT

Aerodynamic properties play a significant role in the textiles across a wide range of sports including cycling, skiing, bobsleigh, and speed skating. Considerations in this aerodynamic performance include the textile weave or knit, seam and fastener placement and air permeability. Elite competition usually involves very short winning time margins in events that often have much longer timescales, making aerodynamic resistance and its associated energy loss during the event significant in the outcome. In fact, a two fold increase in athlete velocity results in a fourfold increase in the drag force needing to be overcome. This paper describes the impact of textile surface employing a standard cylindrical arrangement in wind tunnel studies to provide precise data on aerodynamic drag and lift as a function of athlete's body positions together with garment seam placement and apply these optimized data to cycling apparel design for elite cyclist.

**Keywords:** Wind Tunnel Testing, Drag, Lift, Aerodynamic, Cycling, Fabric.

### 1. INTRODUCTION

The suitability of materials for sports applications, including textiles for sports garments, must meet a range of performance parameters dictated by the specific sport. As such, the minimization of detrimental effects of sports garments on sporting performance is becoming an important aspect of sports technology and product design. The demands on garment design for high performance in dynamic sports and particularly those associated with aerodynamic resistance and its associated energy loss during an event, extend the conventional design methodology of synthesis, form, and function to new requirements for quantitative understandings of materials performance, textile construction and surface texture [1]. As such, garment design and its engineering modelling requires detailed information on the textile and surface physics of the materials as well as systematic evaluation of the aerodynamic behaviour in the wind tunnel and modelling. Strangwood [2] points out that the close interplay of design and sports materials science brought about by engineering modelling is only as good as the data on which it is based. Since the early work of Kyle [3] and Brownlie [4] in the 1980s and more recently studies by Chowdhury on the aerodynamic effects of sport clothing [8, 9], systematic progress has resulted in aerodynamic apparel being associated with success at the highest elite levels in, for example, sprint running, speed skating, and cycling as they reported more recently. Considerations in this aerodynamic performance include the textile weave or knit, seam and fastener placement and air permeability. Elite

competition usually involves very short winning time margins in events that often have much longer timescales, making aerodynamic resistance during the event significant in the outcome [4]. There have been a series of research studies over the last two decades progressively identifying reductions of aerodynamic drag in sports garments [5, 7, 8].

Kyle and Brownlie [6] carrying out systematic wind tunnel studies utilizing both mannequins with athletic apparel and cloth covered cylinders, showed that cylinders could evaluate drag and flow transitions. Recently, Faria [7] and Chowdhury [8] have extensively reviewed both the exercise protocols and the factors that influence performance where aerodynamic resistance was considered in terms of both sports equipment and athlete body position [7].

The surface texture as well as garment construction, e.g. seam placement, can potentially exhibit subtle yet significant influences on drag, lift and flow transitions. Surface roughness is an important parameter for lift and drag due to the transitional properties at the boundary layer. In this paper we report an experimental wind tunnel arrangement that provides precise information on the aerodynamic drag and lift characteristics of a series of sports textiles covering a standardized cylindrical geometry able to be deployed at various angles of attack. Here, we apply these studies to aerodynamic effects encountered in time-trial cycling where medium to high velocities are achieved and resistance results in significant associated energy losses. The influence of the aerodynamic characteristics of cycling garments, fabric texture and seam placement, are given through

the standard cylindrical geometry in the wind tunnel.

## 2. EXPERIMENTAL PROCEDURE

The aerodynamic properties, such as drag, lift, side force and their corresponding moments, of four fabrics (shown in Figure 8) were measured in the RMIT Wind Tunnel, which was a closed return circuit with a maximum air speed of approximately 150 km/h. The rectangular test section dimension is 3 m (wide) x 2 m (high) x 9 m (long) with a turntable to yaw suitably sized objects. The tunnel was calibrated before conducting experiments with air speeds measured via a modified NPL ellipsoidal head Pitot-static tube (located at the entry of the test section) connected to a MKS Baratron pressure sensor through flexible tubing. Purpose made computer software was used to compute all 6 forces and moments (drag, side, lift forces, and yaw, pitch and roll moments) and their non-dimensional coefficients.

Figure 1 gives the 3-D CAD model used showing various segments as semi-cylindrical elements and typical athlete body angles in time-trial cycling.

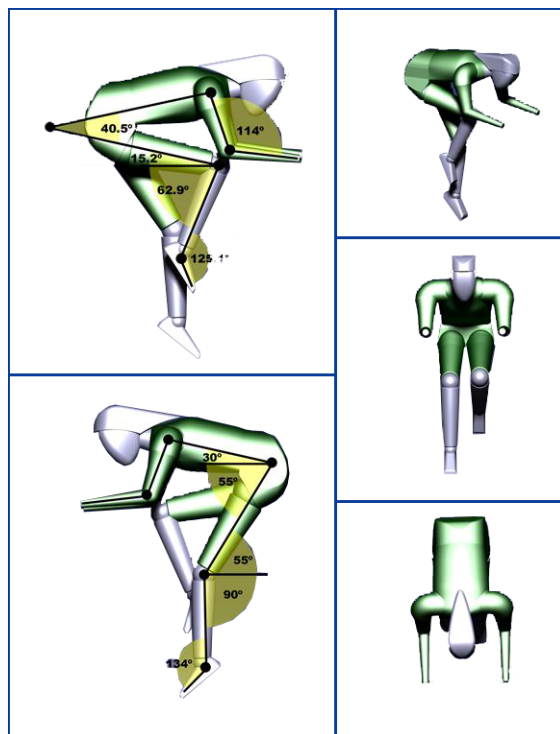


Fig 1. 3D-CAD model of typical body angles in time-trial cycling

A standard cylindrical geometry was adopted to evaluate textiles and garment features e.g. seams which consisted of an active central section (yellow) connected to the load cell and passive upper and lower sections (red) assembled to minimize end effects as shown in Figure 2, details of which are given elsewhere [7, 8]. The active cylinder has a diameter and length of 110 mm and 400 mm respectively, while the 6-axis force transducer (type JR-3) had a sensitivity of 0.05% over a range of 0 to 400 N. To examine the impact of non-vertical athlete body positions, which can generate

aerodynamic drag, lift and down-force, the lower section the cylinder arrangement was designed to provide a rotating mechanism to allow the cylinder to assume any angle from 30° to 150° relative to the wind direction (Figure 2).

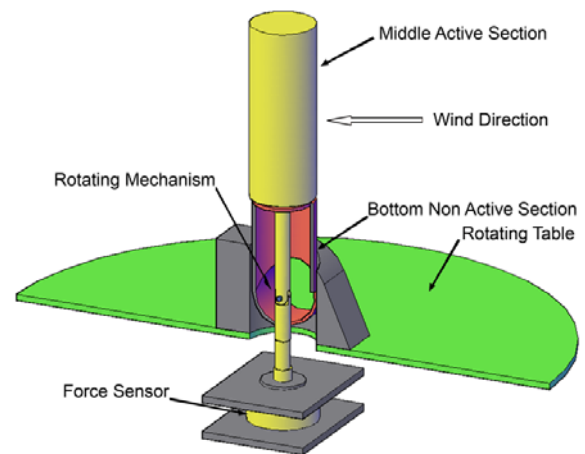


Fig 2. Standard cylindrical geometry arrangement for wind tunnel studies

Textile sleeves were fabricated for the cylinders such that each fabric had similar tensions when installed on the cylinder. The surface textures showed two length scales of features, optical microscopy showed features in the range 500 to 1000  $\mu\text{m}$  and environmental scanning electron microscopy ESEM (QUANTA 200 FEI) provided resolution down to the single micron scale (see Figure 8). Bulk textile moduli (stretch) were determined for each textile using an Instron device.

## 3. RESULTS AND DISCUSSION

The aerodynamic properties such drag, lift and side forces were measured for a range of wind speeds (20 km/h to 120 km/h with an increment of 10 km/h) under angles of attack (30°, 60° and 90° from horizontal). Four textiles with varied surface topology were studied. Two textiles: LT-1 & LT-2 are so called low transition textiles for their relatively rough surfaces (see Figure 8a). Other two textiles: HT-1 and HT-2 are so called high transition textiles for their relatively smooth surfaces (see Figure 8b).

The aerodynamic properties of the bare cylinder were measured first initially and hereafter, the properties of all textiles (HT-1, HT-2, LT-1 & LT-2). The aerodynamic properties were converted to non-dimensional parameters such as drag coefficient ( $C_D$ ), lift coefficient ( $C_L$ ), side force coefficient ( $C_S$ ) and their corresponding moments. Only  $C_D$  and  $C_L$  values are presented in this study.

The drag coefficients for a smooth cylinder (bare cylinder) and all four textiles are plotted against the speeds under 90°, 60° and 30° angles of attack from horizontal which are shown in Figures 3, 4 and 5 respectively. The figures indicate that the airflow around the smooth cylinder remains relatively laminar at speeds below 90 km/h at 90° angle of attack, 80 km/h



at 60° angle of attack and 30 km/h at 30° angle of attack. However, the laminar boundary layer much earlier undergoes transition to turbulent boundary layer for LT-1 & LT-2 at 40 km/h under 90° angle of attack, 30 km/h under 60° angle of attack. No notable transition was observed at 30° angle of attack (see Figures 3 to 5). On the contrary, the airflow around the HT-1 & HT-2 textiles undergoes transition much later at 70 km/h under 90° angle of attack, 60 km/h under 60° angle of attack and 30 km/h under 30° angle of attack compared to LT-1 and LT-2. The bare cylinder possesses higher  $C_D$  value at almost all speeds tested. With an increase of angle of attack, as expected, the drag coefficient increases for all textiles and bare cylinder as shown in Figures 3 to 5.

The lift coefficients against speeds for all textiles and bare cylinder are shown in Figures 6 and 7 for 60° and 30° angle of attack. The LT-1 and LT-2 demonstrate more lift coefficients at high speeds (above 70 km/h under 60° angle of attack and 50 km/h under 30° angle of

attack) compared to HT-1 and HT-2 textiles. A notable variation in lift coefficients between LT-1 and LT-2 was also observed at low speeds below 50 km/h at 60° angle of attack and at all speeds under 30° angle of attack. A similar variation was also noted between HT-1 and HT-2 textiles at slightly different speeds and angle of attacks (see Figures 6 and 7).

In order to take the aerodynamic advantage (eg, lower aerodynamic drag), it would be appropriate to use LT-1 and LT-2 textiles between 40 km/h to 80 km/h speeds for the body parts facing the angle of attack at around 90°, 30 km/h to 70 km/h at around 60° angle of attack and at all speeds under 30° angle of attack. On the other hand, the use of HT-1 and HT-2 will be favourable at speeds over 80 km/h at 90° and 30° angles of attack.

The LT-1 and LT-2 textiles would be better to use for generating lift at speeds over 70 km/h under 60° angle of attack and at all speeds under 30° angle of attack as shown in Figures 6 and 7.

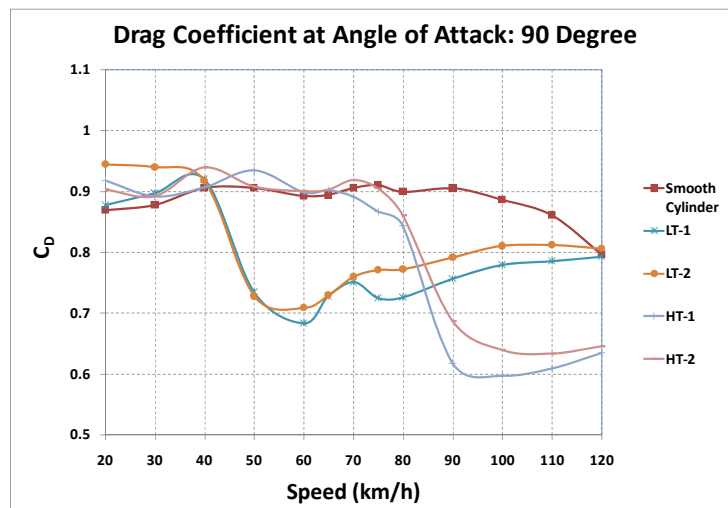


Fig 3. Drag coefficients for various textiles under the angle of attack  $\alpha = 90^\circ$

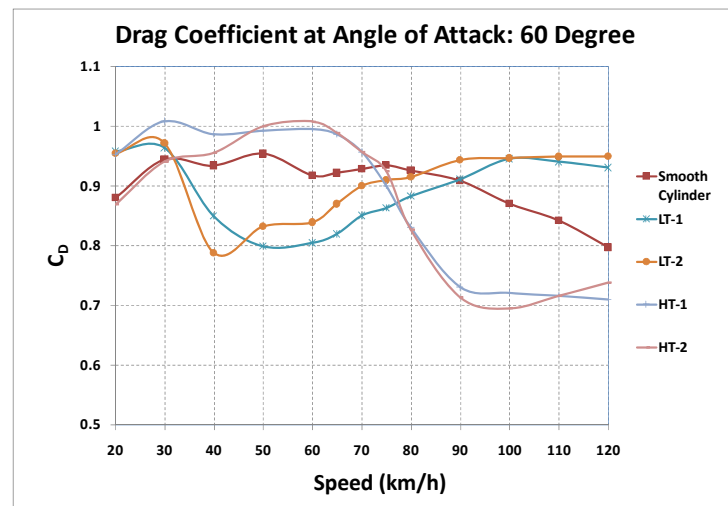


Fig 4. Drag coefficients for various textiles under the angle of attack  $\alpha = 60^\circ$

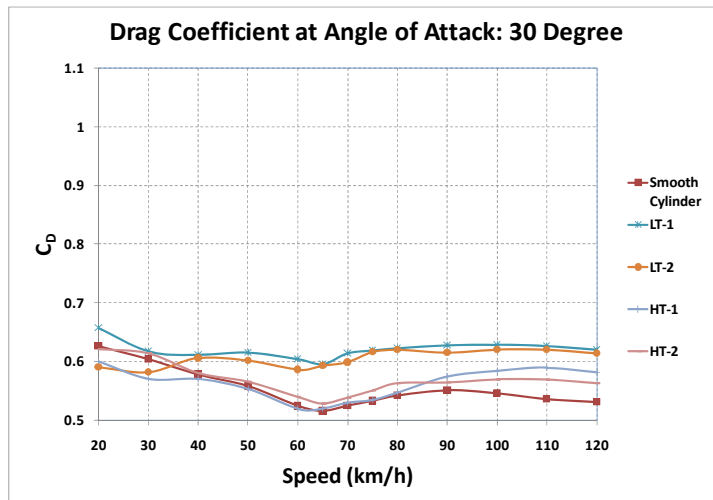


Fig 5. Drag coefficients for various textiles under the angle of attack  $\alpha = 30^\circ$

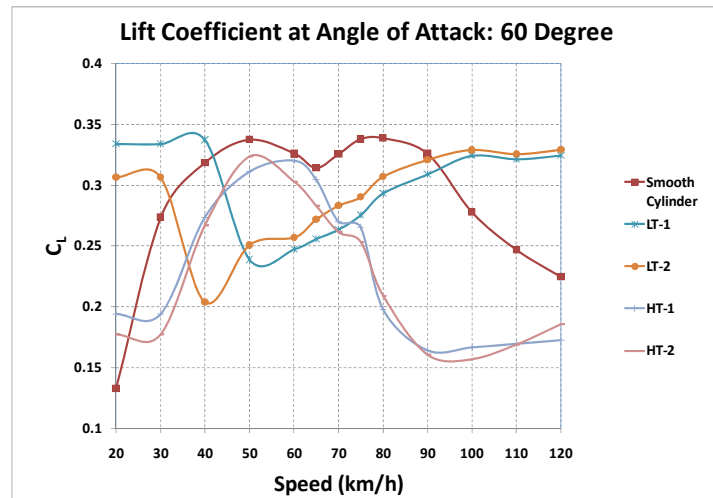


Fig 6. Lift coefficients for various textiles under the angle of attack  $\alpha = 60^\circ$

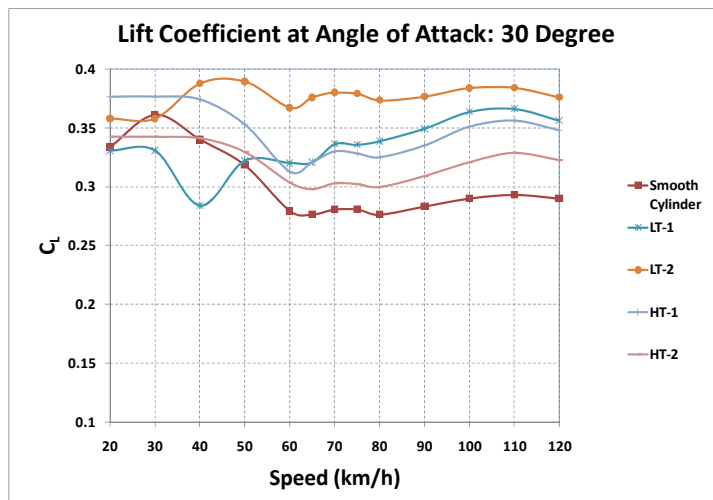


Fig 7. Lift coefficients for various textiles under the angle of attack  $\alpha = 30^\circ$

Examination of the high and low transition textiles by ESEM (Figure 8) showed a marked difference in surface texture. The surface topology of the high transition samples were made up of ~600  $\mu\text{m}$  linear arrays of regular yarn bundles (~250  $\mu\text{m}$ ) composed of fibres (~20  $\mu\text{m}$ ) forming the knitted fabric warp, while

the low transition textiles showed weft fibres straggling the warp array decreasing isotropy and increasing surface roughness at this scale. As noted, sleeves were produced so that they provided a constant fabric tension when placed on the cylinders in order to maintain these surface characteristics.

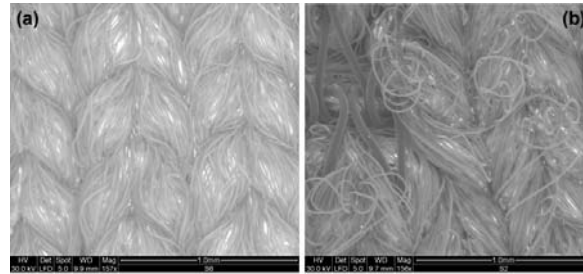


Fig 8. Scanning microscope images of high transition (a) and low transition (b) textiles (156X)

#### 4. CONCLUDING REMARKS

The following conclusions were drawn from the work presented here:

- The bare smooth cylinder possesses higher aerodynamic drag at all speeds compared to rough surface topology textiles.
- The surface morphology plays a key role in the reduction of drag and lift
- Right selection of textiles for athletes is utmost important for achieving aerodynamic advantages.

#### 5. ACKNOWLEDGEMENT

The authors would like to express their sincere thanks to Mr Patrick Wilkins and Mr Gilbert Atkin, School of Aerospace, Mechanical and Manufacturing Engineering, RMIT University for their technical assistance with the wind tunnel testing.

#### 6. REFERENCES

1. Gross, A., Kyle, C.R. and Malewicki, D., 1983, "The Aerodynamics of Human-powered Land Vehicles", *Scientific American*, 249:142-152.
2. Strangwood, M. and Subic, A., 2007, "Modelling of Materials for Sports Equipment", *Materials in Sports Equipment, Volume 2*, Woodhead Publishing Ltd., Cambridge, UK.
3. Kyle, C.R. and Caiozzo, V.J., 1986, "The effect of athletic clothing aerodynamics upon running speed", *Medicine and Science in Sports and Exercise*, 18:509-515.
4. Brownlie, L.W., 1992, "Aerodynamic Characteristics of Sports Apparel", Ph.D. thesis, University of British Columbia, Canada.
5. Brownlie, L.W., Kyle, C.R., Harber E., MacDonald, R. and Shorten, M., 2004, "Reducing the Aerodynamic of Sports Apparel: Development of the Nike Swift Sprint Running and Swift Skin Speed Skating Suits", *The Engineering of Sport 5, Volume 1*, International Sports Engineering Association, UK.

6. Kyle, C.R., Brownlie, L.W., Harber, E., MacDonald, R. and Norstrom, M., 2004, "The Nike Swift Spin Cycling Project: Reducing the Aerodynamic Drag of Bicycle Racing Clothing by Using Zoned Fabrics", *The Engineering of Sport 5, Volume 1*, International Sports Engineering Association, UK.
7. Faria, E., Parker, D. and Faria, I., 2005, "The Science of Cycling Factors Affecting Performance – Part 2", *Sports Medicine*, 35: 313-337.
8. Chowdhury, H., Alam, F., Mainwaring, D.E., Subic, A., Tate, M. and Forster, D., 2008, "Methodology for aerodynamic testing of sports garments", *The Proceedings of the 4th BSME-ASME International Conference for Thermal Engineering*, 1:409-414.
9. Chowdhury, H., Beneyto-Ferre, J., Tate M., Alam, F., Mainwaring, D., Forster, D., and Subic, A., 2009, "Effects of Textile and Garment Design on Aerodynamic Characteristics Applied to Cycling Apparel", *The Impact of Technology on Sports III*, ISBN 13: 978-1-921426-39-1, pp. 131-136.

#### 7. NOMENCLATURE

Symbol	Meaning	Unit
D	Drag Force	(N)
L	Lift Force	(N)
$C_D$	Drag Coefficient	-
$C_L$	Lift Coefficient	-
Re	Reynolds Number	-
V	Velocity of Air	m/s
$\rho$	Density of Air	$\text{kg}/\text{m}^3$
$\nu$	Kinematic Viscosity of Air	$\text{kg}/\text{m}^3$
A	Projected Area	$\text{m}^2$

#### 8. MAILING ADDRESS

Harun Chowdhury  
 School of Aerospace, Mechanical and Manufacturing  
 Engineering, RMIT University  
 Plenty Road, Bundoora, VIC 3083, Australia  
 Telephone: +61 3 99256215  
 Fax: +61 3 99256108  
 E-mail: [harun.chowdhury@rmit.edu.au](mailto:harun.chowdhury@rmit.edu.au)

## REDISTRIBUTED GAS EXCHANGE MECHANISM IN HUMAN LUNG'S PERIPHERALS

M. U. Ahmmed, H. Hirahara and T. Yamamoto

Graduate School of Science and Engineering,  
Saitama University, Shimo-Okubo, Sakura, Saitama,338-8570, Japan

### ABSTRACT

The velocity distribution was investigated with particle image velocimetry (PIV) in a real size model of human's lung peripherals. The working gas is air and the oil mist was used as a tracer. The unsteady velocity profile was obtained with phase locked image capturing, and the data was processed in statistically. The target region of this study is between the 18th to 20th bifurcations in lung's airway. The fundamental respiratory flow was investigated in the present experiment under the high frequency oscillatory ventilation (HFOV) mode for the different compliance conditions, which is important for the clinical treatment. According to the mean flow analysis, the phase delay was estimated theoretically and obtained experimentally. The phase delay in the mean flow was very small, however the obvious flow mixing was observed in the air path lines.

**Keywords:** Human lung, PIV, Compliance, HFOV, Redistribution of Gas.

### 1. INTRODUCTION

A Gas flow in the mammal lungs is simply reciprocal, however, the efficient gas exchange was carried out through this simple air motion. In order to establish the effective gas exchange between oxygen and carbon dioxide, the mammals have developed the sophisticated mechanism in a process of evolution. The gas flow in lungs is so complicated that the flow mechanism has not yet been cleared in the view of the micro or molecular scale. The damage of lung's function arise the critical situation to the human. For these treatments, a lot of effective artificial ventilation devices have been proposed for the lung diseases. HFOV is one of the effective devices for this treatment.

The aim of the present study is to analyze the air trajectory and gas mixing process in the peripherals of lung under the HFOV condition. The fresh air distribution in the bronchial tree is a very important factor in the gas exchange controls of lungs. The heterogeneous compliance distribution will form a different response in the periodic flow motion, thus the time constant in the unsteady flow is different in each branch.

In the present paper, the delay time was compared to the theoretical prediction of electric circuit similarity analysis. The fresh air distribution is associated with the complex flow pattern due to the asymmetric bronchial configuration. In medical treatment, HFOV has a advantage for the minimal pressure fluctuations with a small tidal volume which can avoid the risk of lung injury associated with cyclic opening and closing of

alveolar units, especially for very early born infants who are suffered with respiratory distress syndrome (RDS). Since the tidal volume in HFOV is usually much smaller than the anatomical dead space volume, the prompt gas exchange shown in this operation cannot be explained in terms of simple advective bulk transport to the alveoli. The air transport mechanism has not been cleared, the more detailed fluid dynamical research for HFOV system will be desired to develop the clinical treatment under the optimum condition.

According to the previous researches, it was found that the gas exchange efficiency depends on the Taylor's dispersion, pendelluft and molecular diffusion etc. The fundamental mechanism of pendelluft is attributed to the difference of time constant between lung units due to airway resistance and compliance. In HFOV, it is expected that pendelluft plays an important role on gas exchange; however, all mechanisms of gas transport and exchange have not been yet clarified in detail.

Asymmetry and irregularity of the peripherals has the significant roles in the gas mixing and exchange mechanism. In order to investigate the flow mixing mechanism in the gas exchange zone, many studies have been carried out by considering the human airway models. Otis et al. [1] predicted that asynchronous fluid flow with associated inter-regional convection between parallel respiratory units can result from non-homogeneities in tissue mechanics, and such flows are known as 'pendelluft' flows which are now regarded as an important factor in gas mixing during high frequency ventilation [2]. Ultman et al. [3] and High et al. [4] carried out a study of pendelluft and mixing in a

single bifurcation lung model during HFOV. They obtained the mixing coefficients and the pendelluft volume fraction. They also show that asymmetries in compliance and in inertance produce much greater pendelluft than an asymmetry in resistance. Elad et al.[5] developed a nonlinear lumped-parameter model to investigate the dependency of airflow distribution in asymmetric bronchial bifurcations on structural and physiological parameters. They derived the modified time-dependent expressions of resistance and compliance of each compartment. They also showed that asymmetry in compliance of peripheral airways might affect the flow distribution in daughter tubes and induced larger degrees of pendelluft.

To facilitate investigation of gas mixing and exchange in bronchial tube, efforts have been directed towards the development of air path trajectory. The ensemble mean velocity vectors were obtained through the experiment. The Lagrangian path line of air from the time mean velocity distribution data was reconstructed.

## 2. PULMONARY PHYSIOLOGY AND ANALOGY

### 2.1 Anatomical Background

The air way of human lung is divided into 23 generations. These airways consist of successive two zones, conducting zone and the respiratory zone. From trachea to the bronchioles (G0 to G16, where G is generation), no alveoli exists and no gas exchange occurs so that this space is called anatomical dead space. Down to the conducting zone the respiratory zone (G17 to G23) starts and continues to respiratory bronchioles, alveolar ducts and alveolar sacs. In this region a vast number of alveoli exist and hence suitable gas exchange occurs.

Gas diffusion is dominated in the bottom of the lung, whereas, in the respiratory region an active gas mixing will be expected to maintain the effective molecular diffusion. The end part of lung in which the inhaled air contacts with the residual air, has complicated bronchial tissue with bifurcated micro-channels where the complicated gas exchange mechanism occurs by not only molecular diffusion but also convective motion.

Oscillatory air flow generated by artificial ventilation system HFOV is an important process to develop the rate of gas exchange in deeper branches of bronchial tube. The oscillatory flow exhibits an important characteristic

length as Stokes layer thickness,  $\delta = \sqrt{\frac{2\nu}{\omega}}$ , where  $\nu$  ( $= 1.513 \times 10^{-5} \text{ m}^2/\text{s}$ , 20 degrees in Celsius for air) is the kinematic viscosity,  $\omega$  ( $= 2\pi f$ ,  $f$  is the frequency) is the angular frequency. Two fundamental dimensionless parameters for the oscillatory flow are Reynolds number and Womersley number. They are

defined as  $Re = \frac{u d}{\nu}$  and  $\alpha = \frac{d/2}{\sqrt{\frac{2\nu}{\omega}}}$ , respectively.

Where,  $u$  and  $d$  are averaged flow speed and the diameter of channel respectively.

Under the normal breathing condition,  $Re$  is about

4000 at the trachea and about 30 at terminal bronchus where it is less than 0.04 in the alveolar region. Hence the average fluid velocity at the centre of the alveolar sac closes to zero so that the velocity in the alveoli is assumed to be slow streaming velocity. As described above, the flow features are very different in each generation. Furthermore, under HFOV driving condition, the flow regime should be changed drastically. In order to clarify the gas exchange mechanism both in the case of normal respiration and HFOV, the accurate flow measurement should be required. The frequency is 25~100 times of the normal breath for HFOV condition.

Since  $\alpha$  is proportional to the root of frequency, for large number of  $\alpha$ , the phase delay is increased in velocity profiles between the main flow and the boundary layer. Consequently, the local disturbance will be induced near the bronchus.

### 2.2 Lump Parameter Analysis

The air flow distribution in the bronchial tree is associated with the complex flow pattern and subjected to the nonlinear features of lung's mechanics. Direct in vivo study of airflow in lung is almost impossible and has been limited to evaluation of the frequency response of the respiratory system. The increasing of ventilation frequency or stroke volume increases the time and percentage of pendelluft in each cycle (Elad et al. [5]). Time constant difference or phase delay measurement between two sections of bronchial tube is another important assignment for better understanding of pendelluft motion. The generation of the pendelluft is predicted with the lump parameter analogy. The circuit of this analogy was demonstrated in Figure 1 for the present experiment.

The simulated synthetic impedance ( $Z_{19}$ ) in the first junction may be expressed as

$$\begin{aligned} Z_{19} &= \frac{1}{(\sum R_i)^2 + (\sum S_i)^2} \left[ \frac{(R_1|Z_2|^2 + R_2|Z_1|^2)}{+ j(S_1|Z_2|^2 + S_2|Z_1|^2)} \right] \\ &= X_{19} + jY_{19} \\ &= \sqrt{X_{19}^2 + Y_{19}^2} e^{j\phi_{19}} \end{aligned} \quad (1)$$

$$\text{where } \phi_{19} = \tan^{-1} \left( \frac{Y_{19}}{X_{19}} \right)$$

$$|Z_i|^2 = (X_{20i} + R_{19i})^2 + (Y_{20i} + S_{19i})^2$$

$$S_i = \omega L_i, \quad \text{for } G19$$

$$S_i = \omega L_i - \frac{1}{\omega C_i}, \quad \text{for } G20$$

$$i = 1 (\text{for left branch}), 2 (\text{for right branch}). \quad (2)$$

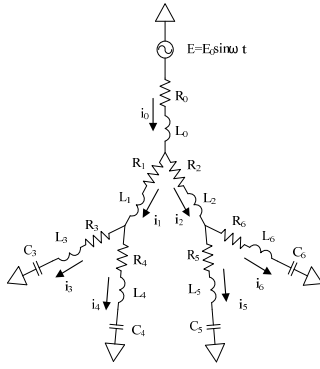


Fig 1. RLC circuit analogy

To simulate the present investigation, the resistive, inertial and elastic properties of the respiratory system have been replaced with RLC electrical circuits. We adopted the empirical resistance law of Collins et al. [6] for each airway which is time-dependant and reflects the influence of curvature and the boundary layer development. This law is defined as in equation (3).

$$R = R_L (0.556 + 0.067 \sqrt{Re}) \quad (3)$$

Here,  $R_L = \frac{128 \mu l}{\pi d^4}$  is the laminar flow resistance in a circular tube,  $l$  the length of the tube and  $\mu$  the viscosity of the air.

In an oscillatory flow the pressure gradient that drives the fluid makes the inertia (acceleration and deceleration). The inductance corresponds to the fluid acceleration and can be expressed in terms of tube dimensions (Van der Tweel[7]), thus,

$$L = \frac{4 \rho l}{\pi d^4} \quad (4)$$

where  $\rho$  is the density of air. Since, air is practically incompressible within the real scale of bronchial tube, the inductance is independent of time.

In our experiment, the bronchial branches of G20 are connected to the rubber tubes which have the

volume-dependant compliance,  $\frac{dV}{dP}$  of peripheral airways and lung tissue, whereas G18 and G1<sup>h</sup> hold the constant volume as rigid tube made of metal plate and glass. According to the investigation of Sharp et al. [8], the net lung's compliance has a range in value

$$C_{lung} = 0.128 \times 0.81 \left[ \frac{l}{cm H_2 O} \right]$$

The compliance per unit length of rubber tube used in the experiment is

$$C_{Tube} = 7.86 \times 10^{-3} \left[ \frac{ml}{cm H_2 O} \right] \quad (5)$$

The compliance below G20 was estimated from the number of the blanch and the length of the tube was adjusted for the equivalent compliance.

The combined resistance of bronchial model tube is simulated as

$$R_{combined} = R_{metal} + R_{glass} + R_{fittings} + R_{rubber\ tube} \quad (6)$$

The combined results for  $R$  and  $L$  are also obtained by employing the equation (6).

The impedance of G19 depends on the real resistance and inductance only. So, the local pendelluft in the first junction is generated by the influence of inductance which may induce the lateral mixing of air particles.

### 3. EXPERIMENTAL METHOD AND SETUP

#### 3.1 Bronchial Model

In order to investigate the flow mechanism in lung, the instantaneous velocity vector fields are obtained for the different phase timing through the influx and efflux. By using these data, the periodic velocity distributions were obtained and fluid tracking was conducted for two cycles. According to the anatomical structure, a multi-bifurcated micro channel was used in the experiment as shown in Fig.2.

The test channels made of aluminum plate were pre-processed with black coating in order to reduce optical scattering. The channel widths of the G18, G19, and G20 generations were 500 $\mu$ m, 450 $\mu$ m and 400 $\mu$ m respectively as shown in Fig.2. The depth of each channel was 500 $\mu$ m.

The length of the G19 was 1.2mm along the centre line. The angles of first and second junction were 70 and 60 degrees respectively.

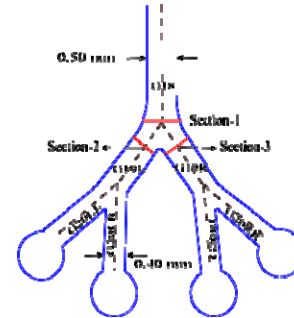


Fig 2. Bronchial model tube

Each branch of G20 was terminated with closed flexible tube which represents the peripheral alveoli. The tube is TYGON R-3603 (SAINT-GOBAIN Co'LTD).. The standard compliance of human under G20 is

$$2.0 \times \frac{10^{-3} ml}{cm H_2 O}$$

Hereafter, we call this compliance as 1-unit standard compliance. By changing its length, we can obtain the desired compliance to match the standard human lung. The driving system of HFOV was connected to a chamber. The chamber was connected to the test section and served a premixed mixture of air and tracer particles. The tidal volume and the amplitude of pressure variation were controlled by the controller of HFOV system.

#### 3.2 Experimental Apparatus

Fig.3 shows schematic of the experimental setup for  $\mu$ -PIV, which is consisted of ventilation system (HFOV),



test channel, image acquisition system, and illumination laser.

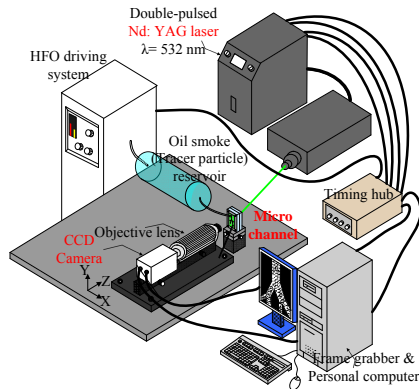


Fig.3 Schematic of experimental setup

The ventilation mode was generated by HFOV driver. The signals from pressure sensor were used for phase locking image acquisition.

The  $\mu$ -PIV system for 2D velocity field measurements was consisted of high speed CMOS camera (IDT, XS-5), a macro lens with long working distance (KEYENCE, VQ-Z50A,  $\times 500$ ), double-pulsed Nd-YAG laser (New Wave Research, Solo III), timing hub, and computer for image capturing. The test section was illuminated by Nd-YAG laser with 532 nm wavelength, 50mJ/pulse output and 5ns duration from the backside of the micro channel at angle of 60 degree to prevent the damage of camera. The resolution of CMOS is 1280(H) $\times$ 1024(V) pixels in space and 8 bits in depth of intensity. The maximum frame rate is 1000 frames per second. In our experiment, the oil-mist particles in the order of 1 $\mu$ m in diameter generated by Laskin nozzle were used as seeding particles. These particles are mixed in the premix chamber which connected to the inlet of the test channel.

## 4. RESULTS AND DISCUSSIONS

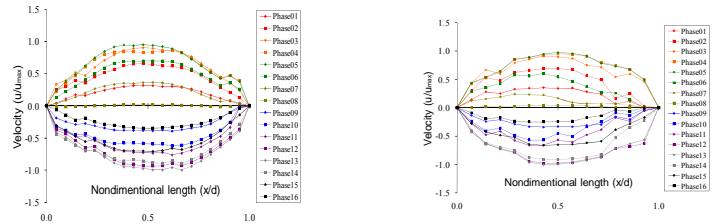
### 4.1 Instantaneous and Time Mean Velocity Distributions

The phase locked measurement was carried out in order to investigate the periodic oscillatory flow in multi-bifurcated airway models during HFOV condition at 10, 15, and 20 Hz. The phase locked signal was synchronized with the pressure signal and the delay time,  $n\Delta T$  ( $n = 0, 1, 2, \dots, 15$ ).

Here,  $T$  is the period of oscillatory flow, and  $\Delta T = \left(\frac{1}{16}\right)T$ . 500 pair images were acquired for each delay time. The time mean velocity fields were obtained with these data. The size of the observation area was 2.8 $\times$ 2.3 mm, the image size recorded by micro-PIV system was 1280(H)  $\times$  1024(V) pixels and the interrogation window size for velocity reconstruction was 16 $\times$ 16 pixels.

Fig.2 shows the measurement sections of velocity profiles and Fig.4 exhibits the velocity profiles at sections 1, 2 and 3. The velocity profiles in the parent

tube (Section-1) are approximately parabolic and oscillated in phase with driving force. If frequency increases, Womersley number also increases and a little unsteady nature of velocity profiles are observed in identical sections. As a result, we notice the asymmetric flow patterns in the daughter channels (Section-2, 3). This unsteadiness depends on time constant difference between parallel branches. In order to clarify the effect of phase delay we use two different volume ratios (4:4:4:4) and (4:4:1:1) and we perform our entire experiment by fixing a constant inspiration phase as a critical ventilation.



(a) Section-1

(b) Section-2

In case of even ratio (4:4:4:4), the vectors did not show symmetrical distribution. This was attributed to the difficulty of the fabrication of the model channels and the contamination of particle mist.

From Fig.4, if frequency are increased for symmetric volume ratio, the velocity profiles are about to parabolic. This happens for unsteadiness of flow and the phase delay occurs. This effect is noted in first junction of particle trajectory as shown in Fig.5. Also a very small pendelluft (small vortices) was observed in first junction, thus it is called a local stream. Moreover, this phase delay may occur by the combined effect of bifurcated junction, the oscillating viscous boundary layer and the tendency of lateral mixing. The phase delay is revealed from experimental results and RLC analogy model as shown in Table.1

Table: Comparison of phase delay

Frequency	Volume ratio	Phase delay [ms] (Experiment)	Phase delay [ms] (RLC circuit)
10 Hz	4:4:4:4	5.95E-01	6.78E-01
	4:4:1:1	6.01E-01	6.77E-01
15 Hz	4:4:4:4	6.10E-01	6.67E-01
	4:4:1:1	5.08E-01	6.68E-01
20 Hz	4:4:4:4	7.25E-01	6.53E-01
	4:4:1:1	2.52E-01	6.46E-01

observed during an oscillatory flow through a Y-shaped tube bifurcation model. This is the effect of the



asymmetric geometry on the oscillating velocity vector field. It can be deduced that the quasi-steady redistribution is greatest for fluid elements that experience the highest velocity through the bifurcation junction. The redistributed field contributes to a complex

## 5. CONCLUSION

Ensemble mean velocity distributions under the HFOV condition were obtained for a bronchial model tube for generation 18th to 20th of human lung with micro-PIV

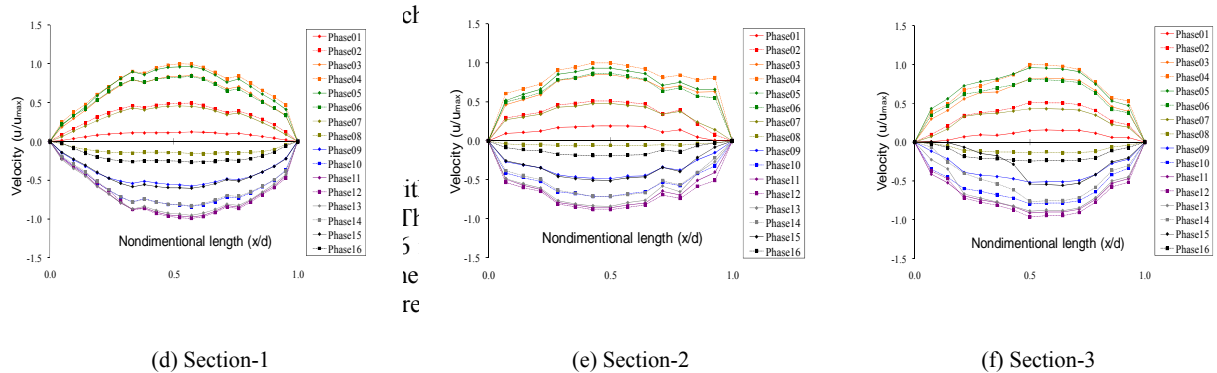


Fig.4 Velocity profiles at sections 1, 2 and 3 for 10 Hz (a, b, c) and 15 Hz (d, e, f)

vector maps of time interval  $\frac{1}{8}\Delta T$  were obtained by interpolation of the experimental data.

Fig.5 shows, at the start of inspiration, 13 red markers were introduced in the parent channel (G18). For a complete cycle, the red dots for inspiration and the blue dots for expiration are air trajectory. For  $f=15$  Hz and the volume ratio (4:4:4:4), the path lines seem to be almost symmetric as shown in Fig. 5(a).

The obtained path lines are so complicated and interesting. The markers go down along the bifurcated channel in the inspiration phase and come back in the expiration phase. We see that the markers are deviated to the centre side and most of them overcome the starting positions. The markers which were introduced inner side, they moved back by a little deviation and few of them could not reach the initial position. As mentioned here, this is an important mixing mechanism for this respiratory condition. During several cycles, the outer side air moves to the centre side and the centre side air moves to the deep location. Other words, the markers turn anticlockwise in left branch and clockwise in right branch. This mixing mechanism should be the most important reason on the redistribution of air. Fig. 5(b) shows that the compliance of left branch is four times larger than that of right branch by the conditions (4:4:1:1) and 15 Hz. So, flow rate becomes uneven for this asymmetric ratio and the markers of right branch show the quasi laminar behavior. Then, all markers returned to the starting position and exceeded their initial line.

By similar condition, if frequency is increased by 20 Hz, the path lines show the different features as shown in Fig.5(c). The markers of both branches penetrate to more deep location. The markers of right branch do not reach their starting position whereas almost all particles of left branch exceed their initial position. The small period for larger frequency and smaller flow rate does not effect on pendelluft but a very little time constant difference may induce a vortex generation which leads to the different path of the particles thus called redistribution.

system. The phase delay was discussed for the different compliance and driving frequencies. The identical phase delay is observed from experiment and RLC analogy circuit model. By using the experimental velocity data, air trajectories were determined for several experimental conditions. We observe that oscillatory flow pattern changes for increasing of the driving frequency and for decreasing of Stoke's layer thickness.

The lines show the very complicated trajectories and these characteristic behaviors give a very important insight for the air redistribution in human airway of lung.

## 6. REFERENCES

1. Otis, A.B., McCarron, C.B., Bartlett, R.A., Mead, J., McIlroy, M.B., Selverstone, N.J., and Radford, E.P., 1956, "Mechanical factors in distribution of pulmonary ventilation", *Journal of Applied Physiology*, 8: 427-443.
2. Chang, H.K., 1984, "Mechanisms of gas transport during ventilation by high-frequency oscillation", *Journal of Applied Physiology*, 56: 553-563.
3. Ultman, J. S., Shaw, R.G., Fabiano, D.C. and Cooke, K.A., 1988, "Pendelluft and mixing in a single bifurcation lung model during high frequency oscillation", *Journal of Applied Physiology*, 5:146-155 .
4. High K.C., Ultman J.S. and Karl S.R., 1991, "Mechanically induced pendelluft flow in a model airway bifurcation during high frequency oscillation", *Journal of Biomechanical Engineering*, 113:342-347.
5. Elad, D., Shochat, A. and Shiner, R.J., 1998, "Computational model of oscillatory airflow in a bronchial bifurcation", *Respiration Physiology*, 112:95-111.
6. Collins, J.M., Shapiro, A.H., Kimmel, E., Kamma, R.D., 1993, "The steady expiratory pressure-flow relation in a model pulmonary bifurcation", *J. Biomech. Eng.*, 115:299-305.
7. Van der Tweel, L.H., 1957, "Some physical aspects of blood pressure pulse wave, and blood pressure

- measurements”, Am. Heart J., 53:4-22.
8. Sharp, J.T., Henry, J.P., Sweany, S.K., 1964, ” The total work of breathing in normal and obese men”, Journal of Clinical Investigation, 43:728-739.

## 7. NOMENCLATURE

Symbol	Meaning	Unit
$G$	Generation	
$d$	Diameter of each compartment	(mm)
$f$	Frequency	(Hz)
$\omega$	Angular frequency	(rad /s)
$\nu$	Kinematic viscosity	(m <sup>2</sup> /s)
$u$	Average flow speed	(mm/s)
$\alpha$	Womersley number	(Dimensionless)
$\delta$	Stokes layer thickness	(Dimensionless)
$R_i$	Resistance of each compartment	(ohms)
$Z_i$	Impedance of each compartment	(ohms)
$S_i$	Total reactance of each compartment	(ohms)
$R$	Airway resistance	(cmH <sub>2</sub> O.L <sup>-1</sup> .sec)
$R_L$	Laminar resistance	(cmH <sub>2</sub> O.L <sup>-1</sup> .sec)
$\rho$	Air density	(kg/m <sup>3</sup> )
$l$	Tube length	(mm)
$L$	Inertance	(cmH <sub>2</sub> O.L <sup>-1</sup> .sec <sup>2</sup> )
$\varphi$	Phase delay	(sec)
$C$	Compliance	(L/cmH <sub>2</sub> O)

## STENOSIS LENGTH AND ITS IMPACT ON FLOW OF BLOOD THROUGH RECTANGULAR STENOSED CORONARY ARTERY

S. Chakrabarti<sup>1</sup> and D. K. Mandal<sup>2</sup>

<sup>1</sup>Dept. of Mech. Engg., Bengal Engineering and Science University, Shibpur, India

<sup>2</sup>Dept. of Basic Science & Humanities, College of Engg. & Management, Kolaghat, India

### ABSTRACT

Impact of stenosis length on flow of blood through rectangular stenosed coronary artery has been investigated in case of non dimension stenosis lengths of 0.1, 0.5, 1.0 and 2.0 for the restriction of 50% (by diameter) and Reynolds number of 200. Effect on streamline contour and wall shear stress has been discussed and presented along with its possible physiological aspects. It is revealed that the wall shear stress is dependent upon the stenosis length but reattachment length is relatively independent of stenosis length.

**Keywords:** Stenosis, Wall pressure, Wall Shear Stress, Stenosis Length

### 1. INTRODUCTION

Atherosclerosis is a progressive disease characterized by localized plaques that form within the artery wall. One of the fundamental causes of the plaque development is believed to be the abnormal enlargement of the intima by infiltration and accumulation of macromolecules such as lipoproteins, and the associated cellular and synthetic reactions. As the disease progresses, these plaques enlarge and, either directly or indirectly, lead to impairment of blood flow. This in turn can have serious consequences, such as blockage of the coronary arteries. Both clinical reports and numerical simulations show that haemodynamics play an important role in the pathogenesis of atherosclerosis. It is widely believed that atherosclerosis development and progression are affected by many risk factors, such as static pressure, wall shear stress, blood viscosity, flow velocity etc.

Some attempts to study across rectangular stenoses have been done by different researchers numerically and experimentally. Among them, the numerical work have been done by Cheng [1, 2] for steady, oscillatory and pulsatile flow, Coder and Buckley[3] for unsteady flow, Wille [4] for steady, laminar, Newtonian flow conditions for several models of stenosed vessels with different constriction ratios of 50%, 75% and 90% with Reynolds numbers 10, 100 and 200, and Liou et al.[5] for steady flow with Reynolds numbers of 25 and 150. The experimental work have been done by Seeley and Young [6] for steady flow with Re varying from 0 to 1000 with 60%, 75%, 85% and 90% area reduction considering different stenosis lengths, Solzbach et al. [7] have investigated experimentally the influence of stenosis geometry in steady flow conditions for Re varying from 1 to 500 with percentage lumen area reduction of 77%, 87% and 94% for two stricture lengths. Liepsch et al. [8] have studied experimentally the flow behavior under

steady flow condition in four models of cylindrical stenosis with rectangular cross section at Re varies from 150 to 920 and percentage of restriction of 21%, 45%, 49% and 73% approximately for a fixed stenosis length.

From brief review of literature, it is noted that a number of researchers have studied the effect of percentage of restriction, Reynolds number and stenosis length on pressure drop and flow separation for rectangular shaped constriction. Very few of them have discussed the flow separation with the variation of stenosis length. None of them has investigated the effect of stenosis length of a rectangular stenosis on the wall shear stress. Therefore, in this work, an attempt has been made to study systematically the effect of stenosis lengths of 0.1, 0.5, 1.0 and 2.0, on stream line contour and shear stress typically for Reynolds number of 200 and percentage of restriction of 50% respectively.

### 2. MATHEMATICAL FORMULATION

#### 2.1 Governing Equations

A schematic diagram of the computational domain is illustrated in Fig. 1. The flow under consideration has been assumed to be steady, two-dimensional and laminar. In the study, the blood is considered as Newtonian and incompressible, and the arterial wall is rigid.

The following dimensionless variables are defined to obtain the governing conservation equations in the non-dimensional form;

$$\text{Lengths: } x^* = x/D \quad y^* = y/D \quad L_i^* = L_i/D$$

$$L_{ex}^* = L_{ex}/D \quad L_s^* = L_s/D$$

$$\text{Velocities: } u^* = u/V_1 \quad v^* = v/V_1$$

$$\text{Pressure } p^* = (p + \rho gy)/\rho V_1^2$$

With the help of these variables, the mass and momentum conservation equations are written as follows,

$$\frac{\partial u^*}{\partial x^*} + \frac{\partial v^*}{\partial y^*} = 0 \quad (1)$$

$$\frac{\partial(u^*u^*)}{\partial x^*} + \frac{\partial(v^*u^*)}{\partial y^*} = -\frac{\partial p^*}{\partial x^*} + \frac{1}{\text{Re}} \left[ \frac{\partial}{\partial x^*} \left( \frac{\partial u^*}{\partial x^*} \right) + \frac{\partial}{\partial y^*} \left( \frac{\partial u^*}{\partial y^*} \right) \right] \quad (2)$$

$$\frac{\partial(u^*v^*)}{\partial x^*} + \frac{\partial(v^*v^*)}{\partial y^*} = -\frac{\partial p^*}{\partial y^*} + \frac{1}{\text{Re}} \left[ \frac{\partial}{\partial x^*} \left( \frac{\partial v^*}{\partial x^*} \right) + \frac{\partial}{\partial y^*} \left( \frac{\partial v^*}{\partial y^*} \right) \right] \quad (3)$$

Where, the flow Reynolds number,  $\text{Re} = \rho V_1 D / \mu$

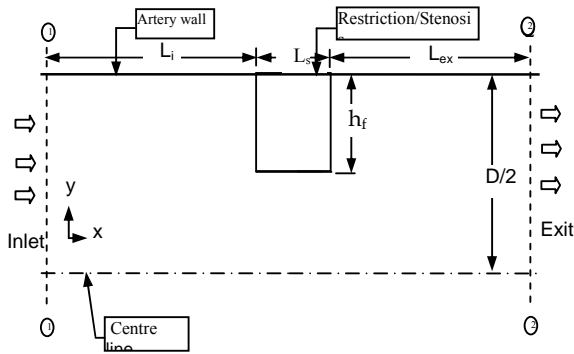


Fig 1. Computational Domain

## 2.2 Boundary Conditions

Four different types of boundary conditions have been applied to the present problem. They are as follows,

1. At the walls:  $u^* = 0, v^* = 0$ .
2. At the inlet: Fully developed flow condition has been specified at the inlet, i.e.,  $u^* = 1.5 \left[ 1 - (2y^*)^2 \right]$
3. At the exit:  $\frac{\partial u^*}{\partial x^*} = 0, \frac{\partial v^*}{\partial x^*} = 0$
4. At the line of symmetry:  $\frac{\partial u^*}{\partial y^*} = 0, v^* = 0$

## 2.3 Numerical Procedure

The partial differential equations (1), (2) and (3) have been discretised by a control volume based finite difference method. Power law scheme has been used to discretise the convective terms as per Patankar<sup>9</sup>. The discretised equations have been solved iteratively by SIMPLE algorithm, using line-by-line ADI method. The convergence of the iterative scheme has been achieved when the normalized residuals for mass and momentum equations summed over the entire calculation domain will fall below  $10^{-8}$ .

In the computation, flow has been assumed fully developed at the inlet and exit and therefore, the inlet and exit have been chosen far away from the restriction. For all calculations, the non-dimensional inlet and the exit lengths have been considered to be 50. The distributions

of grid nodes have been considered non-uniform and staggered in both coordinate direction allowing higher grid node concentrations in the region close to the wall and restriction.

## 3. RESULTS AND DISCUSSION

### 3.1 Variation of Streamline Contour

A detailed knowledge associated with the flow pattern is essential for detection of stenosis. The recirculation zone in the post stenotic region is considered to be an important phenomenon for the formation and

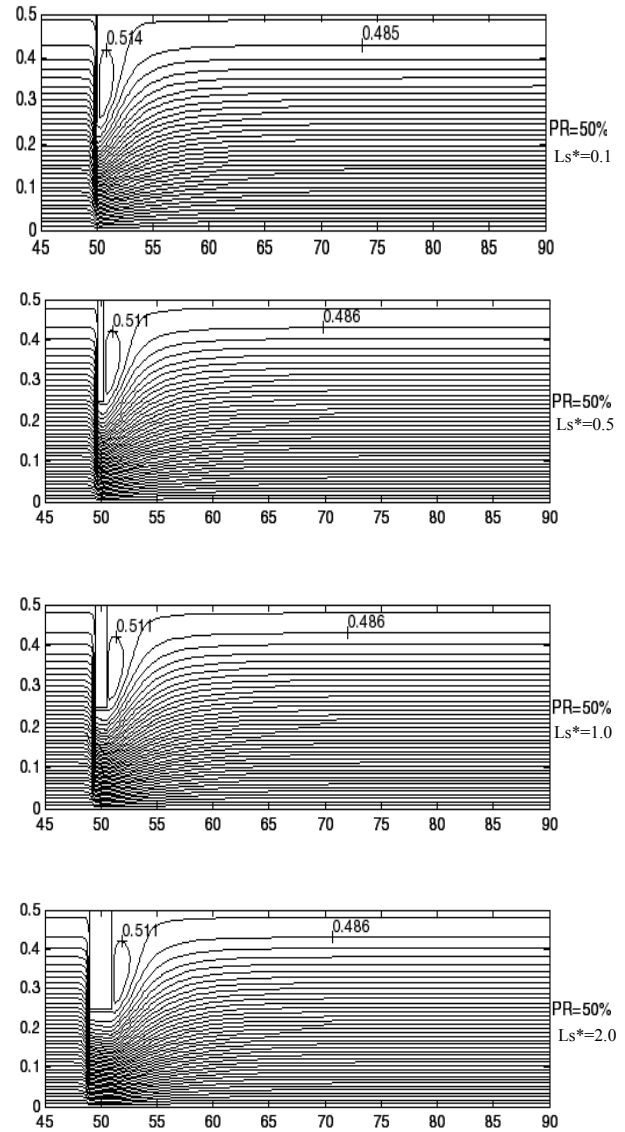


Fig 2. Effect of stenosis length on streamline contour at Reynolds number of 200 for PR of 50%.

atherosclerosis. The physiological significance of the recirculation zone is that the bloodstream stagnates locally in this area and allows platelets and fibrin to form a mesh at the inner wall in which lipid particles become trapped and eventually coalesce to form atheromatous

plaque, this may tend to accumulate to cause a more severe stenosis (Tu et al. [11]). Apart from that, the reattachment point is having also significance on the formation and propagation of atherosclerosis. The high cell turnover rate takes place near the reattachment point due to high cell division and low cell density near that region. For this, a leaky junction may develop which is considered to be the possible pathway for transport of low-density lipoprotein through the arterial wall, (Weinbaum and Chien [12]).

Figure 2 depicts the streamline contours for all the considered stenosis lengths of 0.1, 0.5, 1.0 and 2.0 for typical flow Reynolds number of 200 and 50% restriction. From the study of streamlines, it is noted that, at downstream to the throat section, separation phenomenon takes place and then it reattaches at some distal location. For considered PR and Re, no change in reattachment length is noted with the change in stenosis length. Solzbach et al. [7] have experimentally observed the same nature of flow stabilization with stenosis length. It indicates that once the stenosis is developed, there is no further disturbance of flow characteristics in terms of the length of the recirculation zone with the propagation of stenosis length for the considered geometry of stenosis. It is also observed that the reattachment point moves downstream with increase in stenosis length which indicates the movement of cell turnover point on the arterial wall with the progression of stenosis length.

### 3.2 Variation of Wall Shear Stress

Fry [13, 14] has first postulated that high wall shear stresses do mechanical damage to the arterial wall and consequently initiate the process for formation of atherosclerosis but Caro et al [15] have claimed that such lesions occur in regions of low wall shear stress. It has been found that initially blood cells are damaged or their surface changes in a high shear field, and then the particles stick to wall and form deposits at low shear stress fields, (Chakraborty [16]). Apart from that, RBC damage and thrombosis formulation are thought to occur due to combination of low and high shear stress. Therefore, both high and low wall shear stress regions have been considered to be important aspects in respect to atherogenesis.

The non-dimensional wall shear stress at any position is computed with the help of the following expression:

$$\tau_w^* = \frac{\tau_w}{\tau_{wref}}$$

Where,  $\tau_{wref}$  is the reference wall shear stress, which is considered to be the wall shear stress far away from the stenosis.

Figure 3 represents the wall shear stress distributions for the considered stenosis lengths of 0.1, 0.5, 1.0 and 2.0 for typical flow Reynolds number of 200 and 50% restriction only. Curves of wall shear stress show that, at the restriction zone, rise of wall shear stress occurs due to high velocity gradient and then, at the downstream of restriction, it attains negative wall shear stress due to adverse pressure gradient.

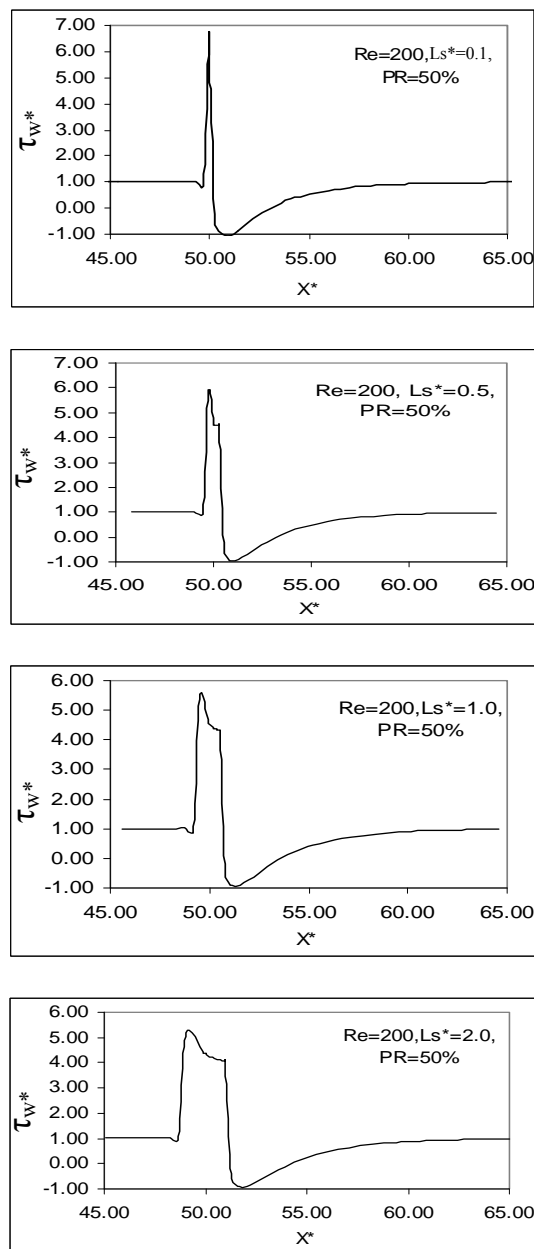


Fig 3. Effect of stenosis length on wall shear stress at Reynolds number of 200 for PR of 50%.

In this study, it is noted that the magnitude of non-dimensional peak wall shear stress is very high for the stenosis length of 0.1 compared to other stenosis lengths of 0.5, 1.0, and 2.0 for the considered Reynolds number and PR, and the magnitude of peak wall shear stress decreases with increase in stenosis length. It is also observed that the magnitude of maximum negative value of wall shear stress remains more or less same with the increase in stenosis length. From the observations, it can be stated that the combined effect of both the peak and low wall shear stress can be considered as the effect of peak wall shear stress only. Therefore, at the time of initiation, i.e. for low value of stenosis length, the chance of damaging to the arterial wall due to peak wall stress is high but it decreases when the stenosis length increases.

#### 4. CONCLUSION

From the present numerical study, it is revealed that during initiation of stenosis length, peak wall shear stress increases appreciably and then its magnitude decreases with the progression of stenosis length. There is no change in the size of recirculation zone with stenosis length.

It is also noted that the size of recirculation zone is not depending on stenosis length. Therefore, it may be mentioned that during initiation of the stenosis length, there may be maximum possibility of lipid deposition on the wall, but the progression of this phenomenon may not take place with further increase in stenosis length. However, the maximum cell turnover point on the arterial wall, due to reattachment point, moves downstream with stenosis length.

#### 5. REFERENCES

1. Cheng, L. C., Clark, M., E., and Robertson J. M., 1972, "Numerical Calculations of Oscillating Flow in the Vicinity of Square Wall Obstacles in Plane Conduits", *Journal of Biomechanics*, 5: 467-484.
2. Cheng, L. C., Robertson, J. M., and Clark, M. E., 1974, "Calculation of Plane Pulsatile Flow Past Wall Obstacles", *Computers & Fluids*, 2:363-380.
3. Coder David, W., and Buckley, Jr. Frank T., 1974, "Implicit solutions of the unsteady Navier-Stokes equation for laminar flow through an orifice within a pipe", *Computers & Fluids*, 2:pp.295-315.
4. Wille, S. O., 1980, "Pressure and Flow in Arterial Stenosis Simulated in Mathematical Models", *Appl. Math. Modelling*, 4:483-488.
5. Liou, R. J., Clark, M. E., Robertson, J. M., and Cheng, L. C., 1981, "Three-Dimensional Simulation of Steady Flow Past a Partial Stenosis", *Journal of Biomechanics*, 14(5), pp. 325-337.
6. Seeley, B. D., and Young, D. F., 1976, "Effect of Geometry on Pressure Losses Across Models of Arterial Stenoses", *Journal of Biomechanics*, 32:439-48.
7. Solzbach, U., Wollschläger, H., Zeiher, A., and Just, H., 1987, "Effect of Stenotic Geometry on Flow Behaviour Across Stenotic Models", *Medical and Biological Engineering and Computing*, 25: 543-550.
8. Liepsch, D., Singh, M., and Lee, M., 1992, "Experimental Analysis of the Influence of Stenotic Geometry on Steady flow", *Biorheology*, 29(4):419-31.
9. Patankar, S. V., 1980, "Numerical Heat Transfer and Fluid Flow", Hemisphere Publication.
10. Gessner, F. B., 1973, "Haemodynamic Theories of Atherogenesis", *Circulation research*, 3: 259-266.
11. Tu, C., Deville, M., Dheur, L., and Vanderschuren, L., 1992, "Finite Element Simulation of Pulsatile Flow Through Arterial Stenosis", *Journal of Biomechanics*, 25(10):1141-1152.
12. Weinbaum, S., and Chien, S., 1993, "Lipid Transport Aspects of Atherogenesis", *J. Biomech. Eng.*, 115:602-10.

13. Fry, D. L., 1968, "Acute Vascular Endothelial Changes Associated with Increased Blood Velocity Gradients", *Circ. Res.*, 12:165-97.
14. Fry, D. L., 1969, "Certain Histological and Chemical Responses of the Vascular Interface to acutely induced Mechanical Stress in the Aorta of the Dog", *Circ. Res.*, 24(1):93-108.
15. Caro, C. G., F-G, J. M., and Schroter, R. C., 1971, "Atheroma and Arterial wall Shear: Observation, Correlation, and proposal for a shear dependent mass transfer mechanism for atherogenesis", *Proc R Soc Lond [Biol]*, 117:109-159.
16. Chakraborty. S., 1987, "Effects of stenosis on the Flow-Behaviour of Blood in an Artery", *Int. J. Engng. Sci.*, 25:1003-1016.

#### 6. NOMENCLATURE

Symbol	Meaning	Unit
A	Area at any section	(m <sup>2</sup> )
D	Diameter of the artery	(m)
h <sub>f</sub>	Depth of the restriction	(m)
L <sub>i</sub>	Inlet length (i.e., length between inlet section and middle of restriction)	(m)
L <sub>ex</sub>	Exit length (i.e., length between middle of restriction and exit section)	(m)
L <sub>s</sub>	Stenosis length	(m)
P	Static pressure	(Nm <sup>-2</sup> )
PR	Percentage of restriction or Percent stenosis = $\frac{2h_f}{D} \times 100\%$	
P <sub>w</sub>	Wall pressure	(Nm <sup>-2</sup> )
u	Velocity in x-direction	(ms <sup>-1</sup> )
v	Velocity in y-direction	(ms <sup>-1</sup> )
V <sub>i</sub>	Average velocity in x-direction at inlet	(ms <sup>-1</sup> )
τ <sub>w</sub>	Wall shear stress	(Nm <sup>-2</sup> )
x, y	Cartesian co-ordinates	
ρ	Density	(kg m <sup>-3</sup> )
μ	Dynamic viscosity	(kg m <sup>-1</sup> s <sup>-1</sup> )
Ψ	Stream function	
Subscri pts*	Dimensionless terms	
1-1	Inlet	
2-2	Exit	

#### 7. MAILING ADDRESS

S. Chakrabarti  
 Dept. of Mech. Engg.,  
 Bengal Engineering and Science University, Shibpur,  
 Howrah-711 103, W. B., India  
 Email: [somnathbec@rediffmail.com](mailto:somnathbec@rediffmail.com)

## AERODYNAMICS OF FOOTBALLS

Firoz Alam, Harun Chowdhury, Christopher Whyte and Aleksandar Subic

School of Aerospace, Mechanical and Manufacturing Engineering, RMIT University, Australia

### ABSTRACT

Ball sports are becoming faster and more demanding than ever before, pushing traditional ball designs to their limits. In order to meet the increasing performance requirements, the ball manufacturers are producing new designs that can display better aerodynamic performance, geometric symmetry and balance. Since the inception of football game-the most popular and widely played game in the world, the centre piece of the game- the spherical ball which has gone through significant structural changes over the decades. A traditional spherical ball made of 32 leather panels stitched together in 1970s has now become only 14 synthetic curved panels thermally bonded (without stitches). Currently Adidas, the official supplier and manufacturer of footballs to FIFA is believed to be more spherical and it performs more uniformly regardless of where it is hit. Therefore, the primary objectives of this study were to evaluate aerodynamic performances of a current Adidas 14 curved panel football ball and a traditional Nike made 32 leather panels football ball. The aerodynamic forces and moments were measured experimentally for a range of wind speeds (20 km/h to 130 km/h) and the non-dimensional drag coefficient was determined and compared

**Keywords:** Aerodynamics, Football, Wind Tunnel, Drag Coefficient.

### 1. INTRODUCTION

Aerodynamics plays a prominent role in defining the flight trajectory of all high speed ball sports. Depending on aerodynamic behaviour, the ball can be deviated from its anticipated flight path significantly resulting in a curved and unpredictable flight trajectory. Lateral deflection in flight, commonly known as swing, swerve or curve, is well recognized in cricket, baseball, golf, tennis, volleyball and football (soccer). In most of these sports, the lateral deflection is produced by spinning the ball about an axis perpendicular to the line of flight. Therefore, the aerodynamic properties of a sport ball is fundamental for the players, coaches (trainers), regulatory bodies, ball manufacturers and even the spectators. It is no doubt that the game of football is the most popular in the world. No other game is so much loved, played and excited spectators than football. It is played in every corner by every nation in the world. Although, the football among all sport balls traditionally has better aerodynamic properties and balance, however, over the years, the design of football has undergone a series of technological changes, in which the ball has been made to be more accurate and aerodynamically efficient by utilizing new design and manufacturing processes. Adidas, the official supplier and manufacturer of soccer balls to FIFA (Federation Internationale de Football Association), has applied thermal bonding to replace conventional stitching to make a seamless surface design and an improved carcass shape by using 14 curved panels (making the ball topologically

equivalent to a truncated octahedron) instead of 32 panels previously used in the ball since 1970. It is claimed that the ball is more spherical and performs more uniformly regardless of where it is hit. However, no independent studies have been reported in support of this statement. Although the aerodynamic behaviours of other sports balls have been studied by Alam [2, 3, 5, 6], Mehta [5], and Smits & Ogg [6], scant information is available to the public domain about the aerodynamic behaviour of new seamless football except studies by Asai [7, 8]. Moreover, no comparative study of the new ball (seamless, 14 panels) and traditional ball (32 panels with stitches). Therefore, the primary objective of this work is to experimentally study the aerodynamic properties of a new seamless ball and also a traditional 32 panel ball.

### 2. EXPERIMENTAL PROCEDURE

#### 2.1 Description of Balls

Two new balls: Nike made traditional 32 panel leather ball and a new Adidas made 14 panel thermally bonded synthetic ball have been selected for the study. Both are FIFA approved balls. The diameter of the 32 panel ball is approximately 220 mm which is inflated with three different pressures. The size the ball is 5. The 32 panel ball is stitched together to provide a truncated icosahedron archimedean spherical shape. The 14-panel Adidas ball is thermally bonded machine-pressed ball without any stitches or seams, which is believed to be



more spherical compared to a 32 panel ball. The diameter of the ball is approximately 220 mm and the size of the ball is 5. A sting mount was used to hold the ball, and the experimental set up in the wind tunnel test section is shown in Figure 3. The aerodynamic effect of sting on the ball was measured and found to be negligible. The distance between the bottom edge of the ball and the tunnel floor was 420 mm, which is well above the tunnel boundary layer and considered to be out of significant ground effect.



Fig 1. Nike made 32 panels Football (with seam and stitches)



Fig 2. Adidas made 14 panels Football (seamless)

## 2.2 Experimental Set Up

In order to measure the aerodynamic properties of two footballs experimentally, the RMIT Industrial Wind Tunnel was used. The tunnel is a closed return circuit wind tunnel with a maximum speed of approximately 150 km/h. Two mounting studs (stings) holding the ball

with a six component force sensor (type JR-3) in the wind tunnel were manufactured and purpose made computer software was used to digitise and record all 3 forces (drag, side and lift forces) and 3 moments (yaw, pitch and roll moments) simultaneously. More details about the tunnel can be found in Alam [4]. The experimental set up of both balls in the wind tunnel is shown in Figures 3 & 4.



Fig 3. Experimental setup of a 32 panels football in the test section of RMIT Industrial Wind Tunnel



Fig 4. Experimental setup of a 14 panels football in the test section of RMIT Industrial Wind Tunnel

Each ball was fixed to the sting with an adhesive in order to make it very rigid. Three forces (drag, lift and side force) and their corresponding moments were measured simultaneously under a range of speeds (20 km/h to 130 km/h within an increment of 20 km/h). The aerodynamic forces are defined as drag ( $D$ ) acting in the opposite direction to the wind, lift ( $L$ ) acting perpendicular to the wind direction, and the side force acting ( $S$ ) sideways based on a frontal view. The measured aerodynamic forces were converted to non-dimensional drag coefficient ( $C_D$ ), the lift coefficient ( $C_L$ ) and the lateral-force coefficient ( $C_S$ ), using the formula as defined in Eqs. 1 to 3.

$$C_D = \frac{D}{\frac{1}{2}\rho V^2 A} \quad (1)$$

$$C_L = \frac{L}{\frac{1}{2}\rho V^2 A} \quad (2)$$

$$C_s = \frac{S}{\frac{1}{2}\rho V^2 A} \quad (3)$$

Here,  $\rho$  is the density of air ( $1.2 \text{ kg/m}^3$ ),  $V$  is the flow velocity ( $\text{m/s}$ ) and  $A$  is the projected area of the soccer ball ( $A = \frac{\pi D^2}{4}$  where  $D$  is the diameter of the ball).

### 3. RESULTS

#### 3.1 Flow Visualisation

In order to understand the flow structure around a 32 panel ball and a 14 panel seamless ball, the airflow was visualised using smoke (see Figures 5 and 6).



Fig 5. Airflow structure around a 32 panels football



Fig 6. Airflow structure around a 14 panels football

Due to the roughness created by the seams in 32 panel ball, the airflow over ball became turbulent and subsequently generated favourable pressure gradient and

delayed flow separation as shown in Figure 5. The airflow appears to be separated at around  $100^\circ$  from horizontal direction. Generally, the flow separates at around  $90^\circ$  from the horizontal for a smooth surfaced sphere. For the 14 panel seamless and stitch-less ball, the surface is more spherical and smooth. The ball behaviour is very similar to a smooth sphere. As shown in Figure 6, the airflow separates at around  $90^\circ$  from the horizontal as in the case of a smooth sphere. Therefore, the 14 panel ball can potentially generate more aerodynamic drag at low speeds.

#### 3.2 Aerodynamic Drag

The aerodynamic drags for the 32 panel Nike ball under 14.5 pound per square inch (PSI) air pressure, 14 panel Adidas ball under two different air pressures (13 and 14.5 PSI) and a sphere for a range of Reynolds number varied by wind speeds are shown in Figure 7. Two different pressures were chosen to see if there was any significant effect of pump up pressure on aerodynamic properties. There is no notable variation in drag for the Adidas ball. Both balls have similar trend, however, a minor fluctuation of drag was noted for the 32 panel Nike ball. The Nike ball displayed more aerodynamic drag compared to the Adidas ball in the range of 60 km/h to 120 km/h. No transition was noted for both types of balls. The aerodynamic drag for the smooth sphere has clearly demonstrated notable variation and also undergone transition from laminar to turbulent flow.

The drag coefficient,  $C_D$  for the Adidas, Nike and a sphere is shown in Figure 8. The average  $C_D$  value for both balls is around 0.23 at speeds above 60 km/h. The transition (laminar boundary layer to fully turbulent boundary layer) for both balls occurs in the range of Reynolds numbers  $1.1 \times 10^5$  to  $3.2 \times 10^5$ . In contrast, the boundary layer undergoes transition for a smooth sphere at Reynolds numbers of  $2.9 \times 10^5$  to  $4.6 \times 10^5$  (see [1]), which is notably different from flow regime around a football.

The boundary layer transition for a football is occurred much earlier compared to a smooth sphere. The results from this study have agreed well with the published data [7, 8]. Although, the Nike 32 panel ball displays relatively higher  $C_D$  between 60 to 120 km/h speeds, the variation in drag coefficients for the Adidas 14 panel ball and Nike 32 panel ball was not significant. It is clear from Figures 8 and 9 that the  $C_D$  for the 32 panel ball fluctuates more compared to the  $C_D$  value of the 14 panel Adidas ball as it is believed to be more spherical than the Nike 32 panel ball.

The small variation in pump up pressure has minimum effect on the aerodynamic drag as shown in Figure 10.

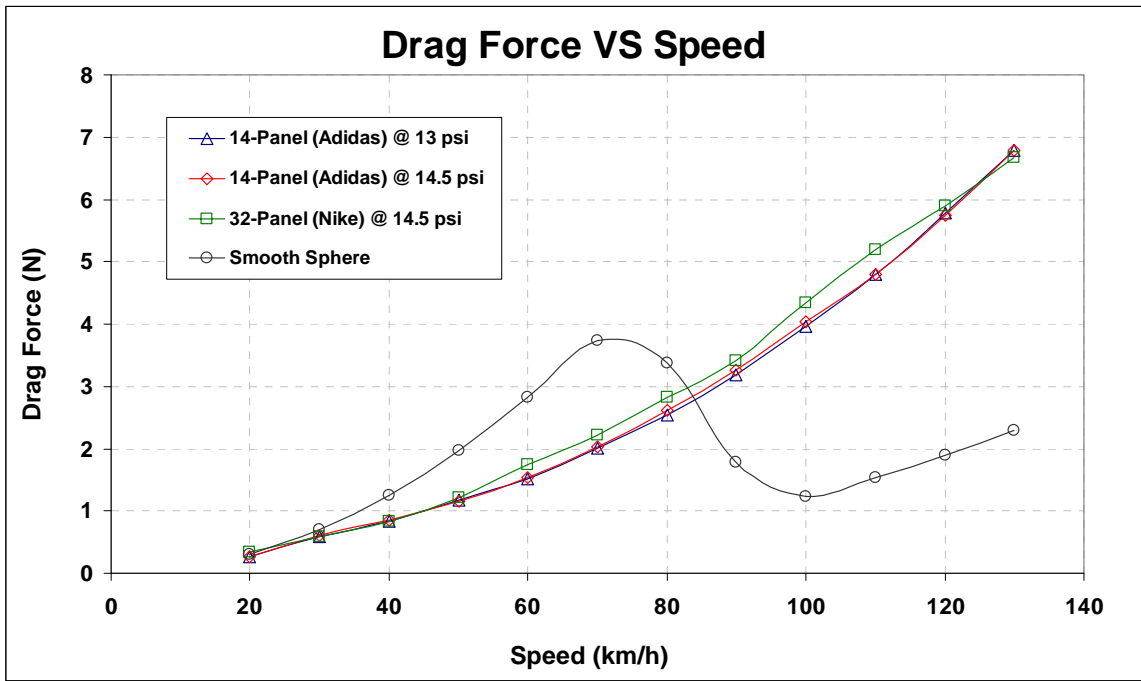


Fig 7. Aerodynamic drag of balls and a smooth sphere

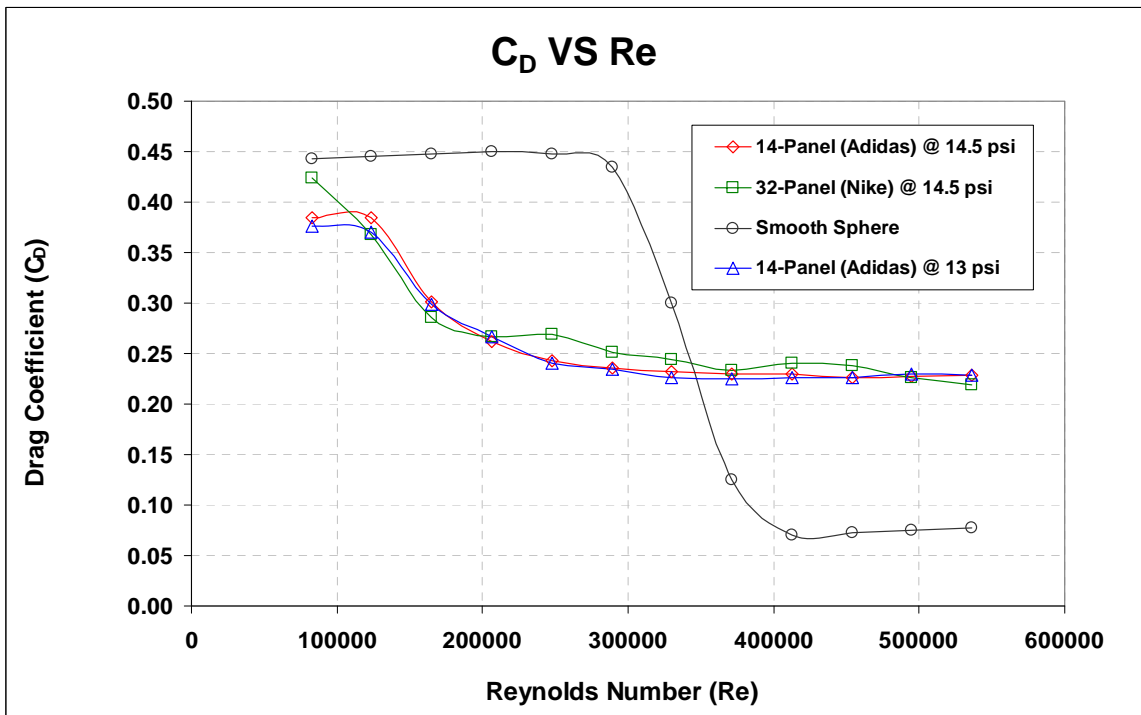


Fig 8. Drag coefficients of balls and a smooth sphere

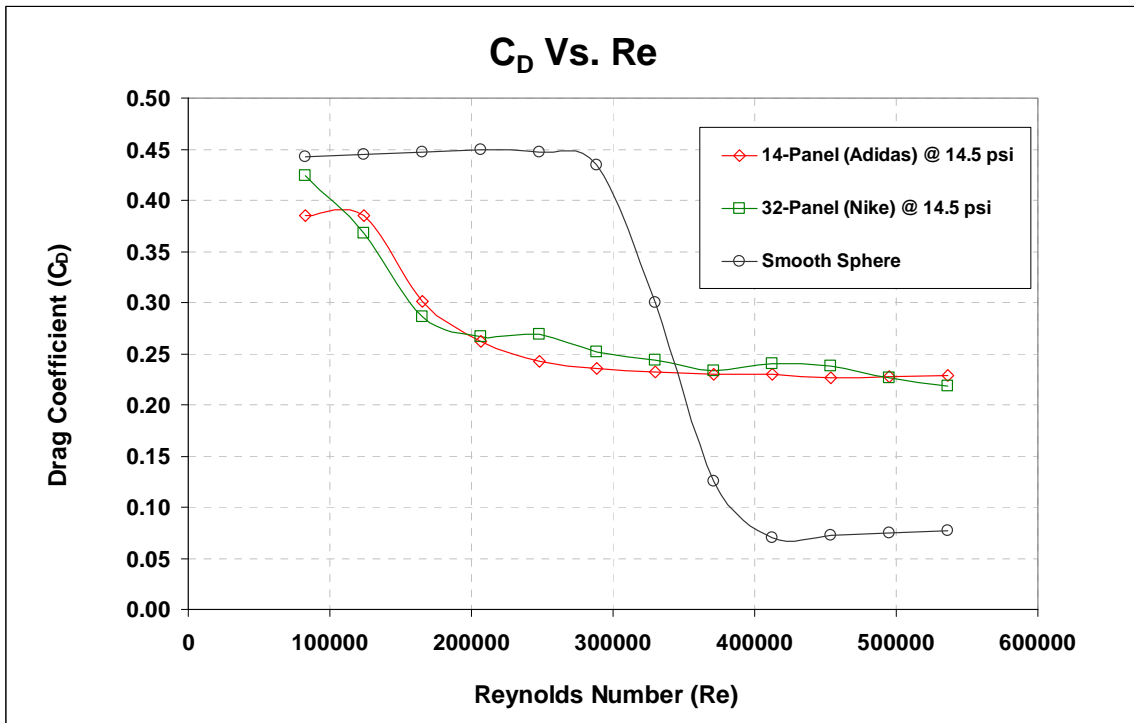


Fig 9. Drag coefficients of balls and a smooth sphere

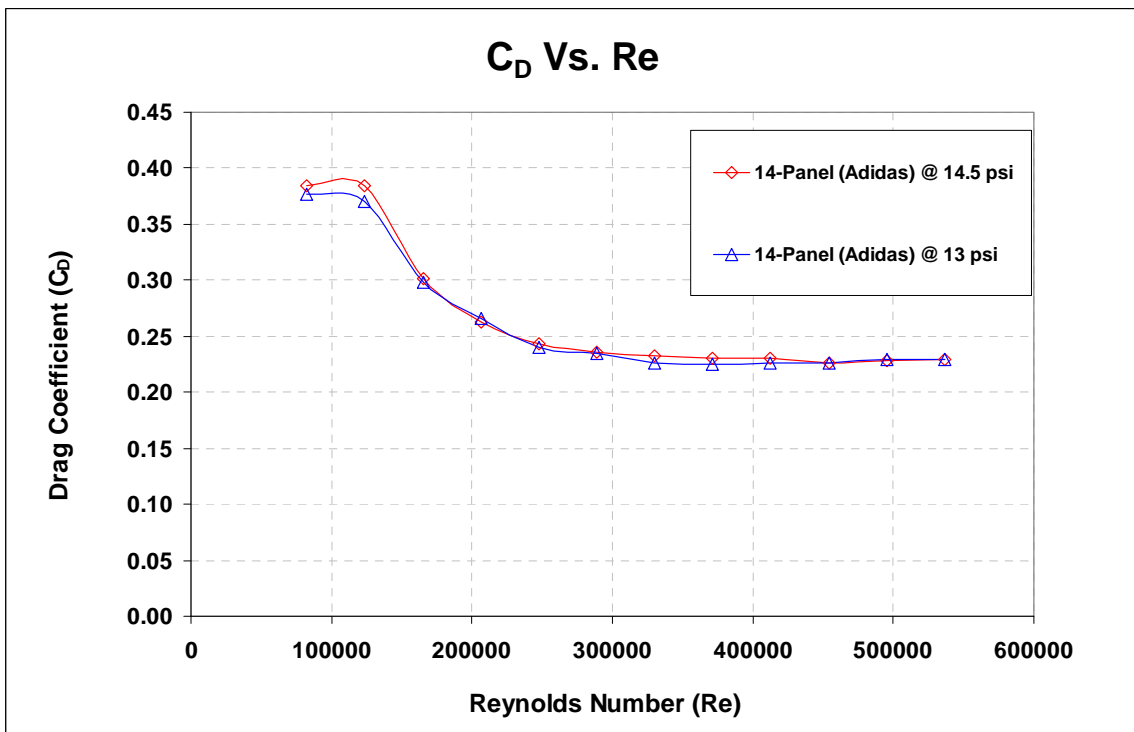


Fig 10. Drag coefficients of 14-panel ball under two different pressures

#### 4. DISCUSSION

The  $C_D$  value largely depends on the roughness of the ball exterior surface and the seams can cause additional drag due to the boundary-layer separation. The results indicate that the  $C_D$  value for a football is in

between a smooth sphere and a golf ball. The golf ball data was not shown here, however for more details, see [6]. As the speeds of football are generally in the range of 90 km/h to 130 km/h during a free kick or long shot, the  $C_D$  value of 32 panel or 14 panel balls are expected to be

the same. However, the  $C_D$  value can be in the transition zone when the ball is kicked for a short pass.

## 5. CONCLUSION

The following concluding remarks have been made based on the experimental study presented here:

- The drag coefficient of a non-spinning football is approximately 0.40 at low speeds (below 30 km/h) and 0.23 at high speeds (over 60 km/h).
- The 32 panel ball has slightly higher drag at high speeds compared to the 14 panel ball.
- The drag coefficient of the 32 panel ball fluctuates more as it is believed to be less spherical compared to a 14 panel seamless and stitch-less ball.
- A small pump up pressure variation has negligible effect on aerodynamic properties.

## 6. ACKNOWLEDGMENT

The authors are highly grateful to the Australian Football Federation for providing the balls for this study and their strong support. The authors also express their thanks to Mr Patrick Wilkins and Mr Gilbert Atkin, School of Aerospace, Mechanical and Manufacturing Engineering, RMIT University, Melbourne, Australia for their technical assistance with the wind tunnel testing.

## 7. REFERENCES

1. Achenback, E., 1972, "Experiments on the flow past spheres at very high Reynolds numbers", *Journal of Fluid Mechanics*, 54:565–575.
2. Alam, F., Subic, A., Watkins, S., Naser, J. and Rasul, M. G., 2008, "An Experimental and Computational Study of Aerodynamic Properties of Rugby Balls", *WSEAS Transactions on Fluid Mechanics*, 3:279-286.
3. Alam, F., Subic, A., Watkins, S. and Smits, A. J., 2009, "Aerodynamics of an Australian Rules Foot Ball and Rugby Ball", *Computational Science and Engineering (edited by M. Peters)*, Springer, Germany.
4. Alam, F., Zimmer, G. and Watkins, S., 2003, "Mean and Time-Varying Flow Measurements on the Surface of a Family of Idealized Road Vehicles", *Journal of Experimental Thermal and Fluid Sciences*, 27:639-654.
5. Mehta, R. D., Alam, F. and Subic, A., 2008, "Aerodynamics of Tennis Balls- a Review", *Sports Technology*, 1:1-10.
6. Smits, A. J. and Ogg, S., 2004, "Golf Ball Aerodynamics", *The Engineering of Sport 5*, ISBN 0-9547861-0-6, pp 3-12.
7. Asai, T., Carré, M. J., Akatsuka, T. and Haake, S. J., 2002, "The Curve Kick of a Football", *Sports Engineering*, 5:183–192.
8. Asai, T., Akatsuka, T. and Haake, S. J., 1998, "The Physics of Football", *Physics World*, 11:25–27.

## 8. NOMENCLATURE

Symbol	Meaning	Unit
D	Drag Force	(N)
L	Lift Force	(N)
S	Side Force	(N)
$C_D$	Drag Coefficient	-
$C_L$	Lift Coefficient	-
$C_S$	Lateral-Force Coefficient	-
Re	Reynolds Number	-
V	Velocity of Air	m/s
$\rho$	Density of Air	kg/m <sup>3</sup>
A	Projected Area	m <sup>2</sup>

## 9. MAILING ADDRESS

Dr Firoz Alam  
 School of Aerospace, Mechanical and Manufacturing  
 Engineering, RMIT University  
 Plenty Road, Bundoora, Melbourne, VIC 3083,  
 Australia  
 Telephone: +61 3 99256103  
 Fax: +61 3 99256108  
 E-mail: [firoz.alam@rmit.edu.au](mailto:firoz.alam@rmit.edu.au)



## EFFECT OF A HEATED HOLLOW CYLINDER ON COMBINED FREE AND FORCED CONVECTION IN A VENTILATED CAVITY

M. M. Rahman, M. A. Alim and M. A. H. Khan

Department of Mathematics, Bangladesh University of Engineering and Technology (BUET),  
Dhaka, Bangladesh

### ABSTRACT

Effect of a heated hollow cylinder on combined free and forced convection in a ventilated cavity is studied numerically. The wall of the cavity is assumed to be adiabatic. Flows are imposed at the bottom of the left wall and exited at the top of the right wall of the cavity. The heated cylinder is placed at the center of the cavity. The present study simulates a practical system such as an air-cooled electronic equipment with a heat component or an oven with heater. Emphasis is sited on the influences of the cylinder diameter and thermal conductivity of the cylinder in the cavity. The consequent mathematical model is governed by the coupled equations of mass, momentum and energy and is solved by employing Galerkin weighted residual method of finite element formulation. A wide range of pertinent parameters such as Reynolds number, Richardson number, cylinder diameter and the solid-fluid thermal conductivity ratio are considered in the present study. Various results such as the streamlines, isotherms, heat transfer rates in terms of the average Nusselt number and average fluid temperature in the cavity are presented for different parameter. It is observed that the cylinder diameter has significant effect on both the flow and thermal fields but the solid-fluid thermal conductivity ratio has insignificant effect on the flow field.

**Keywords:** Hollow Cylinder, Ventilated Cavity, Combined Free And Forced Convection.

### 1. INTRODUCTION

Convection in enclosures containing blocks has gained recent research significance as a means of heat transfer enhancement. One of the systematic numerical investigations of this problem was conducted by House et al. [1], the authors considered natural convection in a vertical square cavity with heat conducting body, placed on center in order to understand the effect of the heat conducting body on the heat transfer process in the cavity. They found that the heat transfer across the enclosure enhanced by a body with thermal conductivity ratio less than unity. Lacroix [2] performed a numerical study of natural convection heat transfer from two vertically separated heated cylinder to a rectangular cavity cooled from above. Later on, Lacroix and Joyeux [3] conducted a numerical study of natural convection heat transfer from two horizontal heated cylinders confined to a rectangular enclosure having finite wall conductance's. They indicated that wall heat conduction reduces the average temperature differences across the cavity, partially stabilizes the flow and decreases natural convection heat transfer around the cylinders. Ha et al. [4] conducted a comprehensive numerical study to investigate the transient heat transfer and flow characteristics of the natural convection of three different fluids in a vertical square enclosure within which a centered, square, heat conducting body generates heat. Later on, Ha and Jung [5] conducted a comprehensive

numerical study to investigate three dimensional steady conjugate heat transfers of natural convection and conduction in a differentially heated in a vertical cubic enclosure within which a centered, cubic, heat-generating cubic conducting body. They concluded that for the presence of a conducting body in the enclosure, a larger variation of the local Nusselt number at the hot and cold walls in the z-direction is seen. Roychowdhury et al. [6] analyzed the natural convective flow and heat transfer features for a heated cylinder kept in a square enclosure with different thermal boundary conditions. Dong and Li [7] studied conjugate of natural convection and conduction in a complicated enclosure. They investigated the influences of material character, geometrical shape and Rayleigh number on the heat transfer in overall concerned region and concluded that the flow and heat transfer increase with the increase of thermal conductivity in the solid region; both geometric shape and Rayleigh number affect the overall flow and heat transfer greatly. Buoyancy induced flow and heat transfer inside a square cavity due to a thin baffle on the hot wall was analyzed numerically in Tasnim and Collins [8]. They investigated the effects of baffle height, length and Rayleigh number on heat transfer performance. It was found that adding baffle on the hot wall increased the rate of heat transfer. Braga and Lemos [9] numerically studied steady laminar natural convection within a square cavity filled with a fixed amount of conducting solid

material consisting of either circular or square obstacles. They showed that the average Nusselt number for cylindrical rods is slightly lower than those for square rods. Bhave et al. [10] were investigated the effect on the steady-state natural convection heat transfer enhancement of a centrally-placed adiabatic block within a differentially heated square cavity with a fixed temperature drop between the vertical walls. Kumar and Dalal [11] studied natural convection around a tilted heated square cylinder kept in an enclosure in the range of  $103 \leq Ra \leq 106$ . They reported detailed flow and heat transfer features for two different thermal boundary conditions and found that the uniform wall temperature heating is quantitatively different from the uniform wall heat flux heating.

The studies of mixed convection in a partially divided rectangular enclosure were respectively carried out by Hsu et al. [12], How and Hsu [13]. The simulation was conducted for wide range of Reynolds and Grashof numbers. They indicated that the average Nusselt number and the dimensionless surface temperature depended on the location and height of the divider. Combined free and forced convection in a square enclosure with heat conducting body and a finite-size heat source was simulated numerically by Hsu and How [14]. They concluded that both the heat transfer coefficient and the dimensionless temperature in the body center strongly depend on the configurations of the system. Recently Rahman et al. [15] studied of mixed convection in a square cavity with a heat conducting square cylinder at different locations. At the same time Rahman et al. [16] studied mixed convection in a vented square cavity with a heat conducting horizontal solid circular cylinder. Very recently Rahman et al. [17] analyzed mixed convection in a rectangular cavity with a heat conducting horizontal circular cylinder by using finite element method.

Most of the previous studies were done on natural convection in a closed cavity with a heat conducting body. There has been little study on mixed convection in an obstructed vented cavity. In the present study, a numerical simulation of flow and temperature fields in a square cavity with a heated hollow cylinder is carried out. We investigate the flow and thermal characteristics of the system by observing variations in streamlines and isotherms for different values of the cylinder diameter and solid fluid thermal conductivity ratio at the three convective regimes. We also investigate the heat transfer characteristics by calculating the average Nusselt number on the hot surface.

## 2. MODEL SPECIFICATION

The schematic of the system considered in this paper is shown in Fig. 1. The system consists of a square cavity with sides of length  $L$ , within which a heated hollow cylinder with diameter of  $d$  and thermal conductivity of  $k_s$  is centered. The sidewalls of the cavity are assumed to be adiabatic. It is assumed that the incoming flow is at a uniform velocity,  $u_i$ , and at the ambient temperature,  $T_i$ . An inflow opening located on the bottom of the left vertical wall, whereas the out flow opening at the top of the opposite side wall and the size of the inlet port is the

same size as the exit port which is equal to  $w = 0.1L$ . The outgoing flow is assumed to have zero diffusion flux for all variables i.e. convective boundary conditions (CBC). All solid boundaries are assumed to be rigid no-slip walls.

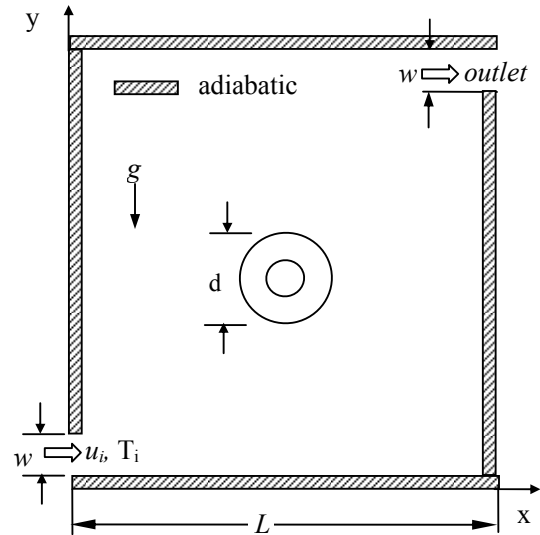


Fig 1. Schematic diagram of the problem considered and coordinate system

## 3. MATHEMATICAL FORMULATION

The equations describing the problem under consideration are based on the laws of mass, momentum and energy. All physical properties of are assumed to be constant except the density variation in body force term of the  $v$ -momentum equation according to the Boussinesq approximation. The flow within the cavity is assumed to be steady, laminar and two-dimensional incompressible. The radiation effects, viscous dissipation and pressure work are taken as negligible. Taking into consideration the above mentioned assumptions the equations can be written in dimensionless form as follows:

$$U \frac{\partial U}{\partial X} + V \frac{\partial V}{\partial Y} = 0 \quad (1)$$

$$U \frac{\partial U}{\partial X} + V \frac{\partial U}{\partial Y} = -\frac{\partial P}{\partial X} + \frac{1}{Re} \left( \frac{\partial^2 U}{\partial X^2} + \frac{\partial^2 U}{\partial Y^2} \right) \quad (2)$$

$$U \frac{\partial V}{\partial X} + V \frac{\partial V}{\partial Y} = -\frac{\partial P}{\partial Y} + \frac{1}{Re} \left( \frac{\partial^2 V}{\partial X^2} + \frac{\partial^2 V}{\partial Y^2} \right) + Ri\theta \quad (3)$$

$$U \frac{\partial \theta}{\partial X} + V \frac{\partial \theta}{\partial Y} = \frac{1}{RePr} \left( \frac{\partial^2 \theta}{\partial X^2} + \frac{\partial^2 \theta}{\partial Y^2} \right) \quad (4)$$

For solid cylinder the energy equation is

$$0 = \frac{K}{RePr} \left( \frac{\partial^2 \theta_s}{\partial X^2} + \frac{\partial^2 \theta_s}{\partial Y^2} \right) \quad (5)$$

Here the Reynolds number, Grashof number, cylinder diameter, Prandtl number, Richardson number and solid fluid thermal conductivity ratio are given respectively by Eq. (6).



$$Re = u_i L / \nu, Gr = g \beta \Delta T L^3 / \nu^2, D = d / L \quad (6)$$

$$Pr = \nu / \alpha, Ri = Gr / Re^2 \text{ and } K = k_s / k$$

Using the following variables the above equations were non dimensionalized

$$X = \frac{x}{L}, Y = \frac{y}{L}, U = \frac{u}{u_i}, V = \frac{v}{u_i}, P = \frac{p}{\rho u_i^2},$$

$$\theta = \frac{(T - T_i)}{(T_h - T_i)}, \theta_s = \frac{(T_s - T_i)}{(T_h - T_i)}$$

Where X and Y are the coordinates varying along horizontal and vertical directions, respectively, U and V are, the velocity components in the X and Y directions, respectively,  $\theta$  is the dimensionless temperature and P is the dimensionless pressure.

The boundary conditions for the present problem are specified as follows:

At the Inlet:  $U = 1, V = 0, \theta = -0.5$

At the outlet: Convective boundary condition  $P = 0$

At all solid boundaries:  $U = 0, V = 0$

At the cavity walls:  $\frac{\partial \theta}{\partial N} = 0$

At the inner surface of the cylinder:  $\theta = 1.0$

At the outer surface of the cylinder:  $\left(\frac{\partial \theta}{\partial N}\right)_{fluid} = K \left(\frac{\partial \theta_s}{\partial N}\right)_{solid}$

Where  $N$  is the non-dimensional distances either  $X$  or  $Y$  direction acting normal to the surface.

The average Nusselt number at the heated surface is calculated as

$$Nu = -\frac{1}{L_h} \int_0^{L_h} \frac{\partial \theta}{\partial N} dS$$

and the average temperature of the fluid is defined as

$$\theta_{av} = \int \theta d\bar{V} / \bar{V}$$

where  $L_h$  is the surface area of the of the heated wall and  $\bar{V}$  is the cavity volume.

#### 4. COMPUTATIONAL PROCEDURE

The solution of the governing equations along with boundary conditions are solved through the Galerkin finite element formulation. The continuum domain is divided into a set of non-overlapping regions called elements. Six node triangular elements with quadratic interpolation functions for velocity as well as temperature and linear interpolation functions for pressure are utilized to discretize the physical domain. Moreover, interpolation functions in terms of local normalized element coordinates are employed to approximate the dependent variables within each element. Substitution of the obtained approximations into the system of the governing equations and boundary conditions yields a residual for each of the conservation equations. These residuals are reduced to zero in a weighted sense over each element volume using the Galerkin method. More details are available in and Rahman *et al.* [17] and Zienkiewicz Taylor [18]

Grid independency test is important for this study due to complexity of the computational domain. We made

several test on Grid independency by using the following grid dimensions: 30049 nodes, 4738 elements; 37248 nodes, 5876 elements; 38821 nodes, 6118 elements and 48495 nodes, 7634 elements. The results are obtained for average Nusselt numbers and average fluid temperature at  $Re = 100, D = 0.2, Ri = 1.0, K = 5.0$  and  $Pr = 0.71$  and listed in Table 1. The table shows that average Nusselt numbers and average fluid temperature do not change significantly with grid dimensions. Based on the results from the table 38821 nodes and 6118 elements can be chosen throughout the simulation.

Table 1: Grid Sensitivity Check at  $Re = 100, D = 0.2, Ri = 1.0, K = 5.0$  and  $Pr = 0.71$

Nodes (elements)	30049 (4738)	37248 (5876)	38821 (6118)	48495 (7634)
$Nu$	0.736641	0.737751	0.745781	0.754781
$\theta_{av}$	0.088298	0.087330	0.087296	0.086298
Time(sec)	408.859	563.203	588.390	793.125

For the purpose of code validation, the natural convection problem in an enclosure with a square heat conducting body in the center of the enclosure was tested for Rayleigh number,  $Ra = 0.0, 10^5$  and two values of  $K = 0.2$  and  $5.0$ . The calculated average Nusselt numbers at the hot wall for the test cases were compared with the values calculated by House *et al.* [1]. The calculated average Nusselt numbers as shown in the Table 2 have an excellent agreement with the results obtained by House *et al* [1].

Table 2: Nusselt Number Comparison for  $Pr = 0.71$

$Ra$	$K$	$Nu$		
		Present work	House <i>et al.</i> [1]	Error (%)
0	0.2	0.7071	0.7063	0.11
0	1.0	1.0000	1.0000	0.00
0	5.0	1.4142	1.4125	0.12
$10^5$	0.2	4.6237	4.6239	0.00
$10^5$	1.0	4.5037	4.5061	0.00
$10^5$	5.0	4.3190	4.3249	0.14

#### 5. RESULTS AND DISCUSSION

The effect of a heated hollow cylinder on mixed convection flow in a ventilated square cavity is tested using a numerical technique. Inspection of the foregoing analysis indicates that the flow and heat transfer characteristics in the present study depend on 5 parameters. These are the Reynolds number  $Re$ , Richardson number  $Ri$ , Prandtl number  $Pr$ , solid fluid thermal conductivity ratio  $K$  and dimensionless cylinder diameter  $D$ . Since a number of governing dimensionless parameters are required to characterize the system, a comprehensive analysis of all combinations of parameters is not practical. So the objective here is to present the effects of  $D, K$  and  $Ri$  on the convective heat transfer in the cavity. In particular, air ( $Pr = 0.71$ ) flowing through the cavity with  $Re = 100$ .

The effect of cylinder diameter on the flow field at  $K = 5.0$  and three different values of  $Ri$  is displayed in fig. 2. The flow structure in the absence of free convection effect ( $Ri = 0.0$ ) and for the four different values of  $D$  is shown in the left column of the fig.2. Now at  $Ri = 0.0$  and  $D = 0.2$ , it is seen that a comparatively small uni-cellular vortex appears just at the top of the inlet in the cavity, due to the effect of buoyancy driven flow. Further with the increase of  $D$  at fixed  $Ri$  ( $Ri = 0.0$ ) the size of the vortex decreases. This is due to increasing the size of the cylinder which gives rise to a decrease in the space available for the flow induced by the heat source. Next for  $Ri = 1.0$  and the different values of  $D$  ( $D = 0.2, 0.3, 0.4$  and  $0.5$ ), it is clearly seen from the figure that the natural convection effect is present, but remains relatively weak at the higher values of  $D$ , since the open lines characterizing the imposed flow are still dominant. As  $Ri$  increase from 1.0 to 5.0, the size of the vortex increases sharply and another vortex is appear just at the below of the outlet port for the lower values of  $D$  ( $D = 0.2$  and  $0.3$ ). On the other hand, the uni-cellular vortex become two cellular for the higher values of  $D$  ( $D = 0.4$  and  $0.5$ ). The effect of cylinder diameter on the thermal field at  $K = 5.0$  and three different values of  $Ri$  is displayed in fig. 3. From these figures it is seen that the size of the cylinder influences the shapes of the isotherms at the three convective regimes. A thermal boundary layer near the bottom of the cylinder is found for the selected values of  $D$  and  $Ri$ . However, a careful observation indicates that the thermal boundary layer on the bottom part of the cylinder become thinner with increasing the values of  $D$  at the three convective regimes. Also, a plume shape isotherms are found at the top of the cylinder.

The effect of the solid-fluid thermal conductivity ratio  $K$  on streamlines at  $D = 0.2$  and various  $Ri$  ( $= 0.0, 1.0$  and  $5.0$ ) are presented in fig. 4. At low  $Ri$  ( $Ri = 0.0$ ) and relatively small values of  $K$  ( $K = 0.2$ ), a small recirculating cell is located just at the top of the inlet port of the cavity. The formation of circulation cell is because of the mixing of the fluid due to the buoyancy driven and convective currents. From the left column of fig. 4, it is also be seen that the streamlines for the different values of  $K$  ( $K = 0.2, 1.0, 5.0, 10.0$ ) at  $Ri = 0.0$  are almost identical. This is because thermal conductivity ratios have insignificant influence on velocity distribution. When  $Ri$  increases from 0.0 to 1.0, i.e. the natural convection effect is comparable with forced convection effect, then the size of the recirculating cell increases, compared with that for  $Ri = 0.0$  and different values of  $K$ . Further when  $Ri$  increases to 5.0, the effect of natural convection is far more compared to the forced convection effect. In this case, conditions are strongly favoring the phenomena of natural convection and significant increase in recirculating cell is found. The effect of the solid-fluid thermal conductivity ratio  $K$  on isotherms for various  $D$  ( $= 0.2, 0.3, 0.4$  and  $0.5$ ) and  $Ri$  ( $= 0.0, 1.0$  and  $5.0$ ) is presented in fig. 5. From the fig. 5, it is clearly seen that the thermal conductivity of the inner cylinder affects strongly on the isotherm structures in the cavity. Now at different values of  $Ri$  ( $= 0.0, 1.0$  and  $5.0$ ) and large  $K$  ( $K = 10.0$ ), the isotherms move out of the inner cylinder and a thermal boundary layer is formed

near the bottom part of the cylinder. On the other hand, plume shape isotherms are observed at the top of the cylinder. When we compare the results for the distribution of isotherms for the case of  $K = 10.0$  with those for  $K = 5.0$  and  $1.0$ , the distribution of isotherms for  $K = 10.0$  is generally similar to that for  $K = 5.0$  and  $1.0$ , for all the Richardson number considered, except slight difference around the solid body due to the difference in the thermal conductivity of the solid. However, at small  $K$  ( $K = 0.2$ ) various values of  $Ri$ , the isothermal lines are crowded in the cylinder, due to lower thermal conductivity of the solid. Moreover, the isotherms are qualitatively similar for different Richardson number considered.

The effects of cylinder diameters on average Nusselt number  $Nu$  at the heated surface and average temperature  $\theta_{av}$  of the fluid in the cavity as a function of  $Ri$  are shown in fig.6. From these figures it is seen that the values of average Nusselt number  $Nu$  decreases monotonically with increasing  $Ri$  for the higher values of  $D$ , but the values of  $Nu$  decreases in  $Ri \leq 0.5$  and beyond these values of  $Ri$  it is increases with  $Ri$ . On the other hand, average Nusselt number  $Nu$  is always highest for  $D = 0.5$ . Average temperature  $\theta_{av}$  of the fluid in the cavity increases slowly with increasing  $Ri$  for all values of  $D$ .

The effect of thermal conductivity ratio  $K$  on average Nusselt number  $Nu$  at the heated surface and average temperature  $\theta_{av}$  of the fluid in the cavity with  $D = 0.2$  is shown in fig. 7. From these figures it is clearly observed that as  $Ri$  increases, average Nusselt number  $Nu$  at the hot surface slowly increases for all values of  $K$ . Maximum average Nusselt number is always found for the higher values of  $K$ . However, as  $Ri$  increases average temperature  $\theta_{av}$  of the fluid decreases slowly in the forced convection dominated region and increases sharply in the free convection dominated region with increasing  $Ri$  for all values of  $K$  in the cavity. On the other hand, the average temperature  $\theta_{av}$  of the fluid in the cavity is the lowest for the highest values of  $K$ .

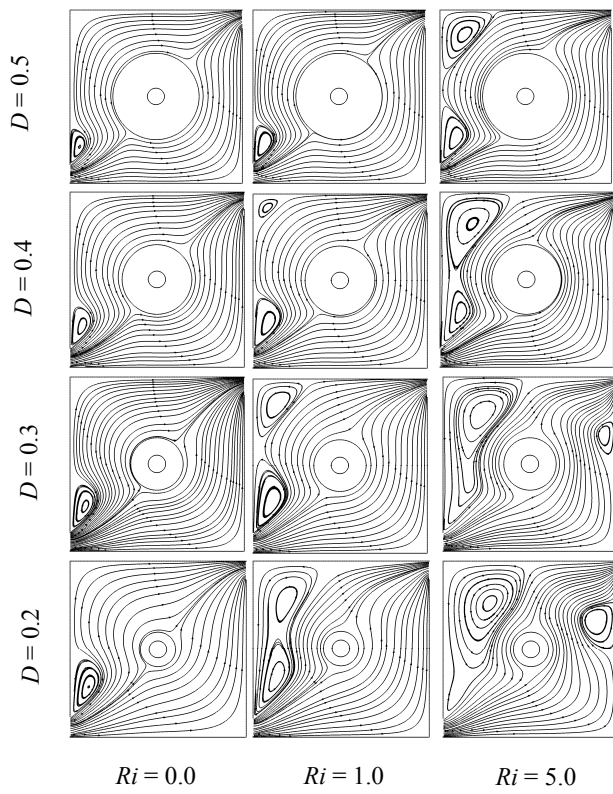


Fig 2. Streamlines for different values of cylinder diameter  $D$  and Richardson number  $Ri$  while  $K = 5.0$ .

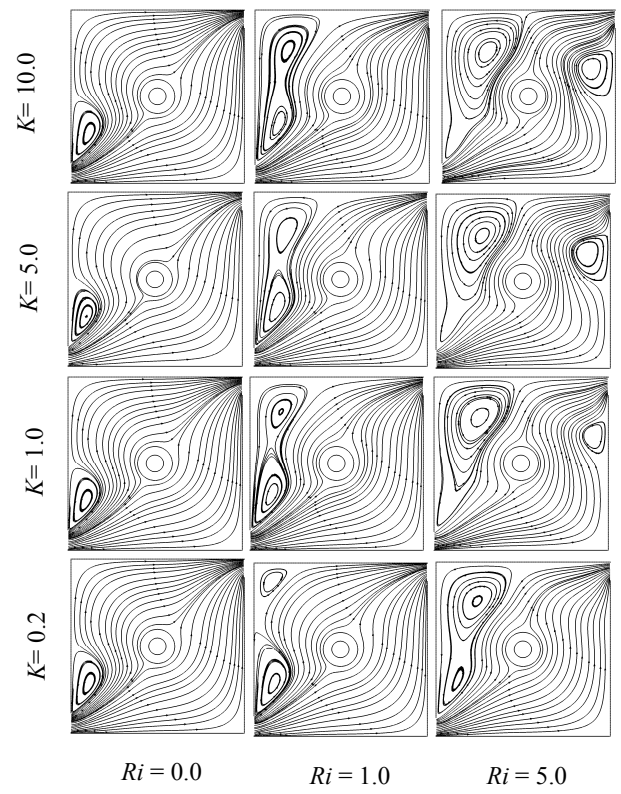


Fig 4. Isotherms for different values of solid fluid thermal conductivity ratio  $D$  and Richardson number  $Ri$  while  $D = 0.2$

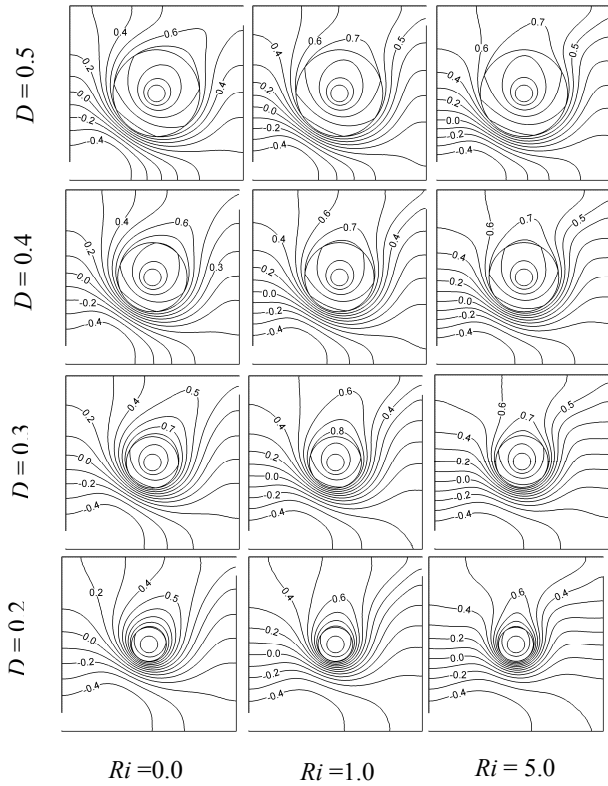


Fig 3. Isotherms for different values of cylinder diameter  $D$  and Richardson number  $Ri$  while  $K = 5.0$ .

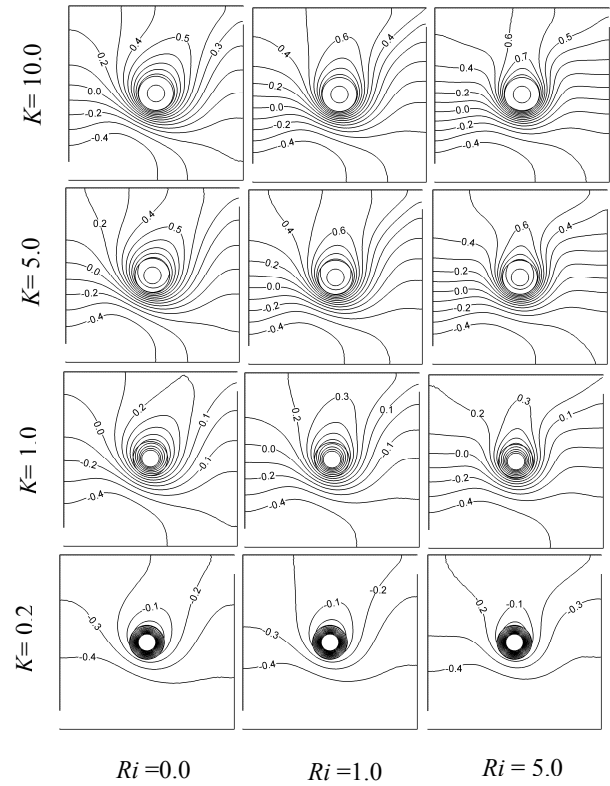


Fig 5. Isotherms for different values of solid fluid thermal conductivity ratio  $D$  and Richardson number  $Ri$  while  $D = 0.2$ .

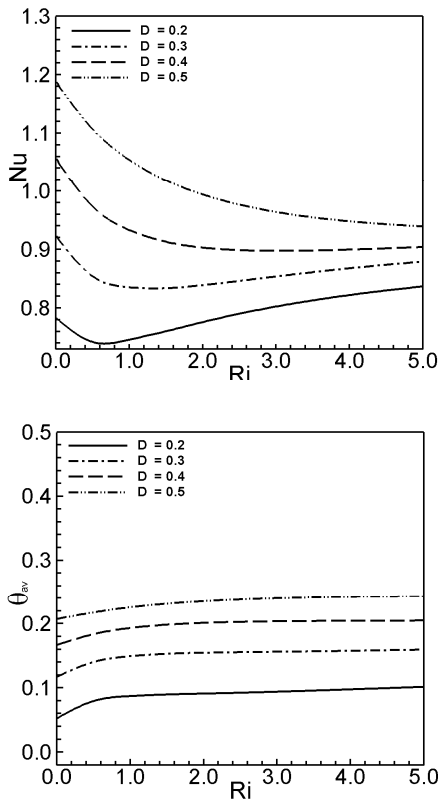


Fig 6. Effect of  $D$  on average Nusselt number (top) and average fluid temperature in the cavity (bottom), while  $K = 5.0$ .

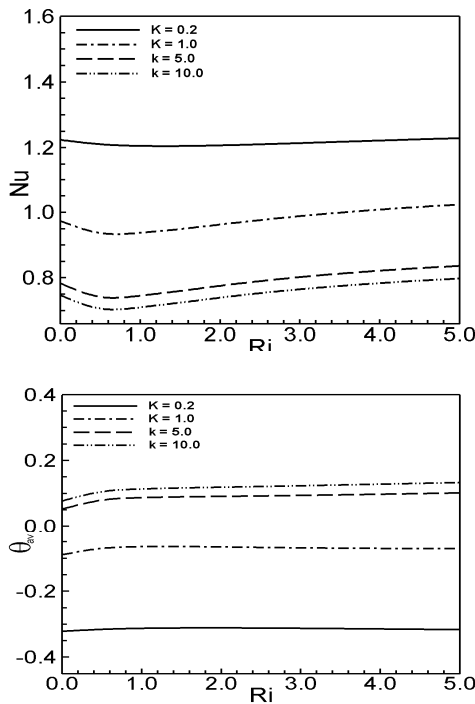


Fig 7. Effect of  $K$  on (i) average Nusselt number and (ii) average fluid temperature in the cavity, while  $D = 0.2$ .

## 6. CONCLUSION

The present study investigates numerically the characteristics of a two dimensional mixed convection problem in a ventilated cavity with an inner heated hollow circular cylinder. A detailed analysis of the distribution of streamlines, isotherms, average Nusselt number and average fluid temperature in the cavity was carried out to investigate the diameter of the cylinder and solid fluid thermal conductivity ratio on the fluid flow and heat transfer in the mentioned cavity for different Richardson number  $Ri$ . The following conclusions may be drawn from the present investigations

- Cylinder diameter has significant effect on the flow and thermal fields at the three convective regimes. Maximum average Nusselt number and average fluid temperature are found for the largest value of the Cylinder diameter.
- Solid fluid thermal conductivity ratio has insignificant effect on the flow and has significant effect on thermal fields at the three convective regimes. Maximum average Nusselt number and minimum average fluid temperature is found for the largest value of  $K$ .

## 7. REFERENCES

1. House, J. M., Beckermann, C. and Smith, T. F., 1990, "Effect of a Centered Conducting Body on Natural Convection Heat Transfer in an Enclosure", Numerical Heat Transfer, Part A, 18: 213–225.
2. Lacroix, M., 1992, "Natural convection heat transfer around two heated horizontal cylinders inside a rectangular cavity cooled from above", Numer. Heat Transfer, Part A, 21: 37-54.
3. Lacroix, M. and Joyeux, A., 1995, "Natural convection heat transfer around heated cylinders inside a cavity with conducting walls", Numer. Heat Transfer, Part A, 27: 335-349.
4. Ha, M. Y., Jung, M. J. and Kim, Y.S., 1999, "Numerical study on transient heat transfer and fluid flow of natural convection in an enclosure with a heat-generating conducting body", Numer. Heat Transfer, Part A, 35: 415-434.
5. Ha, M. Y. and Jung, M. J., 2000, "A numerical study on three-dimensional conjugate heat transfer of natural convection and conduction in a differentially heated cubic enclosure with a heat-generating cubic conducting body", Int. J. of Heat and Mass Transfer, 43: 4229-4248.
6. Roychowdhury, D.G, Das, S.K. and Sundararajan, T.S., 2002, "Numerical simulation of natural convection heat transfer and fluid flow around a heated cylinder inside an enclosure", Heat and Mass Transfer, 38: 565-576.
7. Dong, S. F., and Li, Y.T., 2004, "Conjugate of natural convection and conduction in a complicated enclosure", Int. J. of Heat and Mass Transfer, 47: 2233-2239.

8. Tasnim, S. H. and Collins, M. R., 2004, "Numerical analysis of heat transfer in a square cavity with a baffle on the hot wall", *Int. Commun. Heat Transfer*, 31 (5): 639-650.
9. Braga, E. J., and de Lemos, M. J. S., 2005, "Laminar natural convection in cavities filed with circular and square rods", *Int. Commun. in Heat and Mass Transfer*, 32: 1289-1297.
10. Bhave, P., Narasimhan, A. and Ress, D. A. S., 2006, "Natural convection heat transfer enhancement using adiabatic block: Optimal block size and Prandtl number effect", *Int. J. of Heat and Mass Transfer*, 49: 3807-3818.
11. Kumar De, A. and Dalal, A., 2006, "A numerical study of natural convection around a square, horizontal, heated cylinder placed in an enclosure", *Int. J. of Heat and Mass Transfer*, 49: 4608-4623.
12. Hsu, T.H., Hsu, P.T., How, S.P., 1997, "Mixed convection in a partially divided rectangular enclosure", *Numerical Heat Transfer, Part A*, 31: 655-683.
13. How, S.P. and Hsu, T.H., 1998, "Transient mixed convection in a partially divided enclosure", *Comput. Math. Appl.*, 36: 95-115.
14. Hsu, T.H., and How, S. P., 1999 "Mixed convection in an enclosure with a heat-conducting body", *Acta Mechanica*, 133: 87-104.
15. Rahman, M. M., Alim, M. A., Saha, S. and Chowdhury, M. K., 2008a, "A Numerical Study of Mixed Convection in A Square Cavity with A Heat Conducting Square Cylinder at Different Locations", *J. of Mechanical Engineering, The Institution of Engineers, Bangladesh*, ME 39 (2): 78 - 85.
16. Rahman, M. M., Alim, M. A., Saha, S. and Chowdhury, M. K., 2008b, "Mixed Convection in a vented Square Cavity with a Heat Conducting Horizontal Solid Circular Cylinder", *Journal of Naval Architecture and Marine Engineering*, 5 (2): 37 - 46.
17. Rahman, M. M., Alim, M. A. and Mamun, M. A. H., 2009, "Finite element analysis of mixed convection in a rectangular cavity with a heat-conducting horizontal circular cylinder", *Nonlinear analysis: Modeling and Control*, 14 (2): 217-247.
18. Zienkiewicz, O. C. and Taylor, R. L., 1991, "The finite element method", Fourth Ed., McGraw-Hill.

## 8. NOMENCLATURE

Symbol	Meaning	Unit
d	Dimensional cylinder diameter	(m)
D	Nondimensional cylinder diameter	
g	gravitational acceleration	( $ms^{-2}$ )
Gr	Grashof number	
h	Convective heat transfer coefficient	
$K_f$	Thermal conductivity of fluid	$Wm^{-1}K^{-1}$
$K_s$	Thermal conductivity of solid	$Wm^{-1}K^{-1}$
K	Solid fluid thermal conductivity ratio	
L	Length of the cavity	(m)
$L_h$	Surface area of the of the heated wall	( $m^2$ )
Nu	Nusselt number	
p	Dimensional pressure	( $Nm^{-2}$ )
P	Dimensionless pressure	
Pr	Prandtl number	
Re	Reynolds number	
Ra	Rayleigh number	
Ri	Richardson number	
S	Distance along the square enclosure	(m)
T	Dimensional temperature	(K)
$u, v$	Dimensional velocity components	$ms^{-1}$
$U, V$	Dimensionless velocity components	
$\bar{V}$	Cavity volume	( $m^3$ )
w	Height of the opening	(m)
x, y	Cartesian coordinates	(m)
X, Y	Dimensionless Cartesian coordinates	
<b>Greek symbols</b>		
$\alpha$	Thermal diffusivity	( $m^2s^{-1}$ )
$\beta$	Thermal expansion coefficient	( $K^{-1}$ )
$\nu$	Kinematic viscosity	( $m^2s^{-1}$ )
$\theta$	Non dimensional temperature	
$\rho$	Density of the fluid	( $kgm^{-3}$ )
<b>Subscri</b>		
pts		
av	Average	
i	Inlet state	
s	Solid	

## 9. MAILING ADDRESS

M. M. Rahman  
 Department of Mathematics,  
 Bangladesh University of Engineering and Technology  
 (BUET), Dhaka, Bangladesh

## AN EXPERIMENTAL INVESTIGATION OF THE EFFECT OF VEHICLE SPACING ON BOUNDARY LAYER CHARACTERISTICS IN THE 2-VEHICLES PLATOON

A.Motin and M.A.T. Ali

Department of Mechanical Engineering, Bangladesh University of Engineering and Technology, Dhaka,  
Bangladesh.

### ABSTRACT

Aerodynamic shape of a moving object is a major concern of the researchers from many years. Though different accessories, engine parts and passenger compartment for example in the moving vehicle are needed to be available, perfect aerodynamic shape of any body, like passenger car, is not possible to maintain. In this circumstance, alternate factor other than body shape which can affect the vehicle performance is required to be kept in consideration. For this, aerodynamic characteristics of two vehicles moving in platoon maneuver are investigated as the function of vehicle spacing (space between two vehicles) in this study. To conduct this investigation, 1/32 scale models of a saloon car are tested in the 300x300 mm wind tunnel facility of the Department of Mechanical Engineering, BUET. Velocities in the vertical plane through the centre of the wind tunnel are measured by pitot static tube which is interfaced with a computer through pressure transducer for data acquisition and is traversed by a computer controlled 3-axes co-ordinate positioning device. The integral analysis of the boundary layer is used to quantify the behavior of the aerodynamic characteristics and the effects of vehicle spacing on the boundary layer characteristics and skin friction. The zone of flow separation approaching laminar-turbulent transition is also investigated. In this study the displacement and momentum thicknesses on the trailing vehicle are found to be higher for smaller vehicle spacing. The flow strikes the front of the vehicle and is accelerated over the bonnet and is observed to be separated from the rear zone of the bonnet but reattaches in the leading edge of the roof. The flow reattachment becomes little bit earlier in the trailing vehicle than that in the leading vehicle.

**Keywords:** Boundary Layer, Flow Separation, Platoon Vehicle, Friction Drag, Friction Coefficient.

### 1. INTRODUCTION

The aerodynamic forces on automotive vehicles traveling in close proximity to each other are investigated in a wind tunnel. Scaled vehicle models are longitudinally aligned in a "platoon" configuration with various separation distances between the models. The velocity distributions along stream wise direction are measured by Pitot-static tube (United Sensor, U.S.A) along with pressure transducer (FC014-Micromanometer, Furness Controls, U.K.) interfaced with computer to quantify the transient interactions of the vehicle flow fields [1]. The integral analysis of boundary layer proposed by Theodore Von Karman and K. Pohlhausen in separate papers in 1921[2] is used to quantify the aerodynamics parameters. Due to friction present on the surface, the flow near the surface is retarded, so that the streamlines must be displaced outward to satisfy continuity. The flow separation is frequently quite sensitive to small changes in the shape of the body, particularly if the pressure distribution is strongly affected by the change of shape of the body as found by

H. Schlichting [2]. There is always a possibility of separation in regions where the pressure increases, and it is even greater when the rate is larger, particularly for bodies with blunt rear sides. As a result of the backflow close to the wall, a strong thickening of the boundary layer takes place and with this boundary layer mass is transported away into the outer flow. At the point of separation, the streamlines leaves the wall at a certain angle and the wall shear stress  $\tau_w$  vanishes. As a result fluid from the outer downstream zone moves towards the wall and fluid near the boundary is drawn right into the main flow leading to flow separation. Thus the separation point is defined as the boundary between the forwards and backflow in the layer closest to the wall.

Aerodynamics has a strong influence on the design and performance of a vehicle. The components of aerodynamic forces and moments experienced by a vehicle are shown in figure 1.1. In characterizing the aerodynamic behavior of road vehicles, a drag force is one of the most important factors from the viewpoint of

fuel economy as found by JL. Tsuei et.al.[3]. From control and stability point of view, however, the side force and yawing moment are the most crucial aerodynamic characteristics of a vehicle [3]. Lift force and pitch movement is especially important to light weight and high speed vehicles used in racing cars [4] and roll movement is critical in some specific circumstances where strong gust occurs, Skibor-Rylski [5]. Earlier publications discussed the issues related to road vehicle aerodynamics can be found in Scibor Rylski[5], Hucho & Sovran [6].

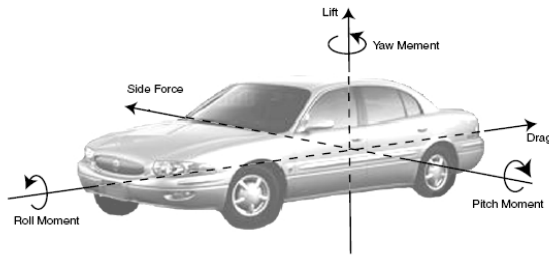


Fig 1. Force and moment on a vehicle.

These reviews discussed the fundamentals of fluid dynamics, experimental results and various automobile designs related to vehicle aerodynamics. However, their results are found mostly on the performance of single vehicle and covered relatively less material of the aerodynamic interactions involved with more than one vehicle. Several studies have discovered that a running car experiences a significant change of drag, side force and yaw moment induced by an overtaking vehicle, which may severely affect the overtaken car control [7], [8].

## 2. EXPERIMENTAL

The investigations of the study are conducted only on the top surface of the vehicle and at  $Z=0$  along the axial direction along with available  $Y$  direction. The velocity profiles underneath the vehicle and in the side wall are not considered in this investigation. Hence, the total effect of boundary layer around the model car can not be analyzed. But the interaction of flow through ground clearance of the vehicle with the wake/eddies and vortex is observed by taking velocity profiles behind the vehicle at  $Z=0$  but different  $X$  and  $Y$  positions. Before performing the experiment with the test model, the accuracy of the data acquisition system and the continuity of the test section are checked [9]. The flow stability and flow variation in the test section of the wind tunnel is also analyzed with the help of this investigation.

The model cars are placed along axial direction in the centre line of the bottom plane of the wind tunnel maintaining vehicle ground clearance of 25 mm. Testing is carried out at three different vehicle spacing i.e.  $\frac{1}{4}$ ,  $\frac{1}{2}$  and 1 car length and at  $U_\infty = 21.5$  m/s (78 km/hr). The data are taken by Pitot - static tube which is interfaced with computer through pressure transducer. The Pitot - static tube is traversed by the computer controlled 3-axes co-ordinate positioning device [1]. The velocity distributions along vertical axis are taken at the number

of planes in the stream wise direction from 150 mm ahead of the leading vehicle to 50 mm behind the trailing vehicle in the platoon maneuvers. The model car used for this experiment has the length of 130 mm including spare wheel casing in the rear of the vehicle.

The local velocities along the stream wise direction are made dimensionless by dividing the corresponding free stream velocity ( $U_\infty$ ). The  $X$ -axis is taken zero at the front edge of the leading vehicle and  $Y$ -axis is taken zero at the bottom surface of the wind tunnel. The  $X$ -axis and  $Y$ -axis are made dimensionless by dividing it by the car length ( $l_c$ ). Two different length scales i.e  $x/l_c$  and  $x_c/l_c$  are introduced to analyze the flow characteristics of the model in the test section. The  $x/l_c$  is used for indicating the location of the vehicles in the test section with respect to zero ( $X_0$ ) position. The  $x_c/l_c$  is introduced to investigate and compare the boundary layer characteristics with respect to individual positions of each vehicle. The car dimension is shown in fig. 2.

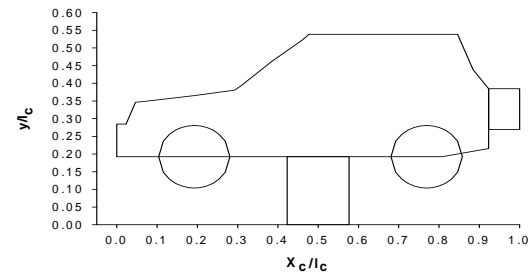


Fig 2. Model car dimension

From the number of velocity profiles along the stream wise direction, the contours of velocity are plotted for different experimental conditions. The numerical integration techniques are used for calculating the displacement thickness and momentum thickness and the finite difference techniques are used for calculating the friction coefficient. All the aerodynamic parameters are plotted in the non-dimensional form.

## 3. RESULT AND DISCUSSION

Fig.3 and fig.4 show the velocity profiles ahead of the leading vehicle and on the leading vehicle respectively of 2-vehicles platoon which are found to be similar in nature with those of single vehicle for  $U_\infty = 21.5$  m/s investigated by A.Motin [10][11]. In figure it is seen that when the vehicle spacing is small i.e.  $\frac{1}{4}$  car length, the front of the trailing vehicle is affected by the wake generated behind the leading vehicle. As a result, no air thrust is present in the front of the trailing vehicle causing reduction of pressure drag on the front of the trailing vehicle. As the vehicle spacing increases, this effect reduces and it is observed for 1 vehicle spacing that the air flow strikes to the front of the trailing vehicle with a velocity of around  $U/U_\infty = 0.6$  producing more resisting force in the front in comparison to the small vehicle spacing. As a result, it can be said that the trailing vehicle with small vehicle spacing requires less amount of fuel on this count to drive the vehicle due to comparatively small restricting force present in the front.

Fig.6 shows that for  $\frac{1}{4}$  vehicle spacing in the leading edge of the trailing vehicle ( $x/l_c = 1.25$ ), there is no air



flow from  $y/l_c = 0.39$  to  $0.46$  due to generation of wake behind the leading car. In the case of  $1/2$  vehicle spacing the flow pattern in the same position of the vehicle ( $x/l_c = 1.5$ ) is found similar with the smaller vehicle spacing. But the magnitude of  $U/U_\infty$  is greater i.e.  $U/U_\infty = 0.43$  at  $y/l_c = 0.39$  and  $0.46$  and at  $y/l_c = 0.54$  the  $U/U_\infty$  is found to be about  $0.73$ . When the vehicle spacing is equal to 1 car length, the  $U/U_\infty$  at  $y/l_c = 0.46$  is reduced to about  $0.67$  from about  $0.72$  at  $y/l_c = 0.39$ . This means that in the case of 1 vehicle spacing comparatively high air velocity strikes in front of the trailing vehicle and is circulated. On the half way of the bonnet of the trailing vehicle ( $x/l_c = 1.40, 1.65$  and  $2.15$  for  $1/4, 1/2$  and 1 vehicle spacing respectively) the flow velocity gradually increases in the vertical direction from the surface for  $1/4$  vehicle spacing but for  $1/2$  and 1 vehicle spacing it reduces from the surface up to the point of  $y/l_c = 0.46$  and then increases smoothly. It can be illustrated from that the air flow just attaches on the half away of the bonnet for  $1/4$  vehicle spacing. It is also observed that the maximum flow velocity is attained at the level of the roof wall  $x/l_c = 0.54$  on the bonnet for all the vehicle spacing. The velocity profiles on the top wall of the vehicle for all the vehicle spacing is observed similar in nature and magnitude. From fig.7, it is seen that the velocity profiles behind the trailing vehicle of 2-vehicles platoon is almost similar in nature with the velocity profiles in between the leading and trailing vehicle illustrated in fig.5. But the magnitude of air velocity in the level of bottom surface of the trailing vehicle is less than that of the leading vehicle.

The contour plots of velocity for 2-vehicles platoon at different vehicle spacing are shown in fig. 8. For  $1/4$  car spacing, it is seen that in the leading vehicle the maximum flow velocity occurs just on the surface of the top wall. But for the trailing vehicle the maximum velocity of flow is observed about 30 mm above the surface of the top wall of the vehicle. This phenomenon occurs due to the boundary layer formation in the downward direction. It is also observed that the wake generated behind the leading vehicle is interfered up to about mid point on the bonnet of the trailing vehicle for  $1/4$  vehicle spacing. As a result the flow circulation occurs on the bonnet in the trailing vehicle when the vehicle spacing is low ( $1/4$  vehicle length). For  $1/2$  car spacing it is seen that the wake generated behind the leading vehicle affects the zone up to the front edge of the trailing vehicle when the vehicle spacing is  $1/2$  of the vehicle length. Hence, the flow circulation i.e the back flow occurs at the leading edge of the trailing vehicle.

For 1 car spacing the flow circulation due to wake generated behind the leading vehicle occurs in the front of the trailing vehicle and the slow moving air strikes at the front of the vehicle. When the vehicle spacing is small, the wake generated behind the leading vehicle in platoon interfere more to the trailing vehicle than that of larger vehicle spacing. As a result, pressure drag can be reduced as vehicle spacing becomes small. On the other hand, the thickness of boundary layer on the trailing car is a function of vehicle spacing but inversely related (shown in fig.8). It is clearly seen that the boundary layer in the down stream of the trailing vehicle for  $1/4$  vehicle spacing is greater than that for  $1/2$  and 1 vehicle spacing.

According to the boundary layer principle, higher the boundary layer thickness higher the mass flux and momentum flux deficit [2]. Since, the momentum flux is directly related to the skin-friction drag; hence the skin-friction drag may be more for shorter vehicle spacing although the pressure drag is reduced with smaller vehicle spacing.

Fig.9 shows that both the magnitude and variation of displacement thickness of the leading vehicle remain nearly the same as that of the single vehicle found by A.Motin [10][11]. In the trailing vehicle the variation pattern remains the same as the leading vehicle but its magnitude increases about 2 times than those of the leading vehicle. It is seen that the displacement thickness for  $1/4$  vehicle spacing is greater than that for  $1/2$  and 1 vehicle spacing. As the wake generated behind the leading vehicle interferes more for smaller vehicle spacing (as described earlier), the displacement thickness on the trailing vehicle becomes higher for  $1/4$  vehicle spacing than that of  $1/2$  and 1 car spacing.

In fig.10, it is seen that in the case of trailing vehicle, it is observed that up to about  $x_c/l_c = 0.15$  in the downward direction from the leading edge of the trailing vehicle, the momentum thickness for  $1/4$  vehicle spacing is smaller than that for  $1/2$  and 1 vehicle spacing. After this point the trailing vehicle at  $1/4$  vehicle spacing in platoon maneuver shows higher momentum thickness than that at  $1/2$  and 1 vehicle spacing. From velocity profile for  $1/4$  vehicle spacing described earlier in, it is observed that there is no flow on the bonnet of the vehicle. Since, the flow velocity is zero there is no momentum on the surface of the bonnet. As a result, the momentum thickness is low in the front of the trailing vehicle for  $1/4$  vehicle spacing than that of  $1/2$  and 1 vehicle spacing. It is also observed that the momentum thickness on the trailing vehicle (from  $x_c/l_c = 0$  to 1) decreases with the increase in vehicle spacing. From fig.10, it is seen that the momentum thickness for a specific location in the stream wise direction in the trailing vehicle is higher than that in the same location in the leading vehicle.

Fig.11 shows that the friction coefficient is observed zero at  $x_c/l_c = 0.1, 0.27$  and  $0.5$  in the downward direction of the leading vehicle which indicates that the point of flow separation and flow reattachment respectively. The highest friction coefficient is observed on the bonnet where the flow tends to separate and the minimum friction coefficient is found to be at  $x_c/l_c = 0.325$ . It is also seen that the friction coefficient is observed negative from  $x_c/l_c = 0.27$  to  $0.5$  in the downward direction which means that the back flow occurs here. In the case of trailing vehicle it is seen that for  $1/2$  and 1 vehicle spacing the friction coefficient is negative from the leading edge of the top wall. This is because of flow circulation which occurs due to wake generated behind the leading vehicle in the leading edge and in the front of the trailing vehicle for  $1/2$  and 1 vehicle spacing respectively. But in the case of  $1/4$  vehicle spacing the flow separation occurs in the mid point of the bonnet in the trailing vehicle as observed earlier in fig.8. For this reason, the friction coefficient for  $1/4$  vehicle spacing is observed positive and maximum at the leading edge of the trailing vehicle and zero at about the mid point of the bonnet (about  $x_c/l_c =$

0.15 in the downward direction). For both leading and trailing vehicle, after the flow reattachment at  $x_c/l_c = 0.5$ , the friction coefficient is observed positive due to boundary layer development on the top wall of the vehicle.

Fig.11 also shows that the friction coefficient on the leading vehicle in platoon maneuver is positive up to  $x_c/l_c = 0.27$  in the downward direction. At  $x_c/l_c = 0.27$  of the vehicle the flow is separated and reattaches at  $x_c/l_c = 0.5$  in the downward direction. On the other hand, for the trailing vehicle the friction coefficient is found to be negative up to  $x_c/l_c = 0.5$  from the leading edge of the trailing vehicle and at this point the flow is reattached. After that point the trend of friction coefficient for leading vehicle and trailing vehicle is almost identical.

Fig.12 shows the variation of local friction drag coefficient as a function of vehicle spacing for leading and trailing vehicles. From both the curves it is seen that the variation of vehicle spacing in platoon maneuver has no significant effect on the local friction drag coefficient. From fig.12 it is observed that the friction drag on the leading vehicle is high on the front of the vehicle and reduces up to the mid point of the bonnet. After that point the value of drag coefficient rises up to  $x_c/l_c = 0.31$  in the downward direction. It indicates that in the intersection zone of bonnet and front wind shield the momentum flux deficit is occurred. It is also observed that at the leading edge of the trailing vehicle the friction drag coefficient for  $1/4$  vehicle spacing is slightly lower than that for  $1/2$  and 1 vehicle spacing and it observed reduces exponentially.

In fig.12, it is seen for the  $1/4$  vehicle spacing that the friction drag coefficient in the trailing vehicle is higher than that in the leading vehicle. It is also observed that in the trailing vehicle the friction drag coefficient decreases exponentially. For  $1/2$  and 1 vehicle spacing, it is seen that the local friction drag coefficient in the trailing vehicle is higher than that in the leading vehicle up to  $x_c/l_c = 0.31$  of the vehicle. After that point the friction coefficient in the leading and trailing vehicle remains almost the same.

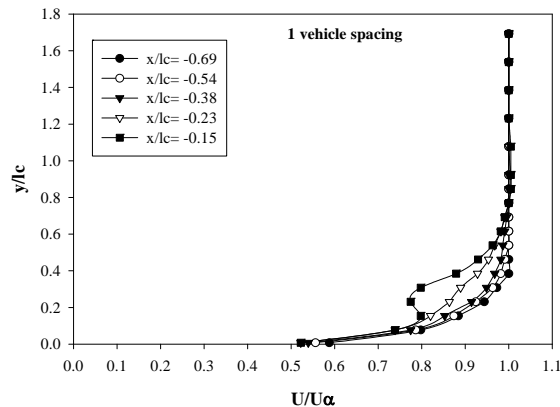


Fig 3. Velocity profiles ahead of the leading car

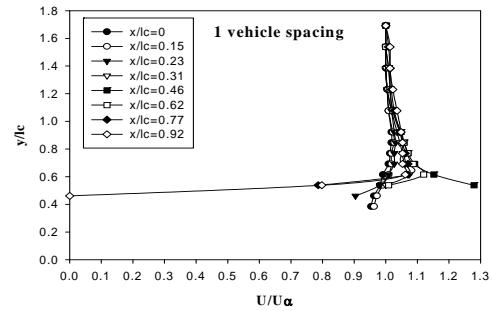


Fig 4. Velocity profiles on the leading car.

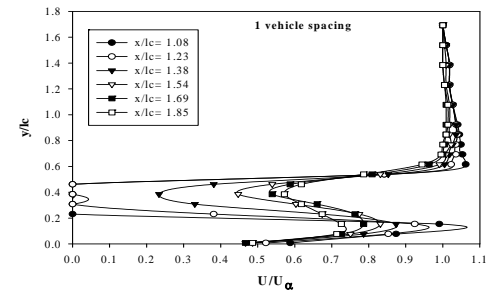
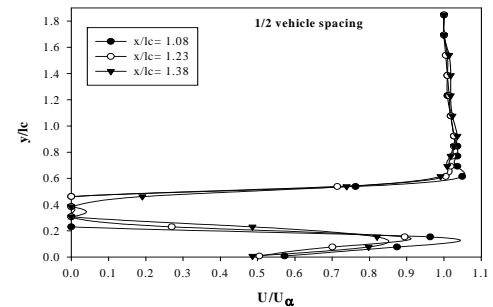
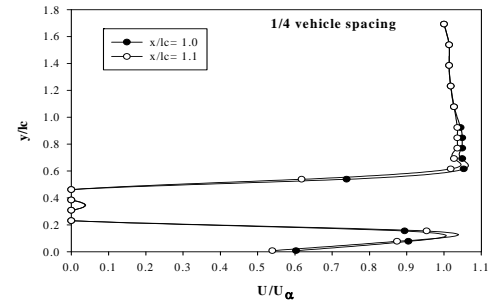
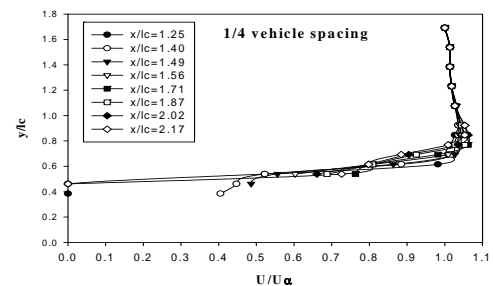


Fig 5. Velocity profiles in between leading and trailing car.



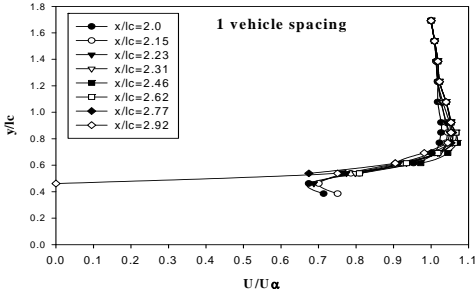
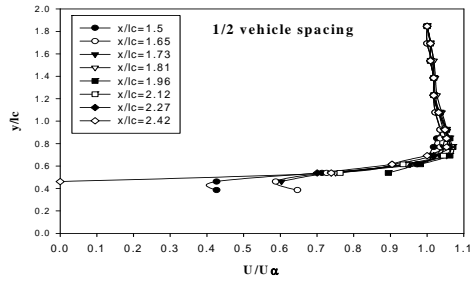


Fig 6. Velocity profile on the trailing car

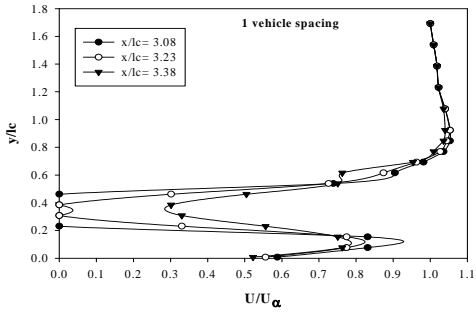
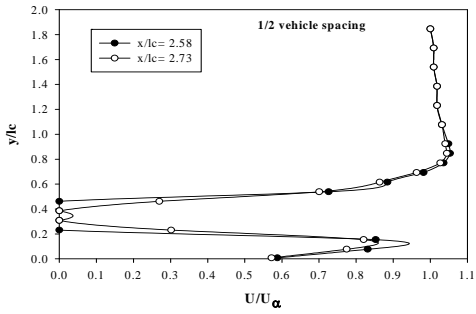
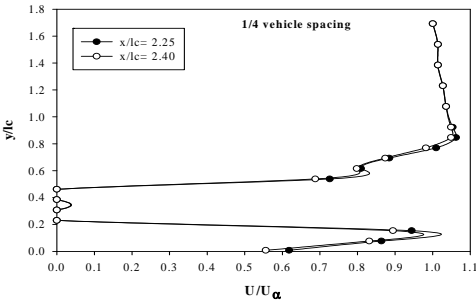


Fig 7. Velocity profiles behind the trailing car

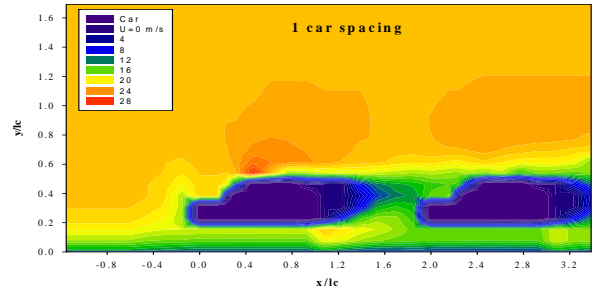
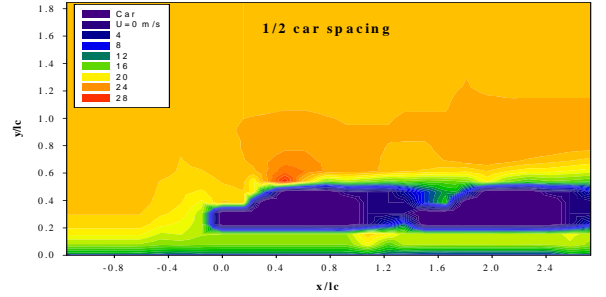
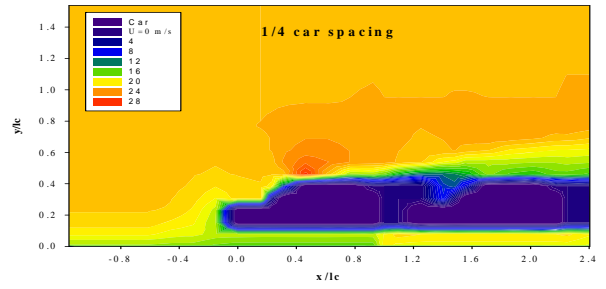


Fig 8. Contour plot of velocity for 2-cars in platoon.

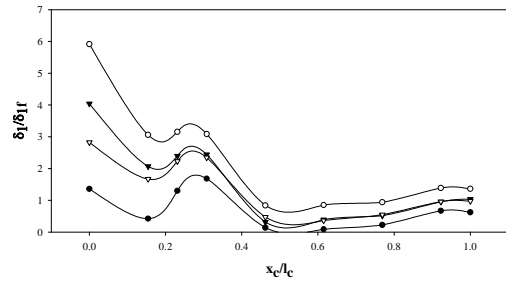


Fig 9. Variation of displacement thickness.

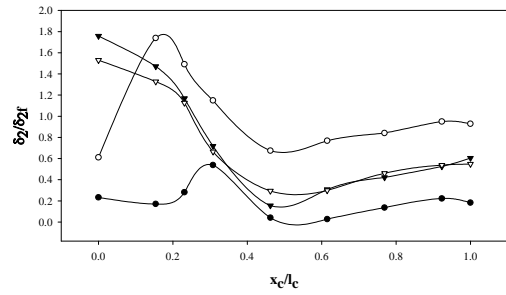


Fig 10. Variation of momentum thickness.

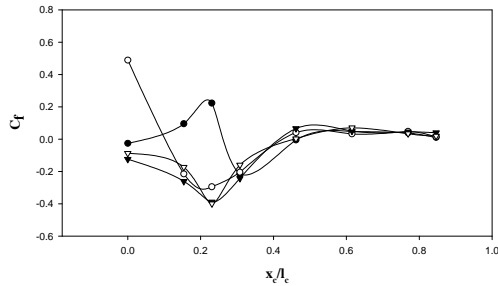


Fig 11. Variation of skin friction coefficient.

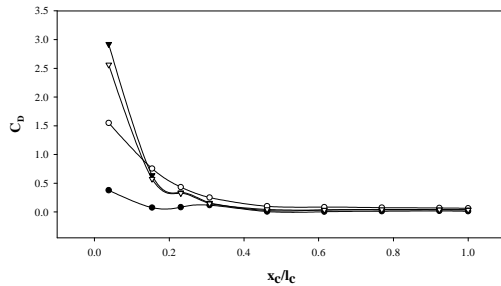


Fig 12. Variation of local friction drag coefficient.

#### 4. CONCLUSION

From the present research work the following conclusions may be drawn.

1. Effect of boundary layer developed on the platoon vehicles at all the vehicle speed and spacing vanishes at  $y/lc > 1.0$ .
2. The displacement and momentum thickness over the 2<sup>nd</sup> car is more than that over the leading car
3. The displacement thickness on the 2<sup>nd</sup> decreases with the increase of vehicle spacing. At the leading edge of the 2<sup>nd</sup> vehicle ( $x_c/lc=0.0$ ) the  $\delta_1$  reduces to 50% as the vehicle spacing increases from  $1/4$  to 1 car length.
4. At  $x_c/lc=0$ , the momentum thickness on the 2<sup>nd</sup> vehicle increases by 2.7 times as the vehicle spacing increases from  $1/4$  to  $1/2$  car length and reduces to 90% as the vehicle spacing increases from  $1/2$  to 1 car length.
5. The separation of flow in the leading vehicle occurs at the end of the bonnet ( $x_c/lc=0.3$ ) and the flow reattaches at the leading edge of the roof ( $x_c/lc=0.5$ ).
6. At  $x_c/lc > 0.5$  the change of vehicle spacing has no significant effect on the friction coefficient and friction drag coefficient.
7. On the 2<sup>nd</sup> vehicle at  $x_c/lc=0$  the friction drag increases by 45% as the vehicle spacing increases from  $1/4$  to  $1/2$  car length and reduces by 11% as the vehicle spacing increases from  $1/2$  to 1 car length.

#### 5. REFERENCES

1. A. Motin, et.al. "Development and Accuracy Test of Computer Controlled Sensing Probe Positioning Device Paired with Data Acquisition System", 5<sup>th</sup>

CISCON -2008, P-53, 7-8 November, 2008, Manipal, India.

2. H. Schlichting, et.al. "Boundary Layer Theory" ISBN: 3-540-67939-I, Reprint-2003.
3. J.L. Tsuei, et.al. "Transient Platoon Aerodynamics During Passing Maneuvers and In-line Oscillations" California PATH Research Report, UCB-ITS-PRR-2000-26
4. Howell, J., "Catastrophic lift force on Racing cars" J. Wind Eng. Ind. Aerodyn., Vol. 9, 1981
5. Skibor-Rylski A.J. ,Road vehicle aerodynamics, Pentech press, London, 1975.
6. Hucho, W-H., Sovran, G; 1993; Aerodynamics of Road Vehicles; Annu. Rev. Fluid Mech.; 2.No. 25; p. 485-537/
7. Abdel Azim, A. F., "An Experimental study of the Aerodynamic Interference Between Road Vehicles" SAE Paper, No. 940422, 1994.
8. Sano, M., et.al., "Unsteady Aerodynamical Forces by Interference of Two Bluff Bodies Moving Closely", Bulletin of JSME, Vol. 27, No.226, 1984.
9. A. Motin, M.A.T. Ali, "Flow Characteristics in the Test Section of a Wind Tunnel", 4<sup>th</sup> BSME-ASME International Conference on Thermal Engineering, (p-75), 27-29 December, 2008, Dhaka, Bangladesh.
10. A. Motin, M.A.T. Ali, "An Integral Analysis of Boundary Layer and Skin Friction of Moving Vehicle" 4<sup>th</sup> BSME-ASME International Conference on Thermal Engineering, (p-71), 27-29 December, 2008, Dhaka, Bangladesh.
11. A.Motin "An Experimental Study of Boundary Layer Characteristics around Platoon Vehicle" M.Sc. Thesis published in the dept. of Mechanical Engineering, BUET, January 2009.

#### 6. NOMENCLATURE

Symbol	Meaning	Unit
$U$	Local velocity	m/s
$U_{\infty}$	Free stream velocity	m/s
$\delta_1$	Displacement thickness	mm
$\delta_{1f}$	Free stream displacement thickness	mm
$\delta_2$	Momentum thickness	mm
$\delta_{2f}$	Free stream momentum thickness	mm
$C_f$	Skin friction coefficient	--
$C_D$	Friction drag coefficient	--
$l_c$	Characteristic car length	mm
$x_c$	Stream wise distance along the model car from the front of the car.	mm

#### 7. MAILING ADDRESS

A.Motin  
 Department of Mechanical Engineering,  
 Bangladesh University of Engineering and Technology,  
 Dhaka-1000, Bangladesh  
 E-mail: amotin@me.buet.ac.bd

## CHARACTERISTICS OF TWIN AXISYMMETRIC FREE JETS

Mohammed A. Azim

Department of Mechanical Engineering, Bangladesh University of Engineering and Technology  
Dhaka, Bangladesh

### ABSTRACT

Axisymmetric single free jet and twin identical free jets with three nozzle spacing have been investigated numerically. Flow characteristics of single jet, twin jets and two superimposed individual jets are compared, and effect of nozzle spacing on twin jet flows is studied. Turbulence closure in those jet flows was achieved by one equation model. The governing equations were solved by using Implicit  $\theta$ -Scheme and Tridiagonal Matrix Algorithm. Mean motion augmentation and turbulence attenuation occur on the axis of symmetry of twin jets compare to single jet and two superimposed individual jets. Both converging and combining points of twin jets are found to move downstream with the increase in nozzle spacing. It also appears that increase in nozzle spacing is associated with mean motion attenuation and turbulence augmentation at any axial location of the flows between the nozzle centerlines.

**Keywords:** Axisymmetric Twin Jets, Numerical Study, Vortex Breakdown.

### 1. INTRODUCTION

Most of the published data on axisymmetric turbulent free jets describe the developed region. There are few experimental data on the developing region of these jets [1-3]. The flow structure in developing region of the jet is important in many engineering applications, for instance, impinging jets are used for augmentation of convective heat or mass transfer process.

Compared to single jet, there is little information available in literature on the flow characteristics of interacting twin jets [4]. Interaction and mixing of twin jets are fundamental problems of turbulent shear flows that occur in a wide variety of engineering applications such as burners and thrust augmenting ejectors for V/STOL aircrafts, premixers for gas turbine combustors, chemical reactors, chemical lasers, propulsion systems, pollutant disposal devices, air conditioners and fluidics.

Twin jets are classified in literature as ventilated if they are issued from two free-standing nozzles or unventilated if the space between the two nozzles is blocked by a wall. The flow of twin axisymmetric turbulent jets is schematically shown in figure 1. In general, twin interacting jets develops through three successively distinct regions: converging region, merging region and combining region. In the converging region, the inner layers of the individual jets merge towards the centerline between the nozzles. Converging region terminates at the initiation of merging point and the two individual jets continue to merge until the combined point appears where the mean

axial velocity becomes maximum on the axis of symmetry. Far downstream from the combined point, the twin jet flow resembles a single jet. Mutual entrainment of the surrounding fluid creates a subatmospheric region between the unventilated jets that causes their convergence and reversal of considerable fraction of the total flow at the axis of symmetry against a strong downstream force of turbulent shear. The same mechanism of mutual entrainment of the surrounding fluid is also operative in ventilated twin jets that converge into an atmospheric region prohibiting the formation of vortices upstream of the merging region [5-6]. Flow characteristics in the merging region of twin axisymmetric jets are three-dimensional, highly anisotropic and non-self-preserving, and these characteristics in the combining region are similar to a single jet.

Detail knowledge of flow characteristics of twin jets in the converging and merging regions is essential to the understanding of many observed complex phenomena in the aforesaid applications. For this reason, initial region of twin jets draw interest of the researchers. The lengths of converging and combining regions depend on the configuration of twin jets, i.e. plane jets converge and combine faster than axisymmetric jets, unventilated jets converge and combine faster than ventilated jets, and small spacing jets converge and combine faster than large spacing jets. Literature shows substantial discrepancies in the published data for converging and combining lengths of twin jets with small nozzle spacing [7].

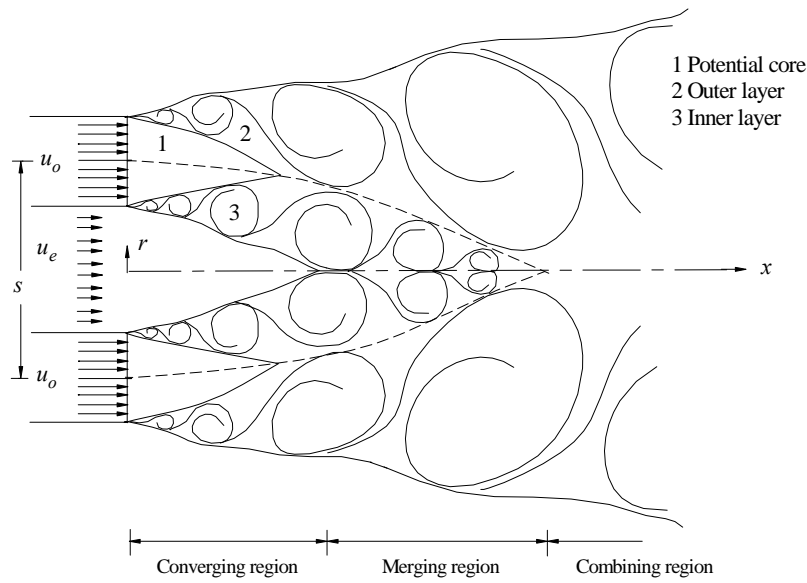


Figure 1. Schematic of twin axisymmetric free jets.

Studies show that nozzle spacing affects the flow structure, development and degree of mixing of twin jets quantitatively. On the other hand, Reynolds number ( $Re$ ) does not affect the flow structure of twin jets [7], moreover, the structure of high speed twin jets is identical to that of low speed twin jets [8]. One of the objectives of the present study is to compare the structure and development of the flows for single jet and twin jets in the merging region. Another objective is also to investigate the effect of nozzle spacing on the flow characteristics in the same region.

## 2. GOVERNING EQUATIONS

The merging region of the interacting twin axisymmetric jets is three-dimensional. However, flow in the vicinity of the symmetry plane connecting the nozzle centerlines is fairly two-dimensional. Hence the mean governing equations for such single phase, steady state and constant property fluid flow ( $\bar{v}, \theta, \bar{u}$ ) in cylindrical co-ordinates ( $r, \theta, x$ ) by thin shear layer approximation under uniform pressure are

$$\frac{1}{r} \frac{\partial}{\partial r} (r \bar{v}) + \frac{\partial \bar{u}}{\partial x} = 0 \quad (1)$$

$$\bar{v} \frac{\partial \bar{u}}{\partial r} + \bar{u} \frac{\partial \bar{u}}{\partial x} = \frac{1}{r} \frac{\partial}{\partial r} \left[ r \left( \bar{v} \frac{\partial \bar{u}}{\partial r} - \overline{u'v'} \right) \right] \quad (2)$$

The closure between Eqs. (1)-(2) is achieved through one equation turbulence model by expressing Reynolds shear stress  $\overline{u'v'}$  as

$$-\overline{u'v'} = 0.38k \quad (3)$$

and solving  $k$  from the kinetic energy equation [9]

$$\bar{v} \frac{\partial k}{\partial r} + \bar{u} \frac{\partial k}{\partial x} = \frac{1}{r} \frac{\partial}{\partial r} \left[ r \left( \bar{v} + v_t / \sigma_k \right) \frac{\partial k}{\partial r} \right] +$$

$$v_t \left( \frac{\partial \bar{u}}{\partial r} \right)^2 - C_D \ell_m^{-1} k^{3/2} \quad (4)$$

There  $v_t$  Boussinesq's eddy viscosity is expressed by

$$-\overline{u'v'} = v_t \frac{\partial \bar{u}}{\partial r} \quad (5)$$

$\ell_m$  Prandtl's mixing length is expressed by

$$v_t = \ell_m^2 \frac{\partial \bar{u}}{\partial r} \quad (6)$$

and  $k$ ,  $\nu$ ,  $\sigma_k$  and  $C_D$  are the turbulence kinetic energy, fluid viscosity, turbulence Prandtl number and constant of proportionality.

## 3. NUMERICAL PROCEDURE

The closed set of Eqs. (1), (2) and (4) is solved by using Implicit  $\theta$ -Scheme, which is the Crank-Nicolson Scheme for  $\theta=0.5$  [10] where  $\theta$  is the weighting factor, and by using Tridiagonal Matrix Algorithm [11]. The flow domain due to two identical axisymmetric jets, with nozzle spacing  $s$ , is symmetric about  $x$ -axis allowing computation in half of the flow domain. The boundary conditions are  $\partial \bar{u} / \partial r(0, x) = \partial k / \partial r(0, x) = \bar{v}(0, x) = \overline{u'v'}(0, x) = 0$  and the initial conditions are  $\bar{u}(r \leq r_o, 0) = u_o$ ,  $\bar{u}(r > r_o, 0) = u_e$  and  $k(r, 0) = \bar{v}(r, 0) = \overline{u'v'}(r, 0) = 0$  where  $r_o$  is the jet radius, and  $u_o$  and  $u_e$  are the uniform jet exit velocity and uniform external velocity, respectively. Grid spacings are uniform in  $x$ -direction with  $\Delta x = 1.6 \Delta r_j$  and variable in  $r$ -direction such that  $\Delta r_{j+1} = K \Delta r_j$  where

$$\Delta r_l = r_o (K - 1) / (K^{nj-1} - 1) \quad (7)$$

and number of grid points  $n_j = 31$  for single jet over  $r_o = 20 \text{ mm}$  with  $K = 1.01$ .

#### 4. RESULTS AND DISCUSSION

The set of Eqs. (1), (2) and (4) is solved numerically for the initial and boundary conditions appear in the free shear flow of single jet and twin jets, and for  $\sigma_k = 1.0$  and  $C_D = 0.18$ . All the presently investigated air jets are identical with respect to the flowing fluid, jet diameter and its velocity, i.e., the jets are of the same Reynolds number. Implicit  $\theta$ -Scheme is found to work well with  $\theta = 0.3$  for the axisymmetric jets in the present study. The obtained results from computation are presented in this section for single free jet and twin free jets in the moving ambient of  $u_e = 0.1u_o$ .

##### 4.1 Comparison of Single Jet and Twin Jets

Twin jets are characterized by converging, merging and combining regions. Combining region initiates when merging of two jets is complete and flow in this region resemble a single jet. In the initial region of single free jet, the vortices are separated by the potential core and rotate outwardly whereas vortices in the inner layers of twin free jets rotate inwardly (figure 1). This makes the flow physics of single jet different from that of twin jets in the initial region.

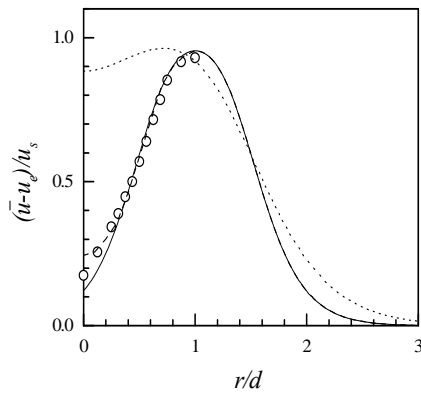


Figure 2. Mean axial velocity distributions at  $x/d=6$  for different jets. — Single free jet, - - - - Superposition of two jets with  $s=2d$ , ..... Twin jets with  $s=2d$ ,  $\circ$  Single free jet data [1].

Mean axial velocity  $\bar{u}$ , Reynolds shear stress  $\overline{u'v'}$  and turbulent kinetic energy  $k$  are plotted against the radial distance  $r/d$  in figures 2-4 at axial location  $x/d=6$ . In figure 2,  $(\bar{u} - u_e)/u_s$  against  $r/d$  is presented for single free jet and twin free jets with  $2d$  nozzle spacing between the nozzle centerlines where  $d$  is jet diameter and  $u_s = u_o - u_e$ . The mean velocity profile of the twin jets with depression on the axis of symmetry

indicates that the profile is located in the merging region. This velocity profile compare to that of single jet shows mean motion augmentation in twin jets. Mean velocity profiles of two individual jets with  $2d$  nozzle spacing are superimposed which show that the flow of the twin jets between the nozzle centerlines is not a simple superposition. Sami et al data [1] for circular jet ( $Re=22 \times 10^4$  at jet exit) in quiescent ambient are found to decay a bit higher and as a consequence spread a bit higher than the single free jet ( $Re=1.6 \times 10^4$ ) in the present study. Otherwise, the data show good agreement with the present results for mean axial velocity

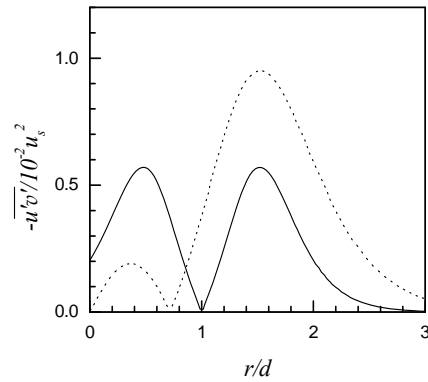


Figure 3. Reynolds shear stress distributions at  $x/d=6$  for different jets. See figure 2 for legends.

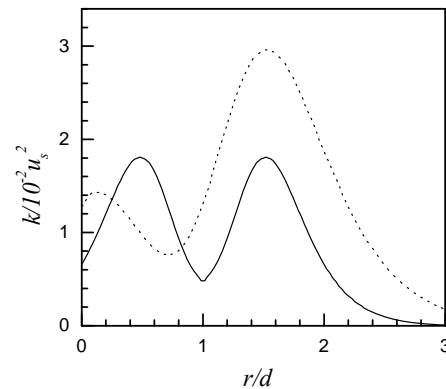


Figure 4. Turbulent kinetic energy distributions at  $x/d=6$  for different jets. See figure 2 for legends.

indicating the effectiveness of the numerical scheme used for solving the governing equations.

Figures 3-4 show that  $\overline{u'v'}/u_s^2$  and  $k/u_s^2$  are weakened in the merging region of twin jets compare to single jet. This is due to intense vortex breakdown by the inwardly counter rotating vortices and also by the squeezing of inner layers resulting from reduction in volume flux due to momentum flux constancy.



## 4.2 Structure and Development of Twin Jets

The profiles of  $(\bar{u} - u_e)/u_s$ ,  $\overline{u'v'}/u_s^2$  and  $k/u_s^2$  are plotted in figures 5-7 against  $r/d$  for twin jets with  $2d$

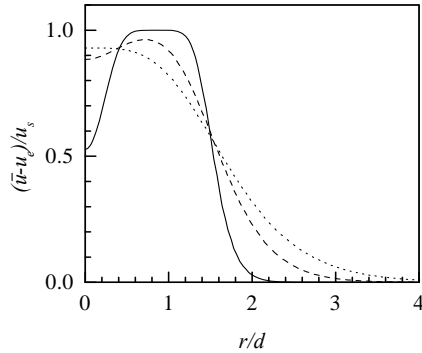


Figure 5. Mean axial velocity distributions for twin jets with  $s=2d$ . —  $x/d=1$ , - - -  $x/d=6$ , .....  $x/d=13$ .

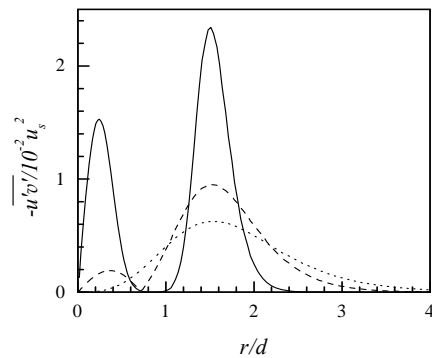


Figure 6. Reynolds shear stress distributions for twin jets with  $s=2d$ . See figure 5 for legends.

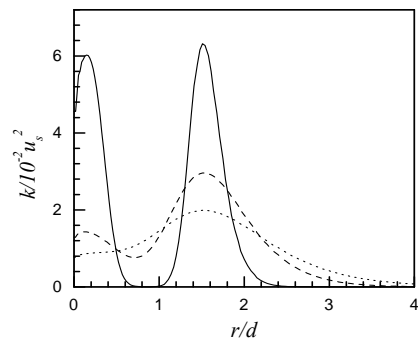


Figure 7. Turbulent kinetic energy distributions for twin jets with  $s=2d$ . See figure 5 for legends.

nozzle spacing. The profiles of mean velocity in figure 5 show that inner layers converge on the axis of symmetry for  $x/d < 1$  and combine into a single jet at  $x/d=13$ . Beyond the combine point this twin jet flows as a single

free jet. Figures 6-7 show that the profiles of  $\overline{u'v'}/u_s^2$  and  $k/u_s^2$  decay in the downstream and resemble a single jet at  $x/d=13$ .

## 4.3 Effect of Nozzle Spacing on Twin Jet Flow

Twin jets with three nozzle spacing  $1.5d$ ,  $2d$  and  $2.5d$  are investigated numerically to discern the effect of nozzle spacing on their flows. The profiles of

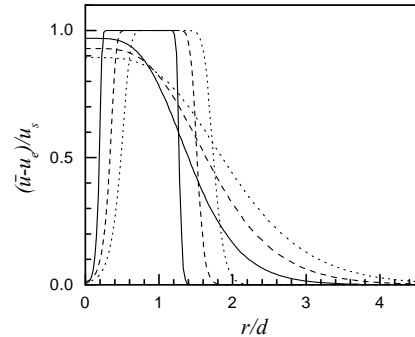


Figure 8. Mean axial velocity distributions at converging and combining points for twin jets. —  $s=1.5d$ ,  $x/d=0.04, 10$ ; - - -  $s=2d$ ,  $x/d=0.12, 13$ ; .....  $s=2.5d$ ,  $x/d=0.32, 17$ .

$(\bar{u} - u_e)/u_s$  at the converging and combining points of twin jets for three nozzle spacing are plotted against  $r/d$  in figure 8. The converging and combining points of the jets are found to appear in the figure as: converge at  $x/d = 0.04, 0.12$  and  $0.32$ , and combine at  $x/d = 10, 13$  and  $17$ , respectively, for  $1.5d, 2d$  and  $2.5d$  nozzle spacing. This implies that both converging and combining points of twin jets move downstream with increasing nozzle

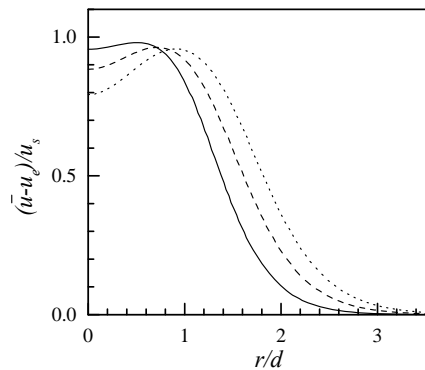


Figure 9. Mean axial velocity distributions for twin jets at  $x/d=6$ . —  $s=1.5d$ , - - -  $s=2d$ , .....  $s=2.5d$ .

spacing. The figure also indicates that peak of the mean velocity profile at combined point reduces with increasing nozzle spacing. Ko and Lau [12] made measurements on unventilated twin plane jets with small nozzle spacing of  $2.5d$  where  $d$  is jet width and

obtained combining point at  $10.5d$  but did not mention the distance of converging point. This discrepancy in the data of combining length may be attributed to the difference in jet's configuration.

Figures 9-11 describe the profiles of  $(\bar{u} - u_e)/u_s$ ,  $\overline{u'v'}/u_s^2$  and  $k/u_s^2$  against the radial distance  $r/d$  at  $x/d=6$  for three different nozzle spacing. It appears from these figures that increase in nozzle spacing attenuates mean motion and augments turbulence at any axial location of the flows in the merging region. The figures also show that the peaks of mean velocity, shear stress and kinetic energy are offset radially outward with increasing nozzle spacing.

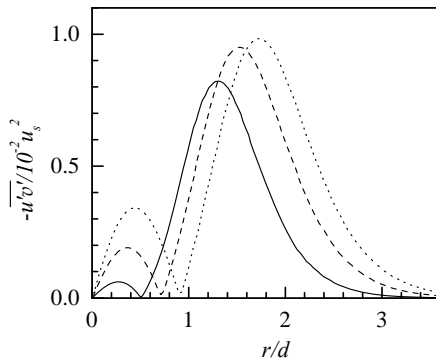


Figure 10. Reynolds shear stress distributions for twin jets at  $x/d=6$ . See figure 9 for legends.

## 5. CONCLUSIONS

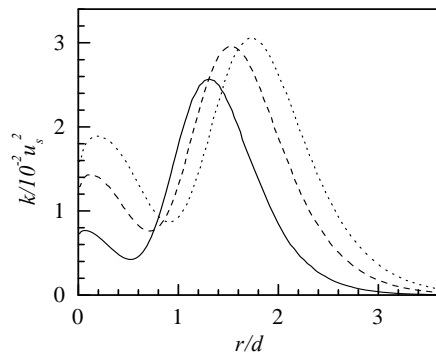


Figure 11. Turbulent kinetic energy distributions for twin jets at  $x/d=6$ . See figure 9 for legends.

Comparison of single and twin axisymmetric jet flows reveals that inner layers of twin jets converge much earlier than if the flow of two individual jets were superimposed. Turbulence quantities in the flow between the nozzle centerlines of twin jets reduce due to intense vortex breakdown by the counter rotating vortices and squeezing of the inner layers by the reduction in volume flux as a result of momentum flux constancy. Thus in the merging region of twin jets mean motion becomes stronger and turbulence becomes

weaker than those of a single jet. This stronger mean motion can cause thrust augmentation and weaker turbulence can cause sound attenuation in aircrafts.

With increased nozzle spacing, both converging and combining points of twin jets move downstream. Increase in nozzle spacing reduces the degree of mixing in the merging region due to reduction in vortex breakdown leading to an increase in segregation of the jet fluid.

## 6. REFERENCES

1. Sami, S., Carmody, T. and Rouse, H., 1967, Jet Diffusion in the Region of Flow Establishment, *J. Fluid Mech.* 27: 231-252.
2. Crow, S. C. and Champagne, F. H., 1971, Orderly Structure in Jet Turbulence, *J. Fluid Mech.* 48: 547-591.
3. Boguslawski, L. and Popiel, Cz. O., 1979, Flow Structure of the Free Round Turbulent Jet in the Initial Region, *J. Fluid Mech.* 90: 531-539.
4. Stapountzis, H., Westerweel, J., Bessem, J. M., Westendorp, A. and Nieuwstadt, F. T. M., 1992, Measurement of Product Concentration of Two Parallel Reactive Jets Using Digital Image Processing, *Appl. Sci. Research* 49: 245-259.
5. Marsters, G. F., 1977, Interaction of Two Plane Parallel Jets, *AIAA Journal* 15: 1756-1762.
6. Elbanna, H., Gahin, S. and Rashed, M. I., 1983, Investigation of Two Plane Parallel Jets, *AIAA Journal* 21: 986-991.
7. Nasr, A. and Lai, J. C. S., 1997, Two Parallel Plane Jets: Mean Flow and Effects of Acoustic Excitation, *Exp Fluids* 22: 251-260.
8. Moustafa, G. H., 1994, Experimental Investigation of High-Speed Twin Jets, *AIAA Journal* 32: 2320-2322.
9. Launder, B. E. and Spalding, D. B., 1972, *Mathematical Models of Turbulence*, Academic Press, London.
10. Anderson, D. A., Tannehill, J. C. and Pletcher, R. H., 1984, *Computational Fluid Mechanics and Heat Transfer*, McGraw-Hill.
11. Thomas, L. H., 1949, *Elliptic Problems in Linear Difference Equations Over a Network*, Watson Sci Comput Lab Report, Columbia University, New York.
12. Ko, N. W. M. and Lau, K. K., 1989, Flow Structures in Initial Region of Two Interacting Parallel Plane Jets, *Exp Fluid Sci* 2: 431-449.

## 7. MAILING ADDRESS

Mohammed A. Azim  
Department of Mechanical Engineering,  
Bangladesh University of Engineering and Technology  
Dhaka-1000, Bangladesh

## AERODYNAMICS OF VEHICLE ADD-ONS

Firoz Alam, Harun Chowdhury and Simon Watkins

School of Aerospace, Mechanical and Manufacturing Engineering, RMIT University,  
Melbourne, Australia

### ABSTRACT

Over 80% of the required total vehicle power is essential to overcome the aerodynamic drag and the remaining power is used for rolling resistance. An aerodynamically streamlined shape significantly reduces the aerodynamic drag thus lowering the fuel consumption. Although aerodynamics of road vehicles has been well studied, scant studies on aerodynamic effects of vehicle add-ons were reported to the public domain. Due to the life style demands, most modern passenger cars use various add-ons including roof-rack, ski-rack, bicycle rack, advertising signboard, police and ambulance siren, and portable ladder. The aerodynamic impact on fuel consumption was not well studied, fully understood and quantified. Therefore, the primary objectives of this study were to experimentally measure the aerodynamic drag generated by the use of various vehicle add-ons under a range of vehicle operating speeds and cross winds conditions. The study was conducted using a reduced scale (25%) detailed model of a production large family size passenger car manufactured in Australia. The aerodynamic drag coefficient was related to fuel consumption and a detailed analysis of fuel consumption was conducted.

**Keywords:** Vehicle Aerodynamics, Wind Tunnel, Drag Coefficient, Vehicle Add-ons.

### 1. INTRODUCTION

Since the inception of the modern motor vehicle in early 1900's, vehicle manufacturers have shown little interest to streamline vehicle body shape for better aerodynamic efficiency as their priority was to make stylish cars. The oil crisis due to Middle East oil embargo in 1970s compelled vehicle manufacturers first brought sound aerodynamic design to the forefront for practical and scientific uses rather than for aesthetic purposes as in previous decades. A study by Snyder [8] indicated that in the US, if it was possible to reduce fuel consumption by as little as 1% (which typically equates to merely 0.1L/100km for a standard car) then US\$30 million could be saved, which given today's car numbers could only have dramatically increased. Additionally, the economic benefit of fuel consumption reduction is also an equally important environmental upside. The world's oil resources are not infinite. As of 2009, the world burnt over 1.3 trillion litres of petrol and diesel each year for powering hundred of millions cars and trucks. If this is coupled with un-sustainable depletion and the high levels of pollution (namely  $CO_2$ ) generated by burning petrol it becomes overwhelmingly apparent as to why reducing fuel consumption, if only by a small percentage, is so important to the world we live.

The primary objective of this study is to investigate the aerodynamic effects of vehicles add-ons and their impact on fuel consumption. Therefore, the primary focus will be on vehicle aerodynamic drag that is

generated by various add-ons such as antenna, roof-rack, taxi sign, ladder and spoiler. A motor vehicle travelling at a constant velocity on a level road, the power required to overcome the aerodynamic drag (approximately 80%) and tyre rolling resistance (around 20%). However, with an increase of speeds, the required power increases significantly to overcome aerodynamic resistance (drag) while power required for rolling resistance remain almost constant.

$$Power_{Required} = \frac{D \times S}{t} = D \times \frac{S}{t} = D \times V = (C_D \frac{1}{2} \rho V^2 \times A) \times V = C_D \frac{1}{2} \rho A V^3$$

The aerodynamic effects on current designs of vehicle add-ons spoilers, roof racks, taxi signs and ladders were not well studied and documented. Although the primary focuses of vehicle manufacturers and researchers have been concentrated on fuel saving devices of the commercial vehicles till to date [2, 3-7]. As the number of passenger cars have been increased significantly worldwide, it is utmost important to study the effects of passenger car's various add-ons on fuel cost as well as environmental impact.

### 2. EXPERIMENTAL PROCEDURE

#### 2.1 Description of Vehicle Add-Ons

In order to keep the airflow around the test vehicle as practical as possible, a 25% scale model of a family size passenger production vehicle was used. The model is a true replica of a General Motors Holden VT Commodore family size passenger vehicle (see Figure 1). Various

vehicle add-ons such as antenna, taxi sign, roof-racks, roof-racks with ladder attached were designed, manufactured and attached with the base car. These add-ons were 25% scale of their full size to match the scale model. Figures 1-5 show the base vehicle with various add-ons.



Fig 1. 25% Scale Model of GMH Commodore Vehicle (test vehicle) in the test section of RMIT Industrial Wind Tunnel



Fig 2. A taxi sign on the roof top of the test vehicle



Fig 3. Roof-racks on the roof top of the test vehicle



Fig 4. A ladder attached to the Roof-racks of the test vehicle



Fig 5. An antenna attached to the rear of the test vehicle

## 2.2 Experimental Set Up

In order to measure the aerodynamic properties of the test vehicle and vehicle add-ons experimentally, the RMIT Industrial Wind Tunnel was used. The tunnel is a closed return circuit with a maximum speed of approximately 150 km/h. The test vehicle was mounted on a six component force sensor type (type JR-3) in the test section (see Figure 1). All three forces (drag, lift and side force) and their corresponding moments were measured. The vehicle was tested alone first and then tested with each set of add-ons. A plan view of RMIT Industrial Wind Tunnel is shown in Figure 6. More details about the tunnel can be found in Alam et al. [1]. Tests were conducted at a range of wind speeds (60 km/h to 120 km/h with an increment of 10 km/h) under three yaw angles ( $0^\circ$ ,  $10^\circ$  and  $20^\circ$  yaw angles) to simulate the crosswind effects. Yaw angle can be defined as the angle between the vehicle centreline and the mean direction of airflow experienced by the vehicle.

## 3. RESULTS AND DISCUSSION

The percentage of aerodynamic drag increases due to antenna, taxi sign, roof rack and roof rack with a ladder over the base vehicle drag as shown in Tables 1-3 for three yaw angles (eg,  $0^\circ$ ,  $10^\circ$  and  $20^\circ$ ) respectively. As expected, the antenna has minimum aerodynamic drag increase (an average of 3% at  $0^\circ$  yaw angle, 4% at  $10^\circ$  and  $20^\circ$  yaw angles). The yaw angles have virtually no effect

on the antenna due to its circular shape. The taxi sign has increased aerodynamic drag an average of 11% at 0° and 10° yaw angles and 9% at 20° yaw angle (see Tables 1-3). A 2% reduction of aerodynamic drag at 20° yaw angle was noted compared to other two yaw angles due to the oblique angle of taxi sign to the wind direction thereby lowered the projected frontal area of the taxi sign. Similar effect was also noted for the roof rack. However, the roof rack with a ladder had significant impact on aerodynamic drag. As shown in Tables 1-3, an average 12%, 14% and 17% aerodynamic drag increase over the base vehicle were noted at 0°, 10° and 20° yaw angles respectively. With an increase of yaw angles, the roof rack with a ladder generated more drag as its projected frontal area increased. Additionally, the airflow around

the roof rack with a ladder became more complex and chaotic with yaw angle increase.

For a passenger car with an annual travelling distance of 25,000 km with an average speed of 60 km/h, estimated fuel consumption, fuel cost and the amount of  $CO_2$  due to vehicle add-ons (antenna, taxi sign, roof rack and roof rack with a ladder) are shown in Tables 4-6. The tables clearly indicates that with an increase of yaw angles, the aerodynamic drag, fuel consumption, cost and greenhouse gas ( $CO_2$ ) emission increases. The roof rack with a ladder and the bare roof rack have more impact on aerodynamic drag, fuel consumption and environment than the antenna and taxi sign.

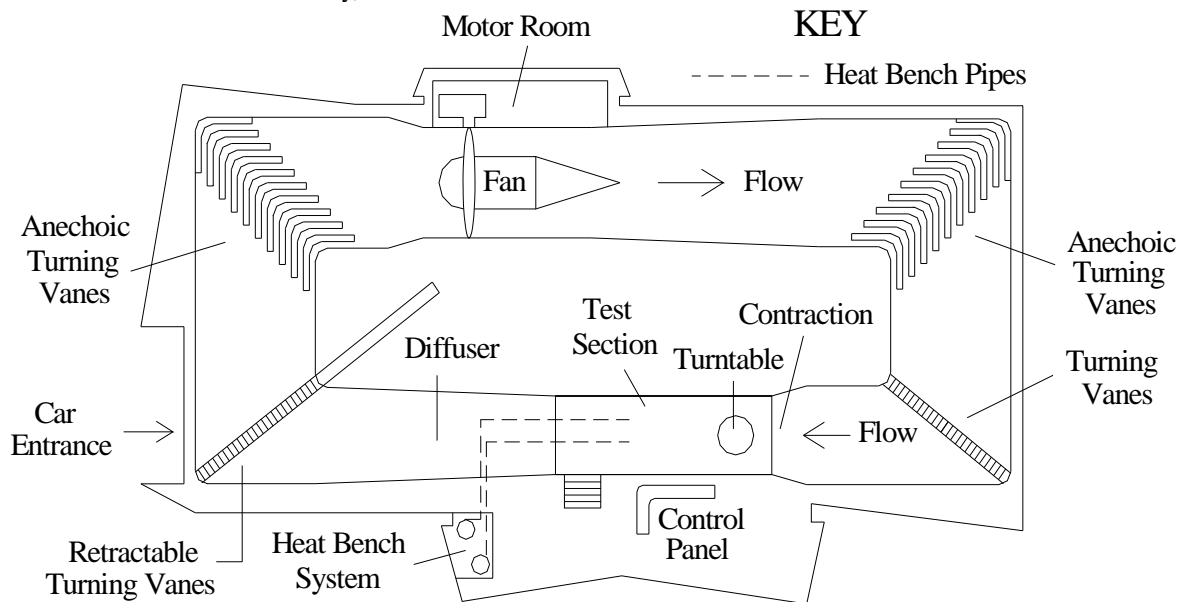


Table 1: Drag increase over base vehicle in percentage for 0° yaw angle

Speed	Antenna	Taxi sign	Roof rack	Roof rack w/ladder
km/h	%	%	%	%
60	5.57	11.49	5.48	13.14
70	3.61	9.28	7.30	11.30
80	2.73	10.64	7.88	10.71
90	2.46	10.59	7.82	13.60
100	3.99	11.22	6.52	12.17
110	2.31	13.77	5.49	11.17
120	3.82	11.89	6.42	12.59
Average	3	11	7	12

Table 2: Drag increase over base vehicle in percentage for 10° yaw angle

Speed	Antenna	Taxi sign	Roof rack	Roof rack w/ladder
km/h	%	%	%	%
60	2.08	10.34	8.40	13.06
70	3.62	7.91	6.70	13.87
80	4.89	9.44	5.95	13.71
90	4.24	8.57	6.04	10.18
100	3.01	13.27	10.41	9.47
110	5.50	13.04	11.25	16.62
120	5.42	12.97	8.09	17.83
Average	4	11	8	14

Table 3: Drag increase over base vehicle in percentage for 20° yaw angle

Speed	Antenna	Taxi sign	Roof rack	Roof rack w/ladder
km/h	%	%	%	%
60	-1.63	12.73	3.58	9.64
70	-3.77	11.36	5.42	15.44
80	5.77	6.08	3.69	21.95
90	4.36	6.27	7.17	17.62
100	7.19	7.53	4.72	18.07
110	7.85	8.17	5.37	17.66
120	6.61	7.95	6.67	17.90
Average	4	9	5	17

Table 4: Fuel cost and CO<sub>2</sub> emission at 0° yaw angle

Average mileage 25000 km/year for 60 km/h average speed at 0 deg yaw angle					
	Base	Antenna	Taxi	Roof rack	Roof rack w/ladder
drag (N)	102	105	113	109	114
Fuel (L)	241	249	268	258	270
Cost @\$1.2/L (\$)	290	298	322	310	325
CO <sub>2</sub> (kg)	596	614	662	638	668

Table 5: Fuel cost and CO<sub>2</sub> emission at 10° yaw angle

Average mileage 25000 km/year for 60 km/h average speed at 10 deg yaw angle					
	Base	Antenna	Taxi	Roof rack	Roof rack w/ladder
drag (N)	119	124	132	129	136
Fuel (L)	282	293	313	304	321
Cost @\$1.2/L (\$)	338	352	375	365	385
CO <sub>2</sub> (kg)	696	724	772	752	793

Table 6: Fuel cost and CO<sub>2</sub> emission at 20° yaw angle

Average milage 25000 km/year for 60 km/h average speed at 20 deg yaw angle					
	Base	Antenna	Taxi	Roof rack	Roof rack w/ladder
drag (N)	136	141	148	143	159
Fuel (L)	322	335	351	338	377
Cost @\$1.2/L (\$)	386	402	421	406	452
CO <sub>2</sub> (kg)	795	827	867	835	930

#### 4. CONCLUSIONS

The following concluding remarks have been made based on the experimental study presented here:

- The vehicle add-ons have notable impact on aerodynamic drag as they can generate 5 to 20% more aerodynamic drag depending on yaw angles.
- The antenna has minimum impact and the roof rack with a ladder has highest impact on aerodynamic drag. The roof rack with a ladder generates higher drag compared to antenna and taxi sign.
- The average fuel consumption considerably increases due to vehicle add-ons, especially due to rook rack and roof rack with ladders.
- The removal of vehicle add-ons can not only save fuel consumption but also reduce significant amount of greenhouse gas emission.

#### 5. ACKNOWLEDGMENTS

The authors are highly grateful to Mr Darren Scari and Mr Shameera De Livera, final year B.Eng students, School of Aerospace, Mechanical and Manufacturing Engineering, RMIT University, Melbourne, Australia for conducting wind tunnel testing and data collection.

#### 6. REFERENCES

1. Alam, F., Zimmer, G. and Watkins, S. 2003, Mean and time-varying flow measurements on the surface of a family of idealized road vehicles, *Journal of Experimental Thermal and Fluid Sciences*, 27, No. 5, pp 639-654.
2. Alam, F. and Watkins, S. 2004, Aerodynamics of Trucks and Drag Reducing Devices, *Journal of Mechanical Engineering, Khulna University of Engineering and Technology, Khulna, Bangladesh.*
3. Hucho, W. H., 1998, *Aerodynamics of Road Vehicles*, 4th edition, Society of Automotive Engineers (SAE), ISBN 0-7680-0029-7, Warrendale, USA
4. Cooper, K R. 2006, Full-Scale Wind Tunnel Tests of Production and Prototype, Second-Generation Aerodynamic Drag-Reducing Devices for

Tractor-Trailers, SAE Paper No. 2006-01-3456, USA

5. Landman, D., Wood, R. M, Seay, W. S. 2009, Understanding Practical Heavy Truck Drag Reduction Limits, SAE Paper No. 2009-01-2890, USA.
6. Schoon, R. E. 2007, On-road Evaluation of Devices to Reduce Heavy Truck Aerodynamic Drag, SAE Paper 2007-01-4294, USA
7. Watkins, S., Saunders, J. W. and Hoffmann, P. H. 1987, "Wind Tunnel Modelling of Commercial Vehicle Drag Reducing Devices: Three Case Studies", SAE Paper No. 870717, Detroit, USA
8. Snyder R. H. 1977, Tire Rolling Losses and Fuel Economy, SAE Special Publication, P-74, Detroit, USA

#### 7. NOMENCLATURE

Symbol	Meaning	Unit
D	Drag Force	(N)
L	Lift Force	(N)
S	Side Force	(N)
C <sub>D</sub>	Drag Coefficient	-
C <sub>L</sub>	Lift Coefficient	-
C <sub>S</sub>	Lateral-Force Coefficient	-
Re	Reynolds Number	-
V	Velocity of Air	m/s
$\rho$	Density of Air	kg/m <sup>3</sup>
A	Projected Area	m <sup>2</sup>
S	Distance Travelled by vehicle	m

#### 8. MAILING ADDRESS

Dr Firoz Alam  
 School of Aerospace, Mechanical and Manufacturing Engineering, RMIT University  
 Plenty Road, Bundoora, Melbourne, VIC 3083,  
 AUSTRALIA  
 Phone: +61 3 99256103  
 Fax: +61 3 99256108  
 E-mail: firoz.alam@rmit.edu.au



## A MODIFIED EULERIAN-LAGRANGIAN APPROACH FOR SOLVING MULTI-PHASE FLOW APPLIED TO A COMPACT DOWN-HOLE SUB-SEA GAS-LIQUID SEPARATOR

Shakil Ahmed<sup>1</sup>, Gerardo Sanchez Soto<sup>1</sup>, Jamal Naser<sup>2</sup> and Edson Nakagawa<sup>1</sup>

<sup>1</sup>CSIRO Earth Science and Resource Engineering, Technology Park Kensington, Perth

<sup>2</sup>School of Engineering and Industrial Sciences, Swinburne University of Technology, Hawthorn, Melbourne

### ABSTRACT

This paper presents a modified Eulerian-Lagrangian approach for solving multi-phase flow applied to a laboratory scale gas-liquid separator designed for high gas content. The separator consists of two concentric pipes with swirl tube in the annular space between the pipes. The gas-liquid mixture comes from the tangential side inlet and the system works with a combination of gravity and centrifugal forces to achieve a high-efficient gas-liquid separation. In the modified Eulerian-Lagrangian method, gas flow is coupled with the spray and wall film models. Spray model involves multi-phase flow phenomena and requires the numerical solution of conservation equations for the gas and the liquid phase simultaneously. With respect to the liquids phase, discrete droplet method (DDM) is used. The droplet-gas momentum exchange, droplet coalesces and breaks-up, droplet-wall interaction with wall-film generation and entrainment of the water droplet back into the gas stream are taken into account in this investigation. To be consistent with the experiments the same air water mixture is used for the present work. The standard k- $\epsilon$  turbulence model is used for turbulence closure. The predicted results from the modified Eulerian-Lagrangian multi-phase model explain the complex flow behavior inside the separator and are in good agreement when compared with experiments.

**Keywords:** Modified Eulerian-Lagrangian Approach, Compact Gas-liquid Separator, Multi-Phase Flow.

### 1. INTRODUCTION

The gas-liquid separation technology currently used by the petroleum industry is mostly based on the gravity driven vessel type separator which is large, heavy and expensive to purchase and operate especially in the subsea. This brought a lot of attention to academic researchers as well as field operators [1-4] to develop a compact gas-liquid separator suitable for off-shore application and potentially in sub-sea in order to enhance the recovery of the gas fields. A separator has to be simple, reliable with low maintenance requirements, minimal footprint, low pressure loss and easy to install. Considering all of these characteristics the swirl tube technology could be best suited to design a gas-liquid separator. Gas-liquid cylindrical cyclone separator (GLCC) and a gas-liquid separator being developed by CSIRO (CS-T) are excellent examples of designs for this kind of applications. GLCC has been implemented in a number of applications as reported recently by Kouba et al. [5]. Experimental data of GLCC operational envelope and a mechanistic model for GLCC separators have been reported by Arpandi et al. [6]. On the other hand laboratory scale experimental investigation has just been completed by Wong et al. [7] for the CSIRO's gas-liquid CS-T. However, more investigation is required to

develop a mechanistic model for the gas-liquid CS-T.

Simulation of the flow behavior in GLCC separator applying a computational fluid dynamics (CFD) approach was presented for single-phase and two-phase flow by Erdal [8] and Erdal et al. [9]. Motta et al. [10] presented a simplified CFD model for rotational two-phase flow in a GLCC separator. The model assumes an axisymmetric flow and three velocity components, applicable to steady-state and isothermal conditions. Ahmed et al. [11] presented the numerical modeling of gas-liquid CS-T separator where they used Eulerian-Eulerian approach for modeling the complex behavior of the multi-phase flow. The predicted pressure drop, flow field and volume fraction were reasonably matched when compared with experiments. The presence of liquid droplets and a possible liquid film poses new challenges to the separation phenomena regarding the two-phase flow pattern and droplets break-up/coalescence which cannot be modeled using Eulerian-Eulerian approach of multi-phase flow. Ahmed et al. [11] concluded in their paper to use a new modified Eulerian-Lagrangian approach with specific sub model for wall film and droplets break-up/coalescence and that is the motivation of this present work.

The current investigation presents a modified

Eulerian-Lagrangian approach for solving multi-phase flow applied to a laboratory scale gas-liquid separator designed for high gas content. The separator consists of two concentric pipes with helical swirl tube in the annular space between the pipes. The gas-liquid mixture enters tangentially from a side inlet into the separator and passes through the annular swirl tube. While passing through the swirl tube the liquid separates from the gas due to the centrifugal action, strikes at the inner wall of the outer pipe, and creates a liquid film at the wall, which ultimately descends due to gravity. On the other hand the lighter gas rises through the inner tube and the separation occurs with a combination of centrifugal force and gravity. The unique feature of the gas-liquid CS-T separator is its simple design without any moving parts. The performance of the gas-liquid CS-T separator is visually established by observing the liquid carry over (LCO) regime in which liquid is carried out in the gas stream. The liquid and gas flow rates at which the LCO is observed defines the upper operational range of the separator. To be consistent with the experiments, the same air-water mixture is used for the current numerical investigation.

## 2. NUMERICAL MODELING

Three-dimensional, transient and incompressible multiphase flow fields are obtained by solving the continuity and Navier-Stokes equations. The modified Eulerian-Lagrangian multiphase model is used where gas flow is coupled with the spray and wall film models available in commercial software FIRE [12]. Spray model involves multi-phase flow phenomena and requires the numerical solution of conservation equations for the gas and the liquid phase simultaneously. With respect to the liquid phase, discrete droplet method (DDM) is used. DDM operates by solving ordinary differential equations for the trajectory, momentum, heat and mass transfer of single droplet, each being a member of a group of identical non-interacting droplets termed a 'parcel'. Thus one member of the group represents the behavior of the complete parcel. Droplet parcels are introduced in the flow domain, along with the gas flow, with initial conditions of position, size, velocity, temperature and number of particles in the parcel. The droplet-gas momentum exchange, turbulent dispersion, secondary break-up, droplet collision and droplet-wall interaction are covered with a comprehensive set of models which allow the usage of the module very suitable for gas-liquid separation. The droplets are tracked in a Lagrangian way through the computational grid used for solving the gas phase partial differential equations. Full two-way coupling (interaction) between the gas and liquid phases is taken into account.

In a gas-liquid separator, a significant amount of the liquid can be deposited on the walls as a thin liquid film due to wall collisions of liquid. Some amount of this liquid is sheared off and entrained back into the gas flow. The coupling between the liquid film phase and the air flow is accomplished in FIRE by setting up modified and refined boundary conditions at the interface. At high air velocity, the shear force at the film surface tears droplets entrained back into the air flow. The wall film

entrainment model is simulated within the wall film module. The governing equations used for DDM spray and wall film modeling are described in the following section.

### 2.1 DDM Spray Model

The governing equations for the trajectory and velocity of a particle parcel are as follows:

$$m_p \frac{du_{ip}}{dt} = F_{idr} + F_{ig} \quad (1)$$

where  $F_{idr}$  is the drag force, given by:

$$F_{idr} = D_p \cdot u_{irel} \quad (2)$$

$D_p$  is the drag function, defined as:

$$D_p = \frac{1}{2} \rho_g A_p C_D |u_{rel}| \quad (3)$$

$C_D$  is the drag coefficient which generally is a function of the particle Reynolds number  $Re_p$  and  $A_p$  is the cross-sectional area of the particle.  $F_{ig}$  is a force including the effects of gravity and buoyancy and is given by:

$$F_{ig} = V_p \cdot (\rho_p - \rho_g) g_i \quad (4)$$

Substituting the above forces in Eq. (1) the equation for the particle acceleration can be obtained and the integration of that equation will give the particle velocity.

### 2.2 Secondary Chu Break-up Model

The theoretical correlation is constructed in order to predict droplet sizes on the basis of an exponential function. The model implemented in this simulation represents a modified version of Chu's [13] original model in that it includes a Taylor-series expansion of the exponential term to first order, and subsequently an explicit discretization in time in which particle diameter correlation is written as:

$$\frac{dD}{dt} = -C_o \cdot C_1 We^{C_2} (u_{rel} \varepsilon^{0.5}) T^{*(C_1-1)} \quad (5)$$

where  $C_o$  is the function of the density ratio  $\varepsilon$ :

$$C_o = 0.1708 - 0.149 \varepsilon^{0.5} \quad \varepsilon = \rho_g / \rho_p \quad (6)$$

and  $T^*$  is a non-dimensional accumulated time within the particle integration time step when using sub-cycling method for solving Eq. (5).

$$T^* = \frac{\varepsilon^{0.5} u_{rel} t}{D_o} \quad (7)$$

The stable particle radius should exist if the critical Weber number  $We_{crit}$  is below 12

$$r_{stable} = \frac{2 \cdot We_{crit} \sigma}{\rho_g u_{rel}^2} \quad (8)$$

The values for the constants  $C_1$  and  $C_2$  used in this simulation are 0.772 and 0.246 respectively.

### 2.3 Schmidt-O'Rourke Coalescence Model

The Schmidt-O'Rourke coalescence model [14] performs the collision calculation for pairs of particles only if they are in the same computational cell. For description the particles with larger radius are called *collectors* and those with smaller radius are called *droplets*. The collision frequency  $\nu$  between a particle of parcel 1 and all particles associated with another parcel,

within the computational volume, is used to calculate the probability  $P$  that a particle of parcel 1 will collide with a particle of the other parcel (pairs). The collision frequency  $\nu$  of a *collector* with all (surrounding) *droplets* is calculated according to:

$$\nu = \frac{N_2}{V_{cell}} \frac{\pi}{4} (d_1 + d_2)^2 |u_1 - u_2| \quad (9)$$

the subscripts 1 and 2 refer to the properties of the *collectors* and *droplets* respectively.  $N_2$  is the number of particles in parcel 2 and  $V_{cell}$  is the volume of the computational cell in which both parcels are located. The probability  $P$  that a *collector* undergoes  $n$  collisions with *droplets* follows a Poisson distribution:

$$P_n = e^{-\bar{n}} \frac{\bar{n}^n}{n!} \quad (10)$$

with the mean value (number of expected collisions)  $\bar{n} = \nu \Delta t$ , where  $\Delta t$  is the computational time step. Thus the probability of no collisions is  $P_0 = e^{-\bar{n}}$ . A random number  $R_{n1}$  in the range  $0 \leq R_{n1} \leq 1$  is then used to decide whether a collision takes place or not. If  $R_{n1} < P_0$  then no collisions are calculated for the particular pair of particles in associated parcels. If  $R_{n1} \geq P_0$  then all the *collectors* will undergo one or more collisions with the *droplets*, where each collision is of the same type.

In the case of collisions a second random number  $R_{n2}$  also in the range  $0 \leq R_{n2} \leq 1$  is used to determine which type of collision takes place. For this, a collision impact parameter is defined as:

$$b = (d_1 + d_2) \sqrt{R_{n2}} \quad (11)$$

if  $b < b_{cr}$ , where  $b_{cr}$  is the critical impact parameter below which coalescence may occur, then the result of every collision is coalescence. If  $b \geq b_{cr}$ , then each collision is a grazing collision, i.e. the particles maintain their sizes and temperature but undergo velocity changes. The value of  $b_{cr}$  depends on the particle diameter, the relative velocity between the particles and the liquid surface tension coefficient:

$$b_{cr}^2 = (d_1 - d_2)^2 \min[1.0, 2.4(f(\gamma)/We_d)] \quad (12)$$

$$f(\gamma) = \gamma^3 - 2.4\gamma^2 + 2.7\gamma, \quad \gamma = \frac{d_2}{d_1} \quad d_2 > d_1 \quad (13)$$

$$We_d = \frac{\rho_p |u_{d1} - u_{d2}|^2}{2\sigma} d_1 \quad (14)$$

the random number  $R_{n2}$  is used to determine the number of coalescences  $n$  for each *collector*:

$$\sum_{k=0}^{n-1} P_k \leq R_{n2} < \sum_{k=0}^n P_k \quad (15)$$

for each *collector* particle,  $n$  *droplets* are removed from their associated parcel and the properties of the *collector* particles, diameter, velocity and temperature are appropriately modified due to conservation of mass, momentum and energy. If there are an insufficient number of *droplets* to have  $n$  coalescences with the *collector*, then  $n$  is recomputed so that all  $N_2$  *droplets* coalesce, and the parcel associated with the *droplets* is removed from the calculation.

In the case of grazing collision, only one collision is calculated for each particle. Grazing collisions are

calculated between  $N$  pairs of particles, where  $N$  is the minimum of  $N_1$  and  $N_2$ . The  $N$  *collectors* and *droplets* are then return to their parcels in such a way that mass, momentum and energy are conserved. The expression giving the velocity of each particle after a collision is:

$$u_{d1}^* = \frac{u_{d1} d_1^3 + u_{d2} d_2^3 + d_2^3 (u_{d1} - u_{d2}) R_{n3}}{d_1^3 + d_2^3} \quad (16)$$

where  $R_{n3}$  is a further random number defined as:

$$R_{n3} = \frac{b - b_{cr}}{(d_1^3 + d_2^3) - b_{cr}} \quad (17)$$

## 2.4 Particle Wall Interaction/Splashing Model

The splashing model used for particle wall interaction is heavily based on systematic empirical investigations carried out with a wide variety of initial conditions. The predominant influence of particle momentum and properties such as viscosity and surface tension is taken into consideration by introducing the dimensionless groups Reynolds number and Ohnesorge number for the particular particle:

$$Re_D = \frac{\rho d_0 u_{\perp 0}}{\mu} \quad (18)$$

$$Oh = \frac{\mu}{\sqrt{\rho \sigma d_0}} \quad (19)$$

the Reynolds number compares momentum to viscous forces, whereas the Ohnesorge number relates viscous forces to surface tension. For the Reynolds number, only the wall normal component  $u_{\perp 0}$  of the initial particle velocity  $u_0$  is used, which accounts for impact angle effects. Additionally, a  $K$ -value is defined as:

$$K = Oh \cdot Re_D^{1.25} \quad (20)$$

this  $K$ -value is used as the key parameter for the splashing model. The criterion for inception of splashing is given at  $K=57.7$ . Consequently, for  $K < 57.7$  the particles are deposited completely at the wall without bouncing or breakup. The kinetic energy of the particle is dissipated.

## 2.5 Wall Film Model

The basic governing equation for wall film flow is the film thickness equation. It is a slightly modified formulation of the continuity equation, which is transformed to conservation of film thickness. For simplicity, just the Cartesian formulation is presented here, but the wall film model is capable of dealing with distorted cells as well.

$$\frac{\partial \delta}{\partial t} + \frac{\partial \delta u_1}{\partial x_1} + \frac{\partial \delta u_2}{\partial x_2} = \frac{1}{\rho A} (S_{mD} - S_{mV}) \quad (21)$$

Instead of employing the momentum equations for solving the velocity components  $u_1$  and  $u_2$ , wall film model uses the analytical film velocity profiles developed by AVL and implemented in FIRE [12]. If the velocity components as well as the source term  $S_m$  are

known then the convection terms  $\frac{\partial \delta u_1}{\partial x_1}$  and  $\frac{\partial \delta u_2}{\partial x_2}$  can be

evaluated and Eq. (21) can immediately be solved explicitly.

## 2.6 Wall Film Entrainment Model

The entrainment model used in this simulation is the Schadel-Hanratty model [15] where the critical Weber number, specifying the onset of entrainment is defined as:

$$We_{cr,SH} = \frac{\rho_g u_{rel}^2 \delta}{\sigma} \quad (22)$$

and the limit is set to  $We_{cr}=17.0$ . The relative velocity  $u_{rel}$  is:

$$u_{rel} = |\bar{u}_{gas} - \bar{u}_f| \quad (23)$$

the model calculates the entrainment rate as the amount of mass sheared off the film per unit area and unit time according to the Eq. (24).

$$R_{A,SH} = X_{RA} u_{\tau} \sqrt{\rho_g \rho_f} \cdot 10^{-3} \quad [\text{kg/m}^2\text{s}] \quad (24)$$

where:

$$X_{RA} = 0.4 \ln(150 I_R We_{SH} + 1) + 1.4 \sqrt{I_R We_{SH}} \quad (25)$$

with the roll wave intermittence factor as a function of excess film flow rate  $\Gamma_E$ :

$$I_R = 0.15 + 0.75 \Gamma_E \quad I_R \leq 0.5 \quad (26)$$

In Eq. (25) an alternative definition of Weber number is used by replacing relative velocity with friction velocity  $u_{\tau}$ :

$$We_{SH} = \frac{\rho_g u_{\tau}^2 \delta}{\sigma} \quad (27)$$

the mass ripped off the film per unit area per unit time acts as a mass sink to the film and consequently as a mass source to the spray DDM. To introduce these new particles to the spray, particle diameter is calculated by Kataoka droplet correlation model [16] where a volume mean diameter is defined as:

$$D_{vm,K} = 0.028 \frac{\sigma}{\rho_g \bar{u}_g^2} Re_{f,IM}^{-1/3} Re_g^{2/3} \left( \frac{\rho_g}{\rho_f} \right)^{-1/3} \left( \frac{\mu_g}{\mu_f} \right)^{2/3} \quad (28)$$

with the film Reynolds number

$$Re_{f,IM} = \frac{4 \bar{u}_f \delta \rho_f}{\mu_f} \quad (29)$$

## 3. BOUNDARY CONDITIONS AND MESH

The inlet boundary condition is set by introducing flow rates for both air and water at the tangential side inlet. The top outlet of the inner pipe, from where the air comes out after separation, is open to atmosphere in the experiments. So a pressure boundary condition is applied in the numerical simulation and the atmospheric pressure is set to  $10^5$  Pa. Experimental investigation reveals that gas (1-5%) in the form of bubbles is trapped and discharged with the downward flowing liquid. This phenomenon is known as gas carry under (GCU). GCU boundary condition is imposed at the bottom outlet of the outer pipe by assuming that 1% of the total gas is trapped as bubbles in the liquid flowing downward along the wall of the outer pipe.

The volume mesh consists of hexahedral elements. The solutions are grid independent when the total number of elements is 651,975. The interval step used for this simulation is 0.0025 s. The simulation was run until the

solution had reached the steady-state. The convergence criterion for the momentum equations and turbulent parameters are  $10^{-4}$  and for the continuity equation is  $10^{-3}$ .

## 4. RESULTS AND DISCUSSIONS

The modified Eulerian-Lagrangian approach of multi-phase flow with specific sub-models for wall film and droplets break-up/coalescence is applied to gas-liquid CS-T separator. Two points, one on the experimental LCO curve (point 1) and one above (point 2) are selected for the simulations (Fig 1). For the point 1, an air flow rate of 383 L/min and water flow rate of 25 L/min are used. The air flow rate is then increased by 20% for point 2. The modeling is carried out in transient or time dependent fashion and hence the results presented represent a snapshot in time.

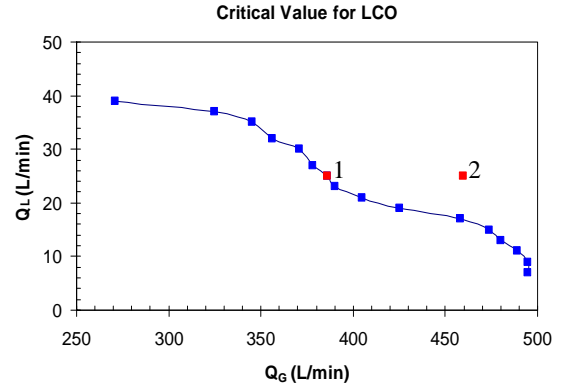


Fig 1. Two points for which simulations are performed

Velocity streamlines showing the flow path of air and velocity in the near wall regions for the point 1 are shown in Fig 2(a) and 2(b).

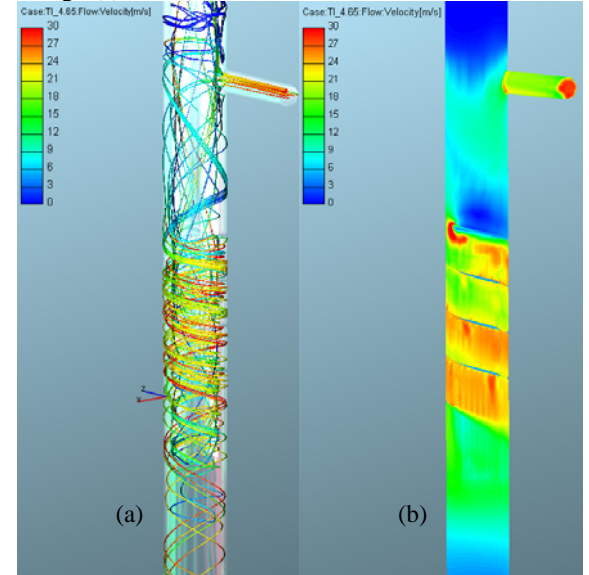


Fig 2. (a) Velocity streamlines showing the flow path of air and (b) velocity in the near wall regions for the point 1

The air-water mixture enters the annular space of the separator from the tangential inlet and strikes at the outer pipe. It then accelerates and moves downward towards

the swirl tube and reaches the maximum velocity (30 m/s) at the entrance of the swirl tube. The velocity then decreases to 25 m/s (Fig 2(b)) and almost constant inside the swirl tube. While passing through the swirl tube, the water gets separated from the air due to the centrifugal action and creates a liquid wall film at the outer pipe, which ultimately descends due to gravity. The lighter air rises, travels through the inner pipe and comes out from the air outlet.

Figure 3(a-b) shows the formation of the wall film by the spray droplets impinging on the outer pipe wall for point 1.

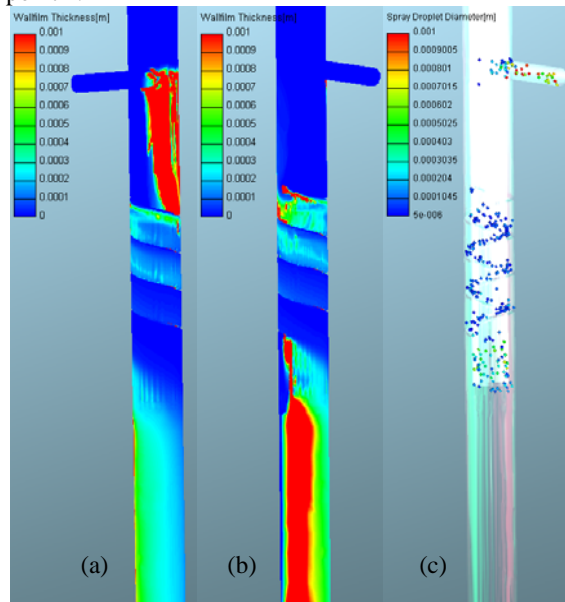


Fig 3. (a-b) Formation of the wall film by the spray droplets impinging at the outer pipe wall and (c) entrainment of the water droplets back into the air stream inside the swirl tube and at the entrance of the inner pipe

As the air-water mixture strikes the outer pipe wall in the annular space, most of the water droplets convert into wall film as shown in Fig 3(a). This wall film then moves downward towards the swirl tube. Inside the swirl tube the wall film thickness reduces and the entrainment of the water droplets back into the air stream occurs (Fig 3(c)). This phenomenon is more important at the entrance of the inner pipe where most of the water droplets along the periphery of the inner pipe coalesce, get bigger, and ultimately go down due to gravity. Only a couple of them are carried into the inner pipe due to the higher drag force dominating over the gravity and occasionally come out through the air outlet. This is the onset of LCO state which is captured in the simulation and consistent with the experiments. The size of the droplets is exaggerated in Fig 3(c) for visual comfort. The actual size of the droplet can be obtained from the color key. Each droplet represents a cluster of droplets or one member of the group or parcel. The wall film at the exit of the swirl tube moves downward (Fig 3(b)) along the outer pipe of the separator and thus the separation of the air-water mixture is completed.

The LCO curve shown in Fig 1 defines the upper operational range of the separator which indicates that for a point above this curve, a constant LCO occurs. To

gain more confidence in this new approach another point (point 2) is simulated above the LCO curve, where the air flow rate is increased by 20% (459 L/min), and the results are explained in the next section.

Figure 4(a-b) shows the velocity in the near wall regions and wall film generation for the point 2. As expected, like point 1, the maximum velocity occurs (Fig 4(a)) at the entrance of the swirl tube but the magnitude is higher than the point 1 (36 m/s) because of increased air flow rate. No significant change occurs in the wall film formation between the point 1 and 2 (Fig 3(a-b) and 4(b)) as the water flow rate is same for both cases but the difference is clear when the LCO are compared.

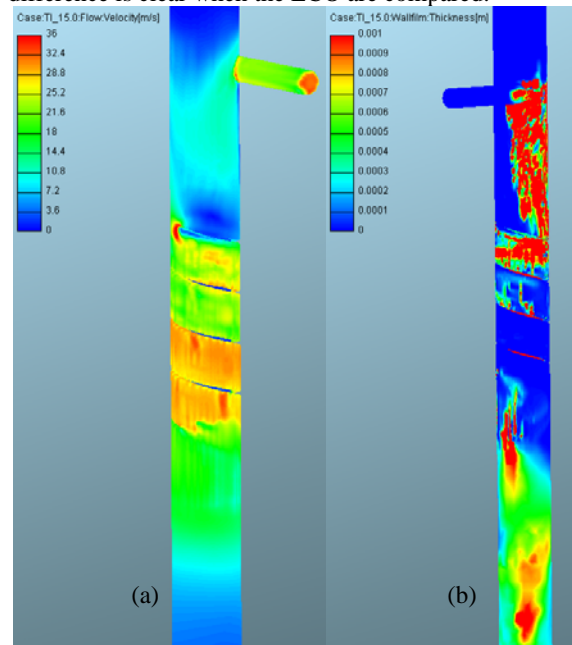


Fig 4. (a) Velocity in the near wall regions and (b) formation of the wall film for the point 2

Figure 5(a-b) compares the LCO in the inner pipe for the point 1 and 2. Point 1 represents the onset of LCO state where at the entrance of the inner pipe the water droplets are in unstable condition. At this region an increase in drag force over gravity carries a couple of droplets inside the inner pipe and ultimately through the air outlet. On the other hand point 2 is well above the LCO curve. An increase in air flow rate (20%) results in higher tangential velocity inside the swirl tube. Lots of water droplets are entrained back into the air stream inside the swirl tube due to the high shearing action between the wall film and the tangential air velocity. At the exit of the swirl tube air stream carries most of these water droplets in the inner pipe and a constant LCO occurs. This phenomenon is well captured in the simulation and consistent with the experiments.

## 5. SUMMARY AND CONCLUSIONS

This paper presents a modified Eulerian-Lagrangian approach for solving the complex multi-phase flow. The air flow was coupled with the spray droplets, wall film, break-up/coalescence and wall film entrainment model available in commercial software FIRE. The multi-phase model is applied to a gas-liquid CS-T separator to



understand the complex flow behavior inside it.

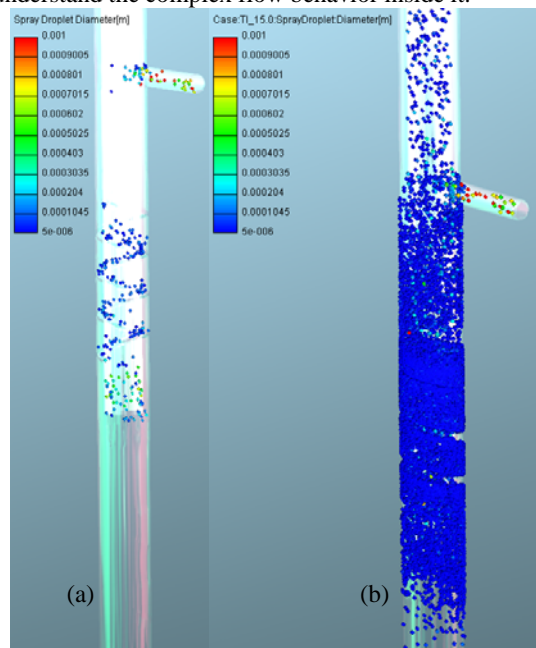


Fig 5. (a) Onset of LCO state for the point 1 shows unstable water droplets at the entrance of the inner pipe and (b) Increased air flow rate for the point 2 shows lots of water droplets in the inner pipe

The simulations are performed for two points: one on the experimental LCO curve (point 1) and the other well above the LCO curve (point 2). The onset of the LCO state is visually observed for the point 1. The air-water mixture is introduced into the separator from a tangentially side inlet and strikes the outer wall in the annular space where all the water droplets form the wall film. The wall film moves downward towards the swirl tube and passes through it. The thickness of the wall film reduces inside the swirl tube and due to the high tangential velocity, the shear force at the film surface tears droplets entrained back into the air flow. The entrainment phenomenon is more important at the entrance of the inner pipe, where all the water droplets are in unstable condition and a small increase in the drag force over the gravity results in LCO at the air outlet. The whole physics is well captured in this simulation and consistent with the experiment. The point 2 is well above the upper operating range of the LCO curve which indicates a constant LCO. The simulation of the point 2 shows (Fig 5(b)) a constant LCO and consistent with the experiment. This modified Eulerian-Lagrangian model can now be used to understand the flow phenomenon for complex multi-phase flow like gas-liquid CS-T separator

## 6. ACKNOWLEDGEMENTS

The authors gratefully acknowledge the financial and other support received for this research from the Western Australian Energy Research Alliance (WA: ERA) and Chevron Energy Technology Pty Ltd.

## 7. REFERENCES

1. Powers, M.L., 1993, "New perspective on oil and gas separation performance", SFE prod. & facilities, pp. 15: 77-83
2. Talavera, P.G., 1990, "Selecting gas/liquid separator", Hydrocarbon Process, pp. 10: 80-85
3. Choi, M.S., 1990, "Prediction of separator performance under changing field conditions", Annual Technical Conference and Exhibition, Sep. 23-26, New Orleans, LA, SPE 20703
4. Noui-Mehidi, M.N., Wu, J., Cueille, P.V., Sanchez-Soto, G., Rivero, M. and Nakagawa, E., 2007, "Effect of Salinity on the performance of Gas Liquid Cyclonic Separators", AIChE Journal, October, 53 (10), 2722-2725
5. Kouba, G., Wang, S., Gomez, L., Mohan, R., Shoham, O., 2006, "Review of the state-of-the-art gas/liquid cylindrical cyclone (GLCC) technology-field applications", SPE J. Dec., SPE 104256
6. Arpandi, I. A., Joshi, A.R., Shoham, O., Shirazi, S., and Kouba, G.E., 1996, "Hydrodynamics of two-phase flow in gas-liquid cylindrical cyclone separators", SPEJ, December, pp: 427-436
7. Wong, C.Y., Wu, J., Graham, L., Ahmed, S., Bowditch, P., Kilpatrick, T., and Sanchez-Soto, G., 2009, "Optimization of the CS-T gas-liquid separator- Final Report", Confidential, CSIRO Material Science and Engineering (C), Highett, Melbourne, Australia
8. Erdal, F. M., 1996, "CFD simulation of single-phase and two-phase flow in gas-liquid cylindrical cyclone separator," M.S. thesis, The University of Tulsa
9. Erdal, F. M., Shirazi, S. A., Shoham, O., and Kouba, G.E., 1996, "CFD simulation of single-phase and two-phase flow in gas-liquid cylindrical cyclone separator", 71<sup>st</sup> SPE Annual Meeting, Denver, CO, October 6-9, SPE paper: SPE 36645
10. Motta, B.R.F., Erdal, F.M., Shirazi, S.A., Shoham, O., and Rhyne, L.D., 1997, "Simulation of single-phase and two-phase flow in gas-liquid cylindrical cyclone separators", Proceedings of the ASME Summer Meeting, Vancouver, Canada, June 22-26, FEDSM97-3554
11. Ahmed, S., Noui-Mehidi, M.N., Naser, J., Sanchez-Soto, G., and Nakagawa, E., 2009, "Evaluation of numerical modeling for a compact down-hole sub-sea gas-liquid separator for high gas content", APPEA Journal, pp: 433-440
12. Fire, Version 8, 2006, CFD Solver V8.5-Multiphase flow, Spray and Wall film Modeling
13. Chu, Cho-Chone C., 1986, "One-dimensional transient fluid model for fuel-coolant interaction analysis", Thesis, University of Wisconsin-Madison
14. O'Rourke, P.J., 1989, "Statistical properties and numerical implementation of a model for droplet dispersion in turbulent gas", J. Comput. Physics, 83
15. Schadel, S. A. and Hanratty, T.J., 1989, "Interpretation of atomization rates of the liquid film in gas-liquid annular flow", Int. J. Multiphase Flow, 15 (6), pp. 893-900

## MIXING OF SUPERSONIC JETS WITH DIFFERENT MERGING ANGLES FOR CONSTANT INLET PRESSURE AND VELOCITY

Mohammad Ali, M. Quamrul Islam, TAGN Jubery and S. M. Nazrul Islam

Department of Mechanical Engineering, BUET, Dhaka, Bangladesh

### ABSTRACT

In present investigation mixing of two supersonic non parallel gaseous streams has been simulated numerically. The streams are of air and hydrogen, which come into contact after passing over a finite thickness base. The gases are considered to be fed from a high-pressure reservoir. Two-dimensional unsteady state Navier-Stokes equations, energy, mass diffusion and species continuity equations are numerically simulated to analyze two-dimensional shear layers in supersonic flow field. An explicit Harten-Yee Non-MUSCL Modified flux-type TVD (total variation diminishing) scheme has been used to solve the system of equations. An algebraic turbulence model was used to calculate the eddy viscosity coefficient. Keeping constant the inlet pressure and velocity of the streams, the merging angle is varied to observe the physics of the mixing flow fields, mixing of shear layers and mixing efficiency. The result shows that when merging angle increases interaction between two streams increases and high momentum exchange occurs and eventually high mixing occurs for the pressure ratios considered here.

**Keywords:** Supersonic Combustor, Mixing, Shear Layers, Merging Angle

### 1. INTRODUCTION

Turbulent mixing layers occur in flow fields of many engineering applications e.g., combustion chambers, pre-mixers for gas turbine combustors, chemical lasers, propulsion systems and flow reactors. Particularly, the mixing of reactants and their complete combustion in supersonic combustion ramjet (scramjet) engines has drawn special attention of present scientists. In supersonic combustion systems, the flow speeds are so high that the fuel and oxidizer have little time to mix. The shear layers are naturally unstable and usually lead to a large scale mixing. The higher the Mach number, the longer length it takes the shear layers to become unstable. This reduces mixing accomplished in a given length. Several configurations of combustor have been studied to seek the enhancement of mixing. Generally parallel, normal or oblique type mixing is used. Most of the researchers studied two parallel supersonic streams.

Guirguis et al. [1] performed two-dimensional time-dependent numerical simulation of the mixing of two supersonic parallel streams of air. They simulated a supersonic shear layer in a two dimensional channel, 20 cm long and 2.4 cm high. They used flux corrected transport algorithm and neglected all diffusion transport processes. They considered only inviscid or convective mixing. They compared the vorticity, density and pressure contour of confined and unconfined shear layer. Farouk et al. [2] performed numerical simulation of the mixing of two supersonic streams of air. They simulated 25cm x 3cm flow field. Brown et al. [3] experimentally investigated the effects of density ratio on plane turbulent

mixing between two streams of different gases. It was observed that, for all ratios of densities in the two streams, the mixing layer was dominated by large coherent structures. These structures made convection at nearly constant speed, and increased their sizes and spacing discontinuously by the process of amalgamation with neighboring ones. Thus these structures would grow in large scale and roll up in coherent manners that greatly increase the mixing surface. Finally it was concluded that large changes of the density ratio across the mixing layers have relatively small effect on the spreading angle, when one stream was supersonic. Papamoschuo et al. [4] observed that the spreading rate was dependent of Mach number but independent of transverse density gradients. This was in agreement with the experimental results of Debieve et al. [5] on different aspects of supersonic turbulent flows.

Gai et al. [9] experimentally studied the development of large-scale organized motions in compressible mixing layers. The mixing layer was formed behind the base of a parallel strut with a Mach 2 air stream and a co-flowing two dimensional slot jet of helium at a Mach number of 1.2. They observed that the thickness of the primary boundary layer had a strong influence on the growth and structure of the mixing layer. They showed that the injector lip could have significant effect on the subsequent flow development. Gerlinger et al. [10] found that increase in injector lip thickness resulted in increased shear layer thickness and also total pressure losses because of the stronger recompression shocks. They also found that increase in mixing layer thickness



did not have significant effect on the mixing efficiency. In another investigation Guirguis et al. [11] studied the effect of bluff center bodies on mixing enhancement in supersonic shear layers. They observed that the shear layer became unstable faster than with the streamlined body. As a result, a large amount of convective mixing occurred within the length of the domain. Azim et al. [12] investigated plane mixing layers from parallel and non-parallel merging of two streams. The authors reported that both types of mixing layers were found to decrease in growth with increasing velocity ratio, though they spread more at the high speed side.

The air stream is at the upper side of the base plate whereas the hydrogen stream is underneath the base plate as shown in Fig.1. After separating from the base, the streams form shear layers and mix with one another. The length and width of the calculation domain is chosen to be 0.208m and 0.024m, respectively. In this study the effect of merging angles on the physics of fluid dynamics and mixing efficiency is studied. The merging angles are varied from  $0 \sim 20^\circ$  with the increment of  $5^\circ$ . The calculations of flow field with different merging angles are denoted as case 1 (merging angle  $0^\circ$ ), case 2 (merging angle  $5^\circ$ ), case 3 (merging angle  $10^\circ$ ), case 4 (merging angle  $15^\circ$ ), and case 5 (merging angle  $20^\circ$ ). For all cases the pressure of both streams is considered as 1.0 atmosphere. The objectives of this investigation are (i) to increase the mixing efficiency of a supersonic combustor and (ii) to study the physics of fluid dynamics including shocks and turbulence. The results and discussion are presented in the following articles: (i) the physics of free shear layer (ii) mixing of hydrogen with air stream (iii) identification of the parameters that affect the free shear layer growth and mixing, and (iv) finding out the way of increasing the mixing efficiency.

## 2. GOVERNING EQUATIONS

The flow field is governed by the two-dimensional full Navier-Stokes equations with conservation equations of species. Body forces are neglected. For non-reacting flow, these equations can be expressed by

$$\frac{\partial U}{\partial t} + \frac{\partial F}{\partial x} + \frac{\partial G}{\partial y} = \frac{\partial F_v}{\partial x} + \frac{\partial G_v}{\partial y}$$

Where

$$U = \begin{pmatrix} \rho \\ \rho u \\ \rho v \\ E \\ \rho Y_i \end{pmatrix}, F = \begin{pmatrix} \rho u \\ \rho u^2 + p \\ \rho uv \\ (E + p)u \\ \rho Y_i u \end{pmatrix}, G = \begin{pmatrix} \rho v \\ \rho v^2 + p \\ (E + p)v \\ \rho Y_i v \end{pmatrix}$$

$$F_v = \begin{pmatrix} 0 \\ \sigma_x \\ \tau_{xy} \\ \sigma_x u + \tau_{yx} v - q_x \\ -m_x \end{pmatrix}, G_v = \begin{pmatrix} 0 \\ \tau_{yx} \\ \sigma_y \\ \tau_{xy} u + \sigma_y v - q_y \\ -m_y \end{pmatrix}$$

The following terms are expressed as

$$\sigma_x = \lambda \left( \frac{\partial u}{\partial x} + \frac{\partial v}{\partial y} \right) + 2\mu \left( \frac{\partial u}{\partial x} \right)$$

$$\sigma_y = \lambda \left( \frac{\partial u}{\partial x} + \frac{\partial v}{\partial y} \right) + 2\mu \left( \frac{\partial v}{\partial y} \right)$$

$$\tau_{xy} = \tau_{yx} = \mu \left( \frac{\partial u}{\partial y} + \frac{\partial v}{\partial x} \right)$$

$$q_x = -k \frac{\partial T}{\partial x} - \sum_{i=1}^{ns} D_{iml} h_i \frac{\partial Y_i}{\partial x}$$

$$q_y = -k \frac{\partial T}{\partial y} - \sum_{i=1}^{ns} D_{iml} h_i \frac{\partial Y_i}{\partial y}$$

$$m_x = -\rho D_{iml} \frac{\partial Y_i}{\partial x}$$

$$m_y = -\rho D_{iml} \frac{\partial Y_i}{\partial y}$$

$$\lambda = \frac{2}{3} \mu$$

## 3. RESULTS AND DISCUSSION

### 3.1 Physics of Fluid dynamics

Figure 2 shows the velocity vectors with streamlines just behind the finite base for case 1~5. In Fig.2(a) the upper recirculation rotates clockwise while the lower recirculation rotates counterclockwise. The flows expand and high interaction occurs after recirculation. The recirculation zones spread downstream, increasing its length in longitudinal direction. The stream lines indicate that both of the recirculations are created by the hydrogen flow. For other cases in Figs.2 (b) to (e), after entering into the first recirculation, portion of the hydrogen flow can not complete the recirculation. This portion of hydrogen makes intimate contact with air and deflects  $180^\circ$  due to the high momentum of air stream. The velocity in recirculation is low and therefore hydrogen has much time to contact with air resulting in high diffusion. Throughout the study, the momentum of air is higher than that of hydrogen, due to which the expansion of hydrogen is high behind the base while the expansion of the air stream is low. Due to expansion and interaction between two streams hydrogen enters in the recirculation region and mixes with air by diffusion and convection. By means of this, recirculation plays a vital role to enhance mixing.

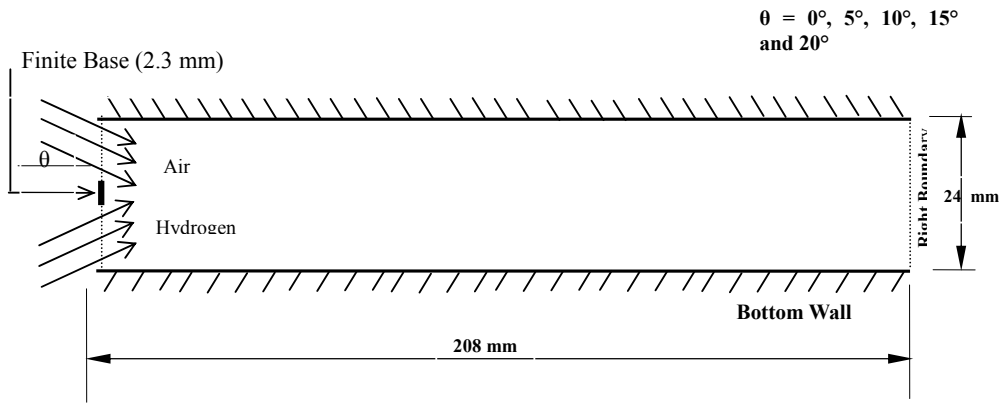


Fig 1. Schematic diagram of calculation domain

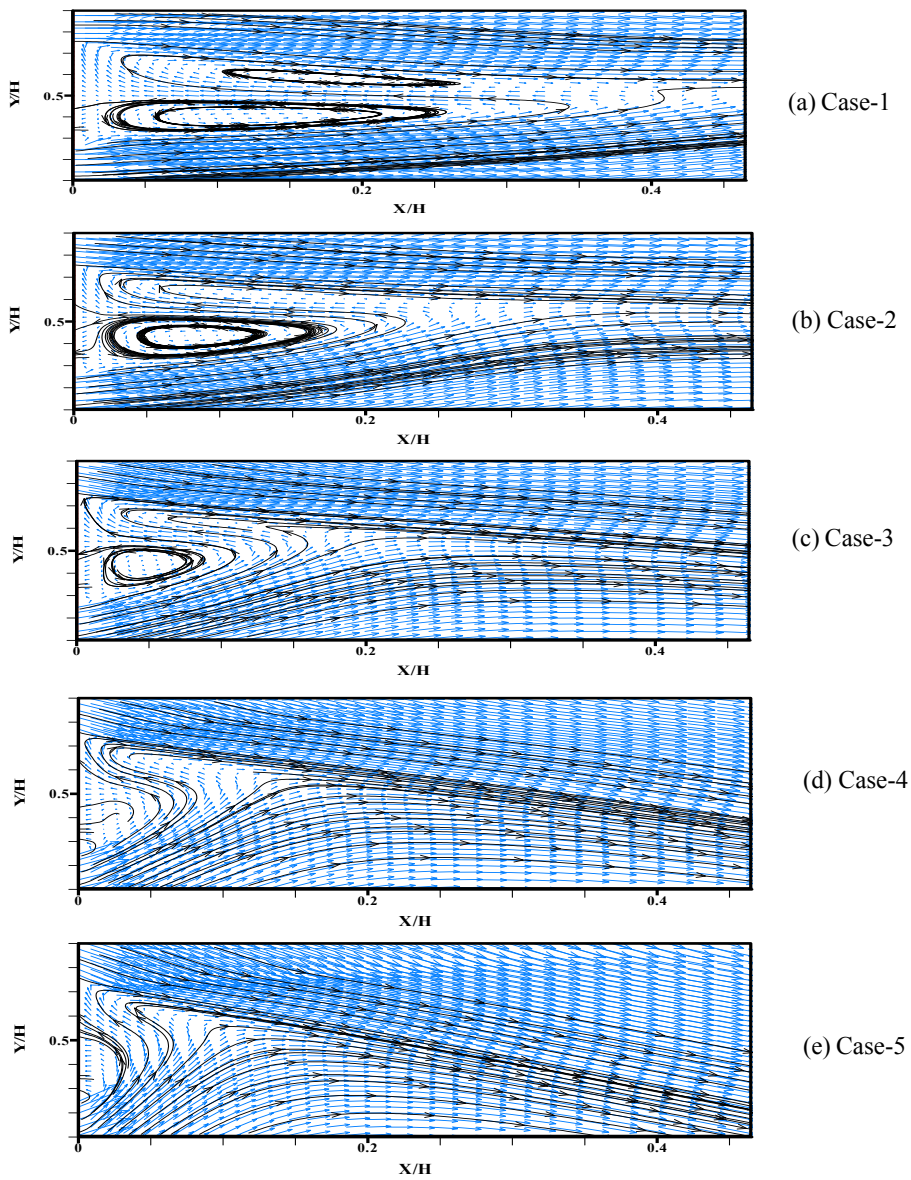


Fig 2. Vector and streamline representation of near flow circulating region for Case -1~5

Figure 2(b) shows the shear layer mixing regions spread with longitudinal distance until impingement occurs at approximately  $X/H = 0.22$ , which is shorter than case 1. Therefore, the area of recirculation zones in case-2 are smaller than case-1. Figures 2 (a~e) shows that with the increment of merging angle the size of both recirculations diminishes but more hydrogen molecules are entering in the recirculation region due to strong interactions and eventually more molecular and convection diffusion occurs. Another observation is that in Fig. 2(a) two recirculations are very clear but in Fig. 2(b) the upper recirculation vanishes and the size of lower recirculation decreases. Moreover, the streamlines generated from the same location of Fig. 2(a) and (b) indicate that more hydrogen molecules enter into the upper side of the recirculation region and make intimate contact with the air stream for case 2 than that of case 1.

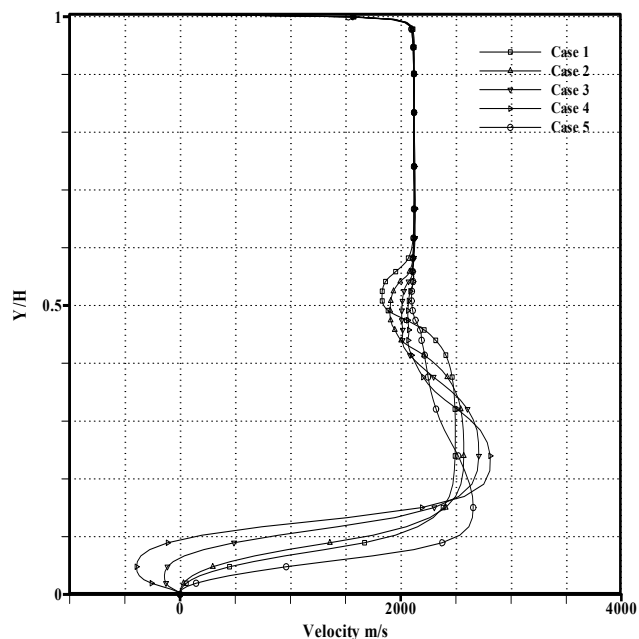


Fig.3 Velocity distribution at section  $X/H=5.98$  for Case 1 to Case 5

Velocity distribution curves in Fig.3 show that velocities of the upper section are similar to all merging angles at constant pressure ratio. But the velocity of the lower part (hydrogen) increases at the downstream. The maximum velocity occurs at merging angle of  $5.0^\circ$ .

### 3.2 Structure of Shear Layers

The mole fraction contours give a structure of free shear layers created by the mixing of the two streams. Figure 4 shows the mole fraction contours of hydrogen. The mole fraction of hydrogen close to bottom wall is 0.95 and the contour line varies from 0.95 to 0.05 towards the upper wall. The increment of mole fraction between two adjacent contour lines is 0.05. As stated earlier, a thin base is located from  $Y/H = 0.45$  to  $0.55$  in the middle of the two streams. Throughout the study hydrogen has less momentum than that of the air stream and eventually hydrogen will occupy more space after the thin base. For case 1 there is no initial deflection of

shear layer due to identical pressure. But for cases 2~5 the shear layer deflects towards the bottom wall due to non-parallel mixing and higher density of air. The deflection angle is measured with respect to X-direction. The deflection angles for case 2, 3, 4 and 5 are  $5.0^\circ$ ,  $8.0^\circ$ ,  $10.0^\circ$  and  $18.0^\circ$ , respectively. The spreading of free shear layers also increases with the increment of merging angle. Further deflections of shear layer at downstream are fairly understandable for higher merging angles. The spreading of free shear layers is the highest for case 5 and case 1 it is the lowest. For all cases, the spreading of hydrogen increases as mixing angle increases. After this initial deflection all the shear layers deflect towards the upper boundary. In order to investigate how the details of the structure are affected by the mixing angles, the computational domain should be long enough to allow the shear layer to become unstable naturally. So it is found that the deflection angles as well as spreading of free shear layer increase with increases the merging angle.

### 3.3 Mixing Efficiency

Mixing efficiency has been calculated on the basis of flammability limits of hydrogen and air. So, in the calculation of mixing efficiency the region having the mole fraction range of hydrogen from 0.05 to 0.75 has been taken into consideration. The mixing of hydrogen in air can be occurred by means of (i) interaction between two streams, (ii) turbulence and convection due to recirculation and velocity of the flow, or (iii) molecular diffusion due to density gradient. The performance of different cases is evaluated by calculating the mixing efficiency. Figure 5 shows the mixing efficiency along the physical model for different cases. For all cases the mixing efficiency increases sharply just behind the base due to expansion at the thin base corner and recirculations. The sharp increment in efficiency is caused by the interaction of two streams. In downstream the mixing is very slow in shear-layer caused by weak molecular diffusion for supersonic nature of the flow. From Fig.5 it can be observed that the strong interaction of the two streams in case 5 causes high penetration of air in the hydrogen. Consequently, case 5 has the highest increment of mixing efficiency near the left boundary. Whereas at lower merging angle, weak interaction of two streams causes weak penetration and lower mixing efficiency. In Fig.5 at  $X/H=2$  the mixing efficiencies of the cases 1,2,3,4 and 5 are 4.9, 6.5, 11.5, 18.0 and 24.0%, respectively i.e. in upstream mixing efficiency increases as merging angle increases. In the downstream increase of mixing for case 1 is higher than that for case 2, whereas for case 3, 4 and 5 it remains almost constant. This increasing trend indicates that case 1 has the maximum hydrogen diffusion in the downstream. So, for the cases 3~5 the longer combustor might increase the cost of construction of combustor, provided that other parameters are identical. The overall mixing efficiency at outflow for cases 1, 2, 3, 4 and 5 are 7.5, 9.0, 13.5, 20.0 and 25.0%, respectively. So, overall mixing efficiency at the outflow boundary increases with the increase of merging angle.

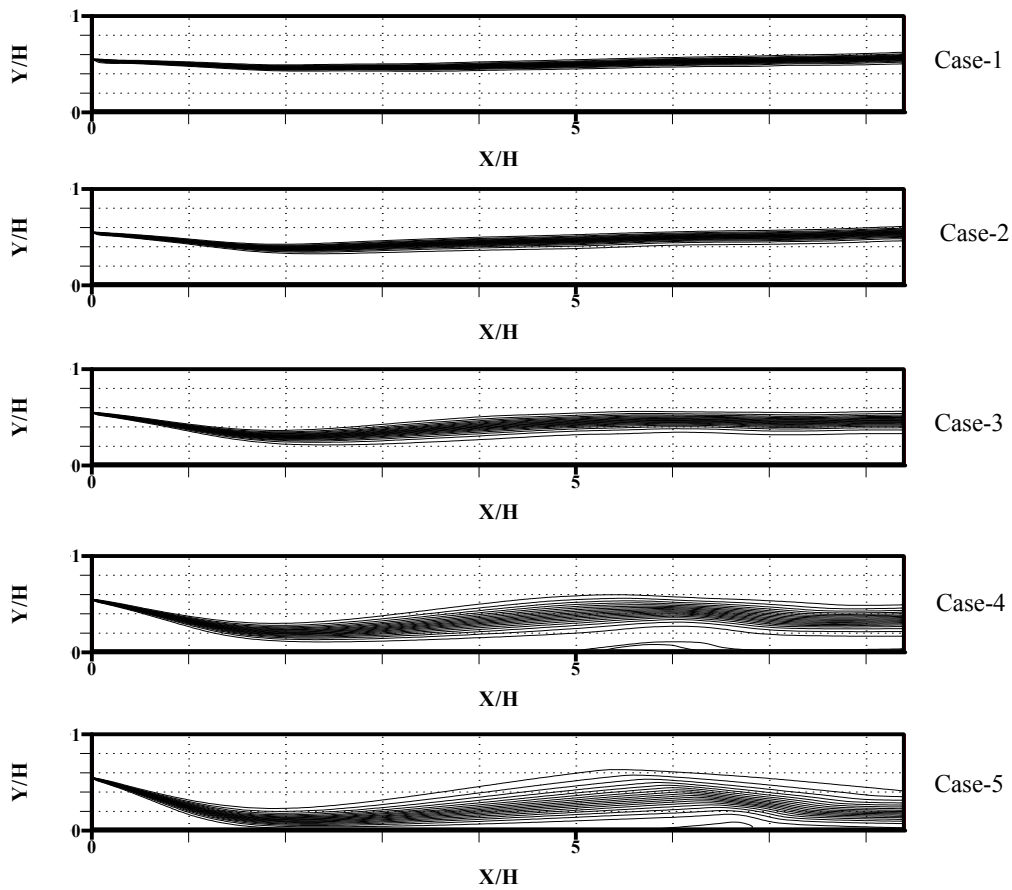


Fig 4. Mole fraction contour of hydrogen  $\phi(0.05,0.95,0.05)$  for Case 1 ~ 5

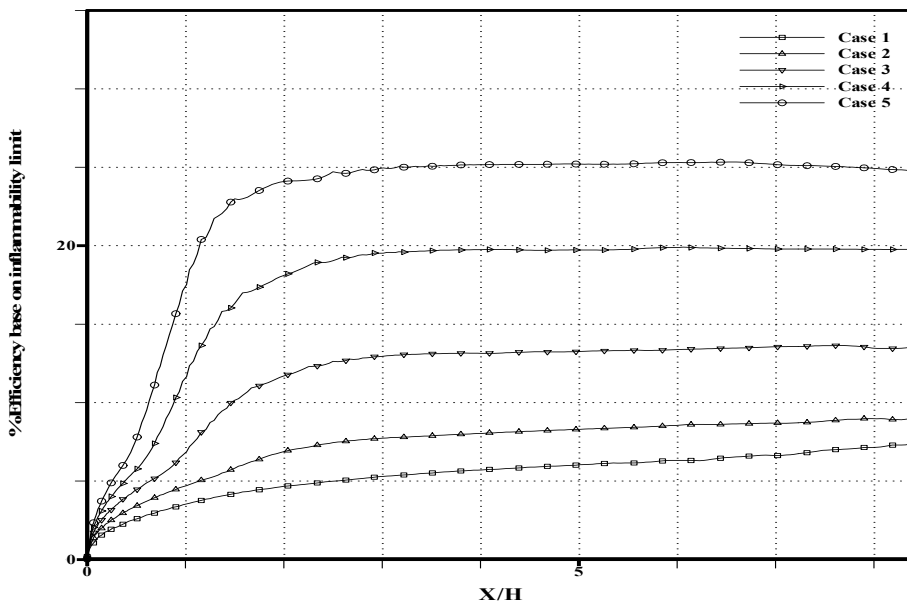


Fig 5. Mixing efficiency base on inflammability limit for Case 1 ~ 5

#### 4. CONCLUSION

For good combustion in a supersonic combustor the need of efficient mixing is mandatory. Many experiments, theoretical and numerical studies have been performed on mixing, ignition and combustion in supersonic flow. In supersonic combustion, high penetration and mixing of fuel with oxidizer is difficult due to their short residence time in combustor. In the present study the effects of merging angle in a limited range of values on supersonic mixing have been studied and some information extract from this study. Due to finite base, hydrogen and air expand behind the base creating a separation region and a recirculation region. Both hydrogen and air streams move to each other and strike behind base. The velocity in recirculation is low and therefore hydrogen has much time to contact with air resulting in high diffusion. By varying merging angle it has been found that, interaction between the two streams increases with increase of merging angle but the area of recirculation increases. By the investigation of the recirculation region in detail, it has been found that although recirculation area decreases with the increase of merging angle, high amount of hydrogen enters into the recirculation region and eventually mixing efficiency increases. Due to high interaction of the streams high momentum exchange occurs and eventually high mixing occurs at upstream for high merging angle. At high merging angle shocks created in the flow-field are strong. Due to these strong shocks, pressure loss increases as the merging angle increases. Strong interactions and shocks in high merging angles reduce the pressure in outflow boundary.

#### 5. REFERENCES

1. Guirguis, R.H., Girnstein, F. F. Young, T. R. Oran, E. S. Kailashanath, K. and Boris, J. P., 1987, "Mixing Enhancement in Supersonic Shear Layers", AIAA 87-0373.
2. Farouk, B., Oran, E. S. and Kailashanath, K., 1991, "Numerical Simulations of the structure of supersonic shear layers", Physics of Fluids, A, Vol. 3, No. 11, pp. 2786-2798.
3. Brown, G.L., Roshko, A., 1974, "On Density Effects and Large Structure in Turbulent Mixing Layers", Journal of Fluid Mechanics, Vol. 64, No. 4, pp. 775-816.
4. Papamoschuo D., Roshko, A., 1988, "The Compressible Turbulent Shear Layer: An Experimental Study", Journal of Fluid Mechanics, Vol. 197, pp. 453-477.
5. Debieve, J., Dupont, P., Laurent, H., Mena, M and Dussauge, J., 2000, "Compressibility and Structure of Turbulence in Supersonic Shear Flows", Eur. J. Mech.B-Fluids, Vol. 19, pp. 597-614.
6. Ali, M. and Islam, A.K.M.S., 1999, "Effect of Main flow Inlet Width on Penetration and Mixing of Hydrogen in Scramjet Combustor", Proceedings of the Eighth Asian Congress of Fluid Mechanics, pp. 647-650, December 6-10, Shenzhen, China.
7. Ali, M. Fujiwara, T. and Leblanc, J.E., 2000, "Influence of Main Flow inlet Configuration on Mixing and Flame Holding in Transverse Injection into Supersonic Air Stream", International Journal of Engineering Science, Vol. 38, pp.1161-1180.
8. Ali, M. Fujiwara, T. and Parvez, A., 2002, "A Numerical Study on the Physics of Mixing in Two-dimensional Supersonic Stream", Indian Journal of Engineering and Materials Sciences, Vol. 9, pp.115-127.
9. Gai, S.L., Tranopolsky, A. and Riley, A.J., 2002, "Study of a Mixing Layer Formed by a Supersonic Main Stream of Air and a Co-Flowing Supersonic Helium Jet", Flow, Turbulence and Combustion, Vol. 68, pp.195-226.
10. Gerlinger, P. and Bruggemann, D., 2000, "Numerical Investigation of Hydrogen Injections into Supersonic Airflows", Journal of Propulsion & Power, Vol. 16, pp.22-28.
11. Guirguis, R.H. Girnstein, F. F. Young, T. R. Oran, E. S. Kailashanath, K. and Boris, J. P., "Mixing Enhancement in Supersonic Shear Layers: II. Effect of Bluff Centre Bodies", Laboratory for Computational Physics and Fluid Dynamics, Naval Research Laboratory, Washington, D.C., Report-20375.
12. Azim, M. A. and Islam, A.K.M.S., 2003, "Plane Mixing Layers from Parallel and Non-parallel Merging of Two Streams", Experiments in Fluids, Vol. 34, pp. 220-226.

#### 6. MAILING ADDRESS

Mohammad Ali  
Department of Mechanical Engineering  
BUET, Dhaka – 1000, Bangladesh  
Email: mali@me.buet.ac.bd

## EFFECT OF GAS WEBER NUMBER ON LIQUID SHEET BREAKUP

Mohammad Ali, M. Quamrul Islam and R. Mahamud

Department of Mechanical Engineering, Bangladesh University of Engineering and Technology  
Dhaka, Bangladesh

### ABSTRACT

In this study dynamic behavior of liquid sheet of thermoplastic with co flowing air is discussed and numerically simulated. The Navier-Stokes systems associated with surface tension forces are solved by the Volume of Fluid (VOF) technique with a Continuum Surface Force (CSF) manner. The velocity of liquid is kept constant throughout the study whereas the velocity of air is varies which eventually varies the gas Weber number. Sulphur hexa fluoride ( $SF_6$ ) and high density polyethylene (HDPE) are considered as liquid to investigate the physics of breakup process. The effects of gas Weber number on liquid sheet breakup process are discussed to reveal the underlying physics of liquid disintegration. It is found that under any flow conditions a range of gas Weber number controls the instability for the breakup of liquid sheet. The pressure as well as velocity distribution of the flow field are also discussed to study the breakup processes in details.

**Keywords:** Weber Number, VOF, CSF, Sulphur Hexa Fluoride, HDPE.

### 1. INTRODUCTION

A thermoplastic is a polymer that turns to a liquid when heated and freezes to a very glassy state when cooled sufficiently. Most thermoplastics are high-molecular-weight polymers whose chains are associated through weak Vander Waals forces (polyethylene); stronger dipole-dipole interactions and hydrogen bonding (nylon); or even stacking of aromatic rings (polystyrene). One of the advantages of thermoplastic polymers is that they can be re-melted and re-moulded. Many thermoplastic materials are addition polymers; e.g., vinyl chain-growth polymers such as polyethylene and polypropylene. Thermoplastic is widely used for injection molding, sheet forming, thermal coating, foam processing etc. In previous many experiments and numerical simulations were done on thermoplastic processing. Pham et al [1] performed an experiment to understand the formation of Polyethylene Terephthalate (PET) bottles. He also conducted numerical simulations to study the effects of temperature and strain rate on the strain-hardening properties of the polymer during the stretch blow molding process.

Yijie Wang [2] studied the gas assisted injection molding technique. The displacement of a low viscosity fluid in higher viscosity material causes the formation of a long bubble penetrating through the high viscosity fluid. This left a thin coating on the wall, which had important application in gas-assisted injection molding. The effect of fluid rheological properties on the fractional coverage left by the bubble was studied under isothermal conditions. The polymer solutions of different shear thinning properties were used as high viscosity fluids,

and silicon oil was used as the displacing fluid in his experiment. The result showed that as the absolute viscosity increased, the thickness of the high viscosity fluid on the wall also increased. Gas-assist injection molding is a process that utilizes an inert gas (normally nitrogen) to create one or more hollow channels within an injection-molded plastic part. At the end of the filling stage, the gas ( $N_2$ ) is injected into the still liquid core of the molding. The gas then follows the path of the least resistance and replaces the thick molten sections with gas-filled channels. The gas pressure packs the plastic against the mold cavity surface, compensating for volumetric shrinkage until the part solidifies. Finally, the gas is vented to atmosphere or recycled. Gas-assist injection molding has been around for well over two decades. Now; gas-assist injection molding is widely practiced. Design engineers and processors alike are discovering that this technology is an attractive option for certain applications and offers many benefits.

Early studies of droplets and spray formation from liquid jets issuing into ambient gases can be traced back to the late nineteenth century. Rayleigh [3] showed that liquid jet break-up in still gases is a consequence of hydrodynamic instability. Research on the break-up of liquid jets was continued with much of the theoretical work based on linear instability analysis of absolute and convective instabilities of liquid jets issuing into gaseous environments by Tomotika [4], Chandrasekar [5], Reitz and Bracco [6], and laterly Teng et al. [7], Gordillo and Perez-Saborid [8], Lozano et al. [9] and Lin [10]. Recently, Mehring and Sirignano [11, 12] presented a nonlinear analysis of the spatial temporal development of

axisymmetric capillary waves in a thin annular liquid sheet sheared by fast co-flowing gas streams. Their study showed that the break-up of the annular liquid sheet is initiated by sheet modulation in sinusoidal and dilatational modes. Numerical simulation of the problem showed that there was a nonlinear coupling between the dominant sinusoidal and dilatational mode.

Ali [13] found that the disturbances occurred by the gas Weber number controls the instability process for the liquid sheet breakup. Two modes of forces for liquid stretching were found; one was shear force causing the stretching of liquid by shear velocity and the other was normal force causing the stretching of liquid by gas velocity ahead the tip of the liquid sheet. Stretching of liquid by shear force caused the protrusion of liquid from the tip of liquid sheet at initial stage. The surface tension force made the tip of the sheet to become round and gradually the aerodynamic normal force at the tip of the sheet played an important role to continue the stretching of sheet and controls the formation of droplet and occurrence of sheet breakup.

In this work the dynamical behavior of SF<sub>6</sub> and High Density Polyethylene (HDPE) sheet at high temperature and pressure is discussed in context of capillary phenomena. A linear polymer, HDPE is prepared from ethylene by a catalytic process. High density polyethylene lends well to blow molding, e.g. for bottles, cutting boards, dipping baskets, dippers, trays and containers. HDPE is also somewhat harder and more opaque and it can withstand rather higher temperatures (120° Celsius for short periods, 110° Celsius for continuous). Almost same dynamical behavior of HDPE can be found as SF<sub>6</sub>.

## 2. MATHEMATICAL MODELING

The flow field is governed by time dependent three-dimensional Navier-Stokes equations with surface tension force. Body forces are neglected. These equations can be expressed as

$$\frac{\partial \vec{U}}{\partial t} + \frac{\partial \vec{P}}{\partial x} + \frac{\partial \vec{Q}}{\partial y} + \frac{\partial \vec{R}}{\partial z} = \frac{\partial \vec{P}_v}{\partial x} + \frac{\partial \vec{Q}_v}{\partial y} + \frac{\partial \vec{R}_v}{\partial z} + \vec{F}_{sv} \quad (1)$$

$$U = \begin{pmatrix} \rho \\ \rho u \\ \rho v \\ \rho w \end{pmatrix}, \quad P = \begin{pmatrix} \rho u \\ \rho u^2 + p \\ \rho uv \\ \rho uw \end{pmatrix}, \quad Q = \begin{pmatrix} \rho v \\ \rho uv \\ \rho v^2 + p \\ \rho vw \end{pmatrix},$$

$$R = \begin{pmatrix} \rho w \\ \rho uw \\ \rho vw \\ \rho w^2 + p \end{pmatrix}$$

$$P_v = \begin{pmatrix} 0 \\ \tau_{xx} \\ \tau_{xy} \\ \tau_{zx} \end{pmatrix}, \quad Q_v = \begin{pmatrix} 0 \\ \tau_{xy} \\ \tau_{yy} \\ \tau_{yz} \end{pmatrix}, \quad R_v = \begin{pmatrix} 0 \\ \tau_{zx} \\ \tau_{yz} \\ \tau_{zz} \end{pmatrix}$$

$$F_{sv} = \begin{pmatrix} 0 \\ \sigma \kappa f n_x \\ \sigma \kappa f n_y \\ \sigma \kappa f n_z \end{pmatrix}$$

Where,  $F_{sv}$  is the surface tension force,  $\sigma$  the surface tension,  $\kappa$  the curvature of surface,  $n$  the unit normal to the surface and  $f$  is a function for continuous change of the color variable (here density) across the thickness of fluid interface.

## 3. NUMERICAL SIMULATION

A numerical analysis is performed on moving liquid sheet in a gaseous medium (Nitrogen) of much higher velocity compared with the liquid. The effects of co-flowing gas with different Gas Weber number on the dynamical behavior of the liquid sheet of thermoplastic are included in the analysis. For numerical simulation, volume of fluid (VOF) method based on a simplified treatment of the Navier-Stokes equation with a fixed, regular, uniform grid is used to solve the problem. Piecewise Linear Interface Calculation (PLIC) is implemented for the advection of the liquid interface. The treatment of surface tension consists of artificially smoothing the discontinuity present at the interface by Continuum Surface Force (CSF) manner. In the present work the surface tension force is estimated by a volume force which gives the correct surface tension. The volume force is calculated with the area integral over the portion of the interface lying within the small volume of integration. The construction of algorithm for calculation of normal vector is based on the idea that a normal vector together with the fractional volume of one fluid contained by the cell determines a unique planar surface cutting the cell into two parts as shown in Fig.1. Each part of the cell contains proper volume of one of the two fluids. Figure 1 shows a planar surface ABCD, under which the liquid lies in the cell.

To determine the fractional volume and interface position, a parameter is searched which is related to the smallest distance between the planar surface of liquid and the origin of the cell. Therefore this parameter represents the distance along the normal and also defines the planar surface of liquid in the cell. Utilizing this parameter we can determine the area of different sides of the cell occupied by the liquid. A comprehensive description of this calculation can be found in Gueyffier et al. [14], where the description is started with two-dimensions and later it is generalized to three



dimensions for calculation of area as well as volume of the fluid. Both area and volume calculations are continuous, one-to-one, and have a functional relationship with volume inside the cell lying below the planar surface and the parameter which characterizes the plane. For easy calculation of area and volume of the liquid, the cells are identified as three categories: (i) cells with zero value of one component of normal to the planar surface, (ii) cells with zero values of two components of normal to the planar surface, and (iii) cells with non-zero normal components. Algorithm is constructed for these categories of cells with the implementation of all possible logics.

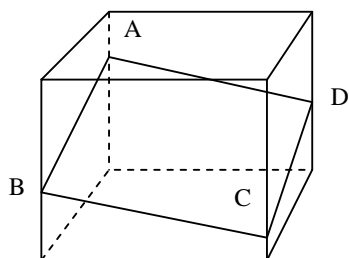


Fig 1. Liquid planar surface, ABCD cuts the cubic cell into two parts

After the construction of liquid interface in cell, its motion in the underlying flow field must be introduced in the algorithm by a suitable advection method. Since the atomization process is very fine and rapid, the simulating code should be capable of capturing all the phenomena behind the atomization process. It can be pointed out that the proper and precise computation of this type of problem is a complex one even when it is two-dimensional case. More complexity arises when the problem is three dimensional. Therefore, calculation of fluid flux should be precise for accuracy of the result. By the motion of the fluid, flux of fluid from one cell to its neighboring cells is calculated. Using the expression described in Gueyffier et al. [14], we can determine the “wetted” area occupied by the liquid in the cell through which the flux of fluid occurs. But this area does not remain constant during one time step. To incorporate this change of flux area, first we need to search the cells in which the “wetted” area is changing during the time step and then calculate the changing area as well as flux of the liquid. It can be pointed out that during calculation, different critical shapes of the cut cube can occur as shown in Fig. 2 where six critical shapes of the cut cubes are presented. Special care must be taken for the advection of liquid from one computational cell to neighboring cells during this occurrence. In present calculation after finding out the cells, the change of flux is calculated with the conjunction of normal to liquid planar surface and geometry of the interface position

The interface where the fluid changes from one fluid to the other discontinuously is replaced by a continuous transition. It is not appropriate to apply a pressure jump induced by surface tension at the interface. Rather, the surface tension should act everywhere within the transition region. In fact, the surface tension contributes a

surface pressure which is the normal force per unit interfacial area. In present work the surface tension force is estimated by a volume force which gives the correct surface tension. The volume force is then calculated with the area integral over the portion of the interface lying within the small volume of integration. A suitable color function (density for present investigation) is chosen for smooth variation over the thickness across the interface. A detail description and the formulation for numerical simulation can be found in Gueyffier et al. [14]. The model is implemented in the algorithm for present investigation.

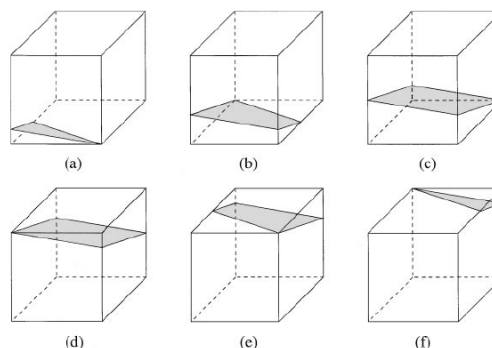
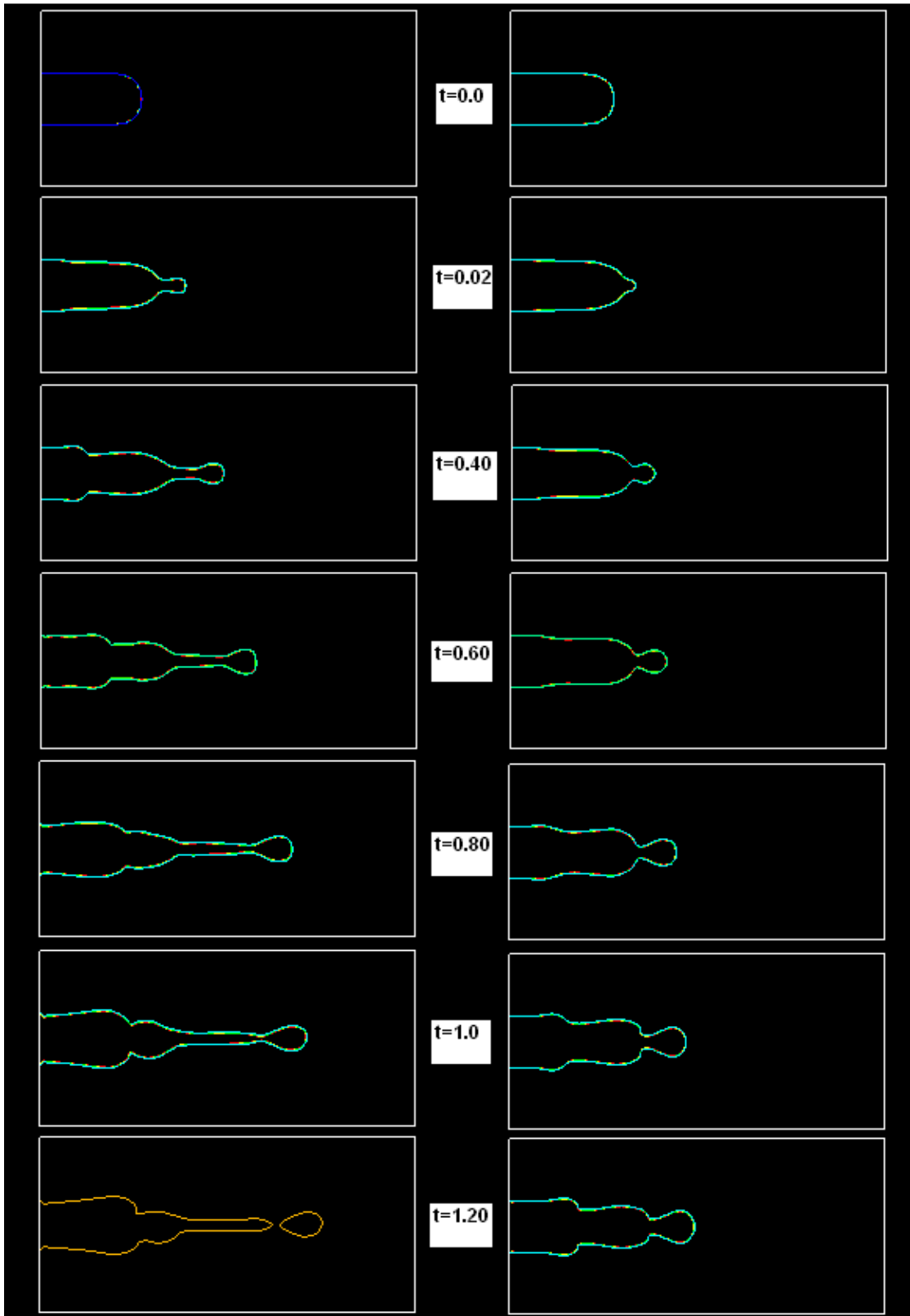


Fig 2. The different critical shapes of the cut cube (Gueyffier et al. [14]). The liquid in the cube changes shape with time and the plane crosses vertices.

## 4. RESULTS AND DISCUSSION

### 4.1 Effect of gas Weber Number

To study the effects of gas Weber number, a numerical study is carried out on water sheet with co-flowing air. It is seen that water sheet does not break without co-flowing air or gas flow. There is a minimum value of gas Weber number for a fixed liquid Weber number below which liquid sheet does not break. This critical value of gas Weber number is 14 for  $SF_6$ . Numerical calculation on various liquid also indicates the similar value of gas Weber number. Over this value of gas Weber number after certain time liquid sheet of HDPE breaks up. It is also found that if velocity of surrounding gas is increased which consequences to the increase of the Weber number of gas tends to precede the breakup processes of liquid sheet. Also if the gas Weber number is increased liquid sheet becomes thinner as the sheet is stretched by the surrounding gas. Throughout the calculation, at the inlet boundary the uniform gas velocity is imposed on top and bottom of the liquid sheet and constant gas pressure is considered for all boundaries of calculation domain. For liquid sheet, at inlet boundary the constant pressure is used. To investigate the effect of Gas Weber number on the liquid sheet breakup mechanism the Weber number of gas is varied from 10 to 100 by keeping constant liquid ( $SF_6$ ) Weber number,  $W_{el}=1$ . Figure 3 shows the breakup process for Gas Weber number of 14 at different time and the velocity profile of the flow field. On the other hand, below the critical gas Weber number only the shape of a drop is forming but no droplet is occurred.



(a) Gas Weber Number 14

(b) Gas Weber Number 10

Fig 3. (a) Weber Number 14 (b) Weber Number 10, Surface contour for SF6 with co-flowing Nitrogen gas (t=dimensionless time)

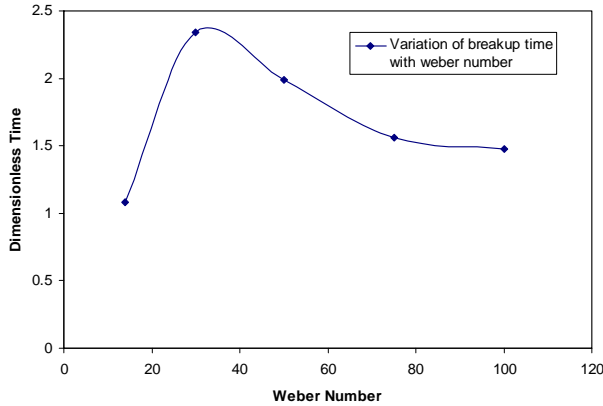


Fig 4. Variation of breakup time with gas Weber Number (SF<sub>6</sub>).

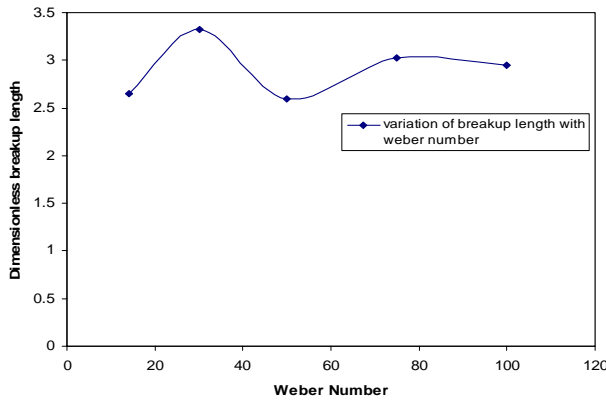


Fig 5. Variation of breakup length with gas Weber number.

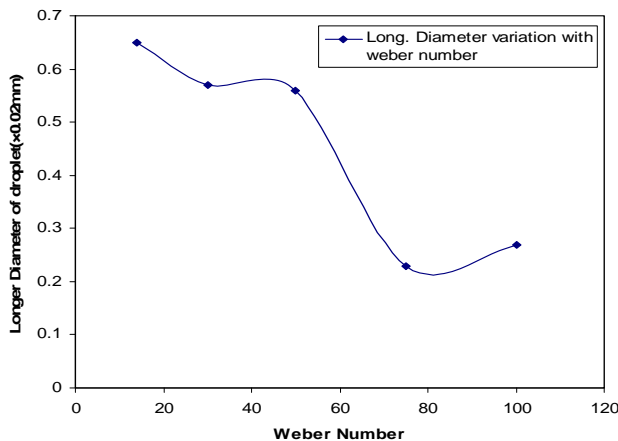


Fig.6 Variation of droplet diameter (along longitudinal direction) with gas Weber Number

#### 4.2 Effect Of Gas Weber Number On Breakup Time

If the gas Weber number increases gradually, the time for breakup decreases as shown in Fig. 4. The increasing of gas Weber number means the gas velocity is increased.

The aerodynamic force, which is the effect of gas velocity, would be dominant if gas Weber number increases. For low gas Weber number the breakup occurs earlier caused by the capillary instability. For much higher gas Weber number the aerodynamic force is dominant which acts on the surface of the liquid sheet and also on tip of the liquid sheet. The interaction between liquid and air also increases. It causes the breakup to be held earlier.

#### 4.3 Effect of gas weber number on breakup length

The length at which breakup occur increases if the gas Weber number increases as shown in Fig.5. Since liquid sheet is stretched at high gas Weber number, it causes the liquid sheet elongated at high gas Weber number.

#### 4.4 Effect of gas weber number on droplet diameter

The droplet diameter decreases at high gas Weber number as shown in Fig.6 caused by the aerodynamic force. The shape changes from round to rectangular at high gas Weber number.

### 5. CONCLUSIONS

A two dimensional study has been performed to discuss the pattern of liquid SF<sub>6</sub> as well as thermoplastic sheet for the study of injection molding and coating of thermoplastic and some other uses. The Navier-Stokes equations with surface tension force are used for numerical simulation and volume-of-fluid (VOF) techniques are applied for the advection of liquid from one computational cell to the neighboring cell. For smoothing the discontinuity present at the interface of the cells, a Continuum Surface Force (CSF) manner is adopted for the treatment of surface tension. The velocity of liquid and gas are determined from liquid and gas Weber number, respectively. Keeping constant the liquid Weber number, the gas Weber number is varied to investigate the range of gas Weber number under which breakup and droplet are possible. Two effects are activated on the flow field: aerodynamic effect and surface tension effect. The aerodynamic effect is caused by the interaction between the gas and liquid surface of the sheet and plays an important role for the formation and breakup of liquid droplet. When aerodynamic effect prevails over surface tension effect, the disturbances grow on liquid surface and eventually break up and droplet occurs. In that case surface tension force helps to form a droplet and make it bigger in diameter, and keeps it in a round shape. But when surface tension force is prevailing no breakup is occurred.

The aerodynamic force acts on both surfaces of the liquid sheet as well as on the tip of the liquid sheet. Due to interaction of aerodynamic force with the liquid on the surface of the sheet, liquid sheet is stretched and a protrusion on the tip of the sheet occurs. If the aerodynamic force is insufficient to keep the drop as its regular shape, the drop gradually losses its shape and eventually the drop are merged into the liquid sheet by surface tension force. The gas velocity ahead the liquid sheet, which is the consequences of aerodynamic effect,

varies with time. If the gas velocity is low enough, no droplet and breakup of liquid occur. If the gas velocity is high enough, the liquid protrusion length increases so much which causes the reduction of droplet diameter and losses the usual breakup procedure. This causes the stretching the liquid sheet so much and create an uneven pattern of sheet. Hence, a range of velocity can produce droplet and make a breakup of the liquid.

## 6. REFERENCES

1. Pham, X.-T. ; Thibault, F.; Lim, L.-T., 2004, "Modeling and simulation of stretch blow molding of polyethylene terephthalate", *Polymer Engg. and Science*, Vol.44, No.8, pp.1460-1472.
2. Yijie Wang, 2003, "The Effect of Non-Newtonian Rheology on Gas assisted Injection Molding Process", Ph. D. Thesis, Ohio State University, USA.
3. Rayleigh, L., 1879, "On the capillary phenomenon of jets", *Proc Royal Soc. London, Math* 29, pp.71–97.
4. Tomotika, S., 1935, "On the instability of a cylindrical thread of a viscous liquid surrounded by another viscous fluid", *Proc. Royal Soc. London, Series A* 150, pp.322–337.
5. Chandrasekar, S., 1961, "The capillary instability of a liquid jet with Hydrodynamic and Hydromagnetic stability", Oxford University Press, pp 537–542.
6. Reitz R. D, and Bracco, F. V., 1982, "Mechanisms of Breakup of Round Liquid Jets", *Phys Fluids*, Vol. 25, pp.1730–1742.
7. Teng, C. H., Lin, S. P., and Chen, J. N., 1997, "Absolute and convective instability of a viscous liquid curtain in a viscous gas", *J. Fluid Mech* Vol. 332, pp.105–120.
8. Gordillo, J. M., and Perez-Saborid, M., 2005, "Aerodynamic effects in the break-up of liquid jets: on the first wind-induced break-up regime"; *J. Fluid Mech.*, Vol. 541, pp.1–20.
9. Lozano, A., Barreras, F., Hauke, G., Dopazo, C., 2001, "Longitudinal instabilities in an air-blasted liquid sheet", *J. Fluid Mech.*, Vol. 437, pp.143– 173.
10. Lin, S. and Reitz, R., 1998, "Drop and spray formation from a liquid jet", *Annu. Rev. Fluid Mech.* Vol. 30, pp.85–105.
11. Mehring, C., and Sirignano, W. A., 1998, "Nonlinear capillary wave distortion and disintegration of thin planar liquid sheets", *J. Fluid Mech.*, Vol. 388, pp.69–113.
12. Mehring, C., and Sirignano, W. A., 2000, "Axisymmetric capillary waves on thin annular liquid sheets I: temporal stability", *Phys. Fluids*, Vol. 12(6), pp.1417–1439.
13. Mohammad Ali and Akira Umemura, 2008, "Dynamics and Breakup of Liquid Sheet", Research report, Department of Aerospace Engineering, Graduate School of Engineering, Nagoya University, Japan.
14. Gueyffier, D., Li, J., Nadim, A., Scardovelli, R. and Zaleski, S., 1999, "Volume-of-Fluid Interface Tracking with Smoothed Surface Stress Methods for Three-Dimensional Flows", *J. Computational Physics*, Vol. 152, pp.423-456.

## 7. MAILING ADDRESS

Mohammad Ali  
 Department of Mechanical Engineering,  
 Bangladesh University of Engineering and Technology  
 Dhaka – 1000, Bangladesh,  
 Email: mali@me.buet.ac.bd.

## EFFECTS OF RADIATION AND PRESSURE WORK ON MHD NATURAL CONVECTION FLOW AROUND A SPHERE

M. A. Alim<sup>1</sup> and Tahmina Akhter<sup>2</sup>

<sup>1</sup>Department of Mathematics, Bangladesh University of Engineering and Technology, Dhaka, Bangladesh

<sup>2</sup>Department of Mathematics, The University of Asia Pacific, Dhaka, Bangladesh

### ABSTRACT

The effects of radiation and pressure work on magnetohydrodynamic (MHD) natural convection flow on a sphere have been investigated in this paper. The governing boundary layer equations are first transformed into a non-dimensional form and the resulting nonlinear partial differential equations are then solved numerically using finite-difference method with Keller-box scheme. We have focused our attention on the evaluation of shear stress in terms of local skin friction and rate of heat transfer in terms of local Nusselt number, velocity as well as temperature profiles. Numerical results have been shown graphically and tabular form for some selected values of parameters set consisting of radiation parameter  $R_d$ , pressure work parameter  $G_e$ , Magnetohydrodynamic parameter  $M$  and the Prandtl number  $Pr$ .

**Keywords:** Thermal Radiation, Natural Convection, Pressure Work, Magnetohydrodynamics.

### 1. INTRODUCTION

Radiative energy passes perfectly through a vacuum thus radiation is significant mode of heat transfer when no medium is present. Radiation contributes substantially to energy transfer in furnaces, combustion chambers, fires and to the energy emission from a nuclear explosion. Radiation must be considered in calculating thermal effects in rocket nozzles, power plants, engines, and high temperature heat exchangers. Radiation can sometimes be important even though the temperature level is not elevated and other modes of heat transfer are present. Radiation has a great effect in the energy equation which leads to a highly non-linear partial differential equation. Magnetohydrodynamic (MHD) is the science, which deals with the motion of conducting fluid in presence of a magnetic field. Study of the flow of electrically conducting fluid in presence of magnetic field is important from the technical point of view and such types of problems have received much attention by many researchers. The specific problem selected for study is the flow and heat transfer in an electrically conducting fluid adjacent to the surface. The interaction of the magnetic field and the moving electric charge carried by the flowing fluid induces a force which tends to oppose the fluid motion.

The pressure work effect plays an important role in natural convection in various devices which are subjected to large deceleration or which operate at high rotational speeds and also in strong gravitational field processes on large scales and in geological processes. It is established that pressure work effects are generally rather more important both for gases and liquids.

The problems of natural convection boundary layer flow have been studied by many researchers. Amongst

them Nazar et al [1], Huang and Chen [2] considered the free convection boundary layer on an isothermal sphere and on an isothermal horizontal circular cylinder both in a micropolar fluid. Alim et al. [3-4] considered the pressure work effects along a circular cone and stress work effects on MHD natural convection flow along a sphere. Alam et al [5-7] considered the pressure work effects for flow along vertical permeable circular cone, vertical flat plate and along a sphere.

Soundalgekar et al. [8] have studied radiation effects on free convection flow of a gas past a semi-infinite flat plate using the Cogley-Vincenti-Giles equilibrium model Cogley et al. [9], later Hossain and Takhar [10] have analyzed the effects of radiation using the Rosseland diffusion approximation which leads to non-similar solutions for free convection flow past a heated vertical plate. Akhter and Alim [11] studied the effects of radiation on natural convection flow around a sphere with uniform surface heat flux.

In the present work, the effects of radiation and pressure work on MHD natural convection flow around a sphere have been investigated. The transformed boundary layer equations are solved numerically using implicit finite difference method together with Keller box scheme describe by Keller [12] and later by Cebeci and Bradshaw [13]. Numerical results have been shown in terms of local skin friction, rate of heat transfer, velocity profiles as well as temperature profiles for a selection of relevant physical parameters consisting of heat radiation parameter  $R_d$ , Prandtl number  $Pr$ , Magnetic parameter  $M$  and the pressure work parameter  $G_e$  have been shown graphically.

## 2. FORMULATION OF THE PROBLEM

It is assumed that the surface temperature of the sphere is  $T_w$ , where  $T_w > T_\infty$ . Here  $T_\infty$  is the ambient temperature of the fluid,  $T$  is the temperature of the fluid in the boundary layer,  $g$  is the acceleration due to gravity,  $r(x)$  is the radial distance from the symmetrical axis to the surface of the sphere

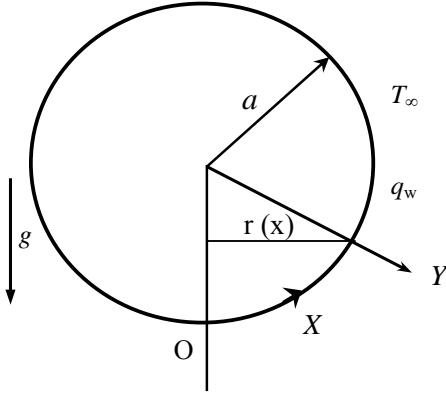


Fig 1. Physical model and coordinate system

and  $(u, v)$  are velocity components along the  $(x, y)$  axis. Under the usual Boussinesq approximation, the equations those govern the flow are

$$\frac{\partial}{\partial X}(rU) + \frac{\partial}{\partial Y}(rV) \quad (1)$$

$$U \frac{\partial U}{\partial X} + V \frac{\partial U}{\partial Y} = \nu \frac{\partial^2 U}{\partial Y^2} \quad (2)$$

$$+ \rho g \beta (T - T_\infty) \sin\left(\frac{X}{a}\right) - \frac{\sigma_0 \beta_0^2}{\rho} U$$

$$U \frac{\partial T}{\partial X} + V \frac{\partial T}{\partial Y} = \frac{k}{\rho C_p} \frac{\partial^2 T}{\partial Y^2} \quad (3)$$

$$- \frac{1}{\rho C_p} \frac{\partial q_r}{\partial Y} + \frac{T \beta}{\rho C_p} U \frac{\partial p}{\partial X}$$

We know for hydrostatic pressure,  $\partial p / \partial X = \rho g$ .

The boundary conditions of equation (1) to (3) are

$$U = V = 0, \quad T = T_w \quad \text{at} \quad Y = 0 \quad (4)$$

$$U \rightarrow 0, \quad T \rightarrow T_\infty \quad \text{as} \quad Y \rightarrow \infty$$

where  $r$  is the density,  $k$  is the thermal conductivity,  $b$  is the coefficient of thermal expansion,  $m$  is the viscosity of the fluid,  $C_p$  is the specific heat due to constant pressure and  $q_r$  is the radiative heat flux in the  $y$  direction. In order to reduce the complexity of the problem and to provide a means of comparison with future studies that will employ a more detail representation for the radiative heat flux; we will consider the optically dense radiation limit. Thus the Rosseland diffusion approximation proposed by Siegel and Howell [15] and is given by simplified radiation heat flux term as:

$$q_r = -\frac{4\sigma}{3(\alpha_r + \sigma_s)} \frac{\partial T^4}{\partial Y} \quad (5)$$

We now introduce the following non-dimensional variables:

$$\xi = \frac{X}{a}, \quad \eta = Gr^{1/4} \left( \frac{Y}{a} \right),$$

$$u = \frac{a}{\nu} Gr^{-1/2} U, \quad v = \frac{a}{\nu} Gr^{-1/4} V, \quad (6)$$

$$\theta = \frac{T - T_\infty}{T_w - T_\infty}, \quad Gr = g\beta (T_w - T_\infty) \frac{a^3}{\nu^2}$$

where  $\nu (= \mu/\rho)$  is the reference kinematic viscosity and  $Gr$  is the Grashof number,  $\theta$  is the non-dimensional temperature function.

Substituting variable (6) into equations (1)-(3) leads to the following non-dimensional equations

$$\frac{\partial}{\partial \xi}(ru) + \frac{\partial}{\partial \eta}(rv) = 0 \quad (7)$$

$$u \frac{\partial u}{\partial \xi} + v \frac{\partial u}{\partial \eta} = \frac{\partial^2 u}{\partial \eta^2} + \theta \sin \xi - Mu \quad (8)$$

$$u \frac{\partial \theta}{\partial \xi} + v \frac{\partial \theta}{\partial \eta} =$$

$$\frac{1}{Pr} \frac{\partial}{\partial \eta} \left[ \left\{ 1 + \frac{4}{3} Rd (1 + \Delta \theta)^3 \right\} \frac{\partial \theta}{\partial \eta} \right] \quad (9)$$

$$+ Ge \left( \theta + \frac{T_\infty}{T_w - T_\infty} \right) u$$

Where  $M = \frac{\sigma_0 \beta_0^2 a^2}{\rho \nu Gr^{1/2}}$  is the Magnetohydrodynamic

parameter and  $\Delta = \frac{T_w}{T_\infty} - 1$

With the boundary conditions (4) as

$$u = v = 0, \quad \theta = 1 \quad \text{at} \quad \eta = 0$$

$$u \rightarrow 0, \quad \theta \rightarrow 0 \quad \text{as} \quad \eta \rightarrow \infty \quad (10)$$

where  $Rd$  is the radiation-conduction parameter and  $Pr$  is the Prandtl number defined respectively as

$$Rd = \frac{4\sigma T_\infty^3}{k(\alpha_r + \sigma_s)} \quad \text{and} \quad Pr = \frac{\mu C_p}{k} \quad (11)$$

To solve equations (8)-(9), subject to the boundary conditions (10), we assume the following variables

$$\psi = \xi r(\xi) f(\xi, \eta), \quad \theta = \theta(\xi, \eta) \quad (12)$$

where  $\psi$  is the non-dimensional stream function defined in the usual way as

$$u = \frac{1}{r} \frac{\partial \psi}{\partial \eta} \quad \text{and} \quad v = -\frac{1}{r} \frac{\partial \psi}{\partial \xi} \quad (13)$$

Substituting (13) into equations (8)-(9), after some algebra the transformed equations take the following form

$$\frac{\partial^3 f}{\partial \eta^3} + \left(1 + \frac{\xi}{\sin \xi} \cos \xi\right) f \frac{\partial^2 f}{\partial \eta^2} - \left(\frac{\partial f}{\partial \eta}\right)^2 + \frac{\sin \xi}{\xi} \theta - M \frac{\partial \theta}{\partial \eta} = \xi \left( \frac{\partial f}{\partial \eta} \frac{\partial^2 f}{\partial \xi \partial \eta} - \frac{\partial f}{\partial \xi} \frac{\partial^2 f}{\partial \eta^2} \right) \quad (14)$$

$$\frac{1}{\text{Pr}} \frac{\partial}{\partial \eta} \left[ \left\{ 1 + \frac{4}{3} \text{Rd} (1 + \Delta \theta)^3 \right\} \frac{\partial \theta}{\partial \eta} \right] + \left(1 + \frac{\xi}{\sin \xi} \cos \xi\right) f \frac{\partial \theta}{\partial \eta} + \text{Ge} \left( \theta + \frac{T_\infty}{T_w - T_\infty} \right) \xi f' = \xi \left( \frac{\partial f}{\partial \eta} \frac{\partial \theta}{\partial \xi} - \frac{\partial \theta}{\partial \eta} \frac{\partial f}{\partial \xi} \right) \quad (15)$$

Along with boundary conditions

$$f = \frac{\partial f}{\partial \eta} = 0, \theta = 1 \text{ at } \eta = 0$$

$$\frac{\partial f}{\partial \eta} \rightarrow 0, \theta \rightarrow 0 \text{ as } \eta \rightarrow \infty \quad (16)$$

The physical quantities of principal interest are the wall-shear-stress, the heat transfer rate in terms of the skin-friction coefficients  $C_f$  and Nusselt number  $Nu_x$  respectively, which can be written as

$$C_f = \frac{Gr^{-3/4} a^2}{\rho \nu} \tau_w \text{ and } Nu = \frac{a Gr^{-1/4}}{k(T_w - T_\infty)} q_w \quad (17)$$

$$\tau_w = \mu \left( \frac{\partial u}{\partial y} \right)_{y=0} \text{ and } q_w = -k \left( \frac{\partial T}{\partial y} \right)_{y=0} \quad (18)$$

Here we have used a reference velocity  $U = \frac{\nu Gr^{1/2}}{a}$

Using the variables (6) and (13) into (17)-(18), we get

$$C_f = \xi f''(\xi, 0) \quad (19)$$

$$Nu = - \left( 1 + \frac{4}{3} \text{Rd} \theta^3 \right) \theta'(\xi, 0) \quad (20)$$

The values of the velocity and temperature distribution are calculated respectively from the following relations:

$$u = \frac{\partial f}{\partial \eta}, \quad \theta = \theta(\xi, \eta) \quad (21)$$

### 3. RESULTS AND DISCUSSION

The present problem has been solved numerically for different values of relevant physical parameters and for a fixed value of  $\Delta = 0.1$ . Results have been obtained in terms of local skin friction and the rate of heat transfer in terms of local Nusselt number, velocity as well as temperature profiles.

Velocity and temperature profiles are shown in figures 2 for different values of radiation parameter  $\text{Rd}$  while  $\text{Pr} = 7.0$ ,  $M = 1.0$  and  $\text{Ge} = 1.5$ . It is also observed that for higher values of radiation the velocity and

temperature becomes higher and there is no significant change found in the boundary layer thickness.

Effects of the variation of pressure work on velocity and temperature profiles are shown in the figures 3. Significant changes have been found in maximum velocity and temperature due to the change of  $\text{Ge}$ . For  $\text{Ge} = 0.1$  the maximum velocity is .19573 which occurs at  $\eta = 0.88811$  and for  $\text{Ge} = 2.5$  the maximum velocity is 0.77787 which occurs at  $\eta = 0.78384$ . Thus we observe that due to the change of  $\text{Ge}$  from 0.1 to 2.5 the velocity rises up 297.4%. Again small value of  $\text{Ge}$  ( $= 0.1$ ) gives the typical temperature profile which is maximum temperature at wall then it gradually decrease along  $\eta$  direction and finally approaches to the asymptotic value (zero). But larger values of  $\text{Ge}$  do not show the typical temperature profiles. In this case along  $\eta$  direction temperature gradually increased from the wall value to the peak and then decrease and approach to the asymptotic value.

Moreover, in the figure 4 it is observed that the velocity decrease with increasing  $M$  but the temperature increase along  $\eta$  direction up to the maximum value and then gradually decreases to zero.

Figure 5 show the skin friction and rate of heat transfer against  $\xi$  for different values of radiation parameter  $\text{Rd}$ . From this figure we observe that skin friction becomes lower for higher values of radiation, also along  $\xi$  direction skin friction always positively increasing and no separation occurs within the region of our consideration that is  $0 \leq \xi \leq \pi/2$ . There may be flow separation beyond this value of  $\xi$  which has not been investigated in this study due to numerical instability. Again the rate of heat transfer increase, between  $\xi = 0.0$  to 0.125 intersect at  $\xi = 0.125$  and then decrease for higher values of  $\text{Rd}$  within the region  $\xi > 0.125$ . In this figure we found both positive and negative Nusselt numbers. When the wall temperature is higher that the fluid the Nusselt number is positive but when the fluid temperature is higher than the temperature of wall the Nusselt number will be negative which may occur due to the imposed conditions on the problem.

Figure 6 shows the skin friction coefficient  $C_f$  for different values of pressure work parameter  $\text{Ge}$ . It is observed from the figure that the pressure work have great influence on skin friction as well as on the rate of heat transfer. Frictional force at the wall becomes much higher towards the downstream for higher values of  $\text{Ge}$  and the rate of heat transfer as shown in 6 gradually decreased for higher values of pressure work parameter.

From figure 7 it is observed that the rise of magnetohydrodynamic parameter,  $M$  leads to decrease the skin friction and the rate of heat transfer. Which also reduce the gradient of heat transfer and the rate of heat transfer at the leading edge, as a result the rate of heat transfer becomes same at the point  $\xi = 1.0$ . That is, the rate of heat transfer increases between  $\xi = 0.0$  to 1.0 intersect at  $\xi = 1.0$  and then decrease for increasing  $M$  while  $\xi > 1.0$ .



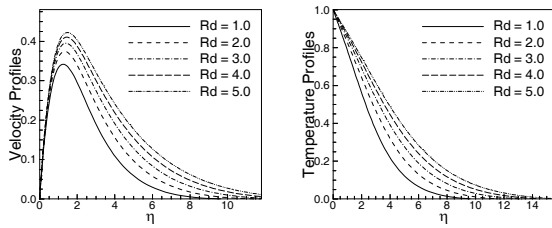


Fig 2. Velocity and temperature profiles for different values of  $Rd$  when  $Pr = 7.0$ ,  $M = 1.0$  and  $Ge=0.1$

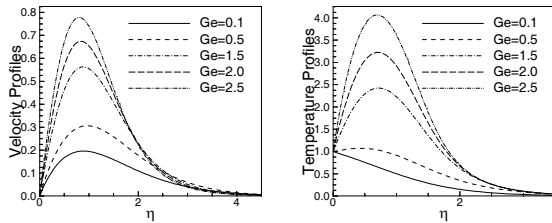


Fig 3. Velocity and temperature profiles for different values of  $Ge$  when  $Pr = 7.0$ ,  $M = 1.0$  and  $Rd = 1.0$

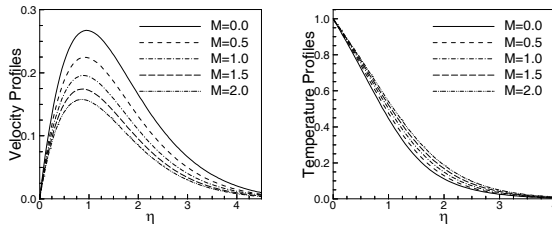


Fig 4. Velocity and temperature profiles for different values of  $M$  when  $Pr = 7.0$ ,  $Rd = 1.0$  and  $Ge=0.1$

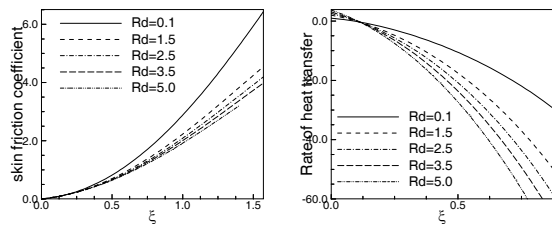


Fig 5. Skin friction and Rate of heat transfer for different values of  $Rd$  when  $Pr = 7.0$ ,  $M = 1.0$  and  $Ge=0.1$

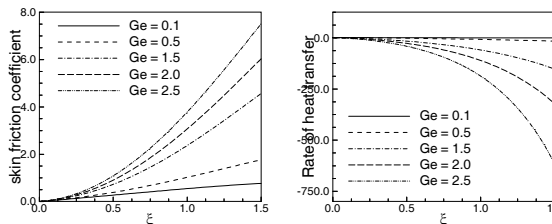


Fig 6. Skin friction and Rate of heat transfer for different values of  $Ge$  when  $Pr = 7.0$ ,  $M = 1.0$  and  $Rd=1.0$

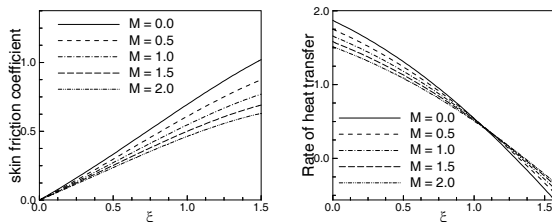


Fig 7. Skin friction and Rate of heat transfer for different values of  $M$  when  $Pr = 7.0$ ,  $Ge=0.1$  and  $Rd=1.0$

#### 4. CONCLUSION

MHD Natural convection flow around a sphere has been studied with the effects of pressure work and radiation. From the present investigation the following conclusions may be drawn:

The velocity as well as the temperature becomes higher for higher values of radiation, which also leads to increase the boundary layer thickness. Also the skin friction becomes lower for higher values of radiation and rate of heat transfer increase near the wall and then decrease for higher values of  $Rd$ .

Due to the increase of pressure work parameter  $Ge$  the velocity rises up. For larger values of  $Ge$  the temperature profiles change its typical nature, such as along  $\eta$  direction temperature gradually increase from the wall value to the peak and then decrease and approach to the asymptotic value. Also the frictional force at the wall becomes much higher towards the downstream for higher values of  $Ge$  and the rate of heat transfer gradually decreased for higher values of pressure work parameter.

The rise of magnetohydrodynamic parameter,  $M$  leads to decrease the velocity, increase the temperature and also reduce the skin friction. The rate of heat transfer shows regular profile before they cross at the point  $\xi = 1.0$  and then show an irregular form.

#### 5. REFERENCES

- Nazar, R. Amin, N. Grosan, T. and Pop, I., 2002, "Free convection boundary layer on an isothermal sphere in a micropolar fluid", *Int. Comm. Heat Mass Transfer*, 29 (3): 377-386.
- Huang, M.J. and Chen, C.K., 1987, "Laminar free convection from a sphere with blowing and suction", *J. Heat Transfer*, 109:529-532.
- Alim, M. A., Alam, Md. M. and Chowdhury, Md. M. K., 2006, "Pressure work effect on natural convection flow from a vertical circular cone with suction and non-uniform surface temperature", *Journal of Mechanical Engineering, The Institution of Engineers, Bangladesh*, 36:6-11.
- Alim, M. A., Alam, Md. M. and Chowdhury, Md. M. K., 2008, "Work Stress Effects on MHD Natural Convection Flow Along a Sphere", *Thammasat International Journal of Science and Technology*, 13(1):1-10.
- Alam, Md. M., Alim, M. A. and Chowdhury, Md. M. K., 2007, "Free convection from a vertical permeable circular cone with pressure work and non-uniform surface temperature", *Nonlinear Analysis: Modelling and Control*, 12(1):21-32.
- Alam, Md. M., Alim, M. A. and Chowdhury, Md. M. K., 2006, "Effect of pressure stress work and viscous dissipation in natural convection flow along a vertical flat plate with heat conduction", *Journal of Naval Architecture and Marine Engineering*, 3(2):69-76.
- Alam, Md. M., Alim, M. A. and Chowdhury, Md. M. K., 2007, "Viscous dissipation effects with MHD natural convection flow on a sphere in presence of

heat generation, Nonlinear Analysis: Modelling and Control”, 12(4):447-459.

8. Soundalgekar, V. M., Takhar, H. S. and Vighnesam, N.V., 1960, “The combined free and forced convection flow past a semi-infinite vertical plate with variable surface temperature”, Nuclear Engineering and Design , 110:95-98.
9. Cogley, A.C., Vincenti, W.G. and Giles, S.E.,1968, “Differential approximation for radiation transfer in a nongray near equilibrium”, AIAA Journal, 6:551–553.
10. Hossain, M. A. and Takhar, H. S, 1996, “Radiation effect on mixed convection along a vertical plate with uniform surface temperature”, Heat and Mass Transfer, 31:243-248.
11. Akhter, Tahmina and Alim, M. A., 2008, “Effects of Radiation on Natural Convection Flow around a Sphere with Uniform Surface Heat flux”, Journal of Mechanical Engineering, The Institution of Engineers, Bangladesh, 39(1):50-56.
12. Keller, H. B., 1978, “Numerical methods in boundary layer theory”, Annual Rev. Fluid Mechanics, 10:417-433.
13. Cebeci, T. and Bradshaw, P., 1984, “Physical and Computational Aspects of Convective Heat Transfer”, Springer, New York.
14. Siegel, R. and Howell, J. R., 1972, “Thermal Radiation Heat Transfer”, McGraw-Hill, New York.

## 6. NOMENCLATURE

Symbol	Meaning	Unit
a	Radius of the sphere	(m)
$C_f$	Skin-friction coefficient	
$C_p$	Specific heat at constant pressure	( $\text{Jkg}^{-1}\text{k}^{-1}$ )
f	Dimensionless stream function	
g	Acceleration due to gravity	( $\text{ms}^{-2}$ )
Gr	Grashof number	
k	Thermal conductivity	( $\text{wm}^{-1}\text{k}^{-1}$ )
M	Magnetohydrodynamic parameter	Dimensionless
Nu	Nusselt number	Dimensionless

Symbol	Meaning	Unit
Pr	Prandtl number	Dimensionless
$q_r$	Radiative heat flux	( $\text{W/m}^2$ )
$R_d$	Radiation parameter	Dimensionless
r	Distance from the symmetric axis to the surface	(m)
T	Temperature of the fluid in the boundary layer	(K)
$T_\infty$	Temperature of the ambient fluid	(K)
$T_w$	Temperature at the surface	(K)
U	Velocity component along the surface	( $\text{ms}^{-1}$ )
V	Velocity component normal to the surface	( $\text{ms}^{-1}$ )
u	Dimensionless velocity along the surface	
v	Dimensionless velocity normal to the surface	
X	Coordinate along the surface	(m)
Y	Coordinate normal to the surface	(m)
$\alpha_r$	Rosseland mean absorption co-efficient	( $\text{cm}^3/\text{s}$ )
$\beta$	Volumetric coefficient of thermal expansion	( $\text{K}^{-1}$ )
$\eta$	Dimensionless Coordinates	
$\theta$	Dimensionless temperature	
$\mu$	Dynamic viscosity of the fluid	( $\text{kgm}^{-1}\text{s}^{-1}$ )
$\nu$	Kinematic viscosity	( $\text{m}^2/\text{s}$ )
$\xi$	Dimensionless co-ordinates	()
$\rho$	Density of the fluid	( $\text{kgm}^{-3}$ )
$\sigma$	Stephan Boltzmann constant	( $\text{js}^{-1}\text{m}^{-2}\text{k}^{-4}$ )
$\sigma_s$	Scattering coefficient	( $\text{m}^{-1}$ )
$\tau_w$	Wall-shear-stress	( $\text{N/m}^2$ )
$\psi$	Stream function	( $\text{m}^2\text{s}^{-1}$ )

## 7. MAILING ADDRESS

M. A. Alim  
 Department of Mathematics,  
 Bangladesh University of Engineering and Technology,  
 Dhaka-1000, Bangladesh.  
 E-mail: maalim@math.buet.ac.bd

## NUMERICAL STUDY ON MIXING FLOW FIELD WITH DIFFERENT ANGLES INTO A SUPERSONIC FLOW

Rafiqul Hoque<sup>1</sup>, Mohammad Ali<sup>2</sup> and Quamrul Islam<sup>2</sup>

<sup>1</sup>Institute of Information and Communication Technology, BUET, Dhaka, Bangladesh

<sup>2</sup>Department of Mechanical Engineering, BUET, Dhaka, Bangladesh

### ABSTRACT

This paper investigates the performance of fuel combustion with the help of computer based simulation system. The simulation is carried out using huge volume of data analysis. A numerical study on mixing of hydrogen injected into a supersonic air stream has been performed by solving Two-Dimensional full Navier-Stokes equations. An explicit Harten-Yee Non-MUSCL Modified-flux-type TVD scheme has been used to solve the system of equations, and a zero-equation algebraic turbulence model to calculate the eddy viscosity coefficient. The main objectives of this study are to increase the mixing efficiency and the flame holding capability of a supersonic combustor. The performance of combustor has been investigated by varying the injection angle, keeping constant the backward-facing step height and other calculation parameters. The investigation shows that, small and large injecting angles increase the flame holding capability but mixing efficiency is poor. For moderate injecting angle, the configuration might act as a good flame holder and become efficient in mixing.

**Keywords:** Navier-Stokes Equations, Flame, Mixing Efficiency, Mach no

### 1. INTRODUCTION

Mixing of fuel with oxidizer and their combustion are encountered in many engineering applications. Particularly, the fuel injection in both supersonic and hypersonic streams requires special attention for efficient mixing and stable combustion. Though a considerable number of researches have been carried out on mixing and combustion of fuel with supersonic air stream, still it faces many unresolved problems. The main problems that arise in this regard, concern mixing of reactants, ignition, flame holding, and completion of combustion. More investigations are required to overcome these problems. In fact, in supersonic combustion, high penetration and mixing of injectant with main stream is difficult due to their short residence time in combustor. In an experimental study, Brown et al. [1] showed that the spreading rate of a supersonic mixing layer decreased drastically with increasing free stream Mach number. A similar conclusion was drawn by Papamoschou et al. [2] on the basis of a theoretical analysis of shear-layers. Furthermore, they showed that the reduction in spreading rate correlated most closely with the convective Mach number, where convective Mach number is defined as the differential velocity normalized by the speed of sound. An independent linear stability theory analysis of Ragab et al.[3] reached the same conclusion. These investigations showed that difficulty exists in achieving a high degree of mixing in high Mach number flows. As

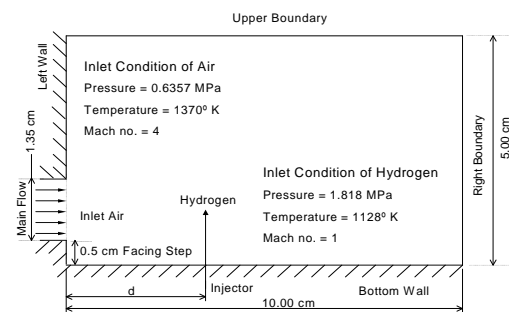


Fig 1. The geometric configuration of the calculation domain

an injectant, gaseous hydrogen is used because it is the most suitable fuel and has high potential of heat release. This is why a considerable number of researches [4-5] has been performed their investigations using hydrogen as an injectant. Therefore, it is necessary to investigate all the parameters that affect the mixing of hydrogen in supersonic airstreams. There exist several methods of fuel injection in the supersonic air stream. Perpendicular injection causes rapid mixing of injectant with main stream and is used to some degree at all flight Mach numbers to promote mixing particularly in upstream portion of the combustor. This study is a part of M.Sc. thesis done by Hoque [6]. Here the effect of injecting angle is investigated for a constant mach number. The geometric configuration of the calculation domain and the inlet conditions of main and injecting flows is shown

in Fig. 1. In this investigations all cases, the left boundary of domain consists of a backward facing step of height 5 mm, a main flow inlet of height 0.9 cm and a solid wall of height 3.6 cm. The backward facing step of 5 mm used because it was found most efficient in mixing investigated by Ali et al [7]. Using Mach 4 we varied the angle 30°, 60°, 90°, 120° and 150°.

## 2. MATHEMATICAL DESCRIPTION

The flow field is governed by the unsteady, two-dimensional full Navier-Stokes and species continuity equations. The body forces are neglected. With the conservation-law form, these equations can be expressed by

$$\frac{\partial U}{\partial t} + \frac{\partial F}{\partial x} + \frac{\partial G}{\partial y} = \frac{\partial F_v}{\partial x} + \frac{\partial G_v}{\partial y}$$

The different terms of this equation can be found in Hoque et al [8].

## 3. RESULTS AND DISCUSSION

Results of varying angle are to be analyzed and discussed under the following contexts; (i) penetration and mixing of hydrogen under the variation of these parameters and (ii) characteristics of the flow field.

### 3.1 Penetration and Mixing of Hydrogen

Figures 2(a~e) show the penetration and mass concentration of hydrogen in the flow field. The definition of “penetration” is given earlier. Penetration and mixing of hydrogen in a numerical simulation can occur by means of (i) turbulence and convection due to recirculation and velocity of the flow (ii) molecular diffusion. For all cases (case 1 ~ 5) the mole fraction contours of hydrogen are concentrated in a narrow region on the top of the injector, as shown in figure 2(a~e), which might became a high heat release zone in the reacting flowfield. The backward facing step associated with upstream recirculation brings the injected hydrogen up to the left boundary in all cases. The hydrogen penetration height at different downstream locations can also be compared from Fig 2(a~e). Longer recirculation zone containing stoichiometric mixture strength results in a longer residence time and leads

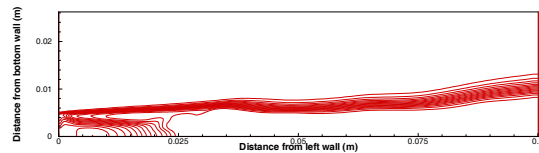


Fig 2a. Mole fraction counter of Hydrogen,  $\Phi(0.05, 1.0, 0.05)$ ; Case-1( $\theta=30^\circ$ )

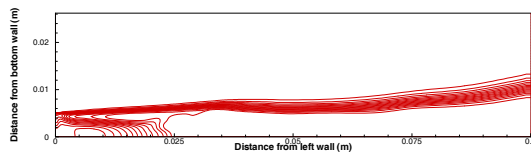


Fig. 2b. Mole fraction counter of Hydrogen,  $\Phi(0.05, 1.0, 0.05)$ ; Case-2( $\theta=60^\circ$ )

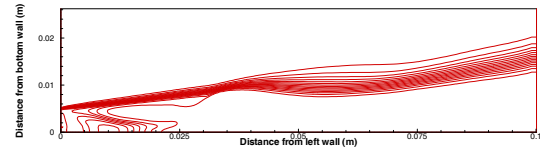


Fig 2c. Mole fraction counter of Hydrogen,  $\Phi(0.05, 1.0, 0.05)$ ; Case-3( $\theta=90^\circ$ )

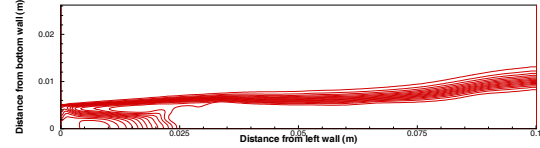


Fig 2d. Mole fraction counter of Hydrogen,  $\Phi(0.05, 1.0, 0.05)$ ; Case-4( $\theta=120^\circ$ )

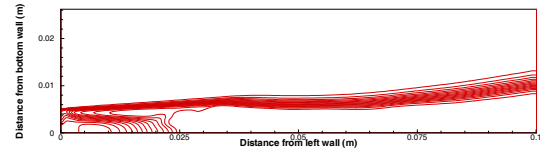


Fig 2e. Mole fraction counter of Hydrogen,  $\Phi(0.05, 1.0, 0.05)$ ; Case-5( $\theta=150^\circ$ )

to a more stable flame. Accordingly case-3 ( $\theta=90^\circ$ ) and 4 ( $\theta=120^\circ$ ) have good flame holding capability, because they can produce larger and elongated upstream recirculation where most of the region contains good proportion of hydrogen and oxygen exists. Again in cases having  $\theta = 30^\circ$  and  $150^\circ$  upstream region contains lower mass concentration of hydrogen which is not good for flame holding. In downstream hydrogen distribution is seemed to be better in case 3~4 as mentioned earlier because of higher expansion of side jet.

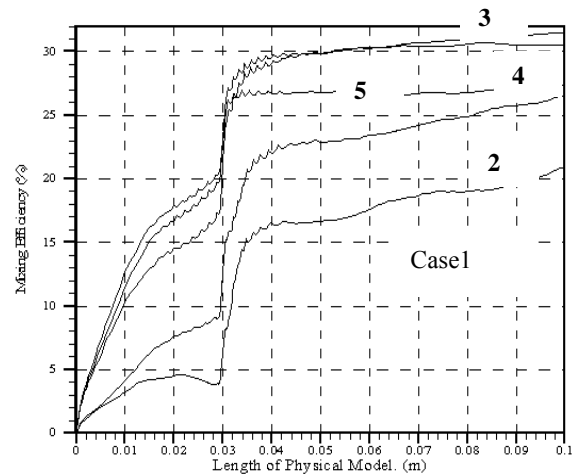


Fig 3. Mixing efficiency along the length of physical model

Figure 3 shows the mixing efficiency along the length of physical model for different cases (case 1~5). Physically mixing efficiency indicates the ratio of hydrogen mass flow rate capable of burning to its total mass flow rate at the exit of side jet. Figure 4 shows that mixing efficiency increases sharply at injector position of respective cases. Generally, in upstream region, the increasing of mixing is moderate and in downstream it is

very slow. Individually, case-3( $\theta=90^\circ$ ) and 4( $\theta=120^\circ$ ) have the highest increment of mixing efficiency at injector position due to strong upstream recirculation. In downstream the increasing rate of mixing along the length of physical model for case-3( $\theta=90^\circ$ ) is higher than case-4 ( $\theta=120^\circ$ ) whereas for case 5( $\theta=150^\circ$ ) it remains almost constant which indicates that for case 5. The larger combustor might increase the cost of construction of combustor provided the other parameters are identical. So case 3( $\theta=90^\circ$ ) has the maximum increasing rate of mixing in downstream.

### 3.2 Characteristics of the flow field

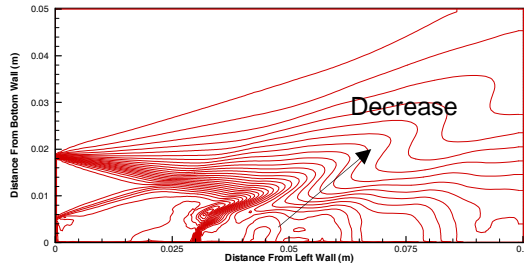


Fig 4a. Case-1( $\theta=30^\circ$ )

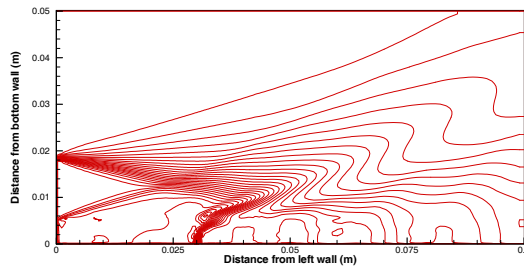


Fig 4b. Case-2( $\theta=60^\circ$ )

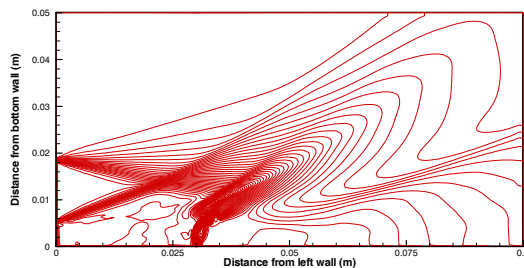


Fig 4c. Case-3( $\theta=90^\circ$ )

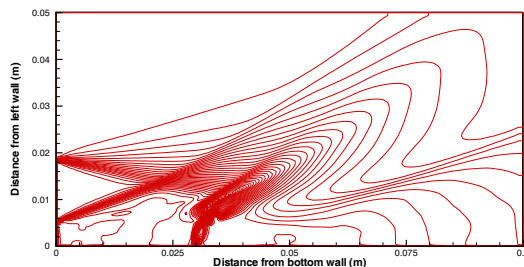


Fig 4d. Case-4( $\theta=120^\circ$ )

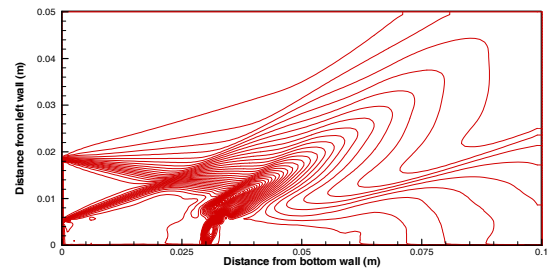


Fig. 4e. Case-5 ( $\theta=150^\circ$ )

The characteristics of the flow field are shown in figs. 4 (a-e). For case 3 ( $\theta=90^\circ$ ) the pressure in the downstream is relatively lower, at upper part of the flow field. Various characteristic phenomena such as separation shock, bow shock, Mach disk, reattachment shock can be seen in figures. The figure shows the pressure contours by which the pressure distribution and different shocks can be understood. Flow separation is initiated by the backward facing step at left boundary. The main flow is deflected upward by the existence of wall at the upper part of the left boundary. The deflection angle is maximum for case 3( $\theta=90^\circ$ ) caused by strong interaction. Under expanded side jet rapidly expands and forms a Mach disk and a bow shock due to the interaction with main flow. This increasing Mach disk is caused by higher expansion of side jet. For the injecting angle  $\theta=90^\circ$  the slope of the bow shock is steeper indicating high interaction between the main and side jet. Due to strong interaction, high gradient of mass concentration exists and this indicates more uniform mixing. The maximum pressure and temperature in the flow field rises immediately behind the intersection of separation shock and bow shock. In the downstream region the reattachment shock is more visible in the pressure contour of figure 4 (a-e). The reattachment shock starts more or less at the same point for all cases (case 1-4). The pressure is higher in the upstream recirculation region while it is much lower immediately behind the injector caused by the suction of injection

### 4. CONCLUSION

The investigation showed that for varying injector angle small and large injecting angles have no significant upstream recirculation. Upstream recirculation is dominant for moderate injecting angle. Perpendicular injection angle increases the both mixing efficiency and flame holding capability. Small injecting angle and very large injecting angle have good flame holding capability but mixing efficiency is poor. It has been found out that for moderate injecting angle ( $\theta=90^\circ$ ) the combustor might act as a good flame holder and become efficient in mixing.

### 5. REFERENCES

1. Brown, G. L. and Roshko, A.: On Density Effects and Large Structure in Turbulent Mixing Layer, *J. Fluid Mechanics*, Vol. 64, No. 4, pp.775-816, (1974).
2. Papamoschou, D. and Roshko, A.: Observation of Supersonic Free Shear Layers, *AIAA Paper 86-0162*,

January (1986).

3. Ragab, S. A. and Wu, J.L.: Instabilities in the Free Shear Layer Formed by Two Supersonic Streams, AIAA Paper 88-0038, January, 1988.
4. Rogers, R. C.: A Study of the Mixing of Hydrogen Injected Normal to a Supersonic Airstream, *NASA TN D-6114*, (1971).
5. Yokota, K. and Kajii, S.: The Injection Methods and Mixing Characteristics in the Two-Dimensional Supersonic Free Stream, *Trans. Japan Soc. Aero. Space Sci.*, Vol. 38, no. 122, pp. 383-393, (1996).
6. Hoque, M. R.: A Numerical Study on Mixing and Injection Systems in Supersonic Combustors, M.Sc. Engineering thesis, Department of mechanical engineering, BUET, January, 2004, Dhaka, Bangladesh.
7. Ali, M., Fujwara, T. and Leblance J. E.: The Effects

of Backward-facing step on Mixing and Flame holding in Supersonic Combustor, *Journal of Energy, Heat and Mass Transfer*, Vol. 23, 2001, pp.319-338.

8. Hoque, M. R. and Ali, M., "Numerical Simulation on Mixing Flow Field with Different Mach Numbers", *4th BSME - ASME International Conference, December 27-29, 2008, Dhaka, Bangladesh.*

## 6. MAILING ADDRESS

Rafiqul Hoque  
Institute of Information & Communication Technology,  
BUET, Dhaka 1000, Bangladesh  
Phone: +8801971707580  
E-mail: rafiqul@iict.buet.ac.bd,

## CONTROLLING THE SIZE DISTRIBUTION OF EXHALED BIOAEROSOL DROPLETS BY MODULATING THE VISCOELASTIC PROPERTIES OF HUMAN AIRWAY MUCUS

Md Anwarul Hasan<sup>1</sup>, Carlos F. Lange<sup>1</sup> and Malcolm King<sup>2</sup>

<sup>1</sup>Department of Mechanical Engineering, University of Alberta, Canada

<sup>2</sup>Pulmonary Research Group, Department of Medicine, University of Alberta, Canada

### ABSTRACT

Effect of the viscoelastic properties of artificial mucus simulant samples on the volume size distribution of bioaerosol droplets generated during simulated coughing has been investigated through in-vitro experiments. The mucus simulant samples had similar viscoelastic properties as real human airway mucus. The mucus simulant gels were prepared by mixing various proportions of 1% Locust bean gum solution and 0.1 M sodium tetraborate (XLB) solution. The viscoelastic properties of the samples were measured using a Bohlin Gemini (Malvern) nano rheometer with peltier plate assembly. An artificial cough machine was used to simulate human cough, generating aerosol droplets in a model trachea attached to the front of the cough machine. The size distribution of the droplets generated through simulated cough was measured using a laser diffraction particle sizer (Malvern SprayTec). Results confirm that the viscoelastic properties of mucus have substantial effect on the size distribution of bioaerosol droplets generated during coughing. The experimental results showed an increase in particle size as the sample changed from an elastic solid type to a viscoelastic type to viscous fluid type sample.

**Keywords:** Bioaerosol droplets, Mucus, Viscoelasticity, Surface Tension, Cough machine.

### 1. INTRODUCTION

Bioaerosol droplets generated and exhaled by humans during breathing, sneezing and coughing may carry airborne pathogens, which upon inhalation by others spread certain contagious infectious diseases, such as influenza, measles, swine flue, chickenpox, smallpox, SARS and so on. Such airborne transmission of respiratory infections through the bioaerosol droplets poses a major public health threat and it is a subject about which surprisingly very little is known. Recent theoretical studies [1] support the hypothesis that the number and size distribution of the bioaerosol droplets generated during coughing can be controlled by altering viscoelastic and surface properties of the airway surface liquid. However, the detail about the correlations between the viscoelastic properties of mucus and the characteristics of the generated bioaerosol droplets are still unknown. In order to mitigate the airborne transmission and to control the generation of bioaerosol droplets during coughing, sneezing etc., it is important to understand the detail mechanisms underlying these events (coughing, sneezing etc) as well as the structure and properties of the airways surface mucus, and the correlations between the relevant viscoelastic properties of mucus with the size distribution of the generated droplets.

#### 1.1 State of the Art Knowledge about Coughing and Bioaerosols

A cough can generate some 3000 droplet nuclei, as can talking for 5 minutes [2]. A sneeze can generate as many as 40,000 droplets [3]. IRSST - Guide on respiratory protection against bioaerosols [4] reports these numbers to be even higher, according to which, during a sneeze, close to two million droplets can be expelled at a velocity of 100 m/sec (200 miles/hour), compared to fewer than 100,000 droplets from a cough. This significant difference is based on the origin of the secretions, which is deeper in the case of a cough [5]. During a forceful cough airspeeds as high as 200 m/s can be attained [6]. Many of the generated droplets may be large enough to contain thousands of microorganisms [7].

During the expulsion, the diameters of the droplets vary between 1 and 2,000  $\mu\text{m}$ , 95% of which are in the order of 2 to 100  $\mu\text{m}$ . However, they dry very rapidly. The drying times for 100 and 50  $\mu\text{m}$  droplets in air at 50% relative humidity are 1.3 and 0.3 seconds, respectively [8]. After being exhaled these droplets can evaporate to particles in the size range of 0.5 to 12 micron [3]. Others reported that the infectious particles generated from human respiratory sources occur primarily as droplet nuclei of 0.5 to 5.0 micron in



diameter [9]. On complete evaporation, the particles may be small enough to remain airborne in the indoor air flow.

The size of microorganisms, on the other hand, span wide size ranges i.e. from 0.3 to 10 micron for bacterial cells and spores, 2.0 to 5.0 micron for fungal spores, and 0.02 to 0.30 micron for viruses [10]. Others report these numbers to be slightly different. For example: According to Lee et al. [11], most bacteria and molds are between 0.7 and 10  $\mu\text{m}$  in size. According to AIHA (American Industrial Hygiene Association) the sizes of bioaerosols are in the order of 0.02 to 0.25  $\mu\text{m}$  for viruses, 0.3 to 15  $\mu\text{m}$  for bacteria, and 1 to 50  $\mu\text{m}$  for the majority of molds and yeasts [12]. Yassi and Bryce [5] and ACGIH [7] report that the size of infectious bioaerosols is probably between 0.1 and 10  $\mu\text{m}$  [5], [7]. It even appears that the majority of viruses and bacteria that cause respiratory diseases in humans are usually inside bioaerosols with diameters greater than 5  $\mu\text{m}$ .

Depending on aerosolized droplet size, airborne pathogens can quickly be deposited on nearby external surfaces or the expired bioaerosols can travel great distances and remain airborne for an extended period of time, particularly when droplet diameters are too large for diffusive deposition ( $>200$  nm) or too small for gravitational deposition ( $<2$   $\mu\text{m}$ ) [13], [14]. Bioaerosols consisting of solid or liquid particles smaller than 10  $\mu\text{m}$  in diameter remain suspended in the air for a sufficient time (a few hours) and are likely to be inhaled [7], [15], [5]. Table 1 presents the time required for a bioaerosol to be deposited by sedimentation from a height of three meters. As shown in table 1, solid or liquid particles between 6 and 10  $\mu\text{m}$  can take a few hours before being deposited from a height of 3 meters [8], [5].

Some researchers make a distinction between micro droplets with diameter less than or equal to 5 micron, and those with diameter  $> 5$  micron, with a belief that droplets larger than 5 micron sediment before traveling a distance of one meter. Such a distinction has no solid foundation (Lenhart et al., 2004b).

Table 1: Behavior of bioaerosols in the air (Yassi and Bryce, 2004)

Diameter in micron	Time required for deposition from a height of 3 meters
100	10 sec
40	1 min
20	4 min
10	17 min
6 to 10	A few hours
0.06 to 6	Several hours

## 1.2 Literature Review on Bioaerosol Research

To date, few studies have carefully examined the nature of the bioaerosols that humans exhale on a daily basis (Table 1). Early researchers assumed the upper respiratory tract (nose, mouth and throat) was the primary location of droplet formation [16], [17], [18]. In these early studies, the mouths and throats of volunteers were coated with a dye and breathing, talking, sneezing

and coughing maneuvers were monitored and any resulting droplets were collected directly onto a slide. Only droplets  $>1$   $\mu\text{m}$  were measured by microscopic observation. Duguid [16] found that droplets ( $>1$   $\mu\text{m}$ ) produced by speaking, coughing and sneezing were sufficiently small enough to remain airborne. Normal breathing, however, produced no measurable droplets ( $>1$   $\mu\text{m}$ ). In a second series of experiments Duguid [17] determined that coughing produced an average droplet size of 14  $\mu\text{m}$  and geometric standard deviation (GSD) = 2.6 and for sneezing GM = 8.1  $\mu\text{m}$  and GSD = 2.3. On the other hand, Loudon and Roberts [18] showed that the estimated lognormal parameters were GM = 12.1  $\mu\text{m}$  and GSD = 8.4 for cough. More recently, Papineni and Rosenthal [19] measured expired bioaerosol droplets (in nose and mouth breathing, coughing and talking) to be  $<2$   $\mu\text{m}$  in size, with no droplets  $>8$   $\mu\text{m}$ .

An interesting common finding from these studies was the high variability in the levels of bioaerosol production from different individuals. More-recent experiments have utilized optical particle counting (OPC) to determine the size and concentration of droplets exhaled from all parts of the respiratory tract [19], [20], [21]. In a similar experiment to that of Papineni and Rosenthal, Edwards et al. [20] observed 11 healthy human subjects. Results from this study confirmed Papineni and Rosenthal's findings because they suggested exhaled particles during normal mouth breathing are predominantly  $<1$   $\mu\text{m}$  in diameter. Edwards' results also showed that expired particle numbers vary substantially from subject to subject, with two distinct populations: low producers (those exhaling an average of  $<500$  droplets per liter over a six hour measurement period) and super producers (those exhaling an average of  $>500$  droplets per liter over a six hour measurement period) of expired bioaerosols. Remarkably, the super producers (six people from this test group) expired 99% of the total amount of bioaerosols that were expired by the entire group,

In their study, Edwards et al. [20] further found that delivering  $\sim 1$  g of isotonic saline (orally via nebulized aerosols, 5.6  $\mu\text{m}$  in diameter) reduces the total amount of expired aerosols (among the super-producing individuals) by  $\sim 72\%$  over a six hour period and markedly diminishes total expired bioaerosol production for the entire group. In vitro results, obtained using a simulated cough machine, also indicated that a mucus mimetic nebulized with saline produces a larger droplet size after the forced convection of air over its surface than when air is forced over the mucus mimetic alone (i.e. without saline nebulization). These results led Edwards and co-workers to conclude that saline delivered onto lung surfactant increases its surface tension, and potentially other dynamic physical properties of the lung surfactant, thereby changing the droplet breakup dynamics. In another study, Clarke et al. [22] report that delivering isotonic saline aerosols (in 5.6  $\mu\text{m}$  droplets) into the endotracheal tube of anesthetized bull calves showed a dose-responsive effect on exhaled bioaerosols; six minutes of treatment resulted in a decrease  $\leq 50\%$  of exhaled bioaerosols for at least 120 minutes, compared with pre-treatment.

The idea of inhaling saline for medical benefit has existed since the time of Hippocrates. However, the mechanism of this phenomenon remains unclear, as does the reason for the dramatic exhaled aerosol differences among human individuals [23].

In explaining why certain individuals in Edward's study breath out many more bioaerosol particles than do others, Wiwik et al suggested that possibly transient and/or durable intersubject variations in the ionic composition of airways surface liquid produce the intersubject variations in the number of expired bioaerosol particles, and potentially in airborne disease infectiousness. They reasoned that the gelation of the free surface of airways surface liquid mimetic owing to deposition of salt-based solutions should diminish the propensity of the airways surface liquid to break up into droplets in the cough machine.

## 2. EXPERIMENT

### 2.1 Material and Specimen

Mucus simulant gels having similar viscoelastic properties as real human airway mucus [24] over a wide range were used. The gels were prepared by mixing various proportions 1% Locust bean gum (LBG) solution and 0.1 M sodium tetraborate (XLB) solution. For preparation of locust bean gum solution, 100 ml of saline ( $\text{Na}_2\text{NO}_3$ ) solution was heated to 80 °C. The required amount of LBG powder was added to the saline solution little by little while the solution continuously being stirred using a magnetic stirrer. The weight of the beaker with the saline solution was measured both before and after heating and mixing LBG powder. Mass balance was ensured by adding additional saline solution to compensate the losses due to evaporation whenever necessary. Compositions of locust bean gum solution used in the experiments was 1%, 0, 10, 15, 20, 30, 45, 60 and 90 microlitre of 0.1M tetraborate solution was added to 1.5 ml of locust bean gum solution. The mixture was then vortexed for 2 minutes on a vortex meter.

### 2.2 Viscoelastic Properties

Viscoelastic properties of the samples were measured using a Bohlin Gemini Malvern Nano-Rheometer with a peltier plate assembly and parallel plate geometry. The frequency of the oscillation was varied between 0.1 Hz and 10 Hz. All measurements were performed at constant strain within the linear viscoelastic region i.e. within the limit of shear stress where viscosity is independent of applied shear stress. This region was obtained for each sample by performing an amplitude sweep test before the actual measurement of viscoelastic properties. The temperature was kept constant at 25 °C. A solvent trap was used to avoid drying out of the samples during measurement.

### 2.3 Cough machine experiment

Cough machine experiments were performed to mimic bioaerosol generation during a human cough. The artificial cough machine comprised of an 8-liter Plexiglas tank equipped with a Wilmot Castle pressure gauge. The Gas release was controlled by an Asco solenoid valve located at the start of the outflow line. A

model trachea 35 cm long with an interior width of 2.0 cm and an interior height of 1.0 cm was attached to the outlet after the solenoid valve. A small rectangular slot 3 cm long by 1.76 cm wide and 1 mm deep was engraved on the upper surface of the bottom plate of the model trachea to hold the mucus simulant sample in place. The slot size was large enough for holding 1.5 ml sample. Mucus simulant samples were placed inside the trachea at the sample slot and a normal adult cough was simulated by suddenly releasing the air from the tank stored at a pressure of 8.5 psi.

### 2.4 Measurement of Droplet Size Distribution

The size distribution of the droplets was measured using a laser diffraction based size measuring device, Malvern Spraytec. In our case, the droplets generated from the cough machine were passed through the laser beam of of about 1cm diameter. The droplets scatter the light, smaller droplets scattering the light at larger angles than bigger droplets. The scattered light is measured by a series of photodetectors placed at different angles. This is known as the diffraction pattern for the sample. The diffraction pattern is used to measure the size of the droplets using light scattering theory developed by Mie. Laser diffraction is sensitive to the volume of the droplets. For this reason, droplet diameters are calculated from the measured volume of the droplets, assuming a sphere of equivalent volume.

## 3. RESULTS AND DISCUSSION

The viscous modulus and elastic modulus versus amount of cross linking graphs for the mucus simulant samples are shown in Fig 1 (a) and (b) respectively. The Figure shows that the change in viscous modulus with increase in cross linking follows different pattern at different frequencies (i.e. at different shear rate). Even though at low frequencies ( $\leq 0.1$  Hz) the change in viscous modulus with increase in cross linking is considerably high, at moderate to high frequencies ( $\geq 0.5$  Hz), which are more likely relevant to coughing, change in viscous modulus with increase in cross linking is not significant. The elastic modulus of the samples, on the other hand increases continuously by up to two orders of magnitude as shown in Fig. 1(b). Figs. 2 (a) and (b) present the complex viscosity of the samples against frequency and amount of cross linking respectively. The shear thinning behavior is evident in Fig. 2 (a) while Fig. 2 (b) shows that the complex viscosity increases with increase in cross linking at all frequencies. Figs. 3 (a) and (b) show the phase angle of the samples against frequency and amount of cross linking respectively. As expected due to the non-Newtonian behavior of the samples, the phase angle values are different at different shear rate for the same sample. It is worth mentioning here that a zero degree phase angle means a pure elastic (solid) material, a ninety degree value of phase angle indicates a purely viscous (Newtonian fluid) material while the values between zero and ninety indicates a viscoelastic material. Based on the phase angle at a particular shear rate, the samples can be classified into (i) elastic solid like samples (0 to <30 degree), (ii) strongly

viscoelastic samples (30 to 60 degree), and (iii) viscous liquid like samples (60 to 90 degree). A simulated Cough is considered to be a high shear rate phenomenon as is a real human cough considered. However since the actual value of the shear rate that governs the droplet generation is unknown, for convenience we will subsequently refer all viscoelastic properties at a frequency of 0.1 Hz. Thus based on the phase angle values at 0.1 Hz, from Fig. 3 (a) we find that 0 micro liter sample was a viscous fluid type sample, 10 micro liter and 15 micro liter samples were strongly viscoelastic samples while the 30 and 45 micro liter samples were elastic solid type samples.

The volumetric size distribution of the droplets generated during simulated cough experiments for addition of 0, 30, 45 and 60 micro liter cross linking agent (Sodium Tetraborate solution) are presented in

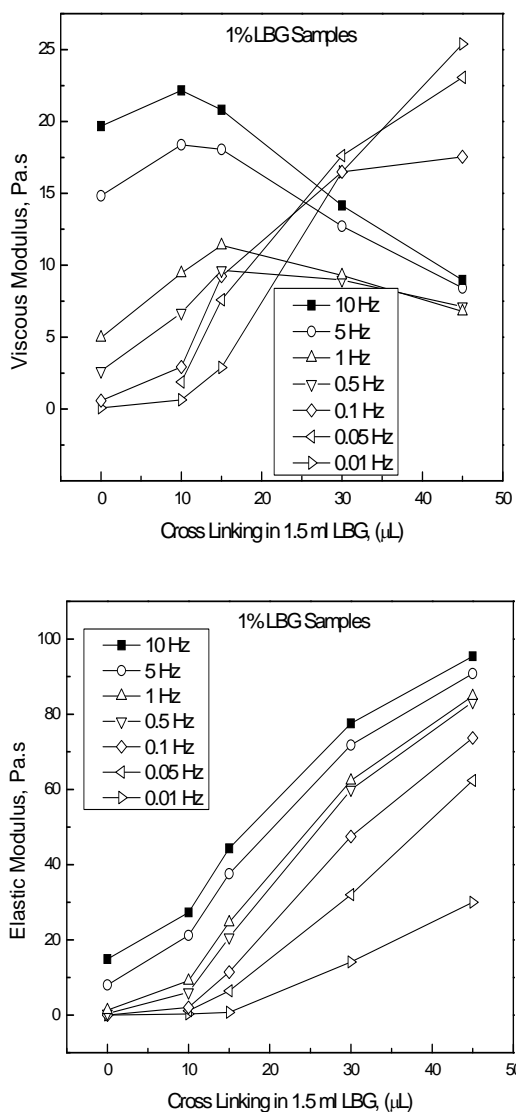


Fig 1. Viscous modulus and elastic modulus versus amount of cross linking graphs for 1% LBG samples.

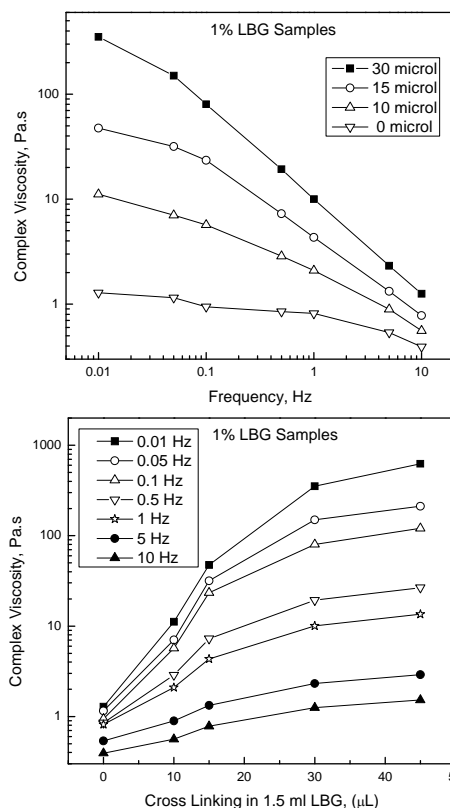


Fig 2. Complex viscosity versus (a) frequency, and (b) amount of cross linking graphs for 1% LBG samples.

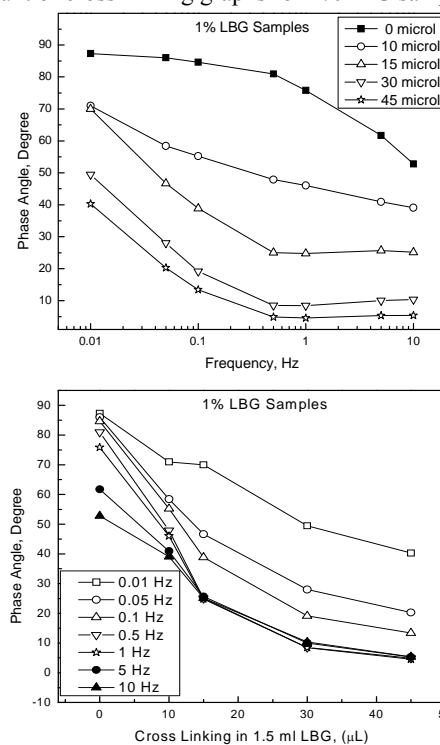


Fig 3. Phase angle for 1% LBG samples. Figs. 4 (a), (b), (c), and (d) respectively. Each figure presents results for at least three repeated test runs for one sample. Figure 4 confirms that the viscoelastic properties of mucus have substantial effect on the size distribution of droplets generated during coughing. Three

distinct type of droplet size distribution are apparent in Figure 4. While the viscous liquid like sample, Fig. 4(a), shows a bimodal droplet size distribution with a smaller peak at around 0.4 micron and a larger peak at around 10 micron, the viscoelastic type sample, Fig. 4 (b), shows a single mode of size distribution. The smaller peak in the submicron size range apparent for the viscous liquid like sample is no longer apparent for strongly viscoelastic sample. For elastic solid type samples, Figs. 4 (c) and (d), the size distribution is again a bimodal distribution with a much stronger peak at a relatively smaller size.

In another word, the size distribution of the droplets apparently shifts rightward as the sample changes from an elastic solid like sample (large amount of cross linking) to a viscoelastic sample to a viscous fluid like sample as shown in Fig. 5.

#### 4. CONCLUSIONS

This study confirms that the viscoelastic properties of mucus have substantial effect on the size distribution of droplets generated during coughing. The experimental results showed an increase in particle size as the samples changed from an elastic solid type to a viscoelastic type to viscous fluid type samples.

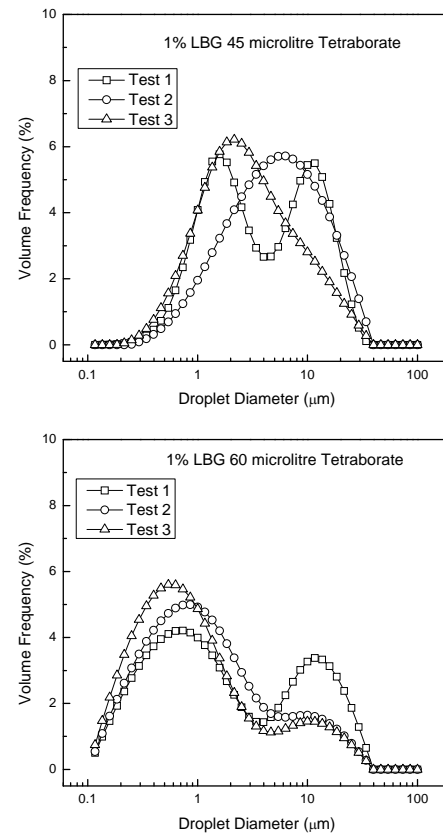
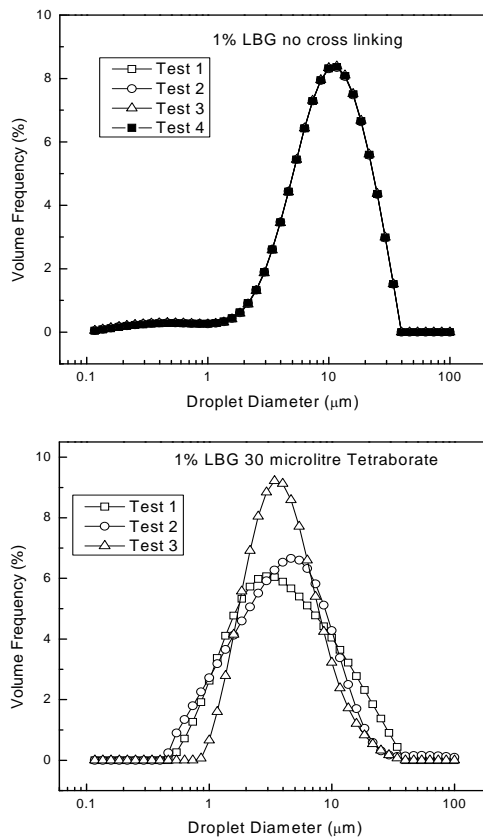


Fig 4. Complex viscosity versus (a) frequency, and (b) amount of cross linking graphs for 1%LBG samples.

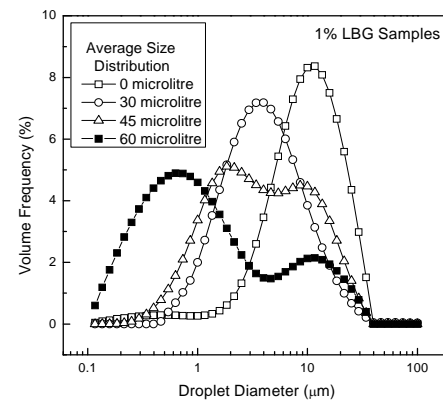


Fig 5. Complex viscosity versus (a) frequency, and (b) amount of cross linking graphs for 1%LBG samples.

#### 5. ACKNOWLEDGEMENT

The authors would like to thank Dr Gustavo Zayas for his assistance in the lab with sample preparation. The Nanotechnology scholarship of the Alberta Ingenuity fund and FS Chia PhD scholarship from the Faculty of Graduate Studies and Research, University of Alberta as well as the Alberta Lungs Association PhD scholarship for MD Anwaul Hasan are also gratefully acknowledged.

## 6. REFERENCES

1. Vasudevan M., and Lange C. F., 2007, "Surface Tension Effects on Instability in Viscoelastic Respiratory Fluids", *Mathematical Biosciences*, 205: 180-194.
2. Des Prez R., and Heim C., 1990. Mycobacterium Tuberculosis. In: Mandell, G, Douglas, J. R., and Bennett, J., (Eds.), *Principles and Practices of Infectious Diseases*. Churchill Livingstone, New York, pp. 1877-1906.
3. Cox C. S., 1987. *The Aerobiological Pathway of Microorganisms*. John Wiley and Sons Ltd, Chichester (UK).
4. Lavoie J., Cloutier Y., Lara J., and Marchand G., 2007. *Guide on Respiratory Protection against Bioaerosols - Recommendations on Its Selection and Use, Studies and Research Projects/Technical Guide RG-501 IRSST, Montréal*, pp. 40 pages.
5. Yassi A., and Bryce E., 2004, "Protecting the Faces of Health Care Workers: Knowledge Gaps and Research Priorities for Effective Protection against Occupationally-Acquired Respiratory Infectious Diseases. The Change Foundation, Ontario Hospital Association and Occupational Health and Safety Agency for Healthcare in Bc, 103 Pages".
6. Ross B. B., Gramiak R., and Rahn H., 1955, "Physical Dynamics of the Cough Mechanism", *J. Appl. Physiol.*, 8: 264-269.
7. ACGIH, 1999. *American Conference of Governmental Industrial Hygienists (Acgih), (1999), Bioaerosols: Assessment and Control.*, Cincinnati, OH, pp. 322 pages.
8. Lenhart S. W., Seitz T., Trout D., and Bollinger N., 2004b, "Issues Affecting Respirator Selection for Workers Exposed to Infectious Aerosols: Emphasis on Healthcare Settings", *Applied Biosafety*, 9: 2-36.
9. Owen M. K., Ensor D. S., and Sparks L. E., 1992, "Airborne Particle Sizes and Sources Found in Indoor Air", *Atmos. Environ.*, 26: 2149-2162.
10. Cole E. C., and Cook C. E., 1998, "Characterization of Infectious Aerosols in Health Care Facilities: An Aid to Effective Engineering Controls and Preventive Strategies", *American Journal of Infection Control*, 26: 453-464.
11. Lee S.-A., Adhikari A., Grinshpun S. A., McKay R., Shukla R., Zeigler H. L., and Reponen T., 2005, "Respiratory Protection Provided by N95 Filtering Facepiece Respirators against Airborne Dust and Microorganisms in Agricultural Farms." *Journal of Occupational and Environmental Hygiene*, 2: 577-583.
12. Goyer N., Lavoie J., Lazure L., and Marchand G., 2001. *Les Bioaérosols En Milieu De Travail : Guide D'évaluation, De Contrôle Et De Prévention. Études Et Recherches, Guide Technique T-23.*, Institut de recherche Robert-Sauvé en santé et en sécurité du travail, pp. 63 pages.
13. Gerrity T. R., 1979, "Calculated Deposition of Inhaled Particles in the Airway Generations of Normal Subjects", *J. Appl. Physiol.*, 47: 867-873.
14. Stahlhofen W, Gebhart J, Heyder J, Philipson K, and P. C., 1989, "Intercomparison of Experimental Regional Aerosol Deposition Data", *J. Aerosol Med.*, 2: 285-308.
15. Hinds W. C., 1982. *Aerosol Technology. Properties, Behavior, and Measurement of Airborne Particles*. John Wiley and Sons, Toronto.
16. Duguid J. P., 1945, "The Numbers and Sites of Origin of the Droplets Expelled During Expiratory Activities", *Edinburgh Med. J.*, 52: 385-401.
17. Duguid J. P., 1946, "The Size and Distribution of Air-Carriage of Respiratory Droplets and Droplet-Nuclei", *J. Hyg.*, 4: 471-480.
18. Loudon R. G., and Roberts R. M., 1967, "Droplet Expulsion from the Respiratory Tract", *American Review of Respiratory Disease* 95: 433-442.
19. Papineni R. S., and Rosenthal F. S., 1997, "The Size Distribution of Droplets in the Exhaled Breath of Healthy Human Subjects", *J. Aerosol Med.*, 10 105-116.
20. Edwards D. A., Jonathan C. Man, Brand P., Katstra J. P., Sommerer K., Stone H. A., Nardell E., and Scheuch G., 2004. *Inhaling to Mitigate Exhaled Bioaerosols*, *Proc. Natl. Acad. Sci. U. S. A.*, pp. 17383-17388.
21. Fairfield C. I., and Stampfer J. F., 1987, "Particle Concentration in Exhaled Breath", *Am Ind Hyg Assoc J.*, 48: 948-949.
22. Clarke S. W., Jones J. G., and Oliver D. R., 1970, "Resistance to Two-Phase Gas-Liquid Flow in Airways", *J. Appl. Physiol.*, 29: 464-471.
23. Watanabe W., Thomas M., Clarke R., Klibanov A. M., Langer R., Katstra J., Fuller G. G., Griel L. C., Fiegel J., and Edwards D., 2007, "Why Inhaling Salt Water Changes What We Exhale", *Journal of Colloid and Interface Science*, 307: 71-78.
24. King M., Brock G., and C. Lundell C., 1985, "Clearance of Mucus by Simulated Cough", *J Appl. Physiol*, 58: 1776-1982.

## 7. MAILING ADDRESS

Md Anwarul Hasan  
Department of Mechanical Engineering, University of  
Alberta, Canada.

# MHD NATURAL CONVECTION FLOW FROM A POROUS VERTICAL PLATE

Amena Ferdousi<sup>1</sup> and M. A. Alim<sup>2</sup>

<sup>1</sup>Department of Electronics and Electrical Engineering, Eastern University, Bangladesh

<sup>2</sup>Department of Mathematics, Bangladesh University of Engineering and Technology, Dhaka, Bangladesh.

## ABSTRACT

An analysis of MHD natural convection flow from a porous vertical plate is carried out by using finite difference method together with Keller-Box scheme. This method is applied successfully to predict the surface shear stress, the rate of heat transfer, velocity and temperature profiles. The governing boundary layer equations are first transformed into a non dimensional form and the resulting non linear system of partial differential equations are then solved numerically. The numerical results of the surface shear stress in terms of skin friction coefficient and the rate of heat transfer in terms of local Nusselt number, velocity as well as temperature profiles are shown graphically and tabular form for a selection of parameters set of consisting of magnetohydrodynamic parameter  $M$ , Prandtl number  $Pr$ . MHD affects the boundary layer flow, so velocity decreases and temperature increase for this the skin friction coefficient and the rate of heat transfer decreases. Increasing value of MHD serves to thin the boundary layer.

**Keywords:** porous plate, natural convection, magnetohydrodynamic.

## 1. INTRODUCTION

The study of the flow of electrically conducting fluid in presence of magnetic field is also important from the technical point of view and such types of problems have received much attention by many researchers. The specific problem selected for study is the flow and heat transfer in an electrically conducting fluid adjacent to the surface. The interaction of the magnetic field and the moving electric charge carried by the flowing fluid induces a force, which tends to oppose the fluid motion. And near the leading edge the velocity is very small so that the magnetic force, which is proportional to the magnitude of the longitudinal velocity and acts in the opposite direction, is also very small. Consequently the influence of the magnetic field on the boundary layer is exerted only through induced forces within the boundary layer itself, with no additional effects arising from the free stream pressure gradient. MHD was originally applied to astrophysical and geophysical problems but more recently to the problem of fusion power, where the application is the creation and containment of hot plasmas by electromagnetic forces, since material wall be destroyed. Astrophysical problems include solar structure especially in the outer layers, the solar wind bathing the earth and other planets and interstellar magnetic fields. In the presence of MHD natural convection boundary layer flow from a porous vertical plate of a steady two dimensional viscous incompressible

fluid has been investigated. In the present work following assumptions are made:

- Variations in fluid properties are limited only to those density variations which affect the buoyancy terms
- Viscous dissipation effects are negligible and
- The radiative heat flux in the  $x$ -direction is considered negligible in comparison with that in the  $y$  direction, where the physical coordinates  $(u, v)$  are velocity components along the  $(x, y)$  axes.

Merkin [1] studied free convection with blowing and suction. Lin and Yu [2] studied free convection on a horizontal plate with blowing and suction. Singh [3] concluded on MHD free-convection flow in the Stokes problem for a porous vertical plate. Chowdhury and Islam [4] considered MHD free convection flow of visco-elastic fluid past an infinite vertical porous plate. Hossain and Takhar [5] studied radiation effect on mixed convection along a vertical plate with uniform surface temperature. Hayat et al [6] pursued the influence of thermal radiation on MHD flow of a second grade fluid. Alam et al. [7] investigated numerical study of the combined free-forced convection and mass transfer flow past a vertical porous plate in a porous medium with heat generation and thermal diffusion. Hossain [8] computed effect of Hall current on unsteady hydromagnetic free convection flow near an infinite vertical porous plate. Hossain et al. [9] studied the effect of radiation on free convection flow from a porous vertical plate. They [9]

analyzed a full numerical solution and found an increase in Radiation parameter  $R_d$  causes to thin the boundary layer and an increase in surface temperature parameter causes to thicken the boundary layer. The presence of suction ensures that its ultimate fate if vertically increased is a layer of constant thickness. Duwairi and Damseh [10] studied magnetohydrodynamic natural convection heat transfer from radiate vertical porous surfaces. None of the aforementioned studies considered MHD effects on laminar boundary layer flow of the fluids along porous plate.

In the present study, we have investigated MHD natural convection flow from a porous vertical plate numerically. The results will be obtained for different values of relevant physical parameters and will be shown in graphs as well as in tables.

The governing partial differential equations are reduced to locally non-similar partial differential forms by adopting some appropriate transformations. The transformed boundary layer equations are solved numerically using implicit finite difference scheme together with the Keller box technique [11]. Here, we have focused our attention on the evolution of the surface shear stress in terms of local skin friction and the rate of heat transfer in terms of local Nusselt number, velocity profiles as well as temperature profiles for selected values of parameters consisting of the magnetic parameter  $M$ , Prandtl number  $Pr$ .

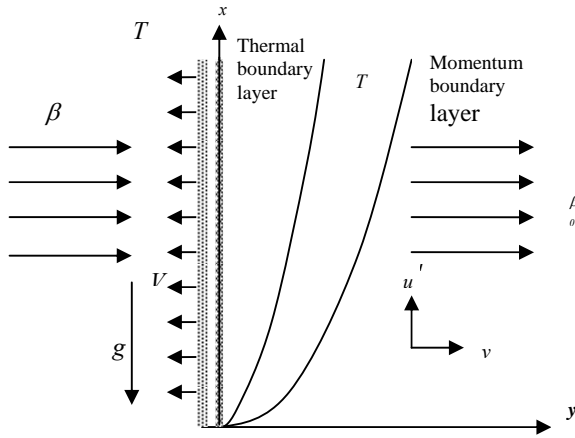


Fig 1. The coordinate system and the physical model

We have investigated MHD natural convection flow from a porous plate. Over the work it is assumed that the surface temperature of the porous vertical plate,  $T_w$ , is constant, where  $T_w > T_\infty$ . The physical configuration considered is as shown in Fig.1:

The conservation equations for the flow characterized with steady, laminar and two dimensional boundary layer; under the usual Boussinesq approximation, the continuity, momentum and energy equations can be written as:

$$\frac{\partial u}{\partial x} + \frac{\partial v}{\partial y} = 0 \quad (1)$$

$$\rho(u \frac{\partial u}{\partial x} + v \frac{\partial u}{\partial y}) = \mu \frac{\partial^2 u}{\partial x^2} + \rho g \beta (T - T_\infty) - \sigma_0 \beta_0^2 u \quad (2)$$

$$\rho c_p (u \frac{\partial T}{\partial x} + v \frac{\partial T}{\partial y}) = k \frac{\partial^2 T}{\partial y^2} \quad (3)$$

With the boundary conditions

$$x = 0, y > 0, u = 0, T = T_\infty,$$

$$y = 0, x > 0, u = 0, v = -V, T = T_w \quad (4)$$

$$y \rightarrow \infty, x > 0, u = 0, T = T_\infty$$

where  $\rho$  is the density,  $\beta_0$  is the strength of magnetic field,  $\sigma_0$  is the electrical conduction,  $k$  is the thermal conductivity,  $\beta$  is the coefficient of thermal expansion,  $\nu$  is the reference kinematic viscosity  $\nu = \mu/\rho$ ,  $\mu$  is the viscosity of the fluid,  $C_p$  is the specific heat due to constant pressure. Over the work it is assumed that the surface temperature of the porous vertical plate,  $T_w$ , is constant, where  $T_w > T_\infty$ . Here  $T_\infty$  is the ambient temperature of the fluid,  $T$  is the temperature of the fluid in the boundary layer,  $g$  is the acceleration due to gravity, the fluid is assumed to be a grey emitting and absorbing, but non scattering medium.

Now introduce the following non-dimensional variables:

$$\eta = \frac{Vy}{\nu \xi}, \xi = V \left\{ \frac{4x}{v^2 g \beta \Delta T} \right\}^{\frac{1}{4}}$$

$$\psi = V^{-3} v^2 g \beta \Delta T \xi^3 \left\{ f + \frac{\xi}{4} \right\} \quad (5)$$

$$\theta = \frac{T - T_\infty}{T_w - T_\infty}, \theta_w = \frac{T_w}{T_\infty} \quad (6)$$

Substituting(5) and (6) into Equations (1), (2) and (3) leads to the following non-dimensional equations

$$f''' + \theta - 2f'^2 + 3ff'' + \xi f'' = \xi \left( f' \frac{\partial f'}{\partial \xi} - f'' \frac{\partial f'}{\partial \xi} \right) - \frac{\sigma_0 \beta_0^2}{\rho} v^{-2} \xi^2 f' \quad (7)$$

$$\frac{1}{Pr} \frac{\partial}{\partial \eta} \left[ \frac{\partial \theta}{\partial \eta} \right] + 3f\theta' + \xi \theta' = \xi \left( f' \frac{\partial \theta}{\partial \xi} - \frac{\partial f}{\partial \xi} \theta' \right) \quad (8)$$

Where  $Pr = \nu C_p / k$  is the Prandtl number is the heat generation parameter and  $M = \beta_0^2 \sigma_0 / \nu \rho$  is the magneto hydrodynamic parameter.

The boundary conditions (4) become

$$f = 0, f' = 0, \theta = 1 \text{ at } \eta = 0 \quad (9)$$

$$f' = 0, \theta = 0 \text{ as } \eta \rightarrow \infty$$

The solution of equations (7), (8) enable us to calculate the nondimensional velocity components  $u, v$  from the following expressions

$$(1)$$



$$\bar{u} = \frac{v^2}{Vg\beta(T_w - T_\infty)} u = \xi^2 f'(\xi, \eta) \quad (10)$$

$$\bar{v} = \frac{v}{V} = \xi^{-1} (3f + \xi - \eta f' + \xi \frac{\partial f}{\partial \xi})$$

In practical applications, the physical quantities of principle interest are the shearing stress  $\tau_w$  and the rate of heat transfer in terms of the skin-friction coefficients  $C_{fx}$  and Nusselt number  $Nu_x$  respectively, which can be written as

$$Nu_x = \frac{V}{V\Delta T} (q_c)_{\eta=0}, C_{fx} = \frac{V}{g\beta\Delta T} (\tau)_{\eta=0} \quad (11)$$

$$\text{where } \tau_w = \mu \left( \frac{\partial u}{\partial y} \right)_{\eta=0} \text{ and } q_c = -k \left( \frac{\partial T}{\partial y} \right)_{\eta=0} \quad (12)$$

$q_c$  is the conduction heat flux.

Using the Equations (6) and the boundary condition (9) into (11) and (12), we get

$$C_{f_x} = \xi f''(x, 0) \quad (13)$$

$$Nu_x = \xi^{-1} \theta'(x, 0)$$

The values of the velocity and temperature distribution are calculated respectively from the following relations:

$$\bar{u} = \xi^2 f'(\xi, \eta), \quad \theta = \theta(x, y) \quad (14)$$

## 2. NUMERICAL PROCEDURE

Solutions of the local non similar partial differential equation (7) to (8) subjected to the boundary condition (9) are obtained by using implicit finite difference method with Keller-Box Scheme. which has been described in details by Cebeci [12].

Discussion on the advancement of algorithm on implicit finite difference method is given below taking into account the following Equations (15-16).

$$f''' + 3ff'' - 2(f')^2 + \theta - \xi f''' - Mf'\xi^2 = \xi \left( f' \frac{\partial f'}{\partial \xi} - \frac{\partial f}{\partial \xi} f'' \right) \quad (15)$$

$$\frac{1}{Pr} \frac{\partial}{\partial \eta} \left[ \frac{\partial \theta}{\partial \eta} \right] + 3f\theta' + \xi\theta' = \xi \left( f' \frac{\partial \theta}{\partial \xi} - \frac{\partial f}{\partial \xi} \theta' \right) \quad (16)$$

To apply the aforementioned method, we first convert Equations (15)-(16) into the following system of first order equations with dependent variables  $u(\xi, \eta)$ ,

$v(\xi, \eta)$ ,  $p(\xi, \eta)$  and  $g(\xi, \eta)$  as

$$f' = u, u' = v, g = \theta, \text{ and } \theta = p \quad (17)$$

$$v' + p_1 f v - p_2 u^2 + g - \xi v - p_5 u \xi^2 = \xi \left( u \frac{\partial u}{\partial \xi} - \frac{\partial f}{\partial \xi} v \right) \quad (18)$$

$$\frac{1}{Pr} [p'] + p_4 g + \xi p + p_1 f p = \xi \left( u \frac{\partial g}{\partial \xi} - p \frac{\partial f}{\partial \xi} \right) \quad (19)$$

$$\text{Where } p_1=3, p_2=2, p_5 = M \quad (20)$$

The corresponding boundary conditions are

$$f(\xi, 0) = 0, u(\xi, 0) = 0 \text{ and } g(\xi, 0) = 0 \quad (21)$$

$$u(\xi, \infty) = 0, g(\xi, \infty) = 0$$

We now consider the net rectangle on the  $(\xi, \eta)$  plane and denote the net point by

$$\eta_0 = 0, \eta_j = \eta_{j-1} + h_j, \quad j = 1, 2, \dots, J$$

$$\xi^0 = 0, \quad \xi^n = \xi^{n-1} + k_n, \quad n = 1, 2, \dots, N$$

We approximate the quantities  $(f, u, v, p)$  at the points  $(\xi^n, \eta_j)$  of the net by  $(f_j^n, u_j^n, v_j^n, p_j^n)$ .

$$\xi^{n-1/2} = \frac{1}{2} (\xi^n + \xi^{n-1}) \quad (22)$$

$$\eta_{j-1/2} = \frac{1}{2} (\eta_j + \eta_{j-1})$$

$$g_j^{n-1/2} = \frac{1}{2} (g_j^n + g_j^{n-1})$$

$$g_{j-1/2}^n = \frac{1}{2} (g_j^n + g_{j-1}^n)$$

Now we write the difference equations that are to approximate Equations (17) - (18) by considering one mesh rectangle for the midpoint  $(\xi^n, n_{j-1/2})$  to obtain

$$\frac{1}{2} \left( \frac{v_j^n - v_{j-1}^n}{h_j} + \frac{v_j^{n-1} - v_{j-1}^{n-1}}{h_j} \right) + (p_1 f v)_{j-1/2}^{n-1/2} - (p_2 u^2)_{j-1/2}^{n-1/2} + (g)_{j-1/2}^{n-1/2} - (\xi v)_{j-1/2}^{n-1/2} - (p_5 u \xi^2)_{j-1/2}^{n-1/2} \quad (23)$$

$$= (\xi)_{j-1/2}^{n-1/2} \left( (u)_{j-1/2}^{n-1/2} \frac{u_j^n - u_{j-1}^n}{k_n} + (v)_{j-1/2}^{n-1/2} \frac{f_j^{n-1} - f_{j-1}^{n-1}}{k_n} \right)$$

$$\frac{1}{Pr} [h_j^{-1} (p_j^n - p_{j-1}^n) + \xi_{j-1/2}^n p_{j-1/2}^n + (p_1)_{j-1/2}^n (f p)_{j-1/2}^n - M_{j-1/2}^{n-1} + \alpha_n [-(u g)_{j-1/2}^{n-1} + (f p)_{j-1/2}^{n-1}] + \alpha_n [(u g)_{j-1/2}^n - (f p)_{j-1/2}^n] \quad (24)$$

$$- u_{j-1/2}^n g_{j-1/2}^{n-1} + u_{j-1/2}^{n-1} g_{j-1/2}^n + p_{j-1/2}^n f_{j-1/2}^{n-1} - p_{j-1/2}^{n-1} f_{j-1/2}^n]$$

Similarly Equations (18) - (19) are approximate by centering about the midpoint  $(\xi^{n-1/2}, n_{j-1/2})$ , Where

$$L_{j-1/2}^{n-1} = (p_1)_{j-1/2}^{n-1} (f v)_{j-1/2}^{n-1} - (p_2)_{j-1/2}^{n-1} (u^2)_{j-1/2}^{n-1}$$

$$+ g_{j-1/2}^{n-1} - (\xi p)_{j-1/2}^{n-1} + h_j^{-1} (v_j^{n-1} - v_{j-1}^{n-1})$$

$$- (p_5)_{j-1/2}^{n-1} u_{j-1/2}^{n-1} (\xi^2)_{j-1/2}^{n-1}$$

$$\text{and } R_{j-1/2}^{n-1} = -L_{j-1/2}^{n-1} + \alpha_n \left\{ -(u^2)_{j-1/2}^{n-1} + (f v)_{j-1/2}^{n-1} \right\}$$

where

$$M_{j-1/2}^{n-1} = \frac{1}{Pr} [h_j^{-1} (p_j^{n-1} - p_{j-1}^{n-1}) + [\xi_{j-1/2}^{n-1} p_{j-1/2}^{n-1} +$$

$$(p_4)_{j-1/2}^{n-1} g_{j-1/2}^{n-1} + (p_1)_{j-1/2}^{n-1} (f p)_{j-1/2}^{n-1}]$$

$$T_{j-1/2}^{n-1} = -M_{j-1/2}^{n-1} + \alpha_n [(f p)_{j-1/2}^{n-1} - (u g)_{j-1/2}^{n-1}]$$

The corresponding boundary conditions become

$$f_0^n = 0, u_0^n = 0, g_0^n = 1, u_J^n = 0, g_J^n = 0$$

Now the system of linear Equations momentum and energy equations together with the boundary conditions can be written in matrix or vector form, where the coefficient matrix has a block tri-diagonal structure. The whole procedure, namely reduction to first order followed by central difference approximations,

Newton's quasi-linearization method and the block Thomas algorithm, is well known as the Keller-box method.

### 3. RESULT AND DISCUSSION

In this exertion MHD natural convection flow on a porous vertical plate is investigated. Numerical values of local rate of heat transfer are calculated in terms of Nusselt number  $Nu_x$  for the surface of the porous vertical plate from lower stagnation point to upper stagnation point, for different values of the aforementioned parameters and these are shown in tabular form in Table:1 . The effect for different values MHD parameter  $M$  on local skin friction coefficient  $C_{fx}$  and the local Nusselt number  $Nu_x$ , as well as velocity and temperature profiles are displayed in Fig.2 to 5. The aim of these figures are to display how the profiles vary in  $\xi$ , the selected streetwise co-ordinate.

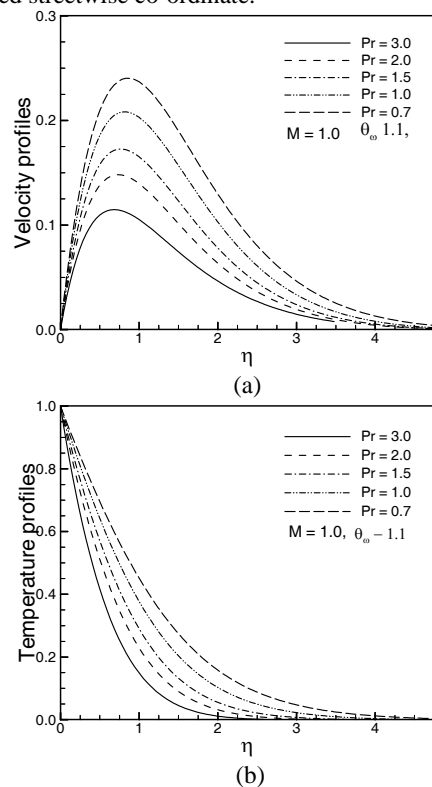


Fig 2. (a) Velocity and (b) temperature profiles for different values of prandtl number Pr with others fixed parameters

In figures 2(a)-2(b) it has been shown that when the Prandtl number  $Pr = 0.7, 1.0, 1.5, 2.0$  and  $3.0$  increases with  $\theta_w = 1.1$  and  $M=1.0$ , both the velocity and temperature profiles decrease.

Figures 3(a) display results for the velocity profiles for different values of magnetic parameter  $M$  with Prandtl number  $Pr = 1.0$  and surface temperature parameter  $\theta_w = 1.1$ . It has been seen from figure 3(a) that as the magnetic parameter  $M$  increases, but th velocity profiles decrease with the increase of magnetic parameter. It is also observed from figure 3(a) that the changes of velocity profiles in the  $\eta$  direction reveals the typical velocity profile for natural convection boundary layer flow, i.e., the velocity is zero at the boundary wall then the velocity

increases to the peak value as  $\eta$  increases and finally the velocity approaches to zero (the asymptotic value) . The maximum values of velocity are recorded to be 0.14712 , 0.16024, 0.17466, 0.19259 and 0.21244 for  $M = 20.0, 15.0, 10.0, 5.0,$  and  $0.0$ , at  $\eta=0.73363, \eta=0.78384$  and  $\eta=0.83530$ . Here, it is observed that the velocity decreases by 27.77% as the magnetic parameter  $M$  changes from 0 to 20.0. . Figure 3(b) displays results for the increasing temperature profiles, for different values of magnetic parameter  $M$  while Prandtl number  $Pr = 1.0$  and surface temperature parameter  $\theta_w = 1.1$ .

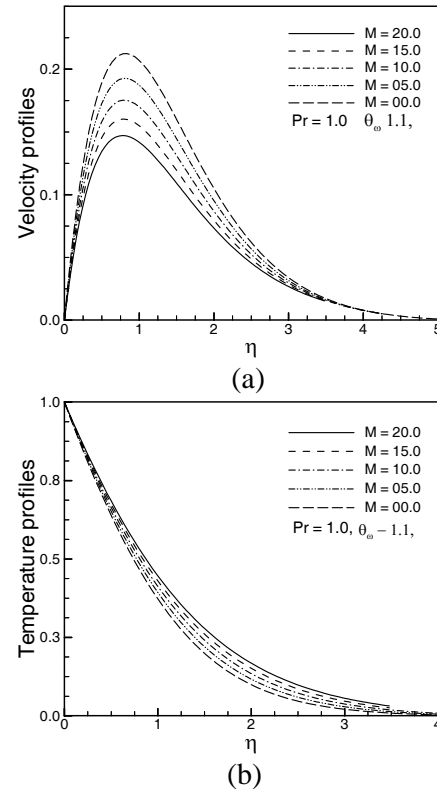


Fig 3. (a) Velocity and (b) temperature profiles for different values of magnetic parameter M with others fixed parameters

The variation of the local skin friction coefficient  $C_{fx}$  and local rate of heat transfer  $Nu_x$  for different values of Prandtl number  $Pr$  while  $\theta_w = 1.1, Q = 1.0$  and  $M=1.0$  are shown in Figures 4(a)-4(b). We can observe from these figures that as the Prandtl number  $Pr$  increases, the skin friction coefficient decreases and rate of heat transfer increases.

Figures 5(a)-5(b) show that skin friction coefficient  $C_{fx}$  and heat transfer coefficient  $Nu_x$  decreases for increasing values of magnetic parameter  $M$  while Prandtl number  $Pr = 1.0$ , and surface temperature parameter  $\theta_w = 1.1$ . The values of skin friction coefficient  $C_{fx}$  and Nusselt number  $Nu_x$  are recorded to be 0.27168, 0.30664, 0.36150, 0.46883 and 0.84175 and 1.00479, 1.00477, 1.00465, 1.00527 and 1.05097 for  $M=20.0, 15.0, 10.0, 5.0$  and  $0.0$  respectively which occur at the same point  $\xi = 1.5$ . Here, it observed that at  $\xi = 1.5$ , the skin friction decreases by 67.72% and Nusselt number  $Nu_x$  decreases by 4.39% as the magnetic parameter  $M$  changes from 0.0 to 20.0.

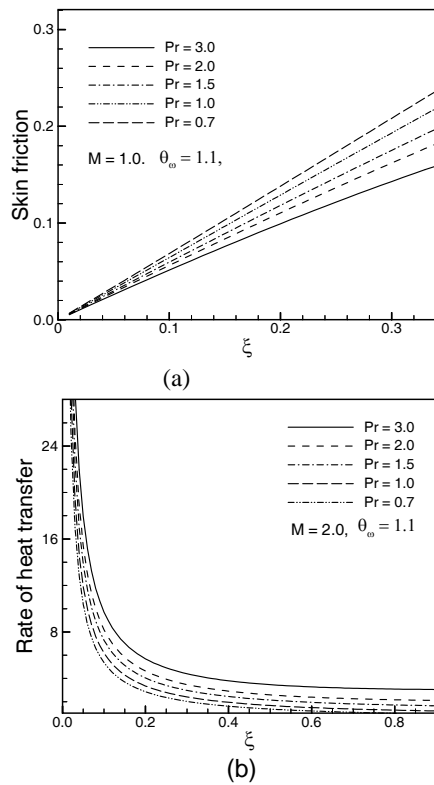


Fig 4.(a) Skin friction and (b) rate of heat transfer for different values of prandtl number Pr with others fixed parameters.

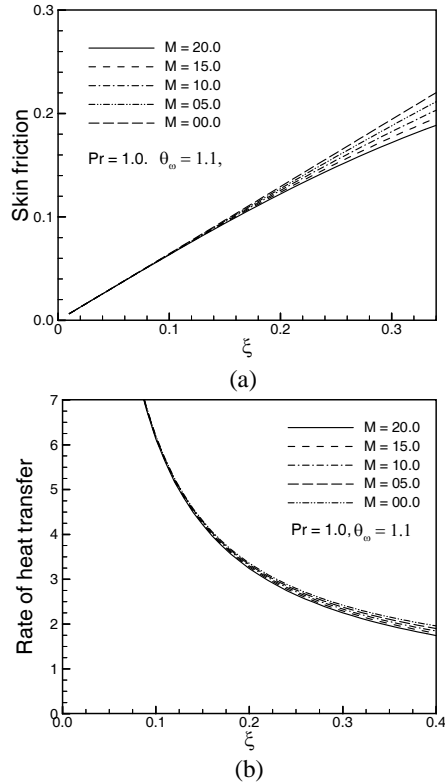


Fig 5.(a) Skin friction and (b) rate of heat transfer for different values of magnetic parameter M with others fixed parameters. Numerical values of rate of heat transfer  $Nu_x$  and skin friction coefficient  $C_f$  are calculated from Equations (13)

from the surface of the vertical porous plate. Numerical values of  $C_{fx}$  and  $Nu_x$  are shown in Table 1.

Table 1: Skin friction coefficient and rate of heat transfer against x for different values of magnetic parameter M with other controlling parameters  $Pr = 1.1$  and  $\theta_w = 1.1$ .

$\xi$	M=00.0		M=05.0	
	$C_{fx}$	$Nu_x$	$C_{fx}$	$Nu_x$
0.01	0.00642	57.68614	0.00642	57.68336
0.05	0.03219	11.90384	0.03216	11.89554
0.10	0.06441	6.18952	0.06417	6.17415
0.50	0.32307	1.68751	0.29579	1.61497
1.00	0.61989	1.18088	0.44698	1.08005
1.10	0.67172	1.14138	0.45801	1.04684
1.20	0.72014	1.11037	0.46458	1.02581
1.30	0.76484	1.08588	0.46784	1.01378
1.40	0.80545	1.06641	0.46892	1.00779
1.50	0.84175	1.05097	0.46883	1.00527

$\xi$	M=00.0		M=05.0	
	$C_{fx}$	$Nu_x$	$C_{fx}$	$Nu_x$
0.01	0.00642	57.67780	0.00642	57.67502
0.05	0.03209	11.87897	0.03206	11.87071
0.10	0.06370	6.14360	0.06347	6.12841
0.50	0.25337	1.49227	0.23693	1.44212
1.00	0.30773	1.02211	0.27312	1.01591
1.10	0.30813	1.01152	0.27298	1.00955
1.20	0.30786	1.00744	0.27261	1.00708
1.30	0.30742	1.00590	0.27224	1.00596
1.40	0.30700	1.00518	0.27194	1.00525
1.50	0.30664	1.00477	0.27168	1.00479

In the above table the values of the values of skin friction coefficient  $C_{fx}$  and Nusselt number  $Nu_x$  are recorded to be 0.27168, 0.30664, 0.36150, 0.46883 and 0.84175 and 1.00479, 1.00477, 1.00465, 1.00527 and 1.05097 for  $M=20.0, 15.0, 10.0, 5.0$  and  $0.0$  respectively which occur at the same point  $\xi = 1.5$ . Here, it observed that at  $\xi = 1.5$ , the skin friction increases by 67.72% and Nusselt number  $Nu_x$  decreases by 4.39% as the magnetic parameter  $M$  changes from 0.0 to 20.0.

## 5 Comparison of the results

Table 2: Comparison of the present result with [9]

$\xi$	$\theta_w = 1.1$			
	Hossain		Hossain	
	$C_{fx}$	$Nu_x$	$C_{fx}$	$Nu_x$
0.1	0.0655	6.4627	0.06535	6.48306
0.2	0.1316	3.4928	0.13138	3.50282
0.4	0.2647	2.0229	0.26408	2.03018
0.6	0.3963	1.5439	0.39519	1.55522
0.8	0.5235	1.3247	0.52166	1.32959
1.0	0.6429	1.1995	0.64024	1.20347
1.5	0.8874	1.0574	0.88192	1.06109

$\xi$	$\theta_w = 2.5$			
	Hossain		Hossain	
	$C_{fx}$	$C_{fx}$	$C_{fx}$	$C_{fx}$
0.1	0.0709	8.0844	0.07078	8.10360
0.2	0.1433	4.2858	0.14313	4.29682
0.4	0.2917	2.4003	0.29120	2.40669
0.6	0.4423	1.7863	0.44145	1.78912
0.8	0.5922	1.4860	0.59080	1.48991
1.0	0.7379	1.1098	0.73590	1.31822
1.5	1.0613	1.1098	1.05693	1.11262

In order to verify the accuracy of the present work, the values of Nusselt number and skin friction for  $R_d = 0.05$ ,  $Pr = 1.0$ ,  $M = 0$  and various surface temperature  $\theta_w = 1.1$ ,  $\theta_w = 2.5$  at different position of  $\xi$  are compared with Hossain [9] as presented in Table 2. The results are found to be in excellent agreement.

## 6. CONCLUSION

For different values of relevant physical parameters including the magnetic parameter  $M$  on natural convection flow from a porous vertical plate has been investigated. The governing boundary layer equations of motion are transformed into a non-dimensional form and the resulting non-linear systems of partial differential equations are reduced to local non-similarity boundary layer equations, which are solved numerically by using implicit finite difference method together with the Keller-box scheme. From the present investigation the following conclusions may be drawn:

- For increasing values of Prandtl number  $Pr$  leads to decrease the velocity profile, the temperature profile and the local skin friction coefficient  $C_{fx}$  but the local rate of heat transfer  $Nu_x$  increases.
- An increase in the values of  $M$  leads to decrease the velocity profiles, the local skin friction coefficient  $C_{fx}$  and the local rate of heat transfer  $Nu_x$  but the temperature profiles increases. Electrically conducting fluid increases the temperature so the rate of heat transfer decreases. An increase of  $M$  increase the Lorentz force, which opposes the flow also increases and leads to enhanced deceleration of the flow. So velocity as well as skin friction decrease.

## 7. REFERENCES

1. J. H. Merkin, 1972, "Free convection with blowing and suction", International journal of heat and mass transfer, 15: 989-999.
2. H. T. Lin, W. S. Yu, 1988, "Free convection on horizontal plate with blowing and suction", Transactions on ASME journal of Heat Transfer 110: 793-796.
3. AK. Singh, 1982, "MHD free-convection flow in the Stokes problem for a porous vertical plate", Astrophysics and Space Science, 87: 455-461.
4. A Chowdhury, MK, A Islam, MN, 2000, "MHD free convection flow of visco-elastic fluid past an infinite vertical porous plate", Journal of Heat and mass transfer, 36: 439-447 .
5. M. A. Hosain, H.S. Takhar, 2001, "Radiation effect on mixed convection along a vertical plate with uniform surface", Journal of Temperature, Heat and Mass Transfer, 31: 243-248.
6. A Hayat, T, A Abbas, Z, A Sajid, M, Asghar, S, 2007, "The influence of thermal radiation on MHD flow of a second grade fluid", International Journal of Heat and Mass Transfer, 50: 931-941.
7. A Alam, MS, A Rahman, MM, A Samad, MA, 2006, "Numerical study of the combined free-forced convection and mass transfer flow past a vertical porous plate in a porous medium with heat generation and thermal diffusion", Journal of Nonlinear Analysis, 11: 331-343 .
8. A Hossain, MA, 1986, "Effect of Hall current on unsteady hydromagnetic free convection flow near an

infinite vertical porous plate", Journal of the Physical Society of Japan, 55: 2183-2190.

9. M. A. Hossain, M. A. Alim, D. A. S. Rees, 1999, "The effect of radiation on free convection flow from a porous vertical plate", International Journal of Heat and Mass Transfer, 42:81-91.
10. A Duwairi, HM, A Damseh, RA, 2004, "Magnetohydrodynamic natural convection heat transfer from radiate vertical porous surfaces", Journal of Heat and Mass Transfer, 40: 787-792.
11. H.B. Keller, 1978, "Numerical methods in boundary layer theory", Annual Review of Fluid Mechanics, 10: 417-433.
12. T. Cebeci, P. Bradshaw, 1984, "Physical and Computational Aspects of Convective Heat Transfer", Springer, New York,.

## 7. NOMENCLATURE

### Nomenclatures

- $C_f$  Local skin friction coefficient  
 $C_p$  Specific heat at constant pressure( $J.kg^{-1}k^{-1}$ )  
 $f$  Dimensionless stream function  
 $g$  Acceleration due to gravity( $m.s^{-2}$ )  
 $k$  Thermal conductivity( $W.m^{-1}K^{-1}$ )  
 $Nu_x$  Local Nusselt number  
 $Pr$  Prandtl number  
 $q_w$  Heat flux at the surface( $W.m^{-2}$ )  
 $q_c$  Conduction heat flux  
 $T$  Temperature of the fluid in the boundary layer(K)  
 $T_\infty$  Temperature of the ambient fluid(K)  
 $T_w$  Temperature at the surface(K)  
 $(u, v)$  Dimensionless velocity components along the  $(x, y)$  axes  
 $V$  Wall suction velocity  
 $(x, y)$  Axis in the direction along and normal to the surface respectively

### Greek symbols

- $\beta$  Coefficient of thermal expansion( $K^{-1}$ )  
 $\eta$  Similarity variable  
 $\theta$  Dimensionless temperature function  
 $\theta_w$  Surface temperature parameter  
 $\mu$  Viscosity of the fluid( $kg.m^{-1}s^{-1}$ )  
 $\nu$  Kinematic viscosity( $m^2s^{-1}$ )  
 $\xi$  Similarity variable  
 $\rho$  Density of the fluid( $kg.m^{-3}$ )  
 $\sigma$  Stephman-Boltzman constant( $W.m^{-2}K^{-4}$ )  
 $\mu_f$  absolute Viscosity at the film temperature  
 $\tau$  Coefficient of skin friction  
 $\tau_w$  Shearing stress  
 $\psi$  Non-dimensional stream function

### Subscripts

- $w$  wall conditions  
 $\infty$  Ambient temperature

## 8. MAILING ADDRESS

Amena Ferdousi  
 Senior Lecturer, Department of Electronics and Electrical Engineering,  
 Eastern University, R#4, Dhanmondi, Dhaka-1207, Bangladesh  
 E-mail: amena@easternuni.edu.bd

## EXPERIMENTAL STUDY OF THERMALLY STRATIFIED CO-AXIAL JETS WITH TRIP RING EXCITATION

M. A. T. Ali and Sukanta Bhattacharjee

Dept. of Mechanical Engineering, Bangladesh University of Engineering & Technology,  
Dhaka, Bangladesh

### ABSTRACT

The experimental investigation of thermally stratified coaxial jet with trip ring excitation is presented. Isothermal as well as thermally stratified or non-isothermal co-axial jet flows are developed by issuing two jets with different unidirectional velocities from a concentric compound nozzle. Enhanced mixing of coaxial free jets of different temperature and different velocity ratio is achieved with the help of vortex generation influenced by inner and outer trip ring placed around the central nozzle. The spatio-temporal velocity fields along with the temperature of the jets are studied by a pitot-static tube with an embedded thermocouple and a high-resolution pressure transducer. The inner dynamic and thermal potential core lengths become much shorter, and mixing between the inner and the outer fields is markedly enhanced by the wake produced after introducing the trip rings. Among the different combinations inner trip ring is found most efficient in mixing non-isothermal co-axial jets.

**Keywords:** Non-Isothermal, Coaxial Jets, Trip Ring, Potential Core.

### 1. INTRODUCTION

Jet flow is one of the basic flow configurations that are found both in nature and in industrial applications. Most of the jets encountered in our daily life are turbulent in nature. Simple flow cases are relatively easy to handle and solve theoretically but when it involves two or more turbulent fluid streams then the flow structure becomes too complicated to solve theoretically. Therefore, experimental investigation is the best option to know about the flow field of interacting flows. Experimental investigation of the mean flow characteristics of velocity field as well as thermal field of thermally stratified trip ring excited co-axial jets have been carried out for different initial conditions. The hot central jet comes out from a 19 mm central nozzle while the annular ambient jet is emitted through the annular space between the outer and the central nozzle. Outer nozzles having inner diameter of 63mm is used that results in the area ratio of annular to central jet as 3.57. Four outer to inner jet velocity ratios ranging from 0.0 to 0.75 have been considered for each nozzle configuration. The temperature of the central jet is varied to establish different temperature gradient between the central jet and the annular jet by varying supply voltage to the heater placed upstream of the central nozzle. Three different values of temperature ratio of the annular jet to the central jet have been considered as 1.0, 0.974 and 0.925 on the basis of absolute temperature scale. The excitation is made by two trip rings. One placed outside the inner nozzle, trips the flow of annular jet is called outer trip ring and the other placed inside of the inner

nozzle, trips the flow of the central jet is called inner trip ring. Measurements of mean velocity and mean temperature in the mixing zone of these two jets are taken with the help of a pitot-static tube with embedded thermocouple.

### 2. FLOW STRUCTURE OF CO-AXIAL FREE JETS

As represented in figure 2 the initial region of co-axial jets consist of two potential cores separated by an annular mixing region. In the streamwise direction the central jet interacts only with the annular jet but the later interacts with both the central jet and the ambient room air at the boundary. Thus, near the exit of co-axial jets two distinct potential cores exist, one at the center and the other along the mean circumference of the annular jet forming a wedge shaped ring. Of the two mixing regions, one is between the central and inner boundary of the annular jet and the other is between the ambient room air and the outer boundary of the annular jet. As the flow proceeds, the width of each core decreases approximately linearly. This zone is in a state of intense mixing and afterward it becomes fully turbulent in its developed state. In the developing stage, the inner mixing layer spreads towards the outward direction more rapidly to meet the outer one and further in the downstream distance, the co-axial jets produce a velocity profile identical to that produced by a single axisymmetric one indicating the complete mixing and fully developed flow condition. The characteristics of flow properties in this region become self-preserving.

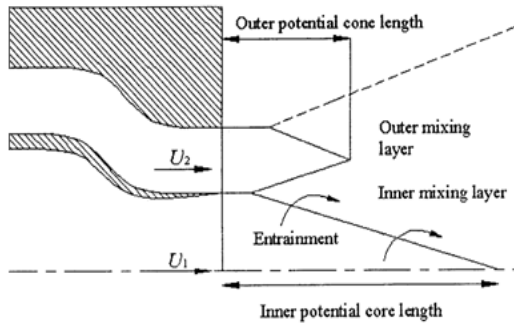


Fig 1. Schematic Diagram of the Mixing Layers in the Near Field of Co-axial Free Jets

### 3. EXPERIMENTAL SET UP

The experimental study has been carried out by using the circular co-axial air jet facility as shown in the figures 2 and 3. To make the flow of hot central jet to produce non isothermal single jet as well as thermally stratified co-axial jets, a series of heaters are installed in the upstream of the central jet. The overall length of the flow facility (Fig. 2) is 8.1 m. It has axial flow fan unit, two settling chambers, two diffusers a silencer and a flow nozzle. The fan unit consists of three Woods Aerofoil fans of the same series. The fan unit receives air through the butterfly valve and discharges it into the silencer of the flow duct. Flow from the silencer passes on to the settling chamber through a diffuser. At the discharge, side of this chamber there is a flow straightener and wire screen of 12 meshes to straighten the flow and to breakdown large eddies present in the air stream. Air from this chamber then flows to the second settling chamber through a nozzle and second diffuser. The flow straightener and wire screens are used here to ensure a uniform axial flow free of large eddies which may be present in the upstream side of the flow. The flow from the second settling chamber then enters the 100 mm long and 80 mm diameter circular nozzle. At the farthest end the diameter of the flow facility is reduced from 475 mm to 80 mm where the experimental nozzle is fitted. A centrifugal blower is placed below the main flow system to supply air to the central nozzle. A 100 mm discharge line of the blower is connected to the heating/settling chamber. A 62 mm PVC pipe is connected to the delivery side of this chamber and enters radially into the 2<sup>nd</sup> settling chamber of the main flow system placed concentrically with the 475 mm diameter main flow set up by means of four pin centralizers in three different locations. The distances between the three consecutive centralizers are 520 mm and 460 mm respectively. In between the centralizers, a 100 mm PVC pipe having length of 520 mm is placed and it is connected to the 62 mm radial pipe insertion through a 62 mm×100 mm diffuser. The outlet of the 100 mm PVC pipe is connected with a 29 mm steel pipe acting as the central nozzle via another diffuser. This 100 mm PVC pipe acts as a plenum chamber with two pairs of wire screens of 24×24 mesh inside it. These wire screens are placed at the entry and exit of this 100 mm PVC pipe to break the big eddies created in the upstream side and thereby to

produce smooth uniform flow with low levels of turbulent intensity.

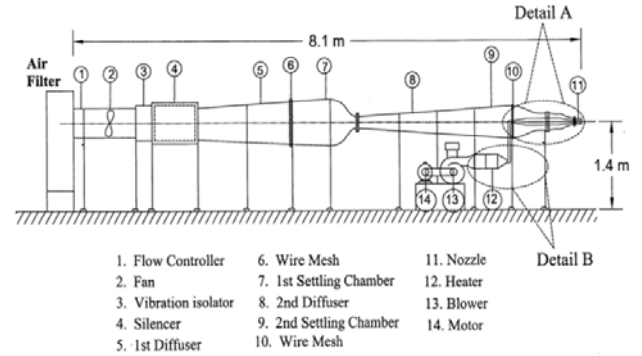


Fig 2. Schematic diagram of the jet flow facility

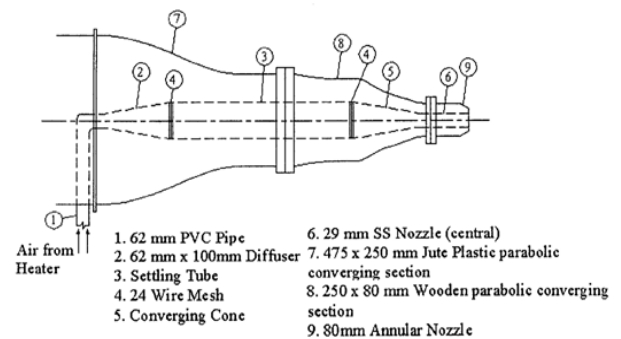


Fig 3. Enlarged View of Co-axial Flow System

The heating system has a capacity of 3 kW and consisted of four different sections as divergent entry section, heater section, settling chamber and convergent exit section. Air from the centrifugal blower comes to the heater section through the divergent entry section. There are six heating elements in the heater section that are made of electric resistance wire and mica sheet and placed to ensure uniform heating to the flowing air throughout the section. After passing over the heaters, the hot air enters into the settling chamber where the temperature of the hot air attains more uniformity because of intermixing. The whole air heating system is insulated with asbestos cloth and glass wool to prevent the heat loss to the surrounding from the hot air. Finally, the hot air is passed to the co-axial jet flow system through the exit section. The flow through the central nozzle is regulated by controlling the supply frequency to the centrifugal blower whereas airflow through the annular nozzle is controlled by the butterfly valve and/or by regulating the speed of the fan units. The temperature of the central jet is regulated by controlling the supply voltage to the heaters by means of a variac. The whole setup is mounted on rigid frames of M.S. pipes and plates and these frames are securely fixed with the ground so that any possible unwanted vibration of the system may be reduced to a minimum. To avoid the effect of ground shear, the set is installed at an elevation of 1.4 m from the ground. For the present investigation, an outer nozzle of 63 mm diameter is used. The diameter

of the central nozzle jet is kept fixed at 29 mm, which makes the area ratio of 3.57. The trip rings used for the excitation is made of nylon and are placed at the exit of the co-axial nozzle. The outer trip ring is attached around the outside periphery of the central nozzle, which has an inner diameter of 29.2 mm and outer diameter of 39 mm. The inner trip ring is attached with the inner side of the central nozzle, which has an outer diameter of 29mm, inner diameter of 19mm. Each trip ring has a wedge shaped edge and is 4mm thick.

#### 4. CENTERLINE VELOCITY

The fundamental axis of any jet flow is its centerline. Different important aspects of flow field such as the potential core length, momentum transfer amongst fluid streams; virtual origin etc. can be identified from the flow characteristics along the centerline of a jet. In figure 4 the effect of different types of excitation for the same velocity ratio is shown. For the velocity ratio of 0.25 the unexcited jet has a core length of 6d and that of for outer trip ring excitation is 4d and inner trip ring excitation is 2d. The inner trip ring also decrease the centerline velocity of the central jet at a very faster rate. For the velocity ratio of 0.50 there is a clear indication that inner trip ring tends to accelerate the fluid at lower x/d value while external trip ring decelerates it. For higher velocity ratio this effect is increased initially for excited jets. However, for inner and outer trip ring excited co-axial jets the decrease of change of velocity occurs in the same manner.

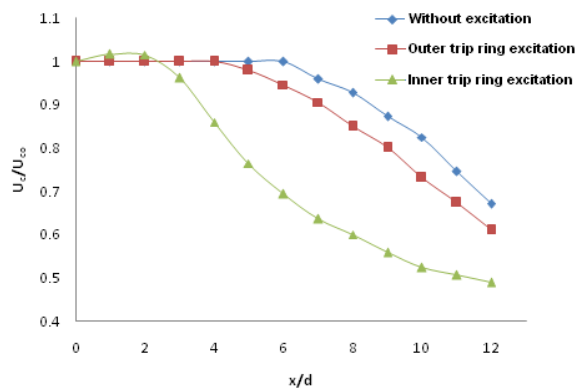


Fig 4. Non-dimensional centerline velocity profiles of isothermal co-axial jet with a velocity ratio ( $U_2/U_1$ ) of 0.25 at different excitation method

#### 5. EXIT VELOCITY

Figure 5 present a comparative study between the non dimensional exit velocity profiles of isothermal co-axial jets for different excitation at a velocity ratio of 0.75. There is a negative pressure zone in the exit velocity profile of the excited jets, created by both outer and inner rings. This reverse flow creates some wakes indicated by the dotted line in the graphs. In case of the outer ring excitation the region is formed around 0.6d to 0.7d and in case of the inner ring excitation the region is formed around 0.4d to 0.5d. At lower velocity ratio the velocity profiles at the annular jet region is like top hat shape and as the velocity ratio increases the shape changes to parabolic shape gradually.

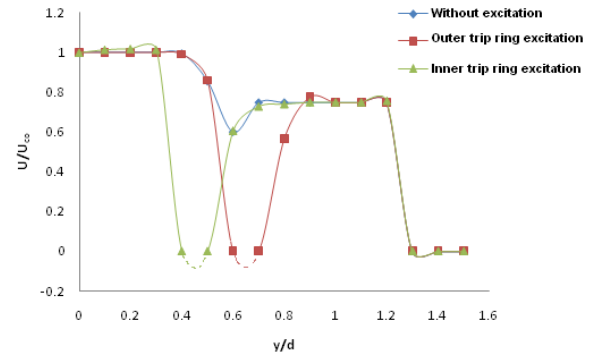


Fig. 5: Non-dimensional exit velocity profiles of isothermal co-axial jets ( $Re= 3.72 \times 10^4$ ) at velocity ratio ( $U_2/U_1$ ) of 0.75 with different excitation method

#### 6. EXIT TEMPERATURES

In figure 6 the effect of different types of excitation is shown. It is clearly visible that the temperature gradient is more prominent in unexcited co-axial jets than the excited ones. This is due to the enhanced mixing by the wake produced by the excitation rings.

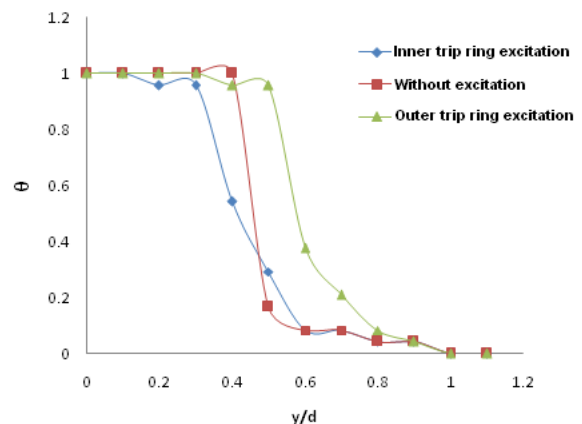


Fig 6. Non-dimensional exit temperature profiles of Non-isothermal co-axial jet ( $Re= 3.72 \times 10^4$ ) at temperature ratio ( $T_2/T_1$ ) of 0.925 and velocity ratio ( $U_2/U_1$ ) of 0.25 with different type of excitation

Moreover, the thermal potential core for outer trip ring excited jets is longer than that of inner trip ring excited or unexcited jets. This is caused by the convex nature of the outer trip ring, which gives an expanding effect on the cooler outer jet and prevents the hot jet from the central nozzle to mix with it. While in inner trip ring excited co-axial jets the inner ring tends to compress the jet due to its concave nature.

#### 7. CENTERLINE TEMPERATURE

The centerline mean temperature of non-isothermal jet flows is one of the most important parameters that reveal different important aspects of the thermal field of non-isothermal jets like thermal core length, diffusion mixing amongst the fluid streams etc. In the current investigation the centerline temperature of the jet is expressed as:



$$\theta_c = \frac{T_c - T_2}{T_1 - T_2} \quad (1)$$

For both of the temperature ratios ( $T_2/T_1 = 0.974$  and  $0.925$ ) thermal potential core is found to be of length  $4d$  for unexcited non-isothermal co-axial jets. It is also observed that, the centerline temperature of non-isothermal single jet decreases more rapidly at lower temperature ratio. The fluctuation of temperature is found to be more prominent at its lower range than that in the higher one. It indicates that the instability of temperature is more at lower value of temperature ratio.

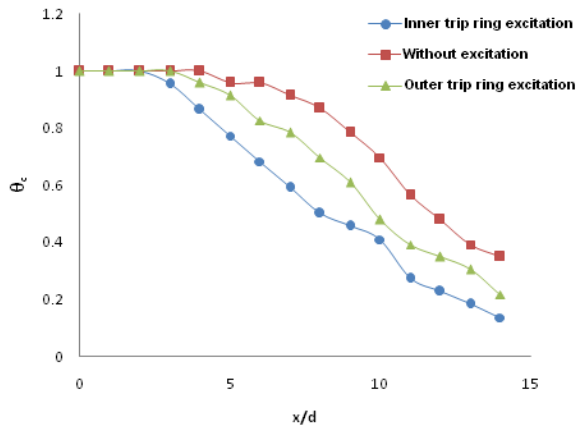


Fig 7. Centerline temperature profile of co-axial jets at velocity ratio of 0.75 and temperature ratio of 0.925 with different type of excitation

It is evident that the centerline temperature at lower velocity ratio of unexcited and outer trip ring excited co-axial jets follows the same path. With the increase of velocity ratio the difference of centerline temperature profiles between them is increasing. In the present investigation the inner trip ring excited co-axial jets have the shortest thermal potential core and the rate of change of temperature is also greater than other two cases i.e. without excitation and outer trip ring excitation.

## 8. CONCLUSIONS

From the study of trip ring excited non-isothermal co-axial jets it is found that inner trip ring is most efficient in mixing co-axial jets. The lengths of both dynamical and thermal potential core are shorter than that of outer trip ring excited or unexcited co-axial jets. In the case of dynamical potential core it is less than  $3d$  and for thermal potential core it is less than  $2d$  for most of the cases. However, outer trip ring excited co-axial jets and unexcited co-axial jets have almost the same thermal potential core length in lower velocity. Temperature gradient is more prominent in unexcited non-isothermal co-axial jets than the excited ones.

In trip ring excited co-axial jets a negative pressure zone is created at the exit of the jets due to formation of wake and reverse flow in the place between the central and annular jets. The place of the wake depends on the thickness of the trip ring and the type of the ring i.e. outer or inner.

## 9. REFERENCES

- Ahmed, R. A. and Sharma, A. D., "Effect of Velocity Ratio on the Turbulent Mixing of Confined Co-axial Jet", *Experimental Thermal and Fluid Science*, Vol. 22, Issue 1-2, pp. 19-33, August 2000.
- Alpinieri, Louis J., "Turbulent Mixing of Co-axial Jets", *AIAA Journal*, Vol. 2, No. 9, pp. 1560-1567, 1967.
- Begum, R., "Experimental Study of Co-axial Free Jets", M.Sc. Thesis, Mechanical Engineering Department, BUET, Dhaka, 2004.
- Buresti, G., Talamelli, A. and Patenga P., "Experimental Characterization of the Velocity Field of a Co-axial Jet Configuration", *Experimental Thermal and Fluid Science*, Vol. 9, Issue 2, pp. 135-146, August 1994.
- Champagne, F. H., and Wygnanski, I. J., "An Experimental Study of co-axial Turbulent Jet", *International Journal of Heat and Mass Transfer*, Vol. 14, pp. 1445-1464, 1971.
- Gamma, B. A., "Study of the Effect of Excitation on A Circular Air Jet", M.Sc. Thesis, Mechanical Engineering Department, BUET, Dhaka, 1993.
- Lenzo, C. S., and Dala, T. N., "Center-Line Velocity Decay in Co-axial Free Jets", *Journal of Applied Mechanics*, Transaction of ASME, pp. 514-516, June 1975.
- Obot Y. Nalma, Trabold A. Thomas, Graska L. Michael and Gandhl Faroukh, "Velocity and Temperature Fields in Turbulent Jets Issuing from Sharp-Edged Inlet Round Nozzle", *Ind. Eng. Chem. Fundam.*, Vol. 25, no. 3, 1986.
- Villermaux, E., and Rehab, H., "Mixing in co-axial jet", *Journal of Fluid Mechanics*, Vol. 425, pp. 161-185, 2000.
- Yue, W., "Air Jets in Ventilation Application", [Source: The Internet]
- Hasan, Mohammad Nasim, "Experimental Study of Flow Characteristics in the Near Field of a Thermally Stratified Co-axial Free Jet" M.Sc. Thesis, Mechanical Engineering Department, BUET, Dhaka, 2008.

## 10. NOMENCLATURE

Symbol	Meaning	Unit
$d$	Central jet diameter	(mm)
$D_2$	Annular jet diameter	(mm)
$T$	Local mean temperature	(K)
$T_1$	Mean temperature of inner jet	(K)
$T_2$	Mean temperature of outer jet	(K)
$T_c$	Centerline temperature	(K)
$U$	Mean jet velocity	(m/s)
$U_1$	Central mean jet velocity	(m/s)
$U_2$	Annular mean jet velocity	(m/s)
$\theta$	Non-dimensional temperature	

## 11. MAILING ADDRESS

M. A. T. Ali  
 Dept. of Mechanical Engineering,  
 Bangladesh University of Engineering & Technology,  
 Dhaka, Bangladesh.

## ANALYSIS OF A NEGATIVELY BUOYANT JET

Chandan Kumar, D. Das and M.M. Razzaque

Department of Mechanical Engineering, Bangladesh University of Engineering and Technology (BUET),  
Dhaka, Bangladesh.

### ABSTRACT

The behavior of plane fountains, resulting from the injection of dense fluid (water) upwards into a large container of homogeneous fluid of lower density (air), is investigated. In this study we experimentally examine the behavior of fountains for different Froude and Reynolds numbers. The fountain inlet flow rate and nozzle diameter of the inlet fluid is varied to cover a wide range of Reynolds and Froude numbers. Fountain behavior is observed by changing the inclination angle of the fountain for different nozzle diameter and flow rate. We found that the penetration height greatly depends on Froude number. We develop an empirical correlation of the non-dimensional fountain height with Froude number ( $\frac{H}{D} = 1.452Fr^{1.94}$ ). But well defined by both Reynolds and Froude number. Finally we also develop an empirical correlation of the non-dimensional fountain height Reynolds and Froude number ( $\frac{H}{D} = 0.0001Re^{-0.72}Fr^{2.26}$ ) by numerical regression. The result are compared with previous numerical and experimental results and found consistent.

**Keywords:** Buoyant Jet, Negatively Buoyant Jet, Fountain, Positively Buoyant Jet, Reynolds Number.

### 1. INTRODUCTION

Negatively buoyant jets occur when a fluid is injected into another fluid of differing density where the buoyancy force opposes the momentum of the flow. In our case water (denser) is injected upward into air (lighter).

The injected fluid penetrates a distance into the environment before stagnating and falling back around itself. The characteristics of the fountain flow, such as the penetration height and the amount of mixing, depend on the Froude number and Reynolds number, which for round fountains are defined as

$$Fr = \frac{v}{\sqrt{Dg}}$$

and

$$Re = \frac{\rho v D}{\mu}$$

respectively, where 'D' is the characteristics dimension or hydraulic diameter of the source and. The characteristic velocity 'v' is defined here as  $v = Q_0/\pi r^2$ , where  $Q_0$  is the volume flow rate at the fountain source;  $\mu$  is the dynamic viscosity of the fluid at the fountain source, and  $\rho$  is the density of fluid of fountain source .

In this study we experimentally examine the behavior of a negatively buoyant jet for wide range of Froude and Reynolds numbers.

There have been numerous studies investigating fountain behavior. Significant contributions have been made by Turner (1966), Abraham (1967), Mizushima et al. (1982),

Baines et al. (1990) and Bloomfield & Kerr (2000). The consensus in these works, on both dimensional (Turner 1966), analytical (Abraham 1967) and experimental grounds (Turner 1966; Mizushima et al. 1982; Baines et al. 1990.

Some of them correlate non-dimensional fountain height with Froude number and both with Reynolds and Froude number. Most of the previous work was done in the context of Boussinesq approximation where density differences are sufficiently small to be neglected. For example they study the fountain created by injecting salt water up into fresh water (n.williamson, n.srinarayana, s.armfield, g,d Mcbain), flow of hot gas downward into air. In this case densimetric Froude number is used.

Our objectives are to study the fountain created by non-Boussinesq approximation injecting water up into air. In our study density difference is not small. We aimed to investigate the behavior of the jet with different Reynolds number and Froude number. Our also aimed to see the effect of inclination angle on the fountain behavior.

Finally the effect Reynolds number and Froude number on penetration height of jet is investigated. By numerical regression analysis we develop an empirical correlation of penetration height with Reynolds and Froude number.

## 2. EXPERIMENTAL SETUP

Experiments have been performed by injecting water into air up in an observation tank. The observation tank is 12inch deep with 12 inch square base. The water is fed from a header tank to the base of the observation tank as shown in the arrangement in figure 1. The water is injected from a sudden start and maintained at a constant flow rate throughout the experiment. A ball valve is used to control the flow.

The observation is made of transparent plastic glass to observe the jet behavior. In the base of the observation tank there are two holes. One is to collect the dispersed water from nozzle and another is to supply water to nozzle.

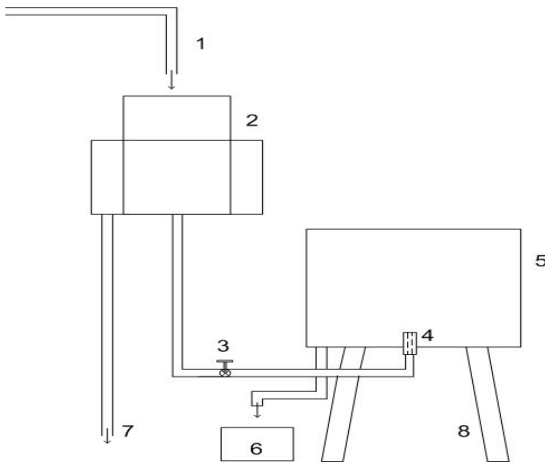


Fig 1. Schematic representation of experimental setup with 1: supply line, 2: header tank, 3: control valve, 4: nozzle, 5: observation tank, 6: collection bucket, 7: drain line, 8: stand.

A protractor is attached at the lower part of the observation tank inline with base. Inclination angle is measured by this protractor by holding a set square vertically and take the reading.

Header tank consist of two tank one act as a supply tank and another is act as an overflow tank. In the supply tank the head of water remains always constant thus supplying constant flow throughout the experiment. The excess water of the supply tank flow to overflow tank. The water in overflow tank is drained by a pipe. In the supply tank water is supplied at a rate higher than the flow rate need to make the fountain. The excess water spill over from the supply tank to overflow tank thus the head of water remains same in the supply tank.

Water flows from header tank to observation tank through a pipe. In the middle of this pipe a ball valve is connected to control the flow rate. A solid ball with hollow section is rotated with to adjust the flow. Here ball valve is used to control the flow rate for to vary Reynolds and Froude number.

The nozzle in our experiment was a straight nozzle there is no variation of cross sectional area. In the source side of the nozzle is stepped as Christmas tree to prevent leakage. Diameter of middle section of the nozzle is higher than two sections to fix with the observation tank. We use five nozzle of different diameter. Nozzle inner diameter of 2.50mm, 3.00mm, 3.50mm, 4.00mm and 4.70mm were used. The outer side of the nozzle is same for all nozzles. Five nozzles are manufactured at BUET machine shop and are made of mild steel.

Platform scales are instruments used for measuring weight. It may be various types. In our experiment portable beam scale type platform scale was used.

## 3. OBSERVATIONS

The experiments were performed over the ranges  $3.00 < Fr < 13.00$  and  $1500 < Re < 8500$ , and the penetration height and the fountain behavior was observed carefully. It is observed that when the nozzle is purely vertical i.e. no inclination in jet there is rapid fluctuation in fountain height but in case of inclined jet height is constant for a Reynolds and Froude number. In case of vertical jet fountain front continually rises until its kinetic energy becomes zero, then stagnates here kinetic energy is zero but potential energy is maximum, and then collapses around the next rising front, so the next rising front can not reach its maximum height. As a result fluctuation occurs in a vertical jet. On the other hand height of inclined jet remains almost constant in all time for a Reynolds and Froude number.

But a peculiar and very interesting phenomenon occurs in the low Reynolds number for every nozzle. We observed that inclined jet also fluctuate for a Reynolds and Froude number. This is due to cohesion between rising and falling water. As the height decrease the distance between the falling and rising column decreases for some certain angle. It is observed that at some state the rising and falling column mix at the top of the jet due to cohesion. Due to this interaction and mixing between rising and falling column, decreased in vertical momentum of the injected fluid occur, the fountain height decrease. The height of the fluctuation depends upon inclination angle and nozzle diameter. This Fluctuation height increases with diameter decrease. And fluctuation height increases with inclination angle increases. This behavior is due a combination of the decreased interaction between the up-flow and the down-flow when inclination angle increase.

The rising column of every fountain can be categorized of three segments as rising or initial stage, intermediate or wobbling stage and stagnating stage. At rising stage fluid column is pure stream of jet no variation in diameter of the jet. But in intermediate stage fluid column starts wobbling. In this stage diameter of jet increases gradually as height increases. In the final stage fluid particle starts to reverse its direction and they disperse disorderly. In the wobbling stage it is observed that the fluid column twisted as it rises. This is due to Coriolis effect of earth. In the north hemisphere fluid column twisted counterclockwise, but in the south hemisphere fluid column twisted clockwise.

#### 4. ANALYSIS

We tried to find whether the height is dependent on Reynolds number or Froude number or both in Reynolds and Froude number. For this reason we observe the variation of non-dimensional parameter Height /radius (H/r) with respect to Reynolds (Re) and Froude (Fr) number.

We also correlate the non-dimensional fountain height (Height/radius) with Froude number. And for both Reynolds and Froude number.

The non-dimensional fountain height (Height/radius) and Reynolds number is plotted for different diameter (in figure 2). From this graph it is observed that the fountain height increases as the Reynolds number increases for a diameter of nozzle. But as the diameter increases fountain height decreases for a Reynolds number. Because if the diameter increases then flow area increases as a result velocity decreases. So fountain height decreases.

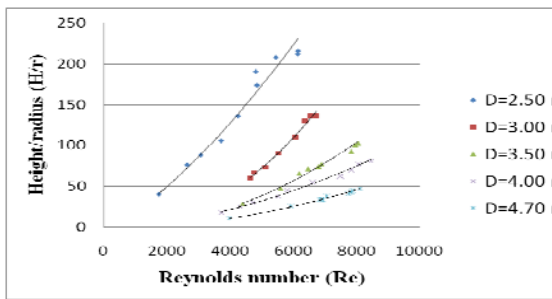


Fig 2. Non-dimensional penetration Height/radius (H/r) as a function of Reynolds number (Re).

The variation of non-dimensional fountain height (H/r) for all the experiment in this study is plotted (figure 3) against Froude number. It is observed that a relationship can be obtained between the non-dimensional fountain height (H/d) and Froude number. By numerical regression analysis we find a nonlinear relationship of non-dimensional fountain height (H/d) with Froude number. 
$$\frac{H}{r} = 1.452 Fr^{1.915}$$

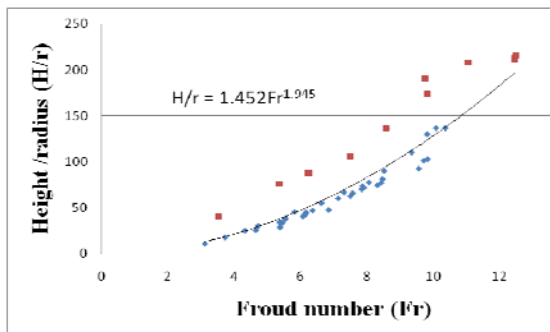


Fig 3. Non-dimensional fountain height (H/r) as a function of Froude number (Fr).

In the above figure it is observed that some data are scattered from the regression line. So we find another

correlation of non-dimensional penetration height including both Reynolds and Froude number. By numerical regression analysis we found that the non-dimensional penetration height is well described by the following relationship,

$$\frac{H}{r} = 0.374 Re^{-0.072} Fr^{2.26}$$

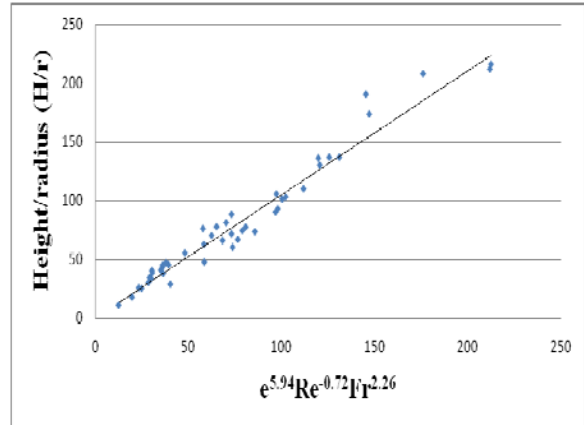


Fig 4. Comparison of experimental non-dimensional fountain height with correlation obtained.

#### 5. DISCUSSION AND RESULT

Turner(1966) performed the first experimental work on turbulent round fountains using salt-water solution injected upwards into a fresh-water tank and found maximum penetration depth  $Z_m$  scales as  $Z_m/R_0 = C Fr$ , where  $C=2.46$  over the range  $2 \leq Fr \leq 30$ . Other experimental studies followed which confirmed the linear relationship, albeit with some small variation in the magnitude of the coefficient.

Mizushima et al. (1982) obtained  $C = 2.35$  for  $5 < Fr < 260$  and  $1130 < Re < 2710$ ; ampbell & Turner (1989) found  $C = 2.46$ ; Baines et al. (1990) found  $C = 2.46$  for  $10 < Fr < 300$  and  $Re = 2000$ ; and Pantzloff & Lueptow (1999) found  $C = 2.1$  for  $15 \leq Fr \leq 78$  and  $1250 \leq Re \leq 7500$ .

Lin & Armfield (2000a) numerically simulated fountains with  $0.2 \leq Fr \leq 1.0$  and  $Re = 200$ . At these very low Froude numbers the fountain flow is very weak and penetrates only a very small distance before reversing and flowing radially out from the source. In this study the authors found that a linear Froude number scaling for the penetration height, i.e.  $Z_m/R_0 = C Fr$ , is still valid. The authors also simulated fountain flow for  $1.0 \leq Fr \leq 2.0$  and found the linear scaling to be invalid.

Kaye & Hunt (2006) later re-plotted these results and found them to be well fitted by  $Z_m/R_0 = C Fr^{2/3}$  for  $Fr < 1$  and  $Z_m/R_0 = C Fr^2$  for  $Fr > 1$ .

But recently baines et al obtained an analytical scaling  $H/r = C Fr^{1.915}$ . Campbell and turner obtained  $C=1.64-1.97$  from their experiment on turbulent round fountain.

Our investigation shows that the non-dimensional fountain height varies as the following relationship 
$$\frac{H}{r} =$$

1.452  $Fr^{1.843}$ . This is very similar to above studies.

Recently Lin and Armfield investigated the effect of the Reynolds number on the height of plane fountains. They found that for  $Re \leq 200$  the non-dimensional fountain height was dependent on the Reynolds number with the following scaling:  $\frac{H}{r} = C Fr^{0.8}$ .

We conduct our experiment in the following range  $3.00 < Fr < 13.00$  and  $1500 < Re < 8500$ . The relationship in this range is  $\frac{H}{r} = 0.264 Re^{-0.72} Fr^{0.85}$ .

From the above relation we can predict the fountain height for a Reynolds and Froude number for any diameter of the nozzle.

## 6. CONCLUSION

The behavior of negatively buoyantly jet (fountain) has been investigated experimentally. It has been found that the pure vertical jet of water always fluctuates because falling front falls upon the nest rising front.

Inclined jet remains at a constant height up to a minimum height for a fixed flow and nozzle diameter. But at that minimum height interaction between falling and rising front occur and fluctuation of inclined jet starts.

For high Reynolds number the jet stream can be divided into three segments. Rising stage here the flow is streamlined no variation in the diameter of the jet, Intermediate stage with increasing diameter and wobbling of fountain occur and at final stage jet stagnates and reverse its direction.

Non-dimensional fountain height ( $H/r$ ) is greatly depend on the Froude number ( $Fr$ ) by the correlation  $\frac{H}{r} =$

$$1.452 Fr^{1.843}$$

But it is relatively well fitted by  $\frac{H}{r} = 0.264 Re^{-0.72} Fr^{0.85}$ ,

## 7. REFERENCE

1. n.williamson, n.srinarayana, s.armfield, g.d McBain (2008) Low-Reynolds-number fountain behavior
2. Philippe, C. Raufaste, P. P Kurowski, and P. Petitjeans (2005) Penetration of a negatively buoyant jet in a miscible liquid.
3. T. Mizushina, F. Ogino, H. Takeuchi, and H. Ikawa, Kyoto, Japan(1982) An Experimental Study of Vertical Turbulent Jet with Negative Buoyancy.
4. N. Srinarayana, S. W. Armfield1 and W. X. Lin (2007) Numerical Simulation of Free-fountains in a Homogeneous Fluid (AUS JMF).
5. Williamson, N.1, Srinarayana, N.1, Armeld, S.W.1, McBain, G.1 and Lin,(2007) Characterization of Low Reynolds Number Fountain Behavior.
6. Abraham, G. 1967 Jets with negative buoyancy in homogeneous fluid. J. Hydraul Res. 5, 235-248.
7. Lin, W. and Armeld, S. W., Direct simulation of fountains with intermediate Froude and Reynolds numbers, ANZIAM J., 45(E), 2004, C66.C77.
8. Baines, W. D., Turner, J. S. & Campbell, I. H. 1990 Turbulent fountains in an open chamber. J. Fluid Mech. 212, 557-592.
9. Bloomfield, L. J. & Kerr, R. C. 2000 A theoretical model of a turbulent fountain. J. Fluid Mech. 424,197-216.
10. Zhang, H. & Baddour, R. E1998 Maximum penetration of vertical round dense jets at small and large Froude numbers. J. Hydraul. Engg.
11. Friedman, P. D. 2006 ,Oscillation height of a negatively buoyant jet. Trans. ASME J:J.FluidsEngng 128,880-882.

## 8. MAILING ADDRESS

Chandan Kumar  
Department of Mechanical Engineering, Bangladesh University of Engineering and Technology (BUET), Dhaka-1000,Bangladesh.

## **SMALL ENERGY TECHNOLOGY FOR EMPOWERING RURAL POOR: BANGLADESH CONTEXT**

**S. M. N. Islam**

Department of Mechanical Engineering,  
Bangladesh University of Engineering and Technology, Dhaka, Bangladesh

### **ABSTRACT**

About half of the population of Bangladesh lives within poverty level. The Millennium Development Goal (MDG) of UNO requires to reduce poverty by one half by 2015, and Copenhagen Declaration demands environmental protection. About 80% of the population lives in rural area and use poor cooking fuel which creates pollution. Most of them are landless and day labor. They have insufficient income to provide for their basic needs. A business model has been designed which the people may use for sustainable rural development in Bangladesh. Sustainable development comprises types of economic and social development that protect and enhance natural environment and social equity. The scanty energy resources of rural area shall be used to attain development to provide basic needs for the poor and to meet MDG target. This paper explores possibilities of attaining rural development through fostering rural power companies based on Renewable Energy Technologies (SET). This will create village businesses for selling power generated from renewable energy technologies. An integrated ecological, economic and social model is proposed to assist sustainable rural development. People of all classes will be a party to share business under this model. The renewable energy technologies (RET) create income generating activities for landless and marginal farmers and for women from such households. The use of renewable technology will reduce deforestation, health hazards and indoor air pollution for cooking with poor quality fuels. The capital cost of Renewable Energy Technology (RET) is little high. This model proposes an extension of well-known micro-credit approach developed by Grameen Bank or BRAC. The target group of village people would form a village organization (VO) like cooperative with the

assistance of an external agency composed of NGO, business group and government representatives. The village organization may borrow money from a bank or a large NGO and purchase a RET. The RET may be based on biogas, solar or wind depending upon available sources and locations. The village organization shall sell power to weather members of the society and would repay the loans. Thus they will gain direct ownership and control of the technology and its applications. Here the model is proposed with biogas plant. This will be used to generate power and cooking gas. This is one of the best uses of rural technology to empower the rural poor investing their indigenous skills and resources. Probably the model of this kind can establish gender equity and alleviates poverty to empower the landless poor and protects environment. This model now needs field testing as pilot project.

**Keywords:** Small Energy Technology, Renewable Energy Technology, Poverty Alleviation.



**ICME09-KEY-02**

**THERMAL MANAGEMENT OF CRYOGENIC  
STORAGE VESSELS TO PREVENT BOIL OFF**

**M. M. Rahman**

Dept. of Mech. Engg, University of South Florida, Tampa, FL 33620, USA

**ABSTRACT**

In the recent years, cryogenic storage techniques for liquid hydrogen as well as other liquefied gases are of widely increasing interest. Liquid storage of hydrogen has very significant advantage over gaseous or chemical storage because of much lower storage volume and ease of regeneration of the fuel with its demand. Because of its very low normal boiling point and high latent heat of vaporization, hydrogen's most challenging aspect in cryogenic storage is the losses due to boil-off under the effect of the heat leak through the insulation layers of the tank from the surrounding environment. Conventional cryogenic storage tanks suffer loss of hydrogen due to boil-off of the cryogen induced by heat leak. In order to control the tank pressure within its structural limits, the stored fluid needs to be bled off periodically. The Zero Boil Off (ZBO) concept has evolved as an innovative means of storage tank pressure control by a synergistic application of passive insulation, active heat removal, and forced mixing within the tank. A cryocooler (with a power supply, radiator, and controls) is integrated into a traditional cryogenic storage subsystem to reject the storage system heat leak. Therefore, the fuel can be stored for a very long time without any loss. This paper presents both steady-state analysis of an active heat dissipation system and the transient analysis of a passive heat dissipation system. The active system includes a tank with cylindrical wall and oblate spheroidal top and bottom and a cold-spray nozzle head whose face is set perpendicular to the axis of the tank. The nozzle head has many nozzles on its down face. The cold fluid from the cryocooler enters the inlet opening at the top of the tank, follows an axial supply tube to the nozzle head and injects into the heated fluid inside the tank through the nozzles. The displaced fluid exits the tank through an annular outlet opening (also at the top of the tank and co-axial to the inlet opening) then goes back to the cryocooler. The passive system includes a tank with cylindrical wall

KEY-02

and oblate spheroidal top and bottom, a heat pipe located along the axis of the tank, and an active circulator, which is a pump-nozzle unit including a pump body, a suction tube, and a spray nozzle facing the evaporator section of the heat pipe. The evaporator section removes heat from liquid hydrogen inside the tank and transports it to the external condenser section of the heat pipe that dissipates heat to the ambient via a cryocooler and radiator. The entire system has been modeled numerically by solving equations for the conservation of mass, momentum, and energy. Simulations with different on/off periods for the operation of the pump and different normal speeds of fluid discharged at the nozzle face are run for a parametric analysis. Typical distributions of velocity and temperature are presented. Average speed and maximum temperature are evaluated for assessing mixing and boiling effects, respectively. The effectiveness of the combination of operating parameters is estimated for the optimization of the tank design. The results provide valuable guidelines for the design of ZBO cryogenic storage systems.

**Keywords:** Cryogenic Storage, Liquid Hydrogen, Active Storage System.

## **TRANSONIC TONES AND EXCESS BROADBAND NOISE IN OVEREXPANDED SUPERSONIC JETS**

**K. B. M. Q. Zaman**

NASA Glenn Research Center, Cleveland, OH 44135, USA

### **ABSTRACT**

Noise characteristics of convergent-divergent (C-D) nozzles in the overexpanded regime are the focus of this paper. The flow regime is encountered during takeoff and landing of certain airplanes and also with rocket nozzles in launch-pad environment. Experimental results from laboratory-scale single nozzles are discussed. The flow often undergoes a resonance accompanied by emission of tones (referred to as 'transonic' tones). The phenomenon is different from the well-known screech tones. Unlike screech, the frequency increases with increasing supply pressure. There is a staging behavior – odd harmonic stages occur at lower pressures while the fundamental occurs in a range of relatively higher pressures. A striking feature is that tripping of the nozzle's internal boundary layer tends to suppress the resonance. However, even in the absence of tones the broadband levels are found to be high. That is, relative to a convergent case and at same pressure ratio, the C-D nozzles are found to be noisier, often by more than 10dB. This excess broadband noise (referred to as 'EBBN') is further explored. Its characteristics are found to be different from the well-known broadband shock-associated noise ('BBSN'). For example, while the frequency of the BBSN peak varies with observation angle no such variation is noted with EBBN. The mechanisms of the transonic tone and the EBBN are not completely understood yet. They appear to be due to unsteady shock motion inside the nozzle. The shock drives the flow downstream like a vibrating diaphragm, and resonance takes place similarly as with acoustic resonance of a conical section having one end closed and the other end open. When the boundary layer is tripped, apparently a breakdown of azimuthal coherence suppresses the resonance. However, there is still unsteady shock motion albeit with superimposed randomness. Such random motion of the internal shock and its interaction with the separated boundary layer produces the EBBN.

**Keywords:** Transonic Tones, Supersonic Jet, Broadband Noise.

KEY-03

## **REVIEW AND SOME RESEARCH RESULTS ON JET FLOW CHARACTERISTICS**

**M. A. T. Ali**

Department of Mechanical Engineering,  
Bangladesh University of Engineering and Technology, Dhaka, Bangladesh

### **ABSTRACT**

Jet is a common flow situation occurred both in nature and in engineering installations. It is also a simple flow to study and to understand the basic characteristics of flow, particularly its mixing process. In this paper review of some of the works on jet flow is presented and some research findings on the effect of different flow conditions like upstream flow excitation, wedge shape nozzle exit, vertical flange at the nozzle discharge, spline shape nozzle surface, upstream swirl and coaxial jets, without and with trip ring excitation are discussed. In all the cases measurements were taken in the Reynolds number range  $Rd = 2 \times 10^4$  to  $1 \times 10^5$ . For each case axial mean velocity and static pressure were measured by pitot-static probe and axial turbulence intensity by constant temperature hot-wire anemometer. For the jets in general, the mean static pressure within the potential core was positive and that in the mixing region was negative. The decay of centerline mean velocity was maximum at the preferred mode of excitation and was minimum at the suppression mode. Near the exit, the streamwise mean velocity profiles were saddle shaped which disappeared at the end of the potential core. Turbulence intensity was enhanced in presence of vertical flange, wedge shape exit and splined nozzle surface. The central line turbulence intensity decreased due to the presence of vertical flange and wedge angle. But for upstream excitation the centerline turbulence intensity increased with increase of excitation frequency, reached its maximum value at  $Std = 0.58$  and with further increase of excitation frequency it started to decrease and reached its minimum value at  $Std = 1.8$ . In the case of helical swirling jet, there was no existence of potential core due to intense mixing which was completed within two diameter down-stream from the nozzle exit. In the case of coaxial jets two distinct mixing zones, one between the central jet

and inner boundary of the annular jet and the other between the outer boundary of the annular jet and the surrounding air, existed in coaxial jets. Potential cores of these jets were longer ( $6d$ ) than that of the single jet ( $5d$ ). After nine diameters downstream the two jets merged together and behaved like a single jet for the area ratio 3.57 but this value increased with the increase of area ratio. For trip ring excited coaxial jets the effect of inner trip ring excitation in mixing two jets was more prominent than the outer one.

**Keywords:** Preferred Mode, Suppression Mode, Trip Ring.

Proceedings of the  
International Conference on Mechanical Engineering 2009  
(ICME2009) 26-28 December 2009, Dhaka, Bangladesh

**ICME09-KEY-05**

**TITLE & TOPIC TO BE SUPPLIED BY THE  
KEYNOTE SPEAKER DURING THE KEYNOTE  
SESSION**

**Shaik Jeelani**

Director, Center for Advanced Materials  
Vice President, Research and Sponsored Programs  
jeelanis@tuskegee.edu  
Ph.: (334) 727-8970  
Fax: (334)-724-4224

## STUDY OF MICROSTRUCTURE AND TEMPERATURE DEPENDENT LOW FREQUENCY AC PROPERTY OF $\text{Ni}_{0.46}\text{Zn}_{0.54}\text{Ca}_{0.05}\text{Fe}_2\text{O}_4$ FOR MECHATRONICS AND ELECTRONIC DEVICE APPLICATION

H. M. Iftekhar Jaim<sup>1</sup>, F A Khan<sup>2</sup>

<sup>1</sup>Department of Mechanical Engineering, Bangladesh University of Engineering and Technology, Dhaka, Bangladesh

<sup>2</sup>Department of Physics, Bangladesh University of Engineering and Technology, Dhaka, Bangladesh

### ABSTRACT

By solid state reaction method  $\text{Ni}_{0.46}\text{Zn}_{0.54}\text{Ca}_{0.05}\text{Fe}_2\text{O}_4$  compound was prepared. By XRD the crystal structure was revealed and by SEM the microstructure was studied. At different temperatures the ac parameters such as conductivity and capacitance were studied from 1 KHz to 6 MHz. Q factor was measured to find the specific frequency range for switching property. All these experimental results are found to be useful in fabrication of future MEMS technology since the industry is taking new approaches for miniaturizing circuit elements for control and mechatronic applications. The minute addition of Calcium enhanced the electrical properties required for such applications.

**Keywords:** Ni Zn Ferrite Composites, Control System, Mechatronic Device Material, SEM, XRD

### 1. INTRODUCTION

Nickel Zinc Ferrite solid composites are the well known spinel ferrites. These composites prepared by different techniques and with different levels of doping are widely been used in the soft ferrite industry. Ni Zn Ferrite composites have become a major concern of research for several decades for their extensive uses in high-frequency transformers and inductors [1], signal transformer, power transformer, pulse transformer, input/output filter chokes [2], deflecting yokes and flyback transformer for TV receivers, antenna rods for radio set [3] and recording heads [4]. Recent interest is focused on the development of miniaturization of electronic components to downsize various electronic packages and thus to reduce the size/weight ratio. Although high-frequency Mn Zn ferrite is used in most cases to develop mini dc-dc converters and inductors [5] for higher electric resistance exceeding  $10^7\Omega\text{ m}$ , Ni Zn ferrite core is a good competitor in this field. Electronic and magnetic applications sensitive to eddy current losses and usable at moderate permeability, Ni Zn ferrite offers better performance than Mn Zn ferrites. For commercial EMI suppression Ni Zn ferrite composites are already in the market. [6] Another use of it is magnetic switching where it shows much better performance than electrically switched systems. All these inventions and researches are very important for control system and mechatronic applications. Ni Zn

Ferrite is spinel type soft magnetic material combining tetrahedral A site and octahedral B site in  $\text{AB}_2\text{O}_4$  crystal structure. It consists of a combination of normal and inverse spinels which has very important magnetic properties for applications above 1MHz. [7] In this paper we investigated the ac properties at different temperatures and micro structure of the  $\text{Ni}_{0.46}\text{Zn}_{0.54}\text{Ca}_{0.05}\text{Fe}_2\text{O}_4$

### 2. EXPERIMENTAL PROCEDURE

$\text{Ni}_{0.46}\text{Zn}_{0.54}\text{Ca}_{0.05}\text{Fe}_2\text{O}_4$  sample was synthesized using standard solid state reaction technique using powder NiO, ZnO, CaO and  $\text{Fe}_2\text{O}_3$  as raw materials from Baker, Germany. Stoichiometric amount of required powders were pressed into disk shaped and toroid shaped samples. The samples were sintered at  $1200^\circ\text{C}$ . The temperature ramp was at  $5^\circ\text{C}/\text{min}$  for both cooling and heating. The samples were of two sizes: sample A was a solid flat disc and sample B was a toroid. Microstructural properties have been investigated by XRD and SEM. X ray diffraction was carried out with a Philips X'pert automatic powder diffractometry system using  $\text{Cu-K}_\alpha$  radiation. The Philips XL30 Scanning Electron Microscope with an accelerating voltage of 15 KV was used for SEM imaging. Conductivity and capacitance were measured at  $25^\circ\text{C}$ ,  $50^\circ\text{C}$ ,  $75^\circ\text{C}$  temperatures at low frequency range (typically from 100 KHz to 6 MHz



with an Agilent low frequency impedance analyzer 4291A model where the circuit was in series connection with the material under test.

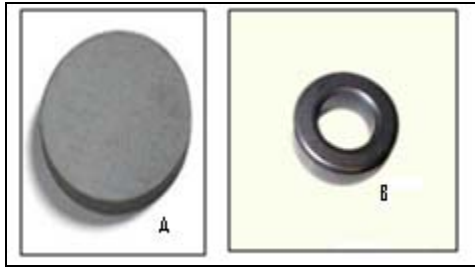


Fig 1. Prepared samples A and B

Table 1: Dimensions of the samples

Sample	A	B
Thickness (mm)	2.92	3.0
Outer diameter (mm)	11.3	15.0
Inner diameter (mm)	6.05	-

### 3.1 MICROSTRUCTURE STUDY

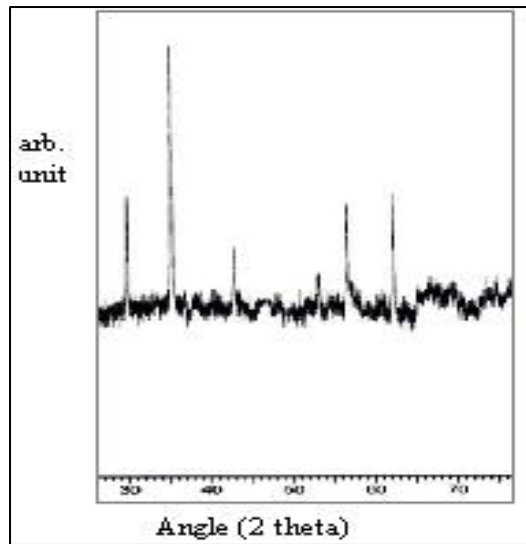


Fig 2. XRD of  $\text{Ni}_{0.46}\text{Zn}_{0.54}\text{Ca}_{0.05}\text{Fe}_2\text{O}_4$

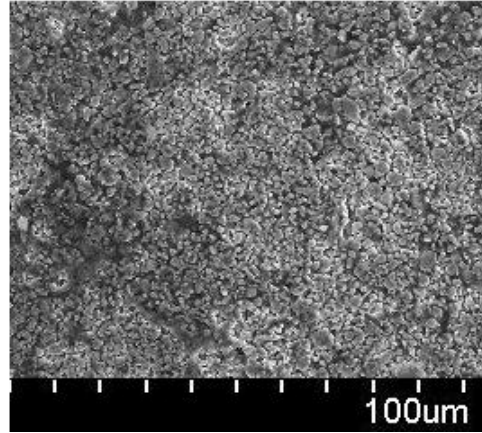


Fig 3. SEM image at 100 μm resolution

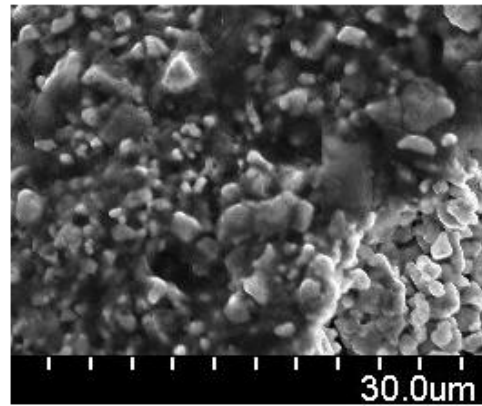


Fig 4. SEM image at 30 μm resolution

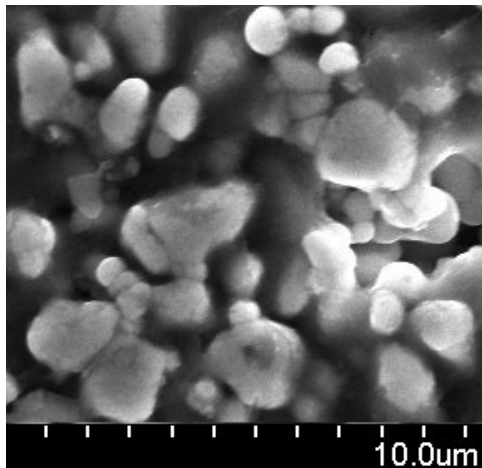


Fig 5. SEM image at 10 μm resolution

### 3.2 XRD RESULT

X-ray diffraction (XRD) pattern showed the polycrystalline phase and formation of spinel crystal structure. The angles of the peak values correspond to (111), (222), (220), (440) planes due to the atoms present at octahedral and tetrahedral sites. Because the ionic radii of  $\text{Ca}^{2+}$  ions are greater than that of Ni the replacement of Ni by  $\text{Ca}^{2+}$  ions is expected to increase the lattice constant of ferrite. [8] Redistribution of tetra- and octahedral sites are evident from the increase of intensities of (111) and (222) peaks and decrease of (220) and (440) peaks. By applying scherrer formula the size of the crystallite size is measured and found around  $8.42^{\circ}$  A.

The calculation was made as followings:

$$d = \frac{0.9 \lambda}{\beta \cos \theta} \quad (1)$$

Where, d= crystalline diameter  
 $\lambda$  = wavelength of the XRD =  $1.56^{\circ}$  A  
 $\theta$  = angle of the highest peak =  $18^{\circ}$   
 $\beta$  = half line width of the maximum peak

### 3.3 SEM IMAGE

Scanning electron microscope is a powerful tool of studying microstructure. In our case SEM was done at 15 K Electron Volt and at three different resolutions  $100\mu\text{m}$ ,  $30\mu\text{m}$  and  $10\mu\text{m}$ . From these images the grain size was measured. The average grain size was about 5 micro meter. The images showed inhomogeneity in the crystal structure. The black spaces are the voids created during solidification.

### 4. CONDUCTANCE MEASUREMENT

Frequency dependent ac parameters such as conductivity and capacitance were measured at  $25^{\circ}\text{C}$ ,  $50^{\circ}\text{C}$ ,  $75^{\circ}\text{C}$  temperatures at low frequency range with an Agilent low frequency impedance analyzer 4291A model. The flat disc sized sample was in series circuit during the measurement. Joule heating was done by variable external voltage. By calibrating the voltmeter with the thermocouple the temperature was measured. The specimen sample A was subjected to high pressure to make better contact in the circuit. Temperature dependent conductance was measured at  $25^{\circ}$ ,  $50^{\circ}$  and  $75^{\circ}$  C. It is found that with the increasing temperature the conductivity decreases. The difference between  $50^{\circ}$  C and  $75^{\circ}$  C is slight but these two show big differences with the room temperature measurement. The conduction process in ferrites with excess ferrous content (*n*-type semiconductors) is usually attributed to electronic

jumps between  $\text{Fe}^{2+}$  and  $\text{Fe}^{3+}$  in the octahedral sites. [9] The electrical conductivity of these materials can be approximately described by:

$$\sigma = (ne^2 l^2 \nu_0 / kT) \exp(-E/kT) \quad (2)$$

Where, *n* = density of charge carriers,

*e* = electron charge,

*l* = length of a jump (usually assumed to be 0.3 nm, representing the distance between the octahedral positions),

$\nu_0$  = characteristic frequency ( $10^{12}$ – $10^{14}$  s<sup>-1</sup>),

*k* = Boltzmann constant,

*T* = absolute temperature,

*E* =activation energy of the conduction process (“electron hopping”)

The addition of calcium in the Ni Zn ferrite composite enhances resistance and impedance by introducing glassy behavior in the grains boundaries. From the graphs (Fig 6-8) of our experiment frequency dependent conduction behavior was revealed which is necessary for finding the eddy current losses in the system. Each ferrous ion can be considered as a donor containing an extra electron, which jumps to the adjacent ferric ion easily and constitutes the electronic conduction process. The variation of temperature changes dc conductivity. The oxidation of divalent iron reduces the donor concentration in the material such that the electrical resistivity is increased. The grain boundary resistivity is, generally, expected to be higher than the bulk resistivity. [10] Thus the material preparation techniques have a great role in determining the ac parameters and in a rich area for experimental researchers.

### 5. CAPACITANCE MEASUREMENT

The capacitance of the sample increased with the increasing temperature. All the graphs (Fig 9-11) showed exponential decay of the capacitance with the increasing frequency. These curves showed the dynamic behavior of charge concentration in the composite with varying frequency at three different temperatures.

### 6. Q FACTOR MEASUREMENT

In control system and mechatronics remote magnetic switching to avoid the wiring and reduce size of the components often spinel ferrite is a good choice. To make band pass filter and tuning operated circuit, oscillating circuit and varactors Quality factor measurement is an important aspect. In our experiment Q factor was measured in LRC precision meter 4285 A. Various type of band pass filters can be designed from 0.3 to 0.7 MHz frequency range.

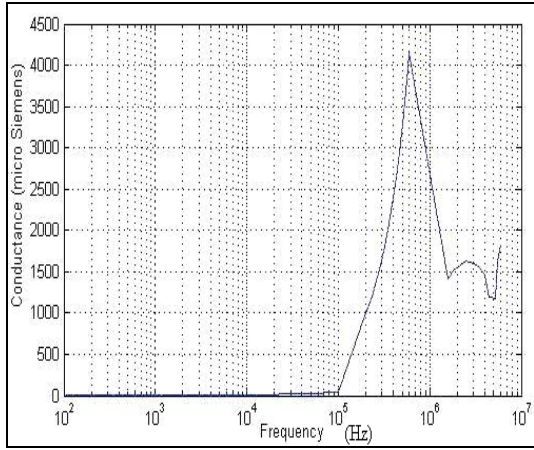


Fig 6. Frequency vs Conductivity at room 25° C

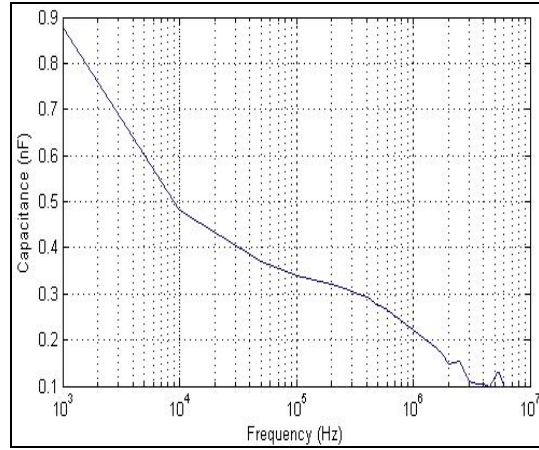


Fig 9. Frequency vs Capacitance at room 25° C

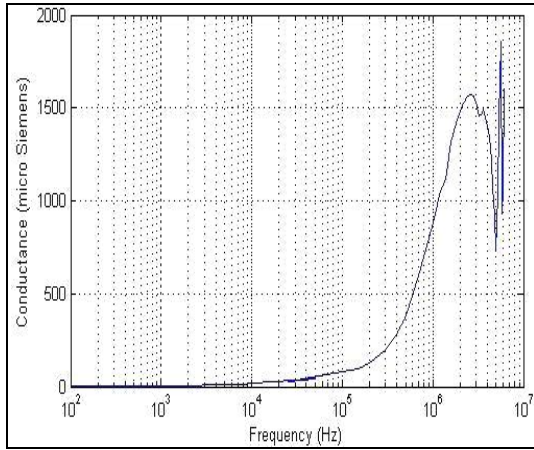


Fig 7. Frequency vs Conductivity at room 50° C

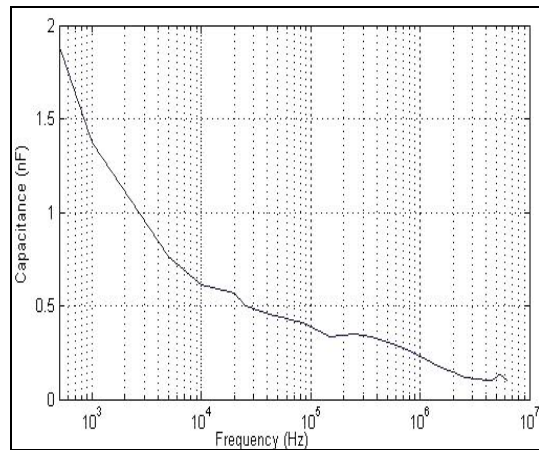


Fig 10. Frequency vs Capacitance at room 50° C

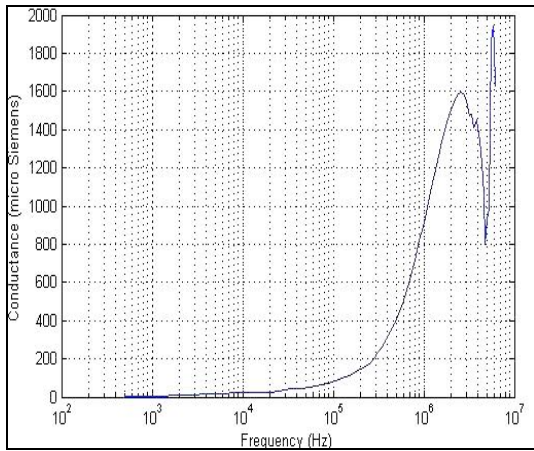


Fig 8. Frequency vs Conductivity at room 75° C

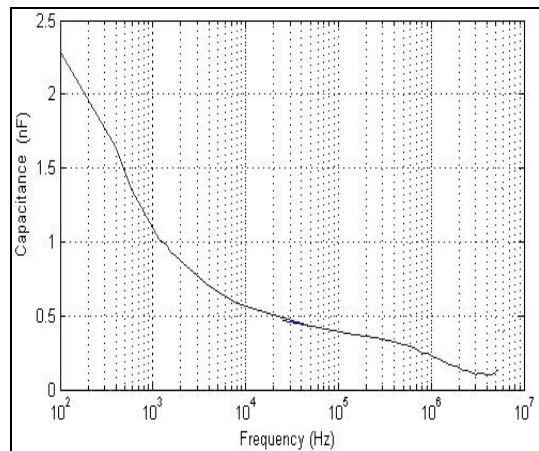


Fig 11. Frequency vs Capacitance at room 75° C

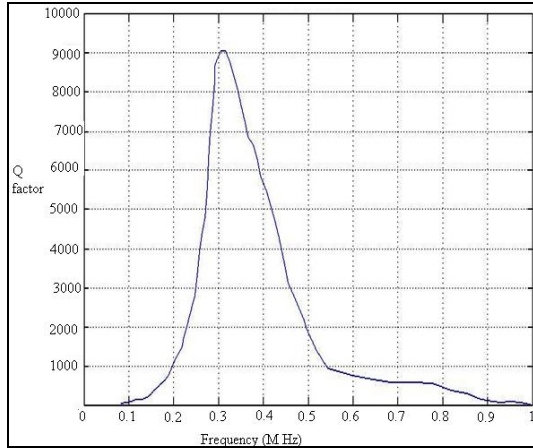


Fig 12. Q factor vs frequency at 25<sup>0</sup> C

## 7. CONCLUSION

The study of  $Ni_{0.46}Zn_{0.54}Ca_{0.05}Fe_2O_4$  shows that samples prepared by solid state reaction techniques is appropriate for practical applications in control system and mechatronics application. The results found in this experiment is well suited with the theoretical study of spinel ferrites. The studied ac characteristics are important for designing miniature circuits at varying temperatures and recent MEMS technology.

## 8. REFERENCES

1. Wendy Middleton, Mac E. Van Valkenburg, 2002 Reference Data for Engineers: Radio, Electronics, Computers and Communications, 2.
2. Haim Taraseiskey, 1996, Power hybrid circuit design and Manufacture, 24
3. Magnetic Materials: Report By National Research Council (U.S.), 1985, Committee on Magnetic Materials, National Research Council (U.S.). National Materials Advisory Board, Commission on Engineering and Technical Systems, National Academy Press, 38
4. William F. Smith, Javad Hashemi, Foundations of Materials Science and Engineering, 2003 McGraw-Hill Professional , 867

5. Y.Matsuo et al., "Decreasing core loss of Mn-Zn ferrite," 1996, J. Magn. Soc. Jpn., vol. 20, no. 2, 429.
6. The use for soft ferrite for interference suppression, application note by Ferroxcube
7. M. I. Rosales ,M.P.Cuautle, V. M. Castano, Microstructure and magnetic properties of Ni-Zn ferrites ,Journal of Material Science 33:1414, 3665-3669.
8. R. D. Shannon, "Revised effective ionic radii and systematic studies of interatomic distances in halides and chalcogenides," 1976, Acta Cryst. A, vol.32, 751-769.
9. I. I. Zyat'kov, V. P. Miroshkin, and Y. I. Panova, 1988, Sov. Phys. Sol. State 30, 748.
10. A. Dias et al.: Conductivity behavior of n-type semiconducting ferrites, Aug 1998, J. Mater. Res., Vol. 13, No. 8.

## 9. NOMENCLATURE

Symbol	Meaning	Unit
d	Crystallite diameter	(m)
$\theta$	Angle of peak	( <sup>0</sup> )
$\beta$	Half line-width of peak	(rad)
$\lambda$	Wavelength of the XRD	(m)
T	Absolute temperature	(K)
n	density of charge carriers	(C/m <sup>3</sup> )
l	the length of a jump	(m)
E	Activation energy of conduction process	(J)
$\nu_0$	Characteristic frequency	(s <sup>-1</sup> )
C	Capacitance	(F)
G	Conductance	(S)
Q	Quality factor	Dimensi- on less

## 10. MAILING ADDRESS

H. M. Iftekhar  
 Department of Mechanical Engineering,  
 Bangladesh University of Engineering and  
 Technology, Dhaka, Bangladesh



## FRICITION BEHAVIOUR OF ELECTROLESS Ni-B COATINGS

Prasanta Sahoo and S. Kalyan Das

Department of Mechanical Engineering, Jadavpur University, Kolkata, India

### ABSTRACT

This paper presents an experimental study of friction characteristics of electroless Ni-B coatings sliding against steel and optimization of coating process parameters based on the Taguchi method to minimize the same. Experiments are carried out by utilizing the combination of process parameters based on the  $L_{27}$  Taguchi orthogonal design with four process parameters, namely, bath temperature, concentration of reducing agent, concentration of nickel source and annealing temperature. It is observed that concentration of reducing agent has the most significant influence in controlling friction characteristics of Ni-B coating. The optimum combination of process parameters for minimum coefficient of friction is obtained from the analysis. The surface morphology and phase content of coatings are also studied with the help of scanning electron microscopy and x-ray diffraction analysis respectively. The wear mechanism is also studied and found to be abrasive in nature.

**Keywords:** Electroless Coating, Ni-B, Taguchi Method, Friction.

### 1. INTRODUCTION

In 1946, Brenner and Riddell [1] discovered a revolutionary coating process, which did not require electricity for its operation and hence was popularized as electroless coating. Electroless plating is an autocatalytic process where the substrate develops a potential when it is dipped in electroless solution called bath that contains a source of metallic ions, reducing agent, complexing agent, stabilizer and other components. Due to the developed potential, both positive and negative ions are attracted towards the substrate surface and release their energy through charge transfer process.

Among the various types of electroless plating, electroless nickel has gained immense popularity due to its ability to provide a hard, wear and corrosion resistant surface [2,3]. Hypophosphite reduced Ni-P coating [4-9] has already been widely accepted and the quest for achieving a superior hard and wear resistant surface has brought Ni-B coatings at the focus of research [10-17]. Aerospace, automotive, chemical and electrical industries utilize electroless nickel-boron plating due to its good solderability, lubricity, high hardness, high wear and abrasion resistance [2].

### 2. TAGUCHI METHOD

Taguchi techniques were developed by G. Taguchi [18]. Taguchi method uses a set of orthogonal arrays to reduce the number of experiments required which may otherwise increase the time and cost of the experiment. Taguchi offers the use of S/N (Signal/Noise) ratio to identify the quality characteristics applied for engineering design problems. The S/N ratio characteristics can be divided into three categories:

lower-the-better (LB), higher-the better (HB) and nominal-the best (NB). For the case of minimization of friction, LB characteristic needs to be used. Furthermore, a statistical analysis of variance (ANOVA) [19] is performed to find which process parameters are statistically significant. With the S/N ratio and ANOVA analysis, the optimal combination of coating parameters can be predicted. Finally, a confirmation experiment is conducted to verify the optimal process parameters obtained from the parameter design.

### 3. EXPERIMENTAL DETAILS

#### 3.1 Coating Procedure

Mild Steel (AISI 1040) is used as the substrate material (square blocks of size 20 mm × 20 mm × 8 mm) for the deposition of Ni-B films. The substrates are carefully prepared so that their sizes are maintained with precision. The samples are cleaned of any foreign particles and corrosion products prior to coating. Then the samples are cleaned with distilled water. The specimens after thorough cleaning are given a pickling treatment with dilute (18%) hydrochloric acid for one minute to remove any surface layer formed like rust. Finally they are cleaned with distilled water prior to coating. A large number of trial experiments were performed before deciding on the bath composition with the ranges of the coating parameters. Table 1 indicates the bath composition and the operating conditions for successful coating of electroless Ni-B. The cleaned samples were activated in palladium chloride solution at 55°C temperature and placed in the bath for a deposition time of 1 hour. For each sample, the procedure is

repeated twice except for the palladium chloride activation in the second round. The range of coating thickness was found to lie between 20-25 microns. After deposition, the samples were taken out of the bath and cleaned using distilled water. Then the samples were heat treated in a box furnace (for 1 h) separately according to the OA. After annealing, the samples were cooled to room temperature (about 25°C) and no artificial cooling is employed. Depending on annealing temperature, it takes 10–15 min time for cooling.

It is important to note that the present study does not consider substrate roughness as the input variable. Thus it is essential that all samples after different stages of processing and prior to coating should have same roughness. But this is extremely difficult to achieve. Thus large numbers of samples are prepared and after all the processing prior to coating these are subjected to roughness evaluation (centre line average,  $R_a$ ). Only those specimens that show insignificant variation (less than 0.1%) in roughness are used for coating deposition.

Table 1: Bath constituents and ranges of values for electroless Ni-B coating

Parameters	Ranges of parameters
Nickel chloride	15 – 25 g/l
Sodium	0.6 – 1.0 g/l
Ethylenediamine	59 g/l
Lead nitrate	0.0145 g/l
Sodium hydroxide	40 g/l
Bath temperature	85 – 95 °C
pH of solution	12.5
Deposition time	1 hr
Annealing	250 – 450 °C

### 3.2 Choice of Process Parameters

There are a large number of factors that can affect the quality of EN coating viz. bath temperature, reducing agent concentration, nickel source concentration, stabilizer concentration, pH of the solution, etc. Based on an intensive literature review it was found that the first three factors (bath temperature, reducing agent concentration and nickel source concentration) were mostly used by the researchers to control EN coating. These three factors were chosen as the main design factors along with their interactions in the present study. The literature review also reports that annealing greatly influences the tribological characteristics of electroless nickel coatings. Hence annealing temperature has been considered as the fourth design factor in this study. Table 2 shows the design factors along with their levels. Three levels, having equal spacing, within the operating range of the parameters were selected for each of the factors. By selecting the three levels, the curvature or non-linearity effects could be studied.

Table 2: Design factors and their levels

Design Factors	Unit	Levels		
		1	2	3
Bath Temperature (A)	°C	85	90 <sup>a</sup>	95
Reducer conc. (B)	(g/l)	0.6	0.8 <sup>a</sup>	1.0
Nickel source conc. (C)	(g/l)	15	20 <sup>a</sup>	25
Annealing temp (D)	°C	250	350 <sup>a</sup>	450

a : initial condition

### 3.3 Response Variable

This study is carried out to consider the friction characteristics of EN coatings as the performance characteristics. The response variable used to accomplish this study is the coefficient of friction (COF). Hence the coating process parameters are optimized with the objective to minimizing the coefficient of friction of electroless Ni-B coatings.

### 3.4 Design of Experiment

The DOE using Taguchi approach can economically satisfy the needs of problem solving and product/process design optimization projects in the manufacturing industry. By learning and applying this technique, engineers, scientists and researchers can significantly reduce the time required for experimental investigations. Based on the Taguchi method, an OA (orthogonal array) is employed to reduce the number of experiments for determining the optimal coating process parameters. An OA provides the shortest possible matrix of combinations in which all the parameters are varied to consider their direct effect as well as interactions simultaneously. Taguchi has tabulated several standard OAs. In this investigation, an  $L_{27}$  OA, which has 27 rows corresponding to the number of tests and 26 degrees of freedom (DOFs) with 13 columns at three levels, is chosen. As per the requirements of the  $L_{27}$  OA, the 1st column is assigned to bath temperature (A), the 2nd column is assigned to concentration of reducing agent (sodium borohydride) (B), the 5th column is assigned to concentration of source of nickel (nickel chloride) (C), the 9th column is assigned to the annealing temperature (D) while the rest of the columns are assigned to the two-way interactions of the factors and error terms.

### 3.5 Friction Measurement

Friction characteristics of the electroless Ni-B coated specimens are studied under dry, non-lubricated conditions and at ambient temperature of about 28°C and relative humidity of about 85% in a multitrilater apparatus (TR-25, DUCOM, INDIA) using a plate-on-roller configuration. The experiments are conducted with a constant load of 25N and at 60 rpm and for a constant time of 300 s considering the smaller thickness (around 25 $\mu$ m) of the coatings. The roughness measurement of the coatings prior to the tribological testing is done using a stylus and skid type profilometer, Talysurf (Taylor Hobson, Surtronic 3+). The centre line average roughness values are obtained in the range 0.2–0.8 $\mu$ m.

### 3.6 Surface Morphology and Compound Analysis

Surface morphology of the EN coatings is studied by SEM (JEOL, JSM-6360) in order to analyse the microstructure of the deposited coatings before and after annealing at different heat treatment temperatures to see the effect of annealing temperature. SEM is also done after the tribological testing to see the sliding track patterns. The different precipitated phases of the deposits both before and after annealing were analyzed by X-ray diffraction (XRD) analyzer (Rigaku, Ultima III).

## 4. RESULTS AND DISCUSSION

### 4.1 Analysis of Signal to Noise Ratio

As an evaluation tool for determining robustness, the signal-to-noise (S/N) ratio is preferred to simple averages of results as the former can capture the variability of the results within a trial condition. Hence Taguchi technique utilizes the S/N ratio approach to measure the quality characteristic deviating from the desired value. In the present work S/N ratio analysis is done with coefficient of friction as the performance index. The S/N ratio for coefficient of friction is calculated using LB (Lower the better) criterion and is given by

$$S/N = -10 \log(\sum y^2 / n) \quad (1)$$

where  $y$  is the observed data and  $n$  is the number of observations. Table 3 shows the experimental COF values along with their S/N ratios. As the experimental design is orthogonal, it is possible to separate out the effect of each coating parameter at different levels. The mean S/N for each level of the factors A, B, C and D is summarized in Table 4. All the calculations are performed using Minitab® [20]. The response table includes ranks based on Delta statistics, which compare the relative magnitude of effects. The Delta statistic is the highest average for each factor minus the lowest average for the same. Ranks are assigned based on Delta values; rank 1 is assigned to the highest Delta value, rank 2 to the second highest Delta value, and so on. The corresponding main effects and interaction effects plots between the process parameters are also shown in Fig 1 and Fig 2 respectively. In the main effects plot if the line for particular parameter is near horizontal, then the parameter has no significant effect. On the other hand, a parameter for which the line has the highest inclination will have the most significant effect. From the main effects plot (Fig 1) it is clear that factor B i.e. the concentration of the reducing agent is the most significant factor while factor A i.e. bath temperature is moderately significant. In case of interaction plots non-parallelism of the parameter effects are observed. If the lines on the interaction plots are non-parallel, interaction occurs and if the lines cross, strong interactions occur between parameters. From the interaction plots (Fig 2) it can be observed that the interaction between A and C and that between B and C are somewhat significant as far as the friction characteristics are concerned. Thus from the present

analysis it is clear that the concentration of reducing agent (B) is the most influencing parameter for COF of electroless Ni-B coatings. The optimal process parameter combination is the one that yields maximum mean S/N ratio i.e. minimum COF and is found to be A1B1C1D3.

Table 3: Experimental results along with S/N ratio

Exp. No.	COF	S/N Ratio
1	0.184	14.72728
2	0.107	19.41232
3	0.132	17.58852
4	0.314	10.06141
5	0.411	7.723164
6	0.108	19.33152
7	0.300	10.45757
8	0.131	17.65457
9	0.571	4.867278
10	0.093	20.63034
11	0.282	10.99502
12	0.209	13.59707
13	0.083	21.61844
14	0.246	12.1813
15	0.311	10.14479
16	0.368	8.683044
17	0.326	9.735648
18	0.310	10.17277
19	0.207	13.68059
20	0.449	6.955073
21	0.274	11.24499
22	0.409	7.765534
23	0.124	18.13157
24	0.267	11.46977
25	0.364	8.777972
26	0.255	11.8692
27	0.477	6.429632

Table 4: Response table for mean S/N ratio

Level	A	B	C	D
1	13.536	14.315	12.934	11.925
2	13.084	13.159	12.740	12.556
3	10.703	9.850	11.650	12.842
Delta	2.833	4.465	1.284	0.917
Rank	2	1	3	4

Total mean S/N Ratio = 12.441 dB



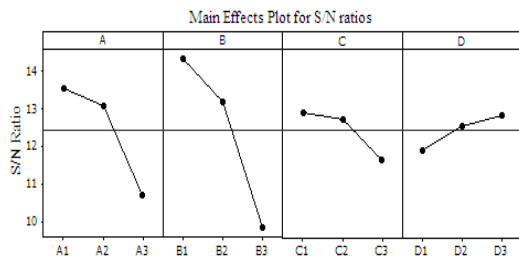
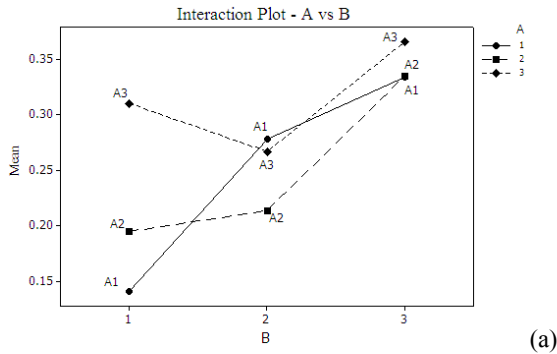
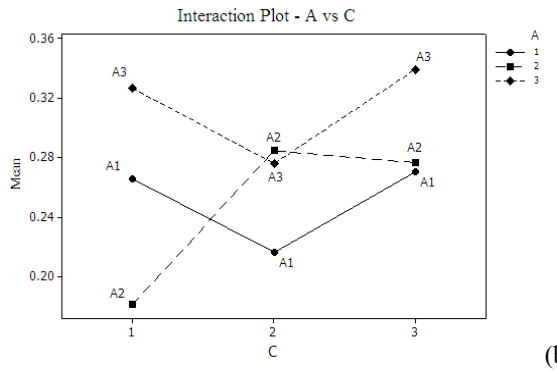


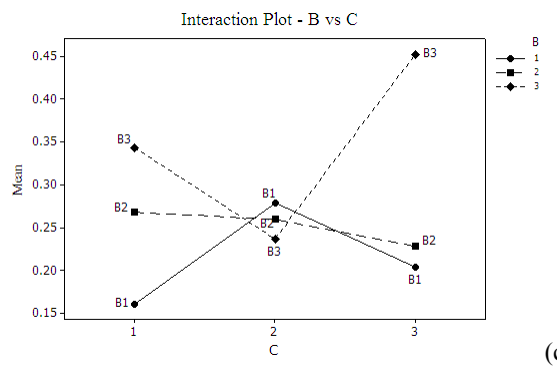
Fig 1. Main effects plot for mean S/N ratio



(a)



(b)



(c)

Fig 2. Interaction effects plot for mean COF (a) A versus B, (b) A versus C and (c) B versus C.

#### 4.2 Analysis of Variance (ANOVA)

The purpose of the ANOVA is to investigate which of the process parameters significantly affect the performance characteristics. This is accomplished by separating the total variability of the S/N ratios, which is measured by the sum of the squared deviations from the

total mean of the S/N ratio, into contributions by each of the process parameters and the error. In the present study ANOVA is performed using Minitab® [20]. ANOVA results for COF of electroless Ni-B coating is shown in Table 5. In ANOVA a ratio called F-ratio, which is the ratio between the regression mean square and mean square error is used to measure the significance of the parameters under investigation with respect to the variance of all the terms included in the error term at the desired significance level,  $\alpha$ . A calculated F-ratio which is higher than the tabulated F-ratio indicates that the factor is significant at desired  $\alpha$  level. ANOVA table also shows the percentage contribution of each parameter. It is seen that parameter B, i.e. concentration of reducing agent has got the most significant influence on coefficient of friction at the confidence level of 65% within the specific test range. No other parameter is significant at the said level of confidence. Also none of the interaction is found to have significant effect on the friction characteristics of electroless Ni-B coating but interaction between bath temperature and concentration of nickel source ( $A \times C$ ) and that between concentration of reducing agent and concentration of nickel source ( $B \times C$ ) have got somewhat contribution in controlling the friction coefficient.

Table 5: ANOVA table for coefficient of friction

Source	DF	SS	MS	F	% contribution
A	2	41.71	20.85	0.57	7.33
B	2	96.66	48.33	1.33*	17.00
C	2	8.62	4.31	0.12	1.52
D	2	3.96	1.98	0.05	0.70
A*B	4	42.80	10.70	0.29	7.52
A*C	4	87.56	21.89	0.60	15.39
B*C	4	69.72	17.43	0.48	12.25
Error	6	217.94	36.32		38.30
Total	26	568.97			100

\* - significant parameters and interactions  
( $F_{0.35, 2, 6} = 1.26$ )

#### 4.3 Confirmation Test

Once the optimal level of the process parameters is selected, the final step is to predict and verify the improvement of the performance characteristic using the optimal level of the process parameters. The estimated S/N ratio  $\hat{\gamma}$  using the optimal level of the process parameters can be calculated as

$$\hat{\gamma} = \gamma_m + \sum_{i=1}^o (\bar{\gamma}_i - \gamma_m) \quad (2)$$

where  $\gamma_m$  is the total mean S/N ratio,  $\bar{\gamma}_i$  is the mean S/N ratio at the optimal level, and  $o$  is the number of the main design parameters that significantly affect the COF

of electroless Ni-B coating. Table 6 shows the comparison of the estimated S/N ratio with the actual S/N ratio using the optimal parameters. The increase of the S/N ratio from the initial coating parameters to the optimal coating parameters is 9.742 dB which means friction is reduced by about 67%.

Table 6: Result of the confirmation experiment for friction coefficient

	Initial parameters	Optimal Parameters	Experiment
Level	A2B2C2D2	A1B1C1D3	A1B1C1D3
COF	0.396		0.129
S/N ratio (dB)	8.046	12.441	17.788

Improvement of S/N ratio = 9.742 dB

#### 4.4 Surface Morphology and Phase Structure

Surface morphology study of the coatings is done by SEM in order to analyse the effect of heat treatment on the microstructure of the coatings for some of the samples at random and they show similar qualitative change in microstructure. Fig 3 shows the SEM micrographs of the samples in as deposited and under heat treated conditions. It is seen that the electroless Ni-B coatings in general exhibit a defect free surface with distribution of Ni-B nodules, more like that of a cauliflower surface which indicates that the coating possesses a lubricious behaviour. The surface of the coating appears dense and light grey in colour with low porosity. When heat treated, the Ni-B nodules grow in size giving rise to a coarse-grained structure. This indicates that in as deposited condition the structure is a mixture of amorphous and microcrystalline which becomes crystalline with heat treatment. This is further supported by the XRD patterns of Ni-B deposits in as deposited and heat treated condition (Fig 4). The XRD patterns in as deposited condition is a collection of microcrystalline peaks. But with heat treatment at 450°C for one hour, broad peaks of Ni, Ni<sub>2</sub>B and Ni<sub>3</sub>B are produced.

SEM micrograph of the worn surface is shown in Fig 5. The presence of longitudinal grooves along the sliding direction with high degree of plasticity can be clearly observed. This is indicative of the occurrence of micro-cutting and micro-ploughing effect and characterized as ductile failure. Almost no pits or prows are observed on the worn surface. Hence it can be concluded that the abrasive wear is the predominant phenomenon. The same trend is observed for other combinations of deposition parameters within the experimental regime considered in this study.

The influence of four factors, viz., bath temperature, concentration of nickel source, concentration of reducing agent and annealing temperature is considered in the present study. Future study may attempt to evaluate the influence of other factors viz. concentration of stabilizer, pH of solution, substrate roughness, etc on the friction characteristics of electroless Ni-B coating.

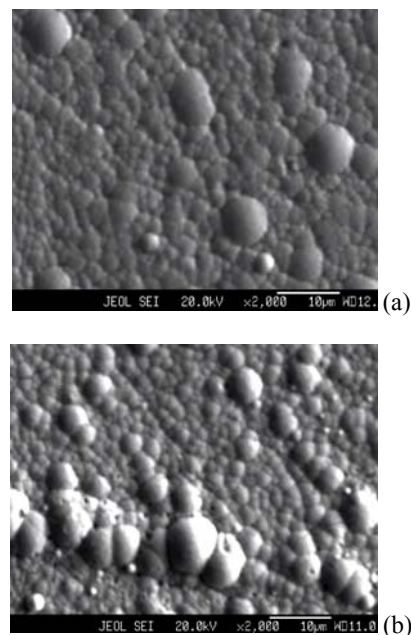


Fig 3. SEM micrographs of the coating surfaces: (a) as-deposited and (d) heat treated at 450°C.

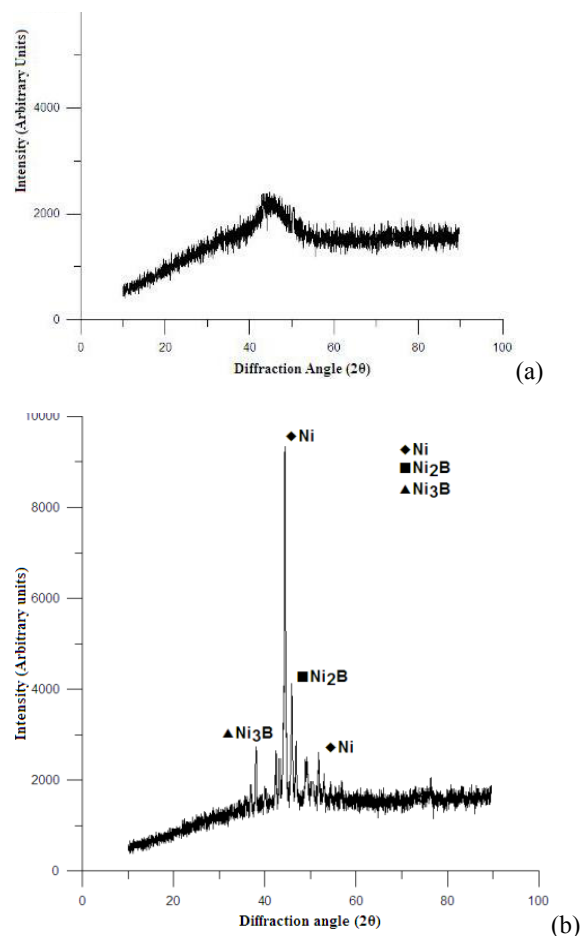


Fig 4. XRD patterns of electroless Ni-B deposit in

(a) as-deposited and (b) heat treated at 450°C

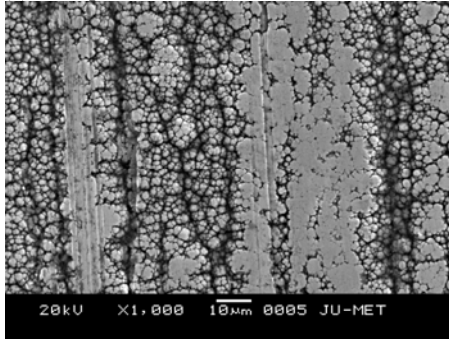


Fig 5. SEM micrograph of coating surface after friction testing

## 5. CONCLUSION

In the present study Taguchi orthogonal array is used to optimize the coating process parameters (bath temperature, concentration of reducing agent and concentration of nickel source) together with annealing temperature in order to minimize coefficient of friction of electroless Ni-B coating. The following conclusions can be drawn:

- Concentration of reducing agent (B) is the most important parameter that significantly affects the coefficient of friction at a confidence level of 65%.
- Interaction between bath temperature and concentration of nickel source ( $A \times C$ ) and that between concentration of reducing agent and concentration of nickel source ( $B \times C$ ) have got somewhat contribution in controlling the friction coefficient.
- The optimal parameter combination for minimum friction is A1B1C1D3.
- The coefficient of friction is reduced by about 67% at the optimal condition compared to the initial condition.

The microstructural study through SEM micrographs reveals that the coating has a cauliflower like structure with no obvious surface damage and low porosity. XRD analysis shows that the coating is in general amorphous in as deposited condition and turns crystalline with heat treatment. The sliding tracks show that abrasive failure is the predominant phenomenon.

## 6. REFERENCES

1. Brenner, A. and Riddell, G. E., 1950, "Nickel plating by chemical reduction", US Patent US2532282.
2. Mallory, G. O. and Hadju J. B., 1991, *Electroless Plating: Fundamentals and Applications*, AESF, Orlando.
3. Riedel, W., 1991, *Electroless Plating*, ASM International, Ohio.
4. Agarwala, R. C. and Agarwala, V., 2003, "Electroless alloy /composite coatings: A review", *Sadhana*, 28(3 & 4):475–493.
5. Sahoo, P., 2008, "Friction performance optimization of electroless Ni-P coatings using Taguchi method", *Journal of Physics D: Applied Physics*,

41:095305(11pp)

6. Sahoo, P. and Pal, S. K., 2007, "Tribological Performance Optimization of Electroless Ni-P Coatings Using the Taguchi Method and Grey Relational Analysis", *Tribology Letters*, 28: 191-201.
7. Staia, M. H., Castillo, E. J., Puchi, E. S., Lewis, B. and Hintermann, H. E., 1996, "Wear performance and mechanism of electroless Ni-P coating", *Surface & Coatings Technology*, 86–87:598–602.
8. Taheri, R., Oguocha, I. N. A. and Yannacopoulos, S., 2001, "The tribological characteristics of electroless Ni-P coatings", *Wear*, 249:389–396.
9. Ramalho, A. and Miranda, J. C., 2005, "Friction and wear of electroless Ni-P and Ni-P + PTFE coatings", *Wear*, 259:828–34.
10. Delaunois, F. and Lienard, P., 2002, "Heat treatments for electroless nickel-boron plating on aluminium alloys", *Surface and Coatings Technology*, 160:239–248.
11. Oraon, B., Majumdar, G. and Ghosh, B., 2008, "Improving hardness of electroless Ni-B coatings using optimized deposition conditions and annealing", *Materials and Design*, 29:1412–1418.
12. Krishnaveni, K., Sankara Narayanan, T. S. N. and Seshadri, S. K., 2005, "Electroless Ni-B coatings: preparation and evaluation of hardness and wear resistance", *Surface & Coatings Technology*, 190:115–121.
13. Anik, M., Körpe, E. and Şen, E., 2008, "Effect of coating bath composition on the properties of electroless nickel-boron films", *Surface & Coatings Technology*, 202:1718–1727.
14. Vitry, V., Delaunois, F. and Dumortier, C., 2008, "Mechanical properties and scratch test resistance of nickel-boron coated aluminium alloy after heat treatments", *Surface & Coatings Technology*, 202:3316–3324.
15. Ziyuan, S., Deqing, W. and Zhimin, D., 2004, "Surface strengthening pure copper by Ni-B coating", *Applied Surface Science*, 221:62–68.
16. Di Giampaolo, A. R., Ordonez, J. G., Gugliemacci, J. M. and Lira, J., 1997, "Electroless nickel-boron coatings on metal carbides," *Surface and Coatings Technology*, 89:127-131.
17. Delaunois, F., Petitjean, J. P., Lienard, P. and Jacob-Duliere, M., 2000, "Autocatalytic electroless nickel-boron plating on light alloys", *Surface and Coatings Technology*, 124(2–3):201-209.
18. Taguchi, G., 1990, *Introduction to quality engineering*, Asian Productivity Organization.
19. Montgomery, D. C., 2001, *Design and Analysis of Experiments*, Wiley, New York.
20. Minitab User Manual (Release 13.2), 2001, *Making data analysis easier*, MINITAB Inc, State College, PA, USA,

## 7. MAILING ADDRESS

Prasanta Sahoo  
Professor, Department of Mechanical Engineering,  
Jadavpur University, Kolkata 700032, India  
Email: [psjume@gmail.com](mailto:psjume@gmail.com)

## OPTIMIZATION OF ELECTROLESS Ni-B COATINGS BASED ON MUTIPLE ROUGHNESS CHARACTERISTICS

S. Kalyan Das and Prasanta Sahoo

Department of Mechanical Engineering, Jadavpur University, Kolkata, India

### ABSTRACT

This paper presents an experimental study of multiple roughness characteristics of electroless Ni-B coatings. Optimization of coating process parameters based on the Taguchi method combined with grey relational analysis is done to minimize roughness. Experiments are carried out by utilizing the combination of process parameters based on the L<sub>27</sub> Taguchi orthogonal array design with three process parameters, namely, bath temperature, concentration of reducing agent and concentration of nickel source. It is observed that concentration of reducing agent has the most significant influence in controlling roughness characteristics of electroless Ni-B coating. The optimum combination of process parameters for minimum roughness is obtained from the analysis. The surface morphology and phase structure of coatings are also studied with the help of scanning electron microscopy and x-ray diffraction analysis.

**Keywords:** Electroless Coating, Ni-B, Roughness, Taguchi Method, Grey Analysis.

### 1. INTRODUCTION

The invention of Electroless Nickel (EN) coating is mainly credited to Brenner and Riddell [1]. Borohydride reduced coatings or Ni-B coatings have found extensive applications in aerospace, automotive, chemical and electrical industries especially due to their high hardness, wear resistance, solderability, abrasion resistance, etc.[2-10].

Surface roughness has a large impact on the mechanical properties such as fatigue behaviour, corrosion resistance, creep life, etc. It also affects other functional attributes of machine components such as friction, wear, light reflection, heat transmission, lubrication, electrical conductivity, etc. As a result, there is a need for research on modeling surface roughness and optimization of the controlling parameters to obtain a surface finish of the desired level. Hence the present study is directed towards roughness optimization of Ni-B coatings.

The present study uses Taguchi method to optimize the process parameters in order to minimize the surface roughness of Ni-B coating. Taguchi method [11] is a powerful tool for design of high quality systems based on orthogonal array (OA). Taguchi makes use of S/N (Signal to Noise) ratio to denote the quality characteristics. The S/N ratio characteristics can be divided into three categories: lower-the-better (LB), higher-the better (HB) and nominal-the best (NB). Grey relational analysis is done to have an optimum coating parameter combination that yields optimum roughness characteristics. A statistical analysis of variance (ANOVA) [12] is performed to find which process parameters are statistically significant. Finally, a confirmation experiment is conducted to verify the

optimal process parameters obtained from the parameter design.

### 2. EXPERIMENTAL DETAILS

#### 2.1 Coating Deposition

Mild Steel (AISI 1040) is used as the substrate material (square blocks of size 20 mm × 20 mm × 8 mm) for the deposition of Ni-B films. The samples are cleaned of any foreign particles and corrosion products prior to coating. Table 1 indicates the bath composition and the operating conditions for successful coating of electroless Ni-B. The cleaned samples were activated in palladium chloride solution and placed in the bath for a deposition time of 1 hour. For each sample, the procedure is repeated twice except for the palladium chloride activation in the second round. The range of coating thickness was found to lie between 20-25 microns. After the deposition the samples were taken out of the bath and cleaned using distilled water. To see the effect of heat treatment on the characteristics of the coating, some of the samples were heat treated at 450°C (for 1 hour) in a box furnace.

It is important to note that the present study does not consider substrate roughness as the input variable. Hence it is required that all samples have uniform roughness. This is achieved by preparing large number of samples and selecting those which show insignificant variation (less than 0.1%) in roughness.

#### 2.2 Design Parameters

Although many factors can affect the quality of EN coating, the present study considers (A) bath temperature

(B) reducing agent concentration and (C) nickel source concentration as the process parameters based on an intensive literature review. These three factors were chosen as the main design factors along with their interactions in the present study. Table 2 shows the design factors along with their levels.

Table 1: Bath constituents and ranges of values for electroless Ni-B coating

Parameters	Ranges of parameters
Nickel chloride	15 – 25 g/l
Sodium	0.6 – 1.0 g/l
Ethylenediamine	59 g/l
Lead nitrate	0.0145 g/l
Sodium hydroxide	40 g/l
Bath temperature	85 – 95 °C
pH of solution	12.5
Deposition time	1 hr

Table 2: Design factors and their levels

Design Factors	Unit	Levels		
		1	2	3
Bath Temperature (A)	°C	85	90 <sup>a</sup>	95
Reducer conc. (B)	(g/l)	0.6	0.8 <sup>a</sup>	1.0
Nickel source conc. (C)	(g/l)	15	20 <sup>a</sup>	25

a : initial condition

### 2.3 Response Variable

The present study is carried out to consider the roughness characteristics of electroless Ni-B coatings as the performance characteristics. Since a single parameter can't totally describe the quality of a surface, five roughness parameters are considered. It is a multiresponse problem and the five roughness parameters considered are: Centre line average roughness ( $R_a$ ), Root mean square roughness ( $R_q$ ), Skewness ( $R_{sk}$ ), Kurtosis ( $R_{ku}$ ) and Mean line peak spacing ( $R_{sm}$ ).

### 2.4 Design of Experiment

Taguchi method uses a set of orthogonal arrays (OA) to reduce the number of experiments required which may otherwise increase the time and cost of the experiment. An OA provides the shortest possible matrix of combinations in which all the parameters are varied to consider their direct effect as well as interactions simultaneously. Taguchi has tabulated several standard OAs. In this study, a  $L_{27}$  OA, which has 27 rows corresponding to the number of tests and 26 degrees of freedom (DOFs) with 13 columns at three levels, is chosen. As per the requirements of the  $L_{27}$  OA, the 1st column is assigned to bath temperature (A), the 2nd column is assigned to concentration of reducing agent (sodium borohydride) (B), the 5th column is assigned to concentration of source of nickel (nickel chloride) (C) while the rest of the columns are assigned to the two-way interactions of the factors and error terms.

### 2.5 Roughness Measurement

Roughness measurement is done using a portable stylus and skid type profilometer, Talysurf (Taylor Hobson, Surtronic 3+). The profilometer is set to a cut-off length of 0.8 mm, Gaussian filter, and traverse speed 1 mm/s with 4mm evaluation length. Roughness measurement on the electroless coatings is repeated four times and the average of four measurements is recorded. The measured profile is digitized and processed through the dedicated advanced surface finish analysis software Talyprofile for evaluation of the roughness parameters.

### 2.6 Surface Morphology and Compound Analysis

Study of surface morphology of the EN coatings is obtained by SEM (JEOL, JSM-6360) to analyse the microstructure of the deposited coatings both before and after annealing at 450°C, in order to see the effect of annealing temperature. The different precipitated phases of the deposits both before and after annealing were analyzed by X-ray diffraction (XRD) analyzer (Rigaku, Ultima III).

## 3. RESULTS AND DISCUSSION

### 3.1 Grey Relational Analysis

The objective of the present study is to minimize the five roughness parameters ( $R_a$ ,  $R_q$ ,  $R_{sk}$ ,  $R_{ku}$ ,  $R_{sm}$ ) simultaneously by optimizing the coating process parameters. Hence it is a case of multiresponse optimization which cannot be handled by Taguchi method alone. Hence the Grey relational analysis [13] is used together with Taguchi method to solve the problem. The Grey theory has been proven to be useful for dealing with poor, incomplete and uncertain information. In Grey analysis black represents having no information and white represents having all information. A grey system has a level of information between black and white and hence the name “Grey” is associated with it. The main objective of grey system theory is to supply information so that one can whiten the greyness.

In grey relational analysis the first step is to perform the grey relational generation in which the results of the experiments are normalized in the range between zero and one. The second step is to calculate the grey relational coefficient from the normalized data to represent the correlation between the desired and actual experimental data. The overall grey relational grade is then computed by averaging the grey relational coefficient corresponding to each performance characteristic. Overall evaluation of the multiple performance characteristics is based on the calculated grey relational grade. As a result, optimization of the complicated multiple performance characteristics is converted into optimization of a single grey relational grade. The optimal level of the process parameters is the level with the highest grey relational grade. Furthermore, a statistical ANOVA is performed to find which process parameters are statistically significant. With the grey relational analysis and statistical ANOVA, the optimal combination of the process parameters can be predicted. Finally, a confirmation experiment is conducted to verify



the optimal process parameters obtained from the analysis. For conciseness, the details of the Grey analysis and the intermediate calculations are omitted here. Only the final values for the grey relational grade and their order are listed in Table 3.

### 3.2 Analysis of Signal to Noise Ratio

Signal to noise ratio is preferred by Taguchi instead of mean since the former can capture the variability within a trial condition. In the present work S/N ratio analysis is done with grey relational grade as the performance index. The S/N ratio for grey relational grade is calculated using HB (Higher the better) criterion and is given by

$$S/N = -10 \log \left( \frac{1}{n} \sum_{i=1}^n \frac{1}{y_i^2} \right) \quad (1)$$

where  $y$  is the observed data and  $n$  is the number of observations. As the experimental design is orthogonal, it is possible to separate out the effect of each coating parameter at different levels. For example, the mean grey relational grade for factor A at levels 1, 2 and 3 can be calculated by averaging the grey relational grades for the experiments 1–9, 10–18 and 19–27, respectively. The mean grey relational grade for each level of the other factors can be computed in the similar manner. The grey relational grade for each level of the factors A, B, and C is summarized in Table 4. All the calculations are performed using Minitab® software [14]. The mean response table also includes ranks based on Delta statistics, which compare the relative magnitude of effects. The Delta statistic is the highest average for each factor minus the lowest average for the same. Ranks are assigned based on Delta values; rank 1 is assigned to the highest Delta value, rank 2 to the second highest Delta value, and so on. The corresponding main effects and interaction effects plots between the process parameters are also shown in Fig 1 and Fig 2 respectively. In the main effects plot if the line for particular parameter is near horizontal, then the parameter has no significant effect. On the other hand, a parameter for which the line has the highest inclination will have the most significant effect. From the main effects plot (Fig 1) it is clear that factor B i.e. the concentration of the reducing agent is the most significant factor while factor A i.e. bath temperature is also very significant. In case of interaction plots non-parallelism of the parameter effects are observed. If the lines on the interaction plots are non-parallel, interaction occurs and if the lines cross, strong interactions occur between parameters. From the interaction plots (Fig 2) it can be observed that the interaction between A and B are somewhat significant. Thus from the present analysis it is clear that the concentration of reducing agent (B) is the most influencing parameter for roughness parameters of electroless Ni-B coatings. The optimal process parameter combination for minimum roughness characteristics is found to be A2B1C2.

Table 3: Grey relational grade and its order

Exp. No.	Grey relational grade	Order
1	0.5365	21
2	0.7204	8
3	0.6224	16
4	0.5053	23
5	0.6739	13
6	0.4997	24
7	0.5270	22
8	0.4436	27
9	0.5767	19
10	0.7752	2
11	0.7326	6
12	0.7701	3
13	0.6179	17
14	0.6936	10
15	0.6740	12
16	0.5600	20
17	0.7570	5
18	0.6969	9
19	0.7572	4
20	0.6753	11
21	0.8553	1
22	0.6474	14
23	0.7314	7
24	0.6238	15
25	0.5937	18
26	0.4541	26
27	0.4545	25

Table 4: Response table for the grey relational grade

Level	A	B	C
1	0.5673	0.7162	0.6134
2	0.6975	0.6297	0.6536
3	0.6437	0.5627	0.6415
Delta	0.1302	0.1535	0.0402
Rank	2	1	3

Total mean grey relational grade = 0.6361

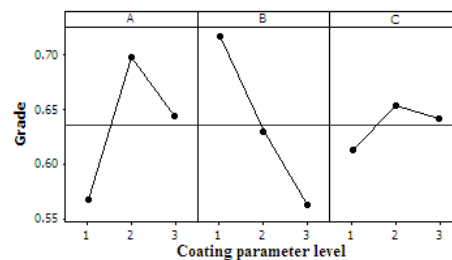


Fig 1. Main effects plot for mean grey relational grade

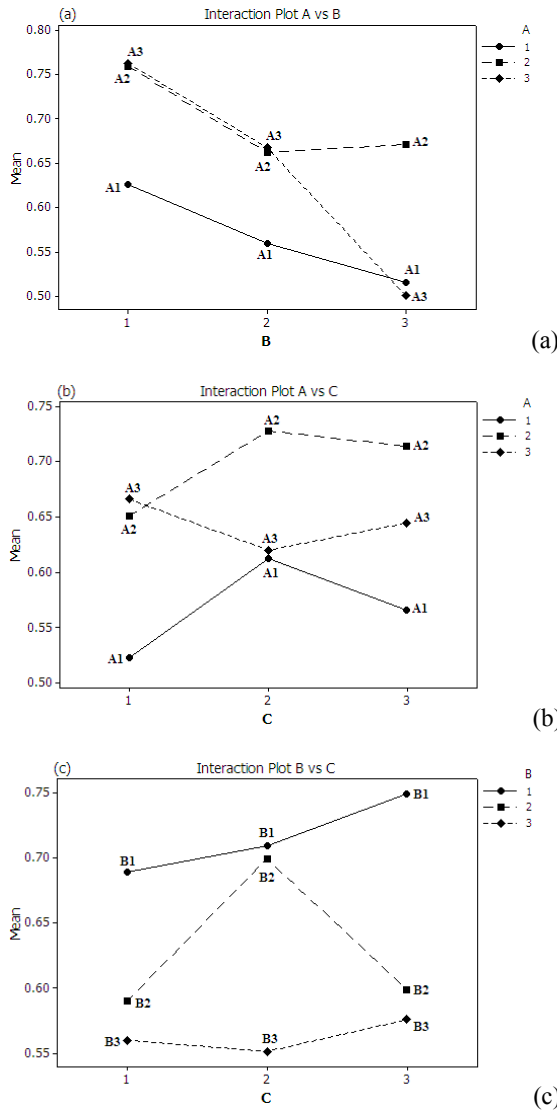


Fig 2. Interaction effects plot for mean grey relational grade (a) A versus B, (b) A versus C and (c) B versus C.

### 3.3 Analysis of Variance (ANOVA)

ANOVA is used to quantify the significance of the process parameters and their interactions, on the performance characteristics considered. This is accomplished by separating the total variability of the response which is measured by the sum of the squared deviations from the total mean of the response, into contributions by each of the process parameters and the error. In the present study ANOVA is performed using Minitab. ANOVA results for grey relational grade are shown in Table 5. In ANOVA a ratio called F-ratio, which is the ratio between the regression mean square and mean square error is used to measure the significance of the parameters under investigation with respect to the variance of all the terms included in the error term at the desired significance level,  $\alpha$ . A calculated F-ratio which is higher than the tabulated F-ratio indicates that the factor is significant at desired  $\alpha$  level. ANOVA table also shows the percentage contribution of each parameter. It is seen that parameter B, i.e. concentration of reducing

agent has got the most significant influence on roughness at the confidence level of 95% within the specific test range. Also parameter A, i.e. bath temperature is significant at the same confidence level. None of the interaction is found to have significant effect on the roughness characteristics of electroless Ni-B coating but interaction between the bath temperature and the concentration of reducing agent ( $A \times B$ ) has got somewhat contribution in controlling the roughness parameters.

Table 5: Results of ANOVA for grey relational grade

Source	df	SS	MS	F	% contribution
A	2	0.077	0.038	5.18*	24
B	2	0.106	0.053	7.16*	33
C	2	0.008	0.004	0.51	2.5
A*B	4	0.035	0.018	1.17	11
A*C	4	0.018	0.004	0.59	5.5
B*C	4	0.021	0.005	0.70	6.5
Error	8	0.059	0.007		
Total	26	0.324			

\* - significant at 95% confidence level ( $F_{0.05,2,8} = 4.46$ )

### 3.4 Confirmation Test

After the optimal level of the process parameters is selected, the final step is to predict and verify the improvement of the performance characteristic using the optimal level of the process parameters. The estimated grey relational grade  $\hat{\gamma}$  using the optimal level of the process parameters can be calculated as:

$$\hat{\gamma} = \gamma_m + \sum_{i=1}^o (\bar{\gamma}_i - \gamma_m) \quad (2)$$

where  $\gamma_m$  is the total mean grey relational grade,  $\bar{\gamma}_i$  is the mean grey relational grade at the optimal level, and  $o$  is the number of the main design parameters that significantly affect the roughness characteristics of electroless Ni-B coating. Table 6 shows the comparison of the estimated grey relational grade with the actual grey relational grade using the optimal parameters. It can be observed that there is a good agreement between the estimated and the actual grey relational grade. The increase of the grey relational grade from the initial coating parameters to the optimal coating parameters is 0.04 which is about 6% of the mean grey relational grade.

### 3.5 Surface Morphology and Phase Content

Surface morphology of the coatings is done by SEM in order to analyse the effect of heat treatment on the microstructure of the coatings for some of the samples at random and they show similar qualitative change in microstructure. Fig 3 shows the SEM micrographs of the samples in as deposited and under heat treated conditions. It is seen that the electroless Ni-B coatings in general exhibit a defect free surface with distribution of Ni-B nodules, more like that of a



cauliflower surface which indicates that the coating possesses a lubricious behaviour. The surface of the coating appears dense and light grey in colour with low porosity. When heat treated, the Ni-B nodules grow in size giving rise to a coarse-grained structure. This indicates that in as deposited condition the structure is a mixture of amorphous and microcrystalline which becomes crystalline with heat treatment. This is further confirmed by the XRD patterns of Ni-B deposits in as deposited and heat treated condition (Fig 4). The XRD patterns in as deposited condition is a collection of microcrystalline peaks. But with heat treatment at 450°C for one hour, broad peaks of Ni, Ni<sub>2</sub>B and Ni<sub>3</sub>B are observed.

Table 6: Results of confirmation test

Level	Initial parameter combination	Optimal parameter	
		Prediction	Experimentation
	A2B2C2	A2B1C2	
R <sub>a</sub>	0.420		0.405
R <sub>q</sub>	0.526		0.522
R <sub>sk</sub>	0.651		0.397
R <sub>ku</sub>	6.100		3.620
R <sub>sm</sub>	0.050		0.084
Grade	0.693	0.777	0.733

Improvement of grey relational grade = 0.04

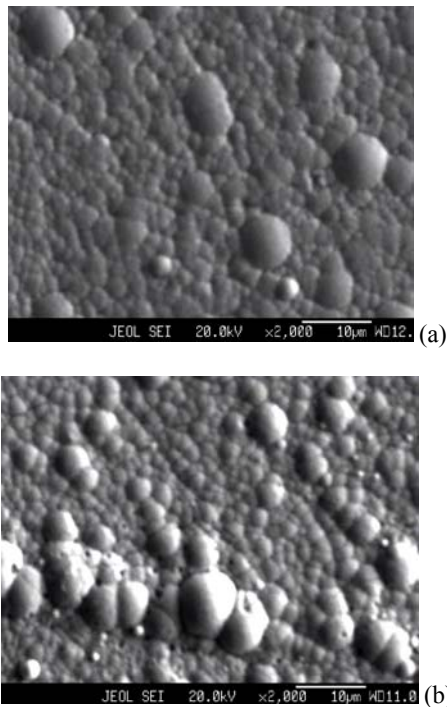


Fig 3. SEM micrographs of the coating surfaces: (a) as-deposited and (d) heat treated at 450°C.

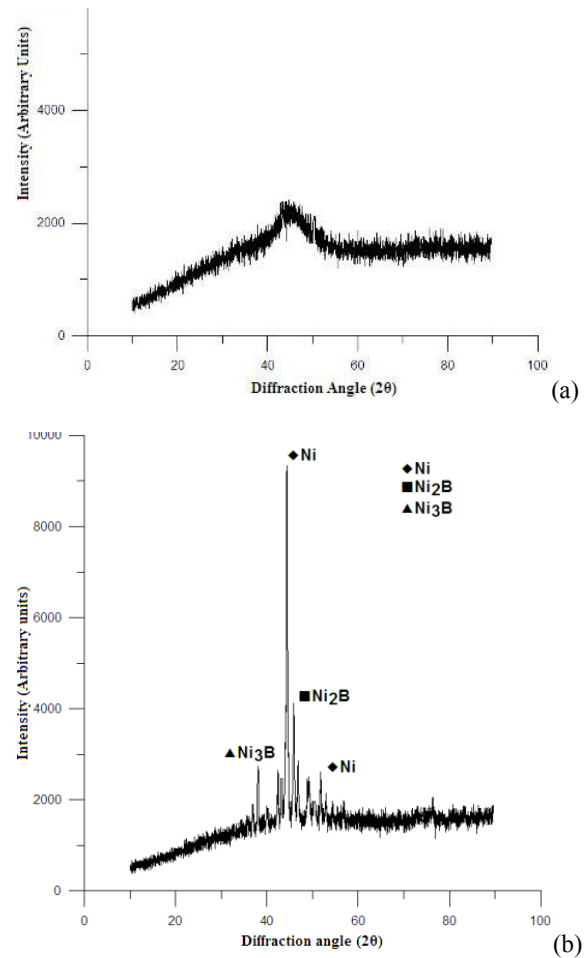


Fig 4. XRD patterns of electroless Ni-B deposit in (a) as-deposited and (b) heat treated at 450°C

#### 4. CONCLUSION

In the present study Taguchi orthogonal array together with grey relational analysis is used to optimize the coating process parameters (bath temperature, concentration of reducing agent and concentration of nickel source) together in order to optimize multiple roughness parameters (R<sub>a</sub>, R<sub>q</sub>, R<sub>sk</sub>, R<sub>ku</sub>, R<sub>sm</sub>) of electroless Ni-B coating. The following conclusions are reported :

- Concentration of reducing agent (B) is the most important parameter that significantly affects the roughness characteristics at a confidence level of 95%. Also the bath temperature (A) is very significant at the same level of confidence.
- Interaction between bath temperature and concentration of reducing agent (A × B) has got somewhat contribution in controlling the roughness features.
- The optimal parameter combination for minimum friction is A2B1C2.
- The optimal parameter combination yields about 0.04 grey relational grade more than the initial condition.

The microstructural study through SEM micrographs reveals that the coating has a cauliflower like structure with no obvious surface damage and low porosity. Also

the coating is dense and light grey in colour. In as deposited condition the coating is a mixture of amorphous and microcrystalline structure which generally turns crystalline with heat treatment. This is confirmed by the presence of Ni<sub>2</sub>B and Ni<sub>3</sub>B phases in the XRD plot of Ni-B coating annealed at 450°C.

## 5. REFERENCES

1. Brenner, A. and Riddell, G. E., 1950, "Nickel plating by chemical reduction", US Patent US2532282.
2. Agarwala, R. C. and Agarwala, V., 2003, "Electroless alloy /composite coatings: A review", *Sadhana*, 28(3 & 4):475–493.
3. Delaunois, F. and Lienard, P., 2002, "Heat treatments for electroless nickel–boron plating on aluminium alloys", *Surface and Coatings Technology*, 160:239–248.
4. Oraon, B., Majumdar, G. and Ghosh, B., 2008, "Improving hardness of electroless Ni–B coatings using optimized deposition conditions and annealing", *Materials and Design*, 29:1412–1418.
5. Krishnaveni, K., Sankara Narayanan, T. S. N. and Seshadri, S. K., 2005, "Electroless Ni-B coatings: preparation and evaluation of hardness and wear resistance", *Surface & Coatings Technology*, 190:115–121.
6. Anik, M., Körpe, E. and Şen, E., 2008, "Effect of coating bath composition on the properties of electroless nickel–boron films", *Surface & Coatings Technology*, 202:1718–1727.
7. Vitry, V., Delaunois, F. and Dumortier, C., 2008, "Mechanical properties and scratch test resistance of nickel–boron coated aluminium alloy after heat treatments", *Surface & Coatings Technology*, 202:3316–3324.
8. Ziyuan, S., Deqing, W. and Zhimin, D., 2004, "Surface strengthening pure copper by Ni-B coating", *Applied Surface Science*, 221:62–68.
9. Di Giampaolo, A. R., Ordonez, J. G., Gugliemacci, J. M. and Lira, J., 1997, "Electroless nickel-boron coatings on metal carbides," *Surface and Coatings Technology*, 89:127-131.
10. Delaunois, F., Petitjean, J. P., Lienard, P. and Jacob-Duliere, M., 2000, "Autocatalytic electroless nickel-boron plating on light alloys", *Surface and Coatings Technology*, 124(2–3):201-209.
11. Taguchi, G., 1990, *Introduction to quality engineering*, Asian Productivity Organization.
12. Montgomery, D. C., 2001, *Design and Analysis of Experiments*, Wiley, New York.
13. Deng, J., 1989, "Introduction to grey system", *Journal of Grey System*, 1(1):1-24
14. Minitab User Manual (Release 13.2), 2001, *Making data analysis easier*, MINITAB Inc, State College, PA, USA,

## 6. MAILING ADDRESS

Suman Kalyan Das  
Research Scholar, Department of Mechanical  
Engineering, Jadavpur University,  
Kolkata 700032, India  
E-mail: [psjume@gmail.com](mailto:psjume@gmail.com)

# NONLINEAR DYNAMICS OF ELECTROSTATICALLY ACTUATED MICROSTRUCTURES UNDER THE EFFECT OF SQUEEZE FILM DAMPING

S. Chatterjee and G. Pohit

Department of Mechanical Engineering, Jadavpur University, Kolkata, India

## ABSTRACT

The electrostatic force being inherently nonlinear, characterization of oscillations induced by large DC and/or AC loads is not possible with a linearized model. Moreover, electrostatic microstructures actuated by large electrostatic loads and operating in fluidic environments are subjected to nonlinear damping. Under the effect of these nonlinearities, electrostatic MEMS exhibit interesting dynamic characteristics. A reduced order model (ROM) of an electrically actuated microcantilever formulated accounting for the nonlinearities of the system is numerically simulated to observe the nonlinear dynamics. The presented model and methodology enable simulation of the transient as well as the steady-state dynamics for slip flow conditions. Nonlinear phenomena such as softening, nonlinear resonance, superharmonic resonance of second order, and dynamic pull-in are predicted. Squeeze film damping is found to considerably affect the observed nonlinear phenomena.

**Keywords:** MEMS, Squeeze Film Damping, Superharmonic Resonance, Dynamic Pull-In.

## 1. INTRODUCTION

The coupled electrical-mechanical nature of electrostatic MEMS gives rise to interesting dynamic characteristics of these devices [1-4] which can have significant impact in their applications as capacitive switches, resonators, tunable capacitors, and actuators. The electrostatic MEMS devices are inherently nonlinear due to the nonlinear nature of the electrostatic forces [5]. Manifestations of this nonlinearity have resulted in various nonlinear phenomena like pull-in instabilities [6-10], jump phenomenon and hysteresis [10, 11], superharmonic [12, 13] and subharmonic [11, 13] resonances, period-doubling bifurcations [10-12], and chaos [12]. Moreover, the damping of electrically actuated microstructures vibrating in presence of fluid trapped in the narrow gap between deformable and fixed electrodes is dominated by nonlinear squeeze film damping [14] and needs to be taken into account for effective simulation of the system dynamics. Several approaches to model and numerically simulate these nonlinear devices have been reported in open literature. In [6, 7], MEMS dynamics were investigated for purely DC loads under damped operating conditions. Purely DC loads and undamped operating conditions were dealt in [8, 9]. Effects of electrostatic actuation by a combination of DC and AC loads in presence of linear viscous damping were studied in [10, 11, and 13]. Full-Lagrangian based relaxation and Newton schemes were presented in [12] for dynamic analysis of nonlinearly damped electrostatic MEMS devices. Few studies in the existing literature deal with a unified yet

simple model to successfully tackle the varying range of loading and damping conditions.

In this paper, numerically simulated dynamics of electrostatic microcantilevers actuated by purely DC load or a combination of DC and AC loads, and, operated under damped or undamped conditions are investigated and comparisons are drawn. A reduced order model (ROM) formulated accounting for the nonlinearities of the system, arising out of electric forces and the damping terms, is successfully employed to predict the nonlinear dynamics. Squeeze film damping is found to considerably affect the observed nonlinear phenomena.

## 2. GOVERNING EQUATIONS

The model (Fig 1) shows a damped cantilever beam of length  $l$ , width  $b$ , thickness  $h$  separated from the ground plane by a small initial air-gap of  $d_0$ .

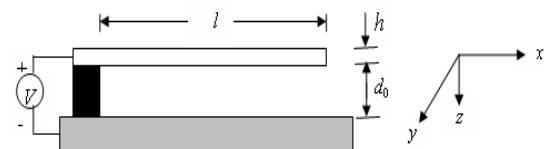


Fig 1. A schematic diagram of an electrostatically actuated microcantilever beam model.

When subjected to a driving voltage  $V(t)$  comprising of a DC voltage  $V_{DC}$  and an AC component  $V_{AC} \cos(\omega t)$ , the beam undergoes oscillatory motions

and these oscillations redistribute pressure in the air trapped in the non-uniform gap spacing causing a damping effect. Let  $w(x,t)$  denote the transverse displacement of the beam being dependent on the position  $x$  along the beam length and time  $t$ . Following the elastic beam theory, and, adding terms representing electrostatic excitation and squeeze film effect, the governing equation of the one-dimensional Euler-beam for small air gap is given by

$$\rho A \frac{\partial^2 w}{\partial t^2} + EI \frac{\partial^4 w}{\partial x^4} = \frac{1}{2} \frac{\epsilon_0 b V^2}{(d_0 - w)^2} - f_d(x,t) \quad (1a)$$

with the boundary conditions as

$$\begin{aligned} w(0,t) = \left. \frac{\partial w}{\partial x} \right|_{x=0} &= 0, \\ \left. \frac{\partial^2 w}{\partial x^2} \right|_{x=l} = \left. \frac{\partial^3 w}{\partial x^3} \right|_{x=l} &= 0 \end{aligned} \quad (1b)$$

where  $\rho$  is the density of the beam material; permittivity constant for free space  $\epsilon_0 = 8.854 \times 10^{-12}, Fm^{-1}$ ; plate modulus for wide beams  $E = E'/(1-\nu^2)$ ,  $E'$  is the Young's modulus,  $\nu$  is the Poisson's ratio. The beam is assumed to be prismatic with rectangular cross section, thereby the moment of inertia and the area of the cross section can be given by  $I = bh^3/12$  and  $A = bh$ , respectively. The first term on the right hand side of Eq. (1a) represents the excitation force per unit length while the second term represents the force acting on the beam owing to the pressure of the squeezed gas film between the beam and the ground plane.

The one-dimensional force due to squeeze film damping is obtained by integrating the two-dimensional pressure distribution along the width of the beam, and, is given by

$$f_d(x,t) = \int_0^b [p(x,y,t) - p_a] dy \quad (2)$$

where  $p(x,y,t)$  is the absolute pressure in the gap and  $p_a$  is the ambient pressure. For slow viscous motion within small gaps and the motion of the beam being restricted to normal approach, the pressure  $p(x,y,t)$  is governed by the nonlinear Reynolds equation [14]

$$\frac{\partial}{\partial x} \left( \frac{\rho_a g^3}{12\mu} \frac{\partial p}{\partial x} \right) + \frac{\partial}{\partial y} \left( \frac{\rho_a g^3}{12\mu} \frac{\partial p}{\partial y} \right) = \frac{\partial}{\partial t} (\rho_a g) \quad (3a)$$

with the trivial boundary conditions, applicable for small air-gaps, as

$$\begin{aligned} p(x,0,t) = p(x,b,t) = p(l,y,t) = p_a, \text{ and,} \\ \frac{\partial p(0,y,t)}{\partial x} = 0 \end{aligned} \quad (3b)$$

where  $\rho_a$  is the density of ambient air; the non-uniform gap spacing  $g(x,t) = d_0 - w(x,t)$ ;  $\mu$  is the dynamic viscosity of air under standard temperature and pressure.

Assuming the flow to be incompressible, and, considering an effective air viscosity  $\mu_{eff}$  [14] to take into account the slip-flow conditions, Eq. (3a) can be reduced to

$$\frac{\partial}{\partial x} \left( g^3 \frac{\partial p}{\partial x} \right) + \frac{\partial}{\partial y} \left( g^3 \frac{\partial p}{\partial y} \right) = 12\mu_{eff} \frac{\partial g}{\partial t} \quad (4)$$

where effective viscosity  $\mu_{eff} = \mu/(1+6Kn)$ , calculated using Burgdorfer's model; Knudsen number  $Kn = \lambda_a/g$ ;  $\lambda_a = \lambda_0 p_0/p_a$  is the mean free path at ambient pressure  $p_a$ . The mean free path  $\lambda_0$  at standard temperature and pressure  $p_0 = 1.013 \times 10^5, Pa$  conditions is about  $65 \times 10^{-9}, m$ . Using Eq. (2) and the nondimensional variables  $\bar{x} = x/l, \bar{y} = y/b, \bar{w} = w/d_0, \bar{g} = g/d_0, \bar{p} = p/p_a, \bar{t} = t/s, s = l^2(\sqrt{\rho A}/\sqrt{EI})$ , Eq. (1) and Eq. (4) can be expressed as

$$\frac{\partial^2 \bar{w}}{\partial \bar{t}^2} + \frac{\partial^4 \bar{w}}{\partial \bar{x}^4} = \frac{\alpha_2 V^2}{(1-\bar{w})^2} - \hat{P} \int_0^1 (\bar{p}-1) d\bar{y} \quad (5a)$$

$$\begin{aligned} \bar{w}(0,\bar{t}) = \left. \frac{\partial \bar{w}}{\partial \bar{x}} \right|_{\bar{x}=0} &= 0, \\ \left. \frac{\partial^2 \bar{w}}{\partial \bar{x}^2} \right|_{\bar{x}=1} = \left. \frac{\partial^3 \bar{w}}{\partial \bar{x}^3} \right|_{\bar{x}=1} &= 0, \end{aligned} \quad (5b)$$

and

$$\begin{aligned} \left( \frac{d_0}{l} \right)^2 \frac{\partial}{\partial \bar{x}} \left( \bar{g}^3 \frac{\partial \bar{p}}{\partial \bar{x}} \right) + \left( \frac{d_0}{b} \right)^2 \frac{\partial}{\partial \bar{y}} \left( \bar{g}^3 \frac{\partial \bar{p}}{\partial \bar{y}} \right) \\ = \frac{12\mu_{eff}}{p_a s} \frac{\partial \bar{g}}{\partial \bar{t}} \end{aligned} \quad (6a)$$

respectively, where  $\alpha_2 = (1/2)(\epsilon_0 b l^4 / E I d_0^3)$ ,  $\hat{P} = l^4 b p_a / E I d_0$ ,  $V(\bar{t}) = V_{DC} + V_{AC} \cos(s\omega\bar{t})$ ; with the pressure boundary conditions, Eq. (3b), can be rewritten as

$$\bar{p}(\bar{x}, 0, \bar{t}) = \bar{p}(\bar{x}, 1, \bar{t}) = \bar{p}(1, \bar{y}, \bar{t}) = 1, \quad \frac{\partial \bar{p}(0, \bar{y}, \bar{t})}{\partial \bar{x}} = 0 \quad (6b)$$

Taking into consideration the boundary conditions, Eq. (6b), absolute pressure underneath the vibrating plate can be written as

$$\bar{p}(\bar{x}, \bar{y}, \bar{t}) = 1 + P^*(\bar{x}, \bar{y}, \bar{t}) \quad (7)$$

where  $P^*(\bar{x}, \bar{y}, \bar{t}) = \psi(\bar{x})(\bar{y} - \bar{y}^2)e^{j(s\omega)\bar{t}}$  is used assuming, as in earlier works [6, 7], the spatial distribution of pressure to be separable being the product of a parabolic function along the beam width and an unknown function  $\psi(\bar{x})$  along the beam length.

Substituting Eq. (7) in Eq. (6a) and integrating the resulting equation across the width of the beam leads to

$$\left(\frac{d_0}{l}\right)^2 \frac{1}{2} \bar{g}^2 \frac{\partial \bar{g}}{\partial \bar{x}} \frac{\partial \psi}{\partial \bar{x}} e^{j(s\omega)\bar{t}} + \left(\frac{d_0}{l}\right)^2 \frac{1}{6} \bar{g}^3 \frac{\partial^2 \psi}{\partial \bar{x}^2} e^{j(s\omega)\bar{t}} - \left(\frac{d_0}{b}\right)^2 2 \bar{g}^3 \psi e^{j(s\omega)\bar{t}} = \frac{12\mu_{eff}}{p_a s} \frac{\partial \bar{g}}{\partial \bar{t}} \quad (8)$$

For air-gap to length ratio  $d_0/l$  less than 0.3 [9], the  $(d_0/l)^2$  terms in the expression for the electrostatic force [9] can be safely neglected. As expressed in Eq. (1a), the present model neglects the  $(d_0/l)^2$  terms in the expression for the electrostatic force and thus assumes parallel plate capacitance. For compatibility of the fluid model with the electrostatic model, the  $(d_0/l)^2$  terms in Eq. (8) are neglected to obtain the pressure function  $\psi(\bar{x})$  as

$$\psi(\bar{x}) = \frac{6\mu_{eff} b^2}{d_0^2 p_a s} \frac{1}{(1-\bar{w})^3} \frac{\partial \bar{w}}{\partial \bar{t}} e^{-j(s\omega)\bar{t}} \quad (9)$$

Using Eqs. (7) and (9), Eq. (5a) can be rewritten as

$$\frac{\partial^2 \bar{w}}{\partial \bar{t}^2} + \frac{\partial^4 \bar{w}}{\partial \bar{x}^4} = \frac{\alpha_2 V^2}{(1-\bar{w})^2} - \frac{\gamma}{(1-\bar{w} + 6\bar{\lambda})(1-\bar{w})^2} \frac{\partial \bar{w}}{\partial \bar{t}} \quad (10)$$

where  $\gamma = (\mu l^2 / \sqrt{EI\rho A})(b/d_0)^3$ ;  $\bar{\lambda} = \lambda_a/d_0$ . The second term on the right hand side of Eq. (10) is proportional to the beam velocity with the coefficient being a nonlinear function of the beam displacement.

### 3. REDUCED ORDER MODEL (ROM)

The method of Galerkin decomposition is employed to approximate the system Eq. (10) by a reduced order model composed of a finite number of discrete modal equations. The process of Galerkin decomposition starts

with separating the dependences of the deflection of the deformed beam,  $\bar{w}(\bar{x}, \bar{t})$ , into temporals and spatial by functions  $a_i(\bar{t})$  and  $\phi_i(\bar{x})$  respectively, in the form of a series of products, i.e.,

$$\bar{w}(\bar{x}, \bar{t}) = \sum_{i=1}^N a_i(\bar{t}) \phi_i(\bar{x}) \quad (11)$$

where  $N$  represents the number of modes retained in the solution.  $\phi_i(\bar{x})$  is the  $i^{th}$  linear undamped mode shape of the undeflected microcantilever obtained from the following linear undamped eigenvalue problem of a straight beam

$$\frac{d^4 \phi_i}{d\bar{x}^4} = (s\omega_i)^2 \phi_i \quad (12a)$$

$$\phi_i(0) = \frac{d\phi_i}{d\bar{x}} \Big|_{\bar{x}=0} = \frac{d^2 \phi_i}{d\bar{x}^2} \Big|_{\bar{x}=1} = \frac{d^3 \phi_i}{d\bar{x}^3} \Big|_{\bar{x}=1} = 0 \quad (12b)$$

It is worth mentioning that  $\phi_i(\bar{x})$  is normalized such that  $\int_0^1 \phi_i^2 d\bar{x} = 1$ .

Multiplying Eq. (10) by  $(1-\bar{w} + 6\bar{\lambda})(1-\bar{w})^2$ , substituting Eq. (11) and (12a) into the resulting equation, multiplying by  $\phi_n(\bar{x})$ , and integrating the outcome from  $\bar{x} = 0$  to 1, the set of coupled nonlinear algebraic equations can be derived as

$$\begin{aligned} & (1+6\bar{\lambda}) \frac{\partial^2 a_n}{\partial \bar{t}^2} + \gamma \frac{\partial a_n}{\partial \bar{t}} + \left[ (1+6\bar{\lambda})(s\omega_n)^2 + \alpha_2 V^2 \right] a_n \\ & - (3+12\bar{\lambda}) \sum_{i=1}^N \sum_{j=1}^N \frac{\partial^2 a_i}{\partial \bar{t}^2} a_j \int_0^1 \phi_n \phi_i \phi_j d\bar{x} - (3+12\bar{\lambda}) \\ & \sum_{i=1}^N \sum_{j=1}^N a_i a_j (s\omega_i)^2 \int_0^1 \phi_n \phi_i \phi_j d\bar{x} + (3+6\bar{\lambda}) \sum_{i=1}^N \sum_{j=1}^N \sum_{k=1}^N \frac{\partial^2 a_i}{\partial \bar{t}^2} \\ & a_j a_k \int_0^1 \phi_n \phi_i \phi_j \phi_k d\bar{x} + (3+6\bar{\lambda}) \sum_{i=1}^N \sum_{j=1}^N \sum_{k=1}^N a_i a_j a_k (s\omega_i)^2 \\ & \int_0^1 \phi_n \phi_i \phi_j \phi_k d\bar{x} - \sum_{i=1}^N \sum_{j=1}^N \sum_{k=1}^N \sum_{p=1}^N \frac{\partial^2 a_i}{\partial \bar{t}^2} a_j a_k a_p \\ & \int_0^1 \phi_n \phi_i \phi_j \phi_k \phi_p d\bar{x} - \sum_{i=1}^N \sum_{j=1}^N \sum_{k=1}^N \sum_{p=1}^N a_i a_j a_k a_p (s\omega_i)^2 \\ & \int_0^1 \phi_n \phi_i \phi_j \phi_k \phi_p d\bar{x} - (1+6\bar{\lambda}) \alpha_2 V^2 \int_0^1 \phi_n d\bar{x} = 0, \end{aligned} \quad (13)$$

$$n = 1, 2, \dots, N$$

#### 4. RESULTS

The entire analysis is carried out using the ROM retaining five ( $N = 5$ ) modes in Eq. (13). As shown in earlier work [9], at least five modes are required to correctly simulate the pull-in instabilities using reduced order models. The dynamic analysis is carried out by numerically solving the set of nonlinear ODEs obtained retaining five ( $N = 5$ ) modes in Eq. (13). Static analysis can be done by numerically solving the set of nonlinear algebraic equations obtained from Eq. (13) with  $a_i(\bar{t})$  being let independent of time,  $V_{AC}$  equal to zero, and all the time derivatives set equal to zero. The design properties used in the present analysis are  $l=150\ \mu m$ ,  $b=22\ \mu m$ ,  $h=4\ \mu m$ ,  $d_0=1.4\ \mu m$ ,  $E=160e9\ Pa$ ,  $\rho=2330\ kg/m^3$ ,  $p_a=1.013e5\ Pa$ ,  $\mu=1.8e-5\ Ns/m^2$  as used in [15].

The present procedure has been validated by comparing the numerical results with the experimental results of [15]. For the above mentioned design properties of the beam, experiments were carried out in [15] to extract the damping ratio under excitation voltage ( $V_{DC} + V_{AC}$ ) in the range of 10% to 20% of the static pull-in voltage [9]. The experimentally obtained first resonance frequency was reported to be  $240\ kHz$ . To facilitate comparison, the present numerical simulation is carried out for  $V_{DC}$  equal to  $5\ V$  and  $V_{AC}$  equal to  $1\ V$  with the excitation voltage ( $V_{DC} + V_{AC}$ ) about 14% of the static pull-in voltage ( $41.94\ V$ ). As shown in Fig 2, the resonance frequency is obtained to be  $236\ kHz$  which is very close to the experimental observation of [15].

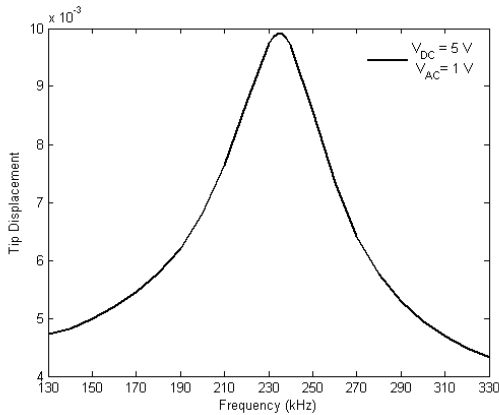


Fig 2. Frequency response curve.

Next, the microcantilever is subjected to purely DC ( $V_{DC}$ ) load and the transient dynamics is investigated for both damped and undamped conditions. For the undamped case, periodic motion is observed (Figs 3 & 4) below a certain critical value of the voltage known as the dynamic pull-in voltage ( $V_{DPI}$ ).

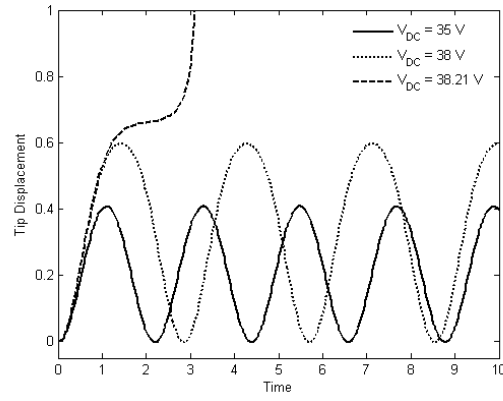


Fig 3. Undamped deflection time history.

Increase in time period (Fig 3) with  $V_{DC}$  indicates softening effect of electrostatic nonlinearity. As  $V_{DC}$  is increased to  $V_{DPI}$  ( $38.21\ V$ ), the motion diverges and the beam abruptly collapses onto the electrode.

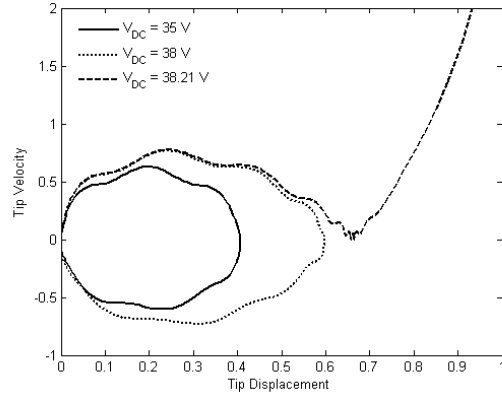


Fig 4. Undamped phase plot.

In interpreting the results in Figs 3 & 4, it may be noted that the normalized tip displacement equal to unity corresponds to collapse of the cantilever into the fixed electrode.

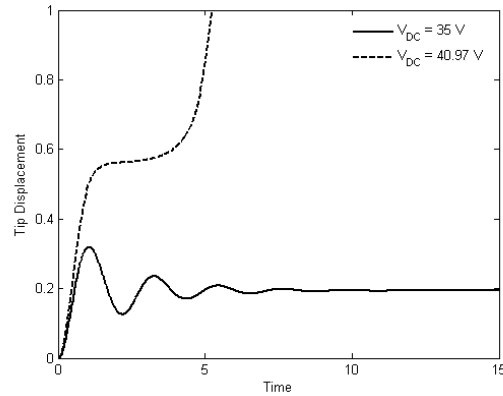


Fig 5. Damped deflection time history.

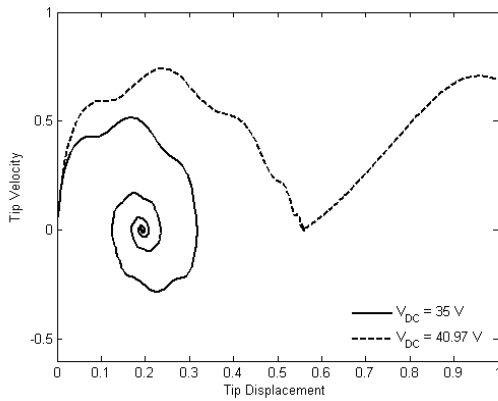


Fig 6. Damped phase plot.

Under squeeze film damping, the beam performs a decaying oscillatory (Figs 5 & 6) motion for  $V_{DC}$  below the damped dynamic pull-in voltage ( $V_{DDPI}$ ), and, finally settles to a steady deformed state.  $V_{DDPI}$  (40.97 V) has been observed to be higher than  $V_{DPI}$  (38.21 V) and approaches the static pull-in voltage (41.94 V). The pull-in displacement for the undamped case (0.6–0.7) is found to be higher than for the damped case (0.5–0.6), thus shrinking the region of stability. The separatrix on the phase plane (Figs 4 & 6) separates the stable and unstable regions.

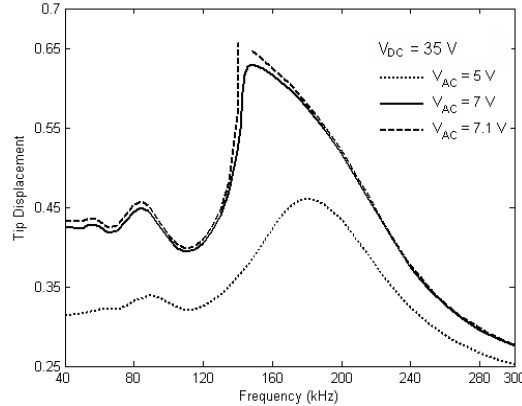


Fig 7. Frequency response curve.

The nonlinear dynamic behaviour is then studied for combined DC and AC loads in the primary and superharmonic frequency range. Frequency-response curve (Fig 7) obtained for a certain DC bias and varying AC amplitudes shows primary as well as possible existence of second order superharmonic resonances. With increase in  $V_{AC}$ , the resonant peaks shift towards the left indicating softening behaviour. As shown in Fig 7, the dynamic pull-in is observed at  $V_{DC}$  equal to 35 V and  $V_{AC}$  equal to 7.1 V for which the left and right branches of the frequency-response curve do not close-in and both the branches terminate as normalized

tip displacement exceeds 0.65 .

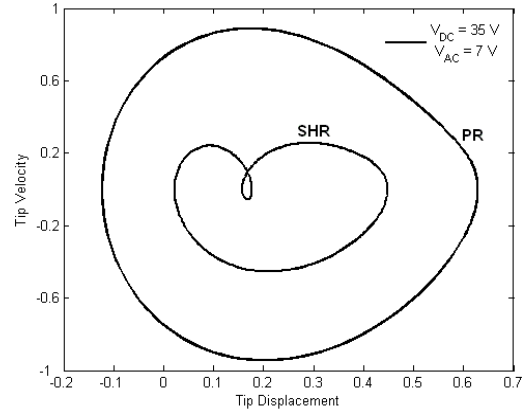


Fig 8. Phase plot at resonance.

Fig 8 shows the phase plot for primary (PR) as well as superharmonic (SHR) resonances just before dynamic pull-in. When actuated by a combination of DC and AC loads, dynamic pull-in of the cantilever beam occurs at a much lower  $V_{DC}$  (35 V) (Fig 7) than when actuated by a purely DC ( $V_{DC}$  equal to 40.97 V) (Fig 5) load.

## 5. CONCLUSION

Nonlinear phenomena of resonance shift, superharmonic resonance, and dynamic pull-in associated with electrostatic MEMS have been presented in this paper. The present model is valid for incompressible flow in the slip flow regime. The nonlinear electrostatic force is found to be responsible for the nonlinear dynamic properties observed while the nonlinear damping force influences a quantitative shift in the design parameters like time period, oscillation amplitude, dynamic pull-in voltage and pull-in displacement. The present approach enables selection of DC bias and the amplitude and frequency of harmonic AC loading for realization of both pull-in and non-pull-in devices.

## 6. REFERENCES

1. Gaillard, J., Skove, M. J., Ciocan, R. and Rao, A. M., 2006, "Electrical detection of oscillations in microcantilevers and nanocantilevers", *Review of Scientific Instruments*, 77: 073907.
2. Zhao, J. P., Chen, H. L., Huang, J. M. and Liu, A. Q., 2005, "A study of dynamic characteristics and simulation of MEMS torsional micromirrors", *Sensors and Actuators A*, 120: 199–210.
3. Jin, Z. and Yang, Y., 1998, "Electrostatic resonator with second superharmonic resonance", *Sensors and Actuators A*, 64: 273-279.
4. Fischer, M., Giousouf, M., Schaepperle, J., Eichner, D., Weinmann, M., von Miinch, W. and Assmus, F., 1998, "Electrostatically deflectable polysilicon micromirrors – dynamic behaviour and comparison with the results from FEM modeling with ANSYS", *Sensors and Actuators A*, 67: 89-95.



5. Pelesko, J.A. and Bernstein, D.H., 2003, *Modeling MEMS and NEMS (Chapter 7)*, Chapman&Hall/CRC Press, London/New York/Washington, DC.
6. McCarthy, B., Adams, G., McGruer, N. and Potter, D., 2002, "A dynamic model, including contact bounce, of an electrostatically actuated microswitch", *Journal of Microelectromechanical Systems*, 11: 276–283.
7. Krylov, S. and Maimon, R., 2004, "Pull-in dynamics of an elastic beam actuated by continuously distributed electrostatic force", *Journal of Vibration and Acoustics*, 126: 332–342.
8. Xie, W.C., Lee, H.P. and Lim, S.P., 2003, "Nonlinear dynamic analysis of MEMS switches by nonlinear modal analysis", *Nonlinear Dynamics*, 31: 243–256.
9. Chaterjee, S. and Pohit, G., 2009, "A large deflection model for the pull-in analysis of electrostatically actuated microcantilever beams", *Journal of Sound and Vibration*, 322: 969–986.
10. Nayfeh, A. H., Younis, M. I. and Abdel-Rahman, E. M., 2007, "Dynamic pull-in phenomenon in MEMS resonators", *Nonlinear Dynamics*, 48: 153–163.
11. Mestrom, R.M.C., Fey, R.H.B., van Beek, J.T.M., Phan, K.L. and Nijmeijer, H., 2008, "Modelling the dynamics of a MEMS resonator: Simulations and experiments", *Sensors and Actuators A*, 142: 306–315.
12. De, S. K. and Aluru, N. R., 2006, "Complex nonlinear oscillations in electrostatically actuated microstructures", *Journal of Microelectromechanical Systems*, 15: 355–369.
13. Nayfeh, A. H. and Younis, M. I., 2005, "Dynamics of MEMS resonators under superharmonic and subharmonic excitations", *Journal of Micromechanics and Microengineering*, 15: 1840–1847.
14. Bao, M. and Yang, H., 2007, "Review of squeeze film air damping in MEMS", *Sensors and Actuators A* 136: 3–27.
15. Pandey, A. K. and Pratap, R., 2007, "Effect of flexural modes on squeeze film damping in MEMS cantilever resonators", *Journal of Micromechanics and Microengineering* 17: 2475–2484.

## 7. NOMENCLATURE

Symbol	Meaning	Unit
$l$	Beam length	$\mu\text{m}$
$b$	Beam width	$\mu\text{m}$
$h$	Beam thickness	$\mu\text{m}$
$d_0$	Air-gap	$\mu\text{m}$
$x$	Length co-ordinate	$\mu\text{m}$
$y$	Width co-ordinate	$\mu\text{m}$
$t$	Time	sec
$V(t)$	Excitation voltage	V
$V_{DC}$	DC voltage	V
$V_{AC}$	AC voltage	V
$\omega$	Excitation frequency	rad/s
$w$	Beam displacement	$\mu\text{m}$
$\rho$	Density of beam material	$\text{Kg/m}^3$
$f_d$	Damping force	N/m
$\epsilon_0$	Permittivity constant for free space	F/m
$E$	Plate modulus	$\text{N/m}^2$
$E'$	Young's modulus	$\text{N/m}^2$
$\nu$	Poisson's ratio	-
$I$	Area moment of inertia	$\text{m}^4$
$A$	Cross sectional area	$\text{m}^2$
$P$	Absolute pressure	$P_a$
$P_a$	Ambient pressure	$P_a$
$\rho_a$	Density of ambient air	$\text{Kg/m}^3$
$g$	Non-uniform gap spacing	$\mu\text{m}$
$\mu$	Coefficient of viscosity	$\text{Ns/m}^2$
$\mu_{eff}$	Effective coefficient of viscosity	$\text{Ns/m}^2$
$Kn$	Knudsen number	-
$\lambda_a$	Mean free path at ambient pressure	m
$\alpha_2$	Strength of electric actuation	-
$\hat{P}$	Non-dimensional pressure	-
$P^*$	Pressure variation	-
$\psi$	Pressure function	-
$\gamma$	Damping factor	-

## 8. MAILING ADDRESS

S Chaterjee  
 Department of Mechanical Engineering, Jadavpur  
 University, Kolkata 700032, India.  
 Email: [gpohit@vsnl.net](mailto:gpohit@vsnl.net)  
 Telefax: +91 33 2414 6890)

## INVESTIGATION OF STRUCTURAL AND MAGNETIC PROPERTIES OF $Co_{1-x}Zn_xFe_2O_4$ PREPARED BY COMBUSTION TECHNIQUE

M. H. R. Khan<sup>1</sup>, Farhad Alam<sup>2</sup>, M. N. I. Khan<sup>3</sup>, M.A. Hakim<sup>3</sup>, D.K. Saha<sup>3</sup>, and  
A. K. M. Akther Hossain<sup>4</sup>

<sup>1</sup>Department of Arts & Sciences, Ahsanullah University of Science & Technology, Dhaka, Bangladesh  
<sup>2</sup>School of Engineering and Computer Science, Independent University, Bangladesh, Dhaka, Bangladesh.  
<sup>3</sup>Materials Science Division, Atomic Energy Centre, Dhaka, Bangladesh  
<sup>4</sup>Department of Physics, Bangladesh University of Engineering & Technology, Dhaka, Bangladesh

### ABSTRACT

A series of polycrystalline  $Co_{1-x}Zn_xFe_2O_4$  ( $x = 0, 0.1, 0.2$  and  $0.3$ ) ferrites powders were prepared by combustion technique. Obtained fine nano-sized powders were calcined at low temperature ( $\sim 973K$ ). From the fine calcined powders, toroid and disk-shaped samples were prepared and sintered at various temperatures ( $1473K, 1523K$  and  $1573K$ ) in air for 5 hours. The bulk density and porosity of sintered samples were measured by Archimedes principle. The x-ray diffraction analysis confirmed that the samples are single-phase cubic spinel structure. The lattice parameter increases with increasing  $Zn$  content. This is due to the effect of ionic radii. Microstructural studies were carried out by high-resolution optical microscope. It is observed that grain size increases with increasing  $Zn$  content. The magnetic properties of these ferrites were studied in the frequency range  $100Hz$  to  $100MHz$ . It was observed that initial permeability increases with increasing sintering temperature up to  $1523K$  and above  $1523K$  permeability decreases. The experimental density, porosity, quality factor, and temperature dependent permeability of  $Co_{1-x}Zn_xFe_2O_4$  are also investigated. The aim of these studies is to synthesize new materials with enhanced magnetic permeability for the creation of new technology.

**Key words:** Cubic spinel, Grain Size, Permeability, Ferrimagnet.

### 1. INTRODUCTION

Ferrites are extensively studied because of several interesting properties. They have spinel type crystal structure. It has tetrahedral  $A$ -site and octahedral  $B$ -sites in  $AB_2O_4$  crystal structure. Depending on  $A$ -sites and  $B$ -sites cations they exhibit ferromagnetic, antiferromagnetic, spin (cluster) glass, and paramagnetic behaviour [1-6]. Polycrystalline spinel ferrites are widely used in many electronic devices. These are preferred because of their high permeability in the radio- frequency (RF) region, high electrical resistivity, mechanical hardness and chemical stability. These types of ferrites are subjects of intense theoretical and experimental investigation due to their remarkable magnetic and electric properties [7-9].

The  $Co$ - $Zn$  ferrites are quite important in the field of microwave industry [10]. The  $ZnFe_2O_4$  is normal spinel ferrites, while  $CoFe_2O_4$  is inverse spinel; therefore,  $Co$ - $Zn$  ferrite is mixed spinel type with interesting properties. Many efforts have been made to improve the basic properties of these ferrites by substituting or adding various cations of different valence states depending on the applications of interest [11-13]. In our present research we are interested to investigate the effect of

substitution of divalent  $Zn$  in  $Co$  site on structural and magnetic properties of  $Co_{1-x}Zn_xFe_2O_4$ .

### 2. EXPERIMENTAL

The powders of  $Co_{1-x}Zn_xFe_2O_4$  with ( $x = 0-0.3$ ) were prepared through auto combustion method. The stoichiometric amounts of  $Co(NO_3)_2 \cdot 6H_2O$ ,  $Zn(NO_3)_2 \cdot 6H_2O$ ,  $Fe(NO_3)_3 \cdot 9H_2O$  were dissolved in ethanol. Then the solution was heated at a constant temperature bath ( $343K$ ) to transform into gel, the dried gel burnt out to form fluffy loose powders. The resultant powders were calcined at  $973K$  for 5h and then pressed uniaxially into disk-shaped (about  $0.01$  m outer diameter,  $0.02-0.03$  m thickness) and toroid-shaped (about  $0.01$  m outer diameters,  $0.005$  m inner diameter, and  $.003$  m thickness) samples. The samples were sintered at  $1473K, 1523K$  and  $1573K$  for 5 h in air. The temperature ramps were  $0.16Ks^{-1}$  for heating and  $0.08Ks^{-1}$  for cooling. Microstructural properties were investigated with a high-resolution optical microscope. The bulk density was measured by  $\rho_B = M/V$ , where  $M$  is the mass of the sample and  $V$  is the volume. Average grain sizes (grain diameter) of the samples were determined from optical micrographs by linear intercept technique [14]. The

frequency dependent initial permeability of  $Co_{1-x}Zn_xFe_2O_4$  was investigated using an Agilent Impedance Analyzer (Model no. 4192A). The complex permeability measurements on toroid-shaped samples have been carried out at room temperature in the frequency range 100Hz-100MHz. The values of the real part of the initial complex permeability ( $\mu'_i$ ) have been calculated using the following relations:  $\mu'_i = L_s/L_o$ , where  $L_s$  is the self inductance of the sample core and  $L_o = (\mu_0 N^2 h/2\pi) \ln(r_o/r_i)$  is derived geometrically, where  $L_o$  is the inductance of the winding coil without the sample core,  $N$  is the number of turns of the coil ( $N = 5$ ),  $h$  is the thickness,  $r_o$  is the outer radius and  $r_i$  is the inner radius of the toroid-shaped sample. The relative quality factor (or  $Q$  factor) was calculated from the relation:  $Q = \mu'_i / \tan \delta$ , where  $\tan \delta$  is the loss factor.

### 3. RESULTS AND DISCUSSION

#### 3.1 Structural and Surface Morphology

The x-ray diffraction (XRD) patterns for the polycrystalline  $Co_{1-x}Zn_xFe_2O_4$  compositions are presented in figure 1. The XRD peaks can be indexed to (111), (220), (311), (222), (400), (422), (511), (440) planes of spinel structure. The XRD patterns for these compositions confirm the formation of cubic spinel ferrites having no significant impurity. From XRD pattern the lattice parameters have been calculated with the help of Nelson-Riley function [2]. The lattice parameters of  $Co_{1-x}Zn_xFe_2O_4$  compositions are plotted as a function of Zn content, as shown in figure 2a. The measured lattice parameter 'a', bulk density ' $\rho_B$ ' and porosity 'P' for different samples sintered at different temperatures are given in table 1. It is observed from the figure 2a that the variation of 'a' with Zn contents in the  $Co_{1-x}Zn_xFe_2O_4$  obey Vegard's law in the whole composition range under present investigation. 'a' increases with increasing Zn content for all compositions. The increase in 'a' with increasing Zn content can be explained on the basis of the ionic radii. The ionic radii of the cations used in  $Co_{1-x}Zn_xFe_2O_4$  are 0.074 nm ( $Zn^{2+}$ ), 0.072 nm ( $Co^{2+}$ ) and 0.069 nm ( $Fe^{3+}$ ) [15,16]. Since the ionic radius of  $Co^{2+}$  is less than that of the  $Zn^{2+}$ , increase in lattice constant with the increase in Zn substitution is expected.

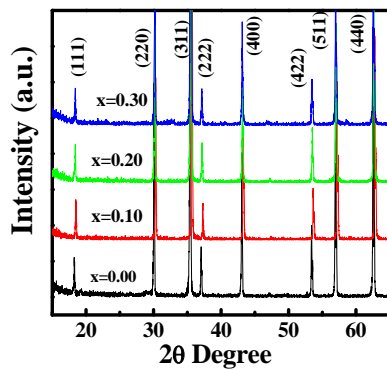


Fig 1. The x-ray diffraction pattern of polycrystalline  $Co_{1-x}Zn_xFe_2O_4$ .

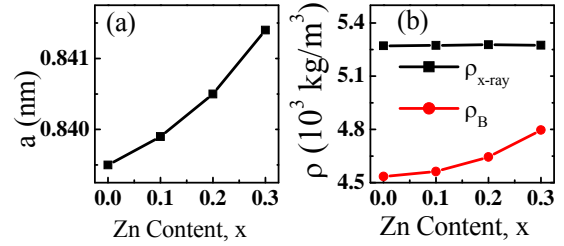


Fig 2. Variation of (a) lattice constants and (b) x-ray density and bulk density with Zn content of polycrystalline  $Co_{1-x}Zn_xFe_2O_4$  sintered at 1473K.

The x-ray density  $\rho_{x-ray}$  was calculated using following expression:

$$\rho_{x-ray} = \frac{8M_A}{N_A a^3}, \quad (1)$$

where  $N_A$  is Avogadro's number ( $6.02 \times 10^{23}$ ),  $M_A$  is the molecular weight. The porosity was calculated from the relation,  $P \% = \frac{\rho_{x-ray} - \rho_B}{\rho_{x-ray}} \times 100\%$ , where  $\rho_B$  is the

bulk density. The composition dependence  $\rho_{x-ray}$  is shown in figure 2b. The  $\rho_B$  of the polycrystalline samples increases with increasing Zn content since the mass of  $Co^{2+}$  less than the mass of  $Zn^{2+}$ . Also  $\rho_B$  and  $P$  depends on sintering temperature,  $T_s$ . For different sintering temperatures such as 1473K, 1523K and 1573K, the  $\rho_B$  increases up to 1523K then decreases with further increasing sintering temperature. On the other hand,  $P$  of the sample decreases as increasing sintering temperature up to 1523K, and above 1523K the porosity increases as shown in the figure 3. This increase in density with increasing Zn content can be explained on

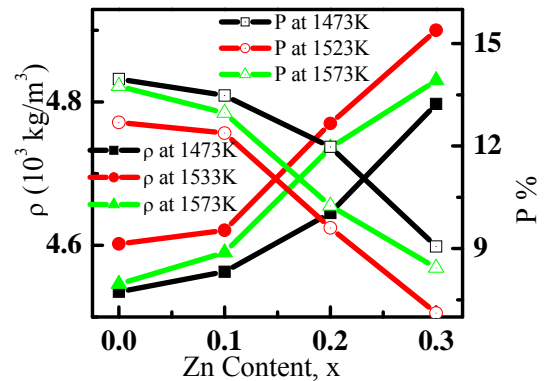


Fig 3. Variation of density and porosity as a function of Zn content for polycrystalline  $Co_{1-x}Zn_xFe_2O_4$  sintered at different temperatures.

the basis of the atomic weight. It is observed that the porosity of ceramic samples originates from two sources, intragranular porosity and intergranular porosity. The total porosity could be written as  $P = P_{intra} + P_{inter}$ . The

intergranular porosity mainly depends on the grain size [9,17]. During the sintering process, the thermal energy generates a force that drives the grain boundaries to grow over pores, thereby decreasing the pore volume and densifying the samples.

Table 1: The lattice parameter, density, porosity and average grain size of  $Co_{1-x}Zn_xFe_2O_4$  sintered at various temperatures,  $T_s$ , for 5 hours in air.

x	a (nm)	$T_s$ (K)	$\rho_{x-ray} 10^3$ (kg/m <sup>3</sup> )	$\rho_B 10^3$ (kg/m <sup>3</sup> )	P (%)	$\mu_i'$	Grain Size ( $\mu m$ )
0.0	0.8395	1473	5.271	4.54	14.0	26	1.57
		1523		4.60	12.7	27	2.10
		1573		4.55	13.7	25	2.96
0.1	0.8399	1473	5.274	4.56	13.5	31	1.84
		1523		4.62	12.4	34	2.45
		1573		4.59	12.9	28	3.10
0.2	0.8405	1473	5.277	4.65	11.9	33	2.06
		1523		4.77	9.60	38	2.98
		1573		4.74	10.3	30	3.56
0.3	0.8414	1473	5.275	4.80	9.10	38	2.45
		1523		4.90	7.10	40	3.12
		1573		4.83	8.40	36	3.86

At higher sintering temperatures the density decreases because of increasing intragranular porosity resulting from discontinuous grain growth. Such a conclusion is in agreement with that previously reported in case of Ni-Zn ferrites [9].

Figure 4 shows micrographs of various  $Co_{1-x}Zn_xFe_2O_4$  samples sintered at different temperatures. Well-developed grains with fewer pores were observed for all samples. The grain size is found to increase with increasing Zn content and different sintering temperatures. The microstructure becomes more uniform and compact with increasing Zn content as a result intergranular pores disappear and grains become large. The average grain size for different sintering temperatures is presented in table 1.

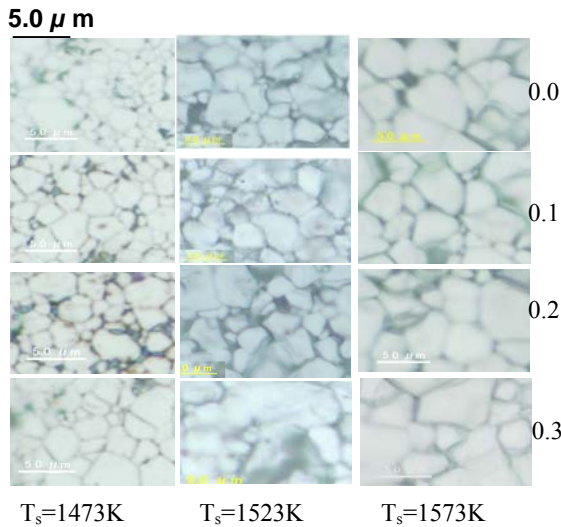


Fig 4. The optical micrographs of polycrystalline  $Co_{1-x}Zn_xFe_2O_4$  ( $x=0.0-0.3$ ) samples sintered at various temperatures.

### 3.2 Initial Permeability

Figure 5 shows the frequency dependent real part of initial permeability,  $\mu_i'$ , values of  $Co_{1-x}Zn_xFe_2O_4$  sintered at 1523K. From this figure we observed that the  $\mu_i'$  increases with increasing Zn content. Similar observation is observed at samples sintered at 1473K and 1573K. Figure 6 represents the frequency dependent  $\mu_i'$  for  $Co_{0.7}Zn_{0.3}Fe_2O_4$  sintered at different temperatures. It is observed that the  $\mu_i'$  for all samples increase as the  $T_s$  increases up to 1523K and above 1523K it decreases. Therefore,  $\mu_i'$  is related to the  $\rho_B$ , P and microstructure of the samples.

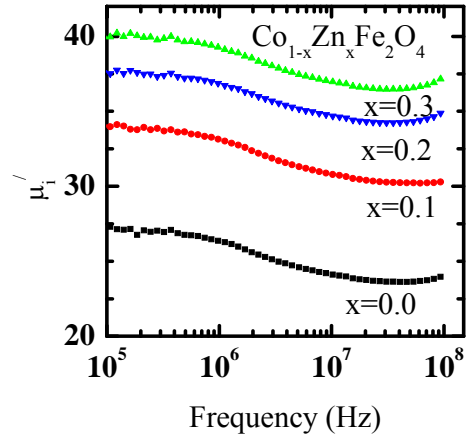


Fig 5. Real part of initial permeability of polycrystalline  $Co_{1-x}Zn_xFe_2O_4$  samples sintered at 1523K.

It is well known that the magnetization process can be characterized as superposition of domain wall motion and spin rotation [12].

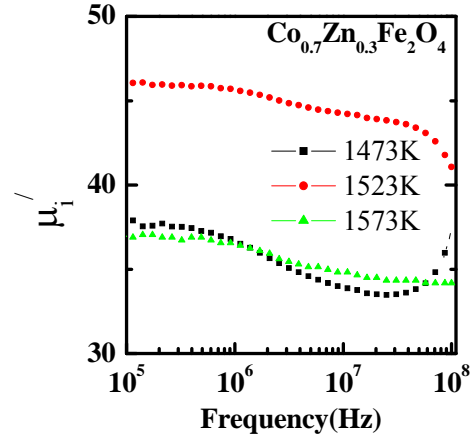


Fig 6. Real part of initial permeability of polycrystalline  $Co_{0.7}Zn_{0.3}Fe_2O_4$  sample sintered at 1473K, 1523K and 1573K.

So, the permeability can be described as [5,6]

$$\mu_i' = 1 + \chi_{spin} + \chi_{dw} \quad (2)$$

where  $\chi_{spin}$  and  $\chi_{dw}$  denote the magnetic susceptibility of spin and domain wall motion, respectively.  $\chi_{dw}$  and  $\chi_{spin}$  can be written as:  $\chi_{dw} = 3\pi M_s^2 D/4\gamma$  and  $\chi_{spin} = 2\pi M_s^2/K$ ,

where  $M_s$ ,  $K$ ,  $D$  and  $\gamma$  are the saturation magnetization, total anisotropy energy, average grain diameter and domain wall energy, respectively [18]. Since the magnetic anisotropy field  $H_A = 2K/M_s$ ,  $\chi_{spin}$  can be represented by,  $\chi_{spin} = 4\pi M_s/H_A$  [19].

For polycrystalline ferrites, pores and other imperfections are unavoidable, which generate a demagnetizing field. So, anisotropy field consists of magnetic anisotropy field  $H_A$  and demagnetizing field  $H_d$ . Therefore,  $\chi_{spin}$  should be represented by  $\chi_{spin} = 4\pi M_s/(H_A + H_d)$ . In our present investigation  $H_d$  decreases because pores decrease and grains become bigger with increasing Zn content consequently  $\chi_{spin}$  increases. The sample doped with Zn content possesses the most compact and uniform microstructure in all samples. The grain size increases with Zn content and therefore the increasing permeability with Zn content could be attributed to grain size. Our results agree with the results reported by Yan, M *et.al.* [19] and Karche, B. R. *et.al.* [20] in Ni-Cu-Zn and Mg-Cd ferrites.

From the figure 5, it is observed that the resonance peaks are beyond 100MHz. This indicates that these materials are useful for fabrication of devices up to 100MHz.

From the observed loss factor we have calculated the  $Q$  factor for the polycrystalline  $Co_{1-x}Zn_xFe_2O_4$  compositions sintered at various sintering temperatures. The  $Q$  factors at 1523K are shown in figure 7. It is observed that  $Q$  factor increases with increasing Zn content. The highest  $Q$  factor is observed for  $Co_{0.7}Zn_{0.3}Fe_2O_4$  sintered at 1523K.

### 3.3 Temperature Dependent Initial Permeability

The variation of  $\mu'_i$  with temperature for various  $Co_{1-x}Zn_xFe_2O_4$  samples sintered at 1473 K is shown in figure 8. The temperature dependent  $\mu'_i$  of the samples is measured

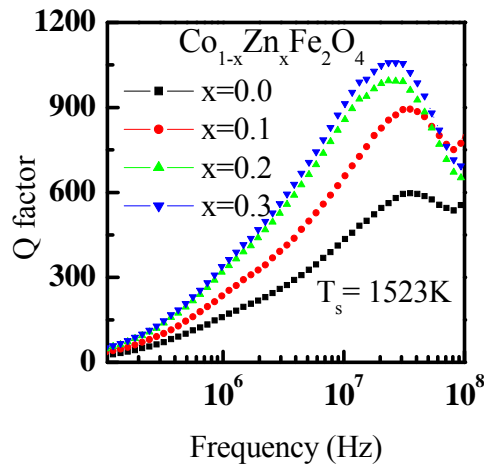


Fig 7. The  $Q$  factor of polycrystalline  $Co_{1-x}Zn_xFe_2O_4$  sintered at 1523K.

at an arbitrary constant frequency (100 kHz). The  $\mu'_i$  slowly increases with temperature, reaches a maximum and then sharply drops to lower value at certain temperature. This temperature is called Néel temperature,  $T_N$ . The increase  $\mu'_i$  with temperature can be explained as

follows: The anisotropy field usually decreases with temperature much faster than  $M_s$  [4, 21]. The intrinsic parameters of the sample that affect  $\mu'_i$  are saturation magnetization and magnetocrystalline anisotropy. It is also dependent upon the degree of wall continuity across the grain boundaries as shown by Globus *et.al* [22]. Since saturation magnetization and anisotropy constant vary with temperature,  $\mu'_i$  is a complicated function of temperature and it is difficult to derive any qualitative inference.

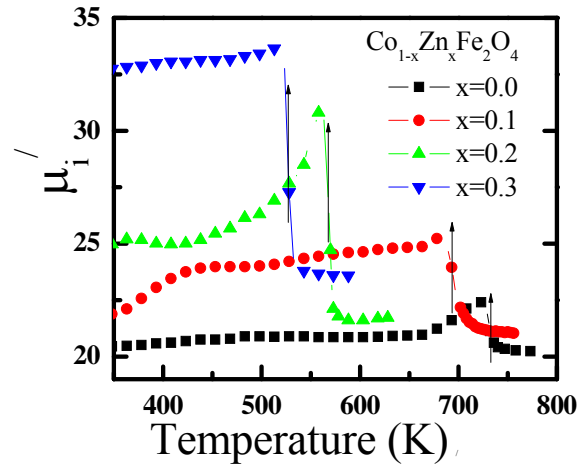


Fig 8. The initial permeability as a function of temperature for  $Co_{1-x}Zn_xFe_2O_4$  samples sintered at 1473K.

From the figure 8 we observed that  $\mu'_i$ - $T$  curves suddenly drop to lower value at  $T_N$ . The  $T_N$  values decrease continuously with Zn content due to weakening of the A-B interaction on additions of non-magnetic Zn content. Similar observation has been reported in the case of Zn substituted Ni-Cu and Li-Cu ferrites [23,24].

### 4. CONCLUSION

Phase pure  $Co_{1-x}Zn_xFe_2O_4$  ferrites are prepared by combustion method. The XRD pattern confirms that all the samples exhibit cubic spinel structure. The  $\mu'_i$  values are strongly depend on the density, sintering temperature and microstructures of the samples. Ferrimagnetic to paramagnetic transition is observed in all the samples. Substitution of Zn increases permeability values but lowers the Néel temperature. The appropriate amount of Zn substitution helps to improve the magnetic properties of these ferrites.

### 5. REFERENCES

1. Tsutaoka, T., 2003 "Frequency dispersion of complex permeability in Mn-Zn and Ni-Zn spinel ferrites and their composite materials" *J. Appl. Phys.*, Vol. 93, No. 5.
2. Akther Hossain, A. K. M, Seki, M., Kawai, T., and Tabata, H., 2004 "Colossal magnetoresistance in spinel type  $Zn_{1-x}Ni_xFe_2O_4$ ," *J. Appl. Phys.*, **96**, 1273.



3. Snoek, J. S., 1949, *New Developments in Ferromagnetic Materials*, Elsevier Publishing Company, Inc., New York.
4. Valenzuela, R., 1994, *Magnetic Ceramics*, Cambridge University Press, Cambridge.
5. Ahmed, M. A., Okasa, N. and Salah, L., 2003, "Influence of yttrium ions on the magnetic properties of Ni-Zn ferrites," *J. Magn. Magn. Mater.* 264: 241.
6. Verma, A., Goel, T. C., Mendiratta and Kishan, P., 2000, "Magnetic properties of nickel-zinc ferrites prepared by the citrate precursor method," *J. Magn. Magn. Mater.*, 208: 13.
7. El-Shabasy, M., 1997, "DC electrical properties of Ni-Zn ferrites," *J. Magn. Magn. Mater.*, 172:188.
8. Rosales, M. I., Amano, E., Cuautle, M. P. and Valenzuela, R., 1997, "Impedance spectroscopy studies of Ni-Zn ferrites," *Materials Science and Engineering*, B 49: 221.
9. Mahmud, S.T., Akther Hossain, A.K.M., Abdul Hakim, A.K.M., Seki, M., Kawai, T. and Tabata, H., 2006, "Influence of microstructure on the complex permeability of spinel type Ni-Zn ferrite" *J. Magn. Magn. Mater.*, 305 : 269–274.
10. Josyulu, O.S., Sobhanadri and Viswanatham, B., 1981, *Rev. Roum. Chim.* 26(5):687.
11. Shukla, S.J., Jadhav, K.M. and Bichile, G.K., 1999, "Influence of Mg substitution on magnetic properties of Co-Fe-Cr-O spinel ferrite system" *J. Magn. Magn. Mater.*, 195: 692-698.
12. Arulmurugan, R., Jeyadevan, B., Vaidyanathan, G. and Sendhilmathan, S., 2005, "Effect of zinc substitution on Co-Zn and Mn-Zn ferrite nanoparticles prepared by co-precipitation" *J. Magn. Magn. Mater.*, 288 : 470–477.
13. Brabers, V.A.M., 1995, *Handbook of Magnetic Materials*, ed. By. K. H. Buschow (Elsevier Science B.V.) Vol. 8, p 189.
14. Verma, A., Goel, T. C., Mendiratta, R. G. and Kishan, P., 2000, "Magnetic properties of nickel-zinc ferrites prepared by the citrate precursor method," *J. Magn. Magn. Mater.*, 208:13.
15. James E. Huhecy, *Inorganic Chemistry (Principles of structure and Reactivity)*, Fourth edition.
16. Shannon, R.D., 1976, *Acta Crystallogr.* A 32: 751.
17. Sattar, A. A., El-Sayed, H. M., El-Shokrofy, K. M. and El-Tabey, M. M., 2005, "Improvement of the magnetic properties of Mn-Ni-Zn ferrite by the non-magnetic Al<sup>3+</sup> ion substitution," *J. Appl. Sci.*, 5(1):162.
18. Slick, P.I., 1980, *Ferromagnetic Materials*, vol.2, in: E.P. Wohlforth (Ed.), North-Holland, Amsterdam.
19. Yan, M., Hu, J., Luo, W. and Zhang, W.Y., 2006, "Preparation and investigation of low firing temperature NiCuZn ferrites with high relative initial permeability" *J. Magn. Magn. Mater.*, 303 : 249–255.
20. Karche, B. R., Khasbardar, B. V. and Vaingankar, A.S., 1997, "X-ray, SEM and magnetic properties of Mg-Cd ferrites" *J. Magn. Magn. Mater.*, 168: 292-298.
21. Cullity, B. D., 1972, *Introduction to Magnetic Materials*, Addison-Wesley Publishing Company, Inc., California.
22. Glubus, A. and Duplex, P., 1969, "Size of bloch wall and parameters of the magnetic susceptibility in ferrimagnetic spinels and garnets", *Phys. Stat. Sol.* A 31: 765
23. Ahmeda, M.A., and EL-Sayed, M.M., 2007, "Magnetic characterization and thermoelectric power of Ni<sub>1-y</sub>Zn<sub>y</sub> Cu<sub>0.3</sub>Fe<sub>1.7</sub> O<sub>4</sub>" *J. Magn. Magn. Mater.*, 308:40–45.
24. Jadhav, S. A., 2001, "Magnetic properties of Zn-substituted Li-Cu ferrites" *J. Magn. Magn. Mater.*, 224: 167-172.

## 6. NOMENCLATURE

Symbol	Meaning	Unit
$\rho_{x\text{-ray}}$	X-ray density	(kg/m <sup>3</sup> )
$\rho_B$	Bulk density	(kg/m <sup>3</sup> )
$\mu_i$	Real part of initial permeability	Dimensionless
a	Lattice parameter	(nm)
P	Porosity	Dimensionless
Q	Relative quality factor	Dimensionless

## 7. MAILING ADDRESS

M. H. R. Khan  
 Department of Arts & Sciences,  
 Ahsanullah University of Science & Technology,  
 Dhaka, Bangladesh

## BIOGAS FROM ANAEROBIC DIGESTION OF FISH WASTE

B. Salam, M. Islam and M. T. Rahman

Department of Mechanical Engineering  
Chittagong University of Engineering & Technology, Chittagong, Bangladesh

### ABSTRACT

Biogas is a by-product of the biological breakdown of organic wastes under oxygen free condition. Research work was conducted to investigate the production ability of biogas from anaerobic digestion of fish waste. This paper presents results of research work conducted in laboratory scale to produce bio gas from fish waste and cow dung. Five laboratory scale digesters were made to co-digest fish waste (FW) and cow dung (CD) in various proportions. The digesters were made of plastic container of four liter capacity each. Fish wastes were used 200 gm and 250 gm, and cow dung were used 0 - 300 gm to make fish waste to cow dung ratios in the range (wt.) of 1:0 to 1:1.5. The digester were fed on batch basis and operated at ambient temperatures for 15 days. Total solid contents of 8% were used for all the experiments. The highest gas yield was obtained about 2 L/kg waste from a fish waste and cow dung ratio of 1:1.2. It was observed that when only fish waste was used, gas yield obtained was 150 ml/kg waste and it took 10 days to start bio gas generation. Whereas when cow dung was mixed with fish waste, gas production starting time reduced to 7 days.

**Keywords:** Biogas, Anaerobic, Fish Waste.

### 1. INTRODUCTION

Anaerobic digestion (AD) is a complex biological process in which anaerobic bacteria decompose organic matter in environments with little or no oxygen. The products of anaerobic digestion are biogas and digested substrate, commonly named digestate, and used as fertilizer in agriculture. The biogas generally composes of 55-65% methane, 35-45% carbon dioxide, 0-3% nitrogen, 0-1% hydrogen, and 0-1% hydrogen sulfide [1]. By AD process the significant methane emission resulting from the uncontrolled anaerobic decomposition of organic waste into atmosphere would be stopped, where methane has 21 times more global warming potential than carbon dioxide [2]. Moreover, production of biogas will reduce the use of fossil fuels, thereby reducing the carbon dioxide emission. This is thus in accord with Kyoto Summit agreement [3].

Production of biogas from organic fraction of municipal solid wastes, different animal manures, fish waste, agricultural waste etc. were reported by different researchers. Not much works of fish waste digestion were reported. Lanari and Franci [4] produced biogas from rainbow trout biomass (faecal sludge) using up-flow anaerobic recirculating digester made from fiber-glass cylindrical tank of 1.5 m height and 0.6 m diameter, which was randomly packed with cubes in reticulated polyurethane. McDermott et al. [5] reported biogas production during investigating the effect of ultrasonication as pre-treatment of the aquaculture waste for anaerobic digestion. Marchaim et al. [6] to treat the solid waste from the Yona Tuna and Sardines fish

processing factory by a combined method of digestion by thermophilic anaerobic bacteria and by flesh flies, produced biogas. Gebaur [7] reported anaerobic treatment be the preferred method of stabilization and hygienization of sludge from saline fish farm effluents because of its energy (biogas) production. Gebaur carried out mesophilic treatment of sludge of total solids (TS) 8.2-10.2 (wt.%) in 15 L continuous stirred tank reactors at 35°C. Batchwise digestion of fish waste and sisul pulp was studied by Mshandete et al. [8] both with the wastes separately and with mixtures in various proportions in 1000 mL bioreactors constructed by using conical glass flasks. Gebaur and Eikebrokk [9] investigated the treatment of concentrated sludge (10–12 wt.% TS) collected from Atlantic Salmon smolt hatchery with biogas production in order to reduce the high energy demands of smolt hatcheries.

The scope of this present work was to conduct research work in laboratory scale to produce biogas from mesophilic anaerobic digestion of fish waste and co-digestion of fish waste and cow dung.

### 2. MATERIALS AND METHODS

#### 2.1 Waste Sources

The fish waste in this experiment was collected from the Pahartali Bazar, Choumuhoni, in Chittagong, consisted of offals and gills. The cow dung was collected from local area around CUET. The total solids of fish waste and cow dung were considered to be 32.2 wt.% [8] and 18 wt.% [10] respectively.



Figure 1 shows the fish waste used.

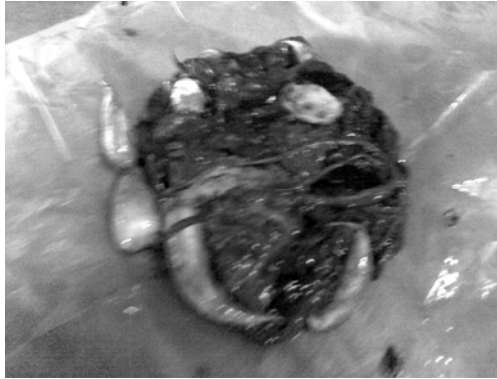


Fig 1. Fish waste used for anaerobic digestion

## 2.2 Experimental Set-up and Procedure

The anaerobic digestion of fish waste and co-digestion of fish waste and cow dung were tested in 4 L plastic digesters with different working volumes below around 2 L. Five laboratory scale digesters were made to digest fish waste, and co-digest fish waste and cow dung mixture in various proportions. Fish wastes were used 200 gm and 250 gm, and cow dung were used 0 - 300 gm to make fish waste to cow dung ratios (wt.) in the range of 1:0 to 1:1.5. The schematic diagram of the set-up is shown in figure 2. The digesters were set-up with other equipments such as displacement tank/gas collector and

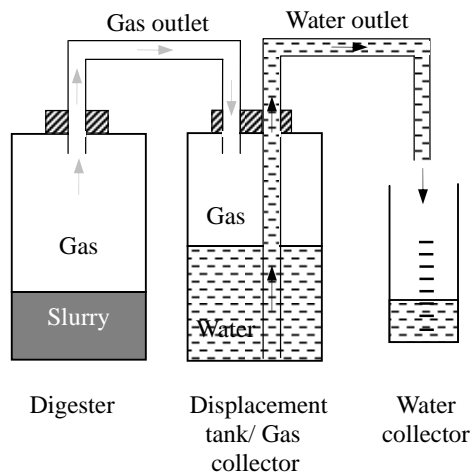


Fig 2. Schematic diagram of the experimental set-up for anaerobic digestion

water collector. Plastic pipe was used to connect digester and displacement tank. The pipe allowed the gas produced in the digester to pass to displacement tank and was fitted air tight in both the tanks and inserted at top positions. The gas was collected by water displacement method [5, 7]. The digesters were operated in batch mode at room temperature for 15 days and fed manually. Total solid contents of 8%(wt.) [10, 11] were used for all the experiments. To make the slurry of total solid content 8%(wt.), required amount of water was added. Table 1

shows the amounts of water and waste/s for different mixture. In water displacement method, initially the displacement tank/gas collector was kept full of water. When the gas started coming to the gas collector it displaced the water out of the collector to make its space inside. Another plastic pipe was used to take the displaced water from the displacement tank to the water collector which was fitted air tight in the displacement tank and inserted up to bottom part of it. The gaseous yield was measured by measuring the displaced water volume.

## 3. RESULTS AND DISCUSSION

Figure 3 shows the total gas yields for different fish waste to cow dung ratios. For all the co-digestion processes the gas generation started on the 7th day. For anaerobic digestion of fish waste gas generation started on the 10th day and generation continued only for 2 days.

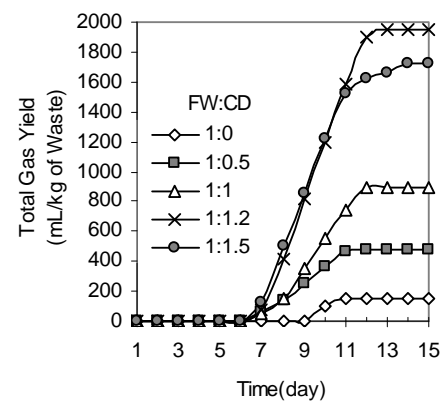


Fig 3. Total gas yield from anaerobic digestion

Figure 4 shows the daily gas production for each ratios and it is clear that highest gas production rates lie between the 8th and 10th days for all the co-digestion

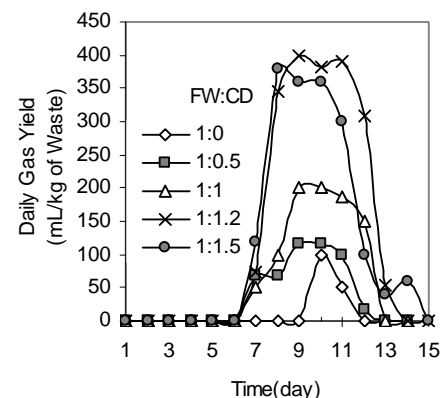


Fig 4. Daily gas yield from anaerobic digestion

processes. The maximum daily gas yield was observed from 1:1.2 (FW:CD) ratio (wt.) and on the 9th day maximum gas yield was found to be 400 ml/kg waste. For 1:1.5 (FW:CD) ratio (wt.) the maximum gas yield was observed on the 8th day of 380 ml/kg waste and higher than 1:1.2 ratio. At ratios of 1:1, 1:0.5 and 1:0 the

maximum daily gas yields were 200, 117, and 100 ml/kg waste respectively.

Figure 5 shows the ultimate gas yield and total retention time for different ratios. It is observed that with the increase of cow dung fraction the retention time was increased. For fish waste digestion retention time was 11 days. Whereas for co-digestion of fish waste and cow dung with 1:1.5 (FW:CD) ratio (wt.) the retention time was 14 days. The maximum ultimate gas yield was obtained from 1:1.2 (FW:CD) ratio (wt.) and amounted to 1955 ml/kg waste.

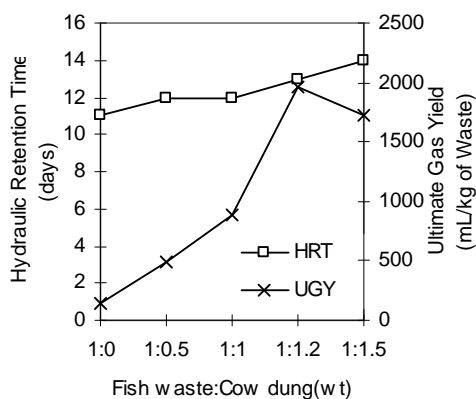


Fig 5. Ultimate gas yield and hydraulic retention time for anaerobic digestion

#### 4. CONCLUSION

Biogas was produced from anaerobic digestion of fish waste and also from anaerobic co-digestion of fish waste and cow dung. The results indicated anaerobic co-digestion of fish waste and cow dung with 1:1.2 (FW:CD) ratio (wt.) gave the highest gas yield of about 2 L/kg waste. The total gas yield from anaerobic digestion of fish was 150 ml/kg waste. More work should be done with proper slurry volume to digester volume ratio for the purpose of producing more gas.

#### 5. REFERENCES

1. Milono, P., Lindajati, T. and Aman, S., 1981, "Biogas Production from Agricultural Organic Residues". *The First ASEAN Seminar-Workshop on Biogas Technology, Working Group on Food Waste Materials*, pp. 52-65.
2. Environmental Protection Agency Methane Web Page, [www.epa.gov/methane/](http://www.epa.gov/methane/)

3. Mata-Alvarez, J., Macé, S. and Llabrés, P., 2000, "Anaerobic Digestion of Organic Wastes. An Overview of Research Achievements and Perspectives", *Bioresource Technology*, 74, pp. 3-16.
4. Lanari, D. and Franci, C., 1998, "Biogas Production from Solid Wastes Removed from Fish Farm Effluents", *Aquat. Living Resour.*, 11(4), pp. 289-295.
5. McDermott, B. L., Chalmers, A. D. and Goodwin, A. S., 2001, "Ultrasonication as a Pre-Treatment Method for the Enhancement of the Psychrophilic Anaerobic Digestion of Aquaculture Effluents", *Environmental Technology*, 22, pp. 823-830.
6. Marchaim, U., Gelman, A. and Braverman, Y., 2003, "Reducing Waste Contamination from Animal-Processing Plants by Anaerobic Thermophilic Fermentation and by Flesh Fly Digestion", *Applied Biochemistry and Biotechnology*, 109, pp. 107-115.
7. Gebaur, R., 2004, "Mesophilic Anaerobic Treatment of Sludge from Saline Fish Farm Effluents with Biogas Production", *Bioresource Technology*, 93, pp. 155-167.
8. Mshandete, A., Kivaisi, A., Rubindamayugi, M. and Mattiasson, B., 2004, "Anaerobic Batch Co-digestion of Sisal Pulp and Fish Wastes", *Bioresource Technology*, 95, 19-24.
9. Gebaur, R. and Eikebrokk, B., 2006, "Mesophilic Anaerobic Treatment of Sludge from Salmon Smolt Hatching", *Bioresource Technology*, 97, pp. 2389-2401.
10. Chowdhury, M. S., 2008, "Study of a Stirling-Generator Using Alternative Fuels", M.Sc. Thesis, Department of Mechanical Engineering, BUET, Dhaka.
11. Santana, A. and Proud, B., 1980, "The Production of Biogas from Cattle Slurry, the Effects of Concentration of Total Solids and Animal Diet", *Trop Anim Prod*, 5(2), pp. 130-135.

#### 6. MAILING ADDRESS

B. Salam  
 Department of Mechanical Engineering  
 Chittagong University of Engineering & Technology  
 Chittagong-4349, Bangladesh  
 Email: [bsalam@cuet.ac.bd](mailto:bsalam@cuet.ac.bd)

Table 1: Relative wastes and water amounts in the slurry

FW:CD(wt. ratio)	1: 0	1:0.5	1:1	1:1.2	1:1.5
Fish waste (gm)	200	200	200	250	200
Cow dung (gm)	0	100	200	300	300
Water (gm)	605	720	835	1101	950

# THERMODYNAMIC ANALYSIS OF HIGH TEMPERATURE STEAM GASIFICATION OF BLACK LIQUOR FOR POWER GENERATION

M. M. Rahman<sup>a</sup>, W. Yang<sup>b</sup>

<sup>a</sup>Department of Mechanical Engineering, CUET, Chittagong-4349, Bangladesh

Phone & Fax: +88-031-714953, E-mail: [mmrahman@cuet.ac.bd](mailto:mmrahman@cuet.ac.bd)

<sup>b</sup>Division of Energy and Furnace Technology, Royal Institute of Technology, Stockholm, Sweden

Tel: +46 8 790 8402 Fax: +46 8 20 76 81 , Email: [weihong@mse.kth.se](mailto:weihong@mse.kth.se)

## ABSTRACT

Today gasification of Black liquor at high temperature is a promising alternative to the conventional recovery boiler process used in chemical pulping. This study aims to develop a new conceptual model for black liquor gasification. The mixture of black liquor vapour and water vapour is passed through a regenerative system where the mixture is heated up at high temperature. The regenerative system uses an additional preheating system combusting part of the produced syngas. Hydrogen production increases with increase in steam/fuel ratio and decreases with increase in gasification temperature. For steam/fuel ratio 1.30, maximum hydrogen production is about 55.5%. The mass balance, energy balance of the system has computed to evaluate the efficiency of the system. Also the exergy value of produced syngas has computed. The result shows that both the energy value (LHV) and exergy value increases with the increase of gasification temperature. The maximum exergy 72.5% is achieved at 1100C and steam/fuel ratio 0.30. The largest part of exergy loss occurs in the gasifier which is 23.5%. The analysis also shows that power generation efficiency of the system is favoured by higher gasification temperature but disfavoured by higher steam/fuel ratio at a constant temperature. But in both cases the cold gasification efficiency (CGE) increases.

**Keywords:** Black liquor, Gasification, Syngas

## 1. INTRODUCTION

Today it has become very significant to use renewable and CO<sub>2</sub> natural fuels like biomass and waste due to the increased world energy demand and the alarming global warming. In paper industry when wood is converted to pulp by the Kraft process (or sulphate method), the fibre is released by dissolving the other organic constituents of the wood or nonwood lignocellulosics into an aqueous solution containing sodium hydroxide and sodium sulphide. After removal of the fibre product, the remaining spent solution, which is called black liquor, is an important industrial fuel in papermaking countries. It consists mainly of dissolved lignin degradation products from reacting an aqueous solution containing sodium hydroxide and sodium sulfide along with the hemicellulosic and cellulosic hexose and pentose sugars degradation products. Pulp and paper industry producing huge amount of black liquor can play an important role in the respective country energy system.

Gasification of Black liquor at high temperature is a promising alternative to the conventional recovery boiler process used in chemical pulping. Compared to the conventional recovery process, i.e. combustion of black liquor in a recovery boiler, the primary advantage of gasification is the potential to produce bio-fuels and chemicals. Black liquor with an integrated combined

cycle has the potential to double the amount of net electrical energy for a Kraft pulp mill compared to an ordinary recovery boiler with a steam turbine. Among the several gasification processes, they can roughly be categorized into two processes. One is low temperature processes that work below 715°C and the other one is high temperature processes which operate above 900°C. For low temperature processes the inorganic salts are removed as dry solid and for high temperature processes the inorganic salts are removed as smelt. The main principal behind these technologies is to spray the black liquor as fine particles into the reactor where the temperature is high enough to gasify the black liquor droplets.

In this study, a conceptual model-high temperature steam gasification of black liquor (HTSG-BL)-has been developed as shown in figure 1. Chemical equilibrium calculation by using CEA code has been done to get the composition of syngas from black liquor gasification for different operational parameters (gasification temperature, steam/fuel ratio and gasifier pressure). Finally mass balance, energy balance, exergy and efficiency have been calculated to evaluate the model.

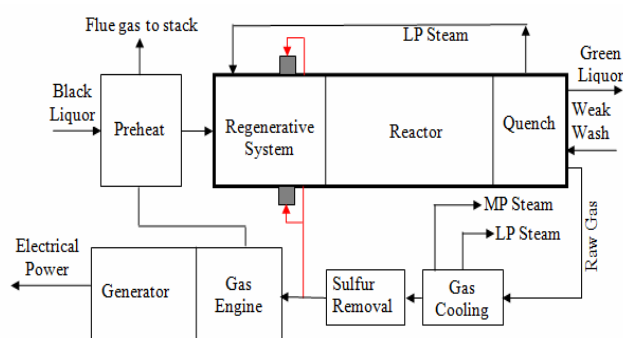


Figure 1: A new conceptual model of high temperature steam gasification of black liquor (HTSG-BL)

A compact regenerative system where a part of product gas is combusted to provide the necessary heat, can be used to produce a preheated mixture of black liquor vapour and steam above 1000C [1]. Figure 2 shows a conceptual model of such equipment.

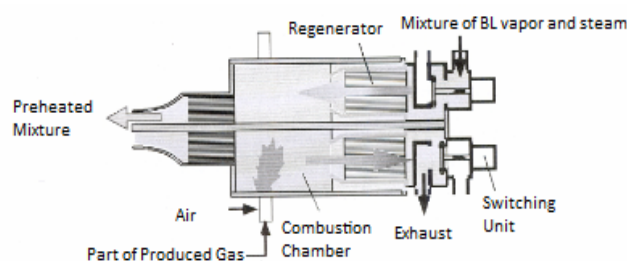


Figure 2: Concept of regenerative system for high-temperature gasification

The regenerator is located at the bottom of a combustion chamber and is heated up by the flue gases. The mixture of BL vapour and steam to be heated passes the regenerator on top and takes up previously stored heat. Heat storage and heat release in the regenerator are repeated periodically when combustion gases and cold BL vapour-agent are alternatively provided to the two regenerators by on-off action of a switching valve located on the low temperature side. The preheated gas continuously discharges from each exit nozzle on the left-hand side section and combustion gas exhausts from the right-hand side section.

## 2. METHODOLOGY

### 2.1 Gasification Equilibrium Model

The composition of a mixture at equilibrium can be estimated using different methods. The gasification equilibrium model used here is based on the **CEA** (Chemical Equilibrium with Applications) **code**. This code is suitable for calculations of the equilibrium state of systems comprising of one or more phases. The chief advantage of this method is that it does not require selecting a number of “representative”

chemical reactions allowing the formation of (equilibrium) products; it is nevertheless necessary to establish a list of chemical species inclusive of the ones expected in the product mixture. Other approaches to estimate the product composition are available, such as kinetic/dynamic models [2] and neural network applications [3] allowing in some instances to obtain a better accuracy. Nevertheless, the proposed approach has a more general application with predictive capability, without requiring an extended set of data to fit/train the model itself.

The model considers 78 chemical species. The chosen compounds are combinations of C, H, O, Na and S that are the typical elements of black liquor. The model results show that only a small number of species is present in the product of mixture after gasification in a significant fraction. The black liquor composition was assumed to be  $CH_{1.25}O_{0.70}Na_{0.24}S_{0.04}$  which corresponds to typical Kraft liquor with a molar ratio of S/Na is 0.30. The following assumptions were made during the simulation:

1. The residence times of reactants were considered as high in order to reach the chemical equilibrium.
2. Whole carbon contained in fuel is gasified. Therefore, charcoal was not formed
3. The reactions are at thermodynamic equilibrium
4. The reactions proceeds iso-thermally
5. The gasification reactor temperature varied between 700C and 1200C
6. The pressure varied between 1 bar and 35 bar.
7. Steam/fuel ratios varied between 0.30 and 1.30 [mol/mol]

### 2.2 Model Equation

The steam gasification is represented by the following equation:



Where, n, m and p are number of moles of feedstock compositions; carbon, hydrogen and oxygen respectively. w is Number of moles of steam ( $H_2O$ ). a, b, c and d are number of moles of the fuel gases; carbon monoxide, hydrogen, carbon dioxide and methane respectively.

The LHV of fuel gases was calculated by using the following equation [4,5]:

$$LHV [kJ/Nm^3] = (30 * CO + 25.7 * H_2 + 85.4 * CH_4 + 151.3 C_nH_m) * 4.2$$

Where, CO,  $H_2$ ,  $CH_4$  and  $C_nH_m$  are molar ratio of the CO,  $H_2$ ,  $CH_4$  and hydrocarbon ( $C_2H_4$  and  $C_2H_6$ ) in the gas product. The energy balance was calculated by the following equations:

$$\sum H_{input} = \sum H_{output}$$

The energy input was calculated by the formulas:

$$\sum H_{input} = H_{CH,BLV} + H_{SG,RS}$$

The chemical energy of feedstock was calculated as follows:

$$H_{CH,BLV} = LHV_{Feedstock} * m_{DryFeedstock}^o$$

Where,  $LHV_{Feedstock}$  - Lower heating value of feedstock [MJ/Kg feedstock]

Energy required for the regenerative system:

$$H_{SG,RS} = H_{SS} + H_{BLV}$$

The sensible heat of gaseous mixture at a defined temperature was calculated as the weighted average of the sensible heat for the pure species:

$$H_{mix} = \sum_i h_i$$

$$h_i = h_{i,sensibleheat} + h_{i,latenheat}$$

The sensible heat at a defined temperature relative to the standard state can be computed by the Shomate equation:

$$h_{i,sensibleheat} = A * t + B * \frac{t^2}{2} + C * \frac{t^3}{3} + D * \frac{t^4}{4} - E * \frac{1}{t} + F - H$$

Where  $t = T/1000$

The energy output has calculated by the following formulas:

$$\sum H_{output} = H_{CH,SG} + H_{PH,CG} + H_G + H_{FG}$$

The fuel gas energy was calculated from the following equations:

$$H_{CH,SG} = LHV_{SG} * m_{Syngas}^o$$

$$H_{PH,SG} = \sum_i \left[ m_{Gi} * \int_{T_{in}}^{T_{out}} Cp dT \right]$$

Assumptions made during the energy balance:

1. The energy loss in gasifier was assumed to be 10% of the chemical energy of the syngas, i.e.

$$H_G = 10\% * H_{CH,SG}$$

2. The thermal loss through flue gas was assumed to be 5% of energy used in the regenerative system, i.e.

$$H_{FG} = 5\% * H_{CG,RS}$$

The electrical power output from the system is,

$$P_{Electrical} = H_{SGE} * \eta_E * \eta_G$$

Where,  $H_{SGE}$  -Energy of syngas used in engine [KW],  
 $\eta_E$  -Efficiency of engine 30%,  $\eta_G$  -Efficiency of generator 95%

Total exergy of syngas can be found as:

$$E_{total,SG} = E_{CH,SG} + E_{PH,SG}$$

The chemical exergy relative to a standard environmental state (298K and 1 bar) was calculated with:

$$E_{CH,SG} = m_{SG}^o \left[ \sum x_i \epsilon_{0,i} + RT_0 \sum x_i \ln(x_i) \right]$$

The physical exergy relative to a standard environmental state (298K and 1 bar) was calculated with:

$$E_{PH,SG} = m_{SG}^o \left[ (h_i - h_{0,i}) - T_0 (s_i - s_{0,i}) \right]$$

The entropy of species at different temperatures was also calculated by using the Shomate-equation:

$$s_i = A \ln(t) + B * t + C * \frac{t^2}{2} + D * \frac{t^3}{3} - E * \frac{1}{2t^2} + G$$

Where  $t = T/1000$

For black liquor fuel, thermodynamic properties are not available. Therefore, the statistical correlation of Kotas was used to calculate the exergy of formation for black liquor [6]:

$$E_{BL} = LHV_{BL} \left[ \frac{1.0438 + 0.1882 \frac{g_{H_2}}{g_C} - 0.2509 * \left( 1 + 0.7256 \frac{g_{H_2}}{g_C} \right) + 0.0450 \frac{g_{Na}}{g_C}}{1 - 0.3035 \frac{g_{O_2}}{g_C}} \right]$$

Where,  $LHV_{BL}$  is the lower heating value i.e net enthalpy of combustion of black liquor and  $g_{H_2}$ ,  $g_C$ ,  $g_{O_2}$ ,  $g_{Na}$  are the mass fraction of hydrogen, carbon, oxygen and sodium respectively.

The net electrical efficiency of the system [%]

$$\eta_{Total} = \frac{P_{Electrical}}{m_{Feedstock} * LHV_{Feedstock}} * 100 \%$$

The cold gasification efficiency (CGE) is a measure of gasifier performance. It is defined as the ratio of energy in the gas and the energy contained within the fuel.

$$\eta_{CGE} = \frac{LHV_{gas} * V_{gas}^0}{m_{Feedstock} * LHV_{Feedstock}} * 100 \%$$

### 3. RESULT AND DISCUSSION

#### 3.1 Syngas Composition

The CEA code enabled to obtain the syn gas composition after gasification of black liquor. Among the 78 species only several species are presented in the gasification product in a significant percentage. The quench-cooler is used to separate the products exiting the reactor (gases and smelt). Table 1 shows the syngas molar composition equilibrium calculations for different operational parameters (reactor temperature, steam/fuel ratio and reactor pressure). Smelt generally consists of inorganic salts like  $Na_2CO_3$ ,  $Na_2SO_4$ ,  $Na_2S$ ,  $NaOH$ ,  $Na^+$ ,  $COS$  etc.

Table 1: Gasification conditions and syn gas compositions for black liquor

Case number	1	2	3	4	5	6	7	8
Temperature(°C)	900	1000	1100	1100	1100	1100	1100	1100
Pressure(bar)	1	1	1	1	1	1	5	10
Steam/fuel ratio	0.30	0.30	0.30	0.48	0.66	0.84	0.30	0.30
CH <sub>4</sub> (mole %)	0.59	0.25	0.11	0.0044	0.0021	0.0011	0.71	1.44
CO(mole %)	43.17	47.23	51.86	46.65	39.35	32.88	45.22	43.73
CO <sub>2</sub> (mole %)	0.52	0.16	0.06	1.21	2.64	3.89	0.23	0.44
H <sub>2</sub> (mole %)	54.88	52.07	47.86	49.33	50.97	51.92	53.29	53.32
H <sub>2</sub> O(mole %)	0.84	0.29	0.11	2.80	7.03	11.33	0.55	1.06
H <sub>2</sub> S(mole %)	0.00	0.00	0.00	0.0012	0.0032	0.0081	0.00	0.0011
LHV(MJ/Nm <sup>3</sup> )	9.66	10.06	10.52	10.00	9.50	9.20	9.90	9.80

The yields of the different species as a function of steam-fuel ratio is presented in figure 3. Analyzing the thermodynamic equilibrium composition of syngas in figure 3, it can be seen that hydrogen and carbon dioxide formation are favoured at higher steam-fuel ratio and at lower steam-fuel ratio carbon monoxide and methane are the dominant equilibrium products. It also can be seen that the LHV decreases from 10.52 MJ/Nm<sup>3</sup> to 8.20 MJ/Nm<sup>3</sup> with increasing steam-fuel ratio from 0.30 to 1.30 respectively.

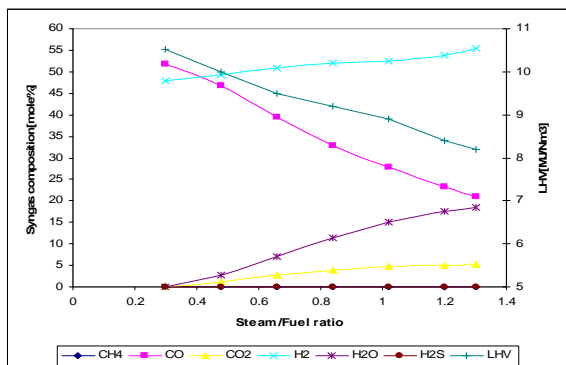


Figure 3: Syn gas equilibrium composition and LHV vs. steam/fuel ratio at temperature 1100°C and pressure 1 bar.

Analyzing the thermodynamic equilibrium composition of fuel gas as a function of temperature, it can be seen that carbon monoxide formation is favoured at higher temperature and at lower temperature hydrogen, carbon dioxide and methane are the dominant equilibrium products. The LHV also increases with increasing temperature.

#### 3.2 Quality of Syngas

Figure 5 shows the energy value (LHV), the exergy value of the produced syngas, hydrogen/carbon monoxide ratio and carbon dioxide/ carbon monoxide ratio as a function of the gasification temperature. By analyzing the figure it is clear that the higher gasification temperature has beneficial effect on the both energy and exergy density of the produced gas. This is mainly due to the fact that as the gasification temperature increases the dilution by carbon dioxide decreases. The figure also shows that the hydrogen/carbon monoxide ratio and carbon dioxide/ carbon monoxide ratio also decreases from 2.38, 27.52 to 0.86, 0.04 respectively as the gasification temperature increases from 700<sup>0</sup> C to 1200<sup>0</sup> C respectively. It is also clear that the decreasing ratio for carbon dioxide/ carbon monoxide is more steeper than the decreasing ratio for hydrogen/carbon monoxide. Figure 4 also shows that for a corresponding temperature rise the exergy value increases more rapidly than the energy value of produced syngas for the same temperature rise.

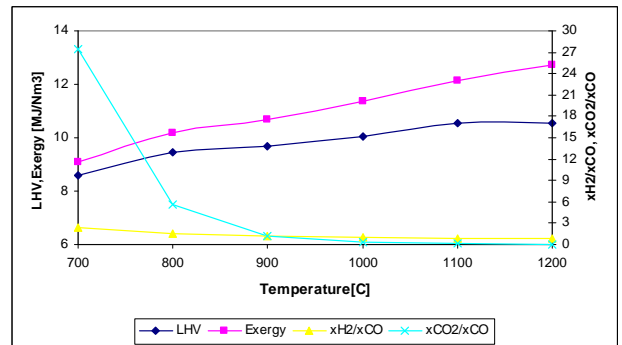


Figure 4: Energy value (LHV), Exergy value, xH<sub>2</sub>/xCO, xCO<sub>2</sub>/xCO of the produced syn gas as a function of temperature at pressure 1 bar, steam/fuel ratio 0.30

The quality of syngas has also been analyzed for different steam/fuel ratio. Figure 5 shows the hydrogen/carbon monoxide ratio, carbon dioxide/ carbon monoxide ratio as a function of the steam/fuel ratio. Analyzing the figure it can be seen that both the hydrogen/carbon monoxide ratio and carbon dioxide/ carbon monoxide ratio increases with increasing steam/fuel ratio. This increase is mainly due to the fact

that hydrogen and carbon dioxide formation are favoured at higher steam/fuel ratio and at the same time carbon monoxide formation is disfavoured at higher steam/fuel ratio which is well described in figure 3. Actually, hydrogen and carbon dioxide formation is favoured mainly for the so-called water gas reaction ( $C+H_2O = CO+H_2$ ) and the water gas shift reaction ( $CO+H_2O = CO_2+H_2$ ) by the addition of steam as a gasification agent.

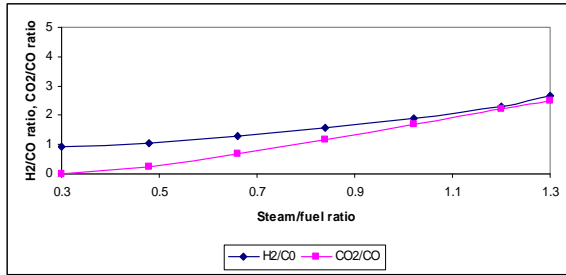


Figure 5: H<sub>2</sub>/CO ratio and CO<sub>2</sub>/CO ratio of the produced syn gas as a function of steam/fuel ratio at pressure 1 bar and temperature 1100<sup>0</sup> C

### 3.3 Energy and Exergy Flow

In figure 6, an energy flow diagram of the gasifier model with T=1100C, P=1 bar and steam/fuel ratio 0.30 is shown. Also in figure 7, an exergy flow diagram of the gasifier model with T=1100C, P=1 bar and steam/fuel ratio 0.30 is shown. It is seen that energy loss in gasifier is higher than loss through flue gas. The physical energy of syngas is 15% of the total out put energy which could be utilized to produce steam.

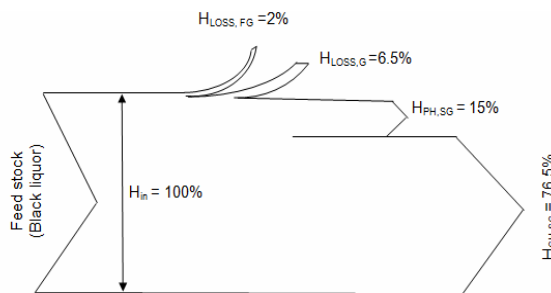


Figure 6: Energy flow diagram for gasifier energy model at temperature 1100<sup>0</sup>C, pressure 1 bar and steam/fuel ratio 0.30

The largest part of exergy loss occurs in the gasifier, where the highly order chemical energy of feedstock converted into chemical energy of fuel gas and heat. The exergy loss in the gasifier decreases with the increase of gasification temperature. In this gasifier model total exergy loss is 27.5%. But from figure 6 it is clear that total energy loss for the same model is only 8.5% of the total out put energy.

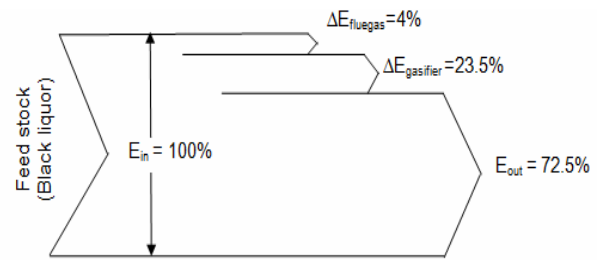


Figure 7: Exergy flow diagram for gasifier model at temperature 1100<sup>0</sup> C, pressure 1 bar and steam/fuel ratio 0.30

### 3.4 Efficiency

The total system efficiency and cold gasification efficiency as a function of gasification temperature is presented in the figure 8. Both the system efficiency and cold gasification efficiency increases with the increase of temperature.

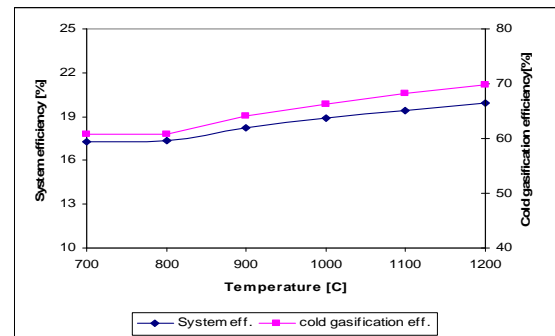


Figure 8: System efficiency and cold gasification efficiency vs. temperature at pressure 1 bar and steam/fuel ratio 0.30

The total system efficiency and cold gasification efficiency as a function of steam/fuel ratio is presented in the figure 9.

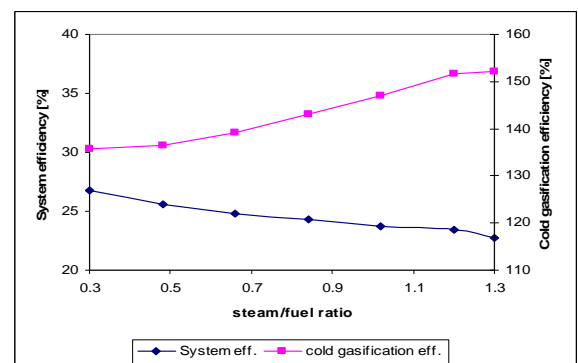


Figure 9: System efficiency and cold gasification efficiency vs. steam/fuel ratio at temperature 1100C and pressure 1 bar.



increase in gasification temperature from 700C to 1200C.

- The Cold Gasification Efficiency (CGE) of gasifier system increases for both the increase in steam/fuel ratio and gasification temperature. The CGE increases from 135.73% to 152.24% for the increase in steam /fuel ratio from 0.30 to 1.30

#### 4. CONCLUSIONS

This study aimed to understand the thermodynamic limitations and advantages of a new conceptual black liquor gasification model-direct heating of black liquor vapour and steam mixture by using an additional preheating system that uses part of the syngas produced. The system has been studied both for varying steam/ fuel ratio and gasification temperature.

- Though thermodynamic equilibrium calculation does not give the full picture of the real process but it shows the trend of the results. To get the better result it should be supported with kinetic studies.
- The steam/fuel ratio and gasification temperature has a strong influence on syngas quantity and quality. Hydrogen/carbon monoxide ratio increases from 0.92 to 2.66 for the increase in steam/fuel ratio from 0.30 to 1.30 respectively.
- Hydrogen production increases with increase in steam/fuel ratio and decreases with increase in gasification temperature. For steam/fuel ratio 1.30, maximum hydrogen production is about 55.5%.
- LHV decreases from 10.52 MJ/Nm<sup>3</sup> to 8.20 MJ/Nm<sup>3</sup> with increase in steam-fuel ratio from 0.30 to 1.30 and it increases from 8.57 MJ/Nm<sup>3</sup> to 10.55 MJ/Nm<sup>3</sup> with increase in gasification temperature from 700C to 1200C respectively.
- Both the energy density and exergy density of produced gas increases with the increase in gasification temperature.
- The maximum exergy 72.5% is achieved at 1100C and steam/fuel ratio 0.30. The largest part of exergy loss occurs in the gasifier which is 23.5%.
- The net electrical power generation efficiency decreases with increasing steam/fuel ratio but it increases with increasing gasification temperature. Power generation efficiency increases from 17.30% to 19.90% with the

#### 5. REFERENCES

- [1] Ponzio A., Yang W., Lucas C., (2006) Development of a thermally homogeneous gasifier system using high-temperature agents, Clean Air, Vol. 7,pp.363-379.
- [2] Gøbel, B., Henriksen, U., Jensen, T.K., Qvale, B., Houbak, N., 2007. The development of a computer model for a fixed gasifier and its use for optimization and control. Bio resource Technology 98, 2043–2052.
- [3] Guo, B., Li, D., Cheng, C., Lu, Z., Shen, Y., 2001. Simulation of biomass gasification with a hybrid neural network. Bio resource Technology 76, 77–83.
- [4] X. Dai, C. Wu, H.B. Li, Y. Chen, The fast pyrolysis of biomass in CFB reactor, Energy and Fuels 14 (2000)552–557.
- [5] Zabaniotou A; Rapeseed residues utilization for energy and 2nd generation biofuels, Fuel (2007).
- [6] Kotas T.J. The exergy method of thermal plant analysis. Butterworths, London, 1985.

#### 6. NOMENCLATURE

Symbol	Meaning	Unit
LHV	Lower Heating Value	Kj/Nm <sup>3</sup>
$H_{CH,BLV}$	Chemical energy of feedstock	KW
$H_{SG,RS}$	Syngas used in reg. system	KW
$H_{CH,SG}$	Chemical energy of syngas	KW
$H_{PH,SG}$	Physical energy of syngas	KW
$m_{SG}^o$	Mass flow of syngas	Kg/s
$x_i$	Mole of different species	
R	Molar gas constant	Kj/KG-k
$h_{0,i}$	Enthalpy at standard state	KJ/kg

## LASER CLEANING AND METAL CHARACTERIZATION IN AID OF ARTEFACT PRESERVATION AND ARCHAEO-METAL TECHNOLOGY INVESTIGATION

Barnali Mandal<sup>1</sup>, P. K. Chattopadhyay<sup>2</sup>, Dipten Misra<sup>3</sup> and Prasanta K. Datta<sup>4</sup>

<sup>1</sup>Research Scholar, Dept. of Met. & Mat. Engg. Jadavpur University, Kolkata-700032

<sup>2</sup>Fellow, Centre for Archaeological Studies & Training, Kolkata-700016,

<sup>3</sup>Director, School of Laser Science & Engg. Jadavpur University, Kolkata-700032,

<sup>4</sup>Professor, Dept. of Met. & Mat. Engg. Jadavpur University, Kolkata-700032, INDIA

### ABSTRACT

Two *bronze* icons, one *Radha* and one *Krishna*, were supplied by a West Bengal Museum for restoration and investigation of their manufacturing technology. After laser cleaning with Quanta system laser both the items recovered the dull initial appearance of yellowish brass metal. On material characterization of the metals it was established that the alloy used was leaded  $\alpha$ -brass, cast possibly in hot clay molds. To understand that manufacturing process, a complete foundry design of one cast item *Radha* has been worked-out to reconstruct the probable methoding route followed by medieval Bengal workers.

**Keywords:** Laser Cleaning, Characterization, Methoding.

### 1. INTRODUCTION

Few years back some *bronze* artefacts were recovered by villagers in South 24-Paraganas District of West Bengal during excavation, as chance finds. Two of the artefacts were of *bronzes*, one *Radha* and one *Krishna*, and were in heavily corroded state, needing restoration for display at the museum gallery of Sundarban Anchalik Sangrahasala, Baruipur. Jadavpur University was approached to help in the restoration work and so, laser cleaning was applied to clean the surface of the items. Small fragments of each item were collected to undertake metallurgical characterization for investigation of metal technology. The investigation revealed cast metal technology in hot molds, and, on that basis a reconstructed methoding design for manufacturing the castings has been attempted.

### 2. LASER CLEANING OF BRONZES

Both the *bronzes* before cleaning had hard dark corrosion coating over the surface. The dark coating was removed by laser cleaning method with Q-switched Nd:YAG laser. After removal of the coating, *bronze* castings showed dull yellow color with shallow irregular poke marks over few areas. A slow removal rate, by Quanta System Q-switched Nd:YAG Laser (Model: PALLADIO, Serial No. PLLOOI-0207) was used. The laser heating was countered by cooling under water. Under wet condition, laser cleaning yielded better contaminant removal rate than dry condition.

By repeated laser cleaning for two hours per seating it took 4 to 5 seating, for arriving at a dull but clear appearance (Figs. 1, 2). The dull appearance comes from the presence of a thin layer of patina. The patina is deliberately left on the artefacts as it helps in protecting the substrate against further degradation. Details are shown in Table 1.

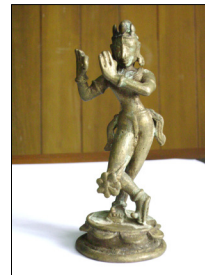


Fig.1. *Krishna* (as received) Fig.1(a). Laser Cleaned

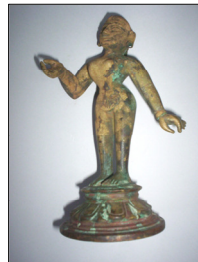


Fig.2. *Radha* (as received) Fig.2(a). Laser Cleaned

Table 1: Details of Laser Cleaning Operation.

Exp. No.	Sample	Time (sec.)	Frequency (Hz)	Energy (J)
1.	*Bronze	30	10	0.155
2.	Bronze	5	10	0.151
3.	Bronze	60	10	0.157
4.	Bronze	30	10	0.155
5.	Bronze	60	10	0.156
6.	Bronze	30	10	0.154
7.	Bronze	30	10	0.152
8.	Bronze	30	10	0.151

\*Bronze here signifies Copper-Alloy items as is the convention of Archaeologists and does not represent the scientific Copper-Tin alloy understood by Metallurgists.

### 3. CHARACTERIZATION OF BRONZES

Two small inner fragments of the bronzes were collected and then investigated using common metallurgical tools like Scanning Electron Microscopy (SEM) with Energy Dispersive X-Ray Analysis (EDX), Hardness Measurement, X-Ray Diffraction Crystallography and Differential Thermal Analysis.

#### 3.1 Chemical Composition by SEM-EDX

The average chemical composition analyzed using EDX of Scanning Electron Microscopy has been given in Table 2. Chemical compositions identify the bronzes as Copper-Zinc alloy, having  $\alpha$ -brass signature coupled with generous amount of lead and a small bit of tin, arsenic, iron, etc. Might be it was the attempt of the medieval metal workers to reach the popular iconic, *Astadhat*, [1] Octo-alloy composition (Cu, Sn, Zn, Pb, Fe, As + [Au & Ag]). All these come close to modern Gun-Metal (Cu-Sn-Zn-Pb system). Bulk hardness values conform to cast leaded brass data [2]. The Bulk Hardness and Micro-Hardness of bronze icons, *Radha* and *Krishna* were obtained by Vickers' Macro Hardness Machine, Model no. HPO-250, 10 kgf, and Vickers' Micro Hardness Machine, Leica make, 15 gf load, respectively. The impressions of the bulk-hardness indentation of icon *Radha* are shown in Fig. 3.

#### 3.2 Characterization of Icon *Radha*

The typical cast single phase, microstructure of  $\alpha$ -brass, showing dendritic morphology produced in a casting process, predominates the photograph (Fig.4). Dendrites being the marker of a cast product, no doubt, the artefact was manufactured by a cast metal technology. The distribution of elements, when analyzed by SEM and EDX, shows clearly Cu-rich  $\alpha$ -phase dendrites (black) as matrix. Last-to-freeze solute rich, Cu-lean  $\beta$ -phase can be seen as shaded areas (white to grey).

Lead particles are shown as white round or roundish spots. Micro-Hardness data of  $\alpha$ - and  $\beta$ -phases show high HV values due to the high concentrations of many complex solutes.

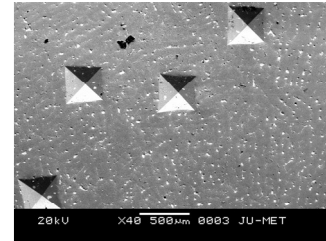


Fig.3. Vickers' Pyramidal Indentations of the Bulk-Hardness measurements show sinking-in effect of soft materials.

Table 2: Chemical Compositions and Bulk Hardness of bronzes.

Elements (Weight %)	Radha	Krishna
Copper (Cu)	69.45	64.13
Zinc (Zn)	19.08	20.76
Lead (Pb)	6.18	9.75
Tin (Sn)	3.60	1.86
Arsenic (As)	0.69	0.95
Antimony (Sb)	0.30	-
Iron (Fe)	0.34	2.55
Nickel (Ni)	0.36	-
Bulk Hardness (HV)	76.5	74.3

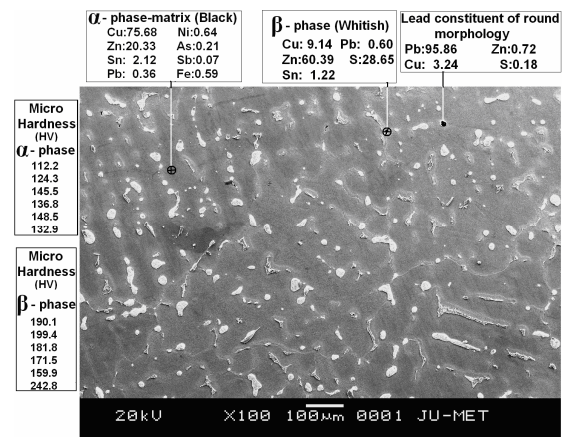


Fig. 4. Etchant:  $\text{FeCl}_3$  in HCl. Compositions of  $\alpha$ ,  $\beta$  and lead constituents are given above in wt.%. Micro hardness of phases is shown in left hand side. The microstructure reveals typical serial grains, known as dendrites, commonly found in a cast product. This matrix is of  $\alpha$ -phase (Black), while inter-dendritic regions (White) become solute rich  $\beta$ -phase. White round particles are mainly lead rich insoluble phase.

For clarification of uneven distribution of solute elements like zinc and tin in the given  $\alpha$ - and  $\beta$ -phases further SEM-EDX analyses were undertaken as shown in Fig.5. The lower percentage of zinc and tin in primary  $\alpha$ -phase and spike in percentages of solutes in last-to-freeze  $\beta$ -phase (Table 3), as expected in normal dendritic material, known as coring [3], are observed. So, the production process as casting is confirmed again.

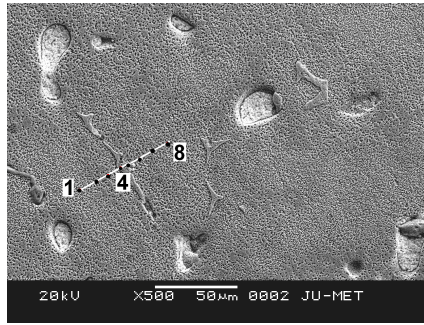


Fig.5. Marking points on the microstructure of icon *Radha*, where SEM-EDX analyzes were made to determine the distribution of percentages of Copper, Zinc and Tin. Markings 1-3 and 6-8 are in  $\alpha$ -phase and 4, 5 are in  $\beta$ -phase.

Table 3: Chemical Compositions of icon *Radha* in the microstructure at points 1 to 8.

Pts.	Phase	Copper (Wt. %)	Zinc (Wt. %)	Tin (Wt. %)
1.	$\alpha$	75.68	20.33	2.12
2.	$\alpha$	75.50	19.88	2.50
3.	$\alpha$	71.97	18.63	4.73
4.	$\beta$	59.95	8.38	29.31
5.	$\beta$	61.53	8.83	29.02
6.	$\alpha$	72.09	18.29	5.03
7.	$\alpha$	74.52	19.93	2.98
8.	$\alpha$	75.40	19.32	2.63

Analyzing the X-Ray diffraction data for icon *Radha* (Table 4) a number of phases have been identified [4] by RIGAKU ULTIMA-III machine. From the X-Ray Diffractogram, (Fig.6) the presence of dominant  $\alpha$ -Cu phase (solid solution of Zn, Sn in FCC Cu) is confirmed. Some minor  $\beta$ -phase (solid solution of Sn, Zn in BCC Cu) can also be seen. Insoluble lead as separate phase can be found in the analysis.

DTA analysis (Fig.7) was made in Pyris Diamond DTA instrument for icon *Radha*. Differential Thermal Analysis of the sample points towards the occurrence of early phase change. Obviously it vindicates the presence of low melting point elements (few are also insoluble) present in the alloy.

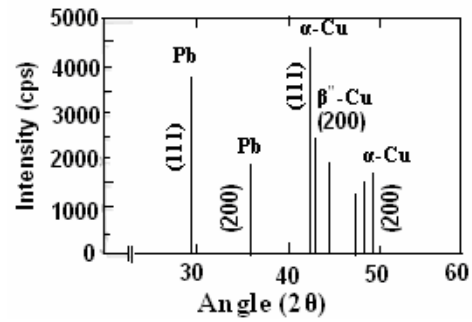


Fig.6. XRD Pattern of icon *Radha*, shows major constituents as  $\alpha$ -Cu phase.

Table 4: Details of X-Ray Diffractogram of icon *Radha*.

Peak No.	Angle (2 $\theta$ ) (Deg)	d <sub>space</sub> (Å)	I / I <sub>0</sub>	Identified Phase and Plane (hkl)
1.	29.40	3.0355	87	Pb (111)
2.	39.40	2.2851	36	Pb (200)
3.	42.50	2.1253	100	$\alpha$ -Cu (111)
4.	43.20	2.0924	41	$\beta$ -Cu (200)
5.	48.50	1.8754	26	$\alpha$ -Cu (200)

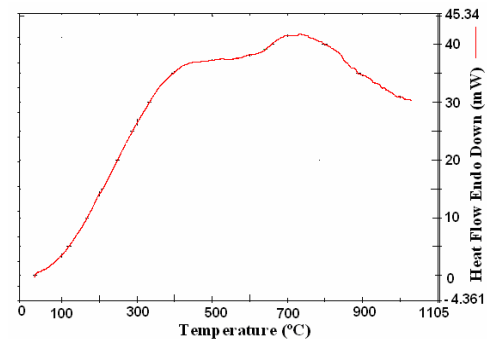


Fig.7. DTA analysis of icon *Radha*, points to an early phase change due to low melting constituents, lead & tin, etc.

### 3.3 Characterization of Icon *Krishna*

The microstructure (Fig.8) of *bronze icon Krishna* reveals coarse dendrites with lots and lots of lead precipitated within or around dendrites. Coarseness of dendrites leads to the conclusion that the castings were produced in hot molds. The reason is poor heat dissipation rate can only provide long solidification time, necessary for grain growth. With respect to *bronze Radha*, the amount of lead can be seen to be significantly higher. The insoluble lead effectively fills up pores between dendrites and made the casting more sound.



The chemical compositions of  $\alpha$ -Cu (black areas) and  $\beta$ -Cu phases show Cu-rich and solute rich elements respectively, as shown earlier. The insoluble lead constituent was also analyzed. The Micro-Hardness of  $\alpha$ - and  $\beta$ -phases were measured and shown in Fig.8.

Though the hardness of the  $\alpha$ -phase was similar to that of icon *Radha*, the hardness of  $\beta$ -phase is slightly higher than that of *Radha*. As usual lead constituent shows very low hardness values of soft lead.

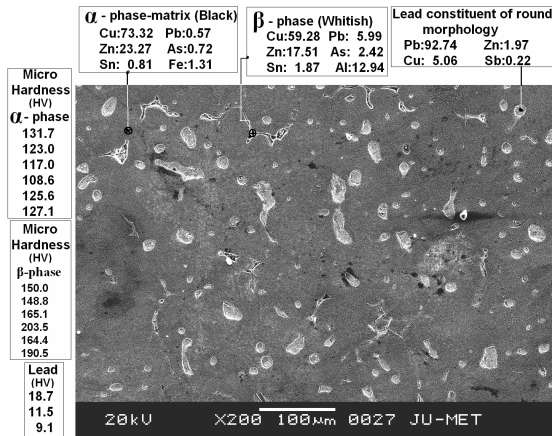


Fig.8. Etchant: FeCl<sub>3</sub> in HCl. All compositions of respective phases given above are in wt.%. Micro hardness of phases are shown in left hand column. Coarse dendrites (black area) engulf the microstructure, as major  $\alpha$ -phase. Like earlier microstructure of icon *Radha*, white areas consist of lead bearing phase and minor  $\beta$ -phase, in which the former amount is large.

For X-ray Diffraction analysis (Table 5), in case of *Krishna*, (Fig.9) all the comments about the *bronze Radha* are valid — that is the major phase is  $\alpha$ -Cu phase and minor phase is  $\beta$ -Cu phase.

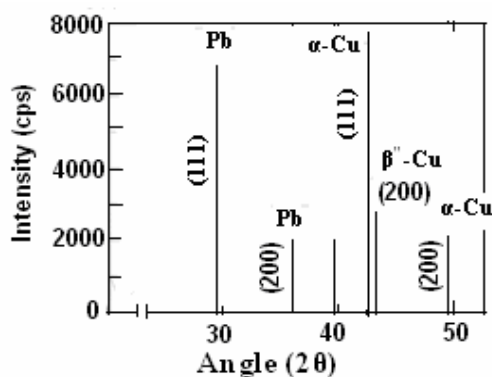


Fig.9. XRD Pattern of icon *Krishna* almost similar to earlier *Radha* sample.

DTA of *Krishna* is shown in Fig.10. The same comment mentioned in case of *Radha* is validated here also.

Table 5: Details of X-Ray Diffractogram of *Krishna*

Peak No.	Angle (2θ) (Deg)	d <sub>space</sub> (Å)	I / I <sub>0</sub>	Identified Phase and Plane (hkl)
1.	29.50	3.0254	88	Pb (111)
2.	36.00	2.4927	43	Pb (200)
3.	42.50	2.1253	100	$\alpha$ -Cu (111)
4.	43.20	2.0924	57	$\beta$ -Cu (200)
5.	48.60	1.8718	38	$\alpha$ -Cu (200)

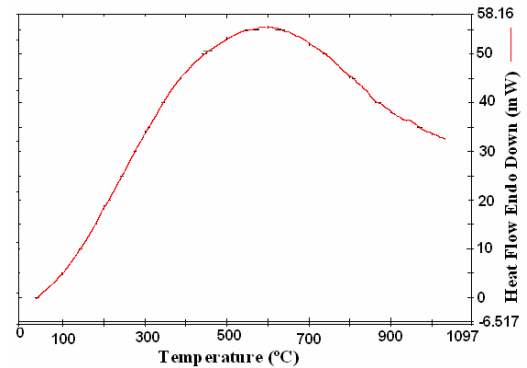


Fig.10. DTA analysis of icon *Krishna*, exhibits the early transformation of low melting constituents.

#### 4. ARCHAEO-TECHNOLOGY CONSTRUCTION

Based on the characterization of metals, there is little doubt that *bronzes* were produced using Cast Metal Technology of hot molds. Following the medieval practice, the molds should be made of Silica sand with alluvial clay as binder, as reported in literature [5]. After joining those hard piece-molds together, liquid metal was poured in the hot assembly, through a gating system, and a riser was probably provided to compensate for the liquid-solid contraction during solidification. The total system of medieval foundry practice has been visualized here under.

The casting process starts with methoding in which pattern, core, gating and riser are designed in successive order. The reconstructed methoding for one casting, *Radha* has been described to get a glimpse of that technology.

#### 5. METHODING DESIGN

Details of icon *Radha*, as received.

Weight of the Casting,  $\times 10^3$ , kg = 716

Volume of the Casting,  $\times 10^6$ , m<sup>3</sup> = 110

Height of the Casting,  $\times 10^3$ , m = 150

On the basis of recovered casting, the pattern and core volumes with the associated heat dissipating areas have been estimated. Considering simple geometry the estimation has been made and these are totally approximate which is given in Fig.11.

**(1) Pattern and Core parameters:**

Height of the Pattern, $\times 10^3$ , m	= 155
(3% contraction allowance considered)	
Volume of the Pattern, $\times 10^6$ , $m^3$	= 111
Outside Area of the Pattern, $\times 10^3$ , $m^2$	= 17
Volume of the Core, $\times 10^6$ , $m^3$	= 24
Outside Area of the Core, $\times 10^3$ , $m^2$	= 5
Heat dissipating area of the casting, $(A_c + A_{co})$ , $m^2 = 22$	

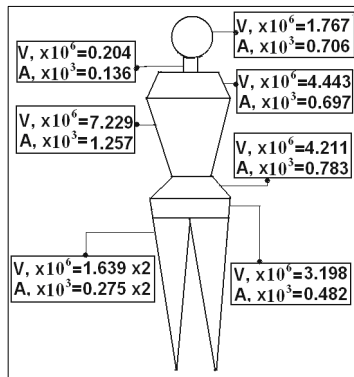
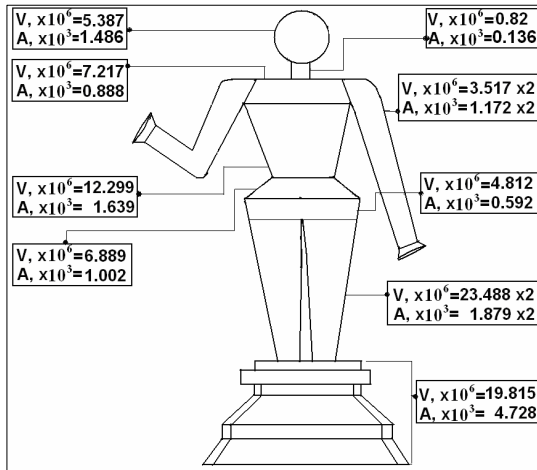


Fig.11. Calculated Volume ( $m^3$ ) and Area ( $m^2$ ) of the Pattern (top) and the Core (bottom) of reconstructed sample.

**(2) Gating Design:**

Assumptions: Top Gating	
Sprue Diameter, $\times 10^3$ , m	= 4
Sprue Height, $\times 10^3$ , m	= 70
Cup Height, $\times 10^3$ , m	= 20
Discharge coefficient,	= 0.9

For Bronze: Viscosity [6], mPa.s = 3.8  
 and Density [7],  $kg/m^3$  = 7826  
 On the basis of above,  
 Sprue Area,  $\times 10^6$ ,  $m^2$  = 12.566  
 Velocity @ Sprue,  $v_s$ , m/sec, =  $C\sqrt{2gh_s}$  = 1.0547  
 Liquid metal flow rate,  $A_s v_s$ ,  $\times 10^6$ ,  $m^3/sec$  = 13.2534

Time of filling,  $t_f = \frac{V_c}{A_s v_s}$ , sec,  $\approx 8$   
 Check by Reynolds's No.,  $R = \frac{v_s \rho d_s}{\mu} = 8688$

$t_f$  is small and  $R < 10,000$ ,  
 So,

**Design satisfactory**

**(3) Sprue Design:**

Aspiration Correction,  $A_s / A_{cu} :: \sqrt{h_{cu}} / \sqrt{h_s}$   
 $\Rightarrow \frac{d_s}{d_{cu}} = \sqrt[4]{\frac{h_{cu}}{h_s}}$   
 $\Rightarrow$  Cup Diameter,  $d_{cu}$ ,  $\times 10^3$ , m  $\approx 6$

**(4) Riser Design:**

Volume of the liquid Metal,  $(V_c - V_{co})$ ,  $\times 10^6$ ,  $m^3 = 87$   
 $M_c = \text{Modulus of the Casting} = \frac{\text{Volume}}{\text{Area}} = \frac{V_c - V_{co}}{A_c + A_{co}}$   
 $\Rightarrow M_c$ ,  $\times 10^3$ , m = 3.954

Let,  $M_r = \text{Modulus of Riser} = 1.3 M_c$   
 $\Rightarrow M_r \times 10^3$ , m = 5.1402

Assume Cylindrical Riser,  $d_r = h_r$   
 $M_r = \frac{d_r}{4}$

$\Rightarrow d_r$ ,  $\times 10^3$ , m  $\approx 20$

Table 6: Design Summary ( $\times 10^3$ , m)

Sprue diameter	Sprue height	Cup height	Cup diameter	Riser diameter
4	70	20	6	20

**(5) Placement of Riser and Sprue:**

The feeding distance ( $f_d$ , inch) is given by  $5.61 T^{0.53}$ , when,  $T$  is the thickness of the casting in 'inch' [8].

Here,  $T_c, \times 10^3, m = 3$

$\Rightarrow f_d, \times 10^3, m = 46$

The complete gating and riser dimensions with their placement position are shown in Fig.12.

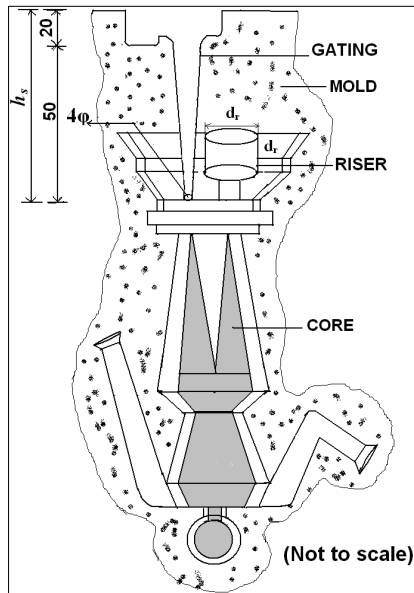


Fig.12. Gating and Riser dimensions are given with locations in the probable mold for *bronze icon, Radha*.

## 6. CONCLUSIONS

Laser cleaning using Nd:YAG laser has been successful in restoration of two museum *bronzes* in West Bengal and can be considered a viable alternative to chemical cleaning route.

*Bronzes* of medieval Bengal, in this case, constitute a copper alloy of primarily leaded  $\alpha$ -brass composition, although coming close to modern Gun-Metal.

The metallurgical investigation further reveals a hot mold casting practice, probably executed by medieval Bengal metalworkers, to produce the artefacts. Using present knowledge, the prospective foundry design of the castings has been reconstructed to understand the manufacturing process, practiced in archaeological period.

## 7. REFERENCES

1. Saraswati, S.K, 1962, *Early Sculpture of Bengal*, Sambodhi Publications Privated Limited, Calcutta, 27-28.
2. West, E.G., 1982, *Copper and its alloys*, Ellis Horwood Limited, 137.

3. Shewmon, P.G, 1962, *Transformations in Metals*, McGraw-Hill Book Co., 166-69.
4. JCPDS (Joint Committee for Powder Diffraction System) file, 1978, *Selected powder diffraction data for metal and alloys*, Volumes-I and II, file nos. 23-0345, 19-0179 and 4-0836.
5. Mukherjee, M, 1978, *Metalcraftmans of India*, Anthropological Survey of India, Calcutta. 314-18.
6. Ruud, C.O., D. Chandra, J.M. Fernandez, and M.T. Hepworth, 1976, "Copper and Copper Alloy Viscosity", *Metallurgical Transaction*, 7B: 497-498.
7. Gale, W.F. and T.C. Totemeier, 2004, *Smithells Metals Reference Book*, 8<sup>th</sup> edition, Butterworth – Heinemann an imprint of Elsevier, Vol.14, 10.
8. Sylvia, 1972, *Cast Metal Technology*, Addison Wesley Lakeville Mass., 171.

## 8. NOMENCLATURE

Symbol	Meaning	Unit
$V_c$	Volume of the Pattern	(m <sup>3</sup> )
$A_c$	Outside Area of the Pattern	(m <sup>2</sup> )
$V_{co}$	Volume of the Core	(m <sup>3</sup> )
$A_{co}$	Outside Area of the Core	(m <sup>2</sup> )
$d_s$	Sprue Diameter	(m)
$A_s$	Sprue Area	(m <sup>2</sup> )
$h_s$	Sprue Height	(m)
$h_{cu}$	Cup Height	(m)
$C$	Discharge coefficient	(-)
$\mu$	Viscosity of Bronze	(mPa.s)
$\rho$	Density of Bronze	(kg/m <sup>3</sup> )
$v_s$	Sprue Velocity	(m/sec)
$t_f$	Time of filling	(sec)
$R$	Reynolds's No.	(-)
$A_{cu}$	Cup Area	(m <sup>2</sup> )
$d_{cu}$	Cup Diameter	(m)
$M_c$	Modulus of the Casting	(m)
$M_r$	Modulus of the Riser	(m)
$d_r$	Riser Diameter	(m)
$h_r$	Height of the Riser	(m)
$T$	Thickness of the Casting	(m)
$T_c$	Thickness, Actual Casting	(m)
$f_d$	Feeding Distance	(m)

## 9. MAILING ADDRESS

**Ms Barnali Mandal**

Department of Metallurgical & Material Engineering  
Jadavpur University, Kolkata – 700 032, INDIA

**Phone No:** +91 33024146940,  
+91 33024146666 (Extn. 2176),  
09474053996 (cell).

**E-mail :** [barnali\\_ju@yahoo.co.in](mailto:barnali_ju@yahoo.co.in) and  
[dokra\\_pkd52@yahoo.co.in](mailto:dokra_pkd52@yahoo.co.in).



## UNUSUAL WIND BEHAVIOUR AT SITAKUNDU OF BANGLADESH

A. K. Azad<sup>1</sup>, Dr. M. M. Alam<sup>2</sup>

Department of Mechanical Engineering,  
Bangladesh University of Engineering & Technology (BUET), Dhaka, Bangladesh

### ABSTRACT

Wind energy is a non polluting cost-effective renewable energy source. The science of exploration of wind power is not a new one. For the past few centuries, people have been extracting energy from the wind in various ways. One means of converting wind energy to a more useful form is through the use of windmills. Wind power technology in Bangladesh has been growing significantly in the last decade. Capacity of wind turbines has been increased significantly and at the same time, the cost of generating power from wind has come down. For the purpose of wind data, first of all the wind data of the coastal areas in Bangladesh from January to December, 2006 is to be collected and sorted in sequence in appropriate frequency. The data are further analyzed and converted into several useful parameters, like daily mean wind speed, monthly mean wind speed, and mean annual wind speed. After that, the velocity frequency bar graph, energy bar graph, velocity duration curve, etc. have been plotted and analyzed. During the analysis, it has been found that an unusual wind characteristic at sitakundu on September, 2006 with respect to other month. This unusual wind behavior further analysis for determining wind gusts and Weibull parameters. The wind speed data of a location has been fitted to Weibull function to find different parameters for that site. The value of Weibull shape factor (k) and Weibull scale factor (c) have been calculated by different methods and compared and plotted them by employing different methods. Although the peak wind velocity, the equivalent pressure on rigid bodies, and the dynamic along wind response of flexible structures are component parts of the gust buffeting problem, different procedures have been developed in the technical literature with reference to each of these subjects.

**Keywords:** Wind energy, Weibull distribution, Weibull shape factor (k), Weibull scale factor (c), Wind Gusts.

### 1. INTRODUCTION

Sitakundu has been developing a wind load meteorological background to support Sitakundu standards. Wind impact is one of the major loads affecting buildings and other constructions, among which the most affected are the power-transmission pylons of the electrical energy network which can be seriously damaged by wind, resulting in serious collateral damage in different areas. Croatia has to harmonise its standards with European standards and one of its biggest problems is that there is an insufficient number of locations with long-term continuous measurements of wind direction and speed averaged to 10-minute intervals. Namely, the pre-drafts of European standards (ENV 1991.2.4, 1995; CENELEC/TC 11 (SEC) 40, 1997) recommend the use of 10-minute averaged wind speed in the calculation of many parameters. In Croatia, such data are available from 21 locations, for periods longer than three but shorter than ten years. They have been used as the basis for the development of a meteorological background for Croatian standards. However, within this project, for the estimation of locally expected maximal wind speeds, it has been decided to also use wind speed and

direction averaged over hourly periods. Hourly averaged data for longer periods are available at another 24 locations and they are particularly useful to achieve better territorial coverage of the Croatian area observed.

This paper presents a direct application of hourly averaged wind speed data (instead of the recommended 10-minute average) for defining the maximal local instantaneous wind speed (wind gust). Such application has been researched on the example of hourly data from April to September in Sitakundu, 2006. where some of the strongest Croatian gusts had been measured. It is therefore important to know the persistency of strong wind. To define the wind conditions at the Sitakundu that might jeopardise the power-transmission lines, an analysis has been made of the wind speed data for one day in each month when two kinds of maximal monthly speeds were identified for the same month. These are the maximal monthly mean hourly wind speed and the maximal monthly instantaneous wind speed. The relationship of these two maximal speeds has been analyzed. The analysis has been performed by a methodology derived from the methodology for defining

gusts based on mean ten-minute wind speeds as recommended by the pre-draft of European standards for building European power-transmission lines. The simplest form of the relations has been applied to get a first insight into the local gust characteristics and computations. Generally, in attempting to define the local characteristics of gusts in detail, many kinds of analyses have been applied so far. For instance, for an Argentinean location, gusts have been computed for different averaging intervals, their variation with height and the time of year has been analysed, the general form of the vertical wind profile and its dependence on stability conditions have been analysed and compared with those of typical episodes of severe winds (Labraga, 1994). One of the newest physically based parameterization schemes for the computation of wind gusts has been implemented in a numerical Canadian regional climate model (Goyette et al, 2003). A parameterization scheme has been developed in order to use the quantities available at each model time step, including the wind gust computation for each of these time steps. There have been many attempts to relate wind gusts to mean wind speeds averaged over different time scales, and even to mean daily wind speeds.

## 2. WIND DATA

In the present study, the objective is to statistically analyze of wind characteristics in some coastal region of Bangladesh and make a comparison between various methods to determine Weibull parameter. Wind data of some coastal areas in Bangladesh such as Kuakata, Munshigonj, Khagrachari, Kishorgonj, Naogaon, Pakshey, Panchagarh, Rauzan, Sitakundu, Kutubdia (Cox's Bazar) and Teknaf (Cox's Bazar) from January to December, 2006 have been considered [4]. The wind data measured in ten minutes interval and then further processed to hourly time series. All data are supplied by LGED, Renewable energy department.

## 3. OUTLINE OF METHODOLOGY

First of all the wind data of the coastal areas in Bangladesh from January to December, 2006 is to be collected and sorted in sequence in appropriate frequency. The data are further analyzed and converted into several useful parameters, like daily mean wind speed, monthly mean wind speed, and mean annual wind speed. After that, the velocity frequency bar graph, energy bar graph, velocity duration curve, etc. have been plotted and analyzed. During the analysis it has been found that frequently increase the wind characteristic at Sitakundu on August and September, 2006 than other months. This abnormal wind behavior further analyzed for determining wind gusts and other Weibull parameters at that unusual wind behavior at Sitakundu. The wind speed data of a location has been fitted to Weibull function to find different parameters for

that site. The value of Weibull shape factor (k) and Weibull scale factor (c) have been calculated by different methods and compared and plotted them by employing different methods.

Except in the short period of gusts, was on the average relatively high over a longer period, i.e. at least over an hour. The days thus chosen are days when substantial material damage can be expected due to the great strength and relatively long duration of strong wind, and this was the main reason for this research.

For application to the building of electrical power-transmission equipment in Europe, the estimation of wind gusts based on mean ten-minute wind speed values has been initially suggested to be processed as follows

$$V_g = K_g V_{mean} \dots\dots\dots(1)$$

where  $V_g$  is the gust speed (m/s), i.e. the instantaneous maximal wind speed in a measuring interval (T) of 2 seconds,  $V_{mean}$  is the mean ten-minute wind speed (m s<sup>-1</sup>) and  $k_g$  is the gust factor. The gust factor is defined as:

$$k_g = 1 + \frac{2.28}{\ln\left(\frac{z}{z_0}\right)}, \dots\dots\dots(2)$$

where z (m) is the height above ground and  $z_0$  is the roughness length (m), which depends on terrain characteristics. At the Sitakundu and other prospective locations, wind measurements are performed at the usual height above ground, 10m and 20m. i.e. z=10m. The value of the roughness length,  $z_0$ , has been taken as 0.3 m, which is the value defined in most Asian countries for woodland areas like the Bangladeshi area observed.

In equation (2), the log wind profile is used to define the gust. The mean wind speed as a function of height above the ground can be computed by the logarithmic profile.

$$V_{mean} = \frac{u^*}{k} \ln\left(\frac{z}{z_0}\right), \dots\dots\dots(3)$$

where k is the von Karman constant, approximately equal to K= 0.4;  $u^*$  is the friction velocity;  $z_0$  is the surface roughness length; and z is the height above the ground.

The peak gust speed ( $V_g$ ) at height z is computed using Durst's statistical model (Durst, 1960) as follows:

$$V_g(z) = V_{mean}(z) + g(T)\sigma_v(z), \dots\dots\dots(4)$$

where T is the averaging period,  $g(T)$  is the gust peak factor which is a function of T and  $\sigma_v(z) = \sqrt{\beta}u^*$  is the root-mean-square value of the longitudinal fluctuating wind speed at height z, in which  $\beta$  is a terrain dependent coefficient. For  $g(T)$ , the Eurocode uses alternatively factors of 3.7 and 3.5. By including equations (3) and (4) into equation (1), the following gust factor equation is obtained:

$$k_g = \frac{V_g}{V_{mean}} = 1 + g(T)I(z), \dots\dots\dots(5)$$

where  $I(z)$  is the longitudinal turbulence intensity and  $I(z)$  is defined as:

$$I(z) = \frac{\sigma_v(z)}{V_{mean}(z)} \dots\dots\dots(6)$$

Equations (4), (5) and (6) indicate that the constant 2.28 in (2) is calculated as:

$$2.28 = g(T) \sqrt{\beta k} \dots\dots\dots(7)$$

Strong gusts have been assumed to characterize the daily weather conditions which significantly affect the values of the individual mean hourly wind speeds during the whole day and not only the value of the mean ten-minute speed at the time of the gust. Because of this assumption, and because there are no ten-minute data available for many locations in Croatia, the recommended equation (1) has been modified and the following modification has been tested:

$$V_g = k_g V_{MAX} \dots\dots\dots(8)$$

where  $k_g$  is the same parameter value as in equation (2),  $V_{MAX}$  is the maximal mean hourly speed for a particular month and  $V_g$  is the expected maximal gust on the same day.

The values of the maximal monthly gusts estimated on the basis of equation (8) have been compared with the measured maximal monthly gusts. It has been established that this equation should be further modified for all maximal mean hourly wind speed classes, for both bura and jugo. The modification of equation (8) has been carried out for all wind speed classes. All equations, derived individually for every maximal mean hourly wind speed class, have the following form:

$$V_g = k_g V_{MAX} + C \dots\dots\dots(9)$$

where  $C$  is the constant, which is different for each particular wind speed class and for the same wind speed. Constant  $C$  represents the mean difference between the individual measured wind gusts in the particular speed class considered and the associated wind gusts calculated by using equation (8).

#### 4. ESTIMATION OF THE WEIBULL PARAMETERS FROM THE PROCESSED DATA:

The Weibull distribution shows its usefulness when the wind data of reference station are being used to predict the wind regime in the surrounding of that station. The idea is that only annual or monthly average wind speeds are sufficient to predict the complete frequency distribution of the year or the month. This section deals with methods to extract the Weibull parameter  $k$  and  $c$  from a given set of

data. There are several methods by which  $k$  and  $c$  can be determined. Three different methods are described below.

1. Weibull paper/ Regression analysis
2. Standard - deviation analysis
3. Energy pattern factor analysis.

### 5. RESULT AND DISCUSSION

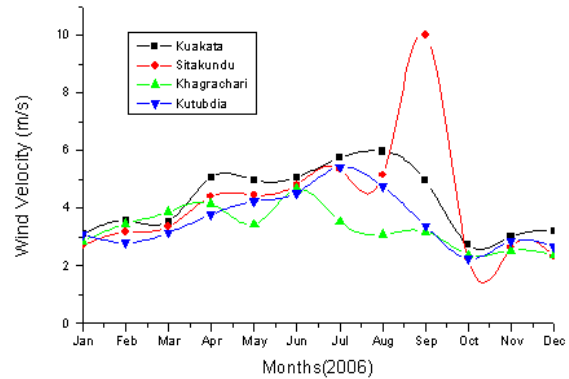


Fig 1. Monthly Average Wind Speed Curve for most Prospective Wind Sides at 2006.

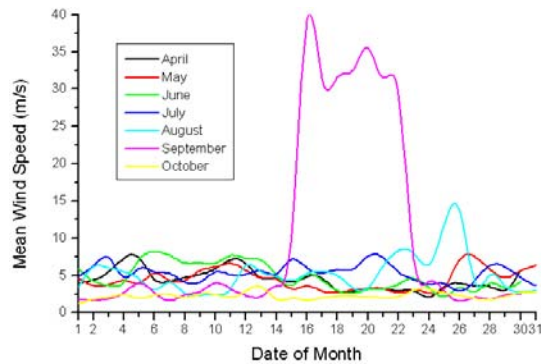


Fig 2: Daily Average Wind Speed Curve at Sitakundu, 2006.

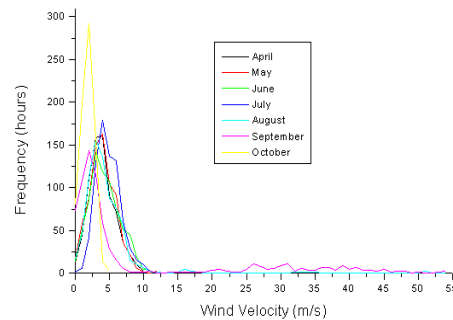


Fig 3: Frequency Vs. Wind Speed Curve at Sitakundu, 2006.

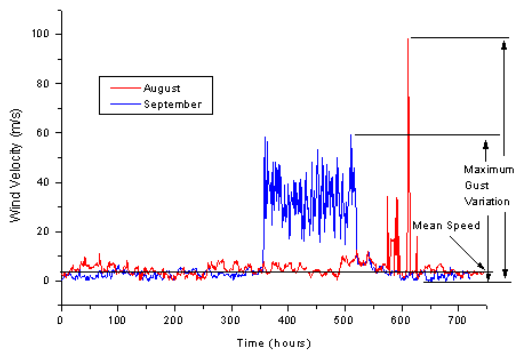


Fig 4: Instantaneous Variation of Wind Velocity at Sitakundu, 2006.

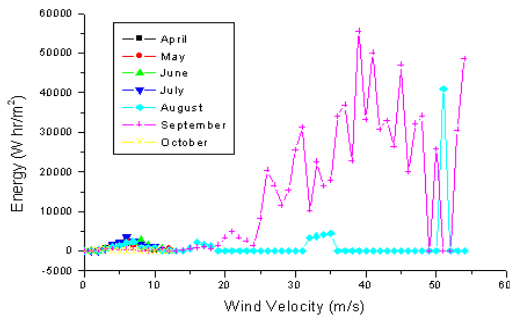


Fig 5. Energy Vs. Wind Velocity Curve at Sitakundu, 2006

### 5.1: Find Out Of Weibull Parameters

Weibull Parameters i.e shape factor 'K' and scale factor 'C' is very important for wind data analysis. Where shape factor 'K' is a dimensionless number and scale factor 'C' in m/s.

Value of  $k$  and  $C$  by Various Methods

Table 1: Weibull paper Method.

Location	Month	K	C
Sitakundu,06	April	2.10	4.97
	May	1.90	5.03
	June	2.00	5.43
	July	2.20	6.02
	August	1.95	5.66
	September	1.32	10.83
	October	1.90	2.56

Table 2: Standard Deviation Method

Location	Month	K	C
Sitakundu,06	April	2.40	4.98
	May	2.41	5.04
	June	2.32	5.43
	July	3.19	4.88
	August	2.09	3.47
	September	1.10	2.23
	October	2.19	2.57

Table 3: Energy Method

Location	Month	K	C
Sitakundu,06	April	2.40	4.97
	May	2.42	5.04
	June	2.28	5.43
	July	3.00	5.97
	August	Out of Range	Not Applicable
	September	Out of Range	Not Applicable
	October	2.52	2.56

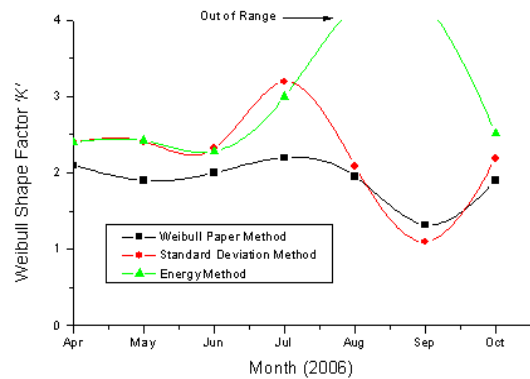


Fig 6: Weibull Shape Factor 'K' curve by different Methods.

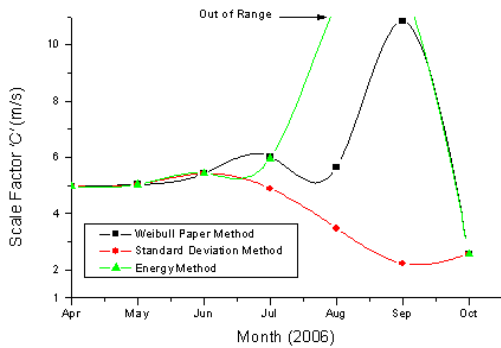


Fig 7: Weibull Scale Factor 'C' curve by different Methods.

## 6. DISCUSSION

From the Table and graphs, it is clear that the wind behavior at Sitakundu (August to October), 2006 is irregular than any other prospective sides (Fig 1). Then the analysis has been carried out on seven month from April to October. The diurnal variation of wind speed has shown in (Fig 2), where hourly average wind speed has been plotted and it shown that Sitakundu, August and September wind behavior is so rough. At September, 14 to 24 average wind speed is above 32 m/s which is very harm full for wind turbine, constructions and power transmission lines ect. Frequency Vs. Wind Speed Curve shown in (Fig 3:), which shown that most of the month wind speed 2-5 m/s is higher frequency and August and September some frequency have wind speed 10 to 54 m/s. Maximum wind Gust is clearly shown in (Fig 4), where at sitakundu 350<sup>th</sup> to 530<sup>th</sup> hours i.e 180 hours wind Gust is higher than 42 m/s. Weibull Parameters i.e shape factor 'K' and scale factor 'C' has been calculated by Weibull Paper method (Table -1), Standard deviation method (Table -2) and Energy method (Table -3). By Energy method, both K and C value at August and September is out of range. Because of the irregularity of wind velocity and high magnitude of wind Gust.

## 7. CONCLUSION

In this study, assessments of wind characteristic for Coastal region of Bangladesh were made. The following conclusion can be drawn from the present analysis. The shape factor (k) and scale factor (c) are determined for each month. It is found that the value of k remains between 1.90 to 3.19 and that of c remains between 2.56 to 10.89. The most of the Weibull functions follow very close to the Raleigh function (k=2) for the selected sites. The Weibull probability distribution scale parameters (c) are consistently higher in values and variability than the shape parameters (k) monthly distributions. Both steps of the modification developed proved usable. In the first step, the mean ten-minute wind speed data input in the pre-draft of the European standard model was replaced by a mean hourly

data input, because of the availability of long-term hourly averaged data for a large part of the Sitakundu. Long-term data provide an insight in the climatological characteristics of the location observed. Therefore, in the few cases where the derived relations for Sitakundu proved unsuitable (Fig 2,4,5,6 and 7), they point at a cluster of cases which have to be taken as locally exceptional and rare but possible. In further wind gust investigations some other forms of relationship between gust speed and mean hourly speed will be investigated for the Selected location. The intention is to find a universally applicable form of wind gust calculation.

## 8. REFERENCES

1. "Wind Energy Resources Mapping (WERM), 2003", a project of Local Government Engineering Department (LGED) financed by United Nation Development Program (UNDP).
2. Choi, E. C. C. and Hidayat, F. A. (2002): Gust factor for thunderstorm and non-thunderstorm winds, Journal of wind engineering and industrial aerodynamics, 90, 1683–1696.
3. Davenport, A. G. (1965): The relationship of wind structure to wind loading. Proc. of Conf. On Wind Effects on Structures., National Physical Laboratory 54–102.
4. Chowdhury, S.C., Ramana Rao, B.V. and Sharma P. (1981) "Performance of low-cost Sail-Wing Windmill", Journal of Agriculture Mechanization in Asia, Africa and Latin America, Vol. 12, No. 1: pp 66-68
5. Goyette S., Brasseur, O. and Beniston, M. (2003): Application of a new wind gust parameter sation: Multiscale case studies performed with the Canadian regional climate model – art. no. 4374, J. Geophys. Res. – Atmos. 108.
6. Jungo, P., Goyette, S. and Beniston, M. (2002): Daily wind gust speed probabilities over Switzerland according to three types of synoptic circulation, Int. J. Climatol., 22, 485–499.
7. Panda, R.K. and Clerk, R.N. (1999), "Stochastic Study of Windpumps with Reservoir in Southern High Planes", Journal of Energy Engineering. Vol. 125, No. 3: pp79-93
8. Alam, M. M. and Burton, J. D. (1998) "The Coupling of Wind Turbine to Centrifugal Pumps", Journal of Wind Engineering. Vol. 22, No. 5: pp223-234
9. Siddig, M. H. (1997). "The Feasibility of Using Wind Pump in Zimbabwe", Journal of Wind Engineering, Vol. 21, No. 4: pp 227-236
10. Suresh, R. and Block, D.S. (1998), "Field Testing of Geared Type Deep Well Wind Pumps in India", Journal of Wind Engineering. Vol. 22, No. 2: pp117-129

11. Hussain, M., Alam, S. Reza, K.A. and Sarkar, M, “A Study of Wind Speed and Wind Energy Characteristics in Bangladesh”, Journal of Conversion Management.. Vol. 26, No. 3/4: pp 321-327
12. Robert, G., Kortenkamp, R. and Twele, J. (1997), “A Simple Method for Near Optimum Design of Wind Turbines with Centrifugal Pumps”, Journal of Wind Engineering. Vol.11, No. 5, pp: 293-312
13. Siddig, M.H. (1996), “Design Optimization of Wind Powered Piston Pumps”, Journal of Wind Engineering. Vol. 20, No. 25: pp 63-71
14. Sarkar, M. and Hussain, M. (1991), “The Potential of Wind Electricity Generation In Bangladesh”, Journal of Renewable Energy. Vol. 1, No. 5/6: pp 855-857
15. Hussain, M., Alam, S. Reza, K.A. and Sarkar, M, “A Study of Wind Speed and Wind Energy Characteristics in Bangladesh”, Journal of Conversion Management.. Vol. 26, No. 3/4: pp 321-327.

## 9. NOMENCLATURE

Symbol	Meaning	Unit
K	Shape factor	...
C	Scale factor	m/s
$K_E$	Energy pattern factor	...
$f(v)$	Provability density function	...
A	Area	$m^2$
E	Available energy	$wh/m^2$
$\rho$	Air density	$Kg/m^3$
$\sigma$	Standard Deviation	....
v	Velocity of Air	m/s
N	Total number of hours	hurs
T	Total time	hurs
$P(v)$	Wind Power	W
$p(v)$	Wind power density	$W/m^2$
P	Power	wat
$V_{mean}$	Mean wind Speed	m/sec
R	Correction Co-efficient	...
$V_g$	Gust Speed	m/s
$K_g$	Gust Factor	....
Z	Height above the ground	m
$Z_0$	Roughness length	m
$g(T)$	Gust peak factor	....
$I(z)$	Longitudinal turbulence intensity.	....

## FIXED BED PYROLYSIS OF DATE SEED WASTE FOR LIQUID OIL PRODUCTION

M. Nurul Islam, S. M. Najmul Hoque and M. U. Hossain Joardder

Department of Mechanical Engineering  
Rajshahi University of Engineering & Technology, Rajshahi, Bangladesh

### ABSTRACT

The conversion of biomass waste in the form of date seed into pyrolysis oil by fixed bed pyrolysis reactor has been taken into consideration in this study. A fixed bed pyrolysis has been designed and fabricated for obtaining liquid fuel from these date seeds. The major component of the system are fixed bed pyrolysis reactor, liquid condenser and liquid collector. The date seed in particle form is pyrolysed in an externally heated 7.6 cm diameter and 46 cm high fixed bed reactor with nitrogen as the carrier gas. The reactor is heated by means of a biomass source cylindrical heater from 400°C to 600°C. The products are oil, char and gas. The reactor bed temperature, running time and feed particle size are considered as process parameters. The parameters are found to influence the product yield significantly. A maximum liquid yield of 50 wt. % is obtained at a reactor bed temperature of 500°C for a feed size volume of 0.11- 0.20 cm<sup>3</sup> with a running time of 120 minutes. The pyrolysis oil obtained at this optimum process conditions are analyzed for some fuel properties and compared with some other biomass derived pyrolysis oils and also with conventional fuels. The oil is found to possess favorable flash point and reasonable density and viscosity. The higher calorific value is found to be 28.636 MJ/kg which is significantly higher than other biomass derived pyrolysis oils.

**Keywords:** Renewable Energy, Pyrolysis Oil, Fixed Bed, Date Seeds.

### 1. INTRODUCTION

Biomass has been recognized as a major renewable energy source to supplement declining fossil fuel sources of energy [1]. It is the most popular form of renewable energy and currently biofuel production is becoming very much promising [2]. Transformation of energy into useful and sustainable forms that can fulfill and suit the needs and requirements of human beings in the best possible way is the common concern of the scientists, engineers and technologists. From the view point of energy transformation, pyrolysis is more attractive among various thermo chemical conversion processes because of its simplicity and higher conversion capability of biomass and its solid wastes into liquid product. Pyrolysis is generally described as the thermal decomposition of the organic components in biomass wastes in absence of oxygen at mediate temperature (about 500°C) to yield tar (bio oil, bio fuel, bio crude), char (charcoal) and gaseous fractions (fuel gases). Pyrolysis may be either fixed bed pyrolysis or fluidized bed pyrolysis. In fixed bed pyrolysis, a fixed bed pyrolyser is used. The feed material in the reactor is fixed and heated at high temperature. As the feed is fixed in the reaction bed (reactor), it is called fixed bed pyrolysis. In this process, the feed material is fed into the reactor and heat is applied externally. Usually nitrogen is used as

inert gas for making inert condition and for helping the gaseous mixture to dispose of the reactor. The losses in fixed bed pyrolysis are relatively less than fluidized bed pyrolysis. A possible reaction pathway of pyrolysis process is shown in Figure 1. This technology is spreading with research and experimental work in many countries of the present world [3]. Energy is the major requirement of modern society, its development and management carries a lot of significance in the economic development of any country. There is a close relationship between the level of energy consumption in a country and its economic development. The energy consumption in the world has been growing at an alarming rate. By the year 2100, the world population is expected to be more than 12 billion and it is estimated that the demand for energy would increase by five times the current demand [4]. Under such circumstances, man has to find out some sources of energy for his survival that be able to meet considerable part of the energy demand in future. In this contest, fixed bed pyrolysis system from the date seed is one of the promising sources of energy. Dates are grown extensively in the whole world especially in Middle East and Asia. According to UN Food & Agriculture Organization in 2005, the top ten date producer countries produced 1.67 billion tons of dates. The seeds of these dates are almost unutilized. This waste may be used for



energy recovery as fuel.

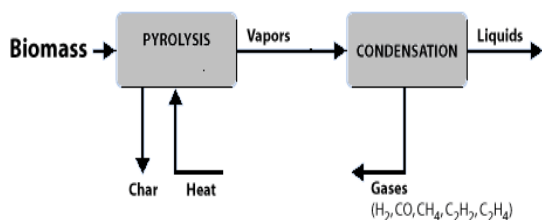


Fig 1. A possible reaction pathway of pyrolysis of organic solid waste

The pyrolysis oil is of moderate heating value, is easily transported, can be burnt directly in the thermal power plant, can possibly be injected into the flow of a conventional petroleum refinery, burnt in a gas turbine or upgraded to obtain light hydrocarbons for transport fuel [5]. Besides these, there are scopes to upgrade the oil to obtain high grade fuel and valuable chemicals. The solid char can be used for making activated carbon. The char has its potential as a solid fuel [5].

## 2. MATERIALS AND METHODS

### 2.1 Material

Date seed is collected locally in Rajshahi (Bangladesh). The feedstock is ground and cut into three different volume sizes and is finally oven dried for 24 hours at 110 °C prior to pyrolysis. The higher heating value of date seed is found to be 18.936 MJ/kg. The proximate analysis of date seed is presented in Table 1.

Table 1: Higher heating value and proximate analysis of date seed [6]

Moisture	Oil	Crude fiber	Carbohydrates	Ash
5-10%	7-10%	10-20%	55-65%	1-2%

### 2.2 Experimental Setup

Date seed is pyrolyzed in an externally heated stainless steel fixed bed reactor system. The main components of the system are fixed bed reactor, liquid condenser and ice cooled liquid collectors. The effective length of the reactor is 46 cm and the diameter is 7.60 cm. The schematic diagram of the fixed bed pyrolysis system is shown in Figure 2. The reactor is heated externally by a biomass heater at different temperatures ( 400, 450, 500, 550 and 600°C) and this temperature is measured by means of a mercury thermometer. Nitrogen gas is supplied in order to maintain the inert atmosphere in the reactor, and to dispose of the pyrolyzed vapor products to the condenser. Pyrolysis vapor is condensed into liquid in the condenser and then is collected in the liquid collectors. The non-condensed gas is flared to the atmosphere.

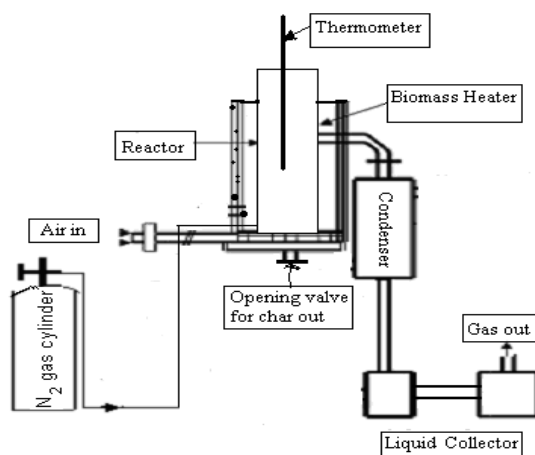


Fig 2. Schematic diagram of fixed bed pyrolysis system

## 3. RESULT AND DISCUSSION

### 3.1 Product Yield

The products obtained from the pyrolysis of date seed are liquid oil, solid char and gas. At an operating temperature of 500 °C for a feed size volume of 0.11-0.2cm<sup>3</sup> (quarter of date seed) at a gas flow rate of 5 liter/min with a running time of 120 minute, liquid production is found to be the maximum (50 wt%) of the dry feedstock.

### 3.2 Effect of Operating Temperature

The relationship between the variation of percentage of mass of liquid, char, and gaseous products at different reactor bed temperature is presented in Figure 3. The results show that as the operating temperature is increased, the liquid yield is increased up to 500 °C at a liquid yield of 50 wt%. After this temperature, the liquid yield decreased. At a lower temperature of 400 °C, the liquid product is found to be 30 wt% of the dry feedstock. The higher temperature above 500<sup>0</sup> C may cause secondary cracking reaction of the vapors, yielding more gas at the cost of liquid product. On the other hand the reason for the lower liquid yield at lower temperature may be due to fact that the temperature is not enough for complete pyrolysis to take place.

### 3.3 Effect of Feed Particle Size

Figure 4 represents the percentage mass of liquid and solid char products for different feed particle size of feed at a bed temperature of 500 °C and an operating time of 120 minutes. It is observed that at 500 °C the percentage of liquid collection is maximum at 50% of total biomass feed for particle size volume of 0.11-0.20 cm<sup>3</sup>. Liquid yield is found to be maximum for the smaller particles because the larger size particles might not be adequately heated up so rapidly causing incomplete pyrolysis.

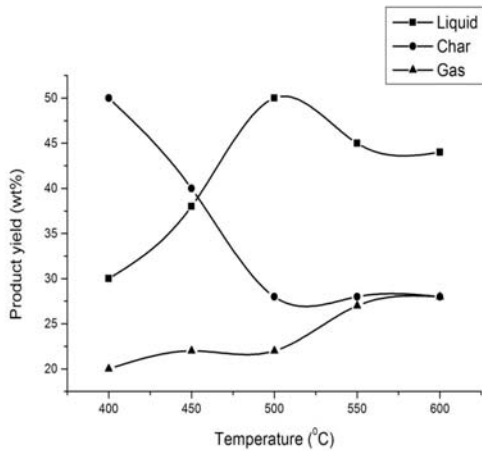


Fig 3. Effect of operation temperature on product yield.

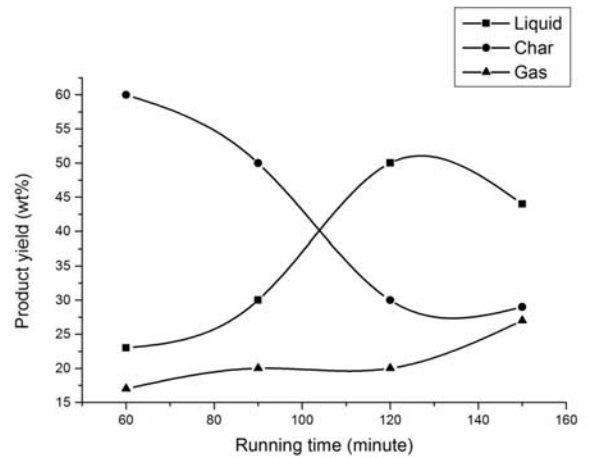


Fig 5. Effect of running time on product yield

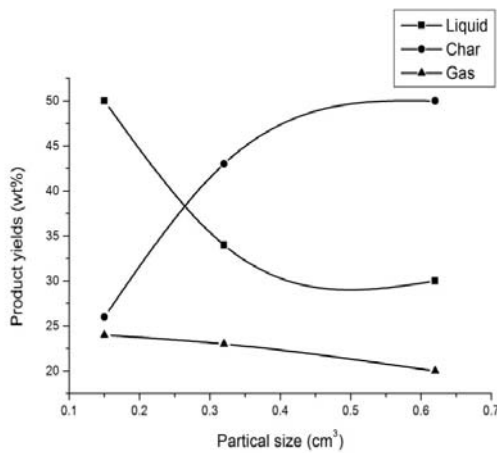


Fig 4. Effect of feed particle size on product yields.

plotted result shows that the liquid yield increases with the increase of running time. The maximum liquid product is found to be 50 wt% of biomass feed while the solid char product is 32 wt% of dry feed at 120 minutes. After this, the liquid product yield is not optimum that may be due to complete devolatilization of the feedstock and higher rate of gas discharge.

#### 4. ANALYSIS OF PYROLYSIS OIL

##### 4.1 Physical Property Analysis of Pyrolysis Oil

The energy content of the oil is 28.636 MJ/kg. The oil is found to be slightly heavier than water with a density of 1042.4 kg/m<sup>3</sup> at 26 °C. The flash point of the oil is 126 °C and hence precautions are not required in handling and storage at normal atmosphere. The low viscosity of the oil of 6.63 cSt at 26 °C is a favorable feature in the handling and transportation.

##### 4.2 Comparison with other Biomass Derived Oil and Diesel Fuel

Table 2 shows the characteristics of the pyrolysis oil derived from date seed in comparison with other biomass derived oils and diesel fuel. It is evident that the density and viscosity of date seed oil is favorable than other pyrolysis oils and very much closer to diesel. The higher heating value of date seed oil is found to be higher than other biomass derived oil.

Table 2: Comparison of date seed pyrolysis oil with biomass derived pyrolysis oil

Analysis	Date seed oil	Waste paper oil [7]	Sugarcane bagasse oil [8]	Jute stick oil [8]
Kinematic viscosity at 26°C (cSt)	6.63	2.00	89.34	12.8
Density (kg/m <sup>3</sup> )	1042.4	1205	1198	1224
Flash Point (°C)	126	200	105	>70
HHV(MJ/kg)	28.636	13.10	20.072	21.091

Table 3: Comparison of date seed pyrolysis oil with diesel fuel

Analysis	Date seed oil	Diesel [9]	Heavy fuel oil [10]
Kinematic viscosity at 26°C (cSt)	6.63	2.61*	200 <sup>#</sup>
Density (kg/m <sup>3</sup> )	1042.4	827.1*	980*
Flash Point (°C)	126	53	90-180
HHV(MJ/kg)	28.636	45.18	42-43

## 5. CONCLUSION

The biomass solid waste in the form of date seed is successfully converted into liquid, char and gas by fixed bed pyrolysis system. The heating value of the pyrolysis oil is found to be 28.64 MJ/kg, which is higher than other biomass derived pyrolysis oils and also significantly higher than that of solid date seed waste. The maximum liquid yield is found to be 50 wt% of dry biomass feedstock at the temperature range of 500 °C. The density and viscosity of the liquid are greater than that of diesel. However, the oil from the date seed may be considered as an important candidate of potential source of alternative fuel,

## 6. REFERENCES

1. Williams, P.T., Halim, S. And Taylor, D.T., 1992, "Pyrolysis of Oil Palm Solid Waste", in: Grassi G, Collina A, Zibetta H, Editor. Biomass for Energy, Industry and Environment, London: Elsevier Applied Science. PP 757-761.
2. M. N. Islam and F. N. Ani, 1998 "Characterization of Bio-Oil from Palm Shell Pyrolysis with Catalytic Upgrading," Renewable Energy Congress, Elsevier Science, PP 1977-1990.
3. A.V. Bridgwater and S. A. Bridge, 1991 "A Review of Biomass Pyrolysis and Pyrolysis Technologies," In Biomass Pyrolysis Liquids Upgrading and Utilization, Edited by A. V. Bridgwater and G. Grassi, Elsevier Applied Science London, , PP LI-92.
4. A. T.Marshall,. & J. M. Morris, August,2006. "A Watery Solution and Sustainable Energy Parks", CIWM Journal. P22-23.
5. P.A. Horne, and P.T Williams. 1994. "Premium Quality Fuels and Chemical from The Fluidized Bed Pyrolysis of Biomass with Zeolite Catalyst Upgrading". Renewable Energy 5(2): 810-812,
6. Julia F. Morton, Miami FL, 1987 " Fruits of Warm Climates" Chapter-Date.PP 5-11.
7. M. N.Islam, M. N.Islam, M. R.A. Beg, M. R. Islam 2004 "A Work on Pyrolytic Oil from Fixed Bed Pyrolysis of Municipal Solid Waste and Its Characterization". Renewable Energy 30, PP 413-420.
8. M.R Islam, M.N. Nabi, and M.N.Islam, 2001, "Characterization of Biomass Solid Waste for Liquid Fuel Production", 4th International Conference on Mechanical Engineering (ICME 2001), Bangladesh, PP 77-82.
9. R.G.Andrews, and P.C. Patniak, 1996 "Feasibility of Utilizing A Biomass Derived Fuel for Industrial Gas Turbine Applications ",in: Bridgwater AV, Hogan EN, Editor. Bio-Oil Production & Utilization, Berkshire: CPL Press, PP 236-245.
10. F. Rick, and U. Vix,2000 " Product Standards For Pyrolysis Products for Use as Fuel in Industrial Firing Plants", in Bridgwater AV, Grassi G, Editor. Biomass And Bio Energy Journal.

## 7. NOMENCLATURE

Symbol	Meaning
cm	Centimeter
°C	Degree Celsius
wt%	Weight Percentage
MJ	Mega Joule
Kg	Kilogram
cSt	Centistokes

## 8. MAILING ADDRESS

Mohammad Nurul Islam  
Department of Mechanical Engineering  
Rajshahi University of Engineering & Technology,  
Rajshahi-6204, Bangladesh  
Phone & Fax: +880721-750319,  
E-mail: [shumon99234@yahoo.com](mailto:shumon99234@yahoo.com)

## OPTIMIZATION STUDY OF A SOLAR-OPERATED LITHIUM BROMIDE-WATER COOLING SYSTEM WITH FLAT PLATE COLLECTORS

K. K. Datta Gupta<sup>1</sup>, D. N. Basu<sup>1</sup> and S. Chakravarti<sup>2</sup>

<sup>1</sup>Dept. of Mechanical Engg., Bengal Engg. & Science University, Howrah, West Bengal, India

<sup>2</sup>B.P. Poddar Institute of Management & Technology, Kolkata, West Bengal, India

### ABSTRACT

A general theoretical study on the design and optimization of the solar-operated LiBr-H<sub>2</sub>O cooling system has been undertaken. The results of the study show that, in general for fixed initial conditions and given system cooling capacity, there exists an optimum generator temperature at which the required collector area is minimum. From the study it has also been revealed that for a single-stage LiBr-H<sub>2</sub>O cooling system flat plate collectors with two covers are preferable.

**Keywords:** Absorption Cooling Cycle, Flat Plate Collector, COP.

### 1. INTRODUCTION

Solar energy is gaining popularity because it increases energy independence and sustainability leaving no negative impact on the environment. Absorption cooling is one of the first and oldest forms of air-conditioning and refrigeration system which uses thermal energy to produce cold, and thus solar energy, waste heat and other forms of low grade heat can be employed. Since the demand for cooling, whether for comfort or food preservation, is greatest at the time of maximum solar radiation, the seasonal and diurnal variations of solar insolation matches very well with the demand for cooling. Thus the utilization of solar energy for absorption cooling systems has been a very popular field of research for the scientific communities. The basic findings of these activities is the demonstrative ability of flat plate collectors to achieve required temperatures necessary for operation of LiBr-H<sub>2</sub>O cooling system.

Alizadeh et al.[1] have carried out performance comparison of solar operated LiBr-H<sub>2</sub>O and NH<sub>3</sub>-H<sub>2</sub>O cooling systems, and concluded that LiBr-H<sub>2</sub>O system is simpler and operates with higher cooling ratio and heat exchanger parameter. Ward [2] has studied the technical and economic feasibilities of solar operated absorption cooling system viz-a-viz the conventional vapour compression cooling systems. Results indicate that the thermodynamic efficiency of solar absorption cooling is very nearly equivalent to that of an electrically-driven vapour compression system and economically solar absorption cooling is marginal, but improves significantly with tax incentives. Mansoori and Patel [3] have presented a comparative study for different combinations of refrigerant-absorbent: NH<sub>3</sub>-H<sub>2</sub>O,

NH<sub>3</sub>-NaSCN and LiBr-H<sub>2</sub>O and concluded that LiBr-H<sub>2</sub>O combination is preferred for localities with high environmental temperatures. Li and Sumathy [4] have carried out simulation of a solar air conditioning system with a single storage tank, and concluded that a system with a partitioned hot water storage tank results a quicker early-hour cooling effect and higher overall system COP as compared to a normal stratified storage tank. Using TRANSYS software and weather parameters of Cyprus, Florides et al.[5] have carried out modeling and simulation to compare the performance of a solar assisted LiBr-H<sub>2</sub>O cooler powered by three different types of solar thermal collectors, and concluded that for a cooling load of 1.5 ton, the optimized system consists of a 15m<sup>2</sup> compound parabolic collector with a 600l capacity hot water storage tank. Liu and Wang [6] have presented performance prediction of a solar/gas driven double effect LiBr-H<sub>2</sub>O cooling system where solar energy together with high pressure water vapour from high pressure generator supply heat to the low pressure generator. Simulation results demonstrate that this kind of double effect absorption system is feasible both technically and economically. Fathi et al.[7] have presented performance analysis of a solar absorption refrigerator by considering four temperature reservoirs and both internal and external irreversibilities to predict optimal design and operating conditions. Assilzadeh et al.[8] have carried out modeling and simulation for a LiBr-H<sub>2</sub>O cooler using TRANSYS program and solar radiation data for Malaysia. The results presented show that the system performance is in phase with the diurnal variation of solar radiation. For optimum generator temperature and higher system reliability, a hot water storage tank has been recommended. Mittal et al.[9] have

reported the the effects of hot water inlet temperatures on COP, contributed solar fractions and surface areas of cooling system components. Ardehali et al.[10] developed a computer code to simulate the performance of a solar assisted LiBr-H<sub>2</sub>O cooling system, and examined the effect of clearness index on the auxiliary heating source. Based on experimental results of a solar absorption cooling system in Spain, Rodriguez et al.[11] have reported saving in conventional energy and economy, and reduction in CO<sub>2</sub> emission. Mazloumi et al.[12] have carried out simulation of a single effect LiBr-H<sub>2</sub>O cooling system for a city in Iran powered by parabolic trough collectors with a hot water storage tank. For a cooling load of 5 ton, they have recommended a minimum collector area of 57.6 m<sup>2</sup>.

The objective of this paper is the conjugate analyses of the solar collector and LiBr-H<sub>2</sub>O cooling systems to predict the overall system performance with the help of a computer program. Finally, schemes have been evolved to determine the relative amount of collector material required for optimum system performance, and to observe the influence of number of glass cover(s) on the performance of the whole system in the operating regime of the generator.

## 2. MATHEMATICAL MODEL

### 2.1 Absorption Refrigeration System

Fig.1. illustrates the schematic diagram of a solar operated LiBr-H<sub>2</sub>O absorption cooling system which operates on two pressure levels: low pressure in the

extracting heat ( $Q_E$ ) from the cooling load, and enters the absorber where it is absorbed by the strong solution returning from the generator via the liquid-liquid heat exchanger and the expansion valve. The weak solution thus formed in the absorber is pumped back to the generator via the heat exchanger. In the generator external heat addition ( $Q_G$ ) from the solar collector causes boiling of the solution resulting in the formation of water vapour which enters the condenser and leaves as saturated liquid, thus completing the cycle.

In order to relate the characteristics of the cooling cycle to the properties of the working fluids, mass and energy balances are to be performed on each component by taking a control volume around each of them. Several assumptions are made to simplify the analysis, two important ones are that the system is operating under the steady state condition and the pump work is negligible. The following equations are obtained:

$$\text{Evaporator: } Q_E = m_w (h_{10} - h_9) \quad (1)$$

$$\text{Absorber: } Q_A = m_{ss} h_6 + m_w h_{10} - m_{ws} h_1 \quad (2)$$

$$\text{Generator: } Q_G = m_w h_7 + m_{ss} h_4 - m_{ws} h_3 \quad (3)$$

$$\text{Condenser: } Q_C = m_w (h_7 - h_8) \quad (4)$$

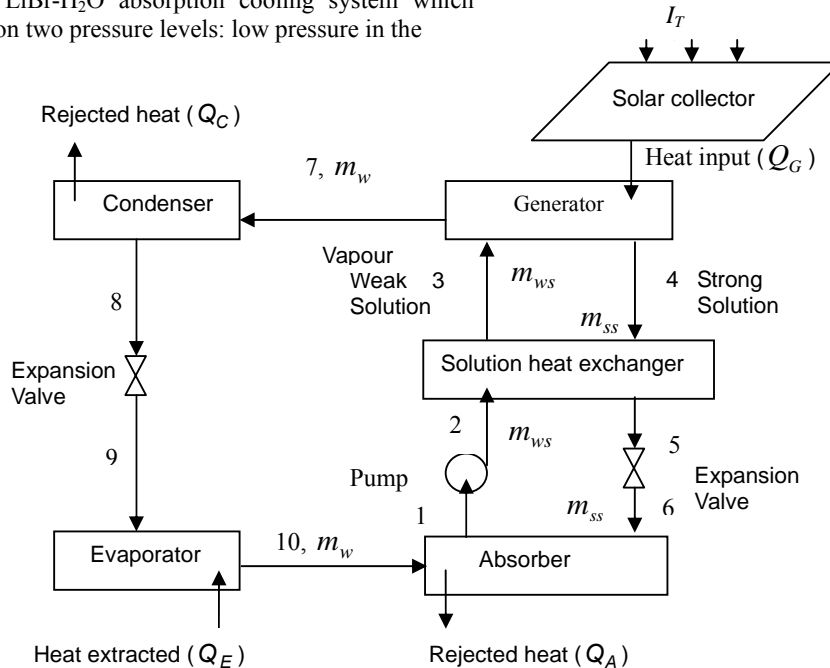


Fig 1. Schematic of solar-operated LiBr-water absorption system

evaporator and absorber, and high pressure in the generator and condenser. High pressure liquid refrigerant (water) leaving the condenser undergoes a throttling process in the expansion valve and enters the evaporator as a low-pressure, low-quality wet vapour. The refrigerant leaves the evaporator as saturated vapour after

From the mass balance the relation between the mass of refrigerant (water),  $m_w$ , and the mass of weak solution leaving the absorber,  $m_1$ , is obtained as

$$m_w = m_1 (X_4 - X_3) / X_4 \quad (5)$$

where  $X_4$  and  $X_3$  are the concentrations of LiBr in the solution at the generator outlet and inlet respectively. The ratio of mass of weak solution leaving the absorber,  $m_{ws}$ , to the ratio of mass of refrigerant,  $m_w$ , is called circulation factor.

Finally,

$$(COP)_{cycle} = \frac{Q_E}{Q_G} \quad (6)$$

$$(COP)_{system} = \frac{Q_E}{Q_S} \quad (7)$$

where  $Q_S$  is the solar radiation incident on the collector plane. It can be easily shown that

$$(COP)_{system} = (COP)_{cycle} \times \eta_c \quad (8)$$

where  $\eta_c$  is the collector efficiency.

## 2.2 Solar Collector

A flat plate collector is the most simple and widely used means to convert solar radiation into useful heat. The useful heat gain ( $Q_U$ ) by the working fluid is given by [13]

$$Q_U = A_c F_R [S - U_c (T_{fi} - T_a)] \quad (9)$$

where  $A_c$  is collector area,  $F_R$  is collector heat removal factor,  $S$  is absorbed solar radiation,  $U_c$  is collector loss coefficient,  $T_{fi}$  and  $T_a$  are collector fluid inlet and ambient temperatures respectively. Absorbed radiation,  $S$  is given by

$$S = I_T (\tau\alpha)_e \quad (10)$$

where  $(\tau\alpha)_e$  is the effective transmissivity-absorptivity product and  $I_T$  is the solar radiation flux on the collector plane.

Collector loss coefficient,  $U_c$  is given by [13]

$$U_c = U_t + U_b + U_s \quad (11)$$

where  $U_t$ ,  $U_b$ , and  $U_s$  are top loss, bottom loss and side loss coefficients respectively.

Top loss coefficient  $U_t$  is given by [14]

$$U_t = \left[ \frac{N}{\left( \frac{C}{T_{PM}} \right) + \left( \frac{T_{PM} - T_a}{N + f} \right)^{0.252}} + \frac{1}{h_w} \right]^{-1} + \left[ \frac{\sigma (T_{PM}^2 + T_a^2) [T_{PM} + T_a]}{1 + \frac{2N + f - 1}{\varepsilon_c + 0.0425N(1 - \varepsilon_c)} + \frac{2N + f - 1}{\varepsilon_g} - N} \right] \quad (12)$$

In the above equation  $N$  is the number of cover(s),  $T_{PM}$  is mean plate temperature,  $\sigma$  is Stefan Boltzman constant,  $\varepsilon_c$  and  $\varepsilon_g$  are emissivity of collector plate and glass cover respectively, and

$$f = \left( \frac{9}{h_w} - \frac{30}{h_w^2} \right) \left( \frac{T_a}{316.9} \right) (1 + 0.091N) ,$$

$$C = \frac{204.429 (\cos\beta)^2}{L^{0.24}} , \text{ and}$$

$$h_w = 0.86(\text{Re})^{-1/2} \rho_a C_{pa} V_a \text{Pr}^{-2/3}$$

Collector heat removal factor,  $F_R$  is given by [14]

$$F_R = \frac{\dot{m}_w C_{pw}}{U_c A_c} \left[ 1 - \exp \left( - \frac{F' U_c A_c}{\dot{m}_w C_{pw}} \right) \right] \quad (13)$$

where  $A_c$  is the collector area and  $F'$  is the collector efficiency factor. Ignoring collector bond resistance, collector efficiency factor,  $F'$  is given by [14]

$$F' = \frac{1}{W U_c \left[ \frac{1}{U_c (2L_f F + D_o)} + \frac{1}{\pi D_i h_i} \right]} \quad (14)$$

where  $W$  is collector tube spacing,  $L_f$  is fin length,  $h_i$  is tube to fluid heat transfer coefficient,  $D_i$  and  $D_o$  are collector tube inner and outer diameters.  $F$  is fin efficiency and is given by [13]

$$F = \frac{\tanh \{ m (W - D_o) / 2 \}}{m (W - D_o) / 2} \quad (15)$$

$$m = \sqrt{U_c / K_c t_c} \quad (16)$$

where  $K_c$  is the thermal conductivity of collector plate material,  $t_c$  is thickness of collector plate.

Thermal efficiency of the collector is given by [13]

$$\eta = F_R(\tau\alpha)_e - U_c F_R \frac{T_{fi} - T_a}{I_T} \quad (17)$$

### 3. COMPUTATIONAL SIMULATION

LiBr-H<sub>2</sub>O cooling cycle has been analysed by evaluating the properties of the working fluids expressed in polynomial equations given by [15, 16]. The simulation has been carried out for specific temperatures and pressures in the evaporator and condenser, while the generator temperature has been varied from 65°C to 95°C taking a step of 1°C. For solar collectors, the transmissivity-absorptivity product  $(\tau\alpha)_e$  of the cover-absorber system has been taken from [14]. Top loss coefficient,  $U_t$  for N number of covers, bottom loss,  $U_b$  and side loss,  $U_s$  coefficients have been evaluated from the equations given by [14]. The collector heat removal factor  $F_R$  has been calculated using the procedure followed by [13]

### 4. RESULTS AND DISCUSSION

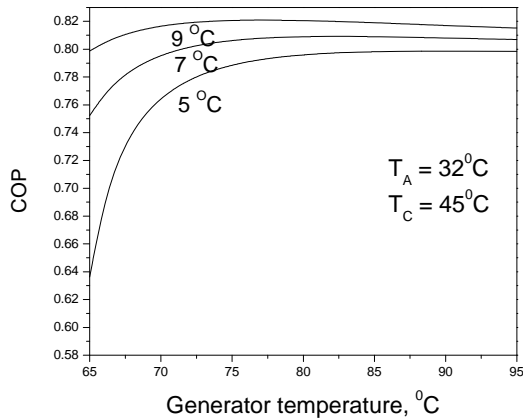


Fig 2. Effect of generator temperature on COP for different evaporator temperatures

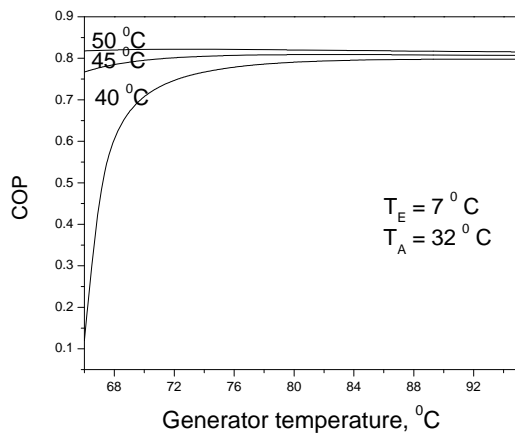


Fig 3. Effect of generator temperature on COP for different condenser temperatures

Figure 2 illustrates the variation of COP with generator temperatures for three evaporator temperatures

of 5°C, 7°C and 9°C. The improvement of COP with higher values of evaporator temperatures may be attributed to the fact that as the evaporator temperature is raised, the refrigeration capacity per unit mass of refrigerant increases. Figure 3 depicts the variation of COP with

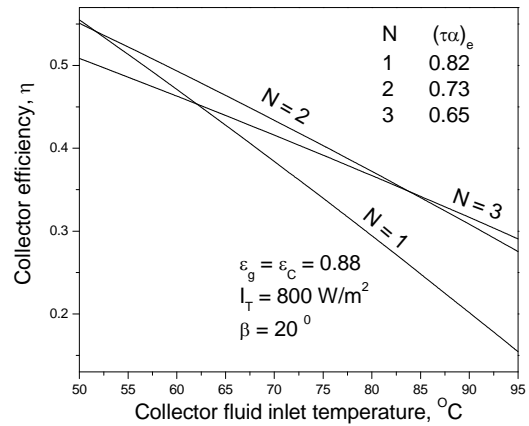


Fig 4. Collector efficiency as a function of collector fluid inlet temperature

generator temperature for condenser temperatures of 40°C, 45°C and 50°C. The variation of collector efficiency with fluid inlet temperatures is shown in Fig.4 for one cover, two cover and three cover systems. This figure demonstrates the effect of number of cover(s) on the collector performance. Normally increase in the number of cover glasses increases the optical losses, but to a greater extent decreases the thermal losses, thus increasing the stagnation temperature of the collector. So for higher operating temperatures, multi-cover flat plate collectors will operate at higher efficiency and thus are preferred.

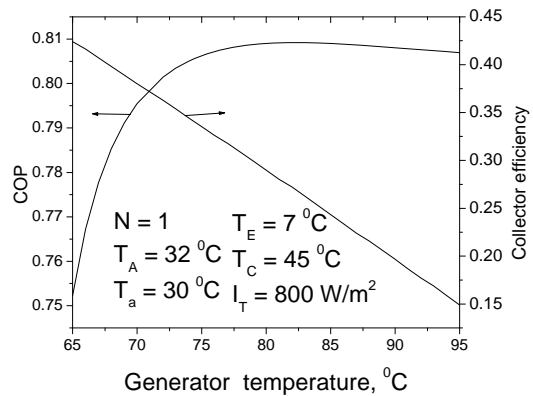


Fig 5. Effect of generator temperature on system performance

The variation of cycle COP and collector efficiency with generator temperature is depicted in Fig.5. The break even point indicates the optimum generator temperature for the solar operated absorption cooling system.



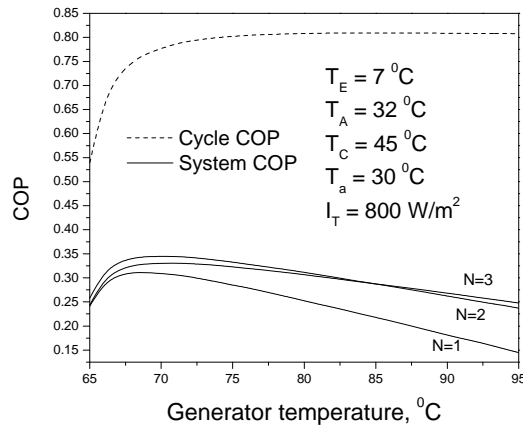


Fig.6. Effect of generator temperature on system and cycle COP

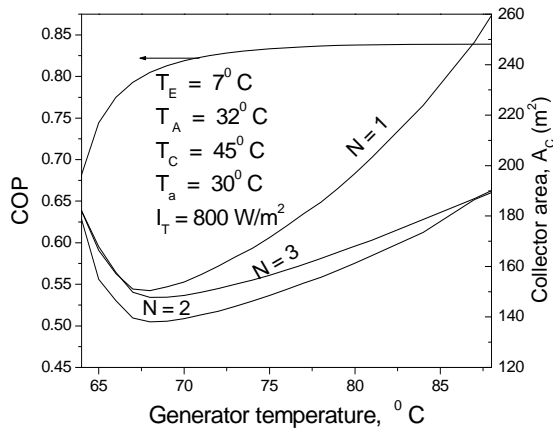


Fig.7. Effect of generator temperature on COP and collector area

Figure 6 illustrates the variation of cycle COP and system COP with generator temperatures for the cooling system driven by solar flat plate collectors having one, two and three glass covers. It is seen that the highest system COP is obtained when flat plate collectors with two glass covers are used. Finally in Fig.7 is shown the variation of required collector area with generator temperatures for one, two and three glass cover systems. If the design generator temperature is assumed to be 5°C below the fluid inlet temperature of collector, then the system could be designed for this generator temperature, and the collector area required for a cooling load of 10 ton can be determined from Fig. 7. It is seen that the required collector area is least for flat plate collectors built with two glass covers.

## 5. CONCLUSION

The coupling of solar thermal collectors and thermally driven chillers needs a sophisticated control since both components exhibit a reverse dependence of their figure of merits from the operating temperatures. In the design and optimization of the performance of such system the most important variable which has to be taken into

account is the temperature of the generator because the other parameters of the system depend on the existing initial conditions, and consequently are fixed. The operating temperature range of hot water supplied to the generator of a solar-operated LiBr-H<sub>2</sub>O absorption cooling system is restricted between 72 and 95°C. The lower limit is imposed for two reasons. Firstly, the hot water temperature must be sufficiently high to ensure effective boiling to produce sufficient water vapour from the weak solution in the generator. Secondly, the temperature of the concentrated lithium bromide solution on its passage back to the absorber must be kept high enough to prevent crystallization of lithium bromide. The upper limit is imposed to avoid boiling of water in an unpressurized flat plate collector and formation of crystals in the strong solution after the heat exchanger. Determination of the generator temperature is influenced by several factors. For the optimum design temperature of the generator, the choice of right type collector is essential so that the overall system COP exists near the maximum. Before carrying out analysis of the coupled systems, it is important to know the values of  $F_R(\tau\alpha)_e$  and  $F_R U_c$  products for different types of collectors which are determined by testing of collectors and are provided by collector manufactures.

## 6. REFERENCES

1. Alizadeh, S., Bahar, F. and Geoola, F., 1979, "Design and Optimization of an Absorption Refrigeration System Operated by Solar Energy", *Solar Energy*, 22:149-154.
2. Ward, D.S., 1979, "Solar Absorption Cooling Feasibility", *Solar energy*, 22:259-268.
3. Mansoori, G. A. and Patel, V., 1979, "Thermodynamic Basis for the Choice of Working Fluids for Solar Absorption Cooling Systems", *Solar Energy*, 22:483-491.
4. Li, Z. F. and Sumathy, K., 2001, "Simulation of a solar absorption air conditioning system", *Energy Conversion and management*, 42:313-327.
5. Florides, G. A., Kalogirou, S. A., Tassou, S. A. and Wrobel, L. C., 2002, "Modeling and Simulation of an Absorption Solar Colling System for Cyprus", *Solar Energy*, 72:43-51.
6. Liu, Y. L. and Wang, R.Z., 2004, "Performance prediction of a solar/gas driving double effect LiBr-H<sub>2</sub>O absorption system", *Renewable Energy*, 29:1677-1695.
7. Fathi, R., Gumimi, C. and Ouaskit, S., 2004, "An irriversible thermodynamic model for solar absorption refrigerator", *Renewable Energy*, 29:1349-1365.
8. Assilzadeh, F. Kalogirou, Ali, Y. and Sopian, K., 2005, "Simulation and optimization of a LiBr solar absorption cooling system with evacuated tube collectors", *Renewable Energy*, 30:1143-1159.
9. Mittal, V., Kasana, K. S. and Thakur, N. S., 2006, "Modeling and Simulation of a Solar aaAbsorption Cooling System for India", *Journal of Energy in South Africa*, 17:65-70.

10. Ardehali, M. M., Shahrestani, M and Charles, C. A., 2007, "Energy simulation of solar assisted absorption system and examination of clearness index effects on auxiliary heating", Energy Conversion and Management, 48:864-870.
11. Rodriguez Hidalgo, M. C., Rodriguez Aumente, P., Izquierdo Millan, M., Lecuona Neumann, A. and Salgado Mangual, R., 2008, "Energy and carbon emission savings in Spanish housing air-conditioning using solar driven absorption system", Applied Thermal Engineering, 28:1734-1744.
12. Mazloumi, M., Naghashzadegan, M. and Javaherdeh, K., 2008, "simulation of a solar lithium bromide-water absorption cooling system with parabolic trough collectors", Energy Conversion and Management, 49: 2820-2832.
13. Duffie, J. A. and Beckmen, W. A., 1991, Solar Engineering of Thermal Processes, Wiley, New York.
14. Sukhatme, S.P., 1996, Solar Energy, Tata McGraw-Hill, New Delhi.
15. Jeter, S. M., Lenard, J. L. Y. and Teja, A. S., 1992, "Properties of lithium bromide-water solutions at high temperatures and concentrations-part IV: vapour pressure", ASHRAE Transactions, 98:167-172.
16. Talbi, M. M. and Agnew, 1992, "Exergy analysis of an absorption refrigerator using lithium bromide and water as the working fluids", Applied Thermal Engineering, 20:619-630.

## 7. NOMENCLATURE

Symbol	Meaning	Unit
$A_c$	Collector Area	(m <sup>2</sup> )
$C_{p_w}$	Specific heat of water	(kJ/kg. K)
$D_i$	Inner diameter of collector tube	(m)
$D_o$	Outer diameter of collector tube	(m)
$F$	Fin efficiency	(Dimension less)
$F'$	Collector efficiency factor	(Dimension less)
$F_R$	Collector heat removal factor	(kJ/kg)
$h$		(W/m <sup>2</sup> K)
$h_i$	Specific enthalpy	(W/m <sup>2</sup> )
$h_w$	Tube to fluid heat transfer coefficient	(W/m <sup>2</sup> K)
$I_T$	Wind heat transfer coefficient	(W/m K)
	Solar radiation flux on collector plane	(m)

		(m)
$K_c$		(kg)
$L$	Thermal conductivity of collector plate	(kg)
$L_f$	Spacing between collector plate and glass cover	(kg)
$m_w$		(kg/s)
$m_{ss}$		(Dimension less)
$m_{ws}$	Fin length	(Dimension less)
$m_w$	Mass of refrigerant	(kW)
$N$	Mass of strong solution	(kW)
	Mass of weak solution	(kW)
	Collector fluid flow rate	(kW)
$P_r$	Number of covers	(kW)
		(kW)
$Q_A$	Prandtl number	(Dimension less)
$Q_C$		(kW)
$Q_E$		( <sup>0</sup> C)
	Heat rejection in the absorber	( <sup>0</sup> C)
$Q_G$		
$Q_S$	Heat rejection in the condenser	(K)
$Q_U$		(m)
$R_e$	Heat extraction in the evaporator	(W/m <sup>2</sup> .K)
	Heat addition in the generator	(m/s)
$S$		(m)
$T_a$	Incident solar radiation	(kg/kg of ol.)
$T_{fi}$	Useful heat gain by collector	(Dimension less)
	Reynolds number	(W/m <sup>2</sup> .K <sup>-4</sup> )
$T_{PM}$		(Dimension less)
$t_c$	Absorbed solar radiation	(Dimension less)
$U_c$	Ambient temperature	(Dimension less)
$V_a$	Collector fluid inlet temperature	(kg/m <sup>3</sup> )
$W$		(Dimension less)
$X$	Mean plate temperature	
	Thickness of collector plate	
$(\tau\alpha)_e$	Collector loss coefficient	
	Wind velocity	
$\sigma$	Collector tube spacing	
$\epsilon_c$	Mass concentration of LiBr in the solution	
	Effective transmissivity – absorptivity product	
$\epsilon_g$	Stefan Boltzman constant	
$\rho_a$	Emissivity of collector plate	
$\eta$	Emissivity of glass plate	
	Density of air	
	Efficiency	

## 8. MAILING ADDRESS

K. K. Datta Gupta  
 Dept. of Mechanical Engg.  
 Bengal Engg. & Science University, Howrah-711103,  
 West Bengal, India.  
 Email: [k.dattagupta@rediffmail.com](mailto:k.dattagupta@rediffmail.com)

## A MODEL FOR PREVENTIVE MAINTENANCE SCHEDULING – A STEP TO IMPLEMENT TPM IN ORGANIZATIONS

A. M. Mohammad Mukaddes, N. F. Ahmed Chowdhury and M. Moin Uddin

Department of Industrial and Production Engineering, Shahjalal University of Science and Technology,  
Sylhet, Bangladesh

### ABSTRACT

Maintenance is essential for machines or equipments. Without maintenance machine or equipment cannot work properly throughout its service life. To perform maintenance activities, the organization needs to ensure maintenance scheduling in time. Case study shows that, in Bangladesh most of the organizations are practicing preventive maintenance even some are still practicing only breakdown maintenance. Among them most of the organizations perform the maintenance scheduling manually which is time consuming and which is also troublesome for record keeping. In order to overcome those problems, this research proposes a model for preventive maintenance scheduling. Application database software using C# and MySQL is developed supporting the proposed model. This software may be treated as a helping tool to establish TPM partially in organization by sharing information for autonomous maintenance program and a scheduled/periodic maintenance program.

**Keywords:** Preventive Maintenance, Automatic Scheduling, Information Sharing.

### 1. INTRODUCTION

Maintenance management plays a vital role in manufacturing or even in service industries. Commercial organizations strive to make a reasonable profit; public and non-profit organizations strive to operate in a cost-effective manner. Either way, the businesses must deliver products or services at optimum cost and on schedule in order to be judged effectively [1]. To achieve these goals, organizations use enormous mechanical, electrical, structural equipment, which need maintenance activity for their proper functioning. Almost every organization has a maintenance department for the maintenance of the equipments or machines.

There are different ways used to manage the maintenance activities. An important one is preventive maintenance (PM) which is a schedule of planned maintenance actions aimed at the prevention of breakdowns and failures. It is the maintenance carried out at predetermined intervals, or other prescribed criteria, and intended to reduce likelihood of an item not meeting an acceptable condition [2]. The primary goal of preventive maintenance is to prevent the failure of equipment and machine before it actually occurs. The ideal preventive maintenance program would prevent all equipment failure before it occurs. In most organization, this type of maintenance scheduling activity is paper based as well as manual. We also found that the histories of maintenance are not kept in an organized way in most of organizations. Some of them keep the maintenance history according to machine / equipment, some according to date. Though some organizations use ERP

software for maintenance scheduling, but they are still much more expensive and cost ineffective for most of the industries of Bangladesh. Moreover, most of the ERP software is client server based [3], which needs internet connection but in Bangladesh still now internet connection with proper data transfer rate is not available everywhere. In this paper we propose a model for preventive maintenance scheduling which can help to maintenance in an effective manner. We also develop application database software, which can help to automate periodic scheduling. The commercial software C# and MySQL [4] is used in creating the database. In order to select the features provided in the software, some field data are collected from different organizations. The developed software for preventive maintenance scheduling eliminates paper work and cost and makes the periodic scheduling more accurate. It also includes maintenance history, spare parts inventory control and list of break down maintenance. From the maintenance history, one can analyze the previous data and can change the periodic schedule and take necessary steps.

The proposed model and database software will also decrease cost of replacement, system downtime and better spares inventory management. It is shown that the developed model and database support some goals and pillars of TPM (Total Productive Maintenance) [5]. Thus it might help to implement TPM in an organization. two-line space between the keywords and the top of body of the text.

### 2. PRESENT SITUATION OF MAINTENANCE MANAGEMENT

A case study is performed in several manufacturing

and service industries in Bangladesh to collect information of maintenance management. The case study sort out the following points:

- There are three types of maintenance performed. They are preventive maintenance, breakdown maintenance and predictive maintenance. Preventive maintenance is considered as most important among three.
- Most of the organizations have separate persons engaged for scheduling the preventive maintenance. Most of them have manual scheduling process.
- The maintenance history is recorded manually.
- Most maintenance activities are done daily basis.
- The maintenance duration of each distinct machine or equipment is selected according to manual of machine/equipment and some times according to experience of experts.
- Operators are not trained properly in maintenance activities. Operators have little knowledge about the basic maintenance activities like lubrication, inspection, tightening etc.
- There is little cooperation between the operation and maintenance department. The operator's philosophy is "I operate, you fix".
- Operators are not responsible for cleaning and tidiness of the equipments area.
- The daily maintenance task sheet is prepared manually.

### 3. PROPOSED MODEL FOR PM SCHEDULING

From the analysis of data collected, we have found that an automatic maintenance scheduling can remove some drawbacks of maintenance management exists in the industries of Bangladesh. To satisfy those drawbacks, we proposed a model for preventive maintenance management as shown in figure-1.

The relation between the maintenance department and operation department is also defined. In our proposed model, maintenance department is the centre of control where a data base is kept. Maintenance department entries information to the database after a new machine or equipment is launched. The information might be collected from the following three sources.

- manual of machines/equipments
- maintenance history analysis
- experience of experts

The database keeps the records of inserted information and according to the inserted information, the software automatically prepare a maintenance schedule in daily basis. The input and output (automatic) of the database are shown in figure-3.

The maintenance department could retrieve the equipments which should be considered for maintenance for a specific date. A task sheet of those machines could be printed. According to the information in the task sheet, maintenance department would decide whether this task is done by the department itself or send it to the operations department for the basic maintenance activities. Once the maintenance for that day is finished, the feed back of the scheduled maintenance is updated in the database by the maintenance department. Database

automatically changes the maintenance schedule for the following days.

The maintenance history of a specific machine or equipment is also maintained in the database. Thus by sorting major breakdowns and reoccurring breakdowns from the maintenance history, the maintenance department can take corrective actions. Beside these activities, maintenance department also performs time based maintenance activity. The operation department mainly operates the plant, beside it in our proposed model operation department performs basic maintenance activities which are given in the task sheet. The maintenance department would train the people of operation department for these basic maintenance activities. Our proposed interaction of the maintenance department with the database is shown in figure-3.

We also propose the following activities of the maintenance department and operation department-

#### Maintenance department

Repairs & Engineering	Preventive maintenance
Safety	Planning and scheduling
Estimating	Stores control
Perform time based maintenance	Quality Assurance
Employee relations	Training (the people of operation dept.)
Record keeping and Data base management	Budgeting & financial planning
Reports and analysis	Construction and rescheduling

#### Operation department

Keep the operation smooth	Perform Basic Maintenance Activities such as: Cleaning, Lubrication, Adjust, Inspection
Receive and deliver work order to maintenance department.	Get training from maintenance department.
To achieve better safety, health and environment work with EHS department	Report abnormalities to the maintenance department.

### 4. APPLICATION DATA BASE SOFTWARE

In order to implement the proposed maintenance model, a huge class of software is needed for various developing stages. Much commercial software is available which should be purchased to implement the system. Of course some software should be developed to provide desired feature to the maintenance department. An important task is to create database software. A large class of database is a significant criterion for such a model. One thing should be kept in mind during the development of software is that software should be

flexible to use and be simple to suit the existing infrastructure in organization [6].

The steps given in figure-4 are followed to create a database supporting the proposed model described in the preceding section where the input and output of the data base are shown in figure-3.

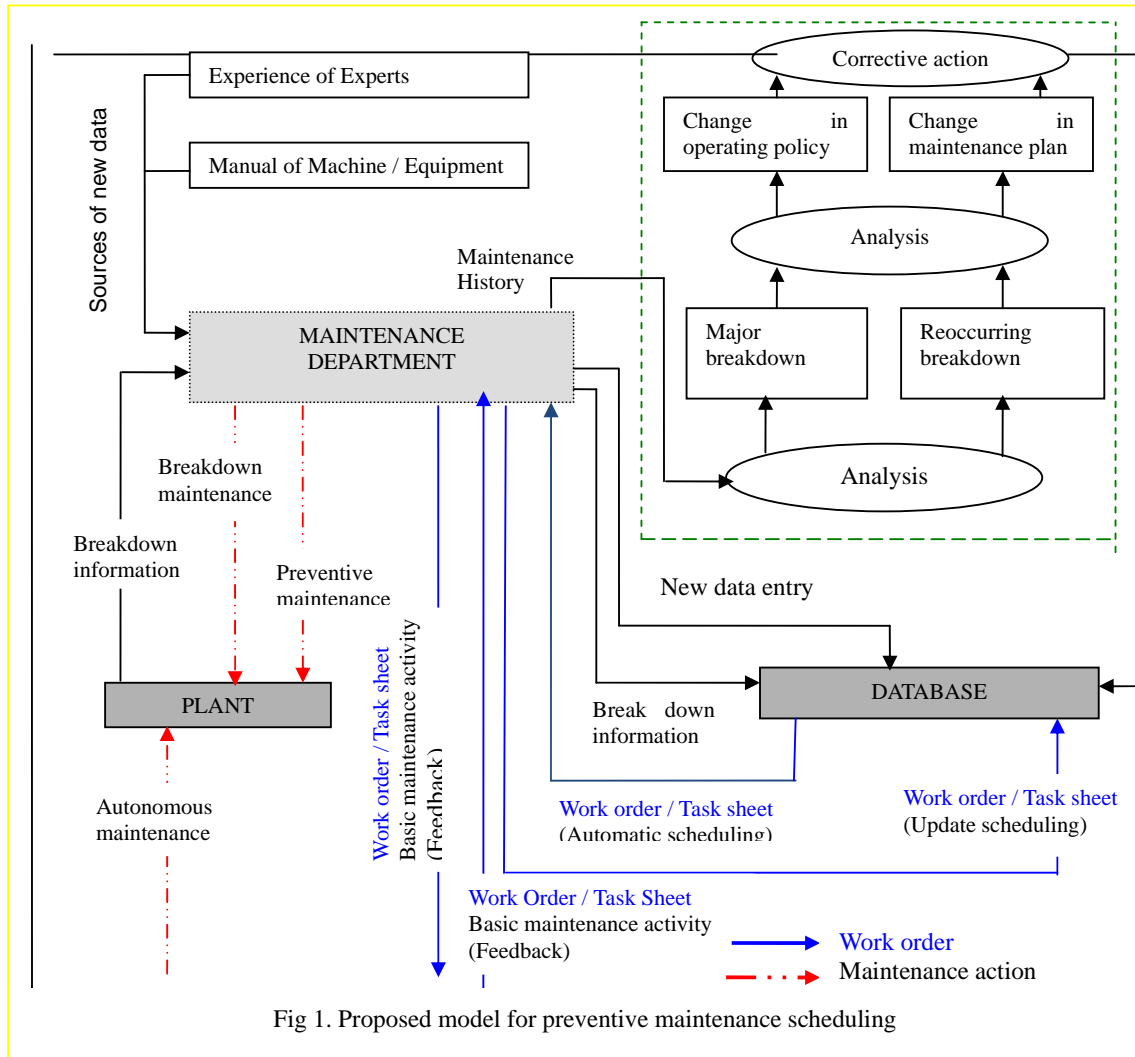


Fig 1. Proposed model for preventive maintenance scheduling

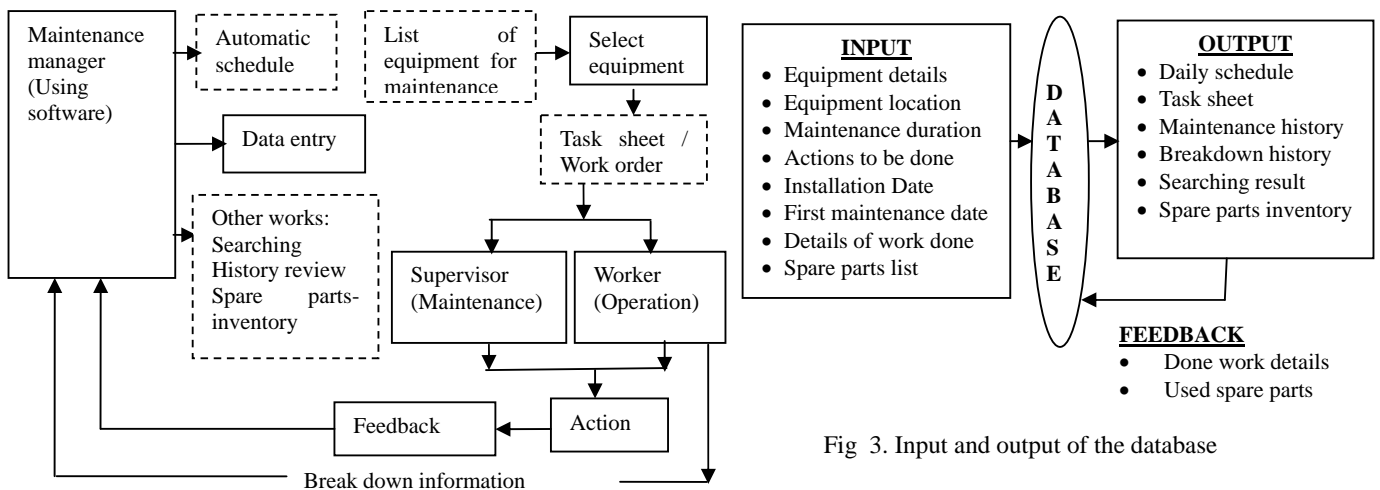


Fig 3. Input and output of the database

Fig 2. Interaction of maintenance manager with

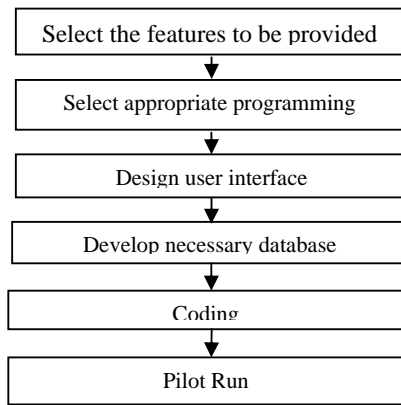


Fig. 4 Steps of developing software

The features provided in the database, are selected from the information collected from different industries with the help of some questionnaires. With its intuitive and user-friendly design the developed database integrates preventive maintenance work order, scheduled work orders, spare parts inventory control, maintenance history and equipment searching to benefit the maintenance manager.

Database schema is created using columns and rows in tables. We use My SQL database software [5]. Computer code was written in C# language using visual studio 2008.[6].

The first window of our created database are shown in figure-5. Some pictorial view of the features of the developed application database software is given below. It includes new data entry (figure-6), automatic scheduling for a specific date (figure-7), specification of a item (figure-8), a task sheet (figure-9) that will be given to the maintenance people for proper action. It also provides the searching options of any equipment or spare parts (figure-10 and figure-13). The database maintains the history of previous maintenance (figure -11 and figure-12) and spare parts inventory (figure-14). Huge number data could be kept in the developed database. The database manager should update the data base after the maintenance work every day through figure-8. It will automatically reschedule for the following days.

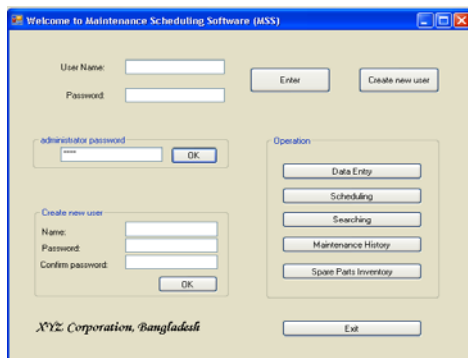


Fig 5. First window of the database software

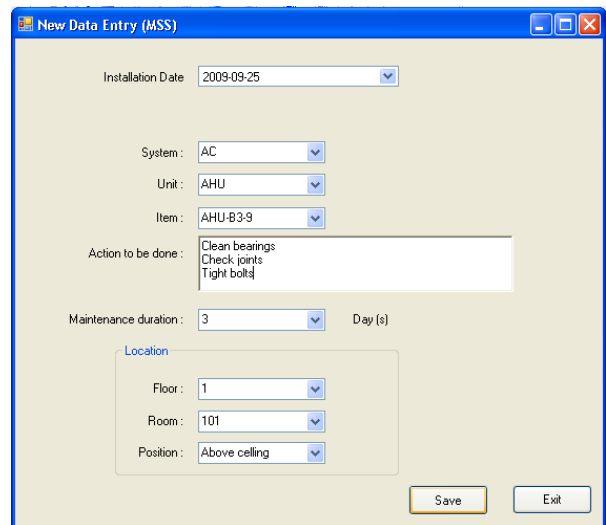


Fig 6. New data entry

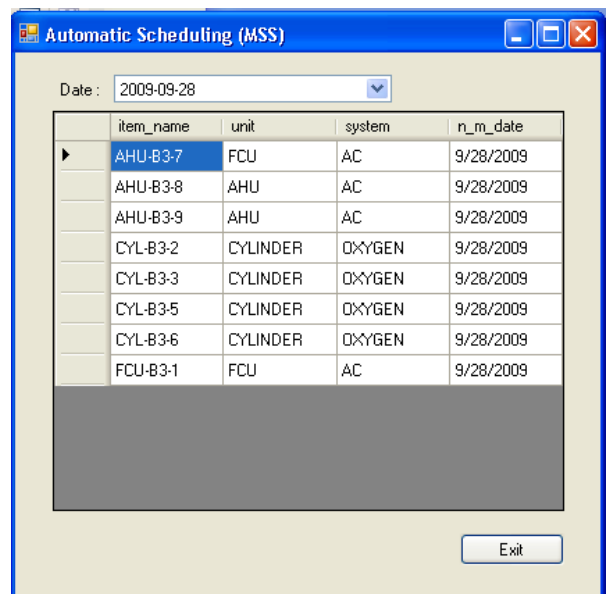


Fig 7. Automatic scheduling

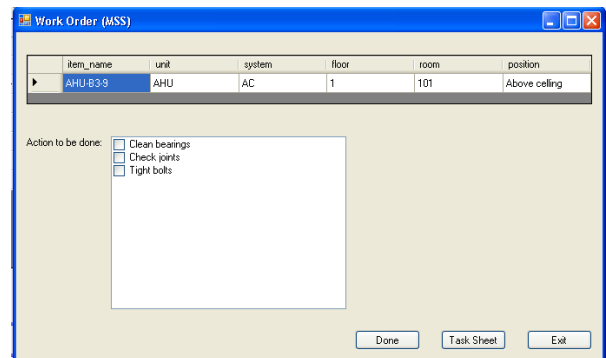


Fig 8. Work order

**xyz Corporation**

*Task Sheet*

Date: Monday, September 28, 2009, 2:11 PM Previous maintenance date: 10/1/2009 12:00:00 AM

Record ID : 28-09-2009-AHU-B3-9

Item  
Item name: AHU-B3-9 Unit: AHU System: AC

Location  
Floor: 1 Room: 101 Position: Above ceiling

Action to be done:  
 Clean bearings  
 Check joints  
 Tight bolts

comment (if any) name & signature (action done by) name & signature (engineer)

Print

Fig 9. Task sheet

Item name: AHU-B3-9 Search History Other search List of all Item

Description  
Unit: AHU System: AC

Location  
Position: Above ceiling Room: 101 Floor: 1

Action to be done:  
 Clean bearings  
 Check joints  
 Tight bolts

Maintenance duration: 3 Day(s)

First installation date: 25-Sep-2009

Next maintenance date: 19-Oct-2009

Previous maintenance date: 16-Oct-2009

Revised maintenance date: 2009-09-28 Reset

Delete List of revised maintenance Exit

Fig 10. Searching

Date: Monday, September 28, 2009 Search by Item

item_name	unit	system	done_date
AHU-B3-7	FCU	AC	9/28/2009
AHU-B3-8	AHU	AC	9/28/2009
AHU-B3-9	AHU	AC	9/28/2009
CYL-B3-2	CYLINDER	OXYGEN	9/28/2009
CYL-B3-3	CYLINDER	OXYGEN	9/28/2009
CYL-B3-5	CYLINDER	OXYGEN	9/28/2009
CYL-B3-6	CYLINDER	OXYGEN	9/28/2009
FCU-B3-1	FCU	AC	9/28/2009

Exit

Fig 11. Maintenance history

Item Name: AHU-B3-9 Search

item_name	unit	system	done_date	action_done
AHU-B3-9	AHU	AC	9/28/2009	
AHU-B3-9	AHU	AC	10/1/2009	Clean bearings
AHU-B3-9	AHU	AC	10/4/2009	Clean bearings
AHU-B3-9	AHU	AC	10/7/2009	Check joints
AHU-B3-9	AHU	AC	10/10/2009	Clean bearings
AHU-B3-9	AHU	AC	10/13/2009	Check joints Tight bolts
AHU-B3-9	AHU	AC	10/16/2009	Clean bearings

Exit

Fig 12. Item history

List of all item

sl_no	item_name	unit	system	ins_date
66	AHU-B3-9	AHU	AC	9/25/2009
67	AHU-B3-8	AHU	AC	9/25/2009
68	AHU-B3-7	FCU	AC	9/25/2009
69	CYL-B3-5	CYLINDER	OXYGEN	9/25/2009
70	CYL-B3-3	CYLINDER	OXYGEN	9/25/2009
71	FCU-B3-1	FCU	AC	9/25/2009
72	CYL-B3-6	CYLINDER	OXYGEN	9/25/2009
73	CYL-B3-2	CYLINDER	OXYGEN	9/25/2009
74	CYL-B3-8	CYLINDER	OXYGEN	9/28/2009
75	FCU-B3-6	FCU	AC	9/28/2009
76	AHU-B1-18	AHU	AC	9/28/2009
77	CYL-B3-23	CYLINDER	OXYGEN	9/29/2009
78	AHU-B1-14	AHU	AC	9/29/2009
79	AHU-B3-19	AHU	AC	9/29/2009
80	CYL-B3-9	CYLINDER	OXYGEN	9/29/2009

OK

Fig 13. List of all items

System (Spare): Bolt

Item (Spare): B0-4-15

No. of Item (Spare): 19

Add Use

Search by System  
 Search by Item

Search See all

system	item	no_of_item
Oxygen Cylinder	100 liter	23
Oxygen Cylinder	50 liter	23
Oxygen Cylinder	70 liter	43
Bearing	B-DC-10	123
Bearing	B-DS-10	17
Bearing	B-DS-12	14
Bolt	B0-4-13	62
Bolt	B0-4-15	19
Bolt	B0-5-12	56
Photocopy	Cartage	3

Exit

Fig 14. Spare parts inventory



## 5. RELATION WITH TPM

The proposed model and data base software agrees with some objectives and goals of TPM. Those are summarized in Table-1 and Table-2.

Table 1

S / L	TPM goals [5]	Relation with proposed model
1.	Elimination of the six big losses (down time, speed, and defect)	
2.	An autonomous maintenance program	Interaction of the maintenance department with operations department
3.	A scheduled maintenance program for the maintenance department	Automatic scheduling of preventive maintenance
4.	Increased skills of operations and maintenance personnel	The maintenance department will train the worker of operations department in regular basis
5.	An initial equipment management program	

Table 2

S/L	TPM pillars [7] [8]	Relation with proposed model
1.	Planned Maintenance	Proper maintenance scheduling
2.	Training & Education	
3.	Focused Improvement	
4.	Quality Maintenance	Analysis from the maintenance history helps in quality maintenance.
5.	5s (Sort, Systematic, Shine the workplace, Standardization, Self discipline)	.
6.	Office TPM	
7.	Safety Health & Environment	Trained operators
8.	JISHU HOZEN = Autonomous Maintenance	Basic maintenance activities of the operation department and correlation with maintenance department

## 6. CONCLUSION

A case study on the present situation of maintenance management in several industries in Bangladesh is performed. Based on the information from the case study, a model for preventive maintenance scheduling is proposed as well as database software is developed supporting the model. In the developed software we tried to automate preventive maintenance the scheduling. The developed software will generate the information of previous maintenance history that helps in decision making of predictive maintenance. We tried to introduce an easy and convenient model of maintenance scheduling with the help of a simple but effective maintenance scheduling software. So the outcome of this research will benefit first and foremost the maintenance manager of industries in Asian developing countries like Bangladesh.

## 7. REFERENCES

1. E. Hartmann, D. J. Knapp, J.J. Johnstone & K.G. Word, "How to Manage Maintenance", American Management Association
2. Anthony Kelly, 1991 "*Maintenance Planning & Control*", Affiliated East West Press Ltd
3. Derek L Waller, 2003 "Operations Management – A supply chain approach", International Thomson Business Press
4. Luke Welling, Laura Thomson, "*PHP and MySQL Development*", Sams Publishing.
5. Seiichi Nakajima, 1984 "*Introduction to TPM*", Japan Institute for Plant Maintenance
6. Karli Watson, Eric White, 2006 "*Beginning Visual C# 2005*", Wiley Publishing, Inc
7. Dr. M Ahsan Akter Hasin, 2007, "*Quality Control and Management*", Bangladesh Business Solution
8. A.K.M. Masud, Abdullah-Al-Khaled, Seratun Jannat, A.K.M. Sajedul Arefin Khan & Kingshuk Jubaer Islam, June 2007, "Total Productive Maintenance in RMG sector. A case: Burlingtons limited, Bangladesh" Journal of Mechanical Engineering, vol. ME37.

## FACTORS AFFECTING PRODUCTIVE EFFICIENCY OF THE APPAREL INDUSTRY OF BANGLADESH

S. Nadeem Ahmed,<sup>1</sup> A. Akhter Hasin<sup>2</sup>,

<sup>1</sup> Secretary, BIDS, Bangladesh

<sup>2</sup> Department of IPE, BUET, Dhaka, Bangladesh

### ABSTRACT

Although labor productivity is a popular productivity (partial) measure for any production system but the factors which are responsible for augmenting its value, needs careful attention. Evaluation of performances of any production systems definitely depends upon various factors for its subsequent improvement. The apparel industries in Bangladesh suffer from poor productivity due to several factors, or variables. On many occasions, these variables are not only complex in nature by itself, but interacting too, thereby multiplying the complexity further. These factors or variables have never been analyzed econometrically. As a result, accurate performance, in terms of productivity, could never be known. This impedes subsequent improvement drive. This study is part of bigger research aimed at analyzing the factory performances, finding out the weak variable linkages and identifying the efficient frontier of apparel industry of Bangladesh. The study focuses on fifteen parameters in order to determine their influences upon the output of the workers as a whole. Five among them have been found to be influencing the output produced, which are: Gender, Age Group, Work Experiences, Satisfactions and Qualifications of the workers.

**Keywords:** Labor Productivity, Apparel Industry, Worker's Performances

### 1. INTRODUCTION

It is a well known phenomenon that there exists a greater need for the productivity enhancement of the abundant labor force of the country, specially in the apparel sector. With the increase in the productivity per unit cost of the product is reduced which leads the company to remain competitive in both the inside and outside markets of the country. The unproductive workers are burdensome to the company and in the long run could destroy the organization. Productivity provides information about the performance, quality of individuals, work groups and processes. It presents current operational results and comparisons to past history.

In this study an attempt is being made to explore the affects of various parameters which positively or negatively influence the productive efficiency of any apparel industry. A questionnaire suitably designed to incorporate factors thought to be influencing the productive efficiency of the apparel factory have been analyzed in a sequential manner. After obtaining detailed answers analysis was carried out to find which factors are significant contributors to the productive efficiency [1]. The analysis was done using the SPSS.

Fifteen factors such as: Gender, Age Group, Work Experiences, Level of satisfactions, Fatigue, Relation with Fatigue, Number of hours worked, Compensation, Comfort, Skillness improvement, Nonpayment, Deferred payment, Qualifications, Need for training, Mode of learning, were analyzed against the output produced.

### 2. OBJECTIVES OF THE STUDY

To study the affects of various labor related factors affecting the productive efficiency of apparel industry.

### 3. METHODOLOGY AND DATA COLLECTION

A suitably designed questionnaire, incorporating labor related various factors thought to have affects on the productive efficiency, have been used to collect the primary data. These data have been collected from the apparel factories around the greater Dhaka city.

### 4. FACTORS AFFECTING THE PRODUCTIVE EFFICIENCY

#### 4.1 Gender

Gender plays a major role in the factory environment. In Bangladesh, women's employment in export-oriented industry has narrowed the gender gap in many spheres [2]. The percentage of male and female and their individual contribution is necessarily a big issue for augmenting the productivity. In Table 1 the number and percentage of male and female working in the factory are shown. In Table 2 the p-value shows that the relationship found between outputs produced in number of pieces and gender is significant.

Table 1: Gender distribution

Gender	Number	Percent
Male	120	29.6
Female	285	70.4
Total	405	100.0

Table 2: Output related to gender

Gender	pieces produced per hour			p-value
	60-79	80-99	100+	
Male	10.0	24.4	36.3	0.013
Female	90.0	75.6	63.7	
Total	100.0	100.0	100.0	

Here the outputs produced have been divided into three groups and analyzed accordingly. From the analysis it can be seen that in the higher producing categories the percentage of male workers are increasing proportionately i.e. the male workers are performing better than their counterpart.

#### 4.2 Age Group

In considering the age of the workers as have been shown in the Table 3 the total numbers of workers are divided against four age groups (19-24, 25-30, 31-36 and 37+) and three output producing groups (60-79, 80-99 and 100+). In Table 4 the p-value shows that the relation between output produced in number of pieces and the different age groups are significant.

Table 3: Output distribution

PCSPHR GROUP	Age Group			
	19-24	25-30	31-36	37+
	Number of workers			
60-79	8	2	0	0
80-99	55	123	18	9
100+	12	159	7	12
Total	75	284	25	21

Table 4: Output related to age group

Age Group	% Output			p-value
	pieces produced per hour			
	60-79	80-99	100+	0.0
19-24	80.0	26.8	6.3	
25-30	20.0	60.0	83.7	
31-36	0	8.8	3.7	
37+	0	4.4	6.3	
Total	100.0	100.0	100.0	

It can also be seen that the better performing group is the group having the age between 25 to 30 years.

#### 4.3 Work Experiences

In a factory undoubtedly work experiences of the workers augments the output of the factory as whole [3]. This has also found true in this case. The work experiences of the workers are divided into three groups (less than 3 years, 3 to 10 years and more than 10 years)

against output produced in pieces into three groups (60 to 79, 80 to 99 and more than 100) as shown in Table 5. The patterns of workers following into different groups are analyzed and when these data are run has been found to have very significant relationship, which can be seen from the p values in the Table 6.

Table 5: Distribution of Work Experiences of the workers.

Work Exp. Group	Number of workers				Total
	<3	3-10	10+		
PCSPHR GROUP	60-79	1	0	9	10
	80-99	45	25	135	205
	100+	26	103	61	190
Total	72	128	205	405	

Table 6: Output related to Work Experiences

WEXPGR	pieces produced per hour				P Value
	60-79	80-99	100+	Total	
<3	10.0%	22.0%	13.7%	17.8%	0
3-10	0	12.2%	54.2%	31.6%	
10 and above	90.0%	65.9%	32.1%	50.6%	
Total	100.0	100.0	100.0	100.0	

#### 4.4 Level of Satisfactions

The fourth factor has been analyzed is the level of satisfactions of the workers, which is divided into five levels (Very satisfied, Satisfied, Neither satisfied nor dissatisfied, Dissatisfied and Very dissatisfied) against the three output produced in pieces in hour (60 to 79, 80 to 99 and more than 100) as shown in Table 7. When these levels of satisfactions of the workers are analyzed against the output produced it was found to have no significant relationship as shown in Table 8.

Table 7: Satisfaction distribution

PCSPHR		Numbers of workers			
		60-79	80-99	100+	Total
SATIS GROUP	Very much satisfied 81%>	8	178	165	351
	Satisfied 61%-80%	1	15	9	25
	Neither satisfied nor dissatisfied 51%-60%	1	5	5	11
SATIS GROUP	Dissatisfied 30%-50%	0	2	5	7
	Very much dissatisfied <30%	0	5	6	11
Total		10	205	190	405

Table 8: Output related to satisfactions

	PCSPH RGR	pcs produced per hour			P Value
		60-79	80-99	100+	
SATIS FACT ION GRO UP	Very much satisfie d 81%>	2.3	50.7	47.0	0.001
	Satisfie d 61%-80 %	4.0	60.0	36.0	
	Neither Satisfd nor Dissatis fied 51%-60 %	9.1	45.5	45.5	
	Dissatis fied 30%-50 %	0	45.5	54.5	
	Very much Dissatis fied <30%	2.5	50.6	46.9	

#### 4.5 Qualifications

The qualification of the workers plays an important role, since uneducated person are able to learn the skills and techniques very slowly, which in turn lead the overall performance of the factory to remain in a low level. The qualifications of the workers have been classified into three tiers: below Class V, Class VI to VIII and above Class VIII. The pattern distributions are shown in Table 9. When the values of the output are analyzed against the qualifications it is found that there exists a significant relationship as shown in Table 10.

Table 9: Qualifications distribution.

Class interval	Number	Percent
Below class V	243	60.0
Class VI to VIII	121	29.9
Above class VIII	41	10.1
Total	405	100.0

Table 10: Output related to relationship to qualifications.

Qualifi cation	% Output pieces produced per hour				
	60-79	80-9 9	100+	Total	P Value
Below class V	90.0	74.1	43.2	60.0	2 cells (22.2%) have expected count less than 5.The minimum expected count is 1.0
Up to Class VIII	10.0	13.7	48.4	29.9	
Above Class VIII	0	12.2	8.4	10.1	

#### 5. CONCLUSION

After carrying out the analysis Gender, Age Group, Work Experiences, Satisfactions of the workers and Qualifications of the workers have been found to have positive influences on the output produced. From the values after conducting individual linear regressions it has been found that approximately 3.4 percent of the variation in output is explained by the gender factor, approximately 4.2 percent of the variation in output is explained by the age group factor, approximately 3.7 percent of the variation in output is explained by the work experiences, approximately 0.05 percent of the variation in output is explained by the satisfactions, 4.9 percent of the variation in output is explained by the qualifications factor. Also it is understood that there are other factors besides these contributing factors which have influences on the output produced. The differences between R Square and Adjusted R Square are very small. The error quantity indicates that the misspecification is very small. It can be seen that in the higher producing categories, the percentage of male workers are increasing proportionately i.e. the male workers are performing better than their counterpart. These values have been shown in Table 11.

Table 11: Gender Model Summary

Model	R	R Squar e	Adjuste d R Square	Std. Error of the Estimate
Gender	0.185	0.034	0.032	0.53631
Age Group	0.206	0.042	0.040	0.53401
Satisfaction	0.074	0.005	0.003	0.54418
Work Exp.	0.19	0.037	0.034	0.535
Qualificns	0.221	0.049	0.046	0.53218

#### 6. RECOMMENDATIONS

1. The data set considered have been collected from around the greater Dhaka city. The analysis may be carried out collecting the data from outside the Dhaka city e.g. Chittagong and other parts of the country.

2. In finding the factors, responsible for augmenting the productive efficiency of the Apparel factories, fifteen factors have been considered, mostly related to labor productivity of the workers and working conditions of the factory. Other factors such as style of leadership, management quality etc. may be incorporated.
3. Multiple Regression Analysis may also be applied taking into account all the parameters which may influence the output.

Dr. Syed Nadeem Ahmed  
Secretary  
Bangladesh Institute of Development Studies(BIDS)  
E-17, Agargaon, Sher-e-Bangla Nagar  
Dhaka, Bangladesh  
E-mail: [secy10bids@sdnbd.org](mailto:secy10bids@sdnbd.org)

## **7. REFERENCES**

1. Rios, Ana R. and Gerald E. Shively(2005), “Farm size and Nonparametric Efficiency Measurements for Coffee Farms in Vietnam,” Department of Agricultural Economics, Purdue University, Department of Agricultural Economics, Purdue University 403 West State Street, West Lafayette, IN 47907.
2. Majumder, Pratima Paul and Begum , Anwara (2000) The World Bank Development Research Group/ Poverty Reduction and Economic Management Network, “ The Gender Imbalances in the Export Oriented Garment Industry in Bangladesh” .
3. USAID (June 2005), Measuring Competitiveness and Labor Productivity in Cambodia’s Garment Industry.

## **8. MAILING ADDRESS**

# STUDIES ON TIN OXIDE ( $\text{SnO}_2$ ) AND CU DOPED $\text{SnO}_2$ THIN FILMS DEPOSITED BY SPRAY PYROLYSIS TECHNIQUE FOR WINDOW MATERIALS IN SOLAR CELLS

S. S. Roy<sup>1</sup> and J. Podder<sup>2</sup>

<sup>1</sup>Department of Physics, Dwarika Paul Mohila Degree College, Sreemongal

<sup>2</sup>Department of Physics, Bangladesh University of Engineering and Technology,  
Dhaka, Bangladesh

## ABSTRACT

$\text{SnO}_2$  thin films have been deposited onto glass substrates by spray pyrolysis technique. Tin chloride and copper nitrate were used as source of Sn and Cu respectively. The structural, optical and electrical properties of  $\text{SnO}_2$  films have been investigated as a function of Cu-doping (1~8 wt. %). The SEM micrographs of film show uniform deposition and EDX results show the stoichiometry and elemental composition of the films (viz. Cu, Sn and O, etc.). The optical transmission was found to increase from 71 % to 79 % for 200 nm thickness with the addition of Cu up to 4 % and then decreased for higher concentration of copper doping. The optical band gap for pure  $\text{SnO}_2$  film was found 3.75 eV. Due to Cu doping, the band gap was shifted to lower energies and then increased with further increasing of doping concentrations. X-ray diffraction studies show the polycrystalline nature of the films with preferential orientation along the (101) planes and an average grain size of 7.244 Å. The resistivity of  $\text{SnO}_2$  films was found to decrease initially from  $4.5095 \times 10^{-4} \Omega\text{m}$  to  $1.1395 \times 10^{-4} \Omega\text{m}$ . The experimental results discussed the suitability of this material for using as transparent and conducting window materials in solar cells.

**Keywords:** Spray Pyrolysis,  $\text{SnO}_2$  Thin Film, Optical Band Gap

## 1. INTRODUCTION

Transparent and conducting oxides (semiconductors) have been extensively studied because of their novel properties and wide range of applications including architectural windows, polymer-based electronics, etc. [1].  $\text{SnO}_2$  semi-conducting transparent thin films have various appealing features for technical applications in solar energy conversion, flat panel displays, electro-chromic devices, invisible security circuits, LEDs, etc. Hence large area  $\text{SnO}_2$  films on cheap and easily available substrates are of considerable interest for the formation of most of the photonic structures.

There are various methods such as chemical vapour deposition, sol gel, spray pyrolysis, electron beam evaporation, vapour deposition, pulsed laser deposition, molecular beam epitaxy, thermal evaporation, reactive evaporation and magnetron sputtering, etc. for the preparation of pure or doped

thin films [2-6]. The structure of  $\text{SnO}_2$  in its bulk form is tetragonal rutile with lattice parameters of  $a = b = 4.737 \text{ \AA}$  and  $c = 3.816 \text{ \AA}$  [7]. However, in thin film form, depending on the deposition technique, its structure can be polycrystalline or amorphous. Generally,  $\text{SnCl}_4$  is used as a precursor for Sn, and limited work had been reported using  $\text{SnCl}_2$  instead of  $\text{SnCl}_4$ . The  $\text{SnO}_2$  films close to stoichiometric conditions have low free carrier concentration and high resistivity, but non-stoichiometric  $\text{SnO}_2$  films have high carrier concentration, high conductivity, and high transparency. Usually there is an oxygen vacancy in the structure, so that the formula for the thin film of the material is  $\text{SnO}_{2-x}$ , where x is the deviation from stoichiometry. Conventional n-type transparent conducting oxide (TCO) thin films are  $\text{In}_2\text{O}_3$ : Sn (ITO),  $\text{SnO}_2$ : F (FTO), and  $\text{ZnO}$ :Al (AZO) [8].  $\text{SnO}_2$  thin films with electrical resistivity of  $2.7 \times 10^{-4} \Omega\text{-m}$  at a deposition temperature of 500°C and the minimum resistivity for the doped  $\text{SnO}_2$  films was found to be  $0.381 \times 10^{-4} \text{ m}$  deposited

at 575° C with 3 wt. % of Fe doping [9]. The transmittance value for the pure tin oxide films is found to increase from 42.24 % to 54. 48 % (at 800 nm) on the addition of 0.5 wt. % of antimony. But the transmittance is found to decrease gradually if the antimony concentration is increased above 0.5 wt. % [10]. The highest transmission observed in the films was 75% and the band gap varied between 2.7 and 3.4 eV for Mn doped tin oxide [11]. The main objective of this work is to prepare high conducting Cu doped SnO<sub>2</sub> thin films from SnCl<sub>2</sub> precursor and to explore its optical and electrical properties. In this paper we are reporting the effect of Cu doping on the structural, optical, and electrical properties of SnO<sub>2</sub> films prepared by a simple spray pyrolysis technique (SPT).

## 2. EXPERIMENTAL DETAILS

Pure SnO<sub>2</sub> and SnO<sub>2</sub>: Cu films were deposited using a locally fabricated spray pyrolysis system.

0.2M SnCl<sub>2</sub>.2H<sub>2</sub>O was added with 50 ml water and 50 ml ethanol for precursor solution of pure SnO<sub>2</sub> thin film. 1~8 wt % of Cu (NO<sub>3</sub>)<sub>2</sub>.3H<sub>2</sub>O was dissolved in SnCl<sub>2</sub>.2H<sub>2</sub>O solution for Cu doped thin film. To enhance the solubility of prepared solution, a few drops of HCl were added [12]. The distance between substrate to nozzle was 30 cm. Air pressure was 1 bar, spayed time was 5 min. and spray rate was kept constant at 5 ml/min. For each concentration the reproducibility of the films were verified by repeating the experiments several times. Microscope glass slides were used as substrates. The substrate temperature was fixed at 350 °C. Scanning Electron Microscope (SEM) model HITACHI, S-3400N JAPAN, was used to see the surface morphology. The transmission and absorption spectra for the as-deposited films were recorded using a UV-1631 spectrophotometer (SHIMADZU) as a function of wavelength ranging from 290 to 1100 nm. The electrical resistivity was measured using Van der Pauw method in the range of 300~475K.

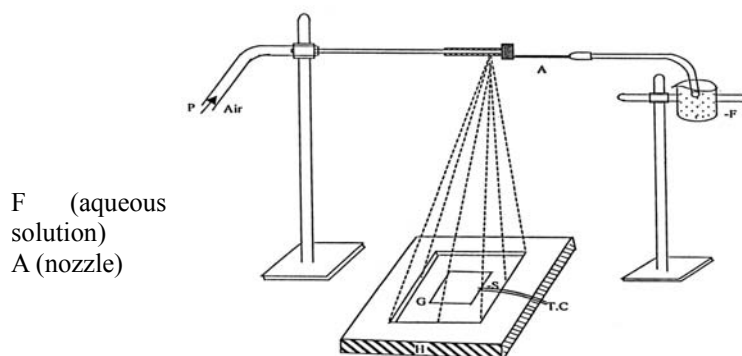


Fig 1. Experimental setup of spray pyrolysis technique.

## 3. RESULTS AND DISCUSSION

The thickness of the as de-posed film was estimated to be about 200 nm by Fizeau fringes method. Weight % of Sn, O and Cu are found as 69.52, 20.50 and dopant concentration was increased, the films became denser and closely packed. This clearly indicates that the metal dopant inhibits grain growth. The micro structural analysis shows grain sizes of 9.98 nm and 9.45 nm respectively. The morphology of the films was found that for lower dopant concentration, films were non-uniform. As the images are shown in Figure 3. In pure SnO<sub>2</sub> films, weight % of Sn and O are found to be 90.55 and 9.45 respectively. On the other hand for 4% Cu doping,

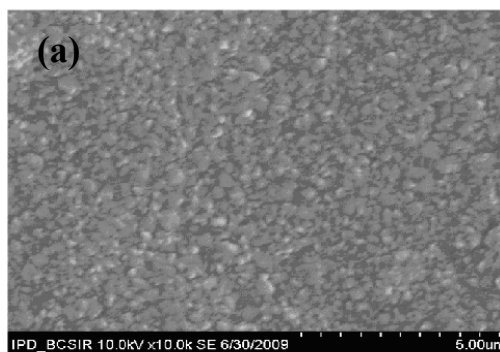


Fig 2. SEM images for 4 wt. % Cu doped SnO<sub>2</sub> thin film



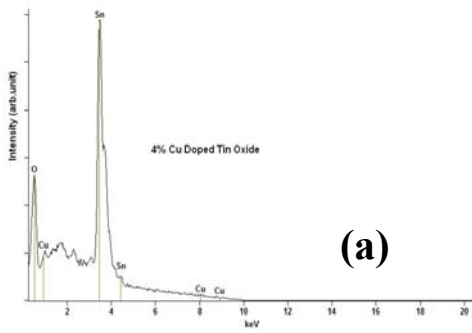


Fig 3. EDX images for 4 wt. % Cu doped SnO<sub>2</sub> thin film.

Further evidence is found in the X-ray diffraction patterns shown in Figure 4. From this figure it is observed that the reflection peaks in the doped films shifted from their standard positions in the presence of the dopant. The deviation in the lattice parameters is mainly due to occupying of doping atoms into the interstitial positions of the lattice. Hence from the EDX, optical absorption spectra and X-ray diffraction patterns, it is clearly

observed that the Cu<sup>2+</sup> ions are acting as dopants in the SnO<sub>2</sub> thin film. The XRD patterns of pure SnO<sub>2</sub> and 4% Cu doped SnO<sub>2</sub> thin film are shown in Figure 4. The XRD patterns were recorded at room temperature. From the XRD patterns, it is observed that there is a shift in the diffraction peaks of the doped film compared to the pure SnO<sub>2</sub> film. This shift is due to the substitution of Sn<sup>4+</sup> ions by Cu<sup>2+</sup> ions, which leads to a decrease in the lattice parameters. The optical absorption spectra were recorded at room temperature. The absorption spectra of pure SnO<sub>2</sub> and 4% Cu doped SnO<sub>2</sub> thin film are shown in Figure 5. From the absorption spectra, it is observed that there is a shift in the absorption edge of the doped film compared to the pure SnO<sub>2</sub> film. This shift is due to the substitution of Sn<sup>4+</sup> ions by Cu<sup>2+</sup> ions, which leads to a decrease in the band gap energy. The transmittance spectra of pure SnO<sub>2</sub> and 4% Cu doped SnO<sub>2</sub> thin film are shown in Figure 6. The transmittance spectra exhibit a transmission of > 80% in the visible and IR region, again it is found > 70% in the visible and IR region for Cu doped film, which is found to be greater than that of undoped film. The refractive index of pure SnO<sub>2</sub> thin film has been obtained 1.6316 and refractive index became 1.5417 for 4% Cu doping (Figure 6.). This low value of refractive index may probably due to the smaller density of the films. It is observed that refractive index increases further for higher doping of Cu. Among these transmittance plots it is seen that films deposited at 4% Cu doped have the highest transmittance value.

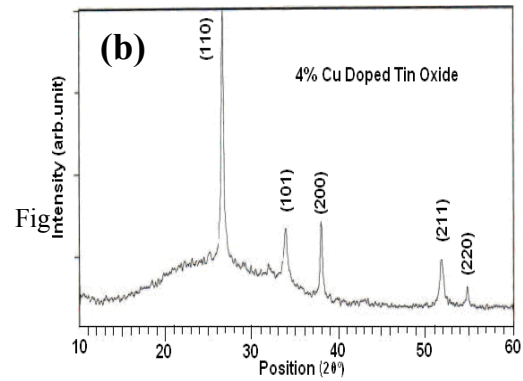
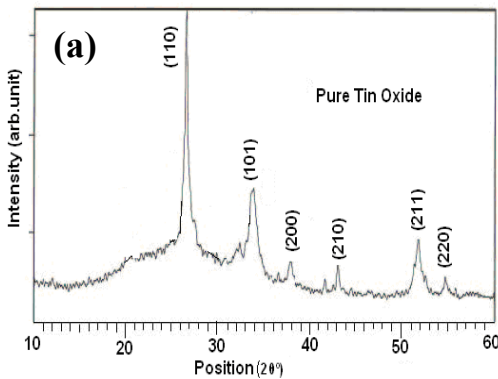
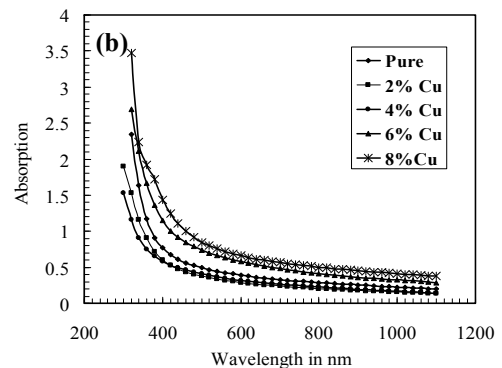
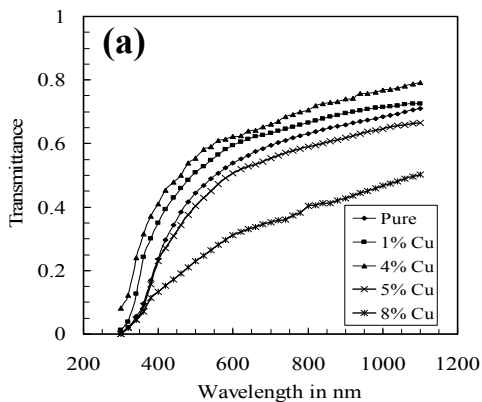
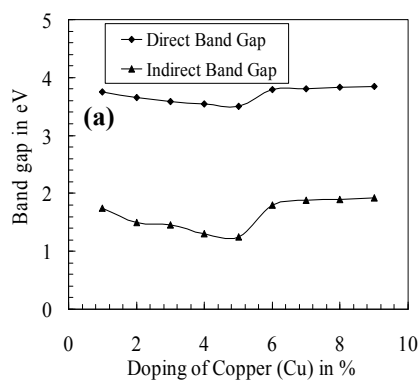


Fig 4. XRD images (a) for pure and (b) for 4% Cu doped SnO<sub>2</sub> thin film



The lowest direct optical transition corresponds to energy about 3.75–3.50 eV. The indirect transitions dominate as Sn<sup>2+</sup> increases in the system and occurs within the conduction band at 1.75–1.25 eV causing transparency in the visible range (Figure 6). The resistivity of the as-deposited SnO<sub>2</sub> thin films is decreased (close to linear) with increasing temperature. This behavior indicates the semiconducting nature of the films. All the films exhibited resistivity in the range of 10<sup>-4</sup> ohm-cm. The resistivity was dependent on dopant concentration and similar oscillatory behaviour in resistivity has been observed in the case of Sb doped SnO<sub>2</sub> thin films. In this work the variation has been related to the increase in mobility at a particular concentration. Other work on Nb and Al doped SnO<sub>2</sub> thin films also report similar resistivity behavior. It is clear that the doped SnO<sub>2</sub> films in the current study exhibit the properties of transparency and semiconductivity.



At room temperature, the electrical resistivity and sheet resistance of pure SnO<sub>2</sub> films is found to be 5.1065 × 10<sup>-4</sup> Ω-m, and 2.5532 × 10<sup>3</sup> Ω/□ respectively. Conductivity of pure films is varied in the range of 1.9582 × 10<sup>3</sup> (ohm-m)<sup>-1</sup> to 2.4065 × 10<sup>3</sup> (ohm-m)<sup>-1</sup> in the temperature range 305-475K. For Cu doping the resistivity is reduced and then its range becomes 1.1395 × 10<sup>-4</sup> Ω-m to 0.5080 × 10<sup>-4</sup> Ω-m (Figure 7). On Cu doping, carrier concentration increases and conductivity enhances remarkably. The conductivity behaviour is, however, an oscillatory nature depending on the level of dopant concentrations. It was proposed that Sn interstitials produce a donor level inside the conduction band due to their loosely bound outer electrons which gives rise to donor ionization and conductivity. Oxygen vacancies on the other hand would tend to produce deep levels inside the band gap. Sn interstitials have very low formation energy, therefore, they can exist in significant quantities and they are stable due to the intrinsic multivalency of Sn.

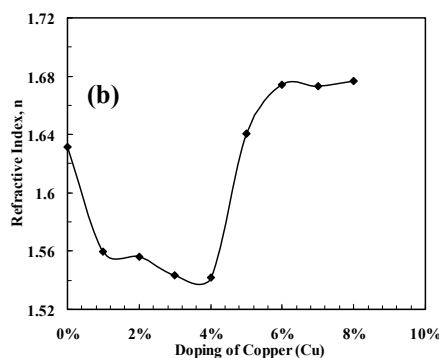


Fig 6. Variation of (a) band gap (b) refractive index of pure and Cu doped SnO<sub>2</sub> thin films

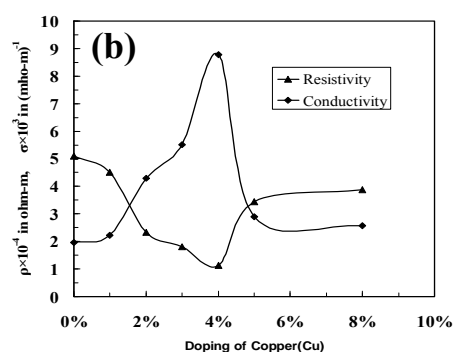
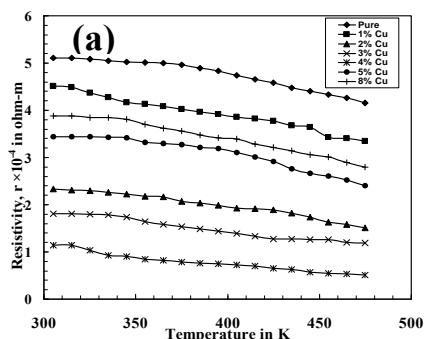


Fig 7. Variation of resistivity with (a) temperature and (b) Cu doping.

#### 4. CONCLUSION

The pure and Cu doped tin oxide thin films are prepared by spray pyrolysis technique from SnCl<sub>2</sub>

precursor. XRD patterns of SnO<sub>2</sub> films is found to have a better polycrystalline nature oriented along the (110), (101), and (200), (211) planes at 2θ = 26.591°, 33.888°, 37.959 and

51.787° respectively with single phase of SnO<sub>2</sub>. Average grain size of the film is found to be 7.244579 Å, which is agreed well with previous reported value. The transparency is ~ 80% for the best films with resistivity of the order of 10<sup>-4</sup> ohm-m. The transmittance increases initially with increase in doping concentration and then decreases for higher doping levels which is attributed to light absorption. The behaviour of the films has been explained within the frame work of current model for the coexistence of transparency and conductivity in SnO<sub>2</sub> based systems. The sheet resistance of the undoped films is

decreased with 4% doping of copper to attain a minimum value and increased for higher level of doping. The direct band gap of pure film is found to be 3.75 eV and reduces to 3.50 eV for 4% Cu doped SnO<sub>2</sub> films. The refractive index of the pure films is being into 1.63 and for 4% Cu doped film is 1.54. The obtained experimental results infer the suitability of this material as transparent and conducting window materials in thin film solar cells and optoelectronic devices.

## 5. REFERENCES

1. Joseph, J., Mathew, V., Mathew, J., and Abraham, K.E., 2008, "Studies on physical properties and carrier conversion of SnO<sub>2</sub>: Nd thin films", Turk J. hysics, Vol. 32, pp. 1-10.
2. Rusu, R. S., Rusua, G. I., 2005, "On the electrical and optical characteristics of CdO thin films", Journal of Optoelectronics and Advanced Materials Vol.7, No.2, pp. 823 – 828.
3. Islam, M. R. and Podder, J., 2009, "Optical properties of ZnO nano fiber thin films grown by spray pyrolysis of zinc acetate precursor", Cryst. Res. Technol. Vol. 44, No. 3, pp. 286 – 292.
4. Mishra, S., Ghanshyam, C., Ram, N., Singh, S., Bajpai, R. P. and Bedi, R. K., 2002, "Alcohol sensing of tin oxide thin film prepared by sol-gel process", Bull. Mater. Sci., Vol. 25, No. 3, pp. 231–234.
5. Shadia, J. I. and Riyad, N., Bitar, A., 2008 "Effect of Processing on the Electrical Properties of Spray-Deposited SnO<sub>2</sub>: F Thin Films", American Journal of Applied Sciences, 5(6), pp. 672-677.
6. Yuelan, Z., Ying, L., and Meilin, L., 2006, "Nanostructured Columnar Tin Oxide Thin Film Electrode for Lithium Ion Batteries", Chem. Mater., 18, pp. 4643-4646.
7. Hong, N. H., Sakai, J., Prellier, W. and Hassini, A., 2005, "Transparent Cr doped SnO<sub>2</sub> thin films: ferromagnetism beyond room temperature with a giant magnetic moment", Journal of Physics: Condensed Matter, Vol. 17, pp. 1697-1702.
8. Shanthi, E., Banarjee, A., Dutta, V. and Chopra, K. L., 1982, "Electrical and optical properties of tin oxide films doped with F and (Sb+F)", J. Applied Phys. Vol. 53, pp.1651-1621.
9. Joseph, J., Mathew, V., and Abraham, K. E., 2007, "Studies on Cu, Fe, and Mn Doped SnO<sub>2</sub> Semi-Conducting Transparent Films Prepared by a Vapour Deposition Technique", Chinese Journal of Physics, Vol. 45, No. 1. pp. 84-97.
10. Elangovan, E., and Ramamurthi, K., 2003, "Studies on optical properties of polycrystalline SnO<sub>2</sub>: Sb thin films prepared using SnCl<sub>2</sub> precursor", Cryst. Res. Technol. 38, No. 9, pp. 779–784.
11. Rajeeb Brahma, R., Krishna, M. G., and Bhatnagar, A. K., 2006, "Optical, structural and electrical properties of Mn doped tin oxide thin films", Bull. Mater Sci., Vol. 29, No. 3, pp. 317–322.



## AUTOMATION OF TESTING FACILITIES USING MATLAB

M. M. Rahman<sup>1</sup>, Z. M. Hasib<sup>2</sup>

<sup>1</sup>Esolutions Training Center, Dhaka

<sup>2</sup>Bangladesh University of Engineering & Technology, Dhaka.

### ABSTRACT

MATLAB is a powerful tool for engineering and scientific analysis. Experimental analysis and testing is must for engineers and researchers to carry on advanced engineering and scientific research works as well as to take decisions on different practical aspects. Thus it is obvious the result of any experimental analysis should be error free and well presented. This paper examines how to develop an automated testing facility using MATLAB with the help of a parallel port and as well as com port in PC and microcontroller with proper sensory arrangement. **The forced convection over a flat plate** experimental setup has been taken as a model. Software with MATLAB GUI has been developed to make the system more user-friendly. The total system contains the hardware arrangement for the data acquisition from the setup and to control the setup via MATLAB and an automated report generation based on the data received from the DAQ part. The system also has emergency data saving capability if the PC somehow fails to work or shut down unexpectedly. The developed automated system has the capability of starting the whole testing facility itself, check the required parameters needed to carry out the experiment, control the inputs given by the experimenter and finally take the result. The automated system also provides the experimenter, the facility for the statistical analysis of the result.

**Keywords:** MATLAB, GUI, Auto Calibration, Automation.

### 1. INTRODUCTION

Engineers and researchers frequently need to carry out numerous experiments within a very short time. A highly automated testing facility [1] widens the scope of achieving an error free result and also acute analysis of the result. Moreover, sensors used during the experiment may require calibration from time to time, to ensure minimum error in the result.

The automation of a testing facility should be such that, it encompasses all the aspects of testing process, from the test planning to the test execution, storage of results for statistical analysis, and finally to print out the data tables, graphs, and results.

The endeavor of our work was to show, the detailed hardware and software arrangement for automation of a testing facility and to depict the advantages, obtained due to this automation. There are numerous important engineering applications in which heat transfer for flow over bodies such as flat plate, a

sphere, a circular tube or tube bundle are needed. That's why in our present work, we have taken '**Forced Convection over a Flat Plate**' as a model. The testing panel is interfaced with PC, and is programmed, using MATLAB. GUI has been used to make the system more user-friendly. Microcontroller is used for the storage of results, if the PC fails to work or shut down unexpectedly. For the permanent storage of the results, we have used Microsoft Excel, in affiliation with MATLAB.

The hardware & software arrangement facilitates the experimenter, to start/stop and control the air velocity, to regulate the heat input to the plate, and to auto-calibrate the sensors, by means of computer control. The system arrangement also enables the experimenter, to perform the experiment, at different angles of the heated plate.

## 2. SENSOR ARRANGEMENT

Sensors are generally used to convert a physical signal into a corresponding electrical signal, which by proper amplification or attenuation is converted into a numeric quantity. Forced convection analysis over a flat plate consists of temperature sensors in the plate that is under experiment. The sensors (Fig 1) are connected to the control unit. The experimental setup contains two types of sensors, a pressure sensor and temperature sensors. Piezo-electric [2] sensor is used to measure pressure inside the duct. For temperature sensing, two types of sensors are used, namely DS18B20 (-55°C to 125°C) and LM34 (-45°C to 145°C) and the ultimate working range of the testing facility is from -45°C to 125°C. DS18B20 acts as the primary temperature sensor, which provides output in °C. LM34 acts as the secondary temperature sensor, which provides output in milli volt (mv). ADC channels of a Microcontroller chip ATMEGA 8 connected to the secondary sensors convert milli volt (mv) unit into a suitable 10 bit digital value. Secondary sensors are calibrated by comparing it with the primary sensor output value during calibration. The components used in the experiment can be listed as below:

- 1) Piezo-electric pressure sensor.
- 2) DS18B20 temperature sensor.
- 3) LM34 temperature sensor.
- 4) ATMEGA 8-microcontroller chip

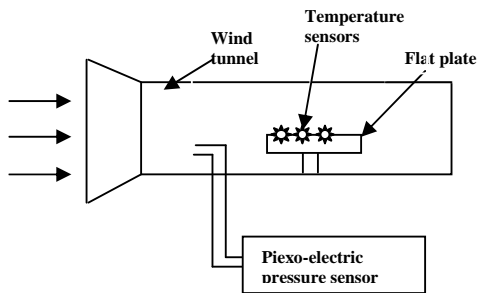


Fig 1. Sensor arrangement

## 3. HARDWARE ARRANGEMENT

The hardware part of the system covers the whole electrical system apart from the hardware of the testing facility itself. Hardware sections used here can be divided into following parts,

- A. Circuit to control testing equipments.
- B. Circuit for intermediate processing and feedback control.
- C. Circuit for storing transferring and monitoring data (Data logging circuitry).

Well developed hardware arrangement is the backbone of automation. The hardware part should contain control unit, feedback unit, and processing unit. The feedback unit and the intermediate processing unit contains microcontroller which is programmed by C/C++. All these units should have interconnection with one another. PC sends primary control data associated to the experiment and fixed by the experimenter to both the intermediate processing unit and the feedback unit. Intermediate processing unit then processes the data and

sends command to the control unit. And based on the command, control unit controls fan speed and heat input to the plate. The feedback unit receives feedback from the velocity and pressure sensors, and sends it to both the PC and control unit. Once the test is started, intermediate processing unit takeover all the task for processing and controlling based on user input and sends data to the PC where MATLAB based software shows the ongoing data for monitoring and controlling of parameters, if needed, by the user. To make the software more user friendly, GUI has been introduced. The software facilitates the experimenter, to store the data in (.xls) file. Finally, the experimenter has scope to print out the data table, graphs and also to generate a detailed report based on the experimental data.

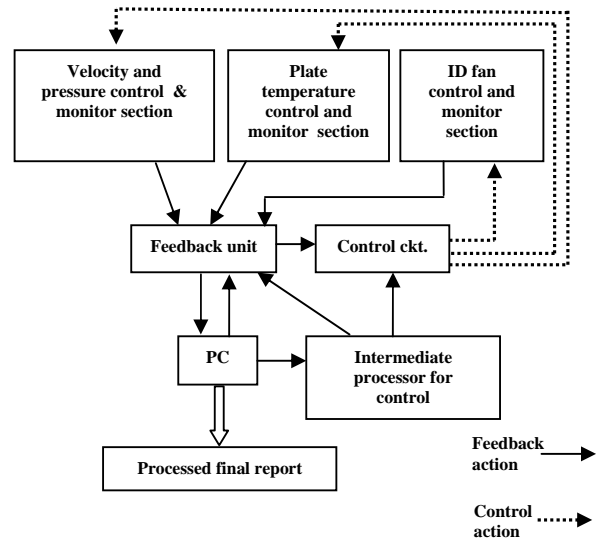


Fig 2. Schematic diagram of hardware arrangement.

### 3.1 Inter-Connection between Fan\* Speed and Velocity/Pressure Sensing Arrangement

In this work, the endeavor was to develop a highly atomized testing set-up. The hardware and software arrangement facilitates the experimenter to perform the experiment at different air velocity (Fig 3). The experimenter sets the air velocity in which he needs to perform the experiment. And based on the given air velocity, the control unit changes the fan speed to achieve that air velocity. Until the system reaches the desired given velocity (steady state) it takes the feedback from the pressure sensor which in turns calculate the instantaneous velocity of air in the tunnel and sends it back to the control unit. Control unit, based on the feedback changes the fan speed until the desired velocity is achieved.

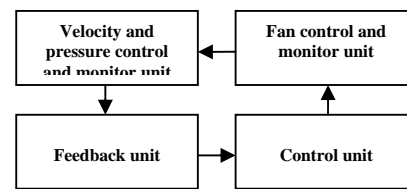


Fig 3. Schematic diagram to set air velocity

\*ID Fan has been used in this model

### 3.2 Inter-Connection between Plate Temperature and Control Section

The hardware and the software setup facilitate the experimenter to perform the experiment at different plate temperatures (Fig 4). The experimenter has option to select the plate temperature. And based on the selected plate temperature, the control unit changes the heat flux to the plate. Until the system reaches the desired plate temperature (selected by the experimenter), it takes the feedback from the temperature sensors. Control unit, based on the feedback, changes heat flux to the plate until the desired plate temperature is achieved.

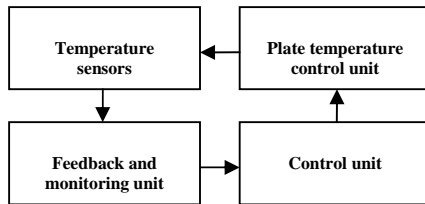


Fig 4. Schematic diagram to control the plate temperature

## 4. SOFTWARE DEVELOPMENT

To make the testing facility more efficient and user-friendly, an object oriented GUI based software has been developed (Fig 5) using MATLAB GUIDE tool and the MATLAB programming and mathematics tool for the setup. To decrease the complexity and to make the testing procedure conspicuous, experimenter has been given the privilege to stop control and change the parameters at any time and if necessary shutdown the whole process. The object oriented analysis is a faster and efficient way, to develop software and systems. The object-oriented software divides the system into well defined units. For example as in this study: setup checking, data recording [3], initialization, graph plotting etc. are the different units present in the system with the capability of each unit performing independently.



Fig 5. Initial GUI of the software

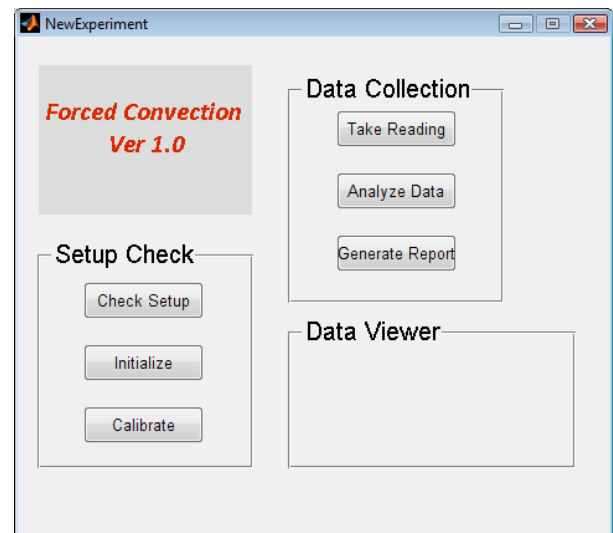


Fig 6. GUI of the software when a new experiment would be conducted

### 4.1 Setup Checking

The very first task of an experiment is to check the setup. (i.e. if any of the functional components of the setup is ok or not). The GUI for the setup checking has been developed with a proper arrangement to check the availability and the functionality of the equipments (Fig 7). The software provides a pictorial view of the setup, and each of the components, along with their specifications. The software facilitates the experimenter, to check the availability of all the components. Such as: copper plate, blower, temperature sensors, etc. And if any of the components does not respond, then the software apprises the experimenter to check that specific component.

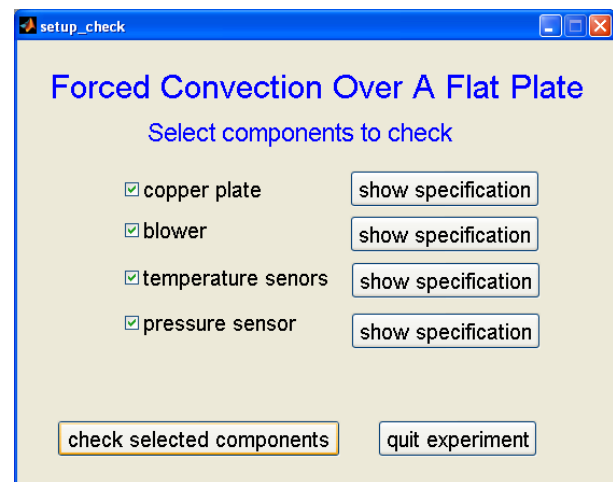


Fig 7. GUI for setup check

### 4.2 Auto-Calibration

To record the temperature, at different points of the plate, two types of temperature sensor have been used. **DS18B20** has been used as the primary sensor and **LM34** has been used as the secondary sensor. The primary sensor has good accuracy level ( $\pm 0.5$  °C). And it provides



the temperature in digital unit. The secondary sensors are calibrated by comparing it with the primary sensor. GUI for auto-calibration has been developed (Fig 8). The software contains built-in auto- calibration code to simplify the calibration process.

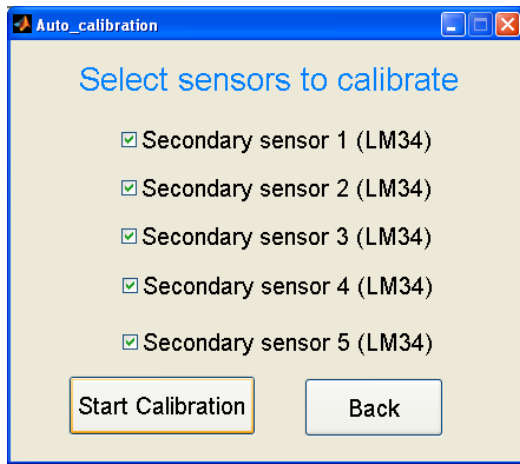


Fig 8. GUI for auto calibration

#### 4.2.1 Advantages of Auto-Calibration

Every sensor shows fluctuation in performance. So for better accuracy the sensors used in an experiment needs calibration from time to time. The conventional process of calibration needs physical access to the sensors which usually means disassembling the system, which is an inconvenient and time consuming process. Moreover in auto-calibration process all the sensors are calibrated simultaneously. Auto calibration shows far better performance than the conventional calibration process. Auto-calibration reduces the error level to a significant level [4]. In this model, specifically Dallas semiconductor designed DS18b20 has been used but if needed other primary sensors can also be used with a proper transducing arrangement to employ auto- calibration in the system.

#### 4.2.2 Method of Auto-Calibration

MATLAB code has been developed to auto calibrate the secondary sensors. Each secondary sensor is connected to ADC channels of a Microcontroller chip ATMEGA 8 which converts milli volt (mv) input to a suitable 10 bit digital value. To calibrate the secondary sensors, the copper plate is heated to a higher temperature (about 100 °C) and the software records the actual temperature and digital values for each secondary sensor at an interval of 250 milli second. Based on these data, the software plots the temperature vs. digital output curve (Fig 9) and generates equation for each secondary sensor. However, for higher accuracy and low response time, LM34 can be replaced by thermocouples or other temperature sensors [5] such as TSIC-301(response time 0.1 second) can also be used. Following table shows the data recorded to calibrate 2(two) LM34 (secondary sensor) sensors automatically, the program itself generates the table and generates necessary curve for the calibration purpose.

Table 1: Digital values of the sensors at different temp.

DS18b20 (°C)	LM34 (sensor 1) (Digital value)	LM34 (sensor 2) (Digital value)
50	122.16	123.2
55	127.45	126.56
60	130.54	129.85
65	133.25	134.26
70	136.88	137
75	139.90	140.12
80	143.25	144.4

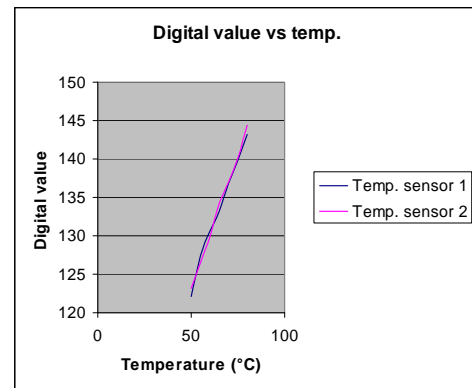


Fig 9. Digital value vs. temp. graph

#### 4.3 Initializing the Process

In every experiment, the experimenter has to provide some standard test data, based on which the experiment is performed. GUI for the initialization of the test has been developed (Fig. 10). The experimenter has to initialize the specifications of the plate which is going to be used in the experiment i.e. plate material, plate length, thickness etc. The software provides option to change the air velocity and plate temperature.

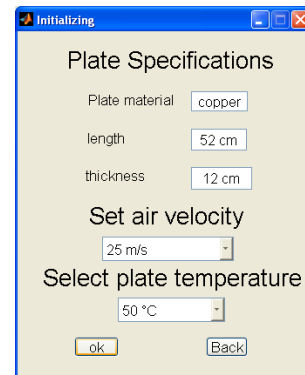


Fig 10. GUI for initializing.

#### 4.4 Data Recording

After the prompt from the experimenter, the software records data, sent by the hardware arrangement. The software has collaboration with 'Microsoft Excel'. So the software records each data set to a new (.xls) file. This arrangement facilitates the experimenter to compare the data with the previous experiments. (Fig. 11) shows the GUI for data recording. The data table shows each data along with their units. The user also has the option to remove wrong or unwanted data, from the table. In an experiment, several data are needed to record simultaneously. So there runs a risk of missing some data. To prevent this problem, hand shake [6] with parallel port is used to ensure that, the system records each necessary data. And if somehow a single data is missing the software will notify the experimenter regarding the missing data. The calculation would not start until the experimenter confirms the system to proceed and the system would apprise the experimenter to perform the experiment from the beginning.

obs n	power input	Emperical co-relation		Theoretical (hc)	Experimental (hc)
		Rel	Pr		
1	50	801000	0.706698	49.99	91.21
2	100	756000	0.7061	46.28	72.63
3	150	748000	0.7055	45.88	66.98

Fig 13. Calculation table

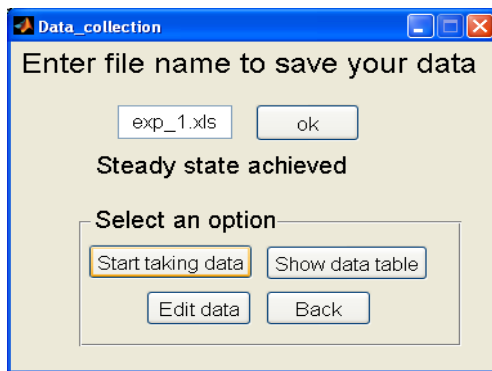


Fig 11. GUI for data collection

#### 4.5 Calculations and Graphs

The final step of an experiment is calculation. Well programmed software enhances the scope of performing numerous complex calculations within a very short time. (Fig. 12) shows the GUI for calculations and graphs. For the calculation purpose, air property table is needed. And the property table has been attached with the software by using MATLAB database [7]. However, the software has facility to view the results (Fig 13), graphs (Fig 14) and also to generate report of the experiment.

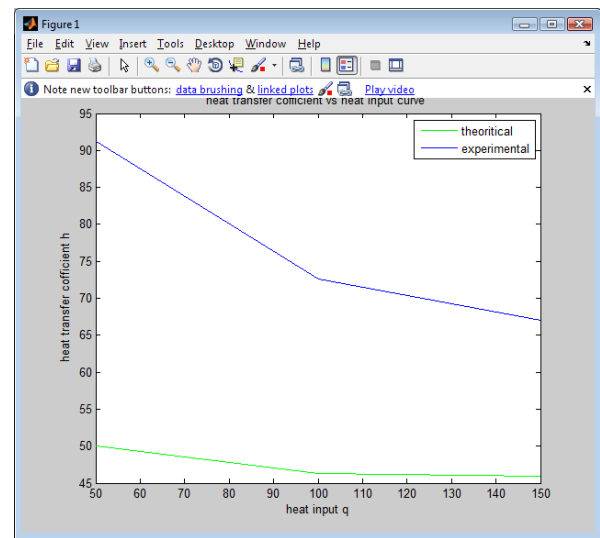


Fig 14. Heat transfer coeff. vs. heat input curve

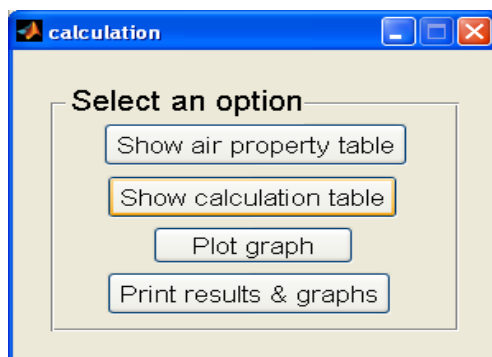


Fig 12. GUI for calculation

#### 5. FURTHER DEVELOPMENT

Further development of this work would facilitate the experimenter, to perform the experiment at different plate angles. Stepper motors can be connected with the flat plate, for the inclination of the plate at different angles [8]. Software can also be developed which would facilitate the experimenter, to choose the range of the plate angles at which the experiment would be carried out. And the results of heat transfer coefficient, for different plate angles would help the experimenter to find out the plate angle for which heat transfer coefficient would be maximum / minimum. And this would make the experimental setup, as an universal setup [9].

#### 6. CONCLUSION

MATLAB is a user-friendly and a powerful tool that can carry out various engineering applications and calculations within a very short period of time. So

MATLAB has been chosen in this work, to develop the software for automation purpose. GUI is used to make the software more user-friendly. This paper shows the gateway to atomize any testing setup. The objective of this study and present work is entirely to give the students and as well as researchers the idea of the MATLAB automation tool [10] and how to automate a testing facility for the ease of experiment. **The forced convection over a flat plate** experimental setup has been taken as a model for the work. However, any testing facility can be atomized, by following these general steps [11], as described in this paper. The **auto-calibration** process as described in this paper can be used to calibrate any type of sensors. A highly atomized testing setup widens the scope of achieving error free result [12] and performing a test within a very short time. That's why a highly atomized setup can commercially be used for testing purposes.

## 7. ACKNOWLEDGEMENT

This work was supported in part by R&D department of E-Solutions BD.

## 8. REFERENCES

The references related to this paper are listed as below:

1. Nelson, G. B., Gresse,B., Wright,J., 2004, "Automated Testing and Real Time Event Management: An Enterprise Notification", *proc. SUGI-29, Montreal Canada*, PP 228-29.
2. Beckwith, G. T., Marangoni, D. R. and Lienhard,H. J., 2001,*Mechanical Measurements*. Pearson Education, Singapore.
3. Spall,J., and Downing,D., 2002, *Automated Testing of Oracle Applications Release 11i (v 11.5.7)*. Atlanta, U.S.A.
4. Milar Jonathan, "The Benefits of Auto-Calibration". 2006, Diamond Group, U.S.A. <http://www.diamondsystems.com/files/binaries/Benefits-of-Autocalibration.pdf>
5. Pan,X. D. and Sui, Q., 2009, "A Novel Configuration of Temperature Compensation in Rectangular Wavelength Resonant Cavities". *Proc. PIERS 2009, Beijing, China*. PP 318-322.
6. M. L. Bailey, J. V. Briner and R. D. Chamberlain, 2004, "Parallel Logic Simulation of VLSI System". *Acm computer surveys* 26(3):255-294, September 1994.
7. Klysburn, P. and Netsai, C., 2006, "Development of MATLAB based Data-Logging System ai Siam Photon Source". *Proc. EPAC 2006, Edinburg, Scotland*. PP 3098-3100.
8. Onate,E. and Zarate,F., 2000, "Rotation-free Triangular Elements and Plates", *Int. J. Num. Mech. Engg.* 47, 557-603 (2000).
9. Kroposki,B. and Englebretson,S., "Testing of GE Universal Interconnection Device", NREL/TP-560-34676.
10. Pieres, J. N., "Using MATLAB for Industrial Robots and Automatic Equipment" , *IEEE robotics and automation magazine*, 2009.
11. Butchet, T., Clebi, Y., Wei, G., and Kamath, B., "Small oil burner concepts based on Low Pressure Air Atomized". *Proc. Second European conference on heating and burner technology, University of Stuggat, march 16-17, 2000*. PP BNL 2267.
12. Linden, W. J., Glass, C. A., "Capitalization in Item Calibration Error in Computer Adaptive Test", Ph.D. thesis, University of Twente, Enschede, The Netherlands.

## 9. MAILING ADDRESS

Zannatul Moiet Hasib  
 Student no: 0510111.  
 Department of Mechanical Engineering  
 BUET, Dhaka-1000, BANGLADESH.  
 Phone: 01811965493.  
 Email: moiet\_0510111@yahoo.com

## SAVING ELECTRICAL ENERGY USING INTELLIGENT AUTOMATION TECHNOLOGY

M. N. Ekram Tamim, Fazle Rabbi and M. A. A. Shoukat Choudhury

Department of Chemical Engineering  
Bangladesh University of Engineering and Technology

### ABSTRACT

The primary objective of this study was to reduce electricity consumption by automation of the switching system of a room. A motion sensor was used which senses human movement by change in heat flux in a confined space. Appropriate circuitry has been developed to control the switching system of the room in such a way that when motion is sensed the circuit gets closed, fans and lights starts operating. When motion ceases, the circuit opens and all appliances shut down after two minutes of delay. The automation device was implemented for testing purpose in a room and data of energy consumed in KWh were collected for both manual and automatic modes. Observed data indicated that approximately 40% of electrical energy can be saved by adopting such automation systems. This study showed that a total of 140 MW of electricity can be saved by implementation of such automation systems in commercial offices in Bangladesh.

### 1. INTRODUCTION

#### 1.1 Electricity Problem in Bangladesh:

Bangladesh is in a dire strait because of its recent crisis for electricity. As an under-developing country uninterrupted power supply to its industrial, commercial and residential sectors is a must to achieve higher GDP growth. To increase productivity of the existing infrastructures, to attract foreign and local investments and to create new industries, uninterrupted power supply must be ensured. According to the authority about 1400 MW to 1800 MW electricity shortage is about to be occurred in 2009, which is almost twice more than that of last year and the country need approximately 5000 MW of electricity in total [1]. The projected demand of electricity in the year of 2012 is 7900 MW and by 2020 it is believed to reach 14600 MW [2]. Therefore, the amount of electricity shortage may increase more rapidly in near future unless something is done now. Installation of new power plants and reduction of system loss may improve the situation. But gas crisis limits the possibility of new power plant implementation as right now power generation capacity of about 500 MW per day remains unutilized due to gas shortage. The present gas demand is about 2400MMCFD while our production capacity is about 1950MMCFD [3]. So it is essential that electricity consumption in different sectors should be reduced by considerable amount to improve the current situation. The electricity consumption sectors can be divided into four groups – 1.Residential, 2.Industrial, 3.Commercial and 4.Others. Electricity consumption pattern for the year 2007-08 has been shown in Fig. 1.

The figure shows that in 2007-08 approximately 47% of total energy was consumed in residential section while electricity consumption in industrial and commercial sectors was 41% and 9%, respectively. The consumption

pattern is believed to be remained same in the recent years. The figure shows that in 2007-08 approximately 47% of total energy was consumed in residential section while electricity consumption in industrial and commercial sectors was 41% and 9%, respectively. The consumption pattern is believed to be remained same in the recent years.

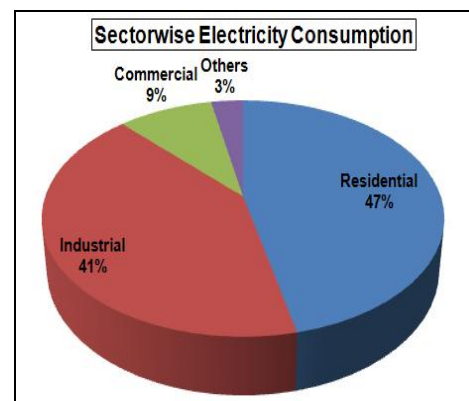


Fig 1. Electricity Consumption Pattern [4]

The focus of this study is the energy being consumed in the commercial sector. Energy consumption in commercial sector refers energies consumed in buildings and facilities of both government and private sectors -- wholesale and retail trades; the operation of hotels and restaurants; renting and business activities; financial intermediations, bank and insurance companies; public administration and defense offices; education institutes; community halls, health and social service activities. The

detail data of sectorwise electricity consumption is presented in table A.1 in Appendix 1. From this table it is quite clear that electricity consumption in different sector is increasing and in the case of commercial sector the rate increase is even higher.

In 2007-2008, commercial sector consumed nine percent (9%) of total electricity while electricity consumption in this sector has increased by 30% over the year of 2006-07 [4].

## 1.2 Saving Electricity

Electricity is being wasted in our country in various ways. As it has been stated earlier, we are having a huge shortage of electricity. Saving electricity and restricting its wastage are utmost necessary. Some steps have already been taken recently to save electricity:

1. Disconnecting illegal power connections
2. Introducing Day Light Saving (DST) to maximize the use of day light
3. Implementing a new dress code which allows government officials to wear light clothing instead of formal suits and ties
4. Keeping air conditioners thermostat level at 24 degrees Celsius.

However the amount of electricity wasted due to ignorance and careless behavior of people is large. A noticeable portion of electricity can be saved by disallowing this type of wastage. It is of common practice that people do not play active role on reducing consumption of electricity by carefully switching off the electrical devices while they are not in use. Most of the time people do not switch off lamps, fans and other appliances while leaving the room for a short period of time. As a result the more the time spent outside the room, the more energy is wasted.

## 2. OBJECTIVE

In this study the primary focus was the wasted energy due to careless behavior in the commercial office buildings. It is mentioned earlier that about nine percent of total consumption of electricity is consumed in the year of 2007-08 at commercial sector. So a considerable portion of electricity can be saved if wasting of electricity in commercial buildings is reduced. This wastage could be easily prevented if we become more conscious to turn off the electrical appliances when they are not in use. But bringing change in human behavior is not easy. In this project an alternative measure is attempted through automation of the switching system of the room. If the switching system can be so that the presence and absence of human inside a room is detected and automatic switch off occurs during absence of people inside the room, the waste of energy can be minimized.

Automation of the switching system can be performed in many ways. The following are two probable options:

1. By using a motion sensor which senses human movement by change in heat flux in a confined space.
2. By using two door sensors which will count people entering and leaving the room with the help of appropriate circuitry.

In this current project a motion sensor with

appropriate circuitry was used for automation of switching system of a closed room. Appropriate circuitry was developed to control the switching system of the room so that when motion is sensed the circuit kept closed; fans and lights starts operating. When motion sensor does not detect human motion for two minutes, the circuit breaks and appliances shut off. The automation device was implemented for testing purpose in a room containing three tube lights and a fan. Theoretically each of these tube lights consumes 40 W and the fan consumes 60 W. The modes of operation were conventional manual mode without sensor and the auto mode operating with the sensor. Data for energy consumed in KWh was collected for each of the two modes of operation for 7-10 days in rotation.

## 3. THEORY OF OPERATION

### 3.1 Block Diagram

The simplified block diagram of the set-up for automation of switching system is shown in figure 2.

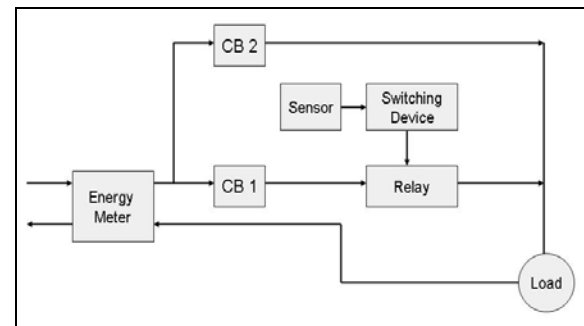


Fig 2. Block Diagram of the Automation Process

In this diagram, CB 1 refers to the circuit breaker which has been used to operate the circuit in the automatic mode and CB 2 has been used for conventional operation of the circuit.

### 3.2 Working Principle

The working principle for this project is simple. For this project only a few equipments were used. The block diagram of the project is shown in Figure 2. When there is human movement in the room, sensor senses movement by change in heat flux due to the heat radiated from human body and closes the circuit for operation. But when there is no movement in the room for a set time period, an electrical pulse is sent to the switching device which turns off the power supply by breaking the circuit with the help of a relay. The time delay was set to two minutes for this study. This system is capable of turning on the electrical appliances instantaneously when it senses human movement again. Energy meter was used to monitor the consumption of electrical power for both operational modes.

## 4. PROJECT SET-UP

The automation circuit implemented in the room consists of mainly the motion detector, controlling circuit, circuit breaker switch and an energy meter.

The Motion Detector which can sense human

movement in a confined space by change in heat flux is shown in figure 3. This motion detector, which was mounted on the wall, can sense the human movement over a range of 15ft by 10 ft.



Fig 3. Motion detector mounted on the wall

The switching system controlling circuit has been shown in Figure 4.

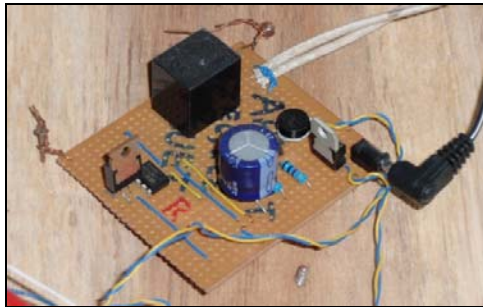


Fig 4. Controlling Circuit to Automate Electricity Switching

This control circuit is the heart of this intelligent automation switching system technology. This drives the switching system in the ON or OFF modes based on the motion detected by the sensor.

## 5. OBSERVATIONS

### 5.1 Data Presentation

Data for electricity consumption in KWh per day for each of the two operation modes were collected for two summer months. A part of such data is shown in Figures 5 and 6.

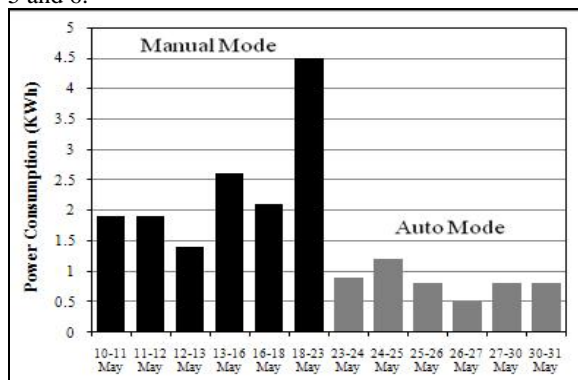


Fig 5. Power Consumption in Both Operating Modes

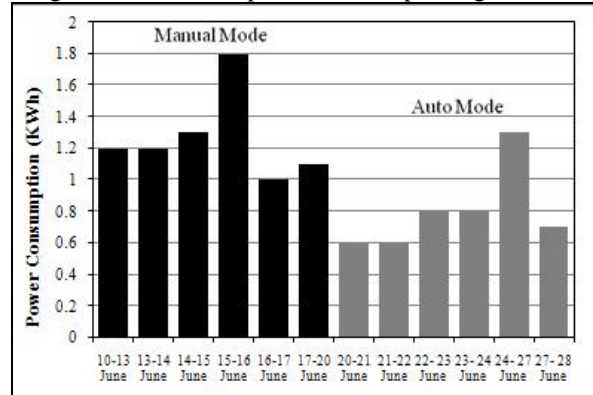


Fig 6. Power Consumption in Both Operating Modes

From Figures 5 and 6, it is clear that energy consumption in KWh per day for automation mode is much lesser than that of manual mode. Two largest bars in Figures 5 and 6 include energy consumed in the weekend too. Therefore, data for energy consumed in the working days are separated and presented in Figure 7. This figure now represents power consumption data only for regular working days excluding all the weekends and vacations. From Figures 5, 6 and 7, it can be observed that a considerable drop in power consumption occurred by using switching system automation device in the room.

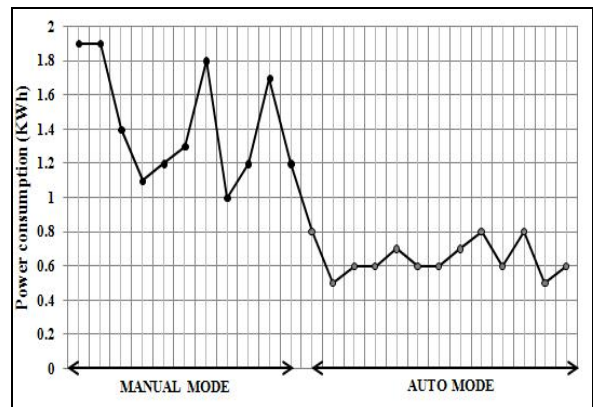


Fig 7. Power consumption per working days in both modes

### 5.2 Results

The results of implementing switching system automation device are highlighted in Table 1 and energy consumption data for manual mode operation is presented in Table 2.

In Table 1 power consumption in auto mode is listed with hours of operations.



Table 1: Calculated data of power consumption at Auto Mode

Hours in operation (hr)	Working hours (hr)	Power consumed (KWh)	Comments
24	8	0.7	-
24	8	0.9	-
24	8	1.2	-
24	8	0.8	-
29	13	0.5	-
67	4	0.8	Including weekend
24	8	0.8	-
24	8	1.0	-
24	8	0.6	-
24	8	0.6	-
72	8	1.1	Including weekend
24	8	0.7	-
24	8	0.6	-
24	8	0.6	-
24	8	0.8	-
24	8	0.8	-

From table 1, it is seen that power consumption per day in auto mode ranges between 0.5-1.2 KWh.

Table 2: Calculated data of power consumption at Manual Mode

Hours in operation (hr)	Working hours (hr)	Power consumed (KWh)	Comments
24	8	1.9	-
24	8	1.9	-
24	8	1.4	-
72	8	2.6	Including weekend
118.5	-	4.5	Including mid-term break
24	8	0.8	-
24	8	0.7	-
24	8	1.1	-
72	8	1.2	Including weekend
24	8	1.2	-
24	8	1.3	-
24	8	1.8	-
24	8	1.0	-
72	8	1.1	Including weekend
24	8	0.9	-
24	8	1.2	-
24	8	1.7	-

From Table 2, it is seen that power consumption in

normal manual mode ranges between 0.7-2.6 KWh.

By calculation of percentage of electricity savings following results are obtained-

1. Average saving in power based on total runtime (Including vacations and weekends)  
Percentage of electricity saving per day = 36.2 %
2. Average saving in power based on total runtime (Excluding long time absence)  
Percentage of electricity saving per day = 41%
3. Average saving in power (time-weighted average)  
Percentage of electricity saving per day = 40%

## 6. PROJECT FINDINGS

The major findings of this study can be listed as in the following:

1. Bangladesh is having a huge shortage in electricity as electricity demand outruns electricity generation. In the current year (2009), the expected electricity shortage is expected to be approximately 1400 MW- 1800 MW.
2. The amount of electricity shortage is increasing day by day. As the projected electricity demand is 7900 MW in 2012, where the current estimated demand is 5000 MW, the situation will become more complicated unless effective steps are taken to reduce consumption.
3. A total 9% of total electricity consumption is consumed by commercial sector last year and in domestic sector the consumption rate is 47%. 9% of total electricity corresponds to 450 MW of electricity, which is being consumed by commercial sector now while 2350 MW of electricity is being consumed by domestic sector. Consumption rates in commercial sector as well as in domestic sector are also increasing quite rapidly day by day than the other sectors.
4. A considerable amount of electricity is being wasted due to unconscious behaviour of people. By minimizing this wastage a good amount of electricity can be saved thus the amount of “electricity shortage” can be reduced.
5. In the case of confined places, about forty percent (40%) of electricity can be saved by automation of switching system developed in this project.

The facts mentioned above indicates that the problem of electricity shortage can be made a little better by adopting the automation of switching system of the electrical devices used in a room. The circuit with motion detector developed in this study can be used in commercial offices, offices of educational institutions and other sectors, conference rooms, drawing room or leaving room of our. The circuit is quite flexible for use in different sectors as the delay time is adjustable and it is very easy to implement even in the existing system.

Treatment of raw data indicates that 40% of electricity can be saved by adopting the switching automation system in a room. Assuming 90% of total energy consumed in the commercial sector is used by commercial offices and rooms and 90% of total commercial offices are covered by such switching automation devices developed in this project, a total of 145 MW electrical energy can be saved nationwide ( $450 \times 0.9 \times 0.9 \times 0.4$ ). If 3% of domestic sector rooms are equipped with such switching automation devices, another 28 MW can be saved ( $2350 \times 0.03 \times 0.4$ ).



Therefore, a total 173 MW of electricity is expected to be saved by using such automation devices.

Saving 145-175 MW electricity can be quite beneficial to our country in several aspects such as-

1. Saving of 145-175 MW electricity means, a power plant of medium capacity may not be needed. So the cost of implementation and operation of one power plant can be prevented and huge amount of money can be saved.
2. One less power plant means, a considerable amount of saving in natural gas consumption.
3. Again minimization of operation of a power plant means, lesser pollutant emission to air and water bodies.
4. This amount of electricity saving can be used for carbon trading and the country can get a considerable amount of foreign exchange money from United Nations (UN).

## 7. ECONOMIC FEASIBILITY OF THE AUTOMATION DEVICE

The power saving ability of the switching system automation device developed in this project has already been demonstrated above. Now the economic aspects of the device are studied below for checking the feasibility of such devices. Let us consider a room containing of the following devices:

1. An air conditioner (1350 watt)
2. A fan (75 watt)
3. 2 light bulbs (100x2 watt)
4. 2 low energy lights (20x2 watt)

Therefore, the total energy consumption of this room can be calculated as 1665 Watt.

### 7.1 Calculation of Monthly Saving

Assume, the working time for offices be 7 hours per day, 5 days per week and 20 days a month. In manual mode,

Monthly bill for this particular room will be 1433.6 Tk based on Tk. 6.15 per unit of electricity cost in commercial sector ( $1665 \times 7 \times 20 / 1000 \times 6.15$ ).

If automation device were used,

Monthly bill for this particular room will be= 860 Tk

Monthly saving by using automation device for a room  
 $= (1433.6 - 860) \text{ Tk} = 573.6 \text{ Tk}$

### 7.2 Break-Even Analysis

The total cost to implement the automation device for this current project was 4000 Tk. The expected service life of the device is 10 years.

Now, considering the case of the office room, the break-even point, where the cost of the device is equal to the money saved due to the use of automation device, can be found graphically as shown in Figure 8. Therefore, the fixed capital investment will be equal to the amount of savings after 140 working days. This corresponds to 7 months with the assumption of 20 working days per month. Therefore, it can be concluded that the economic feasibility of the switching system automation device is justified

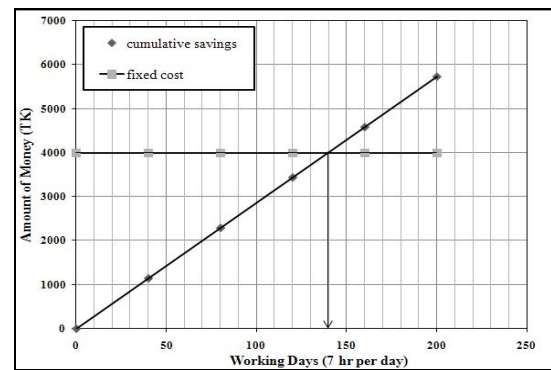


Figure 8: Break-even Analysis

## 8. CONCLUSION AND FUTURE WORK

This study aimed to reduce the consumption of electricity by minimizing electricity wastage due to unconscious human behavior. The study suggests that using automated switching system can save up to 40% of electricity. If all office rooms are equipped with such automation systems approximately 145 MW of electricity can be saved. This will not only help reducing the load-shedding but also increase the productivity. It will also save natural gas by eliminating one moderate size power plant. This will result in less pollution too. Thus it can be concluded that considering the critical energy situation through which Bangladesh is going through now, the implementation of such automation systems will reduce the electricity load and ensure an efficient use of energy.

Though the economic feasibility of the automation device is justified, the cost for the implementation of the automation device is relatively high for our country. If the fixed cost is reduced by 50-60% the device would become more economically attractive and popular. So the main challenges of wide use of automation devices for switching system controlling are cost reduction, easy and flexible implementation. The major cost of the device is for the sensor, which is 3000 Tk. If door sensors are used, the cost of the device can be significantly reduced.

## 9. REFERENCES

1. "Load Shedding of Electricity in Bangladesh", Khaled Saifullah, <http://freshclick.wordpress.com/>. Accessed: 4 pm, September 29, 2009.
2. Power System Master Plan Update, Power Cell, Power Division, Ministry of Power, Energy & Mineral Resources.
3. "Bangladesh Energy Scenario – Current Priorities", Engr. Khondkar Abdus Saleque, [www.energybangla.com](http://www.energybangla.com). Accessed: 4:30 pm, September 29, 2009.
4. Annual Report 2008, Dhaka Electric Supply Company Limited (DESCO), 2008.

**APPENDIX - 1**

Table A.1: Sector wise energy consumption data [4]

<b>Year</b>	<b>Domestic Service (MKWh)</b>	<b>Industrial Service (MKWh)</b>	<b>Commercial Service (MKWh)</b>	<b>Others (MKWh)</b>	<b>Total (MKWh)</b>
1994-95	4090	4546	915	1345	<b>10896</b>
1995-96	4681	4867	951	1336	<b>11835</b>
1996-97	3208	8646	586	550	<b>12990</b>
1997-98	3612	5217	714	633	<b>10176</b>
1998-99	4217	5603	742	699	<b>11261</b>
1999-00	4023	5795	770	764	<b>11352</b>
2000-01	4891	5125	824	794	<b>11634</b>
2001-02	5511	5432	876	748	<b>12567</b>
2002-03	5969	6003	1007	738	<b>13717</b>
2003-04	6598	6682	1157	898	<b>15335</b>
2004-05	6946	7153	1243	994	<b>16336</b>
2005-06	8910	9175	1595	1274	<b>20954</b>
2006-07	9006	9275	1612	1288	<b>21181</b>
2007-08	10642	9489	2095	705	<b>22931</b>

## WEAR BEHAVIOUR OF NODULAR CAST IRON

N. Fatima and M.A. Islam

Materials and Metallurgical Engineering Department  
BUET, Dhaka, Bangladesh.

### ABSTRACT

For many applications of nodular cast irons, wear properties of the component parts are very important. However, the wear resistance of as-received (as-cast) nodular cast iron is not so encouraging, because of its lower hardness. In this research work, initiative has been taken to improve the surface hardness as well as the wear resistance of the as-received nodular cast iron by pack carburizing technique. Using pin-on-disc type wear test apparatus, wear behaviour of both as-received and pack carburized nodular cast irons were carried out at room temperature in the ambient air. For both cases, various dead loads such as 0.5, 1.0 and 2.0 kg were used. After wear tests, worn surfaces of both pin (specimen) and disc (counter body) were observed in metallurgical microscope and they were photographed. Weight losses of pins under different test conditions were also measured. Experimental results reveal that carburized nodular cast irons are unbelievably more wear resistant compared to that of as-received one under similar test conditions. For both samples, wear patterns were also found to be different.

**Keywords:** Nodular cast iron, Wear, Surface hardening, Automotive parts.

### 1. INTRODUCTION

Nodular cast iron is a cast ferrous alloy. Its advantages are numerous. The main advantages of nodular cast irons among all other cast alloys are evident in the area of mechanical properties. It offers designers the option of selecting high ductility (more than 18%) with high tensile strength exceeding 120 ksi, which are comparable to many steels used for various structural applications and tool manufacturing [1-5].

Nodular cast irons are used for manufacturing many critical automobile and agricultural parts such as crankshafts, engine connecting rods, truck axels, power transmission yokes and gears, etc. [3-5]. Because, it offers a unique combination of a wide range of high strength, wear resistance, fatigue resistance and ductility [6,7]. Wear is always a major industrial problem for all transmission parts. In nodular cast irons, graphite nodules are embedded in the ferrous matrix. These graphite nodules behave as a solid phase lubricating agent and minimize the wear rate of the component. But, its matrix hardness (which is very important to provide higher wear resistance) is relatively low. As a result, as-received, i.e. as-cast nodular cast iron cannot provide satisfactory wear resistance. So, various initiatives have been taken to increase the matrix hardness through different heat treatments. In this regard, so far, the popular heat treatment techniques used for hardening nodular cast irons are austempering, martempering, quenching and tempering, etc. [3,8,9]. In the case of traditional hardening treatments, components are

hardened thoroughly. As a result, the overall toughness of the component is reduced. In the case of carburizing treatment, the surface hardness of the component is increased selectively through adding more carbon from the external source keeping the core soft and ductile. This technique might be a potential heat treatment process for heavy duty transmission gears and other automobile parts. The aim of this work is to investigate possibility of surface hardening of nodular cast iron by pack carburizing and to characterize the wear properties of carburized nodular cast iron.

### 2. MATERIALS AND HEAT TREATMENT

In this present research work, wear behaviour of commercially available nodular cast iron was used. The composition of this ferrous cast alloy has been presented in Table 1. Wear test specimens of length 8.7 mm and diameter 4.66 mm were prepared and carburized 1050°C for 4 hours. After carburization, test samples were cooled in the furnace. The carburized samples were then observed in the microscope to confirm the selective increase in carbon content at surface layer of the specimens. One carburized sample was also quenched in water in order to reveal carburized layer from surface toward the core of the test piece as detection of carburized layer is not always easy for furnace cooled samples. The heat treatment schedule is shown in Fig.1.

Table 1: Chemical compositions of nodular cast iron (weight percent).

C	Mn	Si	S	P
3.6	0.21	2.6	0.025	0.036

### 3. EXPERIMENTAL PROCEDURE

After heat treatment, surface hardness values of as-received and carburized samples were measured, which have been presented in Table 2. Surface hardness of the counter body has also been measured (Table 2). Dry sliding wear tests of all samples of both as-received and carburized and furnace cooled nodular cast iron were carried out at room temperature in the laboratory air. Here it is to be mentioned that, for samples of both conditions, the total sliding distances were kept constant to 8500 m. However, variable dead loads as 0.5, 1.0 and 2.0 kg were used for both groups of samples to know the effect of applied load on the wear rate and wear morphologies.

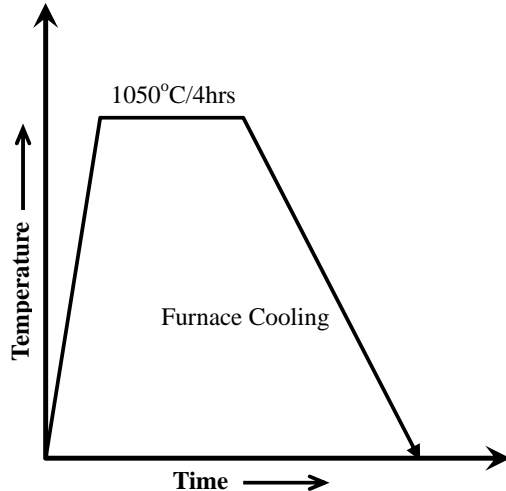


Fig 1. Schematic diagram showing the heat treatment cycles used for carburizing.

Table 2: Hardness values of as-received cast iron, carburized cast iron and steel counter body.

Sample Identification	Hardness Value (RC)
As-received Cast Iron	24
Carburized Cast Iron	33
Steel Counter Body	50

After wear tests, weight losses were measured. Worn samples were also observed under microscope to know the wear behaviour and they were photographed.

### 4. RESULTS AND DISCUSSION

The average surface hardness values of steel counter body and as-received nodular cast iron samples were respectively RC50 and RC24. After carburizing and air cooling, the surface hardness of the as-received nodular cast iron increased to RC33. The reason of this increased surface hardness was due to increase in the carbon

content during pack carburizing. During carburizing, carbon diffused in the ferritic matrix of the cast iron from the carburizing media and changed the microstructure as shown in Figs.2 and 3. Before carburizing as-received nodular cast iron showed ferritic matrix embedded with graphitic nodules of various sizes and distributions. After carburizing, the shape, size and distribution graphite nodules were almost unchanged, however, austenite grains near the surface area absorbed more carbon from the surrounding pack carburizing media at high temperature. As a result of higher carbon content in the austenite grains at surface area of the specimens, austenite of surface area transformed to pearlite rather than to ferrite. The carburized case with higher carbon content is clearly visible in Fig.3.

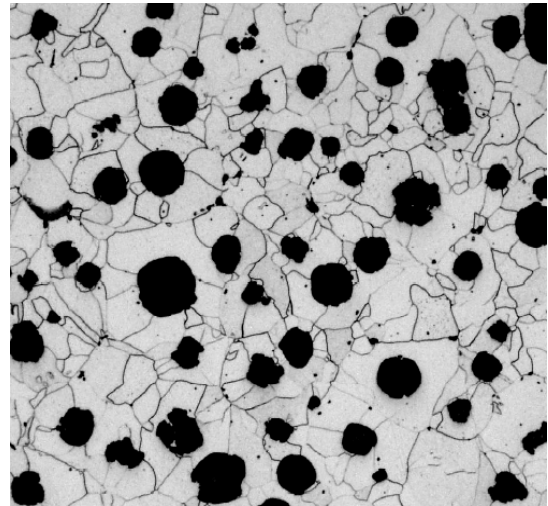


Fig 2. Micrograph of as-received (as-cast) nodular cast iron with ferritic matrix.

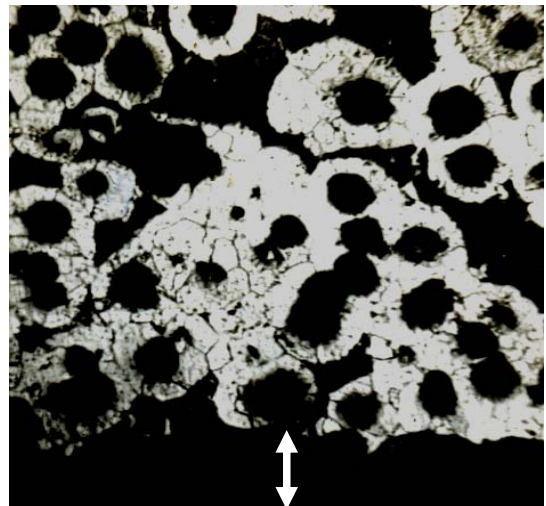


Fig 3. Micrograph of carburized and furnace cooled nodular cast iron. Here, carburized zone is pearlitic (indicated by arrow), whereas core is ferritic.

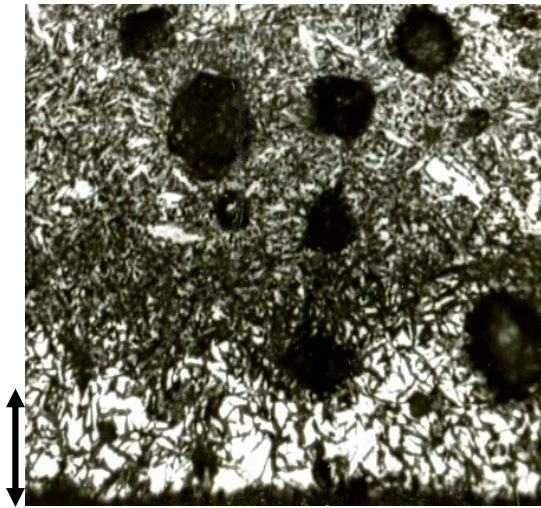


Fig 4. Micrograph of carburized and quenched nodular cast iron. Arrow is indicating the zone of high carbon needle-like martensitic structure (carburized case) at surface and low carbon lath martensitic structure is seen in the core.

When high carbon ferrous alloy is quenched from sufficiently high temperature, the high carbon zone transforms to needle-like martensitic structure, however, low carbon area either remains unchanged or transforms to low carbon lath martensitic structure, which is also very clear in Fig.4.

Wear tests were carried out on pin-on-disc type apparatus schematic diagram of which is given in Fig.5. Many investigators used this type of set-up for dry sliding wear test [8,9]. Here, hardened steel block was used as counter body and test specimen was as pin.

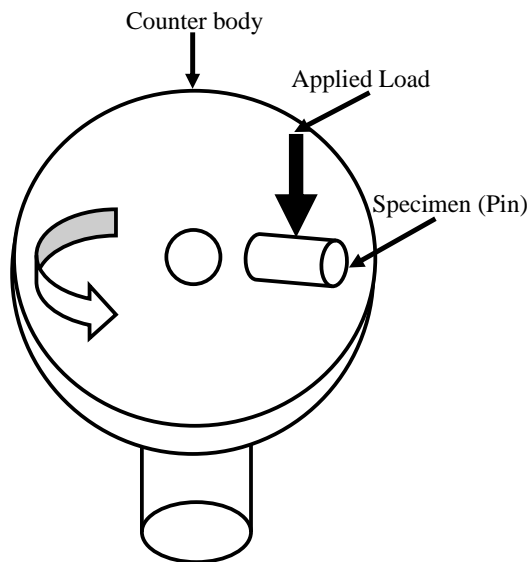


Fig 5. Schematic diagram showing pin-on-disc type wear test set-up.

In order to know the effect of applied load on the wear rate, wear tests were carried out under three different

applied loads as 0.5, 1.0 and 2.0 kg. The test results have revealed that increased hardness by carburizing caused significant decrease in the wear rate. The reason is that during carburization, carbon diffused from the surrounding carburizing media and increased the carbon content at the surface area. In the case of ferrous alloys of similar structures, increase in carbon means increase in hardness and strength. Increase in hardness means reduced wear rate, which can be easily understood from the following equation [10]:

$$v = kWx/H \quad (1)$$

Where  $v$  is volume of worn material,  $k$  is non-dimensional wear co-efficient,  $W$  is applied load,  $x$  is sliding distance and  $H$  is the hardness of the worn surface.

Table 3: Weight loss of as-received and carburized nodular cast iron samples after 8500 m sliding friction in contact of steel counter body under various applied loads.

Applied Load	Weigth Loss, gm	
	As-received Sample	Carburized Sample
0.5 kg	0.01	0.007
1.0 kg	0.06	0.010
2.0 kg	0.95	0.060

With increase in applied load, wear rate of samples of both conditions increased, Table 3. The reason is that with increase in load means increase in stress on contact surface of the test specimen. As a result, specimens under both conditions gradually experienced more intensive friction. So, specimens of both conditions showed more weight losses as dead loads were gradually increased.



Fig 6. Wear pattern on steel counter body used for as-received nodular cast iron sample.

Detail investigation on worn steel counter body revealed that the wear patterns of counter body used for cast iron samples of both conditions were almost similar



(microcutting type abrasive wear), Figs.6-7. However, wear patterns on worn samples were somewhat different, Figs.8-9. For as-received condition adhesive type wear morphology was dominant. On the other hand, carburized samples showed mixed (adhesive and abrasive) type wear mechanisms. In most cases of dry sliding wear test, wear patterns of samples and counter bodies are controlled by the surface hardness of the respective component. It has been mentioned that the average hardness of counter body was around RC50. Compared to this value, the hardness values of as-received and carburized test specimen (respectively RC24 and RC33) were very low, which could not dominate over hardness of counter body. As a result, worn particles from counter body of sufficiently high hardness could not be plastically deformed or adhered with the counter body. So, counter body showed abrasive type wear patterns for both sample conditions.

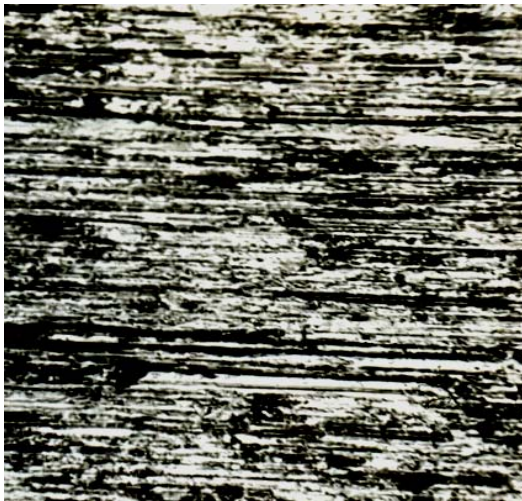


Fig 7. Wear pattern on steel counter body used for carburized nodular cast iron sample.

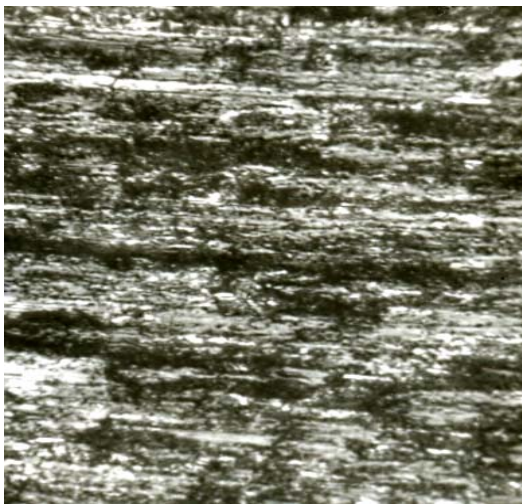


Fig 8. Wear pattern on as-received cast iron tested in contact with steel counter body.

However, hardness of carburized sample specimen

(RC33) was significantly higher than that of as-received specimen (RC24). As a result, as-received sample showed adhesive wear and the carburizing effect changed the wear pattern to mixed mode.

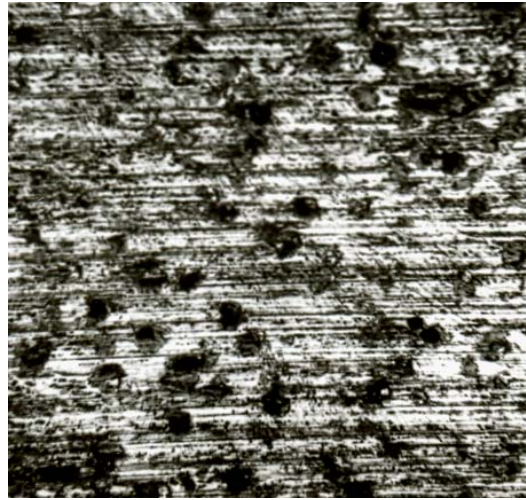


Fig 9. Wear pattern on carburized nodular cast iron tested in contact with steel counter body.

## 5. CONCLUSIONS

In this present work the effects of carburizing on the wear behaviour of as-received nodular cast iron has been investigated. After experimental work, the following conclusions have been drawn.

1. Experimental results showed that surface modification by carburizing encouragingly increased the wear resistance of the as-received nodular cast iron under similar test conditions.
2. Carburizing increased the surface hardness of the cast iron and changed the wear pattern of as-received nodular cast iron from adhesion dominating one to mixed mode.
3. For both sample conditions, wear pattern of steel counter body was found to be abrasive type.

## 6. ACKNOWLEDGEMENT

The author is grateful to Bangladesh University of Engineering and Technology (BUET), Dhaka for giving necessary fund and permission to conduct this research work in the laboratories of Materials and Metallurgical Engineering Department.

## 7. REFERENCES

1. Gonzaga, R.A., Landa, P.M., Perez, A., and Villanueva, P., 2009, "Mechanical Properties Dependency of the Pearlite Content of Ductile Irons", *Journal of Achievements in Materials and Manufacturing Engineering*, vol.33, pp.151-158.
2. Hafiz, M., 2001, "Mechanical Properties of SG-Iron with Different Matrix Structures, *Journal of Materials Science*, vol.36, pp.1293-1300.

3. Gilbert, G.N.J., 1968, "Report on Engineering Data on Nodular Cast Iron", British Cast Iron Research Association, United Kingdom.
4. Kohout, J. and Stanislav, V., 2008, "Shift of S-N Curves of Ferritic Nodular Cast Iron Due to Loading Cycle Asymmetry, The Arabian Journal of Science and Engineering, vol.33, no.1B, pp.213-222.
5. Dorazil, E., 1991, Report on "High Strength Austempered Ductile Cast Iron", Chichester, Horwood.
6. "A Design Engineer's Digest of Ductile Iron", 1983, 5<sup>th</sup> Edition, QIT-Fer et Titane Inc., Montreal, Quebec, Canada.
7. "Ductile Iron", Metals Handbook, American Society for Metals, 9<sup>th</sup> Edition, vol. 15.
8. Islam, M.A., Haseeb, A.S.M.A and Kurny, A.S.W., 1995, "Study of Wear of As-Cast and Heat-Treated Spheroidal Graphite Cast Iron Under Dry Sliding Condition", Journal of Wear, Elsevier Science Ltd., vol.188, pp.61-65.
9. Haseeb, A.S.M.A., Islam, M.A. and Bepari, M.M.A., 2000, "Tribological Behaviour of Quenched and Tempered and Austempered Ductile Iron at the Same Hardness Level", Journal of Wear, Elsevier Science Ltd., vol.244, pp.15-19.
10. Bhushan, B., 1999, "Principles and Applications of Tribology, John Wiley & Sons, Inc.

## 8. MAILING ADDRESS

N. Fatima  
 Materials and Metallurgical Engineering Department  
 BUET, Dhaka-1000, Bangladesh.  
 E-mail: aminulislam@mme.buet.ac.bd



## DEVELOPMENT OF THE CONCEPT OF OVERALL WORK COMPATIBILITY: INTEGRATING IMPORTANT WORK VARIABLES

F. Afreen Prama<sup>1</sup>, M. A. Akhtar Hasin<sup>2</sup> and Tahera Yesmin<sup>3</sup>

<sup>1,3</sup>Lecturer, Department of Industrial and Production Engineering, BUET, Dhaka

<sup>2</sup>Professor, Department of Industrial and Production Engineering, BUET, Dhaka

### ABSTRACT

A work environment consists of a complex array of work factors that jointly influence work outcomes. Based on previous human performance models and theories, researchers have introduced the guideline principles of “Work Compatibility Theory”, which is a comprehensive quantitative approach to solving the problem of human performance outcome. In the previous theories, work compatibility has been represented by a Work Compatibility Matrix (WCM) for each of the Work Compatibility variables. In this research, we tried to find out the Overall Work Compatibility (OWC) of a work environment (floor/shop/ organization) for each worker, taking into account all the WC variables and their mixed effects on human. Since the idea behind the WCM model is based on the positive and negative (or both) effects of a web of elements which might or might not be interrelated, an Artificial Neural Network (ANN) model was created to produce a comprehensive and holistic result.

**Keywords:** Work Compatibility, Overall Work Compatibility, Artificial Neural Network.

### 1. INTRODUCTION

Ever since the advent of scientific management theories, it has been clear to researchers that human’s capacity to work or work productivity can be influenced unpredictably by multifaceted variables. It is not necessary that all humans are positively influenced by the same work variable, say management’s concern. Managements’ concern for an employee can have positive influence on some, but there are some employees who may think of it critically and reduce their productivity. Similar is the case with other work related variables. In fact, it is not solely positive or negative influence; a work variable can have somewhat positive and somewhat negative influence on a single employee. In attempt to measure this integrated influence, came the concept of Work Compatibility (WC) [1]. In previous research by Genaidy et al, a mathematical concept of work compatibility has been developed, where the WC of each work related variable is expressed in form of a matrix named Work Compatibility Matrix [2]. The WC Matrix represents the WC of a single variable. As we all would agree, a work environment is a complex situation where many work related variables are intertwined. The integrated effect of all the variables finally determines the work productivity of an individual. We seek to find this integrated effect of all the WC variables in a particular work situation. This is what we call the “Overall Work Compatibility” (OWC) of an organization. It has been taken in previous literatures that work productivity is directly proportional to WC [2].

Therefore, we represent the Overall Work Compatibility in terms of productivity of each employee, rather than a complex matrix. Also, with the concept of Overall Work Compatibility, we attempt to find the inter relation between the work related variables in terms of relative weights.

In computation of such a critical web of variables, the Artificial Neural Network (ANN) approach has been chosen. ANN has been used for a long time for prediction of values that emanate from variables that have seemingly capricious relationships. An ANN can be trained using past data and with the artificial intelligence thus developed, it can predict future data.

Past data from a local garments industry has been used to train the ANN, and thus the relative weights existing in the present variables were established. Using this information, the ANN can be used to predict future OWC of a situation.

### 2. LITERATURE REVIEW

As the practical life is approached, many of the challenges in the field of Human Factors are found in the complex interaction among man, machine, environment and the socio-technical systems [3]. The researchers are now approaching towards studying the interactions themselves rather than the factors or interfaces in a person’s environment [4].

Today, the work environment presents unique challenges to different professionals because it consists

of a complex web of work factors that jointly influence work outcomes. The goal of system design with respect to work compatibility is to simultaneously maximize work productivity, quality and safety outcomes of work environment. Based on previous human performance models and theories, researchers have introduced the guideline principles of “Work Compatibility Theory”, which is a comprehensive quantitative approach to solving the problem of human performance outcome [1].

Work compatibility allows the assessment of workplace characteristics (including both physical and psychosocial factors) using a common metric [4]. According to the model, work-related variables can exert both a positive and a negative effect; the integration of both determines the final outcome. Also, 12 specific variables were identified as Work Compatibility Variables [2].

A mathematical model was established by Wallace et al., giving an empirical solution to the Work Compatibility (WC) matrix. Based on that, an equation for WC matrix was proposed [5]. Furthermore, an operating zone was developed in which there was a region of optimality for the employee to function with good degree of efficiency. S. Salem et al. developed the *Work Compatibility Model* (WCM) as a multidimensional diagnostic tool of human performance that measures the level of synchronization between the workforce and the work environment [6]. The authors proposed a quantitative model and a graphic-based framework to implement the work compatibility model at the operational level. Using the proposed approach, managers can identify smart solutions that contribute to personnel development.

Researchers have measured the work compatibility of different work related variables among 147 construction workers using a Demand –Energizer Instrument (DEI) [7]. In this questionnaire based study, the association between the exposure variables (work energizer and work compatibility) and outcome variables were determined using a *multivariate logistic regression model*.

In the context of industries in Bangladesh, the work compatibility variables are yet to be identified and established. The present WCM, with appropriate customization, can very well be used in this regard. There is a scope of extending the research with the use of a new tool in identifying the priority areas for future intervention strategies [7]. Since the idea behind the WCM model is based on the positive and negative effects of a web of elements and each of these elements are correlated, the application of Neural Network approach can be considered to produce a more comprehensive and holistic result [8, 9]. Use of ANN for Work Compatibility Modeling can be considered for a number of reasons [10].

### 3. THEORETICAL BACKGROUND

Two important concepts were combined in the study, necessitating theories regarding two different concepts- Work Compatibility and Artificial Neural Networks.

### 3.1 Work Compatibility

Depending upon positive or negative impacts, work related factors are classified into two major categories. Variables in the work environment that positively affect the energy supplies in the human system such as financial incentives, social recognition etc. are coined as “Work energizers”. Variables that negatively affect energy supplies of human system are termed as “Work Demands”, e.g, work conflict, making decision etc [1]. The relationship between the positive and negative impact factors results in the important work design parameter, named Work Compatibility (WC). All individual factors in the system are integrated to produce the work compatibility. It is derived from the concept of an integrator as in control systems.

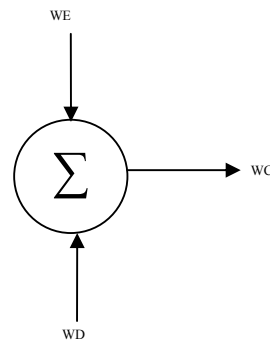


Fig 1. Work compatibility theory

Later, a mathematical model for WC was developed by Wallace et al., where WC for a particular work variable was found in the form of a matrix called the WC matrix [2]. It was a two dimensional matrix, where Work Demand (WD) was taken as row values and Work Energizer (WE) was taken as a column value, both on a 5- step scale. Thus a five- by- five matrix resulted, in which each particular position denoted the state of WC of a particular work related variable. Some contours with significant Work Compatibility characteristics were also identified in the matrix [5].

### 3.2 Artificial Neural Networks

Artificial neural networks, originally developed to mimic the basic biological neural systems- the human brain particularly, are composed of a number of interconnected simple processing elements called neurons or nodes [9]. Each node receives an input signal which is the “total” information from other nodes or external stimuli, processes it locally through an activation or transfer function and produces a transformed output signal to other nodes or external outputs. Collectively a number of neurons can perform a surprising number of tasks quickly and quite efficiently. This information processing characteristics makes an ANN a powerful computational device.

In the graphical presentation of a neural network, the signals are interconnected at certain points. These points are called *nodes*. An activation function or a firing rule determines the way to decide whether a neuron should fire or not for any input pattern. Most frequently, a

sigmoid function is used. Usually a network is trained by providing it with input and matching output patterns. The architecture of an ANN is very important. A “*feed forward back propagation*” network, as shown in Fig. 2, is most often used, in which there are three layers of neurons. The first or lowest layer is an *Input Layer*, where external information is received. The last or the highest layer is an *Output Layer*, where the output value is obtained. In addition to the input and output layers, one or more *Hidden Layers* may be present in these networks, comprising of a number of *Hidden Neurons*. The purpose of hidden neurons is to intervene between external input and network output so that the network is enabled to reduce prediction error.

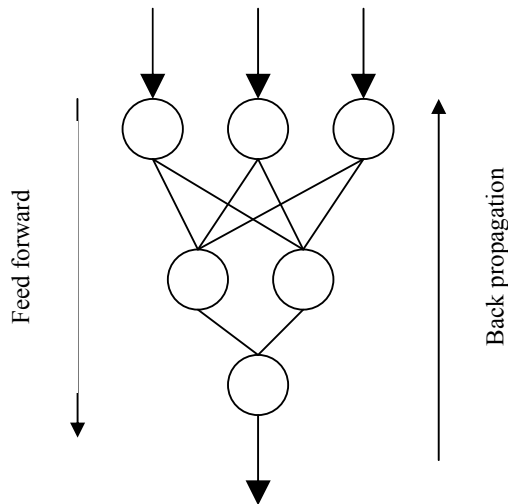


Fig 2. A feed forward back propagation neural network

#### 4. DEVELOPMENT OF THE CONCEPT OF OVERALL WORK COMPATIBILITY

Work Compatibility is a variable- based compatibility matrix. For each work variable, there will be a different WC matrix assigning the WE and WD values of the concerned variable. From the WC matrix, an area of WC can be found.

The Overall Work Compatibility (OWC), on the other hand is a concept based on the theory of Work Compatibility, but this is an employee- specific value. For each employee, different work- related factors are rated and based on a previously trained Artificial Neural Network, the productivity of that employee is calculated. This rate of output or productivity is termed as the Overall Work Compatibility (OWC) of that employee. This is a concept where all the work related variables are integrated together to produce, not a matrix, but a single value that can be used as an indicator of work compatibility. Here, it is assumed that, the more compatible an employee is, the greater will be his/ her work productivity. The OWC, thus is expressed as work output such as pieces per unit time or hours of work done per day etc.

#### 4.1 Methodology

The study was conducted to develop a model based on Artificial Neural Network (ANN) in order to find out the

Overall Work Compatibility (OWC) of workers in a certain work environment. To analyze how compatible a work situation is for a particular worker, the work related variables were crucial. Selection of appropriate variables was very important. A representative sample of workers was selected and the data regarding all the work variables and work output were collected. By feeding the data in a computer program to analyze neural networks, a best neural network model was chosen. This was later validated with more data. The outcomes of the network were analyzed. Thus, relative importance of different work related variables were obtained.

#### 4.2 Analysis using ANN

To develop the OWC of a particular work environment, data was taken from the production floor of an eminent garments industry of Bangladesh. Eight variables, regarded as important work related components, were chosen.

Table 1: Input and output variables and their units

		Name	Unit
Input variables	1	Experience Level	years
	2	Education Level	years
	3	Salary	taka
	4	Age	years
	5	Gender	(1/-1) =(Male/ Female)
	6	Difficulty level of work	Scale of 3
	7	Management's opinion about the worker	Scale of 3
	8	Worker's attitude towards management	Scale of 5
Output variable	1	Overall Work Compatibility	Pieces per hour

The 80-20 rule was used to divide the data into training set and testing set for neural network. Using different combinations of training and testing sets, a number of ANNs were developed. The best ANN was chosen based on the performance characteristic called R- Squared value. The formula for R<sup>2</sup> is:

$$R^2 = 1 - (SSE/SS_{yy})$$

Where  $SSE = \sum (y - \hat{y})^2$ , and

$$SS_{yy} = \sum (y - \bar{y})^2$$

y is the actual value,  $\hat{y}$  is the predicted value of y, and  $\bar{y}$  is the mean value of all y the values.

R<sup>2</sup> compares the accuracy of the model to the accuracy of a trivial benchmark model wherein the prediction is just the average of all of the example output values. A perfect fit would result in an R Squared value of 1, a very good fit near 1, and a poor fit near 0. The characteristics of the ANN with the best performance is presented in Table 2.

Table 2: Neural network characteristics

Number of input variables	8
Number of output variables	1
R <sup>2</sup> value for best network performance	0.9214
Number of hidden neurons trained	10
Optimal number of hidden neurons	10

**5. RESULTS**

The R- squared value of the selected ANN, as seen from above, was 0.9214, which indicated a very good fit. The ANN could be said to be a good model. Therefore, the relative importance values obtained from this model was taken as the relative importance of corresponding WC variables. Basically these values were the weights put on various WC variables in the ANN by trial and error, a combination of which produced the best fit. Table 3 depicts the relative importance values of various WC variables found from the selected ANN model. These importances are depicted pictorially in Figure 3. In Figure 4, the actual and predicted values of the selected ANN have been shown. It is evident that the values match well, indicating that the selected model is good enough.

Table3: Relative importance of variables

Variable	Initial	Relative importance obtained
Experience	experience	0.530
Difficulty Level	diffclt lvl	0.167
Gender (Male/Female)	M/F	0.091
Managements' Opinion about	mgt's opnn	0.069
Salary	salary	0.064
Age	age	0.036
Attitude towards management	attitude twrds mgt	0.028
Education	education	0.016

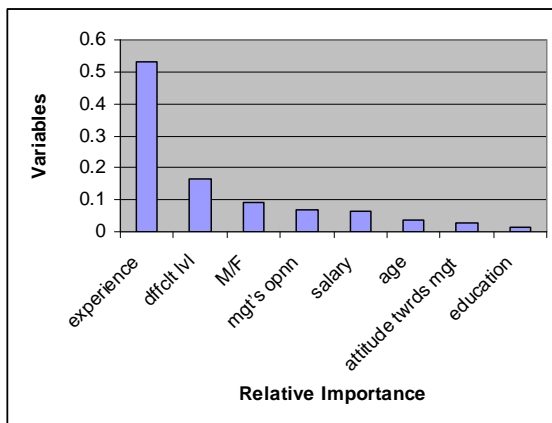


Fig 3. Relative importances of the input WC variables

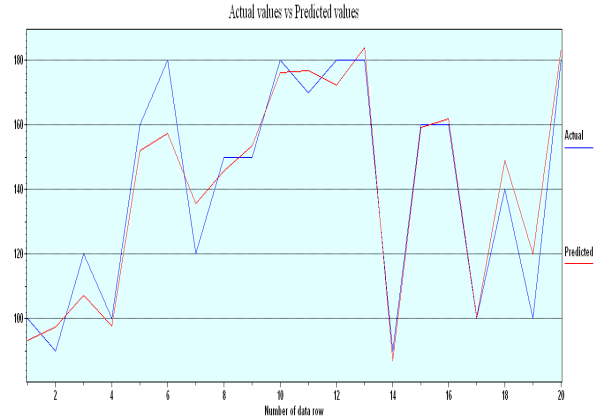


Fig 4. Prediction by the selected ANN model

As evident from the results, Experience level of workers is the factor in the particular work situation, that influenced work outcomes the most. The second most influential WC variable was difficulty Level of work. Although these comparisons may seem capricious, but the fact is, when considering their combined effects, it is very much possible that an unlikely work variable may succeed to influence more.

**6. DISCUSSIONS**

This analysis has been done using 10 variables that may affect Work Compatibility. These were the variables that varied most from worker to worker. Also, according to their opinion, these variables had immediate affect on work productivity. But there are many more variables, especially psychosocial ones, which could be incorporated in such analysis. Further scopes lie in that area.

It is to be kept in mind that results provided by ANN mostly depends on what it is taught with. Therefore, data integrity is a crucial factor when we are using ANN. For each worker, original data has been collected and used. But still judgmental data such as managements' rating may vary from person to person. Such trivial details were ignored.

**7. CONCLUSION**

Thus an ANN model can possibly be developed for a particular work situation in order to straighten the seemingly capricious and intertwined relationships among work related variables. The model would also predict output values in terms of pieces produced per hour when a future unknown situation in provided. The output thus obtained could be taken as the OWC value for that particular situation.

Future scope of further research in this field lies in exploring more work situations and work variables, and a common platform could be established.

**8. REFERENCES**

1. Genaidy, A.M., Karwowski, W., and Shoaf, C.,”

- The fundamentals of work system compatibility theory: An integrated approach to optimization of human performance at work”, Theoretical Issues in Ergonomics Sciences, Vol.3, pp 346–368, 2002.
2. Wallace,W., Shoaf, C., Genaidy,A., and Karwowski,W., “Assessing the compatibility of work system factors through an integrative model: A case study”, International Journal of Occupational Safety and Ergonomics, Vol. 9, pp 25–33, 2003.
  3. Wilson, J. R., and Corlett, N., “Evaluation of human work”, CRC press, Taylor and Francis Group, Boca Raton, 2005.
  4. Wilson, J. R., And Nichols, S.C., “Cognitive work investigation and design in practice: the influence of social context and social work artifacts”, Laurence Erlbaum Assoc., NJ, 2003.
  5. Abdallah, S., Genaidy, A., Salem, O., Karwowski, W. and Shell, R., “The concept of work compatibility: An integrated design criterion for improving workplace human performance in manufacturing systems”, Human Factors and Ergonomics in Manufacturing, Vol. 14, No. 4, pp 379-402, 2004.
  6. Salem, S., Paez, O., Holley, M., Tuncel, S., Genaidy, A., and Karwowski, W., “Performance tracking through work compatibility model”, Human Factors and Ergonomics in Manufacturing, Vol. 16, No. 2, pp 133-153, 2006.
  7. Salem, O., Sobeih, T. M., Genaidy, A., Shell, R., Bhattacharya, A., and Succop, P., “Work compatibility and musculoskeletal disorders in the construction industry”, Human Factors and Ergonomics in Manufacturing, Vol. 18, No. 2, pp 230-252, 2008.
  8. Tsoukalas, L., H., and Uhrig, R., E., “Fuzzy and neural approaches in engineering”, John Wiley and Sons, Inc. NY, 1997.
  9. Simon Haykin, “Neural networks: A comprehensive foundation”, Prentice Hall, Inc. NJ, 1999.
  10. Guoqiang Zhang, B. Eddy Patuwo, and Michael Y. H., “Forecasting with artificial neural networks: The state of the art”, International Journal of Forecasting, Vol. 14, pp35-62, 1998.

**9. NOMENCLATURE**

Symbol	Meaning
WC	Work Compatibility
OWC	Overall Work Compatibility
ANN	Artificial Neural Network

**10. MAILING ADDRESS:**

Farhana Afreen Proma  
 Lecturer, Department of Industrial and Production Engineering,  
 BUET, Dhaka- 1000.

## ENVIRONMENTAL POLLUTION OF BANGLADESH – IT’S EFFECT AND CONTROL

G. M. Jahangir Alam

Bangladesh Air Force, Dhaka Cantonment, Dhaka.

### ABSTRACT

Environmental pollution is as old as the civilization itself. It has become a major concern in the last few decades. It is the by product of the development of civilization and in fact a price for the progress. It is more prone in case of Bangladesh. Air pollution of Bangladesh is mainly caused by the vehicle emission, industrial discharge and burning of fossil fuel. The water resource of Bangladesh becomes a major health hazard due to arsenic contamination, inadequate solid waste and industrial effluent management. Necessary steps are to be taken to protect the environment for our own existence. This paper provides an overview of different environmental problems of Bangladesh and discusses the ways to improve it

**Keywords:** Environmental Pollution, Air Pollution, Water Pollution, Noise Pollution

### 1. INTRODUCTION

**1.1** Pollution has become the first enemy of the mankind. Industrial revolution of 19th century led to environmental disaster. The whole world is now more afraid of pollution rather than nuclear blast. Technological advancement has brought revolutionary changes in life style and national economy with overwhelming power over nature. The protection of environment has become a major issue around the global for the well being of the people and economic development.

**1.2** The present environmental condition of Bangladesh is not at all equilibrium. Severe air, water and noise pollution are threatening human health, ecosystems and economic growth of Bangladesh. Air pollution caused due to increasing population, burning fossil fuels, industrialization and associated motorization. The water pollution caused due to industrialization. The under ground water of Bangladesh has been polluted due to arsenic. The inhabitants of major cities of Bangladesh are also exposed to high level of noise pollution. Environmental degradation of Bangladesh is also caused due to poverty, over-population and lack of awareness on the subject. It is manifested by deforestation, destruction of wetlands, soil erosion and natural calamities. Few steps have been taken by the government to improve the environmental degradation and pollution control. This paper analyzes the different types of environmental pollution and associated health hazard in Bangladesh. It also discusses the different governmental steps as well as some suggested steps to improve the pollution control.

### 2. DIFFERENT ASPECTS OF ENVIRONMENTAL POLLUTION

#### 2.1 Air Pollution.

Air pollution is a serious environmental health hazard affecting the populations of Bangladesh. Air pollution of Bangladesh is caused due to increasing population and associated motorization. Indoor air pollution is mainly associated with the use of biomass fuels during cooking with poor ventilation. Industrial emissions and automobiles are the principle sources of outdoor air pollution. The national ambient air quality standards of Bangladesh and amount of pollutants in the air of Dhaka city is shown below:

Table – 1: Bangladesh National Ambient Air Quality Standards

Land use Category	8-hour average concentration in $\mu\text{g}/\text{m}^3$			
	CO	NO <sub>2</sub>	SPM	SO <sub>2</sub>
Industrial/mixed use	5,000	100	500	120
Commercial/mixed use	5,000	100	400	100
Residential/rural use	2,000	80	200	80
Sensitive use *	1,000	30	100	30

\*Sensitive areas include national monuments, health resorts, hospitals, archeological spots, and educational institutions. *Source:* Department of Environment (DOE), 1997.

Table – 2A: Pollutants in the Air of Dhaka City

Location at Dhaka City	Sulfur Dioxide (SO <sub>2</sub> )		Nitrogen Dioxide (NO <sub>2</sub> )	
	Concentration (µg/m <sup>3</sup> )	Permissible (µg/m <sup>3</sup> )	Concentration (µg/m <sup>3</sup> )	Permissible (µg/m <sup>3</sup> )
Gulistan	800	100	500	100
Jatrabari	1300		500	
Pantho-Path	900		500	
Mohakhali	1200		500	

Table – 2B: Pollutants in the Air of Dhaka City

Location at Dhaka City	Carbon Monoxide (CO)		Suspended Particulate Matter (SPM)	
	Concentration (µg/m <sup>3</sup> )	Permissible (µg/m <sup>3</sup> )	Concentration (µg/m <sup>3</sup> )	Permissible (µg/m <sup>3</sup> )
Gulistan	33200	5000	1332	400
Jatrabari	67000		4667	
Pantho-Path	85100		2666	
Mohakhali	69300		2111	

## 2.2 Main Sources of Air Pollution.

### 2.2a. Burning of Fossil Fuel.

Air pollution mainly occurs due to burning of fossil fuels like coal, petroleum etc and associated black smoke. Over 99% of the brick kilns use fossil fuel but don't comply with the "Brick Kiln Ordinance" and pollute enormous air.

### 2.2b. Industrial Discharge.

Industries cause air pollution through smoke emission. Agro based industries like sugar, pulp, paper, tanneries and value added industries like textile, garments, pharmaceuticals, oil refineries, fertilizer and chemical industries are the major contributors for air pollution. The air pollution percentage of most five industrial sectors of Bangladesh in the year 2001 is shown below:

Table-3: Air Pollution Percentage of most Five Industrial Sectors of Bangladesh in the Year 2001

Industry	Emission (Tons/yr)	Pollution (%)
Food Industry	1,46,356.06	38.7
Cement/Clay	62,725.88	16.6
Pulp and Paper	51,963.92	13.7
Textile	39,831.01	10.5
Tobacco	16,992.22	4.5

Source: Research Work by Islam Faisal on "Industrial Pollution in Bangladesh" in the year 2002.

### 2.2c. Emission from Vehicles.

One of the major sources of air pollution in urban areas of Bangladesh is due to the unburned fuel from two stroke engine vehicles. Dhaka has been rated as one of

the most polluted cities of the world. Bangladesh Atomic Energy Commission reports that automobiles in Dhaka emit 100 kg lead, 3.5 tons SPM, 1.5 tons SO<sub>2</sub>, 14 tons HC and 60 tons CO in every day. The contribution of air pollution by different types of vehicle and the amount of pollutants emitted from vehicles in Dhaka city is as follows:

Table-4: Contribution of Air Pollution by Vehicle Type

Type of Vehicle	CO (%)	HC (%)	NOx (%)	PM (%)	Annual Growth
Truck	13.4	8.6	59.7	47.5	7.8
Bus	10.3	9.7	18.5	29.4	2.5
Mini bus	7.3	3.9	6.5	19.1	6.8
Utility	6.3	4.4	2.8	0.7	10.2
Car	38.2	18.2	6.5	1.2	9.4
Three wheeler	10.6	26.9	6.0	1.2	31.0
Motor cycle	14.0	28.3	0.3	1.0	8.1

Source: Country Profile on Environment of Bangladesh by Japan International Cooperation Agency in the Year 1999.

## 2.3 Water Pollution.

Water pollution creates serious health hazard for Bangladesh. The dumping of municipal wastes, hospital wastes and toxic environmental discharges from mostly industries pollute both surface and ground water sources. The most dangerous threat emanating from environmental degradation is the arsenic contamination of ground water.

## 2.4 Main Sources of Water Pollution.

### 2.4a. Industrial Waste and Effluent.

The main industrial areas of Bangladesh are at Dhaka, Chittagong, Khulna, and Bogra districts. The mostly contributing industries for water pollution are pulp and paper, pharmaceuticals, metal processing, food industry, fertilizer, pesticides, dyeing and painting, textile, tannery etc. More than 200 rivers of Bangladesh directly or indirectly receive a large quantity of untreated industrial wastes and effluent. Everyday approximately 700 tanneries of Dhaka city are discharging about 16,000 cubic meters of toxic wastes. The Department of Environment (DOE) has listed 1,176 factories that cause pollution throughout the country. Water pollution percentage of most five industrial sectors of Bangladesh in the year 2001 is shown below:

Table-5: Water Pollution Percentage of most Five Industrial Sectors of Bangladesh in the Year 2001

Industry	Emission (Tons/yr)	Pollution (%)
Pulp and Paper	91,768.10	47.4
Pharmaceuticals	30,866.72	15.9
Metal	27,174.61	14.0
Food Industry	23,403.39	12.1
Fertilizers/Pesticides	12,715.00	6.6

Source: Research Work by Islam Faisal on "Industrial Pollution in Bangladesh" in the year 2002.



#### 2.4b. Solid Waste and Sewage Disposal.

The indiscriminate discharge of solid waste, domestic and hospital sewage are the major source of water pollution in Bangladesh. About 4,000 to 4,500 tons of solid wastes are generated daily and only half of the generated wastes are disposed of in low lying areas or into river water. These solid wastes are associated with the problems of littering on roads, spilling around the bins, clogging of drains, indiscriminate dumping on vacant plots and cause serious environmental pollution. More than 500 hospitals and clinics of Dhaka city generate and release hazardous and toxic wastes without any treatment. The generated solid waste of six famous hospitals / clinics of Dhaka city is shown below:

Table-6: Solid Waste Generation from Six Famous Hospitals/Clinics of Dhaka City

Name of Hospital / Clinic	Generated waste (Kg/bed / day)	Non hazardous waste		Hazardous waste	
		Qty	% of Total waste	Qty	% of Total waste
DMCH	1.19	1.07	90	0.12	10
SSMCH	1.23	1.09	89	0.14	11
RIHD	1.20	0.91	76	0.29	24
HFRCH	1.59	1.29	81	0.30	19
DNMCH	0.80	0.70	88	0.10	12
SAHL	0.83	0.72	87	0.11	13

Source: M Shehab Ullah on "A study of hospital waste management in Dhaka city" in the year 1999.

#### 2.4c. Inadequate Sanitary Facilities.

Inadequate sanitation facilities pose a serious environmental threat in Bangladesh. Dhaka Water and Sewerage Authority (DWASA) can serve only for 15 to 20% of city population. In absence of the sanitation and infrastructural services, 40% having septic tank and soak pit, 15% using pit latrines and 30% using open latrines. The sewage is mostly released into low-lying areas and river water in untreated manner causing great environmental hazards.

#### 2.4d. Arsenic Contamination of Ground Water.

Arsenic in ground water poses a serious environmental hazard for Bangladesh. About ninety-seven percentages (97%) of Bangladesh people have been using ground water as the main source of drinking water but the water has been threatened by arsenic contamination. More than half (52%) of the studied population drink well-water containing >50ug/L of arsenic and more than two-thirds (70%) drink well-water containing >10ug/L of arsenic. The acceptable level of arsenic in drinking water is 0.05 mg/L for Bangladesh but some places it is found more than 70 times higher than that standard. About 80 million people are at a risk of arsenic contamination. The arsenic level of ground water over 0.05 mg/L surveyed in 1998 by the British Geological Survey team is as follows.

Table-7: Percentage of Ground Waters Surveyed in 1998 by the British Geological Survey Team with Arsenic Levels over the Limit

District	% of ground water surveyed	District	% of ground water surveyed
Bagerhat	66	Madaripur	93
Barisal	63	Magura	19
Brahmanbaria	38	Manikganj	15
Chandpur	96	Meherpur	60
Chittagong	20	Moulvibazar	12
Chuadanga	44	Munshiganj	83
Comilla	65	Narail	43
Cox's Bazar	3	Narayanganj	24
Dhaka	37	Nawabganj	4
Faridpur	66	Noakhali	75
Feni	39	Pabna	17
Gopalganj	94	Pirojpur	24
Jessore	51	Rajbari	24
Jhalakati	14	Rajshahi	6
Jhenaidah	26	Satkhira	73
Khulna	32	Shariatpur	80
Kushtia	28	Sylhet	19
Lakshmipur	68		

Source: Allan H Smith, Elena O Lingas & Mahfuzar Rahman on "Contamination of drinking-water by arsenic in Bangladesh: a public health emergency" in 1998.

#### 2.5 Noise Pollution.

The noise pollution is also a major health hazard in Bangladesh. According to World Health Organization (WHO), 60 decibel (DB) sound can make a man deaf temporarily and 100 DB sound can cause complete deafness. According to the Department of Environment (DOE), the perfect sound condition for Bangladesh is 45 dB for the daytime and 35 dB for the night in peaceful areas and 50 dB for the daytime and 40 dB for the night in residential areas. The main sources of noise pollution are industries, motorized vehicles, construction works and indiscriminate use of loudspeaker. At present noise level in Dhaka city are estimated ranging from 60 to 100 decibel. If present situation continues then by the year 2017, 50% people of Dhaka city will loss 30 decibel of hearing power. The daily variation of noise level near the road at some of the key locations of Dhaka city is shown below:

Table – 8A: Pollutants in the Air of Dhaka City.

Time Interval	Location		
	Gulistan Commercial	Science Lab Mixed	Saydabad Commercial
7am -11am	80.08	76.24	83.27
11am -3pm	79.34	75.19	83.89
3pm -7pm	81.13	77.23	84.37
7pm -1pm	78.52	75.32	82.08

Source: Nazmul Chowdhury research on noise pollution in Dhaka city on Feb 2002.

Table – 8B: Pollutants in the Air of Dhaka City.

Time Interval	Location			
	Farmgate	Dhan- mondi	Gulshan	Uttara
	Commer- cial	Residen- tial	Residen- tial	Residen- tial
7am - 11am	80.07	75.87	76.16	76.25
11am - 3pm	78.86	74.38	74.83	74.81
3pm - 7pm	81.96	75.21	76.11	76.81
7pm - 1pm	80.28	76.30	74.31	73.36

Source: Nazmul Chowdhury research on noise pollution in Dhaka city on Feb 2002.

### 3. EFFECT OF ENVIRONMENTAL POLLUTION

**3.1** Severe environmental pollution is threatening human health and economic growth of Bangladesh. Air pollution mostly affects the urban children. Indoor air pollution is a greater threat to health than outdoor air pollution. Bangladesh could avoid 10,000 deaths and save between 200 and 500 million dollars a year if indoor air pollution in four major cities can be reduced to acceptable limits.

**3.2** Immediate effect of smoke inhalation causes headache, vertigo, burning sensation of the eyes, sneezing, nausea, tiredness, cough etc. It's long term effect may cause asthma and bronchitis. Lead affects the circulatory, nervous and reproductive systems as well as affects kidney and liver including liver cancer or cirrhosis. Carbon monoxide hampers the growth and mental development of an expected baby. Nitrogen oxides cause bronchitis and pneumonia.

**3.3** Industrial emissions cause different waterborne disease and damage to health. Arsenic poisoning is slow and cumulative. It causes melanosis, kurtosis and conjunctivitis. Subsequently respiratory problem, gangrene, skin, kidney and lung cancer would arise. The Arsenic effect not only causes serious health hazards but also creates a widespread social problem. The inadequate sanitation facilities also pose a serious health threat in Bangladesh.

**3.4** Noise pollution causes mental and physical illness among the people. Sound pollution causes deafness to heart attack. Any sort of noise pollution seriously affects expecting mothers. It also causes high blood pressure, tachycardia, headache, indigestion, and peptic ulcer.

**3.5** Many people died every year in many diseases due to environmental pollution. The death rate in the year 1996 mainly due to environmental pollution is as follows.

Table-9: The death rate in the year 1996 due to environmental pollution

Causes of Death	National Level	Dhaka City
Death: All Ages (%)		
Cardiovascular	7.87	17.5
Asthma	5.2	4.3
Diarrhea	1.66	7.8
Cancer	4.05	5.3
Dysentery	4.05	5.5
Viral Hepatitis	2.14	3.4
Death: Less than One Year Infant (%)		
Anemia	4.77	6.5
Breathing problem	1.87	2.8
Diarrhea	18.96	17.5
Cancer	4.05	5.0
Dysentery	1.66	3.9
Viral Hepatitis	2.14	3.4

Source: Bangladesh Bureau of Statistics (BBS), Statistical Yearbook of Bangladesh 2001, Ministry of Planning, Dhaka 2002.

### 4. GOVERNMENTAL STEPS FOR POLLUTION CONTROL IN BANGLADESH

**4.1** The 'Ministry of Environment and Forest (MOEF)' of Bangladesh is primarily responsible for environmental protection. It was created in 1989. The MOEF has taken some steps to control the environmental pollution of Bangladesh.

#### 4.2a. National Environmental Management Action Plan (NEMAP).

The government has taken a project named NEMAP to integrate environment with the development in a policy framework. It provides a guideline for promoting effective management of resources, raising awareness among the people and improvement of environmental degradation.

#### 4.2b. Environmental Acts, Rules and Laws.

The government of Bangladesh has modified environmental acts, rules and laws to improve environmental condition. Environment court has already been established to take prompt legal action against environmental pollution. The DOE has been empowered to punish the offenders of environmental rules.

#### 4.2c. Control of Air Pollution.

Recently the DOE has taken some measures to carry out surveys on identification and control of polluting industries, protecting habitats, examining the use of compressed natural gas in industries, setting environmental standards and controlling river and automobile pollution on environmental management. It also conducts vehicular emission measurements at Dhaka city.

#### 4.2d. Banning of Polyethylene Bags.

Most of the sewage lines of Dhaka city have been blocked by indiscriminate dumping of polyethylene bags over the years. As such, the government has banned the production, marketing and use of polyethylene bags up to 20 microns thick or less from 01 March 2002.

#### 4.2e. Urban Transport Project.

An Urban Transport Project has been launched by the Government to improve traffic system, envisage good bus services, improve road networks by constructing over-bridges, fly-overs, underpasses and envisage a positive role for non-motorized transport.

#### 4.2f. Embargo on Import of Items.

The government has banned the import of leaded petrol, high sulfur diesel and high sulfur coal. The government has also encouraged to use Compressed Natural Gas (CNG) to the automobiles. Bangladesh Road Transport Authority (BRTA) has restricted the registration on two stroke three wheelers.

#### 4.2g. Control of Arsenic Pollution.

The Government has taken four Strategies to mitigate the arsenic problem. These are as follows:

- (1). Immediate detection of the arsenic effected patients and ensure their proper treatment.
- (2). Identify the arsenic contaminated tube wells, labeled them with red colour for danger ones and green with safe ones.
- (3). Detect the reasons for arsenic contamination in soil water and find out the sources of safe drinking water.
- (4). Conduct health education campaigns and grow awareness among the people.

#### 4.2h. Knowledge Enrichment Programme.

Environmental education program has been incorporated in primary and higher education. Many universities have introduced various curriculum and projects on environmental issue. Government organizations as well as NGOs present meetings and seminars to arise public awareness on the environmental issue.

#### 4.2j. Rural Sanitation Programme.

The Bangladesh Government has taken a rural sanitation programme from October 2003 to implement the facilitation, construction and installation of twin pit latrine. It improves rural sanitation coverage and reduces infectious diseases in rural areas.

### 5. AIR POLLUTION IN MEGA-CITIES

5.1 Environment problems differ from country to country. Cities in the South East Asia such as Delhi, Bangkok and Manila suffer from high levels of lead, particulate matter, and oxides of sulfur. Central and

South American cities such as Mexico City and Santiago experience frequent ozone problems. A comparison of air pollution in mega cities of the world is as follows:

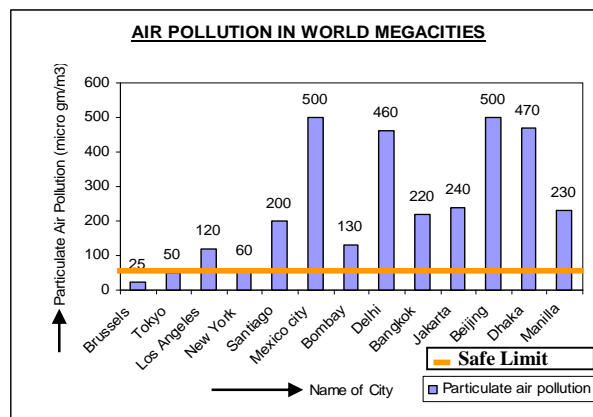


Fig 1. Comparison of Air Pollution in World Mega cities

### 6. SUGGESTED STEPS FOR POLLUTION CONTROL

6.1 The government has taken some steps to improve the pollution control of Bangladesh. But the steps are not adequate. As such, few more steps may also be taken to improve the environmental degradation:

#### 6.2 Use of Environmental Technologies and Methods.

Environmental technologies and methods such as Geographic Information Systems (GIS), remote sensing and environmental impact assessment might be used for integrated policy formulation, decision-making, evaluation and monitoring of environment.

#### 6.3 Development of Environmental Database.

A comprehensive environmental database may be made and the environmental planners might have the access for environmental up-gradation, planning and management. The database is to be updated regularly.

#### 6.4 Environmental Education and Awareness.

Formal and informal methods of education might be adopted through local media, seminars, celebrations, workshops, walks and student competitions to aware the people regarding the process of environmental degradation.

#### 6.5 Industrial and Solid Waste Management.

The government might take appropriate measures to monitor emission limits and Market Based Incentives (MBI) for reducing pollution control. The industries might be given both technical and financial support for introducing mitigation measures, promoting green technologies, using less pollution technologies and recycling the waste.

#### 6.6 Enforcement of Rules and Regulation.

Environmental Conservation Rules of 1997, traffic rules and other relevant environmental laws might be

enforced further to punish the violation of the emission limits.

### 6.7 Urban Transport Management.

Government must strengthen vehicle emission standards, complete the emission inventory and conduct an investigation on the emission control measures. Auto-rickshaw must be restricted in Dhaka city. Government must replace old vehicles, two-stroke engine vehicles, improve traffic conditions and promote an equivalent and efficient alternative public transportation services to improve urban transport management.

### 6.8 Reduce Sulfur in Diesel.

Government must take necessary steps to remove sulfur content from diesel through hydro-desulphurization (HDS) process. The government must also enforce the vehicle manufacturers to install catalytic converters in every vehicle to reduce the vehicular emissions.

## 7. CONCLUSION

**7.1** Environmental issues have become a major concerns due to impact on public health and development of Bangladesh. Air and water pollution, groundwater contamination, nuisance from solid wastes and noise pollution are the main environmental pollutions of Bangladesh. Dhaka City is one of the most polluted cities in the world. Environmental problems occur mainly due to population growth, urbanization, industrialization, rapid rise in transportation, inadequate and improper traffic management, poor sanitation systems and inefficient solid waste management.

**7.2** Air pollution from transportation systems in urban areas mainly occurs due to smoke emission from automobiles, burning of fossil fuel, use of low lead gasoline, high sulfur in diesel, increasing number of two stroke engine and overall poor traffic management. Industries cause air and water pollution through smoke emission, inadequate solid waste management and dumping of untreated effluent to lakes, rivers and ground water. The arsenic pollution of groundwater has become a major disaster for Bangladesh. The noise pollution is a major health hazards in the country. It is a serious but neglected issue throughout Bangladesh. Government as well as other organizations must take adequate steps to reduce the environmental pollution of Bangladesh.

## 8. REFERENCES

1. Md Mahbubur Rahman, "Environmental Pollution in Dhaka City and It's Effects on Public Health", 2003.
2. KM Nurul Huda, "Air Quantity Management Policy and Vehicle Emission Control", 1998.
3. Khan Morshed Ali, "Toxic Trap - Thousands Exposed to Stagnant Tannery Waste", The Daily Star, 16 July 2002.
4. Islam Faisal, "Industrial Pollution in Bangladesh", The World Bank Dhaka office, 2001.

5. Tariq Bin Yousuf, "Solid Waste and Sewerage Disposal of Dhaka", 1998.
6. Nazmul Chowdhury, "Noise pollution in Dhaka city", 2002.
7. Allan H Smith, Elena O Lingas & Mahfuzar Rahman on "Contamination of drinking-water by arsenic in Bangladesh: a public health emergency", 1998.
8. A survey report by British Geological Team on "Percentage of Ground Waters with Arsenic Levels over the Limit", Bangladesh, 1998.
9. A survey report by British Geological Team on "Sustainable Development Networking Project", Bangladesh, 1999.
10. Kafiluddin and Rawshan Ara Begum, "Noise Pollution Epidemic for Dhaka City", The Daily Prothom Alo, 13 June 1999.
11. Bangladesh Bureau of Statistics (BBS), Statistical Yearbook of Bangladesh 2001, Ministry of Planning, Dhaka 2002.
12. KM Nurul Huda, "Air Quantity Management Policy and Vehicle Emission Control", 1998.
13. Khan Morshed Ali, "Toxic Trap - Thousands Exposed to Stagnant Tannery Waste", The Daily Star, 16 July 2002.
14. M Shehab Ullah, "A study of hospital waste management in Dhaka city", 1999.

## 9. ABBREVIATION

Abbreviated Form	Full Form
SO <sub>2</sub>	Sulfur Dioxide
NO <sub>x</sub>	Nitrogen Dioxide
CO	Carbon Monoxide
HC	Hydro Carbon
SPM	Suspended Particulate Matter
DOE	Department of Environment
DWASA	Dhaka Water and Sewerage Authority
WHO	World Health Organization
DB	Decibel
BBS	Bangladesh Bureau of Statistics
MOEF	Ministry of Environment and Forest
NEMAP	National Environmental Management Action Plan
CNG	Compressed Natural Gas
BRTA	Bangladesh Road Transport Authority
GIS	Geographic Information Systems
MBIs	Market Based Incentives
HDS	Hydro-desulfurization
DMCH	Dhaka Medical College Hospital
SSMCH	Sir Salimullah Medical College Hospital
RIHD	Rehabilitation Institute & Hospital for Disabled
HFRCH	Holly Family Red Cresent Hospital
DNMCH	Dhaka National Medical College Hospital
SAHL	South Asia Hospital Limited



# MULTI-OBJECTIVE OPTIMIZATION OF CUTTING PARAMETERS FOR SURFACE ROUGHNESS IN CYLINDRICAL GRINDING USING RESPONSE SURFACE METHOD

B. C.Routara<sup>1</sup>, P. Sahoo<sup>2</sup> and A. Bandyopadhyay<sup>2</sup>

<sup>1</sup> Department of Mechanical Engineering, KIIT University, Bhubaneswar

<sup>2</sup> Department of Mechanical Engineering, Jadavpur University, Kolkata.

## ABSTRACT

In the present research, response surface methodology (RSM) has been applied to determine the optimum cutting conditions leading to minimum surface roughness in cylindrical grinding operation on AISI 1040 mild steel. The second order mathematical models in terms of machining parameters were developed for surface roughness prediction using RSM on the basis of experimental results. The model selected for optimization has been validated with F-test. The adequacy of the models on surface roughness has been established with Analysis of Variance (ANOVA). An attempt has also been made to optimize cutting parameters using multi-objective characteristics for the surface roughness prediction models.

**Keywords:** Cylindrical Grinding, Optimization, Surface Roughness, ANOVA.

## 1. INTRODUCTION

Surface finish is an important attribute of quality in any machining operation. The accuracy of mating surface is directly proportional to the surface finish produced on the machined part. Good surface finish, especially in grinding contributes to the aesthetic appeal of the product. Grinding is a complex machining process with a lot of interactive parameters, which depend upon the grinding type and requirements of products. However, surface quality produced in grinding is influenced by the following parameters.

- (i) Workpiece: Mechanical properties, chemical composition and fracture mode etc.
- (ii) Wheel: Abrasives, grain size, grade, structure, binding material, shape and size etc.
- (iii) Process: Wheel speed, workpiece speed, longitudinal feed (feed rate), radial infeed (depth of cut) and dressing conditions etc.
- (iv) Machine: static and dynamic characteristics, spindle system, and table system etc.

It is very difficult to consider all these parameters that control the surface roughness. In grinding operation, it is essential to select the process parameters to achieve the high quality performance. A lot of attempts have been made to study the grinding process effectively to evaluate the factors affecting surface roughness in cylindrical grinding. Kwak [1] investigated the various grinding parameters that affected the geometric error in surface grinding process using combined Taguchi method and RSM. Kwak *et al.* [2] analyzed the surface roughness of the product and grinding power spent during the process in the external cylindrical grinding of hardened SCM440 steel using RSM. The findings of this research work are that the depth cut is more influential

factor than the traverse speed for the grinding power and an increase in infeed changes the maximum height of the surface roughness more than the centre line average height. Shaji and Radhakrishnan [3] presented a study on Taguchi method to evaluate the process parameters in surface grinding with graphite as lubricant. The effect of process parameters such as speed, feed, infeed and modes of dressing are analyzed. Dhavlikar *et al.* [4] reported that the Taguchi and dual response method can be used effectively to determine robust condition for minimization of roundness error of workpiece for centerless grinding operation. Hecker and Liang [5] put a thought on prediction of the  $R_a$  based on a probabilistic undeformed chip thickness model. In this model, surface roughness is expressed as the function of wheel microstructure, the process kinematic conditions, and the material properties. A simple expression has been derived to correlate the surface roughness with the chip thickness. Zhong *et al.* [6] characterize the surface finish of thermally sprayed and precision machined WC-Co and alloy-625 coating on the grinding operation. They characterized the scaling behavior of the surfaces using various cut-off lengths, sampling lengths, numbers of sampling and cut-off lengths for measuring the surface roughness parameters  $R_a$  and  $R_q$  (root mean square roughness value). The surface roughness heights of the machined surfaces were found to be dependent on the scale of cut-off length as a power law. Sun *et al.* [7] investigated that the level of surface roughness and depth of sub-surface damage vary differently for different grinding modes. Atzeni and Iuliano [8] developed mathematical model for  $R_a$  and kinematic parameters using regression analysis. The developed model shows that the roughness is mainly influenced by the feed per

grain and cutting speed. A smoother surface is produced by decreasing the feed per grain, though the spacing between successive peaks along the workpiece and depth of engagement decreases. Choi *et al.* [9] established the generalized model for power, surface roughness, grinding ratio and surface burning for various steel alloys and alumina grinding wheels. It has been shown that these models can predict process conditions over a wide range of grinding conditions. Liu *et al.* [10] designed a force control system in a CNC grinding machine to reduce the grinding force variation and surface roughness. They conducted series of experiments using Taguchi method. The experimental result showed that surface roughness decreased with a slower feed rate and also with larger grinding force. Review of available literature shows that  $R_a$  has been the focus of most of the studies. The present study aims at consideration of five different roughness parameters, namely centre line average roughness ( $R_a$ ), root mean square roughness ( $R_q$ ), skewness ( $R_{sk}$ ), kurtosis ( $R_{ku}$ ) and mean line peak spacing ( $R_{sm}$ ) for the surface texture generated in grinding operation.

## 2. RESPONSE SURFACE METHOD

Response surface method (RSM) adopts both mathematical and statistical techniques which are useful for the modelling and analysis of problems in which a response of interest is influenced by several variables. RSM attempts to analyze the influence of the independent variables on a specific dependent variable (response). The mathematical model commonly used for the machining response  $Y$  is represented as

$$Y = \psi(d, N, f) + \varepsilon \quad (1)$$

where,  $d, N, f$  are depth of cut, spindle speed and feed rate respectively and  $\varepsilon$  is the error which is normally distributed about the observed machining response  $Y$ . Let  $\psi(d, N, f) = \eta$ . The surface represented by ' $\eta$ ' is called response surface.

Second order polynomial Model (Quadratic model)

$$Y_u = b_0 + \sum_{i=1}^n b_i x_{iu} + \sum_{i < j} b_{ij} x_{iu} x_{ju} + \sum_{i=1}^n b_{ii} x_{iu}^2 \quad (2)$$

where  $Y_u = f(Y - \varepsilon)$ , is proposed expected response on higher-order polynomial and  $x_i$ s are process variables such as depth of cut, spindle speed and feed rate respectively, and  $b$ 's are regression coefficients can be calculated by linear multiple regression analysis.

## 3. DESIGN OF EXPERIMENTS

The design of experiments is a very powerful tool, which permits us to carry out the modeling and analysis of the influence of process variables on the response variables. For the present work the factors considered for experimentation are workpiece speed ( $N$ ) in rpm, longitudinal feed ( $f$ ) in mm/rev and radial infeed ( $d$ ) in mm. Other parameters were assumed to be constant over the experimental domain. Machining has been carried out by varying one of the process parameters while keeping the rest at constant values.

Based on  $4^3$  factorial design, the selected design matrix constitute a four level three factor full factorial design consisting of 64 sets of coded conditions.

The process variables with their units, notations and values on different levels are listed in the Table.1. The selection of the values of the variables is limited by the capacity of the machine used

Table1: Machining process parameters levels

Parameter	Unit	1	2	3	4
Work speed(N)	rpm	56	80	112	160
Long. Feed(f)	mm/rev	11.33	17.00	22.66	28.3
Radial infeed(d)	mm	0.02	0.04	0.06	0.08

### 3.1 Work piece material

The present study is carried out with AISI 1040 mild steel specimens. The chemical composition of AISI 1040 steel is given as follows: 0.42%C, 0.48%Mn, 0.17%Si, 0.02%P, 0.018%S, 0.1%Cu, 0.09%Ni, 0.07%Cr and balance Fe. The physical properties are as follows: Hardness-201 BHN, Density-7.85 g/cc, Tensile strength-620 MPa. All the specimens are in the form of round bars of diameter 48 mm and length 50 mm.

### 3.2. Response variables

The response variables used to accomplish the present study on surface roughness are the following: Centre line average roughness ( $R_a$ ), Root mean square roughness ( $R_q$ ), Skewness ( $R_{sk}$ ), Kurtosis ( $R_{ku}$ ), Mean line peak spacing ( $R_{sm}$ ).

## 4. RESULTS AND DISCUSSION

All the experiments have been conducted in a HMT made (model K130U) cylindrical grinding machine as per the design of experiment with random order and the surface parameters have been measured using the stylus-type profilometer, Talysurf (Taylor Hobson, Surtronic 3+). The measured roughness parameters have been shown in Table 2 for mild steel. The results are put into the Minitab software for further analysis. The second order model was postulated in obtaining the relationship between the surface roughness parameters and the machining variables. The analysis of variance (ANOVA) was used to check the adequacy of the second order model.

The second order response surface equations have been fitted using Minitab software for all the five response variables ( $R_a, R_q, R_{sk}, R_{ku}$  and  $R_{sm}$ ). The equations can be given in terms of the independent variables as the following:

$$R_a = 0.6297 - 0.0786N + 0.1796f + 0.082d + 0.0505Nf + 0.0251Nd + 0.0136fd - 0.01N^2 - 0.0378f^2 - 0.0086d^2 \quad (3)$$

$$R_q = 0.7226 - 0.0805N + 0.2236f + 0.164d + 0.0623Nf + 0.029Nd + 0.0127fd - 0.0136N^2 - 0.0444f^2 - 0.0198d^2 \quad (4)$$



$$R_{sk} = -0.3068 + 0.2525N - 0.3059f + 0.4594d + 0.003Nf - 0.0107Nd - 0.0448fd \quad (5)$$

$$- 0.0498N^2 + 0.0878f^2 - 0.055d^2$$

$$R_{ku} = 2.331 + 1.2921N - 0.6016f + 0.291d - 0.0758Nf + 0.0126Nd + 0.0327fd \quad (6)$$

$$- 0.2072N^2 + 0.1618f^2 - 0.0879d^2$$

$$R_{sm} = 0.0526 - 0.0022N + 0.0018f + 0.0012d + 0.001Nf - 0.0001Nd + 0.0002fd \quad (7)$$

$$- 0.0001N^2 - 0.0005f^2 + 0.00006d^2$$

Analysis of variance (ANOVA) technique is used to check the adequacy of the developed models at 95% confidence level. As per this technique, if the calculated value of the  $F$ -ratio of the regression model is more than the standard tabulated value of table ( $F$ -table) for 95% confidence level, then the model is considered adequate within the confidence level.

Table 2: Experimental results of roughness parameters

Std. order	$R_a$ ( $\mu m$ )	$R_q$ ( $\mu m$ )	$R_{sk}$	$R_{ku}$	$R_{sm}$ (mm)
1	0.869	1.090	-0.164	3.47	0.054
2	0.919	1.172	0.361	3.84	0.050
3	1.135	1.540	1.686	3.45	0.066
4	1.177	1.487	0.268	3.39	0.052
5	0.725	0.915	-0.202	3.23	0.055
6	1.066	1.337	-0.136	2.97	0.062
7	0.969	1.230	0.074	3.86	0.054
8	1.270	1.587	0.188	3.24	0.066
9	1.152	1.460	0.365	3.66	0.050
10	1.270	1.622	0.532	4.22	0.058
11	1.174	1.477	0.295	3.16	0.060
12	1.417	1.760	0.256	3.11	0.056
13	0.974	1.235	-0.010	3.53	0.057
14	1.280	1.615	0.334	3.78	0.056
15	1.222	1.632	0.755	7.15	0.061
16	1.140	1.427	0.094	3.48	0.058
17	0.875	1.092	0.204	3.49	0.050
18	1.012	1.292	0.323	4.01	0.055
19	0.906	1.162	0.259	3.62	0.054
20	1.172	1.517	0.613	4.69	0.052
21	0.805	1.015	-0.113	3.26	0.058
22	1.197	1.490	0.205	3.21	0.060
23	1.282	1.625	0.167	3.94	0.066
24	1.395	1.747	0.094	2.98	0.071
25	1.102	1.390	-0.046	3.26	0.052
26	1.166	1.477	0.276	4.03	0.053
27	1.490	1.912	0.716	3.96	0.068
28	1.645	2.065	0.474	3.51	0.063
29	1.330	1.685	0.310	3.87	0.058
30	1.515	1.950	0.839	7.75	0.055
31	1.357	1.717	-0.182	3.49	0.056
32	1.512	1.957	0.317	4.59	0.064
33	0.823	1.063	0.096	3.90	0.050
34	0.739	0.990	1.128	4.75	0.045
35	0.891	1.129	0.001	3.38	0.048

36	0.897	1.156	0.069	3.67	0.056
37	0.849	1.057	0.030	3.28	0.050
38	1.205	1.560	0.176	4.11	0.052
39	1.287	1.760	1.437	3.31	0.055
40	1.542	1.922	-0.113	2.92	0.052
41	1.525	1.925	0.291	3.22	0.058
42	1.217	1.567	0.187	3.70	0.050
43	1.745	2.180	0.218	3.29	0.059
44	1.897	2.392	0.201	3.53	0.059
45	0.995	1.380	1.779	3.44	0.064
46	1.111	1.385	-0.130	3.31	0.062
47	1.365	1.740	0.374	4.48	0.067
48	1.575	1.985	0.281	3.59	0.062
49	0.936	1.192	0.317	3.45	0.053
50	1.033	1.322	0.384	3.94	0.050
51	1.018	1.302	0.386	3.35	0.051
52	1.112	1.412	0.277	3.33	0.054
53	0.847	1.084	-0.171	3.74	0.054
54	1.195	1.507	0.039	3.83	0.054
55	1.365	1.810	-0.558	3.59	0.057
56	1.372	1.727	0.336	3.36	0.054
57	0.777	1.017	-0.032	4.21	0.050
58	1.392	1.852	0.502	3.44	0.065
59	1.320	1.690	0.421	3.99	0.053
60	1.655	2.110	0.470	3.59	0.065
61	1.390	1.757	-0.118	3.19	0.058
62	1.817	2.282	0.320	3.34	0.055
63	1.720	2.155	0.256	3.46	0.062
64	2.075	2.605	0.369	3.92	0.067

From Tables 3, 5, 7, 9 and 11, it is observed that surface roughness models are adequate at 95% confidence level. Further, it is necessary that residuals should be normally distributed in order that the regression analysis is valid. The accuracy of the models has been checked by the complete residual analysis. The normal probability plots for centre line average clearly demonstrate that the residuals closely follow a straight line, denoting a normal distribution as shown in Fig. 1. All the statistical measures as explained above show that the non-linear relationships between the factors ( $N$ ,  $f$ , and  $d$ ) and the responses ( $R_a$ ,  $R_q$ ,  $R_{sk}$ ,  $R_{ku}$  and  $R_{sm}$ ) are adequate regression models. Tables 4, 6, 8, and 10 are present ANOVA tables for individual parameters. The significant effect of individual and interaction terms is shown in the summary Table 13. The longitudinal feed is the most influential factor for all surface roughness parameters except  $R_{ku}$ . Similarly, radial infeed is significant for all surface roughness parameters except  $R_{sk}$  and  $R_{ku}$ . Workpiece speed is significant for  $R_a$ ,  $R_q$  and  $R_{ku}$ . The main effect plots of surface roughness parameters with process variables are shown in the Fig. 2. It reveals the same results as explained in ANOVA tables. The parametric analysis has been carried out to study the influence of the individual process parameters such as workpiece speed, longitudinal feed and radial infeed on the surface roughness parameters during cylindrical grinding based on the developed empirical models as established through RSM and response surface plot using

MATLAB software.

Table 3: ANOVA for model of  $R_a$  in mild steel

Source	DF	SS	MS	F	P
Regression	9	4.03	0.44	15.07	0.000
Linear	3	3.59	0.03	1.01	0.395
Square	3	0.11	0.03	1.15	0.336
Interaction	3	0.33	0.11	3.78	0.015
Residual					
Error	54	1.60	0.03		
Total	63	5.64			

Table 4: ANOVA for individual parameter of  $R_q$

Source	df	SS	MS	F	P
$N$	3	0.33	0.11	7.69	0.001
$f$	3	1.96	0.65	44.4	0.000
$d$	3	1.52	0.50	34.46	0.000
$N*f$	9	0.96	0.10	7.31	0.000
$N*d$	9	0.20	0.02	1.55	0.180
$f*d$	9	0.24	0.02	1.87	0.101
Error	27	0.39	0.01		
Total	63	5.64			

Table 5: ANOVA for model of  $R_q$

Source	DF	SS	MS	F	P
Regression	9	6.33	0.70	15.18	0.000
Linear	3	5.67	0.05	1.15	0.338
Square	3	0.16	0.05	1.17	0.328
Interaction	3	0.48	0.16	3.52	0.021
Residual					
Error	54	2.50	0.04		
Total	63	8.83			

Table 6: ANOVA for individual parameter of  $R_q$

Source	DF	SS	MS	F	P
$N$	3	0.57	0.19	6.97	0.00
$f$	3	3.06	1.02	37.30	0.00
$d$	3	2.36	0.78	28.76	0.00
$N*f$	9	1.40	0.15	5.69	0.00
$N*d$	9	0.32	0.03	1.31	0.27
$f*d$	9	0.35	0.03	1.44	0.21
Error	27	0.74	0.02		
Total	63	8.83			

Table 7: ANOVA for model of  $R_{sk}$

Source	DF	SS	MS	F	P
Regression	9	5.48	0.60	5.46	0.005
Linear	3	0.25	0.08	0.75	0.291
Square	3	0.84	0.28	2.52	0.047
Interaction	3	0.21	0.07	0.63	0.594
Residual					
Error	54	6.01	0.11		
Total	63	12.81			

Table 8: ANOVA for individual parameter of  $R_{sk}$

Source	DF	SS	MS	F	P
$N$	3	0.17	0.05	0.53	0.66
$f$	3	1.09	0.36	3.25	0.03
$d$	3	0.36	0.12	1.09	0.36
$N*f$	9	0.47	0.05	0.47	0.88
$N*d$	9	1.47	0.16	1.46	0.21
$f*d$	9	0.70	0.07	0.7	0.70
Error	27	3.02	0.11		
Total	63	7.32			

Table 9: ANOVA for model of  $R_{ku}$

Source	DF	SS	MS	F	P
Regression	9	12.27	1.36	3.30	0.016
Linear	3	1.65	0.55	1.34	0.030
Square	3	4.91	1.63	3.97	0.018
Interaction	3	0.69	0.23	0.56	0.673
Residual					
Error	54	22.27	0.41		
Total	63	41.81			

Table 10: ANOVA for individual parameter of  $R_{ku}$

Source	DF	SS	MS	F	P
$N$	3	5.40	1.80	4.13	0.016
$f$	3	2.47	0.82	1.89	0.155
$d$	3	1.19	0.39	0.92	0.447
$N*f$	9	4.56	0.50	1.16	0.357
$N*d$	9	3.81	0.42	0.97	0.483
$f*d$	9	2.30	0.25	0.59	0.796
Error	27	11.77	0.43		
Total	63	31.54			

Table 11: ANOVA for model of  $R_{sm}$

Source	DF	Seq SS	Adj MS	F	P
Regression	9	0.000835	0.000093	4.2	0.000
Linear	3	0.000694	0.000007	0.33	0.803
Square	3	0.000022	0.000007	0.34	0.799
Interaction	3	0.000118	0.000039	1.78	0.162
Residual					
Error	54	0.001194	0.000022		
Total	63	0.002029			

Table 12: Summary of ANOVA for roughness parameters

	$N$	$f$	$d$	$*f$	$N*d$	$f*d$
$R_a$	#	#	#	#		
$R_q$	#	#	#	#		
$R_{sk}$		#				
$R_{ku}$	#					
$R_{sm}$		#	#			

#-Significant parameter

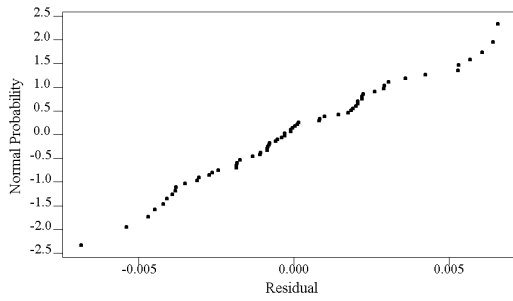
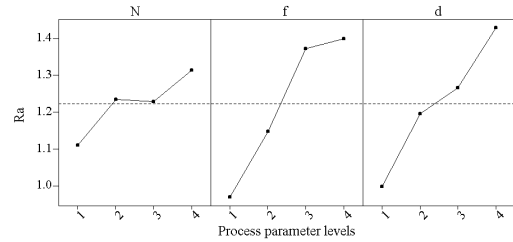
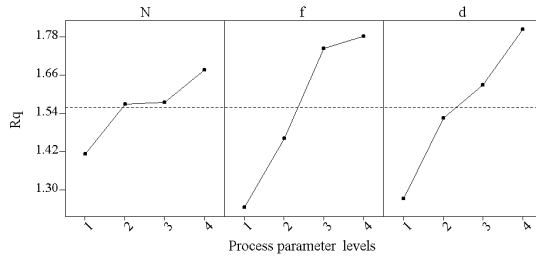


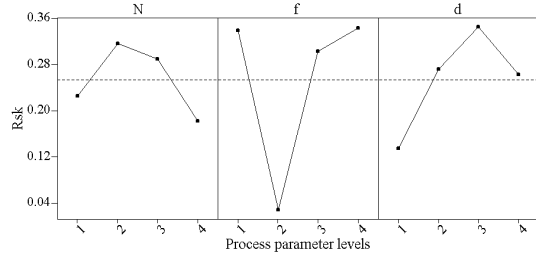
Fig 1. Normal probability plot of residuals of  $R_a$



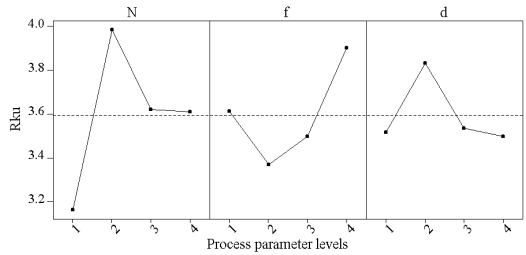
(a)



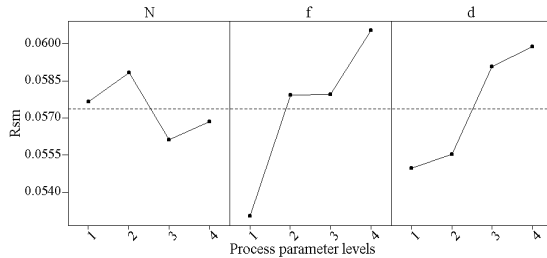
(b)



(c)



(d)



(e)

Fig 2. Main effect plots of surface roughness parameters

The three dimensional surface plots and contour plots for the five roughness parameters ( $R_a$ ,  $R_q$ ,  $R_{sk}$ ,  $R_{ku}$  and  $R_{sm}$ ) are shown in Figs. 3-7. In each of the plots, two cutting parameters are varied while the third one is held at its mid value. It is seen from these plots that there is significant amount of curvature indicating non-linearity in the variation.

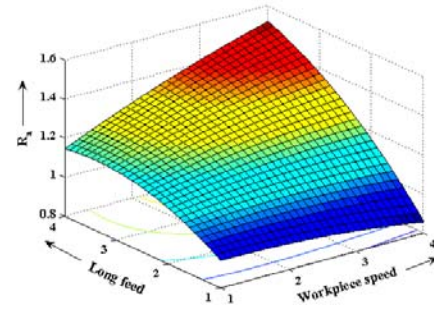


Fig 3. Surface and contour plots for  $R_a$  in cylindrical grinding of mild steel

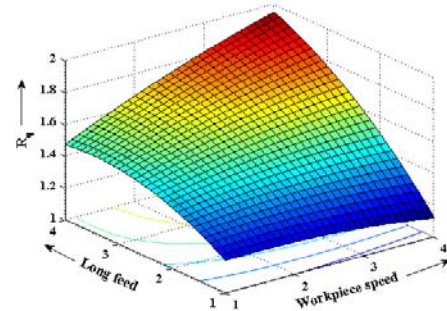


Fig 4. Surface and contour plots for  $R_q$  in cylindrical grinding of mild steel

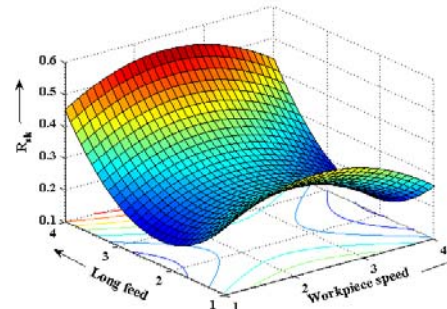


Fig 5. Surface and contour plots for  $R_{sk}$  in cylindrical grinding of mild steel

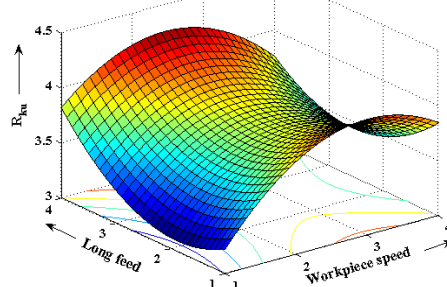


Fig 6. Surface and contour plots for  $R_{ku}$  in cylindrical grinding of mild steel

## grinding of mild steel

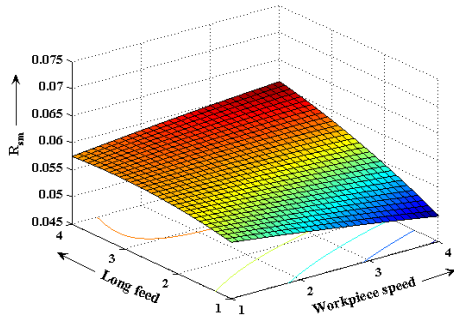


Fig 7. Surface and contour plots for  $R_{sm}$  in cylindrical grinding of mild steel

For some plots, e.g., Fig. 3, 4 and 6 there is switching of the curvature effect. It indicates the reversal in behaviour depending on the combination of the machining parameters. It also points towards significant contribution from the interaction of the machining parameters.

Optimization of machining parameters increases the utility for machining economics; a response surface optimization is attempted using Minitab software for individual roughness parameters in cylindrical grinding. Table 13 shows the RSM optimization results for the roughness parameters in mild steel grinding. It also includes the results from confirmation experiments conducted with the optimum conditions. It is found that the error in prediction of the optimum conditions for different roughness parameters individually is about 3 to 6%. Thus the response optimization predicts the optimum conditions fairly well.

**Table 13** RSM optimization for roughness parameters

Parameter	Objective func.	Optimum combination			Predi response	Expt. value	% of error
		$N$	$f$	$d$			
$R_a$	min	58.12	12.44	0.03	0.765	0.811	-6.01
$R_q$	min	62.23	15.45	0.05	0.964	1.024	-6.22
$R_{sk}$	Tar. 0	82.32	26.23	0.06	0.031	0.033	-6.45
$R_{ku}$	Tar. 3	141.55	16.23	0.07	3.12	3.22	-3.21
$R_{sm}$	min	142.85	22.25	0.04	0.023	0.024	-4.35

## 5. CONCLUSION

In this study an experimental investigation performed to evaluate the surface roughness parameters of AISI 1040 mild steel in grinding operation has been presented. A plan of experiments has been prepared in order to test the influence of cutting speed, longitudinal feed and radial infeed on the surface roughness parameters. The obtained data have been statistically processed using response surface method. The empirical models of roughness parameters are established and tested through the analysis of variance to validate the adequacy of the models. It is found that the roughness parameters greatly

depend on workpiece materials.

## 6. REFERENCES

1. Kwak, J.S., 2005, "Application of Taguchi and response surface methodologies for geometric error in surface grinding process", International Journal of Machine Tools & Manufacture, 45:327-334.
2. Kwak, J.S., Sim, S.B. and Jeong, Y.D., 2006, "An analysis of grinding power and surface roughness in external cylindrical grinding of hardened SCM440 steel using the response surface method", International Journal of Machine Tools & Manufacture, 46:304-312.
3. Shaji, S. and Radhakrishnan, V., 2003, "Analysis of process parameters in surface grinding with graphite as lubricant based on the Taguchi method", Journal of Materials Processing Technology, 141:51-59.
4. Dhavlikar, M.N., Kulkarni, M.S. and Mariappan, V., 2003, "Combined Taguchi and dual response method for optimization of a centerless grinding operation", Journal of Materials Processing Technology, 132:90-94.
5. Hecker, R.L. and Liang, S.Y., 2003, "Predictive modelling of surface roughness in grinding", International Journal of Machine Tools & Manufacture, 43:755-761.
6. Zhong, Z.W., Khoo, L.P. and Han, S.T., 2006, "Prediction of surface roughness of turned surfaces using neural networks", International Journal of Advanced Manufacturing Technology, 28:688-693.
7. Sun, X., Stephenson, D.J., Ohnishi, O. and Baldwin, A., 2006, "An investigation into parallel and cross grinding of BK7 glass", Precision Engineering, 30:145-153.
8. Atzeni, E. and Iuliano, L., 2008, "Experimental study on grinding of a sintered friction material", Journal of Materials Processing Technology, 196:184-189.
9. Choi, T.J., Subrahmanya, N., Li, H. and Shin, Y.C., 2008, "Generalized practical models of cylindrical plunge grinding process", International Journal of Machine Tools and Manufacture, 48:61-72.
10. Liu, C.H., Chen, A., Chen, C.A. and Wang, Y.T., 2005, "Grinding force control in an automatic surface finishing system", Journal of Materials Processing Technology, 170:367-373.
11. Montgomery, D. C., 1991, Design and Analysis of experiments, Wiley, India.

## 7. MAILING ADDRESS:

B. C.Routara  
 Department of Mechanical Engineering, KIIT University,  
 Bhubaneswar-751024  
 E-mail: bharat\_routray@rediffmail.com

## IDENTIFICATION OF INSTABILITIES OF CHIP FORMATION BY IMAGE PROCESSING TECHNIQUE

M. A. U Patwari<sup>1,2</sup>, A.K.M. Nurul Amin<sup>2</sup>, W. Faris<sup>3</sup>

<sup>1</sup>Department of Mechanical and Chemical Engineering, Islamic University of Technology, Dhaka  
<sup>2</sup>Department of Manufacturing and Materials Engineering, <sup>3</sup> Department of Mechanical Engineering,  
Faculty of Engineering, International Islamic University Malaysia

### ABSTRACT

Metal cutting is a chip forming process. Different types of chips are formed during machining. The nature of chip formation process is extremely complicated. This paper includes the findings of an experimental study on instabilities of the chip formation process during end milling operation of Ti6Al4V alloy at different cutting conditions. The instabilities of chip formation process are expressed in terms of primary or secondary serrated frequency. The chip formed at different cutting conditions is analyzed considering the chip cross-section and microstructure under the optical microscope and scan electron microscope. The image obtained from the microscope is further analyzed to identify the serrated teeth elements by detecting the edge using image processing technique. The developed technique can detect the serrated element identifying the boundary of the each teeth element. It has also been observed that the primary serrated frequency is more prominent in end milling of Ti6Al4V alloy compared to other materials. This developed technique will be useful to calculate the chip serration frequency during machining operation which is the primary cause of chatter formation.

**Keywords:** Image Processing, Chip Formation, Instabilities of Chip

### 1. INTRODUCTION

In metal cutting, the term “chip formation” has been used since the nineteenth century. Its initial meaning is the formation of the chip in the primary and secondary deformation zones. Primary attention was devoted to the kinematics relationships, cutting force and contact processes at the tool–chip interface. Later on, the chip-breaking problem became increasingly important with increasing cutting speed, the development of new difficult to-machine materials. Even though the term “chip formation” is still in use, its original meaning has been transformed. The modern sense of this term implies the chip, which just left the tool–chip interface and is yet to be broken [1-2]. The chip is enormously variable in shape and size in industrial machining operations. Chip morphology and segmentation play a predominant role in determining machinability and chatter during the machining operation of materials. In metal cutting, the present tendency is toward achieving increased material removal rates with a high degree of automation and without close human supervision. This requires very reliable machining processes, where the predictability of chip formation is very important.

Much research work has been done on the chip formation in turning, drilling and face milling. Komanduri [3-4] has made some remarkable progress in the research of chip segmentation and instability in chip formation. Nevertheless it appears that very few works

have been done to investigate the nature of chip formation in end milling because of its complexity and geometrical difficulty. Toenshoff [5] proposed the basic chip formation mechanism as “adiabatic shear” at high cutting speed. Amin [6] earlier established that the instability of chip formation could be lowered by preheating the work material during turning. Ekinović et.al [7] mentioned in their work that cutting speed has significant effect on chip formation models. Similar influence of the cutting speed on the chip structure and chip compression ratio was revealed in the experiments conducted by Tonshoff et al. [8]. Problems with surface finish, work-piece accuracy, chatter and tool life can be caused even by minor changes in the chip formation process. At lower cutting speeds the chip is often discontinuous, while it becomes serrated as the cutting speeds are increased. But to maintain stable machining, much attention must also be paid to the formation of the desired type of chip and chip controls to facilitate its easy removal. This is because the chip formation and breaking aspect is very significant in machining.

### 2. EQUIPMENT

Cutting tests was conducted mainly on Vertical Machining Center (VMC ZPS, Model: 1060) powered by a 30 KW motor with a maximum spindle speed of 8000 rpm. SANDVIK grade PM1030 Insert code: R390-11 T3 08E-PL, Insert coating material: carbide, Working

condition: light to medium milling is used for cutting. Insert shape and geometry with their values are shown in Fig.1 and Table 1.

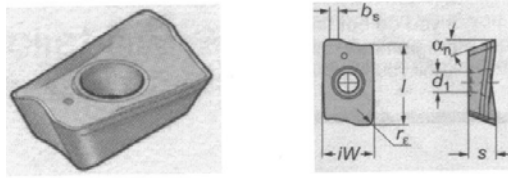


Fig 1. Insert Shape and Geometry

Table1 Insert Geometry Values

L	iW	d <sub>1</sub>	s	b <sub>s</sub>	r <sub>e</sub>	α <sub>n</sub> °
11	6.8	2.8	3.59	1.2	0.8	21

### 3. OBSERVATION OF SEM TOP VIEW OF CHIP

The chip morphology at different cutting conditions is different. The primary and the secondary serrated teeth are observed under the scan electron microscope. A sample view of the chip (SEM) at particular cutting condition is shown in Fig 2.

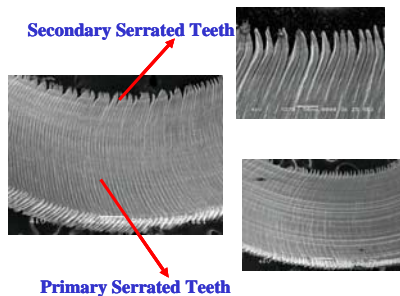


Fig 2. Sample SEM View of the chip showing the primary and secondary serrated teeth.

#### 3.1 Observation of Primary Saw Tooth Formation:

Fig 3.below shows a schematic of the chip showing where the chips were sectioned (along the line A-A) to be observed under the microscope. This sectioning is done in order to observe more clearly the primary chip serration. The lengthwise cross-section view of the chips under optical microscope is shown in Fig 4.

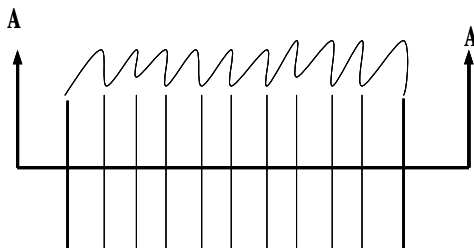


Fig 3. Schematic of chip showing sectioning for viewing side cross sectional view

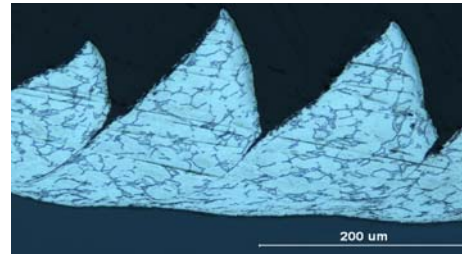


Fig 4. Section of chip formed by cutting the specimen at certain cutting conditions

### 4. IMAGE PROCESSING TECHNIQUE: CHIP ANALYSIS

Image processing is any form of signal processing for which the input is an image, such as photographs or frames of video; the output of image processing can be either an image or a set of characteristics or parameters related to the image. Most image-processing techniques involve treating the image as a two-dimensional signal and applying standard signal-processing techniques to it. Image processing usually refers to digital image processing, but optical and analog image processing are also possible. The whole image process of the chip analysis for identifying the serrated teeth is divided into three steps. They are image acquisition, image editing, edge identifications and extraction. A visual basic code is used to analysis the chip for serrated teeth identification. The steps are described below:

#### 4.1 Image Acquisition:

A color image of a chip is acquiesced by optical microscope or scan electron microscope, has different mode of dot per inch. Image editors can resize images in a process often called image scaling, making them larger, or smaller. High image resolution can produce large images which are reduced in size for use in the image processing code. Image editor programs use a mathematical process called resampling to calculate new pixel values whose spacing is larger or smaller than the original pixel values. Acquiesced image is resized 15% both horizontally and 25% vertically. The resized chip picture is opened in the specified area for further processing of the image as shown in Fig 5.

#### 4.2 Image Pre-processing/Editing:

Image editing encompasses the processes of altering images, whether they be digital photographs, traditional analog photographs, or illustrations. Traditional analog image editing is known as photo retouching, using tools such as an airbrush to modify photographs, or editing illustrations with any traditional art medium. Due to the popularity of cameras, image editing programs are readily available. The more powerful programs contain functionality to perform a large variety of advanced image manipulations.





Fig 5. Image acquisition of the chip

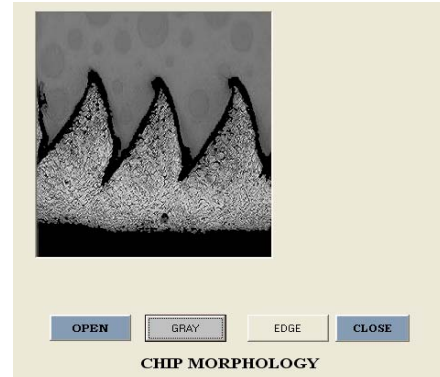


Fig 6. Image editing for chip analysis

### 4.3 Image orientation:

Image editors are capable of altering an image to be rotated in any direction and to any degree. Mirror images can be created and images can be horizontally flipped or vertically flopped. A small rotation of several degrees is often enough to level the horizon, correct verticality, or both. Rotated images usually require cropping afterwards, in order to remove the resulting gaps at the image edges. Image dimension may vary due to the irregularities in the image scanning and capturing process. A normalized size of 360×270 pixels has been used for all images. Subsequently, the color image is converted to a grayscale image. A color image consists of a coordinate matrix and three color channels. Coordinate matrix contains,  $x$ ,  $y$  coordinate values of the image. The color channels are labeled as Red, Green and Blue. Since our approach demands chip images in gray scale, by converting the color image into gray scale. The color image is converted to gray scale using the equation (1) as shown in Fig 6.

$$\text{Gray color} = (\text{Red} + \text{Green} + \text{Blue})/3$$

### 4.4 Edge detection Technique:

Edge detection is a terminology in image processing, particularly in the areas of feature detection and feature extraction, to refer to algorithms which aim at identifying points in a image at which the image brightness or pixel coordinates changes sharply or more formally has discontinuities. The purpose of detecting sharp changes in image is to capture important events and changes in properties of the chip. It can be shown that under rather general assumptions for an image formation model, discontinuities in image are likely to correspond to:

1. discontinuities in depth,
2. discontinuities in surface orientation,
3. changes in material properties and
4. variations in scene illumination.

In the ideal case, the result of applying an edge detector to an image may lead to a set of connected curves that indicate the boundaries of objects, the boundaries of surface markings as well curves that correspond to discontinuities in surface orientation. Thus, applying an edge detector to an image may significantly reduce the amount of data to be processed and may therefore filter out information that may be regarded as less relevant, while preserving the important structural properties of an image. If the edge detection step is successful, the subsequent task of interpreting the information contents in the original image may therefore be substantially simplified. Subsequently, thick boundary (edge) outside the chip is generated using edge detection algorithm [9] given in following equation (2). The result is depicted in Fig 7.

$$X_n = (X_{n+2} + 2X_{n+3} + X_{n+4}) - (X_{n-4} + 2X_{n-3} + X_{n-2}) \dots (2)$$

Where,  $X_n$  is the new pixel value for the detected edge. For the edge detection the pixels of the image of the chip are considered as a 3 X 3 matrixes as shown below.

$X_1$	$X_2$	$X_3$
$X_4$	$X_5$	$X_6$
$X_7$	$X_8$	$X_9$

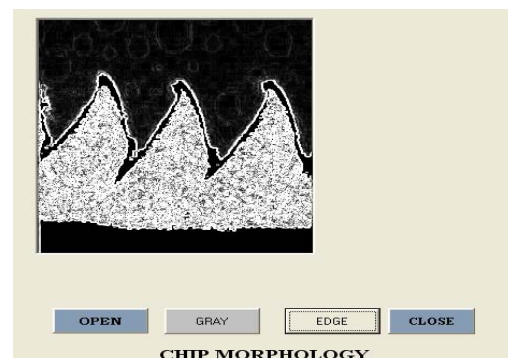


Fig 7. Edge detecting for chip analysis



## 5. CONCLUSIONS:

It can be concluded from the above analyses of chips that the chip formation process is accompanied with an inherent instability and the tendency to form discrete elements. In majority of the cases chips with primary/ secondary serrated teeth are formed. Each such tooth comprises a certain number of smaller sheared grains. The number of deformed grains forming a serrated tooth may identified by the image processing techniques. This technique will be useful for chip analysis and identification of the serrated elements.

## 6. REFERENCES

1. Nakayama, K., Arai, M., Comprehensive chip form classification based on the cutting mechanism, *Annals of the CIRP*, 71, 1992 (1992), 71–74.
2. Nakayama, K., Chip Control in Metal Cutting, *Bulletin of Japanese Society of Precision Engineering*, 18 (1984), 97–103.
3. Komanduri R., On the mechanism of chip segmentation in machining, *J. Eng. Ind.* 103 (1981).
4. Komanduri R., T. Schroeder, 1982, On the catastrophic shear instability of high speed machining of an AISI 4340 steel, *J. Eng. Ind.* 104

5. Tonshoff, H.K., Amor, P.B., Amdrae, P.1999, Chip formation in high speed cutting (HSC), *SME Paper MR99–253*.
6. Amin, A. K. M. N., and Talantov, N. V., 1986, “Influence of the Instability of Chip Formation and Preheating of Work on Tool Life in Machining High Temperature Resistant Steel and Titanium Alloys,”
7. Ekinovic, S., Dolinsek, S., Brdarevic, S., Kopac, J. 2002, Chip formation process and some particularities of high-speed milling of steel materials. In *Trends in the Development of Machinery and Associated Technology, TMT 2002*, B&H, Neum.
8. Tonshoff, H.K., Amor, P.B., Amdrae, P.1999, Chip formation in high speed cutting (HSC), *SME Paper MR99–253*.
9. Rafael C. Gonzalez and Richard E. Woods, “Digital Image Processing,” 2<sup>nd</sup> Edition, Addison-Wesley Longman Publishing Co. Inc, 2001.

## 10. MAILING ADDRESS:

Md. Anayet U Patwari  
Department of Mechanical and Chemical Engineering,  
Islamic University of Technology, Dhaka.  
E-mail: aupatwari@hotmail.com

## FABRICATION OF HIGH-ASPECT-RATIO EDM MICROELECTRODES USING ON-THE-MACHINE TOOL FABRICATION TECHNIQUES

M.P. Jahan, M. Rahman, Y.S. Wong and L. Fuhua

Department of Mechanical Engineering, National University of Singapore, Singapore.

### ABSTRACT

The concept of fabricating on-machine high-aspect-ratio microelectrodes arise from the need of machining small and deep micro-holes in micro-electro-discharge machining (micro-EDM). In recent years, the need for fabricating microelectrodes has gained much importance owing to the wide industrial applicability of micro-EDM technology for precise micro-hole fabrication and micro mold making. Therefore, present study aims to investigate the feasibility of fabricating high-aspect-ratio microelectrodes using block- $\mu$ EDM and turning- $\mu$ EDM processes. The process description and important aspects in fabricating successful, small diameter and high-aspect-ratio microelectrodes have been presented. Finally, a comparative study on the capabilities of the two processes and the application of fabricated microelectrodes in deep-hole micro-EDM drilling of WC has been presented.

**Keywords:** High-aspect-ratio Microelectrodes, On-the-machine Tool Fabrication, Turning- $\mu$ EDM Hybrid Process, Block- $\mu$ EDM Process, Micro-EDM Drilling, Tungsten Carbide.

### 1. INTRODUCTION

Electrical discharge machining, more commonly known as EDM or spark machining, removes electrically conductive material by means of rapid, repetitive spark discharges from electric pulse generators with the dielectric flowing between the tool and the workpiece. Micro-electrodischarge machining (Micro-EDM) is the application of EDM in micro field. The low energy range is becoming important when the EDM process is used in micro field. Micro-EDM has similar characteristics as EDM except that the size of the tool, discharge energy and movement resolutions are at micron level.

In recent years, the need for fabricating microelectrodes has gained much importance owing to the wide industrial applicability of micro-EDM technology for precise micro-hole fabrication and micro mold making [1-3]. Several researches have been carried out on the on-machine fabrication of microelectrodes. A number of EDM based processes for fabricating microelectrodes have been reported; such as wire electro-discharge grinding (WEDG), mesh electrode method and block electrode method [4]. With the development of WEDG technology, micro-EDM has become the machining process of choice for fabricating micro/miniature parts [5]. However, the process requires design and installment of WEDG device on the machine, which needs investments and special design consideration. Multiple electrodes have been fabricated successfully using reverse EDM for different application

like punching of arrays of micro-holes, ECM etc. [6]. In addition, mesh electrode method of fabricating multiple electrodes has also been reported [7]. However, the reverse EDM process is very time consuming and it is very difficult to fabricate very high-aspect-ratio micro-electrodes using reverse EDM. Similarly, machining down to a few tens of microns using mesh electrode method may be exigent due to the difficulty of flushing the debris from the micro tool electrode consisting of a micro-hole [4]. Besides, micro-EDM based processes; there are processes for fabricating microelectrodes, like LIGA [8-9] and micromechanical machining method [10-11]. However, the LIGA process requires very expensive and special facilities, and the maximum achievable thickness is relatively small.

Among all the microelectrode fabrication processes, the use of a conductive block as a cutting electrode and the rod as a workpiece of the block electrode method has been identified as being a simple and useful approach for producing microelectrodes due to its low investment cost and quick set-up [4,12]. However, there are several problems of block-EDM process like maintaining desired diameter and taperness of the fabricated microelectrodes due to occurrence of the wear in both electrode and the block [4]. Therefore, it requires further investigation for improving the performance. Moreover, in recent years, a new technology, turning-EDM hybrid machining technology has been reported to be a successful process for fabrication of microelectrodes

[13]. However, a number of issues remain to be solved for successful fabrication of microelectrodes with high-aspect-ratio and improved dimensional accuracy.

Therefore, investigations have been conducted for fabricating high-aspect-ratio microelectrodes using block- $\mu$ EDM and turning- $\mu$ EDM processes and to apply the microelectrodes in deep-hole micro-EDM drilling of difficult-to-machine tungsten carbide (WC).

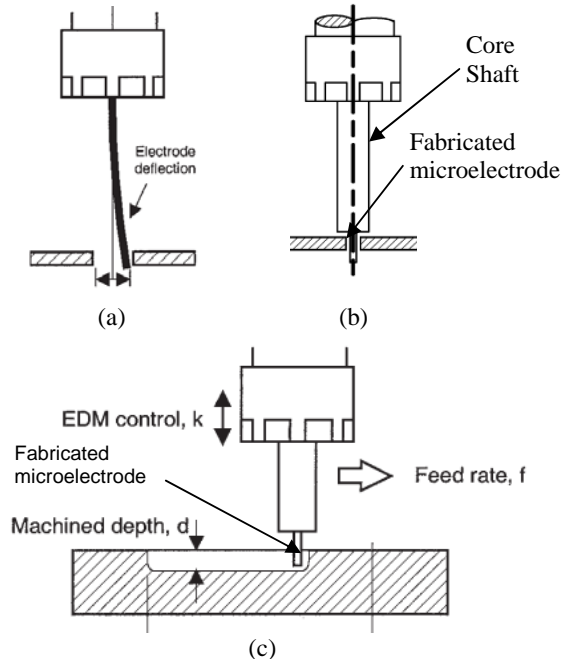


Fig 1. (a) Machining with longer electrodes introduces deflection due to low stiffness, (b) Micro-EDM drilling with on-machine fabricated microelectrode, (c) micromold fabrication using on-machine fabricated microelectrode.

## 2. PROBLEM STATEMENT

With the growing trends towards the miniaturization of machined parts and developments in the area of micro-electromechanical systems (MEMS), fabrication of micromold cavities has become the most important part for mass production of microcomponents. The microcomponents can be made easily using the injection molding process. However, hard-to-machine work piece materials should be machined very precisely in three-dimensional forms over the range of microns for the purpose of microinjection. In recent years, micro-EDM has become one of the alternative machining processes that can be used successfully for the fabrication of complex three-dimensional molds using very tough die materials. Micro-EDM can machine almost every conductive material, regardless of its stiffness. Using a very thin electrode and controlling the EDM contour, micromolds can be produced successfully.

Although micro-EDM plays an important role in the field of micromolds, it has disadvantages, including a high electrode wear ratio and a low material removal rate. The wear of the electrode must be compensated either by changing the electrode or by preparing the longer electrode from the beginning or fabricating the electrode in situ for further machining. Changing the

microelectrode during machining is not recommended, because it may reduce the accuracy due to clamping. However, machining longer electrodes introduces deflection due to low stiffness, as illustrated in Fig. 1.

Moreover, in the micro-EDM process, the electrodes used are in micron level and their handling becomes difficult, as there is huge chance of bending the electrode during putting it into the collets. Therefore, it is more desirable that microelectrodes should be fabricated on-machine and will be used in micro-EDM directly without changing the tool; so that clamping and run out error could be minimized as well as machining accuracy can be improved.

## 3. EXPERIMENTAL SETUP

### 3.1 Machine tool

A multi-purpose miniature machine tool, developed for high-precision micro-machining at the National University of Singapore, was used for both on-machine fabrication of microelectrodes and micro-EDM drilling. The machine is capable of micro-EDM, micro-turning, micro-milling, micro-grinding, and micro-ECM by using suitable attachments. The maximum travel range of the machine is 210 mm ( $x$ -direction)  $\times$  110 mm ( $y$ -direction)  $\times$  110 mm ( $z$ -direction) with a resolution of 0.1  $\mu$ m in all three directions. A full closed-loop-feedback control system ensures sub-micron accuracy. Fig. 2 shows the schematic diagram of the setup with multipurpose miniature machine tool.

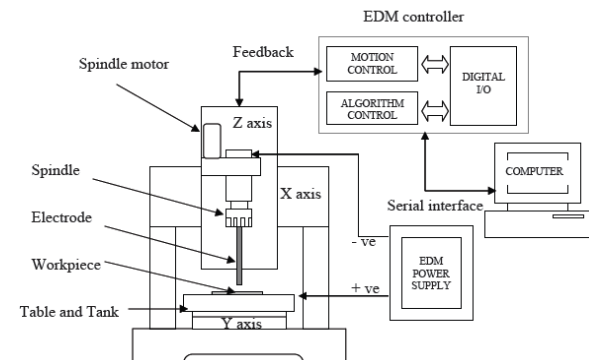


Fig 2. Schematic diagram of the setup with multi-purpose miniature machine tool.

### 3.2 Materials for Turning- $\mu$ EDM process

For fabrication of microelectrodes using Turning- $\mu$ EDM hybrid process, commercially available brass and CuW shafts of 6 mm diameter was used as workpiece. The cutting tool used were commercially available SumiDIA PCD positive rake insert type TCMD73X (0.1 mm nose radius, 7° front clearance and 10° rake angle). The tool shank used was Sumitomo type STGCR1010-09.

### 3.3 Materials for Block- $\mu$ EDM process

For fabrication of microelectrodes using Block- $\mu$ EDM process, commercially available W and CuW (40% Cu, 60% W) of 0.5 mm diameter was used as workpiece and a carbide block with composition

WC-10wt%Co was used as sacrificial block. For the on-machine micro-EDM drilling, WC-10wt%Co workpiece of different thickness (0.1, 0.3, 0.5 and 1 mm) was used.

#### 4. TURNING- $\mu$ EDM HYBRID PROCESS

##### 4.1 Modification of PCD cutting tool using micro-EDG process

Commercially available PCD tools usually have relatively large tool nose designed for general-purpose machining. The tool nose resolves the cutting force into two main components with one of them generating the essential cutting motion ( $F_y$ ) while the other one producing radial force ( $F_x$ ) causing deflection to the micro-shaft [Fig. 3(a)]. Hence, in order to fabricate straight shaft at small diameter, commercial PCD tool nose is modified to reduce the nose radius thus minimizing the force component ( $F_x$ ), that causes the shaft deflection during microturning.

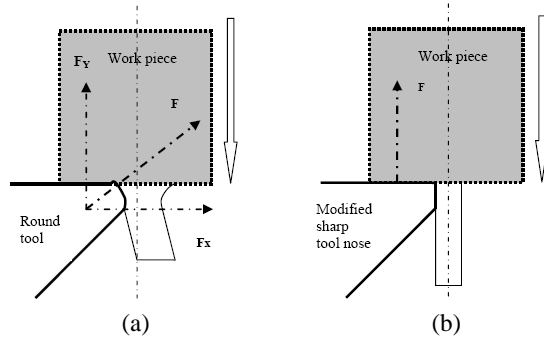


Fig 3. (a) Resolution of cutting forces for microturning with a radius tool nose of commercial PCD insert, (b) Modified sharp tool nose to reduce  $F_x$  component.

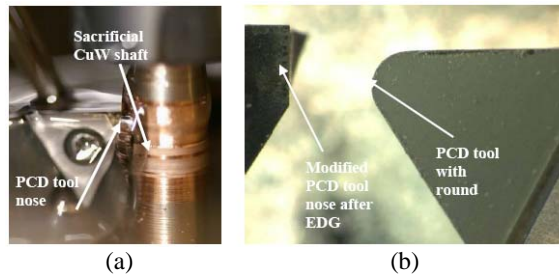


Fig 4. (a) On-machine EDG on PCD cutter, (b) PCD cutter before and after modification using EDG.

Micro-Electro-discharge grinding (EDG) is carried out by first setting the polarity of sacrificial copper tungsten (CuW) shaft to be negative and the PCD cutter to be modified as positive. A visual centering and pre-experimental dressing of the sacrificial CuW electrode has been done to ensure that any surface irregularity of the shaft is eliminated. The EDG of the PCD cutter was conducted using slow feed rate of sacrificial electrode towards the cutter nose and using different scanning motion to ensure precise sharpening and good surface finish of the nose and to avoid any possible formation of circular contours on the PCD cutter's surface mapped from the electrode's circular geometry. Figs. 4(a) and (b) present the on-machine

photographs of the EDG process and the PCD tool before and after modification. The experimental settings for the modification of PCD tool using micro-EDG are listed in Table 1.

Table 1: Parameters used for electrical discharge grinding (EDG) of PCD tool nose

Machining parameters	Rough Cut		Final Cut	
	Gap voltage	120 V	High MRR	80 V
Capacitor	470 pF	100 pF		
Feed rate	20-25 $\mu\text{m}/\text{min}$		10 $\mu\text{m}/\text{min}$	
Spindle speed	1200 rpm		1200 rpm	
Electrode advance in X-axis	140 $\mu\text{m}$		10 $\mu\text{m}$	

##### 4.2 Centering process

The centering process is the most important step for fabricating accurate and high-aspect-ratio microelectrodes. Without proper centering, the micro-shaft becomes tapered and can break at any point of machining, especially when a micro-shaft of less than 100  $\mu\text{m}$  is attempted. Another important thing before centering is the reduction of wobbling effect for the initial electrode. With the help of a superimposed cross-hair as the datum under the on-machine microscope, the degree of run-out can be observed and thus reduced. Fig. 5 presents the schematic diagram and photograph of the approach taken in this study to remove the wobbling effect of the shaft. The centering is done for both the round and sharp edged PCD cutter mounted in two different positions.

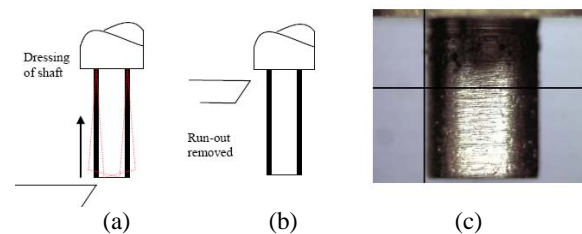


Fig 5. (a) Schematic representation of dressing in X and Z-axis to reduce wobbling effect, (b) removed wobbling (b) Cross-hair check before centering.

##### 4.3 Microturning

In this study, for the fabrication of high-aspect-ratio microelectrodes, three steps were used: straight microturning, taper microturning like pencil sharpener cutting, and final cutting using the modified PCD tool. In the first approach of straight turning, a small depth is dressed in order to reduce the wobbling effect of the initial shaft. The amount of materials removal using this straight turning was kept lower in order to avoid the stress concentration effect at the critical places of varying diameter. Before final cut, another necessary step is to carve out a tapered surface called the pencil sharpener to provide a strong support to the shaft with smooth gradient. The tapered surface is generated by gradual

removal material turning along the taper surface by a limited depth of cut to protect the cutting edge from chipping. There are two reasons for choosing the taper turning process along the taper surface. Firstly, there is a chance of remaining the cutting marks on the surface in case of stepped taper turning parallel to the axis, which can act as the point of stress concentration. Secondly, from the view point of efficient and fast micro fabrication, turning parallel to the taper surface is preferable than that of parallel to the workpiece axis [14].

The final fabrication of the micro-shaft is done in a single pass at the tapered tip, reducing the diameter to the intended diameter. The purpose of creating the tip prior to the final cut is to allow a shallow depth of cut that prevents possible chipping of the cutter as well as to reduce the amount of debris that might interfere with the final turning process. Fig. 6 shows the on-machine images obtained during turning showing different steps of microturning at machining conditions listed in Table 2. Figs. 7(a) and (b) show the images of a fabricated 45  $\mu\text{m}$  CuW shaft and 19.3  $\mu\text{m}$  brass shafts respectively.

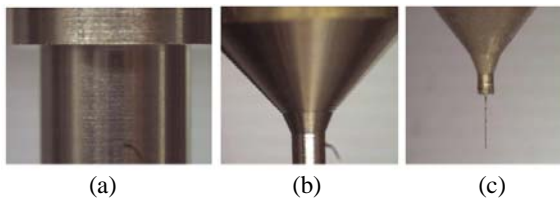


Fig 6. On-machine images of the shaft at different state of micro-turning (a) straight turning, (b) taper turning and (c) final shaft.

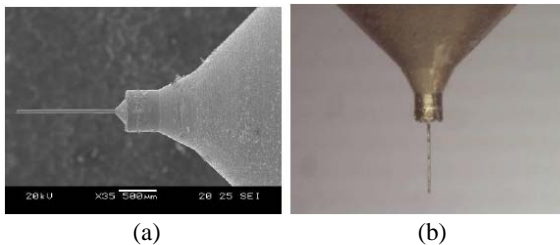


Fig 7. (a) CuW microshaft of about 45  $\mu\text{m}$  diameter, (b) brass shaft of 19.3  $\mu\text{m}$  diameter fabricated by Turning- $\mu\text{EDM}$  hybrid process

Table 2: Microturning with minimized tool wear

Material	Feed rate using round nose (mm/min)	Feed rate using modified nose (mm/min)	Depth of cut (mm)
CuW	1 - 40	1 - 5	Roughing: 0.2-0.3 Finishing: 0.05-0.1
Brass	1 - 100	1 - 40	Roughing: 0.3-0.7 Finishing: 0.1-0.3

## 5. BLOCK- $\mu\text{EDM}$ PROCESS

### 5.1 Stationary Block- $\mu\text{EDM}$ process

Block- $\mu\text{EDM}$  is a simple process requiring very little arrangement in the setup. Fig. 8 shows the schematic diagram of the Block- $\mu\text{EDM}$  process. It needs a precise sacrificial rectangular block with high wear resistance (WC was used in this study due to its high resistance to wear), and a commercially available electrode. However, one important thing is the alignment of block respective to the electrode. It is very important that sacrificial block should be aligned properly (within an accuracy of  $\pm 2 \mu\text{m}$ ) in order to avoid electrodes being more taper, thus reducing dimensional accuracy. It has been found that due to wear of the sacrificial block also, the diameter of the fabricated electrode is sometimes difficult to predict. Therefore, an on-machine camera with measuring unit is installed in the setup to measure on-machine. In this method, the block is used as a cutting electrode and a cylindrical rod is used as the workpiece in the EDM process. The microelectrode that needs to be machined is fed against the conductive block. The machining is carried out at different conditions [shown in table 3] by applying a controlled electric spark and by forcing the dielectric medium to flow through the spark gap between the block and the rod.

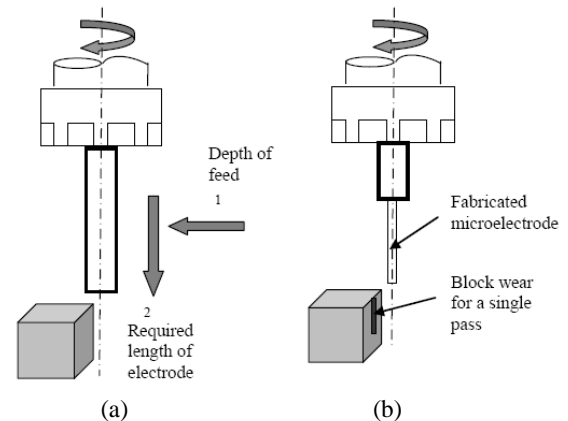


Fig 8. Schematic diagram of Block- $\mu\text{EDM}$  process; (a) at the beginning of process; (b) fabricated microelectrode

### 5.2 Moving-electrode Block- $\mu\text{EDM}$ process

Although, the process is simple in mechanism, it needs several important considerations to fabricate successful, dimensionally accurate and very high aspect ratio microelectrodes. The major problem of block- $\mu\text{EDM}$  is the taperness of the fabricated microelectrodes. Therefore, a new and modified block- $\mu\text{EDM}$  process was developed using the scanning movement of the electrode in addition to downward movement. The introduction of scanning motion significantly reduces the taperness of the microelectrodes. The reason for taperness in stationary block is because, at the start of machining more surface area are exposed to spark zone, which decreases with the block wear. However, if the electrode is moved along the block, then the wear of the block is uniformly distributed which reduces the taperness of the microelectrodes. Fig. 9 shows Block- $\mu\text{EDM}$  process with moving electrode.

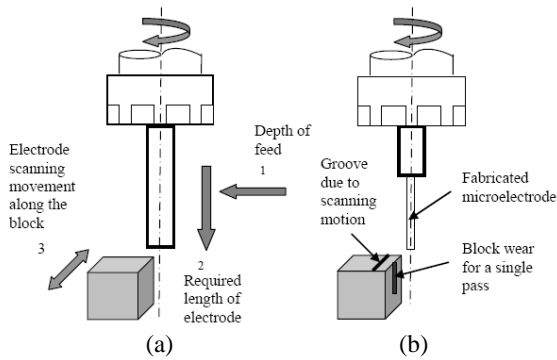


Fig 9. Schematic diagram representing the Block- $\mu$ EDM process with moving electrode; (a) at the beginning of process; (b) fabricated microelectrode

Table 3: Machining conditions for the fabrication of microelectrode using Block- $\mu$ EDM

Electrode materials	CuW, W
Block material	WC-10wt%Co
Dielectric material	TOTAL FINA ELF EDM oil 3
Polarity	Electrode : +ve
Spindle speed	1500
Gap voltage (V)	80, 90, 100, 110, 120,
Capacitance (pF)	47, 100, 470, 1000, 2200, 4700
Feed length ( $\mu$ m)	12.5, 25, 50, 75, 100

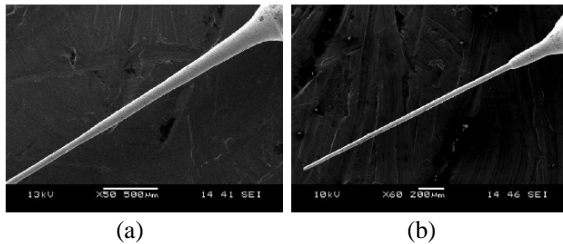


Fig 10. CuW microelectrode; (a)  $\varnothing$  50  $\mu$ m, L 3 mm (a.r. 60) fabricated by stationary Block- $\mu$ EDM process, (b)  $\varnothing$  40  $\mu$ m, L 2 mm (a.r. 50) fabricated by Block- $\mu$ EDM process with moving electrode [steps: see table 4].

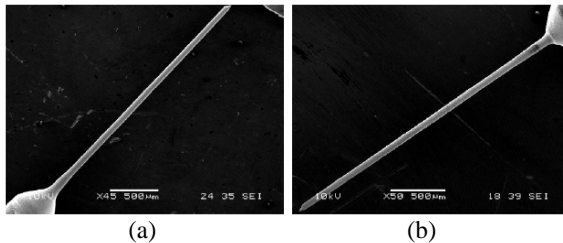


Fig 11. W microelectrode; (a)  $\varnothing$  60  $\mu$ m, L 3 mm (a.r. 50) fabricated by stationary Block- $\mu$ EDM process, (b)  $\varnothing$  40  $\mu$ m, L 3 mm (a.r. 75) fabricated by Block- $\mu$ EDM process with moving electrode.

Fig. 10(a) shows the fabricated CuW electrode of about 50  $\mu$ m diameters and 3 mm long (a.r. 60) obtained using stationary Block- $\mu$ EDM. The improvement in taperness can be observed from Fig. 10(b) where the microelectrode presented has been fabricated using Block- $\mu$ EDM process with electrode movement. Figs. 11(a) and (b) show the fabricated W electrode using stationary and moving block- $\mu$ EDM process. It has been

observed that, moving block- $\mu$ EDM process can provide microelectrodes with less taperness, thus providing better dimensional accuracy.

Table 4: Machining steps for fabricating a CuW microelectrode of  $\varnothing$  40  $\mu$ m, L 3 mm (Fig. 10b)

Machining step	Volta ge (V)	Capacitance (pF)	Feed length (mm)	Average Machining Time (h:mm)
1	120	4700	0.050	0:13
2	120	4700	0.050	0:13
3	120	2200	0.050	0:18
4	120	2200	0.025	0:20
5	100	470	0.025	0:25
6	100	100	0.025	0:30
7	80	47	0.013	0:37
Total average machining time				2:40

## 6. COMPARISON OF TWO PROCESSES

A comparative evaluation on the capabilities and performance of the two processes is listed in Table 5.

Table 5: Comparative evaluation of Turning- $\mu$ EDM and Block- $\mu$ EDM processes for microelectrode fabrication

Factors of comparison	Turning- $\mu$ EDM hybrid process	Block- $\mu$ EDM process
<i>Applicable Materials</i>	Softer and easily machinable materials; e.g. Brass	Difficult-to-cut and soft/easily machinable materials with good electrical conductivity; Brass, CuW, W
<i>Average fabrication time</i>	Depends mainly on centering time PCD cutting tool modification: 10 mins Centering process: 15-30 mins Microturning process: 10 mins Total fabrication time: 30-45 min	Depends on the discharge energy used and number of machining passes For 4 passes of rouging and 3 passes of finishing: Total fabrication time: 2.5 hours
<i>Dimensions</i>	Brass: $\varnothing$ 20 $\mu$ m, L < 1 mm CuW: $\varnothing$ 45 $\mu$ m, L < 800 $\mu$ m	CuW: $\varnothing$ 45 $\mu$ m, L: > 3 mm W: $\varnothing$ 45 $\mu$ m, L: > 3 mm
<i>Aspect ratio</i>	Brass: 45-55 CuW: 15-20	CuW: >70 W: >75
<i>Taperness</i>	Less taper	Comparatively more taper
<i>Distortion</i>	Suffer distortion	No distortion



<i>Surface finish</i>	Depends mainly on microturning conditions; e.g. feed rate and depth of cut  $R_a: < 1 \mu\text{m}$ (optical)	Depends mainly on energy used in finishing steps  $R_a: 0.5\text{-}1.5 \mu\text{m}$ (optical)
-----------------------	--	---

## 7. APPLICATION OF MICROELECTRODES

During the micro-EDM, for fabricating small and high-aspect-ratio micro-holes it requires several times higher electrode length than the thickness of the workpiece. It has been found that, the wear of the brass microelectrodes are very high compared to W and CuW microelectrodes during machining WC. This may be due to the reason that, the melting point of brass is much lower compared to that of WC. Therefore, to remove same unit of material from WC, more materials are removed from the brass. It was observed that electrodes obtained using turning- $\mu$ EDM process is of limited height thus, are not capable of fabricating deeper micro-holes in WC. Fig. 12(a) shows a  $30 \mu\text{m}$  hole in a WC strip of  $0.1 \text{ mm}$  machined by an  $\text{Ø}: 20 \mu\text{m}$ , L:  $1 \text{ mm}$  microelectrode fabricated using Turning- $\mu$ EDM process.

On the other hand, for fabricating deep micro-holes, microelectrodes fabricated using block- $\mu$ EDM process can perform well. As there is no force in this process, micro-electrodes of more than  $3 \text{ mm}$  in length  $40 \mu\text{m}$  diameters can be used for deep-hole drilling in difficult-to-cut WC. Fig. 12(b) shows a micro-hole of  $50 \mu\text{m}$  diameter in  $0.5 \text{ mm}$  WC sheet by a microelectrode ( $\text{Ø}: 45 \mu\text{m}$ , L:  $3 \text{ mm}$ ) fabricated using Block- $\mu$ EDM.

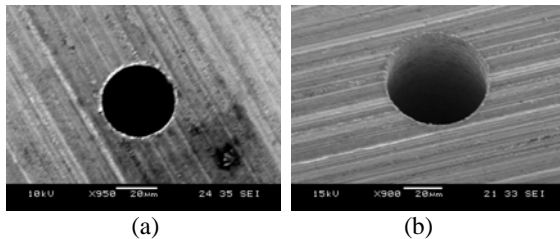


Fig. 12: SEM images of micro-holes machined at  $100 \text{ V}$ ,  $100 \text{ pF}$ ; (a) Microelectrode: Turning- $\mu$ EDM hybrid process; Micro-hole:  $\text{Ø} 30 \mu\text{m}$  hole in  $0.1 \text{ mm}$  WC strip, (a.r. 3.33); (b) Microelectrode: Block- $\mu$ EDM process, Micro-hole:  $\text{Ø} 50 \mu\text{m}$  hole in  $0.5 \text{ mm}$  WC sheet, (a.r: 10).

## 8. CONCLUSIONS

The following conclusions can be drawn from this experimental study of on-machine fabrication of microelectrodes for micro-EDM application:

- Turning- $\mu$ EDM is more suitable for fabricating smaller micro-holes with lower aspect ratios. This study shows that micro-electrodes of diameter down to  $20 \mu\text{m}$  can be machined by this method.
- For fabricating deep micro-holes, micro-electrodes can be fabricated using block- $\mu$ EDM process. As there is no force in this process, micro-electrodes can be fabricated more than  $3 \text{ mm}$  in length with less than  $40 \mu\text{m}$  diameters.
- A newer process, Block- $\mu$ EDM with scanning

movement of the electrode can reduce the taperness significantly; thus reduce the shortcoming of stationary Block- $\mu$ EDM process.

- Very small and high-aspect-ratio micro-holes in difficult-to-cut materials can be machined using micro-EDM drilling by means of the on-machine fabricated microelectrodes.

## 9. REFERENCES

1. Rajurkar, K. P. and Yu, Z. Y., 2000, "3D micro-EDM using CAD/CAM", *Ann. CIRP*, 49:127–130.
2. Mohri, N., Takezawa, H., Furutani, K., Ito, Y. and Sata, T., 2000, "A new process of additive and removal machining by EDM with a thin electrode", *Ann. CIRP*, 49:123–126.
3. Yeo, S. H. and Nachiappan, R., 2001, "Investigation of micro-EDM controllable factors on machined silicon surface quality", *Proc. IMech (Part B), J. Eng. Manufacture*, 215:811–817.
4. Ravi, N. and Chuan, S. X., 2002, "The effects of electro-discharge machining block electrode method for microelectrode machining", *J. Micromech. Microeng.*, 12:532–540.
5. Masuzawa, T., Fujino, M., Kobayashi, K. and Suzuki, T., 1985, "Wire electro-discharge grinding for micro machining", *Ann. CIRP*, 34:431–434.
6. Kim, B. H., Park, B. J., Chu, C. N., 2006, "Fabrication of multiple electrodes by reverse EDM and their application in micro ECM", *J. Micromech. Microeng.*, 16:843–850.
7. Masuzawa, T., Tonshoff, H. K., Zentrum, L., 1997, "Three-dimensional micro-machining by machine tools", *Ann. CIRP*, 46:621–628.
8. Takahata, K., and Gianchandani, Y. B., 2002, "Batch mode micro-electro-discharge machining", *J. Microelectromech. Syst.*, 11:102–110.
9. Takahata, K., Shibaie, N. and Guckel, H., 1999, "A novel micro electro-discharge machining method using electrodes fabricated by the LIGA process", *Proc. Micro Electro Mechanical Systems (MEMS '99) (Piscataway, NJ: IEEE)*, pp 238–243.
10. Liu, W., Rahman, M. and Wong, Y. S., 2001, "Micro machining of silicon by electrical discharge machining", *SME Tech. Paper MR01-237*, pp 1–7.
11. Matsui, S., Kaito, T., Fujita, J.-I., Ishida, M., Ochiai, Y., 2001, "Three-dimensional nanostructure fabrication by focused-ion-beam chemical vapor deposition", *J. Japan Soc. Precis. Eng.*, 67(9):1412–1415 (in Japanese).
12. Ravi, N. and Huang, H., 2002, "Fabrication of symmetrical section microfeatures using the electro-discharge machining block electrode method", *J. Micromech. Microeng.*, 12:905–910.
13. Rahman, M., Lim, H.S., Neo, K.S., Senthil Kumar, A., Wong, Y.S., Li, X.P., 2007, "Tool-based nanofinishing and micromachining", *J. Mater. Process. Technol.*, 185:2–16
14. Rahman, M. A., Rahman, M., Kumar, A. S., Lim, H.S., Asad, A.B.M.A., 2006, "Development of micropin fabrication process using tool based micromachining", *Int. J. Adv. Manuf. Technol.*, 27: 939–944.



## DEFECTS IDENTIFICATION AND ANALYSIS OF A PHARMACEUTICAL PRODUCT USING PARETO AND CAUSE-EFFECT ANALYSIS

S. K. Paul and Abdullahil Azeem

Department of Industrial and Production Engineering,  
Bangladesh University of Engineering and Technology, Dhaka, Bangladesh

### ABSTRACT

Pareto and cause-effect analysis are two major tools to address quality issues. This paper focuses on the process of identifying and analyzing the defects of a pharmaceutical product using these tools. Pareto analysis is used to find out the major problems of the defective products and cause-effect analysis is considered to find out the main causes and sub causes behind that problems. To eliminate the causes and sub causes which are responsible to make defective products, it is very important to identify causes, sub causes and their exact location in the system. In this paper the main problems, causes, sub causes and exact location of causes and sub causes are identified using pareto and cause-effect analysis. Capping, edge-chipping and broken tablets have been found as the vital problems for producing defective products. Few root causes are identified though cause-effect analysis which are responsible for the mentioned problems.

**Keywords:** Defect Identification, Quality Improvement, Pareto Analysis, Cause-Effect Analysis.

### 1. INTRODUCTION

Pareto chart is a simple statistical chart, also known as Pareto diagram. It is useful for quality control. In the early nineteenth century, the famous Italian Economist Vilfredo Pareto developed this. Now a days, it is widely used in quality management to identify the vital few and trivial many. It looks like a cumulative bar chart. The lengths of the bars represent frequency or cost and arranged with the longest bars on the left and the shortest bar to right. The longest bar represents the vital few.

Pareto analysis is a statistical technique in decision making that is used for selection of a limited number of tasks that produce significant overall effect. It uses the Pareto principle - the idea that a large majority of problems (80%) are produced by a few key causes (20%). Pareto analysis is a formal technique useful where many possible courses of action are competing for your attention. In essence, the problem-solver estimates the benefit delivered by each action, then selects a number of the most effective actions that deliver a total benefit reasonably close to the maximal possible one. This is graphical tool for ranking problems from most significant to least significant. It depicts a series of vertical bars lined up in a descending order- from high to low- to reflect frequency, impertinent, or priority.

There must be many potential reasons, or "causes" which ultimately lead to create an adverse "effect". Here, the 'effect' is the quality problem. Cause Effect (CE) analysis is a tool for analyzing and illustrating a process by showing the main causes and sub-causes leading to an effect (symptom). It is sometimes referred to as the "Ishikawa Diagram", because Kauro Ishikawa developed

it, and the "Fishbone Diagram", because the complete diagram resembles a fish skeleton. The fishbone diagram is easy to construct and invites interactive participation. A cause-effect analysis generates and sorts hypotheses about possible causes of problems within a process by asking participants to list all of the possible causes and effects for the identified problem. This analysis tool organizes a large amount of information by showing links between events and their potential or actual causes and provides a means of generating ideas about why the problem is occurring and possible effects of that cause. Cause-effect analyses allow problem solvers to broaden their thinking and look at the overall picture of a problem. Cause-and-effect diagrams can reflect either causes that block the way to the desired state or helpful factors needed to reach the desired state. It is a graphic presentation, with major branches reflecting categories of causes, a cause-and-effect analysis stimulates and broadens thinking about potential or real causes and facilitates further examination of individual causes. Because everyone's ideas can find a place on the diagram, a cause-and-effect analysis helps to generate consensus about causes. It can help to focus attention on the process where a problem is occurring and to allow for constructive use of facts revealed by reported events. However, it is important to remember that a cause-and-effect diagram is a structured way of expressing hypotheses about the causes of a problem or about why something is not happening as desired. It cannot replace empirical testing of these hypotheses: it does not tell which the root cause, but rather what the possible causes are.

Major two types of cause effect diagram include and Process Analysis. Cause Enumeration is the most commonly used CE diagrams in industries. This indicates one by one all possible caused from brainstorming sessions and then classifies into groups. Specialists from concerned departments like engineering and design, procurement, quality assurance, maintenance, production etc. from the group. Participants in brainstorming session are encouraged to think freely and suggest from experience, judgment, anticipation etc. This method has the advantage that the list of possible causes will be more comprehensive because the process has a more free-form nature. The disadvantage is that it is more difficult to draw the diagram from this list rather than from scratch. This method of drawing a CE Diagram can be used in conjunction with brainstorming by using it to distil the brainstorm output down into a logical and useable set of information. A simple cause enumeration may not identify exact location of occurrence in complete process. A process analysis type CE diagram can do that. Its structure is totally different form the earlier type of CE analysis. It follows the process step by step and causes are listed as per process step. This, prior to developing a CE diagram, process flow chart is a must. Additionally, participation of the process owners is also must in the brainstorming session. The main advantage of creating this type CE diagram is its ability in pinpointing the exact location of occurrence. Both types of CE diagram can be used to determining cause. Both types of CE diagram can be used to determining causes. Finding out a cause and pinpointing its location may require both CE diagrams at a time.

Sanders [1] discussed the relevance of the rule of 80/20 and developed from the Pareto principle. Karuppusami and Gandhinathan [2] used Pareto analysis to identify and propose a list of few vital critical success factors (CSFs) of total quality management (TQM) for the benefit of researchers and industries. Jiang and Gainer [3] reported cases of robot accidents involving fatality, injury and non-injury were gathered from several sources (U.S., West Germany, Sweden and Japan) using cause- effect analysis. A method for cause- effect analysis of chemical processing systems has been developed on the concept of a signed directed graph by Umeda et. al. [4]. Sambasivan and Soon [5] used cause-effect analysis to identify the delay factors and their impact (effect) on project completion Malaysian construction industry. Gill [6] used Effect-cause-effect (ECE) methodology of theory of constraints (TOC) to examine the assumptions behind successfully managing business projects. Emery [7] developed a cause-effect-cause model to identify prerequisites for sustaining effective cross-functional integration as well as their temporal inter-relationships. The performance of milling and boring operation on ‘Gear Housing’ in CNC Milling Machine (DC-45), in terms of positional error and accuracy of the job, and a wide variation of the job in terms of quality improvement have been investigated by Dipak et. al. [8] using Pareto and cause-effect analysis. In this paper, Pareto analysis is used to identify the main problems and Cause- effect analysis is used to find out the causes behind the main problem. Pareto analysis is

used to find out the vital problem occurring in processing & compression, coating and blistering of products. Cause effect diagram is developed for the vital problem occurring in processing & compression, coating and blistering. Process type cause effect diagram is also developed to find out exact location of the problem. Data are taken after completing the production in processing & compression, coating and blistering.

## 2. METHODOLOGY

The processing & compression, coating and blistering sections have been taken for analyzing the defects of the product. During processing ingredients are mixed homogeneously and during compression the shape of the product is formed using compression machine. After completing the compression, products are sent to coating section to give a thin coating layer on products. In blistering products are filled into packets. In these sections, lots of defective products are produced. Data has been taken from these sections to identify and analyze the quality of the product. For Pareto analysis, samples of products are taken in consecutive ten batches and numbers of defective products from each batch are identified and defectives products are separated according to the types of problems. Then major problems are identified considering the percentage of defective. The causes and sub causes behind the main problem have been analyzed using cause-effect analysis.

## 3. PARETO AND CAUSE EFFECT ANALYSIS IN PROCESSING & COMPRESSION

Processing and compression are important steps to produce the pharmaceutical products. But lots of defective products are produced here. So, these two steps are taken for analyzing. Data are taken after completing the processing and compression of the product.

### 3.1 Pareto analysis

Data have been taken for the product after completing the Processing and Compression. Samples of products are taken in consecutive ten batches and numbers of defective products from each batch are identified and defectives products are separated according to the types of problems. The data for the product after processing and compression are shown in Table 1.

Table 1: Data for Pareto analysis (processing and compression)

Problems	Frequency	Percent defect (%)	Cumulative percent defect (%)
Capping	173	51.64	51.64
Weight variation	51	15.22	66.87
Mottling	46	13.73	80.6
Chipping	22	6.57	87.16
Friability problem	18	5.37	92.54
Thickness variation	12	3.58	96.12
Lamination	6	1.79	97.91
Others	5	1.49	99.41
Sticking	2	.59	100

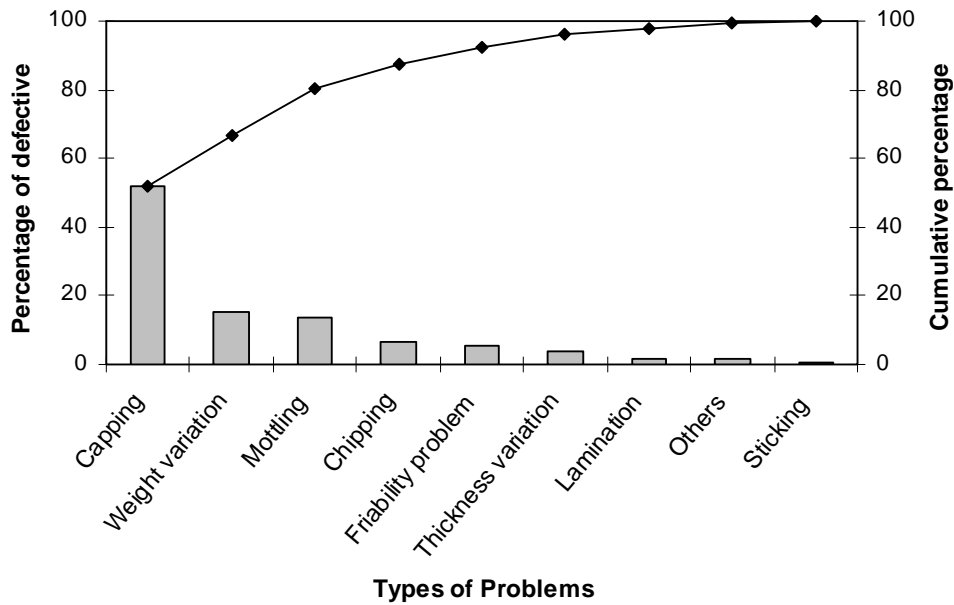


Fig 1. Pareto chart for processing and compression

After identifying the different types of problems and corresponding number of defectives a Pareto chart is drawn to identify the main problems which is shown in Fig. 1. From the Pareto diagram, the major problems are identified which are Capping, Weight variation and Mottling. These problems are responsible for 80.6 % of total defectives. Among these problems, capping is responsible for 51.64% of total defectives which is highest among all the problems. So, cause- effect analysis is performed only for “Capping”.

### 3.2 Cause- Effect analysis

This technique is used for identifying the causes associated with this particular problem. The causes have been identified through brainstorming and then establishing different cause categories like man, machine, method, measurement, material and environment.

Then all the causes have been allocated and placed under the appropriate major cause category. The root causes have been identified and these root causes should be amenable to action. After identifying the main problem, a cause- effect (CE) diagram is developed to find out causes and sub causes for the “Capping”. The cause-effect diagram is shown in Fig. 2. The main causes behind the capping are machine speed, wear and tear of die and punch, mixing, over drying and percentage of powder which are shown in Fig. 2.

### 4. PARETO AND CAUSE EFFECT ANALYSIS IN COATING

Coating, after processing and compression, is also an important step to produce the pharmaceutical products. But lots of defective products are produced here. Data are taken after completing coating of products.

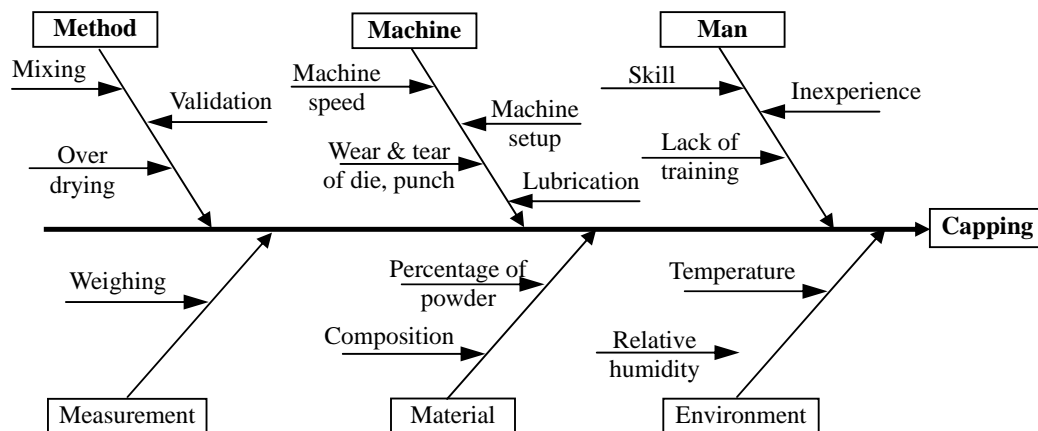


Fig 2. Cause-Effect Diagram of “capping” problem in processing and compression

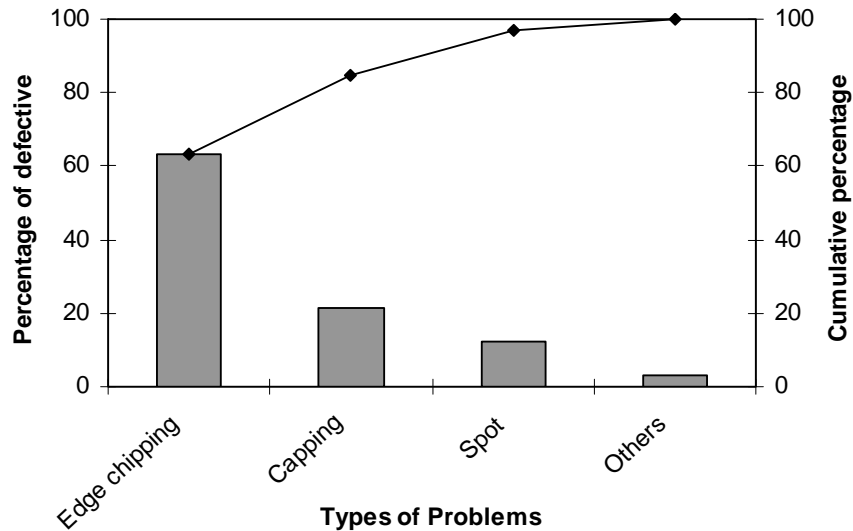


Fig 3. Pareto chart for coating

#### 4.1 Pareto analysis

Data have been collected for the product after completing the coating. Samples of products are taken in consecutive ten batches and numbers of defective products from each batch are identified and defectives products are separated according to the types of problems. The data for the product after coating are shown in Table 2.

Table 2: Data for Pareto analysis (coating)

Problems	Frequency	Percent defect (%)	Cumulative percent defect (%)
Edge chipping	165	63.22	63.22
Capping	56	21.46	84.67
Spot	32	12.26	96.93
Others	8	3.07	100

After identifying the different types of problems and corresponding number of defectives a Pareto chart is developed to identify the main problems for coating which is shown in Fig. 3.

From the Pareto diagram, the main problem in coating is identified due to “Edge chipping”. This problem is responsible for 63.22 % of total defectives. So, cause-effect analysis is performed only for “Edge chipping”.

#### 4.2 Cause- Effect analysis

After identifying the main problem, a cause-effect (CE) diagram is developed to find out causes and sub causes for “edge chipping” problem. The cause- effect diagram is shown in Fig. 4. The main causes behind the “edge chipping” are low solid content in solution, improper drying, low spray rate, high pan speed, low mechanical strength of coating and coating material which are shown in Fig. 4.

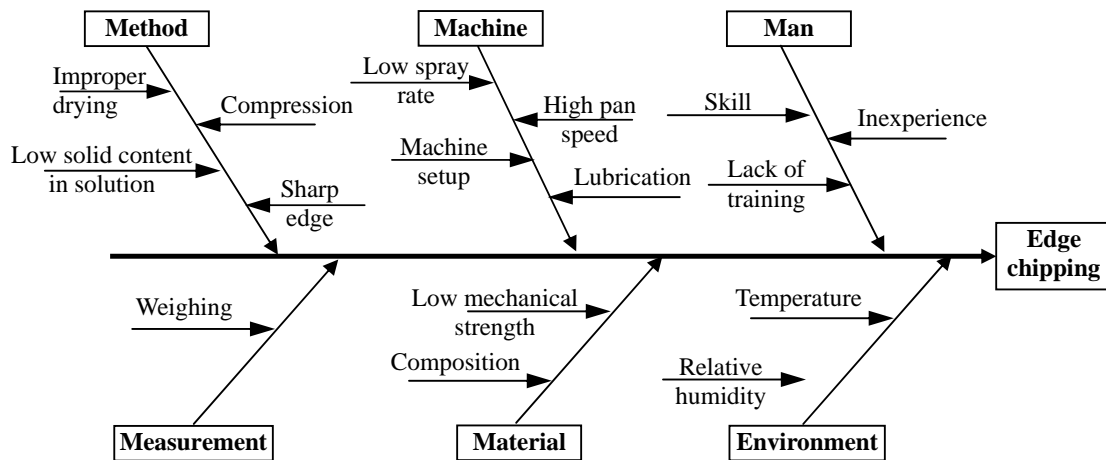


Fig 4. Cause-effect diagram of “edge chipping” problem in coating

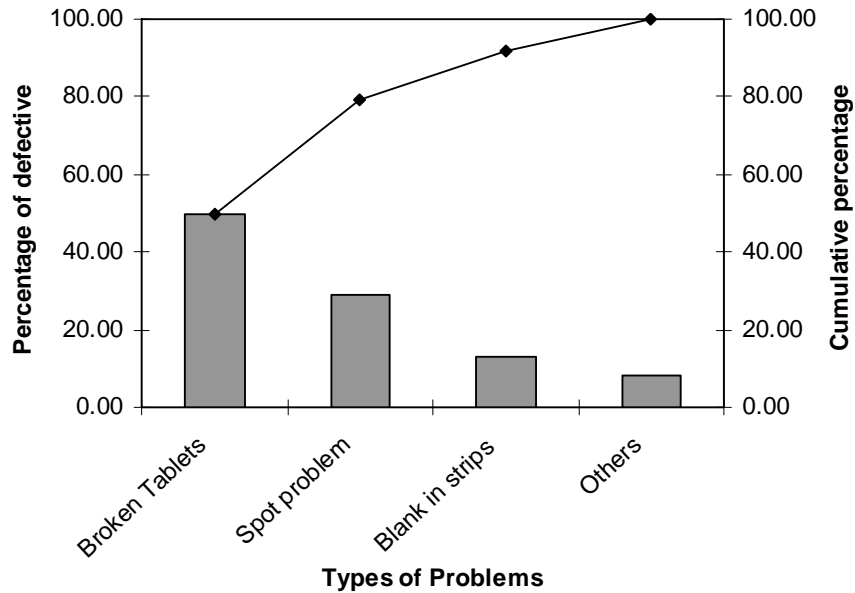


Fig 5. Pareto chart for blistering

## 5. PARETO AND CAUSE EFFECT ANALYSIS IN BLISTERING

Blistering, after coating, is the last step to produce the pharmaceutical products. But lot of defective products is produced here. Data are taken after completing blistering of the product.

### 5.1 Pareto analysis

Data has been collected for the product after completing the blistering of products. Samples of products are taken in consecutive ten batches and numbers of defective products from each batch are identified and defectives products are separated according to the types of problems. The data for the product after blistering are shown in Table 3.

From the Pareto diagram (Fig 5), the main problem is identified due to "Broken Tablets". This problem is responsible for 50% of total defectives. So, cause- effect analysis is performed only for "Broken Tablets".

Table 3: Data for Pareto analysis (blistering)

Problems	Frequency	Percent defect (%)	Cumulative percent defect (%)
Broken Tablets	74	50.00	50.00
Spot problem	43	29.05	79.05
Blank in strips	19	12.84	91.89
Others	12	8.11	100

### 5.2 Cause- Effect analysis

After identifying the main problem, a cause- effect (CE) diagram is developed to find out causes and sub causes for "Broken Tablets" problem. The main causes behind the "Broken Tablets" are processing, compression, sorting, skill and vibration during auto filling which are shown in Fig. 6.

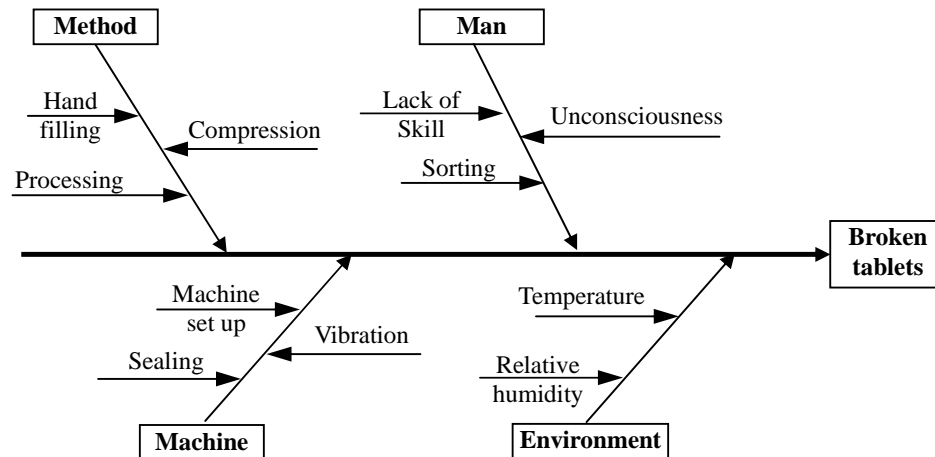


Fig 6. Cause-effect diagram of "broken tablets" problem in blistering

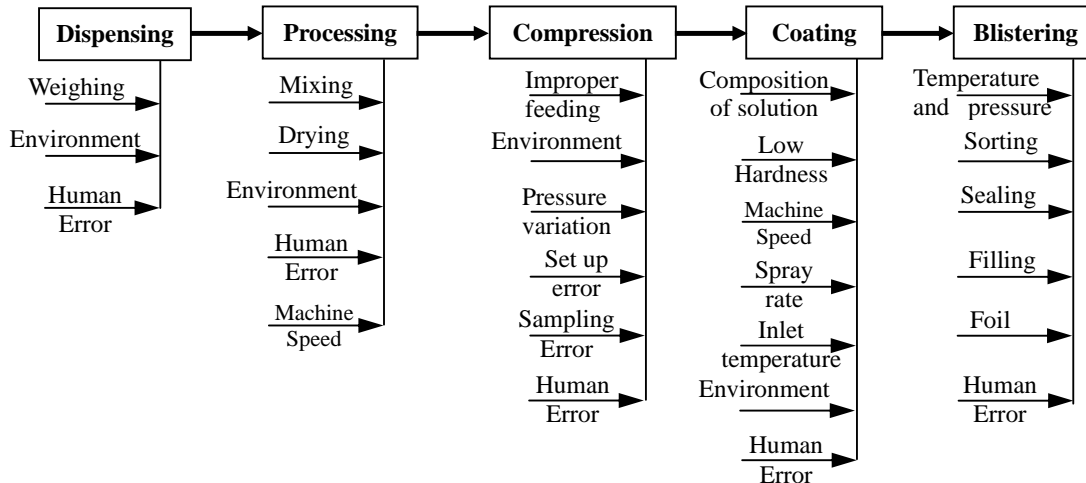


Fig 7. Process flow cause and effect diagram for product defects

Finally, a process flow cause- effect analysis is drawn for the total process to identify exact location of occurrence in complete process. In the manufacturing of the pharmaceutical products, the process is started from the dispensing and completed after packaging. The intermediate stages are processing, compression, coating and blistering. The process flow cause- effect diagram is developed to identify the causes, sub causes and exact location of causes for the defects in tablets. As defects in product may occur any where in the total process, so it is very necessary to identify and eliminate the causes which are responsible for defects in the product. The process flow cause- effect diagram is shown in Fig. 7.

## 6. CONCLUSIONS

Elimination of defects and maintaining the quality of the pharmaceutical products are very important as it deals with the human life. Pareto and cause effect analysis are two important industrial engineering tools which involve solving the quality problems. In this paper, Pareto and cause effect analysis are used to solve the quality problems for one pharmaceutical product. Causes and location of the causes are identified with the help of these analyses. Then some corrective actions are taken to eliminate causes which ultimately lead to create an adverse effect. Quality of the product is improved through eliminating the causes behind defects. These analyses can be used for other products where quality is one of the important considerations. Some others tools like control chart, check sheet, stratification analysis, scatter diagram etc. can be also used to analyze and solve the quality problem of the pharmaceutical product.

## 7. REFERENCES

1. Sanders, R., 1992, "The Pareto Principle: its Use and Abuse", *Journal of Product & Brand Management*, 1(2): 37-40.
2. Karuppusami, G. and Gandhinathan, R., 2006, "Pareto analysis of critical success factors of total quality management: A literature review and analysis", *The TQM Magazine*, 18(4).
3. Jiang, B. C. and Gainer, C. A. Jr., 1987, "A cause-and-effect analysis of robot accidents", *Journal of Occupational Accidents*, 9: 27-45.
4. Umeda, T., Kuriyama, T., O'Shima, E. and Matsuyama, H., 1980, "A graphical approach to cause and effect analysis of chemical processing systems", *Chemical Engineering Science*, 35(12): 2379-2388.
5. Sambasivan, M., and Soon Y. W., 2007, "Causes and effects of delays in Malaysian construction industry", *International Journal of Project Management*, 25(5): 517-526.
6. Gill, A., 2008, "An effect-cause-effect analysis of project objectives and trade-off assumptions", *International Journal of Managing Projects in Business*, 1(4): 535-551.
7. Emery, C. R., 2009, "A cause-effect-cause model for sustaining cross-functional integration", *Business Process Management Journal*, 15(1): 93-108.
8. Dipak, R. J., Anjani, K. and Amaresh, K., 2008, "Positional Accuracy Improvement through Pareto and Cause and Effect Analysis in CNC Machine Tools", *Engineering: Indu*, 4(4): 213-225.

## PARAMETRIC OPTIMIZATION OF CNC WIRE CUT EDM USING GREY RELATIONAL ANALYSIS

B. C. Routara, B.K. Nanda, D.R.Patra

Department of Mechanical Engineering, KIIT University, Bhubaneswar, India

### ABSTRACT

In this present study a multi response optimization method using Taguchi's robust design approach is proposed for wire electrical discharge machining (WEDM) operations. Experimentation was planned as per Taguchi's L9 orthogonal array. Each experiment has been performed under different cutting conditions of gap current (I), gap voltage (V), wire feed rate (W) and duty factor (D). Two responses namely material removal rate and surface roughness have been considered for each experiment. The machining parameters are optimized with the multi response characteristics of the material removal rate and surface roughness, using the grey relational analysis. Multi response S/N (MRSN) ratio was applied to measure the performance characteristics deviating from the actual value. Analysis of variance (ANOVA) is employed to identify the level of importance of the machining parameters on the multiple performance characteristics considered. Finally experimental confirmation was carried out to identify the effectiveness of this proposed method. A good improvement was obtained.

**Keywords:** CNC WEDM, Optimization, Surface Roughness, MRR, ANOVA.

### 1. INTRODUCTION

Wire cut EDM (electrical discharge machining) is an exceptionally precise, efficient and economical manufacturing route in many applications, allowing customers to design parts for optimum function, without the many restrictions of other metalworking processes. Wire cut EDM produces exceptionally precise, parallel sidewalls, allowing stacking when machining multiple parts from sheet material. Usually, the desired machining parameters are determined based on experience or handbook values. However, it does not ensure that the selected machining parameters result in optimal or near optimal machining performance for that particular electrical discharge machine and environment.

Lot of works is going on to increase the efficiency and the cost effectiveness of the WEDM process. As the process depends of different parameters it is very tedious task to analyze the effectiveness of all the parameter for the process. So, different techniques are used to analyze the parameters for better utilization of the process. The material removal rate (MRR) is an important indicator of the efficiency and cost-effectiveness of the process. Several experiments are conducted to consider effects of power, time-off, voltage, wire speed, wire tension, and rotational speed on the MRR (response). A Taguchi standard orthogonal array is chosen for the design of experiments. Analyses of variance (ANOVA) as well as regression analysis are performed on experimental data. The signal-to-noise (S/N) ratio analysis is employed to find the optimal condition [1].

The study of surface roughness ( $R_a$ ), roundness and material removal rate (MRR) on the cylindrical wire electrical discharge turning (CWEDT) has been carried out on AISI D3 tool steel due to its growing range of applications in the field of manufacturing tools, dies and molds as punch, tapping, reaming and so on in cylindrical forms. This study was made only for the finishing stages and has been carried out on the influence of four design factors: power, voltage, pulse -off time and spindle rotational speed, over the three previous mentioned response variables. For MRR,  $R_a$  and roundness regression models have been developed by using the response surface methodology [2].

One of the main challenges in wire electrical discharge machining (WEDM) is avoiding wire breakage and unstable situations as both phenomena reduce process performance and can cause low quality components. The proposed methodology establishes the procedures to following in order to understand the causes of wire breakage and instability. In order to quantify the trend to instability of a given machining situation, a set of indicators related to discharge energy, ignition delay time, and peak current has been defined. Wire breakage risk associated to each situation is evaluated comparing the evolution of those indicators with some previously defined threshold values. The results of work used to develop a real-time control strategy for increasing the performance of the WEDM process [3-5].

A closed-loop wire tension control system for Micro-Wire-EDM is presented to guarantee a smooth



wire transport and a constant tension value. In order to keep smooth wire transportation and avoid wire breakage during feeding, the reel roller is modified and the clip reel is removed from the wire transport mechanism. A genetic algorithm-based fuzzy logic controller is proposed to investigate the dynamic performance of the closed-loop wire tension control system [6].

The surface integrity generated in AISI 01 tool steel by wire electro-discharge machining, hard turning and production grinding is studied and compared. Production grinding generates compressive stresses at the surface, and a slight tensile peak, accompanied by a decreased in hardness beneath it. No structural changes are noticeable. Hard turning generates slight tensile stress in the surface, accompanied by an increase in hardness and in the amount of retained austenite [7].

The issues of machining speed and machined surface quality are interlinked in WEDM with respect to the fundamental mechanism of material removal at the scale of a single discharge. The removal of molten workpiece material is presently understood to be due to the implosion of the plasma channel, and it is estimated that indeed only about 10% of the molten material is actually removed from the parent material, due to inadequate ejection forces. Near dry EDM shows advantages over the dry EDM in higher material removal rate (MRR), sharper cutting edge, and less debris deposition. Compared to wet EDM, near dry EDM has higher material removal rate at low discharge energy and generates a smaller gap distance [8-10].

In order to obtain good surface roughness, the traditional circuit using low power for ignition is modified for machining as well. With the assistance of Taguchi quality design, ANOVA and F-test, machining voltage, current-limiting resistance, type of pulse-generating circuit and capacitance are identified as the significant parameters affecting the surface roughness in finishing process. In addition, it is found that a low conductivity of dielectric should be incorporated for the discharge spark to take place. The performance characteristics of the turning operations such as tool life, cutting force and surface roughness are improved together by using Taguchi method and grey relational analysis [11].

The present study aims at consideration of two response variable such as material removal rate and surface roughness in the machining of die steel on WEDM.

## 2. ANALYSIS OF TAGUCHI METHOD

According to the name of the developer, this method is called as Taguchi Method [12-13]. This method has been utilized widely in engineering analysis to optimize performance characteristics within the combination of design parameters. Taguchi technique is also a powerful tool for design of high quality systems. It introduces an integrated approach that is simple and efficient to find the best range of designs for quality, performance and computational cost. In this optimization technique, the process or product should be carried out in a three -stage approach such as system design, parameter design and

tolerance design. System design reveals the usages of scientific and engineering information required for producing a part. This design includes the product design stage and process design stage. The parameter design is used to obtain the optimum levels of process parameters for developing the quality characteristics and to determine the product parameters values depending optimum process parameter values. In addition, it is expected that the optimal process parameter values obtained from parameter design are insensitive to variation in the environmental conditions and other noise factors. Therefore, the parameter design has the key role in the Taguchi method to achieve high quality without increasing the cost factor. Lastly, the tolerance design is employed to determine and to analyze tolerances about the optimum combinations suggested by parameter design. Tolerance design is required if the reduced variation obtained by the parameter design does not reach the required performance.

The experimental design methods, which were developed by Fisher having some complexity and not easy to use and another important thing is that, whenever the number of process parameters increases, a large number of experiments have to be carried out. To eliminate such problems, the Taguchi method uses a special design of orthogonal arrays to study the entire parameter space with a small number of experiments only. After obtaining the experimental results, these values transformed into a signal - to- noise ratio.

Taguchi offers the use of the signal-to-noise (S/N) ratio to identify the quality characteristics applied for engineering design problems. The S/N ratio characteristics can be divided into three categories such as the smaller- the- better; nominal –the- better and larger the better. The S/N ratio for each level of process parameter is calculated based on the S/N analysis. Irrespective of the category of quality characteristic, a greater S/N ratio seems to be better quality characteristics. Here, it is suggested that the optimal level of process parameters is the level with the greatest S/N ratio. A statistical analysis of variance (ANOVA) can be utilized to verify the influences of the process parameters on surface roughness. With S/N ratio and ANOVA analysis the optimal combinations of process parameters are predicted. Lastly, a verification test is conducted to verify the optimal process parameters obtained from the parameter design.

## 3. EXPERIMENTAL DETAILS

### 3.1 Selection Of Process Parameters

In the present study the following parameters are selected as the control factors in the WCEDM machining: Gap current (I), Gap voltage (V), Wire feed rate (W) and Duty factor (D) is the ratio of pulse on time ( $T_{on}$ ) and pulse off time ( $T_{off}$ )

### 3.2 Design of Experiment

In this study, an  $L_9$  orthogonal array has been used. The experimental layout for the four cutting parameters using  $L_9$  orthogonal array is shown in Table .1

Mo 1.1%, Si 0.3%, V 4.5%, Mn 0.7% and balance Fe 85.35%.

Table1: Experimental layout using L<sub>9</sub>, OA

Expt. No	Gap Volt (V)	Wire feed Rate (W)	Gap Current (I)	Duty factor (D)
1	1	1	1	1
2	1	2	2	2
3	1	3	3	3
4	2	1	2	3
5	2	2	3	1
6	2	3	1	2
7	3	1	3	2
8	3	2	1	3
9	3	3	2	1

The process variables with their values on different levels are listed in the Table 2. The selection of the values of the variables is limited by the capacity of the machine used in the experimentation as well as recommended specification. The experimental results along with process variables levels are shown in Table 3.

Table 2: Process variable values with different levels

Machining parameter	Level1	Level 2	Level 3
Gap current (amp)	10	15	18
Gap voltage (volt)	20	30	40
Wire feed Rate (mm/min)	90	100	130
Duty factor	4	6	9

Table 3: Experimental results for material removal rate (MRR) and Surface roughness (SR)

Expt. No	(V)	(W)	(I)	(D)	MRR	SR
1	20	90	10	4	3.26	1.13
2	20	100	15	6	3.50	1.87
3	20	130	18	9	4.06	0.73
4	30	90	15	9	3.60	0.83
5	30	100	18	4	4.80	1.90
6	30	130	10	6	4.16	2.25
7	40	90	18	6	4.93	1.06
8	40	100	10	9	5.60	2.39
9	40	130	15	4	5.94	2.56

### 3.2 Wedm Machined Used

All the experiments are conducted in a CNC Wire cut EDM (AGIECUT 220) of Switzerland make. The schematic diagram of WEDM is given in the Fig.1.

### 3.3 Workpiece Used

High carbon medium chromium die steel (AISI A7) is used as work piece material for experimentation. The hardness of work piece material was measured on "Rockwell hardness tester" and found to be 56.4 HRC. Composition of work piece material: C 2.8%, Cr 5.25%,

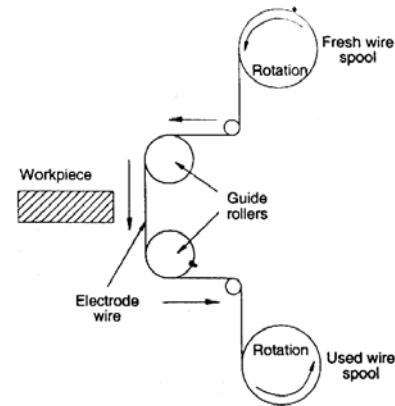


Fig 1. Schematic diagram of WEDM machine

### 3.4 Tool Electrode Used

A wire electrode is required to have a sufficient tensile strength and should be of uniform diameter of 0.25 mm. The electrode wire material is brass with tensile strength more than 45 Kgf / mm<sup>2</sup>.

### 3.5 Surface Roughness Measurement

Surface roughness measurement was done using a portable stylus-type profilometer (Taylor Hobson, Surtronic- 25). The profilometer was set to a cut-off length of 0.8 mm and 4mm evaluation length. The least count of the profilometer is 0.01 micron.

### 3.6 Material Removal Rate (Mrr) Measurement

The material removal rate of the workpiece can be calculated by using the following relations and listed in the Table 3. The width of cut calculated from the relation,

$$b = 2W_g + d$$

where  $W_g$  is spark gap,  $d$  is diameter of wire and  $b$  is width of cut

The material removal rate calculated by using the equation (1)

$$MRR = V_c \times b \times h \text{ mm}^3/\text{min}$$

Where  $V_c$  = cutting speed,  $b$  = width of cut mm

$h$  = height of work-piece 10mm for all 9 experiments

Here the wire diameter is taken as 0.25mm

### 3.7 Grey Relational Analysis For The Experimental Results

In the grey relational analysis, the experimental results are first normalized in the range between zero and unity. This process of normalization is called the grey relational generation. After then, the grey relational coefficient is calculated from the normalized experimental data to express the relationship between the desired and actual experimental data. Then, the overall grey relational grade is calculated by averaging the grey relational coefficient corresponding to each selected process response. The overall evaluation of the multiple process responses is based on the grey relational grade.

This method converts a multiple response process optimization problem into a single response optimization problem with the objective function of overall grey relational grade. The corresponding level of parametric combination with highest grey relational grade is considered as the optimum process parameter [11].

In this grey relational analysis, the normalized data processing for surface roughness corresponding to lower- the-better criterion can be expressed as

$$x_i(k) = \frac{\max y_i(k) - y_i(k)}{\max y_i(k) - \min y_i(k)} \quad (1)$$

Similarly, the normalized data processing for MRR corresponding to larger-the-better criterion can be expressed as

$$x_i(k) = \frac{y_i(k) - \min y_i(k)}{\max y_i(k) - \min y_i(k)} \quad (2)$$

where  $x_i(k)$  is the value after the grey relational generation,  $\min y_i(k)$  is the smallest value of  $y_i(k)$  for the  $k^{\text{th}}$  response, and the  $\max y_i(k)$  is the largest value of the  $y_i(k)$  for the  $k^{\text{th}}$  response. The normalized data processing, after grey relational generation is tabulated in the Table. 4. An ideal sequence is  $x_0(k)$  where ( $k=1$  & 2 for surface roughness and MRR). The definition of grey relational grade in the course of grey relational analysis is to reveal the relational degree between the nine sequences [ $x_0(k)$  and  $x_i(k)$ ,  $i=1,2,\dots,9$ ].The grey relational coefficient  $\xi_i(k)$  can be calculated as

$$\xi_i(k) = \frac{\Delta_{\min} + \xi \Delta_{\max}}{\Delta_{oi}(k) + \xi \Delta_{\max}} \quad (3)$$

where  $\Delta_{0i} = \|x_0(k) - x_i(k)\|$  =difference of the absolute value between  $x_0(k)$  and  $x_i(k)$ ;  $\xi$  =distinguishing coefficient in between zero and one.

$\Delta_{\min} = \forall j \min_{i \forall k} \|x_0(k) - x_j(k)\|$  = the smallest value of  $\Delta_{0i}$  ;

and  $\Delta_{\max} = \forall j \max_{i \forall k} \|x_0(k) - x_j(k)\|$  =largest value of  $\Delta_{0i}$ .The grey relational coefficient results for the experimental data are shown in the Table 5.

After averaging the grey relational coefficients, the grey relational grade  $\gamma_i$  can be calculated as follows

$$\gamma_i = \frac{1}{n} \sum_{k=1}^n \xi_i(k)$$

where  $n$  = number of process responses. Table 6 shows the experimental results for the grey relational grade. The higher the value of grey relational grade considered as the stronger relational degree between the ideal sequence  $x_0(k)$  and the given sequence  $x_i(k)$ . Earlier it has mentioned, the ideal sequence  $x_0(k)$  is the best process response in the experimental layout. Here, it may conclude, the higher relational grade means that the corresponding parameter combination is closer to the optimal.

Table 4: Data processing of each performance characteristic (Grey relational generation)

Exp. No	MRR	SR
Ideal		
Sequence	1	1
1	0.000000	0.781421
2	0.089552	0.377049
3	0.298507	1.000000
4	0.126866	0.945355
5	0.574627	0.360656
6	0.335821	0.169399
7	0.623134	0.819672
8	0.873134	0.092896
9	1.000000	0.000000

Table 5: Grey relational coefficient of each performance characteristics (with  $\psi= 0.5$ )

Exp. No	MRR	SR
Ideal		
Sequence	1	1
1	0.333333	0.695817
2	0.354497	0.445255
3	0.416149	1.000000
4	0.364130	0.901478
5	0.540323	0.438849
6	0.429487	0.375770
7	0.570213	0.734940
8	0.797619	0.355340
9	1.000000	0.333333

Then, the grey relational grade that is computed by averaging the grey relational coefficient corresponding to each performance characteristic. The overall evaluation of the multiple performance characteristics is based on the grey relational grade. The higher grey relational grade represents that the corresponding experimental result is closer to the ideally normalized value. In other words, optimization of the complicated multiple performance characteristics can be converted into optimization of a single grey relational grade. The grey relational grade is shown in the Table 6.

Table 6: Grey relational grade of performance characteristic

Exp. No	Grade
1	0.514575
2	0.399876
3	0.708075
4	0.232804
5	0.489586
6	0.402629
7	0.652576
8	0.576479
9	0.666667

### 3.8. Analysis of Variance

The purpose of the analysis of variance (ANOVA) is to investigate which machining parameters significantly affect the performance characteristic. This is accomplished by separating the total variability of the grey relational grades, which is measured by the sum of the squared deviations from the total mean of the grey relational grade, into contributions by each machining parameter and the error. First, the total sum of the squared deviations  $SS_T$  from the total mean of the grey relational grade  $\gamma_m$  can be calculated as:

$$SS_T = \sum_{j=1}^p (\gamma_j - \gamma_m)^2 \quad (4)$$

Where  $p$  is the number of experiments in the orthogonal array and  $\gamma_j$  is the mean of the grey relational grade for  $j_{th}$  experiment.

The total sum of the squared deviations  $SS_T$  is decomposed into two sources: the sum of the squared deviations  $SS_d$  due to each machining parameter and the sum of the squared error  $SS_e$ . The percentage contribution by each of the machining parameter in the total sum of the squared deviations  $SS_T$  can be used to evaluate the importance of the machining parameter change on the performance characteristic. In addition, the Fisher's  $F$ -test can also be used to determine which machining parameters have a significant effect on the performance characteristic. Usually, the change of the machining parameter has a significant effect on the performance characteristic when  $F$  is large is shown in Table 8. It is found that gap voltage and current are the significant one where as the wire feed rate is not significant as the  $P$  value for wire feed rate is more than 0.05.

Table 8: ANOVA for grey relational grade

Source	DF	Adj SS	Adj MS	F	P
Volt(V)	2	0.101	0.050	12.38	0.025
Current	2	0.052	0.026	6.33	0.046
Wire feed rate	2	0.027	0.013	3.3	0.233
Error	2	0.008	0.004		
Total	8				

Table 9: Results of the confirmation experiment

	Initial parameters	cutting	Optimal cutting parameters	
			Prediction	Experiment
Setting Level	$V_1W_1I_1D_1$		$V_3W_3I_3D_1$	$V_3W_3I_3D_1$
Surface roughness		1.13		1.11
Material removal rate		3.26		4.96
Grey relational grade		0.5145	0.5524	0.6420

Improvement of grey relational grade =0.1275

Table 7: Mean response table of grey relational grade

Level	V	W	I	D
1	0.540	0.466	0.497	0.556
2	0.375	0.488	0.433	0.485
3	0.631	0.592	0.616	0.505
Max				
-min	0.256	0.125	0.183	0.071
Rank	1	3	2	4

In the grey relational grade graph, it is clearly mentioned that third level voltage, third level wire feed rate, third level of current and first level of duty factor( $V_3W_3I_3D_1$ ) are the optimal combination of process parameters for multiple performance characteristics.

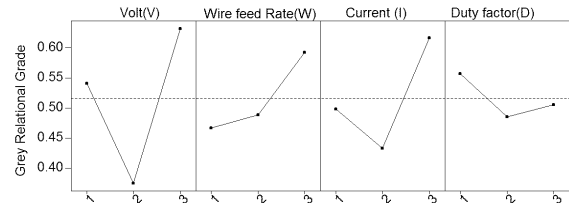


Fig 2 Grey relational grade graph of multiple performance characteristics

### 4. CONFIRMATION TESTS

Once the optimal level of the machining parameters is selected, the final step is to predict and verify the improvement of the performance characteristic using the optimal level of the machining parameters.

The estimated grey relational grade  $\hat{\gamma}$  using the optimal level of the machining parameters can be calculated as:

$$\hat{\gamma} = \gamma_m + \sum_{i=1}^q (\bar{\gamma}_i - \gamma_m) \quad (5)$$

where  $\gamma_m$  is the total mean of the grey relational grade,  $\bar{\gamma}_i$  is the mean of the grey relational grade at the optimal level, and  $q$  is the number of the machining parameters that significantly affects the multiple performance characteristics.

Table 9 shows the comparison of the predicted grey relational grade with the experimented grey relational grade using the optimal process parameter combinations and found that a good agreement between the predicted and actual grey relational grade. The increase of grey relational grade from initial factor setting to the optimal process parameter setting is of 0.1275. Here, it may conclude that the multiple performance characteristic of the WEDM process such as material removal rate and surface finish are improved together by using this approach.

## 5. CONCLUSION

The use of the orthogonal array with grey relational analysis to optimize the WEDM process with the multiple performance characteristics has been reported here. A grey relational analysis of the experimental results of material removal rate and surface roughness can convert optimization of a single performance characteristic called the grey relational grade. As a result, optimization of the complicated multiple performance characteristics can be greatly simplified through this approach. It is shown that the performance characteristics of the WEDM process such as material removal rate, surface roughness are improved together by using this study.

## 6. REFERENCES

1. Mohammadi, A, Tehrani, A.F., Emanian, E. and Karimi, D., 2008, "Statistical analysis of wire electrical discharge turning on material removal rate", *Journal of materials processing Technology*, 205:283-289.
2. Haddad, M.J, and Tehrani, A.F., 2008, "Investigation of cylindrical wire electrical discharge turning (CWEDT) of AISI D3 tool steel based on statistical analysis", *Journal of materials processing Technology*, 198:77-85.
3. Haddad, M. J, and Tehrani, A.F., 2008, "Material Removal rate (MRR) study in the cylindrical wire electrical discharge turning (CWEDT) process",

*Journal of Materials Processing Technology*, 199:369-378.

4. Cabanes, I., Portillo, E., Marcos's, M. and Sanchez, J.A., 2008, "An industrial application for on-line detection of instability and wire breakage in wire EDM", *Journal of Materials Processing Technology*, 195:101-109.
5. Shinji I., Kushiya, M., Nakashima, T. and Sugihara, K., 2008, "Generation of cutter paths for hard material in wire EDM", *Journal of Materials processing technology*, 206:453-461.
6. Yan, M.T, and Fang, C., 2008, "Application of genetic algorithm-based fuzzy logic control in wire transport system of wire-EDM machine", *Journal of Materials Processing Technology*, 205:128-137.
7. Lauwers, B., Brans, K., Liu, W., Vleugels, J., Salehi, S. and K. Vanmeensel, 2008, "Influence of the type and grain size of the electro-conductive phase on the Wire-EDM performance of ZrO<sub>2</sub> Ceramic Composites", *CIRP Annals- Manufacturing Technology*, 57:191-194.
8. K. H. Ho, Newman, S.T., Rahimifard, S., Allen, R.D., 2004, "State of the art in wire electrical discharge machining (WEDM)" *Int. J. Machine Tools Manuf.*, 44:1247-1259.
9. Kao, C. C., Jia Tao and Shih, A.J., 2007, "Near dry electrical discharge machining". *International Journal of Machine Tools & Manufacture*, 47:2273-2281.
10. Liao, Y.S., Huang, J.T. and Chen, Y.H., 2004, "A Study to achieve a fine surface finish in Wire-EDM". *Journal of materials processing Technology*, 149:165-171.
11. Lin, J.L. and Lin, C.L., 2002, "The use of the orthogonal array with grey relational analysis to optimize the electrical discharge machining process with multiple performance characteristics", *International Journal of machine Tools & Manufacture* 42, pp.237-244.
12. Phadke, M. S., 1989, "Quality Engineering using Robust Design", Prentice Hall international, Inc.
13. Montgomery. D. C., 1991, *Design and Analysis of experiments*, Wiley, India.

## 7. MAILING ADDRESS

B. C. Routara  
 Department of Mechanical Engineering,  
 KIIT University, Bhubaneswar-751024  
 E-mail: bharat\_routara@rediffmail.com

## HYDRODYNAMIC INTERACTION FOR A LONG ARRAY OF FREELY FLOATING 3-D RECTANGULAR BOXES

Mir Tareque Ali and Tasnuva Anan

Department of Naval Architecture and Marine Engineering, Bangladesh University of Engineering and  
Technology, Dhaka, Bangladesh.

### ABSTRACT

This paper investigates the first order wave exciting forces and moments and motion responses due to hydrodynamic interactions between an array of twenty-one freely floating three dimensional rectangular bodies in regular waves. The rectangular bodies are identical, and equally spaced along the array. In the present study, the three dimensional source-sink method has been adopted to carry out the numerical investigation. The validation of the computer code developed for this purpose has been justified by comparing the present results with that of the published ones for simple geometrical shaped floating bodies. The numerical computations have been carried out for different wave heading angles and separation distances between the floating rectangular bodies and the hydrodynamic interactions on different members in the array have been studied by calculating the first order wave exciting forces and moments as well as motion responses. Finally some conclusions have been drawn on the basis of the present analysis.

**Keywords:** Hydrodynamic Interaction, Three Dimensional Source-Sink Method, Wave-Exciting Forces, Hydrodynamic Coefficients.

### 1. INTRODUCTION

In recent years, there is a significant increase in the number of activities that involves applications of offshore structures, where two or, more bodies are floating in sufficiently close proximity, experiencing significant interactions. The hydrodynamic interactions occur as a result of the wave motion between neighbors in the array of floating bodies. The number of individual structures as well as their geometry, within such arrangement can vary greatly. Hydrodynamic analysis of multiple floating bodies is different from that of a single floating body, because one body is situated in the diffracted wave field of others. The bodies will experience incident as well as scattered waves impinges upon them. Now if these waves arrive in phase then there will be a considerable escalation in the magnitude of the wave exciting forces on the floating bodies compared to a body in isolation. On the other hand, if these waves arrive out of phase then there will be a significant reduction of wave force. Moreover, each body will also experience radiated waves due to the motion of other bodies. The actual importance of interaction effect depends on the configuration of the multi-body system, which means the size and shape of the floating bodies and the separation distances between them.

Understanding hydrodynamic interaction is particularly important while designing floating bridges. Floating bridges have various advantages comparing to

land based structures. They are minimally influenced by water level fluctuations due to tide and storm surge. These structures are not influenced by soil/seafloor condition, so they do not suffer from differential settlement and can easily be relocated. The deck of a floating bridge is usually supported on a number of rectangular floating boxes. To assist the proper design of a floating bridge, it is quite important to study the wave exciting forces and moments and motion responses on an array of freely floating rectangular boxes.

There are many investigations related to the hydrodynamic interaction between multiple floating bodies in waves. Ohkusu [1] extended the classical solution for a single heaving circular cylinder to the case of two cylinders in a catamaran configuration. Faltinsen & Michelsen [2] used panel method for direct numerical solution of wave effects on 3D floating bodies. The panel method was further extended for two independent bodies by van Oortmerssen [3]. Lee & Newman [4] and Kim *et al.* [5] used panel method for more complex structure like MOB (Mobile Offshore bases). Maniar & Newman [6] presented results for the diffraction past an array of 100 vertical cylinders. Chakrabarti [7] used multiple-scattering method in combination with panel method, while Choi & Hong [8] used higher-order boundary element method to solve the interactions problem between multiple floating bodies.

In this paper, a frequency domain analysis has been carried out to calculate the first order wave exciting forces and moments and motion responses to study hydrodynamic interactions between an array of twenty-one identical freely floating 3D rectangular bodies in regular waves. Using 3D source sink method a computer code has been developed to investigate the hydrodynamic interaction phenomena. In order to justify the validity of the code, some published results have been verified for two freely floating vertical cylindrical bodies. First order wave exciting forces and moments and motion responses for each member of the array comprised of twenty-one rectangular boxes have been computed for different wave heading angles as well as for various separation distances between the members. It is observed from the present study that hydrodynamic interactions vary with the position of a member in the array and with the separation distance between the members of this long array of rectangular boxes.

## 2. MATHEMATICAL FORMULATION OF THE PROBLEM

Consider a group of  $N$  3-dimensional bodies of arbitrary shape, oscillating in water of uniform depth. The amplitudes of the motions of the bodies and waves are assumed to be small, whereas the fluid is supposed to be ideal and irrotational. Two right-handed Cartesian coordinate systems are considered: one fixed to the bodies and another fixed to the space. In regular waves a linear potential  $\Phi$ , which is a function of space and of time, can be written as a product of space-dependent term and a harmonic time-dependent term as follows:

$$\Phi(x, y, z; t) = \phi(x, y, z) \cdot e^{-i\omega t} \quad (1)$$

The wave circular frequency  $\omega$  can be written

$$\omega = \frac{2\pi}{T} \quad (2)$$

where  $T$  is the wave period. The potential function  $\phi$  can be separated into contributions from all modes of motion of the bodies and from the incident and diffracted wave fields as follows:

$$\phi = -i\omega \left[ (\phi_0 + \phi_7)\zeta_a + \sum_{m=1}^N \sum_{j=1}^6 (X_j^m \phi_j^m) \right] \quad (3)$$

where  $\phi_0$  is the incident wave potential,  $\phi_7$  is the diffracted wave potential,  $\phi_j^m$  represent potentials due to motion of body ' $m$ ' in  $j$ -th mode i.e., radiation wave potentials,  $X_j^m$  is the motion of body ' $m$ ' in  $j$ -th mode and  $\zeta_a$  is the incident wave amplitude. The incident wave potential can be expressed as

$$\phi_0 = \frac{g}{\omega^2} \frac{\cosh[k(z+h)]}{\cosh kh} e^{ik(x \cos \chi + y \sin \chi)} \quad (4)$$

where  $\chi$  is the wave heading angle measured from  $+X$  -axis,  $h$  is the depth of water,  $g$  is the acceleration due to gravity and  $k$  is the wave number. The individual potentials are all solutions of the Laplace equation, which satisfy the linearized free surface condition and the boundary conditions on the sea floor, on the body's surface and at infinity.

### 2.1 Source Density and Velocity Potentials

The potential function at some point  $(x, y, z)$  in the fluid region in terms of surface distribution of sources can be written as:

$$\begin{aligned} \phi_j^m(x, y, z) \\ = \frac{1}{4\pi} \sum_{n=1}^N \iint_{S^n} \sigma_j^m(\xi, \eta, \zeta) G(x, y, z; \xi, \eta, \zeta) dS \end{aligned} \quad (5)$$

where  $(\xi, \eta, \zeta)$  is a point on surface  $S$  and  $\sigma(\xi, \eta, \zeta)$  is the unknown source density. The solution to the boundary value problem is given by Eq. (5), which satisfies all the boundary conditions. And since Green's function ( $G$ ) satisfies these conditions, applying the kinematics boundary condition on the immersed surface yields the following integral equation:

$$\begin{aligned} \frac{\partial \phi_j^m(x, y, z)}{\partial n} = -\frac{1}{2} \sigma_j^m(x, y, z) \\ + \frac{1}{4\pi} \sum_{n=1}^N \iint_{S^n} \sigma_j^m(\xi, \eta, \zeta) \frac{\partial}{\partial n} G(x, y, z; \xi, \eta, \zeta) dS \end{aligned} \quad (6)$$

### 2.2 Numerical Evaluation of Velocity Potentials

A numerical approach is required to solve the integral Eq. (6), as the kernel  $\frac{\partial G}{\partial n}$  is complex and it does not permit any solution in closed form. The wetted surface of body is divided into  $l$  number of quadrilateral panels of area  $\Delta S_l^m$  ( $l=1, \dots, E_n$ ) and the node points are considered at the centroid of each panel. The continuous formulation of the solution indicates that Eq. (6) is to be satisfied at all points  $(x, y, z)$  on the immersed surface but in order to obtain a discretized numerical solution it is necessary to relax this requirement and to apply the condition at only  $N$  control points and the location of the control points are chosen at the centroids of the panels. Consequently, discretization process allows Eq. (6) to be replaced as



$$-\frac{1}{2}(\sigma_j^m)_l + \frac{1}{4\pi} \sum_{n=1}^N \sum_{k=1}^{E_n} \iint_{\Delta S_k^n} (\sigma_j^m)_k \frac{\partial G}{\partial n}(l,k) dS$$

$$= \begin{cases} \left( -\frac{\partial \phi_0}{\partial n} \right)_l, & j=7 \\ \left( n_j^m \right)_l, & j=1,2,\dots,6 \\ 0, & j=1,2,\dots,6 \\ \text{(if panel 'l' belongs to body 'm')} \\ \text{(if panel 'l' does not belong to body 'm')} \end{cases} \quad (7)$$

### 2.3 Hydrodynamic Coefficients and Wave Exciting Forces and Moments

Once the velocity potentials have been determined, then the added-mass coefficients ( $a_{kj}^{mn}$ ), fluid damping coefficients ( $b_{kj}^{mn}$ ) and first order wave-exciting forces and moments ( $F_k^m$ ) can be calculated as follows:

$$a_{kj}^{mn} = -\Re e \left[ \rho \iint_{S^m} \phi_j^n n_k^m dS \right] \quad (8)$$

$$b_{kj}^{mn} = -\Im m \left[ \rho \omega \iint_{S^m} \phi_j^n n_k^m dS \right] \quad (9)$$

$$F_k^m = -\rho \zeta_a \omega^2 e^{-i\omega t} \iint_{S^m} (\phi_0 + \phi_j) n_k^m dS \quad (10)$$

For  $m=n$ , the added mass and damping coefficients are due to body's own motion, on the other hand for  $m \neq n$ , the coefficients are due to the motion of other bodies.

Using 'Haskind Relation', first order wave-exciting forces and moments ( $F_k^m$ ) can also be calculated as follows:

$$F_k^m = -\rho \zeta_a \omega^2 e^{-i\omega t} \iint_{S^m} \left( \phi_0 \frac{\partial \phi_j^m}{\partial n} - \phi_j^m \frac{\partial \phi_0}{\partial n} \right) dS \quad (11)$$

### 2.4 Equations of Motions in Frequency Domain

The equations of motion can be expressed by using the following matrix relationship:

$$(M + a)\ddot{X} + b\dot{X} + cX = F \quad (12)$$

where  $M$  is the inertia matrices,  $a$  is the added mass matrices,  $b$  is the fluid damping matrices,  $c$  is the hydrostatic stiffness matrices,  $F$  is the wave exciting force vector and  $X$  is the motion response vector. The above equations of motion are established at the centers of gravity of each body of the multi-body floating system. Since each body is assumed rigid and has six degrees of freedom, each matrix on the left-hand side of Eq. (12) has

a dimension of  $(6N \times 6N)$  and  $X$  and  $F$  are  $(6N \times 1)$  column vectors for  $N$  floating body system. The elements of matrices and vectors in Eq. (12) are discussed in details by Inoue & Seif [9].

## 3. RESULTS AND DISCUSSIONS

On the basis of above formulations, a computer code written in F77 has been developed considering double precision variables. To justify the validity of the computer code, the numerical results are checked for two freely floating vertical cylinders. To study the interaction effects, a detailed computation is then conducted for twenty-one identical freely floating rectangular boxes in regular waves.

### 3.1 Two Freely Floating Vertical Cylinders

The diameter and draft of each cylinder is 40.0 m and 10.0 m respectively and the separation distance or, gap between them is 20.0 m. The water depth is considered as 200.0 m. The wetted surface of each cylinder is divided into 234 panels as shown in Fig 1. For  $0^\circ$  wave-heading angle, body 1 and body 2 represent the lee side and weather side cylinder respectively.

The non-dimensional surge wave exciting forces on body 1 and body 2 are shown in Fig 2. To verify the accuracy of the present computations, the wave exciting forces are computed using diffraction potential as well as Haskind relationship. Fig 3 presents the surge motions of body 1 and body 2. The results are plotted against  $ka$ , where  $k$  and  $a$  denote the wave number and radius of each cylinder respectively. Fig 2 and 3 also depict comparisons between the present results with Goo and Yoshida [10] results and the agreement between both the results are found quite satisfactory.

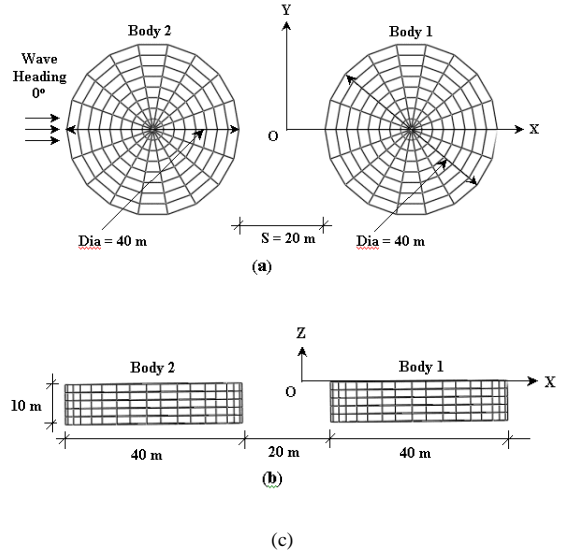


Fig 1. Mesh arrangements of the wetted surfaces of two floating vertical cylinders (a) Top view, (b) Side view and (c) 3-D view

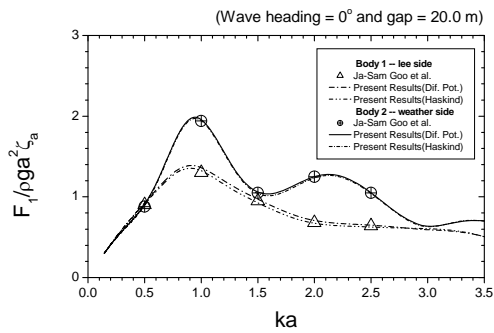


Fig 2. Surge wave exciting forces on floating cylinders

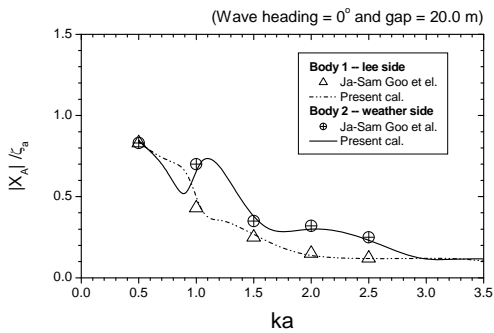


Fig 3. Surge motions of vertical floating cylinders

### 3.2 Twenty-One Identical Freely Floating Rectangular Boxes

Twenty-one identical freely floating rectangular boxes have been considered to study the first order wave exciting forces and moments on individual members for a long array of floating bodies. A frequency domain analysis has been carried out to compute the motion responses of the floating boxes in regular waves. The length, breadth and draft of each box are 109.7 m, 101.4 m and 30.0 m respectively. The C.G. of each body is considered 0.2 m below still water level. The water depth is taken as 100.0 m. The wetted surface of each body is divided into 188 panels. The numbering and arrangement of rectangular boxes in the array is shown in Fig 4. Body 1, Body 11 and Body 21 represent the first, middle and last body in the array for a wave heading of  $180^\circ$ .

Fig 5 shows the variation of non-dimensional surge wave exciting forces with wave circular frequency for Body1 at  $180^\circ$  wave heading angle. The separation distances between the members in the array are varied as 25m, 50m and 75m. Strong and complicated hydrodynamic interaction is observed for these three separation distances. To demonstrate the interaction effect, surge wave exciting forces for an isolated rectangular body is also plotted in these figures. It is observed that the magnitude of wave exciting forces in the frequency range is higher or, close to that of an isolated body. Fig 6 shows the variation of non-dimensional surge wave exciting forces with wave circular frequency for Body21 at  $180^\circ$  wave heading angle. Hydrodynamic interaction is also evident in this

figure. However, the magnitudes of surge wave exciting forces show sharp and significant reduction in amplitude for Body21. Since the number of shielding bodies is more for Body 21 compared to other bodies in the array, so, the magnitude of surge exciting force rapidly approaches to zero. Sharp peaks appear in the figures, which may be due to locally resonated waves in confined fluid domain.

Fig 7 show the variation of non-dimensional heave wave exciting forces with wave circular frequency for Body1 and Body21 at  $180^\circ$  wave heading angle. Similar to previous figures, the results are plotted for the separation distances of 25m, 50m and 75m. Hydrodynamic interaction for Body1 for the three separation distance is quite weak as revealed in these figures. The magnitude of heave exciting force for Body1 is nearly close to that of an isolated body. Hydrodynamic interaction is also weak for Body21. However, for Body21 the magnitude of heave wave exciting forces show gradual decrease in magnitude as the number of shielding body is maximum for this body.

Fig 8 show the variation of non-dimensional pitch wave exciting moments with wave circular frequency for Body1 and Body21 at  $180^\circ$  wave heading angle. Hydrodynamic interaction for the three separation distances is also prominent as revealed in these figures. The magnitude of pitch exciting moment for Body1 is also nearly close to that of an isolated body. Similar to surge and heave forces, pitch wave exciting moment for Body21 show sharp decline in magnitude as the number of shielding body is increased for this body.

Fig 9 show the variation of non-dimensional surge motions with wave circular frequency for Body1 and Body21 at  $180^\circ$  wave heading angle. Hydrodynamic interaction for the three separation distance is quite strong as revealed in these figures. The magnitude of surge motion for Body1 is nearly close to that of an isolated body, whereas for Body21 the magnitude of surge motion shows gradual decrease in magnitude.

Finally, Figs 10 and 11 show the variation of non-dimensional heave and pitch motions with wave circular frequency for Body11 at  $180^\circ$  wave heading angle. The figures clearly show that the hydrodynamic interaction for the three separation distance is quite weak. Resonance is quite prominent for the pitch motion that occurs in between the frequency range of 0.35 rad/s and 0.40 rad/s. The probable reason may be the presence of pitch natural frequency of motion of the floating box within this range. Due to the dominance of resonance, interaction effect is almost absent for pitch motion.

## 4. CONCLUSIONS

3D source sink method has been adopted to compute the first order wave exciting forces and moments and motion responses by taking into account the effect of hydrodynamic interactions among the different floating bodies for an array of twenty-one freely floating rectangular boxes in regular waves. The hydrodynamic interaction effect is strong and complicated for surge exciting forces, pitch exciting moments and surge motions, while it is very weak for heave exciting forces and heave and pitch motions. The variation of the

separation distance between the boxes in the array shows interaction effect near lower frequency region. Sharp peaks appear in the results, which may be due to locally resonated waves in confined fluid domain. In general, the magnitude of wave exciting forces and moments and motions show gradual decline in magnitude as the number of shielding body is regularly increased.

## 5. REFERENCES

1. Ohkusu, M., 1969, "On the heaving motion of two circular cylinders on the surface of a fluid", *Reports of Research Institute for Applied Mechanics*, XVII, No. 58, pp. 167-185.
2. Faltinsen, O. and Michelsen, F., 1974, "Motions of large structures in waves at zero Froude number", *Proc. Intl. Symp. on the Dynamics of Marine Vehicles and Structures in Waves*, London, pp. 91-106.
3. van Oortmerssen, G., 1979, "Hydrodynamic interaction between two structures, floating in waves", *Proc. 2nd. Intl. Conf. on Behaviour of Offshore Structures (BOSS'79)*.
4. Lee, C. H. and Newman, J. N., 2000, "An assessment of hydroelasticity for very large hinged vessels", *Proc. 2nd Intl. Conf. on Hydroelasticity in Marine Technology*, Kyushu, pp. 27-36.
5. Kim, D., Chen, L. and Blaskowski, Z., 1999, "Linear frequency domain hydroelastic analysis for McDermott's mobile offshore base using WAMIT", *VLFS'99*, Honolulu.
6. Maniar, H. D. and Newman, J. N., 1997, "Wave diffraction by a long array of cylinders", *J. Fluid Mec.*, Vol. 339, pp. 309-330.
7. Chakrabarti, S., 2000, "Hydrodynamic interaction forces on multimodulated structures", *Ocean Engineering*, Vol. 27, pp. 1037-1063.
8. Choi, Y. R. and Hong, S. Y., 2002, "An analysis of hydrodynamic interaction of floating multi-body using higher-order boundary element method", *ISOPE'2002*, Kitakyushu, Japan.
9. Inoue, Y. and Seif, M. S., 1997, "Nonlinear responses of multiple floating systems", *OMAE'97*, Yokohama.
10. Goo, J. and Yoshida, K., 1989, "Hydrodynamic interaction between multiple three dimensional bodies of arbitrary shape in waves", *Journal of the Society of Naval Architects Japan*, Vol. 165, pp. 193-202.

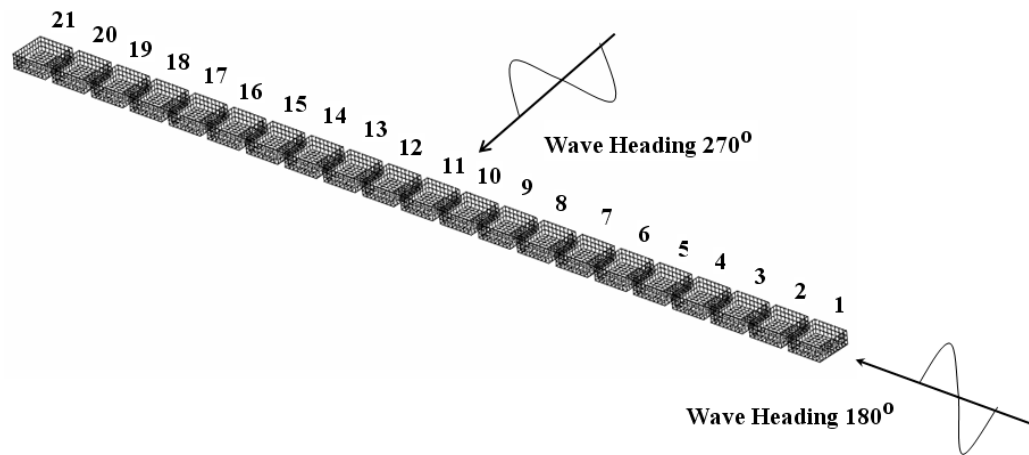


Fig 4. Mesh arrangements and numbering of a long array of 21 freely floating identical rectangular boxes

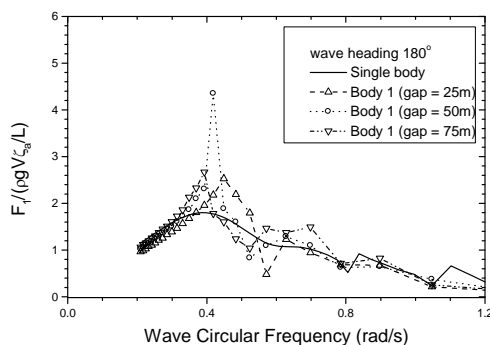


Fig 5. Surge wave exciting forces on Body 1 for a long array of 21 identical freely floating rectangular bodies

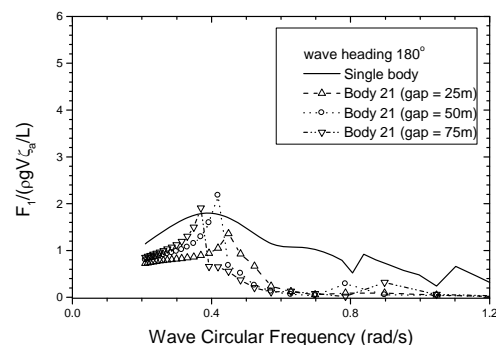


Fig 6. Surge wave exciting forces on Body 21 for a long array of 21 identical freely floating rectangular bodies

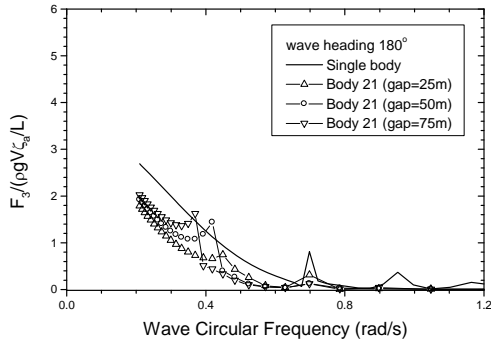
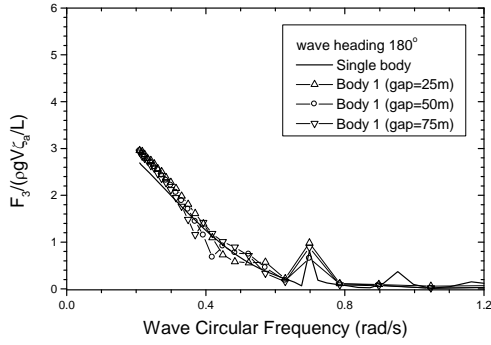


Fig. 7. Heave wave exciting forces on Body 1 and Body 21 for a long array of 21 identical freely floating rectangular boxes

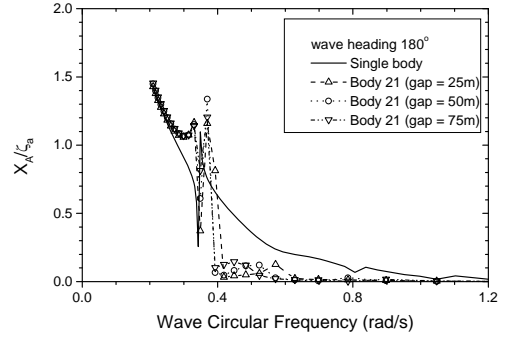
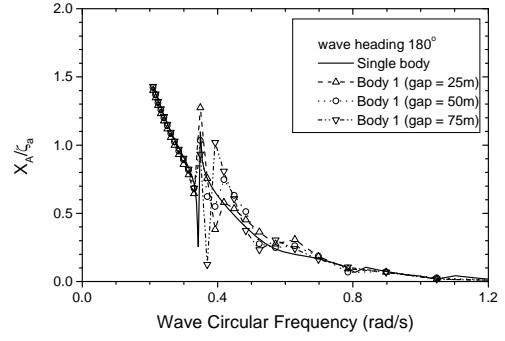


Fig. 9. Surge motions for Body 1 and Body 21 for a long array of 21 identical freely floating rectangular bodies

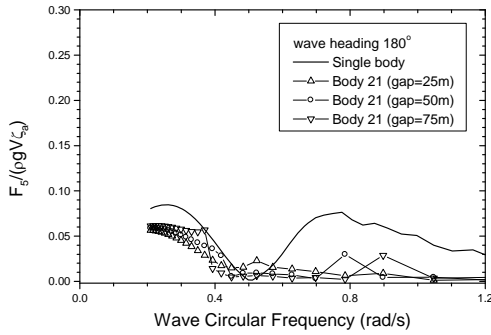
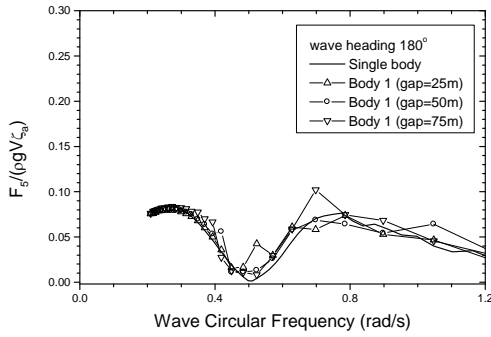


Fig. 8. Pitch wave exciting moments on Body 1 and Body 21 for a long array of 21 identical freely floating rectangular boxes

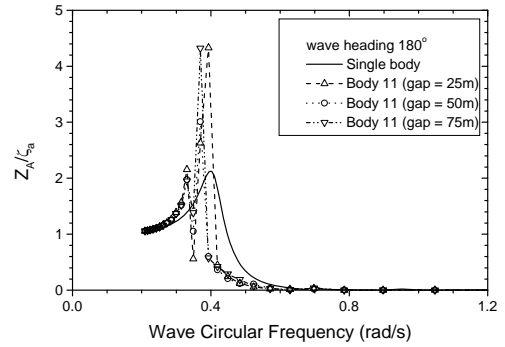


Fig. 10. Heave motion for Body 11 for a long array of 21 identical freely floating rectangular boxes

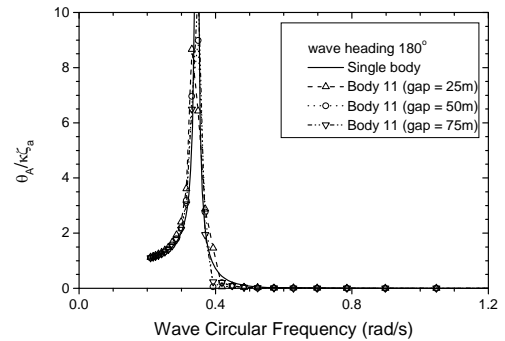


Fig. 11. Pitch motion for Body 11 for a long array of 21 identical freely floating rectangular boxes

## ANALYSIS OF TRANSOM STERN FLOWS BY MODIFIED RANKINE SOURCE PANEL METHOD

Md. Shahjada Tarafder, G. Md. Khalil and G. Kumar Saha

Department of Naval Architecture and Marine Engineering  
Bangladesh University of Engineering and Technology, Dhaka, Bangladesh

### ABSTRACT

The paper presents a numerical method for calculating a potential flow around a ship of transom stern with respect to the double-body potential. The method of solution is based on the distribution of Rankine sources on the hull as well as its image and on the free surface. An iterative algorithm is used for determining the free surface and wave resistance using Dawson's upstream finite difference operator. A verification of numerical modeling is made using R V Athena hull and the validity of the computer program is examined by comparing the wave making resistance with NPL-100A hull.

**Keywords:** Wave Resistance, Transom Hull, Rankine Source Panel Method, R V Athena, NPL-100A

### 1. INTRODUCTION

A large number of vessels currently being used in Bangladesh in passenger service share the characteristics of possessing a cut-off or transom stern. This feature of the vessel defies simple hydrodynamic analysis because the extent and detailed shape of the flow behind the transom is unknown and must be a part of the mathematical solution to the problem. In principle, the pressure acting on the free surface behind the transom must be atmospheric and the flow must separate from the transom tangentially.

High speed displacement vessels are frequently used as patrol boats because of their speed capability combined with good seakeeping characteristics. These vessels have a high length-beam ratio and a transom stern. A practical computational method for such transom stern vessels is of special interest to ship hydrodynamicists due to the peculiar property of the flow pattern. If the ship speed is high enough, (Froude numbers,  $F_n > 0.4$  approximately), the transom clears the surrounding water and the entire transom area is exposed to the air. The transom flow detaches smoothly from the underside of the transom and a depression is created on the free surface behind the transom.

Tulin and Hsu [1] developed a theory for high-speed displacement ships with transom sterns. The flow was assumed to be smooth at the aft waterline and to have a trailing wake. The trailing wake resulted in substantial residuary resistance at high speeds for normal waterline ships. Cheng [2] presented a practical computational method for 3-dimensional transom stern flows. The boundary condition for dry transom stern was derived within the framework of a free surface potential flow. The transom was treated as an inflow boundary and the

transom boundary condition was used to specify the starting values of linearized free surface conditions.

Telste and Reed [3] presented a method of calculating the flow near a transom stern ship moving forward at a moderate to high steady speed into otherwise undisturbed water. Modified free-stream linearization was used to obtain a Neumann-Kelvin boundary value problem in which the usual linearization about the mean free surface level was replaced in the area behind the transom stern by linearization about a surface originating at the hull-transom intersection. A Rankine singularity integral equation was presented for obtaining the solution of the resulting mathematical boundary value problem.

Wang et al. [4] calculated the wave resistance of a fast displacement hull with a transom stern using several different theoretical methods. The results of the calculations were compared with experimental data for a hull from the National Physical Laboratory (NPL) round-bilge hull series.

Sireli and Insel [5] investigated the effects of transom stern on the wave resistance of high speed marine craft by using a series of five monohull forms by both experimental and numerical methods. The wave resistance of the hull was calculated by potential flow theory based on Dawson's algorithm and the viscous resistance by boundary layer calculations.

Doctors and Day [6] used the linearized near field solution for the flow past a vessel with a transom stern. The hollow in the water behind the stern was represented by an extension to the usual centre-plane source distribution employed to model the hull itself. The resistance, sinkage and trim were computed by means of an integration of the resulting pressure distribution over the wetted surface of the vessel.

Millward et al. [7] developed a numerical method to calculate the flow past light displacement ships hulls with a transom stern for Froude numbers ranging from 0.4 to approximately 1.0. The hull was allowed to trim and heave in calculations and the results of the calculations were compared with experimental data available for the Model 100A of NPL round bilge hull series.

The objective of the present research is to develop a numerical model for calculating the flow around the transom stern of a high speed vessel by the modified Rankine source panel method. The special boundary condition is applied to the transom and to the portion of the free surface downstream of the stern. The physical constraints imposed by this transom boundary condition require that the static pressure be atmospheric and that the flow leave tangentially at the transom. The computational method has been applied to R V Athena and NPL 100A hulls and then compared the results with the existing results available in the literature.

## 2. MATHEMATICAL FORMULATION

Let us consider a ship moving in an infinite depth of water with a constant speed  $U$  in the direction of the negative  $x$ -axis as shown in Figure 1. The  $z$ -axis is vertically upwards and the  $y$ -axis extends to starboard. The origin of the co-ordinate system is located in an undisturbed free surface at amidship. The total velocity potential  $\phi$  is the sum of the double body velocity potential  $\Phi$  and the perturbed velocity potential  $\varphi$  representing the effect of free surface wave.

$$\phi = \Phi + \varphi \quad (1)$$

Now the problem for a ship can be constructed by specifying the Laplace equation

$$\nabla^2(\Phi + \varphi) = 0 \quad (2)$$

with the following boundary conditions:

(a) Hull boundary conditions: The normal velocity component on the hull surface must be zero.

$$\nabla(\Phi + \varphi) \cdot \mathbf{n} = 0 \quad (3)$$

where  $\mathbf{n} = n_x \mathbf{i} + n_y \mathbf{j} + n_z \mathbf{k}$  represents a normal to the hull surface in the outward direction.

(b) Free surface condition: The velocity potential needs to satisfy the dynamic and the kinematic conditions on the free surface

$$g\zeta + \frac{1}{2} \nabla\phi \cdot \nabla\phi = \frac{1}{2} U^2 \quad \text{on } z = \zeta(x, y) \quad (4)$$

$$\phi_x \zeta_x + \phi_y \zeta_y - \phi_z = 0 \quad \text{on } z = \zeta(x, y) \quad (5)$$

Eliminating  $\zeta$  from equations (4) and (5)

$$\frac{1}{2} \phi_x (\nabla\phi \cdot \nabla\phi)_x + \frac{1}{2} \phi_y (\nabla\phi \cdot \nabla\phi)_y + g\phi_z = 0 \quad \text{on } z = \zeta(x, y) \quad (6)$$

The free surface condition equation (6) is nonlinear in  $\nabla\phi$  and should be satisfied on the free surface at  $z = \zeta(x, y)$ , which is unknown and can be linearized about the double body solution  $\Phi$  by neglecting the non-linear terms of  $\varphi$ . After linearization the free surface boundary condition (6) can finally be expressed as

$$\Phi_1^2 \varphi_{11} + 2\Phi_1 \Phi_{11} \varphi_1 + g\varphi_z = -\Phi_1^2 \Phi_{11} \quad \text{on } z = 0 \quad (7)$$

where the subscript 1 denotes the differentiation along a streamline of double body potential  $\Phi$  on the symmetry panel  $z = 0$ . The free surface boundary condition given in equation (7) involves the gradient of the velocity potential along a streamwise direction designated by 1 and differentiation is carried out along the corresponding double body streamlines. Finally it is necessary to impose a radiation condition to ensure that the free surface waves vanish upstream of the disturbance. The solution of the Laplace equation in connection with the boundary conditions (3), (7) and the radiation condition for the flow around the cruiser stern is given in Tarafder and Suzuki [8].

## 3. SOLUTION FOR DRY TRANSM STERN

For the case of a transom stern, another constraint to be satisfied at the transom is the exit flow that must be tangential to the hull surface. The free surface of the transom stern is considered to be consisted of two parts. The main section of the free surface is handled in the same way as for cruiser sterns. The fluid domain behind the transom is treated as an inflow boundary and the starting values of a free surface calculation are specified at the transom. The transom stern solution begins with a double model computation. After getting cruiser stern solution, the flow direction for the transom geometry is specified by a local tangential unit vector:

$$\Gamma_x = \frac{\Phi_x}{\sqrt{\Phi_x^2 + \Phi_y^2 + \Phi_z^2}} \quad (8)$$

$$\Gamma_y = \frac{\Phi_y}{\sqrt{\Phi_x^2 + \Phi_y^2 + \Phi_z^2}} \quad (9)$$

$$\Gamma_z = \frac{\Phi_z}{\sqrt{\Phi_x^2 + \Phi_y^2 + \Phi_z^2}} \quad (10)$$

where the vector  $\Phi_x, \Phi_y$  and  $\Phi_z$  represents the velocity for a hull panel whose centroid lies just forward of the sharp corner at the transom. Ensuring the flow tangential to the hull surface, the velocity components at the transom are approximated as (see Cheng, 1989):

$$u_T = 2U_\infty \sqrt{1 - \frac{2g}{U_\infty^2} z_T} \Gamma_x \quad (11)$$

$$v_T = 2U_\infty \sqrt{1 - \frac{2g}{U_\infty^2} z_T} \Gamma_y \quad (12)$$

$$w_T = 2U_\infty \sqrt{1 - \frac{2g}{U_\infty^2} z_T} \Gamma_z \quad (13)$$

The streamwise velocity on the free surface is computed by

$$\phi_{11} = \frac{\Phi_x}{\sqrt{\Phi_x^2 + \Phi_y^2}} \varphi_x + \frac{\Phi_y}{\sqrt{\Phi_x^2 + \Phi_y^2}} \varphi_y \quad (14)$$

Note that the differentiation scheme approximates the free surface flow direction by the double model flow direction. In the numerical calculation of the convective term, finite differencing is used to calculate derivatives between adjacent panels along a double model streamline. A three point upstream finite differencing scheme is used to eliminate upstream propagating disturbances as recommended by Dawson [9]. For the foremost upstream point, a two point upstream finite difference operation is used.

#### 4. RESULTS AND DISCUSSIONS

To investigate the effect of the transom stern on the wave resistance and wave pattern, the method has been applied first for NPL-100A hull. Since the body is symmetric one-half of the computational domain is used for numerical treatment. The extent of free surface domain is 3.0 ship-lengths upstream to 8.0 ship-lengths downstream. The transverse extension of the free surface domain is about 2.0 ship-lengths. The NPL-100A hull is discretized by  $2 \times 20 \times 10$  and is shown in Fig. 1. The free surface is discretized by  $2 \times 1985$  panels (main domain:  $2 \times 90 \times 19$ , domain behind stern:  $2 \times 55 \times 5$ ) and is given in Fig 2.

Figure 3 gives a side-view of the computed wave profiles behind the transom for RV Athena at various Froude numbers. The vertical and horizontal axes are normalized by  $L$  and are plotted to the same scale. The figure indicates that the transom clears the surrounding water and the assumption of a dry transom stern is valid.

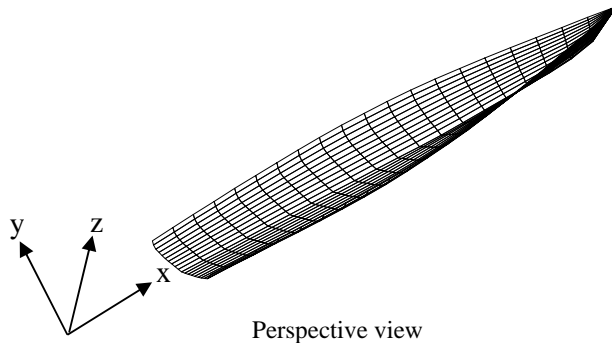


Fig 1. Discretization of NPL-100A by  $2 \times 20 \times 10$  panels

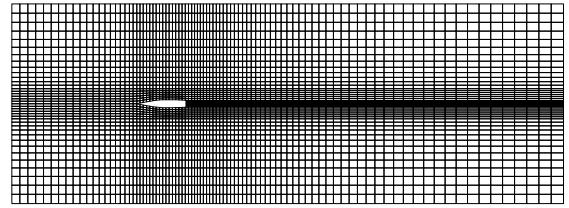


Fig 2. Discretization of free surface for NPL-100A by  $2 \times 1985$  panels (main domain:  $2 \times 90 \times 19$ , domain behind stern:  $2 \times 55 \times 5$ )

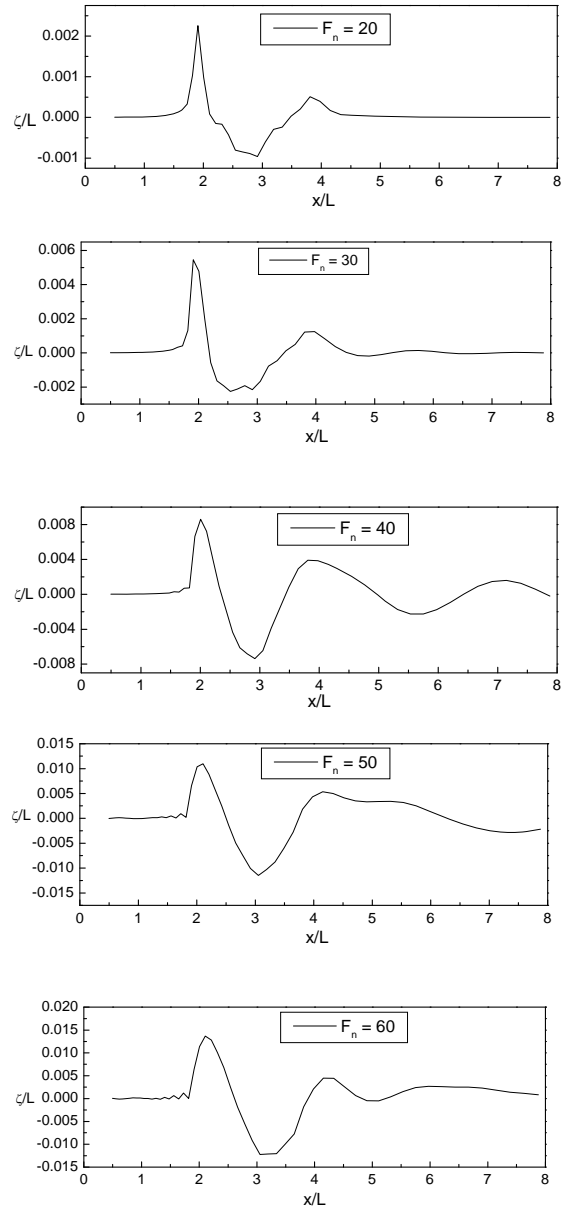


Fig 3. Wave profile at the central line behind the transom stern of NPL-100A hull at various Froude numbers

The comparison of computed wave resistance and measured wave pattern resistance is presented in Fig 4. The computations were performed for Froude numbers



from 0.2 to 1.0 at increment of 0.05. The hull form was held in fixed at the even keel position for these computations. The calculated wave resistance and measured residual wave resistance show general agreement in respect of hump and hollow but the significant difference is found between the present numerical result and Millward's calculated results.

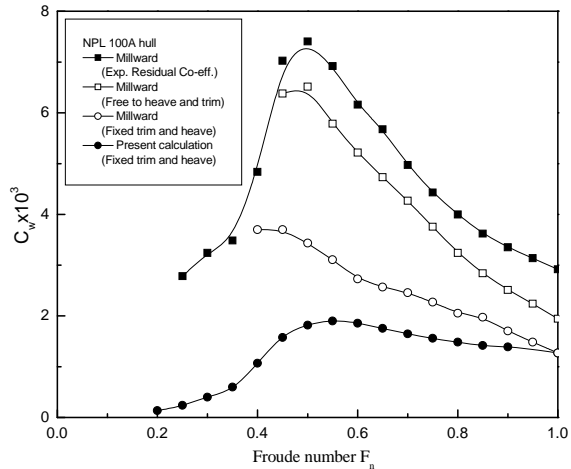


Fig 4. Comparison of calculated wave resistance with Millward's results for NPL-100A hull

The discretization of R V Athena hull and its corresponding free surface are given in Fig 5 and 6 respectively. The calculated wave-making resistance of Athena hull is shown in Fig 7.

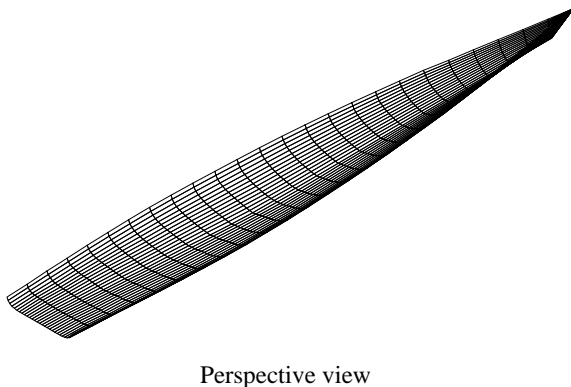


Fig 5. Discretization of R V Athena hull by 2x25x14 panels

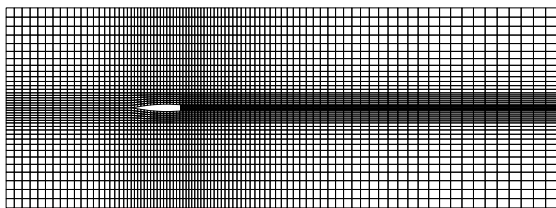


Fig 6. Discretization of free surface for R V Athena hull (main domain: 2x90x19, domain behind stern: 2x55x5)

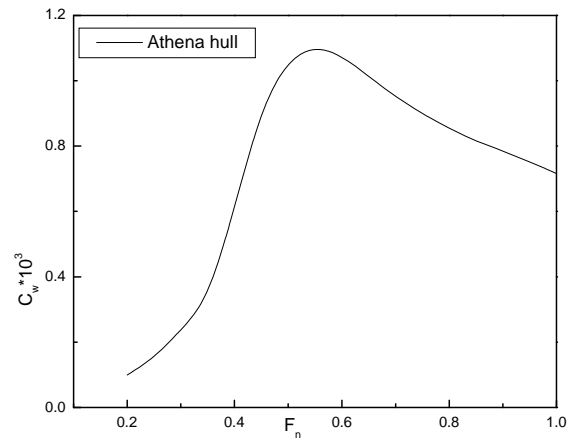


Fig 7. Calculated wave-making resistance of Athena hull

## 5. CONCLUSIONS

The paper presents the modified Rankine source panel method for calculating the flow of transom stern ship using double body linearization of the free surface boundary condition. The following conclusions can be drawn from the present numerical analysis:

1. The present method could be an efficient tool for evaluating the flow field, wave pattern and wave resistance for practical ship forms.
2. The trend of the calculated and measured wave making resistance curve for NPL-100A hull is quite satisfactory but a significant difference is found in magnitude.
3. The calculated results depend to a certain extent on the discretization of the hull and the free surface. Similar panel arrangement should therefore be used if relative merits of different competing ship designs are to be judged.

## 6. REFERENCES

1. Tulin, M. P. and Hsu, C. C. (1986): Theory of high-speed displacement ships with transom sterns, *The Journal of Ship Research*, Vol. 30, No. 3, pp. 186-193.
2. Cheng, B. H. (1989): Computation of 3D transom stern flows, 5<sup>th</sup> International Conference on Numerical Ship Hydrodynamics, pp. 581-591.
3. Telste, J. G. and Reed, A. M. (1994): Calculation of transom stern flows, 6<sup>th</sup> International Conference on Numerical Ship Hydrodynamics, pp. 79-92.
4. Wang, Y., Sproston, J. L. and Millward, A. (1995): A theoretical determination of the wave resistance of a fast displacement hull with a transom stern, *The Journal of Ship Research*, Vol. 39, No. 2, pp.103-107.
5. Sireli, E. M. and Insel, G. M. (1999): The effects of transom stern on the resistance of high speed craft, Naval Technical Congress, IMAM, Naples.

6. Doctors, L. J. and Day, A. H. (2000): The squat of a vessel with a transom stern, 15<sup>th</sup> International Workshop on Water Waves and Floating Bodies (15 IWWWFB), Caesarea, Israel, pp. 40-43.
7. Millward, A., Nicolaou, D. and Rigby S. G. (2003): Numerical modeling of the water flow around a fast ship with a transom stern, International Journal of Maritime Engineering, The Royal Institute of Naval Architects, pp. 21-34.
8. Tarafder, M. S. & Suzuki, K. (2008): Numerical Calculation of Free Surface Potential Flow around a Ship Using the Modified Rankine Source Panel Method, Ocean Engineering, Elsevier Science, UK, Vol. 35, No. 5-6, pp. 536-544.
9. Dawson, C. W. (1977): A practical computer method for solving ship-wave problems, Proceedings of Second International Conference on Numerical Ship Hydrodynamics, pp.30-38.

## 7. NOMENCLATURE

$\phi$	Total velocity potential
$\phi_x$	velocity of the fluid in the x-direction
$\phi_y$	velocity of the fluid in the y-direction
$\phi_z$	velocity of the fluid in the z-direction
$\Phi$	Double body velocity potential
$\varphi$	Perturbation velocity potential
$n$	Unit normal vector
$\zeta$	Wave elevation
$\Gamma$	Tangential unit vector
$u_T$	Velocity component at the transom along x-direction
$v_T$	Velocity component at the transom along y-direction
$w_T$	Velocity component at the transom along z-direction

## MOLECULAR DYNAMICS STUDY OF AFM BASED MACHINING PROCESS

H. Muhammad Khan and Sung-Gaun Kim

Division of Mechanical and Automotive Engineering, Kongju National University, Cheonan, South Korea

### ABSTRACT

Molecular dynamics study has been performed on a three dimensional model to evaluate the machining process on nickel substrate for Nano-Electro-Mechanical System (NEMS) based applications. Some unique macro level properties of Nickel have attracted attention which might be very useful if considered during nano level fabrication especially NEMS based application. Atomic force microscope (AFM) based diamond tool of 4 nm diameter has been used to simulate the whole process varying the cutting depth and effects of cutting depth on deformation, cutting forces, friction coefficient, specific speed and dislocation have been studied. It has been found that, cutting depth has significant relation on different parameters during nanometric machining process. Increasing cutting depth offers more plastic deformations and dislocations induced in the substrate material and consequently result in a rough surface, which satisfies the results obtained by earlier investigations.

**Keywords:** Molecular Dynamics, Nanomachining, NEMS.

### 1. INTRODUCTION

After the first approach to investigate the nanometric machining process with copper in late 1980s, several researches have been already performed to explore the insight of machining process in nanocrystalline materials [1-3]. MD simulation has been a reliable technique over the years for its best suited analyzing ability. Komanduri et al. [4-5] has performed MD simulation of the nanometric machining of mono crystalline aluminium to study material deformation, cutting forces, chip formation, exit failure. Also he has performed some methodology like effect of tool geometry on single crystal copper to study the cutting processes [6]. Those works help tremendously to understand the nanometric machining processes. But small models were adopted in most of the cases which can show lot of boundary effects resulting in unreliable results. Also, due to the small models, most of the previous models were based on two dimensional machining process or quasi-three-dimensional (plane strain) machining process. In previous reported works Morse potential is widely used to study the pair wise interaction between metal atoms and to model interatomic force. It is a pair potential considering only two body interactions. So it cannot properly describe the metallic bonds. But many body EAM potential can describe the phenomenon of metals more precisely and that is why it has been adopted for this simulation purpose [7].

Due to advancement of scanning probe microscopy (SPM) techniques, fabrication of Nano-electro-mechanical system (NEMS) has been proposed to fabricated by atomic force microscope

(AFM) based nanomachining process [8]. As material property changes with the reduction of its size to nano level, macro level cutting behavior cannot be applied to analyze nano level fabrications. Therefore, not only the theoretical analysis but also the experimental or high performance simulation methodology should be used to study the micro world cutting processes which will provide sufficient knowledge to explore the frictional behavior, elastic -plastic deformation behavior, cutting mechanisms.

During any kind of machining process, friction plays a significant role. Atomic scale friction covered by the area is known as Nanotribology. Nanotribology involves dynamic atomic interactions at the interface of two materials in relative contact. The difference arising between tribology and nanotribology is primarily due to the involvement of atomic forces. So it is not possible to use conventional tribological method to evaluate the characteristics during nanomachining processes. As nanotechnology is on its developing stage, mechanical characterization and tribological behavior demands careful observations and standardization.

In this paper, AFM based 3D model has been used for MD (Molecular Dynamics) simulation and EAM (Embedded Atom Method) potential has been used instead of Morse potential. A velocity of 50m/s has been chosen to carry out the simulation process. Effects of cutting depth on deformation, cutting forces, friction coefficient, specific speed and dislocation have been studied. A constant cutting length of 7.0 nm has been maintained throughout the machining process to put all the results on same length scale and towards a better comparison.

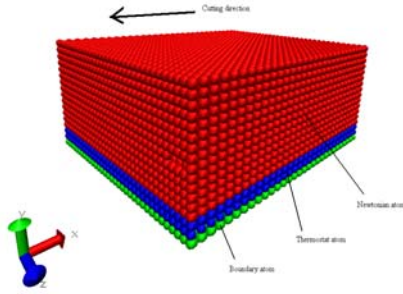


Fig 1. MD simulation model of nanometric machining.

## 2. SIMULATION METHOD

Fig.1 shows the model for the simulation process. Monocrystalline nickel workpiece has been illustrated out on different zones. Size of the workpiece is  $10.56 \times 4.23 \times 8.5$  nm and contains 34680 atoms. The lattice constant of Nickel is 0.352nm. An AFM based spherical diamond pin tool has been used as the cutting tool. The cutting process was along negative x-direction, which is taken as the [-100] direction of the FCC lattice of nickel and on (010) surface. Previously, Komanduri et al has been suggested that the (001) [100] combination should be used for performing simulation of machining, if only one orientation has to be used, based on nanometric machining on various cutting directions and crystal orientations[9]. Workpiece consists of three types of atoms- Newtonian atoms, thermostat atoms and boundary atoms. To reduce the size effects, the boundary atoms are kept fixed at their lattice space. Thermostat atoms have been introduced to the system to ensure the heat dissipation which is generated during the machining process [10]. The temperature of the thermostat atom has been kept at 0 K by rescaling the velocities of the thermostat atoms using velocity rescaling method every hundred computational time which corresponds to 0.3 ps. Newtonian atoms obey the Newton's second law of motion. In molecular dynamics, motions of these atoms are determined by the direct integration of the classical Hamiltonian equations of motion using Velocity-Verlet method [11]. A timestep of 3 fs has been used for the velocity Verlet algorithm. Another boundary condition that has been maintained is – periodic boundary condition which has been maintained along the z direction. It provides the means to minimize effects of simulation scale. All models were subjected to relaxation for equilibrium state at zero temperature by energy minimization using the conjugate gradient method to allow the models to reach natural and dynamical equilibrium status consistent with the specified temperature.

The AFM tool used in this simulation has the shape of a sphere and constructed with perfect diamond lattice with a diameter of 4.0 nm. A constant cutting speed of 50 m/s has been used along a cutting distance of 7.0 nm. Cutting depth has been varied from 0.5 nm to 2.0 nm. The initial temperature of the workpiece is 0 K.

The force acting on the system is obtained by calculating the forces acting on the atom by the surrounding atoms

and encapsulating them. This calculation has been performed using interatomic potentials. Morse potential is a pair wise potential and not only computationally inexpensive but also simple compared to EAM potential [12].

The EAM method has been originated from the density-function theory and based upon the approximation that the cohesive energy of a metal is governed not only by the pair-wise potential of the nearest neighbor atoms, but also by embedding energy related to the “electron sea “ in which the atoms are embedded. This electron density is approximated by the superposition of atomic electron densities. For EAM potential, the total atomic potential energy of a system is expressed as:

$$E_{tot} = 1/2 \sum_{i,j} \phi_{ij}(r_{ij}) + \sum_i F_i(\bar{\rho}_i) \quad (1)$$

Where  $\phi_{ij}$  is the pair-interaction energy between atoms  $i$  and  $j$  and  $F_i$  is the embedding energy of atom  $i$ .  $\rho_i$  is the host electron density at site  $i$  induced by all other atoms in the system, which is given by:

$$\bar{\rho}_i = \sum_{j \neq i} \rho_j(r_{ij}) \quad (2)$$

There are three different atomic interactions in this simulation of nanometric machining process - the interaction in the workpiece, the interaction between the workpiece atoms and the tool atoms, the interaction in the tool atoms. The EAM potential function for nickel developed by Foiles [13] is used here for the interaction of the substrate atoms. EAM potential has been used instead of pairwise morse potential because the EAM provides a more realistic description of the metallic cohesion, although using morse potential the energetics of an arbitrary arrangements of atom can be calculated quickly, but the ambiguity inherited by the volume dependency is avoided on EAM method. For the Ni-C atoms interaction, morse potential has been adopted as there is no existing EAM potential available to describe the behavior of interactions between Ni-C atoms. It has been adopted from Fang et al. [14] as  $D=1.0094$  eV,  $\alpha=0.19875$  nm<sup>-1</sup> and  $r_0=2.559$  nm. The Lorentz-Berthelot mixing rule was used to estimate the interatomic Morse potential for Ni-C interactions. For the interactions between the tool atoms, also Morse potential has been adopted where  $D=2.4230$  eV,  $\alpha=0.25550$  nm<sup>-1</sup> and  $r_0=2.522$ nm. But as stiffness of Diamond tool is much harder than the stiffness of Nickel atoms, the tool can be considered as a rigid body. In this approximation, the interaction force between tool atoms will have no effect on tool atoms. All the simulations of this model use parallel molecular dynamics program LAMMPS [15].

## 3. RESULTS AND DISCUSSIONS

A three-dimensional model has been used for current study of AFM-based nanometric machining process on monocrystalline nickel using an AFM spherical tool. Cutting depths of 0.5, 1.0, 1.5 and 2.0 have been simulated and their effects on deformation, machining forces, tribological behavior and dislocations have been observed. The atoms have been subjected to relaxation to

minimize the energy of the system and to allow the system to reach equilibrium condition. It has been done

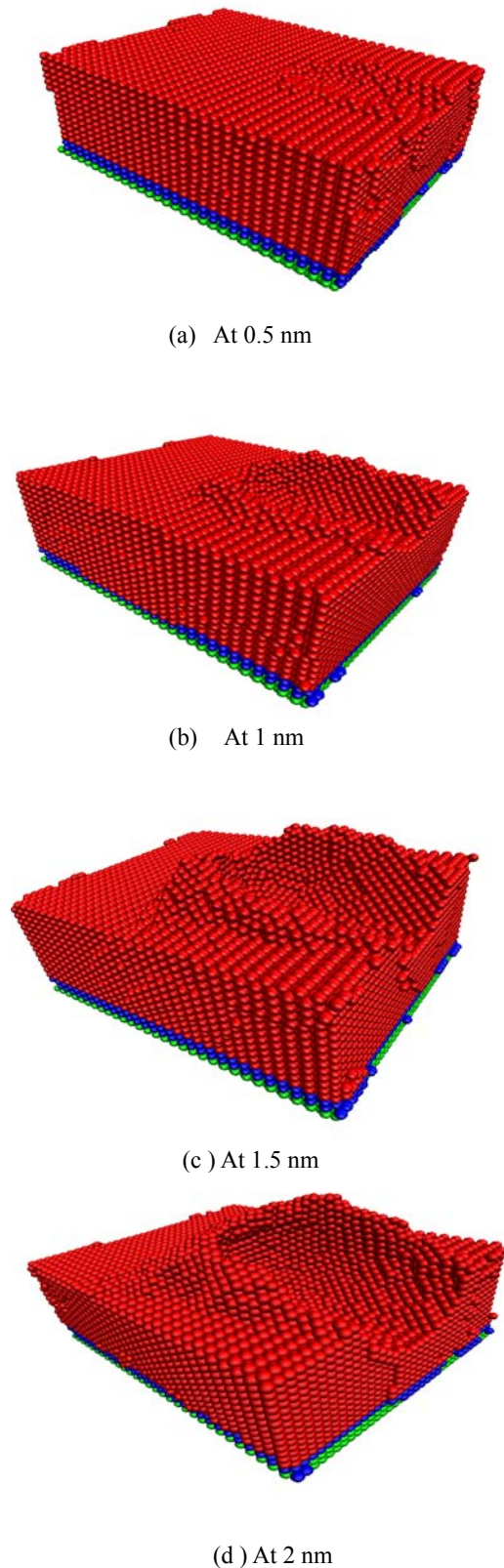


Fig 2. Deformation behavior of machining process at different cutting depths of 0.5, 1, 1.5 and 2 nm.

after configuring the workpiece and tool atoms in their perfect lattice structures. The MD simulation code uses LAMMPS, which is an open source code. The discussion provided below is not only from the plots of MD simulations but also from careful observations of the MD simulations. For visualization, an open source molecular visualization program namely VMD- Visual Molecular Dynamics has been used [16].

### 3.1 On the Nature of Deformation

Fig: 2 shows the different states of cutting process during tool travel along the workpiece material with varying cutting depth. The effects have been observed carefully. As it has been known from solid state physics, as a result of attractive and repulsive forces, metallic atoms are not only arranged in a specific pattern but also they maintain an equilibrium distance in their crystal structures. Conducting a cutting process on a crystallographic material structure will generate disturbance throughout the metallic structure. The arrangements of the atoms will be changed to create room for the tool to travel along its surface. Hence the term deformation takes place. As the tool touches the surface, the crystal structure of the workpiece shows adhesion features with the tool atoms. But with the advancement of the tool on its surface, this adhesion feature no longer exists. Rather it turns into repulsive nature and the interatomic bonds between workpiece material breaks due to the advancement of tool atoms. Accumulation of workpiece atoms takes place in front of the tool. It has been found from the simulation that the accumulation not only takes place in front, but also beneath the tool edge and thus chip is formed. Also with the advancement of tool atoms on substrate material surface, atoms pile up on both side of the tool. As tool goes forward, these atoms flow towards their respective piling directions to allow the tool to travel. As cutting depth increases, this accumulation and piling up occurs in greater scale. So deformation occurs in large scale. To allow the workpiece to reach relaxed state, after certain period, atoms in workpiece rearrange in crystal structure. Thus dislocation nucleates and the atoms slip past each other.

### 3.2 On the Nature of Forces

In the current study, force in the direction parallel to cutting direction has been considered as the Tangential force(x axis) and force in the direction perpendicular to the cutting direction has been considered as Normal force(y axis). The variation of tangential force  $F_x$  with cutting distance for the different cutting depth has been plotted in Fig.3. Sudden rise in the forces in the initial stage can be explained as, as the tool atoms and the workpiece atoms pass the adhesion period, repulsion takes place and workpiece material undergoes complex elastic and plastic deformation. After that, it gradually reaches to a steady state. Although for different cutting depths the magnitude is different. The variation is still there in the steady state. More precisely, the variation can be termed as “quasi-periodic variation.” The same phenomenon has been reported by Buldum and Ciraci et al [2]. That MD simulation was performed using a sharp Ni tip on a Cu substrate. It can be seen from the MD

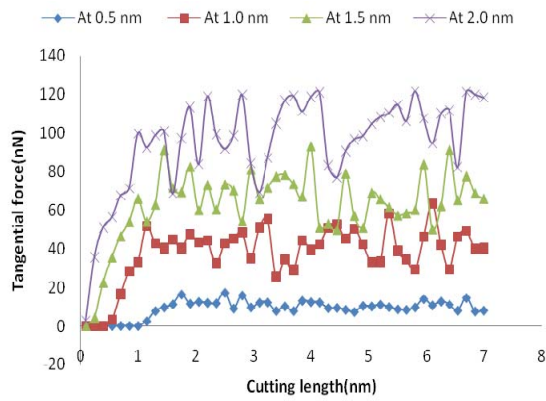


Fig 3. Variation of tangential force for four different cutting depths of 0.5, 1, 1.5 and 2 nm.

simulation of current study that as the cutting depth is less, the nature of the steady state is more periodic. With the increase of cutting depth, steady state tends to deviate and presence of rapid fluctuations can be identified. And increased cutting depth requires more cutting force for material removal. That can be explained as; more material accumulates in front of the tool as cutting depth increases and more the cutting force is required for the advancement of the tool and material removal. The time averaged cutting forces has been presented in Fig.4 with the variation of cutting depth. It has been considered after reaching the steady state which is from 1.5 to 7.0 nm of travelling distance and sudden fluctuating components has been cut off. Although it has been found that, the natures of the curves are similar only varying in magnitude. Both the tangential force and normal force increases with the increase of cutting depth. But the tangential cutting force increases rapidly comparing to the normal force. The ratio of normal force to tangential force changes from more than 6 to almost 1. It seems that with increase of cutting depth, contribution of forces is more in tangential force rather than in normal force as higher cutting force is required for the larger cutting depth.

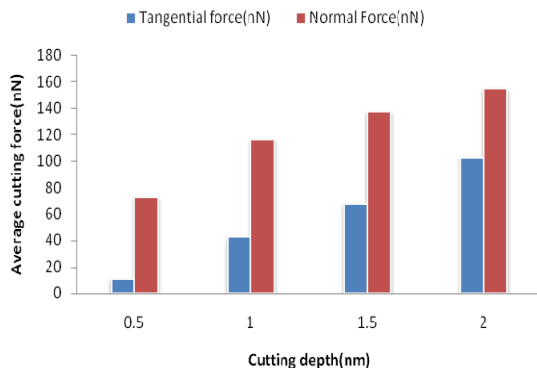


Fig 4. The time averaged cutting forces for the different cutting depths of 0.5, 1, 1.5 and 2 nm.

### 3.3 On the Nature of Friction

As friction arises from the contact followed by relative movement of two surfaces, it is of obvious need to realize the role of friction in any sort of machining process. And nevertheless, for a sophisticated process

like nanomachining it is of immense importance. The values of tangential force and normal force obtained in steady states are listed in Table 1. The friction coefficient is also listed, which is the ratio of tangential force to

Table 1. MD simulation results for varying cutting depths.

Cutting depth(nm)	Tangential force(nN)	Normal force(nN)	Friction coefficient
0.5	10.906	72.455	0.15
1.0	42.597	116.338	0.366
1.5	67.505	137.228	0.492
2.0	102.752	154.573	0.665

normal force. Fig. 7 shows the relation between co-efficient of friction with the variation of cutting depth which has been found to vary from 0.15 to 0.66. Individual cases have not been plotted to save the length of the paper. It has been found that it in individual cases, after reaching the steady state, the friction coefficient is constant but larger in magnitude for larger cutting depth. The co-efficient of friction increases almost linearly with the variation of cutting depth. It can be interpreted as, with the increase of cutting depth, more tangential force is required for tool travel. Because, more material

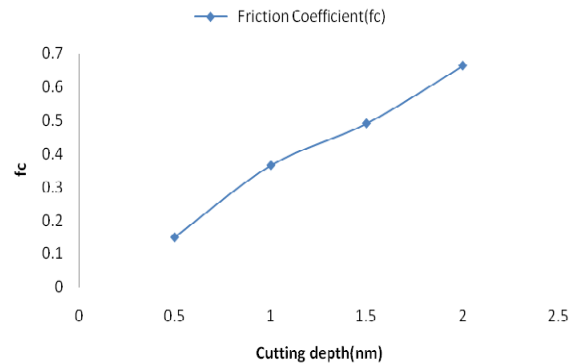


Fig 5. Variation of friction coefficient ( $f_c$ ) with different cutting depths of 0.5, 1, 1.5 and 2 nm.

accumulates in front of the cutting tool and requires more external force in cutting direction to remove them. As well as the friction coefficient increase. As friction is the measure of the resistance, this can be utilized to understand the resisting behavior during AFM-based machining. The friction coefficient has been found to be more dependent on the tangential force than normal force.

## 4. CONCLUSIONS

3D molecular dynamics simulation using EAM (Embedded Atom Method) has been carried out on single crystal Nickel using AFM-based nanomachining process for NEMS based application. Possibilities has been evaluated varying the cutting depths (0.5, 1, 1.5 and 2 nm) and observing its effects on forces, deformation behavior, tribological behavior. On the basis of obtained results from the MD simulation, following conclusions can be drawn:



The smaller is the cutting depth, the earlier the cutting force reaches to the steady state. Still the variation exists which can be termed as a “quasi-periodic” variation [2]. Further study should be carried on to explain this nature and put that into a specific and well-defined function with different cutting parameters. Cutting depth has a major role in nano-machining process, especially in AFM-based machining process. With the increase of cutting depth, machining process is followed by more complex not only elastic deformation but also plastic deformation. The more is the cutting depth, more dislocations generates and nucleates affecting more workpiece material. The frictional coefficient is more dependent on tangential force than the normal force. As with the increase of cutting depth, magnitude of both tangential and normal force increases, but significant contribution goes to tangential force which results in increased frictional coefficient.

## 5. ACKNOWLEDGEMENT

The authors gratefully acknowledge financial support by Brain Korea 21. The authors are also grateful to Long Trandinh for his invaluable comments.

## 6. REFERENCES

1. L. Zhang and H. Tanaka, 1997, “Towards a deeper understanding of wear and friction on the atomic scale- a molecular dynamics analysis”, *Wear* 211: 44-53.
2. A. Buldum and S. Ciraci, 1998, “Contact, nanoindentation, and sliding friction”, *Phys. Rev. B* 57: 2468-2476.
3. K. Maekawa and A. Itoh, 1995, “Friction and tool wear in nano-scale machining- a molecular dynamics approach”, *Wear* 188: 115-122.
4. R. Komanduri, N. Chandrasekaran and L.M. Raff, 2000, “Molecular dynamics simulation of atomic-scale friction”, *Phys. Rev. B* 61: 14007-14019.
5. R. Komanduri, N. Chandrasekaran and L.M. Raff, 1999, “Orientation Effects in Nanometric Cutting of Single Crystal Materials: An MD simulation Approach”, *Ann. CIRP* 48: 67-72.
6. R. Komanduri, N. Chandrasekaran and L.M. Raff, 1998, “Effect of tool geometry in nanometric cutting: a molecular dynamics simulation approach”, *Wear* 219: 84-97.
7. M.S. Daw and M.I. Baskes, 1984, “Embedded-atom method: Derivation and application to impurities, surfaces, and other defects in metals”, *Phys. Rev. B*

- 29: 6443-6453.
8. L.L. Sohn and R.L. Willett, 1995, “Fabrication of nanostructures using atomic-force-microscope-based lithography”, *Appl. Phys. Lett.* 67: 1552-1554.
9. R. Komanduri, N. Chandrasekaran and L.M. Raff, 2000, “M.D. Simulation of nanometric cutting of single crystal aluminium-effect of crystal orientation and direction of cutting”, *Wear* 242: 60-88.
10. W.C.D. Cheong, L. Zhang and H. Tanaka, 2001, “Some Essentials of Simulating Nano-Surfacing Processes Using the Molecular Dynamics Method”, *Key Engg. Mater. Vols.* 196: 31-42.
11. L. Verlet, 1967, “Computer “Experiments” on Classical Fluids. I. Thermodynamical Properties of Lennard- Jones Molecules”, *Phys. Rev.* 159: 98-103.
12. Q.X. Pei, C. Lu, F.Z. Fang and H. Wu, 2006, “Nanometric cutting of copper: A molecular dynamics study”, *Comput. Mater. Sci.* 37: 434-441.
13. S.M. Foiles, M.I. Baskes and M.S. Daw, 1986, “Embedded-atom-method for the fcc metals Cu, Ag, Au, Ni, Pd, Pt, and their alloys”, *Phys. Rev. B* 33: 7983-7991.
14. T.H. Fang and J.H. Wu, 2008, “Molecular dynamics simulations on nanoindentation mechanisms of multilayered films”, *Comput. Mater. Sci.* 43: 785-790.
15. S.J. Plimpton and B.A. Hendrickson, 1993, “Parallel molecular dynamics with the embedded atom method”. In: Broughton J, Bristowe P, Newsam J, (editors). *Mater. Theory and Modelling*, MRS Proceedings 291: 37.
16. W. Humphrey, A. Dalke and K. Schulten, 1996, “VMD: Visual Molecular Dynamics”, *J. Mol. Graph.* 14: 33-38.

## 7. NOMENCLATURE

Symbol	Meaning	Unit
F <sub>x</sub>	Tangential Force	(nN)
F <sub>y</sub>	Normal Force	(nN)
f <sub>c</sub>	Friction coefficient	---

## 8. MAILING ADDRESS

Hanif Muhammad Khan  
 Division of Mechanical and Automotive Engineering,  
 Kongju National University,  
 275 Budae-dong, Cheonan, South Korea, 331-717.



## RESPONSE SURFACE MODELING OF FRACTAL DIMENSION IN CNC TURNING

T. K. Barman, P. Sahoo

Department of Mechanical Engineering, Jadavpur University, Kolkata, India

### ABSTRACT

In the present study, a second order response surface model is developed in CNC turning of mild steel materials. Work-piece speed, feed rate and depth of cut are considered as the process parameters and corresponding fractal dimension ( $D$ ) is considered as the response. For the experimentation, a rotatable central composite design is selected. The developed model is also checked for adequacy. ANOVA table shows that work speed, feed rate, interaction of depth of cut with work-piece speed and feed rate with work-piece speed are significant at 95% confidence level. It is also seen that with increase in work speed, fractal dimension ( $D$ ) increases but with increase in feed rate, fractal dimension decreases in mild steel turning.

**Keywords:** Fractal Dimension ( $D$ ), CNC Turning, RSM.

### 1. INTRODUCTION

In a metal removal process, the generated surface consists of inherent irregularities which are commonly termed as surface roughness which is generally, expressed by some statistical parameters such as centre line average value ( $R_a$ ), root mean square value ( $R_q$ ), mean line peak spacing ( $R_{sm}$ ) etc. The surface roughness is widely used as an index of product quality which has an impact on the mechanical properties like fatigue behavior, corrosion resistance, creep life etc. It also affects other functional attributes of parts like friction, wear, light reflection, heat transmission, lubrication, electrical conductivity etc. Thus the quality of the generated surfaces in machining is very important in manufacturing science. In order to get prescribed surface finish, selection of proper combination of process parameters is mandatory.

As the surface topography is a non-stationary random process, the variances of slope and curvature depend strongly on the resolution of the roughness-measuring instrument or any other form of filter and these conventional roughness parameters are strongly depend on the resolution and filter processing of the instrument. In this context to express surface roughness the concept of fractal is applied. The concept is based on the self-affinity and self-similarity of surfaces at different scales. Roughness measurements on a variety of surfaces show that the power spectra of the surface profiles follow power laws. This suggests that when a surface is magnified appropriately, the magnified image looks very similar to the original surface. Fractals may retain all the structural information and are characterized by single descriptor, the fractal dimension,  $D$ . This fractal dimension, which forms the essence of fractal geometry,

is both scale-invariant and is closely linked to the concepts of self-similarity and self-affinity [1]. It is therefore essential to use fractal dimension to characterize rough surfaces and provide the geometric structure at all length scales [2]. In a material removal process, mechanical intervention happens over length scales, which extend from atomic dimensions to centimeters. The machine vibration, clearances and tolerances affect the outcome of the process at the largest of length scales (above  $10^{-3}$  m). The tool form, feed rate, tool radius in case of single point cutting and grit size in multiple point cutting affect the process outcome at the intermediate length scales ( $10^{-6}$  to  $10^{-3}$  m). The roughness of the tool or details of the grit surfaces influence the final topography of the generated surface at the lowest length scales ( $10^{-9}$  to  $10^{-6}$  m). It has been shown that surfaces formed by electric discharge machining, milling, cutting or grinding [3, 4, 5, 6, 7], and worn surfaces have fractal structures, and fractal parameters can reflect the intrinsic properties of surfaces to overcome the disadvantages of conventional roughness parameters.

In the literature review, some relevant literatures in connection with surface roughness modeling in turning are presented here. Grzesik [8] presents how tribological interactions at the interface between the chip and the tool control the surface roughness generation in finish turning with a single point tool. Yang & Tarn [9] have developed a model to find the optimal cutting parameters for turning operations to minimize the surface roughness using Taguchi method. Abouelatta & Madl [10] have found a correlation between surface roughness and cutting vibrations in turning and mathematical models are developed. They have considered three conventional roughness parameters (center line average roughness

value, maximum height of the profile and skewness). Davim [11] presents a study of the influence of cutting velocity, feed and depth of cut on the surface roughness obtained in turning using Taguchi design. Conventional roughness parameters, center line average roughness value ( $R_a$ ) and maximum height of the profile ( $R_t$ ) have been considered for the analysis. It is shown that the cutting velocity has a greater influence on the roughness followed by the feed rate. Lin et al. [12] used regression analysis to predict surface roughness and cutting force in turning. Suresh et al. [13] have developed a surface roughness prediction model in turning of mild steel using response surface methodology. They have also attempted to optimize the surface roughness prediction model using genetic algorithm (GA). Arbizu and Perez [14] have developed models, which permit to determine surface quality of parts obtained through turning processes. They have also shown from the developed model that the depth of cut and feed rate have negative influence on surface roughness. Feng and Wang [15] have presented a nonlinear multiple regression analysis and neural network algorithm to predict surface roughness in finish turning. Sahin and Motorcu [16] have developed a surface roughness model for turning of mild steel with coated carbide tools using response surface methodology. Kirby et al. [17] have applied Taguchi design to optimizing the surface finish in a turning operation. Palanikumar et al. [18] have focused on the parametric influence of machining parameters on the surface roughness in turning of glass fiber reinforced polymer. Nalbant et al. [19] (2007) have tried to optimize cutting parameters (insert radius, feed rate and depth of cut) in turning using Taguchi approach. Ramesh et al. [20] have tried to minimize the surface roughness in machining titanium alloy using RSM while Palanikumar [21] have used both RSM and Taguchi techniques to minimize the surface roughness in machining glass fiber reinforced. Sahoo et al. [22] have applied Taguchi method to determine optimum fractal dimension in CNC turning. But the most of the available literatures deal with conventional roughness parameters.

In this study, a second order response surface equation has been developed to predict fractal dimension using Minitab software in turning of AISI 1040 materials. A rotatable central composite design of experiments is used for carrying out the experiments. Work-piece speed (N, rpm), feed rate (f, mm/rev) and depth of cut (d, mm) are the three cutting parameters considered in the study. The developed model has been tested for adequacy by carrying out ANOVA test. The effects of cutting parameters on surface roughness are also analyzed

## 2. FRACTAL CHARACTERIZATION

Multi-scale property of the rough surfaces including machining surfaces is characterized as self similarity and self affinity in fractal geometry implying that when the surface or the profile is magnified more and more details emerge and the magnified image is statistically similar to the original topography. Statistical self-similarity means that the probability distribution of a small part of a profile will be congruent with the probability distribution of the whole profile if the small part is magnified equally in all

directions. On the other hand, self-affinity implies unequal scaling in different directions. The qualitative description of statistical self-affinity for a surface profile is shown in Fig. 1.

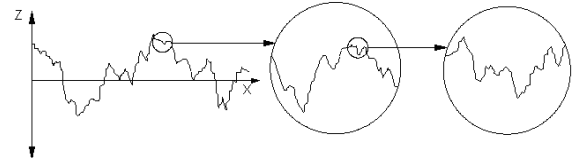


Fig 1. Qualitative description of self-affinity of a surface profile

The property of self-affinity can be characterized by the profile fractal dimension  $D$  ( $1 < D < 2$ ). Isotropic and homogeneous rough engineering surface of dimension  $D_s$  ( $2 < D_s < 3$ ) is considered in this study. The property of isotropy means that the probability distribution of heights is invariant when the coordinate axes are rotated and the surface is reflected on any plane. The property of homogeneity of a surface indicates that the probability distribution of the height is independent of the location on the surface. Therefore, the profile,  $z(x)$ , of such a surface along a straight line and in any arbitrary direction is of dimension  $D = D_s - 1$  and is a statistically valid representation of the surface. Thus the profile fractal dimension  $D$  is adopted to characterize the fractal nature of the surface in this paper. The profile  $z(x)$  in Fig. 1 has the mathematical properties of being continuous everywhere but non-differentiable and is self-affine in roughness structure. These properties are satisfied by the Weierstrass–Mandelbrot (W-M) fractal function, which can be used to characterize the roughness of surface profile and is given as

$$z(x) = G^{(D-1)} \sum_{n=n_1}^{\infty} \frac{\cos 2\pi\gamma^n x}{\gamma^{(2-D)n}}; 1 < D < 2; \gamma > 1 \quad (1)$$

where  $G$  is a characteristic length scale,  $\gamma$  where  $L$  is the sampling length.  $\gamma^n = \omega$ , where frequency  $\omega$  is the reciprocal of wave length and  $n$  is called wave number. To provide both the phase randomization and high spectral density  $\gamma$  is selected to be 1.5. The parameters  $G$  and  $D$  form the set to characterize profile  $z(x)$ . The methods for calculating profile fractal dimension mainly include the yard-stick, the box counting, the variation, the structure function and the power spectrum methods. Out of these, the power spectrum and structure function methods are most popular. Sahoo et al. [22] have presented the procedure to calculate fractal dimension using power spectrum and structure function methods.

## 3. EXPERIMENTAL DETAILS

The design of experiments technique is a very powerful tool, which is used for modeling and analysis of the influence of process variables on the response variables. There are a large number of factors that can be considered for machining of a particular material in turning. However, the review of literature shows that the

following three machining parameters are the most widespread among the researchers and machinists to control the turning process: depth of cut ( $d$ , mm), spindle speed ( $N$ , rpm) and feed rate ( $f$ , mm/rev). In the present study these are selected as design factors while other parameters have been assumed to be constant over the experimental domain. A rotatable central composite design (CCD) is selected for the experimentation. The basic central composite design for  $k$  variables consists of a  $2k$  factorial design with each factor at two coded levels:  $-1, +1$ . For a given number of variables, the  $\alpha$  required to achieve rotatability is computed as  $\alpha = (n_f)^{1/4}$ , where  $n_f$  is the number of points in the  $2^k$  factorial design ( $k$  is the number of factors). In rotatable designs, all points at the same radial distance ( $r$ ) from the centre point have the same magnitude of prediction error. A rotatable CCD consists of  $2^k$  fractional factorial points (usually coded as  $\pm 1$ ), augmented by  $2k$  axial points  $[(\pm\alpha, 0, \dots, 0), (0, \pm\alpha, \dots, 0), (0, 0, \dots, \pm\alpha)]$  and  $n_c$  centre points  $(0, 0, 0, \dots, 0)$ . The centre points vary from three to six. With proper choice of  $n_c$  the CCD can be made orthogonal or it can be made uniform precision design. It means that the variance of response at origin is equal to the variance of response at a unit distance from the origin. Hence, a CCD with uniform precision has been selected for investigation. For three factor experimentation, eight ( $2^3$ ) factorial points, six axial points ( $2 \times 3$ ) and six centre runs, a total of 20 experimental runs have been considered. The value of  $\alpha$  is chosen as 1.682. The process variables with their values on different levels are listed in Table 1. The experimental design matrix is shown in Table 2. The CNC turning operations on AISI 1040 materials have been carried out using a JOBBERXL CNC lathe having the control system FANUC Series Oi Mate-Tc and equipped with maximum spindle speed of 3500 rpm, feed rate 15-20 m/rev and KVA rating 16 KVA. For generating the turned surfaces, CNC part programs for tool paths are created with specific commands. Commercially available CVD coated carbide tools are used in this investigation. The tool holder used is PTG NR-25-25 M16 050, WIDIA and insert used is TNMG 160404 –FL, WIDIA. The tool is coated with titanium nitride coating having hardness, density and transverse rupture strength as 1570 HV, 14.5 g/cc and 3800 N/mm<sup>2</sup>. The compressed coolant WS 50-50 with a ratio of 1:20 with water is used as cutting environment. The response variables used to accomplish the present study on surface topography characterization is the profile fractal dimension  $D$ . Roughness profile measurement is done using a portable stylus-type profilometer, Talysurf (Taylor Hobson, Surtronic 3+). The profilometer is set to a cut-off length of 0.8 mm, filter 2CR, traverse speed 1 mm/sec and 4 mm traverse length. The measured profile is digitized and processed through the dedicated advanced surface finish analysis software Talyprofile.

Table 1: Process parameters levels used

Parameters	Levels					
	-1.682	-1	0	1	1.682	-1.682
Depth of cut	0.032	0.1	0.2	0.3	0.368	0.032
w/p speed	528	800	1200	1600	1872	528
Feed rate	0.0224	0.07	0.14	0.21	0.2576	0.0224

#### 4. RESPONSE SURFACE METHOD

Response surface methodology (RSM) adopts both mathematical and statistical techniques, which are useful for the modeling, and analysis of problems in which a response of interest is influenced by several variables and the objective is to optimize the response [23]. RSM helps in analyzing the influence of the independent variables on a specific dependent variable (response) by quantifying the relationships amongst one or more measured responses and the vital input factors. The mathematical models thus developed relating the machining responses and their factors facilitate the optimization of the machining process. In most of the RSM problems, the form of the relationship between the response and the independent variables is unknown. Thus the first step in RSM is to find a suitable approximation for the true functional relationship between response of interest 'y' and a set of controllable variables  $\{x_1, x_2, \dots, x_n\}$ . Usually when the response function is not known or non-linear, a second order model is utilized [24] in the form:

$$y = b_0 + \sum_{i=1}^n b_i x_i + \sum_{i=1}^n b_{ii} x_i^2 + \sum_{i < j} b_{ij} x_i x_j + \varepsilon \quad (2)$$

where,  $\varepsilon$  represents the noise or error observed in the response  $y$  such that the expected response is  $(y - \varepsilon)$  and  $b$ 's are the regression coefficients to be estimated. The least square technique is being used to fit a model equation containing the input variables by minimizing the residual error measured by the sum of square deviations between the actual and estimated responses. To check the adequacy of the model Analysis of Variance (ANOVA) test for the regression model is carried out. ANOVA calculates the F-ratio, which is the ratio between the regression mean square and the mean square error. The F-ratio, also called the variance ratio, is the ratio of variance due to the effect of a factor (the model) and variance due to the error term. This ratio is used to measure the significance of the model under investigation with respect to the variance of all the terms included in the error term at the desired significance level.

#### 5. RESULTS AND DISCUSSION

In the present study, the second order response model is developed using Minitab in terms of coded values of the independent machining parameters, viz., work-piece speed, feed rate and depth of cut. The response model for the AISI 1040 material is given in the following equation.

$$\begin{aligned}
D_{MS} = & 1.40674 + 0.00453 d + 0.02446 N \\
& - 0.00883 f + 0.005745 dN + 0.002873 df \\
& + 0.006850 Nf - 0.00697 d^2 - 0.00510 N^2 \\
& - 0.00947 f^2
\end{aligned}
\tag{3}$$

The developed model is also checked for adequacy. Table 3 represents the ANOVA table for the second order response model developed for D. It is clear that the developed model is significant at 95% confidence level. The calculated value of F ratio is greater than the tabulated value of F ratio and it can be concluded that the model is adequate at 95% confidence level. ANOVA table for mild steel (Table 4) shows that work speed, feed rate, interaction of depth of cut with work-piece speed are significant factors at 95% confidence level. The  $R^2$  value for the model is 0.9385 and it is a clear indication of good correlation. The main effects plots for fractal dimension are shown in Fig. 2. From the main effect plots, it is concluded that with increase in work speed, D increases but with increase in feed rate, D decreases in mild steel turning. Response surface plots are also generated using Minitab. Figure 3 shows the surface plots for fractal dimension as functions of two independent machining parameters while the third machining parameter is held constant at central value. All these figures clearly depict the variation of fractal dimension with controlling variables within the experimental regime. The normal probability plot of the residuals for D is shown in Fig. 4. It is seen that the residuals generally fall on a straight line implying that the errors are distributed normally.

Table 2: Experimental results

Std. order	Coded Values			D
	d	N	f	
1	-1	-1	-1	1.370
2	1	-1	-1	1.300
3	-1	1	-1	1.362
4	1	1	-1	1.410
5	-1	-1	1	1.267
6	1	-1	1	1.282
7	-1	1	1	1.390
8	1	1	1	1.417
9	-1.682	0	0	1.320
10	1.682	0	0	1.370
11	0	-1.682	0	1.300
12	0	1.682	0	1.420
13	0	0	-1.682	1.360
14	0	0	1.682	1.290
15	0	0	0	1.397
16	0	0	0	1.400
17	0	0	0	1.415
18	0	0	0	1.415
19	0	0	0	1.402
20	0	0	0	1.412

Table 3: ANOVA for second order model for D

Source	DF	SS	MS	F	F <sub>0.05</sub>	P
Regression	9	0.049	0.005409	16.96	3.02	0
Residual Error	10	0.0032	0.000319			
Total	19	0.052				

Table 4: Full ANOVA table for the model

Source	Sum of Squares	df	Mean Square	F Value	P value
Model	0.049	9	0.005409	16.96	0.0001
A-d	0.0007933	1	0.0007933	2.49	0.1458
B-N	0.023	1	0.023	72.48	0.0001
C-f	0.003009	1	0.003009	9.44	0.0118
AB	0.00211	1	0.00211	6.62	0.0277
AC	0.0005281	1	0.0005281	1.66	0.2271
BC	0.003003	1	0.003003	9.42	0.1190
A <sup>2</sup>	0.005608	1	0.005608	17.59	0.0018
B <sup>2</sup>	0.002998	1	0.002998	9.40	0.0119
C <sup>2</sup>	0.010	1	0.010	32.46	0.0002
Residual	0.00318	10	0.0003189		
Lack-of-fit	0.002871	5	0.0005742	9.04	0.0152
Pure Error	0.0003177	5	0.00006354		
Cor Total	0.05186	19			

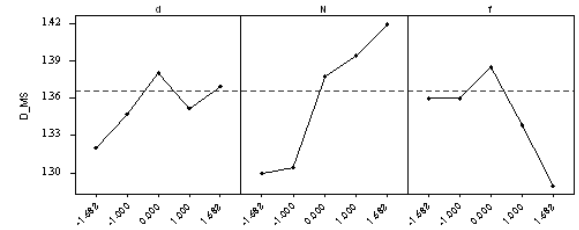
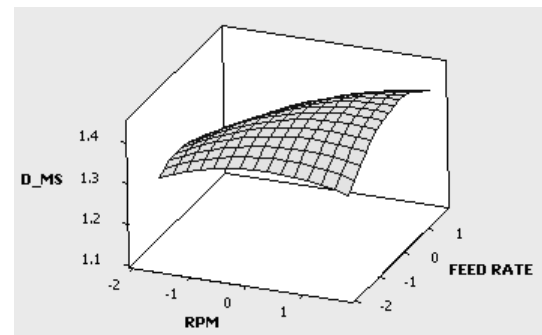
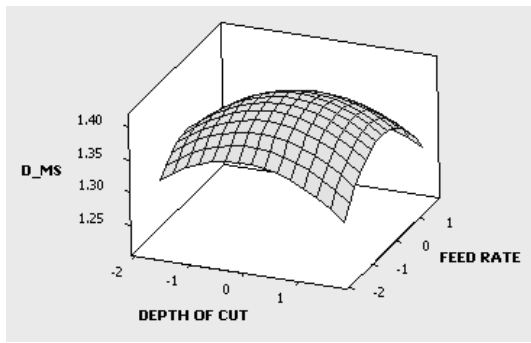


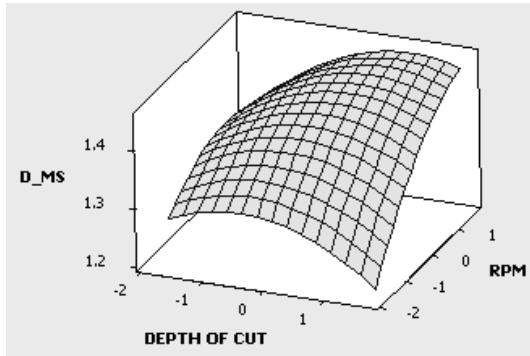
Fig 2. Main effect plots for mild steel



(a)



(b)



(c)

Fig 3. Surface plots for  $D$  in CNC turning of mild steel

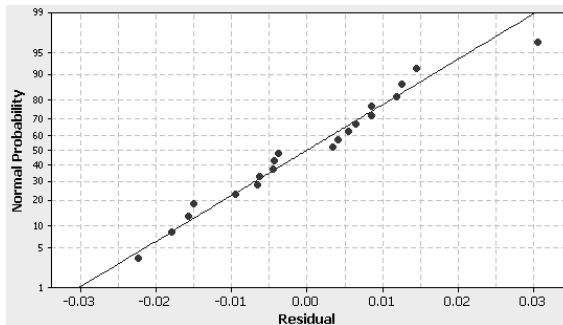


Fig 4. Normal probability plot of the residuals for  $D$

## 6. CONCLUSION

This study presents the development of a second order response surface model for fractal dimension in CNC turning of AISI 1040 material. The second order model is also checked for adequacy using ANOVA. It is seen that the developed model is adequate at 95% confidence level. The normal probability plot of the residuals shows that the errors are distributed normally. From the analysis, it is also seen that the spindle speed is the most significant factor affecting the fractal dimension. It can be concluded from the analysis that with increase in work-piece speed,  $D$  increases but with increase in feed rate,  $D$  decreases in mild steel turning. With increase in spindle speed, fractal dimension also increases.

## 7. REFERENCES

1. Mandelbrot, B.B., 1982, "The fractal geometry of nature", W H Freeman: New York.
2. Bigerelle, M., Najjar, D. and Iost, A., 2005 "Multiscale functional analysis of wear a fractal model of the grinding process", *Wear*, 258: 232-239.
3. Zhang, Y., Luo, Y., Wang, J.F. and Li, Z., 2001, "Research on the fractal of surface topography of grinding", *International Journal of Machine Tools and Manufacturing*, 41: 2045-2049.
4. Jiang, Z., Wang, H. and Fei, B., 2001 "Research into the application of fractal geometry in characterizing machined surfaces", *International Journal of Machine Tools and Manufacturing*, 41: 2179-2185.
5. Jahn, R. and Truckenbrodt, H., 2004, "A simple fractal analysis method of the surface roughness", *Journal of Materials Processing Technology*, 145: 40-45.
6. Kang, M.C., Kim, J.S. and Kim, K.H., 2005, "Fractal dimension analysis of machined surface depending on coated tool wear", *Surface & Coatings Technology*, 193(1-3): 259-265.
7. Han, J.H., Ping, S. and Shengsun, H., 2005, "Fractal characterization and simulation of surface profiles of copper electrodes and aluminum sheets", *Materials Science and Engineering A*, 403: 174-181.
8. Grzesik, W., 1996, "A revised model for predicting surface roughness in turning", *Wear*, 194: 143-148.
9. Yang, W.H. and Tarnag, Y.S., 1998, "Design optimization of cutting parameters for turning operations based on the Taguchi method", *Journal of Material Processing Technology*, 84: 122-129.
10. Abouelatta, O.B. and Madl, J., 2001, "Surface roughness prediction based on cutting parameters and tool vibrations in turning operations" *Journal of Material Processing Technology*, 118: 269-277.
11. Davim, J.P., 2001, "A note on the determination of optimal cutting conditions for surface finish obtained in turning using design of experiments", *Journal of Material Processing Technology*, 116: 305-308.
12. Lin, W.S., Lee B.Y. and Wu, C.L., 2001, "Modeling the surface roughness and cutting force for turning", *Journal of Material Processing Technology*, 108: 286-293.
13. Suresh, P.V.S., Rao, P. V., and Deshmukh, S.G., 2002, "A genetic algorithm approach for optimization of surface roughness prediction model", *International Journal of Machine Tools Manufacture*, 42: 675-680.
14. Arbizu, I. P. and Pérez, C.J.L., 2003, "Surface roughness prediction by factorial design of experiments in turning processes", *Journal of Material Processing Technology*, 143-144: 390-396
15. Feng, C. X. and Wang X. F., 2003, "Surface roughness predictive modeling: neural networks versus regression", *IIE Transaction*, 35: 11-27.
16. Sahin, Y. and Motorcu, A.R., 2005, "Surface roughness model for machining mild steel with coated carbide tool", *Materials & Design*, 26: 321-326.

17. Kirby, E.D., Zhang, Z., Chen, J.C. and Chen, J., 2006' "Optimizing surface finish in a turning operation using the Taguchi parameter design method" *International Journal of Advanced Manufacturing Technology*, 30: 1021–1029.
18. Palanikumar, K., Karunamoorthy, L. and Karthikeyan, R., 2006, "Parametric optimization to minimise the surface roughness on the machining of GFRP composites", *Journal of Materials Science Technology*, 22 (1): 66-72.
19. Nalbant, M., Gokkaya, H. and Sur, G., 2007, "Application of Taguchi method in the optimization of cutting parameters for surface roughness in turning", *Materials & Design*, 28: 1379–1385.
20. Ramesh, S., Karunamoorthy, L. and Palanikumar, K., 2008, "Surface Roughness Analysis in Machining of Titanium Alloy", *Materials & Manufacturing Process*, 23: 174–181.
21. Palanikumar, K., 2008, "Application of Taguchi and response surface methodologies for surface roughness in machining glass fiber reinforced plastics by PCD tooling", *International Journal of Advanced Manufacturing Technology*, 36: 19–27.
22. Sahoo, P., Barman, T. K. and Routara, B. C., 2008, "Taguchi based fractal dimension modelling and optimization in CNC turning", *Advances in Production Engineering & Management*, 3(4): 205-217.
23. Mayers, R.H and Montgomery, D.C., 1995, "*Response surface methodology*", Wiley, New York.
24. Montgomery, D. C., 2001, "*Design and analysis of experiments*", John Wiley, New York.

## 8. MAILING ADDRESS

T K Barman  
 Department of Mechanical Engineering, Jadavpur  
 University, Kolkata- 700032, India  
 FAX : +91 33 2414 689  
 E-mail: tkbarman@gmail.com

## FRACTAL DIMENSION MODELING IN CNC MILLING USING TAGUCHI METHOD

T. K. Barman, P. Sahoo

Department of Mechanical Engineering, Jadavpur University, Kolkata, India

### ABSTRACT

This paper presents an experimental study of fractal dimension characteristics of surface profile produced in CNC milling and optimization of machining parameters based on Taguchi method. To express the surface roughness, fractal dimension ( $D$ ) is used which is advantageous over the conventional roughness parameters like centre line roughness value ( $R_a$ ), root mean square roughness ( $R_q$ ), skewness, kurtosis etc as fractal dimension is scale independent. Experiments on AISI 1040 steels are carried out by utilizing the combination of machining parameters using  $L_{27}$  Taguchi orthogonal design with three machining parameters, viz., spindle speed, depth of cut and feed rate. From Taguchi analysis, it is observed that spindle speed has got the most significant influence in controlling fractal dimension characteristics of surface profile. It is also observed with increase in spindle speed the fractal dimension increases. Taguchi analysis is also employed to identify optimum machining parameter combination that yields maximum fractal dimension.

**Keywords:** Fractal Dimension ( $D$ ), CNC Milling, Taguchi Method.

### 1. INTRODUCTION

CNC end milling is the most popular metal removing machines in industries which includes aerospace and automotive sectors, where quality is an important factor in the production of slots, pockets, precision moulds and dies. In end milling, multi point cutting tool removes material at a faster rate from the surface of the work-piece with a reasonably good surface quality. Several factors influence the final surface roughness in a CNC milling operation. In end milling, the parameters such as the tool geometry including the tool nose radius and flank width, run-out error and various cutting conditions including feed rate, depth of cut and cutting speed are influencing factors for the surface roughness.

Generally, the surface roughness is expressed by conventional roughness parameters such as centre line average value ( $R_a$ ), root mean square value ( $R_q$ ), mean line peak spacing ( $R_{sm}$ ) etc. As the surface topography is a non-stationary random process, the variances of slope and curvature depend strongly on the resolution of the roughness-measuring instrument or any other form of filter and these conventional roughness parameters are strongly depend on the resolution and filter processing of the instrument. In this context to express surface roughness the concept of fractal is applied. The concept is based on the self-affinity and self-similarity of surfaces at different scales. Roughness measurements on a variety of surfaces show that the power spectra of the surface profiles follow power laws. This suggests that when a surface is magnified appropriately, the magnified image

looks very similar to the original surface. Fractals may retain all the structural information and are characterized by single descriptor, the fractal dimension,  $D$ . This fractal dimension, which forms the essence of fractal geometry, is both scale-invariant and is closely linked to the concepts of self-similarity and self-affinity [1]. It is therefore essential to use fractal dimension to characterize rough surfaces and provide the geometric structure at all length scales [2]. In a material removal process, mechanical intervention happens over length scales, which extend from atomic dimensions to centimeters. The machine vibration, clearances and tolerances affect the outcome of the process at the largest of length scales (above  $10^{-3}$  m). The tool form, feed rate, tool radius in case of single point cutting and grit size in multiple point cutting affect the process outcome at the intermediate length scales ( $10^{-6}$  to  $10^{-3}$  m). The roughness of the tool or details of the grit surfaces influence the final topography of the generated surface at the lowest length scales ( $10^{-9}$  to  $10^{-6}$  m). It has been shown that surfaces formed by electric discharge machining, milling, cutting or grinding [3, 4, 5, 6, 7], and worn surfaces have fractal structures, and fractal parameters can reflect the intrinsic properties of surfaces to overcome the disadvantages of conventional roughness parameters.

There are a number of researchers who have analyzed a lot relating to the surface roughness of the fine products and developed surface roughness prediction models. Fuh and Wu [8] developed a model for prediction of surface quality in end milling process using RSM and Takushi



method. Lou et al. [9] have used multiple regression models to develop a surface roughness model to predict Ra in CNC end milling. Tsai et al. [10] have developed an artificial neural networks (ANN) model using spindle speed, feed rate, depth of cut, and the vibration average per revolution as four input neurons, to predict the output neuron-surface roughness  $R_a$  values for end milling operation. Yang and Chen [11] have found out optimum cutting parameters for milling of Al 6061 material using Taguchi design. Benardos and Vosniakos [12] have developed a neural network model to predict the surface roughness ( $R_a$ ) in CNC face milling operation. Mansour and Abdalla [13] have developed a process of a surface roughness for end milling using RSM. Ghani et al. [14] have outlined the Taguchi optimization methodology, which is applied to optimize cutting parameters in end milling when machining hardened steel AISI H13 with TiN coated P10 carbide insert tool. Oktem et al. [15] have developed an effective methodology to determine the optimum cutting conditions leading to minimum roughness in milling using RSM. Reddy and Rao [16] have developed a mathematical model in terms of machining parameters for surface roughness prediction using RSM and optimization is done using GA. Sahoo et al. [17] have carried out fractal dimension modeling in CNC end milling using RSM. El-Sonabaty et al. [18] have used fractal geometry approach for predicting surface roughness using neural network. Routara et al. [19] have developed a prediction model of surface roughness in CNC end milling using response surface methodology. Samanta [20] has also applied different soft computing technique to model surface roughness. But most of these papers deal with the conventional roughness parameters and there are a few literatures which deal with fractal dimension.

In this study, a model is developed using Taguchi's orthogonal array with three cutting parameters, viz. depth of cut (A, mm), spindle speed (B, rpm) and feed rate (C, mm/min) to determine optimum fractal dimension, D in CNC end milling of AISI 1040 material. Confirmation test is conducted to verify the optimal machining parameter combination as predicted by Taguchi analysis. ANOVA test is also carried out to find out the significant factor affecting fractal dimension.

## 2. FRACTAL CHARACTERIZATION

Multi-scale property of the rough surfaces including machining surfaces is characterized as self similarity and self affinity in fractal geometry implying that when the surface or the profile is magnified more and more details emerge and the magnified image is statistically similar to the original topography. Statistical self-similarity means that the probability distribution of a small part of a profile will be congruent with the probability distribution of the whole profile if the small part is magnified equally in all directions. On the other hand, self-affinity implies unequal scaling in different directions. The qualitative description of statistical self-affinity for a surface profile is shown in Fig. 1.

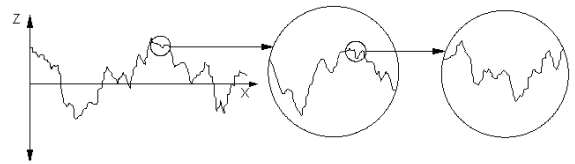


Fig 1. Qualitative description of self-affinity of a surface profile

The property of self-affinity can be characterized by the profile fractal dimension  $D$  ( $1 < D < 2$ ). Isotropic and homogeneous rough engineering surface of dimension  $D_s$  ( $2 < D_s < 3$ ) is considered in this study. The property of isotropy means that the probability distribution of heights is invariant when the coordinate axes are rotated and the surface is reflected on any plane. The property of homogeneity of a surface indicates that the probability distribution of the height is independent of the location on the surface. Therefore, the profile,  $z(x)$ , of such a surface along a straight line and in any arbitrary direction is of dimension  $D = D_s - 1$  and is a statistically valid representation of the surface. Thus the profile fractal dimension  $D$  is adopted to characterize the fractal nature of the surface in this paper. The profile  $z(x)$  in Fig. 1 has the mathematical properties of being continuous everywhere but non-differentiable and is self-affine in roughness structure. These properties are satisfied by the Weierstrass-Mandelbrot (W-M) fractal function, which can be used to characterize the roughness of surface profile and is given as

$$z(x) = G^{(D-1)} \sum_{n=n_1}^{\infty} \frac{\cos 2\pi\gamma^n x}{\gamma^{(2-D)n}}; 1 < D < 2; \gamma > 1 \quad (1)$$

where  $G$  is a characteristic length scale,  $\gamma$  where  $L$  is the sampling length.  $\gamma^n = \omega$ , where frequency  $\omega$  is the reciprocal of wave length and  $n$  is called wave number. To provide both the phase randomization and high spectral density  $\gamma$  is selected to be 1.5. The parameters  $G$  and  $D$  form the set to characterize profile  $z(x)$ . The methods for calculating profile fractal dimension mainly include the yard-stick, the box counting, the variation, the structure function and the power spectrum methods. Out of these, the power spectrum and structure function methods are most popular. Sahoo et al. [18] have presented the procedure to calculate fractal dimension using power spectrum and structure function methods.

## 3. EXPERIMENTAL DETAILS

There are a large number of factors that can be considered for machining of a particular material in end milling. However, the review of literature shows that the following three machining parameters are the most widespread among the researchers and machinists to control the milling process: depth of cut (A, mm), spindle speed (B, rpm) and feed rate (C, mm/min). In the present study these are selected as design factors while other parameters have been assumed to be constant over the experimental domain. Considering  $L_{27}$  orthogonal array, total 27 experiments are carried out on AISI 1040

material. The process variables / design factors with their values on different levels are listed in Table 1. The selection of the values of the variables is limited by the capacity of the machine used in the experimentation as well as the recommended specifications for different work - tool material combinations. The machine used for the milling tests is a 'DYNA V4.5' CNC end milling machine having the control system SINUMERIK 802 D with a vertical milling head and equipped with maximum spindle speed of 9000 rpm, feed rate 10 m/min and 10kW driver motor. For generating the milled surfaces, CNC part programs for tool paths are created with specific commands. Commercially available CVD coated carbide tools are used in this investigation. The tools used are flat end mill cutters (8 mm diameter, 300 helix angle, TiAlN coated solid carbide, parallel shank, 4 flutes) produced by WIDIA (EM-TiAlN). The tools are coated with TiAlN coating having hardness, density and transverse rupture strength as 1570 HV, 14.5 g/cc and 3800 N/mm<sup>2</sup>. The compressed coolant servo-cut is used as cutting environment. All the specimens are in the form of 100 mm x 75 mm x 25 mm blocks. The response variables used to accomplish the present study on surface topography characterization is the profile fractal dimension D. Roughness profile measurement is done using a portable stylus-type profilometer, Talysurf (Taylor Hobson, Surtronic 3+). The profilometer is set to a cut-off length of 0.8 mm, filter 2CR, traverse speed 1 mm/sec and 4 mm traverse length. The measured profile is digitized and processed through the dedicated advanced surface finish analysis software Talyprofile.

Table 1: Cutting parameters and their levels

Levels	Depth of cut (A, mm)	Spindle speed (B, rpm)	Feed rate (C, mm/min)
1	0.15	2500	300
2	0.20	3000	400
3	0.25	3500	500

#### 4. TAGUCHI METHOD

Taguchi technique [21, 22] is a powerful tool for design of high quality systems based on orthogonal array experiments that provide much reduced variance for the experiments with an optimum setting of process control parameters. It introduces an integrated approach that is simple and efficient to find the best range of designs for quality, performance and computational cost. This method achieves the integration of design of experiments (DOE) with the parametric optimization of the process yielding the desired results. The orthogonal array (OA) provides a set of well balanced (minimum experimental runs) experiments. Taguchi's method uses a statistical measure of performance called signal-to-noise ratios (S/N), which are logarithmic functions of desired output to serve as objective functions for optimization. The S/N ratio takes both the mean and the variability into account and is defined as the ratio of the mean (signal) to the standard deviation (noise). The ratio depends on the quality characteristics of the product/process to be optimized. The three categories of S/N ratios are used:

lower-the-better (LB), higher-the-better (HB) and nominal-the-best (NB). The parameter level combination that maximizes the appropriate S/N ratio is the optimal setting. Furthermore, a statistical analysis, ANOVA [23] is performed to find which process parameters are statistically significant. With the S/N ratio and ANOVA analyses, the optimal combination of the process parameters can be predicted. Finally, a confirmation experiment is to be conducted to verify the optimal process parameters obtained from the parameter design.

#### 5. RESULTS AND DISCUSSION

Based on the Taguchi and ANOVA analysis, the results are listed below. The signal to noise analysis is carried out with the fractal dimension (D) as the performance index. The S/N ratio for D is calculated using Higher the Better (HB) criterion as higher the fractal dimension D gives a smoother surface topography and for this S/N ratio is given by

$$S/N = -10 \log \left( \frac{1}{n} \sum \frac{1}{y^2} \right) \quad (2)$$

where y is the observed data and n is the number of observations. Experimental results for fractal dimension of machined surfaces (D) and the corresponding S/N ratios are provided in Table 2. The mean S/N ratio for each level of three factors (A, B and C) and the total mean S/N ratio for the 27 experiments are summarized in Table 3. The main effect plot for mean S/N ratio for AISI 1040 material is also presented in Fig. 2. From the main effect plot, it is observed that the parameters A and B are the significant factors because in the main effect plot, lines for these two parameters have the highest inclination. Whereas parameter C is less significant as the line of C parameter in the main effect plot is near horizontal. It is clear from the figure that the optimum machining parameters combination for maximum fractal dimension (D) is A2B3C3. For estimating the interaction among the parameters, interaction plots are drawn. When the lines on the interaction plots are non-parallel, interaction occurs and when the lines cross, strong interaction occurs. It is seen from the figure that there are interactions between A and C and between B and C.

To check the accuracy of analysis, a verification test needs to be carried out. The estimated S/N ratio,  $\hat{\gamma}$ , using the optimal level of the machining parameters can be calculated as:

$$\hat{\gamma} = \gamma_m + \sum_{i=1}^o (\bar{\gamma}_i - \gamma_m) \quad (3)$$

where  $\gamma_m$  is the total mean S/N ratio,  $\bar{\gamma}_i$  is the mean S/N ratio at the optimal level, and o is the number of the main design parameters that significantly affect the fractal dimension. Table 4 shows the comparison of the estimated S/N ratio with the actual S/N ratio using the optimal parameters. It is seen that there is good agreement between the estimated and actual S/N ratios observed. The increase of the S/N ratio from the initial machining parameters to the optimal machining parameters is 0.50367dB, which means the fractal dimension is improved by about 20%. In other words, the experimental results confirm the prior design and

analysis for optimizing the machining process parameters.

Table 2: Experimental results and corresponding S/N ratio

A	B	C	D	S/N ratio (dB)
1	1	1	1.31	2.34543
1	1	2	1.28	2.14420
1	1	3	1.32	2.41148
1	2	1	1.32	2.41148
1	2	2	1.37	2.73441
1	2	3	1.38	2.79758
1	3	1	1.39	2.86030
1	3	2	1.41	2.98438
1	3	3	1.37	2.73441
2	1	1	1.37	2.73441
2	1	2	1.43	3.10672
2	1	3	1.40	2.92256
2	2	1	1.37	2.73441
2	2	2	1.34	2.54210
2	2	3	1.37	2.73441
2	3	1	1.43	3.10672
2	3	2	1.40	2.92256
2	3	3	1.42	3.04577
3	1	1	1.30	2.27887
3	1	2	1.38	2.79758
3	1	3	1.39	2.86030
3	2	1	1.38	2.79758
3	2	2	1.34	2.54210
3	2	3	1.40	2.92256
3	3	1	1.40	2.92256
3	3	2	1.40	2.92256
3	3	3	1.36	2.67078

Table 5 shows that ANOVA results for fractal dimension. ANOVA calculates the F ratio, which is the ratio of the regression mean square and the mean square error. In general, when the F value increases the significant of the parameters also increases. From the table it is clear that the parameter B is the most significant factor at 95% confidence level within the specific test range whereas other terms are not so significant at 95% confidence level.

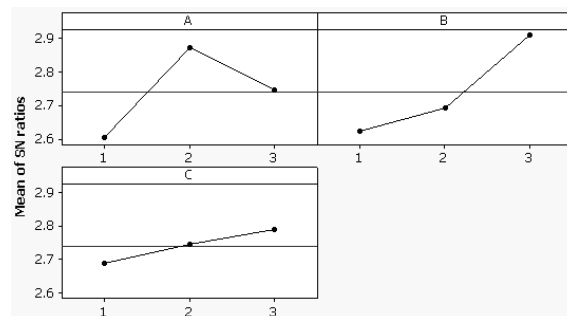
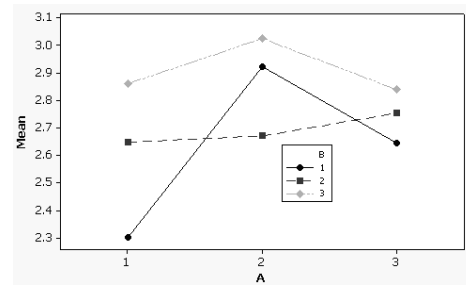
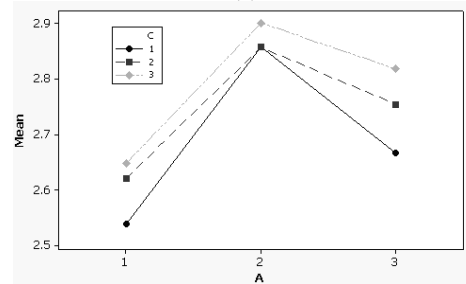


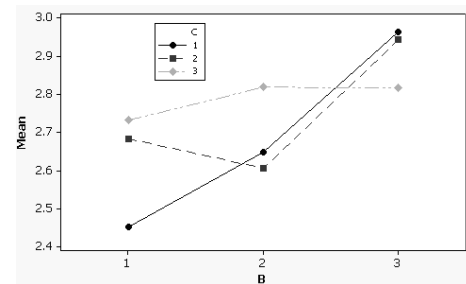
Fig 2. Main effect plots for mean S/N ratio



(a)



(b)



(c)

Fig 3. Interaction effect plots for mean S/N ratio: (a) A vs. B, (b) A vs. C and (c) B vs. C.

Table 3: S/N Ratio response table for mild steel

Level	A	B	C
1	2.603	2.622	2.688
2	2.872	2.691	2.744
3	2.746	2.908	2.789
Delta	0.270	0.285	0.101
Rank	2	1	3

The total mean S/N ratio= 2.7403

Table 4: Result of confirmation experiment for fractal dimension of mild steel material

	Initial machining parameters	Optimal machining parameters	
		Prediction	Experiment
Level	A2B2C2	A2B3C3	A2B3C3
Fractal Dimension (D)	1.34		1.42
S/N ratio (dB)	2.54210	3.08840	3.04577

Improvement of S/N ratio = 0.50367 dB

% improvement= 19.81%

Table 5: ANOVA table for AISI 1040 material

Source	DF	SS	MS	F	P
A	2	0.008030	0.004015	4.00	0.062
B	2	0.009785	0.004893	4.87	0.041
C	2	0.001096	0.000548	0.55	0.599
AXB	4	0.008126	0.002031	2.02	0.184
AXC	4	0.000281	0.000070	0.07	0.989
BXC	4	0.004993	0.001248	1.24	0.366
Error	8	0.008030	0.001004		
Total	26	0.040341			

## 6. CONCLUSION

In this paper, a has been carried out to optimize the machining parameters with respect to fractal dimension using Taguchi method in CNC milling of AISI1040 material.  $L_{27}$  orthogonal array is taken for the analysis. From the analysis, it can be concluded that the spindle speed is the most significant factor affecting the fractal dimension. With increase in spindle speed, fractal dimension also increases. An optimum cutting parameter combination is found out for maximum fractal dimension and it may be useful in computer aided process planning.

## 7. REFERENCES

1. Mandelbrot, B.B., 1982, *"The fractal geometry of nature"*, W H Freeman: New York.
2. Bigerelle, M., Najjar, D. and Iost, A., 2005, "Multiscale functional analysis of wear a fractal model of the grinding process", *Wear*, 258: 232-239.
3. Zhang, Y., Luo, Y., Wang, J.F. and Li, Z., 2001, "Research on the fractal of surface topography of grinding", *International Journal of Machine Tools and Manufacturing*, 41: 2045-2049.
4. Jiang, Z., Wang, H. and Fei, B., 2001 "Research into the application of fractal geometry in characterizing machined surfaces", *International Journal of Machine Tools and Manufacturing*, 41: 2179-2185.
5. Jahn, R. and Truckenbrodt, H., 2004, "A simple fractal analysis method of the surface roughness", *Journal of Materials Processing Technology*, 145: 40-45.
6. Kang, M.C., Kim, J.S. and Kim, K.H., 2005, "Fractal dimension analysis of machined surface depending on coated tool wear", *Surface & Coatings Technology*, 193(1-3): 259-265.
7. Han, J.H., Ping, S. and Shengsun, H., 2005, "Fractal characterization and simulation of surface profiles of copper electrodes and aluminum sheets", *Materials Science and Engineering A*, 403: 174-181.
8. Fuh, K.H. and Wu, C.F., 1995, "A proposed statistical model for surface quality prediction in end-milling of Al alloy", *International Journal of Machine Tools Manufacture*, 35 (S): 1187-1200.
9. Lou, M.S., Chen, J.C. and Li, C.M., 1998, "Surface roughness prediction technique for CNC end-milling", *Journal of Industrial Technology*, 15

- (1).
10. Tsai, Y.H., Chen, J.C. and Lou, S.J., 1999 "An in-process surface recognition system based on neural networks in end milling cutting operations", *International Journal of Machine Tools Manufacture*, 39: 583-605.
11. Yang, J.L. and Chen, J.C., 2001, "A systematic approach for identifying optimum surface roughness performance in end-milling operations", *Journal of Industrial Technology*, 17(2).
12. Benardos, P.G. and Vosniakos, G.C., 2002, "Prediction of surface roughness in CNC face milling using neural networks and Taguchi's design of experiments", *Robotics and Computer-Integrated Manufacturing*, 18: 343-354.
13. Mansour, A and Abdalla, H., 2002, "Surface roughness model for end milling: a semi-free cutting carbon casehardening steel (EN32) in dry condition", *Journal of Materials Processing Technology*, 124: 183-198.
14. Ghani, J.A., Choudhury, I.A. and Hassan, H.H., 2004, "Application of Taguchi method in the optimization of end milling parameters", *Journal of Materials Processing Technology*, 145: 84-92.
15. Oktem, H., Erzurumlu, T. and Kurtaran, H., 2005, "Application of response surface methodology in the optimization of cutting conditions for surface roughness", *Journal of Materials Processing Technology*, 170: 11-16.
16. Reddy, N.S.K. and Rao, P.V., 2006, "Selection of an optimal parametric combination for achieving a better surface finish in dry milling using genetic algorithms", *International Journal of Advanced Manufacturing Technology*, 28: 463-473.
17. Sahoo, P., Barman, T. K., Routara, B. C., 2008, "Fractal dimension modelling of surface profile and optimisation in CNC end milling using response surface methodology", *International Journal of Manufacturing Research*, 3 (3): 360-377.
18. El-Sonabaty, I.A., Khashaba, U.A., Selmy, A.I., Ali, A.I., 2008, "Prediction of surface roughness profiles for milled surfaces using an artificial neural network and fractal geometry approach", *Journal of Materials Processing Technology*, 200: 271-278.
19. Routara, B. C., Bandyopadhyay, A. and Sahoo, P., 2009, "Roughness modeling and optimization in CNC end milling using response surface method: effect of workpiece material variation", *International Journal of Advanced Manufacturing Technology*, 40 (11-12): 1166-1180.
20. Samanta, B., 2009, "Surface roughness prediction in machining using soft computing", *International Journal Computer Integrated Manufacturing*, 22 (3): 257-266.
21. Taguchi, G., 1990, *"Introduction to quality engineering"*, Asian Productivity Organization, Tokyo.
22. Ross, P. J., 1996, *"Taguchi techniques for quality engineering (2e)"*, McGraw-Hill, New York.
23. Montgomery, D. C., 2001, *"Design and analysis of experiments"*, John Wiley, New York.

## **8. MAILING ADDRESS**

T K Barman  
Department of Mechanical Engineering, Jadavpur  
University, Kolkata- 700032, India  
FAX : +91 33 2414 689  
E-mail: tkbarman@gmail.com

## A HOLISTIC APPROACH FOR DUST PREVENTION: COMBINATION OF LEV AND PREVENTION UNITS

Abdullah-Al-Mamun, F. Mahboob Nijhoom and Farzana Khurshid

Department of Industrial and Production Engineering,  
Bangladesh University of Engineering and Technology, Dhaka, Bangladesh

### ABSTRACT

The complex industrial process flow, magnitude of the enormous tasks carried out and the dependence upon relatively old setup leave open doors for further improvements in the industrial sectors in Bangladesh. In this paper the detergent plant of a reputed chemical company of Bangladesh is assessed and possible solutions are proposed to minimize the emanation of detergent dust from different sources. Here a Local Exhaust Ventilation (LEV) system is designed over the mixing chamber which is the main source of dust emission. A proper duct-fan combination is modeled and a new filter design is proposed. Analysis shows that, designing the ductwork considering the properties of dust particle and maintaining a steady pressure difference between inlet and outlet can increase the exhaust capability with optimum power requirement. Some prevention units are also designed to further keep the dust away from the worker. The main focus of this study is to increase the human comfort level inside the plant which can be achieved by providing the workpeople a cleaner and safer air to breath.

**Keywords:** Dust Minimization, LEV, Human Comfort, Ventilation.

### 1. INTRODUCTION

Ventilation in workplaces can include both general (fresh air) ventilation and ventilation used to control airborne contamination of the workplace. Ventilation used to control airborne contamination can be either dilution ventilation or local exhaust ventilation (LEV). Dilution ventilation provides a flow of air into and out of the working area and does not give any control at the source of the contaminant. LEV intercepts the contaminant as soon as it is generated and directs it into a system of ducting connected to an extract fan [3]. To achieve the same degree of control, far less air is extracted using a LEV system than with an equivalent dilution system, with considerable cost savings.

LEV can be defined as a system that uses extract ventilation to prevent or reduce the level of airborne hazardous substances from being breathed by people in the workplace, which draws pollutants away from a process or operation that is likely to release a hazardous substance into the air and which consists of an inlet, such as a hood, slot, booth or cabinet placed around or close to the point of release of the substance. This device is connected via ducting to the inlet of a fan or air mover. The extracted air is usually discharged to the atmosphere or returned elsewhere in the workplace, having first been cleaned to make it safe for release. The LEV system designed here is for the mixing chamber of detergent in a detergent plant. The standard calculations are made for a specific application. But the procedure can be used for other types of LEV system where the particles are fine,

light, generally corrosive and hazardous for human health.

### 2. VENTILATION SYSTEM DESIGN

Local exhaust ventilation is needed when employees are exposed to high toxic chemicals and when large amounts of dusts or welding fumes are generated. In detergent production Soda ash and LABSA (Linear Alkyl Benzene Sulfonic acid) are the main ingredients. High exposure to the organic solvent may cause Nervous System Damage (Central and peripheral), kidney and liver damage and adverse reproductive effect [1]. American Conference of Governmental Industrial Hygienist (ACGIH) recommends Local Exhaust Ventilation system for high toxic material of threshold limit values (TVLs) less than 100 ppm (such as Toluene or Benzene) [4]. So a proper local exhaust ventilation system is necessary for the effective removal of air born contaminants that would otherwise pollute work environment resulting health hazards or nuisance or air pollution.

Local exhaust ventilation operates on the principle that air moves from an area of high pressure to an area of low pressure. The difference in low pressure is created by a fan that draws or sucks air through the ventilation system. Local exhaust systems are located as close as possible to the source of contamination to capture the contaminant before it is released into the work area. A local exhaust system operates in the same manner as a household vacuum cleaner.

A local exhaust system has five basic elements:

1. A "hood" or opening that captures the contaminant at the source,
2. Ducts that transport the airborne chemicals through the system,
3. An air cleaning device (not always required) that removes the contaminant from the moving air in the system,
4. A fan that moves the air through the system and discharges (blows) it outdoors,
5. An exhaust stack through which the contaminated air is discharged.

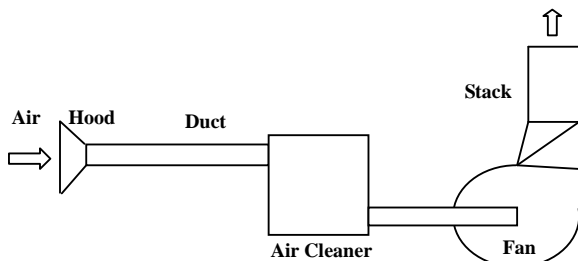


Fig 1. Components of a LEV System

### 3. PROBLEMS OF EXISTING LEV

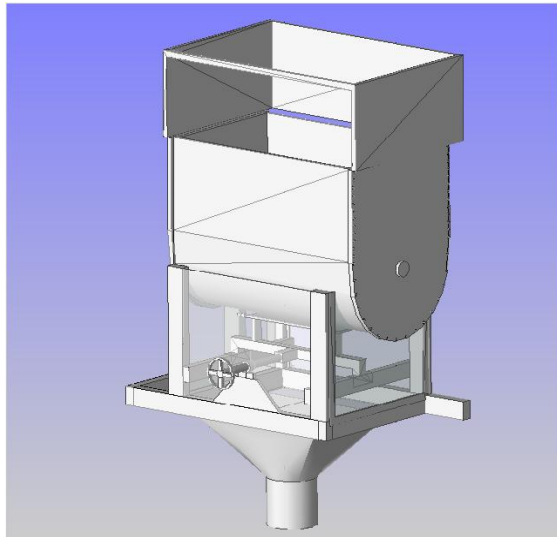


Fig 2. Schematic of the Mixing Chamber

In the mixing chamber (fig.2) different types of chemicals are mixed to form the granular detergent powder. Large powder lump remains in the chamber but the fine dust of detergent evolves and stays in the air inside the plant. This fine dust powder is detrimental for human health and may cause breathing problem of the worker. So it is desirable to remove the dust from the mixing chamber preventing to enter in the plant environment.

The volume of the mixing chamber

$$(81 \times 121.5 \times 45) + (70 \times 111.5 \times 59) + \left( \frac{\pi \times 35^2}{2} \times 111.5 \right)$$

$$= 1117914.145 \text{ cm}^3$$

$$= 1.1179 \text{ m}^3$$

Considering the air inside the hood as well as the coming air through the opening, the total volume is assumed to be (1+1.1179) or 2.118 m<sup>3</sup>.

The existing LEV system has following shortcomings:

- Inadequate dust removal capacity.
- Long ducting causes huge pressure drop across the pipe.
- No stack at the outlet of the exhaust system.
- No filter to purify exhaust air or separate the dust particle.
- The exhaust dust is collected in a cotton sack in the storage area which makes the area dustier.

### 4. NEW DESIGN OF LEV

Each component of the LEV is designed in detail to minimize the dust inside the plant area. Each component is designed so that it meets the functional requirements and standards of different international occupational health and safety organizations like NIOSH and.

#### 4.1 Hood

The hood (fig.3) is used to suck the fume, dust, and smoke out of the workstation or the area from where these things evolve. The existing hood over the mixing chamber is enclosure type hood.

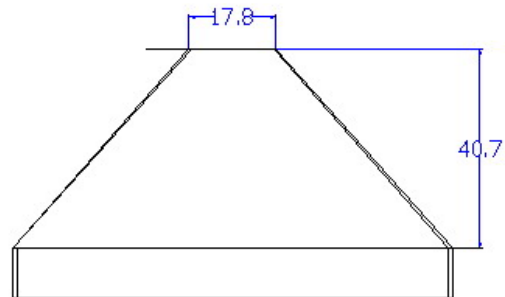


Fig 3. Side View of the Hood (cm)

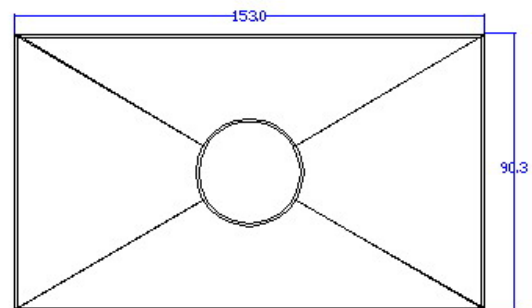


Fig 4. Top View of the Hood (cm)



The hood totally enclosed the emission source except the opening for pouring raw material. There are small opening on both side of the mixing chamber to induce the air flow through the exhaust system. The dust that evolves during mixing is taken away from the breathing zone of the worker. For above reasons the hood design is kept unchanged with small change in height.

#### 4.2 Filter

The proper filtration system for a LEV system depends on the characteristics of air stream and nature and quantity of the contaminants. Here a low cost filter (fig.5) is designed which is efficient to separate the detergent dust particles from the environment.

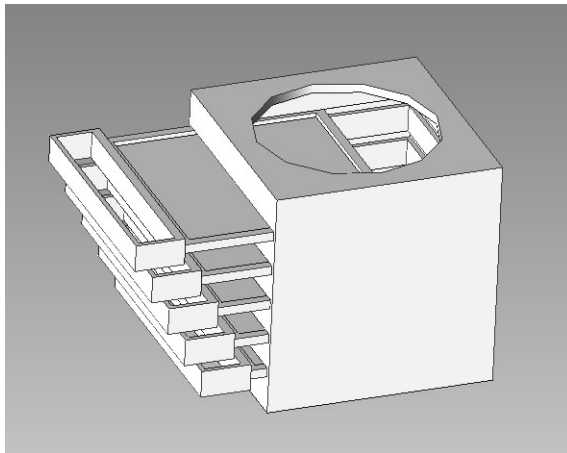


Fig 5. Schematic View of Cubic Filtration Device

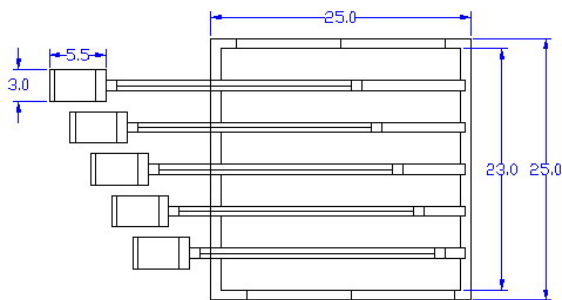


Fig 6. Dimensions of the Filtration Device (cm)

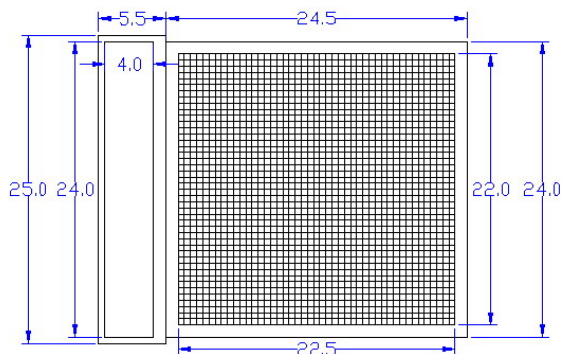


Fig 7. Top View of a Filter (cm)

The filter is placed prior to the fan to avoid degradation and corrosion of blades. They are designed in the form of trays that can be inserted into a cubic hollow box. The filter trays can be pulled out for cleaning purpose. It consists of five filters of consecutively larger mesh size.

Mesh size increases from bottom to top to capture large particles first and smaller particles successively. Very small particles are left to discharge with air through the exhaust system. The filter is made from thin metal wire. Different offset distances are used to put up different mesh size. Sequential perforations of filters from bottom to top are selected to be 50, 70, 90, 100 and 120 meshes. The fine dust particles which are usually smaller than 120 meshes are carried with the air flow out to the environment.

#### 4.3 Duct

Ductwork provides a channel for flow of the contaminated air exhausted from the hood to the point of discharge. If the air contains dust, the air velocity in the duct must be high enough to prevent the dust from settling out and plugging the ductwork. The location and construction of the ductwork must provide sufficient protection against external damage and corrosion, but be accessible for servicing and maintenance.

Air in motion encounters resistance along any surface confining the flowing air volume, and some of the energy of the air is lost by conversion to heat in overcoming this resistance. Friction losses increase with:

- Increasing roughness of the surface walls
- Increasing length of ducting
- Increasing air velocity
- Decreasing diameter of ducting

Energy is also lost from air flowing turbulently - these are termed dynamic losses. Turbulence is caused by changes in direction in a duct like Elbows and angles. The pressure drop in a duct system due to dynamic losses increases with the number of elbows or angles.

In the designed exhaust system the duct length is reduced from **8m to 3.32m** to reduce the pressure drop. Vertical duct is designed to discharge dust outside the plant area rather than in the storage. The duct of LEV system is classified as **class-2**[2] according to concentration and abrasiveness of dust particle. For duct diameter ranging from 100-200mm the steel sheet thickness should be **22-18 mm** [2]. The design duct velocity for "fine and light dust" should be between **10-12.5 m/s** [2] to avoid settling of particles. The appropriate duct diameter and associated pressure drops are calculated in following section for efficient and optimum air removal.

#### 4.4 Fan

Air is moved through the ductwork by a motor-driven fan. There are two major types of fans used in industrial ventilation:

- Axial flow types where the airflow is parallel to the fan shaft.

- Centrifugal flow types, where the airflow is perpendicular to the fan shaft.

Though centrifugal fan is quieter and can operate in higher static pressure, axial fan is more efficient in moving large volume of air. In the new LEV system an axial fan is proposed because the static pressure requirement is low. The appropriate duct-fan arrangement is determined in the following section for an available standard axial exhaust fan. The calculations may vary according to the data provided by the fan manufacturer regarding different fan model.

#### 4.5 Stack

Exhaust stacks also need to be designed and located properly for the most efficient operation of a local exhaust system. The proposed stack design(fig.8) is following:

- In the design 'Discharge cap' is used instead of 'weather cap' because it tends to force the contaminant back down to the building.
- The stack is designed to be horizontal to avoid rain fall into the duct. Another advantage of discharge cap is that, it creates an induced air flow at the exhaust terminal.
- The exhaust stack should not be too close to fresh air intake. According to WISHA (Washington Industrial Safety and Health Act) they should be located no closer than 50 feet to prevent re-circulation of contaminants. In the proposed design the distance between this two is nearly 26m (86ft) which meets the requirement.

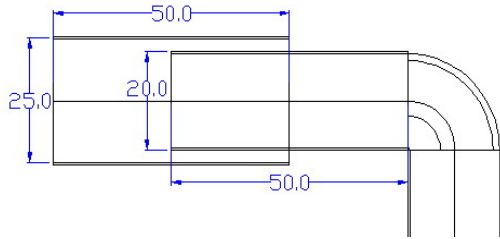


Fig 8. Dimension of the Stack (cm)

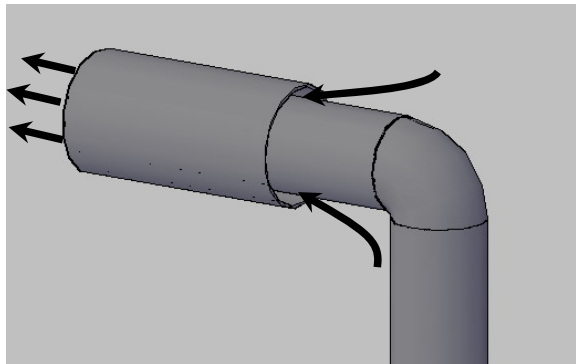


Fig 9. Induced Air Flow through the Stack

In addition to that, the exhaust end is directed opposite to the fresh air intake terminal. As a result, the

air flow is boosted away from the air intake. It ensures that, no dust particle is circulated back into the plant area.

#### 5. CAPACITY OF THE EXHAUST SYSTEM

If the total air inside the chamber is to be changed 4 times per minute then the required capacity

$$= 2.118 \times 60 \times 4$$

$$= 508.32 \text{ m}^3 / \text{h}$$

In order to force air to flow through a duct, it has to be blown or sucked. There must be a difference (p) between the pressures at opposite ends of the duct. For straight ducts, the magnitude of the difference is proportional both to the square of the required volumetric flow  $V$  and to the length  $L$  of the duct.

$$p(V, L) = kLV^2$$

Any change in the cross-section of the duct, or its direction (e.g. inlet or exhaust terminals, bends, etc.) requires an additional pressure difference to maintain the air flow. This is again proportional to the square of the flow(fig.10).

$$p(V) = cV^2$$

Fans for use in ducted ventilation systems can be characterised by the air flow  $V_f(p)$  that they will produce against a given pressure difference  $p$ . The performance of a particular combination of fan and duct system will be determined by finding the values of pressure  $p$  and flow  $V$  that simultaneously satisfy the following two conditions:

$P$  = Total pressure difference required for duct and terminals to deliver a flow  $V$

$V$  = Flow delivered by fan working against a pressure difference  $p$

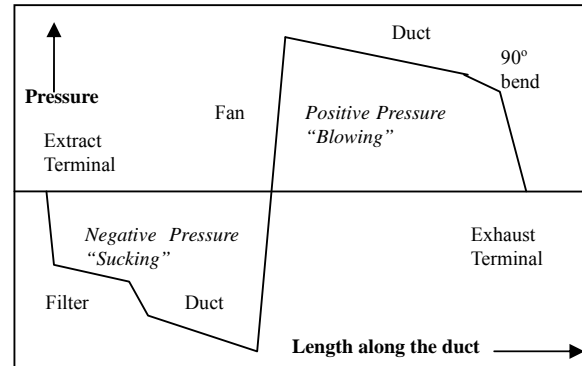


Fig 10. Pressure Variation along the length of the duct

For dry detergent dust classified as "very fine and light dust", the inside duct velocity should be between 10-12.5 m/s [2]. As the powder itself is the product, we have considered maintaining the minimum value of that range. To keep the mean air velocity (preferred) in the duct m/s, the duct diameter  $d$  must satisfy:

$$\text{Flow / area} = \text{Velocity}$$

$$508.32 / (3600 \times \pi d^2 / 4) = 10$$

$$d = ((4 \times 508.32) / (10 \times 3600 \times \pi))^{\frac{1}{2}} = 0.13408 \text{ m} = 134.08 \text{ mm}$$

No pressure data is available for 134.08 cm duct diameter. So the next standard diameter 200mm can be considered for duct. Though velocity will be decreased slightly due to increased diameter it will not affect much the capacity of the LEV system. Pressure drop along the proposed ducting arrangement for 1000 m<sup>3</sup>/h flow rate is calculated as follows for a particular fan model.

Table 1: Pressure drop in ductwork  
(Data obtained from manufacturer of ACM200 Fan)

Component	Pressure drop (Pa)
Extract terminal	624
2.82 m straight duct (10 Pa/m)	28.2
Filter	20*
90° bend	21
0.5 m straight duct (10 Pa/m)	5
Exhaust terminal	66
<b>Total</b>	<b>764.2</b>

So, for a flow of 508.32 m<sup>3</sup>/h, the total pressure drop is  $764.2 \times (508.32/1000)^2 = 197.46$  Pa. The performance chart below shows that the point (508.32, 197.46) is inside the performance envelope of the recommended ACM200 fan (fig.11). It therefore can deliver the target flow.

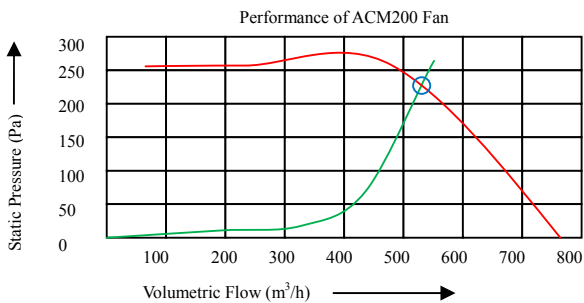


Fig 11. Performance curve of ACM 200 Fan

To determine what actual ventilation can be achieved, write  $v$  for the normalised flow  $V/1000$ , so that  $p = 764.2v^2$ . This relationship is the **system operating curve** for flow in the duct, and is shown in green on the above chart. As the flow increases, the pressure will increase until, at the point where the curves intersect, the fan reaches its performance limit. To determine the intersection for static pressures between 0 and 220 Pa, the flow rate for the fan (in m<sup>3</sup>/h) is given approximately by

$$V = 778 - 1.14p$$

Or, equivalently,

$$v = 0.778 - 0.00114p$$

Substituting for  $p$  gives a quadratic equation for  $v$

$$v = 0.778 - .00114(764.2v^2)$$

That is,  $.871188v^2 + v - .778 = 0$

With positive solution,  $v = .53171$

This corresponds to a flow rate 531.71 m<sup>3</sup>/h

$$\begin{aligned} &= \frac{531.71 - 508.32}{508.32} \times 100\% \\ &= 4.6\% \end{aligned}$$

So, our obtained flow from the specified fan-duct combination is 4.6% better than the target.

Maximum air change per hour achievable,

$$\begin{aligned} &= \frac{531.71 \text{ m}^3 / \text{h}}{2.118 \text{ m}^3} \\ &= 251.04 \text{ times / hr} \\ &= 4.2 \text{ times / min} \end{aligned}$$

## 6. COMPLETE VENTILATION ARRANGEMENT

All the components together along with appropriate fan-duct arrangement form the proper ventilation system that will minimize the toxic detergent dust to stay inside the plant. The cubic filtration device is placed at a height so that a person of average height can reach it without any physical strain. Five trays can be removed, washed and placed back to the filter in minimum time without hampering the production.

The complete arrangement should look like the following:

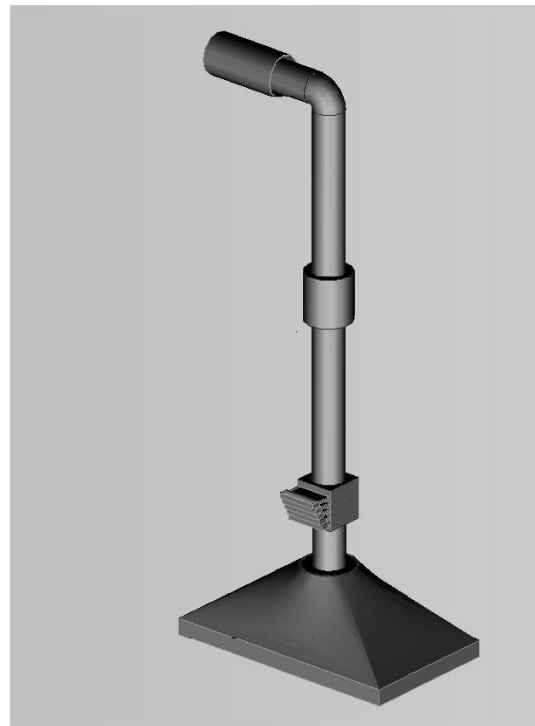


Fig 12. The complete LEV System

## 7. DUST PREVENTION UNITS

In a manufacturing facility where workers have to work in a toxic material, dust prevention unit adds to the process for creating a better workplace. In addition to the top of the mixing chamber, other openings from where dust is evolved can be covered with suitably designed case. It will be appropriate to use transparent plastic sheet to make the inside visible. A slide type opening can be used to clean the inside without extensive physical effort.

## 8. CONCLUSION

The designed LEV system here is suitable for any type of dust particle that evolve from a small area or workstation. The ducting material, thickness of metal, Capture velocity, and type of filter to be used depend on the particle diameter, nature of contaminant and condition of dispersion. So the system can be modified for above conditions to expel any type of dust that is harmful for human health and detrimental to the workplace equipments.

In a detergent plant where the overall ventilation is satisfactory, a good material handling system carries the product from place to place, storage of toxic organic chemicals are secured and dust emission spots are well covered, the new LEV system will work great. But if those factors are not maintained with care, even a sophisticated, well designed LEV system has little to contribute in health and environmental issue. So to maintain a safe and hazard free working environment and smooth operation the above factors also need necessary attention.

## 9. REFERENCES

1. M. J. Jafari, Ali Karimi, M.R. Azari, 2008, "The role of exhaust ventilation system in reducing occupational exposure to organic solvents in a paint manufacturing factory", Indian Journal of

Occupational and Environmental Medicine Vol-12:22.

2. "Guidelines on Design, Operation and Maintenance of Local Exhaust Ventilation System" 2003, Occupation, Safety and Health Division, Ministry of Manpower, Singapore.
3. "Workplace (Health, Safety and Welfare) Regulations" Nuneaton and Bedworth Borough Council, Environmental Health Services, Council House, Cotton Road, Nuneaton, Sep 2003, Issue 3.
4. ACGIH, Industrial Ventilation a manual of recommended Practice, 22 ed ACGIH, 1995.
5. ASHRAE Handbook of Fundamentals, Chapter 26 by American Society of Heating, Refrigeration and Air-Conditioning Engineers (ASHRAE). Atlanta, GA: 2001.
6. D. Jeff Burton, 1997, "Industrial Ventilation: A Self-Directed Learning Workbook (4th Edition)"

## 10. NOMENCLATURE

Symbol	Meaning	Unit
V	Velocity	(m/s)
d	Diameter	(m)
P	Pressure	(Pa)
V	Volumetric Flow	(m <sup>3</sup> /h)
L	Length	(m)

## 11. MAILING ADDRESS

Abdullah-Al-Mamun

Lecturer,

Department of Industrial and Production Engineering,  
Bangladesh University of Engineering and Technology,  
Dhaka-1000

E-mail: [abdullah-al-mamun@ipe.buet.ac.bd](mailto:abdullah-al-mamun@ipe.buet.ac.bd)

## PERFORMANCE EVALUATION OF CARBIDE INSERTS IN TURNING C-60 STEEL AND 42CrMo4 STEEL UNDER HIGH-PRESSURE COOLANT (HPC) CONDITION

M. Kamruzzaman<sup>1</sup> and N. R. Dhar<sup>2</sup>

<sup>1</sup>Department of Mechanical Engineering  
Dhaka University of Engineering & Technology (DUET), Gazipur

<sup>2</sup>Department of Industrial & Production Engineering  
Bangladesh University of Engineering & Technology (BUET), Dhaka, Bangladesh

### ABSTRACT

High temperature during machining causes tool wear and premature failure of cutting tools, dimensional deviation and impairs the surface integrity of the product. In high speed machining, conventional cutting fluid fails to penetrate the chip-tool interface and thus cannot remove heat efficiently. Moreover, it has become problematic in terms of both employee health and environmental pollution. High pressure coolant (HPC) can solve the problems of traditional machining associated with convention coolant. This paper deals with the experimental investigation on the role of high pressure coolant on cutting temperature, tool wear, surface roughness and dimensional deviation in turning C-60 steel and 42CrMo4 steel by uncoated carbide inserts and a comparison between them. The encouraging results include significant reduction in tool wear rate, dimensional inaccuracy and surface roughness by high pressure coolant mainly through reduction in the cutting zone temperature and favorable change in the chip-tool and work-tool interaction.

**Keywords:** Turning, HPC, Tool Wear and Surface Roughness.

### 1. INTRODUCTION

The energy dissipated in machining operation is converted into heat which raises the temperature in the cutting zone. Excessive temperature adversely affects the strength, hardness and wear-resistance of the cutting tool which eventually leads to tool failure. Additionally, tool-wear increases with the increase of speed, feed and depth of cut, though their effects are different [1]. On the other hand, if the tool becomes dull or worn, heat is also generated when the tool tip rubs against the machined surface. So, it's a cyclical process. Increasing heat can cause dimensional inaccuracy and also cause distortion of the machine tool resulting poor dimensional control of the work piece. With the increase of cutting temperature and tool wear, surface roughness increases significantly. Cutting force is also increased with tool wear which results the increase of power consumption. All these problems increase further with the increase in hardness of the work material [2].

For reducing the cutting zone temperature through cooling and lubricating action cutting fluid (soluble oil) may be applied to the tool/work piece interface. In the high speed-feed machining, which inherently generated high cutting zone temperature, cutting fluid can't reach to the chip-tool interface to reduce the temperature [3]. Machining of ductile material in high speed produces long chips, where the length of chips affects the cutting

temperature and thermo-chemical tool wear [4].

Cutting fluid systems are used in industry to deliver fluid to the cutting process, re-circulate fluid, separate chips and collect fluid mist. In flood cooling method, fluid is used in very large amount (6-10 l/hr). The cost associated with the use of cutting fluid is estimated to be about 16% to 20% of the total manufacturing costs [5, 6], where only 4% of the total manufacturing cost is associated with cutting tools [2]. So, in respect of costs, it is very important to reduce the amount of cutting fluid. Some conditions like machining steels by carbide tools, the use of coolant may increase tool wear [7].

Furthermore, the permissible exposure level (PEL) for metal working fluid aerosol concentration is 5 mg/m<sup>3</sup> as per the U.S. Occupational Safety and Health Administration [2] and is 0.5 mg/m<sup>3</sup> according to U.S. National Institute for Occupational Safety and Health [8]. The oil mist level in U.S. automotive parts manufacturing facilities has been estimated to be generally on the order of 20-90 mg/m<sup>3</sup> with the use of traditional flood cooling and lubrication [9]. This suggests an opportunity for improvement in coolant application during machining.

Moreover, for using cutting fluid environment becomes polluted. Because, for improving the lubricating performance Sulfur(S), Phosphorus(P), Chlorine(Cl) or other pressure additives are mixed with

cutting fluid [10]. If the cutting fluids are not handled appropriately, it may damage soil and water resource, which can cause serious environment pollution. Additionally in the factory cutting fluid may cause skin and breathing problem of the operator [11]. So, dry machining is now considered as an environment friendly manufacturing [2]. But some times dry machining cannot show better performance if higher machining efficiency, better surface finish and other special cutting conditions are required. For these cases many special techniques can be used.

The cutting temperature can be reduced by selecting proper tool-work piece combination, improving the metallurgical property of the tool / work piece and proper selection of process parameters. Cubic Boron Nitride (CBN) can maintain its hardness and resistance to wear at elevated temperatures and has a low chemical reactivity to the chip/tool interface [12]. The CBN tool, if properly manufactured, provides less cutting forces, temperature and less tensile residual stresses [13]. Polycrystalline Cubic Boron Nitride (PCBN) also displays a unique combination of hardness, toughness and thermo-chemical stability, properties which are increasingly important in a cutting tool material to meet the demands of machining hard materials. But these tools are so much expensive and recommended to use in that case where other tool materials are not effective.

Coolant is supposed to cool and lubricate but it can only perform these functions at the point of chip formation if the coolant actually reaches the cutting zone. When coolant is turned to steam or otherwise fails to reach the target, it does not perform its two essential functions (cooling and lubricating). This problem increases at the time of high speed machining [16]. If the coolant is applied at the cutting zone through a high speed nozzle, it could reduce the contact length and co-efficient of friction at chip-tool interface then cutting force and temperature may be reduced and tool life can be increased [17, 18]. High-pressure is often the solution to get the coolant to the target so it can cool, lubricate, and sometimes perform its third function- chip breaking that do not break neatly with ordinary machining processes [19].

In drilling operations when temperature is increased a large amount of tool wear appears at the drill bit. Such high cutting temperature not only reduces dimensional accuracy and tool life but also impairs the surface integrity of the product; either it affects roundness of the hole or chip shape and color of chip. High-pressure coolant has reduced temperature as well as improving roundness and also provides lubrication in the tool tip and surface interface [20].

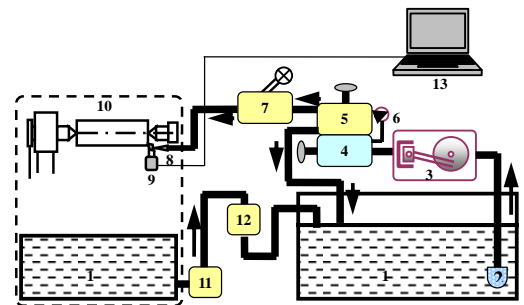
In Grinding operation material is generally removed by shearing and ploughing in the form of micro sized chips by the abrasive grits of the grinding wheel. As a result, high temperature is produced in the grinding zone due to large negative rake and high cutting speed of the grinding wheel. High-pressure coolant jet effectively reduces cutting zone temperature entering into chip tool interface maintaining a good surface integrity [21].

The present work intends to clarify some points relating temperature, tool wear and surface roughness

when turning C-60 steel and 42CrMo4 steel at high cutting speeds and feed rates.

## 2. EXPERIMENTAL INVESTIGATION

The experiment was carried out on a center lathe of 10 hp and maximum spindle speed of 1400 rpm. The schematic view of the experimental set-up is shown in Fig. 1. The tool holder provided negative 6° side and back rake angles and 6° side cutting-edge and end cutting-edge angles. The ranges of the cutting speed (V) and feed rate (f) were selected based on the tool manufacturer's recommendation and industrial practices. Depth of cut, being less significant parameter, was kept fixed (1.0 mm for temperature and 1.5 mm for wear). The experimental conditions are given in Table-1.



- |                      |                           |                 |
|----------------------|---------------------------|-----------------|
| 1 Coolant tank       | 6 Pressure gauge          | 10 Machine tool |
| 2 Foot valve         | 7 Direction control valve | 11 Supply pump  |
| 3 High-pressure pump | 8 Nozzle                  | 12 Filter       |
| 4 Flow control valve | 9 Dynamometer             | 13 Computer     |
| 5 Relief valve       |                           |                 |

Fig 1. Schematic view of experimental set-up

Table 1: Experimental conditions

<b>Machine tool</b>	: Lathe, 10 hp (China)
<b>Work material</b>	: C-60 steel and 42CrMo4 steel
<b>Cutting tool</b>	: SNMG 120408 and SNMM 120408
<b>Process parameters</b>	
Cutting speed, V	: 93,133, 186, 193 and 266 m/min
Feed rate, f	: 0.10, 0.14, 0.18 and 0.22 mm/rev
Depth of cut, d	: 1.00 mm and 1.50 mm
<b>HPC supply</b>	: 80 bar with a flow rate of 6.0 l/min
<b>Environment</b>	: Dry and HPC (VG 68 cutting oil)

High-pressure coolant jet impinged at the chip-tool interface zone for removing temperature through the nozzle at an angle from a suitable distance. The cutting fluid needs to be drawn at high pressure from the coolant tank and impinged at high speed through the nozzle. Considering the conditions required for the present research work and uninterrupted supply of coolant at pressure around 80 bar over a reasonably long cut, a coolant tank has been designed, fabricated and used. The high-pressure coolant jet is directed in such a way that it reaches at the rake and flank surface and to protect auxiliary flank to enable better dimensional accuracy.

The application of high-pressure coolant jet is expected to affect the various machinability characteristics mainly by reducing the cutting temperature. Simple but a reliable tool-work thermocouple technique with proper calibration was used

to measure the average cutting temperature under both dry and high-pressure coolant condition.

The cutting insert was withdrawn at regular intervals to study the pattern and extent of wear on main and auxiliary flanks for all the trials. The average width of the principal flank wear, VB and auxiliary flank wear, VS were measured using an inverted metallurgical microscope (Carl Zeiss) fitted with a micrometer of least count 1.0  $\mu\text{m}$ . The surface roughness was monitored by a Talysurf (Surtronic 3+, Rank Taylor Hobson) using a sampling length of 0.8mm. At the end of full cut, the cutting inserts were inspected under a scanning electron microscope (Philips XL 30, Belgium).

### 3. RESULTS AND DISCUSSION

The average cutting temperature measured by the tool-work thermocouple technique during turning at different cutting speeds and feeds under both dry and high-pressure coolant (HPC) condition is shown in Fig.2 and Fig.3. It shows how and to what extent the average cutting temperature has decreased due to high-pressure coolant application under different experimental conditions. With the increase in V and f, the average temperature increased as usual, even under HPC condition, due to an increase in energy input. It can clearly be observed from Fig.2 and Fig.3 that HPC is able to reduce the average cutting temperature for both C-60 steel and 42CrMo4 steel compared to dry machining. At  $V \leq 100$  m/min and all feed ranges, the reduction in cutting temperature is more than moderate speed used ( $V = 100\text{--}200$  m/min and all feed ranges). At higher speed ( $V > 200$  m/min) and all feed ranges, the reduction in average temperature is minimum.

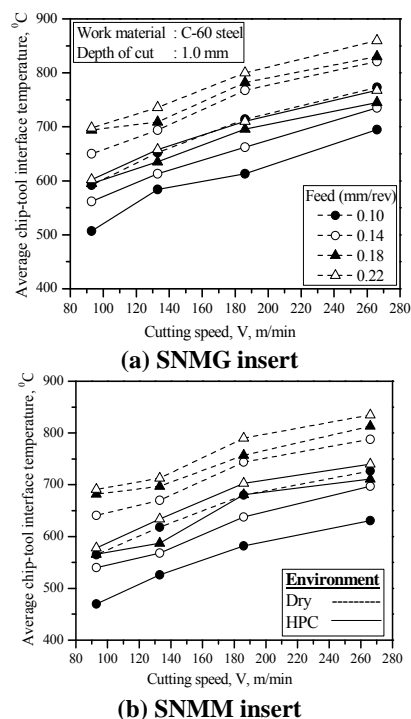


Fig. 2. Variation in temperature in turning C-60 steel

It is evident from Fig.2 and Fig.3 that as the cutting speed and feed rate increases, the rate of reduction in

average cutting temperature decreases. It may be for the reason that, with the increase in V and f, the bulk contact of the chips with the tool did not allow significant entry of high-pressure coolant jet. Only possible reduction in the chip-tool contact length by the high-pressure coolant jet, particularly that which comes along the auxiliary cutting edge, could reduce the temperature to some extent, particularly when the chip velocity was high due to higher V and f, this amount of reduction in average cutting temperature is quite significant in pertaining tool life and surface finish.

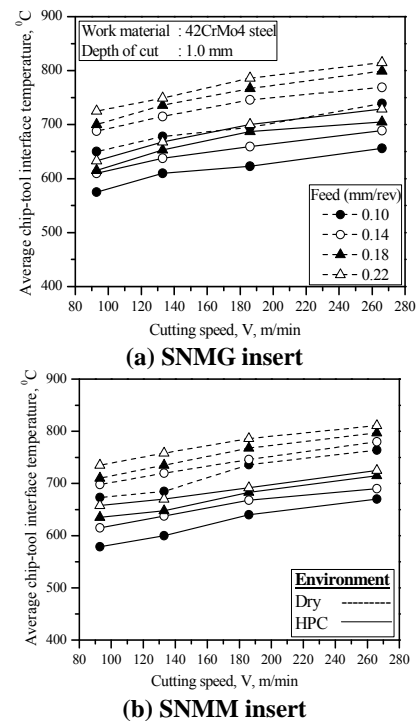
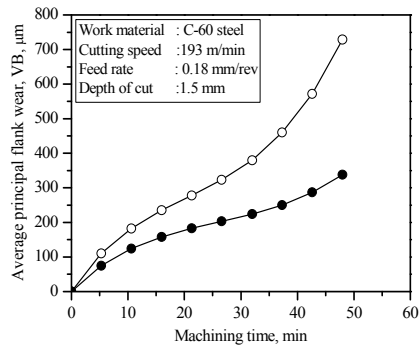


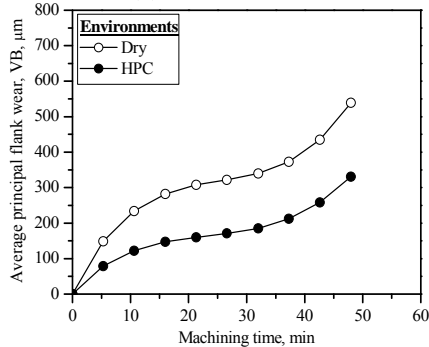
Fig. 3. Variation in temperature in turning 42CrMo4 steel

Productivity and economy of manufacturing by machining are significantly affected by the life of the cutting tools. Cutting tools may fail by brittle fracturing, plastic deformation or gradual wear. Turning carbide inserts having enough strength, toughness and hot hardness generally fail by gradual wear. With the progress of machining, the tools attain crater wear at the rake surface and flank wear at the clearance surfaces due to continuous interaction and rubbing with the chips and the work surfaces respectively. Among the aforesaid wears, the principal flank wear is the most important because it raises the cutting forces and the related problems. The life of carbide tools, which mostly fail by wearing, is assessed by the actual machining time after which the average value (VB) of its principal flank wear reaches a limiting value, like 0.3 mm. Therefore, attempts should be made to reduce the rate of growth of principal flank wear (VB) in all possible ways without much sacrifice in MRR. The cutting insert was withdrawn at regular intervals to study the pattern and extent of wear on main and auxiliary flanks under both dry and high-pressure coolant conditions.



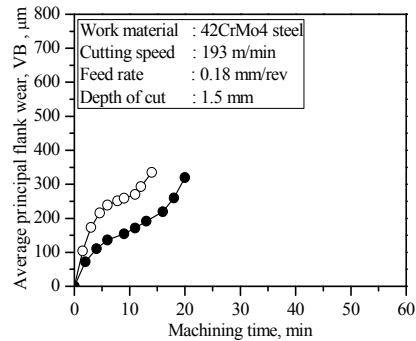


(a) SNMG insert

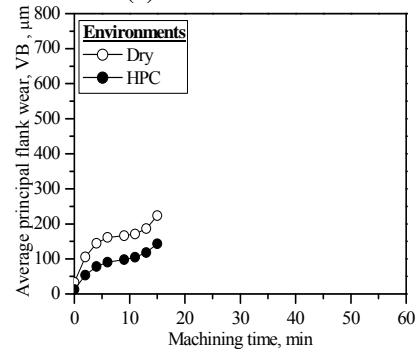


(b) SNMM insert

Fig 4. Growth of VB during turning C-60 steel



(a) SNMG insert

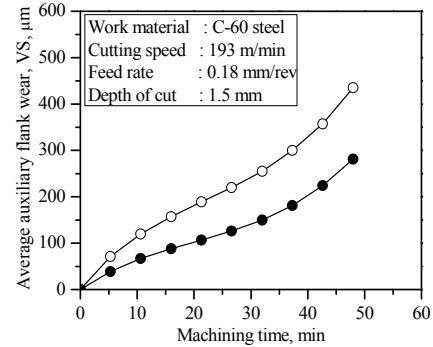


(b) SNMM insert

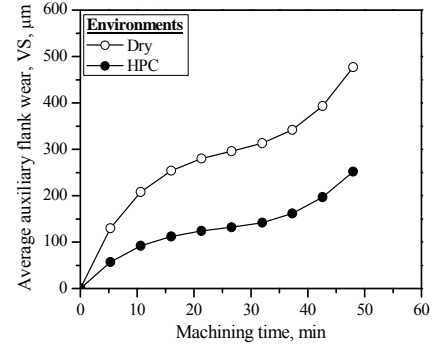
Fig 5. Growth of VB during turning 42CrMo4 steel

The growth of principal flank wear (VB) with progress of machining was recorded during turning at moderately high cutting speed, feed and depth of cut under both dry and high-pressure coolant condition have been shown in Fig.4 and Fig.5. Fig.4 and Fig.5 clearly show that flank wear (VB) particularly its rate of growth, decreases substantially by high-pressure coolant jet. The

cause behind reduction in VB observed may reasonably be attributed to reduction in the flank temperature by high-pressure coolant jet impinged along the auxiliary cutting edge, which helps in reducing abrasion wear by retaining tool hardness and also adhesion and diffusion types of wear which are highly sensitive to temperature. Because of such reduction in rate of growth of flank wear, the tool life would be much higher if high-pressure coolant is properly applied.



(a) SNMG insert



(b) SNMM insert

Fig 6. Growth of VS during turning C-60 steel

The auxiliary flank wear affects dimensional accuracy and surface finish has also been recorded at regular intervals of machining under all the conditions undertaken. The growth of average auxiliary flank wear (VS) with machining time under both dry and high-pressure coolant conditions have been shown in Fig.6 and Fig.7. It appears from Fig.6 and Fig.7 that auxiliary flank wear (VS) has also decreased significantly due to application of HPC jet.

The flank wear occurred quite fast due to rapid attrition wear followed by adhesion and diffusion in addition to usual abrasion particularly at the tool tip where stresses and temperature are high. Rapid start of flank wear causes more intimate contact at the work-tool interface and initiates severe rubbing which again aggravates flank wear further. Flank wear grow so fast in turning by carbide insert that notching and grooving type wear do not appear separately.

The SEM views of the worn out insert after being used under both dry and high-pressure coolant conditions are shown in Fig.8 and Fig.9. Under all the environments, abrasive scratch marks appeared in the flanks. There have also been some indications of adhesive wear especially under dry condition, which produced unfavorable chips as compared to high pressure coolant

condition that produced favorable chips.

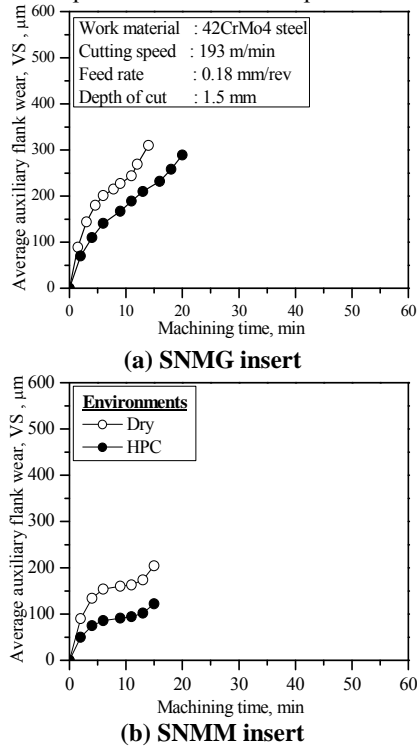


Fig 7. Growth of VS during turning 42CrMo4 steel

But it is clearly evident from Fig.8 and Fig.9 that high-pressure coolant jet machining caused lesser wear than that produced by dry machining. Such reduction in wear is seemingly indebted to reduction of the cutting temperature sensitive wear phenomenon like diffusion and adhesion enabled by direct and indirect cooling by high-pressure coolant jet.

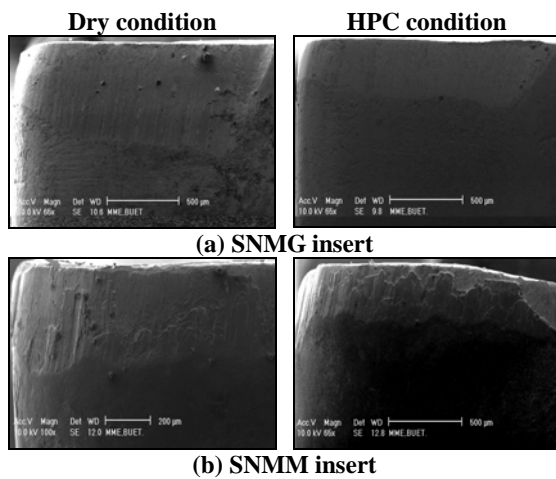


Fig 8. SEM views of worn out insert during turning C-60 steel

In machining research, a cutting tool is generally said to have failed when its VB reaches a specific value, mostly 300 μm. The life of the turning insert is generally evaluated on the basis of this limiting value of average flank wear, VB. Considering VB=300 μm as tool life criteria, the tool life values obtained in machining C-60 steel for both the inserts under both conditions have been

represented in three dimensional wire frame graph in Fig.10. Fig.10 shows that the tool life decreases with the increase of V and f as usual under all the environments undertaken. Tool life improved to some extent particularly when this material was machined at relatively lower V and f but high-pressure coolant jet enhanced tool life more pronouncedly though the benefit gradually decreased with the increase in cutting velocity and feed rate. The high-pressure coolant system increased tool life by approximately twice when turning C-60 steel by the inserts.

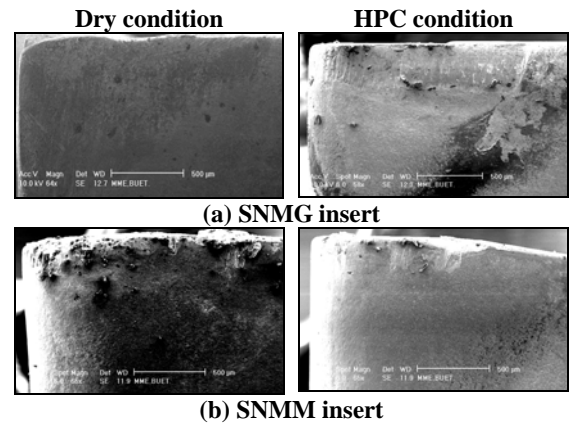


Fig 9. SEM views of worn out insert during turning 42CrMo4 steel

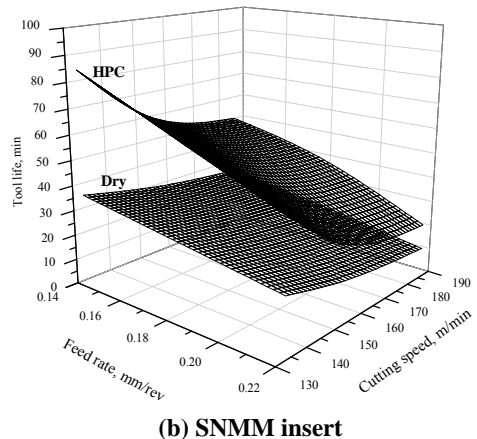
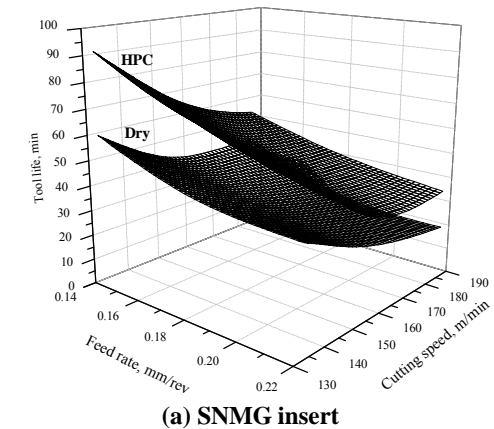


Fig 10. Effect of dry and HPC on tool life during machining C-60 steel

The nature and extent of surface roughness in the longitudinal direction of the turned job depend mainly upon the geometry and condition of the auxiliary cutting edge including a part of the rounded nose. The value of surface roughness increases sharply with the increase in feed and decreases with increase in  $V$ . Built-up edge formation and vibration worsen the surface further.

The resulting surface finishes under both dry and high-pressure coolant conditions are shown in Fig.11 and Fig.12. As high-pressure coolant jet reduced average auxiliary flank wear (VS) on auxiliary cutting edge, surface roughness also grew very slowly under high-pressure coolant condition.

The results shown in Fig.11 and Fig.12 indicate that surface roughness increased substantially with the increase in feed when machined by both the tools and under both the environments. This can be attributed mainly to the roughness caused by the feed marks as explained earlier. It is also noted that surface roughness decreased to some extent with the increase in  $V$  possibly due to smoothing of the nose profile by adhesion and diffusion types wear. However, incase of both the tools surface roughness decreased to some extent when the job was machined under HPC. This can be attributed to reduction in VS due to retention of tool hardness through reduction in temperature by the HPC jet.

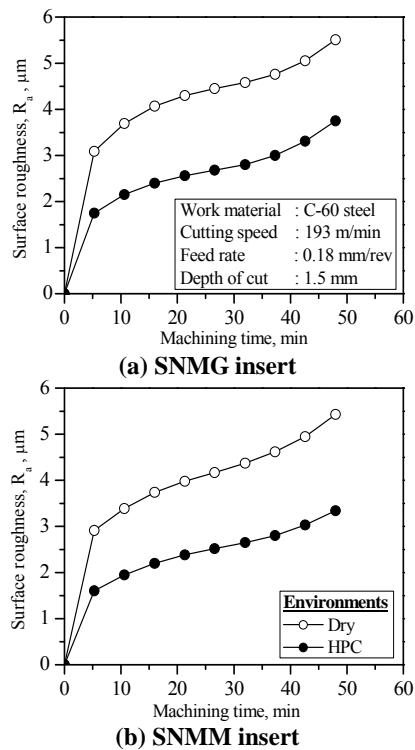


Fig 11. Surface roughness ( $R_a$ ) developed with progress of machining of C-60 steel

High pressure coolant provided remarkable benefit in respect of controlling the increase in diameter of the finished job with machining time as can be seen in Fig.13 and Fig.14. In plain turning, the finished job diameter generally deviates from its desired value with the progress of machining i.e. along the job-length mainly for change in the effective depth of cut due to several

reasons which include wear of the tool nose. With the increase in temperature the rate of growth of auxiliary flank wear and thermal expansion of the job will increase. HPC takes away the major portion of heat and reduces the temperature resulting decrease in dimensional deviation desirably.

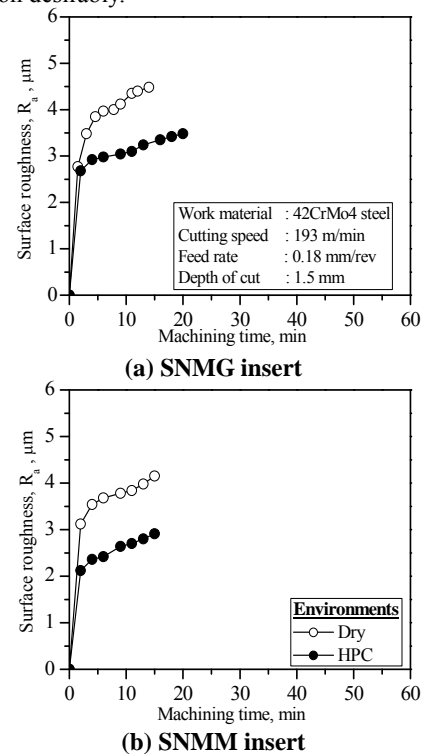


Fig 12. Surface roughness ( $R_a$ ) developed with progress of machining of 42CrMo4 steel

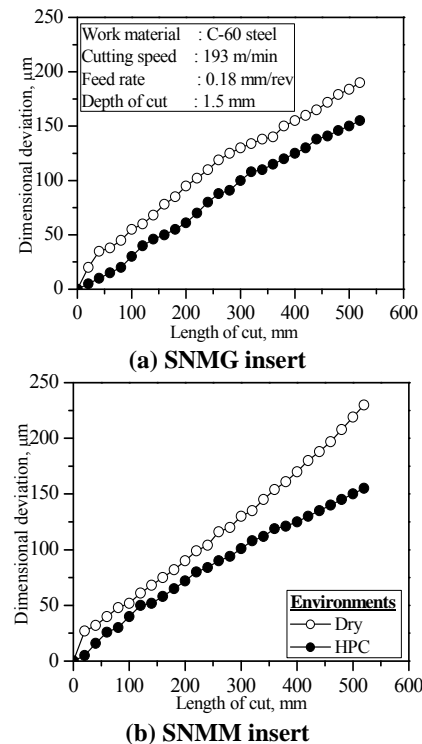


Fig 13. Dimensional deviation observed after one full pass turning of C-60 steel

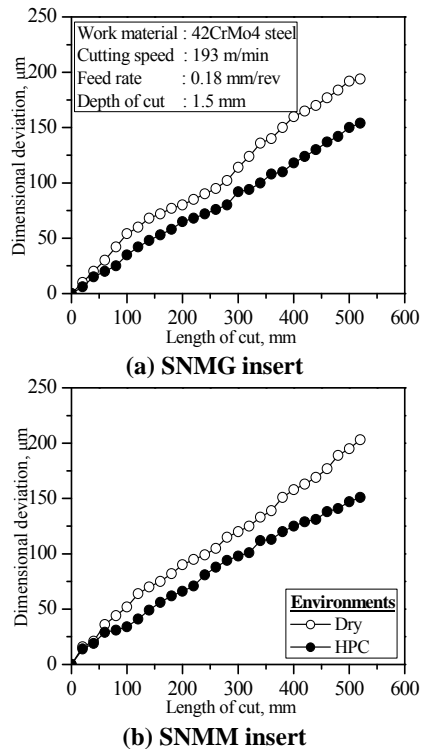


Fig 14. Dimensional deviation observed after one full pass turning of 42CrMo4 steel

#### 4. CONCLUSIONS

- i. The cutting performance of HPC jet assisted machining is better than that of dry machining.
- ii. HPC provides the benefits mainly by substantial reducing the cutting temperature, which improves the chip-tool interaction and maintains sharpness of the cutting edges.
- iii. HPC machining of steel caused lesser tool wear in comparison to dry machining and increased tool life.
- iv. HPC cooling by insoluble oil jet provided better surface finish and higher dimensional accuracy as compared to dry machining.

#### 5. ACKNOWLEDGEMENTS

This research work has been funded by Directorate of Advisory Extension and Research Services (DAERS), BUET, Dhaka, Bangladesh. The authors are also grateful to the Department of Industrial and Production Engineering, BUET for providing the facilities to carryout the experiment.

#### 6. REFERENCES

1. Muraka, P.D., Barrow, G. and Hinduja, S., 1979, "Influence of the Process Variables on the Temperature Distribution in Orthogonal Machining using the Finite Element Method", *Int.J.Mach. Tool Des. Res.*, 21: 445.
2. Aronson, R.B., 1995, "Why Dry Machining", *Manufacturing Engineering*, 114: 33-36.
3. Dhar, N. R., Paul, S., Chattopadhyay, A.B., 2002, "Role of Cryogenic Cooling on Cutting Temperature in Turning Steel", *J. Manuf. Sc. Engg.*, 124(1): 146-154.
4. Nedess, C. and Hintze, W., 1998, "Characteristics Parameters of Chip Control in Turning Operations with Indexable Three dimensionally Shaped Chip Formers", *Annals of CIRP*, 38/1: 75-79.

5. Byrne, G. and Scholta, E., 1993, "Environmentally Clean Machining Processes-A Strategic Approach", *Annals of CIRP*, 42 (1): 471-474.
6. Brockhoff, T. and Walter, A., 1998, "Fluid Minimization in Cutting and Grinding", *Abrasives*, 38-42.
7. Paul, S., Dhar, N. and Chattopadhyay, A.B., 2001, "Beneficial Effects of Cryogenic Cooling over Dry and Wet Machining on Tool Wear and Surface Finish in Turning AISI 1060 Steel", *J. Mat. Process. Technol.*, 116: 44-48.
8. Thornberg, J. and Leith, D., 2000, "Mist Generation During Metal Machining" *J. Tribology, Transaction of ASME*, 122(3): 544-549.
9. Bennett, E.O. and Bennett, D. L., 1985, "Occupational Air Way Diseases in the Metal-Working industry", *Tribology International*, 18(3): 169-176.
10. Peter, C.R., Steven, C. and David, L., 1996, "Evaporation of Poly-disperse Multi-component Oil Droplets", *AIHAJ*, 57.
11. Sokovic, M. M. and Mijanovic, K., 2001 "Ecological Aspects of the Cutting Fluids and its Influence on Quantifiable Parameters of the Cutting Processes", *J. Mater. Process. Technol.*, 109(1-2): 181-189.
12. Narutaki, N. and Yamane, Y., 1979, "Tool Wear and Cutting Temperatures of CBN Tools in Machining Hardened Steels", *Annals of CIRP*, 28/1: 23-27.
13. Davies, M.A., Chou, Y. and Evans, C.J., 1996, "On Chip Morphology, Tool Wear and Cutting Mechanics in Finish Hard Turning", *Annals of CIRP*, 45/1: 77-82.
14. Dhar, N. R., Islam, M. W., Islam, S. and Mithu, M. A. H., 2006, "The Influence of Minimum Quantity of Lubrication (MQL) on Cutting Temperature, Chip and Dimensional Accuracy in Turning AISI 1040 Steel" *J. Mater. Process. Technol.*, 171: 93-99.
15. Dhar, N. R., Kamruzzaman, M. and Ahmed Mahiuddin, 2006, "Effect of Minimum Quantity Lubrication (MQL) on Tool Wear and Surface Roughness in Turning AISI-4340 Steel" *J. Mater. Process. Technol.*, 172: 299-304.
16. Kitagawa, T., Kubo, A. and Maekawa, K., 1997, "Temperature and Wear of Cutting Tools in High Speed machining of inconel 718 and Ti-6V-2Sn", *Wear*, 202: 142-148.
17. Mazurkiewicz, M., Kubula, Z. and Chow, J., 1989, "Metal Machining with High Pressure Water Jet Cooling Assistance-A New Possibility", *J. Eng. Ind.* 111: 7-12.
18. Kumar, A. S., Rahman, M. and Ng, S. L., 2002, "Effect of High-Pressure Coolant on Machining Performance", *Int J Adv Manuf. Technol.*, 20: 83-91.
19. Lo'pez de Lacalle, L.N., Pe'rez-Bilbatua, J., Sa'nchez, J.A., Llorente, J.I., Gutie'rriz, A. and Albo'niga, J., 2000, "Using High Pressure Coolant in the Drilling and Turning of Low Machinability Alloys", *Int J Adv Manuf Technol.*, 16: 85-91.
20. Dhar, N. R., Rashid, M.H. and Siddiqui, A. T., 2006, "Effect of High-Pressure Coolant on Chip, Roundness Deviation and Tool Wear in Drilling AISI-4340 Steel" *ARNP Journal of Engineering and Applied Sciences*, 1(3):53-59.
21. Dhar, N. R., Siddiqui, A. T. and Rashid, M.H., 2006, "Effect of High Pressure Coolant Jet on Grinding Temperature, Chip and Surface Roughness in Grinding AISI-1040 Steel", *ARNP Journal of Engineering and Applied Sciences*, 1(4): 22-28.

## EFFECTS OF HIGH-PRESSURE COOLANT (HPC) JET ON TEMPERATURE, CHIPS AND FORCES IN TURNING AISI 1060 STEEL AND AISI 4320 STEEL

M. Kamruzzaman<sup>1</sup> and N. R. Dhar<sup>2</sup>

<sup>1</sup>Department of Mechanical Engineering  
Dhaka University of Engineering & Technology (DUET), Gazipur

<sup>2</sup>Department of Industrial & Production Engineering  
Bangladesh University of Engineering & Technology (BUET), Dhaka, Bangladesh

### ABSTRACT

Usually cutting fluid is used to remove generated heat or to reduce friction. But the conventional types and method of application of cutting fluid have been found to be less effective under high speed machining as it can not enter into the interface efficiently where maximum temperature attains. Moreover, it pollutes the environment. In this situation, high pressure coolant may be the viable solution to control the cutting temperature and. The present work deals with experimental investigation in the role of HPC on tool-chip interface temperature, chips and cutting forces in plain turning of AISI 1060 steel and AISI 4320 steel at different speed-feed combination by two types of carbide inserts of different geometric configurations. High pressure coolant is more effective in respect of reduction in cutting zone temperature, increment in chip thickness ratio. Also cutting force is decreased sizably as chip load and cutting temperature are decreased.

**Keywords:** Turning, HPC and Forces.

### 1. INTRODUCTION

During machining generation of heat and high cutting temperature is inherent. At such elevated temperature the cutting tool if not enough hot hard and tough may lose their form stability quickly or wear out rapidly resulting in increased cutting forces, dimensional inaccuracy of the product and shorter tool life. The magnitude of this cutting temperature increases with the increase of cutting speed, feed and depth of cut; as a result, high speed machining is constrained by rise in temperature [1]. This problem further intensified with the increase in strength and hardness of the work material [2]. Due to such high temperature and pressure the cutting edge deforms plastically and wears rapidly, which lead to dimensional inaccuracy, increase in cutting forces and premature tool failure. On the other hand, the cutting temperature, if it is high and is not controlled, worsens the surface topography and impairs the surface integrity by oxidation and introducing residual stresses, surface and sub-surface micro-cracks and structural changes of the work material [3].

High cutting temperature is conventionally tried to be controlled by employing flood cooling by soluble oil. Machining under high speed-feed condition conventionally applied coolants fails to penetrate into the chip-tool interface and thus cannot remove heat

effectively [4-6]. Addition of extreme pressure additives in the cutting fluids does not ensure penetration of coolant at the chip-tool interface to provide cooling and lubrication [7].

In high speed machining of exotic materials like Inconel and Titanium alloys, cutting fluids failed to reduce cutting temperature and improve tool life effectively [8]. However high pressure jet of water, if applied at the chip-tool interface, could reduce cutting temperature and improve tool life to some extent [9]. In machining ductile metals even with cutting fluid, the increase in cutting speed reduces the ductility of the work material and causes production of long continuous chips, which raises the cutting temperature further [10]. However, the advantages caused by the cutting fluids have been questioned lately, due to the several negative effects they cause. When inappropriately handled, cutting fluids may damage soil and water resources, causing serious loss to the environment. Therefore, the handling and disposal of cutting fluids must obey rigid rules of environmental protection. On the shop floor, the machine operators may be affected by the bad effects of cutting fluids, such as by skin and breathing problems [11]. For the companies, the costs related to cutting fluids represent a large amount of the total machining costs. Several research workers [12, 13] state that the costs

related to cutting fluids is frequently higher than those related to cutting tools.

Cryogenic cooling by liquid nitrogen jet provides environment friendly, clean technology for suitable control of cutting temperature but it is not cost effective due to high cost of cryogen [3]. In normal cutting condition MQL provides better performance but at higher feed and speed condition performance is not good [6]. Some recent techniques have enabled partial control of the machining temperature by using heat resistant tools like coated carbides, CBN etc. However, CBN tools are very expensive and the practices in the industry are still not wide spread [14].

In line with growing environmental concerns involved in the use of cutting fluids in machining processes, as reported by several researchers and manufacturers [15, 16] of machine tools, strong emphasis is being placed on the development of environmentally friendly technology, i.e., on environmental preservation and the search for conformity with the ISO 14000 standard. On the other hand, despite persistent attempts to eliminate cutting fluids, in many cases cooling is still essential to the economically feasible service life of tools and the required surface qualities. This is particularly true when tight tolerances and high dimensional and shape exactness are required, or when the machining of critical and difficult to cut materials is involved. This makes high pressure coolant, an interesting alternative, because it combines the functionality of cooling, lubrication and reuse of coolants. Lubrication helps to reduce the tool's friction and to prevent the adherence of materials.

The coolant jet under such high-pressure is capable of creating a hydraulic wedge between the tool and the work piece, penetrating the interface deeply with a speed exceeding that necessary even for very high-speed machining. This phenomenon also changes the chip flow conditions [17]. The penetration of the high-energy jet at the tool–chip interface reduces the temperature gradient and minimizes the seizure effect, offering an adequate lubrication at the tool–chip interface with a significant reduction in friction. Excellent chip breakability has been reported when machining difficult-to-cut materials with high-pressure coolant supply [18, 19]. This is attributed to a coolant wedge which forms between the chip and the tool forcing the chip to bend upwards giving it a desirable up curl required for segmentation. Coolant supply at high-pressure tends to lift up the chip after passing through the deformation zone resulting to a reduction in the tool–chip contact length/area. This tends to enhance chip segmentation as the chip curl radius is reduced significantly; hence, maximum coolant pressure is restricted only to a smaller area on the chip. Similar observation with chip segmentation was made while machining steel. It was observed that the power of the coolant jet and the lateral position of the point where the jet hits the line where the chip exits the tool rake face has significant influence on the chip segmentation process with high-pressure coolant supplies [20].

The present work experimentally investigates the role of high pressure coolant (HPC) jet on cutting temperature, chip thickness ratio and cutting force in plain turning of

AISI 1060 steel and AISI 4320 steel at industrial speed-feed condition by uncoated carbide inserts with ISO tool designations SNMG 120408 and SNMM 120408 and compares the effectiveness of HPC with that of dry machining as well as among the steels used.

## 2. EXPERIMENTAL PROCEDURE

The machining was carried out by turning two steel rod of AISI 1060 steel (Size: Ø178 X 580 mm, BHN: 195) and AISI 4320 steel (Size: Ø200 X 520 mm, BHN: 201) in a powerful and rigid lathe (10 hp) at different cutting speeds (V) and feed rates (f) under both dry and high pressure coolant (HPC) condition. The ranges of the cutting speed (V) and feed rate (f) were selected based on the tool manufacturer's recommendation and industrial practices. Depth of cut, being less significant parameter, was kept fixed at 1.0 mm. Uncoated carbide inserts with ISO tool designations SNMG 120408 and SNMM 120408 was used for the machining trials. PSBNR2525M12, Sandvik tool holder was used for the experimentation. The experimental conditions are given in Table-1.

Table 1: Experimental conditions

<b>Machine tool</b>	: Lathe (China), 7.5 kW
<b>Work material</b>	: AISI 1060 and AISI 4320 steel
<b>Tool geometry</b>	: -6°, -6°, 6°, 15°, 75°, 0.8 (mm)
<b>Tool holder</b>	: PSBNR 2525 M12 (Sandvik)
<b>Process parameters</b>	
Cutting speed, V	: 93, 133, 186 and 266 m/min
Feed rate, f	: 0.10, 0.14, 0.18 and 0.22 mm/rev
Depth of cut, d	: 1.00 mm
<b>HPC supply</b>	: 80 bar with a flow rate of 6.0 l/min
<b>Environment</b>	: • Dry and • HPC with VG 68 Cutting oil



Fig 1. Photographic view of experimental set-up

The HPC needs to be supply at high pressure and impinged at high speed through the nozzle at the chip-tool interface. Considering the conditions required for the present research work and uninterrupted supply of HPC at constant pressure (80 bars) over a reasonably long cut, a HPC delivery system has been designed fabricated and used. The thin but high velocity stream of HPC was projected along the auxiliary cutting edge of

the insert, so that the coolant reaches as close to the chip-tool and the work-tool interfaces as possible. The photographic view of the experimental set-up is shown in Fig.1. The HPC jet has been used mainly to target the rake and flank surface and to protect the auxiliary flank to enable better dimensional accuracy.

The average cutting temperature was measured under all the machining conditions undertaken by tool-work thermocouple technique with proper calibration. The calibration curve is shown in Fig.2. The thickness of the chips directly and indirectly indicates the nature of chip-tool interaction influenced by the machining environment. The chip samples were collected during short run and long run machining for the speed and feed combinations under dry and HPC conditions. The thickness of the chips was repeatedly measured by a digital slide caliper to determine the value of chip thickness ratio,  $r_c$  (ratio of chip thickness before and after cut).

The cutting forces were measured with a force dynamometer (Kistler) mount on carriage via a custom designed turret adapter (Kistler) for the tool holder creating a very rigid tooling fixture. The charge signal generated at the dynamometer was amplified using charge amplifiers (Kistler). The amplified signal is acquired and sampled by using data acquisition on a laptop computer at a sampling frequency of 2000 Hz per channel. Time-series profiles of the acquired force data reveal that the forces are relatively constant over the length of cut and factors such as vibration and spindle run-out were negligible.

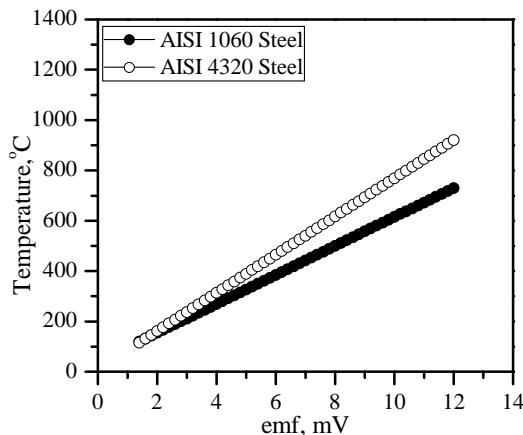


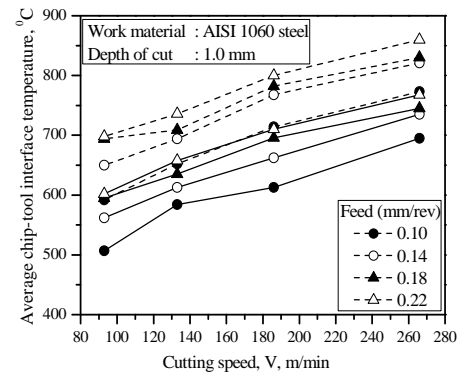
Fig 2. Tool-work thermocouple calibration curve

### 3. RESULTS AND DISCUSSIONS

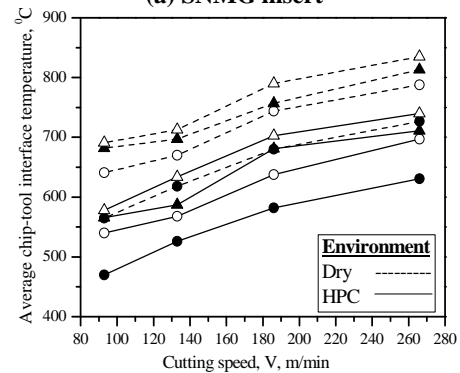
During machining heat is generated at the primary deformation zone, secondary deformation zone and the flank (clearance) surfaces but temperature becomes maximum at the chip-tool interface by accumulating all the heat sources. The cutting temperature measured or evaluated in the present work refers mainly to that chip-tool interface temperature. Any cutting fluid applied conventionally cannot reduce this chip-tool interface temperature effectively because the fluid can hardly penetrate into that the interface where the chip-tool contact is mostly plastic in nature particularly at higher value of  $V$  and  $f$ . However, it was observed that during machining of AISI 1060 steel and AISI 4320 steel with

SNMG and SNMM inserts the high pressure coolant jet in its present way of application enabled reduction of the average cutting temperature depending upon the levels of the process parameters,  $V$  and  $f$  and the types of the cutting inserts. Even such apparently small reduction in the cutting temperature is expected to have some favourable influence on other machinability indices. SNMM insert provided more reduction than SNMG insert and harder AISI 4320 steel provided lower reduction due to higher cutting temperature.

The cutting temperature generally increases with the increase in  $V$  and  $f$ , though in different degree, due to increased energy input and it could be expected that high pressure coolant would be more effective at higher values of  $V$  and  $f$ . But actually it had been otherwise as can be shown in Fig.3 and Fig.4.



(a) SNMG insert



(b) SNMM insert

Fig 3. Variation in temperature in turning AISI 1060 steel

The reduction in the average cutting temperature gradually decreased with the increase in speed more or less truly under all the values of feed when the steel rods was machined under HPC by both type insert unlike when machined by the SNMG type (Fig.3 and Fig.4). This indicates that the geometry of the cutting insert plays significant role on the effectiveness of HPC. It seems the increased bulk contact of the chips with the tool with the increase in speed did not allow significant entry of even the high pressure coolant jet in case of the SNMG insert whose cutting edge geometry allowed intimate contact of the chip over the chip-tool contact length. Only possible reduction in the chip-tool contact length by the HPC jet particularly that which comes along the auxiliary cutting edge could reduce the



temperature to some extent particularly when the chip velocity was high due to higher cutting speed.

Almost all the parameters involved in machining have direct and indirect influence on the thickness of the chips during deformation. The degree of chip thickness which is assessed by chip thickness ratio  $r_c$ , plays an important role on cutting forces and hence on cutting energy requirements and cutting temperature. Fig.5 and Fig.6 shows that HPC has increased the value of  $r_c$  due to reduction in friction at the chip-tool interface and reduction in deterioration of effective rake angle by built-up edge formation and wear at the cutting edges mainly due to reduction in cutting temperature. It appears from Fig.5 and Fig.6 that the chip thickness ratio increases throughout the V-f range undertaken in case of both the inserts when the material machined under HPC condition. The increasing rate of chip thickness ratio is more when machined steel rod under HPC condition by the SNMM type insert due to chip breaking effect of the hill.

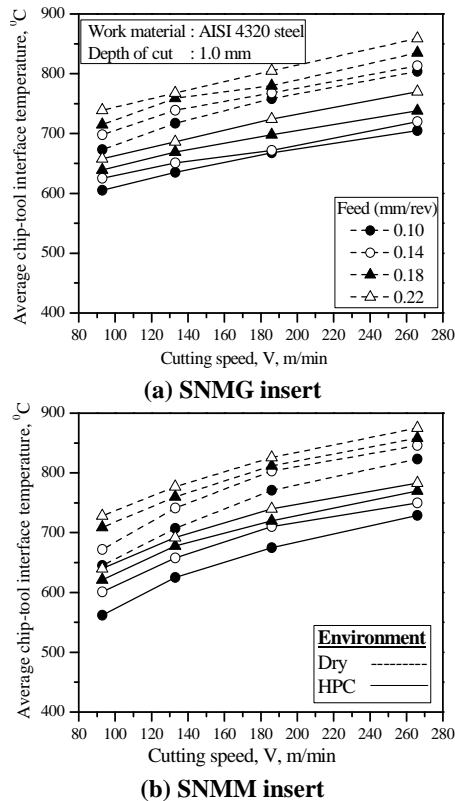
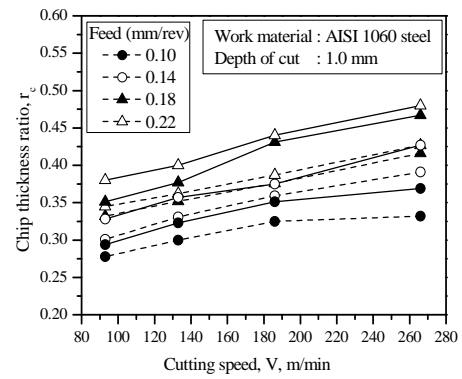
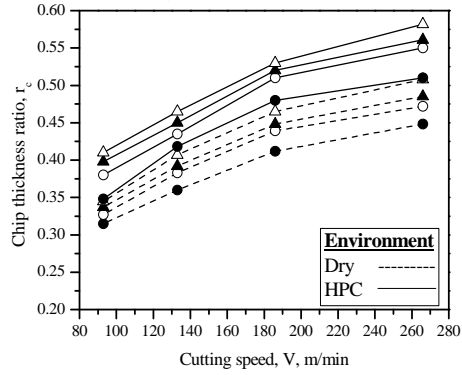


Fig 4. Variation in temperature in turning AISI 4320 steel

A sample of some chips produced during machining both the steels with both the inserts under lower, moderate and higher speeds and feeds are incorporated in Table 2 and Table 3 to show the actual shape and color of the chips under both the environments. Table 2 and Table 3 show that under dry condition chips are basically blue in color and long ribbon shaped. Chips become lighter in color due to reduction in temperature and shapes become loose arc type due to increase in breakability by the application of high velocity HPC jet.

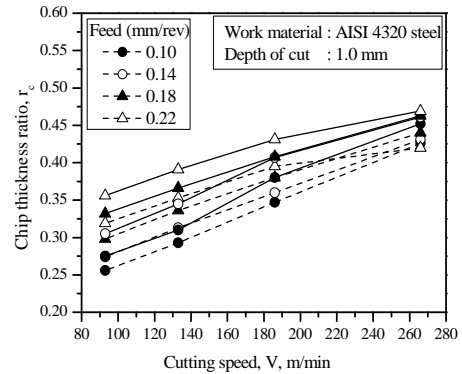


(a) SNMG insert

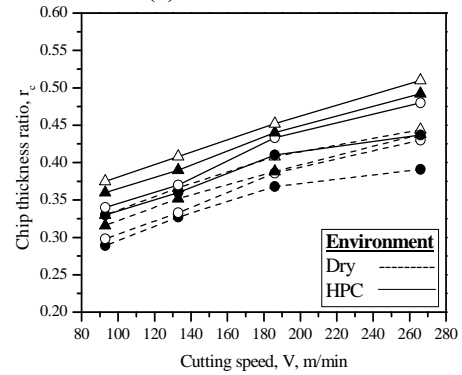


(b) SNMM insert

Fig 5. Variation in  $r_c$  in turning AISI 1060 steel



(a) SNMG insert



(b) SNMM insert

Fig 6. Variation in  $r_c$  in turning AISI 4320 steel

Table 2: Shape and color of chips produced during turning AISI 1060 by different inserts




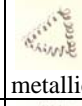




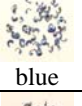


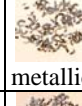


















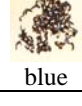
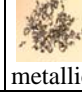
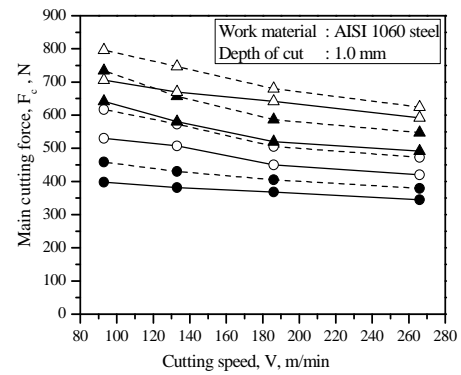
f (mm/rev)	V (m/min)	Insert			
		SNMG		SNMM	
		Environment		Environment	
		Dry	HPC	Dry	HPC
shape/ color	shape/ color	shape/ color	shape/ color		
0.10	93	 blue	 metallic	 blue	 metallic
0.14	133	 blue	 metallic	 blue	 metallic
0.18	186	 blue	 metallic	 blue	 metallic
0.22	266	 blue	 metallic	 blue	 metallic

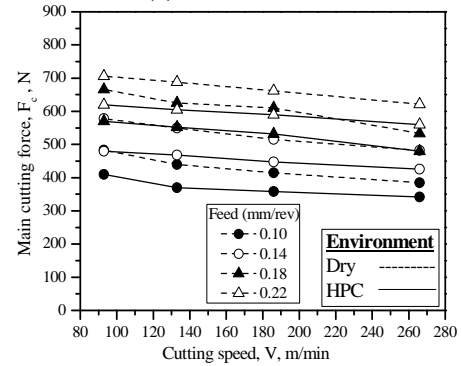
Table 3: Shape and color of chips produced during turning AISI 4320 by different inserts

f (mm/rev)	V (m/min)	Insert			
		SNMG		SNMM	
		Environment		Environment	
		Dry	HPC	Dry	HPC
shape/ color	shape/ color	shape/ color	shape/ color		
0.10	93	 blue	 metallic	 blue	 metallic
0.14	133	 blue	 metallic	 blue	 metallic
0.18	186	 blue	 metallic	 blue	 metallic
0.22	266	 blue	 metallic	 blue	 metallic

The magnitude and pattern of the cutting forces is one of the most important machinability indices because that plays vital roles on power and specific energy consumption, product quality and life of the salient numbers of the Machine-Fixture-Tool systems. Design of the M-F-T-W systems also essentially needs to have the knowledge about the expected characteristics of the cutting forces. Therefore, it is reasonably required to study and assess how the cutting forces are affected by HPC. The force data acquired for the steels machined under both environments with both the inserts are plotted against cutting velocity, shown in figure Fig.7 and Fig.8.

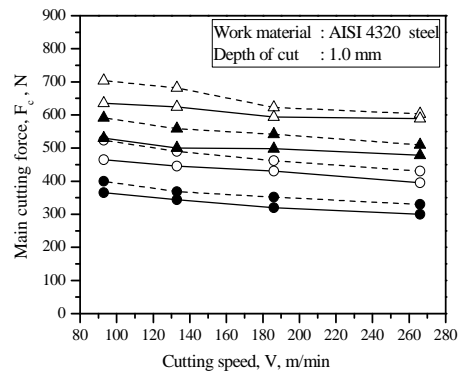


(a) SNMG insert

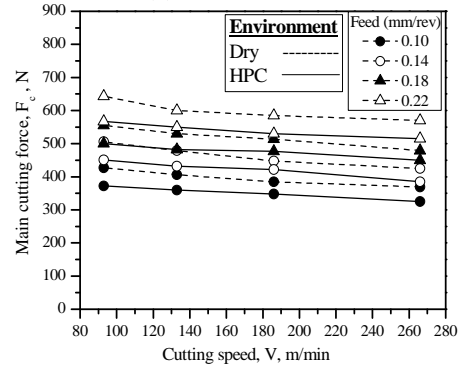


(b) SNMM insert

Fig 7. Variation in main cutting force ( $F_c$ ) in turning AISI 1060 steel



(a) SNMG insert



(b) SNMM insert

Fig 8. Variation in main cutting force ( $F_c$ ) in turning AISI 4320 steel

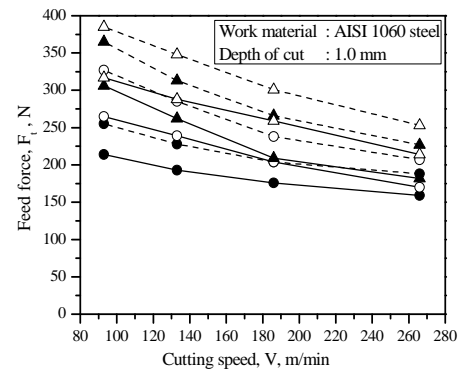
Fig.7 and Fig.8 are clearly showing that  $F_c$  have

uniformly decreased with the increase in cutting speed more or less under all the feeds, for both the inserts and environments undertaken as usual due to favorable change in the chip-tool interaction resulting in lesser friction and intensity or chances of built-up edge formation at the chip-tool interface. It is evident from Fig.7 and Fig.8 that  $F_c$  decreased appreciably due to application of high pressure coolant jet more or less at all the speed-feed combinations when machined steel rods by the SNMM insert. This is the indication of effectiveness of HPC due to the geometry of the cutting insert. It seems that increased bulk contact of the chips with the tool with the increase in speed did not allow significant entry of even the HPC jet in case of the SNMG insert whose cutting edge geometry allowed intimate contact of the chip over the chip-tool contact length.

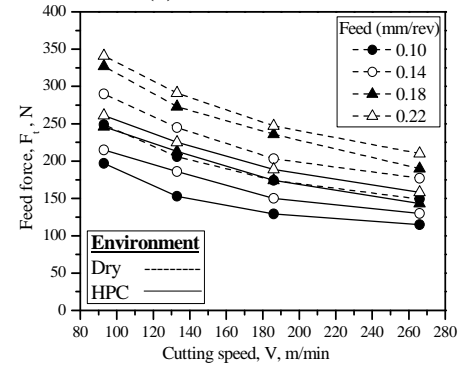
This improvement can be reasonably attributed to reduction in the cutting temperature particularly near the main cutting edge where seizure of chips and formation or tendency of formation of built-up edge is more predominant. Favorable change in the chip-tool interaction and retention of cutting edge sharpness due to reduction of cutting zone temperature seemed to be the main reason behind reduction of cutting forces by the high pressure coolant jet.

Fig.9 and Fig.10 representing the feed force acquired during machining the steels under aforesaid process parameter and conditions. It is evident from Fig.9 and Fig.10 that  $F_t$  decreased sizeably due to application of high-pressure coolant more or less at all the V-f combinations. This improvement can be reasonably attributed to reduction in the cutting temperature particularly near the main cutting edge where seizure of chips and formation or tendency of formation of built-up edge is more predominant. In this respect, the high-pressure coolant jet impinged along the rake surface seems to be more effective in cooling the neighbourhood of the main cutting edge.

Fig.9 and Fig.10 are clearly showing that  $F_t$  has also uniformly decreased with the increase in cutting speed more or less under all machining trial undertaken as usual due to favourable change in the chip-tool interaction. In machining ductile metals like steels by carbide tools, which are not chemically inert like ceramics, the chip material under elevated temperature and high pressure sticks in their layer on the tool surface by adhesion and diffusion and often resulting in gradual piling of the strain hardened layers forming built-up edge near the cutting edge. After growing to certain size, the built-up edge gets separated from the tool by the increased transverse force. Both the formation and frequent separation of built-up edge are detrimental because it not only raises and fluctuates the cutting force but also impairs the finished surface and reduces tool life.

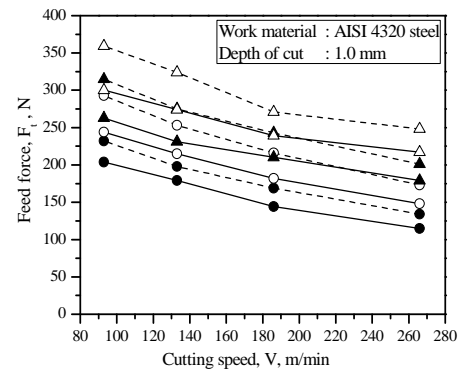


(a) SNMG insert

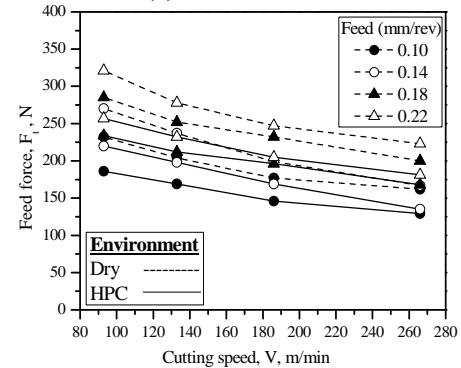


(b) SNMM insert

Fig 9. Variation in Feed force ( $F_t$ ) in turning AISI 1060 steel



(a) SNMG insert



(b) SNMM insert

Fig 10. Variation in Feed force ( $F_t$ ) in turning AISI 4320 steel

#### 4. CONCLUSIONS

Based on the results of the present experimental investigation the following conclusions can be drawn:

- i. The cutting performance of High pressure coolant jet assisted machining is better than that of dry machining with uncoated carbide cutting tools.
- ii. High pressure coolant provides the benefits mainly by substantial reducing the cutting temperature and chip-tool and/or work-tool interface friction which improves the chip-tool interaction and maintains sharpness of the cutting edges.
- iii. Due to HPC cooling, the form and color of the steel chips became favorable for more effective cooling and improvements in nature of interaction at the chip-tool interface.
- iv. High-pressure coolant provides reduction in the cutting forces. Lower cutting forces were recorded when machining at high-pressure coolant supply due to improved cooling and lubrication (low frictional forces) at the chip-tool interface.

#### 5. ACKNOWLEDGEMENTS

This research work has been funded by Directorate of Advisory Extension and Research Services (DAERS), BUET, Dhaka, Bangladesh. The authors are also grateful to the Department of Industrial and Production Engineering, BUET for providing the facilities to carryout the experiment.

#### 6. REFERENCES

1. Muraka, P. D., Barrow, G. and Hinduja, S., 1997, "Influence of the Process Variables on the Temperature Distribution in Orthogonal Machining using the Finite Element Method", *Int. J. Mach. Tool Des. Res.*, 21:445.
2. Aronson, R. B., 1995, "Why Dry Machining", *Manufacturing Engineering*, 114:33-36.
3. Dhar, N. R., Paul, S. and Chattopadhyay, A. B., 2002, "The Influence of Cryogenic Cooling on Tool Wear, Dimensional Accuracy and Surface Finish in Turning AISI 1040 and E4340C Steels", *Wear*, 249: 932-942.
4. Merchant, M. E., 1958, "The Physical Chemistry of Cutting Fluid Action", *Am. Chem. Soc. Div. Petrol Chem. Preprint* 3, 4A:179-189.
5. Dhar, N. R., 2003, "Environmentally Reducing of Conventional Cutting Fluids in Metal Machining", *J. of Mech. Eng., IEB, Bangladesh*, ME 32: 94-107.
6. Dhar, N. R. and Islam, S., 2005, "Improvement in Machinability Characteristics and Working Environment by Minimum Quantity Lubrication", CASR Project, BUET.
7. Cassin, C. and Boothroyd, G., 1965, "Lubrication Action of Cutting Fluids", *J. of Mech. Eng. Sci.*, 7(1): 67-81.
8. Kitagawa, T., Kubo, A. and Maekawa, K., 1997, "Temperature and Wear of Cutting Tools in High Speed Machining of Inconel 718 and Ti-6V-2Sn", *Wear*, 202: 142-148.
9. Mazurkiewicz, M., Kubula, Z. and Chow, J., 1989, "Metal Machining with High-Pressure Water-Jet Cooling Assistance- a New Possibility", *J. Eng. Ind.*, 111: 7-12.
10. Nedess, C. and Hintze, W., 1989, "Characteristics Parameters of Chip Control in Turning Operations with Indexable Three Dimensionally Shaped Chip Formers", *Anns. of CIRP*, 38(1): 75-79.
11. Sokovic, M. and Mijanovic, K., 2001, "Ecological Aspects of the Cutting Fluids and Its Influence on Quantifiable Parameters of the Cutting Processes", *J. Mater. Process. Technol.*, 109(1): 181-189.
12. Byrne, G. and Scholta, E., 1993, "Environmentally Clean Machining Processes-a Strategic Approach", *Anns. of CIRP*, 42(1): 471-474.
13. Klocke, F. and Eisenblaetter, G., 1997, "Dry Cutting", *Anns. of CIRP*, 46(2): 519-526.
14. Narutaki, N., Yamane, Y. and Okushima, K., 1979, "Tool Wear and Cutting Temperature of CBN Tools in Machining of Hardened Steels", *Anns. of CIRP*, 28(1): 23-28.
15. Sahn, D. and Schneider, T., 1996, "The Production without Coolant is Interesting and must be More Known", *Machines and Metals Magazine*, 367: 38-55.
16. Klocke, F., Schulz, A., Gerschwiler, K. and Rehse, M., 1998, "Clean Manufacturing Technologies-The Competitive Edge of Tomorrow?", *Int. J. Manuf. Sci. Prod.*, 1(2): 77-86.
17. R. Kovacevic, C. Cherukuthota, and M. Mazurkiewicz, 1995, "High Pressure Waterjet Cooling/Lubrication to Improve Machining Efficiency in Milling", *Inter. J. Mach. Tools and Manuf.*, 35 (10): 1459-1473.
18. R. Werthein, and J. Rotberg, 1992, "Influence of High Pressure Flushing through the Rake Face of Cutting Tool" *Anns. of CIRP*, 41 (1): 101-106.
19. R. Crafoord, J. Kaminski, S. Lagerberg, O. Ljungkrona, and A. Wretland, 1999, "Chip Control in Tube Turning using a High-Pressure Water Jet", *Proceedings of IMechE 213 (Part B)*: 761-767.
20. J. Kaminski, and B. Alvelid, 2000, "Temperature in the Cutting Zone in Water-Jet Assisted Turning" *J. Mater. Process. Technol.*, 106: 68-73.

#### 7. MAILING ADDRESS

M. Kamruzzaman  
Assistant Professor,  
Department of Mechanical Engineering  
Dhaka University of Engineering & Technology  
(DUET), Gazipur  
E-mail: zaman440n@gmail.com

## EVALUATION OF PROCESS CAPABILITY USING FUZZY INFERENCE SYSTEM

Zakia Farhana, M. Ahasan Habib ,H. Binte Mohsin, S. Mithun Ali and S. Kumar Paul

Department of Industrial and Production Engineering,  
Bangladesh University of Engineering and Technology, Dhaka, Bangladesh

### ABSTRACT

In many industrial instances product quality depends on a multitude of dependent characteristics and as a consequence, attention on capability indices shifts from univariate domain to multivariate domain. In this research fuzzy inference system is used to determine the process capability index. Fuzzy sets can represent imprecise quantities as well as linguistic terms. Fuzzy inference system (FIS) is a method, based on the fuzzy theory, which maps the input values to the output values. The mapping mechanism is based on some set of rules, a list of if-then statements. In this research Mamdani fuzzy inference system is used to derive the overall output process capability when subjected to six crisp input and one output. This paper deals with a novel approach to evaluating process capability based on readily available information using fuzzy inference system.

**Keywords:** Process Capability, Fuzzy Inference System, Design of Experiment.

### 1. INTRODUCTION

In manufacturing industry, Process capability analysis is designed to monitor the proportion of items which are expected to fall outside the engineering specifications in order to prevent an excessive production of nonconforming output. Capability analysis is typically performed by evaluating capability indices which relate the allowable spread of the process, defined by the engineering specifications, to the natural spread of the process. Capability of a process may not depend on only one variable. The process depends on the combined effect of different factors which are known as multivariate process. The process potential index, one of process capability indices depends upon the process variability. To determine the value of process capability index the traditional method is not suitable. Because it can not show the combined effect of different factors affect the process capability. For measuring the capability of this type of process, fuzzy inference system is a good tool. Fuzzy inference is the process of formulating the mapping from a given input to an output using fuzzy logic. The mapping then provides a basis from which decisions can be made, or patterns discerned. The expert based fuzzy inference system makes it easy to measure the process capability. The membership function and the range of process specification help to produce the inference system.

### 2. LITERATURE REVIEW

Process Capability Indices (PCIs) have generated extensive attention in statistical and quality control

publications in recent times. Juran [1] introduced the first process capability index is a simple relative number comparing the value of the required process capability. Capability index

$$C_p = \frac{USL - LSL}{6\sigma} \quad (1)$$

Where USL and LSL are upper and lower specification limit respectively and  $\sigma$  is the process standard deviation.

Kane [2] proposed capability index  $C_{pk}$  that reacts to deviation of the measurement process average mean from check standard nominal value G.Taguchi and T.C. Hsiang [3] designed a loss function as a new approach to production process quality improvement. Yeh and Bhattacharya [4] proposed use of process capability indices based on the ratios of expected proportion NC to actual observed or estimated proportion NC. Flaig [5-8] strongly supports the use of 'fractional conforming' [=1-proportion NC] as a basis for PCIs which will be suitable for any uni modal distribution of X, using Camp-Meidell inequality. Singpurwalla [9] uses the even broader Chebyshev inequality, applicable for any distribution of X.

Clements [10] suggested that  $6\sigma$  be replaced by the length of the interval between the upper and lower 0.135 percentage points of the distribution of X (this  $6\sigma$ ' for a normal N (distribution). Wright [11] suggested PCIs sensitive to skewness. Bai and Choi [12] have constructed PCI for use with possibly skewed distribution of X, based on a 'Weighted variance' (WV)

approach. When the capability of the process depends on many variables, then the calculation of multivariate indices needed to be took place. In this way, Taam, Subbaiah and Liddy [13] generated the first multivariate capability index for the bivariate case. Pal [14] proposed the index. Bothe [15] proposed a method in order to compute the multivariate  $C_{pk}$  index. Wang and Cheng [16] proposed multivariate equivalents for  $C_p$ ,  $C_{pk}$ ,  $C_{pm}$  and  $C_{pmk}$  based on PCA (Principal Component Analysis) decomposition. Wang and Du [17] proposed the same indices and one extension to the multivariate case.

Shahriari et al. [18] and Hubel proposed a process capability multivariate vector in order to evaluate the process performance. The multivariate characteristics of the processes that specify geometric dimensions have led to much research and new capability indices for analyzing the multivariate processes. Nuehard [19] proposed a method for calculating capability indices for multivariate processes in which the variance is adjusted for correlation by multiplying it by a factor, and then the adjusted variance is used to calculate the indices. Hubele et al [20] discussed the disadvantage of using univariate capability index and the advantage of the bivariate process capability vector. They considered the bivariate normal distribution and analyzed the process for its capability.

For non-normal processes, Rogowski [21] proposed to transfer the data into normal and then to use the Ordinary  $C_p$  of the normally distributed process. The type of transformation is obtained by goodness-of-fit tests.

Geometric Dimensioning and Tolerancing (GD&T) is the engineering standard that provides a unified terminology and approach to describe both the geometry of the features and the associated tolerance of the product. GD&T contains different types of tolerances such as form, orientation, profile, position, and run-out. Gruner [22] explained how to calculate a PCR for a specified variable tolerance (tolerance varies as the actual size of the feature varies) using GD&T. Methods for generating the PCR for a spherical or circular tolerance zone and concentricity was studied by Davis[23] et al. Sakar and Pal[24].

Process capability measures that have been introduced in the past years can be generally classified into three categories: process capability measures for coordinate tolerance specifications, process capability measures for geometric tolerance specifications, and process capability measures for multivariate processes.

The above methods didn't use fuzzy logic to find out the process capability index  $C_p$ . In this paper some factors which has significant impact on process capability is considered to calculate  $C_p$  using fuzzy inference system.

### 3. OBJECTIVE OF THE STUDY

The objective of the present work is to compute the process capability of a soap production process. Six input variables which has effect on the process capability of a soap production and one output variable that is the process capability are considered. The input variables are mixing temperature, coolant temperature, flow rate, moisture content, urea content and free fatty acid content.

moisture content, urea content and free fatty acid content.

## 4. METHODOLOGY

The work has been carried out in a soap factory to do this job. Six factors have been identified which affect the process capability of soap production by doing the Design of Experiment (DoE). Those are: mixing temperature, coolant temperature, flow rate of coolant, percentage of fatty acid, percentage of urea, and the moisture content. The combined effect of these six factors of this process is shown in figure 1.

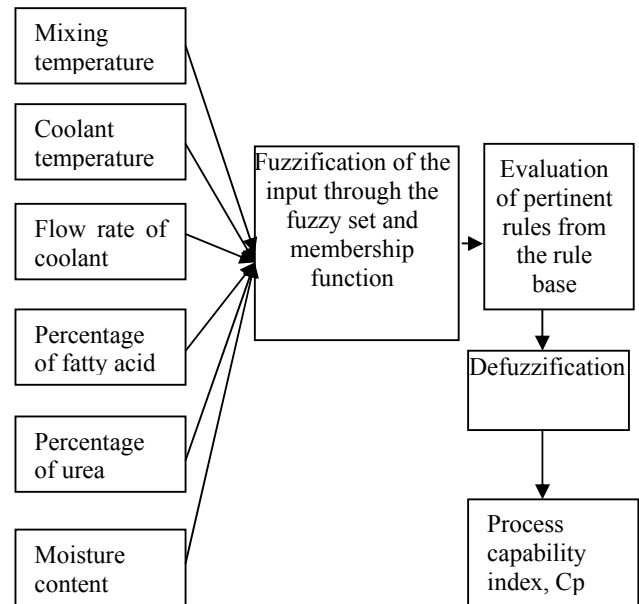


Fig 1. Fuzzy Model of proposed system

### 4.1 Membership Function

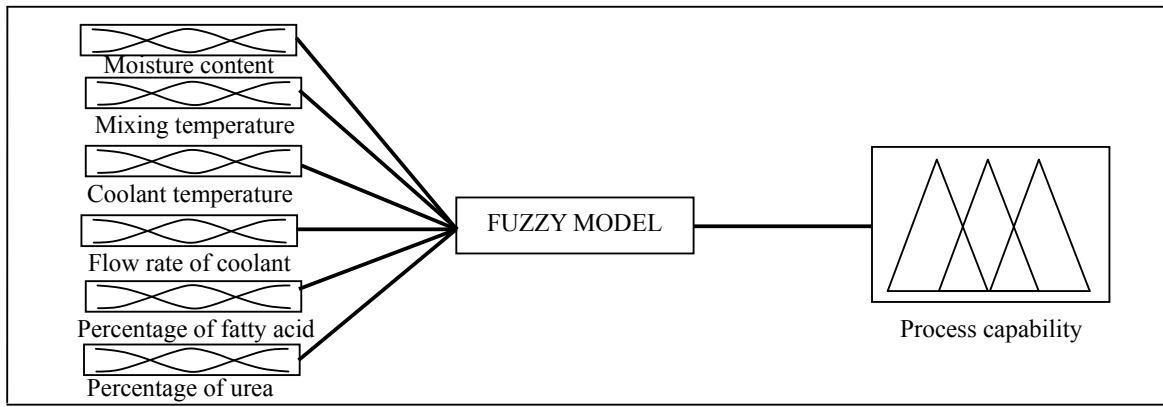
Membership function is the mathematical function which defines the degree of an element's membership in a fuzzy set. The Fuzzy Logic Toolbox of MATLAB includes 11 built-in membership function types. These functions are built from several basic functions:

- Piecewise linear functions,
- The Gaussian distribution function,
- The sigmoid curve and
- Quadratic and cubic polynomial curve.

### 4.2 Input Fuzzification

The step is to take the inputs and determine the degree to which they belong to each of the appropriate fuzzy sets via membership functions. Here the input variables are mixing temperature, coolant temperature and flow rate of coolant, moisture content, urea content and free fatty acid content.

The membership function and the linguistic variables of input and output variables are entered in Matlab Fuzzy Toolbox' Membership Function Editor. Gaussian membership function is used for each linguistic variable. Figure 3 represents the membership function and linguistic variables for one input mixing temperature. Similarly membership function and linguistic variables are entered for other variables.



FIS Name:	Fuzzy model	FIS Type:	mamdani
And method	min	Current Variable	
Or method	max	Name	<input type="text"/>
Implication	min	Type	
Aggregation	max	Range	
Defuzzification	centroid	<input type="button" value="Help"/> <input type="button" value="Close"/>	

Fig 2. FIS model for Process capability analysis

Table 1: The variation of input linguistic variables

Input variable	Low	Medium	High
Mixing temperature	[17.00,60]	[21.2,150]	[10.6,225]
Coolant temperature	[2.12,2.5]	[6.37,5]	[4.25,20]
Flow rate of coolant	[318.5,750]	[424.7,2000]	[318.5,3250]
Percentage of fatty acid	[1.7,6]	[1.06,12.5]	[2.12,20]
Percentage of urea	[5.3,17.5]	[4.25,40]	[5.31,62.5]
Moisture content	[1.7,4]	[1.50,11.5]	[1.66,19]

Table 2: The variation of output linguistic variables

Output variable	Totally incapable	Semi incapable	Almost incapable	Semi capable	Almost capable	Capable	Highly capable
Process capability	[0.064, 0.15]	[0.074,0.425]	[0.053,0.675]	[0.042,0.9]	[0.042,1.1]	[0.11,1.45]	[0.06,1.85]

Different input variables and corresponding values of low, medium and high range in terms of standard deviation and mean are shown in table 1. Output variable and different ranges are shown in table 2.

The membership function and the linguistic variables of input and output variables are entered in Matlab Fuzzy Toolbox' Membership Function Editor. Gaussian membership function is used for each linguistic variable. Figure 3 represents the membership function and linguistic variables for one input; mixing temperature. Similarly membership function and linguistic variables are entered for other variables.

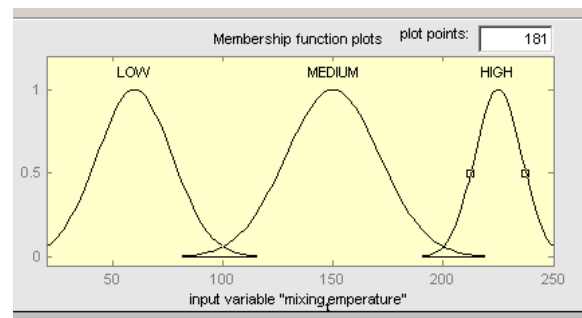


Fig 3. Membership function and linguistic variables for mixing temperature



### 4.3 Antecedent Matching

Once the inputs have been fuzzified, the degree to which each part of the antecedent has been satisfied for each rule is known. If the antecedent of a given rule has more than one part, the fuzzy operator is applied to obtain one number that represents the result of the antecedent for that rule. This number will then be applied to the output function. The input to the fuzzy operator is two or more membership values from fuzzified input variables. The output is a single truth value. Here AND operation has been used.

### 4.4 Rule Fulfillment

After the membership functions are determined, the rules are designated and written in Matlab Fuzzy Toolbox for evaluation. And after the needed data are entered, inputs are solved according to change of input positions for solving of fuzzified systems. Here an example of rule is given:

If (mixing \_temperature is Low) and (coolant \_temperature is Medium) and (flow \_rate is Low) and (urea \_content is Low) and (moisture \_content is Low) and (free fatty acid \_content is High) then (process is semi incapable)

### 4.5 Consequent Aggregation

Since decisions are based on all the rules in a fuzzy inference system, the rules have been combined in some manner in order to make a decision. Aggregation is the process by which the fuzzy sets that represent the outputs of each rule are combined into a single fuzzy set.

### 4.6 Output Defuzzification

Taking fuzzy sets as input, defuzzification outputs a crisp value, which is suitable for analysis and control. There are usually two types of fuzzy inference systems differing in defuzzification part, namely Mamdani-type and Sugeno-type. Here Mamdani-type has been used.

Mamdani-type inference expects the output membership functions to be fuzzy sets. After the aggregation process, there is a fuzzy set for each output variable that needs defuzzification. In this work, the weight of each factors have been taken as one.

## 5. RESULT AND DISCUSSION

The data are taken from a soap manufacturing industry. The measurements are done for 30 data and the sample size for each time is 4. Then the result is analyzed on the basis the data has been performed.

### 5.1 Goodness of Fit Test

To check whether the taken data fit the normal distribution, Kolmogorov-Smirnov goodness of fit test For hypothesis testing, the null hypothesis is

$H_0$  : Data fit normal distribution.

$H_1$  : Data don't fit normal distribution.

According to the basic of Kolmogorov-Smirnov goodness of fit test, D is calculated. If the calculated value of D is less than that of critical value than the null hypothesis is accepted.

For 95.5% confidence level D (upper tail percentage point) is 0.895. The formula for calculating modified D

is: The maximum value of D from the 9<sup>th</sup> column ( $\sqrt{n} \cdot 0.01 + .85 / \sqrt{n}$ ) Here 'n' is the no of samples:

Table 3: Value of Upper tail Percentage Point (D)

Factors	Modified value of D
Mixing temperature	0.8865
Coolant temperature	0.6645
Flow rate	0.862

As rejection region starts from 0.895 so it can be said that the data for above factors are fit for normal distribution. At the same way for other three factors, it can be said that the data are normally distributed.

### 5.2 The Rules Editor

Total 25 rules are developed and the Matlab Fuzzy Toolbox Rule Editor is used to develop these rules.

### 5.3 Surface Viewer

The results which have been obtained from Matlab Fuzzy Toolbox are shown below in figure 4, 5 and 6. These figures show the effects of the inputs to the output. Figure 4 shows the how process capability is varied with the input variables mixing temperature and coolant temperature. In figure 4, the step wise changes of the variables are shown. If the mixing temperature is taken as 150, it is seen from the surface viewer that the process is semi capable. If the coolant temperature is taken as 0, it will also show semi capable. Some time it is seen that the actual results don't match with the surface viewer. This is because of the combined effect. Figure 5 represents the process capability is varied with flow rate and mixing temperature. Moreover figure 6 shows the change of process capability with changing of input; moisture content and mixing temperature. The variation of process capability against the input variables depends on the developed rules.

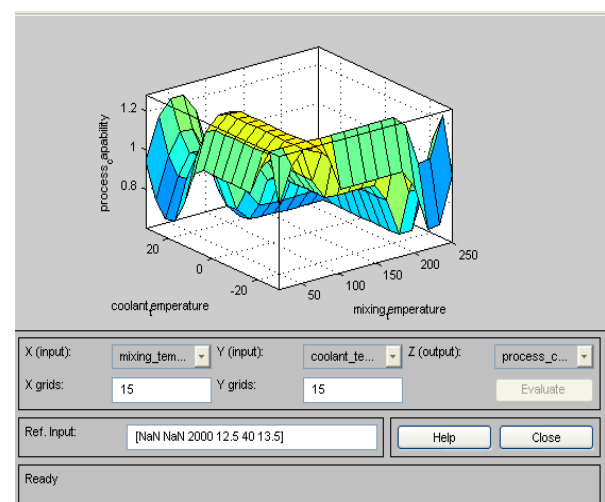


Fig 4. Surface Analysis between mixing temperature and coolant temperature with process capability

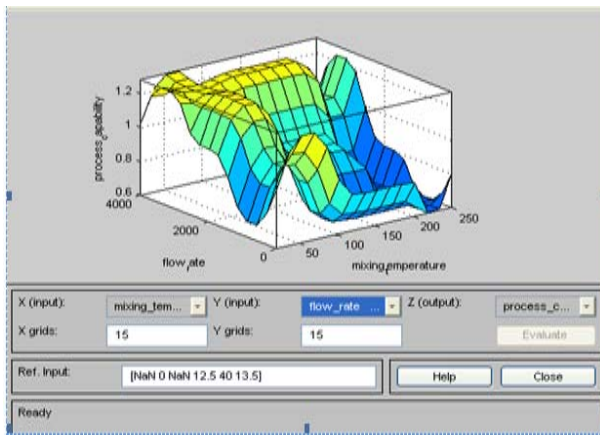


Fig 5. Surface Analysis between flow rate and mixing temperature with process capability

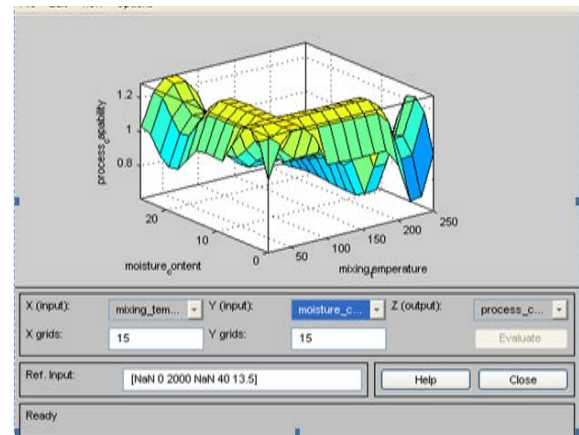


Fig 6. Surface analysis between moisture content and mixing temperature with process capability

### 5.4 Case Study

A case study is done to show the effect of the factors on process capability. The inputs for the six factors are feed in a rule viewer of MATLAB fuzzy inference system.

The rule viewer is shown in figure 7. Different output (process capability) can be measured in response to changing input parameters. The values of input variables and measured output (process capability) are shown in table4.

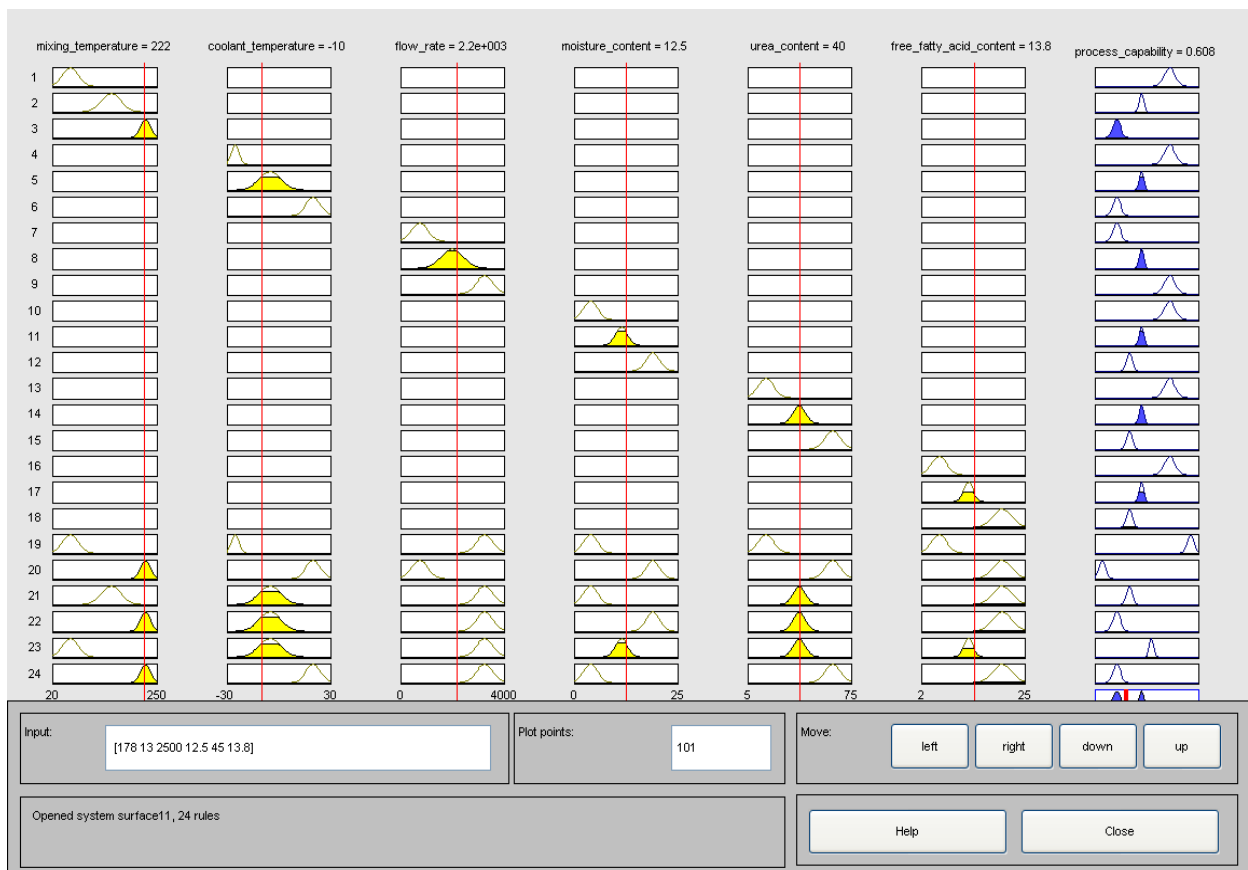


Fig 7. Rule Viewer for case study

Table 4: Values of different parameters for case study

SL. No	Factors	Value
1.	Mixing temperature( <sup>0</sup> c)	222
2.	Coolant temperature( <sup>0</sup> c)	-10
3.	Flow rate of coolant(lt/s)	2500
4.	Moisture content (%)	12.5
5.	Urea content (%)	40
6.	Free fatty acid content (%)	13.8
Output variable	Process capability	0.608

The rule viewer of MATLAB fuzzy inference system is used to feed the inputs and to get the output; that is the process capability.

## 6. CONCLUSION

In this paper, the process capability is obtained by considering moisture content, mixing temperature, flow rate of coolant, urea content, free fatty acid content and moisture content using the fuzzy logic is important as it gives the optimal result. The manufacturing companies should use the optimal result which reduce the total cost and increase the overall profit. Fuzzy logic helps to find these optimal results if the company's expert provided data are available. In this research, using data of a soap manufacturing company the final result is obtained by which process capability is determined. Here, six input variables are considered to find the process capability. For each input and output variable Gaussian membership functions are considered to design the model.

## 7. REFERENCES

- Juran, j.m., "Juran's quality control handbook", 3rd edition, McGraw hill, New York.N.Y.197
- Kane, V.E., 'process capability indices'. Journal of quality control, Vol.18 , pp.41-52, 1986.
- Hsiang , T.C. and Taguchi, G,'tutorial on quality control and assurance – the taguchi method 'joint meeting of the American statistical association, las vegas,Nevada,pp.188
- Yeh, A.B and Bhattacharya, S., 'A robust capability index'. Communications in statistics-simulation and computation. Vol27, pp.565-589, 1998
- Flaig, j.j., "Issues related to compatibility indices"process capability analysis software manual, section 6, applied technology, san jose, CA, 1992
- Flaig,j."A new approach to process capability indices".Quality Engineering.Vol. 9, pp. 200-211, 1996/7
- Flaig,j."Process Capability Sensitivity Analysis". Quality Engg. Vol. 11, pp.587-592, 1999
- Flaig, j.j., "Issues related to compatibility indices" process capability analysis software analysis. section 6, applied tech.,san jose,CA.,2000
- Singapurwalla, N.D.,"The Stochastic Control of Process Capability Indices". Test, pp.1-33, 1998

- Clements, J.A., "Process Capability Calculations for Non Normal Distributions". Quality Progress, Vol.22, pp.95-100, 1989.
- Wright, P.A., "Process Capability Index Sensitive to Skewness", Journal of statistical computation and simulation. Vol.52, pp.195-203, 1995.
- Bai,D.S. and Choi, S.S. "Process Capability Indices For Sewed Populations". Masters thesis. Department of Industrial Engineering, Advanced Institute of Science and Technology, Taejon, South Korea, 1997.
- Taam, W., Subbiah, P. and W.Liddy, J.,"Anote on multivariate capability indices". Journal of applied statistics, Vol.20 (3), pp.339-351, 1993.
- Pal. S., "Performance Evaluation of a Bivariate Normal Process". Quality Engineering. Vol.11 (3), pp.379-386,1999.
- Bothe, D.R.,"Composite capability index for multiple product characteristics",. Quality Engineering, Vol.12(2),pp.253-258,1999.
- Wang, F.K. and Chen, J.C., "Capability index using principal component analysis". Quality Engineering, Vol.11 (1), pp.21-27, 1998.
- Wang, F.K. and Du, T.C.T., "Using principal component analysis in process performance for multivariate data". Omega: the international journal of management science, Vol.28, pp. 184-194, 2000.
- Shahriari,H.,Hubele, N.F. and Lawren ce, F.P., "A multivariate process capability vector", Procc. of the 4<sup>th</sup> Industrial Engineering Research Conference, pp.303-308, 1995.
- Neuhard, J.B., 1987, "Effects of Correlated Subsamples in Statistical Quality Control," IEE Transactions, 19(2), 208- 214.
- Hubele, N.F., Shahriari, H., and Cheng, C-S., 1991, "A Bivariate Process Capability Vector," Ap
- Rogowski, D., 1994, "Non-Normal Distributions, Capability Indices, Specification Limits, DPMO and DPU," TI Technical Journal, pp. 84-95.
- Rogowski, D., 1994, "Non-Normal Distributions, Capability Indices, Specification Limits, DPMO and DPU," TI Technical Journal, pp. 84-95.
- Gruner, G., 1991, "Calculations for Cpk under Conditions of Variable Tolerances," Quality Engg., 3(3), pp. 281-291.
- Sakar, A., and Pal, S., 1997, "Estimation of Process Capability Index for Concentricity," Quality Engineering, Vol. 9, pp. 665

## 8. NOMENCLATURE

Symbol	Meaning
FIS	Fuzzy Inference System
MF	Membership Function
DoE	Design of Experiment
PCI	Process Capability Index

## 9. MAILING ADDRESS

Syed Mithun Ali  
 Department of Industrial and Production Engineering,  
 BUET, Dhaka, Bangladesh  
 Email: [mithun@ipe.buet.ac.bd](mailto:mithun@ipe.buet.ac.bd)

## AN INDUSTRIAL APPLICATION OF DMECA APPROACH TO MANAGEMENT PROCESS ANALYSIS

Azizur Rahman<sup>1</sup>, M. Kutub Uddin<sup>2</sup>

<sup>1</sup>Dept. of IEM, KUET, Khulna, Bangladesh

<sup>2</sup>Dept. of ME, KUET, Khulna, Bangladesh.

### ABSTRACT

This paper presents an industrial application of “Dysfunction Mode and Effects Critical Analysis” (DMECA) to determine and analyze possible dysfunctions in a complex management process. The approach conceptually derived from the Failure Mode and Effect Critical Analysis (FMECA) technique. DMECA enables user to analyze all possible dysfunctions of management processes, identify the subsequent effects of each potential dysfunction, make a list of priority interventions for all the dysfunctions, prioritize and classify the dysfunctions by the Risk Priority Number (RPN) which represents the severity of the consequences, investigate potential causes of dysfunctions and determine the improvement actions. In order to illustrate the performance of the technique, an industrial application concerning analysis of management process in a power plant is presented. It is identified 175 potential causes for the whole management processes and found that 60% of the dysfunctions can be corrected by solving only 15% of the causes.

**Keywords:** Dysfunction Mode and Effect Critical Analysis (DMECA); Failure Mode and Effect Critical Analysis (FMECA); Total Quality Management (TQM).

### 1. INTRODUCTION

Following the principles of the Total Quality Management (TQM) philosophy, the ISO 9000:2000 standard emphasizes the process approach to manage an organization’s quality system. ‘Process approach’ means that all the activities must be identified, managed and controlled. In particular, the organization must: (i) define the interrelations between processes, and (ii) monitor how a dysfunction in a process (or activity) influences the results of other processes (or activities). Another TQM concept emphasized by ISO 9000 norms is related to continuous improvement of processes, and involves applying Deming’s Plan-Do-Check-Act (PDCA) paradigm. Therefore, the organization must correctly select the most important and critical processes, which need improvement actions.

The literature to date does not provide a unique suitable technique that is able to represent a systematic and logical approach to (i) describe and analyze management processes, and (ii) select improvement actions. Two main classes of techniques are adopted to analyze processes. The first class constitutes methodologies to represent a process or more interrelated processes based on graphical methods [1]. Unfortunately, although this technique can identify the correlation between activities and define the ‘father-child’ relationship between processes, it cannot define the criticalities of possible dysfunctions, nor does it permit the establishment of criteria or the definition of

priorities of improvement actions. According to Goulden and Rawlins (1995), by using this approach, activities could be mapped together to build an integrated picture, however this can be a time consuming task with visually confusing results and so can fail to engender a sense of ownership and widespread understanding of management processes[2]. Similar conclusions regarding the limitations of the IDEF type models for process analysis have been reached by Dale and Plunkett (2000)[3]. The second type of approach is represented by problem solving techniques, which are generally able to define the priorities and criteria of improvement actions by adopting structured approaches composed of brainstorming sessions, decision-making support methods, correlation and pondering matrixes and flow diagrams for example. Unfortunately, they neither permit the correlation of the results obtained from improvement actions with other processes, or the evaluation of their impact.

In summary, the literature to till date provide an approach name Dysfunction Mode and Effects Critical Analysis (DMECA) which is able to support description and analysis of processes and, contemporaneously, able to investigate dysfunction consequences, their impact on whole process efficiency, and also the definition of improvement actions. In this paper according to this new approach a case study is presented to evaluate the effectiveness of the DMECA approach.

## 2. DYSFUNCTION MODE AND EFFECT CRITICAL ANALYSIS (DMECA)

The DMECA method proposed is conceptually derived from the Failure Mode Effect and Criticality Analysis (FMECA) approach which was originally developed and used in reliability and maintenance activities [4]. Similar to FMECA, the DMECA methodology is fundamentally the result of two sequential phases:

### 1. DMEA phase:

A dysfunction modes and effects analysis (DMEA) is a procedure for analysis of potential failure modes within a system for classification by severity or determination of the effect of failures on the system.

- Management processes identification – the result is a list of the main processes in relation to the firm’s organizational chart (functional department and their activities)
- Process Breakdown Structure (PBS) definition, where the functional structure of the processes consists of:
  - a. System → macro-processes identification
  - b. For each macro-process → processes identification
  - c. For each process → sub-processes identification
  - d. For each sub-process → activities identification.
- Criteria judgments definition – by applying DMECA, a new correlation matrix between value of probability, severity and detection parameters, and their relative evaluation criteria, has been determined in place of the value reported in product FMECA applications.

### 2. Criticality Analysis phase:

Criticality analysis is another component of Dysfunction Mode, Effects, and Criticality Analysis (DMECA). It is an extension of Dysfunction Mode and Effects Analysis (DMEA). In addition to the basic DMEA, it includes a criticality analysis, which is used to make the probability of failure modes against the severity of their consequences. They are as follows:

- Risk Priority Number (RPN) evaluation – dysfunction causes (instead of failure) and their relative weight can be defined for each activity in order to determine the most critical and decide improvement actions. The result is a list of critical activities and priorities.
- Corrective actions planning and design – DMECA method provides a structured approach to investigate, plan and apply improvement actions by using a corrective action worktable.

Corrective action results evaluation – on the basis of the results, the DMECA process can restart to implement new or reengineered activities.

## 3. RESEARCH INSTRUMENT

Based on the prepared questionnaire, data on the variables were considered and the information were summarized, compiled to fit those into tables and finally analyzed in accordance with the objectives of the study. In

this way overall picture of the study were identified to point out various dysfunctions of the managerial process.

## 4. MANAGEMENT PROCESS IDENTIFICATION

There are 60 management personnel who are directly involved in management process of the power plant but currently working 40 personnel, 28 of which are directly involved in operation and maintenance [5].

## 5. JUDGMENT CRITERIA, DYSFUNCTION DEFINITION AND CRITICALITY ANALYSIS OF DMECA

It is, necessary to redefine evaluation factors, acceptability limits and conversion criteria for the parameters utilized in order to determine RPNs context of the management process. Each dysfunction had thus been judged according to the following three factors: (i) Occurrence Dysfunction ( $O_D$ ), (ii) Detectability of Dysfunction ( $D_D$ ) and (iii) Severity Dysfunction ( $S_D$ ). For Occurrence Dysfunction ( $O_D$ ), six levels (reported in Table 5-1) was identified, ranging from ‘irrelevant’ to ‘very high’ and described through Arabic numerals 1 to 10 [4]. The Mean Time Between Dysfunction (MTBD) factor was introduced which is similar to the Mean Time Between Failure (MTBF) in FMECA and represents the mean time between two same dysfunctions [5]. The values in the third column of Table 5-1 were obtained by interviewing personnel. Generally, the MTBD values in days can change for different companies and depends on the annual number of jobs. A suitable way of calculating the MTBD value is as follows:

$$MTBD = 36500 / (N_c * D_{100i}) \text{ in days}$$

where:

$N_c$  = mean number of jobs per year (historical data)

$D_{100i}$  = number of dysfunctions of type i per 100 jobs.

Table 1: Conversion table for dysfunction occurrence factor

Qualitative evaluation of the dysfunction occurrence	MTBD value	Percentage happen (%)	$O_D$
Irrelevant	> 1 year (> 365 days)	<= 1	1
Remote	4, 5–11 months (132–331 days)	2 to 5	2–3
Low	2–4 months (66–121 days)	6 to 10	4–5
Moderate	1–2 months (27–60 days)	11 to 24	6–7
High	2 weeks–1 month (14–26 days)	25 to 49	8–9
Very high	< 2 weeks (< 13 days)	>= 50	10

For the Detectability of Dysfunction ( $D_D$ ) judgment, a qualitative linguistic evaluation table was proposed as reported in Table 5-2. Based on these judgments, the detectability of dysfunction was divided into five classes, defined by Arabic numerals 10 to 1 and ranging from ‘very low’ to ‘very high’ [4].

Table 2: Conversion table for detectability of dysfunction factor

Qualitative evaluation of the dysfunction detection	Description	D <sub>D</sub>
Very low	Customers detects dysfunction after commissioning	9–10
Low	Dysfunction detected at final test	7–8
Moderate	Dysfunction detected by inspection or after control	4–6
High	Dysfunction detected after work operation where born	2–3
Very high	Dysfunction detected during work	1

Finally, in traditional FMECA, when studying product reliability, the gravity factor was based on parameters such as security and safety [5]. For DMECA, on the other hand, in the management process the gravity factor can be based on productivity loss, high cost, delay in responding to customer needs and quality loss. This list is not meant to be exhaustive. For this case-study, the mission was suggested considering time and quality results (Table 5-3) as critical variables [4].

Table 3: Conversion table for the dysfunction severity factor (Time and quality parameter)

Qualitative/linguistic evaluation of the dysfunction severity	Description	S <sub>D</sub>
Critical	Job delivery delay > 1 month OR Unacceptable quality level: significant risk to ship inadequate material to the customer	10
Very important	Job delivery delay from 15 days to 1 month OR Unacceptable quality level: unacceptable defect detected during final test	7–9
Important	Job delivery delay from 1 to 2 weeks OR Unacceptable quality level: unacceptable defect detected at its first occurrence	4–6
Unimportant	Job delivery delay from 2 to 6 days OR Acceptable quality but at the standard limit	2–3
Trivial	Job delivery delay ≤ 1 day OR Dysfunction mode does not influence quality	1

The next step was the evaluation of possible dysfunctions and the identification of the related causes, attributing a value to the three factors: probability, detection and gravity. In the process break-down structure defined during the process identification phase (reported in Figure 6-1 for the firms' processes), there are 09 sub-processes and 57 activities of job management process have been identified. Figure 6-2 shortly reported the detailed breakdown structure for the macro-process 'operations' of the function 'job management' located at Level 2 of firm-process as reported in Figure 6-1. For each activity, possible dysfunctions had established and 175 potential causes have been identified for the whole process of 'job management'. A code number was assigned to each dysfunction with the same criteria used to map the processes. Thus, it is possible to judge and evaluate the criticality of the dysfunction causes.

### 6. PROCESS BREAKDOWN STRUCTURE

The input to process mapping is the five-level organization chart reported in Figure 6-1 (processes breakdown structure). In Figure 6-1, the 4th and 5th levels of the operations macro-process were more detailed because this is the objective of the DMECA analysis. The second step consists of breaking down the sub-processes of Figure 6-1 to the level of detail needed for the analysis – that is, down to elementary activities as shown in Figure 6-2(short form). Each activity was distinguished by an alphanumeric identification symbol, which labels each decomposition level. There are 09 sub-processes and 57 activities of job management process have been identified (figure 6-2 shows some of these).

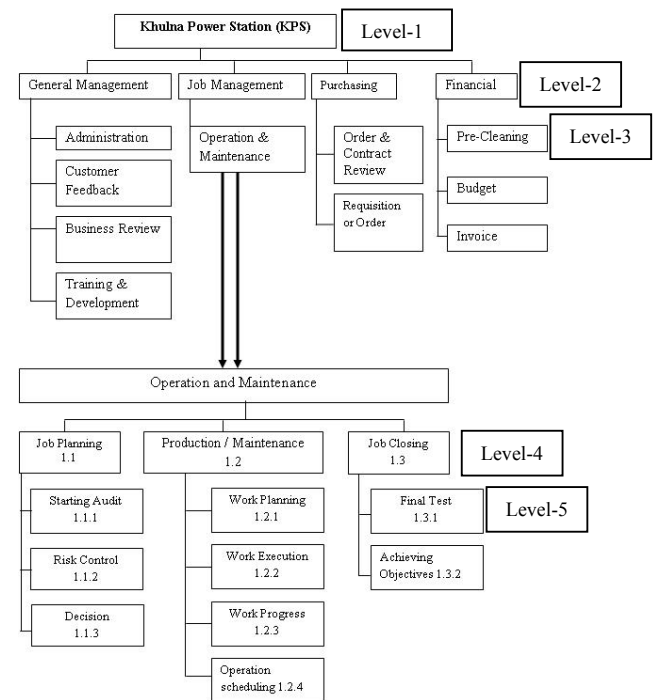


Fig 1. Process (Maintenance and/or Production) breakdown structure (General map of the process)

1<sup>st</sup> level – the firm; 2<sup>nd</sup> level – function; 3<sup>rd</sup> level – macro-process; 4<sup>th</sup> level – process; 5<sup>th</sup> level – Sub-process

ID	MACRO PROCESS	ID	PROCESS	ID	SUB PROCESS	ID	ACTIVITY
1	Operation and maintenance	1.1	Job planning	1.1.1	Starting audit	1.1.1.1	Integrated stock check
						1.1.1.2	Correspondence inventory and transport document
						1.1.1.3	Disassembly
						1.1.1.4	Cleaning components
						1.1.1.5	Visual and dimensional control
						1.1.1.6	Chemical composition analysis
						1.1.1.7	Certification data emission

Fig 2. Process breakdown structure (detailed map of the process but here it is in a short form)

### 7. DATA COLLECTION

Based on the DMEA phase described above, a Criticality Analysis (CA) phase was conducted for every dysfunction identified. As reported in Table 7-2, for each detailed activity, the following are determined:

- all possible and potential causes or problems that can cause dysfunction on activities
- modes of dysfunctions
- the effects of the dysfunction on the whole process or part of it.

To reduce the variability of the answer and the subjective judgment, each personnel completed a questionnaire (table 7-2) independently, with the support of Table 7-1.

Table 4: Indications to complete questionnaire

Column	Indications to complete questionnaire
a	How many times does this kind of cause (reported in the row) of dysfunction happen in every 100 jobs? Write your number.
b	What is the value of gravity of this kind of dysfunction as described in Table 4.4? Write your $S_D$ value.
c	What is the value of detection of this kind of dysfunction as described in Table 4.3? Write your $D_D$ value.

Mean values (from all questionnaires) of the three parameters ( $O_D$ ,  $D_D$  and  $S_D$ ) for each dysfunction then be

calculated. Finally, the respective RPNs was obtained as follows:  $RPN = O_D \times D_D \times S_D$ . The calculated RPN value is given in table 7-2 (short form).

This product may be viewed as a relative measure of the management dysfunctions. Values for the RPN can range from 1 to 1000, with 1 being the smallest management dysfunction possible. This value was then used to rank the various causes in the dysfunctions. In case of process with a relatively high RPN, the engineering team must make efforts to take corrective action to reduce the RPN. Likewise, because of a certain concern has a relatively low RPN, the engineering teams not overlook the causes and not neglect an effort to reduce the RPN. In this case, a low RPN may be extremely misleading, not placing enough importance on a cause where the level of severity may be disastrous. In general, the purpose of the RPN was to rank the various cause. The smaller the RPN the better – and – the larger the worse.

Table 5: Detailed activities, dysfunction causes, modes and effects

ID	Activity	ID	Dysfunctional cause	Dysfunctional mode	Dysfunctional effect	Mean O	Mean D	Mean S	RPN
1.1.1.1	Integrated stock check	1.1.1.1.1	Wrong evaluation of integrity	Work interruption	Money penalty	8	5	8	320
		1.1.1.1.2	Wrong personnel involved			9	4	9	
		1.1.1.1.3	Absence of advanced technology			9	6	7	
									378

### 8. IDENTIFICATION OF CRITICAL ACTIVITIES

The DMECA is a proactive tool, technique and quality method that enables the identification and prevention of management personnel errors. Defect, rework, and miss-management mean loss on material, loss in production time and cost as well. With the help of the DMECA method, it's easy to know what potentially may go wrong with the management personnel-management approach. DMECA can assist to improving overall efficiency of the management personnel. All the dysfunctions are not Sevier. So it was important to identify what are the dysfunctions in the management process that are mainly involved for the loss of material, loss in production time and cost as well. At this point in the structured DMECA process, criticality



analysis according to the procedure described in article 2 was carried out and the critical activities (high RPN) where improvement actions are necessary were found. Dysfunction causes and their relative weights were investigated for each activity in order to determine the most critical and decide improvement actions. The result is shown in a list of critical activities and priorities (Table 8-1). On the basis of these results, the DMECA process can restart to implement on new activities. This will be helpful to run the power plant more effectively and efficiently. For example, Table 8-1 shows some of the activities that receive higher RPNs on its dysfunction causes, these are the critical activities.

Table 6: Some of the critical activities with higher RPN, dysfunction causes, modes and effects

ID	Activity	ID	Dysfunctional cause	Dysfunctional mode	Dysfunctional effect	Mean O	Mean D	Mean S	RPN
1.1.1.1	Integrated stock check	1.1.1.1.1	Wrong evaluation of integrity	Work interruption	Money penalty	8	5	8	320
1.1.1.1.2		Wrong personnel involved	9			4	9	324	
1.1.1.1.3		Absence of advanced technology	9			6	7		
									378

### 9. IDENTIFICATION OF CORRECTIVE ACTION

Management of the Power Plant must focus on defining improvement actions to eliminate the dysfunctional causes of this activities described in table 8-1. A matrix can be used to create, design, plan and control the corrective actions. In the matrix, the following are summarized:

- the critical activity
- the dysfunction cause
- the improvement action proposed
- the frequency of the improvement action
- time necessary to implement action
- a flag to indicate possible interruption of the action implementation
- the responsibility to implement action
- the executor
- the predicted cost
- the benefit

The DMECA approach permits to identify how a corrective action can eliminate a particular dysfunction, also can be used to correct other problems or inefficiencies indirectly. Therefore, at the end of the DMECA structured process analysis, we obtained

schemes where relatively few corrective actions can solve multiple dysfunctions (Table 8-2). This was because there is a strong interrelationship between management processes and activities.

This result is the most important of the DMECA method, as it permits the correction of a group of similar causes of dysfunctions through fewer corrective actions. Evidence of this is illustrated in Table 8-2 for some of the critical activities, where the improvement actions (i) ‘introducing advanced technology and related training course’ can eliminate three dysfunctional causes. The benefits related to the proposed improvement action are  $O_D$  and  $D_D$  reductions.

Table 7: Corrective action planning and design scheme for some of the critical activities

Critical activity		Corrective action								
ID	Activity	ID	Dysfunctional cause	Improvement action	Frequency	Time	Responsible	Executor	Cost (Tk)	Benefit
1.1.1.1	Integrated stock check	1.1.1.1.1	Wrong evaluation of integrity	Introducing advanced technology and related training	6 Months	4 to 5 days	Plant Manager	Executive Engineer	Approximately 50000	Reduction of $O_D$
1.1.1.1.2		Wrong personnel involved								
1.1.1.1.3		Absence of advanced technology								

### 10. CONCLUSION

In every organization (industrial, commercial, services), it is necessary to utilize a method to evaluate possible dysfunctions in managerial processes that can result trouble free operation. The Dysfunction Mode Effects and Criticality Analysis approach which represents an interesting and complete structured tool to find inefficiencies in the management process and consequently define suitable improvement actions. The method allows the user to analyze a process of a power plant in a detailed and structured way. In this case study of the application of DMECA is presented to illustrate the technique in a real business situation of 110 MW, Khulna Power Station (KPS), Bangladesh Power Development Board (BPDB), Goalpara, Khalishpur, Khulna, Bangladesh. The application of DMECA to the power plant helped us (i) to highlight potential criticalities in terms of elementary activities that form the processes and (ii) to define the improvement actions that must be implemented to complete the analysis and the improvement processes. In particular, it will allow the managers to plan, to schedule and to control proposed

actions in terms of responsibility, cost and time. In this study DMECA corrects about 60% of the dysfunction by solving only 15% of the causes. The method may also be useful for repeated applications and reiteration according to Deming's Plan-Do-Check-Act (PDCA) mentality to obtain an effective continuous improvement of the processes. In fact, organizations' needs changes rapidly and some activities can become more critical (i.e., greater RPN). Furthermore, the effects of improvement actions must be correctly evaluated continuously. To analyze the managerial dysfunction in any organization the DMECA approach is very effective and it involves low cost as found in the research work. So, it is cost effective and can be applied to identify management personnel deficiencies which will be helpful for uninterrupted production and/or maintenance. It identifies access and ranks of dysfunctions that are challenges to achieve. Thus, the method prevents the consumption of time and cost of production and/or maintenance.

An application of the DMECA technique in an important power station to analyze, to evaluate and to improve job management process efficiency has already been made. Some typical suggestions that must be looked into by the management personnel to implement the DMECA method are given below:

- Top management commitment is indispensable.
- A motivational campaign from top management is a must.
- Develop a clear cut plan for the use of DMECA.
- Ensure all personnel who are to be involved with the DMECA are made aware of the potential benefits arising out of DMECA and the necessity for corrective action.
- Make it a part of regular job, not an optional one when you are free.
- Make DMECA meetings short but regular, throughout the early stages of the managerial dysfunctions.
- Documents plan and what have been done, review/update plans as per changed requirements.
- It is better to involves personnel from various departments including suppliers for DMECA. In fact it is a recommended part of TQM.
- DMECA is more cost effective at the earlier stage of management plan than at later stage when the plan is almost at the final one.
- It is never wise to prepare DMECA for execution in isolation by one individual.

It is never wise to ignore participation of a less influential individual and allow important dysfunctions modes to be dismissed lightly with comment such as, "we have always done it like this", "don't talk like a fool etc", etc. let everybody to talk without shy and fear.

## 11. REFERENCES

1. Plaia, A. and Carrie, A. (1995) 'Application and assessment of IDEF3 – process flow description capture method', International Journal of Operations and Production Management, Vol. 15, No. 1, pp.63–73.
2. Goulden, C. and Rawlins, L. (1995) 'A hybrid model for process quality costing', International Journal of Quality and Reliability Management, Vol. 12, No. 8, pp.32–47.
3. Dale, B.G. and Plunket, J.J. (2000) "Quality costing" The TQM Magazine, Vol. 12. No. 3, pp.214-217.
4. Bertolini, M. Braglia, M. Carmignani, G. 'An FMEA based approach to process analysis', International Journal of Process Management and Benchmarking, Vol.1, No.2, 2006.
5. Mr. Md. Rezaul Karim, SDE, KPS, BPDB, Khulna.
6. Lindemann, U. 'Specification Risk Analysis: Avoiding Product Performance Deviations Through an FMEA-Based Method', International Journal of Quality and Reliability Management, Vol. 10, No. 4, pp.9-16.

## 12. NOMENCLATURE

Symbol	Meaning
AE	Assistant Engineer
BPDB	Bangladesh Power Development Board
CA	Criticality Analysis
CE	Chief Engineer
D <sub>D</sub>	Detectability of dysfunction
DMECA	Dysfunction Mode and Effect Critical Analysis
Ex-En	Executive Engineer
FMEA	Failure Mode and Effect Analysis
FMECA	Failure Mode and Effect Critical Analysis
ICAM	Integrated Computer Aided Manufacturing
IDEF	Integrated DEFinition
MTBD	Mean Time Between Failure
O <sub>D</sub>	Occurrence Dysfunction
PBS	Process Break down Structure
S <sub>D</sub>	Severity Dysfunction
SADT	Structured Analysis and Design Technique
SDE	Sub-Divisional Engineer
TQM	Total Quality Management

## 13. MAILING ADDRESS

Azizur Rahman  
 Dept. of IEM, KUET,  
 Khulna, Bangladesh

## APPLICATION OF VIKOR BASED TAGUCHI METHOD FOR MULTI-RESPONSE OPTIMIZATION: A CASE STUDY IN SUBMERGED ARC WELDING (SAW)

S. Ajay Biswas<sup>1</sup>, Saurav Datta<sup>2</sup>, Swapan Bhaumik<sup>1</sup>, Gautam Majumdar<sup>3</sup>

<sup>1</sup>Department of Mechanical Engineering, National Institute of Technology (NIT), Barjala, Tripura (W)

<sup>2</sup>Department of Mechanical Engineering, National Institute of Technology (NIT), Rourkela

<sup>3</sup>Department of Mechanical Engineering, Jadavpur University, Kolkata

### ABSTRACT

The term optimization is intensively related to the field of quality engineering. The product quality depends on different quality indices (called attributes) which should reach expected target level in order to meet customer's satisfaction. Deviation from the target results severe quality loss which may not be accepted by the consumers. Therefore, every manufacturing or production unit should have better concern for both quality as well as productivity. High quality can be achieved by optimizing various quality attributes or by selecting an optimal process environment efficient enough to fetch desired requirements of quality. To address this issue several methodologies were recommended in literature but most of the research carried out earlier seeks for optimizing a single objective function. In this context, Taguchi's design of experiment (Orthogonal Array) and Signal-to-Noise (S/N) ratio concept were found to be the most efficient having worldwide application in various fields. This method was proved robust and largely recommended for continuous quality improvement and off-line quality control. However, traditional Taguchi method cannot solve a multi-objective optimization problem. To overcome this shortcoming several hybrid Taguchi techniques were developed. But these methods are based on quality loss of individual attributes from their ideal condition. They fail to consider variations of relative quality loss of multiple attributes. It may so happen that the quality loss associated with some responses is small; but the quality loss associated with rest of the responses is very large, even though the overall average quality loss is small. Such situation may not be accepted by the customers. In consideration of the above, the present study explores application of Taguchi based VIKOR method adapted from Multi-Criteria-Decision Making (MCDM) in order to solve multi-response optimization problem through a case study in SAW. An attempt has been made to evaluate the best process environment (process condition) for achieving desired multi-quality features of the weldment.

**Keywords:** Taguchi Based Vikor Method, Multi-Criteria-Decision Making (Mcdm), Saw

### 1. INTRODUCTION

It is well known that several process control parameters influence weld bead geometry, bead quality and joint performance in Submerged Arc Welding. These parameters should be selected in a judicious manner to reach the desired target or objective which is dictated by the area of application of the weldment. This can be achieved by optimization of welding phenomena.

Literature depicts that the common approaches to tackle simulation modeling and optimization problem in welding include multiple regression analysis, Response Surface Methodology (RSM), Artificial Neural Network (ANN) modeling and Taguchi method, [Unal, R. and Dean, Edwin B., (1991), Rowlands, H., *et al.* 2000, Antony, J. and Antony, F., (2001), Maghsoodloo, S. *et al.* (2004)]. In most of the cases the optimization has been performed using single objective function. For a multi-response process, while applying the optimal

setting of control factors, it can be observed that, an increase/improvement of one response may cause change in another response, beyond the acceptable limit. Thus for solving multi-criteria optimization problem, it is convenient to convert all the objectives into an equivalent single objective function. This equivalent objective function, which is the representative of all the quality characteristics of the product, is to be optimized (maximized).

Optimization using desirability function (DF) approach is very helpful in this context [Asiabanpour, B. *et al.* (2004), Ful-Chiang, Wu. (2005)]. Similarly Taguchi's philosophy has also been recommended as an efficient tool for the design of high quality manufacturing system. However, traditional Taguchi method cannot solve multi-objective optimization problem Jeyapaul, R. *et al.* (2005). Therefore, Taguchi method coupled with grey relational analysis is the

appropriate option. Tarng, Y. S. *et al.* (2002) applied grey-based Taguchi methods for optimization of Submerged Arc Welding process parameters in hardfacing. Apart from desirability function and grey-based Taguchi approach, Genetic Algorithm (GA) and Fuzzy Logic are also found to be useful techniques to solve optimization problem in the field of welding [Al-Aomar, Reid (2002)].

Apart from Genetic Algorithm, fuzzy logic also comes into the scenario of solving optimization problems in material processing technology [Wang, Jen-Ting and Jean, Ming-Der (2006)]. Xue, Y. *et al.* (2005) reported the possibilities of the fuzzy regression method in modeling and optimization of the bead width in the robotic arc-welding process.

Desirability Function (DF) approach coupled with Taguchi method has been used by some researchers to investigate conditions leading to process optimization. In this context, application of other hybrid techniques deserves mention. These techniques are: - (i) Taguchi method coupled with fuzzy logic, (ii) Genetic Algorithm and fuzzy logic, (iii) desirability function approach coupled with fuzzy logic, (iv) Genetic Algorithm in combination with Response Surface Methodology, and (v) Taguchi-Genetic Algorithm [Tsai, Jinn-Tsong (August 2004)]. Tarng, Y. S. *et al.* (July 2000) applied fuzzy logic in the Taguchi method to optimize the submerged arc welding process with multiple performance characteristics. Another approach for optimization is the Controlled Random Search Algorithm (CRS), developed by Price, W. L. (1977).

It has been observed that Taguchi based hybrid methods are based on quality loss of individual quality attributes from their ideal (desired) condition. They fail to consider variations of relative quality loss of multiple attributes. The situation may arise that the quality loss associated with some responses is small; but the quality loss associated with rest of the responses is very large, even though the overall average quality loss is small. Such situation may not be accepted by the consumers.

In order to overcome aforesaid shortcoming, the present study proposes VIKOR method adapted from Multi-Criteria Decision Making (MCDM) hybridized with Taguchi method for solving multi-criteria optimization problem of submerged arc welding. With relevant illustrations, the robustness and application feasibility of the proposed method has been verified through a case study, discussed in the paper.

## 2. VIKOR METHOD

The MCDM method is very popular technique widely applied for determining the best solution among several alternatives having multiple attributes or alternatives. A MCDM problem can be represented by a decision matrix as follows:

$$D = \begin{matrix} & \begin{matrix} Cx_1 & Cx_2 & \dots & \dots & Cx_n \end{matrix} \\ \begin{matrix} A_1 \\ A_2 \\ \vdots \\ \vdots \\ A_m \end{matrix} & \begin{bmatrix} x_{11} & x_{12} & \dots & \dots & x_{1n} \\ x_{21} & x_{22} & \dots & \dots & x_{2n} \\ \cdot & \cdot & \cdot & \cdot & \cdot \\ \cdot & \cdot & \cdot & \cdot & \cdot \\ x_{m1} & x_{m2} & \dots & \dots & x_{mn} \end{bmatrix} \end{matrix} \quad (1)$$

Here,  $A_i$  represents  $i$ th alternative,  $i = 1, 2, \dots, m$  ;

$Cx_j$  represents the  $j$ th criterion,  $j = 1, 2, \dots, n$  ;

and  $x_{ij}$  is the individual performance of an alternative.

The procedures for evaluating the best solution to an MCDM problem include computing the utilities of alternatives and ranking these alternatives. The alternative solution with the highest utility is considered to be the optimal solution. The following steps are involved in VIKOR method [Opricovic, S. and Tzeng, G.-H., 2007]:

### Step 1: Representation of normalized decision matrix

The normalized decision matrix can be expressed as follows:

$$F = [f_{ij}]_{m \times n} \quad (2)$$

Here,  $f_{ij} = \frac{x_{ij}}{\sqrt{\sum_{i=1}^m x_{ij}^2}}$ ,  $i = 1, 2, \dots, m$ ; and  $x_{ij}$  is the

performance of alternative  $A_i$  with respect to the  $j$ th criterion.

### Step 2: Determination of ideal and negative-ideal solutions:

The ideal solution  $A^*$  and the negative ideal solution  $A^-$  are determined as follows:

$$A^* = \left\{ \begin{matrix} (\max f_{ij} | j \in J) \text{ or } (\min f_{ij} | j \in JK') \\ i = 1, 2, \dots, m \end{matrix} \right\} \quad (3)$$

$$= \{f_1^*, f_2^*, \dots, f_n^*\}$$

$$A^- = \left\{ \begin{matrix} (\min f_{ij} | j \in J) \text{ or } (\max f_{ij} | j \in J') \\ i = 1, 2, \dots, m \end{matrix} \right\} \quad (4)$$

$$= \{f_1^-, f_2^-, \dots, f_n^-\}$$

Here,

$$J = \{j = 1, 2, \dots, n | f_{ij}, \text{ if desired response is large}\}$$

$$J' = \{j = 1, 2, \dots, n | f_{ij}, \text{ if desired response is small}\}$$

**Step 3: Calculation of utility measure and regret measure**

The utility measure and the regret measure for each alternative are given as

$$S_i = \sum_{j=1}^n w_j \frac{(f_j^* - f_{ij})}{(f_j^* - f_j^-)} \quad (5)$$

$$R_i = \text{Max}_j \left[ w_j \frac{(f_j^* - f_{ij})}{(f_j^* - f_j^-)} \right] \quad (6)$$

where,  $S_i$  and  $R_i$ , represent the utility measure and the regret measure, respectively, and  $w_j$  is the weight of the  $j$ th criterion.

**Step 4: Computation of VIKOR index**

The VIKOR index can be expressed as follows:

$$Q_i = \nu \left[ \frac{S_i - S^*}{S^- - S^*} \right] + (1 - \nu) \left[ \frac{R_i - R^*}{R^- - R^*} \right] \quad (7)$$

Here,  $Q_i$ , represents the  $i$ th alternative VIKOR value,  $i = 1, 2, \dots, m$ ;  $S^* = \text{Min}_i (S_i)$ ;

$$S^- = \text{Max}_i (S_i) \quad ; \quad R^* = \text{Min}_i (R_i) \quad ;$$

$R^- = \text{Max}_i (R_i)$  and  $\nu$  is the weight of the maximum group utility (usually it is to be set to 0.5). The alternative having smallest VIKOR value is determined to be the best solution.

**3. OPTIMIZATION PROCEDURE ADOPTED**

**Step 1: Estimation of quality loss**

Taguchi defined quality loss estimates for responses using Lower-the-better (LB) and Higher-the-better (HB) criterion are given bellow.

(a) For a lower-the-better (LB) response:

$$L_{ij} = k_1 \times \frac{1}{r} \sum_{k=1}^r y_{ijk}^2 \quad (8)$$

(b) For a higher-the-better (HB) response:

$$L_{ij} = k_2 \times \frac{1}{r} \sum_{k=1}^r \frac{1}{y_{ijk}^2} \quad (9)$$

Here,  $L_{ij}$  is the quality loss associated with the  $j$ th response in the  $i$ th experimental run;  $y_{ijk}$  is the observed  $k$ th repetition datum for the  $j$ th response in the  $i$ th experimental run;  $r$  is the number of repetitions for each experimental run.  $k_1$ ,  $k_2$  are quality loss coefficients,  $i = 1, 2, \dots, m$ ;  $j = 1, 2, \dots, n$ ;  $k = 1, 2, \dots, r$ .

**Step 2:** Calculation of normalized quality loss (NQL) for individual responses in each experimental run. The NQL can be obtained as follows:

$$f_{ij} = \frac{L_{ij}}{\sqrt{\sum_{i=1}^m L_{ij}^2}}, \quad i = 1, 2, \dots, m; j = 1, 2, \dots, n. \quad (10)$$

Here  $f_{ij}$  represents the NQL of the  $j$ th response in the  $i$ th experimental run.

**Step 3:** Evaluation of ideal and negative-ideal solutions.

$$A^* = \{ \min f_{ij} | i = 1, 2, \dots, m \} = \{ f_1^*, f_2^*, \dots, f_j^*, \dots, f_n^* \} \quad (11)$$

$$A^- = \{ \max f_{ij} | i = 1, 2, \dots, m \} = \{ f_1^-, f_2^-, \dots, f_j^-, \dots, f_n^- \} \quad (12)$$

A smaller NQL is preferred, so the ideal and negative-ideal solutions which represent the minimum and maximum NQL of all experimental runs are as follows:

**Step 4:** Calculation of the utility and regret measures for each response in each experimental run using equation (5) and (6) respectively.

**Step 5:** Calculation of VIKOR index of the  $i$ th experimental run. Substituting  $S_i$  and  $R_i$  into equation (7) yields the VIKOR index of the  $i$ th experimental run as follows. A smaller VIKOR index produces better multi-response performance.

**Step 6:** Determination of optimal parametric combination

The multi-response quality scores for each experimental run can be determined from the VIKOR index obtained in step 5, and the effects of the factors can be estimated from the calculated VIKOR values. The optimal combination of factor-level called optimal parametric combination is finally determined, in view of the fact that a smaller VIKOR value indicates a better quality. Taguchi method is to be applied finally to evaluate this optimal setting (by minimizing the VIKOR index). Optimal result is to be verified through confirmatory tests.

**4. CASE STUDY**

**4.1 Experiments and Data Collection**

Bead-on-plate submerged arc welding on mild steel plates (thickness 10 mm) has been carried out as per Taguchi's  $L_{25}$  OA design, with 25 combinations of voltage (OCV), wire feed rate, traverse speed and electrode stick-out. Copper coated electrode wire of diameter 3.16 mm (AWS A/S 5.17:EH14) has been used during the experiments. Welding has been performed with flux (AWS A5.17/SFA 5.17) with grain size 0.2 to 1.6 mm with basicity index 1.6 ( $\text{Al}_2\text{O}_3 + \text{MnO}_2$  35%,  $\text{CaO} + \text{MgO}$  25% and  $\text{SiO}_2 + \text{TiO}_2$  20% and  $\text{CaF}_2$  15%).

The experiments have been performed on Submerged Arc Welding Machine- INDARC AUTOWELD MAJOR (Maker: IOL Ltd., India). Weld being made, the specimens have been prepared for metallographic test. Features of bead geometry: bead width, penetration depth, reinforcement and %dilution have been observed in Optical Trinocular Metallurgical Microscope (Make: Leica, GERMANY, Model No. DMLM, S6D & DFC320 and Q win Software). The domain of experimentation is shown in Table 1. The design of experiment, based on

Taguchi's  $L_{25}$  OA, and the collected experimental data, related to individual quality indicators of bead geometry have been listed in Table 2 and Table 3 respectively.

#### 4.2 Data Analysis

Quality loss estimates for individual responses have been calculated using equations (8 and 9). For penetration depth, %dilution (HB) and for reinforcement and bead width (LB) criterion have been selected. Normalized quality loss estimates have been determined using equation (10). While calculating utility measure of individual responses (criterion) it has been assumed that all responses are equality important. Therefore, 25% weightage has been assigned to each response. Utility and regret measure for each alternative have been calculated next. VIKOR INDEX of each alternative has been evaluated finally. The optimal parametric condition indicates smallest VIKOR INDEX. This has been achieved by optimizing (minimizing) the VIKOR INDEX by Taguchi method.

The S/N ratio of VIKOR INDEX has been calculated using LB (Lower-the-Better) criteria. Optimal parametric setting has been evaluated from Figure 1. The predicted optimal setting becomes: **VI F5 S4 N4**. Mean response table for (VIKOR INDEX) indicates that the most significant factor is wire feed, next traverse speed then voltage. Stick-out showed negligible effect. After predicting the optimal setting, it has been verified through conduction of confirmatory test. It showed satisfactory result. Table 4 represents the result of confirmatory test.

#### 5. CONCLUSIONS

In the present work, multi-response optimization problem has been solved by searching an optimal parametric combination, capable of producing desired quality weld. Four bead geometry features: depth of penetration, reinforcement, bead width and dilution has been optimized using VIKOR based Taguchi method. The study demonstrates the effectiveness of VIKOR's multi-attribute decision making technique hybridized with Taguchi method in relation to parametric optimization of SAW process.

Table 1: Domain of experimentation

Parameters	Units	Notation	1	2	3	4	5
Voltage (OCV)	Volts	V	32	34	36	39	40
Wire feed	cm/s	F	0.42	0.46	0.51	0.79	1.46
Traverse speed	cm/s	S	0.21	0.23	0.24	0.4	0.71
Stick-out	mm	N	20	21	22	23	24

Table 2: Taguchi's  $L_{25}$  OA design

Sl. No.	Levels of factors (Factorial combinations)			
	V	F	S	N
1	1	1	1	1
2	1	2	2	2
3	1	3	3	3
4	1	4	4	4
5	1	5	5	5
6	2	1	2	3
7	2	2	3	4
8	2	3	4	5
9	2	4	5	1
10	2	5	1	2

11	3	1	3	5
12	3	2	4	1
13	3	3	5	2
14	3	4	1	3
15	3	5	2	4
16	4	1	4	2
17	4	2	5	3
18	4	3	1	4
19	4	4	2	5
20	4	5	3	1
21	5	1	5	4
22	5	2	1	5
23	5	3	2	1
24	5	4	3	2
25	5	5	4	3

Table 3: Response data (individual quality attributes related to bead geometry)

Sl. No.	Response data (quality attributes)			
	Bead width	Reinforcement	Penetration	%Dilution
1	9.7722	2.2773	4.1970	35.3825
2	10.0102	1.6683	3.8740	41.9825
3	9.8975	1.5475	3.8475	43.2125
4	9.6303	1.5493	3.9110	43.0625
5	8.6323	1.9203	4.3080	38.6225
6	10.3875	1.4183	3.4545	41.1875
7	10.3522	1.2705	3.4755	44.1950
8	10.0600	1.2780	3.5285	42.2200
9	8.6742	1.4667	3.3670	47.3125
10	13.3842	2.4087	4.9320	46.7725
11	10.7202	1.2280	3.2985	39.5975
12	10.1157	1.1878	3.2430	46.8300
13	8.6950	1.3325	3.2500	44.8250
14	14.5050	1.9793	4.1605	45.4525
15	12.0157	1.7803	4.3830	46.9700
16	10.3557	1.1163	3.1750	41.5325
17	8.9875	1.2717	3.1925	42.0325
18	15.7650	1.7940	3.8205	43.5350
19	13.4857	1.4048	3.7450	42.7625
20	10.9453	1.8085	4.1795	54.0250
21	10.0042	1.3317	3.3450	34.6525
22	18.9743	1.6557	3.5500	37.7525
23	15.0150	1.5340	3.5285	48.6350
24	13.4223	1.4625	3.6315	47.9050
25	11.4425	1.7582	4.0525	47.0425

S/N ratio of VIKOR index

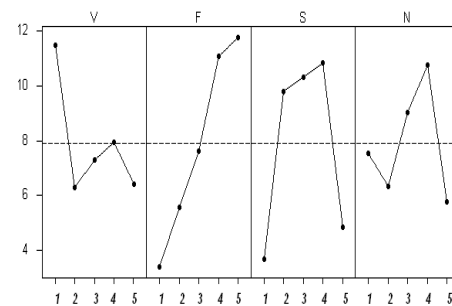


Fig 1. S/N ratio plot for VIKOR INDEX

Table 4: Results of confirmatory test

Level of factors	Optimal setting	
	Prediction	Experiment
S/N ratio of VIKOR INDEX	<b>VI F5 S4 N4</b> 21.2526	<b>VI F5 S4 N4</b> 22.3016

## 6. REFERENCES

1. Antony, J. and Antony, F., 2001, "Teaching the Taguchi Method to Industrial Engineers", *Work Study*, Volume 50, Number 4, pp. 141-149.
2. Al-Aomar, Reid, 2002, "A Robust Simulation-Based Multicriteria Optimization Methodology", *Proceedings of the 2002, Winter Simulation Conference*.
3. Asiabanpour, B., Palmer, K. and Khoshnevis, B., 2004, "An Experimental Study of Surface Quality and Dimensional Accuracy for Selective Inhibition of Sintering", *Rapid Prototyping Journal*, Volume 10, Number 3, pp. 181-192.
4. Ful-Chiang, Wu, 2005, "Optimization of Correlated Multiple Quality Characteristics Using Desirability Function", *Quality Engineering*, Volume 17, Issue 1, pp. 119-126.
5. Jeyapaul, R., Shahabudeen, P. and Krishnaiah, K., 2005, "Quality Management Research by Considering Multi-Response Problems in the Taguchi Method-A Review", *International Journal of Advanced Manufacturing Technology*, Volume 26, pp. 1331-1337.
6. Maghsoodloo, S., Ozdemir, G., Jordan, V. and Huang, C-H., 2004, "Strengths and Limitations of Taguchi's Contributions to Quality, Manufacturing, and Process Engineering", *Journal of Manufacturing Systems*, Volume 23, Number 2, pp. 73-126.
7. Price, W. L., 1977, "A Controlled Random Search Procedure for Global Optimization", *The Computer Journal*, Volume 20, Number 4, pp. 367-370.
8. Rowlands, H., Antony, J. and Knowles, G., 2000, "An Application of Experimental Design For Process Optimization", *The TQM Magazine*, Volume 12, Number 2, pp. 78-83.
9. Tarn, Y. S., Yang, W. H. and Juang, S. C., July 2000, "The Use of Fuzzy Logic in the Taguchi Method for the Optimization of the Submerged Arc Welding Process", *International Journal of Advanced Manufacturing Technology*, Volume 16, pp. 688-694.
10. Tarn, Y. S., Juang, S. C., Chang, C. H., 2002, "The Use of Grey-Based Taguchi Methods to Determine Submerged Arc Welding Process Parameters in Hardfacing", *Journal of Materials Processing Technology*, Volume 128, pp. 1-6.
11. Tsai, Jinn-Tsong, Liu, Tung-Kuan and Chou, Jyh-Horng, 2004, "Hybrid Taguchi-Genetic Algorithm for Global Numerical Optimization", *Evolutionary Computation*, IEEE Transactions, Volume 8, Issue 4, pp. 365-377.
12. Unal, R., and Dean, Edwin B., 1991, "Taguchi Approach to Design Optimization for Quality and Cost: An Overview", Presented at the Annual Conference of the International Society of Parametric Analysis".
13. Wang, Jen-Ting and Jean, Ming-Der, 2006, "Optimization of Cobalt-Based Hardfacing in Carbon Steel using the Fuzzy Analysis for the Robust Design", *International Journal of Advanced Manufacturing Technology*, Volume 28, pp. 909-918.
14. Xue, Y., Kim, I. S., Son, J. S., Park, C. E., Kim, H. H., Sung, B. S., Kim, I. J., Kim, H. J. and Kang, B. Y., 2005, "Fuzzy Regression Method for Prediction and Control the Bead Width in the Robotic Arc-Welding Process", *Journal of Materials Processing Technology*, Volume 164-165, pp. 1134-1139.
15. Opricovic, S. and Tzeng, G-H., 2007, "Extended VIKOR Method in Comparison with Outranking Methods", *European Journal of Operations Research*, Volume 178, pp. 514-529.

## 7. MAILING ADDRESS

Dr. Saurav Datta  
Department of Mechanical Engineering  
National Institute of Technology (NIT),  
Rourkela-769008  
E-mail: s\_bppimt@yahoo.com



## **\*WAREHOUSE DESIGN: A SET THEORETIC APPROACH**

**Mosammat Ferdaushi Sultana, 110 MW Barge Mounted Power Plant, Wartsila Bangladesh Ltd, Khulna.  
Professor Dr. Md. Kutub Uddin, Department of IEM, Khulna University of Engineering and Technology, Khulna**

### **ABSTRACT**

Allocation and assignment of spare-parts is a vital problem for sound operation of a warehouse. Miss-allocation of spare-parts takes huge time to find parts out. This problem causes extra time consumption and money expenditure for the involvement of labor for long time and also creates risk of unavailability of spare parts which lead to improper maintenance or repair of machines. The existing system calls for the location of items in alphanumerical order without regard to issue frequency, size, weight or volume. As a result the plant faces problems in issuing/retrieving the spare parts with minimum waste of time & effort. This paper presents an algorithm based on set theoretic approach for spare parts allocation and assignment in a warehouse of a Barge mounted power plant in Bangladesh. The proposed algorithm classified 4,000 (four thousand approximately) items into 56 (fifty six) spare parts family. A spare parts family is a superset of spare parts required for a particular type of maintenance over the last period of time. The algorithm also calculate the weight for each spare parts family which is the summation of all item's frequency of usages in a year. The weight is used to identify a family as slow or fast moving. Fast moving families are kept near to issue counter. The effectiveness of the proposed algorithm is evaluated by comparing the total transport work and travel distance with respect to present system. It is found that the rearranged system with the help of the algorithm reduces the transport work by 76% and travel distance by 50% approximately. This indicates that the proper allocation and assignment of spare parts will increase the system's performance significantly.

**Key Words:** Allocation, assignment, spare parts, retrieval, total transport work, travel distance, group technology.

***\*Full paper was not received before publication deadline***

## ELCTRO-MECHANICALLY CONTROLLED CONTINUOUSLY VARIABLE TRANSMISSION SYSTEM FOR PASSENGER CARS

A.K.M. Mohiuddin and Md. Ataur Rahman

Department of Mechanical Engineering, International Islamic University Malaysia,  
Kuala Lumpur, Malaysia

### ABSTRACT

Electro-mechanically controlled continuously variable transmission (CVT) system is an automatic transmission system that can change the gear ratio to any arbitrary setting within the limits. This system includes an AC motor, set of power screw, an electromagnetic pick-up sensor, and two DC motors. Electromagnetic wheel speed sensor (WSS) generates the voltage with the travelling speed of the vehicle for operating the DC motor with a double acting magnetic pull-in solenoid switch. The function of power screw mechanism is for shifting movable sheaves axially along the shafts by the DC motor. Both the driving and driven pulleys' moving sheave move at the same time exactly the same linear distance but in opposite directions. The relationship between the DC motor speed and its response time to actuate the moveable sheave was studied. The response time is the time needed for the sheave to travel axially covering all of its stroke length. The response time was derived from motor rpm and its linear speed provided that the whole stroke length equals to 13.6 mm.

**Keywords:** Electromagnetic Sensor, Magnetic Pull-In Solenoid Switch, CVT.

### 1. INTRODUCTION

Predetermined gear ratio as is used in manual transmission obviously does not offer a good solution for all driving conditions of the vehicle [1]. Thus, CVT was introduced to replace the discrete gear ratio manual transmission system and it offers better fuel consumption [2]. The CVT is known as a transmission with literally infinite number of gear ratios which can work at optimal condition for different driving modes. In conventional hydraulic CVT, there is a slippage of the belt which causes loss of power and this behaviour is undesirable. The CVT requires constant force to clamp the belt and control the belt slippage. This results in continuous power consumption which contributes to the major loss to the hydraulic system and reducing its efficiency [3]. The present research is focused on the development of an electromagnetic pick-up sensor operated DC motor position control CVT to eliminate the problems faced by the existing CVT.

### 2. MATERIALS AND METHODS

This system includes an AC motor, set of power screw, an electromagnetic pick-up sensor, and two DC motors as shown in Figure 1. Each of the pulleys movable sheaves is operated by a DC motor in order to maintain the correct transmission ratio with the requirement of the driving torque of the car accompanied with electromagnetic pick-up sensor. Electromagnetic pick-up sensor produces the voltage with the travelling speed of the vehicle which operates the DC motor with a double acting magnetic pull-in solenoid switch. The function of power screw mechanisms is to shift movable

sheaves axially along the shafts by the DC motor. Both movable pulley sheaves move at the same time exactly the same linear distance but in the opposite direction. The system activates only when the transmission ratio change occurs which consume less power compared to the conventional hydraulic CVT [4]. The power screw mechanism makes sure that the pulley is held at its place when there is no changing in gear ratio. No work is extracted from the DC motor during this time. Indeed, it is one of the ideal characteristics for a CVT system. In order to demonstrate the working principle of the proposed CVT system, several designs and components selection were made. The stroke length of the moveable sheave, the driving motor torque and power, torque required to move the moveable sheave were estimated by accounting the vehicle load, travelling speed, tires size, wheelbase, and the location of the CG. A simple pulse width modulation (PWM) was used to control the DC motor speed as it eliminates the heat and the wasted power of the motor and it drives the motor with short pulses. Figure 2 shows the 3-D model of the proposed CVT.

An AC motor is used to drive the system as it replaces the engine in the actual car. While selecting the motor, important characteristics such as the torque and the motor speed are taken into consideration. To find the minimum torque required by the AC motor to run the whole system, components that are linked through the motor up to the wheel are weighted. The secondary pulley shaft is connected with axle shaft through 3:1 straight bevel gear.

### 9 - DC motor control electro-magnetic switch driving axle

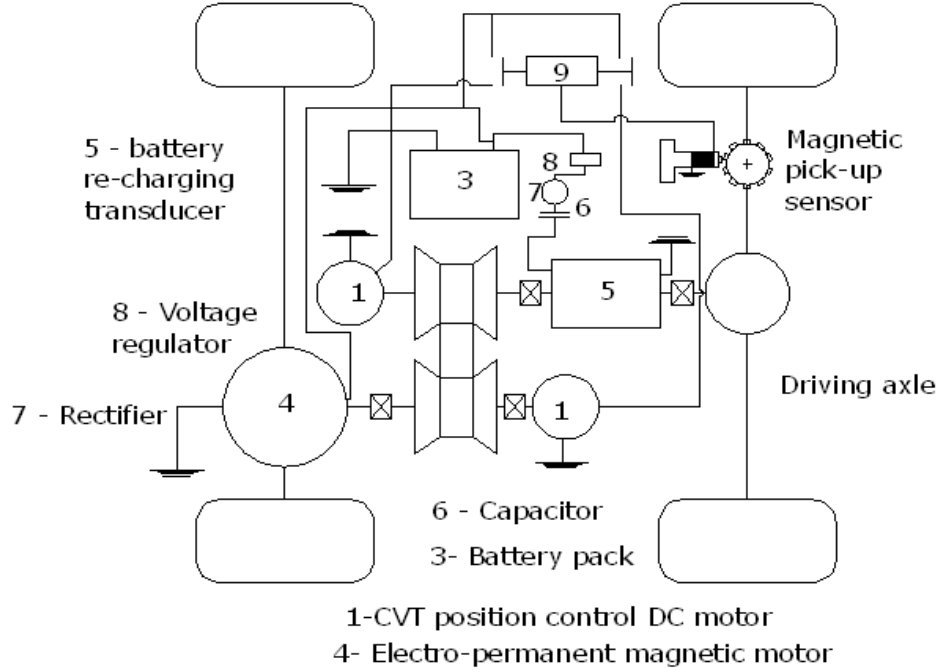


Fig 1. Schematic Diagram of the DC Motor Position Control CVT

Axle shaft's moment of inertia:

$$J_1 = \frac{m_1 R^2}{2} \quad (1)$$

Secondary pulley shaft's moment of inertia:

$$J_2 = \frac{m_2 R^2}{2} \quad (2)$$

Primary pulley shaft's moment of inertia:

$$J_3 = \frac{m_3 R^2}{2} \quad (3)$$

where,  $R$  is the radius of the shaft in m,  $m_1$ ,  $m_2$ ,  $m_3$  are the masses of the shaft of driving axle, secondary pulley shaft, and primary pulley shaft in kg, respectively.

The motor torque can be computed by using the equation,  $T = J_{total} \alpha$ , where  $J_{total}$  is the total moment of inertia in  $\text{kg.m}^2$  [5]. Figure 3 shows the drive pulley. Axial movement of the pulley sheaves is controlled electromechanically. The centrifugal rollers or known as roller weight will be thrown outward by centrifugal force when the pulley is rotating. A roller back contact plane also known as the ramp plate guides the centrifugal rollers so that they will move toward the fixed sheave. As a result, an axial force derived from the centrifugal force pushes the moveable sheave and changes the gear ratio. The clamping force of the pulley can be computed by using the equation of Sheu *et al.* (1999) [6]:

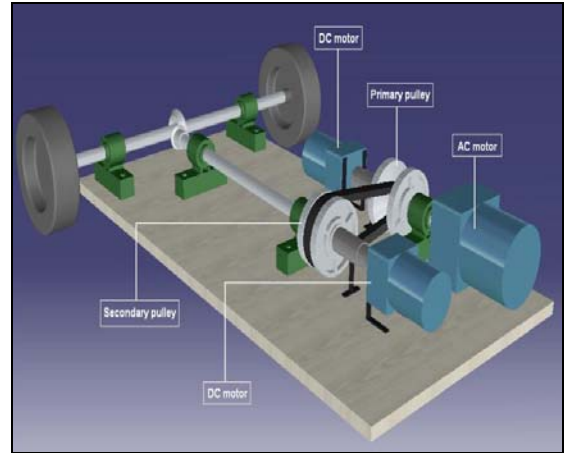


Fig 2. 3-D Model of the Proposed CVT

$$F_d = \frac{m y_m \omega^2}{\left( \frac{\cos \gamma + \mu_c \sin \gamma}{\sin \gamma + \mu_c \cos \gamma} \right) + \left( \frac{\sin \delta + \mu_b \sin \delta}{\cos \delta + \mu_b \sin \delta} \right)} \quad (4)$$

where,  $F_d$  is the axial force of the moveable flange,  $R_c$  is the normal force exerted by the roller housing in kN,  $y_m$  distance between the center of the roller and shaft centerline,  $\delta$  is the angle between the roller contact plate and a line perpendicular to the shaft center,  $\omega$  is the input angular velocity,  $\mu_b$  and  $\mu_c$  are the coefficient of friction between the roller and roller contact plane, and between the roller and roller housing, respectively.

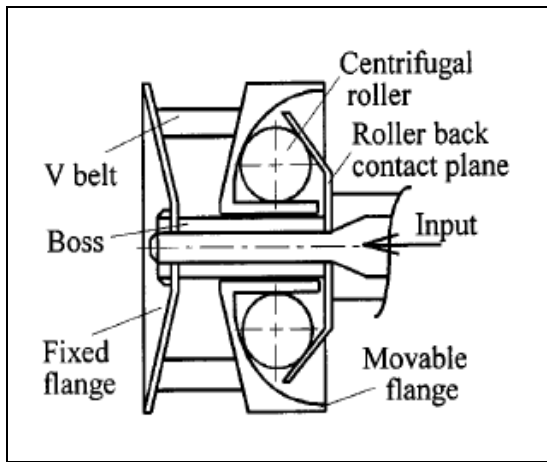


Fig 3. Drive Pulley [6]

Lead screw mechanism for each of the pulleys is developed with a set of nut and a DC motor which moves the movable sheaves of the pulley in correct time for maintaining the desired torque or transmission ration of the CVT. The diameter of the thread is selected based on the pulley's geometrical constraint. The minimum diameter of the sleeve must be slightly greater than the nut that secures the pulleys on the splined shaft. Torque required to drive the screw can be computed by using the equation of [6];

$$T_u = \frac{FD_p}{2} \left[ \frac{\cos \phi \tan \lambda + f}{\cos \phi - f \tan \lambda} \right] \quad (5)$$

$$T_d = \frac{FD_p}{2} \left[ \frac{f - \cos \phi \tan \lambda}{\cos \phi + f \tan \lambda} \right] \quad (6)$$

where,  $\lambda = \tan^{-1} \frac{L}{\pi D_p}$ ,  $\lambda$  is the lead angle,  $f$  is the

coefficient of friction,  $\phi$  is the thread angle,  $L$  is the lead and  $D_p$  is the minimum pitch diameter,  $T_u$  and  $T_d$  are the raise and lower torque, respectively.

The simple pulse width modulation (PWM) was used to control the DC motor speed as it eliminates the heat and the wasted power of the motor and it drives the motor with short pulses. These pulses vary in duration to change the speed of the motor. The longer the pulses, the faster the motor turns, and vice versa. It is due to the fact that most of the available DC motor in the market already posses speed of more than 1000rpm. In this application, the DC motor speed should not be very high because it leads to the abrupt changing of the gear. It is undesirable as it can bring uncomfortable feeling for the driver and passengers of the vehicle. Lowering the DC motor speed is possible in many ways. Basic concept behind it is by varying the supply voltage. Since H-Bridge circuit have already been used, the common practice is to implement another method namely PWM

(Pulse-Width Modulation) used to control the speed of DC motor.

The circuit consists of variable resistor, diode, resistor, capacitor and integrated circuit (IC). Figure 4 shows the completed circuit for controlling the speed of two DC motor. Using this circuit, speed in simply controlled by varying the resistance value through the variable resistor. This will only done once to make sure the speed of the DC motor is constant along the operation. Both DC motor should run at the same speed to maintain the belt tension. Any difference in speed may result in power loss and therefore the efficiency of the system might reduce.

Due to the positioning of the pulley, the rotation of the motors needs to be opposing each other so that if one pulley diameter is increasing, the other should be decreasing at the same rate and vice versa. By doing this

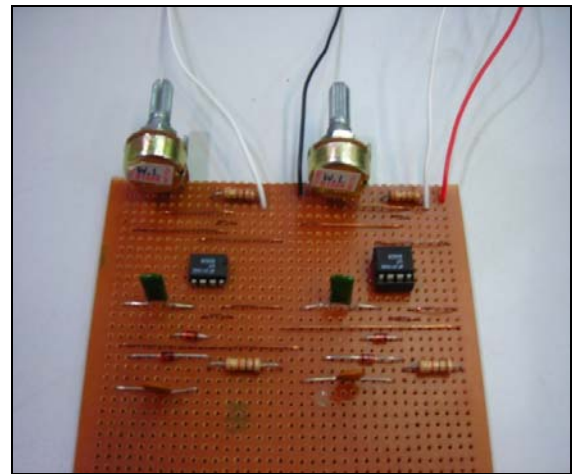


Fig 4. PWM Circuit for 2 DC Motors

gear ratio changing is made possible and belt tension can be maintained all the time. To achieve this, an integrated circuit H-bridge was used. Figure 5 shows the H-bridge circuit consists of only L293B integrated

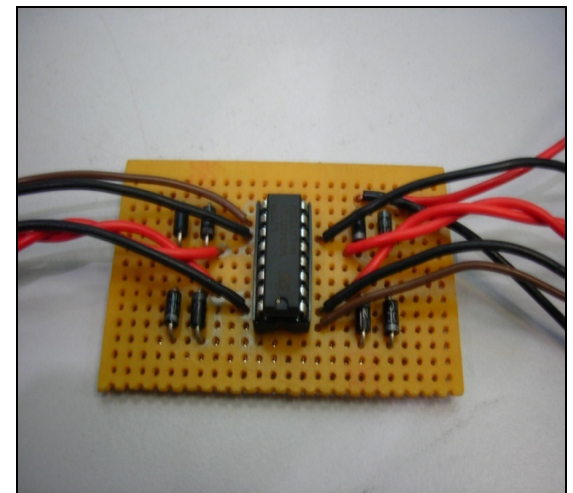


Fig 5. H-Bridge Circuit circuit and diodes. Components on the right side of the

diode are used to control one DC motor while the left side components are for another motor. This is the common method used in most of the automation strategy in controlling the direction of rotation of the motor. Both motors could either rotate in the same or in the opposite direction by changing the polarity.

Figure 6 shows the developed electromagnetic pick-up sensor operated DC motor position control CVT system. This system includes a pair of pulleys, DC motors, main AC motor, a DC battery, PWM circuit and H bridge circuit. After testing with different loading conditions it was found that the system is effective for transferring the power to the driving wheel in any operating condition of the vehicle.

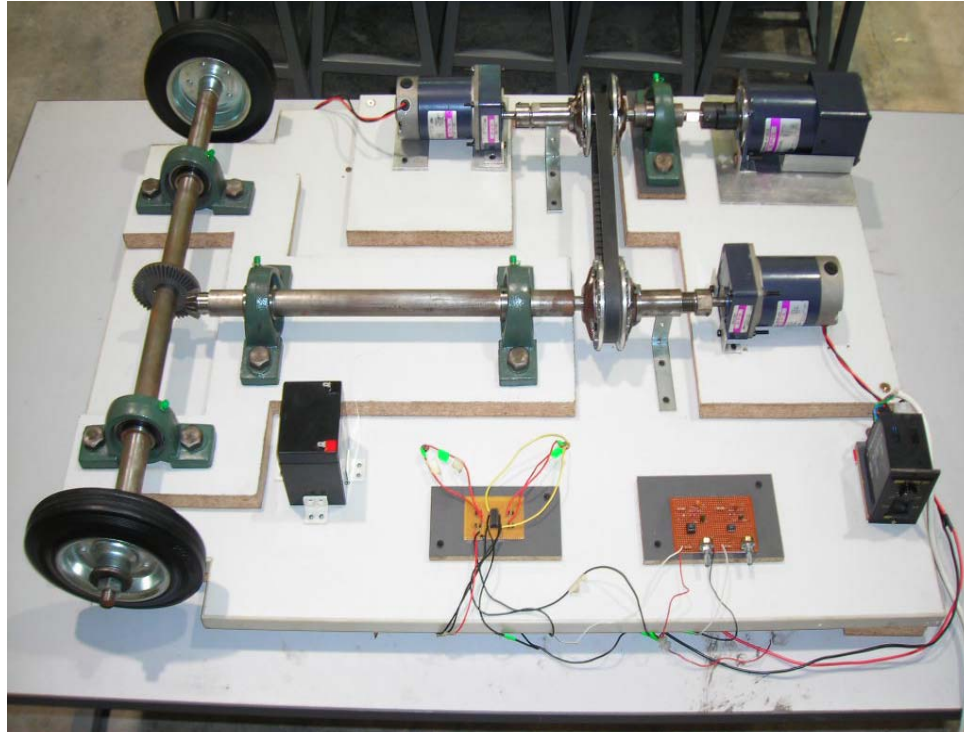


Fig 6. Developed CVT System

### 3. RESULTS AND DISCUSSION

Figure 7 shows the relationship of the linear speed of the sheave and the rotation speed of the DC motor with the developed IC control circuit.

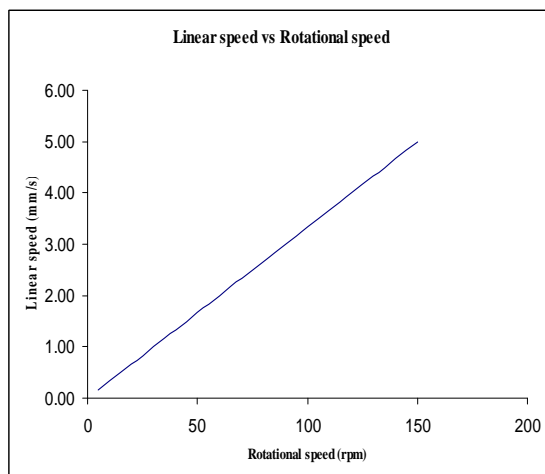


Fig 7. The Relationship Between Linear Speed of the Sheave and Rotational Speed of DC Motor

The speed of both driving and driven shaft is measured for every 2 mm increment of the stroke length which equals to one complete revolution of power screw. The gear ratio can be calculated by dividing the input speed by the output speed. The gear ratio varies from 1.29 up to 2.06 only. The result of the test is represented by Figure 8. All of the torque values are calculated based on gear ratio.

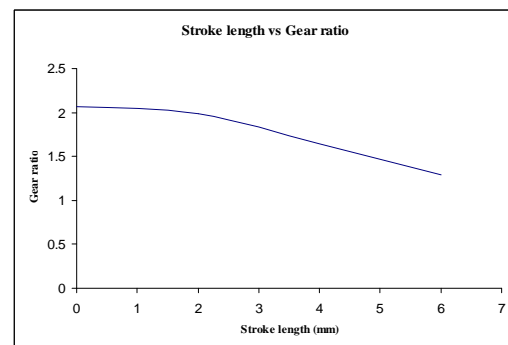


Fig 8. The relationship of the power screw stroke length and the transmission gear ratio.

The relationship between the DC motor speed and its

response time to actuate the moveable sheave was studied. The response time here is the time needed for the sheave to travel axially covering all of its stroke length. Theoretically, high DC motor speed result in low response time. The response time was derived from motor rpm and its linear speed providing that the whole stroke length equals to 13.6mm.

Figure 9 shows the relationship between the torque of the shaft and the transmission gear ratio. Result showed that the small increment to the input torque will result in large decrement of the axle torque. This is because of the underpowered driving motor. It can be concluded that the graph of torque and gear ratio is linearly related unless the over clamping problem arise. Small adjustment is needed to be made to the primary pulley sheave which result in small difference in the stroke length of primary pulley and secondary pulley. Figure 10 shows the relationship of the AC motor speed and the actuator speed.

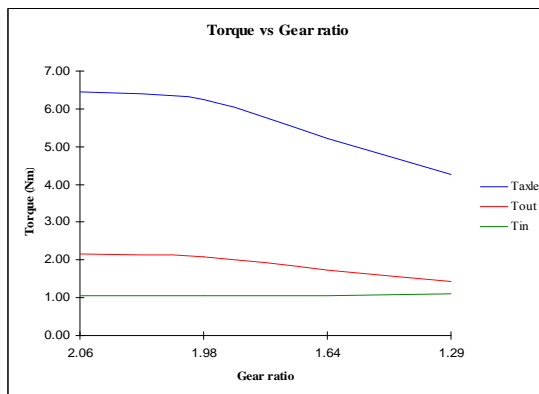


Fig 9. The Relationship Between Torque and Gear Ratio

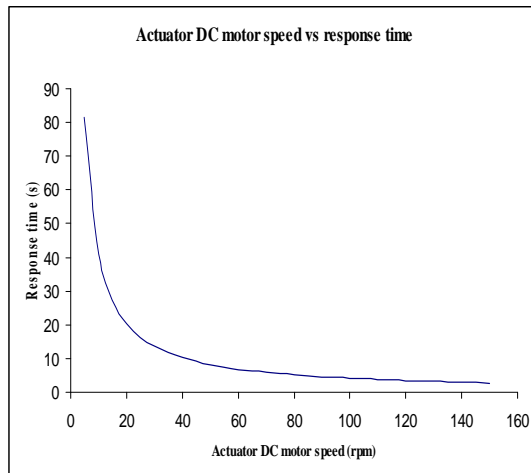


Fig 10. The Relationship of the DC Motor Speed and the Actuator Speed.

#### 4. CONCLUSIONS AND RECOMMENDATIONS

The following conclusions were made based on the content of this paper:

1. Transmission ratio of the CVT is changed to maintain the desired driving torque of the vehicle with the DC motor actuator and the developed power screw mechanism.
2. DC motor speed and rotation can be easily controlled using PWM and H-bridge circuit respectively.
3. The proposed electromechanical CVT system can eliminate the complexity of hydraulic system.

Several recommendations can be made to improve this electromechanical-actuated CVT. The DC motor could be replaced with stepper motor as it has the capability to move the moveable sheave precisely. Furthermore, it can hold torque better than the conventional DC motor. To continue the development of this project, the driving motor should be replaced with a higher powered motor so that CVT can demonstrate its full capability. In addition, the ratio controlling mechanism can be automatically controlled by employing fuzzy logic controlled PID with magnetic pick-up sensors.

#### 5. REFERENCES

1. Aaron, R., Roger, R., Zac, H., & Robert, T., 2004, "Improved recreational vehicle continuously variable transmission", *Small Engine Technology Conference and Exposition*. Retrieved February 23, 2008 from <http://www.sae.org/technical/papers/2004-32-0078>
2. Burke, M., Briffet, G., Fuller, J., Heuman, H. and Newall, J., 2003, "Powertrain Efficiency Optimisation of the Torotrak Infinitely Variable Transmission (IVT)", SAE, 2003-01-0971.
3. Bambang S., Kamarul B. T., Hishamuddin J. and Sugeng A., 2006, "Ratio Control of an Electromechanical Dual Acting Pulley Continuous Variable Transmission (Emdap-CVT) System using PD-Fuzzy Logic Controller", *1<sup>st</sup> Regional Conference on Engineering & Science*. Retrieved April 7, 2008, from [http://eprints.utm.my/239/1/BambangSupriyo2006\\_DCMotorPositionControl.pdf](http://eprints.utm.my/239/1/BambangSupriyo2006_DCMotorPositionControl.pdf).
4. Peggens, M., Vroemen, B., Stouten, B., Veldpau, F. and Steinbuch, M., 2006, "Control of a hydraulically actuated continuously variable transmission", *Vehicle System Dynamics*, 44:5, pp 387 – 406.
5. Wentzell, T. H., 2004, *Machine Design*, New York: Delmar Learning. Croser, P., Ebel, E., (2000). *Basic Level TP 101 Textbook*. Denkdorf: Festo Didactic GmbH & Co.
6. Sheu, K. B., Chiou, S. T., Hwang, W. M., Wang, T. S., and Yan, H. S., 1999, "New automatic hybrid transmissions for motorcycles". *Proceedings of National Sciences Council*, 23(6), pp 716-727.

## 6. NOMENCLATURE

Symbol	Meaning	Unit
$J_1$	Axle shaft's moment of inertia	(kg.m <sup>2</sup> )
$J_2$	Secondary pulley shaft's moment of inertia	(kg.m <sup>2</sup> )
$J_3$	Primary pulley shaft's moment of inertia	(kg.m <sup>2</sup> )
$m_1$	Mass of drive axle shaft	(kN)
$m_2$	Mass of secondary pulley shaft	(kN)
$m_3$	Mass of primary pulley shaft	(kN)
$R$	Radius of the shaft	(m)
$T$	Torque	(kN.m)
$F_d$	Axial force of the movable flange	(kN)
$\mu_b$	Coefficient of friction between the roller and roller contact	
$\mu_c$	Coefficient of friction between the roller and roller	

$R_c$	contact plane Normal force	kN
$\lambda$	Lead angle	°degree
$\phi$	Thread angle	°degree
$L$	Lead	m
$D_p$	Minimum pitch diameter	m
$\omega$	Angular velocity	rad/s
$y_m$	Distance	m
$\delta$	Angle	°degree

## 7. MAILING ADDRESS

A.K.M. Mohiuddin  
 Department of Mechanical Engineering,  
 International Islamic University Malaysia,  
 Kuala Lumpur, Malaysia



## APPLICATION OF THERMAL IMAGE: MACHINE FAULT DIAGNOSIS USING PCA AND ICA COMBINE WITH SVM

Ali Md. Younus, Achmad Widodoa, Bo-Suk Yang

School of Mechanical Engineering, Pukyong National University, Busan, South Korea

### ABSTRACT

A new approach for fault diagnosis of rotating machine based on thermal image investigation using image histogram features is proposed in this paper. By using thermal image, the information of machine condition can be investigated; it is easier than other conventional methods of machine condition monitoring. In the current work, the behavior of thermal image is investigated with different condition of machine. A test-rig that represents the machine in industry was set up to produce thermal image data in experiment. Some significant features have been extracted and selected by means of PCA and ICA and other irrelevant features have been discarded. The aim of this study is to retrieve thermal image by means of selecting proper feature to recognize the fault pattern of the machine. The result shows that classification process of thermal image features by SVM and other classifier can serve for machine fault diagnosis.

**Keywords:** Thermal image, Features, Condition Monitoring, Pattern Recognition.

### 1. INTRODUCTION

Among the excellent condition monitoring tools, infrared thermograph (IRT) is one of the important tool which can assist in the reduction of maintenance time and cost of industry. IRT allows for inspection of mechanical machinery for thermal pattern on pump, motors, bearings, fans, pulleys and other rotating machinery [1]. For new approach of machine condition monitoring, IRT has significant part due to frequently fault diagnosis. Indeed, thermal image is able to indicate whether the machine condition is normal or abnormal. For example, the support bearing contains very useful information on the subject of machine condition so the condition monitoring (CM) data in real application should be experimented on them. Infrared (IR) imaging approach is used in the industry as a part of non-destructive evaluation of machine condition especially to check misalignment, bend shaft and rolling element bearing fault based on thermography (temperature) data [2-4]. Hence, data analysis technique is essential in every approach for machine condition identification.

Fault diagnosis of rotating machinery can be handled as a task of pattern recognition that consists of three steps: data acquisition, feature extraction and final condition identification is the demandable issue of fault diagnosis. In order to obtain correct information whether normal or abnormal, it is important to complete all step of signal processing whatever the signal type such as vibration, image, current, acoustic signal and so on. In this study, the image histogram features have been chosen for pattern classification and condition monitoring because all thermal image features are not useful to fault diagnosis. Images play with many features

such as shape, histogram, colour, spectra texture and others [5]. Fault pattern classification specially for image is typically included of image acquisition, pre-processing, segmentation, feature extraction or dimension reduction, feature selection, classification and decision steps. It is the task of exploring the model that generated the patterns that we must concern with.

Histogram based features such as standard deviation, skew, variance, energy, entropy etc. as dimensionless parameters are effective and practical in fault diagnosis of rotating machinery due their relative sensitivity to early faults and robustness to various load and speed. Here, dimensionless parameters are extracted from the raw IRT data which have unfortunately large dimensionality that may increase the computational burden of a subsequent classifier and degrade the generalize capability of the classifier. Therefore, to overcome these difficulties, a few original features which apparently characterize the machine operating condition need to be selected feature from all features. The methods such as distance evaluation technique [6], genetics algorithm [7, 8], conditional entropy [9] are applied to seek the proper features to established machine characteristics. So after getting normalized features by extracting method, the extracting features are fed into the classification algorithm to identify the machine status as the final step of condition monitoring. Widodo & Yang et al [6] and J.-D. Son et al.[10] used support vector machines(SVM) classifier for vibration and current signal which performed very well to fault diagnosis. Nui & Yang et al. [11] introduced multi-agent decision fusion using several classifier together and B.S Yang et al. [12] showed the new approached of fault

classification which is adaptive resonance theory kohonen neural network (ART-KNN).

This report provides a fault diagnosis scheme for rotating machinery based on thermograph signal by employing histogram features of image. In this experiment, four machine conditions were measured to acquire data. Acquiring data is processed as follows: firstly, features of thermal images are calculated based on Histogram features of Image. Secondly, the feature extraction is conducted by pre-processing techniques by PCA and ICA. Lastly, the extracted data are used for input of the classification algorithms such as support vector machines (SVM), Fuzzy k-Nearest Neighbour (Fk-NN), Adaptive Resonance theory- KOHONEN neural network (ART-KNN) and The Parzen Probabilistic Neural Network (PPNN). The propose method is tested through characterize the different condition of machine fault simulator (MFS). The result from this method validates for assessing the machine state.

## 2. FEATURE EXTRACTION AND EVALUATION

Feature extraction is one of the most important parts used for condition monitoring and fault diagnosis, whose aim is finding a simple and effective transform of original signals. Important features contain in the signal can be extracted for machine condition monitoring and fault diagnosis. The selected features will be the major factor that determines the complexity and success of signal pattern classification process. Detail has been discussed about image features by Umbaugh & Scott [5]. For thermal image analysis, Histogram features of image have been used because data structure of thermograph in temperature scale is similar to the image gray level distribution as like array structure.

### 2.1 Histogram Features

The histogram features can be considered as statistical based features which provide us information about the characteristic of the gray level distribution for the image. Notated that, for thermal image the gray level of image depends on temperature that always varies with temperature. Now let us consider a image I, thus the first-order histogram probability P(g) can be expressed as

$$P(g) = \frac{N(g)}{M} \quad (1)$$

Where M is the number of pixel in the image I or sub image considering that's entire dimension is NxN and N(g) is the number of gray level g.

The mean is the average value which gives some information about general brightness of the image. As the colour distribution varies on temperature so the thermal image can be classified according to its colour intensities. We will use L as total number of gray level available range from 0 to 255 for image but for thermograph signature which is comparable with maximum and minimum temperature as may be mentioned 0<sup>o</sup>K to maximum value of temperature. Therefore, mean can be defined as follows

$$\bar{g} = \sum_{g=0}^{L-1} gP(g) = \sum_r \sum_c \frac{I(r,c)}{M} \quad (2)$$

Variance is defined as a measure of the dispersion of a set of data points around their mean value.

$$\sigma_g^2 = \sum_{g=0}^{L-1} (g - \bar{g})^2 P(g) \quad (3)$$

The standard deviation, which is also known as the square root of the variance, tells us something about the contrast. It describes the spread in the data, so a high contrast image will have a high temperature distribution over image. Using this we can be able to classify various of machine conditions thermal images. Standard deviation is termed as follows

$$\sigma_g = \sqrt{\sum_{g=0}^{L-1} (g - \bar{g})^2 P(g)} \quad (4)$$

The skew S measures the asymmetry about the mean in the gray level distribution. It is defined as

$$S = \frac{1}{\sigma_g^3} \sqrt{\sum_{g=0}^{L-1} (g - \bar{g})^3 P(g)} \quad (5)$$

The energy E tells us something about how the gray levels are distributed

$$E = \sum_{g=0}^{L-1} [P(g)]^2 \quad (6)$$

The energy measure has a maximum value of 1 for an image with a constant value, and gets increasingly smaller as the pixel values are distributed across more gray level values.

The entropy  $E_t$  is a measure that tells us how many bits we need to code the image data, and is given by

$$E_t = \sum_{g=0}^{L-1} P(g) \log_2 [P(g)] \quad (7)$$

As the pixel values in the image are distributed among more gray levels, the entropy increases. A complex image has higher entropy than a simple image.

The kurtosis K is just the ratio of the fourth central moment and the square of the variance.

$$K = \sum_{g=0}^{L-1} \frac{(g - \text{mean})^4}{\sigma^4} \quad (8)$$

### 2.2 Feature Extraction and classification

When the input data to an algorithm is too large to be processed and it is suspected to be notoriously redundant (much data, but not much information) then the input data will be transformed into a reduced representation set of features (also named features vector). Transforming the input data into the set of features is called *features extraction*. If the features are carefully extracted then it is expected that the features set will contain the relevant information from the input data in order to perform the desired task. Two types of feature extraction method have been applied in this current work which are Principal component analysis (PCA) and Independent

component analysis (ICA). PCA is a classical statistical method and is often used to machine fault diagnosis and pattern classification. And ICA is a technique that transform multivariate random signal into a signal having components that as mutually independent in complete statistical sense. For classification, SVMs, ARTKNN FKNN, PPNNs and e.tc. algorithms are used for machine condition diagnosis.

### 3. EXPERIMENT AND MEASUREMENTS

#### 3.1 Experimental setup

Figure1 show the fault simulator with thermo-cam sensor that is apart and a short shaft of 30 mm diameter is attached to the shaft of the motor through a flexible coupling; this minimizes effects of misalignment and transmission of vibration from motor. Using coupling we can set misalignment condition of the fault simulator. The shaft is supported at its ends through two ball bearings. A disk is attached with the shaft that is used for making balanced and unbalanced condition of fault simulator. To get unbalanced extra mass is to add on the disk. A variable speed DC motor (0.5 HP) with speed up to 3450 rpm is used as the basic drive. Table 1 shows the main specification of thermo cam and fault simulator. The sensor used in the experiments for this study is a long-wave IR camera from FLIR with a thermal sensitivity of 0.08 °C at 30 °C.

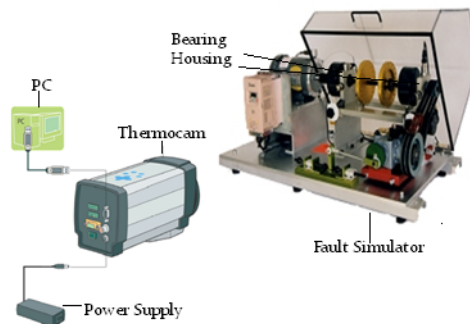


Fig 1. Experimental setup

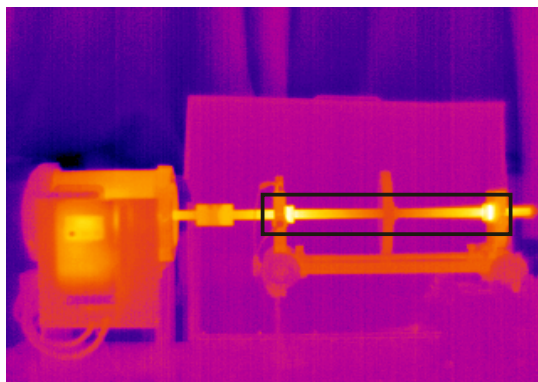


Fig 2. Original Thermal Image

misalignment and transmission of vibration from motor. Using coupling, we can set misalignment condition of the fault simulator. The shaft is supported through two

ball bearings at its ends. Disks are attached on the shaft used to make balanced and unbalanced condition of fault simulator. To get unbalanced, extra mass is added on the disks. A variable speed DC motor (0.5 HP) with speed up to 3450 rpm was used as the basic driver. Table 1 shows the main specification of thermo cam and fault simulator. The sensor used in the experiments for this study is a long-wave IR camera from FLIR with a thermal sensitivity of 0.08 °C at 30

#### 3.2 Experimental procedure

In this experiment, the thermo-cam is the major key device that some parameters are set for data accusation. Some specifications of the thermo cam have been given in the prior section where we can get some idea, regarding thermo-cam. Herein, some parameters are very important to obtain data is emissivity of the object that plays fundamental role for image (signal) accusation but those parameters are put automatically functioning of thermo-cam and all machine's materials about to same. Others parameter of objects, for example, relative humidity, scale temperature, focal length of camera and distance are set as our requirement of experiment. All of these parameters are chosen according to our experiment condition. For all four normal, mass unbalance, misalignment and bearing fault condition, we have put same parameter for accomplished the experiment.

In the current study, we try to analyze different types of faulty condition machine by this experiment. Firstly, the normal condition of machine was set, afterward speed of the motor been increased gradually up to 900 rpm. And then, machine was run for five minutes to get its stable condition then data acquisition was lunched. We conducted experiment of normal, misalignment and mass unbalance condition of machine successively. Data from thermo-cam was saved directly to the notebook or PC. The image from thermo-cam is shown in Figure 2. which carrying only visual inspection of machine condition. Figure 3. shows the data structure from thermo-cam in Kelvin scale which has been processed for fault diagnosis.

....	....	....	....	....	....	....	....	....	....
....	....	....	....	....	....	....	....	....	....
....	....	315.58	315.79	315.39	315.12	314.83	311.94	304.97	....
....	....	315.72	316.35	315.87	315.51	315.16	312.65	305.41	....
....	....	316.51	316.62	316.05	315.69	315.23	312.84	305.46	....
....	....	316.45	316.80	316.41	316.13	315.55	313.55	305.86	....
....	....	316.22	316.41	316.32	316.44	315.87	313.77	306.26	....
....	....	315.89	316.44	316.49	316.60	316.18	314.08	306.23	....
....	....	315.36	316.12	315.90	316.15	316.18	314.51	307.18	....
....	....	315.67	315.82	315.72	315.82	315.94	316.02	314.34	....
....	....	315.10	315.57	315.72	315.74	315.67	322.69	331.09	....
....	....	315.21	315.64	315.95	315.84	316.97	324.40	334.91	....
....	....	....	....	....	....	....	....	....	....
....	....	....	....	....	....	....	....	....	....

Fig 3. Temperature in Kelvin Scale at each pixel of thermal image

Table 1: Specification of thermo-cam and fault simulator

Thermo-cam	• Solid state, uncooled micro
------------	-------------------------------

(FLIR-A 40 series) bolometer detector, 7.5 to 13  $\mu\text{m}$

- 40 °C to +70 °C storage temperature range
- Solid object materials and emissivity: 0.1 to 0.95.
- For short distance, humidity is default value of 50 %.
- 0.08 °C at 30 °C thermal sensitivity

Fault simulator

- Shaft diameter: 30 mm
- Bearing: Two ball bearings
- Bearing housings: Two bearing housings,
- Bearing housing base: Completely movable using jack bolts for easy misalignment in all three planes
- Rotors: Two rotors, 6" diameter with two rows of tapped holes at every 20°.

## 4. RESULT AND DISCUSSION

### 4.1 Feature representation and Feature extraction

In the following feature extraction process, histogram based image features of thermal image data have been used which a new approach to machine condition monitoring.

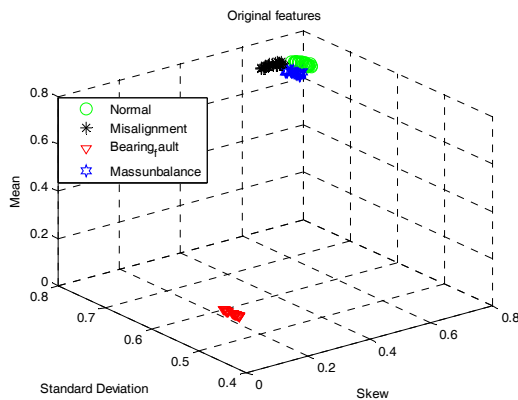


Fig 4. Original features selected randomly

In fact, the original features data could not be possible to cluster well because it is high dimension data structure and being overlapped each other. This phenomenon is shown in the Figure 4, the three features from the original features data(120) has been chosen manually without applying any feature extraction algorithm. The representation of features in figure has possessed as scattered due to large size of data only limited number data having to present. Also different type of faults in figure is overlapped each other. So, these data cannot be separated and also not possible to directly processed into classifier because it will degrade the performance of classifier

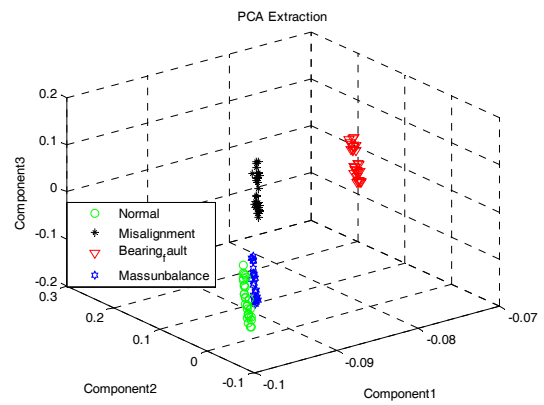


Fig 5. Clustering features by PCA

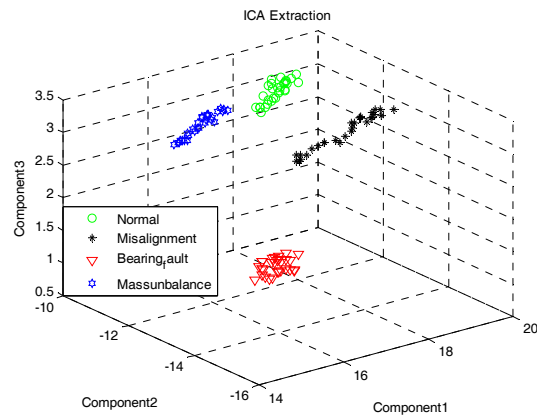


Fig 6. Clustering features by ICA

To overcome these problems and disadvantages, useful features should be extracted and also necessary to reduce the dimension of original data features. Accordingly, the dimension reduction and feature extraction algorithm like PCA and ICA has been employed intending to avoid disorder data. In this study, ICA and PCA is applied based on variation of eigenvalue. The eigenvalues have been chosen according to the biggest value have been selected and remaining were discarded. So, the components of PCA were calculated according to that eigenvalues. The first three principal components of PCA are plotted in Figure 5. It can be mentioned that the different class of data for machine conditions are well separated. If we pay attention to both original features selected randomly (in Figure 4.) and feature by PCA (in Figure 5.), obviously, the using PCA extracting data is showing the better performance than choosing features randomly or manually. The Figure 6. shows the extracting features data by ICA of histogram features of thermal image. Also represents the independent component analysis with four different machine conditions. Data extracting features over ICA compare to PCA and randomly chosen is well. The separation of four types data for machine condition is really appreciable through ICA and every classter data is away eachother in Figure 6.

Table 2: Classifier performance

Features	Data	Classifier Performance			
		Supervised Classifier		Neural Network classifier	
		SVM	FKNN	ARTK NN	PPNN
PCA	Valid	0.9833	0.9167	0.7500	0.8167
	Test	0.8667	0.8333	0.8000	0.7833
ICA	Valid	1.0000	1.0000	0.9660	0.9312
	Test	0.9861	0.9633	0.9425	0.9100
Original Data	Valid	0.7800	0.7837	0.6941	0.6965
	Test	0.7487	0.7600	0.6528	0.6281

#### 4.2 Training and Classification

The relevant parameters setup for the classifier is according to G.Nui et al.[11], Widodo et al. [6], J.-D. Son et al. [10] and B.S. Yang et al.[12]. They have carried out vast and deep researches on classifier for machine fault diagnosis to find out optimum parameters of classifier for achieving good result. With optimum parameters of classifier, in the current work, the RBF kernel is used as the basis function of SVMs which consists of two parameters are  $C$  and  $\gamma$ . As optimal value of these arguments,  $C$  and  $\gamma$  is defined with values 10 and  $2^{-2}$  respectively. ARTKNN is a classifier of neural networks family whose main parameter is number of neurons and also criterion parameter denoted as  $\rho$ . The criterion parameter,  $\rho > 0.96$  indicates the optimal number of neurons because it is directly proportional to the neural numbers. In order to achieve satisfactory performance by this networks, the number of neural networks is 27. The performance of FKNN depends on parameter  $K$  so that it is a important problem to find a suitable  $K$ . To accomplish this job, we have tried the value of  $k < 5$  which gives us satisfactory result of classification. In practice, the parameter value of FKNN differs case to case. Here, PPNNs are a simple type of neural network used to classify data vectors.

In classification processes, features data were input as fifty percent for training and remaining were test validation. After performing classification, from the Table 2 the training and testing accuracy of four classifiers can be observed. For thermal image data, it can be seen that the classification performance using ICA data is much better than PCA and original features data with all classifier. Here, two types of classifier have been shown for classifications that are supervised learning method and neural networks classifier. The best classification accuracy is for thermal image data by SVM and FKNN classifier with trained value of 1.000 where SVM and FKNN are belong to a family of supervised classifier. However, only the SVM test performance is very well over other classifiers. ARTKNN and PPNN belong to family of *neural network classifier*. Performance of this is also appreciable as shown in Table 2. It can be concluded that all classifiers which have been used in this work validate for thermal image data on machine condition diagnosis that is not of course for original features.

## 5. CONCLUSION

By this work, a useful application of thermography in the machine condition monitoring and fault diagnosis area is presented. The thermograph data was taken into account to investigate different types of machine fault. At first, the experiment was carried out for four conditions at the same experimental condition after that raw data was extracted from its original structure to compatibility in data processing technique. Histogram features based on statistical of image were employed as a proper feature for thermal image data. Calculated image features data were taken into feature extraction algorithm due to mass dimensionality. As a result, data extracted by ICA shows better clustering performance compare to PCA. Finally, comparison of classifier accuracy using original, ICA and PCA data shows remarkable result by SVM than other machine learning method.

## 6. REFERENCES

1. Carosena, M., Giovanni, Carlomaggo, M., 2004, "Recent advance in the use of infrared thermography", *Measurement Science and Technology*, 15:R27-R58.
2. Thomas, R., 2007, "The continued and future use of infrared use of infrared thermography", *Proceeding of 2nd WCEAM*. pp. 1897-1907.
3. Abdel-Qader, I., Yohali, S., Abudayyeh, O. and Yehia, S., 2008, "Segmentation of thermal images for non-destructive evaluation of bridge decks", *NDT&E International*, 41:395-405.
4. Epperly, R.A., Herberlin, G.E. and Eads, L.G., 1997, "A tool for reliability and safety: predict and prevent equipment failure with thermography", *IEEE App. Soc. Procs.*, pp 59-68.
5. Umbaugh, S.E., 2005, "*Computer Imaging: Digital Image analysis and processing*", Taylor & Francis, UK.
6. Widodo, A., and Yang, B.S., 2007 "Application of nolinear feature extraction and support vector machines for fault diagnosis of induction motors" *Expert System with Applications*, 33: 241-250.
7. B SAMANTA, 2004, "Artificial neural networks and genetic algorithms for gear fault detection", *Mechanical Systems and Signal Processing*, 18:1273-1282.
8. Jack, L.B. and Nandy, A.K., 2002, "Fault detection using support vector, machines and artificial neural networks, augmented by genetic algorithms", *Mechanical Systems and Signal Processing*, 16:373-390.
9. Lehrman M., Rechester A.B., R.B. White, 1997, "Symbolic analysis of chaotic signals and turbulent fluctuation", *Physical Review Letter*, 78:54-57.
10. Son J.D., Niu G., Yang B.S., Don H.H. and Dong S.K., 2009, "Development of Smart sensors system for fault diagnosis", *Expert System with Applications*, in press.
11. Gang Niu, Tian Han, Bo-Suk Yang and Andy Chit Chiow Tan, 2007, "Multi-agent decision fusion for motor fault diagnosis", *Mechanical Systems and Signal Processing*, 21:1285-1299.
12. Yang B.S., Han and J.L. An T., 2004, "ART-KOHONEN neural network for fault diagnosis of rotating machinery", *Mechanical Systems and Signal Processing*, 18:645-657.

## **7. MAILING ADDRESS**

Ali MD. Younus  
School of Mechanical Engineering,  
Pukyong National University  
San 100, Yongdang-dong, Nam-gu, Busan 608-739,  
South Korea  
Phone: +82-10-8689-7777  
E-mail: md.yali@yahoo.com

## WAVELET CO-EFFICIENT OF THERMAL IMAGE ANALYSIS FOR MACHINE FAULT DIAGNOSIS

Ali Md. Younus<sup>1</sup>, Khairul Alam<sup>2</sup> and Bo-Suk Yang<sup>1</sup>

<sup>1</sup>School of Mechanical Engineering, Pukyong National University, Busan, Korea

<sup>2</sup>Graduate School of Institute of e-Vehicle Technology, University of Ulsan, Nam-gu, Ulsan, Korea

### ABSTRACT

The ultimate goal of this study is to introduce a new method of machine fault diagnosis using different machine conditions data such as normal, misalignment, mass-unbalance and bearing-fault from infrared thermography (IRT). Using thermal image, it is easy to obtain information about the machine condition rather than other conventional methods of machine condition diagnostic technique. Thermal image technique can be successfully applied in the field electrical and electronics system, mechanical system, energy system and medical diagnosis. To get information from the image many techniques of image processing such as discrete Fourier transformation, discrete cosine transformation, neural networks, wavelet transform and many others methods is being used. In this study, our main focal point is to analysis thermal image by discrete wavelet decomposition and tries to find out significant result of machine condition monitoring. In this work, decomposition level of 2 shows satisfactory result for machine condition diagnosis.

**Keywords:** Thermal image, Discrete Wavelet Decomposition, Fault Diagnosis, Machine Condition.

### 1. INTRODUCTION

The fault diagnosis of rotary machinery plays a great role in nondestructive preventive maintenance of rotating part of machine which could save the severe fault even catastrophic failure of machinery during the operating condition. Diagnosis of support bearing by analyzing thermal image signature is the new technique to distinguish machine condition that indicates healthy or unhealthy. Since the support bearing gives very useful information on the subject of machine condition. As typical rotating machinery, support bearing is being widely applied to evaluate machine health condition. Most of the cases, it is difficult to acquire signal from gear box because of its complex structure as well having convolution to evaluate the machine condition so that if the support bearings are examined then the useful information could be found. But more accurate information might be easily found by thermal image that should be processed because appropriate image processing does not create any new information moreover it gives more distinguishable feature [1]. Primarily, we have proposed and used discrete wavelet decomposition (DWT) which gives some significant statistical feature that enable to get machine health condition.

Infrared (IR) imaging approach has been used in the

industry as a part of nondestructive evaluation of machine condition especially to check misalignment, bend shaft and rolling element bearing fault. To evaluate electrical machine fault like cooling system, earth faults, circulating current, air leakage location, water pipe defect location and so on [2-5]. Some researchers have conducted experiment to evaluate the shallow delaminating in concrete bridge decks and they have developed some algorithm for detection that fault [6].

On the other hand, many researchers have been conducted experiment to acquire vibration signals are commonly used in the condition monitoring and diagnostics of the rotating machinery [7-9]. Generally, the vibration measurement of the bearing can be made by some accelerate sensors that are taken place on the bearing house. To analyze these signature usually different approach is been used. To date, some techniques such as envelope analysis, high frequency resonance technique, fast Fourier transformation, wavelet analysis are being used to machine condition diagnosis in bearing fault approach [10-12].

In fact, lots of samples are needed to obtain enough bearing signature because in this field of thermal image signal analysis the reference and sample data are not enough to investigate the machine condition monitoring.

In this study, thermo-cam has specially been used to



obtain the thermal image data at the bearing housing of rotor kit and being measured the four condition of this rotor kit that are normal, misalignment mass unbalance and bearing fault. In these different conditions, the thermal image signature seems to be same it could not be identify what kind fault has occurred. In this paper, DWT has chosen because of complexity of thermal image data that is not conventional vibration signal data. The purpose of this current study is to demonstrate how to extract useful condition indicators (covariates) from raw thermal image signature by using DWT. Primarily, we proposed and used desecrate wavelet decomposition which gives some significant statistical feature that enable to get machine health condition.

## 2. THEORETICAL BACKGROUND

### 2.1 Wavelet Transforms

All wavelet transforms (WT) may be considered forms of time-frequency representation for continuous time (analog) signals and so are related to harmonic analysis. However, in the case of image signal analysis we should be considered the discrete wavelet transformation that might be appropriate tool. Almost all practically useful discrete wavelet transforms (DWT) use discrete-time filter banks. These filter banks are called the wavelet and scaling coefficients in wavelets nomenclature.

The definition of the continuous wavelet transform for a 1-dimensional signal  $f(x) \in L2(\mathbb{R})$ , given by Morlet and Grossmann [13] the space of all square integrable functions, is

$$W(a, b) = \frac{1}{\sqrt{a}} \int_{-\infty}^{+\infty} f(x) \psi^* \left( \frac{x-b}{a} \right) dx \quad (1)$$

Where,  $W(a, b)$  is the wavelet coefficient of the function  $f(x)$ ,  $\psi(x)$  is the analyzing wavelet,  $a (> 0)$  is the scale parameter,  $b$  is the position parameter.

### 2.2 Discrete Wavelet Transform (DWT)

The 2D DWT is a very recent mathematical tool of two-dimensional data handling. A lot of meaningful and awful data is created after calculating the wavelet coefficients at every possible scale. If scales and positions based on powers of 2 called dyadic scales and positions- are chosen then analysis become more efficient and accurate. Such an analysis obtained from the discrete wavelet transforms (DWT) [14]. The analysis start from signal  $s$  and results in the coefficients  $C(a, b)$ .

$$C(a, b) = C(j, k) = \sum_{n \in \mathbb{Z}} s(n) g_{j,k}(n) \quad (2)$$

From the above decomposition fundamental, low frequency and high frequency content signal is generated when original signal is passed through the high pass and low pass filter. For many signals, the low frequency content is the most important part whereas the high frequency content has less importance. The

decomposition algorithm starts with signal  $s$  which is  $n$  by  $m$  dimensions, next calculates the coordinates of approximation (A1), horizontal detail (HD), vertical detail (VD1) and diagonal detail (DD1) then those of A2, HD2, VD2, and DD2 and so on. However, one-dimensional signal being decomposed into two components are approximation (A1) and detail coefficients (D1). The algorithm of 2D DWT is depicted in figure 1.

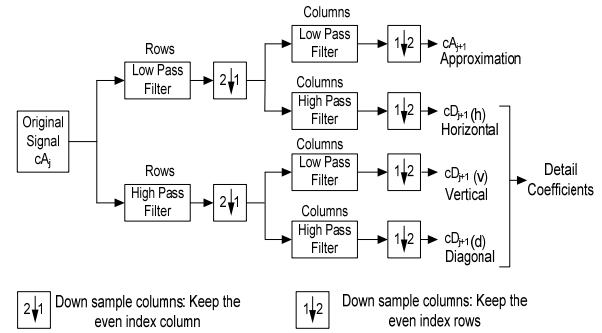


Fig 1. Algorithm of DWT

In this paper, the every level of decomposition and all coefficients have been consider to analysis for finding significant result of machine conditions. Among the huge data, obtained good features data is a great challenge for classify different class data. Primarily, to find out the decomposition level of coefficients is an objective as a part successful application in machine fault diagnosis.

## 3. EXPERIMENT AND MEASUREMENTS

### 3.1 Experimental Setup

Figure 2 shows the machine fault simulator with thermo-cam sensor that is apart. A short shaft of 30 mm diameter is attached to the shaft of the motor through a flexible coupling; this minimizes effects of misalignment and transmission of vibration from motor.

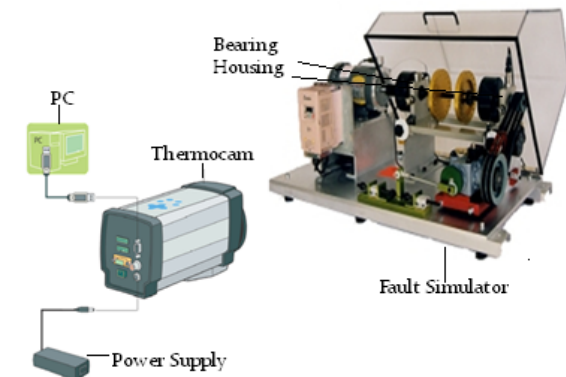


Fig 2. Experimental setup

Using coupling, we can set misalignment condition of the fault simulator. The shaft is supported through two ball bearings at its ends. Disks are attached on the shaft

used to make balanced and unbalanced condition of fault simulator. To get unbalanced, extra mass is added on the disks. A variable speed DC motor (0.5 HP) with speed up to 3450 rpm was used as the basic driver. Table 1 shows the main specification of thermo cam and fault simulator. The sensor used in the experiments for this study is a long-wave IR camera from FLIR with a thermal sensitivity of 0.08 °C at 30.

### 3.2 Experimental procedure

In this experiment, the thermo-cam is the major key device that has some parameters is needed to set for data accusation. Some specifications of the thermo-cam have been given in the prior section where we can get some idea, regarding thermo-cam. There are some parameters of objects very important to obtain data that is especially for thermal image (signal) acquisition. However, those parameters are put automatically functioning of thermo-cam because all machine's materials are considered as similar. The most important parameter is emissivity and other parameters of object are relative humidity, scale temperature, focal length of camera and distance are set as our requirement of experiment in Table 1.

Table 1: Specification of thermo-cam and fault simulator

Thermo-cam (FLIR-A 40 series)	<ul style="list-style-type: none"> <li>• Solid state, uncooled micro bolometer detector, 7.5 to 13 μm</li> <li>• -40 °C to +70 °C storage temperature range</li> <li>• Solid object materials and emissivity: 0.1 to 0.95.</li> <li>• For short distance, humidity is default value of 50 %.</li> <li>• 0.08 °C at 30 °C thermal sensitivity</li> </ul>
Fault simulator	<ul style="list-style-type: none"> <li>• Shaft diameter: 30 mm</li> <li>• Bearing: Two ball bearings</li> <li>• Bearing housings: Two bearing housings,</li> <li>• Bearing housing base: Completely movable using jack bolts for easy misalignment in all three planes</li> <li>• Rotors: Two rotors, 6" diameter with two rows of tapped holes at every 20°.</li> </ul>

All of these parameters are chosen according to our experiment condition. For all four normal, mass unbalance, misalignment condition and bearing fault, we have put same parameters for accomplished the experiment.

In the current study, we try to analyze different types of faulty condition machine by this experiment. Firstly, we set the normal condition of machine, afterward speed of the motor been increased gradually up to 900 rpm. And then, machine was run for five minutes to get its stable condition then data acquisition was lunched. We

conducted experiment of normal, misalignment, mass unbalance condition and bearing fault of machine successively. Data from thermo-cam was saved directly to the notebook or PC.

The original thermal imaging shows in Figs. 3 and 4 the gray level value at each pixel in the thermal image. Fig. 5 presents the temperature value at each pixel of thermal image. The reduced data size 158 by 25 is shown in Fig. 3 by black rectangular marks that have been extracted from original raw images that were 320×240 array.

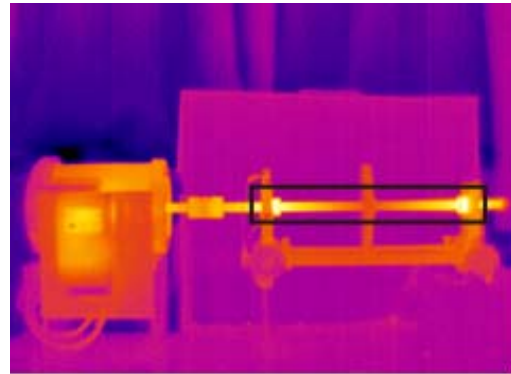


Fig 3. Original thermal image

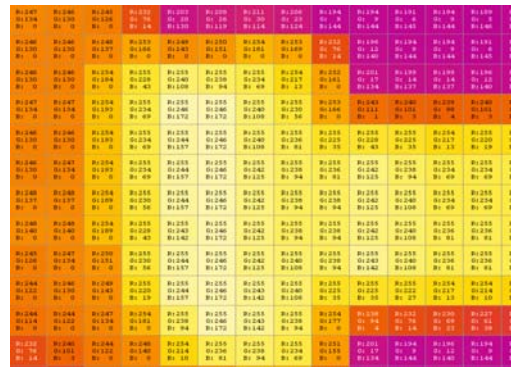


Fig 4. Gray level value at each pixel in thermal image

....	....	....	....	....	....
....	....	....	....	....	....
....	....	315.58	315.39	315.12	....
....	....	315.72	315.87	315.51	....
....	....	316.51	316.05	315.69	....
....	....	316.45	316.41	316.13	....
....	....	316.22	316.32	316.44	....
....	....	315.89	316.49	316.60	....
....	....	315.36	315.90	316.15	....
....	....	315.67	315.72	315.82	....
....	....	315.10	315.72	315.74	....
....	....	315.21	315.95	315.84	....
....	....	....	....	....	....
....	....	....	....	....	....

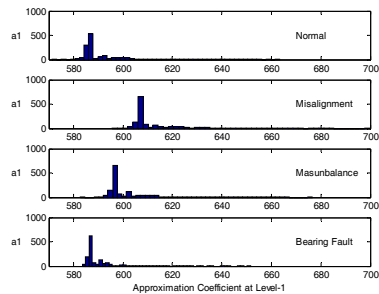
Fig 5. Temperature at each pixel of thermal (Kelvin scale)

## 4. RESULTS AND DISCUSSION

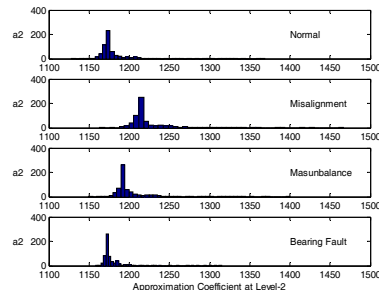
### 4.1 Wavelet Co-efficient Analysis

Select the level N and type of wavelets, and then determine the coefficients of the thermal image signal by 2D DWT. To do decomposition of signals, we have to decide over many selections, such as the types of mother wavelet, the decomposition levels and type of coefficients e.tc. In the decomposition of thermal image data from different condition machines, we apply Bio-orthogonal (bior-3.5) wavelets of degree 3.5 and the decomposition level of 3. Due to the dimension of thermal image data, the decomposition level of 3 is selected because there is no data for decomposition after the selected level. Having performed decomposition, four kinds of wavelet coefficients have found from each class of machine conditions data. Among the coefficients (A, HD, DD, VD), approximation coefficients which passed through the low pass filter is considered for feature extraction because the low frequency signals contain most important part of original signal. However, other wavelet coefficients except approximation may be useful to in machine condition diagnosis. The comparison of approximation coefficients of different class thermal image data at same level is shown in figure 6 (a), 6(b) and 6(c). The histogram of approximation coefficients shows the separates condition of machines by either ranges of histograms or amplitude of coefficients.

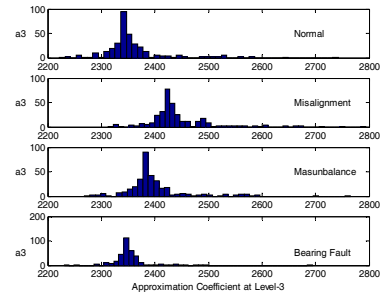
If we closely see, the normal, misalignment and bearing fault can be categorized by ranges. The peak of these conditions of machine lies in different ranges which is the distinguishing feature of machine resonances. In case of bearing fault, the coefficients show the maximum amplitude than other machine conditions. In figure 6, there are only coefficients of one sample presented but we have performed all samples of each machine condition and obtained the similar result.



(a) At level of 1



(b) At level of 2



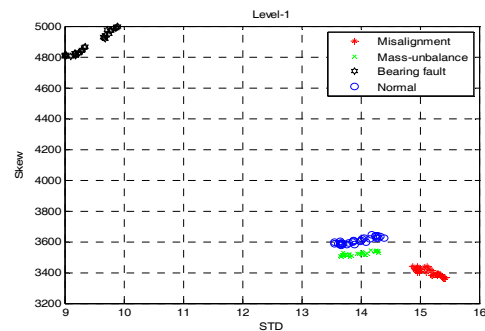
(c) At level of 3

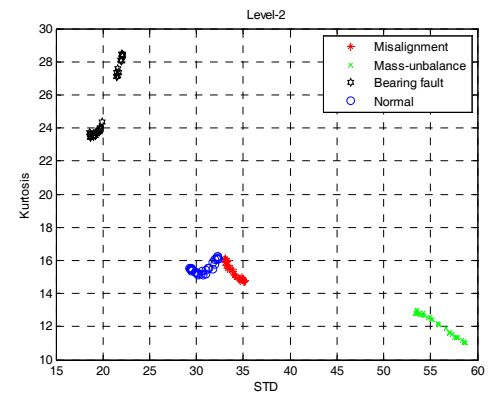
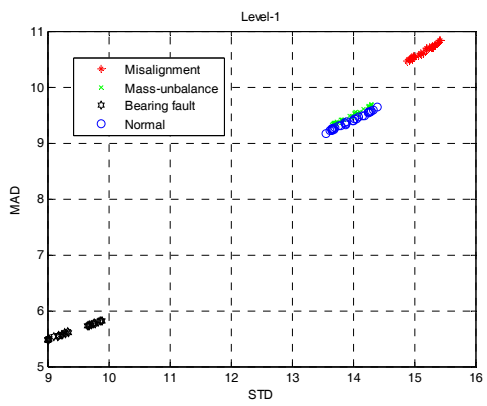
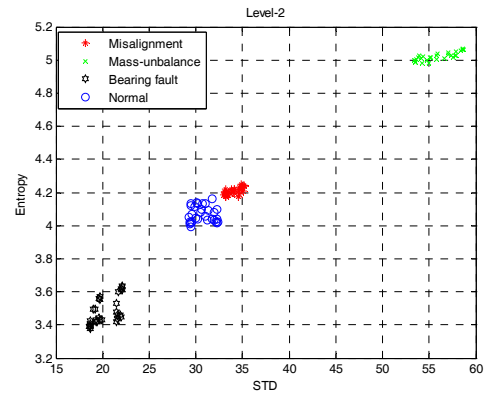
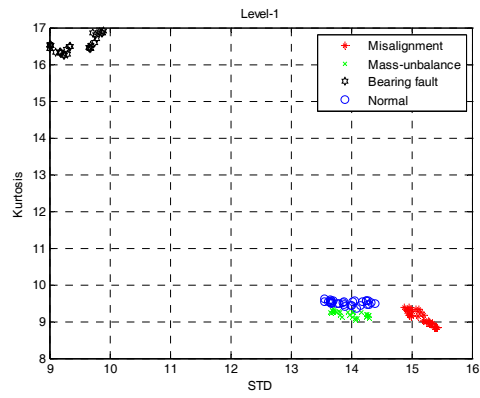
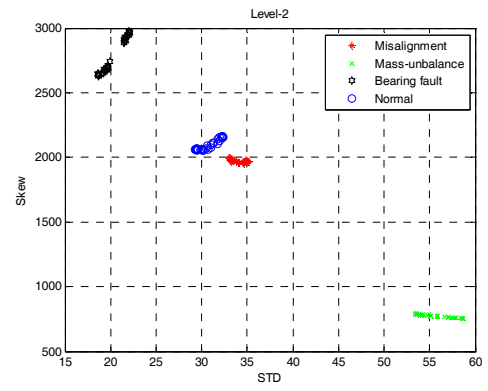
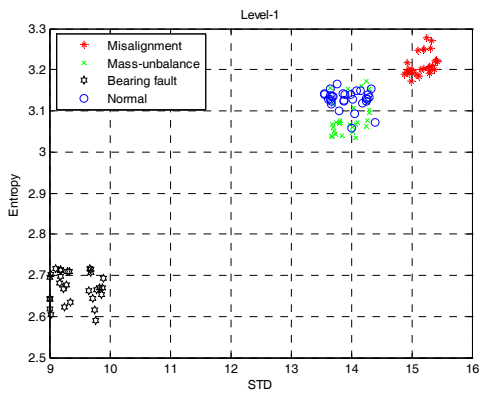
Fig 6. Approximation coefficients at different level and conditions

### 4.2 Feature Extraction

In this work, we work with the 2D signals means of thermal image data. After decomposition by DWT, the 2D coefficients have been found. So feature should be calculated according to 2D statistical features calculation. There are six features have been extracted from four different machine conditions where each condition has thirty samples. The standard deviation, Mean, Entropy, Skew, Kurtosis, Mean absolute deviation are statistical measurement of any kinds of data been used here as feature. The all features from thermal image is shown in figure 7 where wavelet decomposition coefficient of all machine's conditions from level 1 to 3 are presented. All features are plotted against standard deviation to find significant distinguish features of machine condition. First let's come to the coefficient of level 1 in figure 7(a) where machine's conditions are clearly separated for skew versus standard deviation and remaining features are either scattered or overlapped each other.

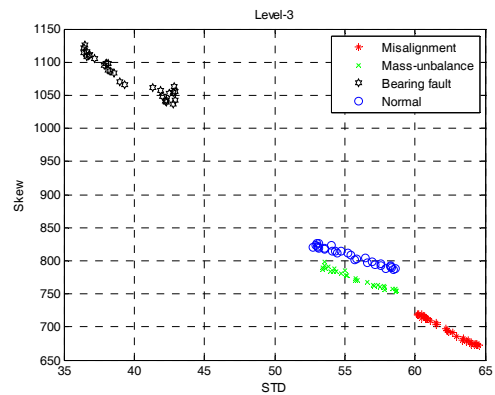
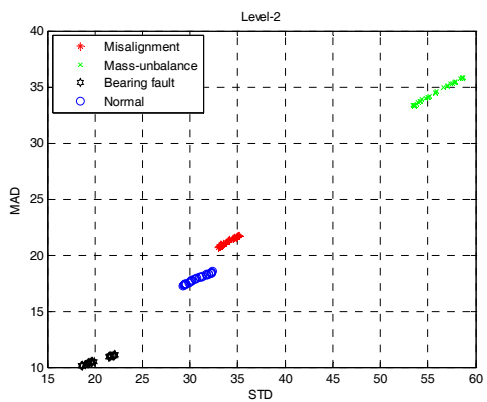
At level of 2, all features are apparently well separated that indicates, in this study, all machine conditions can be understand easily using coefficients of level 2 in figure 7(b). Entropy and Mean absolute deviation versus standard deviation cannot provide the decision about the machine conditions at the coefficients of level 3 because they coincide each other figure 7(c).

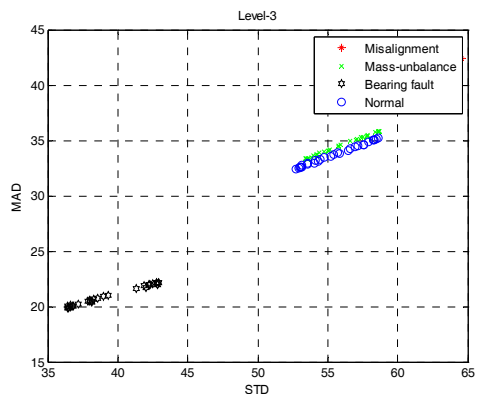
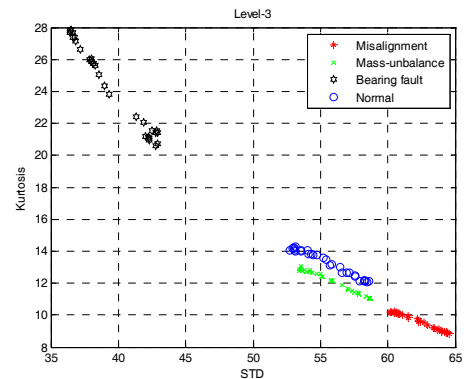
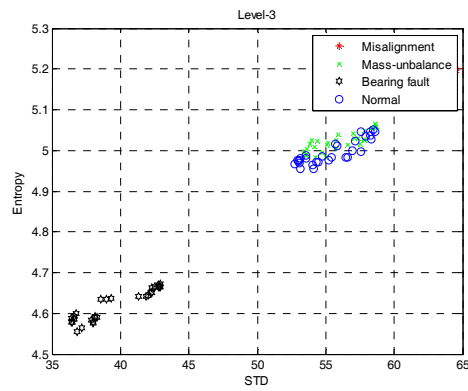




(a) Features at level of 1

(b) Features at level of 2





(c) Features at level of 3

Fig 7. Features at different levels

## 5. CONCLUSIONS

In this study, infrared thermograph has been applied to evaluate the four machine conditions: normal, misalignment, mass unbalance and bearing fault. The goal in image analysis is to extract information useful for application based problem. In this work, bio-orthogonal wavelet algorithm has been successfully implemented to obtain real machine's condition. More clearly get information; we have calculated statistical features that help to make decision to about machine's conditions. Here, coefficients of level 2 shows the best result among the others levels of coefficients. Indeed, the current study demonstrates how to extract useful condition indicators from raw thermal image signature by using wavelet decomposition. In this analysis we also try to show the

behavior of image at operating condition of machine by statistical feature.

## 6. REFERENCES

1. S. Kumar, F. Taheri, 2007, "Neuro-fuzzy approaches for pipeline condition assessment", *Nondestructive Testing and Evaluation*, 22(1):35-60.
2. T. Roderick, "The continued and future use of infrared use of infrared thermography", *Proceeding of 2nd WCEAM*.
3. I. Abdel-Qader, S. Yohali, O. Abudayyeh, S. Yehia, 2008, "Segmentation of thermal images for non-destructive evaluation of bridge decks", *NDT&E International*, 41:395-405.
4. C. Maierhofer, R. Arndt, M. Rollig, C. Rieck, A. Walther, H. Scheel, B. Hillemeier, 2006, "Application of impulse- thermography for non-destructive assessment of concrete structures", *Cem Concr Compos J*, 28:383-401.
5. X.P.V. Maldague, "Theory and practice of infrared technology for nondestructive testing", *New York: Wiley*, 2001.
6. I. Abdel-Qader, S. Yohali, O. Abudayyeh, S. Yehia, 2008, "Segmentation of thermal image for non-destructive evaluation of bridge decks", *NDT&E International*, 41:395-405.
7. J. Shiroishi, Y. Li, S. Liang, T. Kurfess, S. Danyluk, 1997, "Bearing condition diagnostics via vibration and acoustics emission measurement", *Mechanical Systems and Signal Processing*, 11:693-705.
8. N. Tandon, B.C. Nakra, 1992, "Vibration and acoustic monitoring techniques for the detection of defects in rolling element bearings – a review", *Shock and Vibration Digest*, 24(3):3–11.
9. B.A. Paya, I.L. Esat, M.N.M. Madi, 1997, "Artificial neural network based fault diagnostics of rotating machinery using wavelet transforms as a processor", *Mechanical Systems and Signal Processing*, 11:751-76.
10. J.C. Li, J. Ma, 1997, "Wavelet decomposition of vibrations for detection of bearing-localized defects", *NDT&E International*, 30:143-149.
11. K. Mori, N. Kasashima, T. Yoshioka, Y. Ueno, 1996, "Prediction of spalling on a ball bearing by applying the discrete wavelet transform to vibration signals", *Wear*, 195:162-168.
12. R. Rubini, U. Meneghetti, "Use of the wavelet transform for the diagnosis of incipient faults in ball bearings", *Proceedings of the Third International Conference on Acoustical and Vibratory Surveillance Methods and Diagnostic Techniques*, Senlis, France, pp. 371-378, 1998.
13. A. Grossmann and J. Morlet, 1984, "Decomposition of Hardy functions into square integrable wavelets of constant shape", *SIAM Journal of Mathematical Analysis*, 15:723–736.
14. Ibrahim Öz, Cemil Öz, Nejat Yumuşak, "Image compression using 2-d multiple-level discrete wavelet transform (dwt)", *Department of Electrical & Electronics Engineering*, Sakarya University, Sakarya, Turkey.

## **7. MAILING ADDRESS**

Ali Md. Younus  
School of Mechanical Engineering  
Pukyong National University  
San 1000, Yongdang-dong, Nam-gu,  
Busan 608-739, Korea  
Phone: +82-10-8689-7777  
E-mail: md.yali@yahoo.com



## PREDICTION AND EVALUATION OF BOREHOLES SHEAR FAILURES RISK IN SHALE UNDER IN-SITU STRESS STATE - A SENSITIVITY ANALYSIS

Md. Aminul Islam and Pål Skalle

Department of Petroleum Engineering and Applied Geophysics,  
NTNU, S.P Andersens, Trondheim, Norway

### ABSTRACT

Borehole instability during drilling in shale is more pronounced than in any other formations. No well is drilled in shale without problems. A Major instability risk is borehole shear failure. This paper evaluates different shear failure modes under in-situ stress state during underbalanced drilling (UBD). The generation of input data to “geomechanical model” by presenting extensively used correlations for estimating rock strength, in-situ acting stresses and formation pore pressure. Such generated data were used as input to an upgraded analytical model to estimate borehole shear failures. Borehole sensitivity analysis was extended to evaluating the borehole collapse risk of the effect on differential stress and loads, stress anisotropy, cohesion, pore pressure and friction angle. The analytical model relies on the Mohr- Coulomb (M-C) failure criterion. Matlab codes were developed to simulate the analytical model and to validate it through Gullfaks well data. The results showed that the developed geomechanical model is capable of assessing in-situ stresses with a certain degree of quality. The sensitivity analysis results showed that the mud weight and rock strength are the most critical parameters for determining borehole collapse risks for UBD candidates. The borehole collapse model is quantifying the risk of shear failure modes with acceptable accuracy. The generality of this study is to provide a standard workflow to assess in-situ stresses along with borehole failure risks for vertical and horizontal wells.

**Keywords:** Oil Well Drilling, Shale, Geomechanical Model, Borehole Instability.

### 1. Introduction

Shale is specifically mentioned in this setting, due to the fact that borehole instability is more pronounced in such formations than in any other formation [9,10,11, 13 14 & 16]. From field experience, it was found that shales (hard rock) make up of more than 80 % of the sediments and rocks in siliclastic environments and about three quarters of borehole problems are caused by shale instability, troubles such as sloughing shale and stuck pipe. At best, an unstable wellbore would mean that drilling performance is impeded through lost time. At worst it could mean a hole collapse and total loss of a well. All this means extra costs. A significant amount of lost time and extra cost (about 20 billion USD/year) is accounted to overcome shale related problems.

The problem addressed in this study is the borehole shear failures risks in shale during UBD through in- situ stress regimes. Based on in-situ stress magnitudes, Anderson (1951) classified three types of earth's in-situ stress states: extensional ( $\sigma_v > \sigma_H > \sigma_h$ ), strike-slip ( $\sigma_H > \sigma_v > \sigma_h$ ) and compressional ( $\sigma_H > \sigma_h > \sigma_v$ ). Borehole

instability is in most of the cases, a direct reflection of these stress states. An anisotropic stress pattern is characterized by a specific failure position in the borehole circumference, and this position is controlled by in-situ stresses [9-14]. A brief description of these stresses and their impact on stable drilling were presented through previous publications [9, 11 & 15]. This paper aims to evaluate the shear failure risk in shale through in-situ stress regimes. A stress field model is therefore presented in Fig.1. This model represents wellbores drilled in shallow (case-I), medium-deep (case- II) and deep basins (case-III). These three cases are defined based on the in-situ stress magnitudes vs. depth of investigation.

Wellbore stability models that include some aspects of shear failure analysis in shale have already been developed [9-15]. Inspection to these models, found that the assessment of in- situ stress is the focal weak side in borehole instability analysis [9 & 11-15]. A standard geomechanical model is essential for evaluating the



failure modes with reasonable accuracy.

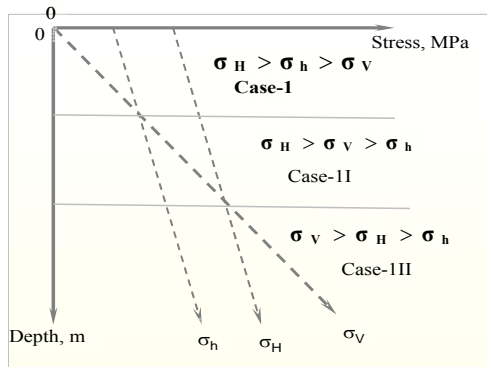


Fig 1. Stress field model.

This paper presents a geomechanical model based on extensively used correlations for estimating rock strength, in-situ acting stresses and formation pore pressure. This current investigation enhanced the insight on borehole collapse risk.

It is not exactly known how rock fails. The processes associated with failure are complex and not subject to convenient characterization through simplified models. The Collapse criterion defines a state where the borehole is no longer stable, but becomes unstable to a degree where it is defined as collapsing. Many different arguments can be used to define collapse criteria, e.g. scientific arguments based on mechanical criteria or operational argument based on practical limitations. Operational arguments which belong to amount of cavings or breakouts present in the drilling fluid, degree of wellbore instability with respect to section of angle & length, and the extension from the borehole. Scientific arguments are fulfillment of a failure criterion, choice of failure criteria with respect to stress conditions, type of formation, and type of analysis method (analytical or numerical).

The selection of a failure criterion for borehole stability analysis is difficult and confusing [5]. Proper selection of failure criteria for borehole stability analysis is therefore unclear to drilling engineers. Rock mechanics experts have applied several failure criteria in an attempt to relate rock strength measured in different simple tests to borehole stability. Some of the predicting methods are M-C criterion, Hoek- Brown criterion, Drucker- Prager criterion, Yield Zone criterion, Cam – Clay model, Modified Lade criterion and Griffith failure criterion. The theoretical backgrounds and limitations of these models have been extensively covered in the literatures [5, 6, 7, 9 & 12]. This study applied M-C failure model due to its simplicity and level of acceptability. For quantifying failure risk the total work is divided into the following phases:

- Develop and investigate the geomechanical model to estimate in-situ stresses.

- Quantify borehole shear failure risk for UBD in shales.
- Conduct sensitivity analysis to define critical parameters on borehole failure state by accounting for the effect of differential stress and loads magnitudes, cohesion, friction angle, pore pressure and well trajectory.

The M-C linear elastic failure model was used to quantify failure risk. Matlab codes were developed to simulate both the geomechanical and the shear failure models dynamically.

## 2. Construction of Geomechanical Model

### 2.1 Generation of input parameters

One challenge for constructing a geomechanical model is the generation of consistent input data. Many of the required parameters can be inferred from different sources, using some of empirical correlations, theoretical expressions, or analogue data previously experienced. Both stress field and rock mechanical properties are part of the GMM. Various methods and techniques have been used to calculate necessary input to generate GMM. This study developed a standard GMM based on updated published work [3, 8, 12 & 16]. Details of present GMM along with data integration techniques are presented through **Table A1**. Our developed model is fairly well structured.

### 2.2 Assessment of the in- situ stresses

For typical depths of oil reservoirs, the ratio of the  $\sigma_h / \sigma_v$  ranges from 0.3 to 1.5, and  $\sigma_H / \sigma_h$  ranges from 1 to 2 [1, 2, 4, 6 & 8]. In particular, the horizontal stress magnitude and orientation are not usually measured. This will definitely increase the uncertainty in the results. This work assesses in- situ stresses based on developed geomechanical model, validated through Gullfaks well data. Estimating results are presented through **Fig. 2**. It is seen that the in-situ stress regimes is identified and varies with depth. For example, at shallow and medium deep formation (1000- 1800 m), the  $\sigma_H$  is largest while at deep formation (2000-3000 m),  $\sigma_v$  dominates. Over pressure zones are identified between 1500- 23000 m. The minimum horizontal stress was estimated by using Breckels and van Eekelen [3] correlation (developed & tested for US Gulf Coast wells). However, the authors experience is that the relation for depths down to 2500 m gives fairly good estimates in most parts of the North Sea with water depths up to approximately 300 m. Though the water depth of this well was greater than 300 m, estimation of  $\sigma_h$  in shallow formation depth up to 1500 m did not show a good trend (**Fig.2**). Thus these relations should only be considered as a first estimate and should always be checked or calibrated against proper data from each field. To get a better accuracy of  $\sigma_h$  we need some adjustment into Breckels empirical correlation. Several well data with regression analysis may provide updated correlations to estimate  $\sigma_h$  in North Sea wells.

The pore pressure assessment is the most critical part of our GMM because up until now, very limited options are found for using prediction pore pressure in shale. The Eaton (1975) correlation was used in this study. The exponent (i.e.,  $n = 3, 3.5, 4, 5$  &  $6$ ) is playing a major role to assess pore pressure in the North Sea area. The assessment of pore pressure vs. different exponents is presented in Fig. 3. The pore pressure trend for exponent  $n = 4.0$  gives reasonable accuracy for Gullfaks well, as supported by others studied also [9, 17 & 18].

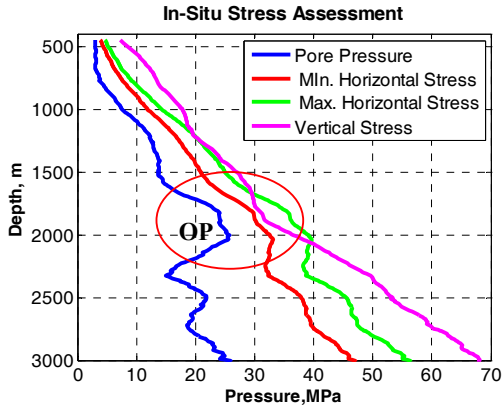


Fig 2. Assessment of the in-situ-stress based on GMM. Data from Gullfaks field (well # 34/10-16)

It is seen that the developed geomechanical model is capable of assessing the in-situ stresses. The accuracy of this GMM can be obtained by verifying it through further investigations. GMM can be revised and upgraded through field data, lab investigation or more case studies throughout this research project. On the other hand, pore pressure prediction in shale is of critical concern, and needs to be focused separately. The combined use of well logs and experimental compaction trends may improve the ability to predict trends of porosity, permeability, density, or velocity versus depth, leading to a prediction of overpressure in shales. Fig. 2 was used as calibration chart for estimating the in-situ stresses at depth of interest. These calibrated data were used for conducting the sensitivity analysis to evaluate the shear failure risks in terms of minimum MW for avoiding borehole collapse. A complete set of wellbore stability analysis data are presented in Table A2. Further verification is essential to improve the confidence of the developed GMM.

### 3. EVALUATION OF BOREHOLE FAILURE MODES

The evaluation of shear failure modes is dependent on the assessment of near borehole stresses. Near wellbore stress are generated after a wellbore drilled to support the rock that was originally supported by the removed solids in the borehole. Near wellbore stresses ( $\sigma_r, \sigma_\theta, \sigma_z$ ) are normally of higher magnitudes and act on the formation at the wellbore wall. It is believed that, the near wellbore stress concentration is created immediately during drilling (unless the far field stresses would change much

during a drilling period). Depending on the prediction of magnitudes and direction of wellbore stresses, prior indications whether a borehole will be failed would be available.

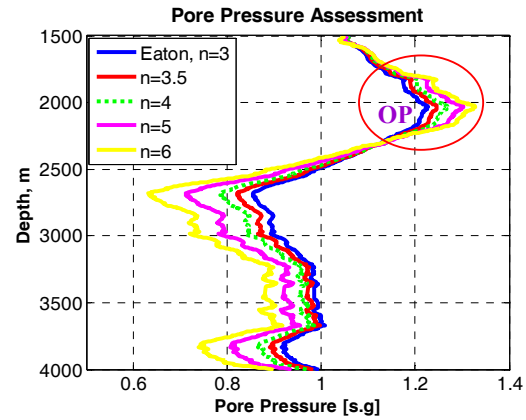


Fig 3. Assessment of the pore pressure based on GMM with different exponents. Data from Gullfaks field (well # 34/10-16)

A near borehole stress model ( $\sigma_r, \sigma_\theta, \sigma_z$ ) is essential to evaluate shear failure risks in shale. Many publications [5, 9-15] have been focused on borehole stress modeling. From their studies, it was found that stress related failures are the major reasons for borehole instabilities. Having anisotropic horizontal stresses, which is the common situation, will change the borehole stress. Detailed and in-depth discussions on the near borehole stress model in shale have been extensively covered through many publications [9-16]. From their studies it was found that hoop stress, rock strength and mud weight design are the more influential parameters to cause shear failure during UBD in shale. Classical Kirch solution [7] explains how hoop stress does lead to shear failure for UBD candidates in shale. At a later part of this paper hoop stress based on Kirch solution are estimated. By arranging permutation and combination of the near borehole stresses, six possible shear failure modes may exist. All modes are influenced borehole instability, but the following three shear failure modes are the most applicable in this study:

- Mode A:  $\sigma_\theta \geq \sigma_z \geq \sigma_r$ ; axial stress is the intermediate concern; M-C failure state =  $f(\sigma'_\theta, \sigma'_r)$ .
- Mode B:  $\sigma_z \geq \sigma_\theta \geq \sigma_r$ ; tangential stress is the intermediate concern; M-C failure state =  $f(\sigma'_z, \sigma'_r)$ .
- Mode C:  $\sigma_z \geq \sigma_r \geq \sigma_\theta$ ; radial stress is the intermediate concern; MC failure state =  $f(\sigma'_z, \sigma'_\theta)$ .

Modes “A” and “B” appear as collapse of the wellbore, but mode “C” appears as collapse of the wellbore first where subjected to excessive internal pressure when compared to the external stress, either in shear or extension mode. This theoretical interpretation was evaluated through analytical simulation based on the M-C failure criteria. The mathematical formulations and

assumptions to determine minimum mud weight to prevent borehole collapse are presented in **Table A3**.

## 4. RESULTS AND DISCUSSION

### 4.1 Assessment of near borehole stresses

#### I. Anisotropy stress effect:

With the assumptions of vertical hole, anisotropic horizontal stress, impermeable wall (shale), perfect mud cake in porous and permeable formation, and steady state condition, classical **Kirsch** equation for stress concentration around a circular elastic hole, the stresses at the borehole wall are [7];

$$\begin{aligned} \sigma_r &= P_w \\ \sigma_\theta &= \sigma_H + \sigma_h - 2(\sigma_H - \sigma_h) \cos 2\theta - P_w \\ \sigma_z &= \sigma_v - 2\nu_{fr}(\sigma_H - \sigma_h) \cos 2\theta \\ \tau_{r\theta} &= \tau_{\theta z} = \tau_{rz} = 0 \end{aligned} \quad [1]$$

Azimuth “ $\theta$ ” is the relative position of horizontal stresses. The tangential ( $\sigma_\theta$ ) and radial ( $\sigma_r$ ) stress in **Eq.1** are a functions of the mud pressure ( $P_w$ ). Hence, any changes in the mud pressure will only affect  $\sigma_\theta$  and  $\sigma_r$ . When  $P_w$  decreases,  $\sigma_\theta$  increases towards the compressive strength, at which  $\sigma_r$  should be less than or equal to  $P_w$ . This is the concern for underbalanced drilling with respect to borehole design. Thus, the lower limit of the mud pressure is associated with borehole collapse and  $\sigma_\theta > \sigma_r$ . It is therefore an effective and useful approach to focus on tangential stress, which incorporates borehole failure mode, regulated by the in-situ stress magnitudes & direction, mud pressure and material intrinsic properties. Investigation of **Eq. 1**, near borehole stresses were evaluated and presented in **Figs. 4 a & b**. From **Figs. 4b**, it is affirmed that horizontal strength anisotropy has significant influence on near borehole stresses to create a strong anisotropic stress environment and lead to borehole stability problems.

#### II. Hoop Stress and borehole instability:

It can be seen from **Fig. 5 (a, b & c)** that at  $\theta = 90^\circ$  or  $270^\circ$ , the predicted hoop stress is maximum. The larger hoop stress at  $\theta = 90^\circ$  position together with magnitudes and direction of the anisotropy in-situ stresses turned the borehole instable. The first borehole breakout may initiate at the peak of the hoop stress. On the other hand, at  $\theta = 180^\circ$ , the borehole stresses are lower where formation fracture may initiates. However, depending of the direction of the in-situ stresses and well trajectory, breakout and fracture initiation positions may be changing. This sensitivity analysis indicates that Mode C gives unrealistic results (i.e. see **Fig. 5a**) which is only valid in the strong tectonic stress regimes. It may be noted that, horizontal wells are more vulnerable under mode B (**Fig. 5c**). In case of vertical well, both modes A and B become closer and equally dominated to lead to borehole instability. Though the axial stress is not a function of mud weight, all modes are changing with similar trend, only anisotropy intensity of the in-situ stresses are exposed to transformed axial stresses. It is recommended that for predicted shear failure at the

borehole wall, “ $\theta$ ” should be equal to  $90^\circ$  while equal to  $180^\circ$  for fracturing of the formation.

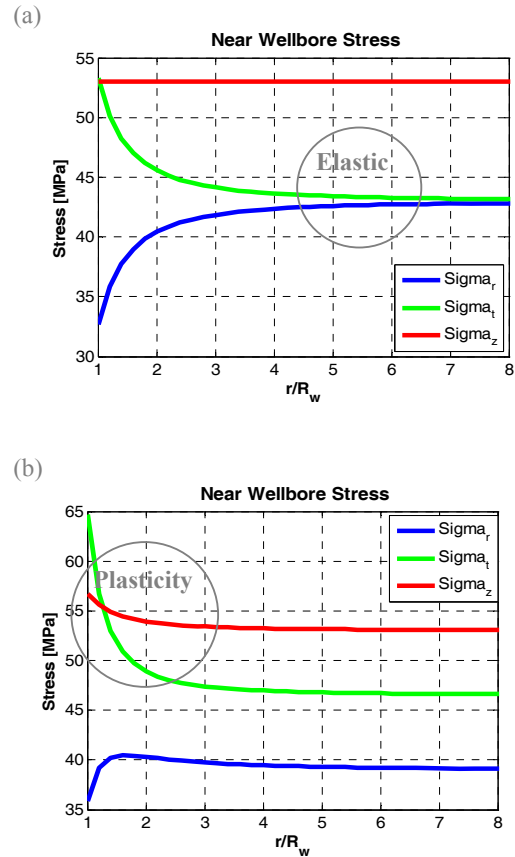


Fig 4a & b. Evaluation of the near wellbore stresses based on Kirsch solution. a) Isotropic b) Anisotropic in-situ stress state. Data from **Table A2** (case III).

#### 4.2. Prediction of Borehole Collapse:

From **Fig. 6 a, b & c**, it is found that predicted borehole collapse pressure through various formation under modes A & B is quantifying borehole collapse pressure (CP) and optimized MW. The predictive observations indicated; CP is determined by the largest in-situ stresses and the material intrinsic properties. In a later sensitivity analysis of this study, it is shown how in-situ stress and material intrinsic properties influences CP. This study results does not concern mud design of UBD, because UBD is a critical issue in shale, which knowledge is necessary for further investigation to capture shale heterogeneity. A 3-D orthotropic shale model is essential, and a separate study is going on within this research project to focus on shale hardening and softening effects. The complete research results on shale instability collectively may give recommendation for UBD. It is observed from the **Fig. 6** that a higher mud weight is required to prevent collapse in mode A. That means tangential stress under mode A is more dominant for determination of MW. Other observations; the rock may be relatively weak or may clay with HC in over pressure zone (@ 1500-2000 m). The estimation of minimum MW becomes equal to formation strength (mode A). It's

indicates an unconsolidated formations with hydrocarbon or the model assumption may not valid in this zones. Mondol et al. [17] is supported our observation. They were seen that in such geological formation in North Sea, formation may with overpressure with mostly quartz formation. The efficient integrated approach (GMM through CPM) in this study may therefore be useful in design of OBD wells.

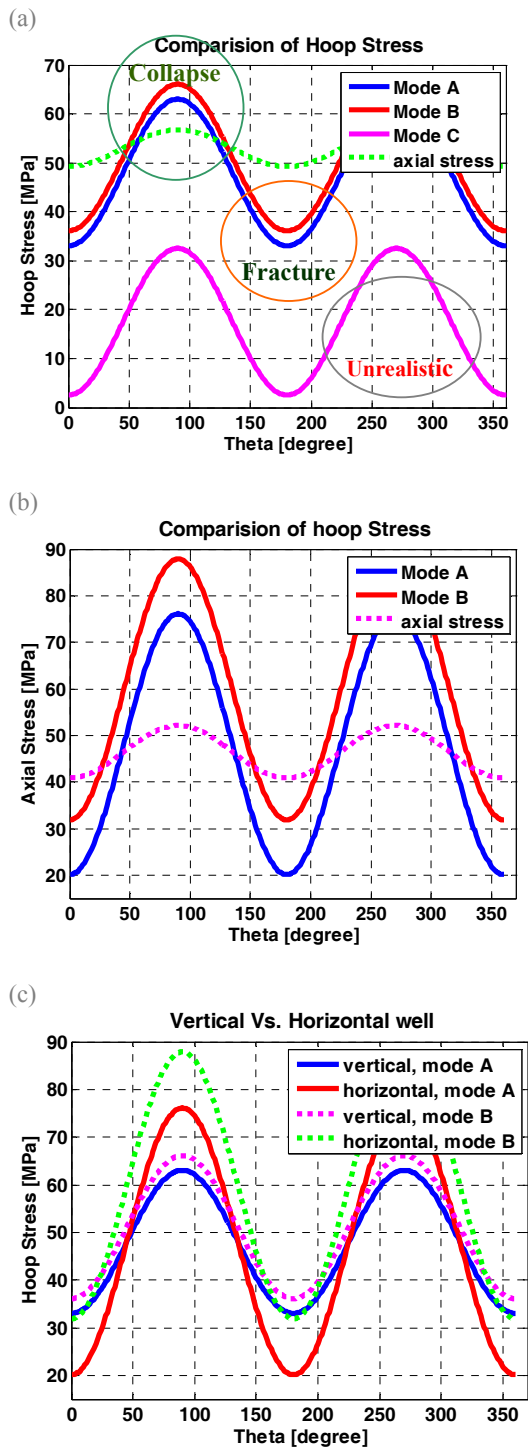


Fig. 5 a, b & c: Evaluation of hoop stresses for vertical & horizontal wells based on Kirsch solution. a) Vertical well

b) horizontal well c) comparison between vertical and horizontal wells. Data from Table A2 (case III).

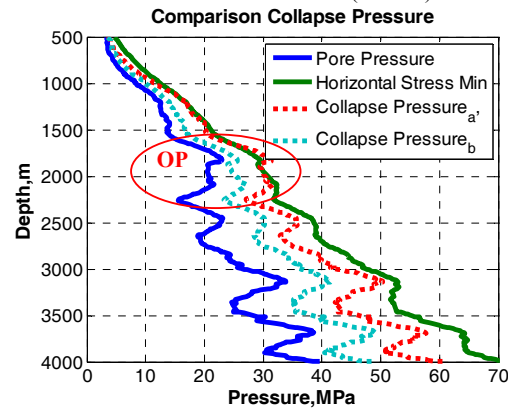


Fig 6. Prediction of the borehole collapse pressure into vertical well through an integrated approach by using GMM & CPM. Data from Gullfaks field (well #34/10-16)

### 4.3 Factors associated with Collapse Pressure

Material intrinsic properties have a significant influence on the M-C failure state. The impacts of the following sensible parameters on the borehole collapse model are:

#### I. Effect of Friction angle and Cohesion on CPM

It is seen that material friction angle and cohesion have remarkable influence on the shear failure modes (Fig. 7 a & b). The required minimum MW to prevent borehole collapse is decreasing considerably with increasing material strength & its internal friction. These results indicate that the accuracy of the borehole instability model to obtain minimum MW strongly depends on the rock strength and material friction. The particular field case study shows that horizontal wells require higher mud weight in normal stress regimes (Fig. 7 a). It is also seen that in lower rock strength ( $\alpha = 1$  degree), the minimum MW difference between horizontal and vertical wells is maximum ( $\Delta$  MW 0.40 s.g). The MW difference is reducing with increasing rock strength (i.e., @  $\alpha = 30$  degree,  $\Delta$  MW = 0.2 s.g). In ultra deep and strong tectonic geological region, horizontal stress anisotropy required relatively higher collapse pressure than vertical [9, 11, 13 & 15]. Mode C gives unrealistic result in normal stress field [Fig. A1]. Material friction angle and cohesion play a major role to estimate MW under different shear failure modes (Fig. A2).

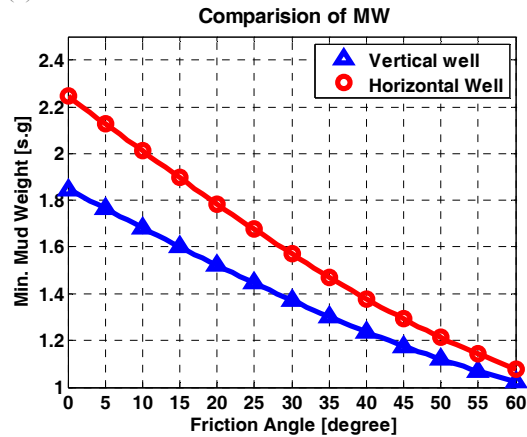
#### II. Effect of Pore Pressure on CPM

Pore pressure prediction in shale, serve as an input to CPM, and produce biggest uncertainties of the model together with determining appropriate mud design to avoid collapse. This is the most unpredictable parameter that was used in GMM. However, its influence on the mud design is vital. Fig. 7c is indicating that MW needs to increase significantly with increasing pore pressure to avoid instability. The horizontal well under mode A and the normal in-situ stress condition is identified as critical

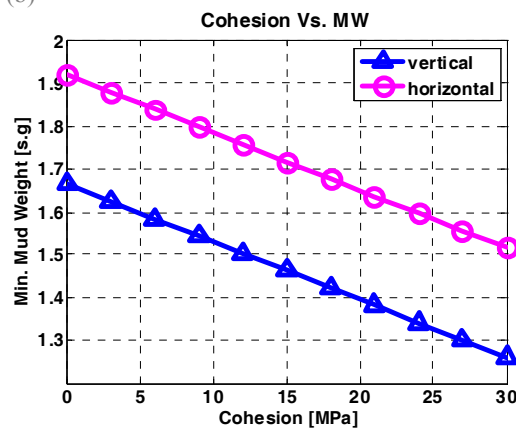


to require biggest mud weight to prevent borehole collapse. But under in strong tectonic stress regimes, vertical wells or drilled well through  $\sigma_H$  are considered as critical borehole instability [9, 15]. The borehole trajectory has trivial impact on mud design while drilling through strong tectonic geological regions, horizontal stress anisotropy determine the collapse risk [9-15].

(a)



(b)



(c)

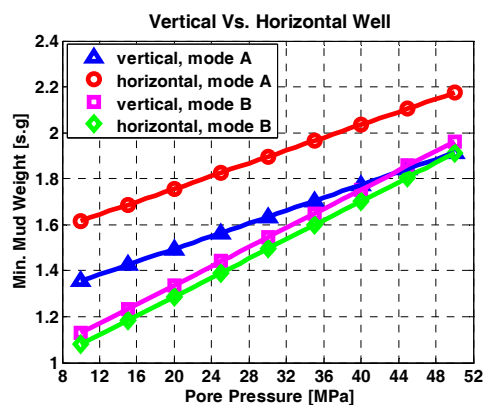


Fig 7. Prediction of the borehole collapse pressure. An integrated approach by using GMM though CPM. a) effect of friction angle , b) effect of cohesion and c) effect of pore pressure on CP. Data from **Table A2** ( case III)

## 5. CONCLUSIONS

- A geomechanical model is under development and has reached a certain level of quality. Predicted in-situ stresses were used as input to the borehole shear failure model to quantify failure risks. The developed model can be revised and updated by using calibrated lab test data, or best fit drilling data.
- Eaton's empirical correlation can be used to predict pore pressure in North Sea wells with  $n$  greater than 3 as the best fit of exponent.
- M-C shear failure criterion can be used for minimum MW design to prevent borehole collapse under the modes A and B but not for mode C. Mode C gives unrealistic results which may only be applicable in strong tectonic geological regions. Under mode A which is the common situation, horizontal wells are most risk to instability (for lower friction angle).
- Failure modes vary with respect to material friction angle and cohesion. Mode A is dominating within friction angle  $0-35^\circ$  while for mode B it is greater than  $35^\circ$ .
- Hoop stress, mud weight and rock strength are the most influential elements in borehole collapse modeling. This study could not recommend UBD in shale. The fact that most horizontal UBD wells are completed open hole may cause a stricter requirement in quantifying rock strength. UBD in shale is risky operation where a separate in-depth study is required.
- Shale is a most heterogeneous substance never expects much accuracy of predictive results through any borehole collapse model. It is impossible to capture the total characteristics of shale behaviour into one stability analysis model.
- This study gives confidence to optimize MW for balanced drilling. The techniques used in this study may apply equally to others wells to optimize model verification.

## 6. REFERENCES

1. Eaton B.A 1972: "Graphical method predicts geopressures worldwide", World Oil 182 (6), 51-56.
2. Eaton B.A 1975: "The equation for geopressure prediction from well logs," paper SPE 5544 presented at the 1975 Fall meeting of the Society of Petroleum Engineers of AIME, Dallas, Sept. 28-Oct.1.
3. Breckels, I.M., van Eekelen, H.A.M. (1982). "Relationship between horizontal stress and depth in sedimentary basins". J.Petr. Tech. 34 (9), 2191-2199.
4. Tan, C.P et al 1993: "An analytical method for determining horizontal stress bounds from wellbore data", Int J Rock Mech Min Sci Geomech Abstracts 30: Page 1103-1109.
5. McLean M, Adis M. 1990 "Wellbore stability analysis; a review of current methods of analysis and their field application. In. Proceedings of the IADC/SPE drilling conference, Houston , Texas, February 27- March 2, 1990, SPE 19941.
6. Grauls D 1998: "Overpressure assessment using a minimum

- principal stress approach". In : Overpressures in petroleum exploration; Proc. Workshop 22. Bull. Centre Rech. Elf Explor. Prod., Pau, France, 137-147.
7. Kirsch, 1898, Die Theorie der Elastizität und die Bedürfnisse der Festigkeitslehre. Zeitschrift des Vereines deutscher Ingenieure, 42, 797–807.
  8. Plumb, R, Edwards, 2000 "The Mechanical Earth Model Concept and its application to high risk well construction product" paper IADC/SPE 59128, held in New Orleans, Louisiana, 23-25 feb 2000.
  9. Aadnøy B.S., 2004 " Bound on In- Situ Stress Magnitudes Improve Wellbore Stability Analyses", SPE 87223, presented in IADC/SPE Drilling Conference held in Dalas, Texas U.S.A.,2004.
  10. Al-Ajmi, A.M.,Sultan Qaboos U.; and Zimmerman, R.W., Imperial collodge, London, 2006." Stability Analysis of Deviated Boreholes Using the Mogi-Coulomb Failure Criterion, With Applications to Some Oil and Gas Reservoirs" presented at the IADC/SPE Asia Pacific Drilling Technology Conference.
  11. Fjær, E., .Holt, M.H., .Hoursrud, P., Raaen, R.M., and Risnes, 2008. Petroleum related rock mechanics" 2<sup>nd</sup> addition.
  12. Afsari, M. et all 2009, M.R. Ghafoori, M. Roostaeian, A. Ataei, R, Masoudi, " Mechanical Earth Model: an effective tool for borehole stability analysis and Managed pressure drilling( case study)" presented at the 2009 SPE Middle East Oil and Gas conference held in the Bahrain international exhibition centre, kingdom of Bahrain, 15-18 march 2009. SPE 118780.
  13. Islam M.A, Skalle P and Tantserev E. NTNU, 2009 "Underbalanced Drilling in Shales- Perspective of Mechanical Borehole Instability" In proceedings of the IPTC 09/SPE drilling conference, Quater, December 7 -9 2009. IPTC/SPE 13475.
  14. Islam M.A, Skalle P. Faruk A.B.M and Pierre. B. NTNU, 2009 "Analytical and Numerical Study of Consolidation Effect on Time Delayed Borehole Stability During Underbalanced Drilling in Shale" In proceedings of the KIPCE 09/SPE drilling conference, Kuwait,14 -16 December 2009. SPE 127554.
  15. Islam M.A, Skalle Pål and Mahmud Shahriar, NTNU, 2009 "In situ stress pattern and its impact on stable drilling operation" In proceedings of the GeoDev 09, Geological and Geophysical conference, Dhaka, 26-30 October 2009.
  16. Hoursrud P. 2001, "Estimation Mechanical Properties of Shale from Empirical Correlations" SPE 56017, J of SPE.
  17. Mondol N.H, Fawad M. Jahren J. and Bjørlykke K." Synthetic mudstone compaction trends and their use in pore pressure prediction" technical article, first break, volume 26, December 08.
  18. Luthje. M, Helset, and Hovland " New integrated approach for updating pore pressure predictions during drilling" SPE 124295, presented in SPE annual technical conference held in Orleans Louisiana, 4-7 october 09.

## 7. NOMENCLATURE

Symbol	Meaning	Unit
$\sigma_v$	Vertical stress	MPa
$\sigma_h$	Min. horizontal stress	MPa
$\sigma_H$	Max. horizontal stress	MPa
$\sigma_\theta$	Tangential or hoop stress	MPa
$\sigma_z$	Axial stress	MPa
$\sigma_r$	Radial stress	MPa
$P_f$	Pore pressure	MPa
$P_{fh}$	Hydrostatic pressure	MPa
$P_w$	Wellbore pressure	MPa
$\nu$	Poissons ratios	

$C_0$	Cohesion strength	MPa
$T_0$	Tensile strength; Pa	MPa
$\tau$	Shear stress	MPa
$\beta$	Orientation of failure angle	Degrees
$\alpha$	Material friction angle	Degrees
$\Delta t_s$	Shear sonic travel time	$\mu\text{s/m}$
$\Delta t_c$	Compressional sonic travel time	$\mu\text{s/m}$
D or h	Depth	m
E	Young's modulus	GPa
$\rho_s$	Formation density	$\text{gm/cm}^3$
$\rho_w$	Water density	$\text{gm/cm}^3$
O	Overburden gradient	KPa/m
H	Hydrostatic gradient	KPa/m
r	Radial distance	m
$R_w$	Borehole radius	m
$V_p$	P- wave velocity	m/s

## Abbreviation:

GMM	: Geomechanical Model
CPP	: Collapse Pressure Prediction
CP	: Collapse Pressure
UBD	: underbalanced drilling
OBD	: Over Balanced Drilling
OP	: Over Pressure
HC	: Hydrocarbon
CPM	: Collapse Pressure Model

## 8. ACKNOWLEDGEMENTS

The authors want to thank NTNU for supporting and giving permission to write this paper. We would like to express our appreciation to Prof. Rune Martin Holt, Erling Fjær, Sintef petroleum research, Per Hoursrud and Ole Ole Kristian Søreide Statoilhydro, for their time to discuss critical issues about this paper work.

## Appendix A:

**Table A1:** Main parameter and sources of information used to build the geomechanical model [3,4, 8, 11, 12].

Parameter	source	Correlation used in this study
$\sigma_v$	Density log	$\sigma_v = \int_0^h \rho_b gh$
$\sigma_H$	Best gauge	$\sigma_H = 1.2 * \sigma_h$ ( best guess)
$\sigma_h$	Breckels, 1982	$\sigma_h = 0.0053D^{1.145} + 0.46(P_f - P_{fh})$ ; D < 3000 m $\sigma_h = 0.0264D - 31.7 + 0.46(P_f - P_{fh})$ ; D > 3000 m
$P_f$	Eaton, 1975	$P_f = O - (O - H) \left( \frac{\Delta t_{normal}}{\Delta t_{observed}} \right)^{3.0}$
$C_0$	Horsrud, 98	$C_0 = 0.77 * V_p^{2.93}$
$\nu$	DSI tool	$\nu_{dy} = 1/2(\Delta t_s/\Delta t_c)^2 - 1)/(\Delta t_s/\Delta t_c)^2 - 1$ $\nu_s = 0.7 \nu_{dy}$
E	DSI tool & Wang, 98	$E_{dy} = \rho_b(4\Delta t_s^2 - 3\Delta t_c^2)/\sqrt{1 - \Delta t_c^2/\Delta t_s^2}$ $E_s = 0.41E_{dy} - 1.059$

**Table A2: Stress field data used in borehole analytical model to predict CP through a sensitivity analysis**

Case #	Stress Criteria, MPa	Others parameters
Case-I; Shallow depth (1200 m) ( manipulated)	$\sigma_H > \sigma_h > \sigma_V$ 22 > 19 > 18	$P_f = 13$ MPa, $C_0 = 8$ , MPa, $T_0 = 1$ MPa, $\nu = 0.20$ , $\alpha = 30^\circ$ , $\theta = 90^\circ$
Case-II; Intermediate depth (2000 m)	$\sigma_H > \sigma_V > \sigma_h$ 40 > 36 > 33	$P_f = 25.5$ MPa, $C_0 = 10$ MPa, $T_0 = 1$ MPa, $\nu = 0.25$ , $\alpha = 30^\circ$ , $\theta = 90^\circ$
Case-III; Deep (2500 m)	$\sigma_V > \sigma_H > \sigma_h$ 53 > 46.5 > 39	$P_f = 23$ MPa, $C_0 = 10$ MPa, $T_0 = 1$ MPa, $\nu = 0.25$ , $\alpha = 30^\circ$ , $\theta = 90^\circ$

### A3: M-C Borehole collapse Model

For borehole collapse it is assumed a M- C shear failure model. This is governed by the maximum and minimum principle stresses. The failure model is:

**Mode A:** Considering the situation where,  $\sigma_\theta \geq \sigma_z \geq \sigma_r$  According to the M- C criterion, failure will occur when;  
 $\sigma'_1 = \sigma'_\theta = C_0 + \sigma'_r \tan^2 \beta$   
 $\sigma'_1 = \sigma_H + \sigma_h - 2(\sigma_H - \sigma_h) \cos 2\theta - P_w - P_f$   
 and  $\sigma'_3 = \sigma'_r = P_w - P_f$ ;

By applying for minimum borehole pressure to prevent borehole collapse, above equations becomes:

$$\sigma_H + \sigma_h - 2(\sigma_H - \sigma_h) \cos 2\theta - P_w - P_f - C_0 - (P_w - P_f) \tan^2 \beta \leq 0$$

and resulting;

$$P_{w,\min}^a \leq \frac{3\sigma_H - \sigma_h - C_0 + P_f (\tan^2 \beta - 1)}{1 + \tan^2 \beta}$$

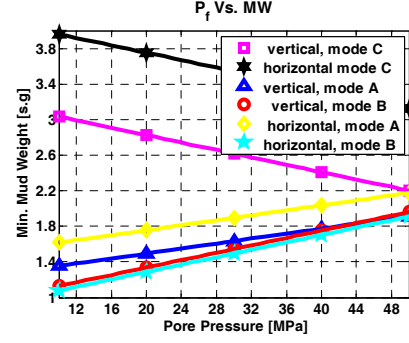
Similarly for mode B and C, collapse pressure equations can be derived. A set of analytical solutions for shear failures is included in **Table A3**.

**Table A3:** An analytical solution of borehole collapse model with the assumption of vertical well, impermeable borehole,

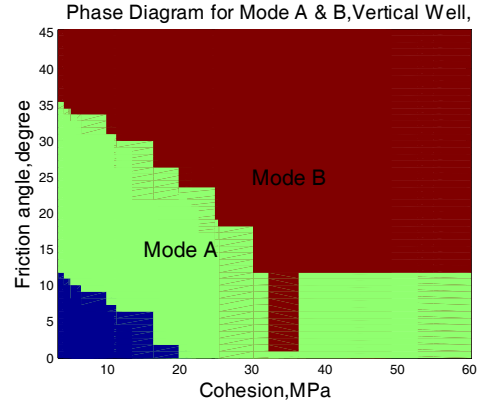
M	Condition	Borehole Failure occurs if	Satisfy the condition
A	$\sigma_\theta \geq \sigma_z \geq \sigma_r$	$P_{w,\min}^{(a)} \leq \frac{3\sigma_H - \sigma_h - C_0 + P_f (\tan^2 \beta - 1)}{1 + \tan^2 \beta}$	$\sigma_r = P_{w,\min}^{(a)}$ $\sigma_\theta = \sigma_H + \sigma_h - 2(\sigma_H - \sigma_h) \cos(2\theta) - P_{w,\min}^{(a)}$ $\sigma_z = \sigma_V - 2\nu_{fr} (\sigma_H - \sigma_h) \cos(2\theta)$
B	$\sigma_z \geq \sigma_\theta \geq \sigma_r$	$P_{w,\min}^{(b)} = P_f + \frac{\sigma_V + 2 \nu_{fr} (\sigma_H - \sigma_h) - C_0 - P_f}{\tan^2 \beta}$	$\sigma_r = P_{w,\min}^{(b)}$ $\sigma_\theta = \sigma_H + \sigma_h - 2(\sigma_H - \sigma_h) \cos(2\theta) - P_{w,\min}^{(b)}$ $\sigma_z = \sigma_V - 2\nu_{fr} (\sigma_H - \sigma_h) \cos(2\theta)$
C	$\sigma_z \geq \sigma_r \geq \sigma_\theta$	$P_{w,\min}^{(c)} = 3\sigma_H - \sigma_h - P_f - \frac{\sigma_V - C_0 - P_f}{\tan^2 \beta}$	$\sigma_r = P_{w,\min}^{(c)}$ $\sigma_\theta = \sigma_H + \sigma_h - 2(\sigma_H - \sigma_h) \cos(2\theta) - P_{w,\min}^{(c)}$ $\sigma_z = \sigma_V - 2\nu_{fr} (\sigma_H - \sigma_h) \cos(2\theta)$

For horizontal well  $\sigma_V$  change to  $\sigma_H$  and  $\sigma_H$  change to  $\sigma_V$ . Mode C is only applicable in strong tectonic stress area where  $\sigma_r$  will

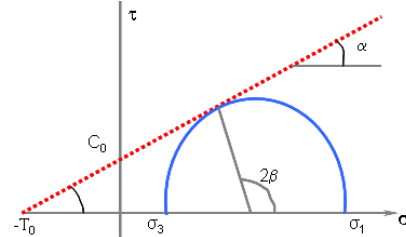
be greater than  $\sigma_\theta$  and  $\sigma_H$  or  $\sigma_h$  also greater than  $\sigma_V$ .



**Fig A1.** Unrealistic results from mode C. data from Table A2 (case III).



**Fig A2.** effect of material cohesion and friction angle on CP



**Fig A3.** M-C failure criterion model



## MEASURING BULLWHIP EFFECT IN A MULTISTAGE COMPLEX SUPPLY CHAIN

Tahera Yesmin<sup>1</sup>, M. A. AKhtar Hasin<sup>2</sup> and F. Afreen Prama<sup>2</sup>

Department of Industrial and Production Engineering, Bangladesh University of Engineering and  
Technology, Dhaka, Bangladesh

### ABSTRACT

Bullwhip effect refers to the amplifications in orders in a supply chain. Industries with reliable demand forecasts waste millions of dollars every year because they are not able to match production to demand. In this research authors conducted the study on a complex supply chain to examine different aspects of bull whip effect with the real data. However, this research is mainly aimed to study the supply chain in an industry which is running in Bangladesh. The supply chain used here is a multistage supply chain consists of three retailers, one distributor, one warehouse and a factory. This research mainly deals with the causes of the supply chain and investigates whether there is any existence of the bullwhip effect in the supply chain or not. After this study it can be easily determined which member is contributing to the presence of bullwhip effect and where to take an effort to mitigate the problems of bullwhip effect.

**Keywords:** Complex Supply Chain, Ordering Quantity, Simulation, Amplification Ratio.

### 1. INTRODUCTION

A supply chain is an integrated process which includes all activities associated with the flow and transformation of goods from raw material stage through to the end user [1]. It involves the integration of information which flows up and down the supply chain. Businesses today are not separate entities; they are all working together in one supply chain, which can improve the quality of goods and services across the supply chain. The primary objective of a supply chain is to satisfy customer while generating profit. The supply chain activities begin with a customer order and end when a satisfied customer has paid for the purchase. The bullwhip phenomenon refers to the amplification in orders in supply chain. It is referred as an incident of demand variability amplification as moving upwards the stages of a supply chain (i.e. moving away from customer demand) [2]. Demand variability causes serious problems for supply chain partners such as excessive inventory, inaccurate demand forecasts, extra production capacity, increased storage space and additional investment cost. Moreover bullwhip effect reduces the profitability of a supply chain by making it more expensive to provide a given level of product availability.

Bull whip effect is not an event for any particular cause. There are many reasons which create bullwhip effect in a supply chain. Forecasting parameters and lead time have direct impact on bullwhip effect. When a product demand exceeds supply, a manufacturer often

ration its product to customers or if the price of products changes dramatically, customers will purchase the product when it is the cheapest. So there are always a number of reasons for which bullwhip effect occurs.

In this research the bullwhip effect is studied in a complex supply chain. The following section reviews relevant different studies on this field. Then we gradually studied the case to find the orders for different members and then after that the amplification ratio is calculated to show the existence of the bullwhip effect.

### 2. LITERATURE REVIEW

Recently there has been a surge of interest and research on the phenomenon popularly called the bullwhip effect. Numerous researches have paid their attention to analyze bullwhip whip effect. Some of the searchers tried to providing empirical evidence supporting the existence of the bullwhip effect. Some tried to analytically demonstrate the existence of bullwhip effect. Some of the researchers tried to find out the causes to minimize it.

The phenomenon named bullwhip effect has its origin in system dynamics theory developed by Forrester [3] where, in many cases, the variance in perceived demand for a manufacturer was several orders of magnitude larger than consumer demand. In addition, Forrester identified that this amplification effect occurred at each stage in the supply chain. One of the major factors which caused the bullwhip was that the information feedback loop between companies was too complex for managers to resolve intuitively. Forrester proposed that the only way to resolve these complex

supply interactions was to treat the supply chain as a complete system. Managers could then model the complete system to determine the appropriate action to be taken.

In an inventory management experimental context, Sterman [4] reports the evidence of bullwhip effect in the “Beer Distribution Game”. The experiment involves a supply chain with four players who make independent inventory decisions without consultation with other chain members, relying only on orders from the neighboring players as the sole source of communications. The experiment shows that the variances of orders amplify as one moves up the supply chain, confirming the bullwhip effect.

Later, Lee et al. [5, 6] shows that a number of major companies also faced problems due to the bullwhip effect. Procter and Gamble were one of them. Logistics executives at Procter & Gamble (P&G) examined the order patterns for one of their best-selling products, Pampers. Its’ sales at retail stores were fluctuating, but the variability was certainly not excessive. However, as they examined the distributors’ orders, the executive were surprised by the degree of variability. When they looked at P&G’s orders of material to their suppliers, such as 3M, they discovered that the swings were even greater. At first glance, the variability did not make sense. While the consumers, in this case, the babies, consumed diapers at a steady rate, the demand order variability in the supply chain were amplified as they moved up the supply chain. P&G then called this phenomenon the “bullwhip” effect.

There have been many researches to quantify the bullwhip on a supply chain. In measuring bullwhip, here are a number of different approaches that can be adopted. At a simple level, a proxy for the level of bullwhip is to consider the maximum order placed during a simulation run and was used by Riddalls and Bennett [7]. While this provides a qualitative idea as to the behavior of bullwhip, it is not necessarily suitable for finding an analytic solution. Another approach is to divide the coefficient of variation for orders placed by the coefficient of variation for orders received [8]. In calculating the variability of orders Cachon [9] have also adopted this coefficient of variation approach.

### 3. CAUSES OF BULLWHIP EFFECT

Bullwhip effect is often created for mainly behavioral and operational causes.

#### 3.1 Behavioral Causes

The behavioral causes are rather straightforward. Supply chain managers may not always be completely rational. Managers over-react (or under-react) to demand changes. Often people are over optimistic and confuse forecasts with targets. Decision makers sometime over-react to customer complaints and anecdotes of negative customer reactions. Moreover, there are cognitive limitations as supply chain networks are often very complicated, operating in a highly uncertain environment with limited access to data.

#### 3.2 Operational Causes

Lee et al. [5, 6] identify five major operational causes of bullwhip. These factors interact with each other in different combinations in different supply chains but the net effect is that they generate the wild demand swings that make it so hard to run an efficient supply chain. These factors must be understood and addressed in order to coordinate the actions of any supply chain. They are,

- *Demand signal processing*

Demand signal processing as the practice of decision makers adjusting the parameters of the inventory replenishment rule. Target stock levels, safety stocks, and demand forecasts are updated in face of new information or deviations from targets.

- *Lead time*

A second major cause of the bullwhip problem is the lead-time. The lead-time is a key parameter for calculating safety stock, reorder points, and order-up-to levels. The increase in variability is magnified with increasing lead-time [5, 6].

- *Order batching*

Order batching occurs because companies place orders periodically for amounts of product that will minimize their order processing and transportation costs. Because of order batching, these orders vary from the level of actual demand and this variance is magnified as it moves up the supply chain.

- *Price fluctuations*

The third major cause of bullwhip as highlighted by Lee et al. [5, 6] has to do with price fluctuations. Retailers often offer price discounts, quantity discounts, coupons or in-store promotions. This results in forward buying where retailers (as well as consumers) buy in advance and in quantities that do not reflect their immediate needs.

- *Product rationing and shortage gaming*

A further cause of bullwhip is connected with rationing and shortage gaming. Inflated orders placed by supply chain members during shortage periods tend to magnify the bullwhip effect. Such orders are common when retailers and distributors suspect that a product will be in short supply. Exaggerated customers orders make it hard for manufacturers to forecast the real demand level.

The following figure shows different causes of bullwhip effect.

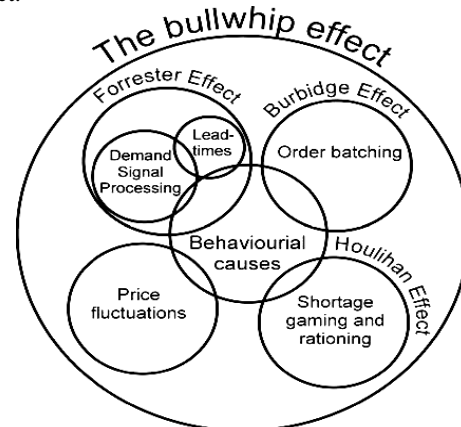


Fig 1. The causes of Bullwhip Effect [10]

#### 4. METHODOLOGY

Theoretically the Bullwhip effect does not occur if all orders exactly meet the demand of each period, otherwise results in greater safety stock which can lead to either inefficient production or excessive inventory as the producer needs to fulfill the demand of its predecessor in the supply chain. This also leads to a low utilization of the distribution channel. Despite of having safety stocks there is still the hazard of stock-outs which results in poor customer service. Furthermore, the bullwhip effect leads to a row of financial costs. It will increase the inventory cost, backorder cost, distribution cost etc.

In this research the study was conducted on a complex supply chain to examine different aspects of bull whip effect as well as measuring it with the real data. The supply chain used here is a multistage supply chain consists of three retailers, one distributor, one warehouse and a factory. The factory is one of the leading manufacturers of Bangladesh which manufactures many products and has many distributors and retailers and one warehouse. In order to make the study more applicable only one product of that particular manufacture is considered. Though this particular product is distributed through many distribution centers to thousands of retailers of all over the country, again to study appropriately we have considered only one distributor and three retailers for this research. To collect more reliable data, three branches of a renowned superstore of Bangladesh are chosen as three retailers for the study. The supply chain network becomes like the following:

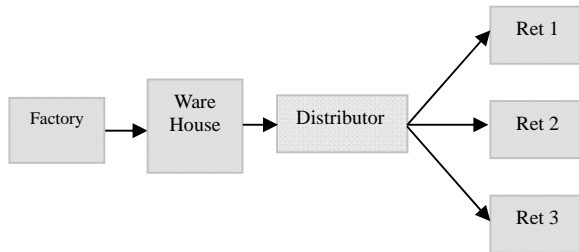


Fig 2. Supply Chain Network of the assigned product

#### 4.1 Data Collection

The customer demand for a particular time period which is 52 weeks of year 2008 is collected. A range of data for the demand are collected which are then generated randomly for the research purpose [11].

#### 4.2 Inventory Policies

To find the ordering quantities for the existing data, information about the inventory policies are essential. Here all the members of the supply chain have their own inventory policy except the customers. Table 1 shows the inventory policy all the members.

To find out the ordering quantities for the members of the supply chain, a fixed amount of beginning inventory for each member of the supply chain is assumed. Ordering cycle time and lead time is set according to the real scenario. Replenishment point is different for different members. Each of the retailers keeps stock equal to one weeks' minimum demand. Distributor keeps 2 week demand of the retailers as a

stock. Warehouse also keeps double of the average demand of the distributor and the factory keeps the stock what ever the ware house keeps.

Table 1: Inventory Policy for each member of the supply chain.

Elements	Ret 1	Ret 2	Ret 3	Distrib- utor	Ware house	Fact.
Beginning Inventory(units)	20	20	20	75	90	100
Lead time (week)	1	1	1	1	1	1
Ordering cycle (week)	1	1	1	1	1	1
Replenishment point (cases)	10	10	10	60	100	100

#### 4.3 Determining Orders for Each Member

Based on the collected customer demand and the inventory policy, ordering quantities are calculated for each of the member of the supply chain by a simulation on the basis of the following equations [12],

$$\text{Order for each member} = \text{Max}(0, \text{Indicated order}) \quad (1)$$

$$\text{Indicated order} = \text{Demand from the immediate downstream} + \text{Adjusted Inventory Stock} + \text{Shortage quantity} \quad (2)$$

$$\text{Adjusted Inventory Stock} = \text{Replenishment Point} - \text{Inventory level} \quad (3)$$

The following figure 3 shows the different ordering patterns for each of the members of the supply chain along with the actual sales. These ordering quantities are obtained from the simulation.

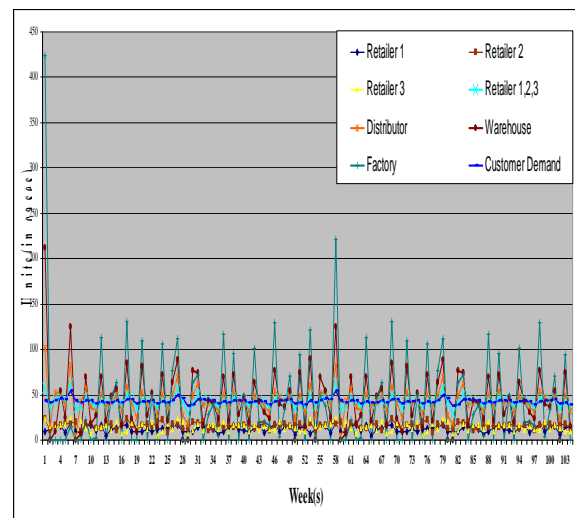


Fig 3. Existing ordering pattern and actual sale for each supply chain member.

## 5. MEASURING BULLWHIP EFFECT

After the computation of the ordering pattern of each of the members for the whole year the next step is to find out the existence of bullwhip effect in the supply chain. The approach taken here to search for the bullwhip effect is measuring the amount of instability an industry contributes to the supply chain: An industry faces unstable demand from its customers, and then imposes its own instability on its suppliers. The bullwhip effect is exhibited by an industry when the variance of its order is greater than the variance of its demand, i.e., if its amplification ratio is greater than one [8].

$$\text{Amplification ratio} = V(q) / V(Q) \quad (4)$$

The variance of customer demand for year 2008 is 7.303 and retailers order's variance is 33.68639. So, the ratio is 4.61, which is greater than 1. Here the variance of retailers is calculated by adding the demands of all three retailers. Since this ratio is greater than 1, which clearly indicated the presence of bullwhip effect in supply chain.

Now like retailers, the variances for the other members are also calculated. The variances for distributor order, warehouse order and factory orders' are 232.803, 1360.785 and 4712.802.

With the help these variances the amplification ratio for each of the member is achieved by the above equation 4. The following table 2 shows the amplification ratio of each members of the supply chain for year 2008.

Table 2: Amplification Measures for Supply chain members for 2008 (yearly)

Supply Chain Member	Amplification Ratio
Retailer Vs Customer	4.61
Distributor Vs Retailer	6.91
Warehouse Vs Distributor	5.85
Factory Vs Warehouse	3.46

## 6. RESULTS

After calculating the variances, it is clearly shown that the variances of orders increased from retailer to factory gradually.

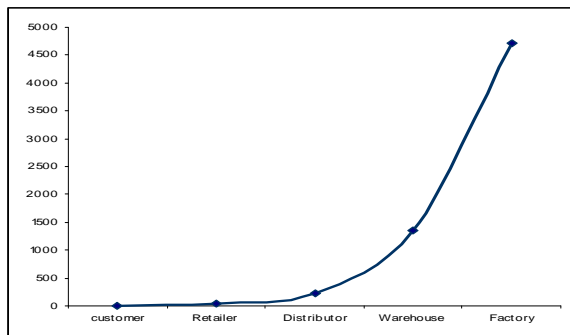


Fig 4. Variances of orders of different supply chain members

The differences between the variances of order from the

downstream supply chain member to upstream supply chain member are huge, which clearly shows afterwards that the amplification ratio is always greater than 1.

Figure 4 shows the gradual increment of variances of orders from downstream to upstream of supply chain member.

Another observation from table 2 shows that bullwhip effect is present in every member of the supply chain as the amplification ratio is always greater than 1. This implies that all the members are asking more to its suppliers than the demands. This clearly makes the presence of bullwhip effect in the supply chain for that particular product.

## 7. PROBLEMS ASSOCIATED WITH BULLWHIP EFFECT

As unnecessary demand variability complicates the supply chain planning and execution processes, the same happened in that particular manufacturing organization and the retailer stores too. The following undesirable effects increase in their severity as bull whip effect negatively impacts operating performances of each member of the supply chain,

- i. Schedule variability increases.
- ii. Capacity for each member of the supply chain (retailer 1, retailer 2, retailer 3, distributor, warehouse, and factory) is sometime under loaded, sometime overloaded.
- iii. Final and the most severe problem of is that the overall costs of supply chain increases

## 8. CONCLUSION

Effective supply chain has already played a very important and significant role in the business area of all over the world. It has always been a very popular topic for the industries and researchers of the developed countries to conduct more and more researches to make their supply chain more efficient, but for a developing country like Bangladesh it is a newly emerging concern of the industries. This conducted study in a manufacturing organization of Bangladesh illustrates that there is the existence of a bullwhip effect which can cause many problems in the supply chain. Our study proves the presence of bullwhip effect in all the member of the supply chain. Now to mitigate its effect, the attention should not be provided to only one member but to all over the supply chain.

## 9. NOMENCLATURE

Symbol	Meaning
q	Order
Q	Demand
V	Variance

## 10. ACKNOWLEDGEMENT

The authors show their whole heart gratitude to the authority of Bangladesh University of Engineering and Technology (BUET) for their support and supervision as this research was conducted partly for the

thesis of M. Sc. Engineering under the department of Industrial and Production Engineering of BUET. The authors are also thankful to the manufacturing organization and the three retail stores of Bangladesh for their continuous cooperation to accomplish this research.

## 11. REFERENCES

1. Chopra, S. and Meindl, P, 2003 “Supply Chain Management”, Pearson Education Inc., Singapore.
2. Kelepouris, T., Miliotis, P. and Pramataris K.,2008, “The impact of replenishment parameters and information sharing on the bullwhip effect: a computational study”, *Computers and Operations Research*, Vol. 35, pp. 3657-3670.
3. Forrester, J.W., 1961, *Industrial Dynamics*, MIT Press: Cambridge.
4. Sterman, J.D.,1989, “Modeling managerial behavior misperceptions of feedback in a dynamic decision making experiment”, *Management Science*, Vol. 35, No. 3, pp. 321-339.
5. Lee, H. L., So, K.C., and Tang, C. S., 2000, “The value of information sharing in a two- level supply chain”, *Management Science*, Vol. 46 (5), pp. 626-643.
6. Lee, H. L., Padmanabhan, V. and Wang, S., 1997, “The bullwhip effect in supply chains”, *Sloan Management Review*, Vol. 38(3), pp. 93-102.
7. Riddalls, C.E. and Bennett, S., 2001. The optimal control of batched production and its effect on demand amplification. *International Journal of Production Economics* 72, 159-168.
8. Cachon, G.P., 1999. Managing supply chain demand variability with scheduled ordering policies. *Management Science* 45 (6), 843-856.
9. Fransoo, J.C. and Wouters, M.J.F., 2000, “Measuring the bullwhip effect in the supply chain”, *Supply Chain Management: An International Journal* 5 (2),78-89.
10. Disney, S. M., and Lambrecht, M. R.,2008, “On Replenishment Rules, Forecasting, and the Bullwhip Effect in Supply Chains”, Hanover: New publishers Inc..
11. Lind, D. A., Marchal, W. G. and Wathen, S. A., 2007-2008, “Statistical Techniques in Business and Economics”, New York: McGraw Hill,
12. Kimbrough, S. O., Wu, D. J. and Zhong, F., 2002, “Computers play the beer game; can artificial agents manage supply chain?”, *Decision Support System*, Vol. 33(3), pp. 323-333.

## 12. MAILING ADDRESS

Tahera Yesmin  
Lecturer, Department of Industrial and Production Engineering,  
Bangladesh University of Engineering and Technology,  
Dhaka, Bangladesh.  
Email: taherayesmin@ipe.buet.ac.

## A MODEL OF A CVT ADJUSTMENT DRIVE BASED ON TRANSIENT RESPONSE

S. C. Banik<sup>1</sup>, S. M. Mahfuzur Rahman<sup>1</sup> and A. K. Mozumder<sup>2</sup>

<sup>1</sup>Department of Mechanical Engineering, CUET, Chittagong, Bangladesh

<sup>2</sup>Department of Mechanical Engineering, BUET, Dhaka, Bangladesh

### ABSTRACT

This paper deals with modeling and simulation of a CVT adjustment drive. The modeling approach is based on the transient response of the system. The transfer function of the system is developed based on some theoretical concepts and experimental data. For the verification of the model various experiments were done at different input voltages (-2V to 2V) for upshift and downshift of the CVT gear with applied forces (600N, 1000N) on driven side. In any case, error in position value is less than 10% with respect to measured value. The causes of small deviation of the results are stated from the model analysis and experimental results.

**Keywords:** Adjustment drive, Cascaded controller, Mechanical transmission, Power drive, Transfer function

### 1. INTRODUCTION

A Continuously Variable transmission (CVT) is a mechanical transmission, which provides a continuous range of speed ratios, unlike a normal transmission, which can provide only a few discrete ratios. It has also some advantages in comparison to other transmission systems due to its simple design. It is necessary to model a system and then to analyze the dynamic characteristics of the system for proper controlling. The mechanical model should be able to describe the mechanical behavior of the real system with an acceptable accuracy. Depending on the goals of analysis and the characteristics of the system, the model can be developed either with the concept of multibody system or the modeling principles of structural dynamics. A real system can be modeled as different elements depending on different views and circumstances. The aim of this work is to develop a computer model of the adjustment drive with which its controllers can be optimized.

### 2. DESCRIPTION OF TEST RIG

The CVT test rig (shown in Fig. 1) mainly has two parts: Prime mover and Adjustment drive. Prime mover is the power transmitting section and adjustment drive controls the speed ratio.

#### 2.1 Prime Mover

Prime mover section includes Main power drives, shaft, pulley, V-belt, etc. Main power drives are two asynchronous motors which have a rated power of 33 kW and a rated torque of 200 N-m. Two parallel shafts are to transmit power from driver to driven set at a distance of 372 mm from each other and having a diameter of 60

mm.

The pulley can adjust its contact diameter from 96mm to 272mm by positioning the shipment of the movable sheave. The V-belt has two different wedge angle: 2° and 18° having some advantages [1].

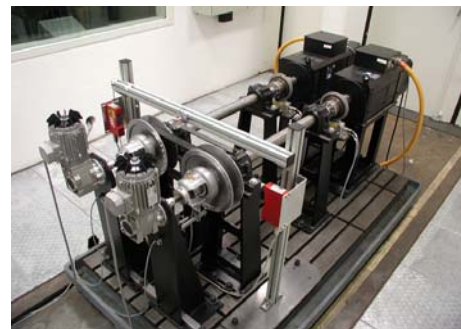


Fig 1. Total view of the test rig [2]

#### 2.2 Adjustment Drive

The adjustment of the speed ratio is accomplished by an electro-mechanical adjustment mechanism which consists of geared motor, coupling, screwed spindle and adjustment housing (shown in Fig. 2). The adjustment has to be done for both the driver pulley and driven pulley simultaneously. The transmission ratio is altered with the change of contact diameter of pulley and belt. This is done by moving one sheave (movable) horizontally along the shaft. For getting the desired ratio, proper pressure has to be maintained to push the sheave to the correct position and to overcome the frictional force.



The adjustment actuator is an asynchronous squirrel-cage AC motor with a rated power of 0.37 kW. Screwed spindle transforms the rotational speed into axial shipment of sheave. The coupling is used to transmit the power required for adjustment from the actuator to the spindle.



Fig 2. Total view of the adjustment drive [2]

### 2.3 Measurement and Control Electronics

For measuring the different parameters of the system different types of sensors are used like displacement, force, rpm, and Temperature. In the CVT test rig a MGCplus amplifier system is used to manipulate the sensor's signal by amplifying, signal conditioning and A/D-conversion to get the values of force, position, rpm etc. with their correct unit. Making the analogue signals continuously available for every measurement channel, the MGCplus provides high speed digital data acquisition at high resolution. The dSPACE (Digital Signal Processing and Control Engineering) / Simulink combination provides an integrated environment for modeling, simulation and real-time implementation. After creating the real-time code for the model, the ControlDesk is set up to acquire data, to watch and change the variables. The ControlDesk provides a graphical user interface (GUI). For adjustment drive the input from 0-10V is applied to the frequency converter (FC) via a dSPACE AutoBox. For the proper control of the system there are four controllers: Position, ratio, force and slip. All these controllers are conventional of PI or PID type [2].

### 3. DEVELOPMENT OF MODEL

The aim of modeling the adjustment drive is to test it with the present controller and then use it for developing an optimized controller. In case of CVT adjustment drive some experimental results are used to simplify the modeling efforts instead of pure theoretical calculations. For a linear system, step response provides all the information needed for developing a state-space representation or an s-domain Laplace representation of the system. Unfortunately, the given system has got some nonlinearities such as slip effects both in the case of motor and the belt. There are also some limitation problems like power limitation of the motor. Moreover, there is a distance limitation after which the sheaves cannot move. We have developed the total model of the

system by elemental behavior analysis of actuator, coupling, screwed spindle, adjustment housing, etc.

#### 3.1 Actuator

As the actuator system consists of some mass inertia, damping and stiffness element, the system can be considered as at least a second order system. The well-known closed-loop transfer function of a second order system is as follows [3]:

$$\frac{C(s)}{R(s)} = \frac{\omega_n^2}{s^2 + 2\omega_n\zeta s + \omega_n^2} \quad (1)$$

where, C(s) is the output, R(s) is the input to the system,  $\omega_n$  is the undamped natural frequency and  $\zeta$  is the damping ratio.

By using a typical step response of a second order system, the parameters  $\omega_n$  and  $\zeta$  can be found out [3, 4]. With the use of step response and formulae [3, 4], we found the value of the natural frequency  $\omega_n = 32.74$  Hz, damping ratio  $\xi = 0.5739$  and the transfer function of the motor is obtained as in Fig. 3.

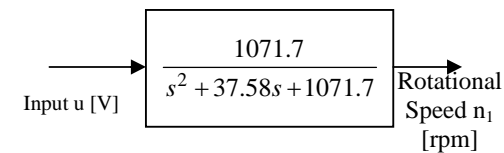


Fig 3. Transfer function for motor

#### 3.2 Coupling

The coupling is a mechanical connection to transmit power from the actuator to the output shaft. It consists of a driver and a driven part and between them there is a toothed plastic connector. It causes a delay in the output, which causes a phase shift between the output and input. In the modeling the coupling is considered as a delay element whose transfer function is as follows (Fig. 4):

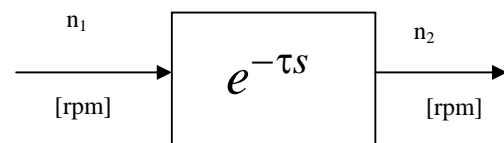


Fig 4. Transfer block for coupling

#### 3.3 Screwed Spindle

The spindle gives 3 mm axial movement to the adjustment housing at each rotation. It is working as an integrator to transmit the rpm into axial distance. So the transfer function for the spindle should be as in Fig. 5.

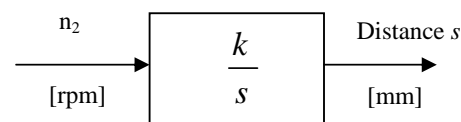


Fig 5. Transfer function for screwed spindle



Where,  $k$  is the pitch of the spindle and  $s$  is the distance traveled by the adjustment housing within a certain integration time.

### 3.4 Adjustment Housing

When the adjustment housing is modeled neglecting the elastic deformation and the material damping, it can be seen as a mass on which some forces are acting. Due to the resultant force, a displacement of the housing occurs. The resultant force is the sum of all forces applied by the belt [5], frictional force between the housing and the spindle thread and the axial force created by the spindle.

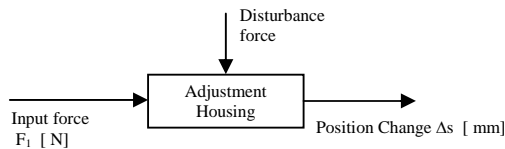


Fig 6. Block diagram of the Adjustment housing

### 3.5 Transformation from Axial Shipment to Radial Change

The total axial shipment  $\Delta s$  of the housing & sheave can be divided into two parts: One sheave has  $\Delta s_1$  and the other has  $\Delta s_2$ . The wedge angles are  $\gamma_1$  and  $\gamma_2$ . Let  $\Delta r$  be the radial displacement of the belt depending on the axial shipment  $\Delta s$  of the sheaves. With some geometrical calculation for the transformation of the axial displacement  $\Delta s$  to the radius change  $\Delta r$ , a proportional block or gain box is considered as follows [6]:

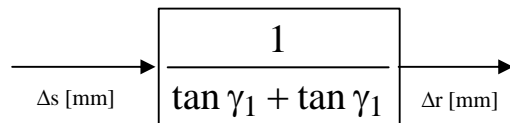


Fig 7. Transformation from displacement to radius change

### 3.6 Model of the Adjustment Drive

The transfer function that was determined before for the actuator did not consider the effect of mass inertia of the housing and the movable sheave. Here transient response is determined when it is connected with these two parts for including their effects. The undamped natural frequency  $\omega_n$  is 7.75 Hz and the damping ratio  $\xi$  is 0.8311.

Table 1: Comparison of  $\omega_n$  and  $\xi$

Parameters	Case1	Case2
$\omega_n$	32.74 Hz	7.75 Hz
$\xi$	0.5739	0.8311

The transfer function for the second case is as follows:

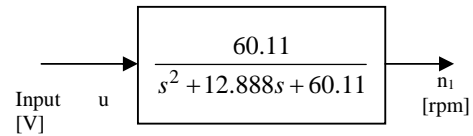


Fig 8. Transfer function for adjustment drive

## 4. SIMULATION RESULT

The simulation was done with the real time interface (RTI) model in the real field. For this, a control layout was made to give input to the system and to see the results of the model and measurement for making comparison. Experiment was performed both in the cases of increasing radius (upshift) and decreasing radius (downshift) during the change of speed ratio.

### 4.1 Upshift of the CVT Gear

When a positive voltage is given to the FC, the sheave moves inwards to the fixed sheave and as a result the contact radius increases. During the closing of the sheave the disturbance torque acts in the opposite direction. The equivalent voltage of the torque is subtracted from the input voltage and the net voltage is passed through the transfer function of the motor. The results obtained when the input voltage is +2V and the force at driven side is 600 N, are shown in Fig. 9, Fig. 10 and Fig. 11:

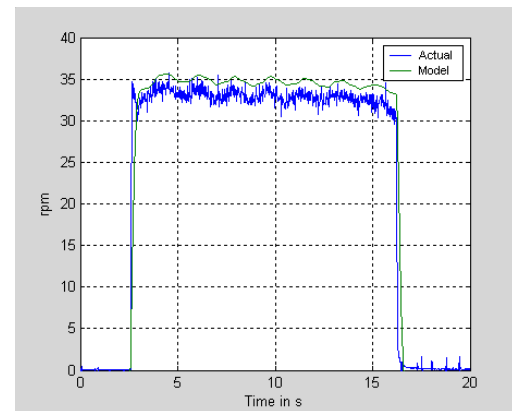


Fig 9. The rpm obtained from the model and motor.

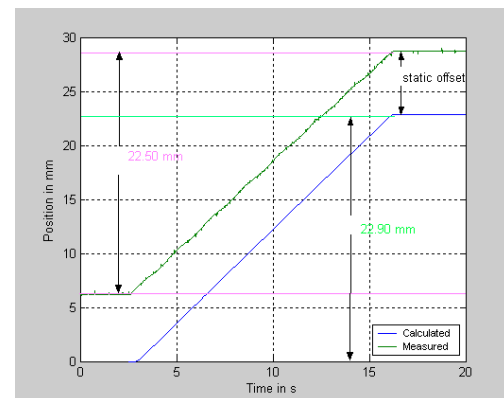


Fig 10. Distance traveled by the movable sheave due to spindle rotation

From the graphs it can be seen that there is a great similarity between calculation and measurement. The small difference between the calculated and measured rpm comes either from the sensor or from the transfer function of the model. The sensor was not fixed to a clamp, it was held by hand. At a high rpm, there is a little movement in the hand which causes an affect on the sensor readings. The time delay due to the coupling block is neglected in the RTI model, because the delay time of the coupling is very small so that it does not create a meaningful deviation to the speed response.

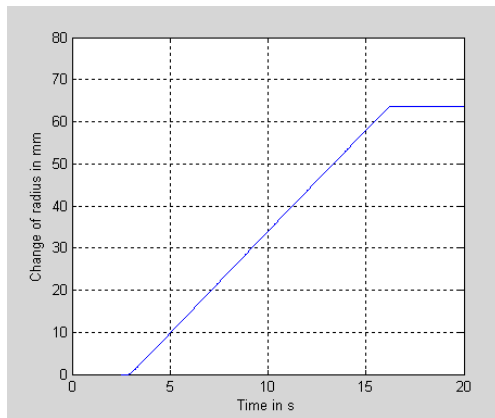


Fig 11. Radius change due to position change of movable shift

There is a swinging response for rpm (Fig. 9) both in the cases of calculated and the measured rpm. It is due to the transverse vibrational effect of the belt [1]. Like the string of a guitar or a violin, the belt can vibrate (as shown in Fig. 12). The frequency of vibration increases with decreasing length of the free span between the pulleys and with increased belt tension. This vibration is transmitted via sheave to the housing when it is measured.

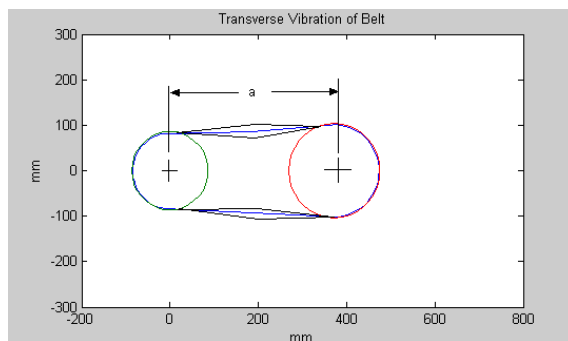


Fig 12. Transverse Vibration of the belt

In the Position vs. Time graph (Fig. 10) it can be seen that, for a certain time period the measured displacement of the sheave is 22.5 mm and the calculated value is 22.90 mm. So the error is as follows:

$$\Delta e = \frac{n_c - n_m}{n_m} \times 100 \% \quad (12)$$

$$= 1.78\%$$

where,  $\Delta e$  is the error,  $n_c$  is the calculated value and  $n_m$  is the measured value of rpm.

This error may also come from the modeling error like as nonlinearities of the system which have not been considered in the model. A part of the error also may come from the inductance sensor due to elasticity and vibrational effects on the attachment part of the housing.

There is a static offset between the measured and calculated position. This is due to the fact that in the RTI model the Integrator subsystem is in *held state*. It holds the position value of the previous experiment. So this acts as a static offset for the next experiment. If a simple Integrator is used in lieu of Enable subsystem in that case also an offset occurs but caused by another reason. In that case, there is a constant negative offset at the entrance of the I-block caused by the disturbance torque. So the I-block's decrement occurs continuously and when an input voltage is given it starts to increase from that offset value. But in both cases, the net increment looks very similar.

There is a linear increment of the radius with respect to time. By adding this increment with a certain reference value, the contact radius of the pulley can be obtained. The radius obtained from the model is calculated as simply a function of the geometry of the pulley. But in reality it depends on other factors too like the speed of the prime mover, load torque, belt properties, etc.

Fig 13 is obtained from the experiment when input Voltage is +2V and the applied force on the driven side is 1000N.

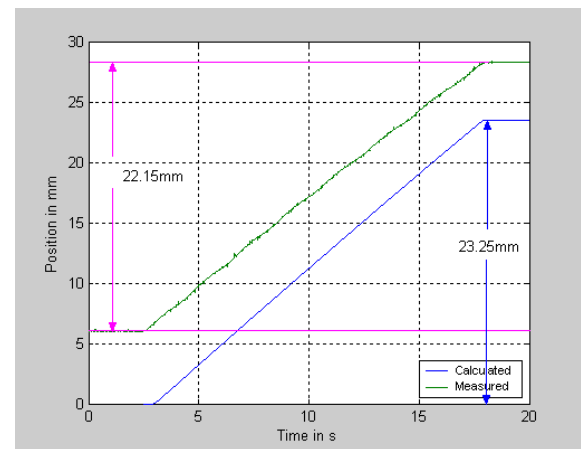


Fig 13. Displacement of sheave when input is +2V and force is 1000N

In this case the actual displacement measured by the sensor is 22.15 mm and the simulation result is 23.25 mm. The error increases to a value of 4.96%. So it can be concluded that there is a relation between the force of the driven side and the rotation of the driver. From the experiment it is observed that high force applied by belt on the driven side causes a decrement of revolution of the driver side. As a result a reduction of displacement occurs for the movable sheave.

## 4.2 Downshift of the CVT Gear

If a negative voltage is given to the FC, the motor rotates in the opposite direction. As a result the movable sheave moves away from the fixed one and the contact radius gradually decreases. In this case the force given by the belt helps the pulley to move faster. In the model, during the negative input voltage the equivalent voltage of the disturbance torque is summed up with the input. So the motor can rotate faster.

An experimental result is shown in Fig. 14 when a input voltage of  $-2V$  and the force on the driven side is  $600N$ . There is a static offset in the rpm diagram due to the disturbance torque, which causes a continuous input voltage to the model of the system. In Fig. 14 the rpm is negative, which means the rotation is in opposite direction. Now it can be compared that when an input voltage is  $+2V$  and force is  $600N$  then the sheave moves  $22.90\text{ mm}$  in  $13.5\text{ s}$ . On the other hand, when input voltage is  $-2V$  and force is  $600N$  the sheave moves  $23.5\text{ mm}$  in  $11.6\text{ s}$  (as shown in Fig. 15). So it is clear that there is a first movement of the sheave during the opening (downshift of CVT gear).

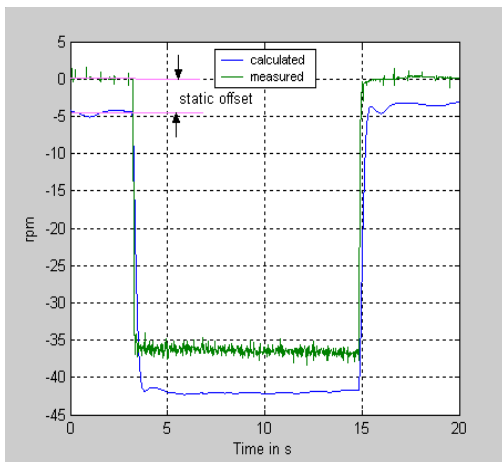


Fig 14. motor's rpm at input  $u = -2V$  and force is  $600N$

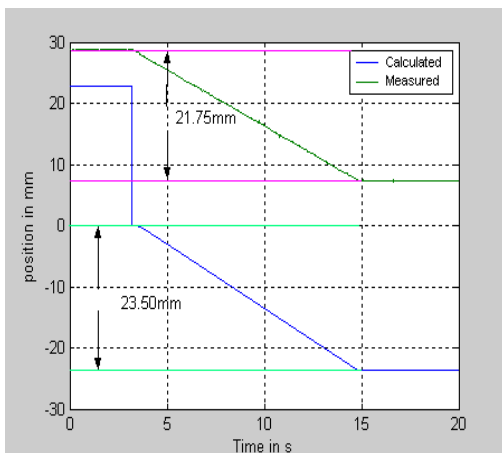


Fig 15. The displacement at  $u = -2V$  & force is  $600N$

## 5. CONCLUSION

In this paper the model of the CVT adjustment drive has been developed by assuming that the system is of 2<sup>nd</sup> order and simulation was performed. The model behaves like the real adjustment drive with a tolerable error at different input voltages in the cases of upshift and downshift of the CVT gear. It gives a good result when the force on the driven side is not so high. A high force affects the other side's rotation. At high force the driver motor has not enough power to overcome this force. By making an interaction between the driver and driven side considering the real behavior, the further development can be carried on. Actually, this small deviation of radius is not a dominant factor for controlling the speed ratio. The changing of the speed ratio depends mainly on the mechanical performance of the electro-mechanical adjustment system.

The error of the rpm sensor can be minimized by making an arrangement for holding it at a fixed position. If the input voltage and current or the torque at the output shaft can be measured, the model can be obtained by pure mathematical formulations. The PID controllers then could be optimized by using the developed model

## 6. ACKNOWLEDGEMENT

This work was conducted at the laboratory for Machine Elements and Material Handling (LMF), Helmut-Schmidt University, Hamburg, Germany. The authors would like to express deep gratitude to Prof. Dr. -Ing Rainer Bruns, Dr. -Ing Oliver Hoepfner and Michael Eisenberg for their conceptual ideas, technical support and valuable advices regarding this research.

## 7. REFERENCES

1. Lodewijks, G., 1996, *Dynamics of Belt Systems*, ISBN 90-370-0145-9, DUT, Netherlands..
2. Banik, S. C., 2004, "Modeling and Simulation of a CVT Adjustment drive", Project Work, Technical University of Hamburg-Harburg (TUHH), Germany
3. Ogata, K., 1997, *Modern Control Engineering*, Third edition, ISBN 0-13-261389-1, Pearson Education, USA.
4. Nise, N. S., 2000, *Control System Engineering*, ISBN 0-471-36601-3, Third Edition, USA.
5. Gerbert, G., 1999, *Traction Belt Mechanics*, ISBN 91-630-7885-6, Kompendiet, Goetenborg, Germany
6. Eisenberg, M., 2004, "Automatisierung eines breitkeilriemen verstellgetrieb e-prüfs- tands unter besonder berücksichtigung der regelung", Diplomaarbeit, HAW, Hamburg,

## 8. MAILING ADDRESS

S. C. Banik  
Department of Mechanical Engineering,  
CUET, Chittagong, Bangladesh.

## CONSIDRATION OF ENGINEERING ETHICS AS A NECESSARY ATTRIBUTE FOR PREPARING ETHICAL ENGINEERS IN PAPUA NEW GUINEA

John Pumwa

Mechanical Engineering Department, Papua New Guinea University of Technology, Papua New Guinea

### ABSTRACT

Unlike developing countries, interest in engineering ethics education has developed significant momentum in almost all advanced countries. The developing countries have not yet paid enough attention to such critical issues and Papua New Guinea is no different. This is probably the reason why corruption activities have become part of the normal activities of politicians, senior public servants and many other higher office holders as reported in the daily news media. As engineering work becomes more complex and diverse, an understanding of engineering ethics becomes an important attribute for adequate and ethical preparation of engineers along with their technical knowledge. This basically means that engineering students have to learn about their ethical obligations towards society, their employers, fellow engineers and themselves. This paper discusses the needs and reasons for integrating ethics into the education of undergraduate engineering students in Papua New Guinea.

**Keywords:** Engineering Ethics, Codes of Ethics, Professional Responsibility.

### 1. INTRODUCTION

Developing countries are striving to catch up with the rapid and vast development in science and technologies to develop competitive economies in the globalization era. It requires an adoption of a world-class balanced engineering program that is effective in producing highly qualified engineers and technologists in their local universities. Curriculum development for engineering programs in developing countries should be informed and guided by the state-of-the-art engineering education in advanced countries but tailored to serve local needs and constraints.

However, developing a balanced engineering curriculum is an enormous task that involves the consideration of several requirements of a graduate engineer such as the industry expectations, the expectations of the accreditation bodies and the interest of a country. Taking into considerations the requirements of industry and the accreditation bodies in the development of a balanced engineering curriculum can be accomplished by considering the inputs from industry and the accrediting professional bodies [1] [2]. However, taking into consideration the interest of a country in the design of a balanced engineering curriculum may be performed by observing the performance of the country in terms of social, economical and political behavior of the population.

It appears that advanced countries have considered ethical competency to be as important as or even more important than technical competencies. Moreover, engineering educators have become more aware of the need to address responsible and ethical behavior

explicitly as part of engineering education curricula. This has led to a recent revision of the requirements of the Accreditation Board of Engineering and Technology in various advanced countries such as USA, UK, and Australia, to have acquired accreditation status only when the engineering programs have evidence that their graduates do have a clear understanding of professional and ethical responsibilities [3]. This has forced the engineering schools to foster in their students an understanding of the ethical and moral characteristics of the engineering profession and practice.

Professional engineers almost always learn ethical and moral lessons only after something has been overlooked or has gone wrong or may have done without realizing that it is unethical and morally wrong. There is no wholly adequate substitute for actual engineering experience. However, having students being aware of ethical issues such as corruption, moral values, ethical values, bribery, whistle blowing, conflict of interest, nepotism, etc. and the requirements of professional institutions like IEPNG and reflect on various realistic case studies can provide some helpful preparation for dealing with ethical and moral issues they are likely to face once they do enter engineering practice. By requiring engineering programs to introduce students to ethical and moral concerns, Accreditation Board of Engineering and Technology is taking the position that students need to begin to think about ethical and moral issues before things may go wrong. In essence, Accreditation Board of Engineering and Technology is advocating a kind of preventive ethics, which is much like preventive medicine in that one doesn't wait until

something is obviously amiss before taking appropriate action. Preventive medicine advocates good health habits as a means for minimizing the need for more serious medical intervention later. Similarly, preventive ethics attempts to anticipate possible consequences of actions in such a way that more serious problems are avoided later during practice.

Our daily news media [4] [5] reports large number of cases of unethical and immoral behavior being committed by white collar professionals including engineers such as corruption, bribery, nepotism (wantok system), conflict of interest and whistle blowing which indicate that Papua New Guinean engineers are in desperate need of preventive ethics that may assist in alleviating further more damaging ethical and moral problems that may be encountered by future engineers. Moreover, general performance and behavior of the population of the country indicates that there is a break down in ethical and moral values and requires an immediate attention if the country is to succeed economically. Therefore, it is vitally important for Papua New Guinea engineers to be made aware of ethical and moral issues such as corruption, moral values, ethical values, bribery, whistle blowing, conflict of interest, etc. and the requirements of professional institutions like IEPNG and reflect on various realistic case studies can provide some helpful preparation for dealing with ethical and moral issues they are likely to face once they do enter engineering practice. In response to this need, the Mechanical Engineering Department at the Papua New Guinea University of Technology has included a course on Ethics and Engineering in its program.

## **2. RELEVANT ATTRIBUTES OF ENGINEERING GRADUATES**

It appears from experience that our engineering graduates tend to lack relevant attributes as desired by industry including ethical and moral behavior. These attributes comprise of technical and non-technical elements. Technical attributes are those related to engineering curriculum while non-technical attributes are mainly related to social science discipline. Technical attributes for engineering graduates are those related to the ability to design and develop a new product or process which includes: i) technical knowledge, ii) the ability to synthesize, iii) the ability to elucidate principles and iv) the ability to evaluate. Technical knowledge is the most important attribute of an engineer which consists of the natural laws and principles. The more natural laws and principles an engineer knows, the greater the choices available to him or her for devising efficient methods to achieve the desired objectives. The second most important attribute of an engineer is the ability to synthesize or combine natural laws and principles to achieve the desired objectives. The ability to elucidate is the third important attribute of an engineer. With this attribute, an engineer is able to discover underlying principles by interpreting data correctly and accurately conducting effective experiments. The fourth most important attribute of a good engineer is the ability to judge between alternative solutions and choose the best and optimum solution for a particular application.

The other attributes of a good engineer are mostly relate to social science disciplines which includes report writing ability, computer literacy, teamwork ability, management and leadership ability, problem solving ability, ability to work under pressure and meet deadlines, commitment to the job, willingness to work overtime, etc. Although these attributes may not seem to be directly related to engineering subjects, they are very relevant in the context of the current competitive business environment.

Similarly, it would be inappropriate to emphasize only on technical expertise without developing parallel engineering ethical framework to safeguard the industrialization conversion. In the absence of ethical abilities, it would certainly lead to high-profile cases of misconduct which may lead to some technical disasters caused by various factors including moral incompetence: negligence and corruption. Therefore, it is necessary for developing countries like Papua New Guinea to adopt engineering education systems that integrate ethics with technical competency and create policies that will aid in its development to eliminate or at least minimize the damaging effects of the adoption of technology on society and environment.

In practice, engineers are expected to know and behave according to professional norms set by their community. This includes evaluation of their worthiness as members of the community by colleagues, collaborators, students and trainees (they teach and mentor) and the society as a whole. It is generally assumed that trainees and students will observe what senior professionals do and follow their example. Unfortunately, modeling of good behavior does not always happen, and even when it does, it may not be sufficient because learning from the behavior of another requires interpretation, which varies from one to another [5]. Moreover, the rationale for any behavior, even exemplary one, is not always obvious, especially when problems are multifaceted and complex and choices must be made among competing interests and concerns. In short, there is more to being an engineering professional than simply being a technical expert [6]. Awareness of and respect for the professional values and standards of the community is a measure of one's standing in that community.

For these reasons, responsible and ethical engineering practices should be addressed explicitly at early stage of engineering engagement during the student's training at the university where the student's will be made to be aware of their ethical and moral responsibilities as well the expectations from their professional institutions. Moreover, as young engineers assume positions of increasing managerial importance, they will face decisions requiring judgments based on ethical reasoning. When this point of decision-making occurs, they should find comfort in a personal memory bank established during their student years---if not earlier---with guidelines for ethical personal conduct. Ethics should be an educational priority for an engineering program.

### 3. WHAT IS ENGINEERING ETHICS?

With the progress of professional societies, the formation of codes of ethics is becoming a necessity to avoid confusions and malpractices within the professions. Generally, ethics is concerned with what is right or wrong, good or bad, fair or unfair, responsible or irresponsible, obligatory or permissible, praiseworthy or blameworthy. It is associated with guilt, shame, indignation, resentment, empathy, compassion, and care. It is interested in character as well as conduct. It addresses matters of public policy as well as more personal matters. On the one hand, it draws strength from our social environment, established practices, law, religion, and individual conscience. On the other hand, it critically assesses each of these sources of strength. Therefore, ethics is complex and often perplexing and controversial which defies concise, clear definition. Nevertheless, it is something with which all of us have a working familiarity and it is everybody's business [7].

Particularly, one may define engineering ethics as the standards of care and values used by engineers in their daily practice of profession towards society, employer and themselves, that is often called professional responsibility that is, moral responsibility based on an individual's special knowledge. Apart from the fundamental commitment of engineers to a fundamental commitment to public health, safety, and welfare, engineering ethics is typically concerned with conflicts of interest, the integrity of data, whistle-blowing, loyalty, accountability, giving credit where due, trade secrets, and gift giving, bribes [8] and nepotism or wantok system.

Engineering ethics is the rules and standards governing the conduct of engineers in their role as professionals. It encompasses the more general definition of ethics, but applies it more specifically to situations involving engineers in their professional lives. Thus, engineering ethics is a body of philosophy indicating the ways that engineers should conduct themselves in their professional capacity. It is critical for an engineer to maintain an ethical reputation within his/her engineering career. The main principles that an engineer should work and live by are to hold paramount the safety, health, and welfare of the public, perform services only in areas of their competence, act for each employer or client as faithful agents of trustees, avoid deceptive acts, and conduct themselves honorably, responsibly, ethically, and lawfully so as to enhance the honor, reputation, and usefulness of the profession. An engineer's negligence may be assessed by measuring the engineer's actions relative to the standard of care of the profession using the five elements of the ethic of care [9]: attentiveness, responsibility, competence, responsiveness, and integrity. It is to be noted that care is identified as an ethical framework suitable to provide guidance for engineering activities [10].

### 4. PROFESSIONAL CODE OF ETHICS

A professional code of ethics state the principles and core values essential to the work of a particular occupational group. One of the characteristics of the professions that distinguish them from other human

endeavors is the habit of developing codes of ethics to guide the actions of their members. The codes of ethics for engineers are intended as guidelines to protect the public, to build and preserve the integrity and reputation of the profession, and to describe proper relations between engineers and their employers and clients. The codes of ethics are intended to play a number of roles which may have negative and positive consequences [11]: i) inspiration and guidance, ii) support, iii) deterrence and discipline, iv) education and mutual understanding, v) contribution to the profession's public image, vi) protecting the status quo and vii) promoting business interests.

A typical code of ethics begins with general introductory section, followed by a series of fundamental statements. Then, the statements are expanded and explained as a means of providing guidance in particular situations. The Code of Ethics of Engineers, published by the Accreditation Board for Engineering and Technology (1985), begins with the following statement of fundamental principles [12]:

Engineers uphold and advance the integrity, honor and dignity of the engineering profession by:

- I. Using their knowledge and skill for the enhancement of human welfare;
- II. Being honest and impartial, and serving with fidelity the public, their employers and clients;
- III. Striving to increase the competence and prestige of the engineering profession; and
- IV. Supporting the professional and technical societies of their disciplines.

Primarily, a code of ethics provides a framework for ethical judgment for a professional. Note that it is only a framework as no code can be totally comprehensive and cover all possible ethical situations that a professional engineer is likely to encounter. It may only serve as a starting point for ethical decision making and it can also express the commitment to ethical conduct shared by members of a profession. It is important to note that ethical codes do not establish new ethical principles but they simply reiterate principles and standards that are already accepted as responsible engineering practice. This is confirmed with the three key concepts being revealed when analyzing several engineering codes of ethics [13]: 1) the public interest, 2) qualities of truth, honesty, and fairness, and 3) professional performance. It can be seen that a code expresses these principles in a coherent, comprehensive, and accessible manner where it spells out the ways in which moral and ethical principles apply to professional practice. Moreover, a code of ethics helps create an environment within a profession where ethical behavior is the norm. It also serves as a guide or reminder of how to act in specific situations and also can indicate to others that the profession is seriously concerned about responsible and professional conduct.

A code of ethics developed from the basic principles of concepts would be acceptable whether it is defended from altruistic or self-improvement motives.

This code is to accept responsibility in making engineering decisions consistent with the safety, health and welfare of the public, and to disclose promptly factors that might endanger the public or the environment. Avoid real or perceived conflict of interest possible, and to disclose them to affected parties when they do exist. To be honest and realistic in stating claims or estimates based on available data, to reject bribery in all its forms. Improve the understanding of technology, its appropriate application, and potential consequences. Maintain and improve technical competence and undertake technological tasks for others only if qualified by training or experience, or after full disclosure of pertinent limitations. Seek, accept, and offer honest criticism of technical work, to acknowledge and correct errors, and to credit properly the contributions of others. Treat fairly all persons regardless of such factors as race, religion, gender, disability, age or national origin. Avoid injuring others, their property, reputation, or employment by false or malicious action. Assist colleagues and co-workers in their professional development and to support them in following this code of ethics. It is anticipated that the development of these types of codes may provide people and officials with guidelines to establish a better corporate ethical and moral culture and to improve management. It may also minimize the risk of white collar crimes and improve ethical decision-making resulting in the promotion of high standards of practice and ethical behavior and enhances trust and respect from the general public.

## **5. TEACHING ETHICS AT ENGINEERING SCHOOLS**

As discussed above, ethics is a framework for making value-laden choices, which basically means that ethics can be taught despite skepticism of the feasibility and legitimacy of this undertaking [14]. A central question, often asked, that raises a fundamental issue is whether or not ethics can be taught in engineering schools. This is because there is a widespread assumption that students at university level have already developed specific moral characters. Skeptics both within academy and without further argue that moral character is formed in the home, church and the community, and cannot be modified in a classroom. This may sound correct to some extent. Although, morality does need to have an early beginning in our lives, the story of moral development is anything but over once we move beyond these early years [15] [16] [17].

However, moral autonomy is the ability to think critically and independently about moral issues and to apply this moral thinking to situations that arise in the course of professional engineering practice. Teaching ethics should foster the moral autonomy of future engineers. Moreover, the various approaches described above can be explained and contrasted, and students can be challenged to apply their own moral values to cases and to learn from the experiences of others. Student engineers can be taught to think ethically and to sensitize them to important ethical issues before they have to confront them during practice.

The following should be the appropriate goals for adopting engineering ethics in engineering programs in a developing country: i) promoting the sense of responsibility; ii) increasing awareness and knowledge of professional ethical standards iii) increasing students awareness of the ethical dimensions of science and engineering; iv) providing students and trainees with experience in making and defending decisions about ethical issues; and v) helping individuals develop strategies for addressing ethical issues and identifying resources to support decisions.

Integrating ethics at all levels of education emphasizes to students and faculty that ethics is a core competency. The content of engineering ethics courses should be widening to cover as much ethical issues and related topics as possible such as ethical implications of public policy relevant to engineering (risk and product liability, sustainable development, health care, and information technology etc.). Accordingly, teaching of engineering ethics courses should cover topics such as basic concepts and methods in ethics, typical professional engineering society code of conduct, history of engineering and technology, organizational loyalty versus professional rights, engineers and the environment, risk and the engineering decision-making process, whistle blowing, and social responsibility versus legal liability [18].

There are a number of ways to present engineering ethics. Studying accidents in terms of historical case studies to analyze both ethical conduct and social implications is a traditional approach in teaching engineering ethics [19]. Developing major-specific interactive cases may help to ensure that students do not ignore the social and environment contexts of engineering while taking engineering science and technical courses. Another approach is to focus more on culturally embedded engineering practice, that is, institutional and political aspects of engineering, such as contracting, regulation, and technology transfer [20]. Knowledge of such non-technical, but nonetheless ordinary engineering practice may provide engineers with the insight to anticipate safety problems before they are escalated into technological disasters.

In order to make the teaching of engineering ethics effective program, the following characteristics have to be considered: i) Ethical issues must be addressed explicitly. Good role models are necessary but not sufficient for teaching ethical behavior and standards ; ii) interactive discussions between students, staff members and senior professionals that may provide ample opportunities for students to think through problems and cases arise in their own projects; iii) the participation of many staff members and senior professionals, demonstrating that the community as a whole values responsible behavior; iv) a focus on topics relevant to the discipline and the local ethical dilemmas; v) programs that begin early in the curriculum and continue throughout graduate and postgraduate education, demonstrating that standards within the community continue to evolve and that, with experience, students and trainees become more sophisticated in addressing complex problems; Activities that are effective in an



educational setting can be adapted for the workplace; and vi) reinforcement of professional standards and ethical and moral values through a variety of programs and activities, including courses, team meetings, informal discussions with advisors and mentors and departmental seminars.

## **6. PREPARATION OF STUDENTS FOR ETHICAL AND MORAL CONDUCT AT THE PAPUA NEW GUINEA UNIVERSITY OF TECHNOLOGY (UNITECH).**

There is an increase of industrial activities throughout the country and engineering is at the heart of all these technological developments. As such any decisions being made and implemented by an engineer is affecting many people, including: consumers, clients, the engineering profession, different communities, different cultures and traditions and the future generations. At the heart of any professional decision making is how the engineer defines and fulfills his or her responsibilities to all of these groups, something that professional codes can clarify but not exhaustively describe.

Therefore, Unitech engineering programs must include engineering ethics in their respective programs where students are made aware of ethical and moral issues such as corruption, moral values, ethical values, bribery, whistle blowing, conflict of interest, etc. and the requirements of professional institutions like IEPNG and reflect on various realistic case studies that can provide some helpful preparation for dealing with ethical and moral issues they are likely to face once they do enter engineering practice.

The Mechanical Engineering Department at Unitech has included a course on Ethics and Engineering (ME 303: Ethics and Engineering) in its program. The course is designed to make the students to be aware of the ethical and moral issues (corruption, moral values, ethical values, bribery, whistle blowing, conflict of interest, loyalty, confidentiality, etc) that they are likely to encounter during practice [21]. The course also covers codes of conduct and the requirements of professional institutions like IEPNG, IMechE, ASME and IEAust. emphasizing that principles are ethical and moral standards that define good behavior. These principles are the tools by which engineers can know they are doing the right thing in the right way. Engineers who work by these principles will build a strong practice, based on professional excellence. Principles underlie laws and societal values such as show respect for individuals and their property, help others, do not cause harm to others, conserve our environment and being honest at all times.

One of the effective methods that have been used to teach engineering ethics is the use of real life case studies such as mining companies dumping mine waste into the rivers, developing huge dams for hydro power generation, dumping palm oil factory waste into the rivers etc. The use of case studies has been found to be successful for students in understanding engineering problems on related ethical issues. This is due to the fact that ethical inquiry begins with problems that professionals can expect to have to face. This is in contrast to beginning at a highly theoretical level and only later considering how

rather general principles and rules might apply to actual situations. By beginning with realistic cases, students have been able to immediately appreciate the relevance and importance of giving serious thoughts to ethics and morality.

Other avenues for ethical and moral development of students being provided by the university on campus include student counseling services, promotion of religious activities such as Tertiary Students Christian Fellowship (TSCF), church services, rallies etc., inviting prominent religious leaders for open lectures to the student population and the university community. The student body is being encouraged to participate in these extra curricula activities that will strengthen their ethical and moral development.

It is of paramount importance that the university community (SEM, HODs, departmental staff - both academic and support, etc.) must create the environment that is conducive to ethical and moral conduct if our graduates are to be ethical and moral. It must be the responsibility of the university community to instill ethical and moral values to the students by being role models on campus. Ethics and morality must be seen as a core value and an ethical environment as fundamental. Note that academic and support staff who are in direct contact with students must “walk the talk”, by initiating and supporting an ethics program that develops, maintains and enhances the ethical work and study environment for students. In addition, the due diligence of faculty and individual staff can be used to show appropriate public accountability in the event of an unanticipated ethics incident or crisis.

## **7. CONCLUSIONS**

It is evident that high quality engineering education is a key ingredient required by developing countries as they strive to develop their economies to allow for effective entry into the global marketplace. Moreover, quality engineering education is vital for effective exploitation of rich natural resources in a developing country like Papua New Guinea. In these countries, teaching of ethics to engineering students have to be considered as part of a strategy for building engineering capacity to secure sustainable development and betterment of the human conditions. Special programs have to be adopted to bring engineering ethics to the mainstream of education with teaching aiming at implantation of professional responsibility and standards of care in daily engineering practices towards employer, society and environment. It is vital for engineering schools to consider various mechanisms that will ensure effectiveness of engineering ethics programs such as interactive discussions, seminars and reviewing of real life case studies of corruption, disasters, etc.

## **8. REFERENCES**

1. Buniyamin, N. and Mohamad, Z., “*Engineering Curriculum Development: Balancing Employer Needs And National Interest – A Case Study*”, TEND 2000 Crossroads of the New Millennium, Workshop, April 8, 2000.

2. Noor, M. J. M.M., Jaafar, M.S., Ghazali, A. H., Aziz, A. A., Ali, A. A. A., “*Outcome-based Civil Engineering Curriculum Development*”, International Journal of Engineering and Technology, Volume 1, Number 2, 2004, pp. 169 – 178.
3. ABET Engineering Accreditation Commission. 2007. *Criteria for accrediting engineering programs: Effective for evaluation during the 2008-2009 accreditation cycle*. Baltimore, MD: Accreditation Board for Engineering and Technology.
4. Papua New Guinea Post-Courier, “*Engineer in Fraud Case*”, Wednesday, June 3, 2009, pp. 6.
5. The National, “*Lae Officer Charged*”, Thursday, June 1, 2009, pp. 4.
6. Hansen, T. B., “*Teaching Ethics to Science and Engineering Students*”, Report Published by the Center for the Philosophy of Nature and Science Studies at the University of Copenhagen, Blegdamsvej 17, DK- 2100 Copenhagen, Denmark, October 2005.
7. McGinn, R. E., “*Mind the Gaps: An Empirical Approach to Engineering Ethics*”, 1997 – 2001, Science and Engineering Ethics 2003, 9, 517.
8. Goldfarb, T. D., Pritchard, M.S., “*Ethics in the Science Classroom. Online instructional guide for Secondary School Science Teachers with Model Lessons for Classroom Use*”, Center for the Study of Ethics in Society, Western Michigan University, 2002.
9. Wujek, J., Johnson, D., “*How to Be a Good Engineer*”, Washington, D. C. IEEE United States Activities Board, 1992.
10. Tronto, J. C., “*Moral Boundaries: A political Argument for an Ethic of Care*”, Routledge, NY, 1993
11. Pantazidou, M., Nair, I., “*Ethic of Care: Guiding Principles for Engineering Teaching and Practice*”, IEEE Technology and Society Magazine, 1993, 12, 19.
12. Martin, M. W., and Schinzinger, R., “*Ethics in Engineering*”, Mcgraw-Hill, 2<sup>nd</sup> Edition, New York, 1989.
13. ABET, Accreditation Board for Engineering and Technology, “*Code of Ethics of Engineers and Suggested Guidelines for Use With the Fundamental Canons of Ethics*”, New York, 1985.
14. Oldenquist, A. G., and Slowter, E. E., “*Proposed: A Single Code of Ethics for All Engineers*”, Professional Engineer, Vol. 49, No. 5, May, 1979.
15. Colby, A., and Sullivan, M. William, “*Ethics Teaching in Undergraduate Engineering Education*”, J. of Engineering Education, July 2008, pp. 327 – 337.
16. Florman, S. C., “*The Civilized Engineers*”, St. Martin’s Press, New York, USA, 1987.
17. Rest, J. R., “*A Psychologist Looks at the Teaching of Ethics*”, Hastings Center Report, Volume 12, February 1982, pp. 29 – 36.
18. Bebeau, M. J., “*Designing and Outcome-Based Ethics Curriculum for Professional Education: Strategies and Evidence of Effectiveness*”, Journal of Moral Education, 1993, 22, 313.
19. Schimmel, K., “*ABET 2000 – Can Engineering Faculty Teach Ethics?*”, The Proceedings of the Christian Engineering Education Conference, 1999. <http://enr.calvin.edu/ces/ceec/schimmel.htm>
20. Billington, D. P., “*Teaching ethics in engineering education through historical analysis*”, Science, Technology and Human Values 2000, 25, 195.
21. Lynch, W., Kline, R., “*Engineering practice and engineering ethics*”, Science, Technology and Human Values, 2000, 25, 195.
22. The Papua New Guinea University of Technology, “*2008 Courses Handbook*”, Public Relations Unit, Unitech Printery, Lae, MP 411, Papua New Guinea, February 2008, pp. 284.

## 9. ACKNOWLEDGEMENTS

The author would like to express his sincere thanks and appreciation to Professor M. A. Satter for his useful assistance in the preparation of this paper. The author would also like to thank the Papua New Guinea University of Technology for their financial assistance in the presentation of this paper in the conference.

## 10. MAILING ADDRESS

John Pumwa  
 Mechanical Engineering Department,  
 Papua New Guinea University of Technology,  
 Lae, MP 411, Papua New Guinea.

## PREPARATION OF CARBON NANOTUBE GAS SENSORS BY INKJET PRINTING PROCESS FOR MONITORING OF POLLUTANT NO<sub>x</sub> GAS IN AIR

M.M.H. Bhuiyan<sup>1</sup>, K. Senba, R. Hayashi, F. Mitsugi, T. Ikegami

Graduate School of Science and Technology, Kumamoto University, Kumamoto, Japan

<sup>1</sup>Institute of Nuclear Science and Technology, Bangladesh Atomic Energy Commission,  
Dhaka, Bangladesh

### ABSTRACT

Single walled carbon nanotube (SWCNTs) gas sensors were prepared by inkjet printing process to deposit controlled less amount of SWCNTs on the substrate in a designed pattern with a view to have higher sensitivity and response time and to produce a large amount of sensor for air pollution monitoring. SWCNTs solution was prepared by mixing with pure water and SDS (sodium dodecyl sulphate) and this solution was used as an ink for the inkjet printing. The method works by ejecting SWCNTs as an ink on the silicon substrate through very fine nozzles to prepare sensor. The sensor surface was characterized by Scanning Electron Microscopy (SEM) and Raman spectroscopy. The sensitivity of the sensors was measured using change of electrical conductance by exposing to different concentrations of NO<sub>2</sub> gases. The resistance of the sensor was found to be decreased with increasing gas concentration. Sensors containing less dense SWCNTs showed higher sensitivity compared to the denser SWCNTs

**Keywords:** Carbon Nanotube, Inkjet Printing, Air Pollution, Gas Sensor, Monitoring, Nox Gas.

### 1. INTRODUCTION

Carbon nanotubes (CNTs) are attractive potential materials for nanotechnology application because of their exceptional electronic properties and mechanical strength. Since their discovery in 1991 by Iijima [1], carbon nanotubes (CNTs) have attracted the scientific interest due to their unique structure and promising properties that make them potentially useful for applications including nanoelectronics, multifunctional composite materials, or field emission devices [2]. CNTs are hexagonal networks of carbon atoms that can essentially be thought of as a layer of graphite rolled-up into a cylinder. Depending on the arrangement of their graphene cylinders, there are two types of nanotubes: single-walled nanotubes (SWNTs) and multi-walled nanotubes (MWNTs). SWNTs have only one single layer of graphene cylinder, while MWNTs have several concentric layers. Their high specific surface area (>1500 m<sup>2</sup>/g), high aspect ratio, size, and hollow geometry also make them promising candidates for their use as components of gas and chemical sensors. As a result of their remarkable physical and structural properties, CNTs are good candidates to be utilized as components of sensors with improved real-time monitoring of combustible gas alarms, gas leak detection, and environmental pollution monitoring, etc. SWNTs and MWNTs as sensitive materials for the detection of gases such as H<sub>2</sub>, NH<sub>3</sub>, NO<sub>2</sub> or O<sub>2</sub> have already been successfully demonstrated [3-7].

The emission of nitrogen oxides (NO<sub>x</sub>, NO and NO<sub>2</sub>) due to the high temperature gas combustion (vehicles, electricity generation, and industrial processes) results

in both smog and acid precipitation, and affect both terrestrial and aquatic ecosystems. Nitrogen monoxide is unstable and quickly forms NO<sub>2</sub>, which is an oxidizing gas that is present in all urban atmospheres. NO<sub>2</sub> is a brownish, highly reactive gas and a deadly poison by inhalation. The NO<sub>2</sub> gas detection has normally been carried out by chemiluminescence or non-dispersive infrared analysis [8-9]. These traditional methods employ large and expensive instruments and require sampling systems as well as complicated maintenance. Therefore, an effective method to monitor NO<sub>2</sub> is demanded for atmospheric environmental measurement and control. Research has been focused on the development of sensors capable of monitoring low NO<sub>2</sub> concentrations.

Functional materials such as polymers or biomolecules are most suitably processed from solution. In this respect, inkjet printing is a particularly attractive technique especially for the controlled solution deposition of small quantities of functional materials in conformity with specific patterns [10]. The technique operates ejecting single drops of an ink through very fine nozzles (with a 20–100 μm in diameter), at ambient temperature and with no contact or vacuum [11-12]. The only constraint is the requirement to have fluids with suitable viscosity (lower than 20 cP) and surface tension (in the range 28–350 mN m<sup>-1</sup>). Important parameters are the ink jet nozzle, the substrate, viscosity and surface tension of printing liquid.

The advantages of ink-jet printing compared with other techniques to deposit thin layers of polymer films onto a variety of solid substrates, such as

electrochemical deposition [13], thermal evaporation [14], spin coating [15], dipping coating [16], photolithography [17], lie in its patterning capability, in the efficient use of material and the low cost of the process, in the compatibility with a wide range of substrates and, finally, in the high level of technical development. Many inkjet applications are now emerging through both patents and scientific literatures in several fields. Recently, different groups have investigated the possibility to use ink-jet technique for chemical sensor applications[18-21], mainly using conducting polymers such as polyaniline as the sensing film. The most advantage of the ink-jet-printed films is a series of partially overlapped droplets that allows rapid diffusion of the vapour molecules into and out of the film, leading to sensor fast response and improved recovery times [22].

CNTs aggregate during preparation and have difficulty in placing controlled small amount of CNTs with high precision in micro or nano electronic device structures. So, inkjet printing process is very effective for fixing a very small amount as a designed pattern on the wafer for gas sensing application. In this work, SWCNTs gas sensors have been prepared for environmental applications especially for the NO<sub>x</sub> gas detection.

## 2. EXPERIMENTAL DETAILS

In this experiment, the inkjet nozzle was used to deposit SWCNTs solution on the Pd prefabricated interdigitated electrodes (called as the sensor substrate) and also on the silicon wafer. The position of the inkjet nozzle was fixed and the sensor substrate was placed on the X-Y stage. The X-Y stage was moved during printing controlled by using a PC to draw designed pattern of SWCNTs dotted line on the sensor substrate. SWCNTs prepared by pulsed laser ablation (PLA) method and commercially available SWCNTs prepared by direct injection pyrolytic synthesis (DIPS) were used in this experiment. At first, different concentration of SWCNTs solutions were prepared by dispersing in 1 wt. % SDS (sodium dodecyl sulphate) adding with pure water. To unbundle SWCNTs and to prepare a homogeneous SWCNTs solution, it was properly ultrasonicated by an ultrasonic homogenizer. These homogeneous SWCNTs solutions were used as an ink to print SWCNTs on the sensor substrate by using inkjet nozzle. The ratio of SWCNTs ink to pure water in three different solutions was 1:100, 1:30, 1:10. The amount of the SWCNTs on the substrate was controlled by the number of inkjet dots per length. The distance between adjacent droplets was controlled by controlling the moving speed of the X-Y stage. Table 1 shows the preparation condition for printing SWCNTs on the silicon substrate for preparing gas sensor. A CCD camera was used to adjust the droplets intervals. One single line of SWCNTs of 5 mm length using different contraptions of SWCNTs solutions was printed on the silicon substrate for single or several times scanning. Figure 1 shows the view of single line of SWCNTs printed by the inkjet printer on the silicon substrate. After printing SWCNTs on the silicon substrate, SDS

was removed from the sensor substrate by rinse in pure water for 10 minutes to measure the sensitivity. .

Table 1: Preparation condition

Inkjet parameters	Value
Nozzle diameter	90 μm
1 <sup>st</sup> Pulse length	50 μs
Pause	10 μs
2 <sup>nd</sup> pulse length	20 μs
Frequency of	20 Hz
Temperature	Room temperature
X-Y stage speed	500-200μm/s

After removing SDS from the SWCNTs line on the Si substrate, silver paste was put at the both ends of the line to form the two terminals. Thin copper wires were connected at the two terminals of the SWCNTs line for measuring electrical conductance by exposing to different concentration of NO<sub>2</sub> gas.

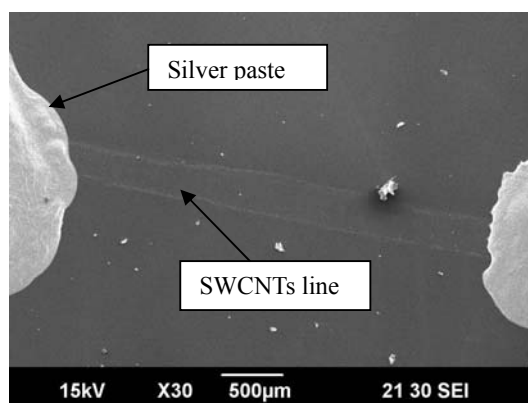


Fig 1. View of single SWCNTs line on silicon substrate printed by inkjet printing for a gas sensor.

## 3. CHARACTERIZATION OF SAMPLES

The sensor surface was characterized by Scanning Electron Microscopy (SEM) and Raman spectroscopy. Raman spectroscopy is a simple and useful technique to characterize the quality of the carbon nanotubes. The Raman spectra were measured using a micro Raman system (Princeton Instrument CCD and a diode laser of 532 nm in wavelength). The results examined for the SWCNTs are shown in Fig.2. The Raman spectra of carbon nanotubes typically consist of two major peaks at  $\sim 1340 \text{ cm}^{-1}$  and  $\sim 1590 \text{ cm}^{-1}$ , or the so-called D- and G-bands, respectively. The D-band is known to be associated with defective, disordered graphite or glassy carbon, while the G-band is related to the  $\text{sp}^2$  vibration of a two-dimensional hexagonal lattice in the graphite. The high G-band with respect to the D-band is a typical feature of the SWCNTs having high crystalline quality. The small D-band peak indicates that the film contains small but finite amount of amorphous carbon (and

defects). The SWCNTs show the vibration peaks of the radial breathing mode (RBM) in the range of 100–300  $\text{cm}^{-1}$ , which are related to the diameters of the nanotubes.

Fig. 3 shows the SEM image of SWCNTs gas sensing line with concentration ratio of SWCNTs ink to water of 1:30. Figures 4, 5 and 6 show the SEM top-view

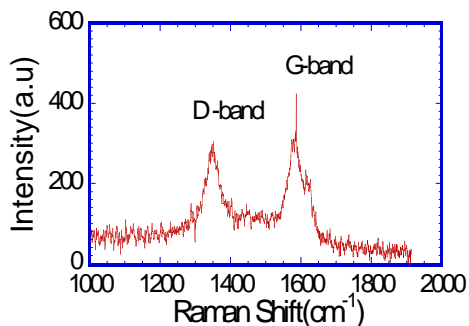


Fig.2. Raman Spectra of SWCNTs used in the gas sensor.

images of the SWCNTs line with concentration ratio of 1:10 at three different positions (at the middle, at the edge and at between middle and edge) on the printed line grown on the silicon substrate for the gas sensor. At the middle position, number of SWCNTs appears to be less compare to the edges. The carbon nanostructures are clearly characterized as a tangled net with a film thickness of 150–250 nm and a diameter of the mats of nanotubules in the range of 10–20 nm. The aspect ratio of the CNTs layer was estimated in the range of ...

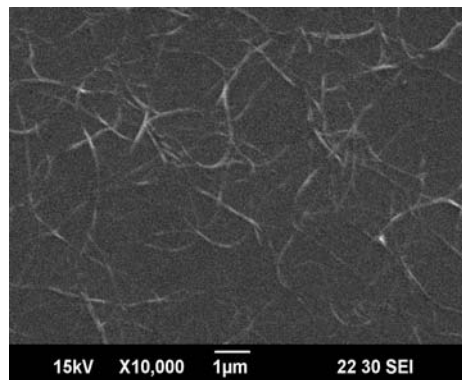


Fig.4.1. SEM view (middle of line )of SWCNTs line printed on Si substrate (CNTs: water=1:10)

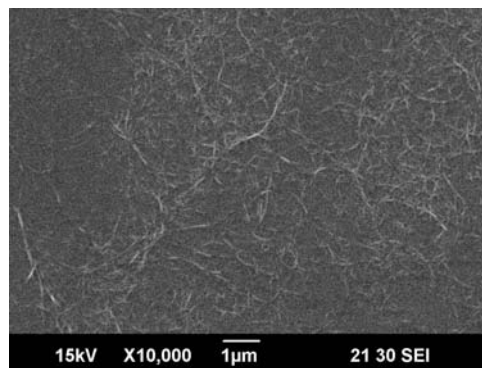


Fig.4.2. SEM view (between edge and

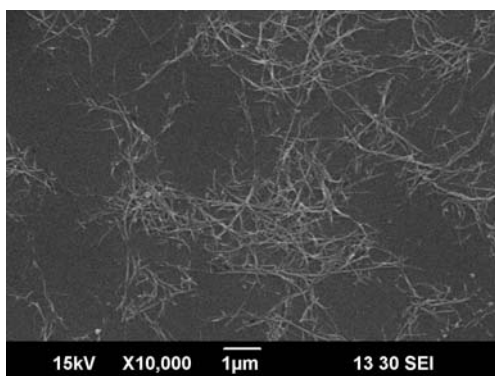


Fig.3. SEM view of SWCNTs line printed on Si substrate (CNTs:water=1:30)

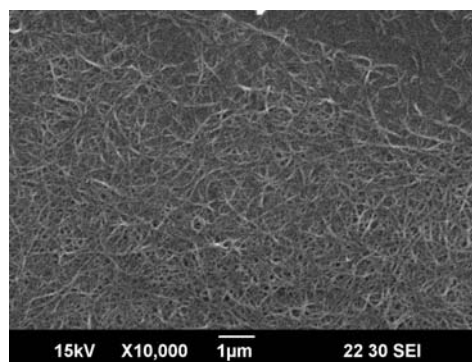


Fig.4.3. SEM view (at the edge of line )of SWCNTs line printed on Si substrate (CNTs: water=1:10)

#### 4. RESULTS AND DISCUSSION

The sensitivity of the sensors were measured by exposing to different concentrations of NO<sub>2</sub> gas. The sensitivity was measured based on change in electrical resistance of the sensor due to exposure to the target gases using the following equation. Sensitivity, S is defined as

$$S = \frac{R - R_0}{R_0} \times 100\% \quad (1)$$

, where  $R$  is the resistance of the sensor in the NO or NO<sub>2</sub> gas and  $R_0$  is the resistance of the sensor in air or N<sub>2</sub> gas. The prepared SWCNTs sensor was annealed in air for three hours, at 150°C to stabilize its gas sensing characteristics. The two terminals of the sensor electrodes were contacted with thin copper wire using silver paste to connect with sensor measurement circuit of the chamber. The resistance of the sensor was found to be decreased with increasing NO and NO<sub>2</sub> gas concentration. For gas sensing, the sensor was loaded in a chamber shown elsewhere [23] and then N<sub>2</sub> was purged for 2 hours to stabilize a base measurement line. The gas responses were performed at different temperatures and also at room temperature. The sensing measurements were done for 10 -30 min exposure to gas followed by a 10 min recovery period in pure N<sub>2</sub> gas. Figs. 5 and 6 show the response for 10 ppm NO<sub>2</sub> gas of the sensors, where the 10 and 2 SWNTs lines were overwritten using SWCNTs solution (1:30), respectively. For the both sensors, resistance values were in the kΩ range and it was higher for single scanning compared to 10 times scanning. For 2 times scanning, the response was unstable compared to 10 times scanning. For 1 time scanning, the response to 10 ppm NO<sub>2</sub> gas which is not shown here. It showed that the gas sensor is sensitive to NO<sub>2</sub> gas exposure at concentration of ppm level at room temperature and atmospheric pressure. The mechanism of SWCNTs gas sensor is that SWCNTs work as p-type semiconductor and when it absorbs oxidizing gas, their electric conductance is modified by the electron transfer from SWCNTs to absorbed molecules.

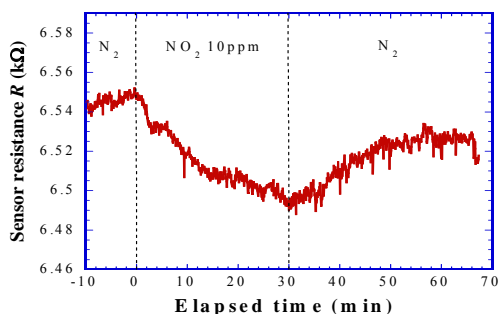


Fig.5. SWCNTs line gas sensor (ratio 1/30 and 10 times scanning) response to 10 ppm NO<sub>2</sub> gas at room temperature.

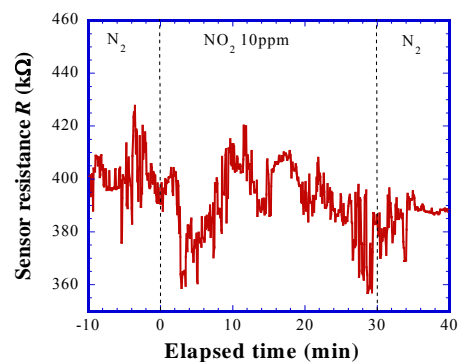


Fig.6. SWCNTs gas sensor (ratio 1:30 and 2 times scanning) response to 10 ppm NO<sub>2</sub> gas at room temperature

Figs.7 and 8 show response of the SWCNTs sensors at room temperature, where SWCNTs lines were put line for 1 and 2 times scanning, respectively using CNT ink (ratio 1:10). For 1 time scanning, the response was not good but for 2 times scanning the response was good to NO<sub>2</sub> gas.

Fig.8 showed that the detection level of sensors was reached to 1 ppm NO<sub>2</sub> with uniform performances at room temperature and atmospheric pressure. The sensitivity was obtained to be 5.0% for 1 ppm NO<sub>2</sub> and it was decreased to 4% and 3% for increasing the

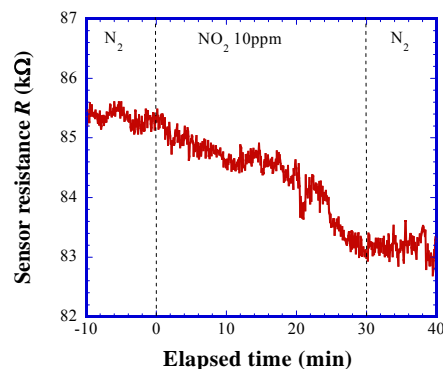


Fig.7. SWCNTs sensor (ratio 1/10 and 1 time scanning) response to 10 ppm NO<sub>2</sub> gas at room temperature and atmospheric pressure.

concentration to 5 ppm and 10 ppm respectively. The electrical resistance of the films decreases with increase in the number of absorbed molecule. Inkjet printing method controls the density of SWCNTs on the substrate and may result in control of resistances. Sensors containing less dense SWCNTs showed higher sensitivity compared to the denser SWCNTs. Detecting target gas at atmospheric condition is an advantage in sensor operation and fabrication as well by simplifying the structures. It applies that the controlling exposing surface area by partially overlapping the droplets of



SWCNTs by inkjet printing process may accelerate the reaction to molecules to improve response time and sensitivity without heating or vacuum. From the above results, SWCNTs sensor prepared with ratio of 1:10 SWCNTs with 2 times scanning single line is the best out of other sensors prepared with other ratios and scanning times.

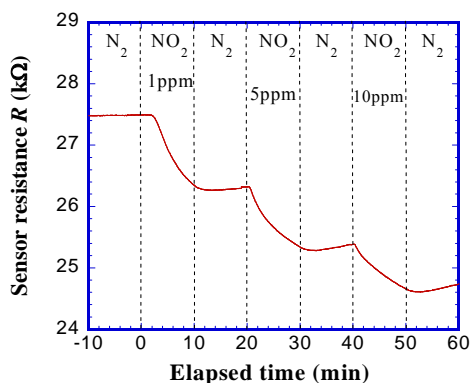


Fig.8. SWCNTs gas sensor (ratio 1:10 and 2 times scanning) response to 1-10 ppm NO<sub>2</sub> gas at room temperature.

## 5. CONCLUSION

SWCNTs gas sensors were prepared by inkjet printing method successfully for air pollutant NO<sub>x</sub> gas monitoring. SEM measurement showed presence of carbon nanotube on the sensor prepared by inkjet printing process. Raman Spectroscopy also confirmed SWCNTs by measuring spectra in the RBM range. From electrical measurement of resistance, i.e., the conductivity, response to NO<sub>2</sub> gas was confirmed. By this method it is possible to fabricate a large amount of gas sensors in a short time with high efficiency. This method is effective to deposit small amount of CNTs at atmospheric pressure and temperature in a designed pattern to fabricate gas sensor with improved sensitivity and response time. SWCNTs sensor prepared with ink CNT ratio of 1:10 with 2 times scanning showed the best performance out of other sensors prepared in this experiment. It has advantages to print droplet of SWCNTs with partial overlapping which may improve the conductance and response time. The prepared sensors showed a response in the range of ppm level of NO<sub>2</sub> gas and it can be apply for detection of NO<sub>x</sub> gas in air at room temperature. By controlling the amount of SWCNTs further and by removing the metallic or graphite property from the SWCNTs it may be possible to detect NO<sub>x</sub> gas in the range of 100 ppb or less with faster response and recovery time.

## 6. REFERENCES

1. Iijima, S., 1991, "Helical Microtubes of Graphite Carbon". *Nature*, 354:56-8.
2. Baughman R.H., Zakhidov A.A. and De Heer, W.A., 2002, "Carbon Nanotubes--the Route Toward Applications", *Science*, 297 : 787-792.
3. Nguyen H.-Q. and Huh, J.-S., 2006, Behavior of Single-walled Carbon Nanotube-based Gas Sensors at Various Temperatures of Treatment and Operation", *Sens. Actuator B* 117: 426-430.
4. Valentini, L., Armentano, I., Kenny, J.M., Cantalini, C., Lozzi L. and Santucci, S., 2003, "Sensors for Sub-ppm NO<sub>2</sub> Gas Detection Based on Carbon Nanotube Thin Films", *Appl. Phys. Lett.* 82: 961-963.
5. Sayago, I., Terrado, E., Lafuente, E., Horrillo, M.C., Maser, Benito, W. K., Navarro, A.M., Urriolabeitia, R., Martínez, E.P. and Gutiérrez, J., 2005, "Hydrogen Sensors Based on Carbon Nanotubes Thin Films", *Synth. Met.*, 148: 15-19.
6. Chopra, S., Pham, A., Gaillard, J., Parker, V. and Rao, A.M., 2002, "Carbon-Nanotube-Based Resonant-Circuit sensor for Ammonia", *Appl. Phys. Lett.*, 80: 4632-4634.
7. Kong, J., Franklin, N.R., Zhou, C., Chapline, M.G, Peng, S., Cho, K., and Dai, H., 2000, *Science*, 287: 625-662.
8. Breuer, J., Waidelich, F., Irtel, C., Von Brenndorff, Sieverding, L., Rosendahl, W., Baden, W., Gass, M. and J. Apitz, J., 1997, "Technical considerations for inhaled nitric oxide therapy: time response to nitric oxide dosing changes and formation of nitrogen dioxide", *Eur. J. Pediatrics*, 156: 460-462.
9. Meléndez, V., De Castro, A.J., López, F. and Meneses, J., 1995, "Spectrally Selective Gas Cell for Electrooptical Infrared Compact Multigas Sensor", *Sens. Actuator A* 47: 417-421.
10. Service, R.F., 2004, *Science* 304: 675.
11. Calvert, P., 2001, "Ink-jet Printing for Materials and Devices", *Chem. Mater.* 13:3299-3305.
12. Tekin, E., De Gans, B.J. and Schubert, U.S., 2004, "Ink-jet Printing of Polymers—from Single Dots to Thin Film Libraries", *J. Mater. Chem.* 14: 627-2632.
13. Segal, E., Tchoudakov, R., Narkis, M., A. Siegmann, A. and Wei, Y., 2005, "Polystyrene/Polyaniline Nanoblends for Sensing of Aliphatic Alcohols", *Sen. Actuators B*, 104 :140-150.
14. Moldovan, C., Hinescu, L., Hinescu, Iosub, M.R., Nisulescu, M., Firtat, B., Modreanu, M., Dascalu, D., V. Voicu, V. and C. Tarabasanu, C., 2003, "Silicon Micromachined Sensor for Gas Detection", *Mater. Sci. Eng. B* 101: 227-231.
15. Fujii, A., Mizukami, H., Hashimoto, Y., Umeda, T., Nishihara, Y., Ozaki, M. and Yoshino, K., 2005, "Highly Efficient Photovoltaic Cells Composed of Interpenetrating Conducting Polymer/c60 Heterojunction", *Synth. Met.* 152:121-124.



16. Zhang, Y., Guan, Y., Liu, J., Xu, J. and Cao, W., 2002, "Fabrication of Covalently Attached Conducting Multilayer Self-assembly Film of Polyaniline by In situ Coupling Reaction", *Synth. Met.* 128: 305–309.
17. Chatzandroulis, S., Andreadis, N., Goustouridis, D., Quercia, L., Raptis, I. and Beltsios, K., 2007, "Composite Chemical Sensors Based on Carbon-filled Patterned Negative Resists", *Jpn. J. Appl. Phys. B* 46: 6423–6428.
18. Bietsch, A., Zhang, J., Hegner, M., Lang, H.P. and Gerber, C., 2004, "Rapid Functionalization of Cantilever Array Sensors by Ink-jet Printing", *Nanotechnology*, 15: 873–880
19. Wenfeng, S., Zhao, Y. and Zhang, C., 2005, "The Preparation of ZnO based Gas-Sensing Thin Films by Ink-jet Printing Method", *Thin Solid Films* 483: 382–387.
20. McCorkle, D. L., Warmack, R. J., Patel, S.V., Mlsna, T., Hunter, S. R. and Ferrell, T. L., 2007, "Ethanol Vapor Detection in Aqueous Environments using Micro-capacitors and Dielectric Polymers", *Sens. Actuators B* 107: 892–903.
21. Carter, J.C., Alvis, R.M., Brown, S.B., Langry, K.C., Wilson, T.S., McBride, M.T., Myrick, M.L., Royall Cox, W., Grove, M.E. and Colston, B.W., 2006, "Fabricating Optical Fiber Imaging Sensors using Ink-jet Printing Technology: a pH sensor proof-of-concept", *Biosens. Bioelectron.* 21: 1359–1364.
22. Mabrook, M.F., Pearson, C. and Petty, M.C., 2006, "Inkjet-Printed Polypyrrole Thin Films for Vapour Sensing", *Sens. Actuators B* 115 : 547–551.
23. Ueda, T., Bhuiyan, M.M.H., Norimatsu, H., Katsuki, S., Ikegami, T. and Mitsugi, F., 2008, "Development of Carbon Nanotube Based Gas Sensors for NOx gas Detection Working at Low Temperature", *Physica E* 40: 2272–2272.

## 7. NOMENCLATURE

Symbol	Meaning	Unit
R	Resistance	Ohm

## 8. MAILING ADDRESS

M.M.H. Bhuiyan  
 Institute of Nuclear Science and Technology,  
 Bangladesh Atomic Energy Commission,  
 Ganak Bari, Savar, P.O.Box.3787,  
 Dhaka-1000, Bangladesh

## ESTIMATION OF VEHICLE INDUCED EMISSIONS OF SELECTED URBAN AREAS IN DHAKA CITY

Armana Sabiha Huq

Accident Research Institute, BUET, Dhaka, Bangladesh.

### ABSTRACT

This study is devoted to assess vehicle induced pollutants ( $\text{NO}_2$ ,  $\text{CO}_2$  and  $\text{SO}_2$ ) in roadside dust and water from fifteen locations in Dhaka City which is carried out by lab experiments. Variation in estimated values of  $\text{NO}_2$ ,  $\text{CO}_2$  and  $\text{SO}_2$  are presented in bar chart. Maximum value of  $\text{NO}_2$  is found to be 0.21 ppm from road side dust at Sayedabad and minimum value is 0.011 ppm from road side water at Nilkhat areas. Maximum value of  $\text{CO}_2$  collected from road side water is found to be 29 ppm at Malibag and minimum value is 3 ppm from road side dust at Nilkhat. The maximum and minimum values of  $\text{SO}_2$  is found to be 49 ppm from road side dust at Sayedabad and 2.01 ppm from road side water at Mugdapara respectively. Expectedly it is observed that the estimated values of vehicle induced pollutants ( $\text{NO}_2$ ,  $\text{CO}_2$  and  $\text{SO}_2$ ) are higher where traffic stream comprises larger sized vehicles i.e. buses, truck etc. Results suggest that in order to tackle vehicle induced pollutants related environmental problems, both vehicle maintenance practice and fuel system should be improved.

**Keywords:** Air Pollution, Emission, Assessment, Traffic, Roadside, Dhaka City.

### 1. INTRODUCTION

An increase in the human population is accompanied with a great increase in the need for the transportation of people and goods, traffic volumes have correspondingly increased. While industrial and domestic emissions have fallen, motor vehicle use has increased, and as a result transportation has rapidly become a dominant source of pollution, particularly in urban environment. Thus the assessment of these emissions to pollution level of urban air is of great interest.

Dhaka City is beset with a number of socio-environmental problems. Of them, increasing emission from the motor vehicles is one of the worst problems posing a serious health threat to the city dwellers. In fact, the main contributor of the deteriorating air quality in city is this transport sector followed by uncontrolled and excessive emission from the huge number of motor vehicles. In addition to the excessive carbon, the amount of other harmful elements like the Suspended Particulate Matter (SPM),  $\text{SO}_x$ ,  $\text{NO}_x$  were found in an intimidating level and the situation is deteriorating day by day. Vehicle pollutants are now regarded as a greater problem than the coal-related emissions whose concentrations are diminishing (Faiz, A. 1994). Concerns about health effects have been much slower in the developing countries than the developed ones (Watkins, H. 1991). Present situation of Dhaka city due to vehicle emissions are as follow:

- The five major primary pollutants of air, including Suspended Particulate Matters (SPM),  $\text{SO}_x$ ,  $\text{NO}_x$ ,

$\text{CO}$ , and Hydrocarbons, account for more than 90 percent of air pollution in the Dhaka City.

- At present Dhaka is the most densely populated city with 12 million people. The life of these people is at stake due to this severe air pollution. About 80 percent of the people are suffering from air pollution related diseases whereas this rate is only 18 percent in the rural areas. The lead level in the blood of the city children is found abnormally high.
- The CO base environmental capacity of vehicles is over-saturated.
- Automobile emissions, particularly unburned carbon, smoke, soot, fumes etc constitute particulate in air. Unburned hydrocarbons and their photochemical reactions involving oxides of nitrogen produce smog.
- A major source of emission of nitrogen oxides is also the exhaust from motorized vehicles.
- The most severe harmful effects of exhaust gas emissions are the formation of tropospheric ozone ( $\text{O}_3$ ), photochemical smog, acid rain, vegetation injuries, and effects on human health.

Development of efficient Transport-Environment interaction requires rigorous planning, appropriate methodology and finally broader technical backup e.g. software related to Transport-Environment interaction which helps to assess the impact of vehicle emissions from numerous source types. The purpose of this paper is to assess the effect of vehicle emissions on the environment.

The Specific Objective of proposed paper is to estimate the concentration of vehicle emissions (SO<sub>2</sub>, NO<sub>2</sub>, and CO<sub>2</sub>) in roadside Dust and Water at different locations in Dhaka City.

## 2. METHODOLOGY

According to the objective, the measurement procedure for concentration of CO<sub>2</sub>, NO<sub>2</sub> and SO<sub>2</sub> are described below:

### 2.1 Procedure for Estimation of the Concentration of Carbon Dioxide

Reagent:

- Phenolphthalein indicator
- Standard N/44 NaOH

Apparatus:

- Beaker : 2 pc
- Measuring Cylinder : 1 pc
- Dropper : 1 pc
- Stirrer : 1pc
- Burette : 1pc

Procedure:

- 100 ml of sample was taken into a beaker & same quality of distilled water into another beaker. 10 drops of Phenolphthalein indicator were added into each beaker, (if a pink color develops, no CO<sub>2</sub> is present in the sample), otherwise, we have to go to the next step. CO<sub>2</sub> was present in the collected sample.
- N/44 NaOH solution was added from a burette to the sample & it was stirred gently until a slight permanent pink color appears as compared with the distilled water. The ml of NaOH used was recorded.

Calculation:

$$\text{CO}_2 \text{ (mg/L)} = (\text{Multiplying Factor} * \text{ml. of N/44 NaOH added})$$

Where,

$$\text{MF} = \text{normality of NaOH} * \text{equivalent weight of CO}_2 * 1000 / (\text{ml. of sample taken})$$

Concentrations of SO<sub>2</sub> & NO<sub>2</sub> are measured by Hach DR/4000 U Spectrophotometer which are as follows:

### 2.2 Procedure for Estimation of the Concentration of Nitrite

Diazotization Method (Using Powder Pillows) USEPA Approval, (May 1, 1979): In Hach DR/4000 U Spectrophotometer, the estimated detection limit for programs 2610 and 2620 are 0.0008 and 0.004 mg/L NO<sub>2</sub><sup>-</sup> - N, respectively.

Reagent:

- One NitriVer 3 Nitrite Reagent Powder Pillow

Procedure:

- The soft key under HACH PROGRAM was pressed. The stored program number was selected for low rang nitrite by pressing 2610 with the numeric keys.
- The display was shown: HACH PROGRAM: 2610 NITRITE, LR. The wavelength (λ), 507 nm was automatically selected.
- A sample cell with 10ml of sample was filled.

- The contents of one NitriVer 3 Nitrite Reagent Powder Pillow were added. Stopper. The cell was shaken to dissolve. (A pink color was developed which indicated the presence of nitrite)
- The soft key under SHIFT TIMER was pressed.
- When the timer was beeped (after 20 minutes reaction time), a second sample cell with 10 ml of sample (the blank) was filled. Then the blank was placed into the cell holder.
- The soft key under ZERO was pressed. Then the display was shown: 0.0000 MG/L NO<sub>2</sub><sup>-</sup> - N.
- The stopper was removed. The prepared sample was placed into the cell holder. Then the light shield was closed. Finally the result in mg/L nitrite nitrogen (NO<sub>2</sub><sup>-</sup> - N) was displayed.

### 2.3 Procedure for Estimation of the Concentration of Sulfur Dioxide

Methylene Blue Method USEPA Approval, (May 1, 1979): In Hach DR/4000 U Spectrophotometer, the estimated detection limit for program 3500 is 800µg/L S<sub>2</sub><sup>-</sup>.

Reagent:

- Sulfide 1
- Sulfide 2

Procedure:

- The soft key under HACH PROGRAM was pressed. The stored program number was selected for sulfide (S<sub>2</sub><sup>-</sup>) by pressing 3500 with the numeric keys.
- The wavelength dial was rotated until the small display was shown: 665 nm. Then the display was quickly shown: ZERO SAMPLE. Then: mg/L S<sub>2</sub><sup>-</sup>.
- A clean sample cell was filled with 25 ml of sample.
- A second sample cell was filled with 25ml distilled water.
- 1 ml of Sulfide 1 Reagent was added into each cell. Swirled to mix.
- 1 ml of Sulfide 2 Reagent was added into each cell. Swirled to mix.
- The soft key under SHIFT TIMER was pressed.
- When the timer was beeped (after 5 minutes reaction time), the blank was placed into the cell holder. Then the light shield was closed.
- The soft key under ZERO was pressed. Then the display was shown: 0.0000 MG/L S<sub>2</sub><sup>-</sup>.
- The prepared sample was immediately placed into the cell holder. Then the light shield was closed. Finally the result in mg/L sulfide (S<sub>2</sub><sup>-</sup>) was displayed.
- Estimated amount of sulfide reacted with oxygen to form SO<sub>2</sub>.

## 3. EXPERIMENTAL RESULTS AND ANALYSIS

From the experimental lab test, variation in estimated values of NO<sub>2</sub>, CO<sub>2</sub> and SO<sub>2</sub> in road side water are presented in Table 1 and Fig 1a to Fig 1c. Besides, Table 2 and Fig 1d to 1f shows variation of the concentration of NO<sub>2</sub>, CO<sub>2</sub> and SO<sub>2</sub> in road side dust.

Table 1: Vehicle emissions in road side water

Locations	Concentration of Nitrogen-dioxide (NO <sub>2</sub> ) in ppm	Concentration of Carbon-dioxide (CO <sub>2</sub> ) in ppm	Concentration of Sulfur-dioxide (SO <sub>2</sub> ) in ppm
Naya Palton	0.08	15.5	10.15
Segun Bagicha	0.10	18.0	11.00
Bijoy Nagar	0.091	17.0	13.00
Motijheel Ba. Bank	0.12	22.1	12.10
Rajar Bagh	0.015	13.0	3.11
Shahjahanpur	0.106	23.0	10.00
Khilgaon R. Crossing	0.113	20.0	10.03
Mugdapara	0.012	14.1	2.02
Azimpur	0.011	15.0	2.10
Nilkhate	0.011	15.3	1.90
Newmarket	0.05	16.0	50.00
Malibag	0.10	29.0	16.00
Sayadabad	0.09	25.0	15.00
Jatrabari	0.013	12.6	5.03
Bokshi Bazar	0.095	16.9	3.01

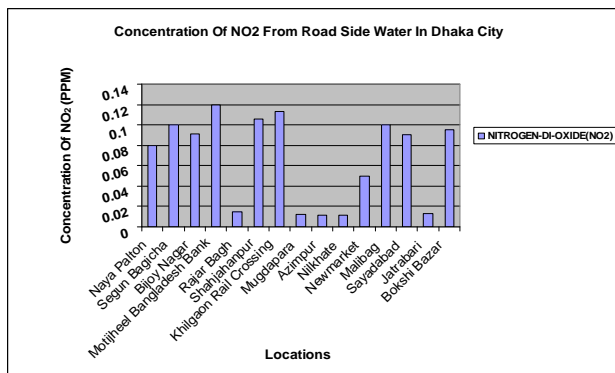


Fig 1a. Concentration of NO<sub>2</sub> from Road Side Water at Different Locations in Dhaka City

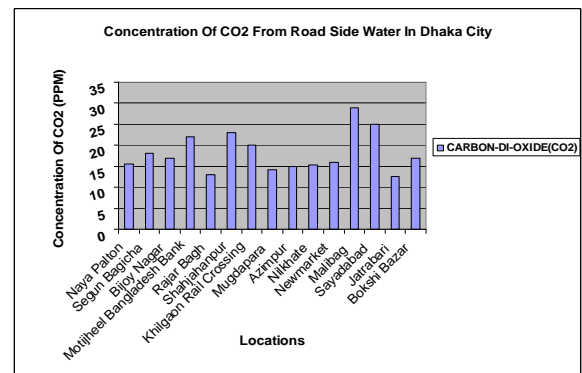


Fig 1b. Concentration of CO<sub>2</sub> from Road Side Water at Different Locations in Dhaka City

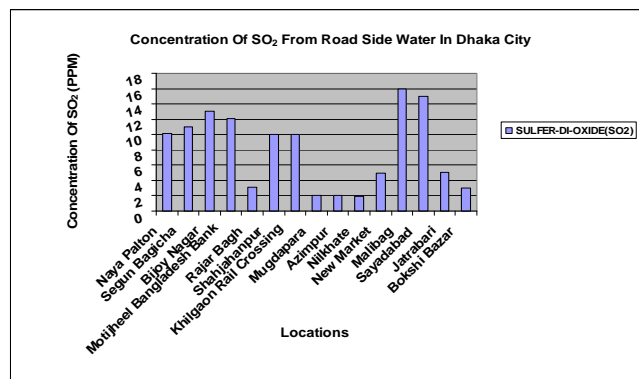


Fig 1c. Concentration of SO<sub>2</sub> from Road Side Water at Different Locations in Dhaka City

From Fig. 1a to 1c, among fifteen observed locations in and around Dhaka City, the concentration of NO<sub>2</sub> found in Road Side Water ranges from 0.011 to 0.12 ppm. The concentration of CO<sub>2</sub> in Road Side Water ranges from 12.6 to 29.0 ppm where as measured concentration of SO<sub>2</sub> varies from 5.03 to 16.0 ppm.

Close observation of Fig. 1a to 1c reveals that road side water collected from Bangladesh Bank areas contains maximum concentration of NO<sub>2</sub> and water collected from Azimpur areas shows minimum concentration of NO<sub>2</sub>. From the same Figures it is also observed that maximum and minimum concentrations of

both CO<sub>2</sub> and SO<sub>2</sub> are found in road side water gathered from the Malibug and Jatrabari areas respectively.

In this study the previous mentioned analysis is also made for road side dust collected from different selected locations of Dhaka City. The results on variation in estimated values of NO<sub>2</sub>, CO<sub>2</sub> and SO<sub>2</sub> in road side dust

are presented in Table 2 and Fig 1d to Fig 1f. From close observation of Table 2, it is evident that the concentrations of NO<sub>2</sub>, CO<sub>2</sub> and SO<sub>2</sub> range from 0.109 - 0.21 ppm, 3.0 - 6.2 ppm and 19.4 - 49.0 ppm respectively for different locations of study area.

Table 2: Emissions of vehicles from road side dust in dhaka city

Locations	Concentration of Nitrogen-dioxide (NO <sub>2</sub> ) in ppm	Concentration of Carbon-dioxide (CO <sub>2</sub> ) in ppm	Concentration of Sulfur-dioxide (SO <sub>2</sub> ) in ppm
Naya Palton	0.11	3.8	29.0
Segun Bagicha	0.12	4.1	32.5
Bijoy Nagar	0.13	4.2	36.0
Motijheel B. Bank	0.16	5.0	42.0
Rajar Bagh	0.13	4.0	20.2
Shahjahanpur	0.15	4.0	31.0
Khilgaon R. Crossing	0.20	4.5	45.0
Mugdapara	0.20	4.1	46.1
Azimpur	0.11	3.1	21.0
Nilkhate	0.109	3.0	19.4
Newmarket	0.15	3.4	21.3
Malibag	0.15	5.0	30.2
Sayadabad	0.21	6.0	49.0
Jatrabari	0.20	6.2	48.3
Bokshi Bazar	0.19	3.8	41.1

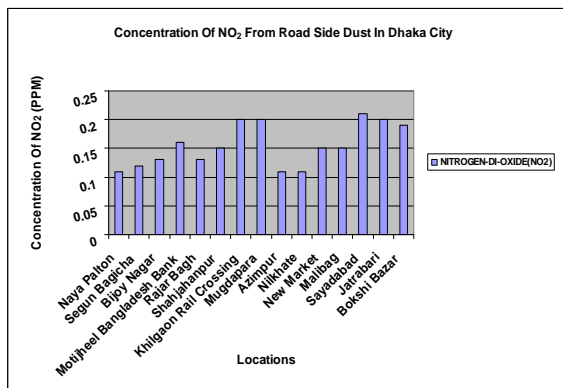


Fig 1d. Concentration of NO<sub>2</sub> from Road Side Dust at Different Locations in Dhaka City

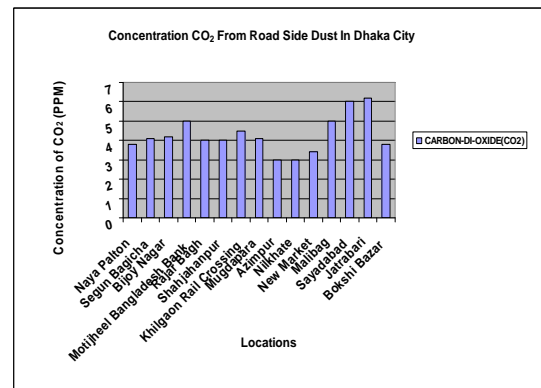


Fig 1e. Concentration of CO<sub>2</sub> from Road Side Dust at Different Locations in Dhaka City

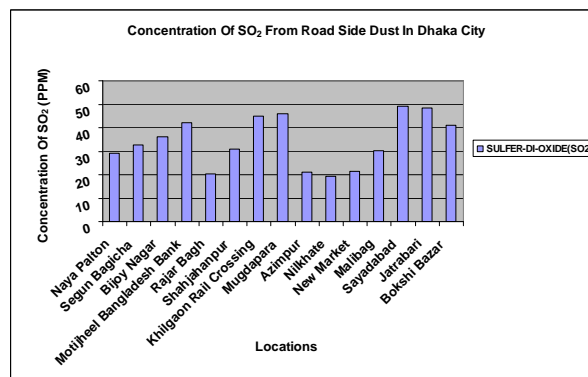


Fig 1f. Concentration of SO<sub>2</sub> from Road Side Dust at Different Locations in Dhaka City

Fig. 1d to Fig. 1f shows that the maximum and minimum concentrations of NO<sub>2</sub> and SO<sub>2</sub> in road side dust are observed at Sayedabad and Nilkhat areas respectively. Whereas, the maximum and minimum concentration of CO<sub>2</sub> are found in Jatrabari and Nilkhat areas respectively.

Therefore, from the above analysis it is observed that the maximum value of NO<sub>2</sub> is 0.21 ppm from road side Dust at Sayedabad and minimum value is 0.011 ppm from road side water at Nilkhat. Maximum value of CO<sub>2</sub> is 29 ppm from road side Water at Malibag and minimum value is 3 ppm from road side Dust at Nilkhat. Maximum value of SO<sub>2</sub> is 49 ppm from road side Dust at Sayedabad and minimum value is 2.01 ppm from road side water at Mugdapara.

#### 4. CONCLUSIONS

This paper was motivated by poor environmental pollution situation prevailing in Dhaka City. Although there exist plethora of opinions regarding improvement of the situation, only few studies had been done on this issue. Due to the lack of scientific and engineering basis, most of the measures undertaken in order to assess the situation failed to produce desired result. In fact, to improve the situation a comprehensive planning is required incorporating various planning options and analyzing their impacts. In this research work attempt had been made to investigate on vehicle induced pollutants (NO<sub>2</sub>, CO<sub>2</sub> and SO<sub>2</sub>) from dust and water collected from different locations of Dhaka City. Details of analyses results are presented in the earlier section. On the basis of the analyses, summary of important findings and recommendations for future probable research study are presented in the following section.

##### 4.1 Findings of the Paper

From investigation on vehicle induced pollutants like NO<sub>2</sub>, CO<sub>2</sub> and SO<sub>2</sub> collected from fifteen different locations of Dhaka City reveals that:

- Maximum value of NO<sub>2</sub> is 0.21 ppm in road side dust at Sayedabad and minimum value is 0.011 ppm from road side water at Nilkhat.
- Maximum value of CO<sub>2</sub> is 29 ppm in road side water at Malibag and minimum value is 3 ppm from road side Dust at Nilkhat.
- Maximum value of SO<sub>2</sub> is 49 ppm in road side dust at Sayedabad and minimum value is 2.01 ppm from road side water at Mugdapara.

The above finding suggests that the estimated values of vehicle induced pollutants (NO<sub>2</sub>, CO<sub>2</sub> and SO<sub>2</sub>) are higher where traffic stream comprises larger sized vehicles i.e. buses, truck etc. Which definitely implies that to tackle vehicle induced pollutants related environmental problems, besides congest management both vehicle maintenance practice and fuel system should be improved.

#### 5. RECOMMENDATIONS

In Bangladesh air pollution monitoring is a very recent phenomenon. Therefore, extensive study on this topic is essential. This is a multi-disciplinary topic. Therefore, people of different disciplines like Engineers, Chemists, Doctors, Geologists, Botanists, etc. should be engaged to this particular study. Undoubtedly, this study has many limitations in terms of data collections, coverage and assumptions. Consequently, in order to acquire better assessment of the impact of vehicle emissions, the study should consider the following suggestions:

- The further study should be like that estimation of the distance of how far a sophisticated building (Hospital, residential are, schools etc) should be installed from roadside to reduce the severity of affected people from air pollution.
- For analyzing the impacts of vehicle emissions a comprehensive planning is essential to incorporate various planning options.
- Reliable and sophisticated equipments should be procured to collect various pollutant concentrations from vehicle emission. Moreover, data should be collected instantaneously.
- Along with vehicle emission estimation, more comprehensive studies should be carried out to find out the effects of changes in the air pollution.
- It is recommended that for mitigation of vehicular emission problems the 3Es approach should be persuaded. Besides Engineering study, both Educational and Enforcement measures ought to be taken to build general awareness among the public as well as to warn the polluters.

#### 6. REFERENCES

1. Faize, A., Walsh, M.P. and Weaver, C.S. (1996), "Air Pollution from Motor Vehicle", The World Bank (WB), Washington, D.C.
2. Watkins, H. (1991), "Air Pollution from Road Vehicle", TRRL, State of the Art Review, U.K.
3. EPA publication, <http://www.epa.vic.gov.au>.
4. Huq, A.S. (2006), "Assessment of Vehicle Induced Pollution by Indirect Measurement in Dhaka City", B.Sc. Engineering Thesis, Department of Civil Engineering, BUET, Dhaka.
5. Raw, S. (1994), "Environmental Pollution Engineering", Wiley Western Limited.

#### 7. MAILING ADDRESS

Armana Sabiha Huq  
Junior Research Fellow/Lecturer,  
Accident Research Institute, BUET  
Dhaka, Bangladesh.

## TIME STUDY OF A FURNITURE INDUSTRY: A CASE STUDY AT NAVANA FURNITURE INDUSTRY

Seratun Jannat<sup>1</sup>, M. Mazharul Hoque, Nazia Sultana, I. Jahan Chowdhury

Department of Industrial and Production Engineering,  
Bangladesh University of Engineering and Technology, Dhaka-1000, Bangladesh

### ABSTRACT

Manufacturing industries are now facing challenges with its competitors and day by day competition is escalating. To deal with these challenges, they have to improve their production efficiency, reduce operations time and incurred cost for each operation. They need to regulate over their production process to continue their production schedule, workforce planning, estimating labor cost, budgeting and time standard for operating a job. To execute all of these efficiently time study is one of the crucial operation need to perform. This paper focuses on developing a time study for a reputed furniture industry. The objective is to establish a time standards for carrying out specified job and thus helping the company in scheduling.

**Keywords:** Time study, Layout design, Cycle time.

### 1. INTRODUCTION

Analysis of operations required to produce a manufactured article in a factory, with the aim of increase efficiency. Each operation is studied minutely and analyzed to set up a benchmark time and it will helpful for production schedule, forecasting etc.

The first effort at time study was made by F. W. Taylor in the 1880s. He published his famous article “The Principle of Scientific Management” which involved getting the best person for each job and trained them to do it in the best possible way. In the early twentieth century Frank and Lillian Gilbreth developed a more systematic and sophisticated method of time study for industry taking into account the limits of human physical and mental capacity and the importance of good physical environment[1]. One problem of time study is the Hawthorne Effect where it is found that employees change their behavior when they know that their being measured. Work Study has conducted in many sectors. One of the hallmarks of leading-edge organizations – be they public or private – has been the successful application of performance measurement to gain insight into, and make judgments about, the organization, and the effectiveness and efficiency of its programmers, processes, and people[2]. To improve productivity and efficiency this technique has been widely used. It is suggested that these techniques are applicable to libraries and librarians and will become increasingly useful as the problems of increased work loads become more severe [3]. Work study is widely used for garments sector in Bangladesh. Time and motion study is used in

radiotherapy[4]. It is also used to reduce accidental cause [5]. A case study on purchasing is also performed by R. Schmelzlee[6].

Though Time Study in furniture industry is not performed yet so the focus of the study is on furniture industry. In Bangladesh furniture industry is growing day by day. They are designing new and new product in every minute. Sometimes they don't know how much time it will take to manufacture the product, they are not sure whether they can accomplish their order within time. The endeavor of this study is to make a clear idea of how much time it will take to manufacture the product. Manufacturer will get a clear idea about the required time to manufacture. This will reduce uncertainty of the industry and planning and scheduling will be trouble-free.

### 2. TIME STUDY: PURPOSE AND PROCEDURE

The technique of random sampling used for analysis of the time spent for rendering each phase of various professional work or services performed by worker of service man is known as time measuring or needed time to perform a work. Organization develops time standards in a number of ways. Most common work measurements are Stopwatch time study, historical time study, predetermined data and work sampling. Among them stopwatch time study is used most frequently. The basics steps in a time study are

- Define the task to be studied and inform the worker will be studied
- Determine the number of cycles to observe



- Time the job and rate the worker performance
- Compute the standard time

Besides the above there are strategies on time study which makes it more efficient. These are:

- Develop a block of time study
- Schedule weekly review and updates
- Prioritize assignment
- Develop a alternative study places free from distractions
- Note every single “Dead Time”
- Review studies and reading just before which was done on previous day
- Schedule special time for critical operations

Time Study will help a manufacturing company to understand its production, investigate the level of individual skill, planning and production control system etc.

### 3. CASE STUDY:

Time study for any furniture industry is very much crucial. The laminated Board (LB) Section of a furniture industry consist of some heavy machines like Auto Panel Saw (APS), Sliding Saw Machine (SSM), Double End Tenoning Machine (DETM), Straight Edge Banding Machine (SEBM), Multiboring Machine (MB), Router Machine (RM), Profile Edge Banding Machine(PEBM) etc. Laminated Board is processed through these machines in various stages. Time Study for each machine is carried out in almost with the same process. The basics time required for each machines are:

- Material loading time
- Machine operation time
- Material unloading time

Material loading time consists of the following things:

- Grasp
- Hold
- Positioning
- Gauge set up time

Machine operation time consists of the following:

- Feed
- Machine operation (depends on cutter travel speed, travel length.)

Material unloading time consists of the following:

- Hold
- Release

### 3.1 Auto Panel Saw and Sliding Saw Machine:

#### Loading Time:

Let,

Initial set up time =  $S_t$  sec

Initial material loading time =  $L_t$  sec

Average intermediate material loading time =  $L_m$  sec

So observed time for a single board input

$$= (S_t + L_t + L_m \times m) \text{ sec ... (1)}$$

Where  $n$  = no. of intermediate loading

If boards are to be input for  $N$  no. of time in a whole lot, then, observe Time,

$$OT(Q) = N(L_t + L_m \times m) + S_t \text{ sec ... (2)}$$

$$\text{Normal Time, } NT = OT \times PR \text{ sec ... (3)}$$

Allowance factor,  $A$  = sum (delay time, personal time, rest time, fatigue time)/Working hour

$$SLT = \frac{NT}{1+A}$$

So Standard Loading Time, ... (4)

#### Unloading Time:

Let,

Average observe unloading time =  $OT(u)$  sec

Normal time for unloading =  $OT \times PR$  sec

So Standard Time for material unloading,

$$SUT = \frac{NT}{1+A}$$

Total Machining Time,

$$MT = N \times (7q_1 + 8q_2 + 9q_3 + 10q_4 + 13q_5) \text{ ... (5)}$$

Here,  $q_1, q_2, q_3, q_4,$  and  $q_5$  are no of operations for range 50-200, 200-900, 900-1500, 1500-1800, 1800-2440 from table-1 respectively

$N$  = No of board input required for one lot

Total time to complete a whole lot =  $SLT + SUT + MT$  ... (6)

### 3.2 Double End Tenoning (DET):

If the running speeds of the belt of DET remains constant  $s$  m/min and the length passed through it is  $d$  mm, then the operation time for one side input

$$= \left( d \times \frac{0.001}{s} \right) \times 60 \text{ Sec ... (7)}$$

Initial loading time,  $LT$  = (machine set up + gauge set up + dimension measurement) time

Standard loading time,  $SLT = LT \times \frac{PR}{1+A} \dots \dots (8)$

For single side tenoning of lot size N:

Total Standard Time

$$= \left( d \times \frac{0.001}{s} \right) \times 60 \times N + SLT \dots \dots (9)$$

But for double side tenoning, it is a matter of considering the difference between the two consecutive stoppers and the distance d becomes fixed depending upon the dimension to be tenoning.

First time tenoning will be same as single end tenoning

$$= \left( d \times \frac{0.001}{s} \right) \times 60 \times N + SLT \dots \dots (10)$$

During Second time tenoning,

Total Standard Time

$$= \left( d \times \frac{0.001}{s} \right) \times 60 \times N + SLT \dots \dots (11)$$

### 3.3 Straight Edge Banding Machine (SEB):

Standard time equation for Straight Edge Banding Machine is same as DET. Here one extra operation is performed and it is to cut the band in each cycle.

Let Time required for this operation =  $T_a$  sec

Standard Intermediate Set Up and Loading Time

■  $SIT$  sec

Then the Standard Time for a dimension of  $d_1 \times d_2$

And lot size of  $N$  will be

$$= \left[ \left( d_1 \times \frac{0.001}{s} \right) \times 60 + T_a \right] \times N + SLT + \left[ \left( d_2 \times \frac{0.001}{s} \right) \times 60 + T_a \right] \times N + SIT \dots \dots (12)$$

### 3.4 Multiboring Machine (MB):

Standard Time depends upon number of workers performing the job.

For two workers:

Standard Time

■  $LT + MSUT + MT + (k - 1) \times SIT \dots \dots (13)$

For three workers:

Standard Time

■  $\frac{LT}{2} + MSUT + MT + (k - 1) \times SIT \dots \dots (14)$

Here

$k$  = How many operations are performed on a single board?

= 1 for single operation

= 2 for double operations

$LT$  ■ Standard Loading Time

$MSUT$  ■ Machine Set Up Time

$MT$  ■ Machining Time

$SIT$  ■ Standard Intermediate Set Up and Loading Time

Time Study for other machines: Router Machine (RM), Profile Edge Banding Machine (PEBM) etc is same as Straight Edge Banding Machine (SEB) that is previously described.

After completing the time study of each machine it is required to measure the necessary time for assembly, cleaning, packaging. Doing all of these the required time of completing a lot of products can easily be calculated. Using this time study required operation time for existing product has been performed. And the result shows the feasibility of this time study conducted at NAVANA FURNITURE.

### 4. CONCLUSION:

Time Study revealed that it has an immense influence over factory planning. The product order usually differs in terms of quantity, material requirement, due date, processing variations, processing time difference and set up time variations. So if the industry seeks to foretell that whether they can meet up customer demand within days or not then this time study will be awfully supportive to them. If the company desires to receive orders from random clients then this study will assist them to check whether they can receive those orders or not. The intension of scheduling is to use of resources in a time frame. Planning department can use this study for trial and error schedule development to get an idea of what different arrangement would involve. Thus a tentative surgery schedule may reveal in sufficient allowance for surgery that takes longer than expected and can be revised accordingly.

The job shop scheduling is somewhat difficult. This requires two basics issues: how to distribute the workload among work centers and what job processing sequence to use. The time study can be used for preparing Gantt charts, assignment method by linear programming, sequencing.

This study can be used to maintain and ensuring the desired rate of output, time management of work shifts and overtime, material handling management, reliability in case of supply delivery, proper inventory management and proper utilization of time and space, to reduce bottleneck, over processing and over production. Further studies can be carried out to enhance its reliability. Company who seek to grow their reputation and

goodwill by sound timing of orders delivery should use this time study.

## 5. REFERENCES

1. The Columbia Encyclopedia, Sixth Edition, 2004, Columbia University Press.
2. Amaratunga, D and Baldry, D and Sarshar, M 2001, 'Process improvement through performance measurement: the balanced scorecard methodology', Work Study (renamed International Journal of Productivity and Performance Management), 50 (5), pp. 179-188.
3. Gilchrist, A, 'Work Study in Libraries', Journal of Librarianship and Information Science, Vol. 2, No. 2, 126-138 (1970).
4. Lievens, Y and Verstraete, J and Pauwels, K and Bogaert, W, V. "Time and motion study of radiotherapy delivery: Economic burden of increased quality

assurance and IMRT" Volume 93, Issue 1, Pages 137-140 (October 2009).

5. Brown, R 'Activities of accident and emergency consultants--a time and motion study' Journal of Accident & Emergency Medicine 2000; 17:122-125; doi:10.1136/emj.17.2.122, (2000).
6. Schmelzlee, R 'Work Study in Purchasing --A Case Study', journal International Journal of Food Sciences and Nutrition, Volume 12, Issue 4 Winter 1958 , pages 145 – 148.

## 6. MAILING ADDRESS

Seraton Jannat  
 Department of Industrial and Production Engineering,  
 Bangladesh University of Engineering and Technology,  
 Dhaka-1000, Bangladesh  
 E-mail: seratonjannat@ipe.buet.ac.bd

Table 1: Operation time for Auto Panel Saw for different travel length

Dimension (mm)	Range	Operation Time (observation 1)	Operation Time (observation 2)	Operation Time (observation 3)	Recommended operation time to be taken (sec)
50-200		6.5	6	7	7
200-900		7	7.5	8	8
900-1500		7.5	8.5	9	9
1500-1800		9	10	8	10
1800-2440		12	11.5	13	13

Table 2: Sample calculation of required time for completing an Executive Table

Comp	No/Pdt	Required time to complete operation at each machine (sec)											
		APS (sec)	DET (sec)	DET-1 (sec)	DET-2 (sec)	Router + band (sec)	SEB (sec)	PE (sec)	MBM (sec)	Assembly (sec)	Cleaning (sec)	packaging(sec)	Total (sec)
Top	1	41.43	23.75				18.86		108		8	37.5	237.59
Top bit	2	5.595	26.50				18.58			34	16	37.5	138.46

Side	2	26.22	26.29					86.86	74.4		16	37.5	267.27
panel	1	32.24	20.79				10.85				8	37.5	109.39
Total	6	105.5	97.38	0	0	0	48.58	86.86	182.4	34	48	150	752.71

## PROBLEM ANALYSIS AND PRODUCTIVITY IMPROVEMENT OF A KNITWEAR CUTTING SECTION: A CASE STUDY OF ABONI KNITWEAR

Seratul Jannat, M. Niaz Sharif, S. Nahar Mithy and S. Alam Khan

Department of Industrial and Production Engineering  
Bangladesh University of Engineering and Technology, Dhaka, Bangladesh

### ABSTRACT

In knitwear industry, quality product with low price is the first preference to the buyers (customers). The buyers always seek quality product from their options (all around the globe) and the manufacturers keeping the best quality gets the green signal. Bangladesh is among those who are keeping the balance between supply and demand of knitwear and other ready made garments by supplying. Its investment friendly environment, comparatively cheap labor cost, availability of resources and high interest attract the global investors to make it their second local. Previously a knitwear industry in Bangladesh faced challenges from only its local counterparts. But now due to the quota free economy the competition is among all companies around the world. For an industrialist, the challenge is to tune up the product with all desirable qualities keeping the cost minimum so that the customers' expectations are met and maximum profit can be earned. This paper focuses on the application of 5S, time study and general concepts of layout on the cutting section of a renowned knitwear industry to minimize its cost of product through keeping the quality as before. The objective of this work is to provide the case company with a methodology that allows them to improve the productivity.

**Keywords:** 5S, Time study.

### 1. INTRODUCTION

5S is the name of a workplace organization methodology that uses a list of five Japanese words which, transliterated and translated into English, start with the letter S. This list is a mnemonic for a methodology that is often incorrectly characterized as "standardized cleanup", however it is much more than cleanup. It is a method for organizing a workplace, especially a shared workplace (like a production floor or an office space), and keeping it organized. It's sometimes referred to as a housekeeping methodology; however this characterization can be misleading, as workplace organization goes beyond housekeeping.

The key targets of 5S are improved workplace morale, safety and efficiency. The assertion of 5S is, by assigning everything (that is needed) a location, time is not wasted by looking for things. Additionally, it is quickly obvious when something is missing from its designated location. Advocates of 5S believe the benefits of this methodology come from deciding what should be kept, where it should be kept, how it should be stored and most importantly how the new order will be maintained. This decision making process usually comes from a dialog about standardization which builds a clear understanding,

between employees, of how work should be done. It also instills ownership of the process in each employee.

The 5S's are:

Phase 1 - **Seiri/Sorting**: Going through all the tools, materials, etc., in the plant and work area and keeping only essential items. Everything else is stored or discarded.

Phase 2 – **Seiton/Straighten or Set in Order**: Focuses on efficiency. When we translate this to "Straighten or Set in Order", it sounds like more sorting or sweeping, but the intent is to arrange the tools, equipment and parts in a manner that promotes work flow.

Phase 3 - **Seisō/Sweeping or Shining or Cleanliness**: Systematic Cleaning or the need to keep the workplace clean as well as neat. At the end of each shift, the work area is cleaned up and everything is restored to its place. This makes it easy to know what goes where and have confidence that everything is where it should be. The key point is that maintaining cleanliness should be part of the daily work - not an occasional activity initiated when things get too messy.

Phase 4 – **Seiketsu/Standardizing**: Standardized work practices or operating in a consistent and standardized fashion. Everyone knows exactly what his or her

responsibilities are to keep above 3S's.

Phase 5 – **Shitsuke/Sustaining the discipline**: Refers to maintaining and reviewing standards. Once the previous 4S's have been established, they become the new way to operate. Maintain the focus on this new way of operating, and do not allow a gradual decline back to the old ways of operating. However, when an issue arises such as a suggested improvement, a new way of working, a new tool or a new output requirement, then a review of the first 4S's is appropriate.[1]

A time study and motion (or time-motion study) is a business efficiency technique. It is a major part of scientific management (Taylorism) [2]. Time Study or Time Measurement (MTM) is a predetermined motion time system that is used primarily in industrial settings to analyze the methods used to perform any manual operation or task and, as a byproduct of that analysis, set the standard time in which a worker should complete that task.[3] Films were taken using constant speed cameras, running at 16 frames per second, of the work performed by qualified workers on the shop floor at the Westinghouse Brake and Signal Corporation. Each sequence was rated during filming by three qualified Industrial Engineers. These ratings had to agree within a close band, otherwise the sequence was not used.

The rating, or Leveling, system used was the Westinghouse or LMS system – so called after its originators Lowry, Maynard and Stegemerten. This system considers four factors independently:

- Skill – Proficiency in following the given method
- Effort – The will to work
- Conditions – The general work surroundings
- Consistency – of performance

Each factor is assigned an alpha rating, e.g. “B-“, “C+”, “A”, etc. which has a numeric value which is applied later. This reduces the possibility of “clock rating” and ensures that all factors are considered in the composite rating. Appendix 1 shows the model for Causes of Difference in Output on which the LMS system is based. Layout, distances, sizes of parts and tools and tolerances were accurately measured and recorded on the shop floor to complement the later analyses.

The films were then projected frame-by-frame and analyzed and classified in to a predetermined format of Basic Motions. These Basic Motions were Reach, Grasp, Move, Position, Release, etc. A motion was taken to begin on the frame in which the hand first started performing the motion and was taken to end on the frame in which the motion was completed. This allowed a time for each recorded motion to be calculated in seconds, by means of a frame count, and then “leveled” to a common performance [4-5].

## 2. CASE STUDY: ABONI KNITWEAR

Aboni Knitwear, a sister concern of Babylon Group has been established in 2001. It is a joint venture knit wear project with Mens Fashion A/S, Denmark for the production of knitted fabrics and garments. It is located at Savar near Dhaka. The knit textile project has been designed with all European best Machinery and

Technical know-how. The garments unit produces about 450,000 pcs of T- shirts/Tank Tops and 300,000 pcs of Polo shirts per month depending on the styles. Its permanent customer list includes, but not limited to Tesco, Zara, H & M, Mono Prix, Wal-Mart etc.

To be a sustainable and consistent industry in knitwear sector Aboni Knitwear is working to achieve the following objectives:

- Better quality product and provide reliable support to buyers.
- Contribute in national income.
- Minimize loss and increase revenue earning to become a profitable business entity.
- Better working environment.

Different concepts of Industrial Engineering tools are employed to assess current condition of cutting section and to improve the findings. Thus, this paper will mainly concentrate on the improvement of productivity (utilizing the space of the storage of cutting section efficiently, allocating manpower in different operations of this section such as lay spreading, numbering, bundling, input-man etc., reduction of fabric wastage, utilization of time properly).

### 2.1 Overview of Cutting Section

Generally in a cutting section of knit wear industry, following steps are maintained:

1. Temporary storage of uncut fabric.
2. Lay spreading.
3. Cutting.
4. Numbering.
5. Bundling.
6. Quality check.
7. Storage of cut fabric.

## 3. PROBLEMS FOUND

### 3.1 Transferring Fabrics from Fabric Storage to Cutting Section

In the knitwear section, the fabric storage is on the 5<sup>th</sup> floor and the cutting section is on the 3<sup>rd</sup> floor. The sewing sections are in 2<sup>nd</sup> and 4<sup>th</sup> floor. Before cutting the fabrics have to be carried by the workers from the storage to cutting section. Extra manpower is used. Time wastage can also be said to be a concerning matter in this matter. If there would have been a simple means of transferring the fabrics there could be some savings in both the manpower and also in time.

This paper suggests a tunnel for transferring the fabrics from the fabric storage to the cutting section. If this tunnel is designed then the whole transferring system can be easier than the previous method. And another important fact is that the time for transferring these fabrics would also be less than the previous method.

Here, the tunnel is designed across two floors. Thus the fabrics have to be passed a long way. A concerning fact in this matter is that there might be a possibility of damage of fabrics. In that case, there has to be a system of trolley on which the fabric will fall. If the bed of the trolley is made of foam, then the damage of the fabric can be prevented.

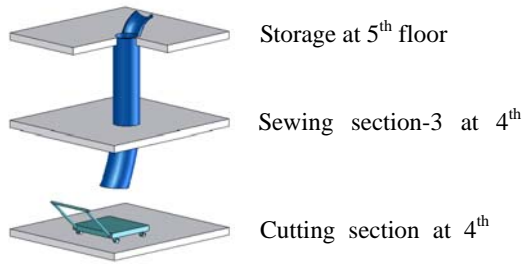


Fig 1. Transfer of fabric.

### 3.2 Storage System

The first stage of the workflow in the cutting section starts from the storage system. The fabrics are brought from the fabric storage and then stored in the sub-store. As the cutting finishes then there is also storage of finished fabrics.

In this section two types of fabrics are stored:

- Uncut fabrics
- Cut fabrics

Before cutting the sacks of fabrics are kept in a haphazard way here and there. So when any fabric is scheduled to cut workers find the appropriate fabric from pile of sacks which wastes time. Besides, workers sometimes select wrong fabric and start cutting which results direct waste of fabric.

In this paper it is suggested to-

- Use selves which are arranged near the cutting table so that the nonproductive time to bring the fabric to cutting table is minimized.
- Arrange fabrics according to their cutting schedule.
- Use different shelves and sacks of different colors for different buyers.
- Use bin card to identify the exact fabric easily.

After cutting the cut fabric are numbered and bundled into sacks again and are kept randomly. The input men of sewing section bear the cut fabrics to the sewing floor according to their sewing schedule. It was observed that nearly half of their time the input men pass in searching the particular sack of fabric. In this paper the shelves for finished fabrics are suggested to be near the exit of the cutting floor which may significantly reduce the wastage

of time.

### 3.3 Problems Faced In Lay Spreading

It was observed that there is no definite rule for allocating workers in the operation of spreading lay. Most of the time 4/5 workers are on each side of the fabric; thus 8-10 workers on the both sides of the fabric. One worker is in the position of throwing fabric and scissoring. And another worker is opposite to this worker (in case of fabric of width more than 60 inch this number is two). Thus a total of 10-12 workers are around fabrics while spreading lays.

The time for each worker to finish their respective jobs was taken, for example the time for the worker to throw the fabric, the time for spreading the lay and level it, the time for scissoring. After studying the workers for a certain time, it was decided that excess workforce is being used in lay spreading. The decision comes from the following points:

- The workers are not acting effectively.
- The work range for each worker is less than enough. They only move their hands to spread. But if they move themselves too they can work in a large range.
- While spreading a fabric of a dia/ width very much less than the width of table the workers have to sit on the table in one side.
- Though sometimes fabrics of about 70-75 inch are dealt with, but maximum time the width of the fabrics are below 50 inch. While spreading these 48 inch width lay workers have to sit down in one side of the table. When labors sit, their comfort zone of working becomes limited. So, excess labors are needed to spread lays.
- When working in the tables of 7ft or 8ft the lays are spread in one side of the table so that at least in one side of the table labors can stand and work comfortably. In such situations on the other side of the table no other lay can be set to spread. For example, if a 48 inch lay is being set in one side of the 84 inch table the remain space is not enough for setting another lay. So there is no difference between a table appropriate for 48in lay and a table of 84in or 96in rather the later one is consuming more space and allows the worker to sit on the table for spreading with in ergonomically harmful.



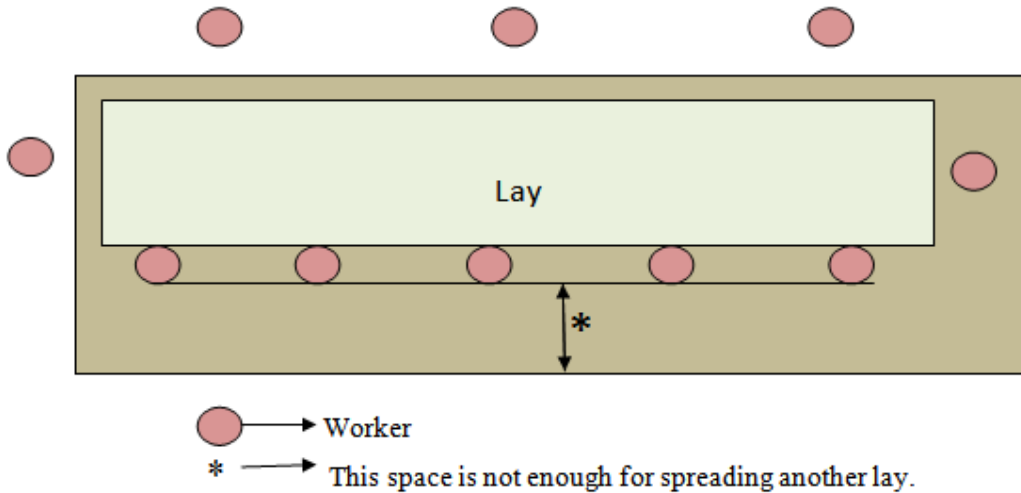


Fig 2. Lays of 64 inch dia is being cut on a table of 84 inch width.

- In some cases three lays are set in one table. In such case the worker who throws the lay in the mid position stands in a very awkward position. It becomes difficult for him to throw the lay. And this job needs extra time.
- Short width tables permits space for more tables and allows workers to spread the lays by standing.
- For fabric of high dia two tables can be joined.
- Shorter tables of about 8 yards can facilitate

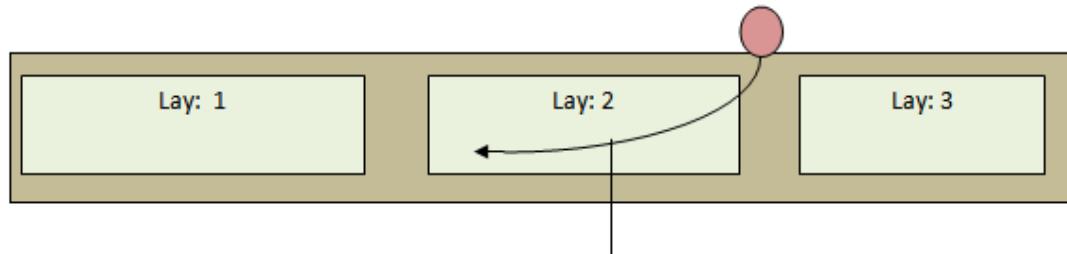


Fig 3. Three Lays are being cutting on a table.

### 3.4 Solution to these problems

The solution of the above problems can be solved by focusing on the followings:

- The comfort zone of the workers can be increased and they can work more efficiently.
- Number of workers for each spreading can be reduced and this worker can be employed to spread more other lays.

The dimensions of the existing tables are:

Table 1: Dimensions of different table (existing)

Table	Length (feet)	Width (feet)
1	70	8
2	90	7
3	80	4
4	80	7

Based on the discussion it is noticed that the tables are not being used effectively. So tables of shorter length and width can be a solution. This is because of the following:

easy movement of tables.

- Long tables cause difficulty for mid position workers.

Finally the follow dimensions of table can be production friendly:

- 11 tables are of 55inch width and 8 yards length.
- One table is of 84inch width and 16 yards length.
- One table is of 84inch width and 8 yards length.

In the new dimensions the workers don't have to sit on any side of the fabric. On both sides of the fabric the workers will be on the standing position.

The number of workers can be redefined for a certain size of the fabric according to the followings:

- Every four yards there will be one worker.
- After every four yards one more worker will be added.

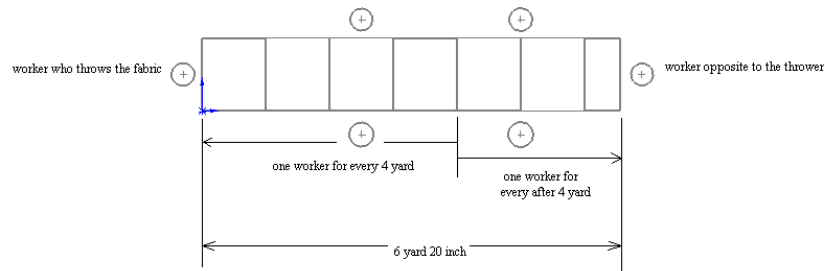


Fig 4. Fabric with width 41 inch and length 6yard 20 inch

Here is an example where the number of worker is redefined for a particular fabric spreading in a particular table.

Thus the total worker in this case = 6, where in the existing dimension the no. of workers is 10.

### 3.5 Proposal for Layout

Layout has a significant role in improving productivity. This paper presents the findings of existing layout and the proposed layout below

#### 3.5.1 Problems in the Existing Layout:

- While fabrics are cut they are needed to pass the quality check. For this all the fabrics are bundled and kept in a sack and brought in front of the QC tables. Here again the sacks are opened and fabrics are checked. Here actually
- These opening of sack are an extra work done two times in the same floor.
- As there is no dedicated place for numbering, bundling and laying the workers have to wander the whole floor when they complete one of their works. These actually hamper the flow of work. If a zone of work could have been created for a group of worker it could have improved the efficiency of the cutting section.

There is no specific place for finished cut fabric. Some fabrics need to be relaxed in specific temperature and humidity. But the fabrics are kept bare for relaxation in a open space which degrade the quality of the fabric.

#### 3.5.2 Proposed Layout

- In our proposed layout the QC tables are decentralized. Here shelves are designed for each table which will provide space for cut fabrics waiting for quality check. These decentralized tables can help to limit too much wandering of a worker.
- Here in between two QC tables one numbering table is set. After cutting, fabrics will be moved to this numbering table and then to the QC shelves.
- A relaxation room is designed beside the temporary storage of uncut fabrics. In this place all the fabrics needing relaxation can be kept which can keep these fabrics dust-free.
- Three areas are specified for keeping finished fabric storage. These storage places are provided with shelves. These shelves not only helps to utilize the space efficiently but also helps the sorting of fabrics easier.



Fig 5: Proposed Layout

#### 4. CONCLUSION

This study revealed the present condition of knitwear or the apparel industry of Bangladesh. During the study many activities that hamper the productivity and working environment have been observed. Among many other problems this study reveals only a few due to its time limitation. This paper suggests the methodology to utilize the manpower, to improve the arrangement of working floor that reduce the time wastage and encourage the working environment.

One severe problem during the study was acute power crisis. It is the main problem behind major anomalies.

Now a day the apparel industry mostly the knitwear industry holds the top most position among the foreign money earners for its reliable status to the buyers. But the primitive concepts and poor work management push the brake of its motion. More studies should be done in order to find the problems in this sector and cut out excess costs incurred in unnecessary steps keeping the quality high. The worker should be trained properly. They have to be satisfied by fulfilling all their demands. Besides, government should subsidize on its necessary demands and provide an uninterrupted power supply. Thus, the economy of Bangladesh can get an expected growth.

#### 5. REFERENCES

1. Imai and Masaaki, 1997, "*Gemba kaizen: a commonsense low-cost approach to management*", New York: McGraw-Hill Professional. P. 64.
2. Taylor, F. W., "*Shop Management*". Harper & Brothers. Free book hosted online by Google Books", <http://books.google.com/books?id=Am4I-N4XN2QC>, 1911.
3. Robbins, S.P., Bergman, R., Stagg, L. and Coulter, M., 2003, "*Management (3rd Edition)*", Sydney, Australia: Prentice.
4. Karger, Delmar, W., Bayha and Franklin, H., "*Engineered Work Measurement, Fourth Edition*". Industrial Press. ISBN (0-8311-) 1170-4.
5. "*MTM-1 Analyst Manual*". UK MTMA Ltd.

#### 6. MAILING ADDRESS

Seratul Jannat  
Assistant Professor,  
Department of Industrial and Production Engineering,  
E-mail: seratuljannat@ipe.buet.ac.bd

## SMALL ANGLE NEUTRON SCATTERING STUDIES ON MIXED MICELLES

I. Kamal<sup>1</sup>, F. U. Ahmed<sup>1</sup>, P.S. Goyal<sup>2</sup> and G .U. Ahmad<sup>3</sup>

<sup>1</sup>Institute of Nuclear Science and Technology, Bangladesh Atomic Energy Commission, Bangladesh.

<sup>2</sup>Inter University Consortium for DAEF, Mumbai Centre, Bhabha Atomic Energy Centre, India

<sup>3</sup>Prime Asia University, Dhaka, Bangladesh

### ABSTRACT

Mixed micelles alkytrimethylammonium halides have been studied using small angle neutron scattering (SANS). In particular, SANS measurements have been carried out on CTAB, DTAB TTAB and mixed micellar solutions of CTAB(m=16)+TTAB(M=14), CTAB+DTAB (m=12) and TTAB+DTAB surfactants with same head group but different chain lengths. The measurements were also made from mixture of surfactants with the same chain but different head groups of CTAB and CDAB. The structural information (shape, size, aggregation number, micellar charge) about alkytrimethylammonium bromide ( $C_mH_{2m+1}N^+(CH_3)_3Br^-$  micelles for a number of systems have been studied. SANS distributions from micellar solutions of different chain length surfactants show a well-defined peak. This peak indicate the presence of strong electrostatic interaction between the micelles. It is found that size, aggregation number and fractional charge on the micelle in the mixed systems have values in between those for the pure component systems. These results are compared with the reported data.

**Keywords:** Mixed Micelles, Chain Length, Head Group, Fractional Charge, Surfactant Concentration

### 1. INTRODUCTION

SANS study of structural aspects of mixed micelles, when two types of surfactant molecules which differ in length or head group size, are simultaneously present in the solution [1]. The micellisation properties of single component surfactant solutions are reasonably well understood. The structural aspects for a number of surfactant solutions have been studied and the effect of temperature, surfactant concentration and the additives ( both organic and organic ) on structural parameters have also been examined [2]. The effect of the relative lengths of the constituents monomer on the aggregate structures in the mixed micelles has been studied by carrying out SANS measurements on cationic alkytrimethylammonium bromide( $C_mH_{2m+1}(CH_3)_3Br^-$  surfactants. In particular, measurements have been carried out on mixed micellar solutions of CTAB(m=16)+TTAB(M=14), CTAB+DTAB (m=12) and TTAB+DTAB. Another set of experiment examine the effect of head group size on the structural parameters of mixed micelles. In this category, the measurements have been carried out on mixed micellar solution of CTAB+CDAB. The length of CDAB ( $C_{16}H_{33}N^+(CH_3)_2C_2H_5Br^-$ ) molecules are similar to that of CTAB. CDAB has bigger head group. Figure 1 gives the pictorial representation of mixed micellar solutions, which have been studied.

### 2. EXPERIMENTAL DETAILS

The micellar solutions were prepared by dissolving known amount of surfactants in D<sub>2</sub>O. The use of D<sub>2</sub>O instead of H<sub>2</sub>O for preparing micellar solutions provides better contrast in SANS experiments. In mixed micellar solutions the solutes were mixed in 1:1 molar proportion and the concentration was kept fixed at 0.2M. SANS measurements were carried out using SANS spectrometer at the guide tube laboratory of Dhruva reactor, [3]. The solutions were held in quartz cell of thickness 0.5cm. The temperature was maintained at 30±0.2°C. The measured SANS distributions were corrected for the background, empty cell scattering and the sample transmission and were normalized to cross section units. The corrected normalized data  $d\Sigma/d\Omega$  Vs. Q are shown in figure 1 to 4.

### 3. THEORY

It has been assumed that constituent surfactants mixed ideally in the micelle for analyzing the SANS data. The coherent differential scattering cross section ( $d\Sigma/d\Omega$ ) for a system of monodispersed ellipsoidal micelles is given by

$$d\Sigma/d\Omega=n(\rho_m-\rho_s)^2V^2[<F^2(Q)>+<F(Q)>^2(S(Q)-1)] \quad (1)$$

where n denotes the number density of micelles,  $\rho_m$  and  $\rho_s$  are the scattering length densities of the micelle and the solvent respectively and V is the volume of the

micelle. The aggregation number  $N$  of the micelle is related to micellar volume by the relation  $V=Nv$ , where  $v$  is the volume of the surfactant monomer. The volume of mixed micelle is given by

$$V=N[x_1v_1+(1-x_1)v_2] \quad (2)$$

where  $x_1$  is the mole fraction of component **1** in the mixed micelle.  $v_1$  and  $v_2$  are the monomer volumes of the components.

The scattering length density of the mixed micelle is calculated by

$$\rho = x_1\rho_1+(1-x_1)\rho_2 \quad (3)$$

where  $\rho_1$  and  $\rho_2$  are the scattering length densities of the components.  $F(Q)$  is single particle form factor and depends on the shape and size of the particles. In the analysis, we assume the micelles to be monodisperse ellipsoids. We recall that for an ellipsoidal micelle

$$\langle F^2(Q) \rangle = \int_0^1 [F(Q, \mu)]^2 d\mu \quad (4)$$

$$\langle F(Q) \rangle^2 = \left| \int_0^1 F(Q, \mu) d\mu \right|^2 \quad (5)$$

$$F(Q, \mu) = \frac{3(\sin x - x \cos x)}{x^3} \quad (6)$$

$$x = Q[a^2\mu + b^2(1-\mu^2)]^{1/2} \quad (7)$$

where  $a$  and  $b$  are the the semimajor axis and semiminor axis of ellipsoidal micelle.  $\mu$  is the cosine of the angle between the direction of major axis and the wave vector transfer  $Q$ .  $S(Q)$  is the interparticle structure factor.  $S(Q)$  specifies the correlation between the centers of different micelles and it is the Fourier transform of the radial distribution function  $g(r)$  for the mass centers of the micelle.

In the analysis,  $S(Q)$  has been calculated by using mean spherical approximation as developed by Hayter and Penfold [4]. In this approximation micelle is assumed to be a rigid equivalent sphere of diameter  $\sigma = 2(ab^2)^{1/3}$  interacting through a screened Coulomb potential. The fractional charge  $\alpha (=z/N$ , where  $z$  is the micellar charge) is an additional parameter in the calculation of  $S(Q)$ . For calculation of the composition of mixed micelles, Clint theory of ideal mixing of surfactant components has been used [5]. In this theory, the mixed CMC ( $C_m$ ), unaggregate monomer concentrations ( $C_1^m$  and  $C_2^m$ ) and the mole fraction ( $x_1$ ) of the component **1** in mixed micelle are given by

$$\frac{1}{C_m} = \frac{\tau}{C_1^m} + \frac{(1-\tau)}{C_2^m} \quad (8)$$

where  $\tau$  is the mole fraction of the surfactant **1** in the total mixed solute.  $C_1^m$  and  $C_2^m$  are the CMC's of pure

surfactants **1** and **2**. The aggregation number ( $N$ ), fractional charge ( $\alpha$ ) and semiminor axis ( $b=c$ ) are the parameters in analysis of SANS data in terms of equation 5.38 The semi major axis is calculated by the relation  $a=3v/4\pi b^2$ .

## 4. RESULTS AND DISCUSSION

### 4.1 Single Component Micellar Solution

SANS distributions from micellar solutions of different chain length surfactants 0.2M CTAB( $m=16$ ), 0.2M TTAB( $m=14$ ) and 0.2MDTAB( $m=12$ ) are shown in figure 1. Each distribution shows a well-defined peak. The fact that peak position  $Q_m$  ( $.048\text{\AA}^{-1}$ ) is different at the same surfactant concentration in CTAB, TTAB and DTAB shows that micelle sizes are different in these systems. The observed values of  $Q_m$ , as one decreases the length of the surfactant molecules for a fixed concentrations, suggest that the number density of CTAB micelles is smaller than those of TTAB and DTAB micelles. That is, micelles of CTAB are larger than micelles of TTAB and DTAB.

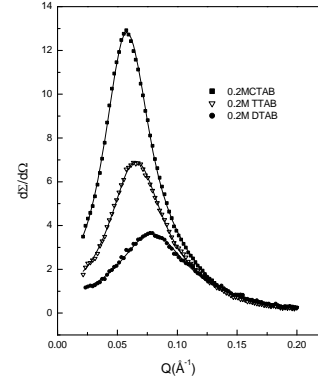


Figure 1: SANS distribution for the 0.2M micellar solution of surfactants with same head group but different chain lengths.

Table 1: Surfactants with same head group but different chains lengths

System	N	Charge ( $\alpha$ )	a ( $\text{\AA}$ )	b ( $\text{\AA}$ )	a/b	d ( $\text{\AA}$ )	$Q = 2\pi/d$
0.2MCTAB	17 5	0.081	48	21	2.2 9	11 3	0.05 5
0.2MTTAB	12 3	0.116	46	18	2.5 6	11 1	0.06 2
0.2MDTAB	72	0.211	35	15	2.3 3	84	0.07 4

Table 2: Surfactants with same chain length but different head groups

System	N	Charge $e(\alpha)$	a ( $\text{\AA}$ )	b ( $\text{\AA}$ )	a/b	d ( $\text{\AA}$ )	$Q = 2\pi/d$
0.2MCTAB	175	0.0814	53	21	2.52	113	0.055
0.2MCDAB	157	0.0996	32	21	1.52	109	0.057

The various structural parameters as obtained from detailed data analysis are given in Table 1. It is seen that micelles are ellipsoidal in all the cases. The values of semiminor axis for CTAB, TTAB and DTAB are 21, 18 and 15 Å respectively. It may be noted that these values are smaller than the corresponding extended length of the surfactant molecules. This shows that surfactant molecules inside micelles are not in extended conformation and they have a tendency to fold. The aggregation number also decreases in the same order. This is due to decrease in the surface area of the micelles with the decrease in length of the surfactant molecule as there is less space for the number of head groups to occupy. However, the fractional charge on the micelle increases as one goes from CTAB to DTAB. The value of fractional charge for DTAB is the largest because of the higher dissociation of surfactant molecules. Figure 2 shows the comparative SANS distribution for CTAB and CDAB, where length of surfactant molecule is fixed and the head group size is varied.

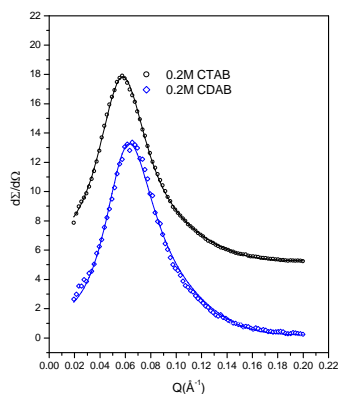


Figure 2: SANS distribution for the 0.2M micellar solution of surfactants with same chain lengths but different head group.

Again, we find that peak position in SANS distribution varies with the change in head group. However, the semiminor axis is same for these two systems. The aggregation number decreases and fractional charge increases from CTAB to CDAB. [Table 2]. The 0.2M CDAB has fractional charge slightly higher than 0.2M CTAB. This is because of the replacement of one of  $-\text{CH}_3$  group in the head group of CTAB by  $-\text{C}_2\text{H}_5$  and this increases the dissociation of  $\text{Br}^-$  ions.

#### 4.2 Mixed Micelles: Effect of Chain Length

Figure 3 shows the SANS distribution from mixed micellar solution of (0.1MCTAB+0.1MDTAB). The SANS patterns from the pure components micellar solutions 0.2M CTAB and 0.2M DTAB are also plotted in the figure. In all these three micellar solutions, total number of surfactant molecules are same. It is observed that two components micellar solution (0.1M CTAB+0.1M DTAB) similar to single component micellar solutions, shows a single peak, which is expected if all the micelles are identical in composition. The intensity and the position of the peak for above mixed micellar solution lies in between those of pure components, namely 0.2M CTAB and 0.2M DTAB. The micellar parameters for these systems are given in Table

3. It is found that size, aggregation number and fractional charge of the mixed system are in between that of single components.

Table 3: The values of various parameters for mixed micellar solutions of surfactants with same head group but different chains lengths.

a. [ 0.1M CTAB+0.1MDTAB) compared with 0.2 CTAB and 0.2M DTAB.

System	N	Charge ( $\alpha$ )	a (Å)	b (Å)	a/b	d (Å)	$Q=2\pi/d$
0.2MCTAB	175	0.08	53	21	2.52	113	0.055
0.1MCTAB+0.1MDTAB	130	0.10	48	18	2.67	103	0.061
0.2M DTAB	72	0.21	35	15	2.33	84	0.0745

b. [ 0.1M CTAB+0.1MTTAB) compared with 0.2 CTAB and 0.2M TTAB.

System	N	Charge ( $\alpha$ )	a (Å)	b (Å)	a/b	d (Å)	$Q=2\pi/d$
0.2MCTAB	175	0.08	53	21	2.52	113	0.055
0.1MCTAB+0.1MTTAB	147	0.09	46	20	2.3	107	0.0587
0.2MTTAB	123	0.12	46	18	2.56	101	0.0623

The value of semi minor axis  $18\text{Å}$  for (0.1MCTAB+0.1M DTAB) micelles is in between  $21\text{Å}$  and  $15\text{Å}$  for 0.2M CTAB and 0.2M DTAB respectively is shown in figure 3. The semi minor axis is usually decided by the length of the surfactant molecule. The variation in semiminor axis thus suggests that in mixed micelles of two different chain length surfactants while the shorter chain length surfactant has a tendency to stretch, the larger chain length surfactant folds to pack inside the micelles. The aggregation number of the mixed micelles has been found to be closer to the one consisting of short chains as compared to the one containing longer chains.

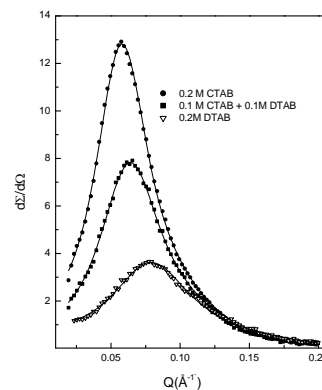


Figure 3: SANS distributions from the mixed micellar solution (0.1MCTAB+0.1M DTAB) and compared with pure surfactant components 0.2M CTAB and 0.2M DTAB solution micellar solutions.

The shifting of peak position towards lower Q shows that micellar size increases on increasing the chain length of mixing surfactants. The aggregation number increases as the chain length of mixing surfactant is increased. (Table 3) in figure 3 and 4.

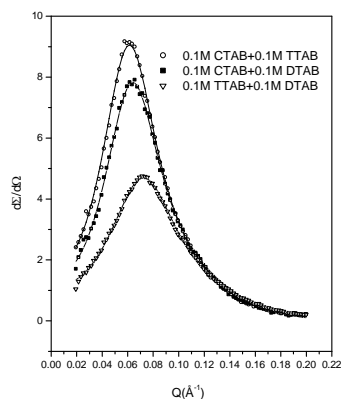


Figure 4 SANS distributions from the mixed micellar solution

## 5. CONCLUSION

The structural information (shape, size, aggregation number, micellar charge) about alkytrimethylammonium bromide ( $C_mH_{2m+1}N^+(CH_3)_3Br^-$ ) micelles has been obtained for DTAB ( $m=12$ ), TTAB ( $m=14$ ) and CTAB ( $m=16$ ) using technique of SANS. That is, the effect of monomer length on structural parameters of a micelle has been investigated. To examine the effect of head group size on micellar structure, measurements have been made on CDAB which are similar to CTAB except that head groups are different. It is seen that micelles are ellipsoidal in all cases. The minor axis of micelle increases with increase in surfactant length but is independent of head group size. However, the major axis and aggregation number depend both on molecular length and the head group size and increase by increasing the chain length by decreasing the head group size. These results are compared with the reported data [1].

## 6. REFERENCE

1. B. Lindman and H. Wennerstrom, *Top. Curr. Chem.* 87, 1 (1980).
2. V.K. Aswal and P.S. Goyal, *Physica B* 245, 73 (1998).
3. P.S.Goyal, V.K. Aswal and J.V. Joshi, BARC/1995/I/018(A report of BARC, Mumbai, 1995).
4. Hayter, J.B., Penfold, J. *Colloid Polym Sci.* 42, 109, (1981).
5. K.M.Lusvardi, A.P. Full and E.W. Kaler, *Langmuir* 11, 487 (1995)

## 7. MAILING ADDRESS

I. Kamal  
 Institute of Nuclear Science and Technology,  
 Atomic Energy Commission, Bangladesh



## DEVELOPMENT AND EVALUATION OF HYDRAULIC SIMULATION MODEL FOR WHEEL LOADER

Khairul Alam<sup>1</sup>, S. Hee Park<sup>2</sup>, C. Don Lee<sup>3</sup> and S. Yong Yang<sup>3</sup>

<sup>1</sup>Graduate School of Institute of e-vehicle Technology,

<sup>2</sup>Graduate School of Mechanical and Automotive Engineering,

<sup>3</sup>School of Mechanical and Automotive Engineering,

Republic of Korea

### ABSTRACT

This paper presents the development of a simulation model for wheel loader hydraulic system. Using the AMESim programming environment as a simulation tool, each component of wheel loader hydraulic system such as main pump, main control valve, compensator, joystick and attachments are modeled according to their specifications and the total simulation model is obtained by a combination of these component models. Analysis and simulation results show that our developed model can simulate wheel loader hydraulic system and its components effectively.

**Keywords:** Hydraulic system, Simulation, Wheel loader.

### 1. INTRODUCTION

Advancement of simulation capabilities made it possible to simulate any physical system before building the prototype to evaluate controls and performance test of components. Simulation results help to improve the design, reliability and operability, thereby reducing cost and time associated with the design significantly. Although hydraulic systems exhibit severe hysteresis and system discontinuities which are often responsible for inaccurate operation, simulation plays an important role in many applications. Therefore, this paper concerns with the development of a hydraulic simulation model for wheel loader.

The wheel loader is a hydraulic machine that has a bucket in the front and can be used for digging, transporting, loading and unloading different type of materials. Wheel loader has obtained popularity in various working fields, especially in urban engineering projects and earthmoving works. Consequently, it has been received much attention by many researchers in order to achieve great gains in efficiency, performance, safety and operator comfort [1-2]. Moreover, an operator of such a vehicle needs a lot of training time and experiences until he can handle a vehicle safely and skillfully. In order to reduce these requirements for the operator as well as to protect from the hazardous working environment, a vehicle should be made as more autonomous way [3]. This work focuses on as a first step in this direction, a wheel loader hydraulic circuit modeling and simulation program to evaluate automatic loading and unloading task.

A wheel loader consists of variable displacement

tandem axis piston pump which is load sensing control type along with maximum pressure regulator, and is operated by signals from joystick that control pilot pressure to spools of the main control valve (MCV). The MCV consists of boom and bucket. Several kinds of hydraulic control systems such as valve control as well as pump control have been examined. Among these, load sensing based pump control system has shown most effective with the control problem of hydraulic wheel loader system. Another remarkable point of this work is to apply flow sharing principle to prevent work stoppage during simultaneous operation of actuators. On the basis of this appropriate and reliable model, wheel loader hydraulic system components can be designed and further optimized conveniently, which can reduce costs.

The remainder of this paper is organized as follows: Section 2 presents description of wheel loader sub-systems. In the following section modeling of hydraulic system including each component's model using AMESim are shown. The results of simulation are in the section 4. Section 5 contains a summary of the work.

### 2. WHEEL LOADER SUB-SYSTEMS

Wheel loaders can be divided into four sub-systems: (1) power-train, (2) brakes, (3) steering (4) hydraulic system for actuators as shown in fig. 1.

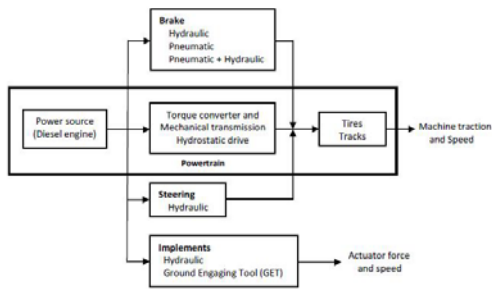


Fig 1. Block diagram of wheel loader sub-systems [1]

The power-train consists of a power source which is typically a diesel engine. Power is transmitted to a mechanical transmission via a torque converter which then connects to differentials, drives and finally tires. Several engine power take-offs provide power via pumps to run the steering hydraulic system, the brake system, and the hydraulic actuation system. The hydraulic actuation system contains the ground engaging tools (attachment) that provides the force and motion to engage the pile that needs to be processed. This paper concerns with the modeling and simulation of hydraulic system. The steering system is out of this paper scope. Figure 2 shows the structure of the simulation model.

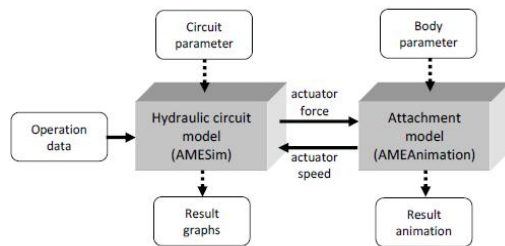


Fig 2. Structure of the simulation model

### 3. HYDRAULIC SYSTEM MODELING

In order to develop the simulation model, at first the main components of a wheel loader hydraulic circuit such as main pump, MCV, compensator, joystick and attachment are modeled using AMESim, a leading commercial simulation software in the field of hydraulic system. These components modeling are based on typical 23-26 ton hydraulic wheel loader.

#### 3.1 AMESim Software Environment

AMESim is multidisciplinary modeling, simulation and analysis software that allows to link between different physics domains as hydraulic, pneumatic, mechanic, electrical, thermal, and electro-mechanical. It was a product of Imagine Corporation of France, and was acquired in June 2007 by LMS International. It has rich module libraries, which can be extended according to demands. Modules are used in accordance with the actual physical system to build simulation model without having to deduce the complex mathematical model. In order to reduce simulation time and improve the accuracy of simulation, its intelligent solver can

automatically select the best integration algorithm from the seventeen algorithms according to the mathematical features of model. AMESim has several interfaces with other computing software like Simulink, Adams, Simpack and dSPACE. In this paper the simulation program is developed using AMESim 4.3.0 version.

#### 3.2 Main Pump Modeling

The main pump modeled in this paper is variable displacement dual tandem axis piston pumps having pump displacement 100 cc/rev and 51 cc/rev respectively with load-sensing controller and maximum pressure regulator.

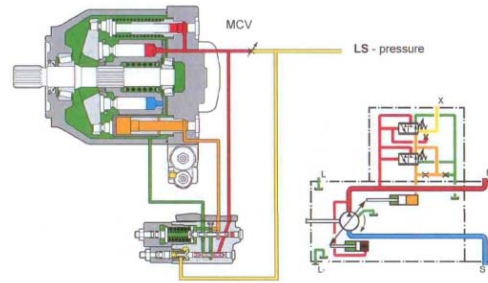


Fig 3. Cross-section of a typical variable displacement load-sensing pump

A load-sensing pump is actuated in dependence on the highest load pressure and only produces the flow demanded by the actuators that makes it energy efficient. Figure 4 shows the AMESim model of one section of the main pump.

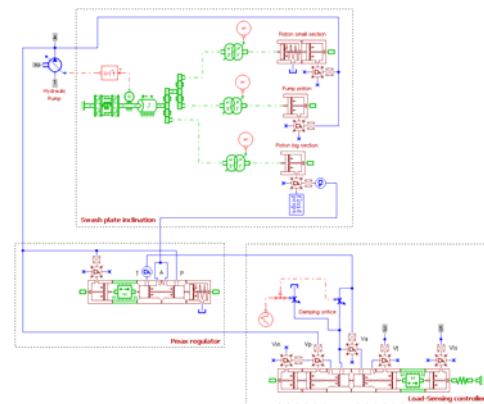


Fig 4. Model of the main pump using AMESim

The pump swept volume is a function of the inclination of the swash plate. The swash plate angle is governed by the resulting torque given by the piston small section, pump pistons and the piston big section, controlled by the flow rate given by the load-sensing controller together with maximum pressure regulator. The main dual tandem pump is formed by coupling two pump sections with single motor having shaft speed 2300 rev/min.

#### 3.3 Joystick Modeling

The employment of joysticks has virtually replaced

the traditional mechanical control lever in nearly all modern hydraulic control systems. Most of the movements of wheel loader are controlled with operation of joystick control lever. Joystick operation decides pilot pressure and direction of movements of MCV spools. The pilot pressure having range 0~45kgf/cm<sup>2</sup> is used in this hydraulic system simulation model. This pressure acts on either side of MCV spools, results respective displacement of spools. Then hydraulic oil passes through the flow area generated by the movement of spools.

In this paper, the operating signal input to joystick is assumed between -10 to 10 and the corresponding pilot pressure generated to port A and port B is directly proportional to the magnitude of input signal. Figure 5 shows the AMESim model of the joystick.

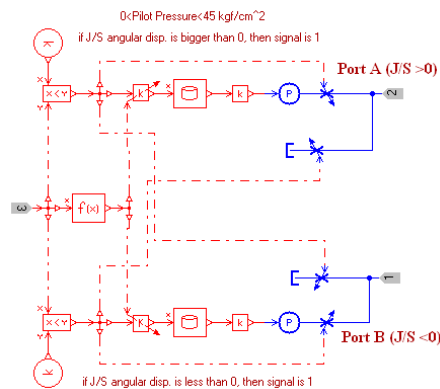


Fig 5. Model of the joystick using AMESim

### 3.4 MCV Modeling

The MCV consists of various valves for boom, bucket and auxiliaries. Only the valves for boom and bucket are modeled in this paper. These valves are 8 ports 3 position types including bypass line as shown in fig. 6.

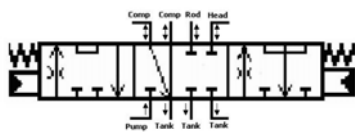


Fig 6. Circuit diagram of boom valve

When pilot pressure acts on one side of a valve selectively, spool is moved in accordance with the pressure. Then the flow area with respect to spool displacement shows a non-linear relation that shown in fig. 7. In course of modeling of MCV valves, the factors considered are the stroke of spool, the mass of spool, the flow area with respect to spool displacement, the diameter of spool, and the end spring stiffness. The model of valves comes from mechanical and hydraulic component design module libraries of AMESim. The valve modeling for bucket is done in a similar way as boom valve. Figure 8 shows the AMESim model of the boom valve.

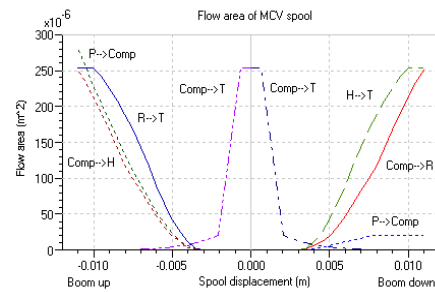


Fig 7. Spool displacement-Flow area characteristics of the boom valve

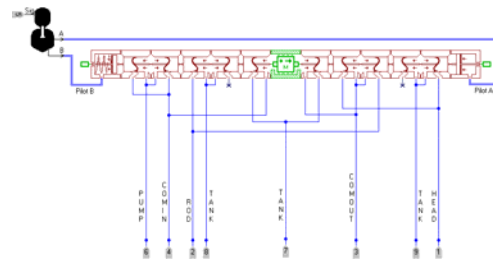


Fig 8. Model of the boom valve using AMESim

### 3.5 Compensator Modeling

The compensator arranged downstream from the orifice (valve spool) is subjected to the pressure downstream from the respective orifice in the opening direction and in the closing keeps to a pressure from the respective actuator. It keeps the pressure drop across the orifice constant, which keeps flow constant and thereby cylinder speed is constant independent of load. Figure 9 shows the hydraulic circuit model of compensator.

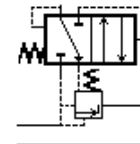


Fig 9. Circuit model of compensator

The compensator keeps the pressure in the pump line to a higher value than the highest load pressure by a pressure difference equivalent to the force of a control spring, so-called  $\Delta p$  control. The value of  $\Delta p$  is assumed to 20 Bar in this paper. Figure 10 shows the AMESim model of compensator.

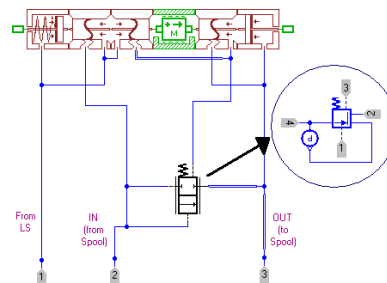


Fig 10. AMESim model of compensator

### 3.6 Attachment Modeling

There are several types of wheel loader implement linkages currently in use. A very common example, called the Z-bar linkage [1], is shown in Fig. 11.

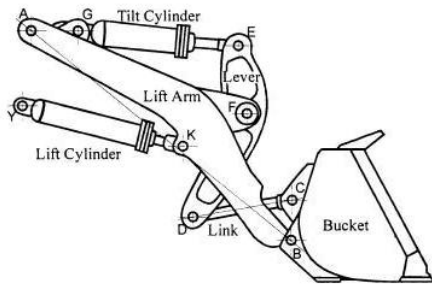


Fig 11. Typical wheel loader attachment

It is a two degrees of freedom (dump and roll back) linkage consisting of four bodies (lifting arm, reversing lever, connecting link, and bucket) and two asymmetric hydraulic cylinders (lift and tilt), all connected together by nine revolute pin joints. The tilt and lift cylinders are double acting type and the specifications are shown in table 1.

Table 1: Specification of cylinders

Parameter	Lift cylinder	Tilt cylinder
Piston diameter	175 mm	150 mm
Rod diameter	50 mm	55 mm
Length of stroke	760 mm	460 mm
Free length	1240 mm	800 mm

In the course of modeling of the Z-bar linkage using AMESim, the size and weight of the bodies are obtained from the specifications of a typical wheel loader. The position of the bodies has defined according to the relative coordinate system of the AMESim planar mechanical library. In order to get actual animation at desired shape of the attachment, this model includes contour data of reversing lever, lifting arm and bucket that confirm the virtual movement of the attachment based on simulation result. Figure 12 shows the AMESim model of the attachment.

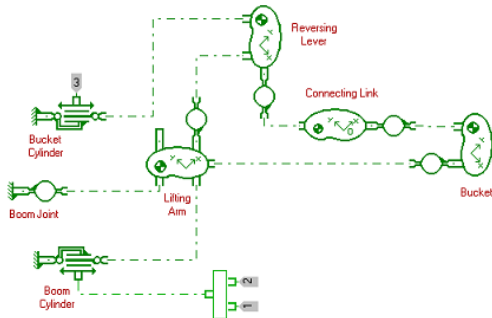


Fig 12. Model of the attachment using AMESim

### 3.7 Total Hydraulic System Modeling

By a combination of models, including the model of pump, MCV spools, compensators, and attachment, coupled with input signal, we get the complete simulation model of the wheel loader hydraulic system, as shown in fig. 13.

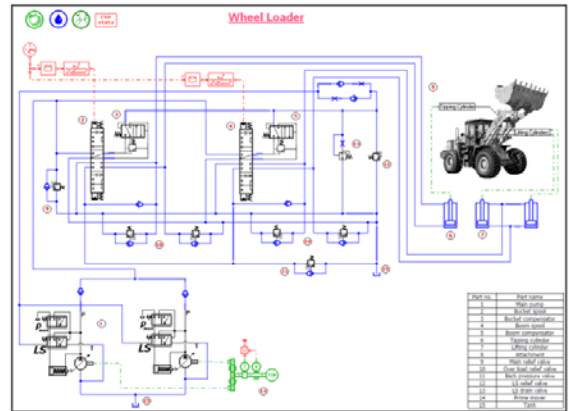


Fig 13. Wheel loader hydraulic system simulation model using AMESim

Simulation runs are carried out to verify the effectiveness of the proposed simulation model when it is applied to wheel loader hydraulic system with different joystick input signals. An additional advantage of this model is that we can rectify the simulation results more quickly and easily by the animation function.

### 4. SIMULATION AND RESULTS

This simulation program works according to the operation of joystick control lever that moves MCV spools. We considered virtual loading and unloading tasks. Then the operating signals input to joystick are assumed between -10 to 10, as shown in fig. 14.

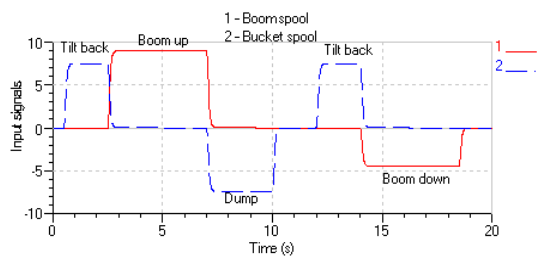


Fig 14. Joystick signals

The movement of attachment according to input signals is decided same order as illustrated in Table 2.

Table 2: Cylinder movement with respect to input signal

Signal	Boom	Bucket
+ (positive)	up	tilt back
0 (zero)	hold	hold
- (negative)	down	dump

A variety of graphs are obtained from the simulation results. Figure 15 shows results for the main pump namely pump pressure and pump flow rate.

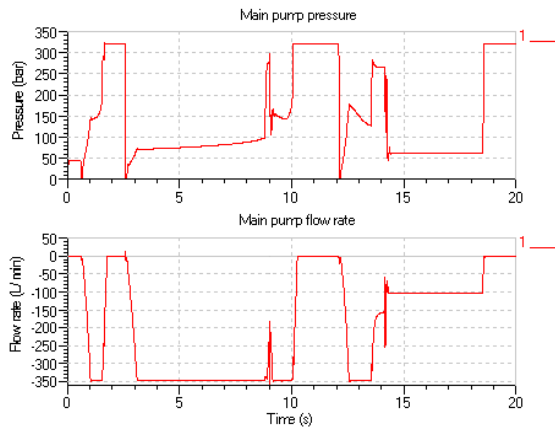


Fig 15. Simulation results of main pump

Figure 16 shows simulation results for the boom namely pilot pressure for boom operation, boom cylinder displacement, pressure and flow rate for boom cylinder head and rod side respectively.

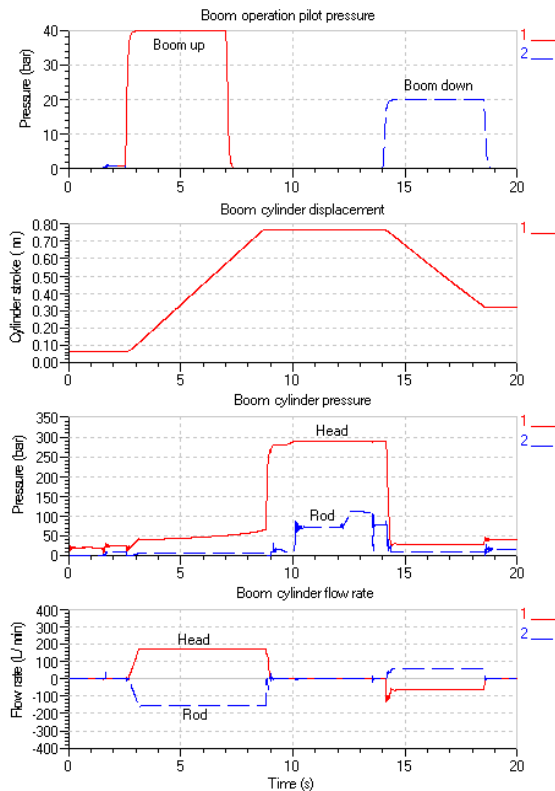


Fig 16. Simulation results of boom

Figure 17 shows simulation results for the bucket namely pilot pressure for bucket operation, bucket cylinder displacement, pressure and flow rate for bucket cylinder head and rod side respectively.

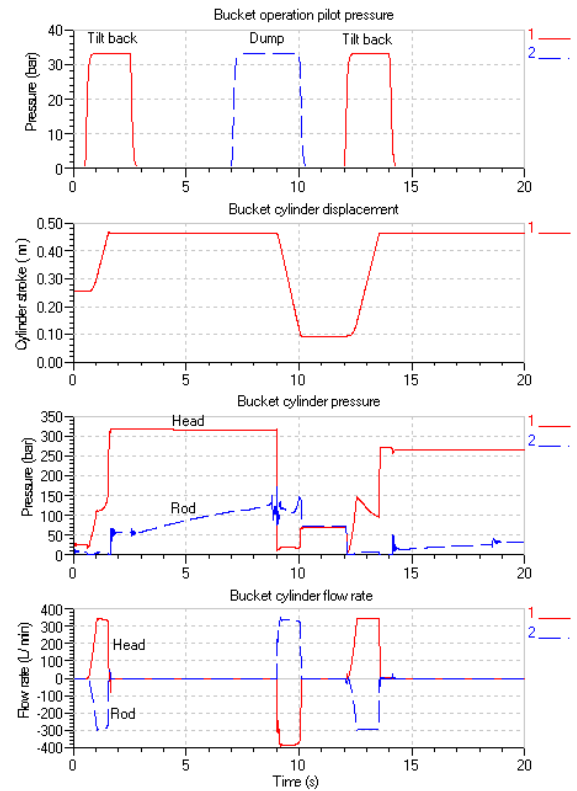


Fig 17. Simulation results of bucket

Figure 18 shows absolute angular position of the attachment according to boom and bucket cylinder displacement.

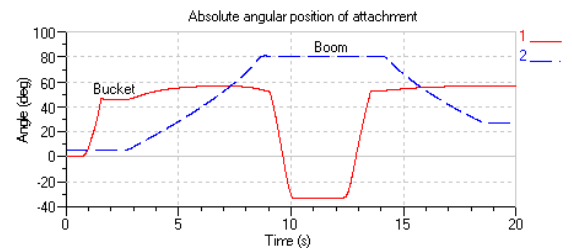


Fig 18. Absolute angular position of attachment

Figure 19 shows attachment model using AMEAnimation based on simulation results.

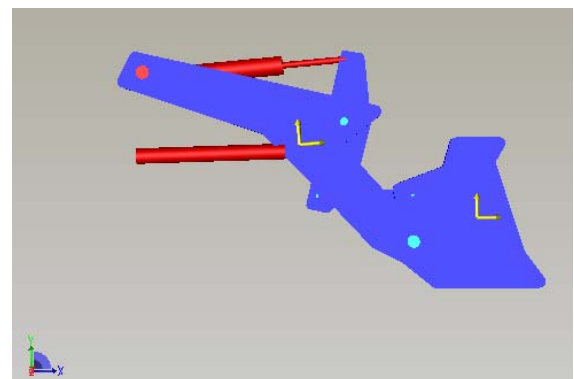


Fig 19. Attachment model using AMEAnimation

In this simulation model the value of  $\Delta p$  is assumed to 20 Bar and it is the compensators' job to fix the pressure drop across the orifice at 20 Bar. As the pressure drop is constant, the flow rate only depends on the valve position. This provides very precise control. Figure 20 and 21 shows the pressure comparison across boom and bucket compensator respectively.

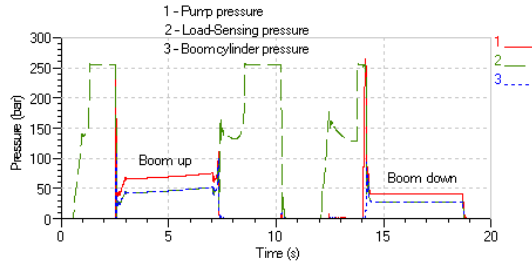


Fig 20. Pressure comparison across boom compensator

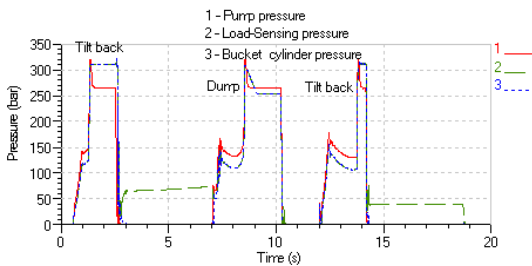


Fig 21. Pressure comparison across bucket compensator

From the above figures we see that the main variable pump adjusts pressure according to load-induced pressure fed back to the pump through load-sensing controller and maintains a higher value equivalent to  $\Delta p$ , thereby making the system energy efficient. Figure 22 shows the result obtained from the field test of a typical wheel loader.

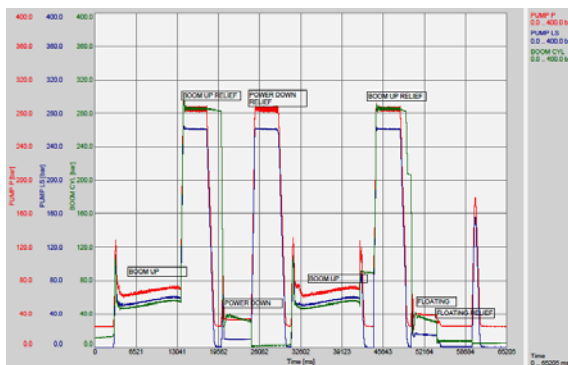


Fig 22. Typical wheel loader experimental test plot

From the Figs. 20-22, obviously, simulation results show a good agreement with experimental results, so the model, as shown in fig. 13, is right.

## 5. CONCLUSIONS

The conclusions of this work are as follows:

1. The developed simulation model can simulate wheel loader hydraulic system and its components effectively. Results of simulations can be used as initial data while building trial versions of real hydraulic system models.
2. In this respect it must be pointed out that the pressure drop across the orifice is not exactly 20 Bar as set. As the shape of the graphs depends mostly on the flow areas of the orifice of the valves, it is very difficult to achieve exact pressure drop.
3. The model in this paper can apply a platform to design and optimize the hydraulic system components, which can save time, reduce costs and improve components quality.
4. Along this research frame, as a future step, we intend to further develop this simulation model so that it will be applicable to the performance test of hydraulic components and automation study of wheel loader. This will hopefully lead in the near future to a modeling tool capable of accurate portrayal of the wheel loader hydraulic system.
5. The approach is original and there is difficult to find similar works. The methods of modeling and simulation possess universal significance to other related hydraulic systems.

## 6. ACKNOWLEDGEMENT

The authors would like to express their gratitude for the financial supports of Hyundai Heavy Industries Co., Ltd. and Post Brain Korea 21, Republic of Korea to conduct this research.

## 7. REFERENCES

1. Mike Cobo, Richard Ingram and Sabri Cetinkunt, 1998, "Modeling, identification, and real-time control of bucket hydraulic system for a wheel type loader earth moving equipment", *Mechatronics*, 8-8:863-885.
2. Sarata, S., Weeramhaeng, Y. and Tsubouchi, T., 2005, "Approach Path Generation to Scooping Position for Wheel Loader", *IEEE Conference on Robotics and Automation, ICRA 2005*, pp.:1809-1814.
3. Soon-Young Yang, Sung-Min Jin and Soon-Kwang Kwon, 2008, "Remote control system of industrial field robot", *6<sup>th</sup> IEE International Conference on Industrial Informatics, INDIN 2008*, DOI 10.1109/INDIN.2008.4618140, pp.:442-447.
4. Sung Hee Park, Khairul Alam, Young Man Jeong, Chang Don Lee and Soon Yong Yang, 2009, "Modeling and Simulation of Hydraulic System for a Wheel Loader using AMESim", *Proceedings of the ICCAS-SICE2009, ICROS-SICE International Joint Conference*, August 18-21, Fukuoka, Japan, pp.:2991-2996.
5. Kazuhide Maehata, "System Simulation for Hydraulic Excavator", 2008, *7<sup>th</sup> JFPS International Symposium on Fluid Power, TOYAMA 2008*, 2:313-316.
6. AMESim solutions guide, 2008, LMS Imagine. Lab, LMS Engineering Innovation.



## THE DEVELOPMENT OF A COMPUTER VISION BASED REAL-TIME INSPECTION SYSTEM TO DETECT THE STATUS OF AUTOMOBILE BREAK TUBE

S. Ahasan Ahammad<sup>1</sup>, E. Naranbaatar<sup>2</sup> and B. Ryong Lee<sup>3</sup>

<sup>1</sup>Graduate School of Institute of e-vehicle Technology, University of Ulsan, Ulsan, Korea

<sup>2</sup>Department of Mechanical & Automotive Engineering, University of Ulsan, Ulsan, Korea

<sup>3</sup>School of Mechanical & Automotive Engineering, University of Ulsan, Ulsan, Korea

### ABSTRACT

Getting high quality products with a rapid and accurate inspection system is the most important aspect in manufacturing field. It is almost impossible to check the fault of all parts coming from part-feeding system, with only human inspection because of time limitation and working hardship as well. Therefore, most of the manual inspections which are applied to specific samples instead of all coming parts can neither guarantee consistent measuring accuracy nor decrease working time. In order to improve the measuring speed and accuracy of the inspection, a computer-aided measuring and analysis method is highly required. In this paper, a computer-vision-based automobile brake tube inspection algorithm is proposed, where a modified Hough transform is applied for calculating the geometry of straight line segments and a line-scanning method is adopted to compute the center points of the inner and outer diameters. Finally, the proposed algorithms are verified by the developed inspection machine to fulfill the inspection requirements demanded from the company.

**Keywords:** Edge Detection, Hough Transform, Computer Vision, Forming-Error Inspection.

### 1. INTRODUCTION

Computer vision systems, as part of factory automation systems, could be used for quality inspection, classification, recognition, etc., instead of human vision [1, 2].

Recently, factory automation technology in manufacturing has been growing rapidly. However, the inspection process, which is the last step of manufacturing, remains at a minimal level of technology. Most part inspection processes still depend on human vision. Conventional human vision-based inspection causes problems such as eye exhaustion, concentration decreases, inconsistent criterion, difficulty in fast feedback, and high labor costs, etc. One alternative method is to apply a computer vision system to the factory automation. Since the mid-1980's, vision inspection systems using CCD cameras have been studied and proven to have advantages of low cost and system simplicity. Exact predictions of the performances of the Hough detection of straight lines in two-dimensional images are presented for rectangular and circular retinas, in Cartesian and normal parameterization [3], in the case of noisy signals, image processing for industrial applications has been studied in Europe [4], vision inspection systems for IC chip fault detection have been studied, in which custom integrated circuits make it possible to realize four basic operations

in a compact way: shape recognition, mask generation, programmable image delay, and subsample filtering [5]. An example that has been processed by a hardware realization of such a pipeline system is provided. Toshiyuki et al. [6] developed an algorithm for a book sorting system using pattern matching. Shapiro et al. [7] developed a failure inspection system for ALC blocks which improved measurement resolution from 0.05 cm to 0.01 cm. As stated above, an inspection system using CCD cameras needs to draw out the feature of the edge for specific parts. The Hough transform among the feature detection methods has been developed to analytically detect definable shapes (line, circle, ellipse etc.) from image data. The main advantage of the Hough transform is achieving robustness against noise; however, one disadvantage if the method is that it requires a large memory and preliminary information of the shape for an exact partition [8-10]. In the matching tasks which form an integral part of all types of tracking and geometrical vision, there are invariably priors available on the absolute and/or relative image locations of features of interest. Usually, these priors are used post-hoc in the process of resolving feature matches and obtaining final scene estimates via 'first get candidate matches, then resolve' consensus algorithms such as RANSAC [11].

In this paper, a computer vision-based inspection



system was developed to inspect the forming status of brake tubes used for automobiles. The system discriminates whether the formed part of the tube is normal or abnormal in both shape and dimension. The inspection algorithm detects line segments from a side-view image using a Hough transform; it finds the slope angle of the formed area, eccentricity and diameters of the tube. Using a front-view image, the center points of the inner and outer diameters are calculated to determine the abnormality of the tubes by applying a line-scanning method.

## 2. TUBE FAULT DETECTION ALGORITHMS

As explained before, tubes considered in this paper were formed at their end point. The formed shape is important to secure the safety in the brake line. If the formed shape is abnormal and combined loosely to the counterpart, there may be high risk in powerful braking because of oil leakage. As a result, it is important to correctly inspect the status of the formed shape to reduce the potential risk of the vehicle. The side-view image of the formed shape of the tube is shown in Fig. 1.



Fig 1. Exemplary side-view image of the formed tube

In this section, a new forming error detection algorithm for a brake tube is proposed. The overall algorithm consists of three main kinds of sub-algorithms: front-view, side-view and threaded nut inspection algorithms. The front-view inspection sub-algorithm calculates inner and outer diameters using a line scanning method. The side-view inspection algorithm extracts line segments of the formed tube-end and calculates the slope angles of the tube-end using a Hough transform technique. From the slope angles, the eccentricity information of the formed area can be acquired. Then, by checking the eccentricity, we can classify the part as either normal or abnormal. The full flowchart of the forming error inspection procedure of the system is shown in Fig. 2.

### 2.1 Side-View Inspection Algorithm

For the side-view inspection, a Hough transform is adopted. Considering line  $y = ax + b$ , parameters  $a$  and  $b$  can have values in the range of  $-\infty < a < \infty$  and  $-\infty < b < \infty$ . Therefore, it is difficult to express the line equation in the parametric space, and a lot of memory quantity is needed to store each line data. If the line  $y = ax + b$  is represented as  $\rho = x \cos \theta + y \sin \theta$  then the range of  $\rho$  and  $\theta$  can be limited between  $-N\sqrt{2} \leq \rho \leq N\sqrt{2}$  and  $-\pi \leq \theta \leq \pi$ , respectively. The quantity of memory and calculation difficulties can be efficiently reduced because of the limited range of the parameters. However, some additional treatment should be considered to further reduce the inspection time. For this purpose, we used a

clustering structure in which a subset area with relatively many points is found.

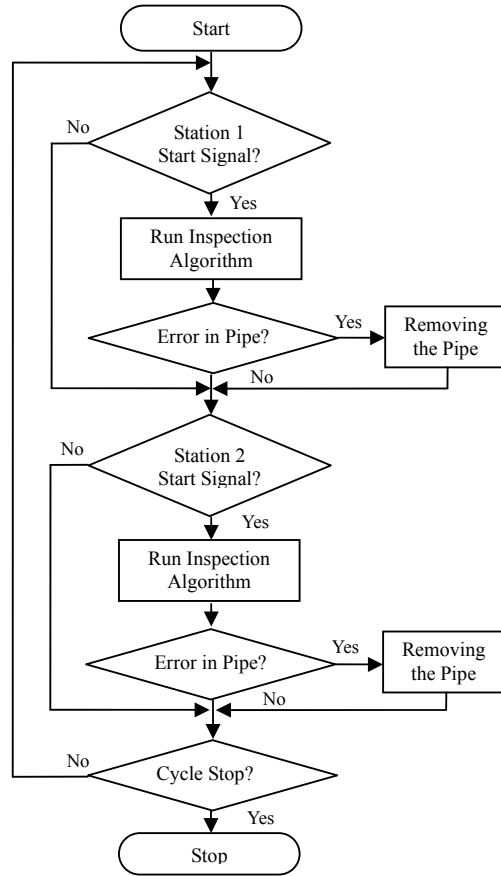


Fig 2. Overall flowchart of tube-fault-detection

The straight line equation obtained from a set of partial points may have some fuzzy distribution because of the noise effect of the Hough transform [13]. Therefore, the line equation needed to be approximated using the Gaussian function [14]. Its center point was calculated with the average of the points belonging to the cluster. Through the side-view inspection, tube type was identified by calculating the diameter of the tube stem. Slope angle of the formed conical shape was also calculated, from which the important eccentricity information was calculated. To classify the tube type, we averaged the diameters given from some sampled diameters as shown in Fig. 3. The average diameter of the tube can be calculated using the Eq. (1).

$$D_{average} = \frac{1}{n} \sum_{i=1}^n (P_{ri} - P_{li}) \quad (1)$$

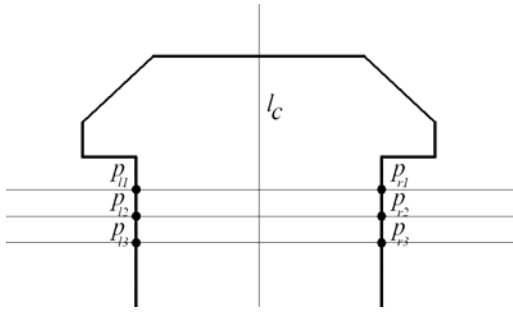


Fig 3. Schematic diagram of diameter calculation using sampled scan data

The inclined lines are determined in the slope surface using Hough transform. Due to noise, in accumulator space, there are several higher voted values (lines) neighboring the real line which is shown in Fig. 4. The accumulator space's highest voted value is used to determine the inclined line which some time does not represent the real line due to noise like sticky scraps on the inclined surface made from forming process. To solve this difficulty, we consider four highest values from the accumulator space and average these values to get the more reliable result. The average parameterized line equation can be calculated using the Eq. (2).

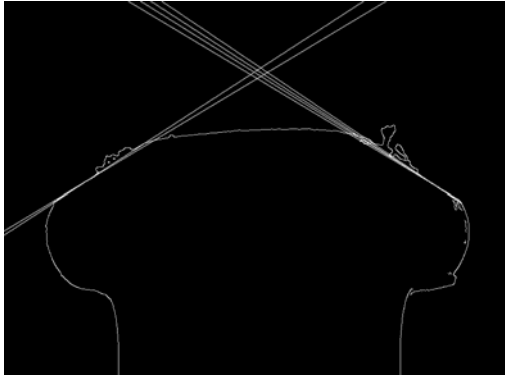


Fig 4. Over lapped inclined lines on slope detection

$$\rho = \frac{1}{n} \sum_{i=1}^n (x_i \cdot \cos \theta_n + y_i \cdot \sin \theta_n) \quad (2)$$

where  $\rho$  is the distance between the line and the origin and  $\theta$  is the angle of the vector from the origin to this closest point.

Once the tube type was identified, the slope angle of the formed area and eccentricity could be calculated using the geometric relations, as shown in Fig. 5.

In Fig. 5, the slope angle of the formed tube, denoted as  $\gamma$ , can be calculated by the Eq. (3).

$$\begin{aligned} \gamma_1 &= \alpha \\ \gamma_2 &= 180^\circ - \beta \\ \gamma &= \gamma_1 + \gamma_2 \end{aligned} \quad (3)$$

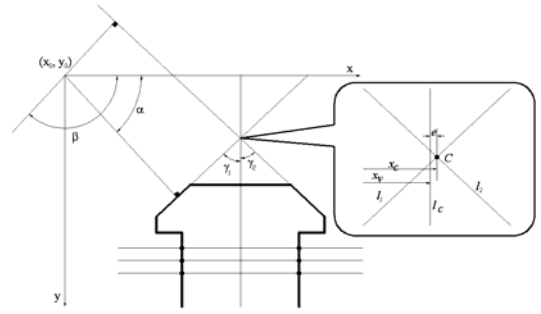


Fig 5. Schematic diagram for finding eccentricity using slope angles and center line of the tube stem

In fact, the slope angle is an important parameter for checking whether the formed tube is normal or not. Another important parameter for the normality test is eccentricity. In Fig. 5,  $l_1$  and  $l_2$  describe the inclined lines representing the slope surfaces of the tube. The intersection point of the two lines is denoted as point  $C$ . When a line  $l_c$  is defined as the line bisecting the tube stem, the eccentricity  $e$  is defined as the off-set displacement from  $l_c$  to the intersection point  $C$  by the Eq. (4).

$$e = |x_c - x_v| \quad (4)$$

where  $x_c$  and  $x_v$  is the x coordinate value of point  $C$  and line  $l_c$  respectively.

Eccentricity is a critical criterion for the normality test. However, it was not easy to calculate the slope angles precisely because of noise on the inclined line due to light reflection. Therefore we adopted the Hough transform to find the correct line information on the lines, even in the presence of considerable noise.

In general, a Hough transform requires abundant memory and time because it considers the whole angular space in the image plane. In our case, we can obtain some pre-determined shape information from the tube. Hence, we can confine the angular space in the image. Since the slope angle of the lines for the normal pipe is known to be  $\pm 28^\circ$ , the search range of the slope angle can be divided by ten:  $0.5^\circ$  interval from  $+26^\circ$  to  $+31^\circ$ , likewise a  $0.5^\circ$  interval from  $-26^\circ$  to  $-31^\circ$ . Hence, a total of 20 parametric spaces were selected for the Hough transform.

## 2.2 Front-View Inspection Algorithm

In the front-view inspection, we calculate the inner diameter and outer diameter as well as the center point of the front image. H. S. Kim and B. R. Lee [15, 16] proposed a line scanning method which scans the front image of the tube in both horizontal and vertical directions inside a specific region. However, when there is an impure material or a lump of dust inside the tube, the method may give the wrong geometric information for the tube. To avoid this weakness, we applied a radial scanning method to measure the radius of the inner circle

of the tube. An exemplary tube image describing the scanning method is shown in Fig. 6.

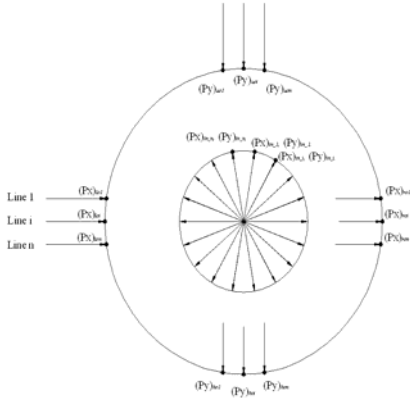


Fig 6. Scanning methods to find the center and radius

Using a number of scanning lines along both x and y directions, the x- and y-coordinate values of the tube center can be calculated. Fig. 5 shows how to find the x-coordinate value of the circle center. Center position and radius are averaged among their values from the scanning lines to increase measuring accuracy. The radius of the outer circle and the coordinate of the center position can be calculated by the Eqs. (5) ~ (7).

$$R_o = \frac{1}{2n} \sum_{i=1}^n [(P_x)_{roi} - (P_x)_{loi}] \quad (5)$$

$$X_{center} = \frac{1}{n} \sum_{i=1}^n \left[ \frac{(P_x)_{loi} + (P_x)_{roi}}{2} \right] \quad (6)$$

$$Y_{center} = \frac{1}{n} \sum_{i=1}^n \left[ \frac{(P_y)_{uoi} + (P_y)_{boi}}{2} \right] \quad (7)$$

When the center position of the circle is known, we can calculate the radius of the inner circle by considering the length between the center position of the circle and points on the circle. Thus, the average radius of the inner circle can be calculated by using Eq. (8).

$$R_i = \left( \sum_{i=1}^n \sqrt{((P_x)_{in_i} - X_{center})^2 + ((P_y)_{in_i} - Y_{center})^2} \right) / n \quad (8)$$

where  $P$  is a point on the inner circle.

### 3. EXPERIMENTAL SETUP AND PIPE-FAULT-DETECTION

To inspect the forming status at both ends of the formed tubes, we implemented computer vision-based experimental equipment. For this purpose, three CCD cameras were used at each end of the tube. Cameras (Sony, model XC-HR70) were used to inspect front-view, side-view and nut-view. The lenses used were TCL 04S-3 for front-view, TCL 04L-3 for side-view, and ML-2514 for nut-view. A Matrox II frame grabber was

used to capture images and transfer them to the computer. The Mil-Lite library was used for communication between Microsoft Visual C++ 6.0 and the Matrox II frame grabber. Open CV Library was used for basic operations such as filtering, feature detection, etc. A clamp and a stopper were operated by an air cylinder to make a position and hold the formed tube at the test bed while the vision inspection process was running. Master K80S PLC was used to control the clamp and stopper, and to receive the inspection-end signal from the computer. The photograph of the implemented computer vision-based inspection system is shown in Fig. 7.



Fig 7. Implemented computer vision-based inspection system

To inspect with good accuracy, we need to secure the pipe and capture the image. To secure the pipe, we used a stopper and clamp. First, the pipe needs to be pushed until it touches the stopper, and then the clamp comes down to fix the pipe in place. After this, the stopper needs to return to its initial position; otherwise it will cover the front view inspection area.

Using the images taken from the front- and side-view profiles and the proposed algorithm, the outer diameter, inner diameter, slope angle, and eccentricity were calculated, and the pipe was determined to be normal or faulty. Table 1 shows the criteria usually used in the tube manufacturing company to determine whether the tested tube is normal or abnormal. To apply the standards in Table 1, a real length per unit pixel had to be found. In this paper, the length per unit pixel was set up as 0.001 mm/pixel based on real experiments, which fitting real measurement as mm in inspection measurement as pixel. In the experiment, image distortion compensation was not considered because the focal length of the lens was too short, distance is constant between camera and object and the view size was very small, at  $5 \times 5 \text{ mm}^2$ , which does not cause big differences between distorted and undistorted images.

Table 1: Parameter criteria for normally formed tubes

Criterion			
Outer Diameter (mm)	Inner Diameter (mm)	Angle (°)	Eccentricity (mm)
7.1±0.18	3.2±0.13	114.5±0.5	0±0.1

### 3.1 Inspection Test for Normal Tube

For the inspection test, normal and abnormal tubes were prepared and the proposed inspection algorithm was tested to prove its feasibility. Fig. 8 shows a processed front-view image after edge detection and radius detection algorithms were applied. The four small circles found on the outer circle represent the core points for left, right, top, and bottom ends which were needed to calculate the radius of the outer circle and its center point based on the line scanning method. Once the center point was known, the radius of the inner circle was calculated by averaging the radial lines between the center point and the inner circle, which were generated by the radial scanning method. The outer and inner diameters were calculated to be 7.078 mm and 3.195 mm, respectively, using Eqs. (5) to (8). The measured dimensions for the inner and outer circles were in the range of the allowance designated in Table 1.

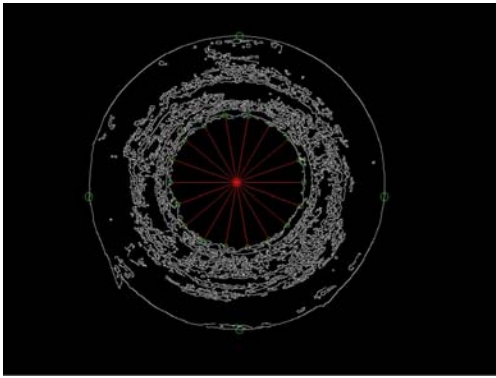


Fig 8. Processed front-view image for a normal tube

Figure 9 shows a processed side-view image after some preprocessing such as edge detection, line scanning, and a Hough transform to draw two inclined lines representing the formed surface of the tube. The lower three thin horizontal lines represent scanning lines for detecting the center line of the tube stem. A reference point was considered in the image. The reference point was decided as an intersection point of a horizontal line passing through the upmost brightest pixels and center line of the tube. All windows for region-of-interests were calculated as relative distances to the reference point. This way, all windows could trace the regions-of-interest even if the tube was placed in a slightly different position than the position preset. The four small squares (upper two and lower two) were regions of interest to find the thickness of the formed area of the tube. The two larger rectangles were regions to calculate the inclined lines of the formed area. The calculated slope angle of the formed area, defined as  $\gamma$  in Eq. (3), was 114.8 degrees. The eccentricity, defined as the off-set displacement from the coaxial line of the tube to the intersection point of the two inclined lines, was calculated as 0.058 mm. The measured two parameters were in the range of the allowable tolerance designated in Table 1.

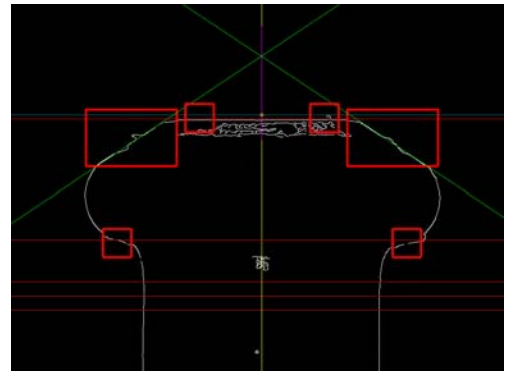


Fig 9. Processed side-view image for a normal tube

### 3.2 Inspection Test for Abnormal Tube

Figure 10 shows the processed image for a front-view inspection for a given abnormal tube, where the dimensions of the inner and outer diameters were 3.158 mm and 7.102 mm, respectively, which satisfies the allowable tolerance for normality regarding inner and outer diameters. However, it is necessary to check the eccentricity of the formed head to prove whether the tube is normal in all parameters.

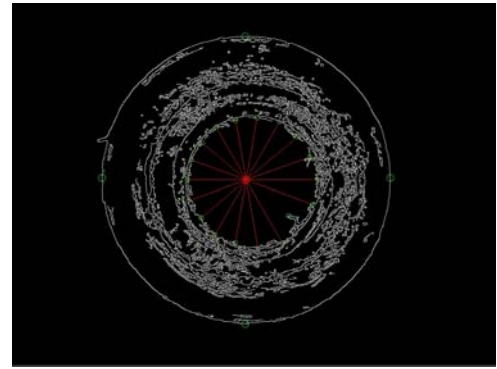


Fig 10. Processed front-view image for an abnormal tube

Figure 11 shows the image of a side-view inspection. As shown in the figure, the eccentricity was relatively big, which means that the tube has a large distance between the intersection point of the slope and center line because

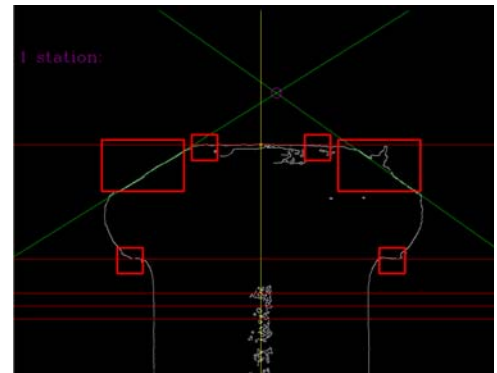


Fig 11. Processed side-view image for an abnormal tube

of a forming fault. The measured eccentricity and the slope angle are 0.348 mm and 112.9 degrees, respectively. According to the front-view and side-view inspections, the forming status of the tube was not normal.

### 3.3 Repeatability and Accuracy Tests

Two kinds of performance tests, repeatability and accuracy, were carried out. In the repeatability test, iterative measurements were performed on the same tube to show the robustness of the measurement. In the accuracy test, dimensions of the measured parts from the proposed vision inspection were compared to those of a 3-D measurement system. Table 2 shows results of the repeatability test, where five parameters of the tube were measured 10 times. As shown in Table 2, the test results were good; there exists no deviations in the outer diameter or angle. Only a 0.01 level of deviation was observed for the inner diameter, thickness, and eccentricity. This level of deviation is below the allowable deviation for most manufacturing lines.

Table 2 Repeatability test results for a sample tube

No	Outer diameter	Inner diameter	Angle	Thickness	Eccentricity
1	7.13	3.21	114.4	2.47	0
2	7.13	3.21	114.4	2.48	0
3	7.13	3.21	114.4	2.48	0
4	7.13	3.20	114.4	2.47	0
5	7.13	3.21	114.4	2.47	0
6	7.13	3.21	114.4	2.48	0.012
7	7.13	3.20	114.4	2.47	0
8	7.13	3.21	114.4	2.47	0
9	7.13	3.21	114.4	2.47	0
10	7.13	3.21	114.4	2.47	0

### 4. CONCLUSION

In this paper, we developed a vision-based fault inspection system and algorithm that can inspect all pipes coming from the forging machine. The system determines whether the pipe is normal or abnormal and the faulty pipe is discarded by a removing actuator. At the same time, the inspection result data and image files are delivered to the server computer. A modified Hough transform and line scanning method are used to analyze the pre-processed image, and the status of the pipe is determined to be satisfactory or defective.

The forging machine takes about 1 sec to draw the pipe, form and release the pipe. That means the whole inspection time could be accomplished in a second. The inspection system spends about 720 milliseconds (ms) to complete the inspection process, including the signaling time from/to the main controller. Therefore, the developed inspection system satisfies the required time. Also, data overflow problems with stacks of data and image files are solved.

In general, the pipes produced in the plant have 0.04 mm of eccentricity. Sometimes this may cause a problem for determining fault status. Since the inspection system can guarantee an accuracy of 0.01 mm, it can remove the decision error from pipe irregularity. Therefore, it is

concluded that the developed inspection can be successfully applied to a real plant system to satisfy all the requirements.

### 5. REFERENCES

- Otsu, N., 1979, "A Threshold Selection Method from Gray-Level Histograms", *IEEE Trans. Syst. Man Cybernet*, SMC-9, pp. 62-66.
- Park, H. J., Hwan, Y. M., 2001, "Dimensional Measurement Using the Machine Vision", *KSPE*, Vol. 18, NO.3, pp. 10-17.
- Maitre, H., 1986, "Contribution to the Prediction of Prediction of Performance of the Hough Transform", *IEEE Trans. on Pattern Analysis and Machine Intelligence*, PAMI-8.5.
- Braggins, D. W., 1990, "Image Processing for Industrial Applications in Europe", *Proc. 5th International Conference on Robot Vision and Sensory Control*, pp. 13-23.
- Persoon, E., 1988, "A Pipelined Analysis System Using Custom Integrated Circuits", *IEEE On Pattern Analysis and Machine Intelligence*, Vol. 10. No.1, pp. 110-116.
- Gotoh, T., Toriu, T., Sasaki, S., 1988, "A Flexible Vision-Based Algorithm for a Book Sorting System", *IEEE On Pattern Analysis and Machine Intelligence*, Vol. 10, No. 3, pp. 393-399.
- Shapiro, S. D., 1975, "Transform for the Computer Detection of Curves in Noisy Picture", *Comp. Graphics Image Process.* 4, pp. 328-338.
- Ballad, D. H., 1981, "Generalizing the Hough Transform to Detect Arbitrary Shapes", *Pattern Recognition*, 13, pp. 111-121.
- Leavers, V. F., 1990, "The Dynamic Generalized Hough Transform", *1st European Conference on Computer Vision (ECCV 1990)*, Antibes, France.
- Califano, A., Tayler, R. W., 1989, "A New Approach to Complex Parameter Feature Extraction", *IEEE on Pattern Analysis and Machine Intelligence*, pp. 192-199.
- Margarita Chli and Andrew J. Davison., 2008, "Active Matching", *10th European Conference on Computer Vision (ECCV 2008)*, Antibes, France.
- P.G.U., 1994, "A Knowledge-Based Inspection Process Planning System for Coordinate Measuring Machines", *Journal of Intelligent Manufacturing*, pp. 351-363.
- Etienne E. Kerre and Mike Nachtgeael, 2000, *Fuzzy Techniques in Image Processing*, pp. 222-246.
- R. Hartley and A. Zisserman, 2003, *Multiple View Geometry in Computer Vision*, Cambridge University Press, Second Edition, pp. 102-104.
- H. S. Kim and B. R. Lee, 2006, "Real-Time Pipe Fault Detection System Using Computer Vision", *International Journal of Precision Engineering and Manufacturing*, Vol. 7, No. 1, pp. 30-34.
- H. S. Kim, E. Naranbaatar, Sheikh Ahasan Ahammad, Y. H. Bae and B. R. Lee, 2009, "Real-Time Forming Error Inspection System using Computer Vision for Small-Sized Tubes", *ICROS-SICE 2009*, Fukuoka, Japan, pp 1950-19554.

## DEVELOPMENT OF A SEPARABLE CAR SEAT TYPE MULTI FUNCTIONAL STROLLER BY OPTIMIZATION

M. Fuhad Hassan and E. Sik Jeon

Graduate School of Engineering, Kongju National University (KNU), Cheonan-si, Chungcheongnam-do,  
South Korea.

### ABSTRACT

In this paper, optimization of a separable car seat type multi functional stroller based on minimizing total weight, subject to the limits on the structural performance measures. The effects of dimensional imperfections of the members on the minimum weight design of a structure. Design sensitivity coefficients of objective function and constraints are computed and supplied to the optimization algorithm. In this Research Paper the components of the separable car seat type multi functional stroller and its cross sectional imperfection are discussed. This paper illustrated with design concept considering the cases with multiple loading options and some means of deterministic analysis. The achieved optimum solutions for designs with admissible tolerances show significant differences in structural weight. In case of these the proper analytical approaches were given by showing the stresses, deformations and weight. Problems are presented to study the performance of the proposed optimization technique as well as the methodology based on approximation optimization concepts.

**Keywords:** Optimization, Sensitivity, Optimization-algorithm, Deterministic Analysis, Structural Weight.

### 1. INTRODUCTION

Structural shape optimization aims to find an optimum shape, defined by a set of design variables, in order to minimize an objective function while satisfying a set of design constraints. Over the past decades, the scope of structural shape optimization has widened considerably. Optimization is to enhance the weight minimizing of structures remains an active area of research.

Intense global competition in the automotive industry has driven automakers to propel the evolution of optimization methods for design applications. The urgent need to improve product performance, shorten design cycles, reduce cost, and meet increasingly stringent government regulations is the main driving force. The performance of an automobile can be improved in a cost-effective manner by integrating optimization techniques in the design process. In the past decade, the automotive industry has extensively used optimization techniques for component design. As a result, almost any structural part of an automobile can now be optimized using such techniques. Examples of optimization of small parts such as mirrors, steering knuckles, rocker panels, mounting brackets, pillars, seat frames, trunk reinforcements, suspension rings and tie rods or large parts such as engine blocks, chassis and whole car bodies, are abundant in the published literature. For instance, Chen et al. [1] performed the shape optimization of the gas tank. White and Webb [2] used shape optimization method to determine the optimum air cleaner shape and rib design for low shell noise. Chen and Usman [3] present

an application of topology optimization for seam weld reduction of an instrument panel. Leiva et al. [4] utilized sizing optimization method to identify optimum location of automobile welds.

Traditional methods for shape optimization are based on the assumption that the geometry of the structure is defined by the shape of its boundary, and that an optimal design can be found by varying the shape of an existing initial design. Even if at first glance such an approach seems very general, this formulation cannot by itself remove existing boundaries or add new boundaries to the design.

The main difficulties encountered in shape optimization are [5], the continuously changing of the model, since it is difficult to ensure that the accuracy of the analysis remains adequate throughout the design process, and the expense involves in to obtain good sensitivity derivatives with respect to shape design variables than with respect other variables (e.g. sizing variables).

The investigation presented in this paper aims to develop a fully automated shape and material layout optimization system for Car Seat type stroller structures. In last year's some research groups had combined successfully these technologies, but the design domain (ground structure) where topology optimization is formulated has always been supposed to be constant in the course of the process, as proposed for instance by Maute and Ramm [6].

This paper will propose an integrated procedure where GDO and shape optimizations are combined in



automation. Shape and GDO optimization steps are alternated during the process, where the Stroller geometry and sizing variables are optimized sequentially (see Fig. 1). This procedure allows predicting the optimum shape of the structure, but also the optimum material distribution on the model. This formulation involves a variable designing domain for the topology optimization problem, since the shape of the shell mid-plane where the material is distributed changes during the process. The presented method will enhance the exploration of better designs for carrying the applied loads, and provide the designer with a tool which would help to conceive the best configuration of the element considered in each situation.

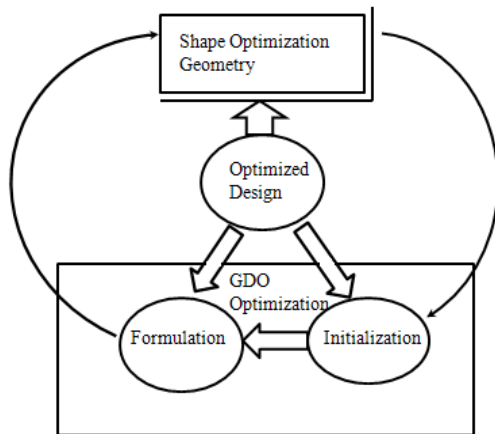


Fig 1. Combined Shape and GDO optimization

The objective of this paper is to present a methodology for Development of a Separable Car seat type by optimizing a Multi Functional Stroller. First, the traditional GDO-based method of optimization using sensitivity analysis is explained. Then the alternative method of optimality criteria is presented. It will be shown that the complex task of shape optimization of nonlinear structures can efficiently be performed by the optimality criteria method. It will also be proved that by this process the structure for the stroller what we get is more efficient and light.

## 2. ADAPTIVE REFORMULATION OF OPTIMIZATION PROBLEMS

A typical design optimization problem for this process can be defined as follows:

$$\text{Minimize } \varphi(b) \text{ Subject to } \psi_i(b) \leq \psi_i^u \text{ and } b_j^l \leq b_j \leq b_j^u \quad (1)$$

Where  $\varphi(b)$  is the objective function;  $b$  is the vector of design variables captured in CAD solid models;  $\psi_i(b)$  is the  $i^{\text{th}}$  structural performance measure with its corresponding upper bound;  $\psi_i^u$ ; and  $b_j^l$  and  $b_j^u$  are lower and upper bounds of the  $j^{\text{th}}$  design variables, respectively.

### 2.1 Goal driven non-linear constrained optimization

Assuming that the objective and constraints are sufficiently smooth functions of the optimization variables  $s$ , the solution of the above constrained optimization problem is characterized by a stationary point of the following Lagrange function:

$$L(s, \beta, \gamma, v) = f(s) + h(s)^t \beta + g(s)^t \gamma \quad (2)$$

where  $\eta$  and  $\gamma$  are vectors of Lagrange multipliers. The Karush–Kuhn–Tucker (KKT) conditions are the first order necessary conditions for a local extremum:

$$\nabla L = \nabla f(s) + \nabla g(s)^t \beta + \nabla h(s)^t \gamma = 0 \quad (3)$$

where  $\nabla(\cdot)$  is the gradient operator with respect to the optimization variables  $s$ . In structural optimization, for example, the objective  $f$  and the constraints  $h$  and  $g$  are typically functions of certain optimization criteria, such as mass, strain energy or stress, which are in turn explicit or implicit functions of the optimization variables  $s$ .

At the optimum,  $\nabla L$  vanishes. For non-optimal designs the norm of the residual together with the norm of the constraint violations can be used to measure the quality of the intermediate result.

### 2.2 Shape optimization

Shape optimization methods provide a powerful tool for challenging design problems in form finding of shell structures. These methods allow to determine the optimum shape of variable contour edges, which define the geometry of the shell mid plane. There are a large number of possible formulations of shape optimization problems.

One may choose to minimize weight, stress, compliance, displacement or any other property that can be derived with the output from a finite element analysis module. In the present study, we formulate the problem as the minimization of the compliance for a fixed volume of material.

In order to incorporate the constraints described above, the penalty method is used. In this method the fitness of an individual design is increased when constraints are violated. Then Eq. (4) can be written in the following way:

$$g_i = W + \lambda |\Delta \sigma|^2 + \mu |\Delta V p|^2 + \eta H_1(g_c, 0) + \xi H_2(g_s, 0) \quad (7)$$

where  $g$  is the penalized weight,  $i$  the structured index,  $|\Delta \sigma|$  the allowed stress minus acting stress,  $|\Delta V p|$  the allowed control-points coordinate minus actual control-points coordinate,  $H_1(g_c, 0)$  the function that measure the elements shape distortion. If there exist some singular or negative Jacobians  $g_c = aW$ , otherwise  $g_c = 0$  and  $H_2(g_s, 0)$  the function that measure the violation of side constraints. If one or several side constraints are violated  $g_s = \gamma W$ , otherwise  $g_s = 0$ .

The parameters  $\lambda$ ,  $\mu$ ,  $\eta$ ,  $\xi$ ,  $\sigma$ ,  $\gamma$  are adjusted by trial and, in this paper, they have been evaluated in such a way that a 10% of violation in every constraint increases the original weight by about of 10%.

### 3. GEOMETRY BASED MODELING

The solid modeling system used herein is based on geometric element modeling. This type of modeling is based on three main aspects [7]: problem formulation through geometry, geometry representation and geometry manipulation.

The formulation of the shape optimization problem by using the geometry is depicted in Fig. 2. The process begins using solid design elements to define the problem



geometry. Then, the mesh control information is defined on the boundary as well as the problem-specific attributes, such as material properties, loads, boundary conditions, etc., are assigned to the model.



Fig 2. Modeling process

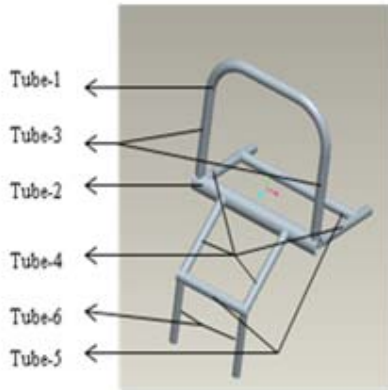


Fig 3. Geometric entities

#### 4. NUMERICAL SIMULATION IMPLEMENTATION

The implementation part is basically consists of 3 parts. These 3 parts are very important for the stroller optimization cases. Three parts are:

1. Space size determination
2. Determination of optimized design criteria by GDO optimization
3. Weight minimization by the Shape optimization

##### 4.1 Space Size Determination

Table 1: Space size dimension of different cars:

Type	Length (mm)	Width (mm)	Height (mm)
1	520	310	330
2	480	300	300
3	560	300	320
4	500	310	310
5	530	320	300
Optimum	518	308	312

#### 4.2 Optimized Design Criterion By GDO

For the optimization by GDO process we consider two criteria for the selection of force

(a) Give the movement force to the stroller.

(b) Give the force to the stroller main edges by the baby. In case of this condition I used the weight of baby considering that the baby is 2 or 2.5 yrs old. The weight of the baby is 6-8.5 kg. So I used the forced as 60N.

Optimization history of tube selections:

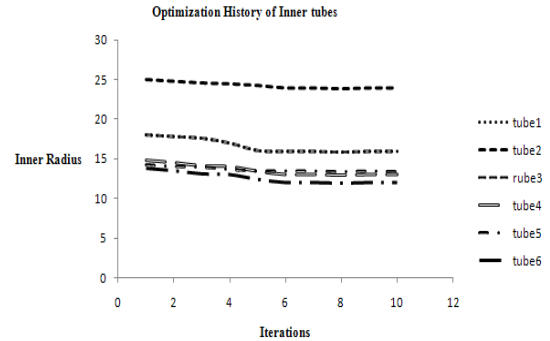


Fig 4. Optimized radius selection (Inner tube)

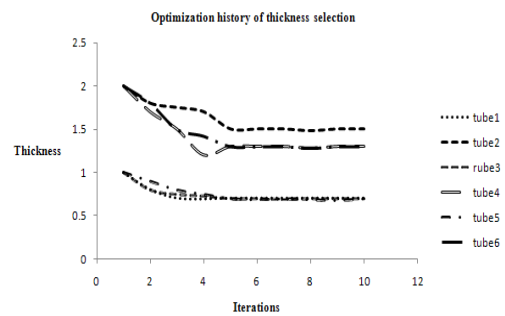


Fig 5. Optimized thickness selection

Sensitivity analysis for selecting the tube radius of optimal value:

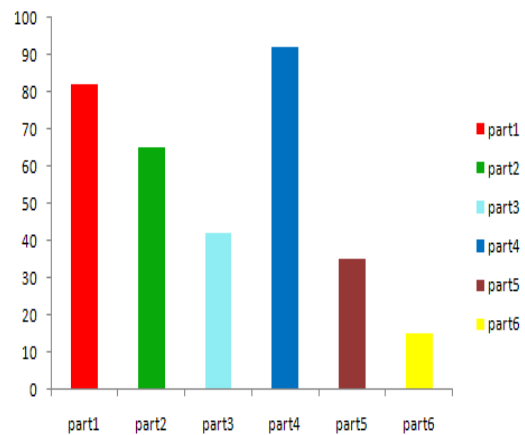


Fig 6. Sensitivity analysis for tube radius selection

Table 2: Optimum dimension of tube inner and outer radius and thickness

Tube	Inner (mm)	Thickness (mm)	Outer (mm)
1	16	0.7	16.7
2	24	1.5	25.5
3	16	0.7	16.7
4	13	1.3	14.3
5	13.5	1.7	15.2
6	12	1.3	13.3

Table 3: Weight minimization from initial condition to GDO optimization

Tube	Initial Dimensions		
	Inner Radius (mm)	Outer Radius (mm)	Thickness (mm)
1	15	17	2
2	15	17	2
3	15	17	2
4	15	17	2
5	15	17	2
6	15	17	2

Optimal dimensions			Weight Reduction (%)
Inner Radius (mm)	Outer Radius (mm)	Thickness (mm)	
16	16.7	0.7	12
24	25.5	1.5	31
16	16.7	0.7	9
13	14.3	1.3	17
13.5	15.2	1.7	20
12	13.3	1.3	13

#### 4.3 Weight Minization By Shape Optimization

Here in the selection of Shape optimization first application of the modeling in the program. Then applied all the conditions and finally by 10% reduction of weight will get the optimized weight of the stroller.



Fig 7. Geometry dimensions, boundary and load conditions for the stroller



Fig 8. Final optimized shape and optimal weight of the stroller

Table 4: Shape optimization data for 10% reduction of weight for the optimal structure

Type	Mass (Kg)	Target Reduction (%)	Support Type
Original	0.580		
Optimal	0.522	10	Fixed

## 5. RESULTS

It is found that in case of our procedure we obtained the optimal dimensions for stroller by the GDO process and optimized mass and final shape by the Shape optimization process. Typical results are shown in Fig. 7, Fig. 8 & Table 4. In fig. 7 it shows the optimized dimensions of the tubes strollers and the modeling and fig. 8 it shows the final shape given by the shape optimization and Table 4 gives the specific optimized result by reducing the original weight by 10%.

## 6. CONCLUSION

A new methodology for shape optimization of a separable car seat type stroller has been developed. Two optimality criteria have been proposed and combined with a geometrically nonlinear analysis. The method changes the shape of the structure so that the average optimized weight (or variation for the case of thickness optimization) for all design variables become uniform. It has been shown that this method converges to the optimum shape in less number of iterations compared to the standard gradient-based methods of optimization. It is concluded that the complex task of shape optimization of nonlinear structures can efficiently be performed by the proposed methodology.

An integrated approach for three-dimensional shape optimal design using genetic algorithms and mesh parameterization has been presented. The definition of geometry through shape geometric entities provides a great versatility for the characterization and control of the body shape. Also, the use of GDO and Shape optimization as optimization technique increases the performance of the developed tool due to its great advantages as compared with traditional optimization techniques.

The use of this combined optimization tool provides

an alternative, effective and realizable way to solve this kind of problem and their encourages its application to more complex three-dimensional shape optimization problems.

More studies are currently conducted by the authors to determine the performance of the proposed algorithm in the design of large scale structures, and also how to consider and modify the imperfection during shape optimization. The results of such studies will be reported in the near future.

## 7. REFERENCES

1. C.J. Chen, S. Maire, M. Usman., "Improved fuel tank design using optimization." ASME McNu97' Design Optimization with Applications in Industry Symposium, Chicago, 1997.
2. J.A. White, J.C. Webb, "Air cleaner shell noise reduction with finite element shape optimization." Proceedings of the Society of Automobile Engineers Noise and Vibration Conference and Exposition, Detroit, MI, 1997.
3. C.J. Chen, M. Usman, "Design optimization for automobile applications." Int. J. Vehicle Des. 25 (2001) 126-141.
4. J.P. Leiva, L. Wang, S. Recek, B.C. Watson, "Automobile design using the GENESIS structural optimization program." NAFEMS Advances in Optimization Technologies for Product Design, Chicago, IL, 2001.
5. R.T. Haftka, R.V. Grandhi, "Structural shape optimization - a survey." Comput. Methods Appl. Mech. Eng. 57 (1986) 91-106.
6. Maute K, Ramm, "Adaptive topology optimization of shell structures." E. AIAA J 1997, 35:1767-73.
7. S. Kodiyalam, V. Kumar, P.M. Finnigan, "Constructive solid geometry approach to three-dimensional shape optimization." AIAA J. 30 (1992) 1408-1415.

## 8. MAILING ADDRESS

Md. Fuhad Hassan  
Graduate School of Engineering,  
Kongju National University(KNU),  
275, Budaе-dong, Cheonan-si,  
Chungcheongnam-do 330-717, South Korea.

## AN EXPERIMENTAL INVESTIGATION OF VEGETABLE OIL BASED CUTTING FLUID ON DRILLING MEDIUM CARBON STEEL BY HSS DRILL BIT

M. A. Islam<sup>1</sup>, M. J. Uddin<sup>1</sup>, M. A. Alim<sup>1</sup> and N. R. Dhar<sup>2</sup>

<sup>1</sup>Department of Industrial and Production Engineering  
Rajshahi University of Engineering and Technology, Rajshahi, Bangladesh

<sup>2</sup>Department of Industrial and Production Engineering  
Bangladesh University of Engineering and Technology, Dhaka, Bangladesh

### ABSTRACT

Drilling is the most prominent machining process, requiring specialized techniques to achieve optimum cutting condition. Drilling can be described as a process where a multi-point tool is used to remove unwanted materials to produce a desired hole. High production machining and drilling with high cutting velocity, feed and depth of cut is inherently associated with generation of large amount of heat and high cutting temperature and power consumption. In Dry condition, such high cutting temperature not only reduces dimensional accuracy and tool life but also impairs the roundness deviation, taper of the hole. Conventional cutting fluid uses for producing cylindrical holes in the work piece can reduce above problems but it pollutes the environment and has high risk of water pollution and soil contamination during disposal. The increasing needs for environmentally friendly production techniques have justified the demand for an alternative to machining process using cutting fluids. Vegetable oil is used as cutting fluid is more effective to reduce temperature and also have good lubrication properties. In this regard the present work has been carried out with a view to study the effects of vegetable oil based cutting fluid on the cutting performance of medium carbon steel, as compared to completely dry and wet in terms of force, torque, chip formation mode and roundness deviation. Compared to the dry and wet, vegetable oil based cutting fluid performed much superior mainly due to reduction in cutting zone temperature, enabling favorable chip formation and improving roundness and taper. It also provides lubrication in the tool tip and work surface interface.

**Keywords:** Vegetable Oil Based Cutting Fluid, Drilling, Chip, Force, Torque, Roundness Deviation.

### 1. INTRODUCTION

Hole making had long been recognized as the most prominent machining process, requiring specialized techniques to achieve optimum cutting condition. Drilling can be described as a process where a multi-point tool is used to remove unwanted materials to produce a hole. It broadly covers those methods used for producing cylindrical holes in the work piece. While removal of material in the form of chips new surfaces are cleaved from the work piece accompanied by a large consumption of energy. The mechanical energy necessary for the drilling operation is transformed in to heat leading to conditions of high temperature and severe thermal / frictional conditions at the tool- chip interface [Ezugwu and Lai 1995]. The magnitude of the cutting temperature increases though in different degree with the increase of cutting velocity, feed and depth of cut. At such elevated temperature the cutting tools if not enough hot hard may lose their form stability quickly or wear out

rapidly resulting in increased cutting force, dimensional inaccuracy of the product and shorter tool life [Kitagawa et al. 1997]. This problem increases further with the increase in strength and hardness of the work material. During drilling process, the most important factor affecting the cutting tool performance and work piece properties is cutting temperature that emerges between drill bit and chip.[Eyup and Babur 2006]. The cutting temperature directly influences hole characteristics such as diameter, perpendicularity and cylindricity, as well as surface roughness and tool wear [Eyup and Babur 2006]. A major portion of the energy is consumed in the formation and removal of chips. The greater the energy consumption, the greater are the temperature and frictional forces at the tool-chip interface and consequently the higher is the tool wear [Senthil Kumar et al 2002]. Drill wear not only affects the surface roughness of the hole but also influences the life of the drill bit [Panda et al. 2006].

Worn drills produce poor quality holes and in extreme cases, a broken drill can destroy almost all finished parts. A drill begins to wear as soon as it is placed into operation. As it wears, cutting forces increases, the temperature rises and this accelerates the physical and chemical processes associated with drill wear and therefore drill wears faster [Sanjay et al. 2005].

Thrust and torque depend upon drill wear, drill size, feed rate and spindle speed. Research results show that tool breakage, tool wear and work piece deflection are strongly related to cutting force [Sanjay et al. 2005]. The application of cutting fluid during machining operation reduces cutting zone temperature and increases tool life and acts as lubricant as well [Beaubien and Cattaneo 1964]. Also Dhar et al. [2004] state that without cooling and lubrication, the chip sticks to the tool and breaks it in a very short cutting time. It reduces cutting zone temperature either by removing heats as coolant or reducing the heat generation as lubricant. In addition it serves a practical function as chip- handling medium [Cassin and Boothroyd 1965]. On the other hand, the cooling and lubricating effects of cutting fluid influence each other and diminish with increase in cutting velocity [Kitagawa et al. 1997].

Manufacturing by machining constitutes major industrial activities in global perspective. Like other manufacturing activities, machining also leads to environmental pollution [Ding and Hong 1998 and Hong et al. 1999] mainly because of use of cutting fluids. These fluids often contain sulfur (S), phosphorus (P), chlorine (Cl) or other extreme-pressure additives to improve the lubricating performance. These chemicals present health hazards. Furthermore, the cost of treating the waste liquid is high and the treatment itself is a source of air pollution. The major problems that arise due to use of cutting fluids are- [Aronson 1995]

- environmental pollution due to breakdown of the cutting fluids into harmful gases.
- biological hazards to the operators from the bacterial growth in the cutting fluids
- disposal of the spent cutting fluids, which also offer high risk of water pollution and soil contamination.

Since beginning of twentieth century people [Welter 1978; Kennedy 1989 and Thony et al. 1975] were concerned with possible harmful effects of various cutting fluid application. During machining process, a considerable amount of heat is generated for which the cutting fluid may attain a temperature sufficiently higher than the saturation temperature. The vapor is produced at the solid-liquid interface as a result of boiling. Vapor may be generated also at the liquid-air interface when the fluid vapor pressure is less than the saturation pressure, namely as evaporation phenomena. Vapor generated then may condense to form mist. Mists are aerosols comprised of liquid particles (less than 20  $\mu\text{m}$ ). [Iowa Waste Reduction Centre 1996] reported that besides potential skin and eye contact, inhalation is also a way to occupational exposure.

From viewpoints of Performance, cost, health, safety and environment, vegetable oils are, therefore, a viable

alternative to petroleum-based metalworking cutting fluids [Skerlos and Hayes 2003; Krahenbuhl 2005], because

- The lubricating film layer provided by vegetable oils, being basically strong and lubricious, improves workpiece quality and overall process productivity reducing friction and heat generation.
- A higher flash point yields opportunities for increased rates of metal removal as a result of reduced smoke formation and fire hazard.
- The higher boiling point and greater molecular weight of vegetable oil result in considerably less loss from vaporization and misting.
- Vegetable oils are nontoxic to the environment and biologically inert and do not produce significant organic disease and toxic effect.
- No sign and symptom of acute and chronic exposure to vegetable oil mist have been reported in human [ACGIH 1991].

The purpose of this research is to investigate the effects of vegetable oil based cutting fluid as an alternative to conventional cutting fluid on the drilling performance of medium carbon steel, as compared to completely dry cutting and wet with conventional cutting fluid. During each test cutting forces, roundness deviation, chips formation mode are measured and compared.

## 2. EXPERIMENTAL PROCEDURE

The photographic view of the experimental set-up is shown in Fig. 1. The coolant used was water soluble cutting oil and vegetable oil based cutting fluid dispensed at a flow rate of 10 l/hour. Drilling metals by high speed steel (HSS) is a major activity in the manufacturing industries. Drilling of steels involves more heat generation for their ductility and production of continuous chips having more intimate and wide chip-tool contact. Again, the cutting temperature increases further with the increase in strength and hardness of the steels for more specific energy requirement. Keeping these facts in view the commonly used steel medium carbon steel has been undertaken for the present investigations.



Fig 1. Photographic view of the experimental set-up

The drilling tests have been carried out on a radial drill machine (RM-U9 Radial Drill Machine, Sweden) by HSS drill under dry, and wet by conventional cutting fluid and vegetable oil conditions. The photographic view of the experimental set-up is shown in Fig.1. The experimental conditions of the present experiments are given in Table-1.

Table 1: Experimental conditions

<b>Machine tool</b>	: Radial Drill Machine (Sweden), 1.5 kW
<b>Work material</b>	: Medium carbon steel
<b>Cutting tool</b>	: High speed steel ( $\phi$ 4.0, 6.0 & 8.0 mm)
<b>Process parameters</b>	
Cutting speed	: 200, 440 and 670 rpm
Feed rate	: 0.16 mm/rev
Length of cut	: 20.0 mm
<b>Cutting fluid</b>	: 10 litter/min
<b>Environment</b>	: • Dry • Wet • Vegetable oil based cutting fluid

### 3. EXPERIMENTAL RESULTS AND DISCUSSIONS

During machining any ductile materials, heat is generated at the (i) primary deformation zone due to shear and plastic deformation, (ii) chip-tool interface due to secondary deformation and sliding and (iii) work-tool interfaces due to rubbing. All such heat sources produce maximum temperature at the chip-tool interface, which substantially influence the chip formation mode, cutting forces and tool life. Therefore, attempts are made to reduce this detrimental cutting temperature. Conventional cutting fluid application may, to some extent, cool the tool and the job but cannot cool and lubricate effectively as expected at the chip-tool interface where the temperature is maximum because it loses its lubricating properties at high temperature.

#### 3.1 Drilling Force and Torque

Drilling force is an important factor in drilling operation. The force exerted by the rotating drill bit on the surface which is to be drilled, referred as drilling force. Force measuring device is used to measure the drilling force and torque. The effect of conventional cutting fluid and vegetable oil based cutting fluid on drilling force and torque with 8 mm HSS drill bit and various rpm at constant feed rate as shown in Fig. 2, Fig. 3, Fig. 4 and Fig 5 respectively. Here drilling force decreases with increasing the rpm of the spindle because with increases rpm material loses its viscous properties and drilling force increases with increasing the depth of cut. Drilling torque also increases with increasing the

depth of cut but it is decreased at higher rpm. Torque and Drilling force increases with hole depth because the drill bit contact surface increases, so friction force is more in higher depth of cut. The investigation shows that the force and torque at dry condition is higher than the wet condition. By using vegetable based cutting oil it is possible to reduce cutting force 6% and torque 6.6 % than using conventional cutting fluid. Fig.6 and Fig.7 show that the drilling forces and torque with the variation of drill diameter. In these Figs. it is cleared that the force and torque increases with increases the drill bit diameter in all environment. Wet with conventional cutting fluid can reduce force and torque than dry condition but with vegetable oil condition force and torque is average 8% more reduced than wet with conventional condition.

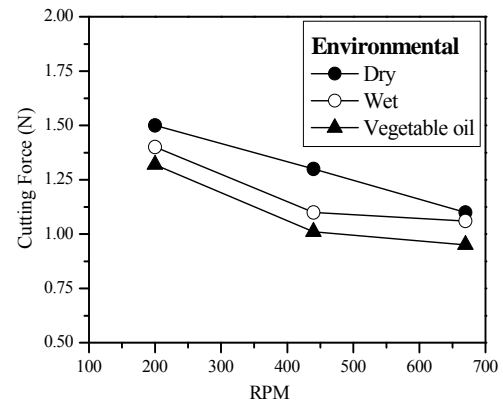


Fig 2. Variation of drilling force with rpm at different environments.

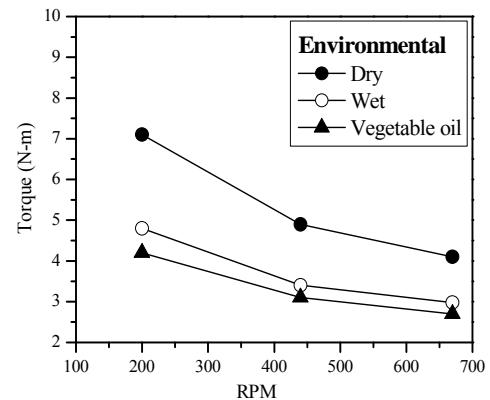


Fig 3. Variation of drilling torque with rpm at different environments.

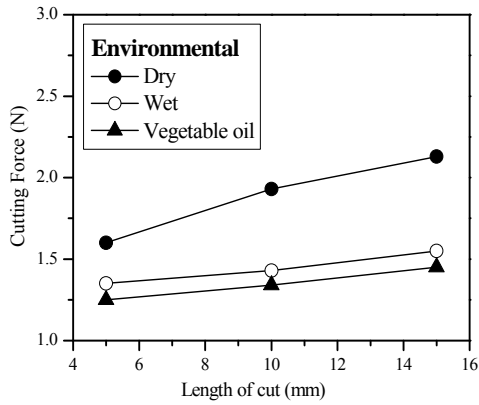


Fig 4. Variation of drilling force with increasing length of cut at different environments.

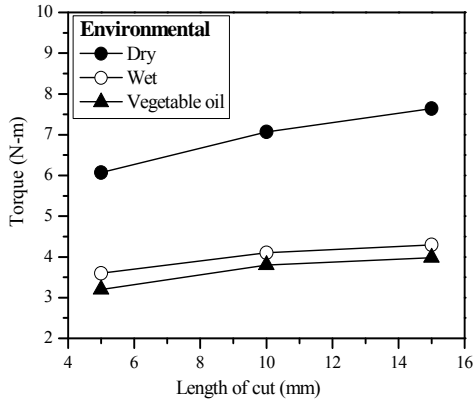


Fig 5. Variation of drilling torque with increasing length of cut at different environments.

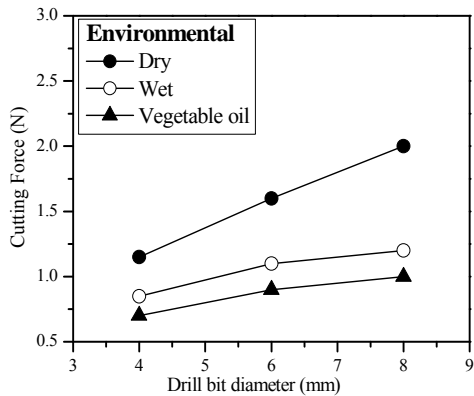


Fig 6. Variation of drilling force with different drill bit size at different environments.

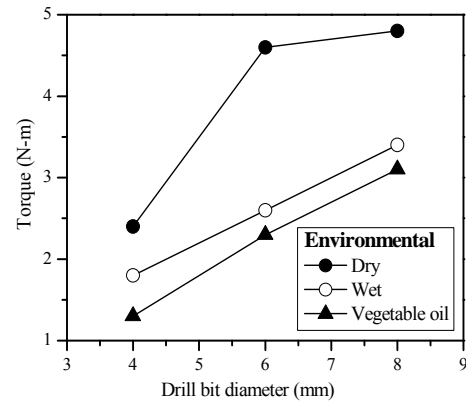


Fig 7. Variation of drilling torque with different drill bit size at different environments.

### 3.2 Roundness Deviation

Before the analysis of the quality parameters of the holes, it is important to note that neither diameter nor any other quality parameter of the hole was influenced by tool wear. Fig. 8 shows that the roundness deviation close to the beginning of the hole occurs with the number of drilling holes. For dry condition roundness deviation is higher than wet condition with conventional cutting fluid and wet with vegetable oil based cutting fluid. Some points fluctuate from the curves nature in case of dry conditions. But for wet condition, these cases are less. Fig. 9 shows the deviation for maximum, average and minimum values of hole diameter. The fluctuation of the curve occurs due to the irregular drilling force; increment of drilling temperature, variation on feed rate, vibration etc. These causes mainly occurred in dry condition. But in case of wet condition, the drilling operation is comparatively smooth. The curve for wet with vegetable oil condition is approximately straighter than the dry condition.

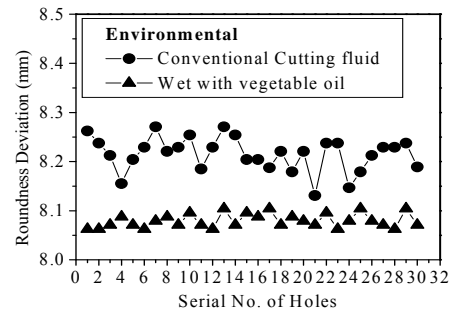


Fig 8. Roundness deviation close to the beginning of holes under dry and wet condition at 440 rpm and 8 mm drill bit.



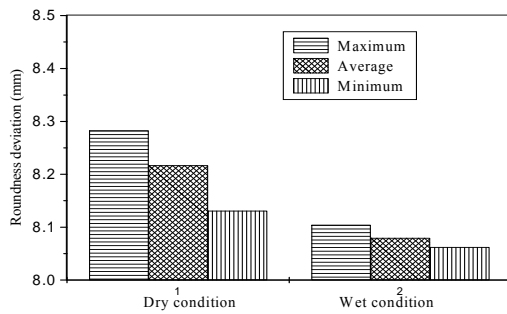


Fig 9. Maximum, average and minimum roundness deviation close to the beginning of holes under different environment at 440 rpm and 8 mm drill bit

### 3.3 Chip morphology

The shape of the chip is the most important factor for the smoothness of a drilling process and study of drilling chip is required to understand the mechanism of chip formation and those of material removal. The chips produced during drilling medium carbon steel eel at 440 rpm is shown in the Fig.10 under the different environments. Dry drilling at both 8 mm and 6 mm and 4 mm diameter drill bit provided different types of chips such as lamellar, spherical, irregular shaped. In dry condition some chips have burn for higher drilling zone temperature and ductility of steel specimens are expected to yield larger number of spherical chips. Chips produced under wet condition at both 8 mm, 6 mm and 4 mm drill bit provided approximately equal width chips but more straight in shape. For 6 mm drill bit the chips has the build up edges, which are harmful for the operation and operator. The rotational motion causes the spiral chips to have difficulty maintaining their shape as the hole gets deeper. If chips cannot keep up with the rotational motion, they will either break or be forced to move along the flute without spinning, and form string chips. Cutting fluid played very effective role for cooling and provided lubrication between drill bit and chip interface. The shape of the chip produced under dry conditions was spiral but wet condition became lamellar. The color of the chips became metallic from burnt blue due to reduction in drilling temperature by wet condition by vegetable oil.

Drill bit Size	Environments	
	Dry	Wet by vegetable oil
8 mm		
6 mm		

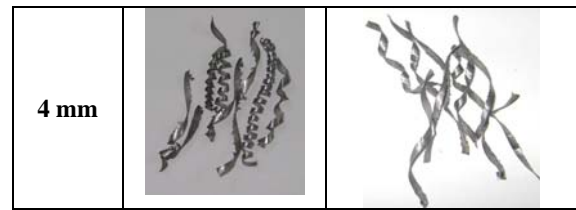


Fig 10. Chips produced by HSS drill bit under dry and wet by vegetable oil based cutting fluid conditions.

## 4. CONCLUSION

The experimentally observed effect of vegetable oil based cutting fluid in drilling medium carbon steel by HSS drill may be summarized as follows:

- The drilling force and torque is higher in dry condition than the wet conditions. Drilling with vegetable oil based cutting fluid is able to reduce more cutting force and torque 6% and 8% respectively than conventional cutting fluid.
- With increasing depth of hole and the drill bit diameter force and torque also increased in all environment but these are relatively low at vegetable oil environment.
- Roundness deviation was smaller at both the entrance of the holes under wet condition in compare to dry condition. When high depth of cut used, the drilling with wet condition was difficult because of poor cooling and lubrication action.
- The formation of chip under wet condition with vegetable oil based cutting fluid is more favorable in compare to dry condition because of high lubricant capacity. The beneficial effects of cutting fluid may be attributed to effective lubrication action, which prevents the chip sticking on the tool and makes the cut feasible and vegetable oil based cutting fluid is not harmful to the environment.

## 5. ACKNOWLEDGEMENT

This research work has been funded by Directorate of Advisory Extension and Research Services, RUET, Rajshahi-6204, Bangladesh. The authors are also grateful to the Department of Industrial and Production Engineering and Department of Mechanical Engineering RUET for providing the facilities to carryout the experiment.

## 6. REFERENCES

- ACGIH, "Documentation of the threshold limit values and biological exposure indices, 6th edition, Cincinnati, Ott: American Conference of Governmental Industrial Hygienist, (2001).
- Aronson, R. B., "Why Dry Machining", Manufacturing Engineering, Vol.114, pp.33-36, (1995).
- Cassin C. and Boothroyd G, "Lubrication Action of Cutting Fluid", J. of Mechanical Engineering Science, Vol. 7(1), pp.67-81 (1965).
- Eyup Bagci and Babur Ozcelik, "Investigation of the effect of drilling conditions on the twist drill temperature during step-by-step and continuous dry

- drilling”, *Materials and Design*, vol. 27; pp. 446–454(2006)
5. Ezugwu E. O. and Lai C. J., “Failure Modes and Wear Mechanisms of M35 High Speed Steel Drills when Machining Inconel 901”, *Journal of materials Processing Technology*, Vol. 49, pp 295-312 (1995)
  6. Kitagawa T., Kubo A. and Maekawa K., “Temperature and Wear of Cutting Tools in High Speed Machining of Inconel 718 and  $T_i-6V-2S_n$ ”, *Wear*, Vol.202, pp.142-148 (1997)
  7. Panda S.S., Singh A.K, Chakraborty D. and Pal S.K. “Drill wear monitoring using back propagation neural network”, *Journal of Materials Processing Technology*, vol. 172; pp. 283–290(2006)
  8. Senthil Kumar A., Rahman M.and Ng S. L., “Effect of High-Pressure Coolant on Machining Performance”, *International Journal of Advance Manufacturing Technology*, Vol.20, pp.83–91(2002)
  9. Sanjay C., Neemab M.L andChin C.W., “Modeling of tool wear in drilling by statistical analysis and artificial neural network”, *Journal of Materials Processing Technology*. Vol.170; pp. 494–500 (2005)
  - 10 Kitagawa T., Kubo A. and Maekawa K., “Temperature and Wear of Cutting Tools in High Speed Machining of Inconel 718 and  $T_i-6V-2S_n$ ”, *Wear*, Vol.202, pp.142-148 (1997).

## 7. MAILING ADDRESS

M. A. Islam  
Department of Industrial and Production Engineering  
Rajshahi University of Engineering and Technology  
(RUET), Rajshahi, Bangladesh  
E-mail: maislam252@yahoo.com

## PERFORMANCE EVALUATION OF DIFFERENT TYPES OF CUTTING FLUID IN MQL MACHINING OF ALLOY STEEL BY COATED CARBIDE INSERT

S. Sultana<sup>1</sup>, Prianka B. Zaman<sup>2</sup>, and N. R. Dhar<sup>2</sup>

<sup>1</sup>Department of Textile Engineering, Daffodil International University (DIU), Dhaka, Bangladesh

<sup>2</sup>Department of Industrial & Production Engineering Bangladesh University of Engineering and Technology (BUET), Dhaka, Bangladesh

### ABSTRACT

The research work studied some aspects of the turning process applied on alloy steel using coated carbide insert at different speed-feed combinations under minimum quantity lubrication (MQL) by different types of cutting fluids (water soluble cutting fluid, vegetable oil and VG68 cutting oil) as compared to completely dry cutting with respect to cutting temperature, chip thickness ratio, cutting forces, tool wear and surface roughness. In this study, the minimum quantity lubrication was provided with a spray of air and cutting fluids at a pressure 23 bars and coolant flow rate of 150 ml/hr. Compared to dry condition, MQL performed better mainly due to substantial reduction in cutting temperature that enabling favorable chip-tool interaction. This also facilitated the significant reduction in tool wear and surface roughness. The results indicated that the use of minimum quantity lubrication (MQL) by VG68 cutting oil reduced cutting temperature, cutting forces, delayed tool wear and lowered surface roughness significantly in compare to other environments.

**Keywords:** MQL, Cutting Fluids, Temperature, Force, Tool Wear And Roughness

### 1. INTRODUCTION

Machining is the process in which a tool removes material from the surface of a less resistant body, through relative movement and application of force. The material removed as chip, slides on the face of tool, called tool rake face, submitting it to high normal and shear stresses. Most of the mechanical energy used to form the chip becomes heat, which generates high temperatures in the cutting region. During machining at high cutting speed and feed, the heat generation [1] also raises the temperature of the cutting tool tips and the work surface near the cutting zone which results in high tool wear rate, reduced tool life. This may occur as these contact conditions become very severe and the tool wear is mainly caused by thermal softening, abrasion and a built-up edge (BUE) formation, which affects the quality of the generated surface and dimensional accuracy [2,3]. Machining under high cutting velocity and unfavorable process parameters require high specific energy. This machining results in very high cutting temperature and reduction of the dimensional accuracy and tool life by plastic deformation and rapid wears of the cutting points [4, 5]. During machining, in complete absence of coolant, chip transportation causes an increase of tool-chip and tool-workpiece friction, which results increased cutting force as well as abrasive wear and attrition. As a result the surface quality of the finished products deteriorates

with the increase in cutting temperature due to built-up-edge formation, oxidation, rapid corrosion, induction of tensile residual stresses and surface. At elevated temperature the cutting tool if not enough hard may lose their form stability quickly or wear out rapidly resulting in increased cutting force, dimensional inaccuracy of the product and shorter tool life [6]. Some recent techniques have enabled partial control of the machining temperature by using heat resistant tools like coated carbides, CBN etc. The improvement in the coatings of carbide tools and in the chemical and mechanical properties of tool materials has caused the increase of tool working life in machining processes.

Due to the fact that the higher the tool temperature, the faster it wears. The use of cutting fluids in machining processes is the most common strategy, as its main goal, the reduction of the cutting zone temperature, either through lubrication reducing friction wear, or through cooling by conduction, or through a combination of these functions. The application of coolant during a machining operation is believed to reduce tool wear [7]. Cutting fluids also act as chip-breaker during machining and chip formation is also affected when coolant is applied during a machining operation. The chip curl changes with the temperature gradient along the thickness of the chip and affects the size of the crater wear and the strength of the tool cutting edge.

It has already been reported [8, 9] that the use of conventional cutting fluids (wet machining) does not serve the desired purpose in machining steels by carbides, rather reduce tool life and often may cause premature failure of the insert by brittle fracture. Cutting with the excess amount of cutting fluids is still very common in conventional machining to control high cutting temperature which adversely affects, directly and indirectly, chip formation, cutting forces, tool life and dimensional accuracy and surface integrity of the products. When inappropriately handled, cutting fluids may damage soil and water resources, causing serious loss to the environment. Therefore, the handling and disposal of cutting fluids must obey rigid rules of environmental protection. On the shop floor, the machine operators may be affected by the bad effects of cutting fluids, such as by skin and breathing problems. Eliminating use of cutting fluids can be a significant economic incentive.

Enormous efforts to reduce or eliminate the use of lubricant in metal cutting are, therefore, being made from the viewpoint of cost, ecological and human health issues. According to Diniz et al. [10] machining processes with the minimum quantity lubrication (MQL) technique or without any cutting fluid (dry cutting) reduced the utilization of cooling lubricants, in order to improve environmental protection, safety of machining processes and to decrease time and costs related to the number of machining operations.

The concept of minimum quantity lubrication (MQL) presents as a possible solution for machining in achieving slow tool wear while maintaining cutting forces/power at reasonable levels, provided that the minimum quantity lubrication parameters can be strategically tuned. The conventional flood supply system demands more resources for operation, maintenance, and disposal, and results in higher environmental and health problems. MQL machining has many advantages in this regard [11, 12, and 13]. Minimal quantity lubrication (MQL) is a technique of supplying lubrication in machining to achieve both environmental and economical benefits. The present work experimentally investigates the role of minimum quantity lubrication (MQL) by different types of cutting fluids (water soluble cutting fluid, vegetable oil and VG68 cutting oil) on cutting temperature, chip thickness ratio, cutting forces, tool wear mechanism and surface finish in continuous turning 42CrMo4 steel using coated carbide insert (SNMM-TN 2000) at industrial speed-feed condition and compares the effectiveness of MQL with that of dry machining.

## 2. EXPERIMENTAL SETUP AND PROCEDURE

The experiment was carried out on lathe, which has a 7.5 kW spindle and maximum spindle speed of 1400 rpm. The work material was alloy steel (42CrMo4) having external diameter of 160 mm and length of 550 mm. The cutting tool used was coated carbide insert (Widia SNMM TN-2000). The tool holder provided negative 6° side and back rake angles and 6° side cutting-edge and end cutting-edge angles. The ranges of the cutting speed (V), feed (f) and depth of cut (d) were selected based on

the tool manufacturer's recommendation and industrial practices. The experimental conditions are given in Table-1.

Table 1 Experimental conditions

<b>Machine tool</b>	: Lathe (China), 7.5 kW
<b>Work material</b>	: 42CrMo4 steel
<b>Tool geometry</b>	: -6°, -6°, 6°, 15°, 75°, 0.8 (mm)
<b>Coating</b>	: TiCN
<b>Tool holder</b>	: PSBNR 2525 M12 (WIDIA)
<b>Process parameters</b>	
Cutting speed, V	: 175, 247 and 352 m/min
Feed rate, f	: 0.10, 0.12 and 0.14 mm/rev
Depth of cut, d	: 1.00 mm
<b>MQL supply</b>	: Air pressure 23 bars, oil pressure 25 bars and flow rate 150 ml/hr
<b>Environment</b>	: • Dry
	• MQL with Soluble oil
	• MQL with Vegetable oil and
	• MQL with VG 68 Cutting oil

The experimental set-up shown in Fig.1, where a minimum quantity lubrication jet was injected through the tool rake face, consists of a compressor, MQL applicator, centre lathe machine, tool-wear thermocouple and hardened steel. In this study, the minimum quantity lubrication was provided with a spray of air and cutting fluids at a pressure 23 bars and coolant flow rate of 150 ml/hr.



Fig 1. Photographic view of the experimental set up

The average cutting temperature was measured by tool-work thermocouple technique with proper calibration [14]. The thickness of the chips directly and indirectly indicates the nature of chip-tool interaction influenced by the machining environment. The chip samples were collected during short run and long run machining for the V-f combinations under dry and MQL conditions. The thickness of the chips was repeatedly measured by a slide caliper to determine the value of chip thickness ratio. The cutting insert was withdrawn at regular intervals to study the pattern and extent of wear on main and auxiliary flanks under both dry and MQL conditions. The average width of the principal flank wear, VB and auxiliary flank wear, VS were measured using

metallurgical microscope (Carl Zeiss, Germany) fitted with micrometer of 1 $\mu$ m resolution. No notch wear was observed during measuring under optical microscope. The surface roughness of the machined surface after each cut was measured by a Talysurf (Surtronic 3<sup>+</sup>) using a sampling length of 0.8mm.

### 3. RESULT AND DISCUSSION

Heat generation at the chip-tool interface is of prime concern in the machining process. The machining temperature at the cutting zone must be reduced to an optimum level. During machining, shearing of work material, friction between the flowing chips and rake face of the tool and friction of auxiliary flank with finished surface are the principal sources of heat generation. The magnitude of the cutting temperature increases with the increase of material removal rate i.e. with the increase of cutting velocity, feed and depth of cut, as a result, high production machining is constrained by the ascend in temperature. This problem increases further with the increase in strength and hardness of the work material.

The variation in average chip-tool interface temperature at different cutting speed, feed and environment combinations is shown in Fig.2. The cutting temperature generally increases with the increase in V, f and d though in different degree due to increased energy input. So, for high-speed machining it is very important to control the cutting temperature. It could be expected that MQL would be more effective at higher values of V, f and d.

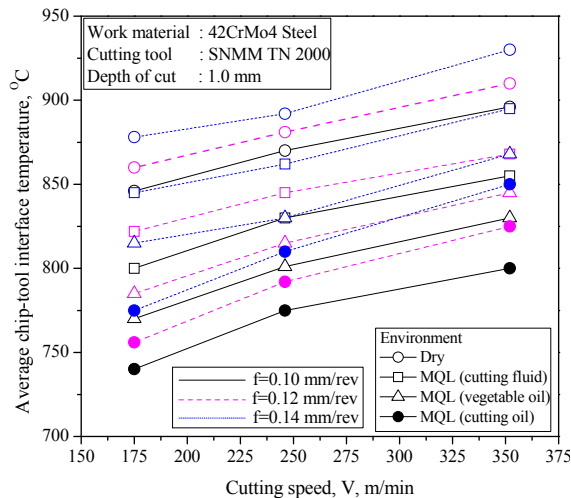


Fig 2. Variation of chip-tool interface temperature with V and f under different environments

Fig.2 shows that MQL is better than dry machining for all the V-f-d combinations but among three fluids used for MQL, cutting oil shows best results, secondly vegetable oil and than cutting fluid. The reduction in cutting temperature among all V-f combinations is more for the set V=175m/min and f = 0.10 mm/rev. In this V-f combination temperature reduction under MQL by cutting oil, vegetable oil and soluble oil varies from 8.60~12.53%, 6.67~8.98% and 3.36~5.44% respectively.

It can be noticed that with the increase in speed and feed MQL becomes less effective. This may be due to the increase in chip load and increase in plastic contact length during cutting prevents the MQL to enter into the chip-tool interface. More over, it shows best reduction at higher cutting speed for lower feed rate. In all the tests through out the entire experiment, MQL with cutting oil (VG-68) shows the best performance due to its better cooling and lubrication irrespective of speed feed and depth of cut. The effects of different environments over dry condition on cutting temperature at different V-f combination have been evaluated by regression analysis using the limited experimental data. The result is shown in Fig.3.

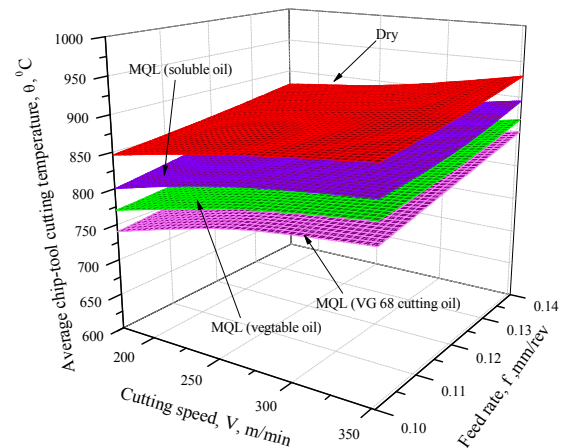


Fig 3. Effect of environment on chip-tool interface temperature evaluated by regression analysis of the experimental data

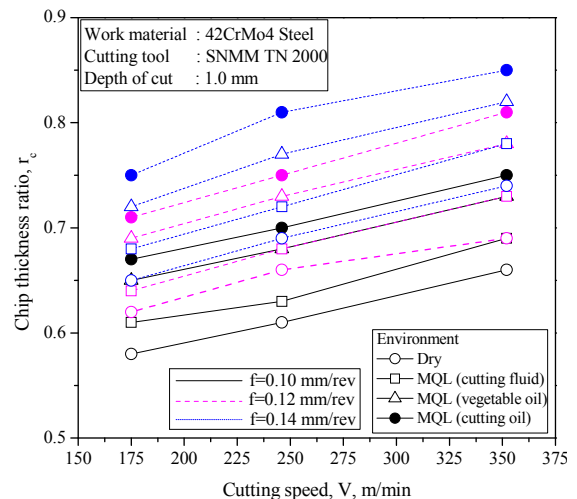


Fig 4. Variation of chip-thickness ratio with V and f under different environments

Chip thickness depends on almost all the parameters involved in machining. The degree of chip thickness which is measured by chip thickness ratio, plays an important role on cutting forces and hence on cutting energy requirements and cutting temperature. Fig.4



shows the effect of increase in  $V$  and  $f$  and the change in environment on the value of chip-thickness ratio ( $r_c$ ) obtained during turning 42CrMo4 steel. MQL has increased the value of chip thickness ratio for all  $V$ - $f$ - $d$  combinations due to reduction in friction at the chip-tool interface, reduction in built-up-edge formation and wear at the cutting edges. The percentage increment of chip thickness ratio for the above mentioned  $V$ - $f$  combinations for MQL by cutting oil, vegetable oil and soluble oil over dry condition are 14~17%, 10~13% and 3~6% respectively.

The magnitude of the cutting force is a major index of machinability which governs productivity, product quality and overall economy in machining. The cutting forces increase almost proportionally with the increase in chip load and shear strength of work material. The magnitude of main cutting force,  $F_C$  and feed force,  $F_f$  have been monitored by dynamometer for all the speed-feed combinations under dry, MQL (soluble oil), MQL (vegetable oil) and MQL (VG 68 cutting oil) machining by coated carbide insert (SNMM-TN2000) which have been shown graphically in Fig.5 and Fig.6 respectively. The figures clearly indicate the influence of feed and cutting speed on main cutting force ( $F_C$ ) and feed force ( $F_f$ ). The main cutting force and feed force are increased though in different degree by increasing feed due to increased energy input and chip load and decreased by increasing cutting speed due to much softening of the work material ahead of the advancing tool.

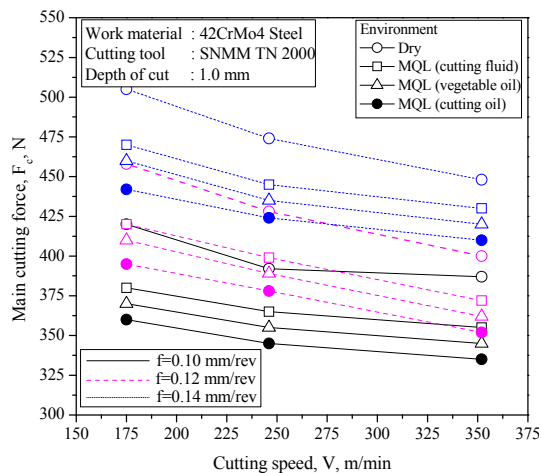


Fig 5. Variation of main cutting force with cutting speeds and feed rates under different environments

The percentage of reduction in main cutting force for the stated  $V$ - $f$  combinations under MQL using cutting oil, vegetable oil and soluble oil over dry condition are 8~14%, 6~11% and 4~9% respectively with an average of 12%, 9% and 7% respectively. Percentage of reduction in feed force for the stated  $V$ - $f$  combinations for MQL using cutting oil, vegetable oil and soluble oil over dry condition are 6~12%, 4~10% and 2~7% respectively with an average of 9%, 7% and 5% respectively. Among the environments MQL cutting oil (VG 68) gives the best performance.

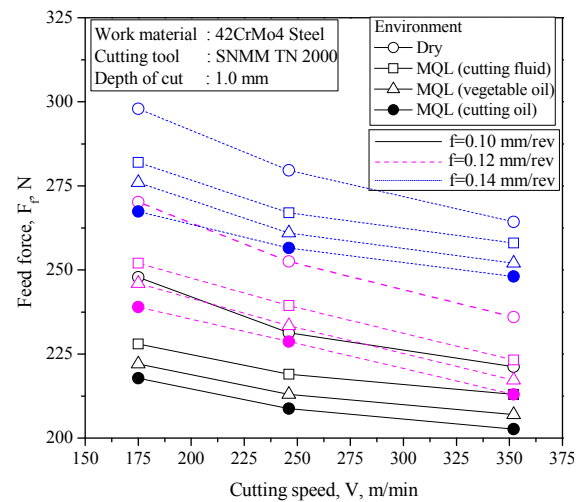


Fig 6. Variation of feed force with cutting speeds and feed rates under different environments

The life of carbide tools, which mostly fail by wearing, is assessed by the actual machining time after which the average value (VB) of its principal flank wear reaches a limiting value, like 0.3 mm. therefore, attempts should be made to reduced the rate of growth of flank wear (VB) in all possible ways without much sacrifice in MMR. The growth of average principal flank wear (VB) and auxiliary flank wear (VS) with progress of machining by SNMM insert under dry and MQL conditions have been shown in Fig.7 and Fig.8 respectively. From the previous discussion it is obtained that MQL by cutting fluid in feed 0.12 mm/rev is more effective, so the wear parameters are selected considering these fact.

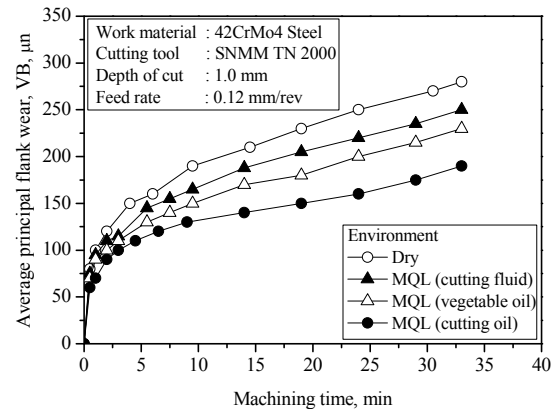


Fig 7. Growth of average principal flank wear (VB) with machining time under different environments

It is clearly appeared from Fig.6 and Fig.7 that flank wears, VB and VS particularly its rate of growth decreased substantially by MQL when turning 42CrMo4 steel by coated carbide SNMM inserts. Pressurized jet of MQL easily dragged into the plastic contact by its high energy jet, cools the interface and lubricate properly. It not only cools the interface but also reduces frictional heat generation by lubricating the friction zones.

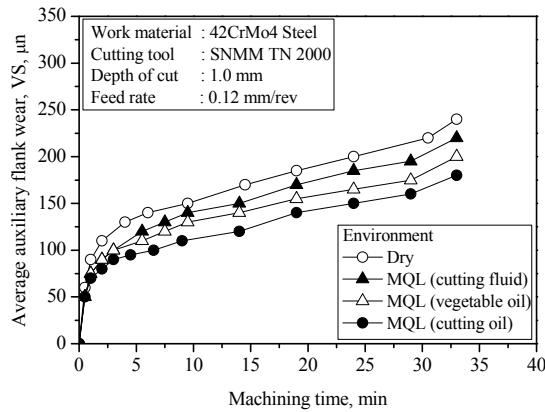


Fig 8. Growth of average auxiliary flank wear (VS) with machining time under different environments

Surface finish is also an important index of machinability. Feed force as well as chip thickness ratio is responsible for surface roughness along the longitudinal direction of the turned job. Usually surface roughness decreases with the increase in cutting velocity as cutting force decreases and chip thickness ratio increases with the increase in cutting speed. It is clear from Fig. 8 that surface roughness is reduced under MQL condition than dry through out the V-f-d combinations but MQL by cutting oil and vegetable oil show better results. In respect of surface roughness MQL is better for  $f=0.12$  mm/rev and  $V=352$  m/min. The value of percentage reduction for cutting oil and vegetable oil are 17~25% and 12~21% respectively.

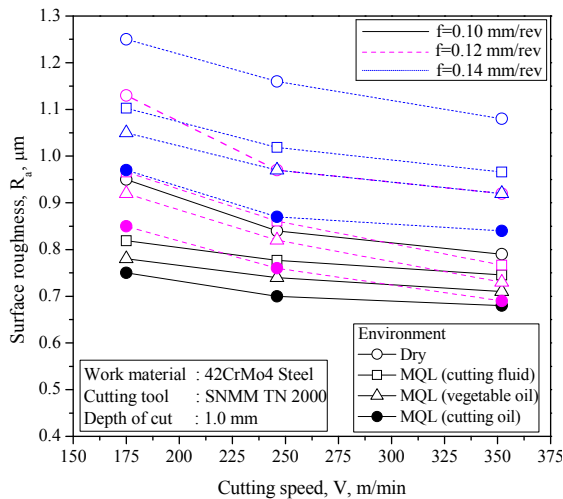


Fig 9. Variation of surface roughness with cutting speeds and feed rates under different environments

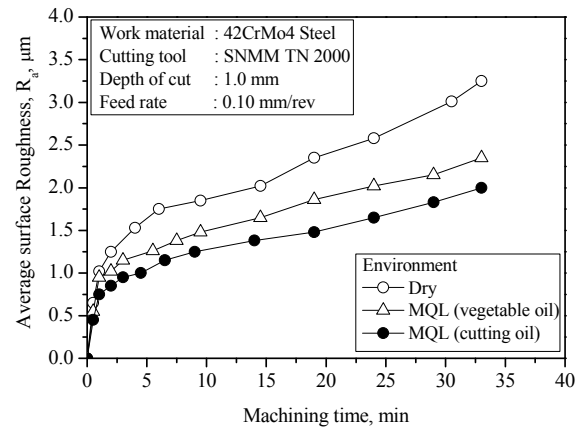


Fig 10. Variation of surface roughness with machining time

The variation in surface roughness observed with progress of machining 42CrMo4 steel at a particular set of cutting speed  $V$ , feed rate  $f$  and depth of cut  $d$ , by the coated carbide SNMM insert under dry and different MQL conditions has been shown in Fig.10. It is clear that surface roughness gradually increases with the machining time due to gradual increases in auxiliary flank wear VS. MQL has appeared to be more effective in reducing surface roughness as it did for auxiliary flank wear. The rate of increase in surface roughness decreases to significant extent when machining has been done under minimum quantity lubrication. MQL jet not only reduce the VS but also possibly of built-up edge formation due to reduction in temperature.

#### 4. CONCLUSION

Based on the results of the present experimental investigation the following conclusions can be drawn:

- i. MQL assisted jet enabled reduction in average chip-tool interface temperature from 3 to 12.5% depending upon the types of cutting fluids. Even such apparently small reduction, enabled significant improvement in the major machinability indices. MQL by VG 68 cutting oil reduced cutting temperature by about 8.6%-12.5% that indicates the effectiveness of cutting oil over other two MQL coolants.
- ii. Among the three MQL coolants VG 68 cutting oil exhibits the best results in respect of chip thickness ratio when 42CrMo4 steel is machined using coated SNMM carbide insert. MQL by VG 68 cutting oil has increased the chip thickness ratio ( $r_c$ ) by 14% - 17%.
- iii. MQL jet provided reduced tool wear, improved tool life and better surface finish as compared to dry and wet machining of steel. Surface finish improved mainly due to reduction of wear and damage at the tool tip by the application of MQL.

#### 5. ACKNOWLEDGEMENT

This research work has been funded by Bangladesh University of Engineering and Technology (BUET) and also partially supported by Bangladesh Council of Science & Industrial Research (BCSIR), Bangladesh.



The authors are also grateful to the Department of Industrial and Production Engineering for providing the facilities to carryout the experiment.

## 6. REFERENCES

1. Trent, E.M., 1984, "Metal Cutting", Butterworths, London & Boston.
2. Leskover, P. and Grun, J., 1986, "The metallurgical Aspect of Machining", Annals of CIRP, Vol. 35, No.1, pp. 537-550.
3. Tonshoff, H.K. and Brinkomier, E., "Determination of the Mechanical and Thermal influences on Machined Surface by Micro-hardness and Residual Stress Analysis", Annals of CIRP, Vol. 29, No.2, pp. 519-532, 1986.
4. Chattopadhyay, A.K. and Chattopadhyay, A.B., 1982, "Wear and Performance of Coated Carbides and Ceramics Tools", Wear, Vol. 80, pp.239-253.
5. Singh, S.B., Chakroborty, A.K. and Chattopadhyay, A. B., 1997, "A Study of the Effects of Inclusion contact on the Machinability and Wear Characteristics of 0.24% Carbon Steel", International Journal of Material Processing Technology, Vol. 66, pp.90-96.
6. Kitagawa, T., Kubo, A. and Maekawa, K., 1997, "Temperature and Wear of Cutting Tools in High-Speed Machining of Inconel 718 and Ti-6Al-6V-2Sn", Wear, Vol. 202, pp.142-148.
7. Shaw, M.C., 1984, "Metal cutting principles", Clarendon Press, Oxford University Press, pp. 324.
8. Paul, S., Dhar, N. R. and Chattopadhyay, A. B., 2000, "Beneficial Effects of Cryogenic Cooling over Dry and Wet Machining on Tool Wear and Surface Finish in Turning AISI 1060 Steel", Proc. of the ICAMT-2000, Malaysia, pp. 209-214.
9. Seah, K.H.W., Li, X. and Lee, K.S., 1995, "The Effect of Applying Coolant on Tool Wear in Metal machining Performance", International Journal of Advanced Manufacturing Technology, Vol. 49, pp. 495-501.
10. Diniz, A.E., Ferreira, J.R. and Filho, F.T., 2003, "Influence of Refrigeration/Lubrication Condition on SAE 52100 Hardened Steel Turning at Several Cutting Speeds", International Journal of Machine Tools and Manufacture, Vol. 43, No.3, pp.317-326.
11. Weinert, K., Inasaki, I., Sutherland, J. W. and Wakabayashi, T., 2004, "Dry Machining and Minimum Quantity Lubrication", Annals of CIRP, Vol. 53, No.2, pp.511-537.
12. Weinert, K., Adams, F. J. and Thamke, D., 1995, "Was kostet die Kühlschmierung?", Technika, Vol.44, No.7, pp.19-23.
13. Dhar, N. R. and Islam, S., 2005, "Improvement in Machinability Characteristics and Working Environment by Minimum Quantity Lubrication", CASR Project, BUET, Bangladesh.
14. Choudhury, S. M. A., 2009, "Study of the Effects of Minimum Quantity Lubricants (MQL) on Turning Steels Using Uncoated Carbide Inserts", Ph.D. Thesis, Bangladesh University of Engineering and Technology, Dhaka, Bangladesh.

## 7. MAILING ADDRESS

S. Sultana  
Department of Textile Engineering  
Daffodil International University (DIU)  
Dhaka, Bangladesh  
Email: [sonia.sultana@hotmail.com](mailto:sonia.sultana@hotmail.com)

## OPTIMIZATION OF RETAIL DISTRIBUTION NETWORK: A CASE STUDY

M. Mazharul Hoque, Abdullahil Kafy and Abdullahil Azeem

Department of Industrial and Production Engineering  
Bangladesh University of Engineering and Technology, Dhaka, Bangladesh

### ABSTRACT

Recently retail business in Bangladesh is expanding in a substantial amount. Supermarket biggies have attempted a massive expansion drive recent years to catch up more shoppers who still depend on unorganized wet market to buy their essentials. To catch up all the customer it is obligatory for retail business to have a good coordination among their business and therefore good coordination between retail outlet and distribution centre is must. A good communication between these two is required for a better schedule and thus a better schedule will reduce transportation cost. Again there incur a huge transportation cost within the retail outlets and distribution centers'. Therefore network distribution for retail industry is so vital. Besides a proper network distribution reduce transportation cost and improve product availability. The objective of the study is to develop a mathematical model for network distribution of a retail business. The study has been conducted at ACI Logistics to facilitate maintaining a proper network distribution.

**Keywords:** Optimization, Network Distribution, Transportation Cost.

### 1. INTRODUCTION

Network distribution is so vital for any kind of industry. In retail business, there incur huge amount of transportation. So transportation cost is also high.

Different studies have been conducted over transportation model over the years. As it is important to identify and protect the essential components of the transportation system of an urban intelligent transportation network to ensure its survivability. A study had been conducted in the critical point identification in the physical and communication layers of a small urban transportation system by Paul Oman and Brian Johnson[1]. Assessment of intermodal transportation planning at state department of transportation is conducted by Andrew R. Goetz[2]. Another study show how decisions concerning transportation programmes and projects can be made in the context of sustainable transportation [3]. Multinational firms face problem of optimal transportation route to inland destination in land locked country and Honkey Mon studied over this issue [4]. Some studied for development of sustainable transportation system which identifies issues related to the definition, evaluation and implementation of sustainable transportation. Significant issues include the range of definitions of sustainability, the range of issues considered under sustainability, the range of perspectives, criticism of sustainability analysis, evaluating sustainability, transportation impacts on sustainability, goals vs. objectives, sustainable transport decision making[5]. Two modeling approaches using spreadsheets for the transportation assignment problem is conducted by Xiang Ye, Xiao Zong [6]. Another study develops a

regional city forecasting model is developed within the national traffic model to ensure that all traffic components, internal and external trips, can be predicted through socio-economic data [7]. Surapati Pramanika presented a priority based fuzzy goal programming approach for solving a multiobjective transportation problem [8].

This study is concern about retail business transportation system. Retail business need to maintain a smooth transportation system. They need to transport products within time to the outlet otherwise business will definitely go down. Again to compete with its competitor they need to reduce their transportation cost, make the product available and reduce inventory cost. This model is concern about the demand of the retail outlet and supply capacity of the warehouses. Coordination is made within these two. The model formulated in this study is solved using MATLAB programming.

### 2. RETAIL BUSINESS IN BANGLADESH

Retail is the sale of goods to end users, not for resale but for use and consumption by the purchaser. The retail transaction is at the end of the supply chain. Manufacturers sell large quantity of products to retailers and retailer sell small quantities of those products to consumers. Retail business may be in the format of convenience store, automatic vending, door to door sales, telephone and direct mail.

In the recent years the retail business like superstore in Bangladesh increased in a massive way. In 2009 ACI logistics has opened 52 outlets named SWOPNO. Meena Bazar, Rahimafrooz, Nandan Mega Shop also set up for

new retail outlet. In Bangladesh, 3S Shopping Mall, Almas General Store, PQS Super Centre, Nandan Mega Shop etc.

### 3. LOGISTICS FOR RETAIL INDUSTRY

A lot of companies all around the world have put up logistics measures. These companies have found that these indicators can actually ensure faster and timelier service. These procedures are quite important to any company, particularly in the retail business. The manufacture and sale of goods all depend on timely execution of all aspects of the whole process. If one part bogs down, then the entire sale process fails as well. These procedures that companies put up in their respective logistics department are there to ensure a smooth transition of operations. Logistics is the portion of supply chain management that encompasses distribution, transportation and inventory management. To put in the context with the simplified description given above regarding the supply chain management functions of plan, buy, make, store, move, sell and return. Logistics is the store and move functions. It is not unusual for transportation cost for alone to be more than 10% of revenue. For many companies, transportation is the single largest cost element on their financial statements. Transportation costs are often double the expense of warehousing and inventory carrying cost (which means that warehousing and inventory costs can be 5% of revenue, which is no small matter). And every single taka saved in transportation cost goes straight to bottom line. The measures of logistics are in the form of key performance indicators. These indicators grade certain aspects of the whole supply chain. It is usually just a selection between pass or fail nothing in between. The failing grades will help managers locate which part of the whole chain needs further work and improvement. Usually the aspect involved the following: warehouse site selection, interplant movement, order processing, inventory, forecasting, packaging, and a whole lot more. Each aspect of these will be grade differently. However time will always be an unchanging factor. Again it is to be realized that the support of logistics of one type of business will be entirely different from another type of business. So the company will put in place must be tailor made to fit the logistical department. In reality policies and measures of logistics are not difficult to make. They are just quite tedious. The point of all about of logistics is to satisfy end user i.e. customer. If it is possible to deliver a product on a timely manner, then supply chain will work properly. It will give and added bonus to the prestige to the company since the customers are satisfied with the deliveries. Logistics measures can really help to ensure the success and productivity of the organization whole.

### 4. TRANSPORTATION NETWORK

The design of a transportation network impacts the performance of a supply chain to establishing the infrastructure within which operational transportation decisions regarding scheduling and routine are made. A well designed transportation network allows a supply chain to achieve a desired degree of responsiveness at

low cost.

Transportation network can be designed to any of the following:

- Direct shipping network
- Direct shipping with milk run
- All shipment via central distribution centre
- Shipping via DC using milk runs

Factors to be considered during transportation are the followings:

- Per week Demand of retail house
- Capacity of the retail house
- Inventory cost of goods
- Availability of product from source, i.e., from warehouse
- Distance between source and destination
- Transportation cost
- How much amount of product can be delivered from each warehouse?
- Time to deliver from source to destination
- Mode of transportation (rail, truck, rented or own vehicle)
- Types of products (sophisticated, solid, sensitive or other types)
- Equality of demand and supply
- Product cost
- Trade off between own or rented vehicle

### 5. CASE STUDY

ACI logistics run distribution strategy with direct shipment network. It has 5 warehouses in 5 different districts – Dhaka, Bogra, Sylhet, Chittagong, Jessore. And they have to deliver goods to their outlet located in 64 districts. So it is necessary for them to develop a schedule by which they can deliver their products from warehouse to outlets with minimum cost.

To develop the mathematical model some assumptions have been considered. These are

- One delivery at each outlet from warehouse
- Sufficient amount of demand at each outlet so it is considered that one vehicle at each outlet
- Per vehicle capacity is constant and it is considered to be 7 ton
- Demand at each retail house is fixed and it is 7 ton per week
- Demand is considered as fixed
- Each warehouse can supply a limited amount of goods to the outlet

The following steps have been performed for model development

- Developing a distance matrix
- Developing cost matrix from the developed distance matrix
- Formulating the model

#### 5.1 Distance Matrix Development

ACI logistics have 5 distribution centers at Dhaka, Bogra, Chittagong, Jessore and Sylhet. It has to distribute products to 64 districts. So the distance matrix is made between 5 districts and 64 districts. The distance matrix is made between warehouses to retail outlets.

Table 1: Part of Distance Matrix (km)

	Dhaka	Bagerhat	Bandorbon	-----	Thakurgaon
Dhaka	0	178	316	-----	407
Bogra	197	328	510	-----	210
Chittagong	242	363	85	-----	646
Jessor	164	93	476	-----	443
Shylet	241	414	454	-----	616

Table 2: Part of Cost Matrix (km)

	Dhaka	Bagerhat	Bandorbon	-----	Thakurgaon
Dhaka	0	6610.67	8634.67	-----	9969.33
Bogra	6889.33	8810.67	11480	-----	7080
Chittagong	7549.33	9324	5246.67	-----	13474.67
Jessor	6405.33	5364	10981.33	-----	10497.33
Shylet	7534.67	10072	10658.67	-----	13034.67

Table 1 shows the distance matrix required for the formulation of the mathematical model.

### 5.2 Cost Matrix Development

Cost matrix is developed considering all the fixed and variable cost for a single trip.

Fixed cost involves wages, servicing, depreciation and miscellaneous whereas the variable cost include per kilometer.

The calculation of cost matrix considers the following fixed and variable costs:

- Depreciation cost =1000 taka
- Miscellaneous cost =500 taka
- Servicing cost = 500 taka
- Personnel cost = 2000 taka
- So total fixed cost for each trip = 4000 taka
- Distance goes for per liter fuel =3 km
- Cost of fuel per liter = 44 taka
- Total variable cost per km =14.667 taka

Part of the cost matrix generated using this calculation is shown in Table 2.

### 5.3 Model Formulation

To formulate the mathematical model, let's consider a sample cost matrix shown in Table 3.

Table 3: A sample cost matrix

	D <sub>1</sub>	.....	D <sub>n</sub>	Supply
O <sub>1</sub>	C <sub>11</sub>	.....	C <sub>1n</sub>	A <sub>1</sub>
.....	.....	.....	.....	.....
O <sub>m</sub>	C <sub>m1</sub>	.....	C <sub>mn</sub>	A <sub>m</sub>
Demand	B <sub>1</sub>	.....	B <sub>n</sub>	

Objective function of the problem can be written as:

$$\begin{aligned}
 \text{Min } Z = & C_{11}X_{11} + C_{12}X_{12} + \dots + C_{1,64}X_{1,64} + \dots \\
 & C_{21}X_{21} + C_{22}X_{22} + \dots + C_{2,64}X_{2,64} + \dots \\
 & \dots \\
 & C_{51}X_{51} + C_{52}X_{52} + \dots + C_{5,64}X_{5,64}
 \end{aligned} \tag{1}$$

Constraints equations for the problem are:

$$\begin{aligned}
 X_{11} + X_{21} + \dots + X_{51} &= 1 \\
 X_{12} + X_{22} + \dots + X_{52} &= 1 \\
 \dots \\
 X_{1,64} + X_{2,64} + \dots + X_{5,64} &= 1
 \end{aligned} \tag{2}$$

and

$$\begin{aligned}
 X_{11} + X_{12} + \dots + X_{1,64} &\leq A_1 \\
 X_{21} + X_{22} + \dots + X_{2,64} &\leq A_2 \\
 \dots \\
 X_{51} + X_{52} + \dots + X_{5,64} &\leq A_5
 \end{aligned} \tag{3}$$

The non-negativity constraints are

$$X_{ij} \geq 0 \text{ for } i = 1 \text{ to } 5; j = 1 \text{ to } 64 \tag{4}$$

In the above equations,  $C_{ij}$  = cost incurred to transport goods from  $i$  locations to  $j$  destinations.

$X_{ij} = 1$ ; if goods are transported from location  $i$  to destination  $j$ ;  
 $= 0$ ; if goods are not transported from location  $i$  to destination  $j$ .

Table 4: Outlets to be supplied from each warehouse

Source (Warehouse)	Destination (Retail Outlet)
<b>Dhaka</b>	Dhaka, Barisal, Bhola, Faridpur, Gazipur, Jamalpur, Madaripur, Manikgonj, Munshigonj, Mymensing, Narayanganj, Potuakhali, Rajbari, Sherpur, Tangail
<b>Bogra</b>	Bogra, Dinajpur, Gaibandha, Joypurhat, Kurigram, Lalmonirhat, Naogaon, Natore, Nawabgonj, Nilphamary, Panchagar, Rajshahi, Rangpur, Sirajgonj, Thakurgonj
<b>Chittagong</b>	Bandorbon, Chandpur, Chittagong, Comilla, Cox's Bazar, Feni, Khagrachari, Lakhshampur, Noakhali, Rangamathi, Shariatpur
<b>Jessore</b>	Bagherhat, Borguna, Chuadanga, Gopalganj, Jessor, Jhalkhati, Jinaydhoho, Khulna, Kustia, Magura, Meherpur, Narail, Pabna, Pirojpur, Shatkhira
<b>Sylhet</b>	Bramhanbaria, Habigonj, Kishorgonj, Moulivibazar, Narshidhi, Netrokona, Sunamgonj, Sylhet

The program to solve this is linear programming problem has been generated using MATLAB software.

Minimization of the function  $f(x)$  is solved by using the following equations

$$Ax \leq B$$

$$Aeq.x = Beq$$

$$ub \leq x \leq lb$$

$$And [x] = linprog(f, A, B, Aeq, Beq, lb, ub)$$

$$Here, f = [C_{11} \ C_{12} \ \dots \ C_{21} \ \dots \ C_{5 \ 63} \ C_{5 \ 64}]$$

$$Let, a = ones(1, 64)$$

$$z = zeroes(1, 64)$$

$$Then A = \begin{bmatrix} a & z & z & z & z \\ z & a & z & z & z \\ z & z & a & z & z \\ z & z & z & a & z \\ z & z & z & z & a \end{bmatrix}$$

Value of B is the limit for each warehouse that how many retail outlets that can be served by each warehouse. It may be equal for all warehouses or can vary. Equal quantity is considered during the problem solution and it is considered as 15, 16, 17, 18 etc.

$$\begin{matrix} 15 & 16 \\ 15 & 16 \end{matrix}$$

So,  $B = 15$  or  $B = 16$

$$\begin{matrix} 15 & 16 \\ 15 & 16 \end{matrix}$$

Again, let,  $a_{eq} = eye(64)$

$$So, a_{eq} = \begin{bmatrix} 1 & 0 & \dots & 0 & 0 \\ 0 & 1 & \dots & 0 & 0 \\ \vdots & \vdots & \ddots & \vdots & \vdots \\ 0 & 0 & \dots & 1 & 0 \\ 0 & 0 & \dots & 0 & 1 \end{bmatrix}$$

$$Then A_{eq} = [a_{eq} \ a_{eq} \ a_{eq} \ a_{eq} \ a_{eq}]$$

$$and B_{eq} = ones(64,1)$$

$$ub = ones(320,1)$$

$$lb = zeroes(320,1)$$

As it is seen that the limit of warehouses distribution capacity can be altered easily to the main program so it is easy to analyze for various conditions. Again the main program read the data from excel spreadsheet and the result of the program will automatically generate in another excel spreadsheet. Thus, this program is user friendly. Each warehouse has certain capacity to supply at the outlet. Varying the capacity limit of the warehouse the programming can be modified and the relevant result can be obtained.

## 6. RESULTS

After execution of the program the result can be obtained. It can be easily seen from the result that which warehouse has to choose to deliver products to a certain retail outlet.

If we consider the limit of warehouse that each can supply at maximum 18 outlets then the result is shown in Table 4.

If it is considered that each warehouse can supply at maximum 15 retail outlet then total transportation cost is 3409000 taka. Table 5 shows total transportation cost for different number of maximum retail outlets.

Table 5: Total transportation cost for maximum outlet

Maximum retail outlet	Total transportation cost (Tk.)
15	3409000
16	334590
17	331080
18	330160
19	330160

For a maximum retail outlet of 18 and above, transportation cost remain same. It is observed that the

minimum cost can be obtained when the limit for the warehouse is set to minimum 18 i.e. if each warehouse can supply at least 18 outlets. So it would be better if each warehouse have a capacity to supply at least 18 retail outlets. Again the inventory cost to hold this capacity need to be considered as well. Overall cost and which warehouse has to deliver to which retail outlet is automatically generated by the program.

## 7. CONCLUSIONS

Retail industries have to make decision about the distribution process i.e. how to distribute their products from warehouse to outlet. Each warehouse has certain capacity to supply to the outlet. Again the outlets have a weekly demand which may vary over time. Retail industries often face the problem that which warehouse will be most economical to supply to a certain retail outlet. They mostly face it when they have a situation where outlet demand, warehouse capacity, delivery times, transportation cost etc vary over time. In this paper, a mathematical model has been developed to find the optimum distribution network of a company. As the model is formulated considering the outlet demands, warehouse capacity and overall transportation cost, it will help the retailers to choose the exact warehouse for the delivery of products to the outlets. Again the result will help to achieve the overall minimum transportation cost for the delivery of products from warehouse to outlet. This will also assist the retailers to smooth their transportation system because it chooses the minimum distance path for the delivery of retail goods.

## 8. REFERENCES

1. Butapati, S., Kalidindi, R., Benke, M., Rahim, A., Oman, P. and Johnson, B., 2006, "A case study of critical point identification in the physical and communication layers of a small urban transportation system" *International Journal of Critical Infrastructures*, 2(4):319-330.
2. Goetz, A. R., Szyliowicz, J. S., Vowels, T.M. and Taylor, G. S., 2007, "Assessing intermodal transportation planning at state departments of transportation", *World Review of Intermodal Transportation Research*, 1(2):119-145.
3. Zietsman, J., Rilett, L. R. and Kim, S. J., 2006, "Transportation corridor decision-making with multi-attribute utility theory", *International Journal of Management and Decision Making*, 7(2/3):254-266.
4. Min, H., Ko, H. J. and Soo, L. C., 2009, "Designing the global inland transportation network" *International Journal of Logistics Systems and Management*, 5(5):457-472.
5. Litman, T. and Burewell, D., 2006, "Issues in sustainable transportation", *International Journal of Global Environmental Issues*, 6(4):331-347.
6. Ye, X. and Zong, X., 2006, "Two modeling approaches using spreadsheets for the transportation assignment problem", *International Journal of Information and Operations Management Education* 1(3):316-325.
7. Ashad, R. H., John, D. H., Piet, C. H. and Kumares, C. S., 2001, "Application of Conventional and Simplified Modeling Techniques under Uncertainty", *A GIS-T Approach for Jerusalem*, *Transportation Research Record*, Paper Number 01-3374.
8. Pramanika, S. and Royb, T. K., 2001, "Multiobjective Transportation Model with Fuzzy Parameters: Priority based Fuzzy Goal Programming Approach", Department of Mathematics, Nandalal Ghosh B.T. College, Panpur, P.O., North 24 Parganas, West Bengal, India.

## 9. MAILING ADDRESS

M. Mazharul Hoque  
 Department of Industrial and Production Engineering  
 Bangladesh University of Engineering and Technology,  
 Dhaka, Bangladesh

## EFFECT OF SCANDIUM ON THE CAST Al-Si-Mg ALLOY

M. S. Kaiser<sup>1</sup>, M. R. Basher<sup>2</sup>, and A. S. W. Kurny<sup>2</sup>

<sup>1</sup>Directorate of Advisory, Extension and Research Services,

<sup>2</sup>Department of Materials and Metallurgical Engineering, Bangladesh University of Engineering and Technology, Dhaka-1000, Bangladesh

### ABSTRACT

Ageing of Al-6Si-0.3Mg alloy doped with varying concentration of scandium ranging from 0.2wt% to 0.6wt% has been carried out. Attempts were made to understand the grain refining effect of scandium in Al-6Si-0.3Mg alloy. As cast samples were naturally aged for 60 days. Some samples were aged isochronally for 60 minutes at different temperature up to 500°C and also isothermally up to 400°C for different periods ranging from 30 to 240 minutes. Hardness of the alloys was measured to study the age hardening effect due to scandium addition. Moreover, a kinetic analysis for precipitation in experimental alloys has been carried out by Differential Scanning Calorimetric Technique to gain a clear understanding about the kinetics of precipitation and recrystallization in Al-6Si-0.3Mg alloy with or without scandium additions.

**Keywords:** Al-Si-Mg alloys, age hardening, grain-refinement, precipitates, recrystallization.

### 1. INTRODUCTION

Scandium is an effective grain refiner and increases the recrystallization temperature in aluminium alloys [1, 2]. Scandium addition in pure aluminium and its alloys also enhance the mechanical properties, thermal properties, corrosion resistance and its weldability and reduce hot cracking susceptibility [3]. Scandium forms a stable  $Li_2$  phase,  $Al_3Sc$  with aluminium. The precipitation of  $Al_3Sc$  is coherent with the matrix. Presences of fine coherent precipitates of  $Al_3Sc$  impede the migration of dislocations and increase the recovery temperature by stabilizing the substructures. The kinetics of recrystallization is also delayed by scandium addition [1, 3]. Scandium does not form any second phase intermetallic compound with other alloying elements such as iron, manganese and chromium [3].

This article discusses the results of investigations on the ageing behavior of Al-6Si-0.3Mg alloys containing varying amounts of scandium. It also presents the results on the evolution of microstructures in the experimental alloys due to change in their chemistry, mechanical and thermal history. Differential Scanning Calorimetry has also been used to understand the precipitation and recrystallization in Al-6Si-0.3Mg alloys.

### 2. EXPERIMENTAL

Four alloys were produced by melting in a natural gas fired pit furnace under suitable flux cover (degasser, borax etc.). Commercially pure aluminium (98.5% purity) was taken as the starting material. First the aluminium, aluminium-silicon and aluminium-scandium master alloy (2%Sc) were melted in a clay-graphite

crucible. Piston head of Toyota car engine was used as aluminium-silicon master alloy (11.2% Si with small amount of magnesium and other trace elements). The final temperature of the melt was always maintained at  $760 \pm 15^\circ C$  with the help of an electronic temperature controller. Then the melt was homogenized by stirring at  $700^\circ C$ . Casting was done in cast iron metal moulds [20.0 mm in dia x 200.0 mm in length] preheated to  $200^\circ C$ . All the alloys were analyzed by wet chemical and spectrochemical methods simultaneously. The chemical compositions of the alloys are given in Table 1. The cast alloys were cut to pieces of suitable size [16.0 mm dia x 10.0 mm length]. As cast samples were aged isochronally for 60 minutes at different temperatures up to  $500^\circ C$ . The samples in the as cast condition were isothermally aged at various temperatures up to  $500^\circ C$  for different ageing times ranging from 30 to 240 minutes. All cast alloys were naturally aged up to 60 days. The aged alloys were then put to hardness testing to assess the age hardening behaviour. A Rockwell F scale [60kg load, 1/16" steel ball indenter] was used and an average of ten concordant readings has been taken as the representative hardness of a sample. The heat treated cast alloys were subjected to optical metallographic studies. The specimens were polished with alumina, etched with Keller's reagent and observed under a Versa met-II Microscope. The alloys, in the form of lumps of 10 to 15mg in weight, have also been subjected to DSC using a Du Pont 900 instrument. Inert  $N_2$  gas atmosphere was used and the DSC scan was conducted over a temperature range from  $50^\circ C$  to  $600^\circ C$ . A fixed heating rate of  $10^\circ K/min$  was used in all scans.



Table 1: Chemical Composition of the Experimental Alloys (wt%)

Alloy	Si	Mg	Sc	Pb	Ti	Cu	Fe	Mn	Ni	Zn	Cr	Sn	Al
1	5.73	0.282	0.00	0.006	0.020	0.765	0.406	0.074	0.402	0.043	0.011	0.027	Bal
2	5.57	0.305	0.20	0.007	0.025	0.838	0.404	0.069	0.404	0.040	0.011	0.029	Bal
3	5.87	0.291	0.40	0.007	0.027	0.839	0.459	0.080	0.454	0.044	0.012	0.027	Bal
4	5.88	0.289	0.60	0.008	0.034	0.875	0.409	0.077	0.393	0.039	0.012	0.026	Bal

### 3. RESULTS

#### 3.1. Optical Microscopy

Optical micrograph of alloy 1 shows dendrites with black second phase particles within inter-dendritic spaces (Fig. 1). Addition of 0.2 wt% scandium to the base alloy showed a diminution in the amount of second phase particles. It further appears that dendrite arm spacing is decreased in alloy 2 and 3 with the consequent refinement of dendrites (Figs. 2-3). The structural fineness is seen to increase with increasing scandium content. In the alloy with 0.6 wt% Sc, the amount of second phase particles is reduced to a great extent. The dendrite fragments are seen to have refined remarkably (Fig. 4).

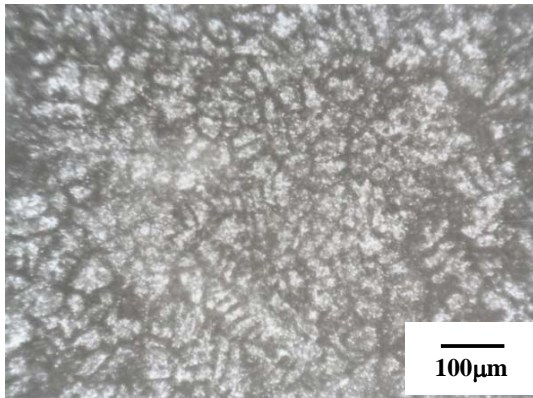


Fig 1. Optical micrograph of cast alloy 1.

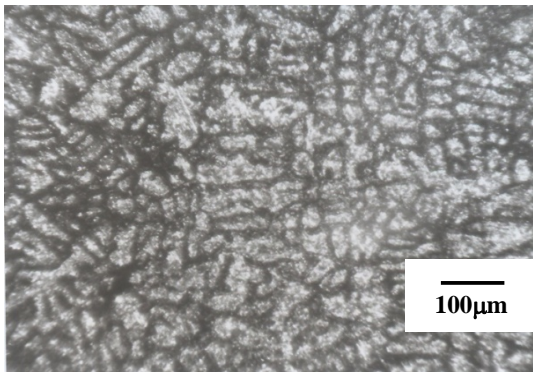


Fig 2. Optical micrograph of cast alloy 2.

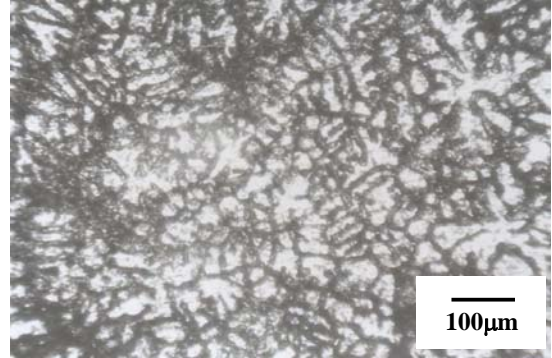


Fig 3. Optical micrograph of cast alloy 3

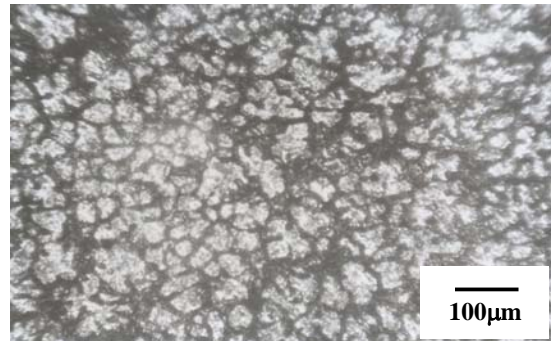


Fig 4. Optical micrograph of cast alloy 4.

If the alloys are annealed at 400°C, the base alloy is seen to be recrystallized almost fully (Fig. 5). The scandium added alloys, on the other hand, do not recrystallize even when annealed at 400°C (Figs. 6-8).

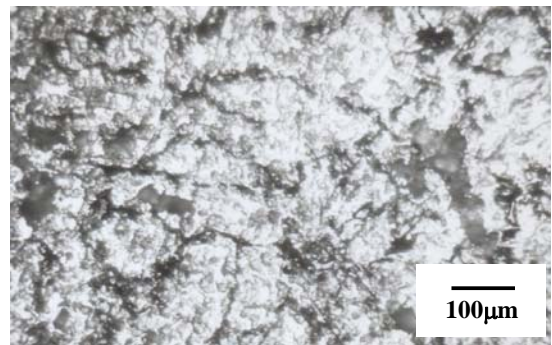


Fig 5. Optical micrograph of cast alloy 1, aged at 400°C for 1 hour.

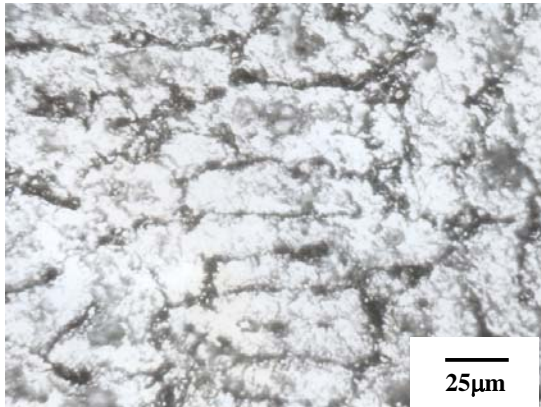


Fig 6. Optical micrograph of cast alloy 2, aged at 400°C for 1 hour.

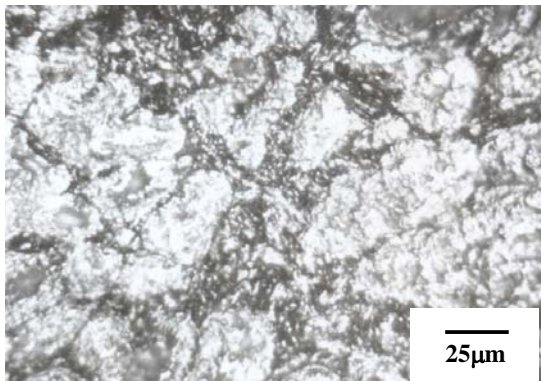


Fig 7. Optical micrograph of cast alloy 3, aged at 400°C for 1 hour.

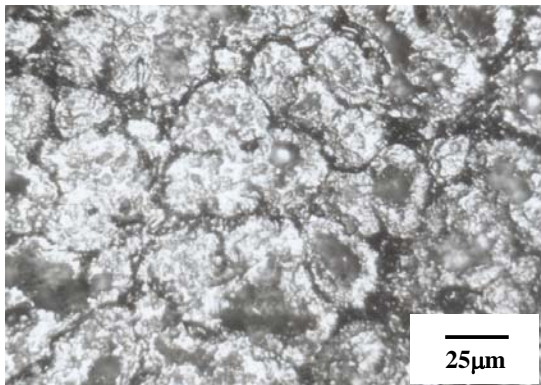


Fig 8. Optical micrograph of cast alloy 4, aged at 400°C for 1 hour.

### 3.2. Ageing

Fig. 9 shows the variation of hardness of the different alloys under natural ageing condition. It is apparent that all the alloys achieve some extent of age hardening after 10 days. However, the Sc containing alloys initially show higher hardness. In the case of Sc bearing alloy the hardness in as cast condition over the period of holding does not vary significantly. Fig. 10 shows the Isochronal ageing behavior for different alloys. For all the alloys the peak ageing condition has been attained at 250°C. Although hardness of the base alloy is lower than the Sc

bearing alloys in the as cast condition, the softening effect above 250°C was found to be much more prominent in the base alloy than in the Sc containing alloys. Figures 11 to 14 show the isothermal ageing behavior of different alloys at different levels of temperature. Up to 200°C the base alloy attains the peak condition after 30 min. In the case of Sc bearing alloys the peak hardness is maintained without any appreciable softening through the duration of ageing. For ageing within the temperature range 250 to 400°C the peak ageing condition has been attained after 30 min. The ageing effect is gradually reduced with increase in temperature above 250°C. However, the Sc bearing alloy exhibits stronger resistant to softening in comparison to the base alloy.

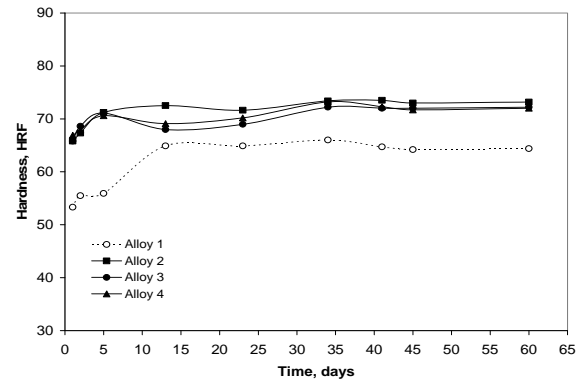


Fig 9. Natural ageing curve of the cast alloys for 60 days.

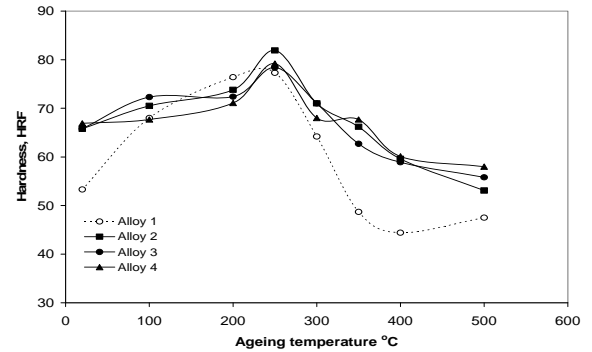


Fig 10. Isochronal ageing curve of the cast alloys, Aged for 1 hour.

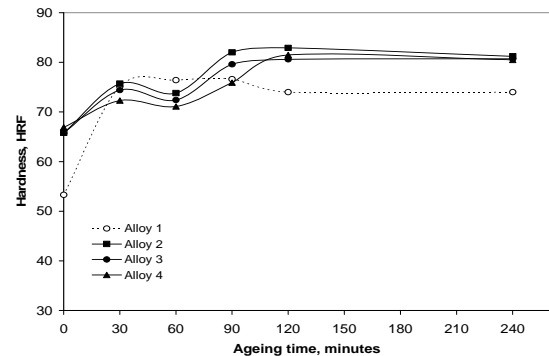


Fig 11. Isothermal ageing curve of the cast alloys, Aged at 200°C.

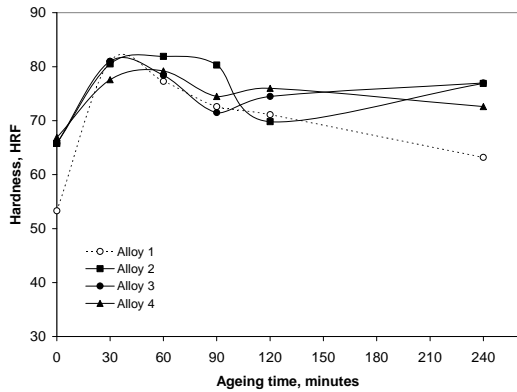


Fig 12. Isothermal ageing curve of the cast alloys, Aged at 250°C.

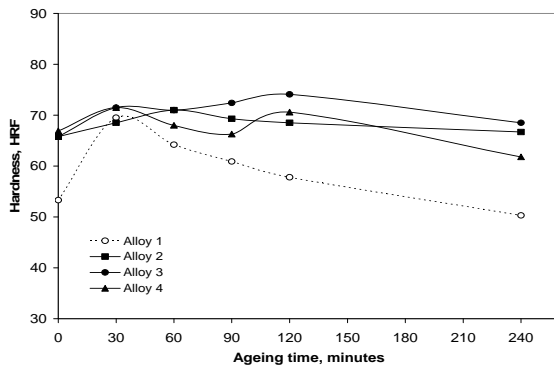


Fig 13. Isothermal ageing curve of the cast alloys, Aged at 300°C.

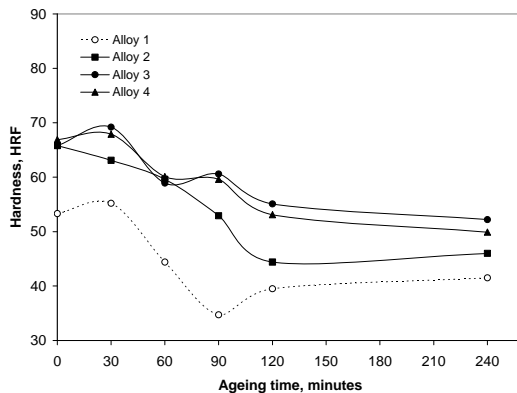


Fig 14. Isothermal ageing curve of the cast alloys, Aged at 400°C.

### 3.3. Differential scanning calorimetry (DSC)

The DSC curve for the base Al-6Si-0.3Mg alloy is shown in Fig. 15. It may be noted that a broad exothermic occurs at 220°C. This is indicative of dissolution of some phase already present in the cast alloy [8]. This is followed by another exothermic peak at 460°C. The exothermic at 460°C corresponds to recrystallization. The DSC heating curve of alloy containing 0.2 wt% Sc is shown in Fig. 16. An exothermic at 225°C corresponds to

the dissolution of some kind of second phase particle presumably  $\beta$ -phase present in the microstructure. Following this a broad exothermic peak is seen to appear at 475°C in the heating curve. This signifies the recrystallization taking place at a higher temperature. The DSC thermogram of the cast alloy containing 0.4 wt% Sc records a superimposition of two exothermics (Fig. 17). The preceding peak occurs at 225°C and is indicative of the formation second  $\beta$ -phase. There is a peak at about 475°C to support recrystallization. The DSC heating curve of the alloy containing 0.6 wt% Sc shows an exothermic peak at 225°C signifying the precipitation of hexagonal  $Mg_2Si$  and another exothermic presents there at 475°C for the recrystallization (Fig. 18).

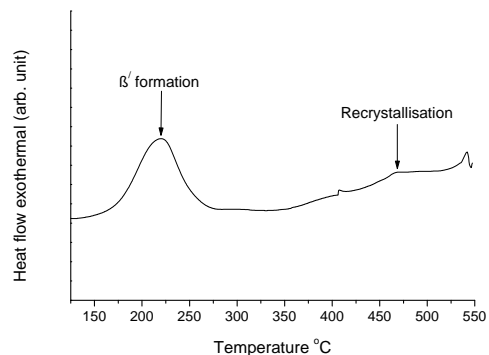


Fig 15. DSC heating curve of cast alloy 1.

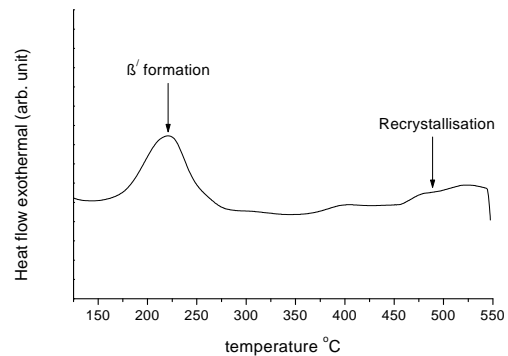


Fig 16. DSC heating curve of cast alloy 2.

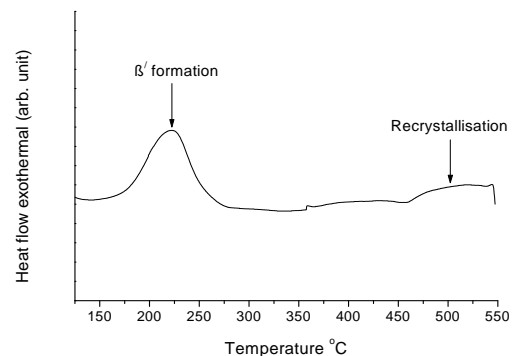


Fig 17. DSC heating curve of cast alloy 3.

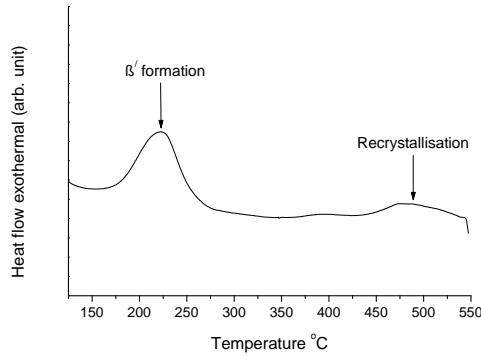


Fig. 18: DSC heating curve of cast alloy 4.

#### 4. DISCUSSION

Observations under optical microscopes have not provided much information; nevertheless the overall appearance of the microstructure resembles what are normally observed in cast aluminium alloy ingot [9]. The dendrites of the cast binary alloy are seen to have refined significantly with the addition of scandium. Reportedly [3], alloy with 0.2 wt% Sc does not provide much grain refinement, but refines the primary dendrites of  $\alpha$  with consequent diminution of dendrite arm spacing. The arm spacing in scandium treated alloys were found to lie within a range of 20  $\mu\text{m}$  to 40  $\mu\text{m}$  against a value of around 45  $\mu\text{m}$  in case of base alloy. This is ascribed to the modification of solidification speed by scandium during the growth of the dendrite structure [10]. Also scandium-containing alloys are seen to contain fewer amounts of intermetallic compounds. Due to increase in solidification speed, the super-cooling effect is weakened. The consequential faster solidification leads to decrement in the amount and size of the second phase constituents with scandium addition. The faster solidification also aids in the retention of more solutes in solution. Since dendrites are refined with scandium addition, the size of individual second phase region becomes smaller as these phases are formed within the inter-dendritic spaces. Increasing amount of scandium leads to a greater increase in solidification speed and hence the related effects on dendrite refinement and fraction and number density of second phase constituents have been realized more as evidenced in the optical microstructures of alloys 2-4. The base alloy however has started recrystallizing as it is known that recrystallization of Al-6Si-0.3Mg alloy becomes completed at about 400°C. However alloys 2-4 have dispersion of fine precipitates of  $\text{Al}_3\text{Sc}$ . These precipitates are coherent with the matrix. It is reported [11], that recrystallization is almost impossible in aluminium alloys when such particles are already present. However at 300°C, the finely dispersed  $\text{Al}_3\text{Sc}$  in alloy 2 is sufficient to inhibit recrystallization fully. The precipitates hinder the movement of sub-boundaries and grain boundaries. On increasing the temperature to 400°C, the second phase constituent is almost dissolved in base alloy and there is nothing to hinder dislocation movement. As a result recrystallization becomes

complete. In alloys containing scandium the supersaturated solution decomposes to form  $\text{Al}_3\text{Sc}$  at around 300°C. These precipitates are known to be resistant to coarsening. There are reports saying that increasing the annealing temperature of Al-Mg-Si-Sc alloy from 300°C to 400°C increases the size of  $\text{Al}_3\text{Sc}$  precipitates from 4 nm to 13 nm. The precipitates of  $\text{Al}_3\text{Sc}$  remain coherent with the matrix even when their size increases to 100 nm due to higher temperature of annealing [2, 3]. In the present case however the precipitate size is around 15 nm when annealed at 400°C. Therefore dislocation pinning force is very large. As a result recrystallization is not possible.

Hardening peak was found for all alloys in 10 days. This is due to formation of hexagonal  $\text{Mg}_2\text{Si}$ . Scandium added alloys show higher hardness due to relatively fine grain. In isochronal ageing for one hour maximum hardness was found at 250°C for all alloys. The peak hardness of alloy 1 falls more quickly than the other alloys. This is because with the increase of temperature alloy 1 starts to recrystallize. But due to the formation of  $\text{Al}_3\text{Sc}$  recrystallization is delayed in alloys 2-4. This is also because of formation of  $\text{Al}_3\text{Sc}$  which results in finer grains and increase of hardness. When alloys are aged at 200°C hardening peak was found in 90 minutes. This is also because of formation of  $\beta'$ . Again hardness of alloy 1 falls quicker than the other alloys because of early recrystallization. When alloys are aged at 250°C maximum hardness was found in 30 minutes.  $\beta'$  is formed in less time due to higher temperature. The effect of  $\text{Al}_3\text{Sc}$  formation is clearly seen the right portion of the graph where hardness of alloy 1 decrease due to recrystallization. Ageing at 300°C gives maximum hardness in 30 minutes. But this maximum hardness is less than the previous maximums. Because in higher temperature the precipitates tend to become coarser and coarse precipitates are not as effective as finely dispersed precipitates to resist the movement of dislocation. Coarse precipitates also do not offer enough resistance to the recrystallization. Effect of high temperature and coarse precipitates are also seen here and in the following graph.

Alloy 1 contains some metastable phase. It is reported that metastable  $\beta'$  phase in Al-Si-Mg alloy gives way to the formation of  $\beta$ -phase [12, 13]. Two separate DSC peaks noted for the alloy is suggestive of the probable dissolution of  $\beta'$  phase for subsequent formation of  $\beta$ -phase at 220°C. The following exothermic occurs at 460°C. Recrystallization temperature is found similar to what has been reported earlier [3, 8]. DSC plot of cast alloys 2-4 are almost similar to cast alloy 1. An exothermic peak denoting the formation of metastable  $\beta'$  is noticed at 225°C because the presence of dislocations might have induced the formation of a metastable phase in higher scandium alloy. This implies that with the greater volume fraction of finely distributed  $\text{Al}_3\text{Sc}$  precipitates, the dislocation movement is restricted. Hence sub structural stability is increased.

Recrystallization takes place at a high temperature viz. 475°C although it is reported that the favorable temperature for recrystallization is 400°C. Thus kinetics of recrystallization is greatly delayed in Al-6Si-0.3Mg-0.4Sc alloy. This is so because fine coherent precipitates of Al<sub>3</sub>Sc have high coherency strains. This severely impedes the migration of dislocations. This may be due to misfit dislocations which are partially annihilated only at high temperatures after sufficient degree of particle coarsening [14].

## 5. CONCLUSION

1. The dendrites of the cast base alloy are refined significantly with the addition of scandium. Increasing amount of scandium leads to a greater dendrite refinement and fraction of second phase constituents is reduced.
2. The age hardening effect shown by the alloys are due to formation of metastable  $\beta'$  phase.
3. Sc addition is effective in respect of improving the hardness during ageing. However Sc addition is most effective in suppressing the softening effect during prolonged ageing treatment.
4. The precipitates delay the recrystallization in scandium bearing alloys. Higher is the volume fraction of precipitates; higher becomes the recrystallization start temperature.

## 6. REFERENCES

1. Kaiser, M. S., Datta, S., Roychowdhury, A. and Banerjee, M. K., "Effect of scandium on the microstructure and ageing behaviour of cast Al-6Mg alloy" *Materials Characterization*, Vol. 59, 2008, pp. 1661-1666.
2. Lathabai, S., Lloyd P. G., "The effect of scandium on the microstructure, mechanical properties and weldability of a cast Al-Mg alloy" *Acta Mater* Vol. 50, 2002, pp. 4275-4292.
3. Toropova L.S., Eskin D.G., Kharakterova M.L. and Dobatkina T.V., "Advanced Aluminum Alloys Containing Scandium, Structure and Properties" Baikov Institute of Metallurgy, Moscow, Russia, 1998.
4. Sawtell, R. R. and Jensen, C. L., "Mechanical properties and microstructures of Al-Mg-Sc alloys", *Metallurgical Transactions A*, Vol. 21A, 1990, pp. 421-430.
5. Kaiser, M. S. and Banerjee, M. K., "Effect of Scandium on Cast Al-6Mg Alloys" *Indian Foundry Journal*, Vol. 52, No. 8, August 2006, pp. 29-43.
6. Royset, J. and Ryum, N., "Scandium in aluminium alloys," *International Materials Reviews*, Vol. 50, No. 1, 2005, pp. 19-44.
7. Drits, M. E., Pavlenko, S. G. and Toropova, L. S., "Mechanism of the Influence of Scandium in Increasing the Strength and Thermal Stability of Alloys in the Al-Mg System", *Sov. Phys. Dokl.* Vol. 26 No. 3, 1981, pp. 344-346.
8. Nagasaki S. and Maesono A., "High Temp. High Press" *Metals Physics*, Vol. 11, 1965, p. 182.
9. Sawtell R. R., Jensen C. L., "Mechanical properties and microstructures of Al-Mg-Sc alloys". *Metall Trans*, Vol. 21A, 1990, pp. 421-430.
10. Tadashi A, Nobutaka S, Miura Y. The effect of scandium on the as-homogenized microstructure of 5083 alloy for extrusion" *Mater Sci Eng*, Vol. 280, 2000, pp. 139-45.
11. Polmear I. J., "Role of trace elements in aged aluminum alloys" *Materials Science Forum*, Trans Tech Publications, Switzerland-Germany-UK-USA. Vol. 13/14, 1987, pp.195-214.
12. Polmear I. J: *Light Alloys, Metallurgy of the Light Metals*, Edward Arnold (Publishers) Ltd 41 Bedford Square, London WC1B 3DQ 1981.
13. Wang, Q. G. and Davidson, C. J., "Solidification and precipitation behaviour of Al-Si-Mg casting alloys," *Journal of materials science*, Vol. 36, No. 1, 2001, pp. 739-750.
14. Kaiser, M. S., Nambissan, P. M. G., Banerjee, M. K., Sachdeva, A. and Pujari, P. K., "Positron lifetime studies and coincidence Doppler broadening spectroscopy of Al<sub>94-x</sub>Mg<sub>6</sub>Sc<sub>x</sub> (x = 0 to 0.6) alloy", *Journal of Materials Science*, Volume 42, Number 8, April, 2007, pp. 2618-2629.

## 7. MAILING ADDRESS

Md. Rashedul Basher  
 House: Y-16(1<sup>st</sup> floor), Road: 1, Block: A, Chandgaon  
 C.D.A Residential Area, Chandgaon, Chittagong.  
 Phone: +8801913484165  
 E-mail: rashed.mme.buet@gmail.com



## EFFECTS OF EGR & MAGNETIC FUEL TREATMENT SYSTEM ON ENGINE EMISSION CHARACTERISTICS IN A BIO FUEL ENGINE

P. Govindasamy<sup>1</sup> and S. Dhandapani<sup>2</sup>

<sup>1</sup>Department of Mech. Engg., Kongu Engg. College, Perundurai, Tamilnadu, India

<sup>2</sup>Institute of Technology, Coimbatore, Tamilnadu, India

### ABSTRACT

The depletion of fossil fuels and the increase in the emission levels has caused a concern globally. An eco-friendly alternate was required to fulfill the growing demand. Bio fuels have proved to be the best alternative. The overall performance and emission tests have given good results except for the NO<sub>x</sub> component of the emission. This experimental work focuses on the reduction of this component to a great extent with the implementation of techniques called Exhaust Gas Recirculation and Magnetic Fuel Treatment system

**Keywords:** Alternative Fuel, Magnetization, Engine, Emission.

### 1. INTRODUCTION

Today the world has realized that fossil diesel stock will almost come to an end within a few decades and if alternatives to these are found out, our vehicles would soon have a new eco friendly fuel to be used in the future. Bio diesel, due to its biodegradable nature, and essentially no sulphur and aromatic contents, offers to reduce particulate and toxic emissions (Avinash kumar agarwal, 2002). Bio diesel when mixed with diesel fuel in small quantities also seems to improve the fuel lubricity, extend engine life and reduce fuel consumption.

Jatropha oil is used as an alternative to diesel. This oil is chosen because it has properties (table 1) similar to that of diesel and mixing with the petroleum diesel would be really easy. Due to higher cetane number and lubricating properties (Gerhard Vellguth, 1983), this fuel gives good performance with any diesel engine. While analyzing the emissions in Jatropha oil and comparing with that of diesel, all the components in the emission got reduced drastically except NO<sub>x</sub>. This work mainly focuses on the methodology of reducing the emission of NO<sub>x</sub> using the technique called Exhaust Gas Recirculation (Avinash kumar agarwal, 2003).

The emissions in general like CO, HC etc., can be reduced (Ruggero, 2000) by fuel magnetization. The fuel is polarized to enhance the mixing of the air and fuel thereby producing a complete combustion. The idea that magnetizing hydrocarbon fuel can improve combustion and engine efficiency has been around since at least the 1930s. In 1936, Chinese fishermen are said to have been

applying magnets to engine fuel lines in fishing boats in order to improve fuel economy (Busch, K.W ,1976).

Table 1: Properties of Jatropha oil

Density (g cm <sup>-3</sup> at 20°C)	0.879
Flash point ( °C)	191
Fire point ( °C)	207
Cetane number	57-62
Viscosity(mm <sup>2</sup> /s at 40°C)	4.20
Calorific value (MJ/L)	32.80

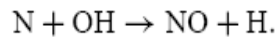
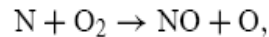
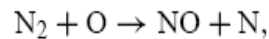
A report entitled, "Investigation of the effects of the use of Magno-Flo magnets on diesel engines", by Dr Joe Cheung, of the Bolton Institute School of Engineering, shows improvements from 5% to 10% in fuel consumption in an engine under load.

In order to study magnetic field effect on fuel oil, kinematic viscosities of fuel oils were measured. From the results of measurement, the analysis was carried out to clarify whether magnetic effect on fuel oils exists or not. Magnetic effects on fuel oils were significant over 95% and especially significant when the magnetic field of 2500 or 9500 gauss was used

### 2. MECHANISM OF NOX FORMATION

A major hurdle in understanding the mechanism of formation and controlling its emission is that combustion is highly heterogeneous and transient in diesel engines.

NO is formed during the post flame combustion process in a high temperature region. The most widely accepted mechanism was suggested by Zeldovich (Heywood 1988). The principal source of NO formation is the oxidation of the nitrogen present in atmospheric air. The nitric oxide formation chain reactions are initiated by atomic oxygen, which forms from the dissociation of oxygen molecules at the high temperatures reached during the combustion process. The principal reactions governing the formation of NO from molecular nitrogen are



Formation of NO<sub>x</sub> is almost absent at temperatures below 2000 K. Hence any technique, that can keep the instantaneous local temperature in the combustion chamber below 2000 K, will be able to reduce NO<sub>x</sub> formation.

### 3. EGR- NOX REDUCTION TECHNIQUE

Exhaust Gas Recirculation is a process developed to reduce a type of harmful air pollution. It is primarily used as an emissions control device on fuel driven engines. EGR systems control the amount of NO<sub>x</sub> expelled from the exhaust of an engine by controlling the temperature of the combustion chamber. Specifically, under heavy engine loads, the internal temperature becomes ideal to create oxides of nitrogen.

Re introducing an inert gas into the combustion process to keep the temperatures down - mainly the Carbon Dioxide, which the engine already expels, does reducing NO<sub>x</sub>. The system is mechanically simple as it is nothing more than a valve, which taps the exhaust gasses and plumbs it into the engines intake manifold (figure 2).

### 4. MAGNETIC FUEL TREATMENT SYSTEM

The magnetic fuel treatment system is fabricated with a stand containing a fuel tank to hold the charged fuel. It also consists of a radiator core, 9500 Gauss (figure 1) ferrite permanent magnet, a fuel pump and some piping. The flow is continuously maintained with the pump for circulation of the fuel for polarizing it (Mcneely, M, 1994).

These devices are external online installations without cutting or modifying the fuel pipes and the magnetic energy generated through the monopole is rendered concentric and exactly perpendicular to the flow of the fuel.

The most important factors in the monopole technology are the magnetic field intensity and the collimation (Marshall, S.V, 1987) of the magnetic lines of flux. The intensity of the magnetic field is far superior to that generated by regular permanent magnets and the collimation of the magnetic fields renders the magnetic lines of flux exactly parallel to each other (Ruggero, 2000) at extremely high densities (to the order of millions of lines of flux per sq. cm.).

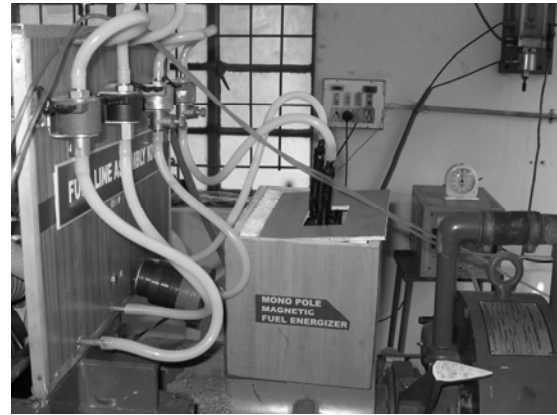
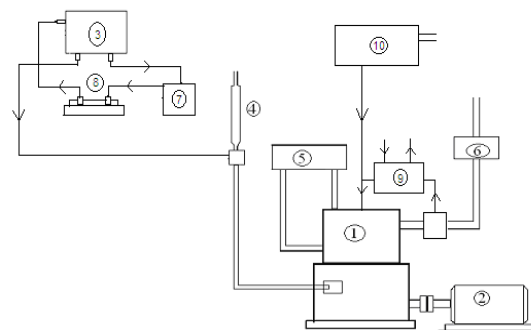


Fig 1. Experimental setup of fuel treatment system

### 5. EXPERIMENTAL PROCEDURE

The following steps were followed in approaching the above said problem of emissions and scope for Jatropha oil in the future as an alternate fuel.

1. Single cylinder four stroke water cooled electrically loaded engine with AVL five gas analyzer and AVL smoke meter was preferred for experiments.
2. The Jatropha oil was procured and blends of 50% and 100% bio diesel were prepared for the testing purpose.
3. A permanent magnet of 2500 Gauss was used in the fuel line, which was used to energize the fuel before injection. Another conditioning magnet of 9500 Gauss was also used in case of bio diesel.
4. EGR system was fabricated with heat exchanger like cooling system to cool the exhaust gas before recirculation
5. Engine modification for EGR was made.



1. Engine 2. Alternator 3. Fuel Tank 4. Fuel metering tube 5. Cooling water Thermometer 6. Exhaust Gas Thermometer 7. Fuel pump 8. Permanent Magnet 9. EGR 10. Air box

Fig 2. Schematic diagram of experimental setup

6. The performance tests and the heat balance tests have been carried out to compare the various



blends and their performance with each other was carried out for the following

- Without any engine modification.
  - With implementation of EGR.
  - Without the fuel conditioning setup.
  - With the fuel conditioning setup
7. A comparison study between the performance of the blends and the emission comparison is also presented.

## 6. CONCLUSIONS

From the experimental results the following conclusions were made:

- The mechanical efficiency of the engine while using Bio diesel is more than the conventional petroleum diesel (figure 6). When the percentage of Bio diesel increases the mechanical efficiency also increases simultaneously. With EGR, the mechanical efficiency was found to increase by 13%.
- No considerable change in the value of the torque was noticed. The torque remained almost the same for all the blends irrespective of EGR.
- There was no considerable change in the value of the brake mean effective pressure though the value of the 50% blend was closer when compared to other blends. The energized blends were also closer to diesel.
- There was a slight decrease in indicated thermal efficiency while using EGR and with various blends of Bio diesel. However, the presence of the magnetic fuel treatment has increased the values by about 5%.
- Other performance characteristics of the diesel engine running with Bio diesel almost remained same with the implementation of EGR and magnetic fuel conditioning.
- The emission of  $\text{NO}_x$  came down drastically with the use of EGR (figure 5). It was zero in some cases. The CO and HC values got reduced with the implementation of the monopole technology (figure 3 & 4).

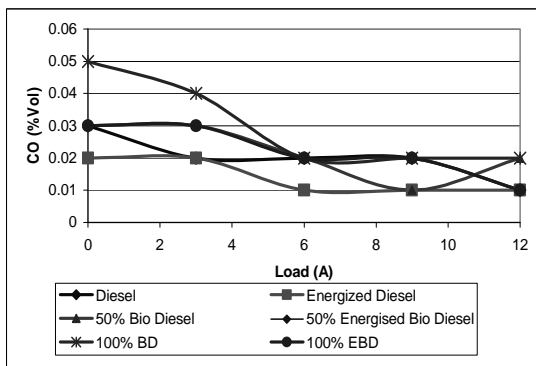


Fig 3. Variation of CO with load (Amps)

With a magnetic field we can increase the internal energy of the fuel, to cause specific changes at a molecular level. Increasing the internal energy means to obtain easier combustion. The molecules fly apart easier, join with oxygen easier and ignite well.

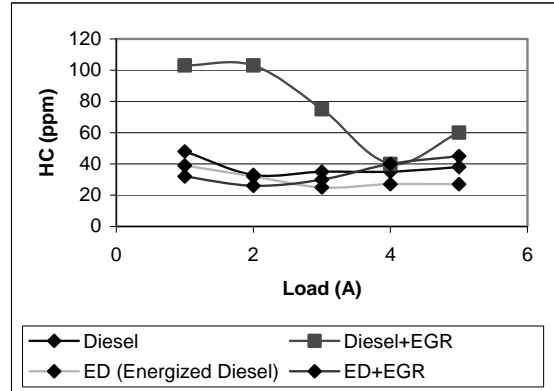


Fig 4. Variation of HC with load(Amps)

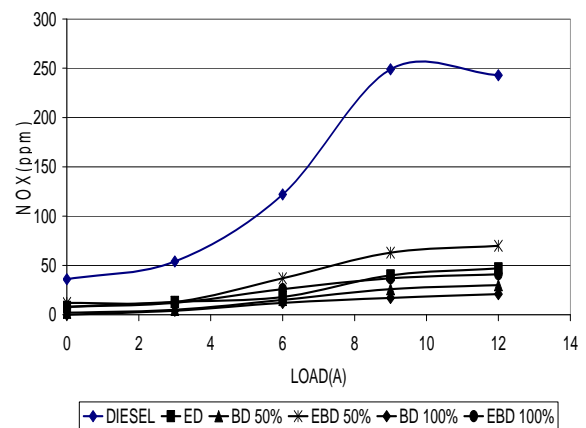


Fig 5. Variation of NOx with load (Amps)

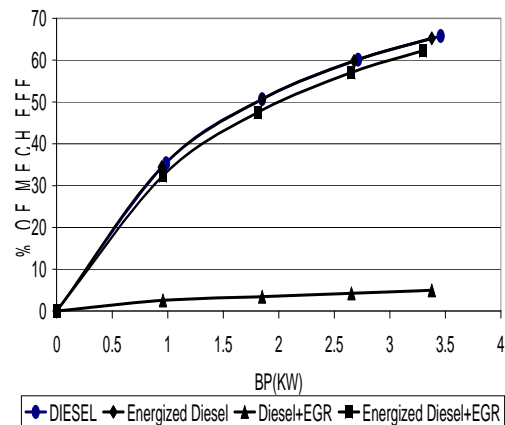


Fig 6. Variation of mechanical efficiency with brake power

The resultant conditioned fuel is magnetized to burn more completely, producing higher engine output, better fuel economy, more power and most importantly reduces the amount of hydrocarbons and carbon monoxide in the exhaust.

Finally, it is concluded that the use of EGR is more effective with the bio diesel and the magnetic fuel treatment system for the diesel for achieving improved emission performance of the engine.

#### ACKNOWLEDGEMENT

We are very grateful for the experimental setup funded by AICTE (All India Council for Technical Education, New Delhi, India). We thank Dr. M.A.Veluswami, Formerly professor, IIT, Chennai, for his guidance towards solving experimental complexity of the work.

#### 7. REFERENCES

1. Ashok K.Raina and B.R.Gaikwad, 2001, "Chemo-Botany of Jatropha species in India", *Publication of Godrej soaps Research Centre, Mumbai, India*
2. Avinsh Kumar Agarwal and Shrawan Kumar Singh, 2003, "Effects of EGR on exhaust gas temperature in CI engine", *Transactions, Indian Institute of Technology, Kanpur, India*
3. Avinsh Kumar Agarwal and L.M.Das, 2002 "Biodiesel development and characterization for use as a fuel in compression ignition engines", *Transactions, Indian Institute of Technology, Kanpur, India*
4. Busch, K.W., Busch, R.E. Darling, S. 1976 "Design of a test loop for the evaluation of magnetic water treatment devices. Process safety and environmental protection", *Transactions of the Institution of Chemical Engineers*
5. Gerhard Vellguth, 1983 "Performance of vegetable oils and their monoesters as fuel for diesel engines", *SAE Paper no. 831358, U.S.A.*
6. Gopalkrishna K.V. and Rao P.S. 2000, "Use of non-edible vegetable oils as alternate fuels in diesel

engines", *DNES Project report, I.C.Engines lab, IIT Madras, Chennai, India*

7. Marshall, S.V., and G.G. Skitek , 1987 "Electromagnetic Concepts and applications", 2<sup>nd</sup> ed. *Englewood Cliffs, N.J: Prentice-Hall, Inc.*
8. Mcneely, M,1994,"Magnetic fuel treatment system designed to attack fuel-borne microbes", *Diesel Progress Engines and Drives.*
9. Pitterson, D. J., 1966, "Cylinder Pressure Variations - Fundamental Combustion Problem", *Society of Automotive Engineers*
10. Ruggero Maria Santilli, 2000,"Recycling liquid wastes and Crude oil into Magnegas and Magne Hydrogen", *Hydrogen International Conference Hy2000, Munich, German.*
11. Samuel, S, Austin, L & Morrey, M, 2002,"Automotive test drive cycles for emission measured and real-world emission levels", *I Mech E Proceedings*
12. Vinayak patil and Kanwarjit singh.,2001, "Oil gloom to oil boom (Jatropha Curcas)", *published by Agro-forestry Federation, Maharashtra, India*
13. Proceedings of the XVIII National conference on IC engines and combustion held at College of Engineering, Thiruvanthpuram, India under the auspices of *the Combustion Institute (Indian Section).*
14. National conference proceedings on Alternative & Renewable energy Technologies held at *Indian Institute of Technology Kanpur, India*

#### 8. MAILING ADDRESS

P. Govindasamy  
Professor and Head,  
Department of Mech. Engg., Kongu Engg. College,  
Perundurai, Tamilnadu, India.

## NATURAL CONVECTION AND RADIATION IN CIRCULAR AND ARC CAVITY

Naheed Ferdous<sup>1</sup>, Md. Tofiqul Islam<sup>2</sup>, Md. A. Hasan Mamun<sup>1</sup>

<sup>1</sup>Department of Mechanical Engineering, Bangladesh University of Engineering and Technology, Dhaka, Bangladesh.

<sup>2</sup>Department of Mechanical Engineering, Wayne State University, Detroit, USA

### ABSTRACT

The radiation effect of gray surfaces on multiple steady-state solutions obtained in circular and arc-square inclined enclosure filled with air has been investigated numerically, by a finite-volume procedure. The left and right surfaces of the cavity are, respectively, heated and cooled at constant temperatures, while its horizontal walls are adiabatic. Parameters of the problem are the Rayleigh number  $Ra(10^2 > Ra > 10^6)$ , the inclination angle  $\gamma$  (0 to 90°), aspect ratio equal to 1 and the surface emissivity (0 <  $\epsilon$  < 1).

**Keywords:** Constant Temperature, Circular And Arc Cavity, Nusselt Number, Radiation

### 1. INTRODUCTION

Heat transfer by combination of natural convection, conduction and radiation occurs when simulating building components, in particular passive heating and cooling systems, cooling of electronic components, design of solar collectors etc. Natural convection, coupled with surface radiation in a square cavity, heated from below [1], the conjugate heat transfer in an inclined square enclosure bounded by a solid wall [2], mixed convection and thermal radiation in ventilated cavities with gray surfaces [3] have been studied numerically. In the past, a great number of studies have focused on a variety of cavity configurations formed with straight walls, but the effects of curving the walls inward to form a derived circular cavity are beneficial because the fluid follows a less convoluted path. The flow and temperature field alters with the shape and orientation of the cavity.

### 2. PHYSICAL MODEL

The Physical diagram of the problem and the boundary conditions are shown in the fig. 1 (a) and (b). They are circular and arc cavities filled with air. Diameter of the cavity is  $H$ , where adiabatic horizontal sides are  $0.57 H$ . The left wall is at a constant temperature  $T_h$  and it is heated. The cold wall is also at a constant temperature  $T_c$ . It is inclined at an angle  $\gamma$  with the horizontal axis. Laminar fluid flow and constant fluid properties are assumed here. The gravitational acceleration is considered in the normal vertical direction. The fluid outside and the horizontal walls are maintained to an ambient temperature  $T_a$ . In the present study, Rayleigh number is varied from  $10^2$  to  $10^6$ ; emissivities from 0 to 1; inclination angles from 0 to 90°. The aspect ratio and Prandtl number are 1 and 0.7 respectively throughout the problem.

### 3. MATHEMATICAL MODELING

It is assumed that the flow is two-dimensional, steady state, laminar and the fluid is incompressible. The thermo-physical properties of the fluid are assumed to be constant except in the buoyancy term of the momentum equation, i.e., the Boussinesq approximation. Radiation heat transfer is taken into consideration along with natural convection mode. The viscous energy dissipation term in the energy equation can be neglected because of the small flow velocities associated with free convection. Continuity Equation:

$$U \frac{\delta U}{\delta X} + \frac{\delta V}{\delta Y} = 0 \quad (1)$$

X-Momentum Equation:

$$U \frac{\delta U}{\delta X} + \frac{\delta U}{\delta Y} = -\frac{\delta P}{\delta X} + \frac{1}{Re} \left( \frac{\delta^2 U}{\delta X^2} + \frac{\delta^2 U}{\delta Y^2} \right) + Ri \theta \sin(\gamma) \quad (2)$$

Y-Momentum Equation:

$$U \frac{\delta V}{\delta X} + \frac{\delta V}{\delta Y} = -\frac{\delta P}{\delta Y} + \frac{1}{Re} \left( \frac{\delta^2 V}{\delta X^2} + \frac{\delta^2 V}{\delta Y^2} \right) + Ri_y \theta \cos(\gamma) \quad (3)$$

Energy Equation:

$$U \frac{\delta \theta}{\delta X} + V \frac{\delta \theta}{\delta Y} = \frac{1}{Re * Pr} \left( \frac{\delta^2 \theta}{\delta X^2} + \frac{\delta^2 \theta}{\delta Y^2} \right) \dots \quad (4)$$

At the surface:

$$Nr \zeta = \left( \frac{\delta \theta_f}{\delta X} - k_r \frac{\delta \theta_s}{\delta X} \right) \quad (5)$$

where  $Nr = \sigma T_\infty^4 / q''$  is the radiation number,  $\zeta$  is dimensionless radiative heat flux,  $\zeta = q_r / \sigma T_\infty^4$ ,  $\delta\theta_f / \delta X$  and  $\delta\theta_s / \delta X$  are the heat flux from the wall surface to the fluid on the right and to the solid on the left, respectively. The governing parameters are  $Ra$ ,  $Pr = \nu/\alpha$ ,  $k_r$ ,  $\varepsilon$ , and  $A = L/H$  and  $w = l/H$ .

The average convective and radiative Nusselt numbers are calculated at  $X = 0$  plane as

$$Nu_c = -\int_0^1 \frac{1}{\theta} \frac{\delta\theta}{\delta X} dY \quad (6) \quad Nu_r = -\int_0^1 \frac{1}{\theta} Nr \zeta_s dY \quad (7)$$

$$\text{The dimensionless temperature } \theta = \frac{T - T_c}{T_h - T_c} \quad (8)$$

#### 4. GRID SENSITIVITY TEST

In order to obtain grid independent solution, a grid refinement study is performed for the cavity under constant temperature considering  $Ra=10^6$ ,  $Pr = 0.71$ ,  $\gamma = 0$  as shown in Table 1.

Table 1: Grid Sensitivity Test

No. of Nodes	$Nu_{av}$
10	0.99587268
30	1.0433495
50	1.0516758
70	1.0532773
90	1.0531155

#### 5. CODE VALIDATION

Figure 2(a) and 2(b) reveals the streamline and isotherm obtained in this present study have excellent agreement with those obtained by El Hassan Ridouane and Antonio Campo [4]. The table 2 shows the comparative values of Nusselt numbers for different Rayleigh numbers.

Table 2: Code Validation

Rayleigh number	Circular cavity Present study Nu	Circular cavity Paper Nu	Arc cavity Present study Nu	Arc cavity Paper Nu
$10^2$	1.281	1.245	1.138	1.114
$10^3$	1.4038	1.32	1.1758	1.175
$10^5$	4.8195	4.94	4.700	4.71
$10^6$	9.1151	9.2	9.0378	9.05

## 6. RESULTS AND DISCUSSION

The numerical results obtained here are governed by several variable influential parameters. Those are Rayleigh numbers varied from  $10^2$  to  $10^6$ , the inclination angles ranged from  $0^\circ$  to  $90^\circ$  and the emissivity of materials changed from 0 to 1.

### 6.1 Effect of Rayleigh Number

From the stream line plots it can be seen that all four configurations contain a single rotating vortex. As the Rayleigh number increases, the circulation evolving from buoyancy inside the cavities gets energetic. It is seen that there are two vortices instead of a single, in the lower right and upper left corners. Vortex rotation is clockwise.

The isotherms are parallel to the gravity field at low Ra that indicates the typical conduction temperature distribution. Marked compression of the isotherms toward the boundary surfaces of the enclosure occurs to a greater extent with increasing Ra. Combined Nusselt number is a strong increasing function of Ra. It is almost horizontal up to critical  $Ra=10^3$ , then the deviation begins.

### 6.2 Effect of Emissivity

The flow pattern and isotherms for the surface emissivity  $\varepsilon = 0.0, 0.6$  and  $0.1$  for circular cavities are shown in fig 3 and 4 for circular and arc cavity respectively. For the case with  $\gamma = 0$  we present  $Nu_c$  as a function of the Rayleigh number in Fig.5. We see the combined nusselt number is an increasing function of  $\varepsilon$ .

### 6.3 Comparison of Heat Transfer Rate for Natural Convection and Radiation

It is seen that generally the temperature field is more brilliant and the gradients much higher for  $\varepsilon = 0$  than  $\varepsilon = 1$ . So it can be anticipated that the convective heat transfer be decreased with surface radiation in spite of enhanced circulation.

The spatial arrangement of temperature field changes creating distance within the isotherms which grows with Ra. The fluid temperature inside the cavity goes toward homogeneity with the existence of wall's radiation.

It is seen from Figure 6(a),  $H_c$  decreases by increasing  $\varepsilon$  for a given Ra. So, radiation affects convection negatively.  $H_r$  increases quickly with  $\varepsilon$  (for a given Ra). So, surface emissivity acts positively for  $H_r$ . The Heat transfer due to radiation, and therefore, the total heat transfer, increases in a drastic manner for highly emissive walls of the cavity (Figure 6(b))

### 6.4 Comparison of Circular and Arc Cavity

The nusselt number for total heat transfer rate considering radiation with natural convection increases at the same course as for only natural convection.  $Nu_t$  is always higher for circular cavity in comparison with arc cavity.

For convection  $Nu_c$  is 0.86% higher for  $Ra=10^6$ ,  $\gamma = 0$ , and  $Nu_t$  is 1.13% higher considering radiation,  $\varepsilon=1$ . Heat transfer increases 1.74% for circular cavity in comparison of arc taking  $Ra=10^6$ ,  $\gamma = 0$  and  $\varepsilon=1$ .

## 6.5 Effect of Inclination Angles

In Figure 7(a), convective Nusselt numbers for circular cavity is presented as a function of the inclination angle,  $\gamma$  with  $Ra=10^2, 10^3, 10^5, 10^6$ ,  $Nu_c$  is an increasing function of  $Ra$  and at  $Ra=10^6$ , it goes through a maximum at 22degree for circular cavity and 9 degree for arc(fig 7(b)). Percent of radiation in total heat transfer is quasi constant for  $\gamma$  from 0 to 20°, thereafter they increase by 6.81% from 30 to 90° in fig 8(a). Invariance of the radiative heat transfer is observed in fig 8(b) where total heat transfer is a decreasing function of  $\gamma$ .

## 7. CONCLUSION

The surface radiation modifies temperatures on all enclosure walls; the velocity and temperature gradients are decreased. Considering radiation, the percentage of radiation heat transfer decreases gradually at low Rayleigh, increases at high Rayleigh and again decreases at higher Rayleigh number. The radiative heat flux is a strong increasing function of the surface emissivity starting at its low values; as a consequence, the convective heat flux is a strongly decreasing function of it. The combined Nusselt number  $Nu_t$  is an increasing function of  $Ra$  as well as surface emissivity,  $\epsilon$ .  $Nu_t$  is always higher for circular cavity in comparison with arc cavity.

The convective Nusselt number  $Nu_c$  goes through a broad maximum at the inclination angle of 22degree for circular cavity and 9 degree for arc cavity at  $Ra=10^6$  while the radiative Nusselt number  $Nu_r$  is unaffected to its fluctuation. At high inclination angle,  $Nu_c$  declines; i.e. total heat transfer rate decays. But the Radiation heat transfer in insensible to angle variation.

The percentage of radiation heat transfer increases with higher inclination angle.

## 8. REFERENCES

- Ridouane, E. H., Hasnaoui M., Amahmid A., Raji, A. , “Interaction between natural convection and radiation in a square cavity heated from below”, Numerical Heat Transfer, Part A:Applications,45:3,289 — 311
- Nouanegue H.F., Muftuoglu A., Bilgen E., 2008, “ Heat transfer by natural convection, conduction and radiation in an inclined square enclosure bounded with a solid wall”, International Journal of Thermal Sciences , doi:10.1016/j.ijthermalsci..06.008
- Raji and Hasnaoui M., 2001 “Combined mixed convection and radiation in ventilated cavities”, Engineering Computations Vol. 18 No. 7, pp. 922-949
- Ridouane E. H., Campo A., 2006, “Free convection performance of circular cavities having two active curved vertical sides and two inactive curved horizontal sides”, Applied Thermal Engineering 26, 2409–2416
- Ramesh N. and Venkateshan S. P.,1999,” Effect of Surface Radiation on Natural Convection in a Square Enclosure”; Journal of thermophysics and heat transfer.Vol. 13, No. 3
- Balaji C. and Venkateshan S. P., 1993, “Interaction of surface radiation with free convection in a square cavityInt”, J. Heat and Fluid Flow, Vol. 14, No. 3

## 9. NOMENCLATURE

Symbol	Meaning	Unit
$C_p$	specific heat capacity at constant pressure	J/kg.K
$k$	thermal conductivity	W/m.K
$Nu$	average Nusselt number; $Nu = hL/k, h\Delta T/ k(\Delta T/L)$	
$Gr$	Grashof number, $Gr = g\beta L^3 (T_w - T_a)/\nu^2$	
$Pr$	Prandtl number, $Pr = \nu/\alpha$	
$Ra$	Rayleigh number, $Ra = Gr * Pr$	
$T$	temperature	°K
$U, V$	non-dimensional x & y velocity component , $U = uH/\alpha_f, V = vH/\alpha_f$	
$Ri$	Richardson number, $Gr/Re^2$	
Symbols		
$\alpha$	thermal diffusivity	$m^2/s$
$\gamma$	inclination angle	degree
$\epsilon$	emissivity	
$\theta$	non-dimensional temperature	
$\nu$	dynamic viscosity	kg/m.s
Subscripts		
$s$	surface	
$h$	hot	
$c$	cold	
$f$	fluid	

## 10. MAILING ADDRESS

Naheed Ferdous  
 Department of Mechanical Engineering,  
 Bangladesh University of Engineering and Technology,  
 Dhaka 1000, Bangladesh.  
 Email: [nfmou\\_104@yahoo.com](mailto:nfmou_104@yahoo.com)

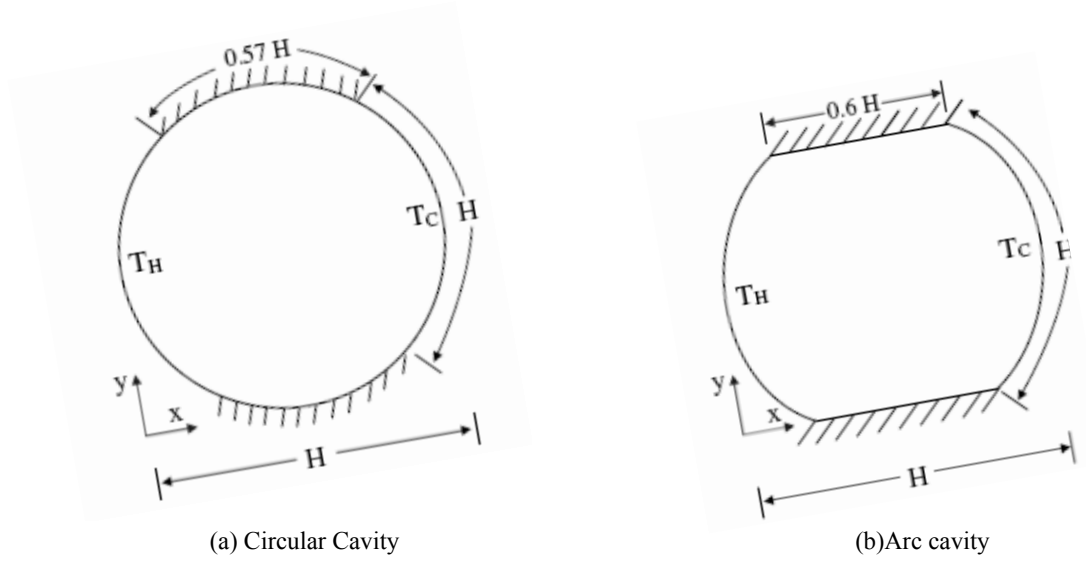


Fig 1. Physical Model of (a) circular (b) arc geometry

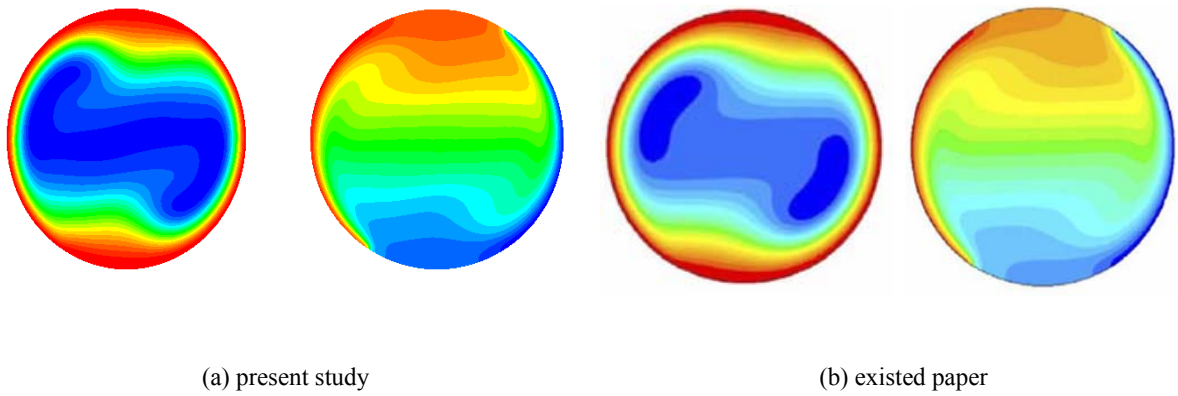
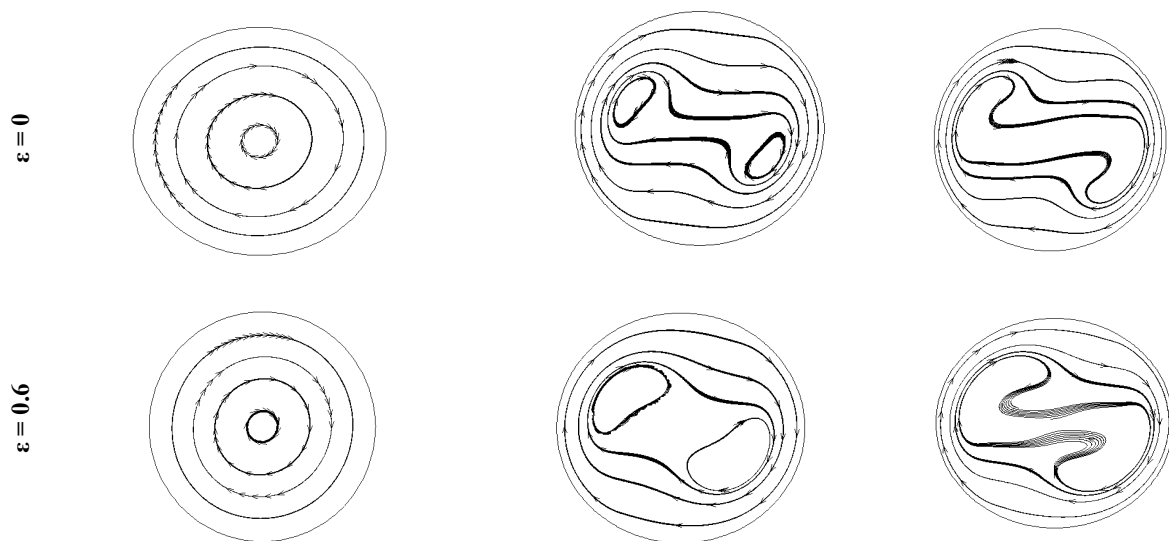


Fig 2. Code Validation; Comparison of stream lines and isotherms for high  $Ra=10^6$  In circular cavity



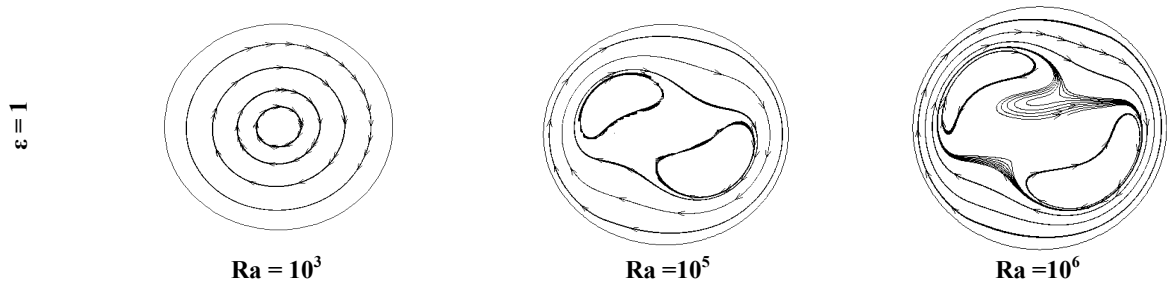


Fig 3. Streamlines Variation of Ra at  $\gamma = 0^\circ$  (circular cavity)

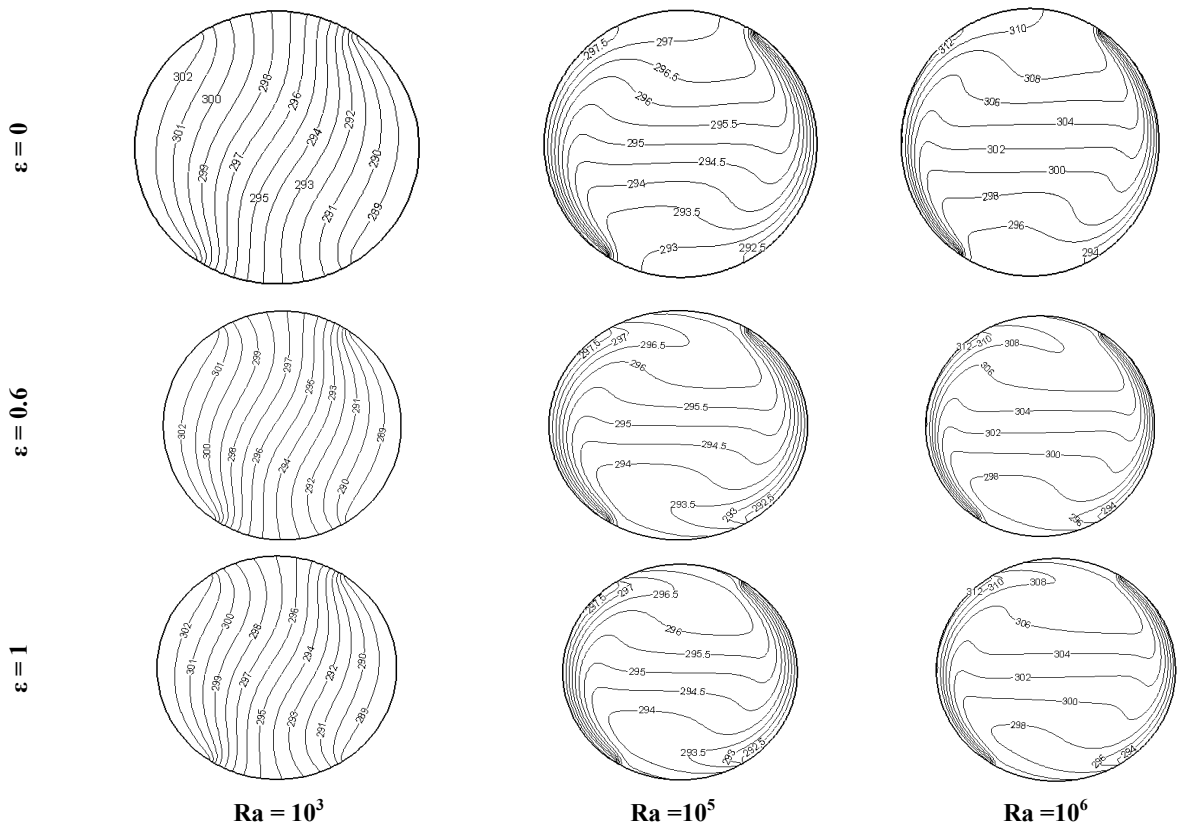


Fig 4. Isotherms Variation of Ra at  $\gamma = 0^\circ$  (circular cavity)



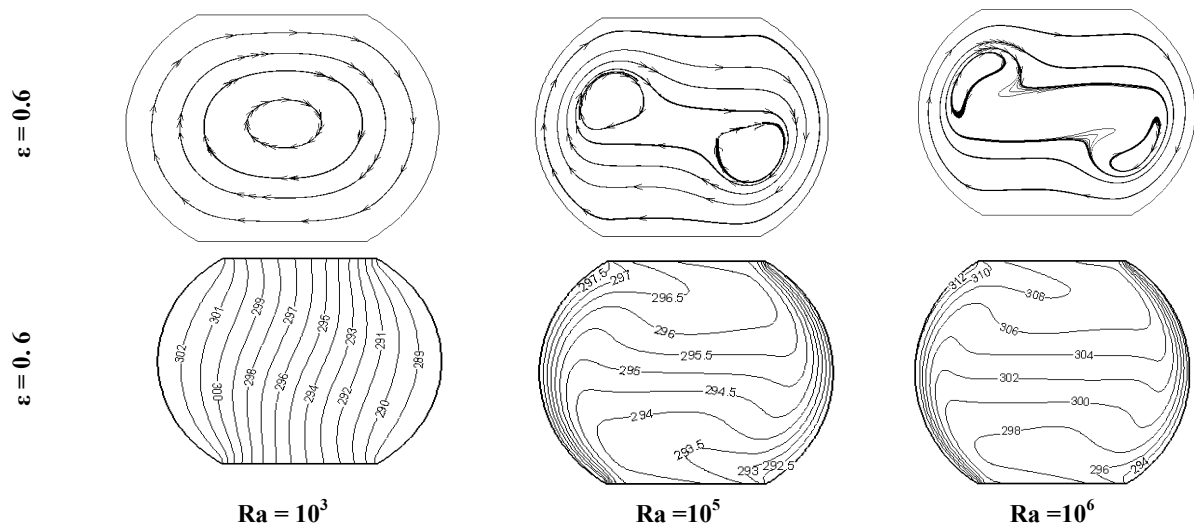


Fig 5. Streamlines and isotherms Variation of Ra at  $\gamma = 0^\circ$  (for arc cavity)

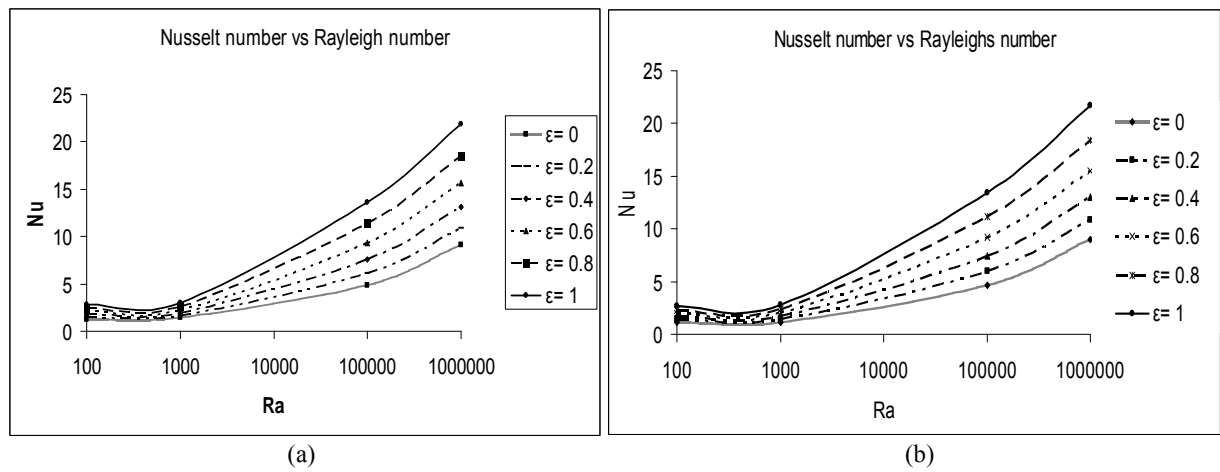


Fig 6. variation of Ra on Nusselt number at different emissivity at  $\gamma = 0^\circ$  (a) for circular cavity (b) for arc cavity

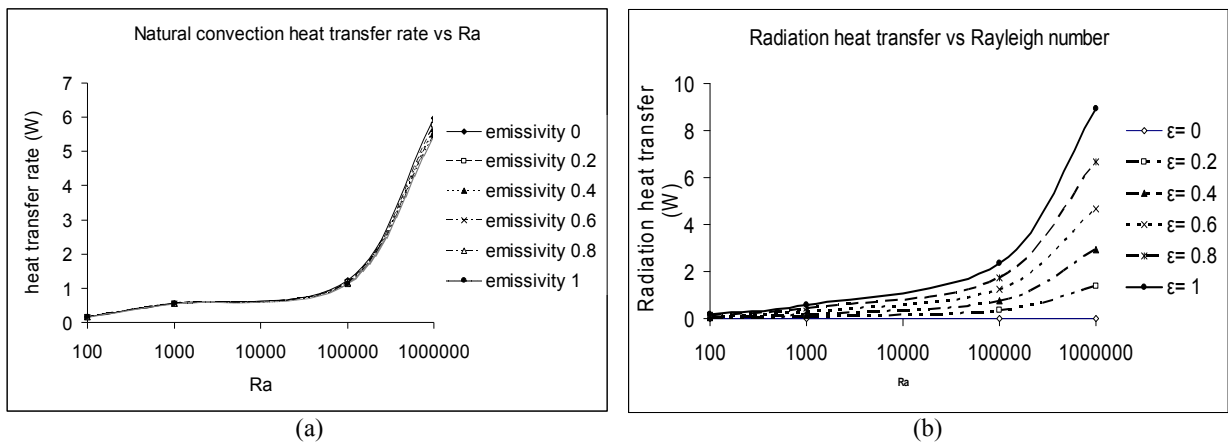
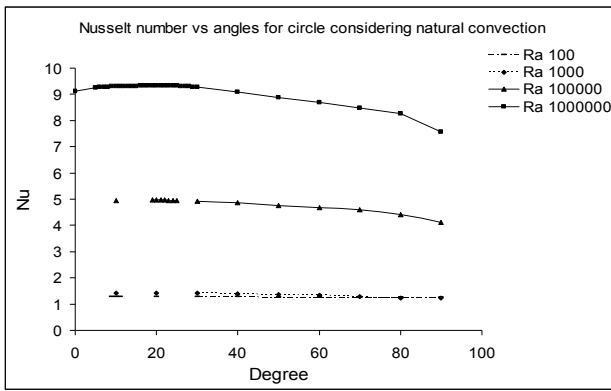
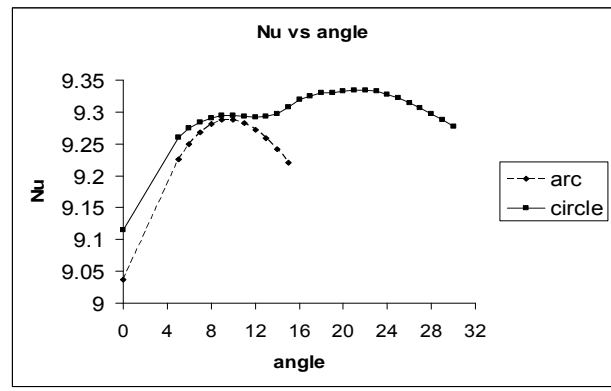


Fig 7. (a) Natural convection heat transfer rate for different emissivities in a circular cavity (inclination angle 0) (b) Radiation heat transfer rate for different emissivities in a circular cavity (inclination angle 0)

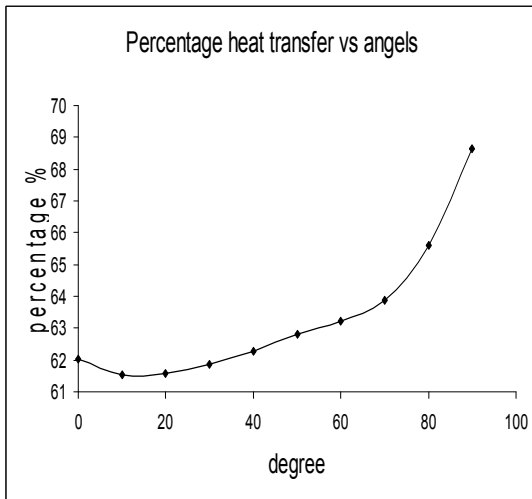


(a)

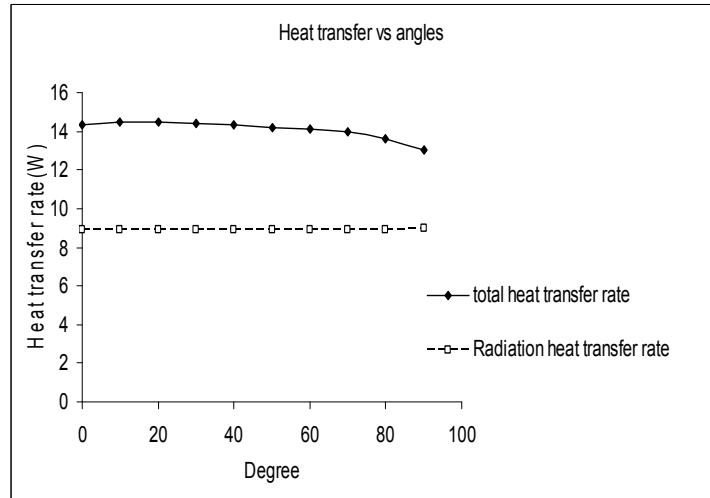


(b)

Fig 8. (a) Nusselt number variation for different inclination angle in a circular cavity considering natural convection; (b) Finding of the optimum inclination angles for maximum Nusselt number for arc and circular cavity considering natural convection ( $Ra 10^6$ )



(a)



(b)

Fig 9. (a) Percentage of radiation heat transfer in the combined heat transfer rate for different  $\gamma$  in a circular cavity for  $\epsilon=1$  and  $Ra 10^6$  (b) combined and radiation heat transfer rate for different  $\gamma$  in a circular cavity, taking  $\epsilon=1$  and  $Ra 10^6$

## PROSPECTS OF BIOMASS GASIFICATION AS AN ENERGY SOURCE IN BANGLADESH

M. Mahadi Hasan, N. N Mustafi and M. Abul Hashem

Dept. of Mechanical Engineering, Rajshahi University of Engg. and Tech., Rajshahi, Bangladesh

### ABSTRACT

Biomass gasification is quite new in Bangladesh and may be considered as a promising technology for the useful conversion of waste biomass. The fuel gas produced by gasification can run engines and thus generate electricity. In the present work, literature survey is performed to compare the available proven gasification technologies around the globe in terms of biomass quality and quantity, system complexities and capacity, and economic factors. The outcome of this study would identify a suitable gasification technology for Bangladesh. To explore the full potentials of biomass gasification, necessary data on biomass availability and quality is discussed. A case study is incorporated which applies biomass gasification technology in Bangladesh, to generate power from rice husk. This will provide a practical impression on the successful use of this technology in this country. Finally useful conclusions and possible recommendations are made in favor of adopting this technology in Bangladesh's perspective.

**Keywords:** Biomass, Gasification, Power generation.

### 1. INTRODUCTION

Electricity is the most useful form of energy. Since all industrial and other economic activities rely on electricity or other means of power, the availability of electrical energy can be considered as an indicator of a country's economic strength. In Bangladesh, the majority electricity is generated from fossil fuel sources: indigenous natural gas and imported petroleum fuels. However, only about 38% of its total population has access to the electricity. The energy situation in rural Bangladesh is characterized by low quality of fuel, low efficiency of use, low reliability of supply and limited access leading to lower productivity of land, water and human effort, ultimately leading to low quality of life and environmental degradation. Therefore access to quality, reliable and affordable energy is critical for promoting economic and social development in rural areas [1]. The Government of Bangladesh aims to provide electricity to its entire rural population by 2020 to help boost social development and economic growth. However, it would be unrealistic and infeasible to use grid electricity to reach the target. In addition to the expansion of the grid, it has to rely on non-grid options such as renewable energy-based small capacity independent power plants.

In supplementing the declining fossil fuel sources of energy, biomass has been recognized as a major renewable and sustainable source of energy with the highest potentials to contribute to the energy needs of modern society world-wide [2]. Like in other parts of the world, biomass has been proved to become the largest source of renewable and sustainable energy in

Bangladesh. About 80% of her people live in rural areas, and the contribution of biomass energy is about 70% of the total national energy consumption in Bangladesh [3]. Different methods have been adopted in the last decades to utilize biomass as a useful source of energy with its full potentials. It includes direct combustion, anaerobic fermentation, briquetting, pyrolytic conversion and gasification. Being agriculture-based country, Bangladesh has huge potentials to utilize agricultural wastes as biomass sources. However, direct combustion is the most common method of biomass utilization in Bangladesh (especially in rural areas), which has very poor energy efficiency.

Amongst the bioenergy technologies, the biomass gasification option for meeting the rural electricity needs of domestic, irrigation and rural small and cottage industrial as well as thermal activities, is shown to have a large potential. Gasification is the technology capable of producing fuel gas from conversion of biomass, which can serve the need of energy in various forms. In recent years biomass gasification technology seems to have given concerns around the world. This technology serves following advantages:

- It uses biomass which is sustainable and renewable sources of energy
- It is an efficient way to utilize waste biomass and the gas produced from gasification can be used for generating electricity
- Gasification produces less harmful exhaust as biomass is very low in sulfur, chlorine or heavy metals, which are detrimental to the environment

- It contributes to global warming - when biomass is grown on a sustainable basis, it does not contribute to carbon dioxide emissions
- It can provide economic development and employment opportunities in rural areas
- The biggest advantage of gasification is the use of variety of feedstock and products, as the syngas can also be used for chemical industry along with power generation.

Biomass gasification is new in Bangladesh and may be considered as a promising technology for the utilization of waste biomass. The fuel gas produced by gasification technology can run internal combustion engines and thus generate electricity. In the present work, literature is reviewed to compare the available proven gasification technologies in terms of biomass quality and quantity, gasification system complexities, system capacity and the associated economic factors, around the world. The outcome of this review would identify a suitable gasification technology that can be adoptable in respect of this country. To explore the full potentials of biomass gasification, necessary data on biomass availability and quality have been incorporated. A case study is also added which is employing agricultural biomass such as rice husk for gasification technology to generate electricity. This is the first successful application of the technology in commercial sector in Bangladesh. This will provide a practical impression on the successful use of this technology in this country. Finally, useful conclusions and possible recommendations are made in favor of adopting this technology in Bangladesh's perspective.

## 2. FUNDAMENTALS OF BIOMASS GASIFICATION

In principle, gasification is the thermal decomposition of organic matter in an oxygen deficient atmosphere, producing a mixture of combustible and non-combustible gases. Typically the gas mixture includes carbon monoxide (CO), hydrogen (H<sub>2</sub>), carbon dioxide (CO<sub>2</sub>), methane (CH<sub>4</sub>), traces of higher hydrocarbons, water, nitrogen (if air is used as gasifying agent). Gasification also produces tar and solid particles like ash and char. Gasification is different from pyrolysis in the sense that gasification is performed to produce gaseous components, whereas pyrolysis is the production of liquid residues and charcoal. The latter normally occurs in the total absence of oxygen, while most gasification reactions take place in an oxygen deficient or starved environment [4m] [5m].

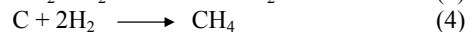
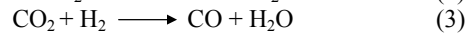
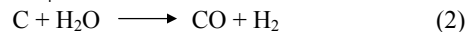
Gasification occurs in a gasifier in which the biomass particle is exposed to high temperatures. As the particle is heated, the moisture is driven off and the weight of biomass fuel reduces to even more than 50%. Further heating of the particle begins to drive off the volatile gases. Discharge of these volatiles will generate CO and a wide spectrum of hydrocarbons ranging from methane to long chain hydrocarbons comprising tars, creosotes and heavy oils. After about 900°C-1000°C, the biomass particle is reduced to ash and char. Typically the char is contacted with air, or oxygen and steam to generate CO, introduced below the grate and diffuse up through the

CO<sub>2</sub> and heat. The total gasification procedure is performed in three stages [6m]:

- Stage 1: Gasification process starts as autothermal heating of the reaction mixture. The necessary heat for this process is covered by the initial oxidation exothermic reactions by combustion of a part of the fuel
- Stage 2: Combustion gases are pyrolyzed by being passed through a bed of fuel at high temperature. Heavier biomass molecules distillate into medium weight organic molecule and CO<sub>2</sub>, through following reaction



- Stage 3: Initial products of combustion, CO<sub>2</sub> and H<sub>2</sub>O are converted by reduction reaction to CO, H<sub>2</sub> and CH<sub>4</sub>:



The combustible gases produced by this technology can be used in power or heat generation shown in Fig.1 [8].

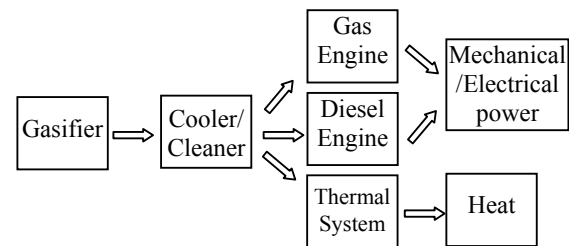
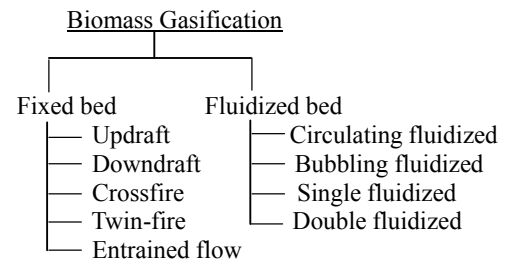


Fig 1. Usage of produced gas in different purposes.

## 3. GASIFICATION TECHNOLOGIES

Several types of gasification methods have been used in the last few decades depending mainly on the type of gasifier. These methods can be summarized in a flow chart:



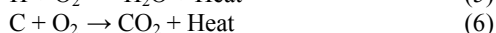
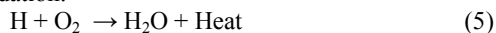
Besides these basic classes, gasification technologies are also classified based on the type of feeding (automatic or manual), amount of pressure applied (atmospheric or pressurized), type of opening (open top or closed), etc. A few of them is discussed in the following sections.

### 3.1 Updraft Gasifier [9m]

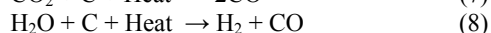
The oldest and the simplest form of gasifier is updraft. It has clearly defined zones for partial combustion, reduction and pyrolysis. Biomass is introduced at the top of the reactor and a grate at the bottom of the reactor supports the reacting bed. Air or oxygen or steam is bed of biomass and char. Complete combustion of char

takes place at the bottom of the bed, liberating CO<sub>2</sub> and H<sub>2</sub>O. These hot gases (~1000°C) pass through the bed upward, where they are reduced to H<sub>2</sub> and CO and cooled to about 750°C. Containing up the reactor, the reducing gases (H<sub>2</sub> and CO) pyrolyze the descending dry biomass and finally dry the incoming wet biomass, leaving the reactor at a low temperature (~500°C). Therefore it has four clearly definer reaction zones and these are oxidation, reduction, pyrolysis and drying zone. The reactions in each zone are:

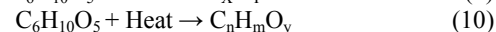
Oxidation:



Reduction:



Pyrolysis:



Drying:



### 3.2 Downdraft Gasifier

Downdraft gasifier is so called as the fuel and gas flow downward direction of the gasifier. It is also known as concurrent-flow gasification. The downdraft gasifier has the same mechanical configuration as the updraft gasifier except that the oxidant and product gases flow down the reactor in the same direction as the biomass [9m]. In the updraft gasifier, gas leaves the gasifier with high tar vapor which may seriously interfere the operation of internal combustion engine. This problem is minimized in downdraft gasifier. This process can combust up to 99.9% of the tars formed. Primarily biomass and air or oxygen is ignited in the hearth zone [10m]. The produced flame generates pyrolysis gas or vapor, which burns leaving 5% to 15% char and provide hot combustion gas.

These gases flow downward and react with the char at 800 to 1200°C, generating more CO and H<sub>2</sub>. Finally, unconverted char and ash pass through the bottom of the grate and are sent to disposal.

### 3.3 Circulating Fluidized Bed Technology

The bed material along with heated biomass particles circulates in the gasifier and hence called circulation fluidized bed [9m]. Gasification temperature ranges from 800 to 950°C. The gas velocity inside the gasifier is higher than that of bubbling bed technology. The approach velocity in the gasifier lies in the order of magnitude of the terminal velocity; as a consequence, the bed material is carried into the freeboard thus forming a gas/solids flow in the entire reactor. With the help of a cyclone, the carried away bed material is separated from the gas stream and recirculated into the reactor [11, 12m].

### 3.4 Bubbling Fluidized Bed Gasification

A bubbling fluidized bed consists of fine, inert particles of sand or alumina as bed material [9m]. As oxidant (oxygen, air or steam) is forced through the inert particles, a point is reached when the frictional force between the particles and the gas counterbalances the

weight of the solids. At this gas velocity (minimum fluidization) bubbling and channeling of gas through the media occur such that the particles remain in the reactor. The fluidized particles break up the biomass feedstock effectively and ensure good heat transfer throughout the reactor [11m]. This is the gasification mode of operation. Typical desired operating temperatures ranges from 900°C to 1000°C.

### 3.5 Comparison among different gasifier systems

Table 1 presents a comparison between the fixed bed and fluidized bed gasification technologies and Table 2 compares the merits and demerits of different fixed bed technologies.

However high rate of tar production in updraft gasifier makes them very impractical for high volatile fuels. On the other hand, downdraft gasifier has been developed for the conversion of high volatile fuels to low tar gas and therefore has proven to be the most successful design for power generation. It is also recommended where a clean gas is required. Downdraft gasifier is very suitable for small-scale power plant as well as preferred for the application in internal combustion engines.

### 3.6 Selection of Gasification System for Bangladesh

Either updraft or downdraft gasifier system can be chosen for Bangladesh's perspective due to their simplicity in construction and low maintenance requirements. Also, the technologies of these systems are quite matured in the world. Based on the above comparative discussions, however, a downdraft gasifier is better than an updraft gasifier system in many aspects. Therefore, "an open top downdraft gasification system" can be chosen as the most suitable one for Bangladesh. This gasifier has some unique advantages like suitability to small scale production (50-150kW), minimum operating labor required, exhaust type (particularly % of tar content), and easy as well as less maintenance required.

## 4. AVAILABILITY OF BIOMASS IN BANGLADESH

Bangladesh is an agriculture-based country and the available biomass is mainly of agricultural wastes. In addition to the agricultural wastes, the other biomass sources are industrial wastes such as saw dust, rice husk, bagasse from sugar industries. The approximate annual biomass production is summarized in Table 3.

### 4.1. Pulse's Rind (A New Option)

The rind of pulses ("dal") can be used as biomass fuel for gasification as it has better uniformity in size and good calorific value. The most common rinds of pulses are Gram, Mug, Masur, Khesari, Mashkalai, Peas etc. The annual pulse production is tabulated below in M.tons in Table 4 [17]. This enormous amount of pulses is capable of producing substantial amount of rind, which can be used as biomass feedstock.

Table 1: Comparison between fixed bed and fluidized bed technologies [13, 14]:

Fixed bed technology		Fluidized bed technology	
Updraft	Downdraft	Bubbling	Circulating
<p><b>Advantages</b></p> <ul style="list-style-type: none"> <li>- Simplicity in design and construction and suitable for small scale production</li> <li>- Easy and less maintenance and thus more economical</li> <li>- Good maturity</li> </ul> <p><b>Disadvantages</b></p> <ul style="list-style-type: none"> <li>- Limited type of biomass fuel can be used</li> <li>- Requires smaller feed size</li> <li>- Allowable moisture content is &lt;20%</li> <li>- Calorific value of gas is low</li> <li>- More tar content</li> <li>- Different scrubber and cleaner are to be employed.</li> </ul>		<p><b>Advantages:</b></p> <ul style="list-style-type: none"> <li>- Excellent gas and solid mixing</li> <li>- Uniform temperature and high heating rates</li> <li>- Large variety of biomass can be used as feedstock</li> <li>- Greater tolerance to particle size range</li> <li>- Safer operation and good control</li> </ul> <p><b>Disadvantages:</b></p> <ul style="list-style-type: none"> <li>- Complex construction and greater maintenance and hence expensive</li> <li>- Fused ash and tar condensation provokes defluidization</li> </ul>	

Table 2: Comparison among fixed bed technologies [9, 13, 14, 15]:

Gasifier type	Advantages	Disadvantages
Updraft	<ul style="list-style-type: none"> <li>- good maturity and have a good thermal efficiency</li> <li>- small pressure drop</li> <li>- little tendency towards slag formation</li> <li>- simpler construction and less installation cost</li> </ul>	<ul style="list-style-type: none"> <li>- great sensitivity to tar and moisture</li> <li>- poor reaction capability with heavy gas load</li> <li>- suitable for small size fuel only</li> </ul>
Downdraft	<ul style="list-style-type: none"> <li>- flexible adaptation of gas production to load</li> <li>- low sensitivity to charcoal dust and tar content of fuel</li> <li>- better quality of gas</li> <li>- simple and low cost process and minimum maintenance required</li> </ul>	<ul style="list-style-type: none"> <li>- design tends to be tall</li> <li>- little complex construction than updraft</li> <li>- suitable only for small scale plant</li> <li>- feed needs to have a fairly uniform particle size</li> <li>- limited access to the type of fuel</li> </ul>
Cross draft	<ul style="list-style-type: none"> <li>- short design height</li> <li>- very fast response time to load</li> <li>- flexible gas production</li> <li>- economy in gasifier size</li> </ul>	<ul style="list-style-type: none"> <li>- very high sensitivity to slag formation</li> <li>- high pressure drop</li> <li>- complex construction</li> </ul>
Twin-fire	<ul style="list-style-type: none"> <li>- clean gas production and no need of extra purification devices</li> <li>- simple in design as well low cost</li> <li>- suitable output gas temperature</li> <li>- economy in gasifier size</li> </ul>	<ul style="list-style-type: none"> <li>- it needs an additional oxygen production plant</li> <li>- limited type of fuel can be used</li> <li>- higher amount of oxidant required</li> <li>- complex construction</li> </ul>
Entrained flow	<ul style="list-style-type: none"> <li>- produced gas is about completely tar free</li> <li>- simple design</li> <li>- clean gas production excluding the need of purification apparatus.</li> </ul>	<ul style="list-style-type: none"> <li>- fuel is ground to very small sizes</li> <li>- it needs an additional oxygen production plant</li> <li>- operates at high temperature.</li> <li>- needs large volume of carrier gas</li> </ul>

Table 3: Yearly biomass (Million in m. ton) from various unorganized sectors [16]

Year	Jute stick	Rice straw	Rice husk	Bagasse	Fire wood	Twigs leaves	Other wastes	Total million in m.ton
1995-96	1.5	18.75	6.2	1.3	1.3	3.60	2.70	44.45
1996-97	1.8	18.95	6.3	1.4	1.4	3.90	2.80	45.45
1997-98	2.1	18.18	6.3	1.4	1.4	5.00	2.90	46.18
1998-99	1.9	18.12	6.3	1.2	1.2	5.60	3.00	46.52
1999-00	2.1	18.04	6.4	1.2	1.2	6.00	3.00	47.54
2000-01	2.2	18.75	6.4	1.3	1.3	6.20	3.10	48.95
2001-02	2.3	18.49	6.5	1.4	1.4	6.40	3.10	49.29
2002-03	2.2	18.60	6.6	1.4	1.4	6.60	3.20	49.80
2003-04	2.1	18.60	6.5	1.5	1.5	7.20	3.20	50.50
2004-05	2.2	18.50	6.5	1.5	1.5	7.80	3.30	51.20
2005-06	2.3	18.65	6.5	1.5	1.6	7.90	3.35	

## 5. CASE STUDY (DREAMS POWER PRIVATE LTD.)

### 5.1. Background

The biomass gasifier-based decentralized power generation system is implemented in Gaspur village in Kapasia of Gazipur district. Gaspur is a non-electrified village. Asaduzzaman Manik, a poultry farmer of this village, experienced difficulties in keeping his business running without electricity. He then decided to generate electricity required his farm by himself. He visited India and learned about small-scale husk-fired power plant. Following his visit, he planned to build such a about the availability of the biomass feedstock as Bangladesh produces plenty of rice-husk throughout the country. He then managed to install a rice-husk based decentralized small-scale power plant with the technical an financial supports of IDCOL (Infrastructure Development Company Limited) and World Bank in 2007. The details of the plant are summarized in Table 5.

### 5.2 Investment

The total investment for creating the entire infrastructure, including installing power generation (gasifier, dual-fuel engine, generator, and other apparatus), distribution cost and end-use (lighting, flour mill, etc.) was about Tk. 25 millions. IDCOL provided concessionary loans and grants about 20%; the World Bank provided 60% of the project cost as grant while the owner himself provided 20% of the total investment.

### 5.3. Plant Capacity

The total capacity of the power pant is 250 kW. It has

Table 4: Yearly produced pulses (M.tons) in Bangladesh [17].

year	2004-05	2005-06	2006-07
Gram	9630	9760	9810
Mung	17935	16870	18675
Masur	121065	115370	116810
Khesari	136085	107250	82735
Mashkalai	17190	17400	18190

Peas	9410	7780	6645
Arharl	1005	1015	1445

two units having equal capacity to supply 125 kW. The plant was originally proposed to supply electricity to the villagers covering more than 50% of its total population (approximately 200 households) and 100 commercial entities of that area, after meeting the demand of the farm.

### 5.4 Type of Biomass Used and Its Availability

The plant is using rice husk as the feed material. It is cheap and easily available. As mentioned above, being, an agricultural based country Bangladesh produces varieties of agricultural residues. Until now they are consuming mainly as domestic cooking purposes in rural areas and industrial (rice parboiling) energy source. Among the various agricultural residues rice husk is ranked the top in terms of its availability, as paddy is the main crop of Bangladesh. Rice husk is a good quality biomass fuel as it has good calorific value, small in particle size having an excellent uniformity.

### 5.5 Economic Analysis

The total project is a profitable one provided that the plant is running with its full capacity and the generated electricity is fully utilized. The estimation is quite simple:

If the project runs in its full capacity it is capable of earning Tk. 900,000 per month (250kW \* 24hr \* 30days \* Tk. 5.0) = Tk. 900,000). Its running costs are about Tk. 600,000 (includes biomass procuring, diesel, mobile, filtering, and others (= 400,000 + 150,000 + 10,000 + 10,000 + others)). Thus it provides a net income of about Tk. 300,000 per month. Based on this simple analysis, the turn over period can be determined as about 7 years.

However, the present situation is quite different. The plant is not running with its full capacity and currently, only from one unit, fractional power is supplied about 336 kWh/day (56 kW \* 6hrs = 336 kWh/day). So it earns only about Tk. 50,000 per month. Whereas the operating costs are about Tk. 90,000 per month. Thus the project is now in running under loss.

According to the management, if there is a rice mill beside the plant, the loss could be minimized. As the rice mill would act as both supplier of biomass and a consumer of the generated electricity.

### 5.6 Problems Encountered During Operation

Being a pioneer entrepreneur in terms of biomass

Table 5: Plant description at a glance [18]

Parameter	Description
Gasifier type	downdraft
Capacity	max. 250 kw
Rated gas flow	625 Nm <sup>3</sup> /hr
Max. gasification efficiency	up to 75 %
Gasification temperature	1050-1100°C
Biomass feeding	manual
Outlet gas temp	250-400°C



Average gas calorific value	>1.05 Kcal /Nm <sup>3</sup>
Rated biomass consumption	up to 300 kg/hr
Typical gas composition	CO-20.6%,H <sub>2</sub> -10.6%,CO <sub>2</sub> -13.6%,CH <sub>4</sub> -4%,N <sub>2</sub> -52.6%

gasification power plant in Bangladesh, this project is now facing different types of problems. Being located in a rural area the project often faces a number of problems: lack of skilled operators, improper guidelines, poor management, technical and financial problems, lack of government patronization, unavailability of biomass, tendency of the customers not to pay the bill in due time etc. Study also identifies that there are some sort of social and political problems that are discouraging this effort.

## 6. CONCLUSIONS

Based on the above discussions the following conclusions can be drawn:

- Biomass gasification can offer an attractive alternative renewable energy system especially in rural areas where biomass fuel is available. Thus can provide community based small-scale independent power plants.
- Between the updraft and downdraft gasifier systems, an open top downdraft gasifier with manual feeding downdraft gasifier is preferred as it provides cleaner gases. This type of system has been identified for Bangladesh's perspective.
- The biggest challenge in these gasification systems lies in developing reliable and economically cheap cooling and cleaning systems.
- For the fuels with high ash content, fluidized bed system may offer a better solution, but they are more complex in design.
- Rice husk can be ranked the top of the available biomass types in Bangladesh. However, other types of biomass such as rind of pulses, saw dust should also be considered for gasification.
- If rice husk is used for gasification, rice mills should be installed beside the power plant to make it feasible.

## 7. RECOMMENDATIONS

Rural electrification is a great challenge for the Government of Bangladesh. Installation of biomass based, small-scale independent power plants around the country could be a feasible solution. Biomass gasification is treated as an emerging technology that can be employed for the purpose. However, there are problems or barriers, which need to be solved or removed for the sustainability of such projects. The following recommendations are made out of the above discussions:

- Provision of government subsidies for the installation of such gasification power plants. Government can seek funds from different foreign aids. Also carbon trade can be an option.
- NGOs and other government organizations that work for the well being and development to the society should be motivated and involved in such projects.
- Rural unemployed people should be educated and trained to the standard that would make them eligible to take part in such projects.

- It is essential to have an access to the database of the available biomass quality and quantity.
- A market should be development so that local and foreign entrepreneurs would convince to invest in such projects.
- Government of Bangladesh would need to amend energy policy so that the gasification plants can run to their full capacity and can sell the surplus electricity to the grid.

## 8. REFERENCES

1. N. H. Ravindranath, H. I. Somashekar, S. Dasappa and C. N. Jayasheela Reddy, "Sustainable biomass power for rural India: Case study of biomass gasifier for village Electrification", Centre for Sustainable Technologies, Indian Institute of Science, Bangalore 560 012, India.
2. K. Maniatis, "Progress in biomass gasification", Directorate General for Energy, European Commission, Rue de la Loi 200, 1049 Brussels, Belgium.
3. M. Rafiqul Islam, "Renewable energy resources and technologies practice in Bangladesh", Department of mechanical engineering, RUET.
4. Don J. Stevens; Pacific Northwest National Laboratory, Richland; Washington, "Hot Gas Conditioning: Recent Progress With Larger-Scale Biomass Gasification Systems". National Renewable Energy Laboratory, Washington.
5. Goran G. JANKES, Nebojsa M. Milovanovic, "Biomass Gasification In Small-Scale Units For The Use In Agriculture And Forestry In Serbia". Review paper, UDC: 662.636/.638:544.45.
6. J. B. Jones, G. Hawkins, "Three main successive stages of biomass gasification source". Engineering thermodynamics 1986,p. 456.
7. Chandrakant Turare, "Biomass Gasification Technology and Utilization, Impact Of Fuel Properties on Gasification", ARTES Institute, University of Flensburg, Flensburg, Germany.
8. SME Renewable Energy, "Financing Biomass Gasification Technology in Rural Cambodia". Cambodian RE Company (2005).
9. Jared P. Ciferno, John J. Marano, "U.S. Department of Energy National Energy Technology Laboratory" June 2002.
10. Emanuele Scoditti, "renewable sourced and innovative energetic cycles. State of the art review on gasification and gas cleaning. Examples of ongoing projects gas cleaning. Examples of ingoing projects world wide and world wide and Italy".
11. Savannah, "Gasification of two biomass fuels in bubbling fluidized bed, Proceedings of the 15<sup>th</sup> international conference on fluidized bed combustion", May 16-19, 1999, Paper No fbc99-0014, Georgia.
12. R Mark Bricka, "Energy-crop Gasification", Mississippi State University, Mississippi State.
13. Bridgwater, A.V., Evans, G.D., "An Assessment of Thermo chemical Conversion Systems for Processing Biomass and Refuse", Energy Technology Support Un (ETSU) on behalf of the

- Department of Trade, ETSU B/T1/00207/REP, 1993.
14. Paisley, M.A., Farris, M.C., Black, J., Irving, J.M., Overend, R.P., “Commercial Demonstration of the Battelle/FERCO Biomass Gasification Process: Startup and Initial Operating Experience”, Presented at the 4<sup>th</sup> Biomass Conference of the Americas, Volume 2.
  15. Anil K. Rajvanshi, “BIOMASS GASIFICATION”, Director, Nimbkar Agricultural Research Institute, PHALTAN-415523, Maharashtra, India.
  16. Islam MN, “Energy security issues of Bangladesh Engineering news”, Institute of Engineers Bangladesh, 2000.
  17. “BANGLADESH BUREAU OF STATISTICS” Agriculture Wing, Summary Crop Statistics of Major Crops 2008.
  18. Publication by Project Developer/Co-sponsor, Dreams Power Private Ltd (DPPL), Infrastructure Development Company Limited (IDCOL), Agargaon, Dhaka 1207.

## **9. MAILING ADDRESS**

Md. Mahadi Hasan  
Dept. of Mechanical Engineering,  
Rajshahi University of Engg. and Tech  
Rajshahi – 6204, Bangladesh

## ROLE OF OXYGENATED FUEL TO REDUCE DIESEL EMISSIONS: A REVIEW

M. Nurun Nabi<sup>1</sup>, Dhandapani Kannan, J. Einar Hustad<sup>1</sup> and M. Mustafizur Rahman<sup>2</sup>

<sup>1</sup>Norwegian University of Science and Technology (NTNU), NORWAY

<sup>2</sup>Rajshahi University of Engineering and Technology (RUET), BANGLADESH

### ABSTRACT

Particulate matter (PM) and oxides of nitrogen (NO<sub>x</sub> emissions) are the two important harmful emissions in diesel engine. Fuel companies and the researchers around the world are devoted to reduce such emissions with different ways. Fuel modification, modification of combustion chamber design and exhaust after treatment are the important means to alleviate such emissions. In this context, engine researchers are hunting suitable alternative fuels for diesel engine. Among different alternative fuels, oxygenated fuel is a kind of alternative fuel. Diethylene glycol dimethyl ether (DGM), dimethoxy methane (DMM), dimethyl ether (DME), diethyl ether (DEE), methyl tertiary butyl ether (MTBE), dibutyl ether (DBE), dimethyl carbonate (DMC), methanol and ethanol have played their role to reduce diesel emissions. These fuels can either be used as a blend with conventional diesel fuel or as a neat fuel. The presence of oxygen in the fuel molecular structure plays an important role to reduce PM and other harmful emissions from diesel engine. The present work reports on the effect of oxygenated fuel on diesel combustion and exhaust emissions. It has been found that the exhaust emissions including PM, total unburnt hydrocarbon (THC), carbon monoxide (CO), smoke and engine noise were reduced with oxygenated fuels. NO<sub>x</sub> emissions were reduced in some cases were increased depending on the engine operating conditions. The reductions of the emissions were entirely depended on the oxygen content of the fuel. It has been reported that the combustion with oxygenated fuels were much faster than that of conventional diesel fuel. This was mainly due to the oxygen content in the fuel molecular structure and the low volatility of the oxygenated fuels. The lower volatile oxygenated fuel evaporated earlier and very good air-fuel mixing was achieved during combustion eventually resulted in lower exhaust emissions.

**Key words:** Diesel Engine, Alternative Fuel, Oxygenated Fuel, Diesel Combustion And Exhaust Emissions.

### 1. INTRODUCTION

Due to price hike in 80's and the rapid depletion of fossil fuels researchers concentrate their research on alternative fuel. Methanol and ethanol were proved to be effective alternative fuels long ago for internal combustion (IC) engines. The oxygen in the methanol and ethanol molecule helps to make complete combustion when combusted with atmospheric oxygen. Most recently DME, oxygen content of 34.7% has been noticed as one of the promising alternative fuels for IC engine. DME can be derived from natural gas, coal or even from biomass sources. Zhang et al. (1) reported lower diesel emissions including smoke, THC, carbon dioxide (CO<sub>2</sub>), NO<sub>x</sub>, while slight increase in CO was noticed with DME compared to those of conventional diesel fuel. Authors reported the reason of reducing exhaust emissions were the presence of oxygen in the DME, absence of C-C bond, shorter ignition delay and

the instantaneous vaporization of DME. Like DME, DEE is another oxygenated fuel that has a very high cetane number. Masoud et al. (2) reported lower smoke and THC emissions due to higher cetane number and oxygen content of DEE. Authors also found lower CO emissions at high load condition, but higher at low load condition Also lower NO<sub>x</sub> emissions were realized with DEE-diesel blends. Kapilan et al. (3) conducted experiments with 5 % DEE and found lower CO, THC and smoke emissions while a slight improvement in thermal efficiency was observed. Yeh et al. (4) investigated the effect of fourteen different oxygenated fuels on diesel emissions, specially PM and NO<sub>x</sub> emissions. Authors found that for PM reduction, the most effective oxygenates on equal oxygen content basis were the C<sub>9</sub> – C<sub>12</sub> alcohols in both the engine and vehicle testing. No significant NO<sub>x</sub> emissions was increased with the oxygenates.

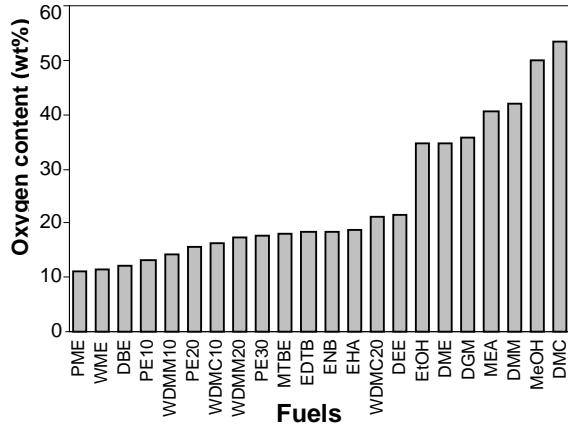


Fig 1 Oxygen content in different fuels

The current work focuses on diesel emissions, special emphasis on PM and NOx emissions with oxygenated fuels. The effects of liquid oxygenated fuels on diesel combustions are discussed in this work as many researchers worked on liquid oxygenated fuels. The advantages of using liquid fuel are: easy transportation, easy injection to the combustion chamber and require less space to store. The role of fuel oxygen on PM and NOx emissions is investigated with the previous research works. The target of the work is to make a correlation between fuel oxygen and the exhaust emissions.

Fujia et al. (5) investigated the effect of fuel oxygen on total PM and other exhaust emissions. Authors used CME, SME, RME, PME, WME and oxygenated fuels like ethanol, DMC and DMM. They reported that the total PM emissions were reduced with all biodiesels compared to that of diesel fuel (D160). THC emissions with all biodiesel reduced from 45-67%. Like THC, CO

emissions were reduced by 4-16% with the biodiesels. On the other hand, NOx emissions were increased with the addition of fuel oxygen content. Authors extended their research with three oxygenated fuels like ethanol, DMC and DMM. 10-30% ethanol was blended with PME, 10-20% DMC was added to WME and 10-20% DMM was added to DMM. The reductions in PM, THC and CO emissions and the increase in NOx emissions were due to the oxygen content in the fuel.

Zannis et al. (6) conducted engine experiments with oxygenated fuels. They used two oxygenated fuels, such as Diethylene Glycol Dimethyl Ether (Diglime – C<sub>6</sub>H<sub>14</sub>O<sub>3</sub>) and Diethylene Glycol Dibutyl Ether (Butyl-Diglime – C<sub>12</sub>H<sub>26</sub>O<sub>3</sub>), and one biodiesel (RME). These two oxygenated fuels and RME were blended with conventional diesel fuel (D1) maintaining oxygen content of 3 to 9%. The blended fuels were termed as DOX1, DOX2 and DOX3. The effect of fuel oxygen content on exhaust emissions at various engine loads was investigated. Authors reported relative changes of emissions between base fuel (diesel fuel) and oxygenated fuels DOX1 and DOX3. Soot, CO and THC emissions were reduced with increasing oxygen content for all loads. The reductions were higher for higher percentage of oxygen (9%) in the fuel blends and at high load condition. Authors reported that the reduction of soot, THC and CO emissions with increased fuel oxygen, which prevent to form soot emissions as less available carbon in fuel molecule. Authors also reported that the increase of local oxygen concentration enhances soot oxidation. On the other hand, NOx emissions were increased for higher oxygen content in the fuel. The additional oxygen in fuel rich region in conjunction with the increase in gas temperature due to the increase of cylinder pressure during combustion phase favors the formation of thermally generated NOx emissions.

Table 1 Oxygen content and molecular formula of different oxygenated fuels

Oxygenates	Oxygen (wt %)	Molecular formula
Dimethyl carbonate (DMC) (7)	53.30	C <sub>3</sub> H <sub>6</sub> O <sub>3</sub>
Diethyl ether (DEE) (8)	21.00	C <sub>4</sub> H <sub>10</sub> O
Diethylene glycol dimethyl ether (DGM) (7)	35.82	C <sub>6</sub> H <sub>14</sub> O <sub>3</sub>
Di-n-butyl ether (DBE) (7)	12.30	C <sub>8</sub> H <sub>18</sub> O
Dimethoxy methane (DMM) (7)	42.10	C <sub>3</sub> H <sub>8</sub> O <sub>2</sub>
Ethyl hexyl acetate (EHA) (7)	18.60	C <sub>10</sub> H <sub>20</sub> O <sub>2</sub>
Methyl tert-butyl ether (MTBE) (7)	18.18	C <sub>5</sub> H <sub>12</sub> O
Ethylene glycol di-t-butyl ether (EDTB) (7)	18.40	C <sub>6</sub> H <sub>14</sub> O <sub>2</sub>
Ethylene glycol mono-n-butyl ether (ENB) (7)	18.40	C <sub>6</sub> H <sub>14</sub> O <sub>2</sub>
Dimethoxy propane (DMP) (10)	-	(CH <sub>3</sub> ) <sub>2</sub> C(OCH <sub>3</sub> ) <sub>2</sub>
2-methoxyethyl acetate (MEA) (13)	40.70	CH <sub>3</sub> COOCH <sub>2</sub> CH <sub>2</sub> OCH <sub>3</sub>
Methanol (MeOH) (7)	50.00	CH <sub>4</sub> O
Ethanol (EtOH) (7)	34.78	C <sub>2</sub> H <sub>6</sub> O
Palm oil methyl ester (PME) (5)	11.20	-
Waste cooking oil methyl ester (WME) (5)	11.30	-
Cottonseed oil methyl ester (CME) (5)	10.60	-
Rapeseed oil methyl ester (RME) (5)	10.50	-
PME 90% +EtOH (10%) (PE10) (5)	13.30	-
PME 80%+EtOH (20%) (PE20) (5)	15.50	-
PME 70%+EtOH (30%) (PE30) (5)	17.70	-
WME 90%+DMC10% (WDMC10) (5)	16.20	-
WME 80%+DMC20% (WDMC20) (5)	21.10	-
WME 90%+DMM10% (WDMM10) (5)	14.20	-
WME 80%+DMM20% (WDMM20) (5)	17.30	-

Nabi (7) also performed engine experiments with different oxygenated fuels. He investigated the effects of fuel oxygen on diesel emissions and combustion. In Figure 2, PM emissions were shown with soluble organic fraction (SOF) and insoluble fraction (ISF), which is actually termed as dry soot. The results in Figure 2 show the PM with neat diesel fuel, DGM100 and ENB100. Remarkable reduction in PM (Figure 2) and other emissions (not shown) were reported by the author. NOx emissions were also reduced with the oxygenated fuels (Figure 3). In Figure 2, only DGM was added to the conventional diesel fuel at volumetric percentages of 0, 25, 50, 75 and 100. Author concluded that it was oxygen, not the kinds or the chemical structures of the oxygenated fuels, was responsible for lower exhaust emissions. He also found the lower adiabatic flame temperature which caused the lower NOx emissions with oxygenated fuels. Author extended their research applying EGR in the exhaust system. Using EGR and an oxygenated fuel DGM, remarkable reductions in both smoke and NOx emissions were realized compared to those of diesel fuel.

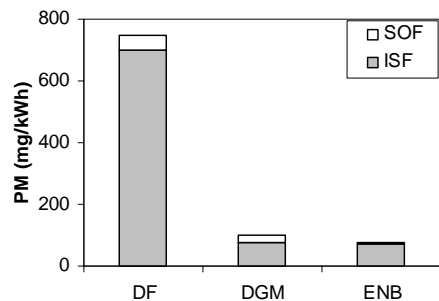


Fig 2. Improvement in PM with oxygenates (BMEP=0.75 MPa) (7)

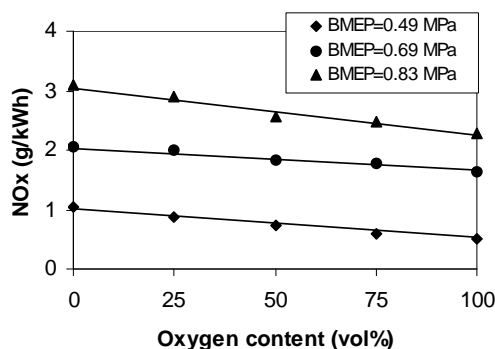


Fig 3. Improvement in NOx emissions with DGM at three BMEP conditions (7)

Nabi (7) attempted smokeless stoichiometric diesel combustion with a combination of high EGR, highly oxygenated fuels and a three way catalyst. Figure 4 shows the smoke emissions with DMM100 and different kinds of highly oxygenated liquid fuels at stoichiometric and high (30 vol%) EGR conditions. The smoke emissions formed easily at these conditions. 100 %DGM

and DGM based fuels blended with ordinary diesel fuel or different kinds of oxygenated fuels shown in Table 1. From Figure 4 it is observed that smoke emissions decreased sharply and linearly and became zero at an oxygen content of 38%. The smoke free diesel combustion was also confirmed with two other oxygenated fuels of oxygen content of 40 and 42%. From this study it was suggested that DGM80+MeOH20 (oxygen content of 38%), DGM80+DMC20 (oxygen content of 40%) and DMM100 (oxygen content of 42%) were suitable for partial load high EGR and high load stoichiometric diesel combustion.

Figure 5 (7) shows the influence of EGR on NOx emissions using DMM100. DMM100 realizes smokefree diesel operation at any engine conditions as discussed in Figure 4. The extreme right end points of Figure 5 represent to the stoichiometric condition where a three-way catalyst is believed to be effectively reduce NOx emissions. Significantly low NOx emissions were achieved by applying high EGR (30%) at different excess air conditions where high NOx emissions reductions with a three-way catalyst are difficult. It can be seen from the Figure that 30 % EGR produces NOx emissions below 100 ppm at any excess air condition. With oxygenated fuel and stoichiometric diesel operation significantly increase the maximum BMEP, which was found to be as high as 0.9 MPa without applying EGR. To achieve ultra low diesel emissions, author incorporated a three way catalyst in a diesel exhaust system. Figure 6 (7) shows the influence of a three way catalyst on three diesel emissions in partial load high EGR and high load stoichiometric diesel operation using DMM100. It can be seen from the Figure that the NOx emissions were reduced to as low as 100 ppm, while the THC and CO emissions were found to be about 200 ppm even at stoichiometric condition and without applying EGR. Thus it can be concluded that extremely low NOx and smokefree diesel operation was realized with the combination of a three way catalyst, high EGR and DMM100.

Anand et al. (8) investigated the influence of EGR and oxygenated fuel on diesel combustion and exhaust emissions. Authors used DEE as oxygenated fuel and blended with diesel fuel up to 30 vol%. Authors incorporated 5% EGR using 20 vol% DEE to diesel fuel. Without applying EGR, lower NOx emissions were resulted from DEE blended fuels compared to diesel fuel, while higher smoke emissions were realized with the same blends. Authors also reported simultaneous NOx and smoke emissions with DEE20 when applied EGR. 80% NOx emissions were reduced with 15% EGR using 20 vol% DEE to diesel fuel. At full load under 15 vol% EGR conditions with 20 vol% DEE, the smoke emissions were reduced to 2.1 Bosch smoke units (BSU) from the baseline smoke level of 4.2 BSU. The reductions were due to the oxygen availability in DEE, which supplies oxygen during combustion.

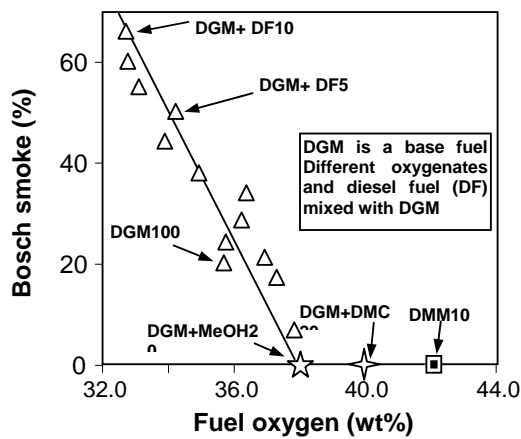


Fig 4. Smoke emissions with highly oxygenated fuels ( $\phi = 1.0$ , EGR = 30%) (7)

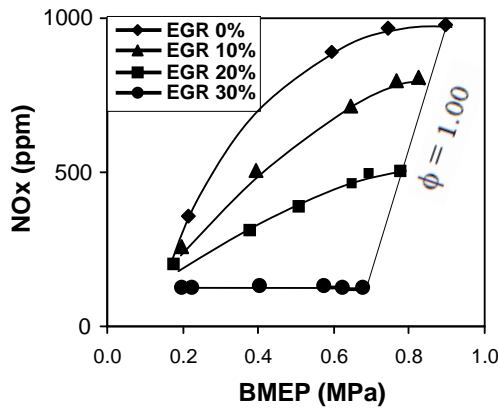


Fig 5. Influence of EGR on NOx emissions with DMM100 (7)

Miyamoto et al. (9) conducted experiments with eight kinds of oxygenated fuels to investigate the effect of low content oxygenate additive (maximum 10 vol%) on diesel emissions. The oxygen contents of the neat oxygenated fuels were ranging from 12.3 to 53.3 wt%. When blended these oxygenates with conventional diesel fuel, particulate and smoke emissions were suppressed significantly without increasing NOx. THC and CO emissions were also decreased slightly. Oxygen content in the blended fuels and the low volatility of the fuel were the reasons for decreasing the emissions.

Sathiyagnanam et al. (10) conducted diesel engine experiments with DMM and dimethoxy propane (DMP). Authors blended DMM and DMP as additives (1 ml to 3 ml) to diesel fuel. They conducted the experiments by introducing a diesel particulate filter (DPF). The experimental results were compared with and without DPF using the two oxygenated additives (DMM and DMP) and diesel as a base fuel. It was found that smoke and PM emissions were reduced with the addition of

DMM and DMP to diesel fuel. Smoke and PM emissions reduction was higher with DPF. NOx emissions, on the other hand were higher with DMM and DMP blended fuels. It was reported that NOx emissions were higher by 13 g/kWh with DMM and 16 g/kWh by DMP.

Lu et al. (11) investigated the spray characteristics and diesel exhaust emissions with three oxygenated fuels, namely ethanol, DMC and DMM. Authors investigated the spray characteristics (Sauter mean diameter (SMD) and axial mean velocity distribution) with DMM-diesel hybrid fuels, while the engine

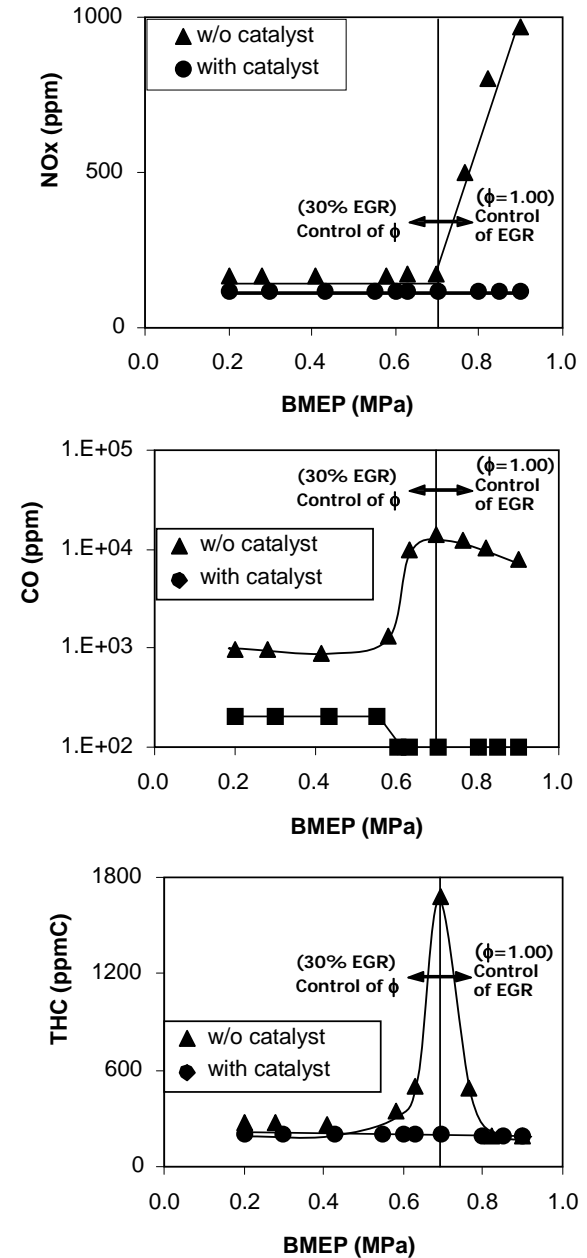


Fig 6. Influence of a three way catalyst on three diesel emissions (7)

experiments were performed with DMC-diesel hybrid fuels. For spray analysis DMM was blended to diesel fuel at blending ratios of 25 and 50 vol%, while for DMC the ratios were 10, 20 and 30 vol%. It was found that the droplet diameter of the DMM-diesel hybrid fuels decreased with increased axial distance from the injector tip. Compared to diesel fuel, the mean axial velocities of DMM-diesel hybrid fuels were higher. The lower SMD and higher axial mean velocity with DMM-diesel hybrid fuels were due to the inherent properties of lower kinematic viscosity and surface tension of neat DMM. Concerning exhaust emissions it was reported that the smoke and NOx emissions were reduced markedly with DMC-diesel hybrid fuels. The reductions were higher with the higher percentages of DMC to diesel fuel. The reduction of NOx emissions was due to the shorter combustion duration, while presence of oxygen in hybrid fuels was additional reason for reduction in smoke emissions.

Wang et al. (12) carried out engine experiments with several oxygenated fuels like biodiesel, ethanol, DMM and DMC. They made different oxygenated blends with diesel fuel. The biodiesels used in the experiments were derived from palm oil, waste cooking oil and acidified oil. It was found that the dry soot in PM emissions decreased significantly as the fuel oxygen content increased. SOF, which is a constituent of PM were found to be higher. Authors also investigated the effect of cetane number on SOF emissions. It was found that with the increase in fuel cetane number SOF emissions decrease. Authors found that an oxygenated fuel blend of 50% biodiesel, 15% DMC and 35% diesel fuel (oxygen content of the blend is 15.46%) met the Chinese 4th stage standard, which is equivalent to Euro IV for heavy duty engines without modifying or using any after treatment device.

Yanfeng et al. (13) did experiments with a new kind of oxygenated fuel, 2-methoxyethyl acetate (MEA) of oxygen content of 40.7 wt%. Authors reported significant reduction in smoke emissions with MEA blends. THC and CO emissions were also reduced with higher blending percentages of MEA to diesel fuel. However, the MEA blends had almost no effects on NOx emissions. Authors suggested that 15% MEA blend is suitable for diesel emissions, engine power and fuel economy.

Guo et al. (14) attempted engine experiments with a new oxygenated fuel, methyl 2-ethoxyethyl carbonate (MEEC) by introducing an ether group to DMC molecule. MEEC was blended with diesel fuel from 15 to 25 vol%. For a 25% MEEC blend with full load condition, CO was lessened by 29.2 to 40.5%, smoke by 0.3 to 0.5 BSU. NOx emissions were also lessened by 15.9% when the 15% MEEC was blended with diesel fuel. Output power of the engine was not noticeably changed with MEEC blends; however 2.5 to 5.5% fuel consumption was increased with 20% MECC. BSEC was improved by 10% when the engine was fuelled with 20%MECC.

Cheng et al. (15) carried out experiments with two oxygenates, DMM and DEE blended with conventional diesel fuel and a Fischer-Tropsch (F-T) diesel fuel to investigate their exhaust emissions reduction potential. Both DMM and DEE reduced PM emissions. Like PM, NOx emissions were also reduced with these blends. 35% less PM was observed with DMM30, while 30% less PM emissions were resulted in with DEE30. Compared to diesel fuel. F-T fuel also reduced PM emissions by 29%. NOx emissions, on the other hand were reduced by 1-10% with F-T, DMM and DEE blends. Fuel conversion efficiency (thermal efficiency) was reduced with the tested fuels compared to diesel fuel.

Chen et al. (16) investigated the effect of fuel oxygen on diesel emissions and performance. Authors blended ethanol and biodiesel to diesel fuel. The blending percentages of ethanol to diesel fuel were 10, 20 and 30%, while the biodiesel percentages were 5 and 10%. Engine torque was reduced and BSFC was increased with blended fuels. Using the diesel ethanol and biodiesel blends the PM was reduced significantly and the reduction was found to be significant at higher percentages of oxygen in the fuels. NOx emissions were slightly increased or the same as baseline diesel fuel. THC emissions with oxygenated blends were reduced under most operating conditions. CO emissions were increased at low to medium load conditions, but reduced at high load condition.

Tat et al (17) investigated diesel exhaust emissions with biodiesel. Authors used soy methyl ester (soy biodiesel) and high oleic methyl ester to investigate the brake specific NOx, THC, CO and smoke emissions. Both biodiesels are some sort of oxygenated fuels as approximately 11 wt% oxygen contain in their molecular structures. The brake specific THC and the smoke emissions were lower with the two biodiesels compared to diesel fuel. The brake specific NOx emissions with two biodiesels were higher than those of diesel fuel. The reasons of higher NOx emissions with biodiesels are as follows: the higher proportion of unsaturated fatty acid compositions in the biodiesels, advance injection timing leads to earlier ignition, which leads to higher peak cylinder temperatures. Biodiesels produce less soot than diesel fuel, which may increase NOx emissions.

## 2. CONCLUSIONS

This paper reports on the role of oxygenated fuels on diesel emissions. The results of the different research papers were analyzed and can be summarized as follows:

1. NOx, smoke and PM emissions with oxygenated fuels were reduced in most cases. However, the increase in NOx emissions were also reported with oxygenated fuels. The reductions in emissions were mainly dependent on fuel oxygen. The reductions were found maximum at the maximum percentage of fuel oxygen.
2. The increase in NOx emissions with biodiesel which is also an oxygenated fuel were the higher percentage of



unsaturated fatty acid compositions, lower soot emissions with biodiesels. Advance injection timing with biodiesels lead to earlier ignition. Earlier combustion with biodiesels resulted in higher peak cylinder temperatures. Higher cylinder temperatures with biodiesels eventually lead to higher NO<sub>x</sub> emissions.

3. CO emissions were reduced with all oxygenated fuels at wide operating load ranges. The reductions were significant at higher load range. The fuel oxygen, which was responsible for reducing CO emissions made complete combustion in the fuel rich region.

4. Like CO emissions, THC emissions were also reduced with oxygenated fuels for all loading conditions, but a few reports showed higher THC emissions at lower load condition.

5. It is established that the reductions in smoke, PM, CO and THC emissions were dependent on fuel oxygen content. Lower boiling points and lower volatility of oxygenated fuels were the additional factors for the reduction in these emissions.

6. The engine thermal efficiency was reduced and in some cases increased with oxygenated fuels.

### 3. ACKNOWLEDGEMENTS

The opinions, findings and conclusions discussed in this paper are those of the authors mentioned in the list of reference and do not reflect opinions or views of the authors of this paper.

### 4. REFERENCES

1. Zhang, JJ., Huang, Z., Wu, JH., Qiao, XQ. and Fang, JH., 2008, "Combustion and performance of heavy-duty diesel engines fuelled with dimethyl ether", IMechE vol. 222 (D), pp. 1691-1703.
2. Iranmanesh, M., Subrahmanyam, JP. and Babu, MKJ., 2008, "Potential of Diethyl ether as supplementary fuel to improve combustion and emission characteristics of diesel engines", SAE paper no. 2008-28-0044.
3. Kapilan, N., Mohanan, P. and Reddy, RP., 2008, "Performance and Emission Studies of Diesel Engine Using Diethyl Ether as Oxygenated Fuel Additive", SAE paper no. 2008-01-2466.
4. Yeh, LI., Rickeard, DJ., Duff, JLC., Bateman, JR., Schlosberg, RH. and Caers, RF., 2001, "Oxygenates: An Evaluation of their Effects on Diesel Emissions", SAE paper no. 2001-01-2019.
5. Fujia, W., Jianxin, W., Wenmiao, C. and Shijin, S., 2008, "Effects of Different Biodiesels and their Blends with Oxygenated Additives on Emissions from a Diesel Engine", SAE paper no. 2008-01-1812.

6. Zannis, TC., Hountalas, DT. and Kouremenos, DA., 2004, "Experimental Investigation to Specify the Effect of Oxygenated Additive Content and Type on DI Diesel Engine Performance and Emissions", SAE paper no. 2004-01-0097.
7. Nabi, MN., 2000, "Study of Diesel Combustion and Exhaust Gas Emissions with Oxygenated Fuels", Ph.D. Thesis, Hokkaido University, Japan.
8. Anand, R. and Mahalakshmi, NV., 2007, "Simultaneous reduction of NO<sub>x</sub> and smoke from a direct-injection diesel engine with exhaust gas recirculation and diethyl ether", IMechE vol. 221 (D), pp. 109-116.
9. Miyamoto, N., Ogawa, H., Arima, T. and Miyakawa, K., 1996, "Improvement of Diesel Combustion and Emissions with Addition of Various Oxygenated Agents to Diesel Fuel", SAE paper no. 962115.
10. Sathiyagnanam, AP., Saravanan, CG., 2008, "Effects of diesel particulate trap and addition of di-methoxy-methane, di-methoxy-propane to diesel on emission characteristics of a diesel engine", Fuel 87, pp. 2281-2285.
11. Lu, XC., Zhang, WG., Qiao, XQ. and Huang, Z., 2005, "Fuel design concept for improving the spray characteristics and emissions of diesel engines", IMechE vol. 219 (D), pp. 547-557.
12. Wang, J., Fujia, W., Xiao, J. and Shuai, S., 2009, "Oxygenated blend design and its effects on reducing diesel particulate emissions", Fuel 88, pp. 2037-2045.
13. Yanfeng, G., Shenghua, L., Hejun, G., Hu Tiegang, H., and Longbao, Z., 2007, "A new diesel oxygenate additive and its effects on engine combustion and emissions", Applied Thermal Engineering, 27, pp. 202-207.
14. Guo, H., Huang, X., Zhang, J., Zhang, H., and Li, L., 2005, "Study on Methyl 2-Ethoxyethyl Carbonate Used as an Oxygenated Diesel Fuel", SAE paper no. 2005-01-3142.
15. Cheng, AS., and Dibble, RW., 1999, "Emissions Performance of Oxygenate-in-Diesel Blends and Fischer-Tropsch Diesel in a Compression Ignition Engine", SAE paper no. 1999-01-3606.
16. Chen, H., Wang, J., Shuai, S., and Chen, W., 2008, "Study of oxygenated biomass fuel blends on a diesel engine", Fuel 87, pp. 3462-3468.
17. Tat, ME., Wang, PS., Van Gerpen, JH., and Clemente, TE., 2007, "Exhaust Emissions from an Engine Fuelled with Biodiesel from High-Oleic Soybeans", Journal of Am Oil Chem Soc 84, pp. 865-869.

### 5. MAILING ADDRESS

Md. Nurun Nabi  
Norwegian University of Science and Technology  
(NTNU), NORWAY  
Email: nahin1234@hotmail.com

## LARGE SCALE THERMAL-SOLID COUPLING ANALYSIS USING INEXACT BALANCING DOMAIN DECOMPOSITION

A. M. Mohammad Mukaddes<sup>1</sup> and Ryuji Shioya<sup>2</sup>

<sup>1</sup>Department of Industrial and Production Engineering, Shah Jalal University of Science and  
Technology, Bangladesh,

<sup>2</sup>Faculty of Information Science and Arts, Toyo University, Japan

### ABSTRACT

In this research, a system of thermal-solid coupling analysis is developed with the implementation of Inexact Balancing Domain Decomposition with a diagonal scaling (IBDD-DIAG) in both thermal and solid analysis. The IBDD-DIAG is an improved version of Balancing Domain Decomposition (BDD), where an incomplete factorization based parallel direct method is employed to solve a coarse space problem, and the diagonal-scaling is employed to precondition local fine space problems instead of the Neumann-Neumann preconditioner. The developed system performed heat conductive analysis to have temperature distributions in solid models and then performed the structural analysis to see deformation or expansion due to temperature differences. Both of the analyses employed the Hierarchical Domain Decomposition Method (HDDM) with parallel IBDD-DIAG. It is shown that the iterative procedure converges rapidly and the convergence is independent of the number of subdomains, namely, numerical scalability is satisfied. The present system is implemented on massively parallel processors and succeeds in solving a thermal-solid coupling problem of 12 millions of nodes.

**Keywords:** Finite element analysis, coupling problems, Incomplete Balancing Domain Decomposition

### 1. INTRODUCTION

Engineering products that have complex geometries may crack during the heating process or fail during operations. To avoid such failures and reduce the cost of production, the behavior that occurs in the products during manufacturing or while operating must be predicted in advance. These behaviors include the stress from external loads as well as the thermal stresses from the temperature difference in the products. The purpose of this research is to develop a system that could be used to analyze heat transfer problems that have complex geometries for the temperature distribution. The predicted temperature combined with the applied external loads is then used to compute the deformation and thermal stresses of the products. The partial differential equation described the thermal and structural problems can be coupled when the stress in the structural problem is a function of temperature from the thermal problem [1]. The motivation of the coupling analysis comes from thermal-fluid coupling problem [1] and the large scale fluid-structure coupling problem [2].

Large scale problems need to be solved for the improvement of accuracy. The conventional algorithm like Domain Decomposition Method (DDM) needs much time to solve the large scale problems and moreover it is not scalable [3]. A preconditioner should be used to reduce the computation time and the number of iterations. A suitable preconditioner might make the DDM scalable.

The present research attempts to develop a system of thermal-solid coupling analysis to address these requirements.

By using the Hierarchical Domain Decomposition Method (HDDM) [4] with a preconditioned iterative solver in order to perform both thermal and solid analyses, it is hoped that the developed system would perform the heat conductive analysis to achieve temperature distributions in solid models and then perform the structural analysis to see deformation or expansion due to temperature differences. The HDDM employs a preconditioned iterative solver in order to perform both thermal and solid analyses.

Moreover Balancing Domain Decomposition (BDD) [5] has received much attention in the last few years. The main reason for the popularity of this method is undoubtedly, the need to take the advantage of parallel computers. BDD is close in spirit to multigrid methods and is a variation of Neumann-Neumann algorithm. It involves solution of a coarse problem in each iteration of iterative DDM. Moreover to efficiently solve a coarse space problem derived from equilibrium conditions for singular problems associated with a number of subdomains appeared in the BDD algorithm, an Inexact Balancing Domain Decomposition with Diagonal Scaling (IBDD-DIAG) is proposed for structural problem [6].

In this paper, this inexact balancing domain

decomposition method is investigated in the analysis of thermal-solid coupling problem. In the IBDD-DIAG formulation, a coarse space problem is approximated by an incomplete factorization coarse operator based parallel direct method, and the diagonal scaling is employed to precondition local fine space problems instead of the Neumann-Neumann preconditioner. The thermal-solid coupling problem of a nuclear pressure vessel model with 12 million nodes is successfully analyzed with this IBDD-DIAG. The numerical results show better performance of IBDD-DIAG.

## 2. THERMAL-SOLID ANALYSIS

By considering a heat conduction equation on a domain  $\Omega$ , defining  $\bar{f}$  as internal heat generation,  $\bar{T}$  temperature applied on the boundary  $\Gamma_T$ ,  $\bar{Q}$  the heat flux applied on the boundary  $\Gamma_Q$ , the fundamental equations of this heat conduction problem is given by:

$$\begin{cases} q = -\lambda \text{grad}T & \text{in } \Omega \\ \text{div } q = \bar{f} & \text{in } \Omega \\ q \cdot n = \bar{Q} & \text{on } \Gamma_Q \\ T = \bar{T} & \text{on } \Gamma_T \end{cases} \quad (1)$$

where  $T$  is temperature,  $q$  the heat flux,  $\lambda$  the thermal conductivity and  $n$  an outer normal unit vector, respectively. The finite element (quadratic tetrahedral) discretization of (1) yielded a linear system of the for

$$Ax = f \quad (2)$$

where  $A$  is the global stiffness matrix,  $x$  is an unknown vector of temperature and  $f$  is a known vector.

Again we considered a structural problem concerning a domain  $\Omega$ . Hence,  $\bar{F}_i$  is the traction force applied on the boundary  $\Gamma_F$ ,  $\bar{B}_i$  the body force applied in the domain  $\Omega$  and  $\bar{u}$  the prescribed displacement on the boundary  $\Gamma_u$ . Fundamental equations of this structural problem are summarized as follows:

$$\begin{cases} \tau_{ij,j} + \bar{B}_i = 0 & \text{in } \Omega \\ \varepsilon_{ij} = (u_{i,j} + u_{j,i})/2 & \text{in } \Omega \\ \tau_{ij} = D_{ijmn} \varepsilon_{mn}^e & \text{in } \Omega \\ \tau_{ij} n_j - \bar{F}_i = 0 & \text{on } \Gamma_F \\ u_i = \bar{u}_i & \text{on } \Gamma_u \end{cases} \quad (3)$$

where,  $i, j$  take the value 1 to 3,  $m, n$  take the value 1 to 3,  $u_i$  is displacement,  $\varepsilon_{ij}$  a strain tensor,  $\tau_{ij}$  stress tensor,  $D_{ijmn}$  a coefficient tensor of the Hooke's law and  $n_j$  an outer normal vector on the boundary  $\Gamma$ ,

respectively. Here, if we consider the high temperature distribution on the whole domain  $\Omega$ , elastic strain as  $\varepsilon^e$ , total strain  $\varepsilon$  and thermal strain  $\varepsilon^t$  then we have:

$$\varepsilon^e = \varepsilon - \varepsilon^t. \quad (4)$$

Again, the thermal  $\varepsilon^t$  is considered as follows:

$$\varepsilon^t = \begin{cases} \alpha(T - T_0) & (m = n) \\ 0 & (m \neq n) \end{cases} \quad (5)$$

where  $T_0$  is the reference temperature,  $\alpha$  the thermal expansion coefficient and  $T$  the temperature which is the output of the thermal analysis. The value of thermal strain  $\varepsilon^t$  in the equation (5) was used in the equation (3) through the equation (4). The thermal strain  $\varepsilon^t$  took the value  $\alpha(T - T_0)$  when  $m=n$  and otherwise it took 0. The finite element (quadratic tetrahedral) discretization of (3) yielded a linear system of the form:

$$Ku = b \quad (6)$$

where  $K$ ,  $u$  and  $b$  are, respectively, the stiffness matrix, the displacement vector and the force vector.

## 3. THERMAL-SOLID COUPLING ANALYSIS

The present system is conducted to predict temperature distributions in solid models and then to investigate the thermal expansion or deformation due to the temperature difference. Analysis steps are as follows:

- 1) Read the input data for the heat conductive analysis and decompose the model by ADVENTURE\_Metis [6].
- 2) Analyze heat conductive problems with IBDD-DIAG based on the HDDM system
- 3) Gather temperature information of all nodes of the model from outputs of heat conductive problems.
- 4) Read temperature information of all nodes and other input data for structural analysis and then decompose the model by ADVENTURE\_Metis.
- 5) Analyze structural problems with IBDD-DIAG based on the HDDM system.

Fig. 1 shows the flow chart of thermal-solid coupling analysis with the developed system. The name of the ADVENTURE module used in each analysis is shown in parentheses.

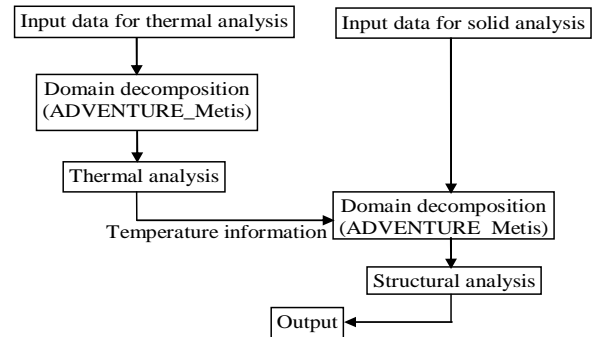


Fig 1. Flow chart of thermal-solid coupling problems.

#### 4. DOMAIN DECOMPOSITION METHOD

In this method the domain  $\Omega$  was decomposed into  $N$  non-overlapping subdomains,  $\{\Omega_i\}_{i=1,\dots,N}$ . As usual the stiffness matrix  $K$  (it represents  $A$  in equation 2 and  $K$  in equation 6) could be generated by subassembly:

$$K = \sum_{i=1}^N R^{(i)} K^{(i)} R^{(i)T} \quad (7)$$

where  $R^{(i)T}$  is the 0-1 matrix which translates the global indices of the nodes into local numbering. Denoting  $u^{(i)}$  as the vector corresponding to the elements in  $\Omega^{(i)}$ , it can be expressed as  $u^{(i)} = R^{(i)T} u$ . Each  $u^{(i)}$  was split into degrees of freedom  $u_B^{(i)}$ , which correspond to  $\partial\Omega^{(i)}$ , called interface degrees of freedom and remaining interior degrees of freedom  $u_I^{(i)}$ . The subdomain matrix  $K^{(i)}$ , vector  $u^{(i)}$  and 0-1 matrixes were then split accordingly

$$K^{(i)} = \begin{pmatrix} K_{II}^{(i)} & K_{IB}^{(i)} \\ K_{IB}^{(i)T} & K_{BB}^{(i)} \end{pmatrix}, \quad (8)$$

$$u^{(i)} = \begin{pmatrix} u_I^{(i)} \\ u_B^{(i)} \end{pmatrix}, \quad (9)$$

$$\text{and } R^{(i)} = \begin{pmatrix} R_I^{(i)} \\ R_B^{(i)} \end{pmatrix}. \quad (10)$$

After eliminating the interior degrees of freedom, problem (2) was reduced to a problem on interface

$$Su_B = g \quad (11)$$

where  $S = \sum_{i=1}^N R_B^{(i)T} S^{(i)} R_B^{(i)}$  is assumed to be positive definite,  $u_B$  is the vector of the unknown variables on the interface,  $g$  is a known vector and  $S^{(i)}$  are the local Schur complements of subdomain  $i = 1, \dots, N$ , assumed to be positive semi-definite. The problem (11) is solved by a preconditioned CG method which solves the problem,

$$z = M^{-1}r \quad (12)$$

where  $r$  is the residual of (11) and  $M$  is a preconditioner. When the interface problem is solved iteratively, of course, an efficient solution of the large scale problems depends on how one chooses an efficient and scalable preconditioner.

ii) *Hierarchical Domain Decomposition Method (HDDM)*

Constructing the DDM algorithms for parallel computers, a good principle is to divide the original domain into parts, which are further decomposed into smaller subdomains as shown in fig.-2. In this research,

Hierarchical Domain Decomposition Method (HDDM) [4] which is a well known parallel DDM is adopted.

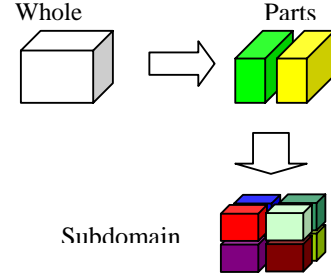


Fig. 2. Hierarchical Domain Decomposition Method

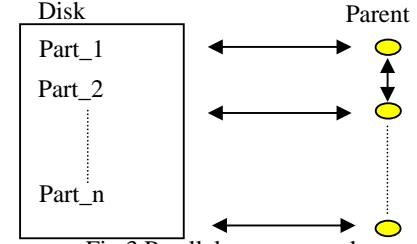


Fig.3 Parallel processor scheme

Fig. 3. shows the parallel processor scheme of HDDM system. In this scheme, the Parent processors perform the FEA by themselves and also coordinate the CG iteration. Here, the number of parts should be the number of processors.

#### 5. BALANCING DOMAIN DECOMPOSITION (BDD)

The BDD preconditioning technique proposed by Mandel [5] uses at each CG iteration solution of the local Neumann-Neumann problems on the subdomains coupled with a coarse problem in a coarse space. The BDD preconditioner is of the form:

$$M_{BDD}^{-1} = Q_c + (I - Q_c S) Q_l (I - S Q_c) \quad (13)$$

where  $Q_l$  is the local level part and  $Q_c$  is the coarse level part of the preconditioner.

##### 5.1 Local level

The local level part of the preconditioner basically involved the solution of local problems, where  $Q_l$  is expressed by

$$Q_l = \sum_{i=1}^N R_B^{(i)} D^{(i)} S^{(i)+} D^{(i)T} R_B^{(i)T} \quad (14)$$

The dagger (+) indicates pseudo-inverse, since the  $S^{(i)}$  is singular for floating subdomain. The BDD method uses a collection matrixes  $D^{(i)}$  that determines partition of unity on interface [5,9],

$$\sum_{i=1}^N R_B^{(i)} D^{(i)} R_B^{(i)T} = I \quad (15)$$

The simplest choice for  $D^{(i)}$  is the diagonal matrix with

diagonal elements equal to the reciprocal of the number of subdomains with which the degree of freedom is associated.

## 5.2 Coarse level

The application of the coarse term  $Q_c = R_0(R_0^T S R_0)^{-1} R_0^T$  amounts to the solution of a coarse problem whose coefficient matrix is  $S_W = R_0^T S R_0$ . The operator  $R_0$  translates the coarse degrees of freedom to the corresponding global degrees of freedom and is defined by

$$R_0 = \left[ R_B^{(i)} D^{(i)} Z^{(i)}, \dots, R_B^{(N)} D^{(N)} Z^{(N)} \right]. \quad (16)$$

For the scalar heat conductive problem,  $Z^{(i)}$  is a column constant vector [8,9] and can be defined by

$$Z^{(i)} = (1, \dots, 1)^T \quad (17)$$

For the structural problem  $Z^{(i)}$  [8] comes from the dof of rigid body of motion.

## 5.3 Simplified diagonal scaling (DIAG)

A diagonal matrix is considered as a preconditioner whose diagonal elements are constructed from the corresponding ones of  $K_{BB}^{(i)}$ . The diagonal matrix is defined as

$$Q_{DIAG} = \sum_{i=1}^N R_B^{(i)} \left( \text{diag} \left( K_{BB}^{(i)} \right) \right)^{-1} R_B^{(i)T}. \quad (18)$$

## 6. INEXACT BALANCING DOMAIN DECOMPOSITION

To implement the coarse grid correction with high parallel efficiency, inexact balancing based on an incomplete parallel Cholesky factorization is employed in the present BDD method. In general, such an incomplete factorized operator is typically used together with some iterative computations to compensate the incompleteness. In this paper, however, the coarse problem is approximated by the incomplete factorized operator without iterations. This incomplete balancing process decreases computation costs for preprocessing and improves parallel efficiency but may reduce the convergence rate compared with exact balancing. However, total computation time is expected to be reduced. Remarkably, with the original exact BDD preconditioner, a coarse grid correction is performed after a local subdomain correction in each iteration. However, with the present inexact BDD preconditioner, a coarse grid correction is also implemented to the CG residual vector before a local subdomain correction due

to incomplete deletion of components of the coarse space. The incomplete balancing technique is applied to the BDD considering a diagonal scaling as a local level preconditioner. The new preconditioning technique is marked as IBDD-DIAG and is defined as:

$$M_{IBDD-DIAG}^{-1} = \tilde{Q}_c + (I - \tilde{Q}_c S) Q_{DIAG} (I - S \tilde{Q}_c) \quad (19)$$

where  $\tilde{Q}_c$  is constructed from the incomplete factorized coarse operator.

The implementation of the IBDD-DIAG preconditioner (19) goes as follows:

**Step 1:** Balance the original residual by approximating the coarse problem using the incomplete coarse operator for an unknown vector  $\tilde{\lambda} \in \mathfrak{R}^N$ :

$$\tilde{S}_0 \tilde{\lambda} = R_0^T r. \quad (20)$$

**Step 2:** Set

$$\tilde{s} = r - S R_0 \tilde{\lambda}. \quad (21)$$

**Step 3:** Perform the diagonal scaling and average these results

$$\tilde{u} = \sum_{i=1}^N R_B^{(i)} \left( \text{diag} \left( K_{BB}^{(i)} \right) \right)^{-1} R_B^{(i)T} \tilde{s}. \quad (22)$$

**Step 4:** Compute

$$\hat{s} = r - S \tilde{u}. \quad (23)$$

**Step 5:** Approximate the coarse problem again for an unknown vector  $\tilde{\mu} \in \mathfrak{R}^N$

$$\tilde{S}_0 \tilde{\mu} = R_0^T \hat{s}. \quad (24)$$

**Step 6:** Find the preconditioned vector

$$z = \tilde{u} + R_0 \tilde{\mu}. \quad (25)$$

The  $\tilde{S}_0$  means the corresponding term of the coarse matrix of  $R_0^T S R_0$ , which is factorized incompletely.

Hence, it is said that the residual is incompletely balanced in (21). The implementation of incomplete balancing reduces the computation costs for factorization of the coarse matrix and for forward elimination and backward substitution of the problem (20) and (24) and consequently the amount of work of each iteration is reduced. For this reason although IBDD-DIAG preconditioner may increase the number of iterations, a

speed up is achieved for large scale problems in the massively parallel computer.

## 7. NUMERICAL RESULTS AND DISCUSSIONS

Thermal and structural analysis on two models shown in Fig. 4 are performed.

### 7.1 HTGR Model [8,9]

#### i) Model description and computational conditions

The HTGR model shown in Fig. 4 is graphite made, helium cooled reactor core whose height was 580 mm. The convergence criterion was that the norm of the relative residual is reduced to  $10^{-6}$ . The mesh sizes of this model are shown in Table 1.

#### ii) Computational performances

The computation performances for both thermal and structural analysis of HTGR model are shown in Table 2. Fig. 5 shows the convergence history for thermal analysis of HTGR model. Both results show that BDD and IBDD-DIAG converges rapidly. Regarding the memory requirements of the various preconditioning approaches, IBDD-DIAG which employ a diagonal-scaling as a local subdomain correction, reduce memory requirements by around 40% compared with BDD preconditioner.

### 7.2 Model B: ABWR [9]

#### i) Model description and computational conditions

In this research, as a large scale and real shape model problem having a bad convergence, the present method is applied to a 12 million node unstructured mesh for a precise model of Advanced Boiling Water Reactor (ABWR)[9] as shown in Fig. 4. The model is expressed with 3,000 subdomains, 7,486,792 elements, 11,794,506 nodes in the HDDM system.

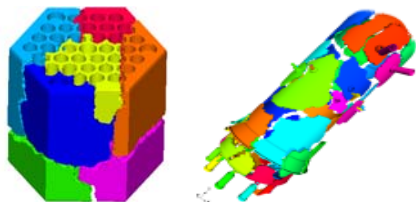


Fig 4. Part decomposition of HTGR (left) and ABWR model (right)

Table 1: Mesh sizes of HTGR model

	Number of nodes (dof)	Number of elements	Number of subdomains
Thermal	1,893,340 (1,893,340)	1,167,268	3,200
Structural	1,893,340 (5,680,020)	1,167,268	4,000

Table 2: Performances of BDD and IBDD-DIAG (HTGR)

		Num. of iteration	Computation time (sec)	Memory /PE (MB)
Thermal Analysis	DIAG	527	777.50	174
	BDD	33	224.61	277
	IBDD-DIAG	70	358.34	185
Structural Analysis	DIAG	1,570	6,895	321
	BDD	118	3,075	544
	IBDD-DIAG	85	2,599	980

Table 3: Performances of BDD and IBDD-DIAG (ABWR) for thermal analysis

	Sub # 3,000			Sub #6,000		
	#Iter.	Time (sec)	Mem. (MB)	Iter.	Time (sec)	Mem. (MB)
DIAG	3,201	1,259		4,295	1,103	
BDD	59	522		58	1,758	
IBDD-DIAG	124	264		105	294	

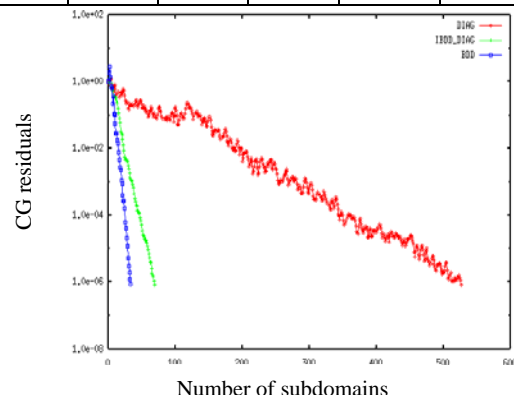


Fig 5. Convergence history of thermal analysis (HTGR)

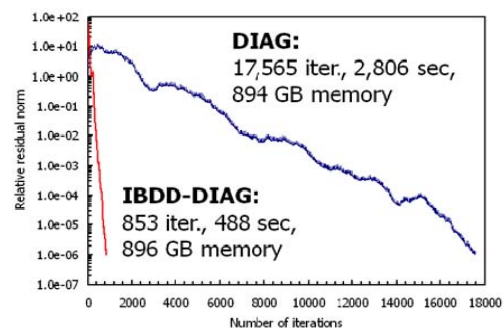


Fig 6. Convergence history (ABWR model)

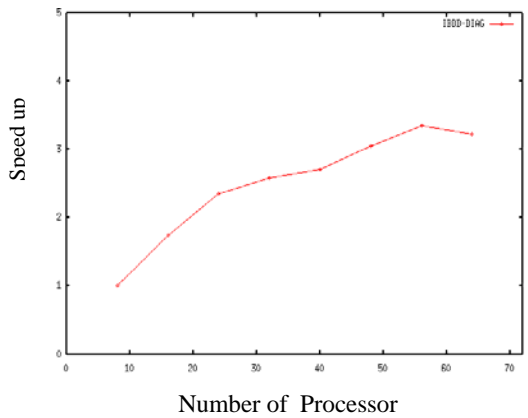


Fig 7. Parallel scalability of IBDD-DIAG

### ii) Computational performances

IBDD-DIAG is investigated in the thermal analysis of ABWR model using two different numbers of subdomains. The results are shown in Table 3. In 3,000 subdomains, the exact BDD type preconditioners reduce the number of iterations to about 2% and the computation time to about 40%. In 3,000 subdomains, the IBDD type preconditioners reduce the number of iteration to about 4% and the computational time to about 22%. It is found that with almost the same memory size as DIAG, IBDD-DIAG shows the best performance in computation time. Next in 6,000 subdomains, the exact BDD type preconditioners are slower than DIAG. It has the reason that the completely Cholesky factorization of a coarse grid operator gives almost all computation time. Here, IBDD-DIAG shows good performance in computational time with less memory size than in the case of 3,000 subdomains. Therefore, the IBDD-DIAG is an effective method to analyze large scale thermal-solid coupling problems. The convergence history for thermal analysis of ABWR model is shown in Fig. 6 which again shows the better convergence of IBDD-DIAG. Again Fig.7 predicts that IBDD-DIAG is parallelly scalable [10].

### 8. CONCLUSION

In this study a thermal-solid coupling system is successfully implemented on a 12 million dof ABWR model. The computational speed of the HDDM system was improved dramatically by employing the IBDD-DIAG method as an efficient preconditioner. The

IBDD-DIAG exhibits an excellent performance in terms of memory requirements, convergence rate and computation time. Furthermore, this system has been successfully implemented on parallel computer.

### 9. REFERENCES

- Reddy, J. N. and Gartling, D. K. 2000. *The finite element method in heat transfer and fluid dynamics*, CRC press, USA.
- Gang, Li., Wenbin, C. and Yaochu, F. 2008. *A fluid-structure coupling analysis of large scale hyperbolic cooling tower subjected to wind loads*. Proc. of 8<sup>th</sup> World Congress on Computational Mechanics (WCCM'8).
- Farhat, C., Chen, P.S. and Mandel, J., 1995, A Scalable Lagrange Multiplier Based Domain Decomposition Method for Time-Dependent Problems, *International Journal for Numerical Methods in Engineering*, Vol. 38 , p. 3831-3853.
- Yagawa, G. and Shioya, R. 1993. Parallel finite elements on a massively parallel computer with domain decomposition. *Comput. Systems Eng.* 4:495-503.
- Mandel, J. 1993. Balancing domain decomposition. *Comm. Numer. Methods Eng.* 9:223-241.
- M. Ogino, R. Shioya and H. Kanayam. 2008, An inexact balancing preconditioner for large scale structural analysis, Vol.2. No. 1
- <http://adventure.q.t.u-tokyo.ac.jp>
- Shioya, R., Ogino, M., Kanayama, H. and Tagami, D. 2003. Large scale finite element analysis with a balancing domain decomposition method. *Key Eng. Materials* 243-244:21-26.
- Shioya, R., Kanayama, H., Mukaddes, A.M.M. and Ogino, M. 2003, Heat conductive analysis with balancing domain decomposition. *Theor. Appl. Mech.* 52:43-53.
- Mukaddes, A.M.M., Ogino, M., Kanayama, H. and Shioya, R. 2006. A scalable Balancing Decomposition based preconditioner for large scale heat transfer problems. *JSME Int. J. Ser. B.* 49:533-540.

### 10. MAILING ADDRESS

Abul Mukid Mohammad Mukaddes  
 Department of Industrial and Production Engineering,  
 Shah Jalal University of Science and Technology,  
 Bangladesh,  
 Email: mukaddes1975@gmail.com



## BIODIESEL FROM JATROPHA OIL AS AN ALTERNATIVE FUEL FOR DIESEL ENGINE

Mohammad Mashud, M. Hasan Ali, Md. Roknuzzaman and Asadullah Al Galib

Department of Mechanical Engineering,  
Khulna University of Engineering and Technology , Bangladesh.

### ABSTRACT

The world is getting modernized and industrialized day by day. As a result vehicles and engines are increasing. But energy sources used in these engines are limited and decreasing gradually. This situation leads to seek an alternative fuel for diesel engine. Biodiesel is an alternative fuel for diesel engine. The esters of vegetable oil animal fats are known as Biodiesel. This paper investigates the prospect of making of biodiesel from jatropha oil. Jatropha curcas is a renewable non-edible plant. Jatropha is a wildly growing hardy plant in arid and semi-arid regions of the country on degraded soils having low fertility and moisture. The seeds of Jatropha contain 50-60% oil. In this study the oil has been converted to biodiesel by the well-known transesterification process and used it to diesel engine for performance evaluation.

**Keywords:** Bio-diesel, Jatropha Oil and Trans-esterification Process.

### 1. INTRODUCTION

As civilization is growing, transport becomes essential part of life. The biggest problem is the growing population & depletion of fossil fuel. About 100 years ago, the major source of energy shifted from recent solar to fossil fuel (hydrocarbons). Technology has generally led to a greater use of hydrocarbon fuels, making civilization vulnerable to decrease in supply. This necessitates the search for alternative of oil as energy source.

Biodiesel is an alternative fuel for diesel engine. The esters of vegetable oils and animal fats are known collectively as biodiesel. It is a domestic, renewable fuel for diesel engine derived from natural oil like Jatropha oil. Biodiesel has an energy content of about 12% less than petroleum-based diesel fuel on a mass basis. It has a higher molecular weight, viscosity, density, and flash point than diesel fuel.

Jatropha curcas is unusual among tree crops is a renewable non-edible plant. From jatropha seeds jatropha oil can be extracted which have similar properties as diesel but some properties such as kinematic viscosity, solidifying point, flash point and ignition point is very high in jatropha oil. By some chemical reactions, Jatropha oil can be converted into biodiesel. Jatropha oil can also be used directly by blending with diesel. Some benefits of jatropha oil are as follows:

- (i) The oil is being extensively used for making soap in some countries because it has a very high saponification value.

- (ii) The oil is used as illuminants as it burns without emitting smoke.
- (iii) The latex of jatropha curcas contains an alkaloid known as "jatrophine" which is believed to have anti cancerous properties.
- (iv) From the bark of jatropha curcas a dark blue dye is produced which is used for coloring cloth, fishing nets etc.
- (v) The byproduct of jatropha seeds contain high nitrogen, phosphorous and potassium which is used for fish foods, domestic animals food and in lands as fertilizer.

Now a day it has found that jatropha may display certain anti tumor and anti malarial properties and research is advancing related to HIV/ AIDS. Alternative fuels, other than being renewable, are also required to serve to decrease the net production of carbon dioxide (CO<sub>2</sub>), oxides of nitrogen (NO<sub>x</sub>), particulate matter etc. from combustion sources.

The production of biodiesel is limited by land area but jatropha curcas trees can be cultivated in any kinds of land. Jatropha is a wildly growing hardy plant, in arid and semi-arid regions of the country on degraded soils having low fertility and moisture. It can be cultivated successfully in the regions having scanty to heavy rainfall even it can be cultivated even on fallow and barren lands. There is huge unused area in southern part of Bangladesh, where jatropha can be cultivated with profitable income. The seeds of jatropha contain 50-60% oil. So Bangladesh can produce a huge amount of biodiesel from jatropha curcas and can save a large amount of importing of petroleum products from foreign countries.

The purpose of this research work is to investigate the fuel properties of Jatropha oil and production of bio-diesel from Jatropha oil. Investigate the fuel properties of bio-diesel and performance test diesel engine by using bio-diesel.

## 2. METHODOLOGY

The use of biodiesel is an effective way of substituting diesel fuel in the long run. One important conclusion that can be drawn from the work done earlier is that the vegetable oils can't be used directly in the diesel engine. Several problems crop up if unmodified fuel is used and viscosity is the major factor. It has been found that transesterification is the most effective way to reduce the viscosity of vegetable oils and to make them fit for their use in the present diesel engines without any modification.

Transesterification is the process by which biodiesel is produced. In this process an ester reacts with an alcohol to form another ester and another alcohol. The catalyst for this reaction is KOH or NaOH. Three mol methanols react with one mol triglyceride which produces mixture of fatty esters and glycerin. The industrial-scale processes for transesterification of vegetable oils were initially developed in the early 1940s to improve the separation of glycerin during soap production.

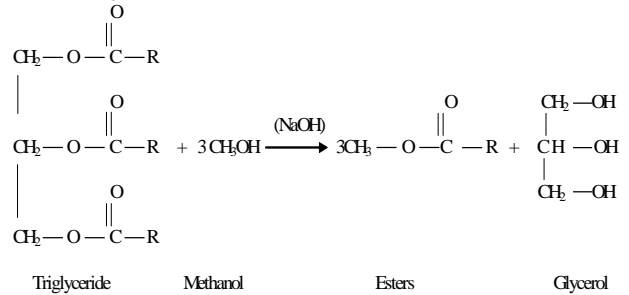
The primary input is assumed to be oil that has previously been extracted from jatropha oilseed. To accomplish the transesterification reaction described above, the oil, methanol, and catalyst are mixed together in a stirred reactor. 55°-60°C temperature will cause the reaction to reach equilibrium more rapidly; in most cases the temperature is kept below the normal boiling point of the methanol(65°C) so the reactor does not need to be pressurized .

As shown in the reaction equation below, three moles of methanol react with one mole of triglyceride. In practice, most producers will use at least 100% excess methanol (6:1 molar ratio) to force the reaction equilibrium towards a complete conversion of the oil to biodiesel. The reaction is slowed by mass transfer limitations since at the start of the reaction the methanol is only slightly soluble in the oil and later on, the glycerin is not soluble in the methyl esters.

Since the catalyst tends to concentrate in the glycerin, it can become unavailable for the reaction without agitation. A common approach to overcome this issue is to conduct the transesterification in two stages. First, the oil is combined with 75% to 90% of the methanol and catalyst and this mixture is allowed to react to equilibrium. Then, the glycerin that has formed is separated by gravity separation and the remaining 10% to 25% of the methanol and catalyst is added for a second reaction period. At the conclusion of this second reaction period, the remaining glycerin is separated and the biodiesel is ready for further processing. The glycerin separation steps are usually accomplished by gravity settling or with a centrifuge

After the biodiesel is separated from the glycerol, it contains 3% to 6% methanol and usually some soap. If the soap level is low enough (300 to 500 ppm), the methanol can be removed by vaporization and this methanol will usually be dry enough to directly recycle back to the reaction. Methanol tends to act as a co-solvent for soap in the biodiesel, so at higher soap levels the soap will precipitate as a viscous sludge when the methanol is removed.

The reaction is given below:



Where R is long hydrocarbon chains, sometimes called fatty acid chains.

After the methanol has been removed, the biodiesel needs to be washed to remove residual free glycerin, methanol, soaps, and catalyst. This is most frequently done using liquid-liquid extraction by mixing water with the biodiesel and gently agitating them to promote the transfer of the contaminants to the water without creating an emulsion that might be difficult to break. The washing process is usually done multiple times until the wash water no longer picks up soap. Although the gray water from later washes can be used as the supply water for the earlier wash steps, the total amount of water will typically be one to two times the volume flow rate of the biodiesel. Sometimes, to reduce the amount of water required, producers will add acid to the wash water. Weaker organic acids, such as citric acid, will neutralize the catalyst and produce a soluble salt.

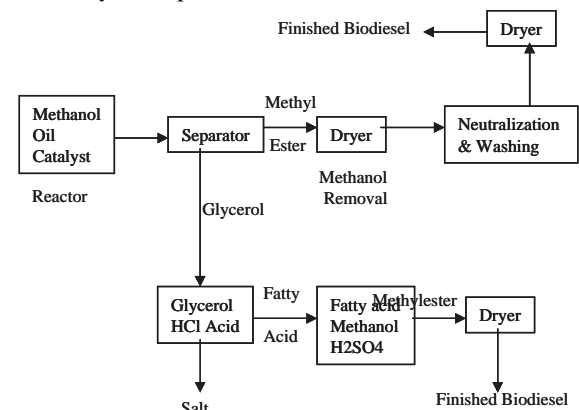


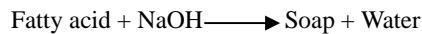
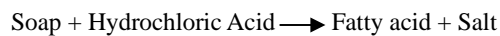
Fig 1. Schematic of Biodiesel Processing.

Stronger inorganic acids, such as hydrochloric, sulfuric, or phosphoric, can be used to split the soap and this reduces the water requirement to 5% to 10% of the biodiesel flow because the salts are easier to remove than the soap. After washing, the biodiesel is frequently

cloudy due to small water droplets suspended in the fuel. While these droplets will eventually settle out, it is much faster to use a flash evaporator to remove the residual water from the fuel.

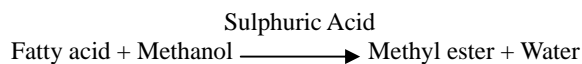
The glycerin that is separated from the biodiesel will contain a substantial amount of methanol, most of the catalyst, soaps that have been formed during the reaction and many of the polar contaminants that were originally present in the oil. These contaminants contribute to a dark brown or black color for the glycerin in spite of it being clear when present as a pure compound. The raw glycerin has very little value and must be upgraded to raise its purity before it can be sold. The usual practice is to add strong hydrochloric acid to the glycerin to neutralize the catalyst and split the soap.

The reactions are given below:



The soaps split into free fatty acids (FFAs) and salt, as shown in the equation. The FFAs are not soluble in the glycerin and can be separated with a centrifuge. The methanol can be removed by vaporization leaving a crude glycerol that is 80% to 90% pure. Most of the impurities will be salts. Only a few of the biodiesel producers in the U.S. have invested in the equipment to refine this crude glycerin to the 99.5% purity required for pharmaceutical and cosmetic applications. The fatty acids are not soluble in the glycerin and can be separated with a centrifuge. These high free fatty acid oils present special challenges when used for biodiesel production. When an alkali catalyst is added to these feed stocks, the free fatty acid reacts with the catalyst to form soap and water as shown in the above reaction. This reaction makes the catalyst unavailable for catalyzing the reaction and if enough soap is produced it can inhibit the separation of the methyl esters and glycerin.

When oils and fats with high free fatty acids are to be used for biodiesel production, an acid catalyst such as sulfuric acid can be used to esterify the free fatty acids to methyl esters as shown in the following reaction.



Then, the Methanol with the FFAs converted to methyl esters, a conventional alkali-catalyzed process can be used to transesterify the triglycerides in the feedstock. While acids can be used to catalyze the transesterification reaction, the reaction is very slow at the 50° to 60°C reaction temperature the two-step approach of acid-catalyzed esterification followed by base-catalyzed transesterification gives a complete reaction at moderate temperatures. A problem with this approach is that the water produced by the esterification reaction should be removed before the base-catalyzed process begins so that soap formation is not excessive. This can be done by settling or centrifuging the

methanol-water-acid layer that separates after the esterification has reached equilibrium. The additional equipment required for the acid-catalyzed pretreatment raises the processing cost, but this approach allows the use of feed stocks containing up to 100% FFA. Finally after drying the found methyl ester is converted to the required biodiesel. Hence, it is seen that 900ml biodiesel is produced from 1 liter of Jatropha oil.



Fig 2. Seeds of Jatropha



Fig 3. Jatropha oil



Fig 4. During the biodiesel production



Fig 5. Biodiesel

### 3. EXPERIMENTAL SET-UP AND PROCEDURE

The final product of biodiesel from Jatropha oil is used as an alternative fuel to operate diesel engine in the Heat Engine Laboratory of Department of Mechanical Engineering, Khulna University of Engineering & Technology. The tested engine specification is shown in Table-A and photograph is shown in Fig. 5. The engine has been run using biodiesel and required data are collected to calculate the engine performance parameters.



Fig 6. Photograph of Experimental Set-Up

Table-A: Engine Specification

Model	06-TCVenaria
Type	Vertical, four cylinder, in line, air –cooled, diesel cycle
Bore or diameter(mm)	76.1
Stroke(mm)	71.5
Total swept volume(cc)	1301
Compression ratio	20
Maximum power(DIN standards)	
Maximum torque(DIN standards)	7.2 kg-m(71 Nm) at 2500 rpm
Method of cooling	Air cooling by fan
Method of lubrication	Centrifugal lubrication, combined oil mist and splash.
Method of starting	By using starting motor
Voltage of electric installation i.e. Battery(v)	12v, 21 plate
Ignition sequence	1-3-4-2
Distribution	Single-shaft in the cylinder head with toothed belt drive
Injection pump	BOSCH rotary pump
Oil sump capacity(l)	4
Clearance of cold tappets (mm)	0.40(intake), 0.50(exhaust)
Optimal utilization of engine speed (R pm)	1500-4000

#### 4. RESULTS AND DISCUSSION

Table-1: The observed properties of oil and fuels:

Properties	Jatropha Oil*	Biodiesel	50% Biodiesel & 50% Diesel	Diesel*
Density [gm/cc]	--	0.62	0.58	0.84
Kinematic viscosity at 30°C	55	5.34	6.86	4.0
Calorific value [MJ/kg]	39.5	41	42.7	45
Cetane number	43	--	--	47
Solidifying point °C	-10	--	--	-14
Boiling point °C	286	255	--	248

Table-2: The observed engine performance using diesel and biodiesel:

Performance	Diesel	Biodiesel	50% Biodiesel & 50% Diesel
Brake power , kw	0.466	0.895	0.339
Specific fuel consumption, g/kw-hr	784	629.74	1298
Mass of fuel, kg/hr	0.712	0.62	0.44
Brake thermal efficiency,%	11.76	24.09	10.8
Mass of air, kg/hr	7.94	5.52	8.49
Air fuel ratio	31.15	8.9	19.3

Table-3: The exhaust Gas analysis by ORSAT apparatus:

% of sample gas	Diesel	Biodiesel	50%Biodiesel & 50% Diesel
CO <sub>2</sub>	9	1.33	5
O <sub>2</sub>	5	17.67	8
CO	1	0	1

From the present research it is found that the calorific value of biodiesel is almost same as the diesel.

It has been found that the performance of biodiesel, mixture of 50% biodiesel & 50% diesel and compared with diesel and found that the brake power, brake thermal efficiency is greater than diesel and mass of air, fuel consumption, mass of fuel of biodiesel and air fuel ratio is less than diesel. It is also found that brake power, brake thermal efficiency, mass of fuel of biodiesel is greater than 50% biodiesel & 50% diesel and mass of air and air fuel ratio of biodiesel is less than mixture of 50% biodiesel & 50% diesel.

From the analysis of exhaust gas it is observed that % of CO<sub>2</sub> gas of biodiesel is very lower than the diesel and also from the mixture of 50% biodiesel & 50% diesel. The % of O<sub>2</sub> of biodiesel is very higher than the diesel and nearly with mixture of 50% biodiesel & 50% diesel. And the % of CO is zero for biodiesel & one for other two compositions.

As far as the utilization of the seed cake is concerned, niche formation processes are hardly present. The seedcake pressed into briquettes, which can be used as fuel in wood stoves or ovens. Using seedcake as fertilizer could be more promising because of its favorable nutritional qualities. Potential actors in this domain are farmers who want to use the cake as fertilizer, and the oil pressing facilities, which generate Jatropha cake as a by-product. It would appear to be highly important for this niche to develop, because Jatropha cultivation itself stands to benefit from it.

The by-products of Transesterification process; glycerin and soap can also be the source of income. By supplying

the processed glycerin in the market money can be made. And small-scale Jatropha soap contributes on the economics. Because, the soap, itself is a good product with strong antiseptic qualities. It commands a high price compared to ordinary soaps, so only a minority of people can afford it. The expectation is that this market will not expand much beyond its current size.

From the above discussion it is clear that biodiesel from Jatropha oil is very necessary to us. It reduces green house effect on our environment by reducing CO<sub>2</sub> gas emission. It is very friendly with environment because it increases percentage of O<sub>2</sub> in exhaust gas than the ordinary diesel. The economics of biodiesel fuels compared to traditional petroleum resources are marginal; public policy needs to be revised to encourage development. As Jatropha curcas is easy to cultivate so by planting of Jatropha, Bangladesh can save a huge amount of importing of petroleum products from foreign countries.

## 5. CONCLUSION

Biodiesel is a viable substitute for petroleum-based diesel fuel. Its advantages are improved lubricity, higher cetane number, cleaner emissions (except for NO<sub>x</sub>), reduced global warming, and enhanced rural development. Jatropha oil has potential as an alternative energy source. However, this oil alone will not solve our dependence on foreign oil within any practical time frame. Use of this and other alternative energy sources could contribute to a more stable supply of energy. Major production centers on the level of modern petroleum refineries have not been developed. The economics of biodiesel fuels compared to traditional petroleum resources are marginal; public policy needs to be revised to encourage development. Increased Jatropha oil production would require a significant commitment of resources. Land for production would need to be contracted, crushing and biodiesel production plants need to be built, distribution and storage facilities constructed, and monitoring of users for detection of problems in large-scale use are all needed to encourage development of the industry. To meet the challenges of excessive import, we have to strengthen our oilseed sector and lay special emphasis on harnessing the existing and augmenting future potential source of green fuel. The organized plantation and systematic collection of Jatropha oil, being potential bio-diesel substitutes will reduce the import burden of crude petroleum substantially. The emphasis should be made to invest in agriculture sector for exploitation of existing potential by establishing model seed procurement centers, installing preprocessing and processing facilities, oil extraction unit, trans-esterification units etc. There is also need to augment the future potential by investing largely on compact organized plantation of Jatropha on the available wastelands of the country. This will enable our country to become independent in the fuel sector by promoting and adopting bio-fuel as an alternative to

petroleum fuels. It is evidenced that there are new work opportunities in Jatropha cultivation and biodiesel production related sectors, and the industry can be grown in a manner that favors many prosperous independent farmers and farming communities.

## 6. REFERENCES

1. Jon H. Van Gerpen, Charles L. Peterson, Carroll E. Goering, Biodiesel: An Alternative Fuel for Compression Ignition Engines, For presentation at the 2007 Agricultural Equipment Technology Conference Louisville, Kentucky, USA 11-14 February 2007.
2. ASTM. 2002. D 6751 – Standard specification for biodiesel fuel (B100) blend stock for distillate fuels. West Conshohocken, Penn.:ASTM International.
3. ASTM. 2006. *Standard Specification for Diesel Fuel Oils*. West Conshohocken, Penn.:ASTM International.
4. Prof. (Dr.) R. K. Khotoliya, Dr. Harminder Kaur & Rupinder Sing, Biodiesel Production from Jatropha (Source- Kurukshetra, volume-55, No-4, February-2007).
5. Bradshaw, G. B., and W.C. Meuly. 1942. Process of making pure soaps. U.S. Patent 2,271,619.
6. Van Gerpen, J. 2005. Biodiesel processing and production. *Fuel Processing Technology* 86: 1097-1107.
7. T. Mirunalini, R.Anand and N.V.Mahalakshmi. JATROPHA OIL AS A RENEWABLE FUEL IN A DI DIESEL ENGINE. Proceedings of the 3rd BSME-ASME International Conference on Thermal Engineering, 20-22 December, 2006, Dhaka, Bangladesh.
8. Janske van Eijck Project Leader Biofuels, Diligent Tanzania and Henny Romijn Eindhoven Centre for Innovation Studies, Prospects for Jatropha Biofuels in Developing Countries: An analysis for Tanzania with Strategic Niche Management.
9. Knothe, G. 2005b. Cetane numbers—The history of vegetable oil-based diesel fuels. Chapter 2 in G. Knothe, J. Van Gerpen, and J. Krahl, eds. *The Biodiesel Handbook*. Champaign, Ill.: American Oil Chemists' Society Press.
10. Peterson, C.L. 1980. Vegetable oils—Renewable fuels for diesel engines. ASAE Paper No. PNW 80-105. St. Joseph, Mich.: ASAE.
11. Peterson, C.L. 1985. Vegetable oil as a diesel fuel – Status and research priorities, ASAE Paper No. 85-3069. St. Joseph, Mich.: ASAE.
12. L.Kritana Prueksakorn and Shabbir H. Gheewala, Energy and Greenhouse Gas Implications of Biodiesel Production from Jatropha curcas, The 2nd Joint International Conference on “Sustainable Energy and Environment (SEE 2006)” 21-23 November 2006, Bangkok, Thailand.
13. Palligarnai T. Vasudevan & Michael Briggs, Biodiesel production—current state of the art and challenges.
14. ISO, (1997) International Standard ISO 14040, Environmental management – Life cycle assessment – Principles and Framework, Retrieved on 5th January 2006, Available online: [www.ce.cmu.edu/~hsm/lca2006/readings/iso14040.pdf](http://www.ce.cmu.edu/~hsm/lca2006/readings/iso14040.pdf)

## 7. MAILING ADDRESS

Mohammad Mashud  
Khulna University of Engineering and Technology  
Khulna-9203, Bangladesh.  
Email: mdmashud@yahoo.com

# DESIGN, CONSTRUCTION AND PERFORMANCE TEST OF A SYNCHRONIZED MULTI-SPARK MODULE FOR ELECTRONIC IGNITION DEVICE

Mohammad Mashud, M. Mostafizur Rahman and S. Hossain Khan

Department of Mechanical Engineering Khulna University of Engineering & Technology, Khulna

## ABSTRACT

Synchronized multi spark module can be used for minimizing fuel loss at the starting of engine. The objective of this project was to design, construction & performance test of a synchronized multi spark module. Multi spark module is very useful at low rpm & low temperature range. Due to voltage fluctuation the pulse width of the module will be vary. Breaker point is opening & creating pulses. These pulses go to shaping block, which producing pulse according to engine speed. Clock generator which Produces 2ms pulse, When p2 (gate) is opened then the counter receive pulse s of 1 ms from clock generator .Then it goes OR Gate that will generate a series of spark.

**Keywords:** Multi-Spark Module, Electronic Ignition Device , Internal Combustion Engine.

## 1. INTRODUCTION

There are many different types of ignition systems. Most of these systems can be placed into one of three distinct groups: the conventional breaker point type ignition systems (in use since the early 1900s); the electronic ignition systems (popular since the mid 70s); and the distributor less ignition system (introduced in the mid 80s). The automotive ignition system has two basic functions: it must control the spark and timing of the spark plug firing to match varying engine requirements, and it must increase battery voltage to a point where it will overcome the resistance offered by the spark plug gap and fire the plug.

### Point-type ignition system:

An automotive ignition system is divided into two electrical circuits -- the primary and secondary circuits. The primary circuit carries low voltage. This circuit operates only on battery current and is controlled by the breaker points and the ignition switch. The secondary circuit consists of the secondary windings in the coil, the high tension lead between the distributor and the coil (commonly called the coil wire) on external coil distributors, the distributor cap, the distributor rotor, the spark plug leads and the spark plugs.

### Electronic ignition systems:

The need for higher mileage, reduced emissions and greater reliability has led to the development of the electronic ignition systems. These systems generate a much stronger spark which is needed to ignite leaner fuel mixtures. Breaker point systems needed a resistor to reduce the operating voltage of the primary circuit in

order to prolong the life of the points. The primary circuit of the electronic ignition systems operates on full battery voltage which helps to develop a stronger spark. Spark plug gaps have widened due to the ability of the increased voltage to jump the larger gap. Cleaner combustion and less deposit have led to longer spark plug life.

The Direct Ignition System (DIS) uses either a magnetic crankshaft sensor, camshaft position sensor, or both, to determine crankshaft position and engine speed. This signal is sent to the ignition control module or engine control module which then energizes the appropriate coil.

The advantages of no distributor, in theory, are:

- No timing adjustments
- No distributor cap and rotor
- No moving parts to wear out
- No distributor to accumulate moisture and cause starting problems
- No distributor to drive thus providing less engine drag

The major components of a distributor less ignition are:

- ECU or Engine Control Unit
- ICU or Ignition Control Unit
- Magnetic Triggering Device such as the Crankshaft Position Sensor and the Camshaft Position Sensor
- Coil Packs

Synchronized multi-spark module is very useful especially in the case of starting of the engine at low rpm range. Basic idea, is to apply to spark plugs instead of only one spark, a "spark-burst" having big energy. Multi-spark is generated repeatedly turning the coil current on and off during the spark sequence. At low RPM, during cranking,

the DMS generates up to 12 sparks. This assures quick starting even under the most adverse conditions. At idle and cruise, the number of sparks fired is adjusted to maintain total spark duration of about 20 degrees (crankshaft), assuring smooth idle, improved throttle response, and eliminating the lean surge characteristic of some late model emission controlled vehicles. During acceleration at higher RPM levels, the DMS generates a single powerful spark with about twice the spark. In this case, combustion of air/fuel mixture is much better and the emissions are more reduced. In addition, through burning improvement, the consumption of fuel can be reduced. The advantage of synchronized multi spark module is reduced starting load system for an automobile engine. According to the engine speeds Spark timing control of multiple fuel engines. The importance of multi spark module is ignition system improvements for internal combustion engines. The application of synchronized multi spark module Late Model Computer Controlled Vehicles with Stock Electronic Ignition, Honda and Acura Integra, Earlier Electronic Ignition Systems without Computer Control

The purpose of this research is to design and construct a Synchronized Multi Spark Module for Electronic Ignition Devices and its performance evaluation.

## 2. WORKING PRINCIPLES OF SMSM

As shown in Fig. 1, shaped pulse triggers directly the EID and act as START pulse for multi-spark module. If rpm of engine is under speed limit, the module will generate a series of supplementary pulses that, through an OR gate, will generate supplementary sparks by EID. When speed limit is reached (for example, 2000 rpm), supplementary pulses stop at module output, thus no supplementary sparks will be generated.

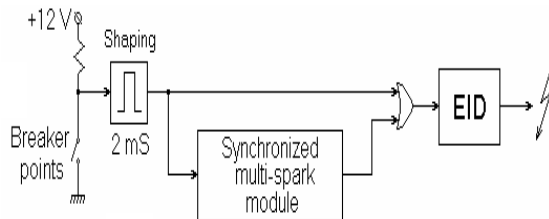


Fig 1. Placement of Synchronized Multi-Spark Module

Fig.2 when 12 V dc power is supplied to the stepup transformer then this transformer is made the power about 40,000 volts & the breaker points open. As a result 2ms puls is generated by shaping block which is produced pulse & sent pulse to EID. As the module parallel with the convectional system. The module is generated a serise of pulse according to engine speed. Sequence timer is used to determine the time interval of pulse generation. Speed sensor is used to sense the speed of crank shaft and sent the sense to the circuit and it is started its work. The pulse is shown in the oscilloscope. The module uses for control the shaped pulses from breaker points. The time between two consecutively pulses depends on rpm engine. From whole T interval, only in the first half of this will be

generated supplementary sparks, after the main spark produced by the breaker points.

This is very important, because generating sparks outside of half of the interval, the spinning distributor could apply these sparks to next cylinder, and this could be very harmful for mechanical parts of engine.

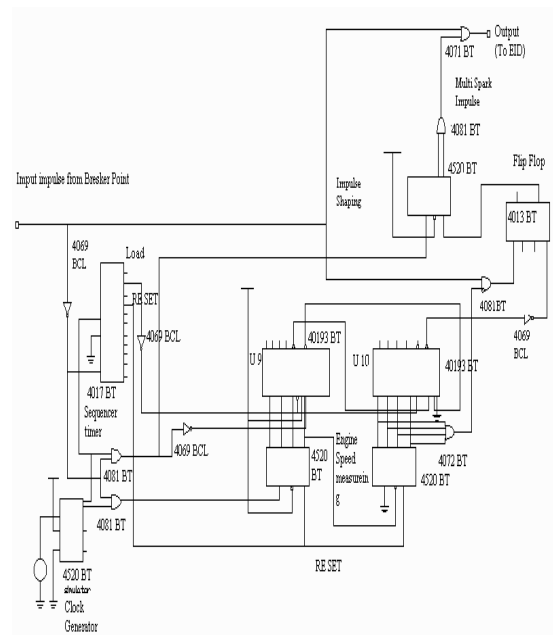


Fig 2. Circuit diagram of Synchronized Multi-Spark Module

At breaker-points opening, the shaping circuit (not shown in drawing) produces a square pulse having 2 m S. This, named BP, is applied to EID by an OR gate and generate the main spark.

In multi-spark module, during 2 msec interval, a sequence timer (a counter with decoded outputs) accomplishes the initialization of circuits (full operations will be detailed later). When impulse BP disappears, the gate P2 is opened and the counter N1 receives pulses with 1 mS period, from clock generator. These 8 bits counter measures, in fact, the duration between two breaker-points pulses. It can count maximum 255 pulses, each having 1 mS (see the table, this correspond to 120 rpm, far below the free running speed!). At next BP pulse, P2 close and the counting stop. The number stored inside N1 is in fact the time length between two BP impulses.

The sequence timer “copy” the number stored in N1 to N2, after this resets counter N1. When BP becomes low level, N1 restarts the counting. In the same time, the up/down counters N2, starts counting the pulses having 0.5 mS period, which comes via gate P1. It counts down, but with double speed. In this way the counter N2 reach to “0” after T/2 time. The counter N4 and gate P5 makes the pulses for supplementary sparks (2 mS length).

This counter works only if INH signal is at low level. The flip-flop FF1 “marks” the interval T/2 in which will be generated supplementary sparks. It is rested when N2 reach “0”. The gates P3 and P4 unlock the flip-flop and start supplementary sparks. Also, these gates switch-off the multi-spark function when engine speed limit is reached (in this case, ~ 2000 rpm). In the upper table we



can see at about 2000 rpm, the time length between two BP pulses is 15 mS.

This means as after a counting cycle, the first 4 bits of counter N1 will be 111 and next 4, 0000. In this case, P3 gate output will be at low level, and the same value for P4 output. The flip-flop FF1 will be not set, and as result, no supplementary sparks. If the speed engine decrease (time length T increase), the last 4 bits of N1 will have at least one 1 and the flip-flop will be set. This allow to appear supplementary sparks until flip-flop will be rested by borrow pulse of N2. The module can be made like a plug-in adapter for an EID.

### 3. EXPERIMENTAL SET-UP

To evaluate the performance of the constructed SMSM a simple experimental set-up, as shown in Fig. 3, has been made and perform the experiment. The key point of our project is to SMSM for electronic ignition device. The disc between sensor and LED define as rpm of crank shaft of the engine. The disc is coupled with a wiper motor. This motor is controlled by an electrical circuit, using regulator.

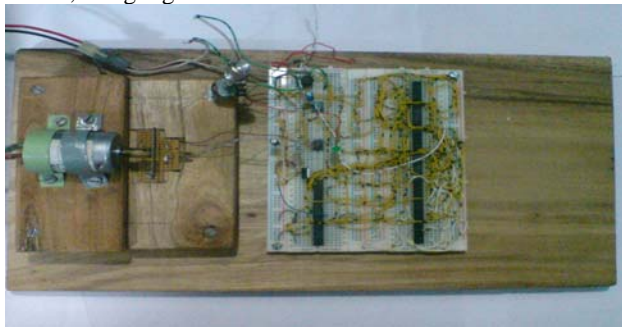


Fig 3. Photograph of the experimental Set-Up

The table 1 shown the relationship between engine speed & spark frequency. The spark frequency is detected by LED. The shape of the pulse is shown in the oscilloscope & also shown the spark frequency. With the varying of variable resistor the spark frequency also

No. of observation	Revolution speed (rpm)	Spark Frequency (Hz)	Time between impulse (ms)
1	400	14	50
2	800	26	30
3	1200	40	20
4	1600	56	15
5	2000	68	9
6	2400	86	7
7	2800	104	4

changed. According to the circuit characteristics, when rpm of the engine increases, then the spark frequency increases.

The module can be controlled under a given speed limit.

Table-1: Experimental Data

The crankshaft velocity of an internal combustion engine is given by following formula:

$$n = \frac{30 * N * M * B}{C}$$

Where:

n = revolution speed of engine crankshaft (rpm)

M = strokes number (2 or 4)

N = number of sparks per second (sparks frequency, in Hz)

B = number of ignition coils

C = cylinder number

For conventional four stroke engines, with 4 cylinders and a single ignition coil, the formula becomes:

$$n = 30 * N$$

From where:

$$N(\text{sparks / sec}) = \frac{n(\text{rpm})}{30}$$

### 4. CONCLUSION

This research work is performed with the most primary technological facilities. Multi spark module is at first Designed and it is constructed successfully. The objective is to start the engine at low temperature & low rpm range. From the experimental data which has found, in the developed rpm is suitable for required output. We get accurate rpm of the crank shaft, as because of coupling propeller with shaft which cuts sensor properly.

### 5. REFERENCES

1. William H. Crouse, Automotive Engine Design, 4<sup>th</sup> edition, McGraw-Hill, NY.
2. Book of Narang, G. B. S., Automobile Engineering, 2<sup>nd</sup> edition, Khanna Publishers, India.
3. Book of Joseph Heitner, Automotive Mechanics, 5<sup>th</sup> edition, McGraw-Hill, NY.

### 6. MAILING ADDRESS

Mohammad Mashud  
Department of Mechanical Engineering  
Khulna University of Engineering & Technology,  
Khulna, Bangladesh



## INTELLIGENT AIR-CUSHION SYSTEM OF SWAMP PEAT VEHICLE CONTROL: FUZZY LOGIC TECHNIQUE

A. Hossain<sup>1</sup>, A. Rahman<sup>2</sup>, A.K.M. Mohiuddin<sup>2</sup>

<sup>1</sup> Department of Mechanical Engineering, Faculty of Engineering, University Industry Selangor,  
,Batang Berjuntai, Selangor, Malaysia

<sup>2</sup>Department of Mechanical Engineering, Kulliyah of Engineering, International Islamic University  
Malaysia

### ABSTRACT

This paper describes the fuzzy logic to control the intelligent air-cushion system of swamp peat vehicle. Focusing on optimizing the total power consumption of the vehicle, two main issues were studied in this paper. First, a theoretical model is developed to minimize total power consumption of the vehicle. Second, a control scheme is proposed to achieve the control targets and to minimize the power consumption by using a fuzzy logic controller. Compared with traditional approach, fuzzy logic approach is more efficient for the representation, manipulation and utilization. Therefore, the primary purpose of this work was to investigate the relationship between total power consumption, clearance height and cushion pressure, and to illustrate how fuzzy logic technique might play an important role in prediction of total power consumption. All experimental values were collected from the field test using a developed prototype hybrid electrical air-cushion tracked vehicle.

**Keywords:** Swamp Peat, Power Consumption, Fuzzy Logic, Cushion Pressure.

### 1. INTRODUCTION

With increasing demands to the wide application of off-road vehicles over soft terrain and swamp peat such as agriculture, forestry, construction and the military, there is a need to increase the knowledge about intelligent air-cushion system of swamp peat vehicle. The performance of air-cushion tracked vehicles travelling in a straight motion with uniform ground pressure distribution is well understood. However, prepared or unprepared tracks inherently have uneven profile for situations of vehicles travelling on deformable road surfaces. The vehicle responses during off-road operation are dependent on the road conditions and vehicle parameters such as clearance height, road roughness, vehicle speed, vehicle weight, and air-cushion pressure [1-3]. Many research works have been carried out and different types of vehicles are introduced to solve the transportation problems on moderate peat terrain [4-6]. But still no one offers any vehicle on low bearing capacity swamp peat terrain in Malaysia. The proposed vehicle could be useful for transporting the palm oil fresh fruit bunches over the swamp peat. A hybrid vehicle which combines intelligent air-cushion system with a driving mechanism has been proven to be an efficient solution for a heavy duty vehicle on severe working conditions [7]. The use of commercial intelligent air-cushion tracked vehicles to test the vehicle parameters is limited due to the difficulties in varying parameters as well as the control of

the air-cushion pressure. A small scale hybrid electrical air-cushion tracked vehicle (HEACTV) was therefore developed based on low bearing capacity of peat swamp [8]. The study has been focused based on the bearing capacity of the peat swamps in Sarawak that has been found as 7.7 kN/m<sup>2</sup> and it has poor trafficability due to the presence of submerged and undecomposed and partially decomposed materials. Other important properties are the very high ground water table, and low bulk density [9-11].

The mobility of the vehicle, cushion pressure and sinkage by vehicle effect on swamp terrain, are complex process with many other factors. For this reason, mathematical models have been introduced to understand the terrain nature and mechanics of track-terrain interaction and the interaction of air-cushion supporting system-terrain [12]. The air-cushion system of this vehicle was designed in such a way that it would not slide on the terrain with the vehicle movement. It only supports the partial load of the vehicle once the vehicle sinkage is closed to 70 mm and makes the vehicle ground contact pressure 7 kN/m<sup>2</sup>. The additional thrust (or tractive effort) is provided to the vehicle by using a propeller to overcome the drag motion resistance of the air-cushion system. As the terrain is unprepared, the air-cushion system was protected by using a novel design supporting system.

## 2. STRUCTURE SKETCH OF VEHICLE

The vehicle comprised mainly with full track system, air-cushion and air-cushion propulsion system, DC motors, two propellers, a battery pack, and a small engine are shown in Fig. 1. The full segmented rubber track mechanism is used as driving system to overcome traveling resistance, and the flexible skirt air-cushion as vehicle body to support vehicle partial weight. The air-cushion pressure is provided by a single compressor to lift the vehicle. Since the total vehicle load is partly supported by the air-cushion system and partly by the driving (also called propulsion system) system, the required total power for the vehicle includes two parts, i.e., the power for propulsion system and the power for lifting system (air-cushion system). Thus, it is important to reduce the total required power consumption that significantly affects transportation efficiency. A fuzzy logic controller is needed to maintain the vehicle in the optimum operation condition that optimizes the total power consumption of the vehicle by using properly selected control parameters. Therefore, an intelligent air-cushion system for a swamp peat vehicle is developed and theoretical analysis is carried out.

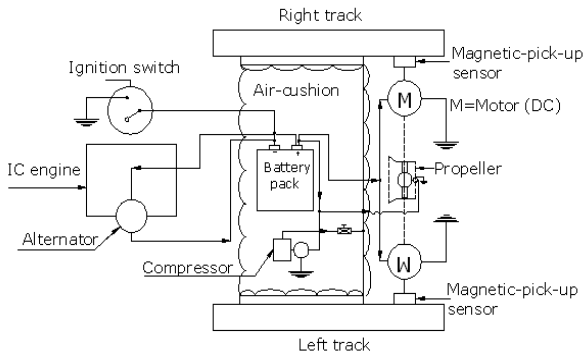


Fig 1. Structure sketch of the vehicle

Like many other real-world optimization, at present, various techniques exist in soft computing method. Based on the studies on wheeled air-cushion vehicles and semi-tracked air-cushion vehicles, an intelligent system using Fuzzy Logic was proposed to predict the power consumption. Fuzzy Logic, a relatively new, intelligent, knowledge based technique performs exceptionally well in non linear, complex systems [13-14].

This work presents the model of fuzzy system, comprising the control rules and term sets of variable, enabling to express vague human concepts using fuzzy sets and also describe the corresponding inference systems based on fuzzy rules [15]. In fuzzy rule-based systems, knowledge is represented by if-then rules. The aim of this study was the construction of fuzzy knowledge-based models for the prediction of the power consumption by controlling air cushion pressure of air-cushion tracked vehicle based on the Mamdani approach. A comparative performance analysis of this approach, by sampling data collected from the operation, was used to validate the fuzzy models.

## 3. THEORETICAL MODELS

When the vehicle with a constant load is subjected to external disturbances, such as uneven or slope of terrain surfaces, the clearance height of the vehicle and the required power on the tracks will change. However, the load distribution between driving system and air cushion pressure also changes, and thus total power requirement changes. Hence, in order to find an optimal range of load distribution which is corresponding to minimum power requirements, the cushion pressure needs to be controlled within optimal range.

The total power requirement  $P$  of the vehicle includes the power for air cushion system  $P_c$  and the power for driving system (propulsion system)  $P_d$ , which is given by:

$$P = P_c + P_d \quad (1)$$

where  $P_c$  is the power consumed by air-cushion used to support the weight of the vehicle body in  $W$  and  $P_d$  is the power consumed by driving system (propulsion system) in  $W$  used to overcome the traveling resistance and maintain normal driving state.

### 3.1 Model of Motion Resistance

In this study, the vehicle is designed mainly as a low speed heavy-duty off road vehicle. Based on established mathematical model, and assuming the vehicle on a level terrain surface, the motion resistances from aerodynamics and track belly drag component in the computations of the total motion resistance can be ignored. Hence, the total resistance  $R_t$  can be assumed to only contain the motion resistance of the vehicle due to terrain compaction  $R_c$ , inner resistance  $R_m$ , and the dragging motion resistance  $R_{drag}$ .

In a particular soil condition, the compaction resistance  $R_c$  in  $N$  is given by [12],

$$R_c = 2B \left( \frac{k_p z^2}{2} + \frac{4}{3D_{htc}} m_m z^3 \right) \quad (2)$$

In the above Eqs.,  $p'$  is the normal pressure of the vehicle in  $N/m^2$  and  $z$  is the sinkage in  $m$ ,  $m_m$  is the surface mat stiffness in  $N/m^3$ ,  $k_p$  is the underlying peat stiffness in  $N/m^3$ ,  $D_{htc}$  is the track hydraulic diameter in  $m$  when air cushion touches the ground,  $A_C$  is the air-cushion effective area,  $W$  is the total weight of the vehicle in  $N$ ,  $W_i$  is the weight supported by the two tracks (weight of driving system or weight supported by propulsion system) in  $N$ , and  $p'_o$  is the cushion pressure in  $N/m^2$ .

The motion resistance of the vehicle due to internal friction losses, deeply affected by the track and the speed of the vehicle,  $R_m$  in  $N$  is computed by [12]:

$$R_m = \left( \frac{W - W_{v(ac)}}{1000g} \right) [222 + 3v_i] \quad (3)$$

where  $v_i$  is the vehicle theoretical speed in  $m/s$ ,  $g$  is the gravitational acceleration in  $m/s^2$ ,  $W$  is the total weight of the vehicle in  $N$ , and  $W_{v(ac)}$  is the weight supported by the air-cushion in  $N$  and is equal to  $W_{v(ac)} = p'_o A_C$ .

The drag motion resistance  $R_{drag}$  of the air-cushion

system in N is calculated by [12],

$$R_{drag} = p'_0 A_C \tan \varphi \quad (4)$$

Depending on Eqns. 2-4, the total travelling resistance  $R_t$  in N is,

$$R_t = R_c + R_{in} + R_{drag} \quad (5)$$

### 3.2 Power Demand for Air-Cushion System

The power demand for air-cushion system  $P_c$  in W can be expressed by [1],

$$P_c = p'_0 Q = p'_0 h_c L_c D_c \left( \frac{2p'_0}{\rho} \right)^{\frac{1}{2}} \quad (6)$$

Where  $Q$  is the volume flow of air from compressor in  $m^3/s$ ,  $h_c$  is theoretical clearance height in m,  $L_c$  is the air-cushion perimeter in m,  $D_c$  is the discharge coefficient,  $\rho$  is the air density in  $kg/m^3$  and  $p'_0$  is the cushion pressure in  $N/m^2$ .

### 3.3 Power Demand for Propulsion System

The power demand for propulsion system  $P_d$  in W can be expressed by,

$$P_d = R_t v_t = \left[ 2B \left( \frac{k_p z^2}{2} + \frac{4}{3D_{htc}} m_m z^3 \right) + \left( \frac{W - W_{v(ac)}}{1000g} \right) [222 + 3v_t] \right] v_t + [p'_0 A_C \tan \varphi] v_t \quad (7)$$

Where  $R_t$  is the total travelling resistance in N,  $v_t$  is the vehicle theoretical speed in m/s,  $p'_0$  is the cushion pressure in  $N/m^2$ .

### 3.4 Total Power Consumption and Optimum State

Based on Eqns. (6) and (7), the total vehicle power requirement  $P$  is rewritten as below,

$$P = P_c + P_d \quad (8)$$

In Eq. (8),  $P_c$  is mainly used to fully or partially support main proportion weight of the vehicle body,  $P_d$  is to overcome the vehicle travelling resistance and to maintain the normal driving state. For a particular soil condition, the existence of an optimal load distribution ratio, which results in minimum total power consumption for the vehicle, could be determined. So for Eq. (8), taking partial derivative of  $P$  with respect to  $p'_0$  and having resultant equation equal to zero, i.e.

$$\frac{\partial P}{\partial p'_0} = 0 \quad (9)$$

The optimal cushion pressure  $p'_0$  can be calculated for given soil condition and vehicle speed.

## 4. CONTROLLER DESIGN

### 4.1 Structure of the Control System

Focusing on optimizing the total power consumption of the air-cushion track vehicle operating on some severe conditions, e.g., soft terrain, wet fields, swamp peat,

many research works have been carried out [17]. However, for most air-cushion vehicles, the air from the cushion chamber is exhausted and wasted. Based on the previous studies on tracked air-cushion vehicles, air from the cushion chamber is fed back to the air accumulator which will reduce the power consumption of the air compressor. The diagram of the air-cushion pressure control system is shown in Fig. 2. In the diagram, controller determines the valve of air-cushion pressure based on the height and determines the value of the air-cushion pressure using pressure sensor and compares with calculated cushion pressure. Finally it takes decision by opening or closing solenoid valve. Distribution of vehicle load is controlled by Fuzzy Logic controller and is actually done by maintaining the inside pressure of the cushion based on the optimum power consumption by the vehicle.

At any instant the sinkage is measured by the high precision (1 mm resolution) distance measuring sensor. Then optimum pressure is determined based on the developed optimum pressure – sinkage relation and the pressure in the cushion chamber is controlled by the Fuzzy controller by maintaining solenoid valve and continuously monitored by the pressure sensor attached with the cushion chamber.

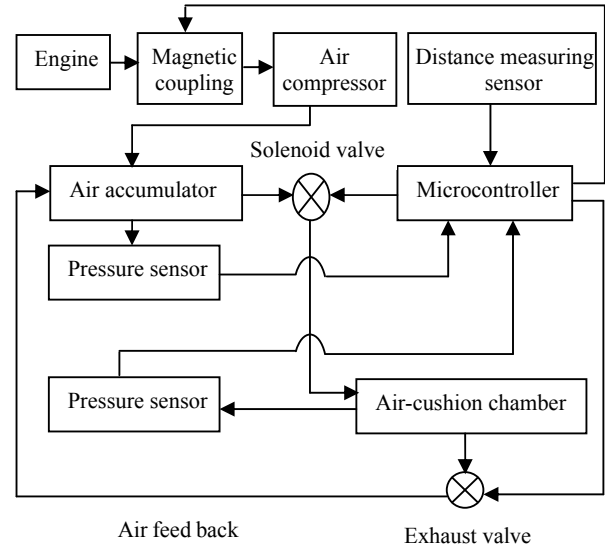


Fig 2. Control system diagram for air-cushion pressure.

### 4.2 Design of Fuzzy Logic Controller

There are a number of different techniques that would work here and therefore a design choice must be made. Some of the techniques require a relatively accurate model of the system in order to develop a satisfactory system. Fuzzy logic, on the other hand, does not require a model of the system. Instead, they rely on the knowledge of an expert for the particular system. Therefore, with all of this in mind, a Fuzzy Logic expert system is introduced for the prediction of total power consumption of the intelligent air cushion track vehicle. The main advantage of Fuzzy Logic is that it can be tuned and adapted if necessary, thus enhancing the degree of freedom of the system

[18]. For implementation of fuzzy values into the of ACTV by using Fuzzy expert system (FES), clearance height (CH) and cushion pressure (CP) were used as input parameters and total power consumption (PC) were used as output parameters. For fuzzification of these factors the linguistic variables very low (VL), low (L), medium (M), high (H), and very high (VH) were used for the inputs and output. The units of the used factors were: CH (m), CP (kPa), and PC (kW). With the fuzzy sets defined, it is possible to associate the fuzzy sets in the form of fuzzy rules. For the two inputs and one output, a fuzzy associated memory or decision (also called rule) table is developed as shown in Table 1.

Table 1: Rule base of fuzzy expert system.

Rules	Input variables		Output variable
	CH	CP	PC
Rule 1	VL	VL	VL
.....	.....	.....	.....
Rule 10	L	VH	H
.....	.....	.....	.....
Rule 15	M	VH	H
.....	.....	.....	.....
Rule 20	H	VH	M
.....	.....	.....	.....
Rule 25	VH	VH	M

The first block inside the fuzzy expert system (FES) is fuzzification, which converts each piece of input data to degrees of membership by a lookup in one or several membership functions. The fuzzification block thus matches the input data with the conditions of the rules to determine how well the condition of each rule matches that particular input instance. There is a degree of membership for each linguistic term that applies to that input variable. Fuzzifications of the used factors are made by aid follows functions. These formulas were determined by using measurement values.

$$CH(i_1) = \begin{cases} i_1; 0.01 \leq i_1 \leq 0.03 \\ 0; otherwise \end{cases} \quad (10)$$

$$CP(i_2) = \begin{cases} i_2; 0.5 \leq i_2 \leq 4 \\ 0; otherwise \end{cases} \quad (11)$$

$$PC(o_1) = \begin{cases} o_1; 2 \leq o_1 \leq 10 \\ 0; otherwise \end{cases} \quad (12)$$

Using MATLAB FUZZY Toolbox, prototype triangular fuzzy sets for the fuzzy variables, namely, clearance height (CH), cushion pressure (CP), and total power consumption (PC) are set up. The membership values used for the FES were obtained from above the formulas and are shown in the Fig. 3 (a), (b), and (c).

The determination of conclusion is taken when the rules that are applied to deciding what the power consumption to the plant (vehicle) should be. In defuzzification stage, truth degrees ( $\mu$ ) of the rules were determined for the each rule by aid of the min and then

by taking max between working rules.

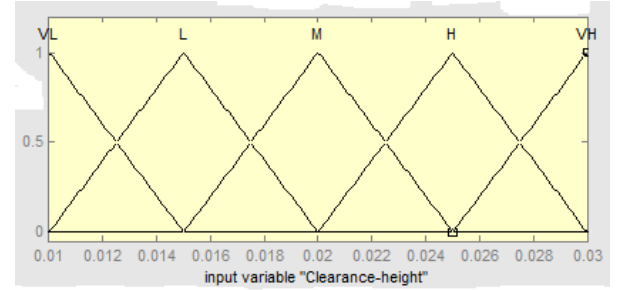


Fig 3 (a). Prototype membership functions for CH.

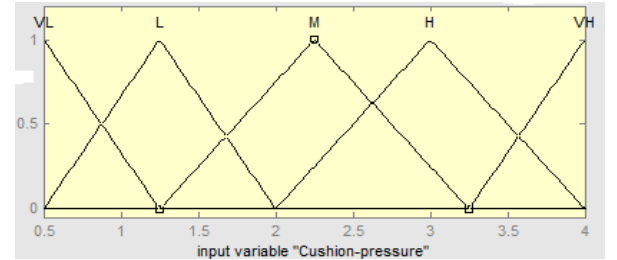


Fig 3 (b). Prototype membership functions for CP.

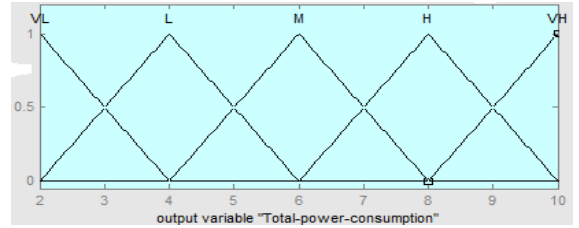


Fig 3 (c). Prototype membership functions for PC.

In this stage defuzzification operation is considered that is the final component of the fuzzy controller. Defuzzification operates on the implied fuzzy sets produced by the inference mechanism and combines their effects to provide the “most certain” controller output (plant input). Due to its popularity, the “center of gravity” (COG) defuzzification method is used for combing the recommendations from all the rules [15].

The output membership values are multiplied by their corresponding singleton values and then are divided by the sum of membership values.

$$output^{crisp} = \frac{\sum b_i \mu_i}{\sum \mu_i} \quad (20)$$

Where  $b_i$  is the position of the singleton in  $i$  the universe, and  $\mu_{(i)}$  is equal to the firing strength of truth values of rule  $i$ .

In addition, the predictive ability of developed system was investigated according to mathematical and statistical methods. In order to determine the relative error ( $\epsilon$ ) of system, the following equation was used:

$$\epsilon = \sum_{i=1}^n \left| \frac{y - \hat{y}}{y} \right| \frac{100\%}{n} \quad (13)$$

Where  $n$  is the number of observations,  $y$  is the

actual value, and  $\hat{y}$  is the predicted value. The relative error gives the deviation between the predicted and experimental values and it is required to reach zero. In addition, goodness of fit ( $\eta$ ) of predicted system was calculated by following equation:

$$\eta = \sqrt{1 - \frac{\sum_{i=1}^n (y - \hat{y})^2}{\sum_{i=1}^n (y - \bar{y})^2}} \quad (14)$$

Where  $\bar{y}$  is the mean of actual values. The goodness of fit also gives the ability of the developed system and its highest value is 1.

## 5. RESULTS AND DISCUSSIONS

### 5.1 Simulation Condition

To optimize the power consumption of HEACTV and some related physical and mechanical parameters about the HEACTV are shown in Table 2 and developed prototype is presented in Fig. 4 (photo). Steering of this vehicle was achieved by means of an individual switch of the DC motor with a power of 0.500 kW @ 2.94 Nm [8]. The dry weight of the vehicle was considered as 2.43 kN and it was designed mainly for operating a maximum load of 3.43 kN including a 1.00 kN payload over the swamp peat terrain. The total ground contact area of the vehicle was 1.052 m<sup>2</sup> including 0.544 m<sup>2</sup> of the air-cushion system. The vehicle was powered by a battery pack comprising eight (8) lead acid batteries, connected in parallel. The vehicle could travel 24 km powered of the single charging battery pack. A small IC Engine power of 2.5 kW @ 4000 rpm was installed on the vehicle to recharge the battery pack with the help of an alternator.

Table 2: Terrain and vehicle design parameters.

Parameters	Notations	Values	Units
Total vehicle load	$W$	3433.5	N
Length of track ground contact	$L_t$	1.00	m
Width of track ground contact	$B_t$	0.254	m
Length of the air-cushion,	$L_{ac}$	0.80	m
Width of the air-cushion	$B_{ac}$	0.68	m
Air cushion effective area	$A_C$	0.544	m <sup>2</sup>
Air cushion perimeter	$L_C$	2.96	m
Vehicle theoretical velocity	$v_t$	2.78	m/s
Air density	$\rho$	1.20	kg/m <sup>3</sup>
Surface mat stiffness	$m_m$	13590	N/m <sup>3</sup>
Underlying peat stiffness	$k_p$	171540	N/m <sup>3</sup>



Fig 4. Developed prototype of hybrid electrical air-cushion track vehicle [8].

### 5.2 Effect of Load Distribution on Total Power Consumption

The present study is focusing on load distribution (defined as the load transferred from the driving system to the air cushion system) for minimizing total power consumption. The effect of load distribution on the total power consumption for the hybrid electrical air-cushion tracked vehicle (HEACTV) are investigated.

Fig. 5 shows the relationship between load distribution ratio and total power consumption. From the Figure, it is observed that the load distribution ratio affects the total power consumption significantly as total power consumption linearly increases with the increase of load distribution ratio. The total power consumption is varied from 1.25 to 8.3 kW. Based on established theoretical model and the designed prototype, corresponding simulation and experimental results were carried out and an optimal load distribution ratio of 0.2 was obtained which could result in prediction of minimum power consumption of 3.5 kW and it was also supported by [8] for the vehicle loading condition of 3.43 kN.

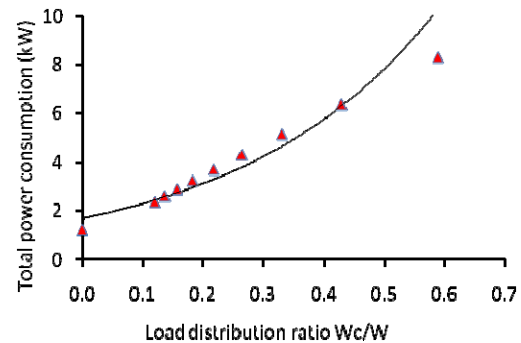


Fig 5. Effect of load distribution ratio on PC.

Fig. 6 shows the relationship between load distribution ratio and total power consumption for the actual and predicted (FES) values. For total power consumption, mean of actual and predicted values are 4.03 and 4.22 kW respectively. Furthermore, the correlation between actual and predicted values (from



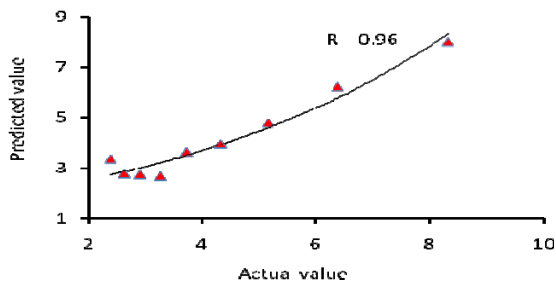


Fig 6. Correlation between actual and predicted values of total power consumption.

FES model) of total power consumption for different load distribution conditions also examined. The relationship is significant for all the parameters in different operating conditions. The correlation coefficient of total power consumption is found as 0.96. The mean relative error of actual and predicted value of total power consumption is found as 10.63 %. For the parameters tested and simulated, the relative error of predicted value is found to be equal to the acceptable limits (10%). The goodness of fit of prediction (from FES model) value of total power consumption is found as 0.97. The value is found to be close to 1.0 as expected.

## 6. Conclusion

This paper presents an adaptive approach based on the use of fuzzy logic for the prediction of total power consumption for the hybrid electrical air-cushion track vehicle in transportation efficiency and energy economy. In this study, according to evaluation criteria of predicted performances of developed fuzzy knowledge-based model was found to be valid. However, the conclusions drawn from this investigation are as follows:

- Load distribution could be controlled by taking cushion pressure as a control parameter using fuzzy logic controller.
- The developed model can be used as a reference for the full scale prototype which is being carried out.
- This system can be developed further by increasing the knowledge rules and by addition of Genetic-Fuzzy and Neuro-Fuzzy to the system.

## 7. REFERENCES

- Wong, J.Y. Theory of Ground Vehicles. 3<sup>rd</sup> Ed., New York, John Wiley & Sons, Inc., 2001.
- Bekker, M.G. Introduction to terrain-vehicle systems. The University of Michigan Press, Ann Arbor, MI., 1969.
- MacFarlane, I. C. 1969. *Muskeg Engineering Handbook*. University of Toronto Press, Toronto.
- Ataur, R., Azmi, Y., Zohadie, M., Ahmad, D and Ishak, W. Design and Development of a Segmented Rubber Tracked Vehicle for Sepang Peat Terrain in Malaysia. *Int. J. of Heavy Vehicle Systems*, Vol.12 (3), p.239-267, 2005.
- Bodin, A. Development of a tracked vehicle to study the influence of vehicle parameters on tractive performance in soft terrain. *Journal of Terramechanics*, 36, pp.167-181, 1999.

- Ooi, H.S. Design and development of peat prototype track type tractor. *MARDI*, Report no.184, 1996.
- Zhe Luo, Fan Yu, and Bing-Chong Chen. Design of a novel semi-tracked air-cushion vehicle for soft terrain. *In. J. of Vehicle Design*, Vol. 31, No. 1, pp. 112-123, 2003.
- A. Al-Anbuky, S. Bataineh, and S. Al-Aqtash. Power demand prediction using fuzzy logic. *Control Engineering Practice*, Vol. 3, No. 9, pp. 1291-1298, 1995.
- Ataur, R., A. K. M. Mohiuddin, Faris Ismail, and Altah Hossain. Development of hybrid electrical air-cushion tracked vehicle for swamp peat. *Journal of Terramechanics*, Vol.xxx, No.xxx, pp.xxx-xxx, 2009. Available online at [www.sciencedirect.com](http://www.sciencedirect.com).
- Ataur, R., Azmi, Y., Zohaide, B., Ahmad, D., and Wan, I. Mechanical properties in relation to mobility of Sepang peat terrain in Malaysia. *Journal of Terramechanics*, Vol.41, No.1, pp.25-40, 2004.
- Jamaluddin, B. J. Sarawak: Peat agricultural use. *Malaysian Agriculture Research and Development Institute (MARDI)*, pp. 1-12, 2002.
- Singh, H., Bahia, H.M., and Huat, B.B.K. Varying perspective on peat, it's occurrence in Sarawak and some geotechnical properties. Proceedings of Conference on Recent Advances in Soft Soil Engineering and Technology, Sarawak, Malaysia, 2-4 July, 2003.
- Ataur Rahman, Altah Hossain, A.K.M Mohiuddin, and Azmi Yahya. *Integrated Mechanics of Hybrid Electrical Air-Cushion Tracked Vehicle for Swamp Peat*. International Journal of Heavy Vehicle System (IJHVS), 2009, INDERSCIENCE (In Press).
- Sreenatha G. Anavatti, Jin Young Choi, and Pupin P. Wong. Design and implementation of fuzzy logic controller for wing rock. *International Journal of Control, Automation, and Systems*, Vol. 2, No. 4, pp. 494-500, 2004.
- K. Carman. Prediction of soil compaction under pneumatic tires a using fuzzy logic approach. *Journal of Terramechanics*, Vol.45, pp.103-108, 2008.
- Kevin M. Passino, and Stephen Yurkovich. Fuzzy control. Addison Wesley Longman, Inc. Menlo park, CA, USA, 1998.
- Zhe Luo, and Fan, Yu. Load distribution control system design for a semi-track air-cushion vehicle. *Journal of Terramechanics*, Vol. 44, No. 4, pp.319-325, 2007.
- A. Rajagopalan, G. Washington, G. Rizzani, and Y. Guezennec. Development of Fuzzy Logic and Neural Network Control and Advanced Emissions Modeling for Parallel Hybrid Vehicles, *Center for Automotive Research, Intelligent Structures and Systems Laboratory*, Ohio State University, USA, December 03

## 8. MAILING ADDRESS

Md. Altah Hossain  
Lecturer, Department of Mechanical Engineering,  
Faculty of Engineering, University Industry Selangor,  
45600 Selangor, Malaysia  
Phone: +6-03-3280 5122 (7187), Fax : +603-3280-6016  
E-mail: [altah75@unisel.edu.my](mailto:altah75@unisel.edu.my)

## NATURAL CONVECTION FLOW ALONG THE WAVY CONE IN CASE OF UNIFORM SURFACE HEAT FLUX WHERE VISCOSITY IS INVERSLY PROPORTIONAL TO TEMPERATURE

Azad Rahman<sup>1</sup>, Sharaban Thohura<sup>1</sup>, M.M.A. Sarker<sup>2</sup>, M. Mamun Molla<sup>3</sup>

<sup>1</sup>Department of Natural Science, Stamford University Bangladesh, Dhaka, Bangladesh

<sup>2</sup>Department of Mathematics, Bangladesh University of Engineering & Technology, Dhaka, Bangladesh

<sup>3</sup>Dept. of Mechanical & Manufacturing Engineering, University of Manitoba, Canada

### ABSTRACT

The effect of temperature dependent viscosity  $\mu(T)$ , on steady two dimensional natural convection flow along a vertical wavy cone with uniform surface heat flux has been investigated. Viscosity is considered to be inversely proportional to temperature. Using the appropriate variables the basic equations are transformed to non-dimensional boundary layer equations and then solved numerically employing implicit finite difference method. The effects viscosity variation parameter on the velocity profile, temperature profile, velocity vector field, skin friction, average Nusselt number, streamlines and isotherm have been discussed. The results have been shown graphically by utilizing the visualizing software Techplot. The present numerical result shows excellent agreement with the published results when the effect of temperature dependent viscosity was passed over.

**Keywords:** Natural convection, wavy cone, viscosity variation parameter

### 1. INTRODUCTION

Wavy surfaces are encountered in several heat transfer devices such as flat plate solar collectors and flat plate condensers in refrigerators. Larger scale surface non-uniformities are encountered, for example, in cavity wall insulating systems and grain storage containers, room heater etc. If the surface is wavy, the flow is disturbed by the surface and this alters the rate of heat transfer.

The only papers to date that study the effects of such non-uniformities on the vertical convective boundary layer flow of a Newtonian fluid are those of Yao [1], Moulic and Yao [2, 3]. Natural convection over a vertical wavy cone and frustum of a cone has been studied by Pop and Na [4, 5]. Cheng [6] have investigated natural convection heat and mass transfer near a vertical wavy cone with constant wall temperature and concentration in a porous medium. Hossain et al. [7, 8, 9] have studied the problem of natural convection flow along a vertical wavy cone and wavy surface with uniform surface temperature in presence of temperature dependent viscosity and thermal conductivity. Wang and Chen [10], have studied mixed convection boundary layer flow on inclined wavy plates including the magnetic field effect. Yao [11] has studied natural convection along a vertical complex wavy surface. Molla et al. [12] have studied natural convection flow along a vertical complex wavy surface with uniform heat flux.

In all of the above mentioned studies except Hossain et al. [7, 8, 9], the authors considered that the viscosity

of the fluids are constant in the flow regime. But the physical properties may change significantly with temperature. For instance, the viscosity of water decreases about 240% when the temperature increases from 10°C to 50°C. Ling and Dybbs [13] have considered the viscosity to vary inversely to a linear function of temperature. On the other hand, Chraudeau [14] has proposed a formula assuming the viscosity of the fluid to be proportional to a linear function of temperature. Hossain et al. [8, 15] investigated the natural convection flow past a permeable wedge and wavy cone for fluid having temperature dependent viscosity. In many application of practical importance, the surface temperature is non-uniform.

The case of uniform surface heat flux, which is often approximated in practical applications, has great importance in engineering applications. Very few of the aforementioned authors have studied natural convection flow for a surface which exhibits the uniform surface heat flux.

In the present study, the natural convection boundary layer flow along a vertical wavy cone with uniform heat flux has been considered. In addition the viscosity of the fluid is taken to be inversely proportional to the temperature. The formula proposed by Ling and Dybbs [13] is used to define the relationship between viscosity and temperature. The current problem is solved numerically by using Straightforward Finite Difference method (SFFD), reported by Yao [1, 2, 11]. Solutions are obtained for

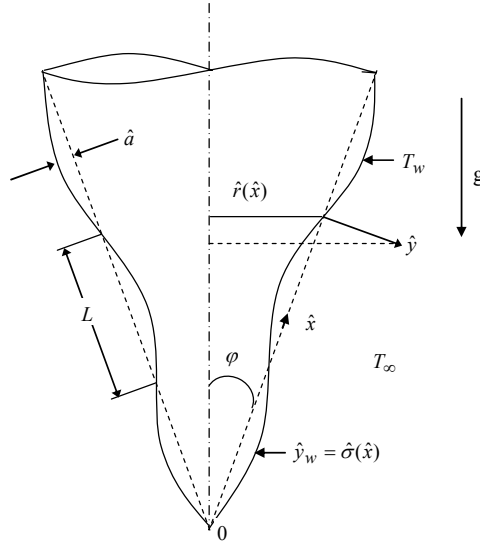


Figure 1: Physical model and the coordinate system

the fluid having Prandtl number  $Pr = 7.0$  (water) and with the different values viscosity variation parameter.

## 2. FORMULATION OF THE PROBLEM

The boundary layer analysis outlined below allows the shape of the wavy surface,  $\hat{\sigma}(\hat{x})$  to be arbitrary, but our detailed numerical work will assume that the surface exhibits sinusoidal deformations. Thus the wavy surface of the cone is described by

$$\hat{y}_w = \sigma(\hat{x}) = \hat{a} \sin(\pi \hat{x}/L) \quad (1)$$

where  $2L$  is the fundamental wavelength associated with wavy surface and  $\hat{a}$  is the amplitude of the waviness.

The physical model of the problem and the two-dimensional coordinate system are shown in Figure 1, where  $\varphi$  is the half angle of the flat surface of the cone and  $\hat{r}(\hat{x})$  is the local radius of the flat surface of the cone which is defined by

$$\hat{r} = \hat{x} \sin \varphi \quad (2)$$

Under the Boussinesq approximation, we consider the flow to be governed by the following equations:

$$\frac{\partial(\hat{r}\hat{u})}{\partial\hat{x}} + \frac{\partial(\hat{r}\hat{v})}{\partial\hat{y}} = 0 \quad (3)$$

$$\hat{u} \frac{\partial\hat{u}}{\partial\hat{x}} + \hat{v} \frac{\partial\hat{u}}{\partial\hat{y}} = -\frac{1}{\rho} \frac{\partial\hat{p}}{\partial\hat{x}} + \frac{1}{\rho} \bar{\nabla} \cdot (\mu \bar{\nabla} \hat{u}) + g\beta(T - T_\infty) \cos \varphi \quad (4)$$

$$\hat{u} \frac{\partial\hat{v}}{\partial\hat{x}} + \hat{v} \frac{\partial\hat{v}}{\partial\hat{y}} = -\frac{1}{\rho} \frac{\partial\hat{p}}{\partial\hat{y}} + \frac{1}{\rho} \bar{\nabla} \cdot (\mu \bar{\nabla} \hat{v}) + g\beta(T - T_\infty) \sin \varphi \quad (5)$$

$$\hat{u} \frac{\partial T}{\partial\hat{x}} + \hat{v} \frac{\partial T}{\partial\hat{y}} = \frac{k}{\rho C_p} \bar{\nabla}^2 T \quad (6)$$

where  $(\hat{x}, \hat{y})$  are the dimensional coordinates and  $(\hat{u}, \hat{v})$  are the velocity components parallel to  $(\hat{x}, \hat{y})$ . Also  $C_p$  is the specific heat at constant pressure and  $\mu$  is the temperature dependent viscosity of the fluid which is defined as a linear function of the temperature.

$$\mu = \mu_\infty [1 + \gamma(T - T_\infty)] \quad (7)$$

where  $\mu_\infty$  is the viscosity of ambient fluid outside the boundary layer and  $\gamma$  is a constant.

The boundary condition for the present problem is

$$\hat{u} = 0, \quad \hat{v} = 0, \quad q_w = -k(\hat{n} \cdot \bar{\nabla} \hat{T}) \text{ at } \hat{y} = \hat{y}_w = \sigma(\hat{x}) \quad (8a)$$

$$\hat{u} = 0, \quad T = T_\infty \text{ as } \hat{y} \rightarrow \infty \quad (8b)$$

where  $q_w$  is the uniform heat flux and  $\hat{n}$  is the unit vector normal to the wavy surface. Now the following non-dimensional variables are introduced to obtain a set of non-dimensional governing equation:

$$x = \frac{\hat{x}}{L}, \quad y = \frac{\hat{y} - \sigma(\hat{x})}{L} Gr^{1/5}, \quad r = \frac{\hat{r}}{L}, \quad a = \frac{\hat{a}}{L},$$

$$\sigma(x) = \frac{\sigma(\hat{x})}{L}, \quad \sigma_x = \frac{d\hat{\sigma}}{d\hat{x}} = \frac{d\sigma}{dx}, \quad p = \frac{L^2}{\rho \nu_\infty^2} Gr^{-4/5} \hat{p},$$

$$u = \frac{\rho L}{\mu_\infty} Gr^{-2/5} \hat{u}, \quad v = \frac{\rho L}{\mu_\infty} Gr^{-1/5} (\hat{v} - \sigma_x \hat{u}),$$

$$\theta = \frac{T - T_\infty}{(q_w L/k)} Gr^{1/5}, \quad Gr = \frac{g\beta q_w \cos \varphi}{k \nu_\infty^2} L^4 \quad (9)$$

where  $\theta$  is the dimensionless temperature function and  $\nu_\infty = \mu_\infty/\rho$  is the kinematic viscosity. Here the new coordinate system  $(x, y)$  are not orthogonal, but a regular rectangular computational grid can be easily fitted in the transformed coordinate. On introducing the above dimensionless dependent and independent variables into the equations (3)-(6) the following dimensionless form of the governing equations are obtained at leading order in the Grashof number,  $Gr$ :

$$\frac{\partial(ru)}{\partial x} + \frac{\partial(rv)}{\partial y} = 0 \quad (10)$$

$$u \frac{\partial u}{\partial x} + v \frac{\partial u}{\partial y} = -\frac{\partial p}{\partial x} + \sigma_x Gr^{1/5} \frac{\partial p}{\partial y} - \frac{\varepsilon}{(1 + \varepsilon \theta)^2} (1 + \sigma_x^2) \frac{\partial \theta}{\partial y} \frac{\partial u}{\partial y} + \frac{(1 + \sigma_x^2)}{(1 + \varepsilon \theta)} \frac{\partial^2 u}{\partial y^2} + \theta \quad (11)$$

$$\sigma_x \left( u \frac{\partial u}{\partial x} + v \frac{\partial u}{\partial y} \right) + \sigma_{xx} u^2 = -Gr^{1/5} \frac{\partial p}{\partial y} + \frac{\sigma_x (1 + \sigma_x^2)}{(1 + \varepsilon \theta)} \frac{\partial^2 u}{\partial y^2} - \frac{\varepsilon \sigma_x (1 + \sigma_x^2)}{(1 + \varepsilon \theta)^2} \frac{\partial \theta}{\partial y} \frac{\partial u}{\partial y} + \theta \tan \varphi \quad (12)$$

$$u \frac{\partial \theta}{\partial x} + v \frac{\partial \theta}{\partial y} = \frac{1}{Pr} (1 + \sigma_x^2) \frac{\partial^2 \theta}{\partial y^2} \quad (13)$$

where  $Pr = \frac{\mu_\infty C_p}{k}$ ,  $\mu = \mu_\infty [1/(1 + \varepsilon \theta)]$  and

$$\varepsilon = \gamma \frac{q_w L}{k} Gr^{-1/5} \quad (14)$$

Here  $\varepsilon$  is a parameter which controls the value of  $\gamma$  and hence the temperature dependent viscosity  $\mu$  as it is defined by equation (7) and (14).

It can easily be seen that the convection induced by the wavy surface is described by equations (10)-(13). Equation (12) represents that the pressure gradient along the  $x$  direction is in the order of  $Gr^{-1/5}$ . In the present problem this pressure gradient is zero because, no externally induced free stream exists. The elimination of  $\partial p / \partial y$  from equations (11) and (12) leads to

$$u \frac{\partial u}{\partial x} + v \frac{\partial u}{\partial y} = \frac{(1 + \sigma_x^2)}{(1 + \varepsilon \theta)} \frac{\partial^2 u}{\partial y^2} - \frac{\varepsilon (1 + \sigma_x^2)}{(1 + \varepsilon \theta)^2} \frac{\partial \theta}{\partial y} \frac{\partial u}{\partial y} - \frac{\sigma_x \sigma_{xx}}{1 + \sigma_x^2} u^2 + \frac{(1 + \sigma_x \tan \varphi)}{1 + \sigma_x^2} \theta \quad (15)$$

The corresponding boundary conditions for the present problem then turn into

$$\begin{aligned} u = 0, \quad v = 0, \quad \partial \theta / \partial y = -1 / \sqrt{1 + \sigma_x^2} \quad \text{at } y = 0 \\ u = 0, \quad \theta = 0 \quad \text{as } y \rightarrow \infty \end{aligned} \quad (16)$$

### 3. NUMERICAL METHODS

Investigating the present problem we have employed the straightforward finite difference method, which is described below. Firstly we introduce the following transformations to reduce the governing equation to a convenient form:

$$\begin{aligned} X = x, \quad Y = y / \left\{ (5x)^{1/5} \right\}, \quad R = r, \quad U(X, Y) = u / \left\{ (5x)^{3/5} \right\}, \\ V(X, Y) = (5x)^{1/5} v, \quad \Theta(X, Y) = \theta / \left\{ (5x)^{1/5} \right\} \end{aligned} \quad (17)$$

Introducing the transformations given in equation (17) into the equations (10), (15) and (13) we have,

$$8U + (5X) \frac{\partial U}{\partial X} - Y \frac{\partial U}{\partial Y} + \frac{\partial V}{\partial Y} = 0 \quad (18)$$

$$\begin{aligned} (5X)U \frac{\partial U}{\partial X} + (V - YU) \cdot \frac{\partial U}{\partial Y} + \left\{ 3 + \frac{\sigma_x \sigma_{xx}}{1 + \sigma_x^2} (5X) \right\} U^2 = \\ \frac{(1 + \sigma_x^2)}{\left\{ 1 + \varepsilon (5X)^{1/5} \Theta \right\}} \frac{\partial^2 U}{\partial Y^2} + \frac{(1 + \sigma_x \tan \varphi)}{1 + \sigma_x^2} \Theta - \\ \frac{\varepsilon (1 + \sigma_x^2)}{\left\{ 1 + \varepsilon (5X)^{1/5} \Theta \right\}^2} (5X)^{1/5} \frac{\partial \Theta}{\partial Y} \frac{\partial U}{\partial Y} \end{aligned} \quad (19)$$

$$5XU \frac{\partial \Theta}{\partial X} + (V - YU) \frac{\partial \Theta}{\partial Y} + U\Theta = \frac{1}{Pr} (1 + \sigma_x^2) \frac{\partial^2 \Theta}{\partial Y^2} \quad (20)$$

The boundary conditions now take the following form:

$$U = 0, \quad V = 0, \quad \frac{\partial \Theta}{\partial Y} = -1 / \sqrt{1 + \sigma_x^2} \quad \text{at } Y = 0$$

$$U = 0, \quad \Theta = 0 \quad \text{as } Y \rightarrow \infty \quad (21)$$

Solutions of the non-dimensional partial differential system given by (18)-(20) and subject to the boundary conditions (21) are obtained by using the straightforward finite difference method developed by L.S. Yao [1, 2, 11]. However, once we know the values of the function  $U$ ,  $V$  and  $\Theta$  and their derivatives, it is important to calculate the values of the average Nusselt number,  $Nu_m$  from the following relation which is obtained by using the set of transformations:

$$Nu_m (5/Gr)^{1/5} = \frac{X^{1/5} \int_0^X \sqrt{1 + \sigma_x^2} dX}{\int_0^X \sqrt{1 + \sigma_x^2} X^{1/5} \Theta(X, 0) dX} \quad (22)$$

Also the skin friction coefficients is defined as

$$C_{f_x} (Gr)^{1/5} / 2(5X)^{2/5} = \left[ \frac{\sqrt{1 + \sigma_x^2}}{\left\{ 1 + \varepsilon (5X)^{1/5} \Theta \right\}} \frac{\partial U}{\partial Y} \right]_{Y=0} \quad (23)$$

The stream function for the wavy cone is defined as

$$u = \frac{1}{r} \frac{\partial \psi}{\partial y} \quad \text{and} \quad v = -\frac{1}{r} \frac{\partial \psi}{\partial x} \quad (24)$$

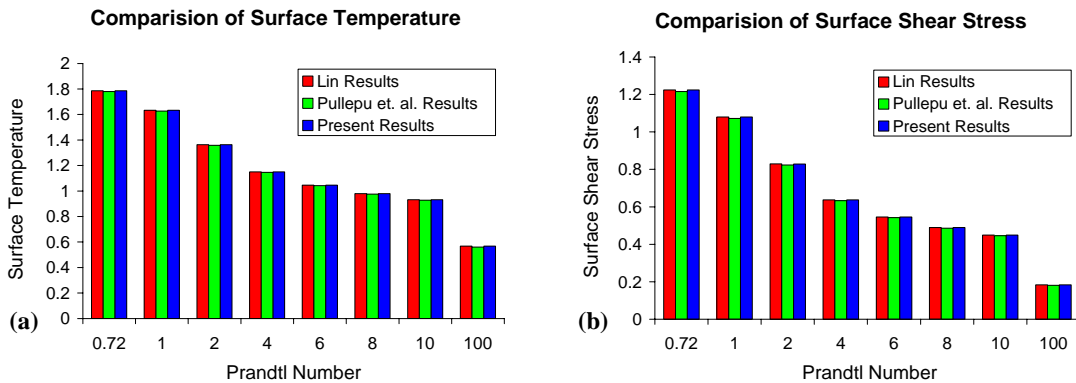


Figure 2: Comparison of present results on a) Surface temperature and b) Surface shear stress with Lin and Pullepu et. al. results

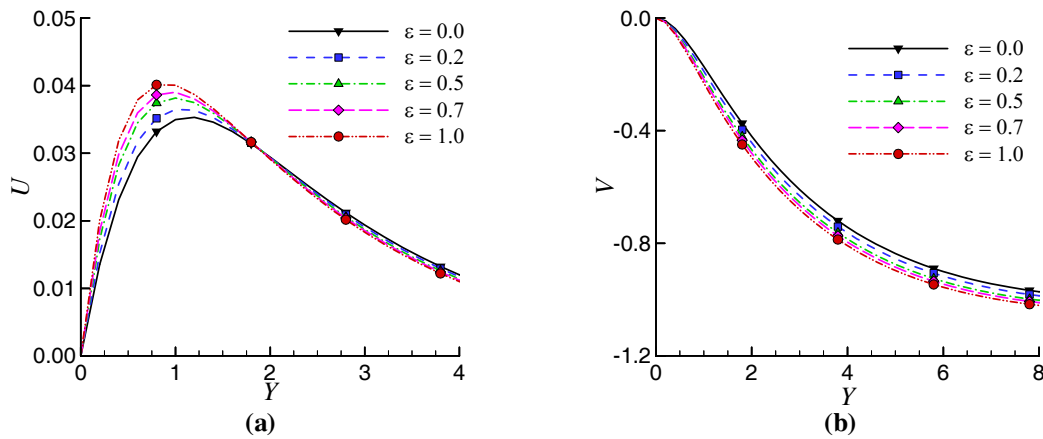


Figure 3: (a) Tangential velocity distribution and (b) Normal velocity distribution at  $X=1.0$  for Prandtl number  $Pr = 7.0$ ,  $a = 0.3$  and  $\phi = 30^\circ$ .

For calculating the stream function  $\psi$ , we have integrated the fluid velocity over the whole boundary layer, which may be defined as

$$\psi = \int_0^Y R(5X)^{3/5} U dY, \text{ where } R = X \sin \phi \quad (25)$$

#### 4. RESULTS AND DISCUSSION

In this paper, the effect of temperature dependent viscosity on a steady two-dimensional natural convection laminar flow of viscous incompressible fluid along a vertical wavy cone has been investigated by using very efficient finite difference method. It is seen that the solutions are affected by the viscosity variation parameter as well as the amplitude of the cone. Here we have focused our attention on the effect of  $\epsilon$  on the average Nusselt number  $Nu_m(5/Gr)^{1/5}$ , skin friction  $C_{fx}$  as well as velocity and temperature distribution. We also show the graphical representation of velocity vectors, stream lines and isotherms of the flow field.

In order to validate the present numerical results, the skin friction coefficient and the surface temperature have been compared with those of Lin [16] and Pullepu et. al. [17]. The present comparison is done for the flat

vertical cone with uniform surface heat flux case. Lin [16] has studied the free convection from a vertical cone with uniform surface heat flux case. On the other hand, Pullepu et al. [17] have studied unsteady laminar free convection from a vertical cone with uniform heat flux case. The comparative studies are illustrated graphically in fig. 2 which shows that the present results have excellent agreement with those results when the effect of viscosity variation parameter was passed over.

The numerical results are presented for the different values of viscosity variation parameter  $\epsilon$  for a suitable fluid having Prandtl number  $Pr = 7.0$  (water). To examine the effect of  $\epsilon$  we also considered that  $a = 0.3$  and  $\phi=30^\circ$  remain constant. Figure 3 (a), (b) represents the non-dimensional tangential and normal velocity distribution for different values of  $\epsilon$  at a fixed point  $X = 1.0$ . It is found that the increasing value of  $\epsilon$  increase the tangential velocity inside the boundary layer slightly. The thickness of the boundary layer remains same as  $\epsilon$  increases. Figure 3(b) shows that the normal velocity decreases slightly when  $\epsilon$  increases.

Fluid temperature distribution at a fixed point  $X = 1.0$  and surface temperature distribution for different values of  $\epsilon$  are shown in fig 4(a) and 4(b) respectively.

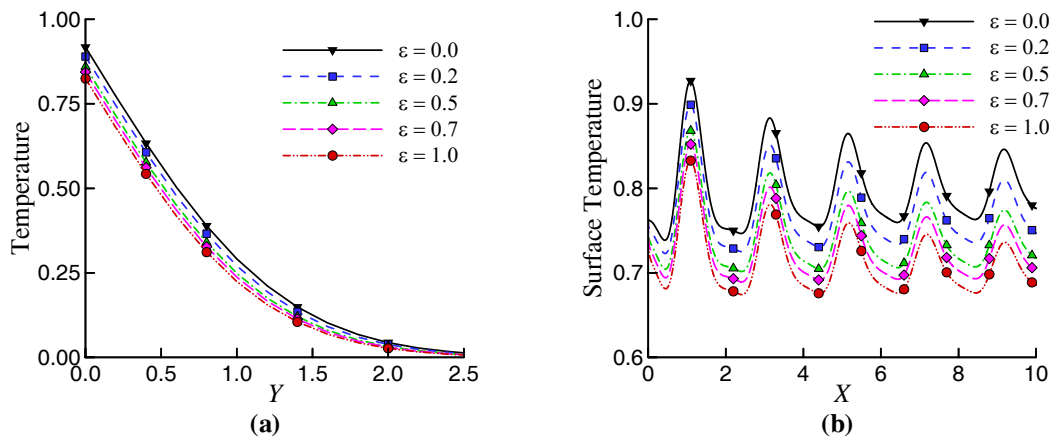


Figure 4: (a) Fluid temperature distribution at  $X=1.0$  and (b) Surface Temperature distribution for  $Pr = 7.0$ ,  $a = 0.3$  and  $\phi = 30^\circ$ .

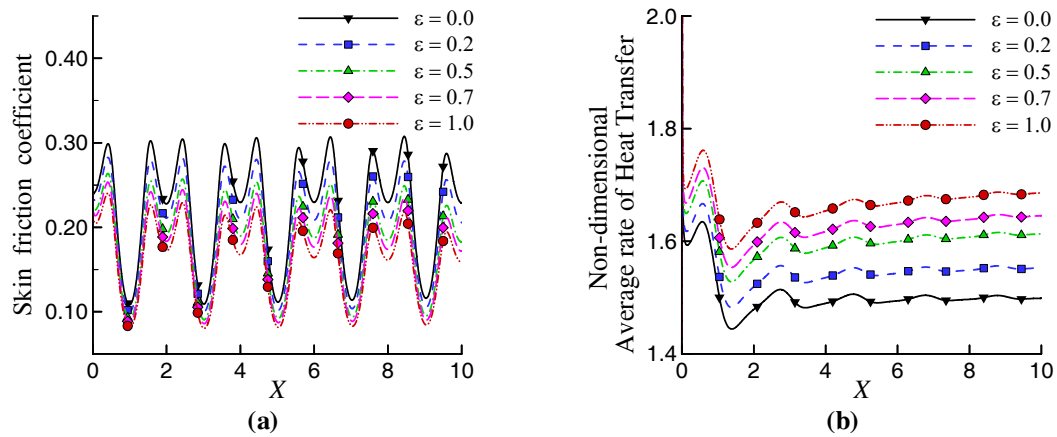


Figure 5: (a) Skin friction coefficient and (b) Average rate of heat transfer for  $Pr = 7.0$ ,  $a = 0.3$  and  $\varphi = 30^\circ$

From the figure it is evident that the temperature distribution inside the boundary layer at any fixed point decreases slightly when  $\varepsilon$  increases. The surface temperature decreases significantly due to the increasing value of  $\varepsilon$  and the surface temperature is found to fluctuate along the wavy surface.

The effect of  $\varepsilon$  on the surface shear stress in terms of skin friction coefficient and on the average rate of heat transfer in terms of average Nusselt number are given in the fig 5(a) and 5(b) respectively. The skin friction decreases faintly with the increase of viscosity variation parameter. While the average rate of heat transfer increases significantly for higher value of  $\varepsilon$ .

Figure 6(a)-(c) show the isotherm for a wavy cone, while the viscosity variation parameter  $\varepsilon$  is taken as 0.0, 0.5 and 1.0 respectively. The figures indicate that the increases of  $\varepsilon$  affect the isotherm and leads to the thinner thermal boundary layer.

#### 4. CONCLUSIONS

The effect of viscosity variation parameter  $\varepsilon$ , on the natural convection boundary layer flow along a vertical wavy surface with uniform heat flux, has been studied numerically. New variables transform the complex

geometry into a simple shape where a very efficient straightforward finite difference (SFFD) method was used to solve the non-dimensional boundary layer equations. From the present investigation the result can be summarized as follows:

- The skin friction decreases within the computational domain for increasing value of the viscosity variation parameter  $\varepsilon$ .
- The average rate of heat transfer enhance significantly with the increases of  $\varepsilon$ .
- Tangential velocity increase slightly with the increasing value of viscosity variation parameter  $\varepsilon$ .
- It was found that the temperature inside the boundary layer at any fixed point decreases slightly when  $\varepsilon$  increases.
- One important finding is that, the increases of  $\varepsilon$  affect the isotherm and leads to the thinner thermal boundary layer.

#### 5. REFERENCES

1. Yao, L. S., 1983, Natural convection along a vertical wavy surface, ASME J. Heat Transfer vol. 105, pp. 465–468.

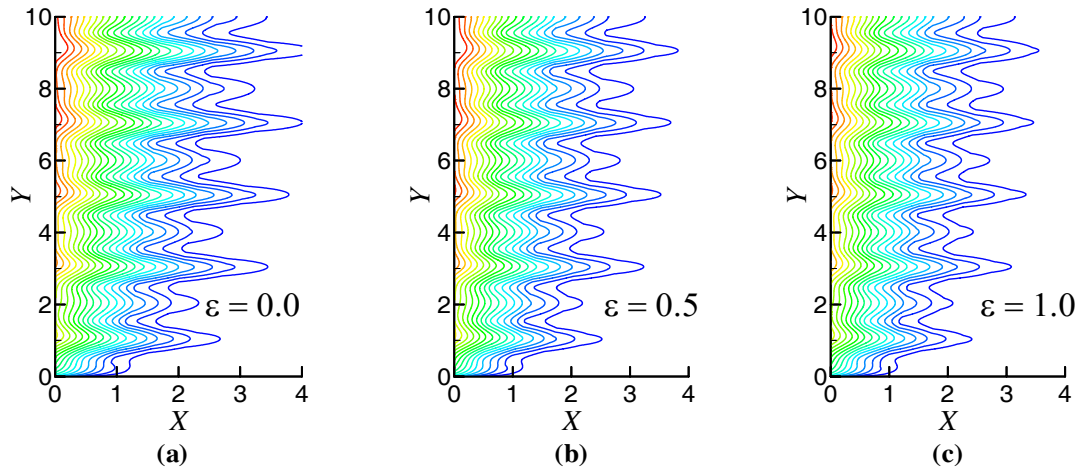


Figure 6: Isotherm for different values of  $\varepsilon$  for a wavy cone with  $a = 0.3$ ,  $\varphi = 30^\circ$  and  $Pr = 7.0$ .

2. Moulic, S. G. and Yao, L. S., 1989, Natural convection along a wavy surface with uniform heat flux, ASME J. Heat Transfer vol.111, pp. 1106–1108.
3. Moulic, S. G. and Yao, L. S., 1989, Mixed convection along wavy surface, ASME J. Heat Transfer vol. 111, pp. 974–979.
4. Pop, I. and Na, T. Y., 1995, Natural convection from a wavy cone, applied Scin. Res. vol. 54, pp. 125–136.
5. Pop, I. and Na, T. Y., 1999, Natural convection over a vertical wavy frustum of a cone, Int. J. Non-Linear Mech. vol. 34, pp. 925–934.
6. Cheng, C. Y., 2000, Natural convection heat and mass transfer near a vertical wavy cone with constant wall temperature and concentration in a porous medium, Mech. Res. Commun., vol. 27, pp. 613–620.
7. Hossain, M. A., Munir, M. S. and Pop, I., 2001, Natural convection flow of viscous fluid with viscosity inversely proportional to linear function of temperature from a vertical cone, Int. J. Therm. Sci. vol. 40, pp. 366–37.
8. Hossain, M. A., Munir, M. S. and Pop, I., 2001, Natural convection of a viscous fluid with variable viscosity and thermal conductivity from a vertical wavy cone, Int. J. Therm. Sci., vol. 40, pp. 437–443.
9. Hossain, M. A., Kabir, S. and Rees, D. A. S., 2002, Natural convection of fluid with temperature dependent viscosity from heated vertical wavy surface, ZAMP 53, pp. 48–52.
10. Wang, C. C., and Chen, C. K., 2005, Mixed convection boundary layer flow on inclined wavy plates including the magnetic field effect, Int. J. Therm. Sci., vol. 44, pp. 577–586.
11. Yao, L. S., 2006, Natural convection along a vertical complex wavy surface, Int. J. Heat Mass Transfer, vol. 49, pp.281–286.
12. Molla, M. M., Hossain, M. A. and Yao, L. S., 2007, Natural convection flow along a vertical complex wavy surface with uniform heat flux, ASME J. Heat Transfer vol. 129 (10), pp. 1403-1407.
13. Ling, J. X. and Dybbs, A., 1987, Forced convection over a flat plate submersed in a porous medium: variable viscosity case, Paper 87 -WA/HT-23, ASME, New York.
14. Chhrraudeau, J., 1975, Influence de gradients de proprietes physiques en convection force application au cas du tube, Int. J. Heat Mass Tran. vol. 18, pp 87–95.
15. Hossain, M. A., Munir, M. S. and Rees, D. A. S., 2000, Flow of viscous incompressible fluid with temperature dependent viscosity and thermal conductivity past a permeable wedge with uniform surface heat flux, Int. J. Therm. Sci., vol. 39, pp. 635–644.
16. Lin, F. N., 1976, Laminar convection from a vertical cone with uniform surface heat flux, Letters in Heat and Mass Transfer, vol. 3, pp. 49-58.
17. Pullepu, B., Ekambavanan, K., Chamkha, A. J., 2008, Unsteady laminar free convection from a vertical cone with uniform surface heat flux,

Nonlinear Analysis: Modeling & Control, vol. 13(1), pp. 47-60.

## 6. NOMENCLATURE

Symbol	Meaning	Units
$a$	Amplitude wavelength ratio	(- -)
$\hat{a}$	Amplitude of the wavy cone	(m)
$C_p$	Specific heat at constant pressure	( $m^2 \cdot s^{-2} \cdot K^{-1}$ )
$C_f$	Skin friction coefficient	(- -)
$g$	Acceleration due to gravity	( $m \cdot s^{-2}$ )
$Gr$	Grashof number	(- -)
$k$	Thermal conductivity	( $m \cdot kg \cdot s^{-3} \cdot K^{-1}$ )
$L$	Half of the fundamental wavelength	(m)
$\hat{n}$	Unit vector normal to the wavy surface	(- -)
$Nu_m$	Average Nusselt number	(- -)
$p$	Dimensionless pressure function	(- -)
$Pr$	Prandtl number	(- -)
$q_w$	Uniform heat flux at the surface	( $kg \cdot s^{-3}$ )
$\hat{r}(\hat{x})$	Local radius of the of the cone	(m)
$r, R$	Dimensionless radius of the cone	(- -)
$T$	Temperature in the boundary layer	(K)
$(\hat{u}, \hat{v})$	Velocity component along $\hat{x}$ and $\hat{y}$	( $m \cdot s^{-1}$ )
<b>Greek symbols</b>		
$\beta$	Volumetric coefficient of thermal expansion	( $K^{-1}$ )
$\varepsilon$	Viscosity variation parameter	(- -)
$\theta, \Theta$	Dimensionless temperature function	(- -)
$\mu$	Viscosity of the fluid	( $m^{-1} \cdot kg \cdot s^{-1}$ )
$\mu_\infty$	Dynamic viscosity of the ambient fluid	( $m^{-1} \cdot kg \cdot s^{-1}$ )
$\nu_\infty$	Reference kinematic viscosity	( $m^2 \cdot s^{-1}$ )
$\rho$	Density of the fluid	( $m^{-3} \cdot kg$ )
$\sigma(x)$	Non-dimensional surface profile function	(- -)
$\hat{\sigma}$	Surface profile function	(m)
$\tau_w$	Shearing stress	( $m^{-1} \cdot kg \cdot s^{-2}$ )
$\varphi$	The half angle of the cone	( $^{\circ}$ )
$\psi$	Stream function	(- -)
<b>Subscript</b>		
$w$	Wall conditions	
$\infty$	Ambient temperature	
$m$	Average condition	
$x$	Differentiation with respect to $x$	



## MIXED CONVECTION ANALYSIS IN A LID DRIVEN TRAPEZOIDAL CAVITY WITH ISOTHERMAL HEATING AT BOTTOM FOR VARIOUS ASPECT ANGLES

Md. N. H. Khan Chowdhury<sup>1</sup>, Sumon Saha<sup>2</sup> and Md. A. Hasan Mamun<sup>1</sup>

<sup>1</sup>Department of Mechanical Engineering, Bangladesh University of Engineering and Technology (BUET), Dhaka, Bangladesh

<sup>2</sup>Department of Mechanical Engineering, The University of Melbourne, Victoria , Australia

### ABSTRACT

Mixed convection heat transfer in a two-dimensional trapezoidal cavity has been investigated with a locally heated lower wall and moving cold top lid. The enclosure represents a practical system where the space requirement is very important factor for efficient electronic cooling system. The numerical study is conducted for several values of aspect angle of the cavity and a range of Richardson numbers with constant Reynolds and Prandtl numbers. The influence of Richardson number on average Nusselt number is investigated for various aspect angles. Results are represented in the form of isotherms and streamlines under different conditions. The solution procedure is conducted using the Galerkin finite element method.

**Keywords:** Mixed Convection, Richardson Number, Aspect Angle, Finite Element Method

### 1. INTRODUCTION

Air cooling is one of the preferred methods for cooling various electrical equipments as well as in some critical places of engineering plants where cooling is very essential for better performance. This study focuses especially on mixed convection heat transfer, which is being used for cooling different devices through worldwide. Various studies and researches are still carried out to make this cutting edge field more advanced as well as developed.

Mixed convection, in which, neither natural convection nor forced convection is dominant but both modes of convection heat transfer are in a balance condition that arises in many technological processes (Incropera, 1988). Various works have already been done on mixed convection heat transfer, where almost all of them are handled with vented cavity and very few considered enclosures having one or two walls are moving. Davis and Jones (1983) studied the pure natural convection with uniformly heated walls. Papaniclaou and Jaluria (1990, 1992, 1993 and 1994) carried out a series of numerical studies to investigate the combined forced and natural convective cooling of heat-dissipating electronic components, located in rectangular enclosure and cooled by an external through flow of air. The results indicated that flow patterns generally consisted of high-or low-velocity recirculating cells because of buoyancy forces induced by

the heat source. Computations for turbulent flow in mixed convection in a cavity by  $k-\omega$  model were later performed by Papaniclaou and Jaluria (1995). Numerical solutions were obtained for  $Re = 1000$  and  $2000$  in the range of  $Gr = 5 \times 10^7$  to  $5 \times 10^8$ . Iwatsu et al. (1992) performed numerical studies for the flow of a viscous, thermally stratified fluid in a square container. Shaw (1993) investigated three-dimensional mixed convection heat transfer in a cavity heated from below. The influences of Reynolds number and Grashof number on the Nusselt number had been discussed extensively. Aydin and Yang (2000) numerically studied mixed convection heat transfer in a two-dimensional square cavity having an aspect ratio of 1.

The physical model has shown in Fig. 1 along with boundary conditions. It consists of base length ( $W$ ), height ( $H$ ) and an aspect angle ( $\phi$ ) between the side walls with the vertical axis. In this study, the bottom wall is heated at a uniform temperature ( $T_h$ ) whereas the upper wall is lid driven maintained at a lower temperature ( $T_c$ ) and constant velocity,  $u_0$  in right-ward (+x) direction and side walls are kept adiabatic. The flow is induced by the combined effect of shear force raised by moving top lid and buoyancy force by the hot bottom wall. The main objective of this study is to observe the flow situation as well as the mixed convection heat transfer characteristics due to the change of aspect angle of the enclosure.

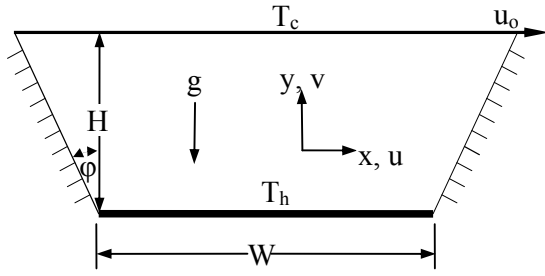


Fig 1. Schematic of the problem with the domain and boundary conditions

## 2. MATHEMATICAL EQUATIONS

The non-dimensional Navier-Stokes equations along with energy equation for two-dimensional, incompressible, steady flow with constant properties and considering the Boussinesq approximation in Cartesian co-ordinates can be written as follows:

$$\frac{\partial U}{\partial X} + \frac{\partial V}{\partial Y} = 0 \quad (1)$$

$$U \frac{\partial U}{\partial X} + V \frac{\partial U}{\partial Y} = -\frac{\partial P}{\partial X} + \frac{1}{Re} \left( \frac{\partial^2 U}{\partial X^2} + \frac{\partial^2 U}{\partial Y^2} \right) \quad (2)$$

$$U \frac{\partial V}{\partial X} + V \frac{\partial V}{\partial Y} = -\frac{\partial P}{\partial Y} + \frac{1}{Re} \left( \frac{\partial^2 V}{\partial X^2} + \frac{\partial^2 V}{\partial Y^2} \right) + Ri\Theta \quad (3)$$

$$U \frac{\partial \Theta}{\partial X} + V \frac{\partial \Theta}{\partial Y} = \frac{1}{Re Pr} \left( \frac{\partial^2 \Theta}{\partial X^2} + \frac{\partial^2 \Theta}{\partial Y^2} \right) \quad (4)$$

Equations (1-4) are normalized using the following dimensionless scales:

$$(X, Y) = \frac{(x, y)}{W}, (U, V) = \frac{(u, v)}{u_0}, P = \frac{p}{\rho u_0^2}, \Theta = \frac{T - T_c}{T_h - T_c}$$

The Grashof number (Gr), Prandtl number (Pr), Reynolds number (Re), and the Richardson number (Ri) are given by

$$Gr = \frac{g\beta(T_h - T_c)W^3}{\nu^2}, Pr = \frac{\nu}{\alpha}, Re = \frac{u_0 W}{\nu}, Ri = \frac{Gr}{Re^2}$$

where  $\alpha$ ,  $\beta$ ,  $\rho$  and  $\nu$  are thermal diffusivity, thermal expansion coefficient, fluid density and kinematic viscosity respectively. The average Nusselt number of the heated wall is calculated as

$$Nu = \int_0^1 -\left( \frac{\partial \Theta}{\partial Y} \right) \Big|_{Y=0} dX \quad (5)$$

## 3. COMPUTATIONAL PROCEDURE

A finite element formulation based on the Galerkin method (Reddy, 1993) is employed to solve the governing equations subject to the boundary conditions for the present study. In the current investigation, triangular elements are utilized to discretize the physical domain. A variable grid-size system is generated in the present investigation to capture the rapid changes in the dependent variables. To ensure convergence of the numerical algorithm the following criteria is applied to all dependent variables over the solution domain

$$\sum |\phi_{ij}^m - \phi_{ij}^{m-1}| \leq 10^{-5} \quad (6)$$

where  $\phi$  represents a dependent variable  $U$ ,  $V$ ,  $P$ , and  $\theta$ , the indexes  $i, j$  indicate a grid point, and the index  $m$  is the current iteration at the grid level. To meet the higher accuracy, a grid refinement study is performed for aspect angle,  $\phi = 45^\circ$  and  $Ri = 1$ . Table 1 shows the accuracy of the average Nusselt number which is become independent of mesh size after 5966 elements.

Table 1: Comparison of the results for various grid dimensions ( $Ri = 1$  and  $\phi = 45^\circ$ )

Elements	$Nu$
2846	4.278
3430	4.285
4958	4.296
5966	4.305
7712	4.305
9008	4.305

## 4. RESULTS AND DISCUSSION

In this computation, the working fluid is chosen as air with Prandtl number,  $Pr = 0.71$ . For aspect angle  $\phi = 0^\circ, 15^\circ, 30^\circ$  and  $45^\circ$ , the computations are performed at  $Ri$  from 0.1 to 10 keeping the Reynolds number ( $Re$ ) and the aspect ratio of the enclosure ( $H/W$ ) fixed at 100 and 1, respectively.

### 4.1 Effect of Richardson Number on the Flow and Heat Transfer

Streamlines for  $\phi = 0^\circ$  shown in Fig. 2 indicate that one large vortex is created rotating in the clockwise direction. It shows that heat is carried out along with the motion of the moving upper wall and the intensity of the flow is increased at the middle region of the cavity with the help of increased buoyancy forces for higher Richardson number. Flow starts from the upper moving wall to the right and it goes downward until the lower region is reached. As soon as it reaches the lower region, it starts to move in the left direction and turns to the upper region as it reaches the left corner of the bottom wall. The flow along the upper and the bottom walls is different for different Richardson number, especially at the lower right corner. And for  $Ri = 1$  and 5, the streamlines are almost same. The difference is that the small vortex at the lower right end increases with the increase in Richardson number which helps the more heat transfer rapidly. Also it is observed that the center of the main large vortex is shifted towards the center of the cavity.

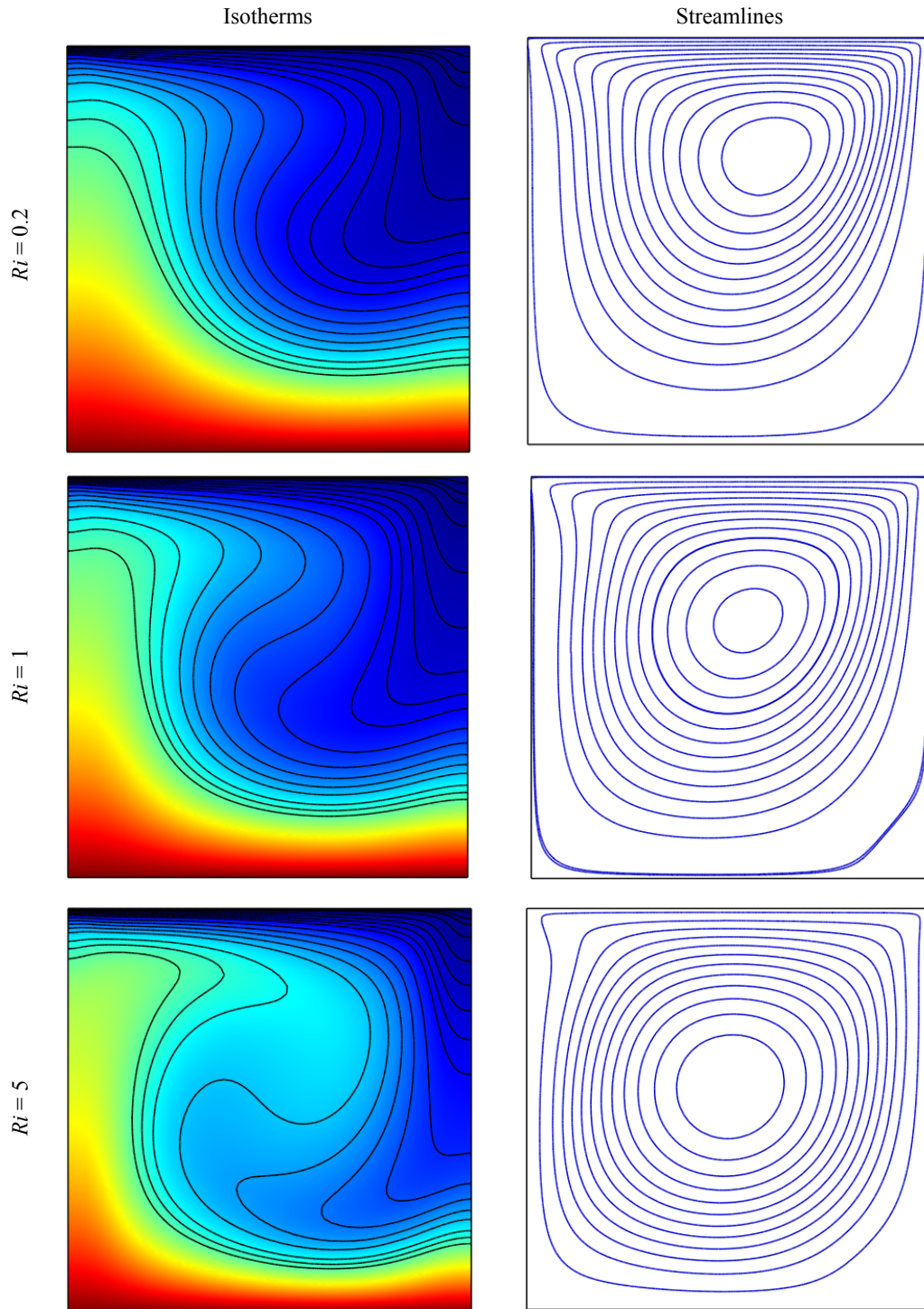


Fig 2. Effect of Richardson number on isotherm and streamline patterns for  $\phi = 0^\circ$ .

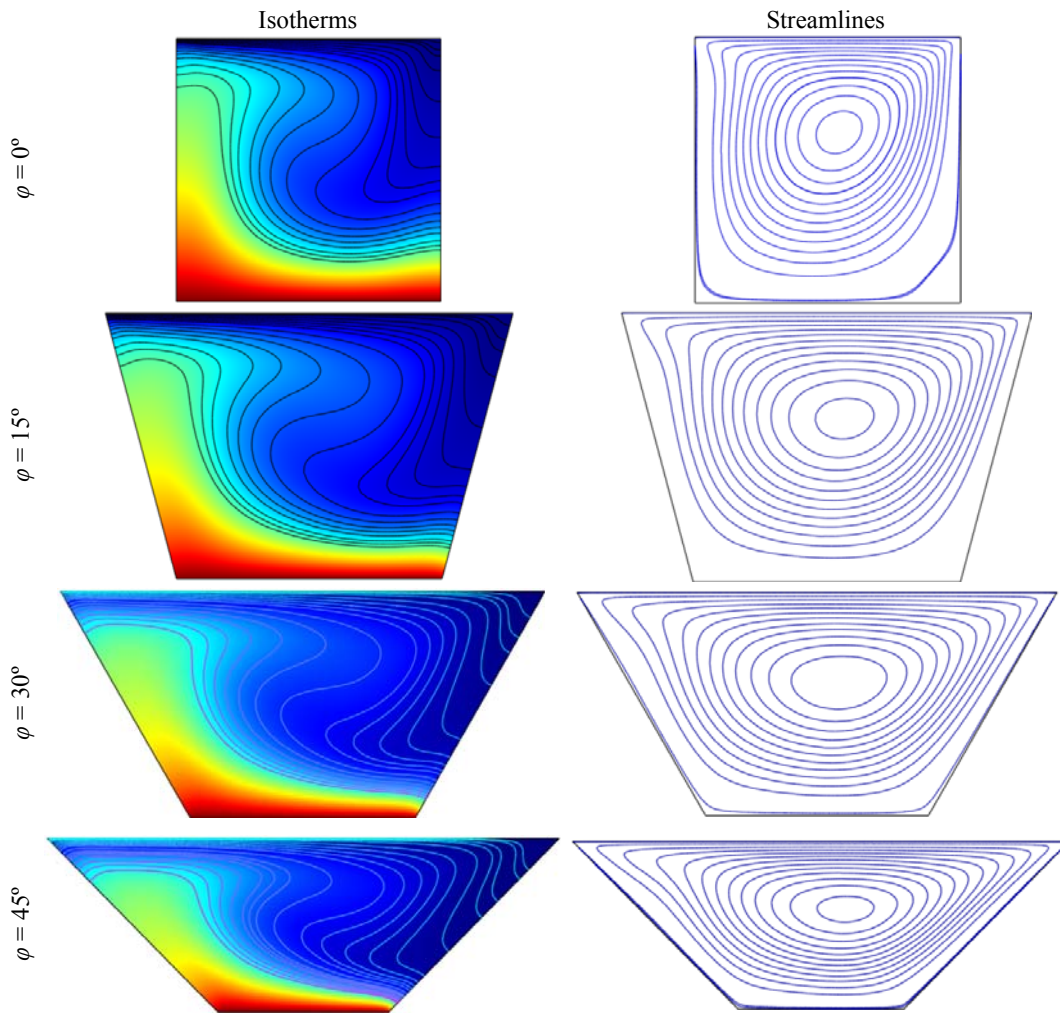


Fig 3. Effect of aspect angle on isotherm and streamline patterns for  $Ri = 1$ .

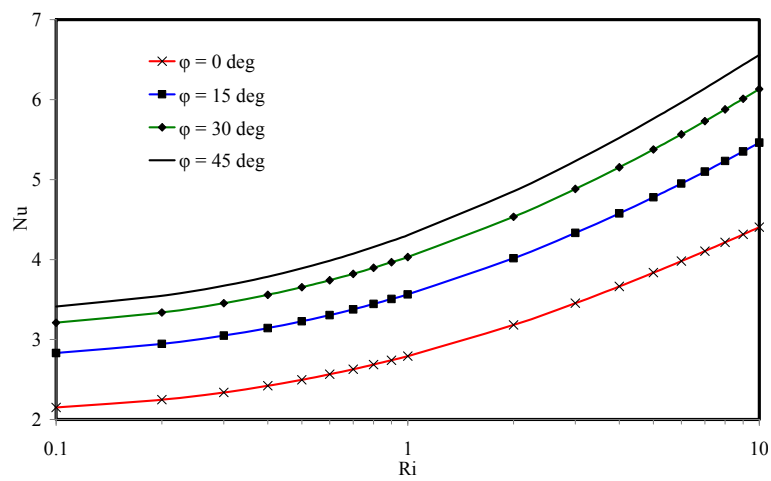


Fig 4. Variation of average Nusselt number as a function of Richardson number for different aspect angles.

Some significant changes in the isotherms are also observed for the different values of the Richardson number (Ri) in Fig. 2. The isotherms also reveal the similar scenario of the heat transfer characteristic within the cavity. The isotherms get stronger near the hot wall with the increasing value of the Richardson number (Ri). The isotherms are at first more uniform in nature. With the increase of Richardson number (Ri), the non-linearity of the isotherms increases at a higher value resulting the higher plume formation and a distorted plume is formed indicating better convective heat transfer for Ri = 5. When Ri = 1, the buoyancy and shear effects are in comparable level and with the further increase of Ri leads to dominant natural convection over mixed convection. However, for lower Ri, where dominant forced convection existed, shows less heat transfer as evident in Fig. 4.

#### 4.2 Effect of Aspect Angle on the Flow and Heat Transfer

The streamlines and isotherms are shown for the aspect angle,  $\phi = 0^\circ, 15^\circ, 30^\circ$  and  $45^\circ$  in Fig. 3. From the observation of these figures, it is implied that the patterns of the streamline and isotherm are almost same in all four configurations but resulting heat transfer enhancement with the increase in aspect angle is different as appeared in Fig. 4. With the increase of aspect angle, average Nusselt number increases to a great extent.

#### 5. CONCLUSIONS

In this investigation, the results of a numerical study of shear and buoyancy induced flow and heat transfer in a two-dimensional trapezoidal cavity with localized heating from below and cooling from the moving upper wall are presented. The main parameters of interest are mixed convection parameters, Richardson number (Ri) and the aspect angle ( $\phi$ ). With the increasing value of Richardson number in the mixed convection regime shows that the behavior of progressively dominant natural convection, which has been analyzed in this study. It has also been shown that for a particular aspect angle of the cavity, the value of average Nusselt number increases with the increase of Richardson number. Again it is found that the maximum value of the average Nusselt number can be attained at the maximum value of the aspect angle ( $\phi = 45^\circ$ ).

#### 6. REFERENCES

1. Incropera, F. P., (1988), Convection Heat Transfer in Electronic Equipment Cooling, *Heat Transfer*, **110**, pp. 1097-1111.

2. Devis, G. D. and Jones, I. P., (1983), Natural Convection in a Square Cavity: A Comparison Exercise, *International Journal for Numerical Methods in Fluids*, **3**, pp. 227-248.
3. Papanicolaou, E. and Jaluria, Y., (1990), Mixed Convection from an Isolated Heat Source in a Rectangular Enclosure, *Numerical Heat Transfer, Part A*, **18**, pp. 427-461.
4. Papanicolaou, E. and Jaluria, Y., (1992), Transition to a periodic regime in mixed convection in a square cavity, *Journal of Fluid Mechanics*, **239**, pp. 489-509.
5. Papanicolaou, E. and Jaluria, Y., (1993), Mixed Convection from a Localized Heat Source in a Cavity with Conducting Walls: A Numerical Study, *Numerical Heat Transfer, Part A*, **23**, pp. 463-484.
6. Papanicolaou, E. and Jaluria, Y., (1994), Mixed Convection from Simulated Electronic Components at Varying Relative Positions in a Cavity, *ASME Journal of Heat Transfer*, **116**, pp. 960-970.
7. Papanicolaou, E. and Jaluria, Y., (1995), Computation of Turbulent Flow in Mixed Convection in a Cavity with a Localized Heat Source, *ASME Journal of Heat Transfer*, **117**, pp. 649-658.
8. Iwatsu, R., Hyun, J. M. and Kuwahara, K., (1992), Convection in a Differentially-Heated Square Cavity with a Torsionally-Oscillating Lid, *International Journal of Heat and Mass Transfer*, **35**, pp. 1069-1076.
9. Shaw, H. J., (1993), Laminar Mixed Convection Heat Transfer in Three Dimensional Horizontal Channel with a Heated Bottom, *Numerical Heat Transfer, Part A*, **23**, pp. 445-461.
10. Aydin, O. and Yang, W.J., (2000), Mixed Convection in Cavities with a Locally Heated Lower Wall and Moving Sidewalls, *Numerical Heat Transfer, Part A*, **37**, pp. 695-710.
11. Reddy, J. N., (1993), *An Introduction to the Finite Element Method*, McGraw-Hill, New York.

#### 7. MAILING ADDRESS

Md. Nafiz Hossain Khan Chowdhury  
 Department of Mechanical Engineering  
 Bangladesh University of Engineering and Technology  
 Dhaka-1000, Bangladesh  
 E-mail: nhkchow@hotmail.com

# MAGNETOHYDRODYNAMIC (MHD)-CONJUGATE FREE CONVECTION FLOW FROM AN ISOTHERMAL HORIZONTAL CIRCULAR CYLINDER WITH JOULE HEATING EFFECT

M. A. Azim<sup>1</sup>, S. Binte Mahtab<sup>2</sup>, M. K. Chowdhury<sup>3</sup>

<sup>1</sup>School of Business studies, Southeast University, Dhaka, Bangladesh

<sup>2</sup>Department of Water Resources Engineering, Bangladesh University of Engineering and Technology, Dhaka, Bangladesh

<sup>3</sup>Department of Mathematics, Bangladesh University of Engineering and Technology, Dhaka, Bangladesh

## ABSTRACT

Magnetohydrodynamic(MHD)-conjugate natural convection flow along the outer surface from the lower stagnation point to the upper stagnation point and from an isothermal horizontal circular cylinder considering Joule heating effect is investigated. The developed governing equations with the associated boundary conditions for this analysis are transferred to dimensionless forms using a suitable transformation. The transformed non-dimensional governing equations are then solved using the implicit finite difference method with Keller box-scheme. Numerical results are found for different values of the Joule heating parameter, Magnetic parameter and Prandtl number. Detail results of the velocity profiles, temperature distributions, the skin friction and the rate of heat transfer are shown graphically.

**Keywords:** Natural Convection, Horizontal Cylinder, Magneto Hydrodynamic, Joule Heating, Conduction.

## 1. INTRODUCTION

Natural convection flow from a horizontal cylinder due to thermal buoyancy was analyzed by a number of researchers [1-4] under diverse surface boundary conditions (isothermal, uniform heat flux and mixed boundary conditions) using different mathematical technique. The conjugate heat transfer process (CHT) formed by the interaction between the conduction inside the solid and the convection flow along the solid surface has a significant importance in many practical application. In fact, conduction within the tube wall is significantly influenced by the convection in the surrounding fluid. Consequently, the conduction in the solid body and the convection in the fluid should have to determine simultaneously. Gdalevich and Fertman[5] studied the conjugate problems of natural convection. Miyamoto et al. [6] analysed the effects of axial heat conduction in a vertical flat plate on free convection heat transfer. Miyamoto observed that a mixed-problem study of the natural convection has to be performed for an accurate analysis of the thermo-fluid-dynamic (TFD) field if the convective heat transfer depends strongly on the thermal boundary conditions. Pozzi et al. [7] investigated the entire TFD field resulting from the coupling of natural convection along and conduction inside a heated flat plate by means of two expansions, regular series and asymptotic expansions. Moreover, Kimura and Pop [8] analysed conjugate natural convection from a horizontal circular cylinder.

MHD flow and heat transfer process are now an

important research area due to its potential application in engineering and industrial fields. A considerable amount of research has been done in this field. Wilks et al. [9] studied MHD free convection about a semi-infinite vertical plate in a strong cross field. Takhar and Soundalgekar [10] investigated dissipation effects on MHD free convection flow past a semi-infinite vertical plate. Hossain [11] studied viscous and Joule heating effects on MHD free convection flow with variable plate temperature. Aldoss et al. [12] analysed MHD mixed convection from a horizontal circular cylinder. El-Amin [13] found out the combined effect of viscous dissipation and Joule heating on MHD forced convection over a non-isothermal horizontal circular cylinder embedded in a fluid saturated porous medium. He observed that both the velocity profiles and temperature profiles shifted down for increasing value of magnetic parameter and that are rise up for increasing value of Joule heating parameter.

In this paper, the MHD-conjugate free convection flow from an isothermal horizontal circular cylinder with Joule heating effect is investigated. The governing boundary layer equations are transformed into a non dimensional form and the resulting non linear partial differential equations are solved numerically using the implicit finite difference method together with the Keller box technique [15,16]. The temperature distributions, velocity profiles, skin friction coefficients and the heat

transfer rates are presented graphically.

## 2. MATHEMATICAL ANALYSIS

Let us consider a steady natural convection flow of a viscous incompressible and electrically conducting fluid from an isothermal horizontal circular cylinder of radius  $a$  placed in a fluid of uniform temperature  $T_\infty$ . The cylinder has a heated core region of temperature  $T_b$  and the normal distance from inner surface to the outer surface is  $b$  with  $T_b > T_\infty$ . A uniform magnetic field having strength  $B_0$  is acting normal to the cylinder surface. The  $x$ -axis is taken along the circumference of

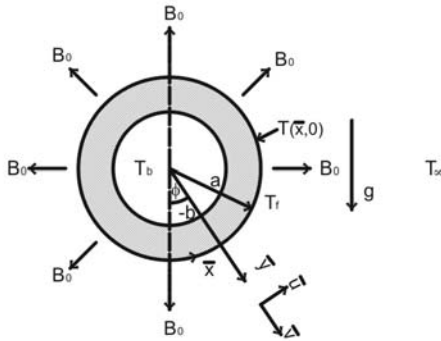


Fig. 1: Physical Model and coordinate system

the cylinder measured from the lower stagnation point and the  $y$ -axis is taken normal to the surface. It is assumed the fluid properties to be constant and the induced magnetic field is ignored. The effects of Joule heating in the flow region and conduction from inner surface to the outer surface considered in the present study. Under the balance laws of mass, momentum and energy and with the help of Boussinesq approximation for the body force term in the momentum equation, the equations governing this boundary-layer natural convection flow can be written as:

$$\frac{\partial \bar{u}}{\partial x} + \frac{\partial \bar{v}}{\partial y} = 0 \quad (1)$$

$$u \frac{\partial \bar{u}}{\partial x} + v \frac{\partial \bar{u}}{\partial y} = \nu \frac{\partial^2 \bar{u}}{\partial y^2} + g\beta(T_f - T_\infty) \sin\left(\frac{x}{a}\right) - \frac{\sigma B_0^2 \bar{u}}{\rho} \quad (2)$$

$$u \frac{\partial T_f}{\partial x} + v \frac{\partial T_f}{\partial y} = \frac{\kappa}{\rho c_p} \frac{\partial^2 T_f}{\partial y^2} + \frac{\sigma B_0^2 \bar{u}^2}{\rho c_p} \quad (3)$$

The physical situation of the system suggests the following boundary conditions

$$\left. \begin{aligned} \bar{u} = \bar{v} = 0, T_f = T(x, 0) \\ \partial T_f / \partial y = \kappa_s (T_f - T_b) / b \kappa_f \\ \bar{u} \rightarrow 0, T_f \rightarrow T_\infty \text{ as } \bar{y} \rightarrow \infty, \bar{x} > 0 \end{aligned} \right\} \text{on } \bar{y} = 0, \bar{x} > 0 \quad (4)$$

The governing equations and the boundary conditions (1)-(4) can be made non-dimensional, using the Grashof

number  $Gr = \frac{g\beta a^3 (T_b - T_\infty)}{\nu^2}$  which is assumed large and

the following non-dimensional variables:

$$\left. \begin{aligned} x = \frac{\bar{x}}{a}, y = \frac{\bar{y}}{a} Gr^{1/4}, u = \frac{\bar{u} a}{\nu} Gr^{-1/2}, \\ v = \frac{\bar{v} a}{\nu} Gr^{-1/4}, \theta = \frac{T_f - T_\infty}{T_b - T_\infty} \end{aligned} \right\} \quad (5)$$

Where  $\theta$  is the dimensionless temperature. The non dimensional form of the equations (1)-(3) are as follows:

$$\frac{\partial u}{\partial x} + \frac{\partial v}{\partial y} = 0 \quad (6)$$

$$u \frac{\partial u}{\partial x} + v \frac{\partial u}{\partial y} + Mu = \frac{\partial^2 u}{\partial y^2} + \theta \sin x \quad (7)$$

$$u \frac{\partial \theta}{\partial x} + v \frac{\partial \theta}{\partial y} = \frac{1}{Pr} \frac{\partial^2 \theta}{\partial y^2} + Ju^2 \quad (8)$$

Where  $M = (\sigma a^2 B_0^2) / (\nu \rho Gr^{1/2})$  is the magnetic parameter,  $J = (\sigma \nu B_0^2 Gr^{1/2}) / \{\rho c_p (T_b - T_\infty)\}$  is the joule heating parameter and  $Pr = \mu c_p / \kappa$  is the Prandtl number.

The boundary condition (4) can be written as in the following dimensionless form:

$$u = v = 0, \theta - 1 = p \frac{\partial \theta}{\partial y} \left\} \text{on } y = 0, x > 0 \quad (9)$$

$$u \rightarrow 0, \theta \rightarrow 0 \text{ as } y \rightarrow \infty, x > 0$$

Where  $p = \frac{b \kappa_f Gr^{1/4}}{a \kappa_s}$  is the conjugate conduction

parameter. The present problem is governed by the magnitude of  $p$ . The values of  $p$  depends on  $b/a$ ,  $\kappa_f / \kappa_s$  and  $Gr$ . The ratios  $b/a$  and  $\kappa_f / \kappa_s$  are less than one where as  $Gr$  is large for free convection. Therefore the value of  $p$  may be zero ( $b=0$ ) or greater than zero. In the present investigation we have considered  $p=1$ .

To solve equation (6)-(8), subject to the boundary condition (9), we assume following transformations

$$\psi = x f(x, y), \theta = \theta(x, y) \quad (10)$$

Where  $\psi$  is the stream function usually defined as

$$u = \partial \psi / \partial y, v = -\partial \psi / \partial x \quad (11)$$

Substituting (11) into the equations (6)-(9), the new forms of the dimensionless equations (7) and (8) are

$$f''' + ff'' - f'^2 - Mf' + \theta \frac{\sin x}{x} = x \left( f' \frac{\partial f'}{\partial x} - f'' \frac{\partial f}{\partial x} \right) \quad (12)$$

$$\frac{1}{Pr} \theta'' + f\theta' + Jx^2 f'^2 = x \left( f' \frac{\partial \theta}{\partial x} - \theta' \frac{\partial f}{\partial x} \right) \quad (13)$$

In the above equations primes denote differentiation with respect to  $y$ . The corresponding boundary conditions take the following form



$$f = f' = 0, \theta - 1 = p \frac{\partial \theta}{\partial y} \text{ at } y = 0, x > 0 \quad (14)$$

$$f' \rightarrow 0, \theta \rightarrow 0 \text{ as } y \rightarrow \infty, x > 0$$

Principle physical quantities, the shearing stress and the rate of heat transfer in terms of skin friction coefficient  $C_f$  and Nusselt number  $Nu$  respectively can be written as

$$C_f Gr^{1/4} = x f''(x,0) \quad (15)$$

$$Nu Gr^{-1/4} = -\theta(x,0) \quad (16)$$

The results of the velocity profiles and temperature distributions can be calculated by the following relations respectively.

$$u = f'(x, y), \theta = \theta(x, y) \quad (17)$$

### 3. METHOD OF SOLUTION

Equation (12) and (13) are solved numerically based on the boundary conditions as described in equation (14) using one of the most efficient and accurate methods known as implicit finite difference method with Keller box scheme [19, 20].

### 4. RESULTS AND DISCUSSION

The main objective of the present work is to analyze the flow of the fluid and the heat transfer processes due to the conjugate heat transfer from an isothermal horizontal circular cylinder. The Prandtl numbers are considered to be 1.63, 1.44, 1.0 and 0.733 for the simulation that correspond to Glycerin, water, steam and hydrogen, respectively. The value of the conjugate conduction parameter  $p$  is considered 1.0 for entire solutions.

A comparison of the local Nusselt number and the local skin friction factor obtained in the present work with  $M = 0.0$ ,  $J = 0.0$ ,  $p = 0.0$  and  $Pr = 1.0$  and obtained by Merkin [1] and Nazar et al. [14] have been shown in Tables 1 and 2 respectively. There is an excellent agreement among these three results.

The magnetic field opposes the fluid flow. As a result the peak velocity decreases with the increasing  $M$  as shown in fig. 2. Consequently, the separation of the boundary layer occurs earlier and the momentum boundary layer becomes thicker. From Fig. 3 it can be observed that the magnetic field decreases the temperature gradient and increases the temperature in the boundary layer for a particular value of  $y$ . Thus, the magnetic parameter increases the thickness of the thermal boundary layer. Temperature at the interface also varies with different  $M$  since the conduction is considered within cylinder.

The variation of the local skin friction coefficient and local rate of heat transfer with  $Pr = 1.0$  and  $J = 0.10$  for different values of  $M$  at different positions are illustrated in Fig. 4 and Fig. 5. The Magnetic force opposes the flow, as mentioned earlier, and reduces the shear stress at the wall as illustrated in Fig. 4. Moreover, the heat transfer rate also decreases as revealed in Fig. 5.

The velocity profiles, temperature distributions, local skin friction coefficients and the heat transfer rate for different values of Joule heating parameter  $J$  are presented in Fig. 6, Fig. 7, Fig. 8 and Fig. 9, respectively

with  $Pr = 1.0$  and  $M = 0.5$ . Increasing value of the Joule heating parameter containing magnetic field strength  $B_0$  increases the temperature and finally the fluid motion is accelerated as plotted in Fig.7 and Fig.6 respectively. The variation of the skin friction coefficient increases for the increasing  $J$  as depicted in Fig. 8 which is expected. The increased temperature for increasing  $J$  within the boundary layer reduced the temperature difference between the boundary layer region and the core region eventually decreases heat transfer rate as illustrated in Fig.9.

In Fig. 10 and Fig. 11 different values of Prandtl number  $Pr$ , with  $M = 0.5$  and  $J = 0.10$ , are considered for the velocity and temperature distributions respectively. It is observed in Fig. 10 that the peak velocity decreases as well as its position moves toward the surface of the cylinder for the increasing values of Prandtl number. The overall temperature profiles shift downward with increasing Prandtl number as shown in Fig. 11. Consequently, temperature difference increases between the boundary layer region and the core region which increases the rate of heat transfer as observed in Fig. 13. This result supports the physical fact that the thermal boundary layer thickness decreases with increasing  $Pr$ . The skin friction coefficient decreases for the increasing values of Prandtl number as plotted in Fig.12.

### 5. TABLES AND FIGURES

Table 1: Numerical values of  $-\theta'(x,0)$  for different values of  $x$  while  $Pr=1.0$ ,  $M = 0.0$ ,  $J=0.0$  and  $p = 0.0$ .

$Nu Gr^{-1/4} = -\theta'(x,0)$			
$x$	Merkin [1]	Nazar et al. [14]	Present
0.0	0.4214	0.4214	0.4216
$\pi/6$	0.4161	0.4161	0.4163
$\pi/3$	0.4007	0.4005	0.4006
$\pi/2$	0.3745	0.3741	0.3741
$2\pi/3$	0.3364	0.3355	0.3355
$5\pi/6$	0.2825	0.2811	0.2811
$\pi$	0.1945	0.1916	0.1912

Table 2: Numerical values of  $x f''(x,0)$  for different values of  $x$  while  $Pr = 1.0$ ,  $M = 0.0$ ,  $J=0.0$  and  $p = 0.0$ .

$C_f Gr^{1/4} = x f''(x,0)$			
$x$	Merkin [1]	Nazar et al. [14]	Present
0.0	0.0000	0.0000	0.0000
$\pi/6$	0.4151	0.4148	0.4139
$\pi/3$	0.7558	0.7542	0.7528
$\pi/2$	0.9579	0.9545	0.9526
$2\pi/3$	0.9756	0.9698	0.9678
$5\pi/6$	0.7822	0.7740	0.7718
$\pi$	0.3391	0.3265	0.3239

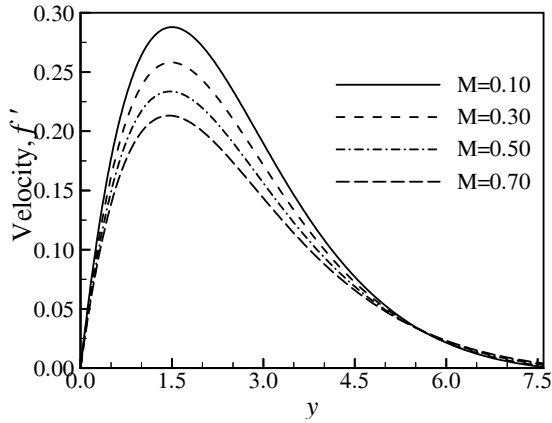


Fig 2. Variation of velocity profiles against  $y$  for varying of  $M$  with  $Pr = 1.0$ ,  $J = 0.10$  and  $p = 1.0$ .

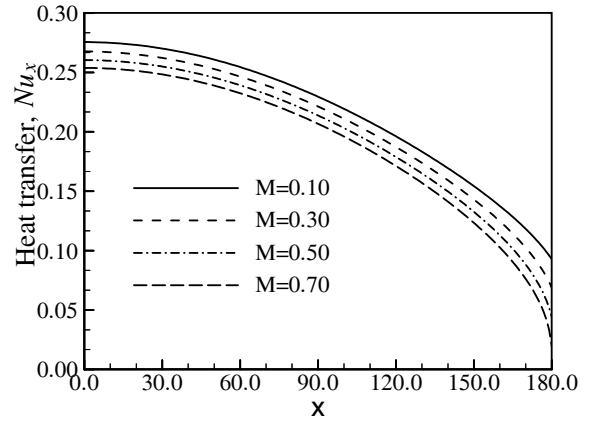


Fig 5. Variation of rate of heat transfer against  $x$  for varying of  $M$  with  $Pr = 1.0$ ,  $J = 0.10$  and  $p = 1.0$ .

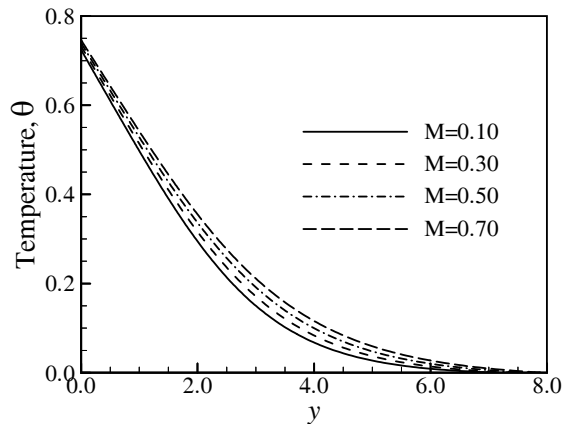


Fig 3. Variation of temperature distributions against  $y$  for varying of  $M$  with  $Pr = 1.0$ ,  $J = 0.10$  and  $p = 1.0$ .

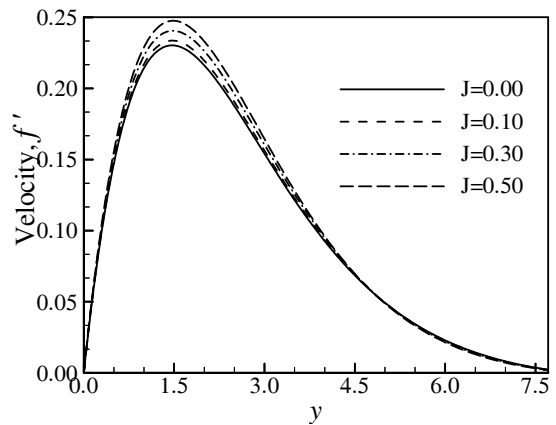


Fig 6. Variation of velocity profiles against  $y$  for varying of  $J$  with  $Pr = 1.0$ ,  $M = 0.5$  and  $p = 1.0$ .

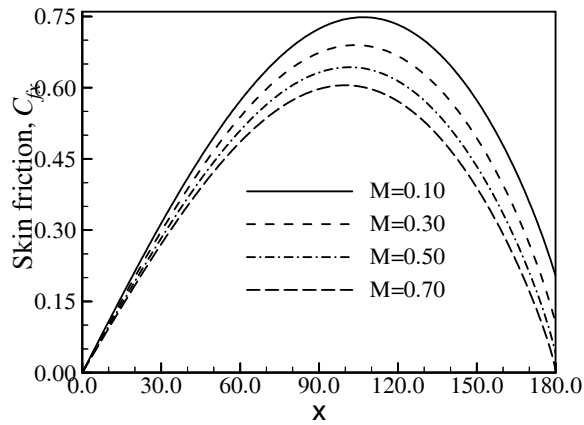


Fig 4. Variation of skin friction coefficients against  $x$  for varying of  $M$  with  $Pr = 1.0$ ,  $J = 0.10$  and  $p = 1.0$ .

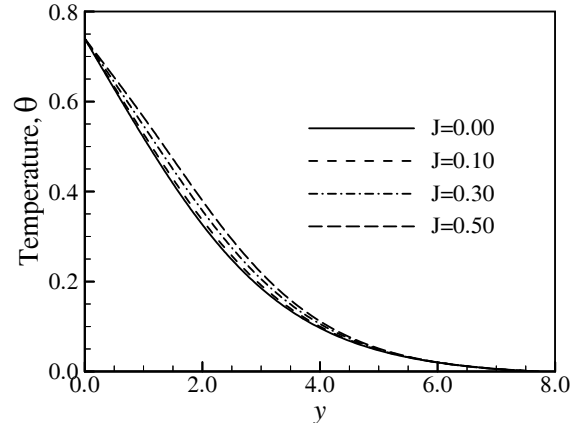


Fig 7. Variation of temperature distributions against  $y$  for varying of  $J$  with  $Pr = 1.0$ ,  $M = 0.5$  and  $p = 1.0$ .

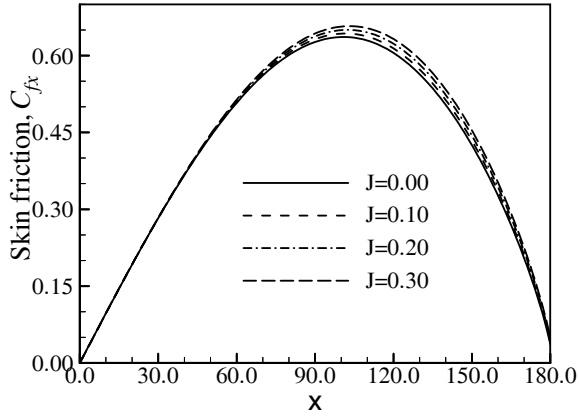


Fig 8. Variation of skin friction coefficients against  $x$  for varying of  $J$  with  $Pr = 1.0$ ,  $M = 0.5$  and  $p = 1.0$ .

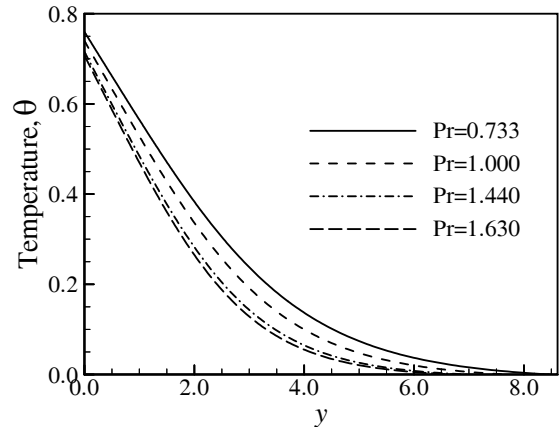


Fig 11. Variation of temperature distributions against  $y$  for varying of  $Pr$  with  $J = 0.10$ ,  $M = 0.5$  and  $p = 1.0$ .

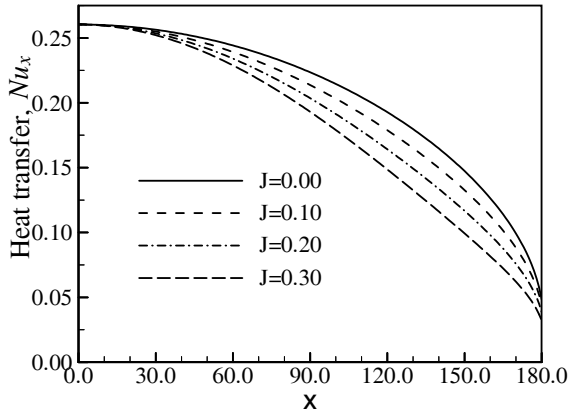


Fig 9. Variation of rate of heat transfer against  $x$  for varying of  $J$  with  $Pr = 1.0$ ,  $M = 0.5$  and  $p = 1.0$ .

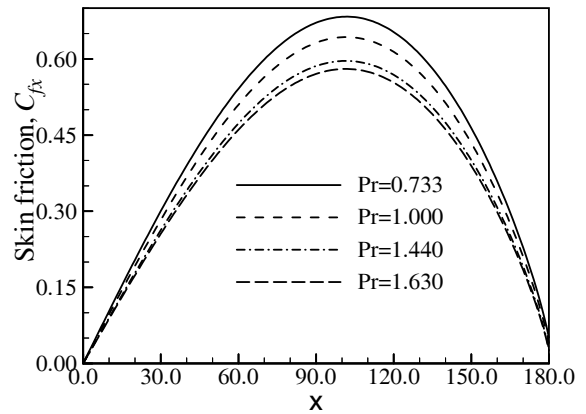


Fig 12. Variation of skin friction coefficients against  $x$  for varying of  $Pr$  with  $J = 0.10$ ,  $M = 0.5$  and  $p = 1.0$ .

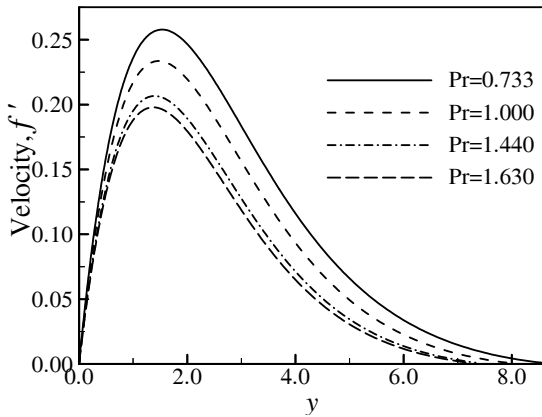


Fig 10. Variation of velocity profiles against  $y$  for varying of  $Pr$  with  $J = 0.10$ ,  $M = 0.5$  and  $p = 1.0$ .

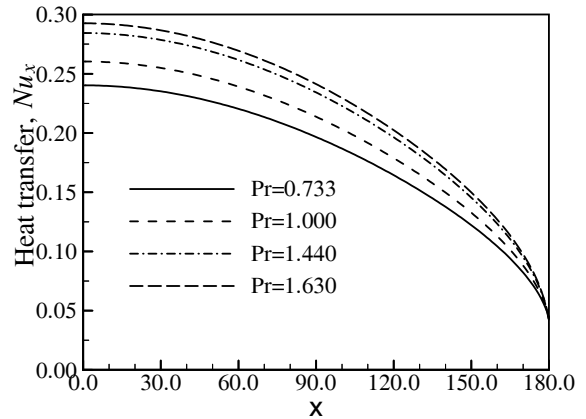


Fig 13. Variation of rate of heat transfer against  $x$  for varying of  $Pr$  with  $J = 0.10$ ,  $M = 0.5$  and  $p = 1.0$ .

## 6. CONCLUSION

A steady, two dimensional, MHD-conjugate free convection flow is studied considering joule heating phenomenon. The effects of the magnetic parameter  $M$ , Joule heating parameter  $J$  and Prandtl number  $Pr$  are analysed on the fluid flow with conjugate conduction parameter  $p = 1.0$ . The velocity of the fluid within the boundary layer and the skin friction coefficients along the cylinder surface decreases with increasing  $M$  and  $Pr$  while it increases with increasing  $J$ . The temperature distribution increases for increasing  $M$  and  $J$  whereas it decreases for increasing  $Pr$ . On the other hand the skin friction coefficients decreases for increasing  $M$  and  $J$  and it increases for increasing  $Pr$ .

## 7. REFERENCES

- Merkin, J. H., 1976, "Free convection boundary layer on an isothermal horizontal cylinder", ASME, paper no.76-HT-16.
- Merkin, J. H. and Pop, I., 1988, "A note on the free convection boundary layer on a horizontal circular cylinder with constant heat flux", Wärme und Stoffübertragung, Vol. 22, pp-79-81.
- Kuehn, T. H. and Goldstein, R. J., 1980, "Numerical solution to the Navier-Stokes equations for laminar natural convection about a horizontal isothermal circular cylinder", Int. J. heat Mass Transfer, Vol.23, pp-971-979.
- Wang, P., Kahawita, R. and Nguyen, T. H., 1990, "Numerical computation of natural convection flow about a horizontal cylinder Using Splines", Numerical Heat Transfer, Part-A, Vol.17, pp.191-215.
- Gdalevich, L. B. and Fertman, V. E., 1977, "Conjugate problems of natural convection", Inzh-Fiz. Zh. 33, 539-547.
- Miyamoto, M., Sumikawa, J., Akiyoshi, T. and Nakamura, T., 1980, "Effects of axial heat conduction in a vertical flat plate on free convection heat transfer", International Journal of Heat and Mass Transfer 23, 1545-1553.
- Pozzi, A. and Lupo, M., 1988, "The coupling of conduction with laminar natural convection along a flat plate", International Journal of Heat and Mass Transfer 31, 1807-1814.
- Kimura, S. and Pop, I., 1994, "Conjugate natural convection from a horizontal circular cylinder", Numerical heat transfer, Part A, Vol.25, pp.347-361.
- Wilks, G., 1976, "Magnetohydrodynamics free convection about a semi-infinite vertical plate in a strong cross field", ZAMP, Vol.27, pp.621-631.
- Takhar, H. S. and Soundalgekar, V. M., 1980, "Dissipation effects on MHD free convection flow past a semi-infinite vertical plate", Applied Science Research, Vol.36, pp.163-171.
- Hossain, M. A., 1992, "Viscous and Joule heating effects on MHD-free convection flow with variable plate temperature", Int. J. heat Mass Transfer, Vol.35, pp.3485-3487.
- Aldoss, T. K., Ali, Y. D. and Al-Nimr, M. A., 1996, "MHD mixed convection from a horizontal circular cylinder", Numerical Heat Transfer, Part A, Vol.30,

pp.379-396.

- El-Amin, M. F., 2003, "Combined effect of viscous dissipation and Joule heating on MHD forced convection over a non-isothermal horizontal cylinder embedded in a fluid saturated porous medium", Journal of Magnetism and Magnetic materials, Vol.263, pp.337-343.

## 8. NOMENCLATURE

Symbol	Meaning	Unit
$b$	Thickness of the cylinder	(cm)
$B_0$	Applied magnetic field	(N)
$C_{fx}$	Skin friction coefficient	...
$c_p$	Specific heat	(J/Kg.K)
$f$	Dimensionless stream function	...
$g$	Acceleration due to gravity	(cm/s <sup>2</sup> )
$J$	Joule heating parameter	...
$l$	Length of the plate	(cm)
$M$	Magnetic parameter	...
$Nu_x$	Local Nusselt number	...
$p$	Conjugate conduction parameter	...
$Pr$	Prandtl number	...
$T_b$	Temperature of the inner cylinder	(K)
$T_f$	Temperature at the boundary layer region	(K)
$T_s$	Temperature of the solid of the cylinder	(K)
$T_\infty$	Temperature of the ambient fluid	(K)
$\bar{u}, \bar{v}$	Velocity components	(cm/s)
$u, v$	Dimensionless velocity components	...
$\bar{x}, \bar{y}$	Cartesian coordinates	(cm)
$x, y$	Dimensionless Cartesian coordinates	...
<b>Greek symbols</b>		
Symbol	Meaning	Unit
$\beta$	Co-efficient of thermal expansion	(K <sup>-1</sup> )
$\psi$	Dimensionless stream function	...
$\rho$	Density of the fluid inside the boundary layer	(Kg/m <sup>3</sup> )
$\nu$	Kinematic viscosity	(m <sup>2</sup> /s)
$\mu$	Viscosity of the fluid	(N.s/m <sup>2</sup> )
$\theta$	Dimensionless temperature	...
$\sigma$	Electrical conductivity	J/msK
$K_f$	Thermal conductivity of the ambient fluid	(kW/mK)
$K_s$	Thermal conductivity of the ambient solid	(kW/mK)

## 9. MAILING ADDRESS

M. A. Azim  
 School of Business studies,  
 Southeast University, Dhaka, Bangladesh,  
 E-mail: nhmarif1@gmail.com

## INFLUENCE OF ENGINE SPEED ON HEAT TRANSFER CHARACTERISTICS OF PORT INJECTION HYDROGEN FUELED ENGINE

M. M. Rahman, Khalaf I. Hamada, M.M. Noor and K. Kadirgama

Faculty of Mechanical Engineering, University Malaysia Pahang , Pahang, Malaysia

### ABSTRACT

This paper presents the numerical investigation of the in-cylinder heat transfer characteristics of port injection hydrogen fueled internal combustion engine. One dimensional gas dynamics was described the flow and heat transfer in the components of the engine model. Special attention is paid to selection and correction of heat transfer which describe of in-cylinder heat transfer to coincide with the practical observations. Engine speed varied from 2000 rpm to 5000 rpm with increment of 500 rpm. The difference between hydrogen and methane revealed in terms of heat transfer rate and the percentage of heat transfer from the total fuel energy are investigated. The acquired results show that hydrogen fueled engine has a higher heat transfer rate with methane because of hydrogen fuel has higher heating value, faster flame speed and small quenching distance. Instantaneous results reveal that the normalized apparent and cumulative heat release is affected by engine speed. The heat transfer rate and coefficient are also affected with engine speed. Beside that the steady state results are presented by examining the dependency of average heat transfer rate and the percentage ratio of heat transfer to the total fuel energy on the engine speed.

**Keywords:** Hydrogen Fuel, Heat Transfer, In-cylinder, Port Injection, Engine Speed.

### 1. INTRODUCTION

In today's modern world, where new technologies are introduced every day, transportation's energy use is increasing rapidly. Fossil fuel is the major contributor to produce energy and the prime fuel for transportation. Rapidly depleting reserves of petroleum and decreasing air quality raise questions about the future. Therefore, alarms about climate contamination and decrease petroleum resources continue to activate research on alternative fuels have been carried out to substitute fossil fuels. With this tendency into account, the use of alternative, renewable fuels and modern vehicle designs has been introduced solution to mitigate these problems. With increasing concern about energy shortage and environmental protection, research on improving engine fuel economy and reducing exhaust emissions has become the major researching aspect in combustion and engine development. Due to limited reserves of crude oil, development of alternative fuel engines has attracted more and more concern in the engine community. Alternative fuels, usually belong to clean fuels compared to diesel fuel and gasoline fuel in the combustion process of engines. The introduction of these alternative fuels is beneficial to slowing down the fuel shortage and reducing engine exhaust emissions. Hydrogen fuel is regarded as one of the most promising alternative fuels for automobiles in future. It is combustion produce no

greenhouse gases, no ozone layer depleting chemicals, and little or no acid rain ingredients and pollution [1]. Hydrogen, produced from renewable energy (solar, wind, biomass, tidal etc.) sources, would result in a permanent energy system which would never have to be changed [2]. Hydrogen Internal Combustion Engines (H<sub>2</sub>ICE) is a technology available today and economically viable in the near-term. This technology demonstrated efficiencies in excess of today's gasoline engines and operate relatively cleanly (NO<sub>x</sub> is the only emission pollutant) [3]. So far, extensive studies were investigated hydrogen fueled internal combustion engines [4-11]. However, most of the previous study regarding the engine performance and combustion process were carried out. Increases efficiencies, high power density and reduce emissions are the main objectives for internal combustion engines (ICE) development [12]. One of the major parameter that effective in the improvement of performance and emission regulation in the ICE is the amount of heat loss from the total heat release during combustion process. Hydrogen can be readily used in spark ignition engines as a clean alternative to fossil fuels. However, the higher burning velocity, higher coefficient of diffusivity, higher thermal conductivity and shorter quenching distance of hydrogen compared with hydrocarbons cause a larger heat transfer from the burning gas to the combustion chamber walls. Because

of this cooling loss, the thermal efficiency of H<sub>2</sub>ICE is sometimes lower than that of conventionally fueled engines. Therefore, reducing the cooling loss is a crucial element in improving the thermal efficiency of hydrogen combustion engines [13]. Based on the analysis of losses that is done by Wimmer et. al. [14]. The authors found that the wall heat transfer has a major influence on overall efficiency in H<sub>2</sub>ICE operation. The significant difference in the physical properties of hydrogen fuel and fossil fuels is the driving force to recognize every behavior for H<sub>2</sub>ICE. A good knowledge about heat transfer characteristics inside the cylinder is very important to accurate descriptions for the heat transfer phenomena inside H<sub>2</sub>ICE. From the above point of view, need to more attention about this matter. The objectives of the present study are to investigate the influence of engine speed on in-cylinder overall heat transfer characteristics for port injection H<sub>2</sub>ICE.

## 2. MATERIALS AND METHODS

### 2.1 Engine Model

A single cylinder, four stroke spark ignition port injection hydrogen fuel was developed in this study. GT-Suite was utilizing the development of engine model. The injection of hydrogen was located in the midway of the intake port. The computational and schematic models of the single cylinder four stroke port injection hydrogen fueled engine are shown in Figures 1 and 2 respectively. The engine specification is listed in Table 1. It is important to indicate that the intake and exhaust ports of the engine cylinder are modeled geometrically with pipes. The air enters through a bell-mouth orifice to the pipe. The discharge coefficients of the bell-mouth orifice were set to 1 to ensure the smooth transition as in the real engine. The pipe of bell-mouth orifice with 0.07 m of diameter and 0.1 m of length are used in this model. The pipe connects in the intake to the air cleaner with 0.16 m of diameter and 0.25 m of length was modeled. The air cleaner pipe identical to the bell-mouth orifice connects to the manifold. A log style manifold was developed from a series of pipes and flow-splits. The total volume for each flow-split was 256 cm<sup>3</sup>. The flow-splits compose from an intake and two discharges. The intake draws air from the preceding flow-split. One discharge supplies air to adjacent intake runner and the other supplies air to the next flow-split. The last discharge pipe was closed with a cup to prevent any flow through it because there is no more flow-split. The flow-splits are connected with each other via pipes with 0.09 m diameter and 0.92 m length. The junctions between the flow-splits and the intake runners were modeled with bell-mouth orifices. The discharge coefficients were also set to 1 to assure smooth transition, because in most manifolds the transition from the manifold to the runners is very smooth. The intake runners for the four cylinders were modeled as four identical pipes with .04 m diameter and 0.1 m length. Finally the intake runners were linked to the intake ports which were modeled as pipes with 0.04 m diameter and 0.08 m length. The overall temperature of the head, piston and cylinder for the engine parts are listed in Table 2. The temperature of the

piston is higher than the cylinder head and cylinder block wall temperature because it is not directly cooled by the cooling liquid. Heat transfer multiplier is used to take into account for bends, additional surface area and turbulence caused by the valve and stem. The pressure losses in these ports are included in the discharge coefficients calculated for the valves. No additional pressure losses due to wall roughness were used.

The exhaust runners were modeled as rounded pipes with 0.03 m inlet diameter, and 80° bending angle for runners 1 and 4; and 40° bending angle of runners 2 and 3. Runners 1 and 4, and runners 2 and 3 are connected before enter in a flow-split with 169.646 cm<sup>3</sup> volume. Conservation of momentum is solved in 3-dimensional flow-splits even though the flow in GT-Power is otherwise based on a one-dimensional version of the Navier-Stokes equation. Finally a pipe with 0.06 m diameter and 0.15 m length connects the last flow-split to the environment. Exhaust system walls temperature was calculated using a model embodied in each pipe and flow-split. Table 3 are listed the parameters used in the exhaust environment of the model.

A simulation of the wall heat transfer is an imperative condition for the accurate analysis of the working process of ICE. The engine model is to estimate the engine heat transfer using Woschni's correlation [15]. The original values of the constant in the correlation were multiplied by factor equal to 1.8, resulting in a better match with the experimental data [16-17]. The authors were found during the analysis that the heat transfer correlation under predicts heat transfer loss.

Table1: Engine specification

Engine Parameter	Value	Unit
Bore	100	mm
Stroke	100	mm
Total displacement	3142	(cm <sup>3</sup> )
Connecting rod length	220	mm
Compression ratio	9.5	
Intake valve close, IVC	-96	°CA
Exhaust valve open, EVO	125	°CA
Inlet valve open, IVO	351	°CA
Exhaust valve close, EVC	398	°CA

Table 2: Engine components temperature

Components	Temperature (K)
Cylinder head	550
Cylinder block wall	450
Piston	590

Table 3: Parameters used in the exhaust environment

Parameters	Value	Unit
External environment temperature	320	K
Heat transfer coefficient	15	W/m <sup>2</sup> K
e temperatureRadiativ	320	K
Wall layer material	Steel	
Layer thickness	3	mm
Emissivity	0.8	

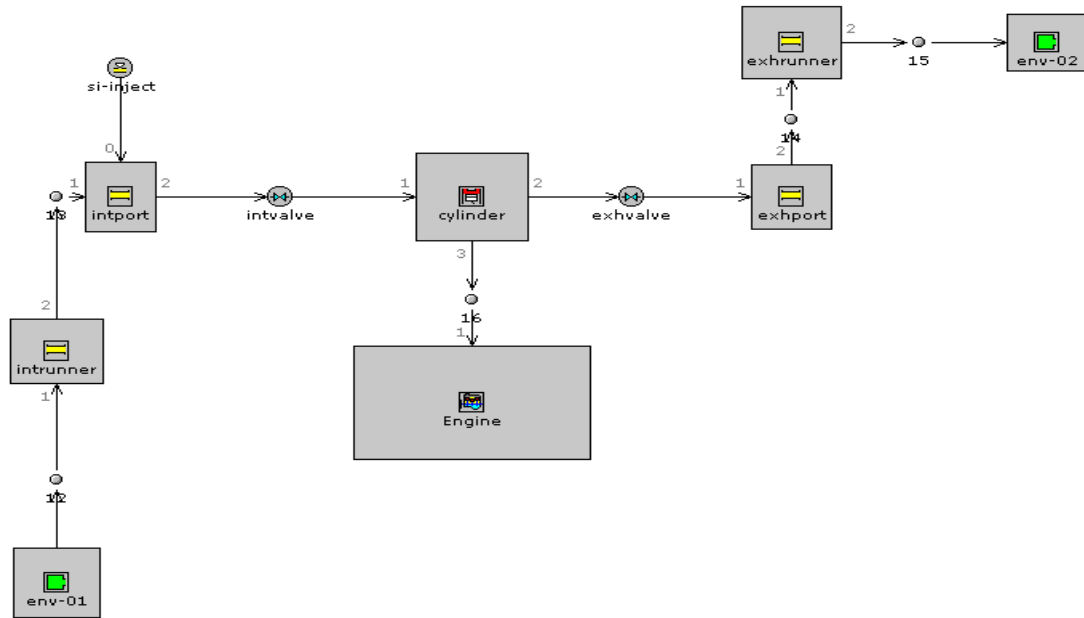


Fig 1. Model of single cylinder, four stroke port injection hydrogen fueled engine

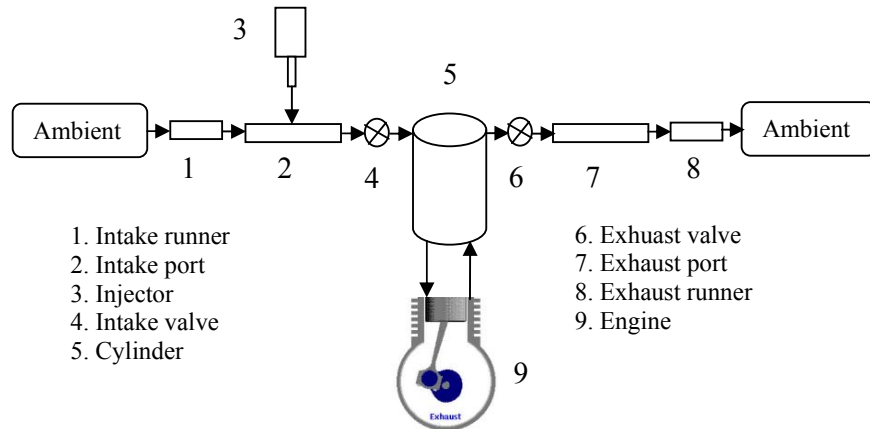


Fig 2. Schematic model of port injection hydrogen fueled engine.

## 2.2 Heat Transfer Governing Equations

One dimensional gas dynamics to represent the flow and heat transfer in the components of the engine model. Engine performance can be studied by analyzing the mass, momentum and energy flows between individual engine components and the heat and work transfers within each component.

The pressure loss coefficient is defined by Equation (1):

$$C_{pl} = \frac{p_1 - p_2}{\frac{1}{2} \rho u_1^2} \quad (1)$$

where  $p_1$  and  $p_2$  are the inlet and outlet pressure

respectively,  $\rho$  the density and  $u_1$  the inlet velocity.

The friction coefficient can be expressed for smooth and rough walls as Equation (2) and (3) respectively:

$$C_f = \frac{16}{Re_D} \quad Re_D < 2000 \quad (2)$$

$$C_f = \frac{0.08}{Re_D^{0.25}} \quad Re_D > 2000$$

$$C_{f(rough)} = \frac{0.25}{\left[ 2 \log \left( \frac{D}{2h} \right) + 1.74 \right]^2} \quad (3)$$



where  $Re$ ,  $D$  and  $h$  are Reynolds number, pipe diameter and roughness height respectively.

The heat transfer from the internal fluids to the pipe and flow split walls is dependent on the heat transfer coefficient, the predicted fluid temperature and the internal wall temperature. The heat transfer coefficient is calculated every time step and it is a function of fluid velocity, thermo-physical properties and wall surface roughness.

The internal wall temperature is defined as Equation (4).

$$h_g = \frac{1}{2} C_f \rho U_{eff} C_p Pr^{-\frac{2}{3}} \quad (4)$$

where  $U_{eff}$ ,  $C_p$  and  $Pr$  are the effective speed outside boundary layer, specific heat and Prandtl number respectively. The Prandtl number can be expressed as Equation (5)

$$Pr = \frac{\mu C_p}{k} = \frac{\nu}{\alpha} \quad (5)$$

where  $\mu$ ,  $k$ ,  $\nu$  and  $\alpha$  are the dynamic viscosity, conduction heat transfer coefficient, kinematic viscosity and thermal diffusivity respectively.

The heat transfer coefficient depends on characteristic length, transport properties, pressure, temperature and characteristic velocity. There is a wealth of heat transfer correlations for describing heat transfer process inside combustion chamber such as Eichelberg's equation [18], Woschni's equation [15] and Annand's equation [19]. The in-cylinder heat transfer is calculated by a formula which closely emulates the classical Woschni correlation. A unique feature of Woschni correlation is the gas velocity term while most of the other correlations use a time averaged gas velocity proportional to the mean piston speed, Woschni separated the gas velocity into two parts: the unfired gas velocity that is proportional to the mean piston speed, and the time-dependent, combustion induced gas velocity that is a function of the difference between the motoring and firing pressures. The heat transfer coefficient can be expressed as Equation (6):

$$h = 3.26 D^{-0.2} P^{0.8} T_g^{0.55} w^{0.8} \quad (6)$$

$$w = 2.28 C_m + 0.00324 \frac{(P - P_m) V_h T_r}{Pr V_r}$$

where  $D$ ,  $P$ ,  $P_m$ ,  $T_g$ ,  $V_h$ ,  $C_m$ ,  $V$  and  $r$  are the bore diameter, pressure, motored pressure, gas temperature, volume, mean piston speed, swept volume and a reference crank angle respectively.

This approach keeps the velocity constant during the unfired period of the cycle and then imposes a steep velocity rise once combustion pressure departs from motoring pressure.

### 3. RESULTS AND DISCUSSION

It has been adequately emphasized that hydrogen fuel possesses some properties which are uniquely different

from the corresponding properties of conventional hydrocarbon fuels. This was primarily the reason why initially the research and development work on. It has usually been found that the first two conditions occur under heavy load conditions. These often cause the engine to stop. The symptoms of unsteady combustion the most pronounced effect in an internal combustion engine. Hydrogen has long since been attempted as a fuel for the internal combustion engine.

#### 3.1 Steady Heat Transfer Characteristics

Steady state heat transfer analysis was carried out for in-cylinder of four stroke port injection spark ignition hydrogen fueled engine model. The engine speed varied from 2000 rpm to 5000 rpm with change step equal to 500 rpm and crank angle varied from  $-40^\circ$  to  $100^\circ$ . The stoichiometric limit (AFR = 34.33) based on mass where the equivalence ratio ( $\phi = 1.0$ ) was considered the air fuel mixture throughout the study. In order to recognize the difference between the in-cylinder heat transfers characteristics for ICE with hydrogen and hydrocarbon fuels, a direct comparison was verify the engine model in terms of heat transfer rate and ratio of heat transfer to total fuel energy which are as shown in Figures 3 and 4 respectively. It can be seen that the increase of heat transfer rate with increases of engine speed for both fuel (Figure 3) and ratio of heat transfer to total fuel energy in percentage decreases with increases of engine speed (Figure 4). It is also clearly seen that the heat transfer rate through the cylinder to the ambient for hydrogen fuel higher than methane for both due to the higher heating value, faster flame speed and small quenching distance for hydrogen. The ratio of heat transfer rate to the total fuel energy is used as another indicator for clarifying that hydrogen fuel gives amount of heat loss more than methane even as a percentage from the total energy supplied by the fuel as shown in Figure 4.

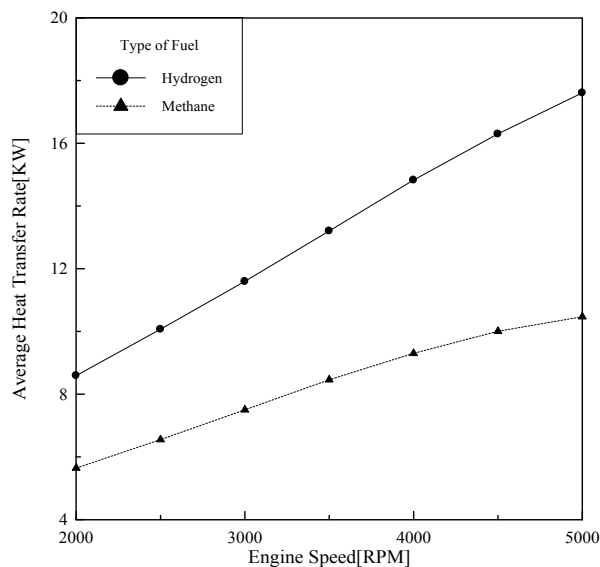


Fig 3. Comparison between hydrogen and methane in term of heat transfer rate for equivalence ratio  $\phi=1.0$ .

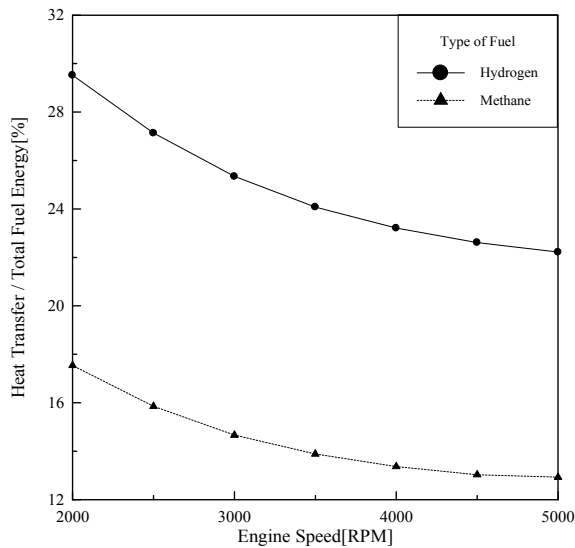


Fig 4. Comparison between hydrogen and methane in term of percentage ratio of heat transfer to total fuel energy

Both of the normalized apparent and cumulative heat release rates are used as indicators for recognizing the in-cylinder heat transfer characteristics for port injection H<sub>2</sub>ICE. Effects of normalized apparent and cumulative heat release rate on engine speed are presented in Figures 5 and 6 respectively. These figures reveal that the dependency of the normalized heat release rate on engine speed are negligible effects because of its related to the amount of energy content in the inlet charge to combustion chamber. The maximum heat release rate decreases with increases of engine speed.

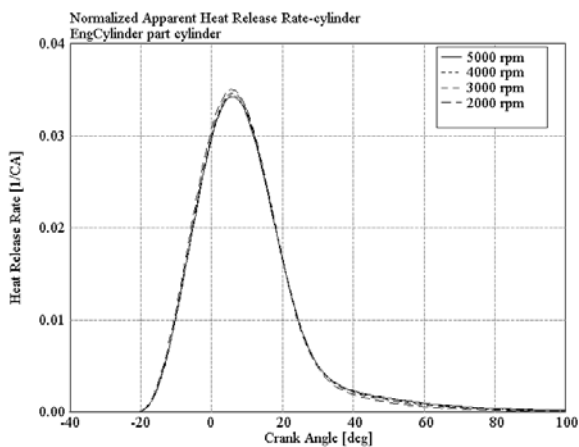


Fig 5. Variation of normalized apparent heat release rate with engine speed

### 3.2 Transient Heat Transfer Characteristics

Transient heat transfer analysis was carried out for in-cylinder of four stroke port injection spark ignition hydrogen fueled engine model. The engine speed varied from 2000 rpm to 5000 rpm with change step equal to 500 rpm and crank angle varied from -180° to 540°. The

air-fuel ratio was varied from rich (stoichiometric) limit (AFR = 34.11:1 based on mass where the equivalence ratio,  $\phi = 1.0$ ) to a very lean limit (AFR =171.65 where ( $\phi = 0.2$ ). The instantaneous behaviors for heat transfer rate and coefficient are employed the in-cylinder heat transfer characteristics for port injection H<sub>2</sub>ICE. Figure 7 shows the instantaneous heat transfer rate from the in-cylinder gases to cylinder walls with various engine speed conditions at AFR=34.33:1 (or equivalence ratio  $\phi=1.0$ ). The obtained results can be seen that the heat transfer rate increases with increases of the engine speed during part of compression stroke, power stroke and most of the exhaust stroke due to increase the turbulence intensity inside the cylinder and lead to increase the forced convection effect which is represent as the main driving force for the heat transfer process between the in-cylinder gases and walls surface. Instantaneous variation of heat transfer coefficient with engine speed at AFR=34.33:1 (Equivalence ratio  $\phi = 1.0$ ) is illustrated in Figure 8. As expected, heat transfer coefficient increased by increasing of engine speed for all cycle strokes where the heat transfer coefficient depends on the forced convection phenomenon. Thus as engine speed increase the effect of forced convection due to increase the in-cylinder gas velocity.

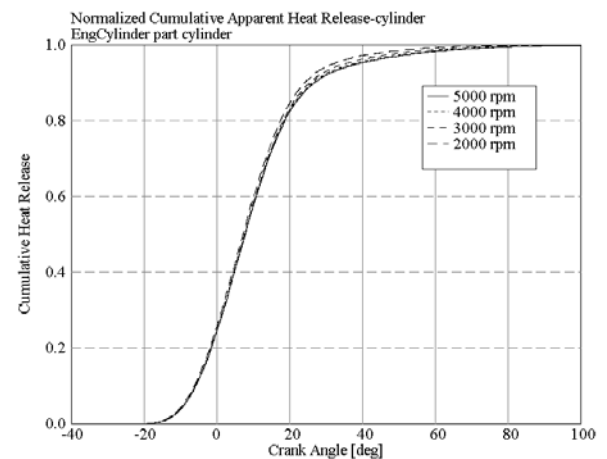


Fig 6. Variation of normalized cumulative heat release rate with engine speed for equivalence ratio ( $\phi$ ) = 1.0

Beside the instantaneous behavior the average heat transfer rate and the percentage ratio for heat transfer to the total fuel energy are used as indicators for the in-cylinder heat transfer characteristics for port injection H<sub>2</sub>ICE. Variation of average in-cylinder heat transfer rate with engine speed is clarified in Figure 9. The average value of heat transfer rate increases as engine speed increases for all AFR values due to increase the driving force (forced convection) for the heat transfer inside the cylinder. While the average value of heat transfer rate increase as AFR decrease for all engine speed and increment in the average heat transfer rate with increasing of the engine speed because of decreasing the energy content for the inlet charge to the cylinder. Variation of the percentage ratio of heat transfer to the total fuel energy with engine speed is presented in figure 10. The ratio of heat transfer rate to total fuel energy

decreases with increases of both engine speed and AFR except AFR=171.65 which has different behavior. For AFR of 171.65, the percentage ratio decreases as engine speed increases until 3500 rpm after that the ratio increases due to the limitation in the energy content for charge interred to the cylinder and continuous increment in the heat transfer rate from the in-cylinder gas to the walls.

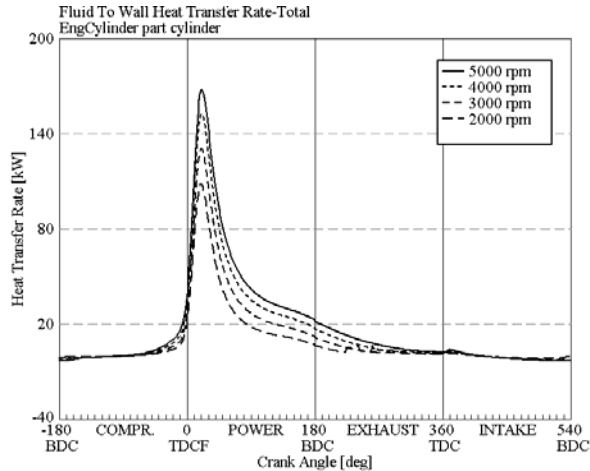


Fig 7. Variation of heat transfer rate with engine speed for equivalence ratio  $\phi=1.0$ .

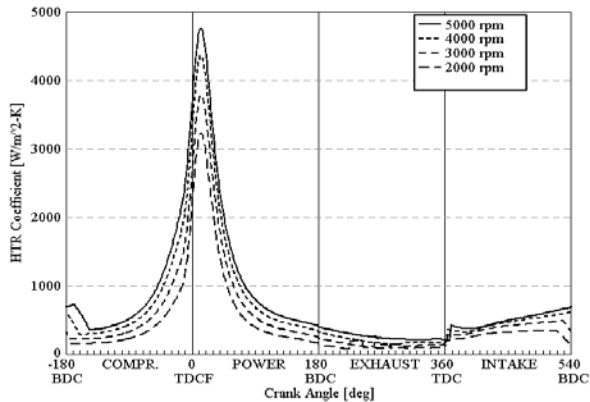


Fig 8. Effect of heat transfer coefficient with engine speed for Equivalence ratio ( $\phi$ )=1.0

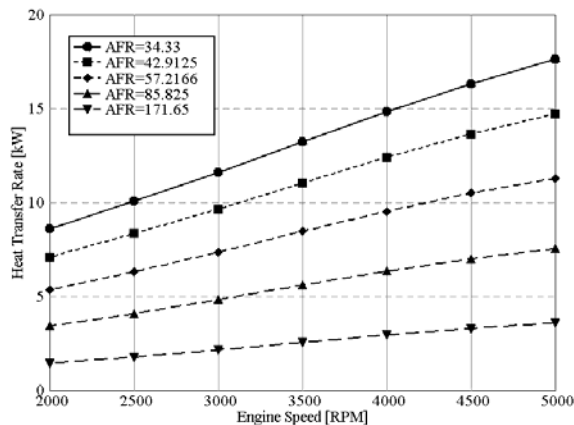


Fig 9. Variation of the average heat transfer rate against engine speed.

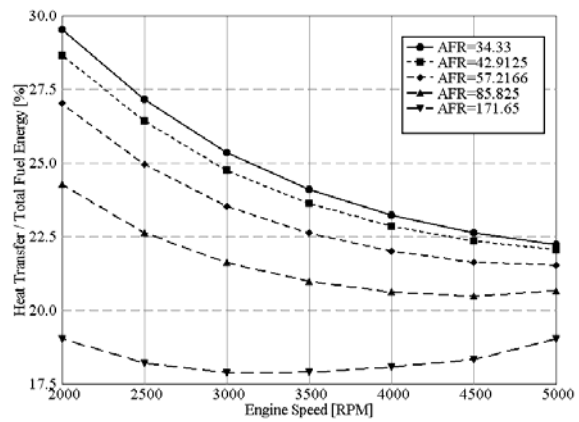


Fig 10. Variation of ratio of heat transfer to total fuel energy with engine speed.

#### 4. CONCLUSIONS

The in-cylinder characteristics of transient and steady states heat transfer process for port injection H<sub>2</sub>ICE have been investigated and quantified. Compression for in-cylinder characteristics between hydrogen and methane fuel in term of heat transfer rate and the percentage ratio for the heat transfer rate to the total fuel energy is clarified. Hydrogen has higher values for the heat transfer rate and the percentage ratio for the heat transfer rate to the total fuel energy due to the difference in physical properties and combustion behavior between of hydrogen and methane. The foregoing results indicate that the dependency both of the normalized apparent and cumulative heat release on engine speed. While for the heat transfer rate and heat transfer coefficient dependency on both of the AFR and engine speed is found. The results show that the average heat transfer rate increases as engine speed increases. As well as the percentage ratio of heat transfer to the total fuel energy variation indicate that decrease with increase of the engine speed.

#### 5. REFERENCES

1. Kahraman, E. 2005, "Analysis of a Hydrogen Fueled Internal Combustion Engine" MSc. Thesis, the Graduate School of Engineering and Sciences of İzmir Institute of Technology.
2. Kahraman, E., Ozcanli, C. and Ozerdem, B., 2007, "An experimental study on performance and emission characteristics of a hydrogen fuelled spark ignition engine", *Int. J. of Hydrogen Energy*, 32(12): 2066–2072.
3. Boretti, A. A., Brear, M. J. and Watson, H. C., 2007, "Experimental and Numerical Study of a Hydrogen Fuelled I.C. Engine Fitted with the Hydrogen Assisted Jet Ignition System" *16th Australasian Fluid Mechanics Conference Crown Plaza, Gold Coast, Australia 2-7 December*.
4. Rahman, M.M., Mohammed, M.K. and Bakar, R.A., 2009, "Effects of air fuel ratio and engine speed on performance of hydrogen fueled port injection engine", *Journal of Applied Sciences*, 9: 1128-1134.

5. Rahman, M.M., Mohammed, M.K. and Bakar, R.A., 2009, "Effects of air fuel ratio and injection timing on performance for four cylinder direct injection hydrogen fueled engine", *European Journal of Scientific Research*, 25: 214-225.
6. Ganesh, R. H., Subramanian, V., Balasubramanian, V., Mallikarjuna, J.M., Ramesh, A. and Sharma, R.P., 2008, "Hydrogen fueled spark ignition engine with electronically controlled manifold injection: An experimental study", *Renewable Energy*, 33: 1324-1333.
7. Ali, M., Shioji, M., Nakai, Y., Ishikura, W. and Tabo, E., 2007, "Performance and combustion characteristics of a direct injection SI hydrogen engine", *Int. J. of Hydrogen Energy*, 32: 296 - 304.
8. Verhelst, S. and Sierens, R., 2001, "Aspects concerning the optimisation of a hydrogen fueled engine", *Int. J. of Hydrogen Energy*, 26: 981-985.
9. Verhelst, S. and Sierens, R., 2007, "A quasi-dimensional model for the power cycle of a hydrogen-fuelled ICE", *Int. J. of Hydrogen Energy*, 32: 3545 - 3554.
10. Li, H. and Karim, G. A., 2006, "Hydrogen Fueled Spark-Ignition Engines Predictive and Experimental Performance", *J. of Engineering for Gas Turbines and Power*, Transactions of the ASME, 128: 230-236.
11. Verhelst, S., Maesschalck, P. , Rombaut, N. and Sierens, R., 2009, "Efficiency comparison between hydrogen and gasoline, on a bi-fuel hydrogen/gasoline engine", *Int. J. of hydrogen energy*, 34: 2504-2510.
12. White, C.M., Steeper, R.R. and Lutz, A.E., 2006, "The hydrogen-fueled internal combustion engine: a technical review", *Int. J. of Hydrogen Energy*, 31(10): 1292-1305.
13. Shudo, T., 2007, "Improving Thermal Efficiency by Reducing Cooling Losses in Hydrogen Combustion Engines", *Int. J. of Hydrogen Energy*, 32: 4285 - 4293.
14. Wimmer, A., Wallner, T., Ringler, J. and Gerbig, F., 2005, "H<sub>2</sub>-direct injection- a highly promising combustion concept", *SAE Paper*, No. 2005-01-0108.
15. Woschni, G., 1967, "A universally applicable equation for the instantaneous heat transfer coefficient in the internal combustion engine", *SAE Paper No. 670931*.
16. Aceves, S. M. and Smith, J. R., 1996, "Hybrid and Conventional Hydrogen Engine Vehicles that Meet EZEVE Emissions", *ASME International Combustion Engine, Fall Conference, Fairborn, Ohio, October 20-23*, pp. 1-13.
17. Aceves, S. M. and Smith, J. R., 1997, "Lean-Burn Hydrogen Spark-Ignited Engines: The Mechanical Equivalent to the Fuel Cell", *Society of Automotive Engineers International Congress and Exposition Detroit, Michigan, February 24-27*, pp. 1-10.
18. Eichelberg, G., 1939, "Some new investigations on old combustion engine problems", *Engineering*, 148: 547-550.
19. Annand, W. J. D., 1963, "Heat Transfer in the Cylinders of Reciprocating Internal Combustion Engines", *Proc. Instn. Mech. Engrs*, 177(36): 973- 996.

## 6. MAILING ADDRESS

M.M. Rahman  
 Automotive Excellence Center  
 Faculty of Mechanical Engineering,  
 University Malaysia Pahang  
 Tun Razak Highway, 26300 Kuantan, Pahang,  
 Malaysia

## EXPERIMENTAL INVESTIGATION OF AN OPEN LOOP CLOSED END PULSATING HEAT PIPE

Tahanee Mujib, Fahim Ahmed and Chowdhury Md. Feroz

Department of Mechanical Engineering, Bangladesh University of Engineering and Technology, Dhaka,  
Bangladesh

### ABSTRACT

This paper presents an experimental study of an open loop pulsating heat pipe (OLPHP) of 0.9 mm inner diameter. The performance characterization has been done for two working fluids at vertical and horizontal orientations. Water and Acetone are employed as the working fluid with 50% fill ratio. The experimental results indicate a strong influence of gravity and thermo physical properties of the working fluids on the performance of OLPHP. Regarding the working fluids, Water has performed better in both vertical and horizontal orientation as lower evaporation temperature has been achieved at all heat loads. Both working fluids perform better at horizontal orientation. OLPHP of 0.9 mm ID in this experiment shows better thermal performance as compared with experimental results of Roger R. Reihl [1] performed with OLPHP of 1.5 mm ID.

**Keywords:** Pulsating Heat Pipe, Inclination Angles, Pulsating Action, Diametrical Effect

### 1. INTRODUCTION

Nowadays the demand of increased capacity of heat transfer devices has risen drastically. One possible solution for power electronics applications is the use of liquid-vapor phase change cooling devices such as the heat pipes. Although the conventional heat pipes (e.g. mini or micro) are one of the proven technologies, the manufacturing of the complex, miniaturized wick structure/geometry of these heat pipes could become the most cost intensive factor. Another common limitation is the capillary limit, which occurs when the wick structure cannot return an adequate amount of liquid back to the evaporator. To overcome these difficulties researchers have come up with pulsating heat pipes (PHPs) which work on principle of oscillation of the working fluid and phase change phenomenon in a capillary tube. PHP is a meandering tube of capillary dimensions with many turns filled partially with a suitable working fluid with no wick structure. PHPs are passive two-phase thermal control devices first introduced by Akachi et al [2]. In this application, reduced diameter channels are used, which are directly influenced by the selected working fluid. The vapor plugs generated by the evaporation of the working fluid push the liquid slugs toward the condensation section and this motion causes flow oscillations that guide the device operation [3].

There are two possible configurations for PHPs, being as an open loop and as a closed loop. In the open loop configuration, one end of the tube is pinched off and welded, while the other end may present a service valve for evacuation and charging. The closed loop configuration has both ends connected and the fluid is

allowed to circulate. On the open loop configuration, the liquid circulation is not possible. In this case, it is believed that a counter-current liquid/vapor flow occurs in order to promote the proper device operation [4]. Therefore, better understanding on this behavior is still a motivation for further investigations. The purposes of this investigation are to study the heat transfer characteristics of an OLPHP and evaluate several issues related to its performance.

### 2. EXPERIMENTAL PROCEDURE

The device used during the experimental tests is shown in Figure 1. A pulsating heat pipe configured as an open loop is built using a capillary copper tubing with 2.30 mm OD, 0.90 mm ID, 4.9 m long to form 13 parallel channels with 12 curves. The apparatus is placed on a support that allowed its adjustment on vertical and horizontal orientations.

The OLPHP as shown in the figure 1 is built with 3 regions: evaporation, adiabatic and condensation, each one is 300 mm wide. The evaporator section is 105mm long, the adiabatic section is 100 mm long and condenser is 95 mm long with filling ratio of 50%. For the tests under vertical orientation, the evaporation section is always below the condensation section. For the tests under horizontal orientation, all sections are at the same plane. Both evaporation and adiabatic sections are thermally insulated, while the condensation section is open to the surrounding air. The condensation section is cooled by forced air, using a fan able to deliver air at a

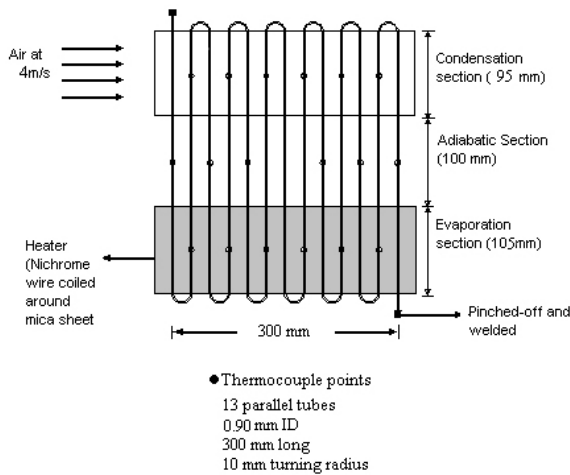


Fig 1. Cross Section of the OLPHP Test Apparatus

velocity of 4 m/s. The evaporation section is in contact with Ni-Cr wire which is coiled around two mica sheets to deliver the desired heat load. The heat loads are administered by an AC power supply. Eighteen K-type thermocouples are used to monitor the device performance during the tests. A total of 6 thermocouples are located at each section. The thermocouples are connected to a digital temperature controller (0°C to 800°C) to monitor wall temperatures. The temperatures are recorded at every 5 minutes. All experimental tests are performed on a heat load profile basis, where the perspective is to evaluate the behavior of OLPHP related to the orientation and applied power.

### 3. RESULTS AND DISCUSSION

#### 3.1 Temperature Profile

When testing the OLPHP with Acetone at vertical orientation as shown in Figure 2(a), it is observed that a more intensive plug/slug pumping action is initiated at 15W. For this working fluid, OLPHP presents even temperature distribution along the evaporation, adiabatic and condensation sections. At horizontal orientation as shown in Figure 2(b) Acetone exhibits more drastic pulsations and intensive oscillations start from 15W. Considering that the channels are of capillary dimension at horizontal orientation, the surface tension and shear stress effects are very expressive.

For Water at vertical orientation as shown in Figure 3(a) oscillations begin from 20W. At the highest heat load of 45W the evaporation section temperature rises to 110°C. So Water is more suitable at lower heat loads than 45W. But at all other heat loads the evaporation section temperature of Water is lower as compared to Acetone. At horizontal orientation as shown in Figure 3(b) temperature distribution of Water is more uniform as compared to vertical orientation. OLPHP does not present an indication of pulsations during its operation at low heat loads, even though some oscillations have been continuously captured and have become more evident after 30W.

From comparison of evaporation section temperature

profile of Acetone it is found that at all heat load levels the evaporator temperature has been considerably lower at horizontal orientation. From comparison between orientations of Water it is observed for low heat loads up to 25W, evaporator temperature is much lower at horizontal orientation and performance is better. At higher heat loads there have been fluctuations and performance is similar or slightly better in horizontal orientation. From comparison of temperature profiles of both working fluids at vertical orientation it is observed that Acetone exhibits the higher evaporation temperature and Water has lower evaporation section temperature at all heat loads. Hence, Water is the better choice for use at vertical orientation. For all heat loads both working fluids show almost similar evaporation temperature with little fluctuations at horizontal orientation.

#### 3.2 Thermal Conductance

Thermal conductance of the heat pipe is calculated by using the evaporation and condensation section temperature.

$$G_{calc} = \frac{Q}{(T_E - T_C)} \quad (1)$$

Figure 4 denotes the comparison of thermal conductance of OLPHP at various orientations using different working fluids. It is observed from the figure 6 that for Acetone at vertical orientation the thermal conductance doesn't change much with heat load. At horizontal orientation thermal conductance of Acetone gradually increases. At 30W heat load there is a sudden drop which could be considered as an anomaly. Water doesn't show any definite trend but mostly the performance is better at horizontal orientation. Water has the higher thermal conductance at almost all heat loads as compared to Acetone. So it is concluded that with regard to thermal conductance Water performs better than Acetone.

#### 3.3 Overall Efficiency

The overall efficiency is determined by the ratio of the thermal conductance of copper tube with working fluids ( $G_{calc}$ ) and empty copper tube ( $G_{ref}$ ).

$$\eta = \frac{G_{calc}}{G_{ref}} \quad (2)$$

Figure 5 indicates the variations of overall efficiency of OLPHP using different working fluids at various orientations. It is observed from the figure 5 that Water has the higher efficiency for both the orientations so it is better than Acetone.

#### 3.4 Diametrical Effect

The findings of this experiment have been compared with the experimental results of Roger R. Reihl [1]. Roger R. Reihl conducted the same experiment with copper tube of 1.5 mm inner diameter. The 0.9mm inner diameter copper tube in this experiment has operated successfully and shown good thermal performance for both the orientations compared with the copper tube of 1.5 mm inner diameter.

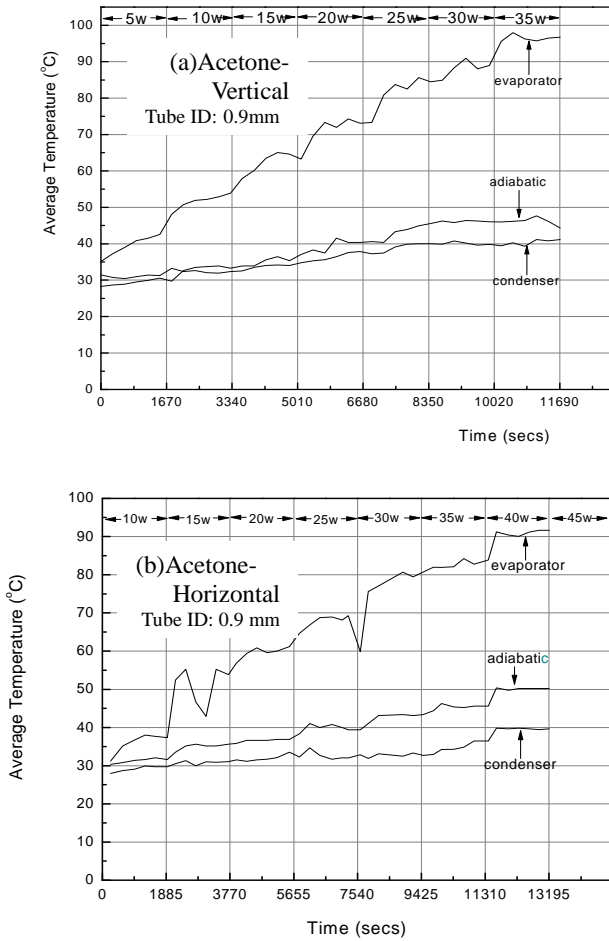


Fig 2. Temperature Profile along the length of OLPHP for Acetone

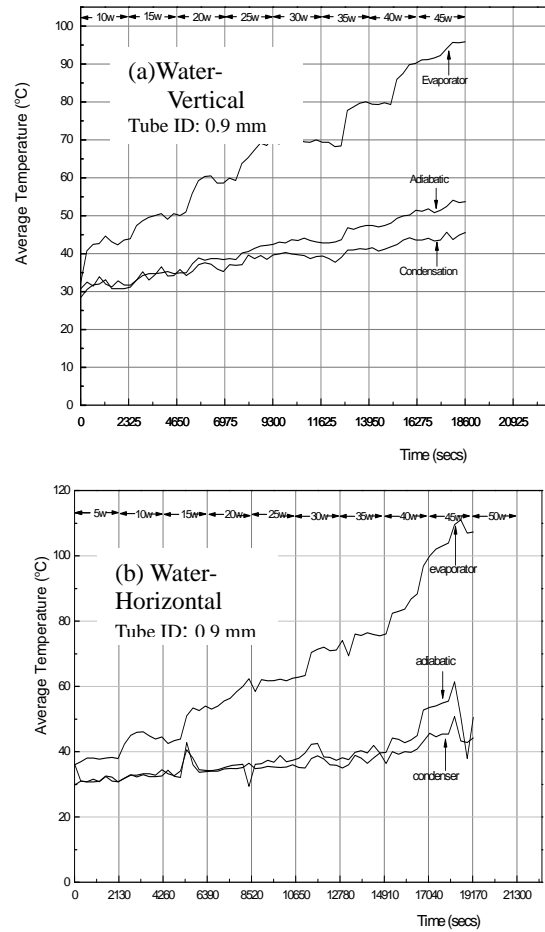


Fig 3. Temperature Profile along the length of OLPHP for Water

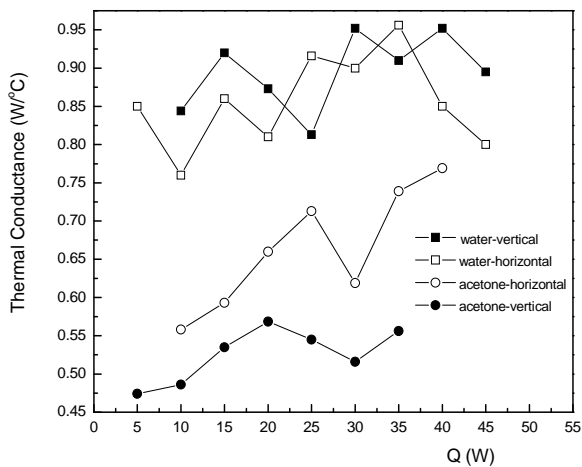


Fig 4. Comparison of Thermal Conductance

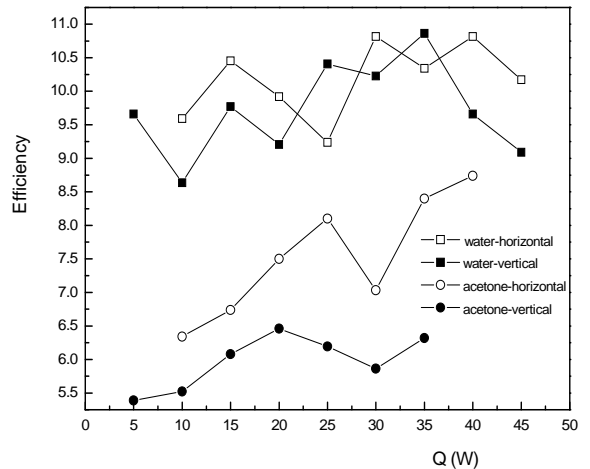


Fig 5. Comparison of Overall Efficiency

Figure 6 signifies the effect of diameter on the performance of OLPHP for different working fluids. For Water, as shown in figure 6(a), the 0.9mm inner diameter

copper tube has operated successfully and shown good thermal performance for both the orientations. In case of Acetone, as shown in figure 6(b), the same result is



obtained again but only for the vertical orientation. For horizontal orientation the 1.5 mm inner diameter copper tube showed better thermal performance.

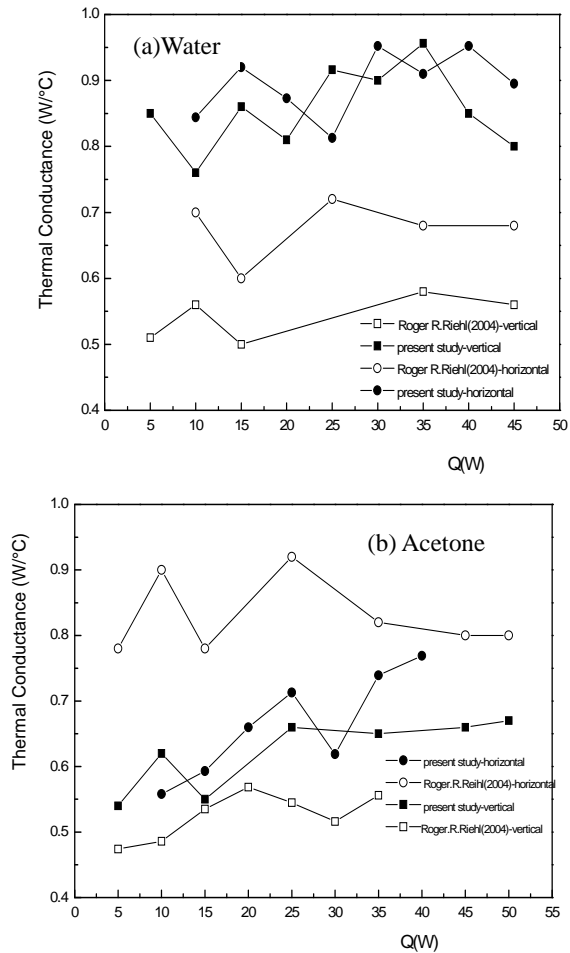


Fig 6. Diametrical effect

#### 4. CONCLUSION

For both the orientations Water shows better thermal performance than Acetone. So Water can be regarded as the better working fluid. Acetone shows drastic pulsations at all heat loads for both the orientations. The plug and slug pumping action started from the very beginning of 5W of power level. In case of Water, for horizontal orientations pulsation started at the very beginning and continued through out all heat loads but for vertical orientation, pulsation did not start till 25W of power level.

The smaller 0.9 mm ID heat pipe shows better thermal performance compared with 1.5 mm ID heat pipe.

#### 5. REFERENCES

1. Roger R. Riehl, "Characteristics of an Open Loop Pulsating Heat Pipe", SAE paper #2004-01-2509.
2. Akachi, H., Polášek F., Štulc P., "Pulsating Heat Pipes", Proceedings of the 5th International Heat Pipe Symposium, 1996, pp.208-217, Melbourne, Australia.
3. Zhang, Y., Faghri, A., "Heat Transfer in a Pulsating Heat pipe with an Open End", International Journal of Heat and Mass Transfer, Vol. 45, 2002, pp. 755-764.
4. Riehl, R. R., "Evaluation of the Thermal-Hydro-Dynamics Behavior of an Open Loop Pulsating Heat Pipe", National Institute for Space Research (INPE) Report, 2003, 35p.

#### 6. NOMENCLATURE

Symbol	Meaning	Unit
G	Thermal Conductance	W/°C
T <sub>C</sub>	Average Condenser Temperature	°C
T <sub>E</sub>	Average Evaporator Temperature	°C
Q	Heat Load	W

#### 7. MAILING ADDRESS

Tahane Mujib  
 Department of Mechanical Engineering,  
 Bangladesh University of Engineering and Technology,  
 Dhaka, Bangladesh

## OPERATIONAL AND PRESSURE CHARACTERISTICS OF A THERMOLOOP DEVICE

K. Sharmin, R. Roy, S. Akhter, M. A. Islam

Department of Mechanical Engineering, BUET, Dhaka, Bangladesh

### ABSTRACT

Thermoloop, a particular kind of two phase pulsated thermosyphon (PTPT) is passive cooling device which can meet high heat flux dissipation requirements. This paper gives emphasis on the analysis of working phenomena and operational characteristics of this device. The PTPT comprises of three components; evaporator, condenser and reservoir connected by flexible tubing. Experiments were carried out for different working fluids and thermal loads for a specific geometry of the device. During each experiment the temperature of the components at different points and pressure at evaporator were measured at steady state condition. Neither mechanical pump nor gravity force is used to assist the flow. Only natural convection was allowed for condensation. It is realized that, the variation of pressure drives the working fluid through the system components. Development of vacuum pressure due to condensation plays key role to refill the evaporator with fresh liquid at the end of each cycle. For a particular working fluid the cycle duration decreases with thermal load but, the  $\Delta T_{\text{sat}}$ , maximum evaporator wall temperature, and maximum cycle pressure increases. The condensate return temperature and maximum vacuum pressure increases slightly with thermal load. The operating cycle can be described by three regions viz. constant volume heat addition, vapor transfer and condensate return region.

**Keywords:** Thermoloop, Evaporator Pressure Drop, Cycle Time.

### 1. INTRODUCTION

Pulsated two phase thermosyphons (PTPT) can meet the demand in electronics industry for its compact size and faster technology to dissipate heat. It is a very effective means of cooling for many purposes. To develop this idea many research works are done. As a result of these series works, conventional heat pipes (capillary driven) were developed by Peterson [1], Faghri [2], Khrustalev et al. [3] which are capable of working against gravity. After heat pipes have been invented, Meidanik et al. [4] and Ku [5] developed loop heat pipe, LHP and capillary pumped loops, CPL, as a part of the research above. In the last few years, Akachi et al. [6], Dobson et al. [7] and Groll et al. [8] have proposed and developed oscillating heat pipes or pulsating heat pipes (OHPs or PHPs), wickless devices able to operate against gravity. But oscillation of temperature occurred in the evaporator section with high frequency [7-8] In 2001, Fillipschi [9] developed an initial idea of implementing PTPT device in electronic and micro-electronic equipments. In 2003, Fillipschi et al. [10] proposed a device for electronic equipment cooling with FC72. That was the first miniature experimental apparatus based on PTPT. In 2005, Fillipschi [11] also carried out a study to find out the influence of main parameters on thermal behavior

and developed a mathematical model to analyze the parameters.

Alam [12], first came with the idea of Thermoloop, made it as a patent and performed few experimental tests identifying the key performance parameters. Later Rahman et al. [13], in May 2008, has conducted some experiment on Thermoloop device in the heat transfer laboratory of Bangladesh University of Engineering and Technology keeping reservoir open to atmosphere and described the effect of evaporator fill ratio and condenser convection condition on evaporator temperature. More recently, Islam et al. [16] completed a research project on PTPT device and extensive data are collected by combining different geometry and sizes of evaporator and condenser for different working fluids. In the project and other recent studies, the system pressure was measured by an indirect means as there was no direct pressure measuring device. Therefore, operating characteristics of the PTPT device is not clearly understood hitherto.

This present study conducted experiments to measure system pressure correctly using a pressure transducer and understood operating characteristics of the thermoloop device more comprehensively. By collecting these experimental data, in this study a description of the pressure characteristics is offered.

And some characteristics curves are also presented here to describe the working principle.

## 2. EXPERIMENTAL SET-UP

### 2.1 Arrangement

The device comprised of three components; an evaporator E(made of copper) with internal volume of 3 cc, a natural cooling copper tube condenser C(4 turns, 25 cc) & a flexible reservoir R, shown in figure 1, placed at a same level to avoid the influence of gravity. The components above were connected by forward lines, FL (7mm) return lines, RL (7mm). These lines are transparent tubes to facilitate flow visualization.

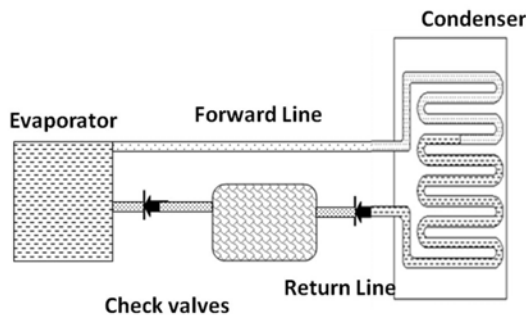


Fig 1. Simple schematic diagram of Thermoloop

Two check valves were placed at the both ends of the reservoir to make the flow unidirectional. The temperature of evaporator wall, fluid (in evaporator) and condensate temperatures were measured by K-type thermocouple. Fluid pressure in evaporator was measured by a pressure transducer. The temperatures and pressure were recorded by a data logger (Pico TC-08). Two cylindrical AC heaters, each of 200 watts were connected in parallel, pressed into a closed flat copper box to apply thermal load to the evaporator. A thermal material coating was applied between the mating surfaces evaporator and heater body to reduce thermal resistance due to air gap.

### 2.2 Experimental Procedure

The study was conducted with three different working fluid viz. Methanol, Ethanol and Water for thermal loads 50W, 75W and 100W. Initially all the components of the thermoloop were filled by a suction pump with working fluid and residual air bubbles were bled out. Then the setup was checked for any possible leakage. All the tests were performed by placing the whole setup horizontally. Then the power connection to the heater was switched on and the desired heat input was ensured by setting the variac to the required level and taking consequent ampere reading. The temperature of the evaporator wall and condenser outlet and pressure inside the evaporator were recorded for certain periods. The total time required for completion of every heat transport cycle was recorded for all the tests performed, along with readings of wall temperature of the evaporator, inlet and outlet temperature of the condenser and voltage of the voltmeter connected with pressure transducer. Almost all the experiments were carried out for about 500 seconds.

## 3. RESULTS AND DISCUSSION

### 3.1 Single Heat Transport Cycle Analysis

The Thermoloop device works in a periodic fashion. The cycle starts with constant volume heat addition of subcooled liquid in the evaporator and when the condensate returns to the evaporator from the reservoir, the cycle is completed. Temperature evolutions for 6 consecutive heat transfer cycles of water for thermal load of 50 W is shown in figure 2.

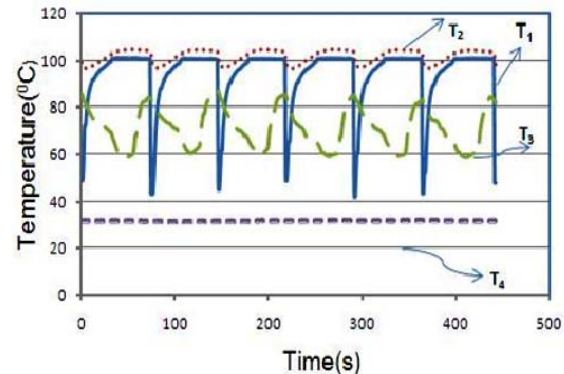


Fig 2. Temperature evolutions of water for 6 consecutive cycles for thermal load of 50 W

The operation of a sample cycle (Methanol, 75W) analyzed here and time expressed in terms of percentage of total cycle duration. The whole cycle can be described through three distinguished regions. These are –

- Constant volume heat addition region
- Vapor transfer region
- Condensate return region

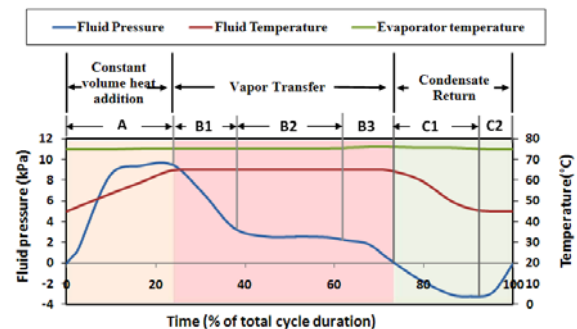


Fig 3. Operating cycle of a Two Phase Pulsated Thermoloop

#### A. Constant volume heat addition region

This region last for 25% of the cycle. At the beginning of this region the evaporator is fully filled with subcooled liquid and the pressure is atmospheric. The temperature of the evaporator wall is higher than the saturation temperature of liquid. The liquid near the evaporator wall first receive heat and free convection current is responsible for rising temperature of the subcooled liquid. Bubbles begin to form near the wall, dissipated in the liquid and pressure in the evaporator gradually increases. Pressure difference required to initiate flow from evaporator which is

$$\Delta P = 32L\mu u_m / D^2 \quad (1) [15]$$

The developed pressure in the evaporator is not enough to make flow and the liquid get heated in a constant volume manner. At end of this region liquid temperature rises to saturation temperature and pressure builds up to maximum in the cycle. The evaporator wall temperature is increases a little.

### B. Vapor transfer region

This region is characterized by removing heat by boiling of liquid and transfer of vapor form evaporator. It lasts for 50% of the cycle. The region can be best described by three sub-regions viz. B1, B2 and B3:

In region B1, the saturated liquid starts to vaporize. The generated vapor moves towards the condenser via forward tube. The vapor carries some liquid causing a mixed flow of liquid and vapor. The pressure in the evaporator drops as the mixed flow poses less viscosity than the liquid flow. The percentage of liquid in mixed flow gradually decreases with time and approaches to zero at the end of sub-region.

Fully vapor flow established in sub-region B2 and pressure in the evaporator is enough to maintain the vapor flow. The check valves direct the vapor towards the condenser and after condensation it returns to flexible reservoir. The generation and transportation of vapor maintains an equilibrium which keeps the evaporator pressure almost constant.

In sub-region B3, evaporator pressure drops back to atmospheric pressure. As only a fixed volume of the liquid is transported into the evaporator in each cycle, when most of the liquid vaporizes the equilibrium of sub-region B2 cannot be maintained. For slower vapor generation rate, pressure drops and descends to atmospheric.

Throughout the Vapor transfer region evaporator wall temperature gradually increases.

### C. Condensate return region

This is remaining 25% time when the evaporator is refilled by fresh subcooled liquid. The system pressure drops due to condensation of vapor, a vacuum creates which sucks a bulk of fresh subcooled liquid from reservoir, then pass through return line, evaporator, forward line and reaches up to condenser inlet. The flexible reservoir collapses during suction to maintain atmospheric pressure. The region briefly analyzed through sub-regions C1& C2.

In region C1, as soon as fresh subcooled liquid comes in contact with superheated evaporator wall, some of the liquid momentarily vaporizes and rest of the liquid carry out heat by heating sensibly. It leads to immediate drop in evaporator body temperature.

At region C2, both the liquid and evaporator temperature holds steady and that seems to be an establishment of thermal equilibrium. The heat removed by flow of fresh subcooled liquid under vacuum pressure is equal to heat rejected by evaporator.

As liquid fills the vacuum created by condensation of vapor the pressure of system recovered to atmospheric again and a new cycle starts.

## 3.2 Variation of Performance Parameters under Different Thermal load and Working Fluid

This study proposes the experimental investigation of thermolooop device to determine the variation of functional parameters on the performance of the thermolooop.

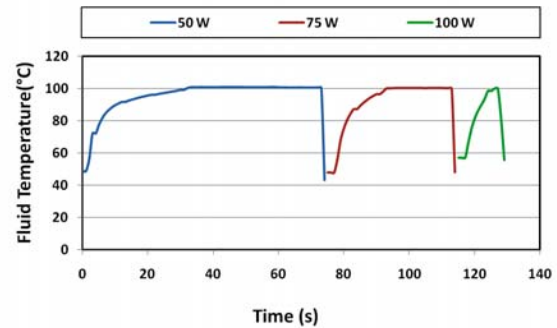
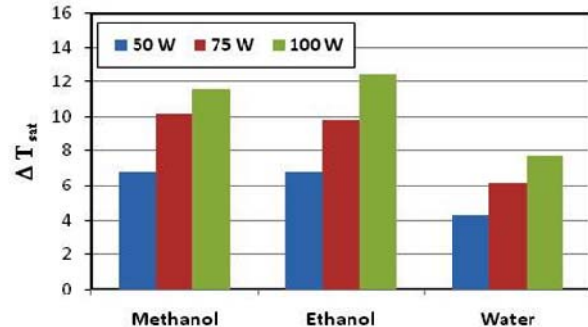


Fig 4. Comparison of cycle times for thermal load of 50W (a), 75W (b), 100W (c)

The figure 4 presents a comparative description of a single cycle for different thermal load. For all working fluid the cycle duration decreases with heat input. For higher thermal load it takes less time to complete the heat transport cycle. because a fixed volume of liquid in the evaporator boils faster. In case of water, for 50 W it takes around 75 seconds, where for 75 W it is 40 seconds and for 100 W it is only 13 seconds. Water exhibits maximum cycle duration for its highest value of latent heat of vaporization and methanol exhibits the minimum for a



certain thermal load.

Fig 5. Variation of  $\Delta T_{sat}$  with Thermal Load.

Figure 5 presents the variation of  $\Delta T_{sat}$  with Thermal Load. The simple law of heat transfer for boiling is heat flux  $q \propto h \Delta T_{sat}$  and the  $\Delta T_{sat} > 0$ . An increment on thermal load increases the heat flux which in terms increases both the  $\Delta T_{sat}$  and  $h$ . Water has a maximum enthalpy of vaporization which poses maximum value of  $h$  and for the same reason ethanol exhibits minimum value of  $h$ . So  $\Delta T_{sat}$  is minimum for water and maximum for ethanol for a certain thermal load.

Figure 6 shows the variation of Maximum Fluctuation of Evaporator wall temperature with Thermal Load. The temperature of evaporator drops in condensate return region when sub-cooled liquid passes through the evaporator and rises during constant volume heat addition and vapor transfer region.

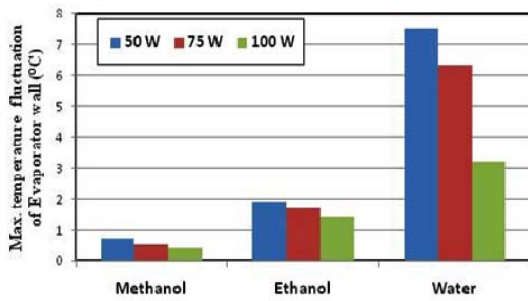


Fig 6. Variation of Maximum Fluctuation of Evaporator wall temperature with Thermal Load

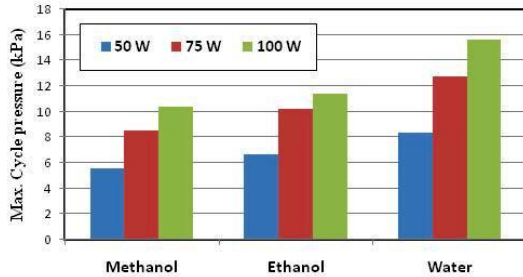


Fig 7. Variation of Maximum Cycle Pressure with Thermal Load

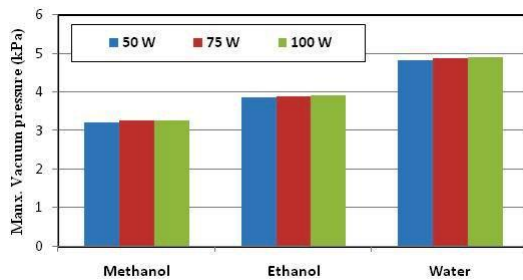


Fig 8. Variation of Maximum Cycle Vacuum Pressure with Thermal Load

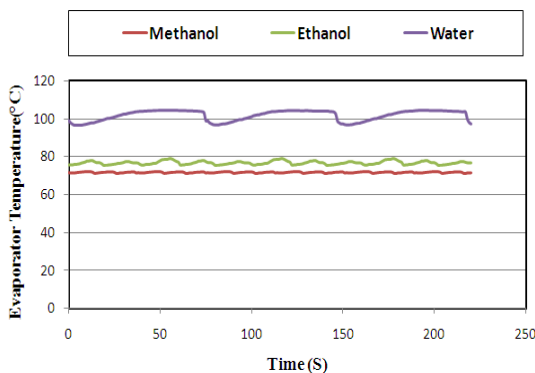


Fig 9. Comparison of evaporator temperature for different working fluid

The temperature drops mostly depends on specific heat  $C_p$  of sub-cooled liquid. As water has the highest value of  $C_p$ , the temperature drops most and the minimum value of  $C_p$  of methanol causes to drop least.

Figure 7 presents comparison of Maximum Cycle Pressure with different Thermal Load. The maximum

pressure increases with thermal load. The maximum cycle pressure develops in sensible heating region which depends on the viscosity of the fluid. The pressure is also depends on change in specific volume due to phase change in some degree and its influence is not realized fully yet. From the observation, water shows maximum pressure and methanol shows the minimum temperature for different working fluid.

Figure 8 shows the variation of Maximum Cycle Vacuum Pressure with Thermal Load. The vacuum pressure develops for condensation of saturated vapor to liquid in the condenser so it depends on the change in specific volume due condensation. Methanol has least change in specific volume for condensation and vacuum creates the minimum among other fluid. The water shows maximum drop in pressure. The maximum vacuum pressure increases with thermal load.

Figure 9 shows a comparative description on cooling process between water and methanol. Methanol boiling point is lower than the boiling point of water. And methanol keeps the evaporator at a lower temperature than that of water. So it is useful to use a working fluid with lower boiling point.

#### 4. CONCLUSION

Periodic two phase thermosyphon (PTPTs) is a special type of unsteady state heat transfer device for high end electronics cooling, capable of operating without gravity support. The maximum thermal load handled were 100W under natural convection. The operational characteristics and influence of various functional parameters on the performance of the thermolooop may be summarized to make following conclusions:

1. The variation of pressure drives the working fluid through the system components. Development of vacuum pressure due to condensation plays key role to refill the evaporator with fresh liquid at the end of each cycle.
2. For a particular working fluid the cycle duration decreases with thermal load but, the  $\Delta T_{sat}$ , maximum evaporator wall temperature, maximum cycle pressure, and condensate return temperature and maximum vacuum pressure increases.
3. Fluid of low boiling temperature (like Methanol 67°C) performs better in cooling purposes and build less thermal stress for the thermolooop device.

#### 5. REFERENCES

1. Peterson, G. P., "An Introduction to heat pipes, Modeling, Testing and Applications", John Wiley & Sons, New York, (1994).
2. Faghri, A., "Heat Pipe Science and Technology, Taylor and Francis", Washington, DC, (1995).
3. Khurstalev, D., Faghri, A., Thermal characteristics of conventional and flat miniature axially-grooved heat pipes, J. Heat Transfer 117 (1995).
4. Maidanik, Y. F., Pastukhov, V. G., Verzhinin, C.V., Korukov, M. A., "Miniature loop heat pipes for electronics cooling", Appl. Thermal Eng. 23, 1125-1135 (2003).

5. Ku, J., "Operating characteristics of loop heat pipes, in: Proc. 29th International Conference on Environmental System", Denver, CO, (1999).
6. Akachi, H., Polasek, F., "Pulsating heat pipe-review of present state of art", Technical Report ITRI ERL, (1995).
7. Dobson, R. T., "Theoretical and experimental modeling of an open oscillatory heat pipe including gravity", Int. J. Therm. Sci. 43, 113-119 (2004).
8. Groll, M., Khandekar, S., "An insight into thermo-hydrodynamic coupling in closed loop pulsating heat pipes", Int. J. Thermal. Sci. 43, 13-20 (2004).
9. Filippeschi, S., "Two phase thermosyphons operating against gravity", phd thesis, Pisa University, Italy, (2001).
10. Fantozzi, F., Filippeschi, S., Latrofa, E., "Miniature pulsated loop thermosyphon for desktop computer cooling: feasibility study and first experimental tests", 5<sup>th</sup> Minsk Seminar on Heat Pipes, Heat Pumps, Refrigerators, Minsk, Belarus, (2003).
11. Filippeschi, S., "On periodic two-phase thermosyphons operating against gravity", Int. J. Thermal. Sci. 45, 124-137 (2006).
12. Alam, M., "Self-Actuating and regulating heat exchange system", Patent Application No: 11/194,420, filed Aug 8, (2005).
13. Rahman, M. A., "Performance Study of Two-phase Loop Thermosyphon", M.Sc. Thesis, Bangladesh University of Engineering and Technology, Dhaka, Bangladesh, (2008).
14. Islam, M. A., Ahmed, R., Bhuiyan, S. M. Y., "Effect of Working Fluids and Evaporator Geometry on the

Performance of Thermoloop", 4th BSME-ASME International Conf. on Thermal Engineering, Bangladesh, 27-29 December, (2008).

15. M. Necati OZISIK, 1985, International Edition, McGraw Hill Book Company, "Heat Transfer: A Basic Approach", page 240.

## 6. NOMENCLATURE

Symbol	Meaning	Unit
E	Evaporator	
C	Condenser	
R	Reservoir	
RL	Return Line	
FL	Forward Line	
L	Line Length	m
D	Line Diameter	m
$P_E$	Evaporator Pressure	Pa
$\Delta P$	Pressure difference	Pa
$\mu$	Viscosity	Ns/m <sup>2</sup>
$u_m$	Fluid Velocity	m/s
q	Heat Flux	Wm <sup>-2</sup>
h	Heat transfer coefficient	W/m <sup>2</sup> K
t	Cycle Time	sec
$T_1$	Temperature of Evaporator Liquid	<sup>0</sup> C
$T_2$	Temperature of Evaporator Body	<sup>0</sup> C
$T_3$	Temperature at condenser Inlet	<sup>0</sup> C
$T_4$	Temperature at condenser Outlet	<sup>0</sup> C
$\Delta T_{sat}$	Temperature difference between evaporator wall and saturation temperature of liquid.	<sup>0</sup> C
$C_p$	Coefficient of heat transfer	J/kg <sup>0</sup> C

## 7. MAILING ADDRESS

K Sharmin  
 Department of Mechanical Engineering,  
 BUET, Dhaka-1000, BANGLADESH  
 E-mail: aislam@me.buet.ac.bd



## ENERGY EXTRACTION FROM CONVENTIONAL BRAKING SYSTEM OF AUTOMOBILE

Aktaruzzaman and Mohammad Ali

Department of Mechanical Engineering  
Bangladesh University of Engineering and Technology  
Dhaka, Bangladesh

### ABSTRACT

Optimization of power consumption is an important subject in the design of automobile. The conventional braking (friction brake) system losses considerable amount of energy during car drive. A model of braking system is designed and constructed to extract and store energy during the braking of a car. Gaseous fluid is compressed in cylinder by a high pressure liquid to store the energy of brake. A positive displacement pump driven by the extraction of energy from brake is used to supply the high pressure liquid. During braking the pump is clutched with the power train of the car. The pump utilizes the inertia energy of the car to compress the gaseous fluid. This stored energy can be used to enhance the acceleration of car and to run other accessories of the car. A performance test of the brake model is conducted and can be found that, during brake approximately 60% of inertia energy can be saved.

**Keywords:** Braking System, Inertia Energy Conservation, Compressible Fluid, Friction Brake.

### 1. INTRODUCTION

Motor vehicle has been the heart of human transportation since the dawn of its creation. Many advances have been made to make the motor vehicle more desirable and friendly for the millions of users throughout the world. It is our goal to design a device that can make their commute an economic one. The Energy extraction from conventional braking system of automobile is a device that can do so by reducing the overall energy required to use. Brake energy is a energy that stops an engine. There are also other opposing forces such as aerodynamic drag force and rolling force. Research of William H. Crouse, "Automotive Mechanics"[1] showed that almost 50% of the total energy was lost as brake energy although this percentage is a bit different from different types of vehicles. Wendel at al. [2] described in Michigan clean fleet conference, Hydraulic Regenerative Braking System has a good power density of 1458 W/Kg and efficiency about 85%. So, this system is more efficient than electric energy storage device.

In 1996 University Wire performed a research onelectric regenerative braking system [3]. In 2002 a new braking system called hydraulic launch assisted to make a stop-and-go driving for large trucks more efficiently by capturing energy [4]. Advanced Technology department at Eaton's Fluid Power Group in 2009 begins a test of Rexroth Hydraulic Hybrid Technology in Refuse Trucks [4] It is sponsored by the New York State Energy Research and Development

Authority (NYSERDA), this evaluation project identifies vehicle fleets which integrate technologies such as HRB (Hydraulic Regenerative Braking system), have high potential for reducing fuel consumption and emissions. The hydraulic hybrid evaluation is a part of a larger program carried out by DSNY that will demonstrate the impact of utilizing multiple alternative drive technologies. In April 2009 Artemis Intelligent Power [5] converted a BMW 530i to capture the energy mechanically resulted from braking (aka "regenerative braking"), and use it in an electrically-hybridized car fashion [6].

### 2. PRODUCT DEVELOPMENT PROCESS

Many decisions are needed to be made in order to produce the most desirable and affordable model to make the highest efficiency and the most unique device. Process has four distinct phases: the Concept Phase, the Design Phase, Mathematical modeling Phase and the Construction Phase. In the Concept Phase, we defined the problem of losing energy while braking on a motor vehicle. We then conceptualized different ways of using that energy with different regenerative braking systems. Through research and customer surveys, we entered the Design Phase knowing consumer preferences. We generated designs based on known preferences, constraints, and parameters. We then made a CAD drawing of our design. We analyzed our model from the viewpoint of the consumer and manufacturer and did mathematical analysis of the optimal designs. After



reviewing our results, we hypothesized how we would start the Construction Phase.

## 2.1 Design Requirements

There are some requirements that needed to produce a product that is both feasible and optimal. There are also some constraints, both geometric and engineering that are also needed to be satisfied. The following list describes these requirements and constraints:

### 1. Store energy while braking

This is the main requirement and the overall objective of the device and must be suitable to meet the customer's needs.

### 2. The system must be fitted on the vehicle for which it is designed

This is one of the most difficult constraints to achieve because we are dealing with a confined spacing. The system contains a few cylinders and other components which are to be fitted on the longest part of the car, particularly between the two axles of wheels.

### 3. Light weight

The importance of having a light weight design is driven by the customer's desire to have a car that is more maneuverable and more portable. This is also a direct trade off with how much energy can be stored in the cylinders.

### 4. Good stopping range

The stopping range is important because the system needs to be usable in real life situations. The product can be optimized to have the shortest stopping distance using dynamic analysis.

### 5. Safe to user and environment friendly

Safety is always a very important aspect whenever there is a consumer product. This requirement will be addressed during the design.

### 6. Reliable

It is important to have a product reliable and this requirement will affect the long term production and needs to be maintained in high regards.

### 7. Manufacturability

In order to make anything profitable, it needs to be easily manufactured, hence important of having a product that can be made easily and economically.

## 2.2 Methodology

Inertia energy of a car is stored as a compressed fluid energy while braking is done. A clutch is used as a brake shoe. During braking this clutch will engage the driveline of the system, then the pump will be activated and it will force hydraulic fluid out of a low pressure cylinder (Reservoir) to a high pressure cylinder. This hydraulic fluid then compress the gaseous fluid in the cylinder and the energy will be stored. This energy can also be used to run a compressor for air conditing, lube oil motor or other hydraulic system.

Power is transmitted from the car drive train to the speed increasing gear box through the clutch. So pump is started to rotate with an increased speed which in turn moves fluid to the accumulator and energy can be stored within a short time, then the car will stop.

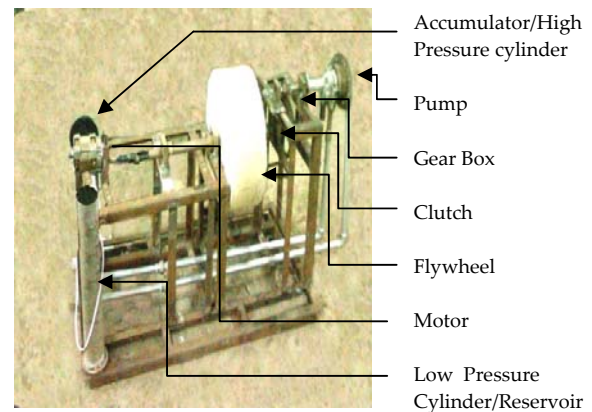


Fig 1. Experimental setup of the system

## 2.3 Design Parameters

Following components are used in model

1. Flywheel  
Diameter = 15in  
Width = 6in  
Material: concrete
2. Gear box  
Diameter of small gear = 1.5in  
Diameter of big gear = 7in
3. Motor: 3-phase ac motor
4. Clutch: 50cc Honda clutch
5. Pump: Oil pump of medium size pick up car
6. Accumulator / high pressure cylinder  
Volume = 75 in<sup>3</sup>
7. High pressure cylinder/Reservoir  
Volume = 100 in<sup>3</sup>

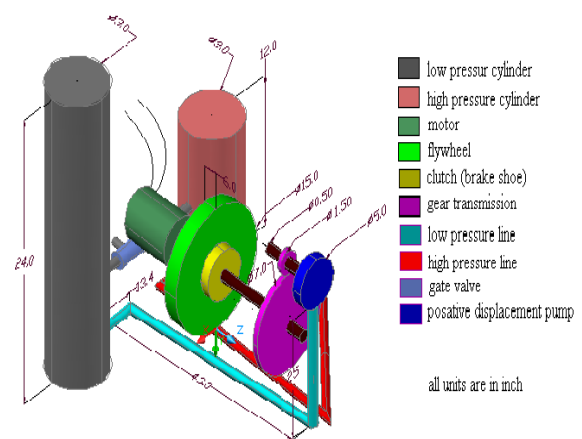
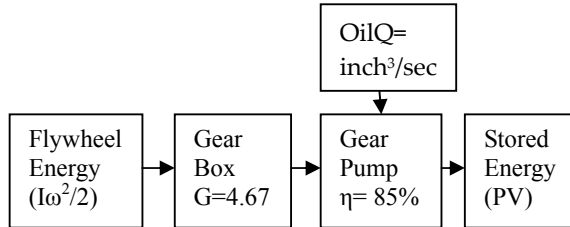


Fig. 2 Components of the model

### 3. MATHEMATICAL MODELING

#### 3.1 THEORETICAL DERIVATION OF THE NECESSARY EQUATIONS

The flow diagram of energy storing system is shown below:



Power flow across the pump,

$$T_p \cdot \omega_p = \Delta P \cdot Q / \eta$$

$$\Rightarrow T_p \cdot 2\pi n = \Delta P \cdot Q \cdot n / \eta$$

$$\Rightarrow T_p = \frac{\Delta P \cdot Q}{2\pi n \eta}$$

$$\text{but } T_i / T_p = G = D_1 / D_2 = 7 / 1.5 = 4.67;$$

$$\Rightarrow T_i = -I\alpha = \frac{\Delta P \cdot Q \cdot G}{2\pi n \eta}$$

$$\Rightarrow I\alpha = - \frac{\Delta P \cdot Q \cdot G}{2\pi n \eta}$$

$$\Rightarrow \alpha = - \frac{d\omega}{dt} = - \frac{\Delta P \cdot Q \cdot G}{2\pi n I \eta} = - \frac{Q \cdot G \cdot (P - P_{atm})}{2\pi n I \eta}$$

Assuming that,

Air compression processes is isothermal process, so pressure volume relation is –

$$PV = P_0 V_0$$

here,  $P_0 = P_{atm}$

$$\Rightarrow \frac{d\omega}{dt} = - \frac{Q \cdot G \cdot (P - P_{atm})}{2\pi n I \eta}$$

$$\frac{d\omega}{dt} = - \frac{Q \cdot G \cdot P_{atm} \left( \frac{P}{P_{atm}} - 1 \right)}{2\pi n I \eta} \quad (1)$$

#### 3.2 Expression of $V_0/V$

Change of Energy in Fly wheel = Energy Stored in Cylinder

$$1/2 I(\omega^2 - \omega_0^2) = 1/\eta \int_{V_0}^V P dV$$

$$= \{RT \cdot \ln(V/V_0)\} / \eta$$

$$V_0/V = e^{- \frac{2\pi n I \eta}{RT} \left( \frac{\omega^2 - \omega_0^2}{2} \right)}$$

$$V_0/V = e^{- \frac{2\pi n I \eta}{RT} \left( \frac{\omega^2 - \omega_0^2}{2} \right)}$$

(2)

From equation (1)

$$\frac{d\omega}{dt} = - \frac{Q \cdot G \cdot P_{atm} \left( e^{\frac{2\pi n I \eta}{RT} \left( \frac{\omega^2 - \omega_0^2}{2} \right)} - 1 \right)}{2\pi n I \eta}$$

when  $t = 0$ ,  $\omega = \omega_0$  &

$t = t$ ,  $\omega = \omega$

After integrating

$$\int_{\omega_0}^{\omega} \frac{d\omega}{e^{\frac{2\pi n I \eta}{RT} \left( \frac{\omega^2 - \omega_0^2}{2} \right)} - 1} = \frac{Q \cdot G \cdot P_{atm}}{2\pi n I \eta} \int_0^t dt \quad (3)$$

Equation (3) represents the variation of angular speed  $\omega$  with respect to time.

#### 3.3 Time Required to Stop The Wheel:

At the time to stop the flywheel,  $t = T$  then  $\omega = 0$ ;

From Equation no (3)

$$\frac{Q \cdot G \cdot P_{atm}}{2\pi n I \eta} \int_0^T dt = \int_{\omega_0}^0 \frac{d\omega}{e^{\frac{2\pi n I \eta}{RT} \left( \frac{\omega^2 - \omega_0^2}{2} \right)} - 1}$$

$$T = \frac{2\pi n I \eta}{Q \cdot G \cdot P_{atm}} \int_{\omega_0}^0 \frac{d\omega}{e^{\frac{2\pi n I \eta}{RT} \left( \frac{\omega^2 - \omega_0^2}{2} \right)} - 1}$$

$$T = \frac{2\pi n I \eta}{Q \cdot G \cdot P_{atm}} \int_{\omega_0}^0 \frac{d\omega}{e^{\frac{2\pi n I \eta}{RT} \left( \frac{\omega^2 - \omega_0^2}{2} \right)} - 1}$$

For getting finite value of integration assuming the limit 0 to 0.991

$$= \frac{2\pi n I \eta}{Q \cdot G \cdot P_{atm}} \int_{\omega_0}^{0.991 \omega_0} \frac{d\omega}{e^{\frac{2\pi n I \eta}{RT} \left( \frac{\omega^2 - \omega_0^2}{2} \right)} - 1}$$

$$= 2.244 \int_{\omega_0}^{0.991 \omega_0} \frac{d\omega}{e^{\frac{2\pi n I \eta}{RT} \left( \frac{\omega^2 - \omega_0^2}{2} \right)} - 1} \quad (4)$$

$$= 2.244 \cdot 3.064$$

$$= 6.8768 \text{ sec}$$

Here

$$a = e^{\frac{2\pi n I \eta}{RT}} = 2.9614$$

$$\omega/\omega_0 = \omega_r$$

$$d\omega = \omega_0 \cdot d\omega_r$$

When  $\omega = 0$  then  $\omega_r = 0$

$$\omega = \omega_0 \text{ then } \omega_r = 1$$

Theoretical stopping time of the fly wheel  $T = 6.8768$  sec for  $N = 200$  rpm

#### 3.4 Volume Calculation

At the time to stop the flywheel,  $t = T$  &  $\omega = 0$ ;  $V = V_2$

For  $\omega = 20.984$ ,  $N = 200$ rpm

From Equation (2)

$$V_0/V = e^{- \frac{2\pi n I \eta}{RT} \left( \frac{\omega^2 - \omega_0^2}{2} \right)}$$

$$\text{So } V_0/V_2 = e^{- \frac{2\pi n I \eta}{RT} \left( \frac{\omega^2 - \omega_0^2}{2} \right)}$$

$$= e^{- \frac{2\pi n I \eta}{RT} \left( \frac{\omega^2 - \omega_0^2}{2} \right)}$$

$$= 2.9768$$

$$V_2 = 75/2.9768 = 25.1958 \text{ in}^3$$

$$P_2 = P_1 V_1 / V_2 = 43.759 \text{ psi}$$

Energy Input

$$E_{in} = 1/2 I \omega_o^2 = 0.5 * 0.7258 * 20.924^2 = 159.8451 \text{ J}$$

Energy Stored

$$E_{st} = -P_o V_o * \ln \frac{V}{V_o} = -101325 * 75 * 0.0234 * \ln \frac{25.1958}{75}$$

$$= 135.8451 \text{ J}$$

For  $\omega = 15.7 \text{ N} = 150 \text{ rpm}$

when  $\omega = 0$  and  $V = V_2$

From Equation (2)

$$V_o/V = e^{-\frac{P_o V_o (V - V_o)}{P_o V_o V_o}} = e^{-\frac{P_o (V - V_o)}{V_o}}$$

$$\text{So } V_o/V_2 = e^{-\frac{P_o (V_2 - V_o)}{V_o}}$$

$$= e^{-\frac{101325 (25.1958 - 75)}{75}} = 1.8417$$

$$V_2 = 75 / 1.8417 = 40.729 \text{ in}^3$$

$$P_2 = P_1 V_1 / V_2 = 27.0732 \text{ psi}$$

Energy Stored

$$E_{st} = -P_o V_o * \ln \frac{V}{V_o} = -101325 * 75 * 0.0234 * \ln \frac{40.729}{75}$$

$$= 76.09241 \text{ J}$$

Energy Input

$$E_{in} = 1/2 I \omega_o^2 = 0.5 * 0.7258 * 15.7^2 = 89.451 \text{ J}$$

Table 1: Theoretical developed Pressure, Volume and Stored Energy

Obs No	N, rpm	P <sub>2</sub> psi	V <sub>2</sub> in <sup>3</sup>	T sec	E <sub>in</sub> (J)	E <sub>st</sub> (J)	Friction Loss	% of Energy Stored
1	200	43.7	25.2	6.8	159	136	24.1	85
2	150	27.1	40.7	5.1	89.4	76.2	13.3	85

## 4. RESULT AND DISCUSSION

### 4.1 Data Collection

Flow rate and efficiency of the rotor pump are taken from J. S. Cundiff [7]

$$\text{Flow Rate } Q = 4.53 \text{ in}^3/\text{rev} = 7.4233 \times 10^{-5} \text{ m}^3/\text{rev}$$

Average efficiency  $\eta_p = 85\%$

$$P_{atm} = 101325 \text{ Pa, Gear Ratio} = D_2/D_1 = 7/1.5 = 4.67$$

Density of concrete,  $\rho = 2000 \text{ kg/m}^3$

$$\text{Diameter of flywheel } D = 15 \text{ in} = 15 * 0.0254 = 0.381 \text{ m,}$$

$$\text{Width, } L = 6 \text{ in} = 6 * 0.0254 = 0.1524 \text{ m}$$

Table 2 : Data Collected

No of Obs	Rotation of wheel N <sub>w</sub> (rpm)	Pressure raise in accumulator $\Delta P$ (Psi)	Time require to stop the wheel T(sec)
1	200	15.5	27
2	150	5.5	15

### 4.2 Calculation

Table 3: Calculated Data

No of Obs	Volume V <sub>2</sub> Inch <sup>3</sup>	Input Energy E <sub>in</sub> ( J )	Stored energy, E <sub>st</sub> ( J )	Friction Loss ( J )	% of input energy stored
1	36.75	159.9	88.2	71	55.5
2	55.1	89.5	38.3	51.17	43

#### Assumptions:

- Isothermal Gas Compression process
- Neglecting Aero and rolling friction Force.

$$\text{Initial Volume } V_o = 75 \text{ inch}^3 = 1.23 \times 10^{-3} \text{ m}^3$$

$$\text{Final pressure } P_2 = \Delta P + P_{atm} = 30.2 \text{ psi}$$

$$\text{Final volume } V_2 = P_1 V_1 / P_2 = (14.7 * 75) / 30.2 = 36.75 \text{ inch}^3$$

Mass of flywheel ,

$$m_w = \rho V + \text{weight of Rod}$$

$$= 2000 * \pi * 0.1905^2 * 0.1524 + \text{weight of Rod}$$

$$= (35+5) \text{ Kg}$$

$$= 40 \text{ Kg}$$

Moment of Inertia,

$$I = 1/2 * m_w (D/2)^2$$

$$= 0.5 * 40 * 0.1905^2$$

$$= 0.7258 \text{ Kg m}^2$$

Energy Input

$$E_{in} = 0.5 * I * \omega_o^2$$

$$= 0.5 * 0.7258 * 20.9485^2$$

$$= 159.9485 \text{ J}$$

Energy Stored

$$E_{st} = -P_o V_o \ln(V_2/V_1)$$

$$= -101325 * 1.23 \times 10^{-3} * \ln(36.75/75)$$

$$= -124.63 \ln 0.49$$

$$= 88.904 \text{ J}$$

$$\text{Friction Loss} = E_{in} - E_{st} = 71.0445 \text{ J}$$

$$\% \text{ of Input energy is stored} = (88.904 / 159.9485) * 100\% = 55.5828\%$$

#### Observation 1

$$\text{Energy Input} = 159.247 \text{ J}$$

$$\text{Theoretical Time Required to stop the wheel} = 6.8768 \text{ sec}$$

Theoretical Energy Stored = 135.8451J  
 Theoretical Frictional Loss = 24.1019J  
 Experimental Time Required to stop the wheel = 27 sec  
 Experimental Energy Stored = 88.204J  
 Experimental Frictional Loss = 71.0429J  
 % of Input energy is stored ( Theoretical) = 85%  
 % of Input energy is stored (Experimental) = 55.58%

$$\% \text{ of Error} = \frac{|\text{Est}_1 - \text{Est}_2|}{\text{Est}_1} = \frac{|135.8451 - 88.204|}{135.8451} = 34.55\%$$

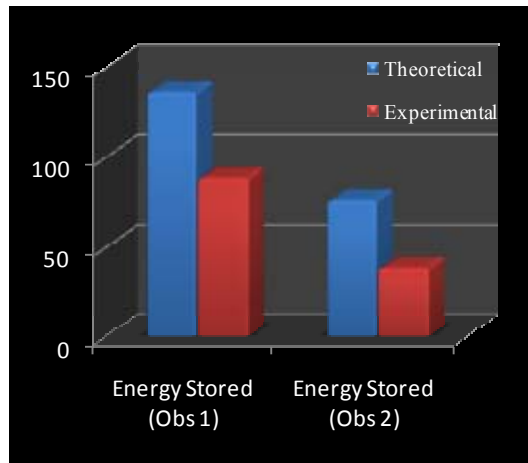


Fig. 3 Stored energy comparison (Theoretical Vs Experimental)

#### 4.3 Discussion

In regenerative braking system works within our expected range. Percentage of input energy stored in theoretical is 85% and the experimental result is 55.5%. It has almost reached our theoretical results. But there are some deviations. These deviations occur due to the following reasons.

1. akage in the Pump:
2. friction in the whole drive train:
3. vibration in the flywheel:
4. leakage in the accumulators and joints:
5. unavailability of the designed components with desired rating in local market:

This deviation will be less in prototype. Because in prototype friction loss will be less, and vibration will be less as all the components will be designed & manufactured as per need.

#### 5. CONCLUSION

In this work, a model of regenerating braking system is designed, manufactured and tested. The data is then compared with theoretical calculation. Two observations are made with rotational speed of the motor. It can be observed that for high speed the percentage of energy store is high and for low speed it is low. This is quite

natural that the system loss due to friction and other possible causes is almost same for all rotational speed. Therefore it affects the lower rotational speed. Hopefully much higher rotational speed of motor in model test will increase the percentage of energy store.

#### 6. RECOMMENDATIONS

To increase the performance of the model the following modifications can be made:

1. In our project regeneration was not done. It can be done by using Hydraulic motor unit.
2. By increasing the number of positive displacement pumps or using more power pumps braking could be done more rapidly.

More sophisticated hydraulic positive displacement pump could be made.

#### 7. REFERENCES

1. Glenn R. Wendel, Simon Basely and Jim O'Brian, 2007 "Hydraulic Hybrid Vehicle System Panel", Michigan Clean fleet Conference, May 17, 2007 NextEnergy Center 461 Burroughs Detroit, Michigan
2. <http://www.google.com/search?q=history+hydraulic+regenerative+braking>
3. William H. Crouse, "Automotive Mechanics".
4. Advanced Technology Department at Eaton's Fluid Power Group, Cleveland, Michigan, USA
5. <http://www.artemisip.com/>
6. <http://www.greenoptimistic.com/2009/02/26/hydraulic-regenerative-braking-saving-527-fuel-in-bmw-530i/>

#### 8. NOMENCLATURE

Symbol	Meaning
$E_{st}$	Energy stored in the Cylinder
$E_{in}$	energy in the flywheel
$m_w$	Mass of the flywheel
$D$	Diameter of the flywheel
$L$	Height of the flywheel
$I$	Moment of Inertia
$\alpha$	Angular Acceleration of the Flywheel
$\omega_0$	Initial Angular velocity (velocity at the start of the braking)
$\omega$	Instantaneous angular velocity
$N_w$	Rotational speed of the flywheel
$N_p$	Rotational speed of the pump
$T_w$	Torque in the Flywheel shaft
$T_p$	Torque in the Pump shaft
$D_1$	Diameter of the big gear
$D_2$	Diameter of the small gear
$G$	Gear ratio
$P_0$	Initial pressure in the cylinder
$P$	Instantaneous pressure in the cylinder
$P_2$	Final Pressure
$\Delta p$	Instantaneous change of pressure in the cylinder
$V_0$	Initial volume in the cylinder

V	Instantaneous volume in the cylinder
$V_2$	Final Volume
Q	Rated flow rate of pump( $m^3/rev$ )
$Q'$	Flow rate ( $m^3/sec$ )
t	Time
T	Stopping time
$\eta$	Efficiency of pump

## 9. MAILING ADDRESS

Aktaruzzaman  
 Department of Mechanical Engineering  
 Bangladesh University of Engineering and Technology  
 Dhaka, Bangladesh  
 E-mail: aman\_04rbt@yahoo.com

# A COMPARATIVE STUDY OF MECHANISTIC PARACHOR MODEL OVER PARACHOR MODEL IN A MULTI-COMPONENT HYDROCARBON SYSTEM

Mohammad Marufuzzaman<sup>1</sup>, Amr Henni<sup>1</sup>, Azizur Rahman<sup>2</sup>

<sup>1</sup>Industrial Systems Engineering (ISE), University of Regina, Canada

<sup>2</sup>Industrial Engineering and Management (IEM), Khulna University of Engineering and Technology (KUET), Khulna, Bangladesh

## ABSTRACT

Interfacial tension is an important property for many processes such as enhanced oil recovery by gas injection and flow through porous media, and in mass and heat transfer applications. The objective of this study is to study four prevalent interfacial tension models along with their governing mechanisms. Also, Mechanistic Parachor model has been studied in comparison with Parachor Model. The trait of the Mechanistic Parachor model is that it considers the mass transfer mechanism responsible for attaining the thermodynamic fluid phase equilibria in multi component hydrocarbon systems, while the other three IFT models doesn't consider the effect. The Mechanistic Parachor model has been tested on Rainbow Keg River (RKR) crude oil-gas systems and showed better IFT prediction over the conventional Parachor model.

**Key words:** Interfacial Tension, Parachor Model, Mechanistic Parachor Model, Gradient Theory.

## 1. INTRODUCTION

Interfacial tension is a physical parameter which plays an important role in many processes in a number of industrial applications, such as heat transfer under boiling conditions, mass transfer during extraction etc. In the petroleum industry, processes such as gas condensate recovery, near critical fluid recovery and secondary and tertiary crude oil recovery, in particular, by gas injection, bring very low surface tension to into play. These surface tensions (i.e liquid/vapour interfacial tensions) must be known because of their dominating influence on capillary pressures, relative permeabilities, one needs reliable theoretical estimates.

While most of the thermodynamic properties refer to individual fluid phases, interfacial tension (IFT) is unique in the sense that it is a property of the interface between the phases. Several models have been proposed for the calculation of interfacial tensions of simple fluids and mixtures in the past few decades. The most important among these models are the Parachor model [1,2], Mechanistic Parachor model [3], Gradient Theory [4], and the linear gradient theory [5,6]. The IFT, being a property of interface, is strongly dependent on the compositions of fluid phases in contact, which in turn depend on the mass transfer interactions between the phases. The commonly occurring mass transfer mechanisms between the fluid phases to attain equilibrium are vaporization, condensation, or a combination of the two. In the vaporizing drive mechanism, the vaporization of lighter components

(C1–C3) from the liquid (crude oil) to hydrocarbon vapor phase promotes the attainment of miscibility of the two phases. In condensing drive mechanism, the condensation of intermediate and heavy components (C4–C8) from hydrocarbon gas to the crude oil is responsible for attaining miscibility between fluid phases. In combined condensation and vaporization drive mechanism, the simultaneous counter-directional mass transfer mechanisms, that is, vaporization of lighter components from crude oil to gas and condensation of intermediate and heavy components from gas to crude oil, are responsible for attaining miscibility of the phases. These mass transfer interactions affect the compositions of both phases and hence their interfacial tension. Therefore, the dynamic changes in IFT can be used to infer information on mass transfer interactions taking place prior to the attainment of thermodynamic fluid phase equilibrium and miscibility.

## 2. OBJECTIVES OF THIS STUDY

The objectives of this study are to (1) study the different existing interfacial theory (2) study of Mechanistic Parachor Model in comparison with Parachor Model which considers the mass transfer interactions occurring prior to attaining fluid phase equilibria. This paper use data from Subash and Rao [3] and Rao [7] to compare Mechanistic Parachor Model with Parachor Model. Subash and Rao [3] proposed the Mechanistic Parachor model where the authors used

Rainbow Keg River (RKR) as a reservoir crude oil-gas system since the fluid compositions and the phase behavior data needed for IFT calculations and the experimental IFT measurements are readily available from Rao [7]. These gas-oil interfacial tension measurements are made using the axisymmetric drop shape analysis (ADSA) technique by fitting the images of the captured pendent drops of crude oil in gas phase with the drop profile calculated using the Laplace capillary equation. An aging period of about 2 h was allowed between the fluid phases to reach equilibrium during these experiments. Flash calculations needed for gas-oil interfacial tension calculations are carried out using QNSS/Newton algorithm and Peng–Robinson equation of state, with CMG Winprop module (Version 2008.10.3118.22139).

### 3. EQUILIBRIUM IFT PREDICTION MODELS

#### 3.1 Parachor Model

This model is the oldest among all the IFT prediction models and because of simplicity is still most widely used in petroleum industry to estimate the interfacial tension between fluids. Empirical density correlations are used in this model to predict the interfacial tension.

The Macleod [1] and Sudgen [2] related surface tension of a pure compound to the density difference between two phases, as

$$\sigma^{1/4} = P(\rho_M^L - \rho_M^V) \quad (1)$$

where  $\sigma$  is the surface tension (dyne/cm),  $\rho_M^L$  and  $\rho_M^V$  are the molar densities of the liquid and vapor phases, respectively ( $\text{g mol/cm}^3$ ), and the proportionality constant P, is known as the Parachor. The Parachor values of different pure compounds are reported in the literature by J.K.Ali [8]. Also one can use the value from the library component of CMG Winprop module (Version 2008.10.3118.22139) on the component selection/ properties option.

The equation proposed by Macleod-Sudgen [1,2] was later extended to multi component hydrocarbon mixtures by Weinaug and Katz [9] using the simple molar average technique for the mixture Parachor,

$$\sigma^{1/4} = \rho_M^L \sum x_i P_i - \rho_M^V \sum y_i P_i \quad (2)$$

where  $x_i$  and  $y_i$  are the mole fractions of the component  $i$  in the liquid and vapor phases, respectively, and  $P_i$  is the Parachor of the component  $i$ . Parachor values of pure compounds are used in Eq. (2) to calculate the interfacial tension of the mixtures, considering the Parachor value of a component in a mixture is the same as that when pure [10]. This model has been extensively used for prediction of surface tension of pure compounds and binary mixtures.

Fanchi [11] proposed the following correlation for calculating the parachor of a hydrocarbon mixture:

$$P = 176.05005 - 7472.9807 v_c - 0.87458088 T_c + 1560.4793 H + 19.309439 H^2 + 0.05013801 H^3 - \frac{25.691718}{H} \quad (3)$$

where,

$$H = v_c^{5/6} T_c^{0.25}$$

Here  $v_c$  is the molar specific critical volume in L/mol and  $T_c$  is the critical temperature in K.

In addition, Firozabadi et al. [12] calculated the parachors of several crude cuts of various crude oils from their surface tensions. They found a quadric relation between the parachor and the molecular weight of each crude cut and proposed the following empirical correlations:

$$P = -11.4 + 3.23 M - 0.0022 M^2 \quad (4)$$

where M is the molecular weight of each crude cut.

Furthermore, Ahmad [13] correlated the parachor of a hydrocarbon mixture with its molecular weight M by

$$P = -4.614873 + 2.558855 M + (3.4004065 \times 10^{-4}) M^2 + \frac{3767.396}{M} \quad (5)$$

#### 3.2 Mechanistic Parachor Model

In the application of the conventional Parachor model to multi component mixtures, Parachor values of pure components are used in IFT prediction, considering each component of the mixtures as if all the others were absent. Significant interactions take place between the various components in a multi component mixture and hence the inability of pure component Parachor values to account for these interactions of each component with the others in a multi component mixture appears to be the main reason for poor IFT predictions from the Parachor model in multi component hydrocarbon systems.

In the Mechanistic Parachor model proposed by Subhash and Rao [3] introduces a ratio of diffusivity coefficients raised to an exponent into the Parachor model to account for mass transfer effects. The mass transfer interactions for phase equilibria between any two fluid phases take place by diffusion due to concentration gradient and by dispersion. Hence diffusivities are used in the Mechanistic Parachor model to account for mass transfer interactions. Furthermore, only diffusivities can reasonably represent mass transfer interactions in complex multi component systems like crude oil-hydrocarbon gas mixtures involving multi components in both the phases. The ratio of diffusivities in both the directions (vaporising and condensing) between the fluid phases raised to an exponent used in the mechanistic model enables the relation of the same dimensions of the original Parachor model. The mechanistic model is given by:

$$\sigma^{1/4} = \left(\frac{D_{os}}{D_{so}}\right)^n (\rho_M^L \sum x_i P_i - \rho_M^V \sum y_i P_i) \quad (6)$$



where  $D_{os}$  is the diffusivity of the oil in gas (solvent),  $D_{so}$  is the diffusivity of the gas (solvent) in oil, and  $n$  is the exponent, whose sign and value characterize the type and extent of governing mass transfer mechanism for fluid phase equilibria. If  $n > 0$ , the governing mechanism is vaporization of lighter components from the oil to the gas phase. If  $n < 0$ , the governing mechanism is condensation of intermediate to heavy components from the gas to the crude oil. The value of  $n$  equal to zero ( $n \approx 0$ ) indicates equal proportions of vaporizing and condensing mass transfer mechanisms to be responsible for fluid phase equilibria. This condition of equal mass transfer in both the directions of vaporization and condensation appear to be most common in binary mixtures where the conventional Parachor model has shown to result in reasonably accurate interfacial tension predictions ( $n = 0$  in the mechanistic Parachor model). The higher the numerical value of  $n$  (irrespective of its sign) the greater the extent of that governing mass transfer mechanism.

Lee [14] compared the diffusivity data of multi component systems at reservoir conditions obtained from various correlations with experiments and concluded that Wilke-Chang equation [15] is the best available empirical correlation to compute the diffusivities in multi component hydrocarbon systems. Hence, equation (7) is used in equation (6) to calculate the interfacial tension in a crude oil-solvent system:

$$D_{AB} = \frac{(117.3 \times 10^{-18})(\varphi M_B)^{0.5} T}{\mu \nu_A^{0.6}} \quad (7)$$

where  $D_{AB}$  is the diffusivity of solute A in very dilute solution in solvent B ( $m^2/s$ ),  $M_B$  is the molecular weight of the solvent (kg/kmol),  $T$  is the temperature (K),  $\mu$  is the solution viscosity (kg/ms),  $\nu_A$  is the solute molar volume at normal boiling point ( $m^3/kmol$ ),  $\varphi$  is the associated factor for solvent, set equal to unity if the solvent used are unassociated.

Equation (7) is extended to multi component hydrocarbon mixtures, using

$$M_B = \sum x_{Bi} M_{Bi} \quad (8)$$

$$\nu_A = \sum x_{Ai} \nu_{Ai} \quad (9)$$

where  $x_i$  is the mole fraction of the component  $i$  in the mixture,  $M_{Bi}$  is the molecular weight of the component  $i$ , and  $\nu_{Ai}$  is the molar volume of the component  $i$  at normal boiling point.

### 3.3 Gradient Theory

The gradient theory [4] states that the surface tension of the planar interface of a mixture is given by

$$\sigma = \int_{-\infty}^{+\infty} \sum_i \sum_j c_{ij} \frac{dn_i}{dz} \frac{dn_j}{dz} dz \quad (10)$$

where  $dn_i/dz$  represents the local gradient in the density of component  $i$ . By analogy with the bulk energy

parameters,  $a_{ij} = (1 - k_{ij})\sqrt{a_i a_j}$ , the crossed influenced parameter  $c_{ij}$  are related to the geometric mean of the pure component influence parameters  $c_i$  and  $c_j$  by

$$c_{ij} = (1 - \beta_{ij})\sqrt{c_i c_j} \quad (11)$$

where  $\beta_{ij}$  is binary interaction coefficients. Stability of the interface requires  $\beta_{ij}$  to be included between 0 and 1. When  $\beta_{ij} = 0$ , the mixing rule is reduced to the geometric mean.

Computation of surface tension with equation (10) also requires knowledge of the gradients in density through the interface. This can be obtained by minimizing the Helmholtz free energy of the planer interface.

$$F = \int_{-\infty}^{+\infty} [f_o(n) + \sum_i \sum_j \frac{1}{2} c_{ij} \frac{dn_i}{dz} \frac{dn_j}{dz}] dV \quad (12)$$

So in the absence of an external potential, the Helmholtz free energy density of an inhomogeneous fluid, given by the gradient theory, is the sum of two contributions: the Helmholtz free energy density  $f_o(n)$  of the homogeneous fluid at the local composition  $n$ ; and a corrective term, which is a function of the local density gradients.

Surface Tension from Equation (10) can be written as:

$$\sigma = \int_{n_{ref}}^{n_{ref}} \sqrt{2 \Delta \Omega(n_1, \dots, n_N) \sum_i \sum_j c_{ij} \frac{dn_i}{dn_{ref}} \frac{dn_j}{dn_{ref}} dn_{ref}} \quad (13)$$

where,

$$\sum_i \sum_j c_{ij} \frac{dn_i}{dz} \frac{dn_j}{dz} = \Delta \Omega(n) = \Omega(n) - \Omega_B$$

and from the chain rule of differentiation,

$$\frac{dn_i}{dz} = \frac{dn_i}{dn_{ref}} \frac{dn_{ref}}{dz}$$

one obtains

$$dz = \sqrt{\frac{\sum_i \sum_j c_{ij} \frac{dn_i}{dz} \frac{dn_j}{dz}}{\Delta \Omega(n_1, \dots, n_N)}} dn_{ref}$$

Thus, the only inputs necessary to use the gradient theory, once the vapor-liquid equilibrium (VLE) has been computed, are the Helmholtz free energy density of the homogeneous fluid  $f_o(n_1, \dots, n_N)$  (that can be derived from the equation of states) and the influence parameters of the various components.

The Helmholtz free energy can be obtained from Peng-Robinson equation of states [16], which is expressed as:

$$P = \frac{RT}{v-b} - \frac{a(T)}{v(v+b) + b(v-b)} \quad (14)$$

where  $b$  is the covolume and  $a(T)$  is the energy parameter. For a mixture, these parameters are related to the ones of the pure fluids by mixing rules.

The parameters of the pure fluid are given by

$$b_i = 0.07780 \frac{RT_{ci}}{P_{ci}} \quad (15)$$

$$a_i(T) = 0.45724 \frac{R^2 T_{ci}^2}{P_{ci}} \alpha(T_{ri}) \quad (16)$$

with,

$$\alpha(T_{ri}) = \{1 + m_i(1 - \sqrt{T_{ri}})\}^2 \quad (17)$$

The coefficient  $m_i$  is function of the acentric factor as

$$m_i = 0.37464 + 1.54226 \omega_i - 0.26992 \omega_i^2 \quad (18)$$

In 1978, Robinson and Peng [17] proposed the following modification of Equation (18) for components heavier than n-decane:

$$m_i = 0.379642 + 1.485030 \omega_i - 0.164423 \omega_i^2 + 0.016666 \omega_i^3 \quad (19)$$

And the influence Parameter is calculated as:

$$\frac{c_i}{a_i b_i^{2/3}} = A_i t_i + B \quad (20)$$

where  $b_i$  is the covolume, and  $a_i(T)$  in the energy parameters in the PR-EOS. The coefficients  $A_i$  and  $B$  are merely correlated with the acentric factor to the component  $i$  by the relations

$$A_i = \frac{-10^{-16}}{1.2326 + 1.3757 \omega_i} \quad (21)$$

$$B_i = \frac{-10^{-16}}{0.9051 + 1.5410 \omega_i} \quad (22)$$

### 3.4 Linear Gradient Theory (Lgt) Model

In the linear gradient theory (LGT), a planer interface is assumed between the bulk liquid and vapor phases. In addition it is assumed that the molar density of each component at the VLE stste is linerly distributed across the liquid-vapor interface [5, 6]. Similar to GT, the LGT calculates the IFT between the bulk liquid and vapor phases by using

$$\gamma_{eq} = \int_{\rho_{r1}^v}^{\rho_{r1}^l} \sqrt{2c[P + \omega(\rho)]} d\rho_1 \quad (23)$$

where  $c$  is the influence parameter,  $P$  is the equilibrium pressure,  $\omega(\rho)$  is the grand canonical free energy density, and  $\rho_1$  represents the integral variable. The subscript “1” denotes a component that has a maximum

molar density difference between its bulk liquid and vapor phases at the VLE state:

$$\Delta\rho_1 = \{\max|\rho_i^L - \rho_i^V|; i = 1, 2, \dots, r\} \quad (24)$$

Here  $\rho_i^L$  and  $\rho_i^V$  are the molar densities of the  $i$ th component in the bulk liquid and vapor phases, respectively,  $i = 1, 2, \dots, r$ .

The influence parameter  $c$  in equation (23) can be calculated by applying the following mixing rule [5]

$$c = \sum_{i=1}^r \sum_{j=1}^r z_i z_j c_{ij} \quad (25)$$

Where  $z_i$  is the mole percentage of the  $i$ th component in the mixture,  $i = 1, 2, \dots, r$ . The influence parameter on the basis of SRK EOS [18] can be calculated as

$$\frac{c_{ij}}{a_i b_i^{2/3}} = (1.403 \times 10^{-16}) A_i (1 - T_{r,i})^{B_i}; i = 1, 2, \dots, r \quad (26)$$

where  $a_i$  and  $b_i$  are the SRK EOS constants of the  $i$ th component;  $T_{r,i}$  is its reduced temperature by its critical temperature;  $A_i$  and  $B_i$  are constant and can be calculated from the following equations respectively:

$$A_i = 0.28367 - 0.05164 \omega_i \quad (27)$$

$$B_i = -0.81594 + 1.06810 \omega_i - 1.11470 \omega_i^2 \quad (28)$$

where  $\omega_i$  is the Pitzer acentric factor of the  $i$ th component. The grand canonical free energy density is defined as

$$\omega(\rho) = f(\rho) - \sum_{i=1}^r \rho_i \mu_i \quad (29)$$

Here,  $f(\rho)$  is the Helmholtz free energy density of a homogeneous mixture with the molar density  $\rho$ . Also,

$$f(\rho) = \rho RT \left[ \int_0^\rho \left( \frac{P}{RT \rho^2} - \frac{1}{\rho} \right) d\rho + \frac{1}{\rho} \sum_{i=1}^r \rho_i \ln \rho_i \right] \quad (30)$$

$$\mu_i = \left[ \frac{\partial f(\rho)}{\partial \rho_i} \right]_{T, V} \quad (31)$$

## 4. PREDICTED IFT FROM THE MECHANISTIC PARACHOR MODEL

The crude oil and hydrocarbon gas compositions and the reservoir temperature from Rao [7] are used in IFT computations for this reservoir. The IFT measurements at various  $C_{2+}$  enrichments in hydrocarbon gas phase and at various pressures reported by Rao [7] are used for comparison with model predictions. A mixture consisting of 10 mol% of crude oil and 90 mol% of hydrocarbon gas is used as the feed composition in the computations to match the composition used in the reported experiments.

Enrichment (mol% C <sub>2+</sub> + CO <sub>2</sub> )	IFT (mN/m)			Weighted squared deviation	
	Experimental (Rao, 1997)	Parachor model	Mechanistic Parachor model	Parachor model	Mechanistic Parachor model
32.86	2.86	1.88	2.37	0.1167	0.0290
37.55	1.89	1.46	1.84	0.0518	0.0007
41.45	1.51	1.14	1.43	0.0610	0.0026
42.61	1.39	1.04	1.32	0.0620	0.0029
47.48	0.70	0.68	0.86	0.0007	0.0518
Objective function ( $\Delta$ ) =				0.2921	0.0871

The comparison of IFT predictions by the original Parachor model with experiments at various C<sub>2+</sub> enrichments in gas phase is given in Tables 1 and 2, respectively for pressures 14.8 and 14.0 MPa. These results are also shown in Figs. 1 and 2, respectively at these pressures. As can be seen, similar trends in IFT are observed for both the pressures. The match between the experiments and the model predictions is not good and IFT under predictions are obtained with the Parachor model.

The disagreement between the experiments and the model predictions, as seen in Figs. 1 and 2, are attributed mainly to the absence of mass transfer effects in the original Parachor model.

Table 1: Comparison of IFT measurements with Parachor and mechanistic Parachor models for RKR fluids at 87 °C and 14.8 MPa

Enrichment (mol% C <sub>2+</sub> + CO <sub>2</sub> )	IFT (mN/m)			Weighted-squared deviation	
	Experimental (Rao, 1997)	Parachor model	Mechanistic Parachor model	Parachor model	Mechanistic Parachor model
17.79	4.26	2.91	3.79	0.1000	0.0123
21.64	3.89	2.59	3.36	0.1124	0.0184
25.85	3.27	2.21	2.88	0.1043	0.0144
30.57	2.69	1.81	2.36	0.1065	0.0155
33.86	2.13	1.54	2.00	0.0762	0.0035
37.70	1.52	1.24	1.61	0.0347	0.0034
43.07	0.97	0.85	1.10	0.0166	0.0175
48.39	0.53	0.50	0.65	0.0028	0.0535
49.28	0.27	0.48	0.63	0.0061	0.0173
Objective function ( $\Delta$ ) =				0.5595	0.1558

The computed diffusivities between the fluid phases at various C<sub>2+</sub> enrichments in hydrocarbon gas phase for RKR fluids at pressures 14.8 and 14.0 MPa are given in Table 3. The mass transfer interactions between the fluid phases declined slightly as the C<sub>2+</sub> enrichment in hydrocarbon gas phase is increased for both the pressures. However, the ratio of diffusivities in both directions (oil to gas and gas to oil) remains almost the same at all C<sub>2+</sub> enrichments in gas phase. The average ratios of diffusivities between the fluids at all C<sub>2+</sub>

enrichments are 3.70 and 3.92, respectively for pressures 14.8 and 14.0 MPa. From the mass transfer enhancement parameters and the average ratios of diffusivities between the fluid phases, the exponents ( $n$ ) characterizing the governing mass transfer mechanism are found to be 0.20 and 0.17, respectively for pressures

Table 2: Comparison of IFT measurements with Parachor and mechanistic Parachor models for RKR fluids at 87 °C and 14.0 MPa

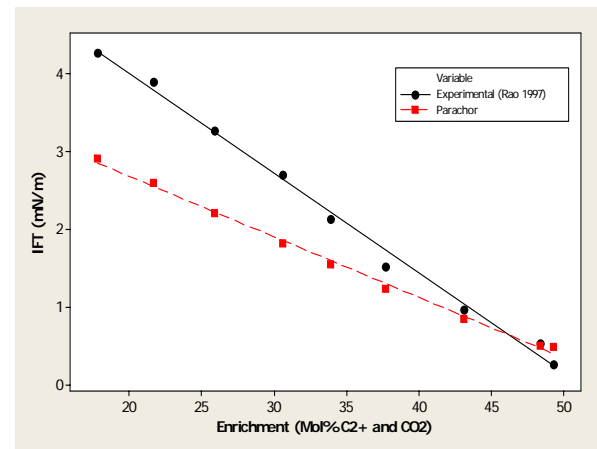


Fig 1. Comparison between IFT measurements and Parachor model for RKR fluids at 87 °C and 14.8 MPa.

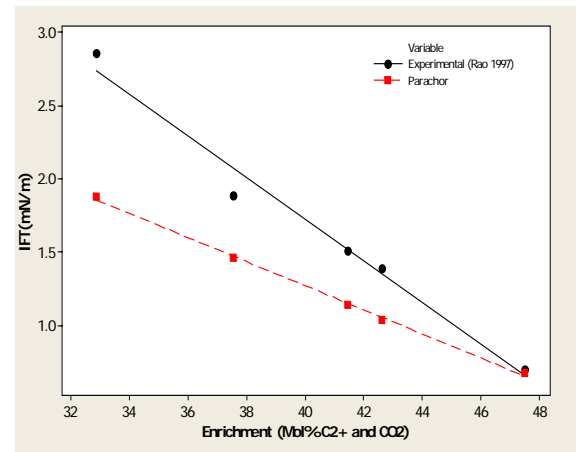


Fig 2. Comparison between IFT measurements and Parachor model for RKR fluids at 87 °C and 14.0 MPa.

14.8 and 14.0 MPa. These values of  $n$  being greater than zero, indicate that the vaporization of light components from the crude oil into the gas phase is the mass transfer mechanism that governs the fluid phase equilibria of these reservoir fluids. This can be attributed to the presence of significant amounts of lighter components (52 mol% C<sub>1</sub>-C<sub>3</sub>) in the crude oil of this reservoir.

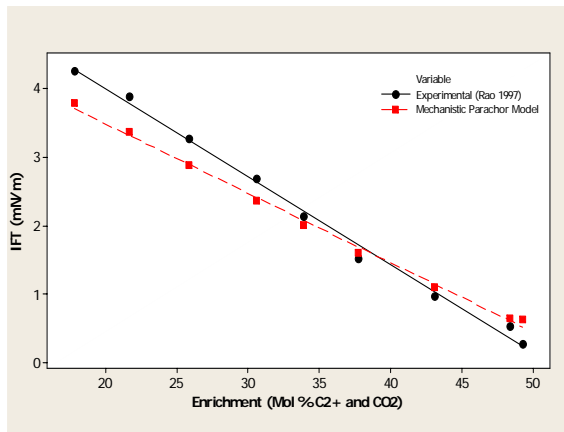


Fig 3. Comparison between IFT measurements and mechanistic Parachor model for RKR fluids at 87 °C and 14.8 MPa.

The comparison between the IFT predictions of mass transfer enhanced mechanistic Parachor model with experiments at various  $C_{2+}$  enrichments in gas phase is given in Tables 1 and 2, respectively for pressures 14.8 and 14.0 MPa. These results are also shown in Figs. 3 and 4, respectively at these pressures. Since the optimization of the mass transfer enhancement parameter ( $k$ ) is based on minimizing the sum of squared deviations between the experimental and calculated values, the mechanistic model prediction matched well with the experiments for both pressures (14.8 and 14.0 MPa)

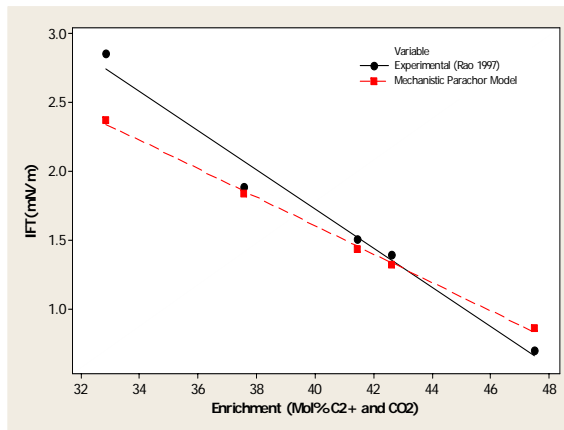


Fig 4. Comparison between IFT measurements and mechanistic Parachor model for RKR fluids at 87 °C and 14.0 MPa.

Table 3: Diffusivities between oil and gas at various  $C_{2+}$  enrichments for RKR fluids

Table 4. Model exponent of different single experimental IFT measurements points in the Mechanistic Parachor Model for RKS fluids at 14.8 MPa.

14.8 MPa				14.0 MPa			
(mol % $C_{2+}$ + $CO_2$ )	Dos (m <sup>2</sup> /s)	Dso (m <sup>2</sup> /s)	Dos/Dso	(mol% $C_{2+}$ + $CO_2$ )	Dos (m <sup>2</sup> /s)	Dso (m <sup>2</sup> /s)	Dos/Dso
17.79	3.45	9.69	3.56	32.68	3.44	8.67	3.97
	E-08	E-09			E-08	E-09	
21.64	3.45	9.40	3.68	37.55	3.34	8.39	3.98
	E-08	E-09			E-08	E-09	
25.85	3.42	9.11	3.75	41.45	3.21	8.18	3.93
	E-08	E-09			E-08	E-09	
30.57	3.36	8.81	3.81	42.61	3.17	8.12	3.91
	E-08	E-09			E-08	E-09	
33.86	3.29	8.62	3.82	47.48	2.99	7.89	3.79
	E-08	E-09			E-08	E-09	
37.70	3.19	8.41	3.80				
	E-08	E-09					
43.07	3.03	8.14	3.73				
	E-08	E-09					
48.39	2.85	7.89	3.61				
	E-08	E-09					
49.28	2.83	7.88	3.59				
	E-08	E-09					

Enrichment (mol% $C_{2+}$ + $CO_2$ )	Average= 3.70			Average= 3.92		
	IFT (mN/m)			k	Dos/Dso	N
	Experimental (Rao, 1997)	Parachor	Mechanistic Parachor Model			
17.79	4.26	2.190	4.26	1.46	3.56	0.30
21.64	3.89	2.590	3.89	1.50	3.68	0.30
25.85	3.27	2.210	3.27	1.47	3.75	0.29
30.57	2.26	1.180	2.69	1.48	3.81	0.29
33.86	2.13	1.540	2.13	1.39	3.82	0.25
37.70	1.52	1.240	1.52	1.23	3.80	0.16
43.07	0.97	0.850	0.97	1.15	3.73	0.11
48.39	0.53	0.500	0.53	1.10	3.61	0.07

## 5. CONCLUSION

In this paper four different IFT models along with their governing equations have been discussed. Then among them the most recent IFT model known as Mechanistic Parachor model has been compared with Parachor model in Rainbow Keg River (RKR) crude oil system. The ratio of diffusivities between the fluid phases raised to an exponent is introduced into the Parachor model for mass transfer effects. The sign and value of the exponent in the mechanistic model characterize the type and the extent of governing mass transfer mechanism for fluid phase equilibria and miscibility. The Mechanistic Parachor Model can be utilized to identify the predominating mass transfer mechanism in the combined vaporizing/condensing mode and to determine dynamic interfacial tension and the miscibility in multi component hydrocarbon system by using the compositional data of the fluid phases.

## 6. REFERENCES

1. Macleod, D. B., 1923, "On a Relation between Surface Tension and Density. Trans. Faraday Soc., 19:38-42.
2. Sudgen, S., 1924, "The Variation of Surface tension with temperature and some related functions". J. Chem. Soc. 125:32-41.

3. Ayirala S. C., Rao D. N., 2006, "A new mechanistic Parachor model to predict dynamic interfacial tension and miscibility in multi component hydrocarbon systems". Journal of Colloid and Interface Science. 299:321-331.
4. Miqueu. C., Mendiboure. B., Lachaise J., 2005, "Modeling of the Surface Tension of Multi component Mixtures with the Gradient Theory of Fluid Interfaces". Ind. Eng. Chem. Res. 44:3321-3329.
5. Zuo Y. X., Stenby, E.H., 1996, "A linear Gradient theory model for calculating interfacial tension of mixtures". J. Colloid Interface Sci. 182:126-132.
6. Nobakht M., Moghadem S., Gu Y., 2008, "Determination of CO<sub>2</sub> Minimum Miscibility Pressure from Measured and Predicted Equilibrium Interfacial Tensions". Ind. Eng. Chem. Res. 47:8918-8925.
7. Rao D. N., 1997, "A new technique for vanishing interfacial tension for miscibility determination". Fluid Phase Equilib. 139:311-324.
8. J. K. Ali., 1994, "Prediction of Parachors of petroleum cuts and pseudo components". Fluid Phase Equilib. 95:383-398.
9. Weinaug C. F., Katz D. L., 1943, "Surface tension of Methane-Propane Mixtures". Ind. Eng. Chem. 35:239-245.
10. A. Danesh, 1998, *PVT and Phase Behavior of Petroleum Reservoir Fluids*. Elsevier, Amsterdam, pp. 281.
11. Fanchi J. R., 1985, "Calculation of Parachors for Compositional Simulation". J. Pet. Technol. 37:2049-2050.
12. Firoozabadi A., Katz D. L., Saroosh H., Sajjadian V. A., 1988, "Surface Tension of Reservoir Crude Oil/Gas Systems Recognizing the Asphalt in the Heavy Fraction". SPE Reservoir Eng. 3:265-272.
13. Ahmed, T. 1989, "Hydrocarbon Phase Behaviour". Gulf Publishing: Houston, TX, 1989.
14. Fayers F. J., Lee S., 1992, "Crossflow Mechanisms by Gas Drive in Heterogeneous Reservoirs". *Proceedings of the SPE 67<sup>th</sup> Annual Technical Conference and Exhibition*, Washington DC, Paper No. SPE 24934.
15. Wilke C. R., Chang P., 1955, "Correlation of diffusion coefficients in dilute solutions". AICHE J. 1:264.
16. Peng D. Y., Robinson D. B., 1976, "A new two constant equation of state". Ind. Eng. Chem. Fundam. 20:58-64.
17. Robinson D. B., Peng D. Y., 1978, "The Characterization of the Heptanes and Heavier Fractions for the GPA Peng-Robinson Programs". Research report RR-28, Gas Processors Association Project 756; University of Alberta, Canada.
18. Zuo Y. X., Stenby E. H., 1998, "Prediction of Interfacial Tension of Reservoir Crude oil and Gas condensate systems". SPE J. 3:134-145.

## 7. NOMENCLATURE

Symbol	Meaning	Unit
P	Pressure	(Pa)
T <sub>c</sub>	Critical Temperature	(K)
V <sub>c</sub>	Molar specific volume	(L/mol)
M	Molecular Weight	(kg/kmol)
σ	Surface Tension	(dyne/cm)
$\rho_M^L$	Molar Density of Liquid	(g mol/cm <sup>3</sup> )
$\rho_M^V$	Molar Density of Vapour	(g mol/cm <sup>3</sup> )
D <sub>AB</sub>	Diffusivity	(m <sup>2</sup> /s)

## 8. MAILING ADDRESS

Mohammad Marufuzzaman  
 Industrial Systems Engineering (ISE),  
 University of Regina, Canada  
 E-mail: marufuzm@uregina.ca

## EXPERIMENTAL INVESTIGATION OF SESSILE DROP EVAPORATION AND ITS RELATION WITH LEIDENFROST TEMPERATURE

A.K. Mozumder, M.R. Ullah and A. Hossain

Department of Mechanical Engg, Bangladesh University of Engineering and Technology (BUET)  
Dhaka, Bangladesh.

### ABSTRACT

This study experimentally investigates the evaporation of sessile drop for four different heated surfaces of Aluminum, Brass, Copper and Mild steel with a combination of four different liquids as Methanol, Ethanol, Water and NaCl solution. The metallic surfaces were polished with a zero grade emery paper and are electrically heated upto temperatures varied from 100 to 400 °C with an increment of 25 °C. The time of evaporation for the droplet on the hot metallic surface was measured. According to the experimental data, the Leidenfrost temperature is within a range of 150 to 200 °C for all the experimental conditions. Sessile drop evaporation time is the maximum for water, then decreases gradually for NaCl solution, Methanol and is the minimum for ethanol for a particular solid material. On the other hand, this time is the highest for copper and the lowest for mild steel for a specific liquid.

**Keywords:** Evaporation, Sessile Drop, Conduction

### 1. INTRODUCTION

The Leidenfrost phenomenon is the film boiling of discontinuous liquid masses on a flat surface. The surface temperature corresponding to minimum heat flux is generally termed as Leidenfrost temperature. Many studies of the Leidenfrost phenomenon have appeared in the literature and a brief review of only the most recent must suffice here. Gottfried [1] have presented evaporation time data for small droplet of five ordinary liquids and have proposed an analytical model which is in fair agreement with the data. The model postulates that heat is transferred to the droplet by conduction from the plate below the drop through the supporting vapor film and by radiation from the plate; mass is removed by diffusion from the outer surface and by bulb evaporation from the lower surface; the drop is supported by the excess pressure above atmospheric in the flowing vapor film under the droplet.

Baumeister [2] analyzed the evaporation rate of larger masses, especially those smaller than the critical size for bubble break-through and obtained good agreement between theory and experiment. Patel and Bell [3] obtained evaporation rate data for masses up to 10ml; they also studied bubble dynamics in the 10ml masses photographically and found that the results were consistent with the submerged surface film boiling studies of Hosler and Westwater [4] and with the prediction of Taylor instability theory. In present study, the total evaporation time was determined for small droplets of four different liquids on four different metal

plates. The temperature of plate ranges from 100° C to 400° C. The longest time among the times of evaporation of a droplet for a particular liquid, particular solid metal and of different temperatures termed as leidenfrost point was determined from the experimental data. Tamura and Tanasawa [5] studied the total evaporation time of a liquid drop on a hot surface at temperature up to 900°C. Ten liquids were used including the pure substances ethanol, benzene and water and the mixtures gasoline, kerosene and heavy oil. Their apparatus consisted of a 16cm diameter stainless steel plate with a concave surface. Small droplets were placed on the plate and the evaporation process observed and photographed. Plate temperatures starting about 50°C below the liquid boiling point and ranging beyond the point where the combustible liquid ignited resulted in evaporation curves that covered all regions of boiling. Since the initial drop sizes in all but one case were smaller than those used in this investigation, it is not possible to compare actual evaporation data, but the general shape of the curves is the same.

The question of the stability of the Leidenfrost phenomenon usually quickly reduces to a discussion of the Leidenfrost point and how it was determined, since the most workers are agreed that film boiling becomes increasingly stable relative to nucleate and mixed modes at increasing surface temperatures. However, very little agreement exists between various workers on the true value of the Leidenfrost point for any given set of conditions.

## 2. EXPERIMENTAL PROCEDURE

The sessile drop apparatus was used to study the evaporation characteristics of droplet on a heated surface. In particular, the liquid-solid interface temperature corresponding to the Leidenfrost Temperature was determined from droplet evaporation curve for different materials of different liquid.

The experimental setup consists of metal block, one stand, two heater, one variac, one thermocouple and one dropper (as shown in the Fig.1). The working fluids were water, NaCl solution, methanol and ethanol. Two 500 watt cartridge heaters were used to heat the metal block and they were placed beneath the test surface by drilling the block. K type Chromel-Alumel thermocouple was used to determine the center temperature of the testing surface. The thermocouple was installed 3 mm below the test surface.

Regulated electrical energy was supplied to the heater by using a variac, connected to the 220 volt laboratory power. A couple of syringes were used to drop the liquid droplets on the test surface. The syringe was held perpendicular to the horizontal test surface and droplets were released from about two inches from the surface. Though the test surface was little concave, it is assumed that heat is transferred to the droplet from a flat surface.

From the schematic of the experimental apparatus it is seen that heating surface was heated from the bottom by using two cartridge heaters. When the temperature reached a predetermined value (around 100°C), a droplet was dropped to the center of the heating surface with a syringe; evaporation time was measured using measured using a stopwatch. The droplet temperature was room temperature when dropped.

The surface temperature was measured using a digital multimeter and a 1-mm-diameter chromel-alumel (type K) thermocouple located 2 mm beneath the center of the test surface. Some of the observation of the evaporation activities was captured using a video camera.

The droplet's initial diameter was calculated as a sphere from the measured average volume of 30 droplets. There may be a little error in measuring the diameter of the droplets. A digital stopwatch was used to record the time. To minimize the timer ( $\pm 0.01\text{sec}$ ) and initial droplet size errors, three evaporation times are recorded for each temperature increment and then average together. This procedure is performed for 25°C surface temperature increment.

## 3. RESULTS AND DISCUSSION

The experimental total vaporization time results are shown in Fig. 2 to Fig. 6. The temperature which gives maximum evaporation time is presumed to be the minimum heat flux at which stable film boiling can exist and is termed as Leidenfrost temperature. To the smaller of the Leidenfrost Temperature, the boiling is in transition regime between nucleate and film.

From Fig. 2, it is shown that water stands out compared with the other liquids by virtue of having a much longer vaporization time. The Leidenfrost time for water and NaCl solution are nearly equal. On the other hand both methanol and ethanol shows small value of Leidenfrost time.

Fig. 3 shows that the Leidenfrost time is the maximum for water when the sessile drop is poured on the brass surface. The other three fluids show similar characteristics on brass surface.

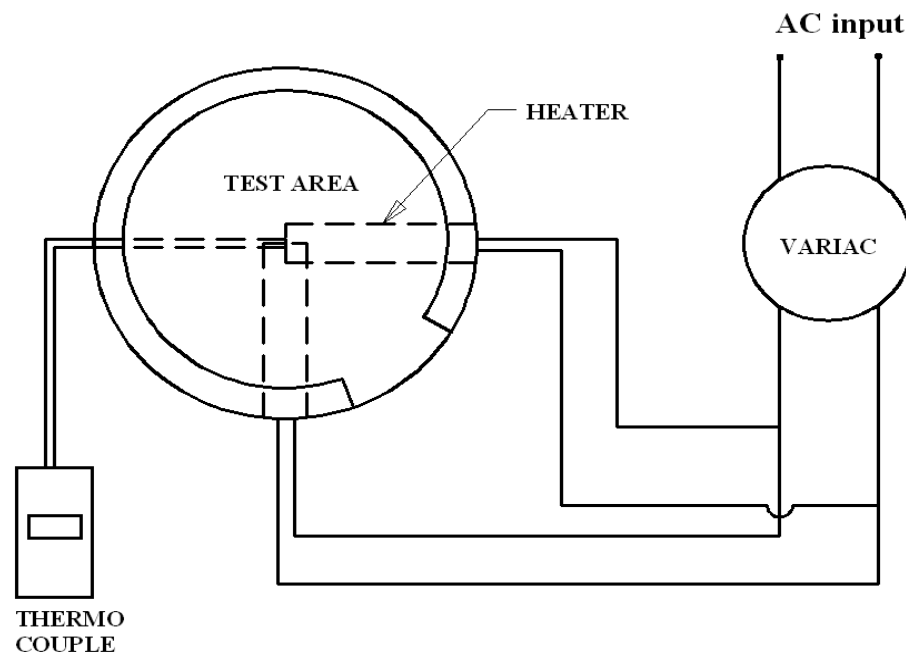


Fig 1. Experimental Setup



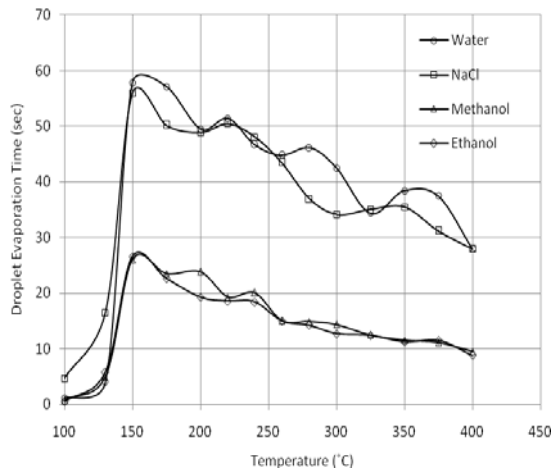


Fig 2. Comparison of Droplet Evaporation Time of Water, NaCl solution, Methanol, Ethanol on Aluminum

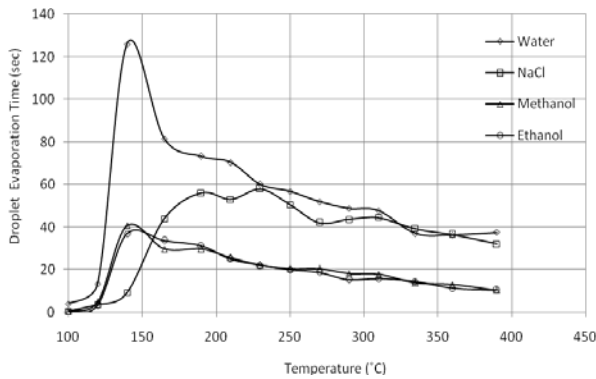


Fig 3. Comparison of Droplet Evaporation Time of Water, NaCl solution, Methanol, Ethanol on Brass

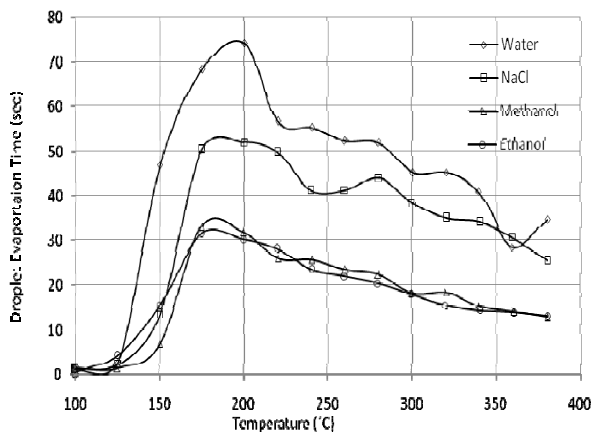


Fig 4. Comparison of Droplet Evaporation Time of Water, NaCl solution, Methanol, Ethanol on Copper

Fig. 4 also shows that the Leidenfrost time is nearly equal for methanol and ethanol. It is also evident from the graph that water shows the highest evaporation time among the four working fluids. Fig. 5 shows the variation of droplet evaporation time on mild steel surface for four different liquids. They show comparable results.

A material of high thermal conductivity would be expected to give a higher and more consistent value of

the Leidenfrost time than one of low thermal conductivity. Few exceptional results were also observed due to uncertainty of the experiment. Leidenfrost temperature values were obtained for water, NaCl solution, methanol and ethanol on aluminum, copper, brass and mild steel surface. The Leidenfrost temperature is nearly identical for aluminum, brass and mild steel surfaces but is slightly higher for the copper surface Bernardin [6].

Fig. 6 represents the variation of evaporation time for NaCl solution on four different metallic surfaces. Aluminum, Brass, and Copper shows comparable times but mild steel results in shorter time which may due to lower value of conductivity of mild steel relative to other materials.

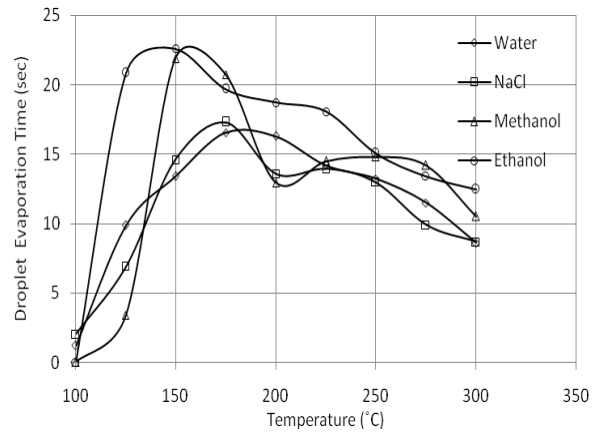


Fig 5. Comparison of Droplet Evaporation Time of Water, NaCl solution, Methanol, Ethanol on Mild Steel

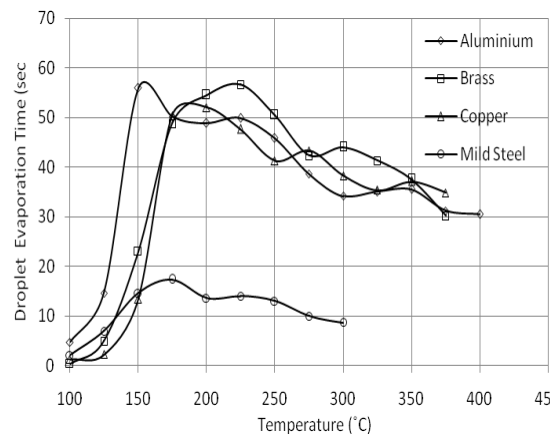


Fig 6. Comparison of Droplet Evaporation Time of NaCl on Mild Steel, Aluminum, Brass, Copper.

Table 1: Experimental Leidenfrost Time

Liquids	Leidenfrost time(sec)			
	Experimental			
	Cu	Al	MS	Brass
Water	74.29	57.79	45.16	126
NaCl solution	51.95	55.89	36.36	56.07
Methanol	33.75	26	21.9	29.65
Ethanol	31.47	26.61	22.58	36.96

Table 2: Experimental Leidenfrost Temperature(C)

Liquids	Leidenfrost temperature(°C)			
	Experimental			
	Cu	Al	MS	Brass
Water	200	150	250	140
NaCl solution	200	150	275	190
Methanol	175	150	150	165
Ethanol	175	150	150	140

Table 1 and Table 2 shows the experimental Leidenfrost time and temperature of four different liquids on the four different metal surfaces. According to the experimental data, the Leidentfrost temperature is within a range of 150 to 200 °C for all the experimental conditions (as also shown in the Figs. 2-6).

The higher drop evaporation value of copper surface is speculated to be the result of higher conductivity than other metal. Higher conductivity means higher heat transfer through the metal. It means, when liquid touch the metal, large amount vapor will produce due to higher heat transfer rate and the surface is completely covered by a vapor blanket and then heat transfer from the surface to the liquid occurs by conduction through vapor. Droplet supported by the vapor film slowly boils away.

From the experimental results, several key conclusions concerning the influential parameters (Leidenfrost Temperature) can be drawn. The major contribution to the heat transfer is the convective and conductive mode. The radiative heat flux cannot be neglected at plate temperatures beyond the Leidenfrost point of liquids.

#### 4. CONCLUSION

On a hot surface, a liquid droplet gets heat by conduction from the vicinity of the surface, by convection between the hot surface and the bottom of the liquid surface and by radiation form the hot surface. After getting heat energy, the droplet starts evaporating. At the bottom of the droplet, the vapor forms and leaves just like a vapor explosion. The reaction force of this vapor ejection made floating the tiny liquid droplet which consequences a gap between the hot surface and the droplet. This separation creates a heat resistance and then naturally the heat transfer between the solid and the

liquid reduces which ultimately reduces the rate of vapor generation. This vapor is not capable to maintain the gap and at last the liquid droplet again falls down to the solid surface and the cycle starts again. This cycle repeats until the volume of the droplet tends to zero.

Sessile drop evaporation time is the maximum for water, then decreases gradually for Nacl solution, Methanol and is the minimum for ethanol for a particular solid material. On the other hand, this time is the highest for copper and the lowest for mild steel for a specific liquid. The radiative heat flux dominates the heat transfer process beyond the Leidenfrost temperature.

#### 5. REFERENCES

1. Gottfried, B. S. "The Evaporation of Small Drops on a Flat Plate in the Film Boiling Regime, " Ph.D. Thesis, 1962, Case Inst. of Technology, Cleveland, Ohio.
2. Baumeister, K. J., T. D. Hamill, and G. J. Schoessow, "Mass Diffusivity Effects on Droplets in Film Boiling" *Proceedings Third International Heat Transfer Conference*, Vol. 4, pp. 66-73 (August 1966).
3. Patel B.M. , and Bell, K.J. , "The Leidenfrost Phenomenon for Extended Liquid Masses," Paper presented at Eighth National Heat Transfer Conference, Los Angeles, August 8-11, 1965. In press for CEP Symposium Series "Heat Transfer-Los Angels."
4. Hosler, er, and Westwater, jw, "Film Boiling on a Horizontal Plate," *ARS J.*, April 1962, pp. 553-558.
5. Z., and Y. Tanasawa 'Seventh International Combustion Symposium,' pp. 509-522, Butterworth's, London, England (1958).
6. Bernardin, J. D. and Mudawar, I., 1999, "The Leidenfrost Point - Experimental Study and Assessment of Existing Models," *ASME Journal of Heat Transfer*, Vol. 121, pp. 894-903.

#### 8.MAILING ADDRESS

A.K. Mozumder  
 Department of Mechanical Engg,  
 Bangladesh University of Engineering and Technology  
 Dhaka-1000, Bangladesh

## EXPERIMENTAL INVESTIGATION OF A HEAT PIPE FOR DIFFERENT WORKING FLUIDS AND FILL RATIOS

A. Kumar Mozumder, A. Fahad Akon and M. S. Hasib Chowdhury

Department of Mechanical Engineering, Bangladesh University of Engineering & Technology,  
Dhaka, Bangladesh.

### ABSTRACT

During last thirty years, component density on integrated circuits has grown from about six thousand on the Intel 8080 microprocessor to over five million transistors on a similar-sized Intel microprocessor. Power and component densities on these integrated circuits have required the development of innovative cooling methods. Miniature heat pipes appear promising for use in microelectronics cooling. The heat pipe though has a wide application; the information available towards the development of an efficient heat pipe is seldom seen in the open literature. In the present study, investigations are carried out for optimizing the fluid inventory in a typical heat pipe. A “flooded” (with exceedingly large amount of working fluid) heat pipe has slow response and has limited lower range of operation in terms of operating temperature. On the other hand, “starving” (with too little amount of working fluid) heat pipe although Exhibits fast response to heat loads, shows severe limit at high temperature conditions. In the present study, an attempt is made to design, fabricate and test a miniature heat pipe with 5 mm diameter and 150 mm length with a thermal capacity of 10 W. Experiments were conducted with and without working fluid for different thermal loads to assess the performance of heat pipe. The working fluids chosen for the study were same as those commonly used namely, water, methanol and acetone. The temperature distribution across the heat pipe was measured and recorded using thermocouples. The performance of the heat pipe was quantified in terms of thermal resistance and overall heat transfer coefficient. The amount of liquid filled was varied and the variation of the performance parameters for varying liquid inventory is observed. Finally, optimum liquid fill ratio is identified in terms of lower temperature difference and thermal resistance and higher heat transfer coefficient. The data reported in this study will serve as a good database for the researchers in this field. Overall heat transfer coefficient of the Miniature heat pipe is found to be the maximum for the Acetone as working fluid.

**Keywords:** Miniature Heat Pipe, Working Fluid Inventory

### 1. INTRODUCTION

Heat pipe is a form of heat exchanger useful for transporting very large quantities of heat with small temperature differences. The heat pipe consists of a hollow tube closed at both ends and partially filled with a liquid that boils at a desired temperature. One end of the tube is immersed in the warm region and the other end in the cold region. The objective is to transfer heat through the pipe from warmer to the colder region. Due to space constraints in most of personal computers and telecommunication systems placed constraints on the size of heat pipes, normally miniature heat pipes of diameter 3 to 6 millimeter and less than 400 millimeters are preferred. The MHP applications for cooling telecom boots and notebooks computers were started in the last decade and now 80% of notebook PCs are using MHP. MHP has unique physical phenomenon contrary to micro heat pipes in view of affects of the operating limit, liquid locking, and length. That is, while the liquid blocking phenomenon occurs in the micro heat pipes of less than 1

mm, the condenser liquid are accumulated at the end of the condenser and heat is not delivered completely. The phenomenon of reducing the vapor temperature and thus reducing the maximum rate of heat transfer occurs in MHP if the condenser is cooled excessively. And there appear significant effects caused by the entire length of a heat pipe and the effect by the capillary limit among operating limits of a heat pipe [1]. The selection of the proper heat pipe cooling solution is dependent upon the developer’s specifications, design constraints and budget. Thermal designers have widely accepted the MHP for their thermal design solution and the utilization as well as area of application of MHP has been increased day by day. But MHP is relatively a new technology; its data and information are quite scarce. So a through comprehension of the heat transfer capability of MHP at different fluid inventory and fill ratio.

Akon and Chowdhury [2] found that fill ratios of working fluid greater than 85% of volume of evaporator show better results in terms of increased heat transfer

coefficient, decreased thermal resistance and reduced temperature difference across the evaporator and condenser. A heat transfer analysis of an inclined two-phase closed thermosyphon was developed by Zuo and Gunnerson [3]. The inclination-induced circumferential flow was unfavorable with respect to dry out because the thin top-side liquid film was easier to boil off, but contrastingly was favorable with respect to flooding because the thick underside film corresponded to a large gravity force. Minimum working fluid inventory remained almost constant for a large range of inclination angles (0-70 °) and then significantly increased for further increase of inclination angle. At a certain inclination angle, the mean heat transfer coefficient of the thermosyphon reached a maximum value, which was related to the heat transfer behavior in both condenser and evaporator. The highest flooding limit was at inclination angle ranging from 30 to 45 o, which corresponded to the best balance of the two opposing effects: secondary circumferential flow and gravity reduction.

Zhang and Wong [4] studied heat transfer and fluid flow in an idealized micro heat pipe with the support of NASA and LaSPACE. They made an analysis for four different values of length to width ratio of an idealized micro heat pipe, viz. 20, 50, 100, and 200. From the liquid temperature distribution along the length of the micro heat pipe, they found that the temperature profile is relatively flat except the region near the evaporator, and for a micro heat pipe with larger length to width ratio, the length of the evaporator is shorter. From the vapor pressure distribution, they found that the pressure goes approximately linearly and is not strongly affected by the length to width ratio. On evaluating the effective thermal conductivity of a micro heat pipe increases with increase in the evaporation area at the evaporator, and length or width of the micro heat pipe. They also added that a fluid with larger latent heat would produce larger effective thermal conductivity.

A network heat pipe concept employing the boiling heat-transfer mechanism in a narrow space was investigated by Cao and Gao [5]. Two flat-plate wickless network heat-pipes (or thermal spreaders) are designed, fabricated, and tested based on this concept. The fabricated thermal spreaders, which are made of copper or aluminum, are wickless, cross-grooved heat transfer devices that spread a concentrated heat source to a much larger surface area. As a result, the high heat flux generated in the concentrated heat source may be dissipated through a finned surface by air cooling. The network heat pipes are tested under different working conditions and orientations relative to the gravity vector, with water and methanol as the working fluids. The maximum heat fluxes achieved are about 40W/cm<sup>2</sup> for methanol and 110W/cm<sup>2</sup> for water with a total heat input of 393 W.

## 2. EXPERIMENTATION

The heat pipe was fabricated using a copper tube of 150 mm length and 5 mm inner dia and 8 mm outer dia as shown in (as shown in the Fig.1). Ni-Cr wire having

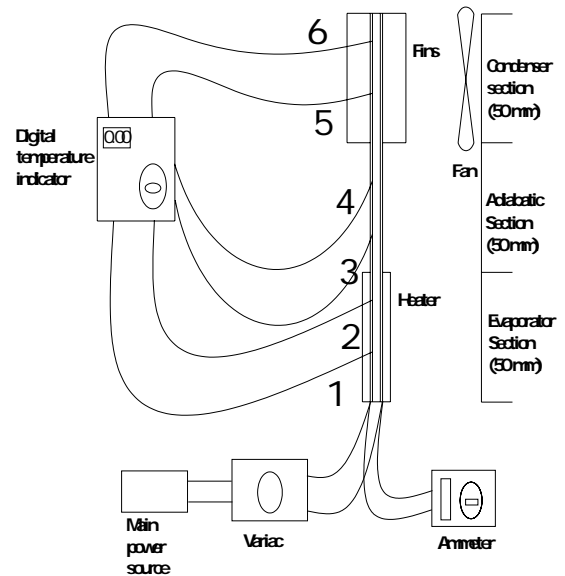


Fig 1. Schematic Arrangement of Experimental Setup

inner diameter 8 mm and length 50 mm was used to make a heater of 230V, 50W capacity and heater was used for providing the required heat source at the evaporator. The evaporator and adiabatic sections of the heat pipe are insulated using asbestos to minimize the heat loss through these portions. Variac and Multimeter were provided to control and measure the power input respectively. K- Type thermocouple wires were used as temperature sensors. A simple 8- channel digital temperature indicator is used to measure the temperature. Five copper fins of length 50mm, width 15 mm, and thickness 0.5mm were brazed on the condenser end. Experiments were conducted with dry run (i.e. without working fluid in the tube) and wet run (with working fluid inside). The heat pipe without working fluid essentially represents metallic conductor. Its performance is considered as the base for the evaluation of heat pipe (i.e. with working fluid in it). The heater is put "on" and the temperature rise was observed at regular intervals till the steady state is achieved, Experiments were repeated for different heat inputs with different fill ratios and various plots were drawn to study the performance of miniature heat pipe to optimize the fluid inventory.

## 3. RESULTS AND DISCUSSIONS

Experiments were carried out in dry mode (without working fluid) and wet mode (with working fluid in it). The dry mode experiment represents the heat transfer characteristics in an ordinary conductor, while the wet mode depicts the live heat pipe characteristics. Three different working fluids namely distilled water, methanol and acetone which have varying useful working range of temperature are tested in this study. The heat pipe was filled with 35%, 55%, 85% and 100% of the evaporator volume tested for different heat input and working fluids.

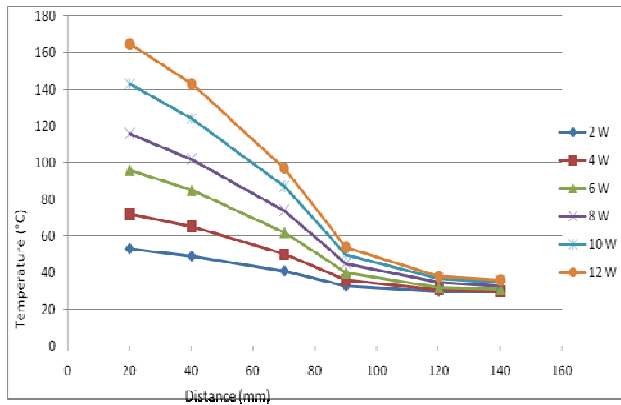


Fig 2. Axial temperature profile for DRY RUN

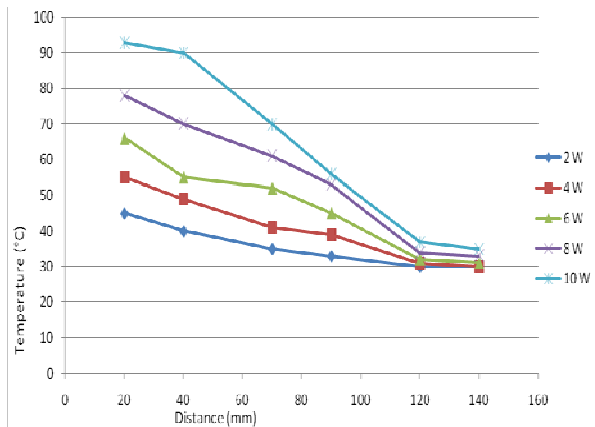


Fig 3. Axial temperature profile for Water With 55% fill ratio

### 3.1 Axial Temperature Profiles

Axial temperature profiles are drawn from the data of temperatures that is obtained at different axial distances on the heat pipe body. The axial temperature distribution along the heat pipe for dry run and water with 55% fill ratio are shown in Figs. 2 and 3 respectively. It shows that the slope of axial temperature distribution increases with heat input and shows larger temperature differences across the condenser and evaporator section. The trend is obvious since greater temperature slope is required for increased heat transfer in case of simple conduction heat transfer.

On the other hand, water shows reduced slopes of axial temperature distribution at similar heat inputs, indicating the effective augmentation of heat transfer at even reduced temperature slopes. The abrupt change in the slope of axial temperature distribution for water at 10W heat input (Fig. 3) indicates the seizure of heat pipe operation. At this stage, the rate of evaporation at evaporator is higher than condensation rate at condenser. Similar trends are found for all other working fluids.

### 3.2 Thermal Resistances and Heat Input

The variations of thermal resistances with different heat inputs for dry run and wet run for 35% are shown in above Fig. 4. In general wet run shows the reduced

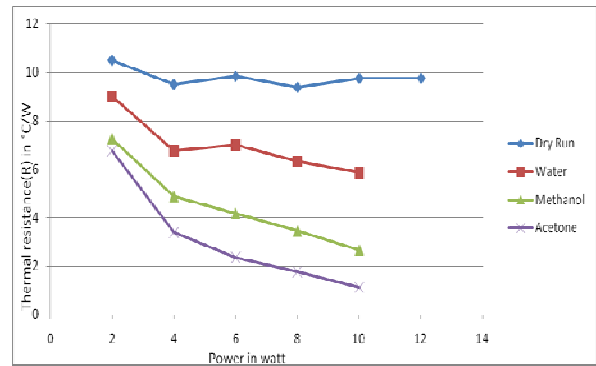


Fig 4. variations of thermal resistances with different heat inputs for 35% fill ratio

thermal resistances for all levels of heat input and all types of working fluids. The dry run shows the largest values of thermal resistances and it is almost constant for varying heat loads. Acetone shows the minimum thermal resistances at all heat inputs for all fill ratios.

### 3.3 Variation of Heat Transfer Coefficient with Heat Input

The dry run shows an overall heat transfer co-efficient of around  $2000 \text{ W/m}^2\text{-}^\circ\text{C}$  corresponding to the forced convective heat transfer at the fin end. When the heat pipe is charged with working fluids, there are remarkable increase in heat transfer co-efficient owing to the augmentation of heat transfer rate by the evaporation and condensation process in side the heat pipe. For 100% fill ratio (Fig. 5), water and methanol shows almost similar pattern of heat transfer co-efficient, but acetone shows greater values for higher heat inputs.

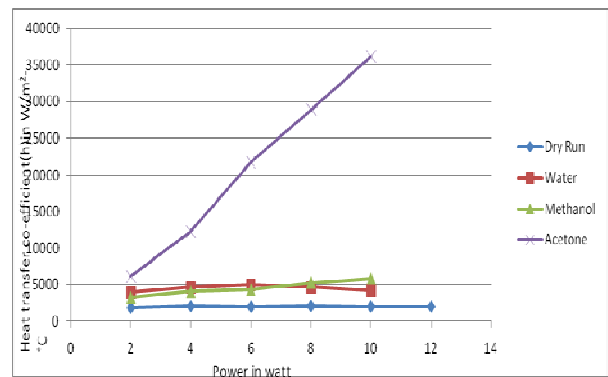


Fig. 5: variations of overall heat transfer co-efficients with different heat inputs for 100% fill ratio

### 3.4 Identifying the Optimum Fluid Fill Ratio

Comparative plot of temperature difference between the evaporator and condenser section at varying fill ratio of working fluid as a percentage of evaporator volume for all the three working fluids with the heat loads of 10 W are shown in the Fig. 6. In case of methanol and water, the fill ratio have minimum effect on the temperature difference between evaporator and condenser. On the other hand, acetone shows reduced temperature difference at higher fill ratios. With acetone as working

fluid, 100% fill ratio of evaporator volume shows the best result with minimum temperature difference across the evaporator and condenser.

### 3.5 Heat Transfer Coefficients and Thermal Resistances

The effect of fill ratio of working fluid on heat transfer co-efficients and thermal resistances for water is shown in Fig. 7. It is observed that it shows maximum value of heat transfer co-efficient and minimum value of thermal resistance at 85% fill ratio. Lower and higher than 85% fill ratio results in lower values of heat transfer co-efficients and higher values of thermal resistances than that of 85%.

### 4. CONCLUSIONS

- The steady state temperature increases with increased heat loads. Slope of axial temperature distribution in dry run increases with the heat input, on the other hand the wet run shows an averaged constant temperature slopes.
- The operating heat pipe with wet run has lesser overall resistance when compared to dry run. For a 2W heat input capacity, the thermal resistance observed in the dry run was 10.5 °C/W and that in wet run was 7.25 °C/W.
- The overall heat transfer coefficient of heat pipe increases with increase in heat input, in the range of inputs tested for acetone and methanol, while water filled heat pipe heat pipe shows a nearly constant.

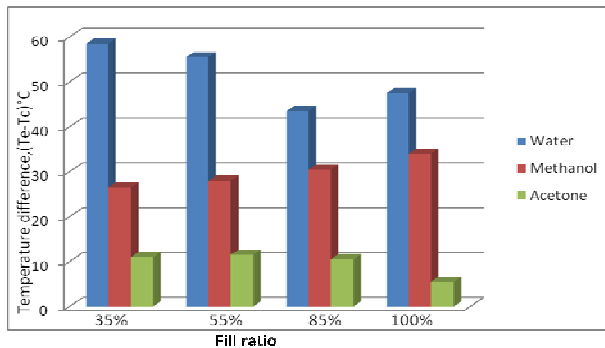


Fig 6. Temperature vs fill ratio for different working fluids for input heat of 10 W

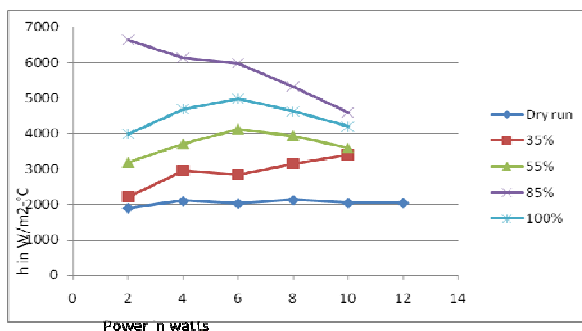


Fig 7. Variations of heat transfer co-efficients with varying heat loads for water

- The fill ratio of working fluid as a percentage of evaporator volume is shown to have minimum effect on the performance of heat pipe with respect to the temperature difference when water and methanol are used as working fluids. However, in case of acetone, the temperature difference across evaporator and condenser continues to drop down with an increase in the fill ratio. With acetone as the working fluid, 100% fill ratio of evaporator volume shows the best result with minimum temperature difference across the evaporator and condenser.
- In general, fill ratios of working fluid greater than 85% of volume of evaporator show better results in terms of increased heat transfer coefficient, decreased thermal resistance and reduced temperature difference across the evaporator and condenser.

### 5. REFERENCES

- Dunn P and Reay D.A., 1982, *Heat Pipes*, Pergamon Press New York, Third Edition, 1982
- Akon, A. F. and Chowdhury M. S. Hasib., "Performance Test of a Heat Pipe for Different Working Fluid and Fill Ratio", Undergraduate Thesis, Dept. of Mechanical Engineering, BUET, Dhaka, 2009
- Zuo, Z. J. and Gunnerson, F. S., 1995, "Heat Transfer Analysis of a Inclined Two Phase Closed Thermosyphon", *Journal of Heat Transfer*, Vol. 117 pp 1073-1075.
- Zhang, J., 2002, "M. S. Thesis: Heat Transfer and Fluid Flow in an Idealized Micro Heat Pipe", 2002 *ME Graduate Student Conference*, LSU.
- Cao, Y. and Gao, M., "Wickless network heat pipes for high heat flux spreading applications Wickless network heat pipes for high heat flux spreading applications", *International Journal of Heat and Mass Transfer*, Volume 45, Number 12, June 2002 , pp. 2539-2547(9)

### 6. NOMENCLATURE

Symbol	Meaning	Unit
$T_e$	Average Evaporator Temperature	°C
$T_c$	Average Condenser Temperature	°C
R	Thermal Resistance	°C/W
h	Overall heat transfer Coefficient	W/m <sup>2</sup> -°C
Q	Heat Input	W
A	Heat transfer surface area at the evaporator	m <sup>2</sup>

### 7. MIALING ADDRESS

A. Kumar Mozumder  
 Department of Mechanical Engineering,  
 Bangladesh University of Engineering & Technology,  
 Dhaka-1000, Bangladesh.

## GENERATION OF BIOGAS FROM ANEROBIC DIGESTION OF VEGETABLE WASTE

M. Islam, B. Salam and A. Mohajan

Department of Mechanical Engineering  
Chittagong University of Engineering and Technology, Chittagong, Bangladesh

### ABSTRACT

Biogas, a renewable form of energy, could be a very well substitute of natural gas which is depleting very fast. A research work was conducted to investigate the production ability of biogas from vegetable waste. Five laboratory scale digesters were made to experiment the effect of co-digestion of vegetable waste and cow-dung in various proportions. The digesters were made of plastic container of four litre capacity each. Vegetable waste was used from 200 gm to 300 gm, and cow-dung was used from 0 gm to 300 gm to make vegetable waste to cow dung ratios from 1:0 to 1:1.5. From 2 to 3 mm sized vegetable waste was used in the experiment. The digester was feed on batch mode and operated at ambient temperature for about 15 days. In the slurry, total solid concentration was maintained 8% by mass for all of the observations. The maximum amount of biogas was yield 1200 ml/Kg of wastes at the vegetable waste and cow dung ratio 1:1.

**Key words:** Anaerobic Digestion, Biogas, Vegetable Waste, Cow Dung.

### 1. INTRODUCTION

Despite rapid globalization, Bangladesh, like other third world countries, is an agro based country. Although her arable land is shrinking gradually because of unplanned urbanization, landslide, flood, cyclone, and other natural calamities; almost 80% of her population directly or indirectly depends on agriculture. Among the total annual harvest a significant portion of land is devoted for vegetable cultivation across the country. In the winter season, a plenty of vegetables are harvested across the country. But, because of the deficiency of efficient transportation and preservation a huge amount of those vegetables are wasted firstly in the land where it was grown and then in the vegetable market. Moreover this waste is not treated properly, which is a consequence of severe environmental pollution. Since methane gas generation from uncontrolled anaerobic digestion of that waste is very threatening to the environment. Investigation is yet to be done to estimate the actual amount of vegetables is destroyed each year, which can be a good source of biogas as a renewable energy, and its residue can be an excellent organic fertilizer. An attempt was done to utilize those wasted vegetables and this paper demarcates briefly the prospect of vegetable waste for biogas generation in Bangladesh.

Numerous studies, researches, and implementation of findings have been going on globally to produce biogas from food waste especially from vegetable waste and India is one of the harbingers in this field. Indian researchers Biswas et al. [1] conducted a comprehensive study on biogas kinetics and they used the municipal wastes as the source of biogas. They used a 10 dm<sup>3</sup>

anaerobic batch digester equipped with a mechanical agitator under controlled environment at pH 6.8 and temperature 40 °C for that purpose. Later Biswas et al. [2] developed a deterministic mathematical model to predict the characteristics of an anaerobic digester of biogas generation satisfactorily. They operated an anaerobic digester of 10 litre capacity in batch mode at an optimum temperature of 40 °C and at a pH of 6.8, feeding vegetable/food residues. Kameswari et al. [3] established a demonstration plant of capacity 30 tonnes per day for biomethanation of vegetable market waste. The biomethanation plant was designed for 30 tonnes per day, organic loading rate of 2.5 kg of VS/day/m<sup>3</sup> with biogas generation of 2500 m<sup>3</sup> of biogas per day. The source of feedstock for Kamaraj [4] study was vegetable market waste. Through the study, he concluded that vegetable waste could be used for biogas production using biphasic system. Kale et al. [5] established a biogas plant in which biogas was produced from kitchen waste using thermophilic microorganisms. The biogas plant was constructed using a mixer/pulper for crushing the solid waste, premix tanks, pre-digester tank, solar heater for water heating, main digestion tank, manure pits, and gas lamps for utilization of the biogas generated in the plant. Italian researcher Cojolon et al. [6] investigated the technical, socio-economical, and environmental aspects of biogas generation using rural household wastes. They found that anaerobic digestion of vegetable waste, daily produced by small households, generated biogas sufficient for daily cooking of those households.

The prime object of this research work was to



investigate the prospect of vegetable waste for biogas generation as a renewable energy source by means of co-digestion with cow dung and ultimate protection of environment from the bad effect of methane gas that would be produced by uncontrolled anaerobic digestion of those wastes.

## 2. EXPERIMENTAL SETUP

A simple experimental setup was fabricated using three container namely digester, water chamber cum gas collector, and expelled water collector. Fig. 1 illustrates a schematic diagram of the setup. Digester was connected with water chamber by a plastic pipe (gas pipe) which was used to allow the produced gas to flow through it to the water chamber and hence expelled the same volume of water from the water chamber, which was then used to flow through another plastic pipe (water pipe) to the water collector. Both the ends of the gas pipe were inserted just at the top of the digester and the water chamber, and one end of the water pipe was inserted up to bottom of the water chamber and the other end of the pipe was inserted into the water collector. Both the gas pipe and water pipe were inserted into their respective container through corks which were maintained air tight firmly.

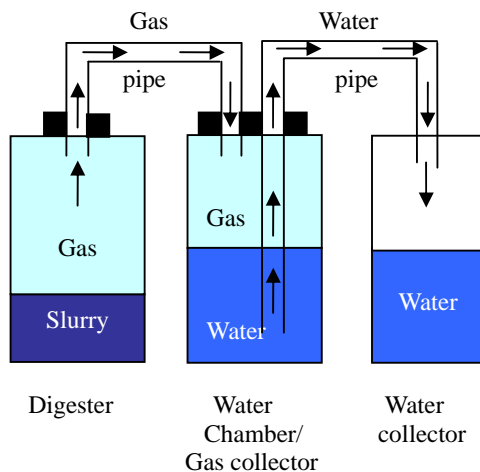


Fig 1. Schematic diagram of the experimental set-up.

## 3. MATERIALS & METHOD

### 3.1 Sources Of Wastes

The vegetable waste and the cow dung for the research work were collected from the student halls and the residential area of Chittagong University of Engineering and Technology, (CUET).

### 3.2 Slurry Preparation

In order to optimize the gas generation, feed stock was maintained 8% [7] of TS concentration by mass. From empirical analysis it was found that fresh cow dung and fresh vegetable waste have the TS of 18% and average 20.5% [7] respectively. So water was added 156.25 gm with each 100 gm of vegetable waste and that was 125 gm with each 100 gm of cow dung.

## 3.3 Data Collection Techniques

In this study the volume of the produced gas was measured by water displacement method considering the volume of the generated gas was equal to that of the expelled water in the water collector. Gas was produced after 7/8<sup>th</sup> operating day of the digester. Data was collected by every three hours from 9:00 AM to 5:00 PM everyday in the Thermal Engineering laboratory of CUET till the generation of the gas become zero.

## 3.4 Observations

Five observations were done feeding the digesters with the mixture of VW and CD with optimum amount of water. After feeding, the digesters were left for anaerobic digestion and gas was started to generate in the 7/8<sup>th</sup> operating day and that was almost terminated within 14/15<sup>th</sup> operating day of the digester. Produced gas was allowed to flow through the gas pipe and accumulated in the gas collector above water surface, which caused to expel the same volume of water (assumed) from water chamber and allowed to flow through the water pipe to the water collector. Volume of the gas was measured directly by measuring the volume of the expelled water in the water collector by a measuring plucks by every three hours. The system was kept air tight and each observation was continued till the flow of the expelled water was terminated. Table 1 bellow shows the amounts of VW, CD and water were added to prepare the slurry of 8% TS for the digesters.

Table 1: Relative wastes and water amounts in the slurry.

Compositions VW : CD	VW (gm)	CD (gm)	Water added for 8% of TS (mL)
1 : 1	300	300	775
1 : 1.5	200	300	635
1 : 0.67	300	200	745
1 : 0.33	300	100	545
1 : 0	300	0	430

## 4. RESULTS AND DISCUSSION

This study was carried out to investigate the generation of bio gas from VW with CD mixture. Data obtained from all of the observations were gas volume. To find out the optimum mixture, variations were done in the ratios of VW and CD. The findings of the observations are represented in the figures Fig. 2, to Fig. 4.

Fig.2 represents the total volume of gas was produced per Kg of wastes during the digester's operation at different proportions of VW and CD mixtures. Next Fig.3 illustrates the amount of gas generation per Kg of wastes per day during that period of time for the same proportions. And finally, Fig.4 shows the influence of the amount of CD in the feed stock on biogas generation.

Analyzing the figure Fig.2 it can be noticed that maximum volume of gas was generated at 1:1 ratio of

VW and CD. But no appreciable amount of gas was produced at 1:0 ratios, that is almost no production while CD was not added in the slurry. Again at the highest proportion of CD that is at 1:1.5 ratios the production was relatively lower.

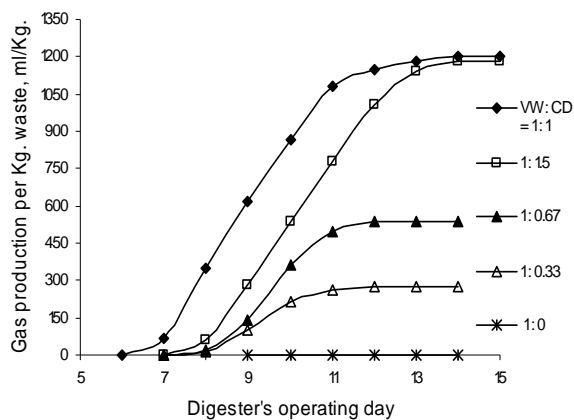


Fig 2. Operating days vs. total volume of gas production per Kg of wastes at different composition of wastes.

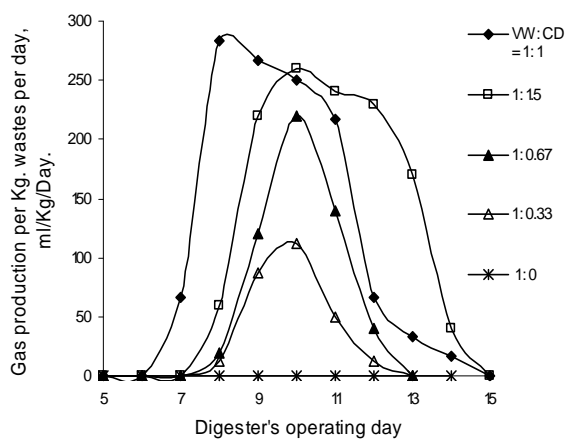


Fig 3. Operating days vs. volume of gas production per Kg of wastes per day at different composition of wastes.

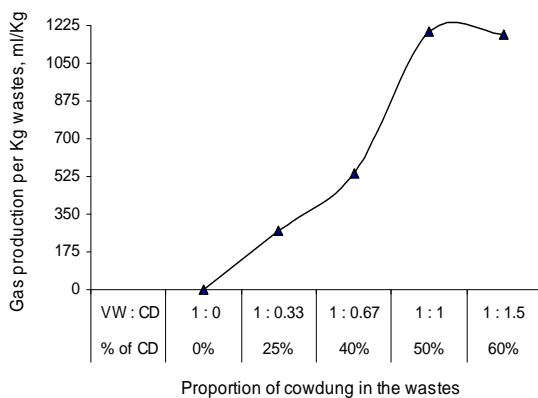


Fig 4. Proportion of CD in the wastes vs. volume of gas produced per kg of wastes.

Similar phenomena are true for Fig.4. When the percentage of CD was increasing the production of biogas per kg of solid wastes also was increasing almost moderately from 0% to 40% of CD. Further this trend was surprisingly rapid at 50% of CD, and the gas production was 1200ml/kg of wastes. However, the generation started to decrease beyond 50% of CD in the mixture. Besides Fig.3 illustrates that the generation of gas was started from 7/8<sup>th</sup> digester's operating day and continued to 14/15<sup>th</sup> operating day. Gas generation was peaked at 9/10<sup>th</sup> operating day to the maximum 170ml/day almost from zero production at 7/8<sup>th</sup> day and that was approximately the mirror view from 9/10<sup>th</sup> to 14/15<sup>th</sup> day.

## 5. CONCLUSIONS

Analyzing the experimental dataset it was found that, the production of gas was not uniform. The bio gas production from vegetable waste largely depends on the proportion of cow dung added with it and the condition of the used vegetable waste. If the amount of cow dung was changed, the production of the gas was also changed. Analyzing the figures it was found that 1:1 mixture of vegetable waste and cow dung was optimum. The maximum gas production was 1200 ml/kg of total wastes. Water was added in order to dilute the organic substances and to increase the breeding of micro-organisms. Addition of cow dung with vegetable waste was beneficiary way to reduce the retention time. It was a primary investigation to learn the production ability of biogas as a renewable source of energy from vegetable waste in Bangladesh, since she has a great potentiality of vegetable waste. It was a mesophilic anaerobic digestion. In the further study thermophilic digestion with periodic stirring into a prescribed digester will be investigated. P<sup>H</sup> level also will be controlled in the next experiment.

## 6. ACKNOWLEDGEMENT

This research work was carried out in the "Thermal Engineering Lab" of the Department of Mechanical Engineering in Chittagong University of Engineering and Technology (CUET), Chittagong-4349, Bangladesh.

## 7. REFERENCES

1. Biswas, J., Chowdhury, R. and Bhattacharya, P., 2006, "Kinetic studies of biogas generation using municipal waste as feed stock", *Enzyme and Microbial Technology*, 38:493-503.
2. Biswas, J., Chowdhury, R. and Bhattacharya, P., 2007, "Mathematical modeling for the prediction of biogas generation characteristics of an anaerobic digester based on food/vegetable residues", *Biomass and Bioenergy*, 31:80-86.
3. Sri Bala Kameswari, K., Velmurugan, B., Thirumaran, K. and Ramanujam, R. A., 2007, "Biomethanation of Vegetable Market Waste – Untapped Carbon Trading Opportunities", *Proceedings of the International Conference on Sustainable Solid Waste Management*, Chennai, India. pp. 415-420.
4. Kamaraj, S., 2008, "Biogas based power generation

from fruit and vegetable waste through bi-phasic digestion”, *NSTI Nanotech, The Nanotechnology Conference and Trade show*, Boston.

5. Kale, S. P. and Mehetre, S. T., 2006, “*Kitchen Waste Based Biogas Plant*”, Nuclear Agriculture and Biotechnology Division, Bhabha Atomic Research Centre, India.
6. Cojolon, C.L., Estrada, Toledo, E. and Ciferri, A., 2008, “Technical, Socio/Economical and Environmental Aspects of Biogas Generation Using Rural Household Waste”, *La Chimica & l’Industria (Milan)*, 90(3):130-134.
7. “Chowdhury, M. S., 2008, “Study of a Stirling-Generator Using Alternative Fuels”, M.Sc. Thesis, Department of Mechanical Engineering, BUET, Dhaka.

## 8. NOMENCLATURE

Symbol	Meaning
VW	Vegetable Waste
CD	Cow Dung
TS	Total Solid

## 9. MAILING ADDRESS

M. Islam  
Department of Mechanical Engineering  
Chittagong University of Engineering and Technology,  
Chittagong-4349, Bangladesh  
E-mail: murad99me@cuet.ac.bd

## THE ROLE OF TRANSESTERIFICATION PERIOD ON THE EFFECT OF ENGINE PERFORMANCE PARAMETERS USING SOYBEAN BIODIESEL AND DIESEL BLENDS

Swarup Paul<sup>1</sup>, P.K. Bose<sup>2</sup> and Bijan Sarkar<sup>3</sup>

<sup>1</sup>Production Engineering Department NIT Agartala, India, <sup>2</sup>Director, NIT Agartala, India

<sup>3</sup>Production Engineering Department, Jadavpur University, Kolkata, India

### ABSTRACT

Gradual depletion of fossil fuel and their harmful combustion effects are compelling to use now-a-days Biodiesel in engines. Transesterification is a method which is used for production of Biodiesel through removal of fatty acid vegetable oil. This Biodiesel can be used as engine fuel mixing with pure diesel with various proportions. In the present work, four types of Soybean Biodiesel have been made just by varying transesterification period. The transesterification periods are 30mins, 60 mins, 90mins and 120 mins respectively. Twenty percent of each type of Soybean Biodiesel is mixed with eighty percent mineral diesel to make B20 fuel. Now these four types of B20 fuels have been used to run the engine. The engine performance parameters viz. Brake power (BP), Specific fuel consumption (SFC) and RPM is tabulated against various load conditions of engine like 0%, 20%, 40%, 50% 80% and 100%. From the experimental observations, nature of each parameter is represented graphically to show which B20 fuel gives the best result. The statistical Analysis by two-way classification (Randomized Block Design) is done to determine whether Variation of Transesterification period is significant on the engine performance parameters.

**Keywords :** Transesterification, Biodiesel, Engine Performance, Randomized Block Design.

### 1. INTRODUCTION

Biodiesel is an alternative fuel for Internal combustion engines that is gaining attraction in terms of the reducing fossil fuel resources of the world and the mitigating of Greenhouse effects due to carbon dioxide. The main advantages of using a biodiesel are that it is one of the most renewable fuels available and it also non-toxic and biodegradable (1). In addition, this fuel can be used directly or mixed with conventional fuel for most Internal Combustion engines without requiring engine modifications to a great extent (2).

Biodiesel is produced from vegetable oils. The major components of vegetable oils are triglycerides. Triglycerides are esters of glycerol with long chain acids, commonly called fatty acids. Problems associated with vegetable oils during engine tests can be classified into two broad groups, viz, operational and durability problems. Operational problems are related to starting ability, ignition, combustion and performance. Durability problems are related to deposit formation, carbonization of injection tip, ring sticking and lubricating oil dilution. It has been observed that the straight vegetable-oils when used for long hours tend to choke the fuel filter because of high viscosity and insoluble present in the straight vegetable oils. The high viscosity, polyunsaturated character and extremely low volatility of vegetable oils are responsible for the operational and durability

problems associated with its utilization as fuels in diesel engines. High viscosity of vegetable oils causes poor fuel atomization, large droplet size and thus high spray jet penetration. The jet tends to be a solid stream instead of a spray of small droplets. As a result, the fuel is not distributed or mixed with the air required for burning in the combustion chamber. This result in poor combustion accompanied by loss of power and economy.

Blending, cracking/ pyrolysis, emulsification or transesterification of vegetable oils may over come these problems. Heating and blending of vegetable oils reduce the viscosity and improve volatility of vegetable oils but its molecular structure remains unchanged hence polyunsaturated character remains. Blending of vegetable oils with diesel, however, reduces the viscosity drastically and the fuel handling system of engine can handle the vegetable oil diesel blends without any problems. On the basis of experimental investigations, it is found that converting vegetable oils into simple esters is an effective way to overcome all the problems associated with the vegetable oils. Most of the conventional production methods for bio diesel use basic or acidic catalyst. A reaction time of 45 min to 1 hour and reaction temperature of 55-65°C are required for completion of reaction and formation of respective esters[3,4,5,6,7,8,9,11, and 12]

But no such exact study related to effectiveness of

transesterification time on the engine performance parameters have been made. In this present study, the authors have tried to find out the effectiveness of transesterification period on engine performance parameters viz. specific fuel consumption, brake power and r.p.m. Four types of soybean biodiesel have been prepared just by varying transesterification period which are 30mins, 60mins, 90mins and 120mins respectively. Then 20% of each type of soybean biodiesel is mixed by volume with 80 percent of mineral diesel to make four types of B20 fuel. The performance parameters of engine run by these four types of B20 fuel is recorded and a statistical model by Randomized Block Design is developed to show significance of transesterification period.

## 2. METHODOLOGY

### 2.1 Randomized Block Design

The essence of this design is that the experimental material is divided into groups, each of which constitutes a single trial or replication. At all stages of the experiment the object is to keep as small as in practicable. Thus, when the units are assigned to the successive groups, all units which go in the same group should be closely comparable. Similarly, during the course of the experiment, a uniform technique should be employed for all units in the same group. Any changes in technique or in other conditions that may affect the results should be made between groups. This division into replications need be recognized only at those stages in the conduct of the experiment where the division may help to reduce experimental errors.

### 2.2 Procedure for Two Way Classification

**Step 1:** To find the treatment totals ( $T_i$ ), the Replicate totals ( $R_j$ ) and the grand total ( $G$ )

**Step 2:** The sums of squares (SS) are obtained as follows :-

$$\text{Correction factor } C = \frac{G^2}{t_r}$$

( $t_r$  = no of observations)

$$\text{Total : } \sum y^2 - C$$

$$\text{Replications : } \sum \frac{R_j^2}{t} - C \quad (t = \text{no of treatments})$$

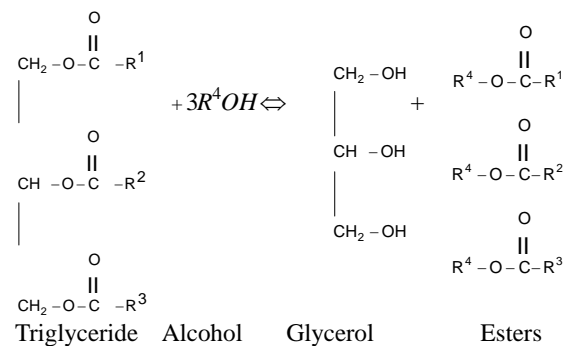
$$\text{Treatments : } \sum \frac{T_i^2}{r} - C \quad (r = \text{no of replications})$$

$$\text{Error : (total SS)-(Replications S.S) - (treatments S.S.)}$$

### 2.3 Transesterification

The formation of methyl esters by transesterification of vegetable oils requires 3 moles of alcohol stoichiometrically. However, transesterification is an equilibrium reaction in which excess alcohol is required to drive the reaction close to completion. The vegetable oil is chemically reacted with an alcohol in presence of a catalyst to produce vegetable oil esters. Glycerol is produced as a by-product of transesterification reaction.

The chemical reaction of the transesterification process is shown below :



The mixture is stirred continuously and then allowed to settle under gravity in a separating funnel. Two distinct layers form after gravity settling for 24hours. The upper layer is of ester and lower layer is of glycerol. The lower layer is separated out. The separated ester is mixed with some worm water (around 10% volume of ester) to remove the catalyst present in ester and allowed to settle under gravity for another 24h. the catalyst gets dissolved in water, which is separated. Moisture is removed from this purified ester using silica gel crystals. The ester is then blended with mineral diesel in various concentrations for preparing bio diesel blends to be used in CI engine for conducting various engine tests. The process of transesterification brings about a drastic change in the density of linseed oil and the linseed oil methyl ester (LOME) has almost similar density as that of mineral diesel.

## 3. EXPERIMENTAL RESULTS AND DISCUSSION

Table 1: Four levels of two factors

% of Load (Nm)	20 (L <sub>1</sub> )	40 (L <sub>2</sub> )	60 (L <sub>3</sub> )	80 (L <sub>4</sub> )
Transesterification period (min)	30 (P <sub>1</sub> )	60 (P <sub>2</sub> )	90 (P <sub>3</sub> )	120 (P <sub>4</sub> )

Table 2 : Performance parameters of Engine run by B20 fuel (Transesterification period : 30mins)

Percentage of Load	SFC (Kg/kwh)	BP (kw)	RPM
L <sub>1</sub>	0.432	1.0	1470
L <sub>2</sub>	0.309	2.1	1440
L <sub>3</sub>	0.324	3.0	1405
L <sub>4</sub>	0.443	3.9	1340

Table 3: Performance parameters of Engine run by B20 fuel (Transesterification period : 60mins)

Percentage of Load	SFC (Kg/kwh)	BP (kw)	RPM
L <sub>1</sub>	0.594	1.0	1470
L <sub>2</sub>	0.334	2.1	1445
L <sub>3</sub>	0.324	3.0	1420
L <sub>4</sub>	0.385	3.5	1270

Table 4: Performance parameters of Engine run by B20 fuel (Transesterification period : 90mins)

Percentage of Load	SFC (Kg/kwh)	BP (kw)	RPM
L <sub>1</sub>	0.486	1.0	1460
L <sub>2</sub>	0.324	2.0	1430
L <sub>3</sub>	0.278	3.1	1405
L <sub>4</sub>	0.496	3.7	1270

Table 5: Performance parameters of Engine run by B20 fuel (Transesterification period : 120mins)

Percentage of Load	SFC (Kg/kwh)	BP (kw)	RPM
L <sub>1</sub>	0.489	1.0	1465
L <sub>2</sub>	0.328	2.0	1430
L <sub>3</sub>	0.296	3.1	1410
L <sub>4</sub>	0.429	3.9	1280

Taking data from table 2,3,4 and 5 graphs have been plotted of specific fuel consumption, Brake power and RPM with percentage of load with increasing rate of transesterification period.

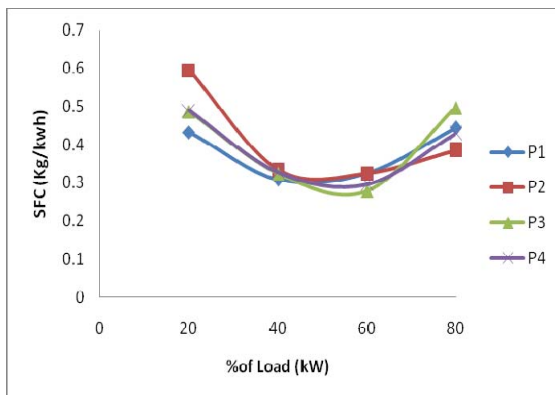


Fig 1. Variation of specific fuel consumption with percentage of load.

Figure-1 shows that specific fuel consumptions are higher for all B20 blends at 20% load of the engine. This is decreasing in nature up to 60% load and then increasing characteristics. At 40% load, specific fuel consumptions are almost same for all the blends. So transesterification period has no effect at this load condition. The B20 fuel for which transesterification is 60 minutes shows maximum variation of specific fuel

consumption.

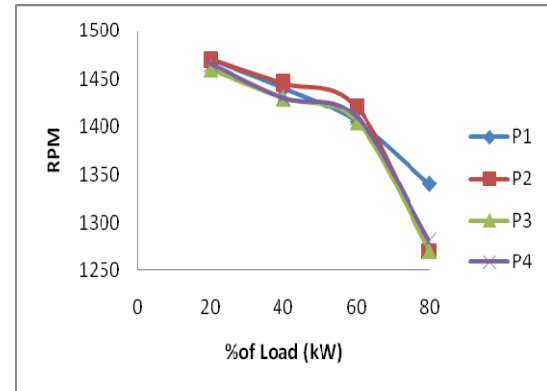


Fig 2. Variation of Brake power with percentage of load.

From figure-2, it can be concluded that Brake power is gradually increasing with higher percentage of loads for all the blends. And for any particular load of the engine, there is negligible variation of Brake power. So transesterification period has no such effect on the Brake power parameter of the engine.

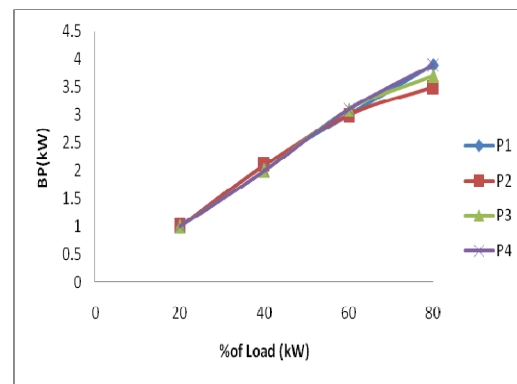


Fig 3. Variation of engine RPM with percentage of load.

From figure 3 – it is seen that at 20% load, RPM of the engine run by all the B20 fuels are almost same which is not true for higher percentage of loads. Maximum variation of RPM for all the B20 fuels occur at 80% load of the engine. And maximum variation of RPM for a particular fuel occurs for the B20 fuel for which transesterification is 60 minute.

From the experimental observations (table 2,3,4 and 5) analysis by Tow way classification has been done and significance of transesterification period on engine performance parameters in shown.

Table 6 : Two-way classification on Specific fuel consumptions .

		Percentage of Load				
		L <sub>1</sub>	L <sub>2</sub>	L <sub>3</sub>	L <sub>4</sub>	Total
Transesterification Period	P <sub>1</sub>	0.43 2	0.30 9	0.32 4	0.44 3	1.508
	P <sub>2</sub>	0.59 4	0.33 4	0.32 4	0.38 5	1.637
	P <sub>3</sub>	0.48 6	0.32 4	0.27 8	0.49 6	1.584
	P <sub>4</sub>	0.48 9	0.32 8	0.29 6	0.42 9	1.542
	Tota l	2.00 1	1.29 5	1.22 2	1.75 3	6.271 6.271

$$C = \text{Correction factor} = \frac{(\text{Grand Total})^2}{\text{Number of observations}}$$

$$= \frac{(6.271)^2}{16} = 2.458$$

Total sum of squares,  
 $SST = [(0.432)^2 + (0.594)^2 + (0.486)^2 + (0.489)^2$   
 $+ (0.309)^2 + (0.334)^2 + (0.324)^2 + (0.328)^2$   
 $+ (0.324)^2 + (0.324)^2 + (0.278)^2 + (0.296)^2$   
 $+ (0.443)^2 + (0.385)^2 + (0.496)^2 + (0.429)^2 ] - C$   
 $= 2.584 - 2.458$   
 $= 0.126$

Treatment sum of squares,  
 $SSA =$   
 $\frac{1}{4} [(1.508)^2 + (1.637)^2 + (1.584)^2 + (1.542)^2] - C$   
 $= 2.460 - 2.458 = 0.002$

Block sum of squares,  
 $SSB =$   
 $\frac{1}{4} [(2.001)^2 + (1.295)^2 + (1.222)^2 + (1.753)^2] - C$   
 $= 2.460 - 2.458 = 0.104$

Error sum of squares,  
 $SSE = SST - SSA - SSB$   
 $= 0.126 - 0.002 - 0.104$   
 $= 0.02$

Table 7 : Analysis of Variance

Source	Degree of Freedom	Sum of Square	Mean Square	Computed f
Factor A	3	0.002	0.00067	0.305 (<1)*
Factor B	3	0.104	0.0347	15.77**
Error	9	0.02	0.0022	
Total	15			

\*\* Significant  
 \* insignificant

Table 8 : Two-way classification on Brake Power : Percentage of Load

		L <sub>1</sub>	L <sub>2</sub>	L <sub>3</sub>	L <sub>4</sub>	Total
Transesterification Period	P <sub>1</sub>	1	2.1	3	3.9	10
	P <sub>2</sub>	1	2.1	3	3.5	9.6
	P <sub>3</sub>	1	2	3.1	3.7	9.8
	P <sub>4</sub>	1	2	3.1	3.9	10
	Total	4.0	8.2	12.2	15	39.4 39.4

$$C = \text{Correction factor} = \frac{(\text{Grand Total})^2}{\text{Number of observations}}$$

$$= \frac{(39.4)^2}{16} = 97.02$$

Total sum of squares,  
 $SST = [1^2 + 1^2 + 1^2 + 1^2$   
 $+ (2.1)^2 + (2.1)^2 + 2^2 + 2^2$   
 $+ 3^2 + 3^2 + (3.1)^2 + (3.1)^2$   
 $+ (3.9)^2 + (3.5)^2 + (3.7)^2 + (3.9)^2 ] - C$   
 $= 114.4 - 97.02$   
 $= 17.38$

Treatment sum of squares,  
 $SSA = \frac{1}{4} [10^2 + 9.6^2 + 9.8^2 + 10^2] - C$   
 $= 97.05 - 97.02 = 0.03$

Block sum of squares,  
 $SSB = \frac{1}{4} [4^2 + 8.2^2 + 12.2^2 + 15^2] - C$



$$= 114.27 - 97.02$$

$$= 17.25$$

**Error sum of squares,**  
**SSE = SST-SSA-SSB**

$$= 17.38 - 0.03 - 17.25$$

$$= 0.10$$

Table 9 : Analysis of Variance

Source	Degree of Freedom	Sum of Square	Mean Square	Computed f
Factor A	3	0.03	0.01	0.909 (<1)*
Factor B	3	17.25	5.75	522.72**
Error	9	0.10	0.011	
Total	15			

\*\* Significant  
 \* Insignificant

Table : 10 : Two-way classification on RPM :

Percentage of Load

	L <sub>1</sub>	L <sub>2</sub>	L <sub>3</sub>	L <sub>4</sub>	Total
P <sub>1</sub>	1470	1440	1405	1340	5655
P <sub>2</sub>	1470	1445	1420	1270	5605
P <sub>3</sub>	1460	1430	1405	1270	5565
P <sub>4</sub>	1465	1430	1410	1280	5585
Total	5865	5745	5640	5160	22410
					22410

$$C = \text{Correction factor} = \frac{(\text{Grand Total})^2}{\text{Number of observations}}$$

$$= \frac{(22410)^2}{16} = 31388006.25$$

Total sum of squares,  
**SST =**  $[1470^2 + 1470^2 + 1460^2 + 1465^2 + 1440^2 + 1445^2 + 1430^2 + 1430^2 + 1405^2 + 1420^2 + 1405^2 + 1410^2 + 1340^2 + 1270^2 + 1270^2 + 1280^2] - C$   
 = 31463400 - 31388006.25  
 = 75393.75

Treatment sum of squares,

$$SSA = \frac{1}{4} [5655^2 + 5605^2 + 5565^2 + 5585^2] - C$$

$$= 31389125 - 31388006.25 = 1118.75$$

Block sum of squares,

$$SSB = \frac{1}{4} [5865^2 + 5745^2 + 5640^2 + 5160^2] - C$$

$$= 31459612.5 - 31388006.25 = 2668.75$$

Error sum of squares,

$$SSE = SST - SSA - SSB$$

$$= 075393.75 - 1118.75 - 71606.25$$

$$= 2668.75$$

Table 11: Analysis of Variance

Source	Degree of Freedom	Sum of Square	Mean Square	Computed f
Factor A	3	1118.75	372.92	1.25*
Factor B	3	71606.25	23868.75	80.49**
Error	9	2668.75	296.53	
Total	15			

\*\* Significant  
 \* Insignificant

#### 4. CONCLUSION

It is evident from the tables 7, 9 and 11 that transesterification period is insignificant where as percentage of load is highly significant. So we must take care of percentage of load. It can be concluded that transesterification period upto 45 minutes to 60 minutes is sufficient to set desirable results using soybean Biodiesel and Diesel blends as Internal Combustion Engine fuels. However, lots of R&D work essential for this.

#### 5. REFERENCES

1. Van Gerpen, J. Shanks, B. Pruszko, R., Clements, D., Knothe, G., 2004. Bio diesel Production Technology. NREL / SR-510-36244, Colorado.
2. Van Gerpen, J. 2005. Biodiesel Processing and Production. Fuel Process. Technol. 86 1097-1107
3. A.K. Agarwal, Vegetable oils versus diesel fuel : development and use of biodiesel in a compression ignition engine, TERI Inf Digest on Energy 8 (1998), pp 191-204.
4. S.Saka and D. Kusdiana, Biodiesel fuel from rapeseed oil as prepared in supercritical methanol, Fuel 80 (2001), pp 225-231
5. T. Murayama, Y. Fujiwara and T. Noto, Evaluating Waste Vegetable Oils as a diesel fuel, Proc Inst Mech Eng D 214 (200) , p.p. 141-148
6. Akasaka Y, Suzuki T, Saurai Y, Exhaust emission of a DI diesel engine fuelled with blends of biodiesel and low sulfur diesel fuel. SAE paper 972998.

7. Marshall W, Schumacher LG, Howell S. Engine exhaust emission evaluation of acummins LIOE when fuelled with biodiesel blend. SAE paper 952363
8. Agarwal AK. Biodiesel for CI engines : an obvious choice for next millennium. In Proceedings of the 12<sup>th</sup> international congress and exhibition on research and development. R&D vision 21<sup>st</sup> Century, 15-16 January 1999
9. Agarwal A.K. Vegetable oils test fuels for diesel engines : formulation and analysis. M. Tech . minor project, centre for Energy Studies, Indian Institute of Technology, New Delhi, 1995-96.
10. M. Diasakou, A. Loulodi and N. papayannakos, Kinetics of the non catalytic transesterification of soybean oil, Fuel 77 (1998), pp 1297-1320.
11. S.S. Marinkovic and A. Tomasevic, Transesterification of sunflower oil in situ, Fuel 77 (1998), pp. 1389-1391.
12. Pelly M. Make fuel from used kitchen grease countryside Magazine, 2001.
13. Cochram & Cox, Experimental Designs, Second Edition, Wiley classics library Edition Published 1992.
14. Walpole, R.E. and myers, R.H., Probability and Statistics for Engineers and Scientists, 1993 (Macmillan : London)

## 6. MAILING ADDRESS

Swarup Paul<sup>1</sup>, P.K. Bose<sup>2</sup> and Bijan Sarkar<sup>3</sup>  
<sup>1</sup>Production Engineering Department NIT Agartala,  
 India, <sup>2</sup>Director, NIT Agartala, India

## EFFECT OF CONDUCTION ON COMBINED FREE AND FORCED CONVECTION IN A VENTILATED CAVITY WITH A HEAT-GENERATING SOLID CIRCULAR BODY

M. A. H. Mamun<sup>1</sup>, M. M. Rahman<sup>2</sup>, and Shuichi Nagata<sup>1</sup>

<sup>1</sup>Institute of Ocean Energy, Saga University, Japan

<sup>2</sup>Department of Mathematics, BUET, Bangladesh

### ABSTRACT

Numerical simulations of the effect of conduction on combined free and forced convection (mixed convection) heat transfer and fluid flow have been performed in a 2-D ventilated cavity with a finite size and finite conductivity solid circular body. The wall of the cavity is assumed to be adiabatic. Flows are imposed at the bottom of the left wall and exit at the top of the right wall of the cavity. The heat generating body is placed at the center of the cavity. The present study simulates a practical system such as air-cooled electronic equipment with a heat component. The developed mathematical model is governed by the coupled equations of mass, momentum and energy and is solved by employing Galerkin weighted residual finite element method. The computation is carried out for wide ranges of Reynolds number, Richardson number. Various results such as the streamlines, isotherms, heat transfer rates in terms of the average Nusselt number and average fluid temperature in the cavity are presented for different parameters. The results indicate that both flow field and temperature distribution strongly depend on Reynolds number, Richardson number. It is also observed that the mentioned parameters have significant effect on average Nusselt number at the heated surface and average fluid temperature in the cavity.

**Keywords:** Solid Circular Body, Ventilated Cavity, Mixed Convection And Finite Element Method.

### 1. INTRODUCTION

Modification of heat transfer in cavities due to introduction of obstacles, partitions and fins attached to the wall(s) has received some consideration in recent years. Many authors have recently studied heat transfer with obstacles, partitions and fins, thereby altering the convection flow phenomenon.

Three related studies of mixed convection in a partially divided rectangular enclosure were respectively carried out by Hsu et al. [1], How and Hsu [2] and Calmidi and Mahajan [3]. The simulation was conducted for wide range of Reynolds and Grashof numbers. They indicated that the average Nusselt number and the dimensionless surface temperature depend on the location and height of the divider. Combined free and forced convection in a square enclosure with heat conducting body and a finite-size heat source was simulated numerically by Hsu and How [4]. They concluded that both the heat transfer coefficient and the dimensionless temperature in the body center strongly depend on the configurations of the system. Shuja et al. [5] numerically studied mixed convection in a square cavity due to heat generating rectangular body and investigated the effect of exit port locations on the heat transfer characteristics and irreversibility generation in the cavity. They showed that the normalized

irreversibility increases as the exit port location number increases and the heat transfer from the solid body enhanced while the irreversibility reduces. The same authors considered heat transfer enhancement due to flow over a two-dimensional rectangular protruding bluff body [6]. Hung and Fu [7] studied the passive enhancement of mixed convection heat transfer in a horizontal channel with inner rectangular blocks by geometric modification. Unsteady mixed convection in a horizontal channel containing heated blocks on its lower wall was studied numerically by Najam et al. [8]. Tsay et al. [9] rigorously investigated the thermal and hydrodynamic interactions among the surface-mounted heated blocks and baffles in a duct flow mixed convection. They focused particularly on the effects of the height of baffle, distance between the heated blocks, baffle and number of baffles on the flow structure and heat transfer characteristics for the system at various  $Re$  and  $Gr/Re^2$ . Turki et al. [10] conducted a numerical investigation to analyze the unsteady flow field and heat transfer characteristics in a horizontal channel with a built-in heated square cylinder. They examined the effects of the blockage ratio, the Reynolds number and Richardson numbers on aerodynamic and heat transfer characteristics. Chang and Shiau [11] numerically investigated the effects of a horizontal baffle on the heat

transfer characteristics of pulsating opposing mixed convection in a parallel vertical open channel. Bhoite et al. [12] studied numerically the problem of mixed convection flow and heat transfer in a shallow enclosure with a series of block-like heat generating component for a range of Reynolds and Grashof numbers and block-to-fluid thermal conductivity ratios. They showed that higher Reynolds number tend to create a recirculation region of increasing strength at the core region and the effect of buoyancy becomes insignificant beyond a Reynolds number of typically 600, and the thermal conductivity ratio has a negligible effect on the velocity fields. Recently Rahman et al. [13] studied of mixed convection in a square cavity with a heat conducting square cylinder at different locations. At the same time Rahman et al. [14] studied mixed convection in a vented square cavity with a heat conducting horizontal solid circular cylinder. Very recently Rahman et al. [15] analyzed mixed convection in a rectangular cavity with a heat conducting horizontal circular cylinder by using finite element method.

The purpose of this study is to examine the effect of a heat generating circular body on mixed convection in a square cavity. Numerical solutions are obtained over a wide range of Richardson numbers and Reynolds number. The dependence of the thermal and flow fields on the Richardson numbers and Reynolds number is studied in detail.

## 2. MODEL SPECIFICATION

The schematic of the system considered in this paper is shown in Fig. 1. The system consists of a square cavity with sides of length  $L$ , within which a heat generating solid circular body with diameter of  $d$  is centered. The cylinder body has a thermal conductivity of  $k_s$  and generates uniform heat per unit volume of  $Q$ . The side walls of the cavity are assumed to be adiabatic. It is assumed that the incoming flow is at a uniform velocity,  $u_i$  and at the ambient temperature,  $\theta_i$ . An inflow opening located on the bottom of the left vertical wall, whereas the out flow opening at the top of the opposite side wall and the size of the inlet port is the same size as the exit port which is equal to  $w = 0.1L$ .

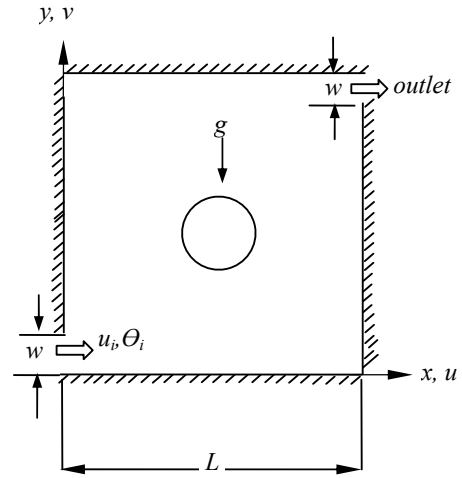


Fig. 1. Schematic diagram of the problem considered and coordinate system

## 3. MATHEMATICAL FORMULATION

The flow within the cavity is assumed to be two-dimensional, steady, laminar, incompressible and the fluid properties are to be constant. The radiation effects are taken as negligible and the Boussinesq approximation is used. The dimensionless equations describing the flow are as follows:

$$\frac{\partial U}{\partial X} + \frac{\partial V}{\partial Y} = 0 \quad (1)$$

$$U \frac{\partial U}{\partial X} + V \frac{\partial U}{\partial Y} = -\frac{\partial P}{\partial X} + \frac{1}{\text{Re}} \left( \frac{\partial^2 U}{\partial X^2} + \frac{\partial^2 U}{\partial Y^2} \right) \quad (2)$$

$$U \frac{\partial V}{\partial X} + V \frac{\partial V}{\partial Y} = -\frac{\partial P}{\partial Y} + \frac{1}{\text{Re}} \left( \frac{\partial^2 V}{\partial X^2} + \frac{\partial^2 V}{\partial Y^2} \right) + \text{Ri} \theta \quad (3)$$

$$U \frac{\partial \theta}{\partial X} + V \frac{\partial \theta}{\partial Y} = \frac{1}{\text{RePr}} \left( \frac{\partial^2 \theta}{\partial X^2} + \frac{\partial^2 \theta}{\partial Y^2} \right) \quad (4)$$

For solid cylinder the energy equation is

$$\frac{\partial^2 \theta_s}{\partial X^2} + \frac{\partial^2 \theta_s}{\partial Y^2} + Q = 0 \quad (5)$$

Here  $\text{Gr} = \frac{\beta g q L^4}{\nu^2 k}$  is the Grashof number,  $\text{Pr} = \frac{\nu}{\alpha}$  is the

Prandtl number,  $\text{Re} = \frac{u_i L}{\nu}$  is the Reynolds number,

$\text{Ri} = \frac{\text{Gr}}{\text{Re}^2}$  is the Richardson number and  $Q$  is the heat generating parameter.

The above equations were non dimensionalized by defining

$$X = \frac{x}{L}, Y = \frac{y}{L}, U = \frac{u}{u_i}, V = \frac{v}{u_i}, P = \frac{p}{\rho u_i^2},$$

$$\theta = \frac{(T - T_i)}{(T_h - T_i)}, \theta_s = \frac{(T_s - T_i)}{(T_h - T_i)}$$

Where  $X$  and  $Y$  are the coordinates varying along horizontal and vertical directions, respectively,  $U$  and  $V$  are, the velocity components in the  $X$  and  $Y$  directions,

respectively,  $\theta$  is the dimensionless temperature and  $P$  is the dimensionless pressure.

The boundary conditions for the present problem are specified as follows:

At the Inlet:  $U = 1, V = 0, \theta = -0.5$

At the outlet: Convective boundary condition  $P = 0$

At all solid boundaries:  $U = 0, V = 0$

At the cavity walls:  $\frac{\partial \theta}{\partial N} = 0$

At the fluid-solid interface:  $\left(\frac{\partial \theta}{\partial N}\right)_{fluid} = K \left(\frac{\partial \theta_s}{\partial N}\right)_{solid}$

Where  $N$  is the non-dimensional distances either  $X$  or  $Y$  direction acting normal to the surface and  $K$  is the dimensionless ratio of the thermal conductivity ( $K_s / K_f$ )

The average Nusselt number at the heated surface is calculated as

$$Nu = - \int_0^{L_H} \frac{\partial \theta}{\partial X} dY$$

and the average temperature of the fluid is defined as

$$\theta_{av} = \int \theta d\bar{V} / \bar{V}$$

where  $L_H$  is the length of the heated surface and  $\bar{V}$  is the cavity volume.

#### 4. COMPUTATIONAL PROCEDURE

The numerical procedure used in this work is based on the Galerkin weighted residual method of finite element formulation. In this method, the solution domain is discretized into finite element meshes, which are composed of triangular elements. Then the nonlinear governing partial differential equations i.e., mass, momentum and energy equations are transferred into a system of integral equations by applying Galerkin weighted residual method. The integration involved in each term of these equations is performed by using Gauss quadrature method. Then the nonlinear algebraic equations so obtained are modified by imposition of boundary conditions. These modified nonlinear equations are transferred into linear algebraic equations by using Newton's method. Finally, these linear equations are solved by using Triangular Factorization method. More details are available in Rahman *et al.* [15]

Geometry studied in this paper is an obstructed cavity; therefore several grid size sensitivity tests were conducted in this geometry to determine the sufficiency of the mesh scheme and to ensure that the solutions are grid independent. This is obtained when numerical results of the average Nusselt number  $Nu$ , average temperature  $\theta_{av}$  and solution time become grid size independent, although we continue the refinement of the mesh grid. As can be seen in Table 1, five different non-uniform grids with the following number of nodes and elements were considered for the grid refinement tests: 24545 nodes, 3788 elements; 29321 nodes, 5900 elements; 37787 nodes, 5900 elements; 38163 nodes, 5962 elements and 48030 nodes, 7516 elements. As is shown in Table 1, 38163 nodes and 5962 elements can be chosen throughout the simulation to optimize the relation

between the accuracy required and the computing time.

Table 1: Grid Sensitivity Check at  $Re = 100, Ri = 1.0$  and  $Pr = 0.71$

Nodes (elements)	24545 (3788)	29321 (4556)	37787 (5900)	38163 (5962)	48030 (7516)
$Nu$	4.46011	4.46014	4.46034	4.46044	4.46149
$\theta_{av}$	0.57855	0.57845	0.57825	0.57815	0.57805
Time(sec)	323.610	408.859	563.203	588.390	793.125

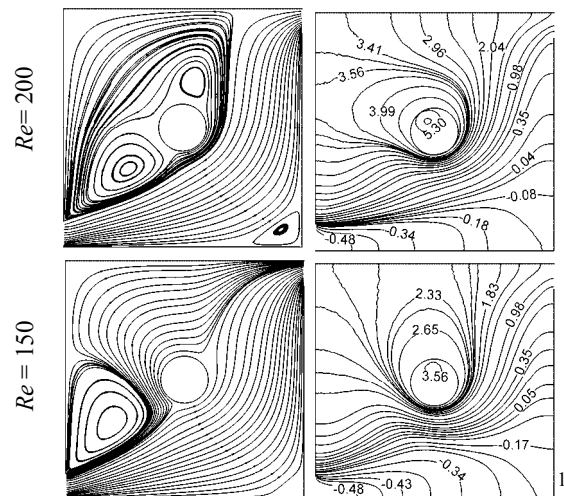
The present code was extensively exercised on the problem of House *et al.* [16] to check its validity. Table 2 compares the present results with the results by House *et al.* for Rayleigh number,  $Ra = 0.0, 10^5$  and two values of  $K = 0.2$  and  $5.0$ . The present results have an excellent agreement with the results obtained by House *et al.*

Table 2: Nusselt Number Comparison for  $Pr = 0.71$

Ra	k	Nu		
		Present work	House <i>et al.</i> [16]	Error (%)
0	0.2	0.7071	0.7063	0.11
0	1.0	1.0000	1.0000	0.00
0	5.0	1.4142	1.4125	0.12
$10^5$	0.2	4.6237	4.6239	0.00
$10^5$	1.0	4.5037	4.5061	0.00
$10^5$	5.0	4.3190	4.3249	0.14

#### 5. RESULTS AND DISCUSSION

The effect of conduction on mixed convection flow in a ventilated square cavity having a heat-generating circular body is tested using a numerical technique. Different governing parameters are used as Reynolds number  $Re$ , Richardson number  $Ri$ , Prandtl number  $Pr$ , solid fluid thermal conductivity ratio  $K$  and heat generating parameter  $Q$ . Two significant parameters such as Reynolds number  $Re$ , Richardson number  $Ri$ , are investigated here for a ventilated square cavity. These



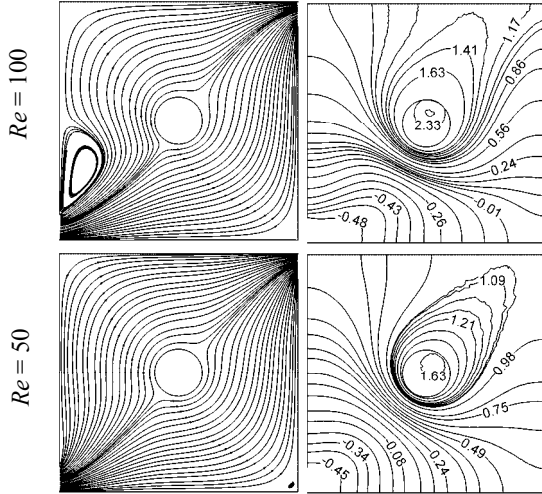


Fig 2. Streamlines and Isotherms for different values  $Re$ , at  $Ri = 0.0$ .

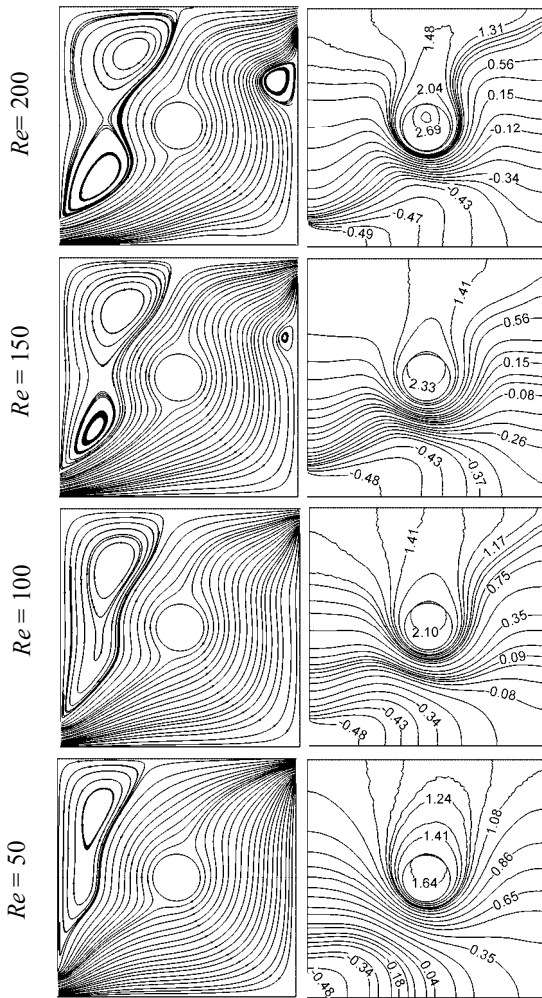


Fig. 3: Streamlines and Isotherms for different values  $Re$ , at  $Ri = 1.0$ .

while the other parameters  $K$ ,  $Pr$  and  $Q$  are keeping fixed at 5.0, 0.71 and 5.0 respectively.

The effect of  $Re$  and  $Ri$  on streamlines and isotherms are shown in Figs. 2-4. The flow structure in the absence of the free convection effect ( $Ri = 0.0$ ) is presented in the left column of the Fig. 2. For  $Ri = 0.0$  and  $Re = 50.0$ , the induced flow enters into the cavity through small inlet and sudden expansion of the fluid is occurred in the cavity due to pressure rise. Thus the fluid occupies the whole cavity and bifurcates near the cylinder. It is also clear that the streamlines are symmetrical about the line joining the inlet and outlet ports. Further, at  $Ri = 0.0$  and  $Re = 100$ , it is seen that a small recirculation cell is developed just at the top of the inlet port, due to increased inertia force. Further more, the size of the recirculation cell increases with increasing  $Re$  at the fixed  $Ri (= 0.0)$ . The corresponding isotherm plots are presented in the right column of the Fig. 2. From the figures it is clear that Reynolds number has significant effect on isotherms at the pure forced convection. Moreover, for  $Ri = 1.0$  and different values of  $Re (= 50, 100, 150$  and  $200)$ , it is seen from the figure 3 that the natural convection effect is

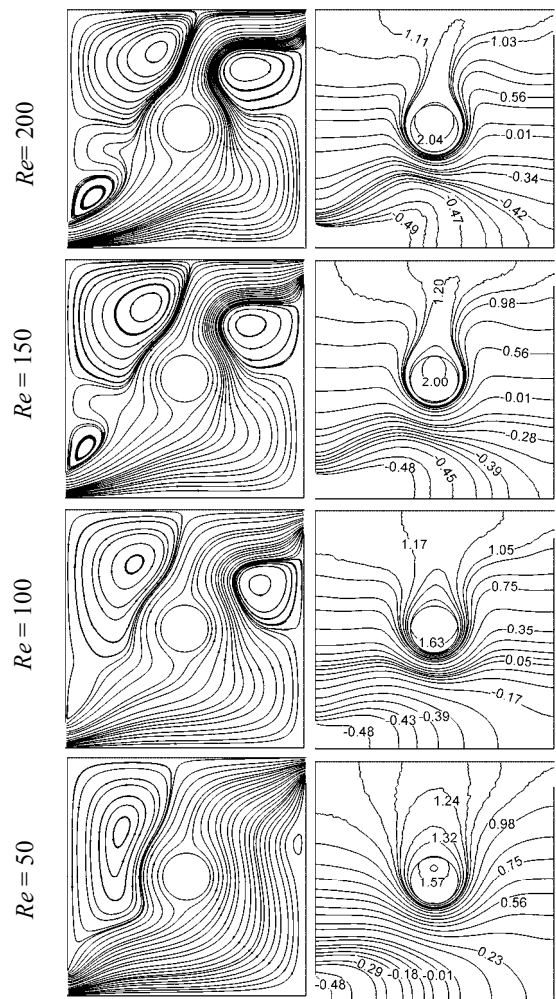


Fig. 4: Streamlines and Isotherms for different values  $Re$ , at  $Ri = 5.0$ .

ranges are varied as to  $50 \leq Re \leq 200$ , and  $0.0 \leq Ri \leq 5.0$ ,

present, but remains relatively weak at the higher values of  $Re$ . Further, increases of  $Ri$  gradually develops the size of the recirculation cell and leads to a large change in the streamline structures. Making a comparison of the isothermal lines for  $Ri = 1.0$  and  $5.0$  and different selective values of  $Re$  with those for  $Ri = 0.0$  and different selective values of  $Re$ , a significant difference is found as shown in the right column of the Figs 3-4.

The effect of the Reynolds number  $Re$  on the average Nusselt number and average fluid temperature in the cavity is shown in Fig. 5. It is noteworthy that the values of average Nusselt number decreases slowly with increasing  $Ri$  for the lower values of  $Re$  ( $= 50$  and  $100$ ) and increases sharply in the forced convection dominated region and slowly in the free convection dominated region for the higher values of  $Re$  ( $= 150$  and  $200$ ). Maximum values of  $Nu$  is found for the highest value of  $Re$ . On the other hand, average fluid temperature in the cavity decreases sharply with increasing  $Re$ , in the forced convection dominated region ( $Ri \leq 0.5$ ) and beyond these values of  $Ri$  it is decreases slowly for the higher values of  $Re$ . But the average fluid temperature in the cavity increases slowly with increasing  $Ri$  for the lowest value of  $Ri$ .

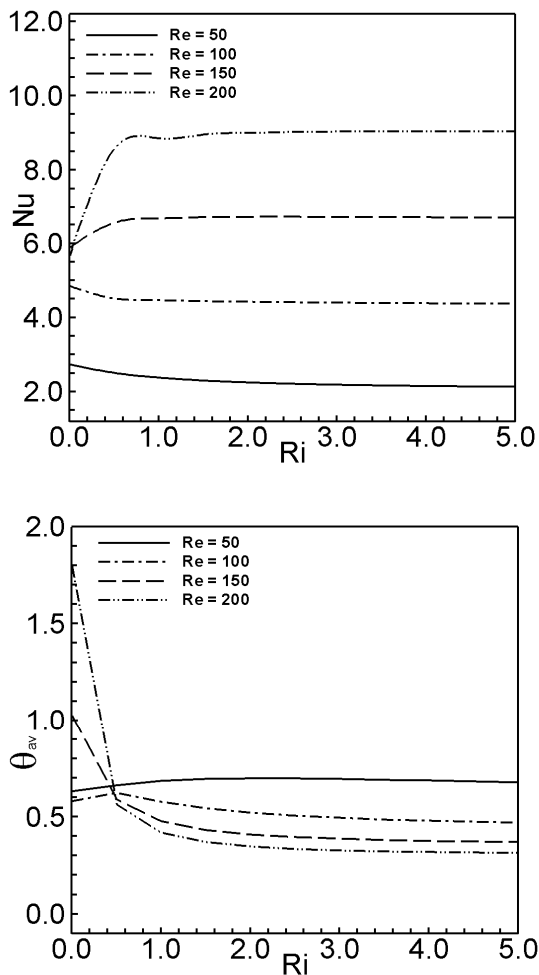


Fig. 5: Effect of  $Re$  on (i) average Nusselt number, (top) and (ii) average fluid temperature (bottom) in the cavity.

## 6. CONCLUSION

The present numerical investigation is made of mixed convection in an enclosure with a heat-generating horizontal circular body. Results are obtained for wide ranges of parameters  $Re$  and  $Ri$ . The following conclusions may be drawn from the present investigations:

Reynolds number has significant effect on the flow and thermal fields at the three convective regimes. Maximum average Nusselt number is found for the largest Reynolds number. On the other hand minimum average fluid temperature is found for  $Re = 100$  in  $Ri \leq 0.5$ , and for for  $Re = 200$  in  $Ri > 0.5$ .

## 7. REFERENCES

- Hsu, T.H., Hsu, P.T., How, S.P., 1997, "Mixed convection in a partially divided rectangular enclosure", Numerical Heat Transfer, Part A, 31: 655-683.
- How, S.P. and Hsu, T.H., 1998, "Transient mixed convection in a partially divided enclosure", Comput. Math. Appl., 36: 95-115.
- Calmidi, V. V., and Mahajan, R. L., 1998, "Mixed convection over a heated horizontal surface in a partial enclosure", Int. J. of Heat and Fluid Flow, 19: 358-367.
- Hsu, T.H., and How, S. P., 1999 "Mixed convection in an enclosure with a heat-conducting body", Acta Mechanica, 133: 87-104.
- Shuja, S. Z., Yilbas, B. S. and Iqbal, M.O., 2000a, "Mixed convection in a square cavity due to heat generating rectangular body effect of cavity exit port locations", Int. J. of Numerical Methods for Heat and Fluid flow, 10 (8): 824-841.
- Shuja, S.Z., Yilbas, B.S. and Iqbal, M.O., 2000b, "Heat transfer characteristics of flow past a rectangular protruding body", Numer. Heat Transfer, Part A, 37: 307-321.
- Hung, T. C., and Fu, C. S., 1999, "Conjugate heat transfer analysis for the passive enhancement of electronic cooling through geometric modification in a mixed convection domain", Numer. Heat Transfer, Part A, 35: 519-535.
- Najam, M., Amahmid, A., Hasnaoui, M., and Alami, M. E., 2003, "Unsteady mixed convection in a horizontal channel with rectangular blocks periodically distributed on its lower wall", Int. J. of Heat and Fluid Flow, 24: 726-735.
- Tsay, Y. L., Cheng, J. C., and Chang, T. S., 2003 "Enhancement of heat transfer from surface-mounted block heat sources in a duct with baffles ", Numer. Heat Transfer, Part A, 43: 827-841.
- Turki, S., Abbassi, H. and Nasrallah, S.B., 2003, "Two-dimensional laminar fluid flow and heat



transfer in a channel with a built-in heated square cylinder”, *Int. J. of Thermal Sciences*, 42: 1105-1113..

11. Chang, T. S., and Shiau, Y. H., 2005, “Flow pulsation and baffle’s effects on the opposing mixed convection in a vertical channel”, *Int. J. of Heat and Mass Transfer*, 48: 4190-4204.
12. Bhoite, M. T., Narasimham, G. S. V. L., and Murthy, M. V. K., 2005, “Mixed convection in a shallow enclosure with a series of heat generating components”, *Int. J. of Thermal Sciences*, 44: 125-135.
13. Rahman, M. M., Alim, M. A., Saha, S. and Chowdhury, M. K., 2008a, “A Numerical Study of Mixed Convection in A Square Cavity with A Heat Conducting Square Cylinder at Different Locations”, *J. of Mechanical Engineering, The Institution of Engineers, Bangladesh*, ME 39 (2): 78 - 85.
14. Rahman, M. M., Alim, M. A., Saha, S. and Chowdhury, M. K., 2008b, “Mixed Convection in a vented Square Cavity with a Heat Conducting Horizontal Solid Circular Cylinder”, *Journal of Naval Architecture and Marine Engineering*, 5 (2): 37 - 46.
15. Rahman, M. M., Alim, M. A. and Mamun, M. A. H., 2009, “Finite element analysis of mixed convection in a rectangular cavity with a heat-conducting horizontal circular cylinder”, *Nonlinear analysis: Modeling and Control*, 14 (2): 217-247.
16. House, J. M., Beckermann, C. and Smith, T. F., 1990, “Effect of a Centered Conducting Body on Natural Convection Heat Transfer in an Enclosure”, *Numerical Heat Transfer, Part A*, 18: 213–225.

## 8. NOMENCLATURE

Symbol	Meaning	Unit
$d$	cylinder diameter	( $m$ )
$g$	gravitational acceleration	( $ms^{-2}$ )
$Gr$	Grashof number	
$h$	convective heat transfer coefficient	( $Wm^{-2}K^{-1}$ )
$K_f$	thermal conductivity of fluid	( $Wm^{-1}K^{-1}$ )
$K_s$	thermal conductivity of solid	( $Wm^{-1}K^{-1}$ )
$K$	solid fluid thermal conductivity ratio	
$L$	length of the cavity	( $m$ )
$Nu$	Nusselt number	
$p$	dimensional pressure	( $Nm^{-2}$ )
$P$	dimensionless pressure	

$Pr$	Prandtl number	
$Re$	Reynolds number	
$Ra$	Rayleigh number	
$Ri$	Richardson number	
$T$	dimensional temperature	( $K$ )
$u, v$	dimensional velocity components	( $ms^{-1}$ )
$U, V$	dimensionless velocity components	
$\bar{V}$	cavity volume	( $m^3$ )
$w$	height of the opening	( $m$ )
$x, y$	Cartesian coordinates	( $m$ )
$X, Y$	dimensionless Cartesian coordinates	

## Greek symbols

Symbol	Meaning	Unit
$\alpha$	thermal diffusivity	( $m^2s^{-1}$ )
$\beta$	thermal expansion coefficient	( $K^{-1}$ )
$\nu$	kinematic viscosity	( $m^2s^{-1}$ )
$\theta$	non dimensional temperature	
$\rho$	density of the fluid	( $kgm^{-3}$ )

## Subscripts

Symbol	Meaning	Unit
$av$	average	
$h$	heated wall	
$i$	inlet state	
$c$	cylinder center	

## 9. MAILING ADDRESS

M. A. H. Mamun  
Institute of Ocean Energy, Saga University, Japan

## EXPERIMENTAL INVESTIGATION OF HEAT TRANSFER CHARACTERISTICS OF CYLINDRICAL FIN WITH DIFFERENT GROOVES

Mohammad Mashud, Md. Shariful Islam, Z. Rahman Arani and Afsanul Tanveer

Department of Mechanical Engineering  
Khulna University of Engineering & Technology (KUET), Khulna, Bangladesh

### ABSTRACT

An experimental study was performed to provide information about the effect of pressure reduction on heat loss from cylindrical fins of three different geometries. A literature review shows that much of work on radiating fins has been carried out analytically and numerically. In this research, a solid cylindrical fin and two other cylindrical fins with circular grooves and threads on their outside surface are investigated experimentally. A test facility with a pressure reduction chamber and instrumentation is fabricated. The heat input to the fin is varied such that the base temperature is maintained constant under steady state. Based on a study of effect of pressure reduction, using available resources, the chamber is designed for a vacuum of 680 mm Hg. The experimental result shows that for cylindrical fin with circular grooves (depth 3.5mm) heat loss is a maximum. The grooved cylindrical fin loses approximately 1.23 times greater heat per unit area, compared to the threaded cylindrical fin, and 2.17 times greater heat per unit area, respectively compared to the solid pin fin at a pressure lower than atmospheric pressure. As pressure decreases heat loss reduces and contribution of radiation heat transfer on total heat loss increases.

**Keywords:** Cylindrical Fin, Grooves, Heat Transfer and Pressure Reduction.

### 1. INTRODUCTION

Heat is energy in transition under the motive force of a temperature difference. If a temperature difference exist between two bodies heat will transfer in the direction of lower temperature. The mechanism of heat exchange is brought about by three methods: conduction, convection and radiation.

Fins are thin strips of metal attached to the heat transfer surface in order to increase heat transfer area. Since there is a certain relation between pressure and heat transfer rate, at low density situation the rate of heat transfer does not remain same as that at atmospheric pressure. To use fins for heat rejection at low density situation it is necessary to observe the heat transfer characteristics of the fin at that situation. Moreover, to reduce high waste heat, it is necessary to increase the heat transfer area of the radiator. But a radiator is generally optimized with respect of mass, since it is difficult and costly to handle a large radiator. The use of grooved or threaded cylindrical fin can be useful in this case.

Most of the work on space radiators has been carried out analytically and numerically. Krishnaprakash presented mass optimized design of a straight rectangular plate fin array extending from a plane wall. Ramesh and Venkatesan numerically optimized the tubular finned space radiator. Krikkis and Razelos presented the correlations for optimum dimensions of longitudinal rectangular and triangular radiating fins with mutual

irradiation. Chung B.T.F.; Nguyen L.D. solved the general equation for radiating spines and studied the spine dimensions and heat transfer characteristics numerically. Razini .A.; Zohoor H. studied a conducting radiating spine with an arbitrary profile to find the optimum dimensions of the spine. Black and Schoenhals, and Black studied the directional radiation properties of specially prepared V groove cavities also optimized the directional emission from V groove and rectangular cavities. Gorchakov and Panevin analyzed the effectiveness and efficiencies of radiating fins having a surface roughness in the form of V grooves oriented in the direction of temperature gradient. Bhise et al. investigated a corrugated fin structure for space radiator applications and presented correlations for the optimum corrugation angle and maximum heat loss to space. Srinivasan and Katte proposed a grooved radiator with higher heat loss per nit mass compared to the flat radiator.

The review shows that there have been a very few attempts to experimentally study the effect of modification of a cylindrical fin on its heat transfer characteristics. In this study, cylindrical fins with grooves and threads on its outside surface are investigated experimentally.

### 2. EXPERIMENTAL SETUP AND PROCEDURE

The experimental setup consists of a pressure

reduction chamber, an air compressor for suction purpose, thermocouples, heating element, digital manometer, multimeter and control valves. The pressure reduction chamber is designed for a maximum vacuum of 680mm Hg. It consists of- a hollow cylinder and two detachable end plates. A 30cm long, 20cm diameter (inner), and 4.5mm thick GI pipe is used as the hollow cylinder. Six passages are made through the cylinder, among which three passages are provided for thermocouples, one for suction inlet of compressor, one for vacuum control valve and one for vacuum measuring instrument. Three passages provided for thermocouples are placed at equidistance. The interior side of the cylinder is painted in black. Two GI plates of thickness 6.5mm are used to enclose the hollow cylinder. The plates are clamped to the cylinder. One of the plates is provided with a passage for the cylindrical fin. The inner side of the passage is threaded so that the cylindrical fin fits perfectly.

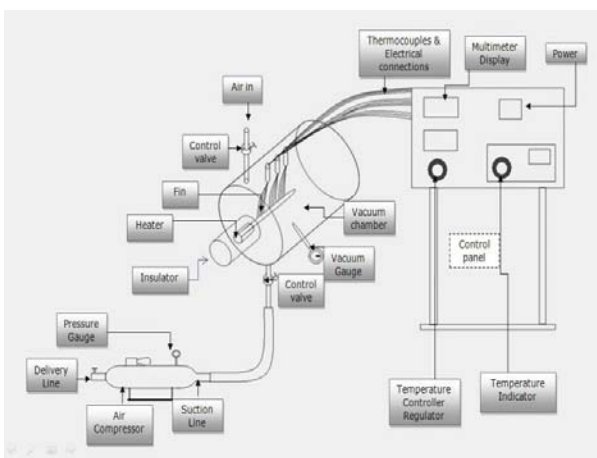


Fig 1. Schematic Diagram of Experimental Setup

Three types of cylindrical fin model are used in present investigation- solid cylindrical fin, circular grooved cylindrical fin, threaded cylindrical fin. Aluminum is chosen as the fin material. The portion of each fin considered for the investigation has the following dimensions- length = 150mm, diameter = 20mm. Each fin is extended 55mm more. This extension is provided for heating and attachment of the fin with the end plate. Among this extension, 15mm length consist external thread which matches the internal threads provided to the passage of the detachable. Rest 40 mm length has a diameter of 32 mm to which heating element is attached. All the three cylindrical fins are painted black. Circular grooves are considered for the analysis. Four rows of grooves, consisting 9 grooves each; total 36 grooves are made through the cylindrical fin. Each groove has depth around 3.5mm. The threaded fin has a tpi of 12.

The control valves are checked and attached to the passages of the pressure reduction chamber. Before attachment the threaded portion of each valve is wrapped with thread tape. The compressor suction line is connected to the control valve provided to the passage at the bottom of the chamber. The delivery valve of the

compressor is remained open so that compress air can escape and the compressor runs with no load. The digital manometer is attached to the control valve at the sidewall of the chamber. The manometer is calibrated before using for ensuring proper functioning. The fin is attached to the endplate, which is then attached to the cylinder and clamped tightly. The thermocouples are inserted to the chamber and are attached to the fin in equidistance. The soldering coil is used as heating element which is attached to the extended end of the fin. The multimeter is calibrated also before using. The outside surface of the soldering coil must be properly insulated to prevent heat loss and to maintain the root of the fin at desired temperature. Glass wool and cork sheet are used for this purpose. The temperature of the root of the fin is controlled by a temperature controller which is connected in series with the soldering coil.



Fig 2. Experimental Setup

After completing the setup the heater (soldering coil) is switched on and the temperature controller is set to 50°C. All experiments are to be carried out under steady state, for a root temperature of 50°C. The root of fin is maintained constant at the desired temperature by adjusting the temperature controller. All the sealed passages must be checked properly before starting the compressor.

For observing the effect of vacuum on heat loss, pressure is varied by controlling the suction of air by the compressor and the corresponding variations of temperature are noted from the multimeter display. The vacuum in the chamber is controlled by adjusting the air flow into the chamber using the control valve. The procedure is continued for each three types of fin. Heat losses corresponding to different pressure are calculated from the data.

### 3. RESULTS AND DISCUSSION

Experimental results are presented graphically with detailed explanations. For each three fins, total heat loss vs. pressure, convective heat loss vs. pressure, radiative heat loss vs. pressure and percentage of heat loss vs. pressure curves are plotted.

#### 3.1 Solid Cylindrical Fin

Experimental data of solid fin gives the following curves shows in the next page –

Figure 3 shows the effect of variation of absolute pressure on total heat loss by a solid cylindrical fin, which includes the effect of convective as well as radiative heat losses. The curve follows an exponential trend line. It is observed that heat loss reduces as pressure falls.

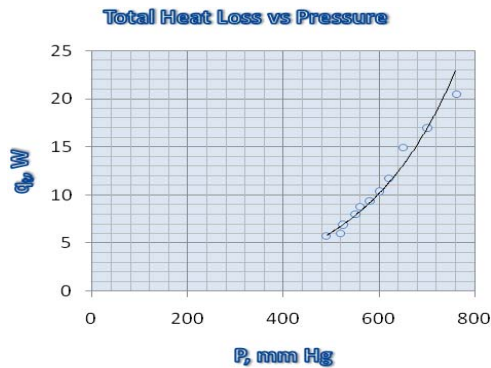


Fig 3. Effect of pressure reduction on heat transfer from solid cylindrical fin

At a pressure of 490 mm Hg heat loss is only about 6.23 W which is only 29.67% of the total heat loss corresponding to the atmospheric pressure. As pressure is reduced by the suction of air, the density of air inside the pressure reduction chamber also reduces. This causes considerable reduction in the rate of convection heat transfer, as a result of which total heat loss is reduced. The curve also indicates that if pressure is further reduced, at a certain vacuum pressure, convective heat loss can reach negligible value.

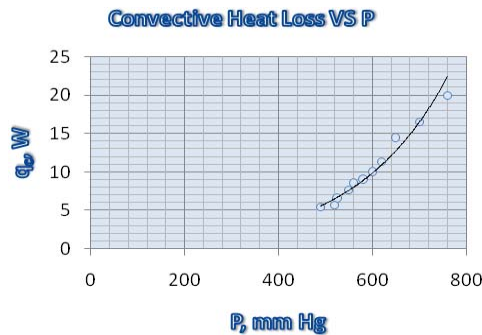


Fig 4. Effect of reduction of pressure on convective heat loss by a solid cylindrical fin

Figure 4 shows that convective heat loss reduces sharply as pressure is decreased. It is because as the pressure inside the pressure reduction chamber is reduced, a low-density situation arises. In low-density circumstances the mean free path of the gas molecules is large enough, and as density reduces this distance increases. The larger this distance becomes, the greater the distance required to communicate the temperature of a hot surface to a as in contact with it. This means, it cannot be assumed that the layer or air in the immediate neighborhood of the surface of the fin will not have the same temperature as the heated surface. This causes a

considerable reduction in convective heat transfer coefficient,  $h$ .

From Fig 5 it is observed that heat loss due to radiation also reduces with the reduction of pressure. During investigation it is noted that, the average temperature of fin also falls with pressure and since temperature inside the pressure reduction chamber remains unchanged, the temperature difference is a little lower than that corresponding to the atmospheric pressure. This causes the reduction in radiative heat loss. It is observed that for a reduction of pressure about 270mm Hg, heat loss by radiation reduces about 46% than that corresponding to the atmospheric pressure.

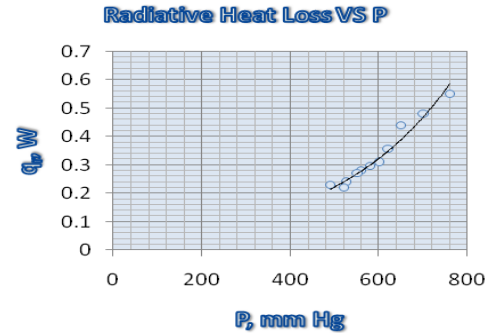


Fig 5. Effect of pressure reduction on radiation from a solid cylindrical fin

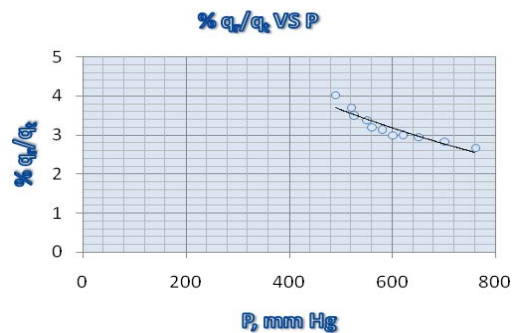


Fig 6. Effect of pressure reduction on the percentage of radiation heat loss to total heat loss for solid cylindrical fin

Figure 6 shows that as pressure is decreased heat loss by radiation plays more vital role in total heat loss. It is observed that at atmospheric pressure heat loss by radiation is only .55 W which is only 2.68% of the total heat loss (which is 21 W). At a pressure of 490mm Hg heat loss by radiation is increased to 3.69% of the total heat loss. A further decrease in pressure will increase the percentage.

### 3.2 Grooved Cylindrical Fin

Grooved fin from the calculated heat loss and pressure following curves are plotted -

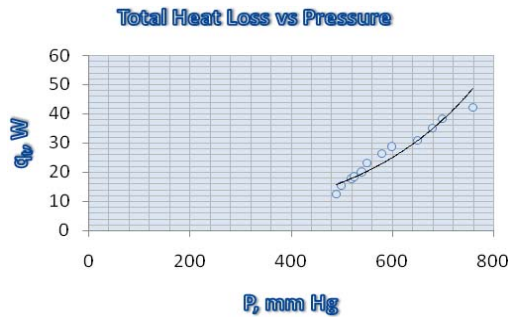


Fig 7. Effect of pressure reduction on heat transfer through the grooved cylindrical fin

Figure 7 shows the effect of pressure reduction on the heat transfer through the cylindrical fin with circular grooves. From the figure it is observed that, with the increase of vacuum pressure there is a considerable reduction in heat transfer rate. At atmospheric pressure heat loss is about 42 W. For a pressure of 490mm Hg heat loss is about 12.4, which is 29.52% of the total heat loss corresponding to the atmospheric pressure.

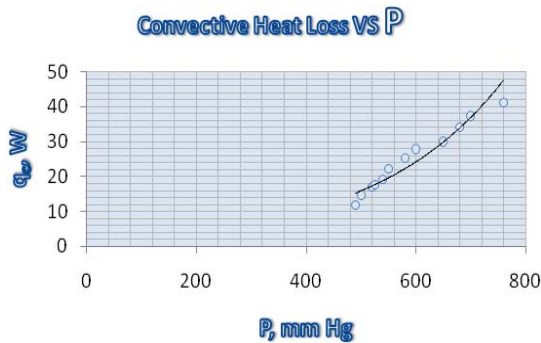


Fig 8. Effect of reduction of pressure on convective heat loss by a grooved cylindrical fin

From figure 8 it is observed that heat loss due to convection reduces more rapidly with pressure for circular grooved cylindrical fin. The curve obtained from above figure has much higher slope than the curve obtained from fig- 29 for solid cylindrical fin. This indicates higher performance of grooved cylindrical fin than solid cylindrical fin.

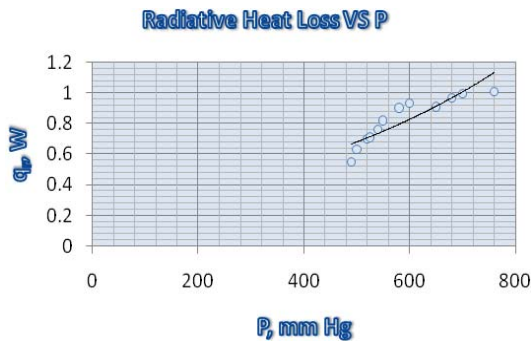


Fig 9. Effect of pressure reduction on radiation from a grooved cylindrical fin

Figure 9 shows that, radiation heat loss reduces with pressure. It is for the same reason as for the solid cylindrical fin which is explained before. In circular grooved fin radiation heat loss is greater than that of a solid cylindrical fin due to greater surface area. It is observed that for a reduction of pressure about 270mm Hg, heat loss by radiation reduces about 54.56% than that corresponding to the atmospheric pressure; which is 46% in case of solid cylindrical fin.

Figure - 10 shows the effect of pressure reduction on the percentage of radiation heat loss to total heat loss for grooved cylindrical fin. It may be noted that at atmospheric pressure radiative heat loss is 2.4% of total heat loss, and at 490mm Hg this value reaches 4.44% of the total value.

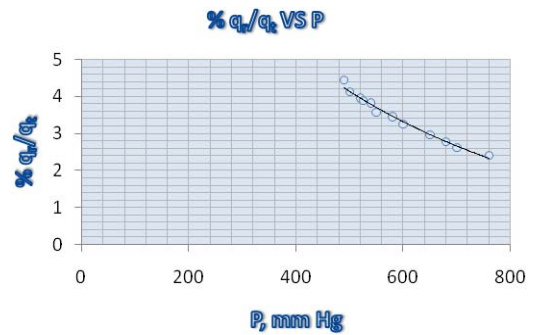


Fig 10. Effect of pressure reduction on the percentage of radiation heat loss to total heat loss for grooved cylindrical fin

### 3.3 Threaded Cylindrical Fin

The curves obtained for threaded fin are discussed below -

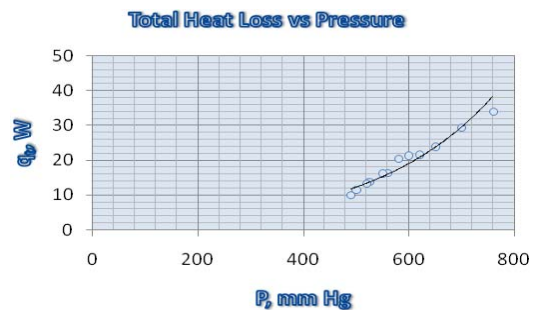


Fig 11. Effect of pressure reduction on heat transfer through the threaded cylindrical fin

The figure -11 shows the effect of variation of absolute pressure on total heat loss by a threaded cylindrical fin, which includes the effect of convective as well as radiative heat losses. From the above figure it is observed that, with the increase of vacuum pressure there is a considerable reduction in total heat transfer rate. At atmospheric pressure heat loss is about 33.9 W. For a pressure of 490mm Hg heat loss is about 10, which is 29.49% of the total heat loss corresponding to the atmospheric pressure.



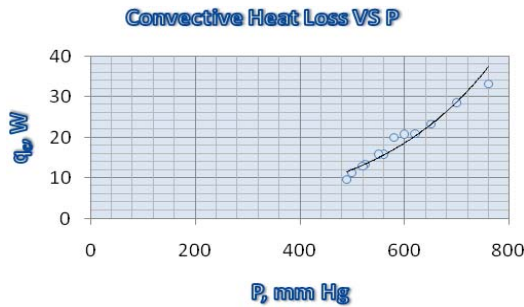


Fig 12. Effect of reduction of pressure on convective heat loss by a threaded cylindrical fin

Figure 12 shows effect of pressure reduction on heat loss due to convection by a cylindrical fin with thread on its outer surface. The curve trend is similar to the trend obtained from fig- 3 (for solid cylindrical fin) and figure - 7 (for circular grooved cylindrical fin). But there is variation in slope from both curves obtained before. This curve from fig- has a larger slope than the curve obtained for a solid cylindrical fin, and a smaller slope than the curve obtained for a circular grooved cylindrical fin. Heat loss by convection from a threaded Cylindrical fin with  $t_{pi}=12$  and thread depth = 1.5mm is less than a Cylindrical fin with 36 circular grooves of 3.5mm depth. At atmospheric pressure convective heat loss by this threaded cylindrical fin is 33.16 W, which is almost 78.95% of the convective heat loss by circular grooved cylindrical fin corresponding to atmospheric pressure.

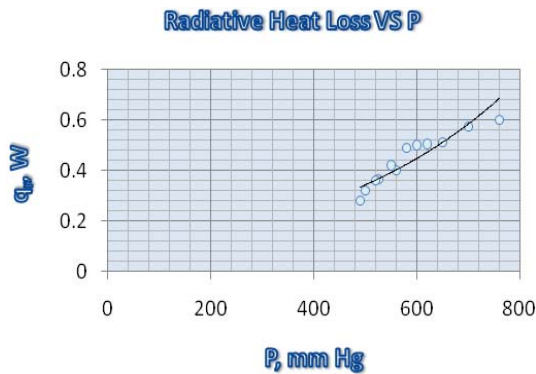


Fig 13. Effect of pressure reduction on radiation from a threaded cylindrical fin

The curve from above Fig.13 has the same pattern as obtained for solid and grooved cylindrical fin. Heat loss due to radiation from the threaded cylindrical fin under consideration is less than that of a circular grooved cylindrical fin. At atmospheric pressure radiation heat transfer for threaded cylindrical fin is .6, which is only about 59.52% than that of a grooved fin. Even this value is less than that of a solid cylindrical fin. It is due the effect of shape factor, since the thread angle is small.

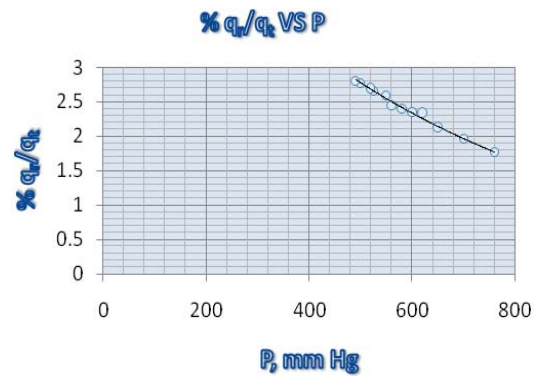


Fig 14. Effect of pressure reduction on the percentage of radiation heat loss to total heat loss for threaded cylindrical fin.

Figure 14 shows that as pressure is decreased heat loss by radiation becomes more prominent in total heat loss. It is observed that at atmospheric pressure heat loss by radiation is only .6 W which is only 1.77% of the total heat loss (which is 33.9 W). At a pressure of 490mm Hg heat loss by radiation is increased to 2.8% of the total heat loss. A further decrease in pressure will increase the percentage.

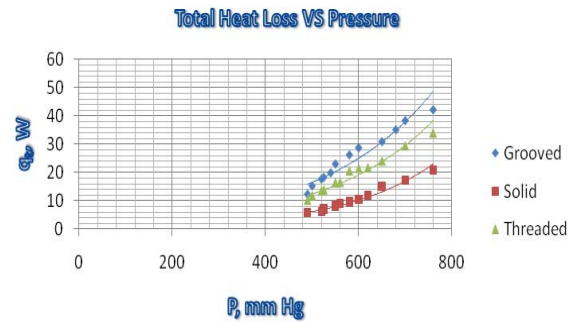


Fig 15. Comparison of total heat loss by solid, grooved and threaded cylindrical fin at different pressure

A comparison is of total heat loss from solid, grooved and threaded cylindrical fin is made. The curves obtained from above figure have the same pattern for all fins. The figure shows that heat loss by grooved cylindrical fin is maximum, which is because heat transfer surface increases as grooves are made, which results in considerable increase in convection heat transfer rate. Moreover due to cavity effect radiation heat transfer also increases. Maximum heat loss obtained from the experiment at atmospheric pressure is 42 W, and at 490mm Hg pressure it is 12.4 W.

For the threaded Cylindrical fin heat loss is greater than solid cylindrical fin but less than grooved cylindrical fin. Heat loss, in this case is larger than solid cylindrical fin due to increased heat transfer area. But since the thread angle and depth is small rate of heat loss is less than grooved Cylindrical fin. Maximum heat loss obtained from the experiment for threaded cylindrical fin at atmospheric pressure is 33.9 W, and at 490mm Hg pressure it is 10 W. these values are close to that for grooved cylindrical fin. So maybe it is possible to

increase heat loss by threaded cylindrical fin than a grooved cylindrical fin by varying thread angle and depth.

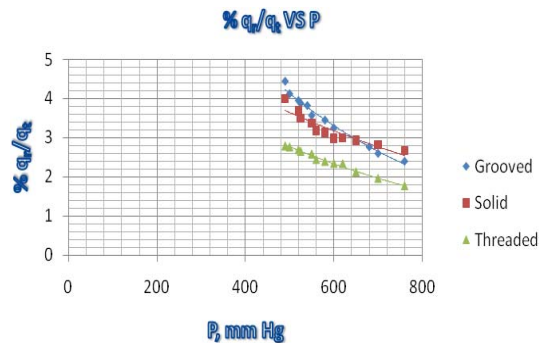


Fig 16. Comparison of participation of radiation on total heat loss for solid, grooved and threaded Cylindrical fin with varying pressure.

Figure 16 shows the comparison of participation of radiation on total heat loss for solid, grooved and threaded Cylindrical fin with varying pressure. It may be noted that at a pressure of 490mm Hg the percentage of radiation to total heat loss is maximum for grooved cylindrical fin, due to cavity effect. But for the solid cylindrical fin it is less than threaded cylindrical fin. This is because of increased heat transfer area due to threads.

#### 4. CONCLUSION

From this experimental study it has been found that the grooved radiating fin loses approximately 1.23 times greater heat per unit area, compared to the threaded pin fin, and 2.17 times greater heat per unit area, compared solid to the solid pin fin at a pressure lower than atmospheric pressure. As pressure decreases heat loss reduces and contribution of radiation heat transfer on total heat loss increases.

#### 5. REFERENCES

1. Holman J.P. , "Heat Transfer", Tata McGraw-Hill Publishing Company Limited, New Delhi, 9<sup>th</sup> edition, 2004.
2. Vasandani , V.P. "Heat Engineering", Metropolitan Book Co. Private Ltd., New Delhi, 4<sup>th</sup> Revised edition, 2001.
3. Wilkins J.E., Jr., "Minimizing the Mass of Thin Radiating Fins", J. Aerospace Science, **27**, 145-146, 1960.
4. Sunil Kumar S. and Venkateshan S.P., "Optimized Tubular Radiator With Annular Fins on a Non-Isothermal Base", Int. J. Heat and Fluid Flow, **15**, 399-409, 1994.
5. Krishnaprakas C. K., "Optimum Design of Radiating Rectangular Plate Fin Array Extending From a Plane Wall", J. Heat Transfer, **118**, 490-493, 1996.
6. Ramesh N. and Venkateshan S.P., "Optimum Finned Tubular Space Radiator", Heat Transfer Engineering, **18**, 69-87, 1997.

7. Krikkis R.N. and Panagiotis Razelos, "Optimum Design of Spacecraft Radiators with Longitudinal Rectangular and Triangular Fins", J. Heat Transfer, **124**, 805-811, 2002.
8. Chung, B. T. F.; Nguyen, L. D., "Thermal analysis and optimum design for radiating spine of various geometries", Heat transfer science and technology; Proceedings of the International Symposium, Beijing, People's Republic of China, Oct. 15-18, 1985 (A87-33101 13-34). Washington, DC, Hemisphere Publishing Corp., p. 510-517, 1987.
9. Razani, A.; Zohoor, H. , "The optimum dimensions of radiative spines", Proceedings of Space 90, the Second International Conference, Albuquerque, NM, Apr. 22-26, 1990. Vol. 2 (A91-27576 10-12). New York, American Society of Civil Engineers, p. 1316-1325, 1990.
10. Schnurr, N. M.; Townsend, M. A.; Shapiro, A. B., "Optimization of radiating fin arrays with respect to weight", ASME, Transactions, Series C - Journal of Heat Transfer, vol. 98, p. 643-648, Nov. 1976
11. Black W.Z. and Schoenhals R.J., "A Study of Directional Radiation Properties Specially Prepared V'-Groove Cavities", J. Heat Transfer, **90**, 420-428, 1968.

#### 6. MAILING ADDRESS

Mohammad Mashud  
 Department of Mechanical Engineering  
 Khulna University of Engineering & Technology  
 (KUET), Khulna-9203, Bangladesh  
 Email: [mdmashud@yahoo.com](mailto:mdmashud@yahoo.com)



# STEADY-STATE SOLUTIONS OF HEAT AND MASS TRANSFER FLOW FROM A VERTICAL POROUS PLATE WITH THERMAL DIFFUSION AND INDUCED MAGNETIC FIELD

M. Mohidul Haque and M. Mahmud Alam

Mathematics Discipline, Khulna University, Khulna, Bangladesh

## ABSTRACT

The unsteady MHD heat and mass transfer flow past a moving semi-infinite vertical porous plate with thermal diffusion has been investigated numerically taking into account the induced magnetic field. The steady-state numerical solutions for the velocity field, induced magnetic field, temperature distribution and concentration distribution are obtained by the explicit finite difference method. The local and average shear stress, current density, Nusselt number as well as Sherwood number are also calculated. The obtained results have been shown graphically. Also the stability and convergence of the explicit finite difference scheme are established. Finally, the comparison of the present results with both analytical and numerical solutions is presented in tabular form.

**Keywords:** MHD, Thermal Diffusion, Induced Magnetic Field, Finite Difference Method.

## 1. INTRODUCTION

The science of magnetohydrodynamics was concerned with geophysical and astrophysical problems for a number of years. In recent years the possible use of MHD is to affect a flow stream of an electrically conducting fluid for the purpose of thermal protection, braking, propulsion and control. From the point of applications, the effect of magnetic field on free convective flows was analyzed by Raptis and Singh[1]. Singh et al.[2] studied MHD heat and mass transfer flow of a viscous incompressible fluid past an infinite vertical porous plate under oscillatory suction velocity normal to the plate. The steady laminar flow and heat transfer characteristics of a continuously moving vertical sheet of extruded material was investigated by Sami and Al-Sanea[3]. The unsteady MHD heat and mass transfer problem with variable suction velocity have studied by Chamkha[4].

The effect of thermal diffusion on MHD free convection and mass transfer flows have many application in separation processes as isotope separation and mixtures between gases with very light molecular weight ( $H_2$ ,  $H_e$ ) and medium molecular weight ( $N_2$ , air) (Eckert and Drake[5]). Transient MHD heat and mass transfer flow with thermal diffusion in a rotating system has analyzed by Alam and Sattar[6]. Recently, Alam et al.[7] have numerically investigated the mass transfer flow past a vertical porous medium with heat generation and thermal diffusion on the combined free-forced convection under the influence of transversely applied magnetic field. The problem becomes more complicated if the

strong magnetic field has been considered. These types of problems have special importance in astrophysical and geophysical engineering.

Hence our main aim is to investigate steady-state solutions of unsteady MHD heat and mass transfer flow of an electrically conducting viscous fluid past a moving semi-infinite vertical porous plate under the action of strong magnetic field taking into account the induced magnetic field with thermal diffusion.

## 2. MATHEMATICAL MODEL OF FLOW

Consider MHD combined heat and mass transfer unsteady flow of an electrically conducting incompressible viscous fluid past an electrically non-conducting continuously moving semi-infinite vertical porous plate with thermal diffusion. The flow is assumed to be in the  $x$ -direction, which is chosen along the plate in upward direction and  $y$ -axis is normal to it. A strong uniform magnetic field is applied normal to the flow region. Initially it is assumed that fluid and the plate are at rest after that the plate is moved with a constant velocity  $U_0$  in its own plane. Instantaneously at time  $t > 0$ , temperature of the plate and species concentration are raised to  $T_w (> T_\infty)$  and  $C_w (> C_\infty)$  respectively, which are thereafter maintained constant, where  $T_w$ ,  $C_w$  are temperature and species concentration at the wall and  $T_\infty$ ,  $C_\infty$  are temperature and species concentration far away from the plate respectively. The physical model of this study is presented in Fig 1.

In addition, the viscous dissipation and joule heating terms in the energy equation have been

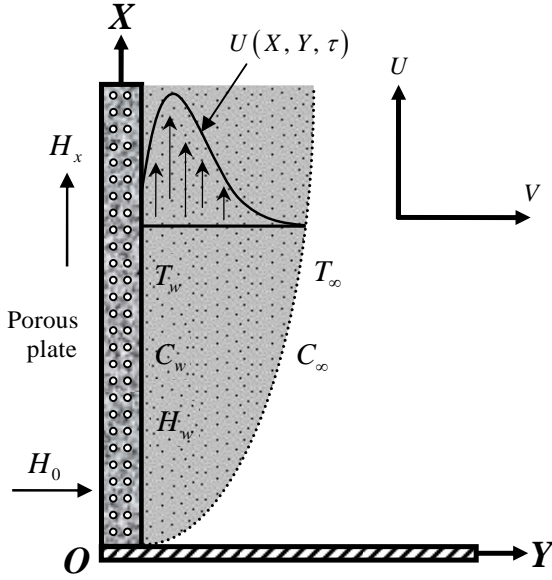


Fig 1. Physical model and coordinate system

considered for high speed flows, the level of concentration of foreign mass has been taken very high for observing the effect of Soret number on flow and the magnetic Reynolds number of flow is taken to be large enough so that the induced magnetic field is not negligible. The divergence equation  $\nabla \cdot \mathbf{H} = 0$  of Maxwell's equation for the magnetic field gives  $H_y = \text{constant} = H_0$ .

Within the framework of the above stated assumptions and using the dimensionless quantities,

$$X = \frac{xU_0}{\nu}, \quad Y = \frac{yU_0}{\nu}, \quad U = \frac{u}{U_0}, \quad V = \frac{v}{U_0}, \quad \tau = \frac{tU_0^2}{\nu},$$

$$\bar{H}_x = \sqrt{\frac{\mu_e}{\rho}} \frac{H_x}{U_0}, \quad \bar{T} = \frac{T - T_\infty}{T_w - T_\infty} \quad \text{and} \quad \bar{C} = \frac{C - C_\infty}{C_w - C_\infty},$$

the equations relevant to the unsteady two dimensional problem is governed by the following non-dimensional system of coupled non-linear partial differential equations under the boundary-layer approximations as;

$$\frac{\partial U}{\partial X} + \frac{\partial V}{\partial Y} = 0 \quad (1)$$

$$\frac{\partial U}{\partial \tau} + U \frac{\partial U}{\partial X} + V \frac{\partial U}{\partial Y} = G_r \bar{T} + G_m \bar{C} + \frac{\partial^2 U}{\partial Y^2} + M \frac{\partial \bar{H}_x}{\partial Y} \quad (2)$$

$$\frac{\partial \bar{H}_x}{\partial \tau} + U \frac{\partial \bar{H}_x}{\partial X} + V \frac{\partial \bar{H}_x}{\partial Y} = \bar{H}_x \frac{\partial U}{\partial X} + M \frac{\partial U}{\partial Y} + \frac{1}{P_m} \frac{\partial^2 \bar{H}_x}{\partial Y^2} \quad (3)$$

$$\frac{\partial \bar{T}}{\partial \tau} + U \frac{\partial \bar{T}}{\partial X} + V \frac{\partial \bar{T}}{\partial Y} = \frac{\partial^2 \bar{T}}{\partial Y^2} + \frac{E_c}{P_r} \left( \frac{\partial \bar{H}_x}{\partial Y} \right)^2 + E_c \left( \frac{\partial U}{\partial Y} \right)^2 \quad (4)$$

$$\frac{\partial \bar{C}}{\partial \tau} + U \frac{\partial \bar{C}}{\partial X} + V \frac{\partial \bar{C}}{\partial Y} = \frac{1}{S_c} \frac{\partial^2 \bar{C}}{\partial Y^2} + S_o \frac{\partial^2 \bar{T}}{\partial Y^2} \quad (5)$$

also the associated initial and boundary conditions are  $\tau \leq 0, U = 0, V = 0, \bar{H}_x = 0, \bar{T} = 0, \bar{C} = 0$  everywhere (6)

$$\tau > 0, U = 0, V = 0, \bar{H}_x = 0, \bar{T} = 0, \bar{C} = 0 \quad \text{at} \quad X = 0$$

$$U = 1, V = 0, \bar{H}_x = h = 1(\text{say}), \bar{T} = 1, \bar{C} = 1 \quad \text{at} \quad Y = 0 \quad (7)$$

$$U = 0, V = 0, \bar{H}_x = 0, \bar{T} = 0, \bar{C} = 0 \quad \text{as} \quad Y \rightarrow \infty$$

### 3. SHEAR STRESS, CURRENT DENSITY, NUSSELT AND SHERWOOD NUMBER

From the velocity field, the effects of various parameters on the shear stress have been calculated. The local and average shear stress,  $\tau_L = \mu \left( \frac{\partial U}{\partial Y} \right)_{Y=0}$  and

$$\tau_A = \mu \int \left( \frac{\partial U}{\partial Y} \right)_{Y=0} dX \quad \text{which are proportional to} \quad \left( \frac{\partial U}{\partial Y} \right)_{Y=0}$$

$$\text{and} \quad \int_0^{100} \left( \frac{\partial U}{\partial Y} \right)_{Y=0} dX \quad \text{respectively. From the induced}$$

magnetic field, the effects of various parameters on current density have been observed. The local and average current density,  $J_L = \mu \left( -\frac{\partial \bar{H}_x}{\partial Y} \right)_{Y=0}$  and

$$J_A = \mu \int \left( -\frac{\partial \bar{H}_x}{\partial Y} \right)_{Y=0} dX \quad \text{which are proportional to}$$

$$\left( -\frac{\partial \bar{H}_x}{\partial Y} \right)_{Y=0} \quad \text{and} \quad \int_0^{100} \left( -\frac{\partial \bar{H}_x}{\partial Y} \right)_{Y=0} dX \quad \text{respectively. From}$$

the temperature field, the effects of various parameters on the Nusselt number have been investigated. The local and average Nusselt number,  $N_{u,L} = \mu \left( -\frac{\partial \bar{T}}{\partial Y} \right)_{Y=0}$  and

$$N_{u,A} = \mu \int \left( -\frac{\partial \bar{T}}{\partial Y} \right)_{Y=0} dX \quad \text{which are proportional to}$$

$$\left( -\frac{\partial \bar{T}}{\partial Y} \right)_{Y=0} \quad \text{and} \quad \int_0^{100} \left( -\frac{\partial \bar{T}}{\partial Y} \right)_{Y=0} dX \quad \text{respectively. And from}$$

concentration field, the effects of various parameters on Sherwood number have been analyzed. The local and average Sherwood number,  $S_{h,L} = \mu \left( -\frac{\partial \bar{C}}{\partial Y} \right)_{Y=0}$  and

$$S_{h,A} = \mu \int \left( -\frac{\partial \bar{C}}{\partial Y} \right)_{Y=0} dX \quad \text{which are proportional to}$$

$$\left( -\frac{\partial \bar{C}}{\partial Y} \right)_{Y=0} \quad \text{and} \quad \int_0^{100} \left( -\frac{\partial \bar{C}}{\partial Y} \right)_{Y=0} dX.$$

### 4. NUMERICAL SOLUTIONS

In order to solve the non-dimensional system by the explicit finite difference method, it is required a set of finite difference equations. For this, a rectangular region of the flow field is chosen and the region is divided into a grid of lines parallel to X and Y axes, where X-axis is taken along the plate and Y-axis is normal to the plate.

Here we consider that the plate of height  $X_{\max} (= 100)$  i.e. X varies from 0 to 100 and assumed  $Y_{\max} (= 25)$  as corresponding to  $Y \rightarrow \infty$  i.e. Y varies from 0 to 25. There are  $m (= 125)$  and  $n (= 125)$  grid spacing in the X and Y directions respectively as shown in Fig 2. It is assumed that  $\Delta X, \Delta Y$  are constant mesh sizes along X and Y directions respectively and taken as follows,

$$\Delta X = 0.8 (0 \leq X \leq 100) \quad \text{and} \quad \Delta Y = 0.2 (0 \leq Y \leq 25)$$

with the smaller time-step,

$$\Delta \tau = 0.005.$$

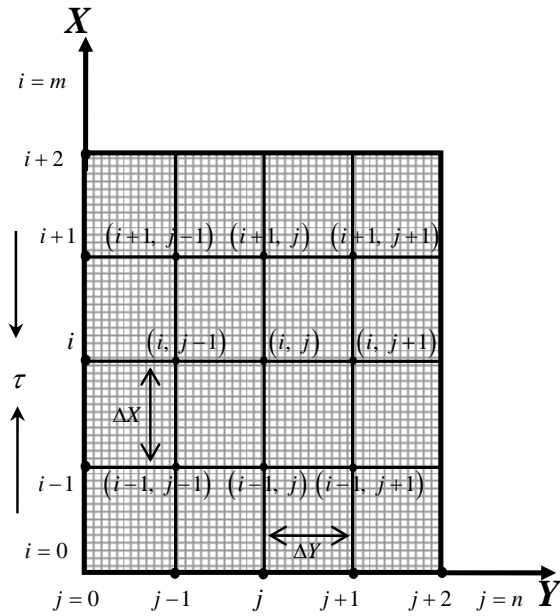


Fig 2. Finite difference space grid

Let  $U'$ ,  $V'$ ,  $\bar{H}'_x$ ,  $\bar{T}'$  and  $\bar{C}'$  denote the values of  $U$ ,  $V$ ,  $\bar{H}_x$ ,  $\bar{T}$  and  $\bar{C}$  at the end of a time-step respectively. Using the explicit finite difference approximation, we obtain the following appropriate set of finite difference equations;

$$\frac{U'_{i,j} - U'_{i-1,j}}{\Delta X} + \frac{V_{i,j} - V_{i,j-1}}{\Delta Y} = 0 \quad (8)$$

$$\frac{U'_{i,j} - U_{i,j}}{\Delta \tau} + U_{i,j} \frac{U_{i,j} - U_{i-1,j}}{\Delta X} + V_{i,j} \frac{U_{i,j+1} - U_{i,j}}{\Delta Y} = G_r \bar{T}'_{i,j} + G_m \bar{C}'_{i,j} + \frac{U_{i,j+1} - 2U_{i,j} + U_{i,j-1}}{(\Delta Y)^2} + M \frac{\bar{H}'_{x,i,j+1} - \bar{H}'_{x,i,j}}{\Delta Y} \quad (9)$$

$$\frac{\bar{H}'_{x,i,j} - \bar{H}'_{x,i,j}}{\Delta \tau} + U_{i,j} \frac{\bar{H}'_{x,i,j} - \bar{H}'_{x,i-1,j}}{\Delta X} + V_{i,j} \frac{\bar{H}'_{x,i,j+1} - \bar{H}'_{x,i,j}}{\Delta Y} = \bar{H}'_{x,i,j} \frac{U_{i,j} - U_{i-1,j}}{\Delta X} + M \frac{U_{i,j+1} - U_{i,j}}{\Delta Y} + \frac{1}{P_m} \frac{\bar{H}'_{x,i,j+1} - 2\bar{H}'_{x,i,j} + \bar{H}'_{x,i,j-1}}{(\Delta Y)^2} \quad (10)$$

$$\frac{\bar{T}'_{i,j} - \bar{T}_{i,j}}{\Delta \tau} + U_{i,j} \frac{\bar{T}'_{i,j} - \bar{T}_{i-1,j}}{\Delta X} + V_{i,j} \frac{\bar{T}'_{i,j+1} - \bar{T}_{i,j}}{\Delta Y} = \frac{1}{P_r} \frac{\bar{T}'_{i,j+1} - 2\bar{T}'_{i,j} + \bar{T}'_{i,j-1}}{(\Delta Y)^2} + \frac{E_c}{P_m} \left( \frac{\bar{H}'_{x,i,j+1} - \bar{H}'_{x,i,j}}{\Delta Y} \right)^2 + E_c \left( \frac{U_{i,j+1} - U_{i,j}}{\Delta Y} \right)^2 \quad (11)$$

$$\frac{\bar{C}'_{i,j} - \bar{C}_{i,j}}{\Delta \tau} + U_{i,j} \frac{\bar{C}'_{i,j} - \bar{C}_{i-1,j}}{\Delta X} + V_{i,j} \frac{\bar{C}'_{i,j+1} - \bar{C}_{i,j}}{\Delta Y} = \frac{1}{S_c} \frac{\bar{C}'_{i,j+1} - 2\bar{C}'_{i,j} + \bar{C}'_{i,j-1}}{(\Delta Y)^2} + S_o \frac{\bar{T}'_{i,j+1} - 2\bar{T}'_{i,j} + \bar{T}'_{i,j-1}}{(\Delta Y)^2} \quad (12)$$

with initial and boundary conditions

$$U^0_{i,j} = 0, V^0_{i,j} = 0, \bar{H}^0_{x,i,j} = 0, \bar{T}^0_{i,j} = 0, \bar{C}^0_{i,j} = 0 \quad (13)$$

$$U^0_{0,j} = 0, V^0_{0,j} = 0, \bar{H}^0_{x,0,j} = 0, \bar{T}^0_{0,j} = 0, \bar{C}^0_{0,j} = 0$$

$$U^0_{i,0} = 1, V^0_{i,0} = 0, \bar{H}^0_{x,i,0} = 1, \bar{T}^0_{i,0} = 1, \bar{C}^0_{i,0} = 1 \quad (14)$$

$$U^0_{i,L} = 0, V^0_{i,L} = 0, \bar{H}^0_{x,i,L} = 0, \bar{T}^0_{i,L} = 0, \bar{C}^0_{i,L} = 0, \quad L \rightarrow \infty$$

Here the subscripts  $i$  and  $j$  designate the grid points with  $X$  and  $Y$  coordinates respectively and the superscript  $n$  represents a value of time,  $\tau = n\Delta\tau$  where  $n = 0, 1, 2, \dots$ . The stability conditions of the method are

$$U \frac{\Delta\tau}{\Delta X} + |V| \frac{\Delta\tau}{\Delta Y} + \frac{2}{P_r} \frac{\Delta\tau}{(\Delta Y)^2} \leq 1,$$

$$U \frac{\Delta\tau}{\Delta X} + |V| \frac{\Delta\tau}{\Delta Y} + \frac{2}{S_c} \frac{\Delta\tau}{(\Delta Y)^2} \leq 1 \text{ and convergence criteria of}$$

the method are  $E_c \ll 1$ ,  $P_r \geq 0.25$  and  $S_c \geq 0.25$ .

## 5. RESULTS AND DISCUSSION

To observe the physical situation of the problem, we have illustrated the steady-state local and average shear stress, current density, Nusselt number and Sherwood number versus  $X$  and  $\tau$  respectively in Figs 3-20. The effect of  $M$ ,  $S_o$ ,  $E_c$ ,  $G_r$ ,  $P_r$  and  $S_c$  on shear stress are shown in Figs 3-8. We see that both steady-state local and average shear stress increase with the rise of  $S_o$ ,  $E_c$  or  $G_r$  while decrease with the increase of  $M$ ,  $P_r$  or  $S_c$ . It is concluded that the shear stress is greater for air and helium than water and carbon dioxide respectively.

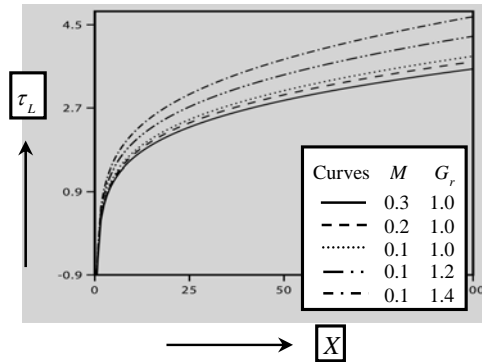


Fig 3. Steady-state local shear stress for  $G_m = 0.4$ ,

$$P_r = 0.71, S_c = 0.6, S_o = 1, P_m = 1 \text{ \& } E_c = 0.01.$$

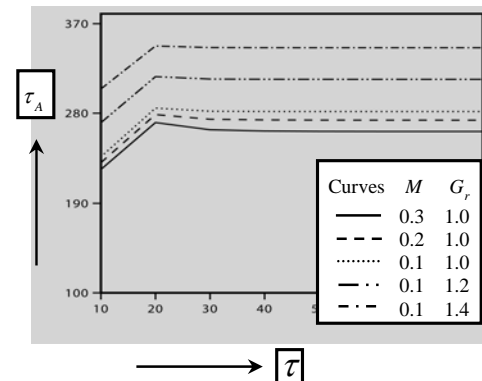


Fig 4. Average shear stress for  $G_m = 0.4$ ,  $P_r = 0.71$ ,

$$S_c = 0.6, S_o = 1, P_m = 1 \text{ \& } E_c = 0.01.$$

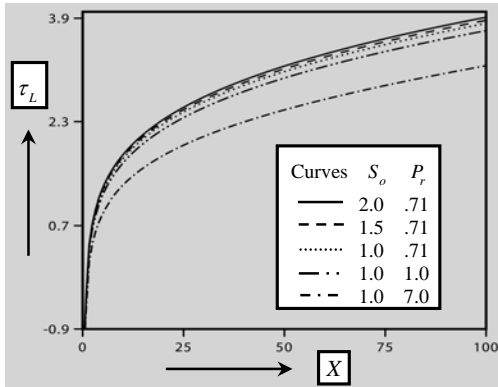


Fig 5. Steady-state local shear stress for  $G_r = 1$ ,  $G_m = 0.4$ ,  $M = 0.1$ ,  $S_c = 0.6$ ,  $P_m = 1$  &  $E_c = 0.01$ .

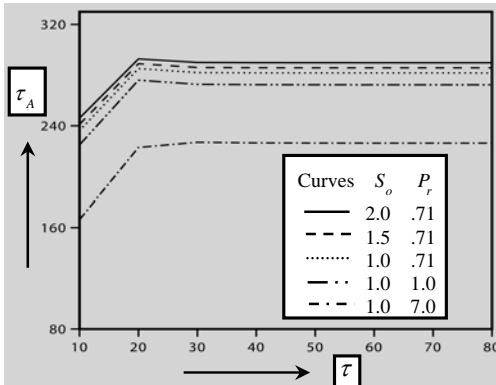


Fig 6. Average shear stress for  $G_r = 1$ ,  $G_m = 0.4$ ,  $M = 0.1$ ,  $S_c = 0.6$ ,  $P_m = 1$  &  $E_c = 0.01$ .

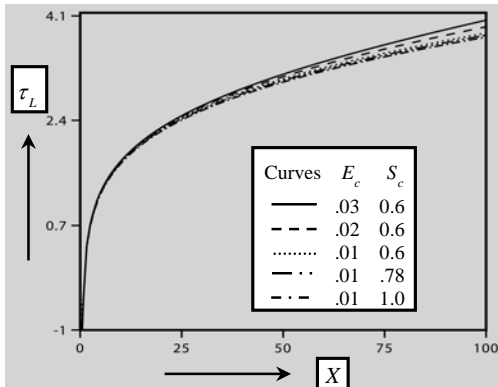


Fig 7. Steady-state local shear stress for  $G_r = 1$ ,  $G_m = 0.4$ ,  $M = 0.1$ ,  $P_r = 0.71$ ,  $S_o = 1$  &  $P_m = 1$ .

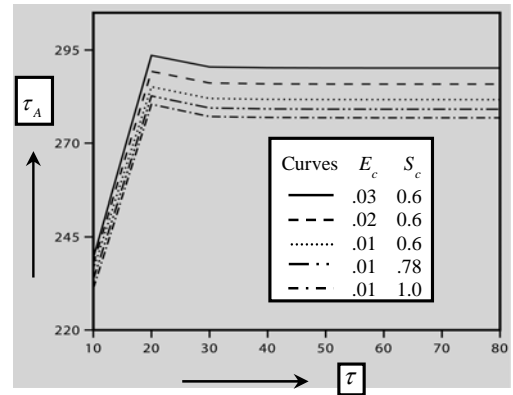


Fig 8. Average shear stress for  $G_r = 1$ ,  $G_m = 0.4$ ,  $M = 0.1$ ,  $P_r = 0.71$ ,  $S_o = 1$  &  $P_m = 1$ .

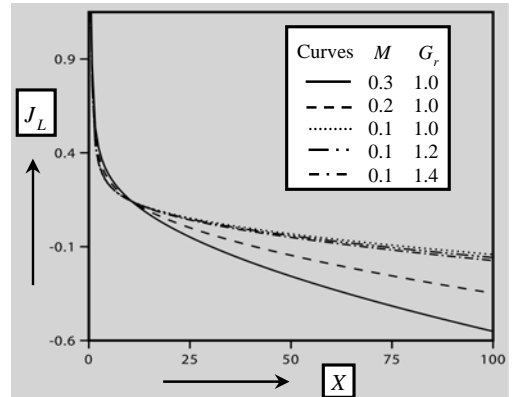


Fig 9. Steady-state local current density for  $G_m = 0.4$ ,  $P_r = 0.71$ ,  $S_c = 0.6$ ,  $S_o = 1$ ,  $P_m = 1$  &  $E_c = 0.01$ .

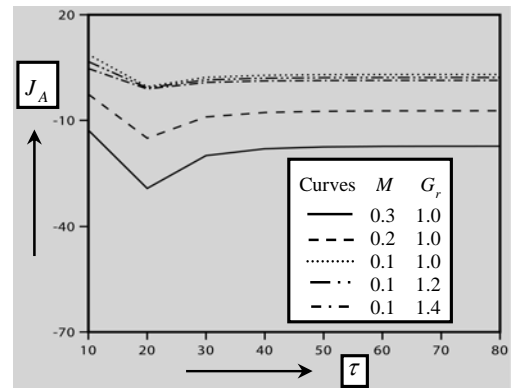


Fig 10. Average current density for  $G_m = 0.4$ ,  $P_r = 0.71$ ,  $S_c = 0.6$ ,  $S_o = 1$ ,  $P_m = 1$  &  $E_c = 0.01$ .

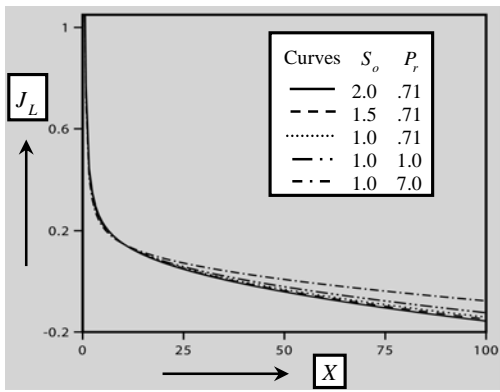


Fig 11. Steady-state local current density for  $G_r = 1$ ,  $G_m = 0.4$ ,  $M = 0.1$ ,  $S_c = 0.6$ ,  $P_m = 1$  &  $E_c = 0.01$ .

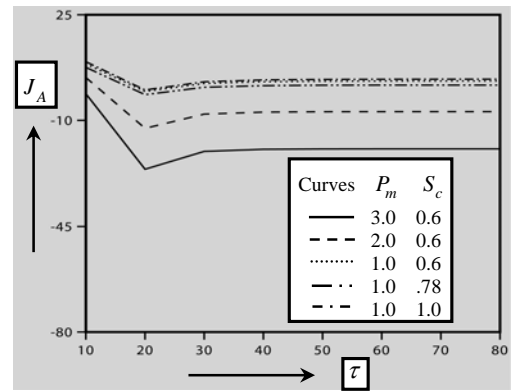


Fig 14. Average current density for  $G_r = 1$ ,  $G_m = 0.4$ ,  $M = 0.1$ ,  $P_r = 0.71$ ,  $S_o = 1$  &  $E_c = 0.01$ .

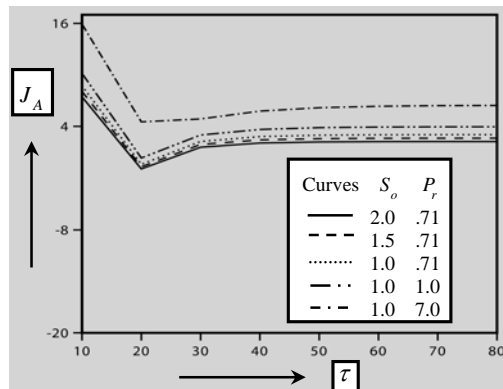


Fig 12. Average current density for  $G_r = 1$ ,  $G_m = 0.4$ ,  $M = 0.1$ ,  $S_c = 0.6$ ,  $P_m = 1$  &  $E_c = 0.01$ .

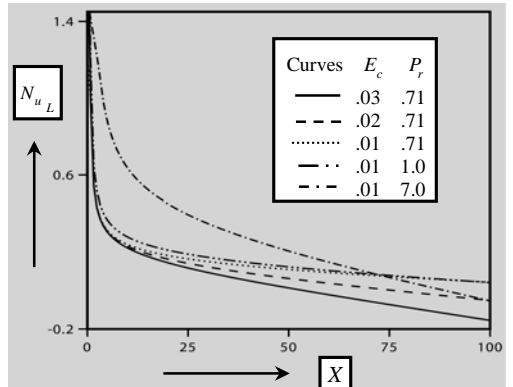


Fig 15. Steady-state local Nusselt number for  $G_r = 1$ ,  $G_m = 0.4$ ,  $M = 0.1$ ,  $S_c = 0.6$ ,  $P_m = 1$  &  $S_o = 1$ .

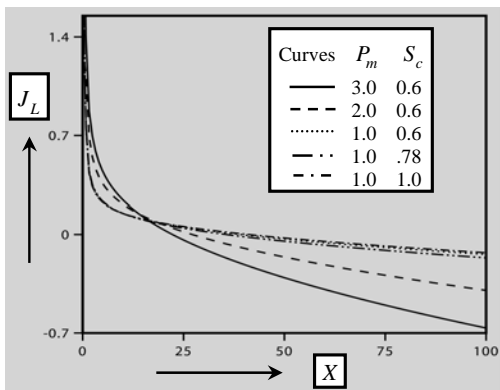


Fig 13. Steady-state local current density for  $G_r = 1$ ,  $G_m = 0.4$ ,  $M = 0.1$ ,  $P_r = 0.71$ ,  $S_o = 1$  &  $E_c = 0.01$ .

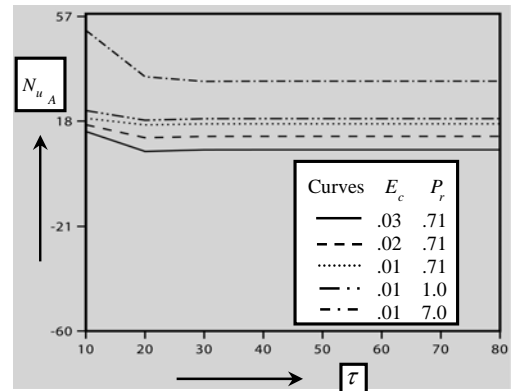


Fig 16. Average Nusselt number for  $G_r = 1$ ,  $G_m = 0.4$ ,  $M = 0.1$ ,  $S_c = 0.6$ ,  $P_m = 1$  &  $S_o = 1$ .

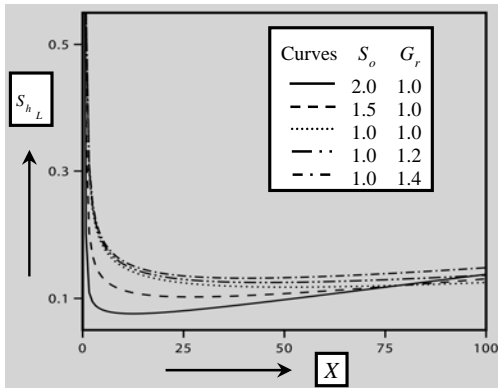


Fig 17. Steady-state local Sherwood number for  $P_m = 1$ ,  $G_m = .4$ ,  $P_r = .71$ ,  $S_c = .6$ ,  $M = .1$  &  $E_c = .01$ .

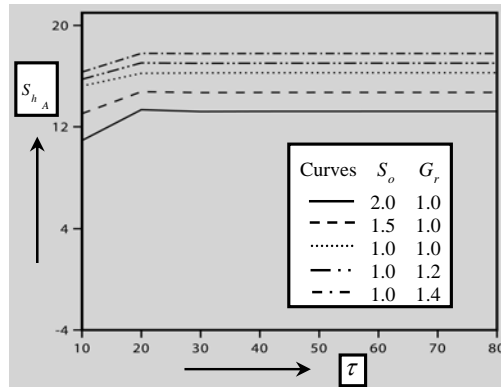


Fig 18. Average Sherwood number for  $G_m = 0.4$ ,  $P_r = 0.71$ ,  $S_c = 0.6$ ,  $M = 0.1$ ,  $P_m = 1$  &  $E_c = 0.01$ .

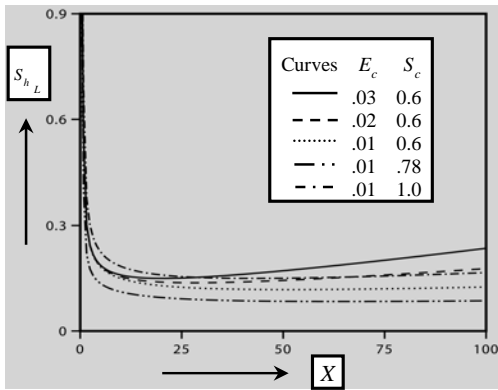


Fig 19. Steady-state local Sherwood number for  $G_r = 1$ ,  $G_m = 0.4$ ,  $M = 0.1$ ,  $P_r = 0.71$ ,  $S_o = 1$  &  $P_m = 1$ .

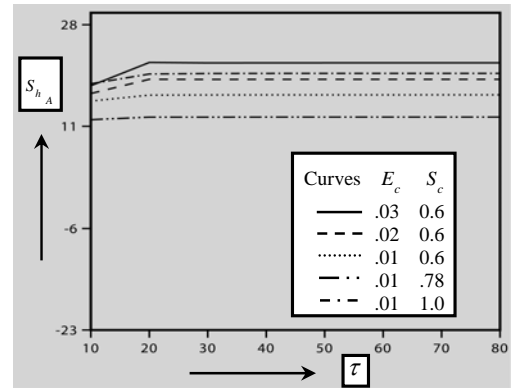


Fig 20. Average Sherwood number for  $G_r = 1$ ,  $G_m = 0.4$ ,  $M = 0.1$ ,  $P_r = 0.71$ ,  $S_o = 1$  &  $P_m = 1$ .

The profiles of steady-state local and average current density for different values of  $M$ ,  $S_o$ ,  $P_r$ ,  $G_r$ ,  $P_m$  and  $S_c$  are presented in Figs 9-14. We observe from these figures, both the steady-state local and average current density increase in case of strong  $P_r$  or  $S_c$  while decrease with the increase of  $M$ ,  $S_o$ ,  $G_r$  or  $P_m$ . It is noted that the current density is more for water and carbon dioxide than air and helium respectively.

The curves of steady-state local and average Nusselt number are displayed in Figs 15-16 for different values of  $E_c$  and  $P_r$ . It is found that both local and average Nusselt number rise with the increase of Prandtl number but fall with the increase of  $E_c$ . It is declared that the Nusselt number is greater for water than air.

The distributions of steady-state local and average Sherwood number have been shown in Figs. 17-20 for the different values of  $S_o$ ,  $E_c$ ,  $G_r$  and  $S_c$ . Both the local and average Sherwood number increase in case of strong  $E_c$ ,  $G_r$  or  $S_c$  while decrease with the rise of  $S_o$ . It is concluded that the Sherwood number is more for carbon dioxide than helium.

Finally, a comparison of our results is made with both analytical solutions for the natural convective problem at a heated vertical plate given by Ostrach[8] and numerical solutions given by Allam and Sattar[6] with no magnetic and rotation effects in their problem. If the viscous dissipation and joule heating terms are neglected in energy equation as well as no magnetic effect, no uniform velocity  $U_0$  are assumed in our problem, it reduces to the problem considered by Ostrach[8]. Hence the comparison of the present results with analytical and numerical results are presented in Table 1 for steady-state  $\tau = 80$ . The accuracy of the present results may be good in case of all the flow variables.

Table 1. Comparison of the present steady-state results

$Y$	0			5.0			10.0			15.0		
Analytical results due to Ostrach [8] 39 × 39 grid, $\Delta\tau = 0.1$	$U$	$V$	$\bar{T}$	$U$	$V$	$\bar{T}$	$U$	$V$	$\bar{T}$	$U$	$V$	$\bar{T}$
	0	0	1	5.3	-1	.5	2.8	-3	.1	.9	-3	.04
Numerical results due to Alam & Sattar [6] 10 × 10 grid, $\Delta\tau = 0.5$	0	0	1	5.0	-1	.5	2.9	-3	.2	1.1	-4	.05
	Truncation error			.3	0	0	-1	0	-1	-2	.1	
Present results 125 × 125 grid, $\Delta\tau = 0.005$	0	0	1	5.4	-1	.5	2.8	-2	.1	.9	-3	.04
	Truncation error			-1	0	0	0	-1	0	0	0	

## 6. REFERENCES

- Raptis, A. and Singh, A. K., 1983, "MHD Free Convection Flow Past an Accelerated Vertical Plate", Int. Communications in Heat and Mass Transfer, 10:313.
- Singh, A. K., Singh, Aj. K. and Singh, N. P., 2003, "Hydromagnetic Heat and Mass Transfer in a Flow of a Viscous Incompressible Fluid Past an Infinite Vertical Porous Plate under Oscillatory Suction Velocity Normal to the Plate", Indian Journal of Pure and Applied Mathematics, 34:429.
- Sami, A. and Al-Sanea, 2004, "Mixed Convection Heat Transfer along a Continuously Moving Heated Vertical Plate with Suction or Injection", Int. J. Heat Mass Transfer, 47:1445.
- Chamkha, A. J., 2004, "Unsteady MHD Convective Heat and Mass Transfer Past a Semi-infinite Vertical Permeable Moving Plate with Heat Absorption", Int. J. Engg. Sci., 42:217.
- Eckert, E. R. G. and Drake, R.M., 1972, "Analysis of Heat and Mass Transfer", McGraw-Hill Book Co., New York.
- Alam, M. M. and Sattar, M. A., 1999, "Transient MHD Heat and Mass Transfer Flow with Thermal Diffusion in a Rotating System", J. of Energy, Heat and Mass Transfer, 21:09.
- Alam, M. S., Rahman, M. M. and Samad, M. A., 2006, "Numerical Study of the Combined Free-forced Convection and Mass Transfer Flow Past a Vertical Porous Medium with Heat Generation and Thermal Diffusion", Nonlinear analysis: Modeling and Control, 11(4):331.
- Ostrach, S., 1953, "An Analysis of Laminar Free-convection Flow and Heat Transfer about a Flat Plate Parallel to the Direction of the Generation Body Force", Natl. Advisory Comm. Aeronautical Technology Report, 1111.

## 7. NOMENCLATURE

Symbol	Meaning	Unit
$x, y$	Cartesian coordinates	
$u, v$	Velocity components	( $\text{ms}^{-1}$ )
$\nu$	Kinematic viscosity	( $\text{m}^2\text{s}^{-1}$ )
$\rho$	Density of fluid	( $\text{kgm}^{-3}$ )
$\mu_c$	Magnetic permeability	
$\tau$	Dimensionless time	
$X, Y$	Dimensionless cartesian coordinates	
$U, V$	Dimensionless velocity components	
$\bar{H}_x$	Dimensionless induced magnetic field vector	
$\bar{T}$	Dimensionless temperature	
$\bar{C}$	Dimensionless concentration	
$G_r$	Grashof number	
$G_m$	Modified Grashof number	
$M$	Magnetic Force number	
$P_m$	Magnetic diffusivity number	
$P_r$	Prandtl number	
$E_c$	Eckert number	
$S_c$	Schmidt Number	
$S_o$	Soret Number	
$\mu$	Coefficient of viscosity	

## 8. MAILING ADDRESS

Md. Mohidul Haque  
 Mathematics Discipline,  
 Khulna University, Khulna, Bangladesh



## THERMAL PERFORMANCE OF PARALLEL MINIATURE HEAT PIPE SYSTEM

C. M. Feroz, M. Mamunur Rahman, Md. Hasibul Alam, and Auvi Biswas

Department of Mechanical Engineering, BUET, Dhaka, Bangladesh

### ABSTRACT

The experimental analysis presented here is based on the heat transfer performance of parallel miniature heat pipe (mHP) system intended for desktop computer processor cooling. The system consists of six single copper tube mHPs slotted into two copper blocks at the evaporator section and fifteen parallel copper sheets at the condenser section. Stainless steel wicks are inserted inside the copper tubes, while methanol and iso-propanol serves solely as working fluids. Heat transfer characteristics of mHPs are determined by conducting the experiment at various levels of heat inputs and analyzed to evaluate the performance. The overall heat transfer coefficient of the system is determined as a performance parameter. The results show that, the behavior of the heat pipe varies significantly for different heat inputs and different working fluids.

**Keywords:** Parallel Miniature Heat Pipes, Heat Flux, Overall Heat Transfer Coefficient, Working Fluids.

### 1. INTRODUCTION

There was a time when people were satisfied with conventional fan cooling in electronic devices despite the huge noise generation and power consumption. But the realization changed quickly because of the increasing heat generation with increasing working speed and also the space constraint. Specially, the cooling of computer processors demanded a whole new outlook. The CPU of a desktop and server computer releases 80 to 130 W and notebook computer 25 to 50W of heat energy [1]. It became more challenging because the chip surface temperature should not be allowed to go beyond 100°C [2]. Scientists started to apply liquid submersion cooling, active and passive heat sink cooling, thermoelectric cooling etc. in computer cooling. But soon these became more or less obsolete for integration and reliability issues. Even the most recent technique of integrated chip cooling is not acclaimed by all because of the huge cost. With massive development in the concept and technology of two-phase and porous media heat transfer systems heat pipes have come up as one of the most potential candidate to meet these challenging needs.

A typical heat pipe consists of a sealed pipe or tube made of a material with high thermal conductivity. After evacuating, the pipe is filled with a fraction of a percent by volume of working fluid, chosen to match the operating temperature. Due to the partial vacuum that is near or below the vapor pressure of the fluid, some of the fluid will be in the liquid phase and some will be in the gas phase. Having a vacuum eliminates the need for the working gas to diffuse through another gas and so the bulk transfer of the vapor to the cold end of the heat pipe is at the speed of the moving molecules. Inside the pipe's walls, an optional wick structure exerts a capillary

pressure on the liquid phase of the working fluid. At the hot interface, the fluid turns to vapor absorbing the latent heat resulting in a phase change, and the gas flows and condenses back to liquid in the cold interface releasing the latent heat. The liquid is moved back by capillary gravity action to the hot interface to evaporate again and repeat the cycle.

The very first advent of heat pipe was in 1944 by R.S. Gauglar [3] of General Motors, which was rediscovered by George Grover and his co-workers [4] of the Los Alamos Scientific Laboratory in 1963. Since then continuous research and development have gone behind heat pipe. Starting in the 1980s Sony began incorporating heat pipes into the cooling schemes for tuners & amplifiers in electronic products in place of both forced convection and passive finned heat sinks. Cao, Y. and Gao, M. [5] designed, fabricated, and tested wickless, cross-grooved thermal spreaders, which were made of Copper or Aluminum. The maximum heat flux achieved was about 40 W/cm<sup>2</sup> for methanol and 110W/cm<sup>2</sup> for water with a total heat input of 393W.

In the development process, as the electronic devices became more mobile in use and tiny in size, scientists started to concentrate more on micro and miniature heat pipes. Zhang, J. and Wong, H.[6] studied heat transfer and fluid flow in an idealized micro heat pipe with the support of NASA and LaSPACE. They made an analysis for four different values of length to width ratio of an idealized micro heat pipe, viz. 20, 50, 100, and 200. In a study of micro and miniature heat pipes, developed by A.R. Anand [7], attempts have been made to develop a one dimensional numerical model of micro heat pipes, taking into account the effect of liquid-vapor interfacial shear stress. In 1991, Wu and Peterson [8] developed a transient numerical model capable of predicting the

thermal behavior of micro heat pipes and compared their results with the steady state results obtained by Babin et al. [9] in 1990.

For electronic equipments, heat pipes of diameter 3 to 6 mm and length less than 400 mm are preferred [10]. Most preferable length is 150 mm [11]. An experimental study is performed by Tanim *et al.* [12] to investigate the performance of cooling desktop processors using miniature heat pipes of 5.78 mm ID and a length of 150 mm with respect to the normal fanned CPU unit. They reported that four mHPs system shows better performance than that of two mHPs. Another experiment has been performed similar to this one by Imtiaz and Feroz [13] on Parallel mHPs for cooling desktop computer processor. They concluded that the addition of a cooling fan in the condenser section provides the lowest temperature of the surface of the processor. This particular experiment is further development of that one. Instead of drawing heat directly from the CPU, external variable heat source is used to observe the performance of the heat pipe under different heating conditions. Finally the performance of the mHPs is also checked for two different working fluids.

## 2. EXPERIMENTAL SETUP

The experimental setup for this study mainly consists of – 6 parallel mHPs along with heating and cooling sections, a variac, 5 selector switches, 30 thermocouples and a temperature controller, as shown in Fig. 1.

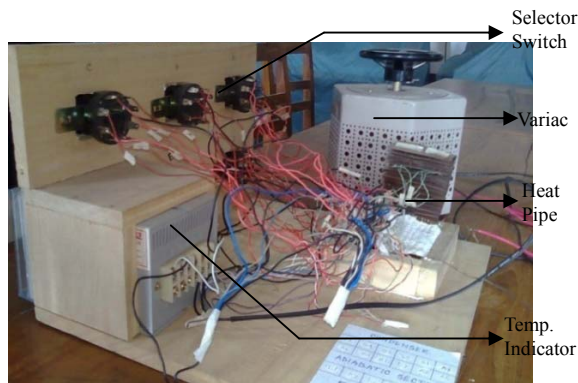


Fig 1. Experimental setup

Six mHPs are placed parallel to each other for cooling purpose. Every mHP has an inner diameter of 1.8 mm and outer diameter of 2.8 mm having a length of 150 mm. There are three sections in every mHP: evaporator, adiabatic section and condenser, as shown in Fig. 2. The condenser sections of MHPs are made of fifteen copper sheets of 67mm×50mm (thickness 0.5mm) placed parallel as extended fins at a constant interval of 5 mm. Plates are joined with the mHPs with Araldite for better heat transfer. Having the space constrain in field of its application in mind, the MHPs are bend at 90° in adiabatic section. The evaporator sections of MHPs are inserted in to the grooves of copper blocks. Two copper blocks of 67mm×50mm×8mm are made very precisely to mate with the MHPs. Grooves are cut inside the blocks. The blocks are precise in dimension and surfaces are finished highly to reduce the contact resistance as well as

to increase the heat transfer rate. Nichrome wires are wound around the evaporator section and then it is electrically and thermally insulated using insulating tape and asbestos respectively.

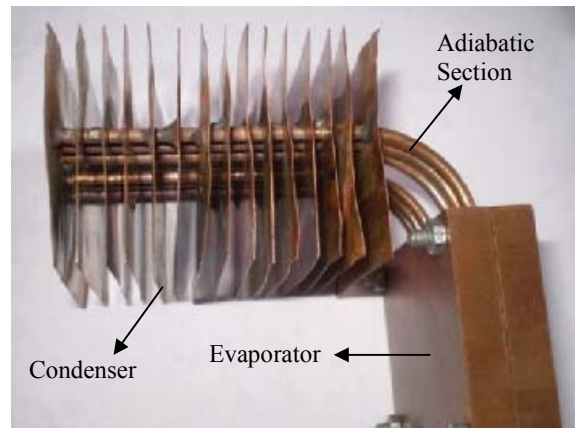


Fig 2. mHPs with Evaporator, Adiabatic and Condenser sections

Before bending, wick of stainless steel of 200 meshes are inserted into the MHPs. After inserting the wick, mHPs are bent to the desired angle. One end of the mHPs is sealed and working fluid with charge ratio 0.9 is poured into that. Five calibrated K-type ( $\Phi = 0.18$  mm) thermocouples are attached to the wall of each mHP using adhesive to measure the wall temperature: two units at the evaporator section, one unit at the adiabatic section and two units at the condenser section. Locations of thermocouples connected on different points along the length of the mHP are shown in the Fig. 3. All thermocouples are connected to a digital temperature indicator through selector switches.

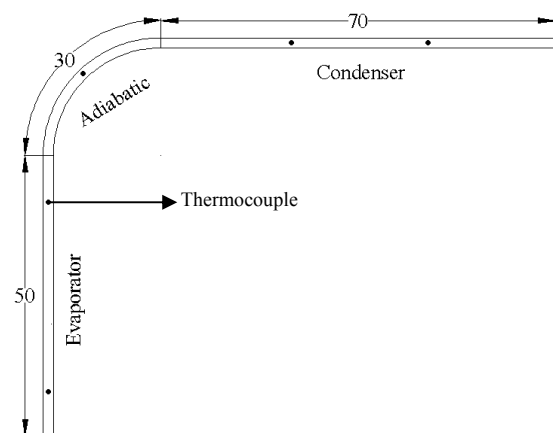


Fig 3. Location of thermocouples

## 3. TEST PROCEDURE

Experiment is conducted for two different working fluids: propanol-2 and methanol. After insertion of the fluid, the mHPs are sealed and alternating current (AC) line is connected to the nichrome wire via a variac. The heat input is increased gradually by changing the voltage

with the variac. Wall temperatures of mHPs are recorded for 40 to 45 minutes (until steady values are attained) at an interval of 5 minutes for each heat input value. The whole procedure is repeated for both the fluids. The experimental parameters are stated in Table 1.

Table 1: Experimental Parameters

Parameters	Condition
Number of the heat Pipes	6
Diameter of the heat pipe(mm)	ID- 1.8; OD- 2.8
Length of the heat pipe(mm)	150
Length of the evaporator section (mm)	50
Length of the adiabatic section (mm)	30
Length of the condenser section (mm)	70
Working fluid	Propanol-2, Methanol
Dimension of the copper block(mm)	67×50×8
Dimension of the copper sheet(mm)	67×50×0.5
Charge ratio	0.9
Wick (SS)	200 meshes

#### 4. TEST RESULTS AND DISCUSSION

As heat load is applied to the evaporator section, the temperature of the evaporator section rises and results in the vaporization of the working fluid. This vaporization of liquid absorbs heat from the evaporator section. The heating value is determined by multiplying the voltage indicated by the variac and the current drawn into the circuit.

Heat flux ( $\phi$ ) is calculated using Eq. (1) where  $Q$  is the input heat power and  $A$  is heating area of the mHP system, i.e. the outer surface area of all six mHPs at the evaporator section.

$$\phi = Q / A \quad (1)$$

##### 4.1 Temperature Profile

Fig. 4(a) and 4(b) shows the temperature profiles along the length of the mHP for propanol-2 and methanol respectively. The temperatures are average of all the readings of the thermocouples in the same horizontal line, i.e. the average of the temperature readings of the six mHPs. Uniformity of temperature in the evaporator and condenser sections indicates the reliability of using mHPs for the cooling of desktop processors.

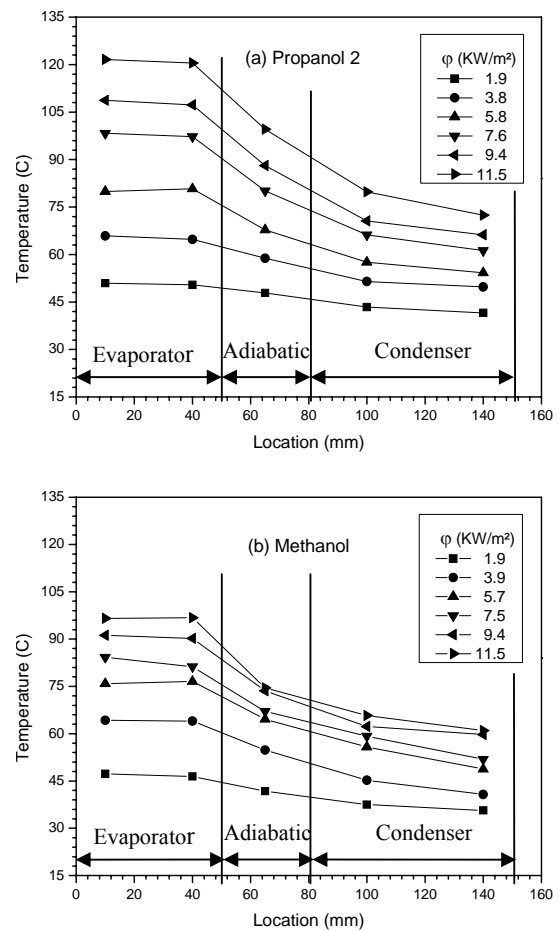


Fig. 4. Temperature Profile along the length of mHPs

##### 4.2 Overall Heat Transfer Coefficient

A graph of overall heat transfer co-efficient vs. heat flux for both the fluids is shown in Fig. 5. The overall heat transfer co-efficient ( $h_{ov}$ ) is determined from Eq. (2). For a particular system, it depends solely on the temperature difference ( $\Delta T$ ) of the evaporator end and the condenser end.

$$h_{ov} = Q / (A * \Delta T) \quad (2)$$

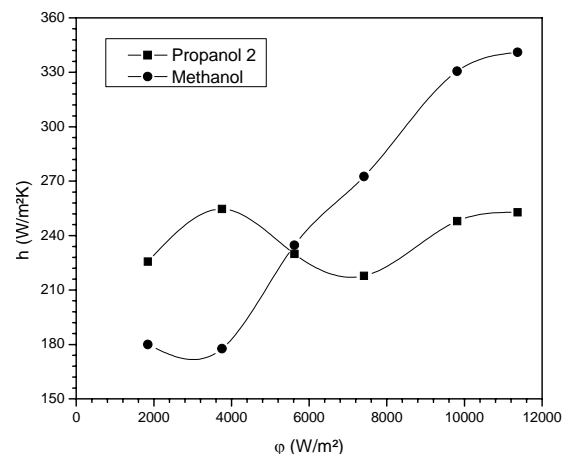


Fig. 5. Overall heat transfer coefficient vs. heat flux

As observed from the graph, at lower heat flux value, the overall heat transfer coefficient for the propanol-2 based system is higher than that of the methanol based system. But for heat fluxes higher than  $5600 \text{ W/m}^2$ , the overall heat transfer coefficient is significantly higher for the later one.

### 4.3 Transient Temperature

Variation of evaporator surface temperature with time is shown in Fig. 6(a) and (b) for the lowest and the highest heat fluxes, respectively. Here, the temperatures of the evaporator section are only considered, because only this section of the mHP system is to be placed on the computer processor and its temperature resembles the temperature of the processor in field of application. The figure indicates that, at a lower heat flux, after attaining the steady state, both the systems show almost the same temperature, but at a higher heat flux, propanol-2 based system shows a little bit higher temperature. It can also be observed that the propanol-2 based system attains steady state temperature a little faster than the acetone based one.

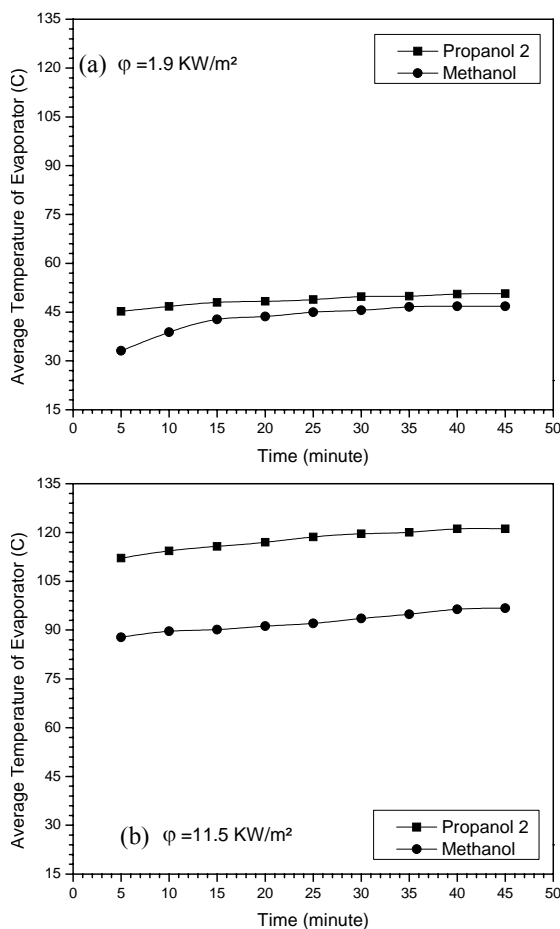


Fig 6. Variation of Evaporator surface temperature with time

## 5. CONCLUSION

The following conclusions can be drawn from the experimental studies:

(1) Insignificant fluctuation of temperature along the length of the MHPs indicates the stability and consistency of the system.

(2) Methanol is the better working fluid to be used in a mHP than propanol-2, as the overall heat transfer co-efficient is higher at higher heat fluxes. Besides, lower evaporator section temperature is achieved with the methanol based system.

## 6. REFERENCES

1. M. Mochizuki, Y. Saito, V. Wuttijumnong, X. Wu, and T. Nguyen, "Revolution in fan heat sink cooling technology to extend and maximize air cooling for high performance processors in laptop/desktop/server application," in Proc. IPACK'05, San Francisco, CA, Jul. 17–22, 2005, [CD ROM].
2. I. Saucius, R. Prasher, J. Chang, H. Erturk, G. Chrysler, C. Chiu, and R. Mahajan, "Thermal performance and key challenges for future CPU cooling technologies," in Proc. IPACK'05, San Francisco, CA, Jul. 17–22, 2005, [CD ROM].
3. Hossain, M. Z. and Haq, M. Z., 2001, "Simulation of Otto Cycle with Multi-Fuel", *Proc. 4<sup>th</sup> Int. Conf. on Mechanical Engineering (ICME2001)*, pp. III:133-137.
4. Gaugler, R. S., "Heat Transfer Device", U. S. Patent 2,350,348.
5. Grover, G. M., Cotter, T. P. and Erikson, G. F., "Structures of Very High Thermal Conductivity", *J. Appl. Phys.*, 35, 1990 (1964).
6. Cao, Y. and Gao, M., 2002, "Wickless network heat pipes for high heat flux spreading applications", *International Journal of Heat and Mass Transfer* 45, 2539-2547.
7. Zhang, J., 2002, "M. S. Thesis: Heat Transfer and Fluid Flow in an Idealized Micro Heat Pipe", 2002 ME Graduate Student Conference, LSU.
8. Anand, A. R., 2002. "Studies on Micro and Miniature Heat pipes", report No. ISRO-ISAC-TR0603.
9. Peterson, G. P., and Wu, D., 1991, "Investigation of the Transient Characteristics of a Micro Heat Pipe," *Journal of thermo physics*, Vol. 5, No. 2, pp. 129-134.
10. Babin, R. B., Peterson, G. P., and Wu, D., 1990, "Steady State Modeling and Testing of a Micro Heat Pipe," *ASME Journal of Heat Transfer* 112, pp. 595-601.
11. S. Yoshiaki, M. Takase, M. Tanabe, N. Teruo, I. Kinoshita, I. Tadashi, K. Namba and S. Masahiro, "A junction block incorporating a micro heat-pipe," *Furukawa Review*, No. 18. 1999.
12. K. S. Kim, S. H. Moon, and C. Gi. Choi, "Cooling characteristics of miniature heat pipes with woven wired wick," in Proc. of the 11th international Heat Pipe Conference –Tokyo 1999, pp 239 – 244.

12. T. R. Tanim., T. Hussain and C. M. Feroz, "Cooling of desktop computer using heat pipes," in Proc. ICME'07, Dhaka, Bangladesh, Dec. 29-31, 2007. [CD ROM, ICME07-TH-01].
13. Imtiaz A. I. and Chowdhury F. Md., "Cooling of Desktop Processor using Parallel Micro heat pipes," Proceeding of the 4th BSME\_ASME International Conference on Thermal Engineering, Dhaka, Bangladesh (2008), pp 98-103.

## 8. MAILING ADDRESS

Prof. Chowdhury Md. Feroz  
 Department of Mechanical Engineering, BUET  
 Dhaka-1000, Bangladesh  
 Email: [cmferoz@me.buet.ac.bd](mailto:cmferoz@me.buet.ac.bd)

## 7. NOMENCLATURE

Symbol	Meaning	Unit
Q	Heat power input	(W)
$\phi$	Heat Flux	(W/m <sup>2</sup> )
$h_{ov}$	Overall heat transfer co-efficient	(W/m <sup>2</sup> K)

## NUMERICAL STUDY OF A TWO-STAGE ADSORPTION CHILLER EMPLOYING RE-HEAT SCHEME WITH DIFFERENT MASS RATIOS

M. Z. I. Khan<sup>1</sup>, SK. Farid<sup>2</sup>, S. Sultana<sup>3</sup>

<sup>1</sup>Bangladesh University of Engineering and Technology (BUET), Bangladesh

<sup>2</sup>Mirpur Girls' Ideal Laboratory Institute, Dhaka, Bangladesh

<sup>3</sup>Stamford University, Bangladesh

### ABSTRACT

This paper deals with the performance investigation of a silica gel/ water-based two-stage adsorption chiller employing re-heat scheme with different mass ratios and compared with that of the two-stage conventional chiller with re-heat scheme using equal mass allocation (upper bed : lower bed = 1:1). The performance of a two-stage adsorption chiller using re-heat scheme with different mass allocation between upper and lower beds have been investigated numerically. Results show that cooling capacity can be improved with the optimum allocation of adsorbent mass to the upper beds than that of lower beds. The improvement in Co-efficient of Performance (COP) values, however, is less significant. It is also seen that the improvement in cooling capacity is more significant for the relatively higher heat source temperature. It is shown that the cooling capacity can be improved up to 8% if the heat source temperature is 80°C.

**Keyword:** Adsorption Cycle, Two-Stage Chiller, Re-Heat, Silica Gel, Water

### 1. INTRODUCTION

With the increasing awareness of global warming and ozone depletion problems, adsorption refrigeration and heat pump systems have received much attention by researchers in many parts of the world; in particular, the low-temperature waste heat sources for cooling energy production. The use of waste heat at near environment temperature is an important contemporary problem. Heat driven sorption (absorption or adsorption) cycle is one of the promising candidates to utilize waste heat at near environment temperature. Though the absorption cycles are predominant in the area of heat driven refrigeration cycles, adsorption cycle has a distinct advantage over absorption systems in their ability to be driven by relatively low-temperature heat source, which cannot effectively regenerate the absorption systems [1]. In the last three decades, extensive investigations on the performances of adsorption refrigeration/heat pump systems have been conducted considering various adsorbent/ refrigerant pairs, such as zeolite/ water [2], activated carbon/ammonia [3], activated carbon/methanol [4] and silica gel/water [5]. It is well known that the performance of adsorption cooling/heating system is lower than that of other heat driven heating/cooling systems specially, absorption system provided that the available heat source temperature is at 75°C or higher. Many authors proposed and/or investigated the adsorption cooling and heating system to improve the performance. To improve the coefficient of performance, Akahira et al. [6]

investigated two-bed mass recovery cycle with novel strategy, which shows that mass recovery cycle with heating/cooling improves the cooling power. To utilize low-temperature waste heat source between 40°C and 60°C, Saha et al. [7] proposed and examined experimentally a three-stage adsorption chiller with silica gel/ water pair. Saha et al. [8] introduced a two-stage adsorption chiller and the required driving heat source temperature is validated experimentally. Alam et al. [9] proposed and analyzed a re-heat two-stage adsorption chiller, which can be operated with driving heat source temperatures between 50°C and 90°C along with a coolant at 30°C. The COP of the re-heat two-stage chiller is higher than that of two-stage chiller without re-heat. Moreover, the re-heat two-stage chiller produces effective cooling even though heat source temperatures are varied between 50°C and 90°C. Recently, Khan et al. [10] studied on a re-heat two-stage adsorption chiller with silica gel/ water as adsorbent/ adsorbate pair. In the present study, the chiller investigated the effect of mass allocation between upper and bottom beds on cooling capacity (CC), Co-efficient of Performance (COP), chilled water outlet and their improvement ratios.

### 2. WORKING PRINCIPLE OF THE TWO-STAGE CHILLER WITH RE-HEAT SCHEME

The schematic diagram and time allocation of the two-stage chiller are shown in Fig. 1 and Table 1, respectively. The design criteria of the two-stage adsorption chiller using re-heat is almost similar to that

of a two-stage adsorption chiller without re-heat, which is developed by Alam et al. [9]. Operational strategy of the re-heat chiller is completely different from the operational strategy of a conventional two-stage without re-heat chiller. In two-stage adsorption chiller, the evaporating pressure lift is divided into two consecutive pressure lifts to exploit low heat source temperature by introducing four adsorbent beds. In the two-stage adsorption chiller using re-heat, the evaporating pressure (temperature) lift, however, can be divided into different ways from the conventional two-stage chiller. To complete one full cycle in re-heat scheme, all adsorbent beds pass through six consecutive steps: (i) desorption (ii) mass recovery process with heating (iii) pre-cooling (iv) adsorption (v) mass recovery process with cooling, and (vi) pre-heating. The two-stage adsorption chiller using re-heat comprises with four adsorbent beds, one condenser, one evaporator, and metallic tubes for hot, cooling and chilled water flows as shown in Fig.1. In a conventional two-stage chiller, lower two beds never interact with the condenser and upper two beds never interact with the evaporator. However, in the two-stage adsorption chiller using re-heat, all beds undergo through all processes and interact with the condenser and evaporator. The chiller can be operated in different strategies. However, only one strategy has been considered in the present study. The chiller has 10 modes, mode A, B, C, D, E, F, G, H, I, and J. Table 1. mode A, B, and C, eva-Hex-2 is in adsorption process and cond-Hex-1 is in desorption process. In the adsorption-evaporation process, refrigerant (water) in evaporator is evaporated at evaporation temperature,  $T_{eva}$ , and seized heat,  $Q_{eva}$  from the chilled water. The evaporated vapor is adsorbed by adsorbent (silica gel), at which cooling water removes the adsorption heat,  $Q_{ads}$ . The desorber (Hex-1) is heated up to the temperature ( $T_{des}$ ) by heat  $Q_{des}$ , provided by the driving heat source. The resulting refrigerant is cooled down by temperature ( $T_{cond}$ ) in the condenser by the cooling water, which removes heat,  $Q_{cond}$ . In mode A, adsorber (Hex-4) is connected with desorber (Hex-3) through pipe with continuing cooling water in Hex-4 and hot water in Hex-3. It is noted that, at the beginning of mode A, Hex-4 was in the end position of evaporation-adsorption process and Hex-3 was in the end position of desorption-condensation process. Due to higher-pressure difference at Hex-3 and Hex-4 in mode A, the refrigerant mass circulation will be higher than that of conventional two stages. This will lead the chiller to provide better performance. In mode B, adsorber (Hex-4) is heated up by hot water, and the desorber (Hex-3) is cooled down by cooling. Mode B is warm up process for Hex-4 and Hex-3. When the pressure of adsorber (Hex-3) and desorber (Hex-4) are nearly equal to the pressure of evaporator and condenser respectively, then Hex-3 and Hex-4 are connected to evaporator and condenser respectively to flow the refrigerant. This mode is denoted as mode C. In mode C, Hex-4 works as desorber and Hex-3 works, as adsorber and this process will continue up to mode E. In mode D, Hex-2 (at the end position of adsorption-evaporation process) and Hex-1 (at the end position of desorption-condensation process) are

connected with each other continuing cooling water and hot water respectively. When the pressure (temperature) of both Hex-1 and Hex-2 nearly equal, then warm up process will start, called mode E. In mode E, Hex-2

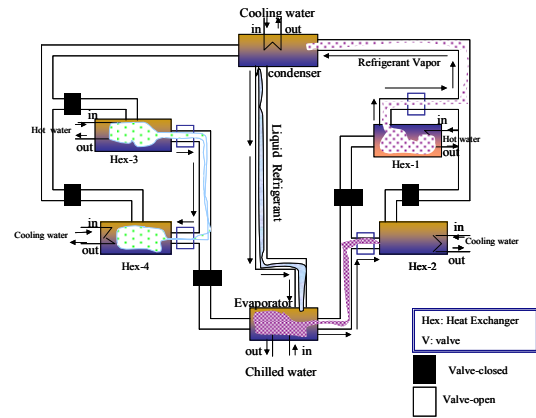


Fig 1. Schematic of a re-heat two-stage chiller

Table 1: Operational strategy of the two-stage chiller using re-heat scheme

Mode	A	B	C	D	E	F	G	H	I	J
Hex-1										
Hex-2										
Hex-3										
Hex-4										

	Adsorption		Mass recovery With heating		Pre-heating
	desorption		Mass recovery With cooling		Pre-cooling

is heated up by hot water, and cooling water-cools down the Hex-1. When the pressure of Hex-1 and Hex-2 are nearly equal to the pressure of evaporator and condenser respectively, then Hex-1 and Hex-2 are connected to evaporator and condenser respectively to flow the refrigerant. This connection will continue up to mode F, G, and H for Hex-1 and Hex-2. In mode F, Hex-3 (at the end position of adsorption-evaporation process) and Hex-4 (at the end position of desorption-condensation process) are connected with each other continuing cooling water and hot water respectively. When the pressure (temperature) of both Hex-3 and Hex-4 are nearly equal, then warm up process will start, called mode G. In mode G, Hex-3 is heated up by hot water, and cooling water-cools down the Hex-4. When the pressure of Hex-4 and Hex-3 are nearly equal to the pressure of evaporator and condenser respectively, then Hex-4 and Hex-3 are connected to evaporator and condenser respectively to flow the refrigerant. This connection will continue up to mode H, I, and J for Hex-3 and Hex-4. In mode I, Hex-1 (at the end position of adsorption-evaporation process) and Hex-2 (at the end position of desorption-condensation process) are connected with each other continuing cooling water and



hot water respectively. When the pressure (temperature) of both Hex-1 and Hex-2 are nearly equal, then warm up process will start, called mode J. In mode J, Hex-1 is heated up by hot water, and cooling cools down the Hex-2. The mode J is the last process and after this mode, all return to mode A (Table-1). The values adapted in simulation are presented in Table. 2 and Table. 3

### 3. MATHEMATICAL FORMALISM

The heat transfer and energy balance equations for the adsorbent beds can be described as follows:

$$T_{out} = T + (T_{in} - T) \exp\left(-\frac{u_{hex} A_{hex}}{\dot{m}_w c_w}\right) \quad (1)$$

$$\begin{aligned} & \frac{d}{dt} \left\{ (w_s c_s + w_s c_w q + w_{hex} c_{hex}) T \right\} \\ & = w_s Q_{st} \frac{dq}{dt} - \delta w_s c_w \left\{ \gamma (T - T_{eva}) + (1 - \gamma) (T - T_w) \right\} \\ & \times \frac{dq}{dt} + \dot{m}_w c_w (T_{in} - T_{out}) \end{aligned} \quad (2)$$

where,  $\delta$  is either 0 or 1 depending whether the adsorbent bed is working as a desorber or an adsorber and  $\gamma$  is either 1 or 0 depending on whether the adsorbent bed is connected with the evaporator or another adsorbent bed.

The heat transfer and energy balance equations for the evaporator can be described as:

$$T_{chill,out} = T_{eva} + (T_{chill,in} - T_{eva}) \exp\left(-\frac{UA_{eva}}{\dot{m}_{chill} c_{chill}}\right) \quad (3)$$

$$\begin{aligned} & \frac{d}{dt} \left\{ (W_{eva,w} C_w + W_{eva,hex} C_{eva,hex}) T_{eva} \right\} = \\ & - LW_s \frac{dq_{ads}}{dt} - W_s C_w (T_{con} - T_{eva}) \frac{dq_{des}}{dt} \\ & + \dot{m}_{chill} C_{chill} (T_{chill,in} - T_{chill,out}) \end{aligned} \quad (4)$$

The heat transfer and energy balance equations for the condenser can be written as:

$$T_{cond,out} = T_{cond} + (T_{cw,in} - T_{cond}) \exp\left(-\frac{UA_{cond}}{\dot{m}_{cw} c_w}\right) \quad (5)$$

$$\begin{aligned} & \frac{d}{dt} \left\{ (W_{cw,w} C_w + W_{cond,hex} C_{cond,hex}) T_{cond} \right\} = \\ & - LW_s \frac{dq_{des}}{dt} - W_s C_w (T_{des} - T_{cond}) \frac{dq_{des}}{dt} \\ & + \dot{m}_{cw} C_w (T_{cw,in} - T_{cw,out}) \end{aligned} \quad (6)$$

The mass balance for the refrigerant can be expressed as:

$$\frac{dW_{eva,w}}{dt} = -W_s \left( \frac{dq_{des-cond}}{dt} + \frac{dq_{eva-ads}}{dt} \right) \quad (7)$$

where, the subscripts des-cond and eva-ads stand for the refrigerant vapor flow from desorber to condenser and evaporator to adsorber, respectively. The adsorption equilibrium equation for silica gel/water pair is taken as:

$$q^* = \{0.8 \times [P_s(T_w)/P_s(T_s)]\} / \{1 + 0.5 \times [P_s(T_w)/P_s(T_s)]\}$$

where  $P_s(T_w)$  and  $P_s(T_s)$  are the saturation vapor pressure at temperatures  $T_w$  (water vapor) and  $T_s$  (silica gel), respectively. The saturation vapor pressure and temperature are correlated by Antoine's equation, which can be written as:

$$P_s = 133.32 \times \exp\left(18.3 - \frac{3820}{T - 46.1}\right)$$

### 4. MEASUREMENT OF SYSTEM PERFORMANCE

The performance of a two-stage adsorption chiller using re-heat is mainly characterized by cooling capacity (CC), coefficient of performance (COP) and can be measured by the followings:

Cooling capacity =

$$\dot{m}_{cw} \int_0^{t_{cycle}} (T_{chill,in} - T_{chill,out}) dt / t_{cycle}$$

Co-efficient of performance (COP) =

$$\dot{m}_{bill} C_w \int_0^{t_{cycle}} (T_{chill,in} - T_{chill,out}) dt / \dot{m}_{ht} C_w \int_0^{t_{cycle}} (T_{ht,in} - T_{ht,out}) dt$$

### 5. RESULTS AND DISCUSSION

In the present analysis, a cyclic simulation computer programme is developed to predict the performance of the innovative two-stage chiller using re-heat. The systems of differential equations (1) - (7) are solved by finite difference approximation with a time step 1 sec. The results taken in the study are from the cyclic steady state conditions. A real chiller starts its operation with unbalanced conditions, however, after a few cycles (typically 2-3 cycles) it reaches its cyclical steady state condition. Therefore, an iteration processes has been

employed in solution procedure to fix all the initial values for the cyclic steady state conditions. In the beginning of the solution process, the initial values are assumed and finally those are adjusted by the iteration process. When two beds are connected with evaporator or condenser, the vapor pressure is unknown that are calculated through the Antoine's equations as the vapor temperature is calculated from the energy balance equation of evaporator or condenser. It is however, difficult to calculate the saturated vapor pressure when two-beds are connected with each other, which are essential for the calculation of adsorption/ desorption rate inside the adsorbent beds. In the state, the pressure is assumed and the amounts of vapor adsorbed/ desorbed beds are calculated. Conceptually, the desorbed vapor is equal to the amount of adsorbed vapor by the other beds. If these amounts are not equal then vapor pressure are adjusted for next iteration. Once the satisfactory convergence criterion is achieved, then process goes for the next time step. The convergence criterion for all cases of present study will be taken as  $10^{-3}$ . The effect of mass allocation between upper and lower beds on cooling capacity (CC), co-efficient of performance (COP), chilled water outlet and their improvement ratio is shown in Fig. (2) – (7). In Figs.2 and 3, numerical values of CC and improvement ratios are depicted against the driving heat source inlet temperature from 50°C to 90°C. The highest cooling capacity is obtained at 3:2 ratio of mass allocation of upper bed to bottom bed. It is seen that the CC and improvement ratio increases with the increase of heat source temperature from 60°C to 90°C in all cases. In Fig.3. It is seen that the improvement ratios are; 5.12%, 5.22%, 6.24% and 7.9%. But the CC and improvement ratio decreases with the increase of heat source temperature from 50°C to 90°C in all cases when the mass allocation is upper bed to bottom bed is 1:2. The decreases ratios are; 2%, 2.8%, 3.18%, 3.23% and 2.47%. In Figs.4 and 5, the effect of heat source temperature on COP, the COP increases with the increase of heat source temperature from 50°C to 90°C in all cases when the mass allocation is upper bed to bottom bed is 1:2 and when the mass allocation is upper bed to bottom bed is 3:2 then COP decreases at 50°C but increases from 60°C to 90°C in all cases. In Figs. 5, it is seen that the improvement ratios are; 37.05%, 26.81%, 20.86%, 15.67% and 11.38% when the mass allocation is upper bed to bottom bed is 1:2. When the mass allocation is upper bed to bottom bed is 3:2 COP decreases 0.59% at 50°C but increase from 60°C to 90°C in all cases 0.35%, 0.67%, 1.12% and 1.84%. Again, when the mass allocation is upper bed to bottom bed is 2:3 then COP increase at 50°C to 60°C but decreases from 61°C to 90°C in all cases. The increasing ratios at 50°C to 60°C are; 0.09%, 0.87% and the decreasing ratios are; 3.22%, 6.09%, 7.26%. In an adsorption chiller, the chilled water for air-condition purposes is obtained from the outlet of the chilled water. Generally, less chilled water outlet temperature is expected, while the requirement of cooling capacity is high. The chilled water outlet temperature, however, affects cooling demand of the demand side. Therefore the requirement

of chilled outlet temperature is very important.

Table 2: Baseline Parameters

Values Adopted in Simulation		
Symbol	Value	Unit
$A_{bed}$	1.45	$m^2$
$A_{eva}$	0.665	$m^2$
$A_{con}$	0.998	$m^2$
$C_s$	924	J/kgK
$C_w$	4.18E+3	J/kgK
$C_{chill}$	4.20E+3	J/kgK
$D_{so}$	2.54E-4	$m^2/s$
$E_a$	2.33E+3	J/kg
$L$	2.50E+6	J/kg
$Q_{st}$	2.80E+6	J/kg
$R$	4.62E+2	J/kg
$R_p$	0.35E-3	M
$UA_{ads}$	2497.6	$Wk^{-1}$
$UA_{des}$	2532.5	$Wk^{-1}$
$UA_e$	989.9	$Wk^{-1}$
$UA_{cond}$	2404.3	$Wk^{-1}$
$W_s$	16	Kg
$W_{cw}$	5	Kg
$W_{eva-w}$	25	Kg

Table 3: Standard operating condition

	Temp.(°C)	Flow rate (kg/s)
Hot water	80	0.5
Cooling water	30	0.3 ( ads) + 0.3 cond)
Chilled water	14	0.3
Cycle time	1300s = ( 480 ads/des + 140 mr + 30 ph/pc )s×2	

Ads/des = adsorption/desorption,  
mr = mass recovery, ph/pc = pre heating/cooling

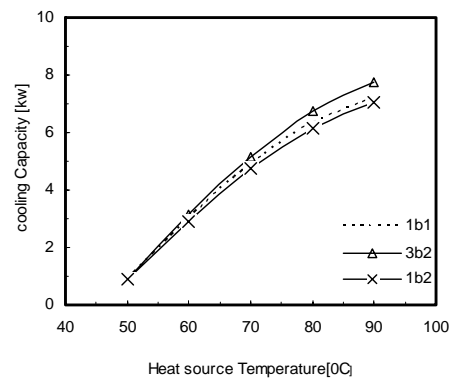


Fig.2. Effect of Heat source Temperature [°C] on cooling capacity

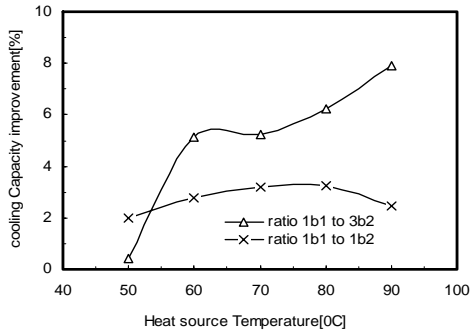


Fig.3. Effect of Heat source Temperature [OC] on cooling capacity improvement

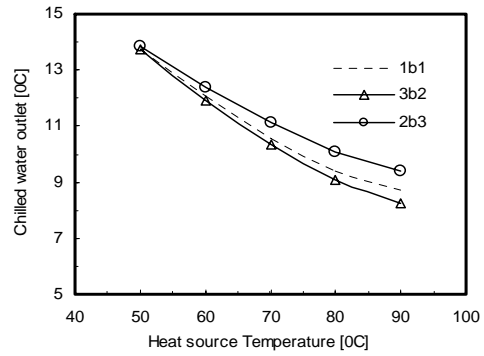


Fig.6. Effect of Heat source Temperature [OC] on chilled water outlet Temperature.

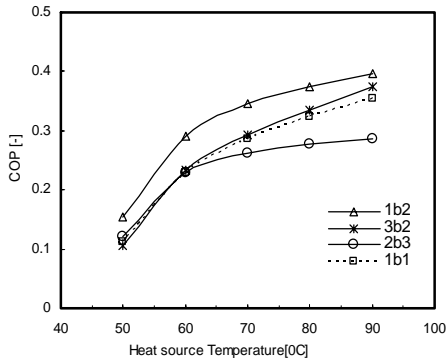


Fig.4. Effect of Heat source Temperature [OC] on cop

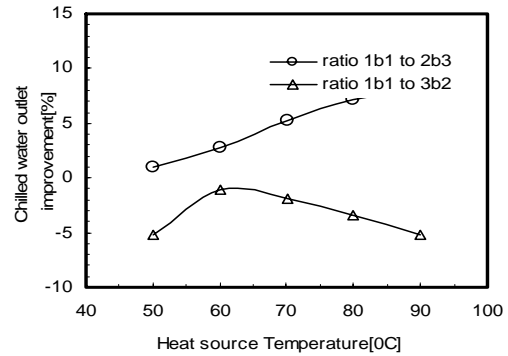


Fig.7. Effect of Heat source Temperature [OC] on chilled water outlet emperature.

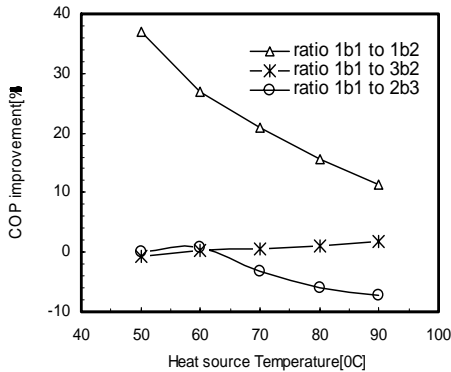


Fig.5. Effect of Heat source Temperature [OC] on cop improvement

From this context, the effect of heat source temperature as well as mass allocation ratios is presented in Figs.6 and 7. Therefore the requirement of chilled outlet temperature is very important. From this context, the effect of heat source temperature as well as mass allocation ratios is presented in Figs.6 and 7. It may be seen that the chiller with different level heat source temperature provides different level chilled water outlet temperature even the other operating conditions are the same. It can be also seen that the higher is the heat source temperature; the lower is the chilled water outlet temperature from the Fig.6, it is also observed that when the mass allocation is upper bed to bottom bed is 3:2 the chilled water outlet temperature is low. In Fig.7, it is seen that chilled water outlet temperature improvement ratios are; 0.97%, 2.74%, 5.26%, 7.2% and 7.82% when the mass allocation is upper bed to bottom bed is 2:3. But the chilled water outlet decreases ratios are; 5.19%, 1.02%, 1.92%, 3.35% and 5.194% when the mass allocation is upper bed to bottom bed is 3:2.

## 6. CONCLUSIONS

The performance of a two-stage adsorption chiller with different mass ratio of upper to bottom cycle was investigated numerically. It is found that the cooling capacity and COP of a two-stage adsorption chiller can be improved by allocating adsorbent mass between upper and bottom cycle. It can be found that the improvement ratio in cooling capacity, however, increases with the

increase of heat source temperature. It is also seen that the two-stage adsorption chiller with re-heat scheme for mass allocation 3:2 upper/bottom provides more cooling capacity than that of two-stage adsorption chiller with re-heat scheme for mass allocation 1:1 upper/bottom for the heat source temperature from 50°C to 90 °C. The COP is also improved significantly. Finally, it may be concluded that if a two-stage adsorption chiller with re-heat scheme is designed at 3:2 (upper/bottom) ratio, the chiller can perform better in terms of cooling capacity than that of conventional two-stage two-stage adsorption chiller with re-heat scheme for mass allocation 1:1 upper/bottom chiller even the heat source temperature is fluctuated between 50°C and 90 °C.

## 7. REFERENCES

1. Kashiwagi, T., Akisawa, A., Yoshida, S., Alam, K. C. A., Hamamoto, Y., Heat driven sorption refrigerating and air conditioning cycle in Japan, In: Proceeding of the International Sorption Heat pump Conference, September 23-27, shanghai china (2002) pp. 50-60,
2. Karagiorgas, M., Meunier, F., The dynamics of a solid adsorption heat pump connected with outside heat sources of finite capacity, J. Heat Recovery Systems CHP, 7(3) ( 1987) pp. 285-299.
3. Critoph, R. E., Vogel, R., Possible adsorption pairs for use in solar cooling, Int. J. Ambient Energy, 7(4) (1986) pp. 183-190.
4. Critoph, R. E., Activated carbon adsorption cycles for refrigeration and heat pumping, Carbon, 27 (1) (1989) pp 63-70.
5. Boelman, E. C., Saha, B. B., Kashiwagi, T., Experimental investigation of a silica-gel water adsorption refrigeration cycle the influence of operating conditions on cooling output and COP , ASHRAE Trans Res,101(2)(1995) pp. 358-366.
6. Akahira, A., Alam, K. C. A., Hamamoto, Y., Akisawa, A., Kashiwagi, T., Mass recovery adsorption refrigeration cycle-improving cooling capacity, International Journal of Refrigeration, 27(2004) pp. 225-234.
7. Saha, B. B., Boelman, E. C., Kashiwagi, T., Computational analysis of an advanced adsorption refrigeration cycle, Energy 20(1995) pp. 983-994.
8. Saha, B. B., Alam, K. C. A., Akisawa, A., and Kashiwagi, T., Ng, K. C., Chua, H. T., Two-stage non-regenerative Silica gel / water adsorption refrigeration cycle, in: proceeding of the ASME advanced energy systems division, Orlando, FL, USA, 40(2000) pp. 65-69.
9. Alam, K. C. A., Hamamoto, Y., Akisawa, A., Kashiwagi, T., Advanced adsorption chiller driven by low temperature heat source, in: Proceeding of 21<sup>st</sup> International Congress of refrigeration (CD ROM), Washington, DC, 2003, paper no. 136,
10. Khan, M. Z. I., Alam, K. C. A., saha, B. B., Akisawa, A., Kashiwagi, T., Study on a re-heat two-stage adsorption chiller-The influence of thermal capacitance ratio, overall thermal conductance ratio and adsorbent mass on system performance. Applied Thermal Engineering, 27 (2007) pp .1677-1685.

## 8. MAILING ADDRESS

M. Z. I. Khan  
Bangladesh University of Engineering and Technology  
(BUET), Bangladesh

## NON-CONVENTIONAL USE OF SMALL DIESEL ENGINES: CASE STUDIES

Md. Ehsan<sup>1</sup>, M. N. Ibne Kabir<sup>2</sup>, Sumon Reza<sup>2</sup>, and M Shahnaz Sultana<sup>2</sup>

<sup>1</sup> Department of Mechanical Engineering, BUET, Dhaka, Bangladesh

<sup>2</sup> Department of Mechanical Engineering, MIST, Dhaka, Bangladesh

### ABSTRACT

Small diesel engines are widely used for producing mechanical or electrical power all over Bangladesh. Apart from conventional use in irrigation, electrical power generation and river transportation, such engines are now having many alternative applications. Because of their huge number they constitute a significant proportion of the consumption of diesel fuel, which needs to be imported. With increasing living costs, the cost of human work force is rising and that has recently opened up some new fields of application of such engines in Bangladesh. Since there is almost no reported formal study of such uses, three such fields have been case studied. These include – Brick-Crushing, Concrete-Mixing and Sugarcane Processing. A number of samples in each category were studied, which included – the engine specification, drive arrangement of the hardware, fuel consumption rate and system transportability. The maximum torque requirement was investigated against the engine capacity. The capital, running and maintenance cost have been analyzed to estimate the economic feasibility of such applications. The sensitivity of prime parameters, on the economic feasibility of replacing each human powered system, have been characterized.

**Keywords:** Diesel Engines, Non-Conventional Use, Alternative Use, Human Powered Systems.

### 1. INTRODUCTION

Small diesel engines, typically producing less than 25 hp, are widely used all over Bangladesh. Although there is no accurate survey, the number of small diesel engine in operation is estimated to be about 0.7 million [1]. Introduced in late 70's such engines are now used in a number of sectors. Diesel fuel is the largest imported energy resource for Bangladesh. Presently about 2.4 million metric tons of Diesel is used every year in Bangladesh. High fuel price, uncertainty of availability of fuel and the question of energy security – requires Bangladesh to justify its use of diesel fuels. Although small consumption per unit, the huge number of the engines create a significant share of the total consumption. About 1 million ton of diesel consumption can be related to small diesel engines in the applications mentioned above [1].

The most important use is in irrigation for driving Low Lift pumps (LLP) and shallow tube wells (STW) in rural Bangladesh. Many of such engines are used for standby power generation to cope up with the frequent failure of main electrical power, as a small community solution. Although electricity have reached in about 60% villages, still more that 2/3rd of the irrigation devices are still run on diesel [1]. Diesel engines have reached wide application in many of about 0.9 million country boats. A large proportion of which is run by diesel now-a-days [1]. In the current decade the cost of human labor has increased, as the cost of living is increasing all across the

country. In a number of non-conventional applications small diesel engines are being used now-a-days, as carrying out the operation with engines replacing human workforce is becoming more productive as well as cost effective. Recently engines have found applications in 'Stone/Brick Crushing' and 'Concrete Mixing' in construction industry; 'Crushing of Rice and Sugarcane' in food industry. Thousands of locally built 3-wheelers are propelled by such engines, which are mostly used in rural transportation. Most of the engines used now are imported from china, but lots of small industries have developed locally which manufacture many spare parts of these engines, creating further employments. As a whole these engines are playing an important role in the overall economy.

Very few studies have been reported regarding the operation of diesel engines in such non-conventional applications. The present work makes group studies of three such applications – Crushing of Sugarcane, Crushing of Bricks and Concrete Mixing machines all run by small diesel engines. The study focuses on the - Engine Specification, Drive Mechanism, Overall Engine Performance and Economic feasibility of the operation. A number of engines used for the particular purpose were visited at different places around Dhaka city. Specification data were collected from the name plate attached to the engines. Information regarding the performance was physically observed for a short period and long-term data were collected from the end users.

For making the cost analysis, average of data collected from a number of selected users was used for each case.

## 2. CASE-1: SMALL DIESEL ENGINES USED IN CRUSHING SUGER CANE

Now-a-days small diesel engines are widely being used for crushing sugarcane for roadside juice vendors. Traditionally this was done using manual labor, now it is being cost effective to drive the crushing mechanism [2] with small diesel engines. Both stationary of 3-wheeler van mounted mechanisms are popular. The device typically consists of a small - single cylinder, water cooled, diesel engine driving a sugarcane crushing mechanism via a pulley-Vbelt speed reduction drive. The engine torque is further increased in the speed reduction gears in the crushing mechanism, where the conveniently sized sugarcane sticks are crushed between mating rollers to squeeze the juice out of them, which is collected in a container.



Fig 1. A 3-wheeler cycle-van mounted sugarcane crushing system used by roadside juice vendors

A number of such sugarcane crushing machines were visited at different places around Dhaka city, however reasonably reliable information could be collected from only 6 samples. The technical specification of a typical system is given below in table-1. Small Diesels engines generally of nearly 3kW capacity and 2600 rpm rated speed, 210 cc displacement volume, manufactured in China were used to drive the crushing mechanism (commonly called the roller mill) using a V-belt and Pulley drive with an effective speed reduction of around 4:1. The drive pulley diameter was found to be 3.5 inch in all samples, but the driven larger pulley diameter was found to range from 13.5 – 17.5 inch with the 14.5 inch size more common. The crushing mechanism had a further speed reduction for which two variants of the mechanisms were found to be in use. Type-I consisted of total four gears in the train with gear teeth ratio of 18:98, resulting about 5.4 times speed reduction. Type-II

consisted of total six gears in the train with gear teeth ratio of 38:73 and 26:90, resulting about 6.4 times speed reduction. Both spur and helical gears were found to be in use.



Fig 2a. Sugarcane Crushing Mechanism, Type-I



Fig 2b. Sugarcane crushing mechanism, Type-II

Table-1: Typical Specification of Sugarcane Crushers

Engine Rating	2.98 kW, 2600 rpm 240 cc
Pulley-VBelt Drive Diameter Ratio Speed Reduction	3.5 : 14.5 (13.5-17.5) inch 4.14 : 1 (3.85-5 : 1)
Crush Mechanism TYPE-I : Teeth Ratios Gear Reduction	(18:98) x (37:37) 5.44
TYPE-II : Teeth Ratios Gear Reduction	(38:73) x (26:90) x (24:24) 6.65
Main Crushing Rollers	Teeth ratio = 37:37 or 24 : 24 Speed ratio = 1: -1
Overall Torque Amplification / Speed Reduction	Type-I = 22.5 times, 115 rpm Type-II = 25.6 times, 102 rpm
Typical Fuel Consumption	2.5 liters/ 12 hours

Finally a pair of 37 teeth (in Type-I) or 24 teeth (in Type-II) gears were used to rotate the main rollers in opposite direction to create the crushing as well as feed motion of the suitably sized sugarcanes (about 2-3 feet in length), extracting the juice. Overall speed reduction achieved is about 23:1 increasing the torque applied significantly, sufficient to extract most of the juice from the sugar cane in 2/3 feeds. The crushing rollers only rotate about 100 rev/min, creating a roller feed rate of about 1.5 feet/sec. The crushing mechanisms are locally made with mild steel gears and the main two 4 inch diameter crushing rollers are made of stainless steel. Figure-2 shows a closer view of the crushing mechanism.

Due to the increased cost of manual labor, the engine driven system is getting more popular. The engine driven system was reported to be more efficient in juice production as well, enhancing its feasibility. For attaining the same juice production rate of the engine driven system one additional worker needed to be employed. A typical engine costs about 11,500-13,000 Taka, the Crushing Mechanism (Ball Mill) costs about 18,000 Taka and incase of a cycle-van mounted system the van costs additional 5,000 Taka. In addition for such capital investment, the fuel consumption was reported to be about 2.5 liters in every 12 hours (effectively 1 day) costing 110 Taka. The lubricating oil and small maintenance cost was about 1000 Taka per month. On the other hand the wage of an additional worker is about 250 Taka/day, which is needed by the owner in order to maintain the level of productivity. The engine driven system could be operated by the owner/employer alone. Table-2 shows the comparison of the cost and additional profit margin per month of an employer using the typical engine driven system. The engine depreciation value was considered as 40% of the purchase cost at the end of one year of operation. For comparison the costing of Sugar Cane, costing for the Crushing Mechanism (Ball Mill) and Cycle-Van, Daily cost/rent for the roadside possession (reported to be 50-60 Taka/day) were considered equal for both cases.

Table-2: Typical monthly cost reduction of an owner per month, using a diesel engine driven system.

Engine Depreciation Per month @5% of 12,500 Tk	625 Tk.
Lubricating Oil & Maintenance	1000 Tk
Fuel Cost : Diesel 44 Taka/Liter 2.5 liters (12 hr day) x 30 x 44 Tk	3300 Tk
Additional cost per month for Diesel engine driven system	4925 Tk
Cost for an additional Labor with a wage of 250 Taka/day	7500 Tk
Cost Reduction (Increase in Profit) per month	2575 Tk
Percentage increase in profit	12 %

The table shows that if a owner/employer have sufficient customers, using the diesel engine driven system instead of the traditional manual labor operated sugarcane crushing mechanism would increase the monthly profit by more than two thousand and five

hundred taka per month, which significant at this level. This could ensure high productivity, but require more investment. Compared to this the manually operated system could be operated by the owner himself only with a limited productivity. Which means his total investment would be only about 13,000 taka less, but the income would be nearly half. The engine driven systems ensures about double productivity without an additional labor. More over it has the advantage that if the business is not so well in few days of the month, the fuel cost would come down accordingly, where the additional labor needs be paid on a flat day/month basis. However one observation was concerning, the diesel exhaust often is blown by a strong wind across the sugar cane, this may degrade the juice quality to some extent, which may need a different sort of investigation.

### 3. CASE-2: SMALL DIESEL ENGINES USED IN BRICK CRUSHING

Conventionally brick was broken down to brick chips manually using a hammer in Bangladesh. In recent years portable brick crushing machines driven by small diesel engines are getting wide popularity. High productivity, uniformity of the chips formed and high labor costs are making its use popular. Typically the entire setup is fitted on a locally built 3-wheeled steel chassis, so that it can be moved (generally using manual labor) to different construction sites. The setup consists of a single cylinder, water cooled Diesel engine, a Belt-Pulley drive for transmitting power at reduced speed, the core crushing mechanism of bricks and accessories for brick feedings and chip collection. The technical specification of a typical system is given below in table-3. Figure-3a shows the typical arrangement mounted on a 3-wheeled chassis.

Table-3: Typical Specification of a Brick Crushers

Engine Rating	13.5 kW, 2200 rpm 1000 cc
Pulley-VBelt Drive Diameter Ratios – Flywheel - Transfer Shaft Transfer Shaft - Crusher	6 : 9 inch 9: 22 inch
Crush Mechanism	Eccentric Crushing Teeth
Overall Torque Amplification / Speed Reduction	3.67 : 1
Typical Brick Crushing Rate	1500 Bricks/hour
Typical Fuel Consumption	10 liters/ 8 hour shift

The Diesel engine typically has a rated capacity of producing 13-14.5 kW power at 2200 rpm. Here all the speed reductions are done using V-belts and four pulleys of different diameters, no gears are used in the transmission. A double grooved pulley of 6 inch diameter is attached with the engine flywheel. This drives a 9 inch diameter pulley fitted at one of the in the transfer shaft. Another pulley of 9 inch diameter is fitted at the other end of the transfer shaft which belt drives a 22 inch diameter fourth pulley mounted on the main drive shaft of the brick crushing mechanism. This creates an overall speed reduction and torque amplification of about 3.67



times. Bricks are manually fed at the top of the crusher 4-6 inserted at a time. An Eccentric metal mass is attached with the drive shaft of the crusher which impacts the bricks against the jaw tooth. The high impact force initially crushes the bricks to several parts first, with vibration it falls down the crusher where a set of loosely meshing gears crush them into smaller pieces [3]. A metal net at the bottom separates the chips from the brick dust and both are collected separately.



Fig 3a. Diesel engine run brick crusher



Fig 3b. Mechanism of a Brick Crusher

Table-4: Typical monthly cost reduction of an owner per month, using a diesel engine driven system.

Engine Depreciation per month @10% of 25,000 Tk	2500 Tk.
Crusher & Chassis Depreciation per month @5% of 130,000 Tk	6500 Tk
Lubricating Oil @200 Tk/liter	1600 Tk
Cost of Investment per month	1500 Tk
Engine Maintenance	5000 Tk
Fuel Cost : Diesel 44 Taka/Liter 10 liters (8 hr day) x 30 x 44 Tk	13200 Tk
Labor Cost per month, 4 person	36000 Tk
Cost of crushing with Diesel run	66300 Tk
No. of Bricks Crushed	360000
Amount of Brick-chips Produced	32000 cft
Chip production cost per 100 cft	185 Tk
Cost Reduction /100 cft brick-chip	915 Tk

Everyday typically the machine is used in 8 hour shifts crushing about 12000 standard bricks. This produces

about 1060 cubic feet (cft) of brick chips. Manual labor cost for producing 100 cubic feet of brick-chip is about 1100 Taka. The cost of producing 100 cft of brick-chip with Diesel run system is about Taka 185. This allows a cost-reduction or profit-increase up to about 900 Taka per 100 cft of chips. Table-4 the components of the monthly cost analysis based on average value of the data collected.

#### 4. CASE-3: USE OF SMALL DIESEL ENGINES IN CONCRETE MIXING

Concrete mixing is an essential operation of modern construction work. Traditionally mixing of cement with brick/stone chips and sand was done manually using hand tools. In recent years concrete mixing machines have been deployed for this operation, which were run from electric mains supply. However the frequent power failures and unavailability of electricity in some construction sites is making diesel run versions of such machines very popular. In small diesel engine run machines the mixing operation do not depend on unreliable electric supply, which often hampers the mixing process and compromise the quality of the concrete mix due to frequent power failure. Typically the entire setup is fitted on a locally built 4-wheeled steel chassis, so that it can be moved (generally using manual labor) to different construction sites. The single cylinder, water cooled, Diesel engine replaces the electric motor and a belt-pulley drive transmits power at reduced speed to the mixing mechanism. The technical specification of a typical system is given below in table-5. Figure-4a shows the typical arrangement mounted on a 4-wheeled chassis. Some machines are fitted with a feeding hopper.



Fig 4a. Diesel engine run concrete mixer



Fig 4b. Drive mechanism of a concrete mixer

Table-5: Typical Specification of a Concrete Mixer

Engine Rating	5.6 kW, 2000 rpm 430 cc
Pulley-VBelt Drive Diameter Ratios – Flywheel – Drive Bevel	3.5 : 16.5 inch
Bevel Ratio	13 : 106
Overall Torque Amplification / Speed Reduction	43 : 1 Drum at 45 rpm
Typical Mixing Rate	1000 cft/ 8 hour shift
Typical Fuel Consumption	16 liters/ 8 hour shift

A pulley-V belt drive is used to transmit the power from the 5.6kW single cylinder diesel engine to the mixing mechanism. A 3.5 inch diameter pulley fitted with the engine flywheel drives a 16.5 inch diameter pulley on the shaft driving the 13 teeth bevel gear. The bevel gear drives the 106 teeth ring gear which finally rotates the mixing drum about a perpendicular axis at about 45 rpm. Speed is reduced 6.7 times in the belt drive and 8.2 times in the bevel gear-train. Typically about 1000 cubic feet of concrete mix is produced in a 8 hour shift, consuming about 16 liters of diesel. In the cost analysis the difference in costing is compared with same mixing machine driven by an electric motor on a month basis. So the costs associated with the – engine, fuel, accessories are compared to the motor and electricity charge. The cost elements are detailed in table-6.

Table-6: Typical monthly cost reduction of an owner per month, using a diesel engine driven system.

Engine Depreciation per month @10% of 15,000 Tk	1500 Tk.
Cost of Investment per month	150 Tk
Lubricating Oil@ 200 Tk/liter	1400 Tk
Engine Maintenance	1000 Tk
Fuel Cost : Diesel 44 Taka/Liter 16 liters (8 hr day) x 30 x 44 Tk	21120 Tk
Cost of mixing with Diesel engine	25170 Tk
Amount of Concrete-Mix Produced	30000 cft
Electricity Consumption / 8 hr shift	48 kWh
Cost of Electricity @6Tk/kWh	8640 Tk
Motor Depreciation per month @5% of 15,000 Tk	750 Tk
Cost of mixing with Elect. Motor	9390 Tk
Difference in cost per month	14380 Tk
Cost increase /100 cft mix with diesel	53 Tk
% of Cost Increase / 100 cft of mix.	20 %

The cost components are comparatively estimated considering the same concrete mixing machine is driven with a small diesel engine replacing an electric motor. Hence the cost involved for the mixing machine would be same in both cases and difference in the cost components for driving the concrete mixer will show the variation of cost. On a monthly basis the cost of driving the mixer with diesel was estimated to be 23,770 Taka, while it would be about 9,390 Taka with an electric motor. This results in an increase of about 48 Taka per 100 cubic

feet of concrete mixture.

## 5. DISCUSSION

In the first case, where small diesel engine are used for crushing sugarcane, the process was found to be cost-effective. Using the engine could eliminate the need of one additional worker, with the same level of Juice productivity. The system with a 3 kW engine required only about 2.5 liters of diesel on a typical (12 hour) day. Observation of the engine exhausts indicated that the engine was frequently subjected to high loads as the bundle of sugarcane is squeezed between the rollers. It reduced the production cost by about 2500 Taka per month, which can be considered as a profit increase also if the same selling price is maintained. Typically it is about 12% rise in the monthly profit. It should be also considered that if the customer demand reduces in several days of the month, or in parts of a day, the fuel and maintenance costs will also reduce to some extent accordingly, however the daily/monthly wage the additional worker needs to be paid at a flat rate. The tri-cycle mounted version has the advantage of changing the location of operation and do not need to pay the fixed rental charges, rather the business is shifted to convenient locations according to customer demand (eg. near the Saheed Minar in the month of February). Cost of manual labor (eg. wage of the worker) is the main parameter influencing the economic feasibility of the diesel run system. Although the economic benefit is making such systems popular, it was observed that often the food materials were exposed to diesel exhaust as a wind blows. The level of food contamination by diesel exhaust could be investigated, to determine the risk of health hazards.

In the second case, where small diesel engines are used for crushing bricks in to chips, the process was found to be very cost-effective. It also reduces the dependency on the labor skill to produce uniformity of the chips produced. The investment cost of the entire setup along with the engine was about 1,55,000 taka. Every 1000 bricks would produce about 85 cubic feet of brick chips, pricing about 1100 taka if done manually. The crushing cost using the diesel run crusher is only about 200 taka per 100 of brick-chip, which can reduce the costing or increase the profit margin very significantly, if the product price is kept the same. Cost of fuel is the main parameter influencing the economic feasibility of the diesel run system, as increase in wage will effect both systems. However to ensure this high economic advantage brick-crushing works must be available throughout the years, the chassis mounted system with wheels helps in this aspect. Although a 15 kW engine was used, the fuel consumption was typically found to be only about 10 liters per 8 hours shift. This indicates although the machine running continuously, it is only subjected to high loads for a fraction of the time, typically during the initial crushing of the bricks in between the crushing tooth. Only for this part the full strength of the relatively larger engine is actually used. The strength of the brick chips made manually and by the engine driven system was reported to be have similar strength [4].

In the third case, where small diesel engines are used

for driving a concrete machine by replacing the electric motor, the process itself was not found to be cost-effective. The production cost of the concrete mix was found to be less compared to the Diesel engine run system. The production cost per 100 cubic feet of concrete mix would increase by 58 Taka, if a diesel engine is used to drive the mixing machine. However the reliability of the electric power supply is of utmost importance in this case, since the quality of the entire lot of the concrete mixture can get compromised if the ongoing process is interrupted for a while. Hence the unreliability of mains electric power, rather than the running cost is making the use of small diesel engines popular in Bangladesh. Reliability of electric supply is the main parameter influencing the economic feasibility of the diesel run system. Another thing to be noticed here is that, although a 5.6 kW engine is used the fuel consumption rate is about 16 liters per 8 hour shift, which is much higher compared to case-2. This indicates the engine is more loaded for most of its operation time, other than loading and unloading. The chassis mounted system with wheels facilitates easier transportability of the system.

## 6. CONCLUSION

Three cases of non-conventional use of small Diesel engines in Bangladesh were investigated. In the first case of crushing sugarcane for producing juice and the second case of crushing bricks to produce brick-chips, the engines are used to replace human manual labor. While in the third case the engines replace the electric motors. For each case 10-15 systems were physically studied first, then specification and performance data were collected from selective apparently more reliable users. In all the three cases it was found that same level of productivity could be maintained with much less manpower involvement. Although the initial investment was more but for crushing of sugarcane and brick-chips the same productivity could be attained at a much lower cost. In the case of concrete mixing the process cost would increase considerably using diesel, provided reliable electric supply is available. However non-reliability of electric power supply is making the use diesel engine run concrete mixers popular. The small diesel engines are already used in huge numbers in areas like – irrigation, standby power generation and river transportation. Further use of such engines in a number non-conventional areas are getting more popular, increasing their cumulative contribution to the overall economy.

## 7. REFERENCES

1. “Statistical Year Book of Bangladesh 2008”, Published by Bangladesh Bureau of Statistics, Ministry of Planning, Govt. of Bangladesh, ISBN No. 984-508-855-4, 2008.
2. Ozkocak T., Mingyue F. and Goodwin, G., 2000, “Maceration Control of a Sugar Cane Crushing Mill”. Proceedings of the American Control Conference, Vol-4, pp. 2255-2259, 28-30 June, Chicago, IL, USA, 2000.
3. Ahmed I. and Ahmed Z. M. “Premature Deterioration of Concrete Structures - Case Study”, Journal of Performance of Constructed Facilities, Vol.-10, No.-4, pp. 164-170, November 1996.
4. Chang P. and Peng Y., M. Z., 2001, “Influence of Mixing Techniques on Properties of High Performance Concrete”, M.Sc Thesis, Department of Civil Engineering, National Chiao Tung University, Taiwan, 2001.

## 8. MAILING ADDRESS

Dr. Md. Ehsan  
Professor  
Department of Mechanical Engineering  
BUET, Dhaka-1000, Bangladesh  
Email : [ehsan@me.buet.ac.bd](mailto:ehsan@me.buet.ac.bd)

## WASTE VEGETABLE OIL AS AN ALTERNATIVE FUEL FOR DIESEL ENGINE

Soma Chakraborty<sup>1</sup>, Amit Adhikary<sup>2</sup> and M. Al Nur<sup>3</sup>

<sup>1</sup> Department of Mechanical Engineering, DUET, Gazipur-1700, Bangladesh,

<sup>2</sup> Dhaka Power Distribution Company Limited and

<sup>3</sup> Department of Mechanical Engineering, BUET, Dhaka-1000, Bangladesh

### ABSTRACT

Vegetable oils are emerging as promising fuel substitute to the conventional petroleum fuels from the view point of the energy crisis and emission problem. In this experiment waste vegetable oil is used as alternative fuel. Waste vegetable oil is used because it loses quality after being burnt several times. The waste vegetable oil's volatility and heat content is found to be lower but density and viscosity to be higher. Viscosity is considered as the main obstacles of using them directly as CI engine fuel. In the present study waste vegetable oil is preheated and blended with 20% diesel fuel and their effects on engine performance is investigated on a direct injection, 4 stroke, single cylinder diesel engine. Engine performance has been evaluated with the help of both conventional performance parameters and availability analysis. It is observed that the engine exhibits better results for higher preheating temperature and performance parameters become comparable with that of diesel when the preheating temperature reaches 80°C. The performance parameters of the blend preheated to 100°C become very close to that of diesel fuel. Exergy analysis shows similar result. Major portion of the fuel chemical availability is wasted in unaccounted factors and nearly 15% is wasted with the exhaust gas which can be directly used for preheating.

**Keywords:** Waste vegetable oil, Engine performance, Exergy analysis

### 1. INTRODUCTION

The world depends mostly on petroleum based fuels but recent concerns over the environment, unstable price and depletion of reserves of petroleum fuels have prompted the interest for development of alternative sources of energy. According to Bangladesh statistical year book 2008, Bangladesh spends about 4.5 billion U.S dollar equivalent to about taka 31 thousand crore as fuel bill for the last fiscal year. This is a huge amount for a country like Bangladesh. If this fuel bill could be reduced through discovery of any economically viable alternative fuel, the money thus spent could be used in development purposes.

The use of vegetable oils as an alternative fuel for diesel engines dates back to around a century. Due to rapid decline in crude oil reserves and increase in price, the use of vegetable oils is prompted again in many countries. Depending upon soil conditions, different nations are looking in different vegetable oils- for example, soybean oil in USA, rapeseed and sunflower oil in Europe, palm oil in Malaysia and Indonesia, coconut oil in Philippines are being considered to substitute diesel fuel [1]. In the context of depleting food production and increasing human population there is very little scope to convert edible oil into fuel in Bangladesh. Lower volatility and

higher viscosity of vegetable oils are the main impediments for possible problems encountered by the CI engines [2]. Viscosity of vegetable oil fuels can be reduced by at least four different ways:

preheating, blending, microemulsion and transesterification [3] [4]. Several investigations have been performed on bio-fuels of which most of them are concerned only on one type of modification technique to reduce viscosity and obtain the optimum point of that technique. Haq [5] has taken up attempts by studying different vegetable oil properties to use those as substitute of diesel fuel. Where kerosene was blended with 4 different vegetable oils (Rapeseed, Soyabean and Linseed) in equal volume to serve the purpose. Uddin [6] observed the behavior of SVO (Soyabean) with various performance parameters at different engine speeds and possibility of using as a substitute of diesel fuel. Morshed [7] carried out performance study of a direct injection, 4 stroke, 3 cylinder diesel engine by blending sesame oil with diesel. Where 80% sesame oil was blended with 20% diesel oil. Islam [8] carried out the performance test of diesel engine run by preheated straight vegetable oil on the basis of both the first and second laws of thermodynamics. Shaheed [9] observed mainly on the possible use of coconut-oil-based fuels as a substitute for

diesel fuel. Diaz [10] has taken up attempts to prove that vegetable oil specially coconut oil is very clean fuel with excellent combustion properties.

None of these experiments were done for waste vegetable oil. In the present work, investigations were performed to explore the optimum technique and optimum point experimentally along with the exergy analysis. The main purpose of this work was to carry out an experiment whether different grades of WVO (waste vegetable oil) could be converted into economically viable fuel. According to WHO (World Health Organization), edible oil after being burnt several time loose quality for human consumption. Such type of oil could be converted into fuel to mitigate the short fall of fuel. For this reason waste vegetable oil two times fried was collected from restaurants, was then tested for its engine related properties.

The experimental works had been divided in two parts a) fuel property testing and b) engine performance testing. Initially different properties (heating value, density, viscosity, flash point, distillation curve, carbon residue, ash content, water and sediment content) of diesel fuel were determined as base data. Those data were then compared with those of pre heated waste vegetable oil at different preheating temperatures, Waste vegetable oil and diesel fuel blends mixed at different proportions by volume and compare their properties with base data.

## 2. EXPERIMENTAL SETUP

A schematic diagram of the experimental set-up is shown in Fig. 1. Experiments are carried out using a 4 kW (6hp) single cylinder diesel engine of model R175A having a rated output is 4 kW at a rated speed of 2400 rpm. A water brake dynamometer has been used to apply desired load on the engine.

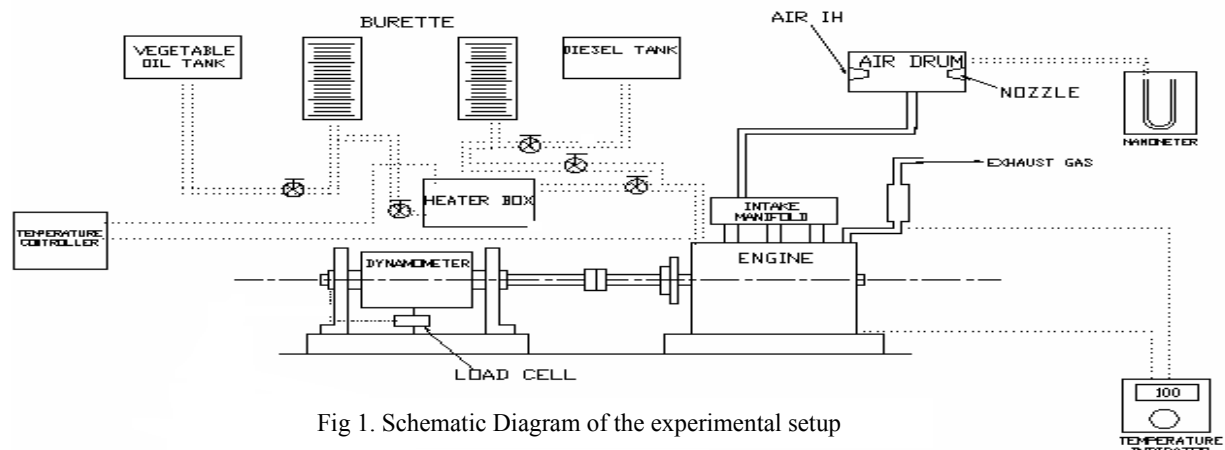


Fig 1. Schematic Diagram of the experimental setup

Initially the test engine is run by diesel fuel at three different speeds of 2400, 2200 and 2000 rpm and all the necessary parameters are recorded and different performance parameters are calculated to check the engine's credibility as a test engine. Then the performance tests are carried out using 100% waste vegetable oil preheated at 80°C and 100°C and 80% waste vegetable oil blended with 20% diesel preheated at 100°C. Engine speed has been maintained within  $\pm 5$  rpm and the temperature was maintained within  $\pm 2^\circ\text{C}$  of the

desired temperature. In this study, BS standards for engine performance test BS 5514: Part I: 1982, equivalent to ISO 3046 and J 1349, ISO and SAE standards for the same respectively, has been followed.

Any other additional guidelines required were taken from the procedures used by Plint and Böswirth [11]. A water brake type dynamometer AN3e model is used to apply desired loads and to measure engine brake power. Lubricant temperature is measured using a thermocouple probe inserted into the lubricant oil sump. All temperatures are measured using digital meter (OMEGA-K), connected to different K-types probes via a selector switch. Diesel and waste vegetable oil supply systems have been modified, so that fuels could be supplied from a graduated burette instead of the fuel tank when needed. Fuel consumption rate is recorded observing the time by a stop watch for every 50cc of fuel. Air flow rate is measured by drawing air through two circular nozzles of 13 mm diameter ( $C_D = 0.92$ ) in accordance with the Plint and Böswirth [11] with an air drum of standard size that is connected to the engine air inlet and pressure drop is measured by means of a manometer, using water as a manometric fluid. The mass flow rate of air is calculated by using the pressure drop in appropriate equation.

## 3. RESULTS AND DISCUSSION

In Fig. 2, variations of fuel densities with temperature are shown. It is found that waste vegetable oil density is 10% higher than that of diesel. When waste vegetable oil is blended with diesel and heated up to 100°C, its density become less than that of diesel fuel at 20°C.

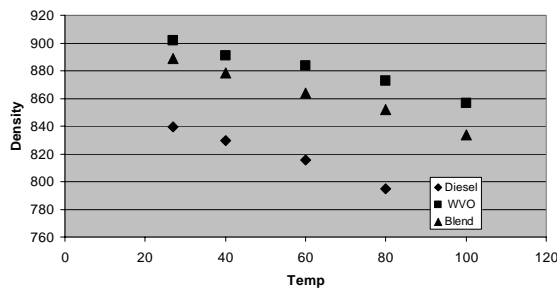


Fig 2. Variations of densities of oil with temperature.

In Fig. 3, viscosities of oils at different temperature are presented. It is seen that the viscosity of waste vegetable oil is nearly 10 times higher than that of diesel fuel at 20°C but when waste vegetable oil is heated up then its viscosity reduces significantly and at 100°C, viscosity of the both waste vegetable oil and its blend become less than that of diesel fuel at 20°C.

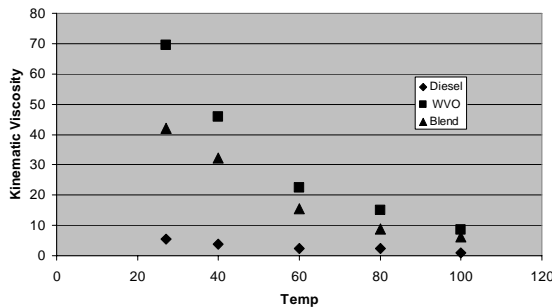


Fig 3. Effect of temperatures on the viscosities of fuels

Fig. 4 shows the volatility of diesel and waste vegetable oil. It is seen that the volatility of waste vegetable oil is much lower than that of diesel fuel but the initial boiling of waste vegetable oil starts earlier than diesel fuel.  $T_{10}$ ,  $T_{50}$  and  $T_{90}$  points on the curves are of special interest. Lower  $T_{10}$  temperature signifies easy starting and a lower  $T_{50}$  point allows the engine to warm up and gain power quickly and  $T_{90}$  temperature associated with crankcase dilution and fuel economy. If the  $T_{90}$  temperature is too high, the larger fuel molecules condense on the cylinder liners and is passed down into the lubricating oil instead of burning. With waste vegetable oil,  $T_{90}$  point is not achievable as chemical decomposition of the fatty acids start before reaching that point.

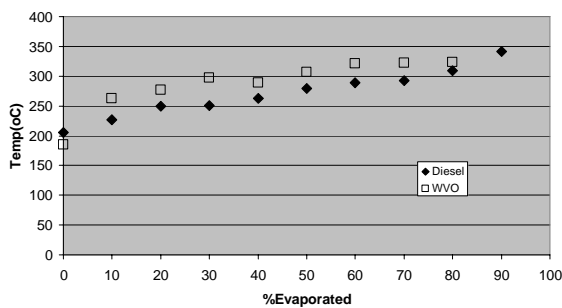


Fig 4. Distillation curves

In order to judge the potentiality of using waste vegetable oil as an alternative to diesel fuel, the experiments are carried out at three different speeds (2400, 2200, and 2000) under variable loading condition using diesel fuel. It is seen that for the same output power, air flow rate increases with engine speed due to the fact that the swept volume per unit time is higher for higher engine speed. Air induction of engine depends on the ratio of intake and exhaust pressures, residual gas volume, intake air velocity, engine speed, size and shape of the passages. Residual gas fraction effect is less in CI engine due to higher compression pressure. As the gas velocity increase pressure drop also increase and breathing reduces. Again, at higher engine speed, intake system or a part of the intake system is choked and once this occurs, further increase in speed does not increase the flow rate significantly and so, volumetric efficiency,  $\eta_v$ , decreases. Again at higher speed, air flow rate per cycle decreases due to short cycle time.

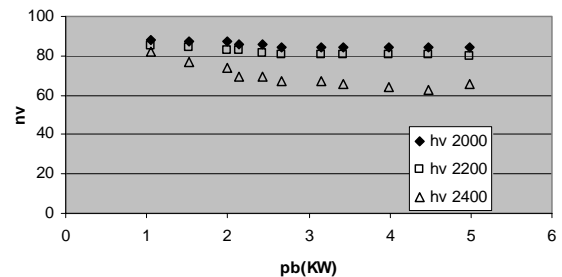


Fig 5. Variation of volumetric efficiency with engine brake power run by diesel

In diesel engine, higher power is achieved by increasing the fuel flow rate. Also, the fuel consumption rate increases with speed. With increase of speed the frictional loss increases and to overcome that more power required inside the cylinder and so, fuel flow rate increases with speed. At part load, more fuel is consumed for higher engine speed but near the rated power, the engine consumes almost the same amount of fuel to generate the same amount of power for all three speeds. This behavior is directly related to friction. Engine friction is either related to engine speed or to peak engine cylinder pressure. At low loading condition the effect of engine cylinder pressure is insignificant and frictional losses are dictated by the energy consumed by the shafts, valves and pumps. These losses increase with the speed of the engine. So, at low loading conditions fuel consumption is higher at higher speed. However, at higher load, the effect of peak cylinder pressure becomes more significant. For the same power output, slower speed generates more pressure and frictional loss increases and so, at higher loading fuel consumption rates become almost the same for all the three speeds. Stoichiometric combustion of diesel fuel requires 14.30 A/F ratio but from experiment it is seen that the air fuel ratio at low load is nearly 55. With the increase of load, A/F ratio reduces and up to 45% of the rated power it reduces steeply. The falling trend continues over the entire range but a lower rate. In CI engine, output power

is increased by increasing the fuel flow rate and at the same time the air flow rate decreases with the increase of load which has already been mentioned. A ‘cross over’ point is observed almost at the middle of brake power  $P_b$ . Variations of brake specific fuel consumption,  $bsfc$  with  $P_b$  at different speed is shown in Fig.6. It is seen that  $bsfc$  is high at low loads and its value decreases with the increase of brake power until the rated output of the engine is reached. Beyond that the value increases again. At lower load, A/F ratio is much leaner. Also that the residual gas temperature and wall temperature is lower and ignition delay period is higher and so, fuel utilization efficiency is less. So,  $bsfc$  value is higher at lower load again at higher load beyond the rated point all the fuel is not burned properly due to scarcity of air. Energy input in the fuel is lost in the form of incomplete combustion that results in higher  $bsfc$ .

It is also observed that, for the same output power, at part load condition  $bsfc$  is higher for the higher rpm but at rated or higher than rated rpm  $bsfc$  is independent of speed. The main reason here is the friction which has been already mentioned earlier.

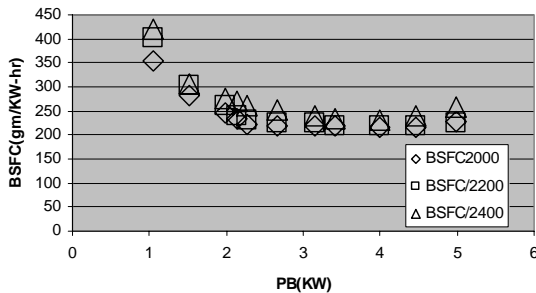


Fig 6. Variations of brake specific fuel consumption with brake power run by diesel fuel

The  $bsfc$  is a measure of overall engine efficiency,  $\eta_b$  and these quantities are inversely related. So, that lower the values of  $bsfc$  higher the overall efficiency of the engine. However, for different fuels with different heating values, the  $bsfc$ 's values are misleading and hence brake thermal efficiency is employed when the engines are fueled with different types of fuels [5]. In Fig.7 brake thermal efficiency,  $\eta_b$  is plotted against the brake power,  $P_b$  for different speeds

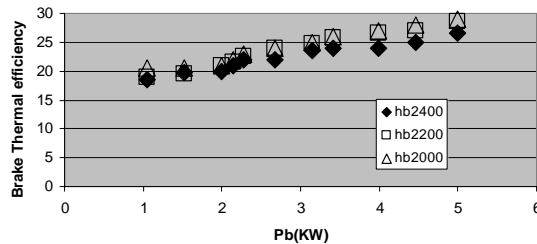


Fig 7. Variations of brake thermal efficiency with engine brake power run by diesel fuel.

The brake thermal efficiency,  $\eta_b$  of the test engine is

plotted against brake mean effective pressure ( $b MEP$ ) in Fig. 8. Engine performance parameters presented as a function of engine brake power is unique for a particular engine at a particular speed. The performance curves for engines of different sizes or for the same engine at different speeds deviates far from each other.

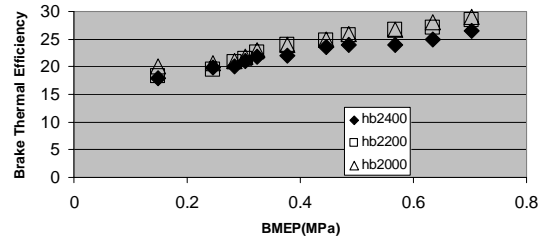


Fig 8. Variations of brake thermal efficiency with brake mean effective pressure run by diesel fuel.

The availability (or exergy) input to an internal combustion engine is contained in its fuel chemical availability. In CI engines, the input availability contained in fuel is converted into: 1. useful brake output availability 2. availability transferred to cooling medium 3. availability transferred to exhaust gases 4. availability destroyed in engines accessories turbocharger, cooling fan, etc. and 5. availability destroyed due to friction and radiation heat loss to surroundings. Szargurt and Styrylska [12] developed the following correlation for computing the chemical availability of liquid hydrocarbons having the general formula  $C_xH_yO_zS_w$ :

$$A_{in} = Q_{in} \left[ 1.0374 + 0.0159 \frac{y}{x} + 0.0567 \frac{z}{x} + 0.5985 \frac{w}{x} \left( 1 - 0.1737 \frac{y}{x} \right) \right] \quad (1)$$

For diesel fuel,  $A_{in} = 1.06489 Q_{in}$ , For waste vegetable oil,  $A_{in} = 1.0724 Q_{in}$ . In the present analysis, due to scarcity of thermo chemical data (specially for waste vegetable oil) ‘percent brake output availability’,  $A_{shaft}$  is used in lieu of second law efficiency,  $\eta_{II}$ . The availability is destroyed or lost due to different irreversibility such as combustion losses, friction losses, heat loss to lubricating oil, power consumed by auxiliary equipment (axial blower in the present test engine), radiation losses, fluid flow losses, etc. Availability transfer to cooling medium (water in this case) has been included into the above category. Availability destruction due to all these sources are combinedly expressed by  $A_{uncounted}$ . This is justified by the fact that availability transfer to cooling medium in an water-cooled engine is only a fraction (less than 2.5%) of the availability input to the engine [13]. Availability destroyed in the exhaust gas is evaluated separately.

In Fig.9, the portion of the input availability converted into brake output power denoted by  $A_{shaft}$  is shown. It may be noted from this figure that at higher  $b MEP$ , availability output show a slightly declining trend after the rated output



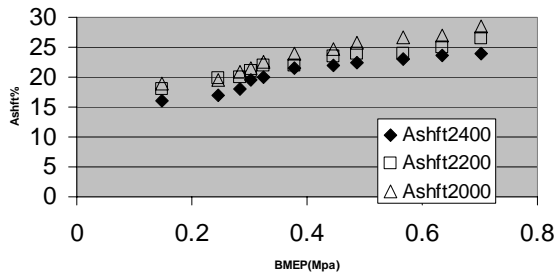


Fig 9. Variations of percent availability output at shaft with engine brake mean effective pressure run by diesel fuel.

The availability input lost in different processes of the engine is shown in Fig. 10. It may be seen that the availability transfer to the exhaust gases (denoted by  $A_{eg}$ ) increases with increasing  $bme_p$ , which is quite a small portion of the availability input, the maximum level having reached approximately 12% of  $A_{in}$ . In contrast, the availability destruction in friction, cooling, combustion etc. (denoted by  $A_{unaccounted}$ ) shows a declining trend. That is, with the increase in  $bme_p$  as  $A_{eg}$  goes up  $A_{unaccounted}$  continues to go down although its extent is far greater. However, the opposite trends of these lines facilitate finding an 'optimum operating point' from the graph. The optimum operating point is around 0.45 MPa

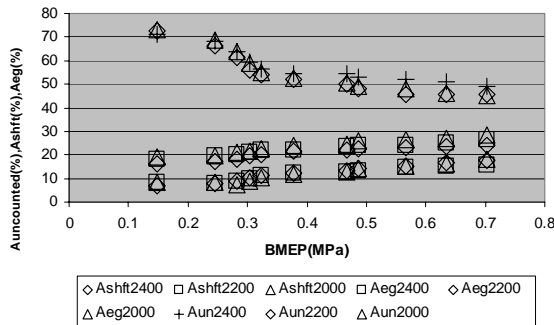


Fig 10. Level of different types of availabilities associated with engine operation as a function of brake mean effective pressure run by diesel fuel.

The comparison of  $\eta_b$  with  $A_{shaft}$  is shown in Fig. 11 to obtain a precise contrast of the two, the curves are plotted at the same plane for a rated speed of 2400 rpm. Observation reveals that  $A_{shaft}$  is somewhat less than  $\eta_b$  throughout the entire range. Both the graphs substantiate the fact that the capability of an engine to utilize the available energy successfully is rather less than that articulated in brake thermal efficiencies. The major reason behind this is that the fuel chemical availability,  $A_{in}$  is about 3.35 to 7.25% as higher (depending on the chemical formula of the fuel) than the heat input  $Q_{in}$  calculated from the lower heating value and this available energy can not be interpreted into shaft work due to inherent irreversibilities.

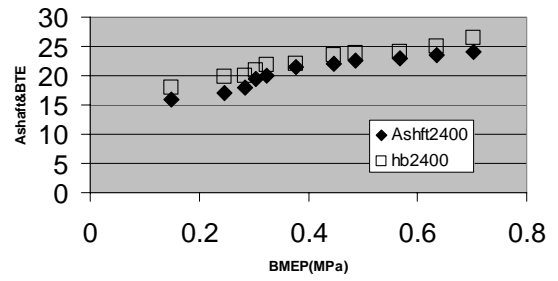


Fig 11. Comparison of percent availability output at shaft with corresponding brake thermal efficiency as a function of brake mean effective pressure run by diesel fuel at 2400 rpm.

Fig. 12, shows the variations of brake specific fuel consumption as a function of brake power for two different preheat temperature 80 °C and 100 °C of waste vegetable oil as well as for 80% waste vegetable oil and 20% diesel blend preheated to 100 °C is compared with that of diesel fuel. From this figure, it is evident that, the specific fuel consumption is higher in the case of vegetable oils. Vegetable oil's heating value is much lower than that of diesel fuel. Again high viscosity and poor volatility of the waste vegetable oil result in poor atomization and mixture formation which, in turn, increase the fuel consumption to maintain the power.

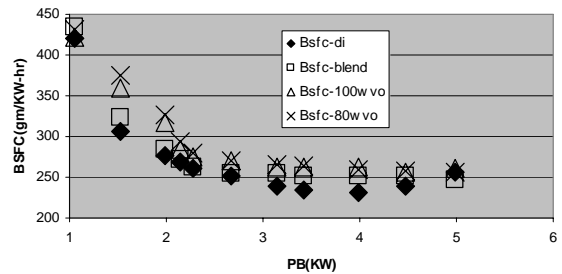


Fig 12. Comparison of the bsfc of different fuels at 2400 rpm as a function of brake power.

With the increase of preheat temperature viscosity of oil greatly reduces to help better fuel injection, atomization and mixing quality of the charge and so, fuel consumption rate decreases. But at high load the temperature effect becomes less significant. At higher load, fuel flow rate and velocity are dominated by the combustion temperature and hence fuels arrive at the point of injection of any preheated temperature with about the same temperature, providing similar injection conditions. Again a blend of 20% diesel and 80% waste vegetable oil preheated to 100°C does not increase the efficiency over 100°C preheated waste vegetable oil. It may be due to the fact that at that temperature extra fine spray formation occurs which reduces penetration and mixing with air offsets the decrease of consumption of fuel.

In Fig. 13, a variation of brake thermal efficiency is shown for the above mentioned conditions. It is seen that the brake thermal efficiency of diesel fuel is lower than that for the waste vegetable oil and the blend preheated at

100°C. Vegetable oil's ignition delay period is also longer than diesel and so, pressure rise inside the cylinder is lower and the frictional loss due to pressure is also less.

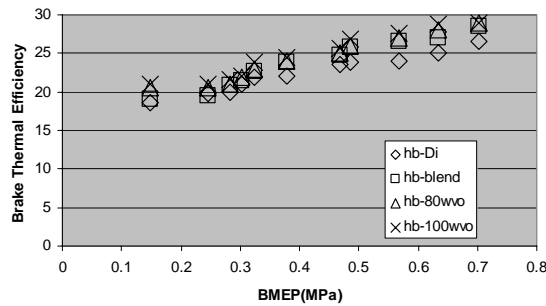


Fig 13. Comparison of the brake thermal efficiency of different fuels at particular speed as a function of brake mean effective pressure.

Brake thermal efficiency as a function of engine brake power is plotted in Fig. 14. The trend of the curve is similar but from the figure it is clear that some power losses are experienced for fuels other than diesel. For each case, the highest efficiency is observed at lower rpm. Ignition delay period is much higher for waste vegetable oil and so, at higher speed fuel gets less time for heat release or heat release occurs late in the expansion stroke and so, effective use of heat becomes less.

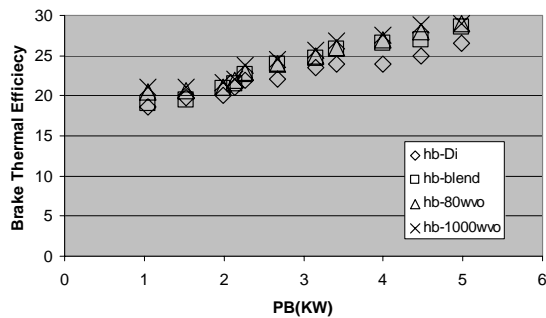


Fig 14. Variations of brake thermal efficiency for 2400 rpm at varying loads for a particular fuel.

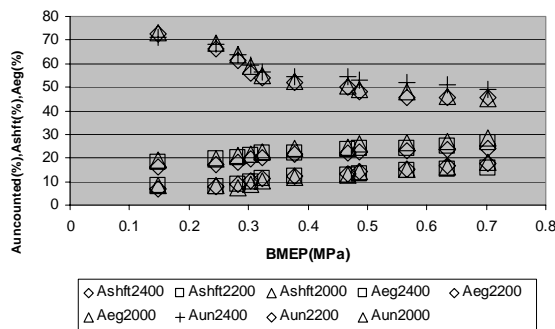


Fig 15. Variations of percent available at shaft and destruction of availability as a function of brake mean effective pressure running by 100°C waste vegetable oil and diesel blend.

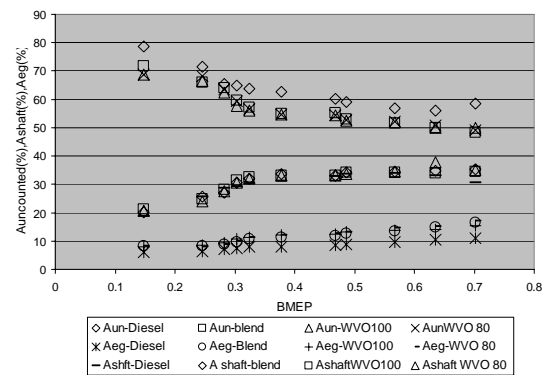


Fig 16. Variations of percent available at shaft and destruction of availability as a function of brake mean effective pressure running for 2400 rpm.

#### 4. CONCLUSION

The obtained results may be summarized to make the following conclusions:

- (1) Without preheating, waste vegetable oil can not be used directly.
- (2) Compared to diesel fuel operation, a little amount of power loss occurs with waste vegetable oil operation.
- (3) Fuel consumption becomes similar for heated and unheated oil operations at higher load.
- (4) At lower rpm operation waste vegetable oil exhibits better results for any preheat temperature.
- (5) The heating energy of waste vegetable oil is almost the same as that of diesel when preheating temperature is 80°C or more than that.
- (6) Preheating the blend of waste vegetable oil with 20% diesel fuel exhibits almost the same result when waste vegetable oil is preheated to the same temperature.
- (7) Availability destroyed with exhaust gas increases with load and is about 15% of the input availability at rated condition. This may be used directly for preheating purpose.
- (8) Major portion of the available energy is lost due to friction, cooling, combustion etc., which is mentioned here as unaccounted factors. So, for engine performance improvement much focus required here.

#### 5. REFERENCES

1. Srivasata, A. and Parasad, R., "triglycerides based diesel fuels," Renewable and Sustainable Energy Reviews 4: 111-133, 2000.
2. Bhattacharyya, S., Reddy,C.S., "Vegetable oils as fuels for internal combustion engines: A Review," Journal of Agriculture Engineering, 57: 157-166,1994.
3. Ali,Y. and Hanna, M. A.," Alternative diesel fuels from vegetable oils," Bioresource Technology, 50: 153-163,1994.

4. Shay, E.G., "Diesel fuel from vegetable oils: status and opportunities," *Biomass and Bioenergy*, 4: 227-242, 1993.
5. Haq M .Z., "Study of the Properties of Vegetable Oil as an Alternative to Diesel fuel" Unpublished M.Sc. Thesis, Dept of ME, BUET, Dhaka, 1995.
6. Uddin M.S., "Performance of a Diesel Engine Using Preheated Vegetable Oil as an Alternative Fuel " Unpublished M.Sc. Thesis, Dept of ME, BUET, Dhaka, 2005.
7. Islam M.M., "Energy –Exergy analysis of a Diesel Engine running on Preheated Straight Vegetable Oil " Unpublished M.Sc. Thesis, Dept of ME, BUET, Dhaka, 2006.
8. Morshed A.K.M, "Sesame Oil as an Alternative Fuel for Diesel Engines in Bangladesh" Unpublished M.Sc. Thesis, Dept of ME, BUET, Dhaka, 1995.
9. Shaheed, A. and Swain, E., "Combustion Analysis of Coconut Oil and Its Methyl Esters in a Diesel Engine" *Proceedings of the I MECH E Part A Journal of Power and Energy*, Volume 213, Number 5, 1 October 1999, pp.417-425(9)
10. Diaz , R.S., "Coconut Oil as Diesel Fuel vs Cocobiodiesel" *Biodiesel Featured Article*, July 2000
11. Plint, M. A., and Bösowirth, L., "Mechanical Engineering Thermodynamics: A laboratory course", Charles Giffin & Company Ltd., London, 1986.
12. Rakopoulos, C.D. and Giakoumis, E. G., "Second-law Analyses Applied to Internal Combustion Engines Operation", *Progress in Energy and Combustion Science*, vol. 32, pp. 2-47, 2006.
13. Al-Najem, N.M. and Diab, J.M., "Energy-Exergy Analysis of A Diesel Engine", *Heat Recovery Sytems & CHP*, vol. 12, No. 6, pp. 525-529, 1992.

## 6. MAILING ADDRESS

Soma Chakraborty  
 Department of Mechanical Engineering,  
 DUET, Gazipur-1700, Bangladesh

## MORPHOLOGICAL STUDY OF THE PARTICULATE MATTER SAMPLED FROM THE EXHAUST OF A DIESEL ENGINE IN DIESEL AND DUAL FUEL MODES

Nirendra N Mustafi<sup>1</sup>, Robert R Raine<sup>2</sup>

<sup>1</sup>Dept. of Mechanical Engineering, Rajshahi University of Engg. and Tech., Rajshahi, Bangladesh

<sup>2</sup>Dept. of Mechanical Engineering, The University of Auckland, Auckland, New Zealand

### ABSTRACT

The particulate matter (PM) of a diesel engine operated on diesel and dual fuel modes are sampled and characterized by size, morphology and fractal geometry by using scanning electron microscopy (SEM) and transmission electron microscopy (TEM). The gaseous fuels used are natural gas and synthetic biogas. The engine operating condition is kept the same to compare the results between diesel and dual fuel PM. SEM images yield PM agglomerate number size distributions and a shape description. TEM images provide the primary particles size distribution in PM agglomerates and the fractal dimensions. Long chainlike PM agglomerates appear for the diesel PM, whereas those for dual fueling are found to be smaller and rounder. All of the measured PM appear to have a bi-modal number size distribution. The average primary particle diameter increases for dual fuel PM (ranging from 26.9 to 29.5 nm) compared to diesel PM (26.4 nm). The average primary particle diameter tends to increase for biogas fueling. Higher fractal dimensions (from 1.73 to 1.88) are obtained for dual fuel PM compared to diesel PM (1.69) implying that diesel PM are more chainlike and elongated. Based on the obtained results, a conceptual model is constructed to understand the phenomena of PM formation for the two types of engine fueling.

**Keywords:** Dual Fuel Engine, Particulate Matter, Morphology.

### 1. INTRODUCTION

Diesel engines are efficient and widely used in both stationary and mobile applications. However, diesel engines emit harmful particulate matter (PM). Exposure to diesel PM occurs within many different occupational groups and diesel PM can make an important contribution to ambient PM [1]. Due to their alleged adverse health and environmental effects, diesel PM have been of great concern in recent times.

Gaseous fuels in diesel engines operate in dual fuel mode where the main energy comes from the gaseous fuel and a minimum amount of diesel acts as the ignition source. A diesel engine can easily be modified to dual fueling condition and the engine can switch over either mode of operation under load. Since diesel engine operates at high compression ratios, it permits the use of low energy content gaseous fuels such as biogas. The benefits of using biogas are two fold: substitution for diesel fuel and proper use of green house gas, methane. The use of natural gas in diesel engines is already in practice because of its availability in many parts of the world. Biogas is a renewable fuel, on the other hand, can be produced from organic wastes.

In addition to gravimetric measurements, PM characterization such as number, and size distributions, shape or fractal dimension is also important to provide

better understanding of particle formation and removal processes. The size and structure of PM influence their atmospheric transport properties, optical properties, deposition behavior, depth of penetration into the lung etc. [2-3].

In diesel engine combustion soot particles are formed as a result of incomplete combustion in fuel rich zones and hydrocarbons are adsorbed or condensed onto their surfaces afterwards [4-5]. Numerous research works are available relative to diesel engine PM emissions and their characterization, research gaps remain, in the case of measurements of PM generated by dual fuel engines.

A light duty diesel engine modified to dual fuel operation is used in this research. Electron microscopy techniques have been used to characterize PM physically and to investigate their morphology as used before [2,6,7]. In this study, scanning electron microscopy (SEM) is used to determine the number size distributions, and the shape of the PM sampled from the engine exhaust. The shape of PM is characterized using a shape factor (SF) as described in [7]. Transmission electron microscopy (TEM) is used to investigate the primary particle diameters and the fractal dimensions of the sampled PM agglomerates. Results are compared between diesel and dual fuel conditions. Based on the

above observations, possible growth mechanisms for the PM agglomerates are identified. Finally, a conceptual model has been constructed to differentiate the insights of PM formation processes between the two types of engine fueling.

## 2. EXPERIMENTAL PARTS

### 2.1 Engine and Fuels

The investigation was carried out on a Lister Petter, direct injection, diesel engine modified to run in either diesel or dual fuel modes (Table 1). The modification is simple and is described in details in [8-9]. Measurements were taken at two different engine loads: low load (3 Nm) and high load (28 Nm) for diesel fueling and only at high load (28 Nm) for dual fueling. For the dual fueling, the amount of diesel fuel was kept the same as for the diesel low load condition and the desired output torque was obtained by increasing the amount of gas flow into the cylinder. About 62% (by volume) diesel fuel was replaced during dual fueling.

New Zealand low sulfur diesel fuel (~50 ppm sulfur) was used for the experiments. Natural gas (NG) was obtained from the pipeline supply and the detailed composition is provided in [9]. Biogas was prepared by mixing NG with CO<sub>2</sub> in order to obtain different types of biogas: biogas-1 (80% CH<sub>4</sub> and 20% CO<sub>2</sub>); biogas-2 (67% CH<sub>4</sub> and 33% CO<sub>2</sub>); and biogas-3B (58% CH<sub>4</sub> and 42% CO<sub>2</sub>).

### 2.2 PM Sampling

PM Samples were collected for electron microscopy analysis using a partial flow dilution system with a dilution ratio of ~10:1; further details of the system are provided in [9]. Collected sample filters were preserved in Petri dishes and sealed carefully until microscopy analysis.

### 2.3 SEM Analysis

For SEM analysis, PM samples were collected on 70 mm Isopore™ polycarbonate membrane filters with 0.4μm pore sizes [10]. These filters have low contrast and very smooth surfaces, which make them suitable for SEM analysis [6]. Prepared samples were examined using a Phillips XL-30S Field Emission Gun. At least 30 SEM images were recorded for each PM sample in this study.

### 2.4 TEM Analysis

Impaction sampling was used for TEM analysis where the TEM grids holder (a thin perforated strip of “post-it”) is attached onto a gravimetric filter through which the diluted exhaust gas passes the existing partial

Table 1: Engine specifications

Engine type	Single-cylinder, DI, water- cooled
Bore/Stroke	87.3/110 (mm)
Swept volume	659 (cm <sup>3</sup> )
Con. rod length	231.9 (mm)
Compression ratio	16.5
Inj. timing by spill	28°bTDC
Engine speed	1750 rpm

flow dilution tunnel system [11]. A CM12 TEM (Philips, FEI Company, Netherlands) was used to examine the PM samples and was operated at an accelerating voltage of 120 kV. TEM images were observed and digitized with the associated image acquisition system equipped with a Model 792 Bioscan digital camera (Gatan Inc., USA) and stored as 1024x1024 pixel computer images. Sufficient images were recorded at both lower and higher magnifications to count about 200 PM agglomerates and at least 300 primary particles respectively for any type of PM sample.

### 2.5 Image Analysis

Digital images obtained from SEM and TEM examinations were analyzed using public domain image processing software ImageJ, Version 1.38l [12]. ImageJ yielded counting, measurement of projected areas ( $A_a$ ), perimeters ( $P$ ), projected area equivalent diameters ( $D_p$ ), fitted best-fit ellipses and measurement of maximum projected length ( $L_{max}$ ) and width ( $W_{max}$ ) of the PM agglomerates. It also provided the means to determine the primary particle diameter ( $d_p$ ) from agglomerates.

## 3. RESULTS AND DISCUSSION

### 3.1 Distribution of Primary Particle Diameters

From the TEM micrographs, primary particles with distinguishable boundaries in the PM agglomerates were selected randomly and their diameters were measured. Results are presented for different engine operating conditions in Fig. 1. The average primary particle diameters,  $\bar{d}_p$ , measured for different fueling, range from 25.9 to 29.5 nm, which are in the range of those obtained for light duty diesel particulates in [13].

As the load increases from low to high, during diesel fueling, the combustion temperature as well as the exhaust temperature remains sufficiently high to provide relatively high oxidation rate of the growing PM and thus reduced  $\bar{d}_p$  is obtained in the latter case [13-14].

The difference in  $\bar{d}_p$  values between diesel high load and dual fuel conditions can be attributed to the combined effects of combustion temperature and duration of combustion. Like high combustion temperature, longer combustion duration can also cause a reduction of the primary particle diameter in diesel high load condition. Higher value of  $\bar{d}_p$  for higher CO<sub>2</sub> containing biogases can be speculated as the negative impact on PM oxidation rate due to the presence of high proportion of diluent CO<sub>2</sub> in fuel. Because CO<sub>2</sub> in biogas results in a low flame temperature as well as a low oxygen content inside the cylinder.

### 3.2 PM Number Size Distribution

SEM images of PM agglomerates were analyzed to yield the projected area equivalent diameter ( $D_p$ ), which is defined as the diameter of a circle having the equal area of the projected agglomerate. Figure 2 shows the measured PM (agglomerates) number size distribution with fitted bimodal lognormal distributions for different engine operating conditions. A bi-modal number size

distribution is obtained irrespective of type of fueling.

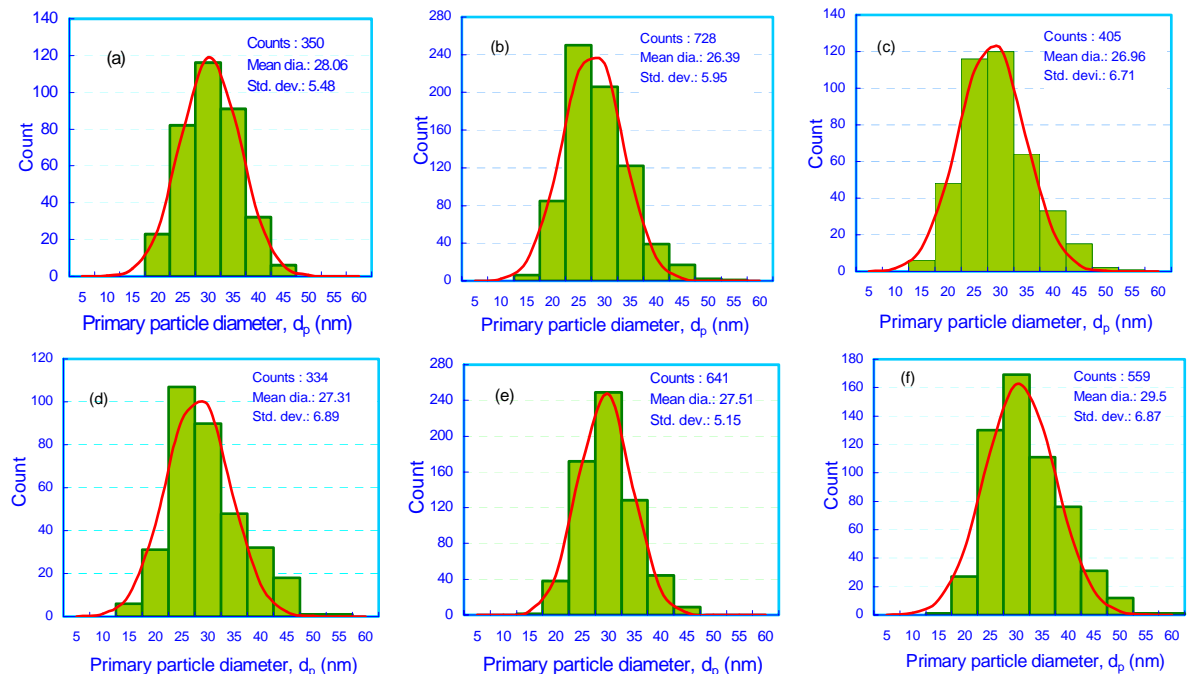


Fig 1. Primary particle size distributions at different engine fueling conditions: (a) diesel low load (3 Nm), (b) diesel high load (28 Nm), (c) diesel-NG (28 Nm), (d) diesel-BG1 (80% CH<sub>4</sub> and 20% CO<sub>2</sub>); (28 Nm), (e) diesel-BG2 (67% CH<sub>4</sub> and 33% CO<sub>2</sub>); (28 Nm), and (f) diesel-BG3B (58% CH<sub>4</sub> and 42% CO<sub>2</sub>); (28 Nm).

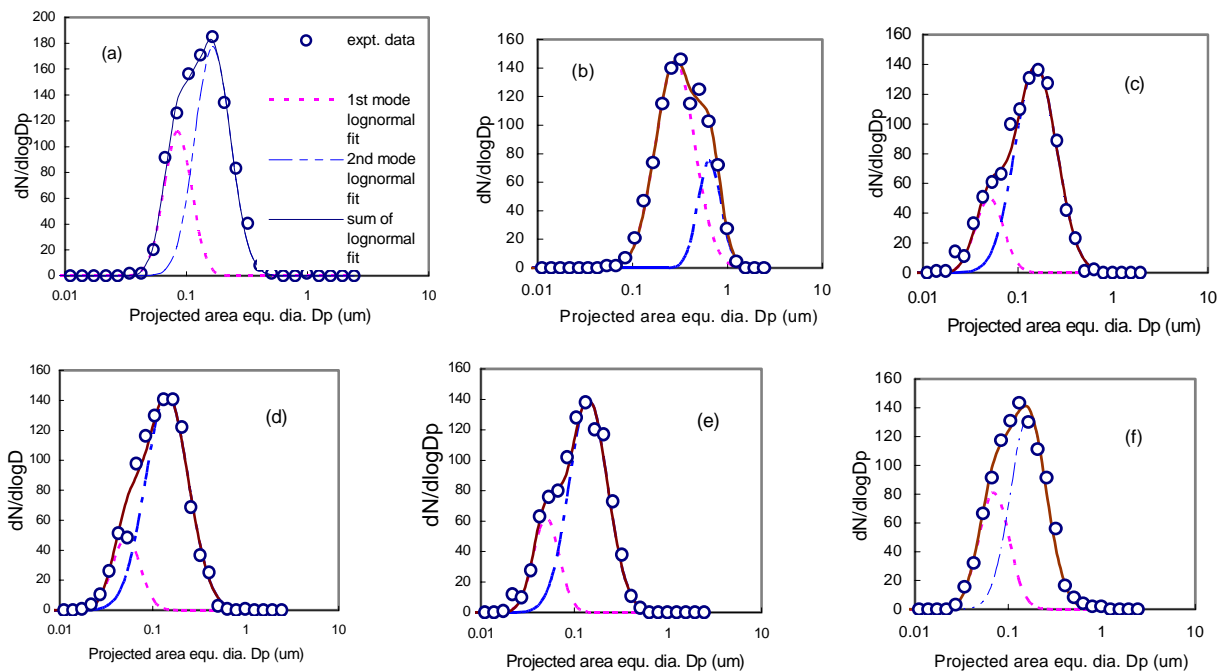


Fig 2.. Number size distribution with fitted bimodal lognormal distribution of the PM agglomerates measured for different engine operating conditions: (a) diesel low load (3 Nm), (b) diesel high load (28 Nm), (c) diesel-NG (28 Nm), (d) diesel-BG1 (80% CH<sub>4</sub> and 20% CO<sub>2</sub>); (28 Nm), (e) diesel-BG2 (67% CH<sub>4</sub> and 33% CO<sub>2</sub>); (28 Nm), and (f) diesel-BG3B (58% CH<sub>4</sub> and 42% CO<sub>2</sub>); (28 Nm). CMD = count median diameter; GSD = geometric standard deviation.

All the measured PM on the SEM filters appear to be in the range of fine particles,  $D_p < 2.5 \mu\text{m}$ , which are composed of ultrafine particles,  $D_p < 0.1 \mu\text{m}$  and nanoparticles  $D_p < 0.05 \mu\text{m}$  [5]. It is observed from Fig. 2 that PM agglomerates size measured on SEM filters has mainly 2 modes of distributions: nuclei ( $D_p$  less than  $0.1 \mu\text{m}$ ) and accumulation mode ( $0.1 < D_p < 1.0 \mu\text{m}$ ) except the diesel (high) where PM size modes are found to be an accumulation and an almost coarse mode ( $D_p$  larger than  $1.0 \mu\text{m}$ ). However, no distinguishable nuclei mode particles are observed for diesel (high) PM. This can be attributed to the fact that a smaller amount of soluble organic fraction (SOF) or volatile fraction (VF) is produced during diesel high load condition as compared to either diesel low load or dual fueling [8], which can contribute to the nuclei mode particles in the exhaust.

The median diameter for dual fueling in nuclei mode region is found to be about  $0.05 \mu\text{m}$ . The second peak (accumulation mode) of the lognormal fits in Fig. 2 are observed at  $D_p = 0.16 \mu\text{m}$  to  $0.14 \mu\text{m}$  for diesel low load and dual fuel operation. But for diesel high load condition, the peak of the accumulation mode is observed at  $D_p = 0.28 \mu\text{m}$ . This indicates that the PM agglomerates measured on SEM filters have significantly larger median diameter for diesel (high) fueling compared to other fueling conditions for the same mode of particles. These results are in good agreement with the previous results reported in [4,15].

### 3.3 Shape Analysis of the Agglomerates

The shape factor, SF, is used to define the external shape of PM agglomerates appear on SEM filters. This SF is calculated from the minor and major axes of the best-fitted ellipses around PM agglomerates [7]:

$$SF = (\text{minor axis length} / \text{major axis length}) \quad (1)$$

SF is sensitive to particulate elongation. SF close to 1.0, indicates that the particles are nearly spherical and SF close to 0.1 indicates that the particles are long-chained or elongated [7].

Figure 3 presents the shape factor of the measured PM for diesel and dual fueling. Comparing the results between diesel high load and dual fuel PM, a significant difference in the nature of the SF curves is noted. In the case of dual fuel operations, all the peaks are close to 0.7, compared to diesel (high) at about 0.5. This indicates that the PM measured for dual fueling are more nearly spherical compared to diesel (high) fueling.

In the coagulation processes, spherical solid soot particles collide with each other and coalesce and form a larger primary spherical particle. When the rate of particle growth slows down, continued collision between the spherical primary particles results in agglomeration to form large clusters of primary particles, which appear to be chain-like. The rate of agglomeration is proportional to the square of the primary particle number density [16]. The major source of PM formation can be

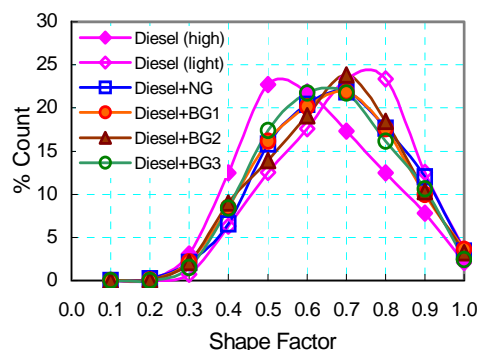


Fig 3. Shape factor (SF) trends of the PM collected on SEM filters for diesel and dual fueling (1750 rpm, and pilot = 0.6 kg/hr for dual fueling).

attributed to the diesel fuel injected into the cylinder. The use of gas during dual fueling is thus expected to produce little PM compared to the diesel (high) as diesel injection is minimized. As number density of the primary particles formed in the case of diesel (high) fueling will be much higher than that for diesel (low) or dual fueling, the corresponding rate of production of agglomerates is also higher in the first case.

### 3.4 Fractal Morphologies of the Agglomerates

Although the primary particles are nearly spherical, the sizes and shapes of PM agglomerates vary significantly. The complex morphology of the agglomerates can be characterized as fractals. PM fractal dimensions are calculated for the different engine operating conditions. The necessary formula and the associated assumptions used in calculation are presented in the Appendix. Fractal dimension based on maximum projected length ( $D_{FL}$ ) is used in this study instead of fractal dimension based on radius of gyration ( $D_f$ ). The two fractal dimensions,  $D_{FL}$  and  $D_f$ , have identical values and can be used interchangeably [3].

Figure 4 shows an example of the results as a plot of the number of primary particles in an agglomerate,  $N$  versus  $L_{max}/\bar{d}_p$  on logarithmic scales (where fractal dimension  $D_{FL}$ , is represented by the slope). Table 2 presents the fractal dimensions for the PM measured for different engine operating conditions.

It can be observed that the fractal dimension values ( $D_{FL}$ ) are in the range 1.69 to 1.88 among which 1.72 is for diesel (low) and 1.69 for diesel (high) fueling. Researchers [13,17] measured fractal dimensions of sampled PM in the range of 1.46-1.70 for a light duty diesel engine while the engine was operated at different low to high speeds and loads. These values are relatively lower than the values obtained in the present study. The main reason is that their calculation did not consider the primary particles overlapping which is an obvious case in any agglomerate. Primary particles overlapping [18] was considered in this study to calculate the fractal dimension. Besides this, the engine and the operating conditions were quite different compared to the present study. However, similar trends in values are obtained: a higher fractal dimension at low load and a relatively lower



fractal dimension at high load condition.

When comparing the fractal dimension between diesel and dual fueling (Table 2), a higher value (1.73 to 1.88) is always obtained for the latter case. No published literature has been found to compare our results for dual fuel PM. However, several articles are found where morphology was studied on PM obtained from premixed

Table 2: Fractal dimensions of the PM sampled for different engine fueling conditions.

Engine fueling	Fractal dimension, $D_{FL}$
diesel low load	1.72
diesel high load	1.69
diesel-NG	1.73
diesel-BG2	1.80
diesel-BG3B	1.84
diesel-BG3A	1.88

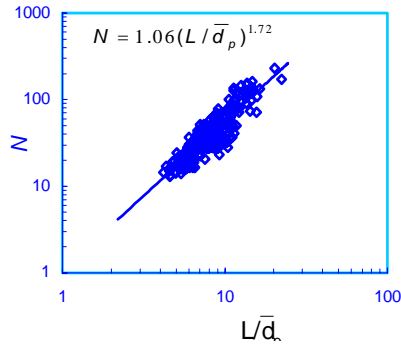


Fig 4. Plot of fractal data of PM agglomerates sampled for diesel low load operation (best fit with  $D_{FL} = 1.72$ ). The number of primary particles per agglomerate  $N$  is correlated with the fractal dimension as

$$N = k_L \left( \frac{L_{max}}{\bar{d}_p} \right)^{D_{FL}} ; \text{ While the fractal dimension, } D_{FL}$$

represents the slope,  $k_L$  (a correlation prefactor) determines the magnitude of the least-squares linear fit to the data in the  $\ln(N)$  versus  $\ln(L_{max}/\bar{d}_p)$  plot.

methane/oxygen flames. Fractal dimensions obtained in these studies by light scattering (LS) and TEM methods are in the range of 1.6-1.82. Therefore our results are in the range of previous values but for methane/oxygen premixed flame instead of dual fuel engine environment.

Fractal agglomerates grow through either primary particle-cluster (PC) or cluster-cluster (CC) collisions in three different growth mechanisms: reaction-limited, ballistic and diffusion-limited [19,20]. It can be speculated that at diesel (high) condition, the particulate agglomeration growth is dominated by the diffusion-limited mechanism since the mean free path is generally smaller than the particulate sizes. On the other hand, at dual fuel condition, the growth may be dominated by the ballistic mechanism since the mean free path would be larger than the particulate size, as the parameter, mainly depends on the number concentrations of the particulates [21]. Typically, smaller fractal dimensions indicate more chainlike and larger fractal

dimensions indicate more spherical particulate agglomerates [20]. Thus diesel (high) PM have more chainlike agglomerates than dual fuel PM.

#### 4. CONCEPTUAL MODELING

Based on the results discussed in the previous sections, a conceptual model can be constructed to differentiate the phenomena of PM formation processes for the two types of engine fueling. Figure 5 interprets the phenomenological model of PM formation and oxidation processes for both cases.

Fuel pyrolysis is the starting process where the organic compounds alter their molecular structure at high temperatures but with the presence of negligible amount of oxygen. The pyrolysis process, which results in the production of PM precursors and PM growth species (such as unsaturated hydrocarbons, polyacetylenes, poly aromatic hydrocarbons (PAHs) and especially acetylene), is a function of temperature and fuel concentration [22]. In the case of diesel (high) fueling, the fuel concentration is higher than the dual fueling and therefore pyrolysis process is dominant compared to the oxidation. On the other hand, for dual fueling, the oxidation can be dominant compared to pyrolysis process, as more oxygen is present (premixed combustion) and the diesel fuel quantity is minimized. Since the amount of PM precursors are significantly higher and especially the PAHs are dominant in diesel (high) pyrolysis, a significantly higher particle inception or nucleation is expected in this case compared to dual fueling.

Nucleation is followed by particle surface growth processes where gas phase hydrocarbons (mostly acetylene) are added to the nucleated particles. These particles then combine by colliding with each other. If the collision results in a bigger particle then it is termed as coagulation. The coagulation process results in the appearance of the primary particles. Agglomeration then follows, where primary particles instead of coalescing, stick together and form particulate clusters or chains. The chainlike agglomeration is common in the case of diesel (high) fueling whereas cluster type agglomeration is common in the case of dual fueling. Among the different parameters, the number of primary particles is the dominant parameter enhancing the formation of chainlike agglomerates, which is significantly higher in the case of diesel (high) fueling. It can also be seen from Fig.5 that the amount of gas phase hydrocarbons are significantly higher in the case of dual fueling.

In the dilution system, further PM formation processes can occur as shown in Fig. 5. As the dual fueling results in significantly higher gas phase hydrocarbons (Fig.5), dilution effects are therefore more significant in this case. A substantial amount of both absorption and condensation of the gas phase hydrocarbons would occur in dual fueling. Condensation can cause particle nucleation and thus can cause more fine particles (nucleation mode) to be emitted in this case compared to diesel fueling. This is why the dual fuel PM contains more SOF or volatile matter than the diesel (high) PM [8]. Particle agglomeration can still occur in the dilution system to form more particulate clusters.

It is important to note that the particulate structure for

dual fueling can be approximated to that for diesel (low) fueling. Therefore, it can be speculated that the final structure of the measured PM primarily depends on the quantity of the diesel fuel injected. Every hydrocarbon fuel tends to produce PM on combustion. However, fuel molecules containing less carbon, high hydrogen and straight chain, such as  $\text{CH}_4$ , would have a lower tendency to produce PM [22]. Also, the contribution of the oxidation processes in dual fueling is more significant which eventually reduces both the production rate and size of the emitted PM agglomerates.

## 5. CONCLUSIONS

Based on the above results the following conclusions can be made:

- As the engine load increased from low to high during diesel fueling, the mean primary particle diameter ( $\bar{d}_p$ ) decreased from 28 nm to 26.4 nm.

The value for dual fueling falls between those for

diesel low load and diesel high load conditions. However, for biogas fueling  $\bar{d}_p$  increases from 27.0 to 29.5 nm as  $\text{CO}_2$  content increases in biogas.

- All the measured PM agglomerates have a bi-modal number size distribution. Two modes of distributions are: nuclei ( $D_p$  less than  $0.1 \mu\text{m}$ ) and accumulation mode ( $0.1 < D_p < 1.0 \mu\text{m}$ ) are observed for all PM except the diesel (high) PM where modes are accumulation and an almost coarse mode ( $D_p$  larger than  $1.0 \mu\text{m}$ ).
- According to shape factor analysis, the dual fuel PM agglomerates are nearly spherical and smaller and the diesel (high) PM are larger and elongated.

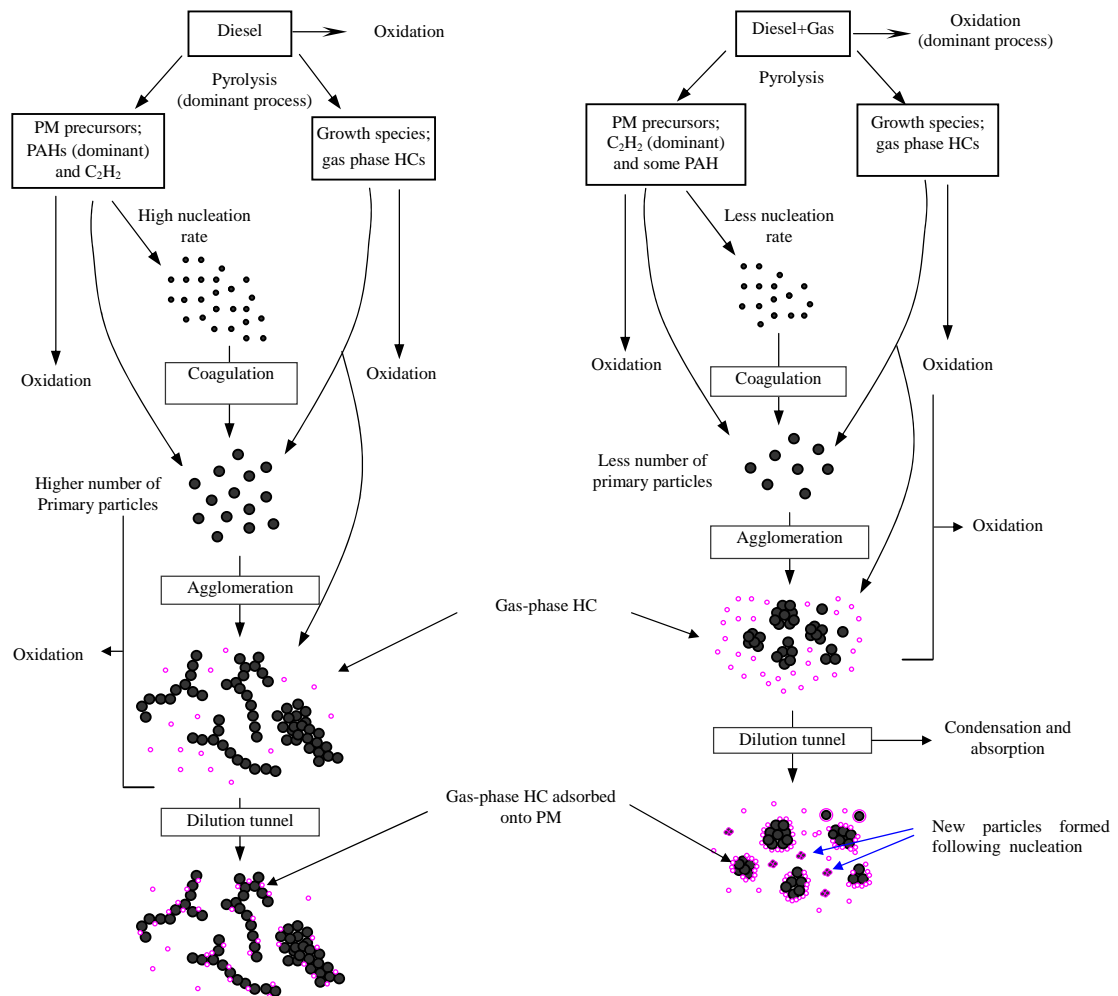


Fig 5. Schematic diagram of the different steps in PM formation process for diesel (high) and dual fueling conditions

Fractal dimension,  $D_{FL}$  of the PM agglomerates are found to be in the range of a light duty diesel engine (1.69 to 1.88). For diesel PM, a higher fractal dimension is measured at low load (1.72) than at high load condition (1.69). However,  $D_{FL}$  is always higher (1.73 to 1.88) for dual fuel PM compared to diesel (high) PM, indicating more chainlike agglomerates in the latter case.

- The particulate agglomeration growth in the case of diesel fueling may be dominated by diffusion-limited mechanism while that for dual fueling may be dominated by the ballistic mechanism.
- Based on these results a conceptual model of PM formation processes in dual fueling condition in comparison to diesel fueling condition can be constructed.

## 6. REFERENCES

1. Vouitsis, E., Ntziachristos, L. and Samaras, Z., 2003, "Particulate matter mass measurements for low emitting diesel powered vehicles: What's next?" *Progress in Energy and Combust. Sci.*, 29:635-672.
2. Park, K., Kittelson, D. B. and McMurry, P. H., 2004, "Structural properties of diesel exhaust particles measured by transmission electron microscopy (TEM): Relationships to particle mass and mobility", *Aerosol Sci. Technol.* 38:881- 889.
3. Chakrabarty, R.K., Moosmüller, H., Arnott, W.P., Garro, M.A. and Walker, J., 2006, "Structural and fractal properties of particles emitted from spark ignition engines", *Environ. Sci. Technol.*, 40:6647-6654.
4. Figler, B., Sahle, W., Krantz, S. and Ulfvarson, U., 1996, "Diesel exhaust quantification by scanning electron microscope with special emphasis on particulate size distribution", *The Science of the Total Environ.*, 193:77-83.
5. Kittelson, D.B., 1998, "Engines and nanoparticles: A review", *J. of Aerosol Science*, 29:575-588.
6. Hinds, W. C., 1999, *Aerosol Technology, Properties, Behavior, and Measurement of Airborne Particles*, John Wiley and Sons, Inc., New York.
7. Nord, K., Haupt, D., Ahlvik, P. and Egeback, K-E., 2004, "Particulate emissions from an ethanol fueled heavy-duty diesel engine equipped with EGR, catalyst and DPF", *SAE Paper 2004-01-1987*.
8. Mustafi, N.N., 2008, "Particulate emissions of a dual fuel engine", PhD Thesis, The University of Auckland, Auckland, New Zealand.
9. Mustafi, N.N. and Raine, R.R., 2008, "A Study of the emissions of a dual fuel engine operating with alternative gaseous fuels", *SAE Paper 2008-01-1394*.
10. Mustafi, N.N., Raine, R.R. and James, B., 2007, "Particulate emissions from a diesel engine operated with gaseous fuels", *Proc. of the conference, Chemeca*, Melbourne, Australia.
11. Mathis, U., Mohr, M., Kaegi, R., Bertola, A. and Boulouchos, K., 2005, "Influence of diesel engine combustion parameters on primary soot particle diameter", *Environ. Sci. Technol.*, 39:1887-1892.
12. Rasband, W.S., 1997-2007, *ImageJ*, U. S. National Institutes of Health, Bethesda, Maryland, USA, Available on the internet at <http://rsb.info.nih.gov/ij/>.
13. Zhu, J., Lee, K. O., Yozgatligil, A. and Choi, M. Y., 2005, "Effects of engine operating conditions on morphology, microstructure, and fractal geometry of light-duty diesel engine particulates", *Proc. of the Combustion Institute*, 30:2781-2789.
14. Jung, H., Kittelson, D.B. and Zachariah, M.R., 2004, "Kinetics and visualization of soot oxidation using transmission electron microscopy", *Combustion and Flame* 136:445-456.
15. Lapuerta, M., Armas, O. and Gomez, A., 2003, "Diesel particle size distribution estimation from digital image analysis", *Aerosol Sci. Technol.* 37:369-381.
16. Smith, O.I., 1981, "Fundamentals of soot formation in flames with application to diesel engine particulate emissions", *Progress in Energy and Combust. Sci.*, 7:275-291.
17. Lee, K. O., Zhu, J., Ciatti, S., Yozgatligil, A. and Choi, M. Y., 2003, "Sizes, graphitic structures and fractal geometry of light-duty diesel engine particulates", *SAE Paper 2003-01-3169*.
18. Oh C. and Sorensen C.M., 1997, "The effect of overlap between monomers on the determination of fractal cluster morphology", *Journal of Colloid and Interface Science*, 193:17-25.
19. Schaefer, D.W. and Hurd, A.J., 1990, "Growth and structure of combustion aerosols: fumed silica", *Aerosol Sci. Technol.*, 12:876-890.
20. Lee, K.O., Cole, R., Sekar, R., Choi, M.Y., Kang, J.S., Bae, C.S. and Shin, H.D., 2002, "Morphological investigation of the microstructure, dimensions, and fractal geometry of diesel particulates", *Proc. of the Combustion Institute*, 29:647- 653.
21. Bird, R.B., Stewart, W.E. and Lightfoot, E.N., 1960, *Transport Phenomena*, John Wiley, New York.
22. Tree D.R. and Svensson K.I., 2007, "Soot processes in compression ignition engines", *Progress in Energy and Combustion Science*, 33:272-309.

## APPENDIX

### Pm Fractal Dimension

The number of primary particles per agglomerate,  $N$ , scales with the overall size of the agglomerate, usually quantified by its radius of gyration,  $R_g$ , with a power  $D_f$  as described by ([A1-A5]):

$$N = k_f \left( \frac{2R_g}{d_p} \right)^{D_f} \quad (A1)$$

where  $d_p$  is the primary particle diameter,  $D_f$  is the fractal dimension, and  $k_f$  is the prefactor of the scaling relationship and both  $D_f$  and  $k_f$  are dimensionless quantities. The primary particle diameter,  $d_p$ , normally enters into the equation as an average value,  $\bar{d}_p$ .

Equation A1 is applicable to an ensemble of agglomerates on the average, i.e. it is statistical in nature [A1]. Essentially, the fractal dimension explains under what mechanism particulate agglomerates are formed and their growth [A6]. The fractal dimension  $D_f$  is generally obtained by evaluating the gradient of a linear regression line fit with the data plot of  $\ln(N)$  versus  $\ln(2R_g/d_p)$ . The number of primary particles,  $N$ , is related to the projected area of the agglomerates as [A2]:

$$N = k_a \left( \frac{A_c}{A_p} \right)^\alpha \quad (A2)$$

where  $A_c$  is the projected area of the agglomerate,  $A_p$  is the average projected area of the primary particles,  $k_a$  is an empirical constant and  $\alpha$  is an empirical exponent.

The estimation of  $N$  using Eq. A2 is also sensitive to the amount of overlap of any two adjacent primary particles.  $N$  is estimated using Eq. A2 with consideration of particle overlap in the present study. The values of  $k_a$  and  $\alpha$  are obtained from [A2]: for diesel (high) fueling  $k_a \sim 1.25$  and  $\alpha \sim 1.09$  and for the other types of fueling  $k_a \sim 1.35$  and  $\alpha \sim 1.1$ .

Once  $N$  is obtained, the other three-dimensional parameter,  $R_g$ , in Eq. A1 is to be determined. The radius of gyration  $R_g$ , can actually be estimated from the projected properties of the agglomerates. The fractal dimension is estimated using a characteristic dimension of the agglomerate, maximum length  $L_{max}$ , (instead of  $R_g$ ) as suggested in [A1,A3-A4]. Hence the outer radius of an agglomerate ( $R_L \cong L_{max}/2$ ) can be used in the

determination of  $D_f$  and the Eq. A2 can be modified as

$$N = k_L \left( \frac{2R_L}{\bar{d}_p} \right)^{D_{fL}} \Rightarrow N = k_L \left( \frac{L_{max}}{\bar{d}_p} \right)^{D_{fL}} \quad (A3)$$

While  $D_{fL}$  represents the slope,  $k_L$  (a correlation prefactor) determines the magnitude of the least square linear fit to the data in the  $\ln(N)$  versus  $\ln(L_{max}/\bar{d}_p)$  plot. The two fractal dimensions  $D_{fL}$  (based on maximum projected length) and  $D_f$  (based on radius of gyration) have identical values and can be used interchangeably [A7]. However, the proportionality constants  $k_L$  and the prefactor  $k_f$  are different.

## REFERENCES

- A1. Koylu, U.O., Xing, Y. and Rosner, D.E., 1995, "Fractal morphology analysis of combustion generated aggregates using angular light scattering and electron microscope images", *Langmuir*, 11:4848-4854.
- A2. Oh, C. and Sorensen, C.M., 1997, "The effect of overlap between monomers on the determination of fractal cluster morphology", *J. of Colloid and Interface Science*, 193:17-25.
- A3. Park, K., Kittelson, D. B. and McMurry, P. H., 2004, "Structural properties of diesel exhaust particles measured by transmission electron microscopy (TEM): Relationships to particle mass and mobility", *Aerosol Science and Technology*, 38:881- 889.
- A4. Neer, A, and Koylu, U. O., 2006, "Effect of operating conditions on the size, morphology, and concentration of submicrometer particulates emitted from a diesel engine", *Combustion and Flame*, 146:142-154.
- A5. Song, J. and Lee, K.O., 2007, "Fuel property impacts on diesel particulate morphology, nanostructures, and NOx emissions", *SAE Paper 2007-01-01239*.
- A6. Lee, K.O., Cole, R., Sekar, R., Choi, M.Y., Kang, J.S., Bae, C.S. and Shin, H.D., 2002, "Morphological investigation of the microstructure, dimensions, and fractal geometry of diesel particulates", *Proceedings of the Combustion Institute*, 29:647- 653.
- A7. Chakrabarty, R.K., Moosmuller, H., Arnott, W.P., Garro, M.A. and Walker, J., 2006, "Structural and fractal properties of particles emitted from spark ignition engines", *Environmental Science and Technology*, 40:6647-6654.

## PERFORMANCE OF A BIOGAS RUN STIRLING GENERATOR

M. Shahzada Chowdhury<sup>1</sup> and Md. Ehsan<sup>2</sup>

<sup>1</sup>Central Locomotive Workshop, Parbatipur, Dinajpur, Bangladesh

<sup>2</sup>Department of Mechanical Engineering, Bangladesh University of Engineering and Technology,  
Dhaka, Bangladesh

### ABSTRACT

New technologies for harnessing power and heat from biomass are being developed to widen such applications. Multi-fuel capabilities, continuous combustion, improved torque and emission characteristics and better part load efficiency are advantages of a Stirling cycle engine. By factoring in the pollution-related environmental and social costs associated with fossil and nuclear fuels, bioelectricity is becoming a competitive energy alternative. A Stirling generator developed by DEKA Research and Development Corp., USA was studied to for small scale (1 kW DC) electricity production using biogas fuel. The project was situated in Manikganj in Bangladesh. Biogas produced from a fixed-dome digester was used as fuel for the Stirling-generator charged with Helium as working fluid. The study focused on performance parameters such as: air-fuel ratio, brake specific fuel consumption, overall efficiency, regenerator heat input, different temperatures, engine speed, and exhaust emissions – at different power levels. The study revealed that the generator performed most efficiently at about 60-70% of the maximum rated load. The overall efficiency ranged 14-24%, which was higher compared to typical petrol engine generators used in small scale power generation. The temperature attained in the hot end was reasonable, although it showed some drop in internal fluid pressure with time, indicating need of improvements in seal durability.

**Keywords:** Stirling-Generator, Stirling Engine, Small Scale Power Generation, Biogas, Alternative fuel

### 1. INTRODUCTION

Stirling engines operate on the principle of compression and expansion of working fluid at two different temperature levels. It incorporates a regenerator heat exchanger, alternately accepting and rejecting heat to and from a working fluid and thus recycling a major fraction of the energy flow from one cycle to the next. The flow of working fluid is controlled by volume changes, so that there is a net conversion of heat energy to work and vice versa. Because of the use of regenerator, Stirling engines can have high thermal efficiencies[1]. A number of attempts have been made to use Stirling technology in small scale power generation, specially for rural areas [2,3,4,5]. The multi-fuel capability, better part load efficiency and less environmental pollution due to continuous combustion are advantages of using a Stirling engine for such applications. DEKA, a technology development company of USA is currently developing a Stirling generator prototype, which was tested for small scale electrical power generation in the rural area of Bangladesh (Tangail and Manikganj) using biogas in 2005. The DEKA Stirling generator was designed to produce up to 1kW of electricity for four hours using biogas generated daily from a 400cft fixed dome digester. The objective of this project was - to evaluate the field level performance of the prototype using biogas and to promote the use of renewable biomass energy for rural power generation.

### 2. EXPERIMENTAL SETUP

The setup consisted of the DEKA Stirling Generator, Biogas fuel supply system and a distributed electrical load bank grid system, as shown in figure 1.

#### 2.1 Stirling Generator

The 1 kW prototype was an external combustion Stirling engine. Helium was used as the working fluid inside the engine. There are two parts in the generator - the core chassis, which consisted of the engine, and the auxiliary chassis, which consisted of the electrical parts and the radiator. The external combustion Stirling engine had two pistons, each having a connecting rod and each undergoing reciprocating linear motion along respective rod axes within respective cylinders and each having a displacement with respect to fixed points along the respective rod axes. Additionally, the engine had a harmonic drive linkage characterized by a net angular momentum. The engine working fluid (Helium gas) was contained within the first and second cylinders, the working fluid undergoing successive closed cycles of heating, expansion, cooling and compression. The engine also had a primary crankshaft, an eccentric crankshaft disposed internally to the primary crankshaft, the eccentric crankshaft was coupled to both the first connecting rod and the second connecting rod, and an epicyclic gear set coupling the eccentric crankshaft to the primary crankshaft in such a manner that the eccentric



crankshaft and the primary crankshaft counter rotate, the eccentric crankshaft is characterized by a forward angular momentum and the primary crankshaft is characterized by a backward angular momentum. The linkage also had a flywheel coupled to the eccentric shaft such that the net angular momentum of the harmonic drive linkage is substantially zero.



Fig 1. Experimental Set-up of DEKA Stirling Gen-set



Fig 2. Components of the Stirling Engine

As shown in figure 2 the engine had the generator coupled to the primary crankshaft for converting mechanical to electrical energy and a processor for controlling a current load on the generator in such a manner as to provide a substantially constant torque on the primary crankshaft. The first and second connecting rods are flexible with respect to bending in a direction transverse to the respective rod axes. The engine also have a heat exchanger for transferring thermal energy across a manifold from a first fluid (combustion gasses) to a second fluid (Helium), the heat exchanger comprising a plurality of pins extending from the manifold into the first and second fluid. The engine was fitted with a burner, which heats the combustion chamber.

The burner burns any gaseous fuel and the heat is transferred to the piston-cylinder combination across a extended surface heat-exchanger. The hot end temperature of the burner was kept about 1000°C at full load. Type-K thermocouples were used for measurement of the temperatures. The intake manifold has a conduit having axial symmetry about the combustion axis with an inlet and an outlet for conveying radially inwardly flowing air. There is an air swirler disposed within the passageway for imparting a rotational component to the inwardly flowing air.

## 2.2 The Electrical System

The following components consisted the electrical system of the Stirling Gen-set:

**Motor / Generator :** Normally used as a generator to extract electric power from the Stirling Engine. Also used initially as motor to start the Stirling Engine.

**Motor Drive :** Used to control the phasing of currents through the motor / generator.

**Boost / Buck Regulator :** Used to boost voltage from battery to HV Bus. This was also used as buck converter when charging battery from HV bus.

**Battery :** Provided power to start stirling engine. Used as a hybrid to briefly power loads exceeding the maximum engine power .

**Shunt :** A heating element immersed in the radiator is used to dissipate excess power on the HV Bus when load is suddenly dropped.

**Output DC/DC Converter :** Provides conditioned power output to the user.

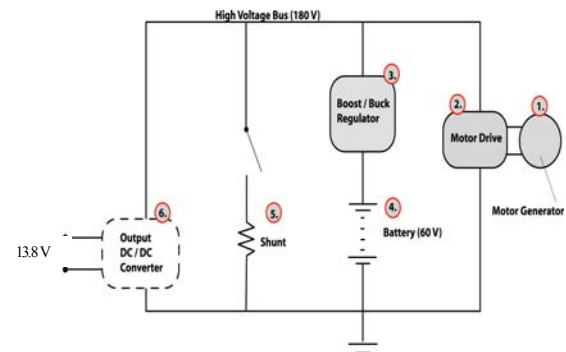


Fig 3. Electrical Block Diagram of Stirling Gen-set

The output terminal of the generator was then connected with 5×100 AH 12 volt deep cycle (Lead-Acid) battery and also with the customer load. So, the Stirling generator at the same time charged the batteries and gave power to the customer loads as shown in figure 3. The engine also has a radiator and a shunt, which is a resistive load immersed in the radiator. If there was any sudden drop in load, heat energy of the engine would be excessive, this was compensated by the shunt connected with the system. The shunt acted as the artificial load during this transition. The shunt is practically a resistive load cooled by water supply in the radiator. The Shunt could handle all of the output (approx 1kW). The radiator cools the shunt and transfers heat from the engine and motor (via the helium) not the burner. The shunt was also used when the unit is idling and the

battery is charged, since some power is being produced and it must be dissipated. It also acts as a buffer between the time when load is removed and the engine rpm is reduced.

### 2.3 Small Distributed Grid System

A mini grid was designed of DC 12 Volt to transmit power to different households and shops were used. Individual wiring lengths from the centrally located generator set was limited to 300 feed. Accessories included - Fuse, Charge Controller and Distribution box.



Fig 4. Grid system (Fuse, Charge controller and Distribution box)

### 2.4 The Fuel System

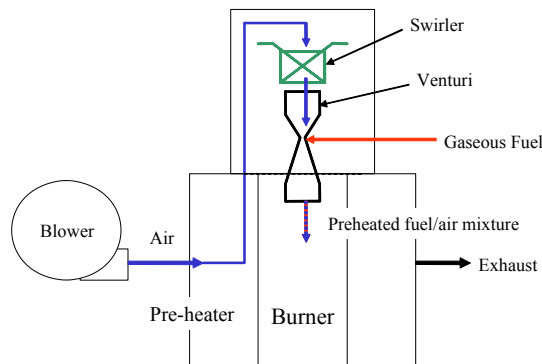


Fig 5. Venturi Fuel System Schematic

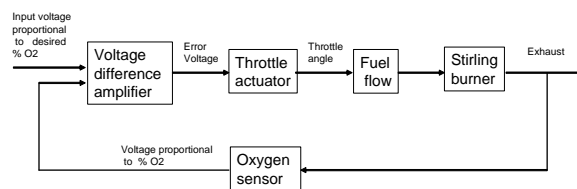


Fig 6. Fuel/Air control strategy.

The burner system was designed for any gaseous fuel. For this study biogas supply from a concrete fixed dome digester, already constructed at the site was used as fuel. The biogas fuel system consisted of a carburetor-type arrangement. With this system vacuum was created at the venturi restriction by air flow through the venturi (driven by the blower) as shown in figure 5. This vacuum was

used to pull the fuel into the combustion chamber. The biogas was obtained from fermentation of cow dung. The bio-digester was fed with 10000 kg cow dung initially and then 400 kg cow dung daily. The peak generation of biogas was found to be about 500 cubic feet, with a hydraulic retention time (HRT) of 40 days.

### 3. PERFORMANCE OF THE GENSET

The DEKA Stirling engine outfitted with a venturi fuel system and performance was tested in the rural area of Bangladesh. “APU controller” converts the 3-phase power from the brushless generator into DC power, which is dissipated into loads. Output power, water temperature and engine head temperatures were recorded using software embedded in the DEKA motor controller. A BACHARACH portable gas analyzer was used to monitor combustion products such as CO, CO<sub>2</sub>, and O<sub>2</sub>. Engine head temperature, swirler temperature, speed, DC load, engine gross power was also measured. Biogas analysis was done from BCSIR (Bangladesh Council for Scientific and Industrial Research) and flow from the digester was measured daily. Biogas methane content was found to vary between 50 – 60% by volume. Air flow rate, fuel flow rate, air-fuel ratios, specific fuel consumption, overall efficiency, exhaust emission components, engine speed, power produced by the generator and temperature of the engine were the main parameters measured. The tests were carried out with a range of variable loads from 400 watt to about 900 watt. The engine was very quite in operation in respect with other internal combustion engine of same capacity. It was found 72dB at 3 meter distance. Table-1 shows the performance parameters when run with biogas having 50% methane content and table-2 the same for biogas with 60% methane content.

Table 1: Parameters at loads, 50% CH<sub>4</sub> content Biogas

Avg. Power (watt)	$\dot{m}_{Biogas}$ (kg/hr)	$\dot{m}_{Air}$ (kg/hr)	Bsfc (g/kW-hr)	$Q_{reg}/Q_{in}$	Overall Efficiency (%)
902	0.55	24.12	610	1.3	14.1
848	0.49	23.2	578	1.4	14.2
780	0.43	19.54	551	1.4	15.3
721	0.37	16.1	513	1.3	16.8
654	0.31	11.88	474	1.2	19.5
553	0.24	8.71	434	1.1	22.0
<b>404</b>	<b>0.24</b>	<b>7.98</b>	<b>594</b>	<b>1</b>	<b>16.8</b>

Table 2: Parameters with load, 60% CH<sub>4</sub> content Biogas

Avg. Power (watt)	$\dot{m}_{Biogas}$ Kg/hr)	$\dot{m}_{Air}$ (kg/hr)	Bsfc (g/kW-hr)	$Q_{reg}/Q_{in}$	Overall Efficiency (%)
902	0.61	24.12	676.3	1.7	15.45
848	0.54	23.2	636.8	1.8	15.55
780	0.47	19.54	602.6	1.74	16.77
721	0.41	16.1	568.7	1.6	18.44
654	0.34	11.88	519.9	1.5	21.66
553	0.27	8.71	488.3	1.3	24.15
404	0.27	7.98	668.3	1.2	18.53



### 3.1 Air and Fuel Flows

The increment of air flow rate with load was almost linear for biogas. The air flow rate was controlled by the blower rpm. The fuel flow was decreased and increased by decreasing and increasing the air flow rate through the venturi and it was done with the demand of the load. The air flow rate varied from 24.1 Kg/hr to 8 Kg/hr with the variation of load of 400 to 900 watt (approximately). Air flow rate was measured with the approximation made with the blower speed of the Stirling generator. Figure 7 shows the variation of the air flow rate and fuel flow rate with load for biogas.

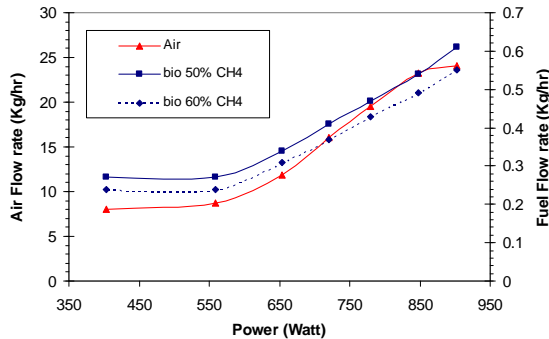


Fig 7. Power vs Flow rate for Biogas.

Figure 7 also shows the variation of the fuel flow rate with load for biogas. The variation of fuel flow rate with load was almost linear. Since the fuel flow measurement was made from system pressure, the calculated mass flow rate is influenced by the value of gas constant ( $R$ ), which is a function of gas composition. For biogas it was found to vary from 0.27 Kg/hr to 0.61 Kg/hr considering 50%  $\text{CH}_4$  content Biogas and 0.3 Kg/hr to 0.55 Kg/hr considering 60%  $\text{CH}_4$  content Biogas with the variation of load from 400 to about 900 watt. Fuel flow rate both for 50% and 60%  $\text{CH}_4$  content Methane content of the Biogas produced was found to be from 50% to 60%.

### 3.2 Air-Fuel Ratio

The variation of the fuel flow rate is shown in figure 8. The air-fuel ratios varied during the range of loads. Mass basis AF ratio varied within a range from 40 to about 30 for 50%  $\text{CH}_4$  content Biogas and 33 to about 44 for 60%  $\text{CH}_4$  content Biogas with load variation from 400 watt to about 900 watt as shown in figure 5 for biogas. The stoichiometric AF ratio for natural gas is 17.2, and for biogas it is only about 5. So the mixture for combustion was very lean. It was due to the fact that the fuel intake system was venturi type, so to draw more fuel it required higher airflow rate.

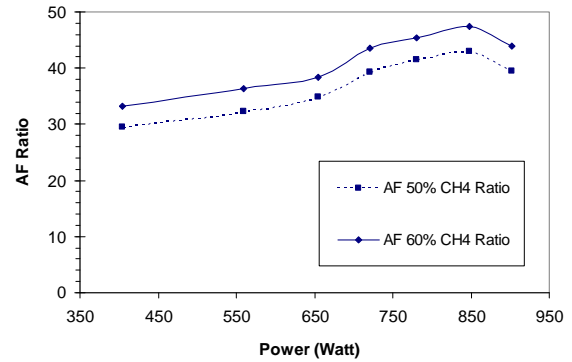


Fig 8. Power vs AF Ratio for Biogas.

### 3.3 Sfc and Overall Efficiency

The specific fuel consumption (sfc) for biogas varied from 676.3 g/kW-hr to 488 g/kW-hr for 50%  $\text{CH}_4$  content biogas and 609.7 g/kW-hr to 594 g/kW-hr for 60%  $\text{CH}_4$  content biogas, the overall efficiency varied from 24.1% to 15.4% for 50%  $\text{CH}_4$  content biogas and 22% to 14.1% for 60%  $\text{CH}_4$  content biogas with a variation of load from 400 watt to about 900 watt. The sfc took a greater value for the highest load and also for the lowest load. The sfc had the lowest value i.e. 488 g/kW-hr for 50%  $\text{CH}_4$  content biogas and 434 g/kW-hr for 60%  $\text{CH}_4$  content biogas at 550 watt (approximately) and at the same load had the highest overall efficiency i.e. 24.1% for 50%  $\text{CH}_4$  content biogas and 22% for 60%  $\text{CH}_4$  content biogas. So, it can be said that the generator works best in the region of 550 to 650 watt load and has less efficiency in the higher and lower loads than that range. As for the Stirling engine a considerable amount of heat is recovered from the regenerator and fed again in to the system. The regenerator heat input,  $Q_{\text{reg}}$  was also accounted for calculation of overall efficiency. For comparison a petrol equivalent of biogas consumption was also. For 50%  $\text{CH}_4$  content biogas it was in the range from 146.7 g/kW-hr to 204 g/kW-hr and for 60%  $\text{CH}_4$  content biogas it was 180.8 g/kW-hr to 255 g/kW-hr with load variation of 400 watt to about 900 watt.

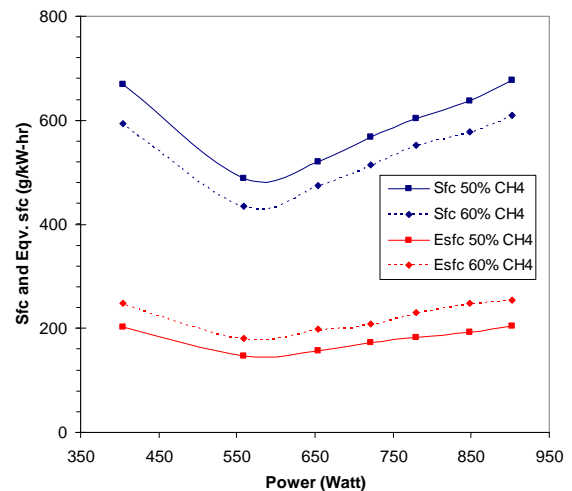


Fig 9. Power vs Bsfc and Eqv. Bsfc for Biogas.

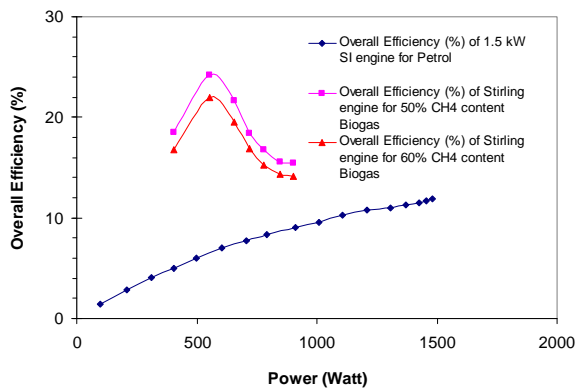


Fig 10. Comparison of Petrol and Stirling engine overall Efficiency

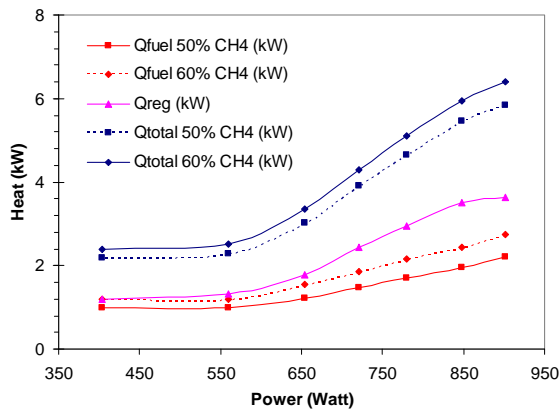


Fig 11. Power vs Heat inputs for Biogas.

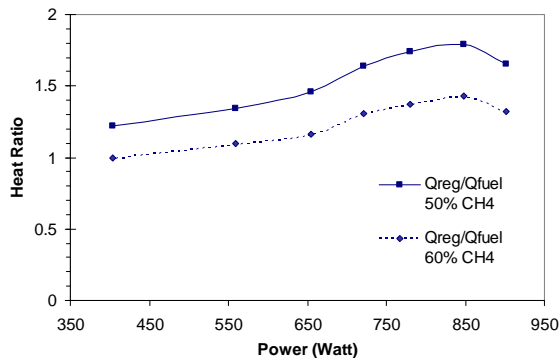


Fig 12. Power vs Heat Ratio for Biogas.

The electrical output of the generator was 13.8 volt dc. The output voltage was almost constant and didn't vary with load the only thing varied was the current. Current varied with the variation of load. As the load varied from 400 to about 900 watt, the current varied from 30 to 70 ampere (approximately). The wirings were designed accordingly.

### 3.4 Temperatures

Measurements of temperatures were at the burner body which was known as "Head Temp", inside the burner (near regenerator) which was known as "Swirler

Temp", and the temperature of coolant (water was used as coolant and it cooled the engine and the radiator (shunt) in a closed loop circuit). Head temperature normally ranged from 700°C to 960°C depending on the load varied from 400 watt to about 900 watt and also on the ambient conditions for biogas. Swirler temperature varied in the range of 400°C to 665°C, but most of the time it was in the range of 500°C to 550°C for biogas. Coolant outlet temperature varied from 34°C to 45°C depending on the ambient conditions and load. But there was a sudden increase in coolant temp when the generator output was dumped into the shunt which was located in the radiator.

### 3.5 Speeds and Torques

There were two rotating components: (a) the Stirling engine and (b) the blower. The engine speed varied from 1400 to 2900 rpm for biogas depending on the load produced by the generator. The blower speed varied from 4,000 to 18,650 rpm for biogas depending on the air demand for combustion. The blower speed was higher for biogas operation as it required more air for combustion. The torque of the Stirling engine was almost flat over the variation of power. It varied from 2.71 N-m to 3.88 N-m in the range of power from 400 watt to about 900 watt. But in 550 watt to 900 watt range it varied between 3.58 to 3.88 N-m. Figure 10 describe Power vs Engine Speed & Torque for Biogas.

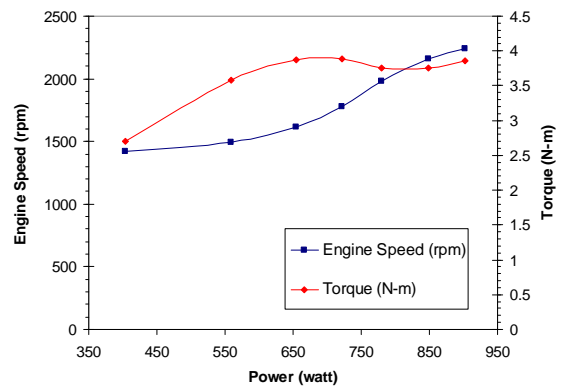


Fig 13. Power vs Engine Speed and Torque for Biogas.

### 3.5 Exhaust Emissions

The exhaust emission was tested by BACHARACH Portable Combustion Analyzer (PCA). Here percentage of O<sub>2</sub>, CO<sub>2</sub>, Excess air, Combustion efficiency and parts per million (ppm) of CO was measured. In the exhaust emission remaining oxygen was 2 to 15.2%, CO<sub>2</sub> was 3.8 to 12.6%, excess air was 4.8 to 24.2%, CO was 22 to 6000 ppm for biogas. The combustion efficiency for biogas was in the range of 79 to 87.4%.

## 4. ENERGY BALANCE IN THE SYSTEM

In a Stirling cycle engine the total heat input  $Q_{total}$  consisted of heat coming from biogas and heat from the regenerator. An energy balance diagram can be constructed where different output and heat inputs can be shown with respect to heat input from fuel ie,  $Q_{fuel}$ . An

energy balance diagrams were constructed, for maximum efficiency condition of operation. Heat recovered from the regenerator  $Q_{reg}$  in the Stirling engine was almost 134% of  $Q_{fuel}$ . Literature showed it could be as high as 400%[1,4]. Total heat input  $Q_{total}$  was 234% of  $Q_{fuel}$ . Mechanical out put was 63% of  $Q_{fuel}$ . Heat loss  $Q_{loss}$  was 171% of  $Q_{fuel}$ . Electrical output was 56% of  $Q_{fuel}$  as shown in figure 14. Overall efficiency was calculated from electrical output to total heat input,  $Q_{total}$ . The maximum overall efficiency was found to be 24%.

Table-3: Heating Components for Maximum Efficiency

Heat input from fuel $Q_{fuel}$	0.98 kW
Heat recovered from regenerator $Q_{reg}$	1.31 kW
Total heat input into the heater head $Q_{total}$	2.29 kW
Electrical output	0.553 kW
If Generator Efficiency $\eta_{gen} = 0.9$ then,	90%
Mechanical output	0.614 kW
Heat loss $Q_{loss} =$ [Assuming all frictional losses converted to heat]	1.676 kW

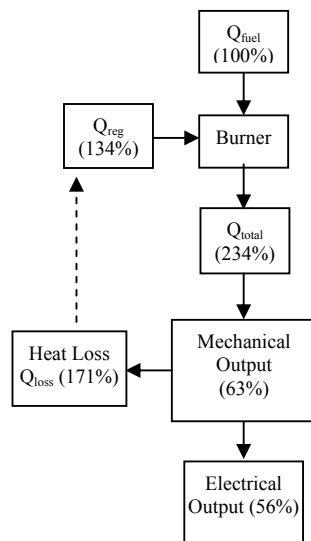


Fig 14. Energy Balance for 553 watt power (Maximum Efficient Operation, 24%).

## 5. DISCUSSION

The fuel and air flow rate increased almost linearly with the load but with different rate and for this reason the AF ratio was not constant and varied with load for biogas. The AF ratio also increased with load but at the peak load it decreased. The value of AF ratio varied between 30 to 44, which indicated very lean burning. The stoichiometric AF ratio for biogas is 5, so the air flow rate was very high due to the fact that more air flow was necessary to increase the fuel flow rate through the venturi and also to maintain the material temperature in the burner within a reasonable range. Here the instantaneous fuel flow rate was not measured, so an average value of fuel flow rate was taken into consideration. The engine speed and blower speed is 1400 to 2900 rpm and 400 to 18650 rpm respectively.

The specific fuel consumption for biogas was found to be higher at high and low load. It was found to be minimum at 550 to 650 watt range and the value was 488.3g/kW-hr considering 50%  $CH_4$  and 434 g/kW-hr considering 60%  $CH_4$  in biogas. The overall efficiency also achieved the highest point at that range i.e. 550 to 650 watt range and the value was 24.1% considering 50%  $CH_4$  and 22% considering 60%  $CH_4$  in biogas. It was found to be less both in high and low loads than that range. The overall efficiency of the Stirling engine was higher compared to SI engine of that range available in the market, that are 12-18% efficient[6].

The torque of the Stirling engine was almost flat over the variation of power. It varied from 2.71 N-m to 3.54 N-m in the range of power from 400 watt to about 550 watt and 3.54 N-m to 3.88 N-m in the range of power from 550 watt to about 900 watt for Biogas. So, the curve is very flat in the working range, which is typical of Stirling engine characteristics. The Helium pressure initially was 550 psi, after 700 hours of operation that was reduced to 450 psi indicating some slow leakage. Part load characteristics of Stirling engine are better compared to internal combustion engine of similar power range. It was found that the part load efficiency of Stirling engine at 40 to 100% of maximum load varied between 14 to 24% and that of 1.5 kW KUBOTA petrol engine varied between 7 to 12% [6]. The output of the generator was 13.8 DC Volt with varying current with load. To make varying current with load the speed of the engine was changed. It is not a problem for DC output but for AC output the speed of the engine needs to be made fixed with variable load.

The different temperatures such as head temperature, swirler temperature, and coolant temperature are within the limits of materials used and the cooling water circulated across cold end and optionally across the shunt resistance, could maintain the water temperature safely below any boiling situation.

## 6. CONCLUSION

The prototype DEKA Stirling engine-genset was capable of satisfactory operation using biogas as fuel. During the engine operation the hot end temperature could be maintained within reasonable limits. The decrease of working fluid pressure if kept running at high loads, indicated need of further sealing improvements. The overall efficiency for small scale electrical power generation was found to be better with respect to comparable gasoline run generators.

## 7. REFERENCES

1. Walker G. et al, "The Stirling Alternative", Gordon and Breach Science Publishers, ISBN: 2-88124-600-1, Switzerland, 1994.
2. Carlqvist S. G. et. al., "Hermetically Sealed Stirling-Electric Generator Set", Paper no. 889434, pp 187-192, Proceedings of 3<sup>rd</sup> International Stirling Engine Conference, Italy, 1988.

3. D H Rix, "Some Aspects of the Outline Design Specification of a 0.5 kW Stirling Engine for a Domestic Scale Co-generation", Journal of Power and Energy, IMechE, 1996
4. Lane N.W., Beale W.T.A., "Biomass-Fired 1 kW Stirling Engine Generator and Its Applications in South Africa", Proceedings of the 9th International Stirling Engine Conference, pp 1-7, June 1999.
5. Hirata K. et. al., "Test Results of Applicative 100W Stirling Engine", Proceedings of the 31st Intersociety Energy Conversion Engineering Conference, Book No. vol. 2, p 1259-1264, 1996.
6. Alam M. S. and Ehsan Md., "Performance of a Gas Run Petrol engine for Small Scale Power Generation", Journal of Energy and Environment, pp.101-107, Vol. 1, November 1999.

## **8. MAILLING ADDRESS**

Md. Shahzada Chowdhury  
Assistant Works Engineer  
Central Locomotive Workshop,  
Parbatipur, Dinajpur, Bangladesh  
Email : [sohag111@yahoo.com](mailto:sohag111@yahoo.com)

## PRODUCTION AND PERFORMANCE OF BIODIESEL AS AN ALTERNATIVE FUEL FOR DIESEL ENGINE

A. Forhad , A. R. Rowshan, M. A. Habib, M. A. Islam

Department of Mechanical Engineering, Bangladesh University of Engineering and Technology,  
Dhaka, Bangladesh.

### ABSTRACT

The increasing demand for fossil fuel can be reduced by introducing renewable and environment friendly bio-fuels, obtained from different vegetable oils. In this study, Soybean oil is used for the production of "bio-diesel" through "Transesterification" reaction. Refined vegetable oil like soybean oil contains less than 0.005% free fatty acid which is very effective for bio-diesel production. Thermo-physical properties of bio-diesel are determined and compared with those of conventional diesel. The density and viscosity of bio-diesel are found higher than diesel, which is considered as the main obstacle for using it directly as CI engine fuel. It can be overcome by preheating. In the present study, preheating technique is employed to the biodiesel blends and their effects on engine performance is investigated on an unmodified direct injection 4 stroke single cylinder engine at different load conditions with rated rpm. Specific fuel consumption increases with the increase of percentage of bio-diesel in the blends at 85°C preheat temperature. Emission quality of the exhaust gas is tested by using IMR2800P Gas Analyzer. CO<sub>2</sub> emission rate shows a decreasing trend with increase of bio-diesel percentage. Unburned O<sub>2</sub>, excess air, NO<sub>x</sub> emission also follows the same trend. Technically diesel fuel can be replaced with preheated bio-diesel but the major obstacle is the high cost of Soybean oil relative to diesel fuel.

**Keywords:** Biodiesel, Transesterification, Diesel Engine, Preheating, Performance, Emission Quality

### 1. INTRODUCTION

Majority of the world's energy needs are supplied through petrochemical sources, coal and natural gases, with the exception of hydroelectricity and nuclear energy. Diesel fuel has an essential function in the industrial economy of a developing country and is used in transports, industrial and agricultural goods, etc. An alternative fuel should be easily available, environment friendly and techno-economically competitive. One of such fuels is triglycerides and their derivatives. This paper presents a comparative performance testing of an unmodified 4 stroke single cylinder diesel engine run by preheated biodiesel produced from soybean oil. Performance test was conducted at rated rpm (2400 rpm) for different loading conditions. Initially the engine was run by diesel fuel. Then the experiments were repeated replacing diesel by biodiesel blends at 85°C preheat temperature. In doing so, various engine performances are obtained, analyzed and reported. The potential of bio-diesel produced from soybean oil have been found to be a very promising fuel for diesel engines in a number of studies [1, 2, 3, 4]. Soybean is mainly used for cooking in Bangladesh. Bio-diesels from a number of other vegetations are also being tried out [5, 6]. Using straight vegetable oils in diesel engines causes a lot of deposition inside the engine and hampers long term operation [6]. Blends of bio-diesel with diesel are used for testing the

engine performance at different proportions termed as B20, B50, B70, B100 etc. B20 contains 20% biodiesel mixed with 80% conventional diesel by volume. This study compares some performance parameters of B20, B50, B70 and B100 based on short term engine tests. Thermo-physical properties such as flash point, fire point, heating value, viscosity, specific gravity of blended bio-diesel are also determined and compared with those of conventional diesel. Exhaust properties are tested by using IMR2800P Gas Analyzer.

### 2. PROCESS OF BIO-DIESEL PRODUCTION

In the following chapter, the process for producing biodiesel using soybean oil and methanol with transesterification reaction is described. The byproduct of this reaction is glycerol which can be used in a number of different ways.

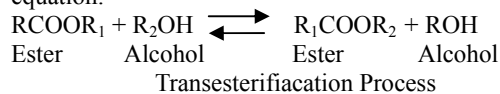
#### 2.1 Biodiesel

Bio-diesel is defined as the mono alkyl esters of long chain fatty acids derived from renewable feed stock, such as vegetable oil or animal fats, for use in compression ignition engines [7]. This name is given to the esters when they're intended for use as fuel.

#### 2.2 Transesterification Reaction

Transesterification [8] also called alcoholysis is the

displacement of alcohol from an ester by another alcohol in a process similar to hydrolysis except that an alcohol is used instead of water [9]. This has been widely used to reduce the viscosity of the triglycerides. The transesterification is represented in the following equation:



The major variables affecting the transesterification reactions are:

- The free fatty acid (FFA) and moisture content[10].
- Type of catalysts[11].
- A literature(Freedman et al. 1984) has revealed that, the rate of reaction is strongly influenced by the temperature.
- Murugesan et al. [12] reported that, after completion of the reaction the product is kept for a certain time interval for separation (approx. 24 h) of bio-diesel & glycerol layer.
- Murugesan et al. [13] reported that, washing is a process to remove entrained glycerol, catalyst, soap and excess methanol.

### 2.3 Producing Biodiesel from Soybean Oil

During the esterification process of soybean oil, first 200 ml (99% pure) methanol was mixed with 3.5 gm NaOH (96% pure). The mixture was shaken until NaOH dissolved completely. This solution is added with 1 litre of soybean oil, which was preheated by an electric heater at 60°C(fig. 1). Then the mixture was blended by a fan coupled with an electric motor as shown in fig. 2. After blending for 3 minutes, this is then left for 24 hours to settle down. This mixture gradually settles down into two distinctive layer as shown in fig. 4. The upper more transparent layer is 100% biodiesel and the lower transparent concentrated layer is glycerol. The heavier layer is then removed.



Fig 1. Preheating Arrangement



Fig 2. Blending setup



Fig 3. B100 just mixed

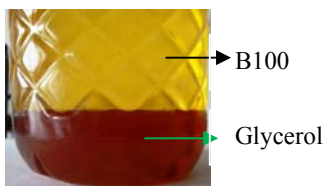


Fig 4. B100 after 24hours

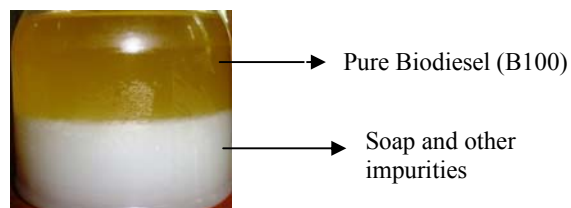


Fig 5. After water washing

### 3. FUEL PROPERTIES OF BIODIESEL

A number of properties of biodiesel blends (B20, B50, and B100) produced are targeted to be studied. The fuel properties of bio-diesel as listed in Table 1 indicate the property variation between bio-diesel produced and conventional diesel fuel.

Table 1: Comparison of properties of biodiesel produced from soybean oil with respect to diesel fuel

Parameter	ASTM method	Diesel	B20	B50	B100
Flash point(°C)	D - 93	67	86	88	98
Fire Point (°C)	D - 93	72	98	102	120
Calorific Value (MJ/Kg)	D-240	44	43.94	43.88	43.7
Specific Gravity	—	0.836	0.844	0.856	0.86
Viscosity (at 32°C) (centi strokes)	D-445	6.4	7.67	8.74	10.34

### 4. PERFORMANCE TESTING AND ANALYSIS

Total experimental works of this study is divided mainly into two groups:

- Performance test of Engine
- Exhaust properties

#### 4.1 Experimental Setup

The experimental setup consisted of engine test bed with fuel supply system, different metering and measuring devices along with the test engine. A four-stroke, single cylinder, and water cooled diesel engine was tested at constant speed. Constant speed tests were carried out at rated 2400 rpm for variable loads, extending from 20% to 100% rated load. Preheating was done manually using gas burner. A hydraulic brake dynamometer directly coupled with the engine was used to load the engine. Load was varied by changing the water flow rate to the dynamometer. Fuel was supplied from externally installed tank, allowing volume measurement of fuel consumed. Speed was measured by digital tachometer and temperatures were measured by using K type thermometer. The experimental setup used for this experiment is showed in fig 8. First tests were carried out using diesel fuel. Then, the tests were



repeated for B20, B50 and B70 blends.



Fig 6. Experimental Setup

#### 4.2 Performance Analysis

Potentiality of using biodiesels produced from soybean oil as an alternative to diesel fuel is judged in the present study. B20, B50, B70 and diesel was used as fuel. B100 is not used directly to the engine as the engine vibrates rapidly. Fig 7 shows the brake specific fuel consumption results over the load range for diesel with B20, B50 and B70. The break thermal efficiency variation with break horse power is presented in fig. 8. Fig 9 and fig 10 shows the temperature variation of exhaust gases and lub oil with power respectively. All the test results are derated as per BS5514 standard.

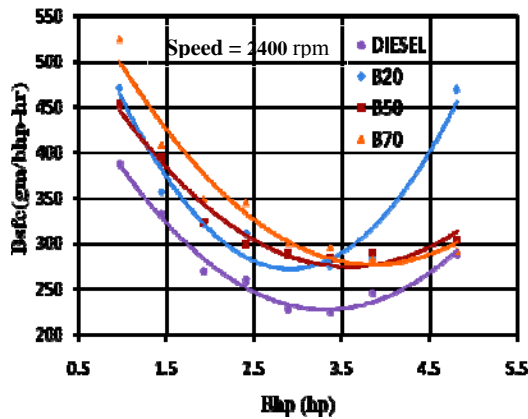


Fig 7. Variation of Bsf with Bhp for different fuels

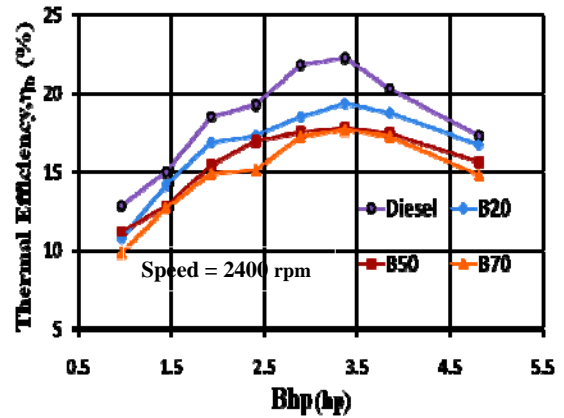


Fig 8. Variation of thermal efficiency with Bhp for different fuels

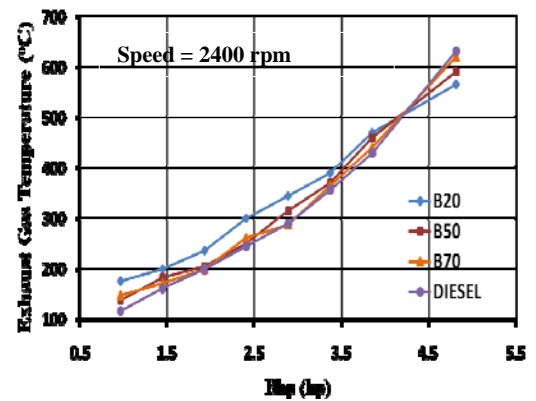


Fig 9. Variation of Exhaust gas temperature with Bhp for different fuels

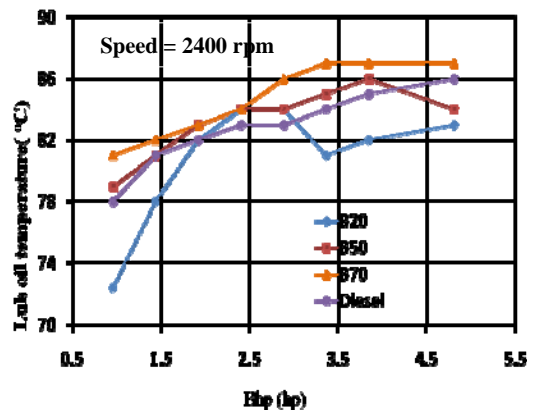


Fig 10. Variation of Lub oil temperature with Bhp for different fuels.

Fuel consumption rates and break thermal efficiency ( $\eta_b$ ) are present respectively in fig 7 and 8 for different fuels and for different loading conditions at 85°C preheat temperature. Without preheating, the operation of the engine was very difficult. This is a major constraint of using biodiesel on unmodified CI engines. For diesel,



the break specific fuel consumption was viewed to vary from 387.91 gm/bhp-hr at near 20% load and reduce to 224.5 gm/bhp-hr at rated capacity which is at 68% loading condition achieving thermal efficiency of 22.28%. Values are typical for diesel engines of this category and the maximum power attained was only slightly less than the manufacturer's specification. Using B20 did not show much difference in rated load performance and thermal efficiency. The bsfc at rated load was 272 gm/bhp-hr for B20 with thermal efficiency of 17.8%. At rated capacity, the bsfc for B50 was 275 gm/bhp-hr and bsfc for B70 was 280 gm/bhp-hr. The thermal efficiencies for B50 and B70 are 17.8% and 17.67% respectively. Results show very little deviations at rated rpm (2400) and rated load. From these figures, it is evident that the specific fuel consumption values are always higher for all biodiesel and in case of thermal efficiency it is always lower for all biodiesel than diesel. One of the reasons could be that, biodiesel has a heating value lower than diesel. Again high viscosity of biodiesel causes poor atomization and mixture formation and increases the fuel consumption rate to maintain the power. Maybe for these reasons, the bsfc for biodiesel was higher than that of diesel and thermal efficiency is lower.

Fig 9 and fig 10 shows the variation of temperature of exhaust gages and lub oil respectively. From fig 11, the exhaust gas temperature for diesel rises tremendously from 116°C to 632°C. The biodiesel blends (B20, B50, B70) also follows the same trend. At starting condition, the exhaust temperature was higher for all three blends. Higher exhaust temperature but lower power output indicates late burning to the high proportion of biodiesel. This would increase heat losses making the combustion a bit less efficient. But for higher loading condition, the exhaust gas temperature for diesel is higher compared to biodiesel blends. But, in case of B20, at starting, the exhaust temperature was higher than the other three and it also deviates at full load condition. At full load, whereas the other two blends have exhaust temperature higher than diesel, the exhaust gas temperature of B20 is lower than diesel. From fig 10, the lub oil temperatures shows similar characteristics for diesel and biodiesel blends, as for biodiesel blends, the lub oil temperature is much higher. With an increase of proportion of biodiesel, the lub oil temperature also increases. One of the reasons could be the preheating treatment of biodiesel needed to run the engine. Exact preheating temperature is not known yet and it needs further investigation.

#### 4.3 Emission Characteristics of Biodiesel

In this thesis, emission characteristics such as, excess O<sub>2</sub>, CO, CO<sub>2</sub>, excess air and heat losses are measured by using IMR 2800P. The NO<sub>x</sub> emission does not show any regular pattern.

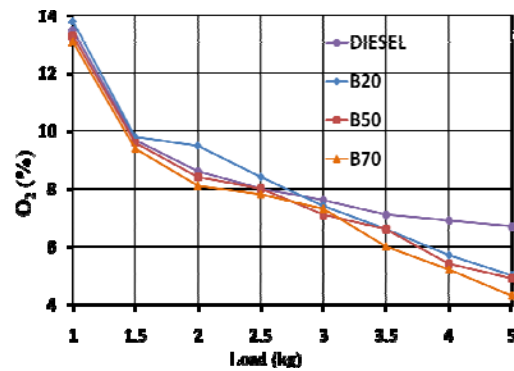


Fig 11. Variation of excess O<sub>2</sub> (%) with load for different fuels

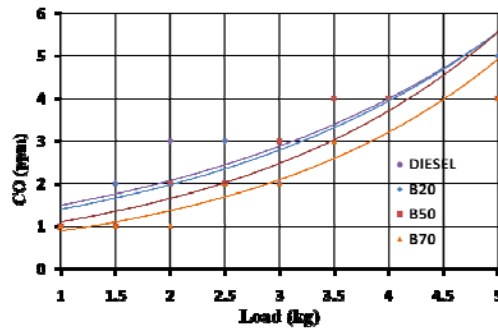


Fig 12. Variation of CO (ppm) with load for different fuels

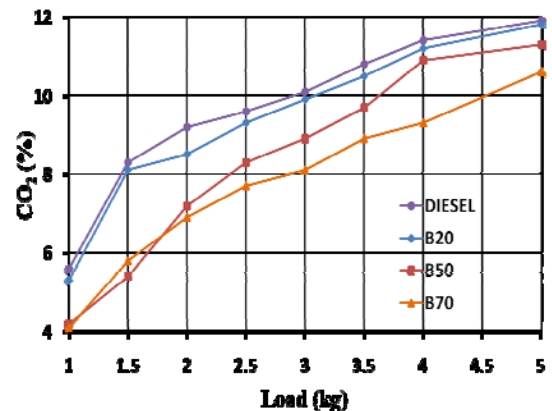


Fig 13. Variation of CO<sub>2</sub> (%) with load for different fuels

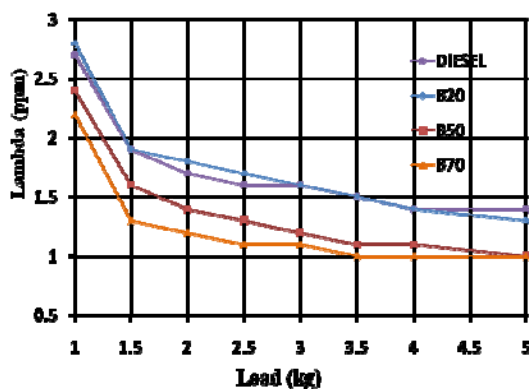


Fig 14. Variation of excess air (ppm) with load for different fuels

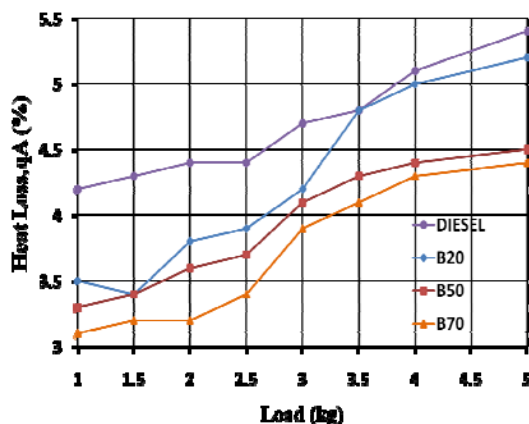


Fig 15. Variation of heat loss (%) with load for different fuels

During experiment the gas probe was inserted at the end of a six feet long exhaust pipe. It was difficult to insert the probe in the actual exhaust port of the engine due to high temperature and vibration. The experimental data such as percentage of  $O_2$ ,  $CO_2$ , Heat loss etc varies from the actual data because of this distance from the exhaust port of the engine. The aim of the experiment is to show the trend of the graphs and the comparison of different bio fuels with the diesel fuel.

Fig. 11 shows the variation of excess  $O_2$  present in exhaust gas with load for different fuel. The  $O_2$  present in the exhaust gas for the biodiesel blends are lower than that of the diesel fuels at all loading conditions. The percentage of  $O_2$  decreases with an increase of biodiesel in the blends.

Fig. 12 shows the variation of CO emission with load for different fuels. The CO emissions for the biodiesel blends are lower than that of diesel fuels, though the characteristics show that the increase or decrease of CO emission is very small. This also maintain the same characteristic as excess  $O_2$ , as the CO emission is higher for lower number biodiesel blend and is lower for higher number.

Fig. 13 shows the variation of  $CO_2$  emissions with load for different fuels. Actual percentage of  $CO_2$  emission is much higher than the experimental data. The

reason behind this variation is the distance of the gas probe from the exhaust point. It is observed that all the  $CO_2$  emission of diesel fuel is higher than that of blended fuels. This may be because the biodiesel blends contains oxygen elements the common context is relatively lower in the same volume of fuel consumed at the same engine load, consequently, the  $CO_2$  emissions from the biodiesel blends are lower.

Fig. 14 shows the variation of excess air present in the exhaust gas with load for different fuels. The excess air present in the exhaust gas decreases with increase in load and biodiesel percentage present in the fuel.

Fig. 15 shows the heat losses by exhaust with load for different fuels. This heat loss does not represent the actual value as the data were collected from a certain distance from the exhaust point. This data does only represent the idea how the heat losses varies with load for different fuels. From the fig, it is clear that heat loss increases with the increase in load. The diesel fuel has higher values for heat loss and it decreases with increase in biodiesel percentage present on the fuel for the same load.

In view of environmental considerations, bio-diesel is considered Carbon neutral because all the  $CO_2$  released during consumption had been sequestered from the atmosphere for the growth of vegetable oil crops. The combustion of bio-diesel has reported to emit lesser pollutants compared to diesel. This indicates that the engine exhaust contains no  $SO_2$ , and shows decreasing emissions of CO, HC, soot and aromatics. The  $NO_x$  emission is reported to be in the range between  $\pm 10\%$  as compared to diesel depending on engines combustion characteristics [14].

## 5. COST ANALYSIS

The present costing of running a diesel engine with biodiesel blends derived from soybean oil are given at the following table:

Table 2: Cost of running engines with different fuels

Fuel	Cost (tk/litre)	At rated load Tk/bhp-hr (Tk/kW-hr)
Diesel	45	10.1 (12.98)
B20	64	17.4 (23.34)
B50	92.5	25.4 (34.1)
B70	111.5	31.2 (41.85)

From Table 2, it is clear that, running diesel engine with biodiesel is costly compared to that of diesel. The main contribution for high cost of per litre biodiesel is the high price of edible oil and high cost of methanol which are used for transesterification reaction. The fuel cost is about 1.4, 2.05 and 2.5 times more expensive compared to diesel for B20, B50 and B70 respectively. Regarding cost of per kWh mechanical power generation, this is about 13 tk/kW-hr for diesel, 24 tk/kW-hr for B20, 34 Tk/kW-hr for B50 and 42 tk/kW-hr for B70 at rated load.

The costing shows that using biodiesel is still very expensive with current market price of diesel, but this situation may change with unavailability of fossil fuel or sharp rise of conventional fossil fuel prices.

## 6. CONCLUSION

Experiments were conducted on a small four stroke, single cylinder, water cooled diesel engine and performance characteristics of the engine was studied using diesel and diesel-biodiesel blends as fuels. The following conclusion can be drawn from this experimental study:

- i). Bio-diesel can be produced from soybean oil using transesterification process.
- ii). It was possible to run the diesel engine with biodiesel blends as the fuel.
- iii). The density and the heating value of bio-diesel from soybean oil were found to be close those of diesel.
- iv). Brake specific fuel consumption for biodiesel increases with increase in its amount in the blend.
- v). The CO, CO<sub>2</sub>, excess O<sub>2</sub> and excess air emissions are reduced with increase in its amount in the blend.
- vi). The B20 seems to be the best alternative fuel for diesel. Because the break specific fuel consumption of B20 (272gm/bhp-hr) is close to diesel (225gm/bhp-hr) and the emission quality is better than diesel.

## 7. REFERANCES

1. Babu A. K. and Devaradjane G., “Vegetable Oils and Their Derivatives as Fuels for CI Engines : An Overview” SAE Technical Paper 2003-01-0767.
2. Reddy, Babu and V.Ganesan, (2000), “Effect of Injection Pressure on Diesel Engine Performance with Vegetable Oil: Diesel Blends”, IC Engines and combustion, 2000.
3. Gerhand vellguth, (1983), “Performance of Vegetable Oils and Their Monoesters as Fuels for Diesel Engines”, SAE Transaction Paper 83153.
4. Peter J.F., Rand, M.C. and Ziemke, M.C. 1982. “Investigation of Soybean Oil as Diesel Fuel Extender”, SAE Paper No.823615.
5. Pramanik. K (2003) “Properties and Use of *Jatropha circus* oil and Diesel Fuel Blends in Compression Ignition Engine”, International Journal of Renewable Energy, 28, pp.239-248.
6. Ehsan, M., Taposh R. M., Islam M.M. “Running a Diesel Engine with Biodiesel” Proceedings of the 7<sup>th</sup> International Conference on Mechanical Engineering, ICME 2007-TH 34, December 2007.
7. Yosimoto. Y, Onodera.M and Tamaki.H (2001), “Performance and Emission Characteristics of Diesel Engines Fuelled by Vegetable Oils”, SAE Paper No. 2001-01-1807/4227.
8. Krawezy T., “Biodiesel - Alternative Fuel Makes in Roads but Hurdles Remain”, INFORM 1996; 7(8):800-15.
9. Otera J., Transesterification Chem Rev, 1993; 93(4):1449-70.
10. Srivastava A, Prasad R, “Triglyceride based Diesel Fuels”, Renew Sustain Energy Rev 2000; 4:111-33.
11. Dorado MP, Ballesteros E, Almeida JA, Schellet C, Lohrein HP, Krause R, “An Alkali Catalysed Transesterification Process for High Free Fatty Acid Oils”, Trans ASAE 2002;45(3):525-9.
12. Freedman B, Pryde EH, Mounts TL. “Variables affecting the yield of fatty esters from Transesterification vegetable oils”, J Am Oil Chem Soc 1984;61(10):1638-43.
13. A.Murugesan, T.R.Chinnusamy, M.Krishnan, PSS.Srinivasan, C.Umarani, C.G.Saravanan, R.Subramanian, N.Nedunchezhian, “Optimization of transesterification process for biodiesel production”, International Conference on I.C Engines and Combustion. Dec 6-9, 2007. pp. 570-576.
14. A.Murugesan, T.R.Chinnusamy, M.Krishnan, V.Chandraprabu, C.Umarani, R.Subramanian, N.Nedunchezhian. “Preparation of methyl ester (bio-diesel) from low cost transesterification unit”, Second International Conference on Resource utilization and intelligent systems, INCRUIS-2008. Jan 3-5, 2008. pp. 38-42.
15. Greeves G,Wang Lucas CHT. CAV Ltd. “Origins of diesel particulate mass emission”, SAE 810260, 1981.
16. Nurannabi MD, Shamim Akhter MD, Zaglul Shahdat MD. “Improvement of engine emissions with conventional diesel fuel and diesel bio diesel blends”, Bio source Technology 2006; 91:372-8.

## 8. NOMENCLATURE

Symbol	Meaning	Unit
T	Temperature	(°C)
$\lambda$	Excess air	(ppm)
q <sub>A</sub>	Heat loss	(%)
Q	Calorific value	(MJ/kg)
A/F	Air Fuel ratio	[-]

## 9. MAILING ADDRESS

M. A. Islam  
 Department of Mechanical Engineering, Bangladesh University of Engineering and Technology, Dhaka, Bangladesh.  
 E-mail: [aislam@me.buet.ac.bd](mailto:aislam@me.buet.ac.bd)

# CARBON STEEL QUENCHING AND MAXIMUM HEAT FLUX WITH WATER JET IMPINGEMENT

A. K. Mozumder<sup>1</sup>, M. Ahmed<sup>1</sup> and M. Monde<sup>2</sup>

<sup>1</sup>Dept. of Mechanical Engineering, Bangladesh University of Engg. & Tech. Dhaka, Bangladesh

<sup>2</sup>Dept. of Mechanical Engineering, Saga University, Saga, Japan

## ABSTRACT

An experimental investigation of jet impingement quenching has been performed for three different block materials copper, brass and steel with jet velocities of 3-15 m/s, jet subcoolings of 5-80K and initial block temperatures of 250-600 °C. The present study has focused to investigate the characteristics of quenching for carbon steel only. The effect of experimental parameters on the maximum heat flux (the maximum value of heat flux from the solid and carried out by the liquid) was investigated in the present study. The value of maximum heat flux increases with the jet velocity and also with liquid subcooling. The maximum heat flux is also found to be almost independent of block initial temperature. A correlation of maximum heat flux for carbon steel together with the dominating parameters is proposed here which well agrees with the experimental data.

**Keywords:** Quenching, Jet Impingement, Heat Flux

## 1. INTRODUCTION

Jet impingement quenching is widely employed in many industrial applications relating to rapid cooling and better control of high temperatures. In the manufacturing world, jet cooling is used in processes such as extrusion, casting, forging and annealing for the purpose of having precise mechanical and metallurgical properties.

Many experimental and analytical works on quenching phenomena have been studied during the last few decades. The quenching process has been defined by researchers in many ways [1]. Chan et al. [2] defined the rewetting as the re-establishment of continuous liquid contact with a hot dry surface. They found that rewetting always occur when the temperature of the hot surface is below a certain value generally referred as the rewetting, sputtering or Leidenfrost temperature.

The quenching by water jet impingement is revealed as a rapid cooling process for high temperature surfaces. The heat transfer rate is significantly greater than other conventional cooling methods. Wolf et al. [3] reported that for single phase convection, the heat transfer coefficient for water jet impingement cooling exceeds 10kW/m<sup>2</sup>. For this reason, the cooling by impinging jets is preferred in many industrial applications.

Filipovic et al. [4] conducted transient boiling experiments where a large preheated specimen was quenched by a water wall jet on its top surface. They observed the propagation of the quench front in the direction of flow along the surface. They reported that the nucleate boiling or single phase convection was present in the upstream of the quench front while the film

boiling was occurred in the downstream of the front.

Mozumder et. al [5-7] conducted the experimental investigations of quenching for three different cylindrical blocks i.e. steel, brass and cast iron using a sub cooled water jet. They observed that the wetting front becomes stagnant for a certain period of time in a small central region before wetting the entire surface and defined this time as the resident time.

## 2. EXPERIMENTAL

The experiment was actually performed by Mozumder [5] and the detailed descriptions of the experiment can be found on there. Different elements of the experimental setup are also shown in Fig.1.

### 2.1 Experimental Setup

The experiment [5] was conducted individually for three different materials of copper, brass and steel. The similar behaviors were found for copper and brass block while bit dissimilarity was found for steel. In this research work, the experimental data was taken from the experiment [5] where a hot cylindrical steel block was quenched by water jet impingement. A water jet of 2 mm was stroked at the center of the heated surface. The temperature readings from the thermocouples recorded by the data acquisition system were used to get the surface parameters i.e. surface temperature and surface heat flux of the heated block. A high speed video camera was used to capture the flow phenomena during quenching. Some video images were available to observe these flow phenomena for this study.

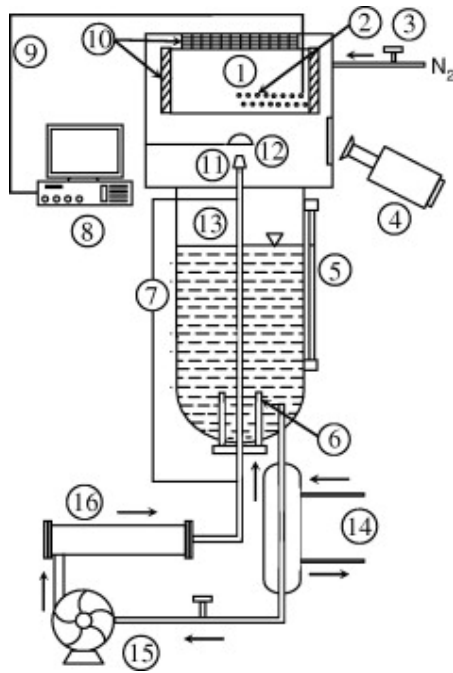


Fig 1. Schematic diagram of the experimental set-up  
 1 – tested block, 2 – thermocouple positions, 3 – nitrogen gas valve, 4 – high-speed video camera, 5 – level gauge, 6 – main heater, 7 – dynamic strain meter (for measuring jet velocity), 8 – data acquisition system, 9 – thermocouple wire, 10 – block heaters, 11 – nozzle, 12 – rotary shutter, 13 – liquid tank, 14 – cooler, 15 – pump, and 16 – auxiliary heater

The present study focuses to investigate the maximum heat flux during quenching of carbon steel block under the same experimental conditions as for copper and brass block.

### 2.2 Analysis of Temperature Data

During quenching of hot surfaces the direct measurement of surface heat flux and temperature is very difficult. It is impossible to get the thermal history directly just from the surface at which the jet is impinged without greatly disturbing the flow and boiling phenomena. An inverse heat conduction technique [8] is proved to get the surface heat flux and temperature from knowing the history of temperatures inside the hot solid surface.

## 3. RESULTS AND DISCUSSION

The effects of dominating parameters have been analyzed in this section. The variation of Maximum Heat Flux (MHF) with radial position, jet velocity, jet subcooling, block initial temperature and with block material are discussed here.

### 3.1 Effect of Radial Position on MHF

The value of maximum heat flux changes with the radial position of the jet impinged point. The solid-liquid interaction region remained fixed up to the radial

position of  $8 \pm 3$  mm for most of the cases and then the wetting front started to move in the radial direction.

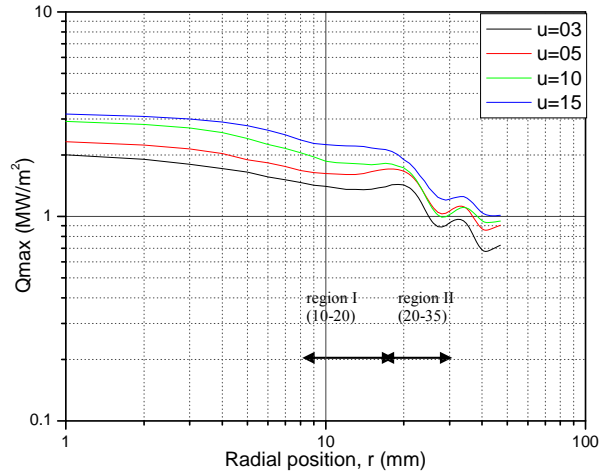


Fig 2. Variation of maximum heat flux with radial position for different jet velocity ( $T_b=300^\circ\text{C}$ ,  $\Delta T_{\text{sub}}=20\text{K}$ )

The heat flux decreases very slowly within this region (Fig.2). In this analysis, the variation of maximum heat flux for these regions has been considered when the wetting front started to move. Two distinctive regions are identified: region I (from 10-20 mm) and region II (from 20-35 mm). In the region I, the maximum heat flux decreases slowly with the radial position. In the region II, the maximum heat flux decreases more rapidly with radial position. It was observed that the area of vigorous boiling region increased when the wetting front started to move outward in the radial direction. The available surface area to become cool is increased and the heat carrying capacity of coolant is decreased when it moves outward in the radial direction. This results in decrease of maximum heat flux with increasing radial position.

### 3.2 Effect of Jet Velocity on Maximum Heat Flux

The effect of jet velocity on maximum heat flux is shown in Fig.3. Maximum heat flux increases with the jet velocity. Maximum heat flux is higher for a smaller

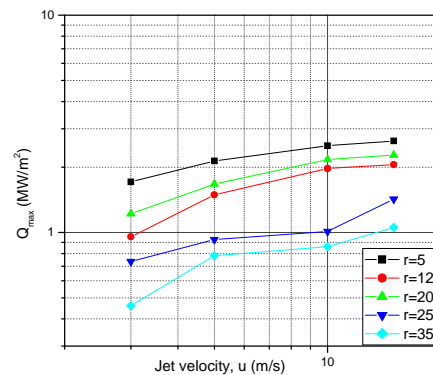


Fig 3. Effect of jet velocity on maximum heat flux ( $T_b=400^\circ\text{C}$ ,  $\Delta T_{\text{sub}}=20\text{K}$ )



radial position for a particular jet velocity which also indicates the maximum heat flux decreases with the radial position. The higher jet velocity means the higher flow rate of coolant supplied to the heated surface which has direct effect on the rate of heat transfer.

### 3.3 Effect of Sub-Cooling on MHF

The variation of maximum heat flux with subcooling of water for different radial position is presented in Fig.4. Higher subcooling means the higher temperature difference between the saturation temperature and liquid temperature. The lower temperature liquid takes more heat from the heated surface to reach its saturation temperature. Therefore the rate of heat transfer is increased. This observation has been found for all experimental conditions.

### 3.4 Effect of Initial Block Temperature on MHF

Mozumder [5] found that the effect of initial block temperature on maximum heat flux is very small. The required time to reach its maximum heat flux point is longer for higher initial temperature. Due to its very small effect it is considered that maximum heat flux is almost independent of block initial temperature  $T_b$ . Figure 5 shows the effect of initial temperature on the maximum heat flux for different radial position. It is also proved that there is very little effect of  $T_b$  on the maximum heat flux. We have ignored some scattering data for the initial temperatures of 450-600°C.

### 3.5 Effect of Block Material on MHF

It is evident that the block material influences strongly the rate of heat transfer. Mozumder [5] experimented on jet impingement quenching of three different block materials (copper, brass and steel) and reported that the maximum heat flux for copper material is more than two times than steel material. The thermal conductivity of copper, brass and steel are 380 W/mK, 112 W/mK and 37.8 W/mK respectively. Therefore, the thermal conductivity of carbon steel is approximates 1/10 times of copper. The maximum heat flux is strongly affected by the block material. In the case of copper, the effects of impinged water quickly reached to the entire surface. The heat of the quenching area is quickly recovered by the stored heat from the nearer surface area due to its higher thermal conductivity. For steel, the surface is cooled locally near the surface at which the jet is impinging. Because of low thermal conductivity heat is locally removed from the heated surface but the total effect of cooling process does not feel immediately over the entire solid body.

### 3.6 Correlation of Maximum Heat Flux

The following two correlations have developed for the initial temperatures of 250-400°C for the two distinct regions:

For region I (radial position of 10-20mm)

$$\frac{Q_{\max}}{\rho_s h_{fg} u} = 55.119 \left( \frac{(\rho c \lambda)_l}{(\rho c \lambda)_s} \right)^{0.674} \left( \frac{\rho_l u^2 (2r_q - d)}{\sigma} \right)^{-0.295} (1 + Ja)^{0.136}$$

For region II (radial position of 10-20mm)

$$\frac{Q_{\max}}{\rho_s h_{fg} u} = 1.106 \left( \frac{(\rho c \lambda)_l}{(\rho c \lambda)_s} \right)^{-1.291} \left( \frac{\rho_l u^2 (2r_q - d)}{\sigma} \right)^{-0.287}$$

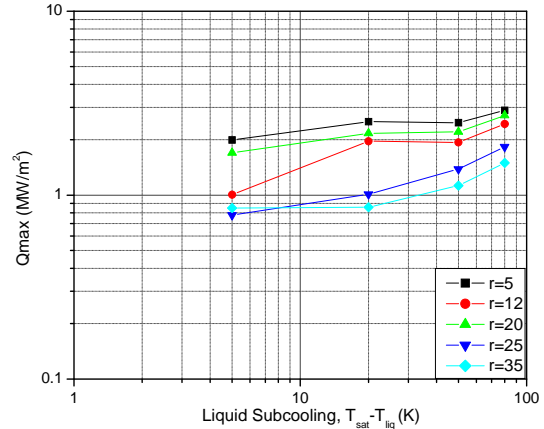


Fig 4. Variation of Maximum surface heat Flux with liquid subcooling ( $T_b=400^\circ\text{C}$ ,  $u=10\text{m/s}$ )

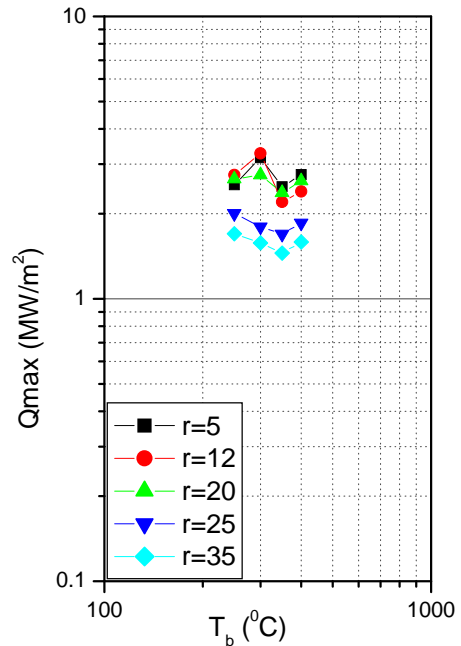


Fig 5. Effect of initial block temperature on maximum heat flux ( $\Delta T_{\text{sub}}=50\text{K}$ ,  $u=15\text{m/s}$ )

The coefficients of these two correlations have been determined by using least square method from the experimental data of maximum heat flux. Experimental data is then compared with these proposed correlations for the two regions. The experimental data is within  $\pm 25\%$  and  $\pm 30\%$  of the proposed correlations for region I and region II respectively.

## 4. CONCLUSION

The present study has focused on the maximum heat flux during jet impingement quenching of steel block. Maximum heat flux is one of the important parameters in

investigating the underlying mechanisms of quenching process. It is a very complicated process. At present the following conclusions can be drawn:

1. The maximum heat flux always occurs during the movement of the wetting front. During this movement the position of the maximum heat flux also moves from the center towards the circumference.
2. The maximum heat flux is reported to be strong function of jet sub-cooling, jet velocity and material property although, it is independent of block initial temperature.
3. The correlations between the maximum heat flux and the important non dimensional groups have been proposed of the steel block for the two regions: region I (10-20mm) and region II (20-35mm).
4. The maximum heat flux for the initial temperatures range of 250-400°C is well predicted within an accuracy of  $\pm 25\%$  and  $\pm 30\%$  for two regions I and II respectively by comparing it with the proposed correlation of maximum heat flux.

## 5. REFERENCES

1. Ahmed, M., 2008, "Maximum Heat Flux and Wetting Delay during Quenching of High Temperature Carbon Steel Block", M. Sc. Thesis, Dept. of Mechanical Engineering, Bangladesh University of Engineering and Technology, Dhaka, Bangladesh
2. Chan, A. M. C. and Banerjee, S., 1981, "Refilling and Rewetting of a Hot Horizontal Tube, Part I: Experiments", Trans. ASME, Journal of Heat Transfer, Vol. 103, pp. 281-286
3. Wolf, D. H., Incropera, F. P. and Viskanta, R., 1993, "Jet Impingement Boiling", In Advances in Heat Transfer (Edited by J. P. Hartnett et al.), Vol. 23, pp. 1-132. Academic Press, New York
4. Filipovic, J., Incropera, F. P., and Viskanta, R., 1995, "Quenching Phenomena Associated with a Water Wall Jet: I. Transient Hydrodynamic and Thermal Conditions", Experimental Heat Transfer 8 pp. 97-117
5. Mozumder, A. K., 2006, "Thermal and Hydrodynamic Characteristics of Jet Impingement Quenching for high temperature surface", Ph.D thesis, Graduate School of Science and Engineering, Saga University, Japan
6. Mozumder, A. K., Monde, M. and Woodfield, P.L., 2005, "Delay of wetting propagation during jet impingement quenching for a high temperature surface", Int. J. of Heat and Mass Transfer 48 pp. 2877-2888
7. Mozumder, A. K., Monde, M., Woodfield, P. I. and Islam, M. A., 2006, "Maximum heat flux in relation to quenching of a high temperature surface with liquid jet impingement", Int. J. of Heat and Mass Transfer 49 pp. 2877-2888
8. Monde, M., Arima, H., Liu, W., Mitsutake, Y. and

Hammad, J.A., 2003, "An analytical solution for two-dimensional inverse heat conduction problems using Laplace transform", Int. J. Heat Mass Transfer 46, pp. 2135-2148

## 6. NOMENCLATURE

Symbol	Meaning	Unit
$d$	Jet diameter	(mm)
$Q_{\max}$	Maximum heat flux	(MW/m <sup>2</sup> )
$h_{fg}$	Latent heat of vaporization	(kJ/kg)
$J_a$	Jackob Number	(-)
$r$	Position in the radial direction of the block	(mm)
$r_q$	Radial position at maximum heat flux point	(mm)
$T_b$	Initial block temperature	(°C)
$T_{liq}$	Liquid temperature	(°C)
$T_{sat}$	Saturated liquid temperature	(°C)
$\Delta T_{sub}$	Liquid subcooling, ( $T_{sat} - T_{liq}$ )	(K)
$u$	Jet velocity	(m/s)
$c$	Specific heat	(kJ/kg K)
$\lambda$	Thermal conductivity	(W/m <sup>2</sup> K)
$\rho$	Density	(kg/m <sup>3</sup> )
$\sigma$	Surface tension	(N/m)
Subscripts		
l	liquid	
s	solid	

## 7. MAILING ADDRESS

A. K. Mozumder  
 Dept. of Mechanical Engineering.  
 BUET, Dhaka, Bangladesh



demand of I-131 is much higher than the current

## NUMERICAL ANALYSIS FOR TEMPERATURE ASSESSMENT OF THE IRRADIATED TeO<sub>2</sub> POWDER IN THE DRY CENTRAL THIMBLE OF THE 3MW TRIGA MARK-II RESEARCH REACTOR

M.S.Islam<sup>1</sup>, S.B.Samee<sup>2</sup>, M.M.Uddin<sup>1</sup> and M.Mamun<sup>2</sup>

<sup>1</sup>Reactor Operation and Maintenance Unit, Atomic Energy Research Establishment, Ganakbari, Savar, ,  
Dhaka, Bangladesh

<sup>2</sup>Bangladesh University of Engineering and Technology (BUET), Dhaka, Bangladesh

### Abstract

Temperature assessment during irradiation of 50g TeO<sub>2</sub> powder in a sealed quartz vial holding with aluminum specimen container (Al-Can) in the dry central thimble (DCT) of the reactor core is performed numerically using a CFD tool. The reactor power is considered full power at 3MW(th). The geometrical configuration of the DCT is; length = 8 m, I.D = 33.88 mm and O.D = 38.1 mm and there is like a dog-leg bend. The length of the quartz vial as well as Al-Can are 75.2 and 95.1 mm, respectively. The gap between the quartz vial and Al-Can, Al-Can and DCT are 0.92 and 4.49 mm, respectively and there is air in the gaps. A 2D and 3D model geometry of the DCT with a narrow gap between quartz vial and Al-Can (0.92 mm) and Al-Can and DCT (4.49mm) is generated by simulating the existing cooling capacity of the DCT. The laminar viscous model and the turbulent RNG  $k-\epsilon$  model are applied for the 2D and 3D models. Radiative heat transfer was modeled using S2S model for the 2D case provided with no hole on the surface of the Al-Can and DTRM is used for the 3D case provided with several holes on the surface of the Al-Can. It has found that the highest centerline temperature of TeO<sub>2</sub> powder is found in the laminar viscous model of the existing cooling geometry which is about 662 °C when no hole is present on the surface of the Al-Can. On the other hand, RNG  $k-\epsilon$  model shows a maximum centerline temperature of 658 °C under the same condition. However, no significant difference has found in temperature distribution between the laminar viscous and the turbulent RNG  $k-\epsilon$  model. In the 3D modeling, when several holes present on the surface of the Al-Can under the same condition, it has found that the centerline temperature along with temperature at different zones decreases considerably. This is because of the more favorable heat transfer atmosphere than the sealed Al-Can (without hole). The detailed numerical analyses under different cases along with experiments under the same cases may really provide a better cooling technique for the DCT of the reactor which consequently does help increasing the I-131 production and other related R&D activities with assured safety of the reactor operation.

**Keywords:** Temperature assessment, Irradiation, Numerical analysis, Safety, Reactor Operation

### 1. INTRODUCTION

Iodine-131 is one of the most important radio-isotopes (RI) that are being used in the fourteen nuclear medicine centers of the country. It is produced by irradiating TeO<sub>2</sub> as a target material in the nuclear research reactor. Bangladesh Atomic Energy Commission (BAEC) is operating a 3MW TRIGA Mark-II research reactor where TeO<sub>2</sub> powder is loaded in a sealed quartz vial and irradiated in the DCT of the reactor core. One quartz vial containing about 40g of TeO<sub>2</sub> powder is irradiated in the DCT at a power level of 2.5 MW. At the end of the irradiation, about 300 mCi of I-131 is obtained by processing the irradiated TeO<sub>2</sub> powder. As the weekly

production level, the need for increasing the production rate of I-131 is always there. One way of doing so is to increase the amount of irradiating TeO<sub>2</sub> in a single quartz vial. Another way is to increase the irradiating time. However the operating cost of the reactor is much higher than the cost of TeO<sub>2</sub> target material. So it is preferable to increase the amount of target material (TeO<sub>2</sub>) loaded in a single vial in the reactor core. But, loading extra amount of target material will produce extra amount of heat energy. Therefore it becomes necessary to conduct a thermalhydraulic safety analysis and ensure that the temperature distribution inside the DCT of the reactor

core is within the operating limit during reactor operation.

On March 19, 2002, the reactor was operated with 50 g TeO<sub>2</sub> powder at DCT at 3MW full power of the reactor power during 8 hours in order to check the cooling system performance of the newly installed plate heat exchanger by replacing shell and tube heat exchanger. After necessary cooling of the irradiated TeO<sub>2</sub> powder, during the unloading period, the level of radioactivity inside the DCT was found much higher than the usual level. After physical investigation, it was found that the lower portion of the Pyrex vial (used to be quartz vial) containing the target material was melted and the Al-Can containing the Pyrex vial was also damaged. To review and analyze the causes of the vial failure, an International Atomic Energy Commission (IAEA) expert mission was conducted at research reactor facility of Bangladesh. The mission recommended using quartz vial instead of Pyrex vial while irradiating TeO<sub>2</sub> powder in the DCT. But when the amount of target material was increased from 40g to 50g and the reactor was operated at full power level, the failure of quartz vial happened in December 2007. Due to these two vial failure incidents it became a necessity to analyze the heat transfer phenomenon inside the DCT of the reactor core with proper approach. In this study, it has evaluated the temperature distribution inside the DCT of the reactor core and determined the temperature at various zones and also checked whether these temperatures are within operating limit.

On the other hand, it is also possible to increase the production rate of I-131 by improving the cooling system in and around the CT. One of the ways is to use perforated Al-Can instead of sealed Al-Can. Furthermore, irradiation channel of central thimble (CT) with water filled is much better than the dry irradiation channel filled in air. This is possible through improving the heat transfer rate from the DCT of the reactor core to the external cooling media (water). For this purpose, it has been modeled and analyzed first only existing and then a modified cooling system. Heat transfer in a narrow channel is of high interest in both theoretical and experimental physics. Many researches have been conducted so far to analyze the thermohydraulic conditions in the narrow channels. Numerical codes are also developed to conduct computational study.

GENGTC<sup>[1]</sup> was one of the first computer programs for calculating capsule temperature in cylindrical geometry. B.G. Jones, N.H. Schilmoeller, D.F. Hang, G.P. Beck<sup>[2]</sup> conducted a study on forced cooling of Illinois advanced TRIGA reactor. M.S. El-Genk, J.S. Philbin, and F.C. Foushee<sup>[3]</sup> investigated the heat transfer and fluid flow at low pressure in narrow channels. This research focuses on heat removal and fluid dynamics in flow regimes characterized by low pressure and low Reynolds number. The program was motivated by a desire to characterize and analyze cooling in a broad class of TRIGA reactors under: (a) typical operating conditions, (b) anticipated, new operating regimes, and (c) postulated accident conditions. It has also provided experimental verification of analytical tools used in design analysis.

M.S. El-Genk, et al.<sup>[4]</sup> also studied the air coolability of TRIGA reactors following a loss-of-coolant accident (LOCA). They conducted experiments on the air-coolability of a heated rod in a vertical open annulus at near atmospheric pressure and later imposed this analogy on to the coolability of reactor fuel rods that are totally uncovered in a LOCA. A.Z. Mesquita and H.C. Rezende<sup>[5]</sup> performed experimental and analytical studies at the Nuclear Technology Development Center to find out the temperature distribution in the IPR-R1 TRIGA Research Nuclear Reactor, as a function of power and position in the reactor core. The basic safety limit for the TRIGA reactor system is the fuel temperature, which is studied in both steady-state and pulsed mode operation.

E. Umar et al.<sup>[6]</sup> conducted the experimental study of natural convection in the hottest channel of TRIGA 2000 kW. The purpose of the experimental study was to verify the theoretical analysis, especially the temperature distribution in the hottest coolant channel using the STAT code. M.Q. Huda et al.<sup>[7]</sup> studied the thermal-hydraulic analysis of the 3 MW TRIGA MK-II Research Reactor under steady-state and transient conditions.

Thermal-hydrodynamic design and safety parameter studies of the TRIGA MK II research reactor were done by M. Q. Huda and M. Rahman<sup>[8]</sup> in 2003. PARET code was used to analyze important thermo-hydrodynamic design and safety parameters of the 3 MW TRIGA MK-II research reactor at Atomic Energy Research Establishment (AERE), Savar, Dhaka, Bangladesh. The loss-of-flow accident (LOFA) scenario of the reactor was also studied to ensure that the existing design and procedures are adequate to assure that the consequences from this anticipated occurrence does not lead to a significant accident. Investigation of thermo-hydraulic parameters during natural convection cooling of TRIGA reactor was done by M.Q. Huda and S.I. Bhuiyan<sup>[9]</sup> in 2006. The experimental results were used for validating NCTRIGA code.

Studies on the overall safety aspects during irradiation of TeO<sub>2</sub> in the central thimble of the TRIGA research reactor was performed by M.Q. Huda et al.<sup>[10]</sup>. They identified safety issues relevant to I-131 radioisotope production and ensured that safety analysis and design are consistent. They evaluated threats developed within the facility during the irradiation process and ultimately ensures establishment of in-core safety limits and conditions at all stages of I-131 production.

TRISTAN, a numerical code for calculating the flow parameters in a coolant channel of reactor core, cooled by natural convection, was developed by I. Mele<sup>[11]</sup>. It was designed for steady-state thermo-hydraulic analysis of TRIGA research reactors operating at low power level of 1-2 MW in an open pool or tank, where normal pressures are not exceeding 2 bars. The objective of this study is to predict the temperature distribution accurately in and around the CT for sustainable I-131 production and other related R&D activities with assured safety of the reactor

operation. Chapt. 2 describes the physical problem in detail and its numerical approach, Chapt.3 describes the numerical results and Chapt. 4 draws a conclusion over whole the investigation.

## 2. PROBLEM DESCRIPTION AND GEOMETRY

The thermal analysis for irradiated target materials of the TRIGA Mark-II research reactor is very necessary for its safe operation. Keeping the temperature of the CT of the reactor core within limit not only ensures safe operation but also strengthens the production of I-131. In the existing irradiation facility, the quartz vial loaded with  $\text{TeO}_2$  is kept inside an Al-Can. The Al-Can is mounted on a stopper plate. Both the Al-Can and stopper plate is inside a CT which is dry. Outside the CT, the cooling fluid (water) is circulated by two primary pumps. Heat from the  $\text{TeO}_2$  powder is first conducted through the quartz vial, and then convection occurs in the air gap between the quartz vial and Al-Can. After that, conduction through Al-Can, convection through air gap between Al-Can and CT and finally conduction through CT wall occurs.

If it is to be looked carefully to the heat transfer phenomenon, then it is obvious that the prime resistance to the heat transfer is the convection through air gaps. To produce I-131 at a higher rate than the present rate without disrupting the safety of the reactor, it needs to be focused on increasing the heat transfer rate through these convection mediums.

One of the ways is to drill sets of radial holes of small sizes (1 mm) at two different levels of the Al-Can for providing the venting in and out of the convective fluid to and from the Al-Can. Air of comparatively less temperature from the outside of the Al-Can enters the Al-Can by the lower level holes, takes heat from the wall of the vial, gets hot and the density decrease. So it climbs up and escapes through the higher level holes. As there is a motion between the inner and outer air of the Al-Can, the heat transfer rate increases to a certain degree. In this study, it is taken two cases; i. CT with no hole over the Al-Can and ii. CT with holes over the Al-Can to model and analyze the situation.

50 g  $\text{TeO}_2$  is kept in a sealed quartz vial (Figs.1 and 2). The quartz vial is 1.75 mm thick. Its inner and outer radii are 9.38 and 11.13 mm, respectively. The height of the quartz vial is 75.2 mm. The quartz vial is kept in an Al-Can. The Al-Can has an inner radius of 12.05 mm and outer radius of 12.45 mm. The height of the Al-Can is 95.1 mm. The Al-Can is in rest on the top of a stopper plate of aluminum. This plate is 3.81 cm thick. Under the plate, there is water at  $60^\circ\text{C}$ . The Al-Can is kept in the CT, which is also made of aluminum. The inner and outer radii of the CT are 16.94 mm and 19.06 mm, respectively. The height of the CT is 8 meter.

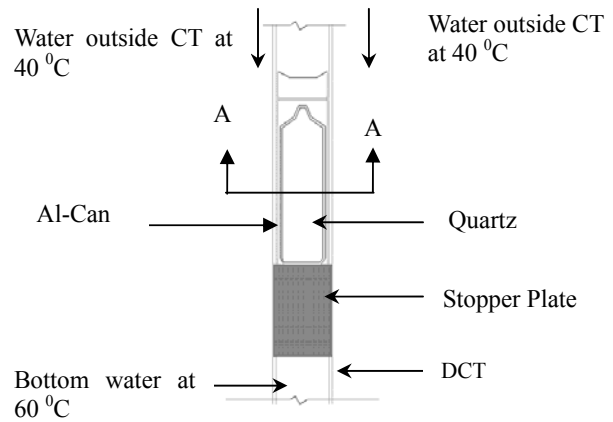
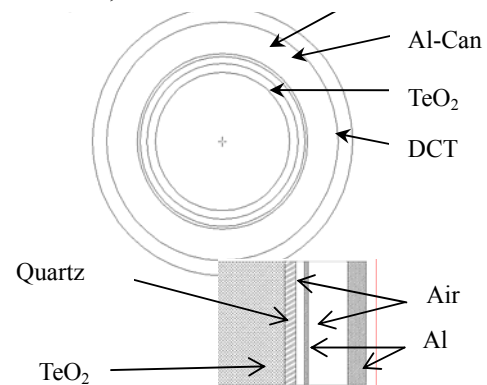


Fig.1 Schematic Diagram of  $\text{TeO}_2$ , Quartz Vial, Al-Can and DCT



$$r_0=0, r_1=9.38, r_2=11.13, r_3=12.05 \quad \text{Unit: mm}$$

$$r_4=12.45, r_5=12.45, r_6=19.05$$

Fig. 2 Sectional View of Quartz, Al-Can and DCT

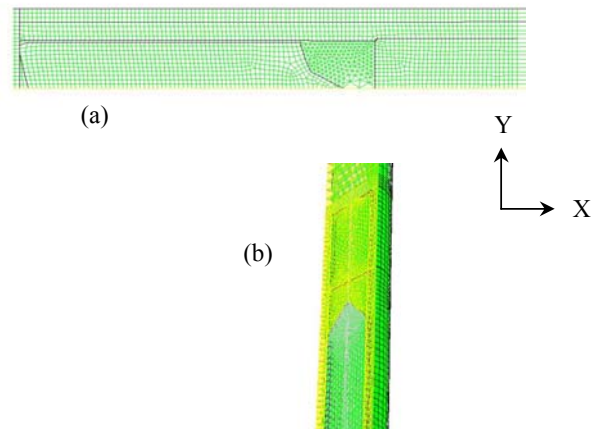


Fig.3 Modeling Geometry

(a) 2D Geometry

(b) 3D Geometry

Outside the CT, w move the heat. The temperature of the circulated water is  $40^\circ\text{C}$ . Holes are drilled at the height of 20 mm and 70 mm of the Al-Can.

The vial is modeled as a heat source with a heat generation rate of  $2.46 \times 10^3$  W/kg. Total 50g of  $\text{TeO}_2$  is kept in the vial. The outside wall of the CT was modeled with a constant temperature of  $40^\circ\text{C}$ . The bottom surface of the stopper plate is modeled with a constant temperature of  $60^\circ\text{C}$ . Except these, all the walls are assumed of “no slip” condition. The top of the CT is assumed to be at  $30^\circ\text{C}$ .

Table 4.1: Thermo-physical properties of the materials

Material	Density, $\rho$ (kg/m <sup>3</sup> )	Thermal conductivity, k (W/m/K)	Heat generation rate, $q'''$ (W/m <sup>3</sup> )	Emissivity, $\epsilon$	Melting temperature ( $^\circ\text{C}$ )
$\text{TeO}_2$	4500	3	$8.7 \times 10^6$	0.89	733
Quartz	2230	1	$34.2 \times 10^6$	0.95	660
Air	1.2	$7.6 \times 10^{-2}$	-	-	-
Water	1000	0.637	-	-	-
Al 6061	2700	230	$0.597 \times 10^6$	0.18	630

First, CAD models are prepared for both “with hole” and “without hole” design. The “without hole” design is modeled as 2D axisymmetric (Fig.3.a). A symmetric 3D model is prepared for the “with hole” geometry (Fig.3.b). The CAD geometries are both transferred to a grid generation program. For the 2D geometry, the grid is made of map, pave and triangular mesh. The grid consists of 5119 nodes. The 3D model describes half of the physical domain with a symmetry boundary condition. The 3D grid consists of map, copper and tetrahedral mesh. The grid contains 225078 cells. One existing design and all three potential designs are analyzed. All the models are analyzed in both the laminar viscous and turbulent RNG  $k-\epsilon$  models. The turbulence is modeled using Renormalization-Group (RNG)  $k-\epsilon$  model.

Natural convection of the fluids is modeled by Boussinesq model. The effect of gravity in the motion of fluid is considered. For the “without hole” models, radiation heat transfer is modeled using Surface-to-Surface (S2S) radiation model. For the “with hole” models, radiation heat transfer is modeled using Discrete Transfer Radiation Model (DTRM). After applying the proper boundary condition to the computational models, flow, momentum and energy equations are solved for each case. Pressure is calculated by SIMPLE pressure-velocity coupling. The discretization of momentum and energy are done by 2<sup>nd</sup> order upwind method. Pressure is discretized by PRESTO! method.

### 3. RESULTS AND DISCUSSION

Temperature profiles are plotted for each case to reveal the temperature distribution inside the DCT of the reactor core. These contours of temperature provide an easy

reasoning of the operating status and whether these conditions are within operating limit. There is not very much difference in temperature distribution of the laminar viscous model and turbulent RNG  $k-\epsilon$  model of each situation. It is seen in Fig. 4(a) that the highest centerline temperature is found in the laminar viscous model of the Al-Can without hole which is about  $662^\circ\text{C}$ .

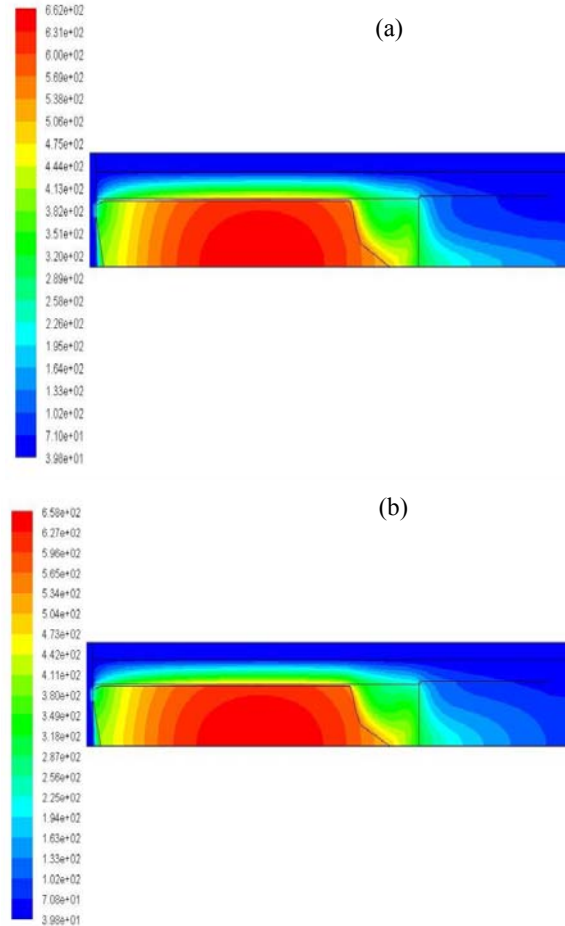


Fig. 4 : Contours of Static Temperature ( $^\circ\text{C}$ )

- (a) DCT without hole over the Al-Can:  
Laminar Viscous Model
- (b) DCT without hole over the Al-Can:  
Turbulent RNG  $k-\epsilon$  Model

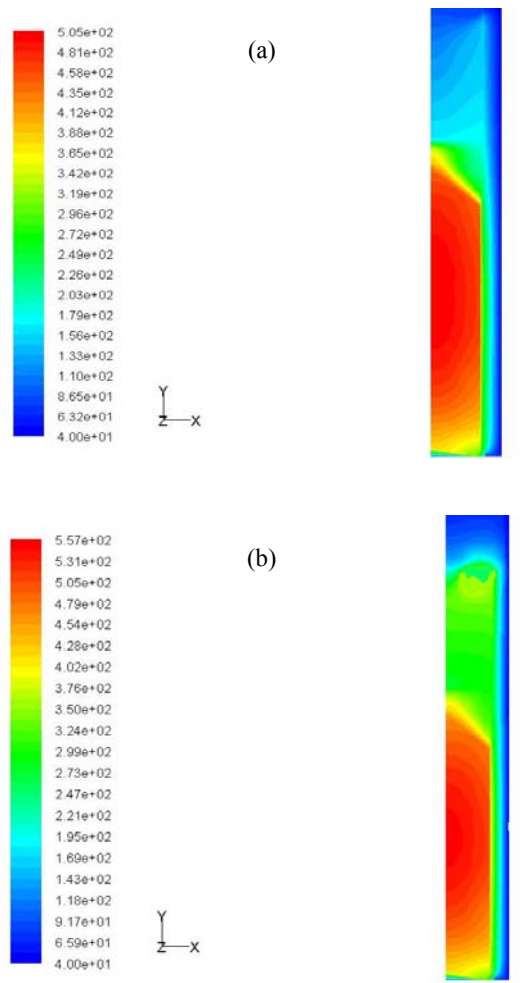


Fig. 5 : Contours of Static Temperature ( $^{\circ}\text{C}$ )

- (a) DCT with hole over the Al-Can:  
Laminar Viscous Model
- (b) DCT with hole over the Al-Can:  
Turbulent RNG  $k-\epsilon$  Model

In Fig.4 (b), the RNG  $k-\epsilon$  model shows a maximum centerline temperature of  $658^{\circ}\text{C}$  under the same situation. In Figs. 5(a) and (b), for 3D model (Al-Can with several holes), laminar viscous model shows a centerline temperature of  $505^{\circ}\text{C}$  and the RNG  $k-\epsilon$  model shows a centerline temperature of  $557^{\circ}\text{C}$ . It is evident from the results that temperature goes down considerably when there are several holes over the Al-Can under the same condition. This is of course, the better situation from the heat transfer view point than that of the sealed Al-Can. The temperature in the walls of the quartz vial and Al-Can is also of great interest. These temperatures should be limited below the melting point of each material. Safety of the reactor core may be disrupted if any melting occurs either in the quartz vial or in the Al-Can. From Figs. 4 and 5, it is clear that the temperature gradient is very high in the radial direction than the axial direction. The maximum temperature is found to be approximately 35 mm to 45 mm Al-Can height in all zones and not

exceeding the melting temperature both the Al-Can and quartz vial when Al-Can is having with several holes on its surface. From the predicted results, it can be mentioned here that perforated Al-Can with 50g  $\text{TeO}_2$  powder at full power ( $3\text{MW}_{\text{th}}$ ) of the reactor operation is a critical situation from the heat transfer view point whereas under the same condition but sealed Al-Can is a catastrophic situation.

#### 4. CONCLUSION

Temperature assessment of the irradiated  $\text{TeO}_2$  powder kept in a sealed Al-Can with hole and without hole has done by numerically using the laminar viscous model and turbulent RNG  $k-\epsilon$  model. It has found that the centerline temperature decreases considerably for the case of Al-Can with several holes. The holes are playing the very important role to convey heat from inside to the outside coolant media (water). It is to be mentioned here that irradiation of  $\text{TeO}_2$  powder was carried out in the past with Al-Can without a hole over its surface. The situation was not good for transferring heat from inside the Al-Can since there is no hole. The heated air is simply confined inside the Al-Can and caused to elevate the temperature. Reactor power, quantity of  $\text{TeO}_2$  powder, geometry of the quartz vial, dry/wet CT and corresponding gap size between the quartz vial and Al-Can, and Al-Can and CT are playing very important role for heat losses. The detailed numerical analysis considering these parameters along with experiments can really provide a better cooling technique for the CT of the reactor which consequently can help increasing I-131 production rate.

#### 5. REFERENCES

- [1] Roland H.C, a one-dimensional ceir computer program for capsule temperature calculations in cylindrical geometry, OSTI (1967).
- [2] B.G. Jones, N.H. Schilmoeller, D.F. Hang, G.P. Beck, Analysis of the forced cooling system of the Illinois advanced TRIGA reactor 14th Annual Meeting of the American Nuclear Society, Toronto, 11, 268-269 (1968).
- [3] M.S. El-Genk, J.S. Philibin, F.C. Foushee, Investigation of heat transfer and fluid flow at low pressure, U.S. TRIGA user's conference; 7 April (1986).
- [4] M.S. El-Genk, J.S. Philibin, F.C. Foushee, S.H. Kim, G.M. Zaki, J. Schulze, Air coolability of TRIGA reactors following a loss-of-coolant accident, U.S. TRIGA user's conference; 7 Apr (1986).
- [5] Amir Zacarias Mesquita and Hugo Cesar Rezende, Thermal behavior of the IPR-R1 TRIGA nuclear reactor, J. Nuclear Energy Science and Technology, Vol.3, No.2, pp.160-169 (2007).
- [6] E. Umar, K. Kamajaya, A. Suwono, N.P.Tandian, T. Hardianto, An experimental study of natural

convection in the hottest channel of TRIGA 2000 kW, National Nuclear Agency of Indonesia.

- [7] M.Q. Huda, S.I. Bhuiyan, T.K. Chakroborty, M.M. Sarker, M.A.W. Mandal, Thermal-Hydraulic Analysis of the 3-MW TRIGA MARK-II Research Reactor Under Steady-State and Transient Conditions, *J. Nuclear Technology*, Vol.135, No.1, pp.51-66 (2001).
- [8] M. Q. Huda, M. Rahman, Thermo-hydrodynamic design and safety parameter of the TRIGA MARK- II research reactor, *Annals of Nuclear Energy*, Vol.31, No.10, pp.1101-1118(2004).
- [9] M. Q. Huda, S.I. Bhuiyan, Investigation of thermodynamic parameters during natural convection cooling of TRIGA reactor, *Annals of Nuclear Energy*, Vol.33, No.13, pp.1079-1086(2006).
- [10] M.Q. Huda, M.S. Islam, M.M. Rahman, A. Haque, M. Uddin, Studies on the overall safety aspects during irradiation of TeO<sub>2</sub> in the central thimble of the TRIGA research reactor, *Annals of Nuclear Energy*, Vol.36, No.2, pp.199-212 (2009).
- [11] I. Mele, "J. Stefan" Institute, Regional Meeting: Nuclear Energy in Central Europe Present and Perspectives, Slovenia (1993).